Fraunhofer Institut
Chemische Technologie

Energetic Materials
Production, Processing and Characterization

29th International Annual Conference of ICT
June 30 - July 3, 1998
Karlsruhe, Federal Republic of Germany

REPORT DOCUMENTATION PAGE

Form Approved OMB No. 0704-0188

1. AGENCY USE ONLY (Leave blank)	2. REPORT DATE	3. REPORT TYPE AND DATES COVERED
	26 June 1998	Conference Proceedings

4. TITLE AND SUBTITLE

29th International Annual Conference of ICT

5. FUNDING NUMBERS

F6170898W0020

6. AUTHOR(S)

Conference Committee

7. PERFORMING ORGANIZATION NAME(S) AND ADDRESS(ES)

Fraunhofer Institute for Chemical Technology
PO Box 1240
Pfinztal 76318
Germany

8. PERFORMING ORGANIZATION REPORT NUMBER

N/A

9. SPONSORING/MONITORING AGENCY NAME(S) AND ADDRESS(ES)

EOARD
PSC 802 BOX 14
FPO 09499-0200

10. SPONSORING/MONITORING AGENCY REPORT NUMBER

CSP 98-1014

11. SUPPLEMENTARY NOTES

12a. DISTRIBUTION/AVAILABILITY STATEMENT

Approved for public release; distribution is unlimited.

12b. DISTRIBUTION CODE

A

13. ABSTRACT (Maximum 200 words)

The Final Proceedings for 29th International Annual Conference of ICT, 30 June 1998 - 3 July 1998

This is an interdisciplinary conference. Topics include Components; Particle Technology; Synthesis, Production and Processing; Characterization of Energetic Materials; Safety Technology; Quality Assurance and Environmental Aspects.

14. SUBJECT TERMS

EOARD, Explosive Devices, Energetic Materials, Propellants

15. NUMBER OF PAGES

Too many to count

16. PRICE CODE

N/A

17. SECURITY CLASSIFICATION OF REPORT	18. SECURITY CLASSIFICATION OF THIS PAGE	19. SECURITY CLASSIFICATION OF ABSTRACT	20. LIMITATION OF ABSTRACT
UNCLASSIFIED	UNCLASSIFIED	UNCLASSIFIED	UL

Herausgeber / Editor:

Fraunhofer-Institut
für Chemische Technologie (ICT)
Joseph-von-Fraunhofer-Straße
Postfach 12 40
D-76318 Pfinztal (Berghausen)

Bundesrepublik Deutschland

Telefon (07 21) 46 40 - 0
Telefax (07 21) 46 40 - 111

Herstellung:

DWS Werbeagentur und Verlag GmbH, Karlsruhe
Printed in Germany

ISSN 0722-4087

Fraunhofer Institut
Chemische Technologie

Energetic Materials
Production, Processing and Characterization

29th International Annual Conference of ICT
June 30 - July 3, 1998
Karlsruhe, Federal Republic of Germany

29th International Annual Conference of ICT
June 30 - July 3, 1998
Karlsruhe, Congress Center
Stadthalle, Weinbrenner-Saal
Federal Republic of Germany

Energetic Materials
- Production, Processing and Characterization

Properties and product quality of propellants and explosives are significantly influenced by the specific features of their components. One possibility to improve the quality of energetic materials in view of less sensitivity and higher performance is a better understanding and control of formation and processing technologies of the components of energetic materials.

The spectrum of tasks comprises synthesis and analysis of energetic materials, their mechanical, chemical and thermal behaviour, components, formation and characterization of particles of energetic materials, processing and manufacturing of propellants and explosives; safety technology, quality assurance and environmental aspects.

The 29th International ICT Annual Conference is aimed at the introduction of new strategies, research and development results and new technologies with special emphasis on production, processing and characterization of energetic materials.

Chairman of the Conference

Ulrich Teipel
Fraunhofer ICT, Pfinztal, D

Vorbemerkung

Die Themen unserer Jahrestagung haben wieder ein breites internationales Echo gefunden. Die große Anzahl von eingegangenen Beiträgen machte, wie in den vorigen Jahren, eine Einteilung in Vorträge und Poster notwendig. Poster ermöglichen eine intensivere Diskussion und eine direkte Rückkopplung von interessierten Tagungsteilnehmern.

Der vorliegende Tagungsband erscheint zu Konferenzbeginn und enthält die schriftlichen Fassungen der Vorträge und Poster. Aus zeitlichen Gründen mußte die Drucklegung vor Eingang sämtlicher Beiträge erfolgen. Nachträglich eingegangene Manuskripte finden sich im Anhang oder wurden durch die Kurzfassung ersetzt.

Preliminary Remark

The subjects of the annual ICT-Conference have again found wide international response. The vast number of contributions necessitated - as in previous years - a division into oral presentations and posters. Posters enable an intensive discussion and direct feedback from interested conference participants.

The Conference Proceedings are published at the beginning of the conference and contain the written versions of the presentations and posters. Due to the shortage of time, printing had to commence prior to receipt of all contributions. Subsequently received manuscripts are either included in the Annex or the abstract is printed instead.

TABLE OF CONTENTS

LECTURES

V10
Synthesis and thermochemistry of diaziridines

N.N. Makhova, V.Y. Petukhova, V.V. Kuznetsov, L.I. Khmelnitskii, V.P. Lebedev, V.I. Pepekin

V11
Reversed Dipole („Umpolung") nitrations: Novel syntheses of polynitroaromatic compounds

R.W. Millar, R.P. Claridge

V12
Herstellung und Charakterisierung von Explosivstoffpartikeln
Production and characterization of particles of explosives

U. Teipel

V13
Characterization of sonochemically-aminated 1,3,5-triamino-2,4,6-trinitrobenzene

J. Bremser, K-Y. Lee

V14
Mahlen von Explosivstoffen
Crushing of solid high explosives

E. Kleinschmidt, H. Späth

V15
Molecular modelling studies of RDX and its morphology

J. Kendrick, W. Leeming, A. Cumming, P. Flower, C. Leach

V16
Metrology tools for the characterization of explosive crystal properties

L. Borne, A. Beaucamp, D. Fendeleur

V17
Untersuchungen zur Kristallisation von Explosivstoffen und zum Einfluß von Ultraschall auf die Keimbildung
Investigation on the crystallization of energetic materials and on the influence of ultrasonic on the nucleation

H. Kröber, U. Teipel

V18
withdrawn

V19
Failure mechanism in PBX

T. Kaully, T. Kimmel

V20
ADN manufacturing technology

T.K. Highsmith, C. McLeod, R.B. Wardle, R. Schmitt, J. Bottaro, P. Penwell, D. Bomberger, J. Brough

V21
Rheological characterisation of castable and extrudable energetic compositions

A.C. Hordijk, R.H.B. Bouma, E. Schonewille

V22
withdrawn

V23
Quantification of microstructural features in HMX using small angle neutron scattering techniques

J.T. Mang, C.B. Skidmore, R.P. Hjelm, P.M. Howe

V24
Alkali metal dinitramides - properties, thermal behaviour and decomposition products

M.D. Cliff, D.P. Edwards, M.W. Smith

V25
Decomposition mechanism of dinitramid salts - Anomalous decomposition of dinitramid metal salts and ammonium salt in the solid phase

A.N. Pavlov, G.M. Nazin

V26
withdrawn

V27
Stabilitätsuntersuchungen einbasiger Treibladungspulver - Mikrokalorimetrie im Grenzbereich
Investigations on stability of single base propellants - microcalorimetry at the limits of sensitivity

U. Ticmanis, G. Pantel, L. Stottmeister

V28
Factors affecting the onset temperature for emulsion explosives

D.E.G. Jones, H. Feng, K.J. Mintz, R.A. Augsten

V29
Thermisches Zersetzungsverhalten von neueren Weichmachern und Bindern untersucht mit der adiabatischen Selbstaufheizung
Decomposition behaviour of azido based and nitric acid ester based plasticizers and binders determined by adiabatic selfheating

M.A. Bohn

V30
Propellant burning rate enhancement and thermal behavior of ultra-fine Aluminum powders (Alex)

M.M. Mench, C.L. Yeh, K.K. Kuo

V31
Observations on the infinite diameter detonation velocities of ammonium perchlorate and its mixtures

R.R. Bernecker

V32
Verwundbarkeitstests mit Splitteraufschlag
Vulnerability tests with fragment impacts

M. Held

V33
Increase of sensitivity of HMX-based pressed explosives resulting of the damage induced by hydrostatic compression

A. Lefrancois, G. Demol

V34
Temperatureinfluß auf die Eigenschaften von Mittelkalibertreibladungen
Influence of temperature on the properties of medium-calibre gun-propellants

E. Rochat

V35
Relation between damage at low velocity impact and mechanical properties and explosive loading of plastic bonded explosives

R.H.B. Bouma, A.C. Hordijk, J.H.G. Scholtes

V36
Processing and characterization of gun propellant formulations containing energetic thermoplastic elastomers

F. Beaupre, G. Ampleman

V37
Effect of process type on propellants properties

C.F. Wiehahn

V38
EI-Technologie - der Schlüssel zum Hochleistungsantrieb
EI-Technology - the key for high performance propulsion design

B. Vogelsanger, K. Ryf

V39
ROWANEX 300 : a new high performance pressable PBX for metal accelerating applications

R.E. Hollands, I.E.P. Murray, C.J. Leach

V40
Laser diode ignition of the combustion of pyrotechnic mixtures. Experimental study of the ignition of $Zr/KClO_4$ and $Zr/ PbCrO_4$

E. Radenac, P. Gillard, M. Roux

V41
Kontrollierte Vernichtung von Datenträgern durch dünne pyrotechnische Schichten als Bestandteil des Datenschutzes in sicherheitskritischen Bereichen
Controlled destruction of data carriers by thin pyrotechnical layers as an element of data protection for high security applications

G. Karametaxas, J. Kutzli, P. Schweizer, M. Tobler

V42
Evaluation of polyNIMMO in a reduced smoke propellant

S. Flynn, D.R. Fossey, D.G. Catton, D. Wagstaff

V43
Festtreibstoffe für den Einsatz in Unterwassertriebwerken
Solid propellants ready for use in underwater rocket-motors

H.P. Hebekeuser, H.P. Mackowiak

V44
Continuous processing of composite propellants (CPOCP)

E. Giraud, J.M. Tauzia, G. Lacroix, C.M. Murphy, R.S. Muscato, W.F. Newton, F.M. Gallant, M.A. Michienzi, S.G. Johnson,

POSTER PRESENTATIONS

P45
Stabilizer consumption by accelerated aging in PEG/RDX propellant

Yoo-Jin Yim, Baek-Neung Ryoo, Young-Chul Park

P46
Synthesis of Cyclodextrin Polymer (Poly CD), a raw material for insensitive, high energy and shock survivable explosives

G.L. Statton, B.M. Kosowski

P47
Nitrotriazole: Chemische Struktur und explosive Eigenschaften
Nitrotriazoles: Chemical structure and explosive properties

H.H. Licht, S. Braun, M. Schäfer, B. Wanders, H. Ritter

P48
withdrawn

P49
New synthesis of TATB - process development studies

R.D. Schmidt, A.R. Mitchell, P.F. Pagoria

P50
Die Reaktion von Ammoniak mit Distickstoffpentoxid
The reaction of Ammonia with Dinitrogen Pentoxide

C. Frenck, W. Janitschek, W. Weisweiler

P51
Isophthalic dimethyloxaziridine as a potential bonding agent for rocket solid propellants

A.M. Kawamoto, M.M. Campbell, M.F. Mahon

P52
A study of some insensitive explosives

P. Marecek, J. Pokorna, P. Vavra

P53
Orientation in the nitration benzoic acid in mixtures of sulfuric and nitric acids

N.V. Yudin, V.F. Zhilin, V.L. Zbarskiy

P54
withdrawn

P55
Novel energetic macrocycle systems of furazan series

L.V. Batog, L.S. Konstantinova, V.Y. Rozhkov, O.V. Lebedev, M.A. Epishina, N.N. Makhova, I.V. Ovchinnikov, L.I. Khmelnitskii

P56
Trinitromethylarenes and trinitromethylhetarenes - synthetic ways and characterization

O.V. Lebedev, L.V. Epishina, T.S. Novikova, N.N. Makhova, T.I. Godovikova, S.P. Golova, A.V. Shastin, E.A. Arnautova, T.S. Pivina, L.I. Khmelnitskii

P57
Synthesis and physical-chemical properties of polycyclic nitropyrazoles

I.L. Dalinger, T.K. Shkinyova, S.A. Shevelev, V.S. Kuzmin, E.A. Arnautova, T.S. Pivina

P58
3,3-Bis(1-Fluoro-1,1-dinitromethyl)difurazanyl ether

A.B. Sheremetev

P59
Synthesis and thermal stability of 5,5´-Bis(tetrazolyl)amine

V.V. Nedelko, B.L. Korsounskii, A.V. Shastin, N.V. Chukanov, T.S. Larikova, A.I. Kazakov

P60
Mechanism of the primary stages of decomposition of aliphatic nitro- and fluoronitronitramines

B.L. Korsounskii, V.G. Matveev, L.D. Nazina, G.M. Nazin

P61
Estimation of nitrate ester bond dissociation energies in Nitrocellulose by molecular modelling

A.L. Lewis, J. Kendrick, S.C. Rogers

P62
TEX: a promising new insensitive high explosive

P.C. Braithwaite, W.W. Edwards, R.M. Hajik, T.K. Highsmith, G.K. Lund, R.B. Wardle

P63
Herstellung von Ammoniumdinitramid-Partikeln
Formation of Ammonium Dinitramide (ADN) particles

U. Teipel, T. Heintz, K. Leisinger, H. Krause

P64
Recrystallization of NTO crystals in a batch cooling crystallizer

Kwang-Joo Kim, Min-Jun Kim, Jung-Min Lee, Hyoun-Soo Kim, Bang-Sam Park

P65
Shock sensitivity of HMX/HTPB PBX's: Relation with HMX crystal density

A.E.D.M. van der Heijden, R.H.B. Bouma

P66
Herstellung fehlstellenarmer Oktogenkristalle durch Rekristallisation aus Lösungen
Formation of HMX-crystals with high internal quality by cooling crystallization

H. Kröber, U. Teipel, K. Leisinger, H. Krause

P67
Recrystallization of HMX with compressed gases as anti-solvent

U. Förter-Barth, U. Teipel, H. Krause

P68
Properties of spray-dried Boron/Potassium nitrate granular

K. Takahashi, N. Asano, K. Ochi

P69
Radiation protective and radiation resistive materials

N. Kalinina

P70
Nanostructured diamonds: Synthesis, characterization and applications

V. Komanschek, A. Pfeil

P71
Feinzerkleinerung von Explosivstoffen
Fine grinding of explosives

P. Gerber, B. Zilly, U. Teipel

P72
Effect of particle size on the detonation regime and its characteristics for azoxydinitrofurazan example

G.T. Afanasev, V.I. Arhipov, M.F. Gogulya, A.A. Sovko

P73
Dilatometrische Messungen an phasenstabilisiertem Ammoniumnitrat mit Hilfe der Röntgenbeugung
Dilatometric measurements of phase stabilized ammonium nitrate (CuPSAN) performed by means of X-ray diffraction

P.B. Kempa, M. Herrmann, W. Engel

P74
Optische Partikelgrößenbestimmung im sub-μm-Bereich in Flammen
Optical measurements of particles less than 1 micrometer in flames

W. Ehrhardt, W. Eckl, M. Weindel, V. Weiser

P75
Einfluß der Partikelgröße auf das Abbrandverhalten von B/KNO_3-Anzündmischungen
Burning behaviour of B/KNO_3-influence of particle size

V. Weiser, D. Kuhn, R. Ludwig, H. Poth

P76
Effect of crystal defects on reactivity of energetic materials:
1. The effect of mechanical deformation

R. Longjohn, M. Cartwright

P77
Characterization of electro-exploded aluminum (Alex)

R. Sanden

P78
Bestimmung der Oberflächenenergie von Polymerbindern und Explosivstoffpartikeln
Determination of surface energy of polymers and particles of explosives

U. Teipel, E. Marioth, T. Heintz, I. Mikonsaari

P79
withdrawn

P80
Mikroverkapselung von Partikeln in einer Wirbelschicht unter Anwendung verdichteten Kohlendioxids
Microencapsulation of fine particles in a fluidized bed

M. Niehaus, W. Weisweiler

P81
Monte Carlo simulation of aluminum agglomeration in composite solid propellants combustion

S.A. Rashkovsky

P82
Simulation of composite solid propellants statistical structure

S.A. Rashkovsky

P83
Finite Elemente Modellierung der Mikromechanik von Festtreibstoffen und Treibladungspulvern
Finite Element Modelling of the micromechanics of solid propellants and gun propellants

E. Geißler, C. Hübner

P84
Characterization for bonding efficiency of the bonding agents in composite solid propellants by dynamic mechanical analysis

Aimin Pang, Jinhan Wu, Huiping Jiang

P85
Characterisation of propellant cure

L. Cribb, A.V. Cunliffe, D.A. Tod

P86
Plasticisers for new energetic binders

P.F. Bunyan, A.V. Cunliffe, P.J. Honey

P87
Evaluation of a homologous series of high energy oxetane thermoplastic elastomer gun propellants

I.A. Wallace, P.C. Braithwaite, A.C. Haaland, M.R. Rose, R.B. Wardle

P88
The modelling of experimental BuNENA/RDX/NC propellant properties

C.F. Wiehahn, M.A.J. Gantana, J.C. Engel

P89
An investigation into the thermal stability of end-modified PolyGlyn

H. Bull, W.B.H. Leeming, E.J. Marshall, M.J. Rodgers, P.F. Bunyan, A.V. Cunliffe

P90
Studies to understand the role of ballistic modifiers in the platonisation of double base propellants

M.P. Sloan, I.A. Duncan, S.F. Dixon

P91
Fast burning rocket propellants with reduced smoke

K. Menke, S. Eisele

P92
Improving the elongation capability of HTPB-based composite propellant

G.J.J. Steyn, G.J. van Zyl

P93
Use of Butacene in composite propellant

D.R. Fossey, D.G. Catton, W.G. Turner-Mutch

P94
Properties of CL-20 based high explosives

H.R. Bircher, P. Mäder, J. Mathieu

P95
Improvements in NTO based PBXs

A. Becuwe, A. Delclos, M. Golfier, G. Donzel

P96
Extrusion trials with a TSK045 twin screw extruder

H.W.R. Sabel, E. Schonewille

P97
Twin screw extrusion compounding of energetic materials - a small scale laboratory facility

P.Q. Flower, M.J. Gough, S.E. Gaulter, R. Clift, B. Murray

P98
withdrawn

P99
Überwachung des Extrusionsprozesses mit Nahinfrarot (NIR)-Spektroskopie
Monitoring of extrusion processes by Near Infrared (NIR) spectroscopy

T. Rohe, S. Kölle, H. Nägele, N. Eisenreich

P100
Deterrent coating of single base powders

V. Pus

P101
Temperature sensitivity of small arm propellant

J. Petrzilek, L. Valenta, L. Velebradsky

P102
A roadmap to very high impetus gun propellants

R. Simmons

P103
Verbrennbare Hülse für RMK 30
Combustible cases for RMK 30

F. Schedlbauer, A. Meßmer, U. Steffens, I. Reuter

P104
Laser cutting of pressed explosives

J.P. Armstrong, P.S. Banks, M.D. Feit, R.S. Lee, M.D. Perry, F. Roeske, B.C. Stuart

P105
withdrawn

P106
Method for experimental study of flame spread along combustible narrow channels

I.G. Assovskii, O.A. Kudryavtsev

P107
Erosive burning of energetic materials - experimental characterization

I.G. Assovskii

P108
Technische Harmonisierung in der Europäischen Gemeinschaft - CE-Kennzeichnung für zivile Treibmittel
Technical harmonization in the European Communities - CE-marking of conformity of civil propellants

H. Michael-Schulz

P109
Betrachtungen hinsichtlich der behelfsmäßigen Anwendung von selbsthergestellten explosiven Materialien

O. Mueller

P110
withdrawn

P111
A new detonation model

Hu Shaoming

P112
Numerical experiment on determination of liquid explosives initiation by impact

A.V. Dubovik

P113
Anomalous detonation of condensed explosives with the CJ condition violation and change in carbon phase state

S.B. Victorov, S.A. Gubin

P114
Development and optimisation of the fiber optic probe; a new optic method for measuring the shock velocity in energetic materials

R.J. van Esveld, M.P. van Rooijen, W.C. Prinse, A.C. van der Steen

P115
Characterisation of booster explosives by flyer impact

W.C. Prinse, R.H.B. Bouma, A.C. van der Steen, T. Jordan, A. Cardell

P116
withdrawn

P117
Determination of the detonation energy and some of the energetic characteristics of various NTO-based formulations

G.J. Ellis, H.C. Bezuidenhout

P118
withdrawn

P119
Shock initiation of nitromethane based explosives in GAP test configuration

S. Cudzilo, A. Maranda, W.A. Trzcinski

P120
Detection of impact time in drop-hammer test

Zijian Lu, Hu Qingxian

P121
Computer model to predict the environmental hazard after explosions

N. Belyaev, N. Kalinina, V. Khrutch

P122
Explosive hazard of gasol mixed with fluorine agent

Xuezhong Xu, Degui Wang, Baotian Hao, Mingjing Pei, Ruifu Yang, Xuefeng Zheng

P123
DETPAR - the catalogue of detonation parameters of explosives

J. Majzlik, V. Dusik

P124
The ICT-Thermochemical Database

H. Bathelt, F. Volk, M. Weindel

P125
ETC plasma-propellant interactions

P.J. Kaste, R.A. Rodriguez-Pesce, M.A. Schroeder, G.L. Katulka, K.J. White, M.L. Leadore, A.E. Kinkennon

P126
Ignition and pyrolysis of explosive components

S. Almada, J. Campos, J.C. Gois

P127
Protocol for the characterization of explosives-contaminated sites

S. Thiboutot, G. Ampleman, P. Dube, J. Hawari, T.F. Jenkins, M. Walsh

P128
Influence of the primary Nitramines´ structure on their thermostability

R.S. Stepanov, A.M. Astachov, L.A. Kruglyakova

P129
Thermal decomposition of 1,9-diazido-2,4,6,8-tetranitro-2,4,6,8-tetraazanonane in liquid and solid phase

J.M. Burov, G.M. Nazin

P130
NMR-spektroskopische Charakterisierung von ADN und CL 20
Characterisation of ADN and CL20 by NMR spectroscopy

M. Kaiser, B. Ditz

P131
Untersuchung der Zersetzung von Pulvervorkonzentrat
Thermal decomposition of nitroglycerin/nitrocellulose mixtures

S. Wilker, U. Ticmanis, M. Kaiser, G. Pantel, K.-F. Elshoff

P132
Internationaler Ringversuch zur Ermittlung der Stabilität zweibasiger Kugelpulver mittels Wärmeflußkalorimetrie
International Round Robin test to determine the stability of DB ball propellants by heat flow calorimetry

S. Wilker, P. Guillaume

P133
Microcalorimetry and chemical studies of double base propellants

P. Guillaume, M. Rat, S. Wilker, G. Pantel

P134
Physikalisch-chemische Charakterisierung der explosiven Eigenschaften von Hydraziniumazid
Physical chemical characterization and explosive properties of hydrazine azide

W.-H. Walther, T.M. Klapötke, G. Holl

P135
Beurteilung der Versprödungsneigung von TLP mit Hilfe des Schlagscherversuchs
Impact sheartest on gun propellants to measure the transition to brittle behaviour

B. Nicklas

P136
BDNPA/F as energetic plasticizer in propellant formulations

G.M. Gore, K.R. Tipare, R.G. Bhatewara, N.M. Walunj, V.K. Bhat

P137
Use of headspace gas chromatography - mass spectrometry to identify and monitor gases evolved during aging of energetic materials

A.N. Agha, J.M. Bellerby, C.S. Blackman

P138
Investigation of lattice imperfections in energetic materials using X-ray diffraction

M. Herrmann, W. Engel

P139
Thermochemical and radiative computation codes linkage using an experimental design method

R. Boulanger, L. Brunet, A. Espagnacq

P140
Radiative calculations on combustion of pyrotechnic compositions

R. Boulanger, A. Espagnacq, P. Gillard, J.M. Souil, M. Roux

P141
A new aspect of relations between differential thermal analysis data and the detonation characteristics of polynitro compounds

S. Zeman

P142
Evaluation of thermochemical parameters of some energetic molecules

V. Prokoudine

P143
Determination of reaction kinetics data from thermodynamic measurements of catalysed composite propellants

M.A. Benmahamed

P144
Characterisation and quantitative determination of trinitrotoluene in mixtures with hexogen by differential scanning calorimetry

M. Suceska, M. Rajic, R. Culjak

P145
Thermal behavior and stability of HNIW (CL 20)

S. Löbbecke, M.A. Bohn, A. Pfeil, H. Krause

P146
Correlations between theoretical and experimental determination of heat of formation of certain aromatic nitro compounds

P.C. Chen, S.C. Tzeng, J.C. Wu

P147
Untersuchung zur Stabilität und Reaktivität von reinem NTO, NTO/TNT- und NTO/RDX-Gemengen zur Beurteilung ihrer sicheren Verwendung
Investigation on the stability and reactivity of pure NTO and mixtures of NTO-TNT and NTO-RDX to assess their safe use

M.A. Bohn, H. Pontius, S. Löbbecke, S. Wilker, G. Pantel

P148
Charakterisierung von Verunreinigungen in neuen energetischen Materialien
Characterisation of impurities in new energetic materials

G. Bunte, H. Pontius, M. Kaiser

P149
Afterburning of TNT detonation products in an explosive chamber

J. Paszula, R. Trebinski, W.A. Trzcinski, P. Wolanski

P150
Comparison of heat effects of combustion and detonation of explosives in a calorimetric bomb

S. Cudzilo, R. Trebinski, W.A. Trzcinski, P. Wolanski

P151
Studies of high energy composites containing Polytetrafluoroethylene

S. Cudzilo, W.A. Trzcinski

P152
LDV-Vermessung reaktiver Strömungsfelder in einer Brennkammer
Reactive flow field diagnostics in a combustion chamber by LDV

J. Backhaus, A. Brock, L. Deimling

P153
Generic qualification of pyrotechnic compositions

P. Fincham

P154
Einfache Modelle der Anzündung von Festtreibstoffen
Simple models of the ignition of solid propellants

W. Eckl, S. Kelzenberg, V. Weiser, N. Eisenreich

P155
Characterization of combustion and stability behavior of solid propellants

M.M. Mench, K.K. Kuo

P156
Study of the flame structure of ADN/HTPB composite propellants using molecular-beam mass-spectrometry

O.P. Korobeinichev, A.A. Paletsky

P157
Entwicklung von Hotspots in energetischen Materialien
Development of Hot Spots in energetic materials

G. Langer, N. Eisenreich

P158
withdrawn

P159
Strahlungsemission instationärer Tankflammen
Time history of radiative heatflux from pool fire

V. Weiser, M. Weindel, N. Eisenreich, W. Eckl

P160
Normal burning rate of polymers

N.N. Bakhman

P161
Untersuchungen zum Verbrennungsverhalten von Festbrennstoffen mittels einer Farbschlierenapparatur
Investigation of the combustion behaviour of solid fuels using Colour Schlieren Apparatus

H. Ciezki, E. Kehringer

P162
Obtaining submicron abrasive powders by pneumatic processing of electric corundum and products of solid rocket propellants combustion

A. Vorozhtsov, Y. Biryukov, L. Bogdanov

P163
Combustion of ammonium nitrate-based compositions
I. Mixtures of ammonium nitrate with catalysts and high explosives

B.N. Kondrikov, V.E. Annikov, L. de Luca

P164
Burning of liquid aliphatic azides

B.N. Kondrikov, M.S. Kozhukh, I.N. Ohotskaya

P165
withdrawn

P166
Catalysis of modern solid propellant combustion

A.A. Zenin, S.V. Finjakov, N.G. Ibragimov, E.K. Aflatulov

P167
Numerical modelling of convective combustion transition to detonation

A.N. Ischenko, J.P. Khomenko

P168
Ash influence on conversion of spherical coal particle reacting with ambient oxidizing gas

T.A. Yarovoy, A.N. Zolotko, N.I. Poletaev, Y.I. Vovchuk

P169
Characterization of self-sustaining combustion of cyclic nitramines

V.N. Simonenko, V.E. Zarko, A.B. Kiskin

P170
Study on combustion of new energetic furazans

V.P. Sinditskii, He Wei Dong, V.V. Serushkin, A.E. Fogelzang, A.B. Sheremetev

P171
Combustion behavior and flame structure of tetrazole derivatives

V.P. Sinditskii, V.Y. Egorshev, A.E. Fogelzang, V.V. Serushkin, V.I. Kolesov

P172
Polyurethanes as a basis for new materials and new process engineerings

V.A. Vilensky, L.A. Goncharenko, S.I. Azarov, L.N. Vilenska

P173
Polyurethane composites for personal safety features and recreation of soils contaminated by radionuclides

V.A. Vilensky, S.I. Azarov, L.N. Vilenska

P174
Phenomenological aspects of detonation in non-ideal heterogeneous explosives

A.J. Tulis, J.L. Austing, R.H. Dihu, R.P. Joyce, D.L. Patel, J. Dillon, D.C. Heberlein

P175
Underwater explosives (I) - Influence of aluminium and ammonium perchlorate on the performance

A. Happ, A. Kretschmer, U. Meyer, T. Keicher, U. Sirringhaus, R. Wild

P176
Modified synthesis of Diethylaluminium azide and the characterization thereof

Zhou Keyan, Gao Zhenxian, Sun Yu, Li Changqing, Huang Yue, Xia Zhongjun

P177
Synthesis and initiation spot-size testings of sonochemically-aminated TATB

K.-Y. Lee, J.E. Kennedy, J.R. Stine

P178
Fragment mine characterized by a directional effect

K. Hel

P179
To the question of the enthalpy of formation for the Nitrocellulose

Y.N. Matyushin, T.S. Konkova, L.I. Korchatova

P180
Thermochemical and explosive properties of Nitropyrazoles

V.P. Lebedev, Y.N. Matyushin, Y.O. Inozemtcev, I.L. Dalinger, S.A. Shevelev, I.V. Fomenkov

FORSCHUNGS-SYNERGIEN ZWISCHEN WEHRTECHNISCHEN UND ZIVILEN ANWENDUNGEN

Peter Eyerer, Peter Elsner

Fraunhofer-Institut für Chemische Technologie (ICT), Postfach 12 40, 76318 Pfinztal

1. Einleitung

Das Fraunhofer ICT forscht seit 1959 in der Wehrtechnik. Schwerpunkte des ICT waren und sind Explosivstoffe (Sprengstoffe, Treibladungspulver, Raketen-Festtreibstoffe und Pyrotechnika). Seit 1994 mußte das ICT, wie alle wehrtechnischen Einrichtungen, Personal abbauen. Doch, entgegen aller Prognosen, gelang die Teilkonversion des ICT in zivile Anwendungsfelder derart positiv, daß wir heute ca. 305 Mitarbeiter beschäftigen können.
Da Explosivstoffe in der Regel höchstgefüllte Kunststoffe sind, lag es nahe, das kunststoff-technische Know-how der ICT-Mitarbeiter auszuweiten und Synergiechancen zwischen Wehr-technik und zivilen Anwendungen zu nutzen.

2. Fraunhofer ICT heute

Anhand des Organigramms, **Bild 1**, des ICT lassen sich die Kernkompetenzen in Stichworten darstellen. **Tabelle 1** vergleicht einige Kenndaten des ICT heute mit denen vor vier Jahren [1].

Die Produktbereiche Umwelt-Engineering und Polymertechnik vertreten neue Themenfelder. In allen fünf Produktbereichen (neben zwei Dienstleistungsbereichen) werden die Chancen von wehrtechnischer und ziviler Forschung für anwendungsnahe Lösungen genutzt. Anhand von Beispielen wird dies im folgenden erläutert.

3. Beispiele zu Forschungs-Synergien zwischen wehrtechnischen und zivilen Anwendungen

Tabelle 2 gibt eine Übersicht zu verschiedenen Beispielen, für die wehrtechnisches oder ziviles Wissen zu neuen Anwendungen im jeweils anderen Bereich führen.

Energetische Demontage

Bild 2 zeigt links die Kosten in DM je Kilogramm Kunststoff-Neuware. Im rechten Teil erkennt man am Beispiel modifiziertem Polypropylen, daß ein Kilogramm Rezyklat etwa in die Größenordnung der Neuware kommt. Somit besteht wenig Anreiz zur Wiederverwertung. Hauptverursacher für hohe Rezyklatkosten ist die überwiegend händische Demontage von beispielsweise Autos, Kühlschränken, Waschmaschinen, Fernseher usw.
Gelingt es, diesen größten Kostenblock zu verringern, gäbe es neue Impulse für die Kreislaufwirtschaft von Kunststoffen.
Bild 3 zeigt prinzipiell einen Lösungsansatz der kosten- und umweltgünstiger ist als heutige Demontagewege. Der Produktentwickler/-konstrukteur sieht an den Stellen des Produktes Hohlkanäle vor, an denen nach Produktnutzen eine Trennung erwünscht wird. Während der Produktnutzung bleiben die Kanäle ungefüllt und dicht verschlossen. Ein "intelligenter" Demontierer füllt das Hohlleitungssystem mit einer kurz vorher zusammengemischten Flüssigkeit, die detonierfähig ist. In einem Schutzbunker werden Produkte zerlegt und können beispielsweise mittels eines mit Sensoren ausgestattetem Roboter sortenrein eingesammelt werden.
Bild 4 zeigt im Rahmen einer Machbarkeit die beginnende Zerlegung einer alten Waschmaschine. Sie wurde mit PVC-Schläuchen und Klebeband so präpariert, daß eine Zerlegung an gewünschten Stellen erfolgte. Um die Sprengung mit einer Hochgeschwindigkeitskamera verfolgen zu können, erfolgte die Zerlegung im Freien. **Bild 5** zeigt die energetische Zerlegung in einem fortgeschrittenem Stadium. Die zerlegten Teile der Waschmaschine zeigt **Bild 6**. Hieraus erkennt man, daß es mittels der beschriebenen energetischen Demontage beispielsweise gelingt, den Kabelbaum, die Kunststoffdichtungen, Stahlteile usw. zu separieren.
Um die Energetische Demontage serienmäßig einsetzen zu können, ist noch umfangreich anwendungsnahe Forschung und Entwicklung erforderlich. In den vergangenen drei Jahren ist es uns am ICT nicht gelungen, deutsche Firmen zur Finanzierung zu gewinnen. Wir arbeiten daher seit kurzem mit einem japanischen Firmenkonsortium zusammen.

Energetisches Prägen

Energetisches Prägen ist seit ca. 1870 in der Wehrtechnik bekannt. Zivile Anwendungen gibt es in Nischen, vor allem im Bereich der Souvenirs, **Bild 7**.

Bild 8 zeigt, wie abbildungsgetreu, beispielsweise ein Eichenblatt, in Metall abgebildet werden kann. Um hohe Abbildungsgenauigkeit zu realisieren, bedarf es viel wehrtechnischem und werkstoffkundlichem Know-how. Dieses Wissen läßt sich jedoch auch für technische zivile Anwendungen einsetzen.

Bild 9 gibt die Oberfläche einer Stahlplatte wieder, in die Leder energetisch geprägt wurde. Zur Herstellung von Lederimitaten, beispielsweise für die Oberfläche einer Instrumententafel im Automobilbau, müssen Formwerkzeuge sehr aufwendig bearbeitet werden, um Kunststoffolien später als Lederimitate abformen zu können. Mit Hilfe der Energetischen Prägung erreicht man ähnliche Oberflächen schneller, wirtschaftlicher und technisch besser, da beim Energetischen Prägen gleichzeitig eine Oberflächenhärtung im Stahl einhergeht.

Verbrennbare Hülsen für Munition (hülsenlose Munition)

Das Beispiel der Herstellung verbrennbarer Hülsen für Geschoßmunition, **Bild 10**, demonstriert, daß nicht nur wehrtechnisches Wissen in die zivile Technik fließt, sondern umgekehrt auch ziviles Wissen in der Wehrtechnik zu wirtschaftlichen und technisch vorteilhaften Lösungen führen kann.

Mittels der in der Polyurethan- und Polyamid-Verarbeitungstechnik bekannten RIM (reaction injection molding)- oder RRIM (reinforced reaction injection molding)-Technik gelingt es durch entsprechende Rezepturentwicklungen "hülsenlose" Munition großserienfähig herzustellen [2].

Ultrafeine Diamanten (UFD)

Volk et al. [3] gelang es bei der Explosion von kohlenstoffreichen Sprengstoff-Rezepturen kugelförmige Diamantpartikel (UFD) herzustellen. **Bild 11** faßt Herstellverfahren und Produkte zusammen. Anwendungsmöglichkeiten wurden bisher kaum erschlossen, obwohl wir am ICT vielfältige Chancen sehen. Beispiele könnten sein: Galvanische oder optische Schichten, Energetisches Einprägen in Metalle, Füllstoffe für Kleber u.v.m.

Gasgeneratoren

Seit etwa zehn Jahren setzt man zunehmend Airbags in vielerlei Varianten zum Schutz von Insassen in Fahrzeugen ein. Beim Zusammenstoß von Autos entfaltet sich ein "Luftsack" vor den Insassen, **Bild 12**. Er wird im Millisekundenbereich durch Gasgeneratoren gefüllt. Das Wissen um diese Gasgeneratoren entstammt der Wehrtechnik. **Bild 13** zeigt einen aufgeschnittenen Airbag-Modul mit den Gasgenerator-Pellets (A) (Tabletten), dem Gasfiltersystem (B) und dem

elektrischen Anzünder (C) samt Boosterladung (Anzündmittel). Derzeitige Forschungen und Entwicklungen beschäftigen sich unter anderem mit der Herstellung azidfreier Gasgenerator-Komponenten und Systemen. **Tabelle 3** macht das Entwicklungspotential von Gasgeneratoren deutlich. Beispielsweise arbeiten wir am ICT neben der Entwicklung neuer Gasgeneratoren für Airbags und Gurtstraffer auch an deren Einsatz in neuen Feuerlösch- und anderen Sicherheitssystemen.

Treibmittel (Gasgeneratoren) mit hoher Gasfreisetzungstemperatur

In der Kunststoffverarbeitung werden Treibmittel zum Schäumen meist auf Basis Natriumcarbonat oder Azodicarbonamid eingesetzt. Die Gasfreisetzungstemperaturen liegen stets unter der Schmelzeverarbeitungstemperatur, so daß der Schäumvorgang während der Verarbeitung erfolgen muß. In der Wehrtechnik kennt man jedoch Gasgeneratoren, deren Gasfreisetzung erst oberhalb 300 °C erfolgt. Sie sind ähnlich kostengünstig wie die üblichen Treibmittel bei Kunststoffen. Dadurch eröffnen sich neue Anwendungsfelder. Mit den neuen Treibmitteln lassen sich, wie in **Bild 14** schematisch angedeutet, lokale Dichteunterschiede innerhalb einer vorgegebenen Wanddicke erzeugen oder örtliche Wanddickenunterschiede durch lokale Energieeinkoppelung (IR-Strahlen, Mikrowellen u. a.) herstellen. Dies kann im Formwerkzeug oder danach erfolgen.

Energetisches Fügen, pyrotechnische Montage

Altbekannt ist beispielsweise im Bauwesen das Setzen von Bolzen, Befestigungselementen und ähnliches mittels Schußapparate. Mit Hilfe neuerer Erkenntnisse läßt sich die Technik des Fügens und/oder Befestigens deutlich erweitert einsetzen.

Durchgängige Simulation bei der Entwicklung und Erprobung von Explosivstoffen

In der Automobiltechnik beispielsweise sind in den vergangenen 20 Jahren große Schritte hin zu virtueller Erprobung von Bauteilen und Fahrzeugen und weg von experimentellen Untersuchungen bzw. Testfahrten umgesetzt worden. Dagegen erfolgt die Entwicklung und Erprobung von neuen Explosivstoffen heute noch weitgehend experimentell. Vereinzelt, nicht miteinander verzahnt, werden wohl Berechnungsprogramme eingesetzt, doch es fehlt an einer durchgängigen Simulation.

Am ICT haben wir begonnen, zusammen mit Partnern aus Industrie und Wissenschaft vorhandenes Know-how zu bündeln und in Richtung einer verstärkt kombinierenden (virtuellen **und** experimentellen) Entwicklung voranzuschreiten.

Schnelle Identifizierung von Kunststoffmüll

Das Messen schneller Vorgänge (Kurzzeit-Physik) spielt in der Wehrtechnik eine große Rolle. Beispiele sind: Explosionen, Innenballistik, Lenken/Erkennen von Flugkörpern usw. Will man beispielsweise den gemischten Inhalt eines "gelben" Sackes schnell sortenrein trennen, braucht man ein zuverlässiges, sehr schnell arbeitendes Identifizierungssystem. Eisenreich et al. [4] haben am ICT seit knapp zehn Jahren auf Basis der Nah-Infrarot-Technik (NIR) ein Erkennungssystem entwickelt, das bis zu 1000 Spektren je Sekunde aufzeichnet. Nachteil war bisher allerdings, daß schwarzeingefärbte Kunststoffe nicht erkannt werden konnten. Mit Hilfe der Röntgenbeugung, **Bilder 15 und 16**, ist es am ICT gelungen, auch schwarze Kunststoffe schnell (innerhalb von einer Sekunde) zu erkennen. Durch eine Koppelung der NIR- mit der Röntgen-Meßtechnik kann man die Lücke schließen. Erste NIR-Systeme sind am Markt im Einsatz.

Überkrititsche Fluide (SCF - Super Critical Fluids)

Der Einsatz von überkritischem CO_2 (oberhalb 31 °C und 74 bar) bei der Hopfenextraktion oder der Entkoffeinierung der Kaffeebohnen ist seit Jahrzehnten Stand der Technik. Überkritisches CO_2 zur Reinigung verseuchter Böden dagegen ist neueren Datums. Dabei ist es gleichgültig, ob es sich um wehrtechnische Altlasten oder zivile Verschmutzungen handelt. In jedem Fall nützt man die hohe Löslichkeit des CO_2 im überkritischen Zustand z.B. gegenüber vieler Organika aus. Was für das CO_2 gilt, läßt sich in anderen Bereichen auch für das Wasser belegen. Im überkritischen Zustand (oberhalb 374 °C und 220 bar) ist Wasser ein sehr gutes organisches Lösemittel auch für umweltkritischste Verbindungen wie halogenierte Kohlenwasserstoffe, Dioxine, polychlorierte Furane, usw. **Bild 17** zeigt Anwendungsfelder für überkritisches Wasser (SCWO - Super Critical Water Oxidation) auf. Bemerkenswert ist, daß die überkritische Fluidtechnik organische Schadstoffe emissionsfrei in handhabbare Gase (CO_2) oder Flüssigkeiten (Säuren, Laugen) umwandelt, **Bild 18**. Eine Vertiefung in SCF gestattet Hirth et al. [5].

Umweltsimulation

Die Untersuchung der Gebrauchstauglichkeit von Produkten (Einfluß der Belastungen während des Transports und des Produktlebenszyklusses) nahm vor Jahrzehnten ihren Ausgang bei Munition, Flugkörpern u. ä. Sie ist heute weder bei wehrtechnischen noch zivilen Produkten erläßlich und gibt uns über die potentielle Lebensdauer von Produkten sowie bei der Schadensanalyse wertvolle Entscheidungskriterien. **Tabelle 4** faßt einige Anwendungsbeispiele der Umweltsimulation zusammen. Die **Bilder 19 und 20** zeigen zwei typische Meßaufbauten für die Ermittlung der Gebrauchstauglichkeit von Produkten.

Leichtbau-Panzerschutz für Fahrzeuge

Der Schutz von wehrtechnischen (Mannschaftswagen, LKW, Hubschrauber u. ä.) sowie von zivilen Fahrzeugen (Politiker, Firmenchefs, sog. VIP) erfolgt heute serienmäßig überwiegend durch Stahlplatten. Sowohl bei den Landfahrzeugen als auch vor allem bei Hubschraubern stößt man an Masse-Transportgrenzen. Am ICT entwickelten wir daher aus der Synergie von wehrtechnischem und polymertechnischem Wissen Leichtbauplatten.

ICT-Leichtbau-Panzerschutzplatten erreichen durch intelligente Kombination von Schichten verschiedener Werkstoffe folgende Daten:

- **B4**
  Beschuß mit Faustfeuerwaffen (.44 Magnum):
  430-450 m/s; Weichkern; 11 mm Ø; 15,6 g Geschoßmasse
  Plattenmasse 6 kg/m² (Stahl 25 kg/m²)
  Die Kosten je m² sind bei besserer Verarbeitbarkeit niedriger als bei technisch vergleichbaren Stahlplatten.
- **B7**
  Beschuß mit Gewehr (G3):
  810-830 m/s; Munition: 7,62 x 51 mm VMS/Hk; 7,62 mm Ø; 9,5 g Geschoßmasse
  Plattenmasse 32 kg/m² (Stahl 80 kg/m²)
  Auch hier sind die Kosten niedriger als bei technisch vergleichbaren Stahlplatten.

Die bessere Verarbeitbarkeit (Umformbarkeit) der ICT-Leichtbau-Panzerschutzplatten (B4) ermöglicht beispielsweise die Dekorbeschichtung einer Fahrzeug-Tür-Innenseite. Die **Bilder 21 und 22** zeigen eine beschossene Fahrzeugtür mit ICT-Leichtbau-Panzerschutzplatten. **Bild 23** verdeutlicht die Energievernichtung des Geschosses über eine ca. 5 cm hohe Ausbeulung der ICT-Schutzplatte. Auch die Forderung nach drei dicht nebeneinanderliegenden Einschüssen kann erfüllt werden.

Seitenaufprallschutz (crash net) für Fahrzeuge

Die Schwachstelle hinsichtlich des Insassenschutzes von Fahrzeugen (PKW) ist der Seitencrash. Wir arbeiten daher am ICT an Machbarkeitsstudien zu folgender Idee: Ein Stahlseil oder -netz wird innerhalb der Karosserie eines PKW von der A- über B- bis C-Säule gespannt. Im Falle eines Seitencrash spannen Gasgeneratoren in definierten Zeitintervallen (intermittierend) derart, daß Aufprallenergie durch stückweises Plastifizieren des gespannten Stahlseiles absorbiert wird. **Bild 24** veranschaulicht den Vorgang prinzipiell.

Wiederaufladbare Hochenergie- und Hochleistungsbatterie

Hambitzer et al. [6] entwickelten am ICT in den vergangenen sieben Jahren ein neues wiederaufladbares Batteriesystem für wehrtechnische und zivile Anwendungen.
Seine Merkmale sind:

- Weltweit höchster Energieinhalt pro Masse und Volumen
- Weltweit höchste Leistung pro Masse und Volumen
- Betrieb bei Temperaturen von ca. -70 °C bis 100 °C (keine Hochtemperaturzelle)
- Schnell- und tiefentladefähig
- unkritisch bei Überladung
- Kreislauffähig/Rezyklierbar
- Kann nicht brennen oder explodieren

Tabelle 6 vergleicht die neue Batterie der Fa. Fortu (ICT-Entwicklung) mit Nickel-Cadmium und handelsüblichen Lithiumionenbatterien. Daraus werden Vorteile für die Fortu-Batterie deutlich. Derzeit erfolgt die Kleinserienherstellung und -erprobung.

Elektrochemische Sensoren

TNT-verseuchte Böden müssen heute mangels langwieriger (Labor)Analytik und wegen umfangreicher Probennahme sehr aufwendig untersucht werden und bei Kontamination relativ großflächig abgetragen werden. Der am ICT entwickelte elektrochemische Sensor auf der Basis potentiometrischer Messungen erlaubt örtliche TNT-Kontaminationen innerhalb weniger zehn Sekunden quantitativ vor Ort zu analysieren.

Weitere wehrtechnische Anwendungen von elektrochemischen (On-Line-)Sensoren können beispielsweise sein:

- Nitro- und Aminoaromaten: vor-Ort Messungen in Böden und Wässern und einfache Handhabung ermöglichen preiswerte und schnelle Messungen
- Minendetektion: positiver Nachweis an Labormuster (Plastikmine) erbracht mit Gasphasensensor (s.u.)
- Chemische Kampfstoffe: positive Erprobung an Vergleichssubstanzen erbracht

Bild 25 zeigt den am ICT entwickelten hochempfindlichen TNT-Sensor. Hiermit lassen sich TNT-Moleküle in Boden und Wässer im Bereich von 1 -6000 ppm quantitativ nachweisen.
In Entwicklung ist ein System, das Moleküle in der Gasphase nachweist. Die Empfindlichkeit liegt im Bereich kleiner 10 ppb. Damit lassen sich die üblichen Landminen mit Kunststoffgehäuse (in geschlossenem Zustand) detektieren. TNT permeiert als Gasmolekül in geringsten Mengen durch das Kunststoffgehäuse.

Eine zivile Anwendung für elektrochemische Sensoren ist ein am ICT entwickelter Alkoholsensor mit dem inline der Alkoholgehalt beim Brauen von Bier verfolgt werden kann. Bisher ist der zielgerichtete Abbruch des Gärprozesses beim Brauen von alkoholfreien Bier nicht sicher möglich, weil die Analytik zu zeitaufwendig ist. Mit dem ICT-Alkohol-Sensor ist nun eine InLine-Analytik möglich.
Weitere denkbare zivile Anwendungen dieser OnLine-Sensortechnologie sind z.B. Explosivstoffsensorik in sicherheitsrelevanten Bereichen (Flughäfen) oder auch das Aufspüren von anderen kritischen Substanzen wie Drogen, Umweltgifte usw.

4. Schlußfolgerung

Die geschilderten Beispiele sind in der Wehrtechnik zum Teil seit längerem bekannte Verfahren, die nun in der zivilen Technik ggf. in neuen Varianten Anwendung finden. Darüber hinaus konnten am ICT jedoch neue Synergiefelder zwischen Wehr- und Ziviltechnik erschlossen werden.
Kreativität und ein starker Wille zur Umsetzung in Machbarkeiten bis hin zu Produkten sind ein wichtiges Element, um Arbeitsplätze am Standort Deutschland zu sichern und neu zu schaffen.

5. Literatur

[1] EYERER, P.; ELSNER, P.; SCHMITT, D.; LUDWIG, CH.: *Wissenschaftsmanagement - Strategien für einen Forschungsverbund Fraunhofer-Institut mit Hochschulinstitut.* ICT-Bericht (unveröffentlicht), Veröffentlichung erscheint demnächst.

[2] EYERER, P.; WALTER, G.: *Stand und Aussichten der PUR-RIM-Technik für Kfz-Außenteile.* In: *Kunststoffe im Fahrzeugbau - Technik und Wirtschaftlichkeit.* Düsseldorf: VDI Verlag, 1988, S. 197-244

[3] GREINER, N.R.; PHILLIPS, D.S.; JOHNSON, J.D.; VOLK, F.: *Diamonds in Detonation Soot.* Nature, Vol. 333 (1988), p. 440-442

[4] EISENREICH, N.; HERZ, J. KULL, H.; MAYER, W.; ROHE, TH.: *Fast on-line identification of plastics by near-infrared spectroscopy for use in recycling processes.* ANTEC 96, Indianapolis, USA, 1996, pp. 3131-3135

[5] HIRTH, TH.; SCHWEPPE, R.; JÄHNKE, S.; BUNTE, G.; EISENREICH, N.; KRAUSE, H.: *Degradation Processes in Sub- and Supercritical Water.* 4th International Symposium on Supercritical Fluids. Volume A. Sendai Japan, May 11-14,1997

[6] Hambitzer, G.: *Wiederaufladbares Hochenergiesystem mit neuem Funktionsprinzip.* Habilitationsschrift, Privat-Universität Witten-Herdecke, 1995

[7] KRAUSA, M.; DOLL, J.; SCHORB, K.; HAMBITZER, G.: Chemie in Labor- und Biotechnik, 49. Jahrgang, Heft 2, 1998

ICT-Institutsleitung
Prof. Dr. Hefer
Dr. Schmitt · Dr. Elsner

Querschnittsaufgaben
Dr. Hefer

- Finanzen
- Personal
- Verwaltung

Zentrales Management
Dr. Ziegahn

- Forschungsplanung
- Öffentlichkeitsarbeit
- ICT - USA

Energetische Materialien Dr.Krause (Dr.Keicher, U. Teipel)	**Energetische Systeme** Dr. Eisenreich (W. Eckl, G. Langer, W. Liehmann)	**Angewandte Elektrochemie** Dr. Hambitzer (Dr. Krausa)	**Umwelt-Engineering** Dr. Hirth (Dr. Ziegahn, Dr. Reichert)	**Polymertechnik** komm. Dr. Elsner (Dr. A. Geißler, Dr. Reichert)
Synthese	Systemorientierte Entwicklung	Energietechnik	Entsorgungsverfahren	Produkte
Komponenten	Verbrennung	Umwelttechnik	Umweltfreundliche Fertigungstechnologien	Verarbeitung
Formulierung	Meßtechnikentwicklung	Leitfähige Polymere	Umweltsimulation	Werkzeugtechnik
Reaktionsmechanismen	Gasgeneratorsysteme		Kreislaufwirtschaft	Werkstoffe
Analytik	Sicherheitsanalysen			
Compounding				

Bild 1: ICT-Organigramm

	1/1994 (Jahr 1993)	12/1997
Finanzen (in Mio DM)		
Gesamthaushalt	23	33,9
• Wehrtechnik	15,5	17
• Polymertechnik	4,8	14
• Industrieanteil	1,5	7
• Investitionen	2,8	2,9
Personal		
Mitarbeiter gesamt	185	298
• Bereich Wehrtechnik	130	116
• Ziviler Bereich	28	82
• Zeit-Angestellte	27	100
davon Doktoranden	18	51
• Lehrlinge	7	13
• Durchschnittsalter	46	38
Leistung		
Erteilte Patente	2	5
Vorträge	72	120
Veröffentlichungen	61	73
ρ-Wi.	34 %	50 %
Tagungen, Workshops	4	8
Baumaßnahmen	0,1	4

Tabelle 1: Kennzahlen ICT - Vergleich

Thema	übergreifende Kooperationen zwischen den Produktbereichen am ICT
Energetische Demontage	EM / PT / UE
Energetisches Prägen	EM / PT / ES
Hülsenlose Munition	EM / PT
Ultrafeine Diamanten	EM / ES / PT
Airbag: azidfreie Rezepturen	ES / UE
Gasgenerator mit hoher Gasfreisetzungstemperatur	ES / PT
Pyrotechnische Montage	ES / PT
Durchgängige Simulation in der Wehrtechnik	ES / EM / PT / UE
Identifizierung NIR / Röntgenbeugung	ES / PT
Überkritische Fluide	UE / EM / PT
Umweltsimulation	UE / ES / PT
Leichtbau-Panzerschutz/Panzerung	PT / EM / ES
Crash-net (Seitenaufprall)	PT / ES
Batterien	AE
Sensorik	AE / ES

Produktbereiche

EM	Energetische Materialien	ES	Energetische Systeme
UE	Umwelt-Engineering	PT	Polymertechnik
AE	Angewandte Elektrochemie		

Tabelle 2: Forschungs-Synergien zwischen wehrtechnischen und zivilen Anwendungen - Übersicht der Beispiele

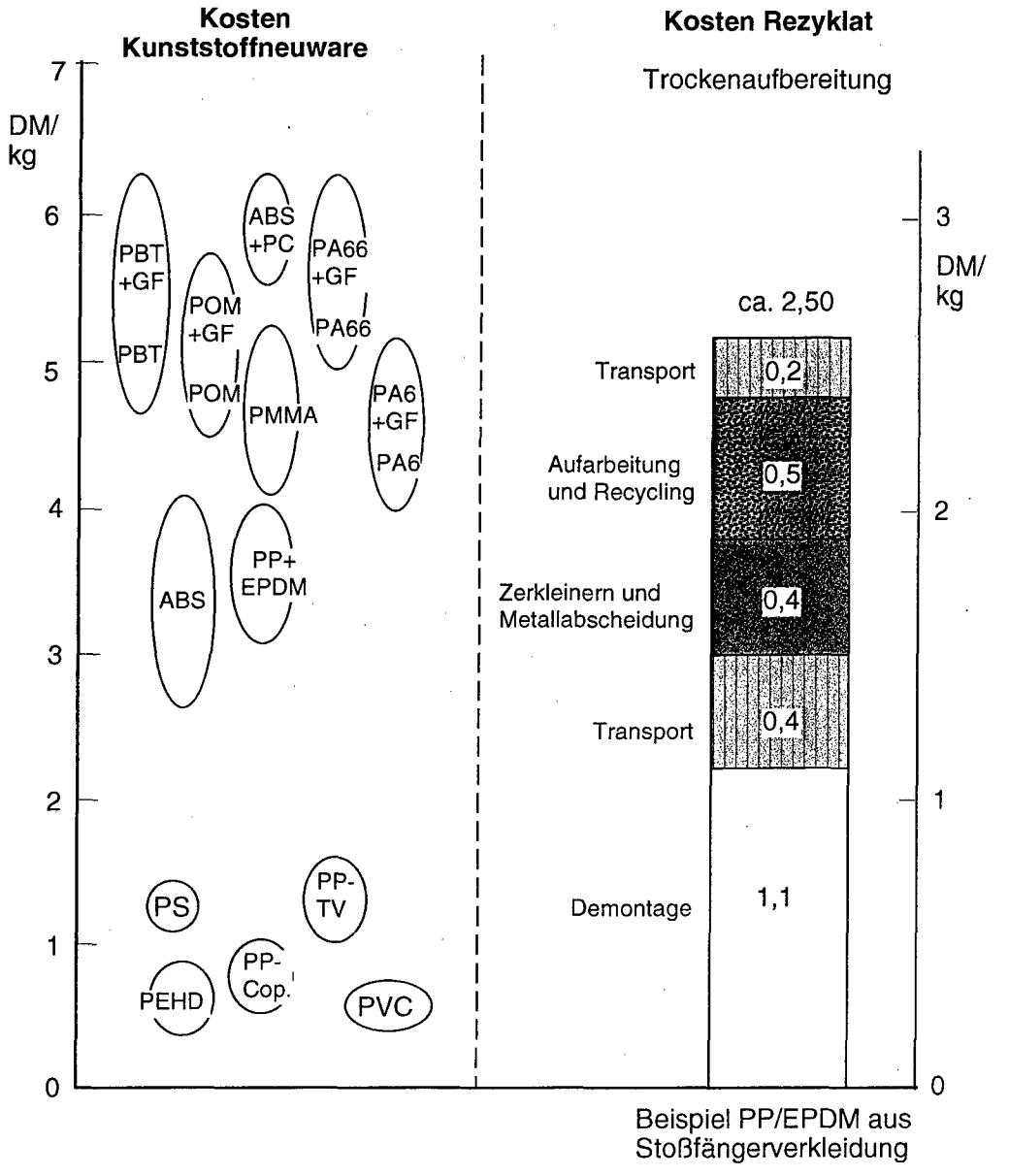

Bild 2: Kostenvergleich:

Neuware mit Rezyklaten aus Fahrzeugteilen

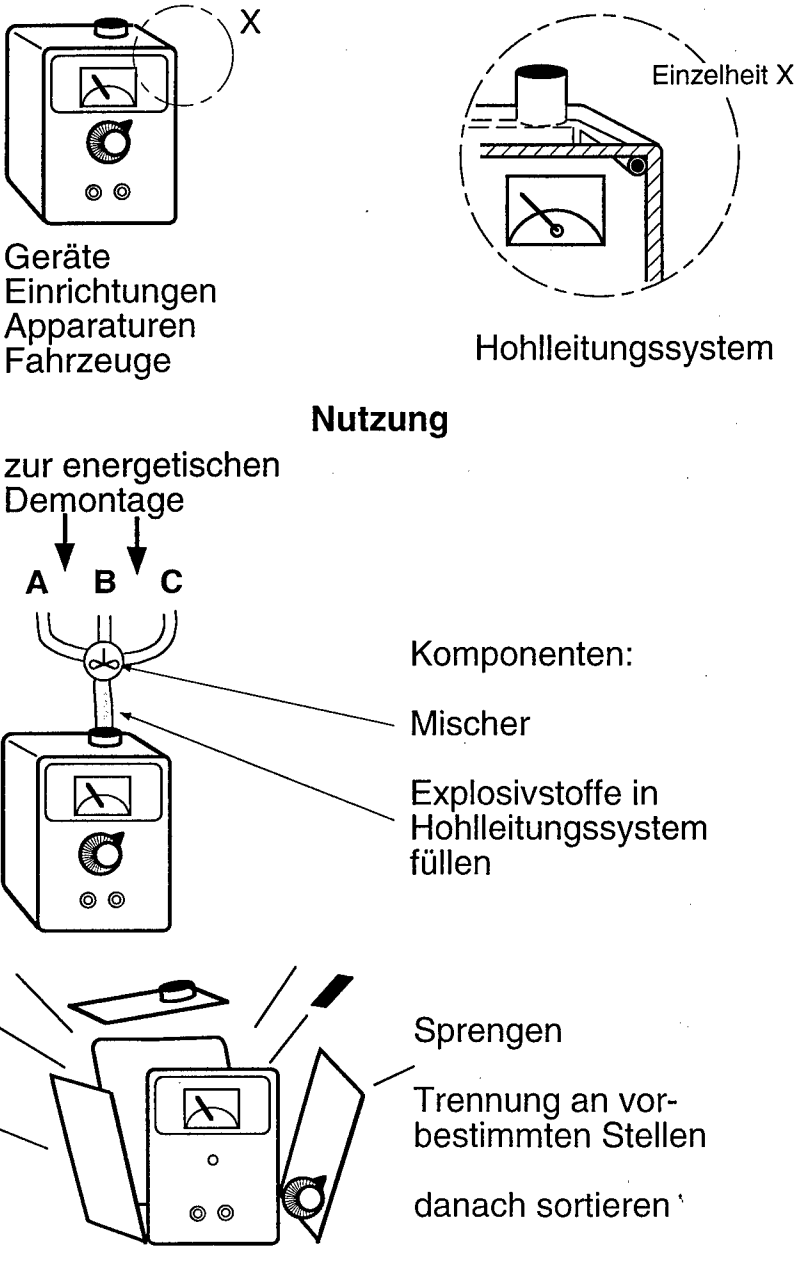

Bild 3: Prinzip der Energetischen Demontage

Bild 4: **Energetische Demontage einer Waschmaschine kurz nach Zündung**

Bild 5: **Energetische Demontage einer Waschmaschine während der Zerlegung**

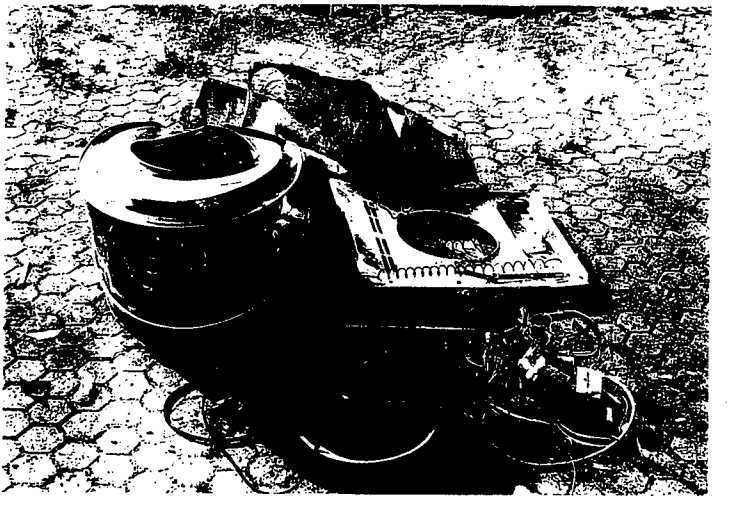

Bild 6: Zerlegte Waschmaschine nach energetischer Demontage

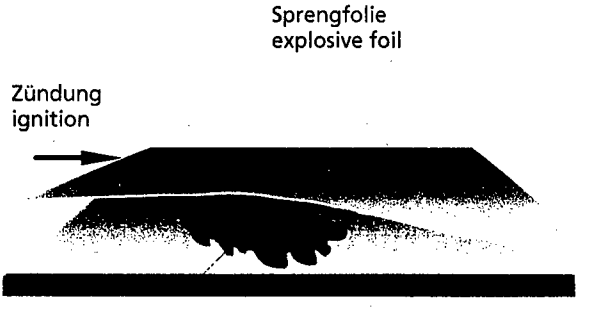

Bild 7: Energetisches Prägen

Bild 8: **Eichenblatt in Stahl energetisch eingeprägt**

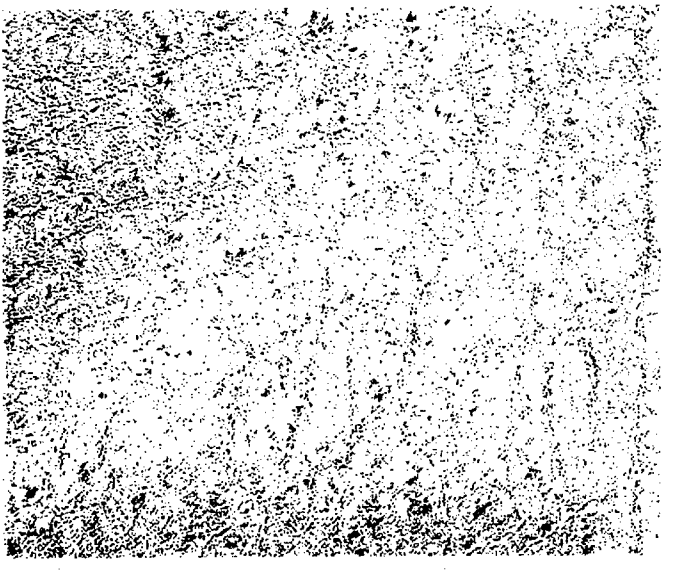

Bild 9: **Ledernarbung in Stahl energetisch eingeprägt**

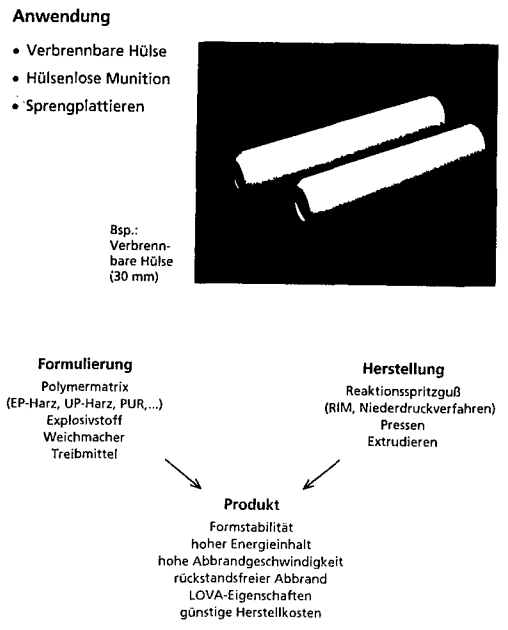

Bild 10: Geschäumte polymergebundene Explosivstoffe

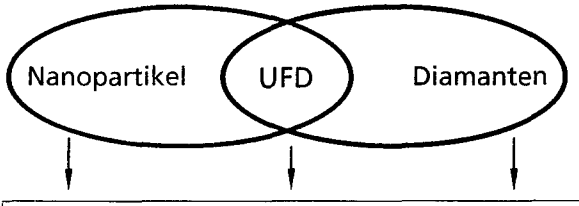

Herstellungsverfahren		
Gasphasen-kondensation Sol-Gel-Prozesse	Detonationssynthese	Graphitumwandlung
Produkte		
z.B.:Metalloxide typisch 30 nm	UFD; Nano-Diamanten Kristallitgröße 5 nm	Diamantpulver bis minimal 100 nm

Marktchancen UFD

Nutzen der Kombination

von Diamant-Eigenschaften und Nanostruktur

Bild 11: Ultrafeine Diamanten UFD

nach ca. 15 ms ab crash nach ca. 50 ms ab crash

Bild 12: Airbags schützen Insassen (hier Versuchspuppen)

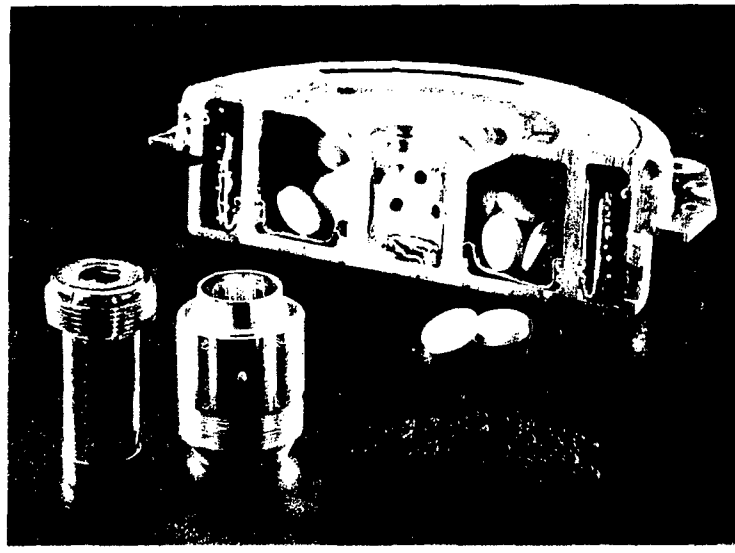

Bild 13: Aufgeschnittener Airbag-Modul eines PKW

Leistungsoptimierte Systeme	Schadstoffreduzierte Systeme
Explosionsschutz Austriebssysteme Membran u. Ventilaktivierung Montagesysteme	Airbag Gurtstraffer Notantriebe Nothydraulik Montagesysteme Aufrichtsysteme Rettungssysteme Auftriebssysteme Feuerlöschsysteme Aerosolgeneratoren Nebelsysteme Werfer Schaummittel für Polymere
Raketenantriebe Unterwasserantriebe	

Tabelle 3: Anwendungen von azidfreien Gasgenerator-Komponenten und Systemen

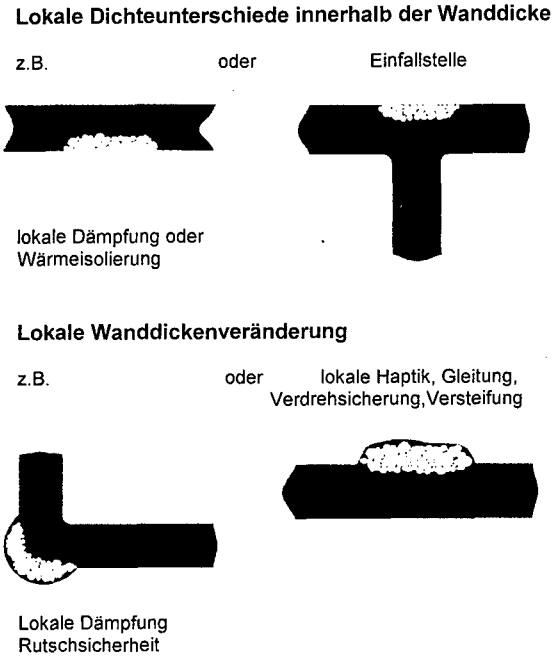

Bild 14: Lokales Aufschäumen nach dem Formfüllvorgang (Thermoplaste, Duroplaste, Elastomere)

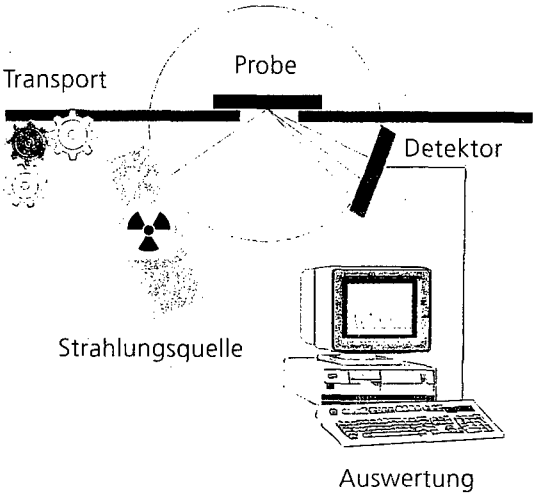

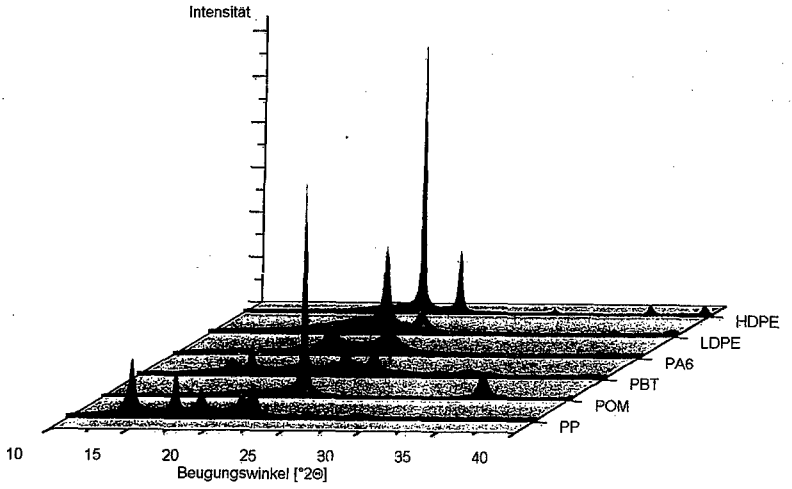

Bild 15 und 16: Kunststoffidentifizierung mit Hilfe der schnellen Röntgenbeugung

Bild 17: Anwendungsfelder für SCWO (super critical water oxidation)

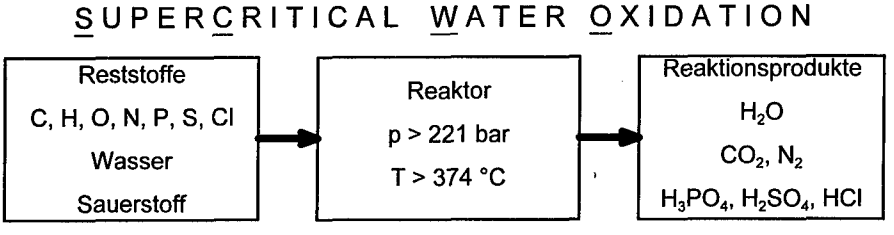

Vorteile:
- Prozeßintegrierter Einsatz
- Geschlossene Anlage
- Kleine Anlagengröße
- Keine Rauchgasreinigung
- Feststoffabscheidung
- Kurze Verweilzeiten
- Hohes Schadstoffzerstörungspotential

Nachteile:
- Anspruchsvolle Verfahrenstechnik
- Kompressionskosten
- Teure Werkstoffe (Korrosion)
- Feststoffablagerung
- Limitierte Feststoffzufuhr

Bild 18: Reststoffbehandlung durch SCWO

Umweltsimulation :=
Nachbildung der Wirkungen von Umgebungseinflüssen

Funktionstest	Lebensdaueruntersuchung	Umweltverträglichkeit
Gasgeneratoren	Gasgeneratoren	Gasgeneratoren und Airbags (Emissionen)
Airbags	Airbags	Kraftstoffbehälter (Permeationssperre)
Treibstoffe	Festtreibstoffe	Autoinnenteile (Fogging)
Zünder	Explosivstoffe	Werkstoffe (indoor air pollution)
Auto-Elektronik	Auto-Elektronik	Treibladungen (NOx-arme)
Nachrichtentechnik	Nachrichtentechnik	
Gebläse	Automobiltanks	
Werkstoffe	Werkstoffe	

Tabelle 4: Umweltsimulation wehrtechnisch und zivil

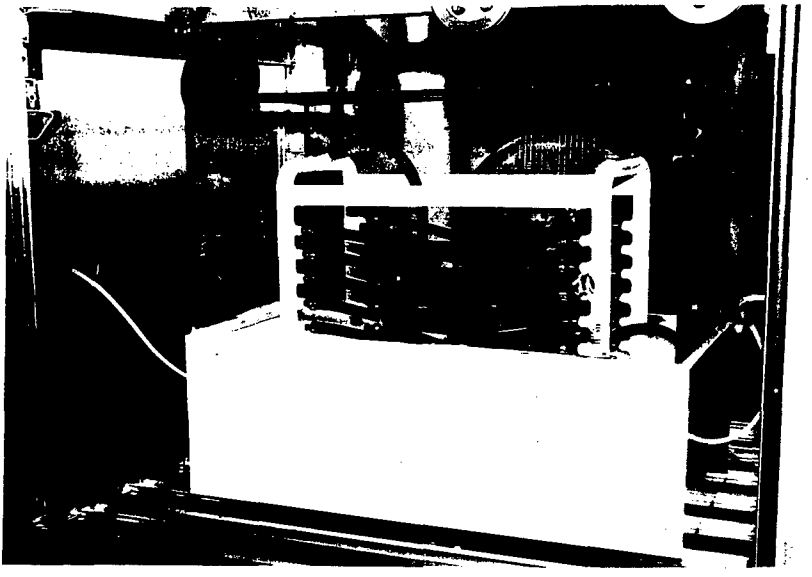

Bild 19: Umwelt Engineering - Untersuchung der Beständigkeit von Kraftstoffschläuchen gegen Ozonrißbildung und Kraftstoffpermeation

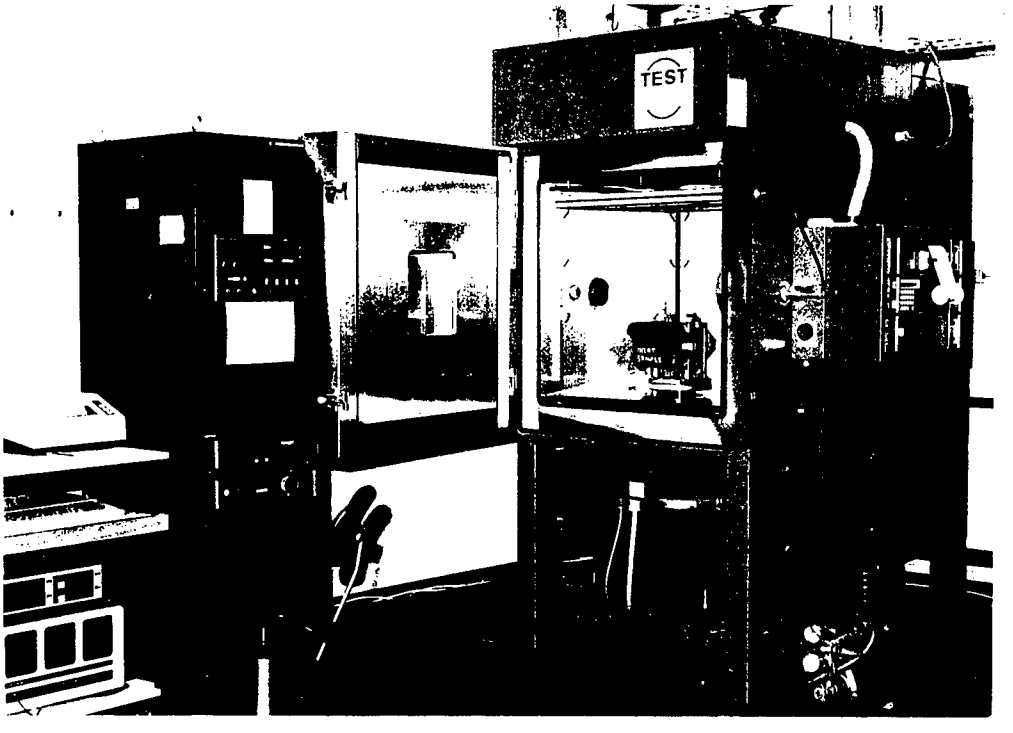

Technische Daten:

Frequenzbereich:	5 Hz ... 5000 Hz
Spitzenkraft:	2100 N
Max. Auslenkung:	25,4 mm
Max. Beschleunigung:	95g
Rechnergesteuert:	Sinus, Rauschen, Schock
Prüfvolumen:	500 l
Temperaturbereich:	- 60 °C ... + 180 °C
Feuchtebereich:	10 % ... 95 %
Taupunktserniedriegung:	bis - 15 °C
Programmgesteuert	

Bild 20: Klima-Vibrations-Kammer für die Umweltsimulation

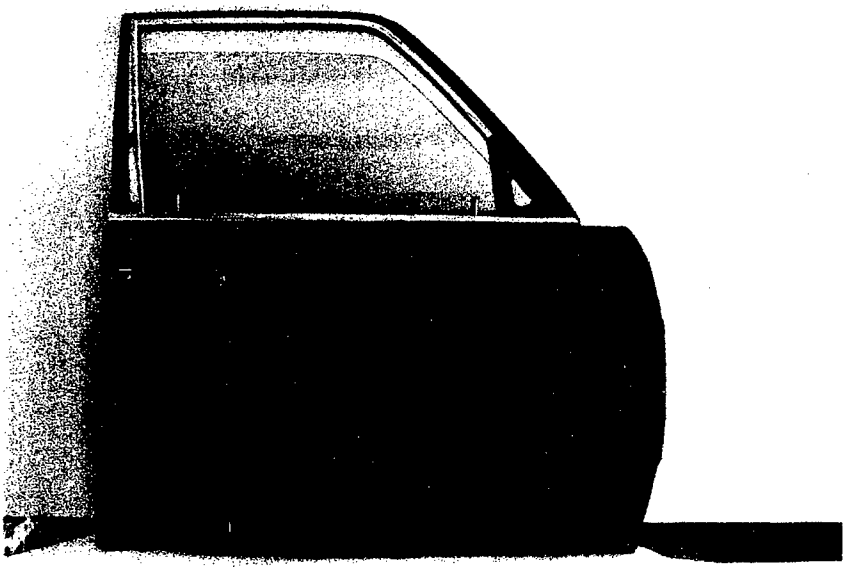

Bild 21: PKW-Tür (Frontansicht), Beschuß mit .44 Magnum

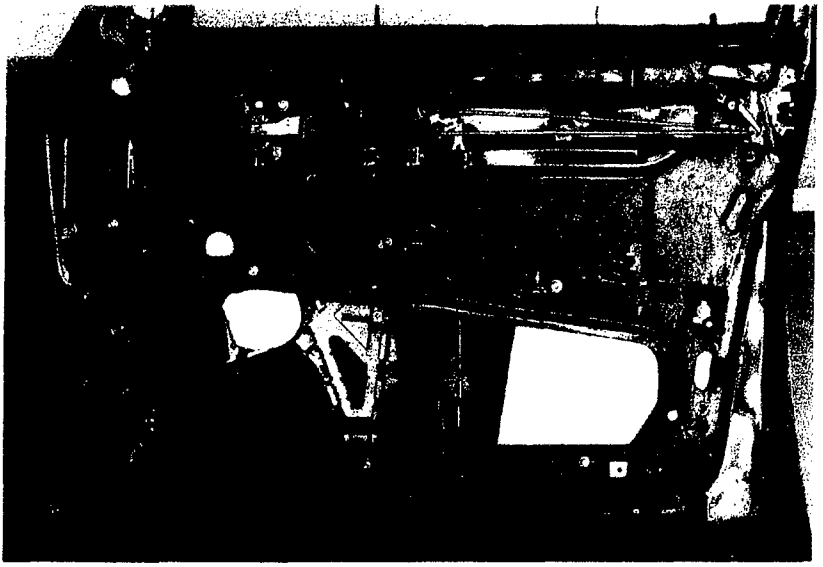

Bild 22: PKW-Tür (Rückansicht), Beschuß mit .44 Magnum

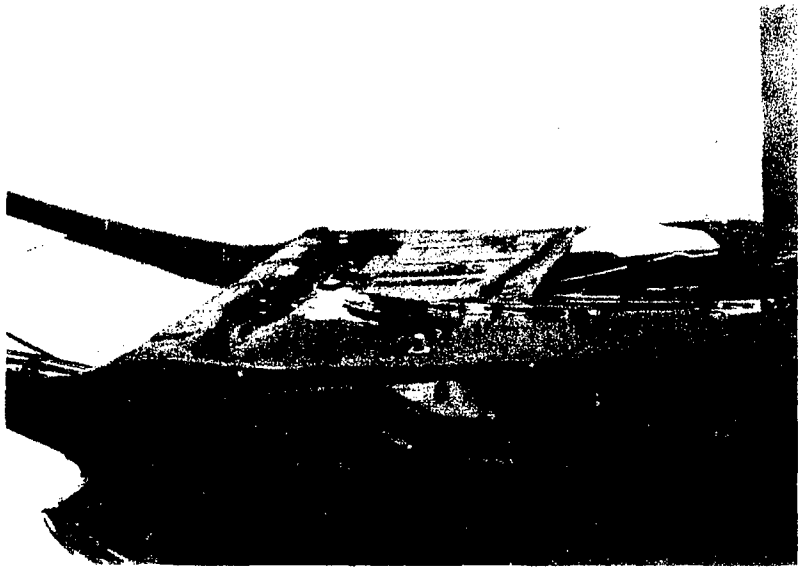

Bild 23: PKW-Tür (Rückansicht liegend), Beschuß mit .44 Magnum

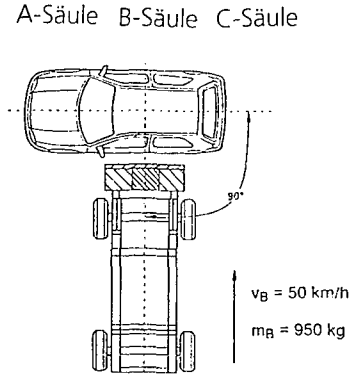

Seitencrash-Versuchskonfiguration

Wirkungsweise:

Stufe 1:

Versteifung der Seitenstruktur durch Anspannen einer Netzstruktur in der Seitenpartie mit einem Gasgenerator

Stufe 2:

Energieaufname durch plastische Verformung der Netzstruktur

Bild 24: Seitenaufprallschutz (Crash Net)

Vergleich mit anderen Systemen I

Gerätebatterien		
Nickel-Cadmium	FORTU	Lithium-Ionen
40 Wh/Kg	Energie > 200 Wh/kg	80 -100 Wh/kg
400 W/kg	Leistung 2000 W/kg	50 W/kg
1000	Zykelzahl 150 (-> 500)	150-500 (-> 1000)
ja, inherent	Überladbarkeit ja, inherent	nein, Sicherheit, Brand
nicht brennbar nicht explosionsfähig	Sicherheit nicht brennbar nicht explosionsfähig	brennbar, Gasentwicklung explosionsfähig

Vergleich mit anderen Systemen II

Electric Vehicle (EV)		
Natrium/Nickelchlorid	FORTU	Lithium-Ionen
780 Wh/Kg	theor. Energiedichte 1100 Wh/kg	460 / 610 Wh/kg
300 kg	Masse einer 30kWh Batterie 150 kg (-> 100 kg)	250 kg
<< 300 km	Reichweite 300 km	< 300 km
nein 90 % in 3 Stunden	Schnelladung ja < 1 Stunde Rückspeicherung der Bremsenergie	nein 3 Stunden
> 250 °C	Betriebstemperatur Raumtemperatur	Raumtemperatur

Vergleich mit anderen Systemen III

Electric Vehicle (EV)		
Natrium/Nickelchlorid	FORTU	Lithiumionen
60 kW/ ?	Dauerleistung/Peakleistung 60 kW / 200 kW	20 kW / 60 kW?
Sicherheitstests bisher erfolgreich aufwendiges Gehäuse brennbar	Sicherheit nicht explosionsfähig einfaches Management nicht brennbar	explosionsfähig aufwendige Zellüberwachung brennbar, HF-Entwicklung
16 % / Tag	Selbstentladung 40 % / Monat (-> 10 % / Monat)	10 % / Monat
Selbstentladung Betriebstemperatur, flüssiges Natrium	Hauptproblem Preis + Verfügbarkeit von Kobalt	Sicherheit; z.Z. Preis von Kobalt

Tabelle 6

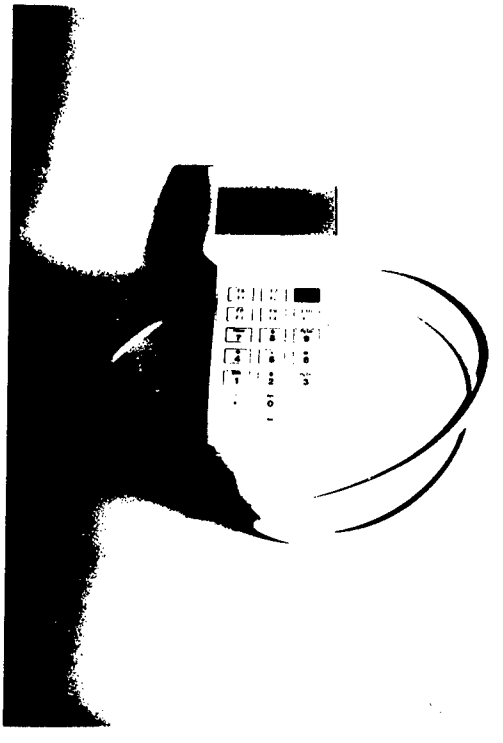

Bild 25: Prototyp des Sensorsystems zur TNT-Bestimmung in Böden und Wässern [7]

29th International Conference of ICT

Plasticisers in Energetic Materials Formulations - A UK Overview

Dr Chris Leach*, **Peter Flower**
Formulation & Processing Group,
Energetic Materials Department
Defence Evaluation and Research Agency,
Fort Halstead, Sevenoaks, Kent TN 14 7BP
United Kingdom

Dr Ron Hollands
British Aerospace plc,
Royal Ordnance Division, Glascoed,
Usk, Monmouthshire, NP5 1XL

Sue Flynn
British Aerospace plc,
Royal Ordnance Rocket Motor Division,
Summerfield, Kidderminster, DY11 7RZ

Dr Eric Marshall
ICI Explosives,
Ardeer Site, Stevenston,
Ayrshire. KA20 3LN

John Kendrick
ICI Wilton Research Centre,
PO Box 90, Wilton , Middlesborough, TS90 8JE

* Presenter Phone 44 1959 515449 Fax 44 1959 516055

Abstract

The energetic material formulator is faced with the need to compromise between often conflicting requirements of performance and safety whilst trying to minimise overall cost and environmental impact. In this, he is often restricted by the ingredients and processing techniques available to him. An area of ingredient and formulation research that has perhaps not received the attention it deserves is that of the design and use of plasticisers in modern composite explosives and propellants. Past research has concentrated on the classical role of the plasticiser as a processing aid and as a modifier of mechanical properties, rather than exploiting other attributes that can be put to good use by formulators. Such attributes include the ability to improve safety characteristics, both of the final formulations and during the manufacturing process; modify the energy or oxygen balance of formulations; and modify

burn rates and ballistics. The roles and ideal attributes of plasticisers are discussed, and illustrated with examples based on UK experience, particularly with polyNIMMO bound composite explosives and propellants.

At present, no ideal plasticiser is commercially available anywhere within the world community and plasticiser choice is often based on the compromise most appropriate to the application. However, the increasing ability to model the action of the plasticiser within the binder matrix represents a tool that can be used in future to design new plasticisers. The relative merits of designing new plasticisers or continuing to exploit existing ones are discussed.

Introduction

The Encyclopaedia of Chemical Technology [1] states "A plasticiser is incorporated in a material to increase its workability, flexibility or distensibility [2]. Addition of a plasticiser may lower the melt viscosity, the secondary-order transition temperature, or the elastic modulus of the plastic." In the past, plasticisers have all too often seen by the energetic material formulator as ingredients required only to perform these classical roles as processing aids and as modifiers of the final mechanical properties of a formulation. As such, past research on composite explosives and propellants may have neglected assessment of these essential ingredients, limiting studies to the effects on formulation viscosity and glass transition temperature. In order to investigate plasticisers in explosive and propellant formulations more rigorously; to be able to compare existing materials more objectively in the same way as explosive fillers have been [3]; and ultimately to design new and hopefully better plasticisers, it is first necessary to fully understand their role, requirements and current limitations.

Ideally, the binder system of an explosive or propellant formulation should not require an external plasticiser. Plasticisers, by their very nature, tend to be low molecular weight molecules, mobile and volatile. Thus, in adding a plasticiser to improve certain formulation characteristics an undesirable feature is introduced, the capacity for plasticiser migration and loss, with the potential for associated deterioration of formulation properties on ageing.

Internally or self- plasticised binders are highly desirable to overcome this potential problem. Plasticiser theory is currently being used to investigate such systems and to indicate whether the concept can be applied to modify existing energetic binders such as polyGLYN. Nevertheless, the need for externally plasticised binders remains a fact of life for the formulator in the near future and most of the energetic materials experience is associated with this type of plasticisation.

Historically, UK experience with composite explosives and propellants has concentrated on three general combinations of plasticiser and binder, shown below in table 1.

	COMBINATION		Plasticiser	Binder	Formulation
	Plasticiser	**Binder**	**Example**	**Example**	**Example**
A	INERT	INERT	DOS	HTPB	AP Composites
				KRATON	ROWANEX 3000 [4]
B	ENERGETIC	INERT	K10	DIOREZ	CPX200
C	ENERGETIC	ENERGETIC	BDNPA/F	polyNIMMO	pN LOVAs [5]

Table 1
Plasticiser/ Binder Combinations

Chronologically the research emphasis has passed from Group A to Group B to Group C, with the bulk of the formulation research interest for future systems use now resting with Group C combinations of an energetic plasticiser with an energetic binder. The group A type formulations represent the most technologically mature group, with HTPB based ammonium perchlorate composites well established in service use and a range of HTPB polymer bound explosives (PBXs) either in UK service or in the process of being introduced [6]. The pure research emphasis, within the UK, on HTPB based systems has shifted mainly from formulation to more advanced means of characterisation, principally to underpin the intelligent ownership of munitions containing such systems and to aid more accurate munition lifetime predictions. However, within an increasing need to address environmental issues and to design formulations with an improved ease of disposal at the end of service life, there has been more recent UK formulation activity on inert plasticised thermoplastic elastomer

systems, particularly for high performance explosives suitable for shaped charge applications [4, 7]. Although only present in a small percentage, the nature of the binder and plasticiser in these pressable explosives can have significant effects on the safety of the final formulation. Experience with inert TPEs is also seen as an essential precursor to research on future energetic TPEs.

UK interest in semi energetic binder systems, as typified by the Group B combination, subsided with the availability of truly energetic polymers such as polyNIMMO and polyGLYN. Today, the bulk of the government sponsored plasticiser and formulation research lies in the evaluation of Group C combinations, although certain Group B combinations are being investigated by Industry, principally for gun propellants.

UK Energetic Plasticiser Experience

Inert plasticisers and inert plasticised systems have been well characterised and are relatively well understood. The energetic material community is able to draw on knowledge from the commercial polymer field and, because of the widespread use of these plasticisers in bulk polymer applications, inert plasticisers are relatively inexpensive. The potential applications of energetic plasticisers are limited to the energetic materials field, thus restricting the body of knowledge and the potential to reduce costs through bulk use. A number of energetic polymers such as polyNIMMO, polyGLYN, GAP and AMMO/BAMO have been developed world wide. Similarly, a large number of energetic plasticisers have appeared. Now instead of being limited to using HTPB with a small choice of well known and freely available plasticisers, the formulator is faced with a complex choice from numerous combinations of plasticisers and binders, potentially with very little information on which to base that choice. In recent years UK energetic binder formulation effort has centred on polyNIMMO [8,9], although an increased emphasis is now being placed on the evaluation of polyGLYN, particularly for rocket propellants. A range of plasticisers have been examined with these two binders but no one commercially available plasticiser has proved to be ideal in all roles and circumstances. Choice of plasticiser has rested more on a compromise between often complex and competing requirements which go much further than the need to lower mix viscosity and binder glass transition temperature. The United Kingdom's experience in this area is not

unique. Similar findings have been reported by other nations in international collaborations such as TTCP and WEAG CEPA14.

The energetic plasticisers investigated in the UK by both DERA and private industry include BDNPA/F, K10 (also known as ROWANITE 8001, a mixture of dinitroethlylbenzene and 2,4,6 - trinitroethylbenzene 65%/35%), NENAs, GAP Azide, BTTN/TMETN, DANPE, and nitro-glycerine, all of which have advantages counter-balanced by real or potential disadvantages. Lack of a single ideal energetic plasticiser has prompted the UK to adopt a more a comprehensive, systematic approach to evaluating plasticisers as formulation ingredients. This approach encompasses reviewing the true role and requirements for plasticisers, understanding and modelling plasticiser action and addressing the need to design and synthesise plasticisers for specific binder systems. A brief overview of the role of plasticisers in energetic material formulations is included below, illustrated with examples mainly drawn from experience of Group C plasticiser / binder combinations but with additional material from Groups A and B.

Plasticiser Roles, Requirements And Effects

Fully energetic binders systems can allow the formulator to achieve one of two objectives, to either directly improve performance without compromising safety or, for a given level of performance, improve the vulnerability of a formulation. The latter objective can be approached in two ways. The energy derived from the binder can be used to reduce the energy required from the more sensitive filler component, either allowing the loading level of a sensitive nitramine filler to be kept to a minimum, as in the case of polyNIMMO composite gun propellants, or allowing the nitramine to be partially substituted with a less vulnerable but less energetic component such as NTO [10]. The contribution of the energy from the plasticiser towards the binder system as a whole is therefore an important consideration in all of these situations. This additional role must be added to those as a process aid and mechanical property modifier. These classical roles can gain additional importance on progressing from Group A to Group C plasticiser / binder combinations. The presence of energetic groups along the polymer chain invariably means that energetic binders are more dense and viscous than HTPB and that their mechanical properties are inferior to HTPB, with higher glass transition

temperatures, Tg. To compensate for this in the final formulation, it is all the more important that the plasticiser has the desired effect in lowering mix viscosity and Tg. The full list of plasticiser roles and attributes are presented below as table 2.

Roles	Essential Attributes	Desirable Attributes
Classical Role -	Stable	Inexpensive, available and
Processing Aid	Safe to Handle	low environmental impact
Modifier of Mechanical Properties	Low toxicity	
Additional Energetic Materials	Physically Compatible	Lower viscosity
Role -	Chemically Compatible	Lower Tg
Improve Energy or Oxygen		No/low migration or loss
Balance		Desired effect on all
Modify ballistics		aspects of performance
Improve safety		and safety

Table 2
Plasticiser Roles and Attributes

Processing Aids

The careful choice of plasticiser and plasticisation level are particularly important if castable compositions are required but plasticiser selection can also be used to aid the mixing as well as the filling process. In the case of ROWANEX 3000, a pressable HMX/TPE explosive, the level of plasticiser was selected to optimise the binder rheology to allow the mixing operation to be carried out by a solventless compounding process, thereby reducing the environmental impact of the production process.

NENA plasticisers have been found to have a much more effective classical plasticisation ability on polyNIMMO than BDNPA/F, leading to lower viscosity uncured binder systems. Figure 1 shows the relative lowering of polyNIMMO viscosity for 10% plasticised BPNPA/F and MEN42 systems. MEN42 is a 42%/58% mixture of methyl NENA in ethyl NENA. In the UK initial studies of ammonium nitrate/ polyNIMMO smokeless composite rocket propellants, under the four power ASNR - TMP programme, were undertaken with BPNPA/F plasticised formulations. Using BPNPA/F, the ASNR performance target of an SI of 240 sec could only be achieved through the formulation of an extrudable composition, AN8 [11] Replacing BDNPA/F with the more efficient plasticiser MEN42 allowed a castable

composition, AN9, to be formulated with the same specific impulse. In the case of polyNIMMO composite gun propellants, the high plasticiser activity of MEN42 has proved to be a processing disadvantage rather than an advantage. Direct substitution of BDNPA/F by MEN42 led to the extruded dough being too soft and caused the propellant to slump and the web to collapse after extrusion.

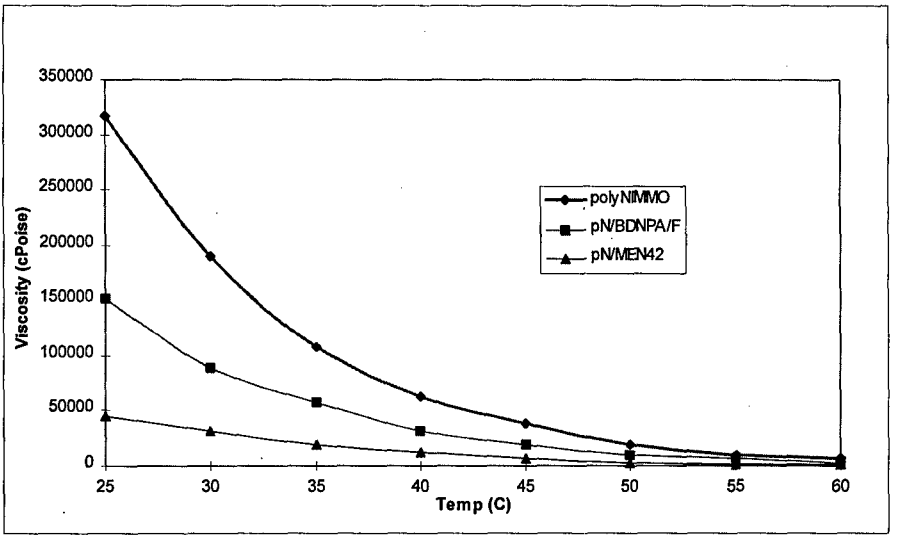

Figure 1
polyNIMMO and 9/1 polyNIMMO/plasticiser viscosity

Effect on Mechanical Properties

Energetic binders have higher glass transition temperatures than established inert binders such as HTPB and efficient plasticisers are required to lower the Tg to an acceptable level, outside the service temperature range, if energetic binders are to find service applications. Tg's as low as - 60 °C or less are desirable for rocket propellants used in air launched missiles, whereas Tg's of around - 35 °C may be acceptable for formulations used in the land or sea environment. Tg also tends to increase with higher formulation solids loading and with the applied strain rate. The desirability of lowering the Tg and its influence on the choice of plasticiser is therefore heavily dependant on the final use of the formulation. A number of studies have been conducted in the UK and other nations [12,13] on the effect of plasticiser on

polyNIMMO glass transition temperature, showing the suitable mechanical properties can be obtained for the binder system, although the air launched requirements are difficult to meet with existing plasticisers. Figure 2 shows the effect of certain plasticisers on polyNIMMO glass transition temperature, cured at a 1/1 polyNIMMO/ Desmodur N100 equivalent weight ratio.

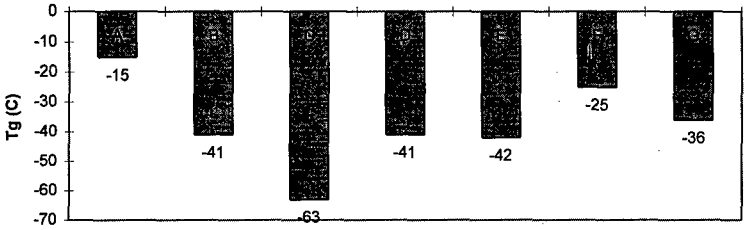

A= polyNIMMO, B= polyNIMMO/MEN42 3/1, C= polyNIMMO/MEN42 1/1,
D= polyNIMMO/ EtNENA 3/1, E= polyNIMMO/ BuNENA 3/1,
F= polyNIMMO/ BDNPA/F 3/1, G= polyNIMMO/ BDNPA/F 1/1,
all measurements by DSC.

Figure 2
Effect of plasticiser on polyNIMMO Tg.

The effect of plasticiser on final formulations can be seen in table 3. LOVA6 formulations were designed only to assess Tg, not as suitable candidates for gun firing. LOVA4, although it has a high Tg, has passed UK low temperature shatter tests prior to gun firing. In this case Tg's were measured by DMTA, which usually gives a higher figure than DSC.

LOVA	Plasticiser	Tg (°C)
4	BDNPA/F	-29
6M	MEN42	-29
6E	Ethyl NENA	-38
6B	Butyl NENA	-38

Table 3
Effect of plasticiser on formulation Tg.

As can be seen from this table the effect on formulation Tg is not as great as might be expected from the binder results, since less NENA plasticiser than BDNPA/F must be used to avoid producing too soft a dough for extrusion purposes.

Effect on Energy and Ballistics

The influence of plasticiser choice on the performance of a final formulation can again be seen from ammonium nitrate based rocket propellants. The reformulation of AN8 to give a castable AN9 formulation was in part due to the superior plasticiser activity of MEN42 compared with BDNPA/F and partly due to it's higher energy content. This also enabled the RDX content to be reduced without reducing the formulation specific impulse, thereby improving the formulation vulnerability. Later use of Nitro-glycerine as the plasticiser allowed the total elimination of RDX, without a significant SI penalty. The use of NG was also found to preferentially increase the burn rate at lower pressures thereby lowering the pressure exponent. The need to control performance and ballistics will again depend on the final application, with potentially widely differing requirements between gun and rocket propellants, and the influence of this will effect the choice of plasticiser to a greater or lesser extent.

Effect on Safety.

As already described above, the plasticiser can have an indirect effect on formulation vulnerability. More direct effects have also been noted. A number of polyNIMMO composite gun propellants using BDNPA/F as the plasticiser have been found to have low vulnerability to shaped charge attack [5]. None containing MEN42 have met that requirement. The choice of plasticiser has also been found to have an effect on the impact sensitiveness of HMX/TPE pressable explosives, with more viscous plasticisers producing more sensitive formulations [14].

Plasticisers can also be used to good effect to improve process safety. The explosive CPX200 is produced using a premix based on RDX and the plasticiser, K10, eliminating the need to load dry RDX into the production mixer. DOS has also been shown to be highly effective at desensitising RDX at levels as low as 3% and research is underway to assess such premixes as feedstock for twin screw extruders [15]. With more sensitive fillers such as CL20 and HNF currently being researched the premix route may be an attractive option for safe future formulation production techniques.

Compatibility

As with all other formulation ingredients, plasticisers must be physically and chemically compatible with other components. Once more MEN42 provides a useful illustration. Although vacuum stability tests highlighted no dramatic compatibility problems at the early stage of ASNR-TMP work, severe stabiliser consumption and gassing problems were observed during the scale up of AN9, containing MEN42. Similar compositions containing BDNPA/F or NG did not suffer from these same problems. MEN42 and other NENA's have also been found to be violently chemically incompatible with NTO and ammonium perchlorate, thereby severely limiting the potential uses of these plasticisers in insensitive high explosive [10] and reduced smoke composite rocket propellant formulations.

All plasticisers must be physically compatible with the polymer matrix, otherwise they will either separate out at the mixing stage or suffer from severe migration problems in the final formulation. Physical compatibility problems can also lead to unforeseen safety problems. A prime example of this is the violent increase in response observed when JA2 propellant is loaded with RDX to produce the JAX series of propellants [16]. RDX is slightly soluble in DEGDN plasticiser and was found to migrate with the plasticiser to the surface of the propellant grain where it was deposited in crystalline form. A similar phenomenon has been reported elsewhere [17].

Migration and Loss

By their very nature efficient plasticisers are small molecules, which can easily migrate and volatilise, leading to a deterioration in formulation properties. A comparative ageing study of castable and extrudable PBXs based on HMX and polyNIMMO showed that the BDNPA/F plasticised systems lost relatively little plasticiser even after one years ageing at 60 °C. The K10 plasticised system lost significantly more than the BDNPA/F system and the MEN42 analogue lost even more, with a mass loss of approximately 8%, expressed as a percentage of the total explosive mass for totally unconfined samples. Confining samples to simulate the effect of explosive enclosed in a sealed warhead significantly reduces plasticiser mass loss but the mass loss of confined samples of K10 and MEN42 PBXs is still greater than that of the unconfined BDNPA/F PBX samples. In an assessment of CPX200, an underwater explosive

with a K10 plasticised Diorez binder, the loss on ageing was considered to be acceptable, provided the explosive was contained in a sealed warhead. Plasticisers such as MEN42 may thus find applications in explosives, but their tendency to migrate may rule them out from use in rocket and gun propellants, where the final applications involve significantly less confinement or expose a large surface area. Thus, once more, the end application has a significant effect on the choice of the plasticiser.

Modelling and the Design of New Plasticisers

The lack of a plasticiser which is capable of fulfilling all of our requirements in all applications has prompted the UK to undertake more comprehensive studies aimed at understanding the plasticisation process using both detailed experimental techniques[18] and modelling [19,20]. This approach is aimed both at making the best use of existing available plasticisers and developing the ability to synthesise new molecules to perform the role. Modelling has already been used to explain differences between the plasticisation ability of BDNPA/F and the NENAs[20]. Simple theory and prediction of Tg lowering using the Fox Equation, suggests that BDNPA/F and Ethyl NENA should have similar plasticisation effects on polyNIMMO, whereas from experiment we know that Ethyl NENA and other members of the NENA family are much better plasticisers in the classical sense than BDNPA/F. The use of the Fox equation predicts similar Tg's to those observed for the NENAs whereas the observed Tg for BDNPA/F plasticised polyNIMMO is much higher than predicted. Molecular modelling targeted at investigating plasticiser / polymer interactions has indicated that BDNPA/F molecules are capable of forming temporary "crosslinks" between polyNIMMO chains whereas the NENA's do not. This potentially explains the low migration rate for BDNPA/F as well as it's poor plasticisation ability to lower Tg and viscosity.

More detailed modelling studies are now underway, using a range of modelling packages commonly used in the more conventional polymer field. In particular this effort is being aimed at predicting the type and geometry of oligomers, based on NIMMO and GLYN, that will best plasticise polyNIMMO and polyGLYN formulations. This approach, allied to practical plasticisation research and synthesis studies should produce plasticisers which

provide the best combination of plasticisation ability with the minimum of migration, physical and chemical compatibility problems.

Discussion

As has been shown, choosing a plasticiser is more than just a question of choosing the one that is most effective at lowering viscosity and glass transition temperature. Other factors need to be taken into consideration. A comparison between BDNPA/F and MEN42 highlights the difficulties facing the formulator. Although MEN42 is very effective at lowering Tg and viscosity and it's energy is greater than BDNPA/F, migration and compatibility problems make it's use impractical for certain applications. Conversely, although BDNPA/F is a poor plasticiser in the classical sense, it has very good characteristics in other respects. Finally cost and availability need to be taken into consideration. At one time the continued availability of both BDNPA/F and the NENA's was in doubt. Now it is likely that there will be future supplies of both. However, K10 has continued to be available from UK sources and although not the ideal plasticiser, it is very stable, any the problems associated with its use are familiar and acceptable and the UK formulator has continued to use it, particularly for explosives. Experience in its use and confidence in availability have had a role to play in plasticiser choice in this case.

It must be considered that it is highly unlikely that one plasticiser can fulfil all the desired roles for all applications, however desirable this might be from a technical and commercial point of view. It is therefore unlikely that plasticiser costs can be significantly reduced through bulk use. The formulator will continue to select the best choice for him based on his own requirements and application. To choose the ideal plasticiser, rather than just the one with the least problems, he needs to fully understand what those requirements are and how plasticisers interact with the rest of the formulation. Modelling provides a useful tool in the latter case and, perhaps, in future it will allow the synthetic chemist to produce not just a new binder but an ideal binder / plasticiser combination. At the moment it is helping him design better oligomeric plasticisers for existing binders, such as polyNIMMO and polyGLYN.

References

1 "Plasticizers" in Kirk Othmer Encyclopaedia of Chemical Technology, Third Edition, Vol 18.

2 ASTM D 883 "Definition of Terms Relating to Plastics", 1980 Book of ASTM Standards, Part 35.

3 R M Doherty & R L Simpson, "A Comparative Evaluation of Several Insensitive High Explosives", 28th International Annual Conference of ICT, 1997.

4 R E Hollands, I E P Murray, C J Leach "Rowanex 300; a New High Performance Pressable PBX for Metal Accelerating Applications", 29th International Annual Conference of ICT, 1998.

5 C J Leach, D F Debenham, J Kelly, K Gillespie, "Advances in polyNIMMO Composite Gun Propellants", 28th International Annual Conference of ICT, 1997, V2.

6 R E Hollands et al, "Reduced Vulnerability High Explosives", ADPA Symposium on Insensitive Munitions Technology, Williamsburg, 1994.

7 WEAG CTP25.2 Working Group, "Collaboration on Pressable Explosives for Shaped Charges - A European Success Story", 28th International Annual Conference of ICT, 1997, V40.

8 A S Cumming et al - Insensitive High Explosives and Propellants - The United Kingdom Approach, ADPA Symposium on Insensitive Munitions Technology, Williamsburg, 1992

9 A S Cumming - Characterisation of Novel United Kingdom Energetic Materials, ADPA Symposium on Energetic Materials Technology, Phoenix, 1995

10 S E Gaulter, A S Cumming, C J Leach "The Formulation of an Insensitive High Explosive based on HMX, NTO and polyNIMMO". ADPA Symposium on Insensitive Munitions Technology, Williamsburg, 1994.

11 D Campbell, A S Cumming, E J Marshall, "Development of Insensitive Rocket Propellants Based on Ammonium Nitrate and polyNIMMO", ADPA Symposium on Insensitive Munitions Technology, Williamsburg, 1994.

12 P Mader "Novel binders for Propellants", 28th International Annual Conference of ICT, 1997, P49.

13 A Messer, J Bohnlien-Mauss, Evaluation of the Application of polyNIMMO in gun propellants, 28th International Annual Conference of ICT, 1997, P116.

14 C J Leach, S B Langston, J Akhavan "A Plasticisation Study of Thermoplastic Elastomer Bound Pressable Explosives", 25th International Annual Conference of ICT, 1994.

15 P Q Flower, M J Gough, S E Gaulter, R Clift, B Murray "Twin screw extrusion compounding of energetic materials - a small scale laboratory facility", 29th International Annual Conference of ICT, 1998.

16 R J Lieb & J M Heimerl - Characteristics of JAX Gun Propellant, 6th International Gun Propellant & Propulsion Symposium, Parsippany, 1994.

17 S Schaefer, J Wilken "Precipitation of RDX on the Surface of High Performance Gun Propellants", 28th International Annual Conference of ICT, 1997, V19.

18 A V Cunliffe, P F Bunyan, P J Honey, "Plasticisers for New Energetic Binders", 29th International Annual Conference of ICT, 1998.

19 E Robson, G A Lieper, A S Cumming, "Molecular Modelling as a Tool to aid the Design of Polymer Bonded Explosives", 24th International Annual Conference of ICT, 1993.

20 E Robson, G A Lieper, E Marshall, A S Cumming, "Molecular Modellimg of polyNIMMO Plasticisation" Life Cycles of Energetic Materials, Del Mar, California 1994.

NEW ENERGETIC MOLECULES AND THEIR APPLICATIONS IN ENERGETIC MATERIALS

M. GOLFIER, H. GRAINDORGE, Y. LONGEVIALLE, H. MACE

SNPE
Centre de Recherches du Bouchet
BP2
91710 VERT LE PETIT (FRANCE)

ABSTRACT

SNPE is involved in the development of energetic materials (space boosters propellants, rocket and gun propellants, high explosives). The operational trends for future applications are :

- to improve performances
- to satisfy insensitive munitions requirements
- to comply with environmental aspects
- and to reduce costs.

In order to develop new energetic materials with characteristics fitting with these above mentioned requirements, SNPE carries out works in the field of new molecules. The most important effort concerns azidopolymers as GAP and derivatives, and new oxidisers as ADN and HNIW.

For oxidisers, the main goal is the adjustment of products quality (chemical and polymorphous purity, particle size, morphology) by using different crystallization or grinding techniques.

For energetic polymers, the aim is to increase weight in order to improve mechanical properties of energetic materials :

The attractive characteristics of energetic materials using these new raw materials are presented :

- profit in the ratio performance/safety behaviour on propellants and high explosives
- mechanical and ballistic properties satisfying operational applications.

1 - Introduction

The operational trends for future applications of energetic materials are :

- to improve performances
- to satisfy insensitive munitions requirements
- to comply with environmental aspects
- and to reduce costs.

These today requirements oriented the research of new molecules and new energetic materials which needed an ongoing effort in chemical synthesis and high energetic materials processing.

Besides usual components like nitro-cellulose, nitro-glycerine, solid oxidisers like ammonium perchlorate, RDX or HMX, a new generation of molecules appeared these last fifteen years. It covers large fields of chemistry from nitration, azidation and more particularly azide chemistry, heterocyclic chemistry (essentially nitrogen), organometallic and polymer chemistry.

The main products developed at SNPE are related both to new oxidisers, binders, plasticisers and additives (table 1). Each of them allows to aim one performance at least above mentioned, when used in energetic materials. Some applications are specific to a family but a common use is generally tried to obtain. Most of them are synthesized either at industrial scale or at industrial pilot scale.

The first results of the synthesis works carried out at SNPE have been already described in a previous paper (1). We present here the most recent progress reports in the field of new energetic molecules with some examples concerning oxidisers as HNIW (CL20) and ADN or azidopolymers as GAP and derivatives.

Their synthesis including crystallization of solid oxidisers and their uses on propellants and high explosives are the main topics developed hereafter.

PRODUCTS	Scale of synthesis (yearly capacity)	PERFORMANCE						Application in energetic materials
		energy	burning rate	mechanical	signature	low vulnerability	environment	
OXIDISERS								
NTO	Continuous process (x. 100T)					X		EXP
HNIW	100 kg (1 T)	X	X		X			COMMON (PRO - PO - EXP)
ADN	Lab	X	X		X	X	X	PRO
BINDERS								
GAP	150 kg (1-3 T)	X	X		X	X		COMMON
BUTACENE ®	100 kg (1-2 T)	X	X			X		PRO
PLASTICISERS								
Nitrated esters	Continuous process (x. 100 T)				X	X		COMMON
Azide plasticizers	Pilot (150-200 kg)		X		X	X		COMMON
ADDITIVES								
MAPO, METHYL BAPO	(1 - 3 T)			X				COMMON
free lead ballistic catalysts	(1 T)						X	PRO

Table 1 **: main new molecules developed at SNPE**

EXP : high explosives PRO : rocket propellants PO : gun propellants

2 - New energetic oxidisers

2.1. - HNIW (CL20)

The hexaaza hexanitro isowurtzitane or HNIW, more commonly called CL20, belongs to the family of high energetic dense caged nitramines. There are about fifty years between the discoveries of HMX and CL20, this last molecule being synthesized for the first time by Arnie NIELSEN in 1987 (2)

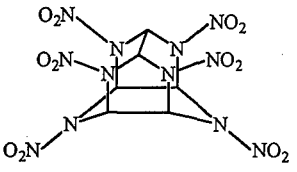

HNIW

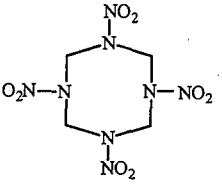

HMX

The first synthesis of CL20 at SNPE was made at SNPE Research Center in 1989. Before this date, the research had been mainly focused on analogs of HMX, incorporating and developing the chemistry of the elementary fragment $-(-N(NO_2)-CH_2-)-$, expecting that new combinations would lead to more energetic and denser compounds. Sorguyl (3), bicyclo HMX (4) and tetranitro-bicyclo-nonanone or K56 (5) are some examples of high energetic dense nitraza polycycles synthesized during this period.

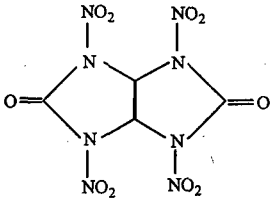

Sorguyl

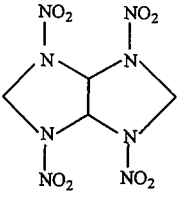

Bicyclo HMX

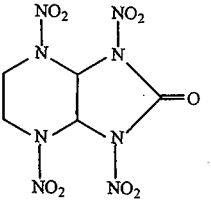

K56

The characteristics of these molecules (table 2) show that only CL20 is superior to HMX both with respect to density, enthalpy of formation and as oxidiser.

Molecule	HMX	Bicyclo HMX	SORGUYL	K56	CL20
Formula	$C_4H_8N_8O_8$	$C_4H_6N_8O_8$	$C_4H_2N_8O_8$	$C_5H_6N_8O_9$	$C_6H_6N_{12}O_{12}$
Molecular weight (g/mole)	296	294	322	322	438
Polymorph	β				γ α β ε
Density	1.91	1.87	2.035	1.975	1.92 1.97 1.99 2.04
Enthalpy of formation (kJ/mole)	+ 84	+ 125	- 292	- 144	+ 339 + 372
Oxygen balance (% O_2/CO, H_2O)	0	+ 5	+ 25	+ 5	+ 11

Table 2 : **characteristics of polycyclic and caged nitramines**

On the synthesis aspect, the hexabenzyl hexaaza isowurtzitane or HBIW was the first derivative of the caged hexaaza isowurtzitane which was described (6) and the only compound of this family which is obtainable from condensation of an amine with glyoxal.

More recently the conversion of HBIW in partly acylated derivatives (7-8) or a mixed acetyl-formyl derivative (9) was described. To obtain CL20 two routes are available : the nitration of a silylated derivative (10) or the original route proposed by Arnie Nielson : the nitrosation followed by a nitration of the tetraacetyl dibenzyl hexaaza isowurtzitane with $NOBF_4/NO_2BF_4$ (11).

The SNPE process also uses HBIW as initial precursor, followed by its conversion and nitration to CL20.

Nowadays at SNPE CL20 is produced at the industrial pilot scale : 50 - 100 kg by batch, the first steps being synthesized by batches of around 150 kg.

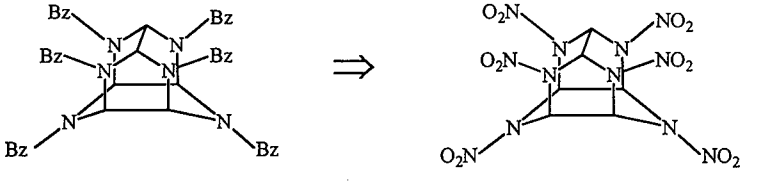

HBIW ⇒ HNIW - CL20

Synthesis is only one step in the preparation of chemical products. A second step is often necessary to adapt the quality of the products to the required specifications : it is the purification step. In the case of solids, crystallization is a well known technique to purify a component : it can eliminate by-products, obtain the right polymorph, access to the right particle size distribution and adapt the morphology of the crystals (shape, porosity, internal defects) which are influential factors in the vulnerability of energetic materials.

CL20 crystallization studies allowed us to access to 4 polymorphs of CL20 characterized by IRFT (fig 1) and X rays (12). Our IRFT traces are analog of characteristic vibrations described by M. Frances FOLTZ (13).

CL20 crystallization studies also aim at the preparation of the ε polymorph with different particle size, up to more than 100 µm. The formation of one of the 4 polymorphs is influenced by thermodynamic phenomena (the least soluble polymorph is the most thermodynamically stable) and kinetic laws (more soluble polymorphs appear because of their higher growth rate).

In a general manner to crystallize a component out of its solution, the equilibrium concentration must be exceeded by some supersaturation method : cooling, evaporating, precipitation...

In order to forecast the influence of the parameter on crystallization, it is essential to know the saturation curve and the metastability zone, where the component solubility is higher than the saturation value.

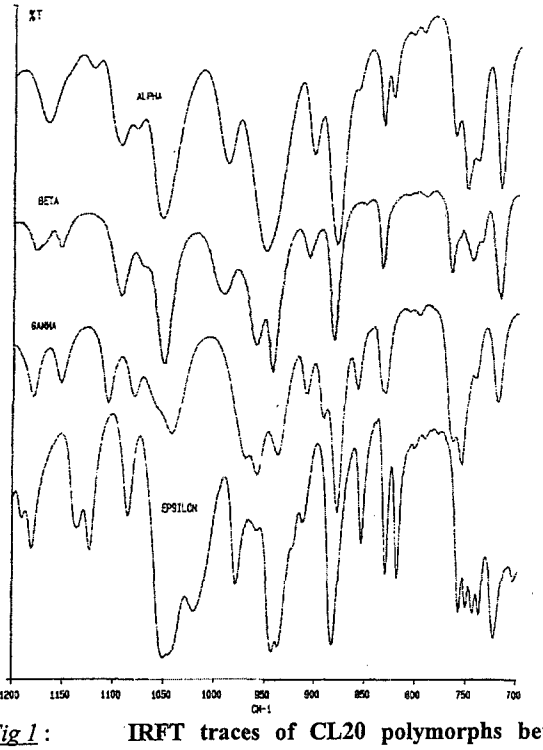

Fig 1 : **IRFT traces of CL20 polymorphs between 700 and 1200 cm^{-1}. 1% dispersion in KBr.**

Then you know the conditions to obtain the right quality for the product, which depends on the nucleation rate, the growth rate, and all other phenomena such as agglomerating. The higher the supersaturation is, the smaller will be the particle size. Generally it is preferred to avoid primary nucleation, that is a hazardous phenomenon, and to seed batch crystallizers so as to master the nucleation and the crystal growth.

The formation of ε CL20 is possible by the classical supersaturation methods, when seeding with ε particles (fig. 2-5) :
- cooling a solution in which the solubility increases with increasing temperature. The particle size may be adjusted between 50 and 100 μm, depending on the seed size,
- adding a less efficient solvent that is miscible with the original solvent : the particle size may be adjusted from 10 to 150 μm, depending on the adding speed,
- evaporating the solvent from a solution of CL20 in a mixture of solvent / non solvent : this systems allow to obtain high or low particle size diameter depending on the type and particle size of the seeds, on the evaporating rate, and of course on the supersaturation.

The smallest particle size (10 μm) may be obtained with ground ε CL20 seeds.

A large range of particle size (20 to 150 μm) can be obtained with crystallized seeds (from 10 to 100 μm), which are more efficient for preparing large particles because of their narrow distribution (no tiny crystals able to act as crystallization centres).

The influence of supersaturation is clear with crystallized seeds : the higher it becomes, the smaller the CL20 particles are, all the more than the concentration rate is high.

Fig. 2 : **ε CL20 d_{50} > 100 μm**

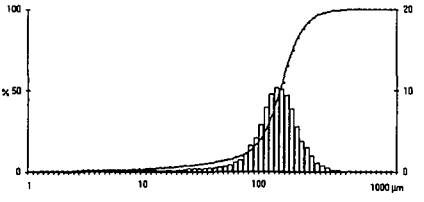

Fig. 3 : **particle size distribution of ε CL20 d_{50} > 100 μm**

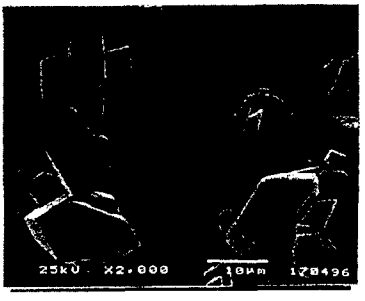

Fig. 4 : **ε CL20 d_{50} = 20- 50 μm**

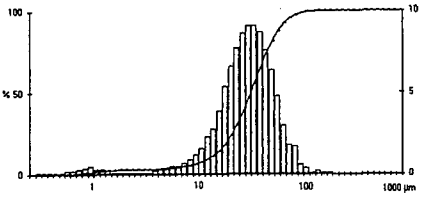

Fig. 5 : **particle size distribution of ε CL20 d_{50} = 20-50 μm**

Some polymorphous impurities may appear depending either on temperature (γ CL20 has been detected when the concentration happens above 70°C, probably due to the transition $\varepsilon \rightarrow \gamma$), either on water content of the solution (α CL20 crystallizes with 0.5 mole of water).

A great number of solvents have been investigated using the concentration process : cetones, esters, aromatic solvents are the best for mastering the ε polymorph formation and the particle size between 10 and 150 µm. The formation of larger particles has still to be studied.

CL20 crystallization studies have already contributed to the improvement of its pyrotechnic behaviour. Nevertheless it is still as sensitive as the most sensitive grades of HMX. That's why today's studies are also largely focused on the understanding of morphological aspects of crystals (shape, internal defects) in relation to chemical purity, polymorphous purity and crystallization systems to be used which are the main parameters influencing the sensitivity of energetic solid oxidisers.

2.2. - <u>ADN</u>

The research of energetic molecules which are able to deliver during the combustion large amount of gas by mass unit, led to structures where the ratio H/C is as high as possible.

Some compounds are in accordance with this criteria.

- Hydrazinium nitroformate (HNF) : this route is studied by APP and TNO in The Netherlands (14),
- the dinitramide salts with ammonium dinitramide (ADN), with parallel development in Russia (15), United States (16) and more recently in Sweden (17)

$H_2N-NH_3^{\oplus}, {}^{\ominus}C(NO_2)_3$ $\qquad$ $NH_4^{\oplus}\,{}^{\ominus}N(NO_2)_2$

ADN is a dense, non chlorine containing, powerful, oxidiser and is an interesting candidate for replacing AP as an oxidiser for composite propellants.

The compared characteristics of ADN (tables 3 and 4) show that ADN is a non carbon compound, as dense as RDX, with a very positive oxygen balance and an enthalpy of formation largely superior to those of ammonium nitrate and ammonium perchlorate.

The present results about its pyrotechnic behaviour show that ADN is less sensitive to impact than RDX and HMX. It is not sensitive to friction and electrostatic spark.

Molecule	RDX	HMX	AP	AN	ADN	HNF
Formula	$C_3H_6N_6O_8$	$C_4H_8N_8O_8$	ClH_4NO_4	$H_4N_2O_3$	$H_4N_4O_4$	$CH_5N_7O_6$
Molecular weight (g/mole)	222	296	117.5	80	124	183
Melting point (°C)	204 d.	280 d.	d.	170	94	115-120
Density	1.805	1.91	1.95	1.72	1.81	1.86
Enthalpy of formation (kJ/mole)	+ 70	+ 84	- 296	- 365	- 150	- 72
Oxygen balance (% O_2/CO_2, H_2O)	-21.6	-21.6	+ 34	+ 20.5	+ 25.8	+ 13.1

Table 3 : **compared characteristics of some energetic oxidisers**

Molecule	RDX "CH" 0-100	HMX 0-100	AP "F"	ADN	HNF
Impact (J) BAM Julius Peters	3.5	4.2	13.7	3.7	1.6
Friction (N) BAM Julius Peters	193	113	30 % at 353 N	11 +/30 at 353 N	29
ESD (mJ)	180 to ≥ 726	225 to ≥ 726	≥ 726	≥ 726	≥ 726

Table 4 : **compared sensitivity of some energetic oxidisers**

The synthesis route performed at SNPE, uses the following chemical scheme.

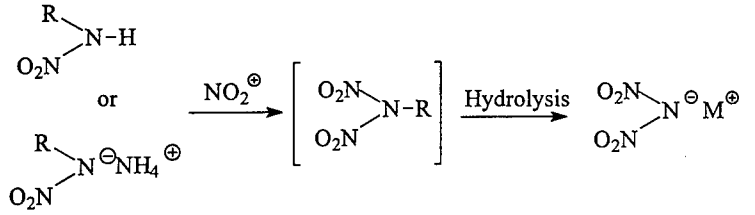

R = hydrolysable group
$M^{\oplus}$ = metallic or ammonium ion

This route needs the use of a new nitrating agent N_2O_5. Because of the difficulties to handle and store N_2O_5, we quickly developed a continuous process including the preparation of N_2O_5 (by ozonolysis of N_2O_4) which gave very good results at lab scale and we are undertaking its scaling up on a pilot equipment (several hundred grams per hour).

About the morphological aspect, no polymorph of ADN has been reported. On the other hand, it naturally crystallizes in needles so that crystallization techniques must be adjusted to avoid this phenomenon. At last some works are also ongoing to improve its chemical stability.

3 - Energetic binders and plasticisers : GAP and derivatives

The chemistry of functional energetic prepolymers (mainly hydroxy terminated) had made large progress these last fifteen years. The substitution of inert prepolymers by energetic prepolymers played either for the increase of energetic performances either for a better compromise energetic performances - vulnerability of the energetic materials.

Among the different energetic prepolymers developed in the world, SNPE has chosen to manufacture azide prepolymers and plasticizers issued from GAP.

Since GAP is classified 1.3, it does not increase the detonability of the materials. GAP is compatible with GAP based plasticisers as well as nitrato esters like BTTN and TMETN which are less sensitive than NG.

PRODUCT	GAP Diol	GAP Triol	GAPA
	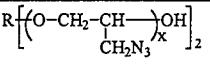	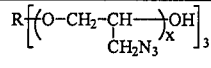	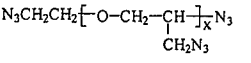
	x ~ 10 R : diol aliphatic residue	x > 3 R : diol aliphatic residue	x > 6
ΔHf (cal/g)	+ 280	+ 280	+ 550
Density	1.29	1.29	1.27
Appearance	light yellow liquid	light yellow liquid	light yellow liquid
GPC (PPG standard)			
$\overline{Mn}$	1700 ± 300	≥ 900	700 - 900
$\overline{Mp}$	2000 ± 300	≥ 1000	800-1000
I	≤ 1.3	≤ 1.3	≤ 1.3
Eq. weight	1200 ± 200	≥ 400	> 15000
Vacuum test 100 °C - 200 h (cm³/g)	≤ 3	≤ 3	≤ 3
Tg (°C)	- 45	- 45	- 69

Table 5 : **characteristics of azide prepolymers and plasticisers**

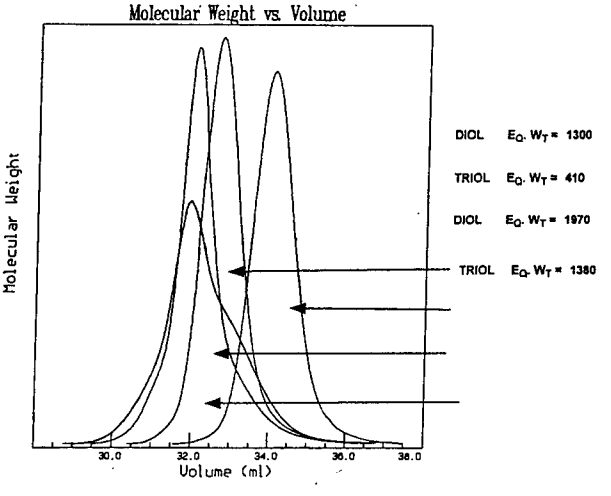

Fig. 6 : **GPC (light scattering) of GAP prepolymers**

Different qualities have been developed (table 5 and fig. 6) : standard GAP diol (Mn ~ 1700), long chain GAP triol (Mn > 2000) or short chain GAP triol (Mn ~ 1000) and azide plasticizers issued from GAP : GAP azide (GAPA).

In 1990, SNPE got a license from ROCKETDYNE to manufacture and sell GAP and GAP derivatives in Europe. More than 3 tons of GAP and GAP derivatives have been produced in a pilot plant located in SNPE SORGUES facility near AVIGNON.

A new simpler process for standard GAP diol is studied at pilot scale at the CRB and will be transferred in a near future in SORGUES pilot plant. This process will allow at least to double the yearly capacity of GAP synthesis and to decrease its cost perceptibly.

The present trends of works concern the research of new qualities of GAP essentially high molecular weight to improve again properties of energetic materials.

Some success has been already registered at lab scale from direct polymerisation of epichlorhydrin by adapting the ratios of reactants and catalyst systems, followed by azidation of the high molecular weight PECH.

3 - Rocket propellants

New energetic ingredients as GAP, CL20 or ADN are very attractive to achieve high performance propellants (18, 19, 20, 21, 22).

SNPE has now a few years experience in the use of GAP and CL20 in the field of rocket propellants.

This experience is presented hereafter on minimum smoke propellants in comparison with a current XLDB propellant.

3.1 - Energetic performances

The use of GAP binder in place of a polyglycol adipate (PGA) binder increases the specific and volumic impulse of the propellant in relation with the higher enthalpy of formation and density of GAP.

CL20 brings additional effect on density and specific impulse.
So, in comparison with the current XLDB propellant (table n° 6), the increase of volumic impulse is higher 11%. This value can be compared with the volumic impulse of current reduced smoke propellant, GAP/CL20 propellant gives a benefit of 7 %, plus low signature and low toxicity (no HCL).

COMPOSITION	binder	PGA/TMETN/BTTN	GAP/TMETN/BTTN	GAP/TMETN/BTTN
	filler	RDX - 63 %	RDX - 60 %	CL20 - 60 %
	ballistic additives	4 %	4 %	4 %
Theoritical specific impulse (s)		238,5	242	251
Volumic impulse (s.g. cm-3)		405	411	452

Table n° 6 : **calculated performances of GAP based propellants**

3.2. - Faisability :

Convenient pot-life to fill rocket motors are obtained with the different propellants :

COMPOSITION	PGA/RDX	GAP/RDX	GAP/CL20
POT LIFE (h)	> 12	> 12	> 12

3.3. - Mechanical properties

Mechanical properties satisfying requirements of rocket motor designers are achieved by current GAP/RDX propellants (table 7).

Unixial traction		Stress	Modulus	Strain et rupture
Temperature (°C)	rate (mm/min)	(MPa)	(MPa)	(%)
+ 20°C	50	0,64	2,6	47
- 47°C	500	7,2	114	29

Table 7 : **mechanical properties of GAP/RDX propellants**

CL20 gives a similar behaviour than RDX in GAP binder propellants

For the same filler content (in weight), in comparison with RDX, the higher density of CL20 induces an higher binder volumic content. It is obvious that this microstructural charge can only improve the mechanical behaviour.

3.4. - Ballistic properties.

A particularity of GAP, as raw material, is its fast burning rate by itself when ignited. This characteristic is again met in propellant. The following tables (Tables n°8 and n°9) exhibit a burning rate increase of near by 20 % at 15 MPa, in comparison with PGA binder propellants.

Composition		Burning rate (mm/s)		Pressure
Binder	Filler (60 %)	7 MPa	15 MPa	Exponent
PGA	HMX	6	11	0,89
PGA	CL20	11,5	23	0,92
GAP	HMX	7,2	13,6	0,91
GAP	CL20	13,4	27,2	0,94

Table N° 8 : **burning rate of uncatalysed compositions.**

Composition		Burning rate (mm/s)			Exponent
Binder	Filler (60 %)	7 MPa	15 MPa	20 MPa	[Pressure range]
PGA	RDX	10,6	15,6	19	0,4 [3-14 MPa] 0,6 [15 - 20 MPa]
GAP	RDX	14,6	18,9	21,4	0,37 [4 - 20 MPa]
GAP	CL20	20	28,3	32,4	0,48 [5 - 25 MPa]

Table N° 9 : **burning rate of catalysed compositions.**

CL20 is now known to lead to a strong effect of the burning rate when used as oxidiser in propellant.

Basic compositions without additives exhibit a burning rate enhancement of more or less twice in comparison with HMX filled compositions. The pressure exponents of these basic compositions are too high for any application. Fortunately burning rate modifiers have been find to be very effective at low pressure. They lead to higher burning rate at the lower pressures, and so, a quite useable pressure exponent is achieved within a large pressure range (pressure exponent = 0,48 - 5/25 MPa).

Use of new ingredients as GAP and CL20 give additional effects on burning of propellants. In comparison with current PGA/RDX propellant, the burning rate is increased by 1,5 - 2 in a large pressure range. In regard with the pressure exponent, the useable pressure range is also significatively improved.

3.5 - Safety behaviour

The handling of new raw materials needs always specific caution. It is also true with neat GAP and furthermore neat CL20. But on this peculiar point, it is noticeable that the safety behaviour becomes quite acceptable for SNPE propellant process when a convenient binder (as GAP binder) wraps the fillers - The safety results obtained on slurry as on propellant (Tables n°10 and 11) show a behaviour included in the range of results obtained with current XLDB and NEPE propellants, with perhaps the exception of burning rate. SNPE has experience from lab scale to 420 Gallon mixes for these reference propellants.

	CL20 Propellant (GAP binder - 60 % CL20)	Current XLDB and NEPE propellants
Bam friction (N)	73 to 161	70 to 0 % 353 N
Electric spark (mJ)	> 726	> 726
30 Kg Fallhammer test (m)	> 4	> 4
Train propagation (mm/s)	10.8	2 to 20
Self ignition (°C)	178 to 181	165 to 185

Table N° 10 : **safety results for CL20 propellants (slurry)**

	CL20 Propellant (GAP binder - 60 % CL20)	Current XLDB and NEPE propellants
Bam friction (N)	56 to 851	70 to 0 % 353 N
Electric spark (mJ)	> 726	> 726
30 Kg Fallhammer test (m)	3.5 < height < 4	3.5 < height < 4
Burning rate at atm.pressure (mm/s)	0.9 to 6.4	< 1 to 3.5
Self ignition (°C)	173	165 to 185

Table N° 11 : **safety results for cured CL20 propellants**

4 - High explosives.

CL20 is also very attractive in high explosives (23) in comparison with HMX filled high explosives, it brings to similar results to Card Gap Test (150-160°C), but to higher density and detonation rate.

An enhancement of measured performances of more than 12 to 15 %, depending on volumic filler content, has been achieved with HTPB binder high explosives.

	HMX	CL20	HMX	CL20
Volumic filler content	66,8	66,8	72,1	72,1
Density	1,575	1,648	1,618	1,710
D (m/s)	8030	8325	8107	8470
$\rho D^2/4$ (GPa)	25,4	28,6	26,6	30,7
Δ CL20/HMX (%)	+ 12,5		+ 15,4	

Table N°12 : **performances of HMX and CL20 filled high explosives**

5 - Conclusions.

SNPE is developing different families of new molecules (fillers, binders, plasticizers and various additives) which meet the requirements of new energetic materials for future application.

Basing its research on modern tools, it has been possible to focus on realistic axes of research and development. The ongoing effort undertaken during the last years on synthesis and techniques of treatment of solids and liquids allowed us to make large progress. Thus, some molecules are already available at industrial scale or industrial pilot scale (CL20, Standard GAP) while others are tested at lab or pilot scale at the Research Center (ADN, others GAP, azide plasticizers).

New energetic ingredients, as GAP or CL20 bring high performance to rocket propellants and high explosives.

GAP improves energetic performances and burning rate of propellants. This enhancement is very useful, peculiarly when low sensitivity but low energy ingredients have to be incorporate in the formulation, i.e. to satisfy I.M. requirements (24). GAP binder propellants achieve mechanical properties satisfying requirements of rocket motor designers.

An attractive profit in the ratio performances/safety behavior has been shown on propellants and high explosives using new energetic ingredients. In comparison with current HMX or RDX filled propellants or explosives :

- the safety behavior of CL20 filled compositions appears roughly similar,
- even though the enhancement of performance is very significant, with an increase of more than 10 % on volumic impulse for rocket propellants and on detonation pressure for high explosives.

Today GAP/CL20 propellants exhibit high burning rate and acceptable pressure exponent in a large pressure range.

In the future the main axes of work will concern the improvement of morphology of energetic oxidisers (CL20, ADN), the development of high molecular weight energetic prepolymers (Mn > 30 000), the synthesis of new molecules mainly in the field of oxidisers with an objective of high performances coupled with a power sensitivity. In this last field, the present research on high nitrogen and oxygen heterocyclic compounds could be considered as an answer.

Future efforts on synthesis and on relation microstructure/properties will be carried on to improve again the quality of raw materials and so, performances of energetic materials.

BIBLIOGRAPHY

[1] - B. FINCK and H. GRAINDORGE.
Energetic Materials. Technology, Manufacturing and processing, 27 th International Annual Conference of ICT, June 25 - 22, 1996, V23, Karlsruhe.

[2] - R.S. MILLER.
"Recherches portant sur les nouveaux matériaux énergétiques", International Defense et Technologie, hors série, 22, (09 - 1994).

[3] - J. BOILEAU, J.M. EMEURY, J.P. KEHREN.
Ger. Coffen 2, 435651 (1975).

[4] - G. ECK. M. PITEAU. FR 2738246, Feb. 22, 1994.

[5] - H. GRAINDORGE. P. LESCOP. F. TERDIER. J.M. POULET.
ACS Symposium series 623 "Nitration, Recent Laboratory and Industrial Developments", 43 - 50, American Chemical Society, Washington DC, 1996.

*[6] - A.T. NIELSEN, R.A. NISSAN, D.J. VANDERAH, C.L. COON, R.D. GILARDI, C.F. GEORGE, J. FLIPPEN - ANDERSON. J.*Org. Chem. 55, 1459 (19990).

[7] - A.J. BELLAMY. TETRAHEDRON LETTERS, 51 (16), 4711 - 22 (1995).

[8] - a) M.IKEDA, T. KODAMA, M.TOJO. WO 9623792 A1, Aug 08, 1996.
b) ASAHI KASEI. Japanese Patent 08208655, Aug 13, 1996.

[9] - W.W. EDWARDS, R.B. WARDLE. WO 9720785 A1, Dec 16, 1997.

[10] - T. KODAMA. Japanese Patent 06321962, May 14 1993

[11] - A.T. NIELSEN. US. 5, 693, 794, Dec. 2, 1997.

[12] - G. JACOB. SNPE/CRB. Personnal communication.

[13] - M.F. FOLTZ. Propellants, Explosives, Pyrotechnics, 19, 63 - 69 (1994).

[14] - a - H.F.R. SCHÖYER, A.J. SCHNOHK, P.A.O.G KORTING and P.J. VANLIT.
"First experimental results of an HNF/Al/GAP solid propellant", AIAA 97 -3131, Seattle, Wa, July 1997.
- b - H.F.R. SCHÖYER, A.J. SCHNORHK, P.A.O.G. KORTING, P.J. VAN LIT, J.M. MUL, E.M.H.H.L. GADIOT and J.J. MEULENBRUGGE
"High performance propellants based on hydrazinium nitroformate", Journal of propulsion and power, vol. 11, n°4, pp 856-869, July - August 1995.

[15] - a - Z. PAK. AIAA paper 93 - 1755, June 28, 1993.
- b - V.A. TARTAKOVSKY, O.A. LUKYANOV, Int Annu. Conf ICT 1994, 25, 13/1 - 13/9.

[16] - a - J.C. BOTTARO, P.E. PENNWELL, R.J. SCHMITT.
Synthetic Communications, 21, 945 (1991).
- b - J.C. BOTTARO, P.E. PENWELL, R.J. SCHMITT. J. Am. Chem. Soc, Vol. 119, n° 40, 9405 - 10, 1997.

[17] - A. LANGLET, H. OESTMARK, N. WING BORG. WO 9706099, A1, Feb 20, 1997.

[18] - S. DEMAY and J.D. BROWN - AGARD. Norway - August 1994 "Use of new oxidizers and binders to meet clean air requirements".

[19] - A.I. ATWOOD and Col. ADPA Symposium on energetic materials technology - March 21 - 24, 1994 - "Combustion of CL20 and CL20 propellant formulations".

[20] - Z.PAK. AIAA - 93 - 1755 - "Some ways to higher environmental safety of solid rocket propellant application".

[21] - Dr. H. ÖSTWARLE and Col - NDIA insensible munitions and energetic materials technology symposium - October 6 - 9, 1997 "Sensitivity, properties and performance of Ammonium dinitramide (ADN).

[22] - M. CHAN and Col. Challenges in combustion and propellants - 100 years after Nobel - May 27-31, 1996 - "ADN propellant technology".

[23] - M.L. CHAN and I. HOOTON. ADPA Symposium on insensitive munitions - June 1994 - "High - energy explosives with desirable sensitibity characteristics".

[24] - Y. LONGEVIALLE and Col. ADPA Symposium on energetic material, technology - September 24 - 27, 1995 - "Low vulnerability minimum smoke rocket propellants".

Development of High Performance CL-20 Explosive Formulations*

P.C. Braithwaite, R.L. Hatch, K.Lee, R.B. Wardle
Thiokol Propulsion
Brigham City, UT 84302-0707

M. Mezger, S. Nicolich
ARDEC
Picatinny, NJ 08806-5000

Abstract

The U.S. Army currently utilizes a family of high energy propellant and explosive systems that range from small high performance shaped charge submunitions to medium caliber kinetic energy tank rounds, to larger diameter explosively formed penetrators. The energetic formulations for these devices were developed with the following driving characteristics: performance requirements of the system, mechanical/ballistic properties of the formulations, system and ingredient cost, vulnerability, and producibility /reliability. Years of effort were expended in developing the formulations and hardware that now define the state-of-the-art in energetic formulations. The full range of commercially available ingredients were examined in developing these formulations and several new ingredients were pioneered during this effort. Formulation capability was pushed to the limit in maximizing the most critical mission capabilities.

Into this arena are now thrust the triple threat requirements of increased performance for applications like advanced kinetic energy gun rounds, future shaped charge, and explosively formed penetrator warheads, of reduced or at least acceptable sensitivity, and of increased concerns for environmental factors spanning the life of a system, particularly the synthesis of ingredients. With current technology stretched to the limit, approaches to meeting these new requirements have quickly focused on a new generation of high energy ingredients including TNAZ and CL-20 and clean manufacturing processes for production of these materials .

Synthesis and Characterization

In the years since the initial synthesis of CL-20, dramatic improvements have been made on the original elegant route of Nielsen[1] (figure 1). At Thiokol, a parallel route[2,3] (figure 2) has been developed that avoids the dinitroso intermediate and leads to an intermediate (tetraacetyldiformylhexaazaisowurtzitane, TADF) that can be nitrated in completely standard nitration equipment. Further, this route allows recovery of all benzyl groups used in the synthesis in the form of toluene which can be recycled as a feedstock for benzylamine synthesis. This reduces the non-recyclable waste stream by completely eliminating the two moles of meta-nitrobenzoic acid made per mole of CL-20 in the

original and related routes. The total of material produced using this synthetic strategy has totaled roughly 12,000 pounds.

The crude product is recrystallized to afford a high density polymorph. The typical particle size obtained is roughly 150 microns as shown in Figure 3. The crude epsilon polymorph can be ground to afford smaller particle sizes as needed for processing and formulating. An exemplary particle size obtained by fluid energy milling is shown in Figure 4.

Significant properties of CL-20 prepared by this process have been described previously.[4] Of considerable interest has been the particle shape and crystal quality. Depicted in Figure 5 are the range of particle shapes that have been observed. While certain shapes are generally preferred, the direct correlation to safety properties has been tenuous particularly when extended to coated explosive formulations where quality of coating seems to be most important. Also of interest is the density of average particles as measured by a flotation method. These data are depicted in Figure 6 and show that the average density of particles is extremely high compared to the theoretical (X-ray) maximum density of 2.044 g/ml. The average density of 2.035 is 99.5 percent of the theoretical and demonstrates a very small percentage of internal voids and lower density defects. This percent density compares favorably with HMX and RDX.

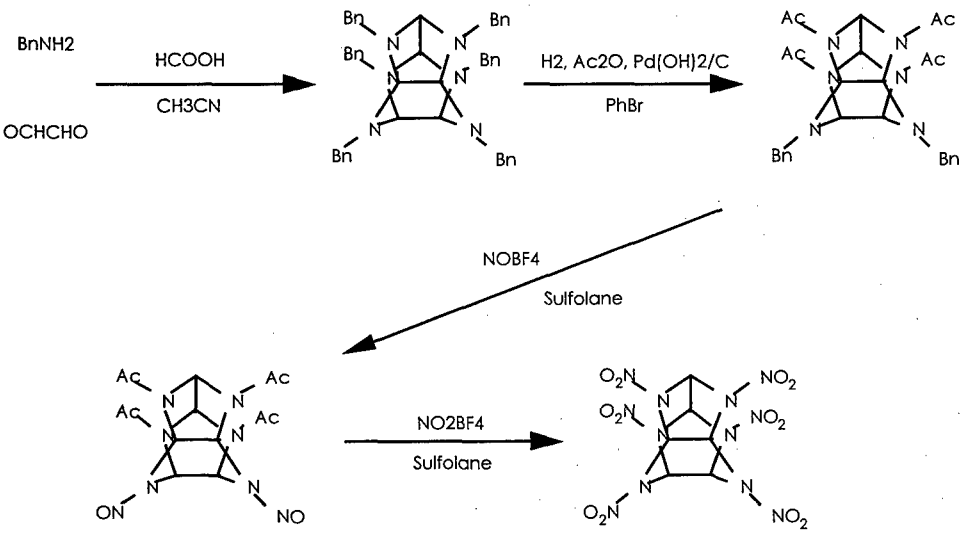

Figure 1. Original Nielsen Route. Depicted here is the original synthetic route to CL-20 as described by Nielsen. This route is elegant but used large amounts of $Pd(OH)_2$/carbon and the expensive BF_4-based nitrating agents.

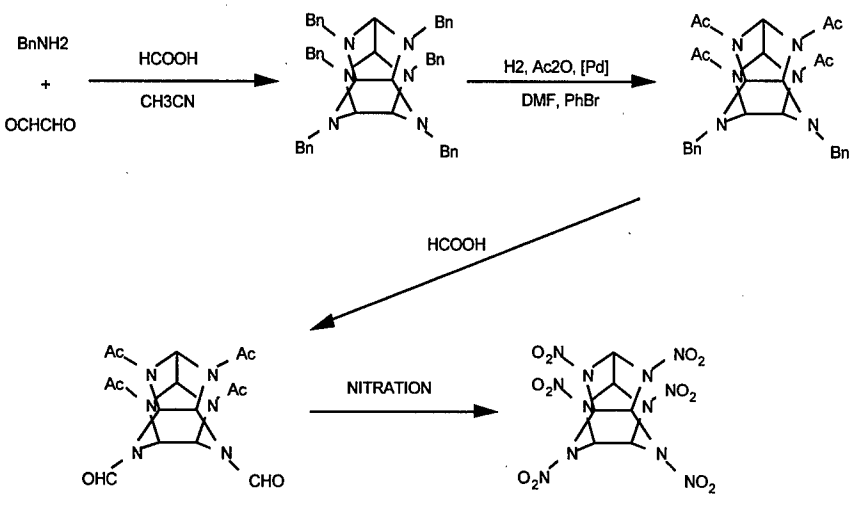

Figure 2. Hexaacyl Route to CL-20. Pictured here is the synthetic route to CL-20 developed at Thiokol. This route differs from Nielsen's route in using a second hydrogenolysis rather than N_2O_4 to remove the final two benzyl groups.

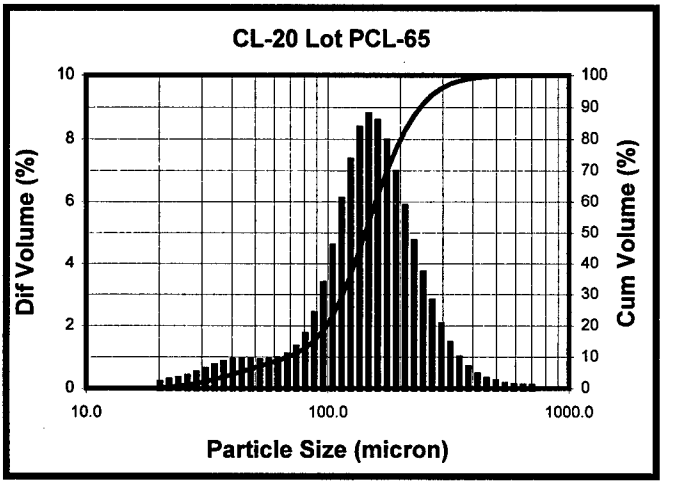

Figure 3. Particle size of crude CL-20. Reproduced here is the particle size distribution for CL-20 as obtained from the crystallization process.

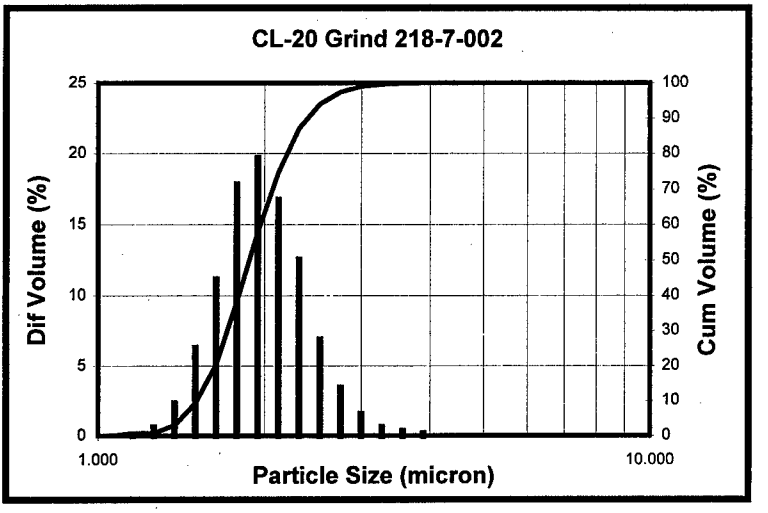

Figure 4. Particle size of ground CL-20. Reproduced here is the particle size distribution for CL-20 as ground using a fluid energy mill.

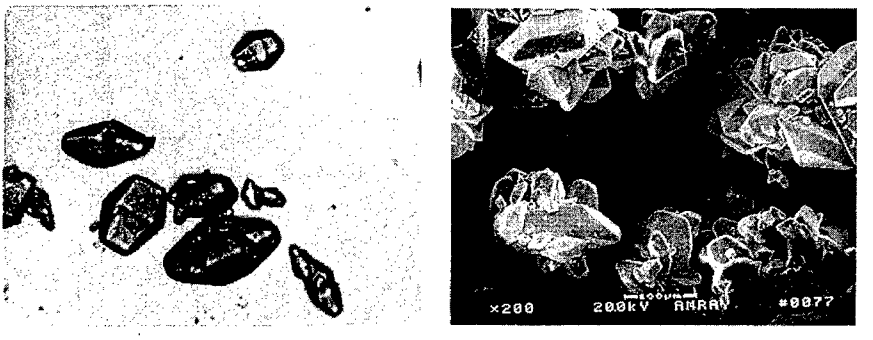

Figure 5. Photomicrographs of CL-20. A variety of particle shapes have been obtained. The particle shape on the left is considered to be superior but the correlation to safety properties is tenuous at best.

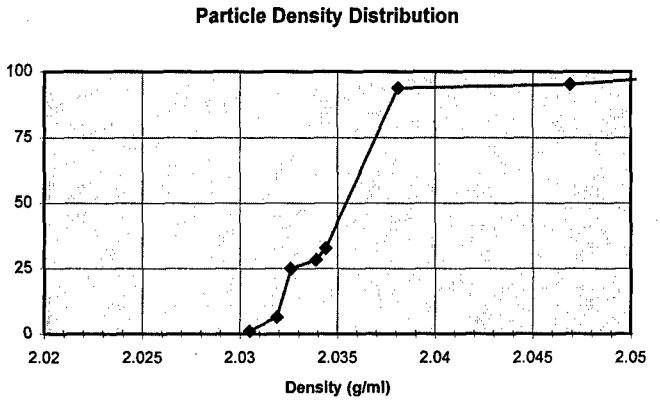

Figure 6. Density Distribution of CL-20. A measure of CL-20 particle quality is shown through the density of particles. The very high percentage of theoretical density provides an upper limit of the quantity of defects in the material. The density of the CL-20 shown above is 99.5 percent of theoretical.

Explosive Formulation and Characterization

Several high solids CL-20 explosives have been developed for evaluation which have very promising theoretical performance values. The calculated performance of several selected CL-20 and two common HMX explosives is shown in Table I. As shown by the data in Table I, the CL-20 based explosives have considerably more energy than analogous HMX compositions.

Table I. Calculated Performance Comparison of CL-20 and HMX Based Explosives

Composition	Density 99%TMD (g/cc)	CJ Pressure (kbar)	Detonation Velocity (km/s)	Cylinder Expansion Energy @V/V0=6.5 (kJ/cc)
PAThX-1 (CL-20 based)	1.944	413	9.37	9.92
PAThX-2 (CL-20 based)	1.923	398	9.22	9.64
PAThX-3 (CL-20 based)	1.958	421	9.50	10.07
PAX-2A (HMX based)	1.773	305	8.42	7.86
LX-14 (HMX based)	1.835	344	8.80	8.59

Processing studies performed using CL-20 have demonstrated that the typical processes used to manufacture explosives containing RDX and HMX may also be used for those

containing CL-20. This was found to be true for mix cast, melt cast and molding powder explosives. A typical water slurry process used to make CL-20 molding powders is shown in Figure 7.

As with HMX and RDX based explosives it has been demonstrated that the quality of coating is directly related to the sensitivity of the molding powder granules. An example of this is shown in Figure 8 for three different mixes of a single explosive which were purposely made using different mix procedures to yield different granules. As shown in Figure 8, as the granules increased in size and became more highly polished their sensitivity to initiation via impact decreased. Laboratory sensitivity data for the CL-20 based formulations listed in Table I have been obtained and are summarized in Table II along with safety data for LX-14, HMX and CL-20. As shown in Table II the laboratory safety characteristics of CL-20 explosives are comparable to those of LX-14 and are much better than either HMX or CL-20 in the uncoated state.

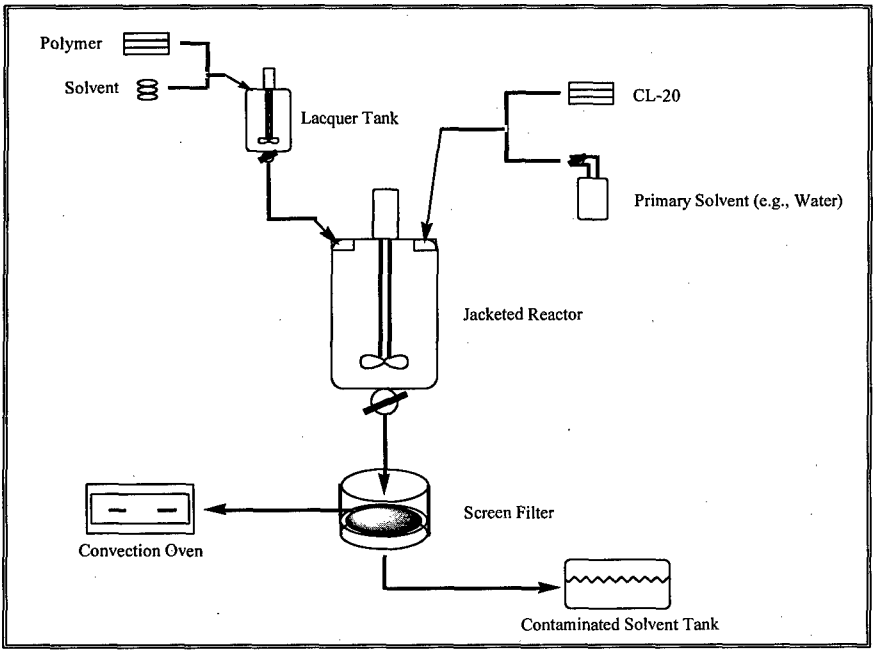

Figure 7. Typical process used to manufacture CL-20 based molding powders.

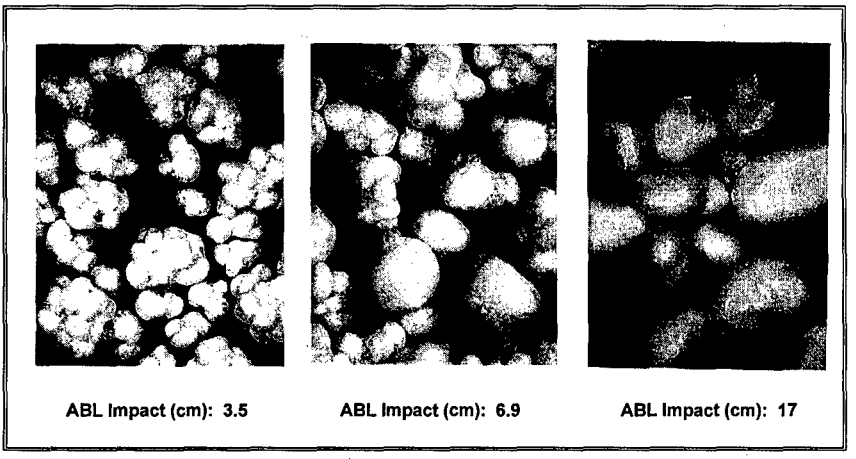

Figure 8. Impact sensitivity for three batches of molding powder of a common formulation.

Table II. Safety Data For CL-20 Pressed Explosives, LX-14, HMX and CL-20.

Material	PATHX-1	PATHX-2	PATHX-3	LX-14	HMX	CL-20
ERL Impact (cm)	35.4	32.5	24.6	30-38	17-25	9-11
ABL Impact (cm)	11	26	26	17	1.8	1-3.5
TC Impact (in)	29.3	21.5	19.4	18.8	27	19-36
BAM Friction (kg)	21.6	21.6	NT	24	11-17	11-15
ABL Friction (psi@ ft/sec)	130@8	240@8	240@8	420@8	100@4	110@2
ESD (Joules)	>8	>8	>8	>8	DOS	DOS

DOS: Depends on size of nitramine.

References:

[1] Nielsen, A.T., U.S. Patent 5,693,794.
[2] Wardle, R.B., Edwards, W.W., U.S. Patent 5,739,325.
[3] Cannizzo, L.F., Edwards, W.W., Wardle, R.B., Highsmith, T.K., U.S. Patent 5,723,604
[4] Wardle, R.B., Hinshaw, JC., Braithwaite, P.C., Rose, M.R., Johnston, H.E., Jones, R., Poush, K., "Synthesis of the Caged Nitramine HNIW (CL-20)," 27th International Annual Conference of ICT, June 25-28, 1996..

SYNTHESIS AND USE OF CYCLODEXTRIN NITRATE

J. P. CONSAGA and R. C. GILL
Indian Head Division
Naval Surface Warfare Center
Indian Head, MD 20640-5035

ABSTRACT

Beta and gamma cyclodextrin (CD) have been nitrated with 98 percent fuming nitric acid yielding 92-95 percent cyclodextrin nitrate (CDN). The cyclodextrin is a non-reducing sugar, which produces a thermally stable nitrate ester. Based on FT-NMR, the majority of the product is fully nitrated, with a small fraction only being partially nitrated. The beta-CD has 18-19 of the 21-hydroxyl groups nitrated, while the gamma-CD has 21 of 24 hydroxyl groups nitrated. The specific impulse of the gamma-CDN is 240 lb.·sec/lb. Nitration process was optimized and scaled up to the 100 lb. level. The CDN was characterized for safety, for thermal stability and analytically. Cyclodextrin nitrate complexes with other nitrate esters, such as TMETN, BTTN, and NG through the glycosidic oxygen bridges in the cavity by dipole-dipole interactions. This complex desensitizes the nitrate ester plasticizers as seen by a reduction in the card of the complex versus the neat plasticizer. The complex formation has been verified by thermogravimetric analysis, where the neat plasticizer comes off approximately 30°C above its boiling point. Work has been on going with various propellant systems during the past three years.

BACKGROUND

Cyclodextrins are cyclic, non-reducing, torus-shaped maltooligosaccharides. They originate from the decomposition of starch by a bacterial enzyme called cyclodextrin glycosyltransferase. Three main types of cyclodextrins are known: alpha-form (6D-glucose molecules), beta-form (7D-glucose molecules), and gamma-form (8D glucose molecules). Functional basis for all application fields is the capability to form inclusion complexes due to the hydrophobic property of the cavity. In principle, the following rule is valid: aliphatic guest molecules-alpha cavity, small aromatic guest molecules-beta cavity, large complex guest molecules-gamma cavity.[1]

NITRATION

When work began on the nitration of cyclodextrin in 1988, the beta compound was selected because of the significant difference in cost: alpha-$200/lb., beta-$6.00/lb. in production quantities, gamma-$2,000/lb. At first, the beta-CD was nitrated with 90 percent nitric acid and using the CD as received. Only the seven primary hydroxyls were nitrated under these conditions. When the CD was dried prior to nitration with the 90 percent nitric acid, the nitration level increased to 12-14 hydroxyls out of 21; however when the CD was dried and nitrated with 98 percent fuming nitric acid, 18-19 out of 21 hydroxyls were nitrated.[2,3] Complete nitration of the hydroxyls was achieved with P_2O_5 and 98 percent fuming nitric acid in methylene chloride. Other types of nitration were tried without success. In order to obtain thermally stable material, the CDN had to be dissolved in acetone and crash precipitated with water. The yields were on the

order of 92-95 percent. The nitration was scaled up from one gram to 8 lb. batches in a 22-liter, round bottom flask at Indian Head Division, Naval Surface Warfare Center (IHDIVNAVSURFWARCEN), while Thiokol Corporation scaled up to 50 lb. batches in a 100-gallon reactor. Wacker Chemie discovered a stereo specific procedure for the synthesis of gamma-CD, which has lowered the cost in production quantities to $6-$9/lb. Since the gamma material became available at the lower cost, our work has only been with the gamma-CD. The nitration procedures for the gamma material are the same as the beta-CD. The major reason for the shift to the gamma-CD is the cavity size increases by 80 percent and allows for a complexation with larger molecules and more of them, while the impulse increases from 226 to 240 lb.-sec/lb.

CHARACTERIZATION OF CDN

A specification was developed as follows.

WATER, % WT	1 percent or less
NITROGEN, % WT	> 13 percent
ACIDITY AS % HNO_3	< 0.0
134.5°C METHYL VIOLET, MIN	≥ 15
VTS, 100°C/48HRS., ML /GM	2 ML MAX

Over 400 lbs. of CDN were produced using the above specification starting with the beta-CD. The CDN was characterized for safety, physical, and analytical values.[3-5] Using high performance liquid chromatography (HPLC), with a solvent ratio of 85/15 acrylonitrile/water, a very condensed curve was obtained. Switching to 75/25 ratio of ACN/H_2O, the HPLC curve was significantly spread out. The nuclear magnetic resonance spectroscopy (NMR) curve for a completely nitrated CD showed six main peaks, while the production material revealed that the CDN was mainly 100 percent nitrated, with a small portion of CD chains only partially nitrated. The properties of the 50 lb. scale-up batch of gamma-CDN are shown in Table 1 and Table 2.

COMPLEXATION

When the CD was first received, physical mixtures of the CD and TMETN were prepared in ratios of 1/1 and ½. On analysis, the CD complexed in both cases at the 1/1 ratio. This was determined by thermogravimetric analysis, as the TMETN came off approximately 30°C higher than its normal boiling point, 134°C. It was also determined that the complexation of CDN with the nitrate ester plasticizer resulted in a lower safety sensitivity.[6] For example, the TMETN plasticizer has a card gap of 15-20 cards and requires a #6 blasting cap for the cap test. When the TMETN is complexed with the CDN in a 2/1 ratio, the card gap is reduced to zero cards and the cap test requires a #8 blasting cap. Similarly, BTTN's card gap is reduced from 55 to 30 cards, when it is complexed with the CDN in a 2/1 ratio. Increasing the plasticizer to CDN ratio requires dissolving CDN and nitrate ester plasticizer in acetone and stripping off the solvent to form the complex. If the complexing capability of the CDN has been exceeded, the neat plasticizer will be evident in the TGA. Usually the complexing capability is exceeded when a ratio of 4-5/1 plasticizer to CDN ratio is obtained. The majority of our propellant work has been done at

ratios Of 2/1. If the complex is not formed , the TGA will only show peaks for the individual components rather than the complex breaking up approximately 30°C higher than the boiling point of the nitrate ester plasticizer plus the decomposition of the CDN.

Table 1. Properties of γ-CDN

TEST PROPERTIES	
Galbraith Analysis	
Carbon, %	25.295
Hydrogen, %	2.595
Oxygen, %	58.055
Nitrogen, %	12.365 (13.0)*
# of OH'S Nitrated	21/24
Density, Gm /CC	1.6539
Molecular Formula	C48H52O40(NO2)21
Empirical Formula	C2.1465H2.3115O3.6706N0.9395
Gram Formula Weight	100
Heat of Formation, KCAL/GFW	50.399
Specific Impulse, lb.-sec/lb.	240

Table 2. Safety Properties of γ-CDN

Impact, mm	
NPP3	75
Bructon	> 49
Friction, PSIG	750
ESD, JOULES	0.015

CHARACTERIZATION OF THE CDN/NITRATE ESTER COMPLEX[7-14]

The most interesting thing about the nitrate ester complex with CDN is that the CDN desensitizes the nitrate ester by forming a dipole-dipole interaction. This is true regardless of the nitrate ester used. The main test that was used to ensure complexation formation was the TGA. The complex peak should be approximately 30 °C higher than the boiling point of the nitrate ester . The safety characterization of the various complexes made are reported in Table 3.

Table 3. Safety Properties of CDN/Nitrate Ester Complexes

MATERIAL	ISP	CARD GAP	DENSITY GM/CC	IMPACT, MM BRUCETON	NPP3	FRICTION PSIG	ESD JOULES	CAVITY DROP
γ-CDN	240	0*	1.65	>49	75	750	0.015	
TMETN	249.4	15-20	1.47		>600	>980	>12.5	
BTTN		55	1.52		100	>980	1.625	
NG			1.60		75	40	>12.5	
CDN/BTTN/1 % BI SALT								
1/1.5	254.3	55,30*	1.56	71	75	>980	8.33	
1 /2.0	254.3		1.55	37	50	>980	8.33	
1 /3.0	257.8		1.54					
CDN/NG/1 % BI SALT								
1/1.5	258.7		1.611					
1/ 2.0	259.6		1.608		70	>30	4.20	
1/ 3.0	260.1		1.603					

*Doesn't have Bi salt in the complex

POLYMER OF CYCLODEXTRIN[15]

A polymer of cyclodextrin was reported in the literature by Hurado in 1993. Attempts to obtain samples from Hurado were unsuccessful. In 1997, MACH I prepared samples of a polymer, which were analyzed by Gel Permeation Chromatography (GPC). The samples had a molecular weight range of 10,000-60,000. Attempts to nitrate the CD polymer by fuming 98 percent HNO_3, mixed acid, and N_2O_5 failed. The only successful nitration was achieved by super critical fluid nitration with N_2O_5 in liquid carbon dioxide. The higher molecular weight samples, when nitrated, were no longer soluble in acetone or dimethylsulfoxide. Normally, when the CD is nitrated, the material increases in molecular weight by 1.75. Therefore, the molecular weight must be in the 150-200,000 range. Future work will determine a more suitable molecular weight range. This is necessary to obtain a soluble poly-CDN material. The poly-CDN will allow the production of solid rocket propellants/explosives, in light of the earlier problems associated with the attainment of mechanical properties with systems containing 80-90 percent liquids using the CDN/NG complex.

APPLICATIONS FOR CDN/COMPLEXES

The original goal was to produce a high energy, insensitive, minimum smoke propellant. Many attempts were made to achieve a solid rocket propellant, but they were unsuccessful, because the mechanical properties were too soft. Part of the reason for the unsuccessful attempts was that no solid oxidizers are used, as they will lower the impulse. Thus, a gumstock was being produced with a plasticizer content on the order of 80-90 percent; however, the liquid complexes could be used in other applications, such as space fuels, torpedoes, and gelled fuels for other rocket motor applications.

CONCLUSIONS

The nitration of cyclodextrin has been very successful using 98 percent fuming nitric acid and has been scaled up to the 50-gallon reactor. Other promising nitration processes include super critical fluid using N_2O_5 in liquid carbon dioxide. Production quantities of 400 lbs. have been successfully reproduced in 22 liter batch reactions and have been fully characterized for safety, thermal stability, aging, and other analytical analyses. Complexes have been made and verified to significantly improve the safety characteristics of the complexes and the propellants made from them. The impulse of 240 lb. sec/lb. for CDN is very high and adds to the attractiveness of this new energetic material. With the advancements made by MACH I in the polymer production of cyclodextrin, many energetic fuels, both liquid and solid, as well as cast and extruded, for both CDN and poly CDN will be explored in the near future.

ACKNOWLEDGMENTS

I want to acknowledge the sponsors, Mr. Steven Mitchell from IHDIVNAVSURFWARCEN and Mr. David Siegel from the Office of Naval Research for the support they gave in allowing the advancement-in-the-state-of-the-art in energetics to progress over the last 10 years. I also want to express my gratitude to Steven Collignon and Morley Shamblen from Dahlgren Division, Naval Surface Warfare Center, Dr. David Flanigan and Dr. Robert Wardle from Thiokol Corporation, Mr. Bernard Kosowski from MACH I, and Dr. Jamie Neidert from Atlantic Research Corporation for their support and guidance, as well as my fellow coworkers at IHDIVNAVSURFWARCEN, who have supported the ongoing efforts.

REFERENCES

1. Schmid, G., Wacker-Chemicals, Adrian, MI., Product Bulletins, 1993.
2. Lang, J. W. and Carr, W. A., "Nitration of Cyclodextrin Nitrate," 1992 JANNAF Propellant Development and Characterization Meeting, Kennedy Space Center, FL, 7-9 Apr 92.
3. Heslop, J. M., "Cyclodextran Nitrate Synthesis and Properties," Third Tri-Service Propellant Formulators Meeting, AMSMI/Redstone Arsenal, AL, 4-5 Sep 91.
4. Richardson, A. C., White, B. R, Bryant, W. F., and Turner, H. E., "Characterization of Cyclodextrin Nitrate," 1992 JANNAF Propulsion Meeting, Indianapolis, IN, 24-27 Feb 92.
5. Boswell, R. F., Tompa, A. S. and Gill, R. C., "Thermogravimetric Differential Scanning Kinetic Analysis of Cyclodextrin Nitrate," 1992 JANNAF PROPELLANT Development and Characterization Meeting, Kennedy Space Center, FL, 7-9 Apr 92.
6. Consaga, J. P. and Collignon, S. L., "Energetic Composites of Cyclodextrin Nitrate Esters and Nitrate Ester Plasticizers," Patent Number 5,114,506 19 May, 92.
7. Consaga, J. P., "Insensitive Minimum Smoke Propellants Using Cyclodextrin Nitrate," Third Tri-Service Propellant Formulators Meeting, AMSMI/Redstone Arsenal, AL, 4-5 Sep 91.
8. Gill, R. C., "Formulation of CDN Propellants," Third Tri-Service Propellant Formulators Meeting, AMSMI/Redstone Arsenal, AL, 4-5 Sep 91.
9. Consaga, J. P., "The Use of Cyclodextrin Nitrate for Insensitive Minimum Smoke Propellants," 1992 JANNAF Propulsion Meeting, Indianapolis, IN, 24-27 Feb 92.
10. Gill, R. C. and Heslop, J. M., "Formulation of Insensitive Low Smoke Propellants Using Cyclodextrin Nitrate," 1992 JANNAF Propulsion Meeting, Indianapolis, IN, 24-27 Feb 92.
11. Gill, R. C., Heslop, J. M., Consaga, J. P., and Newman, L. E., "Formulation of Insensitive Low Smoke Propellants Using Cyclodextrin Nitrate: Part II," 1993 JANNAF Propulsion Meeting, Monterey, CA, 15-19 Nov 93.
12. Consaga, J. P. and Gill, R. C., "β-Cyclodextrin Nitrate," Fourth Tri-Service Propellant Formulators Meeting, Phillips Lab/Edwards AFB, CA, 26-27 May 93.
13. Gill, R. C. and Consaga, J. P., "CDN Ballistic MODIFIERS," Fourth Tri-Service Propellant Formulators Meeting, Phillips Lab/Edwards AFB, CA, 26-27 May 93.
14. Gill, R. C. and Consaga, J. P., "Formulation of Low Smoke Propellant Using Cyclodextrin Nitrate," Fifth Tri-Service Propellant Formulators Meeting, Kennedy Space Center, 11-12 Apr 94.
15. Statton, Dr. G. and Kosowski, B., "Synthesis of Cyclodextrin Polymer (PCD). A Raw Material for Insensitive, High Energy and Shock Survivable Explosives," SBIR Phase I Eglin AFB Contract F08630-97-C-0059 dtd 5 Jan 98.
16. Consaga, J. P., "Cyclodextrin Nitrate/Nitroglycerin/Bismuth Subsalicylate Complex as a Liquid Fuel for Space Motors," Navy Number 78,972, dtd 5 Feb 98.
17. Consaga, J. P., "Chemically Reactive Fragment Warhead," Navy Number 78,973, dtd 9 Feb 98.

SYNTHESIS AND PRODUCTION OF ENERGETIC COPOLYURETHANE THERMOPLASTIC ELASTOMERS BASED ON GLYCIDYL AZIDE POLYMER

Ampleman, G., Marois, A., Désilets, S., Beaupré, F., and [1] Manzara, T.

Presented at the 29th International ICT Conference, June 1998

DEFENCE RESEARCH ESTABLISHMENT VALCARTIER
Department of National Defence, Canada
2459, Pie XI Blvd, North, Val-Bélair
Quebec, Canada, G0A 1R0

[1] 3M, Specialty Chemicals
Division Laboratory, 3M Cottage Grove Center
Building 70-2, 10746 Chemolite Road, Cottage Grove
St Paul, Minnesota 55016, U.S.A

ABSTRACT

For the last few years, DREV has been involved in the synthesis of energetic thermoplastic elastomers (ETPEs) based on linear glycidyl azide polymer (GAP). These polymers are physically-crosslinked rubbery materials which can be solubilized and recycled, and could provide the basis for a new generation of binders for introduction into future formulations of propellants and explosives. Since ETPEs are recyclable, disposal of the new formulations at the end of their life cycle will be less problematic.

Recently, work at DREV in the area of ETPEs has led to a series of three candidates suitable for incorporation in gun propellant formulations. These three different ETPEs are copolymers of type AB and are obtained by macropolymerization from GAPs having molecular weights of 500, 1000 and 2000 with 4,4'-methylenebis-phenyl isocyanate (MDI) . These ETPEs are soluble in ethyl acetate and therefore can be easily processed or recuperated at the end of the munition life time, leading to recyclable materials. Prototypes of these ETPEs have been incorporated in HELOVA formulations and provided good impetus levels. Moreover, the formulations containing the prototypes were easily processed using the current processing technique.

At the moment, an ETPE based on GAP-1000 seems the most promising candidate. The scale-up for the production of these ETPEs was done at the kilogram scale in the laboratory. The transfert of the technology was achieved and the production of the material will be done at the 70 kilograms scale. This paper describes mainly the synthesis and the characterization of these new ETPEs.

1.0 INTRODUCTION

High-energy solid compositions, such as propellants, plastic-bonded explosives or the like, are comprised of an elastomeric binder in which are dispersed particulate solids such as oxidizers, particulate fuel material or crystalline explosives. Glycidyl azide polymer (GAP) serves as an energetic binder (Ref. 1) and is reacted with a curing agent to form a chemically crosslinked matrix for ammonium nitrate in new insensitive low smoke propellant formulations, and for RDX in new insensitive plastic-bonded explosives (Refs. 2-10). To produce this chemically crosslinked matrix, a triol or a triisocyanate, or both, or a polymer having a functionality greater than two reacting with a diisocyanate, must be used to ensure the reticulation (Refs. 11-15). In such systems, different mechanical properties of the binder can be obtained by adjusting the parameters of the curing reaction and the component concentrations, which results in varying the crosslink density of the matrix.

On the other hand, it is desirable to introduce GAP into low vulnerability ammunition (LOVA) formulations in order to obtain higher energy low vulnerability ammunition (HELOVA) formulations. However, GAP must be reacted with a curing agent to form a matrix leading to good mechanical properties (Ref. 16). With the current processing technique used in Canada for propellants, a suitable curing reaction is hard to achieve. Moreover, such a gun propellant would not be recyclable because the crosslinks are covalent chemical bonds and thus irreversible, as they are for composite explosives and rocket propellants. The use of thermoplastic elastomers (TPE) avoids a process that involves curing reactions and hence leads to recyclable LOVA-type gun propellant formulations. DREV has been active in the development of LOVA gun propellant formulations using TPEs, and the incorporation of these polymers as binders has resulted in good mechanical properties, but more energy is still desirable (Ref. 17). The use of GAP-based TPEs in HELOVA gun propellant

formulations led to propellants showing good mechanical properties, low vulnerability and a high impetus. Furthermore, it allowed an easier processing of a gun propellant formulation (Refs. 18-21).

Development at DREV of ETPEs based on glycidyl azide polymer led to a series of three candidates suitable for incorporation into HELOVA gun propellant formulations. These three different ETPEs are copolymers of type AB and were obtained by macropolymerization of GAPs having molecular weights of 500, 1000 and 2000 with 4,4'-methylenebis-phenyl isocyanate (MDI), the monomer giving the hard segment A. This paper describes the synthesis and characterization of these ETPEs.

2.0 THEORY

Thermoplastic elastomers are copolymers of type ABA or AB, where A and B are respectively the hard segment and the soft segment (Ref. 22). The hard segment is capable of crystallization or association and gives the thermoplastic behaviour to the copolymer, whereas the soft segment gives the elastomeric behaviour to the copolymer. The thermoplastic behaviour is the result of crystalline domain formation by chain associations due to reversible interactions such as dipole-dipole interactions, hydrogen bonding, etc. In practice, at room temperature, a thermoplastic elastomer behaves like a rubber because it is crosslinked in the same fashion as a conventional elastomer, but with reversible physical crosslinks. Since the physical crosslinks are reversible, the TPE can be melted or dissolved in a solvent and then mixed with other components of a formulation and processed. A gun or rocket propellant or a composite explosive is obtained upon cooling the TPE or evaporating the solvent. Cooling the TPE or evaporating the solvent lets the broken physical crosslinks re-form and the elastomeric properties are recovered. This also means that obsolete material can be melted or dissolved before the separation of the components, leading to a recyclable composition.

Thermoplastic elastomer copolymers of type ABA are usually obtained by polymerization of a difunctional homopolymer B followed by the addition of monomers of the homopolymer A which is crystallisable. To achieve that type of copolymerization, monomers of both types should have a similar reactivity and most of the time the polymerization is a living one. This technology leads to a

copolymer of controlled structure with suitable adjustable mechanical properties. A good example of this type of polymerization is the preparation of the AMMO/BAMO energetic thermoplastic elastomer. Since 3-azidomethyl-3-methyloxetane (AMMO) and bis 3,3-azidomethyloxetane (BAMO) are both oxetanes with similar reactivities, polymerization of type ABA is possible. Manser *et al.* prepared a wide variety of AMMO/BAMO copolymers of different molecular weights and mechanical properties by varying the monomer concentrations and the polymerization parameters (Ref. 23). On the other hand, copolymers of type AB are usually obtained by mixing monomers of both types having reactive compatible ending groups and represents a simpler technology. For industrial uses, copolymers of type AB are more attractive since the process is often more simple than for copolymers of type ABA.

Polyurethane chemistry is well known and urethane groups are obtained when an hydroxyl group is reacted with an isocyanate group (Fig. 1) (Refs. 15, 24). Water also reacts with isocyanate at a rate similar to a secondary hydroxyl group, yielding a carbamic acid which decomposes to liberate carbon dioxide in the matrix (entrapped bubbles) and form an amine group which is 100 times more reactive than a primary hydroxyl group (Fig. 2). This amine group reacts faster than hydroxyl groups with isocyanate, yielding an urea group which introduces rigidity and brittleness to the polyurethane. Moreover, this urea group can react with a second isocyanate to give a biuret group, introducing covalent crosslinking between two polymer chains (Fig. 3). To obtain linear copolyurethane without bubble formation and covalent crosslinking, the presence of water must be avoided in order to eliminate undesirable reactions.

An important aspect of the polyurethane chemistry is the concentration of isocyanate and hydroxyl groups, i.e. the NCO/OH ratio. An excess of isocyanate will lead to covalent crosslinking by allophanate group formation (Fig. 4) or biuret formation (Fig. 3) if water is present. An excess of hydroxyl groups will lead to incomplete reaction and poor mechanical properties. Thus, the NCO/OH ratio has a direct impact on the molecular weight of the polyurethane and on the mechanical properties. In order to get polyurethane elastomers, covalent crosslinking is needed and is obtained by the use of triol or triisocyanate. The NCO/OH ratio can also be adjusted higher than unity to increase the crosslinking density. At DREV, this type of polymerization was extensively studied with

GAP to lead to a wide variety of thermoset binders with crosslinked chemical structures (Refs. 2-5, 11-14, 25). Theoretically, when a diol is reacted with a diisocyanate at a precise NCO/OH ratio equal to unity, a linear copolyurethane with the highest molecular weight is obtained. Cooper *et al.* used poly(tetramethylene oxide), a dihydroxyl terminated telechelic polyether, as the diol, and polymerized it with MDI (Refs. 26-29). They found that the copolymer when isolated was a copolyurethane thermoplastic elastomer where the hard segment was the result of hydrogen bonding between the urethane groups.

Although many researchers have studied the curing of glycidyl azide polymer with a diisocyanate, this is the first time that urethane groups are used as the hard segments in an energetic thermoplastic elastomer. Glycidyl azide polymer having a functionality of two or less was used as a macromonomer and was polymerized with an aromatic diisocyanate (MDI) at a NCO/OH ratio of 1, to give a linear copolyurethane thermoplastic elastomer which was not chemically crosslinked. This is only obtained using highly controlled conditions. The NCO/OH ratio must be about 1 to avoid chemical crosslinking between the chains and to obtain the best reproducible copolymer. In this copolymer, the elastomeric B segment is provided by the amorphous glycidyl azide polymer, and the thermoplastic A segment is provided by the urethane moieties. Each urethane group within the copolymer is capable of forming hydrogen bonds with the oxygen of another urethane or with the oxygen of an ether. By doing so, physical crosslinks are obtained between the chains and as a result, an energetic copolyurethane thermoplastic elastomer is obtained (Fig. 5).

It has to be noted that this process is not restricted to GAP but can be applied to any dihydroxyl terminated telechelic energetic polymer having a functionality of two or less such as: poly 3-azidomethyl-3-methyloxetane (AMMO), poly bis 3,3-azidomethyloxetane (BAMO), poly 3-nitratomethyl-3-methyloxetane (NIMMO) or poly glycidyl nitrate (GLYN). The process will then lead to a wide variety of energetic thermoplastic elastomers having different mechanical properties.

According to the literature, linear polyurethanes have melting points in the region of 200°C when the thermoplastic content is about 20 to 50% by weight; this is when there are enough hard segments to induce crystallinity (Ref. 26-29). Copolyurethanes with glycidyl azide polymer must not

be melted because the decomposition of GAP occurs at 200°C and can result in an apparatus damage (Ref. 30, 31). However, they can be dissolved in a solvent and used solvated in an energetic formulation such as a gun propellant formulation. Using the copolyurethane thermoplastic elastomer based on GAP in a gun propellant formulation is therefore an elegant way to introduce an energetic binder without the problems associated with conventional cured binders. Moreover, this formulation can be recuperated and recycled.

According to this, GAPs of molecular weights of 500, 1000 and 2000 and having a functionality of two or less were reacted with MDI at a NCO/OH ratio of one to yield copolyurethane thermoplastic elastomers which were used as binders in HELOVA gun propellant formulations. These copolymers were solvated and mixed with the other components of gun propellant formulations using a solvent-type process. After evaporation of the solvent, extrusion, cutting and drying, suitable gun propellant grains were obtained.

3.0 EXPERIMENTAL

Linear difunctional glycidyl azide polymers of molecular weight 500 and 2000 were obtained from 3M. Since linear GAP 1000 was not available commercially, it was obtained by azidation of polyepichlorohydrin (PECH) of molecular weight 1000 synthesized by the process described by Okamoto *et al* (Ref. 33). To adjust the NCO/OH ratio to one, the concentration of the hydroxyl groups related to the functionality of the GAPs must be known. The NMR spectroscopy method was used to determine the equivalent weight of the GAP prepolymers used in the synthesis of the copolyurethane thermoplastic elastomers (Ref. 32). Three energetic copolyurethane thermoplastic elastomers were used to prepare three HELOVA gun propellant formulations with different mechanical properties. GAPs with molecular weights of 2000, 1000 and 500 were used as macromonomers to synthesize the copolyurethane thermoplastic elastomers. The polymerization was achieved in the bulk by reacting stoechiometrically GAP 2000, 1000 or 500 with 4,4'-methylenebis phenyl isocyanate using dibutyltin dilaurate as the catalyst.

All the copolyurethanes synthesized were rubber-like materials which were dissolved in ethyl

acetate in a ratio polymer/solvent of 35/65. Copolyurethane thermoplastic elastomers were dissolved in a large beaker containing ethyl acetate using a glass rod to stir thoroughly the sample until no more material could be dissolved. This stirring was repeated each hour until all the sample was completely dissolved (8 hours). This solution was used as is in the HELOVA formulation.

Copolymerization could also be done in solvent. For production needs, it could be more interesting to perform the polymerization in ethyl acetate in order to avoid the solvatation step before introducing the copolymers into an energetic formulation. The polymerization in ethyl acetate using different polymer concentrations varying from 30 to 70% by weight, was achieved and led to identical copolyurethane thermoplastic elastomers compared to the ones obtained in the bulk. Therefore, the process could be done at different polymer concentrations leading to a wide variety of ETPE solutions suitable for the formulation processes. The solvated thermoplastic elastomers can be used as is in the preparation of high-energy compositions. Since the solvatation step is time consuming, it is recommended to perform the synthesis directly in the preferred solvent.

4.0 RESULTS AND DISCUSSION

Three different linear copolyurethane thermoplastic elastomers were obtained from GAP 2000, 1000 and 500. According to this process, hydrogen bonds were formed between the urethane groups forming the hard segments of the thermoplastic elastomer and therefore a thermoplastic behaviour was observed. All the copolymers synthesized were rubber-like materials which were dissolved in ethyl acetate prior to their inclusion into the gun propellant formulations. Preliminary results obtained with the ETPE based on GAP 2000 showed that the propellant grains were too soft. To increase the hardness of the matrix, a shorter GAP prepolymer was used to increase the hard segment content. By doing so, introducing more hard segments resulted in more hydrogen bonds and therefore, a harder rubber was obtained. The hard segment content of ETPEs with GAP 2000, 1000 and 500 was respectively 10, 20 and 40%. Since the hard segments were not energetic, introducing more of them reduced the total energy of the copolyurethane. It was found that the best compromise energy/ hardness was to use the ETPE based on GAP 1000. The prepolymer GAP 1000 was not commercially available; it was then synthesized according to the procedure developed by Okamoto

et al. (Ref. 33). The polymerization of epichlorohydrin with triethyloxonium hexafluorophosphate (TEOP) was a very efficient system but care had to be taken to control the reaction temperature. If the temperature increased over 30°C, the polymerization would fail to yield polyepichlorohydrin of molecular weight 1000. Azidation of the resulting PECH gave GAP 1000 with an excellent yield. Polymerization of GAPs with MDI yielded copolyurethane thermoplastic elastomers quantitatively.

4.1 Characterization of Thermoplastic Elastomers

The molecular weights of the resulting copolymers were determined by gel permeation chromatography (GPC). Copolymers based on GAP 2000 had number average molecular weights M_n = 35,000 to 40,000, while those obtained from GAPs 1000 and 500 had M_n of 26,000-34,000. This could be explained by the fact that viscosity increased more rapidly when more hard segments were included in the copolymer. When the molecular weight of the macromonomer was small, the content of hard segments increased, leading to a greater viscosity during the polymerization resulting in lower molecular weight copolyurethane thermoplastic elastomers.

Infrared spectroscopy revealed for all copolyurethane thermoplastic elastomers that the urethane groups forming the hard segments were hydrogen bonded, since a strong band at 3320 cm^{-1} corresponding to a NH-bond was observed. It is interesting to note that a small band at 3400 cm^{-1} was observed for ETPE with GAP 2000; this was probably a free N-H band of urethanes. With this particular copolyurethane, the distance between two urethanes was greater compared with the other two copolyurethanes. This implied more freedom for the GAP chains resulting in a disalignment of the urethane groups, therefore, less hard segments were formed. This was in accordance with the fact that this copolyurethane was softer than the others. For the ETPE with GAP 500, no free NH band was observed; moreover, a small decrease in the frequency of the NH-bonded-band at 3310 cm^{-1} was observed. This implied more hydrogen bonds and a better alignment of the urethanes. This resulted in a sample which was very hard compared to ETPE with GAP 2000. In all samples, disappearance of the NCO band at 2270 cm^{-1} confirmed that the polymerizations were complete. Appearance of a carbonyl absorption band at 1730 cm^{-1} was consistent with the formation of urethane groups.

^{13}C-NMR and ^{1}H-NMR spectroscopy confirmed the structure of the copolymers without the presence of chemical crosslinks formed during the polymerization. Only urethane groups were present and no allophanate or biuret were detected in ^{13}C spectra. ^{1}H signals were characteristic of GAP polymers. The aromatic carbon signals of MDI were carefully assigned and compared with polyurethanes in the literature and were consistent with the structure given in figure 5 (Refs. 25, 34-47).

Differential scanning calorimetry measurements were conducted and the glass transition temperatures for the copolyurethane thermoplastic elastomers made with GAP 2000, 1000 and 500 were respectively -28°, -15° and -4°C.. No melting endotherm was observed below 200 °C, the temperature at which GAP decomposed (Refs. 30,31). Nevertheless, all the copolymers obtained using this process were rubbery-like materials soluble in ethyl acetate. Removal of the solvent yielded back the original material showing identical properties.

4.2 Processing of the HELOVA Gun Propellants

Once the ETPE was solvated in ethyl acetate, it was processed with an energetic nitrate ester plasticizer and the other ingredients of a HELOVA gun propellant formulation in a sigma-blade mixer according to the technique presented in Ref. 48. For all formulations, the processing technique used was similar to the one for the reference formulation (LOVA) or one containing an inert TPE (Refs. 17, 48). This aspect was of importance since a modification of the processing would imply an increased amount of effort and expense. The ballistic and mechanical evaluations were done for the most promising formulations and the results could be found in reference 21.

4.3 Production of the ETPEs

An interlaboratory study was initiated between DREV and 3M to evaluate the potential of commercialization of these new copolymers. The technology developed at DREV concerning the copolyurethane thermoplastic elastomers was tranfered to 3M and syntheses were carried out at 3M. Copolymers synthesized at DREV were sent to 3M for comparison with the copolymers prepared by

3M. Since GAP 2000 and 500 were initially obtained from 3M, reproducing the materials obtained at DREV should be feasible. In the case of ETPE 1000, the best compromise for the HELOVA formulations, the GAP 1000 used as starting material was synthesized according to the procedure developed by Okamoto (ref. 33), a procedure different from the 3M procedure. Therefore, it is highly probable that the DREV's material will be different from the one synthesized by 3M. Work is still carried out to evaluate the impact of such differences on the mechanical properties of the copolyurethane thermoplastic elastomers obtained with GAP 1000 from both laboratories. Once the laboratory scale is completed and that the copolymers synthesized by 3M are suitable for the HELOVA formulations, 3M proposed to scale-up and synthesize a larger quantity of the best material (150 lbs). This quantity will be distributed to potential customers for evaluation.

5.0 CONCLUSION

It has been demonstrated that energetic thermoplastic elastomers could easily be obtained by synthesizing copolyurethanes based on linear GAPs having a functionality of two or less. Three different molecular weights of GAP were used as macromonomers to yield three different ETPEs, which were incorporated in HELOVA gun propellant formulations using the current processing technique. To obtain reproducible copolyurethane thermoplastic elastomers, dried reactants and conditions had to be maintained during the polymerization. Infrared and nuclear magnetic resonance spectroscopy confirmed that the copolyurethanes were produced without chemical crosslinking. It was also demonstrated that hydrogen bonding led to the formation of the hard segments. It was also observed that a harder material was obtained when the hard segment content was increased which was accomplished when a GAP macromonomer of lower molecular weight was used. Nevertheless, this lowered the energy content of the copolymer and the best compromise was the use of GAP 1000 to synthesize the ETPE.

Three copolyurethane thermoplastic elastomers were used to prepare high energy gun propellants. Results obtained from processing studies, ballistic and mechanical experiments demonstrated that the use of ETPEs in HELOVA gun propellant formulations can be an improvement over the reference formulation and lead to recyclable materials.

6.0 ACKNOWLEDGMENTS

The authors wish to thank Ms. Nicole Gagnon from the Chemistry and Environment Group for the calorimetric measurements she performed during this study. We want to thank especially Dr S. Thiboutot and Mr. J.F. Drolet who helped us in the patent application process. We would also like to express our appreciation to all of our colleagues in the Energetic Materials Section for their fruitful discussions and encouragement.

7.0 REFERENCES

1. Frankel, M.B., Grant, L.R. and Flanagan, J.E.,"Historical Development of Glycidyl Azide Polymer"; Journal of Propulsion and Power, 8 (3), 560, 1992.

2. Lessard, P., Druet, L., Villeneuve, S., Thiboutot, S., Benchabane, M. and Alexander, D., "Development of a Minimum Smoke Propellant Based on Glycidyl Azide Polymer and Ammonium Nitrate", NATO Advisory Group for Aerospace Research and Development, Conference Proceedings AGARD-CP-511 on Insensitive Munitions, Bonn (Germany), 1991.

3. Hooton, I., Bélanger, C. and Pelletier, P., "Preliminary Studies of Energetic Binder Based PBXs", DREV Memorandum 2996/89, 1989.

4. Hooton, I. and Bélanger, C., "Improvements in GAP-Based Plastic Bonded Explosive Formulations", DREV Memorandum 3154/93, 1993.

5. Villeneuve, S. and Carignan, P., "Binders for Rocket Propellant Formulations Based on Glycidyl Azide Polymers", DREV Report 4631/91, 1991.

6. Henke, K., Böhnlein-Maub, J. and Schubert, H., "Characteristic Properties of AN/GAP-Propellants"; Propellants, Explos., Pyrotech., 21, 139, 1996.

7. Oyumi, Y., Kimura, E., Hayakama, S., Nakshita, G. and Kato, K., "Insensitive Munitions(IM) and Combustions Characteristics of GAP/AN composite Propellants"; Propellants, Explos., Pyrotech., 21, 271,1996.

8. Oyumi, Y. and Nagayama, K., "Development of High Burn Rate Azide Polymer Propellant"; J. Energetic Materials, 15, 59, 1997.

9. Hori, K. and Kimura, M., "Combustion Mechanism of Glycidyl Azide Polymer"; Propellants, Explos., Pyrotech., 21, 160, 1996.

10. Kubota, N., Yano, Y., Miyata, K., Kuwahara, T., Mitsuno, M. and Nakagawa, I., "Energetic Solid Fuels for Ducted Rockets(II)"; Propellants, Explos., Pyrotech., 16, 287, 1991.

11. Ampleman, G., Lee, A.K. and Lavigne, J., "The Curing of GAP with Diisocyanates", DREV M-3023/90, 1990.

12. Ampleman, G., Désilets, S. and Marois, A., "A New Class of Glycidyl Azide Polymers with Increased Functionality and Reactivity: Part I - Synthesis"; DREV R-4680/92, 1992.

13. Villeneuve, S. and Ampleman, G., "Curing and Tensile Mechanical Properties of Binders Based on Increased Functionality Glycidyl Azide Polymer"; DREV M-3142/93, 1993.

14. Désilets, S., Ampleman, G. and Marois, A., "A New Class of Glycidyl Azide Polymer with Increased Functionality and Reactivity: Part II -Characterization"; DREV R-4715/94, 1994.

15. Hepburn, C., "Polyurethane Elastomers", Applied Science Publishers, London, 1982.

16. Stacer, R. and Husband, D.M., "Molecular Structure of the Ideal Solid Propellant Binder"; Propellants, Explos., Pyrotech., 16, 167, 1991.

17. Beaupré, F. and McIntosh, G., "Improvement in Mechanical Properties of LOVA-Type Gun Propellants", Proceedings of the 16th Meeting of TTCP WTP-4, China Lake, 1991.

18. Beaupré, F., Ahad, E. and Ampleman, G., "Preliminary Studies of HELOVA-Type Gun Propellant Containing Energetic Binders"; Proceedings of the American Defense Preparedness Association (ADPA) International Symposium on Energetic Materials Technology, Meeting 450, Orlando, Florida, 1994.

19. Beaupré, F., Ahad, E. and Ampleman, G., "The Use of GAP-Based Binders in HELOVA Gun Propellant Formulations", Proceedings of the 19th TTCP WTP-4 Meeting on New Materials and Processing, DREV, 1994.

20. Beaupré, F., Ampleman, G. et Ahad, E., "Application of GAP-based Binders to Low Vulnerability Gun Propellant Formulations", 6th International Gun Propellant Symposium, ADPA, Event 599, Parsipanny, New Jersey, 1994.

21. Ampleman, G. and Beaupré, F., "Synthesis of Linear GAP-Based Energetic Thermoplastic Elastomers for Use in HELOVA Gun Propellant Formulations"; Proceedings of the 27th Int. ICT Conference (Energetic Materials Tech. Manufacturing), Karlsruhe, Germany, pp 24,1-11, 1996.

22. West, J.C. and Cooper, S.L., "Thermoplastic Elastomers", Science and Technology of Rubbers, Academic Press, Chapter 13, pp. 531-567, 1978.

23. Manser, G.E. and Fletcher, R.W., "Energetic Thermoplastic Elastomers", Summary Report, Office of Naval Research Contract N00014-87-C-0098, 1988.

24. Lenz, R.W., "Organic Chemistry of Synthetic High Polymers", Interscience, NY, pp 180-196, 1967.

25. Désilets, S., Villeneuve, S., Laviolette, M. and Auger, M., "^{13}C NMR Spectroscopy Study of Polyurethane Obtained from Azide Hydroxyl-Terminated Polymer Cured with Isophorone Diisocyanate (IPDI)"; J. Polym. Sci., Part A: Polym. Chem., 35, 2991, 1997.

26. West, J.C. and Cooper, S.L., "Thermoplastic Elastomers", Science and Technology of Rubber, 531, 1978.

27. Lilaonitkul, A. and Cooper, S.L., "Properties of Polyether-Polyester Thermoplastic Elastomers", Rubber Chem. and Tech., 50(1), 1, 1977.

28. Lilaonitkul, A. and Cooper, S.L., "Properties of Thermoplastic Polyurethane Elastomers", Advances in Urethane Science and Technology, 7, 163, 1979.

29. Miller, J.A., Lin, S.B., Hwang, K.K.S., Wu, K.S., Gibson, P.E. and Cooper, S.L., "Properties of Polyether-Polyurethane Block Copolymers: Effect of Hard Segment Length Distribution", Macromolecules, 18, 32, 1985.

30. Kubota, N. and Sonobe, T., "Combustion Mechanism of Azide Polymer"; Propellants, Explos., Pyrotech., 13, 172, 1988.

31. Leu, A.L. and Shen, S.M., "Thermal Characteristics of GAP, GAP/BDNPA/BDNPF, PEG/BDNPA/BDNPF and the Energetics Composites Thereof"; Proceedings 21th International Annual Conference of ICT-Technology of Polymer Compounds and Energetic Materials, Paper 6, 1990.

32. Désilets, S., "Precise Equivalent Weight Determination of Branched Glycidyl Azide Polymers by NMR Spectroscopy"; DREV R-4740/94, 1994.

33. Okamoto, Y., "Cationic Ring-Opening Polymerization of Epichlorohydrin in the Presence of Ethylene Glycol", Polymer Prepr,. 25(1), 264, 1984.

34. Matthews, K.H., McLennaghan, A. and Pethrick, R.A., "^{1}H and ^{13}C Nuclear Magnetic Resonance Studies of the Synthesis of Linear Segmented Polyurethane Elastomers", British Polymer Journal, 19, 165, 1987.

35. Kaji, A., Arimatsu, Y. and Murano, M., "^{13}C NMR Study of Anomalous Linkages in Polyurethane"; J. Polym. Sci. Part A: Polym. Chem. 30 (2), 287, 1992.

36. Sebenik, A., Kastelic, C. and Osredkar, U., "Determination of Allophanate and Biuret Groups in Polyurethane Oligomers by ^{13}C NMR"; Polym. Preprint (Amer. Chem. Soc, Division Polym. Chem.), 25 (1), 120, 1984.

37. Kricheldorf, H.R. and Hull, W.E., "Spectroscopic Characterization of Polyurethanes and Related Compounds"; Makromol. Chem., 182, 1177, 1981.

38. Sebenik, A., Kastelic, C. and Osredkar, U., "Study of the Reaction Between Ethylene Glycol or 1,2-Propylene Glycol with Diphenylmethane-4,4'-Diisocyanate"; J. Macromol. Sci. Chem., A29 (3), 341, 1983.

39. Delides, C., Pethrick, R. A., Cunliffe, A.V. and Klein, P.G., "Characterization of Polyurethane Elastomers by ^{13}C NMR Spectroscopy"; Polymer, 22, 1205, 1981.

40. Mc Lennaghan, A. and Pethrick, R.A., "^{13}C NMR Studies of the Synthesis of Linear Segmented Polyurethane Elastomers"; Polimeri, 7 (6), 155, 1986.

41. Kastelic, C., Sebenik, A. and Vizovisek, I., "Study of Secondary Reaction in Polyurethane Formation"; Hem. Ind., 38 (12), 349, 1984.

42. Kaji, A. and Murano, M., "Sequence Distribution of Segmented Polyurethane-Urea"; Polym. Journal, 22 (12), 1065, 1990.

43. El Ghafari, M.E. et Pham, Q.T., "Cinétique de polycondensation en solution et en masse du polybutadiène hydroxytéléchélique avec le methylène-4,4' di(isocyanate de phényle) en l'absence de catalyseur. Étude par ^{1}H RMN et ^{13}C RMN"; Makromol. Chem. 186, 527, 1985.

44. Kricheldorf, H.R. and Meier-Haack, J., "New Polymer Syntheses. LXX. Synthesis of Multiblock Copolybiurets from Poly(Ethylene-Glycol) and Silylated Diamine"; J. Polym. Sci. Part A: Polym. Chem., 31, 1327, 1993.

45. Kricheldorf, H.R., "^{15}N- NMR Spectroscopy. XVIII Sequence Analysis of Linear Polyureas"; J. Macromol. Sci. Chem., A14 (6), 959, 1980.

46. Okamoto, D.T., O'Connel, E.M., Cooper, S.L. and Root, T.W., "Solid State ^{13}C Nuclear Magnetic Resonance Characterization of MDI-Based Polyurethane", J. Polym. Sci.: Part B: Polymer Physics, 31, 1163, 1993.

47. Okamoto, D.T., Cooper, S.L. and Root, T.W., "^{13}C NMR Investigation of a Poly(Urethane-Urea) System", Macromolecules, 25, 1068, 1992.

48. Beaupré, F. and Durand, R., "Processing Studies of LOVA-Type Gun Propellants", DREV R-4603/90, 1990.

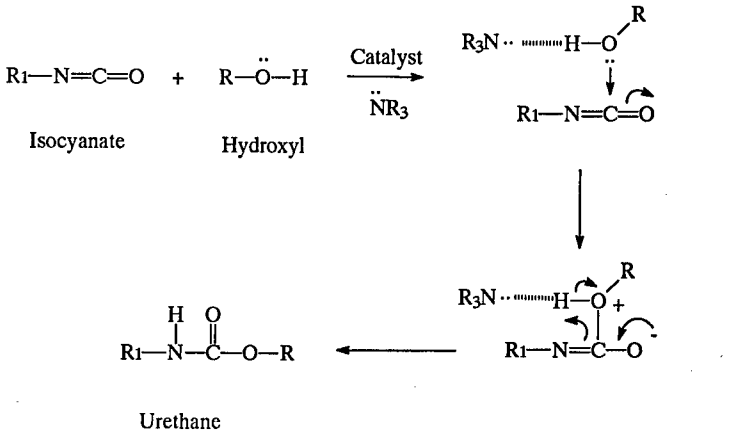

Figure 1: Formation of Urethane Groups

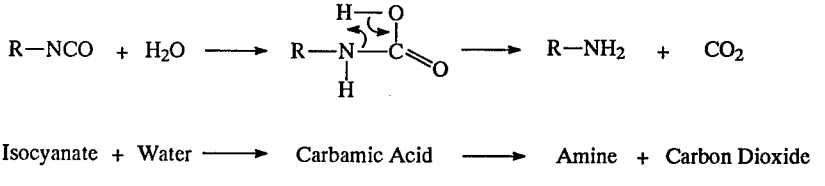

Figure 2: Reaction of Water with Isocyanate

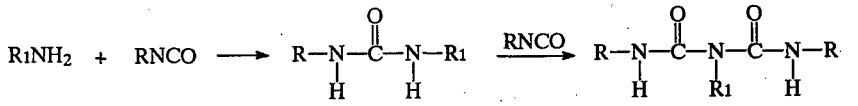

Amine Isocyanate Urea Biuret

Figure 3: Formation of a Biuret Group

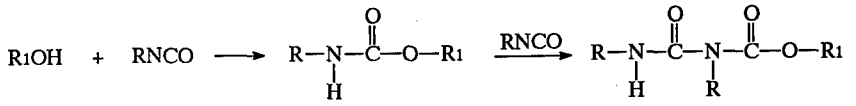

Hydroxyl Isocyanate Urethane Allophanate

Figure 4: Formation of an Allophanate Group

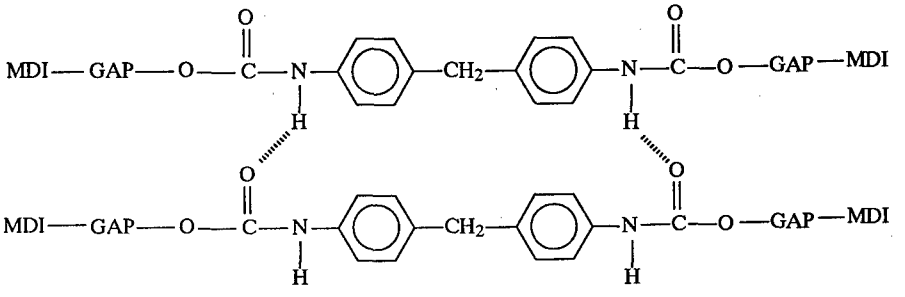

Figure 5: Representation of a Hard Segment in ETPE

NEW HIGH NITROGEN HETEROCYCLES WITH ALTERNATION OF CHARGES: STABILITY AND STRATEGY OF SYNTHESIS

Aleksandr M. Churakov and Vladimir A. Tartakovsky

N. D. Zelinsky Institute of Organic Chemistry, Russian Academy of Sciences
117913 Moscow, Russian Federation

Abstract: Compounds with several linked nitrogen atoms tend to be unstable. The analysis of structure–property relations allow us to form the population of high nitrogen compounds with relatively enhanced stability. These compounds possess the following distinctive properties: cyclic delocalization; alternation of charges in a nitrogen chain; specific Y-type arrangement of atoms in the component units, which impede the degradation of a molecule. The synthetic approach to most of these compounds practically did not exist so far. In this connection, the new methods of intramolecular nitrogen-nitrogen bond formation are discussed. These methods allow to include azoxy units in a cycle. The strategy of synthesizing the following novel heterocycles is exhibited: 1,2,3,4-tetrazine-1,3-di-*N*-oxides fused to benzene and furazan ring; 1-hydroxybenzotriazole 3-*N*-oxides; 1,2,3-triazole 2-*N*-oxides fused to furazan ring.

INTRODUCTION

We are interested in the energetic compounds with high heats of formation. This characteristic depends on the number of N–N bonds in the molecule: the greater the number, the higher the heat of formation. On the other hand, compounds with several linked nitrogens (e. i., nitrogen catenation) are usually unstable [1]. How to stabilize compounds with nitrogen catenation? One of the important factors that could stabilize the molecule, is cyclic conjugation. So herein we consider only cyclic conjugated compounds. Since the energy of the N–N bond is increased by alternation of nitrogen atoms with different electronegativities, alternation of charges in a nitrogen chain could be the other stabilizing factor.

At first, the design and thermodynamic stability of high nitrogen compounds is discussed. The latter is closely connected with electron shell of a molecule and thus with its chemical inertness. Then stability to heat is treated, which strongly depends on a particular degradation path of a molecule. Later on, the strategy of synthesis of some stabilized compounds is described.

DESIGN OF COMPOUNDS WITH ALTERNATING CHARGES

Alternation of charges in a conjugated nitrogen chain can be achieved by alternant addition of substituents to sp^2-hybridized nitrogen atoms resulting in quaternization of these atoms. This procedure can result in neutral compounds, anions or cations, depending on a parent chain (neutral or negatively charged) and on a substituent (neutral or negatively charged). The examples are given in Table 1.

Table 1. Design of nitrogen chains with alternating charges.

parent chain	chain with alternating charges
=N–N=N– ⟷ –N=N–N=	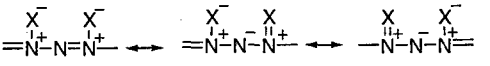
–N=N–N̄–	
=N–N̄–N=	

-X = -O, -NR, $-CR_2$

Bearing this in mind, we have formed a separate population of cyclic compounds. These compounds can be constructed by the following operating sequence:

1. Choose a skeleton, i. e., conjugated alternant hydrocarbon (in our case, naphthalene; Table 2, step 1).

2. Make a replacement of a selected carbon atoms by nitrogens with retention of all cyclic bonds (step 2).

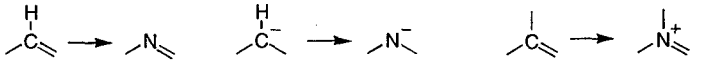

3. Carry out starring procedure (step 3) (for starring procedure of alternant hydrocarbons see ref. 2).

4. Unite all unstarred nitrogen atoms with substituents without exception (in our case, the substituents are oxygen atoms; step 4).

Table 2. The operating sequence of design of AC-compounds.

step 1	steps 2 and 3	step 4
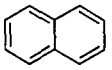	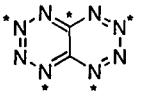	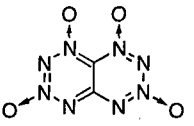

Herein we designate the cyclic conjugated high nitrogen compounds with alternating charges, constructed according to the above rules, the ***AC-compounds***.

These rules are presented for alternant even-membered cycles. However, the odd-numbered nonalternant cyclic anions can also be transformed into AC-compounds on condition that at least one carbon is preserved in a cycle. In this case a nitrogen chain of nonalternant cycle can be regarded as a chain with alternating charges.

Using these basic principles, the population of AC-compounds can by constructed. Some examples are given in Table 3. These compounds possess a number of characteristic features. We shall illustrate them by the examples of AC-compounds **1a** and **2a**, and their non-AC-isomers, i. e., **1a'** and **2a'**.

One of the particularities of the AC-compounds lies in the fact that the distinction in electronegativities of the neighboring N atoms in the nitrogen chain is greater, as compared to their non-AC-isomers. This can be clearly seen from the resonance structures of AC-compound **2a** and its non-AC isomer **2a'** (Scheme 1). This alternation strengthens the σ N–N bonds of a molecule.

Scheme 1

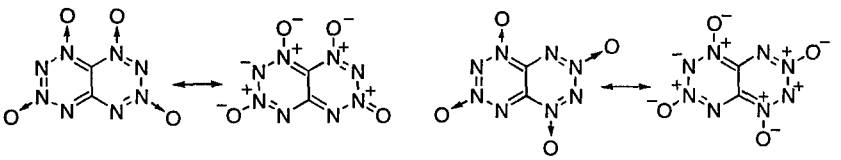

AC-compound **2a**
ΔH_f = 201.2 kcal/mol

non-AC-compound **2a'**
ΔH_f = 213.3 kcal/mol

Table 3. The population of AC-compounds.

run	parent hydrocarbons	AC-compounds
	aromatic HC	
1	 1	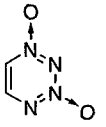 1a 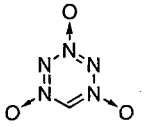 1b 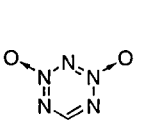 1c 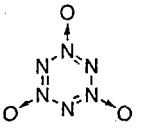 1d
2	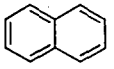 2	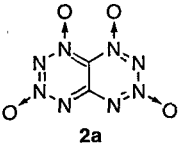 2a 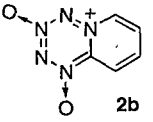 2b
3	 3	 3a 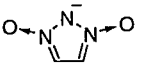 3b
	antiaromatic HC	
4	 4	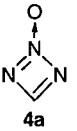 4a 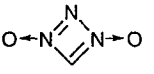 4b 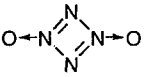 4c
5	 5	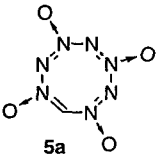 5a 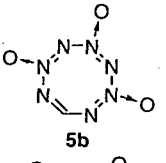 5b 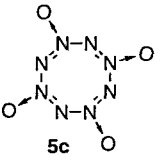 5c
6	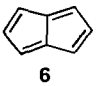 6	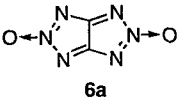 6a 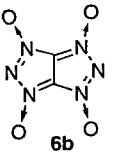 6b
7	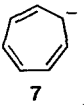 7	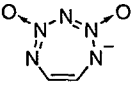 7a 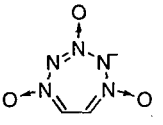 7b

Another characteristic property of AC-compounds is the specific π-electron shell of molecules, which can be readily considered in terms of MO theory. It can be demonstrated that the difference in starred and unstarred atoms in an alternant hydrocarbon is equal to the number of nonbonding MO [2]. Thus, dianion **A'** has one occupied antibonding MO, whereas isomer **A** has two occupied nonbonding MO, which is preferable. Obtained after isoelectronic replacement, neutral isoconjugate compounds **1a** has the electron shell similar to **A**. However, the higher occupied MO in **1a** is a bonding one, due to decrease in orbital energies which results from the distinct electronegativities of N atoms [2]. In other words, we have obtained a compound with a close shell. In the non-AC-isomer **1a'**, the decrease in orbital energies is much less prominent.

Figure 1. Orbital energies (a, b) in parent hydrocarbons; (c) in AC-compound; (d) in non-AC-compound.

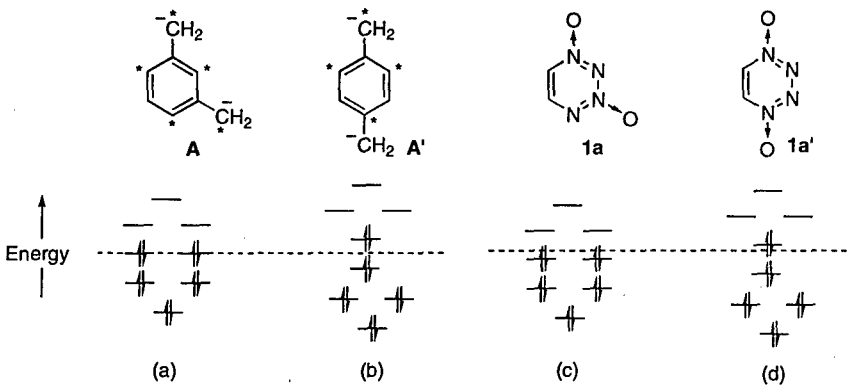

It can be demonstrated that the union of oxygen atom with an unstarred atom of a cycle (Table 2, step 4) always results in molecules with close electron shell.

One more peculiar feature of the AC-compounds structure is the absence of neighboring nitrogen atoms with lone electron pairs and, thus, the absence of destabilizing interaction of these pairs [3].

As the heat of formation is a 'summarizing' measure of the thermodynamic stability, it would be interesting to compare heats of formation of AC- and isomeric non-AC-compounds. For example, despite of the steric hindrance, AC-compound **2a** is more stable than its non-AC-isomer **2a'** ($\Delta\Delta H_f$ = 12.1 kcal/mol, see Scheme 1).

We certainly realize that the actual thermal stability of compounds depends primarily on the specific degradation pathway of a molecule. When comparing the possible decomposition path of AC-compound **1a** with those of its non-AC-isomers **8** and **9** (Scheme), it can be seen, that the latter two compounds have more favorable paths, then the former one. 1,4-Dioxide **8** can easily split off the N_2 molecule to give dinitrosoethylene, followed by furoxan formation. 2,3-Dioxide **9** can take part in ring–chain tautomerism to afford the reactive open-chain isomer **10**. The spatial arrangement of atoms in AC-compound **1a** (as well as in any other AC-compound) does not afford such types of facile decomposition or ring-chain tautomerism.

Scheme 2.

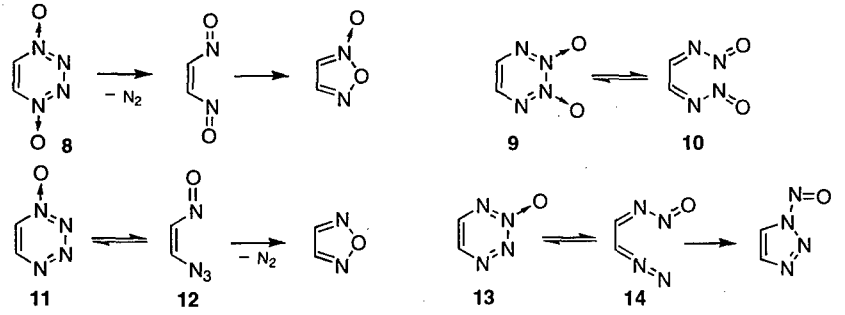

It is noteworthy, that 1,2,3,4-tetrazine mono-N-oxides **11** [4] and **13** cannot be regarded as true AC-compounds in our terms, because not all unstarred nitrogen atoms were united with oxygen atoms (see step 3, Table 2). In fact, both compounds can take part in ring-chain tautomerism to give the highly reactive isomers **12** and **14** followed by ring closure to yield furazan and nitrosotriazole respectively (Scheme 3).

The molecules shown in Table 3 were calculated by MNDO method with full geometry optimization [5]. The molecules obtained from aromatic hydrocarbons (e.g., **1a—d**, **2a,b**) exhibit cyclic delocalization of π-electrons, as expected.

The molecules **4a** and **4b**, resulted from antiaromatic cyclobutadiene, are also antiaromatic (i. e., there is a bond alternation in the cycle), but tetraazacyclobutadiene **4c** is a plane molecule with all cyclic bonds equal, e. i., the cyclic delocalization takes place. Thus, **4c** might by regarded as an aromatic compound. Similarly, molecules **5a—c** and **6a—b**, obtained from antiaromatic hydrocarbons, are also planar delocolized systems.

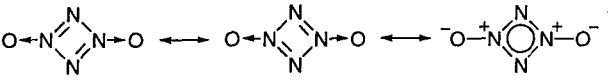

4c

The odd-numbered 6-π-electron (**3**) as well as 8-π-electron (**7**) cyclic anions give anions **3a,b** and **7a,b**, which are also planar systems with cyclic electron delocalization.

SYNTHESIS OF AC-COMPOUNDS

The synthetic approach to most of AC-compounds listed in Table 3, practically did not exist so far. Only a few examples of AC-cycles with three-nitrogen chain are known [1] . The method of N-oxidation is impractical, for the parent nitrogen heterocycles, as a rule, are either not available or not stable [1]. So, the idea was to fulfil ring closure of a chain which would already contain appropriate units.

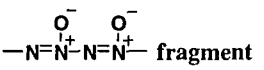

fragment

The most probable way to create the title fragment as part of a cycle, could be forming the N–N bond between two azoxy units. This might be carried out by means of intramolecular coupling of *tert*-butyl-*NNO*-azoxy moiety with diazonio-oxide cation in **B** (Scheme 3), followed by elimination of the *tert*-butyl cation from the intermediate cyclic cation **C**.

Scheme 3

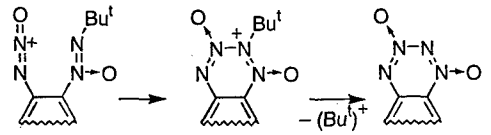

B **C**

The ability of the *tert*-butyl-*NNO*-azoxy group to react with electrofiles with the substitution of the *tert*-butyl group was demonstrated for the first time in the reaction of 1-aryl-2-*tert*-butyldiazene 1-oxides with nitronium cation to yield 1-aryl-2-nitrodiazene 1-oxides [7].

Very little is known about the second reactive fragment in Scheme 3, i. e., the diazonio-oxide cation -N=N=O$^+$ (see ref. [8] and references there). According to calculations [5], it could be rather stable when connected with aryl moiety. The central N atom should be more electrophilic, although the terminal N atom and the oxygen atom could be the electrophilic centers too.

We suggest two new methods for generation of diazonio-oxide cation. The first one (Scheme 4) involves the treatment of aromatic amines with nitrating agents to give nitramine **D**, and then dinitramine **E**. The latter could evidently exist as an equilibrium of covalent forms $\mathbf{E_1}$ and $\mathbf{E_3}$, and ionic form $\mathbf{E_2}$. Herein we propose another, unusual type of ionization of $\mathbf{E_3}$, resulting in diazonio-oxide cation and NO_3^- anion ($\mathbf{E_4}$) formation. This ionic equilibrium resembles ionization of N_2O_5 in polar solvents.

Scheme 4

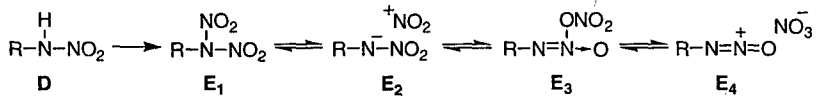

D **E_1** **E_2** **E_3** **E_4**

The second method (Scheme 5) involves the reaction of aryldiazonium cation with the anion of peracid to give the covalent azo compound $\mathbf{F_1}$, which could exist in equilibrium with its ionic form $\mathbf{F_2}$.

Scheme 5

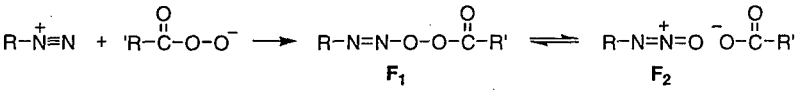

With the first method, 2-*tert*-butyl-NNO-azoxyanilines are the starting compounds for the synthesis of 1,2,3,4-tetrazine 1,3-dioxides fused to benzene ring (BTDOs). The treatment of **15** with excess N_2O_5 in organic solvent gave BTDO **17** along with 5-nitro- (**18**) , 7-nitro- (**19**) and 5,7-dinitro-BTDO **20**. On the first stage of this reaction nitramine **16** was formed. It was isolated when the reaction was carried out with one equiv. of N_2O_5. It was shown by the independent experiment that under reaction conditions BTDO **17** does not afford nitro BTDOs **18**—**20**, therefore the nitration of the benzene ring in nitramine **16** precedes the cyclization.

Scheme 6

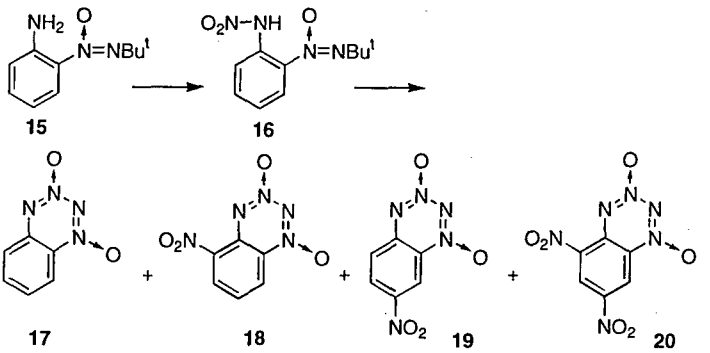

Thus, nitramine **16** undergoes two competitive reactions: *C*-nitration and ring closure. *C*-nitration is supposed to proceed *via* rearrangement of *N*-nitramines in acidic media (see below). The product ratio depends on the reaction conditions, particularly on the nitrating agent and the solvent used. The highest yield of **17** (66%) was reached with N_2O_5 in CH_3NO_2. The ring nitrated BTDOs are predominant in CH_2Cl_2 or in trifluoroacetic acid.

The cyclization of bromo-substituted 2-*tert*-butylazoxy anilines **21a—h** took place in practically similar conditions. Good yields (70—75%) were obtained for 6- and 7-substituted BTDOs **22a,b,f**, in which bromine atoms were removed from the reaction centers. When both *ortho* and *para* positions of aniline **21** were occupied by bromine atoms (as in **21d,h**), the ring nitrated BTDOs were not formed. In other cases the chromatography was used to remove these by-products.

Scheme 7

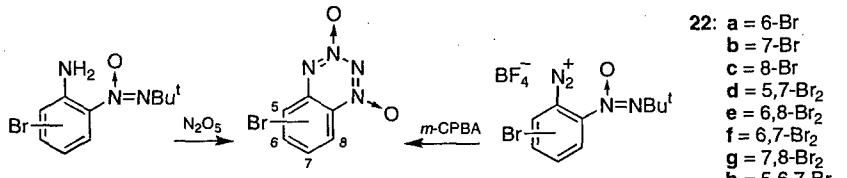

The starting compounds for the second method of BTDO synthesis are diazonium salts **23**, obtained by diazotization of 2-*tert*-butyl-*NNO*-azoxyanilines. The reaction of diazonium salts with *m*-chloroperbenzoic acid can be carried out in acetonitrile as a solvent in the presence of pyridine as a base [9]. The advantage of this method is the absence of nitrated by-products. In this case the yields are comparable to those of the nitration method.

The electrophilic and nucleophilic displacements in BTDO series were investigated. It was shown that in nitration and bromination reactions the positions of BTDO ring are arranged in order of decreasing reactivity almost without exception:

5>7>>8>6

The ring positions in nucleophilic displacement are arranged in the reverse order. Taking this into account, one could synthesize the BTDOs with different substituents. Some examples are given in Scheme 8.

Scheme 8

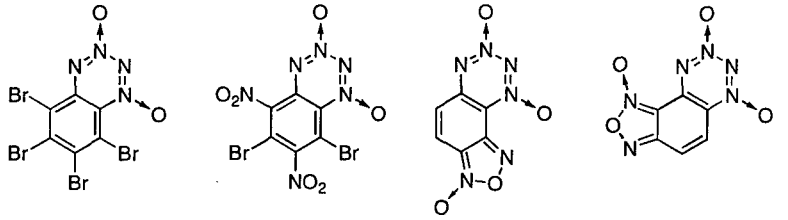

To determine the scope of reaction we endeavored to synthesize tetrazine dioxides fused to the furazan ring. It was found out that the treatment of 3-amino-4-*tert*-butylazoxyfurazan (**25**) with excess N_2O_5 gave 3-nitro-4-*tert*-butylazoxyfurazan (**26**) [8] as a main product (84%) instead of the expected [1,2,5]oxadiazolo[3,4-e][1,2,3,4]tetrazine 4,6-di-N-oxide (**24**). Nevertheless, the latter was obtained when amine **25** was treated with nitronium tetrafluoroborate [10].

Scheme 9

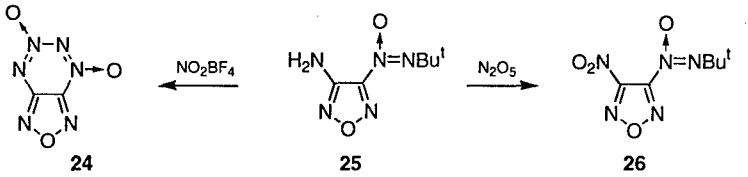

24 **25** **26**

In order to explain such a great difference between N_2O_5 and NO_2BF_4, we suggest that the ring formation is slowed down due to strained transition state of the cyclization reaction. Therefore, NO_3^- anion in $\mathbf{E_4}$ is captured by the terminal N-atom of $N{=}N{=}O^+$ cation to give unstable *O*-nitro-*N*-nitrosohydroxylamine $\mathbf{E_5}$. The latter loses N_2O_3 to give nitroso compound, which is oxidized to nitro compound with excess N_2O_5. When NO_2BF_4 is used, the exchange of ligands results in ionic pair **G**, which is electrophilic enough to react with *tert*-butylazoxy group to produce **24**.

Scheme 10

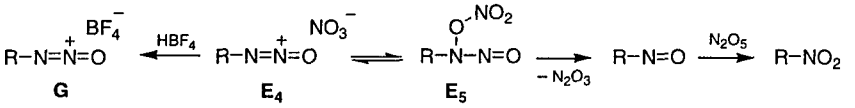

G $\mathbf{E_4}$ $\mathbf{E_5}$

Tetrazine dioxide **24** was obtained as yellow crystals (m.p. 110—112 °C, decomp.) which can be stored at room temperature. It is not as stable as benzo derivatives, but is much more stable than the very similar 2-phenyl-2*H*-[1,2,3]triazolo[4,5-e][1,2,3,4]-tetrazine [6], which does not bear *N*-oxide oxygen atoms.

fragment

The cyclic anion **28**, including the title fragment, was synthesized for the first time by removing the cyanoethyl group from compound **27a** when treated with a base [11]. The key stage in synthesis of the latter, as well as in that of the methyl derivative **27b**, was the intramolecular cyclization of the *N*-nitroso and the azido groups in **30**. The synthetic route involving the formation of the $N{=}N{=}O^+$ cation can also be applied. The treatment of aminofurazan **32** with nitronium tetrafluoroborate afforded **27b**, presumably via cyclization of intermediate **31** followed by loss of NO_2^+ cation. Unfortunately, the yield in this reaction is very low.

Scheme 11

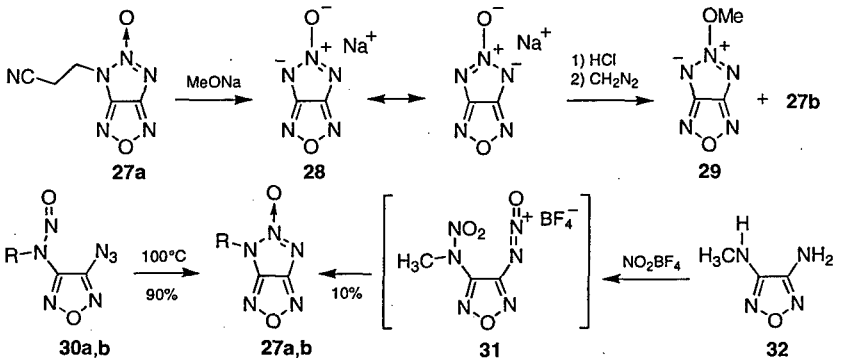

R = CH_2CH_2CN (**a**), Me (**b**)

The methylation of the acid, obtained by acidification of salt **28**, with diazomethane resulted in *N*-methylated (**27b**) and *O*-methylated compound **29**, the latter being predominant. This novel compound is the representative of one more type of AC-compounds.

fragment

The cyclic anion **36**, including the title fragment, was synthesized for the first time by the intramolecular reaction of the N=O group and *tert*-butylazoxy group in **33** [12].

Scheme 12

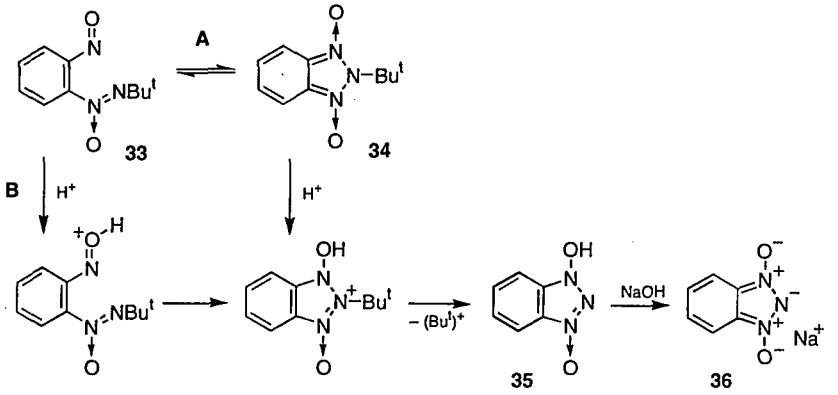

A priori this novel reaction could proceed by route **A** or **B** (Scheme 12). According to route **A**, nitroso compound **33** is supposed to be in equilibrium with cyclic 1,3-dioxide **34**. After protonation, the latter could eliminate *tert*-butyl cation, forming the acid **35**. According to route **B**, the protonation of nitroso compound **33** takes place first, facilitating the cyclization. Route **B** seems more probable because the signals of cyclic compound **34** were not observed in the NMR spectra of **33**.

REFERENCES AND NOTES

1. F. R. Benson. *The High Nitrogen Compounds*; John Wiley and Sons, Inc.: New York, 1984.
2. M. J. S. Dewar, R. C. Dougherty. *The PMO Theory of Organic Chemistry*; Plenum press: New York, 1975.
3. S. Inagaki, N. Goto. *J. Amer. Chem. Soc.*, 1987, **109**, 3234.

4. For decomposition of benzo-1,2,3,4-tetrazine 1-oxides see: A. M. Churakov, O. Yu. Smirnov, S. Yu. A. Strelenko, L. Ioffe, V. A. Tartakovsky, Yu. T. Struchkov, F. M. Dolgushin, A. I. Yanovsky. *Mendeleev Commun.*, 1996, 22.

5. K. I. Rezchikova, Churakov et. all. *Izv. Akad. Nauk, Ser. Khim.*, in preparation. The calculations of compounds **1d** and **4c** has been accomplished previously: (a). (at our request) M. N. Glukhovtsev, B. Ya. Simkin, V. I. Minkin. *Zh. Org. Khim.*, 1988, **24**, 2486; (b). E. G. Gal'pern, I. V. Stankevich, A. L. Chistiakov, V. B. Shur, M. E. Vol'pin. *Dokl. Akad. Nauk SSSR*, 1988, **302**, 1384. For calculations of **6a** see K. I. Rezchikova, A. M. Churakov, V. A. Shlyapochnikov, V. A. Tartakovsky. *Izv. Akad. Nauk SSSR, Ser. Khim.* 1991, 1825 (*Bull. Acad. Sci. USSR, Div. Chem. Sci.* 1991, **40**, 1615).

6. T. Kaihoh, T. Itoh, K. Yamaguchi, A. Ohsawa. *J. Chem. Soc., Perkin Trans. 1*, 1991, 2045.

7. A. M. Churakov, S. E. Semenov, S. L. Ioffe, Yu. A. Strelenko, V. A. Tartakovsky. *Izv. Akad. Nauk, Ser. Khim.*, 1997, 1081 (*Russ. Chem. Bull.*, 1997, **46**, 1042—1043).

8. A. M. Churakov, S. E. Semenov, S. L. Ioffe, Yu. A. Strelenko, V. A. Tartakovsky. *Mendeleev Commun.*, 1995, 102.

9. A. M. Churakov, S. L., Ioffe, Yu. A. Strelenko, V. A. Tartakovsky. *Izv. Akad. Nauk SSSR, Ser. Khim.* 1990, 718 (*Bull. Acad. Sci. USSR, Div. Chem. Sci.*, 1990, **39**, 639).

10. A. M. Churakov, S. L. Ioffe, V. A. Tartakovsky. *Mendeleev Commun.*, 1995, 227.

11. A. M. Churakov, S. L. Ioffe, Yu. A. Strelenko, V. A. Tartakovsky. *Tetrahedron Letters*, 1996, **37**, 8577.

12. E. T. Apasov, A. M. Churakov, Yu. A. Strelenko, S. L. Ioffe, V. A. Tartakovsky. *Tetrahedron*, 1995, **51**, 6775.

NITROLYSIS OF TAT AND DADN WITH N_2O_5/HNO_3: FORMATION OF α-HMX

Anthony J. Bellamy
Department of Environmental and Ordnance Systems,
Cranfield University/RMCS, Shrivenham, Swindon SN6 8LA, UK

Per Lagerkvist
Department XU, Bofors Explosives AB, S-69186 Karlskoga, Sweden

Abstract: Following the reports that nitrolysis of TAT using P_2O_5/HNO_3 gave impact insensitive α-HMX, we have investigated the nitrolysis of both TAT and DADN using N_2O_5/HNO_3. We found that pure α-HMX is only formed from TAT if some product, shown to be α-HMX, separates from the reaction mixture before quenching in water. If the reaction conditions are such that no product separates before quenching, even though nitrolysis is complete, then γ-HMX, as well as α-HMX, can be formed. In the case of DADN nitrolysis, pure α-HMX is only formed if some product separates before quenching **and** the reaction mixture contains more than a critical amount of acetyl nitrate. If product separates before quenching but insufficient acetyl nitrate is present, then the product isolated can be mixtures of α-, β- and γ-HMX. The yield of HMX from DADN was consistently higher than that from TAT. The isolated α-HMX was found to be somewhat less impact sensitive than α-HMX formed by recrystallisation, but significantly more impact sensitive than β-HMX.

The synthesis of HMX by nitrolysis of either TAT or DADN (see Scheme) has been widely studied [1]. However the more recent reports by W.Lukasavage et al [2a, 2b] that nitrolysis of TAT using P_2O_5/HNO_3 gave impact insensitive α-HMX (much less sensitive than β-HMX), prompted us to investigate the nitrolysis of both TAT and DADN using N_2O_5/HNO_3.

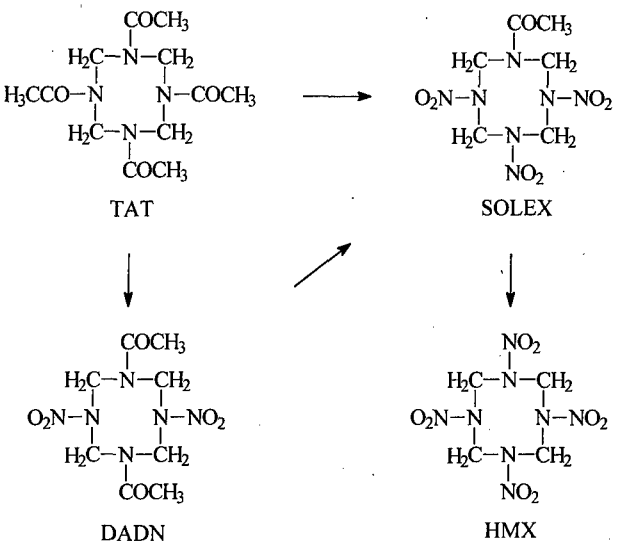

Scheme

The procedures reported by Lukasavage et al in the two patents differ in the quantity of HNO_3 used; the former [2a] uses 10g HNO_3/g TAT whilst the latter [2b] uses only 5g HNO_3/g TAT, with the same quantity of P_2O_5 (1.4g/g TAT) in each case. In repeating these procedures (Table 1) we observed that product only separated from the reaction mixture before quenching in water when the smaller ratio of HNO_3 was used. The product was found by HPLC analysis to be largely (84%) HMX contaminated with the mono-acetylated intermediate (SOLEX [2c], 15%).

In adopting the use of N_2O_5/HNO_3 instead of P_2O_5/HNO_3 we simplistically assumed that one P_2O_5 molecule is equivalent to three N_2O_5 molecules [3], and used 8.4mol N_2O_5/mol TAT instead of 2.8mol P_2O_5/mol TAT, with the same proportions of HNO_3. The first observation was that, as in the P_2O_5 systems, the product only separated before quenching if the lesser quantity of HNO_3 was used. Under the latter conditions the product began to separate after a few hours and was isolated after 24h by addition to water (see Table 2). It was identified by FTIR [4,5] (KBr disc, Figures 1a and 1b) and DSC [4]

as α-HMX , and was isolated in 70-80% yield (98-99% HMX by HPLC). The crystalline appearance (SEM) of authentic α-HMX (recrystallised from 70% HNO_3) and of the isolated α-HMX is shown in Figures 2a and 2b respectively. If the product was filtered off without quenching in water, the product was still α-HMX (Figure 2c) but a much reduced yield (42%) was obtained. This indicates that before quenching in water a significant proportion of the product is still in solution, and that this part is precipitated as α-HMX due to the presence of the α-HMX already separated. This observation led to further experiments in which a saturated solution of HMX in HNO_3 was added to a quenched N_2O_5/TAT reaction mixture, using the latter as a catalyst for the formation of larger amounts of α-HMX (see Table 3 and Figure 2d).

When DADN was used instead of TAT, with the quantity of N_2O_5 being reduced to allow for the reduced nitrolysis requirement, the HMX that was isolated on quenching in water was not pure α-HMX, even though HPLC indicated that the nitrolysis reaction was essentially complete (98+% HMX, 85-92% yield), and that in all cases product had separated before quenching. The crystalline form of the HMX isolated in these cases was unpredictable, the α-, β- and γ-forms all being observed (see Table 4). Pure α-HMX (77-80% yield) was however isolated if Ac_2O was added at the beginning of the nitrolysis. The Ac_2O was added to compensate for the reduced amount of acetyl nitrate that would be released on nitrolysis of DADN compared to TAT. Clearly this was necessary in order to control the crystallisation process. The yield of HMX, whether in the α-form or not, was generally higher when DADN was the starting material.

HPLC analysis of products isolated from TAT when reduced amounts of N_2O_5 and/or shorter reaction periods were employed, demonstrated that both DADN and the mono-acetyl derivative (SOLEX [2c]) are intermediates in the formation of HMX from TAT.

Rotter impact testing (5kg) of authentic α-HMX, and α-HMX isolated from the reactions described above, has demonstrated (Table 5) that the α-HMX isolated in this work is somewhat less sensitive than authentic (recrystallised) α-HMX, but, contrary to the results reported by Lukasavage et al [2b], significantly more sensitive than normal β-HMX.

References

1. V.I.Siele, M.Warman, J.Leccacorvi, R.W.Hutchinson, R.Motto, E.E.Gilbert, T.M.Benziger, M.D.Coburn, R.K.Rohwer and R.K.Davey, *Propellants and Explosives*, 1981, **6**, 67-73.
2. W.Lukasavage, S.Nicolich and J.Alster, (a) US 5 124 493 (June 1992), (b) US 5 268 469 (December 1993), (c) US 5 120 887 (June 1992).
3. J.W.Fischer in Nitro Compounds: Recent Advances in Synthesis and Chemistry, Ed. H.Feuer and A.T.Nielsen (VCH 1990), Ch 3, p268.
4. H.H.Licht, Symposium on the Chemical Problems connected with the Stability of Explosives, Tyringe, 1970, 168-179.
5. C.P.Achthan and C.I.Jose, *Propellants, Explosives, Pyrotechnics*, 1990, **15**, 271-275.

Table 1. Reaction of TAT with P_2O_5/HNO_3*

expt	TAT g	HNO_3 g/g TAT	P_2O_5 g/g TAT	yield g	notes
1	10.0	10.0	1.4	8.90 (85%)	reaction time 43h no product separation (α- + β-HMX)
2	10.0	5.0	1.4	7.11	reaction time 19h product separated (incomplete nitrolysis)

* Condition used in US 5 124 493 and 5 268 469 respectively

Table 2. Reaction of TAT with N_2O_5/HNO_3

Expt	TAT g	HNO_3 g/g TAT	N_2O_5* g/g TAT	yield g	notes
3	1.11	10.0	3.2	0.88 (76%)	reaction period 48h no product separation (mainly α-HMX)
4	1.14	10.0	3.2	0.97 (82%)	reaction period 45h no product separation (γ-HMX)
5	0.94	5.0	3.2	0.75 (77%)	reaction period 24h product separated (α-HMX - VMD 8μm)
6	1.00	5.0	3.2	0.73 (70%)	reaction period 24h product separated (α-HMX - VMD 11μm)
7	1.76	5.0	3.2	1.51 (82%)	reaction period 23h product separated (α-HMX – VMD 14μm)
8	2.12	5.0	3.2	1.07 (48%)	reaction period 23h product separated - filtered off without mixing with water, washed with water (α-HMX - VMD 12μm)
9	0.95	5.0	3.2	0.42 (42%)	reaction period 23h product separated - filtered off without mixing with water, not washed with water (α-HMX - VMD 16μm)
10	1.38	7.5	1.0	1.28	reaction period 6h no product separation (incomplete nitrolysis)

* 3.2g N_2O_5/g TAT ≡ 8.4mol N_2O_5/mol TAT

Table 3. Reaction of TAT with N_2O_5/HNO_3 followed by HMX/HNO_3 addition

expt	TAT g	HNO_3 g/g TAT	N_2O_5 g/g TAT	HMX g	HNO_3 g/g HMX	yield g	notes
11	1.08	5.0	3.2	1.13	7.4	1.96 (87%)	reaction period 24h *HMX-solution added to reaction mixture* - solid redissolved; HMX precipitated by addition to water (γ-HMX)
12	1.70	5.0	3.2	1.77	7.4	3.05 (86%)	reaction period 24h reaction mixture added to water, then HMX solution added to resultant mixture (α-HMX - VMD 13μm)
13	1.57	5.0	3.2	8.17	7.4	8.86 (90%)	reaction period 24h reaction mixture added to water, then HMX solution added to resultant mixture (α-HMX - VMD 24μm)

Table 4. Reaction of DADN with N_2O_5/HNO_3

expt	DADN g	HNO_3 g/g DADN	N_2O_5* g/g DADN	yield g	notes
14	0.77	4.8	2.4	0.67 (85%)	reaction period 23h product separated (β- + α-HMX)
15	1.04	4.8	2.4	0.98 (92%)	reaction period 24h seeded with α-HMX product separated (γ-HMX)
16	1.36	4.8	2.4	1.24 (89%)	reaction period 23h seeded with α-HMX product separated (β- + α- or γ-HMX)
17	0.99	4.8	2.4	0.78 (77%)	1 equiv Ac_2O added reaction period 24h product separated (α-HMX - VMD 10μm)
18	0.85	4.8	2.4	0.69 (80%)	1 equiv Ac_2O added reaction period 24h product separated (α-HMX - VMD 9μm)

* 2.4g N_2O_5/g DADN ≡ 6.4mol N_2O_5/mol DADN

Table 5. Rotter Impact Test Results (5kg)

Authentic α-HMX (VMD 80μm): Figure of Insensitiveness (F of I): <7*

α-HMX from reaction of TAT with N_2O_5/HNO_3

(i) quenched with water (VMD 14μm) : F of I : 17-23*

(ii) not quenched with water (VMD 12μm) : F of I : 13*

α-HMX from reaction of TAT with N_2O_5/HNO_3 followed by quenching with water, and then addition of HMX/HNO_3 (VMD 24μm) : F of I : 33-40*

α-HMX from reaction of DADN with $N_2O_5/Ac_2O/HNO_3$ followed by quenching with water (VMD 17μm) : F of I : 20-27*

* RDX = 80 (reference), β-HMX = 60, PETN = 50, lead azide = 30, lead styphnate = 20

Figure 1a. FTIR (KBr disc) of authentic α-HMX

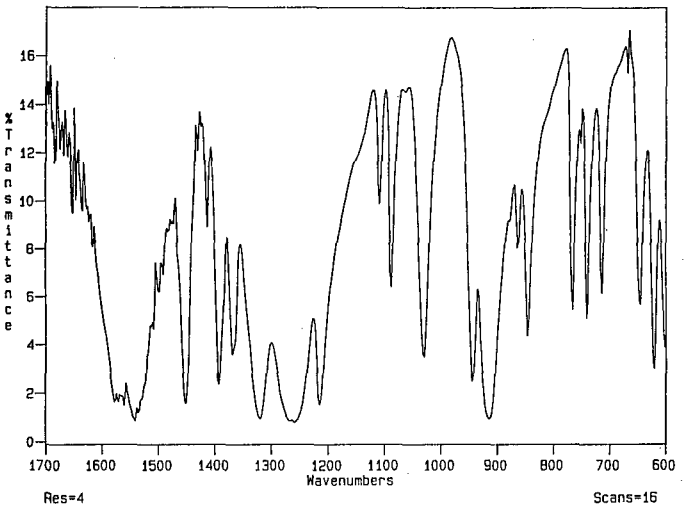

Figure 1b. FTIR (KBr disc) of HMX from TAT/N_2O_5/HNO_3

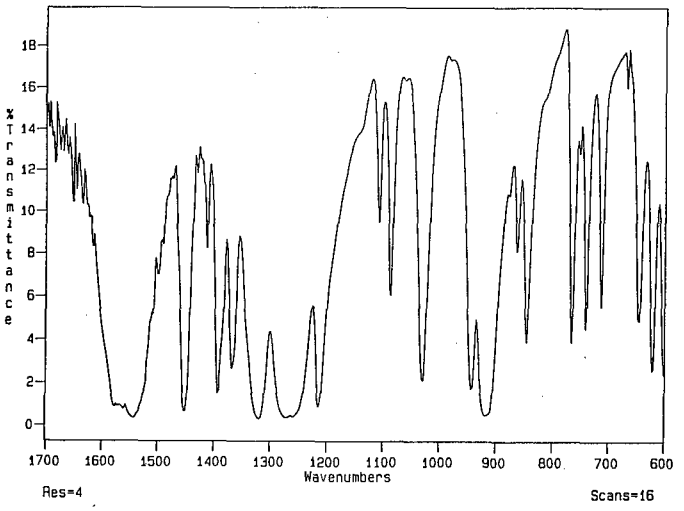

Figure 2a. Authentic α-HMX

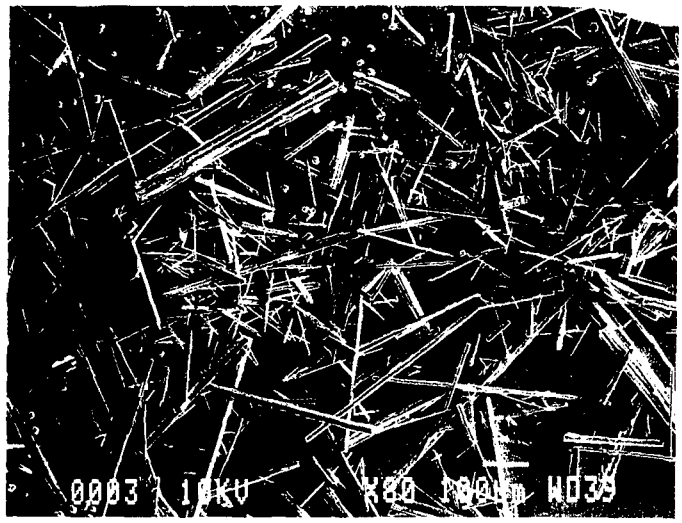

Figure 2b. HMX from TAT/N_2O_5/HNO_3 followed by addition to water

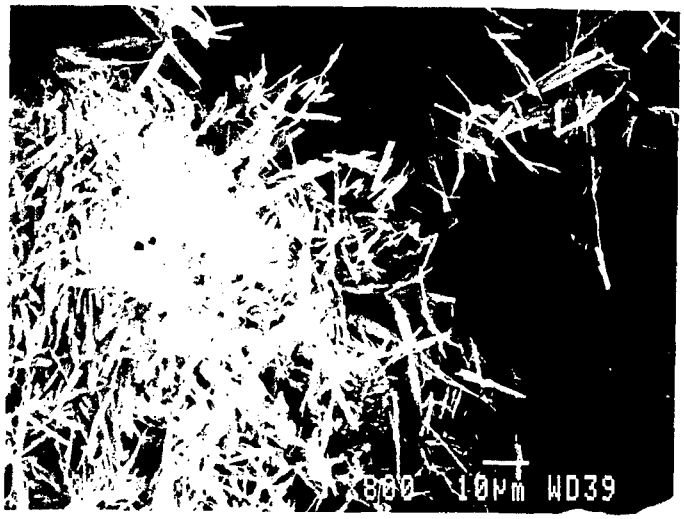

Figure 2c. HMX from TAT/N_2O_5/HNO_3 without contact with water

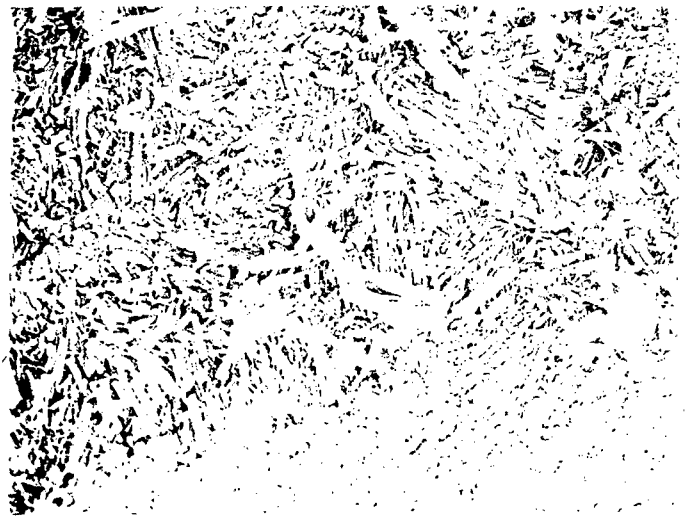

Figure 2d. HMX from TAT/N_2O_5/HNO_3 followed by (i) addition to water, and (ii) addition of HMX/HNO_3

NITRATIONS WITH N_2O_5, ANHYDROUS HNO_3 AND THEIR ADMIXTURES

George W. Nauflett, Robert E. Farncomb, Kurt F. Mueller
Indian Head Division, Naval Surface Warfare Center
Indian Head, Maryland 20640-5035

ABSTRACT

An energetic material synthesis and processing capability has been developed using carbon dioxide in its liquid and supercritical (L-CO_2/SC-CO_2) states as a reaction solvent. This is complimented by our use of newly developed nitration methodologies based on dinitrogen pentoxide, anhydrous nitric acid and their admixture which overcomes many of the drawbacks of conventional mixed acid (HNO_3/H_2SO_4) media. Essential to utilization of these new nitration methodologies is the novel equipment developed for energetic materials processing. Three multipurpose L-CO_2/SC-CO_2 bench scale process development units (PDU's) have been designed and constructed at the Naval Surface Warfare Center, Indian Head, MD for this purpose. In addition, a 100-liter pilot scale plant was developed on a Small Business Innovation Research (SBIR) Contract and will be used for inert L-CO_2/SC-CO_2 process research and development studies. Synthesis and processing in liquid carbon dioxide has been expanded and adapted at NSWC-IHD to include nitration of both liquids and solids. Further, in addition to our use of N_2O_5 generated by the large scale (380 g/h of N_2O_5) oxidation of dinitrogen tetroxide with ozone, we are investigating methods of preparing N_2O_5 by the dehydration of nitric acid with P_2O_5 and extracting it with L-CO_2. The use of L-CO_2 as a solvent for N_2O_5 and HNO_3 offers significant environmental benefits over conventional nitrating agents and the primary focus of this progress report is to elaborate on the development and demonstration of a unique energetic material synthesis and processing capability.

OBJECTIVE

Our principal objective is to develop and implement environmentally benign synthesis and processing methodologies for energetic materials manufacturing using L-CO_2/SC-CO_2 as the processing solvent. This includes the elimination of toxic solvents, volatile organic compounds (VOCs), and hazardous air pollutants (HAPs) during processing.

BACKGROUND

O-Nitration of alcohols is carried out classically with nitric acid alone, or more frequently with mixed acid (mixtures of nitric and sulfuric acid). Selective nitration of materials with acid-sensitive moieties are commonly performed with N_2O_5 at low temperature in halogenated solvents[1]. Even though the use of N_2O_5 in L-CO_2 as nitrating agent is clean, versatile and offers significant environmental benefits, no nitrations using N_2O_5, anhydrous HNO_3 and their admixture in L-CO_2 were previously reported. The primary reason for the lack of progress in the area of L-CO_2 synthesis and processing is that the required equipment has not been commercially available and it is very expensive. The use of N_2O_5, anhydrous HNO_3 and CO_2 require special handling techniques. NSWC-IHD researchers began processing energetic materials in carbon dioxide in its liquid and supercritical states in the early 1980's[2,3]. The initial work was limited to analysis and characterization of energetics that were manipulated using supercritical carbon dioxide. Development of low cost novel SC-CO_2 synthesis and processing equipment was funded by the Small Business Innovation Research Program (SBIR)[3].

Use of liquid carbon dioxide for processing is least developed among the four physical states of CO_2, and it has almost exclusively been used in the beverage and fire-fighting industries. Only within the last few years has it been recognized as a useful processing solvent. Its properties are shown in Figure 1. Use of carbon dioxide in its liquid and supercritical states for the synthesis and processing of polymers for commercial use is seen as an area of unlimited potential and has attracted intense interest within the research and development community. In fact, a research team lead by Professor Joseph M. DeSimone at the University of North Carolina, Chapel Hill, has developed fluorinated surfactants that allow for optimization of the polymers' properties during their synthesis[4,5]. Further, these fluorinated surfactants have also been demonstrated to be useful for the dry cleaning of clothing.

Carbon dioxide exists as a liquid at 5 to 73 atm. (75 to 1070 psi) and -75 to 30 °C, respectively. Its critical temperature (T_C) is 31.1 °C and critical pressure (P_C) is 73 atm. (1074 psi) as shown in Figure 1.

Both N_2O_5 and anhydrous HNO_3 are soluble in L-CO_2 which allows them to be added directly to the substrate being nitrated. Shown in Figure 2 is a diagram of a bench scale PDU used for synthesis and processing of up to 300 grams of energetic materials. Shown in Figure 3 is a diagram of the Center's Pilot Scale Facility currently being developed for the manufacture and processing of 0.5 to 12 kg of energetic materials.

Dinitrogen pentoxide (N_2O_5), was prepared by dehydrating anhydrous nitric acid (HNO_3) with phosphorous pentoxide[6] as shown in eq 1, or by direct ozonolysis of dinitrogen tetroxide[7,8] as shown in eq 2.

$$6\ HNO_3 + P_2O_5 \longrightarrow 3\ N_2O_5 + 2\ H_3PO_4 \qquad (1)$$

$$N_2O4 + O_3 \longrightarrow N_2O_5 + O_2 \qquad (2)$$

The yields for both these reactions are at the 90% level or better. Pure N_2O_5 is a white, thermally labile, crystalline solid. In the pure solid state, N_2O_5 exhibits a half-life of 10 days at 0 °C and 10 hours at 20 °C. The solid readily sublimes, having a vapor pressure of 51 mm at 0 °C, 200 mm at 20 °C, and one atmosphere at 32.5 °C. The chemical properties pure nitric acid are: sp gr 1.51; mp -41.6 °C; bp 86 °C. The apparatus shown in Figure 4 was designed and constructed for the preparation of N_2O_5 and shown in eq 1. It is anticipated that the N_2O_5 can be extracted with L-CO_2, since nitric acid and P_2O_5 have little to no solubility in L-CO_2 at O °C, respectively. Thus we are currently investigating this process. Shown in Figure 5 and 6 are diagrams of apparatus for nitration of liquids and solids with N_2O_5, HNO_3 and their admixtures. A Navy Patent disclosure has been submitted which covers the nitrations of various substrates, including polyols in L-CO_2 with N_2O_5, anhydrous HNO_3 and its admixtures[9].

APPROACH

Carbon dioxide in its gaseous, liquid, solid and supercritical states has been used industrially for several decades. The equipment used for industrial L-CO_2/SC-CO_2 applications is not suitable for energetic material synthesis and processing. The approach chosen was to design, and construct multipurpose L-CO_2/SC-CO_2 process development units for use with energetic materials and to develop those PDU's with the following capabilities:

- Laboratory processing units ~ 1 to 500-mL vessels

- Bench scale processing units ~ 500 to 3,000-mL vessels
- Pilot scale processing units ~ 3 to 100-liter vessels

The vessel sizes for the Laboratory/Bench scale and pilot scale designation were based on engineering and handling considerations. The pumping capacity of the Thar Design P-200 pump is 200 grams of L-CO_2/min, the largest vessel recommended for this pump is 3-liters. Shown in Table 1 are the weight of various vessels and their tops.

Table 1. Thar Design, Inc. Vessel

Vessel i.d. cm	Vol Range	Vessel vol Liter	Vessel wt kg	Top wt kg
2	3 - 50-mL	0.01	0.5	0.1
3	75 - 150-mL	0.1	3.0	0.4
5.4	250 - 750-mL	0.5	6.6	1.1
7.6	0.75 - 2-L	1	15.8	3
10.1	2 - 7.5-L	2.5	45.5	7
15.0	5 - 15-L	16	159	23
20.3	8 - 100-L	100	909	39
40.6	100 - 500-L	300	2,700	181
61	400 - 1,000-L	-	-	400

DEVELOPMENT OF A L-CO_2/SC-CO_2 SYNTHESIS AND PROCESSING CAPABILITY

Considerable attention has been focused on the development of the specialized equipment required to conduct synthesis and processing of energetic materials in liquid and supercritical carbon dioxide. Three modular, multipurpose bench scale L-CO_2 process units were designed and built. The first PDU was painstakingly constructed about ten years ago from components parts from about forty different companies.

The first PDU was implemented with vessels, pumps, valves and fittings made by Autoclave Engineers of Erie, PA, Newport Scientific, Inc. of Jessup, MD, and Fluidtron Inc. of Ivyland, PA. The vessels were very heavy and they were time consuming to open and close. The Newport Scientific compressors, was designed for gaseous nitrogen instead liquid CO_2. The vessels and pumps used in the second and third PDUs, were designed and

built using newly developed equipment from Thar Design, Inc. Pittsburgh, PA. Shown in Table 2 is a list of equipment developed by Thar Design Inc. on a NSWC-IHD phase I & II SBIR contract.

The Thar Design pumps are environmentally benign, containing no oil, pulseless with spring-load Teflon cup seals and special coating for long life. The vessel closure has finger-tight threads (no nuts and bolts). NSWC/IHD received the prototype of each of the items listed in Table 2. The L-CO_2 pump, back pressure regulator, and agitator have been upgraded.

Table 2. Thar Design, Inc. Equipment

- extraction vessels (ranging from 1-mL to 100-liter)
- agitators
- computer controlled L-CO_2 pumps (0.2 and 1 kg/min of L-CO_2)
- cyclone separators
- heat exchangers
- electronic flow meters
- computer controlled back pressure regulators
- PC Control and Software
- Pilot scale, 100 liter plant

The 100 liter L-CO_2/SC-CO_2 pilot plant developed by Thar Design has was recently shipped to Indian Head and is currently being assembled. Plans are being made to transition the SBIR Program to a Phase II add-on for the establishment of a 0.5 to 12 kg energetic materials synthesis and processing facility shown in Figure 3.

EXPERIMENTAL

1. Nitration of a liquid using N_2O_5 in L-CO_2

Preparation of Nitratomethyl methyl oxetane (NMMO)

The equipment used in this study is shown in Figure 5. It consists of a 600-mL pressure vessel equipped with a jacket, a thermocouple, rupture disk, an addition pump, and an agitator (sapphire coated agitator shaft with two impellers blades). The gases exiting the vessel passed through a valve,

product collection U-tube, a U-tube containing sodium carbonate (N_2O_5 trap), a flowmeter, and is vented to a hood.

Solid N_2O_5 (11.3 g, 0.104 mol) was added to the nitration vessel, and the temperature was lowered to 3 °C by circulating ice water through the jacket. At a pressure of 170 atm, 3-hydroxymethyl-3-methyl oxetane (3M3OM; 9.5 g, 0.094 mol) of was pumped into the vessel at 0.5 mL/min. at 2 ± 0.5 °C, while agitating at 250 rpm. The resulting NMMO was removed from the reaction vessel with SC-CO_2. The yield of NMMO was calcd 97% (based on NMMO MW), and was found to contain ca. 2% of a mixture of dimers and trimers.

2. Nitration of a solid using N_2O_5/L-CO_2

Preparation of γ-Cyclodextrim Nitrate (γCDN)

The equipment used in this study is shown in Figure 6. It consists of a 600-mL pressure vessel equipped as in experiment as above, but containing the substrate. An additional 60-mL reaction vessel was used which contained the nitrating mixture. In this experiment no addition pump was used.

(γ-Cyclodextrin (γCD) is a macrocycle containing eight glucose residues connected via alpha 1,4- glycosidic linkages. It has a molecular weight of 1297 and has 24 hydroxyl groups.)

γCD (20 g, 0.015 moles) was added to the 600-mL vessel. N_2O_5 (44 g, 0.407 moles, 10 mole % excess) was added to the 60-mL vessel. The agitator was turned on and carbon dioxide was slowly added to both vessels until the pressure was 68 atm (1,000 psi). The -25 °C cooling fluid was pumped through the jackets of both vessels. The 600-mL vessel's CO_2 addition valve was closed and the valve between the two vessels was opened. For 145 minutes, 1.4 grams of CO_2/minute was passed through the two vessels. The temperature was -5+0.2 °C. The pressure was slowly released and the product was poured into a 2-L beaker containing sodium bicarbonate (80 g, 0.95 moles) and water (1 L). The pressure vessel was rinsed with additional water (ca. 700 mL). The mixture was filtered and the γCDN was washed twice with water (1.7 L). The yield of γCDN was 91% (26.5 g) and the nitrogen content was 13.5%. The DSC had an exotherm (3,090 joules/g) at 192 °C.

3. Nitration of 3M3OM with Anhydrous HNO_3 in L-CO_2

The equipment used in this study is shown in Figure 5. Anhydrous nitric acid, (41 g, 0.65 mol, 20% excess) was added to the 600-mL vessel. Carbon dioxide was added with cooling until the pressure was 68 atm (1,000 psi) at

-5 °C. With the agitator turning at 170 rpm, poly-3-hydroxymethyl-3-methyl oxetane (55 g, 0.54 moles) was pumped into the nitration vessel at 1 mL/min. At end of the addition the pressure was 163 atm (2,400 psi) and the temperature was -3 °C. The pressure was released and extra carbon dioxide was added to flush the oxides of nitrogen from the product. (The equipment was modified, the bottom outlet valve was connected to a 500-mL 2-neck flask, and 10 atm carbon dioxide added to the top. The product was transferred to the 500-mL 2-neck flask by opening the bottom outlet valve with the vessel under 10 atm. The NMMO was washed with 8% sodium bicarbonate solution, water, and was dried. A yield of 57 g of a brown viscous oil was obtained (calcd 72% based on NMMO MW).

RESULTS

NIMMO and γCDN

The monomer, 3-methyl-3-oxetane-methanol were separately nitrated with dinitrogen pentoxide (N_2O_5)[10], anhydrous HNO_3 and also an admixture of N_2O_5 and HNO_3 as shown in eq 3 using L-CO_2 as the processing solvent producing the monomer 3-nitratomethyl-3-methyl oxetane (NIMMO). The corresponding nitration of γCD produced γCDN.

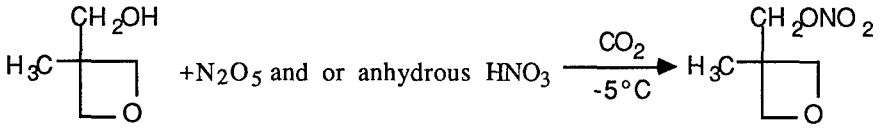

(3)

3-methyl-3-oxetane-methanol

3-nitratomethyl-3-methyl oxetane (NIMMO).

O-Nitration with mixture of N_2O_5 and and anhydrous nitric acid was successfully demonstrated on a starting material.

A black coating formed on the 316 stainless steel parts the first time the equipment was used for N_2O_5 nitration in L-CO_2 and the 17-4-PH stainless steel parts remained unchanged.

The Thar Design carbon dioxide extraction and processing equipment listed in Table 2 has been tested and evaluated at NSWC/IHD and in private industry for about five years, and its performance has been excellent.

CONCLUSION

It has been successfully demonstrated that the L-CO_2/SC-CO_2 PDU's constructed for the synthesis and processing of energetic materials function as designed. This equipment has been found to have a variety applications in the synthesis and processing of various energetic materials. O-Nitrations of liquids and solids were successfully performed using N_2O_5 anhydrous HNO_3 and their admixtures. Carbon dioxide replaced halogenated solvents as the processing solvent in the nitrations.

ACKNOWLEDGMENTS

The financial support and the technical advice provided by Steve Mitchell NSWC/IHD, is gratefully acknowledged. We thank Tom Devendorf, Horst Adolph, and Al Stern, for technical discussions.

REFERENCES

[1]Millar, R.W.; Colclough, M.E.; Desai, H.; Golding, P.; Honey, P.J.; Paul, N.C.; Sanderson, A.J.; Stewart, M.J., "Novel Syntheses of Energetic Materials Using Dinitrogen Pentoxide"; *Nitration Recent Laboratory and Industrial Development* ; Albright, L.F.; Carr, R.V.C.; Schmitt, R.J., Eds.; ACS Symposium Series 623, 1996, pp 104-121.

[2]Nauflett, G. W. and Farncomb, R.E., Processing of Energetic Materials with Supercritical Fluids, CPIA Publication 588; 14 Aug 92; pp 417-435.

[3]Farncomb, R.E.; Nauflett, G. W.; Fauth, M. I.; "Energetic Materials Processing Using Supercritical Carbon Dioxide", CPIA-PUB-634; 4-8 Dec 95; pp 397-404.

[4]DeSimone, J.M.; Maury, E.E.; Menceloglu,Y.Z.; McClain, J.B.; Romack, T.J; Combes, J.R., "Dispersion Polymerizations in Supercritical Carbon Dioxide", Science (Washington, DC), Vol 265, 15 July 1994, pp 356-359.

[5]Farncomb, R.E.; Nauflett, "Development of Procedure for Degreasing of Shipyard Parts", Proceedings of Energetic Materials Technology of American Defense Preparedness Association, 24 March 1994.

[6]Caesar, G.V.; Goldfrank, M., "Nitration of Starches with Nitrogen Pentoxide in Presence of Sodium Fluoride", J. ACS, Vol 68, 1946, pp 372-375.

[7]Devendorf, T.E. and Stacy, J.R., "Pilot-Plant-Scale Continuous Manufacture of Solid Dinitrogen Pentoxide"; *Nitration Recent Laboratory and Industrial Development* ; Albright, L.F.; Carr, R.V.C.; Schmitt, R.J., Eds.; ACS Symposium Series 623, 1996, pp 68-77.

[8]Fischer, J.W., "The Chemistry of Dinitrogen Pentoxide," *Nitro Compounds: Recent Advances in Synthesis and Chemistry*; Feuer, H.; Nielson, A.T., Eds.; VCH Publishers, Inc., NY, 1990; pp 267-365

[9]Nauflett, G.W., Farncomb, R.E., Patent Disclosure Navy Case No. 79,009.

[10]Farncomb, R.E.; Nauflett, G. W.; Innovative Polymer Processing in Carbon Dioxide, Waste Management, Vol 17, No 2/3, Feb 98; pp

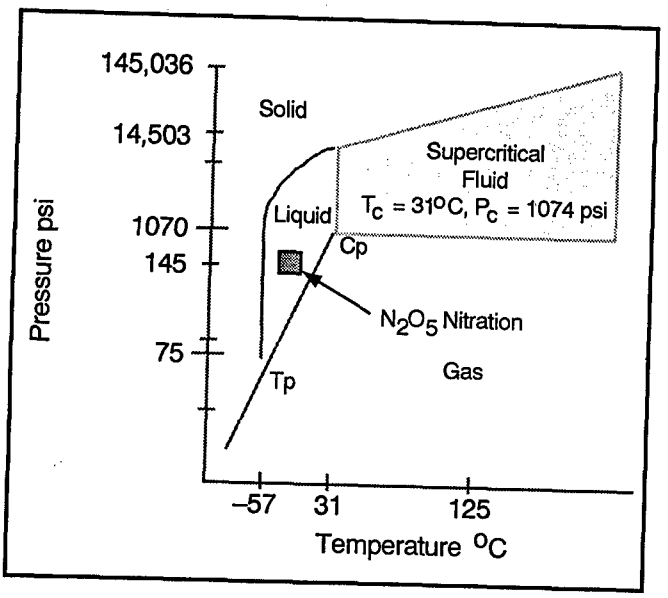

$L\text{-}CO_2$ Properties
Density 0.7 to 1.2 g/mL
t, 10 to 30°C and
p, 800 to 1,050 psi

44 g $L\text{-}CO_2$ = 55 mL (0.8 g/mL)
44 g $G\text{-}CO_2$ = 22,400 mL (STP)

Figure 1. Carbon Dioxide Phase Diagram

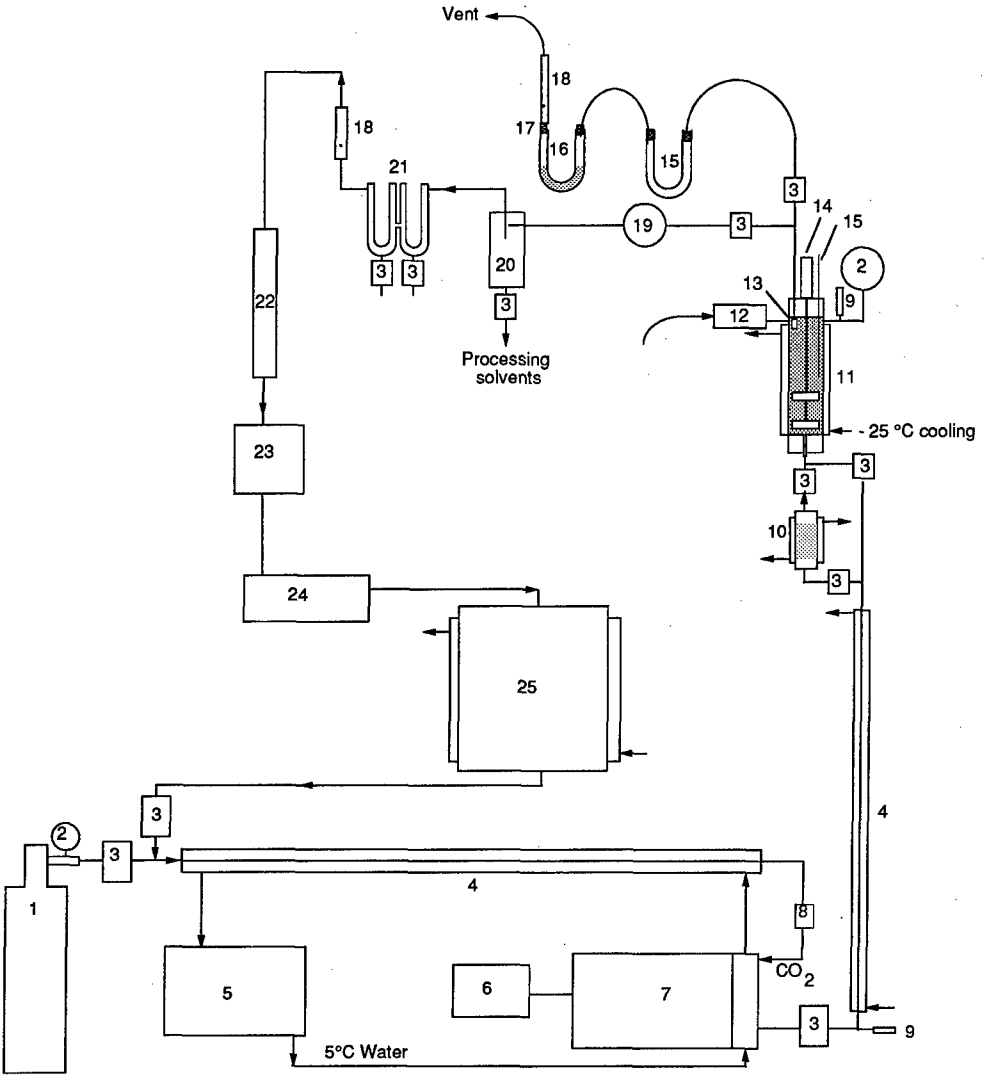

(1) CO_2 cylinder; (2) pressure gauge; (3) valve; (4) heat exchanger (concentric 1/8 and 3/8 inch tubing); (5) water chiller with recirculating pump; (6) computer pump controller; (7) high pressure pump (0 to 200 g CO_2/min); (8) 5µm filter; (9) rupture disk; (10) 100-mL pressure vessel with jacket; (11) 600-mL has three side Inlets (inlet for additions, rupture disk, pressure gauge); (12) addition pump (0 to 40 mL/min); (13) filter; (14) air motor with tachometer and agitator; (15) thermocouple; (15) U-tube; (16) U-tube containing sodium carbonate; (17) rubber stopper; (18) flowmeter; (19) heated depressurization ; (20) cyclone separator; (21) Dry Ice trap; (22) carbon dioxide purification; (23) flowtotalizer (24) compressor; (8-liter carbon dioxide storage.

Figure 2. Bench Scale Carbon Dioxide Synthesis and Processing System

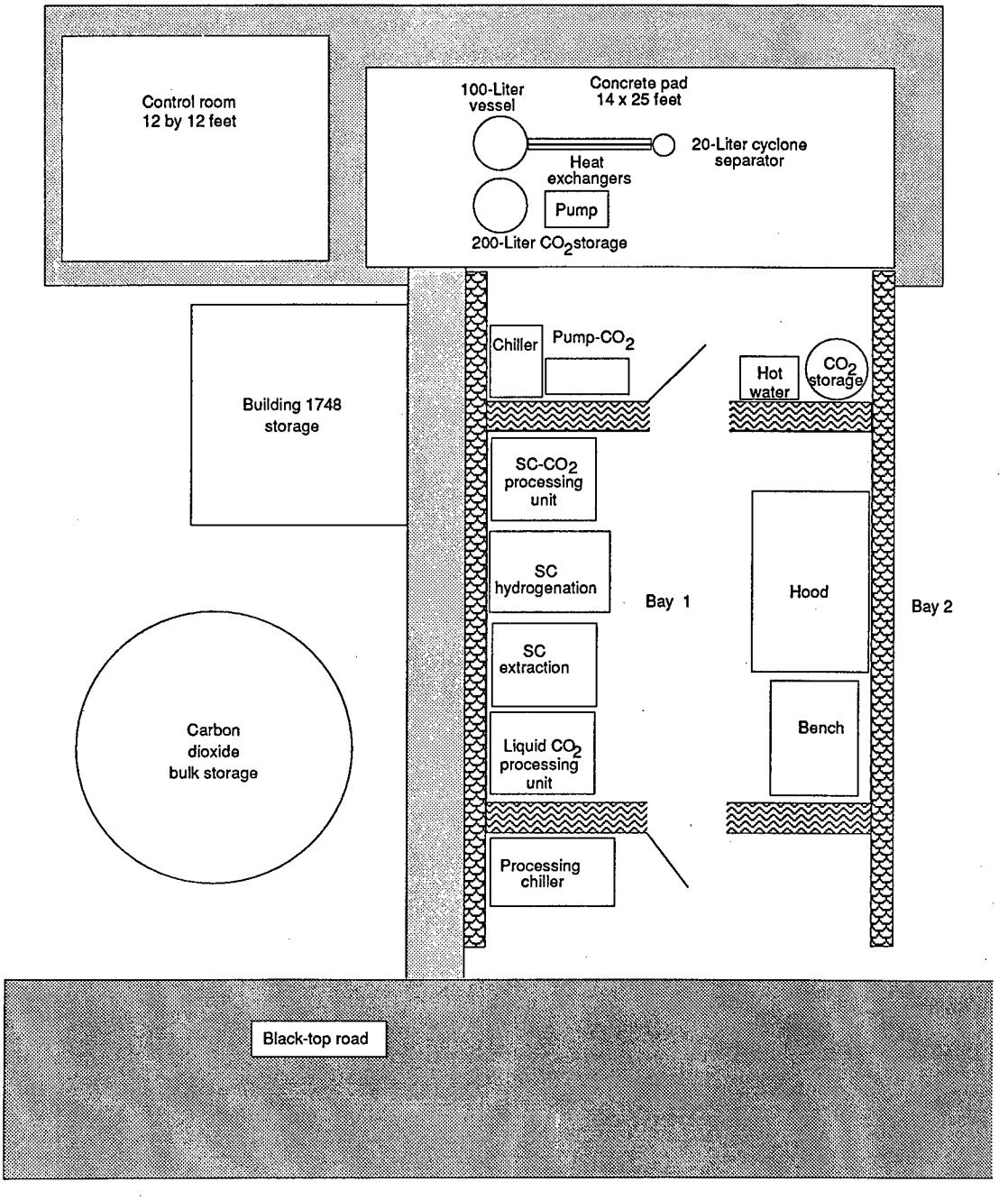

Figure 3. Building 742 Carbon Dioxide Processing Facility

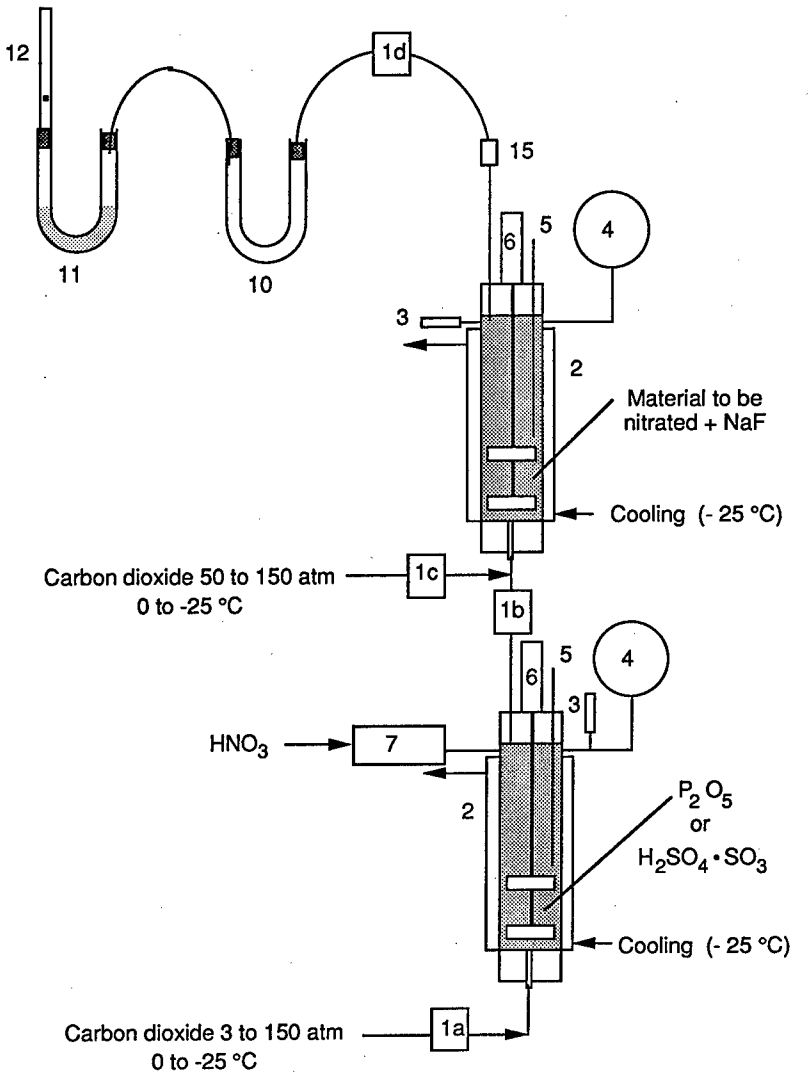

(1) Valves (1a) CO_2 addition to lower vessel; (1b) connecting two vessels; (1c) CO_2 addition to upper vessel ; (1d) pressure release; (2) 600-mL pressure vessel with jacket; (3) rupture disk; (4) pressure gauge; (5) thermocouple; (6) air motor with tachometer; (7) pump; (10) U-tube; (11) U-tube containing sodium carbonate; (12) flowmeter; (15) union.

Figure 4. Preparation of N_2O_5 and L-CO_2 Extraction with Subsequent Nitration

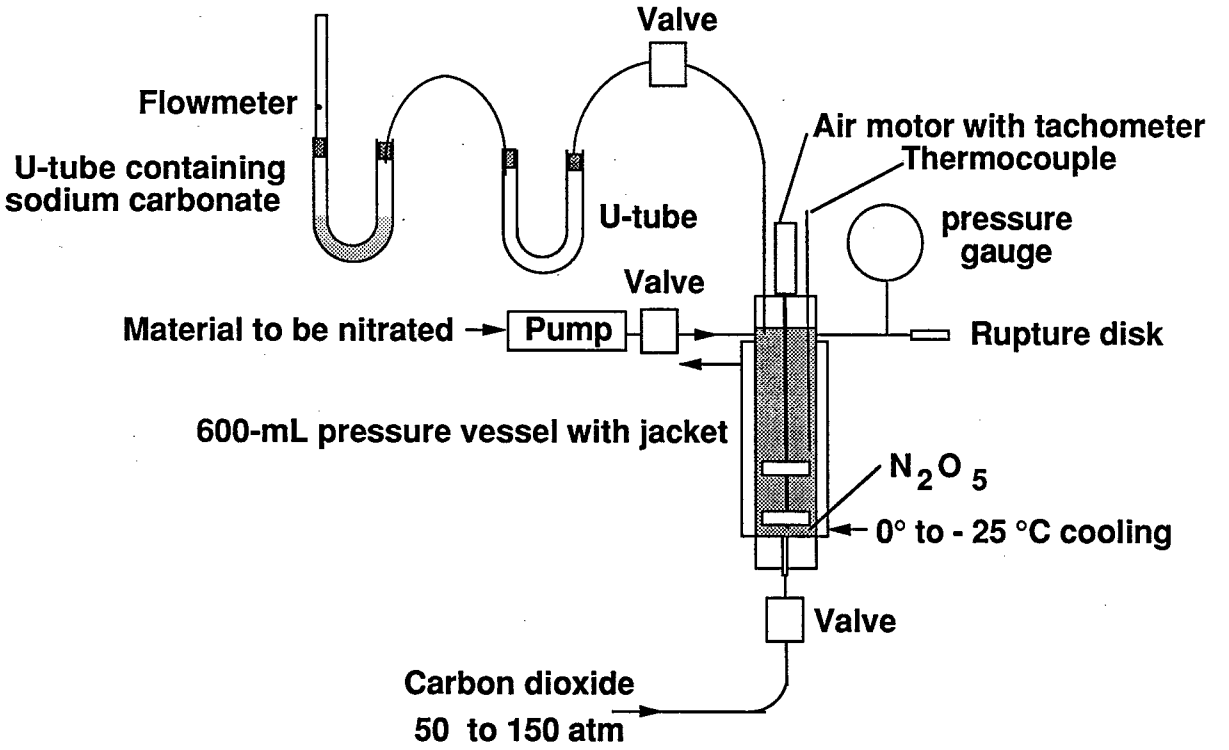

Figure 5. Nitration of Liquids in L-CO_2 with N_2O_5

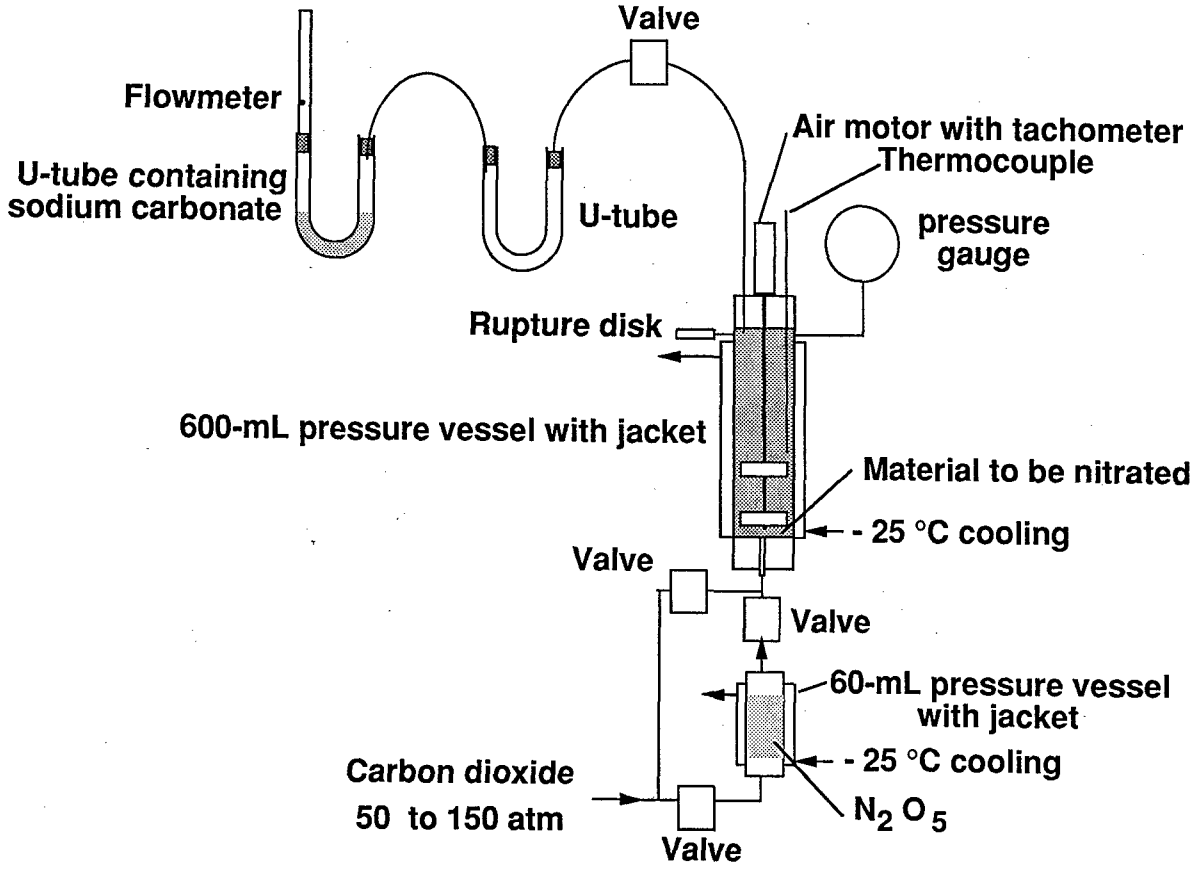

Figure 6. Nitration of Solids in L-CO_2 with N_2O_5

SYNTHESIS AND THERMOCHEMISTRY OF DIAZIRIDINES

Nina N.Makhova, Vera Yu.Petukhova, Vladimir V.Kuznetsov and Lenor I.Khmel'nitskii[✞]

N.D.Zelinsky Institute of Organic Chemistry Russian Academy of Sciences, Leninsky pr. 47, 117913 Moscow, Russian Federation.

Fax: *7-095-135-5328,* ***E-mail****: mnn@cacr.ioc.ac.ru*

Vyacheslav P.Lebedev and Vitally I.Pepekin

N.N.Semenov Institute of Chemical Physics Russian Academy of Sciences, Kosygin str. 4, Moscow, Russian Federation.

Fax: *7-095-137-8297;* ***E-mail****: krupkin@chph.ras.ru*

ABSTRACT

This work includes synthesis and study of thermochemical and some other properties of diaziridines. Different methods for the preparation of alkylic and functional derivatives of diaziridines were develop, in particular, interaction of aldoxime-O-sulfonic acids and other oxime esters with primary aliphatic amines and ammonia along with the most feasible one-step method from carbonyl compounds, amines and aminating reagents in water at controlled values of medium pH. Alkylation and aminomethylation reactions of NH-groups of diaziridines were also

studied. As a result of these investigations the wide series *of compounds with one, two and three diaziridine cycle as well as fused diaziridine-containing systems were synthesized. Among diaziridines obtained, there are structures with the enthalpy formation of more than 1000 Kcal/kg. The combustion and formation enthalpies of a series of model diaziridines were determined by the method of energy measurement in a calorimetric bomb. On the basis of the obtained thermochemical data, diaziridine cycle strain energy was estimated as 16-22 Kcal/mol. An additive-group method was developed for calculating of thermochemical characteristics of diaziridines. The enthalpy of formation and density were calculated for the series both obtained and hypothetic diaziridine structures.*

INTRODUCTION

Diaziridines (cyclic hydrazines) - saturated three-member heterocycles with two nitrogen atoms, were discovered about **30** years ago and since then their chemistry has rapidly developed. In the 60-70s, the most important contribution in this field was made by German chemist Ernst Schmidt [1,2]. Later, other chemists studied these compounds and several reviews were published [3,4]. Schmitz offered several approaches to their preparation, showed that diaziridines were rather stable compounds and found that they were very convenient precursors for the preparation of both unsubstituted and mono- and N,N'-dialkyl hydrazines [5]. The synthesis of hydrazine over diaziridine derivatives is more effective than the Raschig one. The undoubted advantage of diaziridines is their rather feasible synthesis from accessible initial compounds. Yet the known methods allowed to obtain only the simplest types of diaziridine derivatives. Meanwhile it was possible to foresee the high enthalpy of formation of this class compounds as a result of contributions from both the hydrazine fragment and three-member strained cycle and, in this connection, a possibility to prepare energetic materials on their basis. The present work deals with the elaboration of new, common methods for the synthesis and chemical transformation of diaziridines and the study on their thermochemical and some other physico-chemical properties.

SYNTHESIS

The formation of the diaziridine cycle is based on the intramolecular cyclization of N-X-aminal **1**, which can be theoretically obtained through one of three ways: 1) by mixing of three components (primary aliphatic amines or ammonia, carbonyl compounds and aminating reagents), 2) by the interaction of imines (reaction products of carbonyl compounds and amines) with aminating reagents and 3) by the interaction of primary aliphatic amines or ammonia with reaction products of carbonyl compounds and aminating reagents (N-chloroamines or oxime esters) (Scheme 1).

Scheme 1

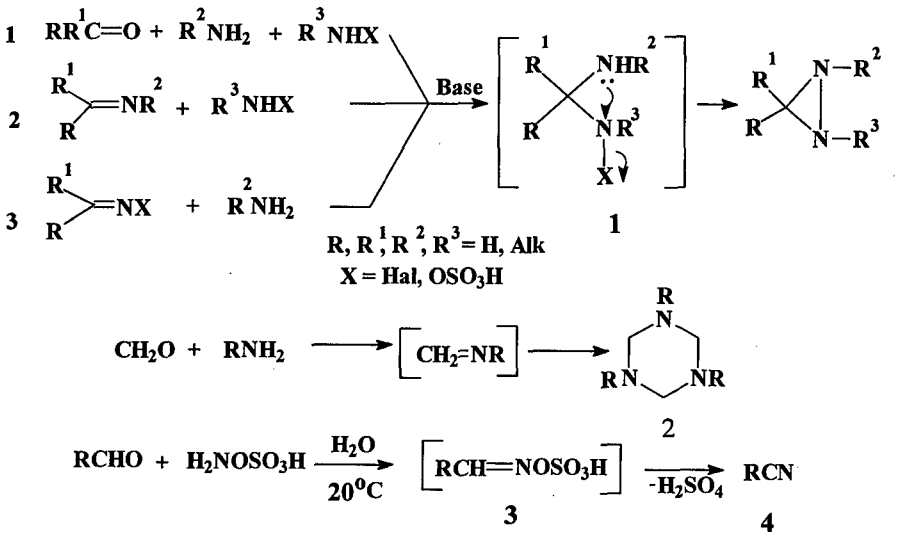

Though not all initial compounds can enter in these three reactions. For example, the interaction of formaldehyde and primary aliphatic amines leads to hexahydrotriazines **2** instead of corresponding imines and interaction of aliphatic aldehydes with hydroxylamine-O-sulfonic acid gives nitriles **4** rather than aldoxime-O-sulfonic acids **3.** Method 1 has the same defects. Some types of diaziridines have not been obtained at all (e.g. 3-monoalkyldiaziridines, diziridines with functional groups, some fused diaziridine systems). Chemical

transformation of diaziridines has not been practically studied. However some reactions, e.g. alkylation, could be very useful for the introduction of suitable substituents. In this work all three variants for the synthesis of diaziridines were studied in detail as well as Mannich and alkylation reactions.

We have shown for the first time that aldoxime-O-sulfonic acids **3** can be stabilized like its salts **5** with primary aliphatic amines or ammonia (the latter - only in 40% solution at lower temperature) and can be used in the diaziridinium synthesis with primary aliphatic amines or ammonia to give 1,3-dialkyldiaziridines **6a** and previously inaccessible 3-monoalkyldiaziridines **6b,** respectively [6] (Scheme 2).

Scheme 2

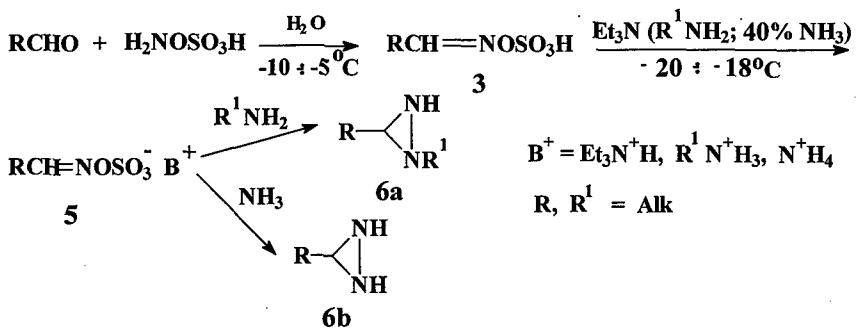

This method was broadened to prepare other diaziridines. Thus a possibility of the preparation of 3,3-dialkyl-(**8a**) and 1,3,3-trialkyl(**8b**)diaziridines from esters of acetone oximes **7** , containing the rests of various acids was studied. Initial **7** were synthesized through the interaction of acetone oxime with chloroanhydrides of corresponding acids. It was shown that only **7** were able to form diaziridines that are stable to Beckman rearrangement and have the central atom of acid rest (heteroatom or carbon one) sterically protected from an attack of amine [7,8]. In this case amine attacks carbon atom of the imino-group of ester **7** followed by the diaziridine formation. It was found that the most appropriate **7** had the rests of arylsulfonyl, alkoxyphosphonic and mesityl acids (**7a-c**). In acyloximes, amine attacks the CO-group with the following formation of corresponding amides (Scheme 3)

Scheme 3

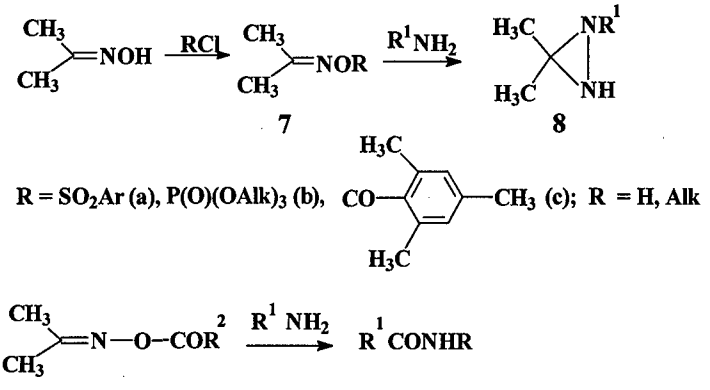

Recently [9,10] we succeeded in creating the simplest one-step method for the synthesis of diaziridines with different substituents at carbon and nitrogen atoms by the interaction of the above components in water with the controlled value of medium pH. It was found that the maximum yield of diaziridines from carbonyl compounds, amines and aminating reagents in water was achieved at a certain pH value shifting towards the less basic region with -I effect of substituents in the carbonyl compound increasing and with pK_{BH+} of amine decreasing. The pH effect can be explained by a possibility of generating of immonium ion **10** from intermediate α-aminocarbinol **9** (Scheme 4).

Scheme 4

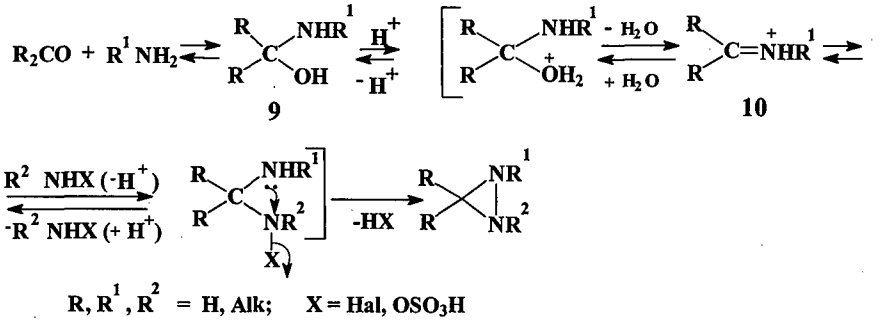

REACTIONS

Diaziridines **6** and **8** have unsubstituted nitrogen atoms that could be used for the introduction of substituents, including those with energetic fragments, e.g. C≡C, C=C, NO_2, ONO_2, N_3. To achieve this, Mannich (aminomethylation) and alkylation reactions were used. It was shown that N,N'-unsubstituted diaziridines and N-monosubstituted diaziridines could enter Mannich reaction only as NH acids. However they successfully yielded Mannich bases with more basic compounds, the reaction proceeding both inter- and intramolecularly [11-13]. Some examples of such transformation are presented in Scheme 5.

Scheme 5

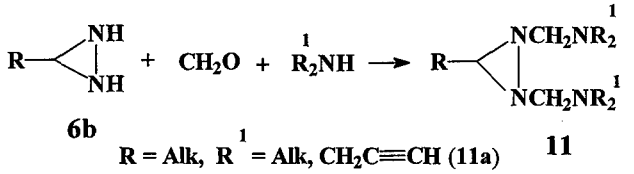

6b **11**

R = Alk, R^1 = Alk, $CH_2C{\equiv}CH$ (11a)

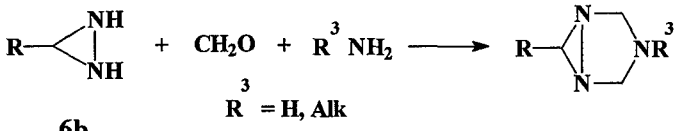

6b

R^3 = H, Alk

12

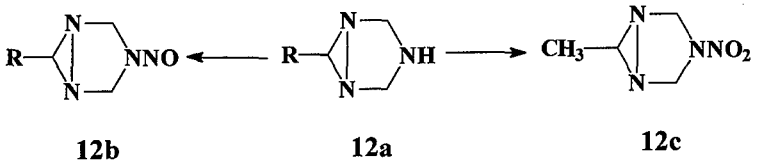

12b **12a** **12c**

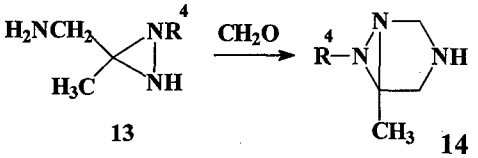

13 **14**

R^4 = H, CH_3

The most convenient object for this reaction proved to be 3-monoalkyldiaziridines **6a.** They were able to form Mannich bases both with two molecules of secondary amines and with one molecule of primary ones (or ammonia). In the former case 1,2-bis(aminomethyl)diaziridines **11** (including 1,2-bis(dipropargilaminomethyl)diaziridine **11a**) and in latter - 1,3,5-triazabicyclo[3.1.0.]hexanes **12** were synthesized. N-Nitroso- and N-nitroderivatives **12b,c** were obtained by nitrosylating and nitration of **12a.** A new heterocyclic system - 1,3,6-triazabicyclo[3.1.0]hexane **14** was synthesized by intramolecular Mannich reaction of 3-aminomethyldiaziridine **13.**

On the study of alkylation it was found that only one nitrogen atom of N,N`-unsubstituted diaziridines **6a** and **8a** is able to enter this reaction. The second molecule of the alkylating reagent attacks the already alkylated nitrogen atom similar to alkylation of hydrazines. Alkylation of N-monosubstituted diaziridines was carried out after obtaining their Na-salt **15** by the interaction with $NaNH_2$ in dipolar aprotonic solvents (tetrahydrofuran, dioxane). N,N'-Di-sodium salts of diaziridines were not obtained, probably, owing to low solubility of initially formed mono-Na-salt **15**. Different functional groups (C=C, C≡C) were introduced into the substituents at nitrogens atoms by means of alkylation.. Chemical transformation of other diaziridines obtained (e.g. compound 16) allowed to broaden their number (NO_2, N_3, ONO_2) (Scheme 6).

Scheme 6

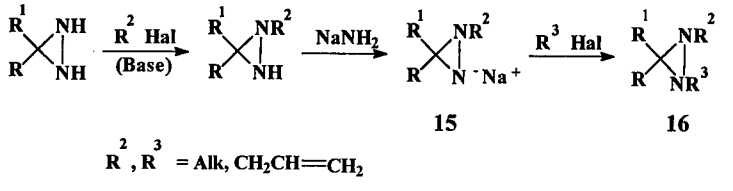

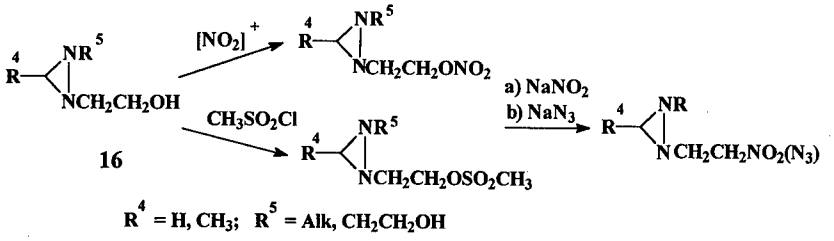

Therefore during the whole cycle of investigations, a wide range of compounds with one, two and three diaziridine cycles in the molecule as well as fused diaziridine-containing systems were synthesized and different functional and energetic groups were introduced into the substituents. It is, however, necessary to note that the synthetic potential of the developed methods is far from being exhausted.

The study of physico-chemical properties of the diaziridines obtained showed that the most of their alkyl derivatives were liquids with amine odor. Fused diaziridines are solid compounds. Diaziridine derivatives are quite stable. Stability is increasing with substitution of the NH-group by the NR-group and decreasing with substitution at carbon atom. They have low toxicity - some of them were proposed as drugs. The basicity of diaziridine alkyl derivatives is equal to that of aniline derivatives. The introduction of electron-withdrawing groups into substituents decreases basicity.

THERMOCHEMISTRY

To estimate energetic properties of diaziridine derivatives it was necessary to determine their thermochemical characteristics. Till now no information on thermochemical properties of diaziridines has been available. We determined experimentally enthalpies of combustion ($-\Delta H_c^o$) for seven model diaziridine derivatives both in solid and liquid state (see Table 1). Enthalpies of formation (ΔH_f^o) for these compounds were calculated from the data obtained. The enthalpies of combustion were found by the method based on the measurement of combustion energy in a calorimetric bomb with a high oxygen excess. The measurement of combustion energy ($-\Delta U_b'$) was carried out with the help of a hermetic half-microcalorimeter with a magnetic mixer, (the design was described in work [14]). The calibration of the calorimeter was carried out by burning standard benzoic acid K-1 mark with combustion energy of 26434.9 j/g. The heat equivalent of the calorimeter was 4212.6 j/conv.grad. The heat equivalent obtained was verified by burning second standard substances - succine and hypure acids. Their combustion energies were in good agreement with the known data.

From these results it was found that the calorimeter in use enabled to measure thermal effects of combustion reactions with ~ 0.02 - 0.03% accuracy.

The core of the method for energetic materials burning was described in details in work [15]. To stabilize combustion, a sample of the investigated substance should be burned together with subsidiary substances - phtalic acid dimehtyl esters and benzoic acid. The calculation of standard $-\Delta H_c^o$ introduced some corrections: on combustion energy of subsidiary substances, on the heat effect of nitric acid formation, on the heat exchange of a calorimetric vessel with an isothermic cover of the calorimeter, on ΔnRT, and the like.

The calculation of standard formation enthalpies for diaziridines was carried out with the help of the following values of formation enthalpies of combustion products (ΔH_f^o): CO_2 (gas): -393.5 kJ/mol and H_2O (liquid): -285.83 kJ/mol. The thermochemical characteristics obtained were used to a calculate strain energy (ΔH_{str}) of the diaziridine cycle. This value was estimated as a difference between the experimental value of combustion enthalpy and the one calculated for the hypothetic nonstrained state of the molecule (Table 1).

The calculation of combustion enthalpy was carried out by the additive-group method developed at the Institute of Chemical Physic RAS. Strain energy manifested in the interval of 63-90 kJ/mol (or 16-22 Kcal/mol) and its middle value is 75 kJ/mol (or 19 Kcal/mol). The obtained thermochemical data could contribute to the progress in calculation methods for thermochemical characteristics of nitrogen-containing organic compounds. Some synthesized diaziridines (both liquid and solid) are presented in Table 2. Formation enthalpies for a series of both obtained and hypothetic diaziridine derivatives were calculated by the developed method (Tables 2 and 3). These tables data allow to recommend some diaziridine derivatives for their investigation as high energetic materials for different purposes.

Table 1. Thermochemical properties of model diaziridines obtained

№	Compounds	$-\Delta U^{l}_{B}$ j/g	$-DH_c^o$ kJ/mol	DH_f^o kJ/mol	DH_{strain} kJ/mol
1	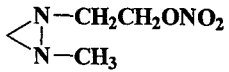 (liq)	19897.4 ± 7.5	2923.7 ± 3.8	63.5 ± 3.8	73.2
2	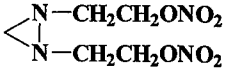 (liq)	15100.9 ± 9.2	3345.5 ± 2.1	-50.2 ± 2.1	87.0
3	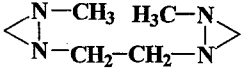 (liq)	33781.6 ± 19.7	4806.2 ± 2.9	444.3 ± 2.9	90.4
4	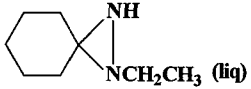 (liq)	39380.9 ± 9.4	5482.7 ± 5.4	48.0 ± 5.4	63.2
5	 (solid)	38919.6 ± 41.7	5846.7 ± 6.3	304.3 ± 6.3	72.4
6	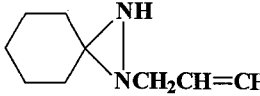 (liq)	39235.4 ± 57.2	5973.2 ± 8.7	145.0 ± 8.7	68.2
7	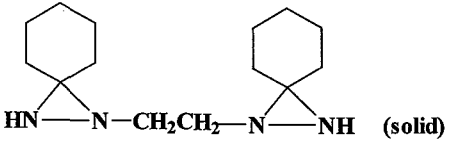 (solid)	37621.5 ± 47.9	9420.0 ± 12.0	195.1 ± 12.0	71.1

Table 2. Synthesized Diaziridine

№	Compounds	B.p. (m.p.) °C	d g/cm^3	DH_f^o Kcal/kg (calculated)
1	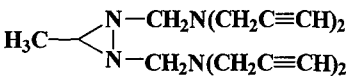	129/0.5 Torr	1.00	940.0
2	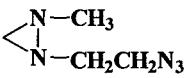	51/10 Torr	1.06	983.0
3	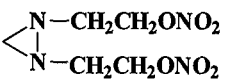	undistill. oil	1.34	-54.0 (exp)
4	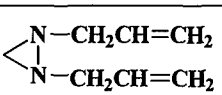	99/170 Torr	0.87	616.0
5		96/80 Torr	0.96	682.0
6	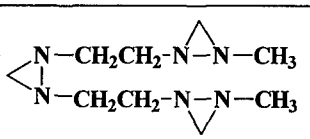	93/1 Torr	1.02	744.0
7	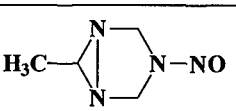	42/1 Torr (30)	1.14	486.0
8	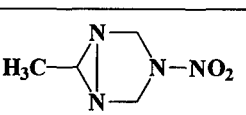	51/0.5 Torr (39)	1.21	347.0
9	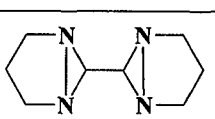	(215)	1.29	610.0

Table 3. Hypotetical Diaziridines

№	Compounds	d* g/cm^3 (calculated)	DH_f^o Kcal/kg (calculated)
1	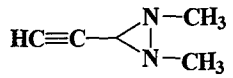	0.89	1070.0
2	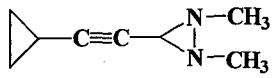	0.94	829.0
3	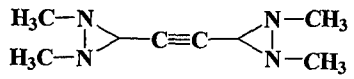	1.00	644.0
4	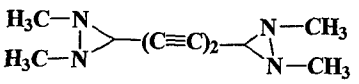	1.02	1076.0
5	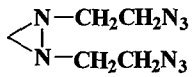	1.17	1088.0
6	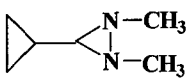	0.89	533.0
7	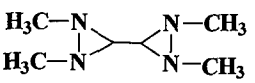	0.97	682.0
8	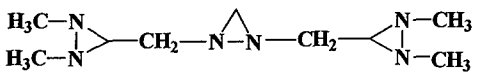	1.06	710.0

*)Density of compounds were calculated on the basis of QSPR (Quantitative Structure - Properties Relationships) approach (Dr. T.S.Pivina, IOCh RAS)

REFERENCES

1. E.Schmitz, "Dreiringe mit zwei heteroatomen", Springer-Verlag-Berlin-Heidelberg-NewYork, 1967.
2. E.Schitz, "Three-Member Rings with two Heteroatoms", Advances in Heterocyclic Chemistry, 1979, V.24,63.

3. H.W.Heine, "Diaziridines, 3H-Diazirines, Diaziridinones and Diaziridinimines", Chem. Het. Comp., 1983, **42**, 547.
4. R.G.Kostianovsky, R.Murugan, M.Sutharchanadevi, Comprehensive Heterocyclic Chemistry II, "Diaziridines and Diazirines", 1996, V.3, 347.
5. E.Schmitz, Angev. Chem., 1959, **71**, 127.
6. A.N.Mikhailyuk, V.Yu.Petukhova, N.N.Makhova, Mendeleev Commun., 1997, 60.
7. N.N.Makhova, V.Yu.Petukhova, L.I.Khmel'nitskii, Izv. Acad. Nauk SSSR, Ser. Khim., 1982, 2107 (Bull. Acad. Sci. USSR, Div. Chem. Sci., 1982, **31**, 1858).
8. A.N.Mikhailyuk, N.N.Makhova, A.E.Bova, L.I.Khmel'nitkkii, S.S.Novikov, Izv. Acad. Nauk SSSR, Ser. Khim., 1978, 1566 (Bull. Acad. Sci USSR, Div Chem. Sci., 1978, **27**, 1367).
9. V.V.Kuznetsov, N.N.Makhova, Yu.A.Strelenko, L.I.Khmel'nitskii, Izv. Acad. Nauk SSSR, Ser. Khim., 1991, 2861 (Bull. Acad. Sci. USSR, Div. Chem. Sci., 1991, **40**, 2496).
10. V.V.Kuznetsov, N.N.Makhova, L.I.Khmelnitskii, Izv. Acad. Nauk, Ser. Khim., 1997, 1410 (Russ. Chem. Bull., 1997,**46**, 1354).
11. N.N.Makhova, A.N.Mikhailyuk, A.E.Bova, V.Yu.Petukhova, T.V.Chabina, L.I.Khmel'nitskii, Mendeleev Commun., 1992, 146.
12. N.N.Makhova, V.Yu.Petukhova, T.V.Chabina, L.I.Khmel'nitskii, Izv. Acad. Nauk. Ser. Khim., 1993, 1665 (Rus. Chem. Bull., 1993, **42**, 1602).
13. N.N.Makhova, A.N.Mikhailyuk, A.E.Bova, T.V.Chabina, L.I.Khmel'nitskii, Izv. Acad. Nauk, Ser. Khim., 1993, 2091 (Rus. Chem. Bull., 1993, **42**, 2004).
14. Yu.N.Matyushin, T.S.Kon'kova, A.B.Vorob'yov, "Modern Calorimeter for Combustion", Proceeding of All-Union Conference on Calorimetrical and Chemical Thermodynamics", Novosibirsk, USSR, 1982 (in Russian).
15. Yu.A.Lebedev, E.A.Miroshnichenko, Yu.A.Knobel, "Thermochemistry of nitrocompounds", M. Nauka, 1970, p.168 (in Russian).

REVERSED DIPOLE ('UMPOLUNG') NITRATIONS: NOVEL SYNTHESES OF POLYNITROAROMATIC COMPOUNDS

Ross W. Millar and Robert P. Claridge
Defence Evaluation & Research Agency, Fort Halstead, Sevenoaks, Kent TN14 7BP, U.K.

Abstract

Nitration reactions are employed to synthesise numerous energetic compounds. Conventional nitrations use electrophilic reagents; electron-deficient molecules, such as certain nitrogen heterocycles and polynitroaromatics, therefore react very slowly, giving low yields and extensive by-product formation. However, such substrates generally react readily with nucleophiles in high yield. Therefore reactions of heterocycles and polynitroaromatics with certain specific nucleophiles were investigated in order to generate intermediates containing 'masked' nitro groups, which could then be converted to nitrated products by simple oxidation procedures.

The method was applied to the nitration of several electron-deficient carbocyclic (i.e. benzenoid) or heterocyclic aromatic compounds, notably pyridines and diazines. The methodology comprised:- i) reacting a haloaromatic with a diarylsulphilimine or its N- alkali metal salt, thereby generating an N-(hetero)aryl-S,S-diarylsulphilimine derivative, and ii) oxidising this intermediate under relatively mild conditions using a peroxycarboxylic acid such as *m*-chloroperbenzoic acid. Moderate to good yields of the corresponding nitro products, including some previously unreported compounds, were obtained. In certain cases the first step could be accomplished without the necessity of a halo precursor, i.e. by vicarious nucleophilic substitution. An attempted extension of the methodology to the aliphatic series, where phosphinimines were also employed as nucleophiles, was, however, largely unsuccessful.

The reversed dipole or 'Umpolung' methodology thus enables nitrations to be carried out in many cases in moderate to good yield where conventional, electrophilic, methods have failed. A further advantage is that the introduction of nitro substituents into the aromatic ring makes it more labile to further substitution, and thus potentially higher degrees of nitration are possible. Consequently, access to novel polynitrated heterocycles, a class of compound particularly useful in energetic materials technology, is facilitated, and indeed some of the polynitroheterocycles so prepared are expected to show potential as novel energetic materials, for instance as thermally-stable explosives.

Introduction

Nitration reactions are employed to synthesise numerous energetic compounds[1]. In conventional nitration reactions, substrates are attacked by an electrophile, usually the nitronium ion NO_2^+, resulting in the substitution, by nitro, of a leaving group which is usually hydrogen (for C-nitration) although other leaving groups are possible (e.g. acyl moieties for N-nitration, etc). The reactions are rapid and high-yielding when the substrate is electron-rich and numerous examples are known[2]; conversely, electron-deficient substrates, for instance certain nitrogen heterocycles, react slowly and only under forcing conditions, giving low yields of the desired nitration products and extensive by-product formation, caused by

reaction at alternative sites in the molecule (e.g. cleavage of rings, etc). For instance, the nitration of pyridine under electrophilic conditions (potassium nitrate/ oleum at 300°C) yields only 4.5% of 3-nitropyridine[3].

On the other hand, electron-deficient substrates generally react readily with nucleophiles in high yield. It is found that nitrite ion is not, however, a useful nucleophile to synthesise nitro derivatives, certainly in aromatic systems[4]. The reason is that the negative charge resides predominantly on the oxygen atoms and hence displacement of for instance halogen gives rise to nitrite esters rather than the desired nitro compounds (Scheme 1); the nitrite esters are hydrolytically unstable and the isolated products in the aromatic series are phenols.

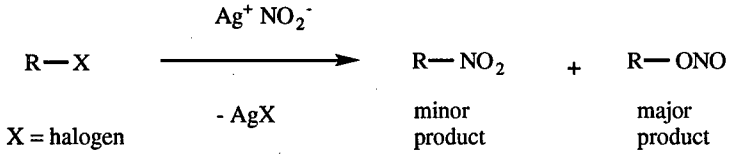

Scheme 1

Therefore a new approach was considered where reactions of heterocycles and polynitroaromatics with other nucleophiles would generate intermediates containing 'masked' nitro groups, which could then be converted to nitrated products by simple oxidation procedures. This novel methodology is outlined in Scheme 2.

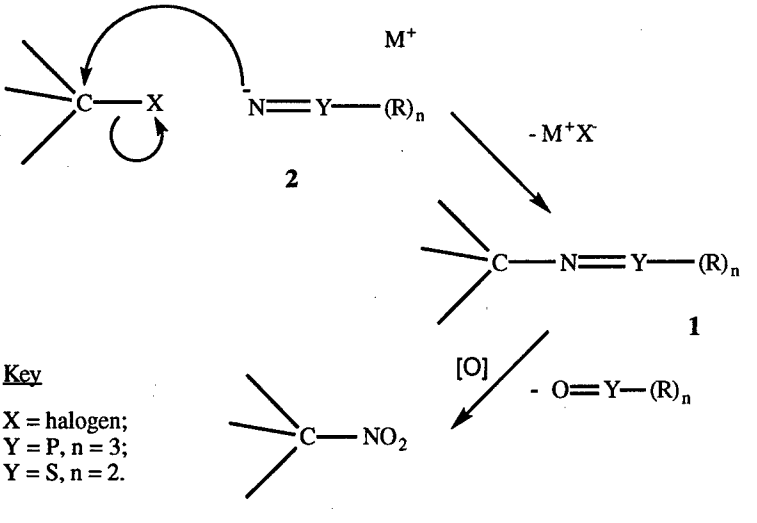

Scheme 2: Principle of 'Umpolung' Nitration

It was known from work in the 1980s that various imine derivatives of general structure **1** could be oxidised to nitro compounds, notably phosphinimines and sulphilimines[5]. More recent reports had indicated that the phosphinimine and sulphilimine precursors (general structure **2**) could act as nucleophiles and effect displacement of leaving groups such as halogen, particularly from heteroaromatic compounds[6]. It was considered that both steps could be combined into a single synthetic sequence wherein displacement of halide from readily accessible aromatic or heteroaromatic halo derivatives (or even displacement of hydrogen - see below) followed by oxidation would give rise to the nitro products directly, without the need for isolation and further elaboration of nitrogenous intermediates such as amines. Such a conversion would be termed an 'Umpolung' nitration because the polarity of the incoming group is reversed in the final product; 'Umpolung' (literally 'reversed dipole') conversions already exist for other functional groups, for instance nucleophilic carbonylation is achieved via dithioacetals[7], and N-chloroamines can effect electrophilic amination[8], reactions which normally occur by electrophilic and nucleophilic attack respectively.

A further advantage of the 'Umpolung' nitration methodology was anticipated, namely, the introduction of nitro substituents into the aromatic ring results in an activating effect which makes the ring more labile to further substitution; thus potentially higher degrees of nitration are possible than under electrophilic conditions. The exact chemistry by which this novel nitration methodology was achieved will now be described.

Results

Nucleophilic Substitutions

Since electron-poor aromatics - pyridines, pyrimidines and pyrazines, as well as polynitrobenzenes - are not readily nitrated by conventional electrophilic nitrating agents, these appeared obvious substrates upon which to investigate the novel methodology (the attempted application to aliphatic systems is described later). In general, halo derivatives of these ring systems were also widely available, and chloro compounds were chosen as the best compromise between cost and reactivity. It was somewhat harder to predict the most suitable nucleophile, however, and some difficulties were encountered in early nucleophilic substitution reactions.

The first nucleophile chosen was N-(trimethylsilyl)triphenylphosphine (**3**), which had been efficacious in the nucleophilic substitution of heterocycles with labile Cl[6a]. However, in our hands it was almost entirely inert (e.g. with 2-chloropyridine), so attention was turned to unsubstituted phosphinimine (**4**) or its salts, e.g. **5**. With these nucleophiles evidence was indeed seen of halide displacement, but the heterocyclic phosphinimine products were, in general, too unstable to be isolated on account of their lability towards hydrolysis; often the

only isolable products were triphenylphosphine oxide and an amino derivative of the starting heterocycle. Hence attention was turned away from phosphinimine nucleophiles in favour of their sulphur analogues, sulphilimines.

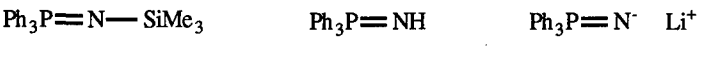

3 **4** **5**

S,S-Diphenylsulphilimine (**6**) was known to react with various heteroaryl halides[6a], as well as polynitrochlorobenzenes[9], in aromatic nucleophilic substitutions to give N-aryl-S,S-diphenylsulphilimine products (Ph_2S=NAr). The reactions with **6** (as the hydrate) were carried out in 100% molar excess (to remove hydrogen halide co-product), and were also found to be sensitive to choice of solvent, a significant improvement over literature yields being obtained when THF was used. The molecule is believed to react through an ylid form (**7**) which enhances the nucleophilicity[10].

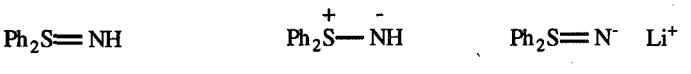

6 **7** **8**

Table 1: Formation of Sulphilimines from Halo Precursors

Substrate	Solvent	Conditions	Product (Yield)
2-Chloro-3-nitropyridine	EtOH	7 hr/ Δ	**9** (76%)
2-Chloro-5-nitropyridine	THF	4 hr/ Δ	**10** (81%)
2-Chloro-3,5-dinitropyridine	"	0.5 hr/ Δ	**11** (100%)
Pentachloropyridine	"	8 hr/ Δ	**12** (44%)*
2,6-Dichloropyrazine	"	18 hr/ Δ	**13** (95%)
2,4-Dichloropyrimidine	"	8 hr/ Δ	**14** (48%)
4,6-Dichloropyrimidine	"	8 hr/ Δ	**15** (72%)
2,4,6-Trichloropyrimidine	"	4 hr/ Δ	**16** (36%) & **17** (53%)
2,4,5,6-Tetrachloropyrimidine	"	4 hr/ Δ	**18** (55%)†
Pentafluoropyridine	"	6 hr/ Δ	**19** (84%)
2,3,5,6-Tetrafluoropyridine	"	4 hr/ Δ	**20** (95%)
2,4-Dichloro-6-(n-propoxy)-s-triazine	"	3 hr/ room temp.	**21**(11%)

* 2-isomer (4%) also formed; † 2-isomer (15%) also formed.

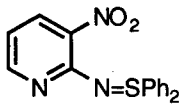

9

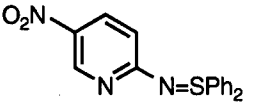

10

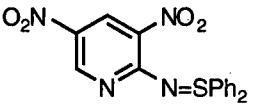

11

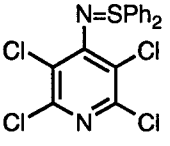

12

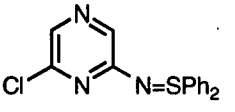

13

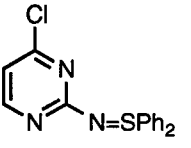

14

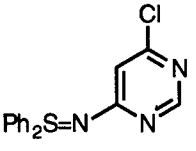

15

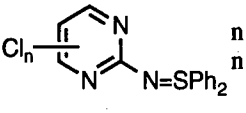

n = 2: **16**
n = 3: **18**

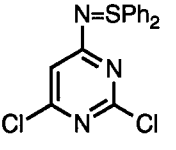

17

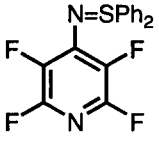

19

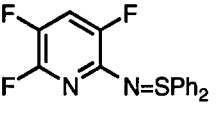

20

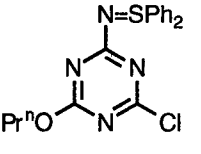

21

The sulphilimines which have been prepared in this way are shown in Table 1[11]. The yields are in general good to excellent, with single products being formed cleanly in many cases. Disubstitution did not appear to occur without further activation of the aromatic nucleus (for example with nitro group(s)). Where by-products were formed, i.e. isomers from attack at a different position on the ring, these were easily separated by column chromatography.

In order to enhance the nucleophilicity of S,S-diphenylsulphilimine (**6**) and thereby extend the range of heterocyclic sulphilimines available, an investigation of the behaviour of N-lithio-S,S-diphenylsulphilimine (**8**) was undertaken. **8** may be prepared either from **6** or from S,S-diphenylsulphonium chloride (**22**), in each case by reaction with butyl lithium. The use of **8** did indeed enable some additional heterocyclic sulphilimines to be synthesised, for example pyrazine **23** was formed in 12% yield, but little advantage was found in other reactions with chloroheterocycles as substrates (notably, a di-(sulphilimino)heterocycle, **24**, was formed, albeit in meagre (3%) yield).

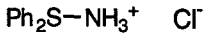

22

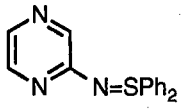

23

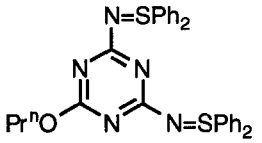

24

However, the greatest advantage in the use of the N-lithio salt, **8**, lay in its reactions with substrates containing nitro groups. In such compounds, for instance 2-chloro-3-nitropyridine, it was found that owing to the higher basicity of **8** compared to **6**, attack took place at the 4-position of the pyridine nucleus (in addition to the 2-position) with the occurrence of displacement of hydrogen. Such a displacement is termed a vicarious hydrogen substitution[12], and the reaction was found to be general for several nitro-containing precursors (Table 2); carbocyclic aromatics (nitrobenzene derivatives) behaved similarly. This is the first reported instance of a vicarious substitution by a sulphur nucleophile of this type.

Table 2: Formation of Sulphilimines by Vicarious Nucleophilic Substitution

Substrate	Conditions	Product (Yield)
1-Chloro-4-nitrobenzene	24 hr/ room temp.	**25** (19%)*
1,3-Dinitrobenzene	" " " "	**26** (20%) & **27** (14%)
2-Chloro-3-nitropyridine	" " " "	**9** (34%) & **28** (49%)
2-Chloro-5-nitropyridine	" " " "	**29** (4%)

* The yield was reduced (7%) upon prolonging the reaction time (72 hr).

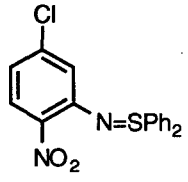

25

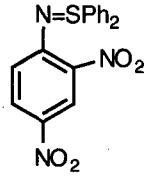

26

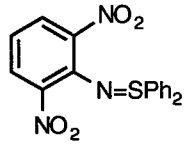

27

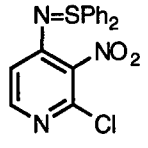

28

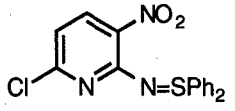

29

Before turning to oxidations, the attempted extension of the methodologies described above to aliphatic systems should briefly be mentioned. The potential benefits of the "Umpolung' nitration methodology to aliphatics would be extensive, permitting a new entry into such compounds without resort to low-yielding 'dirty' reactions such as nitromercuration-demercuration or nitrite additions under Schechter-Kaplan conditions[2d], or alternatively gas phase nitrations[13], which are the usual routes to nitroaliphatics.

The reactions of several alkyl chlorides, bromides and tosylates, particularly tertiary compounds such as *t*-butyl and adamantyl, were investigated using phosphinimine nucleophiles, but little evidence was obtained of nucleophilic substitution. It was presumed that the respective leaving groups were not sufficiently activated towards nucleophilic displacement. Ultimately, attention was turned to allylic systems, and although no phosphinimine could be obtained from allyl chloride or crotyl chloride, the desired reaction occurred with benzyl chloride (Scheme 3), and the phosphinimine (**30**) was obtained quantitatively when triphenylphosphinimine ($Ph_3P{=}NH$) was used (an inferior yield was obtained with the lithium salt, $Ph_3P{=}N^- Li^+$). The subsequent reactions of **30** will be covered in the following section.

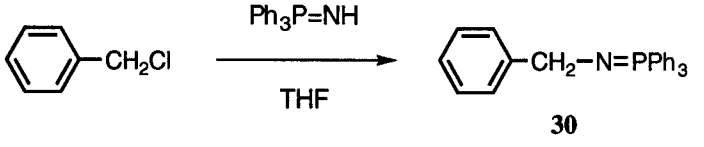

30

Scheme 3

Oxidations

In early work[5a,b] it was reported that ozone was effective as an oxidising agent in the conversion of phosphinimines to nitro compounds. However, in our hands it was found to be almost completely ineffective, and recourse was therefore made to other reported[5c-e] oxidants, notably *m*-chloroperbenzoic acid (mCPBA). The novel clean oxidant dimethyldioxirane (DMD)[14] was also considered, although it was found to be of more limited utility than mCPBA.

Because the conversion of sulphilimines and phosphinimines to nitro compounds depends on oxidation occurring at the nitrogen atom and not the hetero atom, choice of oxidising agent is crucial to the success of this step; the possible products and co-products which may be formed by this reaction are shown (Scheme 4). In practice, because the oxidising agent is always in excess, nitroso compounds are not isolated as products.

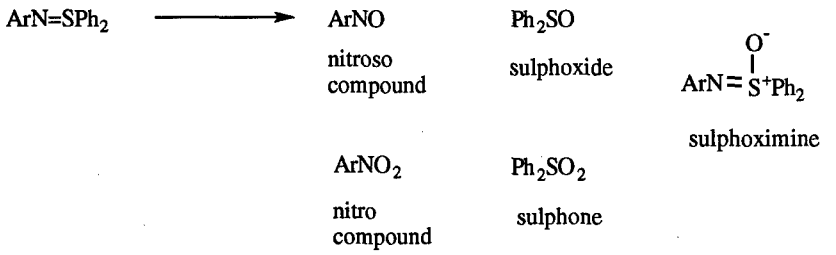

Scheme 4: Sulphilimine Oxidation Products

However, a balance has to be struck between formation of nitro product (oxidation at N) and sulphoximine (oxidation at S), since under the conditions employed in this work further reaction of sulphoximine, to yield the nitro group, does not occur[15]. The sulphoxide and sulphone products are always formed, in variable amounts, as co-products from the N-S bond cleavage which yields the nitroso and nitro products already mentioned. Similar considerations apply to the oxidation of phosphinimines, although of course far fewer of these compounds were studied for the reasons given earlier (see "Nucleophilic Substitutions").

It is found that the oxidation pathway, and hence the nitro:sulphoximine ratio, depends strongly on the nature of the oxidising agent.[16] Thus with electrophilic oxidising agents such as peracids, nitroso/nitro product formation is favoured, whilst with neutral or nucleophilic oxid-ants, such as DMD and peracid salts respectively, sulphoximines are the predominant products. The reason for this effect can best be understood if it is remembered that sulphilimines are effectively ylids, with contributions from dipolar forms (e.g. **7**: see "Nucleophilic Substitutions") which place a partial negative charge on the nitrogen atom; hence electrophilic oxidants, i.e. those where the oxygen bears a partial positive charge, will tend to react on the nitrogen atom. Conversely, nucleophilic oxidants, where the oxygen bears a partial negative charge, will tend to oxidise the sulphur atom. The results of several sulphilimine oxidations are shown in Table 3[17].

It is notable that the yield of nitro products is quite variable (4 to 74%) and in around half of the cases quoted, sulphoximines were obtained as major by-products. In two cases, no nitro products were isolated although clearly S-N bond cleavage had occurred as the formation of diphenylsulphoxide was detected. The behaviour of the sulphilimines towards oxidation is therefore influenced not only by the oxidant used but also by the structure of the sulphilimine itself: hence in some cases (e.g. compounds **13** and **20**) it is a very good route to the nitro derivatives, whilst in others (e.g. **9** and **15**) it is not so efficient. Nevertheless, it

Table 3: mCPBA Oxidations of Sulphilimines

Substrate	Conditions*	Product (Yield)
2-(S,S-Diphenylsulphilimino)-3-nitropyridine (**9**)	2 hr/ Δ/B	**31** (8%)
2-(S,S-Diphenylsulphilimino)-5-nitropyridine (**10**)	0.5 hr/ Δ/B	(Ph_2SO_2 only)
2,3,5,6-Tetrachloro-4-(S,S-Diphenylsulphilimino)pyridine **12**	2 hr/ Δ/B	**32**(24%) & **33**(40%)
2-Chloro-6-(S,S-Diphenylsulphilimino)-pyrazine (**13**)	2 hr/ Δ/C	**34** (60%)
4-Chloro-6-(S,S-Diphenylsulphilimino)-pyrimidine (**15**)	2 hr/ Δ/B	**35** (4%)
2,3,5,6-Tetrafluoro-4-(S,S-Diphenylsulphilimino)pyridine **19**	18 hr/ Δ/A	**36**(21%) & **37**(16%)
2-(S,S-Diphenylsulphilimino)-3,5,6-Trifluoropyridine(**20**)	3 hr/ Δ/B	**38** (74%)
S,S-Diphenylsulphiliminopyrazine (**23**)	2 hr/ Δ/C	(Ph_2SO_2 only)
1-Chloro-3-(S,S-Diphenylsulphilimino)-4-nitrobenzene (**25**)	2 hr/ Δ/C	**39**(32%) & **40**(26%)

Notes to Table 3: * Sulphilimines were refluxed with excess mCPBA in 1,2-dichloroethane for the periods shown. Workup is indicated by A through C as follows:
A: By flash chromatography
B: Product mixture chilled to -5°C and m-chlorobenzoic acid removed by filtration.
C: Product mixture washed with aq. NaOH and water (to remove m-chloro-benzoic acid).

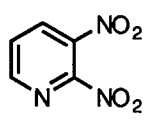

31

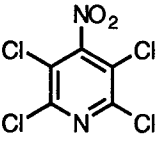

32

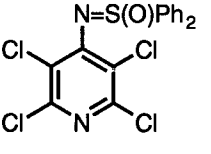

33

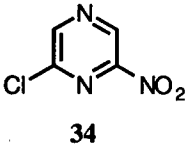

34

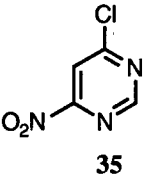

35

36

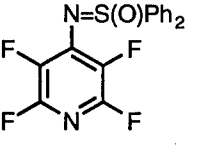

37

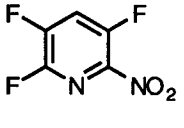

38

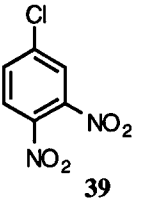

39

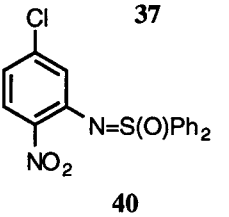

40

should be remembered that, compared with yields in electrophilic nitrations of around 4% (see "Introduction"), yields in the 10 to 30 % category are a significant improvement.

Turning to the behaviour of the aliphatic phosphinimine **30** (see "Nucleophilic Substitutions"), a different behaviour was observed. Oxidation of **30** using either ozone, DMD or mCPBA (Scheme 5) did not give rise to any nitro product (**41**); instead, the only

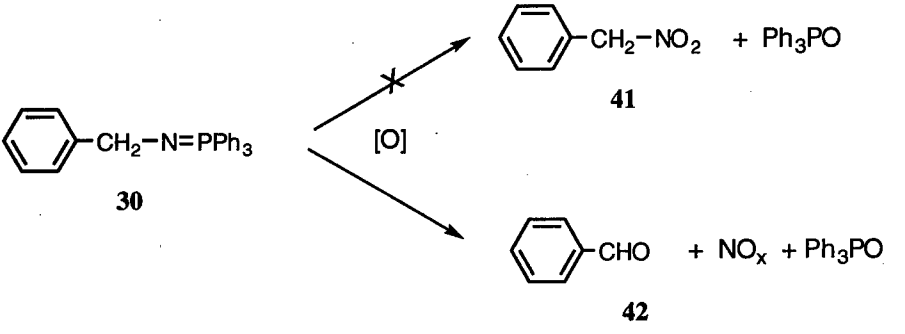

Scheme 5: Oxidation of an Aliphatic Phosphinimine

identifiable products were the aldehyde (**42**) and triphenylphosphine oxide. The reasons for this difference in chemistry from the aromatic systems probably lies in the stability of the carbonyl product (**42**) which drives the reaction along this pathway - one can only speculate as to which intermediates are involved.

Applications to Energetic Materials Synthesis

Two reactions not hitherto mentioned were selected as relevant to this topic; these are based on the reactions reported earlier but use more highly derivatised rings, one carbocyclic (benzenoid) and the other heteroaromatic. The complete reactions are shown at Schemes 6 & 7.

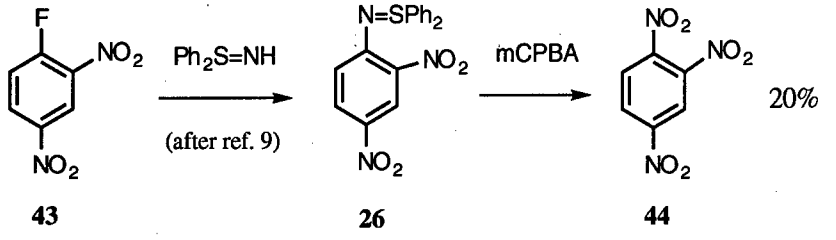

Scheme 6: Synthesis of 1,2,4-Trinitrobenzene

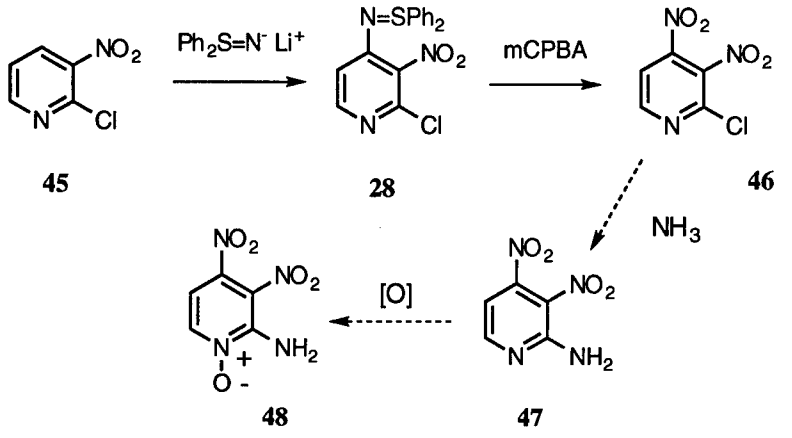

Scheme 7: Synthesis of Dinitropyridine Derivatives

The sulphilimine **26** (Scheme 6), synthesised earlier by vicarious nucleophilic substitution of 1,3-dinitrobenzene (see "Nucleophilic Substitutions"), is also conveniently made by a literature route from the fluoro precursor (**43**)[9]. Oxidation of **26** gives 1,2,4-trinitrobenzene (**44**), a reasonably stable high explosive related to the well known isomer, 1,3,5-trinitrobenzene, which has been suggested as a higher energy replacement for TNT[18]. It is notable that this is the first reported synthesis of a trinitrobenzene which has not required the use of fuming mineral acids, a potential advantage environmentally.

In Scheme 7, two of the elements of the 'Umpolung' nitration methodology are combined, those of vicarious nucleophilic substitution of the chloronitropyridine (**45**), and the oxidation of sulphilimine intermediate **28** by mCPBA (in *ca* 20 % yield). It is anticipated that with further optimisation the yields of such oxidations can be improved. Further functionalisation of the dinitropyridine **46** is then envisaged along the lines indicated to give an aminonitropyridine **47**, which would be susceptible to N-oxidation on the heterocyclic nitrogen to give **48**, a potential insensitive high explosive (molecular formula $C_5H_4N_4O_5$). Compounds with structures of this generic type have been suggested for use in this application[19].

Conclusions

Therefore a new type of nitration methodology has been developed which facilitates the nitration of substrates deactivated towards electrophilic nitration methods, notably electron deficient heterocycles including pyridine and various diazines (pyrimidines, pyrazines) as well as polynitrated benzenes. The nitration, an 'Umpolung' methodology, relies on the introduction of the incipient or 'masked' nitro function as a nucleophile, most

efficaciously a sulphilimine, which is converted to the desired nitro group in a separate oxidation step. Although overall yields as high as 60-70% have been obtained, in some cases yields fall below 10%; nevertheless, these lower figures are still an improvement on those obtained by conventional electrophilic nitration.

The methodology offers promise in the generation of novel energetic materials, or in the improved preparation of known materials, and one example is given of each. With further development, it opens the door to new generations of energetic materials, particularly those with high nitro content, which should fulfil the requirements of future military research programmes.

Acknowledgements

The authors would like to acknowledge the large contribution to this work made by Drs John P.B. Sandall and Claire Thompson of the University of Exeter. Funding was from the Ministry of Defence as part of the Corporate Research Programme.

References and Notes

1. a) T. Urbanski, *Chemistry & Technology of Explosives* (in 4 vols.; Pergamon Press, 1964, 1965 & 1984); b) G. A. Olah & D. R. Squire, *Chemistry of Energetic Materials* (Academic Press, 1991); c) A. T. Nielsen, *Nitrocarbons* (VCH Publishers Inc., 1995).
2. See, for instance, a) G. A. Olah, R. Malhotra & S. C. Narang, *Nitration: Methods and Mechanisms* (VCH Publishers Inc., 1989); b) L. F. Albright, R. V. C. Carr & R. J. Schmitt (Eds.), *Nitration: Recent Laboratory & Industrial Developments* (A.C.S. Symposium Series 623, American Chemical Society, 1996); c) K. Schofield, *Aromatic Nitration* (Cambridge Univ. Press., 1980); d) H. Feuer (Ed.), *The Chemistry of the Nitro and Nitroso Groups* (in 2 vols.; Interscience, 1969); e) S. Patai (Ed.), *The Chemistry of Amino, Nitroso & Nitro Compounds and Their Derivatives* (in 2 vols.; Wiley-Interscience, 1982).
3. R. M. Acheson, *An Introduction to the Chemistry of Heterocyclic Compounds*, 3rd Edit., page 237 (Interscience, 1976). Recent work by Bakke (J. M. Bakke & I. Hegbom, *J Chem. Soc. Perkin Trans. 2* 1211 (1995) and Suzuki (H. Suzuki, M. Iwaya & T. Mori, *Tetrahed. Letts.*, 38(32) 5647-50 (1997)) has shown that pyridine can be nitrated in the 3-position in around 60% yield using either dinitrogen pentoxide or N_2O_4-ozone; however the methodology as reported appears to be specific to pyridine and requires special conditions (SO_2 solvent or bisulphite work-up). It is not, therefore, a method of general applicability such as that described here.
4. See ref. 2a, page 96. Also, a recent report (W. Baik, S. Yun, U. Rhee & G. A. Russell, *J*

Chem. Soc. Perkin Trans. 1 1777 (1996)) has indicated that, under special conditions (DMSO solvent) isoquinolines may be nitrated in the 2-position in yields of around 30%, but no assessment was made of the applicability of this method to other heterocyclic systems.

5. a) E. C. Taylor, C.-P. Tseng & J. B. Rampal, *J. Org. Chem.*, 47 552 (1982); b) E. J. Corey, B. Samuelsson & F. A. Luzzio, *J. Am. Chem. Soc.* 106 3682 (1984); c) M. D. Coburn, *J Het. Chem.* 23 421 (1986); d) M. D. Coburn, *J Het. Chem.* 26 1883 (1989); e) O. A. Rakitin, O. G. Vlasova & L. I. Khmelnitski, *Khim. Geterotsikl. Soedin.* 11 1536 (1990).
6. a) O. A. Rakitin , N. V. Obruchnikova & L. I. Khmelnitski, *Phosphorus Sulphur*, 78, 309 (1993); b) O. A. Rakitin, O. G. Vlasova & L. I. Khmelnitski, *Org. Prep. Proced. Int.* 26 331 (1994).
7. J. March, *Advanced Organic Chemistry*, 4th Edit., page 474 (Wiley-Interscience, 1992).
8. See ref. 7, page 527.
9. Y. Tamura, K. Sumoto, H. Matusumishima, H. Taniguchi & M. Ikeda, *J. Org. Chem*, 38 4324 (1973).
10. J. P. B. Sandall, C. Thompson & N. J. D. Steel, *J Chem. Soc. Perkin Trans. 2* 513-6 (1997).
11. For further details, see R. P. Claridge, R. W. Millar, J. P. B. Sandall & C. Thompson, *J Chem. Res.* 1998 in press.
12. M. Makosza & J. Winiarski, *Acc. Chem. Res.*, 20 282 (1987).
13. A. V. Topchiev, *Nitration of Hydrocarbons and Other Organic Compounds*, Ch. 5 (Pergamon Press, 1959).
14. For recent reviews, see a) R. Curci, A. Dinoi & M. F. Rubino, *Pure Appl. Chem.* 67 811 (1995); b) W. Ando (Ed.), *Organic Peroxides*, Ch. 4 (J. Wiley & Sons, 1992).
15. Very strong oxidising systems, e.g. 90% H_2O_2 in trifluoroacetic acid are capable of cleaving the N-S bond in sulphoximines (M. D. Coburn, personal communication).
16. This effect was first reported by Coburn (see refs. 5c and 5d).
17. For further details, see R. P. Claridge, R. W. Millar, J. P. B. Sandall & C. Thompson, *Tetrahedron* 1998 in press.
18. See ref. 1a, Vol. 1.
19. See, for instance, R. A. Hollins, L. H. Merwin, R. A. Nissan, W. S. Wilson & R. Gilardi, *J Het. Chem.* 33 895 (1996).

Herstellung und Charakterisierung von Explosivstoffpartikeln

Production and Characterization of Particles of Explosives

Ulrich Teipel

Fraunhofer-Institut für Chemische Technologie (ICT)
Joseph-von-Fraunhofer-Straße 7, 76327 Pfinztal

Zusammenmfassung

Bei Festtreib- und Explosivstoffen kommt dem partikulären Füllstoff eine besondere Bedeutung zu. Die Rekristallisation der Explosivstoffpartikel erfolgt je nach stoffspezifischen Eigenschaften mit unterschiedlichen verfahrenstechnischen Prozessen. Neben der Zerkleinerung, der Sprühkristallisation und der Kristallisation aus Lösungen finden auch neue Verfahren wie die Kristallisation unter Anwendung komprimierter Gase und die Emulsionskristallisation immer mehr Anwendung. Zur Beurteilung des Herstellungsprozesses und der Produktqualität ist eine detaillierte Charakterisierung der Partikel notwendig. Ein wichtiges Merkmal bei der Charakterisierung partikulärer Systeme ist die Partikelgröße und die Größenverteilung, die in diesem Beitrag ausführlich diskutiert werden.

1. Einleitung

Festtreib- und Explosivstoffe sind oft hochgefüllte Polymersysteme. Bei diesen partikulären Systemen, die aus bis zu 90 wt. % Füllstoff bestehen können, kommt den Füllstoffpartikeln eine besondere Bedeutung zu. Je nach Anwendungsgebiet werden an die Oxidatoren bzw. die energetischen Füllstoffe spezielle Anforderungen bezüglich der Partikeleigenschaften gestellt.

Die Herstellung der Explosivstoffpartikel bzw. die Rekristallisation der partikulären Füllstoffkomponenten ist ein Verfahrensschritt der zwischen der Explosivstoffsynthese und der Verarbeitung der Festtreib- und Explosivstoffe angeordnet ist (siehe Abb. 1).

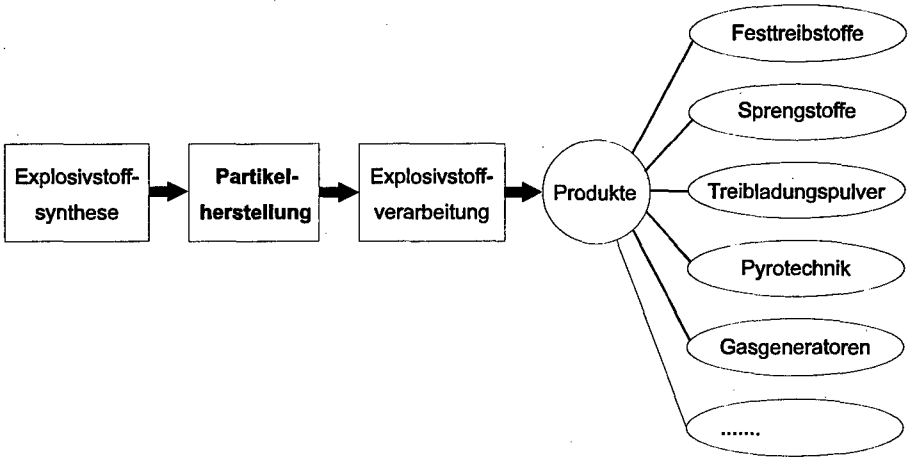

Abb. 1: Teilschritte bei der Herstellung Energetischer Materialien

Durch den Einsatz unterschiedlicher verfahrenstechnischer Prozesse zur Partikelherstellung und Rekristallisation werden die Eigenschaften der synthetisierten partikulären Füllstoffkomponenten so verändert, daß u.a. eine bessere Verarbeitbarkeit der Explosivstoffe erreicht wird oder z.B. durch eine größere spezifische Oberfläche die Abbrandeigenschaften beeinflußt werden. Durch die gezielt auf das Produkt abgestimmte Herstellung der Partikel können unterschiedliche spezifische Eigenschaften der Explosivstoffpartikel realisiert werden:

- unterschiedliche mittlere Partikeldurchmesser
- enge Partikelgrößenverteilungen
- definierte Partikelform, Morphologie
- fehlstellenarme (-freie) Kristalle
- höhere Reinheit

Im folgenden werden verschiedene Verfahren zur Herstellung von Explosivstoffpartikeln vorgestellt. Desweiteren werden in diesem Beitrag einige Möglichkeiten, zur Beurteilung der Qualität der Explosivstoffpartikel und der Charakterisierung dieser partikulären Systeme diskutiert. Eine ausführliche Charakterisierung der Partikel ist sowohl zur Produktverbesserung und zur Qualitätssicherung, als auch zur Verbesserung der Herstellungsprozesse und aller weiteren Verarbeitungsschritte dringend erforderlich.

2. Partikelherstellung

In Abhängigkeit der stofflichen Eigenschaften und der geforderten Zielgrößen, wie die mittlere Partikelgröße o.ä., werden unterschiedliche verfahrenstechnische Prozesse zur Herstellung von Explosivstoffpartikeln eingesetzt :

- Zerkleinerung
- Kristallisation aus Lösungen
- Kristallisation unter Anwendung komprimierter Gase
- Emulsionskristallisation
- Sprühkristallisation/Sprühtrocknung
- Coating von partikulären Systemen

2.1 Zerkleinerung

Bei dem Vorgang der Zerkleinerung wird das Feststoffgefüge unter Einwirkung mechanischer Kräfte zerteilt und somit die Dispersität des Feststoffes erhöht. Da bei der Feststoffzerkleinerung eine Reihe physikalisch schwer zu deutender Effekte, wie z.B. unterschiedliche Materialhärte, Gefügeaufbau und Beanspruchungsart zu-

sammenwirken, ist die Zerkleinerung in hohem Maße eine Domäne der Empirie. Eine theoretische Beschreibung ist heutzutage nur phänomenologisch möglich. Hieraus resultiert, daß eine Vielzahl von unterschiedlichen Zerkleinerungsapparaten mit unterschiedlichen Arbeitsweisen entwickelt worden sind. Folgende Mühlentypen sind zur Zerkleinerung von Explosivstoffen geeignet:

- Zahnkranzdispergierapparate
- Kolloidmühlen
- Kugelmühlen
- Schwingmühlen
- Strahlmühlen

Zur Zerkleinerung von Explosivstoffkomponenten sollte u.a. aus Gründen der Sicherheit der Prozeß der Naßmahlung bevorzugt Anwendung finden. Ein Vorteil der Naßmahlung liegt darin, daß für die gleiche Produktmenge ein geringerer Energieaufwand als bei der Trockenzerkleinerung erforderlich ist, weil durch die höhere Viskosität der Flüssigkeit, im Gegensatz zu Luft als kontinuierliche Phase, günstigere Verhältnisse der Kraftübertragung auf die zu mahlenden Partikel geschaffen werden.

Die Zerkleinerung von RDX, HMX oder CL20 in wäßriger Suspension kann bis zu einem Partikeldurchmesser von $x \geq 5$ µm mit dem in Abbildung 2 dargestellten Zahnkranzdispergierer erfolgen.

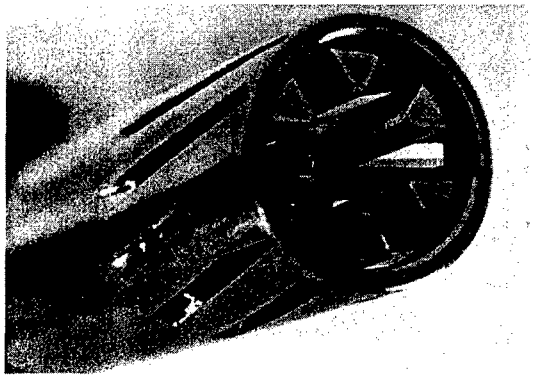

Abb 2: Zahnkranzdispergierer

Dieser Zahnkranzdispergierer besteht aus einem Stator mit 8 schrägen Schlitzen und einem Rotor mit 6 Zähnen. Die Rotordrehzahl kann im Bereich von 3.000 $min^{-1} \leq n \leq 20.000\ min^{-1}$ variiert werden, so daß maximale Umfangsgeschwindigkeiten von u = 16,8 $^{m}/_{s}$ realisiert werden können. Die Partikel und die kontinuierliche Phase der Suspension strömen zentral in den Zahnkranzdispergierer ein und werden nach der Zerkleinerung tangential nach außen gefördert. Abbildung 3 zeigt mittels Zahnkranzdispergierer zerkleinertes CL20. Die mittlere Partikelgröße beträgt $x_m \approx 5\ \mu m$.

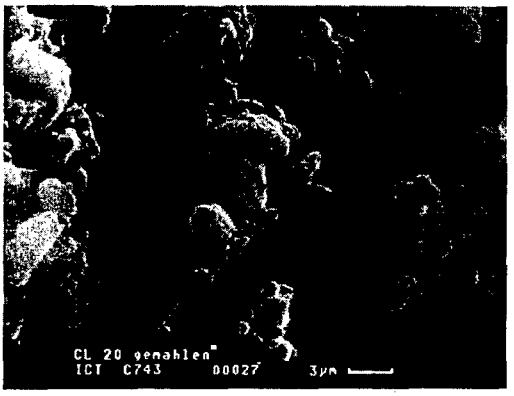

Abb. 3 : CL20 ; Naßmahlung: Zahnkranzdispergierer

Aus dieser Abbildung wird ersichtlich, daß die Partikel nach einem Zerkleinerungsprozeß kein homogenes Oberflächengefüge besitzen. An den Primärpartikeln haften kleine Sekundärpartikel bzw. Kristallbruchstücke. Beim Mahlvorgang werden dem Partikel hohe Scher- oder Prallbeanspruchungen aufgeprägt, so daß sich im Kristallinneren veränderte Spannungszustände aufbauen. Außerdem ergeben sich bei der Zerkleinerung oft breite Partikelgrößenverteilungen, was eine anschließende Klassierung erforderlich macht. Abbildung 4 zeigt die Volumensummen- $Q_3(x)$ und die Volumendichteverteilung $q_3(x)$ von Oktogen, welches mit Ultraschall im Batch-Verfahren zerkleinert wurde.

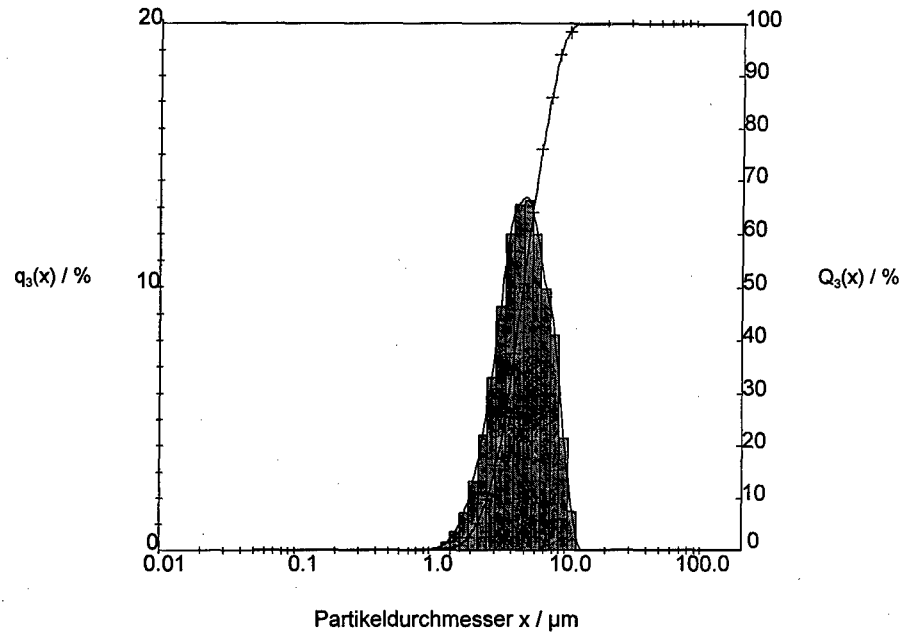

Abb. 4: Volumensummen-$Q_3(x)$ und Volumendichteverteilung $q_3(x)$
Oktogen; Ultraschallzerkleinerung

Der mittlere Partikeldurchmesser beträgt $x_{50,3}$ = 4,8 µm und die Dispersität K = 0,456.

Eine Möglichkeit der Trockenmahlung von Explosivstoffen bieten die Strahlmühlen. In Strahlmühlen wird das Mahlgut in einem expandierten Gasstrahl von Schall- bzw. Überschallgeschwindigkeit suspendiert und durch Prall und Abrieb (Wand und Partikel/ Partikel - Wechselwirkungen) zerkleinert. Bei Strahlmühlen können die Mahlraumabmessungen und somit die Produktmengen sehr klein gehalten werden. Auch die Verweilzeit der Partikel im Zerkleinerungsprozeß ist sehr gering. Diese Besonderheiten der Strahlmahlung machen diesen Prozeß besonders geeignet zur Feinstzerkleinerung von Explosivstoffen. Ein weiterer Vorteil ist, daß Strahlmühlen durch das verwendete Gas einen Selbstkühleffekt besitzen. Besonders geeignet sind Strahlmühlen zur Zerkleinerung von Ammoniumperchlorat (AP) und Kaliumperchlorat (KP), wo Partikelgrößen von ca. 3 µm erreicht werden.

2.2 Kristallisation aus Lösungen

Im Gegensatz zu den Zerkleinerungsverfahren, bei denen die Partikel hohen mechanischen Belastungen unterworfen sind, bietet das Verfahren der Kristallisation zur Herstellung von Explosivstoffpartikeln wesentliche Vorteile. Die Kristalle können relativ langsam spannungsfrei wachsen und besitzen nach Beendigung des Kristallisationsvorgangs eine definierte Kristallstruktur und - form.

Die Kristallisation ist eine verfahrenstechnische Grundoperation, die je nach Lösungsverhalten des kristallisierenden Feststoffes durch Kühlen einer gesättigten Lösung oder Verdampfen von Lösungsmittelanteilen erfolgen kann. Je nach der Art, wie die erforderliche Übersättigung der Kristallisationslösung erzeugt wird, unterscheidet man zwischen:

- Kühlungskristallisation
- Verdampfungskristallisation
- Vakuumkristallisation
- Verdrängungskristallisation

Die Wahl des geeigneten Kristallisationsverfahrens hängt vom Verlauf der Löslichkeitskurve ab. Steigt die Löslichkeit mit der Temperatur, so sollte die Übersättigung durch Kühlen erzielt werden. Eine sehr flache Löslichkeitsfunktion erfordert neben dem Kühlen noch eine Verdampfung des Lösungsmittels.

Die Form des entstehenden Kristallhabitus ist aufgrund der flächenspezifischen Wechselwirkungen zwischen Kristall und Lösungsmittel sehr stark von den eingesetzten Lösungsmitteln abhängig, so daß bei der Kristallisation die Möglichkeit besteht, den Habitus bezüglich der weiteren Verarbeitung zu optimieren. Abbildung 5 zeigt Oktogen-Kristalle, die in verschiedenen Lösungsmitteln rekristallisiert wurden.

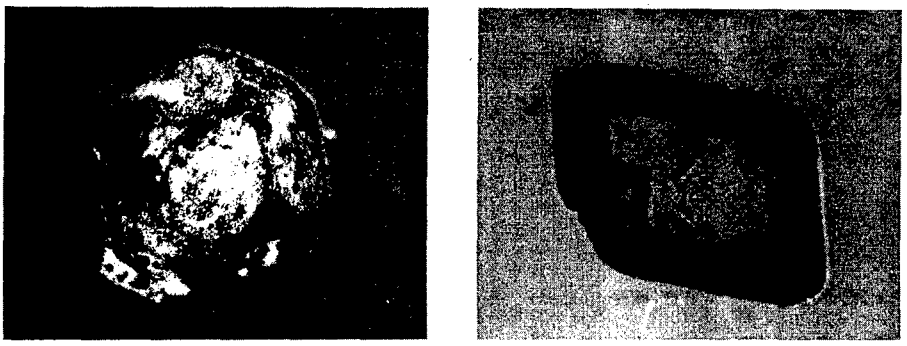

Abb. 5: Oktogenkristalle

In der Kristallisation unterscheidet man zwei wichtige Mechanismen :

- Keimbildung
- Kristallwachstum

Durch Stören des Lösungsgleichgewichts durch Übersättigung der Lösungen kommt es zur Kristallkeimbildung. Durch Anlagerung von Molekülen oder Ionen aus der übersättigten Lösung an den Flächen des Kristallkeims erfolgt dann das Wachstum des Kristalls. Durch Steuerung eines Wachstumsprozesses können die Eigenschaften der Kristalle gezielt beeinflußt werden. So besteht z.B. die Möglichkeit, fehlstellenarme (-freie) Kristalle zu züchten. Abbildung 6 zeigt GAP-Test Ergebnisse von PBX, die aus HTPB und in Propylencarbonat umkristallisierten Oktogen-Kristallen (c=70 wt%) gefertigt worden sind.

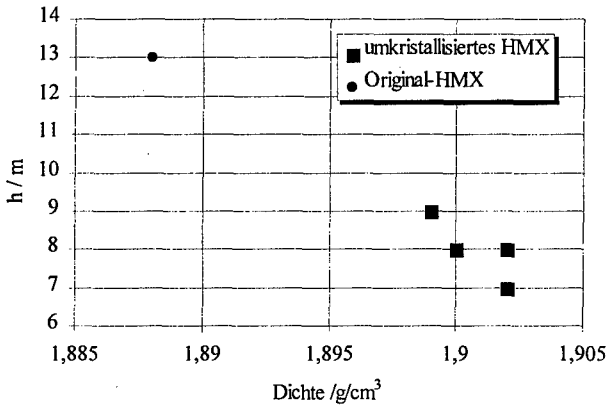

Abb. 6 : GAP-Test: HMX-Kristalle in Propylencarbonat rekristallisiert

Mit zunehmender Dichte wird die innere Qualität der Kristalle verbessert, d.h. es sind weniger Fehlstellen in den Kristallen vorhanden. Abbildung 6 macht deutlich, daß die rekristallierten HMX-Partikel aufgrund der Reduzierung der inneren Fehlstellen wesentlich unempfindlicher sind.

2.4 Kristallisation unter Anwendung überkritischer Fluide

Eine weitere Möglichkeit zur Kristallisation von Explosivstoffkomponenten bieten die Verfahren der Kristallisation unter Anwendung komprimierter Gase.

Diese neuen Verfahren eignen sich insbesondere zur Herstellung von fehlstellenarmen Mikropartikeln (Submikronbereich) mit enger Partikelgrößenverteilung. Die besonderen Eigenschaften hochkomprimierter Gase erlauben es, die Anforderungen an die Explosivstoffpartikel in einem großen Bereich zu variieren /1/.

Zur Herstellung der Explosivstoffpartikel stehen drei unterschiedliche Verfahren zur Verfügung:

Der **RESS-Prozeß** (Rapid Expansion of Supercritical Solutions) wird für die Explosivstoffe eingesetzt, die sich in reinem überkritischem Fluid oder unter Zugabe von Modifiern lösen. Die Bildung der Partikel erfolgt durch schnelle Expansion des mit Feststoff beladenen überkritischen Fluids über eine Düse. Der Druck p und die Temperatur T werden durch die schnelle Expansion stark reduziert, so daß eine hohe, lokale Übersättigung der Lösung und Keimbildung im Freistrahl erfolgen kann. Bedingt durch die schnelle Expansion in der Düse ist das primäre Einsatzgebiet dieses Prozesses die Herstellung feiner, engverteilter Partikel. Da hier keine klassischen Lösungsmittel eingesetzt werden und die Kristallbildung relativ schnell erfolgt, können Kristallfehler durch Lösungsmitteleinschlüsse vermieden werden. Abbildung 7 zeigt schematisch den Aufbau der RESS-Pilotanlage.

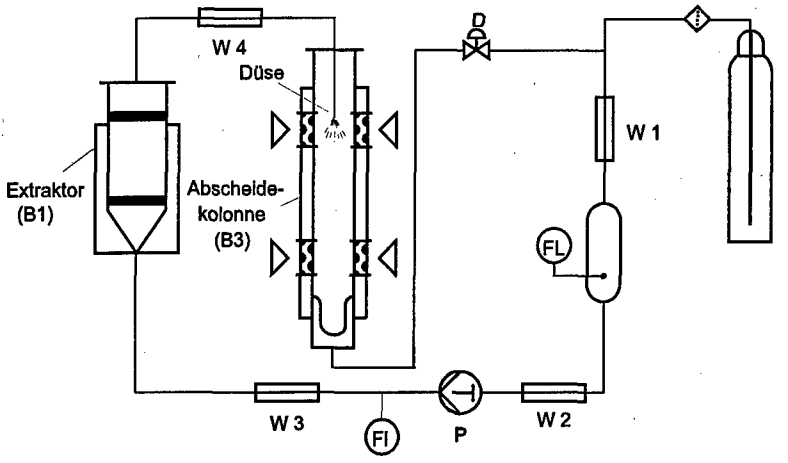

(W 1-4) Wärmeübertrager
(FL) Flüssigkeitsspeicher
(P) Hochdruckpumpe
(FI) Massenstrombestimmung
(D) Druckregelung

Abb. 7 : RESS-Pilotanlage

Mit der im rechten Teil der Anlage dargestellten Pumpen/Wärmetauscher-Einheit erfolgt die Komprimierung und Temperierung des Gases auf überkritische Bedingungen. Das überkritische Fluid löst den im Extraktor (B1) vorgelegten Explosivstoff. Die beladene überkritische Lösung wird dann über eine Düse zerstäubt. Abbildung 8 zeigt zwei Fotos von in überkritischem Kohlendioxid auskristallierten TNT-Partikeln.

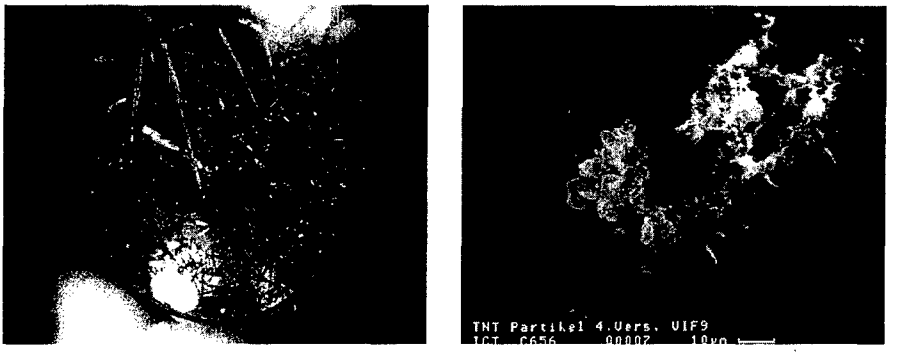

a. statischer Versuch

b. RESS-Prozeß

Abb. 8 : TNT-Partikel

Die in CO_2 (statischer Versuch) kristallisierten TNT-Partikel zeigen das für TNT typische, nadelige Kristallisationsverhalten. Durch den Prozeß der schnellen Expansion beim RESS-Verfahren kann die Ausbildung des Kristallhabitus verifiziert werden (s. Abb. 8, b.). Die mittlere Partikelgröße der TNT-Partikel beträgt $x_{50,3}$ = 10 µm.

Abbildung 9 zeigt NTO-Partikel die mittels RESS-Prozeß und überkritischem CO_2 rekristallisiert wurden.

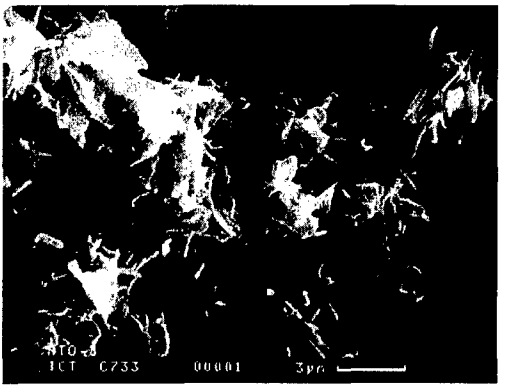

Abb. 9 : NTO-Partikel; RESS-Prozeß

Auch bei NTO können Primärpartikel im Submikronbereich erzeugt werden, allerdings ist in zukünftigen Arbeiten die Agglomerationsneigung von NTO zu untersuchen.

Bei vorliegender NICHT-Löslichkeit der Explosivstoffe in überkritischen Fluiden, wird das verdichtete Gas als **Anti-Solvent** eingesetzt, um den in einem klassischen Lösungsmittel gelösten Explosivstoff zu rekristallisieren. Die Absorption des verdichteten Gases in das Lösungsmittel führt zur Expansion der flüssigen Phase. Die Zunahme des spezifischen Volumens der Lösung, d.h. die Verminderung der Dichte, bewirkt eine Reduzierung des Lösevermögens des Lösungsmittels, so daß Explosivstoffpartikel auskristallisieren. Hierzu stehen zwei Verfahrensvarianten zur Verfügung

- Die beladene Lösung wird in einem Kristallisationsbehälter vorgelegt und das verdichtete Gas zugeführt.

- Die Lösung und das verdichtete Gas werden gleichzeitig, vorzugsweise im Gegenstrom in eine Kristallisationskolonne eingedüst. Diese Vorgehensweise er-

möglicht eine schnelle Diffusion des Gases in die Tropfen, was zu einer „Ausfällung" feiner Explosivstoffpartikel führt. Dieses Verfahren wird als PCA-Prozeß (Preciption with a Compressed Fluid Anti-Solvent) bezeichnet. Abbildung 10 zeigt schematisch das Fließbild der PCA-Anlage.

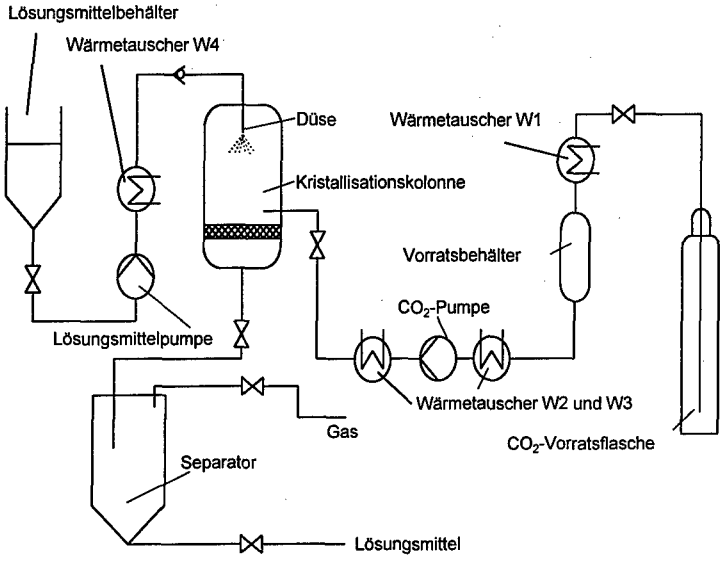

Abb. 10 : PCA-Kristallisationsanlage.

2.4 Emulsionskristallisation

Das Verfahren der Emulsionskristallisation ist insbesondere zur Rekristallisation von schmelzbaren Treib- und Explosivstoffkomponenten geeignet. Mit diesem Prozeß können sphärische Partikel des bei ca. 92 °C schmelzenden Oxidators Ammoniumdinitramid (ADN) hergestellt werden.

Der Emulsionskristallisationsprozeß gliedert sich in zwei wesentliche Teilschritte:

1. Herstellung eines flüssig/flüssig-Mehrphasensystems mit ADN-Schmelze als disperse Phase und einer gegenüber ADN nicht löslichen und nicht mischbaren kontinuierlichen Phase. Der Tropfenaufbruch und die Erzeugung der Emulsion erfolgt durch den Eintrag mechanischer Energie, z.B. durch einen Zahnkranzdispergierer (s. Abb. 2) oder einen geeigneten Rührer.

2. Kristallisation der Emulsionstropfen zu festen, sphärischen ADN-Partikeln. Da die ADN-Tropfen ein stark inhibiertes Materialverhalten zeigen, ist auch im zweiten Teilschritt der Eintrag mechanischer Energie erforderlich. Neben der Abkühlung auf Temperaturen unterhalb der Schmelztemperatur sind zur Rekristallisation der ADN-Tropfen zusätzlich mechanische Energie oder Partikel/Partikel-Wechselwirkungen erforderlich. Durch diesen lokalen Energieeintrag erfolgt die Initiierung des Kristallisationsvorganges.

Mit der Methode der Emulsionskristallisation können ADN-Partikel im Bereich $5\ \mu m \leq x_{50,3} \leq 800\ \mu m$ hergestellt werden. Abbildung 11 zeigt ADN-Partikel, die durch Emulsionskristallisation hergestellt worden sind.

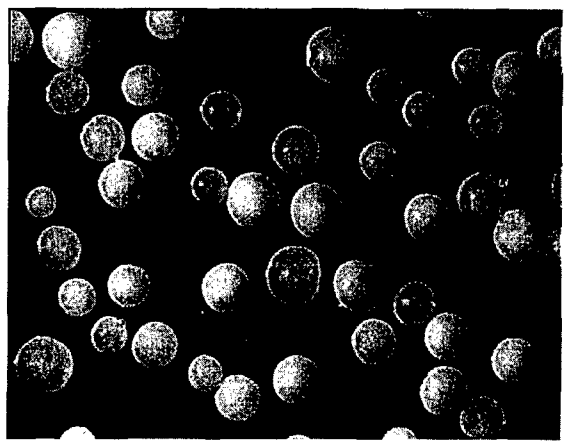

Abb.11 : ADN-Partikel, Emulsionskristallisation

2.5 Sprühkristallisation / Sprühtrocknung

Auch die Sprühkristallisation ist ein aus zwei Teilschritten bestehender Prozeß. Im ersten Teilschritt erfolgt die Zerstäubung der Flüssigkeit zu Tropfen und im Zweiten die Trocknung bzw. die Kristallisation der Tropfen zu sphärischen Partikeln. Beim Einsatz von Zweistoffdüsen mit konzentrischer Gas-und Flüssigkeitsführung ergibt sich in Abhängigkeit der Oberflächenspannung σ und des Volumenstromes $\dot{V}_F$ der Flüssigkeit, der Dichte ρ_G und dem Volumenstrom $\dot{V}_G$ des Gases sowie der Relativ-

geschwindigkeit w zwischen Gas und Flüssigkeit ein mittlerer Tropfendurchmesser x_m von :

$$x_m \approx 0{,}58 \cdot \sqrt{\frac{\sigma}{w^2 \cdot \rho_G}} + 1{,}6 \cdot \left(\frac{\dot{V}_F}{\dot{V}_G}\right)^{1{,}5} \qquad (1)$$

Die Relativgeschwindigkeit ist auch eine Funktion des Zerstäubungsdruckes. Wird die Auslaufgeschwindigkeit u der Flüssigkeit (z.B. durch Verringerung der Flüssigkeitshöhe in der Vorlage) kleiner, erhöht sich die Relativgeschwindigkeit w, was zu kleineren Partikelgrößen führt. In Abbildung 12 ist das Fließbild einer Anlage zur Herstellung von phasenstabilisiertem Ammoniumnitrat (PSAN) dargestellt.

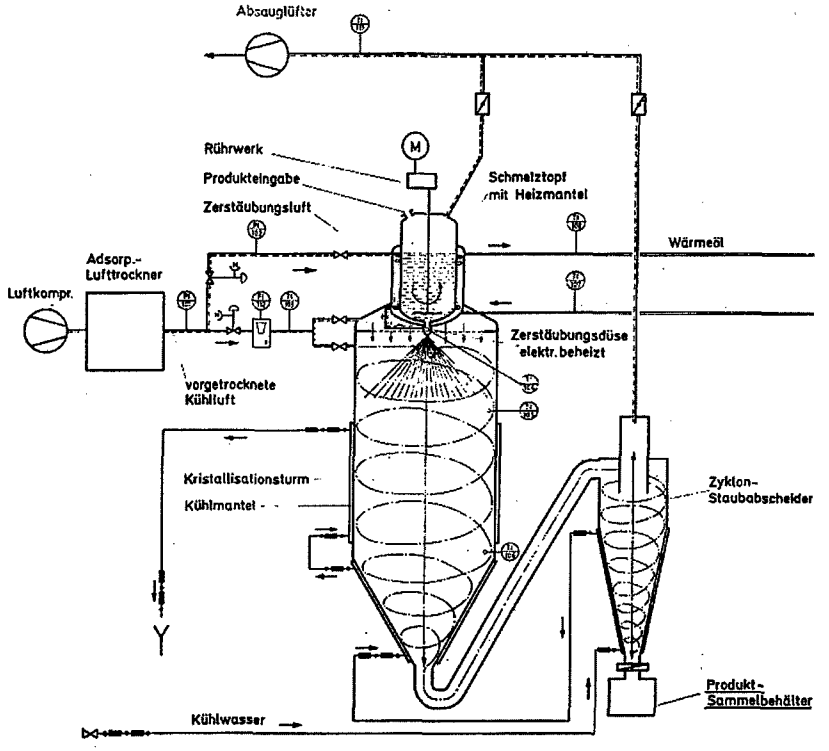

Abb. 12 : Sprühkristallisationsanlage zur PSAN - Herstellung

Die Sprühkristallisationsanlage besteht aus einem Kristallisationsturm mit dem zentralen Bauteil -der Zerstäubungsdüse- und einem Kühlmantel. Dem Kristallisati-

onsturm ist zur Abscheidung der Partikel ein Zyklon nachgeschaltet. Oberhalb des Turmes befindet sich der Schmelztopf incl. Rührwerk.

Phasenstabilisiertes Ammoniumnitrat kann mit verschiedenen Additiven, wie Zinkoxid, Kupferoxid oder Nickeloxid, und ohne Zusatz als SCAN (Sprayed Crystallized AN) in Form sphärischer Partikel mit mittleren Partikelgrößen von x_m = 20 µm, x_m = 50 µm, x_m = 160 µm und x_m = 300 µm durch Sprühkristallisation hergestellt werden.

3. Charakterisierung von Partikeln

Eine detaillierte Charakterisierung der Partikel ist sowohl zur Beurteilung des Herstellungsprozesses und der Produktqualität, als auch im Hinblick auf die Verarbeitung der Explosivstoffpartikel unverzichtbar. In Abbildung 13 sind einige Eigenschaften von Partikeln aufgeführt, welche verschiedenste Auswirkungen auf die Produktqualität, die Verarbeitbarkeit, die Explosivstoffeigenschaften usw. haben und somit in Abhängigkeit der Problemstellung untersucht werden sollten.

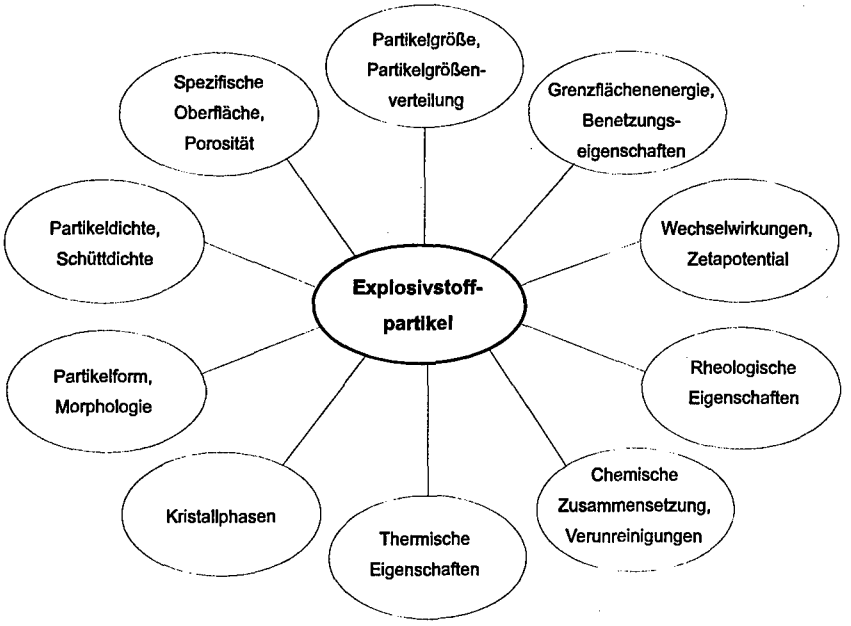

Abb. 13 : Partikeleigenschaften

Da die mittlere Partikelgröße und die Größenverteilung sehr wichtige Partikeleigenschaft sind, die den Verarbeitungsprozeß und die charakteristischen Eigenschaften des Produkts wesentlich beeinflussen, sollen diese Partikeleigenschaften im folgenden diskutiert werden.

Zur Bestimmung von Partikelgrößen und deren Verteilungen stehen verschiedene Meßverfahren zur Verfügung. Sie unterschieden sich insbesondere durch ihr physikalisches Prinzip und durch ihren möglichen Meßbereich. Sie lassen sich einteilen in Trennverfahren (Siebung,Sichten), Sedimentationsverfahren (Schwerkraftsedimentation,Zentrifugieren), Zählverfahren (Coulter-Counter, Extinktion, Bildanalyse), optische Verfahren (Laserbeugungsspektrometrie, dynamische Lichtstreuung, Holographie) und andere Methoden wie die Ultraschallspektroskopie. Abbildung 14 gibt einen Überblick über den möglichen Meßbereich der verschiedenen Verfahren.

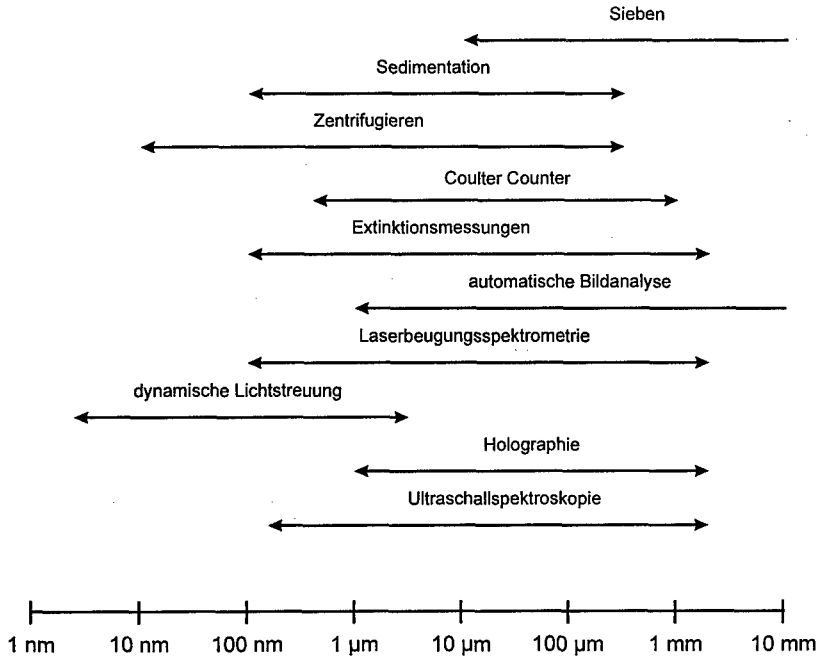

Abb. 14 : Meßbereiche verschiedener Partikelanalysemethoden

Da die Analysemethoden alle auf unterschiedlichen physikalischen Prinzipien beruhen, stimmen die mittelbaren Partikeldurchmesser oft nicht überein. Bei der Sedimentationsanalyse ergibt sich ein Schwerkraft-bezogener Partikeldurchmesser, während z.B. bei den Streulichtverfahren die Information über die Partikelgröße in der durch die Wechselwirkung mit den Partikeln gestörten Ausbreitung der Lichtwellen steckt.

3.1 Darstellung von Partikelgrößenverteilungen

Die Korngrößen von partikulären Systemen können sich über einen weiteren Größenbereich erstrecken.

Die Einzelpartikel lassen sich in sogenannte Größenklassen ordnen. Für eine hinreichende Beschreibung solcher Partikelkollektive ist die Ermittlung und Darstellung der Partikelgrößenverteilung in einem möglichst weiten Bereich notwendig. Zur Kennzeichnung der Einzelpartikel eines Kollektives benutzt man bestimmte meßbare, möglichst die Einzelpartikel eindeutig beschreibende physikalische Eigenschaften, wie z.B. die Masse, das Volumen, die Oberfläche, die Sinkgeschwindigkeit, die Intensität des von Partikeln in einem Lichtstrahl gestreuten oder absorbierten Lichtes oder die Störung eines elektromagnetischen Feldes durch die Anwesenheit von Partikeln. Die durch entsprechende Meßverfahren ermittelbare Verteilung wird durch die in den einzelnen Merkmalsklassen vorhandenen Teilmengen gekennzeichnet. Zu diesen Partikelmerkmalen werden die zugehörigen Mengenanteile bestimmt, woraus sich Mengenverteilungen des entsprechenden Partikelmerkmals ergeben. Entsprechend des verwendeten Meßverfahrens werden unterschiedliche Mengenarten ermittelt. Werden die Partikel bei der Analyse gezählt, so ist die Mengenart eine Anzahl, wiegt man sie, dann ist die Masse die Mengenart. Die Kennzeichnung der Mengenart erfolgt durch den Index r (Tab. 1).

Tab. 1: Kennzeichnung der Mengenart

Mengenart	**Dimension**	**Index**
Anzahl	L^0	**r = 0**
Länge	L^1	**r = 1**
Fläche	L^2	**r = 2**
Masse, Volumen	L^3	**r = 3**

Man unterscheidet zwei Mengenmaße, nämlich die Verteilungssumme $Q_r(x_i)$ und die Verteilungsdichte $q_r(x_i)$. Die Verteilungssumme $Q_r(x_i)$ ist die Teilmenge zwischen der minimalen Partikelgröße X_{min} und dem jeweiligen Wert x_i:

$$Q_r(x_i) = \frac{\text{Menge aller Partikel mit } x \leq x_i}{\text{Gesamtmenge aller Partikel}} \qquad (2)$$

Die Verteilungsdichte $q_r(x_i)$ ergibt sich, wenn der Mengenanteil, der in ein bestimmtes Partikelintervall fällt, auf die Intervallbreite bezogen wird:

$$q_r(x_i) = \frac{\text{Mengenanteil zwischen } x_i \text{ und } x_{i+1}}{\text{Intervallbreite } x_{i+1} - x_i} \qquad (3)$$

Ist $Q_r(x)$ eine stetig differenzierbare Funktion, so ergibt sich

$$q_r(x) = \frac{dQ_r(x)}{dx} \text{ bzw. } Q_r(x_i) = \int_{x_{min}}^{x_i} q_r(x)dx \qquad (4)$$

Zur Charakterisierung von Partikelkollektiven können aus den gemessenen Verteilungen verschiedene Parameter bestimmt werden:

- Medianwert $x_{50,r}$: die Partikelgröße, für die $Q_r(x_{50,r}) = 0{,}5$ gilt; es liegen somit 50 % der Gesamtmenge des Partikelkollektives unterhalb dieses x-Wertes.
- Modalwert x_{mod} : die Partikelgröße, bei der die Dichteverteilung $q_r(x)$ ein Maximum aufweist.
- Die Homogenität bzw. Dispersität eines Partikelkollektives wird durch die Verteilungsbreite gekennzeichnet. Die Breite einer Verteilung kann nach der VDI-Richtlinie 3491 durch den Dispersitätsgrad K beschrieben werden /2/:

$$K = \frac{x_{84,3} - x_{16,3}}{2 \cdot x_{50,3}} \qquad (5)$$

Die Dispersität wird wie folgt unterteilt:

$K < 0{,}14 \rightarrow$ Monodispers
$0{,}14 \leq K \leq 0{,}41 \rightarrow$ Quasimonodispers
$K > 0{,}41 \rightarrow$ Polydispers

- Der Sauterdurchmesser x_s ist ein mittlerer Partikeldurchmesser, der dem Partikelkollektiv den Durchmesser einer Kugel zuordnet, welche das gleiche Verhältnis von Volumen zu Oberfläche besitzt wie das Partikelkollektiv selbst. Mit den gemessenen Werten läßt sich die volumenbezogene, spezifische Oberfläche S_V als Quotient aus Oberfläche S und Volumen V eines Partikelkollektives berechnen. Für kugelförmige Partikel mit dem Durchmesser x berechnet sich die spezifische Oberfläche S_V zu:

$$S_V = \frac{6}{x_S} \qquad (6)$$

3.2 Spezifische Oberfläche

Eine exakte Ermittlung der spezifischen Oberfläche von Partikeln erfolgt mittels der Sorption von Gasen an der Festkörperoberfläche. Das Prinzip dieser Oberflächenmessung beruht darauf, daß an der Oberfläche der Partikel Gasmoleküle adsorbiert werden, und die adsorbierte Gasmenge unter gewissen Bedingungen proportional der absoluten Größe der Oberfläche ist. Mit der Methode der Gasadsorption sind Mikroporen, Risse oder Fehlstellen, die von außen zugänglich sind, detektierbar. Die spezifische Oberfläche steht in direktem Zusammenhang mit der Reaktivität der Partikel und ist somit z.B. für die Abbrandeigenschaften von besonderer Bedeutung.

4. Literatur

/1/ Teipel, U.; Förter-Barth, U.: Gerber, P.: Krause, H.: *Formation of Particles of Explosives with Supercritical Fluids,*
Propellants, Explosives, Pyrotechnics, 22, (1997) p. 165-169.

/2/ VDI-Richtlinie 3491, Blatt 1: *Messen von Partikeln, Kennzeichnung von Partikeldispersionen in Gasen: Begriffe und Definitionen.*
VDI-Verlag GmbH, Düsseldorf, 1980.

CHARACTERIZATION OF SONOCHEMICALLY-AMINTAED 1,3,5-TRIAMINO-2,4,6-TRINITROBENZENE

Julie Bremser and Kien-Yin Lee

Los Alamos National Laboratory
Los Alamos, New Mexico 87545

ABSTRACT

A novel method has been achieved for the preparation of 1,3,5-triamino-2,4,6-trinitrobenzene (TATB) from TCTNB in toluene by amination with ammonium hydroxide solution under the influence of ultrasonic irradiation. Samples of this sonochemically-aminated TATB (FP-TATB) were studied for its powder characteristics. In particular, particle dispersions techniques, such as use of a surfactant, ultrasonic agitation, and sample suspension concentration, were studied to determine the effect on overall particle size distribution and particle stability. It was found that the use of deionized water alone was not sufficient to ensure adequate suspension of the powder. An additional powder dispersion method, such as ultrasonic agitation and/or the use of a surfactant, resulted in a more uniform suspension of the powder and more accurate particle size distribution. It was found that the arithmetic median diameter (vol%) of FP-TATB is ~15 micrometers.

The powder dispersion methods investigated here will be applied to TATB prepared by a different approach. Particle size distribution results on these samples will also be discussed.

INTRODUCTION

The compound 1,3,5-triamino-2,4,6-trinitrobenzene (TATB) is an explosive with a high melting point and thermal stability that has been applied in situations where insensitivity to impact hazards is important. In the past, production grade

TATB (PG-TATB) was prepared by amination of 1,3,5-trichloro-2,4,6-trinitrobenzene (TCTNB) in toluene with anhydrous ammonia gas in a pressurized reactor.[1] TATB thus produced is suitable for most applications with particle size ranging from 30 to 60 micrometers. However, for applications requiring higher sensitivity to shock initiation, fine-grained TATB is desirable. TATB with an arithmetic median of 6 micrometers, produced by Lawrence Livermore National Laboratory (LLNL) and Pantex, has been qualified as an insensitive high explosive (IHE) according to U.S. Department of Energy (DOE) standards.[2] The processes involved in the production of such TATB (UF-TATB) are complicated and time consuming.[3]

Ultrasound is sound with frequencies beyond human hearing, i.e. above 20 kHz. When ultrasound is applied to liquids of either a homogeneous or heterogeneous reaction system, acoustic cavitation results. Rate enhancement of chemical reactions accompanied by higher production yield has been demonstrated under the influence of ultrasonic irradiation (ultrasonication).[4] Recently, the synthesis of nanostructured catalysts with selective hydrogenation reactivity by ultrasonication was reported by Suslick and his coworkers.[5] Ultrasound is also widely used in promoting dispersion of one liquid phase into another through emulsification.

In an attempt to develop a simple method to synthesize TATB that will have particle size comparable to UF-TATB, we have studied the synthesis of TATB by ultrasonication. This presentation will briefly describe the synthesis of FP-TATB, discuss particle dispersion techniques, such as use of a surfactant, and ultrasonic agitation, and their effect on particle size distribution. Results from the particle dispersion and particle sizing of UF-TATB (91190-135m-003), FP-TATB (KYL-I-58s) and PG-TATB (12-11-81-0524-165) powders will be reported.

EXPERIMENTAL

Preparation of FP-TATB (KYL-I-58s)

An ultrasonic liquid processor (Misonix XL2020) equipped with a 0.5-inch probe, operating at 20 kHz with a variable amplitude power-supply output was used for the preparation of FP-TATB. The power output was set at 60% of maximum 550 watts. A solution of TCTNB in toluene was added to an ammonium hydroxide solution in a 300 ml beaker (Pyrex No. 1040). The amination reaction began by immersing the sonicator horn into the two-phase mixture, followed by turning on the processor power. To minimize potential ammonia gas escaping to the air, the beaker was covered with a piece of aluminum foil. After a 40-minute sonication time, the resulting emulsion was left overnight at ambient temperature. The resultant FP-TATB was collected by filtration, followed by washing the solids sequentially with hot water, toluene, and acetone. The resulting lemon-colored solids were then dried at 98°C in a vacuum oven overnight. The amination reaction is shown in Reaction 1.

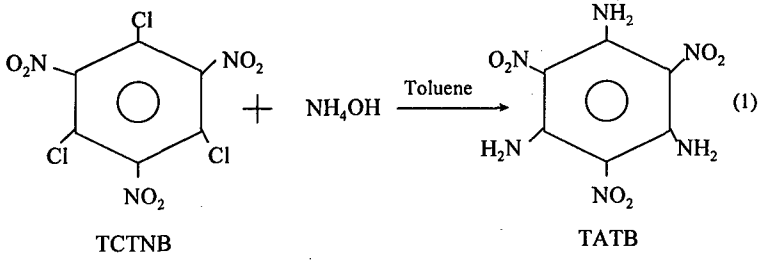

TCTNB TATB (1)

Particle Sizing

All particle sizing was done on a Horiba LA-900 Laser Scattering Particle Size Distribution Analyzer. This instrument uses the principles of the Mie scattering theory for measuring the size and distribution of particles suspended in a liquid medium. Two light sources, a 632.8 nm He-Ne laser and a blue and red

monochromed tungsten lamp, are used in the instrument. After the light beam has been scattered by the particles in the measuring cell, it passes through the condenser lens and is focused on the 18 unit detector. The intensity and angle of scattered light are converted into electrical signals, which are then used to calculate the size distribution of the particles.[6] The instrument is capable of measurements from 0.04 to 1000 μm.

A small sample of the TATB powder was suspended in deionized water for particle sizing. Deionized water was also used as the dispersion fluid (~200ml) in the particle sizer. A peristaltic pump was used to circulate the sample and dispersion medium through the measuring cell. The sample was added drop-wise to the measuring cell until the percent transmission was in the desired range as indicated by the manufacturer. Duplicate samples of FP-, PG- and UF-TATB powders were analyzed three times each.

Various methods of particle dispersion were examined. Samples were dispersed through the use of the instrument's internal pumping system and ultrasonic bath (USB), the use of a 40 Watt ultrasonic probe (USP), and the addition of the dilute non-ionic surfactant Triton®X-100 (TX, manufactured by Rohm & Haas Company). The wattage and time of agitation with the ultrasonic probe were varied to determine the effect on particle dispersion. Samples were agitated for 5 minutes at 40 watts and for 12 minutes at 100 watts using the ultrasonic probe.

Additionally, two sample concentrations were analyzed to examine effect of sample concentration on particle size results. Samples were suspended in water containing dilute Triton X-100, agitated for 10 seconds at 40 watts using the ultrasonic probe and added dropwise to the particle sizer until the percent transmission had dropped to approximately 95% and 70%.

RESULTS AND DISCUSSION

Synthesis of FP-TATB

Lemon-colored TATB was obtained by the amination of TCTNB in toluene with ammonium hydroxide solution under the influence of ultrasonic waves. This method of preparing TATB by ultrasonication is unique and economical. The amination reagent used is an ammonium hydroxide solution (NH_4OH), instead of ammonia gas, thus eliminating the tedious monitoring of gas pressure during amination. This method is more economical since the process is less complicated and time-consuming than previously documented methods, and the hazardous solvent toluene used in the process is regenerated from the waste stream by distillation and can be employed for further amination reactions.

Particle Size Distribution

The samples suspended in deionized water alone, with no additional method of powder disbursement, were difficult to keep in suspension. The high surface tension of the water resulted in a "skin" of powder that tended to adhere to glassware and instrument parts. Powder suspended in deionized water alone tended to re-agglomerate readily, making it difficult to obtain representative particle size distribution data. As a result, both the water alone samples of UF-TATB and FP-TATB resulted in a larger mean and median particle size and wider particle size distribution (see Figure 1) than the same powder when some additional method of powder dispersion was employed. The PG-TATB also resulted in a larger mean and median particle diameters when dispersed in deionized water alone. Figures 2, 3, and 4 compare the particle size distributions for UF-, PG- and FP-TATB samples suspended in deionized water alone with the samples suspended in deionized water plus the use of an additional powder dispersion method.

According to the results obtained in these experiments, for these three powders, the use of deionized water alone was not sufficient to ensure adequate suspension of the powder. An additional dispersion method, such as ultrasonic agitation and/or the use of a surfactant, resulted in a more uniform suspension of the powder. However, the exact method of powder dispersion had little effect on the median particle size or particle size distribution, as also shown in Figures 2, 3,

and 4. Tables 1, 2, and 3 summarize the particle size results. The addition of a small amount of dilute Triton X-100 greatly aided sample dispersion. Although the use of the ultrasonic bath or probe alone were acceptable methods of sample dispersion, the addition of the surfactant made cleaning of the instrument between sample runs much easier.

TABLE 1: UF-TATB Particle Size Results (based on volume)

Preparation	Mean (μm)	Median (μm)
DI water	18.84	8.83
DI water, USB	5.70	5.06
DI water, USP	5.70	5.12
DI water, Triton® X-100	6.35	5.65
DI water, Triton® X-100,USB	5.67	5.01
DI water, Triton® X-100,USP	5.65	4.95

TABLE 2: FP-TATB Particle Size Results (based on volume)

Preparation	Mean (μm)	Median (μm)
DI water	42.04	27.16
DI water, USB	15.95	12.68
DI water, USP	13.77	12.41
DI water, Triton® X-100	16.04	14.70
DI water, Triton® X-100,USB	15.56	13.39
DI water, Triton® X-100,USP	14.91	12.97

TABLE 3: PG-TATB Particle Size Results (based on volume)

Preparation	Mean (μm)	Median (μm)
DI water	75.94	72.86
DI water, USB	56.00	54.86
DI water, USP	54.33	54.36
DI water, Triton® X-100	54.62	56.22
DI water, Triton® X-100,USB	54.18	54.76
DI water, Triton® X-100,USP	54.50	55.18

The particle sizing results for experiments using increased agitation time and wattage during samples preparation indicated there was little, if any, effect on the PG- and UF- TATB powders. The FP-TATB did show some slight reduction in mean particle size when subjected to the same sample preparation. Mean particle size results are shown in Table 4.

TABLE 4: Mean Particle Size Results (based on volume)
for Increased Agitation Time During Sample Preparation

Preparation	FP-TATB	PG-TATB	UF-TATB
10 sec USP/40 watts	14.91 μm	54.50 μm	5.65 μm
5 min USP/40 watts	11.34 μm	55.69 μm	5.89 μm
12 min USP/100 watts	8.85 μm	53.02 μm	5.17 μm

Particle sizing results from the higher sample concentration (lower percent transmission) were very similar to the results from the lower sample concentration

(higher percent transmission). For the powders examined here, there appears to be little, if any, effect due to increased sample concentration. Mean particle size results are shown in Table 5.

TABLE 5: Mean Particle Size Results (based on volume) for Increased Sample Concentration

Preparation	**High Concentration ~70% Transmission**	**Low Concentration ~95% Transmission**
PG-TATB	55.12 μm	54.50 μm
UF-TATB	5.64 μm	5.65 μm
FP-TATB	17.70 μm	14.91 μm

CONCLUSIONS

We have demonstrated that fine-particle TATB can be made by a simple, one-step amination from TCTNB and ammonium hydroxide solution under the influence of ultrasonic irradiation (ultrasonication). This sonochemically-aminated TATB (FP-TATB) has particle size comparable to UF-TATB, an IHE booster material. Results from powder characterization studies on the TATBs illustrated that the arithmetic median particle diameters of FP-TATB is 15 micrometers while that of UF-TATB is 5 micrometers and that of PG-TATB is 55 micrometers.

Further studies on particle dispersion techniques indicated the need for an additional particle dispersion method, such as ultrasonic agitation and/or the use of a surfactant. The addition of a small amount of dilute Triton X-100 greatly aided sample dispersion. Although the use of the ultrasonic bath or probe alone were acceptable methods of sample dispersion, the addition of the surfactant made cleaning of the instrument between sample runs much easier.

Excessive ultrasonic agitation appeared to have little effect on the particle sizing results of both the UF- and PG-TATB powders. However, FP-TATB showed some reduction in mean particle diameters.

Use of heavily concentrated samples did not appear to significantly affect the particle sizing results. However, less concentrated samples are recommended to prevent detector overloading and powder agglomeration, in addition to conserving sample powder.

ACKNOWLEDGMENTS

Work was performed under the auspices of the Department of Energy by the Los Alamos National Laboratory under Contract Number W-7405-ENG-36.

REFERENCES

1. B. M. Dobratz, *The Insensitive High Explosive Triaminotrinitrobenzene (TATB): Development and Characterization—1888 to 1994*, Los Alamos National Laboratory, LA-13014-H, August 1995.

2. R. Lee, et al., *The Relationship Between the Shock Sensitivity and the Solid Pore Sizes of TATB Powders Pressed to Various Densities,* Proc., Eighth Symposium (Intl.) on Detonation, pp. 3-14, NSWC MP 86-194, Albuquerque, NM, July 1985.

3. A. G. Osborn and T. L. Stallings, *Ultrafine TATB - Lot No. 91190-135M-003, PXET-92-03,* Mason & Hanger - Silas Mason Co., Inc., Pantex Plant, Amarillo, TX, August, 1992.

4. K.-Y. Lee, *Study of Chemical Reactions Under the Influence of Ultrasound,* Ultrasonics International 93 Conference Proceedings, pp. 743-746, Vienna, 1993.

5. K. S. Suslick, et al., *Sonochemical Synthesis of Nanostructured Catalysts*, Mater. Sci. Eng., A204 (1-2), pp. 186-92, 1995.

6. Horiba Ltd., *Instruction Manual—Laser Scattering Particle Size Distribution Analyzer, LA-900,* Kyoto, Japan, July 1994.

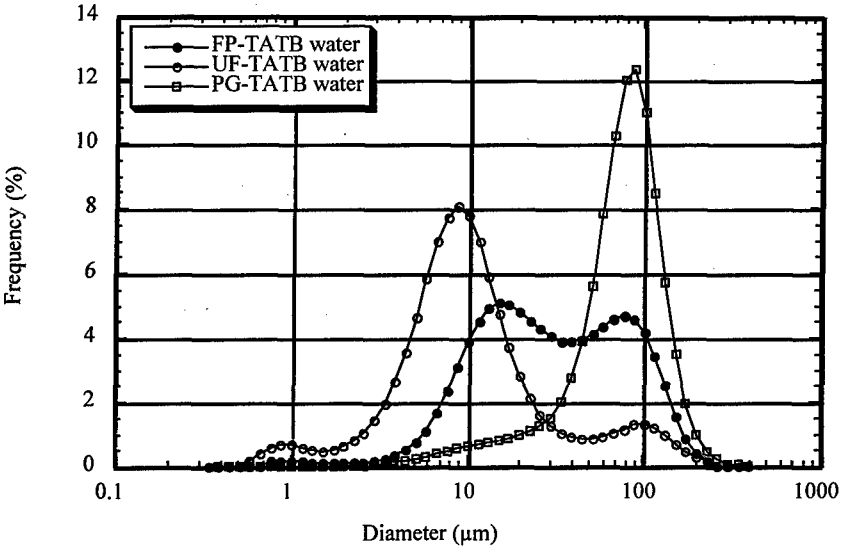

Figure 1

FP-, UF- and PG-TATB, suspended in deionized water, particle size distribution

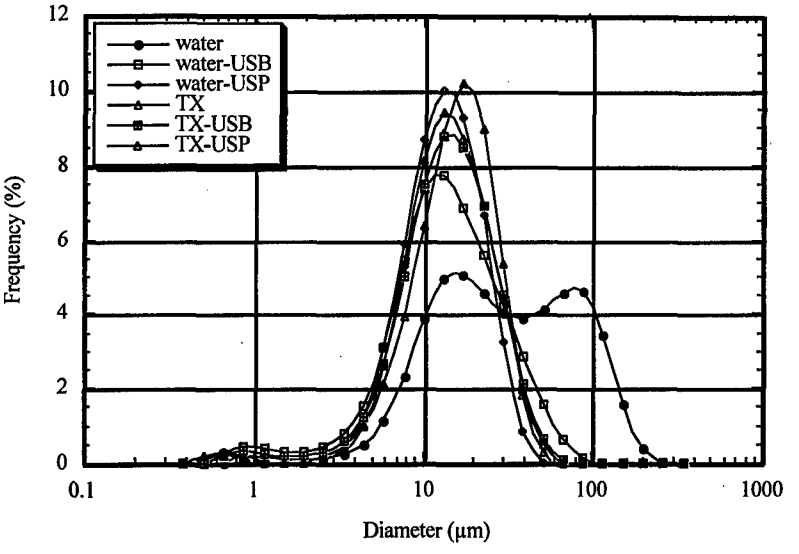

FIGURE 2

Comparison of powder dispersion methods for FP-TATB.

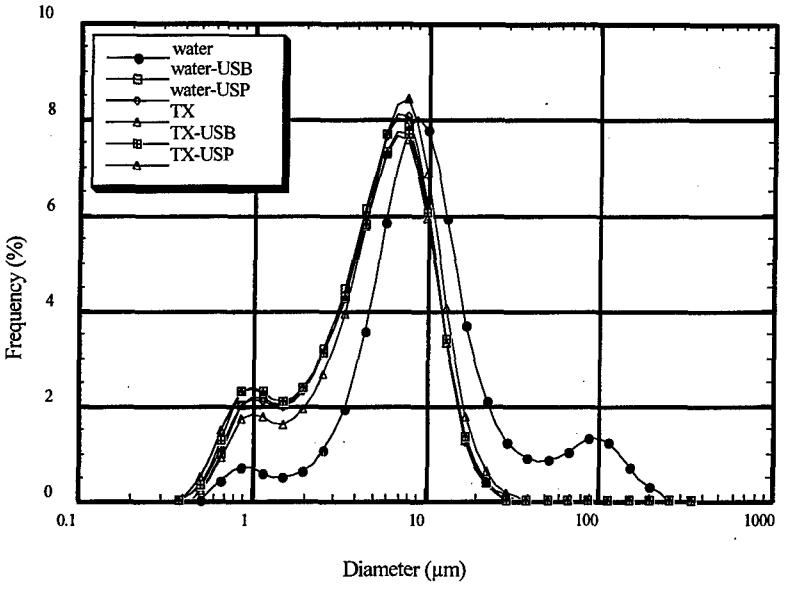

FIGURE 3

Comparison of powder dispersion methods for UF-TATB.

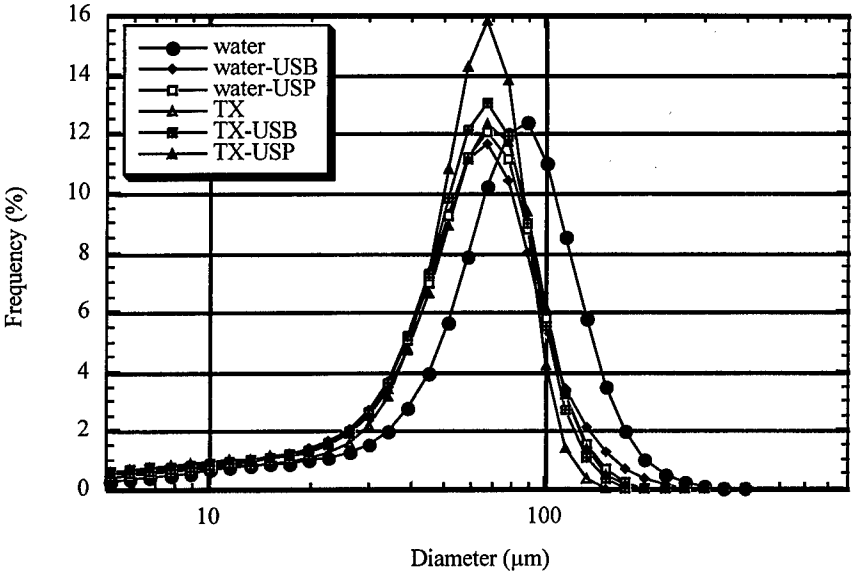

FIGURE 4

Comparison of powder dispersion methods for PG-TATB.

Mahlen von Explosivstoffen

Dr. E. Kleinschmidt, H. Späth
TDW GmbH, 86523 Schrobenhausen, BRD

Zusammenfassung

Beschrieben werden die bei TDW zur Zerkleinerung von festen Explosivstoffen bevorzugten Mühlentypen Kolloidmühle und Kugelmühle. Ihre Möglichkeiten und Grenzen werden im Vergleich zu anderen Zerkleinerungsverfahren dargestellt. Ergebnisse liegen vor allem für Hexogen (RDX) und Oktogen (HMX) vor.
Versuche mit beiden Mühlentypen werden beschrieben. Zur Kontrolle von Zwischen- und Endprodukten werden Laser-Granulometer und Luftstrahlsieb verwendet. Die Aussagefähigkeit beider Verfahren sowie der Einfluß unterschiedlichen Mahlguts auf die Ladungsherstellung werden gezeigt.

Abstract

Colloid-mill and coball-mill, the two at TDW prefered mill-types are introduced. Their possibilities and limits for crushing solid high explosives are shown and compared with other methods. Results are especially available for hexogene (RDX) and octogene (HMX).
Results of tests with both mill-types are shown. Laser-granulometer and air-jet sieve are used for control of intermediates and final products. The suitability for both methods is compared. The ability of different crushed material to manufacture PBX charges is shown.

1. Einleitung

Die Zerkleinerung von Stoffen ist eine Basisoperation der Explosivstofftechnologie. Für die Herstellung von Sprengladungen ist der Einsatz von Feingut in erster Linie aus verfahrenstechnischen Gründen erforderlich. Nur durch den Einsatz von bimodalen Körnungen sind Ladungen hoher Dichte bei minimalem Gehalt an Binder herzustellen. Die Korngrößen des Feingutes liegen zwischen 20 und 150 µm.
Für Treibladungen sind Korngrößen und spezifische Oberflächen zusätzlich von großer Bedeutung für das Abbrandverhalten. Korngrößen ‹ 10 µm sind meist üblich. Durch den verstärkt zu erwartenden Einsatz von Nitraminpulvern gewinnt die Herstellung und Charakterisierung von sehr feinem Hexogen, Oktogen und auch von CL20 zunehmend an Bedeutung (Anlage 1).

2. Zerkleinerungsverfahren

Mahlverfahren sind seit Jahrzehnten Stand der Technik auch für die Zerkleinerung von Explosivstoffen. Die Grundprinzipien des Mahlens sind seit langem bekannt, verbessert hat sich in erster Linie die Leistungsfähigkeit und Sicherheit der Geräte (Anlage 2).
Die Fließbett-Gegenstrahlmühle (fluid energy mill) wird vielfach zum Mahlen von Ammoniumperchlorat (APC) eingesetzt. Das Mahlgut wird in einem Gasstrom fluidisiert. Die Teilchen prallen mit hoher Geschwindigkeit aufeinander und werden zerkleinert. Korngrößen bis zu 1 µm werden damit erzielt. Nachteil dieses Verfahrens ist wie bei allen Trockenmahlverfahren das Fehlen eines phlegmatisierenden Fluids. Risiken wie elektrostatische Aufladung oder Staubexplosionen sind beim Zerkleinern von Explosivstoffen besonders zu beachten.

In Rotor-Stator-Mühlen (colloid mills) wird das Mahlgut als Suspension eingesetzt. Für organische Substanzen (RDX, HMX) dient Wasser als Fluid, für wasserlösliche Salze (APC, AN) kann Isoproponal verwendet werden. Durch Variation des Mahlspaltes kann der Zerkleinerungsgrad beeinflußt werden. Korngrößen bis zu 20 µm sind erreichbar (Anlagen 3, 4).

Ebenfalls in Suspension arbeiten die Kugelmühlen (coball-mills). Das Mahlgut wird als Suspension durch eine mit Mahlkugeln gefüllte Kammer gepumpt. Durch wiederholten Kontakt mit den Mahlkugeln wird das Mahlgut zerkleinert. Mit dem Verfahren werden Korngrößen bis zu 1 µm Durchmesser erzielt. Die Leistung der Mühle kann durch Variation von Kugelfüllung, Durchflußrate der Suspension sowie durch das Verhältnis Mahlgut/ Fluid beeinflußt werden (Anlage 5).

Hohe Bedeutung kommt auch den verschiedenen Kristallisationsverfahren zu. Sie bieten ein hohes Maß an Sicherheit (keine mechanische Belastung des Mahlgutes) bei gleichzeitig hoher Leistungsfähigkeit (Korngrößen von 1 - 1000 µm sind realisierbar). Probleme lassen Stoffe mit mehreren Kristallmodifikationen (HMX, CL20, AN) erwarten.

2.1 Zahnkolloidmühle

Zahnkolloidmühlen werden bei TDW sowohl im Technikum wie in der Produktion eingesetzt. Mahlgut sind in erster Linie RDX und HMX. Die zur Herstellung von Sprengladungen benötigten mittleren Korngrößen liegen meist zwischen 50 und 100 µm. Bei einem

Ausgangsmaterial von 200 - 600 µm Korngrößen werden die gewünschten Werte in einem Mahlvorgang erreicht.
Einflußgrößen sind die Einstellung des Mahlspaltes sowie in geringerem Umfang die aufgegebene Mahlgutmenge (Anlagen 6,7).
Korngrößen von ‹ 50 µm sind in 2 Mahlgängen zu erzielen. Bei geöffnetem Mahlspalt 2 wird das Mahlgut auf ca. 100 µm zerkleinert. Es wird in die Aufnahme zurückgeführt und bei geschlossenem Spalt erneut gemahlen. Die damit erzielte mittlere Korngröße von ca. 30 µm stellt annähernd die Leistungsgrenze des beschriebenen Mühlentyps dar (Anlage 8).

2.2 Kugelmühle

Mit der im Technikum der TDW vorhandenen Kugelmühle können Korngrößen von 1 - 20 µm erzielt werden. Das Ausgangsmaterial ist auf Korngrößen von 50 - 150 µm vorzerkleinert.

Variationsparameter sind:
- Suspensionsgrad (Anlage 9)
- Durchflußrate (Anlage 9, 10)
- Wahl des Fluids (Isoproponal für Salze, Anlage 11)

3. Charakterisierung des Mahlgutes

Unverzichtbare Ergänzung jedes Mahlvorganges ist die Charakterisierung des Mahlgutes. Eine Vielfalt von Verfahren ist bekannt und wird eingesetzt (Anlage 12). Die Auswahl von geeigneten Verfahren hängt vom jeweiligen Anwendungszweck und auch von der jeweiligen Partikelgröße ab. Zur Prozeßkontrolle genügt meist 1 Verfahren, werden dagegen neue Materialien oder Verfahren erprobt, so ist der Einsatz mehrerer Meßverfahren erforderlich (Anlage 13).

Das Luftstrahlsieb (mechanisches Sieb) ist für Korngrößen von ca. 10 µm bis zu mehreren Millimetern geeignet. Zur Erstellung einer Körnungslinie muß mit 4 - 8 Siebgrößen gearbeitet werden. Von Nachteil - vor allem bei sehr teuren Stoffen wie CL20 - ist der hohe Materialbedarf von ca. 20 g pro Sieb.

Laser-Granulometer sind zunehmend Stand der Technik zur Charakterisierung von Feingut. Sie sind für Korngrößen von 0,1 - 100 µm einsetzbar. Die Analysensubstanzen sind in Wasser oder Isoproponal suspendiert, pro Messung genügen wenige mg Substanz. Gemessen wird das Volumen der Partikel, angegeben wird der Durchmesser der volumengleichen Kugel. Ergebnisse können durch stark unterschiedliche Kornformen des Mahlgutes verfälscht werden.

Ein Verfahren für sehr feinkörniges Material (‹ ca. 30 µm) ist die Sedimentationsanalyse. Sie liefert zuverlässige, aussagekräftige Ergebnisse. Wegen des großen Zeitbedarfs von bis zu mehreren Tagen pro Analyse kommt das Verfahren in erster Linie für Forschungszwecke in Frage.

Zur Charakterisierung von Treibstoff Komponenten ist die Bestimmung der spezifischen Oberfläche nach dem BET-Verfahren von Bedeutung. Aussagekräftige Werte erhält man

für Partikel von ‹ 10 µm. Von Nachteil ist der relativ große Zeitaufwand für die Messung sowie der geringe Informationsgrad. Man kann eine Substanz nicht mit einer einzigen Zahl (spezifische Oberfläche: m^2/g) ausreichend charakterisieren.

Mikroskopieverfahren (Lichtmikroskop, Raster Elektronen Mikroskop) sind als Ergänzung zu den vorgenannten Verfahren wichtig. Sie geben Hinweis auf die Form von Partikeln. Die in der Anlage 13 dargestellten Oktogenkristalle sind mit einem Luftstrahlsieb allein nicht zu unterscheiden. Ihre unterschiedliche Kornform kann sich allerdings auf die Verarbeitung auswirken.

4. Einfluß von Korngrößen auf die Ladungsherstellung

Für eine gießbare PBX Rezeptur mit 90 % Oktogen und 10 % HTPB Binder wurde unterschiedlich hergestelltes Feinoktogen eingesetzt. Die beiden Feinoktogene sind bei jeweils 30 µm mittlerer Korngröße mit dem Luftstrahlsieb nicht zu unterscheiden.
Im Laser-Granulometer dagegen zeigt das gemahlene Produkt eine breite Kornverteilung mit mehreren Maxima im Bereich von 1 - 100 µm, das durch Umkristallisation hergestellte Produkt annähernd eine Gaussverteilung mit einem Maximum (Anlagen 14, 15).
Den Viskositätsverlauf beider Mischungen zeigt Anlage 16. Mit dem Mahlprodukt wird die zum Gießen erforderliche niedrige Viskosität nach 30 Minuten, mit dem gemahlenem Produkt dagegen erst nach 75 Minuten erreicht.

5. Zusammenfassung

Es wurden Möglichkeiten aufgezeigt, das zur Herstellung von Spreng- und Treibladungen erforderliche Feingut herzustellen und zu charakterisieren. Bei Nutzung der heute gegebenen technischen Möglichkeiten können hohe Standards an Leistung und Sicherheit erreicht und reproduziert werden.

Anzumerken bleibt, daß von explosiven Gefahrstoffen die Rede ist. Die Einhaltung und gegebenenfalls die Verbesserung von Sicherheitsstandards muß trotz aller technischen Verbesserungen mit an erster Stelle stehen.

Daimler-Benz Aerospace
TDW Gesellschaft für verteidigungstechnische Wirksysteme mbH

Feingut für Spreng- u. Treibladungen

Betrachtete Stoffe

RDX, HMX, CL20 (nicht wasserlöslich)
APC, AN (wasserlöslich)

Erforderliche Korngrößen

Treibladungen:	bevorzugt < 10 µm
Sprengladungen:	bimodale Mischungen
	grobkristallin 200 - 600 µm
	Feingut 30 - 150 µm

Anlage 1

Daimler-Benz Aerospace
TDW Gesellschaft für verteidigungstechnische Wirksysteme mbH

Zerkleinerung von Explosivstoffen

Verfahren	erzielbare Korngrößen [µm]	Bewertung
Fließbett-Gegenstrahl (Fluid energy mill)	1 - 10	Mahlgut nicht phlegmatisiert (Sicherheit!)
Rotor-Stator-Mühle (colloid mill)	20 - 150	Mahlgut phlegmatisiert
Kugelmühle (coball mill)	1 - 50	Mahlgut phlegmatisiert
Kristallisation	1 - 1000	Mahlgut wird mechanisch nicht belastet

Anlage 2

Daimler-Benz Aerospace
TDW Gesellschaft für verteidigungstechnische Wirksysteme mbH

Zahnkolloidmühle

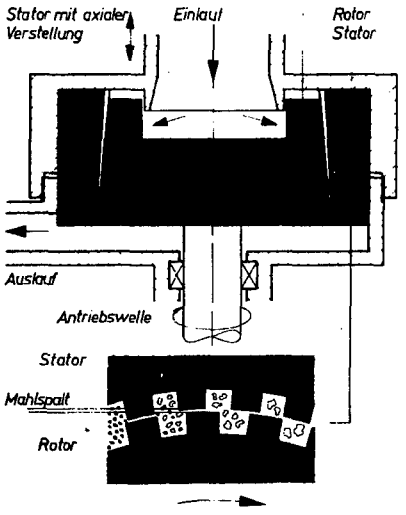

Schematische Darstellung

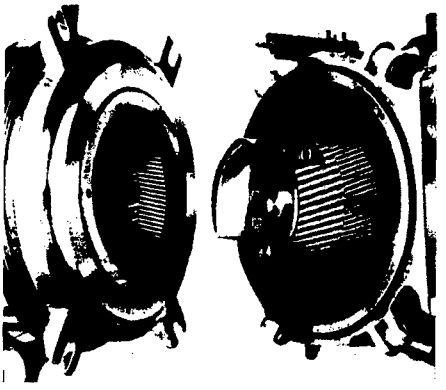

Mühle geöffnet

Anlage 3

Daimler-Benz Aerospace
TDW Gesellschaft für verteidigungstechnische Wirksysteme mbH

Zahnkolloidmühle

Versuchsaufbau

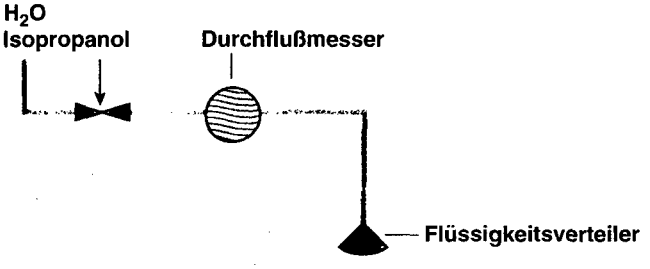

H_2O:
Organische Substanzen (RDX, HMX)

Isopropanol:
Salze (APC, AN)

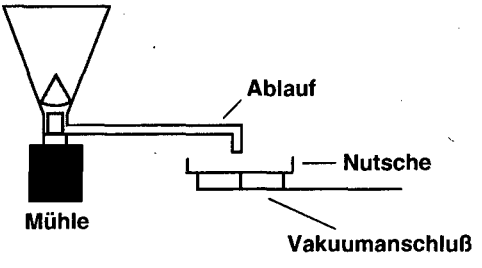

Anlage 4

Daimler-Benz Aerospace
TDW Gesellschaft für verteidigungs technische Wirksysteme mbH

Co-Ball Mill

Rührwerksmühlen für hohe Leistungen im Feinmahlbereich 1 - 50µm

Aufbau - Funktion

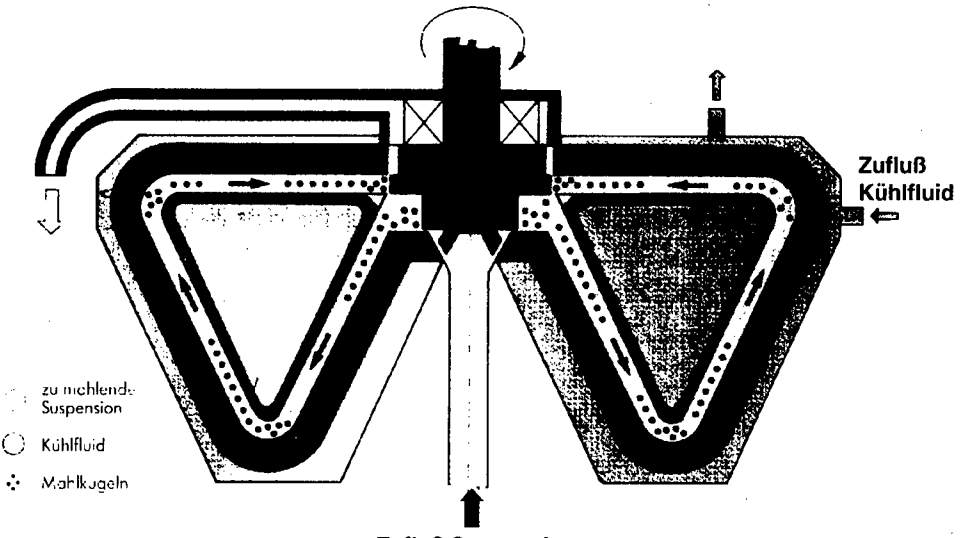

Anlage 5

Daimler-Benz Aerospace
TDW Gesellschaft fur verteidigungs-technische Wirksysteme mbH

Rotor-Stator-Mühle

Einfluß des Mahlspaltes

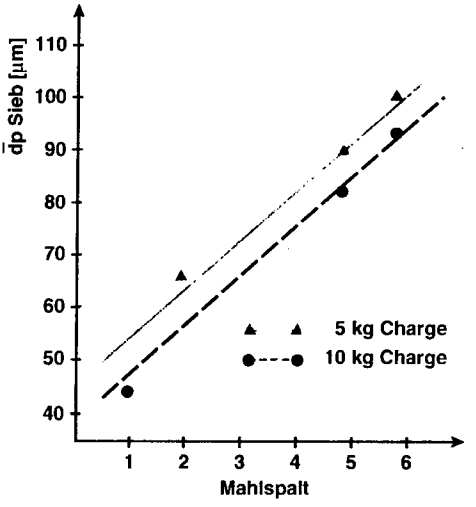

Einfluß der Einwaage

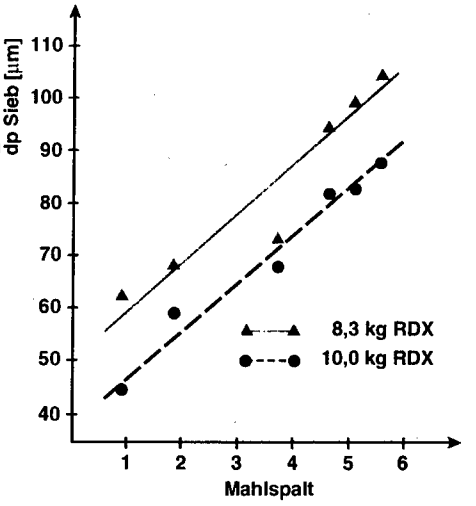

Anlage 6, 7

Rotor-Strator-Mühle

Vorzerkleinern / Mahlen

Mahlgang	Mahlspalt	Korngröße Beginn [µm]	Korngröße Ende [µm]
Vorzerkleinern	4	300	100
Mahlen	0	100	30

Daimler-Benz Aerospace
TDW Gesellschaft für verteidigungstechnische Wirksysteme mbH

Kugelmühle (Einfluß Füllgrad)

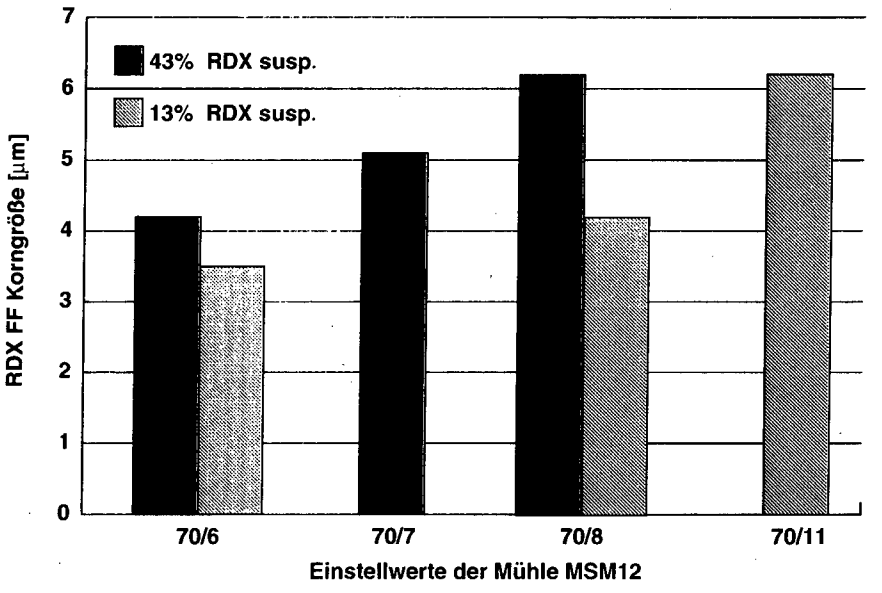

Daimler-Benz Aerospace
TDW Gesellschaft für verteidigungstechnische Wirksysteme mbH

Kugelmühle (Einfluß in Füllgrad u. Durchfluß)

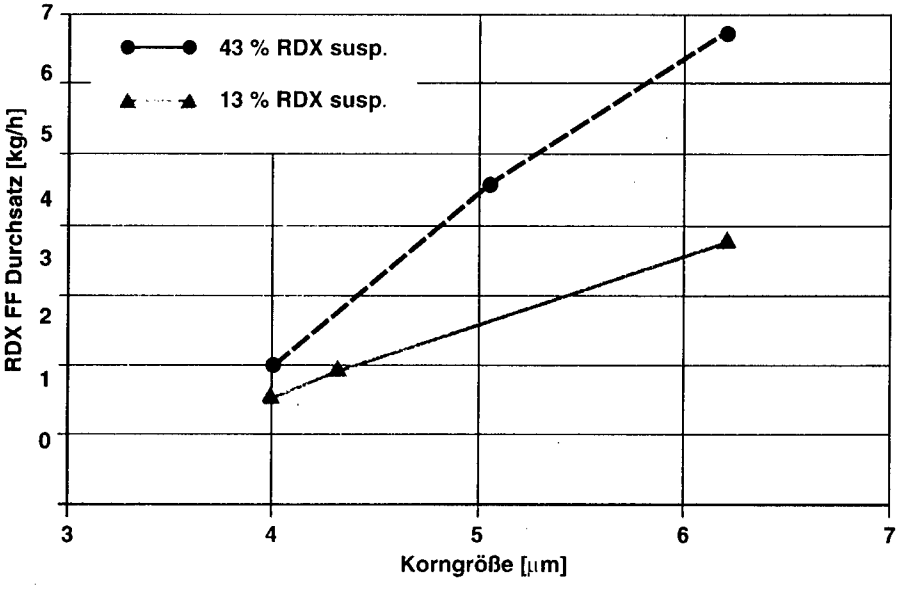

Anlage 10

Daimler-Benz Aerospace
TDW Gesellschaft für verteidigungstechnische Wirksysteme mbH

Kugelmühle (Mahlen von APC)

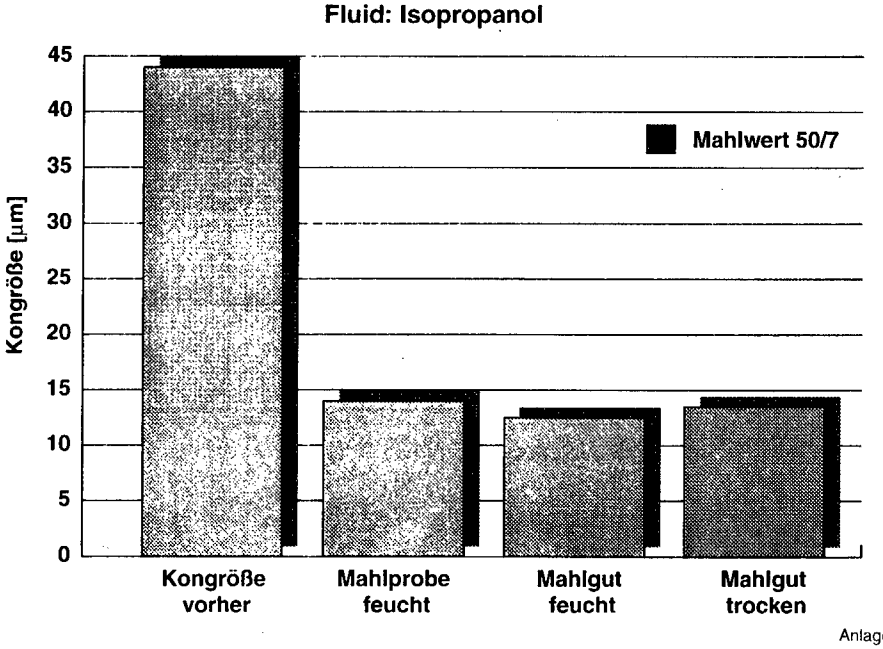

Anlage 11

Charakterisierung von Mahlgut

Verfahren	Meßbereich [µm]	Bewertung
Luftstrahlsieb	10 - 1000	wenig Aussage zur Kornform, hoher Materialbedarf
Laser-Granulometer	0,1 - 100	wenig Aussage zur Kornform, geringer Materialbedarf, schnell
Sedimentation	0,1 - ca. 30	Meßzeit bis zu einigen Tagen
Spezifische Oberfläche (nach BET)	< 10	wichtig für Treibstoff-Komponenten
Mikroskopie	0,1 - 1000	Ergänzung zur Partikelmessung, Aussage über Kornform

Daimler-Benz Aerospace
TDW Gesellschaft für verteidigungstechnische Wirksysteme mbH

Verschiedene Kornformen von HMX

Siebanalyse: nahezu identisch
REM (x100): verschiedene Kornformen

Daimler Benz Aerospace
TDW Gesellschaft für verteidigungstechnische Wirksysteme mbH

Laser-Granulometer

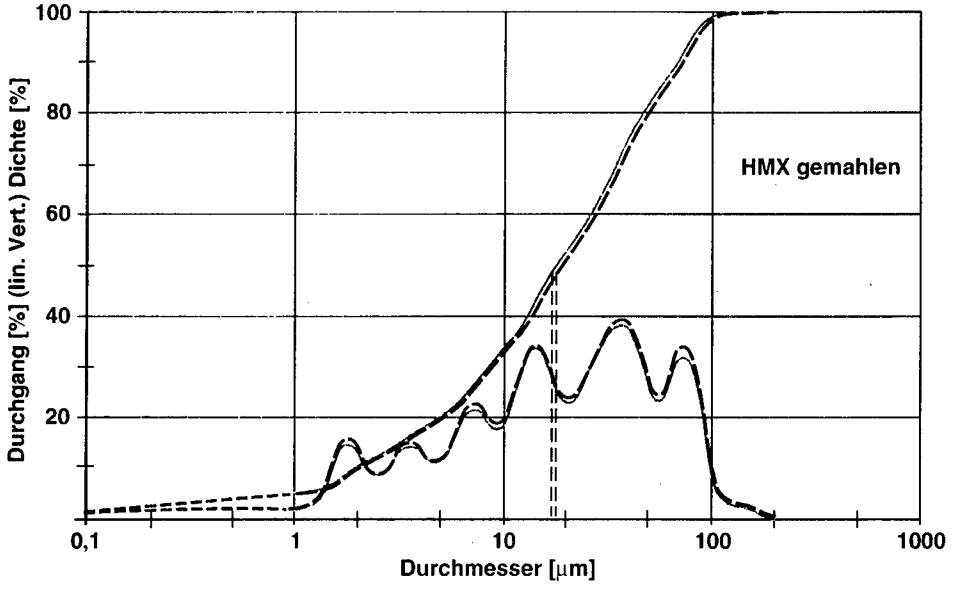

Anlage 14

Daimler-Benz Aerospace
TDW Gesellschaft für verteidigungstechnische Wirksysteme mbH

Laser-Granulometer

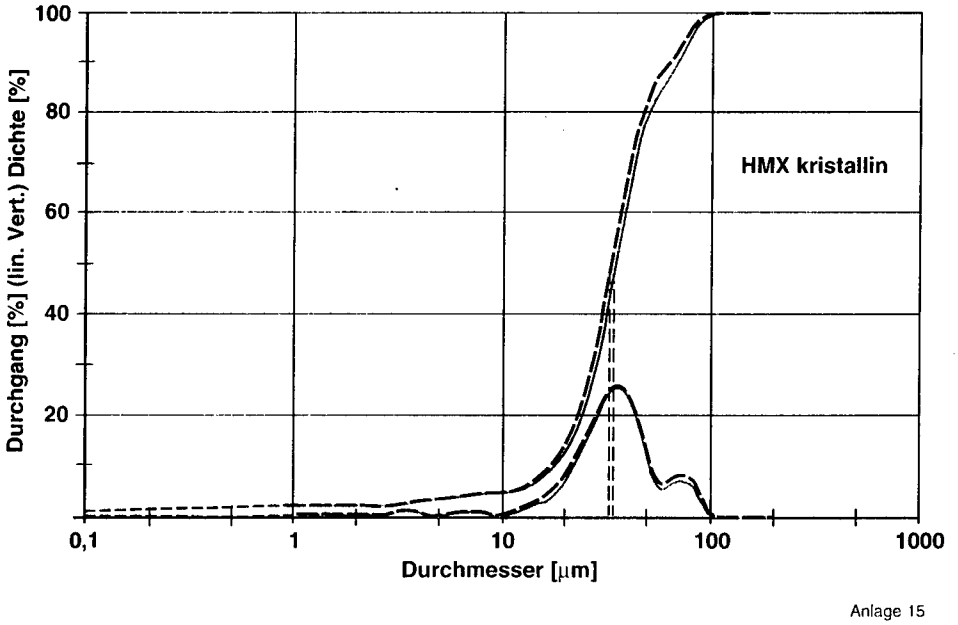

Anlage 15

Daimler-Benz Aerospace
TDW Gesellschaft für verteidigungstechnische Wirksysteme mbH

Kornverteilung und Viskositätsverlauf

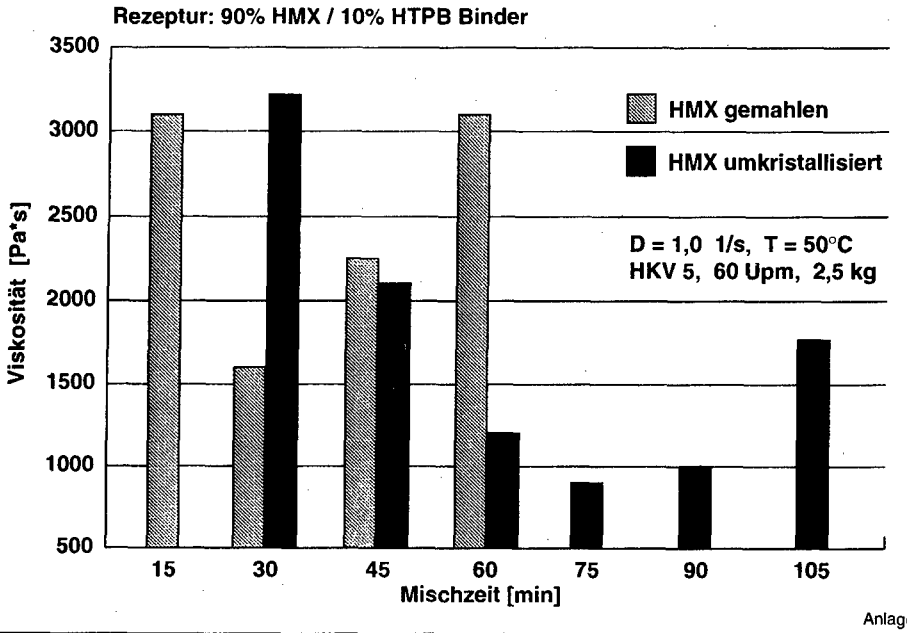

Anlage 16

MOLECULAR MODELLING STUDIES OF RDX AND ITS MORPHOLOGY

John Kendrick

ICI Technology, Wilton, Middlesbrough, TS90 9JE

Bill Leeming

ICI Explosives, Ardeer, UK

Adam Cumming, Peter Flower and Christopher Leach

DERA, Fort Halstead, UK

1. ABSTRACT

The paper reports on some ab initio, molecular orbital and molecular mechanics calculations of the nature of the nitramine group in the energetic material RDX. Preliminary calculations on dimethylnitramine are used to establish the reliability of the calculations used. The calculations are used to understand the nature of the conformation on the nitramine group in the RDX ring and to predict the expected morphology of the RDX crystal.

2. INTRODUCTION

The nitramine group is an important molecular constituent of many of the newer energetic materials. The present calculations on dimethylnitramine and RDX allows comparison of the predictions of theory and computation with the available experimental information, establishing a benchmark for the level of theory which is required to reliably predict the properties of these materials.

In particular the studies of RDX allows the study of the nitramine group in a ring structure. The constraints of the ring imposes additional restraints on the nature of the hybridisation of the nitrogen in the ring, which molecular mechanics may not easily be able to model. The accurate molecular orbital calculations presented here are used to verify the molecular mechanics force field. This force field is the used to calculate the crystalline lattice and molecular structure which can be compared directly with experiment.

Finally information concerning the crystal lattice is used to predict the habit of the crystal. Comparison with previous work indicates that the dielectric constant of the solvent from which the crystals are grown may play an important part in determining the relative stability of the growing surfaces. Consequently estimates are made of the electrostatic nature of the RDX surfaces and the expected changes in stability compared with experiment.

3. METHODOLOGY

3.1 Quantum Mechanics

Molecular Orbital calculations at the Hartree-Fock and 2nd order perturbation theory, MP2, level of theory were carried out using the GAMESS_UK ab initio code (1). Various basis sets were used for the calculations including 6-31G and 6-31G**. Semiempirical calculations were also employed using the AM1 hamiltonian available in MOPAC (2).

3.2 Molecular Mechanics

All molecular mechanics calculations were carried out using the Cerius2 (3) computer program. The Dreiding II force field was used and in some cases was modified in the light of the ab initio calculations. Atomic charges were calculated by fitting the atom centred charges to the electrostatic potential calculated using ab initio theory. The crystal structures were calculated using periodic boundary conditions with the electrostatic energy being calculated using the Ewald technique. Estimates of the crystal habit were made using the method of Donnay and Harker as made available in the Cerius morphology module.

4. DIMETHYLNITRAMINE

The crystal structures of dimethylnitramine (DMN) are available (4-6) and have been obtained from the Cambridge Crystallographic database. All crystal structures reported belong to the P21/m space group, which is monoclinic. Because of the relatively small size of the molecule it has been possible to perform quite accurate ab initio calculations of the gas phase, isolated molecule. These were performed to understand the nature of the nitramine group better and to transfer this learning to the RDX molecule which we will discuss later.

4.1 Ab Initio Calculations

Ab Initio Hartree Fock calculations were performed using a double zeta 6-31G basis set and the results are shown in Table 1 under the column entitled SCF.

Table 1
Gas Phase Energies of DMN

Conformation	Total Energies (Hartree)		Relative Energies (kcals/mole)	
	SCF 6-31G basis	MP2 6-31G**	SCF	MP2
DMN1	-337.706793	-338.731985	1.9	1.7
DMN2	-337.707944	-338.732717	1.2	1.3
DMN3	-337.709879	-338.734766	0.0	0.0
DMN4	-337.673691	-338.697742	22.7	23.2
DMN5	-337.709619	-338.735731	0.16	-0.60

The definitions of the different conformers DMN1 to DMN5 are given in the Table 2 below.

Table 2
DMN Conformers

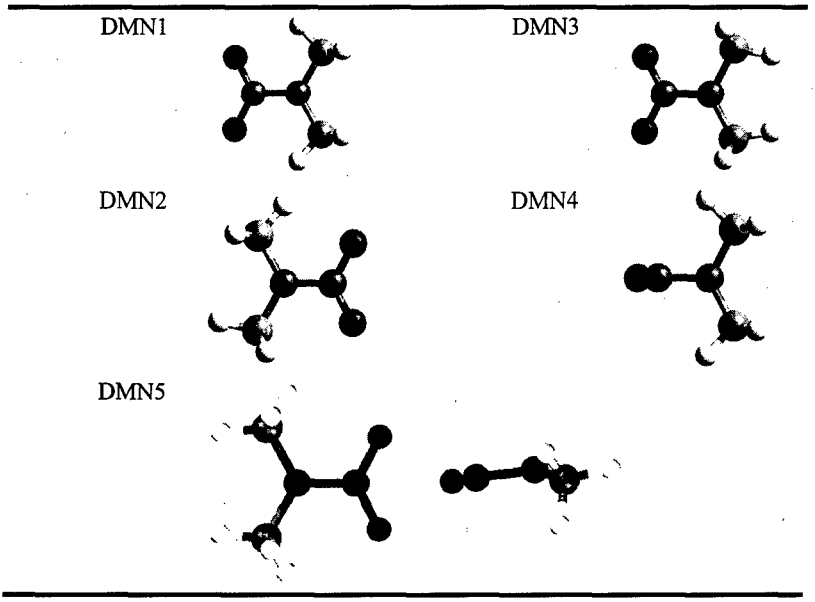

These calculations predict geometries of various conformations of DMN. They predict that the conformation with the N-N-O2 atoms all lying in the same plane is the most stable. Rotation of the -NO2 group, so that the oxygens are lying in a plane perpendicular to the plane of the rest of the molecule, is very expensive energetically (22.7 kcals/mole) and indicates that any complete rotation about the N-N bond will be very slow. The CH_3 groups, on the other hand, appear to be fairly free to rotate. No calculations on barriers to rotation have been performed, but calculations of the three different conformers of DMN, brought about by rotating these groups, indicates that they lie within 2 kcals/mole of each other. The central nitrogen connected to carbon and nitrogen could feasibly by pyramidal and the nature of the calculations so far would not show this, as they maintain the high initial symmetry provided by the starting geometry of the molecule. Consequently, calculations were performed at a lower (Cs) symmetry, which indicated at a Hartree-Fock level that there was a minimum energy conformation with a pyramidal nitrogen only 0.2 kcals/mole higher in energy than the overall minimum energy configuration.

The 6-31G basis is known to favour planar nitrogen conformers over pyramidal ones, so it was decided to repeat the calculations using the 6-31G** basis set and to include correlation effects through the Moller Plesset second order perturbation theory method (MP2). This quite routine calculation is much more expensive than standard Hartree Fock methods, but can be expected to give very accurate bond lengths and angles, given a large enough basis set. Interestingly, this method predicts that the pyramidal nitrogen structure is the most stable by about 0.6 kcals/mole. Its is to be expected therefore that DMN is a fairly flexible structure whose average geometry is a planar one, but whose minimum equilibrium structure, in the gas phase, show a pyramidal central nitrogen.

Table 3 shows the predicted and experimental structural parameters. The table compares the structural parameters for the optimised DMN3 structure, rather than the minimum energy MP2 energy. It can be seen that there is good agreement between the calculated and experimental structures at all levels of theory.

Table 3
A Comparison of Gas Phase, Ab Initio and Molecular Mechanics Results with Experiment Crystal Data for DMN

Bond Length (Å) Bond Angle (degs)	Expt (6)	MP2	RHF	MM Dreiding	MM Modified
N-O	1.23	1.24	1.20	1.21	1.21
N-N	1.33	1.36	1.33	1.33	1.33
N-C	1.45	1.45	1.45	1.45	1.45
C-C	3.12	2.59	2.58	2.49	2.49
O-N-O	124.2	126.5	125.3	113.4	122.3
O-N-N	117.9	116.7	117.4	123.4	118.8
N-N-C	117.7	116.8	117.5	120.9	118.0
C-N-C	124.2	126.4	125.1	118.0	123.9

4.2 Molecular Mechanics

The applications of molecular mechanics to chemicals such as these is difficult, as the force fields available within the packages are not well parameterised for energetic materials. Calculation of the gas phase equilibrium structure of DMN, without any changes to the force fields, illustrates this well, as can be seen in Table 4 in the column labelled; "MM Dreiding", where the prediction of the angles around the central N is poor. Modification of the force

field, by changing the force constant term for the C-N-C bond stretching term, overcame this problem and improved the force field considerably.

Having achieved this, the new force field was used to predict the crystal structure of the DMN. Here, the energy of 3 dimensional periodic structures was minimised with respect to all the atom co-ordinates and with respect to the crystal cell dimensions. The program did not maintain the space group symmetry of the molecule, although this could be achieved if the molecule is assumed to be rigid. Charges from the atoms were taken from potential derived charges (PDC). These charges give the best atom centred point charge model of the electrostatic potential of the molecule that is possible to derive directly from accurate ab initio calculations.

Two experimental determinations of the crystal structure of DMN have been reported (5 and 6). The results of reference 5 are shown using the notation used by reference 6, the so called type II lattice. Using the default force field, there is considerable discrepancy in one of the parameters, namely the lattice parameter along the same direction of the N-N bond. Further exploration of the discrepancy showed that the final structure was exceedingly sensitive to the orientation of the methyl groups. Experience with the ab initio calculations indicated that the methyl groups are probably rotating and a unified atom description of $-CH_3$ was adopted for the van der Waals interaction, whilst maintaining the H atoms as charged atomic centres. The results for this calculation are in much better agreement with the experimental results, being within 2% of the experimental values. No change was made to the C-N-C angle bending force constant to obtain this result.

Table 4
Comparison of Experimental and Calculated Crystal Structures

Cell Parameter	Experimental (Ref 5)	Experimental (Ref 6)	Minimised Default Force Field	Minimised Optimised Force Field
a (Å)	6.56	6.54	6.67	6.65
b (Å)	6.27	6.20	6.37	6.14
c (Å)	6.09	6.06	6.48	6.13
β (degrees)	123.5	123.7	125.7	125.8
Density (gms/cc)	1.44	1.46	1.34	1.47
Energy (kcals/mole)			85.8	77.20

The structure referred to in Table 4 is the so called high temperature form of the crystal as defined by the authors of reference 6. These authors studied a phase transition at 107°K and found that there was a low temperature form consistent with a doubling of the lattice along the c- direction, a change in point group from $P2_1/m$ to $P2_1/c$ and a change in molecular configuration consistent with a N-N bond forming an angle with the C-N-C plane of about 10° at 20°K.

In conclusion it appears that the molecular modelling work is capable of describing the nitramine unit reasonably well at the ab initio level, as long as a sufficiently large basis set is used. The molecular mechanics method has been tuned to predict the average structure of DMN and may still require some development in order to improve the description of the crystal. The final prediction of the crystal density is in good agreement with the experimental value. The changes made to the force field were mainly to account for the molecular motion which is likely to occur in the crystal. In particular, the force field ensures a planar central nitrogen molecule in the nitramine unit and a smeared out description of the repulsive van der Waals interaction for the methyl groups.

5. RDX

RDX is one of the simplest molecules possessing the nitramine group in a ring structure and it was for this reason, along with the extensive experimental information available about the molecule, that modelling work on this system was undertaken.

RDX has a 6 membered ring, with 3 nitramine groups positioned alternating around the ring. The ring itself can exist in a chair or a boat conformation and in addition the nitro groups of the nitramine units can be either orientated axially or equatorially with respect to the ring. This latter feature implies that the central nitrogen is pyramidal in nature, something which is not absolutely clear from the experimental evidence of DMN, but which is supported by the most accurate calculations.

Experimentally (7), RDX crystallises in space group Pbca, an orthorhombic crystal system. The six membered ring of RDX adopts a chair structure. One of the nitramine groups lies in an equatorial position to the ring with an N-N-C-N torsion angle of 145.6°. The other two nitramine groups occupy axial positions on the ring with torsion angles close to 90°. In the

following the various conformers will be referred to by 'aae', for example, which refers to two axial and one equatorial nitrogen in the ring.

Crystal packing effects obviously influence the conformation adopted by the molecule. Thus co-crystallisation with tetramethylene sulphone (8), causes RDX to adopt a chair configuration with one axial and two equatorial nitramines. Additional substitution on the ring also causes a conformation change,
2,4,6-trimethyl-1,3,5-trinitro-hexahydro-1,3,5-triazine (9) where one of the hydrogens of the CH_2 groups in the ring have been replaced by methyl groups, also adopts a configuration with one axial and two equatorial nitramine groups. Carbonylation of the ring results in a similar effect, with 1,3,5-trinitro-2-oxo-1,3,5-triazacylcohexane (10) also having 1 axial and 2 equatorial nitramine groups.

All of the experimental crystal structures found contain the RDX ring in the chair conformation.

5.1 Ab Initio and Semiempirical Calculations

Semiempirical and ab initio calculations using both the 6-31G and 6-31G** basis sets were performed on an isolated RDX molecule. Semiempirical calculations are not usually as reliable but they are very quick, and it was necessary to know whether they might be useful for further calculations. The results are shown together with the ab initio results in Table 5.

In fact the semiempirical calculations were unable to distinguish between the axial and equatorial nature of the nitramine groups and this was put down to its inability to describe the pyramidal nature of the central nitrogen. Only a single chair and a single boat conformer was found by the semiempirical method. The nitramine groups were always best described by an axial conformation, no equatorial conformations were found. The boat conformation was found to be about 6 kcals/mole higher in energy than the chair.

The ab initio Hartree Fock calculations, using a 6-31G basis, were in many ways similar to the semiempirical results. They were also unable to distinguish between the axial and equatorial conformers. The boat optimisations all converged to the same structure, which can probably be best described by *eea*, whilst the chair conformers also all optimised to the

same structure, namely *aaa*. These calculations predict the boat conformer to be slightly more stable than the chair by about 0.4 kcals/mole.

Table 5
Calculated Energies of RDX

Starting Configuration	Heat of Formation MOPAC (kcals/mole)	Hartree-Fock (Hartree) 6-31G	Hartree-Fock (Hartree) 6-31G**
Boat			
aaa	110.5	-892.004315	-892.516079
aae	105.0	-892.004317	-892.516079
eea	110.5	-892.004318	-892.516079
eee	110.4	-892.004317	-892.516079
Chair			
aaa	104.9	-892.002129	-892.514526
aae	104.9	-892.002136	-892.516608
eea	110.5	-892.002136	-892.516425
eee	104.9	-892.002135	-892.510037

The experience with DMN proves useful at this point since it is known that polarisation functions are needed to represent the pyramidal nature of the nitrogen. Calculations on RDX using a 6-31G** basis set do indeed discriminate between equatorial and axial nitrogens in the chair conformation. Calculations at this level still predict that there is only one boat conformer with a conformation best described as *eea*. The overall lowest energy structure found is that observed experimentally, namely the chair *eea* conformer, but this is only 0.3 kcals/mole lower in energy than the next most stable structure, the boat conformation. The agreement is probably fortuitous as there are other energetically low lying conformers and no account has been made of packing energies.

5.2 Molecular Mechanics prediction of Crystal Packing

Taking the lowest energy structure calculated using the 6-31G** basis calculations, the electrostatic potential was used to derive PDC charges which were used in the molecular mechanics minimisation of the full three dimensionally periodic crystal. This minimisation does not maintain the space group symmetry of the system but allows lattice parameters and inter and intra-molecular parameters to adjust so as to minimise the total energy of the

system. Alternatively the molecules can be held rigid and the packing can be adjusted so as to minimise the total energy, whilst maintaining the space group symmetry of the system. Such an approach optimises the energy with respect to the lattice parameters and the intermolecular interactions. The results for both methods are shown in Table 6 and compared with experimental x-ray data.

Table 6
Comparison of Theoretical and Experimental Packing of RDX Crystals

	Experiment[8]	Calculations	
		Packing	Optimised
a (Å)	13.18	13.63	13.41
b (Å)	11.57	11.89	11.78
c (Å)	10.71	10.82	10.74
ρ (g/ml)	1.81	1.68	1.74

The packing approach with rigid molecules is predicting a density which is too low and all lattice dimensions appear to have enlarged somewhat. Full minimisation leads to a lower energy and to an improved density. The agreement to within 3% of the experimental lattice parameter is in line with the expected accuracy of these calculations.

5.3 Crystal Habit

Calculation of the predicted crystal morphology from the crystal data is very straightforward using the Bravais Friedel Donnay Harker Model (BFDH) available within the Cerius package (2). This model assumes a simple inverse relationship between the d-spacing of a growing crystal face and its rate of growth. Based on this and some simple symmetry rules which forbid the existence of certain faces, it is possible to predict the crystal shape. For RDX the calculation predicted that the {200}, {020}, {002}, {11-1} and {210} families of surfaces being visible.

Whilst the BFDH is very useful it is not a quantitative method. Generally surfaces predicted to be visible by BFDH methods are seen, but the size of the surfaces are also affected considerably by the way the crystals are grown, that is, the degree of supersaturation and the solvent used. Some experimental work for RDX has been reported by J.H. ter Horst et al (11). Growing from cyclohexane the crystals show a block like morphology with {200},

{020} and {002} surfaces dominating the crystals. When water is included with the cyclohexane the {111} surface becomes more dominant, but the {200} family of surfaces remains. Water seems to improve the crystal quality and saturation leads to the appearance of {210} surfaces. In γ-butyrolcatone the {210} and the {111} surfaces dominate the morphology with some appearance of the {002} surface.

Comparison with the predicted morphologies is difficult. As expected the visible surfaces are indeed those predicted to be present by both BFDH and attachment energy calculations. However the role of solvent is obviously key to the final morphology and consequently we have investigated the electrostatic nature of the significant surfaces. The electrostatic potential in a plane, 2Å above a surface has been calculated. Interestingly the largest electrostatic separation occurs on the {111} and the {210} surfaces and these are precisely the surface which are likely to be more stabilised by a polar solvent.

6. REFERENCES

1. M F Guest & J Kendrick - GAMESS_UK Manual, SERC Daresbury
2. MSI / BIOSYM Technologies Ltd., 9685 Scranton Rd., San Diego
   Cerius^2 molecular modelling package
3. J.P. Stewart
   MOPAC Program
4. W. Castain and E.G. Cox
   Nature 160 (1947) 826
5. B. Krebs, J. Mandt, R.E. Cobbledick and R.W.H. Small
   Acta Cryst. B25 (1979) 402
6. A. Filhol, G. Bravic, M. Rey-Lafon and M. Thomas
   Acta Cryst. B26 (1980) 575
7. C.S. Choi and E. Prince
   Acta Cryst. B28 (1972) 2857
8. B. Rerat, J. Berthou, A. Laurent and C. Rerat
   C.R. Acad. Sci. Ser. C, 267 (1968) 760
9. E.L. Golod, G.A. Lyushnina, M.A. Porai-Koshits, V.S. Kuzmin, V.A. Shlyapochhikov and V.K. Mikhailov
   Zh. Obshch. Khim. 50 (1980) 2110
10. R. Gilardi, J.L. Flippen-Anderson and C. George
    Acta Cryst. C46 (1990) 706
11. J.H. ter Horst, R.M. Geertman, A.E. van der Heijden and G.M. van Rosmalen, 27th International Annual Conference of ICT, page 126-1, 1996

METROLOGY TOOLS FOR THE CHARACTERIZATION OF EXPLOSIVE CRYSTAL PROPERTIES.

Lionel BORNE, Arnaud BEAUCAMP, Dominique FENDELEUR
French-German Research Institute of Saint-Louis (ISL)
B.P. 34 - 68301 Saint-Louis Cedex France.

Abstract

Explosive crystal microstructure has an influence on the processing and on the reactive behavior of energetic materials. Metrology tools are needed to study and to control the effects of the explosive crystal properties. These tools must provide accurate quantitative measurements. Advanced and sophisticated metrology tools are available for single crystal characterization. For instance, X-ray Lang topography method can be used to analyze the crystallographic volume distortion induced by located defects in a single crystal. But for particle batch processing and control, these very accurate tools are not adapted to extract parameters which must be representative of the set of particles of the batch.

In the field of energetic material processing and control, the main particle parameters to measure are the particle size, the particle shape, the particle surface porosity and the solvent inclusions inside the crystals. The specific needs for energetic material characterization are pointed out. Limits and accuracy of existing methods are discussed. New tools are described for solvent inclusions measurements.

The mercury intrusion porosimetry experiment and the BET gas sorption technique are used for particle surface characterization. Both methods are complementary, but we show that they do not provide all the required information. A small amount of pores whose sizes are located between 0.1 and 10 µm cannot be measured, and could play a role on the reactive behavior of energetic materials.

Solvent inclusions have been found to be an important property of explosive crystals. A good measure of these crystal internal defects is the crystal apparent density distribution curve of a batch of explosive particles. The ISL experimental setup is recalled. Performances and limits of this device are discussed and compared with other existing or potential methods.

1. Introduction

In a wide range of applications using particles, it is more and more important to get a fine control of the various particles properties and accurate metrology tools are needed. The effects of particles properties on the processing of energetic materials are well-known. The sensitivity of energetic materials can be strongly modified by several explosive crystal properties.

Our purpose is to report significant experimental correlations which demonstrate the isolated effect of a well defined explosive crystal property. Experimental works with careful measurements and checking of the explosive crystal properties are underlined.

First the role of the explosive crystal size is recalled. The effect of the solvent inclusions entrapped in the explosive crystals has been demonstrated using the ISL sort experiment. This experimental setup allows to sort the explosive crystals in function of their amount of solvent inclusions. This crystal sort provides also a measure of the explosive crystal apparent density. The accuracy and limits of this tool are discussed. To improve the characterization of crystal internal defects, the use of digital image analysis is investigated using optical microscopy with matching refractive index as the imaging method.

In the last part, the effects of the explosive crystal shape and the explosive crystal surface are carefully investigated. The specific needs to measure these explosive crystal properties are pointed out.

2. Effects of the explosive crystal properties on the sensitivity of the explosive cast formulations.

2.1 The explosive crystal size.

Moulard [1] has shown the effects of the median RDX crystal size on the sensitivity of monomodal cast PBX formulations. Three RDX crystal batches with three separated, narrow, monomodal particle size distributions have been used. In order to process high quality PBX formulations free of any residual extragranular porosity the solid load was 70 percent in weight (~ 56 percent in volume).

Simpson and co-workers [2] have got similar results with formulations containing from 48 to 72 percent by volume HMX and using reactive and non reactive binders.

A detailed analysis of these first results leads to take into account other crystal properties.

Explosive crystal size measurements are usually performed with the following tools: sieving, Coulter counter, laser diffraction apparatus, or digital optical microscopy. These complementary tools are based on different physical principles. Comparison of the results must be performed with care and could provide additional informations such on the crystal shape.

2.3 Effects of the crystal internal defect populations.

Processed batch + **RDX 315/800 µm** **Processed batch -**

Figure 1: Optical microscopy with matching refractive index.

Optical microscopy with matching refractive of explosive crystals like RDX or HMX exhibits closed internal cavities. The amount and size of these crystal internal defects can vary in a large range. Micrographs of figure 1 show two kinds of RDX crystals with two different internal defects populations. These two kinds of RDX crystals have been sorted from a same commercial grade RDX [3].

The study of the shock to detonation transition of two similar high quality cast formulations using these two kinds of RDX crystals shows that these internal defects are potential hot-spots which enhance the formulation sensitivity.

Increasing the amount of internal defects leads to reduce the transit time of an incident plane shock wave across a cast formulation sample [3]. Based on different RDX batches Baillou and co-workers have recorded the same experimental trends [4].

The ISL crystal sort experiment is an accurate tool to measure the internal defects population of an explosive crystal batch. It provides a very accurate measurement of the crystal apparent density. Figure 2 shows the quantitative results associated with the RDX batches of figure 1.

The curves give the amount in weight percent of crystals which have an apparent density higher than the abscissa value. The ISL sort experiment has been presented first in [5] and is discussed in more details in [6].These crystal internal defects are closed cavities. The amount of species entrapped in the cavities (solvent, air and water) have been measured [6]. The experimental correlations recorded between the volume of species entrapped in the cavities and the crystal apparent density records validates the two kind of measurements and underlines their high accuracy.

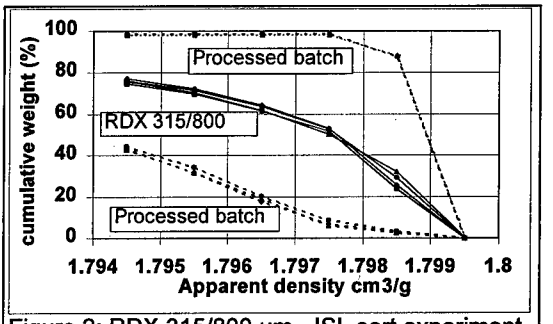

Figure 2: RDX 315/800 µm - ISL sort experiment - crystal internal defect populations.

The ISL sort experiment has allowed us to select, among commercially available batches, three very similar HMX batches (200/300 µm) with large differences between their respective internal defects population. A strong experimental correlation has been recorded between the plane shock wave sensitivity of the high quality cast formulations and the amount of internal defects in the HMX batches [5]. The magnitude of the cast formulation sensitivity variations recorded was significant and interesting for applications.

More recently the same cast formulations using the same HMX batches have been impacted by 20 mm flat ended small projectiles. The initiation threshold variations reach 30 % and are in total agreement with plane shock wave sensitivity results [7].

Increasing the amount of internal defects reduces the small projectile impact initiation threshold. This confirms the important role of the solvent inclusions on the sensitivity of cast formulations.

For both kind of shock sensitivity tests (plane shock wave and small projectile impacts), the sensitivity classification of the cast formulations are very similar. Nevertheless the sensitivity does not vary proportionally to the amount of internal defects. The main difference between the three HMX crystals batches is the global amount of solvent inclusions, but a careful and comparative analysis of the HMX crystals shows some variations of the sizes of the solvent inclusions and of the crystal surface properties (shapes and open porosities).

To measure the sizes of the solvent inclusions of the explosive crystals, we need a new tool. The numerical processing of images of microscopy with matching refractive index is investigated.

Mathematical morphology is a powerful toolbox for image processing and particle morphology analysis. Using these tools robust solutions have been found and some analysis performed [8].

The extraction of the inclusions data is not the main problem. The extraction of the crystal informations is the more difficult task. As the solvent inclusions belong to a crystal, the inclusion properties (amount, sizes) are linked to the studied crystal. This means that extracted inclusions data must be related to crystal data. The matching of the refractive index between the crystal and the surrounding medium leads to enhance the contrast between the inclusions and the crystal. But the contrast between the crystal and the external medium is very low.

Another difficulty is the sampling problem. To extract the desired quantitative informations, the magnification employed often leads to a restricted number of particles in the image. A compromise must be found between the resolution inside the crystal (at

the inclusion level) and the number of crystals in the image. Then the user will have to process several images. This means that the process (data acquisition and analysis) should be automatic to keep its interest. The development of this kind of automatic tool is more difficult and is in progress.

A common drawback of image processing is the compression of the true information on the image plane. But despite the problems, an interest of the image processing methods is the storage of the raw data (the image). This allows to process freely the data, using tools and models which could always be improved.

2.3 Effects of Crystal surface properties: shape and surface porosities.

A first attempt to check the influence of crystal shape and crystal surface is done in[9]. In order to reach a solid load of 85 weight percent, bimodal mixtures of RDX were used. This work provides interesting sensitivity variations between the various cast PBX formulations. Nevertheless the amount of solvent inclusions in the different crystal batches was not checked. Moreover crystal shapes were characterized qualitatively using scanning electron microscopy. Quantitative measurements of the particle surface properties would have improved this study. A quantitative experimental correlation between the surface porosities of explosive crystals and their combustion rate has been published in [10].

The following study has been performed in order to investigate the respective influence of explosive crystal surface properties (crystal shape , open porosities) and explosive crystal volume properties (solvent inclusions) on the shock sensitivities of high quality cast formulations.

2.3.1 Shock-Detonation transition measurements

The explosive formulations use two RDX batches with the same narrow monomodal crystal size distributions: 400/500 µm. To have a very good control of the various parameters, both RDX batches have been processed from a unique commercial grade RDX batch (figure 3). The " processed " batch is obtained by stirring in hot saturated acetone. This leads to a smoothing and a spheroidizing of the RDX crystals.

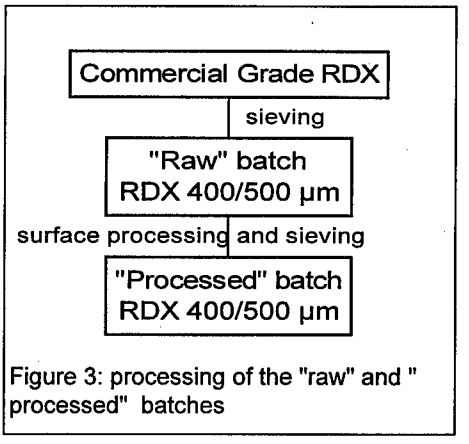

Figure 3: processing of the "raw" and " processed" batches

Finally the RDX processed crystals are sieved in order to keep the narrow monomodal crystal size distribution of the raw batch. A fine characterization of each RDX lot is performed. Figure 4 shows that the crystals of the "processed" batch exhibit more isotropic shapes (twin crystals are removed).

Raw batch **Processed batch**

Figure 4: **RDX 400/500 µm**

The surface porosity is also modified (figure 5). The surface processing reduces the amount of pores on the surface of the explosive crystals.

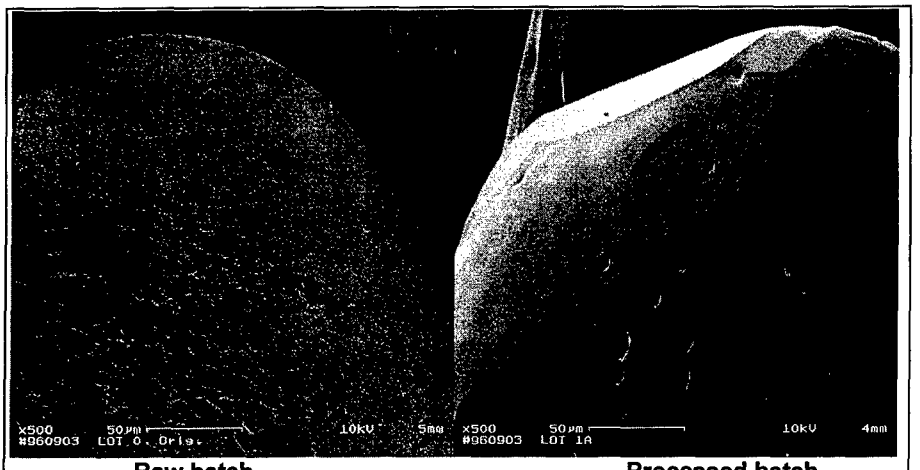

Raw batch **Processed batch**

Figure 5: **RDX 400/500 µm**

Similar high quality cast formulations have been processed based on these two RDX batches: 70 wt percent RDX and 30 wt percent wax . The formulation shock to detonation transition is checked using the records of discrete points of the usual space-time diagram. Chronometric PVDF gauges provide a very accurate recording of the incident plane shock wave transit time across a formulation sample of calibrated thickness. Results are plotted on figure 6. They show that the crystal processing leads to reduce the shock transit time across the formulation sample. Spherical crystal shape and smooth crystal surface contribute to reduce the shock sensitivity of cast formulations.

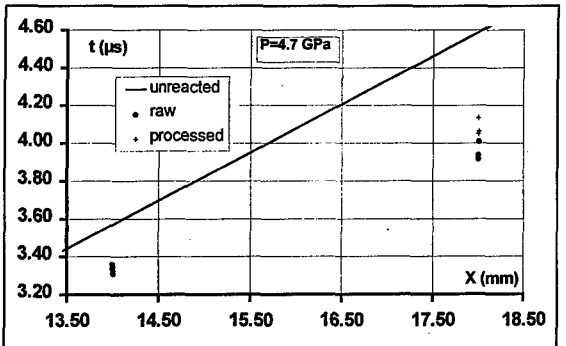

Figure 6: RDX 400/500 µm (70 wt%) + wax (30%) - 1D SDT space time diagram.

2.3.2 RDX crystal internal defects

The crystal internal defects populations of each batch are checked in measuring the crystal apparent density (figure 7). The surface processing leads to a small crystal apparent density decrease: 0.002 g/cm^3. On the basis of spherical particles free of cavities in the vicinity of their surface, this apparent density variation could be explained by a decrease of the particle diameter.

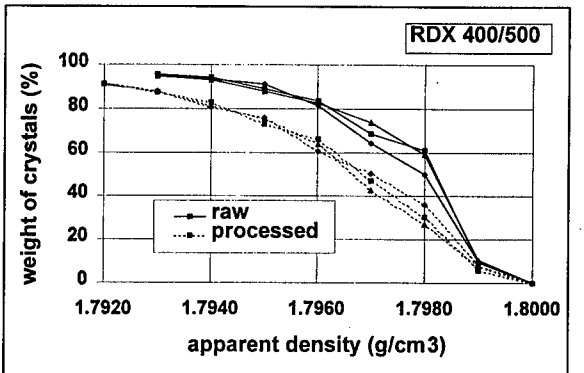

Figure 7: RDX 400 / 500 µm Apparent density distribution- Internal defects population -

The order of magnitude of the particle diameter reduction would be 30 µm. The assumption of a very limited amount of defects in the vicinity of the crystal surface is supported by the optical microscopy images obtained with the matching refractive index method. The sieving performed after the surface processing confirms that the crystal size decrease during the surface processing is very limited.

In conclusion the surface processing is like a peeling process. It does not alter the crystal internal defects. Moreover the results illustrate the high accuracy of the measurements of the explosive crystal apparent density performed at ISL.

2.3.3 RDX crystal surface properties.

There are two usual tools for the measurements of particle surface properties. The first method uses the volumetric adsorption of a gas on a sample of particles. This allows the measurement of the specific surface of these particles (B.E.T method). A porous distribution can be computed using the B.J.H method based on the desorption curve. The range of measured pore sizes is located between about 0.001 µm and 0.02 µm. The second method allows to investigate larger pores (0.1 µm to 50 µm). This is the mercury intrusion experiment.

BET measurements:

Figure 10 gives several specific area measurements (B.E.T method) performed on both RDX batches using increasing amounts of particles to check the accuracy of the measurements. Results show that the RDX raw and processed batches have very low specific areas which are close to the theoretical prediction of non porous RDX spheres of similar sizes. The accuracy of the results is very low because of the use of sample weight below 15 g. Security reasons and the container design do not allow to use RDX sample weight higher than 15 g. This leads to measure a surface of about 0.1 m^2, which is the low limit of the experimental device for measuring areas.

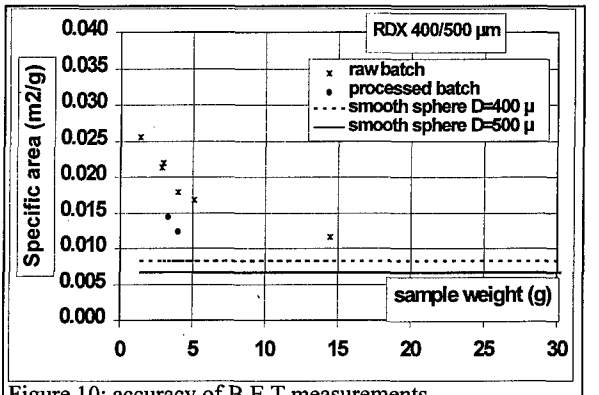

Figure 10: accuracy of B.E.T measurements.

Figure 11 gives a magnification of a porous zone on a RDX particle of the raw batch. According to figure 11 the pores sizes on the particles are located between 0.1 and 10 µm. But it is important to keep in mind that the extent of such porous zone on the particle surface is very low. Similar porous surface does not exist on the RDX particles of the processed batch.

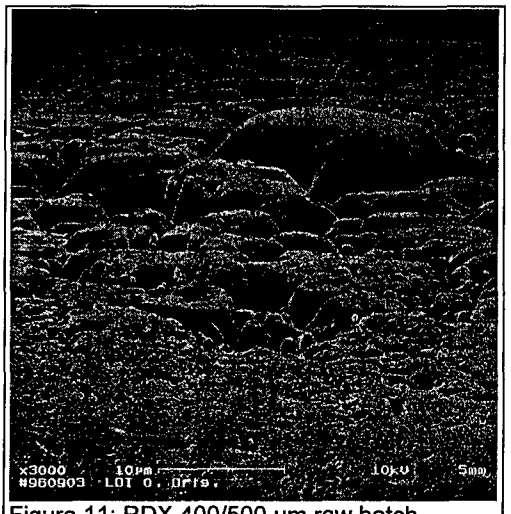

Figure 11: RDX 400/500 µm raw batch

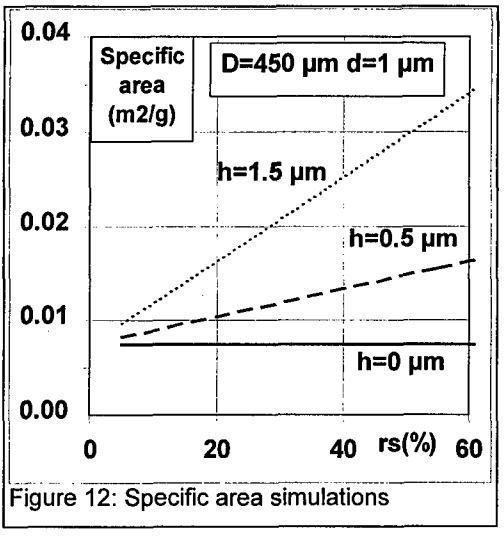

Figure 12: Specific area simulations

Despite the low accuracy of the B.E.T measurements because of the very low specifc area of the particles, a comparison with theoretical predictions gives quantitative informations on the amount of pores on the RDX crystal surface. Figure 12 gives the most significant results of these predictions. The computed specific areas of a 450 µm RDX spherical particle with 1 µm cylindrical pores of height h are plotted in function of the rs parameter which represents the number of pores.

The parameter rs gives the percentage of the surface covered by the pores on the spherical particle. Results are provided for two different pore height h.

Choosing any cylindrical pore diameter d below 10 µm and keeping constant the ratio h/d does not change the results. Figure 12 shows that an amount of cylindrical

pores (d=1 µm, h=1.5 µm) covering more than 20 % of the surface of the sphere would lead to a specific area variation which would be of about 0.01g/cm^3. This variation could be recorded with our experimental apparatus in using a sample weight higher than 10 g, but figure 10 shows that the real crystal shape and surface porosities lead to a smaller variations of the specific surface area:0.005 g/cm^3. This shows that the amount of pores on the surface of RDX particles of the two batches is very limited and does not cover more than 15-20% of the particle surface. This agrees with the qualitative observation on figures 5 and 11.

In conclusion the BET method is inefficient to characterize the surface differences qualitatively observed between the two RDX batches. The comparison between the measurements and the simulations shows only that the amount of the pore on the surface of both RDX batches is very low.

Nevertheless, the measured specific areas of the particles of the processed batch are slightly below the measured specific areas of the particles of the raw batch. This is in agreement with the qualitative observations performed on the electronic microscopic images. Particles of the processed batch exhibit more isotropic shapes and smoother surface than particles of the raw batch.

The BET method is usually employed to record the specific area. Use of the desorption curve provides informations on the size distribution of the smallest pores (in the range: 1 - 20 nm). Data on pores whose sizes are located between 0.1 and 50 µm may be obtained by means of mercury intrusion.

Mercury Intrusion experiment

The mercury intrusion porosimetry experiment provides a measurement of the porous volume in function of the pore radius. The experimental results for the two RDX batches (400/500 µm) are plotted on figure 13. The amount of pores in the processed crystal samples is lower than for the raw crystal samples. This is in agreement with the reduction of the surface porosity and with more isotropic crystal shapes.

The sharp variation of the pore volume for the largest pore diameters (>30 µm) is representative of the narrow monomodal crystal size distribution (400/500 µm). These large pores are the voids between the crystals in the measured sample. They

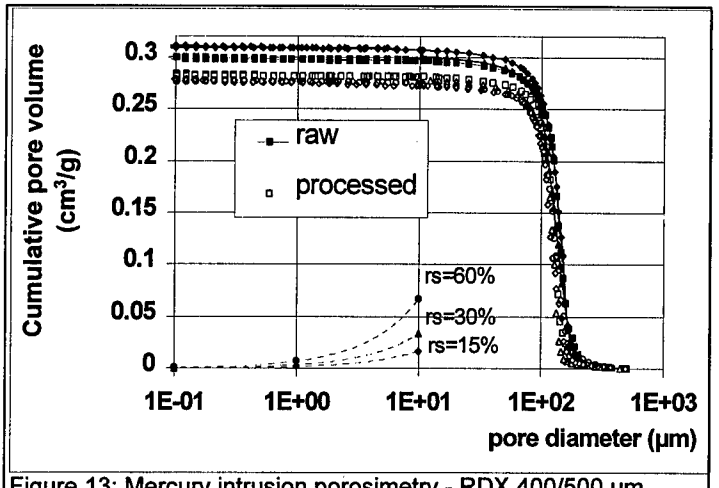

Figure 13: Mercury intrusion porosimetry - RDX 400/500 µm.

are very similar for both RDX batches as the respective crystal size distributions are.

For pores sizes located between 30 and 100 µm, a small difference is recorded for the respective pore volume of the two RDX batches. This is representative of crystal shape variations (for instance the disturbance generated between the two parts of a twin crystal).

For pore sizes below 30 µm, and for the two RDX batches there is no additional pore volume. The surface porosity of both RDX batches and the experimental resolution are too low to record any information in this pore size range. The predicted porous volume for a unit mass of 450 µm spherical RDX particle with n cylindrical pores of various diameter d (height = 1.5 d) is also plotted on figure 13. As previously, n the number of pores on the sphere is represented by the parameter rs. This shows that the amount of pores whose size is located between 1 and 10 µm is very low and that the corresponding rs parameter should be below 15%. This is in agreement with the results obtained with the gas sorption method.

The mercury intrusion experiment provides a measurement of the RDX particle shape variations but does not allow to measure the variations of surface porosities of the two RDX batches.

A very similar work has been performed with another narrow crystal size distribution: 150/200 µm [11]. It leads to the same results and conclusions. Both studies show the effects of RDX crystal surface properties on the shock-to-detonation transition of cast formulations. But it is not possible to distinguish between the respective influence of crystal shape and crystal surface porosities. Scanning electronic microscope shows variations of shapes and surface porosities. Mercury intrusion porosimetry provides measurements of the RDX crystal shape variations, but no accurate measurements of low surface porosities is available. There is a need to measure small amount of surface porosities in the range 0.1 - 10 µm.

3. Conclusions.

Explosive crystal defects are potential hot spots. Among the varieties of crystal defects, which are the critical defects? solvent inclusions? tiny crystallites of secondary growth on the surface of crystals? large or small defects?...

Accurate experimental correlations between explosive crystal properties and the shock sensitivity of the explosive formulations are difficult to get because customizing and measuring crystal properties is an hard work.

Solvent inclusions in an explosive crystal can have large effects on the sensitivity of cast formulations. Increasing the amount of solvent inclusions lead to increase the formulation sensitivity. An accurate measurement tool has been developed to record the global amount of solvent inclusions in an explosive crystal batch. Measures of the sizes of the solvent inclusions could improve the experimental works and help the understanding of the shock to detonation transition.

The effects of explosive crystal surface properties on the sensitivity of cast formulations has been demonstrated. Small variations of the crystal surface properties lead to small but significant variations of the shock sensitivity of cast formulations. Sensitivity variations are higher than the experimental resolution and are significant.

The variations of the crystal surface properties can be observed qualitatively using scanning electronic microscopy, but are to low to be measured with the usual tools. These tools were developed for the characterization of highly porous materials with high specific surface values.

With explosive crystals, the range of specific surface to measure is usually low (from 0.01 to about 10 m^2/g) and the surface porosity is limited.These tools are not adapted to the needs in the field of energetic materials. There is a need for new tools.

References:

[1] H. MOULARD " Particular Aspect of the Explosive Particle Size Effect on Shock Sensitivity of Cast PBX Formulations." Proceedings of the Ninth International Symposium on Detonation, Portland, Oregon, 28 August 1989, pp 18 - 24.

[2] R.L. SIMPSON, F.H. HELM, P.C. CRAWFORD, and J.W. KURY, " Particle size effects in the initiation of explosives containing reactive and non-reactive continuous phases." Proceedings of the Ninth International Symposium on Detonation, Portland, Oregon, 28 August 1989, pp 25 - 38.

[3] L. BORNE " Influence of Intragranular cavities of RDX Particle Batches on the Sensitivity of Cast Wax Bonded Explosives." Proceedings of the Tenth International Symposium on Detonation, Boston, MA, 12-16 July 1993, pp 286 - 293.

[4] F. BAILLOU, J.M. DARTYGE, C. SPYCKERELLE, J. MALA, " Influence of Crystal Defects on Sensitivity of Explosives." Proceedings of the Tenth International Symposium on Detonation, Boston, MA, 12-16 July 1993, pp 816 - 823.

[5] L.BORNE " Microstructure effect on the shock sensitivity of cast plastic bonded explosives." Proceedings of EUROPYRO 95, Tours, France, 5-9 juin 1995, pp 125 - 131.

[6] L. BORNE, J.C. PATEDOYE, C. SPYCKERELLE, " Quantitative Characterization of Internal defects in RDX crystals." in preparation to be submitted to Propellants, Explosives,Pyrotechnics.

[7] L. BORNE " Explosive Crystal Microstructure and Shock-Sensitivity of Cast Formulations." in preparation to be published to the next Eleventh International Detonation Symposium, Snowmass Village, CO, 30 August 1998.

[8] L. BORNE " Caracterisation quantitative des defauts internes dans des cristaux d'hexogene ." ISL report RT 504/96.

[9] A.C. VAN DER STEEN, H.J. VERBEEK, and J.J. MEULENBRUGGE, " Influence of RDX crystal shape on the shock sensitivity of PBXs." Proceedings of the Ninth International Symposium on Detonation, Portland, Oregon, 28 August 1989, pp 83 - 88.

[10] H. CHERIN, D. BOURNISIEN, " Characterization of the porous structure of explosive powders. Correlation with their combustion rate." Proceedings of the 23th Annual International Conference of ICT, Karlsruhe, FRG, 1992.

[11] L. BORNE, D. FENDELEUR, A. BEAUCAMP, " Explosive Crystal Properties and PBX's Sensitivity." DEA 7304 Physics of Explosives, Berchtesgaden, Germany, September 1997 or ISL / PU 358/97 .

UNTERSUCHUNGEN ZUR KRISTALLISATION VON EXPLOSIVSTOFFEN UND ZUM EINFLUSS VON ULTRASCHALL AUF DIE KEIMBILDUNG

INVESTIGATION ON THE CRYSTALLIZATION OF ENERGETIC MATERIALS AND ON THE INFLUENCE OF ULTRASONIC ON THE NUCLEATION

H. Kröber, U. Teipel

Fraunhofer Institut für Chemische Technologie (ICT)

Postfach 1240, D-76318 Pfinztal

e-mail: hkr@ict.fhg.de

Kurzfassung

Ziel dieser Arbeit war es, den Einfluß von Ultraschall auf die homogene Nukleation von Kaliumaluminiumsulfat (Kalialaun) in wäßriger Lösung und 3-Nitro-1,2,4-triazol-5-on (NTO) in verschiedenen Lösungsmitteln zu untersuchen. Hierzu wurden Kristallisationsversuche mit variierenden Abkühlgeschwindigkeiten mit und ohne Ultraschall durchgeführt, die hinsichtlich Induktionszeit, Partikelgröße und Ausbeute ausgewertet und verglichen wurden. Bei diesen Untersuchungen zeigte sich ein unterschiedlicher Einfluß der verschiedenen Lösungsmittel auf die Induktionszeit. So weist NTO in Isopropanol, Methanol und Dimethylformamid gelöst eine Induktionszeit von mehreren Stunden auf, die auch durch den Einsatz von Ultraschall nicht verkürzt werden konnte. Demgegenüber setzte die Keimbildung bei der Kristallisation aus Wasser sowohl beim Kalialaun als auch beim NTO schon nach wenigen Minuten ein. An diesem System konnte die Induktionszeit zudem durch den Einsatz des Ultraschalls beeinflußt werden. Es war also möglich, die Keimbildung gezielt zu starten, was sich deutlich in der Produktqualität bemerkbar machte. So wiesen die Kristalle eine gleichmäßigere Form auf, waren im Mittel deutlich kleiner und hatten eine engere Korngrößenverteilung. Zudem ließen sich reproduzierbarere Ergebnisse erzielen.

1. Einleitung

In der industriellen Kristallisation stellt die Kontrolle der primär homogenen Keimbildung ein großes Problem dar. Ursache hierfür ist vor allem die Tatsache, daß dieser Vorgang ausschließlich unter thermodynamisch metastabilen Bedingungen abläuft. Der Zustand, bei dem es zu einer Phasenbildung durch homogene Nukleation kommt, wird für viele Materialien erst bei sehr hohen Übersättigungen erreicht. Aufgrund dieser hohen Übersättigungen ergeben sich erhebliche Nachteile für den Kristallisationsprozeß. Es kommt z.B. zu sehr langen Induktionszeiten und zu breiten und vor allem nicht reproduzierbaren Partikelgrößenverteilungen. Die Keimbildungsrate, hervorgerufen durch homogene Nukleation, hängt exponentiell von der Höhe der Übersättigung ab, wobei der Exponent Werte von 100 und mehr erreichen kann. Dies bedeutet, daß das Eintreten der Keimbildung schon bei geringfügig unterschiedlichen Übersättigungen zu einer bedeutenden Qualitätsänderung im Produkt führt. Andererseits lassen sich durch die kontrollierte Erzeugung solch stark übersättigter Zustände feine Partikel herstellen, da ein Großteil der vorhandenen Übersättigung durch die Keimbildung abgebaut wird, so daß für das sich anschließende Kristallwachstum nur noch wenig Material zur Verfügung steht, das sich zudem auf sehr viele Partikel verteilen muß. Um dies zu erreichen, muß die homogene Keimbildung kontrolliert initiiert werden. Es ist schon seit längerer Zeit bekannt, daß verschiedene physikalische oder chemische Phänomene Einfluß auf die Keimbildung haben. Hierzu gehört neben der Anwesenheit einer heterogenen Phase, dem mechanischen Energieeintrag durch einen Rührer auch die Kavitation, die z.B. durch Ultraschallwellen hervorgerufen werden kann. Mason [1] und Kapustin [2] zeigten in ihren Arbeiten, daß der Einsatz von Ultraschall in der Kristallisation von besonderem Interesse ist. Insbesondere für Schmelzkristallisationsvorgänge wurde diese Technik bereits intensiv erforscht und hat technische Anwendung in der Metallurgie gefunden.

Gerade bei der Kristallisation von energetischen Materialien (z.B. Hexogen, Oktogen, NTO etc.) kann das gezielte Auslösen der Keimbildung zu einer Produktverbesserung führen. Die sonst in der industriellen Kristallisation häufig verwendete Methode zur gezielten Einleitung der Nukleation durch Einbringen von Saatkristallen ist hier mit Nachteilen für die Produktqualität verbunden, da die Saatkristalle im Produkt verbleiben, wodurch Spannungen im Kristall entstehen können, die wiederum zu einer Erhöhung der Empfindlichkeit des Explosivstoffes beitragen kann.

2. Theorie

Bei der Kristallisation werden feste kristalline Phasen aus Lösungen, Schmelzen oder Gasen abgeschieden. Die am häufigsten angewandte Technik ist die Kristallisation aus Lösungen, es existieren aber auch bedeutende Verfahren zur Kristallisation aus Schmelze oder Gasphase. Die Fällung ist ein Spezialfall der Kristallisation, bei der die selektive Abscheidung einer festen Phase aus einer Lösung durch eine chemische Reaktion erfolgt.

Der Kristallisationsprozeß entsteht aus dem Zusammenwirken der sich zeitlich überlagernden Teilschritte: Keimbildung, Kristallwachstum, Ostwald-Reifung, Agglomeration und Rekristallisation. Die erforderliche treibende Kraft für den Kristallisationsvorgang ist die Übersättigung des Systems. Abhängig von der Art und Weise, wie dieser Ungleichgewichtszustand erreicht wird, spricht man von Verdampfungskristallisation, Kühlungskristallisation, Vakuumkristallisation, Druckkristallisation und Aussalzung oder Fällungskristallisation.

Für die Konzeption eines Kristallisationsverfahrens ist die Kenntnis des Zustands- oder Phasendiagrammes, welches bei der sogenannten Lösungskristallisation auch in vereinfachter Form als "Löslichkeitsdiagramm" bezeichnet wird, von entscheidender Bedeutung.

Jede Phase existiert nur in einem bestimmten Temperatur-, Druck- und Konzentrationsbereich. Die Darstellung dieser Existenzgebiete in Abhängigkeit von der Zustandsvariablen erfolgt in Form von Zustandsdiagrammen.

Das c-T-Diagramm ist für den Übergang Lösung-Festkörper die einfachste Darstellungsart eines binären Systems (Abbildung 1). Darin stellen der Bereich I ungesättigte Lösungen (stabile Lösungen), die Linie 1 die gesättigten Gleichgewichtslösungen und das Gebiet II übersättigte Lösungen (instabile Lösungen) dar, welche in den entsprechenden gelösten Stoff und eine Gleichgewichtslösung zerfallen. Zwei mögliche Phasenübergänge sollen anhand dieses Schaubilds kurz erläutert werden:

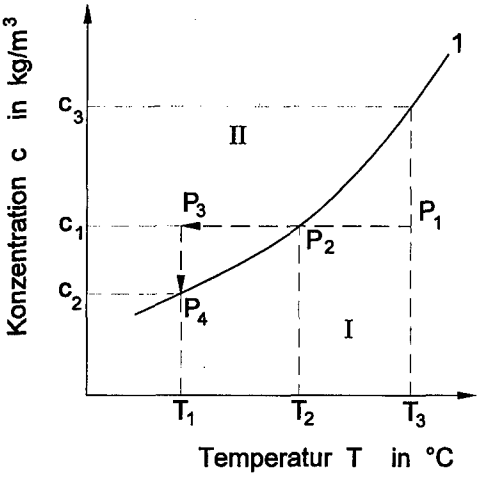

Abb. 1: Schema eines c-T-Diagrammes eines binären Systems

Wird eine untersättigte Lösung, die durch den Punkt P_1 dargestellt und durch die Temperatur

T_3 und die Konzentration c_1 bestimmt ist, abgekühlt, so erreicht diese Lösung im Punkt P_2 (T_2, c_1) die Gleichgewichtskurve. Bei weiterer Abkühlung wird diese überschritten, und es entsteht beispielsweise in Punkt P_3 (T_1, c_1) eine übersättigte Lösung, die in ein Kristallisat und eine Gleichgewichtslösung des Zustandes P_4 (T_1, c_2) zerfällt. Aus der Differenz $\Delta c = c_1 - c_2$ kann die Masse des auskristallisierenden Stoffes bestimmt werden [3].

Als gesättigt wird eine Lösung bezeichnet, die mit einer oder mehreren festen Phasen im Gleichgewicht steht (Sättigungskonzentration). Es lassen sich jedoch auch Lösungen herstellen, die einen größeren Anteil an Feststoff enthalten, als es der Sättigungskonzentration entspricht. Solche Lösungen werden als übersättigt bezeichnet und sind die Voraussetzung für alle Kristallisationsvorgänge. Miers [4] konnte diese Zusammenhänge durch Messungen mit dem Refraktometer während des Kühlungsprozesses von konzentrierten wäßrigen Salzlösungen beobachten. Die daraus abgeleiteten verallgemeinerten Feststellungen gehen aus Abbildung 2 hervor. In dem abgebildeten binären System ist die Kurve 1 die Gleichgewichts- oder Löslichkeitskurve, die Kurve 2 die sogenannte Überlöslichkeitskurve. Die entstehenden unterschiedlichen Gebiete werden als stabil bzw. labil bezeichnet. Der von der Löslichkeits- und Überlöslichkeitskurve eingeschlossene Bereich, wird metastabiler oder Ostwald-Miers-Bereich genannt. Bei genauerer Untersuchung ist es möglich zwei verschiedene Überlöslichkeitskurven zu detektieren. Beim Erreichen der ersten Überlöslichkeitskurve bilden sich die ersten vereinzelten Keime, an der zweiten tritt schlagartig mit hoher Geschwindigkeit die weitere Keimbildung auf, deren Wärmeentwicklung meßbar ist.

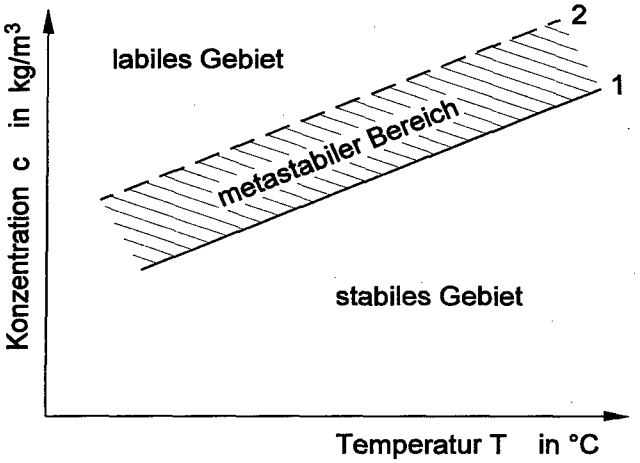

Abb. 2: Löslichkeitsdiagramm eines binären Systems mit Löslichkeits- und Überlöslichkeitskurve

Führt man eine Kühlungskristallisation ohne Saatzusatz durch, so wird die Keimbildung mit zunehmender Abkühlgeschwindigkeit immer weiter von der Sättigungstemperatur entfernt einsetzen. Die Breite des metastabilen Bereichs hängt damit von der Art der Einstellung der Übersättigung ab. Dieses ist insbesondere bei einer dynamischen Einstellung der Übersättigung der Fall, wobei die Breite des metastabilen Bereichs mit abnehmender Abkühlgeschwindigkeit gegen null geht.

Weicht die Konzentration metastabiler Lösungen nur in geringem Maße von der Gleichgewichtslösung ab, so ist durch Zusatz von Saatkristallen ein fast ideales Wachstum eines Korns oder von Körnerkollektiven möglich, da in diesem Zustand die Übersättigung nicht durch Keimbildung abgebaut wird. Dagegen erhält man bei einem Kristallisationsprozeß, der bis in das labile Gebiet geführt wird, auf Grund der hohen Keimbildung ein sehr kleines Kornspektrum.

2.1 Keimbildung

Der Zustand der Übersättigung oder Unterkühlung allein genügt jedoch nicht als Ursache, um eine Lösung auszukristallisieren. Bevor sich Kristalle entwickeln können, müssen in der Lösung eine Anzahl kleinster fester Teilchen, Embryonen, Keime oder Saatkristalle vorhanden sein, die als Kristallisationszentren wirken. Keimbildung kann spontan und plötzlich auftreten oder kann künstlich herbeigeführt werden. Es ist jedoch nicht immer möglich zu entscheiden, ob ein System von selbst Keime gebildet hat oder ob es dies unter dem Einfluß einer äußeren Anregung getan hat.

Keimbildung kann häufig durch Anregungen, wie etwa Rühren, mechanische Stöße, Reibung und extreme Drücke ausgelöst werden. Die noch unvorhersehbaren Auswirkungen äußerer Einflüsse, wie z. B. elektrische und magnetische Felder, Funkenentladungen, UV-Licht, Röntgen- und Gammastrahlen, Schall- und Ultraschallemission, werden seit mehreren Jahren untersucht. Jedoch haben solche Methoden bis heute keine bedeutende Anwendung in der technischen Massenkristallisation aus Lösungen gefunden.

Es ist durch Kavitation möglich, in unterkühlten Lösungen Keimbildung auszulösen. Dies trifft wahrscheinlich ebenso auf eine Reihe der obengenannten Effekte zu. Hunt und Jackson [5] haben mit Hilfe einer neuartigen Versuchstechnik gezeigt, daß die Keimbildung dann erfolgt, wenn die Hohlräume (Kavitäten) kollabieren und in sich zusammenfallen. Dabei können

sehr hohe Drücke (~ 10^5 bar) entstehen. Die Änderung des Drucks setzt die Kristallisationstemperatur der Lösung herab, was die Keimbildung zur Folge hat [6].

In Abhängigkeit von den Bedingungen, unter denen Keime entstehen, werden die in Abbildung 3 dargestellten Arten der Keimbildung unterschieden. Keime, welche aus der Übersättigung der Lösung resultieren, werden als primäre Keime bezeichnet. Tritt Keimbildung in Anwesenheit von arteigenen Kristallen auf, wird der Mechanismus als sekundäre Keimbildung bezeichnet. Bei der homogenen Keimbildung entstehen die Keime spontan und unbeeinflußt von fremden Stoffen. Wird die Keimbildung durch Fremdstoffe, wie z. B. Staub und Rostpartikel in der Lösung, oder Wandrauhigkeiten initiiert, spricht man von heterogener Keimbildung.

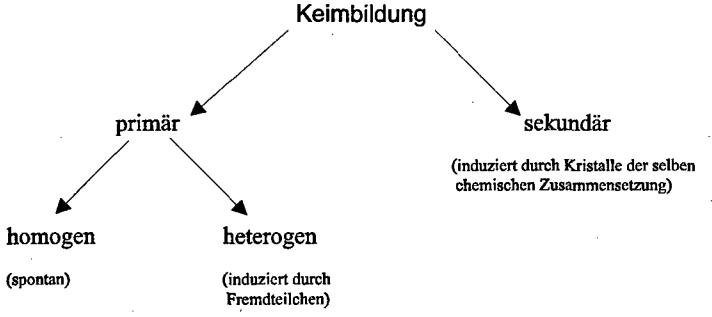

Abb. 3: Schematische Einteilung der Keimbildung

2.2.1 Primäre Keimbildung

2.2.1.1 Homogene Keimbildung

Die Mechanismen, die zur homogenen Keimbildung führen, sind bis heute nicht endgültig erforscht. So muß neben der Zusammenballung der einzelnen gelösten Teilchen auch ihre Orientierung in einem festen Gitter stattfinden. Die Keime sind zu Anfang als ungeordnete Anhäufungen von Atomen, Molekülen oder Ionen (Gitterbausteine) in der übersättigten Lösung vorhanden. Diese ordnen sich dann allmählich innerhalb dieser Anhäufung zu kristallinen Teilbereichen. Die exakte Struktur dieser Anordnungen ist nicht bekannt, da eine direkte Beobachtung wegen der geringen Größe kaum möglich ist.

Damit ein sogenannter kritischer Keim gebildet werden kann, ist eine Zahl von Bausteinen nötig, die etwa zwischen 10 und einigen Tausend variiert. Es ist also praktisch nicht möglich, daß sich eine Zusammenlagerung dieser großen Zahl von Teilchen allein durch Zusammen-

stoß ereignen kann. Mullin [6] beschreibt dies durch bimolekulare Addition von gelösten Molekülen. Bei mikroskopischer Betrachtung einer gesättigten Lösung werden örtlich sowohl Bereiche mit relativ hoher Übersättigung als auch Bereiche mit Untersättigung vorhanden sein, weshalb sich erste Keime wieder auflösen können und überaus instabil sind. In einer übersättigten Lösung dagegen wachsen sie über diese kritische Größe hinaus und werden stabil.

Die klassische Theorie der Keimbildung stammt von Gibbs, der die Bildung von flüssigen Tropfen bei der Dampfkondensation thermodynamisch beschrieben hat. Es ist analog möglich diese Theorie auf die homogene Keimbildung aus Lösungen anzuwenden. Die Überführung von einem weniger geordneten in einen stärker geordneten Zustand (gasförmig → flüssig → fest) hat eine Abnahme der molekularen Beweglichkeit und somit auch der kinetischen Energie des Systems zur Folge. Andererseits ist eine bestimmte Energie zum Aufbau einer höher geordneten Struktur notwendig. So wird bei der Bildung eines kugelförmigen Keimes in einer Mutterphase eine Änderung der freien Enthalpie des Systems ΔG festgestellt, die sich aus der freiwerdenden Energie bei der Bildung eines gewissen Volumens G_V der neuen Phase und der für die Erzeugung der Grenzfläche benötigten Energie ΔG_O zusammensetzt /6/.

$$\Delta G = \Delta G_O + \Delta G_V \qquad (1)$$

$$\Delta G = 4\pi r^2 \sigma - \frac{4}{3}\pi r^3 \frac{\rho_{FS} RT}{M_{FS}} \cdot \ln S \qquad (2)$$

Der Verlauf der Änderung der freien Enthalpie und ihrer einzelnen Terme ist schematisch in Abbildung 4 dargestellt. Das Maximum ΔG_{Kr} ergibt sich für den kritischen Keimradius r_{Kr}. Um ein niedrigeres Energieniveau einzunehmen, werden Keime kleiner als r_{Kr} dazu neigen, ihre Größe zu verringern (Auflösung) und Keime größer als r_{Kr} werden versuchen an Größe zu gewinnen (Wachstum). Um den Wert von r_{Kr} zu ermitteln, wird die erste Ableitung von Gleichung 2 $d(\Delta G)/dr = 0$ gesetzt.

$$\frac{d(\Delta G)}{dr} = 8\pi r_{Kr}^{\ 2} \cdot \sigma - 4\pi r_{Kr}^{\ 3} \frac{\rho_{FS} RT}{M_{FS}} \cdot \ln S = 0 \qquad (3)$$

Der kritische Keimradius r_{Kr} läßt sich aus Gleichung 3 berechnen.

$$r_{Kr} = \frac{2\sigma \cdot M_{FS}}{\rho_{FS} R T \ln S} \qquad (4)$$

Durch Substitution von r_{Kr} in Gleichung 2 erhält man die kritische Keimbildungsarbeit ΔG_{Kr}.

$$\Delta G_{Kr} = \frac{4\pi\sigma \cdot r_{Kr}}{3} \qquad (5)$$

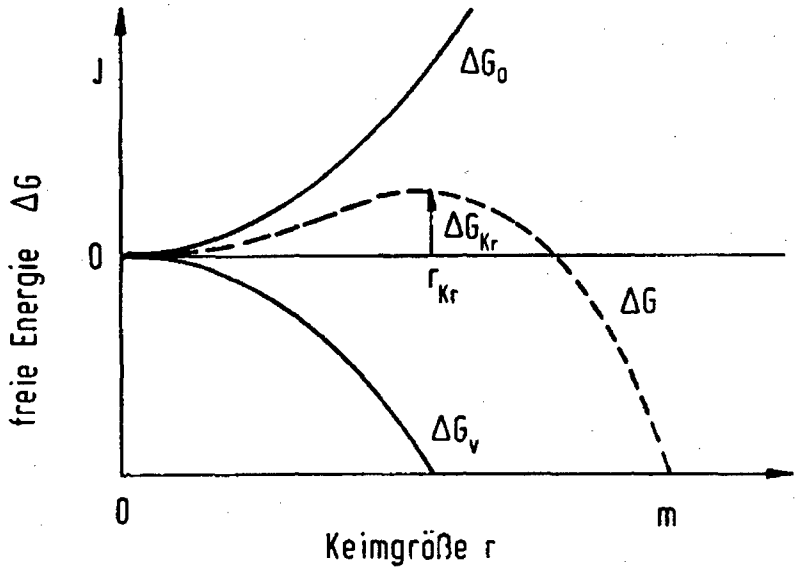

Abb. 4: Verlauf der freien Energie in Abhängigkeit von der Keimgröße r [6]

In der Realität ist es schwierig, die Theorien zur homogenen Keimbildung experimentell zu bestätigen, da die Präparation eines tatsächlich keimfreien Systems praktisch nicht möglich ist.

2.2.1.2 Heterogene Keimbildung

Die Keimbildungsrate kann bereits durch die Anwesenheit geringster Spuren von Verunreinigungen in System beträchtlich beeinflußt werden. Diese können jedoch sowohl zu einem inhibierten Keimbildungsverhalten führen als auch beschleunigend auf die Keimbildung wirken.

Volmer [7] versucht die Keimbildung ausgelöst durch Fremdkörper theoretisch zu beschreiben. Er geht davon aus, daß sich zwischen der artfremden Unterlage (Heterokeim) und einem Tropfen der Mutterphase ein Benetzungswinkel Θ ausbildet. Dieser Winkel kann Werte von 0 bis 180° annehmen, abhängig von der Benetzung des Fremdpartikels durch die Mutterphase (Abbildung 5).

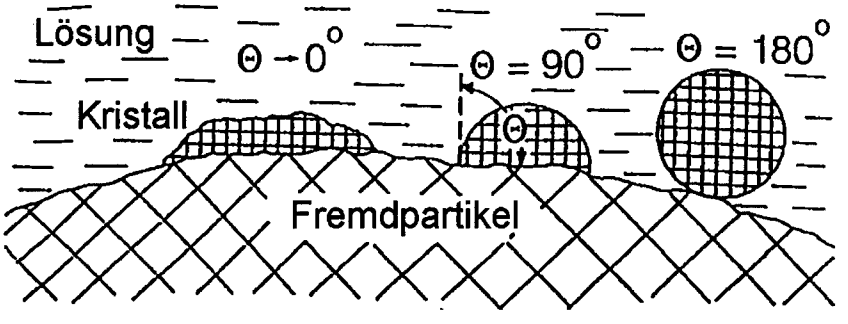

Abb. 5: Keimbildung auf einem Fremdpartikel für verschiedene Benetzungswinkel Θ [8]

Der Keimbildungsprozeß wird dann hauptsächlich durch die Grenzflächenenergie Kristall – Flüssigkeit und damit durch die intermolekularen, interionogenen oder interatomaren Kräfte zwischen den Teilchen der Mutterphase und der "fremden" Oberfläche bestimmt. Volmer nimmt an, daß der sich ergebende Kontaktwinkel Θ ein Maß der Effektivität der fremden Oberfläche in bezug auf die Keimbildung ist, gemäß der Beziehung

$$(\Delta G_{het})_{Kr} = (\Delta G_{hom})_{Kr} \cdot \frac{(2+\cos\Theta)(1-\cos\Theta)^2}{4} \qquad (6)$$

Für die heterogene Keimbildung und vollständige Benetzung (Θ = 0°) ergibt sich

$$(\Delta G_{het})_{Kr} = 0 \qquad (7)$$

Hieraus geht hervor, daß in diesem Fall keine heterogenen Keimbildung in der Lösung stattfindet und alle Keime homogen gebildet werden. Diese Umstände entsprechen dem Impfen einer übersättigten Lösung mit Keimkristallen des gelösten Stoffes, es müssen also keine Keime in der Lösung gebildet werden.

Im Fall einer teilweisen Affinität, d. h. einem Benetzungswinkel im Bereich von $0° < \Theta < 180°$, resultiert Gleichung 8:

$$(\Delta G_{het})_{Kr} < (\Delta G_{hom})_{Kr} \qquad (8)$$

Es zeigt sich, daß heterogene Keimbildung leichter ablaufen kann, da die notwendige freie Energie geringer ist als die für homogene Keimbildung. Anschaulich läßt sich dies damit erklären, daß im Fall einer teilweisen Benetzung im Vergleich zur homogenen Keimbildung eine geringere Oberfläche neu gebildet werden muß.
Im Fall von Nichtbenetzung ($\Theta = 180°$) gilt für die kritische Keimbildungsenthalpie

$$(\Delta G_{het})_{Kr} = (\Delta G_{hom})_{Kr}, \qquad (9)$$

d. h. die benötigte Energie für die heterogene Keimbildung ist gleich der Energie für die homogene oder spontane Keimbildung. Die Fremdstoffteilchen in der Lösung haben in diesem Fall keinen katalytischen Einfluß [3].

2.2.2 Sekundäre Keimbildung

Eine übersättigte Lösung neigt viel eher zur Keimbildung, wenn bereits Kristalle in ihrer arteigenen Lösung vorhanden sind oder bewußt zugegeben werden. Dieser katalysierende Effekt bzw. die Keimbildung bei Vorhandensein von arteigenen Kristallen wird als sekundäre Keimbildung bezeichnet, um sie von der sogenannten primären Keimbildung (anfänglich keine Kristalle vorhanden) zu unterscheiden.
Strickland-Constable [9] beschreibt verschiedene Mechanismen der sekundären Keimbildung, wie:
"initial breeding" (Kristallstaub löst sich von der Oberfläche eingetauchter Saatkristalle),
"needle breeding" (Abbrechen von schwach angewachsenen Kristallnadeln bei hohen Übersättigungen),
"polycrystalline breeding" (Auseinanderbrechen loser polykristalliner Konglomerate bei hohen Übersättigungen),
"collision breeding" (ein komplexer Prozeß, der durch die Wechselwirkung und den Kontakt von Kristallen untereinander und mit Anlagenbauteilen des Behälters, Rührers etc. entsteht).

Heute wird angenommen, daß der Kontakt zwischen Kristallen und Rührorgan der bedeutendste Auslöser für sekundäre Keimbildung in technischen Kristallisatoren ist. Die Wahrscheinlichkeit für einen solchen Zusammenstoß ist direkt proportional zur Rührerdrehzahl [10]. Werden diese Kontakte verhindert, z. B. in einem Fließbett, können neben den oben genannten Mechanismen weitere Phänomene eine Rolle spielen.

Mullin [6] gibt mehrere Gründe für den Größeneinfluß der Saatkristalle bei der sekundären Keimbildung an. Beispielsweise erzeugen große Kristalle, wegen ihrer größeren Kontaktwahrscheinlichkeit und ihrer höheren Kollisionsenergie, mehr sekundäre Keime in gerührten Systemen als dies kleine Kristalle tun. Sehr kleine Kristalle können den Stromlinien auch in turbulenten Wirbeln stark gerührter Lösungen folgen und kommen deshalb nur selten mit dem Rührorgan oder anderen Kristallen in Berührung. Als weiterer Faktor muß bedacht werden, daß Kristalle kleiner als ca. 10 mm wahrscheinlich viel langsamer wachsen als Makrokristalle, und daß stark beschädigte Kristallbruchstücke manchmal gar nicht mehr wachsen.

2.2.3 Induktions- und Latenzzeit

Die sogenannte Induktionszeit, deren Dauer zwischen Mikrosekunden, Tagen und Wochen liegen kann, ist wesentlich von der Übersättigung abhängig und stellt den Zeitraum dar, der zur Bildung eines kritischen Keimes unter den jeweiligen Bedingungen notwendig ist.

In manchen Systemen, besonders bei geringen Übersättigungen, kann eine weitere Zeitdifferenz beobachtet werden. Um sie von der Induktionszeit zu unterscheiden, die oben als Zeitpunkt der ersten Detektion von Kristallen überhaupt im System definiert wurde, wird in Anlehnung an Mullin [6] der Ausdruck Latenzzeit verwendet. Die Latenzzeit soll hier definiert werden als das Auftreten einer bedeutsamen Veränderung im System, d. h. das Einsetzen massiver Keimbildung oder der erkennbar beträchtliche Abbau der Übersättigung in der Lösung.

Das Vorhandensein von Saatkristallen verringert im allgemeinen die Induktionszeit, beseitigt sie aber nicht notwendiger Weise. Sogar wenn ein System zum Zeitpunkt t=0 Saatkristalle enthält, kann eine meßbare Induktionszeit vergehen bevor neue Kristalle entstehen. Diese sind per Definition sekundäre Keime und können in verschiedenen Schüben während der Latenzzeit auftreten. Oft ist es praktisch ratsamer, die Latenzzeit als die für das System charakteristische Größe zu ermitteln. Folgende Faktoren können die Induktions- und Latenzzeit sowie die Geschwindigkeit des Übersättigungsabbaus beeinflussen: Temperatur, Anregung durch Rühren, Wärmeentwicklung während der Kristallisation, Größe der Saatkristalle, Oberfläche

der Saatkristalle und die Anwesenheit von Verunreinigungen. Zur Zeit können hierzu allenfalls qualitative Aussagen über die Abhängigkeiten der einzelnen Einflußfaktoren auf die Induktionszeit getroffen werden.

3. Experimentelle Untersuchungen

3.1 Versuchsaufbau

Die Kristallisationsversuche wurden in einem gerührten Batch-Kristallisator durchgeführt. Die verwendete Versuchsapparatur (Abbildung 6) besteht im wesentlichen aus einer Ultraschallquelle, einem Turbinenrührer, einem Doppelmantelgefäß aus Glas (ca. 750 cm^3 Inhalt) sowie einem daran angeschlossenen Thermostat. Die Zirkulation einer Wärmeträgerflüssigkeit zwischen den beiden letztgenannten Komponenten temperiert die Lösung, ein externer Programmgeber erlaubt die Realisierung vorprogrammierter Aufheiz- bzw. Abkühlphasen. Die tatsächliche Temperatur in der Lösung wird mit Hilfe eines PT 100 Widerstandsthermometers überwacht.

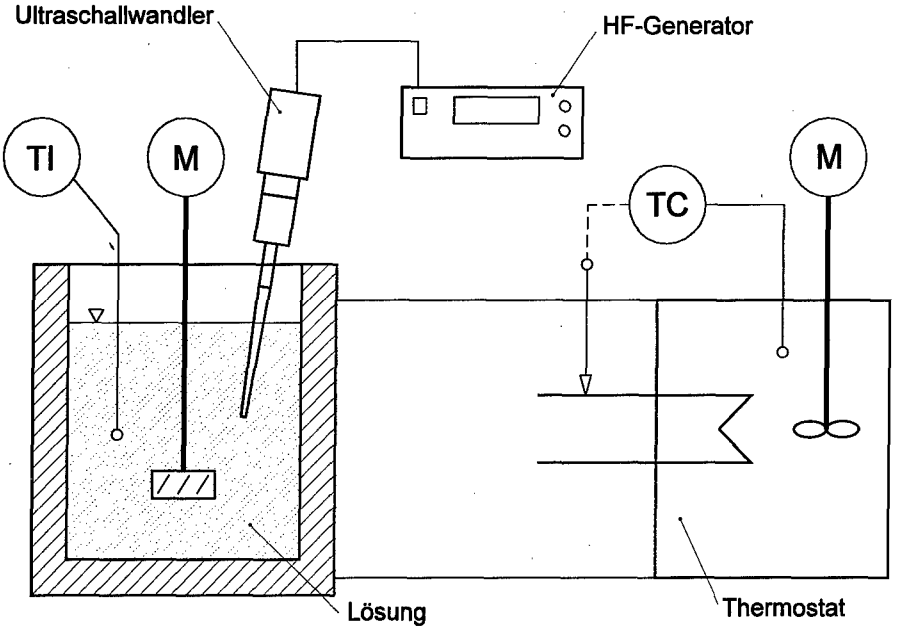

Abb. 6: Versuchsaufbau

Als Ultraschallquelle wurde der "Desintegrator HD 60" der Fa. Bandelin verwendet. Dieses Gerät ist für die Beschallung kleiner Flüssigkeitsmengen mit hoher Schallintensität vorge-

sehen. Der mit einem Wirkungsgrad von mehr als 90% arbeitende HF-Generator wandelt die aufgenommene Netzleistung und Frequenz in Hochfrequenzleistung von 20 kHz um. Der Generator arbeitet mit konstanter Amplitude und einer maximalen HF-Leistung von 60 W.
Der an den Generator angeschlossene Ultraschallwandler (Abbildung 7) setzt mit Hilfe von Piezoelementen die elektrische HF-Energie in mechanische Schwingungsenergie gleicher Frequenz um. Die dabei erzeugte Amplitude wird über eine amplitudenproportionale Frequenznachführung unabhängig von der anliegenden Belastung konstant gehalten.

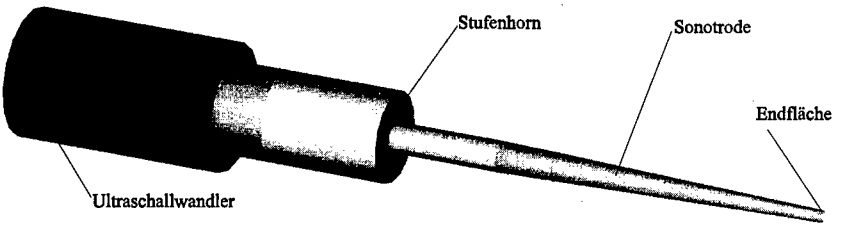

Abb. 7 Eingesetzter Ultraschallwandler mit Stufenhorn und Sonotrode

Das an den Ultraschallwandler angeschraubte Stufenhorn ist geometrisch auf die Frequenz von 20 kHz abgestimmt. Es besteht aus einer hochfesten Titanlegierung und verstärkt die Amplitude auf das ca. 7-fache.
Die Sonotrode überträgt die erzeugte Ultraschalleistung in die Lösung. Sie ist ebenfalls aus einer hochfesten Titanlegierung hergestellt und wird am Stufenhorn festgeschraubt. Sie hat die Form eines Kegelstumpfs und wirkt als Resonanzkörper, der die Ausgangsamplitude des Stufenhorns weiter verstärkt und über eine kleine Endfläche (Durchmesser 6 mm) in das Medium überträgt. Dadurch entstehen hohe Energiedichten an der Endfläche, die zu Kavitation führen.
Zur Beschallung von Flüssigkeiten muß die Spitze der Sonotrode mindestens ca. 10 mm tief eintauchen, um das Ansaugen und Einmischen von Luft zu vermeiden.

3.2 Versuchsdurchführung

Die Anfangstemperatur ϑ_S der Abkühlphase betrug 40 bzw. 60 °C. Es wurden pro Versuch jeweils 300 g Lösungsmittel und die der Sättigungskonzentration bei Anfangstemperatur entsprechende Menge an Substanz eingewogen. Diese Mischung wird mit der beschriebenen Versuchsapparatur auf ca. 3-5 °C über die Anfangstemperatur erwärmt, um das kristalline

Ausgangsmaterial mit Hilfe des Rührers aufzulösen. Nachdem in der Flüssigkeit sichtbar keine Kristalle mehr vorhanden sind, wird die Lösung auf Anfangstemperatur gebracht. Im Anschluß daran wurde die Lösung mit einer vorgegebenen linearen Abkühlgeschwindigkeit b (5, 10 oder 20 K/h) auf Endtemperatur ϑ_u abgekühlt.

Es wurden identische Versuchsreihen, sowohl mit als auch ohne Ultraschall, durchgeführt. Der Einsatz von Ultraschall erfolgte ab der Temperatur ϑ_{US}, also bei einer Unterkühlung $a' = \vartheta_S - \vartheta_{US}$, über einen Zeitraum t_{US}^{ges}, mit dem Ziel eine spontane Keimbildung auszulösen. Der vom Ultraschall verursachte Energieeintrag, erhöht die Temperatur der Lösung je nach Abkühlgeschwindigkeit und Dauer der Beschallung kurzfristig um bis zu 1,5 °C. Die Keimbildungstemperatur ϑ_{Keim} wurde bestimmt, sobald die ersten sichtbaren Keime auftraten. Nach dem Einsetzen massiver Keimbildung, also nach Ablauf der Latenzzeit, wurde die Ultraschallquelle wieder abgeschaltet. Weiterhin wurde die Induktionszeit zwischen dem Einschalten des Ultraschalls und dem Auftauchen erster Keime t_{US}^{Keim} gemessen.

Die entstandenen Kristalle werden mit einem Papierfilter in einer Porzellannutsche von der Restlösung getrennt. Danach wird der Kristallfilterkuchen mit einer Flüssigkeit nachgespült, die mit dem Lösungsmittel mischbar ist, nicht aber das Kristallisat anlöst. So wurde beispielsweise bei der Kristallisation von Kalialaun mit Aceton gespült. Dieser Vorgang entfernt die noch an der Kristalloberfläche haftende Mutterlösung und vermeidet so das Agglomerieren der Kristalle durch Rekristallisation. Darüber hinaus wird in unserem Beispiel die Trocknung drastisch verkürzt.

3.3 Ergebnisse

Die in diesem Beitrag dargestellten Untersuchungen wurden an den folgenden Stoffsystemen durchgeführt:

- Kaliumaluminiumsulfat (Kalialaun) / Wasser
- 3-Nitro-1,2,4-Triazol-5-On (NTO) / Wasser
- 3-Nitro-1,2,4-Triazol-5-On (NTO) / Methanol
- 3-Nitro-1,2,4-Triazol-5-On (NTO) / 2-Propanol
- 3-Nitro-1,2,4-Triazol-5-On (NTO) / Dimethylformamid (DMF)

Die Löslichkeitskurven der fünf Systeme sind in Abbildung 8 wiedergegeben. In diesem Diagramm sind die unterschiedlichen Maßstäbe der beiden Ordinaten zu beachten.

Man erkennt, daß Kalialaun/Wasser und NTO/DMF Systeme mit hohen Löslichkeiten darstellen, während NTO in Wasser, Methanol und 2-Propanol nur gering löslich sind.

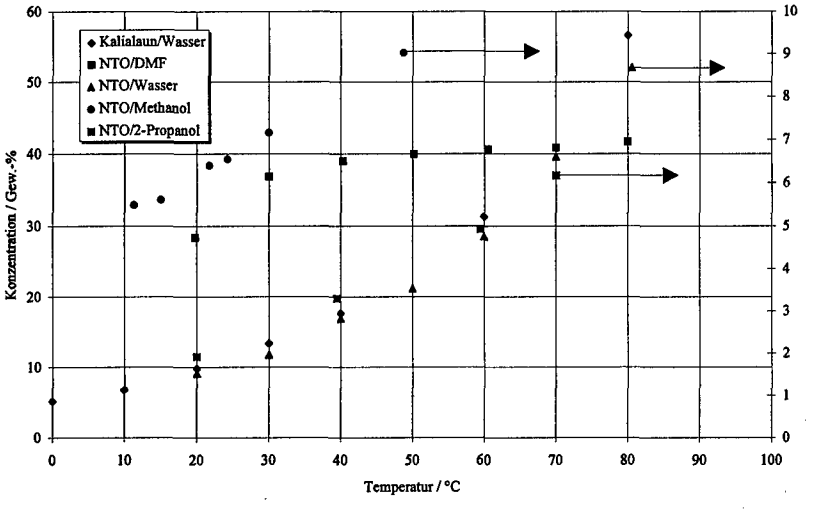

Abb. 8: Löslichkeitskurven der untersuchten Stoffsysteme

3.3.1 Kalialaun / Wasser

In allen untersuchten Fällen des Systems Kalialaun/Wasser konnte durch Ultraschall die Keimbildungstemperatur deutlich reduziert werden, d.h. die Breite des metastabilen Bereichs und Induktionszeit werden verringert.

Abbildung 9 zeigt den Einfluß von Ultraschall auf die Keimbildungstemperatur ϑ_{Keim} bei Versuchen, die mit verschiedenen Abkühlgeschwindigkeiten und einer anfänglichen Sättigungstemperatur ϑ_S = 40 °C durchgeführt wurden. Dabei ist zu erkennen, daß bei den Experimenten mit Ultraschall die Keimbildungstemperatur unabhängig von der Abkühlgeschwindigkeit konstant bleibt. Die Temperatur zum Zeitpunkt der Keimbildung ist unwesentlich höher als die bei Einschalten des Ultraschallfeldes ϑ_{US}. Dies ist auf die schwierige Temperaturkontrolle der Lösung bei Ultraschalleinsatz zurückzuführen. Bei den Versuchen ohne Ultraschall verringert sich, wie zu erwarten, die Keimbildungstemperatur mit zunehmender Abkühlgeschwindigkeit, d.h. man kommt weiter in den metastabilen Zustandsbereich hinein.

Für die Versuche mit einer Anfangstemperatur von ϑ_S = 60 °C sind die Meßergebnisse in Abbildung 10 dargestellt. Hier zeigt sich bei allen Versuchen ein abnehmender Verlauf der Keimbildungstemperatur mit ansteigender Abkühlgeschwindigkeit. Jedoch setzt die Keimbildung bei der Anwendung von Ultraschall zwischen 1,5 und 2,3 °C "früher", d.h. bei geringeren Unterkühlungen, ein als im Vergleichsversuch.

Allen Versuchen mit 60 °C Starttemperatur war eine Zeitdifferenz von etwa 10 Minuten gemein, zwischen der ersten optischen Detektion vereinzelter Keime und dem plötzlichen Einsetzen massiver Keimbildung.

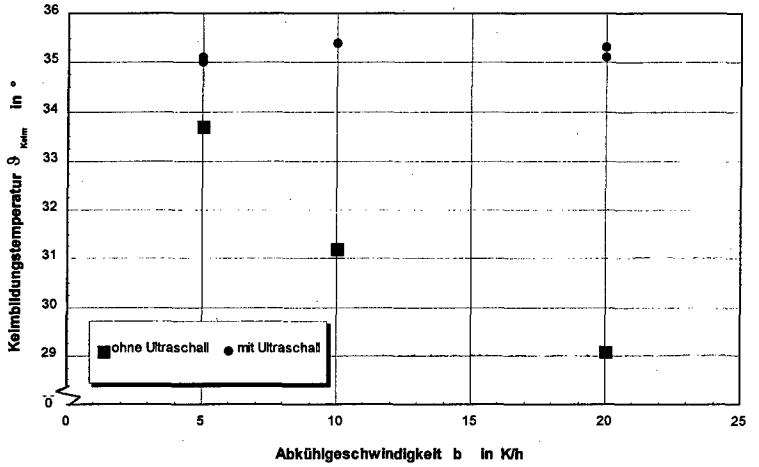

Abb. 9: Keimbildungstemperatur mit und ohne Ultraschall in Abhängigkeit von der Abkühlgeschwindigkeit bei einer Anfangstemperatur $\vartheta_S = 40$ °C

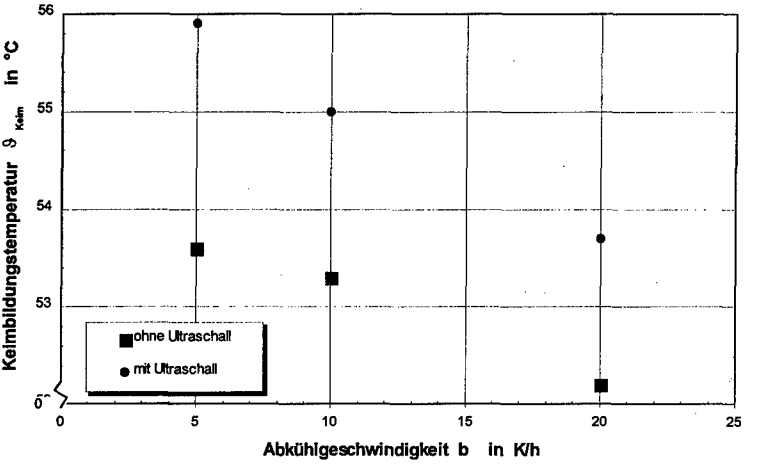

Abb. 10: Keimbildungstemperatur mit und ohne Ultraschall in Abhängigkeit von der Abkühlgeschwindigkeit bei einer Anfangstemperatur $\vartheta_S = 60$ °C

In Abbildung 11 sind die Medianwerte $x_{50,3}$ der kristallisierten Kalialaun-Partikelkollektive bei einer Anfangstemperatur $\vartheta_S = 40$ °C in Abhängigkeit von der Abkühlgeschwindigkeit auf-

getragen. Man erkennt eine lineare Abnahme der mittleren Partikelgröße mit dem Ansteigen der Abkühlgeschwindigkeit bei den Werten ohne Ultraschall. Dagegen bleibt der Medianwert bei der Keimbildung mit Hilfe von Ultraschall auf gleichem Niveau unabhängig davon, wie schnell die Lösung heruntergekühlt wurde. Dies hängt offensichtlich mit der vom Ultraschall vorzeitig eingeleiteten Keimbildung zusammen, wie die Ähnlichkeit mit Abbildung 9 belegt. Die mittlere Partikelgröße des Kollektivs ist also abhängig von der Keimbildungstemperatur und somit von der Übersättigung des Systems bei Beginn der Keimbildung S_{Keim}.

Die Medianwerte der Experimente bei 60 °C Anfangstemperatur zeigt Abbildung 12. Hier ist keine Übereinstimmung mit der Keimbildungstemperatur erkennbar. Es muß daher betont werden, daß die mittlere Partikelgröße nicht nur von der Keimbildungsrate abhängig ist, sondern auch von der Kristallwachstumsgeschwindigkeit. Die Wachstumskinetik hängt wiederum vor allem von Temperatur und Grad der Übersättigung ab.

Zusätzlich zum Einfluß auf den Medianwert des entstandenen Partikelkollektivs wirkte sich der Einsatz von Ultraschall bei der Keimbildung auch auf die Partikelgrößenverteilung aus. Hierbei zeigte sich, daß der Dispersitätsgrad (Maß für die Breite der Verteilung) bei der Keimbildung durch Ultraschall stets kleiner war als bei den Vergleichsversuchen. Zudem hing der Dispersitätsgrad für diese Versuche nicht signifikant von der Abkühlgeschwindigkeit ab, während er ohne den Einsatz von Ultraschall mit steigender Abkühlgeschwindigkeit ebenfalls anstieg.

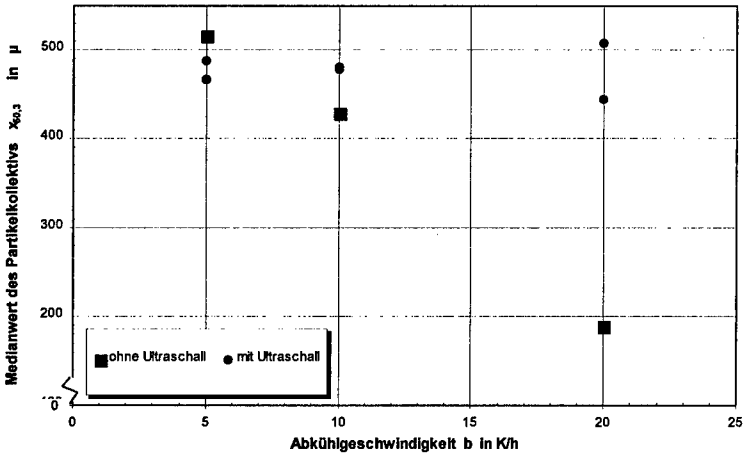

Abb. 11: Medianwerte $x_{50,3}$ der entstandenen Partikelkollektive mit und ohne Ultraschall in Abhängigkeit von der Abkühlgeschwindigkeit b bei einer anfänglichen Sättigungstemperatur $\vartheta_S = 40$ °C

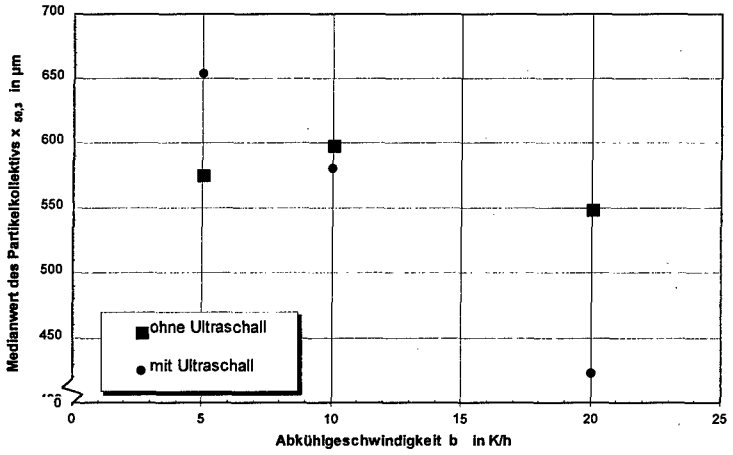

Abb. 12: Medianwerte $x_{50,3}$ der entstandenen Partikelkollektive mit und ohne Ultraschall in Abhängigkeit von der Abkühlgeschwindigkeit b bei einer anfänglichen Sättigungstemperatur $\vartheta_S = 60$ °C

3.3.2 NTO / Lösungsmittel

Bei den Untersuchungen mit NTO zeigte sich, daß es nur mit dem Lösungsmittel Wasser möglich war, die Keimbildung durch den Einsatz von Ultraschall auszulösen. Alle anderen untersuchten Systeme (Methanol, 2-Propanol und Dimethylformamid) wiesen eine extrem lange Induktionszeit auf (bis zu mehreren Tagen). Diese konnte auch durch Einkopplung des Ultraschallfeldes über eine längere Zeitspanne nicht reduziert werden. Dies deutet auf eine starke Inhibierung hin, wobei kein Unterschied zwischen den Systemen mit hoher und niedriger Löslichkeit zu bestehen scheint. Auch die starke Kavitationsbildung beim System NTO/Methanol führte zu keiner Nukleation. Zu beachten ist allerdings, daß der Ultraschallgenerator auf den Einsatz im wäßrigen Medium optimiert ist und keine genaue Anpassung auf andere Lösungsmittel erfolgte. Dies ist allerdings keine grundsätzliche Erklärung für das beschriebene Verhalten, da damit lediglich eine Feinabstimmung erreicht werden kann.

Für die Untersuchungen am System NTO/Wasser wurden 14,5 g NTO in 500 g Wasser bei 40 °C gelöst. Anschließend wurde diese Lösung mit einer konstanten Abkühlgeschwindigkeit von 20 K/h auf 20 °C abgekühlt. Beim Versuch ohne Ultraschall setzte die Keimbildung bei einer Temperatur von 30 °C ein, wobei zunächst nur wenige Keime entstanden. Erst bei einer Temperatur von 28 °C bildete sich der eigentliche Keimschauer. Die mittlere Partikelgröße $x_{50,3}$ betrug für diesen Versuch 345 µm.

Bei dem mit Ultraschall durchgeführten Versuch wurde die Ultraschallquelle bei einer Temperatur von 35 °C, d.h. einer Unterkühlung von 5 K, eingeschaltet. Hier trat die Keimbildung bereits bei einer Temperatur von 33,5 °C ein, wobei auch hier zunächst nur wenig Keime entstanden. Der eigentliche Keimschauer bildete sich nach einer weiteren Abkühlung um 2 K. Die gebildeten Partikel waren deutlich feiner ($x_{50,3}$ = 254 µm) und zeichneten sich durch eine wesentlich engere Partikelgrößenverteilung aus.

Auch die Morphologie der Kristalle konnte durch den Einsatz des Ultraschalls verändert werden. In Abbildung 13 und 14 ist zu erkennen, daß die Kristalle, bei denen die Nukleation unter Ultraschalleinwirkung ausgelöst wurde, eine gleichmäßigere Form aufwiesen als die Kristalle, die dem Ultraschallfeld nicht ausgesetzt waren. Zusätzlich bestätigen die Mikroskopie-Aufnahmen die Aussagen aus der Partikelgrößenanalyse.

Abb. 13: NTO-Kristalle ohne Ultraschall

Abb. 14: NTO-Kristalle mit Ultraschall

4. Zusammenfassung und Ausblick

Ziel der vorliegenden Arbeit war eine systematische, experimentelle Untersuchung zum Einfluß von Ultraschallanwendung auf die Keimbildung bei der Kühlungskristallisation aus Lösungen.

Es wurden verschiedene Stoffsysteme bei verschiedenen Temperaturen unter Veränderung der Abkühlgeschwindigkeit untersucht. Dabei wurde die Keimbildungstemperatur bestimmt und die Induktionszeit zwischen dem Einschalten des Ultraschallfeldes und dem Auftreten erster Keime ermittelt. Da die Partikelgrößenverteilung primär durch die Keimbildung und das Kristallwachstum beeinflußt wird, ist für das entstandene Kristallisat eine Partikelgrößenanalyse mit Hilfe der Laserbeugungsspektrometrie durchgeführt worden.

Bei den Untersuchungen des Systems Kaliumaluminiumsulfat-Wasser zeigte sich, daß durch Ultraschall die Keimbildungstemperatur, im Vergleich zum unbeschallten Versuch, deutlich heraufgesetzt wird, d.h. die Induktionszeit verkürzt wird. Dies wirkt sich bei einer anfänglichen Sättigungstemperatur der Lösungen von 40 °C direkt auf die mittlere Partikelgröße der kristallisierten Kollektive aus. Die Breite der Partikelgrößenverteilung kann durch den Einsatz von Ultraschall reduziert werden.

Die Untersuchungen mit NTO ergaben indifferente Ergebnisse. Lediglich in Wasser konnte ein Einfluß des Ultraschalls gefunden werden. Der Einsatz von Ultraschall reduziert die Partikelgröße und -größenverteilung drastisch und hat einen Einfluß auf die Partikelmorphologie. In weiteren Untersuchungen soll am System NTO/Wasser der Einfluß von Ultraschall auf die Keimbildung durch Variation der Abkühlgeschwindigkeit ermittelt werden. Zudem muß geklärt werden, ob ein solcher Einfluß auch bei organischen Lösungsmitteln zu finden ist.

---

1 Mason, T.J., 1990, *Chemistry with ultrasound*; Elsvier Applied Science, London, 1-25

2 Kapustin, 1962, *Effects of ultrasound on the kinetics of crystallization*; Consultants Bureau New York 1963

3 Baumann, K.-H., Voigt, H.; *Technische Massenkristallisation*; Akademie-Verlag Berlin 1984

4 Miers, H.A., Isaac, F.; *Refractive indices of crystallizing solutions*; J. Chem. Soc. 89, 143 (1906)

5 Hunt, J.D., Jackson, K.A.; *Nucleation of solid in an undercooled liquid by cavitation*; J. Appl. Phys. 37 (1966), 254-257

6 Mullin, J.W.; *Crystallization*; Butterworth-Heinemann Oxford 1993

7 Vollmer, M., Weber, A.; Z. Physik. Chem. (Leibzig) 119 (1926), 277

8 Mersmann, A.; *Chrystallization Technology Handbook*; Marcel Dekker Inc. New York 1995

9 Strickland-Constable, R.F.; *Kinetics ans Mechanism of Crystallization*; Academic Press London 1968

10 Nienow, A.W.; *The effect of aggitation and scale-up on crystal growth rates and on secondary nucleation*; Transactions of the Institute of Chemical Engineers, 54 (1976), 205-207

FAILURE MECHANISM IN PBX

Tamar Kaully, Tamar Kimmel
RAFAEL, Israel

Abstract

Compaction molded PBX are commonly used for warheads. Yet, their poor mechanical properties are of major concern for the users. A thorough understanding of the failure mechanisms in PBX is essential for development of PBX with improved mechanical properties.

PBX is a highly filled particulate composite material with a filler content of approximately 90vol%. In contrast, ordinary polymeric matrix composite materials , including propellants, consist of only ~ 20 - 70 vol% of filler. Therefore, some of the mechanisms in PBX are similar to those in particulate composite materials while others are unique and stem from the fact that high filler concentration cause interactions between particles.

The paper discusses the effects of different parameters like particle size distribution, particle shape, and surface energies of the filler and the elastomer matrix on mechanical behavior of PBX. Mechanical properties under tensile stress and SEM fractographs, as well as surface energies measurements were used as experimental tools.

The results indicate that there are some combined mechanisms that affect failure:

1. There is an interaction between particles, which results in mechanical interlocking. The degree of mechanical interlocking depends on particle size distribution and particle shape.
2. During compression, some of the particles are cracked and fractured, so that the material contains inherent defects.
3. Changes in the degree of adhesion can change the role of dewetting as a failure mechanism.

1. Introduction

A first step in the way of improving mechanical properties of any material (including composite materials), should be understanding the failure mechanism. Reviewing the literature concerning mechanical behavior of particulate composite materials, reveals that there is a variety of parameters influencing this behavior: Particle size, particle shape and size distribution, degree of adhesion and structural defects like microcracks, voids and aggregation (1-4). There are few works that deal with mechanical behavior of PBX' focusing mainly on the effect of adhesion between the binder and the filler(5). Other aspects of mechanical behavior are dealt with in works concerning propellants(6), which are the closest composite materials to PBX'es. The current work will demonstrate that there is a complex of mechanisms that govern mechanical behavior of PBX. Inhomogenieties and degree of adhesion are the main factors that govern failure mechanisms and mechanical properties of PBX.

2. Experimental

The materials that were tested are:

a. PBX based on HMX + Viton A.

b. PBX based on HMX + Kraton + Oil.

The PBX was manufactured in laboratory scale batches by the water slurry method. PBX based on HMX-Viton was manufactured with different granulations (fig 1 - 4).

2.1 Tensile properties and fracture mechanism.

Tensile samples in the shape of cylindrical "dog bones" were machined from pressed bulk material. Three samples were tested of each batch . The tension tests were conducted under room temperature with bridge velocity of 0.05cm/min.

Surfaces of the fractured tensile samples were analyzed with an SEM, as means of understanding crack growth and fracture mechanisms.

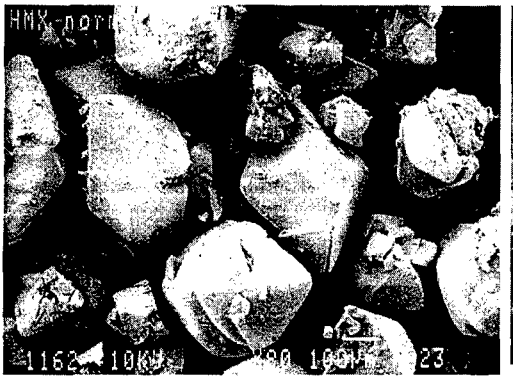

Fig. 1 - HMX-1

Fig 2 - HMX-2

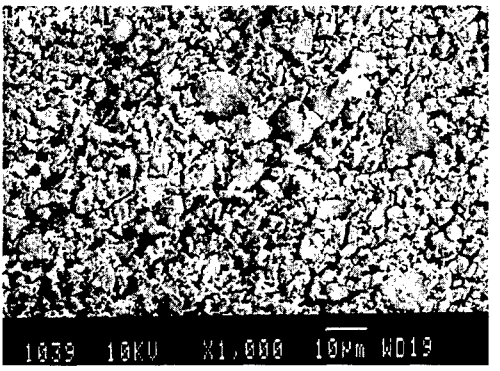

Fig. 3 - HMX-3

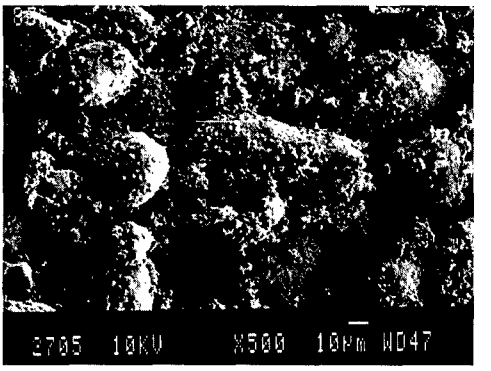

Fig 4 - HMX-4

2.2 Degree of adhesion

The degree of adhesion between the explosive particles and the binder was estimated by interpreting the relevant surface energies. The surface energy of HMX was taken from literature, while surface energies of the binder materials were calculated according to wetting angles measurements and "Owens - Kaelble"(7) model (equation 1). Finally, the interface energy and degree of adhesion were estimated employing equations 2,3.

(1) $1+\cos\Theta = 2\sqrt{\gamma_s^d}(\sqrt{\gamma_1^d})/\gamma_1 + 2\sqrt{\gamma_s^p}(\sqrt{\gamma_1^p})/\gamma_1$

$\gamma_s = \gamma_s^p + \gamma_s^d$

(2) $\gamma_{12} = \gamma_1 + \gamma_2 - 2(\gamma_1^p\gamma_2^p)^{1/2} - 2(\gamma_1^d\gamma_2^d)^{1/2}$

(3) $W_A = \gamma_1 + \gamma_2 - \gamma_{12}$

3. Results and discussion

3.1 Tensile properties

Tensile properties of HMX-Viton A with different granulations and of HMX-Kraton/Oil are listed in table 1.

Table 1 - Tensile properties

PBX	Batch No.	HMX granulation (%)	Density (gr/cm^3)	σ (kg/cm^2)	ε (%)
HMX-Viton	GR-5	50 HMX-1+50 HMX-2	1.847	10.8	0.13 - 0.21
HMX-Viton	GR-6	66 HMX-1+33 HMX-2	1.848	9.4	0.32 - 0.37
HMX-Viton	HV/5	100 HMX-2*	1.796	2.3	0.12 - 0.17
HMX-Viton	GR-2	100 HMX-4*	1.842	16	0.30 - 0.35
HMX-Kr-Oil	HB	66 HMX-1+33 HMX-2	1.763	9.7	1.15 - 1.30

* Size distribution analysis is given in fig. 5.

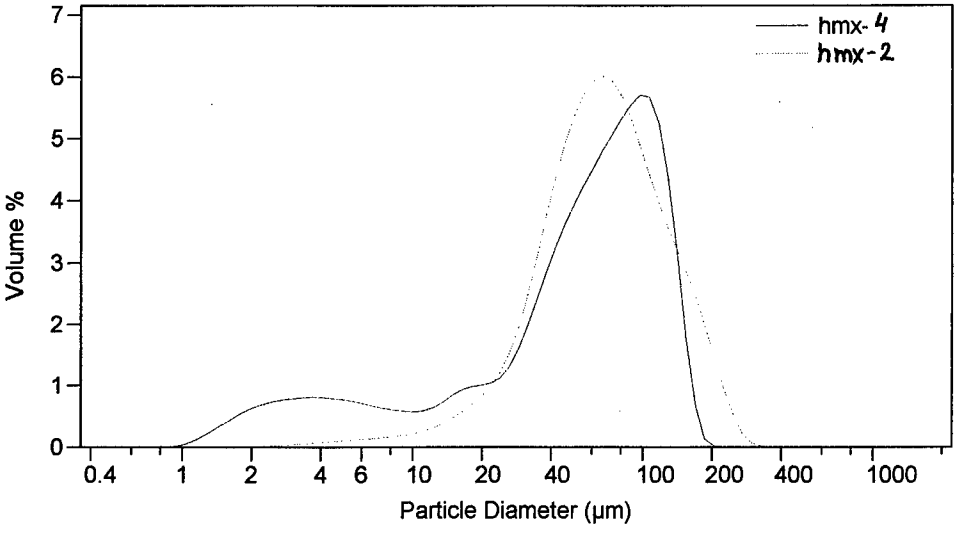

Fig. 5 - Particle size distribution of HMX-2 and HMX-4

3.2 SEM analysis

SEM micrographs of the different PBX'es fracture surfaces were straightforward means for analysing of fracture mechanisms. Generally, similar phenomena are involved in fracture surfaces of PBX'es with different binder or diferent granulations (fig 6-8):

Fig. 6 - HMX-Viton

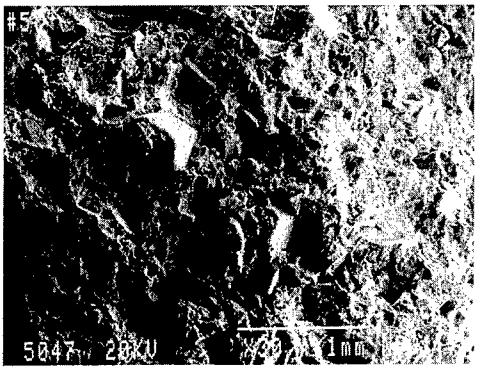

Fig. 7 - HMX - Kr-Oil

Fig.8 - MHX Viton; rounded granulation

a. A dewetting of particles from the binder is spread over a considerable area of the fracture surface. It seems to be a crucial phenomenon especially in the PBX HMX-Kr-Oil.
b. Many particles are fractured, probably due to stress concentration that is developed during compaction. According to the direction of the cracks, they could not be formed as a result of the tension stresses.
c. Some particles touch each other due to a lack of any binder envelope. This can be associated to a more general phenomena in particulate composite materials - aggregation. Aggregation is a type of deffect in the material, but it also contributes to the strength of the material via mechanical interlocking.

It is much easier to see the different phenomenas in the fractured surface of PBX with the rounded particles. Therefore, our discussion from now on will relate to frctographs of this PBX (GR-2).

The relatively large dewetted area (fig. 9) implies that dewetting is a main failure mechanism. The vast dewetting prevents the particles from taking part of the load exerted on the material. The fractured particles behave like a small aglomerate, since there is no binder material between the daghter particles (fig. 10). Mother particles with no binder between them can be related to in a similar manner. The meaning of all the above mentioned phenomenas is that there is no load delivery between binder and particles and mechanical interlocking of particles can be the only mechanism of load delivery. This explains the low strength of HMX-Viton PBX, (about 10kg/cm2) which resembles the strength of polymeric sponges.

By looking at a fractured specimen still under tension and from fig. 10, it is clear that the elastomeric binder continues stretching even after the sample is severly damaged. This means that the mobility of the polymeric chains was not injured considerably, although this is a known phenomena in particulate composite materials with high solid loading, in which the binder layers surrounding the particles are very thin (8). This finding implies that deterioration of chain mobility is not the cause to the poor deformability of the PBX. The poor deformability stems from the fact that the low content of elastomer in the material cannot be dispersed homogeniously throughout the

particles and cracks develop by moving through adjacent particles that are not coated (aggregates or fractured big particles). Generally there is no structure continuity in pressed PBX'es, which is responsible for the poor mecanical properties of the material. There are many samples in literature for effects of different kinds of inhomogenities in particulate composite materials - microcracks, microvoids and aggregation. These can make a composite material with very poor mechanical properties that are much inferior to the properties expected according to properties of the ingredients.

The qualitative analysis of the fractographs can help partially to explain differences in mechanucal properties of PBX with different granulations.

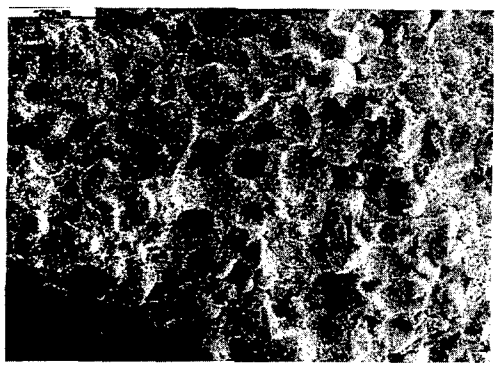

Fig. 9 - Rounded granulation - dewetted areas

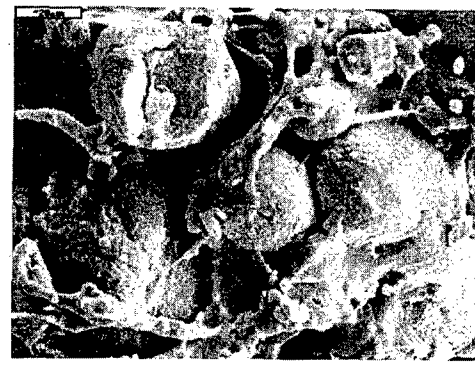

Fig. 10 - Rounded granulation - fractured particl

3.3 Surface energies

The tensile properties depicted in table 1, show that HB has a much bigger strain to failure than GR-6. The granulation of both PBX's is similar, whereas the binder is different. Both Viton A and Kraton-Oil elastomers have an enormous strain to failure in comparison to that of the PBX's. Therefore we assumed that the reason for the better deformability of HB does not stem from the elastomer properties, but from interfacial energies. Table 2 depicts the surface energies of both elastomers and of HMX crystals.

Table 2 - Surface energies

Substance	γ^d(dyne/cm)	γ^p(dyne/cm)	γ(dyne/cm)
HMX*	34.8	6.8	41.6
Viton A	25.9	0.2	26.1
Kr-Oil	0.2	57.3	57.5

Calculating the interfacial energy for HMX-Viton A and HMX-Kr-Oil, gave the following values for work of adhesion between HMX and both kinds of binders:

W_A (HMX-Viton A) = 55.9 dyne/cm

W_A (HMX-Kr-Oil) = 44.7 dyne/cm

This calculation reveals that wicker adhesion can improve deformability considerably. This maybe contradictory to the intuition that better adhesion means better mechanical properties, but it is known also for inert particulate composite materials, that adhesion should be optimised (8). This means that very strong adhesion causes brittleness, while very wick adhesion can cause very low strength that will impart an early failure. Also, we know from the literature, that the dominance of granulation depends on adhesion. The stronger the adhesion, the lower the effect of granulation on mechanical properties.

4. Summary and conclusions

The current work reveals the complex mechanical behavior of PBX's as highly filled particulate composite materials. Crack propagation which leads to failure is influenced by amount of fractured particles in the material during compaction, (which by itself depends on particle size distribution and particle shape) ; the dispersion of the binder material among the particles, and the strength of adhesion that dictates the degree of dewetting.

From the samples given in this work we can conclude that adhesion is a very dominant factor and can change considerably the strain to failure. Granulation parameters seem to have a smaller effect on deformability, but it affects considerably the strength to failure, probably via mechanical interlocking.

A lot of work is still to be done in the field of mechanical behavior of PBX's. The difficulties arise from the facts that it hard to find suitable surfactants from the adhesion point of view ; and it is hard to get powders with similar particle shape, but different particle size distribution, or vice versa.

5. Refferences

1. "Internal Fractures in Model Particle Filled Composites" Bui Loc Vinh Ph.D., The University of Akron, 1993.
2. Bela Pukanszky and Gyorgy Voros, Int Conf. on Interfacial Composite Materials (IPCM) 1995.
3. D. Mahoney et al., J. of Polymer Science: Part B: Polymer Physics, Vol. 31, p. 1029 - 1039 (1993).
4. D.a.Taylor et al., Polymat 94', London U.K. 19 - 27 Sept. 1994, p. 628 - 638.
5. J.M.Bellerby and Ch. Kiriratinkom, Propellants, Explosives, Pyrotechnics, 14, p. 82-85 (1989).
6. R.A.Schapery, DTIC-AD-A225790 Aug. 1990.
7. D.K.Owens et al., J. of Applied Polymer Science, Vol. 13, p.1741 - 1747, (1969).
8. S.H.Saidpour et al., Int. Conf. on Interfacial phenomena in composite materials (IPCM) 1995, p. 141.

ADN Manufacturing Technology*

T.K. Highsmith, C. McLeod, R.B. Wardle
Thiokol Propulsion
Brigham City, UT 84341

R. Schmitt, J. Bottaro, P. Penwell, D. Bomberger
SRI International
Menlo Park, CA 94025

John Brough
Naval Surface Warfare Center, Indian Head Division
Indian Head, MD 20640

Ammonium dinitramide is a novel, non-chlorine containing oxidizer which offers the potential of significant increases in performance in both solid propellants and some types of explosives. Dramatic progress has been made in the very few years since the discovery of ADN in the U.S. in the areas of synthesis and formulation of ADN. Even with these efforts, a chasm still exists between the current state of ADN lab scale production and formulation and the ultimate goal of ADN in a production system. Reports from the Former Soviet Union suggest that ADN and ADN formulation problems resulted in a series of major incidents during production. This program is bringing ADN manufacturing and formulation technology up to U.S. standards for safety and quality. Reported in this paper is progress on ADN made during the first two years of the Manufacturing Technology program.

Summary

The physical and chemical properties of ADN have a significant impact on its viability of a solid propellant ingredient. These properties are presented in Table 1. The properties of most concern are hygroscopicity, thermal instability, and safety characteristics. Various methodologies have been studied in order to overcome these limitations. At Thiokol the combination of additives and a prilling process has significantly improved these properties (see next section).

Table 1. Selected Chemical and Physical Properties of ADN

property	value
melting point	92-94°C
sensitive to light?	yes
hygroscopic?	yes
water solubility	very high
impact sensitivity	moderate
friction sensitivity	low
thermal decomposition (onset)	160°C (20°C/min)
particle dimensions	long needles
incompatibilities	isocyanates

Prilled ADN

To improve the hygroscopicity, thermal stability, and safety properties of ADN a prilling process

was developed at Thiokol under funding from the Navy's ADN MANTECH Program. The proprietary process involves the addition of additives, before the prilling process, to overcome the shortcomings listed above. Improvements in these properties have been realized and these modified properties are presented in Table 2. Further work is ongoing to seek additional improvements.

Table 2. Selected Properties of Thiokol Prilled ADN

property	value
melting point	92-94°C
sensitive to light?	yes
hygroscopic?	no
water solubility	very high
impact sensitivity	low to moderate
friction sensitivity	low
thermal decomposition (onset)	180°C (20°C/min)
particle dimensions	spheres
incompatibilities	isocyanates

The prilled ADN has exhibited improved properties in composite propellants. Most significant is that both the burn rate exponent and temperature sensitivity in a polyether binder system is unchanged from the analogous ammonium perchlorate system. This opens the door for a wide range of uses for the ADN-based propellants. The major obstacle remaining to ADN employment for booster applications is the current propellant hazards properties of ADN-containing propellants. The following vu-graphs exhibit the properties as described.

Ammonium Dinitramide Manufacturing Technology

Robert Wardle, Thomas Highsmith, Corey McLeod, Alan Allred
THIOKOL CORPORATION

Robert Schmitt, David Bomberger, Jeff Bottaro, Paul Penwell, Jason Taylor
SRI INTERNATIONAL

John Brough
NSWC/INDIAN HEAD

June 30, 1998

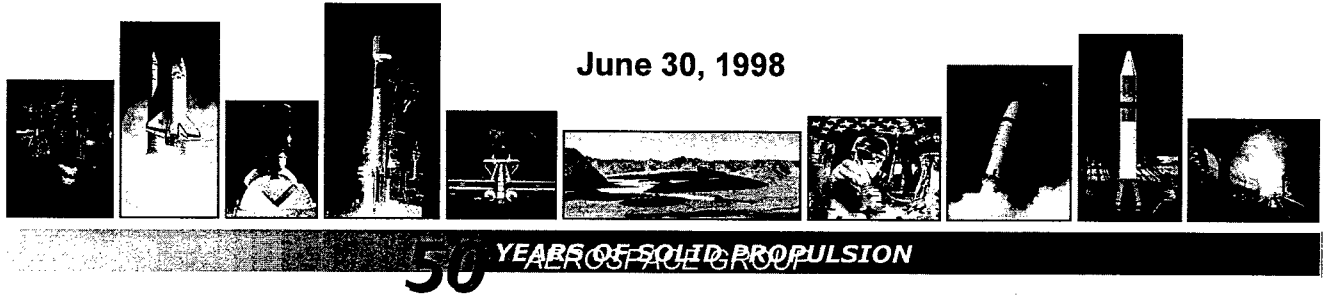

SRI International

THIOKOL
PROPULSION GROUP

NSWC
NAVAL SURFACE WARFARE CENTER
INDIAN HEAD DIVISION
Naval Sea Systems Command

ADN AS AN INGREDIENT

- **Early theoretical performance calculations showed major gains**
  - Isp does increase dramatically
  - Density lower than AP
  - Balance in booster systems a small gain in HTPB-like systems
- **Environmental advantages are not argued**
  - no HCl in exhaust
    - local effects definite
    - booster effects vs. NOx are difficult to quantify
  - demilitarization is very attractive
- **ADN characteristics unsuitable compared to AP**
  - hygroscopicity
  - thermal stability
  - nominally class 1.1 in a 1.3 world

ADN MANTECH PROGRAM

- **Two tasks to answer the two big questions**
  1. Can usable ADN be manufactured economically?
  2. Can propellants and explosives be processed safely, economically, and effectively?

  followed by:

  3. Demonstration of the success at addressing 1 and 2.

- **Critical program results**
  - Potential synthesis routes compared
    - SRI chemical engineering estimates
    - concluded that multiple routes show good economic promise
  - Stabilizer and processing of ADN
    - suitable stabilizer system found
    - safe prilling system developed

SRI International

NSWC NAVAL SURFACE WARFARE CENTER INDIAN HEAD DIVISION

Naval Sea Systems Command

ADN STABILIZER STUDY

- **Thermal stabilizer**
  - Screened at 100°C for 48 hours
    - several classes of potential stabilizers examined
    - neat ADN lost 12% mass and decomposed 10%
    - best system lost 3% mass and no decomposition
  - Verification by simulated bulk autoignition (cheap ARC)
    - with increasing temperature:
      - neat ADN onset at 94.4°C
      - ADN with stabilizer at 120°C
    - with isothermal challenge:
      - neat ADN at 120°C shows immediate exotherm
      - ADN with stabilizer at 120°C shows 7°F exotherm at 11 hours
- **Moisture barrier**
  - Screened at various humidities
    - measured moisture pick-up and decomposition
  - Selected barrier shows no decomposition
    - over 2 weeks at 70% relative humidity
    - maintains shape in prills or crystals
    - neat ADN a liquid

SRI International

NSWC NAVAL SURFACE WARFARE CENTER INDIAN HEAD DIVISION

Naval Sea Systems Command

ADN PRILLING

- **Prilling used to process ammonium nitrate**
  - temperature higher than neat ADN is safe
  - stabilized ADN can survive required conditions
- **Prilling tower constructed and process conditions optimized**
- **Prilled ADN shows markedly improved properties**
  - ABL impact test: 3.5 up to 6.9 cm (T.I.L.)
  - ABL friction test: 420 lbs @ 2 ft/sec up to 560 lbs @ 8 ft/sec
  - dramatic improvements in propellant processing
    - questions remain on ballistic effects of prilling
- **Prill shape is near spherical (lab scale)**
  - see photos

SRI International

NSWC NAVAL SURFACE WARFARE CENTER INDIAN HEAD DIVISION

Naval Sea Systems Command

PRILLING TOWER

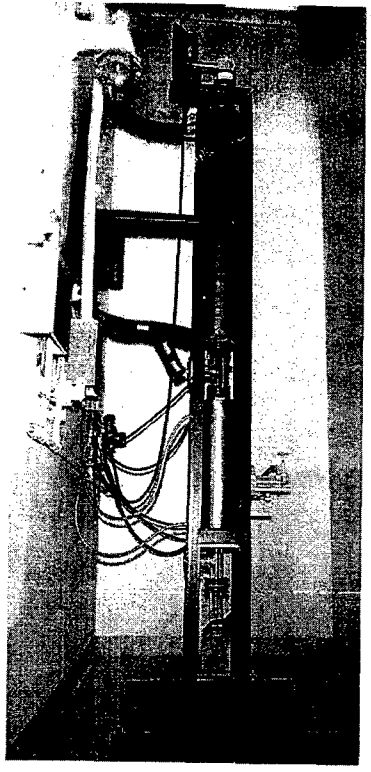

- **Based on work done previously at Thiokol on HP2**
  - heated and cooled zones melt and freeze ADN
  - ADN exposure to heat is very short

SRI International

NSWC
NAVAL SURFACE WARFARE CENTER
INDIAN HEAD DIVISION

Naval Sea Systems Command

PRILLED ADN

Crude

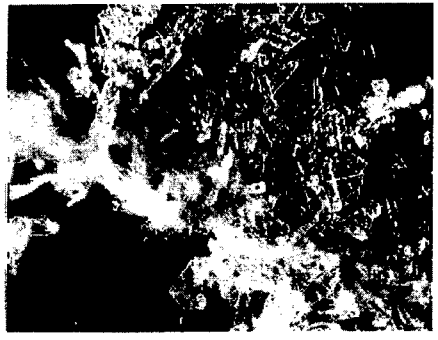

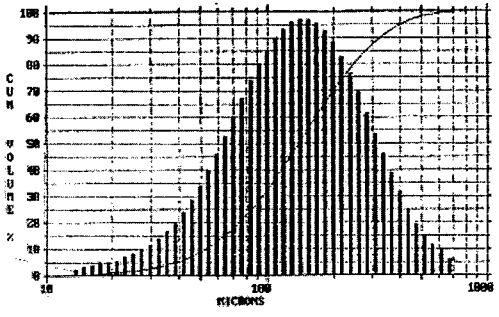

Prilled

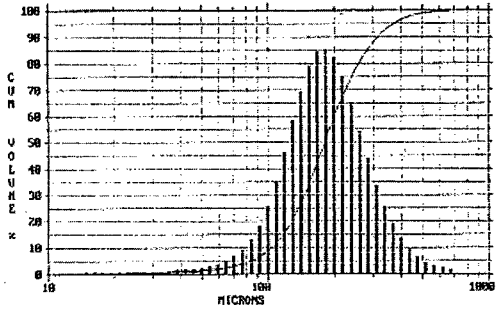

- ADN before and after prilling

SRI International

NSWC NAVAL SURFACE WARFARE CENTER INDIAN HEAD DIVISION

Naval Sea Systems Command

PRILLED ADN

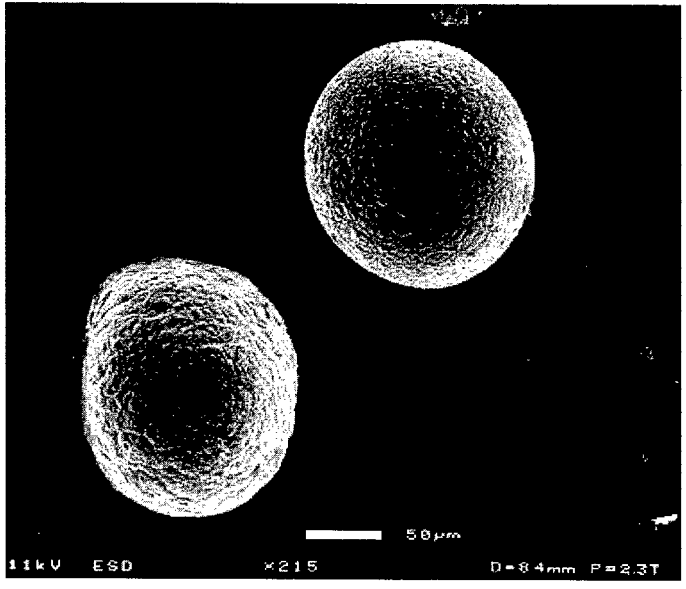

- Electron microscope photo by L. Ramaswamy at University of Maryland at College Park

SRI International

NSWC
NAVAL SURFACE WARFARE CENTER
INDIAN HEAD DIVISION

Naval Sea Systems Command

PRILLED ADN

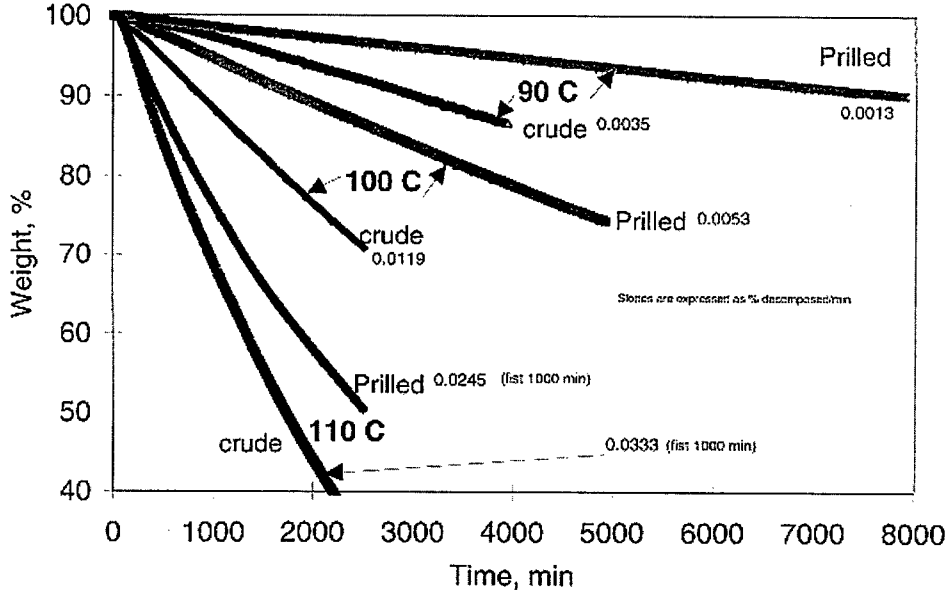

- **Decomposition rates for crude and prilled ADN**
  - Data from Air Force Research Laboratory at Edwards AFB

SRI International

NSWC
NAVAL SURFACE WARFARE CENTER
INDIAN HEAD DIVISION
Naval Sea Systems Command

PRILLED ADN

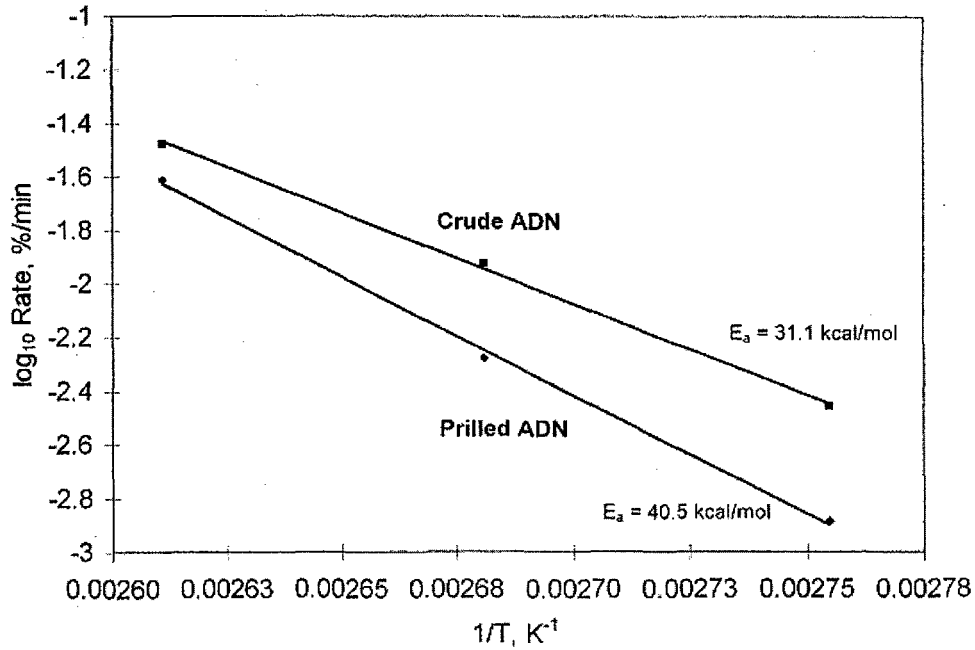

- **Energy of Activation for crude and prilled ADN**
  - Data from Air Force Research Laboratory at Edwards AFB

SRI International

NSWC NAVAL SURFACE WARFARE CENTER INDIAN HEAD DIVISION

Naval Sea Systems Command

SYNTHESIS ROUTES COMPARED

- **Three routes considered potentially viable and examined**
  - viable means projected to \$10-15 per pound cost at 10^6 lbs/yr.
  - pyrosulfate route
  - ANU route
  - mixed acid route
- **All three show significant potential**
  - assumptions define the differences in the cost
  - error bars and potential for improvements say all very close
- **FOA/Bofors scaling up a mixed acid route**
  - delivers quality product (crude ADN)
  - price will be competitive with other current routes

SRI International

NSWC NAVAL SURFACE WARFARE CENTER INDIAN HEAD DIVISION

Naval Sea Systems Command

SUMMARY

- **Met initial ADN MANTECH objectives**
  - stability dramatically improved
  - moisture sensitivity improved
  - particle shape greatly improved
- **Synthesis evaluation completed**
  - numerous routes appear economically viable
  - Bofors/FOA supply will support program
  - Formulation development proceeding

SRI International

NSWC NAVAL SURFACE WARFARE CENTER INDIAN HEAD DIVISION

Naval Sea Systems Command

Rheological characterisation of castable and extrudable energetic compositions

A.C. Hordijk, R.H.B. Bouma and E. Schonewille

TNO Prins Maurits Laboratory, Pyrotechnics and Energetic Materials
P.O. Box 45, 2280 AA Rijswijk, The Netherlands

1. Abstract

Castable compositions are made for over fifteen years now at TNO and there is a four year experience with extrudable compositions, including gun propellants and Plastic Bonded eXplosives. During these years rheological measurements have been carried out not only to characterise batches but also to be able to match the castable and extrudable compositions to the desired processing properties.

Castable compositions are generally characterised by their viscosity. Their flow behaviour is mostly pseudoplastic and the shear rate dependence of viscosity may be described by a power law in which the exponent is larger than 0.6.
The behaviour of castable compositions is never purely viscous. The visco-elastic shear modulus is determined with a dynamic mechanical technique. Well castable compositions are characterised by a relatively low shear loss modulus ($G'' < 100$ Pa, at 0.1 Hz) and an even smaller shear storage modulus (G').
It is observed that both loss and storage modulus rapidly increase with increasing solid load. The storage modulus, however, increases faster than the loss modulus. At a certain solid load both moduli are equal ($G'' \approx G' \approx 10^4$ Pa) and then upon a further increase of the solid load, the storage modulus becomes even larger, indicating that the composition more and more resembles an elastic material. At too high solid loads extrusion becomes an alternative to casting because of the rheological behaviour.
Extrudable compositions show typical shear storage moduli G' in the range of 10^5 to 10^7 Pa.
Apart from the solid load, also the addition of low molecular weight chain-extenders like hexane diols has a significant effect on the visco-elastic properties and thus the applicability of either casting or extrusion techniques.

2. Introduction

This paper deals with two processing techniques, casting and extrusion, and the product and preproduct characterisation. The compositions discussed in this paper, contain an energetic filler and a curable binder to which plasticiser, bonding agent and surface active agents are added. The mean particle size(s) and size distribution, the particle shape as expressed by the specific surface area and the porosity, determine the maximum volume fraction to be obtained.

Three major influences on rheological behavior are discussed:

- chemically and physicochemically induced effects, e.g. curing and the effect of bonding agents
- volume fraction of solids (ϕ_v) or solid load (wt.%)
- surface area of solids (expressed for instance as S_w" in m^2 / ml binder)

The above mentioned effects influence the properties of the composition after processing as well, for instance mechanical properties, but also the performance and the sensitivity to shock.

3. Rheology

The processing of PBXs at TNO-PML is carried out using

- the small scale 300 ml IKA mixer for preliminary processing characterisation,
- the larger HKV 5 (max 3 liter) and HKV 25 (10 liter capacity) mixers for casting of larger test items,
- or the twin screw extruder [1].

The compositions described here are based on PPG or HTPB. Unfilled prepolymers behave as Newtonian fluids. By addition of an energetic filler to the HTPB prepolymer, shear rate dependent behavior such as pseudoplasticity showes up; the stress to be applied is no longer proportional to the shear rate as for a Newtonian fluid [2]. Usually a decrease of viscosity with increasing shear rate is found, so-called shear thinning.

Further filling leads to time dependent behaviour and more elastic behaviour [4]. The latter appears as a yield stress (a relative large stress has to be applied before the mix will flow) or in a oscillatory measurement as a linear viscoelasticity (LVE) region with a corresponding critical stress. Applying a larger stress will result in a

destruction of the structure of the mix – the mixture will become inhomogeneous (e.g. fluid film at the boundary). The extent of these effects increases with increasing solid load.

The rheological behaviour is measured with ;

- a Haake RT 10 Rheometer to determine viscous and viscoelastic properties [2] of the preprocessing compositions
- a Thermal Mechanical Analyser and a draw-bench to determine the mechanical properties for the castcured and extruded compositions [2,3].

In the rotation mode of the Haake RT10 the shear rate dependence of viscosity is determined and data is analyzed according to the power law $\eta = K\dot{\gamma}^{1-n}$, with η is viscosity, K a constant, $d\gamma/dt$ the shear rate and n the pseudoplasticity index. Furthermore the extent or thixotropy or existence of yield stress is determined.
In the oscillation mode one can determine the dynamic viscosity or dynamic shear modulus.

4. Compositions and results

The compositions presented in the tables 1 and 2 have been processed in the small IKA mixer or in the HKV 5 planetary mixer. The extrudable compositions, gun propellants, are mixed in the extruder, while the final propellant grain design (five or nineteen holes) has been realised by hot pressing.

4.1 Castable compositions and castability limits

In table 1 the rheological characterisation results of some of a series of well, moderate and bad castable propellant batches are presented. PPG and HTPB are applied as binders with AP as filler. The percentages bonding agent, cure catalyst and the NCO/OH ratio have been varied. In table 1 the results obtained by rotation mode (viscosity at a shear rate of 1 s^{-1}, K, the power law index n, and the extent of thixotropy) and by oscillation mode (dynamic viscosity, G" and time to max delta – see figures 3 and 4) measurements, are presented and rearranged according to their castability. The phase shift δ is equal to arctan(G"/G'), with G" the shear loss modulus, and G' the shear storage modulus.

When the castability becomes worse the dynamic viscosity, storage modulus, thixotropy and K increase, while the power exponent (n) and time to max. delta decrease. Furthermore it is clear for castable compositions, that G" is typically equal or lower than 100 Pa.

It appears, that although ϕ_v (or solid load) and S_w" only change to a limited extent, the castability changes considerably, thereby demonstrating the importance of chemically and/or physico-chemically induced effects.

Table 1: Relation between castability and rheological parameters (AP based propellants).

	CK 112	CK 122	CK 119	CK 115	CK 127	CK 126	CK 125
	PPG	PPG	HTPB	HTPB	HTPB	HTPB	HTPB
ϕ_v	0.67	0.67	0.73	0.73	0.73	0.73	0.73
Sw"	1.09	1.14	0.65	0.56	-	0.53	0.53
Castability	well	well	moderate	moderate	moderate	bad	very bad
Oscillation mode							
η^* (Pa·s)	50	90	96	85	170	160	500
G" (Pa)	20	50	55	52	100	100	300
Time to max.δ (hrs)	12.6	17	>15	?	6.5	5	<1.5
Rotation mode							
η at 1 s^{-1} (Pa.s)	105	180	200	210	390	-	-
Thixotropy (W/m^3)	15	-	97	44	249	-	-
n	0.66	0.99	0.33	0.56	0.47	-	-
K	93	180	219	221	347	-	-

For an HTPB/AP based propellant, designated CK 45, a series of rheological measurements has been carried on the mix before and after IPDI addition, see table 2. The waiting/rest time after inserting the sample in the Haake RT10 and before starting the measurement is extremely important, because of the ongoing curing reaction. For all experiments a rest time of 10 minutes is used.

It is observed that the mixture before addition of IPDI shows an impressive yield stress (see figure 1) in the rotation mode. In the oscillation mode the measurements show likewise a LVE (Linear Visco-Elastic) region, however, with a smaller critical

stress value because of the different test conditions. Besides, G" is about 10^4 times larger as found as castability limit in table 1. Furthermore, G' >> G", indicating that the rheologic behaviour is predominantly elastic.

Table 2 shows, that after the addition and mixing of the IPDI, the initially non-castable composition can be cast as the yield stress and the critical LVE stress are reduced considerably.

Table 2: Rheological characterisation of CK 45, a moderately castable, AP/HTPB based propellant composition and the effect of isocyanate addition.

	before IPDI addition	after mixing with IPDI	
Castability	does not flow	moderate	
Rotation mode			
η at 0.09 s^{-1} (Pa s)	13,000	2360	
yield stress τ_c (Pa)	7800	200 - 400	
deformation γ_c (%)	4	30	
Oscillation mode, f = 1 Hz			
Stress sweep	large LVE region	small LVE region	
G' (Pa)	3.10^6 (> G")	4.10^5 (> G")	
τ_c (Pa)	470	50 - 100	
Oscillation mode, time curve*		τ < 50 Pa	τ > 100 Pa
η^* (Pa.s)	7.10^5	83000	45
G" (Pa)	-	5.10^5	300
G' (Pa)	-	1.10^5	150

* Measurements are carried out with a serrated plate.

The effect of the isocyanate (IPDI) addition is a reduction in the yield stress from 7800 to about 300 Pa, while applying forces larger than about 100 Pa in oscillatory measurements results in a sharp reduction of the dynamic viscosity making casting possible. It is remarkable to see that the loss modulus G" is reduced by a factor 1000.

Combining the results of tables 1 and 2, well castable compositions are characterised by a viscosity < 200 Pa·s at 1 s^{-1}, a pseudoplasticity index > 0.6 (or 0.4 for THMD containing compositions), and a thixotropic index < 100 Wm^{-3}, in rotation mode measurements. In oscillation mode measurements a castable composition is characterized by an initial dynamic viscosity < 100 Pa·s at 0.1 Hz, or loss modulus < 70 Pa. Furthermore, the pot life, or time to max. δ needs to be more than 10 hrs.

4.2 Extrudable compositions

In table 3 a number of extruded compositions are presented; given are the solid load and Sw", and the results of the rheological characterisation (see also figure 2). Because of the very small particles (< 10 micron) the solid load is lower than for a bimodal filler mix with the usual size distributions. The main reason is that the surface area to be wetted is about a factor of four to six higher than for a bimodal filler mix.

Table 3: Rheological characterisation of extrudable compositions (gun propellants).

	IBK 1001-3	IBK 1007-4	IBK 1007-6
Solid load (wt.%)	79.5	82.0	82.0
Sw" (m^2/ml binder)		2.25	2.25
Castability	not	not	not
Oscillation mode	f = 0.1 Hz	f = 1 Hz	f = 1 Hz
G' (Pa)	2.10^5	2.10^6	6.10^6
τ_c (Pa)	2300	22,000	40,000

* Measurements are carried out with a serrated plate.

Firstly, this table shows, that the G' values are larger than those presented in table 2, while the critical stress values are more than 10 times larger.

Secondly, it is shown, that the stresses to be applied to extrudable compositions to force the mix to flow are in the range of about 3 to 50 kPa. When exceeding these stresses the mix becomes heterogeneous and the moduli are reduced by a factor of about 1000.

This correspond well with those stresses found by others [6]; stresses of 18 – 22 kPa are needed resulting in shear rates of 20 – 70 s^{-1}. In a twin screw extruder as used at TNO-PML the maximum shear stresses are in between 100 and 200 kPa [1] to guarantee save processing of highly energetic materials.

4.3 Mechanical properties of cured compositions

As stated in the introduction the parameters influencing rheology have their effect on the mechanical properties as well. In Table 4 the mechanical data are presented of some of the compositions referred to in this paper as determined with a draw-bench using the tensile and compression mode.

Table 4: Tensile and compression data of several compositions.

	RU 144	RU 130-1	RU 147	RU 146	RU 133
Processing	Casting	Casting	Casting	Casting	Extrusion
Particle size (μm)	10/mono	180/mono	355/mono		180/mono
Solid load (wt.%)	65	65	70	85	86.2
Compression modulus (MPa)		6.4	7.1		80
Max. stress (MPa)		1			4.4
at strain (%)		16.1			22
Young's modulus (MPa)	5.5	8.5	6.4	1.4	-
Max. stress (MPa)	0.66	0.57	0.29	0.30	-
at strain (%)	60	15.7	13.3	28	-
Strain at break (%)			23	45	-
Toughness (MPa)	0.62		0.05	0.15	-

It appears that for the monomodal batches the maximum stress, the strain at maximum stress and the strain at break decrease with increasing particle size. Extruded compositions show a high compression modulus.

5. Conclusions

It is clear that the effect of curing agents and surface active agents are as important as filler volume fraction and filler surface area with respect to the rheological behaviour. Cast-cured compositions show shear rate and time dependent behaviour. The limits of castability in rheological terms have been established, among which a limit for the yield stress.

When a composition has a yield stress, one has to apply relatively large stresses in order to destroy the structure of the compositions, and making it flow. The stresses applied in the twin screw extruder correspond well to and are higher than the yield or critical stresses determined by rheological measurements.

It is common practice to use small particle sizes to reduce the shock sensitivity and to improve the mechanical properties of the product. For castable compositions this implies a reduction in the maximum attainable filler volume fraction. This problem can be solved by extruding instead of casting. For example, a PBX containing 18 μm monomodal RDX may be cast with a solid load up to 65 wt.%, whereas the same composition with 180 μm RDX, can have a solid load up to 78 wt.%. The difference

is the particle surface area to be wetted. Applying extrusion the same composition with 18 μm RDX particles can have a solid load of 86 wt.%.

ACRONYMS.

AP	Ammonium Perchlorate
HDO	Hexane Diol
HMX	octogene
HTPB	prepolymer of Hydroxy Terminated Poly Butadiene
IPDI	IsoPhoron DiIsocyanate
LVE	Linear ViscoElastic region
PBX	Plastic Bonded eXplosives
PPG	prepolymer of PolyPropylene Oxide
RDX	hexogene
TMHD	TriMethyl Hexane Diol

G'	shear storage modulus	(Pa)
G"	shear loss modulus	(Pa)
n	pseudoplasticity index	(-)
$S"_w$	surface area of solids	(m^2/ml binder)
ϕ_v	volume fraction of filler	(-)
η	shear viscosity	(Pa.s)
η^*	dynamic viscosity	(Pa.s)
τ_c	yield stress or critical stress	(Pa)
$\dot{\gamma}$	shear rate	(s^{-1})

LITERATURE.

1 H.W.R. Sabel, E. Schonewille, Extrusion trails with a TSK045 twin srew extruder, ICT 1998.

2 A.C. Hordijk, H.W. R. Sabel, E. Schonewille, The application of rheological equipment for improved processing of HTPB based PBXs, ICT 1996.

3 G. Schramm, A practical approach to rheology and rheometry, Gebr. HAAKE GmbH, 1994.

4 R.R. Miller, E. Lee, Rheology of solid propellant dispersions, J. Rheology 35 (5), July 1991.

5 R.M. Muthiah, V.N. Krishnamurthy, B.R. Gupta, Rheology of HTPB propellant. I. Effect of solid loading, oxidiser particle size and aluminum content, J. of Applied Polymer Science, Vol 44, 2043-2052 (1992)

6 Mueller, Verarbeitung von LOVA-TLP in Doppelschnecken Extruder, ICT 1990.

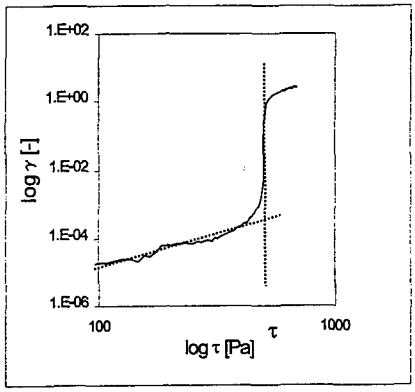

Fig 1. A typical example of a yield stress as meaxured in a CS stress sweep- CK 45 – see table 2.

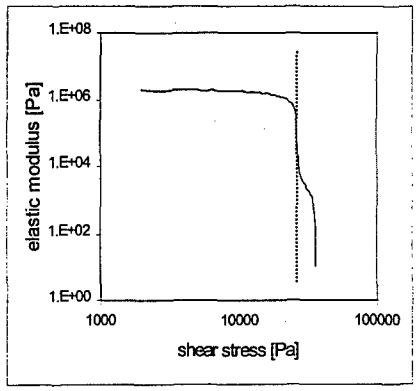

Fig. 2 A typical of a Linear visco-elastic region as found in a osc. Stress sweep - IBK 1007-4 – see table 3.

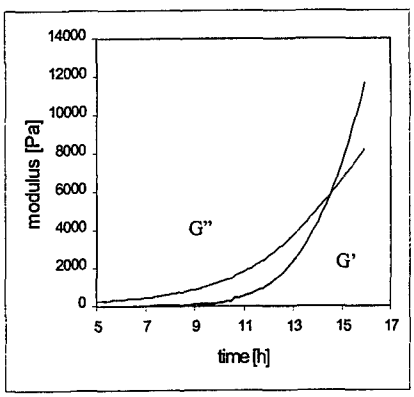

Fig. 3 The storage and loss Moduli as function of time – CK 126 – see table 1

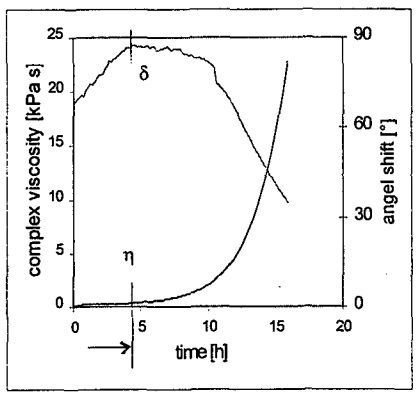

Fig. 4 Time to delta maximum and complex viscosity as function of time for CK 126 –see table 1.

QUANTIFICATION OF MICROSTRUCTURAL FEATURES IN HMX USING SMALL ANGLE NEUTRON SCATTERING TECHNIQUES

Joseph T. Mang and Cary B. Skidmore
DX-2, Los Alamos National Laboratory
Los Alamos, NM 87545

Rex P. Hjelm
Manuel Lujan Jr. Neutron Scattering Center, Los Alamos National Laboratory
Los Alamos, NM 87545

Philip M. Howe
DX, Los Alamos National Laboratory
Los Alamos, NM 87545

Abstract

Microstructural features in raw powders of High Explosives have been qualitatively observed by many researchers, using polarized light and scanning electron microscopy. Here, we present a method for non-destructive quantification of volume fraction and structure of intragranular cracks and crystallization voids in a bulk sample (100-300 mg). By employing Small Angle Neutron Scattering (SANS) in conjunction with the method of contrast variation, we can effectively highlight different structural features of a complex system. The technique of contrast variation relies on immersing the sample in a uniform fluid of known neutron scattering length density. By selectively varying the scattering length density of the immersion fluid, scattering contributions from internal and external structures can be separated. This approach is analogous to varying the index of refraction for immersion oil relative to a sample in polarized light microscopy.

SANS experiments on HMX were conducted using loose powders (261 and 10 micron mean particle diameters) and pellets made by uniaxial consolidation (without binder) to 7 and 10 volume percent porosity respectively. Detailed modeling of the SANS data indicate significant alteration of the intragranular void/crack/pore structure, with pressing, of the HMX powders.

I. Introduction

High explosive (HE) materials are frequently composites, consisting of a crystalline high explosive and a polymeric binder. These materials possess both naturally occurring and process-related defects (cracks, voids, etc.) which can affect their response to certain stimuli. Under conditions of impact or shock for example, locally heated regions, *hot spots*, can occur. The creation of hot spots is thought to occur by conversion of mechanical work into thermal energy through processes such as viscous void collapse[1]. The critical hot spot temperature is known to

be dependent upon both the size and shape of the defect, so shifts in the pore size distribution in an explosive can markedly change the explosive response to shock and impact stimuli[1]. Larger pores (> 1 μm diameter) have lower critical temperatures and are generally thought to be of more consequence in generating hot spots. However, recent molecular dynamics simulations[2] have shown that nanometer sized defects interact strongly with shock waves and thus have profound effects on the shock to detonation transition. In order to quantitatively describe an explosive's response from the lowest ignition thresholds to the development of full detonations and explosions, accurate measurements of a number of structural parameters of the HE composite, particularly porosity and pore size distributions are required.

Experimental efforts at Los Alamos National Laboratory are aimed at providing detailed structural information of high explosives over lengthscales from angstroms to microns. Such efforts require the use of a variety of techniques, including optical microscopy, BET and SEM. However, direct, quantitative determination of structural parameters is needed for an accurate description of HE materials. Standard metallographic techniques, such as cutting and polishing samples are adequate for measuring particle size distributions, but are inadequate for measuring pore size distributions because the softness of the materials may cause the surface pores to be filled in polishing. Techniques such as BET adsorption or mercury porosimetry measure only open pores, which represent only a fraction of the total porosity in design explosives. As part of this ongoing effort, we have performed small angle neutron scattering (SANS) measurements in conjunction with the method of *contrast variation* (to be discussed later in the paper) to measure the shape and internal structure of neat HMX powders. In comparison to other techniques, SANS has a distinct advantage in that it is noninvasive. No special treatment (polishing, grinding, etc.) of samples is necessary for study. A sample can then be examined in its pristine state, exposed to some external insult and then reexamined without further altering the state of the material. In this way, in situ measurements of the effects of external stimuli on structural parameters can be made, allowing for more direct correlation between cause and effect. SANS can provide detailed structural information over length scales between 10 and 1000 Å. As the scattered neutron intensity is proportional to the number and squared volume of the particles present, SANS can provide quantitative information about pore size distributions. Over length scales larger than 0.1 μm, SANS can provide in situ measurements of surface area.

II. Small Angle Neutron Scattering

In a SANS experiment, a collimated beam of neutrons impinges upon a sample, which is characterized by a scattering length density $\rho(\mathbf{r})$. At any point within the sample, the scattering length density is equal to the sum of the atomic neutron scattering amplitudes (scattering lengths) in a small volume around that point, divided by the volume[3]:

$$\rho = \frac{\sum_i n_i b_i}{V_m}. \qquad (1)$$

Here, b_i is the atomic neutron scattering length, n_i the number of a given atom in a molecule and V_m is the molecular volume. A fraction of the incident neutrons will be scattered through an angle, 2θ, from fluctuations in the scattering length density. $\rho(\mathbf{r})$ then reflects microscale structure in the sample in both density and chemical composition.

The scattered intensity, I(Q), is measured as the absolute differential cross section per unit scattering mass (cm^2g^{-1}) as a function of the magnitude of the scattering vector, Q. For elastic scattering events, $Q = (4\pi/\lambda)\sin\theta$, where λ is the wavelength of the incident neutron and θ is half of the scattering angle. I(Q) is related to $\rho(\mathbf{r})$ by a squared Fourier transform[3]:

$$I(Q) = K\left\langle \left| \int \rho(\mathbf{r}) \exp(-i\mathbf{r}\cdot\mathbf{Q}) dr \right|^2 \right\rangle = KP(\mathbf{Q}), \qquad (2)$$

where, the angle brackets indicate a spherical average over all possible particle orientations and $P(Q)$ is the normalized particle form factor, which contains the particle shape information. The constant, $K = NV^2\Delta\rho^2/M$, where N is the number of particles, V is the volume of a particle, M is the scattering mass and $\Delta\rho = \overline{\rho} - \rho_s$ is the contrast between the average scattering length density of the particle, $\overline{\rho}$ and that of the surrounding media, ρ_s.

Eq. 2 describes the observed scattering over all possible length scales. Important approximations to this expression exist which are valid over much more limited ranges. For example, in the range such that $QR < 1$, where R is the average radius of the particles under study, the observed scattering can be described by the Guinier approximation[3]:

$$I(Q) = Ke^{-Q^2R_g^2/3}. \qquad (3)$$

In Eq. 3, R_g is the particle radius of gyration and for spheres, $R_g^2 = 3/5\ R^2$. Over length scales

such that QR >>1, the scattering can be described as a negative power-law[4], $I(Q) = I_o Q^{-\alpha}$, where α and I_o are constants. For rough interfaces, $3 \leq \alpha < 4$. For the special case of smooth interfaces, $\alpha = 4$ and the scattering is termed *Porod scattering*. Under these circumstances,

$$I(Q) = 2\pi S \, \Delta\rho^2 Q^{-4}, \tag{4}$$

where S is the interfacial area per gram of material[3].

Scattering From Simple Shapes

Well-defined particles give rise to distinctive scattering patterns as a function of Q. For example, in the case of a spherical particle of radius R; the particle form factor has the form[3]:

$$P(Q) = \left| \frac{3 j_1(QR)}{QR} \right|^2, \tag{5}$$

where j_1 is the first order spherical Bessel function. The anticipated scattering for an isotropic solution of monodisperse spherical particles is shown in Fig. 1. As seen in the figure, in the low-Q region, the scattering curve follows the Guinier approximation (Eq. 3). This regime is followed by successive maxima which fall-off in intensity as Q^{-4}. The positions of the maxima are indicative of the particle radius. In general, most systems contain some level of size polydispersity, the effects of which can be taken into account by performing the appropriate population average of the form factor. The scattered intensity then has the form:

$$I(Q) = \frac{\Delta\rho^2}{M} \int_0^\infty N(R) V(R)^2 P(\mathbf{Q}, R) dR. \tag{6}$$

As seen by the solid line in Fig. 1, where we have assumed a Gaussian distribution of spherical particles, the effect of polydispersity (even at low-levels) is to wash-out the maxima, resulting in a loss of information.

Method of Contrast Variation

In more complex systems, such as composite materials[5,6], determination of the structure-property relationships is more difficult. This is due to the fact that there are now multiple contributions to the scattering signal. For an HE system, these contributions arise from the

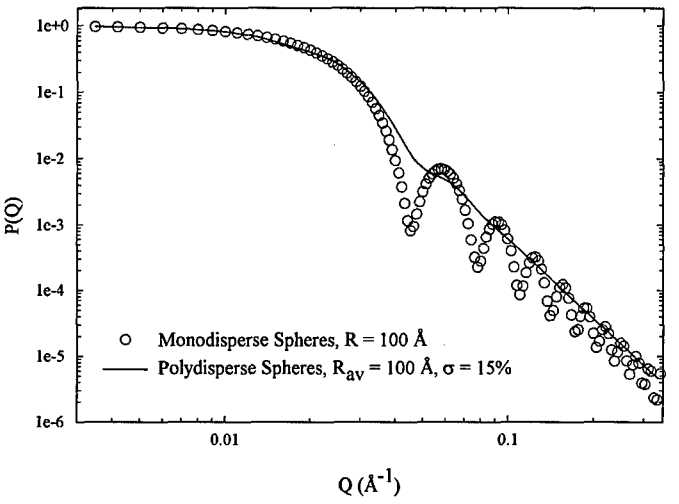

Figure 1 : Modeled SANS scattering for monodisperse spheres (R = 100 Å) and a Gaussian distribution of spheres (R_{av} = 100, σ = 15%).

polymer matrix, the filler (HE material) and the matrix-filler interface as well as from defects, such as (internal and external) voids and cracks. The first step in sorting-out the sources of the observed scattering is to study the isolated components. But, even the investigation of these simplified systems, because of the possibility of internal structure, requires an additional technique, the method of *contrast variation*, to separate the scattering arising from the shape from that of the internal structure. The method takes advantage of the large differences in neutron scattering lengths among isotopes of hydrogen, and the consequential difference in scattering length density between deuterated and non-deuterated materials. Thus, making a fluid mixture of deuterated and non-dueterated species (cyclohexane and deuterocyclohexane in this work) in different proportions, $\Delta\rho$ in Eq. 2 can be varied continuously and different structural features enhanced or suppressed (Fig. 2).

For the purpose of contrast variation we can think of the sample as a collection of particles suspended in a uniform fluid, then the structure of the particles can be modeled as[3,5]:

$$\rho(\mathbf{r}) = \rho_s + (\overline{\rho} - \rho_s)\Omega(\mathbf{r}) + \zeta(\mathbf{r}), \qquad (7)$$

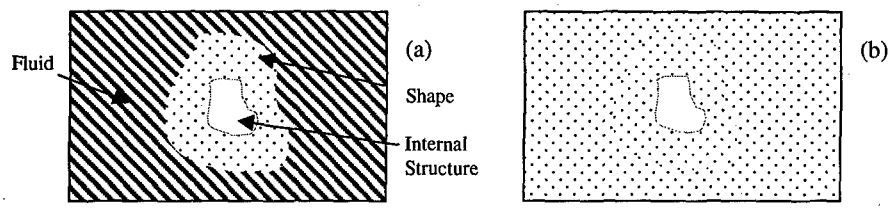

Figure 2 : By varying the scattering length density of the surrounding media, different structural features can be highlighted. At infinite contrast (a) we see the particle shape and at the contrast match point (b), we see the internal structure.

where, ρ_s is the scattering length density of the fluid and $\overline{\rho}$ is the average value of $\rho(\mathbf{r})$ over the entire sample volume, V, given by the expression,

$$\overline{\rho} = \frac{\sum_i n_i b_i}{V}. \tag{8}$$

The scattering contrast is defined as $\Delta\rho = \overline{\rho} - \rho_s$, as before. Now, two important, limiting cases need to be considered. At very high contrast (~ infinite), the internal structure of an object makes no significant contribution to the overall scattering. Under these circumstances, we measure the shape of the particles, represented by $\Omega(\mathbf{r})$ in Eq. 7 (Fig. 2a). This is the shape of the fluid excluding parts of the object. At the other extreme, $\Delta\rho \rightarrow 0$ (the contrast match point), only fluctuations from the internal structure ($\zeta(\mathbf{r})$), contribute to the scattering (Fig. 2b). At any given contrast, the observed scattering intensity is proportional to the square of the Fourier transform of Eq. 7 and can be expressed as a quadratic in $\Delta\rho$:

$$I(\Delta\rho, Q) = \Delta\rho^2 I_{\Omega}(Q) + \Delta\rho I_{\Omega\zeta}(Q) + I_{\zeta}(Q). \tag{9}$$

The coefficients, $I_{\Omega}(Q)$, $I_{\Omega\zeta}(Q)$ and $I_{\zeta}(Q)$ represent the scattering from the shape of the solvent excluding regions, the scattering due to correlations between the shape and internal structure and the scattering from the internal structure, respectively. In an experiment, data is collected as a function of $\Delta\rho$ and Q. The resulting curves are then fit to Eq. 9 at each value of Q and the three scattering functions determined. A minimum of three different contrasts must be studied to make an unambiguous determination of the individual functions. Measurements are typically performed at, above and below the contrast match point.

It should be noted that in arriving at Eq. 9, we have assumed a chemically homogeneous

system. If chemical inhomogeneity exists, the expressions for the individual scattering functions become more complex[6]. To the extent that the system can be approximated as chemically homogenous, Eq. 9 is valid. As will be shown later, the validity of this assumption can be tested in the normal course of data analysis.

III. Experimental

Small angle neutron scattering measurements were performed on the Low-Q Diffractometer (LQD) at the Los Alamos Neutron Science Center (LANSCE). Data were reduced by conventional methods[7] and are reported as differential scattering cross section per unit mass, I(Q) ($cm^2\ g^{-1}$), as a function of the scattering vector, Q.

Experiments were performed on powders of both coarse and fine HMX, having mean particle diameters of 261 and 10 μm, respectively. In addition, pressed pellets, made by uniaxial consolidation of the neat material to 7 (coarse) and 10 (fine) volume percent porosity were investigated in order to determine the effect of pressing on the microstructure. The scattering measurements were performed in conjunction with the method of *contrast variation*, as described previously. To this end, all samples were mixed with cyclohexane and placed in rectangular quartz cells having a 2mm pathlength. The choice of a dispersion fluid was based upon the wide range of contrasts that can be reached with cyclohexane/deuterated cyclohexane mixtures and that HMX is insoluble in cyclohexane. The ratio of deuterated/non-deuterated cyclohexane was varied in order change the total scattering contrast of a sample. Five to six different contrasts were measured for each sample. The data from the individual runs were fit according to Eq. 9. The results obtained for the shape and internal structure functions are discussed below.

IV. Results and Discussion

SANS lineshapes for the loose coarse (HMX-C), pressed coarse (C93), loose fine (HMX-F) and pressed fine (F90) at different contrasts are shown in Fig. 3. As the amount of deuterated solvent is varied (contrast is varied), a change in both intensity and shape of the curves is seen.

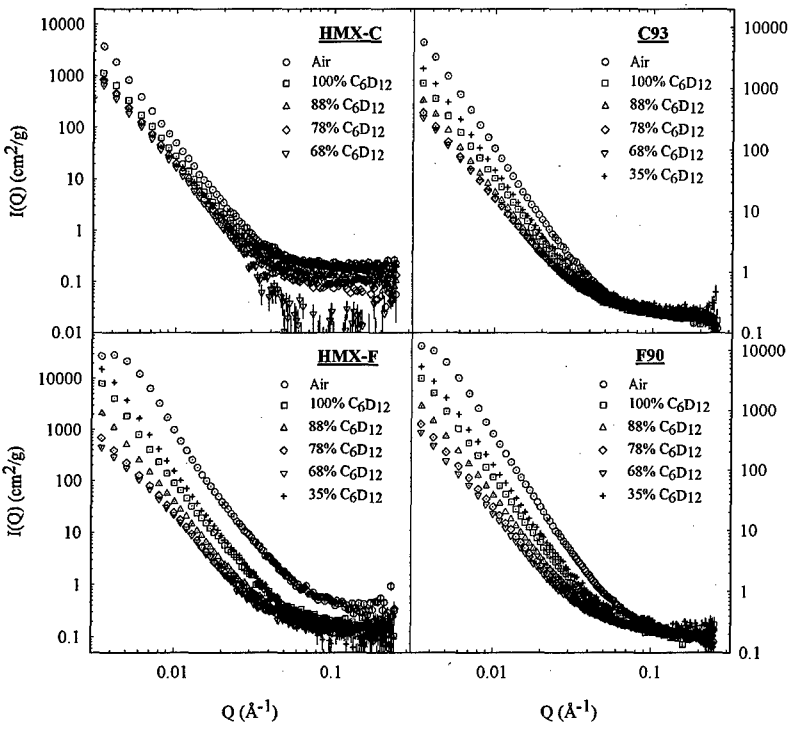

Figure 3 : SANS scattering curves as a function of contrast for HMX powders. Curves change in intensity and shape as contrast is varied because of internal structure.

This initial observation is a good qualitative indication that the HMX crystals possess internal structure over the length scales probed (10 – 1000 Å) and that the SANS technique is sensitive to this structure.

Analysis of the lineshapes according to Eq. 9 is displayed in Fig. 4 in the form of contrast maps, which show clear minima as $Q \rightarrow 0$. The zero of contrast along the vertical axes was calculated using the scattering length density predicted by the chemical composition of HMX ($\rho = 4.5 \times 10^{10}$ cm^{-2}). The positions of the minima indicate the average scattering length density ($\overline{\rho}$) of the HMX material. As can be seen in the figure, in all cases the minima are displaced from zero indicating that $\overline{\rho}$ is different from that predicted by the chemical

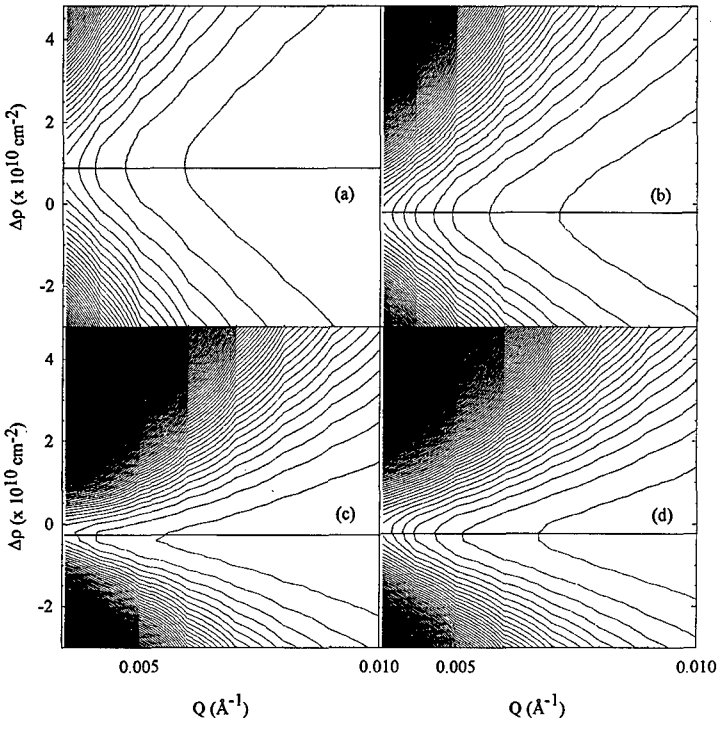

Figure 4 : Contrast maps for HMX powders. (a) HMX-C, (b) C93, (c) HMX-F, (d) F90. Position of contour minima determines $\overline{\rho}$.

composition. Except for the case of HMX-C, the minima appear at negative values of $\Delta\rho$, indicating that $\overline{\rho}$ is less than ρ. This is what would be expected if the differences in scattering length density are due to the presence of voids, internal to the HMX crystals. With the use of Eqs. 1 and 8, we can derive an expression for the void fraction, ϕ_v, in terms of ρ and $\overline{\rho}$:

$$\phi_v = 1 - \frac{\overline{\rho}}{\rho}. \tag{10}$$

Values of ϕ_v calculated from Eq. 10 and the $\overline{\rho}$ determined from the contrast maps are summarized in Table I. In comparing the HMX-F and F90 samples, we see that there is a slight decrease in the void fraction with pressing. This suggests that the internal voids are collapsing

Table I : Summary of internal void fraction and mean internal pore size for HMX powders.

Sample	Internal Void fraction, ϕ_v	Mean Pore Diameter (Å)	Diameter RMS (Å)
HMX-C	----	560	320
HMX-F	0.08	112	104
C93	0.04	98	46
F90	0.05	34	10

under pressure. We were unable to make a clear determination of ϕ_v for the HMX-C sample so we cannot make a direct comparison of the coarse material. However, the value measured for the C93 is very near that of F90, which is consistent with the idea of collapsing voids.

While the contours of Fig. 4 have well-defined minima, a small Q-dependence to the minima positions was found, suggesting the possible influence of chemical inhomogeneity on the experimental results. Chemical analysis of the HMX showed only a small amount (< 1%) of RDX impurity which will have negligible effect on the determination of $\overline{\rho}$. If large chemical inhomogeneities existed in the system, the contours in Fig. 4 would appear to be flattened-out. So the appearance of sharp minima in Fig. 4 is a good indication of chemical homogeneity. The basic scattering functions were calculated for values of ρ ranging from 4.5 – 4.9 x 10^{10}cm^{-2} (as determined from Fig. 4) to determine the influence of ρ on the analysis. Over the range of scattering length densities used, no significant changes in either I_n or I_ζ were observed.

The basic scattering functions derived from the data are shown in Figs. 5-6. Fig. 5a shows the shape functions for all four samples which display power-law scattering with an exponent, α = 4. Analysis of the shape functions was carried-out according to *Porod's* law (Eq. 4) and the total surface area per gram determined. The results are summarized in Fig. 5b. As seen in the figure, the HMX-F sample has a much higher surface area than the HMX-C sample. This is expected as the fine material is made by grinding the coarse HMX into smaller particles. Upon pressing, an increase of surface area was found in the case of the coarse material, suggesting that pressing induces surface cracks and breaks-up crystallites. However, in the case of the fine material, a slight loss of surface area upon pressing is seen. This behavior can be understood by considering that when a material is pressed, several things happen which contribute to the surface area. First, there is a gain in surface area when crystallites are broken-up or when surface cracks are induced. But, at the same time, there is a loss in surface area to the collapse of existing surface cracks and to increased contact of individual crystallites. So, for the coarse

material, the dominant effect is the breaking and cracking of crystallites, resulting in a net gain in surface area, whereas for the fine HMX, the net loss in surface area suggests that the collapsing of cracks and pressing of crystallites together is the dominant behavior. These results differ from those obtained by BET measurements. For the coarse HMX, the SANS results show the same trend of increasing surface area with pressing as BET, but differ in the absolute values measured. However, for the fine HMX, the two techniques differ in both magnitude and trend. The differences between the two techniques may result from the different length scales probed by the individual techniques and are currently under investigation.

The internal structure functions for the coarse and fine HMX samples are shown in Fig. 6. Significant, qualitative changes in the lineshapes are visible upon pressing, indicating that pressing induces structural changes. In order to quantify these changes, the data were fit (solid lines in the figure) to a general model consisting of polydisperse spherical particles (Eq. 6). N(R) in Eq. 6 was assumed to have a Gaussian shape. From the analysis, a mean size for the internal voids (or pores) was determined. The results are summarized in Table I, where we see that the coarse material is characterized by a larger mean pore size than the fine as would be expected. In both cases, there is a shift to a smaller pore size with pressing with smaller root mean deviation

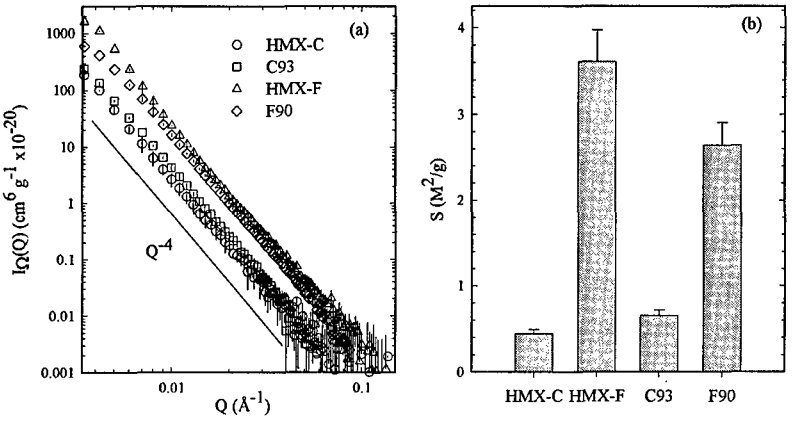

Figure 5 : (a) Shape functions determined by contrast variation analysis. (b) Surface area per gram derived from *Porod* analysis of shape functions.

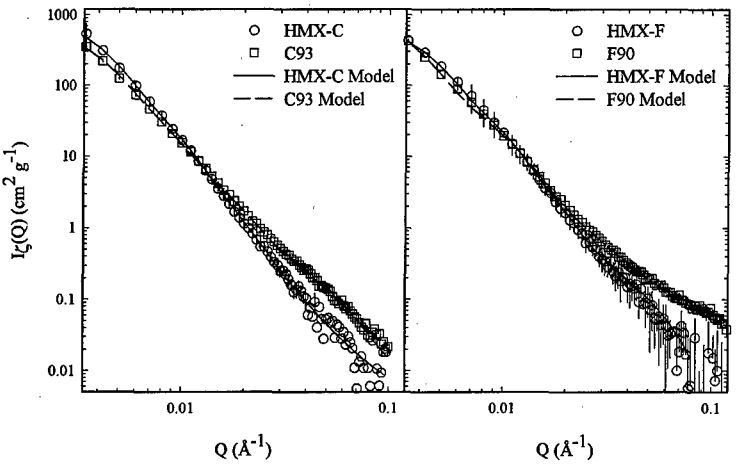

Figure 6 : Internal structure functions. Changes in measured curves indicate pore collapse upon pressing. Solid and dashed lines are fits to a model of polydisperse spheres.

(RMS) about the means. Such a shift can be caused by the collapse of larger pores and/or the induction of elongated structures (internal cracks) and is consistent with the void fraction calculations.

V. Summary and Conclusion

We have used small angle neutron scattering to study the microstructure of a high explosive material. The changes observed in the measured lineshapes as a function of contrast are indicative of structure, internal to the HMX material. With the use of the *contrast variation* technique, we were able to separate the scattering signals arising from this internal structure and that arising from the shape of the HMX crystals. Analysis of contrast maps enabled a determination of the average scattering length density, $\overline{\rho}$, and hence the void fraction. ϕ_v was found to decrease with pressing and sample preparation (grinding), suggesting a collapse of internal voids. The shape functions for all four samples studied display *Porod* scattering, indicating that the lower bound for particle size is > 0.1 μm. Through analysis of the shape

functions we were able to measure systematic changes in the surface area as a function of pressing. By modeling the internal structure functions as a system of polydisperse spherical particles, a mean internal pore size for the different materials and an RMS of the distributions were extracted. A downward shift of the mean pore size was seen, dependent upon pressing, indicating a collapse of larger voids and/or the development of more elongated structures (cracks).

Our results demonstrate that small angle neutron scattering is a powerful tool for use in the characterization and surveillance of high explosive materials. With SANS, we can obtain in situ measurements of surface area and quantitative measurements of internal void populations as well as changes in these quantities dependent upon external insult. These preliminary results indicate that there is significant structure in HMX in the range of 10 - 1000 Å, which may influence the shock to detonation transition[2]. In the future we plan to study the more complex PBX9501 (95 wt.% HMX, coarse:fine - 3:1) system in order to determine the influence of the binding material on changes in the particle structure.

This work was supported in part by the U.S. Department of Energy under contract number W-7405-ENG-36 with the University of California.

References

1. Tarver, C., Chidester, S. and Nichols, A., *J. Phys. Chem.*, **100**, 5794 (1996).
2. White, C., Barrett, J., Mintmire, J., Elert, M. and Robertson, D., *Decomposition, Combustion and detonation Chemistry of Energetic Materials* (Materials Research Society, Pittsburgh, PA, Vol. 418, 1996).
3. Glatter, O. and Kratky, O., *Small Angle X-ray Scattering* (Academic Press, London, 1982).
4. Schaefer, D. and Keefer, K., *Phys. Rev. Letts.*, **56**, 2199 (1986).
5. Hjelm, R., Wampler, W. Seeger, P. and Gerspacher, M., *J. Mater. Res.*, **9**, 3210 (1994).
6. Hjelm, R., Mang, J., Skidmore, C. and Gerspacher, M., *Proceedings of the Materials Research Using Cold Neutrons at Pulsed Sources Conference*, World Scientific Publishing (in press).
7. Seeger, P. and Hjelm, R., *J. Appl. Cryst.*, **24**, 467 (1991).

Alkali Metal Dinitramides - Properties, Thermal Behaviour and Decomposition Products

Matthew D. Cliff, Darren P. Edwards[†] and Matthew W. Smith

Aeronautical and Maritime Research Laboratory (AMRL)-DSTO, P.O. Box 1500, Salisbury, South Australia, 5108, Australia

[†] P.O. Box 4331, Melbourne, Victoria, 3001, Australia

ABSTRACT

In this paper the thermal behaviour and hazard assessment of lithium, sodium, potassium, rubidium and cesium dinitramide are presented. Differential scanning calorimetry, thermal gravimetric analysis, differential thermal analysis and hot stage microscopy were used to examine the thermal decomposition of these five dinitramide salts. The metal dinitramides quantitatively decomposed to their respective metal nitrates, which were identified by mass spectrometry and X-ray diffraction. Hazard assessment showed that the metal dinitramides were insensitive to impact and friction, moderately insensitive to electrostatic discharge but relatively unstable under vacuum stability testing conditions.

INTRODUCTION

The use of ammonium dinitramide (ADN) as a potentially superior oxidant in place of ammonium nitrate and ammonium perchlorate has been recognised for a number of years, with a large body of patents and scientific literature published. In recent years, however, a considerable amount of work has been devoted to the synthesis of ADN analogues. Metal dinitramides may be formed by direct replacement of the ammonium cation in ADN, giving rise to a large family of derivatives[1]. Similar reactions of ADN with organic ammonium bases results in the synthesis of organic salt analogues[2]. The dinitramide anion is an extremely stable species and can be utilised in nucleophilic substitution reactions with organohalides to

form organic dinitramides[3]. This latter technique is able to provide a vast array of dinitramide derivatives for use as high energy materials and oxidants, while the formation of metal dinitramide salts enables high density oxidants to be obtained.

As part of an ongoing investigation into dinitramide chemistry in these laboratories a series of alkali metal dinitramide (MDN) salts was synthesised for incorporation into pyrotechnic flare compositions. Metal dinitramide salts not only provide an energetic oxidant for the composition, but also enable metal salts to be incorporated at a molecular level to provide pyrotechnic effects. This paper presents a hazard assessment of lithium, sodium, potassium rubidium and cesium dinitramides, and examines their thermal behaviour and decomposition products.

SYNTHESIS

All five dinitramide salts were synthesised *via* an acid/base reaction using equimolar quantities of the appropriate metal hydroxide with ADN in water (Scheme 1). Removal of water and liberated ammonia gas by freeze drying gave the salts as white powders. Recrystallisation gave the salts as crystalline plates (NaDN from nitromethane) or needles (KDN, RbDN and CsDN from methanol). The lithium salt could not be recrystallised, and the freeze dried material was used directly for analysis.

Scheme 1

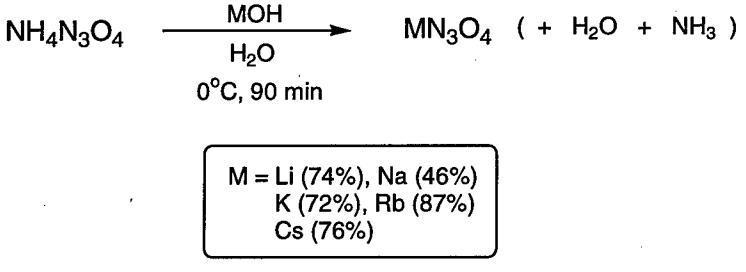

SENSITIVENESS AND VACUUM STABILITY

Sensitiveness to impact and friction were evaluated using Rotter impact[4] and BAM friction[5] tests respectively, with all five dinitramide salts showing insensitivity to both stimuli (Table 1). Sodium, potassium and cesium dinitramide were characterised by Figure of Insensitivity (F of I) values beyond the drop height range of the AMRL instrument. Lithium and rubidium dinitramide displayed F of I values of 140 and 130 respectively, *cf.* F of I of 30 for ADN. Gas evolution was extremely low for both samples (1.6 and 1.1 mL *cf.* 18 mL for RDX with F of I 80). Low gas evolution from energetic materials upon impact initiation usually indicates poor propagation of reaction and hence a low Explosiveness and Hazard Index[6]. For impact results with energetic metal salts, however, care must be taken in drawing such definitive conclusions. Low evolved gas volumes may be a result of oxidant consumption to form metal oxides and give no indication as to the ease of propagation of the event through the material. BAM friction results for all five salts were greater than 360 N.

The MDN salts showed varied responses to electrostatic discharge[4]. LiDN proved to be the most sensitive with initiation occurring above the 0.045 J level. CsDN displayed intermediate sensitivity, while NaDN, KDN and RbDN could not be initiated at a 4.5 J discharge.

All dinitramide salts, with the exception of LiDN, reacted violently under Temperature of Ignition[4] test conditions (duplicate runs of 200 mg samples heated at 5°C/min). Ignition occurred at between 123 - 158°C for sodium, potassium, rubidium and cesium dinitramide and was accompanied by an explosion or smoke. LiDN showed no ignition at temperatures up to 400°C. Differential scanning calorimetry (DSC) for LiDN (Figure 1) showed exothermic behaviour at temperatures of 125°C, yet no violent ignitions were observed under Temperature of Ignition test conditions.

Vacuum stability testing (80°C for 40 hours) of the salts was carried out at a more moderate temperature than the standard 120°C due to the low ignition temperatures discussed above. Despite these mild conditions, however, all five salts liberated considerable volumes of gas. Analysis of both lithium and sodium salts were halted early due to excessive gas pressure. RbDN evolved the least quantity of gas after the 40 hour test period, but considerably more than ADN.

Density measurements on recrystallised sodium, potassium, rubidium and cesium dinitramides showed an increasing density of the salt with increasing molecular weight and, with the

exception of potassium, density of the cation. Lithium dinitramide recorded a density higher than the sodium salt, however, measurements were recorded on a freeze dried sample thereby leading to anomalous results.

TABLE 1. Hazard Assessment for Metal Dinitramide Salts

	LiDN	NaDN	KDN	RbDN	CsDN	ADN
Density (g/cm^3)	2.15-2.19	2.09	2.25	2.63	3.07	1.81
F of I (Gas evolved, mL)	140 (1.6)	>145	>145	130 (1.1)	>145	30 (2.3)
BAM Friction (N)	>360	>360	>360	>360	>360	360
Electrostatic Discharge (J)	0.045	4.5	4.5	4.5	0.45	0.45
Temp. of Ignition (°C)	>400	123	140	158	155	142
Vacuum Stability (80°C / 40 hr, mL/5g)	Excess Gas	Excess Gas	22.9	4.75	25.5	0.73

THERMAL ANALYSIS

Lithium Dinitramide

The DSC trace of LiDN displayed two exotherms at 125°C (-298 J/g) and 182°C (-101 J/g) (Figure 1). The melting endotherm occurred between the two exotherms at 157°C (+83 J/g) and corresponds to melting of an initial decomposition product rather than LiDN itself. This was confirmed by hot stage microscopy where the salt was seen to first darken and then evolve gas before melting. LiDN is extremely hygroscopic and becomes hydrated within a short period upon exposure to the atmosphere. An endotherm at 63°C (+52 J/g) is observed corresponding to the loss of H_2O from $LiDN.xH_2O$. Thermal gravimetric analysis (TGA) of the sample showed a total mass loss of 40.2%, corresponding to the formation of $LiNO_3$ from the dinitramide, with a stoichiometric loss of N_2O.

Sodium Dinitramide

The NaDN salt gave a melting endotherm at 97°C (+54 J/g) followed by major and minor exotherms at 156°C (-946 J/g) and 210°C (-105 J/g) respectively (Figure 2). The minor exotherm at 210°C appeared just below the baseline but was confirmed by a corresponding TG mass loss. A third minor exotherm was observed in the differential thermal analysis

(DTA) trace just prior to melting (91°C) but was not evident in the DSC. TG analysis showed a total mass loss of 38%, matching the formation of $NaNO_3$ with the loss of N_2O.

Additional evidence for nitrate formation was observed in both the DSC and DTA traces as endotherms at 291°C (+61.1 J/g) for the melting of $NaNO_3$. The nitrate melting endotherm observed at 291°C was lower than the corresponding literature value (307°C), however, a significant depression in melting points for ADN and dinitramide salts is observed on inclusion of small quantities of impurities[7].

Potassium Dinitramide

The KDN DSC trace (Figure 3) displayed a large endotherm at 128°C (+96 J/g) corresponding to melting of KDN, however, it was preceded by a smaller exotherm (105°C, -10.5 J/g) and endotherm (108°C, +5.3 J/g). Hot stage microscopy showed the exothermic process from 92 - 108°C to be a breakdown of the crystal structure. The solid was then seen to partially melt from 109 - 115°C, after which no further decomposition or melting was observed until the onset of the KDN melt at 119°C. This partial decomposition / partial melt / quench sequence has been observed by other workers[8,9]. The observed endotherm at 108°C corresponds to the melting point of a KDN/KNO_3 eutectic[8]. Two major exotherms were observed in the DSC, with the first displaying at least two overlapping maxima (range 140 - 182°C, -605 J/g). A final endotherm occurred at 319°C (+51.5 J/g) corresponding to melting of KNO_3, the final decomposition product (KNO_3 lit. mp 334°C); the TGA mass loss of 30.2% corresponded to the formation of KNO_3.

Rubidium Dinitramide

DSC analysis of RbDN gave a similar trace to both the sodium and potassium analogues (Figure 4), with two complex exotherms observed at 141°C (-298 J/g) and 230°C (-60 J/g). The major endotherm observed at 104°C (+78 J/g) corresponds to melting of the dinitramide salt. A smaller endotherm was also observed at 85°C (+4.2 J/g). The TGA trace showed no mass loss at this point, and the exotherm is possibly due to a crystal phase change. Hot stage microscopy clearly showed internal fracturing of the crystal structure from 86.0°C until onset of melting at 100.3°C. Two thermal decompositions with a total mass loss of 28.3% were observed, corresponding to formation of the metal nitrate salt. A melting endotherm was observed at 330°C (+295 J/g, $RbNO_3$ lit. mp 310°C).

Cesium Dinitramide

The DSC melting point endotherm for CsDN appeared as two overlapping maxima (81 and 86°C) rather than as a discrete peak (Figure 5). Thermal treatment of the sample at 100°C resulted in the loss of the first maximum, possibly due to loss of occluded (recrystallisation) solvent molecules. Melting of the crystal structure onset at 85.9°C and was complete at 90.6°C. A complex exotherm was seen at 218°C (-209 J/g) with a corresponding 24.0% mass loss. A sharp endotherm for the $CsNO_3$ melt was seen at 386°C (+48 J/g, $CsNO_3$ lit. mp 414°C).

A summary of the metal dinitramide mass losses and decomposition product melting points is presented below (Table 2).

TABLE 2. Metal Dinitramide Decomposition Data

MDN	Melting point (MNO_3) (°C)		Mass loss (%)	
	DSC	Literature	TGA	Theoretical
LiDN	-	264	40.2	39.0
NaDN	291	307	38.1	34.1
KDN	319	334	30.2	30.3
RbDN	330	310	28.3	23.0
CsDN	386	414	24.0	18.4

With the exception of LiDN which did not show a melting endotherm for the nitrate, the dinitramide salt residues displayed melting endotherms which approximated the literature values for the corresponding metal nitrates. RbDN unexpectedly gave a melting point 20°C higher than the literature value which cannot be explained at this time. Percentage mass losses measured by TGA matched those expected for the formation of MNO_3 from the dinitramide, with differences between the measured and stoichiometric mass losses in the range 0.1 - 5.6%.

Mass spectral analysis of the metal dinitramide salt residues confirmed the presence of the nitrate anion with no detectable dinitramide ion. X-ray diffractometer (XRD) traces were recorded for the five decomposition residues (Figure 6). In each case the only crystalline phase identified corresponded to the metal nitrate. Failure to detect any other significant crystalline

phases (such as nitrites, nitrides or hydroxides) suggests that the formed nitrate salts are essentially pure. Nevertheless, one strong peak in the potassium sample at 3.312Å (2θ=26.9 *) has yet to be identified, although all other notable peaks within the trace have been matched to the nitrate.

SUMMARY

A hazard assessment of the alkali metal dinitramide salts of lithium, sodium, potassium, rubidium and cesium demonstrated that all five salts were insensitive to mechanical, and in most cases, to electrostatic stimuli. They are, however, thermally unstable and capable of being ignited at moderate temperatures. Evolved gas quantities are significant under mild vacuum stability test conditions and hence use of these materials in sealed stores is questionable.

All five salts thermally decompose to their respective metal nitrate salts. Despite similarities in both starting and end compounds, however, the complex DSC traces clearly indicate different thermal behaviour. While there may be similarities in the decomposition pathways, it is clear that all five would require a separate detailed study to examine the decay mechanism.

ACKNOWLEDGMENTS

The authors would like to thank Peter Berry, Mark Fitzgerald and Dr Kim Ide for their assistance in carrying out this investigation and Dr Daniel Whelan for many helpful discussions.

REFERENCES

(1) O. A. Lukyanov, O. V. Anikin, V. P. Gorelik and V. A. Tartakovsky, *Russ. Chem. Bull., 43*, 1457-1461 (1994). V. A. Tartakovsky and O. A. Lukyanov, "Synthesis of Dinitramide Salts", *25th Int. Annu. Conf. ICT*, 28th June - 1st July 1994, Karlsruhe, France.

(2) O. A. Lukyanov, A. R. Agevnin, A. A. Leichenko, N. M. Seregina and V. A. Tartakovskii, *Russ. Chem. Bull., 44*, 108-112 (1995).

(3) O. A. Lukyanov, V. P. Gorelik and V. A. Tartakovsky, *Russ. Chem. Bull., 43*, 89-92 (1994).

(4) Royal Armament Research and Development Establishment, "Sensitiveness Collaboration Committee, Manual of Tests", Test 1A, 3 and 6.

(5) "Recommendations on the Transport of Dangerous Goods, Tests and Criteria", second edition, ST/SG/AC.10/11/Rev.1, United Nations, New York, 1990.

(6) R. J. Spear and L. Montelli, "An Investigation of the Material Hazard of Some Insensitive High Explosives," MRL-TR-91-22, Materials Research Lab., Maribyrnong, Australia, 1991.

(7) J. C. Oxley, J. L. Smith, W. Zheng, E. Rodgers and M. D. Coburn, *J. Phys. Chem. A, 101*, 5646 - 5652 (1997).

(8) F. I. Dubovitskii, G. A. Volkov, V. N. Grebennikov, G. B. Manelis and G. M. Nazin, *Doklady Phys. Chem., 348*, 108 - 109 (1996).

(9) F. I. Dubovitskii, G. A. Volkov, V. N. Grebennikov, G. B. Manelis and G. M. Nazin, *Doklady Phys. Chem., 347*, 106 - 108 (1996).

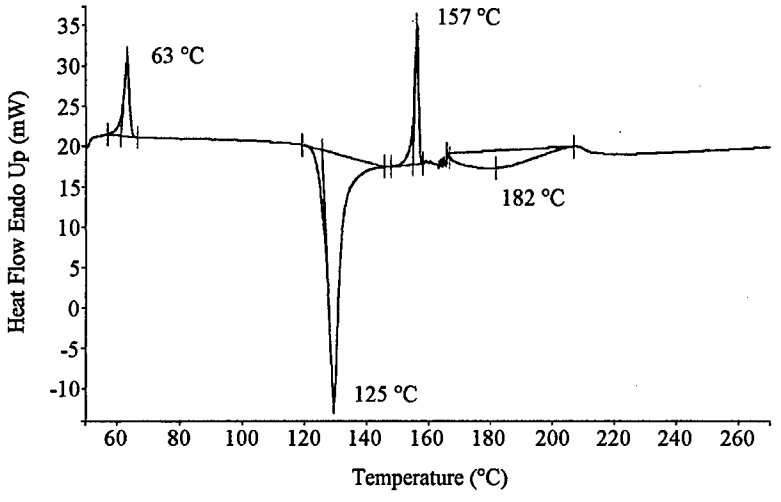

FIGURE 1. DSC Trace of LiDN.xH_2O.

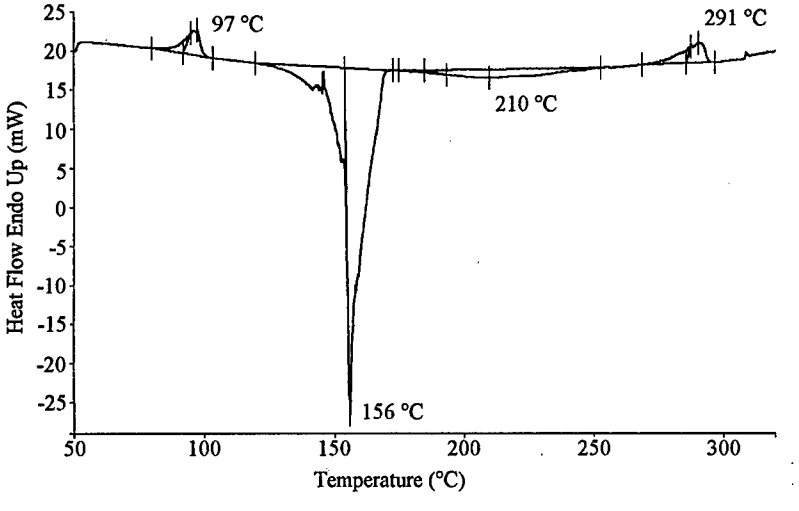

FIGURE 2. DSC Trace of NaDN.

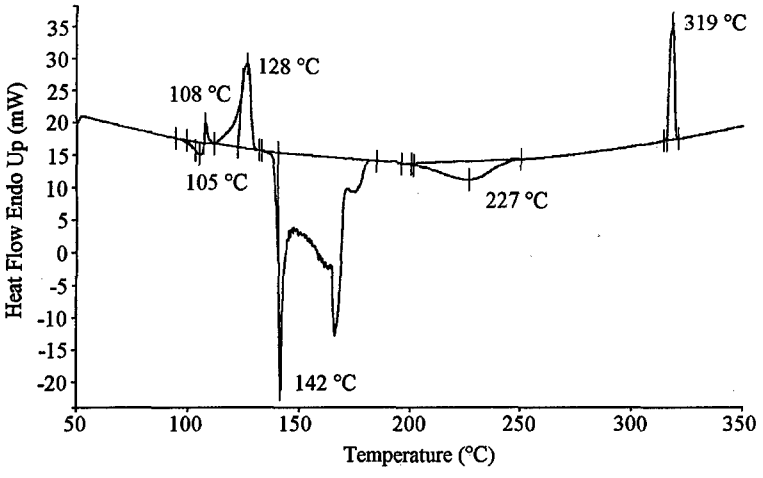

FIGURE 3. DSC Trace of KDN.

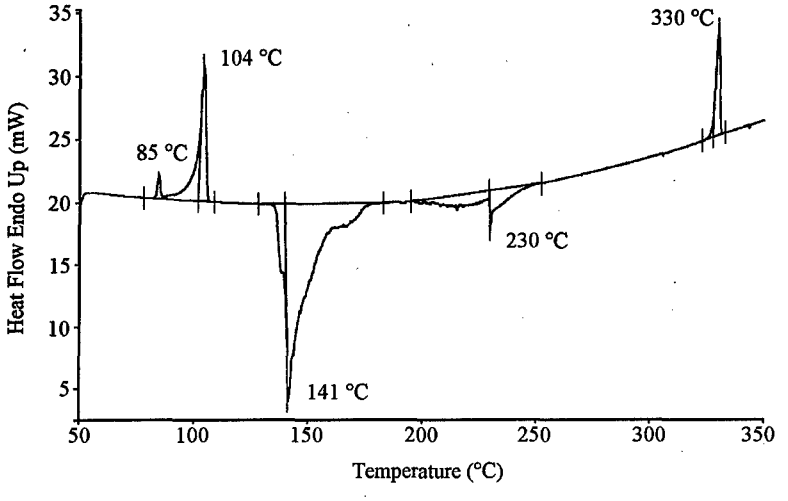

FIGURE 4. DSC Trace of RbDN.

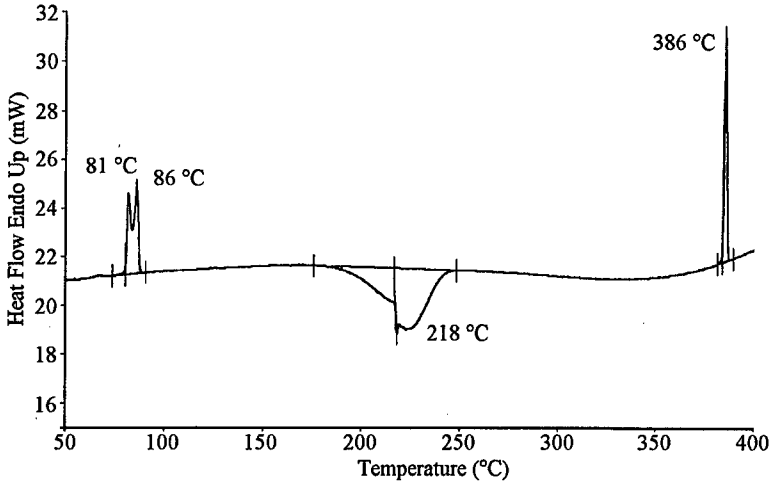

FIGURE 5. DSC Trace of CsDN.

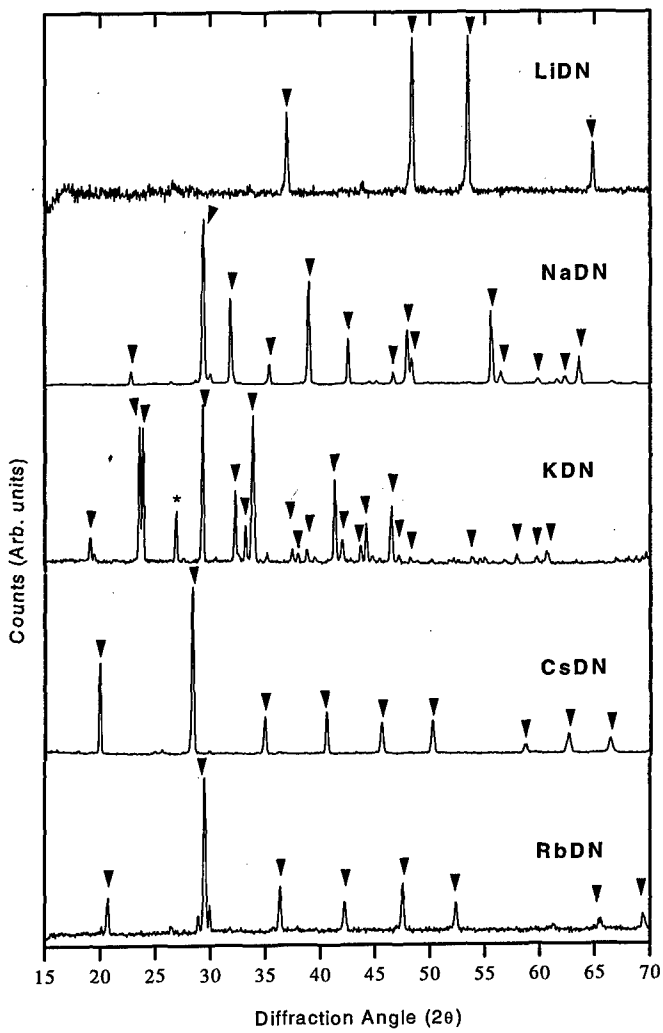

FIGURE 6. X-ray diffractometer traces of decomposed metal dinitramide salts, with the peaks matching the corresponding nitrate salts indicated (▼).

DECOMPOSITION MECHANISM OF DINITRAMID SALTS. ANOMALOUS DECOMPOSITION OF DINITRAMID METAL SALTS AND AMMONIUM SALT IN THE SOLID PHASE

Alexander N. Pavlov, Gennadiy M. Nazin

Institute of Chemical Physics in Chernogolovka,
Russian Academy of Sciences, 142432 Chernogolovka, Moscow Region, Russian Federation
Fax 007(096)5153588 E mail:jubur@icp.ru

Thermal decomposition of dinitramide salts, the new class of highenergetic explosives, are investigated. Thermal decomposition of dinitramid onium salts proceeds via the dissociative mechanism when pKa of the base is lower than 5.0 and via the monomolecular decay of the anion at pKa>7.0.Going from the melt to the solid state, the reaction mechanism does not change(excluding ammonium salt), and the rate decreases by 1-2 orders of magnitude. Unusual regularities are observed for decomposition of ammonium salt and metal salts in the solid phase: the solid phase reaction is $10\text{-}10^4$ times faster than that in the melt, its rate has a sharp peak in the region of eutectics melting with the decomposition product(metal or ammonium nitrate),and it is instantly inhibited by water vapor.In the inhibited regime, the rate in the solid phase is lower than that in the liquid phase. No anomalous effects inherent in dinitramide ammonium salt and metal salts in the solid phase are observed during decomposition of onium salts.

The dinitramide salts were synthesized at 1971[1] . The ammonium salt (ADNA), $NH_4^+N(NO_2)_2^-$ is prospective highenergetic oxidant for ecologicy pure solid roket propellants. At the same time reseach the thermal decomposition of ADNA was initiated by ICPC RAS. As one of the result of the above research in 1972 it was found that the reaction rate in vacuum increases while changing from melted to the solid state, unlike the usually observed dicreasing of the reaction rate for inorganic salts in the same conditions.

The maximum increase of the reaction rate is observed at the melting point of the ADNA and the reaction product NH_4NO_3 eutectic mixture(Fig.8). This

phenomenon was called the anomalous decay. Such ADNA behaviour occurs due to drying out of the substance crystalls. Addition of water vapour immediately terminates decompositioning of the substance. Similar impact on the reaction can be caused by NH_3, CH_3OH, $CH_3C(O)CH_3$, NO, N_2O, CH_3J although the effectiveness will be much less. To understand the nature of such unordinary reaction a detailed research of other salts of dinitramide was undertaken. Thermal decomposition of metal and onium salts in liquid and solid states was widely studied. The results are published[2-7]. DNA salts were synthesized according to the described procedures[8,9].

The products were additionally purified by repeated recrystallizations from suitable solvents and dried in soft conditions. These procedures rapidly decreased the water content to 0.2 - 0.4%, after which the drying process was sharply retarded. More drastic drying conditions down to 0.05% H_2O (60^0-70^0C, vacuum) are accompanied, as a rule, by the partial decomposition of the substance. Lithium and barium salts were sinthesized as lowmelting crystal hydrates. They were dehydrated to 0.5% H_2O by drying over P_2O_5 at 20° C in vacuum (10^{-2} Torr).

The decomposition rate was measured by manometric or gravimetric methods. The products were analyzed by G LC, mass-spectrometry, spectrophotometry.

Metal salts

The metal salts with Li^+, Na^+, K^+, Rb^+, Cs^+, Ba^{++} cations were investigated. The products composition of metal salts conversion is simple and constant at different temperatures and reaction stages: solid salts yield 1 mole of N_2O

$$MeN(NO_2)_2^- = N_2O + MeNO_3$$

(barium salt -2mole N_2O) and liquid salts give l mole of NO + 0.5 mole of N_2O

$$Me\,N(NO_2)_2 = NO + 0.5N_2O + 0.5MeNO_2 + 0.5\,MeNO_3.$$

This fact allows one to obtain rate onstants from the initial regions of kinetic gas evolution curves with a high accuracy. Decomposition of solid salts in a vacuum of 0.1 Torr (permanent pumping out) and in an atmosphere of moist air or at a pressure of neat water vapor of 10-15 Torr was monitored by a thermobalance. In the last two cases, the reactions are slow, and the manometric procedure, which is more sensitive than weighing, was used to study the reaction. Due to the fast escape of residual water vapor, the conditions of decomposition in closed vessels correspond to the decomposition in atmosphere of moist air.

Rate constants of the liquid-phase decomposition at 100°C were estimated to compare decomposition rate constants in the solid phase and in the melt. The extrapolation of data on decomposition[10] in the melt was used for Li,Na,Rb,Cs salts. In addition, the decomposition rates of $RbN(NO_2)_2$ in a low- melting eutectic mixture with rubidium nitrate were measured directly at 100°C. For the barium salt, the parameters of the liquid-phase decomposition were determined from the decomposition of 10-25mol.% solutions of Ba^{++} ions in liquid$KN(NO_2)_2$. Ba^{++} ions were introduced into $KN(NO_2)_2$ as barium nitrate. The observed rate constant of the decomposition of this mixture is described by the equation

$k_{obs} = k(K^+)/[1 + (m_2M_1/m_1M_2)] + k(Ba^{2+})/[1 + (m_1M_2/m_2M_1)]$,

where m is the weighted sample and M is the molecular weight; index 1 refers to $KN(NO_2)_2$ and index 2 refers to $Ba(NO_3)_2$. The $k(K^+)$ value was used for the calculation of $k(Ba^{2+})$ from k_{obs}. The liquid metal salts in the cloused vessels *in vacuo* are decomposed in according to equation of the first order.

The complete kinetic curves and initial regions of the mass loss curves for the decomposition of the solid $RbN(NO_2)_2$ and $CsN(NO_2)_2$ in vacuum of 10^{-1} Torr at different temperatures are presented in Figs. I - 4. The reactions are characterized by a pronounced acceleration, which is typical of topochemical processes, and a very strong retention (this phenomenon appears as follows: after the process is complete,a considerable portion of the starting compound remains unconsumed). The rate peaks are observed in points of eutectic melting on the Arrhenius dependences of the rate constants (Fig.5). The formation of eutectics of DNA salts and the corresponding nitrates was studied by differential scanning colorimetry. Rubidium, cesium,potassium, guanidinium sailts and ADNA give these eutectics with m.p. 84.5, 81.5,102, 106, and 62°C respectively. Other metal salts have the same character of decomposition as $RbN(NO_2)_2$ and $CsN(NO_2)_2$ but they do not give eutectic mixtures with products and have no breaks on the temperature dependences of the rate constants (Fig. 5). Thus, like ADNA, apparent effect of anomalous decay are observed for all metal salts. Other onium salts,guanidinium salt included(Fig.5) manifests no specific features of solid-phase decomposition. The rates in vacuum and in air are equal (Table 2). For guanidinium salt no increase in the rate is observed

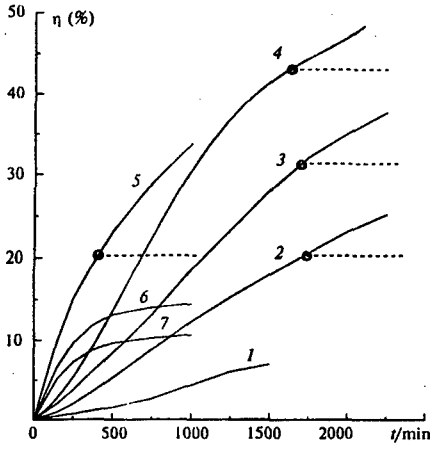

Fig. 1. Decomposition of $RbN(NO_2)_2$ *in vacuo*. T/^{0}C:I-50;2-60;3-70;4-80;5-82; 6-84,5;7-90. Moments of injection of moist air are markedby circles. Dotted lines show the continuation of kinetic curves after injection of air.

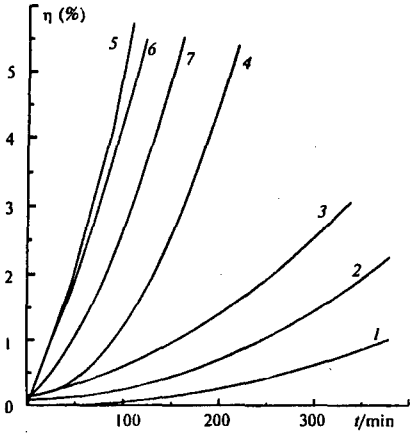

Fig. 2. Initial regions of kinetic curves presented in Fig. 1. Numbers of curves coincide.

(Fig. 5) at the point of eutectic melting with guaniclinium nitrate (106^0 C).

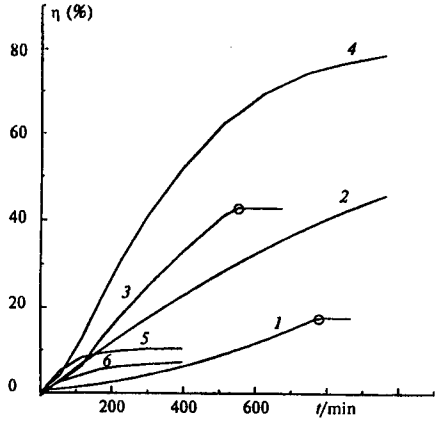

Fig. 3. Kinetic curves of decomposition of $CsN(NO_2)_2$ *in vacuo*.T/^{0}C:1-60.7;2-70; 3-75;4-80,3;5-8l.5;6-84.5. The moinent of injection of 10Torr of H_2O is marked by the circle.

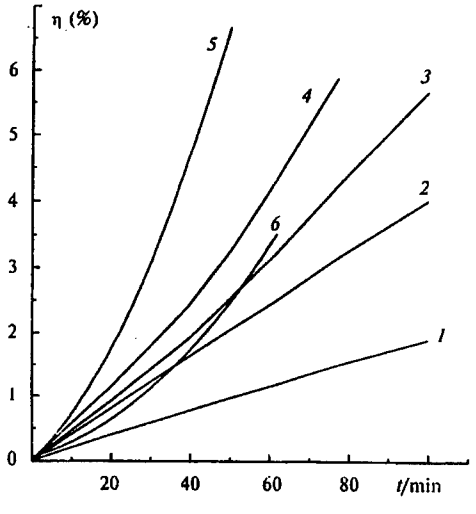

Fig. 4. Initial regions of curves presented in Fig. 3. Numbers of curves coincide.

The retention effect can be explained by one reason: localization of the reaciion on the surface and nonequilibrium defects of the crystal lattice. After "working out" or "recovering" of defect regions by covering them with the product layer, the reaction is stopped.

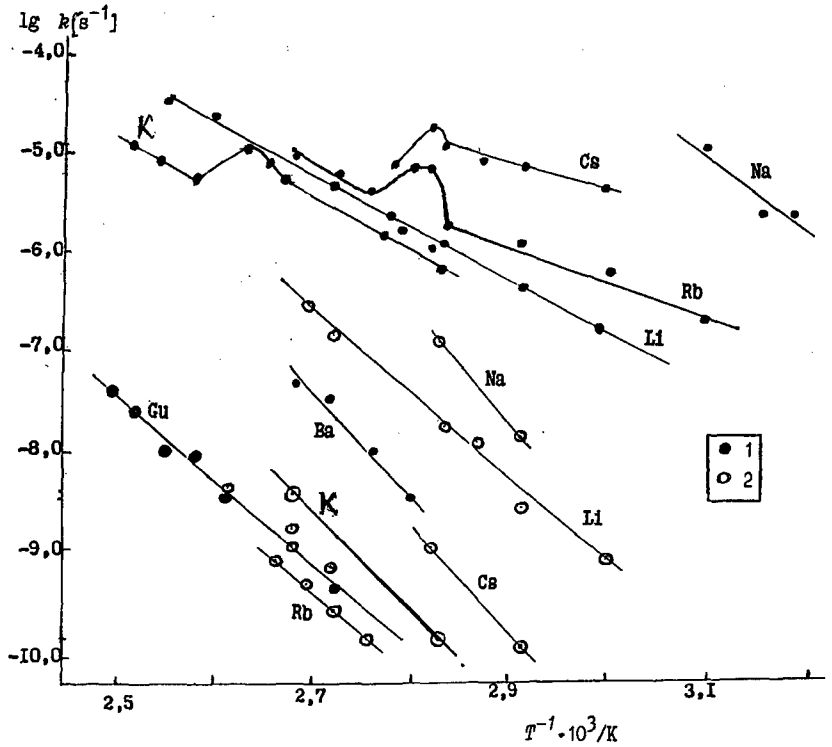

Fig. 5. Temperature dependences of rate constants of decomposition of DNA salts in the solid phase. Symbols near curves correspond to cations; Gu is guanidinium, I- reaction *in vacuo*; 2-decomposition inhibited by water vapor. It can be reinitiated by simple grinding of partially decomposed crystals. The reaction is stopped at the early stages at temperatures higher than the eutectic melting point, because the reaction centers begin to melt.

It can be seen from Table l that the ratio of decomposition rate constants in the solid and liquid phases, k_s/k_l varies(at l00°C) froml0{$(LiN(NO_2)_2$, $Ba[N(NO_2)_2]_2$} to 10^4 ($NaN(NO_2)_2$). The specific feature of all metal salts and ammonium salt is the inhibition of ihe solid-phase reaction by water vapor (Figs. l,3,8, Table l,2). The addition of I0-15 Torr of water vapor at any stage of decomposition immediately stops the reaction. The injection of moist air acts in the same manner.

Table 1. Kinetic parameters of decomposition of dinitramide salts

Cation	M.p. of salt/^{0} C	State	Δ T ^{0}C	E kcal/mol	lgA s^{-1}	k10 $^5/s^{-1}$ (160^{0}C)	k/s^{-1} (100^{0}C)
Li+	158	Melt	____	(36.0)[a]	(15.0)	67[b]	$8.1x10^{-7}$
		S.(0 1)[c]	62 -120	26.0	10.0		$5.7x10^{-6}$
		S. (760)	60 - 98	40.6	17.3		$3.2x10^{-7}$
Na+	lll	Melt		(38.0)[a]	(15.0)	6.4[b]	$5.4x10^{-7}$
		S.(0.1)	30 - 50	40 .0	22.0		$3.6x10^{-2}$
		S. (760)	70 - 80	46.0	21.4		$2.7x10^{-6}$
K	127	Melt	130 - 190	39.5	15.1	1.4	$8.9x10^{-9}$
		S. (0.1)	80 - 100	26.6	10.3		$5.1x10^{-6}$
		S. (760)	80 - 100	41.0	15.6		$3.7x10^{-9}$
Rb+	108	Melt		(39.6)[a]	(15.0)	1.0[b]	$6.2x10^{-9}$
		Melt	130 - 170	40.1	15.3	1.1	$6.3x10^{-9}$
		Eutect. with $RbNO_3$	100				$6.1x10^{-9}$
		S. (0.1)	50 - 100	20.0	6.6		$7.6x10^{-6}$
		S. (760)	70 - 102	38.0	12.8		$3.4x10^{-10}$
Cs+	88	Melt		(39,2)[a]	(15.0)	1.62[b]	$1.0x10^{-8}$
		S. (0.1)	60 - 85	13.0	3.0		$2.4x10^{-5}$
		S. (760)	70 - 80	39.0	14.7		$6.9x10^{-9}$
Ba+		Solution in KN $(NO_2)_2$	160 - 180	50.0	20.8	3.2	$2.8x10^{-9}$
		S. (O.l)	80 - 100	47.3	20.5		$5.6x10^{-8}$

Note. [a] Calculaited trom the k values at 160^{o}C presented in Ref. 10 assuming that logA/s^{-1} has the value 15,0 typical of alkaline salts. [b] Data in ref. 10.

[c] Air pressure (Torr) above the sample.

NH_3,NO, N_2O, and acetone or methanol vapor also retard the decomposition, but considerably more weakly than water vapor. In closed vessels at an initial pressure of 10^{-1}Torr, the reaction occurs rapidly at first as in vacuum but is stopped as N_2 O is accumulated and residual water vapor escapes.

The strong effect of water vapor suggests that decomposition is possible only in dry layers of the substance, and its rate depends on the degree of preliminary drying and conditions of removing residues of the solvent and gaseous products. Tlie lithium and barium DNA salts, which have the smallest k_s / k_l ratios, were obtained from crystal hydrates and, perhaps, the residual moisture retards their decomposition *in vacuo* at the initial stages. These compounds have the maximum degree of acceleration (which can be related to the water loss), and at the acceleration stage, their k_s / k_l values become equal to those of other salts. The water vapor inhibited decomposition of metal salts in the solid phase has a lower rate than that in the melt. Its parameters are presented in Tab1e 1.

Onium salt.

It was studied DNA salts : hydrazinium (**1**), binary ethylenediammonium (**2**), trimethylammonium (**3**), guanidinium (**4**), anilinium (**5**), binary o-henylenediammonium (**6**), tetramethylammonium (**7**), tetra(n-butyl) ammonium (**8**) and ADNA (**9**) salts. The salts were selected in such a way that the decomposition rates in the solid and liquid phases could be measured for the same object (**2**, **4**, **8** and **9**), the solid phase reaction could be carried out in vacuo and in an atmosphere of air (difticultly volatile compound **2**, **4**, **7**, and **8**), the effect of additives of the free base on the rate could be studied for strong and weak amines (**2**, **3**, **5** and **9**), and the rate constants could be correlated with pK_a of the base of the cation in a wide range of pK_a (**1 - 6**, **9**). Based on these data, we can make conclusions on the mechanism of decomposition and anomalies of the solid phase reactions.

The kinetics of decomposition in the liquid phase (meit) was studied manometrically. The reactions of **1**,**3**,**4**-**7** occur according to a first-order equation (Fig. 6). Weak acceleration is observed for compounds **8** and **2** (after 50% decomposition), and very strong acceleration is observed for compound **3**. The ADNA decomposition occur according to a fist-order eguation when the free volume is large ($m/v < 0{,}04$ g/cm ^{3}). If the free volume is small ($m/v_f > 0{,}01$ g/cm^3) the strong acceleration occurs the temperature interval of 95-120 ^{0}C. In the case of the reactions with acceleration, the first-order rate constant (k) for the initial stage was calculated from the time of achieving l% decomposition. The volume of gaseous products at the end of the reaction

$\Delta V\infty$ (cm^3/g^{-1}) brought to normal conditions (0^0C, 760 Torr) was accepted to be 100%. For all other substnces, $\Delta V\infty$ depends slightly on temperature (within 10%), and the use of average $\Delta V\infty$ values (presented in Table 2) does not introduce substantial errors to the calculation of K.

Table 2. Kinetic parameters of decomposition of onium dinitramide salts

Com-pound	M.p. /^{0}C	pK_2 of base	State[a] (p/Torr)[b]	ΔT /^{0} C	E kcalmol^{-1}	logA /s^{-1}	Kx10^5 /s^{-1} (160 'C)	K_I/K_S (160 'C)	ΔV /cm^3g^{-1}
1	80	8.1	I	140 - 180	36.0	17.70	33.0	-	820
2	126	10. I	1	130 - 1 55	35.0	14.00	21.0	-	500
			s (0. 1)	80 - 105	41.6	15.60	0.4	52.5	-
			s (760)	80 - 120	41.6	15.60	0.4	52.5	-
3	13 I.5	9.86	I	135 - 165	34.8	14.00	25.0	-	350
4	144	13.6	1	1 50 - 170	36.9	15.00	23.4	-	450
			s (760)	95 - 140	40.0	14.20	0.1	234	-
5	99	4.58	1	135 - 160	32.0	13.55	245	-	420
6	118	4.37	1	120 - 1 50	30.0	12.50	224	-	500
7	230	-	s (0.1)	160 - 205	39.6	13.80	0.06	-	590
			s (760)	i40 - 170	38.6	13.70	0.16		-
8	153	-	1	160 - 180	38.7	14.60	1.18		-
			s (0. I)	120 - 140	39.6	13.80	0.06	20	306
9	93	9,30	1	95 - 160	35,5	14,40	28,8	-	620
			s (ing)[c]	40 - 83	33,6	11,46	0,3	96	-
			s(anom)[d]	40-83	-	-	-	0,019	

[a]l is liguid, s is solid. [b]The air pressure in in the reaction vessel is shown in parentheses.[c]"nonanomalous" decomposition;[d] anomalous decay;[e]-at 60^0 C.

The main uncertainly in the estimation of k from the time of 1% decomposition is related to a possible dependence of the yield of gaseous products on the degree of conversion.

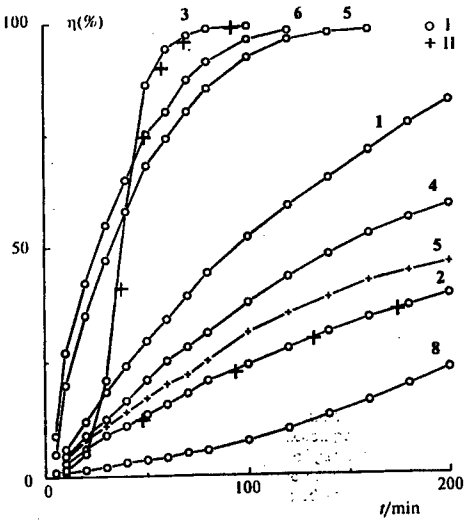

Fig. 6. Kinetic curves of decomposition ot DNA onium sults in melt. Numbers of curves correspond to numbers of compounds at the temperature of the experiment of 140 (**2**, **3**, **5**, **6**), 150 (**1**, **4**), and 160 ^{0}C (**8**). **I** is the pure sall, **II** is 30 mol.% of the free base.

However, the data on the composition of the products, which are presented in Tab.3, suggest that these changes are not great. The $\Delta V\infty$ value can be affected by the pressure-dependent reactions of gaseous products and dissolution of the latter in the condensed phase. To standardize these processes, all experiments were carried out at the same degree of filling the vessel with a substance, $m/v_f = 5x10^{-4}gcm^{-3}$. When solid salts were studied, the thermogravimetric procedure in a constant vacuum (a thermobalance with a sensitivity of 0.1mg) was used along with the manometric procedure. In the case of the solid ADNA decomposition the rate constants were obtaind by only manometric method, because sublimation is observed in constant vacuum. The obtained kinetic parameters of the decomposition of compounds **1-9** in the melt and in the solid phase are presented in Table l. The decomposition products of salts **2**, **4**, **8** and ADNA were analyzed.The data on the ratio of light gases are presented in Table 2. The condensed residue after the decomposition consists mainly of nitrate (but not nitrite) uf the corresponding cation. The products contoin noticeable quantities of the free base and products of the cleavage of cations excluding ADNA decomposition

Table 3, Composition of light gases for decomposition of onium saits

Com-	State	T	η(%)	Composition of light gases (%)					
pound		/⁰ C		N_2+CO	NO	CO_2	$N_2$0	H_2O	NO_2
2	l	135	15	32	-	3	56	9	
	s	95	0.1	30		2	60	8	
4	l	150	50	30		2	33	35	
	s	120	0.1	28		6	20	46	
8	l	160	1.0	25	5	6	38	26	
	l	180	77	28	4	8	32	28	
	s	140	0.4	30	12	8	26	24	
9	l	104	1,0	10(N_2)			90		
	l	170	1,0	26(N_2)	traces		27	45	traces
	s(ing)	80	0,02	10(N_2)			90		
	s(anomal)	60	0,02				100		

along with light gases. For example, in the case of **4**, dicyan is formed, and Me_2NNO, MeCN, and $MeNO_2$ are formed from **4**. The maximum amount of orgauic products (less than 40%) is fonned from compound **8**. At all stages, MeCN, Bu^n OH, $Bu^n{}_3N$, and butene-I are observed.

It can be seen frorn Table 3 that the decomposition rates of salts **1-4,9** are close in the liquid phase, and their activation parameters are typical of the decomposition ot metal salts. Compounds **5** and **6** decompose 10 times more rapidly and compound **8** decomposes considerably more slowly than salts **1-4,9**. The addition of a free base does not affect the rate of decompos ition of the salt of strong base **3** and decreases considerably the decomposition rate of compound **5** (pK_a, of aniline is less than 5.0). The dependence of the rate constants of decomposition of **I- 6** on pK_a of the base (Fig. 2) testifies that when $pK_a > 7$ the rate is independent of the asicity of amine, and when $pK_a < 5$ a sharp increase in the rate is observed. These data allow one to conclude that the mechanism of decomposition of DNA onium salts depends on pK_a of the saltforming base.

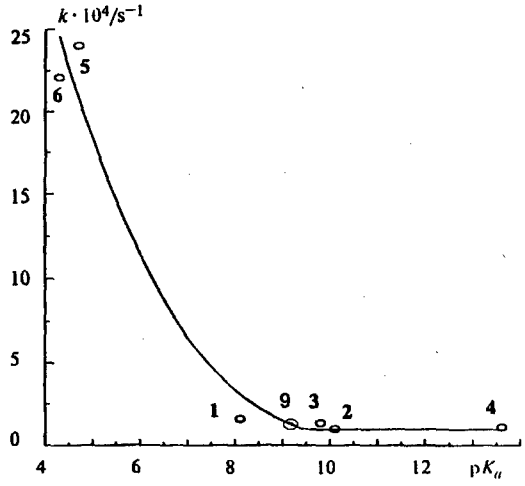

Fig. 7. Dependence of the rate constant of decomposition of DNA onium salts at 160°C on pKa of the base. Figures near points correspond to numbers of compounds (Table 2).

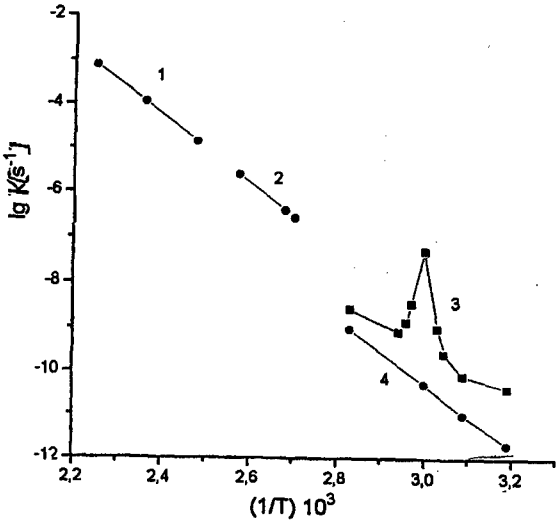

Fig.8 Temperature dependence of rate constance of ADNA decomposition 1-(130-180); 2-(95-120) °C; 3-anomals decay in solid state; 4-in inhibited conditions.

When $pK_a>7$, the decomposition occurs, as for metal salts, via the cleavage of the N--N bond with the ellmination of NO_2, and when $pK_a<5$, the primary dissociation of the salt to the base and acid predominates.

For the monomolecular decomposition of the anion, the difference from metal salts is only in the mechanism of secondary reactions. Instead of the disproportionation of the $O_2NN^{\bullet}$ radical anion (which is a stronger nucleophile than $N(NO_2)^-_2$), the transfer ot proton to this radical anion followed by the formation of the free base is possible. Instead of the oxidation of $O_2NN^{\bullet}$ by nitrogen dioxide, in onium salts cations are oxidized. In salt **8**, at the second stage, the Hofmann reaction type cleavage of the cation occurs

$$Bu^n{}_3N^+(CH_2CH_2C_2H_5)N^{\bullet}NO_2 \rightarrow$$

$$\mathbf{8} \rightarrow Bu^n{}_3N + HN{\bullet}NO_2 + CH_2 = CHCH_2CH_3 .$$

On going from the melt to the solid state, the mechanism of the reactions for **1-8** remains unchanged: the composition of the products is retained, the activation energy changes slightly, and the decomposition rates in vacuum and in air are equal to one another and lower that those in the melt. It is impossible to eliminate that ADNA decomposition occur, at least in part (not more 50%), by salt dissociation way

$$NH_4N(NO_2)_2 \rightarrow NH_3 + HN(NO_2)_2$$

The facts such as a kinetic isotop effect (K_H/K_D at 98 ^{0} C) in the experiments with $ND_4N(NO_2)_2$, the inqibition of initial stage in presence of NH_3 or by strong bases like urotropin and the sublimation in constant vacuum were indicated of it.

Thus, the anomalous decomposition is not inherent in onium salts **1-8**.

The rate of ADNA decompositionin the solid state increases in closed vessel (initial pressure 0,01 Torr) or in inert atmosphere (N_2 ,dry air) when the water content in the samples less than 0.01% H_2O.The single gas product is N_2O in this case.The large peac of rate is observed at melting point (60^{0}C) of eutectic mixture with solid reaction product NH_4NO_3.

The phenomenon of anomalous decomposition, as can be assumed, is related to changes in the structure of the DNA anion on going from the melt to the solid state.

The anion in the crystal can have a structure with a nonsymmetric charge distribution and nonequivalent nitro groups. It is reasonable to expect, that these anions have an increased reactivity, in particular, their thermal stability can change.

A new reaction chanal fast elimination of NO_3^- with ejection of N_2O is opened. The hidrogen bond between anion and H- containing cations or direct solvatation by H_2O molecules and some other dipols decreasis the anion polarisation. These even electron assimetry of anion and prevent intermolecular regrouhing. Local restructuring of cristall lattice occurs while nucleous of eutectic fase are born. Tensions and new defects occur in cristall. It can affect the rate in case the reaction on the surface goes faster than in the cristall's volume. Thus, it may occur in case of unhibited by water the metal salts and ADNA decomposition. It is necessary to accept that the birth of eutectic is folloued by the destruction of hidrogen bonds.

References

1. O. A. Luk'yanov et al. Izv. Akad. Nauk, Ser. Khim., 1994, 1,94-97.

2. A.N.Pavlov,G.M.Nazin,Rus. Chem. Bull.,1997,(Engl.Transl.)]

3. S. B. Babkin, A. N. Pavlov, and G. M. Nazin, Izv. Akad. Nauk, Ser. Khim., 1997, 1947 [Russ. Chem. Bull., 1997, (Engl. Transl.)].

4. F. I. Dubovitskii et al. Dokl. Akad. Nauk, 1996, 347, 763 .

5. F. I. Dubovitskii et al. Dokl. Akad. Nauk, 1996, 348. 205 .

6. A.N.Pavlov,V.N.Grebennikov,L.D.Nazina,G.M.Nazin,G.B.Manelis Izv.Akad.Nauk,Ser.Chem.in print ,1998.

7.G.B.Manelis,26th Jnt.Annu.Conf.JCT, Karlsruhe,July 4-7,1995,15-1.

8. O. A. Luk'yanov et al. Izv. Akad. Nauk, Ser. Khim., 1994, 43,1457.

9. O. A. Luk'yanov et al. Izv. Akad. Nauk, Ser. Khim., 1995, 113 .

10. Z. Pak, AIIA/SAE/ASME/ASEE 29 Joint Propulsion Conf., June 28-30, 1993, Monterey, CA, FllA-93-1755.

Stabilitätsuntersuchungen einbasiger Treibladungspulver – Mikrokalorimetrie im Grenzbereich –

Uldis Ticmanis, Gabriele Pantel, Lutz Stottmeister

Wehrwissenschaftliches Institut für Werk-, Explosiv- und Betriebsstoffe (WIWEB),
ASt Heimerzheim, Großes Cent, D-53913 Swisttal

Kurzfassung

Schätzungen der Einsatzlebensdauer aus dem Stabilisatorabbau bei isothermer Lagerung und aus Wärmeflußmessungen wurden an vier einbasigen Treibladungspulvern (TLP) verglichen. Bei beiden Methoden müssen Schätzfunktionen, die zwei unterschiedliche Werte der Aktivierungsenergie enthalten, eingesetzt werden. Bei Wahl gleicher Referenzpunkte (Mindestgehalt des Stabilisators, Zeitdauer der Wärmeflußmessungen bei der höchsten Meßtemperatur) werden vergleichbare Voraussagen erhalten. Ein Nachteil der Stabilisatormethode ist die sehr lange Lagerdauer.

Abstract

The assessment of service life, based on stabiliser consumption after isothermal storage and on heat flow calorimetry are compared using four single base propellants. Both methods demand kinetics containing two different values for the activation energy. If equal reference points (tolerable stabiliser content, time of heat flow measurements at the highest temperature) are selected, both methods lead to comparable results of the service life. The stabiliser consumption method demands long storage times.

1 Einleitung

Lebensdauerprognosen von TLP basieren meist auf der Bestimmung des Stabilisatorgehalts und seiner Reaktionsprodukte nach Isothermlagerungen mit nachfolgender kinetischer Auswertung der Resultate. Eine derartige Arbeitsvorschrift ist auch in der STANAG 4527 [1] festgeschrieben. Ein nicht zu beseitigender Nachteil dieser Methoden ist die lange Untersuchungsdauer, da signifikante Abbaugrade des Stabilisators bei möglichst niedrigen Lagertemperaturen erreicht werden müssen. Dieses Zeitproblem dürfte sich zukünftig noch beträchtlich vergrößern, weil gründlichere Untersuchungen [2,3] gezeigt haben, daß die Abbaukinetik mit einem einfachen Arrheniusansatz nur höchst ungenügend beschrieben werden kann. Daher soll die o.g. STANAG um die schnellere Methode Wärmeflußkalorimetrie (WFK) ergänzt werden. In dieser Arbeit werden die Ergebnisse beider Verfahren bei der Untersuchung einbasiger TLP verglichen.

2 Autokatalyse, chemische und ballistische Lebensdauer

Die WFK-Methode erfordert das Messen in luftdicht geschlossenen Gefäßen. Die Alterung kann jedoch als munitions-äquivalent betrachtet werden, so daß der Zwang der Methode gegenüber den üblichen „lose verschlossenen" Meßanordnungen ein Vorteil ist. Sowohl der Grad der Autokatalyse als auch die Wirkung des Stabilisators wird – zumindest für geschlossene Systeme – unangemessen überschätzt. Eine WFK-Messung über 8 Tage an einem DPA-stabili-

sierten und einem unstabilisierten einbasigen TLP sonst gleicher Rezeptur zeigt keine nennenswerten Unterschiede im Wärmefluß (Abb. 1).

Eins unserer Modellpulver erreicht bei einer Langzeitmessung nach 25 Tagen bei 80°C einen maximalen Wärmefluß von etwa 50 µW/g, nach 38 Tagen wird ein Energieverlust von 113 J/g (ca. 6 % der totalen Zersetzungswärme) erreicht, ein Zustand, der höchstwahrscheinlich zu merklichen Funktionsverlusten führen würde, andererseits im Realfall kein Sicherheitsrisiko beinhaltet.(Abb.2) Der kritische Durchmesser eines auf 66°C erwärmten Zylinders aus diesem TLP wird nach Frank-Kamenetzkii [4] auf noch 46 cm geschätzt (Eingabedaten s. Tabelle 1).

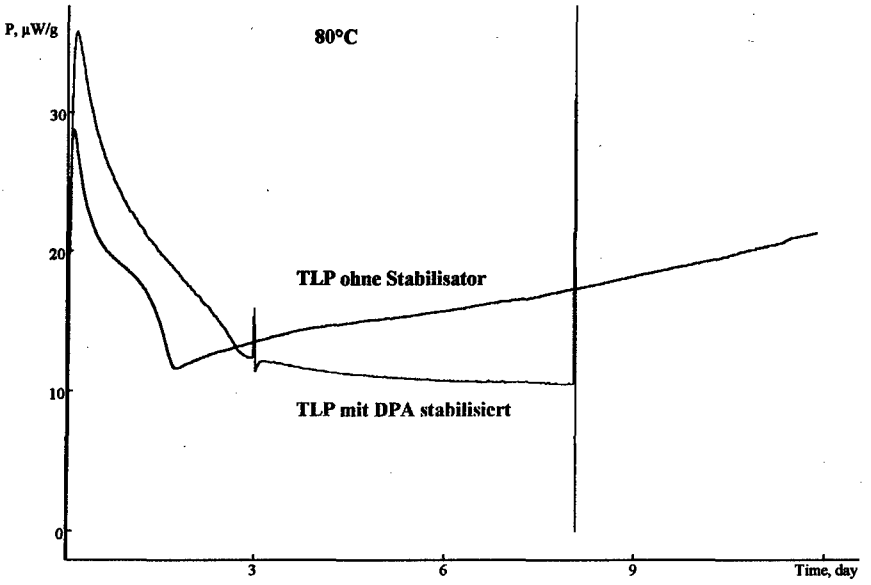

Abb. 1. Vergleich eines einbasigen DPA-stabilisierten TLP mit einem nicht stabilisierten TLP

Tab. 1: Eingabedaten zur Ermittlung des kritischen Durchmessers eines stabilisierten TLP

Aktivierungs-energie	vorexponen-tieller Faktor	Schüttdichte	Radius	Wärmeleit-fähigkeit	geometrischer Faktor
[kJ/mol]	[W/kg]	[kg/m³]	[m]	[W/(m·K)]	-
124,4	1,6E17	800	0,46	0,127	2,00

In Relation zu einem extrem autokatalytisch reagierenden unstabilisiertem Pulvervorkonzentrat (PVK; 85 % Ngl, 15 % Nc) „verschwindet" das TLP (Abb. 3). Als Referenz unserer (sehr konservativen) WFK-Prognosen wurde der Zustand des Minimums (Abb. 2) gewählt, die üblicherweise vorgegebenen Minimalgehalte des Stabilisators [5] findet man jedoch ebenfalls in der Nähe dieses Belastungsbereichs. Der Abbrand im WFK-Minimum belasteter TLP in der manometrischen Bombe ergibt keine signifikanten Unterschiede im Vergleich zu unbelasteten Proben (Abb. 4), so daß man auch auf unveränderte ballistische Eigenschaften schließen kann.

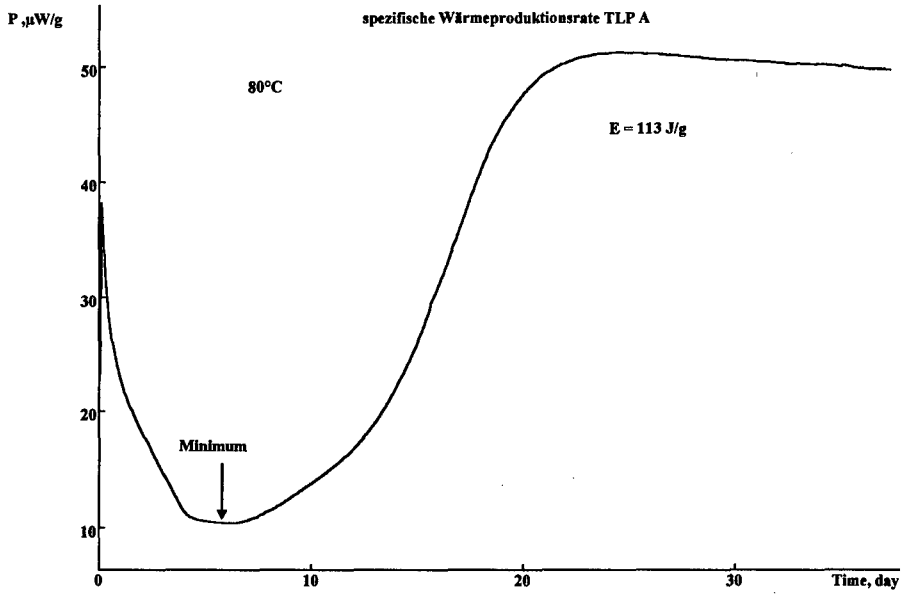

Abb. 2. Wärmeflußmessung an TLP A bei 80°C

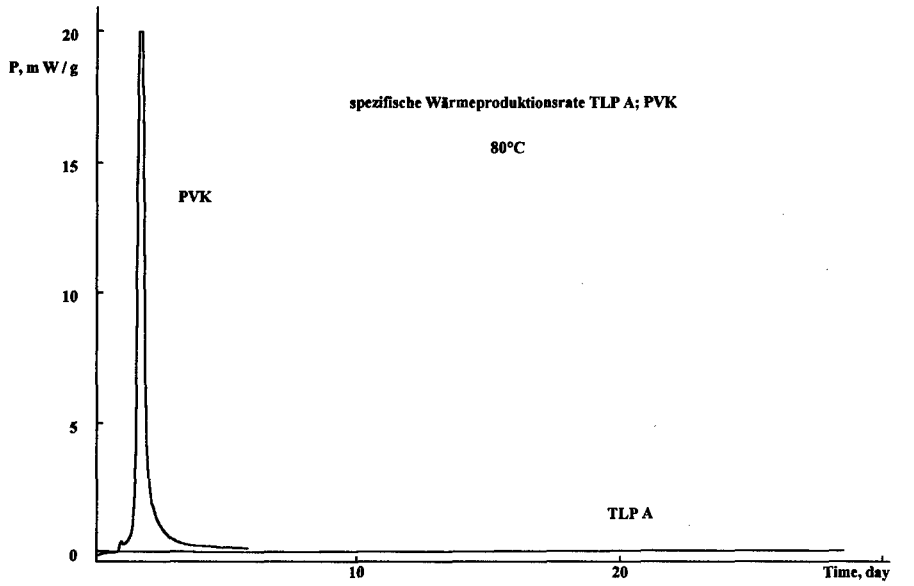

Abb. 3. Vergleich der Wärmeflußmessungen von Pulvervorkonzentrat und einbasigem TLP.

Der Diskussion kurzer Sinn: Unsere Prognosen beziehen sich nicht auf die (sehr lange bis unendliche) Sicherheits- oder chemische Lebensdauer, sondern dienen eher einer vorsichtigen Schätzung der ballistischen Lebensdauer. Diese Betrachtung ist für einbasige TLP, bei denen Diffusionsvorgänge keine Rolle spielen, berechtigt [6].

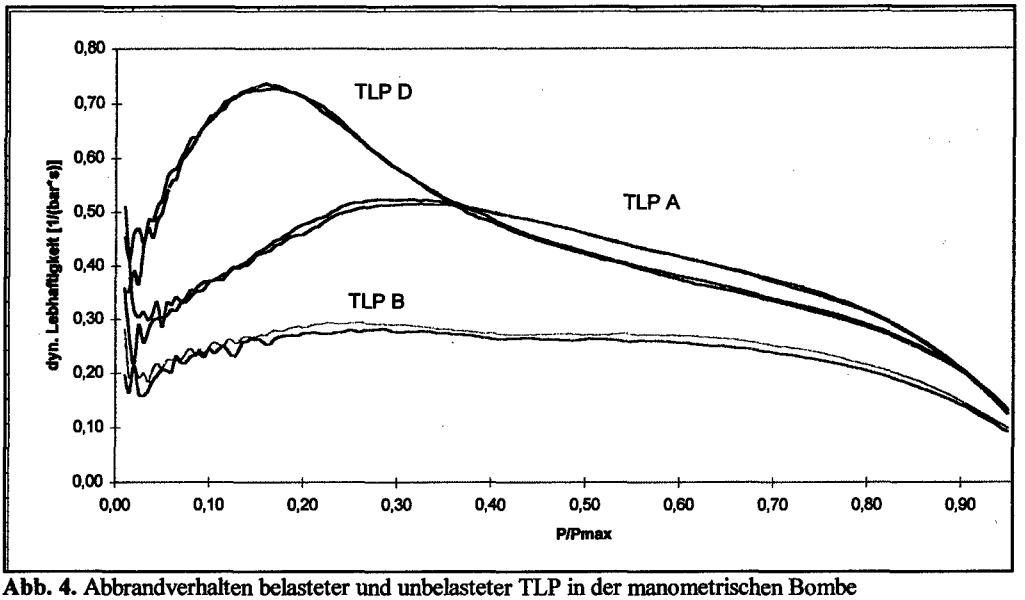

Abb. 4. Abbrandverhalten belasteter und unbelasteter TLP in der manometrischen Bombe

3 Untersuchungsmaterial und -umfang

Die Rezepturen der untersuchten TLP's, deren Bezeichnungen auf Wunsch des Anlieferers zu A, B, C und D anonymisiert wurden, sind in Tabelle 2 zusammengestellt.

Tab. 2: Rahmenrezepturen der untersuchten TLP's mit Angabe des Herstellungsjahrs

Stoff	TLP A (1990)	TLP B (1994)	TLP C (1992)	TLP D (1997)
	[Gew.-%]	[Gew.-%]	[Gew.-%]	[Gew.-%]
Nitrocellulose	94,4 [a)]	91,7 [a)]	ca. 95 [a)]	97,5 [a)]
Diphenylamin [b)]	1,2	1,1	1,2	1,0
Dibutylphthalat	1,0	-	-	-
Campher	-	4,4	-	-
Kaliumsulfat	1,0	0,6	0,8	-
Natriumoxalat	-	-	-	0,6
Feuchte	1,5	1,3	1,7	0,9
Restlösemittel	0,9	< 0,9	< 2,0	-

a) Rest zu 100 %. b) Es sind auch in unbelasteten Proben geringe Anteile an NNODPA enthalten (Tab. 5).

TLP C wurde – um es in die Probengefäße füllen zu können – mittels einer Schneidmühle und Siebung auf Korngrößen von 0,5 bis 2 mm zerkleinert. Das Röhrenpulver D wurde auf Längen von ca. 2 mm geschnitten. TLP A und B wurden im Originalzustand (d.h. unzerkleinert) untersucht.

Die TLP wurden in Glasampullen (ca. 3 ml Volumen) des TAM-Kalorimeters eingefüllt und dicht verschlossen. Die Proben wurden in dieser Form bei 80°C, 70°C, 60°C und 50°C eingelagert, in vorgeschätzten Zeitabständen entnommen und nach folgendem Schema untersucht:

- Bestimmung des Diphenylamins (DPA) und seiner Abbauprodukte mittels HPLC
- WFK-Messung an einer Parallelprobe bei der Einlagertemperatur („Serie 1")
- Folgemessung an derselben Probe bei 80°C bis zum Wärmeflußminimum (vgl. Abb. 2, „Serie 2")

Zur Ermittlung der Arrheniusparameter wurden WFK-Messungen an unbelasteten Proben bei Meßtemperaturen von 80°C bis 40°C durchgeführt („Serie 3").

4 Wärmeflußmessungen

Aufgrund der Änderung der Zersetzungskinetik im Bereich zwischen 50°C und 60°C ist es erforderlich, die WFK-Messungen der Serie 3 möglichst auch noch bei 40°C durchzuführen. Bei dieser Temperatur liegt der Wärmefluß einbasiger TLP nur noch bei ca. 0,1 µW/g (bzw. bei einer Probenmenge von ca. 3 g bei 0,3 µW absolut). Solche Minimalströme können nur unter Beachtung besonderer Maßnahmen erfaßt werden.

Unentbehrlich ist eine Grundlinienkontrolle während des mehrere Tage dauernden Versuchs. Dafür werden für das TAM-Kalorimeter zwei Verfahren vorgeschlagen [7]. Bei der **Parkpositions-Technik** werden Proben- und Referenzampulle aus dem Meßbereich hochgezogen, verbleiben jedoch auf Versuchstemperatur. Somit wird die Basislinie „Luft/Luft" gemessen. Bei der **Switch-Technik** werden Probe und Referenz vertauscht, wobei die Basislinie zwischen dem oberen und unteren Wärmeflußniveau liegt (Abb. 5). Wir halten die Switch-Methode generell für zuverlässiger und nehmen die längeren Einstellzeiten in Kauf.

Die Glasampullen werden mit einer Dichtungsscheibe und einem darüber kragenden Metalldeckel abgedichtet. Nach Einschrauben des Haltehakens ist die Oberseite der Dichtscheibe gegen die Atmosphäre offen, wobei flüchtige Bestandteile der Scheibe verdampfen können und somit in Relation zur Meßgröße große endotherme Effekte auftreten. Dies ist in Abb. 6 anhand einer Messung „Leerampulle mit Scheibe" gegen eine Messung „Leerampulle ohne Scheibe" (nur mit dem Metalldeckel verschlossen) demonstriert. Der Effekt läßt sich durch mehrwöchiges Vorlagern der Scheiben bei 80°C beseitigen.

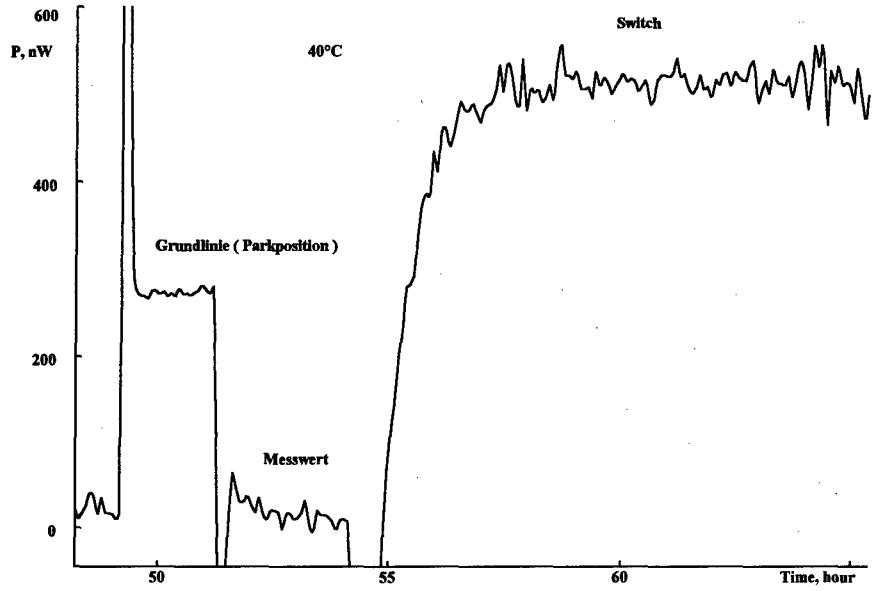

Abb. 5. Messungen eines kombinierten Switch-Parkpositions-Experiments

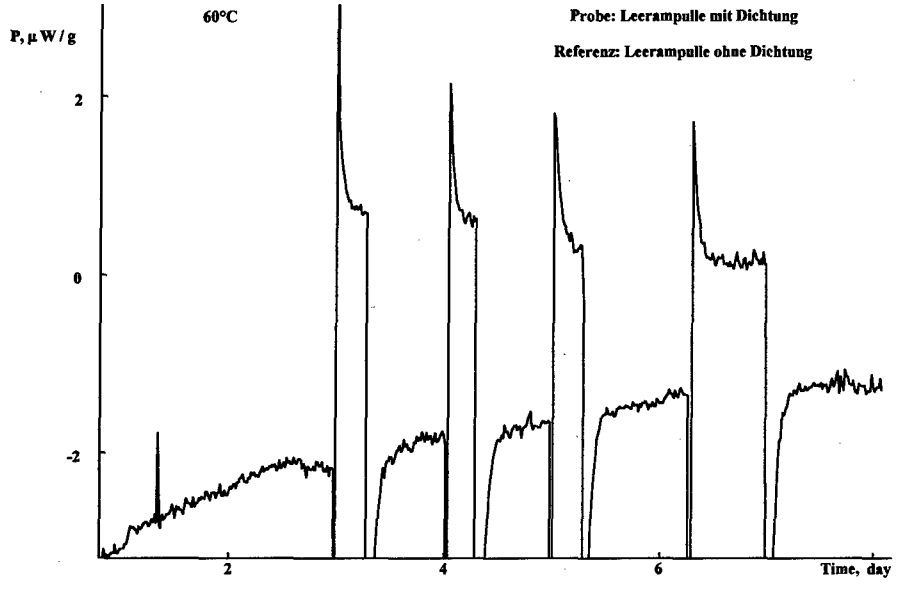

Abb. 6. Messungen einer nicht vorkonditionierten Meßampulle (endothermes Signal durch Verdunstung flüchtiger Bestandteile aus der Dichtung)

Die Notwendigkeit einer guten Regelung der Raumtemperatur veranschaulicht Abb. 7.

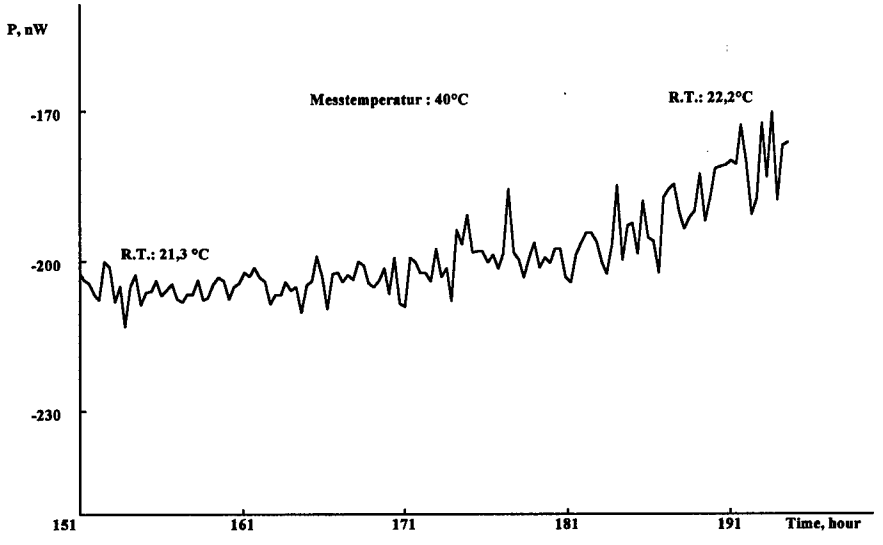

Abb. 7. Messungen der Basislinie mit Korrelation zur Raumtemperatur

Messungen zur Bestimmung der kinetischen Parameter (Serie 3)

Unbelastete Proben der TLP wurden bei 80°C bis zum Erreichen des Wärmeflußminimums gemessen. Dieser Zustand wurde nach rund 4 bis 9 Tagen erreicht. Dieselbe Probe wurde dann bei 70°C, anschließend bei 60°C usw. bis 40°C gemessen (s. Abb. 8).

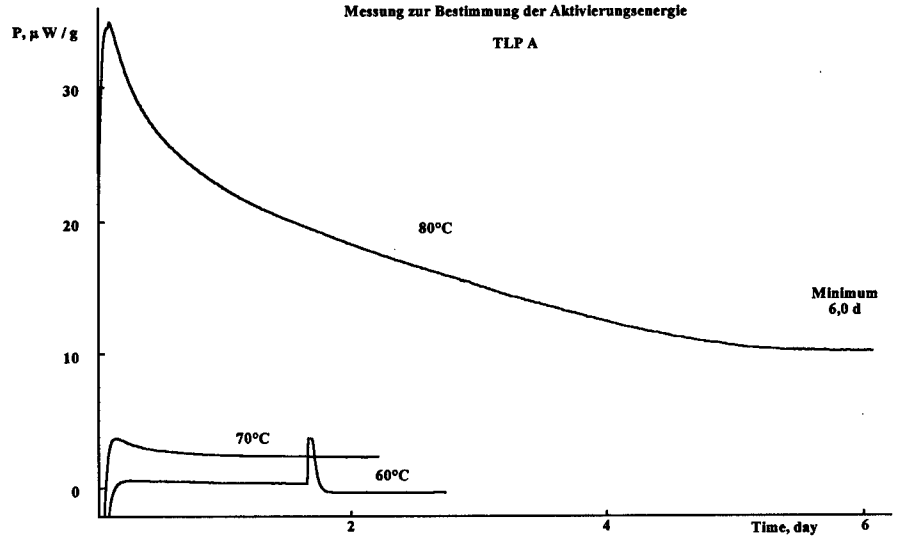

Abb. 8. Messungen zur Bestimmung der Aktivierungsenergie

Die am Ende der jeweiligen Meßperiode erhaltenen konstanten Werte wurden für den Arrhenius-Plot verwendet (Abb. 9-12).

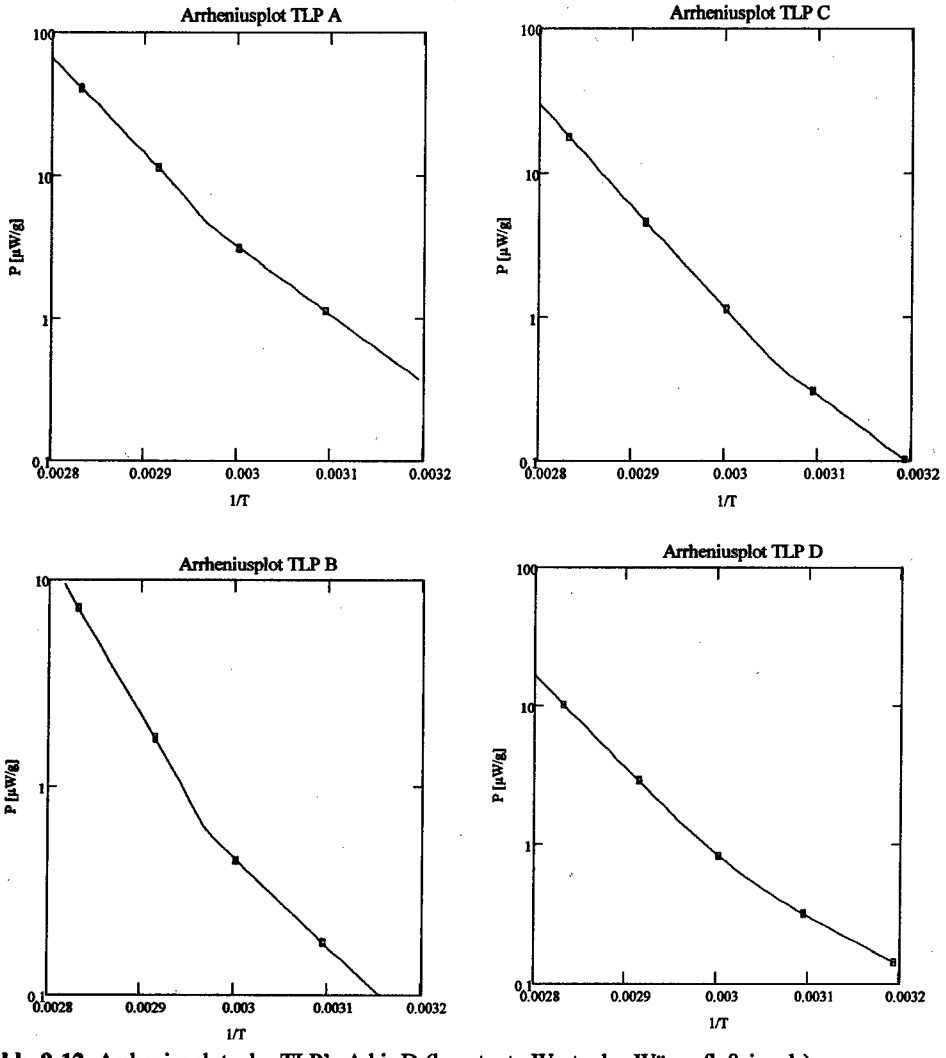

Abb. 9-12. Arrheniusplots der TLP's A bis D (konstante Werte des Wärmeflußsignals)

Abb. 13 zeigt die Auswertung einer Messung an TLP A, bei der die 80°C-Messung (bei sonst analoger Arbeitsweise) über 18,8 Tage, also bis in die Nähe des Maximums (vgl. Abb. 2) ausgedehnt wurde. In allen Fällen wurde ein relativ scharfer Wechsel des Kurvenanstiegs – und somit der Aktivierungsenergie – zwischen etwa 50°C und 65°C festgestellt.

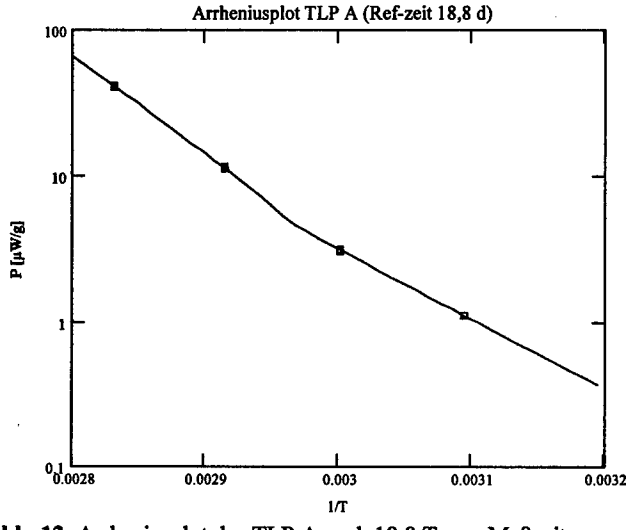

Abb. 13. Arrheniusplot des TLP A nach 18,8 Tagen Meßzeit

Die erhaltenen kinetischen Parameter sind in Tab. 3 zusammengestellt.

Tab. 3: Kinetische Parameter für die TLP's A bis D

TLP	E_1	A_1	E_2	A_2	T_{KN}	t_{ref}	Q_{ref}
	[kJ/mol]	[µW/g]	[kJ/mol]	[µW/g]	[°C]	[d]	[J/g]
A	124,4	3,4E19	88,2	5,1E13	66,4	6,01	8
	127,2	2,7E20	91,2	6,3E14	65,4	18,8	27
B	145,3	2,3E22	81,0	2,2E12	64,6	7,09	7
C	136,0	2,4E21	92,8	3,1E14	53,4	4,23	11
D	127,2	7,6E19	66,3	1,9E11	57,8	8,46	9

A_1, E_1 = Frequenzfaktor und Aktivierungsenergie des Hochtemperaturbereichs

A_2, E_2 = Frequenzfaktor und Aktivierungsenergie des Niedrigtemperaturbereichs

T_{KN} = Übergangstemperatur (gleiche Werte beider Reaktionsratenkonstanten)

t_{ref} = Referenzzeit der Lagerung bei 80°C (= Minimumzeit) mit Ausnahme des zweiten Wertes für TLP A

Q_{ref} = Energieverlust bei der Referenzzeit

Die Werte beider Aktivierungsenergien für das bis zum Minimum und das für 18,8 Tage belastete TLP sind praktisch gleich, lediglich die Frequenzfaktoren des letzteren sind erhöht. Dieses, ebenso wie Untersuchungen über die Form der qualitativ gleich verlaufenden Wärmeflußkurven zweibasiger TLP bei verschiedenen Meßtemperaturen [8] bestätigt die folgende Hypothese. Bis zum Minimum sind die Effekte durch insgesamt unbedeutende Oberlächenreaktionen bestimmt, die kinetisch schwierig darzustellen sind. Über einen weiten Bereich danach ist das Wärmeflußsignal mit einer einheitlichen, wenn auch nicht einfachen Kinetik beschreibbar. Daraus resultiert, daß das Minimum nur den kleinstmöglichen sinnvollen Extrapolationspunkt darstellt. Angesichts des in diesem Zustand gemessenen Energieverlusts von max. 11J/g kann angenommen werden, daß die Wahl eines Bezugspunktes

höherer Zersetzung und entsprechend längerer Lebensdauerschätzung noch zulässig wäre. Dies ist jedoch ohne begleitende Beschußversuche nicht generell quantifizierbar.

Die Zeit bis zum Erreichen des Referenzzustandes (= Minimum des Wärmeflusses) bei isothermer Lagerung kann aus der üblichen Gleichung (1) berechnet werden.

$$t = t_{ref} \times e^{\frac{E}{R}\left(\frac{1}{T}-\frac{1}{Tref}\right)} \qquad (1)$$

mit

t = isotherme Lagerzeit [d]

t_{ref} = Referenzzeit (= Minimumzeit) der 80°C-Messung [d]

T = isotherme Lagertemperatur [K]

T_{ref} = Referenztemperatur (= 353,15 K/80°C)

E = Aktivierungsenergie [kJ/mol]

R = Gaskonstante [0,0083143 kJ/(K·mol)]

Die Lebensdauer für 25°C wurde auf folgendem Weg geschätzt:

Mit E_1, T_{ref} = 353,15 K, t_{ref} = Minimumzeit der 80°C-Messung und T = Knicktemperatur wird t für diese Temperatur berechnet (= t_{KN}). Im zweiten Schritt wird unter Verwendung von E_2, $T_{ref} = T_{KN}$, $t_{ref} = t_{KN}$ und T = 298,15 K die Lagerzeit bei 25°C berechnet. Die Ergebnisse sind in Tabelle 4 aufgelistet.

Tab. 4: Lebensdauerschätzung für 25°C aus WFK-Messungen

TLP	A	A	B	C	D
t_{ref} [d]	6,0	18,8	7,1	4,2	8,5
t_{25} [Jahre]	6,9	26,9	8,5	13,1	6,0

Die auf dem Minimum als Referenz basierenden Zeiten liegen zwischen 6 und 13 Jahren. Falls der Energieverlust von 27 J/g noch ballistisch verkraftbar ist, erhöht sich die Schätzung für TLP A von 7 auf 27 Jahre.

Messungen bei Lagertemperatur (Serie 1)

Diese Messungen dienten vorwiegend zur Überprüfung der Gestalt der Wärmeflußkurven bei niedrigen Temperaturen ohne die Kalorimeter für sehr lange Zeit zu blockieren. Der Kurvenverlauf entspricht qualitativ weitgehend den Messungen bei 80°C, was die Annahme einer einheitlichen Kinetik unterstützt. Ein Beispiel ist in Abb. 14 dargestellt.

Daraus ist auch ersichtlich, daß eine Kontrolle des Alterungsvorganges aus der Höhe des Meßsignals zu absolut falschen Schlüssen führen würde. Bis zum Minimum wird das Meßsignal immer kleiner; dies bedeutet jedoch keineswegs eine Zunahme der Stabilität.

Messungen vorbelasteter Proben bei 80°C bis zum Minimum (Serie 3)

Die Idee dieser Messungen war, zu prüfen, ob sich die Verschiebung des 80°C-Minimumpunktes belasteter TLP als Alterungsmaß für Überwachungstests eignet. Dieser Effekt ist in Abb. 15 dargestellt.

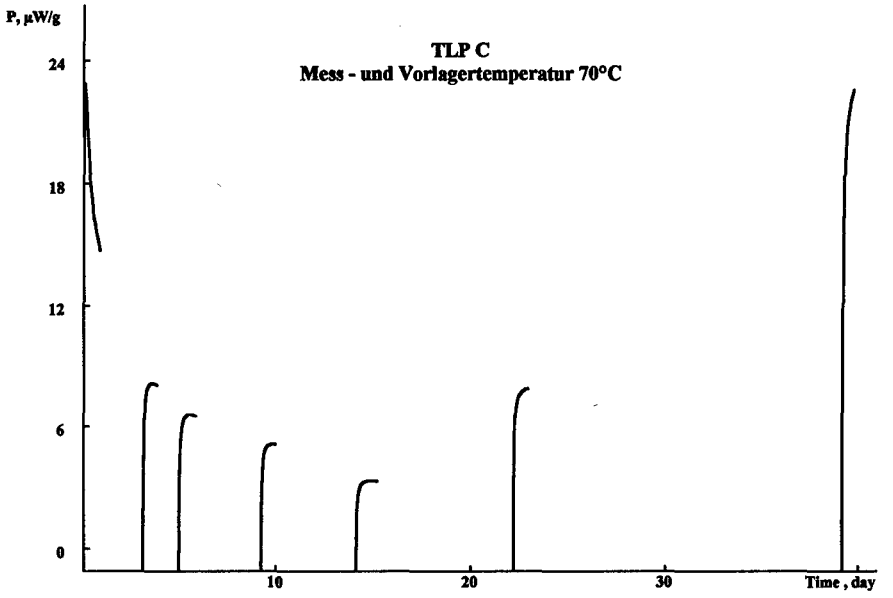

Abb. 14. Wärmeflußmessungen an TLP C bei 70°C nach isothermer Lagerung bei 70°C

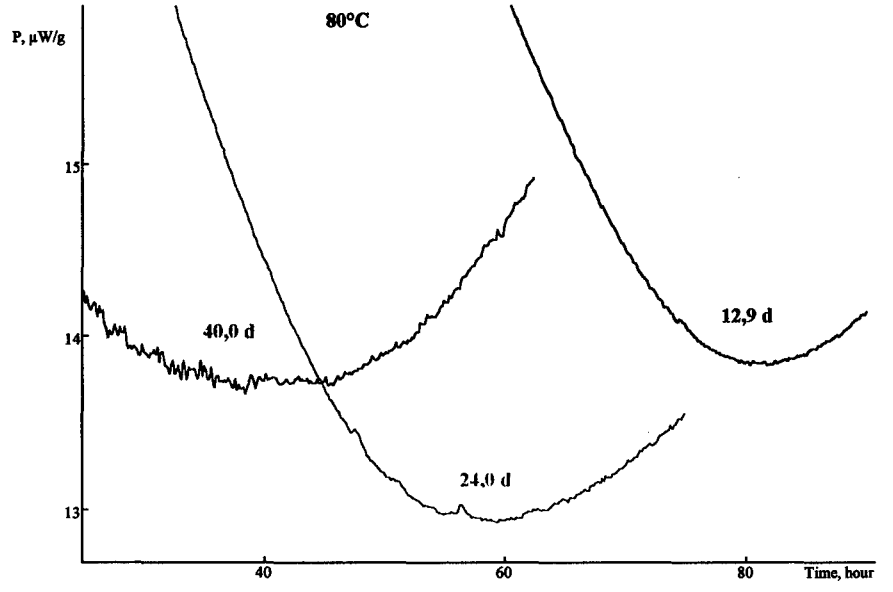

Abb. 15. Minima der 80°C-Messung nach Vorbelastung bei 60°C (TLP C)

In der Tat wurde ein in guter Näherung linearer Zusammenhang zwischen Vorlagerzeit bei niedrigen Temperaturen und der 80°C-Minimumzeit gefunden (Abb. 16)

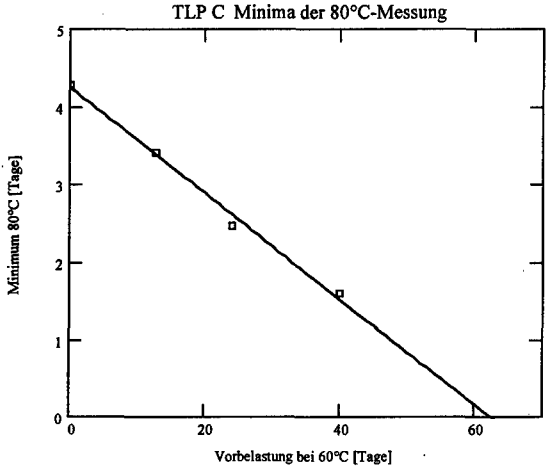

Abb. 16. Minima der 80°C-Messung nach Vorbelastung bei 60°C (TLP C)

Demnach wäre folgende Alternative zum Surveillance-Test denkbar:

- Einlagerung eines frisch gefertigten TLP in WFK-Ampullen bei Raumtemperatur und Messung eines „WFK-Ursignals" (Minimumzeit bei 80°C)
- Messungen bei 80°C der eingelagerten Proben in Zeitabständen von einigen Jahren
- Schnittpunkt der extrapolierten Geraden mit der Raumtemperatur-Achse indiziert den möglichen Ablauf der Einsatzdauer

5 Stabilisatorabbau

Die in Tab. 2 aufgeführten DPA-Gehalte der TLP sind Rezepturwerte. Wie zu erwarten, waren bereits vor der Wärmelagerung merkliche Anteile des DPA zu N-NO-DPA umgesetzt (vgl. Tab. 5). Dieser Vorgang ist auch die Hauptreaktion während der Lagerung, d.h. die Menge des „effektiven Stabilisators" (DPA + 0,85·N-NO-DPA) nimmt im Untersuchungszeitraum nur sehr langsam unter Bildung geringer Anteile 2-NDPA und 4-NDPA ab. Der Zeitverlauf der Hauptumsetzung ist für das TLP C in den Abb. 17-19 dargestellt.

Tab. 5: Stabilisatorgehalt vor Lagerung

TLP	A	B	C	D
DPA [%]	0,90	0,83	0,74	0,66
N-NO-DPA [%]	0,22	0,16	0,33	0,29

Zur Beurteilung der Stabilität wurde entsprechend den Vorgaben der STANAG [1,5] lediglich der DPA-Gehalt herangezogen. Der Zeitverlauf der Kurven über alle Meßtemperaturen ist – wie bereits einleitend erwähnt – mit einer n-Ordnungsreaktion nicht beschreibbar. Beste Anpassung nach der Methode der kleinsten Fehlerquadrate ergibt Abweichungen des DPA-Gehalts von 0,15 bis 0,20 (auf TLP-Masse bezogen), d.h. relative Fehler von ca. 20%. Die „linear-exponential-Formel" von Bohn [2], die zwei Aktivierungsenergien enthält, führt bereits zu einer stark verbesserten Anpassung. Eine genauere Kurvenanalyse zeigt jedoch, daß ein Übergang von nullter zu erster Ordnung nicht signifikant feststellbar ist. Die Reaktionsordnung bleibt eher über alle Temperaturen konstant. Dies ist mit folgendem Ansatz darstellbar:

$$S = S_0 \{1 - (1 - n)[A_1 \times e^{-E1/RT} + A_2 \times e^{-E2/RT}]\, t\}^{(\frac{1}{1-n})} \qquad (2)$$

S = Stabilisatorgehalt [%]

S_0 = Anfangsgehalt des Stabilisators [%]

n = Reaktionsordnung

A_1, E_1 = Frequenzfaktor [d^{-1}] und Aktivierungsenergie [kJ/mol] des bei hoher Temperatur dominierenden Reaktionsmechanismus

A_2, E_2 = Frequenzfaktor [d^{-1}] und Aktivierungsenergie [kJ/mol] des bei niedriger Temperatur dominierenden Reaktionsmechanismus

t = Lagerzeit [d]

T = Lagertemperatur [K]

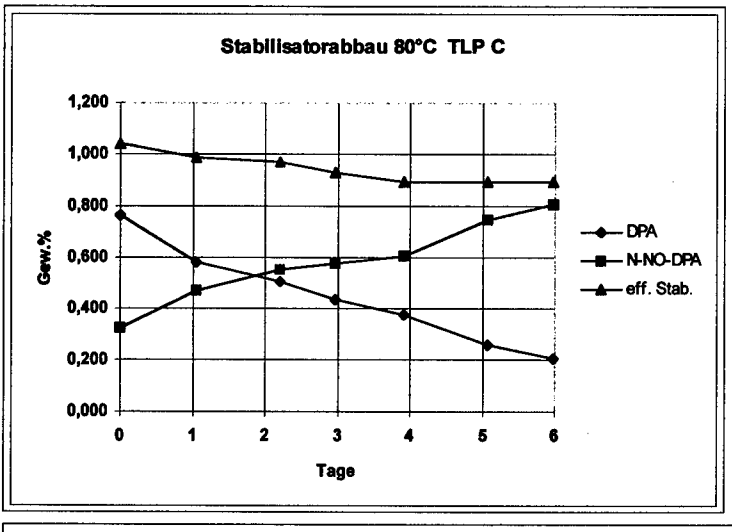

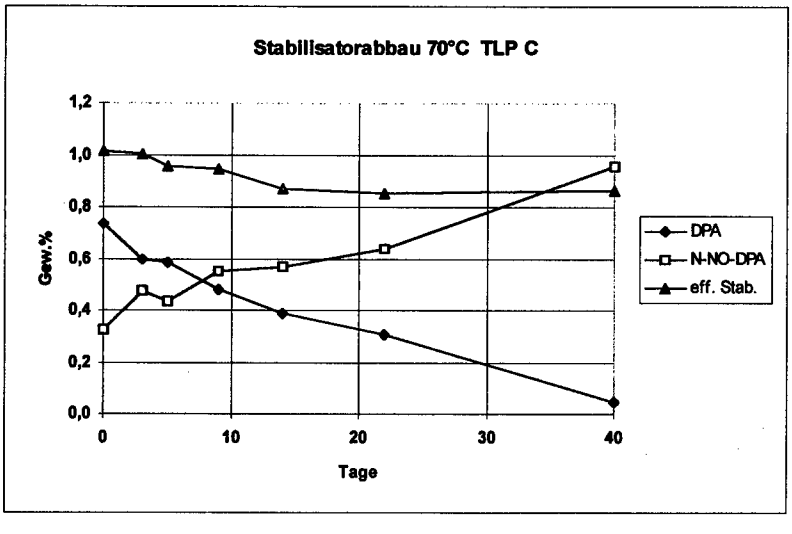

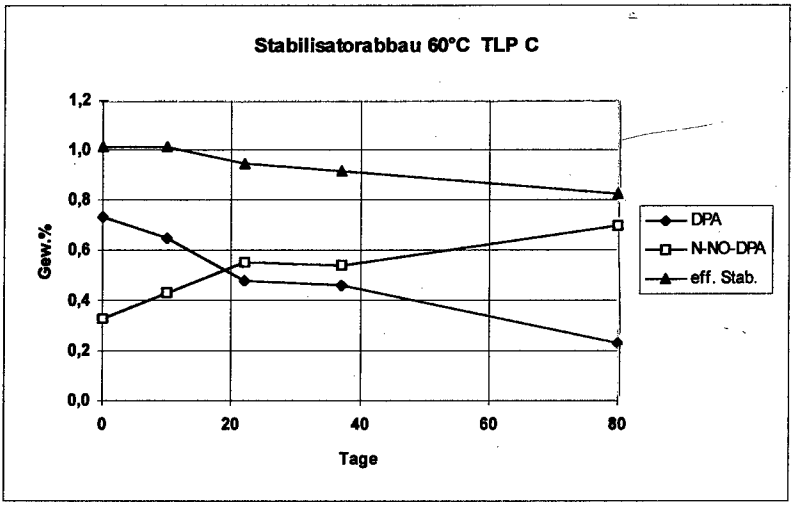

Abb. 17-19. Stabilisatorabbau von TLP C bei 80, 70 und 60°C

Dieser Ansatz liefert eine hinreichende Beschreibung der Meßwerte (vgl. Abb. 20-23). Die relative Standardabweichung liegt mit 0,01-0,03 % DPA im Bereich der Versuchsfehler der HPLC. Die ermittelten kinetischen Parameter sind in Tabelle 6 zusammengestellt. In Anlehnung an die STANAG 4117 fordern wir einen Mindestgehalt von 0,3% DPA und berechnen die diesem Wert entsprechende Lagerzeit bei 25°C als „DPA-Lebensdauer" (Tab. 7).

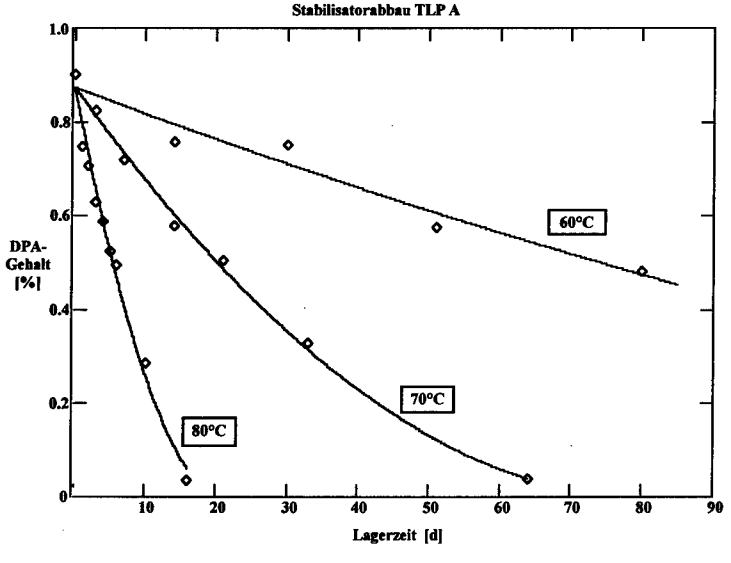

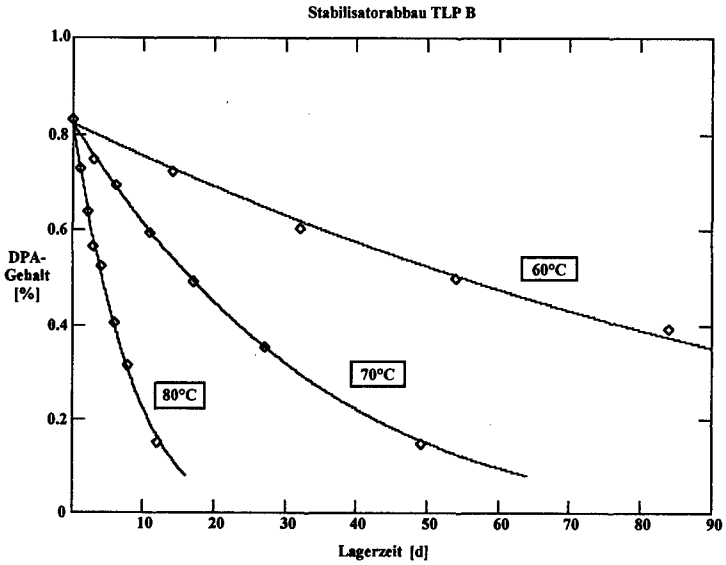
Stabilisatorabbau TLP B
1.0
0.8
0.6
0.4
0.2
0
DPA-
Gehalt
[%]
60°C
70°C
80°C
10
20
30
40
50
60
70
80
90
Lagerzeit [d]

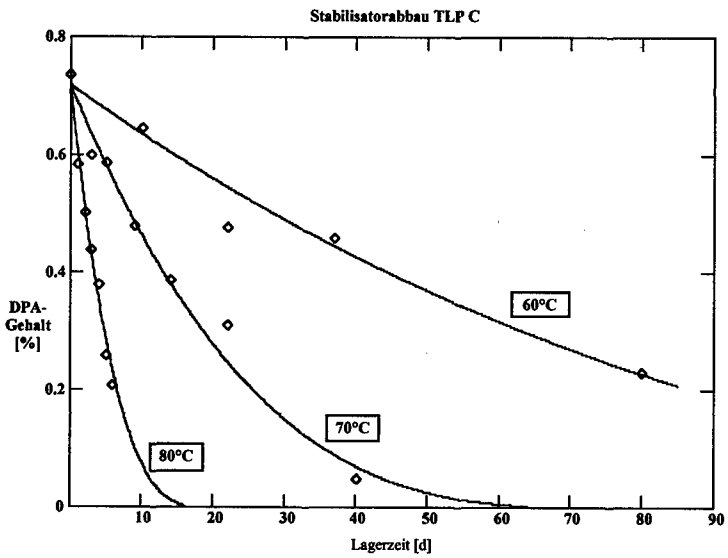
Stabilisatorabbau TLP C
0.8
0.6
0.4
0.2
0
DPA-
Gehalt
[%]
60°C
70°C
80°C
10
20
30
40
50
60
70
80
90
Lagerzeit [d]

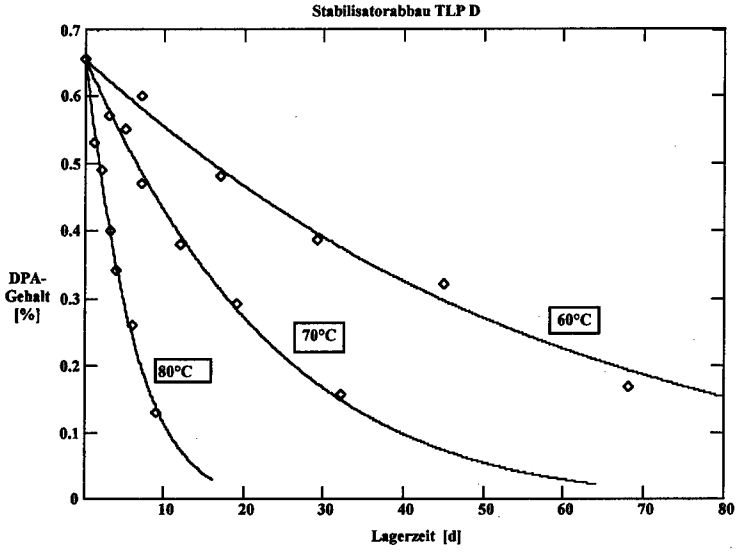

Abb. 20-23. Stabilisatorabbau bei 80,70 und 60°C der untersuchten TLP's

Tab. 6: Kinetische Parameter aus DPA-Abbau

TLP	E_1	A_1	E_2	A_2	n	S_0	STABW
	[kJ/mol]	[d^{-1}]	[kJ/mol]	[d^{-1}]		[%]	[%]
A	147,3	3,7E20	108,7	3,6E14	0,480	0,872	0,030
B	176,8	1,2E25	83,0	6,2E10	0,784	0,822	0,011
C	169,7	1,4E24	89,6	9,1E11	0,679	0,719	0,032
D	193,9	5,4E27	54,9	5,8E06	0,841	0,653	0,017

Tab. 7: Lebensdauerschätzung für 25°C aus DPA-Abbau

TLP	A	B	C	D
S_{ref} [%]	0,300	0,300	0,300	0,300
t_{25} [Jahre]	58,8	13,7	11,5	1,5

Der Wert von TLP A fällt mit fast 59 Jahren aus dem Rahmen. Es kann angenommen werden, daß die Schätzfunktion aufgrund einer ungenügenden Datenmenge aus der 60°C-Lagerung ungenau ist (der höchste verwertete Abbaugrad lag bei nur 37% des Anfangsgehaltes).

6 Vergleich der Schätzmethoden

Beide Schätzfunktionen sind im Prinzip gleichartig. Sie liefern höhere Aktivierungsenergien für höhere Temperaturen und niedrigere Werte für den Tieftemperaturbereich. Die schwerwiegenderen Werte des Tieftemperaturbereichs sind im Mittel angenähert gleich. Die Wahl der

Referenzpunkte ist bei beiden Methoden willkürlich (das WFK-Verfahren liefert jedoch immerhin einen Energieverlust, der einen Bezug zur Funktion hat). Gleicht man die Bezugspunkte an, so werden auch die quantitativen Schätzungen ähnlicher. Berechnet man aus (2) die Zeiten, bei denen bei 80°C der DPA-Gehalt bei 0,3% liegt und verwendet diese Zeiten anstatt der Minimumzeit als Referenz für die WFK-Auswertung erhält man die in Tabelle 8 aufgeführten Werte.

Tab. 8: Vergleich der Lebensdauerschätzung für 25°C

TLP	B	C	D	**Mittelwert**
S_{ref} [%]	0,300	0,300	0,300	
t_{ref} [d]	7,91	4,76	4,77	
t_{25} [Jahre] $_{WFK}$	9,5	14,7	3,4	**9,2**
t_{25} [Jahre] $_{DPA}$	13,7	11,5	1,5	**8,9**

TLP A wurde aus dem o.g. Grund nicht mitgewertet. Die Mittelwerte - nur zur Überprüfung der Tendenz gebildet - sind nahezu gleich, aber auch die Einzelwerte zeigen eine angesichts der Problematik hinreichende Übereinstimmung.

Literatur

[1] STANAG 4527, „Explosives, Chemical Stability, Nc based propellants, procedure for assessment of chemical life and temperature dependence of stabiliser consumption rates", Final edition 1 (July **1996**).

[2] M.A. Bohn, „Systematische Darstellung der Alterung von Rohrwaffentreibmitteln und Raketenfesttreibstoffen", *ICT-Jahrestagung* **1997**.

[3] U. Ticmanis, „Reaktionsordnung und Temperaturabhängigkeit der Aktivierungsenergie des Stabilisatorabbaus in doppelbasigen TLP", *BICT-Bericht* 15134 (**1995**).

[4] V.A. Frank-Kamenetzkii, „Diffusion and Heat-Transfer in Chemical Kinetics", transl. by H. Thon, Princeton Univ. Press 1969.

[5] STANAG 4117, „Explosives, Stability Test Procedures and requirementsfor propellants stabilized with DPA, EC, or mixtures of both", Edition 3 (**1998**).

[6] B. Vogelsanger, R. Sopranetti, „Sicherheits-, Stabilitäts- und Lebensdaueruntersuchungen im Lebenszyklus von Treibladungspulvern", *BICT Workshop Mikrokalorimetrie* (Sept. **1995**), S. 27.

[7] S. Wilker, G. Pantel, U. Ticmanis, P. Guillaume, „Detailed investigation of sensitivity and reproducibility of HFC measurements", *11. Symp. Chem. Probl. Conn. Stabil. Explos.* Båstad **1998**.

[8] P. Guillaume, M. Rat, S. Wilker, G. Pantel, „Microcalorimetry and chemical studies of double base propellants", *ICT-Jahrestagung* **1998**.

PARAMETERS AFFECTING THE ONSET TEMPERATURE OF EMULSION EXPLOSIVES

David E.G. Jones, Hongtu Feng, Kenneth J. Mintz and Rainer A. Augsten
Canadian Explosives Research Laboratory
CANMET
Natural Resources Canada
555 Booth Street
Ottawa, ON K1A 0G1
CANADA

Abstract

There have been numerous international instances over the last several years in which pumping of an emulsion explosive has resulted in an accident. To address the sensitivity of emulsion explosives to various parameters including pressure, a study of a particular ammonium nitrate (AN) based emulsion explosive has been undertaken using the ARC (accelerating rate calorimeter) and a Tian-Calvet heat flux calorimeter (HFC).

The effects of pressure and both inert and oxidizing atmospheres on thermal behaviour were determined and compared with similar results obtained for AN per se. All the results for the emulsion explosive suggest an increased thermal hazard when operating in air in contrast with the observations for the same measurements in Argon. No such difference in the results for AN in air and Argon was observed.

Significantly lower onset temperatures are observed in air from both the ARC and HFC measurements on the emulsion explosive. This observation is believed to be a result of oxidation of the oil phase in the emulsion. Additionally, the ARC results show some dependance on the choice of the initial temperature; a lower initial temperature results in an elevated onset temperature. Sample size also appears to be a factor influencing the onset temperature for both the HFC and ARC results.

At a heating rate of 0.1 °C min^{-1}, the HFC results show a complex exotherm pattern for the emulsion in both Argon and air, but the latter results give a decidedly earlier onset

temperature and a slightly larger ΔH. A complex exotherm pattern is expected for the decomposition of AN but, for the emulsion in air, oxidation of the oil phase further complicates the result.

Introduction

Emulsion explosives are in increasing use at this time because of the advantage that they offer over ANFO and slurry explosives. In spite of their relatively high cost, they have significant benefits such as improved water resistance. Recently, heavy ANFO [1] has been formulated with emulsion filling in the voids between the prills of ANFO, at very little extra cost. It has become common practice to pump these explosives during their manufacture, transfer or loading into boreholes. Two major Canadian and several international accidents [2] have resulted from pumping emulsion explosives.

Perlid has carried out extensive safety tests using a variety of emulsion explosives in a progressing cavity pump in a circulation system against dead head and under dry pumping conditions. He showed that dry pumping a heavy ANFO product resulted in rapid temperature increase over 800 °C, with destruction of both the product and the rubber parts in the pump. When a cap - sensitive emulsion explosive was used under the same conditions, an explosion occurred, damaging the pump and the tubing in the system.

The thermal behaviour of an emulsion explosive is a key property that affects sensitivity and ultimately its safe use. The parameters that determine thermal behaviour are therefore of significant importance. Olson [3] has shown that an increase in initial temperature in an emulsion matrix lowers the minimum burning pressure and raises the linear burning rate.

In Canada, a pumping consortium has been formed for the purpose of focussing on safety issues related to the pumping of explosives. As part of our contribution to this effort, CERL has undertaken, in cooperation with local industry, experimental work aimed at elucidating factors that affect onset temperatures of emulsion explosives.

Experimental

The emulsion explosives were received from ETI Explosives Ltd and used without further treatment. Ammonium nitrate (AN) with a purity of 99% was purchased from Baker

Chemical Company.

A Heat Flux Calorimeter (HFC) and an Accelerating Rate Calorimeter (ARC) were used to study the characteristics of AN and the AN-based emulsion explosives.

HFC

The calorimeter, manifold and special high pressure vessels were used as described in reference [4]. The following two methods were used for loading samples in the HFC: (I) the samples were loaded directly into the high pressure vessel and the pressure change was read by a pressure transmitter during the experiments. In this way, experiments were carried out at ambient and 5.4 MPa pressure of air and Argon. In this method sample size varied from 0.1 to 1.0 g, and (ii) the samples were sealed in a glass ampoule which had an internal volume of about 0.7 cm^3. The glass ampoule was loaded in the high pressure vessel and a helium gas environment was used to provide good thermal conductivity. Sample size was less than 0.1 g. Heating rates for all experiments were 0.1 and 0.3 °C min^{-1}.

ARC

The standard ARC procedure of a heat-wait-search cycle was used for all the experiments. During the search portion of the cycle, the instrument checks for sample self-heating that exceeds a user - definable threshold rate (0.02 °C min^{-1} in this work). Once this condition has been met, the cycle is interrupted but collection of time, temperature and pressure data continues. If the rate drops below the threshold, the heat - wait - search cycle restarts. Data collection stops should some other preselected condition be exceeded. For example, experiments using 2.0 g of sample were programmed to shut down when the rate exceeded 1 °C min^{-1}. Details of the conditions and parameters used in these studies can be found in references [5] and [6].

Thermal hazard studies using the ARC have been published [7, 8] and the thermokinetic information that can be obtained from ARC measurements has been described previously [9]. In this work two sets of conditions (Table 1) were used for the different phases of the program.

Table 1 Experimental Parameters used in ARC Measurements

Reference	Sample mass/g	Vessel mass/g	Step heat/°C	Wait time/min	$P_{initial}$/MPa	$T_{initial}$/°C
[5]	0.5	Titanium 10	10	20	1.0	50
[6]	0.5, 2.0	Hastelloy C 276 40	5	60	0.1-4.0	100,130,150

Table 2 ARC Results For Emulsion Explosives [5]

Sample/run	T_0/°C	P_0/MPa	At maximum rate			
			T_m/°C	P_m/MPa	R_m/°C min^{-1}	t_m/h
1/1	182	1.8	349	6.8	>10	8.3
1/2	175	1.8	375	8.7	2.5	8.1
1*	272	1.2	370	5.2	10	2.8
2/1	204	1.9	358	12	>10	21
2/2	192	1.8	367	11	>10	19
AN*	217	0.68	242	2.4	0.2	4.0

*starting at ambient pressure

Results and Discussion

HFC

High Pressure Vessels

The experimental curves for AN and an emulsion explosive in Argon are compared in Figure 1. From this Figure, the four phase transitions observed for AN disappeared in the emulsion explosive. In fact, observation of crystalline phase transition in an emulsion explosive is not a good sign since this suggests crystallization of AN. The onset temperature for AN appears to be lower than that observed for the emulsion explosive whereas the rate of the reaction for the emulsion explosive is significantly faster than that for AN. A shoulder was observed in the high temperature region of the exotherm for the emulsion explosive, indicating a complex reaction mechanism.

The results for AN at ambient pressure of air, 5.4 MPa of air and Argon are shown in Figure 2. The peak temperatures of the exotherms in the high pressure measurements were shifted to slightly higher values.

The experiments for the emulsion explosive were carried out at ambient pressure of air and 5.4 MPa of air and Argon. All these results are shown in Figure 3. Firstly, comparing the results obtained at ambient pressure of Argon and air, it is found that the real onset temperature for emulsion explosives at ambient pressure of air is lower than that at ambient pressure of Argon by about 15°C. The peak temperature is also shifted to a lower temperature by about 15 °C. These results suggest that early oxidation takes place. From Figure 3, even lower onset temperatures were observed from the results at 5.4 MPa of air and the exothermic reaction is broader, more complex and incomplete at 300 °C. High pressure of inert gas inhibited the exothermic reaction of the emulsion explosive. Clearly, for the experiments carried out at 5.4 MPa of air two factors affect the thermal behaviour of the emulsion explosive: oxidation and inhibition. The former tends to lower the onset temperature whereas the latter tends to delay subsequent reactions.

Experiments were also carried out at a heating rate of 0.1 °C min^{-1} in order to obtain the entire exothermic peak. The results obtained at ambient pressure of air and Argon are

shown in Figure 4. The entire peaks were obtained for both conditions. Similarly, early oxidation and lower onset temperature of the exotherm were obtained from the results at ambient pressure of air. When 1 gram of the emulsion explosive was used, ignition took place in both air and Argon at ambient pressure conditions. These results are shown in Figure 5. At least three peaks were found in the thermogram at ambient pressure of air and the ignition temperature is lower than that at ambient pressure of Argon, in which at least four peaks were observed. Self-heating was considered as the reason for ignition in the larger sample sizes.

Ampoules

The samples were directly loaded into the high pressure vessel in all the above experiments. Because the manifold has a larger free volume than that of the vessel, part of the sample might have vapourized and condensed in the manifold during the experiments. In these experiments, the sample was sealed in air in a glass ampoule in order to avoid material loss and also to simulate a confined condition. All the results are shown in Figure 6. The results for AN show the complete exotherm and a higher rate of reaction, compared with the results from AN obtained using the high pressure vessel. Surprisingly, the results for the emulsion explosive indicate delay of onset temperature by about 50 °C, similar to the results obtained using high pressure of inert gas. This suggests that an increase in pressure from inert products, such as water, is inhibiting the exothermic reaction. The residual of this sample was re-run and the exothermic reaction appeared again, indicating that the reaction was incomplete in the first cycle.

ARC

Table 2 lists the ARC results obtained for the earlier studies [5] on two emulsion explosive products, sample 1 having less AN and more calcium nitrate (CN) than sample 2. It is clear that onset temperatures are lower for emulsion explosives at $P_{initial}$ = 1.0 MPa than at ambient pressure and also lower than the onset temperature for AN. Onset temperatures for AN and emulsion explosive at ambient pressure show the opposite

behaviour.

In a more recent study [6] , a Hastelloy C vessel was used, in spite of its larger mass and lower sensitivity, because there was some independent evidence for a catalytic effect in titanium vessels. The "true" onset temperature in an ARC experiment is typically less than the detected value, since an exotherm cannot be detected in either the heat or wait modes.

A compilation of all the results for two sample masses, at a series of initial temperatures and pressures is given in Table 3. The composition of this emulsion explosive is similar to that of sample 2 in Table 2. Table 3 and Figures 7 and 8 indicate that both rates dT/dt and dP/dt generally increase as the initial pressure increases. This behaviour is also observed for AN per se [10]. Additionally, the initial temperature seems to determine whether or not the first exotherm is detected so that at 100 °C (Table 3) it is not commonly detected. From Figure 8, it appears that the onset temperature decreases with increasing pressure, although there is no such pattern from the results in Table 3 for 0.5 g of emulsion at $T_{initial}$ = 150 °C. Finally, it is apparent that the highest rate in all the tests occurs at the highest initial pressure.

From a comparison of the results in Tables 2 and 3, it appears that a lower initial temperature results in a higher onset temperature but also generally leads to a runaway reaction ie $R_m > 10$ K min^{-1}.

Conclusions

The exothermic reaction for AN is not affected by the nature and pressure of the gas environment. The exothermic reaction for emulsion explosives is dependent on the gas environment. Oxidative decomposition of the oil phase in the emulsion explosive in air is observed. High pressure of inert gas tended to inhibit and delay the exothermic reaction for emulsion explosives, but in air oxidative decomposition resulted in a lower onset temperature with a broadened decomposition caused by the high pressure.

Table 3 ARC results For Emulsion Explosive [6]

Mass/ g	$T_{initial}$/ °C	$P_{initial}$ / MPa	Exotherm # 1			Exotherm # 2			
			T_0^{ext}/°C	R_m/°Cmin^{-1}	ΔP_1/ MPa	T_0^{est}/°C	R_m/°Cmin^{-1}	ΔP_{1+2} /MPa	$10^2(dP/dt)_m$/ MPa min^{-1}
0.5	150	0.70	150	0.06	2.9	252	0.51	6.5	1.8
		1.46	168	0.04	1.8	260	0.26	4.4	1.9
		2.59	155	0.10	1.5	236	0.5	5.0	3.4
		3.99	150	0.16	1.3	246	1.8	>5.7	16
	100	0.10	230	-	(0.4)	235	0.06	3.8	0.6
		0.46	215	0.08	1.9	236	0.47	5.6	4.0
2.0	130	0.10	-	-	(0.4)	218	>1	>2.2	5.4
		1.37	195	0.02	0.2	224	>50	>3.2	28
		3.13	135	0.03	0.0	165	>1	>2.3	6.6
	150	1.43	175	0.08	1.2	220	>1	>4.2	6.6

References

1. D. E. G. Jones, MINTECH 91, p21 - 24
2. H. Perlid, Proc. Annual Conf. Explos. Blasting Tech., 22(1996)101
3. D. Olson, presented at the Fall 1997 Research Center for Energetic Materials Open Safety Seminar, Socorro NM, October 7, 1997
4. D. E. G. Jones, P. Handa and Hongtu Feng, J. Thermal Analysis, accepted for publication
5. D. E. G. Jones and R. A. Augsten, CANMET Report, EXP 95-11(CF)
6. K. J. Mintz and D. E. G. Jones, CANMET Report, EXP 97-06 (TR)
7. R. A. Augsten, K. J. Mintz and D. E. G. Jones, CANMET Report, EXP 95-04 (OP)
8. K. J. Mintz ,D. E. G. Jones and R. A. Augsten, CANMET Report, EXP 96-01 (OP)
9. D. I. Townsend and J. C. Tou, Thermochimica Acta, 37(1980)1
10. K. R. Brower, Symp. Chem. Probl. Connected Stabil. Explos. 8th(1988)273

Figure 1

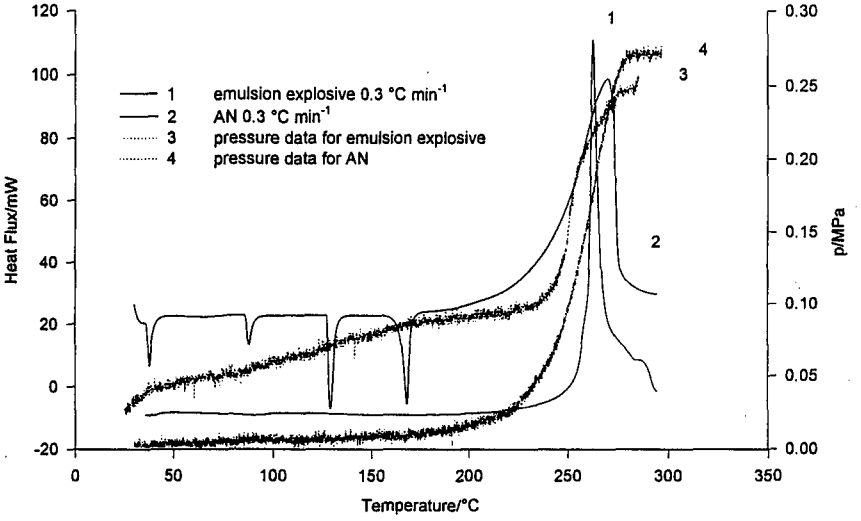

Figure 2

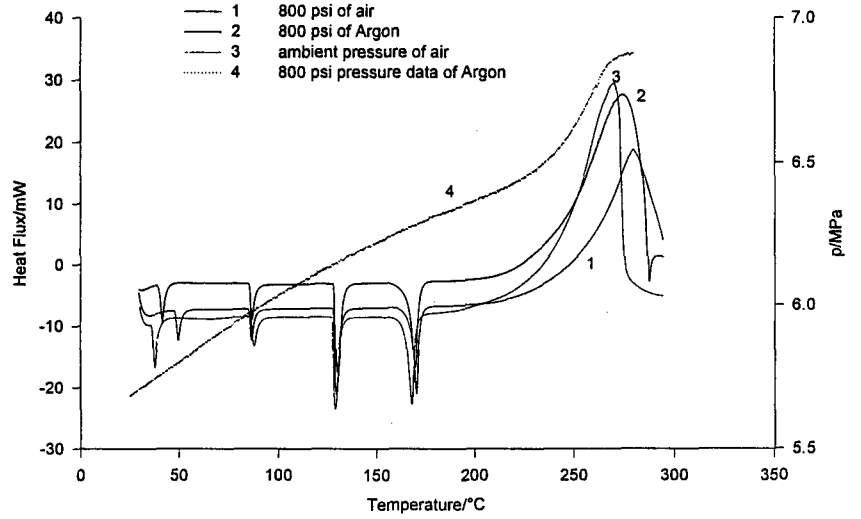

Figure 3

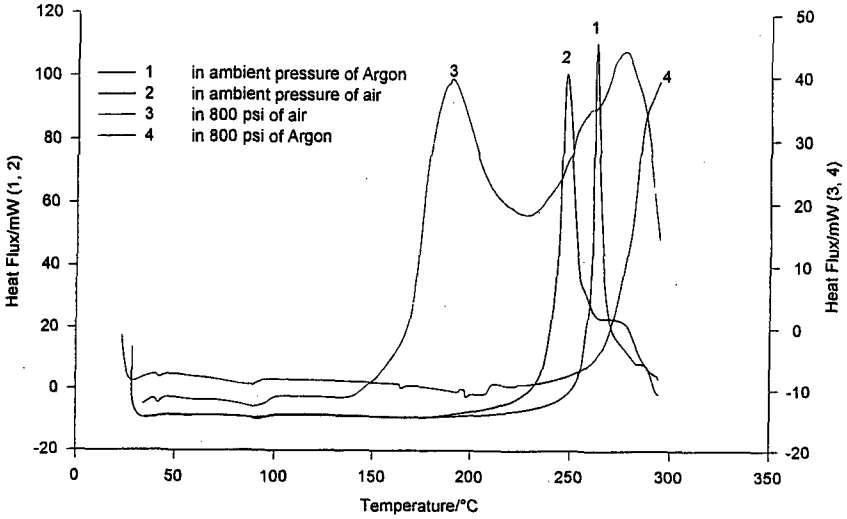

Figure 4

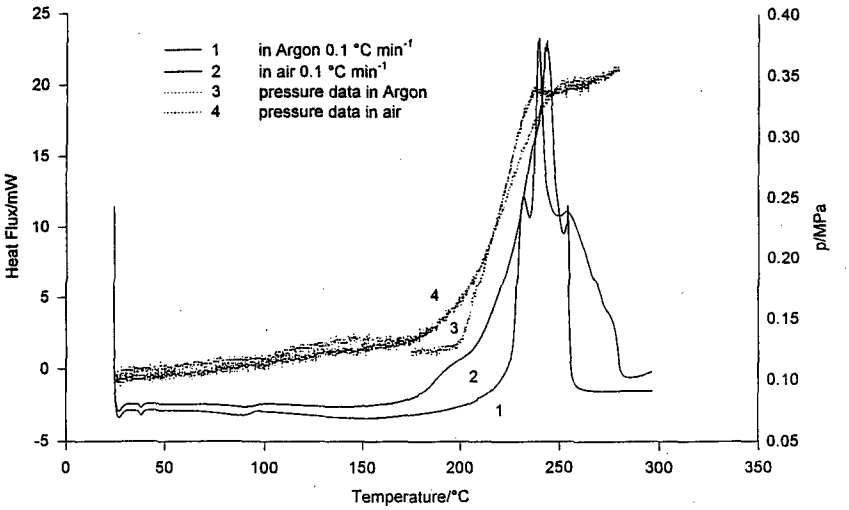

Figure 5

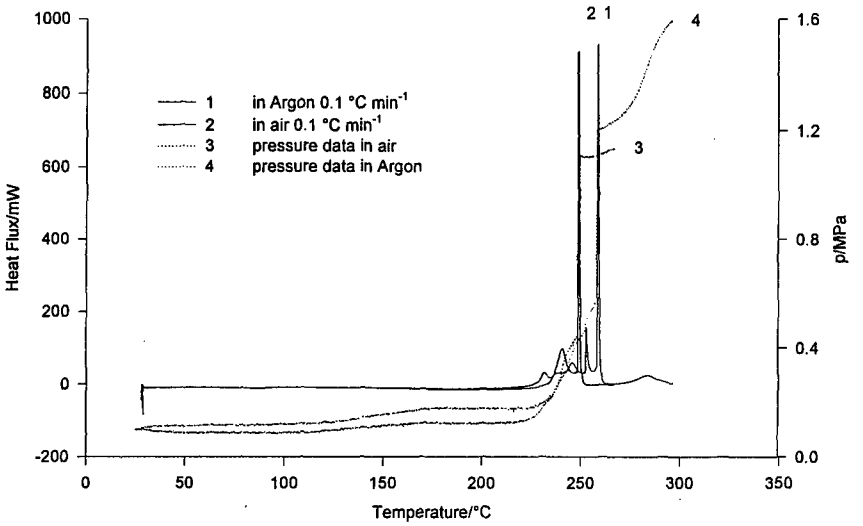

Figure 6

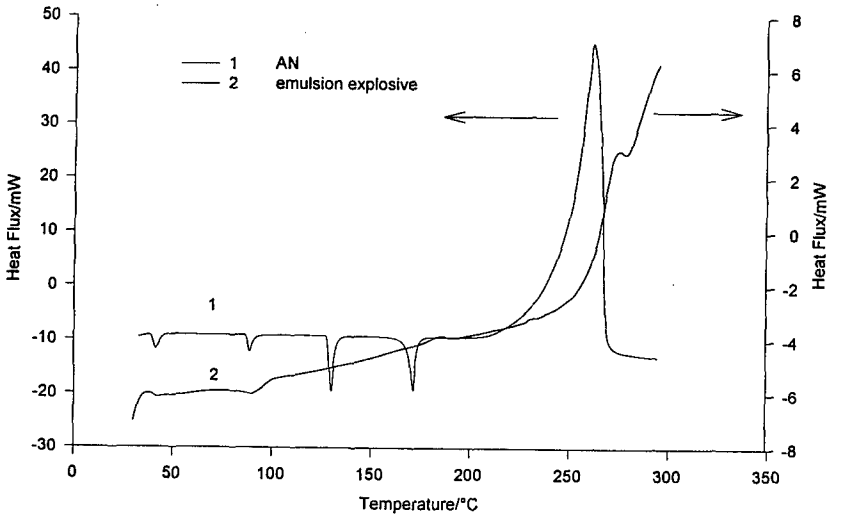

Figure 7

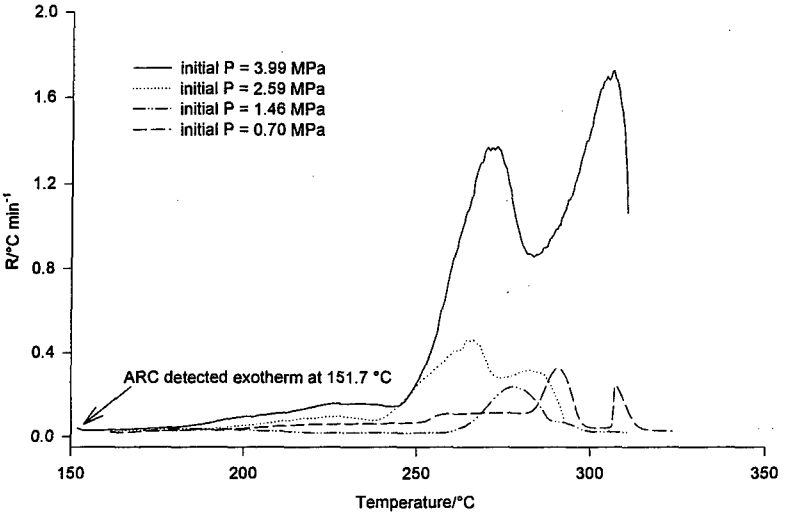

Figure 8

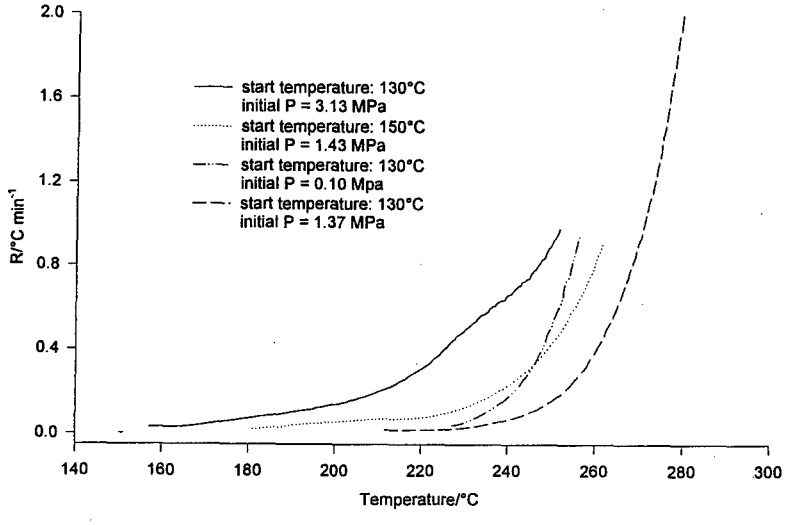

Thermisches Zersetzungsverhalten von neueren Weichmachern und Bindern untersucht mit der adiabatischen Selbstaufheizung

Decomposition Behaviour of Azido Based and Nitric Acid Ester Based Plasticizers and Binders Determined by Adiabatic Selfheating

Manfred A. Bohn

Fraunhofer-Institut für Chemische Technologie, ICT
Postfach 1240, D-76318 Pfinztal-Berghausen, Germany

Abstract

The thermal decomposition behaviour of the following plasticizers and binders was investigated in solutions of toluene (10 mass-%) with an 'Accelerating Rate Calorimeter' (ARC™): N-Methyl-/ N-Ethyl-NENA (58.8 / 41.2 in mass-%), DANPE (1,5-diazido-3-nitraza-pentane), GAPA (short chain GAP with azido end groups), EGBAA (ethylene glycol-bis-(α-azidoacetate), octylazide (not for use in explosives), GAP-AA-2000 (normal GAP, but OH end groups as esters of α-azido acetic acid), GAP-AA-500 (short chain GAP, but OH end groups as esters of α-azido acetic acid), PolyGLYN (poly glycidyl nitrate, uncured), GAP (poly glycidyl azide, uncured) from two manufacturers. Three types of energetic groups are represented with these compounds: nitric acid ester, nitramine and azido group. The amount of weighed-in solution was about 6g. The ARC produces a quasi-adiabatic environment for the sample by counter heating. A closed measuring system was used. This prevent the solutions from evaporation. The advantage of the investigation of the solutions is that the decomposition can be followed in a fully controlled way. The pure energetic substances would deflagrate after a short period of controllable self heating. The characteristic data of the adiabatic self heatings are given: temperature and self heat rate at the onset and at the maximum and the final temperature of the self heat rate curve, the thermal inertia of the system 'toluene solution-measuring cell' and the thermal inertia of the system 'energetic substance-solvent-measuring cell'. Typical values for the two groups of thermal inertia are 1.25 and 12.4. With the self heat rate curves one can distinguish the plasticizers and binders with respect to the decomposition temperature range, the energy generation and the energy generation rate. Different steps in decomposition kinetics can be seen. The Arrhenius parameters and the released heats of reactions have been determined from the self heat rate curves, which could be described with reactions of first order. The self heat rate curves have been scaled to the thermal inertia equal to one, which corresponds to a measurement on a solution without measuring cell and to a measurement on a pure substance without measuring cell. With the data of the simulated situation 'pure substance' the temperatures have been calculated for heat generation rates of 25µW/g and 50µW/g. For 25µW/g the predicted temperatures of Me/Et-NENA and PolyGLYN are 85°C and 90°C. The azido compounds have values above 100°C. DANPE has with 106°C the lowest temperature and the investigated GAP binders have values of about 114°C.

Paper presented at the 29th Internat. Annual Conference of ICT, Karlsruhe, Germany, June 30 - July 3, 1998.

1. Einleitung

Neuere energetische Weichmacher und Binder haben folgende energetische Gruppen: Salpetersäureestergruppe, Nitramingruppe, Azidogruppe. Die grundsätzlichen Ziele der Entwicklung energetischer Binder und Weichmacher sind: (1) erhöhte thermische Beständigkeit, (2) Erhöhung der Energieinhalts, (3) Verbesserung der Weichmacher-Funktionen: Erniedrigen der Glasübergangstemperatur und der Spröd-Duktil-Übergangstemperatur, Vermindern der Migration und des sog. Ausschwitzens, Verbessern der anderen mechanischen Eigenschaften der Treibmittelmatrix und wenn möglich auch des Abbrandverhaltens eines Treibmittels. Azidogruppen sind neben der zusätzlichen Energie auch interessant wegen der hohen Gaserzeugungsrate (Stickstoff) aus der Azidogruppe C-N_3. Dieser Effekt kann z.B. die Abbrandgeschwindigkeit erhöhen und die Druckwellenwirkung verstärken. Von der Salpetersäureestergruppe ist ihre geringere thermische Stabilität von den herkömmlichen Sprengölen und der Nitrocellulose bekannt. Dies ändert sich auch nicht in den neueren Bindern und Weichmachern, die sie als energetische Gruppe enthalten. Der Vorteil ist ein anderes Zersetzungsverhalten. Die ausgeprägte autokatalytische Zersetzung wie bei den herkömmlichen Salpetersäureestern wird bei ihnen nicht beobachtet. Eine vergleichende Untersuchung bezüglich thermisch ausgelöster Zersetzung klassifiziert die untersuchten Substanzen bezüglich ihrer thermischen Beständigkeit und der Freisetzung der Energie. Die Untersuchungsmethode war die adiabatische Selbstaufheizung an Toluollösungen gemessen mit einem 'Accelerating Rate Calorimeter' (ARC^{TM}). Das geschlossene Meßsystem verhindert ein Verdampfen. Der Vorteil der Untersuchung in Lösung ist, daß der Ablauf der Zersetzungsreaktionen in der Geschwindigkeit eingestellt und somit kontrolliert werden kann und auch homogen ist. Die reinen Verbindungen würden alle nach einer kontrollierbaren Selbstaufheizungsphase deflagrieren.

2. Apparatur

2.1 Prinzip der Methode

Das 'Accelerating Rate Calorimeter' (ARC^{TM}) von Columbia Scientific Industries, Austin, Texas, USA (übernommen von Arthur D. Little Inc., Cambridge, Massachusetts, USA) ist in Abb. 1 mit den wichtigsten Komponenten schematisch dargestellt. Der Heizblock besteht aus drei Einzelblöcken H_1, H_2 und H_3, die separat über die Heizblockthermoelemente T_1, T_2 und T_3 geregelt werden. In der Mitte des Heizblocks wird die Meßzelle angebracht. Die kugeligen Meßzellen mit Anschlußstutzen sind aus Titan, Edelstahl, Tantal oder Hastelloy C 276 mit einem Durchmesser von einem oder 0,5 Zoll gefertigt. An der Meßzelle wird das Meßzellenthermoelement T_M mit einer Klemme befestigt. Alle Thermoelemente sind vom Typ N (Nisil/Nicrosil). Über eine dünne Hochdruckkapillare ist die Meßzelle mit dem Druckaufnehmer DA verbunden. In der Regel wird am geschlossenen System gemessen, damit die adiabatische Umgebung möglichst gut gewährleistet ist. Die Meßsignale werden dem ARC-Prozessor zugeführt, welcher das Meßprogramm steuert und während der Selbstaufheizung der Probe die Heizungen nachführt. Durch dieses Nachführen wird eine quasiadiabatische Umgebung erzeugt. Als Temperaturbezugspunkt für die Thermoelemente wird ein hochkonstantes Eispunkt-Gerät verwendet. Der Ablauf einer ARC-Messung ist in der Abb. 2 dargestellt.

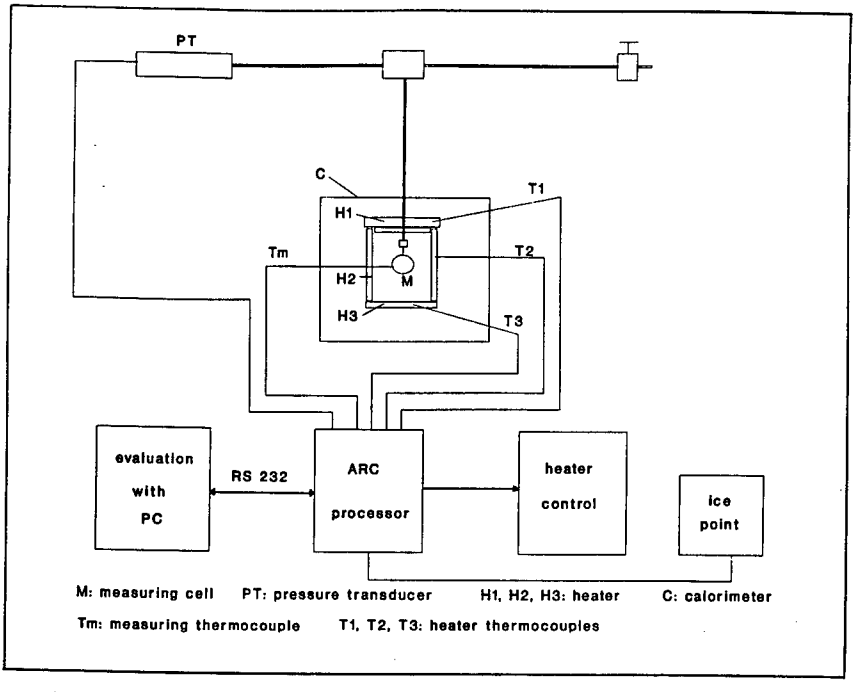

Abb. 1: Schema des 'Accelerating Rate Calorimeter' (ARC).

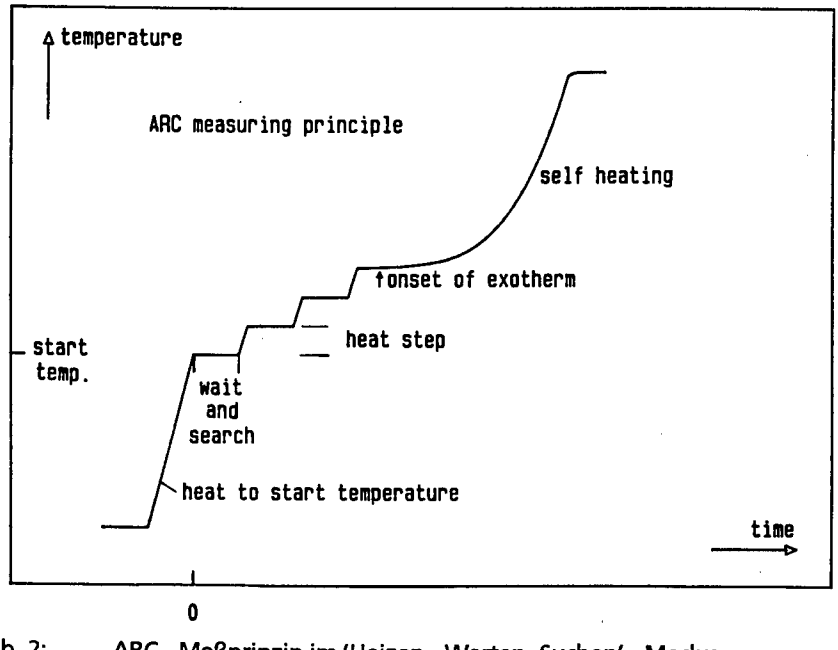

Abb. 2: ARC - Meßprinzip im 'Heizen - Warten- Suchen' - Modus.

Nach dem Hochheizen auf die Starttemperatur oder um einen Heizschritt dient die Warten-Phase zur Equilibrierung der Probe und der Meßzelle mit der Umgebung. Darauf wird in der Suchen-Phase vom Prozessor geprüft, ob die Probe schon eine Selbstaufheizung zeigt. Dazu wird die Temperaturänderung der Meßzelle mit einer vorgegebenen Anstiegsempfindlichkeit verglichen. Ist die Temperaturerhöhung pro Zeit über einen durch Parameter bestimmten Zeitraum größer als diese Schwelle, schaltet das Gerät in die Exotherm-Phase, und die Heizungen werden der nun beginnenden Selbstaufheizung der Probe nachgeführt. Wird während der Suchen-Phase der Schwellenwert nicht überschritten, wird die Probe um den Heizschritt aufgeheizt, worauf wieder die Warten- und Suchen-Phasen folgen. Dies wird solange wiederholt, bis eine Exotherme gefunden oder eine vorgegebene Endtemperatur erreicht wird.

2.2 Berücksichtigung der inerten Massen

Die Probe heizt während der exothermen Zersetzung auch die Meßzelle mit auf. Dadurch wird die Selbstaufheizrate gegenüber einer Messung ohne Meßzelle verkleinert durch die sog. thermisch inerte Masse der Meßzelle und sonstiger inerter Massen. Zur Aufstellung einer Wärmebilanzgleichung wird die Temperaturerhöhung des gesamten Meßzellen-Proben-Systems mit ΔT_{MS} und die der Probe allein mit ΔT bezeichnet. Als spezifische Wärmen werden die bei konstantem Druck verwendet, da das Volumen der Probe eigentlich nicht konstant gehalten wird, was besonders für Feststoffe und Flüssigkeiten gilt. Der Druck ist zwar auch nicht konstant, jedoch sind die Änderungen klein, meist nur wenige bar. Bei reinen Gasreaktionen wäre C_v zu verwenden. Die Bilanzgleichung mit Berücksichtigung der Temperaturabhängigkeit der spezifischen Wärme und der Zersetzung der Probe lautet:

$$(1) \qquad \left(\sum_i m_i(R)\cdot C_i(T)\right)\cdot \Delta T = \left(\sum_i m_i(R)\cdot C_i(T) + m_M \cdot C_M(T) + \sum_j m_j \cdot C_j(T)\right)\cdot \Delta T_{MS}$$

R ist die Reaktionskoordinate (oder der Reaktionsumsatz), über die die Probenmasse m_S und die Massen der Reaktionsprodukte m_i bestimmt werden. Für R = 0 steht in der Summe des linken Ausdrucks der Gl.(1) nur '$m_S \cdot C_S(T)$'. Die Größen mit Index M gelten für die Meßzelle, der Summenausdruck über j erfaßt weitere thermisch inerte Massen. Wenn nur die sich zersetzende Probenmasse auf der linken Seite beachtet wird, steht dort '$m_S(R)\cdot C_S(T)\cdot \Delta T$.

Beim ARC-Versuch ohne Proben- und Zersetzungsproduktanalytik ist der Reaktionsablauf gemäß R unbekannt. Für den linken Ausdruck der Gl.(1) verwendet man daher nur die Probenmasse m_S und eine mittlere spezifische Wärme C_S, wobei auch deren Temperaturabhängigkeit unberücksichtigt bleibt, da ΔT_{MS} in der Regel zwischen 30°C und 70°C liegt. Die vereinfachte Form der Gl.(1) ist die Gl.(2).

$$(2) \qquad m_S \cdot C_S \cdot \Delta T = \left(m_S \cdot C_S + m_M \cdot C_M + \sum m_j \cdot C_j\right)\cdot \Delta T_{MS} \qquad \text{oder umgeschrieben}$$

$$(3) \qquad \Delta T = \phi \cdot \Delta T_{MS} \qquad \text{mit}$$

(4) $$\phi = 1 + \frac{m_M C_M + \sum m_j C_j}{m_S C_S}$$

Die Größe ϕ von Gl.(3) und Gl.(4) wird die thermische Inertheit des Systems Probe-Meßzelle genannt. ϕ wird als Korrekturgröße verwendet, wodurch der Einfluß der inerten Massen näherungsweise eliminiert werden kann /1/. Die exakte Korrektur ist nach Gl.(1) möglich. C_S ist für organische Substanzen im Mittel 2,092 J/g/K.

3. Auswertung und Skalierung adiabatischer Selbstaufheizkurven

3.1 Typen von adiabatischen Selbstaufheizkurven

Die Abb. 3 zeigt typische adiabatische Selbstaufheizkurven für verschiedene Reaktionen. Die zu ihrer Berechnung verwendeten Arrhenius-Parameter sind in der Abb. 3 angegeben. Die Anfangstemperatur T_0 ist 150°C und die Endtemperatur T_f = 250°C. Die Kurven wurden für ϕ = 1 berechnet, also für eine hypothetische Messung ohne Meßzelle oder für eine Messung mit vernachlässigbarem Einfluß der Meßzelle. Die Selbstaufheizraten h(T) sind in den Achsen als lg(h[°C/min]) gegen 1/T [1/K] aufgetragen, auf der Abszisse als °C-Werte zugeordnet. Bei einer Reaktion 0. Ordnung erhält man bei dieser Auftragung eine Gerade, welche wegen des Substanzverbrauchs bei T_f endet. Für die Reaktionen 1., 2. und 3. Ordnung durchlaufen die Kurven ein Maximum und fallen bei Erreichen von T_f auf null zurück. Mit zunehmender Reaktionsordnung n wird der Maximumsbereich breiter. Die Kurven mit $n \neq 0$ liegen bei diesen Bedingungen unter der Kurve mit n = 0. Anhand der Kurvenverläufe wird deutlich, daß die Reaktionsordnungen mit guter Genauigkeit bestimmbar sind. In der Abb. 3 ist auch der Verlauf von h für eine autokatalytische Reaktion nach Gl.(5) und Gl.(6) dargestellt, mit den $\Delta H_{R,i}$ als Reaktionsenthalpien.

(5) $$A \xrightarrow{k_{A1}} B + Z \qquad \Delta H_{R,1}$$

$$A + B \xrightarrow{k_{A2}} 2\,B + Z \qquad \Delta H_{R,2}$$

(6) $$\frac{dA(t,T)}{dt} = -k_{A1}(T) \cdot A(t,T) - k_{A2}(T) \cdot A(t,T) \cdot B(t,T)$$

Die primäre Zersetzung von A ist die Bildungsreaktion des autokatalytisch wirksamen Produkts B als Reaktion 1. Ordnung mit den Arrhenius-Parametern wie für die anderen Kurven in Abb. 3. Die zweite Zersetzungsreaktion ist die autokatalytische Reaktion. Deren Reaktionsgeschwindigkeitskonstante k_{A2} hat die in Klammern angegebenen Arrhenius-Parameter. Autokatalyse bedeutet, daß ein Zersetzungsprodukt B die Zersetzung des Ausgangsstoffs A in einer zweiten Reaktion beschleunigt. B ist im strengen Sinn kein Katalysator, welcher nicht verbraucht wird und die Reaktion zwischen zwei Reaktanten durch Erniedrigen der Aktivierungsenergie und/oder Erhöhen des Vorfaktors beschleunigt, also eine aktivierungsparameterbeschleunigte Reaktion bewirkt. Autokatalyse steht für die reaktive zersetzungsproduktbeschleunigte Zersetzung einer Ausgangssubstanz.

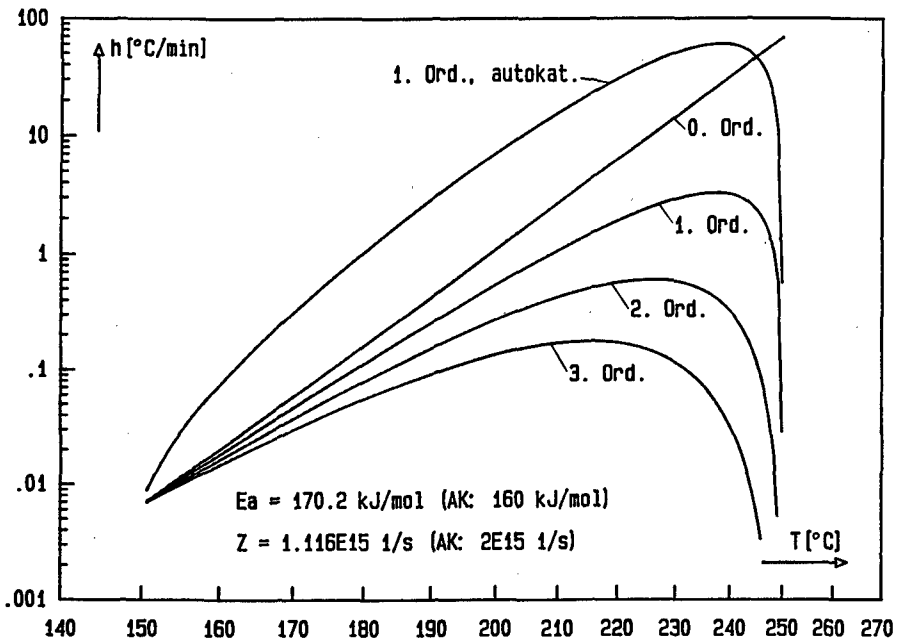

Abb. 3: Selbstaufheizkurven für verschiedene Reaktionsordnungen und bei Autokatalyse.

3.2 Bestimmungen der Arrhenius-Parameter aus der adiabatischen Selbstaufheizung

Zur Bestimmung der Arrhenius-Parameter der Reaktionsgeschwindigkeitskonstanten k(T) der Zersetzung muß diese aus dem Substanzverbrauch als Funktion von Temperatur und Zeit bestimmt werden. Dies wird in der Regel durch Analyse des Substanzverbrauchs mit der Zeit bei verschiedenen Temperaturen durchgeführt. Dies gilt auch bei der adiabatischen Selbstaufheizung. Wenn die Zersetzung nach einer definierten Reaktion abläuft, kann mit einer Bilanzierung von Substanzverbrauch und Temperaturanstieg und mit einem kinetischen Ansatz die Reaktionsgeschwindigkeitskonstante aus der Selbstaufheizrate bestimmt werden. Der Temperaturanstieg entspricht der freigesetzten Reaktionswärme Q_R. Es werden dieselben Approximationen wie zur Formulierung der Gl.(2) verwendet. In Gl.(7) sind die Terme $m_k \cdot C_k$ schon herausgenommen.

$$(7) \qquad \frac{C(t,T)}{C(0)} = \frac{Q_R(T(t_f)) - Q_R(T(t))}{Q_R(T(t_f))} = \frac{T_f - T(t)}{\Delta T} = \frac{T_{fMS} - T_{MS}(t)}{\Delta T_{MS}}$$

C(t,T) Menge (Konzentration, Masse) zur Zeit t bei der Temperatur T = f(t)
C(0) Anfangsmenge bei $T(0) = T_0$
T(t) Temperatur der Probe zur Zeit t bei $\phi = 1$

$T_{MS}(t)$	Temperatur von Probe und Meßzelle zur Zeit t bei $\phi \neq 1$
ΔT	adiabatischer Temperaturanstieg der Probe bei $\phi = 1$ $\Delta T = T_f - T(0)$
ΔT_{MS}	adiabatischer Temperaturanstieg von Probe und Meßzelle bei $\phi \neq 1$ $\Delta T_{MS} = T_{fMS} - T_{MS}(0)$
T_f	erreichte Endtemperatur der Probe bei $\phi = 1$
T_{fMS}	erreichte Endtemperatur von Probe und Meßzelle bei $\phi \neq 1$

Die Kombination mit einem reaktionskinetischen Ansatz mit der Reaktionsordnung n, Gl.(8) bzw. Gl.(9),

$$(8) \qquad \frac{dC(t,T)}{dt} = -k(T)\cdot C^n(t,T)$$

$$(9) \qquad \frac{dC_r(t,T)}{dt} = -k_r(T)\cdot C_r^n(t,T)$$

mit $C_r(t,T) = C(t,T) / C(0)$ und $k_r(T) = k(T)\cdot C^{n-1}(0)$

und Differenzieren von Gl.(7), woraus Gl.(10) folgt,

$$\frac{dC(t,T)}{dt} = -\frac{C(0)}{\Delta T}\cdot\frac{dT(t)}{dt} = -\frac{C(0)}{\Delta T}\cdot h(T(t)) \quad = -\frac{C(0)}{\Delta T_{MS}}\cdot h(T_{MS}(t))$$

(10)

$$\frac{dC_r(t,T)}{dt} = -\frac{1}{\Delta T}\cdot h(T(t)) \quad = -\frac{1}{\Delta T_{MS}}\cdot h(T_{MS}(t))$$

ergibt für die Selbstaufheizrate dT/dt = h(T) die Gl.(11).

$$h(T(t)) = k_r(T)\cdot\Delta T\cdot\left(\frac{T_f - T(t)}{\Delta T}\right)^n \qquad \text{für } \phi = 1$$

(11)

$$h(T_{MS}(t)) = k_r(T)\cdot\Delta T_{MS}\cdot\left(\frac{T_{fMS} - T_{MS}(t)}{\Delta T_{MS}}\right)^n \quad \text{für } \phi \neq 1$$

Mit Gl.(11-1) wurden die Kurven der Abb. 3 mit n = 1, 2, 3 berechnet. Gl.(11-1) wird zu den folgenden Gleichungen für die

- Reaktion 0. Ordnung

$$(12) \qquad h(T(t)) = k_r(T)\cdot\Delta T = \frac{k_0(T)}{C(0)}\cdot\Delta T$$

- Reaktion 1. Ordnung

$$(13) \qquad h(T(t)) = k_r(T)\cdot(T_f - T(t)) = k_1(T)\cdot(T_f - T(t))$$

- Reaktion 2. Ordnung

$$(14)\quad h(T(t)) = k_r(T)\cdot\frac{(T_f - T(t))^2}{\Delta T} = k_2(T)\cdot\frac{C(0)}{\Delta T}\cdot(T_f - T(t))^2$$

Bei einer Reaktion 1. Ordnung ist h(T) explizit unabhängig von C(0), implizit abhängig jedoch über T_f, da T_f mit zunehmender Menge größer wird. Zur Berechnung der autokatalytischen Selbstaufheizung in Abb. 3 wurde folgender reaktionskinetischer Ansatz verwendet, Gl.(15).

$$(15)\quad \frac{dC_r(t,T)}{dt} = -k_1(T)C_r(t,T) - k_2(T)C_r(t,T)(1 - C_r(t,T))$$

Aus Gl.(15) wird mit Gl.(10) die Gl.(16) erhalten, mit der die autokatalytische Selbstaufheizkurve in Abb. 3 berechnet wurde.

$$(16)\quad h(T(t)) = k_1(T)(T_f - T(t)) + k_2(T)(T_f - T(t))\cdot\left(1 - \frac{T_f - T(t)}{\Delta T}\right)$$

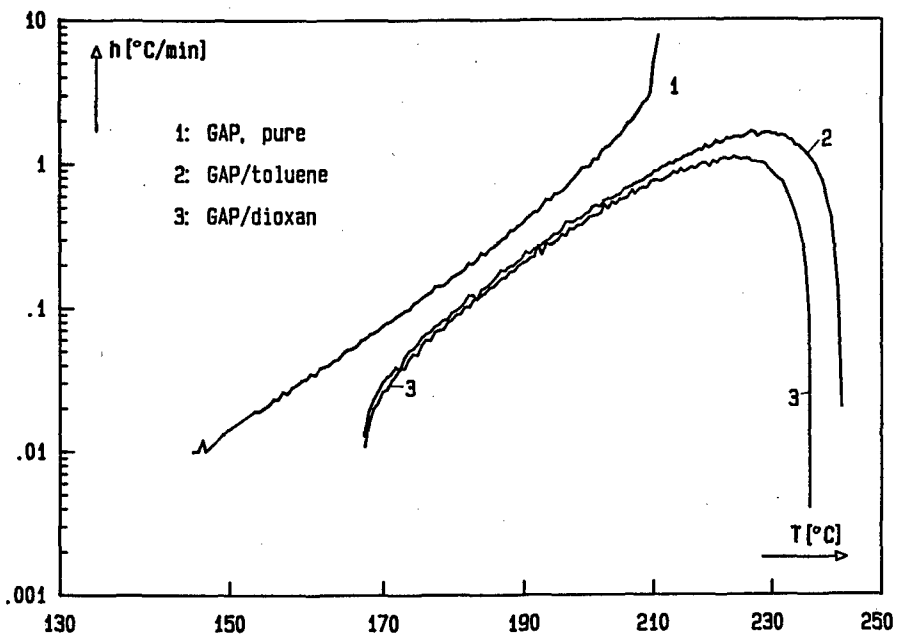

Abb. 4: Selbstaufheizraten von reinem GAP und GAP gelöst in Toluol und Dioxan, jeweils mit 10 Mass.-% GAP /2/.

3.3 Skalierung der Selbstaufheizkurven zu $\phi = 1$

Die Skalierung der Selbstaufheizkurven wird am Beispiel der adiabatischen Selbstaufheizung des reinen ungehärteten GAP (ICT, Charge 1 in Tabelle 2) und der Lösung von GAP in Dioxan gezeigt /2/. Es ist möglich, die Lösungskurven so zu skalieren, daß sie die gemessene Selbstaufheizung des reinen GAP wiedergeben. Somit ist es auch möglich auf $\phi = 1$ zu skalieren, was bedeutet, daß keine thermisch inerte Masse mit aufgeheizt wird und damit die adiabatische Selbstaufheizung der reinen Substanz mit der Messung in Lösung simuliert wird. In der Abb. 4 sind die Selbstaufheizraten für reines GAP und GAP gelöst in Toluol und in Dioxan (jeweils 10 Mass.-% an GAP) angegeben. Die Kurven der Lösungen haben eine definierte Endtemperatur T_{fMS}. Reines GAP hat einen Übergang zur Deflagration, wie auch andere Explosivstoffe /2/. Der vorherrschende, geschwindigkeitsbestimmende erste Reaktionsschritt der GAP-Zersetzung ist die Abspaltung des molekularen Stickstoffs aus der Azidogruppe $C\text{-}\underline{\overset{-}{N}}\text{-}\overset{+}{N}\equiv N$!, wie die Bindungsenergie /3/, die massenspektrometrische Untersuchung der Stickstoffzunahme /4/ und thermoanalytische Untersuchungen /5/ zeigen. Die nachfolgenden Stabilisierungsreaktionen des dadurch entstehenden Nitrens laufen wegen dessen hoher Reaktivität sehr schnell ab. Die Aktivierungsenergie der Azido- bzw. GAP-Zersetzung sollte daher etwa den Wert der Bindungsenergie der $RN\text{-}N_2$-Bindung haben, welche in /3/ mit 163,2 kJ/mol angegeben wird.

Tabelle 1: Arrhenius-Parameter für die GAP-Zersetzung, bestimmt mit verschiedenen Methoden.

Methode	Zitat	m_S [mg]	T_0 [°C]	Temp.bereich [°C]	Ea [kJ/mol]	Z [1/s]	lg(Z[1/s])
N_2-Entwicklung, Massenspektrometrie	/4/	~ 25	~ 120	140-170	176,6	k.A.	k.A.
DTA-Messungen (Heizrate-Peaktemp.)	/5/	(~ 2, k.A.)	~ 190	220-260	174,0	k.A.	k.A.
Isotherme TG	/8/	1,5-2,5	~ 170	180-205	164,9	$1{,}26 \cdot 10^{14}$	14,1
Nichtisotherme TG	/8/	1,5-2,5	~ 170	180-220	164,9	$6{,}31 \cdot 10^{13}$	13,8
Massenverlust/ FTIR	/8/	0,2-0,8	~ 240	240-260	177,0	$1 \cdot 10^{19}$	19,0
NH_3-Entw./FTIR	/9/	k.A.	~ 165	165-260	170,7	$3{,}548 \cdot 10^{15}$	15,55
Isotherme TG	/10/	~ 1	~ 170	170-240	135,7	$8{,}78 \cdot 10^{13}$	13,9
ARC, GAP/Toluol	/2/	592	167	175-230	168,9	$7{,}814 \cdot 10^{14}$	14,89
ARC, GAP/Dioxan	/2/	612	167	175-230	170,2	$1{,}116 \cdot 10^{15}$	15,05
$CH_3\text{-}N_3$ (Gas)	/6/	~ 120	(155)	155-200	170,7	$2{,}850 \cdot 10^{14}$	14,455
$C_2H_5\text{-}N_3$ (Gas)	/7/	~ 40 - 280	(187)	187-230	167,8	$3{,}300 \cdot 10^{14}$	14,519

k.A.: keine Angaben im Zitat

Die gefundenen Aktivierungsenergien stimmen gut mit der Bindungsenergie der RN-N_2-Bindung und den in der Literatur gefundenen Werten, aufgelistet in Tabelle 1, überein. Die für die Zersetzung der Azidogruppe in den gasförmigen Aziden Methylazid und Ethylazid /6,7/ aus Untersuchungen ihres unimolekularen Zerfalls angegebenen Arrhenius-Parametern geben die Aktivierungsenergie des geschwindigkeitsbestimmenden Reaktionsschritts wieder.

Abb. 5 zeigt die gemessene Selbstaufheizrate der GAP-Dioxan-Lösung (10 Mass.-% GAP in 90 Mass.-% Dioxan) mit einem ϕ-Faktor für die Lösung von 1,25. Miteingezeichnet ist die nach Gl.(11) mit n = 1 (entsprechend Gl.(13)) berechnete Selbstaufheizkurve h(T). Die Übereinstimmung mit den Meßdaten ist ab dem Auswertebeginn bei 175°C sehr gut. Die berechnete Kurve ist bis 140°C extrapoliert. Konzentriertere Lösungen haben niedrigere Anfangstemperaturen T_0. Mit Gl.(11) kann h(T) auch für andere ϕ-Faktoren berechnet werden. Für die Faktoren ϕ_1 und ϕ_2 wird die Gl.(11) jeweils für das gesamte Meßsystem als Gl.(17) und Gl.(18) formuliert. Der Index MS wurde weggelassen. Das nichtindizierte T(t) ist laufende Variable.

$$(17)\quad h_1(T(t)) = k_r(T(t)) \cdot \Delta T_1 \cdot \left(\frac{T_{f1} - T_1(t)}{\Delta T_1}\right)^n$$

$$(18)\quad h_2(T(t)) = k_r(T(t)) \cdot \Delta T_2 \cdot \left(\frac{T_{f2} - T_2(t)}{\Delta T_2}\right)^n$$

Nach Gl. (3) gilt:

$$\Delta T = \phi_1 \cdot \Delta T_1 = \phi_2 \cdot \Delta T_2$$

$$(19)\quad \phi_1 \cdot (T_{f1} - T_1(0)) = \phi_2 \cdot \Delta T_2$$

$$T_{f1} = \frac{\phi_2}{\phi_1} \Delta T_2 + T_1(0)$$

Aus der gemessenen $h_2(T)$-Kurve kann damit $h_1(T)$ berechnet werden, Gl. (20).

$$(20)\quad h_1(T(t)) = k_r(T(t)) \frac{\phi_2}{\phi_1} \Delta T_2 \left(\frac{\frac{\phi_2}{\phi_1}\Delta T_2 + T_1(0) - T_1(t)}{\frac{\phi_2}{\phi_1}\Delta T_2}\right)^n \qquad \text{mit } T_1(t) \cong T(t)$$

Mit Gl.(20) wurden die in der Abb. 5 gezeigten 'theoretischen' Selbstaufheizkurven der Lösungen mit $\phi = 1$ und $\phi = 2$ berechnet. Die Zunahme des ϕ-Faktors von 1,25 auf 2 erniedrigt die h(T)-Werte sehr deutlich.

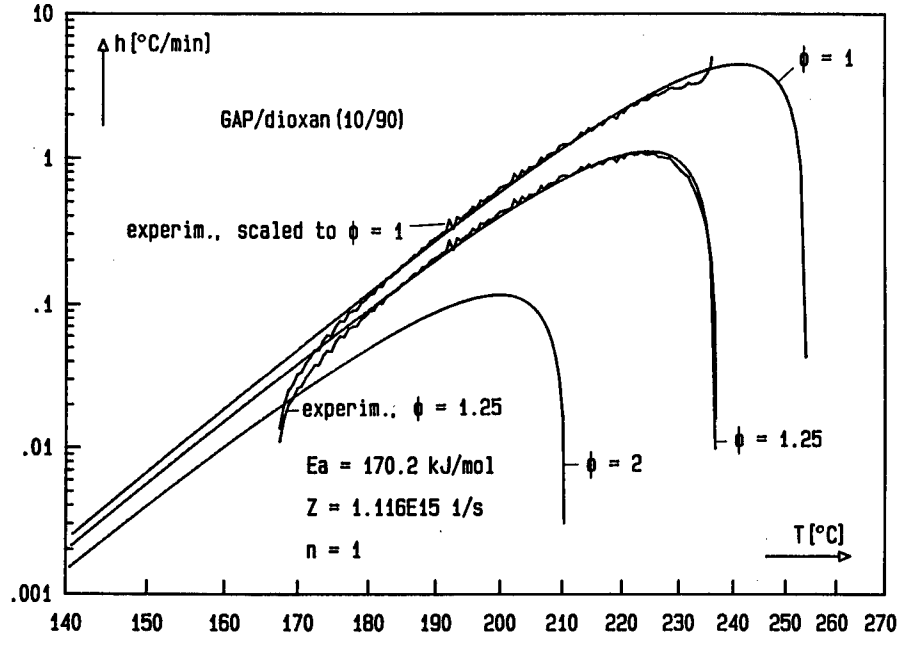

Abb. 5: Skalierung der Selbstaufheizrate der GAP/Dioxan-Lösung auf $\phi = 1$ und $\phi = 2$. Die glatten Kurven sind berechnet, die mit Rauschen sind die Meßkurve mit $\phi = 1{,}25$ und die skalierte Meßkurve mit $\phi = 1$.

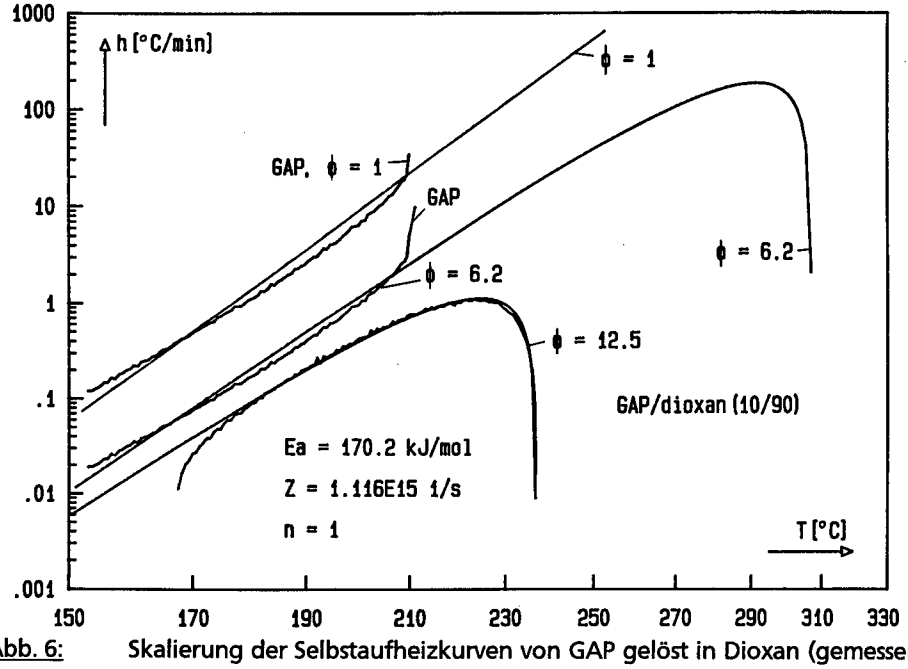

Abb. 6: Skalierung der Selbstaufheizkurven von GAP gelöst in Dioxan (gemessen mit $\phi = 12{,}5$ bezogen auf GAP-Anteil) auf $\phi = 6{,}2$ und $\phi = 1$, beides glatte Kurven, und von reinem GAP gemessen mit $\phi = 6{,}2$ und skaliert auf $\phi = 1$.

Die experimentellen Werte sind auch auf $\phi = 1$ skalierbar. Die entsprechende Formel erhält man durch Division von Gl.(17) mit Gl.(18) und Einsetzen der Ausdrücke von Gl.(19), was Gl.(21) ergibt.

$$\frac{h_1(T(t))}{h_2(T(t))} = \frac{\phi_2}{\phi_1}\left(\frac{\frac{\phi_2}{\phi_1}\Delta T_2 + T_1(0) - T_1(t)}{T_{f2} - T_2(t)} \cdot \frac{1}{\frac{\phi_2}{\phi_1}}\right)^n \qquad (21)$$

mit folgenden Gleichsetzungen: $T_1(t) = T_2(t) \cong T(t)$ und $T_1(0) = T_2(0)$, Größen mit Index 2 für die vorgegebene Messung

Die experimentellen Daten $h_2(T)$ werden nach Gl.(21) zu $h_1(T)$ mit $\phi_1 = 1$ skaliert. Die skalierten experimentellen Daten liegen auf der nach Gl.(20) berechneten h(T)-Kurve für $\phi_1 = 1$. Zu Abweichungen kommt es, wenn T(t) größer als T_M wird, die Temperatur des Maximums der gemessenen Selbstaufheizkurve $h_2(T)$, da dann $h_2(T)$ sehr schnell gegen null geht. Nicht vorhandene Meßdaten sind selbstverständlich nicht rekonstruierbar, so daß die skalierte experimentelle Kurve unvollständig erscheint. Die Selbstaufheizkurve von reinem GAP, Abb. 4, hat im mittleren Teil etwa die gleiche Steigung wie die Kurven der GAP-Lösungen, was auf eine ähnliche Aktivierungsenergie für die Zersetzung des reinen GAP schließen läßt. Der ϕ-Faktor der GAP-Lösungen ist 12,5 bezogen auf die Einwaage an GAP. Das reine GAP deflagriert bei den vorliegenden Meßbedingungen im Gegensatz zu den GAP-Lösungen. In der Abb. 6 sind die h(T)-Kurven berechnet nach Gl.(20) mit $\phi = 12{,}5$, $\phi = 6{,}2$ und $\phi = 1$ für GAP/Dioxan zu sehen. Der Kurve mit $\phi = 1$ entspricht einer 'Lösung mit 100% GAP', also reinem GAP, ohne thermisch inerte Masse. Die Formulierung 'Lösung mit 100% GAP' weist darauf hin, daß die Zersetzung formal wie in der Lösung abläuft, also ohne Deflagration. Die experimentellen Daten der GAP/Dioxan-Lösung werden wie in Abb. 5 sehr gut durch Gl.(20) wiedergegeben. Der ϕ-Faktor der Messung an reinem GAP ist 6,2. Diese Meßdaten liegen noch gut auf der h(T)-Kurve mit $\phi = 6{,}2$. Die auf $\phi = 1$ skalierten Meßdaten des reinen GAP werden gleich gut mit der h(T)-Kurve 'Lösung mit 100% GAP' mit $\phi = 1$ beschrieben. Die Messungen an reinem GAP und die Messungen der GAP-Lösungen sind durch die ϕ-Skalierung in guter Übereinstimmung.

4. Untersuchte Substanzen

Von folgenden Weichmachern und Bindern wurde die adiabatische Selbstaufheizung gemessen:

58,8 / 41,2 in Mass.-% N-Methyl- / N-Ethyl-NENA (Me/Et-NENA), von ICI
DANPE, 1,5-di-azido-3-nitrazapentan, von USA
GAPA, kurzkettiges GAP mit N_3-Endgruppen statt OH-Endgruppen, von USA
A17, EGBAA, Ethylenglykol-bis-(α-azidoacetat), von ICT
Octylazid, von ICT, nur Modellsubstanz, nicht für den Einsatz vorgesehen
GAP-AA-2000, GAP mit α-Azidoessigsäure veresterten OH-Endgruppen, von ICT
GAP-AA-500, wie GAP-AA-2000, jedoch kurzkettig, von ICT

PolyGlyn, (PG), Poly-Glycidylnitrat, von ICI
GAP, Poly-Glycidylazid, von SNPE
GAP, Poly-Glycidylazid, von ICT

Die Substanzen wurden in Lösungen in Toluol p.A. mit 10 Mass.-% Gehalt untersucht. Dies erlaubt die Bestimmung der Zersetzungsparameter der Gesamtreaktion, wie es oben an den Messungen mit GAP gezeigt wurde.

5. Ergebnisse und Diskussion

In der Abb. 7 sind die gemessenen adiabatischen Selbstaufheizungen der untersuchten Substanzen im Überblick gezeigt. Wegen der Überschneidungen mit GAP-AA-500, GAP (ICT) und Octylazid sind diese zusammen mit GAP (SNPE) in Abb. 8 zu sehen. Aus den Abbildungen ist der Temperaturbereich der Zersetzung und über die erreichten Maximalwerte der Aufheizraten und deren 'Kurvenbreite' (Temperaturbereich) in anschaulicher Weise die freigesetzte Energie qualitativ entnehmbar. Die Gesamtzersetzungsreaktion konnte bei allen Substanzen mit einer Reaktion 1. Ordnung beschrieben werden. Bei Me/Et-NENA wurde eine deutliche Nachreaktion gefunden. Die anderen Substanzen zeigten keine oder nur geringfügige Nachreaktionen. Die Abb. 9 zeigt die gesamte Selbstaufheizkurve für Me/Et-NENA. Der zweite Reaktionsbereich ist vermutlich die Zersetzung der Nitramingruppe. Hier wurde nur der erste Reaktionsbereich ausgewertet, der der Zersetzung der Salpetersäureestergruppe zuordnbar ist. Die Einwaagen der Lösungen lagen zwischen 5,8g und 6,7g. Zusammen mit den etwas variierenden Meßzellenmassen ergaben sich thermische Inertheiten zwischen 1,21 und 1,27 für die Lösungen sowie zwischen 12,0 und 12,7 für die reinen energetischen Substanzen. Die Meßbedingungen waren somit für alle Substanzen nahezu gleich. Die Anfangstemperaturen der Zersetzung liegen für die Azidoverbindungen zwischen 159°C und 174°C, bei den Salpetersäureesterverbindungen sind sie für Me/Et-NENA 130°C und für PolyGLYN 146°C. Um die restlichen Einflüsse von Einwaage und ϕ-Faktor für eine Beurteilung der Substanzen zu entfernen, werden die Selbstaufheizraten auf $\phi = 1$ bezüglich der reinen Substanz (Tabelle 2) und bei Bezug auf die Lösung neben $\phi = 1$ auch auf die Einwaage an energetischer Substanz normiert. Die Abb. 10 zeigt einige der Substanzen mit ihren Selbstaufheizraten für $\phi = 1$ bezüglich der Lösung. Im wesentlichen bleibt die Reihenfolge erhalten, aber bei Stoffen, die ein ähnliches Selbstaufheizverhalten haben, kann eine Umkehr erfolgen, wie bei GAPA im Vergleich zu GAP-AA-2000 zu erkennen ist. Die wichtigsten experimentellen Daten der Messungen sind in der Tabelle 2 zu finden, zusammen mit den Arrhenius-Parametern für eine Gesamtzersetzungsreaktion 1. Ordnung und einigen weiteren Daten der Selbstaufheizung für $\phi = 1$ bezüglich der reinen Substanzen, wie die Temperaturen für vorgegebene Selbstaufheizraten h. T_0 und h_0 sind die Anfangswerte der adiabatischen Selbstaufheizung, T_M und h_M die Daten des Maximums und T_f die Endtemperatur. Die Aktivierungsenergien liegen für die Azidoverbindungen zwischen 157 kJ/mol und 169,4 kJ/mol. Me/Et-NENA und PolyGLYN haben eine Aktivierungsenergie von 165,1 kJ/mol und 166,8 kJ/mol. Die Werte liegen in den Bereichen der Bindungsenergien der Bindung CN-NN (163 bis 170 kJ/mol) der Azidogruppe und der Bindung CO-NO_2 (160 bis 170 kJ/mol) der Salpetersäureestergruppe. GAP-AA-500 und Octylazid zeigen etwas niedrigere Aktivierungsenergien. Bei Octylazid könnte dies mit den relativ kleinen gemessenen Selbstaufheizraten zusammenhängen.

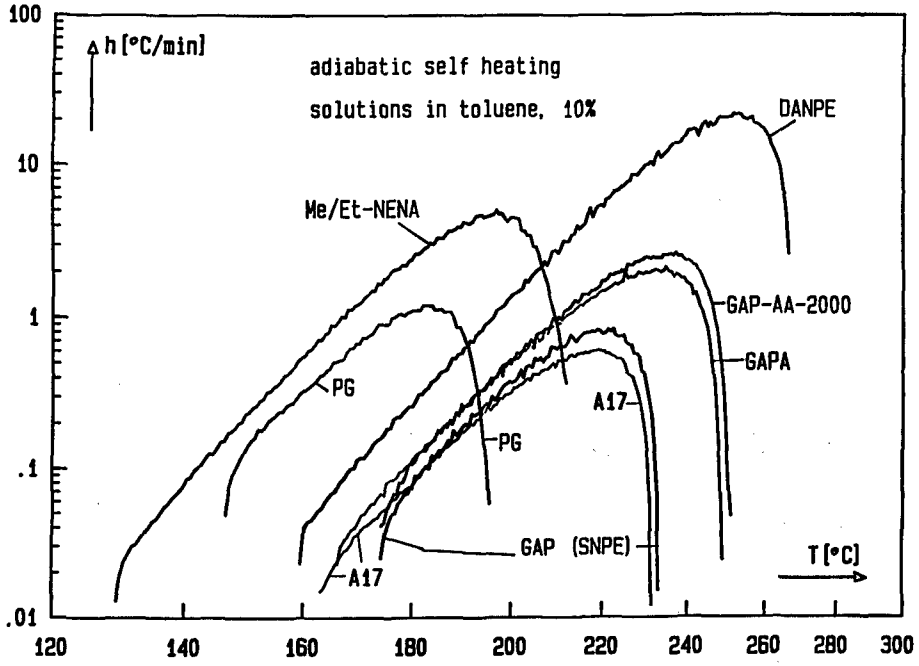

Abb. 7: Adiabatische Selbstaufheizung von Weichmachern und Bindern, gemessen in Toluollösungen mit 10 Mass.-% Gehalt, Teil 1.

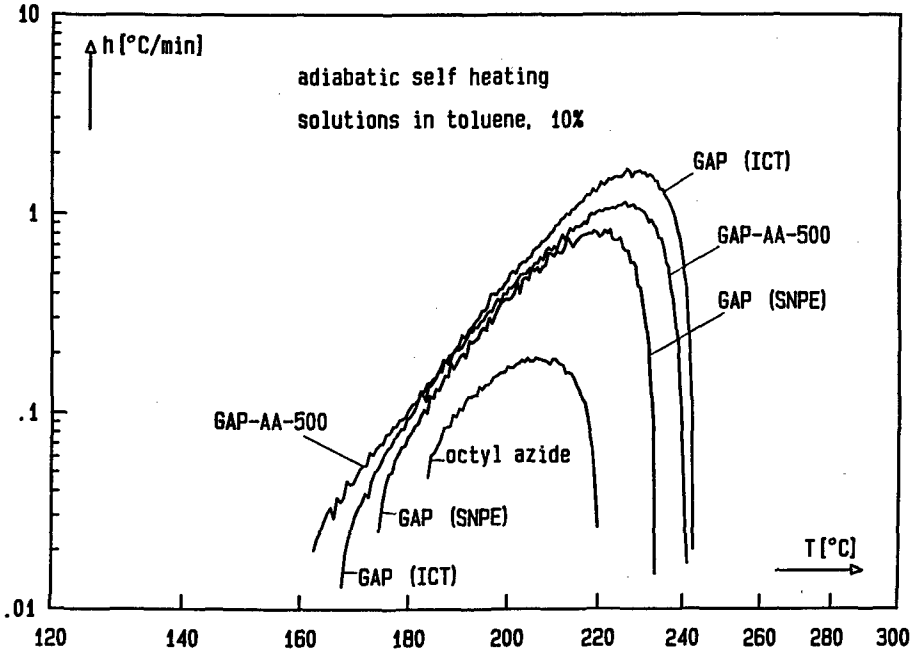

Abb. 8: Adiabatische Selbstaufheizung von Weichmachern und Bindern, gemessen in Toluollösungen mit 10 Mass.-% Gehalt, Teil 2.

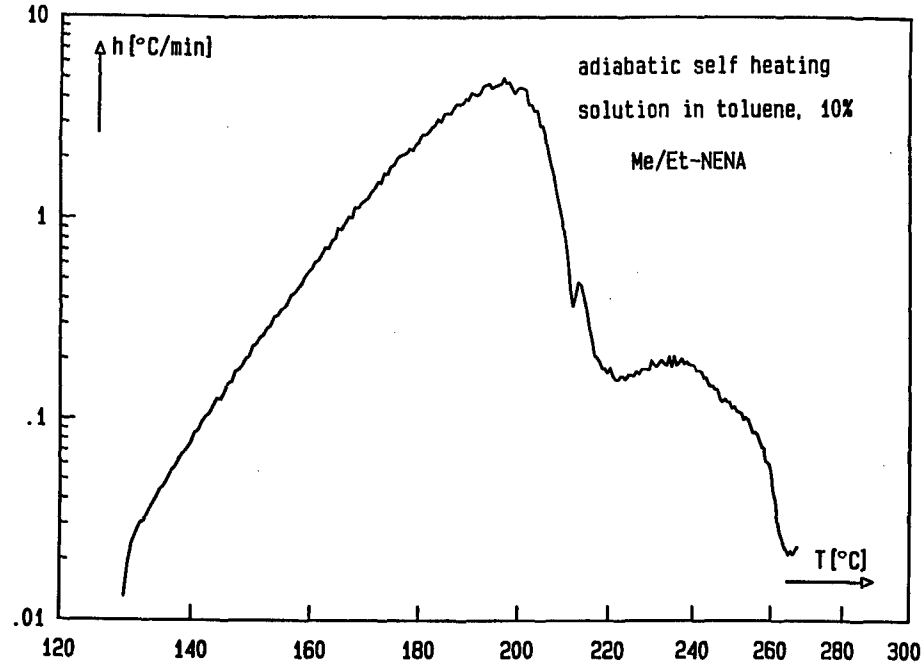

Abb. 9: Gesamte adiabatische Selbstaufheizung von Me/Et-NENA, gemessen in Toluollösung mit 10 Mass.-% Gehalt.

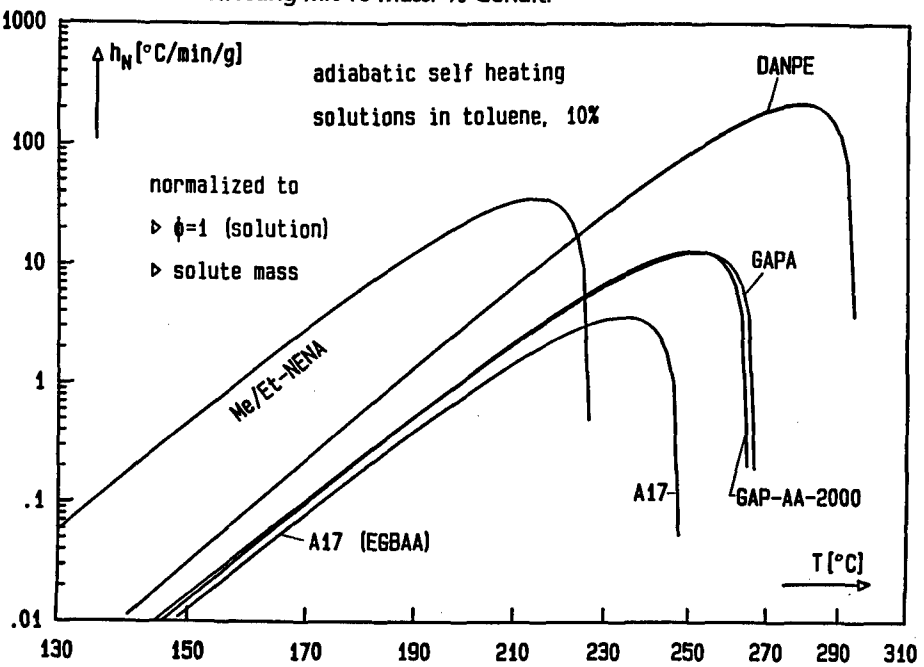

Abb. 10: Berechnete adiabatische Selbstaufheizungen einiger Verbindungen für $\phi = 1$ der Lösung, normiert auf die Einwaage an energetischer Substanz.

Tabelle 2: Charakteristische Daten der adiabatischen Selbstaufheizung von Weichmachern und Bindern aus Messungen an Lösungen in Toluol und Daten für zu $\phi = 1$ skalierte Kurven der reinen energetischen Substanzen (nicht Lösungen).

	GAP Charge 1 ICT	GAP Charge 2 ICT	GAP SNPE	EGBAA (A17) ICT	GAP-AA-2000 ICT	GAP-AA-500 ICT	Octyl-azid ICT	Me/Et-NENA ICI	PolyGlyn ICI	DANPE USA	GAPA USA
Einwaage Lösung [g]	5,920	6,744	5,883	6,005	6,001	6,002	6,003	6,006	5,988	6,143	6,215
Subs.ew. [g]	0,592	0,681	0,591	0,595	0,612	0,597	0,600	0,596	0,596	0,613	0,615
ϕ -Lösung	1,25	1,24	1,27	1,26	1,22	1,27	1,22	1,21	1,21	1,27	1,26
ϕ -Substanz	12,5	12,3	12,6	12,7	12,0	12,7	12,2	12,2	12,2	12,7	12,7
T_0 [°C]	167,4	169,9	174,3	161,4	174,1	162,3	177,6	129,6	146,7	159,0	166,3
h_0 [°C/min]	0,013	0,017	0,025	0,013	0,041	0,020	0,026	0,013	0,049	0,028	0,023
T_M [°C]	229,3	227,6	218,7	218,4	237,1	225,9	205,9	196,9	183,4	251,4	234,7
h_M [°C/min]	1,63	1,55	0,82	0,598	2,62	1,14	0,188	5,00	1,19	21,50	2,12
T_f [°C]	242,5	242,6	233,1	231,5	253,4	243,1	219,7	211,8	205,5	266,4	249,1
	Arrhenius-Parameter und Reaktionswärme Q_R berechnet aus den Selbstaufheizkurven										
Ea [kJ/mol]	168,9	167,7	169,4	162,2	162,4	154,6	157,0	165,1	166,8	167,3	157,9
Z [1/sec]	7,814E14	6,106E14	9,005E14	1,340E14	1,482E14	1,926E13	2,899E13	1,449E16	2,042E16	9,903E14	4,534E13
Q_R [J/g]	1995	1884	1573	1861	2000	2117	1074	2048*)	1290	2822	2204
	Temp. in °C bei der Selbstaufheizrate h, berechnet mit den Arrhenius-Parametern für $\phi = 1$ bez. auf die reine Subs.										
25 µW/g	114,3	113,6	115,7	112,5	111,7	107,6	116,0	85,0	89,6	106,1	115,7
50 µW/g	119,5	118,9	121,0	117,9	117,0	113,1	121,7	89,6	94,3	111,1	121,0
h=0,02	140,8	140,2	142,4	139,9	138,9	135,7	145,2	108,0	113,1	131,6	142,4
h=0,05	148,7	148,2	150,4	148,1	147,1	144,2	154,0	114,9	120,1	139,2	150,4
h=0,10	155,0	154,5	156,7	154,6	153,5	150,8	161,0	120,3	125,6	145,2	156,7
h=0,50	170,2	169,8	172,0	170,5	169,3	167,1	178,1	133,3	139,0	159,8	172,0
h=1,00	177,1	176,7	178,9	177,7	176,4	174,6	185,9	139,2	145,0	166,4	178,9

h in °C/min 25µW/g ≡ 7,2 E-4 °C/min mit C = 2,092 J/K/g *): Me/Et-NENA gesamte Kurve: Q_R = 3517 J/g

Aus den adiabatischen Selbstaufheizkurven ist auch die adiabatische Wärmeentwicklungsrate zu erhalten. Dazu braucht man die Daten der spezifischen Wärmen des Lösungsmittels, des Reaktanten, der Zersetzungsprodukte und der Meßzelle als Funktion der Temperatur. Hinzu kommt die jeweilge Masse der beteiligten Stoffe. Über die Zersetzungsprodukte ist zur Zeit noch nichts bekannt. In erster Näherung werden die spezifischen Wärmen so verwendet wie in Abschnitt 2.2 zur Berechnung des ϕ-Faktors angegeben. Damit werden die Wärmeentwicklungsraten nach Gl.(22) erhalten.

$$(22)\quad \frac{dQ_R(T(t))}{dt} = C_S \cdot m_S \cdot \frac{dT(t)}{dt} + C_{LM} \cdot m_{LM} \cdot \frac{dT(t)}{dt} + C_M \cdot m_M \cdot \frac{dT(t)}{dt}$$

Q_R	freigesetzte Reaktionswärme in Energie, wird unten bezogen auf die Einwaage an energetischer Substanz angegeben, dies ist nicht in Gl.(22) enthalten
C_j	spezifische Wärme der Substanz j in Energie /Masse /Kelvin
m_j	Masse der Substanz j
dT/dt	gemessene Selbstaufheizrate des Systems 'Energiestoff-Lös.mittel-Meßzelle'
Index S:	energetische Substanz
Index LM	Lösungsmittel
Index M	alle zu berücksichtigenden Teile der Meßzelle

Mit der Reaktionsenthalpie $\Delta H_{R,A}$ für die Zersetzung des Stoffes A nach einer Reaktion 1. Ordnung erhält man die Wärmeentwicklungsrate dQ_R/dt nach Gl.(23).

$$(23)\quad \frac{dQ_R(T(t))}{dt} = -\frac{dA(T(t))}{dt} \cdot \Delta H_{R,A} = \Delta H_{R,A} \cdot k_1(T(t)) \cdot A(T(t_0)) \cdot \exp(-k_1(T(t)) \cdot t)$$

In den Abb. 11 und 12 sind mit Gl.(22) berechnete dQ/dT-Kurven für die Weichmacher GAPA und A17 (EGBAA) beispielhaft gezeigt, einmal als Funktion der Temperatur (als 1/T mit T in Kelvin) und einmal als Funktion der Selbstaufheizzeit. In der Zeit-Darstellung wird die unterschiedliche Reaktionsgeschwindigkeit erkennbar. Das A17 reagiert erheblich langsamer als GAPA, da der Temperaturanstieg langsamer ist. Durch Integration der Wärmeentwicklungsrate als Funktion der Zeit erhält man die freigesetzte Reaktionswärme Q_R, welche 2204 J/g für GAPA und 1861 J/g für A17 beträgt. In der Tabelle 2 sind auch die extrapolierten Temperaturen angegeben, bei welchen eine Wärmeentwicklungsrate von 25µW/g und 50µW/g zu messen wäre. Me/Et-NENA und PolyGLYN haben die niedrigsten Temperaturwerte, für 25µW/g sind sie 85°C und 89,6°C. Die Werte der Azidoverbindungen liegen alle deutlich über 100°C, zum Teil über 110°C. DANPE hat mit 106,1°C einen relativ niedrigen Wert, die Werte für GAP liegen um 114°C. Die Abb. 13 zeigt die adiabatische Selbstaufheizrate als Funktion einer normierten Selbstaufheizzeit. Normiert wurde mit dem jeweiligen ϕ-Faktor bezogen auf die energetische Substanz. Die Selbstaufheizraten sind im Zeitbereich von h = 0,05°C/min bis zu ihrem jeweiligen Maximum h_M für einige der untersuchten Substanzen zu sehen.

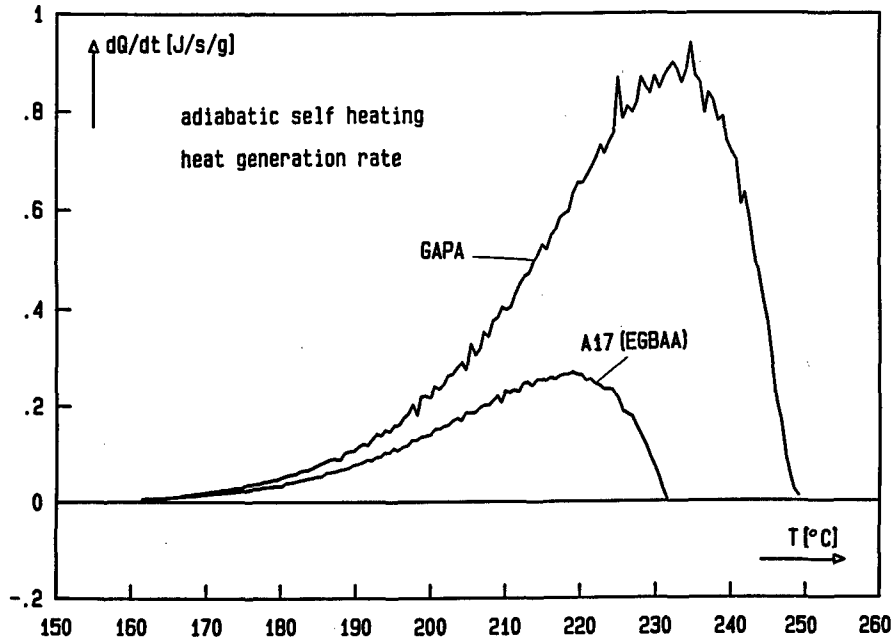

Abb. 11: Adiabatische Wärmeentwicklungsraten als Funktion der Selbstaufheiz-Temperatur der Weichmacher GAPA und A17, berechnet aus den Selbstaufheizraten in den Toluollösungen.

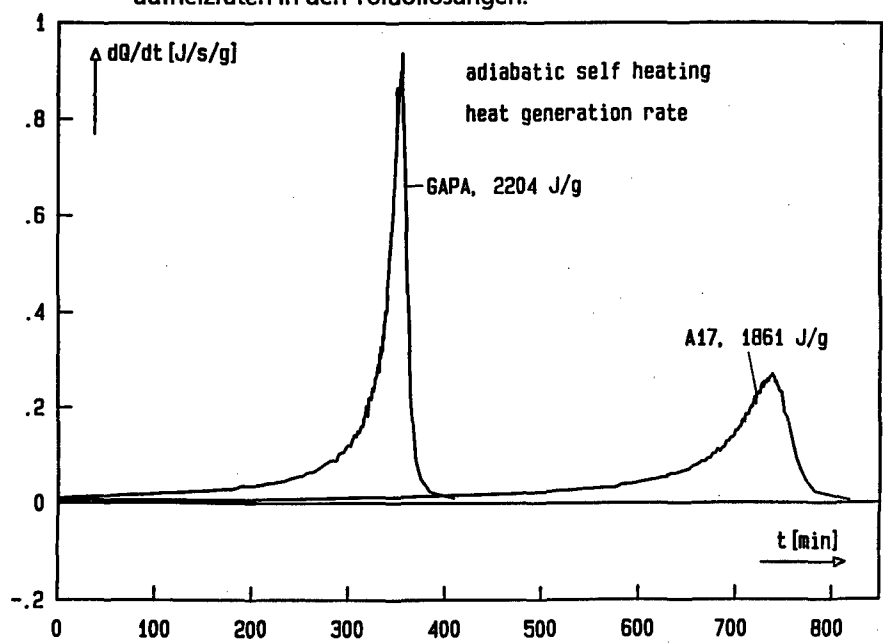

Abb. 12: Adiabatische Wärmeentwicklungsraten als Funktion der Selbstaufheizzeit der Weichmacher GAPA und A17, berechnet aus den Selbstaufheizraten in den Toluollösungen.

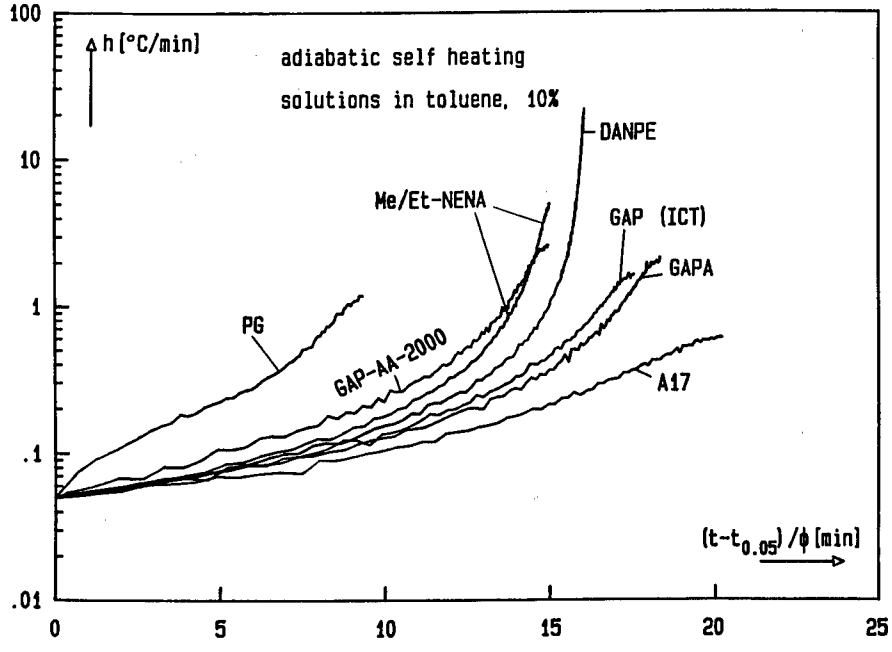

Abb. 13: Adiabatische Selbstaufheizrate als Funktion der mit ϕ bezüglich der energetischen Substanz normierten Selbstaufheizzeit von h = 0,05°C/min bis zum Maximum der Selbstaufheizrate h_M.

6. Zusammenfassung

Von neueren Weichmachern und ungehärteten Bindern mit Azidogruppen, Nitramingruppen und Salpetersäureestergruppen wurden die adiabatischen Selbstaufheizungen in Toluollösungen mit 10 Mass.-% Gehalt an Energiestoff gemessen. Folgende Substanzen wurden untersucht: (1) Mischung (58,8 / 41,2 in Mass.-%) N-Methyl- / N-Ethyl-NENA, (2) DANPE, 1,5-di-azido-3-nitrazapentan, (3) GAPA, kurzkettiges GAP mit N_3-Endgruppen statt OH-Endgruppen, (4) A17, EGBAA, Ethylenglykol-bis-(α-azidoacetat), (5) Octylazid, (nur Modellsubstanz, nicht für den Einsatz vorgesehen), (6) GAP-AA-2000, GAP mit α-Azidoessigsäure veresterten OH-Endgruppen, (7) GAP-AA-500, wie GAP-AA-2000, jedoch kurzkettig, (8) PolyGLYN, Poly-Glycidylnitrat, (9) GAP, Poly-Glycidylazid, erster Hersteller, (10) GAP, Poly-Glycidylazid, zweiter Hersteller.

Mit Einwaagen zwischen 0,59 und 0,67 Gramm an energetischer Substanz wurde eine recht hohe Meßempfindlichkeit erreicht. Da die Messungen am geschlossenen Meßsystem vorgenommen wurden, ist eine Verfälschung durch Verdampfen nicht gegeben. Die Untersuchungen in Lösungen erlauben die kontrollierte Verfolgung der Zersetzungsreaktionen. Die reinen energetischen Substanzen würden deflagrieren. Die Anfangstemperaturen der Zersetzung wurden für die Azidoverbindungen zwischen 159°C und 174°C bestimmt, bei den Salpetersäureesterverbindungen liegen sie für

Me/Et-NENA bei 130°C und für PolyGLYN bei 146°C. Die Meßdaten erlauben eine Einordnung der Substanzen nach dem Zersetzungstemperaturbereich, der Energiefreisetzung und der Energiefreisetzungsrate. Die Arrhenius-Parameter der Gesamtzersetzungsreaktionen und die freigesetzten Reaktionswärmen Q_R wurden aus den Selbstaufheizkurven berechnet. Für alle Substanzen konnte eine Reaktion 1. Ordnung für den Hauptzersetzungsbereich angesetzt werden. Bei Me/Et-NENA wurde eine deutliche Nachreaktion gefunden. Die anderen Substanzen zeigten keine oder nur geringfügige Nachreaktionen. Die Aktivierungsenergien liegen für die Azidoverbindungen zwischen 157 kJ/mol und 169,4 kJ/mol. Me/Et-NENA und PolyGLYN haben eine Aktivierungsenergie von 165,1 kJ/mol und 166,8 kJ/mol. Die Werte liegen in den Bereichen der Bindungsenergien der Bindung CN-NN (163 bis 170 kJ/mol) der Azidogruppe und der Bindung CO-NO_2 (160 bis 170 kJ/mol) der Salpetersäureestergruppe. An einem ausgeführten Beispiel wurde gezeigt, daß die gemessenen Selbstaufheizraten der Lösungen auf die der reinen Substanzen skaliert werden können. Mit solchen skalierten Selbstaufheizungen wurden Temperaturen extrapoliert, bei welchen eine Wärmeentwicklungsrate von 25µW/g und 50µW/g zu erwarten ist. Me/Et-NENA und PolyGLYN haben die niedrigsten Temperaturwerte, für 25µW/g sind sie 85°C und 89,6°C. Die entsprechenden Werte der Azidoverbindungen liegen alle deutlich über 100°C, zum Teil über 110°C. DANPE hat mit 106,1°C einen relativ niedrigen Wert, die Werte für GAP liegen um 114°C.

7. Literatur

/1/ D. I. Townsend, J. C. Tou, Thermochim. Acta 37, 1 (1980).

/2/ M.A. Bohn, F. Volk, Tagungsband der 24. Internat. Jahrestagung des ICT, 1993, Beitrag 8, Fraunhofer-Institut für Chemische Technologie, ICT.

/3/ A. Treinin, Kapitel 1 in „The Chemistry of the Azido Group", Saul Patai (Ed.), Intersciene Publishers, Wiley, 1971.

/4/ M. Farber, S. P. Harris, R. D. Srivastava, Combust. Flame 55, 203 (1984).

/5/ N. Kubota, T. Sonobe, Propell. Expl. Pyrotech. 13, 172 (1988).

/6/ M. S. O'Dell, B. de Darwent, Can. J. Chem. 48, 1140 (1970).

/7/ G. Geiseler, W. König, Z. Phys. Chem. 227, 81 (1964).

/8/ J. K. Chen, T. B. Brill, Combust. Flame 87, 157 (1991).

/9/ H. Krause, A. Pfeil, Tagungsband der 21. Internat. Jahrestagung des ICT, 1990, Beitrag 8, Fraunhofer-Institut für Chemische Technologie, ICT.

/10/ Y. Oyumi, Propell. Expl. Pyrotech. 17, 226 (1992).

PROPELLANT BURNING RATE ENHANCEMENT AND THERMAL BEHAVIOR OF ULTRA-FINE ALUMINUM POWDERS (ALEX)

M. M. Mench, C. L. Yeh, and K. K. Kuo

Department of Mechanical Engineering
The Pennsylvania State University
University Park, PA 16802 USA

ABSTRACT

Alex powder (an ultra-fine aluminum powder produced by the plasma-explosion process) has been shown to be a very effective burning rate enhancer for solid propellants and fuels. The main objective of this study was to examine the effect of replacement of conventional aluminum powder with Alex in a propellant formulation on burning rate and temperature sensitivity. Another objective of this study was to determine if there is a source of stored internal energy in Alex powders that can contribute to the enhancement of propellant burning rates. Two types of aluminized solid propellants (formulation A and B) were tested in this study. Propellant A contains 18% of conventional aluminum particles with average particle diameters of about 30 μm. Propellant B contains 9% of conventional aluminum and 9% of Alex particles with average particle diameters of 0.180 μm. Samples were tested in an optical strand burner at pressures up to 50 MPa and propellant initial temperatures from -32 to 49 °C. The addition of Alex particles to the propellant formulation was shown to substantially enhance the burning rate of aluminized solid propellants. In comparing the temperature sensitivities (σ_p) of the two propellant formulations at the same conditions, it was found that the Alex addition tends to increase the temperature sensitivity of the propellant formulation. A Saint Robert's burning rate law was determined for both propellant formulations at several different initial temperatures. It was found that the pressure exponent of both propellant formulations increases with initial temperature. A DTA was employed to examine the thermal behavior of Alex powders in an inert environment. Two separate batches of Alex powders were tested in helium and argon environments. It was found that there was no exothermic heat release of the Alex powders associated with a release of stored internal energy. It is concluded that the beneficial aspects of Alex addition in terms of enhanced burning rate are

caused by the large specific surface area and small size of Alex particles compared to regular aluminum powders.

INTRODUCTION

Alex powder has been shown to possess unique thermal behavior, which makes it a potential burning-rate enhancer to solid propellants and fuels. Mench et al. [1] have previously shown that Alex particles behave quite differently than conventional aluminum particles. They compared Differential Thermal Analysis (DTA) and Thermogravimetric Analysis (TGA) results of conventional (20 μm average particle diameter) aluminum to Alex particles (average particle diameter 0.183 μm [2]) in air, helium, nitrogen and oxygen environments. According to Mench et al. [1], a rapid weight gain and exotherm of Alex particles in air and nitrogen environment occurred at 548 °C and 700 °C, respectively. The lower temperature reaction in air corresponds to an oxidation reaction. The higher temperature reaction in nitrogen corresponded to an aluminum nitridation reaction. At higher temperatures, the Alex in air also showed weight gain due to a nitridation. In a helium environment, the Alex particle showed no evidence of an exothermic reaction or solid-phase mass changes.

Alex powders was first fabricated by Ivanov of the Institute of Petroleum Chemistry of Russia using a plasma-explosion process. It has been demonstrated by Ivanov and Tepper [3] that propellants containing Alex powders exhibit burning rates 5 to 20 times greater than the same propellant formulations containing regular aluminum powder. It was also found that propellants containing 40% or more regular aluminum powder generally cannot burn successfully. However, propellants containing from 42 to 75 weight percent of Alex were shown to burn at very fast rates. In addition, AP-based propellants containing Alex have been shown to burn cleanly with essentially no residuals, as opposed to a significant amount of condensed-phase particulate and surface residues for AP-based propellants containing conventional aluminum powders.

In the combustion of solid fuels for hybrid rocket applications, Chiaverini et al. [4,5] showed that the mass burning rate of HTPB-based solid fuels can be increased by 70% with a mass addition of 20% Alex powder. For the same weight percentage of conventional aluminum, the increase of mass burning rate is much less than 70%. Also, the recovered burning surface of the sample with Alex powder addition was much smoother than that of the recovered sample with

regular aluminum. It was believed that the Alex powder contributed effectively to the exothermic reaction rate near the fuel surface and thereby enhanced the heat feedback to the unburned solid fuel.

In spite of many benefits associated with the usage of Alex powder described above, the exact mechanisms responsible for its unique burning rate-enhancement behavior have remained unknown. One explanation for the observed combustion behavior of Alex is based upon the fact that the Alex particles are much smaller in diameter than regularly used aluminum particles [1,2]. Ismail and Hawkins [2] used a surface analyzer to construct BET plots from which an average Alex particle diameter of 0.183 μm was determined. This compares to 6 to 100 μm for some typical size of aluminum powders used in propellant formulations. They also determined the Alex particles had an aluminum oxide coating thickness of 0.0019 μm and a specific surface area of around 12.1 m^2/g. The tremendous increase in surface-to-binder contact area was also suggested as a reason for enhanced burning rate phenomena. Ismail and Hawkins [2] found that Alex retains more ambient gas at surface sites than regular aluminum particles; possibly due to the increased specific surface area of the Alex particles.

However, not all of the observed phenomena have been explained on the basis of specific surface area and particle mass. Ivanov and Tepper [3] suggested that the Alex particle contains a certain form of stored internal energy on the order of 400 cal/gram, which can be released in an exothermic reaction at a relatively low threshold temperature. Ivanov has suggested from DTA results a significant exotherm unique to Alex powder in an air environment initiated at a threshold temperature of 450 °C, with the exotherm peaking with partial oxidation at 550 °C.

While most investigations have shown beneficial effects of Alex addition to propellant formulations, few studies have directly compared similar propellant formulations with both Alex and conventional aluminum powders. In addition, it is desired to confirm the conclusion that there is no internal energy released for Alex powder not associated with chemical reaction [1]. These issues are the main focus of this paper.

METHOD OF APPROACH

Burning Rate Measurements in an Optical Strand Burner

A windowed strand burner was used to study the combustion behavior of two types of aluminized solid propellants. A schematic diagram of the strand burner setup is shown in Fig. 1 and detailed descriptions of the testing and operation procedures can be found in Refs. 6 and 7. The strand burner tests were conducted at an initial propellant temperature ranging from -32 to 49 °C and chamber pressures up to around 50 MPa. Two types of aluminized solid propellants (sample A and B) were tested. Propellant A contains 18% of conventional aluminum particles with sizes about 30 μm. Propellant B contains 9% of conventional aluminum and 9% of Alex particles (average particle diameter of 0.18 μm). Cylindrical test strands were prepared to have a length of about 7 cm (2.75 in.) and a diameter of 6.35 mm (0.25 in.). The propellant initial temperature was measured with an embedded fine-wire (bead diameter ~ 25 μm) S or R-type thermocouple.

The steady-state burning rate at each chamber pressure was deduced from the output signal of four breakwires inserted radially within the propellant strand at known separation distances. The time of the nearly instantaneous drop in breakwire voltage was taken as the time of arrival of the burning surface at the known breakwire location. By plotting the regression distance versus breakwire voltage drop times, the steady-state burning rate was determined. In addition to the breakwire data, the burning rate was also deduced from the instantaneous burning surface location of the test sample recorded by a Pulnix CCD camera.

A plot of the natural log of burning rate versus pressure was used to determine the Saint Robert's burning rate law ($r_b = a \cdot P^n$) of the propellants at various initial temperatures. By measuring the burning rate of test propellants at various initial temperatures, the temperature sensitivity (σ_p) of the propellant is determined from the following equation [8],

$$\sigma_p \equiv \left.\frac{\partial \ln r_b}{\partial T_i}\right|_p = \left.\frac{\ln(r_b) - \ln(r_{b,ref})}{T_i - T_{i,ref}}\right|_P \qquad (1)$$

Thermal Analysis

In order to determine if Alex possesses internal energy that can be released at some onset temperature as suggested by Ivanov and Tepper [2], a differential thermal analysis (DTA) of two different batches of Alex powders in argon and helium environments was conducted. The newer batch (stored approximately 6 months at room temperature) was tested in comparison with an older batch (stored approximately 18 months at room temperature) to verify the findings and determine any aging effects. Both batches of Alex were heated in a helium and also an argon environment at a rate of 5 °C/min to a maximum temperature of 1100 °C.

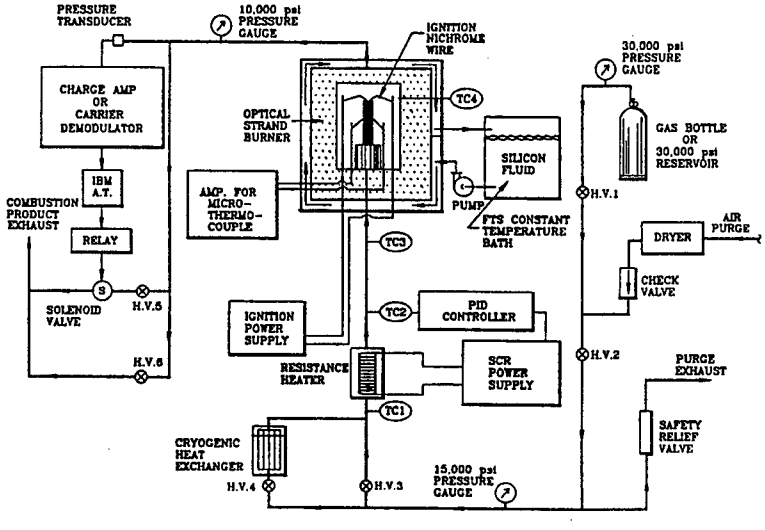

Fig. 1. Schematic diagram of the optical strand burner

RESULTS AND DISCUSSION

Strand Burner Experiments

Figures 2 and 3 show the effect of initial temperature and chamber pressure on the burning rate of propellants A and B, respectively. For each curve shown in Figs. 2 and 3, a pressure exponent (n) and pre-exponential factor (a) for the Saint Robert's law were calculated to describe

the propellant burning rate for a broad range of pressures. The values of a and n for propellants A and B are shown in Tables 1 and 2, respectively. It can be seen that for propellant A, the pressure exponent increases with initial propellant temperature, although the pre-exponential factor remains nearly the same. For propellant B, the pressure exponents are higher than those of A at the same initial temperatures. The same trend of increasing pressure exponent n with increasing initial propellant temperature is seen.

Table 1 Deduced Burning Rate Law Coefficients for Propellant A at Various Initial Propellant Temperatures

Initial Propellant Temp. (°C)	a (cm/s)	n
49	1.995	0.482
25	2.092	0.390
-32	2.125	0.332

Table 2 Deduced Burning Rate Law Coefficients for Propellant B at Two Initial Propellant Temperatures

Initial Propellant Temp. (°C)	a (cm/s)	n
25	2.538	0.618
-32	3.270	0.440

A comparison of the burning rates of propellant A and B at initial temperatures of 25 and -32 °C is shown in Figs. 4 and 5, respectively. The burning rate of propellant B is substantially higher than that of propellant A under the same test condition. This indicates that the addition of

Alex to propellant formulations for partial replacement of conventional aluminum can substantially increase the propellant burning rate over a wide range of propellant initial temperatures and pressures.

The total energy of oxidation released per unit volume of Alex particles is less than that of conventionally used aluminum particles, having a lower volumetric percentage of inert oxide coating [1]. However, the heat release rate of the Alex particles during oxidation is greater than that of regular aluminum particles, resulting in greater heat flux to the metalized propellant samples. It is believed that several effects related to increased heat flux to the unburnt propellant contribute to the enhanced burning rates seen for Alex propellants. First, it is believed that the large surface area of the Alex particle enhances its reactivity with gas-phase species. Secondly, due to small mass of Alex particles, the ignition delay time should be orders of magnitude shorter than those of conventional aluminum particles. Finally, the bulk mass burning rate of the Alex particles is much higher than conventional aluminum particles due to the increased surface area of the Alex particles. These effects result in the Alex particles burning at a high mass consumption rate in locations very close to the burning surface of the propellant. The result is that even though the Alex particle carries a greater volume percentage of inert oxide than conventional aluminum particles, the heat-flux feedback from the burning Alex particles to the unburnt propellant is higher than that of the conventional aluminum particles. This effect contributes to the enhanced burning rate of solid propellants with Alex additives.

The data in Figs. 2 and 3 were used to generate the temperature sensitivity (σ_p) plot shown in Fig. 6. It should be noted that the increasing trend in pressure exponent for both propellants results in a temperature sensitivity that is increasing with propellant initial temperature. This can be illustrated by substituting the Saint Robert's burning rate law into Eq. (1). If the pre-exponential factor is assumed to be constant (which is a more reasonable assumption for propellant A than B), then the functional dependence of the pressure exponent, n, with respect to T_i, is what drives the change in temperature sensitivity with initial propellant temperature. Since n is shown to increase with initial temperature for both propellants, it is expected that the temperature sensitivity will increase with initial temperature. Figure 6 shows the temperature sensitivity of propellant A increases with increasing chamber pressure and initial temperature, as expected. The temperature

sensitivity of the Alex propellant B is greater than that of propellant A at the same initial temperature condition, except for the region of very low pressure. At present, not enough data is available to determine the true reason that Alex propellant B has a higher temperature sensitivity than propellant A.

Thermal Analysis

Figures 7 and 8 are plots of the DTA results in helium and argon environments for the older batch of Alex stored at room temperature approximately one and a half years after manufacture. Testing was conducted on a Perkin Elmer 2050 DTA at a purge rate of 36 cc/min. These results confirm the previous thermal analysis results of Mench et al. [1], conducted using a different DTA machine (Perkin-Elmer Model 7700). There is a slight exotherm that is observed at an onset time of around 112 minutes, which corresponds to 580 °C. This is 130 °C above the onset temperature of exothermic heat release determined by Ivanov and Tepper [2]. The slight exotherms seen in

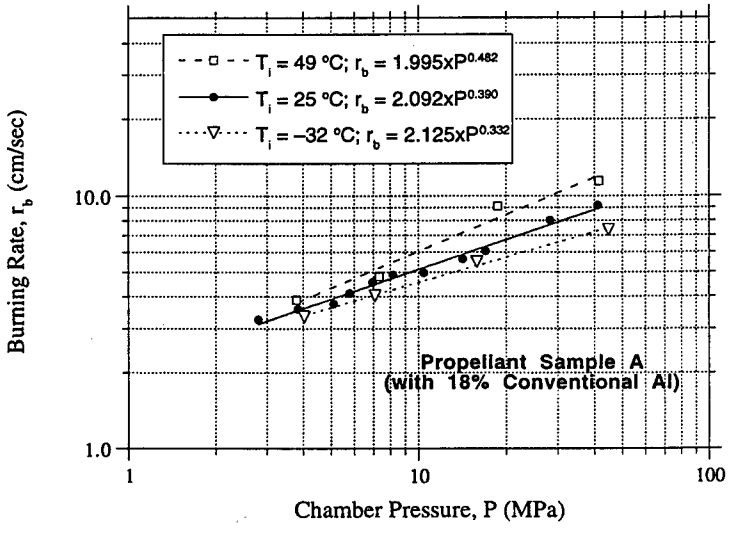

Fig. 2 Measured Burning Rates of Propellant Sample A as a Function of Chamber Pressure at Several Initial Propellant Temperatures

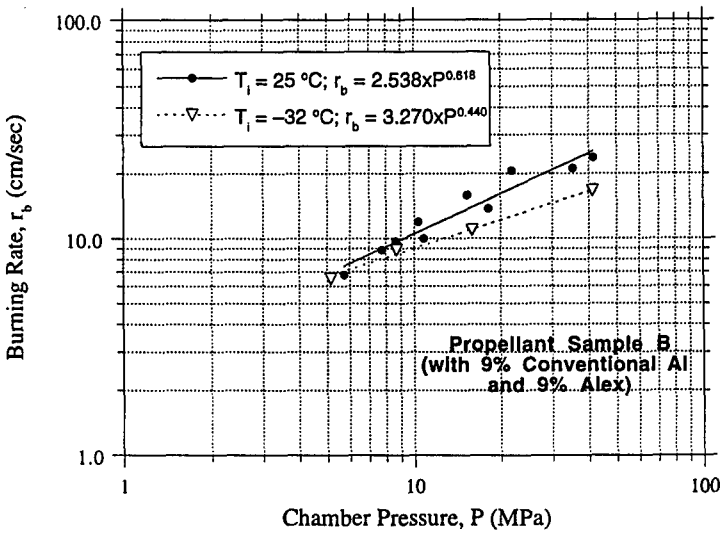

Fig. 3 Measured Burning Rates of Propellant Sample B as a Function of Chamber pressure at Two Initial Propellant Temperatures

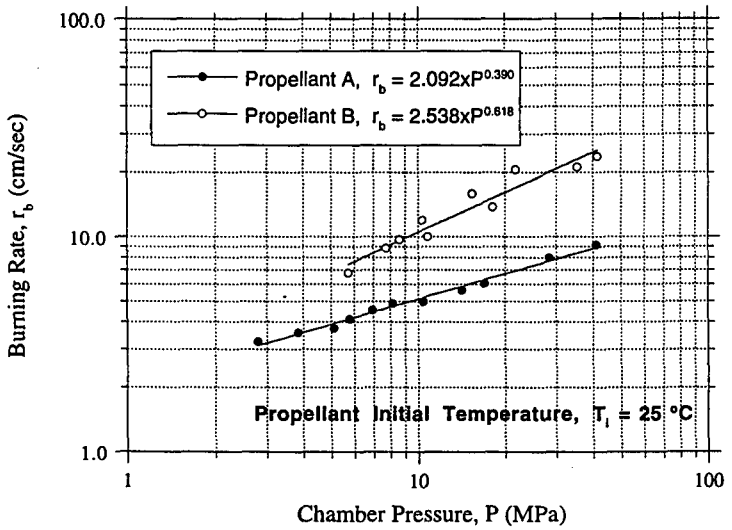

Fig. 4 Comparison of Burning Rates of Propellants A and B at Room Temperature, 25 °C

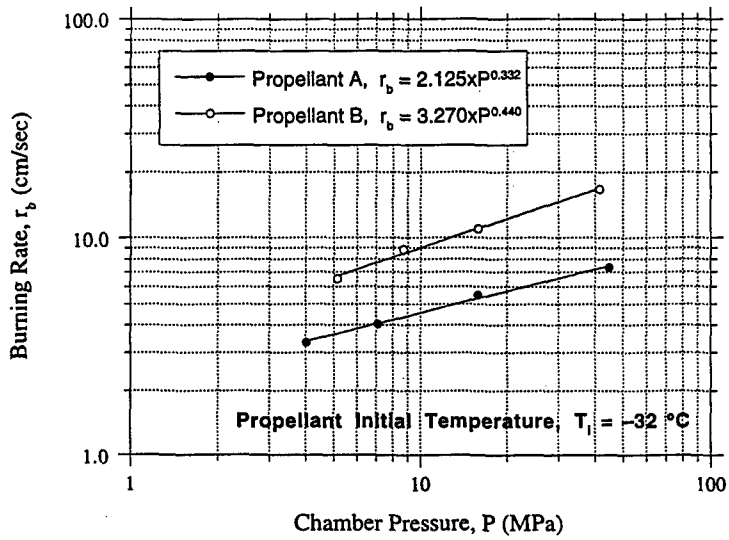

Fig. 5 Comparison of Burning Rates of Propellants A and B at -32 °C

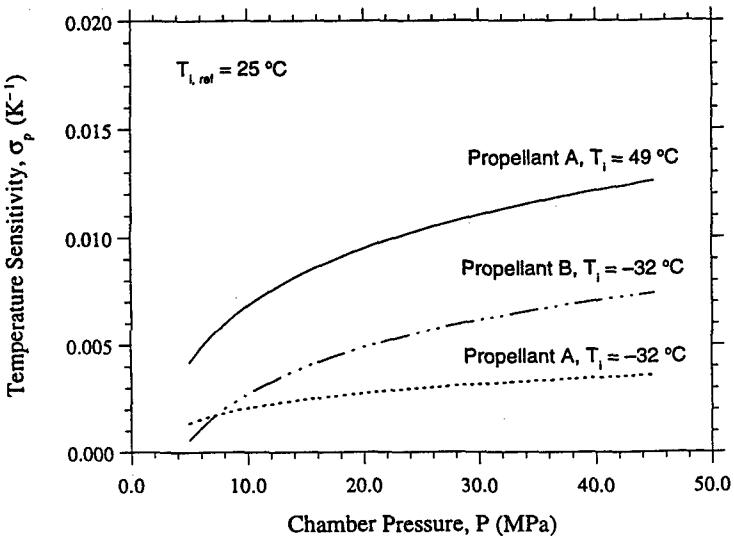

Fig. 6 Temperature Sensitivities of Propellant A and B as a Function of Pressure at Several Initial Propellant Temperatures

Figs. 7 and 8 correspond to the slight oxidation of Alex with the small amounts of impurities in the purge gas as well as possible adsorbed ambient air on the Alex particles because the onset temperature of this small exotherm is consistent with oxidation onset temperatures observed in air environments [1]. It can be seen that the results are the same for both argon and helium environments. No release of stored internal energy was observed from these measurements.

Figures 9 and 10 are plots of the DTA results in helium and argon environments for the newer batch of Alex stored at room temperature approximately six months. This series of tests were conducted to confirm that the older batch of Alex obtained was not somehow tainted, and to check if there could be some observable aging effects. A slight exotherm that is observed at an onset of temperature time of around 112 minutes, which corresponds to 580 °C is shown in both figures. Again, this corresponds to the slight oxidation of Alex with the small amounts of impurities in the purge gas as well as the adsorbed ambient species on the Alex particles. The results are the same for both argon and helium environments. No release of stored energy was observed from these measurements, and no discernible difference was determined between the two batches of Alex aged for different times.

Based upon this comparison, it can be stated that if there is any stored internal energy in Alex powders, the energy is released completely in six months or less. Therefore, it is believed that the beneficial aspects of Alex in propellant formulations can be explained in terms of the large specific surface area and short ignition delay times, associated with the ultra-fine size of Alex particles.

CONCLUSIONS

1. It was shown that the Alex particles substantially enhance the burning rate of aluminized solid propellants. It is believed that several effects related to increased heat flux to the burning propellant surface contribute to the enhanced burning rates seen for Alex propellants. First, it is believed that the large surface area of the Alex particle enhances its reactivity with gas-phase species. Secondly, due to small mass of Alex particles, the ignition delay time is several orders of magnitude shorter than those of conventional aluminum particles. Finally, the bulk mass burning rate of the Alex particles is much higher than conventional aluminum

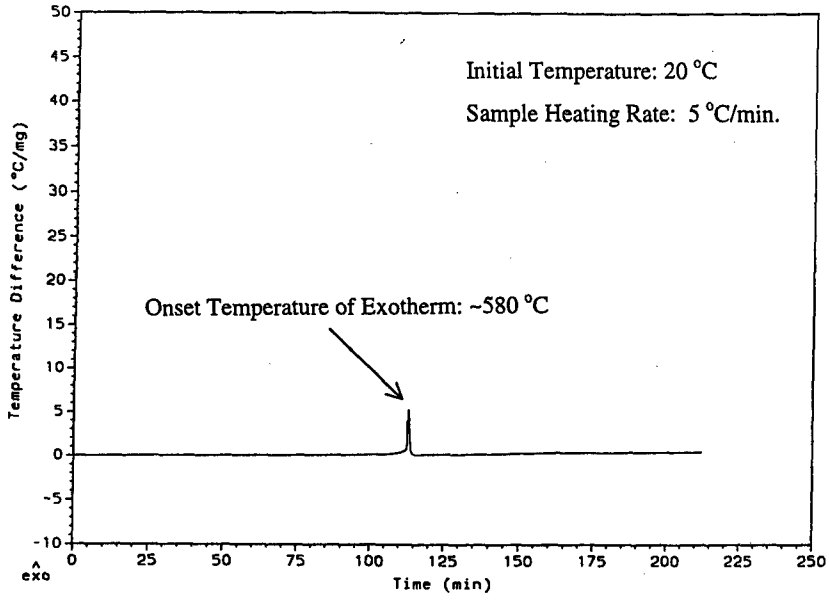

Fig. 7 DTA results for older batch of Alex in Helium environment

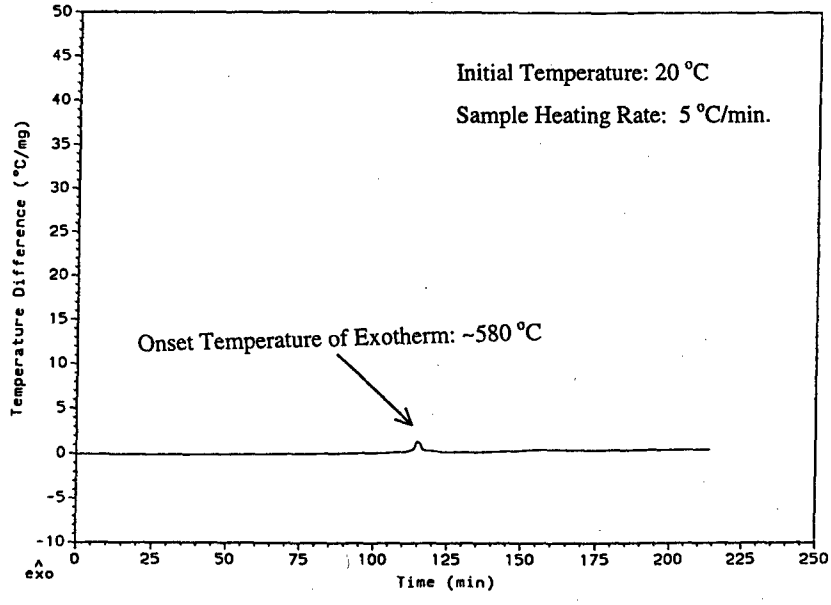

Fig. 8 DTA results for older batch of Alex in Argon environment

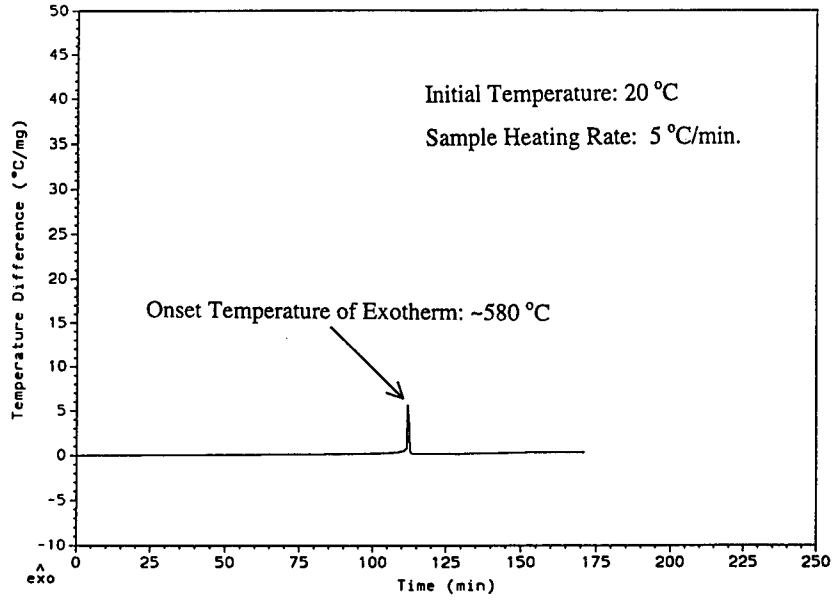

Fig. 9 DTA results for newer batch of Alex in Helium environment

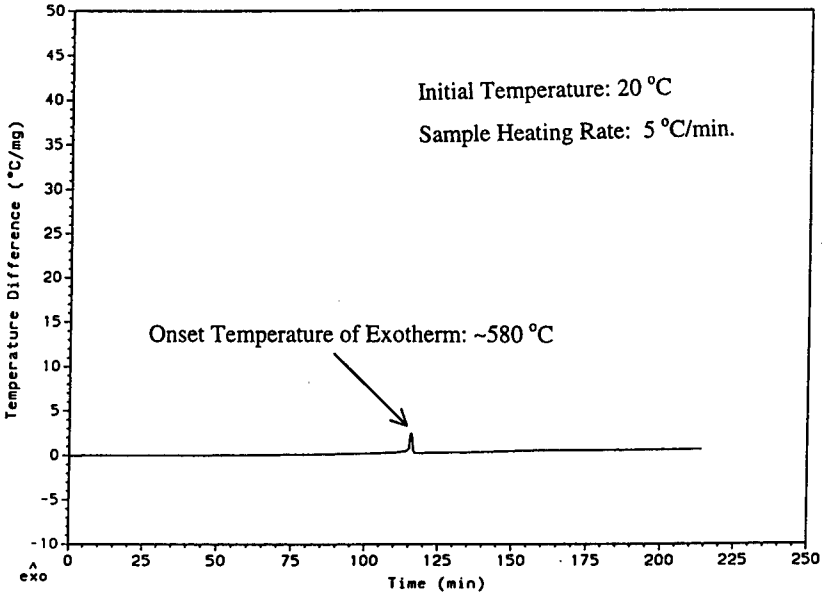

Fig. 10 DTA results for newer batch of Alex in Argon environment

particles. These effects result in the Alex particles burning at a high mass consumption rate in locations very close to the burning surface of the propellant, resulting in greater heat feedback from the burning Alex particles to the propellant surface.

2. For both propellants tested, the pressure exponent is seen to increase with initial propellant temperature, which results in a temperature sensitivity that increases with initial propellant temperature. Both propellants also exhibited an increase in temperature sensitivity with pressure.
3. In comparing the temperature sensitivities of the two propellants at the same initial temperature conditions, it was found that the Alex addition tends to increase the temperature sensitivity of the propellant.
4. Several DTA tests were conducted in argon and helium environments for both an old and a newer batch of Alex. No release of internal energy was observed for both sample batches.

ACKNOWLEDGMENTS

A portion of this work has been sponsored by the Office of Army Research under Grant No. DAAH04-96-1-0054 under the management of Dr. David Mann and the financial support of Mr. Michael A. Natalicchio of the US Army TACOM. The authors would like to thank Dr. Theodore Comfort of AlliantTech Systems for the supply of solid propellants used in this study. A portion of this work was funded through Dr. Richard S. Miller of the Mechanics & Energy Conversion S&T Division of the Office of Naval Research under Grant No. N00014-96-1-0785. The Alex powder used in DTA tests was a donation from Mr. Fred Tepper of the Argonide Corporation. The help of Mr. David K. Johnson in conducting the strand burner experiments is also highly appreciated.

REFERENCES

1. Mench, M. M., Kuo, K. K., Yeh, C. L., and Y. C. Lu, "Comparison Of Thermal Behavior Of Regular And Ultra-Fine Aluminum Powders (Alex) Made From Plasma Explosion Process", accepted for publication in *Combustion Science and Technology*, 1998.
2. Ismail, I. M. K., and Hawkins, T. W., "Evaluation of Electro-exploded Aluminum (ALEX) for Rocket Propulsion," CPIA Publication 650, Vol. II, pp. 25-39, Dec., 1996.

3. Ivanov, G. V., and Tepper, F., "Activated Aluminum as a Stored Energy Source for Propellants," *Challenges in Propellants and Combustion 100 Years after Nobel*, edited by K. K. Kuo, et al., Begell House, 1997, pp. 636-645.
4. Chiaverini, M. J., Kuo, K. K., Peretz, A., and Harting, G.C., "Heat Flux and Internal Ballistic Characterization of a Hybrid Rocket Motor Analog," AIAA Paper No. 97-3080, 33rd AIAA/ASME/SAE/ASEE Joint Propulsion Conference & Exhibit, July 6-9, 1997.
5. Chiaverini, M. J., Serin, N., Johnson, D. K., Lu, Y. C., and Kuo, K. K., "Instantaneous Regression Behavior of HTPB Solid Fuels Burning with GOX in a Simulated Hybrid Motor," *Challenges in Propellants and Combustion 100 Years after Nobel*, edited by K. K. Kuo, et al., Begell House, 1997, pp. 719-733.
6. Salizzoni, R. M., Hsieh, W. H., and Kuo, K. K., "Temperature Sensitivity Measurements and Regression Behavior of a Family of Boron-Based Very High Burning Rate Propellants," Combustion of Boron-Based Solid Propellants and Solid Fuels, Begell House and CRC Press, pp. 438-452, 1993.
7. Kopicz, C., Watson, T. J., Kuo, K. K., and Thynell, S. T., "Combustion Behavior and Thermochemical Properties of JA2 Propellant," Challenges in Propellants and Combustion 100 Years after Nobel, Begell House, pp. 559-573, 1997.
8. Kubota, N. "Survey of Rocket Propellants and Their Combustion Characteristics," Fundamentals of Solid-Propellant Combustion, Progress in Astronautics and Aeronautics, Vol. 90, pp. 1-52, 1984.

OBSERVATIONS ON THE INFINITE DIAMETER DETONATION VELOCITIES OF AMMONIUM PERCHLORATE AND ITS MIXTURES

Richard R. Bernecker
Naval Surface Warfare Center
Indian Head Division
Indian Head, MD 20640-5035

Abstract

Published detonation velocities for ammonium perchlorate (AP) systems have been reviewed in order to determine values for infinite diameter charges. These data have been evaluated in both the detonation velocity - density plane and the detonation velocity - reciprocal diameter plane. The inter-relationship between these two planes is discussed for both intermolecular and intramolecular formulations. The importance of particle size in defining detonation velocities at infinite diameter, D_∞, for AP-containing formulations is discussed and changes the interpretation of previously published conclusions. For AP/wax systems, interesting comparisons have been made for formulations containing 25 and 200 μm AP. Finally, comparisons are made between predictions of detonation velocities (using various BKW parameter sets in TIGER) and experimental data for porous AP.

Introduction

Recent models of the detonation state for two dimensional geometries [1-3] yield predictions showing that a basic tenet of detonics (validated over the years for a wide variety of intramolecular explosive) is invalid for intermolecular explosives. This tenet states that for charge diameters (d's) sufficiently larger than the failure diameter there exists a linear relationship between detonation velocity (D) and the reciprocal of charge diameter (1/d), Eqn. 1. Here D_∞ is the detonation velocity at infinite dia-

$$D = D_\infty + M/d \qquad (1)$$

meter and M, treated herein in a generalized manner, is the slope in this plane and has the units here of $mm^2/\mu s$. The absence of this linear relationship brings into question the ability to predict D_∞, both experimentally and computationally.

For intramolecular explosives (e.g., RDX, HMX, etc.), these models appear to suggest that D_∞ can be determined from a linear D - 1/d relationship. However, for intermolecular explosives (e.g., AN, AP, etc.), these recent models differ among themselves in predicting, for the D - 1/d plane, the variability and magnitude of the slopes at large diameters for similar compositions. Thus, it appears that values of D_∞ can only be determined accurately via a computational model of the detonation state and an experimental data base, that at the mini-

mum, comprises measurements of detonation velocity as a function of charge diameter. But just as importantly, these computations must be based upon a valid - not an approximate - model of the detonation state in order to obtain values of D_∞. The inability to determine experimentally D_∞ for intermolecular explosives affects the ability to calculate detonation state properties from thermoequilibrium codes such as TIGER, CHEETAH, etc. These codes are calibrated against an experimental data base in order to provide some predictive capability for the detonation state of new explosive compositions. Moreover, these calculated detonation properties are then used in models of the performance of these explosive formulations, e.g., late-time reaction (behind the sonic plane) of unreacted ingredients. Thus, the present inability to determine unambiguously values of D_∞ for intermolecular explosives is a significant deficiency in the application of detonation physics and, just as importantly, also in the fundamental understanding of the detonation state in two (or three) dimensions for all explosives. Fortunately, these recent models of the detonation state are being improved to minimize some of the approximations used in their development.

AP Systems

In our ongoing work, we are interested in understanding the detonation state of ammonium perchlorate, AP, and its mixtures. Since AP and its mixtures have not been applied extensively in the calibration of the BKW parameters used in TIGER, etc., one of the initial objectives in this work was to review the data base of D-1/d measurements for AP systems. This in turn determines what reliable data exist for the determination of D_∞ for AP systems and thus for testing TIGER predictions.

AP

The detonation properties of AP have been studied experimentally only for the (very) porous state. Anderson and Pesante reported [4] detonation velocities of porous samples of AP and confirmed the dependence of D on AP particle size; their particle sizes were 6 and 13 μm. (As with all the particle size data herein, these values are the mean particles sizes for the various batches.) Unfortunately, the scatter in the measurements are significantly large at times such that a "valid" values of D_∞ for the various densities of AP can not be determined from their data. (Nevertheless, they reported a summary equation relating D and density.) To have a measure of their values of D for these particles sizes for comparison to data from others, some of their detonation velocities were read from Figs. 1 and 2 in Ref. 4. These data are summarized in Ref. 5 where D(min)and D(max), respectively, represent the minimum and maximum detonation velocities, observed at a given diameter and density.

Price, Clairmont, Erkman and co-workers built upon the work of Anderson and Pesante and took great care in preparing high quality samples for their

measurements and in documenting the particle size distributions of the AP batches. The data for their porous AP samples, where charge densities, charge diameters and particle sizes were varied, are reported in References 6 to 10. Their presentation of the data for these porous AP samples was primarily in the D-density (ρ) plane (Eqn. 2) with occasional representations in the D-1/d

$$D = Do + Y * density \qquad (2)$$

plane. (For intermolecular explosives, no physical meaning is attached to Do by this author.) For intramolecular explosives Do is a point which lies on the TMD curve in the D-ρ plane. Do and Y depend upon charge diameter.

Price, Clairmont and Erkman utilized a variety of batches (and hence particle sizes) of AP in their extensive studies on AP systems. In their summary paper on porous AP [7], it was noted by this author that particle size was not mentioned. This has been found to be a deficiency in their presentation and analyses of their data; see Ref. 5 for a complete discussion of particle size aspects for AP in Refs. 6-10.

Linear fits (Eqn. 2) were defined [5] for the different diameters of porous AP, and used to generate D-1/d data for densities from 0.6 to 1.1 g/cc. The results are shown in Fig. 1, illustrating the agreement between the calculated points from the defined equations and a calculated linear fit to these points. In Fig. 2 the D(min) and D(max) data of Anderson and Pesante are compared with some least square fits (see Fig. 1) and the experimental data of 10 μm AP of Price et al. (symbol x). The dotted lines for the 1.25 and 1.50 g/cc 10 μm AP samples represent an extrapolation of the trends seen in Fig. 1.

AP/Al Systems

Price, Clairmont and Erkman studied several AP/Al formulations to complement their studies of porous AP. Their basic formulations were 95/5 AP/Al, 90/10 AP/Al and 80/20 AP/Al. Their extensive data bases for all their AP/Al systems are documented in Ref. 12 with Ref. 13 being their summary paper.

95/5 AP/Al

As in the case of intramolecular explosives, Al was found by Price, Clairmont and Erkman to decrease the critical diameter when added to AP. Hence, the linear fit to the data in the D-ρ plane extended to slightly higher densities for these AP/Al systems. The detonation velocity measurements for 95/5 AP/Al were stated by Price et al. to be among the more precise measurements in their AP studies. Three lots of AP were used; N-136 with a mean particle size of 7.7 μm, N-141 with a mean particle size of 7.2 μm and N-144 with a mean particle size of 9.3 μm. The latter was used in their main study of 95/5 AP/Al while the other lots were used for a few comparative experiments. The Al particle size used in most of their mixtures was 7 μm. Ref. 12 states "the different lots [of AP] were found to be equivalent in the present work." Unfortunately,

that is not the situation for our objectives (as seen in Fig. 8 of Ref. 5).

Our analyses of their detonation velocity data for 95/5 AP(9.3)/Al(7) are summarized in Fig. 3. For the 76.2 and 50.8 mm diameter charges, very good linear fits were found. Eqn. 3 used data from 0.80 to 1.325 g/cc for the 76.2 mm charges while Eqn. 4 used data from 0.80 to 1.087 g/cc for the 50.8 mm

$$D = 1.147\ (.025) + 2.664\ (.015) * \text{density} \qquad (3)$$

$$D = 1.076\ (.006) + 2.650\ (.006) * \text{density} \qquad (4)$$

charges. All the linear curves in Fig. 3 have Y equal to 2.66. We conclude from Fig. 3 that insufficient data exist for the 1.91 and 25.4 mm diameter charges to generate values for Do and Y (Eqn. 2). For the 34.7 mm charges, a linear fit to the 0.80 and 1.087 g/cc points yields a value of Y of 2.43. However, because the 50.8 mm diameter data depart from Eqn. 4 somewhere between 1.087 and 1.205 g/cc, it is not clear that the 1.087 g/cc datum for the 34.7 mm diameter charges is in its linear region.

For the D-1/d plane, only Eqns. 3 and 4 have been used to define values for the determination of the coefficients of Eqn. 1 for densities between 0.85 and 1.10 g/cc. For the three experimental densities, both the fits and experimental data are shown in Fig. 4. (The dashed lines are extrapolations of the trends seen from Eqns. 3 and 4.)

90/10 AP/Al

In contrast to the 95/5 AP(9.3)/Al(7) measurements, Price et al. noted that there was much more scatter in the detonation velocity measurements for the 90/10 AP/Al samples. The authors used this formulation to explore more extensively the influence of particle sizes on the detonation velocity: both the AP and Al particle sizes were varied. The AP used for their main study on 90/10 AP/Al mixtures was the 7.2 μm batch.

With the addition of additional Al, linear regions in the D-ρ plane extended to higher densities than for 95/5 AP/Al, as can be seen in Fig. 5. In spite of the scatter in these 90/10 AP(7.2)/Al(7) data, it can be seen that the slope decreases with charge diameter. Eqns. 5-8 summarize these linear fits for charge diameters of 25.4, 34.9, 50.8 and 76.2 mm, respectively. These

$$D = 1.366\ (.030) + 2.183\ (.033) * \text{density} \qquad (5)$$

$$D = 1.372\ (.099) + 2.281\ (.097) * \text{density} \qquad (6)$$

$$D = 1.348\ (.074) + 2.484\ (.074) * \text{density} \qquad (7)$$

$$D = 1.291\ (.105) + 2.649\ (.105) * \text{density} \qquad (8)$$

relationships were then used to calculate detonation velocities at various densities and charge diameters. Linear fits (Eqn. 1) were made for densities of 0.60 to 1.40 g/cc. Fig. 6 shows a comparison of some of these linear fits and experimental data for densities of 0.62, 0.90, 1.10 and 1.35 g/cc.

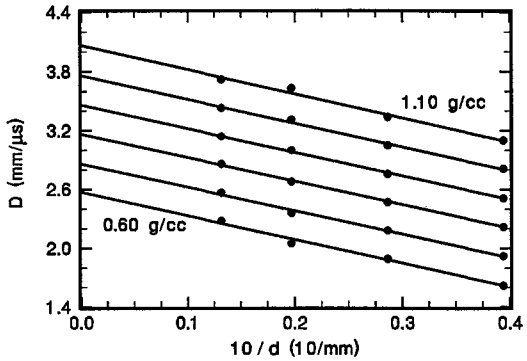

FIG. 1. Calculated Data from D-ρ Curves for 10 μm AP (0.1 g/cc Increments) [6-10]

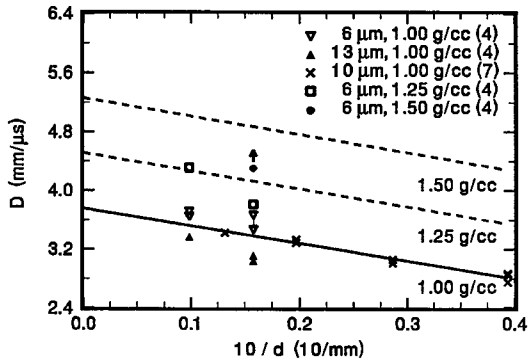

FIG. 2. Influence of Particle Size on Detonation Velocity of Porous AP

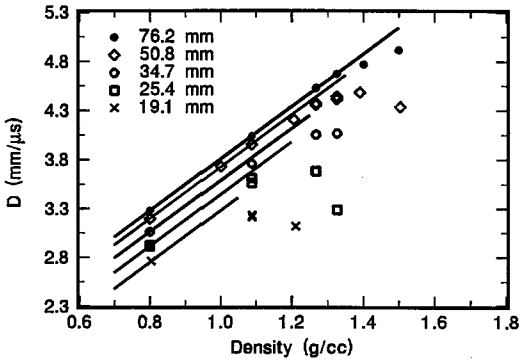

FIG. 3. Influence of Diameter and Density on Detonation Velocity of 95/5 AP(9.3)/Al(7)

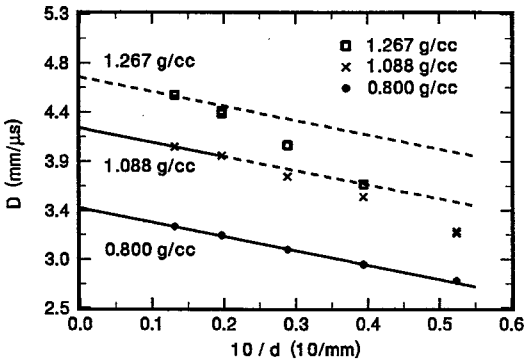

FIG. 4. Calculated Fits from D-ρ Data and Experimental Data for 95/5 AP(9.3)/Al(7)

that is not the situation for our objectives (as seen in Fig. 8 of Ref. 5).

Our analyses of their detonation velocity data for 95/5 AP(9.3)/Al(7) are summarized in Fig. 3. For the 76.2 and 50.8 mm diameter charges, very good linear fits were found. Eqn. 3 used data from 0.80 to 1.325 g/cc for the 76.2 mm charges while Eqn. 4 used data from 0.80 to 1.087 g/cc for the 50.8 mm

$$D = 1.147\ (.025) + 2.664\ (.015) * \text{density} \qquad (3)$$

$$D = 1.076\ (.006) + 2.650\ (.006) * \text{density} \qquad (4)$$

charges. All the linear curves in Fig. 3 have Y equal to 2.66. We conclude from Fig. 3 that insufficient data exist for the 1.91 and 25.4 mm diameter charges to generate values for Do and Y (Eqn. 2). For the 34.7 mm charges, a linear fit to the 0.80 and 1.087 g/cc points yields a value of Y of 2.43. However, because the 50.8 mm diameter data depart from Eqn. 4 somewhere between 1.087 and 1.205 g/cc, it is not clear that the 1.087 g/cc datum for the 34.7 mm diameter charges is in its linear region.

For the D-1/d plane, only Eqns. 3 and 4 have been used to define values for the determination of the coefficients of Eqn. 1 for densities between 0.85 and 1.10 g/cc. For the three experimental densities, both the fits and experimental data are shown in Fig. 4. (The dashed lines are extrapolations of the trends seen from Eqns. 3 and 4.)

90/10 AP/Al

In contrast to the 95/5 AP(9.3)/Al(7) measurements, Price et al. noted that there was much more scatter in the detonation velocity measurements for the 90/10 AP/Al samples. The authors used this formulation to explore more extensively the influence of particle sizes on the detonation velocity: both the AP and Al particle sizes were varied. The AP used for their main study on 90/10 AP/Al mixtures was the 7.2 μm batch.

With the addition of additional Al, linear regions in the D-ρ plane extended to higher densities than for 95/5 AP/Al, as can be seen in Fig. 5. In spite of the scatter in these 90/10 AP(7.2)/Al(7) data, it can be seen that the slope decreases with charge diameter. Eqns. 5-8 summarize these linear fits for charge diameters of 25.4, 34.9, 50.8 and 76.2 mm, respectively. These relationships were then used to calculate detonation velocities at various densities and charge diameters. Linear fits (Eqn. 1) were made for densities of 0.60 to 1.40 g/cc. Fig. 6 shows a comparison of some of these linear fits and experimental data for densities of 0.62, 0.90, 1.10 and 1.35 g/cc.

$$D = 1.366\ (.030) + 2.183\ (.033) * \text{density} \qquad (5)$$

$$D = 1.372\ (.099) + 2.281\ (.097) * \text{density} \qquad (6)$$

$$D = 1.348\ (.074) + 2.484\ (.074) * \text{density} \qquad (7)$$

$$D = 1.291\ (.105) + 2.649\ (.105) * \text{density} \qquad (8)$$

80/20 AP/Al

Charges of 80/20 AP(9.3)/Al(7) were prepared using AP lot N-144. Fig. 7 shows the data for 0.826 and 1.136 g/cc charges and linear fits to the data.

AP/Wax Formulations

Price, Erkman, Clairmont and Edwards studied waxed mixtures of AP. [11,14] The concentrations of the additive were 5, 10, 20 and 31.5%. The particles sizes of AP from the various lots were 25, 28 and 200 μm. The wax had a particle size of 125 μm.

95/5 AP/wax

The 95/5 AP(28)/wax(125) charges were studied at two densities (1.025 and 1.250 g/cc) and various diameters. Their detonation velocity data are shown in Fig. 8. The higher density charges show a feature that was found to be typical of AP/wax and AP/HMX formulations, namely non-linear characteristics in the D-1/d plane (as discussed in the Introduction). A third order polynomial fit to the 1.250 g/cc data is shown in the figure. (In Ref. 11, two linear regions had been fitted to the 1.250 g/cc data.)

90/10 AP/wax

The 90/10 AP(25)/wax(125) charges were studied at two densities (0.940 and 1.201 g/cc) and various diameters. Fourth order polynomial fits have been made to these data as shown in Fig. 9. These data extend to much smaller diameters than found in either the AP or AP/Al studies. (In Fig. 4 of Ref. 11, two linear regions again had been fitted to both data sets.)

80/20 AP/wax

The 80/20 AP(25)/wax(125) charges were studied at two densities(0.901 and 1.101 g/cc) and various diameters. Fourth order polynomial fits have again been made to these detonation velocity data, as shown in Fig. 10. (In Ref. 11, two linear regions again had been fitted to the data.) These data (as well as those for 90/10 AP/wax in Fig. 9) show that at very small diameters the lower density charges have the higher detonation velocities for a given diameter.

68.5/31.5 AP/wax

The 68.5/31.5 AP(28)/wax(125) charges were studied at 0.826 and 1.006 g/cc and various diameters. As seen in Fig. 11, this formulation appears to show the traditional linear relationship in the D-1/d plane. However, the fact that the two curves cross at small diameters, as seen above in Fig. 10 for 80/20 AP(25)/wax(125) charges, suggests the possibility that non-linear behavior may manifest itself at very large diameters.

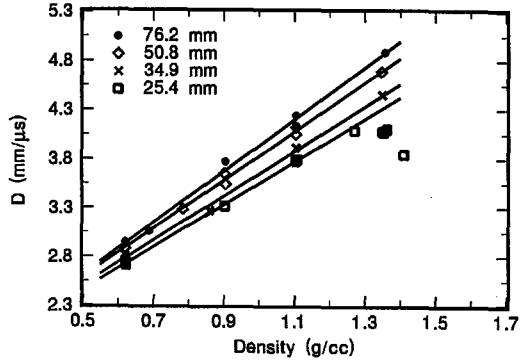

FIG. 5. Influence of Diameter and Density on Detonation Velocity of 90/10 AP(7.2)/Al(7)

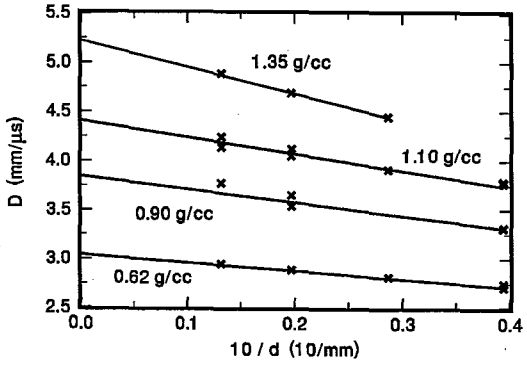

FIG. 6. Calculated Fits from D-ρ Data and Experimental Data for 90/10 AP(7.2)/Al(7)

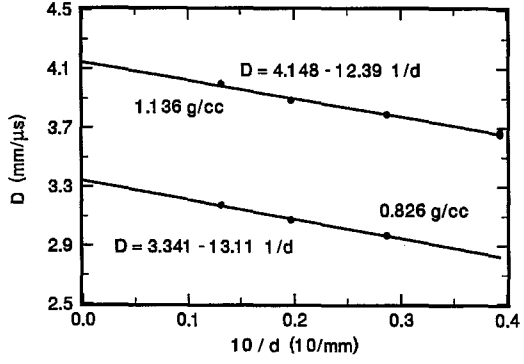

FIG. 7. Influence of Charge Diameter on Detonation Velocity of 80/20 AP(9.3)/Al(7)

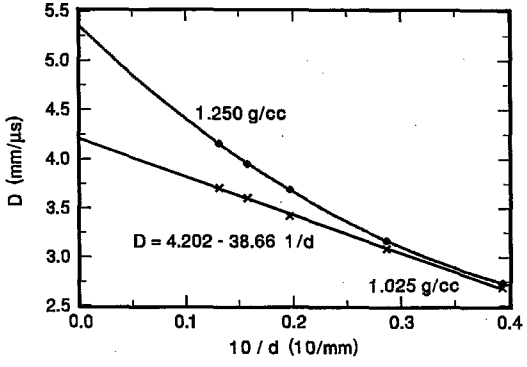

FIG. 8. Influence of Charge Diameter on Detonation Velocity of 95/5 AP(28)/Wax(125)

Discussion

The D-density (D-ρ) plane and the D-1/d plane

Our initial objective for this paper was to select values of D_∞ that could be used to guide the standardization of thermoequilibrium codes for AP systems. Much of the detonation velocity data that we have reviewed herein had been displayed in the D-ρ plane (Eqn. 2) in the original publications. However, it is important to understand how these data transpose to the D-1/d plane (Eqn. 1) since it is the latter where D_∞ selections are made.

For intramolecular explosives, the HBX-1 data set [15] (detonation velocities as a function of density and charge diameter) has served as a reference for Group 1 behavior.[16] The summarized HBX-1 data set [12] has been used to display the HBX-1 data in the D-1/d plane, Fig. 12, for a variety of densities. It is evident that as the density decreases from TMD (1.76 g/cc), the slope (M) increases. This contrasts with the pattern seen herein for AP systems (see Figs. 1 and 4) and is a manifestation of the differences between Group 1 and Group 2 characteristics discussed in Ref. 16. However, in contrast to the general behavior, our analyses have indicated that it is not obvious that the Group 2 systems, as displayed in the D-ρ plane, always have decreasing values of Y (Eqn. 2) as a function of decreasing charge diameters (a major tenet of a Group 2 material). The difficulty when analyzing data in the D-ρ plane is the determination at what density the measurements begin to depart from a linear dependency. This is especially pertinent for the smaller charge diameters where this departure may occurred at densities that are not too far above a "stable packing density" of the granular materials.

The data for 90/10 AP(7.2)/Al(7) in Fig. 5 definitely support the Group 2 description as proposed by Price. In the D-1/d plane, the values of M increase with increasing density, the opposite of that observed for the Group 1 data of Fig. 12. On the other hand, the 10 μm AP data [5] and perhaps the 95/5 AP(9.3)/Al(7) data of Fig. 3 (76.2 and 50.8 mm diameters) show "very similar" values of Y in the D-ρ plane. In the D-1/d plane these data suggest values of M which vary very slightly with increasing densities. Hence, the following generalities have been observed. If values of Y in Eqn. 2 decrease for increasing charge diameters, then values of M decrease with increasing density (Group 1). If values of Y increase for increasing charge diameters, then the values of M increase with increasing density (Group 2). If values of Y are nearly identical, then the values of M are nearly identical for the various densities.

Particle Size and Infinite Diameter Detonation Velocity

It is well known, and illustrated herein and in Ref. 5, that the particle

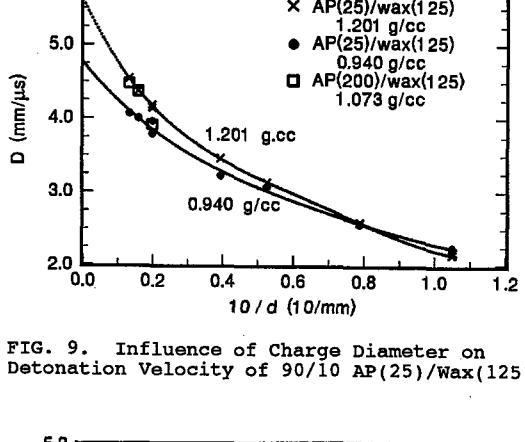

FIG. 9. Influence of Charge Diameter on Detonation Velocity of 90/10 AP(25)/Wax(125)

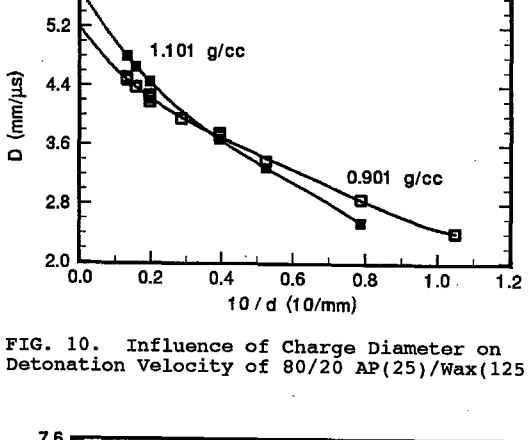

FIG. 10. Influence of Charge Diameter on Detonation Velocity of 80/20 AP(25)/Wax(125)

FIG. 11. Influence of Diameter on Detonation Velocity of 68.5/31.5 AP(28)/Wax(125)

FIG. 12. Linear Fits to Data [12] from D-ρ Equations for Various Densities of HBX-1

sizes of the AP and other ingredients in the AP-containing formulations play major roles in determining the detonation velocities of the systems. Although Price et al. documented very well these particle sizes measurements in the various technical reports, these particles size aspects were not always sufficiently detailed in their literature (summary) publications. Examples of this include the differences between 7.8 and 10 μm AP systems (Fig. 2) and AP/Al systems (see Ref. 5). These latter, and important, observations were not included in the summary paper on AP/Al systems, Ref. 13. For our purposes it is very important to have values of D_∞ that are independent of particle size, as well as to understand how variations in particle size have affected detonation velocities for the various systems that have been studied.

As noted in the Introduction, it should not be assumed that Eqn. 1 will describe experimental data sets. Hence, we have primarily looked for variations to a linear fit before accepting that Eqn. 1 is the best fit to the data. The data of Price et al. from Ref. 7 for porous 10 μm AP samples appear to fit a linear dependency fairly well. Both Anderson and Pesante and Price et al. defined coefficients for Eqn. 2 for infinite diameter charges and, lacking a defined associated particle size, they implied that the coefficients are independent of particle size. We do not agree with their conclusions. Based upon observations from Fig. 2, values of D_∞ for 1.0 g/cc samples will most likely be at least 0.15 mm/μs higher than 3.75 mm/μs, the intercept in Fig. 2. Similar arguments can be made for the 1.25 g/cc samples.

For the AP/Al systems, the same uncertainty exists about the influence of the AP particle size on any extrapolation to infinite diameter. However, there is also the uncertainty of whether the Al is participating (either fully or partially) in the reaction before the sonic plane. Hence, the extrapolation of any AP/Al data set has potential particle size effects associated with both ingredients.

From the Price, Clairmont, Erkman and Edwards data sets for AP/wax it is evident that the selection of any value for D_∞ for these systems is very uncertain. (On the other hand, these data sets are invaluable for understanding the reaction kinetics of the detonation state of these intermolecular formulations.) Price et al. used two linear fits to the data in Figs. 8, 9 and 10. We have used polynomial fits to illustrate the difference in D_∞ values that result from these two different interpretations. Which, if any, of these two procedures is valid is uncertain. As stated in the Introduction, determination of these D_∞ values appears to require numerical calculations using an accurate model of the detonation state and experimental D-1/d data sets, such as shown in Figs. 8-10. (Nevertheless, the experimental data, for AP/Al and AP/wax shown in the various figures, do provide estimates of the lower bounds of D_∞ when extrapolated (1/d = 0) and hence do provide some guidance for standardization of TIGER, etc.)

A very intriguing example of the particle size influence for AP is shown in Fig. 9 for 90/10 AP/wax formulations. For AP and AP/Al formulations having 8-10 μm AP, detonation velocities are higher than for formulations containing larger AP particle sizes (e.g., 25 μm). For 90/10 AP/wax systems, the detonation velocities for 1.07 g/cc 90/10 AP(200)/wax(125) samples at diameters of 63.5 and 76.2 mm are nearly equal to detonation velocities for 1.20 g/cc samples of 90/10 AP(25)/wax(125) at the same (respective) diameter. (The value of D for 90/10 AP(200)/wax(125) at 50.8 mm is indicative of the much larger critical diameter of 90/10 AP(200)/wax(125) relative to 90/10 AP(25)/wax(125).) These observations are most intriguing and allows one to ask questions such as, whether this particle size effect levels off beyond about 30 μm, whether there is a maximum reduction in detonation velocity for a particle size between 30 and 200 μm, whether the fracture of the 200 μm particles during the pressing process produced enough smaller particles to "mimic" a 30 μm mixture or whether a combination of the latter with an earlier possibility is more likely. Only future work can begin to answer these questions.

Prediction of Detonation Velocity

The selection of D_∞ values for AP-containing formulations was to guide the selection of parameters to be used for the BKW EOS in TIGER and/or CHEETAH. Although D_∞ values for these AP system are uncertain (as discussed above), we can explore the trend in predicted detonation velocities resultant from the recent BKW parameter sets, namely BKWR vs. BKWS vs. BKWC. These parameter sets differ in the methodology and data bases used to standardize the parameters.

In Table I are velocities and temperatures calculated for the detonation state for two densities of AP. They were calculated using the three BKW sets

Table I. Calculated Detonation State Values using Three BKW Parameter Sets and the TIGER code

Composition	Density g/cc	D_∞ mm/μs	Temperature °K
		BKWR	
AP	1.00	4.05	1854
	1.95	6.49	1497
		BKWS	
AP	1.00	4.02	2008
	1.95	6.96	1984
		BKWC	
AP	1.00	3.68	1902
	1.95	6.42	1772

(see Ref. 17) and TIGER. A comparison of the 1.00 g/cc detonation velocities with the data in Fig. 2 shows that BKWC yields too low a velocity while the BKWR and BKWS values are consistent with an estimate of D_∞ for infinitely small AP particles. Comparing temperatures among the three sets shows that BKWR has much too low a value at 1.95 g/cc. (One important change from BKWR to BKWS and BKWC is the value for the parameter, θ, that plays a major role in determining the temperature of the detonation state.) The data in Table I illustrate the need and importance to standardize the complete BKW parameters set (including covolumes) for AP-containing formulations. Such an effort is currently underway.

References

1. Kirby, I. J. and Leiper, G. A., "A Small Divergence Detonation Theory for Intermolecular Explosives," Proc. Eighth Symposium (International) on Detonation, NSWC MP 86-194, NSWC, Silver Spring, Maryland, July 1985, p. 176.

2. Bdzil, J. B. and Stewart, D. S., Physics Fluids, *A1*, 1261 (1989).

3. Guirguis, R. H., "Relation between Early and Late Energy Release in Non-ideal Explosives," Proceedings 1994 JANNAF Propulsion Systems Hazards Subcommittee Meeting, CPIA Publication 615, August 1994, p. 383.

4. Anderson, W. H. and Pesante, R. E., "Reaction Rate and Characteristics of Ammonium Perchlorate in Detonation," Eighth Symposium (International) on Combustion, Williams and Wilkins Co., Baltimore (1962), 705.

5. Bernecker, R. R., "Observations on the Infinite Diameter Detonation Velocities of Ammonium Perchlorate and its Mixtures," Proceedings 1997 JANNAF Propulsion Systems Hazards Subcommittee Meeting, CPIA Publication 657, October 1997, p. 193.

6. Price, D., Clairmont, A. R., Jr. and Jaffe, I, "Explosive Behavior of Ammonium Perchlorate," Comb. Flame, *11*, 415(1967).

7. Price, D., Clairmont, A. R., Jr., Erkman, J. O. and Edwards, D. J., "Infinite Diameter Detonation Velocities of Ammonium Perchlorate." Comb. Flame, *13*, 104(1969).

8. Clairmont, A. R., Jr., Jaffe, I, and Price, D., "The Detonation Behavior of Ammonium Perchlorate as a Function of Charge Density and Diameter," NOLTR 67-71, June 1967.

9. Price, D., Clairmont, A. R., Jr., and Jaffe, I, "Particle Size Effect on Explosive Behavior of Ammonium Perchlorate," NOLTR 67-112, Sept. 1967.

10. Price, D., Clairmont, A. R., Jr., Erkman, J. O. and Edwards, D. J., "Ideal Detonation Velocity of Ammonium Perchlorate and its Mixtures with H.E.," NOLTR 68-182, Dec. 1968.

11. Price, D., Erkman, J. O., Clairmont, A. R., Jr. and Edwards, D. J., "Explosive Behavior of a Simple Composite Propellant Model," NOLTR 69-16, March 1969.

12. Price, D., Clairmont, A. R., Jr., and Erkman, J. O., "Explosive Behavior of Aluminized Ammonium Perchlorate," NOLTR 72-15.

13. Price, D., Clairmont, A. R., Jr., and Erkman, J. O., "Explosive Behavior of Aluminized Ammonium Perchlorate," Comb. Flame, *20*, 389(1973).

14. Price, D., Clairmont, A. R., Jr., and Erkman, J. O., "Explosive Behavior of a Simple Composite Propellant Model," Comb. Flame, *17*, 323(1971).

15. Roslund, L. A. and Coleburn, N. L., "Hydrodynamic Behavior and Equation-of-State of Detonation Products Below the Chapman-Jouget State," Proc. Fifth Symposium (International) on Detonation, ACR-184, U. S. Printing Office, Washington, D.C., 1970, p. 523.

16. Price, D., "Contrasting Patterns in the Behavior of High Explosives," Eleventh Symposium (International) on Combustion, The Combustion Institute, Pittsburgh (1967), p. 693.

17. Fried, L. E. and Souers, P. C., "BKWC: An Empirical BKW Parametrization Based on Cylinder Test Data," Propellants, Explosives and Pyrotechnics, *21*, 215 (1996).

<ict 98>
12.03..1998

ICT Jahrestagung 1998

VULNERABILITY TESTS WITH FRAGMENT IMPACTS

VERWUNDBARKEITSTESTS MIT SPLITTERAUFSCHLAG

M. Held
TDW 86523 Schrobenhausen, Germany

Zusammenfassung

Für den Splitterbeschuß nach MIL-STD-2105B sind „Projektilbildende (EFP) Ladungen" mit 16 g Belegungsmasse besonders geeignet. Die geforderte Geschwindigkeit von 2530 m/s wird bereits mit einer Sprengladungsmenge von 80 g erreicht. Drei bis fünf EFP-Generatoren können simultan mit einer zeitlichen Streuung von weniger als 1 µs oder mit jeder gewünschten Zeitdifferenz gezündet werden. Die Splitter treffen den gewünschten Ort auf der Munition mit sehr hoher Genauigkeit. Diese Splittergeneratoren ergeben keine würfelförmigen Splitter von 12,6 mm Kantenlänge. Die Projektile sind halbkugelförmig geformt. Würfelförmige Splitter haben jedoch je nach Trefferlage - Seitenfläche oder Würfelkante - um den Faktor 2 unterschiedliche Grenzgeschwindigkeiten. Deshalb werden mit halbkugelförmigen Splittern weitaus besser reproduzierbare Ergebnisse erhalten.

Summary

EFP charges with 16 g liner mass will be very suitable for the fragment impact tests of the MIL-STD-2105 B. They give the required velocity of 2530 m/s with about 80 g HE. 3 to 5 EFP generators can be fired simultaneously with less than ± 1 µs jitter or with any intended time differences. The fragments can be very accurately aimed to the wanted hit position on the test item. These low cost devices give no cubic fragments with 12.6 mm side length; they are hemispherically shaped. But cubic fragments have more than a factor of 2 threshold velocity differences, depending on side-on, edge-on or tip-on impacts. Therefore much more reliable results are achieved with a hemispherical fragment shape.

1. MIL-STD-2105 B requirements

The MIL-STD-2105 B requires for the acceptance of an „Insensitive Munition" the survivability or at least no violent reactions on fragment impacts <1>. Under the preferred test procedure § 5.2.4.2.1. mild steel cubes of 12,7 mm side length should hit the test item with a velocity of 2530 m/s ± 90 m/s and with at least two fragments, but not more than five fragments.

In USA - a fragment generator FRAGMAT with 50 kgs - 90 kgs high explosive, Composition B, is used with a central point initiation <2>, or with the NAWC FRAGMAT launcher 18,3 kg Octol with a 5 point multi initiation opposite to 25 or only 5 cubic fragments (Fig. 1) <3>. Such a high amount of explosives is not only generating an enormous blast effect but will also load the target additionally. Further such an amount of high explosives can not be used at many test ranges, at least in Europe. Also the hit position of the fragments is not very well controlled. For catching the natural fragments built by the axial confinement originally made of steel, 75 mm to 100 mm thick RHA shielding is necessary to avoid perforation or to overcome spall fragments from the shield <4>. This problem is drastically reduced by using tungsten/epoxy confinement, produced with a special molding process <3>.

Under § 5.2.4.2.2. an alternative test procedure #1 is described where a „single" 16 g mild steel fragment with 12.7 mm diameter and 14.7 mm cylindrical length and an additional cone of 140° on its front side can be used.

Under § 5.2.4.2.3. an alternative test procedure #2 is given where the test setup, fragment characteristics and passing criteria shall be designed, based on the threat hazard analysis (THA) to address fragment threats for tactical situations,.

The author has the impression that the „trial inventors" had problems to test the different items with the 16 g cubical fragments launched by HE generators with 2530 m/s. On one hand, this is an extremely high velocity which may occur on static targets but at least very seldom. On the other hand, the necessary amount of high explosives to launch such fragments creates also a lot of technical problems.

The alternative test procedure #1 is a practical compromise to reduce the requirement now to the impact by a single mild steel fragment with a cylindrical shape and to launch this fragment from a powder gun with 1830 m/s.

The alternative test procedure #2 gives a further compromise, certainly imposed by the threat hazards analysis.

To conduct the multiple fragment impacts with the required velocities - 2530 m/s ± 90 m/s and precise impact location - either on the main charge or on the most shock sensitive location of the munitions, DRI has designed and used a dual powder gun with two extremely long 40 mm barrels arranged in a special mobile shelter <4>. Special problems were coming up to achieve the velocities by changing the test site. No remarks are given on the simultaneity of the two fragments. The reactivity of confined high explosive charges is changing by the time difference of the fragment impacts <5>.

4 such preformed fragments can be also simultaneously launched by a very special laboratory gun <6>. This is generally also an expensive tool. For the installation, the gun needs a concrete base (Fig. 2). The hit positions of the individual fragments on the AURs (all up rounds) are relatively well defined.

Launching of 16 g fragments with an EFP-design to velocities of 2530 m/s is no problem at all. It can be used also mild steel for the fragments. Only the shape will not be cubical. But a cubical shape is also changed to a conical or hemispherical front after perforation, also of thin target material. The orientation of a cubical fragment on a HE surface has a very great influence on the threshold values for initiation (Fig. 3) <7>. More reliable results can definitely be achieved by a hemispherical front face of the fragment.

A large number of tests were conducted by the author with 40 g heavy EFP-fragments to find the threshold values of confined high explosive charges with different barrier or cover plate thickness at 2.400 m/s impact velocities <5>.

2. Fragment threat

The author criticized this unrealistic requirement in his presentations on the „Propulsion and Energetic Panel, 78th Specialist' Meeting held in Bonn 1991 which is published in the AGARD-CP-511 <8> and at the binational German French workshop at the Institute Saint Louis in November 1992 <9>.

Boggs showed in his paper „Hazards of energetic materials and their relations to munitions survivability" the fragment threat as a function of fragment mass and

velocity and in a rough way their probability of occurring <10>. His diagram shows that the 16 g fragment with 2530 m/s is beyond the threat range (Fig. 4). A fragment of exactly 2050 m/s with 73 g has a higher frequency of appearing. A further critical fragment but roughly around 1 % of the frequency compared to the 73 g fragment, is a fragment with 430 g with a velocity of 1280 m/s. These two fragments represent a much higher threat to our munitions compared to the unrealistically fast fragment, as the Fig. 5 and Fig. 6 after Wagenhals show in which the perforation of steel barriers of different wall thicknesses are additionally presented with two different equations (THOR, respectively FATE) <11>.

3. EFP fragment generator

For the layout of the fragment generator as an EFP charge with the liner and charge geometry, assistance was given by Weimann <12>. A mild steel liner (ARMCO-Iron) with a mass of exactly 16 g was used (Fig. 7). To ensure no liner mass is lost by the launch process, a radial confinement or a so-called spallring is used with a hexagonal shape to get also a very well controlled rear or base formation. The weight of the cast high explosive charge of Comp. B 3 is only around 80 g. By firing 2 to 5 charges the total amount of detonating high explosive is 160 g to 400 g which is extremely less compared to FRAGMAT generators of 18300 g to 50000 g. This gives no blast load at all to the test item in a few meters distance.

Three 16 g EFP-fragment generators were fired simultaneously in front of 2 flash X-ray tubes with double exposure after 500 µs and 700 µs (Fig. 8). The axial distances of the fragment generators were 80 mm. They were glued in plastic tubes which were fixed in a 19 mm thick plywood (Fig. 9). Then they were individually oriented to the target by a laser.

The flash X-ray shows the designed velocity of 2500 m/s (Fig. 10). The two externally arranged projectiles are turning both „inwards" which means they are influenced by the middle EFP-fragment generator. This was not expected but can be taken into account. The axial distance from the axis was 80 mm and from the surfaces 40 mm. But still the impacts are very accurate on the target plate at 2100 mm distance (Fig. 11).

On the next test a plywood was installed on the rear side between the two externally arranged 16 g EFP-fragment generators at distances of 160 mm (Fig. 12). As the 500 µs FXR-picture shows the EFP-projectiles are much less tumbling (Fig. 13). The

impacts on the target plate are exactly in the wanted aiming points in 160 mm distance (Fig. 14).

After the first very promising tests a second series of liners was built with a different raw material and new charges cast. To learn something from the test set-up with only 80 mm axial distances, a blast shield was installed between the lower two EFP-fragment generators (Fig. 15). A picture of the total test set-up shows the 16 g EFP-fragment generators on the left side, the protecting cassette for the X-ray film in the background and the windows for the FXR tubes on the far right side. The hazardous fragments of the spall rings are stopped with the wooden blocks around the charges (Fig. 16). The flash X-ray shows that the lower two EFP-fragments are obviously turned to the blast shield which has evidently given some influence to the projectile orientation (Fig. 17). The upper projectile was not very well built by the improper liner material. The impacts are only partially very close to the aiming points on the target plate (Fig. 18).
This test was again repeated where the EFP formation is again less well formed by loosing some small pieces on the rear side which obviously created the tumbling (Fig. 19). The lower EFP-generator had 3.5 g more high explosive weight which has driven this projectile to slightly higher velocities, in the range of 1 %. The impacts of these three projectiles were again good, but not perfectly covering the intended hit positions (Fig. 20). By using the proper liner material, the hemispherical fragment formation and the exact hit point of ± 10 mm at 2 m distance can be achieved, as the first two shots with the first lot of mild steel liners have demonstrated.

4. Conclusion

A 16 g fragment generator can be designed as an EFP charge and can launch a 16 g fragment with 2530 m/s. If wanted the velocity can also be increased, respectively also easily decreased.

With the same design, also other masses can be launched as already demonstrated with 40 g and 240 g fragment masses at 2.400 m/s velocity <6>. This means velocity and masses can be changed relatively easily.

The liner material has to be carefully selected. In further tests it will be demonstrated that shape and impact point can be very well controlled.

But independent from this, these 16 g fragment generators are simple and low cost devices to get one or more impacts on a test item with highly accurate hit positions (Fig. 21). With the low explosive weight it is an ideal tool for testing the survivability of ammunitions by fragment impacts required in MIL 2105 B.

5. References:

<1> Department of Defense. MIL-STD-2105 B Military Standard: Hazard Assessment Tests for Non-Nuclear Munitions (AMSC N6037). Indian Head, MD, NSWC, p. 21, 1994

<2> J. Stotser, „Standard Procedure for Conducting the Multiple Fragment Impact (FRAGMAT) Test („For Score"), NWC-TM 6411, 1988

<3> F. Norris, „FRAGMAT Test Modifications", Naval Weapons Center, China Lake, CA 93555-6001

<4> S.L. Lightsey and D.C. Mann, „A Precision Launch Technique for Insensitive Munitions Fragment Impact Testing", Proceedings of Insensitive Munitions & Energetic Materials Technology Symposium, Tampa, USA, 1997

<5> M. Held, „Initiation Threshold by Fragment Impact", 28th International Annual Conference of ICT, Karlsruhe, Germany, 24:1-13, 1997

<6> Special designed powder gun; if questions, ask the author

<7> D.L. Dickinson and L.T. Wilson, „The Effect of Impact Orientation on the Critical Velocity Needed to Initiate a Covered Explosive Charge", Int. J. Impact Engng 20, 223-233, 1997

<8 M. Held, „MBB Development of Insensitive PBX-Charges", AGARD-CP-511, 7:1-27, 1992

<9> M. Held, „Diskussionsbeitrag zum MIL-STD-2105 A", ISL-Report, S-R 902/93, 3:1-34, 1993

<10> T.L. Boggs, C.W. Dickinson, L.M. Barrington, C. Belanger, P.J. Huskins, „Hazards of Energetic Materials and their Relation to Munitions Survivability", AGARD Conference Proceedings 511, 16:1-7, 1992

<11> M.R. Wagenhals et al., „Three Efforts Concerning Fragment and Shock Hazards to Cast Munitions", AGARD Conference Proceedings 511, 20:1-14, 1992

<12> K. Weimann, EMI, Hauptstraße 18, 79547 Weil am Rhein, Germany
Private communication

Fragment Projector FRAGMAT

TDW

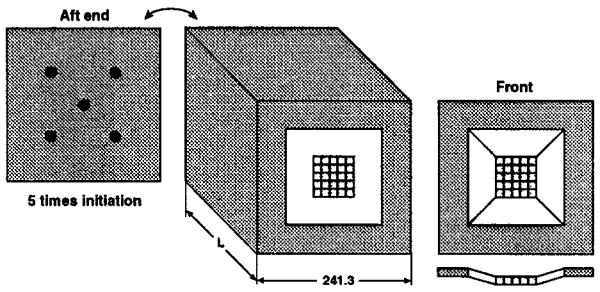

Fig. 1

Special 40 mm Laboratory Gun

TDW

Fig. 2

Detonation Threshold Values for Rotating Platelets

TDW

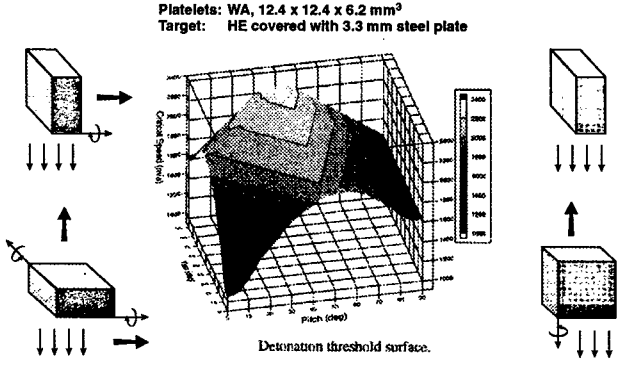

Fig. 3

Overlay of a Fragment Threat Map onto Response Plot

TDW

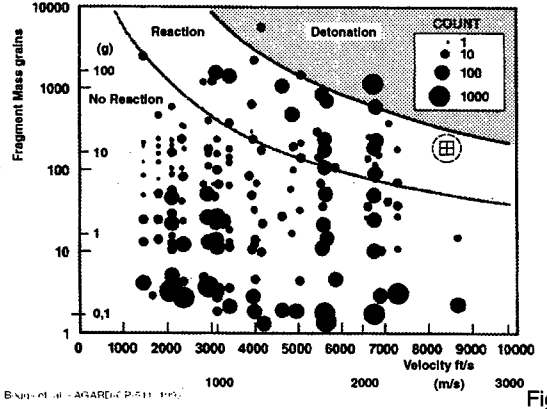

Fig. 4

Degradation of Example Fragments as a Function of Barrier Thickness Using Thor Equations

TDW

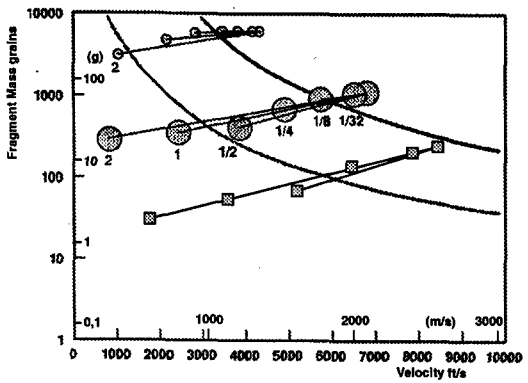

Fig. 5

Degradation of Example Fragments as a Function of Barrier Thickness Using FATE Equations

TDW

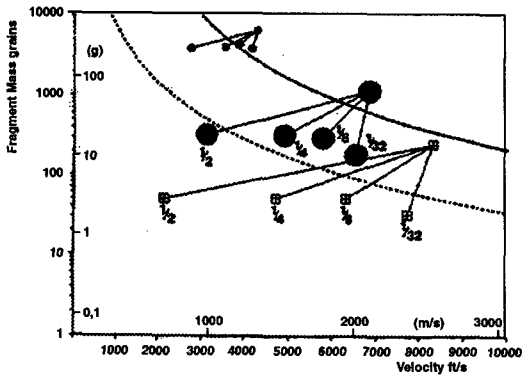

Fig. 6

16 g EFP - Fragment Generator

TDW

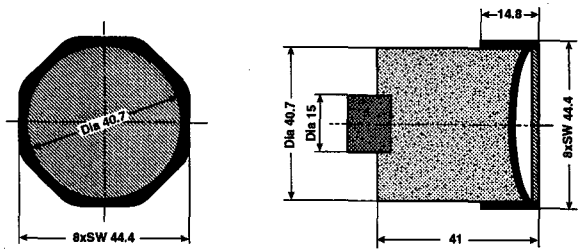

Fig. 7

FXR EFP - Fragment Generator (16 g)

TDW

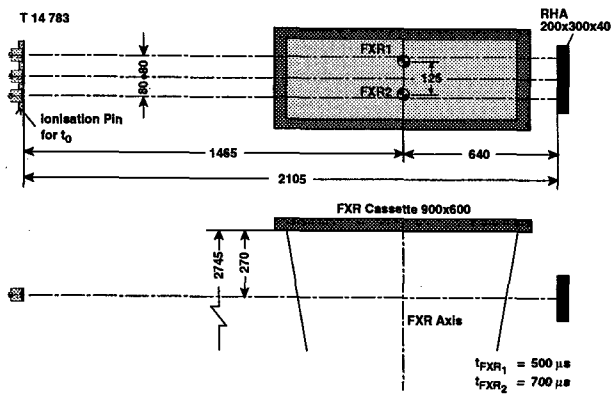

Fig. 8

Three 16 g EFP - Fragment Charges (Det 14 783) TDW

Fig. 9

FXR 14 783 TDW

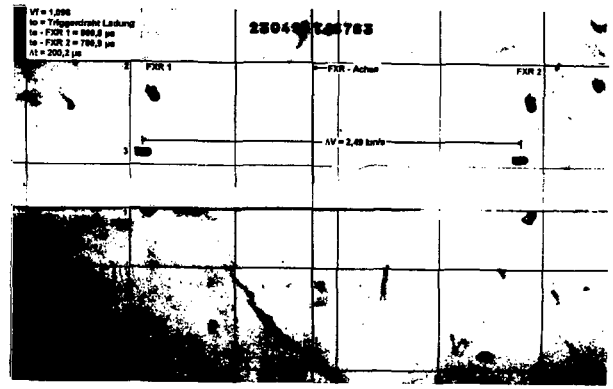

Fig. 10

Impacts at 2100 mm Distance of 16 g Fragments TDW

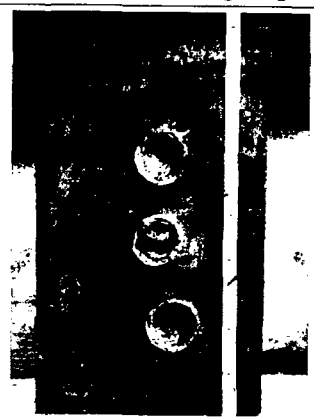

Fig. 11

Two 16 g EFP - Fragment Charges TDW

Fig. 12

FXR 14 784

TDW

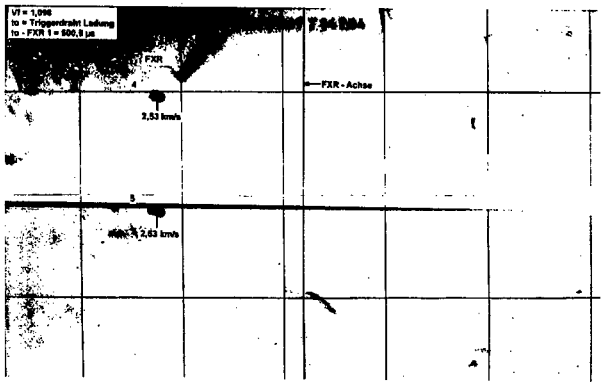

Fig. 13

Impacts at 2065 mm Distance (Det 14 784)

TDW

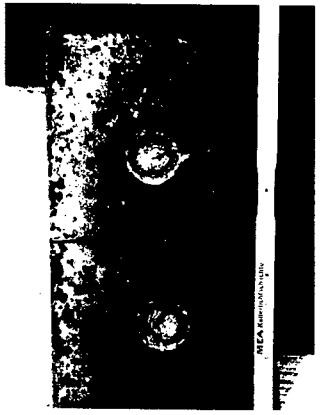

Fig. 14

Three 16 g EFP - Fragment Generators

TDW

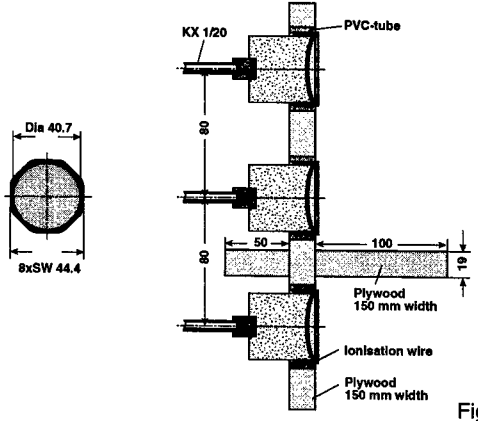

Fig. 15

Test Setup in Front of Double FXR

TDW

Fig. 16

FXR 14 799 TDW

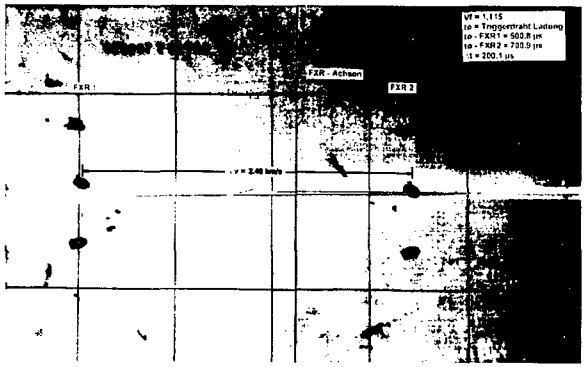

Fig. 17

Impacts at 2100 mm Distance TDW

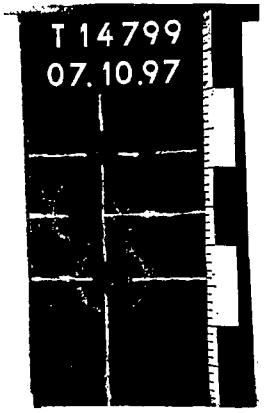

Fig. 18

FXR 14 802 TDW

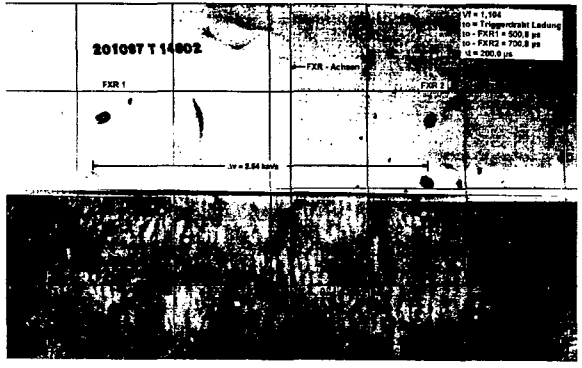

Fig. 19

Impacts at 2100 mm Distance TDW

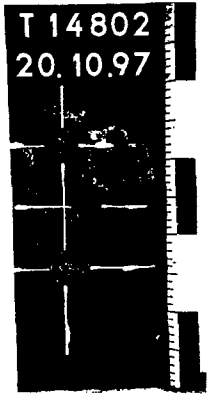

Fig. 20

Conclusions

TDW

FRAGMAT **with Comp B originally needs 50 kgs to 90 kgs**
NAWC FRAGMAT **with Octol and 5 point initiation still needs 18.3 kgs**

Twin *guns* **or 40 mm special laboratory** *gun* **with 4 fragments, launched by sabot, are very special tools and expensive and need special protections**

EFP-FRAGMENT generators

- **have 80 g Comp B3**
- **or 0.4 kg for 5 fragments**
- **no protection necessary**
- **high hit accuracy**
- **simultaneous hits - jitter of about 1 μs - or with any wanted time differences**
- **not expensive**
- **hemispherical shape gives good reproducibility of the reaction levels in contrast to cubical fragments**

Fig. 21

Increase of sensitivity of HMX-based pressed explosives resulting of the damage induced by hydrostatic compression

A.Lefrançois, G.Demol

Centre d'Etudes de Gramat
F-46500 GRAMAT

ABSTRACT

Reflection optical microscopy of polished section of recovered HMX grains submitted to isostatic compression exhibits intragranular defects like microcracks and shear bands. The microstructure of HMX-based pressed explosives thus contains not only porosity but also intragranular damage, that could be responsible for producing additional hot spots, or causing fast decomposition in shock to detonation transition. The influence of intragranular damage on sensitivity was investigated using recovered damaged particles and initial undamaged particles. Interface velocities between 3 mm-thick explosive samples and PMMA windows, separated by a thin (13 μm) aluminium plate, have been recorded with a VISAR. The input shocks were generated by the impact of projectiles launched by a light gas gun and a powder gun. At the calculated pressure of 5 GPa, no difference was observed between the two materials. At higher pressures, the damaged samples showed higher reactivity than the samples made with the initial grains. It is concluded that the additional intragranular defects induced by the isostatic compression process must be taken into account to describe the ignition and growth of the reaction stimulated by shock.

INTRODUCTION

It is widely accepted that initiation of pressed explosives submitted to a shock wave occur in hot spots. Because the energy deposited in the material by the shock wave at the ignition threshold is not sufficient to produce ignition of the bulk, it is necessary to suppose that localization of energy happens in some points of the material. However, the nature of the mechanism(s) involved in this localization is still controversial. Many different processes have been proposed. All heterogeneities of the material have been considered to be potential ignition sites including pores, cracks, contacts between grains or between grain and binder. But the major modeling effort has been made on a mechanism called viscoplastic pore collapse. In this mechanism, when the shock wave has passed, the pore collapses and therefore, the solid material surrounding it strains. This deformation of a viscoplastic material heats the explosive to produce hot spots. However, observing a micrograph of a pressed explosive, let's say of pressed HMX, a lot of defects that can be seen are cracks and deformation bands at the scale of a few micrometers. These microstructural defects are present in the initial moulding powder but they are not so numerous there. We then designed an experimental plan to investigate the influence of the additional defects introduced by the isostatic compression on the sensitivity of the explosive. We will present the experimental procedure used to that respect and the results.

The basic idea of this work is to recover the HMX grains after a hydrostatic compression using a soluble binder. Our aim is to compare the shock-sensitivity of the two batches of HMX grains : the initial one and the recovered one. Firstly, we describe the moulding powder preparation, the compression process and grains recovery. The particle size distribution of "initial and recovered" grains is controlled using laser granulometry and also the microstructure using reflection optical microscopy.

Then, we describe the sensitivity tests. The two batches are separately consolidated the same way with a wax binder. The thickness, the density and also the microstructure are controlled. The sensitivity tests are plane impact experiments. Different projectile velocities are used. VISAR signals measure the particle velocity of the explosive/window interfaces. The observed shock amplification is indeed in relation with the energy release of the explosive. Significant differences in shock sensitivity are recorded. Intragranular defects are reported to influence the shock to detonation transition.

HMX-GRAINS RECOVERY

Preparation of the moulding powder

The formulation of the pressed explosive is 3 % in weight of a water-soluble binder and its plasticizer and 97 % of a bimodal composition of HMX grains.

The water soluble binder is a partially hydrolyzed polyvinyl alcohol. The binder is named Mowiol 10-74 made by Hoechst and the plasticizer is a polyethylene glycol (PEG 300).

The preparation of the moulding powder is composed of the four following steps :

- dissolution of the binder and the plasticizer in water,
- mechanical mixing of HMX powders in the previous solution,
- evaporation of water under vacuum with minimum mechanical agitation,
-manual granulation across sieves and drying.

The coating process itself can severely damage the grains as pointed out by Skidmore [1]. He showed that the particle size distribution can even be affected by such a process. We also experienced a granulometry reduction after a tested magnetic mixing. We had thought previously that this step was rather innocuous but only a careful handling of the grains can allow not to damage the grains. The influence of the process on the microstructure of HMX-grains is controlled with reflection optical microscopy. For the microscopic examination, all the samples are potted in epoxy resin and polished on automated equipment. This technique was designed to reduce artifacts. Polished sections of the moulding powder are prepared and observed with reflection optical microscopy. Figure 1 shows the microstructure of the moulding powder with soluble binder. Even if a crack can be seen in a large grain, the moulding powder is slightly affected by the preparation.

Compression of the powder

The moulding powder is then pressed to produce a damage which is similar to the one usually observed in HMX-based pressed explosives. Some preliminary experiments have been done using uniaxial compression to determine the experimental conditions. However, it is important to remember that the stresses are not comparable in the uniaxial and hydrostatic processes.

The plasticizer effect on the explosive compression is important. This has already been shown in the work by Langston and al [2, 3] and is here confirmed : Table 1 shows the influence of the plasticizer on the density of uniaxial pressed blocks. The measurements are performed using the adapted hydrostatic method with an intermediate oil coating. In 3 % wt.

binder, porosity is almost doubled between the 50 % wt. of plasticizer and no plasticizer. When there is no plasticizer, the binder is rather brittle and the compression introduces a lot of damage in the grains. Adding some plasticizer in the binder allows to obtain a more ductile binder and that reduces significantly the damage created in the grains by compression. The proportion of plasticizer is fixed to 15 %.

Samples	Density ρ_a (g/cm^3)	Porosity $1-\frac{\rho_a}{\rho_{TMD}}$. (%)
Binder and Plasticizer 50 % wt. / 1200 bars	1,76	5,9
Binder only / 1200 bars	1,68	10,1
Binder and Plasticizer 50 % wt. / 1500 bars	1,80	3,7
Binder only / 1500 bars	1,72	8,0

Table 1 : Influence of PEG 300 plasticizer on the density of uniaxial pressed samples.

The temperature of the hydrostatic compression takes into account the influence of the pressure on the glass transition of the binder [4]. The temperature is fixed to 70 °C.

The pressure with two cyclic applications is limited to 1200 bars because HMX grains are too damaged when higher pressures are used during pressing. Figure 2 shows a micrograph of recovered grains after uniaxial compression at 1500 bars. The microscopic investigation reveals crosscracks and open fractures, which lead to the break-up of the coarse grains. At lower pressure, the microstructure is less damaged.

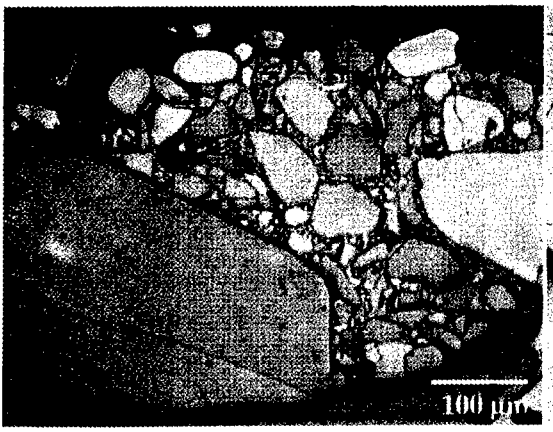

Figure 1 : Microstructure of the moulding powder with soluble binder

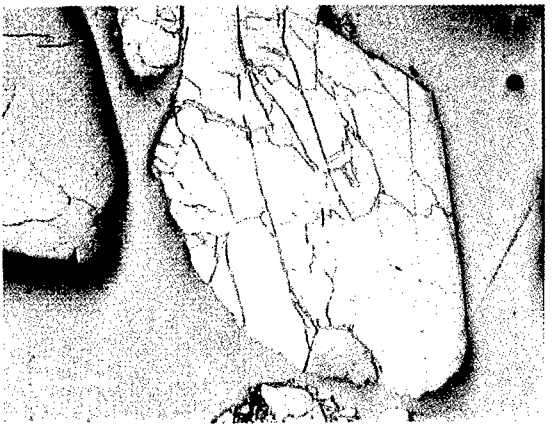

Figure 2 : Microstructure of damaged grains after uniaxial pressing under 1500 bars

After hydrostatic compression, the HMX grains are recovered by dissolving the binder in water. The pressed explosive is placed in distilled water. After a week, the compacted material is completely weathered. The process uses some temperature cycles up to 60°C in double boiler to accelerate the dissolution of the binder in water [5]. Every time the water is changed, the grains are recovered by sieves and filters. Only few balls of grains remain because of undissolved binder.

Particle Size Distribution

The analysis were performed at CEA Le Ripault on a Mastersizer S long bed. The particle size distributions of the initial and recovered grains are compared on figures 3 and 4.

The fine particle distributions are different. The fine volume fraction of recovered grains is smaller than the initial one. The distribution is the same for sizes above 80 µm. But, under this limit, the fine recovered particles diminish rapidly. Different artifacts could interfere with the measurements. The very fine grains could be dissolved in water (the recovered grains have spent more time in water because of the dissolution of binder). They could also pass through the filter. Fine grains could be linked to the coarse grains or to the filter because of undissolved and settled binder. The last explanation is probably the most important one.

The bimodal distribution of the initial grains presents a gap between the fine and coarse grains. This interval is preserved for the recovered grains. So, the coarse grains are not broken during the process of compression.

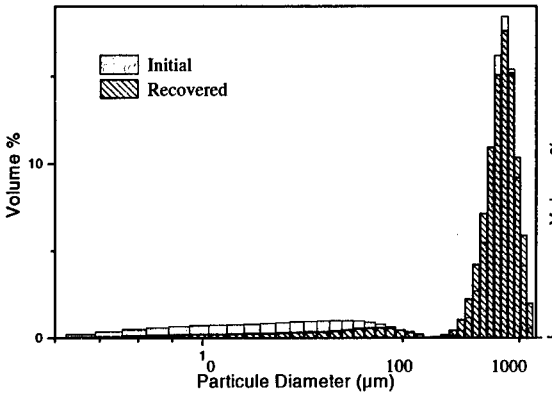

Figure 3 : Particle size distributions of initial and recovered grains

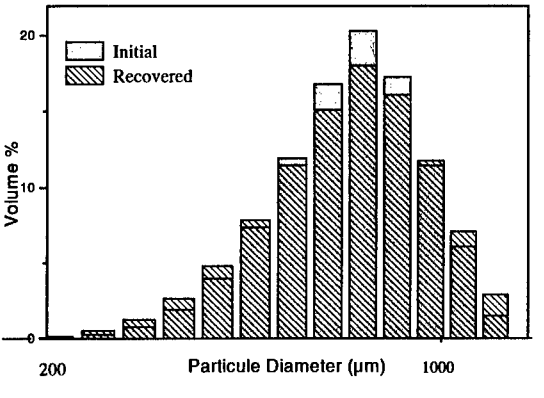

Figure 4 : Particle size distributions of initial and recovered grains taken over a 200 µm sieve

For the coarse fractions of the initial and recovered grains, the median diameter is 682 µm. However, the coarse particle distribution of the recovered grains is larger than the initial one. This slight difference is explained by the microstructure of recovered grains :

- Assemblies of coarse and fine grains remain present after the recovery because of undissolved or settled binder.
- Some grains are broken during the process of compression and recovery.

The results show that the morphology is slightly affected by the hydrostatic compression and the grains recovery. The coarse fractions of the initial and recovered grains whose size is greater than 200 µm are used for the sensitivity test. Because the particle size distribution of the coarse recovered HMX grains is similar to the one of initial coarse grains, the particle size effect on the compared shock sensitivity will be limited.

Additional intragranular Defects

Figures 5, 6 respectively show the microstructure of initial and recovered coarse grains. Different kinds of defects are compared : porosity, twinned bands and cracks. The preparation is very important to avoid artifacts. Bad conditions can lead to many artifacts : for example scratches could be mistaken with porosity.

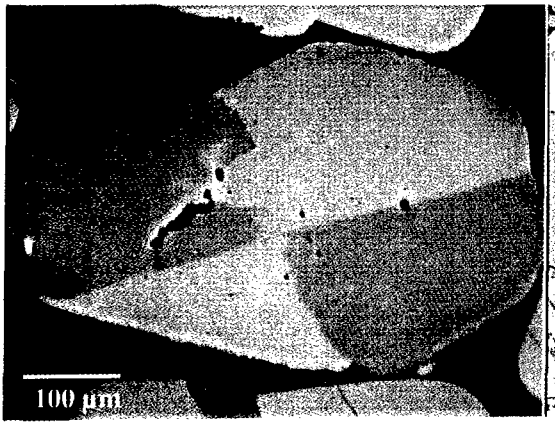

Figure 5 : Microstructure of initial coarse grains

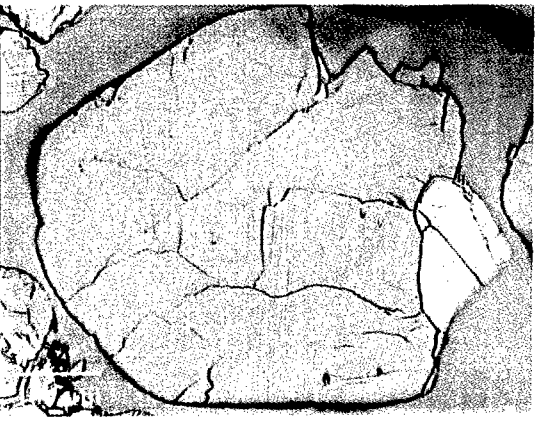

Figure 6 : Microstructure of recovered coarse grains

The intragranular porosity is observed as black spots and the distribution is similar in the two batches : initial and recovered grains. Characterization of the porosity reveals from one to

ten pores with a diameter under ten micrometers in the grains. A few big pores are present with a diameter under 50 µm.

Twinned crystals are observed in both lots. But twinned bands appear only in the recovered coarse grains (see the center of the grain in figure 6). Those bands cover in general a part of the grain. They present no microscopic discontinuity, and are fine, and parallel. Cracks often pass through it. Those bands are probably due to grain plasticity.

Intragranular cracks have already been observed in the initial coarse grains. Their number is limited. For the recovered grains, they are much more numerous. They usually begin from pre-existing heterogeneities : pores, grain border, inclusion. Transgranular cracks are also present. They are often formed by coalescence of intragranular cracks.

SENSITIVITY TESTS

Pressed Explosive formulations

At this point, it is necessary to make explosive formulations from the two HMX powders. For simplicity, we choose to use uniaxial compression of the powder mixed with a wax.

The parameters of the uniaxial compression have been optimized to avoid overdamaging the grains. The following conditions have been tested for compression with initial grains : pressure between 125 and 500 bars, temperature between 40°C and 60°C and wax binder weight fraction between 10 % and 20 %.

Figure 7 : Microstructure of samples pressed at 50 °C, 250 bars and 10 % wax weight fraction made with initial coarse grains

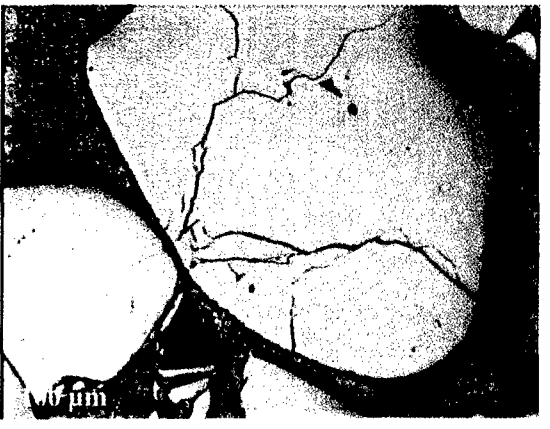

Figure 8 : Microstructure of samples pressed at 50 °C, 125 bars and 15 % wax weight fraction made with initial coarse grains

A wax weight below 20 % and a too high pressure lead to additional cracks, and even fractures. Those defects are generated by contacts between grains. Figures 7 and 8 show the damage caused by contacts between grains under different conditions of compression. The temperature of the process also plays an important role. At 60 °C, the pressed sample is pasty just after the exit of the matrix. At 40 °C it is slightly friable.

The optimized conditions are fixed at 50 °C, 200 bars and a wax weight fraction of 20 %. Both batches of HMX the initial and the recovered ones are separately pressed. Figures 9 and 10 show the microstructure of the two different batches. Cracks and twinned bands are present in the samples made with the recovered grains. Porosity and granulometry are preserved between the two lots. In spite of great care, some grains have been fractured during this step. But this is limited.

The density is also controlled, using the hydrostatic method. The mean porosity of the pressed samples is about 2.3 %. The difference of density between the two different samples is less than 0.01 g/ cm^3.

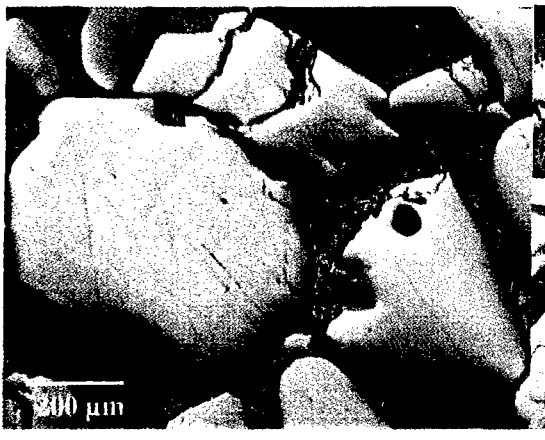

Figure 9 : Microstructure of the pressed explosive made with initial coarse grains and optimized conditions

Figure 10 : Microstructure of the pressed explosive made with recovered coarse grains and optimized conditions

Shock experiments setup

The sensitivity tests are designed to allow a comparison of the shock sensitivities of two explosive blocks.

The experiments are performed using the "ARES" powder and the "DEIMOS" gas launchers at the Centre d'études de Gramat. The two single stage launchers have an inner

diameter of 98 mm. A velocity of 850 to 2400 m/s can be obtained on "ARES". With this gun, velocity reproducibility is better than 1 % and parallelism on impact is about 1.5 mrad. Depending on the breech configuration, a velocity of 50 m/s to 1200 m/s can be reached on "DEIMOS". There, the velocity reproducibility is about 2 % and parallelism on impact is approximately 1.5 mrad.

Plane, one-dimensional impacts take place in an evacuated target chamber. Figure 3 shows the projectile and the target including a support, thin explosives blocks, aluminium films and PMMA windows. The two explosives blocks are glued on the same support, so that the impact velocity is exactly the same for the two explosive samples. The velocity of the explosive/window interface are measured on Push-Pull Valyn VISARs. The parallel measurements allow easy comparisons of the results.

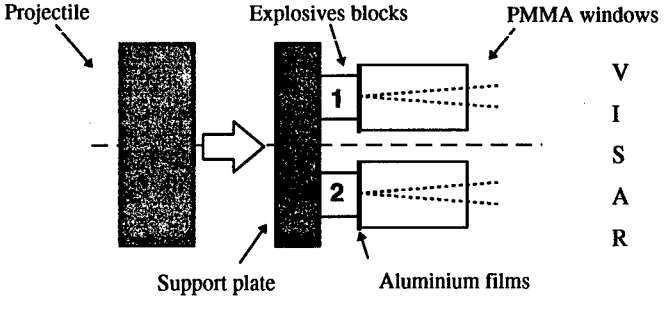

Figure 11 : Layout of the plane impact experiments

Experimental Results

Three projectile velocities were tested, which corresponds to the calculated shock pressure of 5 GPa, 6.5 GPa and 8.5 GPa in the explosive. Figure 12 and 13 show the experimental results for projectile velocities of respectively 880 m/s and 1090 m/s with an explosive thickness of 3 mm. Figure 14 shows a result for an impact velocity of 1305 m/s, with an explosive thickness of 2.2 mm. The presented signals are "raw" and have not been smoothed.

The signals show a kind of hump approximately one microsecond after the shock front. It is due to the aluminium film and corresponds to the reflection of the incident shock wave at the explosive / aluminium film interface and the aluminium film / PMMA interface. A short duration shock is then reflected.

Figures 13 and 14 show a more or less sharp decrease and increase after the hump. The higher the impact velocity, the more important the phenomenon is. It does not happen at low

shock pressure. Therefore, it seems that the reactivity has a great influence on this perturbation. The lateral release wave should affect later.

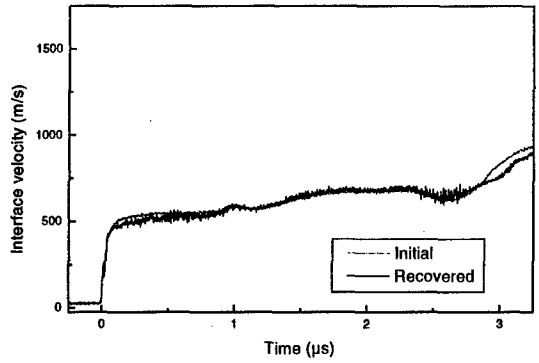

Figure 12 : Experimental results for a projectile velocity of 880 m/s

For Figure 12, during the first microseconds after the passage of the shock front, the slope of the velocity increase is very low and the comparison of the two signals reveals no significant difference. These results show the quality of the fabrication process of the explosive block, and the quality of the test preparation and measurement methods used.

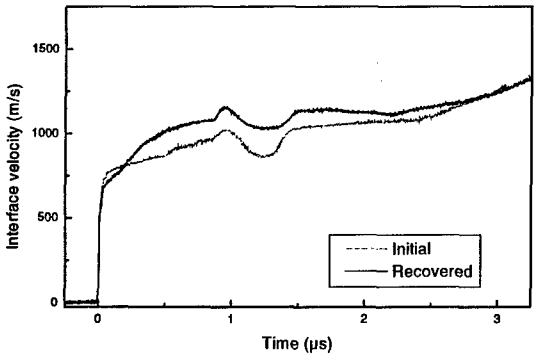

Figure 13 : Experimental results for a projectile velocity of 1090 m/s

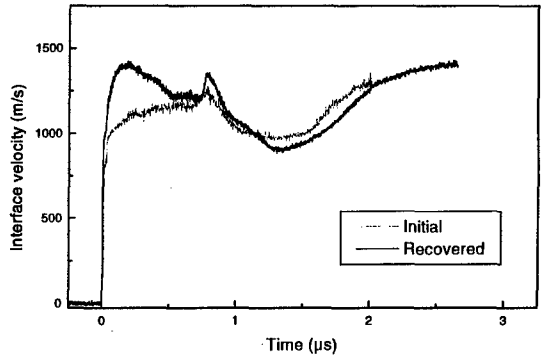

Figure 14 : Experimental results for a projectile velocity of 1305 m/s

For higher projectile velocities, the velocity increase in the block made with the recovered grains is greater than in the one made with the initial grains. Figure 13 shows a higher slope for the recovered grains, but the shock front levels are similar. In Figure 14, the shock front is higher for the block containing the recovered grains. This shock wave is reactive.

When the microstructure is previously damaged by hydrostatic compression, the energy release is much faster. This could be due to an important increase of the ignition sites (hot spots) at high shock levels because of the presence of additional defects created by hydrostatic compression. Alternatively, the presence of defects could play a role in the buildup of detonation because of the increase of specific surface.

CONCLUSION AND DISCUSSION

This study shows the influence of intragranular defects introduced by hydrostatic compression on the shock sensitivity of pressed explosives.

The main kinds of damage created by the process of hydrostatic compression are cracks and twinned bands. Porosity is not changed and the particle size distribution is only slightly affected. Microscopic investigations are performed using reflected optical microscopy and laser granulometry.

Same dimensions, comparable density, comparable particle size distributions and preserved intragranular defects are obtained for the two explosive blocks processed separately with initial and recovered from compression grains. At low shock pressure, no difference is observed between the two blocks. At higher shock pressure the shock sensitivity increases with the presence of additional intragranular defects.

The formation of the hot spots and the hot spots growth and coalescence are the two main stages of the shock to detonation transition [6, 7, 8]. The influence of cracks, and twinned bands is complex on this process. Our results show that the presence of cracks and twinned bands lead to a faster energy release and several explanations are possible. On the one hand, the specific surface area is increased by the opening of cracks and this could accelerate the reaction growth. So, cracks could play a major role in the detonation build-up. On the other hand, the presence of additional intragranular defects could also create additional hot spots. Thus, friction is a potential mechanism involving cracks. At the reactivity threshold (around 5 GPa) there is a hot spots initiation control [9], but the presence of cracks and twinned bands do not increase the chemical reactivity. The influence on the hot spots formation stage could be limited at that level. Other experiments or measurements methods will be necessary.

REFERENCES

[1] SKIDMORE C.B., PHILIPPS D.S., SON S.F., ASAY B.W., Characterization of HMX particles in PBX 9501, 1997 Topical Conference on Shock Compression of Condensed Matter, July 1997.

[2] LANGSTON S. B., AKHAVAN J., CUMMING A. S., Water Soluble Polymers as a Diagnostic Tool for the Examination of Pressed Plastic Bonded Explosives Based on HMX, 25th International ICT-Conference, Karlsruhe, Federal Republic of Germany, 28 June - 1 July 1994.

[3] LANGSTON S. B., Mechanical failure of HMX based PBX's and its relationship to impact sensitivity, 26th Ann. Conf. ICT, Karlsruhe 1995.

[4] JONES PARRY E, TABOR D, Review effect of hydrostatic pressure on the mechanical properties of polymers : a brief review of published data, Journal of Materials Science 8, Chapman and Hall Ltd 1973, pp 1510-1516.

[5] HOECHST Aktiengesellschaft, Mowiol Polyvinyl Alcohol (brochure), Marketing Kunstharze/ Polymerisate, D-6230 Frankfurt am Main 80, December 1991.

[6] KHASAINOV B.A., ERMOLAEV B.S., PRESLES H.-N., VIDAL P., On the effect of grain size on shock sensitivity of heterogeneous high explosives, Shocks Waves, July 1997, pp 89-105.

[7] CHERIN H., The influence of microstructure on the sensitivity of explosive compositions, 10th interna. deto. Symp. 1993, pp 808-815.

[8] SAUREL R., MASSONI J., MAZEL P., DEMOL G., BAUDIN G., Un modèle mécaniste pour la transition choc détonation des explosifs comprimés, rapport interne, 1997.

[9] MOULARD H., Particular aspect of the explosive size effect on shock sensitivity of cast PBX formulations, 9th Symposium (international) on Détonation (1989), 18-24.

ACKNOWLEDGMENTS

The authors wish to acknowledge the Commissariat à l'Energie Atomique - Centre Le Ripault - Laboratoire de physicochimie for their assistance in carrying out the Malvern particle size analysis on the initial and recovered HMX grains. This work has been supported by the Délégation Générale de l'Armement (DGA) of the French Ministry of Defense.

TEMPERATUREINFLUSS AUF DIE EIGENSCHAFTEN VON MITTELKALIBERTREIBLADUNGEN

Etienne Rochat
Oerlikon Contraves Defence
Pyrotec AG, CH-8845 Studen, Switzerland

Abstract

We tested the influence of the heat production in automatic medium-calibre guns on the properties of the propellant and the igniter. The goal was to find a solution without danger of cook-off, overpressure or non-function.

1. Einleitung

Mittelkaliber-Schnellfeuerwaffen mit Hochleistungsmunition erreichen beim Seriefeuer hohe Kammertemperaturen. Bei hoher Feuerbereitschaft werden die Treibladung und die Treibladungsanzündung in der geladenen, heissen Waffe hohen Temperaturen ausgesetzt.
Dadurch kann die Pyrotechnik der Treibladungsanzündung in ihrer Funktionsfähigkeit beeinträchtigt werden und die Innenballistik beim Schuss unvorhergesehene Druck-Werte zeigen.
Die chemische Stabilität der Treibladung ist empfindlich auf lang anhaltende Temperaturbelastung. Nach dem Überschreiten der Verpuffungstemperatur des Treibladungspulvers tritt Cook-off auf.
Im Gegensatz zu konventionellen Waffen führt der Cook-off des Treibladungspulvers in der Trommel von Revolverwaffen meistens zur Zerstörung der Waffe.

Wir erfassten einerseits die Temperaturen an den verschiedenen Orten in der Waffe und der Patrone bei Seriefeuerbeschüssen, anderseits das Selbsterwärmungsverhalten von Treibladungen in ihrer Originalumgebung.
Die Funktionsverlustgrenze der Treibladungsanzündung und die Cook-off Temperatur der Patrone wurden durch Warmlagerversuche ermittelt.
Zur Quantifizierung der Verhältnisse am Geschütz erfolgten Innenballistikbeschüsse mit verschiedenen Treibladungspulvern bei hohen Temperaturen. Dabei wurde auch die Treibladungsanzündung in ihren Ausgangsleistungsparametern variiert.

2. Systembeschreibung

Unsere Untersuchungen erfolgten hauptsächlich mit dem mobilen Low Level Air Defence System **Oerlikon Contraves SkyShield35**. Dieses besteht neben dem Feuerleitmodul und dem ADATS-Lenkwaffenwerfer (1) aus ein bis zwei 35mm Skywhip-Revolverkanonen. Das System verschiesst mit einer Kadenz von 1000 Schuss pro Minute aus jeder Waffe Sprengmunition oder programmierbare AHEAD-Flugkörperabwehrmunition (2) mit je 152 Subprojektilen.
Die verwendeten singlebase Treibladungen (ca. 330g pro Ladung) haben eine Flammtemperatur von ca. 2400 K, eine Explosionswärme von max. 3210 J/g und einen Verpuffungspunkt von +170°C. Die tiefste Cook-off-Temperatur in der Munition ist vorschriftsmässig die der Treibladung.
Jede Waffe hat beim Seriefeuer eine Mündungsleistung über 6'000 kW und während dem Treibladungspulverabbrand werden ca. 265 MW geleistet.
Wenn die Waffe nach mehreren Salven heiss geschossen ist, aber in Schuss-Bereitschaft bleiben muss, darf durch die Erwärmung der geladenen Patronen kein Versagen der Treibladungsanzündung vorkommen, kein Cook-off der Treibladungen in den Patronen in den Revolverkammern eintreten und kein Überschreiten des Konstruktionsgasdruckes beim nächsten Schuss auftreten.

3. Wärmehaushalt in der Trommel der Revolverkanone

Die Konstruktion der Waffe muss möglichst so erfolgen, dass auch nach dem Seriefeuer-Schiessen die Trommeltemperatur +71°C nicht übersteigt. Dann sind automatisch alle Funktionen gewährleistet, weil wir uns im zu erfüllenden MIL-STD-Bereich befinden. Die negative Konsequenz kann aber ein hohes Systemgewicht, eine komplizierte Kühleinrichtung oder ein taktisch unbefriedigender Betrieb sein (Waffe nicht immer durchgeladen, Waffe nach kritischer Wartezeit leerschiessen).
Simulationsrechnungen während der Designphase der Revolverkanone ergaben berechnete Trommeltemperaturwerte, welche dann mittels Experiment an realen Trommeln mit scharfen Patronen überprüft und untersucht werden konnten.
Bei den Experimenten wurden bei Trommeltemperaturen oberhalb 75°C während Langzeiteinwirkungen bereits Temperaturüberhöhungen im Treibladungspulverbett durch Selbsterwärmungserscheinungen beobachtet.

Aus diesem Grunde wurde eine detailierte Überprüfung der folgenden Zusammenhänge:

- Temperaturinput in die geladene Patrone
- Treibladungs-cook-off
- Innenballistik oberhalb 71°C (ausserhalb MIL-STD-Temperaturbereich)
- Anzündsicherheit nach der Temperatureinwirkung im Sinoxidsatz (Tetrazenabbau)

verlangt.

4. Wärmehaushalt im Treibladungspulver-Bett

Zur Ermittlung des Einflusses der verschiedenen TLP-Dimensionen und der verschiedenen Geschosstypen auf das Einstellen des Temperaturgleichgewichtes in der Munition wurden laborierte 35mm-Patronen mit Thermoelementen versehen und im Klimaschrank einer Temperaturpendelprüfung zwischen -54°C und +71°C unterworfen.
Es zeigte sich, dass sowohl Metallgranaten wie Kunststoffgeschosse und sowohl grobkörnige wie feinkörnige Treibladungspulver identisches Aufwärm- und Abkühlverhalten zeigen.
Der Messort innerhalb des Pulverbettes ist aber für die Ermittlung der Einpegelungszeit sehr bestimmend. Bild 1.

Zur Charakterisierung der Hitzestaueffekte unter quasi-adiabatischen Bedingungen wurden Dewartests durchgeführt (schlimmstmöglicher Fall). Das Dewar hatte ein ähnliches Innenvolumen wie eine 35mm Patronenhülse und wurde mit 370g Treibladungspulver geladen. Es wurde festgestellt, dass normalerweise im Zentrum des Pulverbettes bei einer Temperatur oberhalb 145°C der Cook-off eintritt. Darum wurde das Dewar, nach dem Erreichen dieser Temperaturschwelle, automatisch mit Wasser geflutet. Bild 2, Bild 3.

Treibladungspulver	Ofen-Temperatur (°C)	Zeit bis 145°C (h)	Verpuffung?
PGD550MC	130	1.2	ja, 145°C
PGD550MC	120	5.8	geflutet
PGD550Ws	130	1.3	geflutet
PGD550Ws	120	5.7	ja, 145°C
PGD550Ws	100	>> 120	geflutet
PGD550SNPE	130	1.6	geflutet
PGD550SNPE	120	5.6	ja, 140°C
PGD550SNPE	100	>>120	geflutet
PGD375Ws	120	5.5	geflutet
PGD750Ws	120	4.7	geflutet

Die verschiedenen Treibladungspulver-Typen, zum Teil über 10 Jahre alt, zeigten ein relativ einheitliches Bild.

In einem weiteren Versuch unter nicht adiabatischer Umgebung wurden 35mm Patronen mit den oben aufgeführten Treibladungspulvern geladen, mit Thermoelementen bestückt, und im Ofen bei 100°C, 110°C, 115°C und 120°C eingelagert. Sehr interessant ist, dass bei 110°C mit allen Pulvern bis 100 Stunden nichts zu sehen war, bei 120°C aber bei allen Proben nach ca. 5.5 Stunden autokatalytisch-ähnlicher Hitzestau einsetzte. Nach 12 Stunden verfügten alle Pulver noch über genügend Reststabilisator.

Die Sinoxidsätze in den Treibladungsanzündern der belasteten Patronen zeigten bei:

110°C	130°C	
bis 6 h	bis 1 h	volle Funktion
ab 150 h	ab 8 h	keine Funktion

Auf eine theoretische Aufarbeitung dieser Resultate zusammen mit dem ermittelten Stabilisatorabbau im Treibladungspulver und den teilweise vorhandenen Wärmeproduktionsraten im Wärmeflusskalorimeter wurde verzichtet. Die Treibladungspulver differenzieren untereinander zu wenig und das Endresultat würde kaum aussagekräftiger.

Die maximal zulässige Temperatur für Langzeittemperaturbelastungen in Waffen und Wärmeschränken (über Stunden) wurde von uns, unter Beachtung der chemischen Reststabilität älterer Pulver verschiedenster Hersteller und unter der Annahme von adiabatisch-ähnlichen Bedingungen, bei 115°C festgelegt.

5. Innenballistik bei hohen Temperaturen

Zur Ermittlung des Druckverlaufes bei hohen Temperaturen bis 100°C wurden 35mm-Drucklaufbeschüsse mit allen in Frage kommenden Geschoss- und Treibladungspulvertypen bei 21°C, 71°C, 80°C, 90°C und 100°C durchgeführt. Die schonende Treibladungsanzündung (ZSD304) erfolgte mit einer heissen Beiladung mit niedrigem Druckniveau. Bei dieser ersten Versuchsreihe zeigte sich, dass keine Werte über dem zulässigen Gasdruck lagen.

Temp. °C	750g Geschoss TLP Ws		550g Geschoss TLP Ws		550g Geschoss TLP SNPE		550g Geschoss TLP MC		380g Geschoss TLP Ws	
	Max-Druck (bar)	V_0 (m/s)	Max-Druck (bar)	V_0 (m/s)	Max-Druck (bar)	V_0 (m/s)	Max-Druck (bar)	V_0 (m/s)	Max-Druck (bar)	V_0 (m/s)
21	3864	1027	3733	1180	3585	1166	3729	1177	4011	1421
71	3887	1032	4130	1196	4052	1197	4293	1218	4021	1423
80	4015	1041	4175	1197	4203	1206	4441	1224	4186	1436
90	4064	1044	4231	1199	4224	1206	4453	1223	4164	1436
100	4174	1048	4373	1203	4124	1199	4696	1231	4219	1432
	Druckwerte korrigiert auf neues Rohr:									
100°C	4610		4640		4500		4917		4688	

Beschuss mit altem Rohr

Zur Verifizierung erfolgte eine 2. Beschussreihe mit alten Treibladungspulvern (bis 12 Jahre alt) und einer harten und gasreichen Treibladungsanzündung (ZSD301) mit Nitrocellulose-Beiladung.

Versuchs-temperatur	550g Geschoss TLP WS		550g Geschoss TLP MC		380g Geschoss TLP WS	
(°C)	Max-Druck (bar)	V_8 (m/s)	Max-Druck (bar)	V_8 (m/s)	Max-Druck (bar)	V_8 (m/s)
21	3563	1157	4109	1201	3290	1364
71	3851	1172	4792	1238	3745	1408
80	3945	1177	4893	1241	3791	1411
90	3711	1167	4800	1237	3886	1416
100	4125	1186	5212	1253	4062	1421

Beschuss mit neuwertigem Rohr

Relativer Druck (bar) zum 21°C-Niveau mit weicher Anzündung ZSD304

Temperatur	550g Geschoss TLP WS	550g Geschoss TLP MC	380g Geschoss TLP WS
(°C)	(bar)	(bar)	(bar)
21	0	0	0
71	397	564	10
80	442	712	175
90	498	724	153
100	640	967	208

Relativer Druck (bar) zum 21°C-Niveau mit harter Anzündung ZSD301 und alten Treibladungspulvern. Die TLP-Muster, die Ladungsmasse und die Druckrohre sind nicht identisch wie beim Beschuss mit schonender (weicher) Anzündung.

Temperatur	550g Geschoss TLP WS	550g Geschoss TLP MC	380g Geschoss TLP WS
(°C)	(bar)	(bar)	(bar)
21	0	0	0
71	288	683	455
80	382	784	501
90	148	691	596
100	562	1103	772

Erstaunlicherweise unterscheiden sich die zwei Beschussreihen qualitativ nur wenig und die gemessenen Druckkurven zeigen keine Druckresonanzen.

Trotzdem ist auf versteckte Gefahren hinzuweisen, da der gewünschte Druck-Temperaturkoeffizient durch die thermomechanischen Eigenschaften des Pulverkornes programmiert wird. Bei tiefen Temperaturen tritt ein gewisser Kornbruch mit Oberflächenvermehrung auf, bei höheren Temperaturen wird das Korn thermoplastisch verformt und verliert Oberfläche. Bei sehr hohen Temperaturen überwiegt wieder die temperatur- und druckabhängige Brenngeschwindigkeitszunahme und kann nicht mehr durch weitere thermoplastische Verformung kompensiert werden. Weiterhin besteht bei sehr weichem Pulverbett die Gefahr von sich bildenden Drucknestern. Bild 4.

6. Temperaturmessungen in der Waffe

An der 35mm Revolverkanone wurden während Seriefeuerbeschüssen Temperaturmessungen mit Thermoelementen durchgeführt. Die Messorte waren am Rohr vorne, mitte und hinten sowie in einer Messpatrone, welche sofort nach dem Beschuss geladen wurde. Die entsprechenden Messpunkte waren an der Patronenhülsenwand, dem Schulterbereich der Patronenhülse, beim Zünder, beim Treibladungsanzünder und in der Mitte des Pulverbettes. Bild 5, Bild 6. Beim Seriefeuer mit einer Kadenz von 1000 Schuss pro Minute wurden beim folgenden Standard-Programm, beinhaltend 3 x (4 x 18 Schuss) innerhalb von 5 Minuten, folgende Spitzentemperaturerhöhungen gemessen:

- Vorne am Rohr 500 °C nach ca. 3.5 Minuten

Nach weiteren 10 Schüssen zur v_0-Messung wurde nach total 16 Minuten die Messpatrone eingesetzt und neu gemessen:

- Patronenschulter 80 °C nach ca. 13 Minuten
- Im Zünder 95 °C nach ca. 17 Minuten
- Patronenhülsenwand 55 °C nach ca. 22 Minuten
- Treibladungsanzünder 50 °C nach ca. 38 Minuten
- Mitte Pulverbett 60 °C nach ca. 55 Minuten

7. Schlussfolgerung

Die im Experiment an der 35mm Skywhip-Revolverkanone erschossenen Temperaturmesswerte zeigen eine gelungene Waffenkonstruktion. Die Trommel- und die Hitzestauprobleme im Treibladungspulver sowie die Zündsicherheit und Cook-off-Probleme sind unter Kontrolle. Bei weiterer Aufwärmung infolge langanhaltendem Dauerfeuer ist genügend Sicherheits- und Systemreserve vorhanden. Die Innenballistik oberhalb +71°C reagiert gutmütig.

---

(1) ADATS Air Defence Anti-Tank System

(2) AHEAD Advanced Hit Efficiency And Destruction

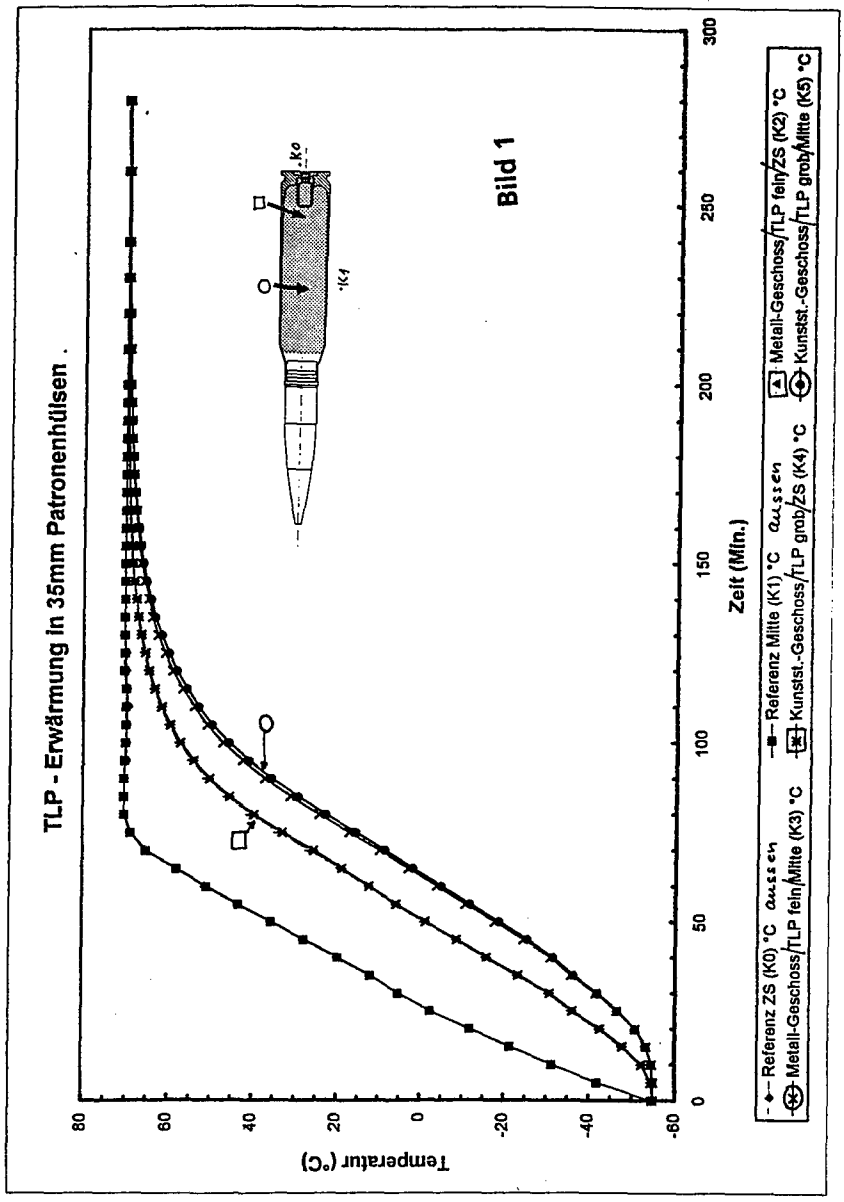
TLP - Erwärmung in 35mm Patronenhülsen .
Temperatur (°C)
Zeit (Min.)
80
60
40
20
0
-20
-40
-60
0
50
100
150
200
250
300
Referenz ZS (K0) °C aussen
Referenz Mitte (K1) °C aussen
Metall-Geschoss/TLP fein/ZS (K2) °C
Metall-Geschoss/TLP fein/Mitte (K3) °C
Kunststst.-Geschoss/TLP grob/ZS (K4) °C
Kunststst.-Geschoss/TLP grob/Mitte (K5) °C
K0
K1

Bild 1

Ofen für Wärmestaumessungen

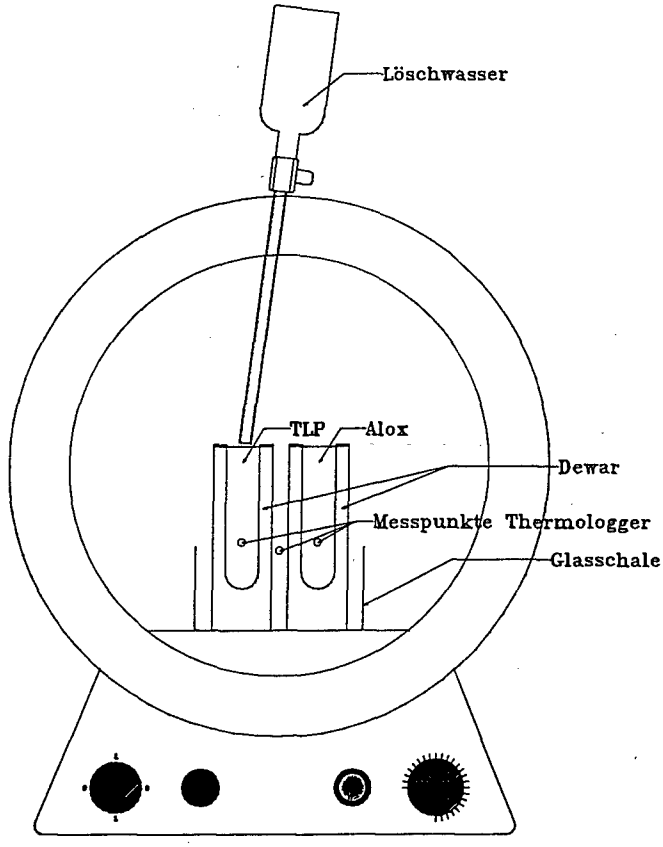

Bild 2

Wärmestau - Messung

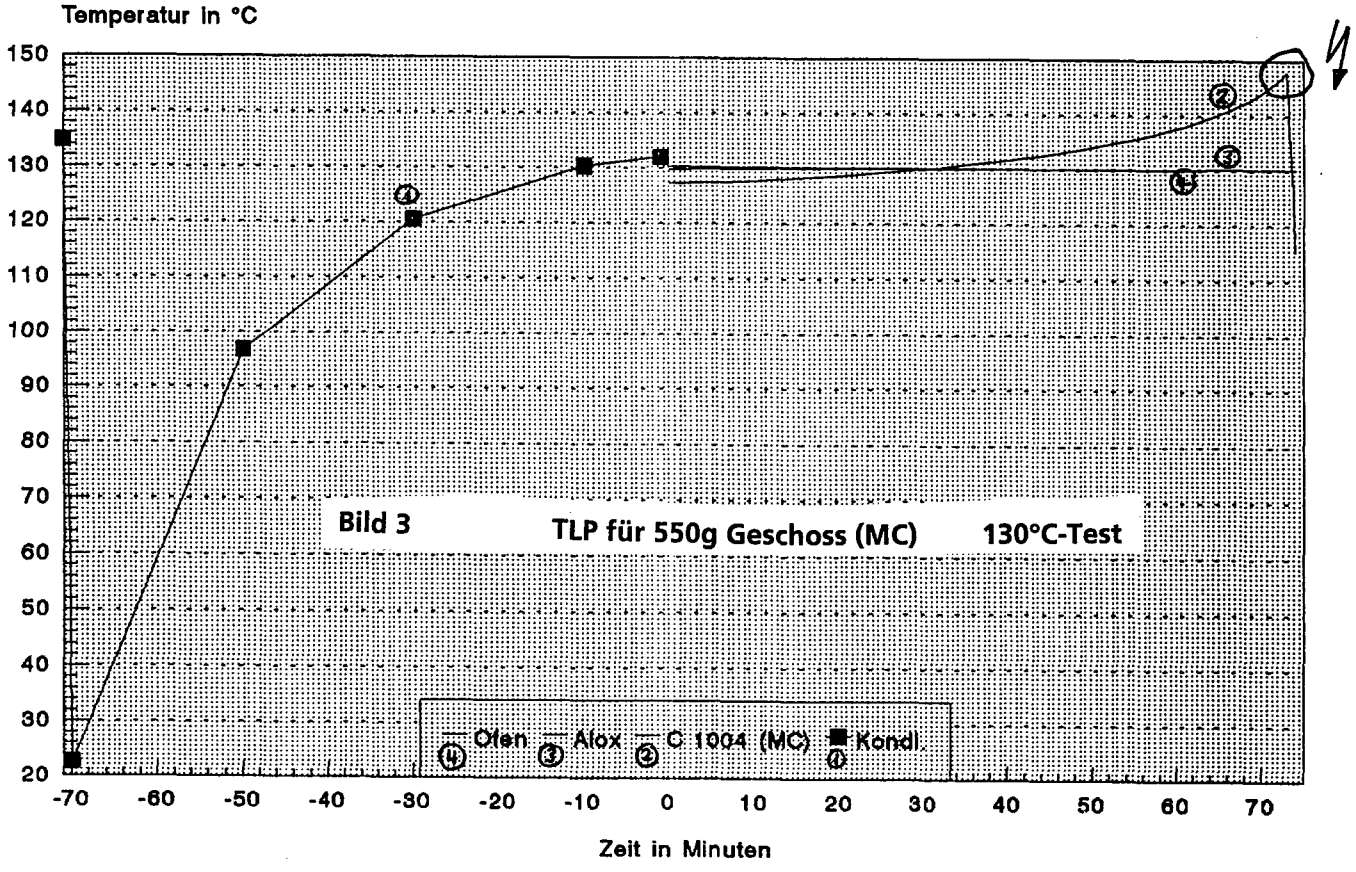

Möglicher theoretischer Druckverlauf

Bild 4

	WK UGD035A 336 g P 2725 WS WU302403 (PGD 550)	Möglicher Theor. Druckverlauf mit Erweichung	Möglicher Theor. Druckverlauf ohne Erweichung
Versuchstemperatu	Max-Druck	Max-Druck	Max-Druck
21	3563	3563	3563
71	3851	3851	3851
80	3945	3945	4045
90	3711	3711	4461
100	4125	4125	5175
110		6350	6350
120		9350	9350

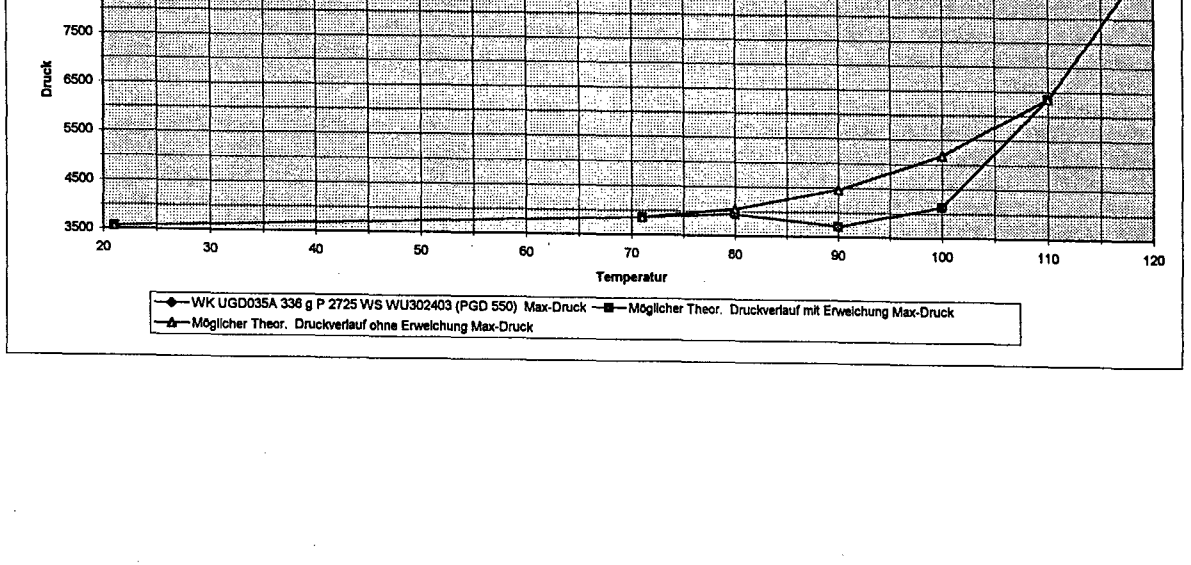

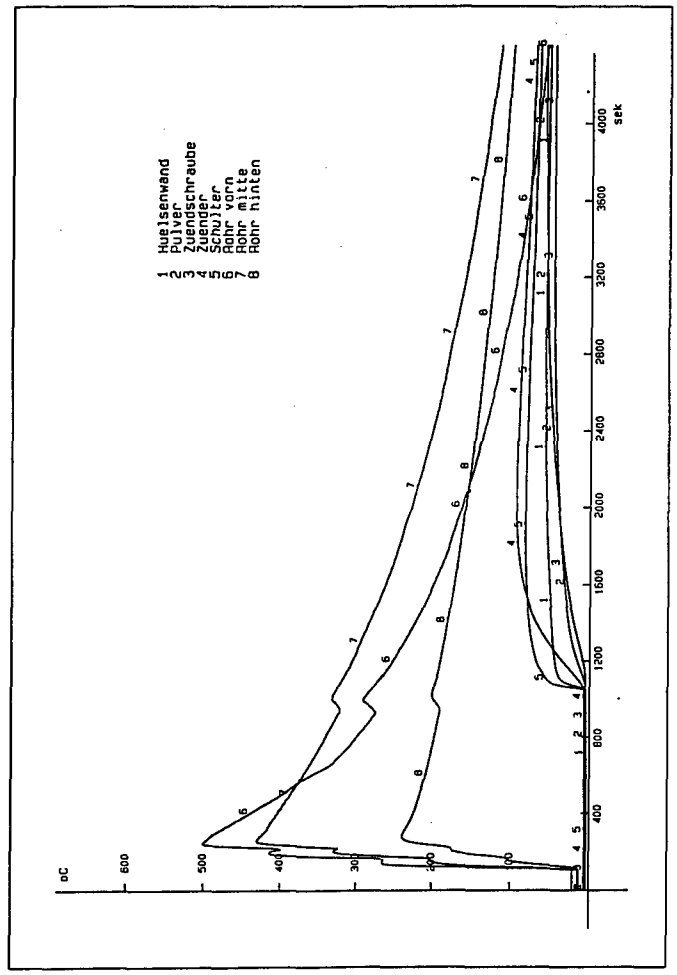

Bild 5 **Aufheizen nach 216 + 10 Schuss**

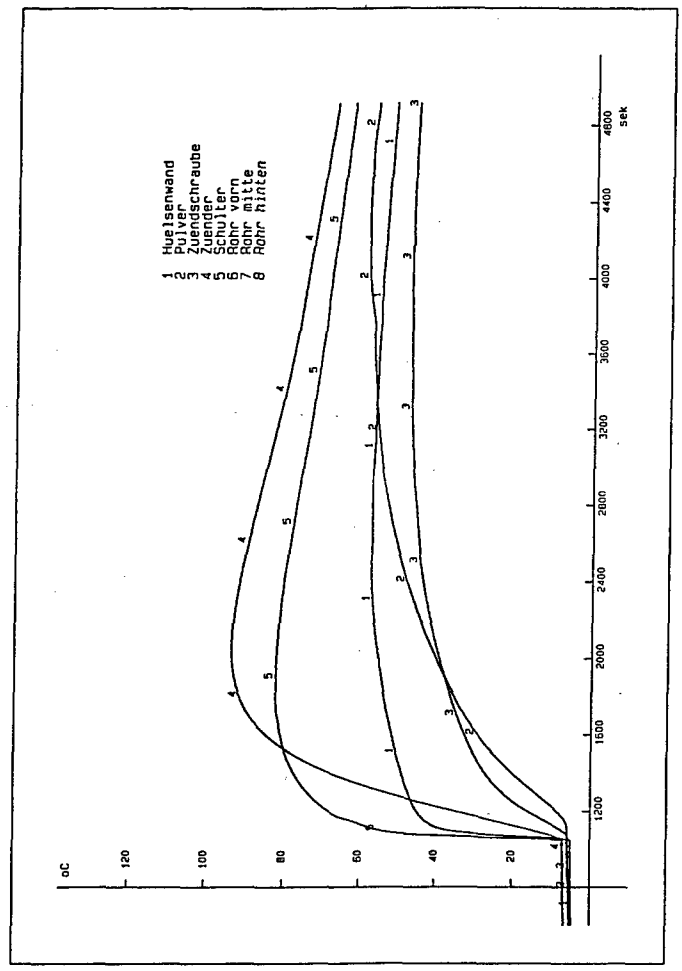

Bild 6 **Aufheizen nach 226 Schuss (Messpatrone)**

RELATION BETWEEN DAMAGE AT LOW VELOCITY IMPACT, AND MECHANICAL PROPERTIES AND EXPLOSIVE LOADING OF PLASTIC BONDED EXPLOSIVES

R.H.B. Bouma, A.C. Hordijk, J.H.G. Scholtes

TNO Prins Maurits Laboratory
P.O. Box 45, 2280 AA Rijswijk, The Netherlands

1. Abstract

At the TNO Prins Maurits Laboratory research is being carried out on the influence of mechanical properties on the response of explosive substances that are thermally and mechanically damaged. Mechanical properties can be determined straightforward with a variety of rheometers. The mechanical moduli depend on temperature and time-scale of the experiment. Furthermore, the mechanical damage at low velocity impact may be correlated to Young's moduli, yield strength, surface under a stress-strain curve, elongation at break, etc...
In order to understand the effect of explosive content, ranging from 65 to 95 % by weight applying processing techniques as pressing, casting and extruding, and the effect of binder properties on the formation of cracks and fragments when explosives are mechanically deformed, a more pragmatic approach has been used to correlate damage to low velocity impact.

The Friability test is one of the tests needed to determine whether an explosive substance can be declared an Extremely Insensitive Detonating Substance (EIDS), see test series 7 of the UN Manual of Tests and Criteria, Transport of Dangerous Goods. In this test a cylindrical sample is firstly projected against a steel plate at about 150 m/s, and secondly the collected fragments are burnt in a manometric bomb. The rate of pressure increase dp/dt is not allowed to exceed 15 MPa/ms. One can assume that with increasing damage to the cylindrical charge dp/dt will increase also due to the higher surface area that can burn.

Experimental work has been directed to the first step of the friability test only. Cylindrical charges are accelerated with a gasgun and impact the steel plate with velocities ranging from 80 to 150 m/s. From high speed video films it is clear that fracture in the charge starts at the interface with the steel plate. Often one big piece is left intact, whereas the impact side of the charge is transformed into a cloud of tiny fragments. The mass of the tiny fragments is determined and plotted against impact velocity. One can clearly distinguish in such a plot the effect of explosive load in the PBX. Furthermore, at an almost constant explosive load, 80 to 85 % by weight, one can see the effect of the mechanical properties of the binder on the damage at low velocity impact.
The low velocity impact experiments require only about 3 charges of 9.0 gram each, and are performed nowadays as another control parameter to adjust the final mix of the binder ingredients for cast-cured compositions.

In paragraph 2 the gas gun used in the experiments is described. In paragraph 3 the compositions and mechanical properties of the plastic bonded explosives are described. And in paragraph 4 the experimental results on the low velocity impact are presented, followed by discussion and conclusions in paragraph 5.

2. Experimental equipment

A gas gun has been constructed at TNO that can accelerate projectiles of about 10 grams to velocities up to 180 m/s. This gas gun is used for example, to perform the impact experiment corresponding to the friability test described in test series 7 in order to determine whether an explosive substance can be declared an Extremely Insensitive Detonating Substance [1]. According to test series 7, the cylindrical charges have a diameter of 9.0 ± 0.1 gram, and a diameter of 18.0 ± 0.1 mm. The same dimensions apply to the experiments presented here. The test series 7 require an 150 ms^{-1} impact velocity of the charge at a steel plate, whereas the impact velocity has been varied here from 60 to 150 ms^{-1}. The impact velocity can be varied by changing the pressure in the pressurization vessel of the gas gun and/or the position of the

charge in the barrel. The actual velocity is determined by measuring the time lapse of the pulses given by two optical sensors.

The lay-out of the gas gun is given schematically in figure 1. The gas gun is mounted at the outside wall of the test cell and consists essentially of a pressurization vessel (2), a barrel (4), and two valves for pressurization (1) and firing (3), respectively. The steel target plate (5) is mounted on the wall opposite side of gas barrel. A polymethylmethacrylate (PMMA) tube (6) is placed in front of the steel plate to collect the fragments after impact. The optical sensors (7) for the velocity measurement are placed in front of this PMMA tube at a fixed position.

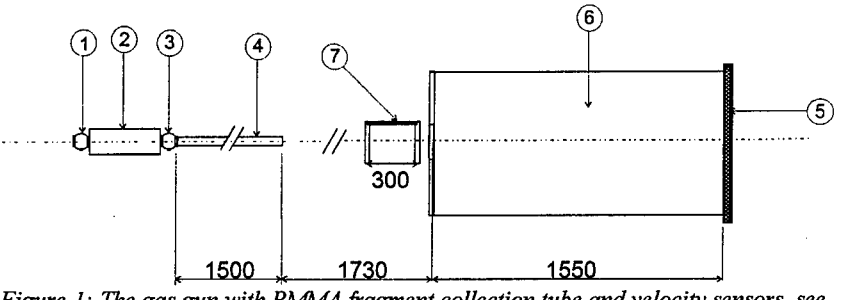

Figure 1: The gas gun with PMMA fragment collection tube and velocity sensors, see also reference 2.

The mass of every charge is determined before every experiment. After impact the mass lost in tiny fragments is calculated from the initial mass and the measured mass of the unfragmented charge.

3. Materials

Plastic bonded explosive (PBX) charges are made with RDX or HMX as the explosive substances, and the corresponding batches will be referred to as RU and HU respectively, followed by a batch number. The explosive charges are made by pressing, extruding or casting, in order to vary the explosive content from 65 tot 95 % by weight. As well monomodal, bimodal as trimodal mixtures of RDX or HMX have been used.

All compositions are based on HTPB (hydroxy terminated polybutadiene), and cured with IPDI (iso-pherondiisocyanate). IDP (iso-dodecane pelargonate) or DOA

(dioctyladipate) is employed as plasticizer. The mechanical properties of the binder are changed by the amount of curing agent IPDI, or the eventual addition of the chain extender TMHD (trimethylhexanediol) or HDO (hexanediol). Batches are produced in quantities of 300 to 400 grams typically.

The mechanical properties are determined with a draw-bench with a shear rate of 0.01 s^{-1} both for the JANNAF specimens (a crosshead speed of 50 mm/min) as well as for cylindrical compression samples. The mechanical properties are determined at room temperature.

In table 1 the compositions of the cast charges are given, and in table 2 the compositions of the pressed and extruded batches. The mechanical properties of the cast compositions are determined in tension, whereas these properties of the pressed and extruded compositions are determined in compression.

In tables 1 and 2 the RDX or HMX solid load is given, the amount of chain extender per unit of prepolymer (only table 1), the volume average explosive crystal diameter, the Young's or compression modulus, and the toughness (only table 1). The toughness is equal to the total area under the stress-strain curve.

Table 1: Description of the cast compositions.

	solid load wt.%	mol chain ext./ mol prepolymer	diameter µm	Young's modulus MPa	toughness MPa
RU 128	65	0	18	5.6	0.53
RU 130	65	0	180	8.5	0.16
RU 144-1	65	0	10	3	0.67
RU 144-2	65	0	10	5.5	0.62
RU 147-2	70	0	355	-	0.05
RU 146-1	85	0.75 (TMHD)	bimodal	1.9	0.12
RU 146-2	85	0.75 (TMHD)	bimodal	1.34	0.15
HU 28	85	0	trimodal	17	0.10
HU 35-2	85	0	16/350 bimodal	12*	-
HU 36-1	85	1.0 (HDO)	16/350 bimodal	7*	-
HU 40-1	80	1.25 (TMHD)	16/350 bimodal	2.0	0.27
HU 41-1	80	1.75 (TMHD)	16/350 bimodal	2.2	0.27
HU 39-1	79	2.5 (TMHD)	16/350 bimodal	40	0.40

* *Compression modulus instead of Young's modulus.*

Table 2: Description of the pressed and extruded compositions.

	solid load wt.%	diameter µm	compression modulus MPa
RU 132-2	86.2	18	68
RU 133-1	86.2	180	79
RU 129-1	95	18	230
RU 131-2	95	180	-
RU 128-2	65	18	5.6
RU 130-2	65	180	6.7

The solid load has a strong influence on the Young's modulus or the compression modulus, because the respective moduli of the explosive and binder phase, differ several orders of magnitude.

From table 1 (RU 128, RU 130 and RU 144) and table 2 it appears that the diameter of the crystal influences the mechanical properties. With increasing mean diameter of the crystal the elastic modulus will increase, while at the same time the toughness will decrease.

The effect of adding TMHD (HU 39, HU 40 and HU 41) is to increase both the modulus as the toughness.

4. RESULTS

In figure 2 the mass of the tiny fragments, referred to as mass loss, is plotted versus the impact velocity of the charge for batch RU 147-2. The mass of the fragments is obtained by subtracting the mass of the remaining intact part of the charge from the initial mass of the charge. Both data of 9 gram samples and 7 gram samples are plotted. The latter have been obtained by decreasing the diameter of charges from the same batch with different dimensions in order to have more charges to measure the influence of impact velocity. There is no difference between 7 and 9 gram samples. The 9 gram samples have a length/diameter ratio of about 1, indicating that the impact time is governed by lateral release waves.

With charges from batch RU 147-2 one can see that within the velocity range of the applied gas gun it is possible to have non-fragmented charges (impact velocity < 75 ms^{-1}) and completely fragmented charges (impact velocity > 150 ms^{-1} for 9 gram samples). The curve in figure 2 is found by a fitting the data to a power law function,

although no model is available describing the fragmentation of a heterogeneous solid, in such an experiment.

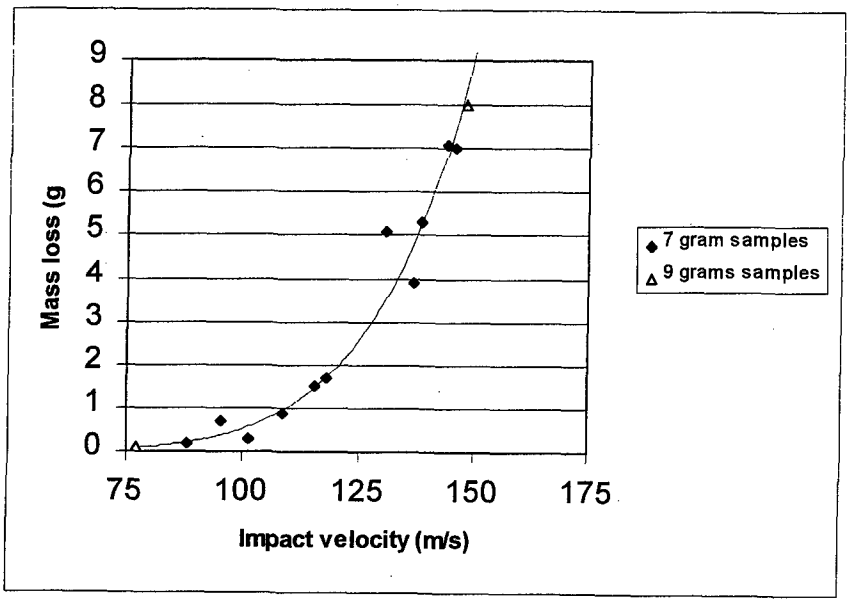

Figure 2: Gas gun experiments with RU 147-2. Mass loss versus impact velocity.

In figure 3 the mass of the fragments is plotted versus impact velocity for RDX-based, monomodal PBXs. Note that the mass of fragments is plotted from 0 to 2.5 grams, in order to show the effect of mechanical properties at small damage levels.

Results for the pressed charges RU 129 and RU 131 are not shown, as the charges are fully fragmented at velocities as low as 70 ms^{-1}. Extruded charges RU 132 and RU 133 have less mechanical damage compared to the pressed charges. Cast charges RU 128 and 130 show less mechanical damage than the extruded charges. The only difference in forementioned batches is the explosive content, RDX crystals have a mean diameter of 18 or 180 μm. The mechanical damage in gas gun experiments seems to be directly related to the explosive content of the explosive, which is in turn directly related to the elastic modulus, see tables 1 and 2.

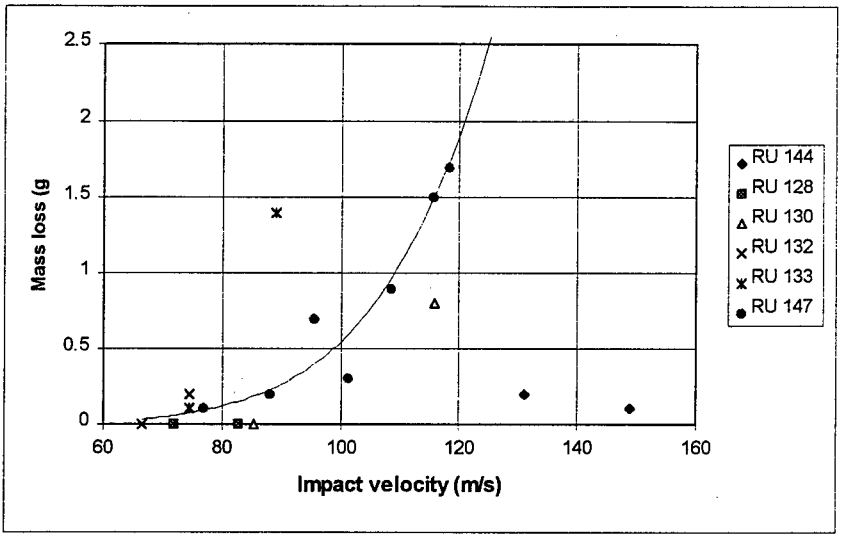

Figure 3: Gas gun experiments with monomodal, RDX-based charges. Mass loss versus impact velocity.

It seems that the size of the RDX crystals has its influence too. RU 144 (10 μm RDX) has the same 65 wt.% solid load as RU 128 (18 μm) and RU 130 (180 μm), and shows the least mechanical damage in the gas gun experiments. RU 144 has a smaller Young's modulus and a higher toughness compared to RU 128 and RU 130.

The value of the Young's modulus is not the only parameter, however, that determines the mechanical behaviour in low velocity impact. RU 146 has a higher explosive content compared with RU 144, but has a smaller Young's modulus. This has been accomplished by using a bimodal distribution of RDX and applying a chain extender. The velocity at which 1 gram of the impacting sample is fragmented is 105 ms^{-1} for RU 146 and more than 150 ms^{-1} for RU 144. RU 144, however, has the largest toughness, i.e. the largest work needs to be performed in order to break the sample.

In figure 4 the mass of the fragments is plotted versus impact velocity for HMX-based PBXs. In this figure the solid load is almost constant, 79 to 85 wt.%. Furthermore, the same bimodal distribution of HMX crystals has been employed, except from batch HU 28.

One can easily rank the batches to their sensitivity for mechanical damage. RU 28 is most sensitive, followed by HU 35, HU 36, and HU 39. HU 40 and HU 41 show the same and least mechanical damage at low velocity impact.

The effect of adding 1.25 or 1.75 mol TMHD per mol prepolymer HTPB on mechanical properties and damage at low velocity imact, seems to be very limited, although addition 2.5 mol TMHD per mol HTPB has a remarkably negative effect on the damage level in the gas gun experiments.

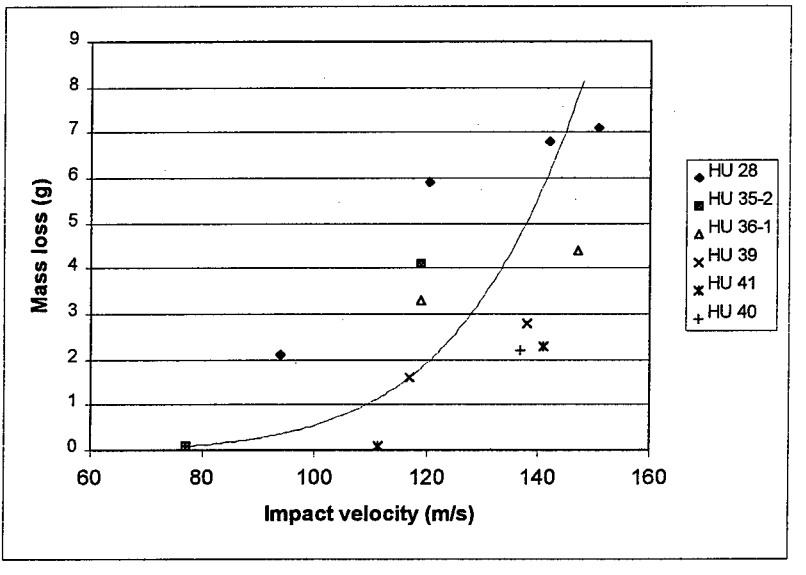

Figure 4: Gas gun experiments with HMX-based charges, effect of binder variations. Mass loss versus impact velocity.

4. Discussion and conclusions

Internal damage can be imposed to plastic bonded explosives already at impact velocities of 20 to 100 ms^{-1}, see reference 3 This internal damage has shown to lower the critical shock initiation pressure of these PBXs. In this paper PBXs have been damaged more severely, to an extent that part of a charge is fragmented.

It is assumed that with increasing damage to the cylindrical charge dp/dt will increase also due to the higher surface area that can burn. In reference 4, for example, the relation between dp/dt and impact velocity has been investigated for the same impact velocity regime as considered here and results confirm the assumption.

In this paper it has been shown that the mechanical damage at low velocity impact is strongly governed by the elastic moduli of monomodal PBXs. A PBX with a lower explosive content and with smaller explosive crystals is less liable to mechanical damage.

When applying bimodal instead of monomodal crystal distributions, however, no direct correlation has been found comparing the mechanical damage in low velocity impact and the Young's modulus of the two crystal size distributions. The Young's modulus is a mechanical property representing the proportion between the force acting on the material and the deformation of the material, in the linear viscoelastic regime. The damage imposed by the low velocity impact experiments is such that the material fragments and one should take into account the work needed to deform the material up to the point of failure, i.e. the toughness of the material.

In reference 5 a rationale is given to obtain so-called damage resistance compositions by application of binder systems with sufficient tensile strength and extremely high elongations, i.e. to have a high toughness.

Even when the relation between mechanical properties (tensile/compression modulus and/or toughness) and damage at low velocity impact is not accurately known, one can easily perform experiments with a gas gun and measure the mass of the unfragmented charge, in order to know how the binder ingredients have to be adjusted to obtain a PBX which is relatively insensitive to mechanical damage. Today this is done at TNO for cast-cured compositions.

5. Abbreviations

DOA	dioctyladipate
HDO	hexanediol
HMX	cyclotetramethylenetetranitramine
HTPB	hydroxy terminated polybutadiene
IDP	iso-dodecane pelargonate
IPDI	iso-pherondiisocyanate
PBX	plastic bonded explosive
PMMA	polymethylmethacrylate
RDX	cyclotrimethylenetrinitramine
TMHD	trimethylhexanediol

6. References

1 UN Manual of Tests and Criteria, Transport of Dangerous Goods.

2 J.H.G. Scholtes, The construction of the friability test at TNO-PML, TNO-report PML 1996-A58, july 1996.

3 H.P. Richter, L.R. Boyer, K.J. Graham, A.H. Lepie, N.G. Zwierzchowski, Shock sensitivity of damaged energetic materials, Ninth Symposium (International) on Detonation, Portland, Ore, August 1989, 574-579.

4 I.E. Hooton, C. Belanger, Curing studies for CX-84 explosives, DREV-TM-9714, December 1997.

5 Russell Reed Jr., B.Y.S. Lee, Tough PBXs, ADPA 1989.

PROCESSING AND CHARACTERIZATION OF GUN PROPELLANT FORMULATIONS CONTAINING ENERGETIC THERMOPLASTIC ELASTOMERS

by

Ms F. Beaupré and Dr. G. Ampleman

Defence Research Establishment of Valcartier

2459 Pie-XI North Blvd. Val-Bélair, Qc

Canada, G3J 1X5

Abstract

Over the last few years, the Defence Research Establishment of Valcartier (DREV) has been involved in the development and synthesis of energetic thermoplastic elastomers (ETPEs) to be incorporated as a binder in energetic materials. One of these ETPEs, based on linear GAP-1000, is presently used in high energy, low vulnerability gun propellant formulations. Several formulations containing this new ETPE and an energetic plasticizer (nitrate ester) have been processed and evaluated. The energies provided by these new formulations are up to 1300 J/g.

A characterization of these formulations is presented in this paper. The properties are also compared to those obtained for a LOVA formulation of reference containing an inert plasticizer as well as an inert binder.

Introduction

Over the last years, the Defence Research Establishment, Valcartier (DREV) has been conducting research work in the replacement of cellulose acetate butyrate (CAB), the inert binder used in the baseline formulation of LOVA-type gun propellants. Gun propellant formulations with CAB are known for not having a good mechanical behaviour and more especially under cold conditions. The preferred way to improve the mechanical properties of the LOVA-type gun propellants developed at DREV was the introduction of thermoplastic elastomers (TPEs) in the formulations. Formulations with inert TPEs were processed and have shown an improvement in the mechanical properties of the gun propellant grains (ref.1). Even if the addition of an inert TPE was already an important improvement over the baseline formulation, there were requirements, expressed and/or expected, for the development of formulations that could still increase the ammunition's performance.

Concurrently to the research work in gun propellants, DREV is also involved in the synthesis of energetic thermoplastic elastomers (ETPEs) to be used in energetic materials. Although these new materials were meant to be used in melt-cast explosives, some have been incorporated as a binder in gun propellant formulations. At DREV, the ultimate aim of using an EPTE in a gun propellant formulation is to see if a formulation containing only energetic ingredients could be achievable and still have low vulnerability characteristics.

Other laboratories have also undertaken similar research work to synthesize and incorporate energetic TPEs (ETPEs) or energetic polymers of other types in gun propellant formulations. In the US, an ETPE which has been studied a lot is the BAMO/AMMO (refs.2,3). In the UK work has been undertaken with a different route and polymers such as Poly-NIMMO and Poly-GLYN are considered for their introduction into the formulations (ref.4).

In Canada, a GAP-based ETPE synthesised at DREV has been incorporated in the gun propellant formulations and has provided very interesting results (refs. 5,6). One of the other aspects of incorporating a TPE energetic or not in a gun propellant formulation is that it opens the door to a recyclable material which is a very interesting feature. Since it is becoming more and more evident that all the new munitions will be designed with the idea to know exactly what to do with them from "cradle to grave", the study of recyclable materials is an important feature.

The object of the paper is to present results obtained so far with gun propellant formulations containing ETPEs formulated at DREV.

ETPEs

In this study, three ETPEs were prepared according to the method presented in ref.5 and incorporated in the formulations. They were all solvated in ethyl acetate prior to their incorporation with the other ingredients. These ETPEs were based on linear GAP and on two other polymers named here A and B.

Theoretical Evaluation

A theoretical evaluation of the impetus of the formulations containing these ETPEs was conducted using the BAGHERRA computer code. This thermodynamic computer code predicts, among other things, the impetus level or the « potential force » of the formulations. The impetus levels of some formulations as well as the one for the reference formulation (for comparison purpose) are presented in Table 1. The theoretical data presented were obtained with a loading density of 0.15 g/cm^3.

Table 1. Theoretical impetus levels of formulations containing ETPEs

FORMULATION	BINDER	IMPETUS (J/g)	FLAME TEMPERATURE (K)
REFERENCE	CAB	1012	2539
36	INERT TPE	1231	3164
73	GAP-based ETPE	1304	3457
90	GAP-based ETPE	1337	3556

As expected and demonstrated in Table 1, the formulations containing ETPEs have higher impetus levels. An energetic nitrate ester plasticizer was used for all formulations except the reference where an inert one was used ATEC (Acetyl Triethyl Citrate). The percentage of the binder in the formulations varied between 9 and 12%. Impetus values up to 1337 J/g are predicted by BAGHEERA. This represents an increase of more than 30% when compared to the reference baseline formulation. Although these impetus levels are very interesting, they do not always directly translate into higher performance when introduced in a gun. Another aspect that should be noted is the predicted values of the flame temperatures. High flame temperatures like the ones in Table 1 are not suitable since they would imply gun barrel erosion. Depending on the application chosen for these high energy propellants, a compromise will certainly have to be made between energy and erosion.

Processing characteristics

All the formulations were processed with an energetic plasticizer and all the other ingredients of LOVA-type formulations in a sigma-blade mixer. The technique described in ref.7 for the preparation of solvent-based formulations was used. Also all

the formulations were extruded in a seven perforation cylindrical geometry. The outside diameter of the grains was 6.35 mm (0.25 in). However, the formulations did not all have the same processing behaviour. One thing was constant though, in all cases, another ingredient had to be incorporated in the formulations to stiffen the propellant grains that were too soft. For the three types of ETPEs, the addition of small quantities were sufficient to solve the problem.

Most of the formulations were processed with GAP-based ETPEs since these materials were available in larger quantities. Their behaviour during the evaporation step differed than what was observed for the reference formulation. The consistency of the dough prior to the extrusion was softer that the one obtained for the baseline formulation. This phenomenon was also noted for the formulations containing polymers A and B but to a more important level. The formulations with the A-based ETPE were more difficult to extrude with a perfect geometry. In some cases, the perforations were not properly formed and tend to collapse. It is not possible at this time to state that one of the three ETPEs was easier to process than the other two due to the limited amount of formulations that were processed. Optimization of the ingredient ratio in these new formulations is still going on as well as their rheological characterization.

The fact that all the formulations could be processed with a technique similar to the one used for the reference formulation is an important aspect. Since a modification in a processing procedure implies a lot of effort, keeping it the same becomes an advantage for the use of these new materials.

Ballistic evaluation

A ballistic evaluation was conducted on the most promising formulations. Some of the results obtained from experiments in a 700 cm^3 closed bomb vessel are reported in Table II. A Kistler piezoelectric gauge was use to take the pressure measurements and a loading density of 0.15 g/cm^3 was selected for all the experiments. Three experiments

were conducted for each of the formulations tested.

Table II. Ballistic evaluation of gun propellant formulations containing ETPEs

FORMULATION	BINDER	P_{MAX} (MPa (psi))	RELATIVE IMPETUS
REFERENCE	INERT	188 (27320)	-
36	INERT TPE	205 (29685)	1.09
73	GAP-based ETPE	225 (32583)	1.19
90	GAP-based ETPE	225 (32600)	1.19
95	GAP-based ETPE	218 (31630)	1.16
133	A-based ETPE	222 (32181)	1.18

As one could expect and shown in Table II, all the formulations containing an ETPE have a relative impetus higher than the formulation of reference. It can also be noted that the rank of the relative impetus is slightly different than the one predicted by the theoretical values reported in Table I by BAGHEERA. However, this ranking is close enough to the one proposed by BAGHEERA that they can be considered similar. Since, as stated in ref.8, care should be taken when comparing data from thermodynamic computer codes, the rank suggested by the ballistic data should prevail. In certain cases, formulations had the same relative impetus. In these cases, preference will be given to the formulations that will demonstrate the best mechanical behaviour. Erosion is also a very important issue. A preference will also be given to the less erosive formulations. In order to study the erosivity of gun propellants, conventional and LOVA-type, a set-up has recently been installed at DREV and will be soon used to test the new formulations containing ETPEs.

Mechanical properties

The mechanical properties of the formulations are also a very important factor to consider when developing low vulnerability or any type of gun propellants. As stated in the introduction, the main purpose of adding a TPE inert or energetic in a formulation is to obtain gun propellant grains with a more elastic behavior. The first results obtained with a Drop-Weight Mechanical Property Tester (DWMPT) according to the method described in ref. 9 are promising. They have shown that these ETPE formulations were not as stiff as the formulation of reference and exhibited a better mechanical behaviour in cold conditions (-20°C). The results of the DWMPT experiments will be available in the near future.

Conclusion

Three energetic thermoplastic elastomers (ETPEs) have been synthesized at DREV and evaluated in high energy LOVA-type gun propellant formulations. The results obtained so far with the formulations containing these new binders are promising.

The formulations containing these new materials were processed with the solvent-based technique currently available for standard LOVE-type gun propellant formulations. Presently, the ones containing GAP-based ETPEs appear to be the easiest ones to process.

The data obtained from the BAGHEERA computer code and the ballistic experiments have demonstrated that these new formulations have an impetus level about 20 to 30% higher than the one for the baseline LOVA formulation.

References

1. Beaupré, F. and McIntosh, G., " Improvement in Mechanical Properties of LOVA-type Gun Propellants ", Proceedings of the 16th meeting of TTCP WTP-4, China Lake, Ca, USA, April 1991.
2. Wardle, R.B., Wallace, I.A. and Bennett, R.R., " Development of and Oxetane Copolymer, BAMO/AMMO, as an Insensitive Propellant Binder", Proceedings of the International Symposium on Energetic Materials Technology, Orlando, Fl, USA, March 1994.
3. Wardle, R.B., Edwards, W.W", Hinshaw, J.C. and Hartwell, J.A., "Polyoxetane Thermoplastic Elastomers as Gun Propellant Binders", Proceedings of the 6th International Gun Propellant and Propulsion Symposium, ADPA and ARDEC, November 1994.
4. Colclough, M.E., Paul, N.C., Desai, H. and Shephard, N., "DRA Approaches to New Energetic Binders", Proceedings of the 6th International Gun Propellant and Propulsion Symposium, ADPA and ARDEC, November 1994.
5. Ampleman, G., Marois, A., Désilets, S., Beaupré, F. and Manzara, T., " Synthesis and Production of Energetic Copolyurethane Thermoplastic Elastomers Based on Glycidyl Azide Polymer", 29th International ICT Conference, Karsruhe, Germany, June 1998.
6. Beaupré, F., Ahad, E. and Ampleman, G., " Preliminary Studies of HELOVA-type Gun Propellant Containing Energetic Binders ", Proceedings of International Symposium on Energetic Materials Technology, ADPA, Orlando, Fl, USA, 1994.
7. Beaupré, F. and Durand, R., " Processing Studies of LOVA-type Gun Propellants ", DREV-R-4603/90, October 1990.
8. Lussier, L.-S., Beaupré, F. and Lavigne, J., " The Use of Thermodynamic Codes for Comparison of Propellant Performance ", ADPA 5th International Gun Propellant and Propulsion Symposium, 19-21 November 1991, Dover, NJ, USA
9. Varga, L., " DREV Drop-Weight Mechanical Property Tester : A Testing Method for LOVA Gun Propellants ", DREV R-4586/90, April 1990

EFFECT OF PROCESS TYPE ON PROPELLANT PROPERTIES

Charles Frank Wiehahn

Somchem, Division of DENEL, (Pty), Ltd, Gun Propulsion – R & D,
PO Box 187, Somerset West, 7129, South Africa

Abstract

Due to environmental pressure because of the solvents used and other factors such as possible cheaper and more reproducible processing, shorter process cycles and improved propellant properties, the solvent-free propellant process was evaluated against the more commonly used solvent process for gun propellant manufacturing. This paper investigates and compares the two processing techniques, the processing limits and the propellant formulation criteria. Various propellant properties such as the chemical, thermochemical, mechanical, dimensional and ballistic properties were determined and evaluated. Certain conclusions are made regarding the advantages and disadvantages of the solvent-free process compared to the solvent process.

1 INTRODUCTION

The propellant formulations presently in production are mostly of a conventional nature and are processed according to the solvent process with ethyl acetate, ether, acetone and ethanol as the typical solvents used. A new generation of propellants are sought which will have improved properties with regards to barrel erosion, combustion characteristics, sensitivity, vulnerability and processability. Because of environmental pressures on the solvents used and to improve the processability, especially regarding the reproducibility of the propellant dimensional parameters such as web and perforation, solvent-free processed propellants are sought.

In order to improve barrel erosion cooler burning propellants are required and therefore formulations with lower flame temperatures were investigated. The ballistic performance of a new propellant should be at least the same or better than that of the currently used propellants and therefore the specific energy of such new propellants must be the same or higher.

The sensitivity and vulnerability of a propellant formulation is a function of the propellant components and by carefully scrutinising and selecting the components the sensitivity and vulnerability of propellant formulations can be greatly improved.

1.1 CRITERIA FOR NEW PROPELLANT PROPERTIES

The following propellant properties have been set as a guideline for the development of new propellant formulations:

- Thermochemical properties:
  - ♦ Specific energy ≥ 1040 J/g
  - ♦ Flame temperature ≤ 2900 K
  - ♦ Molecular mass of combustion gasses ≤ 23 g/mole
- Theoretical density > 1.50 g/cm3

1.2 PROCESSING PARAMETERS

Irrespective of the guidelines for all the other propellant properties, one of the most critical parameters is that the propellant formulations must be processable. At present two basically different types of manufacturing processes are being used, namely:

- The solvent process
- The solvent-free process

The processing parameters for the two types of processes differ considerably and we will concentrate on propellant formulations that can be processed according to both processes. During previous development work the processing parameters for the solvent process, when using nitrocellulose (NC) as binder, have been determined and they are basically as follows:

- Effect of binder : plasticiser ratio on propellant processing:
  - ♦ binder : plasticiser > 2 processing not possible
  - ♦ binder : plasticiser 1- 1.5 good processing
  - ♦ binder : plasticiser < 1 too soft, poor processing
- Crystalline content < 50%

A high crystalline content can be accommodated with the solvent process, but for the solvent-free process the crystalline content should not exceed 50% and because the propellant formulations must be processable with both processes we will strive to maintain the concentration of crystalline material at 50% or less.

2 SELECTION OF CANDIDATE PROPELLANT FORMULATIONS

2.1 THEORETICAL FORMULATIONS

A new generation of propellant formulations with a specific energy and flame temperature that complies with the previously stated thermochemical criteria (refer to 1.1) and which could be processed by the solvent-free process, was investigated. Various series of propellant formulations were investigated and the general guideline for the selection of the formulations were the following:

- binder to plasticiser ratio between 1.0 and 1.5 : 1
- the NC was to be kept between 25% and 40%
- crystalline content < 50%

A series of propellant formulations were selected according to the above criteria for processability and the concentrations of the components were all varied in fixed increments between the upper and lower limits of the feasible processing range. A large number of formulations were generated that complied with the processability and the thermochemical criteria. In order to reduce this list further, tighter constraints were applied. This list was finally reduced to 5 propellant formulations that could be experimentally processed and evaluated.

3 TEST AND EVALUATION RESULTS

All 5 formulations were successfully processed according to both the solvent and the solvent-free process. The results from the various test and evaluation facilities are discussed below.

3.1 CHEMICAL AND SENSITIVITY PROPERTIES

The laboratory analysis of the densities, energy values and tvs (total volatile substances) results of the experimental propellants are reported in Table 1. The solvent processed samples are designated **SOL** and the solvent-free **SF**. The densities of the SOL and SF propellants are graphically presented in Figure 1.

Table 1: Densities, Energy Values and TVS of Experimental Propellant Formulations

Formulation No	Density (g/cm^3)		Energy Value (J/g)		TVS (%)	
	SOL	SF	SOL	SF	SOL	SF
1	1.581	1.582	3738	3716	0.57	1.14
2	1.619	1.604	3759	3753	0.56	1.09
3	1.595	1.580	3743	3703	0.54	0.92
4	1.604	1.588	3748	3725	0.67	1.26
5	1.618	1.595	3708	3726	0.63	0.97

There is a very good correlation between the energy values of the SOL and SF formulations which shows that no variances in the formulations occurred during the processing. This effect is also noticeable from the maximum pressure values recorded during closed vessel firings.

The samples from the solvent process are all drier (lower tvs) than the samples from the solvent-free process. This is because the SOL samples were dried in an oven for a number of days and the SF samples were only dried for a few hours to remove surface water picked up during the cutting process. The difference between the tvs values of the SOL and SF samples will gradually disappear as the samples reach an equilibrium with the atmospheric conditions.

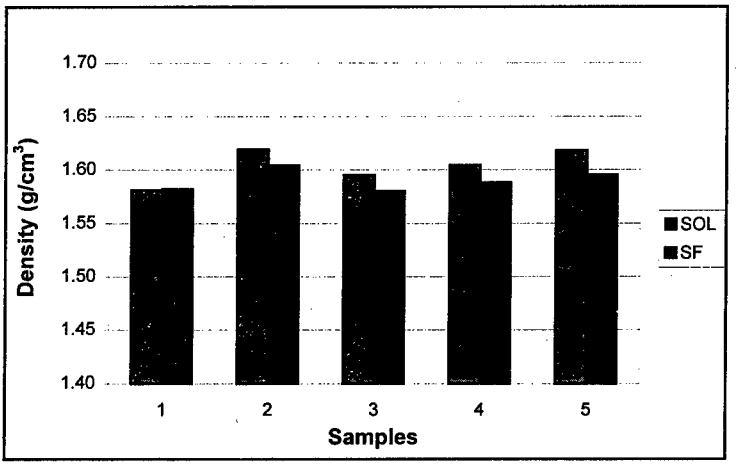

Figure 1: Densities of Solvent and Solvent-Free Processed Propellant Formulations

The densities of the solvent processed samples are in all cases the same or higher than that of the solvent-free samples. Samples 2 and 5 have the highest densities, irrespective if the SOL or SF samples are used, and this correlates with these two samples also having the highest crystalline content.

The methyl violet stability test was performed on all 10 samples (SOL and SF) of the 5 propellant formulations and no sign of a colour change or of fumes after 60 minutes at the test conditions were reported. The stability values of these propellants are therefore at least as good as those of conventional propellants.

3.2 MECHANICAL PROPERTIES

The stress, strain, Young's Modulus and impact tests results of the experimental propellants are reported in Table 2. A graphical presentation of the stress, strain and Young's Modulus of the experimental propellants are given in Figure 2 respectively.

Table 2: Mechanical Properties of Experimental Propellant Formulations

Formulation No	Stress (Mpa)		Strain (%)		Young's Modulus (MPa)		Impact Strength (kJ/m^2)	
	SOL	SF	SOL	SF	SOL	SF	SOL	SF
1	11.9	4.8	31.3	33.5	138.5	24.0	37.7	18.81
2	14.6	5.9	14.8	28.6	352.3	29.6	25.86	11.59
3	13.8	5.9	21.2	33.2	298.8	26.9	38.79	20.00
4	15.6	7.6	24.4	27.0	422.1	80.2	34.70	19.43
5	14.8	6.3	22.0	24.9	407.2	49.9	35.35	15.19

There is a good correlation between the stress values of the solvent processed formulations and between the stress values of the solvent-free formulations. However, the stress values of the solvent processed formulations are approximately double that of the solvent-free formulations. There is far less variance between the different samples of the solvent processed formulations or between the solvent-free processed formulations for that matter, than between the same formulation processed according to the two different processes. In this case the type of process has a larger influence on the stress values than the type of formulation.

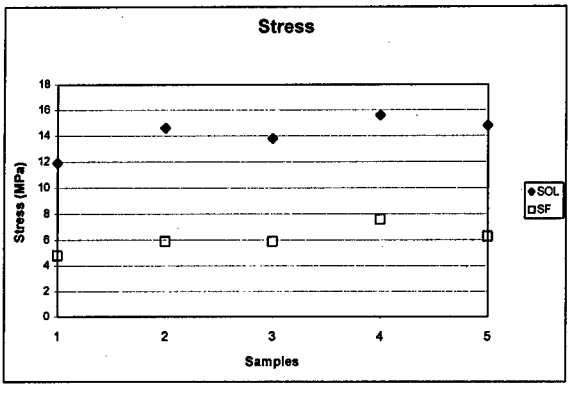

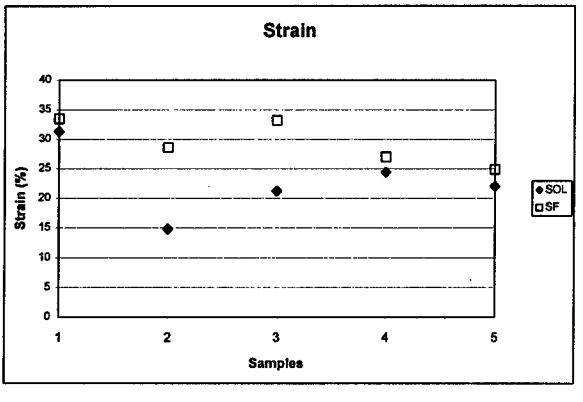

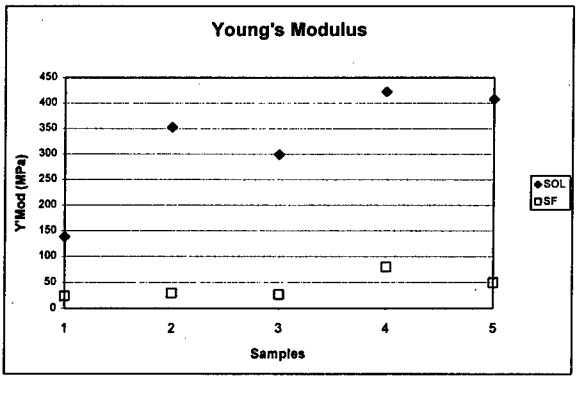

Figure 2: Stress, Strain and Young's Modulus of Experimental Propellant Formulations

More or less the same trend is noticeable for the strain values but here the solvent processed formulations show the lower values for all the formulations. The Young's Modulus values of the solvent-free processed formulations are of more or less the same order of value, but the values of the solvent processed formulations show great variance.

The conclusion can be made that the solvent-free processed samples are softer and perhaps more rubbery and therefore less stress is required before they break than the solvent processed formulations. On the other hand because they are softer and have more "give" they experience far more strain or elongation before breakpoint is reached. It is interesting to note that the two processes create more variance than the different formulations do.

The impact strengths of the experimental propellants are graphically presented in Figure 3.

The impact strength shows the same trend as was the case with the stress values namely that the impact strength of the solvent processed formulations are approximately double that of the solvent-free formulations. Here again the type of process generates more variance in the impact strength values than the type of formulation. The same conclusion as for the tensile tests can be made namely that the solvent processed formulations are harder and need more impact energy (kJ/m^2) before the samples break than is the case with the solvent-free processed formulations.

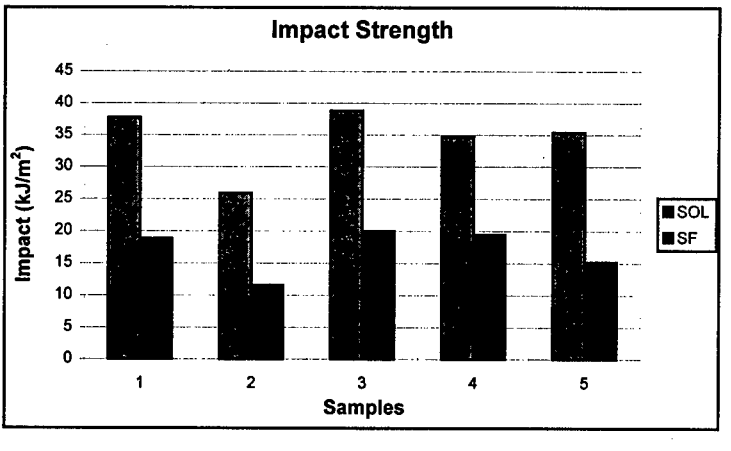

Figure 3: Impact Strength of Experimental Propellant Formulations

3.3 DIMENSIONAL DATA

The length, diameter, web and perforation of each propellant were measured and is reported in Table 3. The diameter, web and perforation dimensions of each propellant relative to the die dimensions are graphically presented in Figure 4.

Table 3: Dimensional Data of Experimental Propellant Formulations

Formulation No	Length (mm)		Diameter (mm)		Web (mm)		Perforation (mm)	
	SOL	SF	SOL	SF	SOL	SF	SOL	SF
1	13.92	13.06	6.30	7.49	1.95	2.37	2.41	2.76
2	13.73	13.34	6.30	7.44	1.92	2.35	2.46	2.74
3	13.66	13.30	6.21	7.89	1.90	2.56	2.41	2.78
4	13.80	13.51	6.41	7.83	1.99	2.56	2.43	2.71
5	14.08	13.33	6.54	7.79	2.00	2.51	2.55	2.78
Die	± 14		7.0		2.15		2.70	

All the solvent processed samples showed web, diameter and perforation shrinkage whereas all the solvent-free processed samples showed web, diameter and perforation swell. These tendencies were expected as the removal of the solvent from the solvent processed samples typically causes shrinkage and the solvent-free processed samples, which are more rubbery, typically show die swell. The shrinkage of the web, diameter and perforation of the solvent processed samples are more or less of the same order with an average value of approximately 10%. The die swell of the diameter and web of the solvent-free processed samples are more or less of the same order but the die swell of the perforations are percentage wise far less and typically of the order of 3% or less.

The web, diameter and perforation of all the solvent processed and the solvent-free processed samples came out differently to the original die configuration. This must be allowed for in the die design. This experiment did not evaluate the consistency or reproducibility of the die swell or shrinkage, but from previous experience the reproducibility or repeatability of the solvent-free process should be better because it is basically only a function of the formulation and not of the formulation and the percentage solvent as is the case with the solvent processed formulations. In the latter case a variation in the percentage solvent used and a variation in the drying conditions can both lead to variations in the percentage shrinkage of the propellant dimensions.

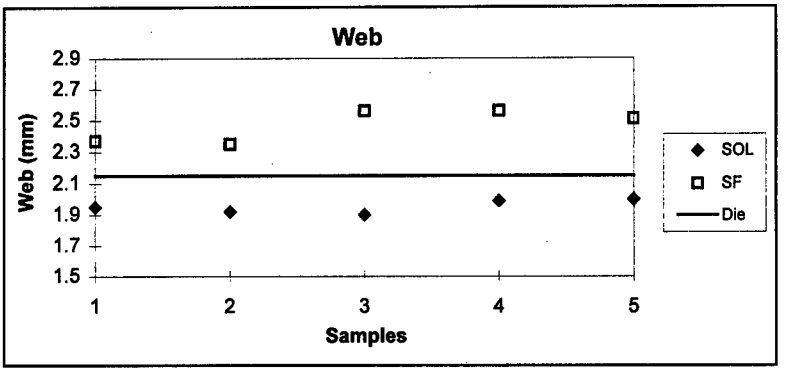

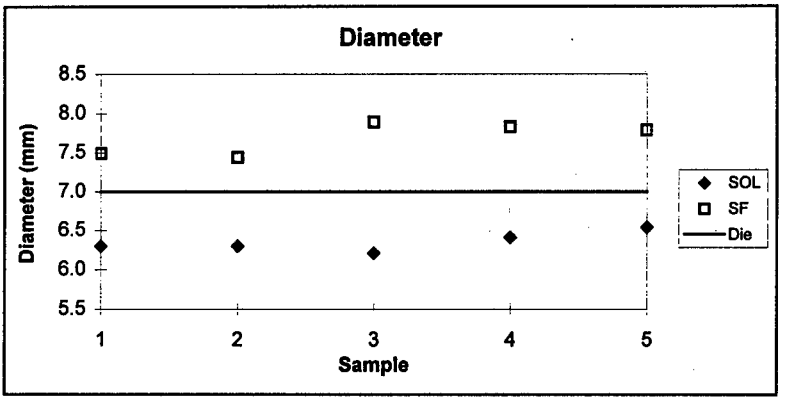

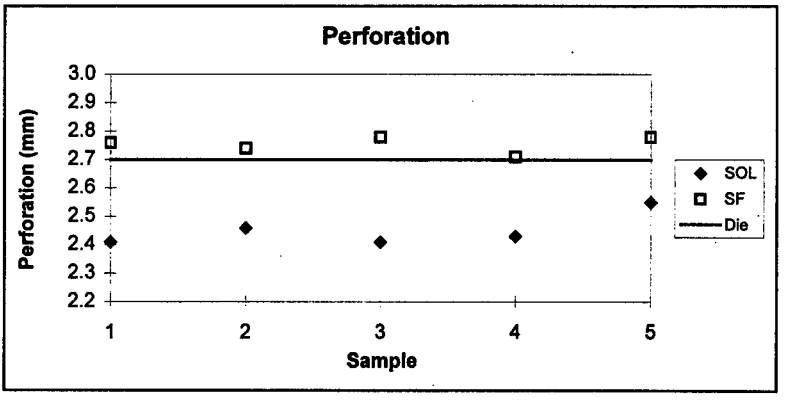

Figure 4: Web, Diameter and Perforation Measurements of Experimental Propellant Formulations

3.4 BALLISTIC PROPERTIES

3.4.1 Closed Vessel Results

Closed vessel test firings were performed in the 300 cm^3 closed vessel at a charge mass of 45g which gives a loading density of 0.150g/cm^3. Because the specific energy of all 5 propellant formulations are similar the maximum pressure generated should be and was approximately the same. Single perforation propellant pellets were used. The maximum pressure, relative quickness and the average dynamic vivacity are given in Table 4. The relative quickness of the experimental propellants are graphically presented in Figure 5.

Table 4: Internal Ballistic Properties of Experimental Propellant Formulations

Formulation No	Max Pressure (MPa)		Quickness		Average D	
	SOL	SF	SOL	SF	SOL	SF
1	155.7	152.5	7108	6127	0.76	0.67
2	155.4	153.5	7139	6146	0.77	0.67
3	151.8	151.5	6335	5183	0.72	0.57
4	155.5	153.6	6201	5236	0.66	0.56
5	155.7	154.3	6480	5482	0.68	0.58

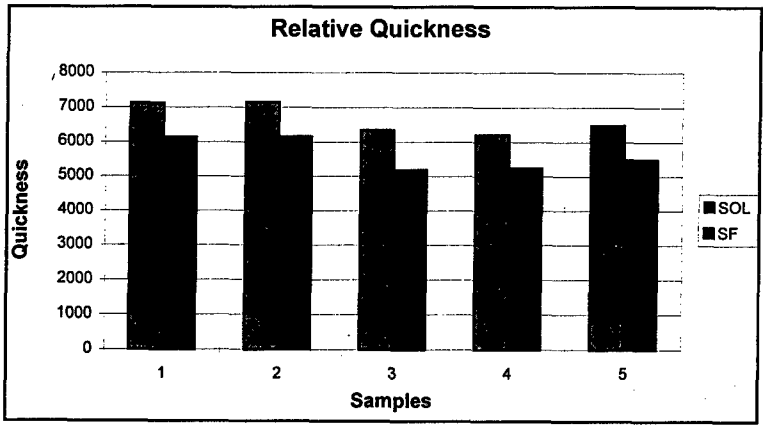

Figure 5: Relative Quickness of Experimental Propellant Formulations

The maximum pressure of all 5 formulations for both processes are very similar and range from 151.5 MPa to 155.7 MPa. This should be so because all 5 formulations have similar specific energy values. The relative quickness and dynamic vivacity of the formulations differ quite considerably with formulations 1 and 2 noticeably higher than the other three formulations. This tendency is the same for both types of processes. The relative quickness of the solvent processed samples are approximately 18% higher than the solvent-free processed samples for all 5 formulations. This trend can be explained by the fact that because of die swell and shrinkage the average web of the solvent processed samples is approximately 25% smaller than the average web of the solvent-free processed samples. It is difficult to deduct if the total trend can be ascribed to the difference in the webs for a specific formulation or if the type of process also influences the quickness of the propellant samples.

3.4.2 Combustion Characteristics

The burning rate of a propellant is represented by the following equation:

$$r = \beta P^{\alpha}$$

Therefore:

$$\log r = \log \beta + \alpha \log P$$

A graph of the log of the measured burning rate, r, versus the log of the measured pressure, P, is a linear relationship for conventional propellants with the slope of the graph equal to α, the burning rate exponent, and the intersection equal to log β, the burning rate constant.

The burning rates were determined from 5 shots fired at different loading densities namely 36g, 42g, 48g, 54g and 60g per 300 cm^3 closed vessel. Four different models were used to determine the burning rates and for comparative reasons the burning rates according to the Nobel Abel method, which uses actual closed vessel parameters, were used. These burning rate parameters are given in Table 5. The burning rate graphs of the solvent-free samples according to the Nobel Abel method (closed vessel parameters) only, are presented in Figure 6.

In samples 3, 4 and 5 a possible break in the linear burning rate curve occurs and if this break-in-the-curve is taken into account and the α's and β's for both sections of the curve are determined separately, the theoretically calculated burning rates at 350 MPa are obtained as presented in Figure 7.

Table 5: Burning Rate Properties of Experimental Propellant Formulations

Formulation No	Burning Rate Exponent (α)		Burning Rate Constant (β)		Burning Rate at 350 MPa	
	SOL	SF	SOL	SF	SOL	SF
1	0.8077	0.8075	1.7049	1.7914	193.4	203.0
2	0.7808	0.7932	1.8557	1.8720	179.9	195.1
3	0.7849	0.8094	1.6897	1.6436	167.7	188.3
4	0.8037	0.8158	1.5449	1.5996	171.2	190.3
5	0.7916	0.7987	1.6742	1.7378	172.9	187.0

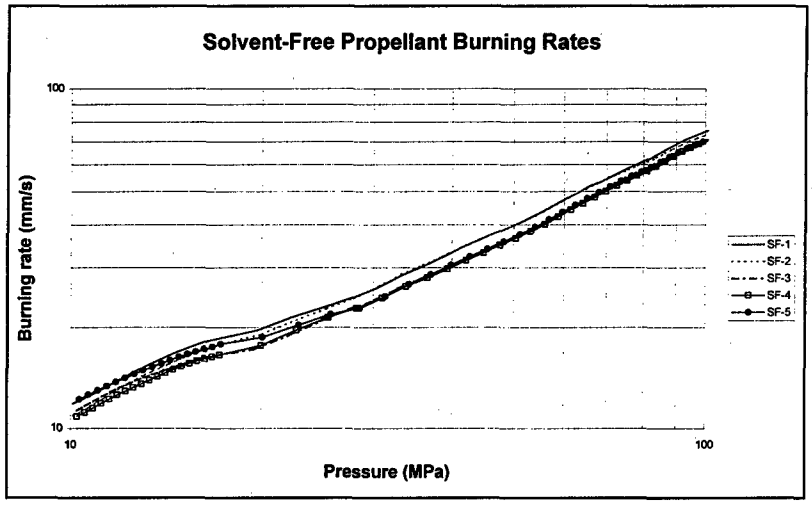

Figure 6: Burning Rates of Solvent-Free Propellant Formulations

In each case the burning rate of the SF propellants are higher than that of the SOL propellants. The difference between the burning rates of the SF and SOL propellants are more or less constant. The effect of the difference in the webs between the samples of the 2 types of processes should not play a role in the determination of the burning rate as was the case with the relative quickness of the propellants. The thermochemical, dimensional and configuration data of the propellant samples are all taken into consideration when calculating the burning rate. It is the linear burning rate in mm/s that is determined and this value should be independent of the propellant sample configuration.

As was the case with the relative quickness, the burning rate of samples 1 and 2 are higher than for samples 3, 4 and 5 for both types of processes. There is a definite break-in-the-curve for samples 3, 4 and 5 and when this is taken into account the burning rate of the solvent-free processed samples are higher than that of samples 1 and 2.

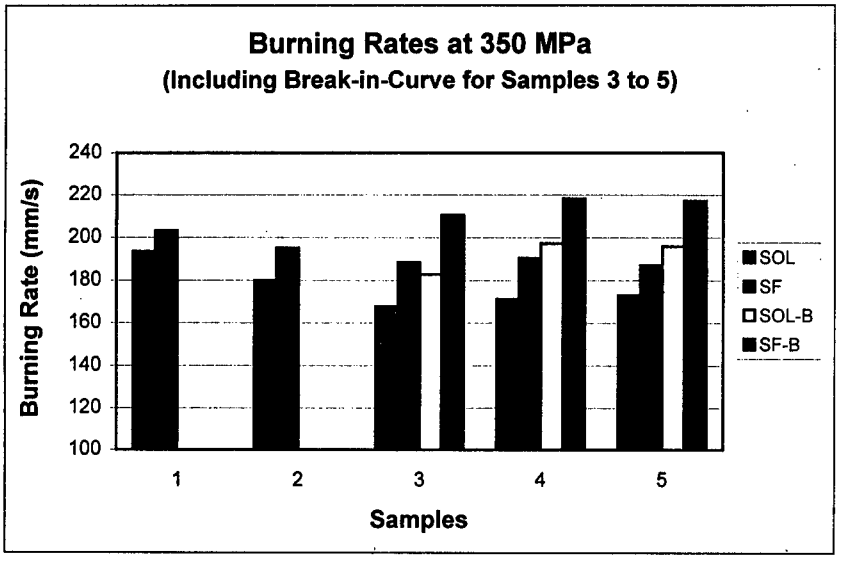

Figure 7: Burning Rates of Experimental Propellant Formulations at 350 MPa

4 CONCLUSIONS

For the same formulation the type of manufacturing process plays an important role in determining the propellant's density and its physical, mechanical and ballistic properties. In general the solvent processed samples are harder and more brittle whereas the solvent-free processed samples are more rubbery and have more "give".

- Five propellant formulations were selected that complied with the thermochemical and theoretical density requirements.
- All 5 propellant formulations were successfully processed with both the solvent and the solvent-free processes. There is a very good correlation between the theoretical specific energy values, the measured energy values and the maximum pressure values recorded during closed vessel firings for all the formulations which indicated that no change occurred in the propellant compositions during the processing phase.

- All 10 samples (SOL and SF) of the 5 propellant formulations passed the Methyl Violet stability test.
- The densities of the formulations processed with the solvent process are the same or higher than that of the same formulations processed with the solvent-free process. Irrespective of the process used the formulations with the highest crystalline content have the highest densities.
- In general the stress values and impact strengths of the SOL formulations are approximately double that of the SF formulations. There is more variance between the same formulation processed according to the two different processes than between different formulations processed with the same process. The type of process generates more variation in the stress and impact strength values than the type of formulation.

  The strain values and Young's Modulus show great variance but here the SOL formulations show the lower values for all the formulations.
- All the solvent processed samples experienced web, diameter and perforation shrinkage whereas all the solvent-free processed samples experienced die swell. These tendencies of shrinkage and die swell are typical of the solvent and solvent-free processes respectively and must be allowed for in the die design. The reproducibility of the propellant dimensions of the solvent-free processed formulations should be better than is the case with the solvent processed formulations.
- The relative quickness of the SOL samples are approximately 18% higher than the SF samples for all 5 formulations. The reason is that the average web of the SOL samples is approximately 25% smaller than the average web of the SF processed samples because of die swell and shrinkage respectively. The type of process might also influences the relative quickness of a specific propellant formulation.
- The burning rates of the SF propellants are constantly higher than that of the SOL propellants. The burning rate curves of the formulations containing RDX show a definite break-in-the-curve at approximately 40 Mpa.

EI- TECHNOLOGY - THE KEY FOR HIGH PERFORMANCE PROPULSION DESIGN

Beat Vogelsanger and Kurt Ryf

NITROCHEMIE WIMMIS AG, CH-3752 Wimmis, Switzerland
Tel: ext - 33 228 13 00 Fax: ext - 33 228 13 30

ABSTRACT

Recently, a new generation of propellants was successfully introduced. The so called "extruded impregnated" EI-propellants overcome several drawbacks connected with conventional propulsion systems and show a significant performance gain under system-compatible conditions in small and medium calibre applications as well as in mortars. EI-propellants are produced from extruded single base propellant grains by impregnation with a blasting oil, followed by deterring with a polymer.

In the medium calibre application range, performance gains of 7 - 12% were attained with the EI-propellant if compared to conventional alternatives. This improvement in interior ballistic performance is achieved by a combination of enhanced bulk density, slightly increased energy content, very progressive burning behaviour and a strongly reduced temperature sensitivity.

A well balanced combination of two different wear reducing agents was found to successfully counteract the adverse effect of the slight increase in flame temperature. The relatively low erosivity of the EI-propellant was confirmed in both erosion bomb tests and in trials with the weapon.

The employment of a well stabilised base grain, proven additives, and a diffusion-stable surface coating kept both chemical and physico-mechanical ageing to a very low level - excellent safe life and ballistic shelf life values are therefore attainable with EI-propellants.

Zusammenfassung

Kürzlich wurde eine neue Generation von Treibladungspulvern eingeführt, welche diverse der bei konventionellen Produkten auftretenden Probleme überwindet und sich, bei systemverträglichen Bedingungen, durch eine signifikante Leistungssteigerung in Klein- und Mittelkaliberwaffen sowie in Mörsern auszeichnet. Die sogenannten "extrudiert-imprägnierten" EI-Pulver werden durch Imprägnierung von extrudierten Ein- und Mehrlochpulvern mit geeigneten Sprengölen, gefolgt von einer Phlegmatisierung mit polymeren Weichmachern, hergestellt.

Insbesondere im Mittelkaliberbereich ist mit der EI-Technologie eine markante Leistungssteigerung möglich (Erhöhung der kinetischen Energie des Geschosses gegenüber herkömmlichen Treibladungen um 7 - 12%). Diese Leistungsverbesserung wird erzielt durch eine Kombination von erhöhter Schüttdichte (höhere Treibladungsmasse bei gegebenem Hülsenvolumen), geringfügig gesteigertem Energieinhalt, stark progressivem Abbrandverhalten und einer reduzierten Temperaturabhängigkeit von v_0 und p_{max} ("TU-Pulver").

Trotz geringfügig höherer Flammtemperatur zeigen EI-Pulver, verglichen mit einbasigen Treibladungen, kaum eine Verstärkung der Rohrerosion. Die effizienten Rohrschonungsmassnahmen (Kombination von zwei gut ausbalancierten Additiven im Innern und auf der Oberfläche der Pulverkörner) vermögen offensichtlich den unerwünschten Einfluss des erhöhten Energieinhaltes zu kompensieren. Dies wird mittels Resultaten aus Erosionsbombe und Waffenbeschuss aufgezeigt.

Dank der Verwendung eines sorgfältig stabilisierten Grundkornes, des Verzichtes auf stabilitätsreduzierende Additive und der Applikation einer diffusionsstabilen Oberflächenbehandlung können sowohl chemische als auch physiko-mechanische Alterungsphänomene stark reduziert werden. Aus diesem Grund zeigen EI-Pulver eine hervorragende Sicherheits- und Gebrauchslebensdauer (oder "chemische" und "ballistische" Lebensdauer).

1. Introduction

During the last few decades, different approaches have been made in order to improve the interior ballistic performance of propellants for medium calibre ammunition. All these "new" developments, such as deterred single and double base propellants, ball powders, consolidated charges and nitramine propellants had serious drawbacks. In the case of single base propellants and ball powders, the gain in performance was limited by the restricted energy content or by the grain geometry. In other propellant types, shelf life was reduced by diffusion of deterrents and blasting oils, or excessive gun barrel wear appeared.

Nitrochemie Wimmis AG has recently successfully introduced a new generation of propellants overcoming the drawbacks mentioned above and showing a significant performance gain under system-compatible conditions in:

- ***small calibres*** (5.56 - 15 mm),
- ***medium calibres*** (20 - 50 mm; sub-calibre / finstabilised ammunition), and
- ***mortars***.

The so called "extruded impregnated" EI-propellant is produced from extruded one-, seven- or nineteen-perforated single base propellant grains by impregnation with a blasting oil, followed by deterring with a polymer. In such EI-propellants, the blasting oil forms an outer layer several hundred micrometers thick. A diagram showing the concentration profiles of blasting oil and deterrent as well as the distribution of energy content within a typical EI-propellant grain is given in Figure 1.

The most important features of EI-propellants for medium calibre application, namely

- ***improved interior ballistic performance***,
- ***increased barrel life***,
- ***excellent safe life*** and ***good compatibility to system environment***, and
- ***excellent ballistic shelf life***

are discussed in some detail in the following chapters. Other advantages include the competitive pricing as well as the high parameter flexibility of the EI-process which allows efficient and quick developments to satisfy the specific demands of our customers.

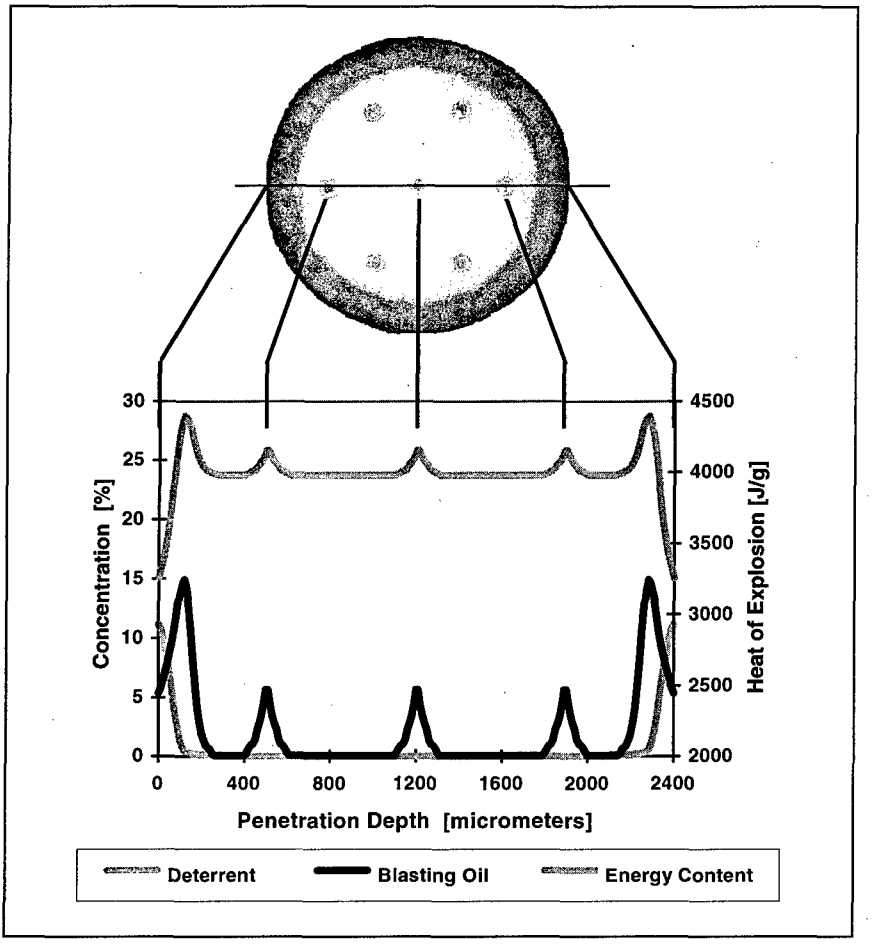

Figure 1: Blasting oil and deterrent concentration profiles as well as corresponding distribution of energy content in EI-propellant. The concentration profiles were determined by Fourier transform infrared (FTIR) microspectroscopy; the energy content was calculated using the ICT code.

2. Interior Ballistic Performance

During the last years, EI-propellants have proven their superiority over competitors' products in different medium calibre ammunition systems (in already qualified applica-

tions as well as in new developments; calibres 25, 27, 30, and 35 mm). In general, performance gains of 7 - 12% were attained compared to conventional alternatives. This improvement in interior ballistic performance is achieved by:

- ***Enhanced bulk density:*** The high bulk density (up to 1100 g/dm^3) allows an increase in the charge weight in the cartridge without consolidation. Enhancement of charge potential directly equals performance gain.

- ***Slightly increased energy content:*** Due to the added blasting oils, the energy content is increased by 200 - 300 J/g compared to single base propellants. This additional chemical energy contributes to the performance gain.

- ***Very progressive burning behaviour:*** The burning characteristic of surface coated propellants is dominated by the distributions of coating agents and energy content (see Figure 1). In case of EI-propellant, the deterred outer surface can be expected to burn much more slowly than the undeterred regions of the grain. This is confirmed by the results of intercepted bomb tests showing that combustion will start mainly from the perforations, whereas the energy-rich, blasting oil containing outer layer burns later in the interior ballistic cycle - exactly at the stage where its energy is needed most. This very progressive burning behaviour further adds to the performance gain.

- ***Reduced temperature sensitivity:*** Thanks to the high parameter flexibility of the EI-process, it is possible to alter the product's properties regarding temperature coefficients of muzzle velocity (v_0) and peak pressure (p_{max}) within certain limits. Therefore, the strong temperature sensitivity known from conventional products can be reduced considerably in EI-propellants. This allows the performance potential given by the system limits of the weapon system to be fully exploited - the maximum performance is obtainable at service temperature.

The excellent interior ballistic behaviour of EI-propellants is demonstrated in Figure 2. An EI- and a single base propellant, both optimised for the specific application, were tested in the APFSDS-T round for the 30 x 173 mm Bushmaster II gun. Thanks to its higher performance level and reduced temperature sensitivity, the EI-propellant enables a gain in kinetic Energy E_0 of 18% at -50°C, and of 12% at +21°C, to be made.

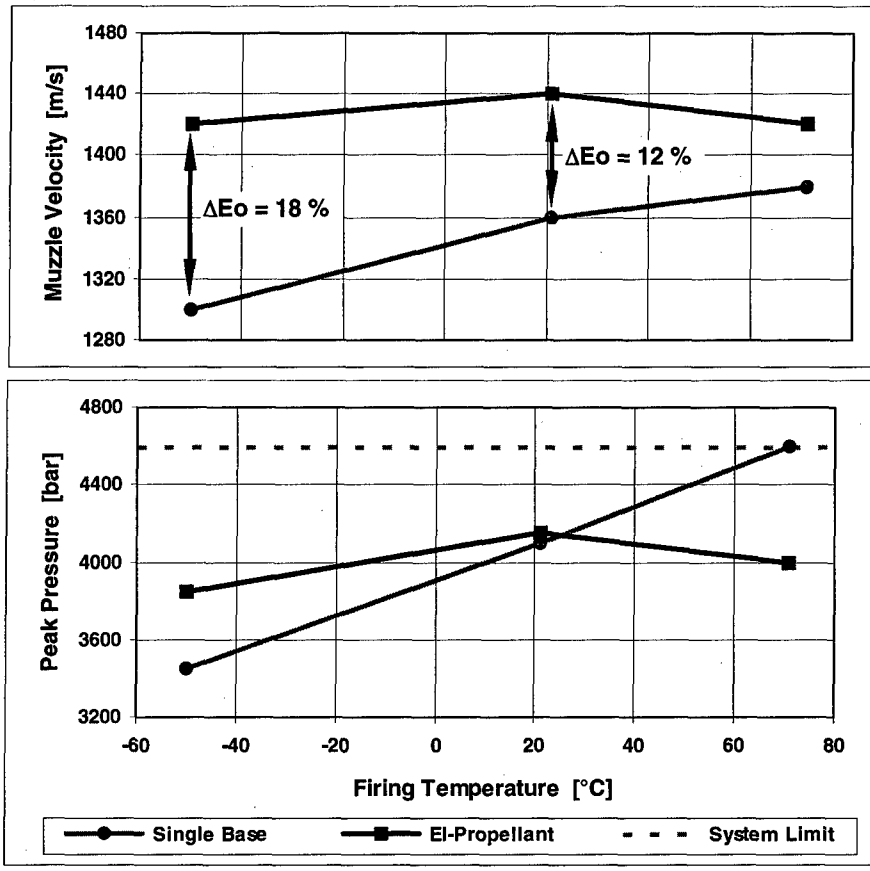

Figure 2: Interior ballistic results obtained with the APFSDS-T round for the 30x173mm Bushmaster II gun. The low temperature sensitivity as well as the significant increase in performance obtainable with the EI-propellant are clearly visible.

3. Barrel Erosion

From practical experience it is known that each increase in the propellant's energy (or flame temperature) will reduce the barrel life considerably. However, with high performance ammunition (especially kinetic energy munitions) one cannot avoid using a charge with a sufficiently high energy content.

In the case of EI-propellant for medium calibre application, the extent of barrel wear is kept to an acceptable level by:

- ***Relatively low flame temperature:*** For an EI-propellant designed for 25 mm ammunition, flame temperatures of around 3000 K are calculated (using the ICT code). This value lies somewhat higher than the 2800 K of a single base propellant for the same application, but is far below the 3500 K calculated for a nitramine propellant already in service.

- ***Optimised barrel protection measures (additives):*** In order to achieve the maximum possible barrel protection over the entire interior ballistic cycle, two different additives are employed ("two-phase design"). One of the additives is located at the surface of the propellant grains to ensure sufficient protection from the beginning of the cycle (effect in transition zone - free flight zone). The second additive, being incorporated in the base grain matrix, is released continuously up to the end of combustion (effect on barrel up to muzzle proximity). The introduction of these additives must be balanced in such a way that no contamination or fouling occurs. It must be noted that the two additives used in small quantities are not exotic ones but known and proven "agents".

The barrel protection concept described above has demonstrated its effectiveness in both erosion bomb and weapon firing tests.

The results of the ***erosion bomb*** tests are given in Figure 3 (diagram of the weight losses of the nozzle as a function of the heat of explosion). From this diagram it is evident that the erosivity of the EI-propellant lies in the same range as for different highly surface-treated and thus so-called "cool" burning single-base charge variants, whereas the "hot" burning nitramine propellant is in the upper investigation range.

During NATO-Homologation at the NATO test centre in the Netherlands, EI-Propellant in a 25 mm APFSDS application ***met the barrel life requirements of STANAG 4173 in both Bushmaster and KBA gun.***

Extensive trials in the 27 mm Mauser gun revealed a ***barrel life*** of substantially more than 3000 rounds for APFSDS ammunition in conjunction with EI-propellant.

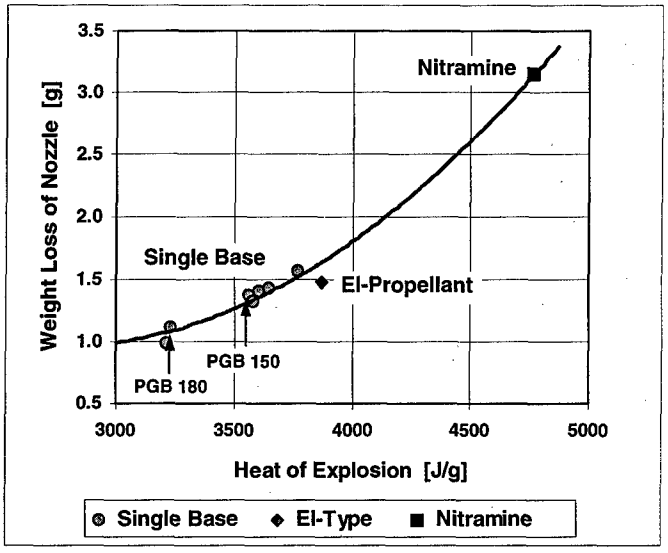

Figure 3: Results of erosion bomb test for different 25 mm calibre propellants (single base, EI-, and triple base / nitramine). As can be seen from the diagram of the weight losses of the nozzle as a function of the heat of explosion, erosivity increases superproportionally to increasing thermal value. The erosivity found for the EI-propellant did not significantly differ from the values obtained for different deterred single-base propellants such as PGB 150. The two propellants PGB 180 and PGB 150 both meet the barrel life values required in STANAG 4173 when the relevant load rates are applied.

4. Chemical Stability / Safe Life

For the production of EI-propellants, a carefully manufactured and well stabilised base grain is used, and only known compatible and proven ingredients or additives are applied. Thus, chemical ageing under normal storage conditions is kept to an almost negligible level, and an excellent chemical shelf life (safe life) will result. This was proven in different experiments:

Conventional stability tests: EI-propellants have been subjected to numerous conventional stability tests during development, qualification and production, e.g. to the 90°C weight loss test, 105°C Dutch test, and 115°C Bergmann-Junk test. All test requirements have been fulfilled.

Microcalorimetry / chemiluminescence: The extremely sensitive microcalorimetry and chemiluminescence detectors, monitoring the actual evolution of heat and nitrogen oxides even at moderate storage conditions (40 - 80°C), confirmed the very low ageing rate of EI-propellants.

Chemical shelf life determination: The chemical shelf life (safe life) of different propellants was determined, whereby the propellant samples were subjected to accelerated ageing for up to 108 weeks at temperatures of 40°C, 50°C, 60°C and 70°C. The remaining stabiliser contents were assayed quantitatively for the unaged propellant as well as for all artificially aged samples by high performance liquid chromatography (HPLC). From the results, the time period for 50% stabiliser consumption was calculated and interpolated to designated storage conditions using the Berthelot equation. This approach is known to be very conservative. The results of these investigations are shown in Figure 4.

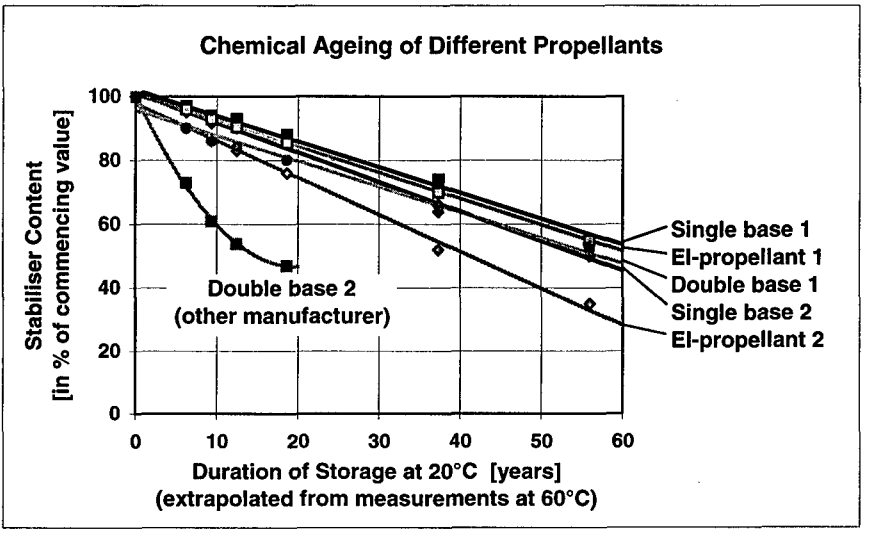

Figure 4: Assessment of chemical shelf life (safe life) for different propellant types. All propellants except "double base 2" have been produced by Nitrochemie Wimmis AG. The safe life values extrapolated from 60°C to 20°C exceed 40 years for all propellants, except for "double base 2" which only manages to reach 15 years (very conservative estimations). The extrapolation was made using the Berthelot approach with an ageing factor of 3.0. The Berthelot law implies that each temperature change of 10°C will increase the rate of propellant ageing by this factor. From numerous investigations it was found that the ageing factor generally extends between 3 and 4.

For ***EI-propellants***, the ***safe storage life*** was determined to be in the range of ***20 - 40 years at 30°C***, and of ***50 - 100 years at 20°C***, respectively.

This excellent behaviour has been confirmed by the recent analysis of two EI-propellants of the same recipe, produced in 1985 and 1995. Despite the older sample having been stored for 10 years under ambient conditions, it was still found to be chemically identical to the new propellant, as can be seen from Table 1. In particular, the concentrations of primary stabiliser as well as the contents of stabiliser derivatives were found to be equal within the accuracy of the method.

Type	Substance	Sample "1985"	Sample "1995"
Primary stabiliser	Acardite II	1.01 %	0.99 %
	2-Nitro-diphenylamine	0.09 %	0.12 %
Stabiliser derivatives	N-Nitroso-diphenylamine	0.01 %	0.02 %
	4-Nitro-diphenylamine	< 0.01 %	< 0.01%
90°C Weight loss test		1.36 %	1.26 %

Table 1: Results of HPLC-analysis of two EI-propellants of the same recipe, produced in 1985 and 1995. Both samples were analysed simultaneously in spring 1996. The results of the 90°C weight loss tests are given as well.

5. Ballistic Shelf Life

In order to guarantee sufficient ballistic shelf life, the phenomena that might contribute to the changes in the interior ballistic behaviour have to be kept to an acceptable level. For surface-coated propellants, the main factors are molecular weight reduction of the nitrocellulose and the diffusion of surface coating agents into the propellant grain. Both processes have been investigated in some detail:

- ***Nitrocellulose degradation***: From experience we know that changes in the ballistic characteristics may occur once the molecular weight of the nitrocellulose has been reduced by more than 45%. Shelf life investigations of EI-propellants, performed by ageing the samples as described in section 4 and monitoring the nitrocellulose degradation using size exclusion chromatography (SEC), predicted a molecular weight reduction of only 40% after approximately 60 years at 20°C. Thus, nitrocellulose degradation does not adversely affect the ballistic properties during the

designated shelf life of the round. The low extent of nitrocellulose depletion corresponds to the other chemical ageing processes (the "chemical" ageing processes, such as stabiliser consumption, nitrocellulose degradation, heat and nitrogen oxide evolution are strongly connected with each other - in a well stabilised propellant, all those processes are of low magnitude).

- ***Diffusion of deterrents and blasting oils:*** The diffusion of numerous deterrents and blasting oils into different propellant matrices during accelerated ageing was investigated using Fourier transform infrared (FTIR) microspectroscopy. The diffusion coefficient values determined by fitting a Fickian diffusion model to the observed concentration profiles correlated to the changes in the interior ballistic behaviour. It was found that the diffusion effects in single base propellants are too small to significantly alter the ballistic performance. In double base propellants, however, the diffusion of deterrents is much faster and will most likely limit the ballistic shelf life. In EI-propellants, the diffusion of surface coating agents can be minimised by carefully balancing type and concentration of both polymeric deterrent and blasting oil. In such EI-propellants, diffusion effects are only marginally higher than in single base propellants, and excellent ballistic shelf life values are achieved. Figure 5 compares the diffusion of the polymeric deterrent in EI-propellant to the diffusion of dibutylphthalate (DBP) in a double base propellant.

Assessment of ballistic stability: Ballistic shelf life is determined using a test plan similar to the one described in section 4. The propellant is aged artificially for up to 36 weeks at temperatures of 40°C, 50°C, and 60°C before being tested in the weapon at different firing temperatures. The results are extrapolated to standard storage conditions using an ageing factor of 3.0 which is known to be a conservative estimation. This test has been performed for ***different weapon / ammunition systems in conjunction with EI-propellant***, revealing ***excellent ballistic shelf life*** values in all cases. Over the entire range of firing temperatures (usually -54°C to +71°C), only marginal changes in peak pressure and muzzle velocity were introduced by artificial ageing periods equivalent to 20 years storage at 20°C. In particular, no dangerous rises in peak pressure (> 150 bar) appeared, and the low temperature sensitivity of the EI-propellant was maintained, thereby proving the effectiveness of the measures to reduce nitrocellulose degradation as well as blasting oil and deterrent diffusion.

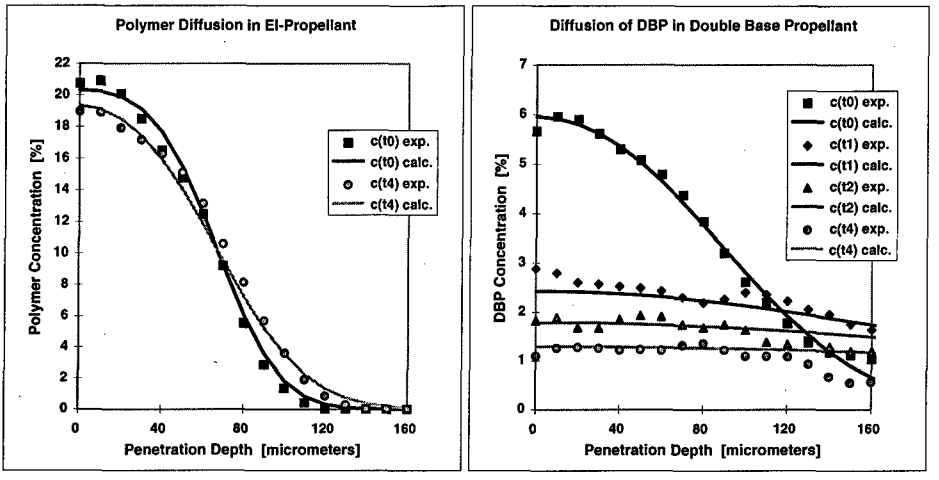

Figure 5: Investigation of the diffusion of deterrents; concentration profiles of polymer in EI-propellant and dibutylphthalate (DBP) in double base propellant, determined by FTIR-microspectroscopy. Measured concentration values (dots) and recalculated concentration profiles (lines) for t_0 (unaged propellant), t_1 (propellant stored at 71°C for 1 week), t_2 (2 weeks at 71°C) and t_4 (4 weeks at 71°C). The deterrent diffusion is very small in the EI- propellant and therefore will not influence the ballistic shelf life (diffusion coefficient determined to be $D = 0.13 \cdot 10^{-15}$ m^2/s). In the double base propellant, however, the diffusion is increased by more than two orders of magnitude ($D = 26 \cdot 10^{-15}$ m^2/s) - such strong diffusion effects will reduce the ballistic shelf life considerably.

The results of ballistic shelf life assessments for five different propellants are depicted in Figure 6. It is evident from this diagram that the single base and all three EI-propellants exhibit shelf life values of more than 20 years, whereas for the propellant with a strongly diffusing surface coating, the ballistic shelf life is reduced to about 10 years at 20°C.

The excellent ballistic stability of EI-propellant was confirmed during different qualification and homologation procedures. In particular, environmental and climatic condition tests such as MIL STD 810 D have been fulfilled without problems. The most severe environmental test program, however, was performed at DGA in Bourges (F). The 30 mm rounds filled with EI-propellant were subjected cumulatively to a "simulation of climatic conditions" (80 days at +71°C / 20% rel. humidity to +60°C / 80% rel. humidity), 30 cycles "simulation of aircraft conditions" (totally 780 hours from -40°C to +100°C), 3 cycles of "complete firing action" (+21°C to +121°C), and a "vibration test",

before being fired in the temperature range -40 to +100°C. Considering the extreme thermal and mechanical stresses involved in this test procedure, the increase in peak pressure found to be within 0 and 200 bar over the entire range of firing temperatures has to be regarded as small. The maximum pressure level obtained with the aged ammunition was still far below the system limits.

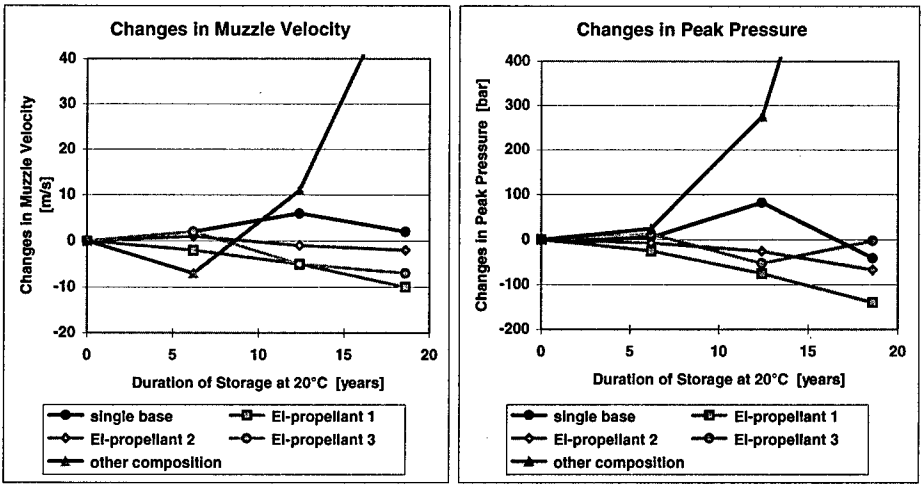

Figure 6: Assessment of ballistic shelf life for different medium calibre propellants. The propellant samples stored for 0, 4, 8 and 12 weeks at 60°C have been tested in the respective weapon systems (temperature during firing test 21°C). The extrapolation from 60 to 20°C was carried out according to the Berthelot equation with an ageing factor of 3.0. The single base as well as the three EI-propellants exhibit only marginal changes in muzzle velocity v_0 and peak pressure p_{max}; a ballistic shelf life of at least 20 years can therefore be guaranteed for all these propellants. In the sample "other composition", however, the diffusion of improperly balanced surface coating agents leads to an excessive rise in peak pressure which significantly reduces the ballistic shelf life of this propellant. The weapon / ammunition systems are: 25mm KBA APFSDS (single base), 25mm KBA APDS (EI-propellant 1), 27mmx155 APFSDS (EI-propellant 2), 30mmx190 APFSDS-T (EI-propellant 3), and 25mm KBB APDS (other composition).

6. Conclusions

EI technology has opened new perspectives in the field of high performance medium calibre ammunition. Thanks to the system-compatible behaviour of this product, a combat rate enhancement can be achieved without drawbacks or undesirable side effects. EI-propellants are equally suited for application in already introduced ammunition systems as well as in new developments.

As a result, EI technology has established itself with much success especially in the following applications:

25 mm x 137	APFSDS, APDS, FAPDS (frangible) qualified according to STANAG 4173 (NATO homologation) for use in Bushmaster (M242) and KBA-gun
27 mm x 155	APFSDS qualified according to STANAG 4170 type classified in Germany for use in TORNADO-gun
30 mm x 173	APDS, APFSDS for use in Bushmaster II and Mauser F-gun
35 mm x 228	APFSDS, FAPDS (frangible) qualified according to STANAG 4170 type classified in Germany for use in RH 503 gun
50 mm CTA	APFSD Development for the RH 503 gun

In recent years, close cooperation has been built up in these field with competent system partners, such as (in alphabetic order) Giat, Mauser, Mecar, Oerlicon Contraves, Primex, Raufoss, Royal Ordnance, Rheinmetall, among others. Such cooperations permitted investigation of system-compatible behaviour of the EI-propellant under a great variety of configurations and performance requirements. As a result, the reliability of this system component can be regarded as being fully established.

Acknowledgements

Financial support by the Gruppe Rüstung (GR), SWIT (different LFP-Projects) is gratefully acknowledged. Special thanks go to Mrs. R. Sopranetti, Mr. B. Ossola, Mr. E. Gurtner, Mr. U. von Mühlenen and Dr. S. De Boni for contributing to this work.

ROWANEX 3000: A NEW HIGH PERFORMANCE PRESSABLE PBX FOR METAL ACCELERATING APPLICATIONS

a
paper
to be presented
at the

29th INTERNATIONAL ICT CONFERENCE
KARLSRUHE, GERMANY
30 JUNE - 3 JULY 1998

ROWANEX 3000: A NEW HIGH PERFORMANCE PRESSABLE PBX FOR METAL ACCELERATING APPLICATIONS

R.E. Hollands, I.E.P. Murray, C.J.Leach*

British Aerospace Defence Limited,
Royal Ordnance Division,
Glascoed,
Usk, Monmouthshire, NP5 1XL.
UK.

*Defence Evaluation and Research Agency,
Energetic Materials Department,
Fort Halstead
Sevenoaks, Kent, TN14 7BP
UK.

ABSTRACT

ROWANEX 3000 is a new polymer-bonded explosive (PBX), developed by Royal Ordnance in conjunction with the Defence Evaluation and Research Agency, which arose from an international WEAG(IEPG) Technical Area 25 collaborative programme on pressable explosives and their associated processing technology [1]. ROWANEX 3000, is a high performance composition capable of being pressed to give the high levels of homogeneity and density required for precision directed energy warheads. In addition it was formulated to have an environmentally friendly manufacturing method and to have reduced vulnerability compared with Octol. The present paper discusses the explosive's formulation, processing method, physical characteristics and stability. Comparison is made between the performance and hazard properties of ROWANEX 3000 and those of conventional melt cast counterparts such as Octol, Composition B and TNT.

1. INTRODUCTION

Pressable polymer-bonded explosive (PBX) compositions with high nitramine solids loadings have been widely developed by explosives formulators in response to demands from directed energy weapon system designers for increased performance. PBXs can possess a number of advantages over traditional explosives based on TNT, such as reduced vulnerability, improved mechanical properties and enhanced survivability in the operational environment.

Reduced vulnerability energetic materials, such as polymer-bonded explosives (PBXs), are seen by Royal Ordnance as central elements in a systems approach to meeting IM requirements [2,3] and research and development in this area forms an important part of the Division's business strategy [4]. Over recent years Royal Ordnance, initially under contract from the UK MOD, has developed a series of PBXs for a broad range of potential main charge applications [5,6].

ROWANEX 3000 is a new polymer-bonded explosive (PBX), developed by Royal Ordnance in conjunction with the Defence Evaluation and Research Agency, which arose from an international WEAG(IEPG) Technical Area 25 collaborative programme on pressable explosives and their associated processing technology. ROWANEX 3000 was formulated to have enhanced performance and reduced vulnerability in comparison with traditional TNT-based Octol compositions, as well as world wide environmental survivability, prolonged service life and ease of processing.

2. ROWANEX NOMENCLATURE

The designation ROWANEX stands for Royal Ordnance Waltham Abbey New EXplosive. Waltham Abbey was the location of the R&D centre where formulation work on new Royal Ordnance explosives commenced and which had historic links with previous Government establishments on the site such as the Royal Gunpowder Factory. Since 1989 research in the explosives area has continued at RO's Glascoed site in South Wales.

The designation code consists of the prefix ROWANEX followed by four digits. The first two digits form a serial number assigned to a general class of formulation which relates both to its processing method and to the predominant explosive ingredient. The remaining two digits of the code are assigned arbitrarily in sequence and relate to specific formulations within the general class. Serial numbers assigned to general classes and sub-classes of formulation are given in Table 1 below.

TABLE 1
ROWANEX NOMENCLATURE

1.1 Serial Numbers for General Classes

Code No	General Class of Formulation
01-09	Melt-Cast TNT-based
10-19	Castable PBXs
20-29	Extrudable PBXs
30-39	Pressable PBXs
40-49	Plastic Explosives
50-59	Sheet Explosives
60-69	)))To be assigned))
70-79	
80-89	
90-99	

1.2 Serial Numbers For Sub-Classes

Sub-class Codes			Formulation Type
Castable PBXs	Extrudable PBXs	Pressable PBXs	
10	20	30	HMX-Based
11	21	31	RDX-Based
12	22	32	PETN-Based
13	23	33	AP/Al-Based
14	24	34	RDX/Al-Based
15-19	25-29	35-39	To be assigned

When an RO explosive is first formulated as part of a research programme and before it has been allocated a ROWANEX designation it is assigned a Research Formulation (RF) Code. No correlation exists between RF and ROWANEX designation sequences.

3. FORMULATION

ROWANEX 3000 is a pressable, HMX-based composition designed for metal accelerating applications, particularly those requiring high levels of homogeneity and density. It has a total solids loading of 95% $^{w}/_{w}$ (91.1% $^{v}/_{v}$) and possesses a theoretical maximum density of 1.83 $Mg.m^{-3}$. The nominal formulation of ROWANEX 3000 and those of selected melt-cast explosives based on TNT are given in Table 2. The composition employs a plasticised thermoplastic elastomer (TPE) binder system derived from a styrene-ethylene/ butylene-styrene (SEBS) block copolymer. TPE binder systems do not involve the use of chemical curing agents such as isocyanates and have the advantage that they can be transformed by a reversible softening process at elevated temperatures. In this way demilitarisation, recovery of expensive hardware and recycling of redundant explosive is facilitated. An antioxidant is included in the copolymer in order to minimise the effects of

ageing due to aerial oxidation and unwanted internal chemical reactions and graphite is added as a processing aid to improve charge quality and reduce the effect of static electricity.

TABLE 2. NOMINAL FORMULATIONS

Ingredient	Nominal Formulations (%w/w)		
	ROWANEX 3000	Octol 75/25	Composition B
RDX	--	--	60
HMX	95	75	--
Binder	5	--	--
TNT	--	25	40

4. PROCESSING

The ROWANEX 3000 moulding powder is prepared in an incorporator in aqueous medium without the use of organic solvents. This method of manufacture has considerable advantages over commonly used lacquering techniques because organic solvents, which are potentially harmful to operators and the environment, are avoided. The TPE binder is smeared onto the nitramine crystals to give an even coating in the course of this operation as evidenced by optical microscopy and scanning electron microscopy (SEM). The moulding powder is dried in heated forced air ovens then coated with graphite in a separate processing stage. Pressing operations are conducted under vacuum and at elevated temperature to ensure void-free, homogeneous fillings. The pressing of explosive charges can be highly automated giving the potential for reduced production costs and higher consistency with respect to traditional melt cast processing methods. However, due consideration must be given to optimisation of pressing and assembly techniques for application in specific weapon systems.

5. PERFORMANCE CHARACTERISTICS

ROWANEX 3000 has been formulated to deliver levels of performance in directed energy applications at least comparable to those given by current in service Octol compositions.

A number of pertinent performance characteristics such as velocity of detonation, detonation pressure and Gurney velocity have been theoretically predicted for ROWANEX 3000 and are presented in Table 3 together with analogous data for Octol 75/25, Composition B and TNT for comparison. It will be seen that the detonation pressure predicted for ROWANEX 3000, at over 34 GPa, exceeds that for Octol 75/25 by 4%. The velocity of detonation of ROWANEX 3000 has been experimentally measured at 8860 $m.s^{-1}$ which is in excess of the predicted value of 8704 $m.s^{-1}$.

As part of the WEAG TA-25 collaboration programme the penetration performance of candidate compositions from participating nations was evaluated in a shared generic shaped charge test vehicle design against a common target plate configuration. Generic reference charges, filled with Octol 75/25 (EDC 1S), were fired under identical conditions for comparison. The shaped charge test vehicles used in penetration trials were 75mm in diameter with a 50° angle, flow formed copper cone, and an aluminium case. Profiled ROWANEX 3000 billets were fabricated by double end pressing and the billet was fitted onto the copper liner. The concentricities of the assembled charges were checked then the shaped charges were fired into stacked 25mm thick mild steel plates at 4, 6, 8, 10 and 15CD

stand off distances. Performance was slightly better than Octol 75/25 at shorter stand-off distances but significant improvement is observed at long stand-off and approached 40% at 15CD (see Table 4 and Figure 1). The improvement in performance at longer stand-off is most probably attributable to the homogeneity of the pressed filling and the symmetry of the density distribution about the principal axis which leads to lower lateral jet drift velocities than for shaped charges filled with melt cast explosives.

TABLE 3. PERFORMANCE DATA[a]

Parameter		Explosive Composition			
		ROWANEX 3000	Octol 75/25	Comp B	TNT
Solids Loading	(%w/w)	95	75	60	--
Solids Loading	(%v/v)	91.1	70.9	57.9	--
Theoretical Maximum Density	(g/cm^3)	1.83	1.81	1.74	1.65
V of D	(m/s)	8704 (8860[b])	8,516	8,071	7,014
Detonation Pressure	(GPa)	34	32.8	28.7	21
Gurney Velocity	(m/s)	2,880	2,820	2,712	2,391
Heat of Detonation	(kJ/g)	6.12	6.09	5.9	5.41
Gas Evolved on Detonation	(cm^3/g)	747	710	681	567

[a] Theoretical data unless stated otherwise. [b] Experimental result

TABLE 4. PENETRATION DATA[a]

Explosive	Performance Parameter[a]	Stand-Off (Charge Diameters)				
		4	6	8	10	15
ROWANEX 3000	Mean Penetration	0•96	1•00	1•02	1•01	0•93
	Maximum Penetration	1•01	1•05	1•10	1•13	1•06
EDC 1S (Octol 75/25)	Mean Penetration	0•95	1•00	1•04	0•97	0•67
	Maximum Penetration	1•01	1•06	1•07	1•07	0•79

[a] Normalised in each case with the mean penetration value at 6CD

FIGURE 1: COMPARATIVE SHAPED CHARGE PLATE PENETRATION RESULTS

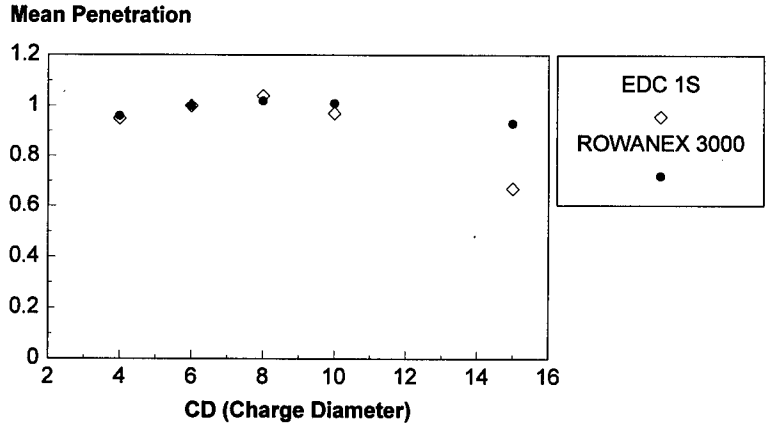

6. HAZARD AND AGEING CHARACTERISTICS

During the course of the development of a new explosive the type and extent of the prescribed testing will depend on the nature of the explosive, its intended role and application, and its similarity to compositions previously assessed [7]. It is normally the case in the UK that formal pass/fail criteria are not applied to test results but judgements on overall safety and suitability for service are made on the basis of comparison with test results of explosives which have been used successfully in similar applications.

An outline of the preliminary hazard assessment programme to which ROWANEX 3000 was subjected is given in Table 5. A full description of the individual tests is beyond the scope of this paper but the test procedures and the apparatus employed are documented elsewhere [8]. The trials programme was divided into three distinct parts:- (a) small scale sensitiveness testing, (b) ageing trial, and (c) charge hazard testing.

6.1 Small Scale Sensitiveness Testing

Sensitiveness is a measure of the ease of accidental initiation of an explosive by a prescribed stimulus. The type of testing undertaken included that generally conducted to generate an explosive hazard data sheet and involved assessment of the sensitiveness of the composition to a range of stimuli such as mechanical impact, friction, heat, naked flame and electric spark. Care was taken to fabricate test samples which maintained, as far as was possible, the integrity of the polymeric matrix encapsulating the energetic fillers so that testing was performed under representative conditions.

TABLE 5. ROWANEX 3000 PRELIMINARY HAZARD ASSESSMENT PROGRAMME

Parameter	Hazard Assessment Test
Sensitiveness	Reaction to mechanical impact (Rotter impact, F of I)
	Reaction to mechanical impact with added grit
	Reaction to frictional impact (mallet friction)
	Rotary friction (F of F)
	Ease of ignition
	Temperature of ignition
	Ignition by flash
	Reaction on inflammation
	Electric spark
	Powder explosiveness
Ageing	12 Months accelerated ageing trial to assess the effect of time and temperature on sensitiveness, chemical stability, mechanical and physical properties.
Charge Hazard	Burning Tube
	Small Scale Fuel Fire
	Large scale gap test

6.2 Ageing Trial

This trial involved accelerating the ageing of the ROWANEX 3000 explosive at elevated temperature (60°C) for periods of up to 12 months. Samples were removed from ovens at

3-monthly intervals for testing and comparison with unaged controls. The ageing explosives were monitored with respect to changes in Shore A hardness, mass, sensitiveness to impact and friction, chemical stability and mechanical properties. At the end of the trial mass loss from unconfined samples over the 12 month period amounted to 0.1% of total composition and the results of vacuum stability tests were well within the limits of acceptability.

6.3 Charge Hazard Trials

The majority of UK charge hazard tests are designed to evaluate the explosiveness of an explosive which is a measure of the magnitude of response to an accidental prescribed stimulus. Since insufficient tests can be carried out under realistic conditions to give statistically significant conclusions on the grounds of cost, tests usually employ stimuli or conditions, such as confinement, which are more severe than would be found in practice. Results from a selection of the charge hazard trials are described below in order to demonstrate the reduction in vulnerability of ROWANEX 3000 when compared with TNT-based counterparts.

6.3.1 Burning Tube Test

The burning tube test was designed to assess the behaviour of an explosive charge when ignited by a propellant under confinement. The results of burning tube tests on ROWANEX 3000, together with those on several melt-cast explosives for comparison, are listed in Table 6. The response of the charge to the test conditions in terms of fragmentation is expressed as a degree of reaction on a scale of 0 to 4 ranging from failure to ignite to full detonation. Descriptions of the experimental observations corresponding to this scale of reaction are given in Table 7. As can be seen from the results, ROWANEX 3000 deflagrated, thereby exhibiting a lower order response than those recorded for comparable TNT-based compositions. Octol 75/25 under the same test conditions gave a very violent explosion.

TABLE 6. COMPARISON OF BURNING TUBE AND SMALL SCALE FUEL FIRE TEST RESULTS

Explosive Composition	Reaction Degree	
	Burning Tube	Fuel Fire
ROWANEX 3000	2	2
TNT	1	2
RDX/TNT 60/40 (Comp B)	3	4
EDC1G (Octol 75/25)	3	4

TABLE 7. DESCRIPTION OF REACTION CATEGORIES FOR BURNING TUBE AND FUEL FIRE TESTS

Degree of Reaction	Reaction Description	Observation
0	Fails to ignite	--
0/1	Burning	End cap not ejected
1	Pressure burst due to burning	End cap(s) ejected
2	Deflagration	2 to 9 tube body fragments
3	Explosion	10 to 100 tube body fragments
4	Detonation	> 100 tube body fragments

6.3.2 Small Scale Fuel Fire Test

This test was developed to examine the behaviour of an explosive charge under the fast cook-off conditions generated in a fuel fire environment. The confinement is provided by a steel tube, similar to that used in the burning tube test, which is suspended over a tray of burning petrol. The results of this test on ROWANEX 3000 and a number of TNT-based explosives are reproduced in Table 5. The scale of response is judged in the same way as in the burning tube test as shown in Table 6. ROWANEX 3000 gave a deflagration response (reaction degree 2) in this test which compares favourably with the detonations (reaction degree 4) observed for Octol 75/25 and Composition B.

6.3.3 Large Scale Gap Test

The large-scale gap test is described in the SCC Manual of Tests (Test No 22) [8]. The large-scale gap test is based on the US NOL large-scale gap test, and is used to measure the shock detonation sensitiveness of explosive materials. Results are expressed as the pressure, P_g, just inside the attenuator at the attenuator/acceptor interface resulting in a 50% probability of detonation of the acceptor. The LSGT results for the candidate formulations, in terms of median gap (in mm) and pressure (in GPa) relative to a 50% probability of detonation. The results for ROWANEX 3000, Octol 75/25, and Tetryl are summarised in Table 8. ROWANEX 3000 exhibited greater sensitiveness to shock in this test than the EDC 1S melt cast reference composition, but its response is still significantly lower than the pressable explosive LX-14.

TABLE 8. COMPARISON OF LSGT RESULTS[a]

Composition	Median Gap (mm)	Pressure (GPa)
EDC 1S	44.7	2.53
OCTOL 75/25	49.5[a]	2.04
ROWANEX 3000	51.2	1.95
LX-14	54.5	1.7
TETRYL	60.6[a]	1.35

a LLNL Explosives Handbook; BM Dobratz

7. CONCLUSIONS

A new pressable polymer-bonded explosive, designated ROWANEX 3000, has been developed for shaped charge and fragmenting warhead main charge applications. The explosive has demonstrated enhanced performance levels and reduced vulnerability against certain hazardous stimuli when assessed against an Octol 75/25 reference composition. ROWANEX 3000 is in the process of being scaled-up and qualified to UK and NATO standards and it is anticipated that it will soon be available to weapon system designers as a fully approved explosive.

8. ACKNOWLEDGEMENT

Ministry of Defence funding for this work is gratefully acknowledged.

9. REFERENCES

1. Collaboration on Pressable Explosives for Shaped Charges - A European Success Story; WEAG Technical Area 25, CTP 25.2 Working Group: Chairman: AS Cumming; 28th International Conference of ICT; V40

2. Insensitive Munitions (IMs), Evaluation. NATO Standardization Agreement STANAG 4439, Brussels (Awaiting ratification by member states).

3. Insensitive Munitions Pillar Proceeding, Ordnance Board Proceeding 42657, 25 Sept 1990.

4. Insensitive Munitions Symposium, Ordnance Board, London, 31 May 1990.

5. Reduced Vulnerability High Explosives. ADPA Insensitive Munitions Technology Symposium, Williamsburg, Virginia, USA; 6-9 June 1994.

6. Pressable TPE-Based Explosives for Metal Accelerating Applications; RE Hollands, IEP Murray, TH Jordan and CJ Leach; 27th International Conference of ICT; P65

7. Introduction of New Explosives to Service, Ordnance Board Proceeeding 41779, 15 Feb 1977.

8. Sensitiveness Collaboration Committee Manual of Tests, October 1988.

Laser diode ignition of the combustion of pyrotechnic mixtures. Experimental study of the ignition of $Zr/KClO_4$ and $Zr/PbCrO_4$

E. RADENAC - Ph. GILLARD - M. ROUX

Laboratoire de Combustion et de Détonique
UPR n° 9028 du CNRS - ENSMA - B.P. 109
86960 Futuroscope Cedex, FRANCE

Abstract

This paper deals with the thermal ignition of some pyrotechnic mixtures by means of a laser diode. It is an interesting way to ignite and study these pyrotechnic mixtures and compositions behavior during ignition. Two experimental setup using an infrared laser beam have been carried out. The first device uses an optical fiber in order to ignite reactions whereas the second one uses lenses to concentrate energy. This work is devoted to the influence of the power of the laser P_{laser}, the pellet porosity $\bar{\epsilon}$, and the mode of ignition on the ignition threshold energy $\overline{E_{50}}$ and on the ignition delay time $\overline{t_i}$. It has been found that the ignition mode have an influence on ignition threshold energies; using optical fiber ignition results in lower energy level than using remote ignition system. The study has shown that P_{laser} increasing causes $\overline{t_i}$ and $\overline{E_{50}}$ decreasing. Concerning the influence of P_{laser}, experimental correlations have been found. It has also been found that an increase of $\bar{\epsilon}$ causes a significant decrease of $\overline{t_i}$ and $\overline{E_{50}}$.

Keywords: laser ignition, pyrotechnic mixture, porosity, ignition delay time, ignition threshold energy

INTRODUCTION

Ignition of explosive reaction with pyrotechnic mixtures may be obtained by means of shock, friction, spark or heat source. Using this last way, numerous detonators have been designed and most of them use hot or explosive wires.

A few years ago, small laser diode were employed in order to provide energy to heat up the surface of explosives. By concentrating the laser beam in some hundred of micrometers diameter, it was then possible to obtain an electronic optical detonator. Advantages of such devices are well known: there are not sensitive to magnetic disruption and their small size and high efficiency allow them to be embarked. Laser diode can be used with

an optical fiber to drive the energy to the explosives. It is also possible to use lenses in order to concentrate energy on the explosive surface.

These principles were used here in order to ignite pyrotechnic mixtures and to caracterize two important parameters during initiation, ignition delay time $\overline{t_i}$ and ignition threshold energy $\overline{E_{50}}$ for two different mixtures: $Zr/KClO_4$ and $Zr/PbCrO_4$.

EXPERIMENTAL SETUP

The pyrotechnic mixtures

Two differents pyrotechnic mixtures supplied by GIAT Industrie have been studied. The grain size of this two products was unknown. The first one was $Zr/KClO_4$, chemically balanced (mass ratio of 60/40) and the second one was $Zr/PbCrO_4$ at the same mass ratio, oxydizer lean. An amount of about 30 ± 2 mg of loose mixture was pelletized at a pressure P_p depending on the porosity ϵ at which the experiment has to be undertaken. The dependency of $\overline{\epsilon}$ versus P_p was found to be linear (Fig.1):

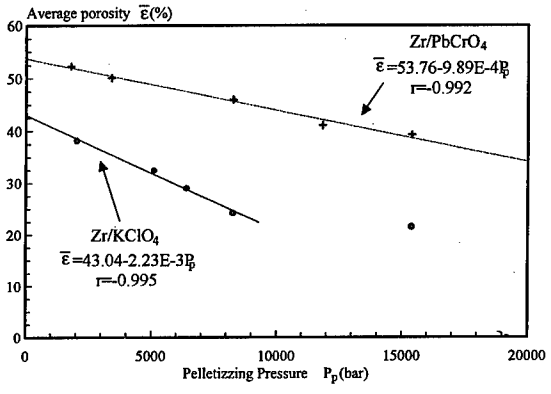

FIG. 1 - *Average porosity $\overline{\epsilon}$ versus P_p*

The porosity was calculated, first by calculating the density ρ_p of the pellet. Therefore, for a cylindrical pellet having a mass of m_p, Φ_p in diameter and a high of d, it results:

$$\rho_p = \frac{4m_p}{\pi \Phi_p^2 d} \tag{1}$$

where: $\Phi_p = 3$ mm, d is measured (round of the 1/100 of millimeter) and m_p is the amount of powder (round of 10^{-5} g). Given ρ_p, it follows:

$$\epsilon = 1 - \frac{4m_p}{\pi \Phi_p^2 d \rho_c} \tag{2}$$

where ρ_c is the density of the compact pyrotechnic mixture. For binary mixtures, it has been found to be equal to:

$$\rho_c = \frac{1}{\frac{X_{oxy}}{\rho_{oxy}} + \frac{X_{fuel}}{\rho_{fuel}}} \tag{3}$$

where X_i and ρ_i are the mass ratios and densities of each component respectively. According to Fig. 1, $\bar{\epsilon}$ decreases as P_p increases and it can be smooth by:

$$\begin{aligned} \bar{\epsilon}_{Zr/KClO_4}(\%) &= 43.04 - 2.23.10^{-3} P_p(bar) \\ \bar{\epsilon}_{Zr/PbCrO_4}(\%) &= 53.76 - 9.89.10^{-4} P_p(bar) \end{aligned} \tag{4}$$

Given $P_p = 0$ in Eq.4, the natural porosity of the powder (in close relation with the grain size) can be calculated; the greater the natural porosity is, the greater the grain size is.

The experimental devices

Two experimental setup (Fig.2 and Fig.3) were carried out in order to use a laser as energy source. Pyrotechnic mixture pellets surface was heated by a laser beam until the ignition temperature is reached.

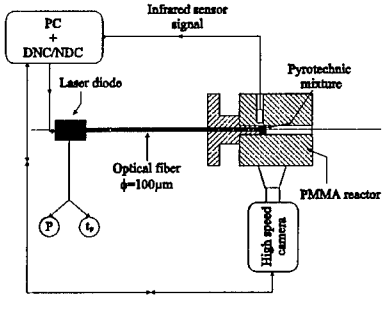

FIG. 2 - *Optical fiber laser ignition (Device 1)*

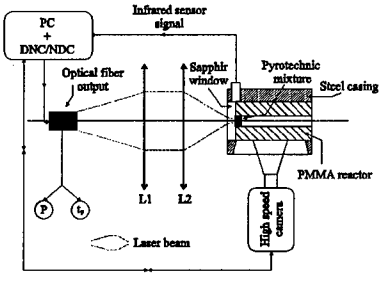

FIG. 3 - *Remote laser ignition (Device 2)*

An electronic box allowed to adjust the laser power and the laser pulse width. The power P_{laser} of the laser is measured by a pyroelectric laser radiometer placed just at the top of the optical fiber for the Device n°1, and after the sapphir window for the second one. A computer drives both the triggering line and the recording data system. The ignition delay time t_i is recorded thanks to an infrared sensor (λ_{max} = 850 nm) placed upon the pellet surface. The sensor voltage is simultaneously recorded on the computer and on a

numerical oscilloscope. These two different systems allowed us high speed photography. Various tests were carried out from 9000 to 18000 frames per seconde on a kodack Ecktapro motion analyser. The camera is also drived by the computer, and the camera photos can be recorded on it.

The first device (Fig.2) uses a laser diode (SDL2262P2). An optical fiber (connected to this diode) of 100 μm allowed to deposit a laser energy flux lower than 7.6 kW/cm^2. The laser beam wavelength is 815 nm. The optical fiber top which is burnt after each shooting has to be cut, and this step is very important for the efficiency of this ignition mode.

The second experimental setup consists of a remote ignition system (Fig.3); the laser source is provided by an other laser diode (OPC-A007-815-FC) on a divergent beam of 1 mm of diameter at the top of the optical fiber. The beam wavelength and the numerical aperture are 815 nm and 0.14 respectively. The laser beam is firstly collimated through a lens (L_1), and then focused by L_2 on the pyrotechnic mixture, which is in contact with a sapphir window (1 mm thick). The top of the optical fiber and the pyrotechnic mixture pellet are placed on the focal length of L_1 and L_2 respectively. Given the optical fiber diameter of D_{fiber} = 1 mm and the focal lens length of L_2, f_2 = 4.6 mm; f_1 changed, various spot diameters on the pellet were obtained (cf Tab.1):

f_1 (mm)	10	16	25	30
D_{spot} (μm)	400	290	185	155

TAB. 1 - *Calculated spot diameters.*

This setup provides a tuning power lower than 4 W on a spot diameter which ranges from 180 to 400 μm. The beam diameters were measured by using a photo paper placed against the sapphire window; as the first device the laser is driven by a control box. In the Device n°2 high speed camera can run through a window made into the cylindrical steel casing. All the experiments, for Device n°2 were carried out for a spot diameter of 185 μm.

STATISTICAL METHODS

Working on reactive heterogeneous materials implies the use of statistical methods in order to determine $E_{c\%}$ (ignition threshold energy correponding to a ignition probability of c%) and the ignition delay time $\overline{t_i}$, both disturbed by this heterogeneousness.

To access the ignition threshold energy $\overline{E_{50}}$ and its standard deviation $\sigma_{E_{50}}$, "Bruceton"

statistical test [1] has been used. This test consists firstly of preliminaries which permit to estimate $E_{5\%}$ (no ignition energy threshold) and $E_{100\%}$ (threshold energy corresponding to an ignition probability of 100%).

Therefore a series of 30 shootings has been undertaken in order to determine $E_{5\%}$, $\overline{E_{50\%}}$ and $E_{95\%}$. The test is validated if the energy step number (resulting from positive and negative shooting) ranges from 4 to 7. Assuming that the ignition energy statistical law is gaussian, it follows:

$$\begin{aligned} \overline{E_{50\%}} &= E_0 + d\left(\frac{A}{N} \pm \frac{1}{2}\right) \\ \sigma_{E_{50}} &= 1.62d\left|\frac{NB-A^2}{N^2} + 0.029\right| \end{aligned} \tag{5}$$

Where: N: Total shooting number

E_0: minimal energy value

d: energy step

A: $\sum_{i=1}^{step} in$, n number of shooting of the less numerous type of shooting (positive or negative) at a level of energy i

B: $\sum_{i=1}^{step} i^2 n$

Given $\overline{E_{50}}$ and σ, the energy and its standard deviation at an ignition probability of c% is $E_c = \overline{E_{50}} + K\sigma_c$ and $\sigma_c = \sigma_{50}Q$, with Q and K tabulated values.

The average ignition delay time $\overline{t_i}$ and the average porosity $\overline{\epsilon}$ (Fig.1) were calculated thanks to an other statistical method. Although these pellet batches are made under identical experimental conditions, a spreading out of these two values due to the powder heterogeneousness has been observed; a method, based on the "3σ statistic law", valid for the large number law, has then been computed. One of the statistical law used for small populations (less than 30) is the "Student law" which tends to a normal law for $n > 30$. In order to translate the "3σ law" into a law for small populations, the tabulated value of t_α (student coefficient) has to be found, which gives, for a number of elements n, a probability of 99.7% to find the "true value" between:

$$m - \frac{t_\alpha \sigma}{\sqrt{n}} < X_0 < m + \frac{t_\alpha \sigma}{\sqrt{n}} \tag{6}$$

Where σ: standard deviation $\sqrt{\frac{\sum_{k=1}^{n}(X_k - m)^2}{n-1}}$

m: mean of n elements $X_k \sum_{k=1}^{n} \frac{X_k}{n}$

Firstly, the mean and the standard deviation are calculated with all the values of X_k (for this study ϵ_k or t_{i_k}); then, regarding to Eq.6, all the X_k which range between the two limits determined by Eq.6 were kept to calculate with a good precision the value of $\overline{\epsilon}$, $\overline{t_i}$ and their standard deviation. Thus, Eq.6 is used as a filter.

For $\overline{t_i}$ measurements, the infrared sensor signal is firstly calibrated to be linked to the ignition phenomenon. In order to do that, both high speed camera and infrared sensor voltage have been used (Fig.4):

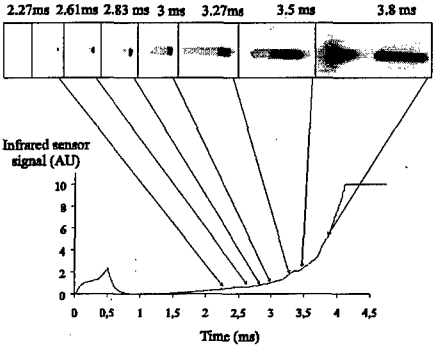

FIG. 4 - *Determination of the ignition criterion*

The ignition delay time $\overline{t_i}$ has been defined as the delay between the beginning of the laser pulse and the very first steps of the ignition corresponding to the first visible light production. For the two mixtures and various experimental conditions the infrared sensor voltage associated with this event was found to be constant: $\boldsymbol{V_{ignition} = 0.338V}$

RESULTS AND DISCUSSION

As said before, the influence of the average porosity $\overline{\epsilon}$, P_{laser} and the ignition mode on $\overline{E_{50}}$ and $\overline{t_i}$ were carried out for $Zr/KClO_4$ and $Zr/PbCrO_4$ mixtures.

The first results concerning the influence of $\overline{\epsilon}$ have shown for $\overline{E_{50}}$ and $\overline{t_i}$ a monotonic decrease as $\overline{\epsilon}$ decreases (Fig.5) for the two studied mixtures.

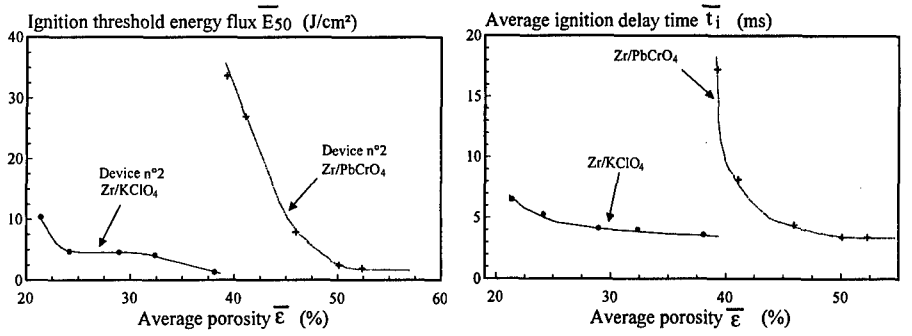

FIG. 5 - *Influence of* $\overline{\varepsilon}$ *on* $\overline{E_{50}}$ *and* $\overline{t_i}$

These results were performed on the Device n°2 with P_{laser1}=2.94 kW/cm^2 for $Zr/KClO_4$ and P_{laser2}=1.84 kW/cm^2 for $Zr/PbCrO_4$; P_{laser} was chosen far enough from the critical value P_c under which no ignition occures and $\overline{E_{50}}$ standard deviation increases. As shown in Fig.5, $\overline{E_{50}}$ and $\overline{t_i}$ tend to a minimal value of 1.5 J/cm^2 and 3.4 ms respectively, when $\overline{\varepsilon}$ tends to the natural porosity. For $Zr/PbCrO_4$, the influence of $\overline{\varepsilon}$ seems to be more pronounced. Some other studies[2, 3, 4] dealing with the influence of $\overline{\varepsilon}$ on $\overline{E_{50}}$ provide support for the results shown in Fig.5. Brochier [2] has shown that decreasing ρ (i.e. increasing $\overline{\varepsilon}$) implies the surface to be rough and dark which leads to minimize the ignition threshold energy flux. More theorical studies[5] have shown the same influence of the surface roughness upon the radiative surface properties. In fact the influence of the porosity on the studied parameters appears to be more complex; radiative and thermal parameters, just like gaz phase reactions may be change by $\overline{\varepsilon}$. Some experimental works (supported by calculations) undertaken in our laboratory[6] have shown that increasing the porosity causes a slight decrease of the thermal diffusivity a; the decrease of a emphasies hot spots growing and facilitates ignition. It can also be thought that surface roughness raising results in surface micro black bodies growing (i.e. surface reflexivity decrease) and thus, minimizing the ignition threshold energy flux. Gaz phase reactions[7, 8] has to be also taken into account because they can be alterred by a porosity decrease. A part of chemical reactions occurs into the gaz phase (ex oxydizer decomposition[7]) which implies that closing porosity causes the solid specific area decrease. This last chemical phenomenon could influence the ignition delay time decrease.

In a second part, the influence of the ignition mode and the influence of the laser power P_{laser} on $\overline{E_{50}}$ and $\overline{t_i}$ have been studied.

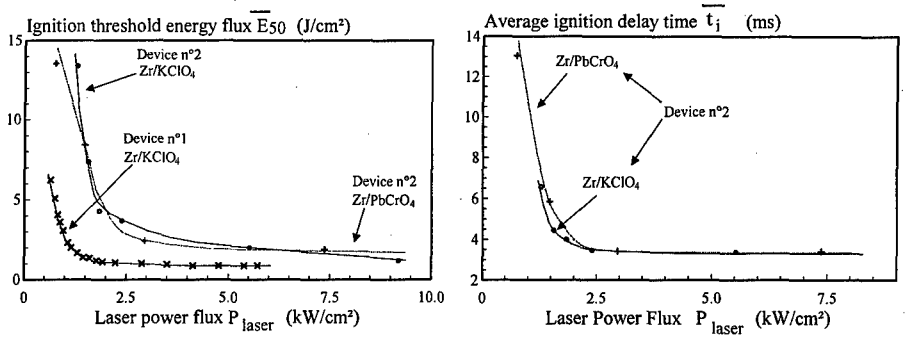

FIG. 6 - *Influence of P_{laser} on $\overline{E_{50}}$ and $\overline{t_i}$*

It can be seen for the results plotted in Fig.6 that, for the two devices and the two mixtures, a P_{laser} increase causes a huge decrease of $\overline{E_{50}}$ and $\overline{t_i}$; it also shows that over P_{laser} =2 kW/cm^2, $\overline{E_{50}}$ and $\overline{t_i}$ tends to fixed numbers, meaning that P_{laser} =2 kW/cm^2 constitutes a boundary limit between two ignition regimes. Fig.6 illustrate the fact that the ignition thresholds obtained from the Device n°1 (Fig.2) are lower than these obtained on device n°2 (Fig.3). This difference may be causes by energetic losses due to the fact that, in device n°1, the optical fiber (which drives the energy to the pellet surface) is put into contact with the reactive mixture; thus optical energetic losses[3] are limited by heat conduction transmission efficiency. This is worth remarkable that for the two devices, the heating diameter is not the same, and it is known [3, 9] that for each composition, the influence of the heating diameter upon the ignition threshold energy is not monotonic; there is a critical diameter corresponding to a minimum ignition threshold energy. The results plotted on Fig.6 demonstrate that there is a critical laser power P_c, below which no ignition occures. It means that, to drive to ignition, P_{laser} has to be far enough from P_c in order to compensate energetic losses represented by P_c . It follows thus that $\overline{E_{50}}$ versus P_{laser} can be represented by:

$$\overline{E_{50}} = \frac{A}{f(P_{laser} - P_c)} \tag{7}$$

The problem is to determinate an accurate value of P_c. An other way to present such results is to plot P_{laser} versus t_{p50}, where $t_{p50} = \frac{\overline{E_{50}}}{P_{laser}}$ (Fig. 7):

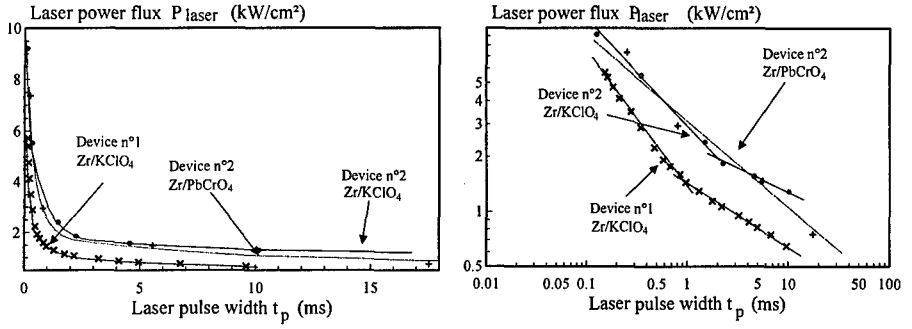

FIG. 7 - *Influence of t_{p50} on P_{laser}*

The results displayed in Fig.7 clearly demonstrate that P_{laser} =2.2 kW/cm^2 constitutes a limit between to ignition zones. A 1D analytical study[10] has shown that it is possible to approach P_{laser} versus t_{p50} by Eq.8:

$$\overline{P_{laser}} = \frac{A}{(t_{p50})^b} \tag{8}$$

with b=0.5.

In our case Eq.8 is verified for:

	A	b	r
Device n°1 $Zr/KClO_4$	1.72	0.519	-0.978
Device n°2 $Zr/KClO_4$	3.22	0.5469	-0.986
Device n°2 $Zr/PbCrO_4$	3.22	0.5102	-0.988

TAB. 2 - *Experimental values of A and b*

Despite of the two regions observed on Fig.7, this experimental output (Tab.2) give results in quite good agreement with those predicted by the thermal ignition equation (Eq.8). Some other experimental works [11, 12] undertaken in our laboratory have shown the same evolution. A 2D numerical simulation carried out by gillard et al.[13], taking into account radial phenomena follows and confirms very well with our experimental results.

In order to determinate P_c, it is very interesting to plot $\frac{1}{t_i}$ versus P_{laser}. Delichatsios[14] et al. have found that, for thermal ignition, $\frac{1}{\sqrt{t_i}} = C^{te} P_{laser}(W/m^2) + C$. By considering our experimental values which correspond to thermal ignition (i.e. P_{laser} <2.2 kW/cm^2), it becomes easier to get P_c (Fig.8):

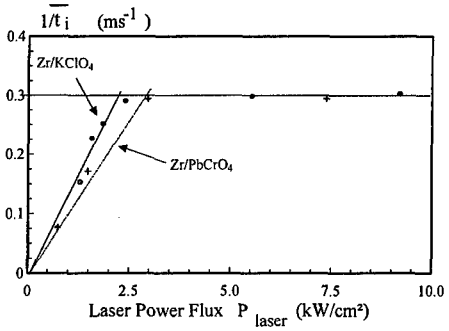

FIG. 8 - $\frac{1}{\overline{t_i}}$ *versus* P_{laser} *(Device n° 2)*

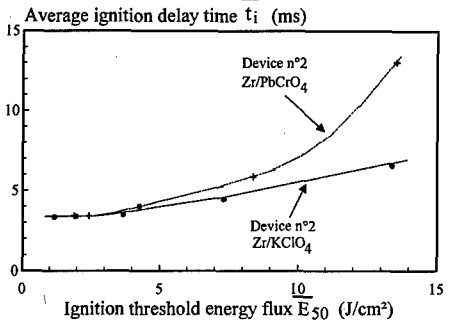

FIG. 9 - $\overline{t_i}$ *versus* $\overline{E_{50}}$ *(Device n° 2)*

When $\overline{t_i}$ tends to infinity, $\frac{1}{\overline{t_i}}$ tends to zero, and P_{laser} tends to P_c. It follows for P_{laser} <2.2 kW/cm^2 and using a linear extrapolation ($\frac{1}{\overline{t_i}} = aP_{laser} + b$):

$$P_c = -\frac{b}{a} \tag{9}$$

It results from Eq.9 and Fig.8 that P_{c1} =0.139 kW/cm^2 and P_{c2} =0.387 kW/cm^2 for $Zr/PbCrO_4$ and $Zr/KClO_4$ respectively. For P_{laser} >2.2 kW/cm^2, the results plotted in Fig.8 show that $\overline{t_i}$ tends to a limit which was 3.39 ms and 3.3 ms for $Zr/PbCrO_4$ and $Zr/KClO_4$ respectively. Therefore smoothing our values with a power function and taking into account the previous results, it follows:

$$\begin{aligned} \overline{t_i}^{Zr/KClO_4}(ms) &= \frac{1.75}{(P_{laser}-P_{c2})^{2.49}} + 3.3 \\ \overline{t_i}^{Zr/PbCrO_4}(ms) &= \frac{2.11}{(P_{laser}-P_{c1})^{3.26}} + 3.39 \end{aligned} \tag{10}$$

Thanks to the results obtained from Eq.9 and replacing them into Eq.7, it follows:

$$\begin{aligned} \overline{E_{50}}^{Zr/KClO_4}(J/cm^2) &= \frac{8.47}{(P_{laser}-P_{c2})^{0.94}} \\ \overline{E_{50}}^{Zr/PbCrO_4}(J/cm^2) &= \frac{8.65}{(P_{laser}-P_{c1})^{0.86}} \end{aligned} \tag{11}$$

Fig.9 shows that an increase of $\overline{E_{50}}$ causes an increase of $\overline{t_i}$. This evolution has been numericaly shown by Gillard et al.[13] in a 2D numerical simulation; it ensues that the understanding of the phenomenon has to consider the radial dimension in order to connect it to the reality.

CONCLUSION

Two experimental setup using two different laser diode were completed in order to initiate pyrotechnic mixtures. Two important parameters, $\overline{t_i}$ and $\overline{E_{50}}$ were studied for $Zr/KClO_4$

and $Zr/PbCrO_4$ mixtures.

It was shown that both mixtures give the same results concerning the study of the influence of P_{laser} and $\bar{\epsilon}$ on $\overline{t_i}$ and $\overline{E_{50}}$. It was found that the ignition mode is very important, and results in huge threshold energy differences: in our case, optical fiber ignition gives lower ignition threshold energy than the remote ignition system. The results shows that an increase of P_{laser} (for both studied mixtures and both devices) causes a decrease of $\overline{t_i}$ and $\overline{E_{50}}$. Calculating P_c, the power under which no ignition occurs, experimental laws have been written by linking all the experimental parameters involved in the ignition. Concerning the influence of the porosity $\bar{\epsilon}$, the results have shown that $\overline{t_i}$ and $\overline{E_{50}}$ decrease when $\bar{\epsilon}$ increases. It has been found some explanations about the results by refering them to physical phenomena such as surface radiation, thermal diffusivity or gas reactions. All this parameters seems to take place into the porosity effect.

Acknowledgements: The autors thank A. Espagnac of GIAT INDUSTRIE for providing various types of pyrotechnic mixtures ($Zr/KClO_4$ and $Zr/PbCrO_4$) for this laser ignition study.

REFERENCES

[1] Groupe de Travail de Pyrotechnie Spatiale. Méthodes statistiques de mesure - test de bruceton. In *Document GTPS n°11C*, pages 1–11. A.D.E.R.A., (1982).

[2] M. Brochier S.N.C. Davey Bickford. Contribution à l'étude de l'initiation de substances pyrotechniques par laser. In *19th International Annual Conference of ICT*, pages 78–89, (1988).

[3] J. Baoren, C. Danming, W. Zuoni, L. Yulian, Z. Kexing, L. Xufa, and L. Yide. Experimental studies on petn detonators initiated by laser radiation. pages 49–55.

[4] F.A. Al-Ramadhan, I.U. Haq, and M.M. chaudhri. Low-energy laser ignition of magnesium-teflon-viton compositions. *J. Phys. D: Appl. Phys.*, 26:880–887, 1993.

[5] A.S. Adorjan and F.A. Wierum. Radiative properties of rough surfaces. *AIAA Journal*, 9(11):2172–2179, 1971.

[6] M. Roux and C. Brassy. Diffusivité thermique de compositions pyrotechniques. In *rapport commande EFAB.* N° 86 A 01117, (1986).

[7] T. Sofue and A. Iwama. Ignition of composite propellants at subatmospheric pressures by means oc carbone dioxide laser. *PEP*, 4:98–106, 1979.

[8] R.K. Kumar and C.E. Hermance. Role of gasphase reactions during radiant ignition of solid propellants. *Combustion Science and Technology*, 14:169–175, 1976.

[9] G. Krassoulia and FX. Thinat. Un initiateur optopyrotechnique d'allumeur et d'application spatiale. In *colloque GTPS*, pages 1–9, (1989).

[10] Société Européenne de Propulsion. Influence de la durée de pulse laser sur l'initiation de compositions pyrotechniques. In *Europyro*, pages 137–141, (1993).

[11] M. Roux and Ph. Gillard. Ignition of pyrotechnic mixture by means of a laser diode part II: Experimental study. *PEP*, 22:351–354, 1997.

[12] E. Radenac, Ph. Gillard, and M. Roux. Initiation thermique de compositions pyrotechniques par une diode laser. In *A.A.A.F*, pages 1–9, (1996).

[13] Ph. Gillard and M. Roux. Ignition of pyrotechnic mixture by means of a laser diode part I: Numerical modelling. *PEP*, 22:256–262, 1997.

[14] M.A. Delichatsios, TH. Panagiotou, and F. Kiley. The use of time to ignition data for characterizing the thermal inertia and the minimal (critical) heat flux for ignition or pyrolysis. *Combustion and Flame*, 84:323–332, 1991.

KONTROLLIERTE VERNICHTUNG VON DATENTRÄGERN DURCH DÜNNE PYROTECHNISCHE SCHICHTEN ALS BESTANDTEIL DES DATENSCHUTZES IN SICHERHEITSKRITISCHEN BEREICHEN

Dr. Georgios Karametaxas, Jörg Kutzli, Philemon Schweizer, Markus Tobler

SM Schweizerische Munitionsunternehmung
Allmendstrasse 74, CH-3602 Thun

SUMMARY

Compact Discs (in their various formats) are now established as the world's number 1 digital information carrier. Their growth will accelerate with the current introduction of the very high capacity DVD formats (working on the same physical principle).

The contents of the CD-ROM go in certain instances from **very confidential** to **top secret**, especially in the domain MILITARY/INTELLIGENCE GATHERING.

So there is need for immediate destruction under emergency conditions. Presently CD-ROM are routinely destroyed under non emergency conditions using microwave ovens or just by disposal at sea. However these ways are not suitable for *Emergency very Rapid complete data destruction.* The CD-ROM has the disadvantage (advantage in most instances) that it is mechanically and chemically resistant. Its weak point is heat.

We have introduced a thin pyrotechnical layer on a surface just above the printed side of the CD-ROM. This pyrotechnic burns at 2000 °C for under 5 seconds and assures that practically 100 % destruction of the information is achieved. There are practically no side effects, ie no fire hazard and no emission of toxic fumes.

Einleitung

Der 5" Compact Disc ist weltweit zum digitalen Informationsträger Nummer Eins geworden. Die nachfolgende Tabelle möge dies veranschaulichen:

	1994	1995	1996	1997
WESTERN EUROPE	1343	1619	1964	2214
USA	1212	1654	1939	2247
JAPAN	491	580	639	673
LATIN AMERICA	89	127	169	203
CANADA	99	152	173	202
ASIA	210	289	453	598
AUSTRALIA	49	66	79	88
EASTERN EUROPE	29	33	44	57
MIDDLE EAST	16	23	36	40
REST OF WORLD	6	10	12	14
WORLD OUTPUT TOTAL (Mio.)	**3544**	**4553**	**5508**	**6336**

Tab 1 Welt CD Produktion 1994 – 1997
Qelle: Understanding & Solutions Ltd., Dunstabel, Bedfordshire LU6 3HS, England

Die Zahlen umfassen CD im Audio- und Videobereich, sowie CD-ROM. Die CD-ROM-Produktion hat alleine von 988.52 Mio. Einheiten 1995 auf 1 580.50 Mio. Einheiten 1996 zugenommen.

Er wird zunehmend zum Träger von Informationen aus sensitiven Bereichen des Gesundheits- und Bankenwesens, sowie dem Verteidigungsbereich. So werden z.B. Mission Profiles von Flugzeugen, U-Booten und unbemannten Flugkörpern ausschliesslich ab CD-ROM gelesen.

Die Forderung nach der Vernichtbarkeit der Information im Bedarfsfalle ist somit gegeben.

Dies kann beim Papier wie auch bei elektromagnetischen Datenträgern auf einfache Weise geschehen. Der CD-ROM hingegen ist unempfindlich gegen Magnetfelder und bedingt durch seinen Aufbau ebenfalls mechanisch äusserst stabil.

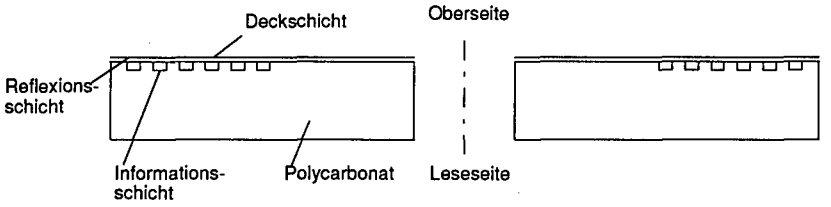

Abb 1 Prinzipaufbau des CD-ROM's

Geringfügige Beschädigungen der Reflexionsschicht, die ein Lesegerät zum «Stottern» bringen, können nicht als informationsvernichtend gewertet werden, denn diese kann mit andern Hilfsmitteln, z.B. mikroskopisch jederzeit wiedergewonnen werden.

In der Praxis hat man sich bis dato denn auch mit «Pfahlbauermethoden», wie erhitzen im Mikrowellengerät oder Versenken im Meer beholfen.

Erste Versuche, das Problem mit Hilfe von Lösungsmitteln oder direktem chemischen Angriff anzugehen, sind gescheitert. Stärkste anorganische und organische Säuren inklusive Königswasser vermochten die Lesbarkeit eines CD-ROM innert nützlicher Frist (< 60") nicht zu beeinträchtigen. Lösungsmittelseitig war einzig Methylenchlorid in der Lage, nach 5 Minuten die Polycarbonatschicht wegzulösen.

Somit bot sich als einzige erfolgversprechende Variante die thermische Vernichtung an und die Pyrotechnik war hier naheliegend.

Problemstellung

1. Ziel

Es ist im Innern des CD-ROM-Behälters (Caddy) oder allenfalls auf der CD-ROM-Oberseite direkt eine pyrotechnische Schicht dermassen anzubringen, dass diese den normalen Betrieb nicht stört, aber im Falle einer Zündung den CD-ROM soweit beschädigt, dass durch keine Massnahme die Information gewonnen werden kann. (no character readable).

2. Randbedingungen

Funktionstemperaturband	–35 °C / +60 °C
Mechanische Belastbarkeit	Falltest) gemäss MIS 810 D/E Schock) Vibration)
Funktion unter Wasser	nicht gefordert
Lagerkondition	60 % rel. Feuchtigkeit
Nebenwirkungen	• Keine Deflagrationen, weder bei Zündung noch bei Abbrand. • Keine Emission von giftigen, oder korrodierenden Gasen • Beim Abbrand darf der Caddy verformt werden, nicht aber zu brennen beginnen • ein Abbrand im Laufwerk darf dieses beschädigen, nicht jedoch die Peripheriegeräte
Caddy	• Dieser muss serienmässig sein. Er darf an Stelle des normalerweise verwendeten Polystyrols aus Polycarbonat bestehen
Zündung	• elektrisch; Zündpille T–7. Als Option kann eventuell eine mechanische Zündung in Betracht gezogen werden

Lösungsansätze

1. Wirkmassen

Infolge den gestellten Randbedingungen musste von vornherein auf gaserzeugende Sätze, wie etwa phlegmatisiertes Schwarzpulver verzichtet werden. Die Auswahl beschränkte sich demzufolge auf

- Thermite mit leichter Zündbarkeit
- Redoxsysteme Metall/Fluorkohlenwasserstoffe
- Metall/Perchlorate (aus Sicherheitsgründen wurden Chloratsätze ausser Acht gelassen)

2. Messgrössen und Beurteilungskriterien

Die Spritztemperatur des allgemeinen CD-Werkstoffes Polycarbonat liegt bei 280–300 °C. Aus Vorversuchen im Wärmeschrank war bekannt, dass sich das Material bei ca. 250 °C dermassen veränderte, dass ein Informationscode nicht mehr erkennbar war. Andererseits waren Wärmeübergangszahlen von abbrennenden Pyrotechnikschichten mit Flammtemperaturen von 1500–2500 K völlig unbekannt, sodass man sich auf eine Trial and Error Methode mit visueller Beurteilung beschränken musste.

3. Anforderungen an die Pyrotechnikschicht

Maximaldicke	0,5 mm (bedingt durch Platzverhältnisse)
Adhäsion	Genügend für Fall- und Vibrationstests
Versiegelung	Keine Bildung von Abrieb und Staub während Betrieb und während der mechanischen Beanspruchung
Substrat	CD-ROM werden während des Lesevorgangs auf maximal 6890 U.p.m beschleunigt. Aus dieser Überlegung kam bevorzugt der Caddydeckel als Substrat in Frage. Damit ergaben sich Probleme, da dessen Material, Polystyrol, thermisch weniger resistent war, als das Polycarbonat des CD-ROM

4. Applikation

Zur Herstellung der Schichten wurden die pyrotechnischen Sätze in Lösungsmittel aufgeschlämmt, Binder zugesetzt und anschliessend mit Pinsel oder Erichsongerät aufgetragen. Der Reproduzierbarkeit kam entscheidend Bedeutung zu. Folgende Binder kamen zum Einsatz:

Binder 14 Compound aus Styrol-Copolymer und modifiziertem Kolophoniumharz bewirkt in kleinen Konzentrationen (3 %) gute satzinterne Bindung. Die Adhäsion auf dem Substrat ist jedoch gering.

Emzelllack (Nitrocellulose/Alkylharz) ergibt verbesserte Adhäsion auf dem Substrat bei jedoch erhöhten Konzentrationen.

Acryllack darf als Kompromiss zwischen Binder 14 und Emzell bezeichnet werden.

Übersicht über die Grundlagenversuche

1. Pyrotechnische Systeme

In einer Grundlagenstudie wurden die folgenden Stoffkombinationen ausgewählt [1–13]

Al/Fe_2O_3; Mg/Fe_2O_3; Al/$MgFe_2O_3$: Mg/MnO_2; $CaSi_2$/MnO_2; Ti/Fe_2O_3; Ti/B; Fe/$KClO_4$; Mg/PTFE

Vor der Applikation wurden mit losem Gemisch erste Abbrandversuche durchgeführt, anschliessend durch Abbrandversuche in dünner Schicht ergänzt. Zum Schluss wurde mit Binder vermischt und auf den Caddydeckel appliziert.

Erwartungsgemäss hatte der gewählte Binder einen starken Einfluss durch übermässige Phlegmatisierung einerseits, oder Veränderung des Abbrandverhaltens durch die bei der Pyrolyse entstehenden brennbaren Gase.

Für alle gewählten Systeme verbindlich konnte zusätzlich beobachtet werden, dass das Durchbrandverhalten der Schicht stark von der Oberflächenbeschaffenheit des Untergrundes abhängig war. Bei glatter Oberfläche (Kunststoff, Karton, Al-Folie) musste die aufgetragene Menge im Schnitt verdoppelt werden, um einen Durchbrand zu erzielen. Dies wiederum hatte unerwünschte Nebenwirkungen auf das Gesamtsystem.

2. Versuchsresultate der Grundlagenphase

Diese seien im folgenden hexagonalen Schema dargestellt.

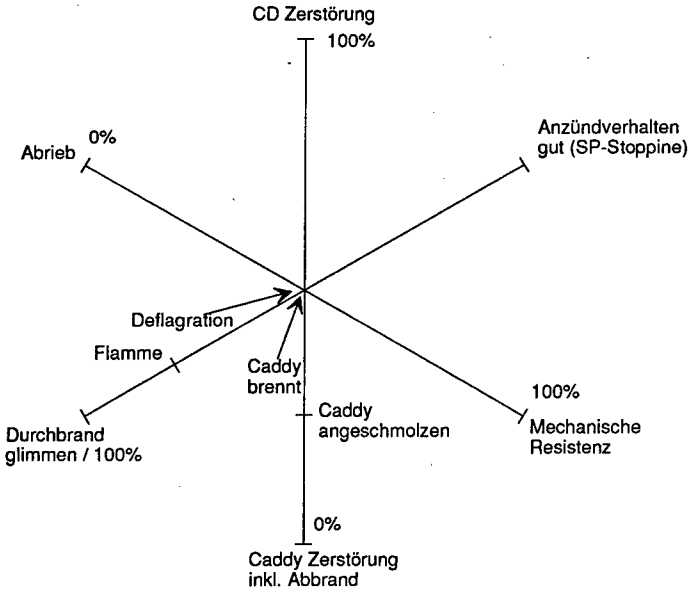

Die 100 % ideale Kombination hätte hier also die Form eines regulären Sechsecks.

Generell kann folgendes bemerkt werden:

Sämtliche Gemische haben in stöchiometrischer Form zu heftig reagiert. Aus diesem Grund musste mit ca. 20 % Überschuss des Reduktors gearbeitet werden.

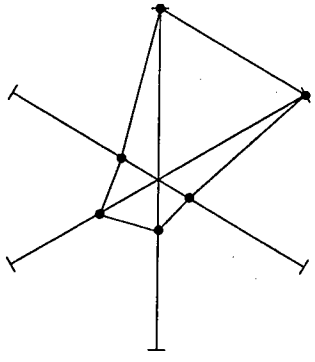

1) Mg/Fe_2O_3 (ca. 60 % Mg)

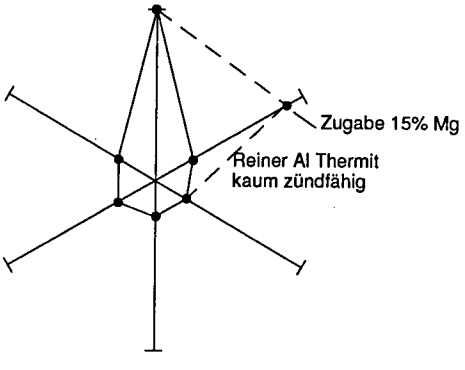

2) Al/Fe_2O_3; $Mg/Al/Fe_2O_3$

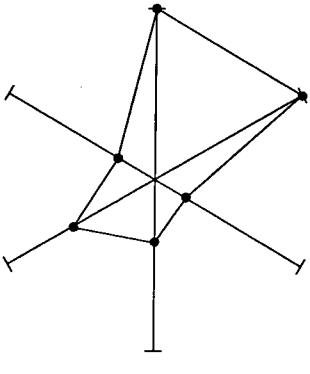

3) Mg/MnO_2

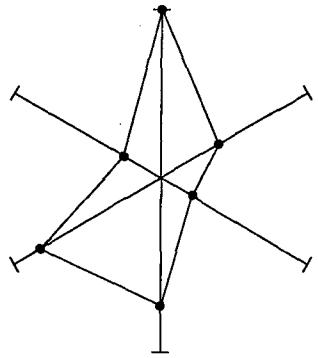

4) $CaSi_2/MnO_2$

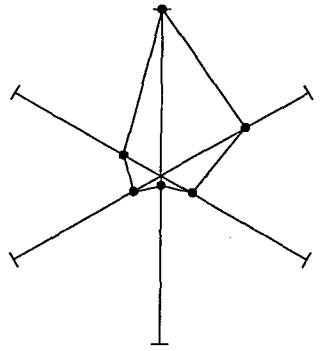

5) Ti/B; Ti/Fe_2O_3

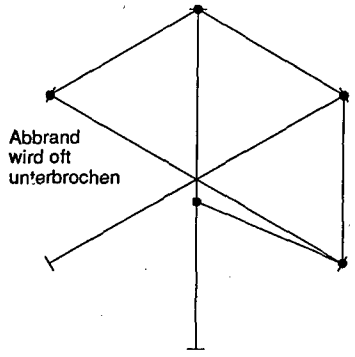

6) Mg/PTFE (Enerfoil)

Da Enerfoil quasi stöchiometrisch zusammengesetzt ist, verläuft der Abbrand zu heftig. Mechanisch hingegen ist das Produkt ideal.

7) Fe/$KClO_4$. Dieses Redoxsystem wird oft in thermoaktivierten Batterien verwendet. Für die vorliegende Anwendung ist es zu energiearm, kann jedoch infolge nachglimmen das Polystyrol des Caddydeckels entzünden.

Aus diesen Grundlagenversuchen geht folgendes hervor:

⇒ Abriebfestigkeit und mechanische Resistenz klar ungenügend
⇒ Substratoberfläche muss aufgerauht sein und soll gegen den Caddydeckel isolieren
⇒ Polystyrol ist als Caddymaterial nicht geeignet. Es muss ersetzt werden durch Polycarbonat
⇒ Als Wirkmasse kann ein aktiviertes Thermitsystem eingesetzt werden. Das System Mg/PTFE fällt aus Emissionsgründen weg

Umsetzung in ein Funktionsmuster

Das als Demonstrator vorgesehene Funktionsmuster ist aus den in den Vorversuchen gewonnenen Erkenntnissen entstanden und verfügt über folgende Konfiguration:

Caddydeckel:	Polycarbonat	
Trägermaterial:	Glasfaservlies /27g/m^2	
Pyrotechnik (3 % Binder 14)	Fe_2O_3:	30 %
	MnO_2:	16 %
	Al:	13 %
	Zr:	21 %
	Fe:	20 %

Das Eisen nimmt nicht aktiv an der Reaktion teil, sondern wirkt als Kühler und gibt die gespeicherte Energie über Strahlung an das CD-ROM ab.

Die Leistungscharakteristik sieht folgendermassen aus:

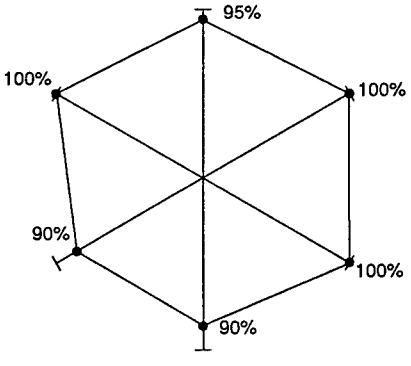

Ein Mittel zur effizienten Informationsvernichtung auf CD-ROM, wie auch auf DVD (Digital Versatile Disc) ist somit gegeben.

Zusammenfassung

Prägnant ausgedrückt war folgende Aufgabe zu lösen:

In einem Kunststoffbehälter ist ohne Auswirkungen auf dessen unmittelbare Umgebung ein Kunststoffgegenstand grossflächig thermisch mittels Pyrotechnik unbrauchbar zu machen.

Dies bedeutet:

- Minimale Energieabgabe an das Substrat; maximale Energieabgabe an das zu zerstörende Objekt
- Erzielung eines stabilen Abbrandes mit Glimmcharakter trotz Energieverluste an das Substrat
- Mechanische Härtung der Schicht, um Beanspruchungen im Rahmen von MIS 810 D zu widerstehen

Durch Verwendung von Glasfaservlies als Isolierschicht zum Kunststoff, beimischen eines metallischen Energiespeichers zur verwendeten Thermit, konnten die Probleme gelöst werden.

Literatur

[1] US Patent 5 439 537, Aug 8, 1995
Thermite composition for use as gas generants

[2] T. Tsuchida, T. Kitagawa, M. Inagaki
Self-combustion rection induced by mechanical activation of Al-Si-C powder mixtures
Europ J of solid State and Inorg Chemistry, 53, No 7–8, 629–638, (1995)

[3] A. Zuhair Munir, A. Debra Odink
The synthesis of intermetallic phases by combustion methods
Konferenz-einzelbericht Metallurgical Processes for the Early Twenty-first Century, Proc. of the 2nd In. Symp., Vol 1, San Diego, USA, Sept 20–23, 1994, Band 1,167–181, (1994) Warrendale TMS

[4] US Patent 5340014 Aug 23, 1994
Combustible slurry for joining metallic or ceramic surfaces or for coating metallic, ceramic and refractory surfaces

[5] R. Orru, B. Simonicini, P.F. Virdis, G. Cao
Int. J Self-Propagating High-Temerature Synthesis, 4, No 2, 137–147, (1995)

[6] C. Bartuli, R.W. Smith, E. Shtessel
J. Advances in science and technology, Ed by P. Vincenzini, Vol 5 Advances in Inorganic Films and Coatings Band, 131–140, (1995)

[7] P. Fragnaud, R. Nagarajan, D.M. Schleich, D. Vujic
J. Powder Sources, 54, 362–266, (1995)

[8] S.C. Deevi, S. Deevi
J Scripta Metallurgica et Materialia, 33, No 3, 415–420, (1995)

[9] A. Leiper Graeme
ENERFOIL Ignition Films as an Ignition Charge
26th International Annual conference of ICT 1995, Karlsruhe, BRD, 58/1–58/14

[10] GB 2 251 434
Pyrotechnic materials (Pyrotechnische Folie aus PTFE und Mg)

[11] Li Hung-Pin
Int. J Self-Propagating High-Temperature Synthesis, 4, No 2, 199–207, (1955)

[12] G.M. Koledinskii, B.V. Novozhilov
J Engineering Physics and Thermophysics, 65, No 5, (1993)

Evaluation of polyNIMMO in a Reduced Smoke Propellant

Poly(3 nitratomethyl-3-methyloxetane or polyNIMMO ($C_5H_9O_4N$) is a new and promising polymer for composite propellants and is a potential replacement for hydroxy-terminated polybutadiene (HTPB).
PolyNIMMO is compatible with the range of newly developed energetic plasticisers such as Glycidyl Azide (GAP-A). Use of such plasticisers allows a reduction in solids loading whilst maintaining performance. In the case of Ammonium Perchlorate (AP) this leads to a reduced secondary smoke level.
This paper presents a study of a polyNIMMO / GAP-A / AP composition. It presents sensitiveness and stability results of the propellant, in both a cured and uncured state. Sensitiveness results show that while the formulation can be more sensitive to impact and friction in the uncured state than a standard HTPB /DOS /AP formulation, once cured there is no significant difference. Results of work undertaken to reduce the sensitiveness of the precure are given.
Ballistic results are given for both burn rate and performance in small scale motors. These show that a high burn rate is possible without the use of ballistic catalysts although their use is not precluded. As AP is the oxidiser all the usual ballistic catalysts can be considered. Pressure exponent results are low which will also be advantageous to rocket designers. Rheological data over a range of temperatures show that, even at these early stages, usable mechanical properties are achievable, especially at low temperatures, and there is no reason to believe that these cannot be improved upon once the cure system is optimised.

Authors
S. Flynn
D. R. Fossey
D. G. Catton
D. Wagstaff

BRITISH AEROSPACE
DEFENCE
ROYAL ORDNANCE

British Aerospace Defence Limited
Royal Ordnance
Rocket Motors
Summerfield, Kidderminster,
Worcestershire DY11 7RZ, England
Telephone (01562) 824061
Fax (01562) 828126

Festtreibstoffe für den Einsatz in Unterwassertriebwerken

H. P. Hebekeuser und H. P. Mackowiak
Dynamit Nobel GmbH Explosivstoff- und Systemtechnik
D-57299 Burbach-Wuergendorf

Abstract

Obwohl Feststoffraketenmotore nur einen relativ geringen rechnerischen Wirkungsgrad gegenüber konventionellen Antrieben aufweisen, zeigen sie doch deutliche Vorteile, nämlich

Kostengünstige und relativ einfache Herstellung
hohe Lebensdauer bei vollständiger Wartungsfreiheit
trotz einfacher konstruktiver Auslegung hohe Zuverlässigkeit
hohe Leistung bei kleinem Bauvolumen

Feststoffraketenantriebe eignen sich auch für die Verwendung in Unterwasserlaufkörpern, die über kurze Laufstrecken bei einmaliger Anwendung eingesetzt werden sollen. Hierzu werden solche Festtreibstoffe benötigt, mit denen sich unter den besonderen Anforderungen für Unterwasserantriebe ine möglichst hohe Leistung erzielen läßt.

Im Rahmen dieser Arbeit[1] wird über die Entwicklung eines hexogenhaltigen Hochleistungstreibstoffs berichtet, der bei extrem hohen Brennkammerdrücken auch noch eine relativ niedrige Abbrandrate besitzt, so daß bei dessen Anwendung auch relativ hohe Reichweiten erzielt werden können.

1. Einleitung und Problemstellung

Die Forderung zu immer höheren Leistungsdaten von Triebwerken führt i.a. ständig zu Verbesserungen der jeweils verwendeten Treibstoffsysteme. Dies gilt insbesondere für Festtreibstoffe, die für die Anwendung in Unterwassertriebwerken vorgesehen sind. Von eminennter Bedeutung ist das Erzielen einer sehr kompakten Bauweise. Daher gehört neben einem hohen spezifischen Impuls auch eine extrem niedrige Abbrandrate bei relativ hohen Brennkammerdrücken zu den wichtigsten Parametern eines Festtreibstoffs, der für den Einsatz in Unterwassertriebwerken für Arbeitstiefen von möglicherweise mehreren 100 m vorgesehen ist.

Im Gegensatz zu Flugkörpern ist bei Unterwasserantrieben selbstverständlich auch noch deren Auftrieb (Wasserverdrängung) zu berücksichtigen, der die Gesamtauslegung eines Unterwasserlaufkörpers stark beeinflussen kann.

Hohe Leistung, d.h. ein hoher spezifischer Impuls ist verständlicherweise auch nur mit einem hochenergetischen Treibstoff erzielbar. Solche Treibstoffe besitzen in der Regel eine günstige Sauerstoffbilanz und liefern daher - wie in nachstehender Tabelle 1 am Beispiel zweier energetisch unterschiedlicher doppelbasiger Treibstoffe gezeigt wird - auch meist relativ hohe Verbrennungstemperaturen.

---

[1] Hierbei handelt es sich um Teilergebnisse einer vom BWB WF I4 finanzierten Studie, die gemeinsam mit dem ICT, Berghausen und der Firma TMS, Bonn bearbeitet wird.

Tabelle 1: Kenndaten zweier energetisch unterschiedlicher doppellbasiger Treibstoffe

		DBE D7150	DBG D731
Sauerstoffbilanz	[% O_2]	-32,5	-45,9
mittl. Verbr. Temperatur	[K]	2680	2018
mittl. spez. Impuls	[Ns/kg]	2400	2130
Explosionswärme	[J/g]	4058	3392

Der Leistungsgewinn führt dann jedoch zu einem für den hier behandelten Einsatzzweck unerwünschten Anstieg der Abbrandrate, wie in der nachstehenden Grafik gezeigt wird.

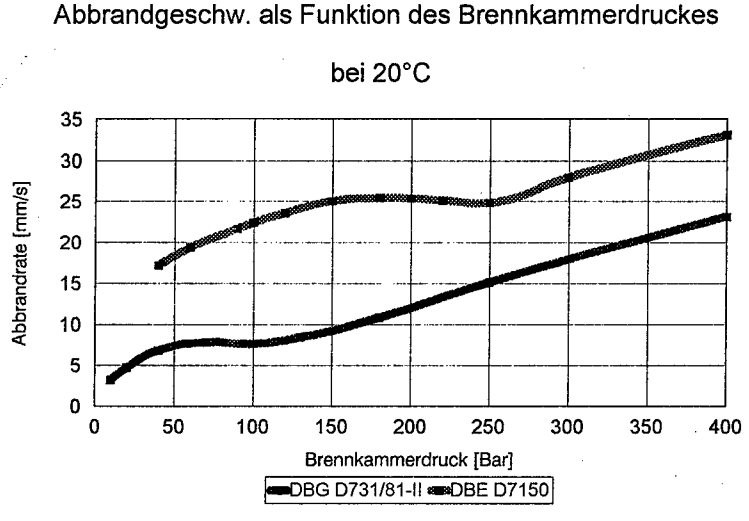

Die Forderung nach einem Hochleistungstreibstoff mit extrem niedriger Abbrandrate bei hohen Brennkammerdrücken erscheint daher zunächst konträr.

Für den Einsatz in einem speziellen Unterwassertriebwerk wurde ein Treibstoff benötigt, mit dem sich ein gerätespezifischer Impuls von etwa 2200 Ns/kg erzielen läßt, d.h. unter der Vorraussetzung eines Wirkungsgrades von η = 0,88 wird min. ein theoretischer spezifischer Impuls von 2500 Ns/kg gefordert. Die Abbrandgeschwindigkeit soll bei einem Brennkammerdruck von 20 bis 25 MPa nur maximal 10 mm/s betragen.

Beide oben aufgeführten doppelbasigen Treibstoffe sind daher verständlicherweise aufgrund des spezifischen Anforderungsprofils nicht geeignet.

2. Problemlösung

Bereits früher in einem anderen Zusammenhang durchgeführte Versuche haben gezeigt, daß der spezifische Impuls hexogenhaltiger Festtreibstofformulierungen durch Ammoniumperchloratzusatz verbessert werden kann, ohne daß die Abbrandrate dadurch wesentlich beeinflußt wird, wenn eine bestimmte Kornzusammensetzung gewählt wird.

Wir haben daher zur Erfüllung der oben genannten Forderungen ein Treibstoffsystem basierend auf Hexogen und Ammoniumperchlorat mit einem zweikomponentigen Bindemittel auf Polybutadienbasis gewählt und verschiedene Formulierungen untersucht, in denen nicht nur die Zusammensetzung sondern auch die Korngrößenverteilung variiert wurde. Insbesondere haben wir im Rahmen einer umfangreichen Meßreihe die Auswirkung des Ammoniumperchloratzusatzes auf die Abbrandgeschwindigkeit $r_{(200)}$ (bei t = 20°C) näher untersucht. Einige Teilergebnisse sind in der Tabelle 2 aufgeführt und in der nachstehenden Grafik visualisiert.

Tabelle 2: Abbrandgeschwindigkeit in Abhängigkeit vom AP/RDX-Verhältnis

	AP: RDX	$r_{(200)}$
1	5,1:1,0[a)]	12,42mm/s
2	5,1:1,0[b)]	9,68 mm/s
3	5,1:1,0[c)]	19,66 mm/s
4	3,0:1,0[d)]	16,0 mm/s
5	5,0:1,0[e)]	8,68 mm/s
6	5,1:1,0[f)]	9,64 mm/s

[a)] Fein- zu Grobkornverhältnis AP = 1:6; [b)] dto. jedoch 1:13; [c)] dto. jedoch 1:3; [d)] dto. jedoch 1:7; [e)] wie [b)] jedoch mit zusätzlichem Weichmacheranteil, [f)] ohne Feinkornanteil.

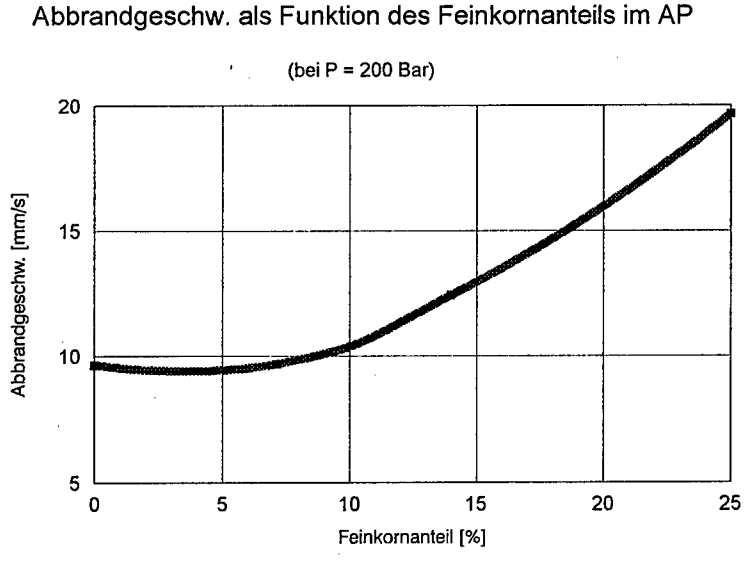

Außerdem haben wir den spezifischen Impuls verschiedener Formulierungen mit unterschiedlichem AP-Gehalt (für eine Entspannung von 200:1) berechnet. Er ist in der nachstehenden Grafik als Funktion des AP-Gehalts (bei konstant gehaltenem Gesamtfeststoffanteil) dargestellt.

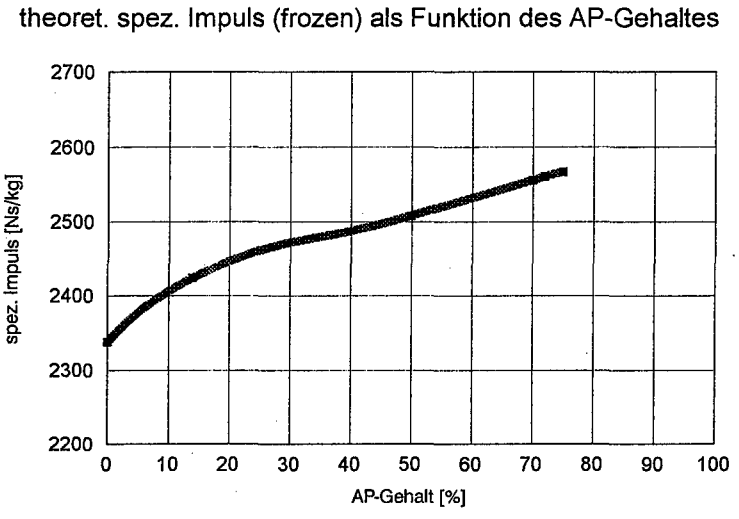

Es ist ersichtlich, daß ein theoretischer spezifischer Impuls oberhalb 2500 Ns/kg nur dann erzielbar ist, wenn die Formulierung mindestens 50 %, optimal jedoch etwa 70% Ammoniumperchlorat enthält. Die günstigsten Abbrandgeschwindigkeiten bei 200 bar Fremdgasdruck werden erhalten, wenn im eingesetzten Ammoniumperchlorat das Verhältnis Fein- zu Grobkorn etwa 1:13 beträgt, und der Weichmacheranteil geringfügig erhöht wird.

3. Charakterisierung des für den speziellen Einsatzzweck entwickelten Treibstoffs „*Schubertit*"[2]

In den nachfolgenden Tabellen und Grafiken sind die Thermodynamischen Leistungsdaten, die Abbrandcharakteristik in der Crawford-Bombe und in der Normbrennkammer sowie einige der im anwendungsnahen Maßstab auf dem Raketenprüfstand ermittelten Leistungsdaten aufgeführt.

[2] Dieser Treibstoff, der im nachfolgenden „*Schubertit*"genannt wird, wurde Herrn Prof. Dr. H. Schubert, ICT, anläßlich seines 70. Geburtstags gewidmet

3.1 Thermodynamische Leistungsdaten

	Entspannung 70:1	Entspannung 200:1
Sauerstoffbilanz (%)	-24,4	-24,4
Bildungsenthalpie (kJ/100g)	-195,13	-195,13
Brennkammertemperatur (K)	2828	2846
Düsenaustrittstemp. (K)	1223	979
spez. Impuls (Ns/Kg)	2376	2546
charakt. Geschwindigkeit (m/s)	1502	1504
$\kappa = C_p/C_v$	1,27	1,29
mittl. Molmasse der Gase (g/mol)	24,3	24,3
Molzahl der Gase	4,11	4,10
Gasvolumen, aktuell (L/Kg)	4188	3343
Gasvolumen, normal (L/Kg)	667	663

3.2 Abbrandcharakteristik
3.2.1 Untersuchung in der Crawford-Bombe

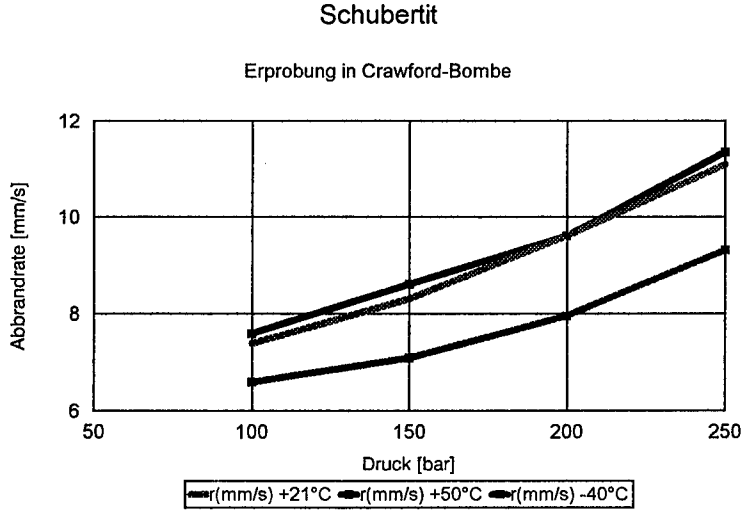

3.2.2 Erprobung in der Normbrennkammer

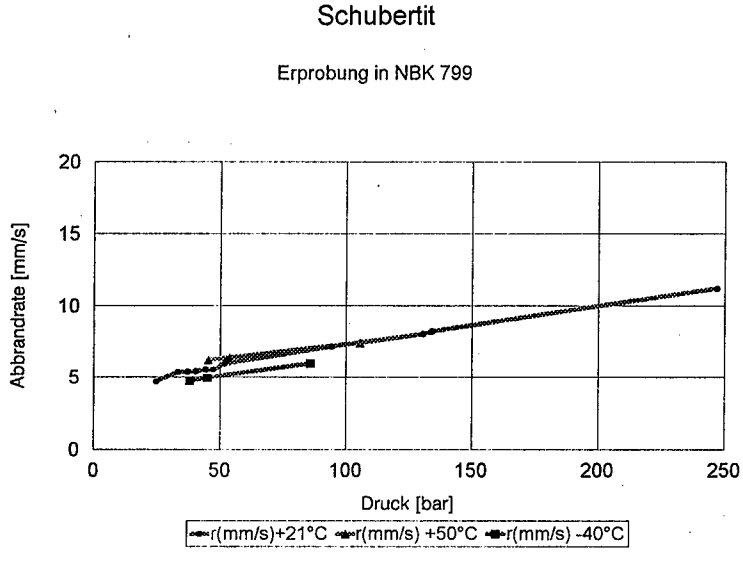

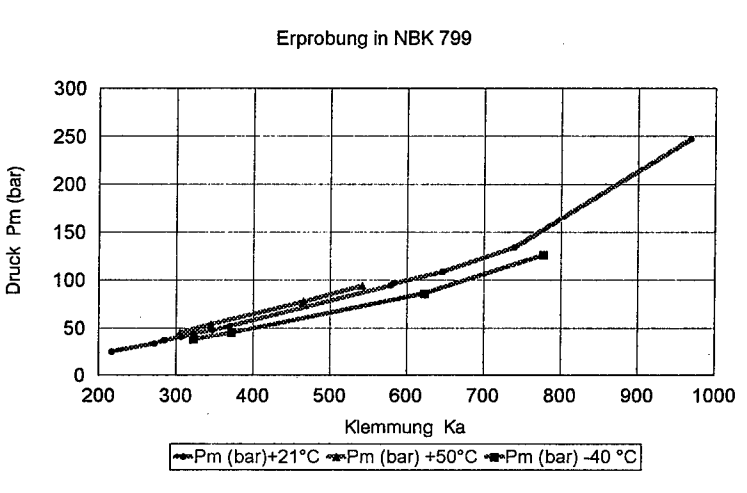

3.2.3 Erprobung im anwendungsnahen Maßstab (Raketentriebwerk mit Sterninnenbrenner)

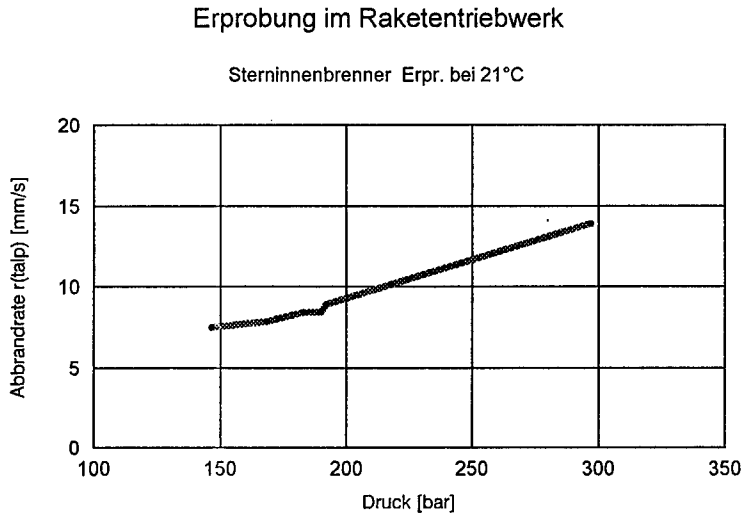

praktisch erzielte Leistungsdaten:

phys. Größe	Wert
mittl. Druck	190 bar
max. Druck	303 bar
spez. Impuls	2324 Ns/kg
Abbr. geschw.	8,5 mm/s

4. Zusammenfassung

Obwohl die Forderung nach einem Hochleistungstreibstoff mit extrem niedriger Abbrandrate zunächst konträr erschien, konnte sowohl durch Korngrößenvariation als auch durch Variation der Zusammensetzung einer Mischung aus Ammoniumperchlorat und Hexogen ein Treibstoff - *Schubertit* genannt - entwickelt werden, der bei einem mittleren Brennkammerdruck von 190 bar einen praktischen spezifischen Impuls von 2324 Ns/kg liefert. Auch liegt dessen Abbrandgeschwindigkeit unterhalb des geforderten Wertes von 10 mm/s. Es steht damit ein neuer Festtreibstoff für vielfältige Aufgaben für Unterwasserantriebe zur Verfügung.

CONTINUOUS PROCESSING OF COMPOSITE PROPELLANTS (CPOCP),

A JOINT PROJECT BETWEEN SNPE AND INDIAN HEAD DIVISION, NAVAL SURFACE WARFARE CENTER (IHDIV, NSWC)

Eric Giraud, Jean-Michel Tauzia, G. Lacroix*
SNPE
BP 57 - 33166 Saint-Medard en Jalles
* Research Center Le Bouchet
France

Constance M. Murphy, Richard S. Muscato, William F. Newton,
Frederick M. Gallant, Mark A. Michienzi, Sharperson G. Johnson
IHDIV, NSWC
101 Strauss Avenue
Indian Head, Maryland 20640-5035

ABSTRACT

The Continuous Processing of Composite Propellants (CPOCP) project is a collaborative research and development effort between the U.S. Department of Defense and the French Department of Defence, respectively represented by IHDIV, NSWC and SNPE. The initial project, which began in September 1994, is nearly complete and has resulted in the development of common technologies and processes for continuously manufacturing both extruded and cast composite propellants.

The technical approach for the project divided the major tasks between the U.S. and France so that each country could brings it's expertise to bear on a focused part of the overall effort. France had the lead on the advancement of state-of-the-art liquid and solid feed systems. The U.S. had the lead on the development and redefinition of state-of-the-art on-line quality control equipment and integration of that equipment into the overall control system for the process.

Both countries have continued to operate and upgrade their own process development scale facilities which are capable of manufacturing rocket motors using a co-rotating twin screw mixer/extruder. The French team has demonstrated the successful mixing, deaeration and continuous casting of their chosen cast composite formulation. The American team has demonstrated the successful mixing, deaeration and extrusion of extruded composite propellant without the use of solvents which are required for conventional batch processing. Finally, these demonstrations have led to full operational tests of each facility to manufacture rocket motors.

The presentation, given jointly by American and French participants, will include a description of each of the two process development facilities and the accomplishments of the project including the results of the rocket motor static testing.

INTRODUCTION

The Continuous Processing of Composite Propellants Project (CPOCP) is an international cooperative research and development effort, between France and the United States, to develop the technology to continuously process solid rocket propellants. This project is governed by a bilateral Memorandum of Agreement (MOA), signed in May of 1994. The official project start date was September 1, 1994 and it was originally scheduled to last 36 months. Due to technical challenges, the project was extended nine months. The total cost of the project is split evenly between the U.S. and France.

The major objectives of this project are to develop continuous processing technology to manufacture both extruded and cast composite propellants and to agree on common standards for the design of continuous processing equipment for the production of these types of propellants The continuous process is applicable to a wide variety of cast and extruded motors ranging in size from small unguided rockets and tactical missile motors to strategic booster motors. Composite propellants were chosen as the focus of this project for two reasons: 1) these types of propellants are of interest to both France and the United States; and 2) composite propellants are the most complicated energetic materials to process in a continuous manner because of multiple feed stream requirements, accuracy requirements of the formulation in order to meet the propellant specifications (burn rate, mechanical properties, etc.), moisture sensitivity, and processing vacuum requirements. This project is specifically directed towards the development of the processing technology for composite propellants, however, the processing technology is directly applicable to PBX explosives, gun ammunition and pyrotechnics.

The management organization for the CPOCP project includes both a Steering Group and a Project Manger appointed by each country. The responsibility of the Steering Group is to provide executive level oversight of the project and to devise solutions to any issues identified and unresolved by the Project Managers. The Project Managers are responsible for the management and execution of the technical portions of the project as well as effective implementation of the project in accordance with the MOA.

Previous experience in the field of continuous processing of energetic materials has revealed two deficient areas which must be improved to achieve a truly effective and viable continuous process for the production of energetic materials. The first area of focus is the accurate metering of solid and liquid ingredients to the continuous processor. The second area of focus is the real time analysis and monitoring of the quality of the final product and using that

information to control the process. The scope of work for the CPOCP project was defined to specifically address these two areas while developing improved mixing and casting or extruding technology to continuously manufacture composite propellants. The two countries have worked jointly to improve the state-of-the-art ingredient feed systems, develop on-line quality analysis and process control technologies, and advance the understanding of the process/quality/safety relationships in a twin screw mixer/extruder. The technology developed has been demonstrated through the testing of propellants and will ultimately be demonstrated through the testing of rocket motors manufactured by the continuous process.

The technical approach for the project divides the major tasks between the U.S. and France so that each country brings its expertise to bear on a focused part of the overall effort. France has the lead for the advancement of state-of-the-art liquid and solid feed systems while the U.S. leads the development of state-of-the-art on-line quality analysis equipment and integration of that equipment into the overall control system for the process. Both countries have continued to operate and upgrade their own pilot scale prototype facilities for both cast and extruded composite propellants. France has concentrated on the development of improved mixing and casting technology for cast composite propellants while the U.S. has concentrated on mixing and extrusion of extruded composite propellants. Both countries have conducted full operational tests of their facility to manufacture rocket motors for testing and will jointly prepare a final technical report summarizing the experiments that have been conducted, results, and recommendations for the design and operation of continuous processing equipment. The overall success of the project will be measured by small scale propellant quality tests and static testing of the rocket motors manufactured by continuous methods.

FRENCH PROJECT ACCOMPLISHMENTS

The continuous processing facility at SNPE, Saint Médard en Jalles

The CPOCP studies are conducted in Saint-Médard plant in a development facility focused on continuous processing. The facility is able to process the all energetic materials handled at SNPE : solvent single, double and triple base, solventless double base, composite propellant, PBX, composite gun powders.

The facility itself is organized around a co-rotating self wiping twin screw mixer extruder built on CLEXTRAL design (French company).

The extruder is an 85 mm diameter equipped with cantilever screws, L/D = 16 .It is exhibiting five different heating/cooling zones : die, screws, and three zones on the barrel. The barrel is a crocodile type opening barrel allowing a perfect cleaning of the whole screws. The mixer extruder is hydraulically powered showing a range of rotation speed from 0 to 50 rpm. It is able to work under vacuum and exhibit two different solid feed ports and five different liquid feed ports.

The chosen formulation for the CPOCP project is a castable HTPB based propellant filled with a bimodal distribution of ammonium perchlorate (68% in mass) and aluminium (18% in mass). The

formulation has been split in three chemically stable components called : oxydizer, binder and curing agent. These three components are continuously fed by two liquid feeders and one solid weighing feeder. Because of the sensitivity of loss in weight feeders to refill operations that occur frequently in a continuous process, the solid feeder is a specific device showing no sensitivity to refill. Moreover in order to minimize the mechanical agressions on ammonium perchlorate it is equipped with vibrating trays.

The total throughput has been set to 60 kg/h (120 lbs/h) of composite propellant. The facility allows eight hours long live runs, with help of two refill systems for binder and oxidizer. In this case the shop is equipped with a specific propellant conveyor used to match with safety requirements.

During extrusion it is possible to regularly take samples and to cast rocket motors. These jobs are realised using a specific three ways valve located at the nozzle of the extruder. Connected to the three ways valve SNPE have developed two different devices used to cast the rocket motors under vacuum.

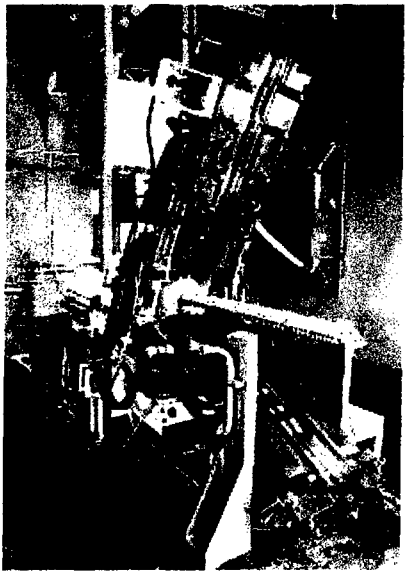

Figure 1 : industrial scale pilot plant

French CPOCP Team

The French portion of the project is managed by the R and D department of SNPE with control of the French Ministry of Defence.

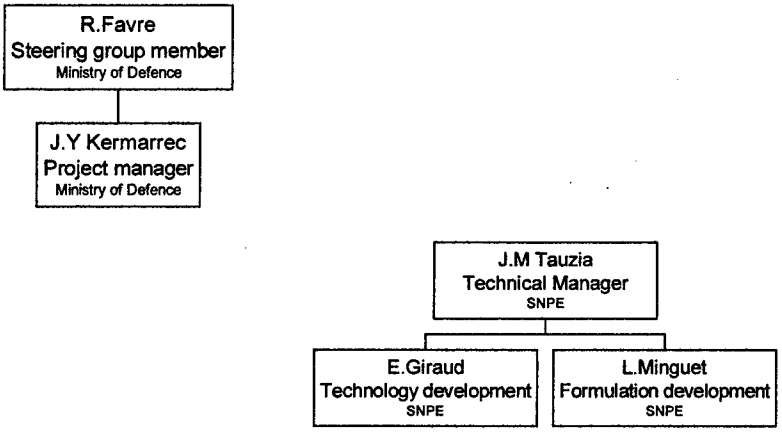

PROJECT ACCOMPLISHMENT

Since the beginning of the project (september 1994), the French team has focused on the following areas :

- Design of the screw profile and choice of the running parameters.
- Design of the propellant stream from extruder nozzle to casting device.
- Split of the propellant formulation in several chemically stable components.
- Calibration and measurement of the feeders accuracy .
- Improvement of the quality control system based on residence time distribution principle (RTD) and on I.R spectroscopy.
- Mathematical design of dies, screws ...
- Design of experiment on the formulation parameters (live propellant).
- Live casting of rocket motors
- Common IHDiv / SNPE live trials in the SNPE facility.
- Development of a continuous to batch filling of rocket motors

Only few items will be described in this paper, we will particularly focuse on

- Live manufacturing of rocket motors and fire testings
- I.R spectroscopy as a method for quality control
- Mathematical modelling of processes

1) Live manufacturing of rocket motors and fire testings.

Several runs have been done in order to manufacture, live Baria rocket motors. The Baria rocket motor are used as control motor for Ariane V propellant, and are able to be manufactured either with batch or continuous process.

Three kinds of live Baria motors have been manufactured with the same raw materials but with three different process :

⇨ Classical batch process with an horizontal mixer and a vacuum casting of the propellant.

⇨ Lab scale continuous process with the SNPE Research Center twin screw extruder and a « Lazy Suzan » casting of the propellant.

⇨ Industrial scale continuous process with SNPE Saint-Medard plant twin screw extruder and a « Lazy Suzan » casting of the propellant.

The lab scale twin screw extruder, is located in the SNPE Research Center in Le Bouchet, it is a Clextral BC45 specifically designed for Energetic applications wich exhibit a ∅ 55 mm diameter screws with cantilever shafts. The total mass flow used during the manufacture of the Baria rocket motors is 10 kg/h (20 lbs/h).

The SNPE industrial scale twin screw extruder is a ∅ 85 mm diameter screws with cantilever shafts. The total mass flow used during the manufacture of the Baria rocket motors is 60 kg/h (120 lbs/h).

During each manufacturing runs some samples have been recovered to check the denstity, and the mechanical properties of the propellant. Fire testings have been done with several rocket motors coming from each process.

Running Parameters of the extruder

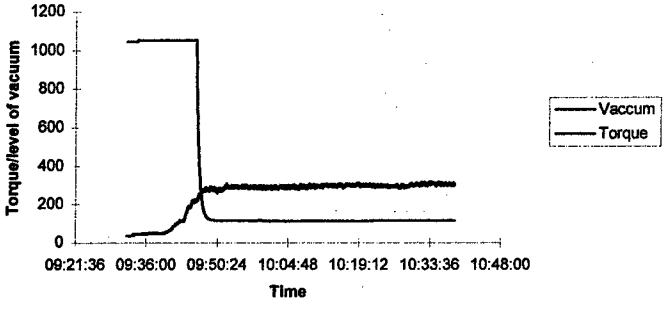

The average burning rate and the standard deviation recorded for each manufacturing are listed in the following table.

Table n°1 : Burning rate results :

Process	Burning rate, mm/s (13 MPa)	Standard deviation
Batch process	10,47	0,08
Lab scale Continuous	10,58	0,1
Industrial scale Continuous	10,37	0,12
Average value for all processes	10,45	0,14

As it can be seen the results of each processes are in a quiet good agreement, with low variations of the burning rate.

Such results make the continuous processing of continuous propellant a trully industrial process. It is also interesting to note that the scale up of processes has been done from a lab scale machine to an industrial machine.

2) I.R spectroscopy as a method for quality control

Chemometric treatment of mid-infrared spectrometry data of propellants has been investigated as a method for quality control.

2.1) Description of propellants standards set

The first step in the definition of chemometric models is the elaboration of the calibration matrix with given well known propellants. In this study, we have modified the original formulation in order to test the accuracy of the I.R methodology.

Just like in the D.O.E on formulation parameters we have modified the filler/binder ratio (+/- 2% of filler content), and the size distribution of the filler +/- 7% on the fine granulometry.

2.2) Description of analysis method

The analytical technique is Fourier Transform Infrared spectrometry (FTIR), in mid wavenumbers region. Two types of analysis method have been evaluated :

Horizontal Attenuated Total Reflexion Analysis (HATR), for macroscopic observations using a ZnSe crystal with multi reflexions. The analysis area is 7 cm2 and the depth of analysis is 10µm

Micro ATR analysis, for microscopic observations using a diamond crystal, with single-reflexion. The analysis area is 50 to 100 μ^2 and the depth of penetration < 10 µ.

2.3) Description of chemometric algorithms

Spectral data are treated by Chemometric techniques. Two types of algorithm have been evaluated : Discriminant analysis and PLS

2.3.1 Discriminant Analysis algorithm

It is a *Spectral Classification* algorithm. The calibrated model determine the known samples class which is nearest from an unknown sample. It is a qualitative analysis based on similarity with known samples, rather than quantitative measures. A distance between unknown sample and nearest class is calculated : this is Mahalanobis distance. Lower is the distance, better is the similarity.

In our application, Discriminant Analysis model is calibrated with 5 standard-class :

- class 68/12 (b=53 - f=15) ⇔ nominal composition
- class 70/10 (b=60 - f=10)
- class 70/10 (b=50 - f=20)
- class 66/14 (b=47 - f=19)
- class 66/14 (b=56 - f=10)

2.3.2 - PLS algorithm

It is a statistical approach for quantitative analysis, based on the Partial Least Square algorithm.

a) It determines spectral area, which are varying statistica lly as a function of components concentrations.

b) It develops a calibration method, using Beer's Law :

$$\text{Absorbance matrix} \;/\; | \text{Abs} | = \text{K} \;|\; \text{x} \;|\; \text{Conc.} |$$

Molar absortivity matrix Component concentrations matrix

c) It predicts concentration values of unknown samples.

In our application, two PLS models have been elaborated :

- one, based on a calibration matrix of :
  . binder concentration in a calibration space of 10 to 14% and
  . fillers concentration in a calibration space of 66 to 70%
- the other, based on a calibration matrix of size particles distribution of fillers, only for macroscopic spectral data, in a calibration space of :
  . 53.4 to 60% for large sizes
  . 10 to 20% for fine size

2.4) Validation procedures

Validation procedures test each model. They allow us to know performances and limits of each elaborated model.

2.4.1) Validation procedure for Discriminant Analysis model (D.A.)

The indicator for a good discrimination in a D.A. model is the Mahalanobis distance of each standard in its own class and face to the other reported classes, with a fixed discrimination threshold of « d (other classes) > 3D (standard classes) ». Results of our D.A. models are given in the table n° 1.

Table n° 2 - D.A. models of ATR spectra and MICRO-ATR spectra.

Class	**MAHALANOBIS DISTANCE AVERAGE**	
	ATR	**ALT**
standard	0.2	0.17
Next	0.52	0.4
70/10 (60.10)	0.74	0.85
70/10 (50.20)	1.2	0.64
68/12 (53.15)	1.0	0.55
66/14 (47.19)	0.66	0.66
66/14 (56.10)	0.8	0.46

We can deduce, from these values, that D.A. models are discriminant enough for the 5 defined classes.

2.4.2) Validation procedures for PLS models

Two types of validation test allow us to validate PLS models :

- Diagnostic tests help us to optimise parameters during elaboration of the method ; the most significant are statistical spectra (variance and correlation spectra) Press test and Outliers diagnostic.
- Cross-validation test quantifies *each calibration standard* as if it were a validation one, by :
  - sequentially removing a standard from calibration set
  - calibrating the new method
  - quantifying removed standard with the new method

Cross validation résults of each PLS model, at macroscopic and microscopic scale, give following accuracy and dispersion relative values :

- 0,8 % for fillers concentration matrix
- 2% for large and medium size particles distribution of fillers

2.5) Conclusion

Chemometric techniques, coupled with IR spectral data, are performing methods to control propellant process, as well at macroscopic as at microscopic scale. However, we can notice some limits for PLS methods :

↳Low accuracy on binder concentration prediction , because of its low rate face to fillers rate or a too large calibration.

↳Bad accuracy on fine particles distribution prediction , at macroscopic scale, and no method at microscopic scale, because of low correlation between spectral and particles distribution informations.

3) Mathematical modelling

Some years ago it appeared mandatory to SNPE to develop Mathematical simulation of processes operations, in order to reduce development cost by decreasing the number of trials.

This has specially been done during the CPOCP project. Four different mathematical tools have been employed to design : the screw profile, the extruder die, and the casting tools. It can be said today that mathematical modeling of processes had been of great help to reach the goals.

The design of the screw profile has been done using LUDOVIC software. This sofware created developped by CEMEF Sophia Antipolis has been used to design the proper screw configuration (conveying elements, number of mixing paddles etc...). It has also been used to choose the screw rotation speed with regards to the total throughput and to the degree of fill of the desaeration chamber.

Moreover, the quality of mixing has been evaluated using the Residence Time Distribution of the different screw profiles and a specific SNPE-CERILOG sofware called ECLIPSE.

The die or extruder nozzle has also been mathematically designed using the RHEOTEK software POLY 3D (see figure n°2). This sofware used by SNPE since 1992, had been applied to the extruder nozzle in order to calculate the pressure drop, and to eliminate all the dead spots in the stream.

Last, the whole casting device has been designed using PROCOP F2D, as a tool for evaluating pressure drops with highly viscous fluid.

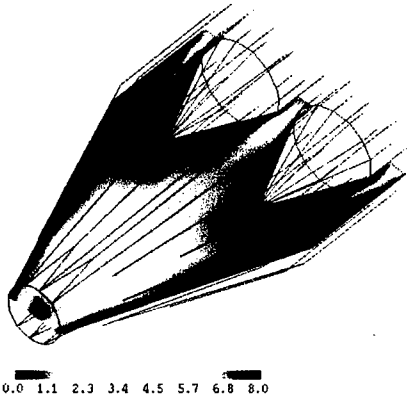

Figure 2 : Extruder nozzle of the Clextral BC 72

Acknowledgment :

CPOCP project would not have become reality without the great support of French Ministry of Defence and especially Mr Jean-Yves Kermarrec, Mr Loic Lallement, Mr R.Favre, Mr P.Lusseyran, Mr P.Andurant.

US PROJECT ACCOMPLISHMENTS

The emphasis of the U.S. team is on the mixing and extrusion of extruded composite propellants as well as the development of on-line, real time quality analysis and monitoring techniques. The overall success of the project will be measured by small scale propellant quality tests and static firing of rocket motors manufactured by the continuous process. These tests will determine the merits of the continuous process. An extruded composite propellant formulation for the 2.75 inch rocket motor was chosen as the test vehicle for the US portion of the project. This grain is approximately 61.5 mm (2.42 inch) in diameter, 762.0 mm (30 inch) in length and has a single star shaped perforation. The propellant formulation is an elastomeric binder filled with a bimodal distribution of ammonium perchlorate and cured with an isocyanate. The solids loading is approximately 86 percent by weight.

The Continuous Processing Facility at Indian Head Division is a small scale facility which is used for process development of both class 1.1 and 1.3 materials. The facility is centered around a Werner & Pfleiderer (W & P) ZSK-40 co-rotating, fully intermeshing twin screw mixer/extruder. The extruder has six segmented barrel sections and three liquid injection plates which can be arranged to serve different ingredient addition locations and operating

requirements. The W&P extruder is equipped with five separate temperature control zones for maintaining process temperature. The facility has an eight feed stream capability. There are four loss-in-weight feeders for feeding solid materials, three volumetric pumps for liquid metering which use closed loop control systems based on mass flow, and one loss-in-weight liquid feeder. The product is extruded through a die mounted in a die holder at the end of the extruder. A variety of extrusion dies and take away systems are available to accommodate different products. The entire process is controlled remotely. A PC-based data acquisition system is utilized to acquire process information. The facility has been operational since July 1988 with inert material and May 1990 with live material. Extruded products, such as Lova nitramine gun propellant, are processed at production rates of 6.8 to 13.6 kg/hr (15 to 30 lb/hr). The anticipated maximum throughput for highly solids loaded castable systems is approximately 45.5 kg/hr (100 lb/hr). Highly solids filled, extruded and castable products have been successfully processed.

Initially the US team focused on the following areas: developing methods of feeding the polymer and other ingredients to the continuous processor, processing of inert propellant to develop operating protocols for live propellant, developing rheological measurement techniques and mathematical models to aid in extrusion die design, and investigating and selecting promising real time, on-line analytical techniques. More recently, the US team focused on using mathematical models to design an extrusion die followed by the fabrication and testing of that die; optimizing the processing of live propellant; and developing near infrared spectroscopy as an on-line quality analysis technique.

The collection of rheology data was necessary to provide input to mathematical models for extrusion die design. The rheological behavior of the extruded composite propellant, manufactured by the twin screw extruder process was characterized. Under the guidance of Dr. Kalyon at HfMI/SIT, the capability to measure rheology data of highly solids filled materials under fully developed flow conditions was established. The shear viscosity function of the formulation was characterized under systematically varied pressure drop and volumetric flow rate conditions. A vertical ram extrusion press was used in conjunction with a series of specially designed, instrumented and jacketed capillary dies. These instrumented capillary dies are unique in that they are capable of directly measuring the propellant pressure and temperature at the entrance of the capillary. A sketch of the die geometry is shown as Figure 1. A Dynisco temperature/pressure transducer (TPT) is inserted into a mounting hole in the die. This method of directly measuring the temperature and pressure of the propellant during steady state extrusion (i.e. constant ram speed or pressure) allows accurate rheological data to be collected.

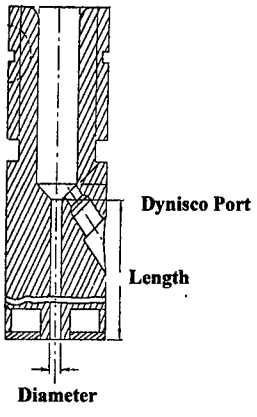

Figure 1

The data collected under isothermal conditions was corrected for capillary entrance and exit effects as well as deviation from Newtonian behavior. The propellant exhibited viscoplastic behavior. The rheology data were fitted with a Herschel-Bulkley type viscoplastic constitutive equation in the high shear rate region (20 - 250 s^{-1}). The best-fit of the Herschel-Bulkley equation generated a yield stress of 150,000 Pa, a consistency index of 31,812 Pa-$s^{0.1}$, and a shear rate sensitivity index (power law) of 0.1. This equation was then used as input to a mathematical model.

A three-dimensional finite element method (FEM) based source code, previously developed at HfMI/SIT, was utilized to design the internal profile of an extrusion die for the continuous processing and shaping of extruded composite propellant using a twin screw extruder. The die design target was a pressure drop of 1000 psi from the screw tips to the die exit. This pressure drop was chosen to ensure good weld line healing after the propellant flowed over the spider legs of the die. Collaboration with Shear Tool, Inc., a die manufacturer, and IHDIV, NSWC yielded a final die design that met the requirements and could be easily manufactured. Initially, the die was designed without consideration for wall slip. This propellant is known to flow as a plug and therefore, slip at the wall. An additional 75 mm (2.96 inches) was added to the length of the die land, increasing the total die length to 305 mm (12 inches), to account for wall slip and result in an extrusion die that would still yield an overall pressure drop of 1000 psi. The actual pressure drop predicted by the model prior to adding the 75 mm was 1041 psi at a throughput of 50 lb/hr and a screw speed of 85.

The first live extruded composite propellant extruder run conducted with the 2.75 inch extrusion die occurred in July 1997. Since then we have conducted six additional extruder runs yielding approximately 500 pounds of propellant. The actual average pressure drop measured at a throughput of 50 lb/hr and a screw speed of 85 rpm ranged from 600 to 650 psi. The last

extruder run was conducted, at those same operating conditions, to manufacture propellant grains for static testing. The average pressure drop measured during this run was 630 psi versus the predicted pressure drop of 1041 psi.

Investigation into the source of error led Dr. Railkar at HfMI/SIT to discover that the rheology data used to design the die was in the high shear rate range when actually low shear rates are experienced in the die. The rheology data in the low shear rate region (1 to 20 s^{-1}), the actual operating shear rate range, were fitted with a Herschel-Bulkley type viscoplastic constitutive equation. The best-fit of the Herschel-Bulkley equation generated a yield stress of 107,331 Pa, a consistency index of 1722 Pa-$s^{0.2}$, and a shear rate sensitivity index (power law) of 0.2. This equation was then used as input to a mathematical model and a pressure of 630 psi was predicted for the die without wall slip (the short die without the additional 75 mm). The original model did not have the capability to incorporate wall slip. However, incorporating wall slip with analytical methods, adjusts the predicted pressure drop to 750 psi. This prediction is within 20% of the observed pressure. HfMI/SIT has developed a new source code which incorporates wall slip for three dimensional geometries. They are currently implementing this source code and anticipate even better agreement with the measured pressure drop from this new code.

The initial live extruded composite propellant extruder runs revealed a variation in the propellant's properties that was unacceptable. The first extruder run with the 2.75" extrusion die was conducted with constant parameters to define the scope of the problem. The parameters were as follows: throughput of 50 lb/hr, screw speed of 55 rpm, vacuum level of 50 mm Hg, mixing temperature of 110°F, and extrusion temperature of 80°F. Six propellant grains were extruded during the course of the 1.5 hour processing run. Each grain was divided into three sections and propellant samples were tested from each. The resulting data was averaged and is presented in Table 1 along with appropriate statistical values.

Table 1

	Density g/cc	Heat of Explosion cal/g	Strand Burn Rate at 77°F, 1000 psi cm/sec (in/sec)
Mean	1.754	1380	1.783 (0.702)
Standard Deviation	0.004	34	0.074 (0.029)
Coefficient of Variation (%)	0.20	2.46	4.10
Minimum Value	1.748	1333	1.623 (0.639)
Maximum Value	1.760	1440	1.892 (0.745)
Range	0.012	107	0.269 (0.106)

Not only was there too much variation in the burn rate from grain to grain, the burn rate was from 6.4% to 20% higher than the typical burn rate obtained from batch mixed extruded composite propellant (1.519 cm/sec or 0.598 in/sec at 77°F and 1000 psi). The high burn rate was not as much of a concern as the variability because we knew we could adjust the formulation to obtain the required burn rate.

The first issue addressed was the feed rate accuracy. Three solid feedstreams and two liquid feedstreams were fed to the extruder for the initial extruder runs. Once the burn rate variability was discovered, the feedstream scenario was evaluated and modified. The graphite coated HyTemp binder was cryogenically ground to a smaller particle size and blended with the burn rate modifier feedstream. This change decreased the feed rate variation of the HyTemp from approximately 16% to a feed rate variation of the combined stream of less than 4%. The feed rate variation of the AP preblend feedstream was approximately 2% which was the best that could be achieved. The liquid feed rate accuracy was satisfactory all along.

A design of experiments (DOE) approach was then used to solve the burn rate variability problem. The goal of the experiment was to understand what process parameter values decreased the burn rate variability. The experimental design used was a full factorial design with replication. The parameters chosen for investigation were those that we felt most likely affected the product variation. All other parameters were held constant (throughput of 50 lb/hr, vacuum level of 10 mm Hg, mixing temperature of 110°F, and extrusion temperature of 80°F). The parameters (factors) and the values evaluated are presented in Table 2.

Table 2

	Low Value (-)	High Value (+)
Binder Mixing Screw Configuration Section	Normal*	Intense
Oxidizer Mixing Screw Configuration Section	Normal*	Intense
Screw Speed (rpm)	50	85

* The normal value of each screw configuration section was the design previously used to make the propellant that exhibited the variable properties.

The DOE involved the evaluation of eight different treatment combinations of the process parameters and the replication of each combination during the course of four extruder trials. The experiment was blocked on screw configuration (i.e. all treatment combinations involving one complete screw design were evaluated during one extruder run) because the screw configuration could not be changed during the course of an extruder run. One propellant grain was extruded for each set of processing conditions. The grains were cured for four days at 170°F and then dissected to provide samples for laboratory analysis. Testing included density, burn rate and heat of explosion.

The analysis of the data revealed that, to a 95% confidence level, the process parameters evaluated do affect burn rate and burn rate variation. The main factors which significantly decreased burn rate variation in descending order of importance were: intense oxidizer mixing screw configuration section, intense binder mixing screw configuration, and a screw speed of 85 rpm. Figures 2, 3 and 4 show the decrease in burn rate variation for each of these factors.

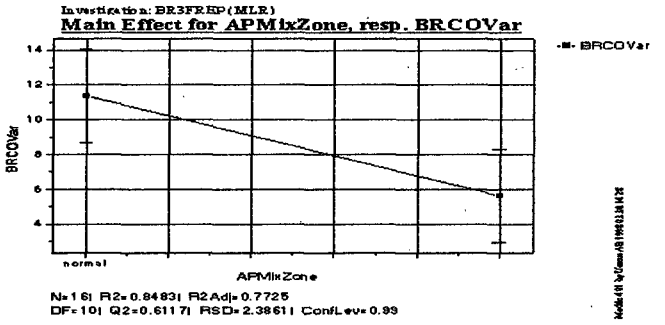

Figure 3

Figure 3 shows a 5.72% decrease in burn rate variability when the oxidizer mixing screw configuration section was changed from normal to intense for all levels of the remaining factors.

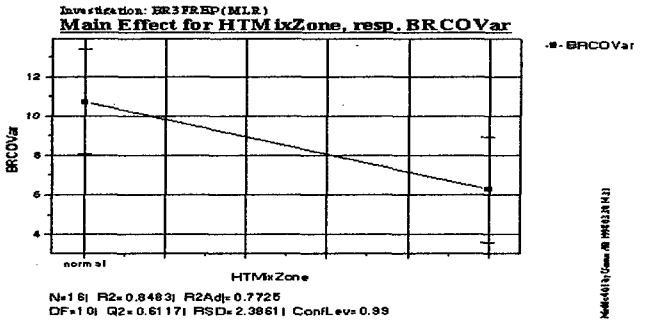

Figure 4

Figure 4 shows a 4.45% decrease in burn rate variability when the binder mixing screw configuration section was changed from normal to intense for all levels of the remaining factors.

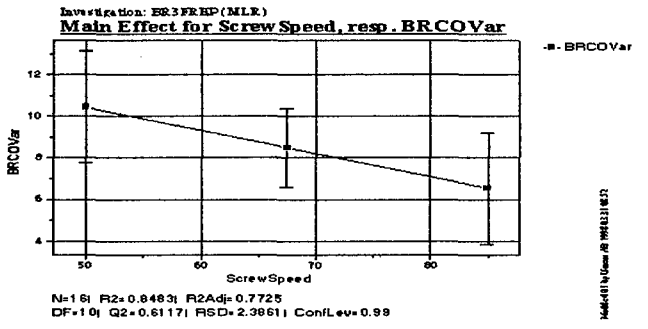

Figure 5

Figure 5 shows a 3.92% decrease in burn rate variability when screw speed was changed from 50 rpm to 85 rpm for all levels of the remaining factors.

Additionally, an interaction effect was discovered which significantly decreased the burn rate variation. The interaction plot for the four different screw configuration sections is shown in Figure 6.

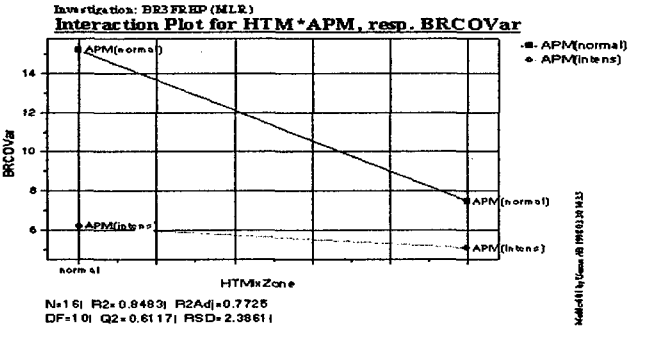

Figure 6

This interaction is extremely important and may not have surfaced during a change one variable at a time experimental design. This plot shows that (at both screw speeds) when the oxidizer mixing screw configuration section and the binder mixing screw configuration section were both normal, the burn rate variation was the highest (15.23%). The burn rate variation is the lowest (5.06%) when both mixing sections are in the intense screw configuration. The effect of the interaction of these two factors on burn rate variability (10.17% reduction) is greater than the greatest effect (5.72% reduction) either of these factors provide individually. Note that the propellant which showed the high degree of burn rate variability initially was manufactured with the oxidizer mixing section and the binder mixing section in the normal screw configuration.

The propellant data obtained at the optimum processing conditions determined by the DOE are presented in Table 3.

Table 3

	Density g/cc	Heat of Explosion cal/g	Strand Burn Rate at 77°F, 1000 psi cm/sec (in/sec)
Mean	1.7493	1375	1.590 (0.626)
Standard Deviation	0.0086	25	0.046 (0.018)
Coefficient of Variation (%)	0.49	1.82	2.84
Minimum Value	1.7335	1341	1.529 (0.602)
Maximum Value	1.7605	1405	1.682 (0.662)
Range	0.0270	65	0.152 (0.060)

The DOE determined the values of the process parameters required to achieve a 38% reduction in the burn rate standard deviation, a 1.26% reduction in the burn rate coefficient of variation and approximately an 11% reduction in burn rate. An extruder trial was then conducted to confirm these results and to manufacture 2.75" extruded composite propellant grains for static firing. The propellant data generated from the confirmation trial is presented in Table 4. Only one propellant sample was tested for HOE, so statistical data is not available.

Table 4

	Density g/cc	Heat of Explosion cal/g	Strand Burn Rate at 77°F, 1000 psi cm/sec (in/sec)
Mean	1.7496	1395	1.663 (0.655)
Standard Deviation	0.0052	N/A	0.036 (0.14)
Coefficient of Variation (%)	0.30	N/A	2.10
Minimum Value	1.7369	N/A	1.631 (0.642)
Maximum Value	1.7594	N/A	1.720 (0.677)
Range	0.0225	N/A	0.089 (0.035)

This data is acceptable and we are going forward with testing the propellant grains. Prior to braiding the inhibitor onto the TSE processed 2.75" extruded composite propellant grains, detailed measurements of the diameter and web thickness at both ends of each grain were taken. The diameter measurements revealed that the grains are slightly under sized with the average diameters ranging from 59.92 mm (2.359 inches) to 60.20 mm (2.370 inches) versus a desired diameter of 61.47 mm (2.420 inches). The outcome will likely be a slightly lower impulse

during the rocket motor firing. This discrepancy is easily rectified by simply enlarging the die by 1.78 mm (0.070 inches). The twin screw processed extruded composite grains are up to 0.79 mm (0.031 inches) out of round. Typically, the batch processed grains are out of round from 0.25 mm (0.010 inches) to 0.51 mm (0.020 inches. This variation is a moot point since the inhibitor braiding and curing process modifies the grains so that they are almost perfectly round. The web thickness are also slightly low, as a result of the small diameters, however their variation is very similar to the web thickness variation measured from batch processed 2.75" extruded composite propellant grains. The variation for both processes is about 0.38 mm (0.015 inches). Overall, the twin screw processed 2.75" extruded composite propellant grains compare dimensionally very well to the batch processed grains.

Near infrared spectroscopy (NIR) was evaluated as a real time, on-line technique for predicting ballistic and physical properties of extruded composite propellant manufactured on a twin screw extruder. NIR was selected because the technology had a high probability of success and of begin easily integrated into the extruder process. The concept was to develop NIR models capable of accurately predicting propellant properties (primary measurements) based on NIR spectra (secondary measurements) and then use those models to predict the propellant's properties from the NIR spectra obtained real time during twin screw processing. Predictive NIR models allow the twin screw processing operator to immediately identify out of specification material (caused primarily by feeder upsets), scrap only the out of specification material, and correct the problem with minimal loss of material or operation time.

The approach taken to develop this on-line analytical tool was to develop and validate the NIR models using small scale batch mixes that were extruded in a two inch vertical ram press, transfer the NIR equipment to the twin screw extruder, and then refine those NIR models with data obtained from the twin screw process. The instrument that was used was a LT Industries Quantum 1200I General Purpose Analyzer equipped with a special reflectance probe designed to interface with existing instrumentation ports on the extruder and also in a set of batch extrusion dies. Prior to model development, depth of penetration and probe fouling studies were conducted to ensure the spectra collected were valid.

Depth of penetration experiments were conducted to determine how deep the probe could "see" into the propellant. In theory, as the limit of the depth of penetration is reached, the absorbance should stop changing as a function of increasing sample thickness. These experiments showed that the absorbance at a given wavelength was inversely proportional to the thickness of the sample up to 250 microns. After that thickness, no correlation exists. This data is shown in Figure 7, a graph of the first derivative single wavelength (1520.5 nm) correlation.

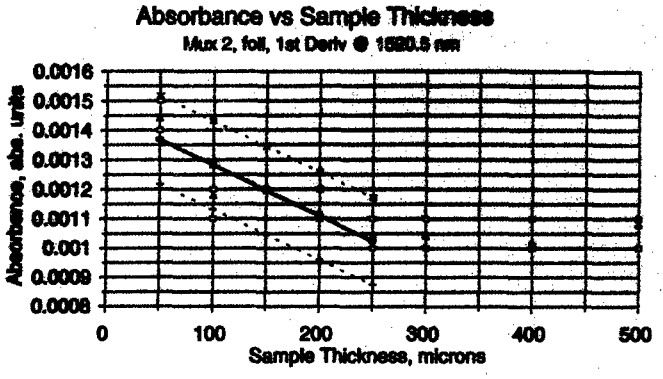

Figure 7

From this data, the conclusion was drawn that 250 microns is the limit of penetration of the infrared light into the extruded composite propellant. These results are significant since the binder rich layer formed during the extrusion process is much less than 250 microns, we are sure that the NIR is analyzing the bulk of the propellant.

Another concern associated with the application of the NIR technology was the extent to which propellant could build up on the lens of the probe, thus fouling it. This effect would result in a false sense that the process is at steady state when in fact the process could be in an upset condition.

An experiment was conducted where two batches of extruded composite propellant, each a variation of the baseline formulation, were extruded using a two inch vertical ram press and a die fitted with the NIR probe. The main variation between the two batches was the amount of oxidizer (79% vs. 89%) and the total solids fill (82.69% vs. 89.12%). NIR spectra was collected as propellant was extruded. The resulting series of spectra, shown in Figure 8, clearly show the difference between the two formulations.

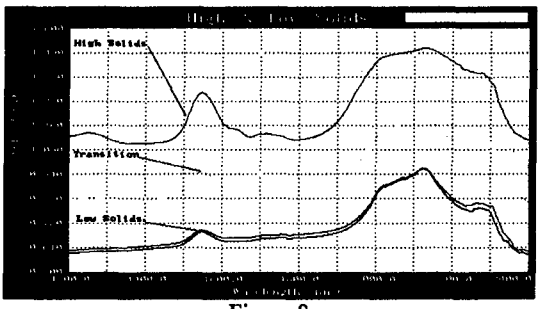

Figure 8

The two *high solids* spectra show higher absorbance overall than the two *low solids* spectra. The spectrum in the middle is the transition from the high solids to the low solids propellant. Looking at 1550 nm (characteristic peak for the oxidizer) also shows the energy absorbed is much higher at that wavelength for the high solids propellant and that the energy absorbed by the propellant decreases with decreasing solids fill. From this data, the conclusion was drawn that the propellant is not fouling the probe lens and the instrument can detect composition variations within a formulation.

Once we were convinced that the data obtained with the NIR was valid, we developed the predictive models by conducting a designed experiment varying the composition of a series of batch mixes of extruded composite propellant; collecting spectra for these mixes as they were extruded; testing each propellant mix for density, burn rate, heat of explosion (HOE) and mechanical properties; and then correlating the spectral data with the tested properties. The composition was varied for this experiment over a range that exceeded anticipated feedstream feed rate variations in the extruder. The predictive models were developed from all of the data and we found that the spectral data did correlate with the propellant density, burn rate and HOE data. Two validation batches were subsequently mixed and the models were used to predict the density, burn rate and HOE of these mixes. The model for density yielded the best results. Figure 9 shows measured versus predicted propellant properties for the validation mixes.

Density (g/ml) Model

PCR/1st derivative data/Kubleka-Monk correction			
Measured	Predicted	Delta	%
1.7537	1.7538	-0.0001	-0.01
1.7434	1.7436	-0.0002	-0.01

Burn Rate (in/sec) Model

PCR/log data			
Measured	Predicted	Delta	%
0.594	0.611	-0.017	-2.86
0.535	0.563	-0.028	-5.23

HoE (cal/g) Model

PCR/log data			
Measured	Predicted	Delta	%
1400	1353	47	3.36
1275	1281	-6	-0.47

Figure 9

The best models developed for all three properties used principle components regression (PCR) analysis. For density, the first derivative absorbance data was used. Also the Kubleka-Monk (K-M) correction was applied. The K-M correction is used to correct for light scattering that occurs with certain materials being scanned. The log(1/T) absorbance data was used for the burn rate and HOE models. The K-M correction did not improve the accuracy of the models for these two properties and was not applied. The density and HOE models predicted accurately.

the burn rate model consistently predicted higher burn rates than the measured values. Sources of error effecting the burn rate model are being investigated. A possible reason is that the iron oxide, a burn rate catalyst, is invisible in the near infrared region.

Following the work using the batch mixed propellant, NIR spectra were collected during a series of extruded composite propellant twin screw processing runs. This data was collected during the designed experiment described earlier. The tested propellant properties were correlated with the spectra that were obtained. The data from both the TSE runs was integrated with the models developed from the batch mixes to refine them.

The spectral data that were collected provided the first glimpse into the twin screw extruder process. During the ramp up process for the extruder, the solid and liquid feed rates are incrementally increased until the full formulation is reached. Once the process stabilizes, vacuum is then applied. A simple plot, shown in Figure 10, of the absorbance at wavelength known to be related to the oxidizer in the propellant clearly shows an increase in absorbance with each increase in the oxidizer feed rate. This data correlates with the ramp up to full formulation on the extruder. This data was very encouraging.

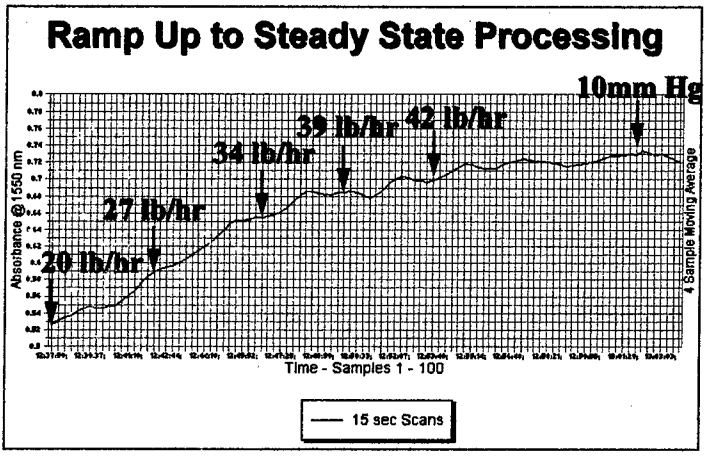

Figure 10

Selected spectra from the extruder runs and the data from the properties tests were incorporated into the original batch models. These models were compared to models based only on TSE data. The data presented in Figure 11 shows the average difference between the measured and the predicted property. The models were based on Kubleka-Monk corrected 1st derivative absorbance data and partial least squares (PLS) correlation.

Average Difference Between Measured and Predicted Property			
Propert/Model	Batch	Batch & TSE	TSE
Density (g/ml)	0.008	0.005	0.004
Burn Rate (in/sec)	0.061	0.035	0.028
HoE (cal/g)	108.9	18.4	11.4

Figure 11

Density continues to be the propellant property that yields the best correlation to the spectral data. Using four sample averaged data, the models generated with batch propellant predicted density with an average error of 0.008 gm/ml. When the TSE data was incorporated into the model, the average difference between the predicted density and the test result decreased to 0.005 gm/ml. The initial burn rate model predicted with an average error of 0.061 in/sec. After this model was revised with data from the TSE runs, the averaged predicted error decreased to 0.035 in/sec.

The validation extruder run conducted early in January 1998 provided an opportunity to test the revised models which incorporate the TSE data. The revised model predicted density with an average error of 0.005 gm/ml. The standard deviation of the tested density samples was 0.005 gm/ml. The revised model predicted burn rates with an average error of 0.019 in/sec. The standard deviation of the tested burn rates was 0.013 in/sec. Both of these models are sufficiently accurate to be useful as a quality and process control tool.

CONCLUSION

The CPOCP project has been a major effort in the development of continuous technology for energetic materials. Major milestones have been reached on both sides of the Atlantic Ocean and the collaboration between, French and U.S teams has been really rich and casual.
If only one aspect should be pointed out, it surely be the manufacture on both side of the Ocean of live material with respect of the specifications and with industrial-like technologies.

STABILIZER CONSUMPTION BY ACCELERATED AGING OF PEG/RDX PROPELLANT

Yoo-Jin Yim, Baek-Neung Ryoo, and Young-Chul Park
Agency for Defense Development, 4-4
Yuseong P.O. Box 35, Taejeon, 305-600
Republic of Korea

ABSTRACT: The depletion rates of MNA and 2-NDPA were investigated by accelerated aging test in PEG/RDX solid propellant containing BTTN and DEGDN as nitrate ester plasticizers. It was found that both MNA and 2-NDPA were depleted by the 0^{th} order reactions and these reactions had two kinds of activation energy which showed the break-point at 60°C for MNA and 70 °C for 2-NDPA from Arrhenius plots in temperature range of 20 ~ 80 °C. Therefore, the stabilizer content in propellant could be predicted much better by using reaction rate in the low temperature range than that in the high temperature range.

NOMENCLATURE

C	Stabilizer content [wt.%]	k_O	Frequency factor [wt.%/week]
C_O	Initial stabilizer content [wt.%]	R	Universal gas constant [J/kmol·K]
E	Activation energy in Arrhenius eq. [J/kmol.]	T	Temperature [K]
k	Reaction rate constant [wt.%/week]		

INTRODUCTION

Solid propellant for military or space application has been improved to have higher performance and density. Recently, the energetic solid propellant has contained nitramine oxidizer and nitrate ester plasticizers such as nitroglycerine(NG) or butanetrioltrinitrate (BTTN) to get the higher

specific impulse[1, 3~5]. By aging for long time, the gaseous holes inside the propellant could be formed or the mechanical properties could be degraded due to the natural decomposition of nitro group in the nitrate ester plasticizer. To prevent this kind of gas fissuring, adequate amount of stabilizer which could react with gaseous products has been used in propellant formulation[1,6,7].

The conventional double base propellant with nitrocellulose and NG used to be formulated with 1 ~ 2% of stabilizer such as ethylcentralite or 2-nitrodiphenylamine(2-NDPA) to keep the sufficient service life especially for military weapon system. But two kinds of stabilizers, 2-NDPA and para-nitro-N-methylaniline(MNA), were found to be more effective than single stabilizer to prevent gas fissuring in not only double base but also nitrate ester plasticizered composite propellant[4,8,9]. Many papers have reported the detail function of stabilizer, but the stabilizer content variation with aging period has shown different results for the formulation of solid propellant. In order to predict the service life, the consumption rate of stabilizer should be measured experimentally and predicted by empirical equation.

Sammour[8,10~12] and Bohn[17] reported how the concentration and their derivatives of stabilizers, 2-NDPA and MNA, changed with accelerated aging at temperature over 60°C for composite modified double base propellant composed with NC and NG as the main ingredients. In this study, the concentrations of these stabilizers in polyethylene glycol(PEG)/cyclo trimethylene trinitramine(RDX) plasticized with BTTN and diethyleneglycol dinitrate (DEGDN) were analyzed during accelerated aging from room temperature to 80°C and better prediction method for their contents was suggested with storage time.

EXPERIMENTAL[6,9,13]

The cured propellant of L130mm x D30mm x W40mm was prepared and 5 sides of this sample were wrapped with aluminum foil. Every edge of aluminum foil was sealed with glue to protect from environmental effects. After samples were stored in ovens controlled at constant temperature of 20, 40, 50, 60, 70, and 80°C for assigned period, 3 grams of each aged propellant was taken in 1 mm thickness like thin chip. The plasticizers and stabilizers were extracted by soxhlet apparatus soaking in 150 ml dichloromethane solution with each thin sample in extraction thimble for 20 hours. Dichloromethane in this extracted solution was removed using nitrogen degassing method and methanol was filled in 100 ml volumetric flask with solvent free solution. Two stabilizers(MNA,

2-NDPA) were analyzed by high performance liquid chromatography(HPLC, Waters Co.) at 270 and 340nm wave length of UV detector. C-18 column(NOVAPAK^R 3.9 x 150mm and BONDAPARK^R 8 x 100mm) of Waters Co. were selected for this experiment with 1.0 ml/min of flow rate and acetonitrile: methanol: water = 45: 10: 45 of moving solution.

RESULTS AND DISCUSSION

Stabilizers Consumption by Aging: The main function of stabilizers was known to react with NO, NO_2, HNO_2, and HNO_3 which were produced from denitration of BTTN and DEGDN and to inhibit the further denitration reactions of nitrate esters and degradation of propellant[11]. The reaction rate of decomposition products and stabilizers in propellant was found to be faster with temperature to general chemical reaction. The propellant containing 15% of BTTN and 5% of DEGDN as the nitrate esters and 0.6% of MNA and 0.5% of 2-NDPA as the stabilizers is selected in this study.

HPLC analysis curves at 340nm wavelength for MNA detection were shown in figure 1 for the original and aged propellant. The peaks at 2.5 minutes of retention time meant MNA and the peaks at 3 minutes were considered to be N-nitroso-MNA which is the derivative from reaction of MNA and denitration products of nitrate esters(BTTN and DEGDN)[1,11]. It was found that MNA levels were lower and the content of N-nitroso-MNA was increased with higher aging temperature. For the same sample, 2-NDPA detection curves analyzed by HPLC at 270nm wavelength were shown in figure 2, where the peaks at about 10 minutes of retention time meant 2-NDPA content which was decreasing with aging temperature and period. Two peaks at about 6 to 8 minutes of curve c were inferred to be the derivatives of 2-NDPA[14-16], where 2-NDPA was decreased by the half of initial content after aging for 7 weeks at 80°C.

MNA content variation with aging temperature and period was plotted in figure 3, which showed slower depletion rate of MNA at 20 ~ 60°C than at 60 ~ 80°C and MNA concentration was linearly decreased with aging period. It meant that reaction order of MNA depletion was 0^{th}. Also 2-NDPA concentration was found to deplete in similar tendency to MNA in figure 4. The stabilizer depletion in CMDB propellant with NC and NG as the main ingredients was reported as combined reaction of 0^{th} and 1^{st} order[10,17]. But in this study, both MNA and 2-NDPA showed the 0^{th} order depletion rate in PEG/RDX propellant with BTTN and DEGDN. The reaction rate constants for each temperature were calculated from figure 3 and 4 and listed in table 1.

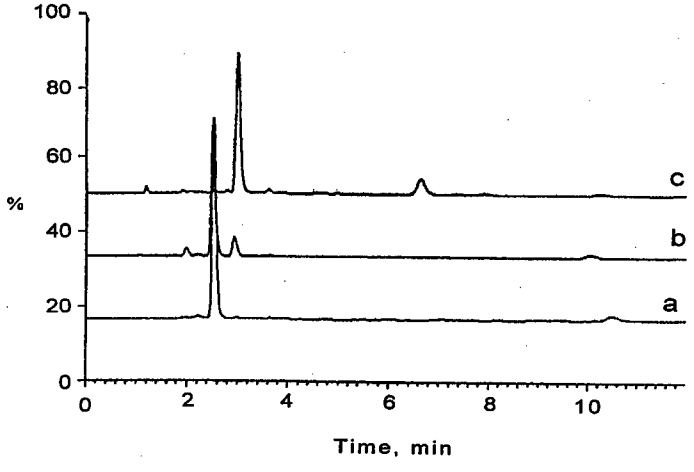

Fig. 1. HPLC chromatograms detected at UV-340nm for MNA analysis, (a) before aging, (b) aged at 60°C for 21 weeks, (c) aged at 80°C for 7 weeks.

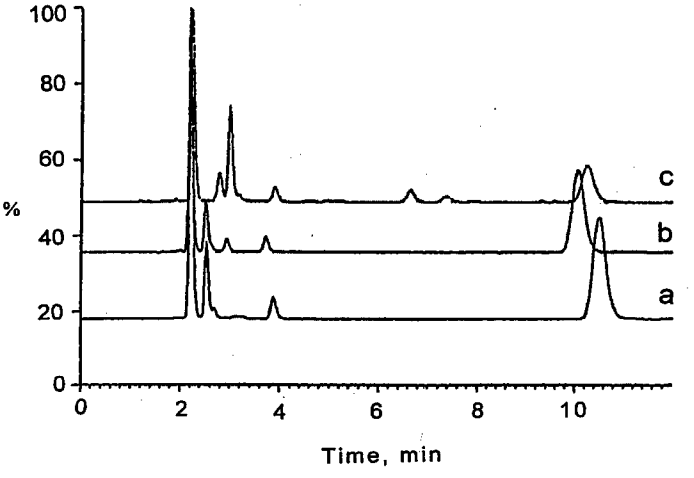

Fig. 2. HPLC chromatograms detected at UV-270nm for 2-NDPA analysis, (a) before aging, (b) aged at 60°C for 21 weeks, (c) aged at 80°C for 7 weeks.

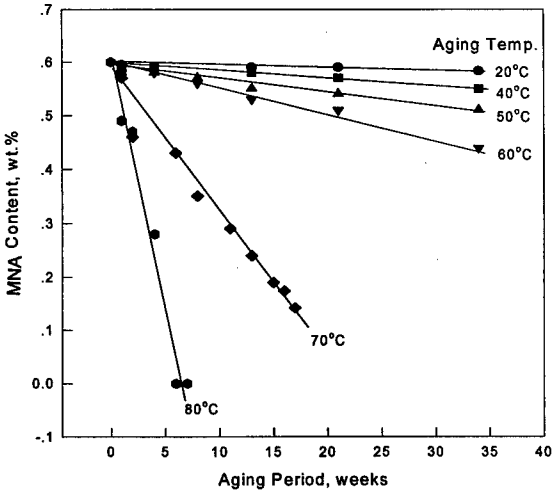

Fig. 3. MNA content variation with aging temperature and period.

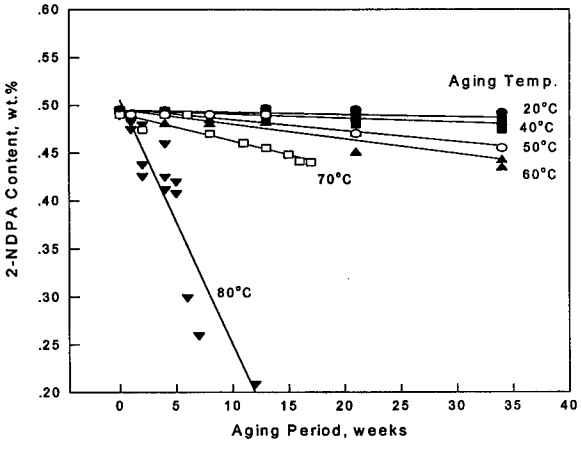

Fig. 4. 2-NDPA content variation with aging temperature and period.

Table 1. Reaction rate constants for MNA and 2-NDPA from fig. 3 and 4

Temperature(°C)	Reaction Rate Constant(wt.%/week)	
	MNA	2-NDPA
20	7.846×10^{-5}	2.249×10^{-4}
40	8.859×10^{-4}	4.104×10^{-4}
50	2.044×10^{-3}	1.151×10^{-3}
60	4.188×10^{-3}	1.539×10^{-3}
70	2.317×10^{-2}	2.882×10^{-3}
80	8.941×10^{-2}	2.548×10^{-2}

Arrhenius Plots for Stabilizers: The depletion rates of stabilizers can be expressed as the following equation (1) because stabilizers content variations showed the 0^{th} order reactions.

$$dC/dt = k$$

$$C = C_o - kt \qquad (1)$$

where C represents the stabilizer concentration, t, the aging period, k, the reaction rate constant, and C_o, the initial concentration of stabilizer respectively. If the reaction rate constant was assumed to follow Arrhenius equation,

$$k = k_O \exp(-E/RT) \qquad (2)$$

In equation (2), k_o represents the frequency factor, E, the activation energy, R, the universal gas constant, and T, the reaction temperature in Kelvin. In order to calculate k_o and E, the reaction rate constant vs. temperature was plotted in figure 5 for MNA and 2-NDPA.

The activation energy for MNA depletion reaction was found to change at the break point of 60°C: E/R=9820K in 20 ~ 60°C temperature range and E/R=18037K in 60 ~ 80°C. For 2-NDPA, the activation energy was shown to change at the break point of 70°C: E/R=5233K in 20 ~ 70°C temperature range and E/R=26411K in 70 ~ 80°C. To predict the remaining content of stabilizer,

accelerated aging tests have been performed at higher temperature in general. Sammour[10], Bohn[17], and Bivin[7] reported that the stabilizer content and the self-life of propellant were predicted based on the results from the accelerated aging at 60 ~ 90°C. Because the depletion rates of stabilizers under 60°C were much slower than those over 60°C in this study, it could make an error when predicting them after long time storage at ambient temperature if these concentrations were calculated from the accelerated aging over 60°C.

The remaining contents of MNA and 2-NDPA of the propellant stored at 25°C were predicted in figure 6 using two kinds of reaction rate equations different with the aging temperature range. Prediction at lower temperature range(lines M1 and N1 in figure 6) was considered to be more reasonable than that at higher temperature range(lines M2 and N2 in figure 6) judging from the experimental data in figure 3 and 4. Therefore it is recommended that the stabilizer content is calculated from aging result under 60°C because the propellant is stored below 60°C in real. Figure 7 showed that the calculated value was coincident with the experimental result for 2-NDPA level change at 60°C.

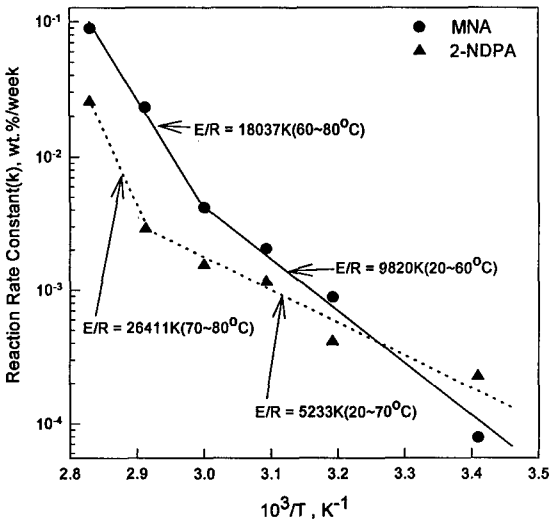

Fig. 5. Arrhenius plot for stabilizer depletion rate.

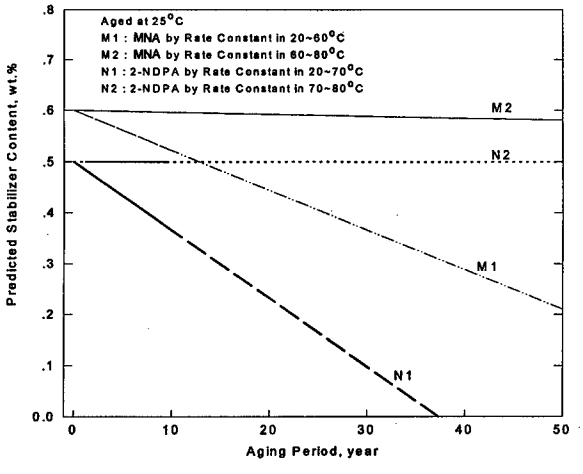

Fig. 6. Predicted stabilizer content of NEPE propellant aged at 25°C .

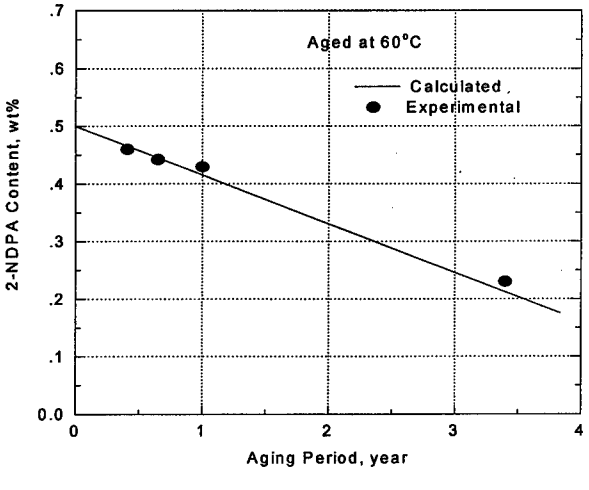

Fig. 7. 2-NDPA content vs. aging period at 60°C.

SUMMARY

The stabilizers content degradation was experimented by accelerated aging at 20 ~ 80°C for PEG/RDX solid propellant containing BTTN and DEGDN as nitrate ester plasticizers. It was found that the stabilizers, both MNA and 2-NDPA were depleted by the 0th order reactions and these reactions had two kinds of activation energy which showed the break-point at 60°C for MNA and 70°C for 2-NDPA from Arrhenius plots. Therefore, the stabilizer content in propellant could be predicted much better by using reaction rate in the low temperature range than that in the high temperature range over 60°C because the propellant is stored below 60°C in real application.

REFERENCES

1. Oberth , A.E.: "Principles of Solid Propellant Development", CPIA Pub. No. 469(1987).
3. Davenas, A.: "Solid Rocket Propulsion Technology", Pergamon Press (1993).
4. Rho, M.K. and Yim, Y.J.: *J. of Kor. Soc. for Aero. and Space Sciences*, **22**, 114(1994).
5. Yim, Y.J.: "Performance Prediction of Aluminized High Energy Propellant", Proceedings of the 6th Symposium of the Society for Korean Propulsion Engineers, pp. 121-127, May (1996).
6. Carver, J.G.: "Selective Detection of Minimum Smoke Stabilizers: Final Report", U.S. Army Missile Command, Technical Report RD-PR-86-3, Jul.(1986).
7. Bivin, R.L., Johnson, J.T., Markovitch, I.L., and Methrotra, A.K.,: "Development of a Class 1.3 Minimum Smoke Propellant", AIAA Paper 92-3724(1992).
8. Bellamy, A.J., Sammour, M.H., and Bellerby, J.M.: *Propellants, Explosives, Pyrotechnics*, **18**, 223(1993).
9. Lee, B.J., Jeong, Y.T., Seo, T.S., and Baek, G.H.: "Analysis of Stabilizers in Minimum Smoke Propellant by HPLC", Agency for Defense Development, MSDC-421-93142, Feb.(1993).
10. Sammour, M.H.: *Propellants, Explosives, Pyrotechnics*, **19**, 82(1994).
11. Sammour, M.H. and Bellamy, A.J.: *ibid*, **20**, 126(1995).
12. Sammour, M.H.: "Effect of Solid Propellant Ballistic Modifiers on the Reaction of Stabilizers", The Proceedings of International ICT Conference, Germany, 104(1994).
13. Kansas, L. and Robertson, D.: *Propellants, Explosives, Pyrotechnics*, **19**, 171(1994).
14. Bellerby, J.M. and Sammour, M.H.: *ibid*, **16**, 235(1991).
15. Bellerby, J.M. and Sammour, M.H.: *ibid*, **16**, 273(1991).
16. Bellamy, A.J. and Sammour, M.H.: *ibid*, **18**, 46(1993).
17. Bohn, M.A.: *ibid*, **19**, 266(1994).

Synthesis of Cyclodextrin Polymer (Poly CD), a raw material for insensitive, high energy and shock survivable explosives

Gary L. Statton and Bernard M. Kosowski

Mach I Inc., 340 East Church Road ,
King of Prussia, PA 19406

Abstract

The U.S. Air Force has a need for high energy, less sensitive shock survivable explosives. The U. S. Navy, Naval Surface Warfare Center, Indian Head, MD has an ongoing program to evaluate nitrated cyclodextrins, as possible components in formulations of propellants which are insensitive, high energy and minimum smoke-producing. By polymerizing the cyclodextrin into higher molecular weight versions and nitrating, the processing characteristics of explosive formulations should improve measurably. This paper describes the polymerization of γ-cyclodextrin using diisocyanates and nitration of the polymers to provide energetic materials.

Introduction

Cellulose is a polysacchharide polymer made up of chains of D-glucose units attached to each other by 1,4 beta linkages. Nitration of cellulose provides a useful energetic compound. Nitrocellulose has long been used as an energetic in a multitude of propulsion and explosive applications. The drawback in its use has been the unstable nature of the material when in the dry state requiring the material to be transported and used while wetted to prevent accidental detonation. Nitrocellulose is classified as a 1.1 class energetic.

Starch is a polysaccharide polymer made up of chains of D-glucose units attached to each other by 1,4 alpha linkages. A recent development is the commercial production of cyclodextrins, a unique group of oligosaccharides, produced from selective enzyme action upon corn starch. Cyclodextrins have the D-glucose units attached to each other to form rings. The most common of these being α, β and γ–cyclodextrin having 6, 7 and 8 glucose units respectively (Figure 1).

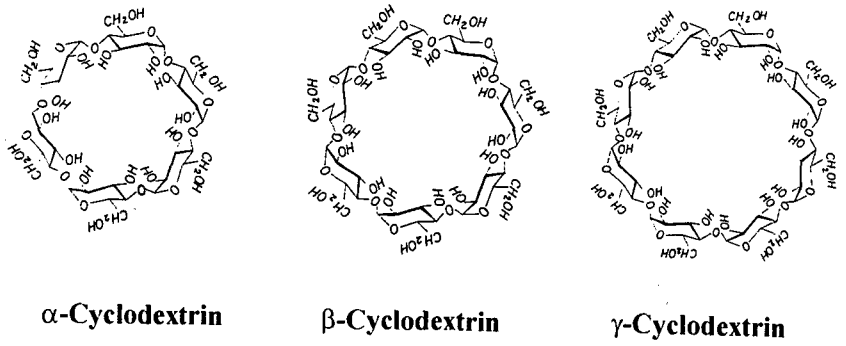

Figure 1. Structure of Cyclodextrins

The cyclodextrins are doughnut shaped molecules constructed so that hydroxyl groups lie along the rims and are hydrophilic while the interior is relatively non-polar and lipophilic. The lipophilic cavity can entrap or encapsulate other chemical compounds without the formation of covalent bonds (Figure 2). The cavity of the cyclodextrins vary in size ranging from 5.3

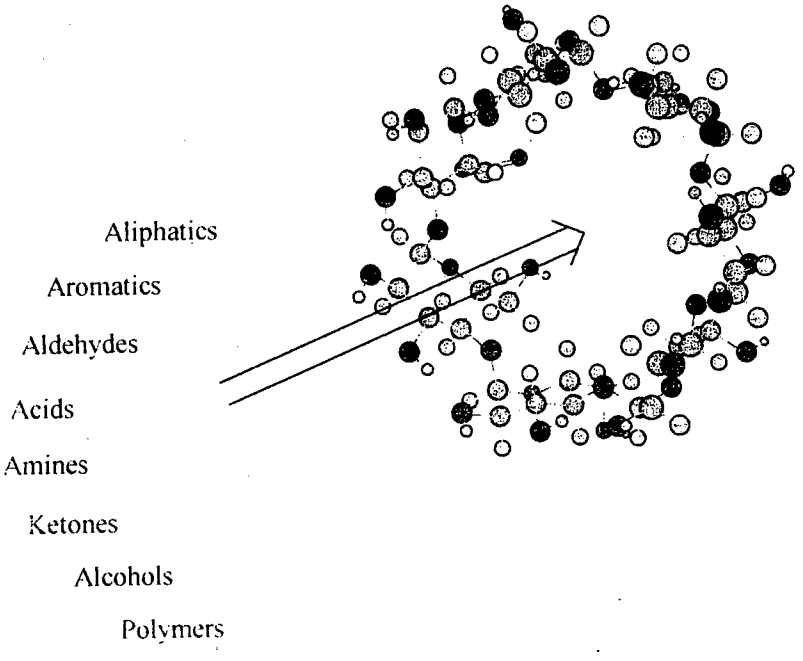

Figure 2. Cyclodextrin Structure and Molecular Inclusion

angstroms for the a-cyclodextrin to about 9.0 for the g-cyclodextrin. Van der Waals forces, hydrogen bonding, dipole forces, release of high enthalpy water and hydrophobic interaction have been offered as hypothesis for the energy, up to 12 kcal/mole, necessary for inclusion of the guest molecules[1]. The nature of the forces for a particular complex thus depends on the guest which occupies the cavity and the host. The thermodynamic stability of a cyclodextrin inclusion complex is generally expressed as a dissociation constant, and this value can often be correlated to physiochemical properties of the guest molecules. The classes of compounds which may be included are quite varied and includes compounds as straight or branched chain aliphatics, aldehydes, ketones, fatty acids, esters, aromatics, amines and recently polymers. Inclusion of the guest molecule in the cavity can give rise to some beneficial modifications of the guest not otherwise achievable, as for example; solubility enhancement, stabilization against degradative

(α-), 21 (β-) or 24 (γ-) hydroxyls. Unlike the nitrated cellulose, the nitrated cyclodextrin is classed as a 1.3C explosive. Similar to the unnitrated cyclodextrin, the nitrated cyclodextrin has a cavity which can be a host for other energetic components such as nitrate esters or nitramines. Figure 3 shows a model of γ-cyclodextrin nitrate with the energetic BTTN in the cavity.

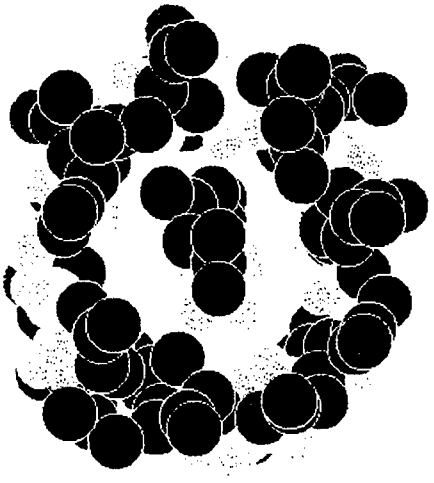

Figure 3. Depiction of γ-Cyclodextrin Nitrate-BTTN Inclusion Complex

The U.S. Navy, Naval Surface Warfare Center, Indian Head, MD has an ongoing program [2] to evaluate nitrated cyclodextrins, as possible components in formulations of propellants which are desired to be insensitive, high energy and minimum smoke-producing.

Mr. John Consaga, of NSWC Indian Head, concluded that his existing program of evaluation of cyclodextrin nitrate demonstrated the following:

- That cyclodextrin nitrate desensitizes nitrate ester plasticizers by complexation
- Scaled-up the gamma cyclodextrin nitrate to the 100 gallon reactor (50 lb.)
- Achieved a 55 cards, high energy, minimum smoke propellant .

The nitrated cyclodextrin which has an Isp of 226 seconds forms an inclusion complex with an energetic organic nitrate ester plasticizer guest increasing the energy of the composition up to an Isp of 250 seconds. However, since the energetic is contained in the inclusion complex, it acts as if partially coated, thus the composition resists detonation due to impact shock, friction or electrostatic discharge [3].

The viscosity of the nitrated gamma cyclodextrin monomer is too low however to be used alone without a binder in many formulations. By polymerizing the cyclodextrin into higher molecular weight versions and nitrating, the processing characteristics should improve measurably and offer explosive chemists new and exciting components. The increased molecular weight of

cyclodextrin polymer nitrate over the nitrated monomer can provide added viscosity and strength to compositions.

Results and Discussion

Polymers may be prepared from cyclodextrins by crosslinking cyclodextrin rings using di or polyfunctional agents as aldehydes, ketones, allyl halides, isocyanates or epoxides (Figure 4)

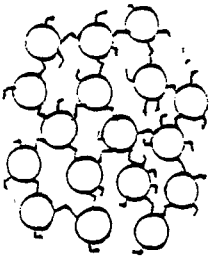

Figure 4. Structures of Cyclodextrin Polymers

where the cyclodextrin rings are connected to other rings by links and can have tails of the linking groups. If the polymerization conditions are judiciously controlled, soluble products may be obtained having weight average molecular weights above 20,000 [4].

We chose to attempt the polymerizations using the diisocyanates, 4,4'-diphenylmethylene diisocyanate (MDI) and hexamethylene diisocyanate (HDI), (Figure 5) as linking groups for γ-cyclodextrin. This cyclodextrin was chosen since it's large cavity could complex several molecules of nitrate ester.

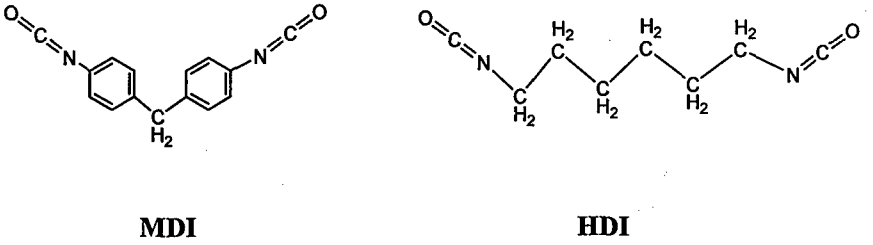

MDI **HDI**

Figure 5. Isocyanate Crosslinkers

Water was a problem since a small amount could essentially react with all or part of the diisocyanate thus reducing polymer yield and molecular weight. γ-Cyclodextrin can crystallize with from 7 to 18 molecules of water [1]. To insure that the cyclodextrin was thoroughly dried, an experiment was run to determine the time necessary to completely dry the material. As figure 6 shows, the water is only slowly released at high temperature and under vaccuum.

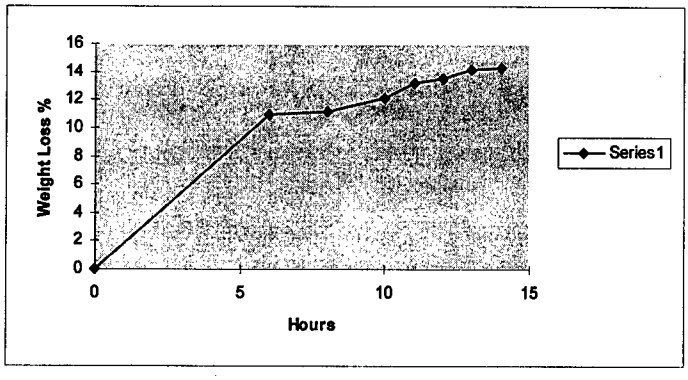

Figure 6. Drying CD at 140° C. under Vacuum

The complete drying of the cyclodextrin at elevated temperatures under vacuum and removal of water in the DMSO solvent by mol sieves did provide high mass spec MW and high weight average molecular weight (Table 1).

Table 1. Polymerization of MDI and γ-CD

Run	Temp. ° C.	MDI/CD	Yield %	MWw	Mass Spec MW	Polymer MDI/CD
7029	20	1.0	33	10,000	3500	3.5
7049	20	1.2	77	--		
7000	40	1.0	33	54,000	4500	4.0

MDI/CD = Molar ratio
%OH reacted = Decrease in OH peaks of polymer by NMR
Mass Spec MW = Highest MW obtained by Mass spec analysis

Aromatic complexes in DMSO solution are known to exist and molecular models of an MDI inclusion complex with γ-cyclodextrin (Figure 7) indicated that the γ-cyclodextrin is of sufficient size to contain the aromatic portion of the MDI but the isocyanate groups, could extend out of the cavity allowing reaction with the outer primary or secondary hydroxyls. This reaction would reduce isocyanate concentration without resulting in polymerization.

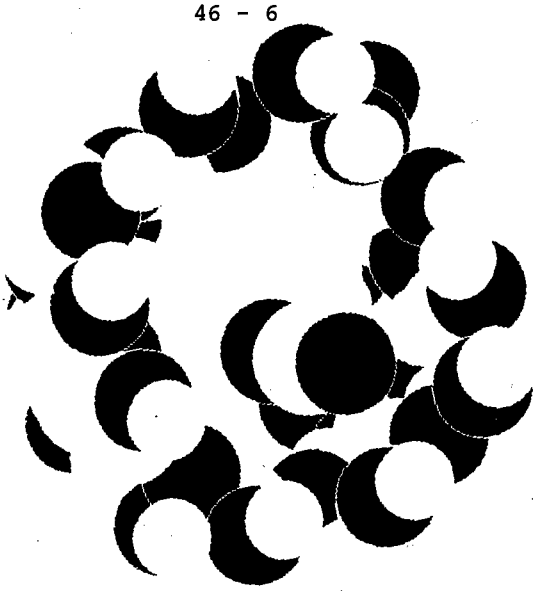

Figure 7. Model of MDI -γ-CD Inclusion Complex

The temperature of the polymerization reaction was thus increased which would destabilize complex formation and the MDI was added dropwise to minimize possible complex formation. These runs are shown in Table 2.

Table 2. MDI γ-Cyclodextrin Polymerization Runs

Run	MDI/CD	Temp. C	Yield %	% OH Reacted	Mass MW
7070	1.0	60	32	12	3500
7075	1.0	80	41	16	4500
7100	1.3	80	58	17	-----
7110	1.0	100	52	17	5000
7112	1.0	80	50	15	6100

MDI/CD = Molar ratio of reactants
%OH reacted = Decrease in OH peaks of polymer by NMR
Mass MW = Highest MW obtained by Mass spec analysis

The higher temperature and dropwise addition of the crosslinker would appear to be providing higher MW as shown by the mass spec.

Correlation of the data with the variables from all of the polymerizations run showed that better drying of the CD and solvent leads to increased yield and % OH reacted. Higher MDI/CD molar ratio of reactants resulted in increased yield but ratios higher than 1.5 resulted in gel.

Hexamethylene diisocyanate (HDI) was also used to prepare a polymer with the γ–cyclodextrin. The aliphatic isocyanate linkages might be expected to be less likely to be cleaved by nitration conditions. The temperature was run at the higher level since the aliphatic isocyanate is less reactive. These results are shown in the following table.

Table 3. HDI γ–Cyclodextrin Polymer

Run	HDI/CD	Temp . °C	Yield %	% OH Reacted	Mass MW
7115	1.0	100	41	~25	7000

MDI/CD = Molar ratio of reactants
%OH reacted = Decrease in OH peaks of polymer by NMR
Mass MW = Highest MW obtained by Mass spec analysis

Small samples of two of the polymers, runs 7112 and 7115 were sent to NSWC Indian Head for nitration. Their procedure for nitration of the cyclodextrin polymer uses liquid carbon dioxide as solvent with the dinitrogen pentoxide.

NSWC nitrated the polymers assuming that 17 hydroxyls were available as suggested by the NMR analyses. They reported that the polymeric crosslinked cyclodextrin nitrates showed increased viscosity over the unnitrated polymer and the cyclodextrin nitrate monomer. Both nitrated polymers were soluble in dimethyl sulfoxide but insoluble in acetone. The molecular weights of the original polymers and the polymer nitrate are indicated by the GPC curves shown in figures 8 -10. Figure 8 shows the GPC curves of the polymer prepared from HDI and γ-cyclodextrin, figure 9, the MDI and γ-cyclodextrin polymer and figure 10, the nitrated polymer from HDI and γ-cyclodextrin.. DSC analysis of the polymer nitrate (Figure 11) from the HDI and γ-cyclodextrin show transitions at 198° C and at 300° C and indicate the energetic nature of the product. Nitrogen analysis of the polymer was 13%.

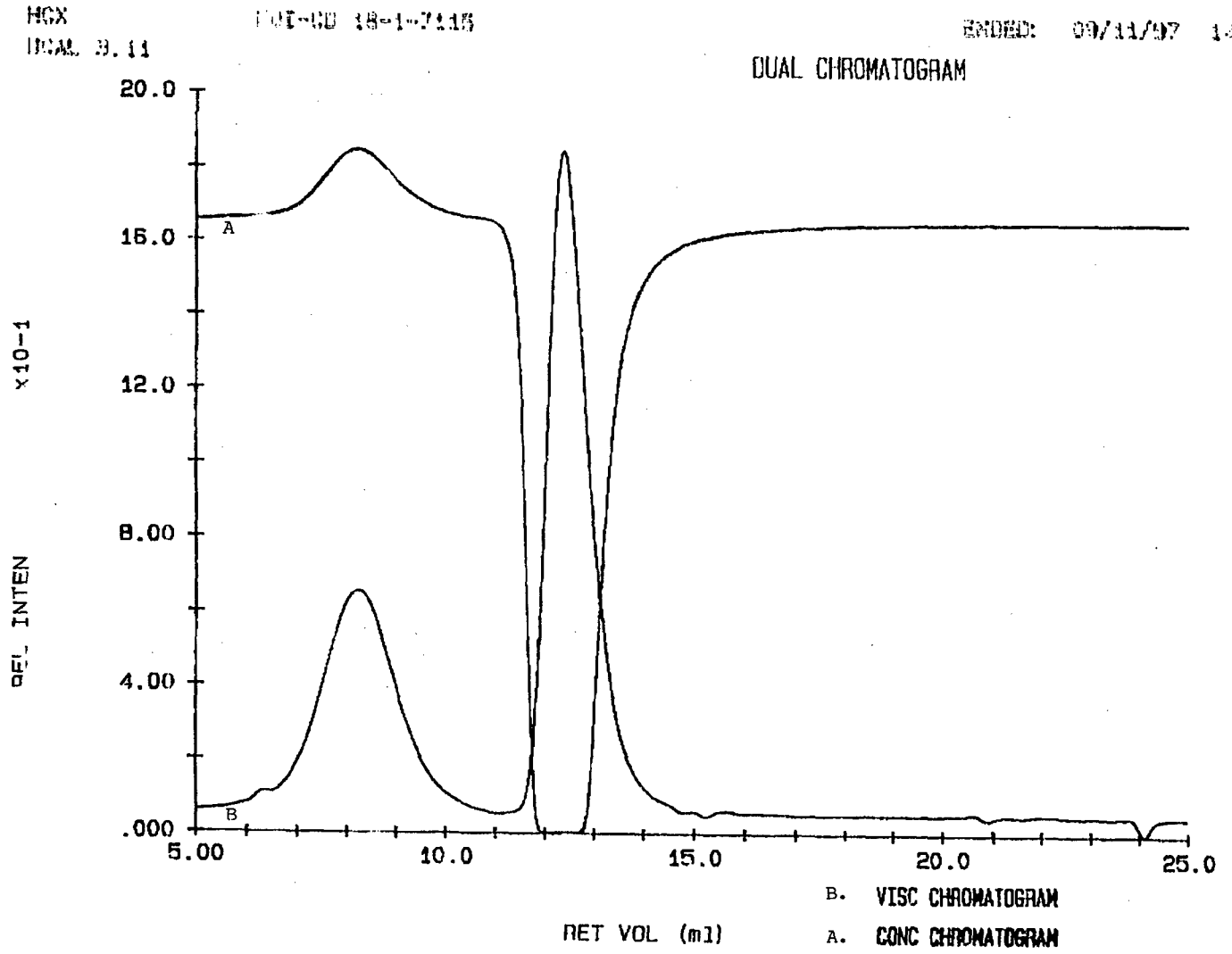

Figure 8. GPC Curves of 7115 HDI-γ-CD Polymer

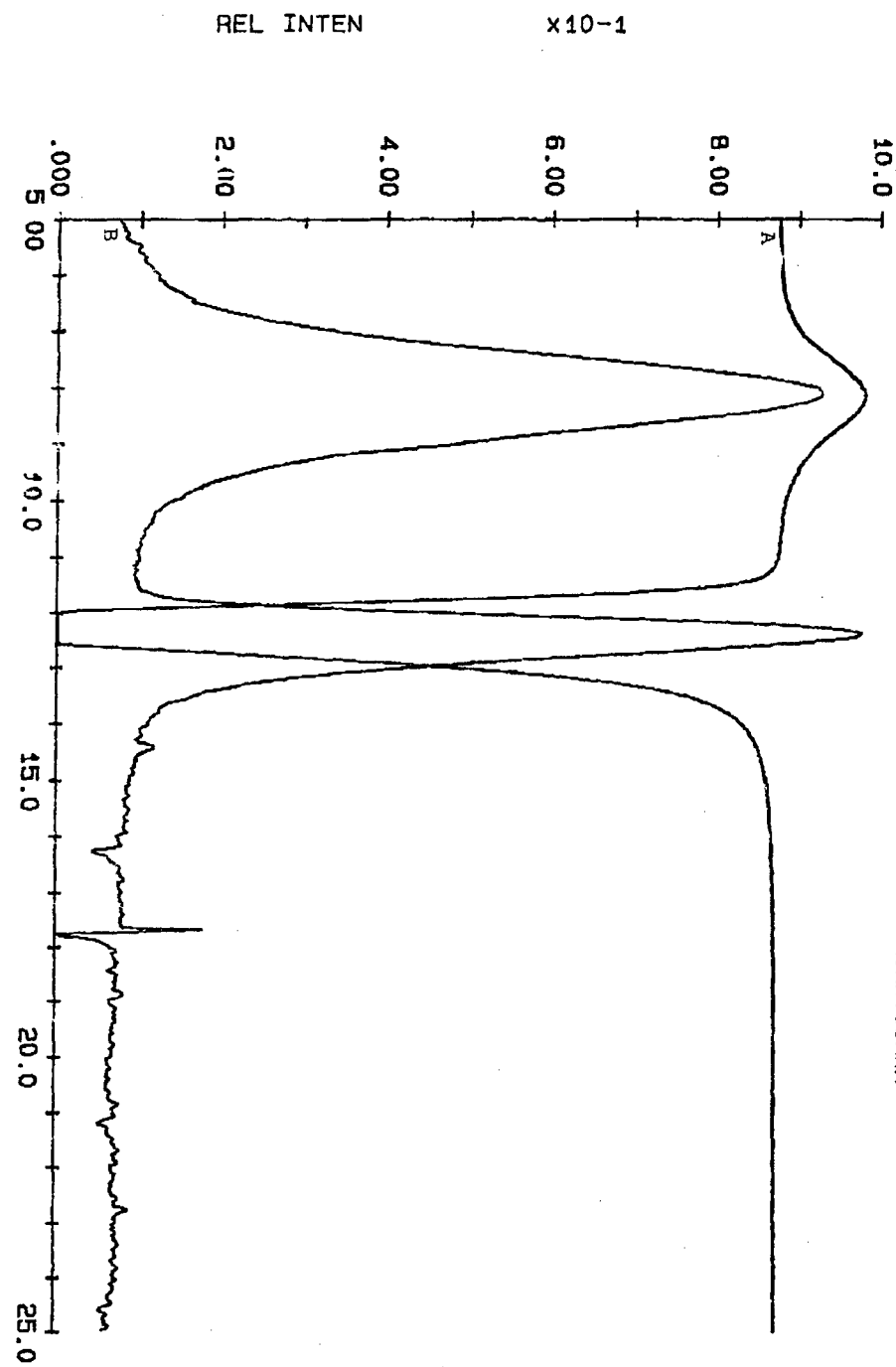

Figure 9. GPC Curves of 7112 MDI-γ-CD Polymer

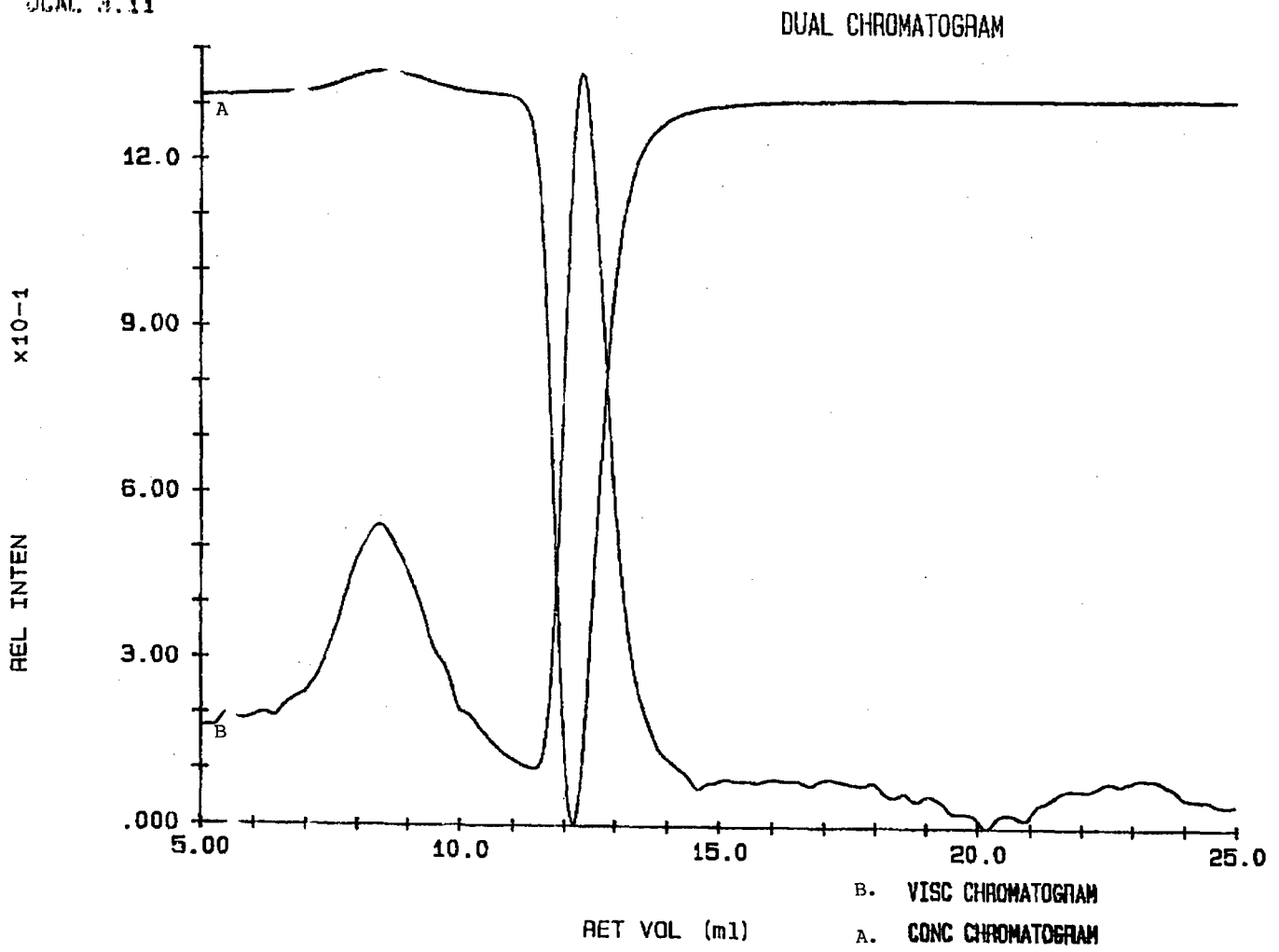

Figure 10. GPC Curves of Nitrated 7115 HDI-v-CD Polymer

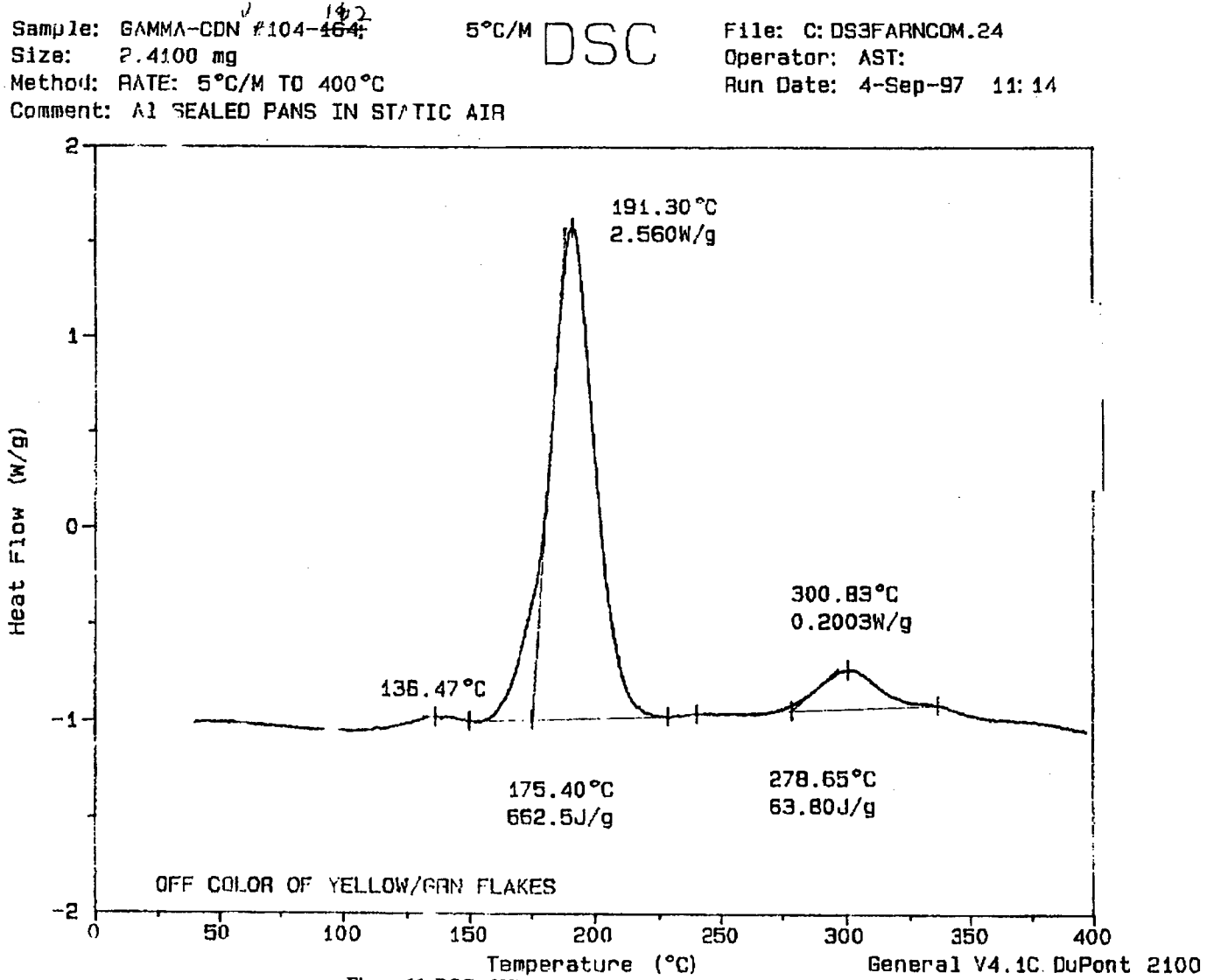

Figure 11. DSC of Nitrated 7115 HDI-γ-CD Polymer

Conclusions

Soluble crosslinked polymers having high weight average molecular weights can be produced from the reaction of diisocyanates and γ-cyclodextrin. These polymers can be successfully nitrated by the procedure used at NSWC Indian Head to provide energetic binders having increased viscosity over the cyclodextrin nitrate monomer. The polymerization procedure is viable to scale up to produce larger quantities of the polymers for nitration and further study in energetic formulations.

References

[1] K. A. Connors, *Chem. Rev.* **97**, 1325-1357 (1997).

[2] J. P. Consaga and R. C. Gill, Naval Surface Warfare Center-Indian Head Division, *AWTP Propulsion Technology Review-Reduce Hazard Binders, Major Accomplishments*, (27-28 April 1995).

[3] J. Eadie, "*The Effect of Wax on the Shock Sensitivity of Explosive Compacts,*" Naval Ordnance Lab, White Oak, Silver Spring, MD, 1965 pp 399-403.

[4] J. Szejtli ,"*Cyclodextrin Technology*", D. Reidel Pub. Co., Dordrecht,1988, p. 62

Acknowledgment

This paper reviews the research carried out by MACH I Inc. of King of Prussia, PA, USA under U. S. Government Small Business Innovative Research (SBIR) Contract F08630-97-C-0059 in support of the U. S. Air Force, Wright Laboratory, Armament Directorate, Eglin Air Force Base, FL, USA.

Nitrotriazole : Chemische Struktur und explosive Eigenschaften

H.H.Licht, S.Braun, M.Schäfer, B.Wanders, H.Ritter

Institut Franco-Allemand de Recherches de Saint Louis — *ISL* — *Deutsch-Französisches Forschungsinstitut Saint Louis*

Postfach 1260, D-79574 Weil am Rhein

Kurzfassung:
Nur gering erscheinende Strukturunterschiede vermögen gravierende Auswirkungen auf die explosiven Eigenschaften von energetischen Materialien zu haben. Das wird am Beispiel einer Reihe verwandter Stoffe demonstriert, die alle zur Klasse der Nitrotriazole gehören und mehr oder weniger ausgeprägte explosive Eigenschaften besitzen.
Da in dieser Stoffklasse Tautomerie- und Isomerie-Erscheinungen berücksichtigt werden müssen, ist bereits die Struktur-Ermittlung an aufwendige analytische Verfahren gebunden. Die Bestimmung der explosiven Eigenschaften ergab auffallende Unterschiede: Es wurden Vertreter aus der Klasse der IHE und Verbindungen mit Primärsprengstoff-Eigenschaften beobachtet.

Abstract:
Already small structure differences may affect the explosive properties of energetic materials in a great extent. This is demonstrated in the case of a series of related compounds which all belong to the group of nitrotriazoles and exhibit more or less distinct explosive properties.

As isomerism and tautomerism had to be taken into account the structure elucidation already implied intense analytical efforts. The investigation of explosive properties yielded striking differences: There were found Insensitive High Explosives and compounds which proved to be primary explosives.

Einleitung.

Das wohl bekannteste Nitrotriazol NTO (Nitrotriazolon) hat inzwischen weltweite Aufmerksamkeit und bereits auch praktische Anwendung als militärischer Sprengstoff gefunden. Obwohl es schon vor 90 Jahren erstmals beschrieben wurde /1/, liegt doch der Nachweis seiner Explosivstoff-Eigenschaften erst 10 Jahre zurück /2/. Damit wurde die ganze Stoffklasse der Nitrotriazole in das Blickfeld der Explosivstoff-Fachleute gerückt, und so sind die Anstrengungen, die bisher nur unvollständig vorliegenden Erkenntnisse zur Chemie und zum Explosivstoff-Charakter dieser Stoffe zu vertiefen, mehr als begründet.

Nach einer von uns durchgeführten eingehenden Untersuchung von Nitrotriazolen wird hier der Versuch unternommen, das Phänomen des Zusammenhangs von chemischer Struktur und Sprengstoff-Eigenschaften eines potentiellen Explosivstoffs zu demonstrieren. Trotz der Begrenzung auf die Grundstrukturen von nur zwei Triazolringen werden alle praktisch bedeutsamen Explosivstofftypen in einer begrenzten Verbindungszahl nachweisbar.

Voraussetzung hierfür war eine entsprechende Anzahl von Substanzen, die verallgemeinernde Schlußfolgerungen überhaupt erst zuließen. Bis auf das NTO sind die hier behandelten Verbindungen keine Handelsprodukte, mußten also im Labor hergestellt werden. Und 7 der 19 im folgenden beschriebenen Verbindungen wurden erstmals im ISL synthetisiert. Detaillierte explosive Eigenschaften wurden von anderer Seite bisher nur für das NTO beschrieben.

Chemie der Triazole.

Triazole gehören zu einer Gruppe von heteroaromatischen Verbindungen, die trotz ihres hohen Stickstoffgehalts - anders als die sonst recht ähnlichen Azidoverbindungen - relativ stabile Stoffe sind. Das liegt daran, daß ihre N-Atome am Aufbau stabiler elektronischer Grundstrukturen beteiligt sind. Ihre Stickstoffatome sind entweder Teil des Doppelbindungssystems (Pyridin-N) oder liegen in Einfachbindung (Pyrrol-N) vor.

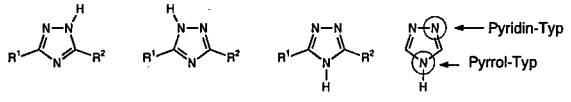

Zwei Arten von Triazolen sind zu unterscheiden: 1,2,4- und 1,2,3-Triazole. Sie haben eine strukturelle Gemeinsamkeit, die Erscheinung der **Tautomerie**: Die Protonen an den Stickstoffatomen sind beweglich. Seine genaue Lage hängt von zwei Faktoren ab, den sonstigen Substituenten und dem Lösungsmittel. Aber es kann auch ein Gleichgewicht tautomerer Strukturen vorliegen. Wird dieses H-Atom durch einen anderen Substituenten ersetzt, kommt zu dem Problem der Tautomerie das der **Isomerie**.

Die Nitrogruppe in Triazolen verleiht dem am Stickstoff gebundenen Wasserstoffatom einen sauren Charakter, dem ganzen Molekül Sprengstoff-Eigenschaften. Alle von uns untersuchten Nitrotriazole zeigen bereits nach Einführung nur einer Nitrogruppe einen mehr oder weniger explosiven Charakter, der zwischen dem eines Insensitive High Explosive (IHE) und dem eines Initialsprengstoffs liegen kann.

Untersuchte Verbindungen.

Die folgenden Nitrotriazole wurden in die Untersuchung aufgenommen (Anlage 2).

Es stand als Handelsprodukt zur Verfügung: 3-Nitro-triazol-5-on (NTO), **7**

Nach Literaturvorschriften wurden hergestellt:

4-Nitro-1,2,3-triazol (4-NT) **2** /3/,
3-Nitro-5-amino-1,2,4-triazol (ANTA) **3** /4/,
4-Nitro-2(1,2,4-triazol-3-yl)-1,2,3-triazol (NBT) **4** /5/,
3-Nitramino-1,2,4-triazol (NITRA) **6** /6/
4,6-Bis(3-nitro-5-amino-1,2,4-triazol-1-yl)-5-nitropyrimidin (DANTNP) **13** /7/,
1-Pikryl-4-nitro-1,2,3-triazol (1-PNT) **14** /3/,
2-Pikryl-4-nitro-1,2,3-triazol (2-PNT) **15** /3/,
1-Dinitrophenyl-3-nitro-1,2,4-triazol **16** /19/.

Für die folgenden Verbindungen haben wir eigene Darstellungsmethoden entwickelt:

3-Nitro-1,2,4-triazol (3-NT) **1** /8/,
2-Dinitrophenyl-4-nitro-1,2,3-triazol **10** ,
1-Dinitrophenyl-4-nitro-1,2,3-triazol **11**.

Die weiteren Stoffe wurden erstmals im ISL synthetisiert:

C,N-Dinitrobitriazol (C,N-DNBTr) **5** /9/,
C,C-Dinitrobitriazol (C,C-DNBTr) **8** /8/,
N-Dinitrophenyl-nitrobitriazol **9**,
4,6-Bis(3-nitro-1,2,4-triazol-1-yl)-5-nitro-pyrimidin **12**,
4,6-Bis(4-nitro-1,2,3-triazol-1-yl)-5-nitropyrimidin **17**,
2,4-Bis(5-amino-3-nitro-1,2,4-triazol-1-yl)-5-nitropyrimidin **18**,
4-Nitro-2-(1,2,3-triazol-4-yl)-1,2,3-triazol **19**.

Synthesen von Nitrotriazolen.

Unsere Synthesen der neuen Verbindungen sind im Anhang I näher beschrieben. Die folgende Übersicht beschreibt zwar nur das Synthese-Prinzip, erlaubt aber bereits Einsichten in den Chemismus der Nitrotriazole.

Nitrotriazole mit ihrem reaktiven Proton können mit geeigneten Partnern wie 2,4-Dinitrochlorbenzol und 5-Nitro-4,6-dichlorpyrimidin, die eine aktivierte Austrittsgruppe tragen, zur Umsetzung gebracht werden. Im Falle derartiger Reaktionen mit 3-Nitro-1,2,4-triazol **1** wurde nur jeweils ein Reaktionsprodukt (**9**, **12**, **16**), mit 4-Nitro-1,2,3-triazol **2** aber ein Gemisch aus dem 1- und dem 2-substituierten Produkt erhalten (**10**, **11**).

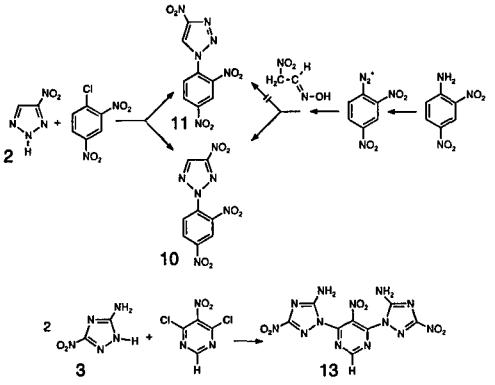

Schema 1

Die Ausnutzung der Diazotierbarkeit von Aminotriazolen stellt den ersten Schritt auf dem Weg zu (unsymmetrischen) Bitriazolen dar. Anschließend werden diese Reaktionsprodukte mit einer Nitroverbindung, der Methazonsäure, gekuppelt und danach zu einem 2-substituierten 4-Nitro-1,2,3-triazol cyclisiert /20/.

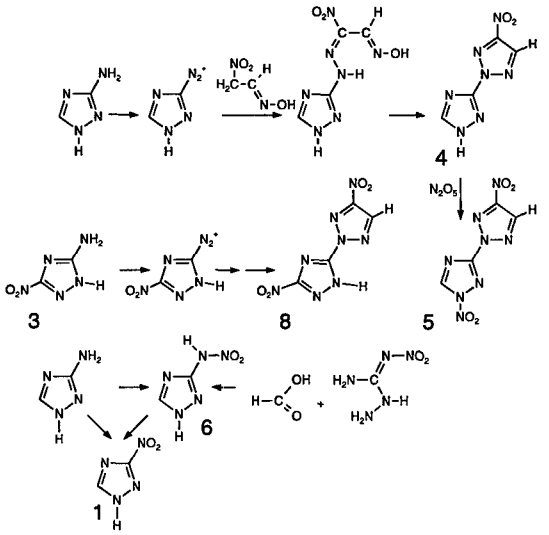

Schema 2

Das 2-Dinitrophenyl-4-nitro-1,2,3-triazol **10** haben wir nach dem o.e. Prinzip /20/ aus Dinitroanilin hergestellt. Dadurch konnte die Struktur der bei der vorher erwähnten Reaktion (Schema 1) entstandenen und chromatographisch getrennten Dinitrophenyl-nitrotriazole **10** und **11** aufgeklärt werden. Das 4-Nitro-1,2,3-triazol **2** läßt sich zum 4-Aminotriazol reduzieren /21/ und entsprechend dem obigem Mechanismus zu einem Bitriazol **19** umwandeln.

Zwei weitere von uns gefundenen Reaktionen, die sich als Alternative zu publizierten Synthesen anbieten, seien erwähnt. Die Nitrierung von Aminotriazol zu NITRA **6** benötigt nicht unbedingt NO_2BF_4 /10/, sondern ist auch mit üblicher Nitriersäure (konz. Salpetersäure / konz. Schwefelsäure) realisierbar. Allerdings haben wir, als es um die Herstellung größerer Mengen von NITRA für die Charakterisierung als Explosivstoff ging, auf die Methode von HENRY /6/ zurückgegriffen, die von Aminonitroguanidin (ANQ) ausgeht.

3-Nitro-1,2,4-triazol ist problemlos in einer SANDMEYER-Reaktion ohne Katalysator zugänglich /11/, liefert aber nur ein verunreinigtes Produkt. Ein Nitrotriazol in hoher Reinheit kann man erhalten, wenn man aus ANQ - nicht aus Aminotriazol - hergestelltes NITRA mit H_2O_2 (84 %) in einer zwar recht unübersichtlichen, aber wirkungsvollen und reproduzierbaren Reaktion /8/ oxidiert.

Die Isomeren **13** und **18**, die durch Umsetzung von 2,4- bzw. 4,6-Dichlor-5-nitropyrimidin mit ANTA **3** dargestellt werden, haben eine auffallende Gemeinsamkeit: Sie sind thermisch stabil und praktisch unlöslich in den gängigen Lösungsmitteln. Trotzdem zeigen sie eine gewisse chemische Labilität insofern, als sie beim Behandeln mit heißem Dimethylformamid oder Dimethylsulfoxid zwar in Lösung gehen, jedoch nicht mehr aus der Lösung ausfällbar sind, was auf chemische Veränderungen hinweist.

Strukturprobleme.

Bei den meisten der hier untersuchten Verbindungen steht die exakte Struktur nicht a priori fest, da unterschiedliche tautomere oder isomere Formen in Erwägung gezogen werden müssen. Ebenso muß - zumindest in Lösungen, und das ist der für chemische Reaktionen wesentliche Zustand - auch ein Gleichgewicht mehrerer Strukturen neben- einander in Erwägung gezogen werden. Die Entscheidung, welche Struktur im Einzelfall vorliegt, ist nicht leicht zu treffen. Die analytische "Methode der Wahl" ist die kernmagnetische Resonanzspektroskopie und zwar besonders ^{15}N-NMR, da es hier um die Charakterisierung von Stickstoff-Atomen geht.

Das ^{1}H-Spektrum des NTO läßt sowohl die Struktur eines Triazolons wie eines Hydroxytriazols (zwei unterschiedliche, mit D_2O austauschbare Signale) zu. Das ^{13}C-Spektrum reicht ebenso wenig für eine Entscheidung aus, da die Signallage von 153 ppm nicht gerade typisch für eine Ketogruppe ist. Erst das ^{15}N-Spektrum ist mit zwei positiven Signalen - entspr. zwei protonentragenden N-Atomen - eindeutig (Fig. 1-3). Die Signale sind in diesem Versuch (Gated Decoupling) positiv, wenn sie ein H-Atom tragen, sonst negativ.

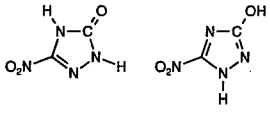

Im Falle des 4-Nitro-1,2,3-triazols - gelöst in DMSO-d_6 - erhält man ein ^{15}N-Spektrum mit 4 Signalen (eines für das N-Atom der Nitrogruppe und je eines für die Ring-N-Atome, da jedes N-Atom sich in einer anderen magnetischen Umgebung befindet). Da **zwei** Signale positiv sind (Fig. 4), also protonentragende N-Atome anzeigen, muß ein **tautomeres Gleichgewicht** zweierr Strukturen vorliegen; denn im Nitrotriazol liegt nur **eine** NH-Gruppe vor. Das gleiche Phänomen beobachtet man beim NITRA und dem C,C-Dinitrobitriazol **8** (Fig. 5). Welche Strukturen dabei beteiligt sind, kann erst durch weitergehende Betrachtungen entschieden werden, wobei oft Signallage und Signalform (Aufspaltungen) Hinweise auf die chemische Umgebung und damit die Struktur liefern. So zeigt das ^{15}N-Spektrum von C,N-Dinitrobitriazol mehrere markante Aufspaltungsmuster (Fig. 6), deren Auswertung (s. /12/) dazu verwendet werden kann, den Ort der N-Nitrierung festzulegen. In Einzelfällen wird das Auftreten von Tautomeren schon im

^{1}H-Spektrum erkennbar, so beim Bitriazol **19**, das allerdings nur im Lösungsmittel Aceton-d_6 die neuen temperaturabhängigen Signale zeigt (Fig. 7).

In anderen Fällen hilft nur eine Inkrementenabschätzung, die dann auf Modellverbindungen basiert, da in einem gewissen Streubereich die Signallage für die jeweiligen Atome reproduzierbar ist. Im allgemeinen beobachtet man, daß das H-Atom an dem Stickstoff zu finden ist, der von der Nitrogruppe am entferntesten liegt. Methodik und Ergebnisse dieser Studie sind in /12/ im Detail dargestellt. Im Anhang II sind in jenen Fällen, wo - zumindest in Lösung - ein tautomeres Gleichgewicht vorliegt, beide tautomere Formen angegeben. Durch Auswertung einer Vielzahl von NMR-Spektren konnten bereits aus den ^{1}H- und ^{13}C-NMR-Signalen der hier betrachteten 19 Verbindungen Zusammenhänge deutlich gemacht werden, die gesicherte Strukturanalysen zulassen:

In den 1,2,3-Triazolen gilt: Im Falle der Substitution an N-1 ist $\delta_{C\text{-}5} < 130$ ppm, bei Substitution an N-2 > 130 ppm. Auch die $^2J_{C\text{-}4\ ,\ H\text{-}5}$ -Kopplungkonstanten unterscheiden sich: Sie sind < 8 Hz im ersten Fall und > 8.5 ppm bei 2-Substitution. Im Falle der 1,2,4-Triazole wird unterscheidbar, ob N-1, C-3 und / oder C-5 ein H-Atom, eine Nitrogruppe oder einen sonstigen Rest tragen, da im einen Fall H-5 < 9 ppm, C-3 > 161 ppm und C-5 < 154 gefunden wird, während im Falle von Substitutionen durch Elektronenacceptoren H-5 > 9.5 ppm, C-3 < 161 ppm und C-5 > 154 ppm ist. Die $^1J_{C\text{-}5\ ,\ H\text{-}5}$ - und die $^3J_{C\text{-}3\ ,\ H\text{-}5}$ -Kopplungskonstanten sind stets > 212 Hz bzw. > 12 Hz (Anhang III).

Bei der Umsetzung von 4,6-Dichlor-5-nitro-pyrimidin mit 4-Nitro-1,2,3-triazol fällt ein Gemisch aus drei Stoffen an, das zu 70 % aus dem 4,6-Bis(4-nitro-1,2,3-triazol-1-yl)-5-nitropyrimidin besteht. Einer der beiden anderen Stoffen konnte als die zu **17** isomere Verbindung identifiziert werden, bei der die Nitrotriazolgruppen am N-2 gebunden sind. Diese Analyse konnte ohne Reindarstellung der Verbindung geschehen, worauf wegen der begrenzten Handhabbarkeit (s. Tab. 1) verzichtet wurde.

Das Bis-nitrotriazolyl-nitropyrimidin **12** erweist sich so als 1-substituiertes 3-Nitrotriazol. Analog kann im Falle der Verbindungen **10** und **11** sicher zwischen 1- und 2-substituierten 1,2,3-Triazolen entschieden werden.

Explosive Eigenschaften.

Als Explosivstoffe wurden bisher NTO /13/, DATNP /7/ und ANTA /14/ beschrieben. Ein Isomeres des ANTA ist das wesentlich leichter zugängliche NITRA, dessen explosive Eigenschaften wir speziell unter dem Aspekt eines Vergleichs dieser Isomeren untersucht haben /15/.

Alle Substanzen sind bei Raumtemperatur kristalline Substanzen von befriedigender thermischer Stabilität (Tab. 1). Die niedrigste gemessene Zersetzungstemperatur (DTA/TG : 6°/min Aufheizgeschwindigkeit) lag bei 207°C. Dem steht ein Höchstwert von 358°C für das Dinitrophenyl-4-nitro-1,2,3-triazol **16** gegenüber. Wesentlich aussagekräftiger ist aber bisweilen die Art der Zersetzung: So beobachtet man bei 1-Pikryl-4-nitro-1,2,3-triazol **14** einen scharfen Zersetzungspeak: Die Substanz zersetzt sich nicht einfach exotherm bei 234°C, sie explodiert. Dagegen gibt das Bis(4-nitro-1,2,3-triazol-1-yl)-5-nitroyprimidin **17** während seiner Zersetzung bei 207°C keinen Hinweis darauf, daß es sich hier um eine nicht mehr handhabbare Verbindung handelt, die schon bei geringster mechanischer Beanspruchung zu explodieren vermag. Sie stellt die empfindlichste Substanz dar, die von den Verfassern je untersucht wurde, und diese Tatsache kann nicht mit dem Hinweis auf die „Verunreinigungen" erklärt werden, da die eher phlegmatisierende Wirkung haben sollten.
Mit den Daten der Schlag- und Reibempfindlichkeit lassen sich drei Klassen von Explosivstoffen unterscheiden :

A : Deutlich reib- und schlagempfindlich, bisweilen Primärsprengstoff-Eigenschaften: **5**, **14**, **7**.
B : Reib- und Schlagempfindlichkeit vergleichbar mit klassischen Sprengstoffen wie Hexogen und TNT: **4, 6, 8 , 11, 15, 19**.

C : Unempfindlich (keine Reib- und Schlagempfindlichkeit nachweisbar), IHE, eventuell ohne Explosivstoff-Eigenschaften: **1, 3, 4, 7, 9, 10, 12, 13, 16, 18**.

Wegen seiner Sensibilität haben wir das C,N-Dinitrobitriazol **5** vor einer Verarbeitung zu einer Ladung aus zylindrischen Preßkörpern mit 7 % Wachs phlegmatisiert. Die metallisch eingeschlossenen Ladungen detonierten problemlos im Durchmesser von 16 mm. Dagegen waren NTO und NITRA auch im unphlegmatisierten Zustand im Durchmesser von 16 mm nicht detonierbar. Auch plattenförmige Ladungen des NTO von 10 mm Dicke, 90 mm Breite und 150 mm Länge, beidseitig mit Metall belegt (Sandwich-Ladungen), detonierten nicht. Diese beiden Sprengstoffe wurden in Metallrohren von 25 mm Durchmesser und 250 mm Länge gesprengt. Im Falle des NITRA wird ein interessantes Phänomen deutlich, die Nicht-Identität von Empfindlichkeit und Initiierbarkeit: NITRA ist kein unempfindlicher Sprengstoff - die Fallhammer- und Reibapparat-Ergebnisse weisen deutlich auf einen Explosivstoff hin -, trotzdem ist es schwer detonierbar.

Auch chemische Stabilität und IHE-Qualifikation gehen nicht immer parallel: DANTNP **13** /7/ wird als IHE beschrieben, zersetzt sich aber beim Erhitzen in Methylpyrrolidinon, dem Lösungsmittel, in dem man seine Konstitution mittels NMR bestimmt hat.

NTO ist auch von seiner Leistung (Tab. 2) her unter den Nitrotriazolen der interessanteste Sprengstoff: Seine gute Zugänglichkeit erlaubte es, NTO einem vertieften Vergleich mit klassischen Sprengstoffen zu unterziehen. Zwar darf seine Leistung (D, GURNEY-Konstante, Plate-Dent-Test) nicht mit Hochleistungssprengstoffen wie Hexogen und Oktogen verglichen werden. Aber als leicht herzustellender und gut zu verarbeitender IHE (Gap-Test) erreicht NTO mühelos die Qualitäten von TATB.

NITRA **6** ist als Isomeres des ANTA mit diesem auch in seiner Leistung gleichwertig. Das geht nicht nur aus theoretischen Berechnungen hervor, die NITRA sogar geringfügig günstiger bewerten, sondern läßt sich auch aus den Meßergebnissen schließen, wenn man die Ladedichte der Prüfkörper, die nur 85 % ihrer Kristalldichte ausmacht, in Rechnung stellt.

Das C,C-Dinitrobitriazol **8** wurde aus dem ANTA hergestellt mit der Idee, auf diesem Weg zu einem zumindest theoretisch leistungsgesteigerten Explosivstoff zu gelangen. Eine experimentelle Überprüfung war erst nach Synthese von dessen Isomeren, dem C,N-Dinitrobitriazol **5**, möglich, das sich besser zur Herstellung der benötigten Stoffmengen eignete. Seine relativ hohe Empfindlichkeit zwang uns allerdings, die Versuche mit einem phlegmatisierten Produkt durchzuführen. Trotz eines Sprengstoffgehalts von nur 93 % und einer dementsprechend niedrigen Ladedichte ist die gemessene Detonationsgeschwindigkeit des Dinitrobitriazols höher als die des ANTA..

Struktur und explosive Eigenschaften.

An mehreren Beispielen konnte in dieser Untersuchung die sonst nur empirisch begründete Tatsache studiert werden, daß bestimmte explosive Eigenschaften wie thermische Stabilität oder mechanische Empfindlichkeit mit (chemischen) Strukturparametern zusammenhängen.

Trotz offensichtlicher Ähnlichkeit können schon Isomere gravierende Unterschiede im Hinblick auf ihre explosiven Eigenschaften aufweisen. Doch sollte hier klar differenziert werden: Nicht alle (explosiven) Eigenschaften werden durch Isomerie, um bei diesem Beispiel für einen scheinbar geringfügigen Struktureinfluß zu bleiben, im gleichen Umfang tangiert. Es gilt im Allgemeinen folgende Regel der abnehmenden Auswirkung:

Mechanische Empfindlichkeit > Dichte > Leistung (D) > thermische Empfindlichkeit.

Beispiel: Die Isomeren ANTA / NITRA, C,C-DNBTr / C,N-DNBTr und 1-Pikryl- / 2-Pikryl-4-N-1,2,3-triazol unterscheiden sich am auffälligsten in ihrer Schlagempfindlichkeit. Bisweilen kann die isomere Struktur deutliche Auswirkung auf die Kristallstruktur und damit die Kristalldichte haben. Aber es fällt auf, daß auch (mechanisch) hochempfindliche Stoffe thermisch oft voll befriedigen und keinen Hinweis auf ihre sonstige Labilität geben.

Bei den nur selten realisierten Fällen einer vergleichenden Leistungsbetrachtung (Detonationsgeschwindigkeits-Messung) ergaben sich - wie auch theoretisch zu begründen -, oft ähnliche Werte, weil sich die Isomerie bisweilen über die Dichte, aber immer nur in begrenztem Umfang über die Bildungsenthalpie auf die Leistung auswirkt. Damit ist eine Strategie für ein Sprengstoff-"Tailoring" aufgezeigt: Ungünstige Eigenschaften können in gewissen Fällen durch Isomerisierung unter Erhalt der Leistung verbessert werden. Der Weg dahin, die chemische Synthese, kann allerdings erheblich komplizierter, eventuell gar ausgeschlossen sein.

In dieser Arbeit wurden mehrere „Composite"-Sprengstoffe untersucht, die aus zwei Explosivstoff-Systemen zusammengesetzt sind: Ausgehend von zwei Nitrotriazolsystemen, wurden mit Dinitrophenyl- und Pikrylverbindungen und der Nitropyrimidyl-Gruppe neue Dinitrophenyl-, Pikryl- und Nitropyrimidyl-nitrotriazole aufgebaut, deren zu erwartende Eigenschaften nicht ohne weiteres vorhersagbar sind. Zur Charakterisierung dieser Einzelbausteine läßt sich folgendes sagen: Die (reinen) **Nitrotriazole** haben wir als meist gutartige, also mechanisch mehr oder weniger unempfindliche Sprengstoffe kennengelernt, deren Brisanz und Leistung sie für eine Verwendung als militärische Sprengstoffe geeignet erscheinen lassen. Unter den **Pikrylverbindungen** befinden sich so populäre Sprengstoffe wie Pikrinsäure und TNT, und auch **Dinitrobenzole** sind bei entsprechendem Einschluß, Ladungsdurchmesser und Initiierung detonationsfähig. Daß **Nitropyrimidin** ein Sprengstoff ist, ergibt sich aus der Beobachtung, daß sein Einbau in andere energetische Systeme (Nitrotriazole) keinen Energieverlust, keine „chemische Phlegmatisierung" zur Folge hat. Allerdings ist reines Nitropyrimidin so schwer zugänglich, daß wir im Augenblick keine Chance sehen, den Beweis über die Messung seiner Detonationsgeschwindigkeit erbringen zu können. Dennoch sind Schlüsse auf den Energieinhalt der Verbindung gerade aus den Daten der hier behandelten Beispiele möglich.

Bei den „Composite"-Sprengstoffen, also Verbindungen, die aus zwei verschiedenen Explosivstoff-Systemen zusammengesetzt sind, ergeben sich die explosiven Eigenschaften nur selten als arithmetisches Mittel oder Summe der Einzelwerte. Die Regeln folgen chemischen, strukturellen Vorgaben:

Wir beobachteten z.B., daß im Falle der Verbindungen **13** und **18** der Ort der Anbindung des ANTA-Teils an den Nitropyrimidinring im Hinblick auf seine Explosivstoff-Eigenschaften unerheblich ist. Die 2,4- und 4,6-Isomeren sind - wie das (eine) Ausgangsprodukt IHE. Wird aber 4-Nitro-1,2,3-triazol mit Nitropyrimidin-Verbindungen substituiert, ist Ort und Art der Substitution entscheidend: 1-substituierte 4-Nitro-1,2,3-triazole sind extrem empfindlich (im Einzelfall nicht mehr handhabbar), während die 2-Isomeren als gutartig eingestuft werden können unabhängig davon, ob der Substituent der hochbrisante Pikryl- oder der (praktisch nicht mehr explosionsfähige) Dinitrophenyl-Rest ist. Wird also das potentiell labile 4-Nitro-1,2,3-triazol an der richtigen Stelle angebunden, kann es dadurch stabilisiert werden.

Die Erklärung für dieses Phänomen ist in der unterschiedlichen Ringöffnung des Nitrotriazolrings zu suchen. Die drei nebeneinanderliegenden Stickstoffatome des Triazolrings stellen im Falle der 1-Substitution eine Gruppierung dar, die offenbar sehr leicht die N-Atome N-2 und N-3 in Form eines Stickstoffmoleküls abspaltet, wogegen im Falle der 2-Substitution dieser Zersetzungsweg blockiert ist, somit eine thermisch und mechanisch stabile Gruppe von drei N-Atomen vorliegt.

Im Falle der Pikrylnitrotriazole **14** und **15** kam eine Untersuchung aus Los Alamos /17/ zu dem Ergebnis, daß sich die unterschiedliche Substitution in differierenden Bindungslängen speziell der N-2- und N-3-Atome auswirkt. Im Falle der 1-substituierten 4-Nitro-1,2,3-triazole erleichtert das eine N_2-Eliminierung nach Ringöffnung zwischen N-3 und C-4. Das so entstandene reaktive Zwischenprodukt ist als Diradikal für die auffallende Empfindlichkeit dieser Verbindung verantwortlich.

Das ANTA-Isomere NITRA **6** stellt nur hinsichtlich seiner mechanischen Empfindlichkeit eine Ausnahme von der Beobachtung dar, daß **1,2,4**-Triazole durchweg IHE-Eigenschaften - ein Hinweis auf die Stabilität dieses Ringsystems - haben. Im Falle der Detonierbarkeit zeigt auch NITRA dieses Charakteristikum.

Zusammenfassung

Neunzehn Nitrotriazole - darunter sieben Verbindungen, die erstmals im ISL synthetisiert wurden, - sind einer vertieften Strukturuntersuchung unterworfen worden, da wegen des Vorliegens von Tautomerie und Isomerie eine verfeinerte Strukturbestimmung (Position eines mobilen Protons) in mehreren Fällen offengeblieben war.

Fast alle Verbindungen erwiesen sich als Explosivstoffe, die Mehrzahl gutartig und problemlos handhabbar, aber es wurden auch einzelne Vertreter von extremer Labilität beobachtet, was sich anhand der jeweiligen Struktur erklären ließ. Dabei spielten isomere (s.o.) Strukturen eine bedeutsame Rolle.

Der anwendungstechnisch wichtigste Vertreter, das NTO, wurde eingehend als unempfindlicher Sprengstoff (IHE) charakterisiert und dem bekanntesten militärisch genutzten IHE, dem TATB, gegenübergestellt, das im NTO einen gewichtigen Konkurrenten (Preis, Leistung) erhalten hat.

Literatur.

/1/ W. Manchot und R. Noll, Lieb. Ann.Chem. 343 (1905) 1 - 27
/2/ K.-Y. Lee, L.B. Chapman, M.D. Coburn, J.Energ.Mat. 5 (1987) 27 -33
/3/ P.N. Neuman, J.Het.Chem. 8 (1971) 51 - 56
/4/ K.-Y. Lee, C.B. Storm, US-Patent, 5,110,380 (1992)
/5/ E.J. Browne, Austr.J.Chem. 22 (1969) 2251 - 54
/6/ R.A. Henry, J.Am.Chem.Soc. 72 (1950) 5344
/7/ Ch. Wartenberg, P. Charrue, P. Laval, Prop.Expl.Pyrot. 20 (1995) 23
/8/ H.H. Licht, H. Ritter, J.Energ.Mat. 12 (1994) 223 - 35
/9/ H.H. Licht, H. Ritter, Prop.Expl.Pyrot. 22 (1997) 333 - 36
/10/ M.S. Pevzner, T.N. Kulibabina, N.A. Povarova, L.V. Kilina, Khim.Geteros.Soedin 1979, 1132 - 35
/11/ L.I. Bagal, M.S. Pevzner, A.N. Frolov, N.I. Sheludyakova, J.Het.Chem.USSR, 6 (1970) 240
/12/ H.H. Licht, H. Ritter, H.R. Bircher, P. Bigler, Magn.Res.Chem. i.Vorb.
/13/ A. Becuwe, A. Delclos, Prop.Expl.Pyrot. 18 (1993) 1 - 10
/14/ R.L. Simpson, P.F. Pagoria, A.R. Mitchell, C.L. Coon, Prop. Expl.Pyrot. 19, 4 (1994), 174 - 79
/15/ H.H. Licht, H. Ritter, B. Wanders, Proc.Int.Conf. ICT 1994, 45
/16/ K.-Y. Lee, C.B. Storm, M.A. Hiskey, M.D. Coburn, J.Energ.Mat. 9 (1991) 415 - 28
/17/ C.B. Storm, R.R. Ryan, J.P. Ritchie, J.H. Hall, S.M. Bachrach, LA-UR 88/927
/18/ B.M. Lynch, T.L. Chan, Canad.J.Chem. 41 (1963) 274
/19/ M.A. Khan, B.M.Lynch, J.Het.Chem. 7 (1970) 1237 - 39
/20/ R.Mohr, M.Zimmermann, DBP 1,168,437 (1964)
/21/ P.N.Neuman, J.Het.Chem. 7 (1970) 1159 - 60

Tab. 1 : Explosive Eigenschaften (Stabilität und Empfindlichkeit)

Verbindung	**Dichte** (g/cm^3)	**Bildungs-enthalpie** (kJ/mol)	T_{ex} [1] (°C)	**Reibempfind-lichkeit** (kp)[2]	**Schlag-empfindlichkeit** (J) [3]
3-Nitrotriazol **1**	1.72	97.9	218	> 36	> 25
4-Nitrotriazol **2**	1.73	167.0	218	29	4.5
ANTA **3**	1.82	70.1	254	> 36	> 25
Nitrobitriazol **4**			267	> 36	> 25
C,N-Dinitrobitriazol **5**	1.82	515.6	258	8.4(Nadeln)	< 1.5
				24 (Pulver)	2.0
5 + 7 % Wachs				> 36	25
NITRA **6**	1.83	93.9	226	19	6.5
NTO **7**	1.91	- 59.9 /2/	236	> 36	25
C,C-Dinitrobitriazol **8**	1.89	189.9	271	> 36	4
N-Dinitrophenyl-nitrobitriazol **9**			> 350	> 36	> 25
2-Dinitrophenyl-4-nitrotriazol **10**			246	> 36	> 25
1-Dinitrophenyl-4-nitrotriazol **11**			247	19	2.0
Bis(3-Nitrotriazolyl)-nitropyrimidin **12**	1.82	638.1	260	> 36	> 25
DANTNP **13**	1.865 /7/	431.2 /16/	328	> 36	
1-Pikryl-4-nitrotriazol **14**	1.75 /17/		234 exp.	7 (Knall)	< 1.5 expl.
2-Pikryl-4-nitrotriazol **15**	1.83 /17/		272	> 36	5.5
1-Dinitrophenyl-3-nitrotriazol **16**			358	> 36	> 25
Bis(4-Nitrotriazolyl)-nitropyrimidin **17**			207	< 0.5 (Knall)	< 1.5 expl
2,4-Bis(5-amino-3-nitro-1,2,4-triazol-1-yl)-5-nitropyrimidin **18**			338	36	> 25
Nitro-(1,2,3-triazolyl)-1,2,3-triazol **19**			258		22.5
Hexogen (RDX)	*1.82*		*230*	*12*	*4.5*
Nitropenta (PETN)	*1.77*		*202*	*6*	*3.0*

Anmerkungen: [1] DTA/TG : 6°/min; [2] Reibapparat J. PETERS: 1. Reaktion; [3] BAM-Fallhammer: 1. Reaktion

Tab. 2 : Explosive Eigenschaften (Leistung)

	Δ (g/cm^3)	**D** (m/s)	$\sqrt{2E}$ (mm/µs)	**Plate-Dent-Test** (mm Kratertiefe)	**Gap-Test** (kbar)
NITRA	1.56	7346	2.28		
ANTA	1.75	7710 /14/			
C,N-Dinitrobitriazol (+ 7 % Wachs)	1.57	7767	2.55		
NTO	1.82	8001	2.34	5.72	> 50
RDX	1.73	8489	2.87	7.71	12.4 (class E)
TATB	1.86	7539	2.34	5.87	> 50
TNT	1.60	6913	2.39	5.51	> 50 (gegossen)

ANHANG I : Experimenteller Teil

2,4-Dinitrophenyl-4-nitro-2-(1,2,4-triazol-3-yl)-1,2,3-triazol **9** :

3.5 g 2,4-Dinitrochlorbenzol und 3.4 g Nitrobitriazol werden in Ethanol suspendiert. Nach Einstellen des pH-Werts auf 7 - 8 durch Zugabe von Triethylamin wird 1 Std. zum Rückfluß erhitzt. Nach dem Abkühlen wird der gebildete Niederschlag filtriert und getrocknet: Ausbeute : 3.24 g (52 %). Nach Umkristallisation aus Ethanol/Aceton hat das beigefarbene Produkt einen Smp. von 194°C.
Bei der Umsetzung von Dinitrochlorbenzol mit 4-Nitrotriazol **2** in Ethanol/Triethylamin entsteht ein durch Säulenchromatographie auftrennbares Gemisch aus zwei Nitrotriazolen **10** und **11**, die sich durch 1- bzw. 2-Substitution unterscheiden. Verbindung **10** mit Schmelzpunkt 118°C wurde durch die nachstehend beschriebene eindeutige Synthese hergestellt. Da LYNCH und CHAN /18/ für ihr Produkt **10** nur einen Schmelzpunkt von 104°C angeben, ist vom Vorliegen eines Gemischs auszugehen.

1-Hydroximino-2-nitroglyoxal-(2,4-dinitrophenyl-1-yl)-hydrazon:

11 g (60 mmol) 2,4-Dinitroanilin werden wasserfeucht (nach Lösen in Eisessig und Ausfällen auf Eis) in eine Mischung aus 90 ml H_2SO_4 (konz.) und 22 ml Wasser eingetragen. Nach Kühlung auf - 5°C wird eine Lösung von 4.5 g Natriumnitrit in 10 ml Wasser zugetropft. Zur Lösung des Diazoniumsalzes läßt man eine gesättigte Lösung von 10 g Natriummethazonat in Wasser zutropfen, wobei die Temperatur nicht über 10°C ansteigen soll. Es bildet sich ein gelber Niederschlag, den man noch eine halbe Stunde bei R.T. rührt. Danach wird filtriert, mit Wasser gewaschen und bei 60°C i.V. getrocknet. 19.9 g Ausbeute (quantitativ). Die Verbindung wird für die weiteren Schritte als Rohprodukt verwendet.

2,4-Dinitrophenyl-4-nitro-(2H)1,2,3-triazol **10** :

2 g (70 mmol) des Hydrazons werden in 40 ml Eisessig suspendiert und mit 30 ml Acetylchlorid versetzt. Die Reaktionsmischung wird so lange unter Rückfluß erhitzt, bis eine klare Lösung entstanden ist. Nach dem Abkühlen liegt ein gelber Niederschlag vor, das Acetat der Hydroxylamin-Verbindung, das abfiltriert und mit Ethanol gewaschen wird. Die Cyclisierung gelingt durch Erhitzen im Vakuum bei 170°C, durch Kochen unter Rückfluß in Ethanol oder durch azeotrope Destillation mit Toluol. Man erhält 0.5 g (25 %) eines Rohprodukts, das aus Ethanol umkristallisiert werden kann.

4,6-Bis(3-nitro-1,2,4-triazol-1-yl)-5-nitropyrimidin **12** :

1.94 g (0.01 mol) 4,6-Dichlor-5-nitropyrimidin und 2.28 g (0.02 mol) 3-Nitro-1,2,4-triazol werden in 30 ml Aceton suspendiert und mit 2.02 g (0.02 mol) Triethylamin versetzt. Nach 2 Std. Rühren bei R.T. wird filtriert, mit Wasser gewaschen und mit 100 ml Aceton ausgekocht. Das Acetonfiltrat wird zur Trockene eingedampft. Es lassen sich 2.3 g (65.9 %) des Rohprodukts isolieren, das nach Umkristallisieren aus Acetonitril einen Zersetzungspunkt von 260°C besitzt.

4,6-Bis(4-nitro-1,2,3-triazol-1-yl)-5-nitropyrimidin **17** :

1.94 g (0.01 mol) 4,6-Dichlor-5-nitropyrimidin und 2.28 g (0.01 mol) 4-Nitro-1,2,3-triazol wurden in 40 ml Tetrahydrofuran (THF) suspendiert und bei R.T. tropfenweise unter Rühren mit 2g (0.02 mol) Triethylamin (TEA) versetzt. Der Niederschlag aus TEA.HCl wurde mit 80 ml Wasser aufgelöst. Nach wenigen Minuten bildete sich ein neuer, gelber Niederschlag, der filtriert, mit Wasser gewaschen und bei 50°C i.V. getrocknet wurde. (Die NMR-Daten wurden mit diesem Rohprodukt erstellt.) Eine Hälfte des Rohprodukts wurde mit Ethylacetat umkristallisiert und filtriert. Das noch nicht völlig getrocknete Produkt explodierte beim Aufrühren mit einem Spatel. Die zweite Hälfte wurde dann unter entsprechendem Sicherheitsaufwand ohne weitere Reinigung für die Prüfung der mechanischen Empfindlichkeit verwendet.

2,4-Bis(5-amino-3-nitro-1,2,4-triazol-1-yl)-5-nitropyrimidin **18** :

1.94 g (0.01 mol) 2,4-Dichlor-5-nitropyrimidin (frisch destilliert) und 2.58 g ANTA **3** wurden in 40 ml THF suspendiert und im Verlauf von 30 Minuten mit 2 g (0.02 mol) TEA (Triethylamin) in 10 ml THF versetzt. Nach Ende der Zugabe hat sich eine rote Lösung gebildet, aus der sich TEA.HCl abscheidet. Nach Zugabe von 80 ml wird eine weitere Stunde bei R.T. gerührt, wobei sich der ursprüngliche Niederschlag weitgehend auflöst und ein neuer entsteht, der filtriert, gewaschen und getrocknet wird. Die Verbindung erwies sich als praktisch unlöslich in allen gängigen Lösungsmitteln, konnte nur unter vollständigem Verlust der Substanz in heißen, hochsiedenden Lösungsmitteln (NMP, DMF) gelöst werden, aus denen sie nicht wieder zurückzugewinnen war. (So entsteht z.B. beim Versuch einer Ausfällung mit Wasser nur ein Gel.)

4-Nitro-2-(1,2,3-triazol-4-yl)-1,2,3-triazol **19** :

1 g (10 mmol) 4-Amino-1,2,3-triazol /21/ werden in verd. HNO_3 (1.4 ml HNO_3 (100 %) + 5.7 ml H_2O) gelöst und bei - 5° tropfenweise mit einer wässrigen Lösung von 0.8 g $NaNO_2$ versetzt. Nach 15-minütigem Rühren wird bei einer Temperatur unter 10° eine wässrige Lösung von 1.4 g Natriummethazonat (mit verd. Natronlauge auf pH = 5 eingestellt) zugegeben, der entstandene Niederschlag abfiltriert und mit Wasser gewaschen. Nach dem Trocknen bei 60° i.V. liegt ein Rohprodukt (60 % Ausbeute) vor, das für die weitere Umsetzung verwendet werden kann.
1.14 g (5.7 mmol) des Rohprodukts werden in 40 ml NaOH (5 %) gelöst, 2 ml Eisessig zugegeben. Bei einer Temperatur von 20 bis 25° werden aus 2 Tropftrichtern gleichzeitig 2 ml Essigsäureanhydrid und soviel NaOH (5 %) eingetragen, daß der pH-Wert immer noch alkalisch bleibt. Nach einer halben Stunde wird mit Eisessig angesäuert und der orange-braune Niederschlag abfiltriert, der neben dem gewünschten Bitriazol (beigefarben) noch ein acetyliertes Zwischenprodukt enthält. Umkristallisieren aus Ethanol ergibt ein Reinprodukt. Aus der Reaktionslösung kann durch Ausäthern weiteres Bitriazol gewonnen werden. Gesamtausbeute 82 %. Schmelzpunkt 194°.

Anmerkung: Elementaranalysen (C,H,N,O ± 0.4 % max.) und IR-Spektren liegen vor und sind mit der angenommenen Struktur vereinbar.

Anhang II : Strukturen der untersuchten Nitrotriazole

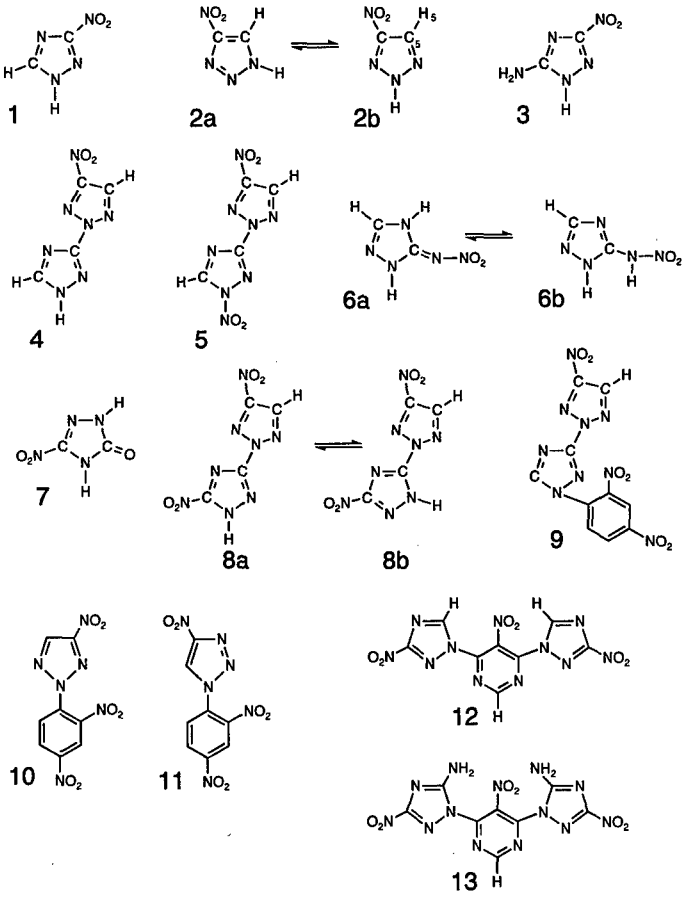

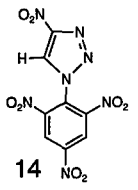
14

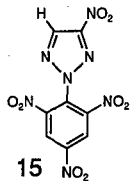
15

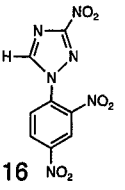
16

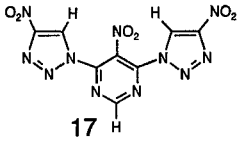
17

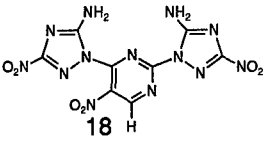
18

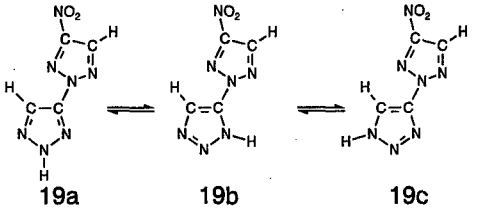
19a 19b 19c

Anhang III : Auswertung der ^{1}H- und ^{13}C-NMR-Signale und Kopplungskonstanten unter Berücksichtigung von Strukturelementen.

I. 1,2,3-Triazole (Lösungsmittel DMSO-d_6; Raumtemperatur)

H-5	C-4	^{2}J	C-5	^{1}J	Verb.	Substituent
9.1	154	9.1	126	206	**2**	R_1 = H
10.1	157	6.3	127	212	**11**	R_1 = dinitrophenyl
10.0	153	7.7	129	212	**14**	R_1 = pikryl
9.2	156	8.1	135	210	**10**	R_2 = dinitrophenyl
9.0	155	9.0	134	208	**4**	R_2 = triazolyl
9.0	156	9.0	135	210	**8**	R_2 = C-nitrotriazolyl
9.2	156	9.1	135	210	**5**	R_2 = N-nitrotriazolyl
9.3	156	9.2	135	210	**15**	R_2 = pikryl
9.0	155	8.0	133	208	**19**	R_2=1,2,3-triazolyl
9.2	158	8.6	137	210	**9**	R_2 = dinitrophenyltriazolyl

II. 1,2,4-Triazole (Lösungsmittel: DMSO-d_6; Raumtemperatur)

H-5	R_1	H-5	R_1	C-3	R_3	C-3	R_3	^{3}J	C-5	R_5	C-5	R_5	^{1}J	Verb.
8.9	H			163	NO_2			14.0	146	H			218	**1**
				161	NO_2						158	NH_2		**3**
8.8	H					157	N-Trz	12.9	146	H			215	**4**
		10.1	NO_2			153	N-Trz	15.6	144	H			234	**5**
	H					151	N-Trz				160	NO_2		**8**
		9.6	DNPh			160	N-Trz	13.4	151	H			224	**9**
		10.1	N-Pym	162	NO_2			14.7	147	H			231	**12**
				162	NO_2						159	NH_2		**13**
		9.6	DNPh	162	NO_2			16.0	148	H			226	**16**

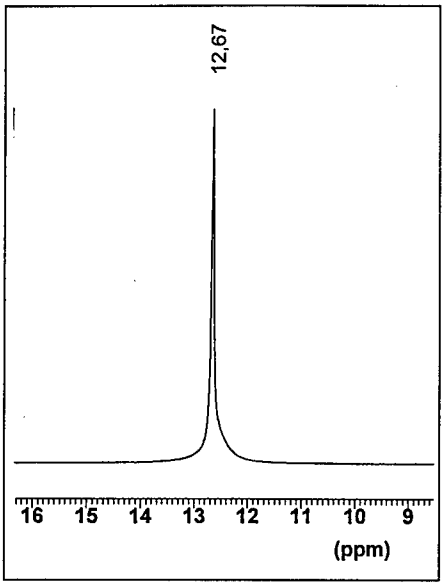

Fig. 1 : ^{1}H-NMR-Spektrum von NTO 7

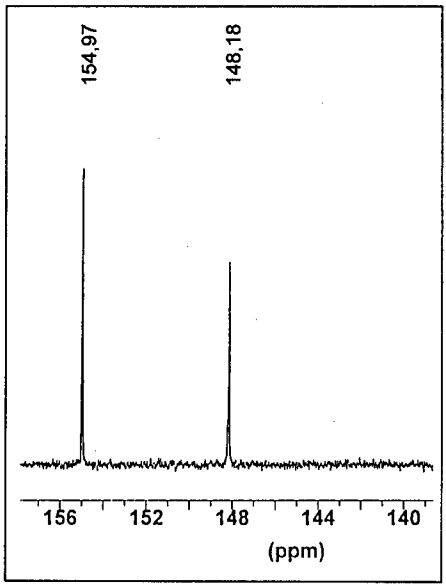

Fig. 2 : ^{13}C-NMR-Spektrum von NTO 7

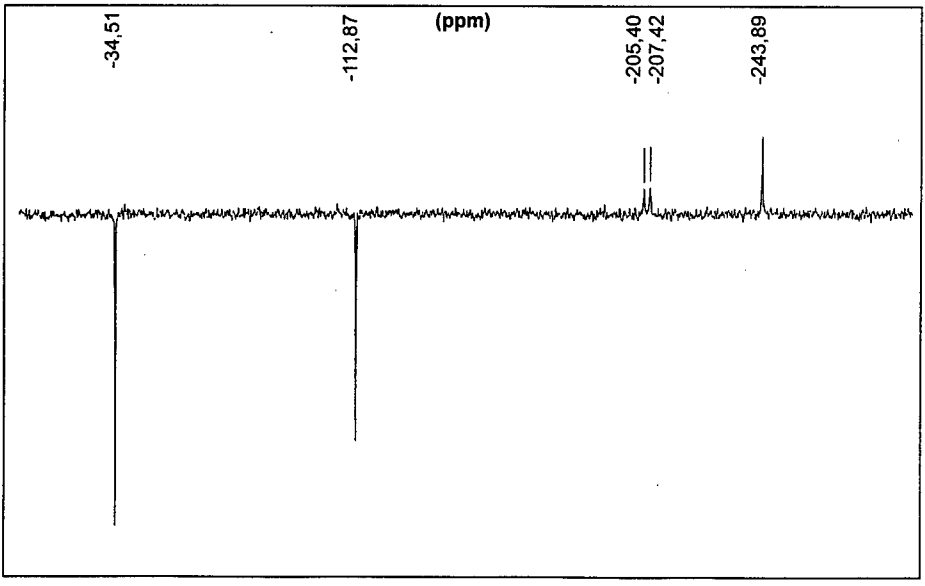

Fig. 3 : ^{15}N-NMR-Spektrum von NTO 7

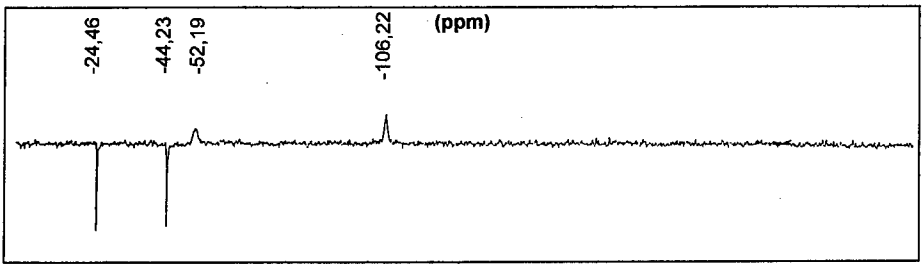

Fig. 4 : ^{15}N-NMR-Spektrum von 4-NT 2

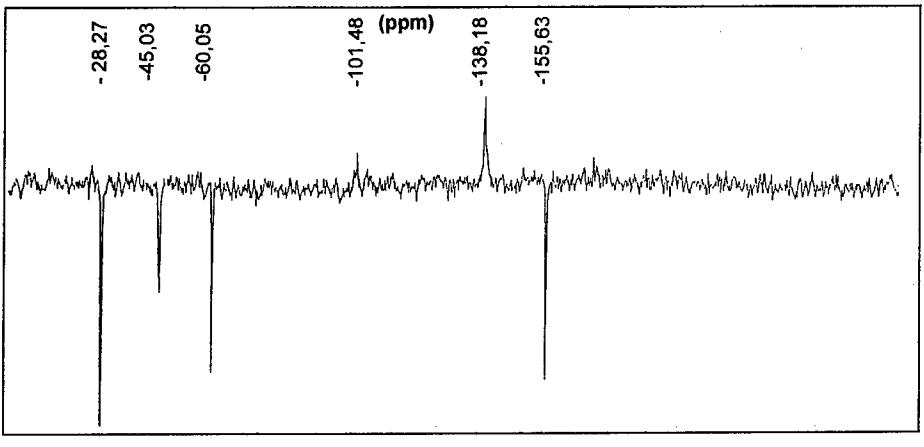

Fig. 5 : ^{15}N-NMR-Spektrum von C,C-DNBTr 8

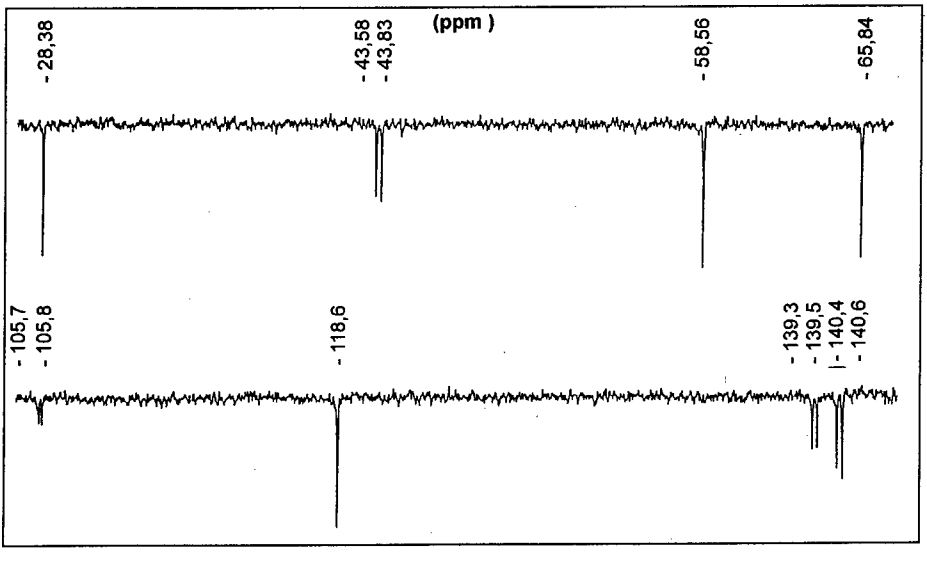

Fig. 6 : ^{15}N-NMR-Spektrum von C,N-DNBTr 5

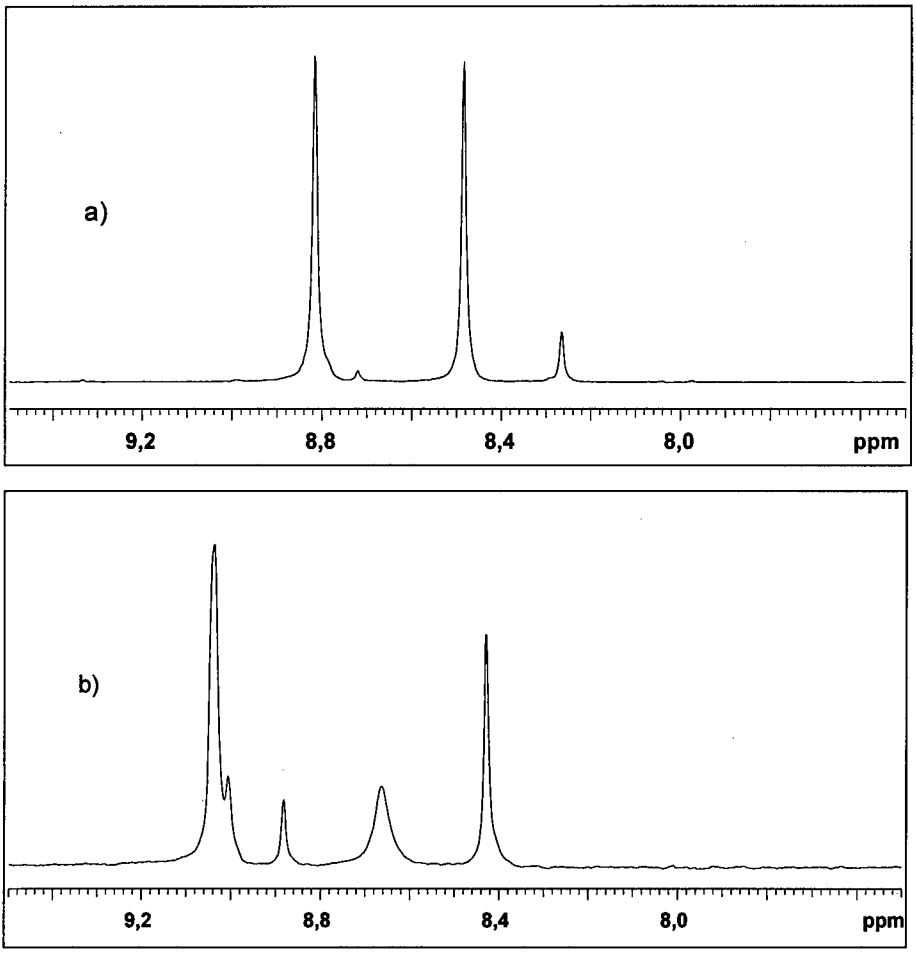

Fig. 7 : **^{1}H-NMR-Spektrum von 4-Nitro-2-(1,2,3-triazol-4-yl)-1,2,3-triazol 19 in Aceton-d_6**
a) bei + 20°C
b) bei - 70°C

NEW SYNTHESIS OF TATB. PROCESS DEVELOPMENT STUDIES

Robert D. Schmidt , Alexander R. Mitchell and Philip F. Pagoria
Lawrence Livermore National Laboratory, Energetic Materials Center, Livermore, California 94551, USA

ABSTRACT

We described a new synthesis of 1,3,5-triamino-2,4,6-trinitrobenzene (TATB) in 1996 at the 27th International Annual Conference of ICT. 1,1,1-Trialkylhydrazinium salts are highly reactive reagents which aminate nitroaromatic compounds through vicarious nucleophilic substitution (VNS) of hydrogen. When applied to picramide, these reagents produce TATB in high yield. Traditionally, TATB has been manufactured in the USA by nitration of the relatively expensive and domestically unavailable 1,3,5-trichlorobenzene (TCB) to give 2,4,6-trichloro-1,3,5-trinitrobenzene (TCTNB) which is then aminated to yield TATB. Elevated temperatures (150° C) are required for both reactions. Our new VNS synthesis potentially affords an inexpensive and a more environmentally benign preparation of TATB. We describe in this report our progress in scaling up the synthesis of TATB from the laboratory to the pilot plant. We will discuss structure and control of impurities, changes in yield/quality with reaction conditions, choice of solvents, workup and product isolation, safety, and environmental considerations. Particle size characterizations as well as small-scale safety and performance testing will also be discussed.

INTRODUCTION

The compound 1,3,5-triamino-2,4,6-trinitrobenzene (TATB) is a reasonably powerful high explosive (HE) whose thermal and shock stability is considerably greater than that of any

other known material of comparable energy.[1] The high stability of TATB favors its use in military[2] and civilian applications[3] when insensitive high explosives are required. In addition to its applications as a HE, TATB is used to produce the important intermediate benzenehexamine.[4-8] Benzenehexamine has been used in the preparation of ferromagnetic organic salts[8] and in the synthesis of new heteropolycyclic molecules such as 1,4,5,8,9,12-hexaazatriphenylene (HAT) that serve as strong electron acceptor ligands for low-valence transition metals.[5,7] The use of TATB to prepare components of lyotropic liquid-crystal phases for use in display devices is the subject of a German patent.[9]

There is a definite need for a less expensive and more environmentally benign production of TATB. Current production techniques for making TATB are expensive and rely on environmentally hazardous reagents and relatively harsh conditions. We recently reported a novel approach to the synthesis of TATB which utilizes relatively inexpensive starting materials and mild reaction conditions.[10-12] This new process relies on amination of nitroaromatic starting materials using a reaction known as Vicarious Nucleophilic Substitution (VNS) of hydrogen.[13] Scheme 1 outlines the approach.

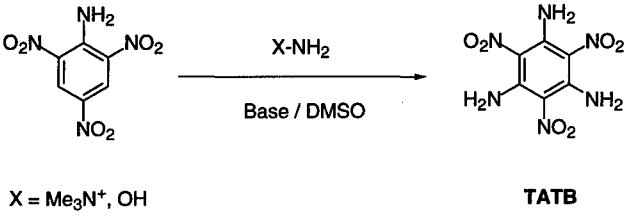

Scheme 1. VNS Synthesis of TATB from Picramide.

We have been working on the scale-up of this new synthesis with the goal of developing a new production of TATB. This paper examines the influence of aminating reagent, base, solvent, temperature, quenching, etc. on yield, purity and morphology of TATB product.

PROCESS STUDIES WITH 1,1,1-TRIMETHYLHYDRAZINIUM IODIDE AS THE VNS AMINATING REAGENT

Initial Studies

We have determined that 1,1,1-trimethylhydrazinium iodide (TMHI) is the most efficient aminating reagent available for the VNS synthesis of TATB.[10-12,14] Picramide and solid TMHI are dissolved in DMSO, and base (sodium methoxide or ethoxide) is added to initiate the reaction. The reaction is conducted at room temperature, and is complete in under 3 hours, giving TATB in 80-90% yield (Scheme 2).

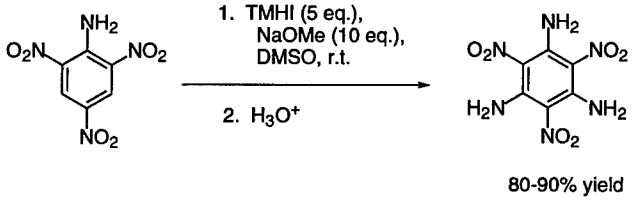

Scheme 2. VNS Synthesis of TATB using TMHI

The major expected impurity is 1,3-diamino-2,4,6-trinitrobenzene (DATB), which results from incomplete amination. Under these reaction conditions, no DATB (≤0.5%) was detected by FTIR spectroscopy or direct insertion solids probe mass spectrometry (DIP-MS).

Studies on Varying Reaction Conditions

The initial studies of this reaction employed picramide concentrations ≤ 0.13 M with large excesses of TMHI and base to drive the reaction to completion. We examined the effects of

decreased solvent and reagents on the reaction. Table 1 summarizes some of the results of this study.

Entry	Mole Ratio of Reagents (Picramide:TMHI: Base)	Base Used	Molarity of Picramide, mol/L	% Yield (Total Product)	Purity of TATB, %
1	1 : 5 : 10	NaOMe	0.13	89	> 99
2	1 : 4 : 8	NaOMe	0.11	82	> 99
3	1 : 4 : 8	NaOMe	0.22	86	≈ 97
4	1 : 4 : 8	NaOEt	0.22	80	≈ 97
5	1 : 2.5 : 5.6	NaOMe	0.27	86	88
6	1 : 3.1 : 8.4	NaOMe	0.11	81	> 99

Table 1. Effect on yield of TATB by varying quantities of reagents.

In general, the reaction will run efficiently up to 0.2 M picramide and using 3 eq. TMHI. The success of the reaction seems most dependent on base, requiring 8 eq. to proceed efficiently. The yield and purity of TATB drop significantly if an insufficient excess of base is used. It was also found that the reaction is very sensitive to the quality of the base, particularly in the case of sodium methoxide: older lots of the base which had been exposed to air, even while retaining the identical physical appearance of fresh material, gave reduced yields (or, in the worst case, no yield at all) of TATB.

Thus far, the largest scale attempted has been the 10 gram level. The reaction appears to scale linearly, delivering 82% yield of TATB at >99% purity. Larger scale work is currently in progress.

Methods of Quenching the Reaction

All initial studies of this reaction used either aqueous mineral acid solutions or water to quench the reaction and induce precipitation of TATB. This method results in a very small particle size, on the order of 0.2-1 μm. It was reasoned that quenching with a weak organic acid

in the absence of water might result in larger particle size. We found that quenching with citric acid monohydrate in DMSO produced particles in the 1-10 μm range. A larger particle size (20 μm) has recently been obtained using other organic acids.[15] It was also noticed that the final color of the product TATB varied when different quenching solutions were used (Table 2).

Entry[1]	TMHI Addition Method[2]	Quench Method	% Yield TATB	Physical Appearance
1	solid	aq. HCl	--	Yellow powder, >99% TATB
2	solid	aq. HNO_3	82	pale tan-yellow powder, >99% TATB
3	in situ	aq. HNO_3	86	pale tan-yellow powder, >99% TATB
4	solid	citric acid/DMSO	80	yellow-maize powder, >99% TATB
5	in situ	citric acid/DMSO	86	yellow-maize powder, >99% TATB

Notes: 1. Reaction conditions were 2 mmol picramide, 4eq TMHI, 8eq NaOMe in 20 mL DMSO.
2. See next section for description of TMHI addition methods.

Table 2. Effects of varying TMHI addition method and quenching method.

In Situ Generation of TMHI

Although TMHI is easy to prepare and handle[12,14] its use in the solid form requires an additional synthesis and isolation step, which would increase the overall product costs at production scale. Therefore, several experiments were conducted which examined the *in situ* generation of the reagent. To accomplish this, the precursor reagents--1,1-dimethylhydrazine and methyl iodide--were sequentially added to DMSO and allowed to react. Picramide was then added to this solution, followed by base, and the reaction was allowed to proceed as before. This method appears to give at least as good results as the original method, and in several cases gave slightly higher yields of TATB (Table 2).

Quality of Starting Materials

As mentioned earlier, the reaction appears to be very sensitive to the condition of the sodium methoxide. Several attempts at making TATB using an older lot of NaOMe failed, even though the base had been stored in a dessicator and the physical appearance of the base was no different from newer material (white, free-flowing fine powder). Analysis of this lot of NaOMe revealed that much of it had been converted to sodium carbonate by absorption of ambient CO_2 which inactivated it in the VNS reaction. Good yields (>85%) were again obtained when fresh NaOMe was employed.

In a few experiments, there was some variation in the purity of the starting picramide, and this appears to have affected the final appearance of the TATB, even though the TATB appears to be chemically >99% pure by spectroscopy. The principal impurity in the picramide was picryl chloride (vide infra). Impurity levels of greater than a few percent cause the product TATB to darken and, of course, reduce the total yield of TATB (although corrected yields are similar to those using pure picramide). High levels of impurities in starting picramide also change the crystal morphology of the product TATB.

Product Analysis

Since TATB is nearly insoluble in most solvents, simpler forms of chemical analysis such as NMR or Gas Chromatography are not practicable. Therefore, other techniques which allow analysis of the solid were investigated. The first of these attempted was Fourier Transform Infrared Spectroscopy (FTIR). The amine N-H stretching modes in TATB produce two characteristic absorptions at approximately 3225 and 3325 cm^{-1}, while those for DATB occur at 3360 and 3390 cm^{-1}. By using Nujol mull preparations for TATB samples, we have found that DATB can be reliably detected at concentrations of 1% or greater.

Another technique for TATB product analysis which we are using is direct insertion solids probe mass spectrometry (DIP-MS). In this technique, a solid sample of TATB is placed

in a sample holder at the end of a probe. The probe tip is inserted into a mass spectrometer, and is heated to cause the solid sample to evaporate into the MS ion volume, thereby allowing analysis of solids. Compounds with differing volatilities will evaporate at different times (a process known "probe distillation") and can thus be resolved to some extent by the MS detector. We have found that DATB can be reliably detected in a TATB sample at 1% concentration, and in some cases in concentrations as low as 0.1%.

Selected samples were submitted for elemental analysis. In early samples, the elemental analysis revealed that the product TATB was contaminated with 1-2% iodine. Unreacted TMHI as a source of iodine contamination was ruled out as TMHI could not be detected in the TATB samples using mass spectroscopy. We are examining the effects of quenching methods on impurities such as iodine, chlorine, etc.

In order to compare the TATB from this VNS process to that from more traditional processes, we have also conducted DSC, CRT, DH_{50}, spark and friction sensitivity tests on this material. In general, results are similar to those observed for TATB, except that thus far, the DSC values run consistently low by about 20-30 degrees. This may be an artifact of the much finer particle size produced by this process, although to confirm this more tests will be needed.

PROCESS STUDIES WITH HYDROXYLAMINE AS THE VNS AMINATING REAGENT

Due to the relative toxicity and cost of reagents used to make TMHI, we reinvestigated the use of hydroxylamine as a VNS aminating reagent. Hydroxylamine is in fact, the earliest known example of a VNS aminating reagent,[16] although the term "VNS" was coined many decades later.[13] Our earliest work in aminating picramide with hydroxylamine was disappointing since the reaction only provided DATB containing trace amounts of TATB at best.[11] The poor reactivity of hydroxylamine was independently confirmed by Seko and Kawamura who were unable to aminate nitrobenzene using hydroxylamine.[17] The low cost of hydroxylamine as an aminating reagent initiated further investigation and recent work in our laboratories showed that

hydroxylamine will aminate picramide to TATB at elevated temperature (65-90°C) to furnish TATB (Scheme 3).[18]

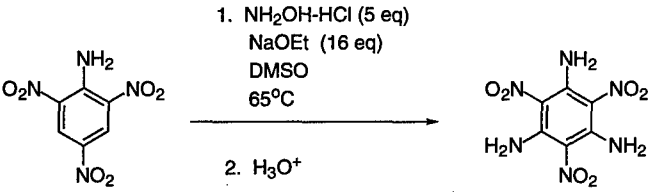

Scheme 3. VNS Synthesis of TATB using Hydroxylamine Hydrochloride.

Although the work with hydroxylamine is preliminary, satisfactory yields of TATB at approximately 97% purity have been achieved. Thus far the best results were obtained using NaOEt as the base in DMSO at 65°C for 6-12 hours. We are in the process of testing other hydroxylamine salts and anticipate the purity of the product will increase to over 99%. The relatively low cost of hydroxylamine salts makes this option very attractive.

STUDIES OF PICRAMIDE SYNTHESIS

As mentioned earlier, picramide is no longer commercially available. Therefore, as part of this project, we were required to reinvestigate methods for its production. One simple method is nitration of 4-nitroaniline, an inexpensive commodity chemical (Scheme 4).[19]

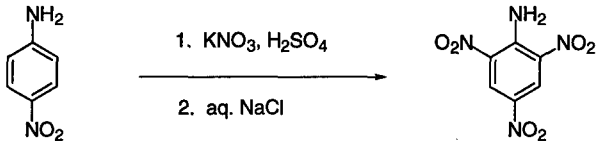

Scheme 4. Synthesis of Picramide.

Early studies in our laboratories using similar conditions gave good results, although some impurities were noted, the most significant being picryl chloride. (The workup of picramide is facilitated by the addition of brine, which apparently gives rise to the picryl chloride impurity.) In one case, picryl chloride was present in up to 20% impurity. Such impurities would require expensive recrystallization processing, since they affect the quality of TATB produced, as discussed earlier. However, our project collaborators at Pantex (Mason & Hanger Corporation, Amarillo, Texas) have improved the process and have prepared picramide in high yields (90%) and purity (>99.5%).

ACKNOWLEDGEMENTS

We wish to acknowledge contributions to this project by Messrs. Ray Thorpe, W. Tim Quinlin, Patrick Phelan and Monty Cates (Mason & Hangar Co., Pantex Plant, Amarillo, Texas, USA), Dr. Michael Coburn (Los Alamos, New Mexico, USA) and Mr. Gregory Lee (LLNL). This work was performed under the auspices of the U.S. Department of Energy by Lawrence Livermore National Laboratory under Contract No. W-7405-ENG-48.

REFERENCES

1. Rice, S. F. and Simpson, R. L., "The Unusual Stability of TATB: A Review of the Scientific Literature," Lawrence Livermore National Laboratory, Livermore, CA, Report UCRL-LR-103683 (July, 1990).

2. Dobratz, B.M., "The Insensitive High Explosive Triaminotrinitrobenzene (TATB): Development and Characterization - 1888 to 1994," Los Alamos Scientific Laboratory, Los Alamos, NM, Report LA-13014-H, (August, 1995).

3. Voreck, W.E., Brooks, J.E., Eberhardt, J.R. and Rezaie, H.A., **U.S. Patent 5,597,974**, "Shaped Charge for a Perforating Gun Having a Main Body of Explosive Including TATB and a Sensitive Primer," January 28, 1997.

4. Kohne, B. and Praefcke, K., "Isolierung farblosen Benzolhexamins," *Liebigs Ann. Chem.*, **1987**, 265.

5. Rogers, D.Z., "Improved Synthesis of 1,4,5,8,9,12-Hexaazatriphenylene" *J. Org. Chem.*, **1986**, *51*, 3904.

6. Kohne, B., Praefcke, K., Derz, T. Gondro, T. and Frolow, F., "Benzotri(imidazole) - a New Ring System Derived from Benzenehexamine," *Angew. Chem. Int. Ed. Engl.*, **1986**, *25* , 650.

7. Nasielski-Hinkens, R., Benedek-Vamos, M., Maetens, D. and Nasielski, J., "A New Heterocyclic Ligand for Transition Metals: 1,4,5,8,9,12-Hexaazatriphenylene and its Chromium Carbonyl Complexes,"*J. Organomet. Chem.*, **1981**, *46*, 179

8. Breslow, R., Maslak, P. and Thomaides, J.S., "Synthesis of the Hexaaminobenzene Derivative Hexaazaoctadecahydrocoronene (HOC) and Related Cations," *J.Am. Chem. Soc.*, **1984**, *106*, 6453.

9. Praefcke, K. and Kohne, B., "Amido Compounds as Components of Lyotropic Liquid-crystal Phases," Ger. Offen. DE 3,612,238; *Chem. Abstr.*, **1988**, *108*, 159109n.

10. Mitchell, Alexander R.; Pagoria, Philip F.; Schmidt, Robert D. " A New Synthesis of TATB Using Inexpensive Starting Materials and Mild Reaction Conditions," in *Energetic Materials-Technology, Manufacturing and Processing*, Keicher, T., Ed., Proc. 27th Int. Annual Conf. of ICT. Karlsruhe, Germany, **1996**, 29.1-29.11.

11. Mitchell, A. R.; Pagoria, P. F.; Schmidt, R. D., **U.S. Patent 5,633,406**, "Vicarious Nucleophilic Substitution Using 4-Amino-1,2,4-triazole, Hydroxylamine or O-Alkylhydroxylamine to Prepare 1,3-Diamino-2,4,6-trinitrobenzene or 1,3,5-Triamino-2,4,6-trinitrobenzene", May 27, 1997.

12. Mitchell, A. R.; Pagoria, P. F.; Schmidt, R. D., **U.S. Patent 5,569,783**, "Vicarious Nucleophilic Substitution to Prepare 1,3-Diamino-2,4,6-trinitrobenzene or 1,3,5-Triamino-2,4,6-trinitrobenzene", October 29, 1996.

13. Makosza, M. and Winiarski, J. "Vicarious Nucleophilic Substitution of Hydrogen", *Acc. Chem. Res.*, **1987**, *20*, 282.

14. Pagoria, P. F.; Mitchell, A. R.; Schmidt, R. D., "1,1,1-Trimethylhydrazinium Iodide: a Novel, Highly Reactive Reagent for Aromatic Amination *via* Vicarious Nucleophilic Substitution of Hydrogen", *J. Org. Chem.* **1996**, *61*, 2934.

15. Dr. Michael D. Coburn, personal communication.

16. J. Meisenheimer, J. and Patzig, E., "Directe Einführung von Aminogruppen in den Kern aromatischer Körper", *Ber.*, **1906**, *39*, 2533

17. Seko, S. and Kawamura, N., "Copper-Catalyzed Direct Amination of Nitrobenzenes with O-Alkylhydroxylamines," *J. Org. Chem.*, **1996**, *61*, 442.

18. Mitchell, A. R., Pagoria, P. F. and Schmidt, R. D, U.S. and Foreign Patent Applications have been filed.

19. Holleman, A. F., "1,3,4,5-Tetranitrobenzene," *Rec. trav. chim.*, **1930**, *49*, 112

DIE REAKTION VON AMMONIAK MIT DISTICKSTOFFPENTOXID

Christian Frenck*, Wieland Janitschek*, Werner Weisweiler**

Abstract

Since 1849 dinitrogen pentoxide (N_2O_5) has been well-known as a powerful nitrating agent. Its reaction with ammonia (NH_3) leads to the formation of ammonium nitrate (AN), nitramide (NH_2NO_2) and ammonium dinitramide (ADN).

The mechanism of this ADN synthesis is described proposing a double nitration of NH_3 via the intermediates nitramide and dinitramide acid. Due to the catalytic decomposition of the intermediates, H_2O and N_2O are formed as further reaction products provable by IR spectroscopy. In addition to the well-known reaction of NH_3 with N_2O_5 forming ADN, nitramide and its decomposition products, a third reaction was dicovered: the reaction of NH_3 with N_2O_5 forming AN and N_2O with the same stoichiometry as it is observed for ADN synthesis. Kinetic modelling of the total reaction scheme leads to a equation for the differential selecticity of ADN. The equation could be confirmed by experimental results.

* Fraunhofer Institut für Chemische Technologie, Josef-von-Fraunhofer-Str. 7, 76327 Pfinztal

** Institut für Chemische Technik an der Universität Karlsruhe, Kaiserstr. 12, 76128 Karlsruhe

1 Einleitung

Seit der Entdeckung von Distickstoffpentoxid (N_2O_5) vor etwa 150 Jahren wird es häufig als Nitrierreagenz in der präparativen Chemie verwendet [1], [2]. Im Vergleich zu den Reaktionen von N_2O_5 mit organischen Substraten ist über die Reaktionen mit anorganischen Substraten, insbesondere mit Nichtmetall-Verbindungen wenig bekannt [3]. Die Reaktion von Ammoniak (NH_3) mit Distickstoffpentoxid ist seit der Entdeckung des Ammoniumdinitramids (ADN), einem potentiellen Oxidator für Raketen-Festtreibstoffe, von besonderem Interesse.

2 Die Reaktionen von Ammoniak mit Distickstoffpentoxid

Sainte-Claire Deville [4] beobachtete die Bildung von Ammoniumnitrat (AN) bei der Reaktion von N_2O_5 mit NH_3. Vast et al. [5] gelang die Synthese von Nitramid (NH_2NO_2) durch dieselbe Reaktion bei -196°C in Ausbeuten bis zu 30%:

$$2\ NH_3 + N_2O_5 \longrightarrow NH_2NO_2 + NH_4NO_3 \qquad \text{Gl. 2-1}$$

Nach der Entdeckung des ADN durch Tartakovsky und Luk'yanov [6] gelang Schmitt et al. [7] dessen Synthese aus NH_3 und N_2O_5:

$$4\ NH_3 + 2\ N_2O_5 \longrightarrow NH_4N(NO_2)_2 + 2\ NH_4NO_3 \qquad \text{Gl. 2-2}$$

Die Ausbeuten betrugen bei Ammoniak-Überschuß und einer Reaktionstemperatur zwischen -20°C und -80°C bis zu 15%.

3 Ableitung eines Reaktionsschemas

Bei den bisher bekannten Reaktionen von NH_3 mit N_2O_5 entstehen die gewünschten Produkte Nitramid bzw. ADN in geringen Ausbeuten; als Hauptprodukt entsteht AN. Wegen des großen Interesses an ADN und der einfachen Einstufen-Synthese aus NH_3 und N_2O_5 ist die Erhöhung der Ausbeute ein vorrangiges Ziel bei dieser Methode. Dazu ist das Verständnis der chemischen Vorgänge im Reaktionssystem von Nutzen.

Schmitt et al. [7] postulierten einen Zweistufen-Mechanismus zur Bildung von ADN über Nitramid als Zwischenstufe, die mit einem zweiten Äquivalent N_2O_5 nitriert wird. Bei einer Temperatur unterhalb von -120°C verläuft diese Reaktion sehr langsam, wodurch Nitramid aus dem Reaktionsgemisch isoliert werden kann. Außerdem ist ein NH_3-Überschuß für die Bildung von ADN notwendig. Die Bildung von ADN ist demnach nach folgendem Mechanismus zu verstehen:

$$NH_3 + N_2O_5 \longrightarrow NH_2NO_2 + HNO_3 \qquad \text{Gl. 3-1}$$

$$NH_2NO_2 + N_2O_5 \longrightarrow HN(NO_2)_2 + HNO_3 \qquad \text{Gl. 3-2}$$

$$HN(NO_2)_2 + NH_3 \longrightarrow \mathbf{NH_4N(NO_2)_2} \qquad \text{Gl. 3-3}$$

$$2\,HNO_3 + 2\,NH_3 \longrightarrow 2\,NH_4NO_3 \qquad \text{Gl. 3-4}$$

In diesem Reaktionsmechanismus treten Nitramid und Dinitraminsäure (HDN) als reaktive Zwischenstufen auf, die sich zersetzen können [8], [9]:

$$NH_2NO_2 \xrightarrow{\text{basenkat.}} N_2O + H_2O \qquad \text{Gl. 3-5}$$

$$HN(NO_2)_2 \xrightarrow{\text{säurekat}} N_2O + HNO_3 \qquad \text{Gl. 3-6}$$

Unter Berücksichtigung dieser beiden Reaktionen läßt sich das in Abbildung 3-1 dargestellte Reaktionsschema für die Reaktion zwischen NH_3 und N_2O_5 formulieren.

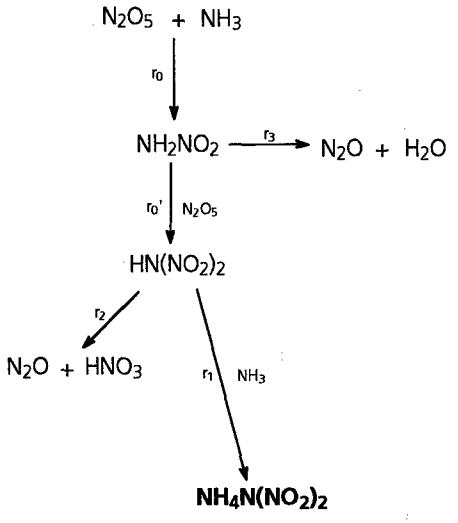

Nebenreaktion der aus r_0, r_0' und r_2 gebildeten Salpetersäure:

$$HNO_3 + NH_3 \xrightarrow{r} NH_4NO_3$$

Abbildung 3-1: Schema für die Reaktion von Ammoniak und Distickstoffpentoxid (r_i sind die Reaktionsgeschwindigkeiten der Teilreaktionen)

Aus diesem Reaktionsschema sind die folgenden Brutto-Reaktionsgleichungen ableitbar:

R_1 : $$4\ NH_3 + 2\ N_2O_5 \longrightarrow NH_4N(NO_2)_2 + 2\ NH_4NO_3$$ Gl. 3-7

R_2 : $$4\ NH_3 + 2\ N_2O_5 \longrightarrow N_2O + 3\ NH_4NO_3$$ Gl. 3-8

R_3 : $$2\ NH_3 + N_2O_5 \longrightarrow N_2O + H_2O + NH_4NO_3$$ Gl. 3-9

Während die Reaktionsgleichung R_1 der bereits bekannten Reaktionsgleichung Gl. 2-2 und die Reaktion R_3 der Brutto-Gleichung aus Gl. 2-1 und Gl. 3-5 entspricht, stellt die Reaktion R_2 eine neue, bisher unbekannte Reaktion von NH_3 und N_2O_5 mit der zur ADN-Bildungsreaktion analogen Stöchiometrie dar.

4 Kinetische Modellierung

Aus dem in Abbildung 3-1 dargestellten Reaktionsschema kann eine Modellgleichung für die ADN-Selektivität in Abhängigkeit der Reaktanten-Konzentration abgeleitet werden. Für die Reaktionsgeschwindigkeiten r_i können die folgenden Ansätze erster Ordnung bezüglich der an den Reaktionen beteiligten Reaktanten machen:

1. Nitrierung: $r_0 = k_0\, c(NH_3)\, c(N_2O_5)$ Gl. (4-1)

2. Nitrierung: $r_{0'} = k_{0'}\, c(NH_2NO_2)\, c(N_2O_5)$ Gl. (4-2)

ADN-Bildung: $r_1 = k_1\, c(HN(NO_2)_2)\, c(NH_3)$ Gl. (4-3)

HDN-Zersetzung: $r_2 = k_2\, c(HN(NO_2)_2)\, c(HNO_3)$ Gl. (4-4)

Nitramid-Zersetzung: $r_3 = k_3\, c(NH_2NO_2)\, c(NH_3)$ Gl. (4-5)

AN-Bildung: $r = k\, c(HNO_3)\, c(NH_3)$ Gl. (4-6)

Bei Gültigkeit des Quasistationaritätsprinzips für die Zwischenprodukte in Gegenwart eines Ammoniak-Überschusses, läßt sich für die Selektivität zur Bildung von ADN die folgende Modellgleichung ableiten:

$$S = -\frac{d\, c(NH_4N(NO_2)_2)}{d\, c(N_2O_5)} = \frac{S_1 S_2}{1 + S_1} \qquad \text{Gl. (4-7)}$$

wobei für die differentiellen Selektivitäten

$$S_1 = \left[1 + \frac{k_3}{k_0'} \frac{c(NH_3)}{c(N_2O_5)} \right]^{-1} \qquad \text{Gl. (4-8)}$$

$$S_2 - 1 = \frac{1}{2S_1} (1 + C - (4\, S_1 (S_1+1) + C (C+2) + 1)^{0,5} \qquad \text{Gl. (4-9)}$$

mit

$$C = \frac{k\, k_1}{k_0\, k_2} \frac{c(NH_3)}{c(N_2O_5)}$$

gilt. Hieraus wird deutlich, daß die differentielle Selektivität S vom Konzentrationsverhältnis, nicht jedoch von den absoluten Konzentrationen der Reaktanten abhängig ist. Die Parameter

$$K_1 = \frac{k_3}{k_0'} \qquad \text{Gl. (4-10)}$$

$$K_2 = \frac{k\, k_1}{k_0 k_2} \qquad \text{Gl. (4-11)}$$

können durch Anpassung der Modellfunktion an experimentelle Werte ermittelt werden.

5 Experimentelle Untersuchungen

Zur experimentellen Untersuchung der Vorgänge im Reaktionssystem NH_3-N_2O_5 wurde in Chloroform gelöstes N_2O_5 mit einem Überschuß gasförmigem Ammoniak in einem kontinuierlich betriebenen Rührkesselreaktor (280 mL) umgesetzt Die kristallinen Reaktionsprodukte wurden abfiltriert und einer Fest-Flüssig-Extraktion mit Essigsäureethylester unterworfen. Die Lösung wurde anschließend im Vakuum bis zur Trockene eingedampft, der Rückstand getrocknet und ausgewogen. Die Identifikation dieses Feststoffes und der kristallinen Raffinatphase der Extraktion erfolgte mittels IR-Spektroskopie. Der Gasraum über

der Reaktionslösung wurde während der Umsetzungen IR-spektroskopisch analysiert. Das nach der Filtration gewonnene Filtrat wurde zunächst IR-spektroskopisch untersucht, zusätzlich wurde eine Wasserbestimmung nach Karl Fischer [10] im Lösemittel sowohl vor als auch nach der Umsetzung durchgeführt. Nach diesen Untersuchungen wurde das Lösemittel im Vakuum verdampft und auf einen eventuell vorhandenen löslichen kristallinen Rückstand hin überprüft.

5.1 Identifikation der Reaktionsprodukte

Gemäß dem Reaktionsschema entsteht durch die Zersetzung des intermediär gebildeten Nitramids Wasser, das in der Lösung nachzuweisen ist. Der Wassergehalt des Lösemittels ändert sich durch die Umsetzung jedoch nur unwesentlich (< 0,01% vor bzw. 0,04 % nach der Umsetzung). Auch läßt sich Wasser IR-spektroskopisch nicht nachweisen. Dies ist auf die hygroskopischen Reaktionsprodukte zurückführen, die der Lösung das Wasser und somit dem Nachweis entziehen. Nach Eindampfen des Filtrats der Reaktionsmischung verbleibt kein Rückstand. Das bedeutet, daß ebenfalls kein Nitramid nachweisbar ist, was auf eine Reaktion im Sinne von Gl. 3-9 hinweist. Die kristallinen Reaktionsprodukte wurden als AN in der Raffinatphase und ADN in der Extraktphase nach der Fest-Flüssig-Extraktion identifiziert. Die Analyse des Gasgemisches über der Reaktionslösung ergab neben der ebenfalls in Lösung auftretenden Komponenten (NH_3, Chloroform) den eindeutigen Nachweis für N_2O (Abbildung 5-1).

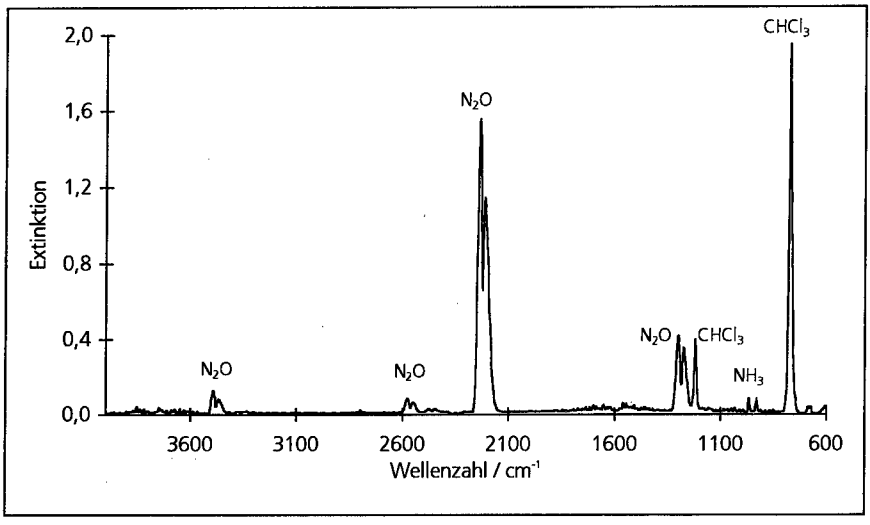

Abbildung 5-1: IR-Spektrum von der Zusammensetzung des Gasraumes über der Reaktionslösung bei der ADN-Synthese aus Ammoniak und Distickstoffpentoxid (bei Ammoniak-Überschuß).

5.2 Bestimmung der Produktverteilung

Mit den drei aus dem Reaktionsschema abgeleiteten Reaktionsgleichungen lassen sich die chemischen Vorgänge im System N_2O_5-NH_3 beschreiben, wenn das Gleichungssystem aus den Stoffbilanzen der Schlüsselkomponenten (N_2O_5, AN, ADN) für die Schlüsselreaktionen R_1, R_2 und R_3 lösbar ist. Zudem läßt sich dann mit den experimentellen Werten für die Stoffmengen in Abhängigkeit des Konzentrationsverhältnisses die Produktverteilung bestimmen. Wie aus der Abbildung 5-2 hervorgeht, nimmt der Anteil der ADN-Bildungsreaktion (R_1) und der Anteil der Reaktion zu AN und N_2O (R_2) mit zunehmendem Konzentrationsverhältnis aus NH_3 und N_2O_5 ab. Dagegen nimmt der Anteil der Reaktion zu Wasser und Lachgas (R_3) zu.

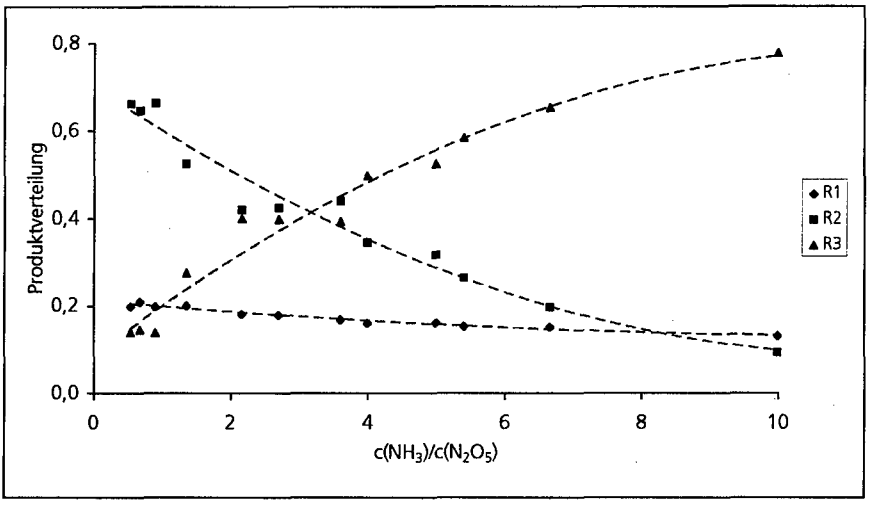

Abbildung 5-2: Produktverteilung als Funktion des Konzentrationsverhältnisses der Reaktanten.

5.3 Anpassung der Modellgleichung an die experimentellen Ergebnisse

Mit Hilfe der Parameter K_1 und K_2 ist eine Anpassung der Modellgleichung an die experimentellen Ergebnisse möglich. In Abbildung 5-3 sind neben den experimentellen Werten und dem Graph der Modellgleichung die differentiellen Selektivitäten S_1 und S_2 angegeben. Die Funktion der Modellgleichung weist eine prinzipielle Überinstimmung mit dem Experiment auf. Während für Konzentrationsverhältnisse von $c(NH_3)/c(N_2O_5) > 5$ ein überwiegender Einfluß durch S_1 zu beobachten ist, ist für kleine Konzentrationsverhältnisse S_2 für die Selektivität bestimmend. Die Abweichung der Modellgleichung von den experimentellen Werten beträgt bis zu 4%. Diese Abweichung ist auf die der Modellierung zugrunde liegenden kinetischen Potenzansätze zurückzuführen, bei denen die Konzentrationen der Reaktanten und Zwischenprodukte nach erster Ordnung eingehen.

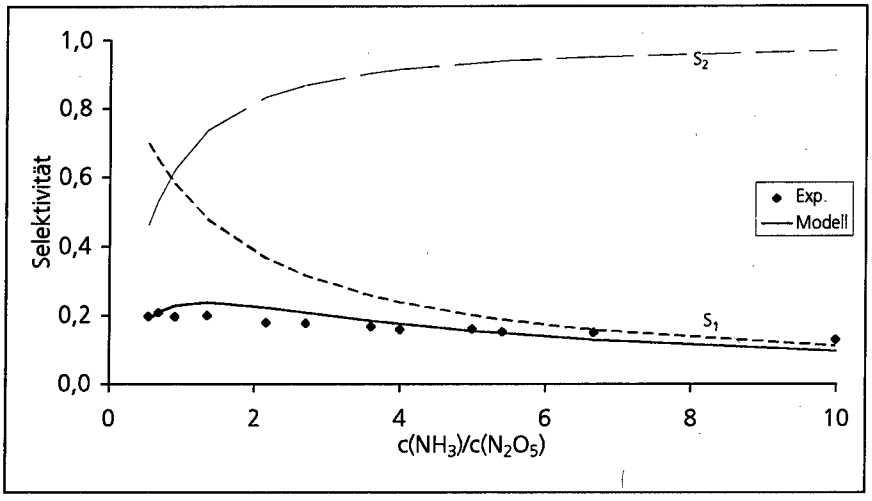

Abbildung 5-3: Abhängigkeit der Selektivitäten S_1, S_2 und S vom Konzentrationsverhältnis der Reaktanten ($K_1 = 0,8$; $K_2 = 3,3$).

Ein verbessertes Modell kann demzufolge durch eine Veränderung der Reaktionsordnung in den reaktionskinetischen Potenzansätzen erreicht werden. Diese Veränderung führt zur Einführung zweier zusätzlicher Parameter p und q. Die Modellgleichung lautet damit

$$S = \frac{S_1 S_2}{[\,1 + S_1]}$$

mit den differentiellen Selektivitäten

$$S_1 = [\,1 + K_1 \left[\frac{c(NH_3)}{c(N_2O_5)}\right]^p\,]^{-1}$$

$$S_2 - 1 = \frac{1}{2S_1}\,(1 + C - (4\,S_1\,(S_1+1) + C\,(C+2) + 1)^{0,5}$$

mit

$$C = \frac{k\,k_1}{k_0\,k_2}\left[\frac{c(NH_3)}{c(N_2O_5)}\right]^q$$

Eine erneute Anpassung der Modellgleichung mit Hilfe der nunmehr vier Parametern (K_1, K_2, p, q) führt zu einer verbesserten Wiedergabe der experimentellen Ergebnisse durch die Modellgleichung (Abbildung 5-4). Die Abweichung von den experimentellen Ergebnissen beträgt maximal 1%.

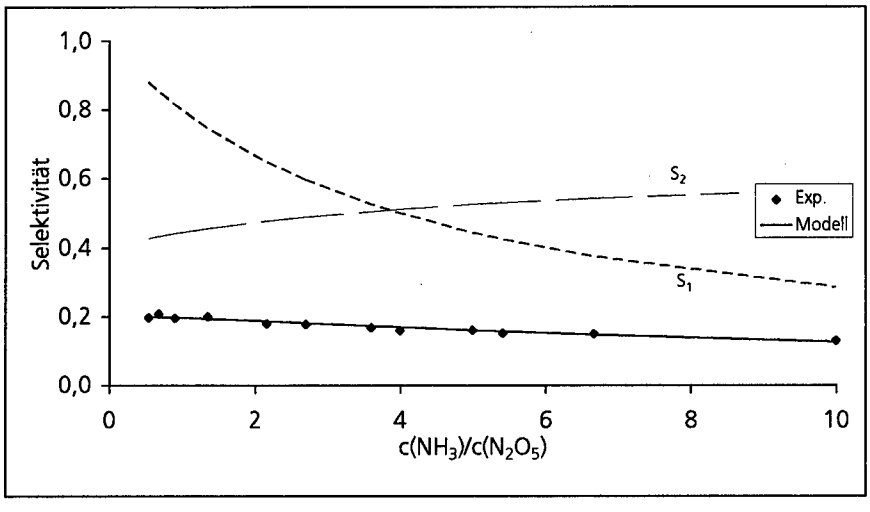

Abbildung 5-4: Funktion der Selektivitäten S_1, S_2 und S vom Konzentrationsverhältnis der Reaktanten (K_1 = 0,25; K_2 = 1,8; p = 1; q = 0,01).

6 Zusammenfassung

Die Reaktionen von Ammoniak (NH_3) und Distickstoffpentoxid (N_2O_5) werden seit der Entdeckung des N_2O_5 untersucht. Neben Ammoniumnitrat (AN) war bisher die Bildung von Nitramid (NH_2NO_2) und Ammoniumdinitramid (ADN) bekannt. Hiervon ausgehend wurde ein Reaktionsmechanismus abgeleitet, bei dem durch eine doppelte Nitrierung des Ammoniak über Nitramid und Dinitraminsäure als reaktive Zwischenstufen nach der Neutralisation neben AN das ADN ensteht. Die Berücksichtigung der Reaktionsmöglichkeiten der Zwischenstufen unter den gegebenen Reaktionsbedingungen (kat. Zersetzungsreaktionen) führte zu einem Reaktionsschema, in dem neben den genannten Reaktionsprodukten Lachgas und Wasser auftreten. Aufgrund der hygroskopischen Eigenschaften von AN und ADN wird das Wasser der Reaktionsmischung entzogen und läßt sich somit nicht in der

Lösung nachweisen. Dagegen konnte das Lachgas eindeutig in der Gasphase über der Reaktionslösung während der Umsetzung nachgewiesen werden. Aus dem Reaktionsschema lassen sich drei Reaktionsgleichungen ableiten. Während eine Gleichung der bereits bekannten ADN-Bildungsreaktion entspricht, stellt eine weitere Gleichung die Bruttoreaktion aus Bildung und Zersetzung von Nitramid dar. Eine dritte Reaktionsgleichung mit zur ADN-Bildungsreaktion analoger Stöchiometrie ist die bisher unbekannte Reaktion von Ammoniak mit Distickstoffpentoxid zu Lachgas und Ammoniumnitrat. Eine reaktionskinetische Modellierung des Reaktionsnetzwerkes ergab eine zweiparametrige bzw. vierparametrige Modellgleichung für die differentielle ADN-Selektivität. Untersuchungen ergaben eine gute Übereinstimmung zwischen Modell und Experiment hinsichtlich der ADN-Selektivität.

7 Literatur

[1] Sainte-Claire Deville, H.: Compt. Rend. 28 (1849), 257.

[2] Feuer, H; Nielsen, A.T.: Nitro Compounds - Recent Advances in Synthesis and Chemistry. VCH Publishers, Inc. New York, 1990.

[3] Colburn, C.: Developments in Inorganic Nitrogen Chemistry. Vol. 2, Elsevier, Amsterdam, 1973.

[4] Sainte-Claire Deville, H.: Lieb. Ann. 74 (1850), 103.

[5] Vast, P. Heubel, J.: C.R. Acad. Sc. 260 (1965), 5799.

[6] Tartakovsky, V.A.; Luk'yanov, O.A.: 25 th Int. Annu. Conf. ICT, Pfinztal/Germany, 1994.

[7] Schmitt, R.J.; Bottaro, J.C.; Penwell, P.E.; Bomberger, D.C.: US Patent No. 5.316.749; 31.05.1994.

[8] Brönsted, J.N.; Pedersen, K.: Z. phys. Chem. 108 (1924), 13.

[9] Löbbecke, S.; Krause, H.H.; Pfeil, A.: Propellants, Explosives, Pyrotechnics 22 (1997), 184.

[10] Scholz, E.: Karl-Fischer-Titration. Springer-Verlag Berlin, Heidelberg, 1984.

ISOPHTHALIC DIMETHYLOXAZIRIDINE AS A POTENTIAL BONDING AGENT FOR ROCKET SOLID PROPELLANTS.

(*)A. M. Kawamoto[a], M. M. Campbell[b] and M.F. Mahon[b]

[a]Chemistry Division, Space Activity Institute, São Jose dos Campos, SP, Brazil

[b]School of Chemistry, University of Bath, Bath, UK

Abstract: The synthesis, reactions and crystal structure of Isophthalic dimethyl oxaziridine are presented here. The synthesis was carried out utilising hydroxylamine-O-sulfonic acid to produce oxaziridine unsubsituted on the nitrogen, which was reacted *in situ* with isophthaloyl dichloride to give the corresponding Isophthatic dimethyl oxaziridine. It is an analogue of Isophthalic 2-methyl aziridine, a product which has been used as a bonding agent for Composite Solid Propellant. The oxaziridine was tested in oxidative reactions of sulfides to sulfoxides, styrene oxide, cyclohexene to cyclohexene oxide, and 1-(2-cyclohexenyl)-2-propanone to [1-(2-cyclohexenyl)-2-propanone] oxide.

Oxaziridines are three-membered rings constructed of three kinds of atoms having different electronegativities in adjacent positions. Oxaziridines have recently received attention as potential anti-tumor agents and as anologues of penicillin[1]. They also have been considered as potential irreversible alkylating inhibitors of the bacterial serine D,D-transpeptidase[2].

The title compound (1) is expected to be capable of oxidizing sulfides to sulfoxides and epoxidizing alkenes.

Besides being used as an oxidizing agent, the title compound is also envisioned to be a potential bonding agent for Rocket Solid Propellants.

Up to the present, many bonding agents, and their mechanism of action, have been studied. Several papers have been reported as to the action mechanism of bonding agents, and it was pointed out that the bond strength between AP and fuel-binder is dominated by the cohesive strength of binder bulk[3,4] and wetting efficiency of binder prepolymer on AP surface[4,5]. Therefore, of particular interest is the interaction mechanism which bonding agents play in the vicinity of the interface between AP and fuel-binder. Oberth[3] concluded that the bonding agents act by forming a tear-resistant layer around the filler particle, thus preventing peel. Nema[6] described that the bonding agents are either chemically reacting with AP or being absorbed by secondary intermolecular attraction.

Aziridine derivatives are known as bonding agents which have a high potential for improving the mechanical properties of the propellant grains composed of the fuel-binder, hydroxyl terminated polybutadiene (HTPB), and the solid fillers ammonium perchorate (AP) and aluminium powder[7]. It can be envisaged that certain analogues of these derivatives, such as the oxaziridines, will provide a propellant with higher performance, due to the oxygen in the three membered ring. The oxygen will increase the intermolecular

attraction (hydrogen-bonded) between the AP and the bonding agent, improving the mechanical properties of the propellants.

Isophthalic 2-methyl aziridine (**2**), a 3M product known as HX-752, has been successfully tested as a bonding agent for ammonium perchorate in composite solid propellants using hydroxyl terminated polybutadiene. This paper reports to the synthesis of its analogue, the Isophthatic dimethyloxaziridine (**1**), by the replacing of the N-C-C group by N-O-C (**Figure 1**).

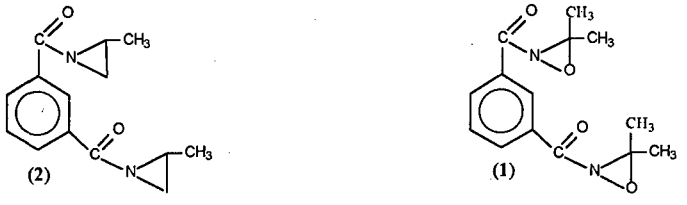

Figure 1 - Structures of Isophthalic dimethyl oxaziridine (**1**) and Isophthalic 2-methyl aziridine (**2**).

Results and Discussion

Isophthatic dimethyloxaziridine (**1**) was prepared from the coupling reaction of 3,3-dimethyloxaziridine with isophthaloyl dichoride (**Scheme 1**).

Scheme 1

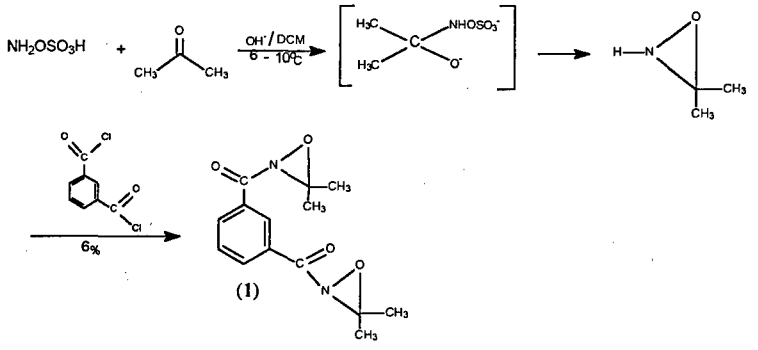

3,3-Dimethyl oxaziridine obtained from hydroxylamine-O-sulfonic acid and acetone, following the method described by Schmitz[8], was not isolated due to its limited stability and it was reacted *in situ* with Isophtahloyl dichloride giving the desired oxaziridine (**1**) in moderated yield.

This new compound was well characterized in the ^{1}H-NMR by a singlet at 1.61 ppm assigned to be the equivalent methyl groups. The ^{13}C-NMR also showed a typical singlet at 84.5 ppm which is characteristic of the oxaziridine function.

The formation of oxime instead of oxaziridine had to be considered (**Scheme 2**), since the ^{1}H-NMR, mass spectrum and elemental analysis for compound **1**, Isophthatic dimethyloxaziridine and compound **3** (oxime) could be the same. However, the resonance of the C=N group in the ^{13}C-NMR normally appears at 155-165 ppm[9].

Scheme 2

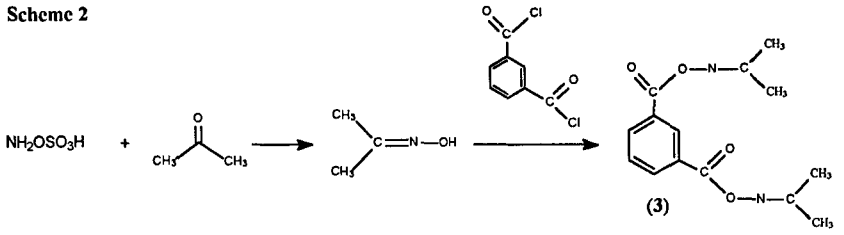

Isophthalic dimethyl oxaziridine was isolated as a crystalline solid which recrystallization from ethyl acetate and light petroleum ether (b.p. 60-80°C), gave crystal of suitable quality for a successful X-ray crystallographic structure determination (**Figure 2**).

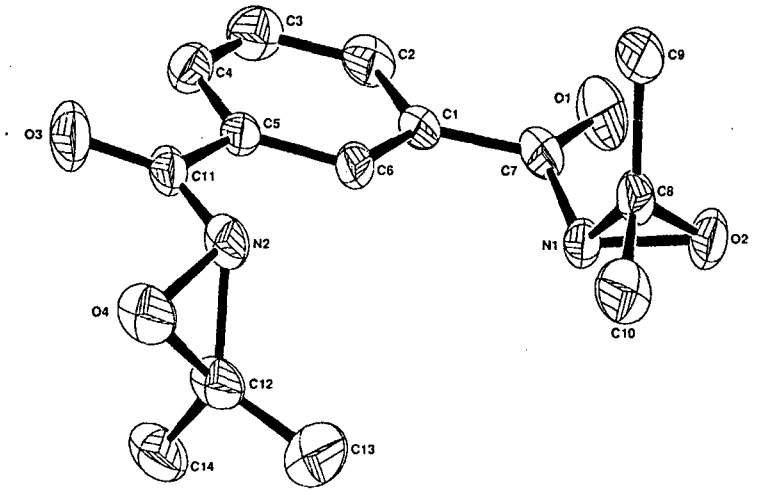

Figure 2 - X-Ray strucuture of Isophthalic dimethyl oxaziridine (**1**).

The methyl group from both oxaziridine rings in the compound appeared as only one singlet at 1.65 ppm at ^{1}H-NMR spectrum, and this indicated that the oxaziridine ring is conformationally mobile and can undergo a "flipping" movement that interconverts the nitrogen lone pair from one side of the XYZ plane to the other, thus converting the molecule between its enantiomer faster than the NMR time scale (**Figure 3**).

Figure 3 - Flipping movement of nitrogen lone pair.

The manufacture of the propellant using Isophthalic dimethyl oxaziridine as a bonding agent for composite solid propellant , is in progress and a comparison of the mechanical properties for propellants manufactured with Isophthalic 2-methyl aziridine (**2**) and Isophthalic dimethyl oxaziridine will be published later.

The oxaziridine was also tested in the oxidative reactions of sulfides to sulfoxides, styrene to styrene oxide, cyclohexene to cyclohexene oxide and 1-(2-cyclohexenyl)-2-propanone to [1-(-cyclohenenyl)-2-propanone] oxide (**Scheme 3**).

Scheme 3

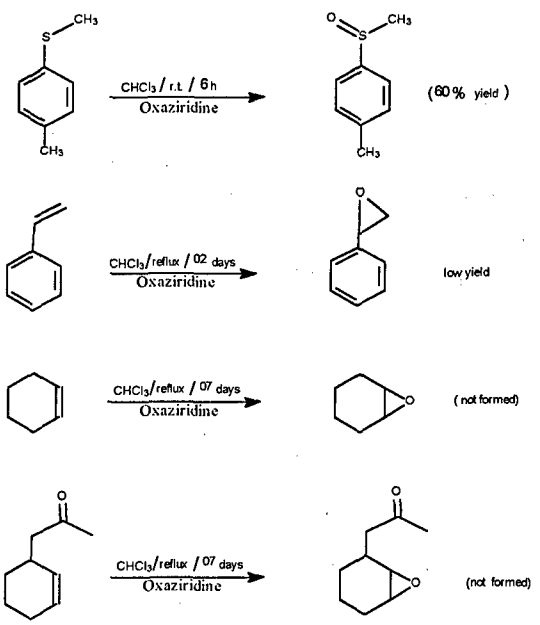

The oxidation of methyl tolyl sulfide proceeded successfully in 60% yield. The ^{1}H-NMR analysis and mass spectrum of the resulting compound confirmed the formation of methyl tolyl sulfide. A strong band at 1039cm^{-1} in the IR spectra also indentified the presence of a sulfoxide.

In the epoxidation of styrene only a low yield of styrene oxide was formed when the reaction was refluxed overnight in chloroform, and the reaction failed for the epoxidation of cyclohexene and 1-(2-cyclohexenyl)-2-propanone.

Future studies should possibly address the possibility of developing a catalytic system for oxidation, employing catalytic quantities of oxaziridine (**Figure 4**).

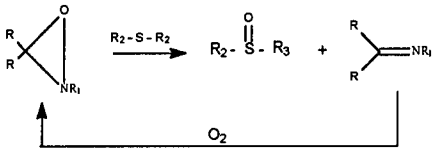

Figure 4 - Catalytic oxidation system for oxaziridine

Experimental Section

Melting points were determined on commercially available apparatus (Electrothermal melting point apparatus), or Büchi 510, and are uncorrected. Elemental microanalysis were carried out using a Carlo Erba 1106 Elemental Analyser. Infrared spectra were recorded in the range of 4000-600cm^{-1}, using a Perkin Elmer 1600 FT-IR spectrophotometer and peaks are reported (ν_{max}) in wave numbers (cm^{-1}). Spectra of liquid samples were taken as nujol mulls, or in chloroform solution, as indicated.

Proton NMR (^{1}H-NMR) spectra were recorded on a Jeol GX FT-270 (270 MHz) spectrometer although, where indicated, a Joel GX FT-400 (400 MHz) spectrometer was used. Carbon 13 magnetic resonance (^{13}C-NMR) spectra were recorded on a Jeol GX FT-270 spectrometer operating at 67.8 MHz and using 90 and 135 DEPT pulse sequences to aid multiplicity determination. Chemical shifts (δ) are expressed in parts per million downfield from internal tetramethylsilane (TMS). Mass spectra were recorded using a VG analytical 7070 E instrument with a VG 2000 data system. Eletron ionisation (E.I.) was produced using an ionisation potential of 70 eV. Chemcial ionistion (C.I.) was empolyed using isobutane as the reagent gas although, where indicated, ammonia was also used.

Isophthalic dimethyl oxaziridine (1). - A solution of hydroxylamine-O-sulfonic acid (0.01mol, 1.12g) in water (10ml) and NaOH 2N (5ml), was added rapidly to a stirred solution of acetone (13.6mmol, 1.0ml) in dichloromethane (30ml) and NaOH 2N (20ml) at 2-5°C. Immediately, a solution of isophathaloyl dichloride (0.005mol, 1.0g) in dichloromethane (10ml) was added, and the stirring was continued for an additional 10 min. The dicholomethane layer was then separated and dried over magnesium sulphate and filtered. Concentration on a rotating evaporator gave a white solid wich was recrystallised from ethyl acetate/light petroleum (b.p. 60-80°C) to give colourless crystals (0,16g, 6.0% yield): m.p. 114-116°C; R_f = 0.27(petrol-ethyl acetate 4:1); $\nu_{max}(CDCl_3)$/cm^{-1} 1716(C=O), 1432(oxaz.), 1200(P=O); $\delta_H(CDCl_3)$ 1.65(s, C$\underline{H}_3$), 7.66-8.61(m, Ar-$\underline{H}$); $\delta_C(CDCl_3)$ 22.14(s, C-$\underline{C}H_3$), 85.12(s, $C_{oxaz.}$), 128.97, 129.54, 132.07, 133.58(4s, Ar). 176.56(s, C=O); *m/z*(C.I.) 277(MH^+, 25%); *m/z*(E.I.) 276(M^+, 2%), 240(M^+ - $NOC(CH_3)_2$, 90), 146(62), 118(100), 90(78), 43(66). Anal. Calcd. for $C_{14}H_{16}N_2O_4$: C, 60.8, H, 5.8; N, 10.1:;Found: C, 60.6, H, 5.8; N, 10.0.

Acknowledgment. We thank the Conselho Nacional de Desenvolvimento Científico e Tecnologico - CNPq and Aerospace Technical Center - CTA, for the financial support of this work.

References

1. G. Sonsnovsky and J. Lukszo, *Eur. J. Med. Chem.*, 1984, **19**, 331
2. J. Marchand-Brynaert; Z. Bounkhala-Khrouz; H. Vanlierde and L. Ghoserz, *Heterocycles*, 1990, **3**, 971.
3. A. E. Oberth and R. S. Bruenner, *Trans. Soc. Rheol.*, 1965, **9**, 165.
4. K. Hori, Doctor Thesis, Tokyo University, 1987.
5. K. Hori, T. Fukuda, and A. Iwama, *Kogyo Kayaku*, 1987, **48**, 65.
6. S. K. Nema, P. R. Nair, A. U. Francic, and V. R. Gowariker, *AIAA Papers*, 1977, **77**, 932.
7. K. Kori and A . Iwama, *Propellants, Explosives, Pyrotechnics*, 1990, **15**, 99.
8. E. Schmitz, *Angew. Chem. Int. Ed. Engl.*, 1964, **3**, 333.
9. M. Cudic and R. Herrmann, *Magn. Reson. Chem.*, 1993, **31**, 461.

A STUDY OF SOME INSENSITIVE EXPLOSIVES

Pavel Mareček, Jiřina Pokorná, Pavel Vávra

SYNTHESIA a.s.
Research Institut of Industrial Chemistry
532 17 Pardubice - Semtín
Czech Republik

ABSTRACT

The conditions of the final stages of nitrotriazolone (NTO) and tetraoxadinitraminoisowurtzitane (TEX) syntheses have been experimentally verified and their effect on the physical properties of the above mentioned substances. The previously found correlation between $F = \rho \cdot \phi$ parameter and detonation enthalpy H has been confirmed using a series of low - sensitive substances. This finding enables the primary estimation of performances and sensitivities for new structures of the substances of this category.

INTRODUCTION

During the last tens of years, insensitive explosives have been receiving a great deal of attention in connection with low vulnerability. Apart from the influence of size and shape of crystals, their defects, compatibility with the binder and physical states on sensitivity to various internal stimuli, such molecule structures are observed that comprise a high energy content and are marked by a low sensitivity.

A very nice surwey of these types of compounds was published by Doherty and Simpson[1] where, in addition to basic characteristics, the values of performance and sensitivity for the individual substances are given as well. With the exception of long known triaminotrinitrobenzene (TATB) and nitroguanidine (NQ), among the suggested structures turned out to be very interesting nitrotriazolone (NTO)[2,3] and tetraoxadinitraminoisowurtzitane (TEX)[4,5] for their relatively simple and cheap preparation and acceptable values of their performance and sensitivity.

EXPERIMENTAL

We have specified the limits of the optimum conditions for the last steps of synthesis of NTO and TEX considering both quality of the products and technological feasibilities.

NTO

Nitration of 1,2,4-triazole-5one (TO) with nitric acid[2] at temperatures above 60°C leads to a high quality product (NTO) but is accompanied with considerable flow of nitrogen oxides. We consider this procedure to be technologically unsuitable.

The acceptable course of nitration of TO with nitric acid[3] is obtained at temperature ranging between 20 and 25°C; the optimum HNO_3/TO nitration ratio has been found 7.7 : 1 . Nitration time 2.5 hours seems to be sufficient, the value of dilution ratio varies around 0.5 . Crystallization has been carried out from water.

TEX

The initial compound for the last stage of synthesis , 1,4-diformyl-2,3,5,6-tetrahydroxypiperazine (DFTP),and glyoxal react in nitric acid and sulphuric acid (HNO_3 - H_2SO_4 mixture)[4] or in nitric acid only[5] forming TEX.We have found that the procedure[4] in mixed acids leads to the product comprising considerable quantity of acid in the crystal (1.5 to 2.5%). Boiling the product in water for 17 hours results in reduction of acid content to 0.44% only.

The reaction in nitric acid[5)] leads, at the same yield, to remarkably lower content of acid in crystal (0.16%) that remains unchanged even after 50 hours boiling in water.

According to our experiments, the optimum conditions are as follows:

* DFTP / glyoxal / HNO_3 ratio : 1 / 0.52 / 9.5

* temperature : 23 to 27°C

* time interval of reaction 24 hours is considered to be sufficient

* utilization of glyoxal in the form of water solution leads to reduced yield

Stability of both compounds has been determined by means of vacuum stability test and the results are given in Table 1.

Table 1 - Vacuum Stability Test NTO and TEX (20 hours)

Temperatura [°C]	NTO [ml.g^{-1}]	TEX [ml.g^{-1}]
110	0.06	0.05

Sensitivity of both compounds has been determined by means of the method of gap test for mixtures with trinitrotoluene (TNT). The results are given in Table 2 where P_{init} is the initiation pressure leading to detonation (50%).

Table 2 Sensitivity to shock wave (GAP TEST)

Specimen	Density [g.cm^{-3}]	P_{init} [GPa]
RDX/TNT (50/50)	1.662	3.65
TNT/NTO (50/50)	1.703	8.60
TNT/TEX (50/50)	1.700	9.50
TNT	1.585	10.75

DISCUSSION

The last stage of preparation of NTO and TEX is not complicated and due to accessibility of the initial compounds it is possible to obtain relatively cheap products. Their stability and low sensitivity enable them to be employed in charges of low vulnerability. It is, however, true that the performance of these compounds is lower than this of the commonly used explosives (RDX,HMX).

From the published set of compounds we have tried to form a new idea of properties of low sensitive molecules with a high performance, see Table 3. Other efficient explosives are also given here for the purpose of comparison; marking of the compounds is the same as in the quoted work[1].

For the given set we have calculated the Kamlet parameter ϕ from the equation:

$$\phi = N \cdot M^{1/2} \cdot Q^{1/2}$$

where N - quantity of gaseous products (mol.g^{-1})
M - mean molecule weight of the gaseous products
Q - heat of explosion (cal.g^{-1})

From the ϕ parameter and density ρ we have defined the F parameter[6]

$$F = \rho \cdot \phi$$

We have verified the existence of a very good correlation between F parameter and specific enthalpy H expressing the working capacity[7,8].

$$H = -0.0847 + 1.3771 \cdot F$$

This equation holds good also for compounds given in Table 3. The performance of the explosive is known to be dependent on the composition, heat of formation and density. The first two quantities are included in ϕ parameter and from Table 3 it can be seen that for each of low sensitive substances $\phi < 6$ and a good performance is gained due to their high densities; the substances with $\phi > 6$ are not likely to belong among the low sensitive ones but their performance will be high. The opposite statement, of course, is not possible to be applied; it cannot be said that all explosives with $\phi < 6$ are insensitive; there is a series of other factors that define the sensitivity of the substance.

The factor of great importance is density; its value for the substances given in Table 3 is altogether high. With one exception only, it is a matter of cyclic substances, predominantly with heteroatoms (N,O) in basic structure. In cases of purely carbon structures, the molecules with high density have relatively great number of substituents. More significant differentiation can be found at cage structures (CL - 20, TEX) at which the source of high density seems to be the presence of heteroatoms in the skeleton; the difference between densities is small compared with the number of - NO_2 substituents.

Even if the number of potential candidates for low sensitive and, at the same time, efficient explosives is relatively small (see Table 3), it is possible to imagine molecules with relatively low energetic content [$\phi < 6$] but with high crystal density. Except the known types of compounds, other heterocycles come on offer as e.g. oxaderivatives, possibly cage structures comprising heteroatoms in the basic skeleton.

REFERENCE

1. DOHERTY, R.M., SIMPSON, R.L.: 28 th. Int. Ann. Conference of ICT, Karlsruhe, 1997, p. 31 - 1
2. SPEAR, R.J., LOVEY, C.N., WOLFSON, M.G.: Technical Report MRL-TR-89-18 Victoria, Australia, 1989
3. BECUWE, A., DELCLOS, A.: Prop. Expl. Pyr. 18, 1 (1993)
4. RAMAKRISHNAN, V.T., VEDACHALAM, M., BOYER, J.H.: Heterocycles 31, 479 (1990)
5. YU, Y. - Z., et al.: 22 th Int. Pyr. Seminar, Colorado 1996, p. 425
6. KAMLET, M.J., JACOBS, S.J.: J. Chem. Phys. 48, 23 (1968)
7. LEE, J., BLOCK-BOLTEN, A.: Prop. Expl. Pyr. 18, 161 (1993)
8. MAREČEK, P., VÁVRA, P.: 28 th. Int. Ann. Conference of ICT, Karlsruhe 1997, p. 59-1

Table 3 Properties of explosives

		ρ [g.cm^{-3}]	ΔH_f [kJ.mol^{-1}]	ϕ	F	H [kJ.kg^{-1}]
1.	CL-20	2,03	415,6	6,85	13,91	19,11
2.	HMX	1,90	92,8	6,76	12,85	17,60
3.	RDX	1,80	60,2	6,78	12,20	16,66
4.	LLM-105	1,91	13,0	5,58	10,67	14,62
5.	LAX-112	1,86	164,0	5,58	10,38	14,21
6.	CL-14	1,94	86,3	5,30	10,30	14,13
7.	ADNBF	1,90	153,9	5,41	10,28	14,09
8.	TEX	1,99	-540,9	5,07	10,06	13,84
9.	2,4-DNI	1,76	20,5	5,70	10,05	13,70
10.	NTO	1,93	-130,0	5,09	9,82	13,47
11.	TATB	1,94	-139,5	5,00	9,70	13,33
12.	NQ	1,71	-92,4	5,58	9,54	13,00
13.	DAAF	1,70	443,5	5,58	9,49	12,92
14.	DATB	1,84	-98,8	5,07	9,33	12,77
15	TNT	1,65	-75,3	4,84	7,98	10,86

Abbreviations:

1. CL-20 - 2,4,6,8,10,12-hexanitro-2,4,6,8,10,12-hexaazatetracyclo [5,5,0,$0^{5,9}0^{3,11}$] dodekane
2. HMX - 1,3,5,7-tetranitro-1,3,5,7-tetraazacyclooktane
3. RDX - 1,3,5-trinitro-1,3,5-triazacyclohexane
4. LLM-105 - 2,6-diamino-3,5-dinitropyrazine-1-oxide
5. LAX-112 - 3,6-diamino-1,2,4,5-tetrazine-1,4-oxide
6. CL-14 - 5,7-diamino-4,6-dinitrobenzofuroxane
7. ADNBF - 7-amino-4,6-dinitrobenzofuroxane
8. TEX - 4,10-dinitro-2,6,8,12-tetraoxa-4,10-diazatetracyclo [5,5,0,$0^{5,9}0^{3,11}$] dodekane
9. 2,4-DNI - 2,4-dinitroimidazole
10. NTO - 3-nitro-1,2,4-tetrazol-5-one
11. TATB - 1,3,5-triamino-2,4,6-trinitrobenzene
12. NQ - nitroguanidine
13. DAAF - diaminoazoxyfuroxane
14. DATB - 1,3-diamino-2,4,6-trinitrobenzene
15. TNT - 2,4,6-trinitrotoluene

Orientation in the nitration benzoic acid in mixtures of sulfuric and nitric acids.

Yudin N.V., Zhilin V.F., Zbarskiy V.L.

Nitrobenzoic acid - important initial substance for synthesis of various chemical compound, including thermally stable (triaminotrinitrobenzene) and high (hexonitrobenzene) explosive substances. The conditions of their synthesis are interesting not only with practical, but also from a theoretical point of view, and thus the study of influence of various factors on isomer chemical composition of obtained products is quite useful.

We carried out nitration of benzoic acid in acid mixtures prepared from 70-107 % H_2SO_4 with a constant low concentration of nitric and benzoic acids. Isomeric composition of the obtained products was determined by the method GLC and HPLC. The outcome of the experiments is partially represented on the figure :

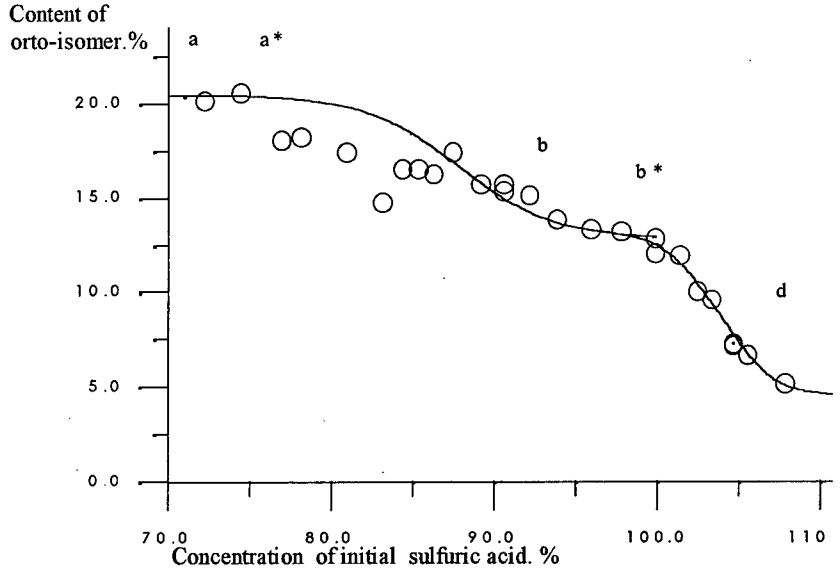

Dependence contents orto-isomer from concentration H_2SO_4, %, with 23°C.

As one can see from the figure raise of concentration sulfuric acid in an indicated interval the diminution content of o-nitrobenzoic acid in a nitration product from 20,2 % down to 5,2% . However the speed of a reaction in oleum area is considerably reduced. Can be explained by assumption that benzoic acid is nitrationed in three forms: by molecular (site a-a* on figure1), protonated (b-b *) and acyl cation (d). On the figure

demonstrate the results of calculation on the basis of the mathematical model composed because of the chemical scheme :

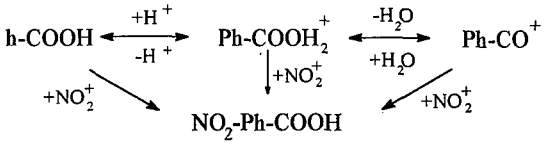

The obtained results show possibility to control isomeric structure of nitration products of oxygen-containing aromatic compounds (on example benzoic acid at the expense changing of medium acidity .)

NOVEL ENERGETIC MACROCYCLIC SYSTEMS OF FURAZAN SERIES

Lyudmila V.Batog, Lidiya S.Konstantinova, Vladimir Yu.Rozhkov, Oleg V.Lebedev, Margarita A.Epishina, Nina N. Makhova, Igor V. Ovchinnikov, Lenor I.Khmel'nitskii*

N.D.Zelinsky Institute of Organic Chemistry Russian Academy of Sciences, Leninsky pr. 47, 117913, Moscow, Russian Federation. Fax: + 7 095 135 5328; E-mail: mnn@cacr.ioc.ac.ru

ABSTRACT

This work deals with the synthesis and characterization of new macrocyclic systems containing different amounts of diazeno- and diazenoxydofurazanyl units (2-8) as well as diazeno- and diazenoxydodifurazanyl units (2-3). Macrocyclic derivatives with diazenofurazanyl fragments were for the first time synthesized by oxidative macrocyclocondensation of various diamines of furazan series: 3,4-diaminofurazan, 4,4'-diamino-3'3-diazenofurazan and diaminodifurazanyl under action of different oxidizers. Macrocycles with diazene oxide groups were obtained by two ways: by oxidation of diazene groups in polydiazenofurazanmacrocyclic derivatives and by oxidative macrocyclocondensation of furazan diamines, already containing diazene oxide fragments. Some characteristics of compounds obtained were studied and it was shown that specific features of these structures are: the high thermic stability (about 200 °C), the high formation enthalpy (700-1200 Kcal/kg) and the quite high density (1.7-1.93 g/cm^3).

INTRODUCTION

Furazan derivatives for a long time have occupied an important place among other nitrogen heterocycles as prospective components of high energetic materials. It is associated with their thermic stability, positive formation enthalpy and presence of active oxygen atom inside the cycle. A special interest in furazan derivatives stands with explosophoric groups, e.g. nitro, nitroxy, diazene and diazene oxide groups. From these groups the two latters make essential especially high contribution to the formation enthalphy of corresponding molecules. According to calculated data the macrocyclic systems of furazan series, containing diazene and diazene oxide groups in macrocycle have the particulary high characteristics [1]. The key purpose of this work consisted of the search of the approaches to design of macrocyclic compounds containing both diazeno- or diazenoxydofurazanyl(difurazanyl) units as well as both these units with different sequence.

SYNTHESIS

As the main approach to design of title macrocyclic systems the interaction of furazan series diamines with different oxidizers [$Pb(OAc)_4$, its mixture with Bu_4NBr, dibromoisocyanurate (DBI) and different hypohaliets] was studied. 4,4'-Diamino-3,3'-azofurazan (DAAF), 3,4-diaminofurazan (DAF) and 4,4'-diamino-3,3'-difurazanyl (DADF) were used as the starting diamines. The investigations were started from $Pb(OAc)_4$. It was shown that the treatment of DAAF with this oxidizer in chloro- and o-dichlorobenzenes at high temperatures gives 5-[4amino-1,2,5-oxadiazol-3-yl]-5H-[1.2.3]triazolo[4.5-c][1.2.5]oxadiazole **1** as a result of intramolecular cyclisation involving the deazene fragment and one of amino groups of DAAF [2]. The oxidation of DAAF with $Pb(OAc)_4$ in the presence of Bu_4NBr (Br^2 or NaOBr) results in essential change in the reaction pathway: instead of **1**, previously unknown macrocyclic compounds **2-4** are formed, products of intermolecular oxidative condensation of two, three and four DAAF molecules, respectively (Scheme 1) [3]. The macrocyclocondensation of DAAF occurs at room temperature in aprotonic solvents (MeCN, EtOAc, CH_2Cl_2, C_6H_6). Macrocycle **2** is a main reaction product and can be isolated in 60-70% yields, while compounds **3** and **4** are formed under the condition studied only in small quantities and can be isolated in < 1% yields.

In addition to DAAF, we also studied the reaction of DAF with $Pb(OAc)_4$ in the presence of Bu_4NBr. This reaction results in a mixture of macrocycles not only with an even number of diazenofurazan units, as is the case in the cyclocondensation of DAAF (compounds **2-4**), but also with an odd number of diazenofurazan units, macrocycles **5** and **6**. It should be noted that tetracycle **2** again predominates in this reaction (Scheme 1) [3].

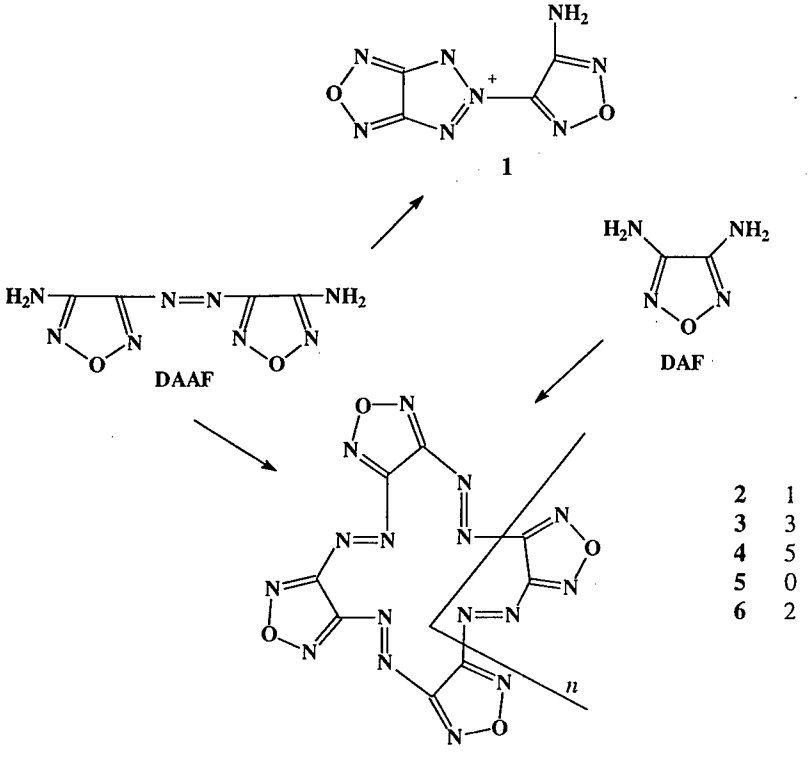

Scheme 1. Oxidizer - $Pb(OAc)_4$

As seen from above mentioned data $Pb(OAc)_4$ is suitable only for the synthesis of compound **2**. The more convenient oxidizer for the preparation of other macrocycles proved to be dibromoisocyanurate (DBI). At first we have used this oxidizer for the intramolecular cyclization of 4,4'-bis(4-aminofurazanyl-3-azo)-3,3'-azofurazan **7** to macrocycle **2** [4]. The oxidative cyclocondensation of DAF and DAAF under the action of DBI has been studied in different solvents (MeCN, C_6H_6, CH_2Cl_2, MeOH and different their mixtures). It was shown that the results of oxidation with this reagent depend significantly on the type of solvent, the diamine: DBI ratio

and their concentrations. The reaction of DAAF with a 2.5-6-fold excess of DBI in MeCN affords a mixture of macrocycle **2-4** with an even number of diazenofurazan fragments. Under the same conditions, DAF affords a mixture of these compounds with macrocycles **5** and **6** containing an odd number of diazenofurazan fragments (5 and 7, respectively), with compound **2** predominating substantially in the reaction products (Scheme 2) [5]. Variing the amount of a solvent, we found both conditions that allow to obtain tetradiazenofurazan macrocycle **2** in a preparative yield (88%) and conditions that increase the yield of macrocycles with six and eight diazenofurazan units **3** and **4** to 35% and 8%, respectively. It has been established that carrying out the reactions in considerably more concentrated (10-15 times) solutions than are needed for the preparation macrocyccle **2** favours the formation of macrocycles with the number of diazenofurazan units >4.

The reaction of DAAF with a two-fold excess of DBI in MeCN or with its 1.7-3-fold excess in other solvents resulted in the formation a mixture of tetracycle **2** and a linear product of the oxidative dimerisation of DAAF - compound **7** in a 15% yield. When the reaction with DAF was carried out in MeOH and DBI was added in portion three-membered macrocycle **5** was formed with 12.5% yield (Scheme 2) [5].

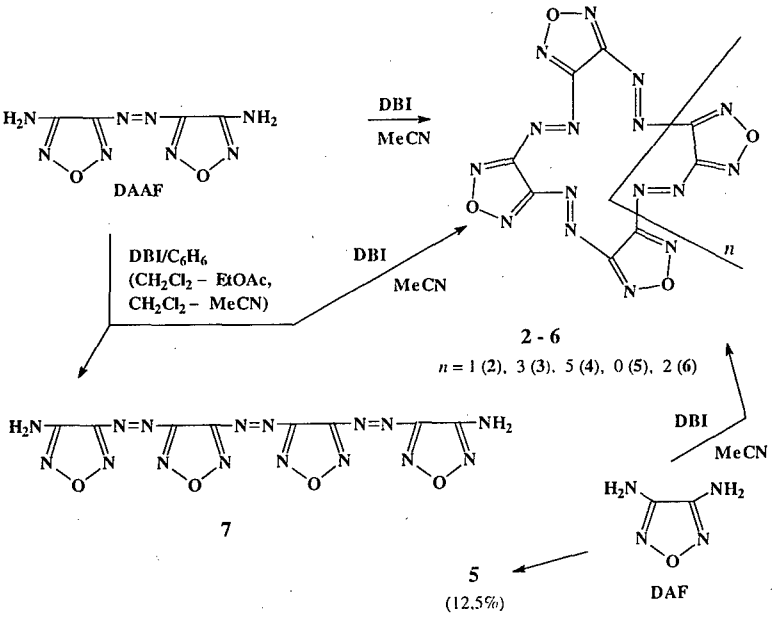

Scheme 2. Oxidizer - DBI

DBI was also used for the oxidative cyclocondensation of diaminodifurazanyl (DADF). The reaction DADF with DBI in MeCN resulted in synthesis of macrocycles **8** and **9**. Both compounds formed simultaneously with similar yields (32.5 and 28%, respectively) (Scheme 3) [6]. The formation of macrocycles with more than three subunits in this reaction is according to ^{13}C NMR data for the third fraction, which was isolated in a small yield by preparative chromatography of the reaction mixture. In this spectrum there are resonance signals due to carbon atoms in the same region as for **8** and **9**. The structure of compound **8** was confirmed by X-ray analysis [7].

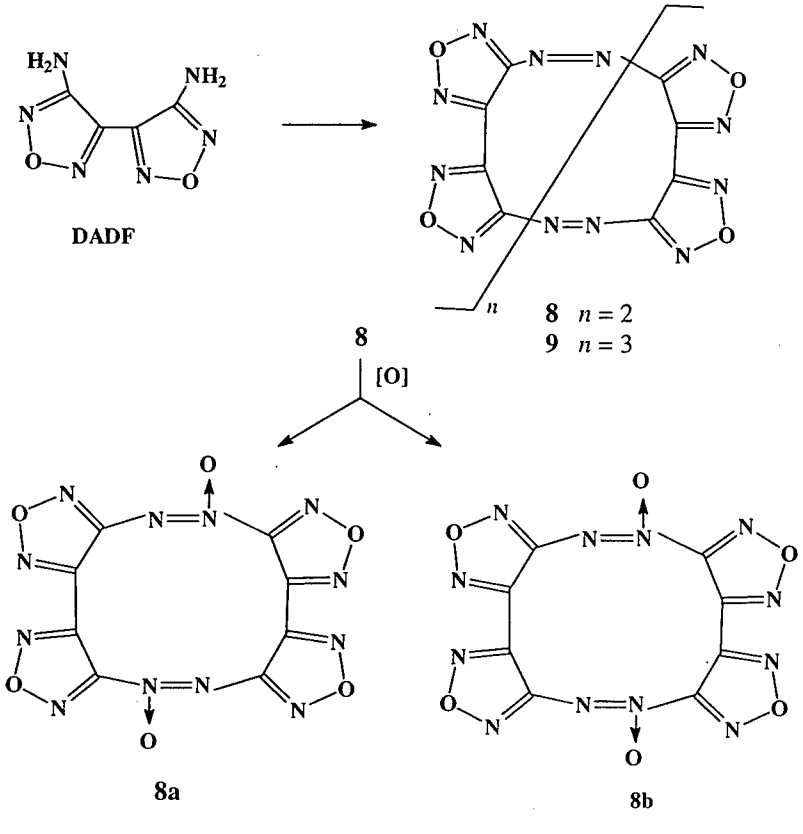

Scheme 3.

During the study of DAAF and DAF oxidation under action of $Pb(OAc)_2$ it has been proposed that acetyl hypobromite (AcOBr) is the oxidizer that directly reacts with these diamines [3]. In order to confirm this assumption, we studied the possibility of oxidative macrocyclocondensation of DAAF and DAF under the action of AcOBr and other hypohaliets (NaOBr, AcOCl and NaOCl). It was shown that the reactions of these diamines with AcOBr or NaOBr (high excess) in MeCN or EtOAc and DAAF with the same hypobromites in aqueous-methanol solution result in the cyclocondensation of both diamines to form polydiazenofurazan macrocycles **2-4** from DAAF and macrocycles **2-6** from DAF. It is noteworthy that the formation of the four-membered macrocycle **2** is the preferential process under the conditions studied upon both the action of DBI and $Pb(OAc)_2$ with Bu_4NBr. The study of the oxidation of the DAAF in AcCN by a small excess AcOBr (1:4) showed that DAAF did not react completely under this conditions, cyclocondensation occurred only insignificantly (6%) and linear product **7** was isolated in a yield of 37%. The same product and DAAF were found in the oxidation of DAF by hypobromites [8].

The study of the reactions of DAAF and DAF with hypochlorites (AcOCl, NaOCl) in aqueous-organic (MeCN, EtOAc) media allowed to establish that the reactivities of these diamines with respect to hypochlorites differ substantially. Macrocycle **2** was mainly obtained from DAAF, while the reaction of DAF resulted in the formation of the previously unknown compound difurazano[*c,g*]-1,2,5,6-tetrazocine **10** as a sole reaction product, the result of the oxidative cyclocondensation of two DAF molecules [8]. The formation of dimer **10** agrees with calculations made on the electrostatic potantials and relative energies of the hypothetic structures **10** and **11** [9]. According to these calculations, structure **10** should have the form of a "boat" with a *cis*-configuration of the furazan units relate to the diazene bridges. These calculations showed that structure **10** is considerably more energetically favourable (by 33 Kcal/mol) than pentalene structure **11**. In the aromatic series the pentalene structure **13** is thermodynamically prefered for the isomeric compound dibenzo[*c,g*]1,2,5,6-tetrazocine **12** [10]. The inversion dependence observed for the corresponding difurazano derivatives **10** and **11** is likely to be related to the instability of the system consisting of four fused five-membered polyheterocycles. Macrocycle **10** is not formed from DAAF, in which furazan cycles have *trans*-configuration to the diazene fragment. It is likely its formation from DAF carries out by another way (Scheme 4) [8].

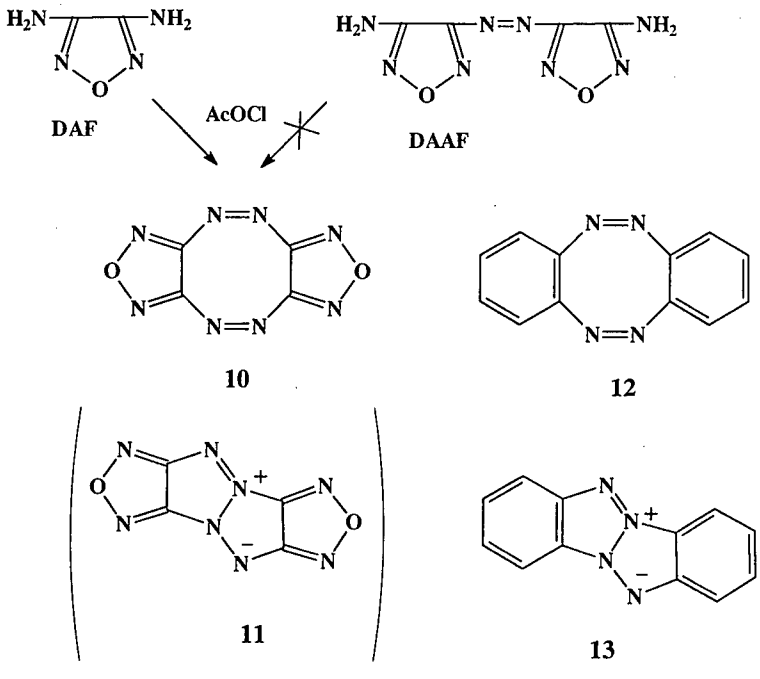

Scheme 4. Oxidizers - hypochlorites.

Among various chemical transformations of the synthesized macrocycles, the possibility of oxidation of the diazene fragments into diazene oxides ones was tested. For this transformation to proceed was found to require quite severe conditions (Karo acid in 20% oleum). The oxidation of macrocycle **2** was studied especially in detail. Since this compound incorporates four diazene groups, its oxidation can lead, in principle, to several species differing either in the number of diazene oxide groups (if the numbers of these groups are the same) or in the position of the N-oxide oxygen atoms with respect to the same furazan rings (whether it is distal or proximal) and in their spatial arrangement with respect to the macrocycle (directed inwards or outwards). It was shown that oxidation of the macrocycle **2** under action of Caro acid in oleum results in the conversion of all four diazene groups into diazene oxides those with formation of macrocycle **2a** (Scheme 5) [11]. Apart from compound **2a,** compound **2b** with one diazenofurazan and three diazene oxide furazan units was isolated in 5% yield. The tetraoxide molecule consists of planar furazan rings joined by strictly alternating diazene oxide bridges. This macrocycle is nonplanar: the furazan rings are

rotated with respect to one another through angles of 11.7, 6.7, 10.1 and 13.9° and the azo bond in each diazene oxide furazan fragment occurs in the ˜sc-ap and ˜sp-ap orientation with respect to the nearest C=N bond of the furazan ring [11].

The same oxidative mixture was used for the oxidation of the diazenes groups into diazene oxides ones in macrocycle **8**. Both diazene groups in compound **8** are subjected to oxidation, resulting in a mixture of isomeric diazene oxide derivatives **8a,b** in the ratio 1:1 (Scheme 3) [6].

To synthesize macrocyclic systems with an *a fortiori* known sequence of oxygen atoms in the diazene oxide groups, oxidation of diamines **14** and **15** through the action of DBI was studied. We found that the diamine **14** undergoes intramolecular oxidative cyclization to give dioxide **2c** whereas in the case of the diamine **15**, intermolecular cyclocondensation occurs yielding two isomeric compounds, namely, the dioxide **2c** (as the major product) and dioxide **2d** with another orientation of N-oxide groups [11].

The most part of macrocycles obtained and some their characteristics are presented in Table. As seen from table data these novel energetic macrocyclic systems of furazan series have the high formation enthalphy, the high melting points and rather high density.

Table
Some characteristics of compounds obtained

11	Compounds	M.p. °C	ρ g/cm³	ΔH_f° Kcal/kg (calculated)
1	**2**	210*	1.80	1093.0
2	**3**	280*	1.74	1093.0
3	**4**	246*	1.70	1093.0
4	**5**	116-117	1.69	1093.0
5	**8**	220	1.80	1095.0
6	**9**	300	1.77	1046.0
7	**10**	232*	1.69	1093.0
8	**2a**	234-235	1.94	796.2
9	**2c**	144-145	1.75	967.3
10	**2d**	105-106	1.75	967.3
11	mixture **8a,b**	137-140	1.86	964.5

*) with decomposition

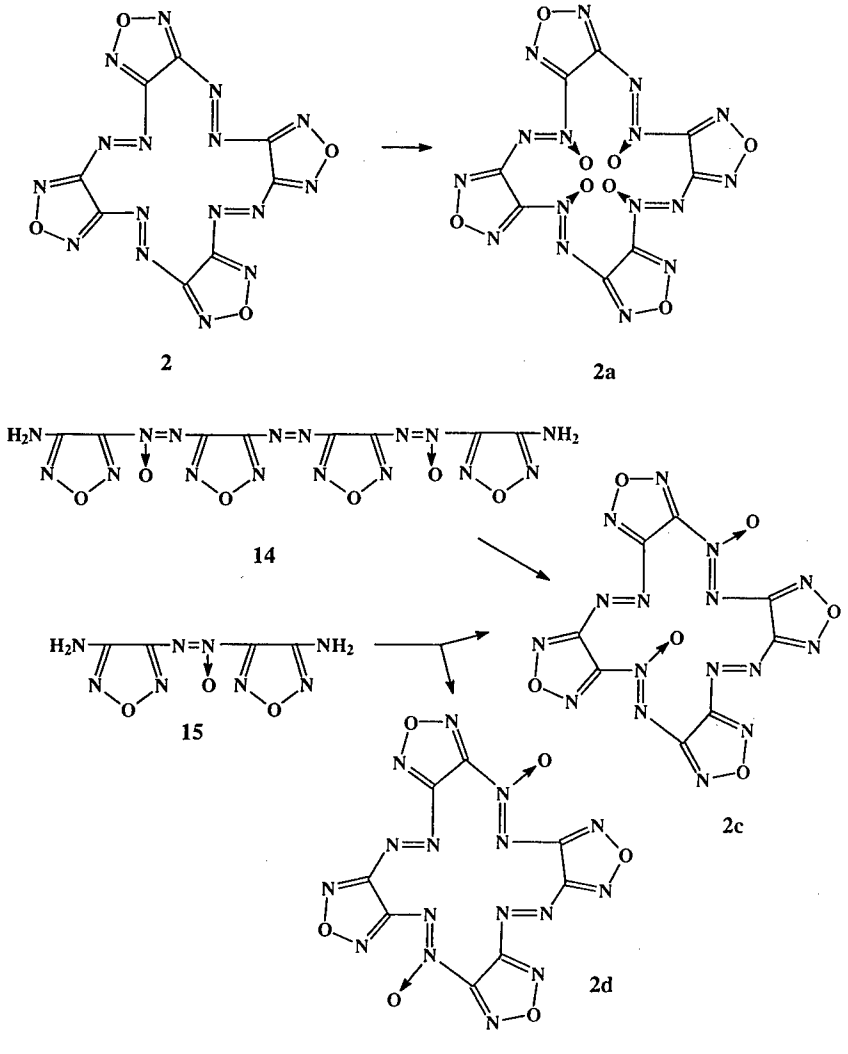

Scheme 5.

REFERENCES

1. T.S.Pivina, D.V. Sukhachev, A.V.Evtushenko, L.I.Khmel'nitskii, Propellant, Explosive, Pirotechnic, 1995, **20**, 5.

2. V.E.Eman, M.S.Sukhanov, O.V.Lebedev, L.V.Batog, L.I.Khmel'nitskii, Khim. Geterotsikl. Soedin., 1996, **344**, 253 (in Russian).

3. V.E.Eman, M.S.Sukhanov, O.V.Lebedev, L.V.Batog, L.S.Konstantinova, V.Yu.Rozhkov, L.I.Khmel'nitskii, Mendeleev Commun., 1996, 66.

4. L.V.Batog, L.S.Konstantinova, V.E.Eman, M.S.Sukhanov, A.S.Batsanov, Yu.T.Struchkov, O.V.Lebedev, L.I.Khmel'nitskii, Khim. Geterotsikl. Soedin., 1996, **345**, 406.

5. L.V.Batog, V.Yu. Rozhkov, L.S.Konstantinova, V.E.Eman, M.O.Decaprilevich, Yu.T.Struchkov, S.E.Semenov, O.V.Lebedev,, L.I.Khmel'nitskii, Russian Chem. Bull., 1996, **45**. 1189.

6. M.A.Epishina, N.N.Makhova, L.V.Batog, L.S.Konstantinova, L.I.Khmel'nitskii, Mendeleev Commun., 1994, 102.

7. L.Chertanova, C. Pascard, Supramol. Chem., 1993, **3**, 71.

8. L.V.Batog, L.S.Konstantinova, O.V.Lebedev, L.I.Khmel'nitskii, Mendeleev Commun., 1996, 193.

9. R.A.Carbony, J.E.Castle, J. Am. Chem. Soc., 1962, **84**, 2453.

10. P.Politzer, J.M. Seminario, Struct. Chem., 1990, **1**, 325.

11. V.E.Eman, M.S.Sukhanov, O.V.Lebedev, L.V.Batog, L.S.Konstantinova, V.Yu.Rozhkov, M.O.Dekaprilevich, Yu.T.Struchkov, L.I.Khmel'nitskii, Mendeleev Commun., 1997, 5.

TRINITROMETHYLARENES AND TRINITROMETHYLHETARENES -SYNTHETIC WAYS AND CHARACTERIZATION

Oleg V.Lebedev, Lija V.Epishina, Tatyana S.Novikova, Nina N.Makhova, Tamara I.Godovikova, Svetlana P.Golova, Aleksei V.Shastin, Elena A.Arnautova, Tatyana S.Pivana and Lenor I.Khmel'nitskii

N.D.Zelinsky Institute of Organic Chemistry, Russian Academy of Sciences, Leninsky pr. 47, 117913, Moscow, Russian Federation. Fax: +7 095 125 5328, E-mail: mnn@cacr.ioc.ac.ru

ABSTRACT

This work deals with different synthetic ways for the formation of trinitromethyl (TNM) derivatives of aromatic and heteroaromatic systems, that were developed at the N.D.Zelinsky Institute of Organic Chemistry. To obtain of TNM-arenes the interaction of N_2O_4 with nitro- and dinitromethyl(DNM)arenes as well as with aromatic aldehyde oximes were used. TNM-hetarenes were obtained through the interaction of N_2O_4 with heteroaromatic carboxaldehyde oximes and destructive nitration of the dicarboxymethylene fragment connected with heterocyclic compounds. As a result of these investigations a wide range of benzene, toluene, imidazole, thiophene, pyridine and 1,3,5-triazine TNM derivatives were synthesized, including bis- and tris-TNM derivatives of benzene, toluene and 1,3,5-triazine. Some characteristics of their compounds were also studied. Among the compounds obtained there are structures with zero oxygen balance, oxidants, hydrogenfree and high density compounds. Calculations of density, enthalpy formation and detonation velocity of obtained compounds and were carried out. Experimental and calculated data proved to be in a good correlation.

INTRODUCTION

The trinitromethyl (TNM) group connected directly with aromatic and heteroaromatic rings has been used for the energetic materials design during many years. Its introduction to the molecule is practically equivalent to the introduction of two nitro groups (one nitro group is necessary for full oxidation of the TNM group carbon atom). The replacement of part of aromatic ring carbon atoms by heteroatoms, e.g. nitrogen ones, could serve as an indirect way for increasing the oxygen balance. Introduction of TNM groups to nitrogen heterocycles could lead to structures with a high content of oxygen, including oxidants. So the key objective of this work is the development of the

methods for the preparation of TNM-arenes and TNM-hetarenes along with the study on some of their characteristics.

SYNTHESIS OF TNM-ARENES

The reaction of N_2O_4 with salts of DNM-arenes is a known method for the preparation of TNM-arenes [1,2]. In its turn, the key method for the synthesis of DNM-arenes is the reaction of N_2O_4 with aromatic carbonyl compounds oximes [3,4a-d]. However literature data on the direct transformation of these compounds into TNM-arenes was lacking till our works. Besides, TNM-arenes with two or three TNM groups in one molecule were not described. To develop the method for the preparation of such compounds we studied in detail the interaction of N_2O_4 with nitromethyl(**1**)- and DNM(**2**)-arenes as well as with aromatic carbonyl compounds oximes (**3**) [5-11]. As a results of these investigations it was stated that:

- Nitromethylarenes, especially their salts **1a**, yield a mixture of the compounds (DNM- and TNM-arenes and arylnitrolic acids) in this reaction, though one of these compounds can be mainly obtained by the alternation of reaction conditions. Arylnitrolic acids **4** were the key products in the reaction of **1a** with N_2O_4 at low temperature and DNM-arenes **2** were obtained at high temperature and in the excess of N_2O_4. Heminal nitronitroso derivatives **5** were isolated with low yield during the investigation of these reactions [10]. Compound **5** is likely to be a precursor of both DNM-arenes **2** and arylnitrolic acids **4.**
- Arylnitrolic acids **4** give TNM-arenes **7** with a high yield by the interaction with N_2O_4, however DNM-arenes **2** do not enter the reaction with this reagent. Precursors of TNM-arenes **7** are probably arylnitrolic acids **4**. We carried out a search of the best method for the preparation of **4** and found that such method is the interaction of aromatic carbonyl compound oximes **3** with 0.5 mole of N_2O_4 in ether [9].
- TNM-Arenes can be obtained in a *one-pot* reaction from aromatic carbonyl compound oximes **3** and N_2O_4.: at first, 0.5 mole of N_2O_4 was added to solution (or suspension) of **3** in ether at low temperature and than an excess of N_2O_4 in dichloroethane was used at 50 °C [9].

A general scheme for the preparation of TNM-arenes **7** was proposed based on the results obtained and literature data (Scheme 1). Consequently TNM-arenes **7** can be obtained by the interaction of N_2O_4 with nitromethylarenes salts **1a**, DNM-arenes salts **2a**, arylnitrolic acids **4** and aromatic carbonyl compound oximes **3.** All the compounds were isolated for the exception of aryldinitronitrosomethanes **6** that had been assumed as direct precursors of TNM-arenes **7.**

Scheme 1

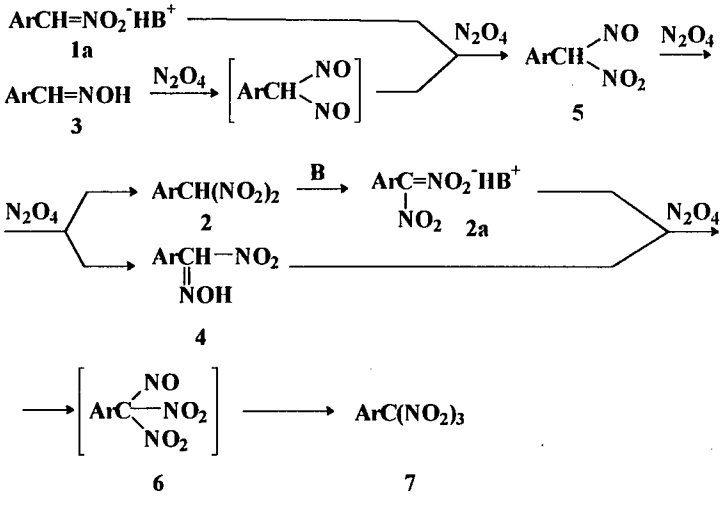

Ar = Ph, MeC_6H_4, m, p- $O_2NC_6H_4$, 3,5-$(NO_2)_2C_6H_3$

Compounds **6** were identified when the reaction of DNM-arenes salts **2a** with N_2O_4 was studied by ^1H, ^{13}C and ^{14}N spectroscopy in the temperature range from -40 to -20 °C. Becides ethoxycarbonyldinitromethane and dinitroethane sodium salts **2b,c** were studied in the same reaction [12,13]. Analysis of the dynamics of NMR spectra and nature of the final reaction products showed that the first step of the interaction of **2a** with N_2O_4 was nitrosylation of the dinitromethane anion to form dinitronitrosomethylene compounds **6a-c** irrespective of substituents. The structure of **6a-c** was confirmed by spectroscopy and blue color of their solutions, and dinitronotrosoethane **6c** was isolated.

The reaction not interrupted, futher transformation of DNM-arene sodium salts **6a** was irreversible oxidation by N_2O_4 to produce TNM-arenes **7**. If the reaction of N_2O_4 with salts **6a** was interrupted after 10 minutes, the key products were benzonitrile oxides **8** followed by their cyclodimerization to yield furoxans **9** (Scheme 2). Thus the reaction of DNM-arene salts with N_2O_4 can serve as both a method for the synthesis of TNM-arenes **7** and a new technique for generating nitrile oxides **8** and obtaining corresponding furoxans **9.**

Scheme 2.

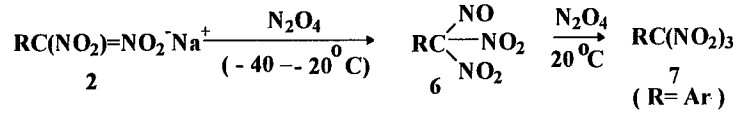

R = Ar(a), EtO_2C(b), Me(c)

Stability of 6: 6a - 2 min, -10 °C; 6b - 10 min, -10 °C; 6c - 7 days, 15 °C

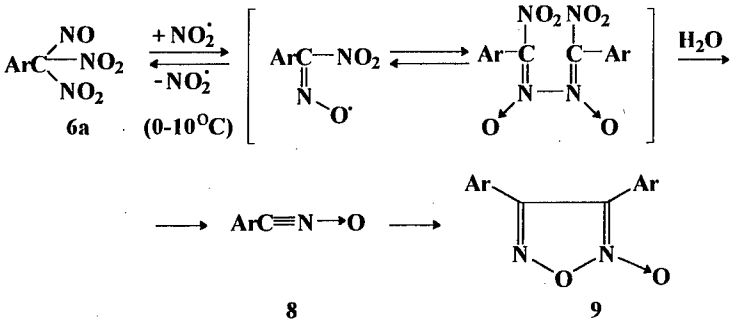

However the method for the synthesis of TNM-arenes 7 and furoxans **9** from DNM-arene salts **2a** and N_2O_4 has some constraints - TNM-arenes and furoxans are not formed in the presence of o-substituents near the DNM-group. 2,4,6-Trinitrophenyl(Pic)DNM sodium salt **2d** gives only corresponding nitrile oxide **8d.** Neither bis(Pic)furoxan **9d** nor Pic-TNM **7d** were obtained.This might be connected with a steric hindrence arising due to two o-nitro-groups. The interaction of 2,4,6-trinitrophenyl carboxaldehyde oxime **3d** gives only Pic-nitrolic acid **4d** (Scheme 3).

To obtain bis(**10**)- and tris-TNM(**11**)-arenes from corresponding bis- and tris-oximes **3e,f,** it was necessary to transform the latter into corresponding bis- and tris-nitrolic acids **4e,f,** though the transformation of three oxime groups needs more than 0.5 mole of N_2O_4. But the excess of N_2O_4 leads to the undesirable formation of DNM-derivatives. This opposition was overcome by the use

Scheme 3

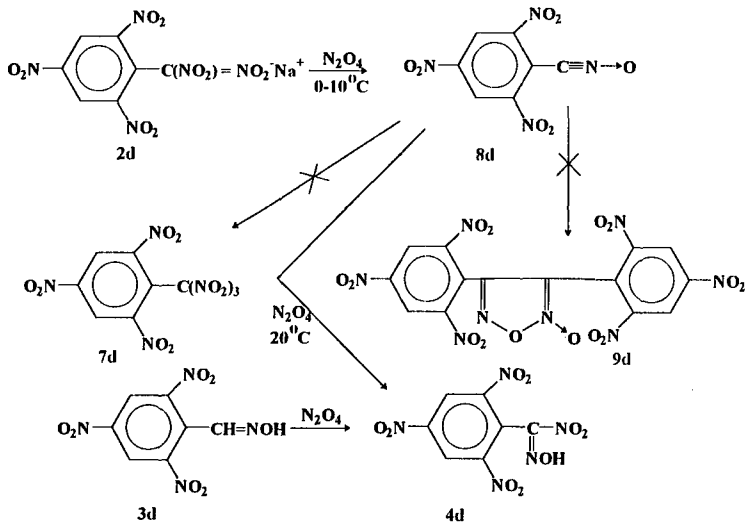

of solvents inclined to the complex-formation with N_2O_4 - dioxane or acetonitrile. Such method allowed to increase the concentration values of N_2O_4 without the DNM-arenes formation and, for the first time, to obtain bis- and tris-TNM-arenes - 1,3-bis(trinitromethyl)benzene **10a**, 3,5-bis(trinitromethyl)toluene **10b** and tris(trinitromethyl)benzene (or nonanitromesitilene) **11** (Scheme 4).

Scheme 4

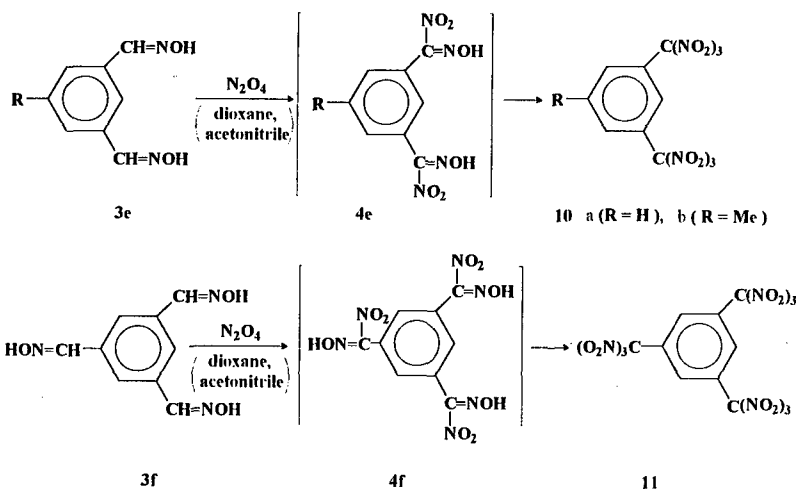

SYNTHESIS OF TNM-HETARENES

Thiophene- and imidazole-2-carboxaldehyde oximes **12a,b** in contrast to arylaldoximes enter readily the reaction with N_2O_4 to yield TNM-derivatives with simultaneous nitration of the heteroaromatic cycle [14, 15]. Nitration proceeds even in positions which are usually inert to electrophylic substitution reaction, e.g., in position 2(4) of the imidazole ring. 3,4-Dinitro-2-(trinitromethyl)thiophene **13** and a mixture of 4(5)-nitro-and 2,4(5)-dinitro-2-(trinitromethyl)imidazoles **14a,b** were obtained in good yields. Natural antibiotic azomichine **15** was synthesized during these investigation.

Furfuryl aldoxime **16** also interacts readily with N_2O_4, though in this case bis-(3,5-dinitrofurfur-2-yl)furoxan **9e** is obtained instead of the TNM derivative. Evidently this reaction proceeds over intermediate furfuryl nitrile oxide **8e.** Nitration of the heterocycle takes place, nevertheless . Pyridine-2- carboxaldehyde oxime **17** gives only TNM derivative **18.** It should be noted that the interaction of **17** with N_2O_4 could evidently proceed by over two different intermediates - nitrolic acid **4g** and DNM derivative **2g**, because of both these compounds are internal salts and structure intermediate product does not matter [14] (Scheme5).

Scheme5

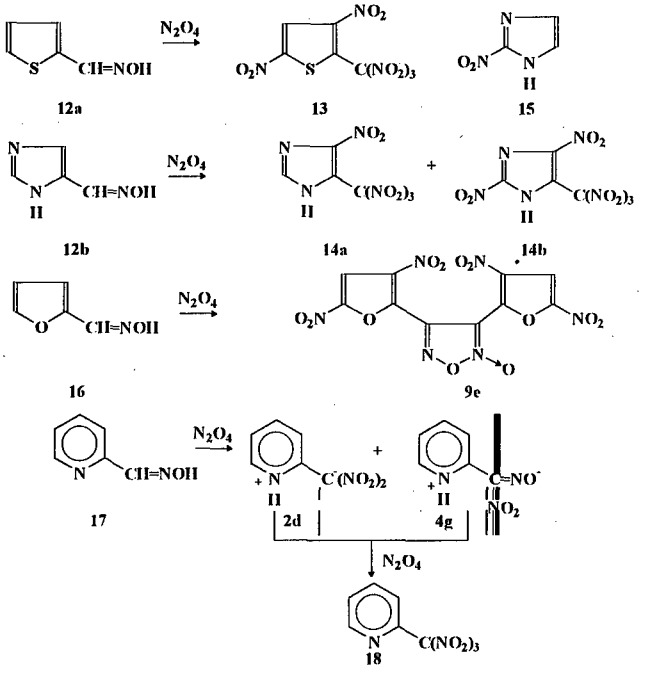

2,4,6-Tris(trinitromethyl)-1,3,5-triazine **20** was obtained by another method - destructive nitration of the carboxyl groups to trinitromethyl entities in 2,4,6-tris(dicarboxymethylene)-1,3,5-triazine **19** by action of concentrated HNO_3 [16]. Compound **20** is an oxidant and has high density - 2.00 g/cm^3, but it is unstable in the air and so is preferably stored as a solution in absolute CCl_4 at 5-10 °C. When undried dioxane is added to the solution of **20** in absolute CCl_4 one trinitromethyl group is subjected to nucleophilic substitution by hydroxyl one due to water present in dioxane. 2-Hydroxy-4,6-bis(trinirtomethyl)-1,3,5-triazine formed was isolated as a stable complex **21** with dioxane in the ratio 2:1 mol (Scheme 6). The structure of this complex was determined by X-ray analysis.

Scheme 6

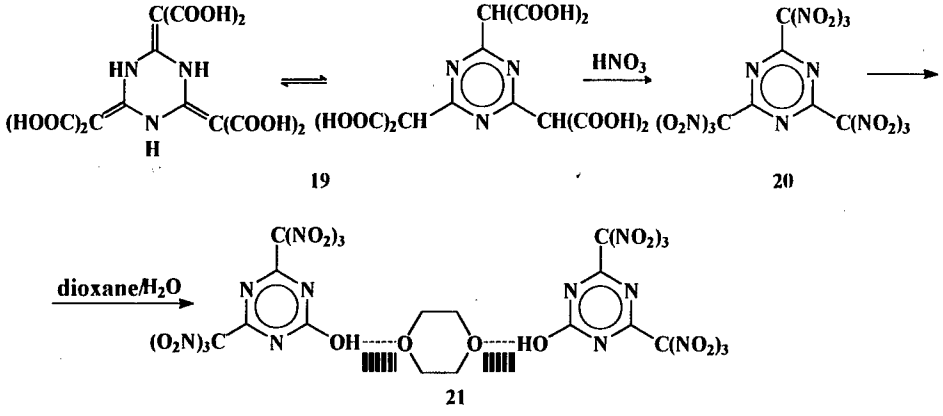

PROPERTIES OF SYNTHESIZED COMPOUNDS

In this section of paper the inclination to hydrolysis and thermic stability as weel as detonation parameters of compounds obtained are discussed in the first instante (Table 1). As a whole, it could be suggested that trinitromethul groups should be connected directly with the aromatic ring influencing each other easier than nitro groups. The most highly nitrated compounds among those synthesized are 3,5-dinitro-1-(trinitromethyl)benzene (Table 1, comp. 3) and tris-(trinitromethyl)benzene **11** (Table 1, comp. 6). All trinitromethyl derivatives obtained are stable to hydrolysis in contrast to hexanitrobenzene, which is quickly hydrolyzed to pentanitrophenol in the air.

There are another situation with heterocyclic trinitromethyl derivatives. The most highly nitrated compounds among these series of compounds are 2,4,6-tris(trinitromethyl)triazine **20** (Table 1, comp.10) and 2,4-dinitro-5-(trinitromethyl)imidazole **14b**. Mono-TNM-pyridine **18** is rather stable compound. So the presence of one pyridine nitrogen atom in molecule does not increase capacity of TNM group for hydrolysis. However the accumulation of pyridine nitrogen atoms in one molecule increases this capacity. The inclination to hydrolysis of the trinitromethyl group in compound **20** is very high (see Scheme 6) - like of one nitro group in hexanitrobenzene. The trinitromethyl group hydrolyses by action even of water traces. In compound **14b,** the influence of both the heterocyclic nitrogen atom and trinitromethyl group takes place. Such combined influence leads to increasing acidity of the "pirrolic" NH-group. Thus compound **14b** is very hydroscopic. This undesirable property disappears after replacing of the NH-group for the N-Me group or by obtaining salts (e.g. compound 8, Table 1).

As seen from Table 1 density of the obtaained compounds is not very high. Probably, it is connected with the influence of the volumetric trinitromethyl group on the crystal packing. Nevertheless, density increases in proportion to the accumulation of trinitromethyl groups both in aromatic and in heterocyclic rings. As was expected density of heterocyclic trinitromethyl derivatives was higher than that of aromatic ones. The compounds with three trinitromethyl groups are oxidants. Their detonation velocity is not very high, however it is not so low for compounds with negative formation enthalpy. These parameters along with density and detonation velocity were calculated by the methods of computer chemistry.

CALCULATIONS

As it is well-known the most important characteristics of explosive materials (as well as energetic compounds in general) are the detonation parameters and, first of all, the detonation velocity (D). For their estimation it is necessary to learn the main chemical-physical characteristics - that is molecular crystal density (d) and energy content (enthalpy of formation in solid state - $\Delta H_f^0(s)$). To estimate these parameters we can use one of the methods of computer chemistry - the Atom-Atom Potentials Method (AAPM) [17]. In this method the enthalpy of formation is calculated as the following:

$$\Delta H_f^0(s) = \Delta H_f^0(g) - \Delta H_s^0, \qquad (1)$$

where $\Delta H_f^0(g)$ is the enthalpy of formation in gas state; ΔH_s^0 is the enthalpy of sublimation. These calculations have been conducted by us in two main stages.

Firstly, we have estimated molecular characteristics in gas phase, since molecular models with optimized structural parameters in this state can be used to construct the elementary cell of crystal structure of compounds and in further calculation of their molecular crystal density. On the other hand, the enthalpy of formation in the gas phase $\Delta H_f^0(g)$ is needed to find the energy content in solid state (see (1)). The structure and energy of molecules in the gas phase were calculated with the use of the set of semi-empirical methods of quantum chemistry (program AMPAC [18]). The molecular geometry of compounds was obtained by one of this set (AM1 calculations). It is necessary to note that compared to other semi-empirical methods the AM1 one provides the best correspondence of experimental and calculated values of torsion angles between nitrogroups and benzene ring for nitro derivatives of benzene. On the other hand, theoretical values of bond length for NO_2-C groups are somewhat different from the average experimental ones available from literature [19]. Considering this fact, we used in our further calculations molecular structures with N=O and C-N bonds lengths equal to 1.22 and 1.48 Å (average experimental values), respectively, i.e. for our calculation we corrected the values of N-O and C-N bonds lengs accordingly to the experimental values and as for the torsion angles we used the AM1 calculated values.

The enthalpy of formation in gas phase was calculated by PM3 method since this method allows to estimate the energy content of nitro-oxygen contained compounds with the most accuracy comparable with the other semi-empirical quantum chemistry methods.

The second stage of our research was the estimation of molecular crystal density and sublimation enthalpy of compounds. It was conducted according to the original technique [20] making use of the method of Atom-Atom Potentials. For search of possible molecular packings of compounds under consideration we employed the PMC (Packing of Molecules in Crystals) program [21,22] of crystal lattice energy minimization.

As a result of these stages, the calculational values of enthalpy of formation in gas, crystal density, and sublimation enthalpy for compounds (1)-(6) were obtained. It gave us possibility to estimate detonational velocities for these compounds. The calculational results as well as the experimental values are presented in Table 1.

For almost all considered compounds, the calculated molecular crystal densities are higher than the experimental ones. Maximum estimated density was obtained for compound (5) and equals to 1.83 g cm^{-3}. The compounds (1) have higher density value than its structural isomer (2). This result is in the contrast to the experimental data (1.62 and 1.64, correspondingly) and the fact

is that the p-derivatives usually form denser packings than the m-derivatives. In comparison with benzene nitroderivatives (m-dinitrobenzene, p-dinitrobenzene and 1,3,5-trinitrobenzene) the trinitromethylarenes have higher crystal density values. For example, crystal density of 1,3,5-trinitrobenzene is 1.68 g cm^{-3}. In the same time, the compound (3) and (5) have densities of 1.83 g cm^{-3}. This differences may be due to higher molecular densities for trinitromethylarenes.

Among compounds under consideration the highest value of energy content was got for compounds (5) and equals to 27.0 kcal mol^{-1}. According to our calculations [23] this compound also has the highest detonational velocity (8.503 km sec^{-1}).

Table 1. Some physico-chemical and detonation characteristics of TNM-arenes and TNM-hetarenes (obtained and calculated (in brackets)).

	Compounds	m.p., °C	d, g/cm^3	D, km/sec	ΔH_f^0 (s), kcal/mol
1.	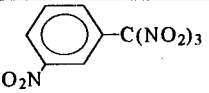	65	1.62 (1.73)	7.35 (7.49)	-82.6 (1.3)
2.	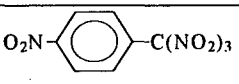	47	1.64 (1.71)	7.15 (6.75)	-105.7 (2.9)
3	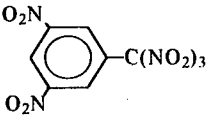	82	1.76 (1.83)	7.93 (8.05)	-140.4 (-4.6)
4	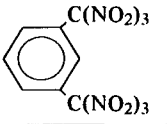	65	1.73 (1.73)	7.90 (7.86)	35.2 (16.9)
5	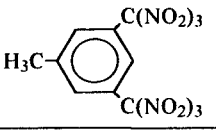	-	1.62	7.40	-207.3
6	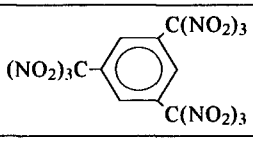	113	1.90 (1.83)	8.80, for $d_{1.85}$ (8.50)	84.9 (27.0)

7	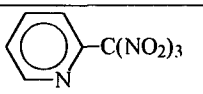	72	1.62 (1.67)	7.00 (7.25)	-10.6 (14.1)
8	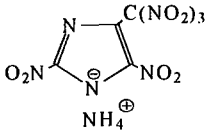	1,35	1.90	8.82, for $d_{1.84}$	-4.3
9	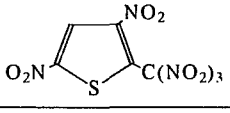	80	1.85	8.10	-
10	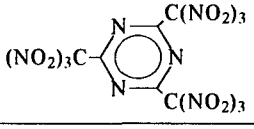	90-91	2.00* (1.91)	-	-

* Additive scheme calculation.

REFERENCES

1. A.N.Titov, V.V.Smirnov, Dokl. Acad. Nauk SSSR, 1952, **83**, 243 [Dokl. Chem., (in Russian), 1952].
2. Z.Fagi, W.Guangyi, Acta Armamentari, 1981,1.
3. G.Ponzio, Atti. Acad.Nat. Lincei (Rendiconf.) (5), 1906, **15**, 111,42,118.
4. a. S.S.Novikov, L.I.Khmel'nitskii, Usp. Khim., 1957, **XXVI**, 459 (in Russian); b. G.L.Rowley, M.B.Frankel, J. Chem. Eng. Data, 1964, **14**, 507; c. L.M.Andreeva, V.V.Perekalin, K.V.Altukhov, Zhurn. Obshch. Khim., 1980, **16**, 2445 (in Russian). d. F.Zhou, N.Fan., Huaxue Xuebao, 1985, **43,** 484.
5. S.S.Novikov, L.I.Khmel'nitskii, O.V.Lebedev, Zhurn. Obshch. Khim., 1958, 2298 (in Russian).
6. S.S.Novikov, L.I.Khmel'nitskii, O.V.Lebedev, Zhurn. Obshch. Khim., 1958, 2303 (in Russian).
7. S.S.Novikov, L.I.Khmel'nitskii, O.V.Lebedev, Yu.P.Egorov, Zhurn. Obshch. Khim., 1958, 2305 (in Russian).
8. S.S.Novikov, L.I.Khme'nitskii, O.V.Lebedev, Izv.Acad Nauk SSSR, Ser.Khim., 1960, 1783 (Bull, Acad. Sci USSR, Div Chem Sci., 1960, 1659).
9. S.S.Novikov, L.I.Khnel'nitskii, O.V.Lebedev, Izv.Acad.Nauk SSSR, Ser. Khim., 1960, 2019 (Bull. Acad. Sci. USSR, Div.Chem. Sci., 1960, 1873).
10. L.I.Khmel'nitskii, S.S.Novikov, O.V.Lebedev, Izv. Acad. Nauk SSSR, Ser. Khim., 1961, 477 (in Russian).

11. S.S.Novikov, L.I.Khmel'nitskii, O.V.Lebedev, V.I.Slovetsky, Izv. Acad.Nauk SSSR, Ser. Khim., 1961, 678 (in Russian).

12. N.N.Makhova, I.V.Ovchinnikov, V.G.Gubonos, Yu.A.Strelenko, L.I.Khmel'nitskii, Mendeleev Commun., 1992, 91.

13. N.N.Makhova, I.V.Ovchinnikov, V.G.Dubonos, Yu.A.Strelenko, L.I.Khmel'nitskii, Izv Acad. Nauk, Ser. Khim., 1993, 147 (Russ. Chem. Bull., 1993, **42**, 131).

14. S.S.Novikov, L.I.Khmel'nitskii, O.V.Lebedev, T.S.Novikova, Khim. Heterocycl. Soedin., 1970, 590 (Chem. Heterocycl. Comds, 1970,).

15. S.S.Novikov, L.I.Khmel'nitskii, O.V.Lebedev, T.S.Novikova, L.V.Epishina, Khim. Heterocycl. Soedin., 1970, 673 (Chem. Heterocycl. Comds, 1970,).

16. A.V.Shastin, T.I.Godovikova, S.P.Golova, V.S.Kuz'min, L.I.Khmel'nitskii, B.L.Korsunskii, Mendeleev Commun.,1995, 17.

17. .I.Kitaigorodsky. Molecular Crystals and Molecules. Academic Press: New York, London, 1973; A.J.Pertsin, A.I.Kitaigorodsky. "The Atom-Atom Potential Method in the Physics and Chemistry of Organic Molecular Solids", N.Y.: Springer 1986.

18. Clark T., A Handbook of Computational Chemistry. Erlangen: Wiley, 1990.

19. Arnautova E.A., Pivina T.S., Gladkikh O.P., Vilkov L.V. Comparative analysis of intramolecular parameters of nitrocompounds. Crystalline and gas phases. J.Mol.Struct., 1996,.**374**, 137-145.

20. Dzyabchenko A.V., Pivina T.S., Arnautova E.A. Prediction of structure and density for organic nitramines. J.Mol.Struct., 1996, **378**, 67-82.

21. Dzyabchenko A.V., Belsky V.K., Zorkii P.M. Kristallografiya, 1979, **24,** 221.

22. Dzyabchenko A.V. Kristallografiya, 1983, **28,** 788.

23. V.I. Pepekin, M.N. Makhov, Y.A. Lebedev, Dokl. Academy of Sciences (Chemistry), 1977, 232.

SYNTHESIS AND PHYSICAL-CHEMICAL PROPERTIES OF POLYCYCLIC NITROPYRAZOLES

Igor L. Dalinger, Tatyana K. Shkinyova, Svyatoslav A. Shevelev, Vladimir S. Kuz'min, Elena A. Arnautova, and Tatyana S. Pivina

N.D. Zelinsky Institute of Organic Chemistry, Russian Academy of Sciences

Leninsky prosp. 47, 117913 Moscow, Russia

Fax: +7 (095) 1355328; E-mail: dalinger@**cacr.ioc.ac.ru**

Abstract

Organic synthesis ways for completely nitrated carbone atom of C-C-bonded bi-, tri- and tetra-pyrazoles have been elaborated. Some characteristics of their properties have been calculated: enthalpy of formation, molecular crystal density, some detonation and combustion parameters as well as some parameters of sensitivity. As it follows from the results of this study, sensitivity of these compounds is comparable with HMX.

Wide-scope investigations of many years in the chemistry of nitrazoles (nitro-containing oxadiazoles, tetra- and triazoles, imidazoles and some others) have shown the prospects for synthesizing high-energy substances on the basis of such compounds. However compounds of the pyrazole sequence have remained actually unstudied so far.

At the same time moderately endothermic pyrazoles, if compared with tetra- and triazoles, in general, could be of high interest for generating materials with high energy capacity on their basis in terms of a current tendency to designing maximally safe, yet high-energy, explosives. Our choice of polycyclic pyrazoles was dictated by their feasibly predicted higher thermal stability.

Only two unsubstituted bipyrazoles 1 [1] and 3 [2] were described before our work. We managed to select conditions under which nitration proceeded on all unsubstituted carbon atoms of bipyrazole 1 (Scheme 1).

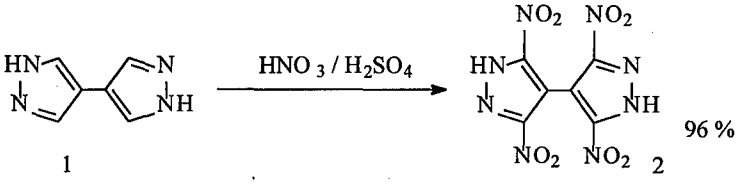

1 2

Scheme 1

As, while nitrating NH-pyrazoles with free-positioned 4 directly by the sulfuric-nitric acid mixture, 4-nitropyrazoles are formed which are not nitrated further on [3], we have chosen an indirect way to obtain tetranitrobipyrazole 6. It has a literature analog [3] and incorporates N-nitration of bipyrazole 3, rearrangement of the obtained N,N'-dinitrobipyrazole 4 and follow-up nitration (Scheme 2).

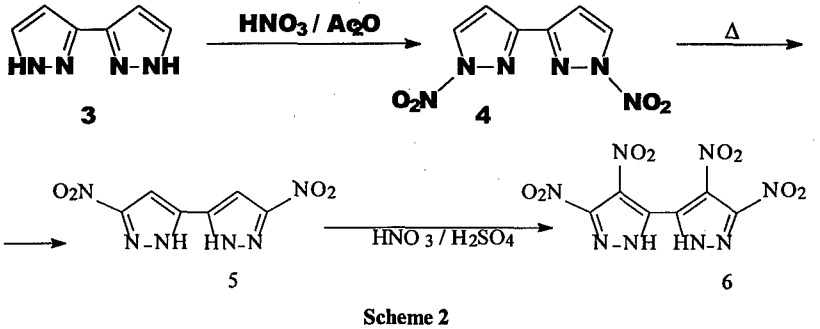

3 4 5 6

Scheme 2

The structure of tetranitrobipyrazoles 2 and 6 was confirmed by NMR ^{1}H, ^{13}C, ^{14}N, ^{15}N, IR, mass spectroscopy and elementary analysis data. The NMR ^{13}C spectrum registered under double heteronuclear resonance with selective unbinding of the nitro group from the

nitrogen atom enabled us to identify the proton position at the cyclic nitrogen atom in bipyrazole 6: it is fixed in position 1.

Tetranitrobipyrazoles 2 and 6 are rather strong two-base acids.

The molecular structure and conformation of tetranitrobipyrazoles 2 and 6 were identified with the help of x-ray analysis.

Crystals of tetranitrobipyrazole 2 crystal hydrate are monoclinal, elementary cell parameters are as follows: *a* = 11.142 (2), *b* = 14.078 (3), *c* = 8.236 (1)A, β = 108.98 (4)^0, V_{cell} = 1209.1 (13)A^3, *Z* = 4, spatial group *Cc*. An autodifractometer "Syntex-P2$_1$" (λMo-K$_\alpha$, graphite monochromator) detected 2,192 non-zero independent reflections. The structure was decoded by a direct SHELX-based method and specified in the anisotropic approximation for each non-hydrogen atom. Coordinates for H atoms were determined from the Fourier differential series. The final value of the R-factor was 0.028. Accuracy for determining bond lengths was ± 0.003 A, that for valence angles - ±0.2^0.

Tetranitrobipyrazole 6 crystals representing potassium salt of crystal hydrate are triclinal. Elementary cell parameters are as follows: *a* = 9.058 (6), *b* = 10.730 (7), *c* = 7.358 (6)A, α = 94.49 (7), β = 108.98 (4)^0, γ = 105.61 (4) ^{0}, V_{cell} = 640 (1)A^3, *Z* = 2, spatial group *P*1. A set of experimental data (1398 non-zero independent reflections) was obtained with the use of an autodifractometer "Syntex-P2$_1$" (λMo-K$_\alpha$, graphite monochromator). The structure was decoded by a direct SHELX-based method and specified in the anisotropic approximation for each non-hydrogen atom, for the exception of H atoms found from the Fourier differential series, up to the R-factor 0.047. Accuracy for

determining bond lengths was ± 0.004 A, that for valence angles - ±0.3°.

In molecule 2 (Fig. 1), to reduce steric hindrance arising from the presence of nitro substituents in ortho-positions to atoms C(4) and C(4a), heterocycle planes are almost straight angled around the C(4)-C(4a) bond and nitro groups are co-planar to respective heterocycles.

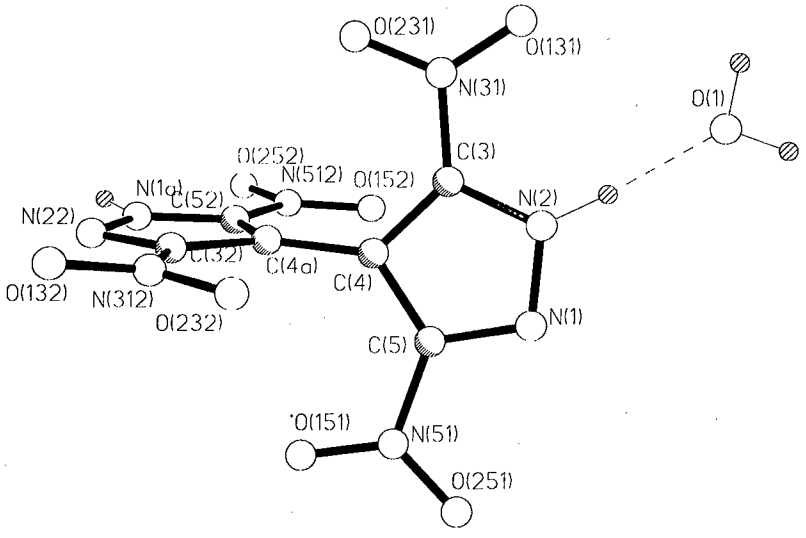

Figure 1. Structure of neutral molecule 2 (crystal hydrate).

The structure of anion 6 is shown in Fig. 2. Bond lengths and valence angles are close to standard values. A dihedral angle between heterocyclic five-member rings is 35.2°, nitro groups [N(3A), N(4A), N(4B), and N(3B)] form 24.4, 28.3, 24.5, and 36.3° dihedral angles, respectively, with heterocycle planes. The identified positions of nitro groups, non-planar to heterocycles they are bonded with, are governed by intramolecular steric contacts between O and N atoms of neighboring nitro substituents: distances O...O and O...N are close to

sums of corresponding Van der Waals radii of O and N atoms (1.4 A for O and 1.5 A for N).

Distinctions in the structure of bicyclic nuclei of tetranitrobipyrazoles 2 and 6 (rotation around the C-C bond that integrates heterocycles and various orientations of nitro groups towards pyrazole ring planes they are bonded to) discovered by the x-ray study evidence to the effect of the steric factor on the molecular conformation.

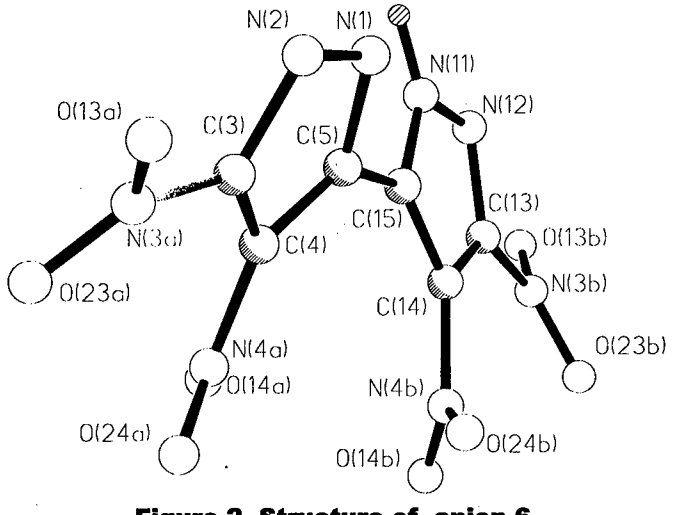

Figure 2. Structure of anion 6.

Till our research no general approaches to the synthesis of C-C-bonded polypyrazoles had been known. We designed a general method for synthesizing such polypyrazoles on the basis of C-(diformylmethyl)nitropyrazoles. To achieve this, in the row of pyrazoles and N-nonsubstituted azoles we pioneered double formulation of the C-polypyrazole methyl group (having employed Wilsmeier's reagent). In so doing, the methyl group should be activated by the nitro group

located at the neighboring carbon atom, i.e. C-(diformylmethyl)nitropyrazoles [4] are generated (Scheme 3).

The structure of 8 and 9 was determined using NMR ^{1}H, ^{13}C and confirmed by IR and UV spectroscopic data and elementary analysis. NMR ^{13}C spectroscopic data evidence that methyl groups in trimethinium salts 8 are not equivalent (proved by NMR ^{1}H data) and malondialdehydes 9 obtained exist fully in the enol form since signals from «carbonyl» and central carbon atoms of the diformylmethyl fragment are in the region of 179 - 180 ppm and 110 - 111 ppm , respectively, which is characteristic of the enol form of malondialdehyde itself [5], and there are no signals detected in the regions of 200 and 60 ppm , respectively, as it takes place in the case of the keto-form of β-diketons [6]. In addition, if dialdehyde 9a is considered, the signal from the «carbonyl» carbon atom at 179.73 in the NMR ^{13}C spectrum has a view of a broadened doublet with coupling constant 176.0 Hz and the signal at 11.14 ppm of the central carbon atom of the C-diformylmethyl grouping - that of a triplet with vicinal coupling constant 20.0 Hz, thus testifying that the latter lacks its own proton. Hence the diformylmethyl grouping was enolized and the proton was positioned between two oxygen atoms. The presence of the chelate-type hydrogen bond is also indicated by a broad band of OH group valence vibrations at 3200 cm^{-1} in IR spectra of compounds 9 obtained in KBr. It may be therefore stated that compounds 9, both in solution and in solid state, are in the enol form.

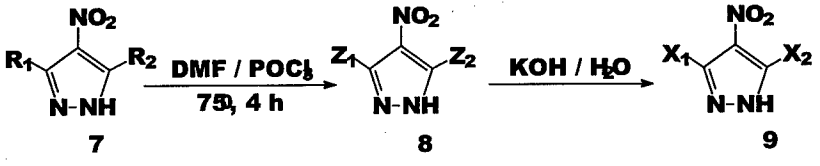

7 **8** **9**

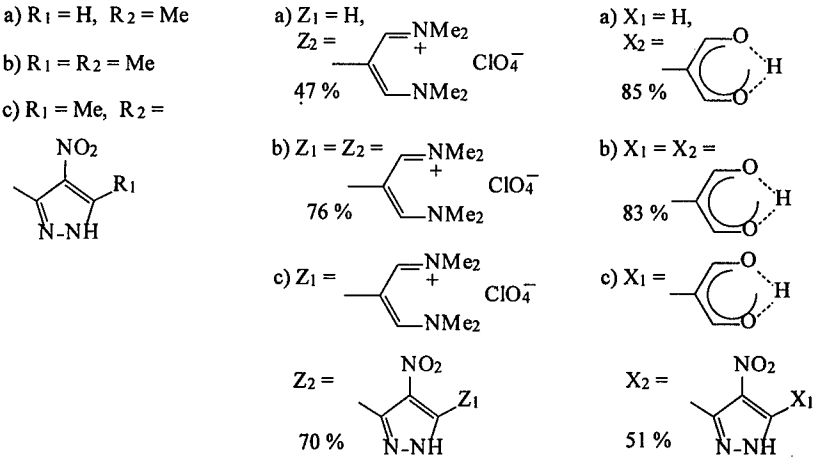

Scheme 3

Having treated C-(diformylmethyl)nitropyrazoles 9 with hydrazine, we obtained relative bi-, tri- and tetracyclic 4-nitropyrazoles 10 (reaction B). Yet it was found that this objective could be successfully attained using precursors of 9 - relative perchlorates of trimethinium salts 8 (reaction A). This would drastically facilitate the method for generating polycycles 10 and increase their yield [7] (Scheme 4).

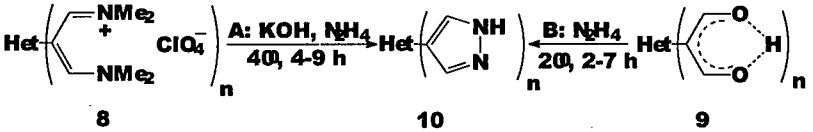

8 **10** **9**

Scheme 4

Het, n	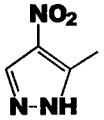 **n = 1**	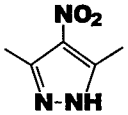 **n = 2**	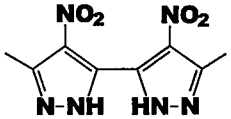 **n = 2**
Yield, %, in A:	**81**	**98**	**91**
Â*:	**91**	**48**	**71**
Â:**	**77**	**40**	**36**

*** yield calculated for compound 9;**

**** yield calculated for compound 8.**

Nitration of the synthesized polypyrazoles was studied. It turned out that bipyrazole 10a could not be nitrated by C atoms in a wide range of varied conditions. At the same time, in nitration of tripyrazole 10b and tetrapyrazole 10c with the sulfuric-nitric acid mixture, we achieved, for the first time, C-C-bonded pentanitrotripyrazole 11 and hexanitrotetrapyrazole 12 with free NH fragments fully nitrated by carbon atoms (Scheme 5). Their structure was confirmed by NMR ^{1}H, ^{13}C, ^{14}N, ^{15}N spectroscopic data.

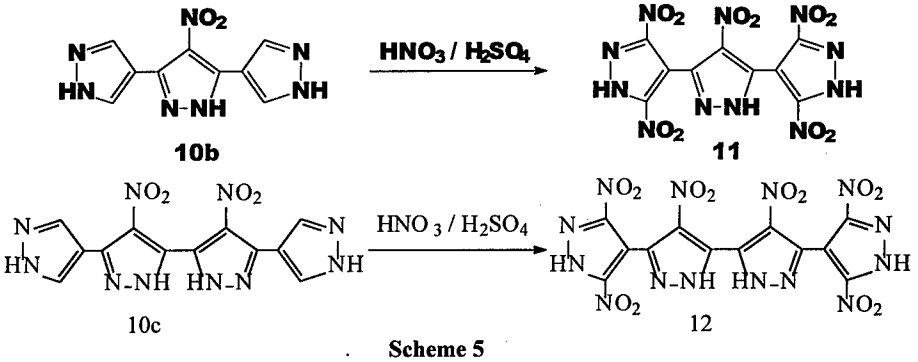

Scheme 5

To evaluate the future usability of the synthesized compounds as energetic materials we calculated their key physical-chemical characteristics (molecular crystal density, energetic and certain performance parameters) and detonation velocity.

Molecular mechanics, quantum chemistry and Atom-Atomic Potential Functions [8] methods were employed for calculating molecular crystal densities (d) and formation enthalpies in the gas phase (ΔH_f^0(g)) necessary for subsequent calculations of the energy content in solid substances (ΔH_f^0(s)).

First, with the help of semiempiric quantum chemical methods we evaluated structural parameters for molecules and formation

enthalpies of the compounds under study (2, 6, 11, and 12) in the gas phase. The evaluation of molecular geometry was conducted by the AM1 method and that of enthalpies of formation by the PM3 method as the former enables to calculate structural parameters of nitrogen-oxygen-containing compounds most realistically and the latter (PM3) is most accurate in the semiempiric pool of methods for estimating the energy content of such compounds in the gas phase. In our calculations we used the known AMPAC program complex [9] that allowed to take advantage of various semiempiric quantum chemical methods with a focus on a specific problem.

As shown by the analysis of theoretical values for intramolecular parameters (bond lengths, valence and torsion angles), those values differ noticeably from the mean experimental ones. The highest deviation refers to bond lengths of N=O nitro groups with the mean theoretical value being 1.18 Å and experimental - 1.22 Å. Yet the AM1 method allows to reproduce the orientation of nitro groups towards heterocycle planes close to the experiment for related compounds. A wide gap between experimental and calculated intramolecular parameters could be narrowed once x-ray analysis data are considered. Having taken into account these data in the calculation of potential crystal packages of the studied compounds, we used molecule geometry obtained from the calculation done by the AM1 method though having corrected the obtained results in terms of mean values known from the experiment (these data were taken from the Cambridge database for X-ray data [10]). As for torsion angles, they were in line with the calculated values.

At the next step we calculated molecular crystal densities and sublimation enthalpies (ΔH_s^0) for compounds 2, 6, 11, and 12. For the evaluation of these characteristics we used a search technique for molecule optimal packing in the crystal developed by us on the grounds of the AAPF method and detailed in [11]. Digital calculations were carried out with the help of the PMC program [12, 13]. Then, basing on the obtained values for ΔH_f^0(g) and ΔH_s^0 and following the known equation ΔH_f^0(s) = ΔH_f^0(g) - ΔH_s^0 , the energy content of compounds 2, 6, 11, and 12 in a solid state was estimated.

Table 1. Physical-chemical and detonational parameters of compounds.

Compound	2	6	11	12
ΔH_f(s), kcal/mol	41.0	42.0	77.9	111.9
d, g/cm^3	1.89	1.82	1.84	1.76
Detonational parameters:				
Velocity, km/s	8.219	7.964	8.232	7.737
Detonation pressure in the Jouget point, kbar	338.3	296.9	309.1	274.6

A further step in our research was the evaluation of detonation characteristics done on the basis of a number of known empiric schemes [14].

The values obtained for physical-chemical and detonation parameters of compounds 2, 6, 11, and 12 are listed in Table 1.

Reviewing the results, it should be noted that among the compounds under consideration compound 2 has the highest molecular crystal density (1.895 g/cm^2). This is likely to have resulted from both this compound having the less molecular volume and a more efficient package of its molecules in the crystal (Fig. 3). In its turn, the lowest density was found with compound 12, this probably being

accounted for by the molecule conformation specifics (namely, the absence of symmetry elements that leads to the inefficient molecule crystal package).

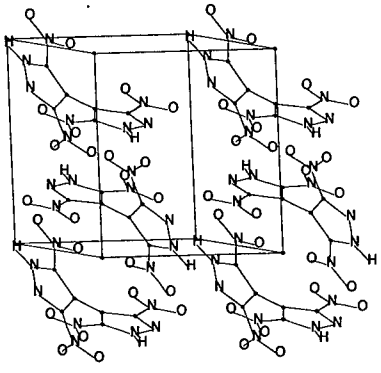

Figure 3. Calculated crystal package for compound 2.

Generally, compounds 11 and 12 were identified to have the highest energy capacity among the discussed substances. The highest detonation velocities however correspond to compounds 2 and 11 (8.219 and 8.232 km/sec, respectively).

It is acknowledged that, in addition to the physical-chemical aspect, the evaluation of performance characteristics of a substance and primarily its sensitivity to mechanic impact is significant for assessing usability of high-energy materials. We accomplished the usability assessment employing the QSPR-based (Quantitative Structure Property Relationships) computational technique described in [15]. As shown by our calculations, compound 6 has the critical thickness of the detonation-capable layer ($^2\Delta_{cr}$ = 66μcm) being approximately equal to HMX (68 μcm (exp)) with the corresponding calculational value [15] of 60 μcm. According to our calculations, compound 2 having $^2\Delta_{cr}$ = 72 μcm is less sensitive than compound 6.

So, we obtained compounds are inferior to HMX by the set of energetic parameters and are close to HMX in sensitivity to mechanical impact.

References

1. **Trofimenco S., J. Org. Chem., 29 (1964) 3046.**
2. **Effenberger F., Chem. Ber., 98 (1965) 2261.**
3. **Kanishchev M.I., Korneeva N.V., Shevelev S.A., and Fainzilberg A.A., Khimiya Geterotsikl. Soed. (in Russ.), (1988) 435.**
4. **Dalinger I.L., Shkinyova T.K., Shevelev S.A., Kral V., and Z. Arnold, Izv. Akad. Nauk, Ser. Khim. (in Russ.), (1993) 1273.**
5. **Bertz S.H., Dalbagh G., J. Org. Chem., 55 (1990) 5161.**
6. **Steigl A., Weith R.W., Braun M., Lieb. Ann. Chem., (1989) 99.**
7. **Shevelev S.A., Dalinger I.L., Shkinyova T.K., and Ugrak B.I., Izv. Akad. Nauk, Ser. Khim. (in Russ.), (1993) 1941.**
8. **Kitaigorodsky A.I., "Molecular Crystals and Molecules". Academic Press: New York, London, 1973; .Pertsin A.J., Kitaigorodsky A.I., "The Atom-Atom Potential Method in the Physics and Chemistry of Organic Molecular Solids". N.Y.: Springer, 1986.**
9. **"A General Molecular Orbital Package (IBM Version)", Stewart J.J.P., QCPE 464, M. Dewar Group, University of Texas, Austin, Texas, 78712.**
10. **Allen F.H., Brice M.D., Cartwright B.A., Doubleday A., Higgs T., Hummelink T., Hummelink-Peters B.G., Kennard O., Motherwell W.D.S., Rodgers J.R., Watson D.G., Acta Cryst., B35 (1979) 2331.**
11. **Dzyabchenko A.V., Pivina T.S., Arnautova E.A., J. Mol. Struct., 378 (1996) 67.**

12. Dzyabchenko A.V., Belsky V.K., Zorkii P.M., Kristallografija (in Russ.), 24 (1979) 221.

13. Dzyabchenko A.V., Kristallografija (in Russ.), 28 (1983) 788.

14. Pepekin V.I., Makhov M.N., Lebedev Y.A., Dokl. Academii Nauk (in Russ.), (1977) 232.

15. Afanas'ev G.T., Pivina T.S., Sukhachev D.V., Propellants, Explosives, Pyrotechnics, 18 (1993) 309.

3,3-Bis(1-Fluoro-1,1-dinitromethyl) difurazanyl Ether

Aleksei B. Sheremetev

N.D.Zelinsky Institute of Organic Chemistry,
Russian Academy of Sciences,
Leninsky Prosp., 47, Moscow 117913, RUSSIA

Fax: +7 (095) 135 5328,
E.mail: sab@cacr.ioc.ac.ru

Despite the fact that 1-fluoro-1,1-dinitromethyl units play important role in construction of energetic plasticizers and polymers, heterocyclic compounds incorporating the unit have received little attention compared to their aliphatic congeners.

Bis(1-fluoro-1,1-dinitromethyl)difurazalyl ether, **FOF-13**, was synthesized and evaluated in terms of insensitivity and performance. The compound is high dense, insensitive to impact, and very stable to thermal stimuli. Performance was found to be higher to bis(2-fluoro-2,2-dinitroethyl)formal, **FEFO**. The synthesis of **FOF-13** is a multy-step pathway using another energetic plasticizer 3,3-dicyanodifurazanyl ether, **FOF-2**, as a precursor.

INTRODUCTION

In an earlier communication[1] we disclosed our initial results on the discovery of analogies and varieties between two series of compounds, namely picryl derivatives (**Pic-R**) and their nitrofurazanyl (**Nif-R**) analogs. The investigation showed that (**i**) the incorporation of **Nif** in place of **Pic** in the molecule decreased *melting point* on 50-200°C; (**ii**) the *density* of **Nif** , as a rule, was 0.1 - 0.2 g/cm^3 greater than for **Pic** analogs; (**iii**) **Nif** compounds possessed high positive *heat of formation*, and **Pic** analogs ranked below them in the parameter from 100 to 500 kcal/kg. A more recent study[2] showed that installation of furazan moieties to pentaerythritol derivatives provides a new and

versatile approach to the synthesis of high energy monomers and polymers which demonstrates excellently compatible both with each other and with earlier prepared by us high energetic furazans.[3-7]

The properties of furazans suggest that they would be potential building blocks for construction of insensitive high energy plasticizer to new and common high energy materials.

As a part of a broad program to developing versatile processes providing syntheses of various high energetic materials from common precursor, we have tested some pathways for modification of 3,3-dicyanodifurazanyl ether (**FOF-2**)[8] which is insensitive high energy co-plasticizer.

RESULTS and DISCUSSION

Because of the interest in the difurazanyl ether derivatives, as insensitive thermal stable energetic materials, the synthesis of the related compound, bis(1-fluoro-1,1-dinitromethyl)difurazanyl ether (**FOF-13**), was investigated. The efficiency and the relative simplicity of the preparation and subsequent base promoted coupling reaction of 3-cyano-4-nitrofurazan **1** to yield **FOF-2** was first noted by us (Scheme 1),[8] and previously discussed in our review.[9] The ready availability of **FOF-2**, combined with the high yields of these reactions, makes the compound highly appealing and very practical, and suggests strongly the possibility of being able to generate more complex molecular assemblies from it.

Scheme 1

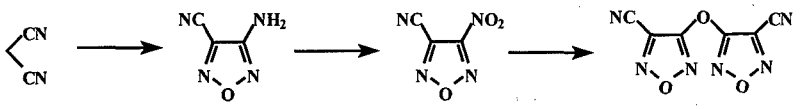

1 **FOF-2**

The synthesis of **FOF-13** involved a multi-step reaction sequence in which **FOF-2** was hydroximated to **2** followed by diatization with sodium nitrite

Scheme 2

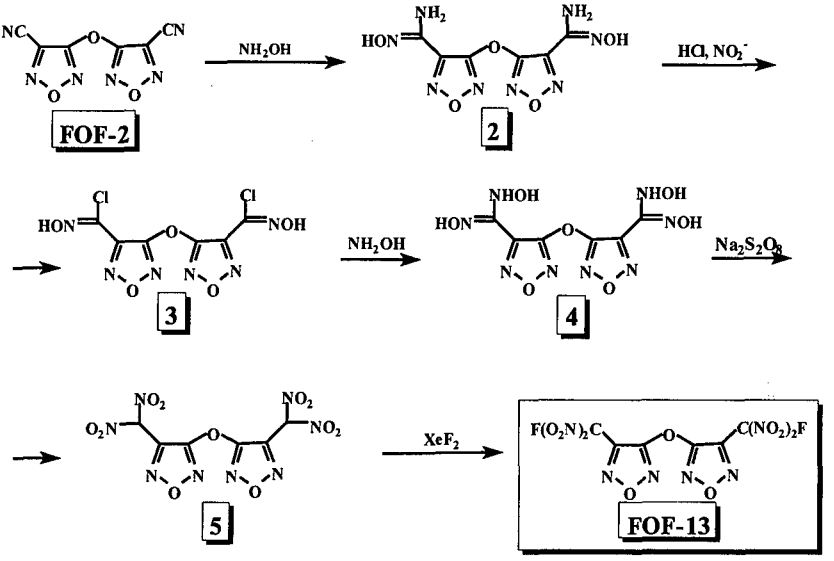

Table 1. Physical and Explosive Properties of **FOF-13** and some analogs.

Structural Formula and Name	Empirical Formula	M.w.	k_O* (%)	Mp (°C)	d (g/cm^3)	ΔH_f (kcal/mol)
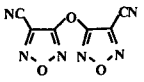 **FOF-2**	$C_6N_6O_3$	204	25	69	1.64	+138
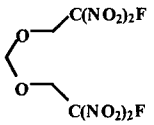 **FEFO**	$C_5H_6N_4O_{10}F_2$	320	84.6	13.4	1.607	-203
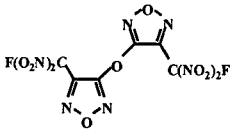 **FOF-13**	$C_6N_8O_{11}F_2$	398	100	48	1.97	-35

* - oxidant coefficient, for explosives that contain carbon, hydrogen, oxygen and fluorine, k_O is given by equation: $(n_O + 0.5n_F)/(2n_C + 0.5n_H)100\%$

in hydrochloric acid to yield bis-hydroxamoil chloride **3** (Scheme 2). The dichloride was converted to tetra-N-hydroxy derivative **4** by the treatment with hydroxylamine. Subsequent oxidation with sodium persulfate gave requisite bis-(dinitromethyl) precursor **5**, which was converted to the desired **FOF-13** by final fluorination with xenon difluoride.

FOF-13 is colorless needles, possesses excellent solubility in all organic solvents, and is not soluble in water and not hydroscopic. Differential scanning calorimetry showed no obvious decomposition of **FOF-13** below 270°C. As starting **FOF-2** decomposes slowly at the temperatures above 250°C, the less conjugated with the furazan ring fluorodinitro group seems to stabililize the desired molecule. Some of the physical and explosive properties of **FOF-13**, together with the data for analogs, are tabulated in Table 1.

The liquid mixtures (with M.p. up to -80°C) in which **FOF-13** is a major part are made by the inclusion of some additions in the compositions. **FOF-13** is excellently compatible both with other high energetic furazans, for example

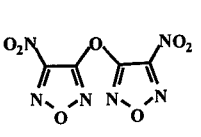

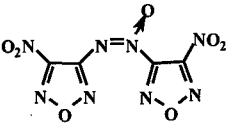

and common ingradients utilized for preparation of explosive and pyrotechnic mixtures, powers and solid rocket propellants (TNT, RDX, HMX, NC, AP, AND and other).

The properties exhibited by **FOF-13** suggests their practical application as energetic plasticizer.

It should be noted that the intermediate **3** is effective building block for a series of other energetic furazans. For example, treatment of **3** with a base afforded the 7- and 14-membered macrocycles **7** and **8**, as well as linear high molecular weight products **9** (Scheme 3). Previous publication from this laboratory have described the design and synthesis of a series of potential high energetic macrocycles based on the furazan block.[4,10,11]

Scheme 3

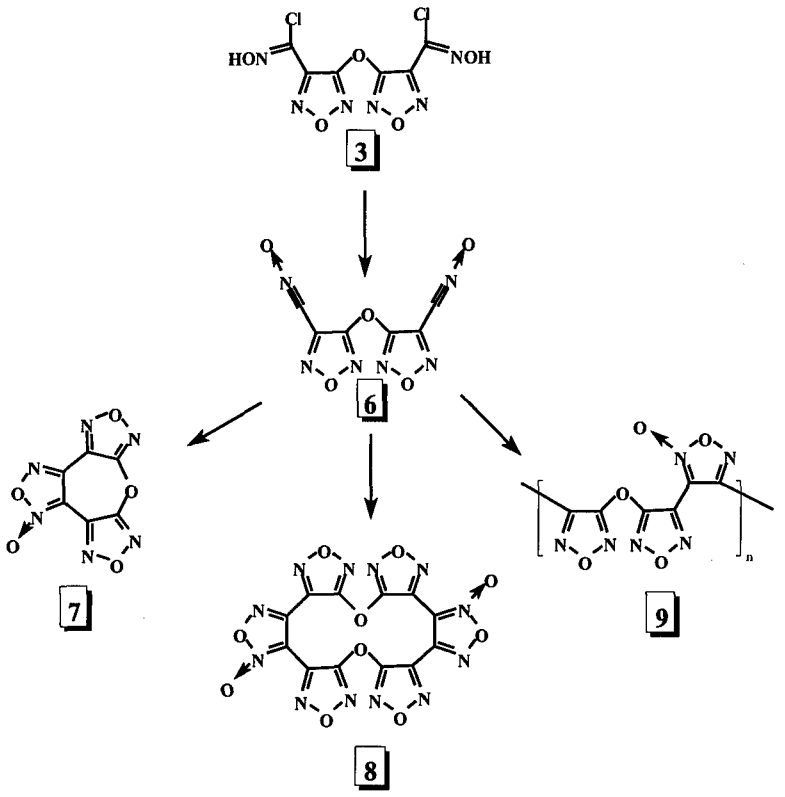

REFERENCES

1. **Sheremetev, A. B**. and **Pivina, T. S**. "Nitrofurazanyl Moiety as an Alternative to Picryl One for High Energetic Materials Construction". *Proc. 27th International ICT-Conference, Energetic Materials - Technology, Manufacturing and Processing*, June 25 - June 28, **1996**, Karlsruhe, FRG, 30/1-30/13.
2. **Sheremetev, A. B.** and **Shatunova, E. V**. "Furazanyl Ethers of Pentaerythritol Derivates". *Proc. 28th International Annual ICT-Conference, Combustion and Detonation*, June 24 - June 27, **1997**, Karlsruhe, FRG, 94/1-8.
3. **Sheremetev, A. B.; Kulagina, V. O.; Aleksandrova, N. S.; Novikova, T. S**., and **Khmelnitskii, L. I**. "Aminofurazans as Key Synthons for Construction of High Energetic Materials". *Proc. 3th International Symposium on Pyrotechnics and Explosives*. November 6-9, **1995**, Beijing, China, 249.
4. **Sheremetev, A. B.; Kulagina, V. O.; Batog, L. V.; Lebedev, O. V.; Yudin, I. L.; Pivina, T. S.; Andrianov, V. G.,** and **Starchenkov, I. B.** "High Energetic Materials from Diaminofurazan", *Proc. Twenty-Second International Pyrotechnics Seminar*, July 15-19, **1996**, Colorado, USA, 377.

5. **Sheremetev, A. B.; Yudin, I. L.; Aleksandrova, N. S.; Andrianov, V. G.,** and **Starchenkov, I. B.** "High Nitrogen Furazan Derivatives for Gas Generators" *Proc. Twenty-Third International Pyrotechnics Seminar,* Sept.30-Oct.4, **1997**, Tsukuba, Japan, 377-388.
6. **Sheremetev, A. B.; Kulagina, V. O.; Aleksandrova, N. S.; Dmitriev, D. E.; Strelenko, Yu. A.; Lebedev, V. P.,** and **Matyushin, Yu. N.** "Dinitro Trifurazans with Oxy, Azo, and Azoxy Bridges". *Propellants, Explosives, Pyrotechnics,* in press.
7. **Sheremetev, A. B.; Semenov, S. E.; Kuzmin, V. S.; Strelenko, Yu. A.,** and **Ioffe, S. L.** "Synthesis and X-ray Crystal Structure of Bis-3,3'-(nitro-NNO-azoxy)-difurazanyl Ether". *Chemistry-European Journal,* **1998**, in press.
8. **Sheremetev, A. B.; Kharitonova, O. V.; Melnikova, T. M.; Novikova, T. S.; Kuzmin, V. S.,** and **Khmelnitskii, L. I.** "Synthesis of Symmetrical Difurazanyl Ethers", *Mendeleev Commun.*, **1996**, (4), 141-143.
9. **Шереметев А.Б.** "Нитро- и нитраминофуразаны. Обзор". *Российский хим. журн. (Журн. Росс. хим. общества им. Д.И.Менделеева),* **1997**, 41 (2), 43-54. [A. B. Sheremetev, "Nitro- and nitraminofurazans". *Ross. Khim. Zhurn. (Zhurn. Ross. Khim. ob-va im. D. I. Mendeleeva),* **1997**, *41*, (2), 43-54 (in Russian)], (English translation in *Mendeleev Chemistry Journal,* **1997**, *in press*).
10. **Chertanova L., Pascard C., Sheremetev A.** "New macrocycles ligand. X-ray study of three macrocycles involving azofurazan subunit." *Supramolec.Chem.*, **1993**, *3*, 71.
11. **Sheremetev, A. B., Kulagina, V. O.,** and **Ivanova, E. A.** "Zero-Hydrogen Furazan Macrocycles with Oxy and Azo Bridges". *J.Org.Chem.*, **1996**, *61*, 1510-1511.

Dr. V.V.Nedelko
Institute of Chemical Physics in Chernogolovka,
Russian Academy of Sciences,
142432 Chernogolovka, Moscow Region, Russia
Fax: (7-096) 515 35 88

SYNTHESIS AND THERMAL STABILITY OF 5,5'-BIS(TETRAZOLYL)AMINE

V.V.Nedelko, B.L.Korsounskii, A.V.Shastin, N.V.Chukanov, T.S.Larikova,
A.I.Kazakov

Institute of Chemical Physics in Chernogolovka,
Russian Academy of Sciences
142432 Chernogolovka, Moscow Region, Russia

5,5'-Bis(tetrazolyl)amine is a stable solid substance with high N-content (>82 wt. %). We consider this tetrazole as a promising gas-generating agent and expedient additive into propellants and other energetic systems. 5,5'-Bis(tetrazolyl)amine has been synthesized in 4-step process from the starting cyanuric chloride. The yield of the final tetrazole was about 40%. 5,5'-Bis(tetrazolyl)amine has been characterized by IR-spectroscopy, ^{1}H and ^{13}C NMR.

Thermogravimetry, volumetry, calorimetry, IR-spectroscopy, and mass spectroscopy were used to study the kinetics and decomposition products (including volatile and condensed products). The kinetic and activation parameters of the decomposition in air and argon have been determined over the temperature range 200 - 242^{0}C. The kinetic curves have an evident S-shape and fit an equation of autocatalysis of the first order $d\alpha/dt = k_1(1 - \alpha) + k_2\alpha(1 - \alpha)$, where the rate constant of noncatalytic decomposition k_1 and the rate constant of catalytic reaction k_2 satisfy the Arrhenius equations $k_1 = 10^{15,6 \pm 0,5}\exp[-(197 \pm 5)/RT]$ s^{-1} and $k_2 = 10^{17,5 \pm 0,7}\exp[-(201 \pm 7)/RT]$ s^{-1} (R is measured in kJ/mol·K). Every 5,5'-bis(tetrazolyl)amine molecule splits out 2,5 molecules of N_2. The purity of nitrogen formed is more than 97,5 vol. %. The evolution of N_2 is accompanied with the formation of the condensed product of unusual structure. The calorimetric data have confirmed the autocatalytic manner of the decomposition. The total reaction heat is about 440 cal·g^{-1}. The critical conditions of the thermal explosion have been evaluated.

We suppose the specific never declared before mechanism of the thermal decomposition of 5,5'-bis(tetrazolyl)amine via the intermediate imino and amino triazoles.

Mechanism of the primary stages of decomposition of aliphatic nitro- and fluoronitronitramines

Boris L. Korsounskii, Vladimir G. Matveev, Ludmila D. Nazina, Gennadii M. Nazin

Institute of Chemical Physics Problems,

Russian Academy of Sciences

142432 Chernogolovka, Moscow Region, Russian Federation

ABSTRACT

The primary stages of the decomposition of compounds $RN(NO_2)$-$CH_2C(NO_2)_2X$ is the homolytic cleavage of the C – NO_2 bond, if X = NO_2, and N – NO_2 bond, if X = F. The inductive effect of substituents decreases the dissociation energies of the C – N and N – N bonds by 1 – 2 kcal/mol. Kinetic effects caused by the spatial interaction of groups and by stepwise decomposition of polyfunctional compounds are described.

INTRODUCTION

Although thermal decomposition of secondary nitramines have been studied in numerous works [1], these reactions are still not adequately investigated. Many problems concerning the influence of substituents and the medium on the rate and the mechanism of decomposition remain unsolved. Decomposition of simple nitramines normally starts with homolytic cleavage of the N – N bond, whose strength depends relatively slightly on the substituents. However, when some substituents, for

example an F atom and carbonyl group [1] or a furazan ring [2] are present in the α- or β-position with respect to the nitramino group or when the decomposition is carried out in a hydrocarbon medium [3], its mechanism and rate sharply changes. The process is accompanied by intramolecular rearrangement and intermolecular interactions, whose mechanisms are unknown. The kinetics of decomposition of nitro-derivatives of nitramines, which constitute a large group of energetic compounds, have not been studied either. The molecules of these compounds incorporate two or several reaction centers, which interact and compete with one another in the primary decomposition reactions.

Therefore, in this work, we studied the kinetics and mechanisms of the initial (non-catalytic) steps of thermolysis of trinitromethyl and fluorodinitromethyl derivatives of secondary nitramines in the liquid phase. As a typical representatives, we chose the following compounds: $MeN(NO_2)CH_2C(NO_2)_3$ (**1**), $(NO_2)_3CCH_2N(NO_2)CH_2C(NO_2)_3$ (**2**), $[(NO_2)_3CCH_2N(NO_2)CH_2\text{-}]_2$ (**3**), $MeN(NO_2)CH_2C(NO_2)_2F$ (**4**), $F(NO_2)_2CCH_2N(NO_2)CH_2C(NO_2)_2F$ (**5**), $[F(NO_2)_2CCH_2N(NO_2)CH_2\text{-}]_2$ (**6**), and $[F(NO_2)_2CCH_2N(NO_2)CH_2\text{-}]_2CH_2$ (**7**).

Decomposition of compounds **2**, **3**, and **5** has been studied previously [4] but only under conditions of fast heating. It was found that NO_2 is formed as a primary thermolysis product; however, this fact hardly makes it possible to elucidate the nature of the primary step of decomposition. Kinetic approach appears more promising for this purpose. We carried out formal kinetic analysis of the decomposition of heterofunctional compounds under isothermal conditions, distinguished the initial step, determined its kinetic parameters, and compared these parameters with known characteristics of the decomposition of monofunctional compounds, *viz.*, nitramines or polynitroalkanes.

For this approach, accuracy of kinetic measurements is an important point. Therefore, the reactions were studied mostly in dilute solutions, *i.e.*, under conditions when the disturbing influences of admixed catalytic or autocatalytic processes is almost entirely eliminated. To analyze the products of decomposition and to elucidate a possible role of intermolecular interactions in the initial stages of the process, some experiments were carried out in a melt.

EXPERIMENTAL

All the solids used were purified by recrystallization from ethanol or aqueous acetone. Decomposition reactions were studied by the manometric method. The pressure in the reaction vessel was measured by the compensation method using sensitive sickle-shaped membranes, usually in the range 5 – 700 Torr with a relative error of <2%. During the experiments, the temperature was maintained with an accuracy of $\pm 0.1^0$C using a liquid thermostat filled with a low-viscosity silicone oil.

When the reaction was carried out in solution, *m*-dinitrobezene, which is a low-melting non-volatile substance, inert toward nitrocompounds and the products of their decomposition at 200^{0}C, was used as the solvent. The melts of the compounds under study in *m*-dinitrobenzene (concentration 0.3 – 3.0 mol.%) were prepared prior to the experiments, usually at 100^{0}C.

The kinetic experiments in solutions were carried out until the degree of conversion of the initial compound was 50 – 100%. The kinetic curves were described satisfactorily by a first-order equation. Decomposition in the melt was studied for nitramines **1**and **2**. In this case, the reactions were autocatalytic. The rate of the catalytic (but not of the initial) stage de-

pended on the degree of filling of the vessel with the substance. The kinetic curves were poorly described by the first-order equation of autocatalysis; the rate constants (k) for the initial step of decomposition were calculated from the time needed to reach a degree of decomposition of 1%. The complete gas evolution (which is convenient to express in the units of adjusted volume ΔV_∞/N cm^3/g) corresponding to 100% decomposition was determined at elevated temperatures. Since ΔV_∞ may depend on the temperature and the compositions of the gas products formed at the initial and autocatalytic stages may be different, errors in the determination of k, activation energy E, and preexponential factor A are possible. Therefore, the data obtained for solutions are, in principle, more accurate, and the measurements for the rest of the compounds were carried out only in solutions.

For compounds **1** and **2**, the ΔV_∞ values equal to 635 and 730 were used in the calculation of k. The stoichiometric coefficients of the reaction (the numbers of moles of gaseous products formed from 1 mole of the initial compound) for compounds **1** and **2** were 6.8 and 12.7, respectively. Large stoichiometric coefficients were also observed for decomposition of all the other compounds. For compound **3** in solution, ΔV_∞ = 565, which corresponds to the evolution of 12 moles of gaseous products.

The manometric procedure chosen provides well reproducible kinetic curves. The experiments showed that the rate constants found in three entries differ by 10 – 15%. For this accuracy of the measurements, 10 – 12 entries carried out in the temperature range from T to T equal to 40^0C are sufficient for the activation energy to be determined with an accuracy of $\pm$1.0 kcal/mol. For a smaller number of entries, the error increased to $\pm$1.5 kcal/mol. The activation energies for the key compounds **1** and **4** and also that for compound **3**, for which it was significant to carry out the most

accurate comparison with compound **1**, were determined with the above-mentioned minimum error.

The products of decomposition of compound **1** were analyzed at 140^{0}C and at degrees of conversion of 2, 15, and 100%. The products were fractionated by freezing at –78 and –195^{0}C. Light gases were analyzed by gas chromatography on columns with Paropack Q, and NO_2 was determined by colorimetry. The products were identified by IR spectroscopy and by chemical analysis. The yields of gaseous products proved to be identical to within 10 – 15% and amounted to (in moles per mole of **1**): CO, 0.3; CO_2, 1.4; NO, 1.0; NO_2, 0.2; N_2O, traces; N_2, 1.25; $MeONO_2$, 1.0; $H_2O \cong 0.8$. Complete decomposition of compound **1** yielded a non-volatile condensed residue (5% w/w) consisting of five products. Due to the small amount of the residue, these products could not be reliably identified. The major compound (65%) was a low-volatile (100^{0}C/0.1 Torr) liquid, whose elemental composition and IR-spectra corresponded most closely to $MeN(NO_2)CH_2C(O)Me$ or $MeN(NO_2)CH_2COOMe$. The second component in order of the content (15%) was an amino acid, probably, $MeNHCH_2COOH$, which catalyzes decomposition of compound **1**. The rest of the condensed products also contained C=O and N=O bonds and might have been carboxy or nitro derivatives.

RESULTS AND DISCUSSION

It follows from the data presented in Table 1 and in Fig. 1 that the rates of decomposition in a dilute solution and in the melt are virtually identical (especially in the case of the most thoroughly studied compound **1**); this indicates that the decomposition of those compounds is not accompa-

nied by any side reactions or bimolecular interactions. The rate constant also does not depend on the concentration of the compound in solution.

Table 1. Kinetic characteristics for the decomposition of nitronitramines

Compound	Medium	$T/^0C$	E/kcal mol^{-1}	Log A/s^{-1}	k/s^{-1} at 150^{0}C	ω *
1	solution	130-180	40.3	16.70	$7.6 \cdot 10^{-5}$	9.1
	melt	90-140	40.4	16.74	$7.4 \cdot 10^{-5}$	8.9
2	solution	110-165	36.1	15.06	$2.6 \cdot 10^{-4}$	31.3
	melt	110-150	36.8	15.59	$3.8 \cdot 10^{-4}$	45.8
3	solution	130-180	40.7	16.80	$5.9 \cdot 10^{-5}$	7.0
4	solution	175-210	40.5	14.90	$9.5 \cdot 10^{-7}$	5.3
5	solution	170-210	39.8	14.92	$2.3 \cdot 10^{-6}$	12.8
6	solution	160-210	40.0	15.29	$3.3 \cdot 10^{-6}$	18
7	solution	160-210	42.3	16.20	$2.2 \cdot 10^{-6}$	12.2
$CH_3C(NO_2)_3$	melt		42.6	16.93	$8.3 \cdot 10^{-6}$	
R_2NNO_2	solution		41.1	14.50	$1.8 \cdot 10^{-7}$	
$CH_3C(NO_2)_2F$	gas [5]		41.7	16.70	$1.1 \cdot 10^{-8}$	

* The ratio of the rate constant of decomposition of the compound under study (k) to that of the reference monofunctional compound (k_{ref}) at 150^{0}C. For **1-3** $k_{ref} = 8.3 \cdot 10^{-6}$ s^{-1} (the data for 1,1,1-trinitroethane in the melt [6], for **4-7** $k_{ref} = 1.8 \cdot 10^{-7}$, the typical value for decomposition of a planar nitramine group [7].

The first-order kinetics of the irreversible decomposition of a complex polyfunctional compound can correspond to a one-step monomolecular reaction, a nonbranched chain process, or a sequence of transformations with the rate-determining first step. Since stoichiometric coefficients are large, the first of these possibilities can be immediately ruled out. Chain mechanisms of decomposition of aliphatic polynitro-compounds are never observed [5]. They are impossible, because the products of thermolysis always contain large amounts of NO and NO_2, which are inhibitors of free-radical processes. Hence, there remains only the third version, *viz.*,

a sequence of transformations, whose rate is limited by the first step. The non-integer stoichiometric coefficient is in agreement with the following sequence of processes: some intermediate compounds are converted according to several pathways characterized by different stoichiometric coefficients (see, for example, Scheme 1), and, therefore, the stoichiometric coefficient for the overall reaction is fractional.

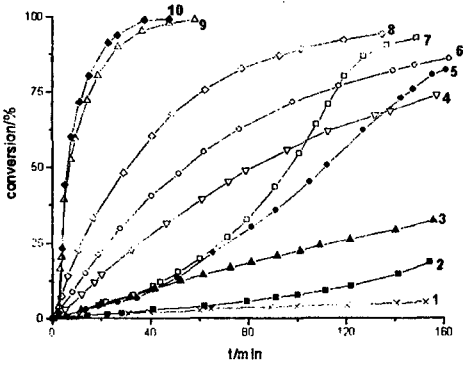

Fig. 1. Examples of kinetic curves of gas evolution during decomposition of compounds **1** and **2**: compound **1**, solution, 130^{0}C (*1*); **1**, melt, 130^{0}C (*2*); **2**, solution, 130^{0}C (*3*); **1**, solution, 155^{0}C (*4*); **2**, melt, 130^{0}C (*5*); **2**, solution, 145^{0}C (*6*); **1**, melt, 140^{0}C (*7*); **1**, solution, 165^{0}C (*8*); **2**, solution, 165^{0}C (*9*); **1**, solution, 180^{0}C (*10*).

Scheme 1

$$\mathbf{1} \rightarrow MeN(NO_2)CH_2C^{\bullet}(NO_2)_2 + NO_2 \quad (1)$$

$$MeN(NO_2)CH_2C^{\bullet}(NO_2)_2 \rightarrow MeN(NO_2)CH_2C(O^{\bullet})NO_2 + NO \quad (2)$$

$$MeN(NO_2)CH_2C^{\bullet}(NO_2)_2 + NO \rightarrow MeN(NO_2)CH_2C(NO)(NO_2)_2 \quad (2a)$$

$$MeN(NO_2)CH_2C(NO)(NO_2)_2 \rightarrow MeN(NO_2)CH_2CN + NO_2 + NO_3 \quad (3)$$

$$MeN(NO_2)CH_2C(O^{\bullet})NO_2 \rightarrow MeN(NO_2)CH_2C^{\bullet}=O + NO_2 \quad (4)$$

$$MeN(NO_2)CH_2C^{\bullet}=O \rightarrow MeN(NO_2)C^{\bullet}H_2 + CO \quad (5)$$

$$MeN(NO_2)CH_2C^{\bullet}=O + NO_2 \rightarrow MeN(NO_2)CH_2COO^{\bullet} + NO \quad (5a)$$

$$MeN(NO_2)C^{\bullet}H_2 + NO_2 \rightarrow MeN(NO_2)CH_2O^{\bullet} + NO \quad (6)$$

$$MeN(NO_2)CH_2COO^{\bullet} \rightarrow MeN(NO_2)C^{\bullet}H_2 + CO_2 \quad (7)$$

$$MeN(NO_2)CH_2COO^{\bullet} + RH \rightarrow MeN(NO_2)CH_2COOH + R^{\bullet} \quad (7a)$$

$$MeN(NO_2)CH_2O^{\bullet} \rightarrow MeN^{\bullet}(NO_2) + CH_2O \quad (8)$$

$CH_2O + NO_2 \rightarrow CO + CO_2 + H_2O + NO$ (9)
$MeN^{\bullet}(NO_2) + NO_2 \rightarrow MeNO + NO + NO_2$ (10)
$MeNO + 2NO \rightarrow Me^{\bullet} + N_2 + NO_3$ (11)
$Me^{\bullet} + NO_2 \rightarrow MeO^{\bullet} + NO$ (12)
$Me^{\bullet} + NO_3 \rightarrow MeONO_2$ (13)
$MeO^{\bullet} + NO_2 \rightarrow MeONO_2$ (14)

The first-order rate constant found experimentally should apparently be attributed to the first step of this sequence provided that all the subsequent reactions are fast. Thus, the mechanism of the thermolysis of compounds **1 – 7** can be analyzed using the kinetic data listed in Table 1.

The activation energies of the decomposition of trinitroalkanes and secondary nitramines are close, whereas the preexponential factors are appreciably dissimilar. In the former case, they always exceed 10^{16} s^{-1}, while in the latter case, they are seldom greater than $10^{14,5}$ s^{-1}. Thus, decompositions of a trinitromethyl group and of a nitramino group can be distinguished from each other only based on the rate constants, which, unlike the *E* values, are measured with high accuracy and can differ by a factor of 60 for monofunctional compounds. Effects of substituents, an increase in the number of reaction groups in polyfunctional compounds, and simply the errors in determination of *E* distort the relationship between the Arrhenius parameters characterizing the cleavage of the C – N and N – N bonds but not between the corresponding rate constants. Thus an error in determination of *E* is always counterbalanced by a change in *A* (false compensation effect), which has only minor influence on the difference between the rate constants.

From a comparison of the magnitudes of rate constants *k* and preexponential factors *A*, it follows that decomposition of compounds **1 – 3** begins with trinitromethyl groups.

In the case of compounds **4 – 7**, the easiest way of choosing between the decomposition of nitramino and fluorodintromethyl groups is to use the *E* values for the reaction. The rates of decomposition of these groups at the temperatures used in our experiments differ by approximately an order of magnitude, and their *E* differ by 6 kcal/mol, which is much greater than the experimental error. The data for compounds **4 – 7** presented in Table 1 (low *E* values and moderate *A* values) unambiguously indicate that decomposition of these compounds begins with nitramino groups.

By comparing groups of compounds **1 – 3** and **4 – 7** one can see that the ratio of the rate constants for key compounds **1** and **4** is equal to 95, *i.e.,* it is larger than that in the case of monofunctional compounds, and that the smallest ratio (between compounds **3** and **6**) is 30. The rates of decomposition of compounds **3** and **6** are 7 and 18 times, respectively, greater than those for the reference monofunctional compounds. Thus, a comparison of the groups of compounds **1 – 3** and **4 – 7** leads to the conclusion that decomposition of polyfunctional compounds **1 – 3** involves the less stable trinitromethyl group.

The results obtained here make it possible to identify a number of fine effects concerning the rate and mechanism of decomposition of the compounds studied.

Compound **1** is 10 times less stable than 1,1,1-trinitroethane, because the C – N bond in it is ~2 kcal/mol less strong. This difference can be fully attributed to the inductive influence of the β-nitramino group on the decomposition of the $C(NO_2)_3$-group.

Using the views on the secondary reactions accompanying decomposition of trinitroalkanes reported in the literature [5] and the data on the transformations of the methylnitramine radical $MeN^{\bullet}NO_2$ in an oxidative

NO and NO_2 medium [8], the detailed mechanism of the decomposition of compound **1** can be represented by Scheme 1. This scheme provides for a qualitative explanation of the composition of the thermolysis products formed from **1** including the high yield of methyl nitrate and the absence of N_2O. It is unlikely that the same products are formed upon the primary cleavage of the N – N bond in compound **1**. Detailed schemes of the fast chemical reactions that accompany decomposition of secondary nitramines have not yet been reliably established. However, it is known [1] that decomposition of these compounds always yields N_2O or stable N-nitroso-derivatives, which have not been detected among the products of decomposition of **1**. Thus, the homolytic mechanism proposed for decomposition of **1**, according to which dissociation of the C – N bond is the first step of the process, is quite justified.

The CO and CO_2 resulting from the thermolysis of 1,1,1-trinitroalkanes are formed from the α-C atom. This carbon atom passes into nitrile or carbonyl groups to only a small extent. The β-C atom is not oxidized at the C – H bonds and enters into the composition of stable compounds in combination with some groups such as OH, NO_2, or ONO_2 [5]. In compounds like **1**, the β-C atom also undergoes complete oxidation due to the low strength of the C – N bond in $H_2C^{\bullet}$- NNO_2R (see Scheme 1). Subsequently, the nitramino group is decomposed, and the reaction stops only at the δ-C atom. Partial oxidation in excess NO_2 yields stable nitro ester. At temperatures of decomposition of nitro esters, they are converted into alcohols and carboxylic acids or undergo the deeper oxidation at the δ-C atom.

The above-presented scheme of secondary reactions can be applied to compounds **2** and **3**. It can be assumed that in the case of compound **2**, the whole molecule immediately decomposes to light gaseous products in

a sequence of rapid secondary reactions, while the destruction of **3** occurs in two steps: after the rate-determining abstraction of one of the nitro-groups, a part of the molecule up to the δ-position is oxidized *via* fast secondary reactions, whereas the rest of the molecule is converted to intermediate **A** of the $RCH_2(NO_2)NCH_2C(NO_2)_3$ type, where R = CN, CH_2OH, COOH, CH_2ONO_2, or CH_2NO_2.

Comparison of the rates of decomposition of compounds **1** and **3** (see Table 1) reveals the following feature that seems strange at first glance. Compound **1** contains one trinitromethyl group acting as a reaction center, while compound **3** contains two groups of this kind. It might be expected that **3** would decompose twice as fast as **1**. However, the gas evolution rate constant found for decomposition of **3** is far from being twice larger than that observed for **1**; conversely, it is even somewhat smaller. This can be explained by the fact that decomposition of **3** occurs stepwise *via* intermediate **A**, whose structure was considered above. The essence of the stepwise decomposition becomes clear from Scheme 2. The first step of the decomposition of compound **3** is characterized by the rate constant, which is twice as large as that for compound **1**. This step involves the cleavage of one of the trinitromethyl groups, and, in addition to gaseous products, it yields a condensed intermediate **A** in which the second $C(NO_2)_3$ group is retained. Decomposition of this intermediate is the second step of process, and its rate is half that observed in the case of **3**.

Scheme 2

$$\mathbf{3} \rightarrow \mathbf{A} + P_1 \ (2k_1) \qquad (1)$$
$$\mathbf{A} \rightarrow P_2 \qquad (k_2) \qquad (2)$$

The curves of gas evolution were calculated assuming that the first and the second reactions yield equal amounts of gaseous products P_1 =

$P_2 = 6P_0$ (P_0 corresponds to the evolution of 1 mole of gaseous products) and $k_1 = k_2 = 7.6 \cdot 10^{-5}$ s^{-1} (as in the case of **1**). As seen from Fig. 2, the calculated gas evolution curve closely simulates a first-order reaction and nearly coincides with the experimental curve for decomposition of compound **3**. The rate constant calculated from the overall curve of gas evolution is $7.6 \cdot 10^{-5}$ s^{-1}, *i.e.*, it coincides with k_1 and is somewhat larger than the observed rate constant for the decomposition of **3** ($5.9 \cdot 10^{-5}$ s^{-1}). Complete agreement between the calculated and experimental curves was obtained for $P_1 = 5P_0$, $P_2 = 7P_0$. This result makes it possible to draw a general conclusion: the rate constant for gas evolution in the stepwise decomposition of compounds with two reaction centers is approximately identical to that for compounds with one decomposition center.

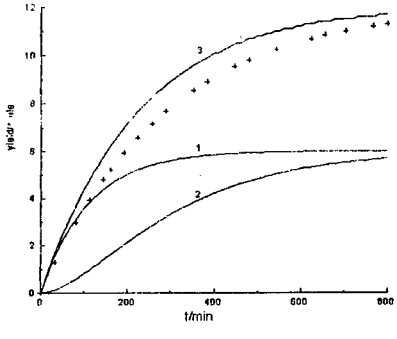

Fig. 2. Kinetic curves for the yield of gaseous products calculated from Scheme 2 (see the text) at $P_1 = P_2 = 6P_0$, $k_1 = k_2 = 7.6 \cdot 10^{-5}$ s^{-1}; reaction (1) (*1*); the curve for P_2 (*2*); the overall curve for $P_1 + P_2$ (*3*); the asterisks mark experimental points ($k = 5.9 \cdot 10^{-5}$ s^{-1}).

Yet another unexpected fact can be discovered by comparing the rates of decomposition of compounds **1** and **2** (see Table 1 and Fig. 1): the decomposition of **2** is characterized by the lower activation energy and occurs at a substantially higher rate than the decomposition of **1**. This differ-

ence between compound **2** and compounds **1** or **3** can be explained by the field effect, which has been observed previously for structural analogs of **2**, namely, for pentane derivatives overloaded with nitro groups [5]. Owing to steric restrictions and electrostatic interactions, the molecule of **2** exists predominantly in a twisted conformation [9], in which one of the O atoms of the nitramine group approaches the C atom of the $-C(NO_2)_3$ group to a distance of 3.09 A (which is smaller than the sum of the van der Waals radii of O and C atoms equal to 3.19 A) and thus stabilizes the free valence in the radical generated on the abstraction of NO_2. This results in a decrease in the *E* value and, to some extent, in the *A* value (since free rotation around the C – C bond in the $RCH_2C^{\bullet}(NO_2)_2$ radical becomes hindered).

The rate of decomposition of compound **4** is 5 times higher than the typical rate of decomposition of a planar nitramine group. This is a result of the inductive influence of the $-C(NO_2)_2F$ group on the $-NNO_2-$ group located in the β-position. Note that in compound **1**, the effect of the nitramino group on the destruction of $-C(NO_2)_3$ is twice stronger.

In the case of compound **5**, the rate constant is approximately twice higher than that for nitramine **4**; this is due to the inductive effect of the two fluorodinitromethyl groups. No conformation effects are manifested in compound **5**. In this respect, compound **5** differs from its analog, compound **2**, in which the nitramino group exerts a strong through-space effect on the cleavage of the C – N bond.

Compounds **6** and **7** contain two nitramino groups each, and the rate constants of their decomposition are 4 and 2 times larger than that for compound **4**, respectively. Possibly, the decomposition of these compounds proceeds stepwise, and the increase in the rate of the process (especially in the case of **6**) is due to the $O...NNO_2$ through-space inter-

action of the nitramino groups separated by two or three methylene bridges. The intermediate six- or seven-membered cyclic structures needed for this interaction are the most accessible nonstrained configurations of atoms linked to one another. In view of this hypothesis, it is of interest to study other polyfunctional nitramines containing the $-N(NO_2)CH_2CH_2N(NO_2)-$ structural fragment.

Thus, in the study of polynitro-substituted nitramines, we found that the decomposition of these compounds always starts from the cleavage of those bonds that are the least strong according to the analysis of the corresponding compounds. The reaction proceeds via a homolytic mechanism that includes the cleavage of the C – N or N – N bonds. The strength of these bonds decreases by 1 – 2 kcal/mol as a result of the inductive effect of groups. In addition, in some cases, spatial interactions (field effect, anchimeric assistance), which are impossible in monofunctional compounds, may also be manifested. In the case of compound **2**, the occurrence of this effect can be regarded as proven, while for compounds **6** and **7**, its role has been assumed. Yet another result of this study is that the kinetic effect of the stepwise decomposition of polyfunctional compounds was demonstrated experimentally as follows. The evolution of the final products imitates the first-order kinetics but is characterized by a smaller rate constant than the destruction of the initial compound. The first-order kinetics is retained for this sequence of transformations if the rate constants for the first and the second steps are close to each other and if the final products are independently produced in approximately equal amounts from the initial compound and from the intermediate.

The scheme for stepwise decomposition can be easily adapted to compounds containing three or four identical reaction groups, and it can be used to interpret numerous published data on the kinetics of decompo-

sition of polyfunctional compounds of various classes (organic azides, nitramines, nitro esters, difluoroamines, polynitro compounds) including explosives: RDX, HMX, nitroglycerol, PETN, trinitrotriazidobenzene, *etc.*

REFERENCES

1. F.I.Dubovitskii, B.L.Korsounskii, *Usp. Khim.,* 1981, **50**, 1228 [*Russ. Chem. Rev.,* 1981, **50** (Engl. Transl.)].
2. D.G.Patil and T.J.Brill, *Thermochim. Acta,* 1994, **235**, 225.
3. J.C.Hoffsommer and D.J.Glover, *Comb. And Flame,* 1985, **59**, 303
4. R.Subramanian and T.B.Brill, *Prop., Explos., Pyrotech.,* 1990, **15**, 187.
5. G.M.Nazin, G.B.Manelis, *Usp. Khim.,* 1994, **63**, 327 [*Russ. Chem. Rev.,* 1994, **63**, 313 (Engl. Transl.)].
6. G.M.Nazin, G.B.Manelis, F.I.Dubovitskii, *Izv. Akad. Nauk SSSR, Ser. Khim.,* 1968, 2628 [*Bull. Acad. Sci. USSR, Div. Chem. Sci., 1968,* **17** (Engl. Transl.)].
7. Yu.M.Burov, G.M.Nazin, *Kinet. Katal.,* 1982, **23**, 1106 [*Kinet. Catal., 1982,* **23** (Engl. Transl.)].
8. V.V.Charskii, A.N.Pavlov, G.M.Nazin, B.L.Korsounskii, A.A.Fedotov, *Izv. Akad. Nauk SSSR, Ser. Khim.,* 1989, 794 [*Bull. Acad. Sci. USSR, Div. Chem. Sci.,* 1989, **38**, 713 (Engl. Transl.)].
9. L.O.Atovmyan, R.G.Gafurov, N.I.Golovina, L.T.Eremenko, B.S.Fedorov, *Zh. Struct. Khim.,* 1980, **21**, 135 [*J. Struct. Chem.,* 1980, **21** (Engl. Transl.)].

ESTIMATION OF NITRATE ESTER BOND DISSOCIATION ENERGIES IN NITROCELLULOSE BY MOLECULAR MODELLING

Authors: Annette L Lewis[*], John Kendrick[+] and Stephen C Rogers[+]

[*] AWE, Aldermaston, Reading, Berks., RG7 4PR, UK

[+] ICI Technology, Wilton, Middlesbrough, Cleveland TS90 8JE, UK

Abstract

A relatively inexpensive molecular orbital method has been developed for estimating bond dissociation energies *ab initio*. The method uses a combination of a small basis set (SV 3-21G*) together with density functional theory (B3-LYP). It may be applied to quite large models by the normal standards of *ab initio* quantum mechanics calculations. Validation of the method has been carried out for a diverse range of bond types for which experimental data is available.

The method has been applied to study the nitrate ester (O-N) bond strengths in model trinitrocellulose. A variation in bond strength with ring position has been predicted. We have also predicted the effect of ring conformation of nitrocellulose on the nitrate ester bond strength.

Introduction

The thermodynamic bond dissociation energy (BDE) is defined as the enthalpy change during the conversion of a molecule into two radical moieties by the scission of a given bond. It is therefore calculated by the difference in enthalpies of formation of the radical moieties and the parent molecule. It is an important property which is often invoked in the kinetics of unimolecular reactions, such as the thermal degradation of explosive materials. The measurement of BDEs involves difficult and expensive experimental thermodynamic techniques.

Molecular orbital (MO) calculations have been used to estimate theoretically bond dissociation energies for over two decades (ref. 1). Over the past ten years methods, such as the G1, G2 and "complete basis" methods (ref. 2), have been developed that now approach experimental accuracy for predicting BDEs. However, such methods are still relatively expensive and may only be applied to small molecules (e.g. a maximum of 5-10 non-hydrogen atoms). An important aspect of such predictions is the necessity to include a good description of electron correlation (i.e. a description of how electrons move under the influence of the other electrons in the molecule - such motions are correlated because of their mutual repulsion). These accurate methods use Moeller-Plesset perturbation theory which scales roughly with the fifth or higher power of the number of atoms or electrons in the molecule.

Recent developments have focussed attention on Density Functional Theory (DFT) methods (ref. 3) which appear to offer a more efficient treatment of electron correlation. Software, such as the Gaussian 94 package (ref. 4) used here, now allows the use of traditional MO description of the wavefunction (linear combination of atomic orbitals themselves described by Gaussian functions) with a variety of density functionals. Among the most successful treatments developed recently are the so-called hybrid functionals, such as those developed by Becke (ref 5.).

In this paper we investigate the prediction of bond dissociation energies of a wide range of small molecules using a hybrid density functional combined with a small Gaussian basis set .

The advantage of this treatment is that it may be applied to larger molecules. We therefore have used the method to predict the nitrate ester (O-N) bond dissociation energies in a model trinitrocellulose ring as a function of ring position of the nitrate group and ring conformation. Such calculations would normally require the use of a supercomputer but the calculations here were carried out on a desktop workstation.

Methods

We have used the B3-LYP hybrid density functional (ref. 6) combined with the Gaussian split-valence basis set, SV 3-21G* (ref. 7). Calculations were performed on the parent molecules and the radical moieties formed by breaking the bonds. Zero point energy changes were included by estimating the harmonic vibrational frequencies of parent molecule and radicals using the Hartree Fock method with the SV 6-31G* basis set (ref. 8). The frequencies were scaled by a well-established factor of 0.8929 (ref. 2). All calculations were performed using the Gaussian 94 program (ref. 4) or the GAMESS_UK program (ref. 9) on Silicon Graphics, IBM or Sun desktop workstations.

Results for Small Molecules

Bond dissociation energies have been predicted for a variety of bond types and are compared with experimental values in Tables 1, 2 and 3. Also shown are predictions made with a more traditional MO method (Moeller-Plesset level 2 treatment with the SV 6-31G* basis set - see ref. 1) and the much more expensive G2 method (ref. 2).

An examination of the statistics from these results is instructive. The G2 results demonstrate the accuracy of this method by having a squared correlation coefficient, R^2, of 0.990 and standard deviation, σ, of 2.6 kcal/mol with the experimental values. The traditional Moeller Plesset level 2 method (UMP2/6-31G*) has $R^2 = 0.900$ and $\sigma = 10.2$ kcal/mol. The density functional method (B3-LYP/3-21G*) is the least expensive technique but has $R^2 = 0.953$ and $\sigma = 6.7$ kcal/mol. Furthermore, much of this error is concentrated in a few cases involving

very small molecules such as HF and water where a very accurate description of electron correlation is probably required.

In most cases the density functional technique outperforms the MP2 method and often rivals the expensive G2 predictions for accuracy. In the few nitrate ester N-O single bonds for which we have found experimental information (ref. 10) there are indications that the density functional method is most accurate (Table 3). It should, however, be noted that the method is not suitable for predicting the full energy surface for bond dissociation because the local density approximation is poor at dealing with extended bond lengths in molecules.

Application to Nitrocellulose

Nitrocellulose has been used as an energetic polymer binder in PBX formulations. The thermal stability of nitrocellulose is therefore of considerable interest (ref. 11) and the breakdown mechanism is not well understood. Three different ring positions are possible for the nitrate groups (Figure 1). Studies have consistently shown that the primary (C6) nitrate ester is most stable. A high resolution Fourier transform nmr study (ref. 12) indicated that the C3 ester is more stable than the C2.

A major advantage of the density functional method described above is its applicability to quite large molecules by *ab initio* MO standards. We have therefore calculated the nitrate ester bond dissociation energies for the three ring positions in a model nitrocellulose. The chosen model was a single ring with the glycidyl linkages capped with methoxy groups (Figure 1). Calculations were performed on this molecule and the corresponding radicals formed by breaking each N-O bond in turn. The zero point energy change was too large to calculate directly and was estimated from equivalent calculations on i-propyl nitrate (for C2 and C3 positions) and $CH_3OCH(CH_3)CH_2ONO_2$ (for C6) as 4.5 kcal/mol, irrespective of ring position of the nitrate group.

The results are shown in Figure 1 as values of the BDE adjacent to each ester bond. The primary (C6) nitrate ester is predicted to the most stable in agreement with experiment. However, the C3 ester is predicted to be less stable than the C2 ester in contrast to the nmr

experimental work. The calculated BDEs are therefore in the stability order C6 = C2 > C3. The difference between C2 and C3 is small and certainly within the likely errors of the calculations.

A further topic of interest lies in the effect of ring conformation on the ester stability. It is generally assumed that ring inversion does not take place in nitrocellulose because of the conformational changes that would be necessitated by the polymer chain. However, studies by ourselves using molecular mechanics and semi-empirical molecular orbital calculations on the isolated ring model described above indicate that at least one boat form and possibly an inverted chair form should be populated at normal temperatures (See Figure 2). Nitrocellulose undergoes a considerable thermal history during nitration and subsequent digestion processes during its manufacture. Perhaps it is possible that ring inversion occurs as an alternative means of relieving strain. Ring inversion would force the nitrate ester groups from equatorial into axial positions. What then are the implications for the nitrate ester bond strength?

This question may only be answered by theoretical modelling. We have estimated the BDEs using the density functional method described above for one boat conformer (boat 1) and the inverted chair conformer shown schematically in Figure 2. The results are shown in Table 4. Inverted the ring to the opposite chair conformation is seen to weaken the secondary nitrate esters, while the primary (C6) stays unchanged. In the inverted chair all the nitrate esters are in equatorial positions. For the "boat 1" form of Figure 2 we have calculated the bond strength of the predicted weakest nitrate ester (C3). The result is intermediate between the two chair forms.

Conclusions

We have evaluated an efficient method of predicting themodynamic bond dissociation energies by *ab initio* molecular orbital methods. While not as accurate as the state of the art methods, our technique may be applied to quite large molecules. In particular, it appears to be particularly accurate for nitrate ester N-O bonds. We have used it to study the strength of

the nitrate esters in model trinitrocellulose, both as a function of ring position and ring conformation.

References

1. See, for example, W J Hehre, L Radom, P v R Schleyer and J A Pople, *Ab Initio Molecular Orbital Theory* (1986), Wiley, New York.

2. (a) L A Curtiss, K Raghavachari, G W Trucks and J A Pople, *J. Chem. Phys.*, **94**, 7221 (1991). (b) J W Ochterski, G A Petersson and J A Montgomery, Jr., *J. Chem. Phys.*, **104**, 2598 (1996).

3. W Kohn and L J Sham, *Physical Review*, **140**, A1133 (1965).

4. Gaussian 94 (Revision D1), M J Frisch et al, Gaussian Inc., Pittsburgh PA (1995).

6. A D Becke, *J.Chem.Phys.*, **98**, 1372 (1993).

7. W J Pietro, M M Francl, W J Hehre, D J DeFrees, J A Pople and J S Binkley, *J. Amer. Chem. Soc.*, **104**, 5039 (1982).

8. P C Hariharan and J A Pople, *Theor. Chim. Acta*, **28**, 213 (1973)

9. M F Guest et al, GAMESS UK Manual, Computing For Science, Daresbury Laboratories, UK.

10. L Batt and G N Robinson, *The Chemistry of the Nitro and Nitroso Groups*, ed. H Feuer, p1076, Interscience, New York (1970).

11. For a good discussion of nitrocellulose decomposition see C Selwitz, *Research in Conservation: Cellulose Nitrate in Conservation*, J. Paul Getty Trust (1988).

12. H R Leider and A J Pane, NTIS DE86016007, UCRL 94049, Rev. 1.

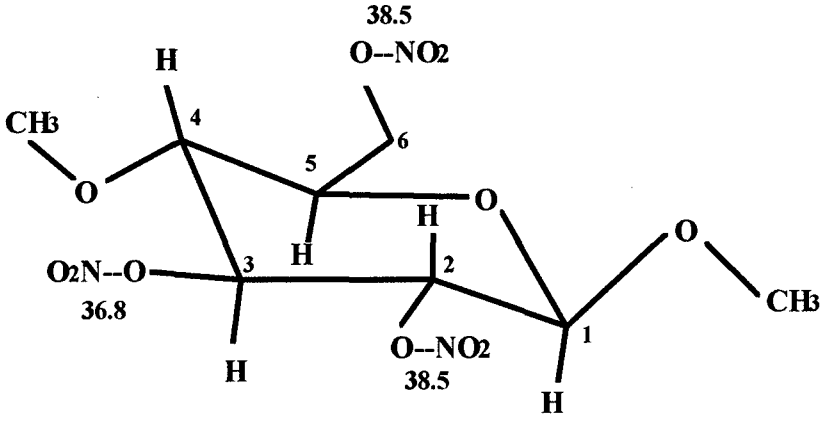

Figure 1 Model used for Trinitrocellulose with Calculated Bond Dissociation Energies (kcal/mol) of Nitate Ester N-O bonds

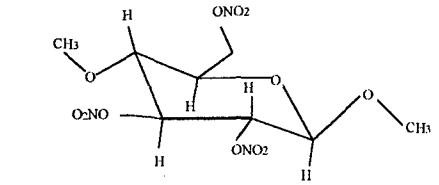

"Normal" Chair

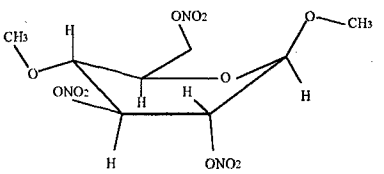

Boat 1

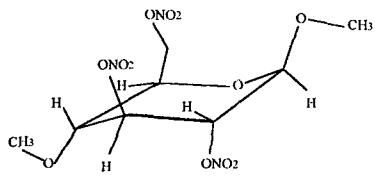

Inverted Chair

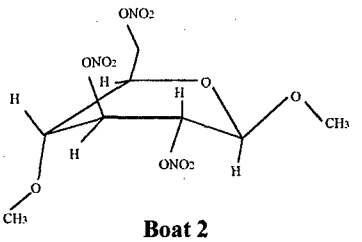

Boat 2

Figure 2 Models used for Different Ring Conformations of Trinitrocellulose

Table 1 Experimental and Predicted H-X Bond Dissociation Energies (kcal/mol)

Bond	Expt.	B3-LYP/3-21G*	UMP2/6-31G*	G2
H-CH_3	103.8	104.8	94.6	104.1
H-CH_2CH_3	101.1	100.4	91.6	100.6
H-$CH(CH_3)_2$	98.6	97.6	91.8	100.6
H-CH_2OH	98.0	93.0	86.7	96.2
H-HC(O)	87.0	86.9	77.3	87.9
H-CN	123.8	127.6	134.8	126.9
H-CH_2F	103.1	97.0	90.7	101.2
H-CHF_2	99.5	97.0	91.9	103.1
H-CF_3	105.9	102.3	97.3	108.5
H-CH_2Cl	100.8	99.4	90.4	99.3
H-$CHCl_2$	98.4	96.6	88.5	97.4
H-CCl_3	93.6	93.8	86.3	
H-CH_2OCH_3	93.0	94.3	87.7	96.2
H-$C(O)CH_3$	89.4	89.2	80.9	90.5
H-$CH=CH_2$	111.3	110.5	107.5	112.3
H-CCH	132.9	133.6	140.8	135.0
H-OCH_3	104.4	91.3	93.2	105.1
H-$C(O)OCH_3$	97.1	97.8	95.6	
H-OH	119.2	102.3	105.0	119.3
H-OOH	88.1	77.5	78.0	87.8
H-$OC(O)CH_3$	105.8	100.8	105.1	
H-NH_2	107.4	102.1	96.1	108.0
H-F	136.2	110.4	118.9	137.2
H-Cl	103.2	97.6	86.0	103.8

N.B. Gaps in the results indicate that the calculation was too large for our resources.

Table 2 Experimental and Predicted Bond Dissociation Energies (nonH-R bonds)

Bond	Expt.	B3-LYP/3-21G*	UMP2/6-31G*	G2
CH_3-CH_3	88.5	88.0	89.1	88.3
CH_3-CH_2CH_3	88.8	86.1	91.5	90.5
$HOCH_2$-CH_2OH	89.1	78.7	86.9	85.4
CH_3-CH(O)	83.4	84.3	85.4	85.7
CH_3-C(O)CH_3	84.3	83.5	72.4	85.7
CH_3-C(O)OH	85.0	90.5	95.1	95.2
CH_3-C(O)OCH_3	93.2	92.4	96.2	
HC(O)-C(O)H	68.5	72.5	72.6	73.0
CH_3-CN	121.8	124.5	140.8	122.5
NC-CN	134.6	151.6	179.2	140.5
CH_2=CH_2 (singlet)*	193.0	207.8	208.8	189.7
CH_2=CH_2 (triplet)*	175.1	173.6	167.4	170.0
CH_3-OH	92.3	84.4	90.0	91.5
$(CH_3)_2$CH-OH	96.0	88.4	97.7	
CH_3-OCH_3	81.9	76.6	85.4	84.1
CH_3C(O)-OH	110.4	108.3	113.9	111.6
HC(O)-OCH_3	97.4	98.1	106.2	103.1
CH_3C(O)O-CH_3	84.0	84.0	96.0	
CH_3C(O)-OCH_3	99.5	97.6	107.2	
F-CH_3	112.8	100.2	106.9	110.7
F-CH_2F	119.5	108.6	120.8	122.1
F-CHF_2	124.5	120.0	131.2	130.4
F-CF_3	129.7	126.4	132.6	133.1
Cl-CH_3	83.4	77.7	78.5	82.8
Cl-CH_2Cl	80.5	71.2	76.6	81.0
Cl-$CHCl_2$	77.0	66.8	72.7	77.6
Cl-CCl_3	68.0	59.8	67.0	
HO-OH	51.2	54.1	50.9	50.5
HC(O)-NH_2	99.5	106.0	101.6	101.1
CH_3C(O)-NH_2	98.9	103.7	101.1	99.8
CH_3-NO_2	60.8	54.4	58.4	62.0

* singlet indicates formation of two single CH2 moieties; triplet indicates formation of two triplet CH2 moieties.

N.B. Gaps in the results indicate that the calculation was too large for our resources.

Table 3 Bond Dissociation Energies for Nitrate Ester Bonds

Bond	Expt.	B3-LYP/3-21G*	UMP2/6-31G*	G2
$CH_3O\text{-}NO_2$	40.7	40.4	45.3	44.7
$CH_3CH_2O\text{-}NO_2$	40.8	40.4	45.3	
$CH_3CH_2CH_2O\text{-}NO_2$	40.5	40.2	45.4	
$(CH_3)_2CHO\text{-}NO_2$	40.9	40.3	43.8	

N.B. Gaps in the results indicate that the calculation was too large for our resources.

Table 4 Predicted Nitrate Ester N-O Bond Dissociation Energy as a Function of Ring Conformation for Trinitrocellulose

Bond	"Normal" Chair	"Inverted" Chair	"Boat 1"
C2O-NO2	38.5	35.0	
C3O-NO2	36.8	30.8	32.4
C6O-NO2	38.7	38.5	

TEX: A Promising New Insensitive High Explosive*

P.C. Braithwaite, W. W. Edwards, R. M. Hajik,
T. K. Highsmith, G. K. Lund, R. B. Wardle
P.O. Box 707, M/S 244
Thiokol Propulsion
Brigham City, Utah 84302

ABSTRACT

It is a continuing objective in the design and production of explosives to provide compositions which are highly energetic when intentionally initiated, but in which the risk of unintentional detonation is minimized. A series of new explosives have been developed based on the new insensitive high explosive 4,10-dinitro-2,6,8,12,-tetraoxa-4,10-diazatetracyclo-[5.5.0.05,903,11]dodecane (TEX). Although the synthesis of TEX was initially reported by Boyer[1] in 1990, it received little attention in the energetic materials community until recently. Thiokol Corporation has recently developed an improved two step synthetic route for the production of TEX which involves the use of readily available, low cost materials. This new synthesis has resulted in sufficient quantity of this material being available to allow some initial evaluations to be conducted.

Characterization of TEX shows it to be more thermally stable and significantly less sensitive to shock, impact and friction than conventional high performance solid nitramines such as RDX, HMX or CL-20. TEX has also been shown to be less likely to proceed from deflagration to detonation than conventional nitramines. Theoretical performance calculations of explosives utilizing TEX predict increased performance relative to NTO, principally due to its high density.

In studies performed to obtain performance characteristics of TEX a simple castable explosive was prepared using an energetic binder system and compared to analogous explosives using RDX and NTO. In instrumented card gap tests the TEX explosive detonated at 0 cards but did not detonate at 70 cards, while RDX and NTO analogues detonated at both 0 and 70 cards. Furthermore, the detonation velocity of the TEX explosive at 0 cards was higher than the NTO explosive. In shock sensitivity studies the go no-go point of a 93% solids TEX pressed explosive was found to be approximately 150 cards less than an analogous HMX composition.

BACKGROUND

During the past decade a significant effort has been made in the development of high explosives which meet the insensitive munitions requirements of MIL-STD 2105,

"Military Standard Hazard Assessment Tests For Non-Nuclear Ordnance." A common formulation strategy used to develop insensitive munitions (IM) explosives is to replace some of the conventional ingredients such as HMX or RDX with less sensitive ingredients such as 3-nitro-1,2,4-triazol-5-one (NTO) and nitroguanidine (NQ). This formulation approach has been successful in the development of less sensitive explosives; however, the performance of these explosives is often not acceptable for the desired application. Clearly there is still a need to develop new ingredients and formulations which are insensitive to common stimuli and still retain the desired performance characteristics.

SYNTHESIS AND CHARACTERIZATION

TEX is a caged nitramine and has the structure shown in Figure 1. The synthesis of TEX reported by Boyer is a two step process in which diformyltetrahydroxypiperazine (DFTHP) is formed by the reaction of formamide and glyoxal. DFTHP is then nitrated by sequential treatment with sulfuric and then nitric acids in the presence of glyoxal to give TEX. Thiokol has made improvements to the synthesis which have increased both the yield and purity. These improvements are the subject of pending patents and have greatly simplified the scale-up of TEX.

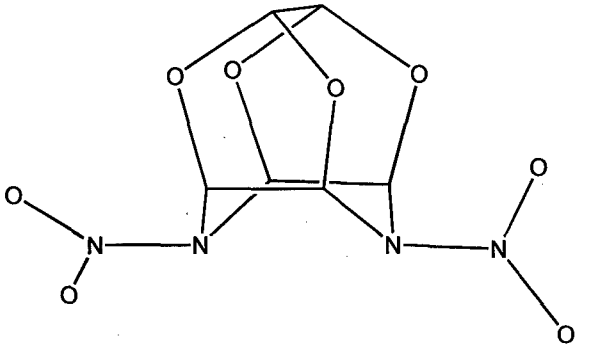

Figure 1. Structure of TEX. The structural similarity of TEX to the well-known CL-20 is obvious. In this depiction, the hydrogen atoms are deleted for simplicity and the carbon atoms are not labeled.

Early samples of TEX produced at Thiokol had a relatively small particle size with a broad distribution. As additional improvements in the synthesis were made, the particle size obtained increased and the particle size distribution became narrower (see Figure 2). Over 100 pounds of TEX has been produced to date for evaluation in explosive and propellant compositions. Efforts with grinding TEX in a fluid energy mill have also proven particularly successful (see Figure 3).

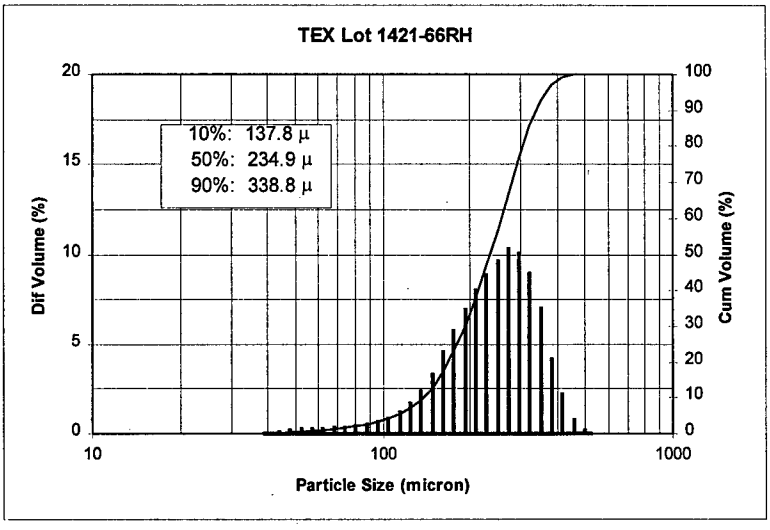

Figure 2. TEX Particle Size Distribution. Shown above is the particle size of TEX as obtained directly from the nitration reaction after quench and washing.

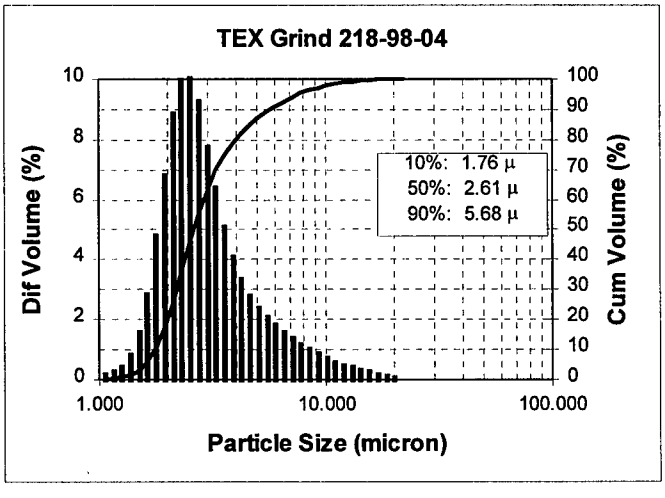

Figure 3. Ground TEX Particle Size Distribution. This material was obtained from the distribution initially obtained from the nitration by fluid energy mill grinding.

Figure 4. Micrograph of TEX. The quality of the individual TEX crystals and the favorable shape are apparent in this photomicrograph.

The heat of formation of TEX was experimentally determined to be -106.5 kcal/mole and its density was reported by Boyer to be 1.99 g/cc. This density is consistent with out experimental data and the high density of TEX can be attributed to its three dimensional caged structure. Laboratory scale safety tests have been conducted which demonstrate that TEX is much less sensitive to friction and impact stimuli than RDX and HMX. TEX has excellent thermal stability, is compatible with common inert and energetic polymers and plasticizers, fuels, and oxidizers. TEX also appears to have a mild cook-off response and evolves very little gas during the vacuum thermal stability test (0.05 ml gas is evolved after 48 hours @ 100°C). Selected safety data for TEX, RDX, HMX, and NTO are shown in Table I (SBAT[2] is a small scale autoignition test which has been developed at Thiokol and successfully used to predict the cook-off temperature of energetic materials in full scale test articles).

Table I. Summary Of Safety Test Results For TEX, RDX, HMX, and NTO.

Material	Impact		ABL Friction	ESD	SBAT onset
	Thiokol (in, 50%)	ABL (cm, t.i.l.)	(psi @ ft/sec, t.i.l.)	(Joules, 50%)	(°C)
TEX (200 μ)	>46	33	800 @ 8	>8	199
RDX (10 μ)	22	3.5	130 @ 4	<0.03	189
HMX (20 μ)	27	1.8	50 @ 4	0.25	208
NTO (250 μ)	43	26	800 @ 8	>8	234

Additional testing which demonstrated the insensitive nature of TEX was performed using a small-scale deflagration-to-detonation transition (DDT) test. This DDT test, initially developed in the former Soviet Union in the early 1970's[2,3] uses a thick walled ductile metal tube which is filled with the energetic material to be evaluated. The tube is sealed at both ends and the energetic material is ignited. If the material transitions from burning to detonation then the detonation wave expands the tube, otherwise the

inner diameter of the tube remains unchanged. The distance between the initiation of the burn and the detonation is an important parameter used in this test to rank the tendency of a material to undergo DDT. When TEX and NTO were evaluated in this test they did not detonate, while materials such as RDX, HMX, TNAZ and CL-20 readily detonate in this test.

THEORETICAL EXPLOSIVE PERFORMANCE

Theoretical computer modeling calculations have been made to predict the performance of TEX as a neat material and in typical explosives. Selected calculations are shown in Table II. As shown by these calculations the predicted performance of TEX is better than NTO and NQ and is similar to RDX. These calculations were performed using TIGER[4] computer program with the BKW equation of state. Similar calculations have been performed using the JCZ3 equation of state. The JCZ3 equation of state predicts the performance of TEX to be better than NQ, similar to NTO and somewhat lower than RDX. Because of the apparently non-ideal detonation reaction of TEX it is suggested that JCZ3 be used to predict the performance of explosives containing appreciable quantities of TEX.

Table II. Performance Predicted By TIGER Using BKW Equation Of State.

Material	Density (g/ml)	Detonation Pressure (katm)	Detonation Velocity (m/sec)
TEX	1.99	370	8665
RDX	1.82	360	8802
NTO	1.91	307	8120
NQ	1.71	286	8348
TEX/TNT (75/25)	1.89	329	8306
RDX/TNT (75/25)	1.77	325	8435
NTO/TNT (75/25)	1.84	288	7938
NQ/TNT (75/25)	1.70	277	8146

INITIAL EXPLOSIVES CHARACTERIZATION

Initial studies performed to obtain performance characteristics of TEX were performed using a simple castable explosive. The composition selected for this evaluation consisted of 70 percent TEX in a poly(glycidyl nitrate) (PGN)/DEGDN binder system. For comparative purposes analogous explosives using RDX and NTO were prepared. Each explosive was mixed and loaded into two standard LSGT card gap pipes. The card gap pipes were instrumented every inch to determine detonation velocity. The results of this test series are shown in Table III. As shown in Table III, the explosive containing TEX detonated at 0 cards but did not detonate at 70 cards, while the RDX and NTO explosives detonated at both 0 and 70 cards. Furthermore, based on the detonation velocity TEX outperformed NTO but fell quite short of the RDX analog

indicating that the non-ideal nature of the TEX detonation reaction is important. This was verified in experiments in which the TEX detonation products were frozen by adiabatic-free expansion followed by mass spec analysis.[5] These experiments showed the production of TEX decomposition products occurred over a period of time roughly 30 times longer than for HMX. This is slower than for TATB. Further, the products included considerable higher molecular weight, complex species typical of non-ideal detonation.

Table III. LSGT Test Results With Castable Explosives

Energetic Solid*	Gap (cards)	Input Pressure (kbar)	Test Results
TEX	zero	213.1	detonation, 6811 m/sec
TEX	70	69.8	no detonation, recovered unburned explosive
NTO	zero	213.1	detonation, 6263 m/sec
NTO	70	69.8	detonation, 5571 m/sec
RDX	zero	213.1	detonation, 7844 m/sec
RDX	70	69.8	detonation, 790 m/sec

* All explosives contained 70% solids in a PGN/DEGDN binder system.

The insensitive nature of TEX was also demonstrated in a composite explosive containing 20% TEX, a PGN/DEGDN binder, ammonium perchlorate and aluminum powder. An similar explosive was prepared in which the TEX was replaced with HMX. These explosives were also cast into two each instrumented LSGT card gap pipes. The results of the card gap tests on these explosives are shown in Table IV. Even though these explosives only contained 20% nitramine a significant reduction in sensitivity was achieved through the use of TEX. As shown in Table IV both explosives detonated at 35 cards, but the explosive containing TEX did not detonate at 70 cards while the explosive which used HMX detonated at 70 cards.

Table IV. LSGT Test Results For Castable Composite Explosives

Composition	Gap (cards)	Input Pressure (kbar)	Test Result
TEX/AP/Al	35	92.0	detonation, 5579 m/sec
TEX/AP/Al	70	69.8	no detonation, ave. reaction rate 2409 m/sec
HMX/AP/Al	35	92.0	detonation, 7432 m/sec
HMX/AP/Al	70	69.8	detonation, 7180 m/sec

TEX has also been successfully formulated into pressed explosives using energetic and non-energetic explosives. For example in a formulation containing 93% TEX and 7% Estane® the go/no-go shock sensitivity in the insensitive high explosives gap test the shock sensitivity was found to be between 63 and 75 cards. The go/no-go shock sensitivity in analogous HMX/Estane® explosive was between 216 and 219 cards.

Because of the favorable response of explosives containing TEX in card gap testing it is expected that these formulations will have milder reactions to sympathetic detonation, bullet impact and shaped charge jet attack than analogous explosives which use conventional nitramines. The mild response of TEX in small, unconfined, cook-off tests is very encouraging and gives the promise of a mild response in confined full scale cook-off testing. Clearly additional testing and evaluation of TEX and TEX based explosives is needed to confirm these trends.

SUMMARY AND CONCLUSIONS

TEX is a new energetic material which is readily synthesized from low cost starting materials. It has a promising blend of insensitivity and performance. It is readily used with inert and energetic binder systems in castable and pressed explosives. It is planned to continue the development of TEX in new high performance, IM explosives.

---

[1] Ramakrishnan, V.T., Vedachalam, M., Boyer, J.H., "4,10-Dinitro-2,6,8,12-tetraoxa-4,10-diazatetracyclo[5.5.0.0^{5,9}0^{3,11}]dodecane," *Heterocycles*, 31, 479, 1990.

[2] Smith, L.D., "Easily Test Thermal Stability an Detonability," *Chemical Engineering Progress*, September 1994, 67-74.

[3] Belyaev, A.F., Bobolev, V.K., Korotkov, A.I., Sulimov, A.A., Chuiko, S.V., "Transition from Deflagration to Detonation in Condensed Phases," *Israel Program for Scientific Translations, Jerusalem*, 1975, 142-148.

[4] Coperthwaite, M. Zwisler, W.H. "TIGER Computer Program and Documentation," *SRI International Publication #Z106*, 1973.

[5] Greiner, R., *Rev. Sci. Instruments*, 64 (1), 1993, and Los Alamos Report 93-1545.

HERSTELLUNG VON AMMONIUMDINITRAMID-PARTIKELN
FORMATION OF AMMONIUM DINITRAMIDE (ADN) PARTICLES

U. Teipel, T. Heintz, K. Leisinger, H. Krause

Fraunhofer-Institut für Chemische Technologie (ICT)
Postfach 1240, 76318 Pfinztal

Abstract

Ammonium dinitramide (ADN) is a powerful oxidizer that should be used in propellants and explosives in future. The particle shape of synthesized ADN is not unique and contains agglomeration. To have an intentional influence on the burning rate, it is necessary to modify the particle shape of the initial material to particles with a defined ratio of surface/volume. Besides, it is necessary to produce particles with predetermined mean particle size and particle size distribution. To keep this demand it is practical and functional to formate spherical particles.

Spheres can be shaped in a two-phase system. In this case, the molten ADN is dispersed in a continuous phase which is not mixable with ADN. Caused by the surface- and interfacial tension the molten droplets take on a spherical shape.

Emulsions from molten ADN and different oils are investigated. The solidification of the molten droplets to spherical particles takes place during the cooling down to a temperture less than the melting point of ADN.

By the choice of suitable substances and optimizing the process parameters, spherical ADN particles with a mean size from 5 µm until 800 µm can be reproduced successfully.

1 Einleitung

Ammoniumdinitramid (ADN) ist ein leistungsstarker Oxidator für Treib- und Explosivstoffe, welcher gegenüber anderen energetischen Materialien wesentliche Vorteile hat /1,2/:

- Signaturarmer Abgasstrahl beim Abbrand von ADN-Raketentreibstoffen
- Geringere Gefährdung der Umwelt da das Abgas frei von Chlor und Salzsäure ist
- Hoher Sauerstoffüberschuß

Das synthetisierte ADN hat i.d.R. eine uneinheitliche Partikelform und ist agglomeriert. Um bestimmte Eigenschaften, wie z.B. das Abbrandverhalten, gezielt zu beeinflussen ist eine Rekristallisation des Ausgangsmaterials zu Partikeln mit definiertem Oberflächen/Volumen-Verhältnis erforderlich. Außerdem ist es notwendig eine definierte mittlere Partikelgröße und Partikelgrößenverteilung herstellen zu können. Daher hat sich die Erzeugung von kugelförmigen Material als praktikabel und zweckmäßig erwiesen.
Zur Erzeugung der Kugelform wird ADN-Schmelze in einer zweiten Phase, die nicht mit ADN mischbar ist, fein verteilt. Die Schmelzetropfen nehmen aufgrund ihrer Ober- bzw. Grenzflächenspannung eine sphärische Gestalt an.
Die Untersuchungen wurden an flüssig/flüssig-Systemen durchgeführt. Dazu wurden Emulsionen aus ADN-Schmelze und verschiedenen Ölen hergestellt. Die Umwandlung der Schmelzetröpfchen zu festen, kugelförmigen Partikeln findet während der Abkühlung der Emulsion auf Umgebungstemperatur statt, also unterhalb der Schmelztemperatur von ADN.
Durch geeignete Stoffauswahl und Optimierung der verfahrenstechnischen Parameter kann kugelförmiges ADN mit einer Partikelgröße von 5 µm bis 800 µm reproduzierbar herzustellen.

2 Chemische und physikalische Eigenschaften von ADN

Summenformel:	$NH_4N(NO_2)_2$
Dichte:	1,82 - 1,84 g/cm^3 /2/
Schmelzpunkt:	91,5 - 92,5 °C /3/
Zersetzungstemperatur:	127 °C /3/

Bildungsenthalpie $-\Delta H_f$:	-150,6 kJ/Mol /2/
Zersetzungsenergie:	255 ± 12,5 kJ/Mol /3/
Massenverlust:	4 % (nach 24 Stunden bei 100 °C) /3/
Wassergehalt:	0,42 % (nach Synthese)
	0,41 % (nach Emulsionskristallisation)
Reibempfindlichkeit:	64 N
Schlagempfindlichkeit:	3,5 Nm

3 Versuchsdurchführung

Die Herstellung von sphärischen ADN-Partikeln aus Emulsionen erfolgt in zwei Teilschritten:

1. Herstellen einer W/O-Emulsion aus ADN-Schmelze als disperse Phase und Öl als kontinuierliche Phase. Eine Bedingung ist, daß die Grenzflächenspannung zwischen ADN-Schmelze und Öl hinreichend groß ist um sphärische Tropfen zu erzeugen und diese auch bei der anschließenden Erstarrung nicht von der Kristallstruktur deformieren zu lassen.
2. Kristallisation der ADN-Tropfen zu festen sphärischen Partikeln. Da ADN-Schmelze ein stark inhibiertes Verhalten aufweist, ist neben der Unterkühlung der Schmelze eine zusätzliche Initiierung durch den Eintrag mechanischer Energie oder durch Partikel-Partikel Wechselwirkung erforderlich. Um bei der Kollision der Tropfen Koaleszenz oder Agglomeration zu vermeiden sind je nach Art der gewählten kontinuierlichen Phase entsprechende Emulgierhilfsstoffe, wie z.B. Stabilisatoren oder Schutzkolloide, beizufügen.

Die vom Rührer eingebrachte Energie darf nicht so groß sein, daß die erstarrenden Partikel bzw. Tropfen deformiert werden. Es ist möglich den Zeitraum des Phasenüberganges von flüssig nach fest über die ADN-Konzentration in der Emulsion zu steuern, da sich die Anzahl der Stöße mit der Konzentration erhöht.

3.1 Versuchsaufbau

Der in Abbildung 1 schematisch dargestellte Versuchsaufbau wird mit maximal 3 g ADN betrieben. Grundsätzlich werden die Versuche nach folgendem Ablauf durchgeführt:

1. Das Öl (kontinuierliche Phase) und evtl. Zusatzstoffe werden unter Rühren aufgeheizt.
2. ADN zugeben und dispergieren.
3. Emulsion abkühlen lassen → Suspension.
4. Fest/flüssig Trennung durchführen und ADN-Partikel trocknen.

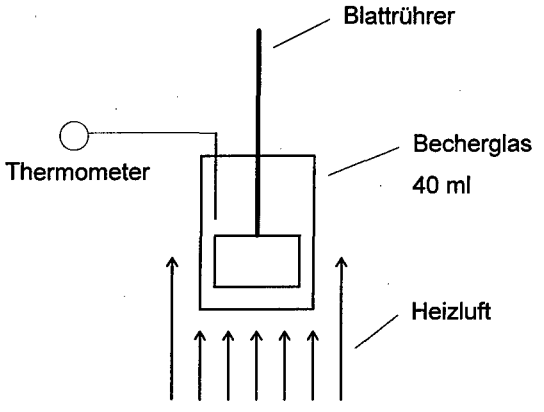

Abbildung 1: Versuchsaufbau im Labormaßstab

3.2 Stoffauswahl

Als kontinuierliche Phase wurde Silikonöl oder Paraffinöl eingesetzt. Es wurden verschiedene Emulgierhilfsstoffe verwendet:
Tenside führen durch Herabsetzung der Grenzflächenspannung zwischen ADN-Schmelze und Öl zu einem leichterem Tropfenaufbruch und somit zu kleineren ADN-Tropfen. Sie lösen sich aber nicht nur in der kontinuierlichen Phase, was wünschenswert ist, sondern ebenfalls in der Schmelze und beeinflussen deren Eigenschaften. So wird bedingt durch die Reduzierung der Grenzflächenspannung der Schmelze die

Kugelform der Tropfen beim Kristallisieren deformiert und die unregelmäßig geformten Partikel neigen zur Agglomeration.
Die verwendeten Stabilisatoren erhöhen die Viskosität der kontinuierlichen Phase durch Wasserstoffbrückenbindungen. Daher kann beim Rühren eine größere Scherspannung auf die Schmelzetropfen übertragen werden, wodurch man die Tropfengröße beeinflussen kann. Der zweite, und noch entscheidendere Vorteil ist, daß die beim Abkühlen und Reduzieren der Rührerdrehzahl wieder ansteigende Viskosität des Öles die Koaleszenz der Tröpfchen verhindert. Die Ober- bzw. Grenzflächenspannung wird nicht verringert, was sich positiv auf die gewünschte Kugelform der Partikel auswirkt. Zu beachten ist allerdings, daß die Konzentration des Stabilisators und die Konzentration der dispersen Phase (ADN-Schmelze) im richtigen Verhältnis stehen, da sich wenige Teilchen in hochviskosem Öl gegenseitig kaum zur Erstarrung anregen. Dies kann dazu führen, daß bei Raumtemperatur noch neben festen ADN-Kugeln noch flüssige Tröpfchen vorliegen.

3.3 Nachbehandlung

Die ADN-Schmelzetropfen erstarren bei ca. 69-76 °C. Aus der Emulsion wird somit eine Suspension aus welcher das feste Produkt abgetrennt werden muß.
Aufgrund der Dichtedifferenz zwischen ADN und Öl sedimentieren die Partikel. Der größte Teil des Öls kann abdekandiert und der Rest mit n-Heptan abgespült werden. Die ADN-Partikel können im Exsikkator getrocknet werden. Bei diesen Vorgängen ist zu beachten, daß das ADN nicht längere Zeit der Umgebungsluft ausgesetzt ist, da es stark hygroskopisch ist und sofort Feuchtigkeit aus der Luft aufnimmt.
ADN-Partikel aus Paraffinölemulsionen lassen sich relativ leicht von der kontinuierlichen Phase trennen, da Paraffinöl weniger polar ist als Silikonöl und sich daher im unpolaren n-Heptan besser löst.

4 Versuchsergebnisse

Abbildung 2 zeigt das als Ausgangsmaterial verwendete ADN aus der Synthese. Die einzelnen Partikel haben eine ungleichmäßige, kristallartige Form und sind stark agglomeriert.

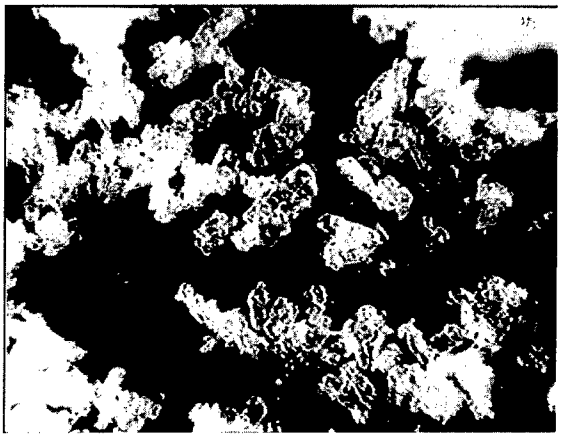

Abbildung 2: Ammoniumdinitramid aus der Synthese

Abbildung 3 zeigt ADN-Partikel aus einer Silikonölemulsion. Zur Erhöhung der Viskosität der kontinuierlichen Phase und zur Vermeidung von Koaleszenz der dispersen Phase wurde dem Silikonöl ein Stabilisator beigemischt. Es können Schmelzetropfen mit einer Größe von 50 bis 300 µm erzeugt werden. Die Anlagerung der Stabilisatormoleküle an den ADN-Tropfen verhindert deren Koaleszenz, wodurch allerdings auch die gegenseitige Anregung zum Erstarren vermindert wird. Versuche haben ergeben, daß ADN-Schmelze auch im stark unterkühlten Zustand erst durch den Kontakt mit kristallinem ADN zur Erstarrung angeregt wird. Somit ist es notwendig eine dem jeweiligen System angepaßte Menge an Emulgierhilfsstoffen zu bestimmen, welche einerseits Agglomeration verhindert und andererseits noch die Wechselwirkungen der Tropfen in der Strömung zuläßt.

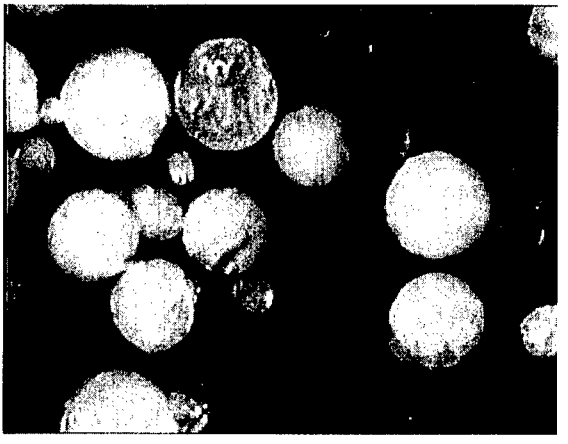

Abbildung 3: Sphärische ADN-Partikel aus Silikonölemulsion mit Stabilisator

Die selben Versuche wurden auch mit Paraffinöl als kontinuierlicher Phase durchgeführt. Verwendet man reines Paraffinöl erhält man relativ große Tropfen (300 µm - 1200 µm), die aber wesentlich weniger agglomerieren als in reinem Silikonöl (Abbildung 4). Der Verzicht auf Zusatzstoffe hat den Vorteil, daß die anschließende fest/flüssig Trennung zwischen Partikel und Öl einfacher ist, da die viskositätssteigernde Wirkung des Stabilisators die Sedimentation hemmt.

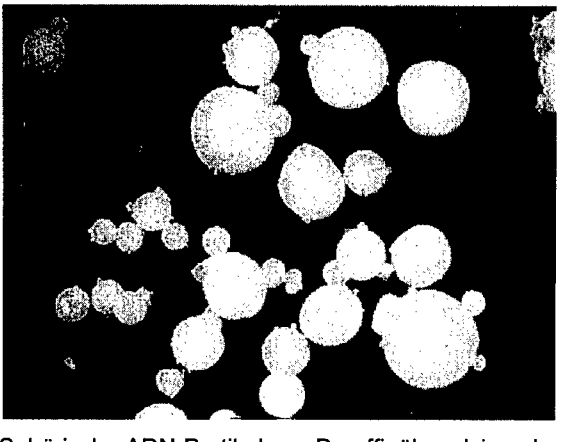

Abbildung 4: Sphärische ADN-Partikel aus Paraffinölemulsion ohne Zusatzstoffe

Die besten Ergebnisse liefert eine Paraffinölemulsion mit geeigneten Emulgierhilfsstoffen. Läßt man die anderen Versuchsparametern konstant entstehen Partikel

mit einem Durchmesser von 80 µm - 600 µm, welche sich durch ihre exakte Kugelform auszeichnen (Abbildung 5).

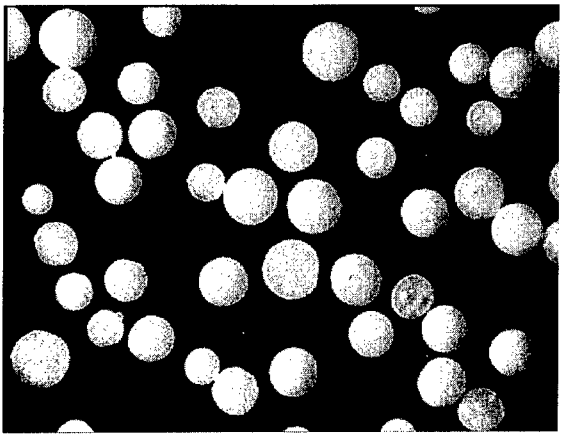

Abbildung 5: Kugelförmiges ADN: Hergestellt aus Paraffinölemulsion mit Emulgierhilfsstoffen

4.1 Partikelgrößenanalyse

Die Partikelgröße läßt sich vor allem über die Eigenschaften des Öles, z.B. dessen Viskosität, die Emulgierhilfsstoffe und die Prozeßparameter beeinflussen.
In Abbildung 6 ist die Volumensummen ($Q_3(x)$)- und Volumendichteverteilung ($q_3(x)$), die mittels Laserbeugungsspektrometrie ermittelt wurde, für feines und grobes ADN dargestellt. Für beide Verteilungen wurden der Medianwert $x_{50,3}$ und der Dispersionsgrad K(84/16) ermittelt.
Der Medianwert $x_{50,3}$ ist derjenige Wert einer Verteilung, bei dem die Verteilungssumme $Q_3(x_i)$ den Wert 50 % annimmt, d.h. die Hälfte der Partikel hat einen größeren Durchmesser als $x_{50,3}$.

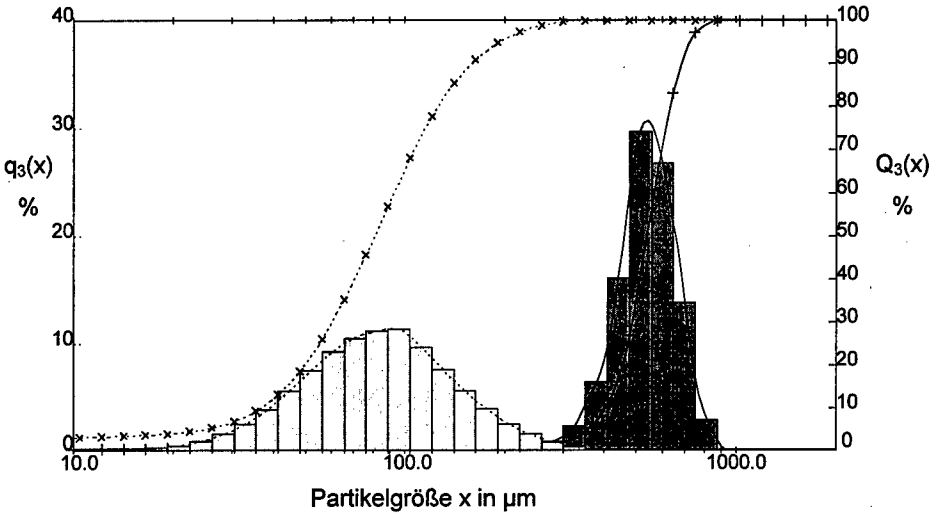

Abbildung 6: Volumensummen- $Q_3(x)$ und Volumendichteverteilung $q_3(x)$ für grobes und feines ADN

..... ADN-Kugeln aus Silikonölemulsion: $x_{50,3}$ = 81 µm; K(84/16) = 0,56

—— ADN-Kugeln aus Paraffinölemulsion: $x_{50,3}$ = 540 µm; K(84/16) = 0,20

Die Charakterisierung der Verteilungsbreite kann z.B. mit Hilfe des Dispersionsgrades K(84/16) erfolgen, welcher nach der Gleichung

$$K(84/16) = \frac{x_{84} - x_{16}}{2 \cdot x_{50}} \qquad (1)$$

definiert ist. Die Ermittlung von x_{84} und x_{16} erfolgt anhand der Volumensummenverteilung, wobei $Q_3(x_i)$ = 84 % bzw. 16 % beträgt.

Nach VDI-Richtlinie 3491 gilt für:

$K(84/16) \leq 0,14$	monodisperse Verteilung
$0,14 \leq K(84/16) \leq 0,41$	quasi-monodisperse Verteilung
$0,41 \leq K(84/16)$	polydisperse Verteilung

Somit hat das grobe Produkt mit K(84/16) = 0,20 eine quasi-monodisperse Verteilung.

In Abbildung 7 sind die Volumensummen- und die Volumendichteverteilungen zweier Partikelkollektive dargestellt, die mit unterschiedlichen Rührergeometrien (Propeller- und Blattrührer) erzeugt wurden dargestellt. Die Rührerdrehzahl und der Rührerdurchmesser, sowie die weiteren Versuchsparameter wurden konstant gehalten. Die Rühergeometrie beeinflußt hauptsächlich die Strömung im Emulgierreaktor. Der Propellerrührer erzeugt eine axiale Strömung, welche die Sedimentation der dispersen Phase verhindert und für eine gute Wärmeübertragung an der Gefäßwand sorgt. Bei der Umwandlung der mechanischen Energie des Rührers in kinetische Energie in der Strömung hat der Propellerrührer weniger Verluste und somit eine größere Scherwirkung, was zu kleineren Tropfen führt.

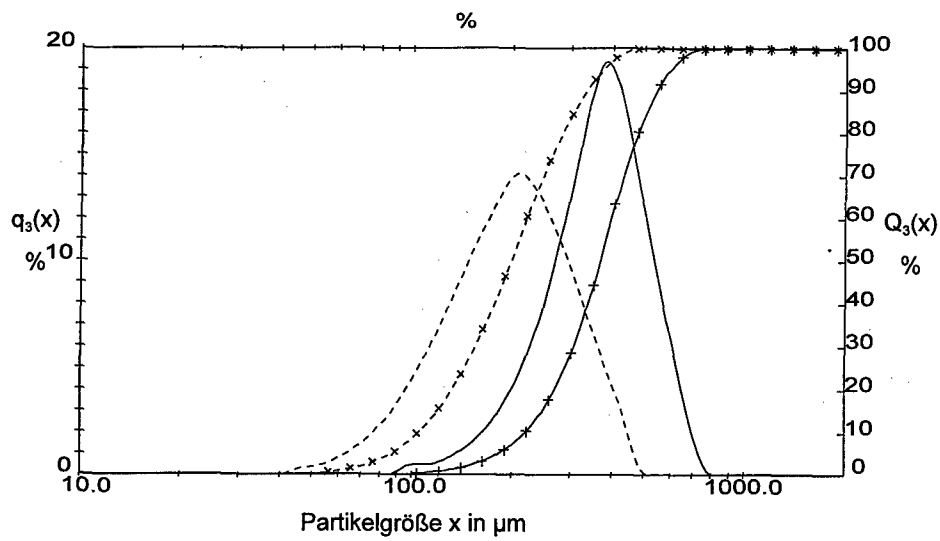

Abbildung 7: ····· Propellerrührer; $x_{50,3}$ = 200 µm; K(84/16) = 0,44

—— Blattrührer; $x_{50,3}$ = 370 µm; K(84/16) = 0,33

Rührerdrehzahl und Rührerdurchmesser sind konstant.

4.2 Produktanalyse

Die Produktequalität kann während des Herstellungsprozesses durch thermische Belastung oder die am Prozeß beteiligten Stoffe beeinflußt werden:
Um dies zu Überprüfen wurden die getrockneten Produkten und das Ausgangsmaterial aus der Synthese mit Hilfe der DSC-Analyse (Differential Scanning Calorimetrie) und der Infrarot (IR)-Spektroskopie untersucht.
Ein Vergleich der IR-Spektren des Ausgangsmaterials (Abbildung 8.1) mit den ADN-Partikeln aus Paraffinölemulsionen (Abbildung 8.2) und den ADN-Partikeln aus Silikonölemulsionen mit Stabilisator (Abbildung 8.3) zeigt keine relevanten Veränderungen durch den Emulsions-Kristallisationsprozeß.
Vergleicht man die DSC-Analysen des Ausgangsmaterials (Abbildung 9.1), der ADN-Partikeln aus Paraffinölemulsion (Abbildung 9.2) und der ADN-Partikeln aus Silikonölemulsion mit Stabilisator (Abbildung 9.3) so haben die aus Emulsionen rekristallisierten ADN-Kugeln einen Schmelzpunkt von etwa 90 °C, während das reine Ausgangsmaterial bei ca. 93 °C schmilzt. Dies ist ein Hinweis darauf, daß sich geringe Mengen des ADN-Zersetzungsproduktes Ammoniumnitrat (AN) gebildet haben.
Desweiteren wurde der Wassergehalt des Ausgangsmaterials und der ADN-Partikel überprüft, da ADN hygroskopisch ist und vor allem bei der Nachbehandlung die Gefahr besteht das Luftfeuchtigkeit aufgenommen wird. Die Messungen ergaben einen Wassergehalt von 0,42 % für das Synthesematerial und 0,41 % für die rekristallisierten ADN-Partikel.

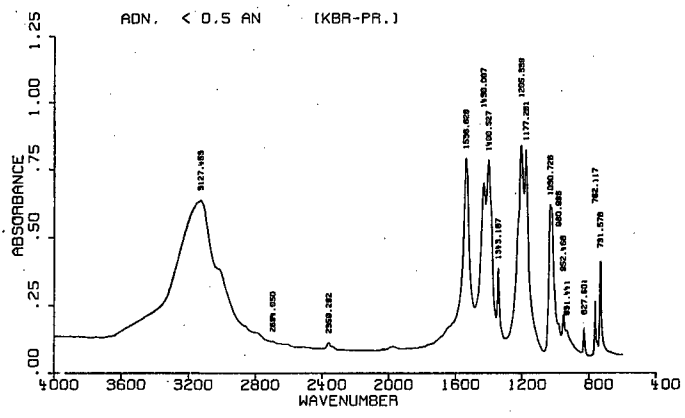

Abbildung 8.1: IR-Spektrum des Ausgangsmaterials aus der Synthese

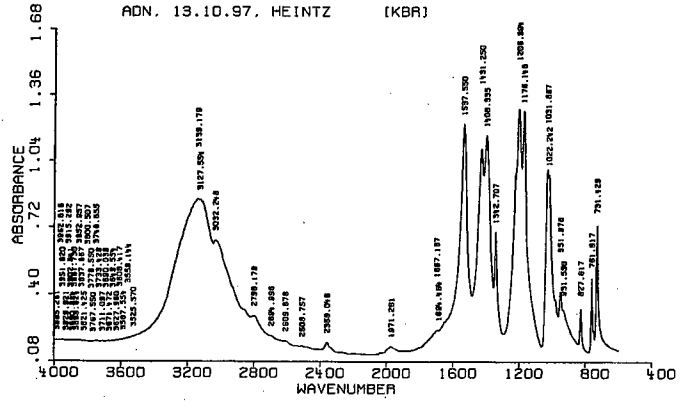

Abbildung 8.2: IR-Spektrum von ADN aus Paraffinölemulsion

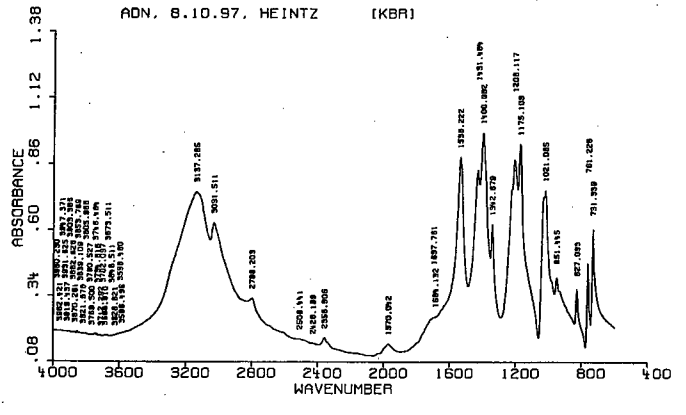

Abbildung 8.3: IR-Spektrum von ADN aus Silikonölemulsion mit Stabilisator

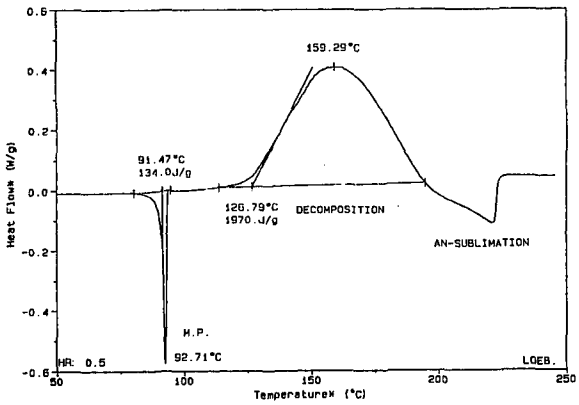

Abbildung 9.1: DSC-Analyse des Ausgangsmaterials aus der Synthese

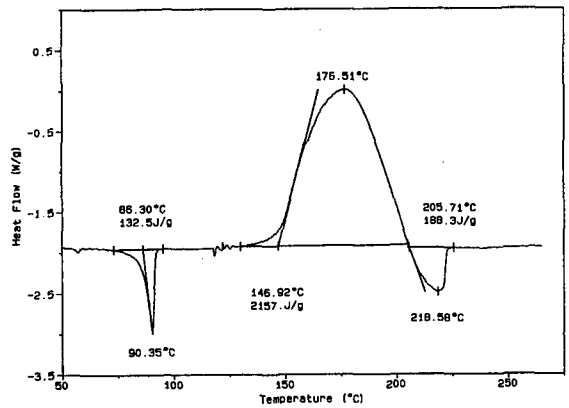

Abbildung 9.2: DSC-Analyse von ADN aus Paraffinölemulsion ohne Zusatzstoffe

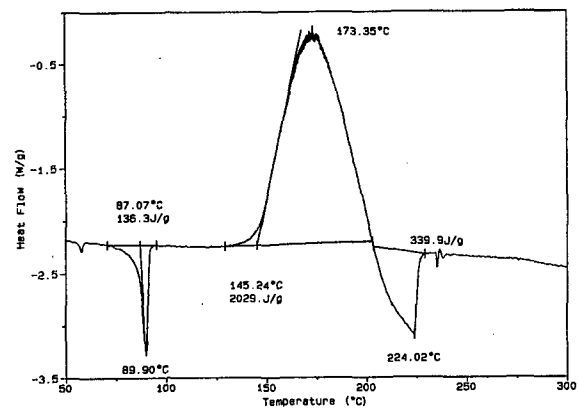

Abbildung 9.3: DSC-Analyse von ADN aus Silikonölemulsion mit Stabilisator

5 Literatur

/1/ Chan, M.L., Turner, A., Merwin, L., Ostrom, G., Mead, C. und S. Wood: ADN Propellant Technology, Challenges in Propellants and Combustion, Hrsg. Kenneth K. Kuo, S. 627 - 635

/2/ Langlet, A., Wingborg, N. und H. Östmark: ADN: A new high performance oxidizer for solid propellants, Challenges in Propellants and Combustion, Hrsg. Kenneth K. Kuo, S. 616 - 626

/3/ Löbbecke, S., Krause, H. H. und A. Pfeil: Thermal Analysis of Ammonium Dinitramide Decomposition, Propellants, Explosives, Pyrotechnics 22, S. 184 - 188 (1997)

RECRYSTALLIZATION OF NTO CRYSTALS IN A BATCH COOLING CRYSTALLIZER

Kwang-Joo Kim[1*], Min-Jun Kim[1], Jung-Min Lee[1], Hyoun-Soo Kim[2], Bang-Sam Park[2]

1. **Chemical Process and Engineering Center Korea Research Institute of Chemical Technology**
   P.O.BOX 107, Yusung, Taejeon 305-600, Korea
2. **Agency for Defense Development, P.O.BOX 35, Taejeon, Korea**

*** Corresponding author**

ABSTRACT

The recrystallization of NTO crystals was investigated in the laboratory scale and the bench scale crystallizers. The effect of additives on NTO morphology in crystallization was also explored. The kinetics of crystallization of NTO in solvents were measured. These kinetic data were employed along with a supersaturation balance to predict the crystal size in cooling crystallization. Some solvents to be acceptable for enhancing of NTO crystal morphology in a cooling crystallizer were selected. It is found that solvent has a large influence on the crystal shape, and the kinetics of crystallization and operating conditions are sensitive the crystal size and its distribution. Performances of a laboratory scale crystallizer and bench scale crystallizer were compared. Results suggest that mean crystal size can be predicted by the model combined with the supersaturation and crystallization kinetics.

INTRODUCTION

3-Nitro-1,2,4-triazol-5-one(NTO) is more attractive than common explosives like hexahydro - 1, 3, 5 - trinitro - 1, 3, 5 - triazine(RDX), octahydro - 1, 3, 5, 7 - tetranitro - 1, 3, 5, 7 - tetrazocine(HMX) and 2,4,6 - trinitrotoluene(TNT) in

terms of its insensitivity and stability. The morphology of NTO crystals coming from the reaction process has typically a jagged rod-like shape, which is easy to agglomerate and ultimately becomes sensitive to a sudden shock. One of the ways to lower the sensitivity toward sudden shock is to control the crystal morphology to be close to spherical. On the other hand, the mother liquors contain additional components from the chemical reaction, in particular formic acid, nitric acid, sulfuric acid and 1,2,4-triazole-5-one. Some of these are trapped into the crystals and are present even after washing. The purification process is necessary to remove these impurities. One attempts to solve these problems is by recrystallization of the NTO in a solvent which allows the control of the crystal size and crystal shape, purity, and narrow crystal size distribution.

EXPERIMENTS

The experiments were performed in a laboratory scale crystallizer as well as a bench scale crystallizer, which were operated batchwise. The crystallizers were a draft-tube type with external baffles and was equipped with an agitator, marine propeller type at a speed in the range of about 400 to 700 rpm. Either heated or cooled medium from a thermostated bath could be circulated through the jacket. An ethylene glycol - water solution was thermostated and controlled by a PID controller, with accuracy of 0.05K. The analysis of CSD, shape and mean crystal size were carried out by image analysis system(VIDAS, Karl Zeiss) with optical and electron microscopes.

RESULTS AND DISCUSSION

Nucleation

For nucleation from solution cooled down at constant rate, Nyvlt[4] proposed the following between the maximum allowable undercooling(i.e. metastable zone width), ΔT_{max} and cooling rate, b

$$\log b = \log(k / a) + n_1 \log(\Delta T_m) \qquad (1)$$

where, $k = k_n (dC_s / dT)^{n-1}$

The maximum allowable undercooling ΔT_{max}, was taken as the difference between the equilibrium temperature and the temperature at which nuclei were detected for each particular cooling rate. The equilibrium temperature was obtained from the experimentally determined solid-liquid diagram. Figure 1 shows the plots of cooling rate against maximum undercooling in log-log coordinates for saturation temperature.

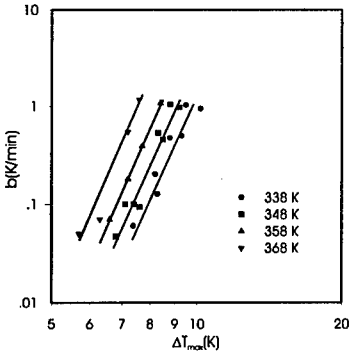

Fig. 1. Plot of b versus ΔT_m

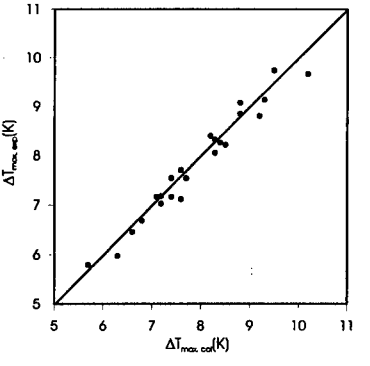

Fig. 2. $\Delta T_{max, exp}$ versus $\Delta T_{max, cal}$

As shown in Figure 1, the maximum allowable undercooling (i.e. maximum allowable supersaturation) varies with cooling rate and equilibrium temperature. The relationship among them can be expressed as the following relation.

$$\Delta T_m = c_1 b^l T_s^m \qquad (2)$$

The values of c1, l and m obtained in this study are 144.6, 0.0905 and -0.47, respectively. All experimental data obtained from this work were correlated from equation 2, shown in Figure 2. Therefore, equation 2 expresses the maximum allowable supersaturation in which the variation of the cooling rate and initial concentration in such a cooling crystallizer considered.

Linear crystal growth rate

The linear crystal growth rate is defined as the change of the characteristic dimension of the crystal with time as equation 3.

It depends mainly on the supersaturation.

$$\bar{G} = \frac{\bar{L}}{t_b} = k'_g \, \Delta\bar{C}^{g} \qquad (3)$$

Where L is crystal size, t_b batch time, k_g rate constant of crystal growth and ΔC average supersaturation working in . Figure 3 shows a plot of the linear growth rate as a function of supersaturation. The crystal growth rate is proportional to the second power of supersaturation.

Calculation of crystal size

The mean crystal size is complex functions of nucleation and growth, which are functions of process variables such as agitation rate, feed composition and production rate. These functions are therefore related to the supersaturation. The average size of crystals obtained in this study was in the range of 5 to 1000 micron, which depends mainly on the supersaturation.

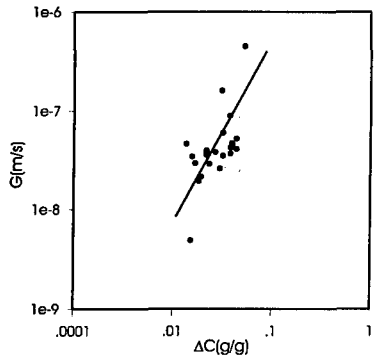

Fig. 3. Plot of G against ΔC

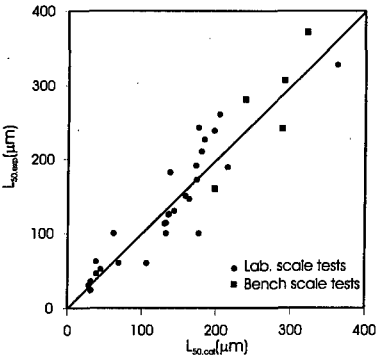

Fig.4. L_{exp} versus L_{cal}

Crystal size depends on the growth rate G, the nucleation rate B, and holdup of crystal φ_s.

$$\bar{L} = f\left(\frac{G\varphi_s}{B}\right) \quad (4)$$

This equation results from the fact that the mean crystal size increases with an increasing growth rate and holdup of crystal and a decreasing nucleation rate. Figure 4 shows the comparison between mean crystal sizes calculated from equation 4 and obtained in bench scale and laboratory scale crystallizers. It is obvious that the results of experiments are reasonably well approximately by relation expressed by equation 4.

Shape of NTO crystals

Figures 5 and 6 show the crude NTO crystals coming from reaction process and NTO crystals crystallized in water under right operating conditions, respectively. Selecting an appropriate operation of crystallizer is thought to be very important to control morphology of NTO crystals.

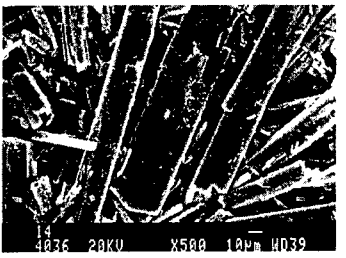

Fig. 5. Crude NTO from reaction

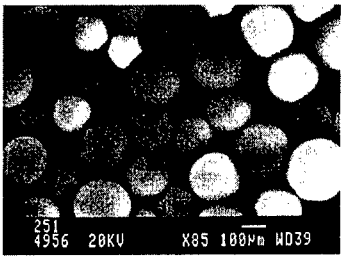

Fig. 6. NTO crystallized

CONCLUSION

The kinetic data of crystallization of NTO in solvents were employed along with a supersaturation balance to predict the crystal size in cooling crystallization. Performances of a laboratory scale crystallizer and bench scale crystallizer were compared. The results suggest that in a scale-up of crystallizer the mean crystal size can be predicted by the model combined with the supersaturation and crystallization kinetics.

SYMBOLS

B	Nucleation rate
b	Cooling rate
ΔC	Supersaturation
L	Crystal size
g	Crystal growth order
k	Nucleation rate constant
n	Nucleation order
T	Temperature
t_b	Batch time
ΔT_m	Metastable zone width

REFERENCES

1. Menapace, J.A. and Marlin, J.E.: J. Phys. Chem., 95, 5509(1991)
2. Lee K. Y. and Coburn M.D.: Los Alamos National Lab. Report, No. LA-10302-MS(1985).
3. Ostmark, H, Bergman, H. and Aqurist, G., Thermochemica Acta, 213, 165(1993).
4. Nyvlt, J.: Crystal Growth J., 3/4, 377-383(1968)
5. Nyvlt, J. et al.: Collect. Czechoslov. Chem. Comm., 38, 3199(1973).

SHOCK SENSITIVITY OF HMX/HTPB PBX'S: RELATION WITH HMX CRYSTAL DENSITY

A.E.D.M. van der Heijden [°] *and R.H.B. Bouma* [*]

TNO Prins Maurits Laboratory, [°] Pyrotechnics and Energetic Materials, [*] Properties of Energetic Materials, P.O. Box 45, 2280 AA Rijswijk, The Netherlands

Abstract

This paper describes the results which were obtained during a two-year cooperation between ICT (FRG) and TNO Prins Maurits Laboratory (NL). During this cooperation, both institutes selected a solvent from which HMX was recrystallized, with the objective to produce two grades of HMX differing in internal crystal quality, predominantly the amount of inclusions in the crystals. After sieving of the particles, casting of the HTPB-based PBX samples, the influence of the internal crystal quality on the shock sensitivity was investigated. As a reference material for these tests, the commercially applied HMX was used.

The results of the shock sensitivity tests point at a direct relation between the HMX crystal density (and hence crystal quality) and shock sensitivity of these particles in the final PBX: the higher the crystal density, the higher the crystal quality and the lower the shock sensitivity. Comparison of the results of ICT and TNO show a very good agreement.

1. Introduction

The objective of this research project is to gain insight in the role of internal defects in nitramine crystals – more specifically the nitramine HMX – in relation to the shock sensitivity of HTPB based PBX's containing 70 wt% solid load [1]. Three different qualities of HMX are used: commercial HMX, and two recrystallized HMX batches. These latter two batches comprise HMX crystals with a difference in their internal defect content, whereas the properties with respect to mean size, shape and surface smoothness should be practically constant. The commercially supplied HMX is included as the reference material.

Section 2 shortly reviews the experimental details of the techniques used during this research programme. In section 3 the HMX production and subsequent characterization of the produced batches with respect to the internal defect content and density of the crystals is reported. This section also includes the results of the shock sensitivity tests and the relation of these data with the product properties of the crystals used in the PBX's. The conclusions are summarized in section 4.

2. Experimental

2.1 Crystallization

The crystallization experiments were carried out in a 2.0 liter jacketed glass vessel, which is temperature controlled by means of a thermostat and computer software. With this equipment a certain temperature profile can be imposed. This so-called bench scale reactor is equipped with a propeller stirrer combined with a draft tube and four baffles. By using a draft tube and a propeller, an axial flow profile of the slurry is built up and maintained throughout the crystallization process. The four baffles divide the vessel in four compartments, in this way breaking up the vortex. A reflux unit prevents the evaporation of the solvent. A mixture of acetone and γ-butyrolactone was used as the crystallization solvent. More details can be found in an earlier paper [1].

2.2 Sieving

In order to prevent influences – other than the internal quality of the crystals – on the shock sensitivity, the width of the crystal size distribution (CSD) of the different batches was kept constant as much as possible. The width of the CSD was controlled by sieving the recrystallized batches as well as the commercial HMX product. The sieve fraction used for preparation of the PBX's is 250 - 425 μm.

2.3 Characterization of HMX crystals

The HMX crystals were characterized with respect to the crystal modification (X-ray powder diffraction), shape (optical microscopy, SEM), size distribution (laser diffraction), surface structure (SEM), defect content (optical microscopy, Laue X-ray difraction), impact and friction sensitivity (BAM), crystal density (fluid pycnometry) and purity (GC). The majority of the results of these characterization tests were reported and discussed earlier [1]. This paper focuses on the relation between the shock sensitivity of an HMX/HTPB PBX and the crystal density of the HMX crystals in the PBX. Therefore, the determination of the crystal density is explained in more detail.

The crystal density is determined by means of liquid pycnometry. The liquid used for the density measurements is dodecane which is saturated with HMX. All the measurements are carried out at room temperature and at least in duplicate. Usually an accuracy of 0.5% or better is reached in this way.

The theoretical density of β-HMX is 1.903 g/cm^3. Measurements deviating from this value point at the presence of inclusions or voids either filled with solvent or with vapour or a combination of these two possibilities. In principle, the vol% of inclusions (V_i/V_{tot}) can be determined if the content of the inclusions is known. This ratio can be calculated on the basis of mass conservation (with ρ the measured density and ρ_S the theoretical density of HMX):

$$\text{total mass} = \text{mass solid} + \text{mass inclusions} = m_S + m_i = m_{tot} \text{ or: } \rho_S V_S + \rho_i V_i = \rho V_{tot}$$

where $V_S = V_{tot} - V_i$. The vol% of inclusions is then known from the equation:

$$\frac{V_i}{V_{tot}} = \frac{\rho_s - \rho}{\rho_s - \rho_i} \approx 1 - \frac{\rho}{\rho_s} \quad \text{for } \rho_i << \rho_S$$

The inclusion density, ρ_i, is – depending on the content of the inclusion – determined by the liquid or vapour density, or some averaged value in case the inclusion contains both liquid and vapour. This can be concluded from the optical microscopic pictures, since generally solvent containing inclusions do not give rise (or to a much lesser extent) to the intensely black spots as can be

observed in the HMX crystals shown in figures 1 to 3. The density of a vapour is much smaller compared to the theoretical solid density ρ_S, hence in the above given equation for the vol% of inclusions, ρ_i can be neglected compared to ρ_S.

2.4 Casting of HMX/HTPB PBX

HMX/HTPB-based PBX's with a solid load of 70 wt% HMX were mixed and cast with help of an HKV5 vertical mixer, equipped with planetary mixing blades. For determination of the shock sensitivity according to the water gap test, samples were required of ∅ 21 mm and 40 mm high. The PBX was cast into PMMA cylinders with these internal dimensions.

***Figure 1:** HMX crystals taken from the commercial product (sieve fraction).*

2.5 Shock sensitivity test

The shock sensitivity is determined according to the BICT or water gap test within the research group Properties of Energetic Materials at TNO PML. This test is described in ref. [2]. As donor charge, an RDX/wax (hexocire) composition was used. The water gap test determines a 'go/no go' level, *i.e.* the water gap distance in mm below which the PBX will detonate. By using a calibration of the water gap and the pressure to which the PBX is subjected, the water gap distance can be translated to a shock initiation pressure. This pressure corresponds to the shock pressure in water, just before impact on the acceptor charge and is therefore not equal to the pressure in the PBX at the

moment of impact. The shock initiation pressure is determined by means of the Bruceton up-and-down method with an accuracy of 1 mm.

3. Results and Discussion

3.1 Crystallization of HMX batches

For the production of sufficient samples required for the shock sensitivity tests, several crystallization batches were needed. After recrystallization of the commercial HMX, the products which were obtained under the same experimental conditions corresponding to a specific quality of the batches, were mixed and sieved.

Figure 2: *HMX crystals taken from the 'bad' quality batch (sieve fraction).*

The HMX particles of the commercial product were non-transparent. Therefore, these crystals were slightly etched in order to smooth the particle surface. An example of a sample of the particles treated in this way is shown in figure 1. The commercial product consists of rounded particles, whereas the recrystallized material comprises more angular particles. Pictures of the two recrystallized batches can be found in figure 2 and 3, respectively. Although the recrystallized particles were much more transparent than the untreated commercial product, also the recrystallized material was slightly etched in order to have a fair comparison. The inclusion content in the recrystallized batches is much lower than in the commercial batch. This is substantiated by the crystal density of the three batches, which is considerably higher for the recrystallized batches (see

section 3.2). The observation that the inclusions are present as dark spots in the crystals suggests that the inclusions do not contain solution, but either vapour or vacuum.

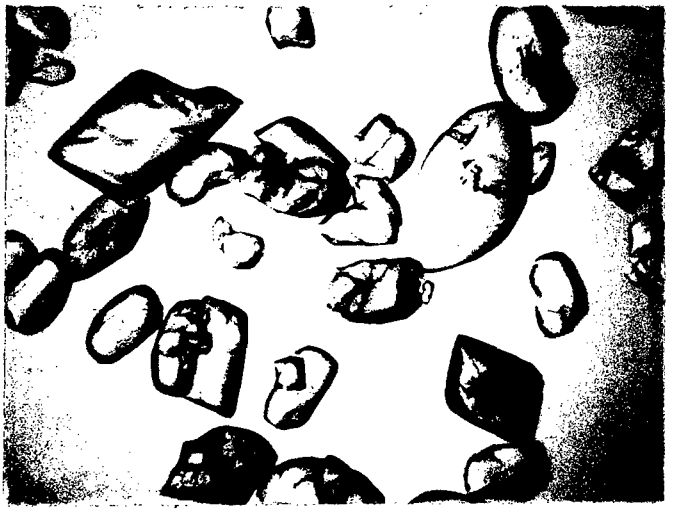

Figure 3: *HMX crystals taken from the 'good' quality batch (sieve fraction).*

3.2 Crystal density

The theoretical density of HMX is 1.903 g/cm^3. The density of the commercial HMX crystals as supplied by DYNO was measured to be 1.868 g/cm^3 (liquid pycnometry), while ICT found a value of 1.871 g/cm^3 (gas pycnometry) [3]. The HMX batches available at TNO and ICT are taken from the same lot as produced by DYNO, hence the starting material is the same for both institutes. For the sieved fraction (250 – 425 μm) of the commercial product the density was found to be 1.886 g/cm^3, so slightly higher than the (mean) density of the crystals comprising the entire size distribution. Also ICT found a slightly higher density for the sieved fraction of the commercial product, namely 1.888 g/cm^3.

The density of the recrystallized batches was always higher than the commercial product (see table 1). The difference between the crystal density of the 'bad' and 'good' quality product was higher for the unsieved batches. Apparently the crystals which contributed the most to the difference in mean crystal density of the entire batches, were sieved from the batches in both cases leading to a fraction of particles with a relatively high crystal density. Also microscopic observations showed a tendency of a higher inclusion content with increasing particle size.

The differences in crystal density are quite small, in particular the densities of the two recrystallized batches. Taking into account an accuracy of ~ 0.5% in the determination of the density, the values of 1.900 and 1.902 g/cm^3 clearly show an overlap. In principle also the density of the sieved commercial product shows a (slight) overlap with the other two crystal densities. However, comparison of the microscopy pictures (figure 1 *versus* figures 2 and 3), shows that the inclusion content in the commercial product is higher than in the recrystallized product, indicating that the difference in crystal density between the reference and recrystallized batches is significant.

Table 1: *Density of the three HMX batches comprising the commercial one and two recrystallized batches. The data refer to the 250 - 425 μm sieve fractions of the batches.*

Batch code (sieve fractions)	density [a] [g/cm^3]	Density [b] [g/cm^3]	inclusion content [c] [vol%]
Reference batch (DYNO)	1.886	1.888	0.89
Low-density ('bad' quality)	1.900	–	0.16
High-density ('good' quality)	1.902	–	0.05

a Density determined by TNO PML by means of fluid pycnometry.
b Density determined by ICT by means of gas pycnometry.
c Inclusion content calculated with help of the equation given in section 2.3, under the assumption that the inclusions contain vapour or vacuum, rather than solvent.

Several parameters characterizing the CSD of the sieve fractions of the recrystallized batches and the commercial product are given in table 2. The data show that the values of d_{10} and d_{90} of the commercial product practically coincide with the sieve meshes of 250 and 425 μm. For the recrystallized batches the cut-off values differ from the sieve meshes applied. Probably this is due to the fact that the shape of the crystals of the commercial product are more spherical than the particle shape of the recrystallized products, which consist of slightly more elongated particles. The size analysis technique is in principle best suited for measuring spherical particles and errors may be introduced when particles are measured which deviate from a sphere. On the other hand, sieving of elongated rather than spherical particles may also result in errors, since then an orientational dependence of the particles is introduced during sieving. Taking into account an accuracy of 5-10% in the size analysis data, this implies that the median sizes of the recrystalllized batches are

comparable. The median size of the commercial HMX batch is lower than that of the recrystallized batches.

Table 2: Median size (d_{50}) and sizes bounding the sieve fractions (d_{10} and d_{90}) of the recrystallized and commercial batches.

Batch code	d_{10} [μm]	d_{50} [μm]	d_{90} [μm]
Reference batch (DYNO)	249	328	430
Low-density ('bad' quality)	328	428	552
High-density ('good' quality)	298	381	498

3.3 Shock sensitivity

Table 3 summarizes the results of the BICT shock sensitivity tests for the PBX's HU32-1, 33-1 and 34-1. The lower the value of the water gap, the less sensitive the PBX is. The shock initiation pressure is plotted versus the crystal density of the HMX particles in figure 4. This figure also contains the data generated by ICT on the shock sensitivity of their PBX's [3]. For the ICT data set a similar tendency is found. Moreover, the TNO and ICT data sets agree very well and appear to fit on a single line.

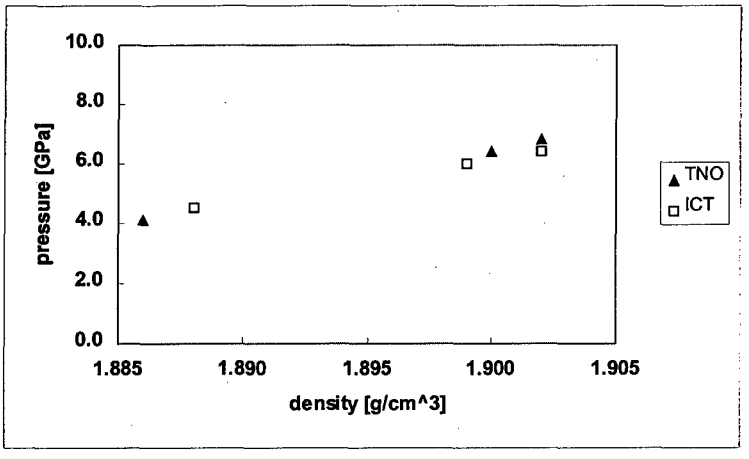

Figure 4: *Plot of the shock pressure vs. crystal density of the HMX particles.*

The finding that the density of the crystals correlates with the shock sensitivity of the PBX in which these crystals have been incorporated, is an important result. Earlier papers by Borne [4,5] pointed at a relation of the inclusion content in RDX and HMX crystals and the shock sensitivity of PBX's containing crystals with different amounts of inclusions. Borne used a flotation technique by means of which he was able to separate crystals of a certain density. These different crystal grades were incorporated in a PBX and subjected to shock sensitivity tests. Borne thus showed that crystals with a high inclusion content were more sensitive to shock than crystals with a low inclusion content.

An effect of ageing of the HU32-1 PBX, which was produced several months earlier than the other two PBX's, might be held responsible for the difference in shock sensitivity. However, the mechanical properties, which in general will change due to *e.g.* oxidation and therefore degradation of the binder during ageing, usually do not influence the shock sensitivity. This implies that the measured differences must be a result of differences in the HMX particle properties, like size, density, internal quality or shape. By using similar sieve fractions of the particles in all of the PBX's, effects of differences in size range are minimized as much as possible. The density of the commercial grade HMX sieve fraction (table 3) is significantly smaller than the density of the recrystallized batches, which are almost the same. This might then explain the fact that HU32-1 is more sensitive than the HU33-1 and HU34-1, assuming that a lower density corresponds to a higher amount of voids which, in turn, triggers the initiation of the PBX. Also, the difference in sensitivity between the latter two PBX's is in line with the density of the HMX crystals: the PBX with the slightly higher density HMX (HU34-1) is less sensitive than the HU33-1, see figure 4.

Table 3: *Results of the shock sensitivity tests. The shock initiation pressure is determined by means of the Bruceton up-and-down method with an accuracy of 1 mm. This implies that the differences in shock initiation pressures are significant.*

PBX code	HMX	water gap [mm]	shock pressure [GPa] [a]
HU32-1	Commercial HMX ρ = 1.886 g/cm^3	13 (go) - 14 (no go)	4.1
HU33-1	'low density' HMX ρ = 1.900 g/cm^3	7 (go) - 8 (no go)	6.4
HU34-1	'high density' HMX ρ = 1.902 g/cm^3	6 (go) - 7 (no go)	6.8

[a] The values given for the shock initiation pressure correspond to the 'no go' levels of the test.

Nevertheless, additional factors might play a role, like the presence of *e.g.* microscopic defects, that might not have been observed by means of the standard optical microscopy techniques. This was not considered further. As can be concluded from the figures 1 to 3, the crystal shape of the commercial product is slightly more spherical compared to the shape of the recrystallized particles. In case particle shape has an influence on shock sensitivity, it might be expected that a more spherical shape leads to a less sensitive explosive [6,7]. Since the reverse effect is found, the shape of the crystals in this particular case, is of less importance compared to the effect of the crystal density on shock sensitivity.

4. Conclusions

The most important conclusion that can be drawn from the results obtained during the cooperation between ICT and TNO is that the shock sensitivity of the PBX's shows a direct correlation with the the HMX crystal density, and hence the internal crystal quality of the HMX particles. The PBX's containing the recrystallized HMX particles is a factor of about 1.5 less sensitive than the reference PBX, containing the commercial grade HMX, and, of much more importance, the shock pressure of the PBX's is linearly dependent on the crystal density of the HMX particles used in the PBX. The same holds for the PBX's cast and characterized by ICT. Moreover, the data obtained by ICT and TNO agree very well.

Acknowledgements

This work was carried out in close cooperation with Dipl.-Ing. V. Komanschek, Dipl.-Ing. H. Kröber and Dipl.-Ing. U. Teipel, within the Fraunhofer Institut für Chemische Technologie, Pfinztal (Berghausen), FRG. The authors acknowledge technical support from J.C. Makkus for the shock sensitivity tests of the PBX's and W. Duvalois and M. Schrader for the characterization of the HMX crystals.

List of abbreviations

CSD Crystal Size Distribution

GC Gas Chromatography

ICT Fraunhofer Institut für Chemische Technologie

HMX $C_4H_8N_8O_8$

HTPB Hydroxy-Terminated PolyButadiene

PBX Plastic Bonded eXplosive

RDX $C_3H_6N_6O_6$

SEM Scanning Electron Microscopy

TNO Netherlands Institute of Applied Scientific Research

References

[1] A.E.D.M. van der Heijden and W. Duvalois, *Characterization of the internal quality of HMX crystals*, Proceedings of the 27th Annual International Conference of ICT, June 25-28, 1996, Karlsruhe, FRG, p. 1-32

[2] F. Trimborn, in: *Explosivstoffe* (Erwin Barth Verlag, Mannheim, August 1967), *Eine einfache Versuchsanordnung zum "Gap Test"*; this test is also described in NATO documents, o.a. AOP-7

[3] H. Kröber *et al.*, Proceedings of the 29th Annual International Conference of ICT, June 1998, Karlsruhe, FRG

[4] L. Borne, Proceedings of the 10th International Detonation Symposium, July 12-16, 1993, Boston, USA, p286

[5] L. Borne, Proceedings of the 5th Congrès International de Pyrotechnie, EUROPYRO 93, June 6 - 11, 1993, Strasbourg, France, p155

[6] A.C. van der Steen and E. Skjold, *RDX particle shape and the sensitivity of PBXes*, Proceedings of the Joint Government/Industry Symposium on Insensitive Munitions Technology, March 13-14, 1990, White Oak, USA, p235

[7] N.H.A. van Ham, A.C. van der Steen and J.J. Meulenbrugge, *Less sensitive explosives*, AGARD Conference Proceedings 511, Insensitive Munitions, October 21-23, Bonn, FRG, p9-1

HERSTELLUNG FEHLSTELLENARMER OKTOGENKRISTALLE DURCH REKRISTALLISATION AUS LÖSUNGEN [1]

FORMATION OF HMX CRYSTALS WITH HIGH INTERNAL QUALITY BY COOLING CRYSTALLIZATION

H. Kröber, U. Teipel, K. Leisinger, H. Krause
Fraunhofer Institut für Chemische Technologie (ICT)
Postfach 1240, D-76318 Pfinztal
e-mail: hkr@ict.fhg.de

Kurzfassung

Für die Weiterverarbeitung und den Einsatz von Festtreib- und Explosivstoffkomponenten kommt den Partikeleigenschaften, z.B. der Partikelgröße bzw. der Partikelgrößenverteilung und der Partikelform, eine besondere Bedeutung zu. Insbesondere im Hinblick auf unempfindliche Explosivstoffe ist die Herstellung fehlstellenarmer Kristalle von großem Interesse. Durch Rekristallisation aus Lösungen lassen sich mittels Variation von Versuchsparameter bestimmte Produkteigenschaften gezielt verändern.

In diesem Beitrag sollen Zusammenhänge zwischen Partikeleigenschaften und Kristallisationsparametern aufgezeigt werden. Des weiteren werden Kristalldefekte und deren Abhängigkeit von den Versuchsparametern qualitativ und quantitativ ermittelt. Durch Empfindlichkeitsuntersuchungen an den umkristallisierten und unterschiedlich fehlerbehafteten Partikelkollektiven soll die Auswirkung von Kristallfehlern auf die Empfindlichkeit dargestellt werden.

[1] In Zusammenarbeit mit der TNO-PML, Rijswijk (NL), Dr. van der Heijden

1. Einleitung

Bei der Formulierung von Treib- und Explosivstoffen werden als energetische Materialien u.a. Nitramine eingesetzt. Hierzu gehören z.B. Hexogen (RDX) und Oktogen (HMX).

Um eine größere Leistungsfähigkeit von kunststoffgebundenen Sprengstoffen (**p**lastic **b**onded explosives, PBX) zu erreichen, muß der Anteil an energetischem Material im PBX möglichst hoch sein. Dies kann durch den Einsatz eines Gemisches mit einer bimodalen Korngrößenverteilung gewährleistet werden, da hierbei die Schüttdichte vergrößert wird. Deshalb müssen energetische Materialien sowohl mit größeren als auch mit kleineren mittleren Korngrößen hergestellt werden. Während kleine Partikel vorwiegend durch Mahlen, aber auch durch Verdrängungskristallisation [1, 2] oder Kristallisation aus überkritischen Fluiden [3] hergestellt werden können, lassen sich größere Partikel durch Umkristallisation aus Lösung gewinnen.

Große Kristalle können eine erhöhte Empfindlichkeit aufweisen, die sich nachteilig auf die Verarbeitbarkeit und den Einsatz des Sprengstoffs auswirken kann. Als Ursache für die höhere Empfindlichkeit ist die vermehrte Anzahl an Fehlstellen im Kristall zu nennen. Die Fehlstellen wirken bei äußerer Beanspruchung als „hot spots", an denen es bei ausreichender Energie zur Reaktion des energetischen Materials und somit zur Detonation des PBX kommen kann [4]. Dieses Verhalten tritt erst bei Fehlstellen mit einer Mindestgröße von etwa 5 µm ein, so daß Partikeln kleiner 5 µm nicht betroffen sind. Bei diesen Partikel kann es allerdings an der Grenzfläche (Partikel/Binder) zu Ablösungen und damit zu „hot spots" kommen. Aus diesem Grund ist es nötig, Kristalle mit möglichst wenig äußeren und inneren Fehlstellen herzustellen. Dies ist durch Mahlen nur schwer zu erreichen, da die durch den Mahlprozeß verursachte hohe äußere Belastung zu Beschädigungen der Oberfläche und Spannungen im Kristall führen. Deshalb sollen zur Formulierung unempfindlicher Explosivstoffkomponenten mit definierten Eigenschaften andere Verfahren eingesetzt werden. Eines davon ist die Rekristallisation aus der flüssigen Phase.

In diesem Beitrag wird die Leistungsfähigkeit dieses Verfahrens aufgezeigt, indem Kristallisationsversuche in einem Batchreaktor unter Variation verschiedener Kristallisationsparameter durchgeführt werden. Anschließend erfolgt eine Charakterisierung der so erzeugten Partikel hinsichtlich ihrer inneren und äußeren Beschaffenheit und hinsichtlich ihres Verhaltens gegen äußere Belastungen, um so eine Optimierung zu erreichen.

2. Grundlagen der Kristallisation

Allgemein wird die Überführung eines Stoffes in den kristallinen Zustand als Kristallisation bezeichnet. Mit ihrer Hilfe können morphologische Stoffeigenschaften gezielt verändert werden. Des weiteren läßt sich der Prozeß zur Reinigung, Stofftrennung und Aufkonzentrierung einsetzen. Die am häufigsten angewandte Technik ist die Kristallisation aus der flüssigen Phase. Die Einteilung der verschiedenen Kristallisationsprozesse erfolgt zumeist nach der Art wie die Übersättigung erreicht wird. Man spricht von Kühl-, Verdampfungs-, Vakuumkühl-, Verdrängungs- und Reaktionskristallisation.

Für den Kristallisationsvorgang ist eine Triebkraft erforderlich, d.h. das System muß in einen Ungleichgewichtszustand gebracht werden. Diese Triebkraft kommt durch die unterschiedlichen chemischen Potentiale, die der gelöste Stoff in der Lösung und in der festen Phase besitzt, zustande. Für das chemische Potential μ_i des gelösten Stoffes i in der Lösung gilt[2]:

$$\mu_{i,Lsg} = \mu_{0,i} + RT \ln a_i \qquad (1)$$

Für den Gleichgewichtszustand muß gelten:

$$\mu^*_{i,Lsg} = \mu_{0,i} + RT \ln a^*_i = \mu_{i,s} \qquad (2)$$

Daraus folgt:

$$\Delta\mu_i = \mu_{i,Lsg} - \mu_{i,s} = RT \ln \frac{a_i}{a_i^*} = RT \ln S = RT \ln \frac{c_i}{c_i^*} = RT \ln \left(\frac{c_i - c_i^*}{c_i^*} + 1 \right) \qquad (3)$$

Das übersättigte System versucht zum einen durch Bildung neuer fester Partikel (Keimbildung), andererseits durch Anlagerung an Partikel (Kristallwachstum) den Gleichgewichtszustand wieder herzustellen.

Zur Steuerung eines Kristallisationsprozesses sind umfangreiche Kenntnisse über das verwendete System notwendig. Dies gilt insbesondere für den Verlauf der Löslichkeits- und Überlöslichkeitskurve. In Abbildung 1 ist der Zusammenhang zwischen Löslichkeit und Temperatur exemplarisch dargestellt. Dem Verlauf der Löslichkeitskurve lassen sich bereits grundlegende Informationen über den zu verwendenden Prozeß entnehmen. Verläuft z.B. die Löslichkeitskurve nahezu waagerecht, besteht also keine Abhängigkeit zwischen der Löslichkeit und der Temperatur, kann durch Abkühlen der Lösung keine Kristallisation ausgelöst werden. Dies ist

[2] Eine Zusammenstellung der verwendeten Formelzeichen befindet sich am Ende des Beitrags

für das System NaCl/Wasser der Fall, weshalb NaCl durch Verdampfungskristallisation gewonnen wird.

Beim Keimbildungsprozeß unterscheidet man zwischen der primären und der sekundären Keimbildung, wobei erstere noch einmal in homogene und heterogene Keimbildung unterteilt wird. Nach welcher Art die Keimbildung im Einzelfall abläuft hängt insbesondere von der Höhe der Übersättigung und dem Energieeintrag in das System ab. Hierbei kommt es bei hohen Übersättigungen zur primär homogenen Keimbildung, bei der die treibende Kraft allein die Übersättigung ist, bei mittleren Werten zur primär heterogenen Keimbildung, die an Fremdstoffoberflächen abläuft, und bei geringen Übersättigungen zur sekundären Keimbildung, die nur bei Anwesenheit arteigener Partikel auftritt. Die absolute Höhe der Übersättigung, ab der die einzelnen Mechanismen auftreten, ist stark stoffspezifisch und läßt sich über die Bestimmung der metastabilen Breite ermitteln.

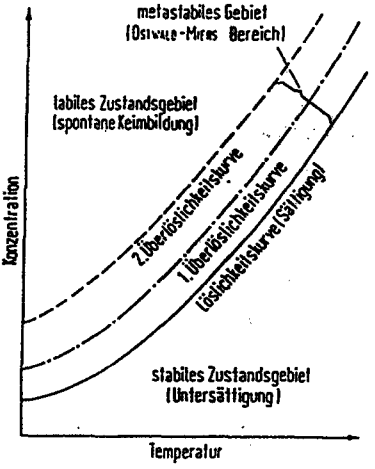

Abb. 1: Löslichkeitsdiagramm [5]

Die Wachstumsgeschwindigkeit eines Kristalls hängt von zahlreichen Parametern ab. Dazu gehören neben der Übersättigung auch die Relativbewegung zwischen Kristall und Lösung. Dies läßt sich mit Hilfe des Zwei-Stufen-Modells erklären. Danach kann der Wachstumsprozeß in zwei Schritte unterteilt werden. Im Diffusionsschritt werden die Kristallbausteine durch die Diffusionsschicht an die Kristalloberfläche transportiert; im sich daran anschließenden Einbauschritt erfolgt der Einbau der Bausteine in die Oberfläche. Formal lassen sich beide Teilschritte durch folgende kinetische Ansätze beschreiben:

$$r_D = k_D \cdot (c_\infty - c_i) = \frac{D}{\delta} \cdot (c_\infty - c_i) \qquad (4)$$

und

$$r_r = k_r \cdot (c_i - c^*)^n \qquad (5)$$

Setzt man n=1, so erhält man für die Gesamtkinetik

$$r_{ges}=k_{ges}\cdot(c_\infty - c^*)=\left(\frac{1}{k_D}+\frac{1}{k_r}\right)^{-1}\cdot(c_\infty - c^*) \qquad (6)$$

Welcher der beiden Schritte die Wachstumsgeschwindigkeit bestimmt, hängt von den Kristallisationsbedingungen ab. Die Abhängigkeit der Wachstumsgeschwindigkeit von der Relativbewegung zwischen Kristall und Lösung ergibt sich über die Abhängigkeit der Diffusionsgrenzschichtdicke δ von der Relativbewegung. Diese läßt sich durch die Rührerdrehzahl und -form beeinflussen.

Die Übersättigung kann durch das Einstellen verschiedener Abkühlgeschwindigkeiten variiert werden. Um eine über die Versuchsdauer konstante Wachstumsgeschwindigkeit zu erhalten, muß bei Annahme einer linearen Löslichkeitskurve die Abkühlgeschwindigkeit kontinuierlich gesteigert werden.

Dieses Zwei-Stufen-Modell stellt eine starke Vereinfachung der tatsächlich ablaufenden Vorgänge dar. Nach Elwell und Scheel [6] läßt sich der Kristallisationsvorgang in bis zu 9 Teilschritte aufteilen. Des weiteren wird in den bisher gängigen Modellen der Einfluß der Kristallisationswärme auf die Löslichkeit in unmittelbarer Oberflächennähe vernachlässigt, obwohl sich die Temperatur nahe der Oberfläche wegen des geringen Volumens, in der die Energie frei oder verbraucht wird, deutlich von der Temperatur in der Lösung unterscheiden kann.

Die Produkteigenschaften werden im großen Maße dadurch beeinflußt, welcher Keimbildungsmechanismus dominiert und in welchem Verhältnis Keimbildung und Kristallwachstum zueinander stehen. So können z.B. feine Partikel erzeugt werden, indem die Prozeßbedingungen so gewählt werden, daß die Keimbildungsrate hohe Werte annimmt, da dann ein Großteil der zur Verfügung stehenden Übersättigung durch die primäre homogene Keimbildung abgebaut wird. Andererseits werden große Kristalle vorwiegend bei Bedingungen gebildet, die sich durch geringe Übersättigungen und einem geringen Energieeintrag auszeichnen.

Ein weiterer wichtiger Parameter, der die Produktqualität beeinflußt, ist das Lösungsmittel, aus dem auskristallisiert wird. Durch die Wahl des Lösungsmittels kann die Form des Kristalls verändert werden. Je nachdem welches Lösungsmittel verwendet wird, entstehen Kristalle unterschiedlichster Formen, obwohl der Aufbau einer Elementarzelle stoffspezifisch und damit unabhängig vom verwendeten Lösungsmittel ist. Erklären kann man dieses Phänomen damit, daß verschiedene Kristallflächen unterschiedlich schnell wachsen, wodurch sich der Kristallhabitus ausbildet. Bei verschiedenen Lösungsmitteln können die Verhältnisse an den einzelnen Flächen stark differieren. Denkbar ist, daß die Fläche A im Verhältnis zur Fläche B im ersten Lösungsmittel sehr rasch, in einem zweiten Lösungsmittel dagegen nur sehr

langsam wächst. Grund dafür sind die flächenspezifischen Wechselwirkungen zwischen Kristall und Lösungsmittel. Aus dem gleichen Grund können auch der Lösung zugesetzte Additive die Kristallform verändern. Bei Kenntnis solcher Wechselwirkungsparameter (z.B. Oberflächenenergie) ist eventuell eine Voraussage der Kristallform möglich. Zu beachten ist, daß im Kristallhabitus diejenigen Flächen dominieren, die die kleinsten Wachstumsgeschwindigkeiten besitzen, und die schnell wachsenden verschwinden.

3. Kristallfehler

In jedem realen Kristall befinden sich Stellen, an denen das regelmäßige Raumgitter gestört ist. Allgemein werden solche Kristallfehler in drei Kategorien eingeteilt:

chemische Verunreinigungen,
Kristallbaufehler und
elektronische Fehlstellen.

So ist für das Kristallwachstum das Vorhandensein von Fehlstellen in Form von Stufenversetzungen unabdingbar, da dadurch Halbkristallagen gebildet werden, an denen sich die Kristallbausteine energetisch günstig einlagern. Grundsätzlich ist anzumerken, daß sich Fehlstellen durch einen erhöhten Energiezustand im Gitter auszeichnen. In kristallinen Explosivstoffkomponenten ist deshalb die zur Detonationsauslösung von außen zuzuführende Energie an Fehlstellen gegenüber ungestörten Kristallbereichen herabgesetzt, weshalb möglichst fehlstellenarme Kristalle im Explosivstoffbereich eingesetzt werden. Je nach Art der Fehlstelle sind unterschiedliche Ursachen für die Entstehung solcher Defekte verantwortlich.

Elektronische Fehlstellen zeichnen sich durch fehlende oder überschüssige Elektronen aus. Diese können durch den Einbau von Fremdatomen, die mehr oder weniger freie Elektronen als die regulären Atome haben, erzeugt werden. Bei der Herstellung von Halbleitern wird dieser Effekt durch eine gezielte Zugabe von Fremdatomen ausgenutzt.

Chemische Verunreinigungen haben unterschiedliche Auswirkungen auf die Kristallstruktur. Bei Fremdatomen, die eine ähnliche chemische Struktur wie die regulären Kristallbausteine besitzen, kommt es nur zu einer geringen Störung. In anderen Fällen kann es zur Bildung von Mischkristallen oder Clustern (Einlagerungen) kommen, die zu Verzerrungen und Spannungen in der Gitterstruktur führen.

Kristallbaufehler bilden sich direkt während des Kristallwachstums. Sie werden gemäß ihrer Dimension in vier Klassen eingestuft.

- Punktdefekte, die auch als nulldimensionale Fehler bezeichnet werden, sind z.B. nicht besetzte oder mit Fremdatomen besetzte Gitterplätze oder in Gitterzwischenräume eingebaute Atome und Moleküle. Punktdefekte kommen sehr häufig vor, da die Gitterbausteine in folge ihrer Wärmebewegung ständig in Bewegung sind.
- Versetzungen sind von eindimensionaler Größenordnung. Dabei unterscheidet man zwischen Stufen- und Schraubenversetzungen, wobei Schraubenversetzungen aus einer um 90° versetzten Aneinanderreihung von Stufenversetzungen entstehen. Die Stufenversetzungen selbst bilden sich infolge starker Scherbeanspruchung auf den Kristall aus. Wie oben erwähnt findet an solchen Versetzungen das Kristallwachstum bevorzugt statt, da der einzubauende Baustein in der „Halbkristallage" bereits von bis zu drei gleichen Nachbarn umgeben ist. Bei einem Einbau in eine ebene Kristallfläche wäre nur ein Nachbar vorhanden, was einen gegenüber der Halbkristallage energetisch ungünstigeren Zustand bedeutet.
- Aneinanderreihungen von Versetzungen kann man als zweidimensionale, flächenhafte Kristallbaufehler interpretieren. Hierzu gehören neben Phasengrenzflächen auch Kleinwinkelkorngrenzen, die sich aus einer regelmäßigen Anordnung von Stufenversetzungen ergeben. Grenzflächen existieren nicht nur zwischen verschiedenen Kristalliten - dann spricht man von Korngrenzen -, sondern werden auch durch Gas- oder Flüssigkeitseinschlüsse gebildet.
- Solche Gas- oder Flüssigkeitseinschlüsse sind dreidimensionale Defekte, die durch unregelmäßiges Wachstum entstehen. Wenn Oberflächenbereiche ihr Wachstum verlangsamen oder gar beenden, Nachbarbereiche dagegen weiterwachsen, kommt es zu einer solchen Lunkerbildung, die verstärkt an Versetzungslinien auftritt.

Zur Detektierung solcher Defekte stehen verschiedene Methoden zur Verfügung. Dabei bieten heute die modernen Analysengeräte prinzipiell die Möglichkeit, sämtliche Arten von Fehlstellen zu erkennen und zu quantifizieren. So können z.B. hochauflösende Elektronenmikroskope selbst Punktdefekte detektieren. Dabei ist zu bedenken, daß solche hochempfindlichen Methoden aufwendig und teuer sind und sich nur selten für Reihenuntersuchungen eignen. Da diese Methoden zumeist für Untersuchungen an Einkristallen entwickelt worden sind, erweist sich eine Übertragung auf Untersuchungen an Kristallkollektiven als schwierig oder gar unmöglich, so daß in diesen Fällen eine Fehlstellenanalyse höchstens qualitativ erfolgen kann.
Als relativ unproblematisch erweist sich die Detektierung chemischer Verunreinigungen, da hierzu auf die Methoden der analytischen Chemie zurückgegriffen werden kann. Dazu gehören chromatographische (Gas- oder Flüssigkeitschromatographie) und spektroskopische Me-

thoden, mit denen die Kristalle auf ihre Reinheit hin untersucht werden können. Diese Methoden sind stoffspezifisch und lassen gegenüber einem definierten Standard quantitative Aussagen zu.

Zur Detektierung von Gas- oder Flüssigkeitseinschlüssen stehen zwei sich ergänzende Methoden zur Verfügung. Mit Hilfe der optischen Mikroskopie können in transparenten Kristallen vorhandene Einschlüsse sichtbar gemacht werden. Da mit dieser Methode nur eine begrenzte Anzahl von Kristallen untersucht werden kann, sollte zur Ermittlung quantitativer Daten eine Dichtemessung durchgeführt werden. Soweit sich das eingeschlossene Material in der Dichte vom reinen Kristall unterscheidet, lassen sich dadurch größere Mengen von Kristallen hinsichtlich Lunkerbildung charakterisieren.

Bei der Detektierung von Kristallbaufehlern treten mit Ausnahme von Volumendefekten erhebliche Schwierigkeiten auf. Lediglich Korngrenzen, also Flächendefekte lassen sich nach aufwendiger Probenvorbereitung mikroskopisch nachweisen. Untersuchungsmethoden, die die Reflexion oder Beugung von Röntgenstrahlen ausnutzen, liefern Aussagen über Gitterstrukturen, woraus Rückschlüsse auf die vorliegende Kristallmodifikation und eventuelle Gitterverzerrungen gezogen werden können.

Da für die Bildung von „hot spots" Fehlstellen mit einer Mindestgröße von 5 µm vorhanden sein müssen, beschränkt sich die Charakterisierung der vorhandenen Fehlstellen auf Volumendefekte, wie z.B. Einschlüsse und Cluster. Die anderen oben genannten Kristallfehler besitzen in der Regel wesentlich geringere Ausdehnungen und können deshalb außer acht gelassen werden.

4. Durchgeführte Versuche

4.1 Versuchsaufbau

Für die Umkristallisationsversuche stand folgende Glasapparatur zur Verfügung, die in Abbildung 2 schematisch dargestellt ist. Die Kristallisation erfolgt in einem zylindrischen Doppelmantelgefäß aus Duranglas, das mit einem passenden Planflansch-Deckel geschlossen werden kann. An diesen Deckel sind über Normschliffhälse ein Tropftrichter, ein Thermoelement, ein Thermometer und das Rührorgan angebracht. Die Temperierung der Lösung erfolgt über einen Kryostaten (Lauda, RUK 90), der mit einem externen Programmgeber (Lauda, PM 351) ausgerüstet ist. Als Wärmeträgermedium dient eine Wasser-Glycerin-Mischung, die durch den Doppelmantel strömt. Die damit erreichbaren Temperaturen liegen im Bereich zwischen 0°C

und 100°C. Mit Hilfe des externen Programmgebers ist es möglich, definierte Aufheiz- und Abkühlkurven vorzugeben. Die jeweilige Temperatur der Lösung läßt sich ständig über das in die Lösung eingebrachte Thermoelement bestimmen und auf einem Schreiber aufzeichnen.

Zum Einsatz kamen zwei verschieden große Kristallisationsbehälter. Zunächst wurden Versuche in einem 1l Gefäß durchgeführt. Die für die GAP-Tests erforderliche größere Menge HMX wurde in einem 2,5l Gefäß umkristallisiert.

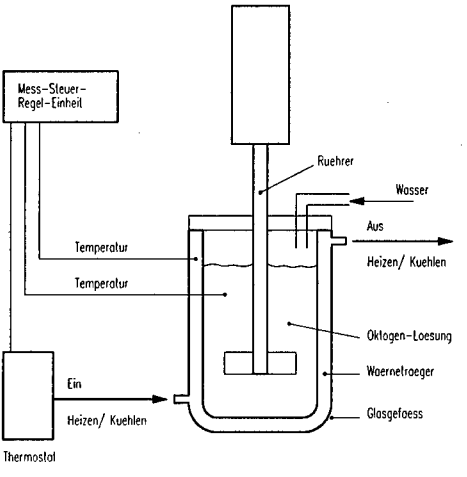

Abb. 2: Schematische Darstellung des Versuchaufbaus

Für die vor den eigentlichen Umkristallisationsversuchen durchgeführten Löslichkeitsversuche wurde ein 400 ml fassendes Doppelmantelgefäß verwendet.

4.2 Versuchsdurchführung und -ergebnisse

Da den Löslichkeitskurven bereits grundlegende Erkenntnisse über den weiteren Kristallisationsprozeß zu entnehmen sind, wurde für Oktogen die Löslichkeit in mehreren Lösungsmitteln bestimmt. Dazu wurde in einem Doppelmantelgefäß ca. 200 ml Lösemittel vorgelegt und temperiert. Dann wurde unter ständigem Rühren solange Oktogen hinzu gegeben, bis sich ein Bodensatz bildete. Diese Suspension wurde anschließend eine Stunde bei gleichbleibender Temperatur gerührt. Nach Abschalten des Rührers setzten sich die ungelösten Partikel am Boden ab (Beruhigungszeit ca. 30 Minuten), so daß sich eine klare Lösung über dem Bodensatz ausbildete, aus der mit einer Pipette eine Probe entnommen werden konnte. Durch Eintrocknen dieser Proben wurde für verschiedene Temperaturen die Gleichgewichtskonzentration in der Lösung gravimetrisch ermittelt. Aufgetragen über die Temperatur ergeben sich die Löslichkeitskurven. Da die verwendeten Lösungsmittel zumeist schwerflüchtige Verbindungen sind, mußte die Trocknung im Vakuumtrockenschrank bei ca. 50 mbar und 90°C stattfinden, damit sichergestellt ist, daß das gesamte Lösungsmittel entfernt wurde (auch aus dem Kristallinneren).

Die Ergebnisse für die untersuchten Lösungsmittel sind in Abbildung 3 dargestellt.

Von sechs Lösungsmitteln kommen vier für weitergehende Untersuchungen in Betracht. Umkristallisationen aus Aceton wurden aufgrund des geringen Lösevermögens genauso wenig weiter durchgeführt wie aus DMSO, da hierbei wegen des hohen Restgehalts an Oktogen am Ende der Abkühlphase nur eine sehr geringe Ausbeute erreichbar gewesen wäre.

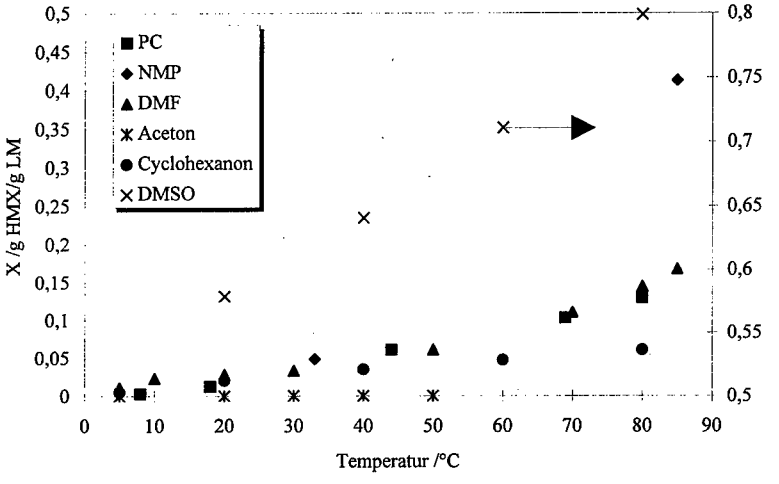

Abb. 3: Löslichkeitsdiagramm von HMX in verschiedenen Lösungsmitteln

4.2.1 Cyclohexanon

Bei der Umkristallisation aus Cyclohexanon zeigte sich, daß nur sehr geringe Ausbeuten erreicht werden konnten. Theoretisch sollten bei einer Abkühlung von 80°C auf 5°C 90% des eingesetzten Oktogens auskristallisieren. Tatsächlich fielen aber nur 15% als kristalline Partikel an.

Abb. 4: HMX aus Cyclohexanon durch Verdampfungskristallisation; x = 55µm

Die als Alternative durchgeführten Verdampfungskristallisationen ergaben zwar eine verbesserte Ausbeute (ca.30%), jedoch waren die so erhaltenen Kristalle sehr klein und unregelmäßig geformt (Abb. 4).

Bei der Verdampfungskristallisation lassen sich generell die Versuchsparameter nur bedingt variieren, so daß der Prozeß nur ungenügend gesteuert werden kann. Dies gilt insbesondere für die im Rotationsverdampfer ablaufenden Versuche, bei denen sich nur die Verdampfungsgeschwindigkeit verändern läßt. Da die mit verschiedenen Verdampfungsgeschwindigkeiten

hergestellten Partikel hinsichtlich der Größe und Form kaum Unterschiede zeigten, wurden diese Versuche vorerst nicht weiter geführt.

4.2.2 N-Methylpyrrolidon (NMP)

Bei den Umkristallisationen aus N-Methylpyrrolidon wurden folgende Parameter eingestellt:

- Temperaturprogramm: Abkühlung von 85°C auf 5°C in 4 h
  isothermes Halten bei 5°C für 30 min
- 4-Blatt-Rührer mit 150 U/min

Dabei stellte sich heraus, daß die Kristalle eine rauhe Oberfläche und unregelmäßige Form haben (Abb. 5). Weiterhin waren die Kristalle teilweise nicht transparent, was auf Lösungsmitteleinschlüsse hindeuten kann. Die Messung der Reib- und Schlagempfindlichkeit zeigte, daß die Umkristallisation keine Verbesserung der Empfindlichkeit mit sich brachte. Auch eine Verringerung der Abkühlgeschwindigkeit (Abkühldauer 8 Stunden), wodurch ein gleichmäßigeres Wachstum erreichbar ist, führte zu keiner Verbesserung der Form und Oberflächeneigenschaften.

Abb. 5: HMX aus NMP umkristallisiert; x = 620µm

4.2.3 Dimethylformamid (DMF)

Die Kühlkristallisation in DMF wurde zunächst unter den gleichen Bedingungen wie die in NMP durchgeführt. Die dabei erhaltenen Partikel zeichneten sich durch eine annähernd sphärische Form und einer glatten Oberfläche aus (Abb. 6).

Aufgrund dieser positiven Ergebnisse sollte durch Variation der Parameter Abkühlgeschwindigkeit, Rührerdrehzahl und Rührerform versucht werden, ob sich eine Optimierung hinsichtlich Korngröße und Form erreichen läßt.

Als Rührer kamen Blattrührer mit zwei bzw. vier schrägen Rührerblättern zum Einsatz. Nachdem sich beim Einsatz des 2-Blatt-Rührers herausstellte, daß die Lösung speziell bei niedrigen Umdrehungszahlen nur unzureichend gut durchmischt wird, und die Gefahr besteht, daß bereits gebildete Kristalle zu Boden sinken, wurden die weiteren Versuche mit dem 4-Blatt-Rührer durchgeführt.

Die Abkühlgeschwindigkeit wurde dahingehend variiert, daß die Abkühlung der Lösung von 85°C auf 5°C in 2, 4 bzw. 6 h bei einer Rührerdrehzahl von 150 U/min erfolgte. Dabei stellte sich heraus, daß eine Verlängerung der Abkühlzeit, also eine Verringerung der Abkühlrate, eine größere mittlere Korngröße und engere Korngrößenverteilung zur Folge hat (der $x_{50,3}$-Wert verändert sich von 252 auf 348 bzw. 365 µm). Dies ist dadurch zu erklären, daß während des Abkühlens keine so hohen Übersättigungen auftreten und sich somit eine geringe Keimbildungsrate einstellt. Die zur Verfügung stehende Übersättigung kann dann überwiegend durch das Kristallwachstum abgebaut werden. Zudem steht für das Wachstum mehr Zeit zur Verfügung, so daß die geringere Wachstumsgeschwindigkeit, bedingt durch die geringere Übersättigung, ausgeglichen wird. Durch die geringe Übersättigung kommt es zu einem langsamen und gleichmäßigen Wachstum, was wiederum zu gleichmäßigeren Kristalle führt.

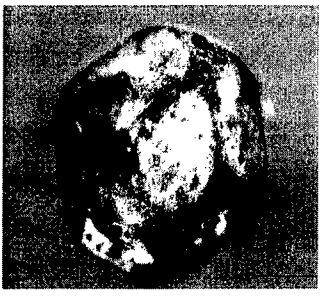

Abb. 6: HMX aus DMF umkristallisiert; x = 1000µm

Die Rührergeschwindigkeit beeinflußt die Relativbewegung zwischen Kristall und Lösung. Eine steigende Drehzahl führt zu einer Verringerung der Diffusionsgrenzschicht und damit zu einer größeren Wachstumsgeschwindigkeit. Dies gilt allerdings nur für den Bereich, in dem die Wachstumskinetik durch den Diffusionsschritt begrenzt wird. Ab einer bestimmten Rührerdrehzahl kann das Wachstum nicht mehr durch eine weitere Erhöhung der Drehzahl gesteigert werden, da dann der Einbauschritt limitierend auf die Wachstumsgeschwindigkeit wirkt.

Es wurden Versuche mit Rührerdrehzahlen von 75, 150 und 225 U/min durchgeführt, wobei jeweils eine Abkühlung von 85°C auf 5°C in 4 h erfolgte. Es zeigte sich, daß eine Erhöhung der Rührergeschwindigkeit eine größere mittlere Korngröße und eine breitere Verteilung bewirkt (der $x_{50,3}$-Wert verändert sich von 284 auf 348 bzw. 407 µm). Die Kristallform nähert sich mit steigender Drehzahl der Kugelform an, was allerdings kein Wachstumseffekt ist, sondern durch Kristallabrieb hervorgerufen wird. Dies wird auch durch die breitere Verteilung bei höheren Drehzahlen bestätigt, da der Feinanteil durch Kristallbruch entsteht.

Aus diesen Ergebnissen ergibt sich, daß durch Umkristallisation aus DMF sowohl hinsichtlich der mittleren Korngröße als auch bezüglich der Kornform eine deutliche Verbesserung gegenüber dem Ausgangsmaterial erreicht werden kann. Dabei ist das Ergebnis um so besser, je größer die Rührerdrehzahl und je länger die Abkühlphase ist. Bezüglich der Abkühldauer ist allerdings anzumerken, daß eine 6-stündige Abkühlphase gegenüber einer 4-stündigen nur

eine geringe Verbesserung bringt, die den Nachteil der längeren Versuchszeit nicht rechtfertigt. Bei Steigerung der Rührerdrehzahl ist zu bedenken, daß vermehrt Kristallabrieb und Kristallbruch auftritt, was zu einer breiten Verteilung führt.

Trotz dieser Ergebnisse wurde die Umkristallisation aus Dimethylformamid eingestellt, da Röntgenbeugungsuntersuchungen zeigten, daß das aus DMF kristallisierte Oktogen nicht in der kristallinen β-Phase, sondern in einer nicht kristallinen Modifikation vorlag. Die Reib- und Schlagempfindlichkeit des umkristallisierten Materials entspricht der des Originaloktogens, wohingegen die Ergebnisse des GAP-Tests eine deutlich gesteigerte Empfindlichkeit des umkristallisierten HMX zeigen.

Die Bildung der nicht kristallinen Modifikation aus DMF kann gegebenenfalls durch Zugabe von Additiven unterdrückt werden, ohne dabei die weiteren Eigenschaften des Oktogens zu beeinflussen. Dies sollte durch weitere Experimente und Simulation verifiziert werden.

4.2.4 Propylencarbonat (PC)

Bei der Kristallisation aus Propylencarbonat trat das Problem auf, daß die Keimbildung erst bei sehr hohen Unterkühlungen (Übersättigungen) einsetzte. Daraus ergab sich eine Vielzahl sehr kleiner Kristalle, was zu Schwierigkeiten bei der Filtration und Trocknung führte, da die Kristalle stark agglomerieren. Außerdem trat die Keimbildung nicht reproduzierbar bei der selben Temperatur ein, so daß stark unterschiedliche Produktqualitäten erzielt wurden. Um reproduzierbar zu größeren Kristallen zu kommen, mußte die Keimbildung zu einem früheren Zeitpunkt ausgelöst werden. Somit konnte die Wachstumsphase verlängert und eine primär homogene Keimbildung unterdrückt werden. Diese Initiierung der Keimbildung läßt sich z.B. durch Zugabe von Wasser in die heiße, übersättigte Lösung erreichen. Durch die Wasserzugabe wird das Lösevermögen des Propylencarbonats bezüglich Oktogen vermindert, d.h. die Übersättigung nimmt spontan zu, wodurch es zur Keimbildung kommt. An diese Keimbildungsphase schließt sich die Abkühlphase an, in der die Kristalle wachsen. Auf diese Weise lassen sich Kristalle, die sich durch eine rhombusartige Form auszeichnen, herstellen (Abb. 7). Röntgenbeugungsuntersuchungen ergaben, daß

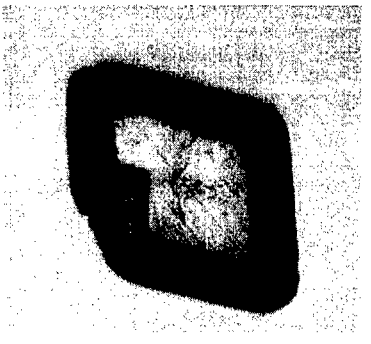

Abb. 7: HMX aus PC umkristallisiert; x = 700 µm

es sich dabei um die gewünschte Kristallmodifikation handelt, so daß weitere Untersuchungen mit diesem System erfolgten.

Für die Versuche wurden eine Lösung bestehend aus 900 g Propylencarbonat und 135 g HMX (X=0,15) auf 95°C erhitzt. Daran schloß sich eine Abkühlung auf 75°C an (dT/dt=0,67 K/min), wodurch sich eine relative Übersättigung von 1,26 bzw. eine Unterkühlung von 17°C einstellte. Über den Tropftrichter wurde der Lösung nun innerhalb von 1 Minute 60 ml Wasser zugesetzt, wobei ein feiner Kristallnebel auftrat. Darauf folgte die eigentliche Abkühlphase, während der das Kristallwachstum stattfand. Im Anschluß an die Abkühlphase wurde die Suspension bei 5°C für 30 Minuten weitergerührt, ehe der Kristallbrei über ein Filter von der Lösung getrennt und mit Aceton nachgewaschen werden konnte.

Bei den Kristallisationsversuchen kam ein 4-Blatt-Rührer bei 250 U/min zum Einsatz. Die Abkühlrate wurde auf 17,5 K/h eingestellt. Es entstanden Kristalle mit einer mittleren Korngröße von 420 µm und einer engen Korngrößenverteilung. Die Partikel waren rautenförmig und hatten weitgehend eine glatte Oberfläche. Bei einigen Kristallen hatte sich die Rautenform noch nicht vollständig ausgeprägt, statt dessen wiesen diese Kristalle eine Kreuzform auf (Abb. 8). Dies deutet auf die Bildung von Twin-Kristallen hin, bei denen in der Twinebene eine innere Spannung auftritt. Die gute Transparenz der Kristalle läßt eine einfache optische Beurteilung des Kristallinneren zu. Durch Untersuchungen im Lichtmikroskop lassen sich keine Einschlüsse nachweisen, was auf ein gleichmäßiges Wachstum hindeutet.

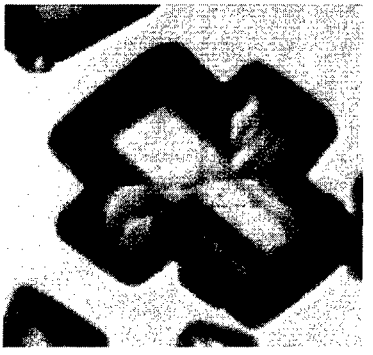

Abb. 8: Twin-Bildung von HMX; x=450µm

Die folgenden Versuche wurden unter Verwendung eines Turbinenrührers durchgeführt, der eine bessere axiale Vermischung ermöglicht.

Um den Einfluß des Rührers zu bestimmen, wurden zunächst die anderen Versuchsparameter konstant gehalten. Es entstand ein deutlich gröberes Produkt mit einem mittleren Korndurchmesser von 527 µm. Dies läßt sich durch den verbesserten Stoffübergang erklären, der zu einer erhöhten Wachstumsgeschwindigkeit und damit zu größeren Kristallen führt. Auf die Form der Kristalle hat die eingesetzte Rührerart keinen signifikanten Einfluß. Es entstanden wiederum rhombusartig geformte Partikel, die allerdings keine glatte Oberfläche besitzen. Vielmehr sind auf der Oberfläche neue Keime zu erkennen, die als Dentriten aus dem Mutter-

kristall heraus wachsen. Verschiedene Kristalle weisen Bruchstellen auf, die auf eine hohe Belastung durch den Rührer hindeuten. Die durchgeführten lichtmikroskopischen Untersuchungen zeigen, daß die Kristalle keine größeren Einschlüsse aufweisen. Es kommt also auch bei der erhöhten Wachstumsgeschwindigkeit zu einem gleichmäßigen Wachstum.

In weiteren Versuchen wurde die Rührerdrehzahl bei 250 U/min konstant gehalten, jedoch erfolgte die Abkühlung von 75 auf 5°C innerhalb von 2 Stunden (dT/dt=35 K/h). Unter diesen Bedingungen entstanden Kristalle mit einer mittleren Korngröße von 390 µm, die in ihrer Größe allerdings sehr breit verteilt waren. Das Vorhandensein kleiner Partikel ist zum einen auf erhöhten Abrieb durch die große Rührerbeanspruchung und zum anderen auf die auf die Hälfte reduzierte Kristallisationszeit zurückzuführen. Zwar ist aufgrund der erhöhten Übersättigung auch die Wachstumsgeschwindigkeit größer, doch scheint dies die verkürzte Wachstumszeit nicht zu kompensieren. Weiter ist anzumerken, daß die Kristalle aufgrund der hohen Wachstumsgeschwindigkeit eine erheblich schlechtere Oberflächenbeschaffenheit aufweisen. Auf der Kristalloberfläche traten Unebenheiten auf, die auf ein dendritisches Wachstum hindeuten. Dieses tritt vor allem bei hohen Übersättigungen auf und führt zu einer verstärkten sekundären Keimbildung, was wiederum eine kleinere mittlere Partikelgröße bedingt.

Um den Einfluß der Rührergeschwindigkeit auf die Produkteigenschaften zu ermitteln, wurden weitere Versuche durchgeführt, bei denen die Abkühlzeit 4 Stunden und die Rührerdrehzahl 350 U/min betrug. Die entstandenen Kristalle hatten eine mittlere Korngröße von 380 µm, wobei es sich dabei allerdings um eine bimodale Verteilung handelt. Bei den kleinen Partikeln handelt es sich um Kristallabrieb, der durch die Zusammenstöße mit dem Rührer oder den Partikeln untereinander entsteht. Diese Kristalle besitzen keine einheitliche Form und haben eine unebene Oberfläche. Dagegen zeigen die durch Abrieb nicht zerstörten großen Partikel (mittlere Korngröße ca. 550 µm) die für die Kristallisation aus PC charakteristische Rautenform. Neben dem Kristallabrieb tritt unter diesen Kristallisationsbedingungen ein weiterer unerwünschter Effekt auf. Viele der Kristalle besitzen im Lichtmikroskop deutlich erkennbare Einschlüsse, die entweder Luft oder Lösungsmittel enthalten. Ursache dafür ist die zu große Wachstumsgeschwindigkeit, die zum einen auf den guten Stoffaustausch zwischen Lösung und Kristall und zum andern auf die hohe Versetzungsdichte auf der beschädigten Oberfläche zurückzuführen ist. Man geht davon aus, daß das Wachstum bei stark beschädigten Kristallen hauptsächlich an den Versetzungen stattfindet, wobei dann vermehrt Lunkerbildung auftritt [7].

5. GAP - Tests

Um einen möglichen Zusammenhang zwischen den Versuchsparametern und der Empfindlichkeit der HMX-Kristalle gegenüber einer Druckwelle zu erhalten, wurden BICT-Wasser-GAP-Tests durchgeführt. Die für diese Tests benötigten PBX hatten einen Füllgrad von 70 Gew.-% HMX, das eine Partikelgröße zwischen 250 und 425 µm aufwies. Als Binder wurde HTPB verwendet. Die eingesetzten Siebfraktionen besaßen unterschiedliche Dichten, was auf unterschiedliche Kristallqualitäten hindeutet. In Abbildung 9 ist das Ergebnis der GAP-Tests graphisch dargestellt.

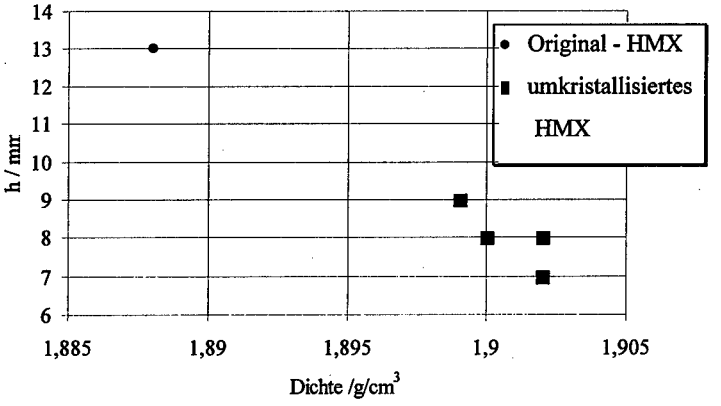

Abb. 9: Graphische Darstellung der Ergebnisse der GAP-Tests

Dargestellt ist die GAP-Distanz h, bei der es gerade noch zur Detonation des PBX kommt, als Funktion der Partikeldichte für das Original-HMX und vier in Propylencarbonat umkristallisierte HMX-Chargen. Je geringer der Abstand zwischen Initiator- und Testladung ist, desto unempfindlicher ist die Ladung. Es zeigt sich, daß die PBX, die mit umkristallisiertem HMX hergestellt wurden, deutlich unempfindlicher gegenüber einer Druckbeanspruchung sind als jene, die Original-HMX enthalten. Da gleichzeitig die Dichte der Partikel durch die Umkristallisierung zugenommen hat, ist eine Korrelation der Empfindlichkeit mit der Partikeldichte möglich. Nimmt man die Dichte als Maß für die innere Qualität der Kristalle, so läßt sich diese durch eine geeignete Umkristallisation deutlich verbessern, d.h. die Anzahl der Fehlstellen kann reduziert werden, wodurch unempfindlichere Ladungen hergestellt werden können. In weiteren Tests ist zu verifizieren, ob dieser Zusammenhang mathematisch z.B. durch eine lineare Abhängigkeit beschrieben werden kann und ob sich für andere engere Siebfraktionen ähnliche Abhängigkeiten finden lassen. Hierbei ist zu erwarten, daß für kleinere Partikel der kritische Abstand, ab dem es zur Detonation kommt, bei gleicher Partikeldichte

größer und die Ladung dementsprechend empfindlicher wird [8]. Umgekehrt sollte eine mit größeren Partikeln gefüllte Ladung unempfindlicher werden.

6. Zusammenfassung

In diesem Beitrag konnte gezeigt werden, daß sich Oktogen in verschiedenen Lösungsmitteln umkristallisieren läßt. Als Lösungsmittel kamen Cyclohexanon, Dimethylformamid, N-Methylpyrrolidon und Propylencarbonat zum Einsatz, wobei die Kristallisation bei Verwendung von Cyclohexanon durch Verdampfen des Lösungsmittels und bei Verwendung der anderen Substanzen durch Abkühlen der Lösung erreicht wurde.

Durch Variation der Prozeßparameter (Rührerform, -drehzahl, Abkühlgeschwindigkeit) ist es gelungen, daß Ausgangsmaterial hinsichtlich der Kristallform, -größe und Oberflächenbeschaffenheit wesentlich zu verbessern. Die Empfindlichkeit wurde mittels GAP-Tests untersucht, wobei sich heraus stellte, daß das in Propylencarbonat umkristallisierte HMX deutlich unempfindlicher gegenüber einer Druckbelastung war als das Originalmaterial. Für das unter verschiedenen Bedingungen aus Propylencarbonat umkristallisierte HMX ergaben sich zwar keine signifikanten Empfindlichkeitsunterschiede, allerdings läßt sich die Empfindlichkeit der PBX mit Hilfe der Dichte der eingesetzten Kristalle korrelieren. Aus den Ergebnissen läßt sich ein linearer Zusammenhang zwischen dem kritischen Abstand (Maß für die Empfindlichkeit) und der Partikeldichte (Maß für die interne Kristallqualität) postulieren, wobei zur Bestätigung weitere Untersuchungen erfolgen müssen.

7. Verwendete Formelzeichen

a	Aktivität	-
c	Konzentration	kg/m^3
D	Diffusionskoeffizient	m^2/s
k	Geschwindigkeitskoeffizient	m/s
n	Wachstumsexponent	-
r	Wachstumsgeschwindigkeit	$kg/s\,m^2$
R	universelle Gaskonstante	J/mol K
T	absolute Temperatur	K
δ	Grenzschichtdicke	m
μ	chemisches Potential	J/mol

8. Literatur

[1] Fels, G.; Ewald, G.
Verringerung der Korngröße von kristallinem Explosivstoff
Patentschrift DE 4200743 A1

[2] Heinemeyer, K.; Redecker, K.; Sassmannshausen, U.
Verfahren zur Herstellung von feinkörnigem Beta-Oktogen
Patentschrift EP 0246526 A1

[3] Gallagher, P.M.; Coffey, M.P.; Krukonis, V.J.
Gas Anti-Solvent Recrystallization of RDX: Formation of Ultra-fine Particles of a Difficult-to-Comminuite Explosive
J. Sup. Fluids, 1992, 5, 130-142

[4] Mellor, A.M.; Wiegand, D.A.
Hot spot histories in energetic materials
Mat. Res. Soc. Symp. Proc. 296, 1993, 293

[5] Matz, G.
Ullmanns Encyklopädie der technischen Chemie; Band 2 (1972); Seite 674

[6] Elwell, D.; Scheel, H.J.
High-Temperature Solutions.
Academic Press, London, 1975

[7] Stepanski, M.
Zur Wachstumskinetik in der Lösungskristallisation
Dissertation an der Universität Bremen, 1990

[8] van der Steen, A.
Shock Wave Interaction with Composite Materials
Journal de Physique IV, 5, 1995, 107-118

RECRYSTALLIZATION OF HMX WITH COMPRESSED GASES AS ANTI-SOLVENT

U. Förter-Barth, U. Teipel & H. Krause

Fraunhofer Institut für Chemische Technologie (ICT), P.O. Box 1240, 76318 Pfinztal, Germany

Abstract

A ternary system consisting of cyclotetramethylene tetranitramine (octogen, HMX) as the solute, acetone respectively γ-butyrolactone as solvents, and carbon dioxide as the anti-solvent was used to investigate the formation of fine particles with the GAS-process as well as the influence of the solvents upon the particle morphology under the same operating conditions. The precipitated particles were examined by infrared radiation spectroscopy (IR), laser light diffraction and light-optical microscopy. The results show that octogen with a narrow particle size distribution was obtained. The crystals are of the same modification as the raw material and of high purity. The modification and the particle size are influenced by the solvent used for the recrystallization.

Keywords: carbon dioxide, anti-solvent, fine particles, GAS-process

Introduction

Compressed gases have been introduced in the near past as solvents for extractive applications. On industrial scale, the decaffeination of coffee beans and the extraction of hops and essential oils with supercritical carbon dioxide as solvent were employed.

A new field of „non-extractive" applications of compressed gases is the formation of fine particles with a narrow particle size distribution. The formation of solid particles with well-defined properties, i.e. the particle size, the particle size distribution, the particle shape and free of solvent inclusions, is of great

importance for many industrial purposes. It is possible to process moderately solids like pharmaceuticals or energetic materials which are difficult to comminute due to their sensitivity to mechanical or thermal stresses. The characteristics of compressed gases allow to vary the morphology of solid particles in a wide range.

Solids which are insoluble in compressed gases can be processed by applying the GAS (Gas Anti-Solvent)-process. For this, a high-compressed gas is added to a solution of a solid in an organic solvent. The GAS-process is based on the ability of a high-compressed gas to dissolve in and expand an organic solvent at moderate pressures and temperatures. Due to the dissolution of the compressed gas, the expanded solvent has a lower solvent capacity towards the solute. The complete miscibility of the organic solvent with the compressed gas is the basic requirement for applying these anti-solvent techniques. Additionally, it is required that the compressed gas has no solvent power towards the solid to be crystallized. Diverse applications have been reported, e.g. the purification and comminution of the energetic materials cyclonite (RDX) [1] and nitroguanidine (NQ) [2], the separation and purification of ß-carotene [3] and the comminution of proteins [4].

Materials and Methods

Materials

Cyclotetramethylene tetranitramine (octogen, HMX) was used to investigate the formation of micron particles by using compressed gases as anti-solvent. The modification that is obtained depends on the solvent used for recrystallization processes. For example, acetone and γ-butyrolactone yield the desired ß-form. Both were taken as solvents to find out how the morphology of the recrystallized particles is influenced by using different solvents, but keeping the process parameters (pressure, temperature) constant. Carbon dioxide was used as anti-solvent. It is not toxic, not flammable, easy available and has low critical parameters (critical pressure p_c = 7,38 MPa, critical temperature T_c = 304,5 K). HMX is sparingly soluble in supercritical carbon dioxide, even when a modifier is added [5].

Methods

The experimental setup of the GAS-process is illustrated in Figure 1. The apparatus consists of three sections: the CO_2-supply unit, the crystallization vessel with a sinter metal filter inside (mean pore size = 0.1 µm) and the separator for the separation of the solvent and the anti-solvent. The CO_2 coming from the supply bottle is liquified in the heat exchanger W1 and is stored in the tank LR. To avoid cavitation in the pump, the CO_2 is undercooled (W2) and afterwards heated up to process conditions (W3). The solution of solvent and solid is put into the crystallization vessel. In the following, CO_2 is let in up to the desired pressure, preferably from the bottom to achieve a better mixing of solvent and anti-solvent. After a holding time CO_2 is supplied via the top of the crystallization vessel, keeping the pressure at the same level as before, to wash and clean the precipitated particles, while the mixture of solvent and CO_2 flushes into the separator to be separated by pressure reduction.

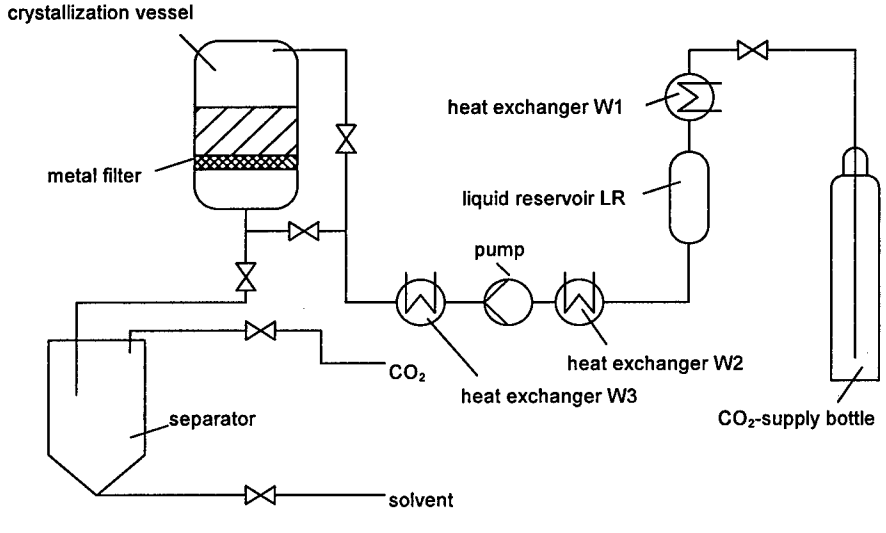

FIGURE 1: Flowsheet of the experimental setup.

All experiments were carried out at p = 8 MPa and T = 313 K. Under these conditions, the expansion of the solvents used for this process, i.e. the dissolution of carbon dioxide in the solvents, is sufficient to lower the solvent capacity that

HMX-particles are precipitated [6]. The amount of HMX dissolved in the solvents was 2 g / 100 g solvent. The solubility of HMX is in acetone 2,8 g / 100g solvent and in γ-butyrolactone 15 g / 100 g solvent at 313 K. The pressure in the crystallization vessel was constantly built up within 60 seconds. After having reached the desired pressure, the system was allowed to sit for about 10 minutes to ensure equilibrium. The washing procedure was conducted for 0,3 hours at the same pressure and temperature level as for the precipitation step.

The degree of saturation of a solution has an effect on the morphology of the recrystallized particles. As it can be seen in Figure 2, the pressure, needed to reach that supersaturation that nucleation occurs, depends on the solid concentration in the solution. Generally, higher temperatures request higher pressures for the onset of nucleation at the same degree of saturation. The time to built up the pressure as well as the degree of supersaturation also effect the number of the nuclei and the growth of the precipitated particles. For the chosen operating conditions which are kept constant for both solvents as described before, it is expected that the morphology of the precipitated particles will vary due to the different solvent capacity of the two solvents towards HMX. This means that the supersaturation of the HMX - acetone solution is higher in comparison to the HMX - γ-butyrolactone solution.

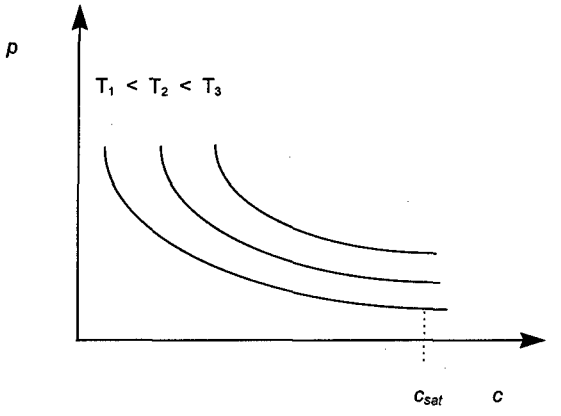

FIGURE 2: Qualitative course of the pressure - concentration isotherms for the beginning of nucleation

Results and Discussion

First of all, investigating the precipitated HMX particles, the most important question was if the crystals are of the same modification as the raw material. For this purpose, infrared radiation spectroscopy (IR) was used to examine the chemical structure and the purity of the received particles compared to the raw material. The results of the IR-spectroscopy are shown in Figure 3 and 4.

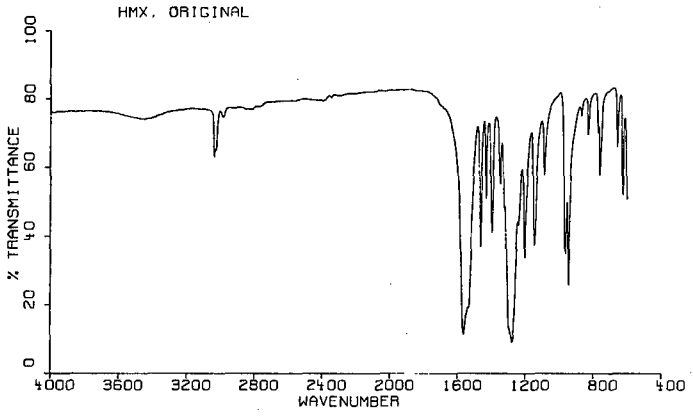

FIGURE 3: IR-spectroscopy of raw ß-HMX.

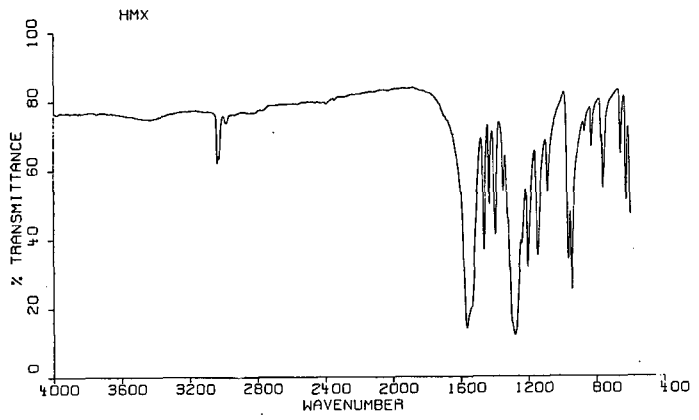

FIGURE 4: IR-spectroscopy of HMX recrystallized from acetone and γ-butyrolactone.

The absorption spectra of the raw HMX and the recrystallized HMX coincide. They correspond to the spectra of ß-HMX as described by Bedard et al. [7] . Due to the resolution of the IR-spectrometer, it can be assumed that the pollution of the particles by solvent residues is less than 1 %.

The particle size and the particle shape were determined by laser light diffraction respectively by light-optical microscopy. The following figures show the results in comparison to the raw material.

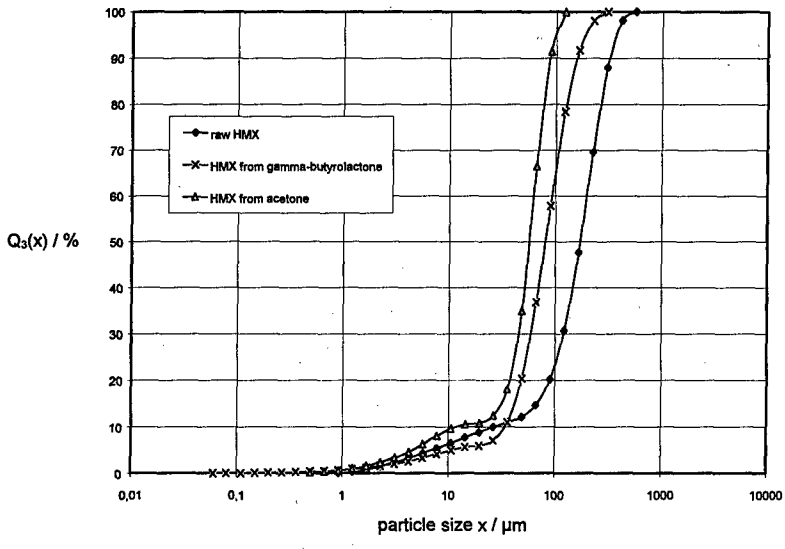

FIGURE 5: Volume sum distribution $Q_3(x)$.

For raw β-HMX, the mean volume diameter $x_{50,3}$ = 200 µm; for β-HMX from acetone, $x_{50,3}$ = 65 µm; for β-HMX from γ-butyrolactone, $x_{50,3}$ = 90 µm. It has to be considered that the particle size distribution of β-HMX from γ-butyrolactone is more spread compared to the distribution of β-HMX from acetone. The raw material has the broadest size distribution.

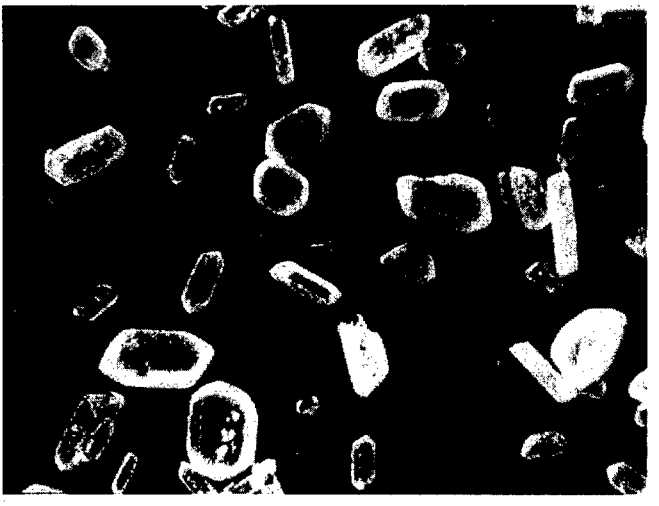

FIGURE 6: Light-optical microscopy of raw β-HMX.

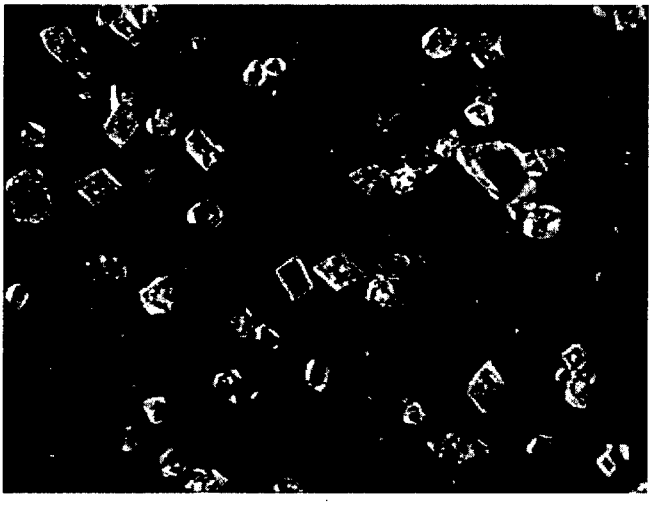

FIGURE 7: Light-optical microscopy of β-HMX from acetone.

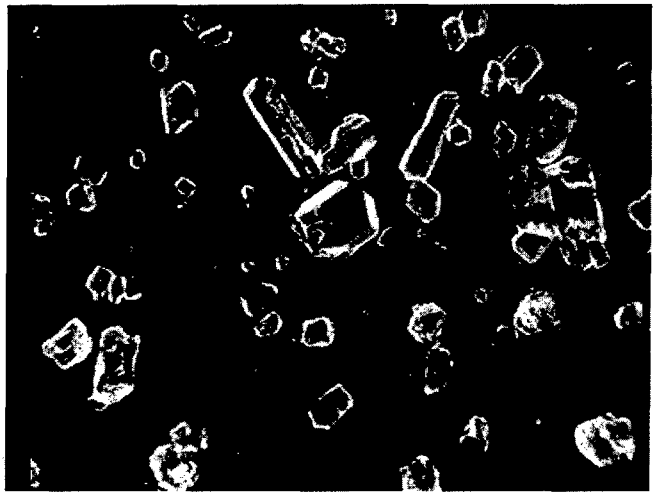

FIGURE 8: Light-optical microscopy of β-HMX from γ-butyrolactone.

Note that the figures are on the same scale. The pictures give an impression of the particle size reduction received by the GAS-recrystallization. The particles precipitated from acetone are more regular shaped and of more uniform size than the particles from γ-butyrolactone. It is noticed that long, rectangular crystals appear when γ-butyrolactone was used as solvent.

Maintaining process conditions (amount of HMX in the solution, pressure, temperature and time to built up pressure), the supersaturation gained is different for the two solvents due to their different solvent capacity towards the solid. The supersaturation for the HMX - γ-butyrolactone solution is high enough to start nucleation. But, for the HMX - acetone solution, the rate of nucleation is higher due to the higher supersaturation. The nuclei grow until the solution is depleted of the solute, and, due to the larger number of nuclei, smaller and more regular-shaped particles are formed in comparison to the HMX - γ-butyrolactone solution.

Conclusion

The GAS-process is well suited for the formation of solid particles which are difficult to handle due to their sensitivity towards thermal and mechanical stresses.

The operation conditions are moderate with regard to pressure and temperature if carbon dioxide is used as anti-solvent. Carbon dioxide itself is non-toxic, not flammable and easy available.

The morphology of the precipitated particles is influenced by the solvent used for recrystallization. The supersaturation that is reached depends on the solid concentration in the solution and the pressure in connection with the corresponding temperature, but the time to built up the pressure within the crystallizer also influences the nucleation and the growth of the particles. The obtained particles are of high purity, probably due to the mechanism of nucleation and particle growing.

References

1. Krukonis, V.J., Coffey, M.P. and Gallagher, P.M., 1988, Exploratory Development on a New Process to Produce Improved RDX Crystals: Supercritical Fluid Anti-Solvent Recrystallization, *Contract Rept. No. BRL-CR-606.*

2. Gallagher, P. M., Coffey, M. P., Krukonis, V. J. and Klasutis, N., 1989, Gas Anti-Solvent Recrystallization: New Process to Recrystallize Compounds Insoluble in Supercritical Fluids, In: Johnston, K. P. and Penninger, J. M. L., Supercritical Fluid Science and Technology, *ACS Symposium Series 406*: Chapter 22.

3. Chang, C.J. and Randolph, A.D., 1991, Separation of ß-Carotene Mixtures Precipitated from Liquid Solvents with High-Pressure CO_2, *Biotechnol. Prog.*, 7: 275-278.

4. Yeo, S-D., Lim, G-B., Debenedetti, P.G. and Bernstein, H., 1993, Formation of Microparticulate Protein Powders Using a Supercritical Fluid Anti-Solvent, *Biotech. and Bioeng.*, 41: 341-346.

5. Niehaus, M., Teipel, U., Bunte, G. and Krause, H., 1997, Suitability of Modified Supercritical Carbon Dioxide as Solvent for Polar Substances, *Propellants Explos. Pyrotech.*, 22: 176-179.

6. Gallagher, P.M., Krukonis, V.J. and VandeKieft, L.J., 1991, Gas Anti-Solvent Recrystallization: Application to the Separation and Subsequent Processing of RDX and HMX, *Proc. 2nd Int. Symp. SCF*, Boston Mass, 45-48.

7. Bedard, M., Huber, H., Myers, J.L. and Wright, G.F., 1962, The Crystalline Form of HMX, *Can. J. Chem.*, 40: 2278-2299.

PROPERTIES OF SPRAY-DRIED BORON/POTASSIUM NITRATE GRANULAR

Katsuhiko TAKAHASHI, Nobukazu ASANO and Koji OCHI
NOF Corporation
61-1 Kitakomatsutani, Taketoyo, Chita-gun, Aichi 470-23, Japan

ABSTRACT

In this report, we will describe the outline of our developed spray-dried process to manufacture Boron/Potassium Nitrate granular, the safety countermeasure which we have introduced in this process and the properties of the product manufactured by this process.

The advantages of the use of spray-dry process to manufacture Boron/Potassium Nitrate granular are mainly; 1) High productivity and low manufacturing cost, 2) Perfect remote control process, 3) Consistency of properties and performance and 4) Easy recycling.

However, it should be noticed that the above advantages will be available when the manufacturing conditions are appropriate and well-controlled. The important safety countermeasures in this process are; 1) Prevention of Boron/Potassium Nitrate to stick on the inner wall of drying chamber duct, cyclone, etc., 2) Control of the electric field inside the drying chamber by real-time sensor, and 3) Installation of an appropriate expansion vent for pressure release.

The Boron/Potassium Nitrate granular manufactured by spray-dried process has good free-flow property, sufficient calorific value and mild burning performance. These characteristics are suitable to ignite various gas generating formulations.

1. INTRODUCTION

Boron/Potassium Nitrate (hereinafter called "BKNO3") granular is popularly used as booster in many type of inflators, usually placed between squibs and gas generants or charged into the squibs, to ignite the gas generants with predetermined output rate at wide range temperature conditions. BKNO3 is a well known ignitor composition and many companies have been manufacturing this composition for many years. The conventional manufacturing process for BKNO3 granular is a batch process and basically consists of four processes, namely, blending, granulation, sieving and drying, which process requires much manpower. In addition, the

conventional process is hard to increase the batch size because of BKNO3's high sensitivity and its violent burning characteristic[1]. From those reasons, the BKNO3 granular manufactured by the conventional process is quite difficult to drastically reduce the cost.

In recent years, many different azide free gas generating formulations have been developed to replace the azide based formulations. Those azide free formulations are generally hard to ignite compared with the azide based formulations. It is considered that the mild burning property of BKNO3, which means the slower burn rate with sufficient calorific output, will help the azide free formulations to be ignited within the prescribed time frame.

Therefore, for customer's satisfaction, the development program to manufacture BKNO3 granular by spray-dry process has been completed in accordance with four steps; 1) Testing by mini-spray-dryer, 2) Full size spray test with dummy formulation, 3) Process hazard evaluation and 4) Full size test production.

This paper describes the outline of our developed spray dry process to manufacture BKNO3 granular, the safety countermeasures which we have introduced in this process and the properties of the product manufactured by this process.

2. ADVANTAGES OF SPRAY-DRY PROCESS TO MANUFACTURE BKNO3

The flow chart of spray-dry process to manufacture BKNO3 granular is shown in Fig.1. This process consists of two step; 1) Preparation of homogeneous water slurry and 2) Spray dry process and BKNO3 granular will be manufactured automatically.

There are mainly four advantages of the use of spray-dried process to manufacture BKNO3 granular.

a) High productivity and low manufacturing cost

In spray-dry process, the productive capacity is generally 20 to 100kg per hour at dried product base. In this process, it is necessary for only few operator to supervisory control the process. In addition, raise of the lot size will be able to reduce not only the cost of quality assurance tests in the manufacturers but also the cost of lot acceptance tests in the customers.

b) Perfect remote control

By isolating the drying chamber in an explosion proof room, and by controlling all the process conditions from the outside of this room, the operator is free from any injuries even if the worst should happen.

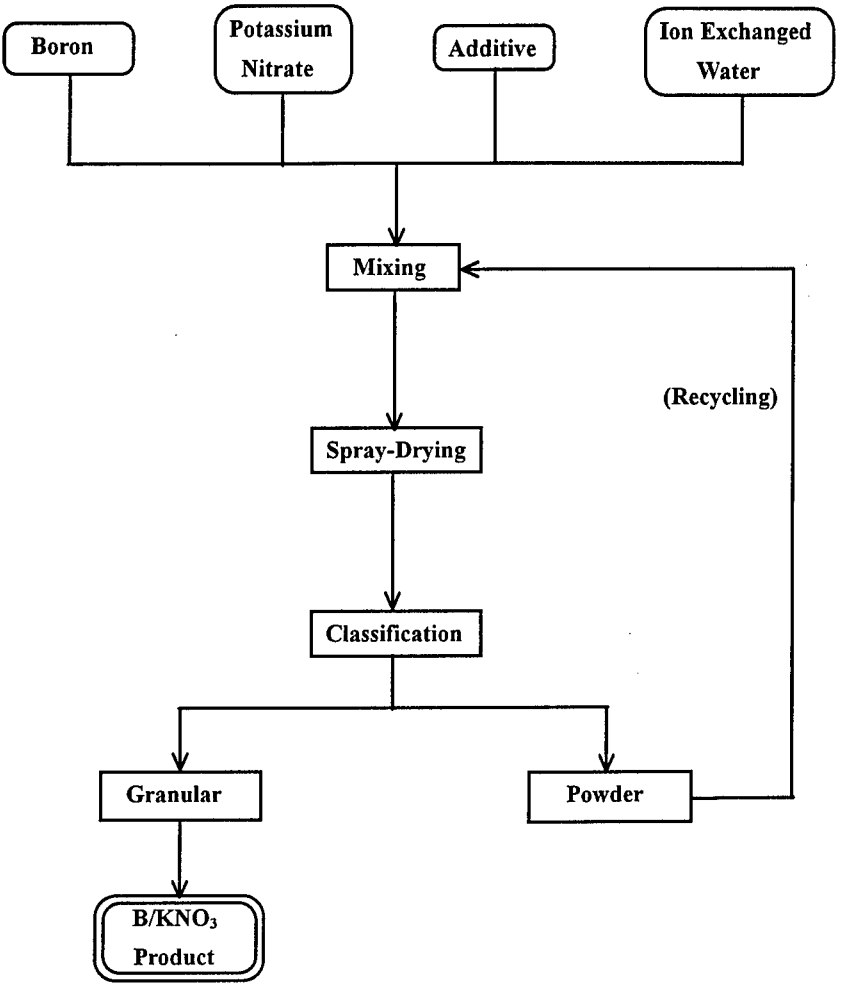

Fig.1 Flow Chart of Spray-Dry Process

c) Consistency of properties and performances

A skilled hand is not necessary to run the spray dry process. Because the BKNO3 granular will be manufactured automatically, the inside lot variability and the lot between variability will be smaller than the conventional processes if the spray drying conditions are fully controlled.

d) Easy recycling

In the conventional processes, a binder (i.e. polyester resin, nitrocellulose or "viton") should be added to make a favorable BKNO3 granular. On the other hand, a binder is not necessary in spray dry process because potassium nitrate dissolved in water slurry will function as binding agent when it recrystallize during the drying process. Therefore, it is easy to recycle the BKNO3 granular or the powderized BKNO3 produced by spray dry process. The spray dried BKNO3 will again form a homogeneous water slurry if the slurry is mixed by an appropriate mixing machine with some water. The product manufactured by using the recycled materials also shows the same properties and performances as the product manufactured by using the virgin materials.

3. SAFETY COUNTERMEASURES

As a result of process hazard evaluation, we may conclude that a considerable origin for unexpected ignition during spray dry process will be an electrostatic discharge. The possibility of unexpected ignition caused by mechanical force (impact, friction) or thermal decomposition of BKNO3 have also been evaluated, the results of which evaluation suggests that those causes will never be a major factor of an unexpected ignition.

3.1 ELECTROSTATIC SENSITIVITY OF BKNO3

The electrostatic sensitivity of BKNO3 in various conditions have been measured in accordance with the test method determined by Research Institute of Industrial Safety, Ministry of Labour, Japan. The sensitivity of BKNO3 dust were measured with 1.2 liters explosion chamber (Hartmann type) at various concentration level. And the sensitivity of BKNO3 layer were measured with a few milligrams quantity at various discharging resistance. The data are summarized in Fig.2.

The sensitivity of BKNO3 layer is rather higher than the sensitivity of BKNO3 dust. This fact means that the prevention of BKNO3 to stick on the inner wall of the drying chamber, duct,

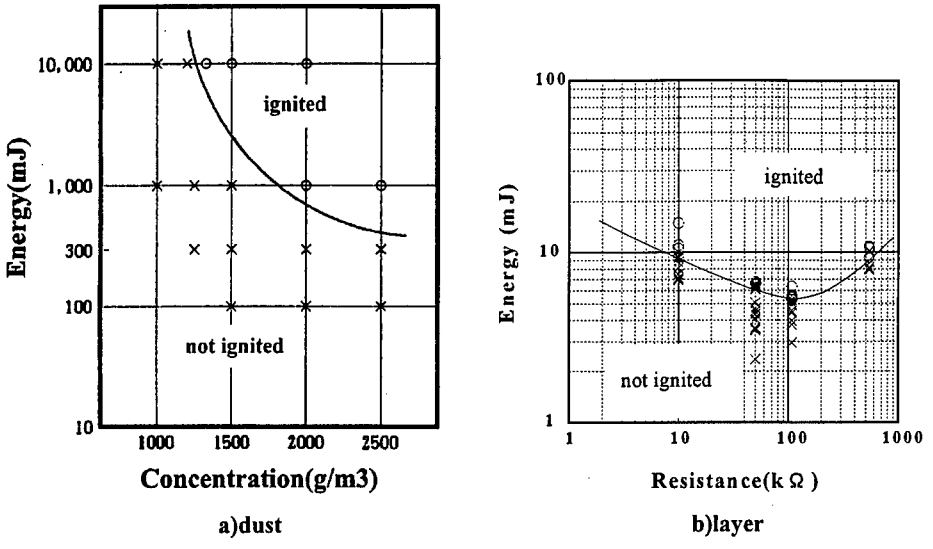

Fig.2 Electrostatic Sensitivity

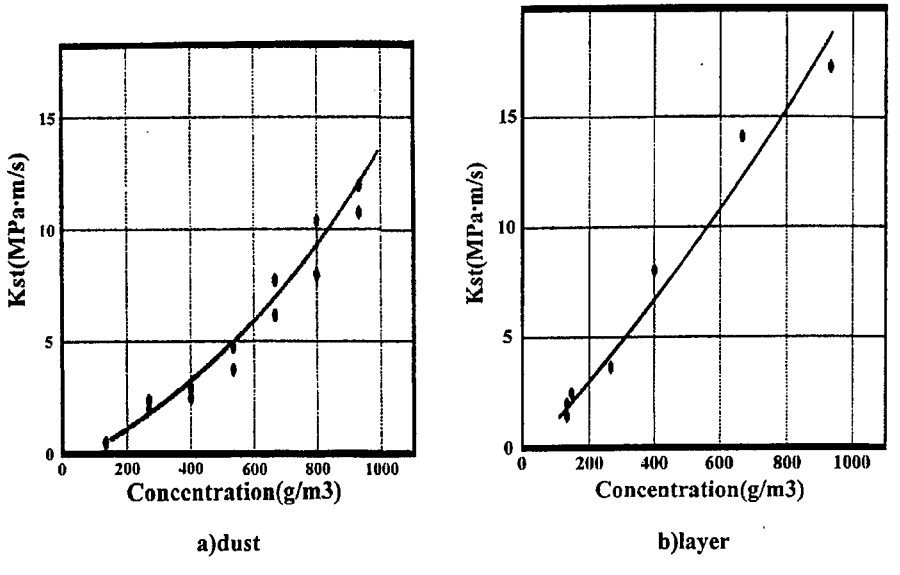

Fig.3 Dust-specific characteristic

cyclone, etc. should be one of the important safety countermeasures to run the spray dry process with safe. To prevent this sticking phenomenon, the below items should be well controlled during the process.

a) Temperature of drying air

b) Blowing rate of drying air

c) Supplying rate of BKNO3 slurry

d) Water content of BKNO3 slurry

e) Atomizing conditions of BKNO3 slurry

3.2 ELECTRIC FIELD INSIDE THE DRYING CHAMBER

It is very hard to suppress the yield of static electricity in spray dry process because the slurry should be atomized anyway by nozzles or disks, and as the result of this atomization, the charged particles will spread inside the drying chamber to form a charged cloud (just like a small thundercloud).

The basic point to maintain the spray dry process with safe is to keep the energy level of this charged cloud lower than the electrostatic sensitivity of BKNO3. The charged energy can be estimated by monitoring the electric field of the drying chamber using the below equation[2].

$$W = \varepsilon_0/2 \int_0^r E^2 * 4\pi r^2 dr$$

$$= \varepsilon_0/2 \int_0^r (r\rho/3\varepsilon_0)^2 * 4\pi r^2 dr$$

$$= 2\pi\rho^2 r^5/45\varepsilon_0 \qquad (1)$$

where ε_0 is vacuum dielectric constant (ε_0=8.854x10^{-12}F/m), r, the relative radius of the drying chamber ($V=4/3\pi r^3$, where V is the volume of the drying chamber), E, the electric field inside the drying chamber, and ρ, the electric charge density inside the drying chamber.

If the level of E is monitored by real time sensor, the level of ρ can be estimated by the law of Gauss ($\rho=3\varepsilon_0 E/r$), and then, the level of W can be estimated by the equation (1), which level should be controlled much lower than the minimum ignition energy of BKNO3.

3.3 EXPLOSION VENT FOR PRESSURE RELEASE

An appropriate explosion vent should be installed for the pressure release of the drying chamber to make provision in case the worst should happen. The required vent area can be obtained from the following equation[3)-6)].

$$A = (a)[V^{2/3}][Kst]^{b}[Pred]^{c} \qquad (2)$$

where:

a = 0.000571exp(2Pstat)

b = 0.978exp(0.105Pstat)

c = 0.687exp(0.226Pstat)

and A is vent area(m^2),V, enclosure volume(m^3), Pred , maximum pressure developed during venting(bar gauge), Pstat, vent closure release pressure(bar gauge) and Kst, dust specific characteristic(bar·m/sec)[7)8)].

It must be noticed that the value of Kst for BKNO3 is not constant, which fact is different from many other inflammable powders. Kst at various BKNO3 concentrations was measured by ASTM-E 1226:Standard test method for pressure and rate of pressure rise for combustible dust with 30 litters spherical tank. Fig.3 shows the experimental Kst data at various BKNO3 concentrations. Considering the process conditions, the appropriate BKNO3 concentration should be estimated to determine the proper Kst, and then, the required vent area can be calculated by the equation (2).

4. PROPERTIES AND PERFORMANCES

Fig.4 shows a typical SEM photograph of spray dried BKNO3. The shape of granular is almost spherical, which fact is important to obtain a free flow property even though the average particle size of the granular is less than 100 microns.

Table 1 shows the main properties of spray dried BKNO3, which properties are comparable with the conventional ones.

One of the unique features of spray dried BKNO3 compared with the conventional BKNO3 is its mild burning performance. Fig.5 shows the comparison of burning characteristic evaluated with 150cc closed bomb testing. In this test, 15 grams BKNO3 was used and ignited by Platinum wire, and then Pressure-time curves was measured. The spray dried BKNO3 showed the better ignitability than the conventional one, however, the quickness of spray dried BKNO3

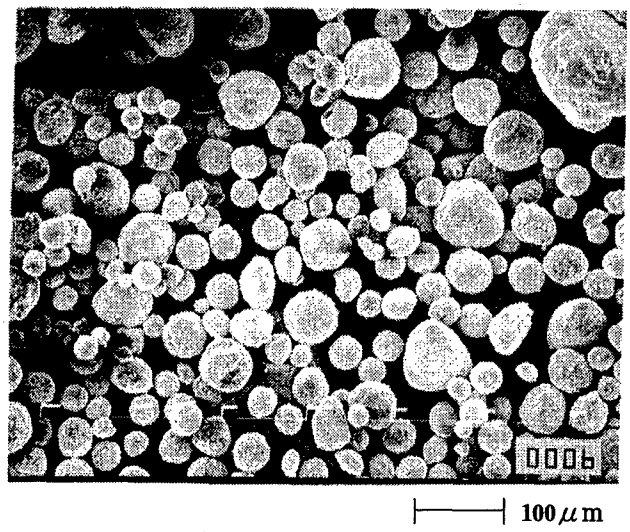

Fig.4 SEM photograph of spray-dried $BKNO_3$

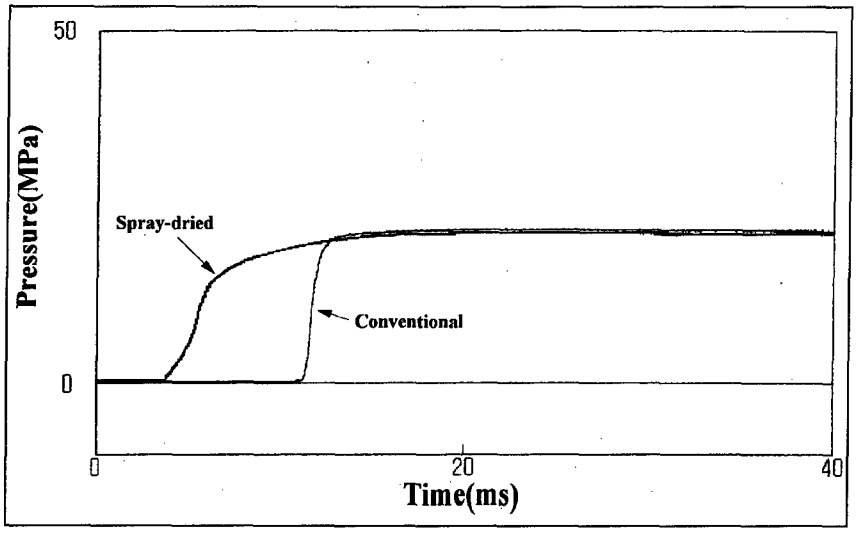

Fig.5 150cc Closed Bomb Data

is lower, and as the results of these characteristics, the time to Pmax are almost the same. Here, the quickness was defined as the time from 0.1 Pmax to 0.9 Pmax. The cause of these differences is not sure at this time, however, we are considering that the presence of binding agent or the difference of the real particle size of potassium nitrate (because of the recrystallization in spray dry process) will be the main cause of these differences.

Fig.6 and Fig.7 show the performance of driver inflator with 60 liters tank at -40°C. There was no difference of inflator performance between spray dried BKNO3 and the conventional one when the charged gas generant was azide based formulation (Fig.6). On the other hand, spray dried BKNO3 showed the better inflator performance when the charged gas generant was azide free based formulation (Fig.7). Those data demonstrate that spray dried BKNO3 which has mild burning characteristic is more suitable than the conventional one to ignite azide free based formulations. In other words, the mild burning characteristic should be a good characteristic to ignite the formulations which has poor ignitability such as azide free based formulations.

5. UN CLASSIFICATION

U.S.DOT has certified our BKNO3 as Propellant, Solid (UN number:0499) and for classification as Explosive 1.3C in accordance with Sections 172.101,173.59 of U.S.DOT Hazardous Materials Regulations.

In addition, 120 grams/box (with special packaging) of our BKNO3 has been certified by U.S.DOT as Articles, explosive, n.o.s. (UN number:0471) and classified as Explosive 1.4E, which enable us to ship the material by air. We hope this classification will help our customers to receive the sample quickly for their evaluation.

6. NEW SPRAY-DRIED BKNO3 GRANULAR

By means of particle size control of BKNO3 and virgin potassium nitrate, a kind of additives and so on, spray dry process will be able to control burning characteristic . The development program of new BKNO3 granular with more mild burning performance has been started.

Table 2 shows an example of burning characteristics of new BKNO3 granular. Modified 1 includes a new additive, aluminum and potassium perchlorate is mixed in Modified 2, and Modified 3 uses new grade of boron. The quickness of Modified 3 is about 5 times lower than that of conventional BKNO3. This means that the use of spray dry process to manufacture

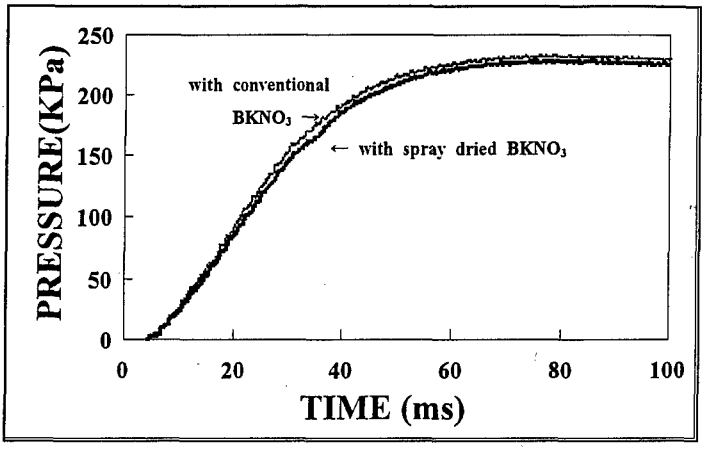

·Gas Generant Formulation NaN_3/MnO_2/Additives=58/34/8
·Pellet Size Diameter=7mm, Thickness=5mm

Fig.6 Inflator Performance (60L Tank Test[-40℃]) with Azide based Gas Generant

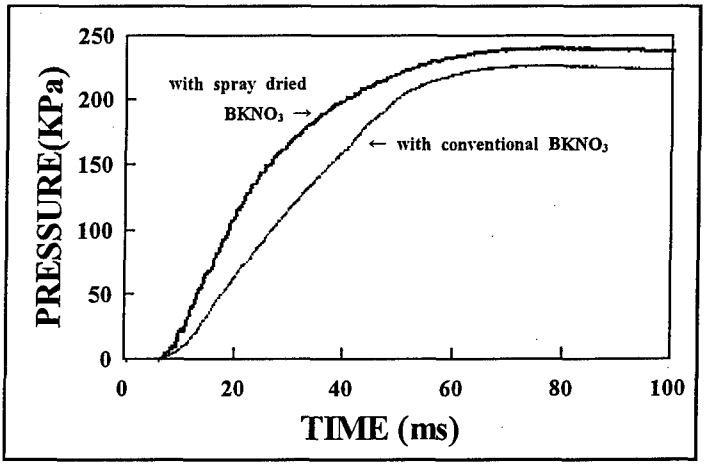

·Gas Generant Formulation HDCA/$KCLO_4$/KNO_3/Additives=27/60/8/5
(HDCA;Hydrazodicarbonamide)
·Pellet Size Diameter=6mm, Thickness=2mm

Fig.7 Inflator Performance (60L Tank Test[-40℃]) with Azide free Based Gas Generant

Table 1 Properties of Spray-dried $BKNO_3$

Testing	Results
Impact Sensitivity	50cm height with 5kg hammer
Friction Sensitivity (BAM Method)	more than 36kgf
DSC Decomposition Temp.	more than 510℃
Detonation Test (ϕ35mm Steel tube)	Detonation not occurred
Aging (107℃-400hrs)	Weight loss: less than 0.1%
Heat of Explosion ·Under 1atm argon gas ·Under 20atm argon gas	 more than 1600cal/g more than 1450cal/g
Apparent Density	between 0.85~1.05g/ml

Table 2 An Example of Burniing Characteristics of new $BKNO_3$ granular

Type of $BKNO_3$	The quickness(ms)
Convwntional $BKNO_3$	3.1
Current Spray-dried $BKNO_3$	5.1
Modified1(including a new additives)	8.4
Modified2(including alminium and Potassium perchlorate)	11.1
Modified3(including new grade of boron)	14.7

BKNO3 will be able to supply BKNO3 granular with several kind of mild burning characteristics to the customers. This characteristics is suitable to ignite various gas generating formulations.

7. CONCLUSION

BKNO3 can be manufactured by spray dry process with safe if some appropriate countermeasures have been taken. The BKNO3 manufactured by spray dry process has almost the same properties as the conventional ones. It was found that, although the spray dried BKNO3's burning characteristic is more moderate than the conventional ones, inflator performances were comparable or better.

REFERENCES

[1] J. M. Smallwood, "Electrical Discharge Incendivity to a Pyrotechnic Powder", The 18th. International Pyrotechnic Seminar (1992)

[2] Tsutomu Kodama, "Measurement of Eletrostatic Charges on Powder cloud in a Fluidized Drier Using a Newly Developed Electrostatic Field Detecting Systcm", The 26th. Safety Engineering Symp. (1993)

[3] Richard Siwek, "New; Revised VDI Guideline 3673", Proceeding of the 28th. Annual Loss Prevention (1994)

[4] Reinhard E. Bruderer, "Advantages of the New Version VDI3673 Part 1 in comparison with the Chapter 7 of NFPA68", Process Safety Progress, Vol.14, No.1 (1995)

[5] Noboru Taguchi, "Experimental Study on the Methods of Explosion Venting" Research Report of the Research Institute of Industrial Safety, RR 19 1 (1970)

[6] NFPA 68 "Guide for Venting of Deflagrations" 1994 Edition

[7] "Hazards of Explosive Dust", Pittsburgh Research Center, Internal Report No.4784, Bereau of Mines (1989)

[8] Toei Matsuda, "The Technical Assessment of Materials Liable to Dust Explosion", Research Report of the Research Institute of Industrial Safety, SD 90 1 (1990)

RADIATION PROTECTIVE AND RADIATION RESISTIVE MATERIALS

Natalija Kalinina

Dniepropetrovsk State University, Ukraine,
320625 Dniepropetrovsk, Nauchny st., 13

It was developed the new superdisperse modificators on the base of carbides nitrides various metals for obtaining radiation protective and resistive materials.

The problem of creation of radiation-protective and radiation-protective and radiation-proof materials is connected with forming a super-fine substructure in the process of their creation. It can be obtained while utilizing special dispersive and ultra-dispersive powders of various materials and their compounds.

On the basis of study of adsorbent, crystallographic, phase, electromagnetic and other characteristics of different powder-like systems we have created new highly effective compounds-modifiers (NiAl, AlN, TiCN, Ni-Co, BV, Ni-V, SiC, WC, VC, MgSi and others) of ultradispersive kind with a particle size = 10...50 nm (100...500 A) for obtaining radiation-protective and radiation-proof materials. Carbides, inter-metalloids, silicids, nitrides and other compounds of the created chemical structure and the proper size-and-crystallographic form were synthesized in special high-frequency plasmochemical plants utilizing waste products of ferroalloys, titanic-magnesium, chemical, carbon and silicon-polymeric industries.

To generate plasma in plasmochemical plants we used whirlwind induction plasmotrons with gas stabilized discharge. Initial powder-like materials measured out in doses were put in the zone of nitrogen plasma flow the temperature of which was 5500...7500 K. As the result the materials got heated, melted and evaporated and came into appropriate chemical interaction. The synthesized gas-powder mixture from the plasmochemical reactor passed through heat exchangers into a catching chamber and further through a plating-protective system into a removable container. Among well-down methods of obtaining ultra-dispersive powders, such as : dispersion, grinding, electrolysis and decomposition of metal solts including those using explosions; emanation and thermoblow only plasmochemical synthesis allows not only synthesizing of compounds with optimum structure and form, but also their output on a large industrial scale in automated and computerized plants.

Obtaining of plasmochemical ultra-dispersive compounds is conditioned by high speed volumetric condensation of gasoplasmic flow which results in unstable state of ultra-dispersive particles /1-3/ : a particle has smaller parameters of its crystalline lattice then massive samples of the same chemical composition and we can find amorphous formations /4/; in the particle itself we can observe lattice parameters decreasing from the centre to the surface due to maximum compression of the surface layer. This results in inhomogeneous arrangement of components and phases in the particle radius direction.

Turning of the material into ultra-dispersive state with the size of particles being decreased causes a steep ride in adsorbent and catalytic activity of the system since a share of surface in a particle volume considerably increases (picture 1, curves 1-3).

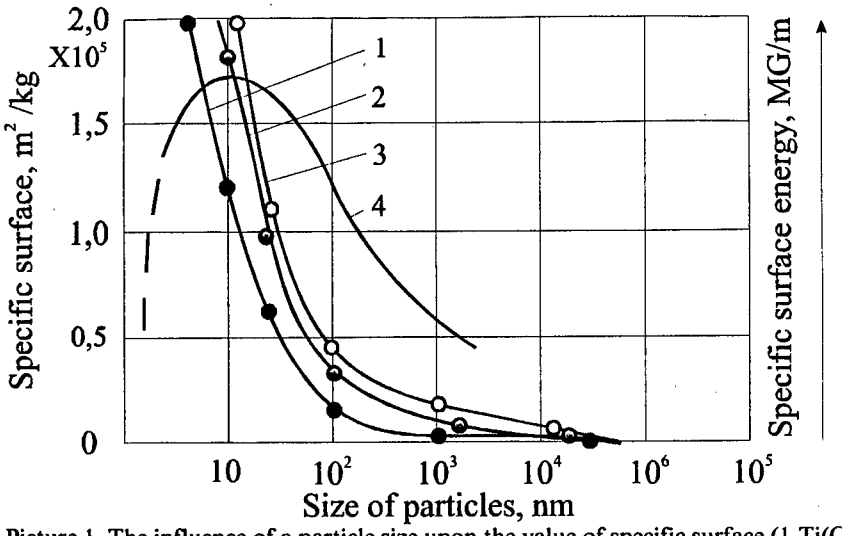

Picture 1. The influence of a particle size upon the value of specific surface (1-Ti(CN), 2-WC, 3-NiAl) and surface energy4.

A steep increase in surface energy while particles is turning into ultra-dispersive state (picture 1, curve 4) and a change in thermodynamic conditions of phase balances result in the following phenomena emerging en ultra-dispersive systems: high temperature super-conductivity /3/, super-paramagnetic and amorphous state /3-4/, temperature shifts in phase transformations, and finally a considerable increase in oxidizing processes.

Ultra-dispersive powders are good hetteras, materials with a developed free surface capable of chemical adsorption and adhesion and at the same time inclined to aggregating in vacuum and neutral medium as well as to oxidation. These peculiarities made it difficult to utilize ultradispersive compounds in the process of smelting of radiation-proof and obtaining radiation-protective materials. As the result of oxidation and diffusion of admixtures the clean active surface of particles is rapidly covered by an absorbed layer which considerably decreases protective characteristics of ultra-dispersive powders in radioactive irradiation. Therefore in the process of obtaining of radiation-protective powders the dominating role belongs to the task of saving clean the surface with high adsorbent and catalytic activity. In this case only ultra-dispersive compounds put into melt will act as centers of crystallization during hardening of smelted radiation-proof materials.

As a result of the carried out researches we have developed and assimilated a method of double-plating of ultra-dispersive powders with covering the processed surface with particles of a micro-layer of solid carbons of methane row /5/. Unlike non-plated ultra-dispersive powders plated ones can be kept in non-hermetic capacities for a long time /picture 2/.

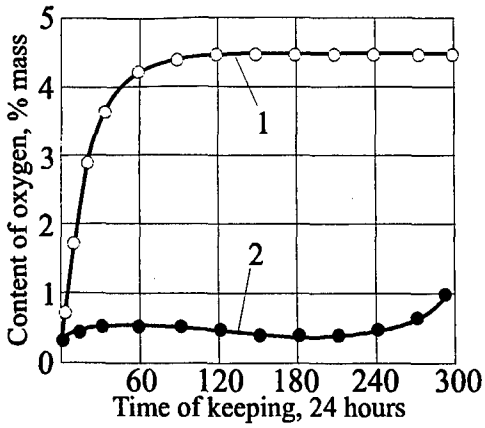

Picture 2. Influence of time of keeping an ultra-dispersive modifier in non-hermetic capacities upon its oxygen content.

1 - non-plated
2 - plated

Radioactive irradiation essentially changes material's structure and characteristics. The basic consequences of radiation are gas and vacancy intumescence of space and nuclear materials accompanied by an essential change in sizes, warping, cracking and destruction of airspace goods. Cosmic irradiation consists mostly of high energetic charged particles (electrons, protons) damaging a surface layer of materials. Apart from ordinary damages beating atoms out and their taking away from the surface of spaceships acquire great importance in high vacuum conditions.

In the created radiation-proof materials obtained with plasmochemically synthesized ultra-dispersive compounds being utilized in the process of smelting we can not find anisotropy of characteristics and can observe a balanced fine-grained structure. They in less degree change their mechanic and anti-friction characteristics and thermal-and elertroconductivity then currently used materials. Ultra-dispersive carbon in a solid solution restrains intumescence of nickels and other alloys of Fe-Cr-Ni system and extends a transition period. The assumed mechanism of carbon atoms activity in a solid solution is their being traps for point defects.

Carbon takes active past in the processes of capture of point defects, diffusion, segregation and dissociation. The optimum carbon concentration in austenite kinds of steel is to be within the limits of 0,5...0,08%. Ultra-dispersive boron carbide has the effect similar to that one of carbon. When in a solid solution boron restrains the development of porosity in austenite kinds of steel and fusions of Fe- C-Ni. The usage of the materials smelted with addition of ultra-dispersive powders of boson carbide, vanadium carbide and wolfram allows to save such expensive materials as molybdenum, zirconium, vanadium, niobium.

Rare earth metals, lead, various compounds of barium are used as the materials for protection against X-radiation. They are applied for common and individual protection. Protective screens are made on their basis. Nevertheless, the effectiveness of their protection combines with the essential technological technological difficulties of manufacturing, with the large weight of goods and toxicity.

After carrying out investigations of the materials containing particles of the size less than 100 nm (1000 A°) it was determined that some metals and their compounds reveal their

aptitude for intensive absorbing of X-radiation (3-5 times). The compounds of wolfram, vanadium, boron and other elements are referred to such compounds.

The difference in the output work of the various crustallographic facets of ultra - dispersive particles attains 1ev. This entails regulating by the crystallographic orientation in the system of interacting particles. The level of the regulated orientation depends on the scale, mutual disposition of the particles and characteristics of the surrounding materials. Dispersion of the X-rays upon the inner surface of ultra-dispersive particles, coherent dispersion upon the particles themselves and diffractive effects on the conglomeration of particles lead to the increase of protons optical length. Correspondingly, photoabsorbing of X-radiation in the ultradispersive compounds of the developed structure and crystallographic form grouse abruptly too.

It is possible to solve not only important problems of the vital activity in the space, but also create conditions for profitable international business through the application of new forward - looking technologies in space equipment engineering, especially in the field of radiation protection.

Literature.

1. Sutugin A.G. Physiochemistry of Ultra - dispersive Systems. M.,"Наука", 1987, p. 15.
2. Morokhov I.P., Trussov L.I., Lapovok V.I. Physical Phenomena in Ultra - dispersive Metal Media. M., "Энергоатомиздат", 1984, p. 224.
3. Petrumin V.F., Andreyev Y.G. Miller T.N. Powder - Metallurgy. 1984, #8, p. 12.
4. Morokhov I.D. and others. The Progress of Physiologic Sciences. 1981, vol. 133, #4, p. 653.
5. Licence # 2069703. /Б.И. 1986, #23, p. 22 c.35/00

Nanostructured diamonds: Synthesis, Characterization and Applications

Volker Komanschek and Achim Pfeil

Fraunhofer-Institut für Chemische Technologie
Joseph-von-Fraunhofer-Str.7, D-76327 Pfinztal

Abstract

Ultrafine Diamond, UFD, is a nanostructured diamond material obtained by processing detonation residues. The structure and properties of this material were verified by combining destinct analytical methods. Promising steps of industrial applications are discussed

1. Introduction

Using energetic materials for the synthesis of diamonds was first demonstrated in the 1960 's by the work of DeCarli et al. [1]. The detonation energy thereby causes a shock compression by which the hexagonal graphite structure is transformed into the cubic diamond structure.

Two decades later detailed analysis showed the presence of diamonds in residues of graphite-free explosives. The explanation forwarded by R. Greiner, F. Volk et al. [2] was that diamond was formed during the detonation process itself. Subsequently the process of direct diamond synthesis was studied by many laboratories over the last twenty years, most of them in the Sowiet Union / GUS [3,4,5].

From the research efforts a new material resulted, called Ultrafine Diamond UFD, which basically is a nanostructured diamond powder displaying unique properties, presently under study for industrial applications.

2. Synthesis and purification

At ICT, UFD are synthesized in a 1.5 m^3 tank using charges of Composition B (60 % TNT / 40 % RDX) up to 300 g weight with confinements consisting of pasteboard or ice. To decrease carbon oxidation the experiments are carried out in an inert atmosphere. After the detonation the tank is washed with water and the UFD containing residue retrieved by an 0,8 µm filter system.

This residue contains three different carbon modifications, namely

- diamond
- carbon black
- graphite.

Besides, the residue contains the impurities copper (from blasting caps), silicium (contained in Composition B), calcium and magnesium (contained in washing water) and iron formed by the erosion of the steel tank during detonation. These impurities are removed by a special purification process with the aim to recover the UFD powder with maximum yield and minimal use of chemistry. The following scheme expresses the different steps involved in the synthesis process:

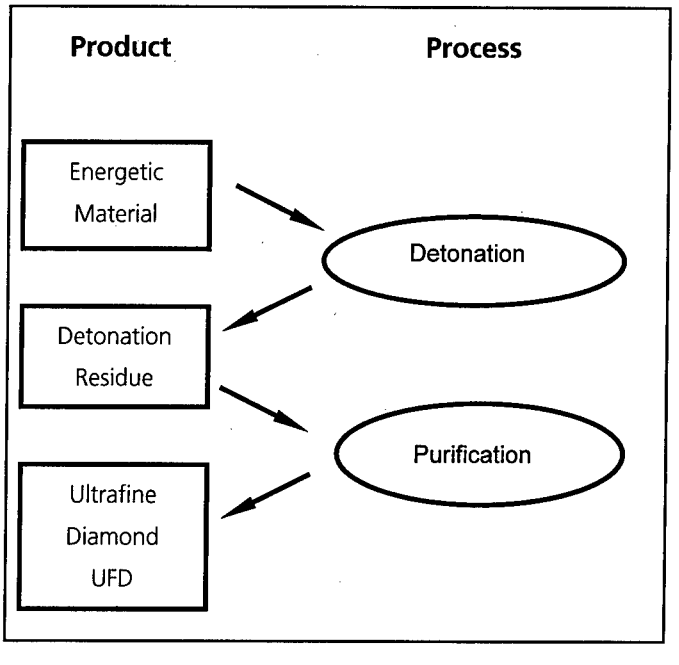

Fig. 1: Scheme of the UFD synthesis.

The purification process at ICT comprises two steps, the first step removes most of the carbon black by a thermal treatment in air. This process requires careful monitoring of the temperature of the residue to prevent loss of UFD. The second step consists of a special acid treatment in a microwave desintegration chamber at reaction conditions up to 240 °C and 30 bar. The conditions enable a short process duration and ensure minimal loss of diamond. The basic chemistry involves is the removal of the impurities by reaction with nitric acid, followed by reaction with hypochloric acid. Certain impurities like silicium oxide, glass, aluminium oxide are removed in an additional chemical step with hydrofluoric or phosphoric acid.

To improve the environmental friendlyness of the purification process, experiments with hydrogen peroxide as a replacement for the acid treatment and / or plasma-treatment of the residue are in progress at ICT.

Since the processes markedly influence the surface properties of the UFD, the purification process is adapted to the particular application sought and will be custom-tailored in cooperation with the UFD material user.

3. Characterization

The characterization of the UFD-material focuses on the following criteria:

- particle size
- chemical purity
- thermal behaviour
- surface properties.

Table 1 summerizes the analytical methods and results of the UFD characterization.

Table 1: Results of UFD characterization

PROPERTY	DETECTING METHOD	MEASURED
size of crystallite area	x-ray diffraction	5 nm
particle size of dry powder	scanning electron microscope	50-100 nm
particle size in dispersion	photon correlation spectroscopy	40-200 nm
density	pycnometer	3,10 g / cm^3
specific surface	BET	247 m^2 / g
zeta-potential at pH 7	laser doppler anemometry	-22 mV
carbon content	CHN automatic analyzer	91 %
decomposition temp. in air	thermogravimetry	390 °C
chemical impurities	energy dispersive x-ray analysis	O, Si

Practice showed that a combination of analytical methods is necessary to get a clear picture of the particle size and structure. For example, X-ray diffraction allows the calculation of the crystallite size by using the Sherrer equation. Typical crystallite diameters are in the range of a few nanometers. These results are verified by visualizing the crystallites using transmission electron microscope (fig.2). These nano-sized crystallites, in turn, form clusters which can be identified by scanning electron microscope (fig. 3). The clusters range between 50 and 150 nm.

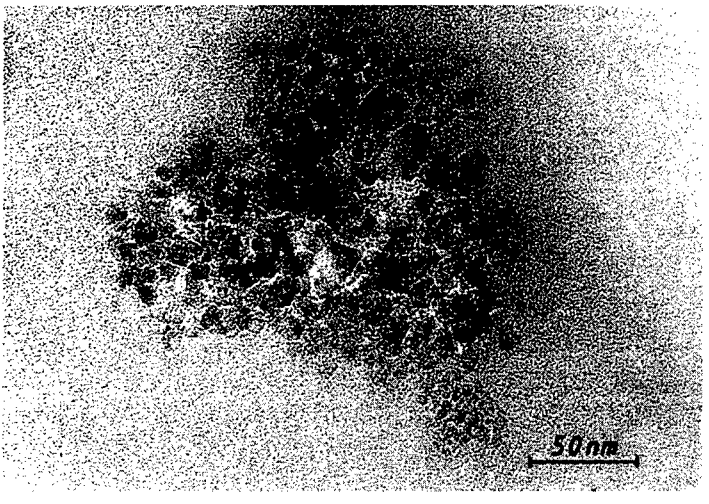

Fig. 2: TEM-picture of UFD

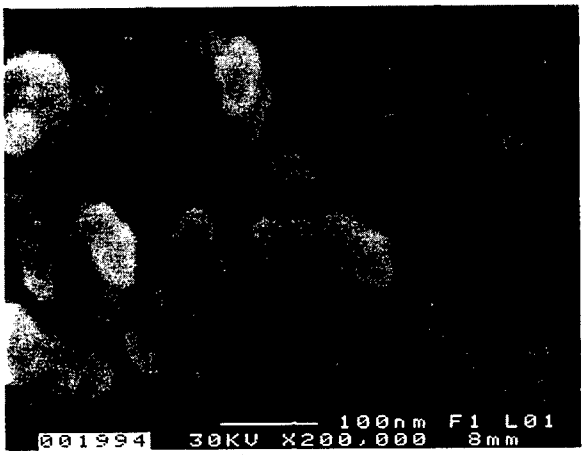

Fig. 3: SEM-picture of UFD

Particles with diameters larger than 40 nm are detected by photon correlation microscopy (PCS) of UFD dispersed in liquids. This method, however, requires effective deagglomeration of the clusters (fig. 4). The deagglomeration of UFD is difficult and not yet completely solved. Typical diameters of UFD-agglomerates are detected above 1 µm.

Hence, UFD purification and characterization have to be linked to the envisaged application.

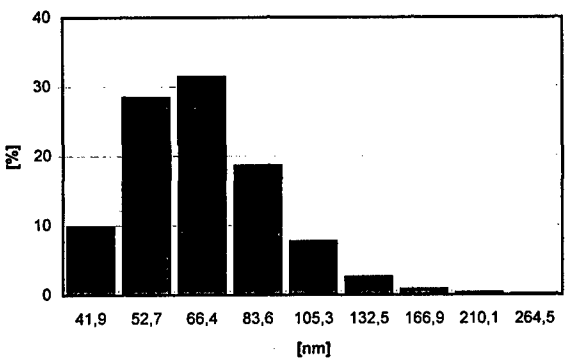

Fig.4: Particle size distribution of UFD (photon correlation spectroscopie)

4. Application

The gap between research results and industrial UFD application is challenging. Although some papers on usable effects are published [6, 7, 8, 9], there is no industrial application established yet in the western industry.

Fields of interest for using UFD are:

- coatings
- composites
- polishing.

To explore applications direct cooperation between industry and institutes is realized by ICT. The efforts resulted in two UFD projects up to now. ICT cooperates with Fraunhofer Institute IST, Braunschweig, to develop anti-wear coatings produced by electroplating. Secondly, UFD/Polymer-composites are produced for testing heat conductivity and tribological properties.

Literature

1. De Carli, P.S.; „Method of making diamond", US Patent No. 3 238 019, 1966
2. Greiner, N.R., Volk, F.; „Diamonds in detonation soot", *Nature*, 1988, 333, pp. 440-442
3. Kuznetsov, V.L., Aleksandrov, M.N.; „ Study of ultradispersed diamond powder obtained using explosion energy", *Carbon*, 29, 1991, pp. 665-668
4. Sakovich, G.V., Petrov, E.A.; „New type of articifial diamond and physical-chemical fundamentals of their creation", *Conversion concepts for commercial applications and disposal technologies of energetic systems*, Moscow, Russia, May 1994, pp. 55-72
5. Le Moigne, C.; „Synthese dynamique de diamants", dissertation, Ecole Nationale Superieure de Chimie de Mulhouse, 1996

6. Jacobs, S.D.; „Nanodiamonds enhance removal in magnetorheological finishing" *Finer points magazine*, 7,1996, pp. 47-53

7. Gubarevich, T.M., Dolmatov, V.Yu.; „Polishing systems based on ultradispersed diamonds", *Russian Journal of Applied Chemistry*, 66, part 2,1993, pp. 1461-1463

8. Xu, Tao, Zhao, Jiazheng; „Study on the Tribological Properties of Ultradispersed Diamond Containing Soot as an Oil Additive", *Tribology Transactions*, 40, 1997, pp. 178-182

9. Ouyang, Q., Okada, K.; „Nano-ball bearing effect of ultra-fine particles of cluster diamond", *Applied Surface Sciene*, 78, 1994, pp. 309-313

Feinzerkleinerung von Explosivstoffen

Fine grinding of explosives

P. Gerber *, B. Zilly, U. Teipel

Fraunhofer - Institut für Chemische Technologie (ICT), Joseph - von - Fraunhofer - Straße 7, D-76327 Pfinztal, e-mail: *ge@ict.fhg.de

Kurzfassung

Zielvorgabe für die folgenden Untersuchung war die Bereitstellung von ε-CL-20 Partikeln mit einer engen Partikelgrößenverteilung und einer mittleren Partikelgröße von 5 µm. Für die Zerkleinerung des Explosivstoffes wurde ein geeignetes Verfahren zur Zerkleinerung ausgewählt. Die Auswahl des Zerkleinerungsprozesses wird in diesem Beitrag erläutert. Um eine möglichst sichere und schonende Zerkleinerung zu gewährleisten wurde ein Zahnkranzdispergierer eingesetzt. Anschließend folgt der Vergleich der Zerkleinerungsergebnisse von ε-CL-20 und Hexogen (RDX).

Abstract

The aim of the following investigations was to produce ε-CL-20 particles with a narrow partice size distribution and an average particle size of 5 µm. For grinding of explosives a suitable grinding process for this task was selected. The selection of the grinding process is studied in this article. To have mild and safe process conditions, a wet grinding process with a rotor-stator mill was used. The results of the experiments for the grinding of ε-CL-20 and Oktogen (RDX) were presented.

* To whom correspondence should be addressed.

1. Einleitung

Für die Herstellung von Raketenfesttreibstoffen, Treibladungspulvern und Explosivstoffen werden ε-CL-20 Fraktionen mit einer mittleren Korngröße $x_{50,3}$ von 5 µm benötigt. Die Partikelgrößenverteilung soll möglichst eng sein; Partikel größer als 100 µm sollten folglich in dem Partikelkollektiv nicht enthalten sein. Die mittlere Partikelgröße $x_{50,3}$ des Ausgangsproduktes (Thiokol, USA) betrug 200 µm. Um zu überprüfen, welches Zerkleinerungsverfahren am geeignetsten erscheint, werden zunächst die Grundlagen des Zerkleinerung und die Auswahlkriterien des Zerkleinerungsprozesses erläutert.

2. Material & Methoden

2.1 Grundlagen der Zerkleinerung

Die Zerkleinerung dient dem Zerteilen von Feststoffen in Teilstücke, wobei immer eine Vergrößerung der spezifischen Oberfläche des zu zerkleinernden Gutes bzw. eine Verringerung der Korngrößen und eine Veränderung ihrer Verteilung erfolgt. Ziel der Zerkleinerung ist die Herstellung bestimmter Körngrößen und Korngrößenverteilungen. Eine physikalische oder chemische Änderung des Explosivstoffes, eine Beeinflussung des Reaktionsverhaltens durch die hohe mechanische Beanspruchung während des Zerkleinerungsprozesses kann ausgeschlossen werden. Zerkleinerungsprozesse lassen sich nach den folgenden Kriterien einordnen:

- stoffliche Widerstandsfähigkeit bei mechanischer Beanspruchung der Zerkleinerungsprodukte

Wie Tabelle 1 zeigt, kann die Zerkleinerungsaufgabe nach der Mohs-Härte oder Ritzhärte des Aufgabegutes eingeteilt werden. Um den Verschleiß während des Zerkleinerungsprozesses zu begrenzen, ist die Kenntnis der Härte des Aufgabegutes unabdingbar. Da Explosivstoffe wie Hexogen oder CL-20 nicht in der Lage sind Stahl (Mohs-Härte: 4) zu Ritzen, handelt es sich bei Zerkleinerung von Explosivstoffen um eine Weich- bis Mittelhartzerkleinerung.

- Korngröße des zu zerkleinerten Produktes

Partikuläre Explosivstoffe weisen in der Regel eine maximale mittlere Partikelgröße von bis zu 500 µm auf. Bei der Zerkleinerung von Explosivstoffen handelt es sich somit immer um eine Fein- oder Feinstzerkleinerung. (s. Tabelle 2)

Tabelle 1: Einteilung des Zerkleinerungsprozesses in Abhängigkeit der Mohs-Härte /1/

	Hart-zerkleinerung	Mittelhart zerkleinerung	Weich-zerkleinerung
Mohs-Härte	10 ... 6	5 ... 2	2 ... 1
Beispiele	Quarz, Topas Zementklinker Korund	Salze, Kalkstein, Kohle, Schwefel	Kalk, Gips, Getreide, Faserstoffe

Tabelle 2: Einteilung des Zerkleinerungsprozesses nach der Partikelgröße des Aufgabegutes /1/

Zerkleinerungsart	Durchmesser des Aufgabegutes d_A
Grobzerkleinerung	$d_A > 100$ mm
Mittelzerkleinerung	5 mm < d_A > 100 mm
Feinzerkleinerung	0,1 mm < d_A > 5 mm
Feinstzerkleinerung	$d_A < 0{,}1$ mm

- Beanspruchungsart

Nach Rumpf /2/ unterscheidet man drei verschiedene Beanspruchungsmechanismen, welche in Abbildung 1 dargestellt sind. Im Fall I erfolgt die Kornzerkleinerung durch Druck zwischen zwei Flächen, im Fall II durch Prallbeanspruchung und im Fall III erfolgt die Zerkleinerung durch das umgebendes Medium (z.B. Schergefälle).

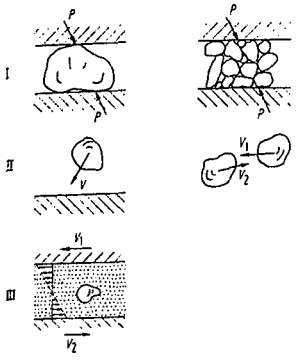

Abbildung 1: Beanspruchungsmechanismen bei der Zerkleinerung

2.2 Eigenschaften der Explosivstoffe

- CL-20

Summenformel: $C_6H_6N_{12}O_{12}$

Kirstallmodifikation: ε-CL-20

Strukturformel:

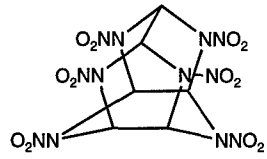

Löslichkeit:	in Wasser	nahezu unlöslich
	in Aceton	gut löslich
Dichte:	2,03 g/ml (theoretische Dichte: 2,04g/ml ε - Phase)	
spez. Oberfläche:	0,16 m²/g	

- Hexogen

Summenformel: $C_3H_6N_6O_6$

Strukturformel:

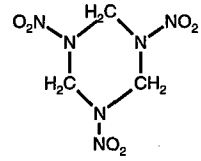

Löslichkeit:	in Wasser	nahezu unlöslich
	in Aceton	gut löslich
Dichte:	1,81 g/ml (theoretische Dichte: 1,82 g/ml)	

Die Dichte wurde mit einem Gaspygnometer gemessen, während die spezifische Oberfläche der Partikel durch Gasadsorption mit dem Quanta Chrome, Nova 2200 ermittelt wurde.

2.3 Zerkleinerungsmaschinen

Die außerordentliche Vielfalt der Zerkleinerungsaufgaben hat eine große Zahl verschiedener Zerkleinerungsmaschinen entstehen lassen. Für die Zerkleinerung von CL-20 lautet die Zerkleinerungsaufgabe:

Weich- bis mittelharte Feinzerkleinerung

Die Zerkleinerung von reib- und schlagempfindlichen Komponenten wie z. B. Hexogen, Oktogen oder PETN in schnellaufenden Mühlen, welche die Explosivstoff-

partikel durch Reibung, Prall oder Schlag beanspruchen, bergen ein gewisses Risiko, weshalb aus Sicherheitsgründen die Naßzerkleinerung dieser Materialien bevorzugt wird /3/. Dies um so mehr, seit bekannt wurde, daß Dispersionen aus reib- und schlagempfindlichen Explosivstoffen in Wasser mit Feststoffanteilen größer 20 % detonationsfähig sind /4/.

Im folgenden werden die Zerkleinerungsmaschinen vorgestellt, mit welchen eine Feinzerkleinerung als Naßzerkleinerung durchführt werden kann.

- Kolloidmühlen

  Als Kolloidmühlen werden etwas großzügig Maschinen für die Feinstzerkleinerung von Suspensionen bezeichnet. Die Partikel verbleiben dabei im allgemeinen im Größenbereich um 1 µm herum, also noch über dem Kolloidbereich. Diese Mühlen sind meistens Scheibenmühlen mit sehr engem verstellbarem Spalt oder besitzen einen Messerrotor, der durch einen feststehenden Rost kämmt. Auch hier sind enge Spalte für eine gute Arbeitsweise notwendig. Die profilierten Scheiben können aus Stahl, Sintermaterialien oder Korund bestehen und rotieren mit Umfangsgeschwindigkeiten von einigen Metern pro Sekunde. Die Spaltweite wird mechanisch oder hydraulisch eingestellt. /2/

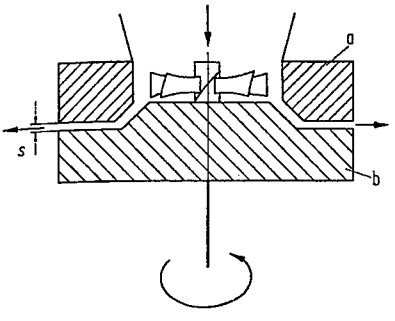

Abbildung 2: Prinzip einer Scheiben-Kolloidmühle, a, b Mahlscheiben
s Spaltweite

- Rührwerksmühle

  Die Rührwerksmühle hat sich für die Zerkleinerung von mittelviskosen Medien bewährt. Sie besteht aus einem vertikal angeordneten zylindrischen Behälter, der mit Sandkörnern, Stahlkugeln, Steatitkugeln oder ähnlichen Mahlkörpern von Abmessungen zwischen einigen Zehntel bis zu einigen Millimetern gefüllt ist. In der

Achse ist ein Rührer angeordnet. Die Suspension durchströmt den Mahlraum von unten nach oben. Ein Sieb oder ein Spalt am Austritt hält die Mahlkörper zurück. Zerkleinert wird durch Druck und Scherung zwischen den Kugeln.

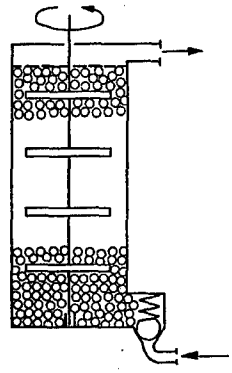

Abbildung 3: Prinzip einer Rührwerksmühle

- Dispergierer, Homogenisator, Turborührer

Dazu gehören Maschinen mit einem schnellaufenden profilierten bzw. zähnebesetzten Rotor-Stator System und Apparate, in denen die Suspension mit großem Druck durch enge Spalte gepreßt werden. Diese Maschinen eignen sich vorwiegend zur Desagglomeration in niedrigviskosen Flüssigkeiten. Mit einem Zahnkranzdispergierer wurden die folgenden Untersuchungen durchgeführt.

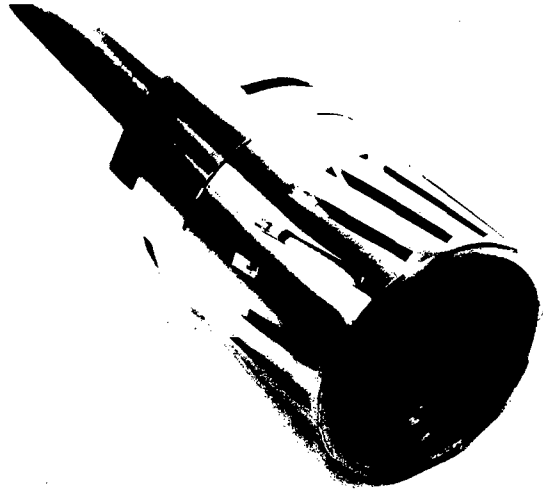

Abbildung 4: Zahnkranzdispergierer, X40, Fa. Ystral

2.4 Versuchsdurchführung

In einem zylindrischen Glasbehälter mit abgerundetem Boden wird demineralisiertes Wasser und der zu zerkleinernde Explosivstoff vorgelegt. Die Verwendung von Glasbehälter erlaubt die Beobachtung und Kontrolle des Zerkleinerungsprozesses. Es ist vorteilhaft die Behältergröße so zu wählen, daß das Volumen des Behälter nur zu ca. ¾ mit Dispergiermedium und Explosivstoff gefüllt ist. Der Zahnkranzdispergierer saugt die Suspension axial an, weshalb ein Mindestabstand von einem Schaftdurchmesser vom Boden des Gefäßes einzuhalten ist. Da sich das Dispergiermedium bei einer Versuchsdauer von zwei Stunden auf über 50°C erwärmt, wurde zur Kühlung der Suspension ein Thermostat eingesetzt. Um eine möglichst hohe Beladung an Explosivstoff zu erzielen, und dennoch mit der Konzentration unterhalb einer detonationsfähigen Suspension zu bleiben, wurde eine Feststoffkonzentration von 15 % gewählt. Zur Erzielung hoher Feinheitsgrade ist ein hoher spezifischer Energieeintrag erforderlich, weshalb es für die Feinstzerkleinerung sinnvoll ist, die Batchgröße so klein wie möglich zu wählen.

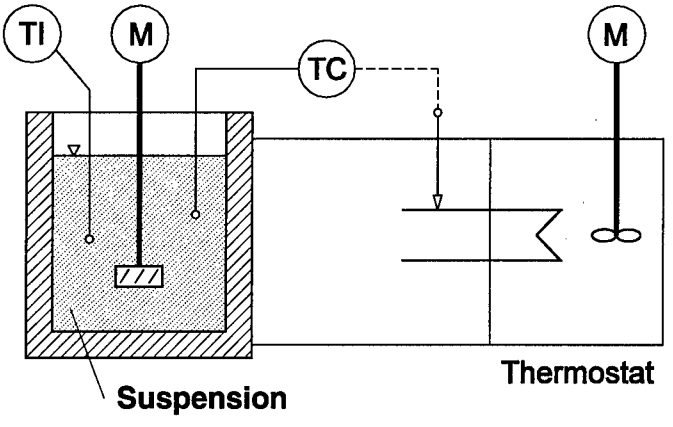

Abbildung 5: Schematische Darstellung der Batch - Zerkleinerungsanlage

3. Versuchsergebnisse

3.1 Zerkleinerung von CL-20

Um die Partikel vor und nach der Zerkleinerung zu vergleichen, zeigen die Abbildungen 6 und 7 die jeweiligen Partikelgrößenverteilung, während Abbildung 8 und 9 die zugehörigen REM - Aufnahmen zeigen. Die Partikelgrößenverteilungen wurden mittels Laserbeugungsspektrometrie (Malvern Mastersizer S) bestimmt.

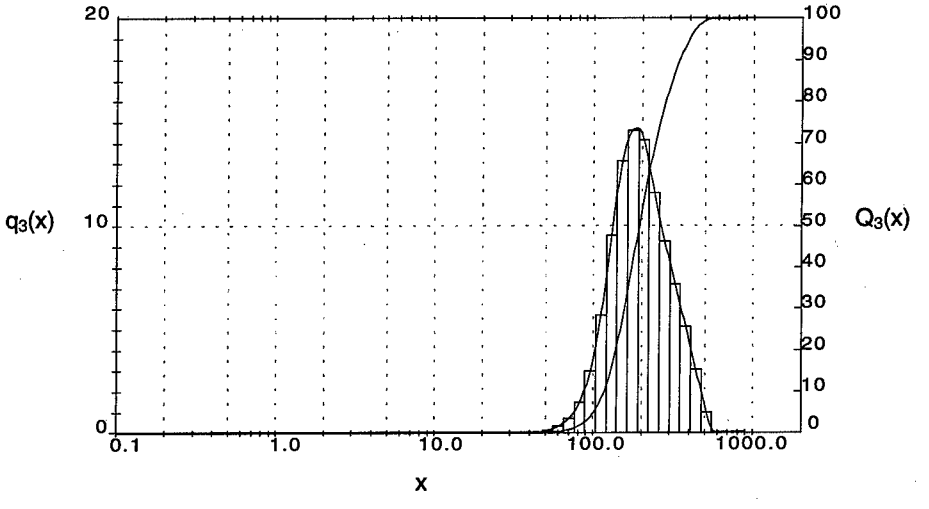

Abbildung 6: Partikelgrößenverteilung, vor Zerkleinerung

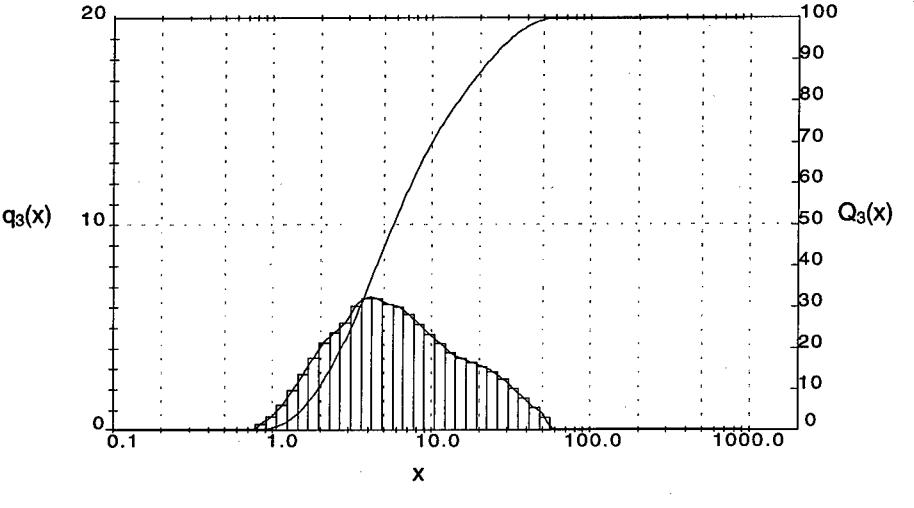

Abbildung 7: Partikelgrößenverteilung, nach Zerkleinerung

CL 20 vor Zerkleinerung

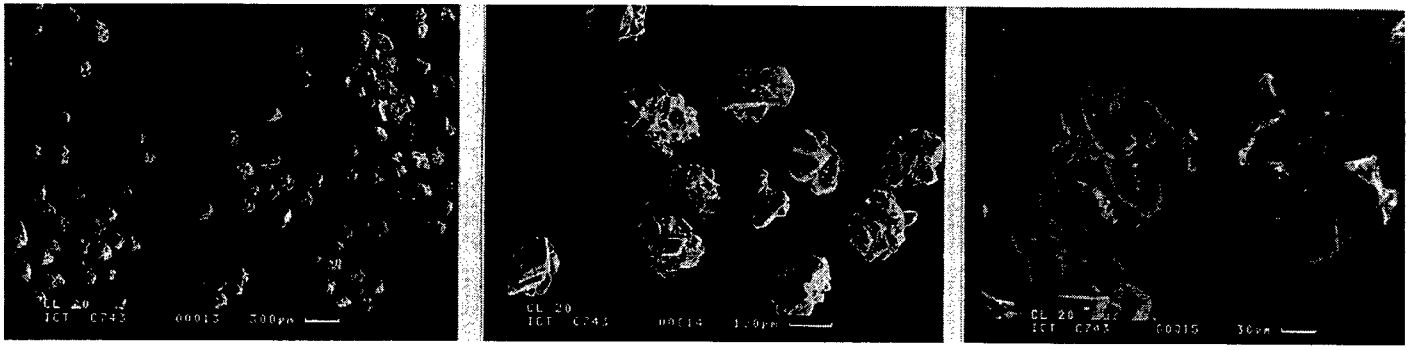

CL 20 nach Zerkleinerung

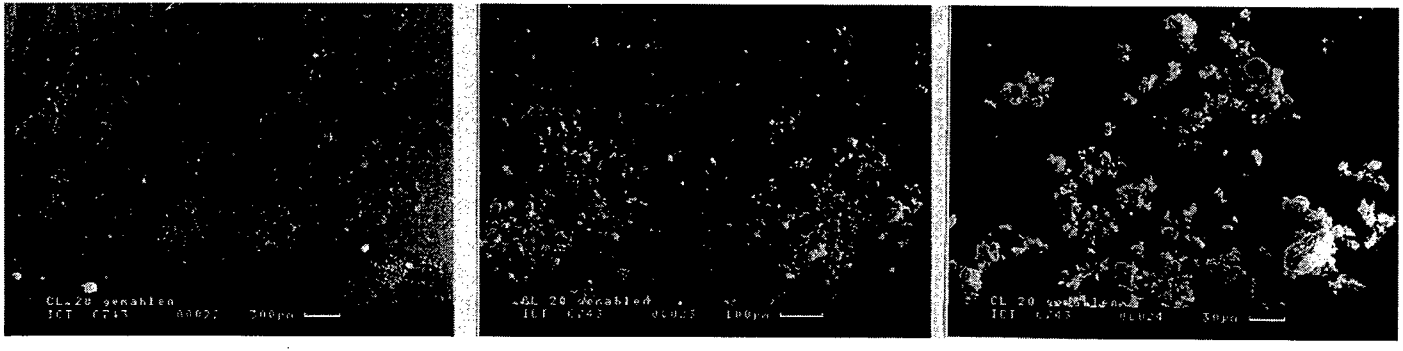

Abbildung 8: CL 20, Vergleich vor und nach der Zerkleinerung

CL 20 vor Zerkleinerung

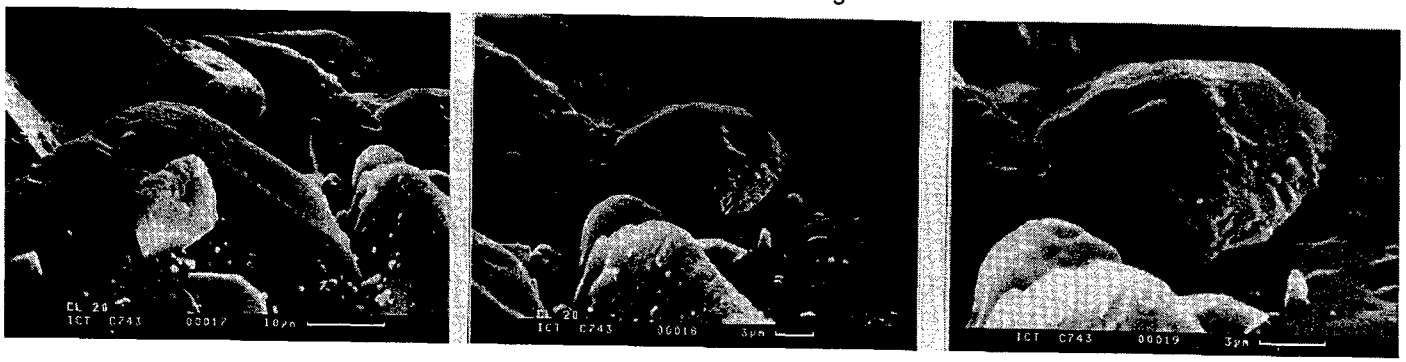

CL 20 nach Zerkleinerung

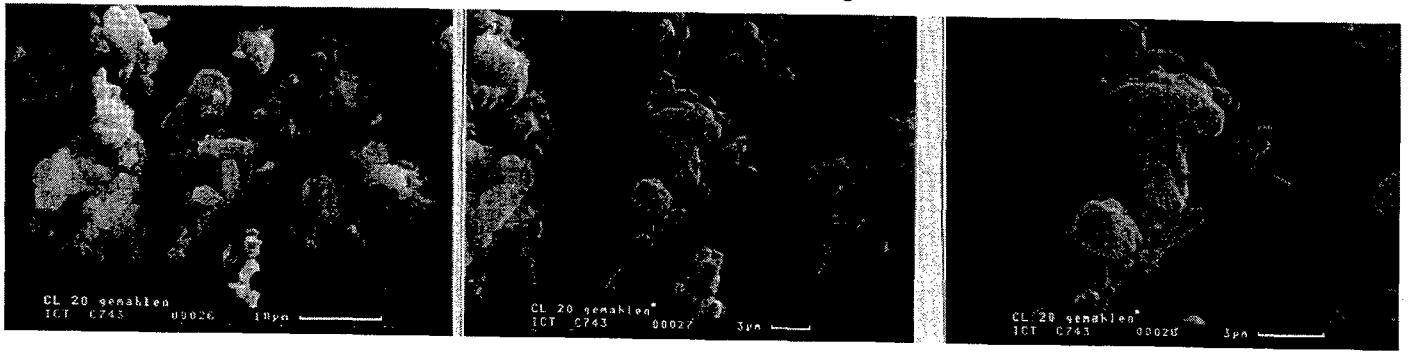

Abbildung 9: CL 20, Vergleich vor und nach der Zerkleinerung

Um die Reproduzierbarkeit des Zerkleinerungsverfahrens zu überprüfen, wurden zwei Zerkleinerungsversuche bei sonst gleichen Versuchsbedingungen durchgeführt. Das Ergebnis ist in Tabelle 3 zusammengefaßt. Da die Abweichungen der Partikelgröße vom Mittelwert (6,1 µm ± 0,4 µm) innerhalb der Reproduzierbarkeit des Meßgerätes liegt, kann die Reproduzierbarkeit des Zerkleinerungsverfahrens als gut bezeichnet werden.

Tabelle 3: Partikelcharakterisierung vor und nach der Zerkleinerung

		Thiokol (USA)	Versuch 1	Versuch 2
Partikelgröße	$x_{50,3}$/µm	117,2	5, 7	6,6
	$x_{10,3}$/µm	190,5	1,9	2,1
	$x_{90,3}$/µm	344,8	23,3	24,4
	x_{max}/µm	< 400	< 60	< 60
BET - Oberfläche	s_V / (m²/g)	0,16 ±0,04	1,27±0,37	1,20±0,44
Dichte	ρ / (g/ml)	2,03	2,04	2,04
Modifikation		ε - Phase	ε - Phase	ε - Phase

3.2 Zerkleinerung von Hexogen

Mit den in Kapitel 2.4 erläuterten Versuchsbedingungen wurden die gleichen Versuche mit Hexogen (RDX) durchgeführt. Abbildung 10 zeigt die Partikelgrößenverteilung nach der Zerkleinerung.

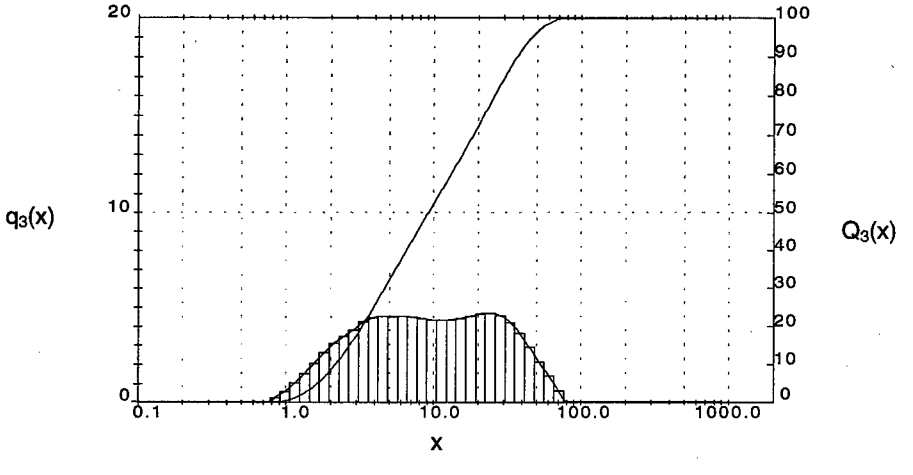

Abbildung 10: Partikelgrößenverteilung, RDX nach Zerkleinerung

Tabelle 4: Vergleich der Partikelgrößenverteilung von CL-20 und Hexogen, nach der Zerkleinerung, bei gleichen Prozeßbedingungen

	CL-20	Hexogen
$x_{50,3}$/µm	5, 7	9,2
$x_{10,3}$/µm	1,9	2,1
$x_{90,3}$/µm	23,3	36,5
x_{max}/µm	< 60	< 75

Das Versuchsergebnis zeigt, daß bei der Zerkleinerung der entstehende Feinanteil bei Hexogen nicht so groß ist, wie für CL-20. Die Ursache hierfür kann in der unterschiedlichen Dichte der Explosivstoffe liegen. CL-20 weist mit 2,04 g/ml eine um ca. 10 % höhere Dichte und somit eine höhere Sinkgeschwindigkeit auf. Je höher die Sinkgeschwindigkeit, desto höher die Wahrscheinlichkeit, daß die Partikel wieder zu Boden sinken und vom Zahnkranzdispergierer angesaugt und zerkleinert werden.

Um die Zerkleinerung von Hexogen zu verbessern kann der Einsatz von Dispergiermedien mit niedrigerer Dichte als Wasser vorteilhaft sein, damit die Sinkgeschwindigkeit erhöht wird. Einen höheren Feinanteil kann durch verkleinern des Batchvolumens erreicht werden, um bei unverändertem Energieeintrag einen höheren spezifisch Energieeintrag zu erzielen.

4. Literatur

/ 1 / Höffel K.
Zerkleinerungs- und Klassiermaschinen, Schlütersche Verlagsanstalt, 2. Auflage, 1997

/ 2 / Rumpf, H.; Schönert K.
Zerkleinern, Ullmanns Encyclopädie der technischen Chemie, 4. Auflage, Band 2, Verfahrenstechnik I, Verlag Chemie

/ 3 / Hommel, H.
Verfahrenstechnik der Herstellung von Hexogen (RDX) feinst, granuliert, ICT-Bericht 7/80, 1980

/ 4 / Santos, J. S.
Hazardous waste disposal through fluidized bed incineration, Min. 16 Explos. Safety Semin., AD - A 007 566, 1974, S. 1051- 1073

G. T. Afanas'ev
Semenov Institute of Chemical Physics RAS,
Kosygin St. 4, Moscow, 117977, Russia.
E-mail: marsh@center.chph.ras.ru

EFFECT OF PARTICLE SIZE ON THE DETONATION REGIME AND ITS CHARACTERISTICS FOR AZOXYDINITROFURAZAN EXAMPLE.

G. T. Afanas'ev, V. I. Arhipov, M.F. Gogulya, A. A. Sovko.

Semenov Institute of Chemical Physics RAS,
Kosygin St. 4, Moscow, 117977, Russia.

Detonation in charges of different initial density and explosive particles grain of size has been studied. Detonation velocity, detonation pressure and detonation propagation critical conditions were obtained in the frame of the work. Failure detonation diameter for azoxydinitrofurazan single crystal was determined as (125 ± 25) μm basing on the obtained discontinuity on the dependence of detonation velocity vs explosive dispersity.

Dilatometric Measurements of Phase Stabilized Ammonium Nitrate (CuPSAN) performed by means of X-ray Diffraction

Paul Bernd Kempa, Michael Herrmann and Walter Engel

Fraunhofer-Institut für Chemische Technologie (ICT), J.-von-Fraunhofer-Str. 7, D-76327 Pfinztal-Berghausen, Germany

Abstract

Ammonium nitrate is used as an oxidizer in solid propellants and gas generators. Its use is hindered by the volume changes caused by the phase transitions of the polymorphic substance under storage conditions. Diammine Copper(II) was incorporated into the ammonium nitrate lattice to improve the phase behaviour.

The thermal expansion and the phase transitions of materials with Diammine copper (II) contents corresponding to 7% CuO were measured with temperature resolved X-ray diffraction. Series of measurements were performed, while the samples were heated with the temperature programs 20/100/-70/100 and 20/143/-70/20 °C. The series were evaluated by Rietveld refinement yielding thermal expansion curves of the phases, which were identified by the known diffraction patterns. In temperature regions with coexisting phases Rietveld refinement was used for quantitative phase analysis.

The obtained data determine unambiguously the stability ranges and the thermal expansion of the phases. They show that the stability of the room temperature phase IV and of phase II is extended to lower temperatures.

Compared to pure AN the elementary cell of phase V of CuPSAN approaches a tetragonal structure like phase II.

Introduction

Ammonium nitrate (AN) is used as oxidizer in solid propellants, gas generators and explosives. Phase transitions, low performance and low burning rates are drawbacks for ist use.

AN crystallizes in five polymorphic phases with well known structures [1-5], stability ranges and phase transition temperatures. The crystallographic data and the stability ranges of the five phases are given in Table 1.

Phase	V	IV	III	II	I
Crystal system	orthorh.	orthorh.	orthorh.	tetrag.	cubic
Space group	Pccn	Pmmn	Pnma	P4mbm	Pm3m
Formula per unit cell [Z]	8	2	4	2	1
Lattice parameters	a = 7.943	a = 5.745	a = 7.7184	a = 5.7193	a = 4.366
	b = 7.972	b = 5.438	b = 5.8447		
	c = 9.832	c = 4.942	c = 7.1624	c = 4.9326	
mesuared at [°C]	-100	22	45	82	150
Stability ranges [°C]					
humid	<-18	-18 - 32	32 - 84	84 - 125	>125
dry	<-18	-18 - 55		55 - 125	>125

Table 1: Crystallographic data and stability ranges of the AN phases

Earlier studies showed that doping ammonium nitrate with small amounts of alkali nitrates [6,7] or diammine complexes of copper, zinc and nickel [8] influences the phase transitions of ammonium nitrate.

In this work we investigated the phase behaviour of samples containing diammine copper. The results obtained with the so called phase stabilized ammonium nitrate (CuPSAN) were compared with those of pure ammonium nitrate [9].

Experimental

The samples were produced by atomizing an ammonium nitrate melt containing diammine Copper (II) corresponding to 7% CuO.

The measuring system consists of a Bragg-Brentano diffractometer D-5000 from Siemens equipped with a copper or a chromium tube, a low temperature device TTK from Paar Inc. and a position sensitive proportional counter produced by Braun.

Series of X-ray diffraction patterns were measured, while the samples were heated with the temperature programs 20/100/-70/100 and 20/143/-70/20 °C. The measurement conditions are shown in Table 2.

Temperature program	20/100/-70/100	20/145/101/-70/20
Radiation	Cu-Tube	Cr-Tube
Profile range	15 - 70 °2Th7eta	20 - 105 °2Theta
Step scan increment	0.02 °2Theta	0.02 °2Theta
Measurring time per pattern	5,5 min	23 min

Table 2: Measuring parameters

Evaluation

The diffraction patterns were evaluated with the Rietveld method [10] using the program WYRIET3 [11]. This refinement technique calculates X-ray diffraction patterns based on stucture models. The calculated patterns are fitted to the measured patterns. Refining and varying the parameters of the structure model yields lattice parameters, volumes, atom coordinates and a quantitative phase analysis of coexistent phases. Further details of the Rietveld method are obtained by ref. 12 and from the literature cited therein.

By plotting the obtained data versus temperature thermal expansion, transition paths, lattice dynamics and volume changes are obtained.

Results and Discussion

Transition paths and temperatures

CuPSAN shows at room temperature the coexisting phases II and IV. On heating phase IV transforms into phase II at 60°C. The transition into phase I is not observed on heating to 143°C. On cooling phase II transforms partially into phase IV. Below 2°C phase II and V can both be fitted to the measured patterns. On the second heating the transitions occur in the reverse order.

By heating until 100°C the same transition path is observed:

IV+II ——— (60°C) ——→ II	heating from 20°C to 143°C
II —— (2°C) ——→ II/V ——→ (-28°C) ——→ II/V+(IV)	cooling from 101°C to -70°C
II/V+IV —— (20°) ——→ IV+II	heating from -70°C to 20°C

Lattice parameters

Table 3 shows the lattice parameters of PSAN measured at defined temperatures. The values for AN are included for comparison.

They are plotted versus temperature in Figure 1 (heating) and Figure 2 (cooling). The linear expansion coefficients are summarized in Table 4. These values were calculated fom the lattice parameters by a linear fit.

		AN	CuPSAN	Difference
	Lattice parameter	Value / Å	Value / Å	Value / Å
Phase I at 150°C	a	4.370		
Phase II at 82°C	a	5.708	5.713	-0.005
	c	4.929	4.916	0.013
Phase IV at 22°C	a	5.755	5.754	0.001
	b	5.444	5.448	-0.004
	c	4.931	4.928	0.003
Phase V at -100°C	a	7.938	7.956	-0.018
	b	7.966	7.960	0.006
	c	9.805	9.799	0.006

Table 3: Lattice parameters

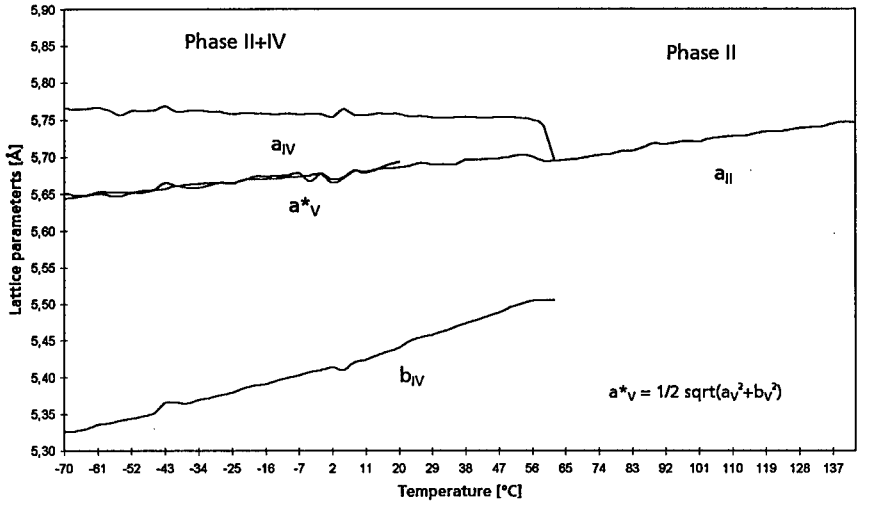

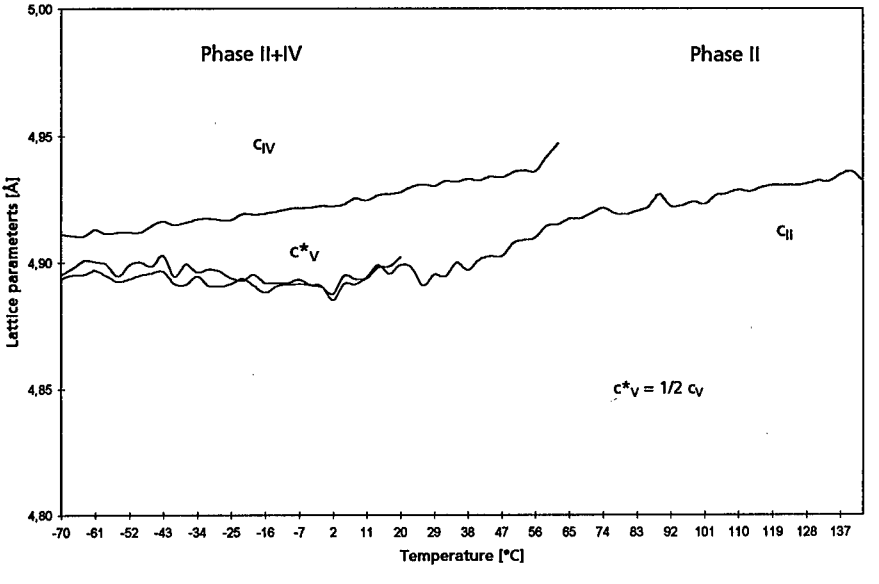

Figure 1: Lattice parameters of the phases II and IV and equivalent distances of the phase V on heating.

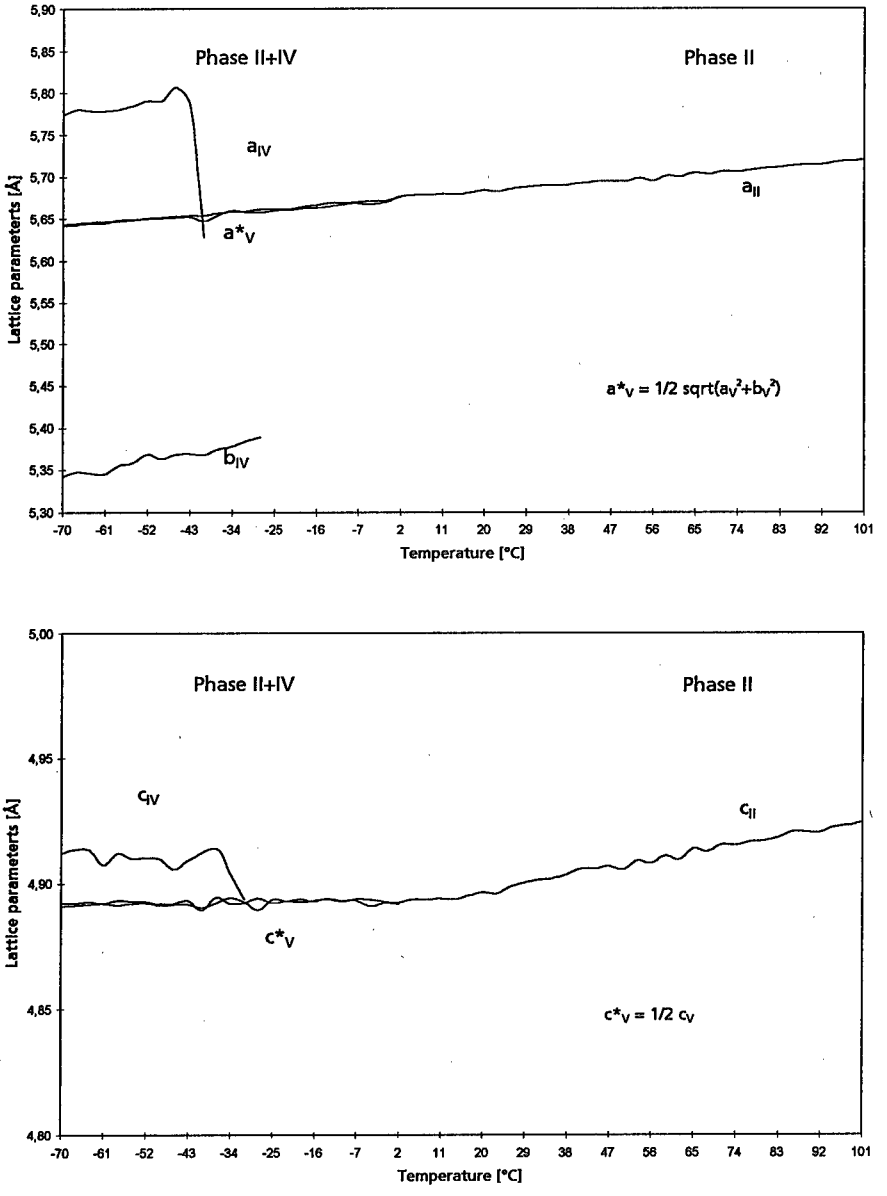

Figure 2: Lattice parameters of the phases II and IV and equivalent distances of the phase V on cooling.

	Lattice parameter			CuPSAN	AN
			Range / [°C]	Expansion / [10^{-6}/K]	Expansion / [10^{-6}/K]
Phase I	a				124
Phase II	a	heating	-70 - 143	79	96
	c		-70 - 2	-22	58
	c		2 - 143	67	
	a	cooling	101 - -70	82	
	c		101 - -70	42	
Phase IV	a	heating	-70 - 62	-17	-25
	b		-70 -62	260	309
	c		-70 -62	45	44
	a	cooling	-37 - -70	186	
	b		-28 - -70	191	
	c		-40 - -70	-79	
Phase V	a	heating	-70 - 20	93	85
	b		-70 - 20	67	66
	c		-70 - 20	-11	-13
	a	cooling	5 - -70	72	
	b		5 - -70	76	
	c		-40 - -70	-7	
	c		5 - -40	7	

Table 4: Linear expansion coefficients

By heating the sample of CuPSAN the lattice parameter b of phase IV increase. Whereas parameter a decreases, and so the elementary cell approaches a tetragonal structure. This occurs by an oscillation of the planar nitrate groups around an axis in direction of c with increasing temperature according to a model of Amoros [13]. The nitrate groups deviate from the position aligned in direction of a causing the transition IV/II.

By heating until 143°C no transformation from phase II to the high temperature phase I is observed.

As the lattice parameters a and b of phase V of CuPSAN are nearly the same, corresponding to a tetragonal basis of the elementary cell, the transition

temperature into the nearly identical phase II cannot be clearly defined. At room temperature phase V as well as phase II is observed.

Compared to AN only the lattice parameter a for the phase V of CuPSAN shows a significant difference.

The linear expansion coefficients are comparable for the corresponding lattice parameters for all phases of AN and CuPSAN. However, for phase IV a difference is observed on cooling. As shown in Figure 2 the thermal expansion for the lattice parameters a and c change. The lattice parameter a increases and c decreases. This point is not clear and requires further investigation.

Specific Volumes

In Figure 3 the specific volumina on heating and cooling are shown. The corresponding values and the volumetric expansion coefficients are shown in Table 5 and 6.

	AN	CuPSAN	
	Volumen / Å^3	Volumen / Å^3	Difference / Å^3
Phase I at 150°C	83.45		
Phase II at 82°C	80.30	80.27	0.03
Phase IV at 22°C	77.27	77.27	0
Phase V at -100°C	77.50	77.58	-0.08

Table 5: Specific volumes

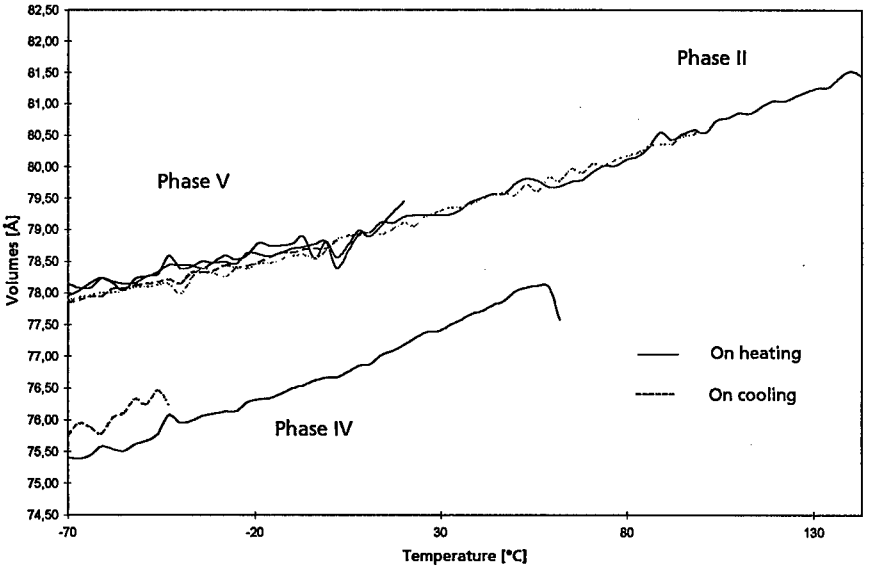

Figure 3: Volumes of the CuPSAN phases.

			CuPSAN	AN
		Range / [°C]	Expansion / [10^{-6}/K]	Expansion / [10^{-6}/K]
Phase I				372
Phase II	heating	-70 - 143	206	250
	cooling	101 - -70	205	
Phase IV	heating	-70 - 62	286	331
	cooling	-37 - -70	312	
Phase V	heating	-70 - 20	170	141
	cooling	5 - -70	162	

Table 6: Volumetric expansion coefficents

Comparing the specific volumes of CuPSAN with AN only small differences are observed. The volumetric expansion coefficients calculated from the curves in Figure 5 are strongest for Phase IV and comparable with those for AN.

Conclusion

The transition paths of CuPSAN distinguish from pure AN by an extended stability range of phase II down to room temperature and up to more then 140°C , so that no transition into phase I is observed on heating to 143°C. Phase IV coexists with the phase II and V decreasing from 40% at -70 °C to <10% at 60°C on heating and from about 1% at -28°C to 10% at -70°C on cooling.
Incorporating diammine copper(II) into the lattice enhances the tendency to a tetragonal structure. The lattice parameters a and b for phase V become nearly the same. The tendency explains the extended stability of phase II and increases the difficulties of distinguishing between the phases II and V.

References

[1] Athee M., Kurki-Suonio K., Lucas B. W., Hewat A. W., Acta Cryst. A35 (1979), 591-597

[2] Choi C. S., Prask H. J., Prince E., J. Appl. Cryst. 13 (1980), 403-409

[3] Lucas B. W., Ahtee M., Hewat A, Acta Cryst. B36 (1980), 2005-2008

[4] Choi C. S., Mapes J. E., Prince E, Acta Cryst. B28 (1971) , 1357-1361

[5] Choi C. S., Prask H. J., Acta Cryst. B39 (1983), 414-420

[6] Müller W., Z. Phys. Chem. 31 (1899), 354-359

[7] Deimling A., Engel W., Eisenreich N., J. Thermall. Anal. 38 (1992), 843-853

[8] Engel W., Explosivstoffe 21 (1973), 9-13

[9] Herrmann M, Engel W., Propellants, Explosives, Pyrotechnics 22 (1997), 143-147

[10] Rietveld H. M., Acta Cryst. 22 (1967),151-152

[11] Schneider J., IUCT Int. Workshop on Rietveld Method, Petten (1989), 71

[12] Kempa P. B., Ph. D. Thesis, Konstanz (1994); Hartung-Gorre Verlag, Constance, Germany (ISBN 3-89191-790-2)

[13] Amorós J. L., Alonso P., Canut M. L., Bol. R. Soc. Esp. Hist. Nat. (G) 56 (1958), 77

OPTICAL MEASUREMENTS OF PARTICLES LESS THAN 1 MICROMETER IN FLAMES

OPTISCHE PARTIKELGRÖßENBESTIMMUNG IM SUB-µm-BEREICH IN FLAMMEN

W. Ehrhardt, W. Eckl, M. Weindel, V. Weiser

Fraunhofer Institut für Chemische Technologie (ICT)
Joseph-von-Fraunhoferstr. 7
76327 Pfinztal

Abstract

An optical system for measuring size and concentration of particles less than Ø1 micrometer in flames, developed at the ICT, is described. The measuring-system is working non-intrusive and has been built up in an experimental scale. The function of the system is based on a multiple-wavelength-extinction-method. In case of sufficient particle-concentration in sooting flames, the system is able to detect particle-sizes in a range of 0.01...0.5µm. Additionally the plume of an Al-filled composite propellant was investigated.

Kurzfassung

In der vorliegenden Arbeit wird ein am ICT entwickeltes optisches Meßsystem zur Bestimmung der Größe und Konzentration von Partikeln im sub-µm-Bereich in Flammen beschrieben. Hierbei handelt es sich um ein berührungslos arbeitendes Meßsystem das im Labormaßstab aufgebaut wurde. Als Meßprinzip kommt ein Mehr-Wellenlängen-Extinktions-Verfahren zum Einsatz. Das System ist in der Lage bei einer genügend großen Konzentration von Partikeln in Flammen den Partikeldurchmesser in einem Bereich von 0.01...0.5µm zu bestimmen. Zusätzlich wurde die heiße Reaktionszone eines Aluminium-Composit-Treibstoffes untersucht.

Einleitung

Im Forschungs- und Entwicklungsbereich der Flammendiagnostik am ICT werden Meßsysteme entwickelt, die die Charakterisierung und Optimierung von Verbrennungsprozessen gestatten. Die Kenntnis von Größe und Konzentrationen der Partikel in rußenden Flammen, speziell derer mit einem Durchmesser kleiner 1µm, ist hierbei von besonderer Bedeutung. Um den Verbrennungsverlauf in den untersuchten Flammensystemen nicht zu beeinflussen, werden berührungslos arbeitende Meßverfahren bevorzugt .

Aus diesem Grund wurde am ICT ein optisches Meßsystem entwickelt, das diesen Anforderungen Rechnung trägt.

Grundlagen

Das Mehr-Wellenlängen-Extinktions-Verfahren, auch Dispersionsquotientenverfahren genannt, beruht auf der Lichtextinktion mehrerer Lichtstrahlen unterschiedlicher Wellenlänge beim Durchgang durch das gleiche Partikelkollektiv. Durchquert ein Lichtstrahl ein Partikelkollektiv, so wird dieser durch Extinktion (Absorption und Streuung) geschwächt.

Unter der Annahme einer monodispersen Partikelverteilung, wird die Extinktion eines monochromatischen Lichtstrahls durch das bekannte Lambert-Beer'sche Gesetz beschrieben:

$$I = I_0 \cdot e^{(-N \cdot L \cdot \pi \cdot r^2 \cdot Q_{ext}(r,\lambda,n))}$$

Dabei bedeuten:

I_0	-Intensität des auf die Partikel treffenden Lichts
I	-Intensität des Lichts hinter dem Partikelkollektiv
N	-Partikeldichte
r	-Partikelradius
Q_{ext}	-Extinktionskoeffizient
n	-Brechungsindex
L	-Meßvolumenlänge
λ	-Wellenlänge des verwendeten Lichtes

Obwohl in der Gleichung sphärische Partikel vorausgesetzt werden, läßt sie sich durch die Betrachtung eines ganzen Partikelkollektivs auch auf andere Partikelformen anwenden. Durch die unterschiedliche räumliche Orientierung der Partikel, innerhalb des vom Lichtstrahl erfaßten Kollektivs, ergibt sich bei von der Kugelform abweichenden Teilchen, im Durchschnitt wiederum ein "mittlerer Radius". Da es sich in der Realität in den seltensten Fällen um kugelförmige Teilchen handelt, wird diese Näherung als hinreichend genau betrachtet und im Dispersionsquotientenverfahren angewendet.

In dem Lambert-Beer'schen Gesetz ist außer der Partikelgröße auch noch die Partikelkonzentration unbekannt. Bildet man jetzt den sogenannten Dispersionsquotienten durch Division der logarithmierten Intensitätsverhältnisse zweier Lichtstrahlen unterschiedlicher Wellenlänge die das gleiche Partikelkollektiv passieren, so kürzt sich die unbekannte Partikeldichte.

$$\frac{\ln\left(\frac{I}{I_0}\right)_{\lambda 1}}{\ln\left(\frac{I}{I_0}\right)_{\lambda 2}} = DQ = \frac{Q_{ext}(r,\lambda_1,n)}{Q_{ext}(r,\lambda_2,n)}$$

Da der Zusammenhang zwischen Dispersionsquotient und Partikelgröße nicht immer eindeutig ist, werden zusätzliche Wellenlängen eingeführt. Nun können weitere Dispersionsquotienten gemessen und eine eindeutige Teilchengröße zugeordnet werden.

Der Extinktionskoeffizient Q_{ext} kann mit Hilfe der Mie-Theorie bestimmt werden und setzt sich additiv aus dem jeweiligen Koeffizienten für Absorption bzw. Streuung zusammen.

$$Q_{ext}(r,\lambda,n) = Q_{abs}(r,\lambda,n) + Q_{str}(r,\lambda,n)$$

Leicht überschaubar sind lediglich die Fälle großer ($r>>\lambda$) bzw. kleiner ($r<<\lambda$) Radien. Im Falle kleinster Teilchen verschwindet die Streustrahlung, da sie in der 4. Potenz von r/λ abhängig ist (Rayleigh-Streuung).

Bei groben Teilchen wirkt sich die Streustrahlung als reflektierte Strahlung aus, die im Falle runder Partikel zwar den gesamten Raum erfüllt, bevorzugt aber entgegen der Einfallsrichtung erfolgt. [1]

Will man nun das zwischen den Extremen liegende Gebiet $r \sim \lambda$ betrachten, so kommt man nicht mehr ohne die exakte Theorie aus, die Gustav Mie (1868-1957) im Jahr 1908 veröffentlichte. Mie hat auf Grundlage der Maxwellschen Theorie die Strahlung von Kugeln berechnet, die von ebenen Wellen getroffen werden. Er löst das Randwertproblem exakt. Den Kugeln werden dabei selbst für die kleinsten Dimensionen die Werte des komplexen Brechungsindex zugeschrieben, wie sie das massive Material besitzt. Die Kugeln werden zu eigenen Schwingungen angeregt, deren Wellenzüge dann mit den ursprünglichen interferieren. Die Lösung ergibt sich als Reihenentwicklung, deren Koeffizienten sich aus Besselschen und Hankelschen Funktionen errechnen.

$$Q_{ext}(m,r,\lambda) = \frac{\lambda^2}{2\pi} \sum_{n=1}^{\infty} (2n+1) * Re(a_n + b_n)$$

Voraussetzung für die Berechnung ist die Kenntnis des komplexen Brechungsindex ($m=m_1-m_2 \cdot i$) des Partikel-Feststoffes.

Da die genauere Berechnung des benötigten Extinktionskoeffizienten nicht Gegenstand dieser Arbeit sein soll, sei an dieser Stelle auf die Literatur [2-4] verwiesen.

Aus dieser Berechnung kann nun für jede der verwendeten Wellenlängen ein Kurve für den Verlauf des Extinktionskoeffizienten in Abhängigkeit von der Partikelgröße abgeleitet werden. Durch die Kombination jeweils zweier Wellenlängen kann dann ein theoretischer Dispersionsquotient DQ_{theor} gebildet und mit dem dazugehörigen gemessenen Quotienten DQ_{exp} gleichgesetzt und letztendlich ein Partikelradius zugeordnet werden.

Aufbau und Funktionsweise

Das von dem Lichtbogen einer Kurzbogenlampe erzeugte Licht, wird durch eine Kondensoroptik am Lampengehäuse parallelisiert. Eine spezielle Einkoppeloptik fokusiert den Lichtstrahl auf die Öffnung eines Lichtwellenleiters mit einem Kerndurchmesser von 200 µm. Am anderen Ende der Faser wird das austretende Licht durch eine Linse auf die Meßebene fokusiert. Dieser Lichtstrahl durchläuft einen Strahlteilerwürfel, der einen Teil des Lichtes um 90° auf eine Silizium-Fotodiode ablenkt. Die Spannung an dieser Detektordiode wird direkt über eine A/D-Wandlerkarte in einen tragbaren Rechner eingelesen.

Der andere Teil des Lichtstrahls trifft auf die Blendenöffnung eines elektronisch gesteuerten, mechanischen Shutters und wird mit dessen Taktfrequenz am Durchtritt gehindert. Im weiteren Verlauf des Strahlengangs befindet sich nun die Meßkammer, die mit Seitenwänden aus Glas versehen ist. In ihr befindet sich das eigentliche Meßobjekt, die Flamme. Das pulsierende Licht trifft hier auf die von der Flamme erzeugten Partikel und wird durch diese in seiner Intensität geschwächt.

Auf der anderen Seite des Meßvolumens befindet sich eine zweite Optik, die den abgeschwächten Lichtstrahl, sowie die Strahlung der Flamme, wiederum auf die Öffnung eines Lichtwellenleiters (Durchmesser 1000µm) fokusiert. Eine Linse bildet den Ausgang des Lichtwellenleiters auf den Eingangsspalt des Monochromators ab. Hier wird nun das auftreffende Licht durch ein Reflexionsgitter in seine spektralen Anteile zerlegt und letztendlich auf die Diodenzeile (1024 Elemente) des Detektors abgebildet.

Im Rechner des Spektrometers (Optical Multichannel Analyser) werden nun die kompletten Spektren des erfaßten Lichtes verarbeitet. Man erhält abwechselnd ein Spektrum der Flammenstrahlung, mit bzw. ohne Überlagerung durch den Meßstrahl.

Synchronisiert wird das gesamte System durch die am Spektrometer eingestellte Integrationszeit. Dieses Triggersignal wird durch einen Funktionsgenerator aufbereitet und dient der Steuerung des zum Shutter gehörenden Controllers. Dieser erzeugt ein Signal, je nach Zustand der Blendenöffnung am Shutter. Mit diesem Signal wird die Meßwerterfassung an dem genannten tragbaren Rechner ausgelöst. Abbildung 1 zeigt in einer schematischen Darstellung den optischen Aufbau und die Datenerfassung.

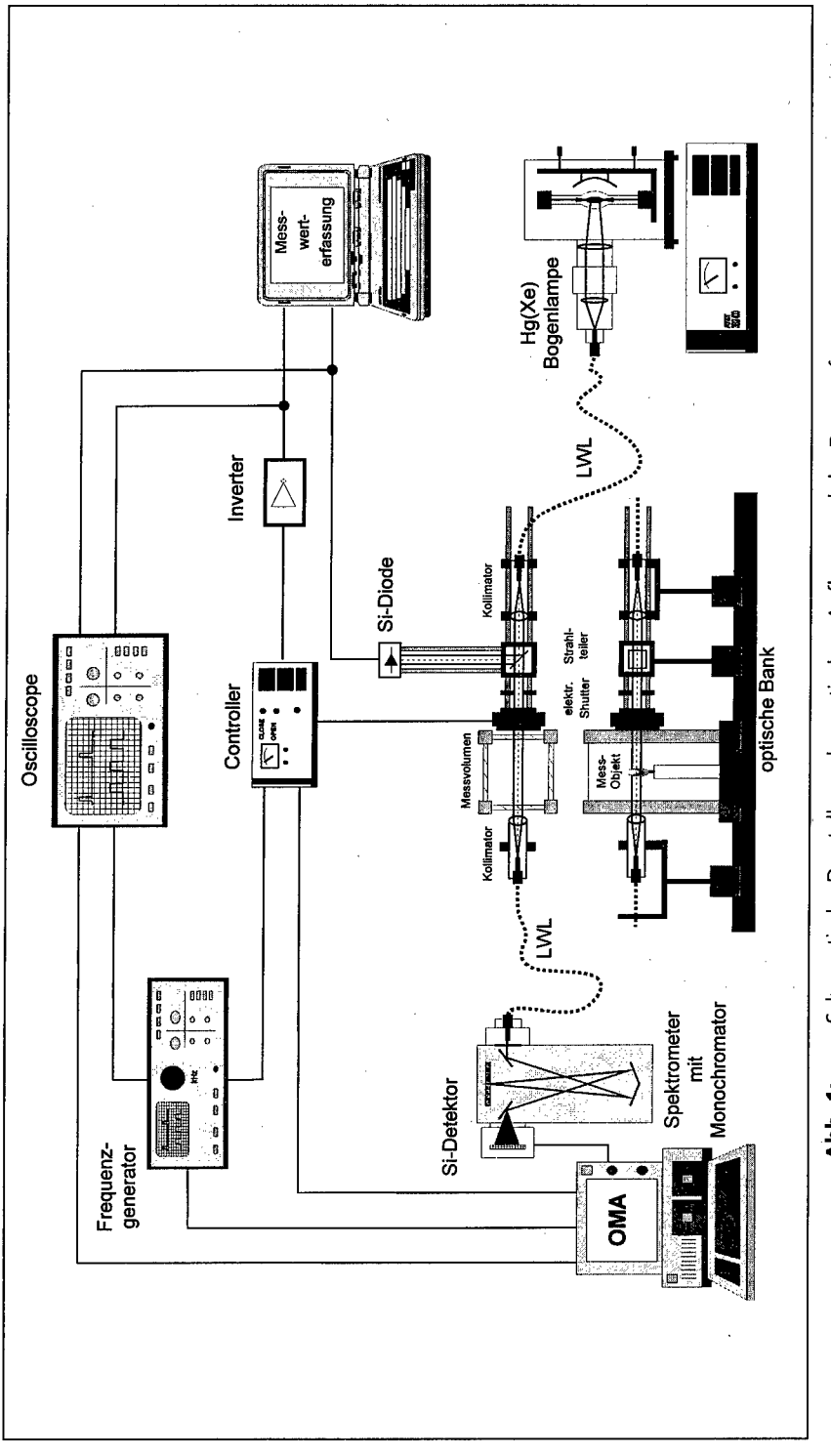

Abb. 1: Schematische Darstellung des optischen Aufbaus und der Datenerfassung

Ergebnisse:

Um die Qualität der Partikelgrößenbestimmung des entwickelten Meßsystem beurteilen zu können, wurde dieses an verschiedenen Flammen getestet. Im Nachfolgenden sind einige Meßergebnisse aus unterschiedlichen Versuchsanordnungen graphisch dargestellt.

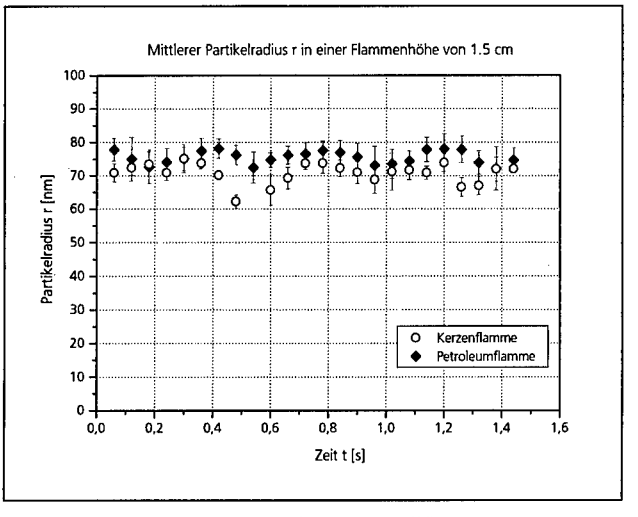

Abb. 2: Rußpartikelgröße in Modellflammen

Abbildung 2 zeigt den Verlauf zweier Meßreihen für unterschiedliche Modellflammen, bei denen der Meßstrahl die Flammenzone in einer festen Höhe von 1,5cm durchdringt.

Weiterhin wurden Messungen an Poolfire - selbst kontrollierten Diffusionsflammen über Brennstofflachen - durchgeführt, bei denen die axiale Lage des Meßstrahls variiert wurde. In Abbildung 3 sind die gemittelten Partikelgrößen (Ruß) in Abhängigkeit von der axialen Flammenposition für unterschiedliche brennende Substanzen dargestellt. Der Basisdurchmesser betrug 5 cm.

Die Meßergebnisse stimme sehr gut mit aus der Literatur bekannten Partikelgrößen überein [1,5]. Man beobachtet ein Partikelwachstum bzw. eine Partikelagglomeration mit zunehmender Flammenhöhe. Der Verlauf der Partikelgröße in Abhängigkeit der horizontalen Flammenposition deckt sich ebenfalls mit durch andere Meßsysteme gewonnenen Ergebnissen [9].

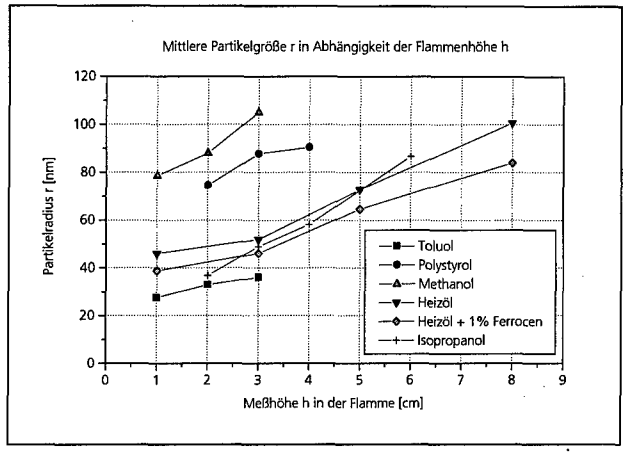

Abb. 3: Rußpartikelgrößen aus Poolfire-Versuchen

Da die Kenntnis des komplexen Brechungsindex des Partikel-Feststoffes die einzige Voraussetzung für das Meßsystem darstellt, können auch andere partikelbeladene Flammensysteme untersucht werden. Als Beispiel hierfür wurde die Größe der Al_2O_3-Partikel beim Abbrand eines Aluminium-Composit-Treibstoffes (HTPB 1029) bestimmt. In Abbildung 4 sind sowohl die gemessenen Teilchengrößen wie auch die Partikelkonzentration dieser Untersuchungen dargestellt.

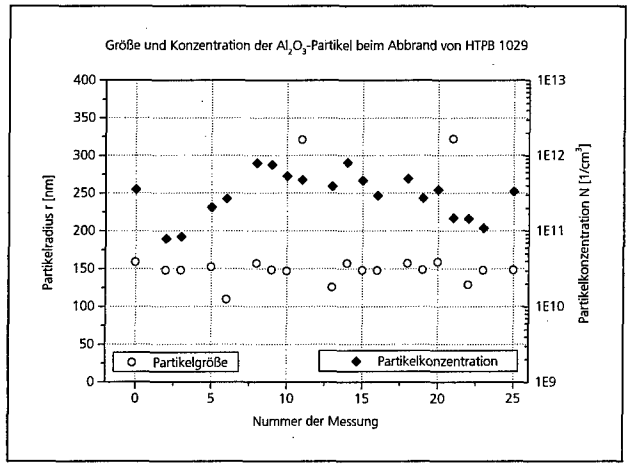

Abb. 4: Al_2O_3-Partikel beim Abbrand von HTPB 1029

Zusammenfassung:

Das hier vorgestellte Meßsystem ist in der Lage den Partikeldurchmesser in einem Größenbereich von 0.01...0.5µm, sowie die Partikelkonzentration im Bereich von $10^5...10^{12}cm^{-3}$ in Flammen berührungslos zu messen.

Ein Vorteil des Meßsystems gegenüber bekannten Systemen ist die Möglichkeit, sehr kleine Partikelgrößen bei hohen Konzentrationen zu detektieren. Durch die Verwendung von fünf und mehr Wellenlängen zu Bestimmung des Dispersionsquotienten, liegt der Hauptvorteil dieses Verfahrens in der hohen Sicherheit der Meßergebnisse. Die Doppeldeutigkeiten im Verlauf des Dispersinsquotienten lassen sich hiermit wesentlich einfacher beseitigen als bei herkömmlichen Meßsystemen, welche mit lediglich zwei bzw. drei Wellenlängen arbeiten. Außerdem ist eine Kalibrierung des Meßaufbaus nicht erforderlich.

In einer nächsten Entwicklungsphase soll das bestehende Laborsystem auf ein kompaktes und handliches Meßsystem reduziert werden. Durch eine direkte Rechneranbindung mit integriertem Spektrometer wird die zeitaufgelöste Online-Auswertung von partikelbeladenen Systemen wie Aerosole, Suspensionen und Emulsionen angestrebt.

Literatur

[1]	F. Rössler	Optische Eigenschaften von Rußteilchen, Optik10, Heft11,1953
[2]	E. Hecht	Optik, Addison-Wesley-Verlag
[3]	Gustav Mie	Beiträge zur Optik trüber Medien, Analen der Physik, 1908
[4]	H. Quenzel/H. Müller	Optical Properties of Single Mie Particles Wissenschaftliche Mitteilung Nr. 34, Universität München,1978
[5]	W.L. Flower	Light-scattering measurements of soot particles in flames International Society for Optical Engeneering, Orlando, 1986
[6]	S. Wittig/H.J. Feld	Particle size measurements in sooting combustion systems Universität Karlsruhe (T.H.), 1987
[7]	P. Bucher/R.A. Yetter	Flame structure mesurements of single Al-particles burning in air 26. Symposium on Combustion / The Combustion Institut, 1996
[8]	K.C. Smyth/C.R. Shaddix	The elusive history of the refraczive index of soot Combustion and flame, 107:314-320, 1996
[9]	S. Schraml/S. Will/A. Leipertz	On-line-Charakterisierung von Nanoteilchen Chemie Ingenieur Technik, 68, 9/1996

Einfluß der Partikelgröße auf das Abbrandverhalten von B/KNO3-Anzündmischungen

V. Weiser, D. Kuhn, R. Ludwig, H. Poth

Fraunhofer-Institut für Chemische Technologie (ICT)
P.O.Box 1240, D-76318 Pfinztal (Berghausen), Germany

Abstract

Gun propellants and particularly LOVA-ammunition with low temperature sensitivity need matched ignitor systems to guarantee reliable and effective ignition. For this systems privileged conditions of the ignitor jet are only partly known like temperature, particles and gas content. Also the influence of the mixture preparation like particle sizes and densities are less investigated. First approaches to investigate these influences to the burning behaviour and ignitor jet of B/KNO_3-mixtures and black powder are presented.

Kurzfassung

Jedes Treibladungspulver benötigt speziell angepaßte Anzündmischungen (AZM), um eine zuverlässige und effektive Anzündung zu gewährleisten. Dies gilt im besonderen Maße für LOVA-Munition und temperaturunempfindliche Pulver. In vielen Fällen sind die effektiven Anzündbedingungen bzgl. der Temperatur oder dem Partikel/Gas-Verhältnis nur unzureichend bekannt. Beim Anzündverhalten spielt die Aufbereitung des AZM bzgl. Partikelgrößenverteilung und Packungsdichte eine ausschlaggebende Rolle. Untersucht wurde der Einfluß dieser Parameter auf das Abbrandverhalten des AZM und der Anzündschwaden.

1 Einleitung

Die konventionelle Anzündung eines Treibladungspulver (TLP) geschieht durch Übertragung thermischer Energie aus dem reagierenden Anzündmittel (AZM) auf die Pulverschüttung über Strahlung und das Auftreffen heißer Gase und Partikel. Diese Vorgänge laufen in wenigen Millisekunden oder schneller ab. Eine hohe kinetische Energie der Gase und Partikel und ihr ausgewogenes, dem TLP angepaßtes Verhältnis sorgt für den Durchgriff auf einen ausreichenden Teil der Pulverschüttung [4].

Das unempfindliche Verhalten von neuen TLPs, insbesondere gegenüber thermischen Einwirkungen, basiert auf der Verwendung von Komponenten, die im Vergleich zu NC erst

bei höheren Temperaturen pyrolysieren. Dies gilt speziell für kalte Hochleistungspulver (KHP) und LOVA-Pulver. Z. B. zeigen Nitramine, die hohe Leistungen aufweisen und häufig bei diesen Pulvern zum Einsatz kommen, eine im Vergleich zu NC um ca. 50°C höhere Zersetzungstemperatur - meist in Verbindung mit einem Schmelzvorgang bei moderaten Heizraten [100K/min]. Binderanteile pyrolysieren z. T. endotherm. Dies erfordert allerdings mehr Energieübertragung und stellt die Entwickler von Anzündern vor das Problem, die Anzündmischungen den neuen Pulvern anzupassen, ohne zu gravierenden Steigerungen der notwendigen Anzündmengen zu kommen.

Ziel der berichteten Arbeiten war es zu untersuchen, wie die Eigenschaften von AZM variiert werden können, ohne ihre chemische Zusammensetzung zu ändern. Dadurch sollen chemische und physikalische Wirkmechanismen voneinander getrennt untersucht werden. Als Parameter zur Variation von Abbrandgeschwindigkeit und Partikeldichten wurde zuerst der Einfluß von Partikelgrößen und Schüttdichten untersucht.

2 Einfluß von Korngrößen und Schüttdichten auf die Umsatzgeschwindigkeit von B/KNO_3

Untersucht wurde der Einfluß der Partikelgrößenverteilung auf das Abbrandverhalten von Anzündmischungen (AZM). Die Partikelgrößenverteilung bestimmt die mikroskopische Vermischung der Reaktionskomponenten und die Größe der reaktionsfähigen Oberfläche. Daher kann erwartet werden, daß Sie einen großen Einfluß auf die Umsatzgeschwindigkeit des AZM ausübt. Auch ist mit einem Einfluß auf die Art und Größe der Schwadenpartikel zu rechnen.

2.1 Versuchsaufbau und Durchführung

Über das Abbrandverhalten von Pulverschüttungen gibt es bislang nur sehr wenige Untersuchungen [1]. Da keine geschlossene Oberfläche auf einem homogenen Material vorliegt, versagt die konventionelle Definition der Abbrandrate, und man beschränkt sich auf die Ermittlung der Umsatzgeschwindigkeit.

Bislang gibt es für derartige Messungen kein einheitliches Meßverfahren. Berger [1] mißt z.B. die Fortpflanzungsgeschwindigkeit einer Verbrennungsfront an einer pyrotechnischen Pulverschüttung in einer Rinne. Dieses Verfahren kann nicht in konventionellen Druckbomben eingesetzt werden. Deshalb wurde ein Verfahren entwickelt, daß Ähnlichkeiten mit der Meßmethode nach Crawford [2] aufweist, die zur Abbrandratenmessung von Festtreibstoffen routinemäßig eingesetzt wird.

Eine definierte Pulvermenge wird in ein 150 mm langes Glasrohr mit 6 mm Innendurchmesser eingefüllt, auf einer Rüttelmaschine möglichst gleichmäßig verdichtet, senkrecht aufgestellt und mit Hilfe einer kurzen Zündschnur angezündet. Die Meßstrecke beträgt 100 mm. Über und unter der Meßstrecke verbleiben etwa 20 mm Vor- bzw. Nachlauf. Der Abbrand wird mit einer Videokamera und eingeblendetem Zeitsignal aufgezeichnet. Die Aufnahmen können manuell und computergestützt ausgewertet werden. Bild 1 zeigt einen

charakteristischen Abbrand; die reagierende Flammenfront beträgt nur wenige Millimeter und verläuft absolut eben; so ist das Meßsignal eindeutig auszuwerten.

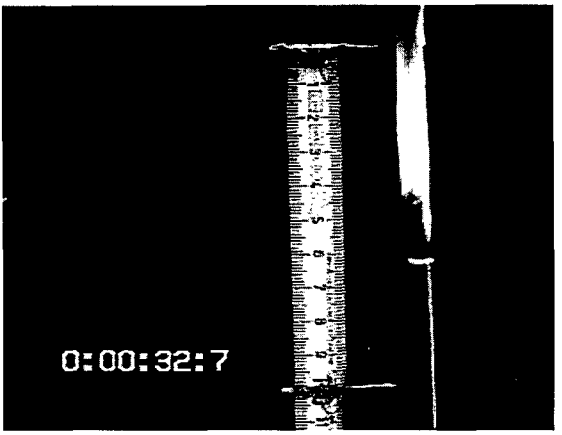

Bild 1 Videoprint eines repräsentativen Abbrandversuchs

2.2 Anzündmischungen und Probenaufbereitung

Untersucht wurden Schüttungen von Bor/Kaliumnitrat (B/KNO_3) in stöchiometrischer Zusammensetzung von 15 zu 85 Massenprozent. Das konventionelle Borpulver hatte einen mittleren Korndurchmesser von x_{50} = 2 µm. Die Kaliumnitratkörner wurden gemahlen und durch Siebung in drei Kornfraktionen aufgeteilt. Die x_{50}-Werte lagen bei 3, 6 und 12 µm.

Es wurden jeweils 3.7 g des Pulvers in ein Röhrchen gefüllt und mit einer Stampfmaschine verdichtet. Durch unterschiedliche Stampfzahlen von 300 bis 2000 Hüben konnten verschiedene Verdichtungen erreicht werden. Die Ermittlung der Schüttdichte erfolgte durch Messen der Füllhöhe nach dem Rütteln.

2.3 Umsatzgeschwindigkeiten

Die unterschiedlichen erreichten Schüttdichten sind in Abhängigkeit vom mittleren Durchmesser der KNO_3-Partikel in Tabelle 1 zusammengestellt. Gleichzeitig ist die maximal erreichte Steigerung der Schüttdichte eingetragen. Die Schüttdichten steigen mit der Größe der KNO_3-Partikel, d.h. mit dem Größenunterschied zwischen Bor und KNO_3. Die kleinen Bor-Partikel fügen sich besser in die Lücken zwischen den KNO_3-Partikeln ein. Durch aufwendiges Rütteln ist nur eine relativ geringe Steigerung der Schüttdichte um etwa 20% erreichbar. Die Reproduzierbarkeit der Schüttdichte bei gleicher Hubzahl war mit Schwankungen von etwa 10% zufriedenstellend.

Tabelle 1 Erreichte Schüttdichten bei unterschiedlichen KNO3-Partikeldurchmessern; x_{50}(Bor) = 2 µm.

x50(KNO_3) in µm	3	6	12
x50(KNO3) : x50(B)	1.5	3	6
Schüttdichte in g/cm³	0.71 bis 0.87	0.79 bis 0.96	0.92 bis 1.06
Steigerung in %	23	22	15

Die Verbrennung verläuft rückstandsfrei. Nur an der Rohrwand findet man eine hauchdünne Ablagerungsschicht. Es werden praktisch keine glühenden Partikel aus dem Rohr geschleudert.

Die bei verschiedenen Schüttdichten gemessenen Umsatzgeschwindigkeiten erweisen sich als mäßig reproduzierbar, wie Bild 2 verdeutlicht. Es zeigt die gemessenen Regressionsgeschwindigkeiten r der einzelnen AZM in Abhängigkeit von der Schüttdichte ρ. Die Abhängigkeit von der Dichte erweist sich als signifikant und ergibt eindeutige Trends.

In Richtung großer KNO_3-Partikel steigert sich die Umsatzgeschwindigkeit von 2 auf 3 mm/s bei niedrigen Schüttungdichten auf von 4 auf 6 mm/s bei hohen Verdichtungsgraden. Als Grund für den Anstieg der Umsatzgeschwindigkeit kann die höhere Packungsdichte bei den 12 µm Pulvern angesehen werden. Durch die bessere Einlagerung und Verteilung der Borpartikel sind Brennstoff und Oxidator besser vermischt; die Reaktionspartner liegen näher beieinander. Dies beschleunigt und optimiert die mikroskopischen Wärme- und Stoffaustauschprozesse bei der chemischen Reaktion.

Die absoluten Werte erscheinen sehr klein im Vergleich zu den Erfahrungen im Anzündsimulator [3] und realen Waffensystemen, in denen sich ähnliche Menge gleichartiger AZM in wenigen Millisekunden umsetzen. Allerdings spielen dabei höhere Inziierungsenergien und starke Verdämmungseffekte eine ausschlaggebende Rolle. Die dargestellten Versuche wurden so konzipiert, daß sich das Abbrandverhalten unabhängig von diesen Effekten möglichst vergleichbar untersuchen läßt. Wie auch bei den Arbeiten von Berger [1] sollen nur isolierte Einflüsse wie die Korngröße und Schüttdichte auf das AZM untersucht und Tendenzen aufgezeigt werden.

Die Umsatzgeschwindigkeit variiert stärker mit der Schüttdichte als mit den untersuchten Korngrößen der KNO_3-Partikel. Mit höhere Schüttdichte steigt die Umsatzgeschwindigkeit überproportional an. Der Anstieg kann nicht als exponentiell betrachtet werden, weil die Steigerung der Schüttdichte nach oben begrenzt ist. Der Anstieg der Umsatzgeschwindigkeit kann, wiederum durch die geringeren mittleren Abstände zwischen den Reaktionspartnern erklärt werden. Als weiterer Effekt muß der gestiegene Strömungswiderstand angesehen werden, der durch die höhere Packungsdichte und die damit verringerten Porendurchmesser entsteht. Die Gase strömen langsamer ab; dies führt zu einer Drucksteigerung im Röhrchen und zu einer schwächeren Wärmeabfuhr aus der Reaktionszone.

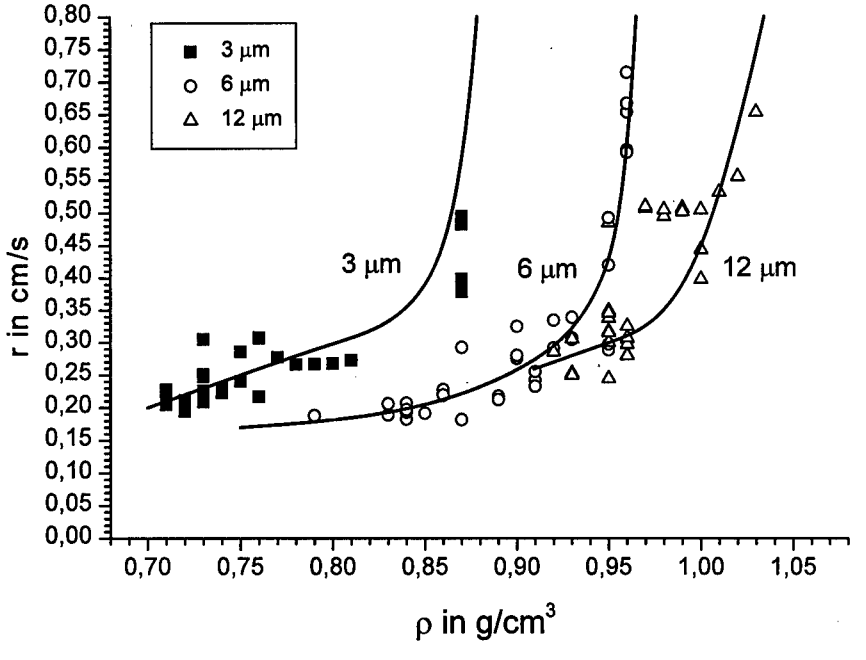

Bild 2 Umsatzgeschwindigkeiten r der AZM unterschiedlicher Korngrößenfraktionen in Abhängigkeit von der Schüttdichte ρ.

3 Untersuchung der Anzündschwaden

Zur Beurteilung der Eigenschaften der Anzündschwaden wurde eine Versuchsapperatur mit 2 cm^3 Füllvolumen aufgebaut, die es erlaubt, AZM-Pulver kontrolliert anzuzünden und einen definierten Schwadenstrahl zu erhalten. Dabei wurden ähnliche Lochdurchmesser gewählt, wie sie z.B. bei der Anzündeinheit Kaliber 76 mm auftreten. Dieser Strahl kann mit optischen Meßmethoden auf Art, Temperatur und Geschwindigkeit von Gas- und Partikeln untersucht werden oder auf ein im bestimmten Abstand befestigtes Pulverkorn gerichtet werden, um das Anzündverhalten des Pulvers während der Anzündphase zu beobachten.

3.1 Aufbau

Das Gehäuse der Apparatur wurde aus Stahl gedreht. Das Füllvolumen beträgt 2 cm^3 und erlaubt eine Befüllung mit verschiedenen Ladedichten. Ein Bodenteil aus Perdinax erlaubt die elektrisch isolierte Durchführung von zwei Anzündelektroden mit 1 cm Abstand. Bild 3 zeigt eine Schemazeichung der Apparatur. Das Gerät ist modular aufgebaut, so daß ohne große Änderungen das Füllvolumen variiert werden kann. Die Modulteile sind gegenseitig verschraubt und erlauben ein einfaches und schnelles befüllen. Dadurch können auch umfangreiche Versuchsreihen schnell durchgeführt werden.

Durch Austausch der oberen Lochplatte kann die Klemmung variiert werden. Sinnvolle Durchmesser liegen bei 1 bis 5 mm. Zwischen Blende und Pulver wird eine dünne Aluminium- oder Kunststofffolie gelegt, um einen definierten Austrittstrahl der Schwaden ab einem bestimmten Innendruck zu gewährleisten.

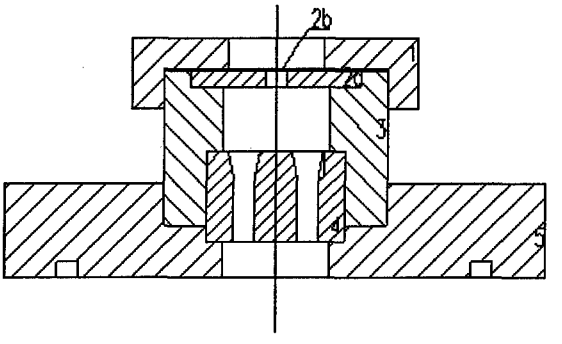

Bild 3 Apperatur zur Untersuchung von Anzündschwaden

Die Anzündung erfolgt nach dem Prinzip der Kondensatorentladung über einen Anzündraht aus einer Nickellegierung. Er ist über eine Strecke von 10 mm doppelt

gewickelt und wird zwischen den beiden Elektroden eingeklemmt. Der gleiche Draht wird technisch in der Kalorimetrie eingesetzt und weist einen Brennwert von nur 6 J/cm auf. Die zugeführte Energie ist wesentlich geringer als der Energieinhalt der eingefüllten Anzündmischungen und beeinflußt kaum das Verhalten des AZM.

3.2 Ergebnisse

Es wurden 20 Versuche mit unterschiedlichen Modell-AZM durchgeführt. Dabei wurden die Klemmung und Ladedichte variiert. Tabelle 2 faßt den Versuchsplan zusammen. Eingesetzt wurden Schwarzpulver, eine konventionelle B/KNO_3-Mischung mit einer angegebenen Zusammensetzung von 66.7-72.7% KNO_3, 22.2-25.2% Bor, 4.6-6.6% Binder und die o.a. B/KNO_3-Mischungen mit verschieden großen KNO_3-Partikel. Bei den Versuchen 7 und 8 wurde der Schwadenstrahl auf ein JA2-Pulverkorn gelenkt. Die Versuche wurden mit Videokamera verfolgt. Beim Abspielen der Videos im Einzelbildmodus erwies sich die Videogeschwindigkeit von 25 Bildern pro Sekunde als gerade noch ausreichend, um die Strahlausbreitung zu verfolgen.

Tabelle 2 Versuchplan zum Einfahren des AZM-Test-Moduls

V-Nr	Stoff	Korngröße in µm	Ladegewicht in g	Klemmungs-durchmesser in mm	Bemerkung
1	BKNO3	3	0,5	4	
2	BKNO3	3	0,5	4	
3	SP		0,5	4	
4	SP		0,5	4	
5	SP		0,75	4	
6	SP		0,75	4	
7	SP		0,5	4	+JA2
8	SP		0,5	4	+JA2
9	SP		0,5	1	
10	SP		0,5	2	
11	SP		0,3	1	
12	SP		0,3	2	
13	SP		0,3	4	
14	BKNO3	3	0,3	2	
15	BKNO3	3	0,3	2	
16	BKNO3	6	0,3	2	
17	BKNO3	6	0,3	2	
18	BKNO3	12	0,3	2	
19	BKNO3	LOS S/X/08/95	0,3	2	
20	BKNO3	LOS S/X/08/95	0,3	2	

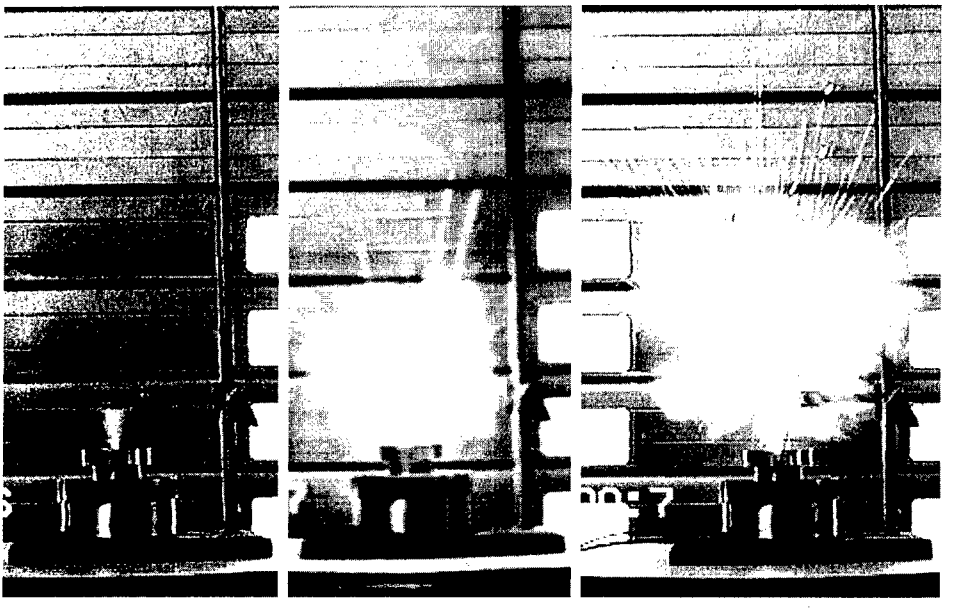

a) b) c)

Bild 4 Videoprints von der Anzündung eines JA2-Pulverkorn mit Schwarzpulverschaden (25 Bilder/s)

Als sinnvolles Ladegewicht erwiesen sich 0.3 g (Δ=0.15) bei einer Klemmungsdurchmesser von 2 mm. Dabei war der Schwadenstrahl einerseits deutlich ausgeprägt, aber für weiterführende Untersuchungen noch nicht zu groß. Die Reproduzierbarkeit der Strahlausdehnung war in allen Fällen zufriedenstellend. Der Strahl zündet JA2 an, wie Bild 4 eindrucksvoll veranschaulicht. Dargestellt ist eine mit Video aufgenommene Bildfolge mit 40 ms Zeitabstand und einer Belichtungszeit von 1/4000 s.

Obwohl die Versuche in erster Linie dem Test der Apparatur dienen sollten, konnten einige, erste Ergebnisse erzielt werden. Dies betrifft im wesentlichen Aussagen über die Strahlgeometrie in Abhängigkeit von den AZM-Substanzen, der Klemmung, und der mittleren Korngröße.

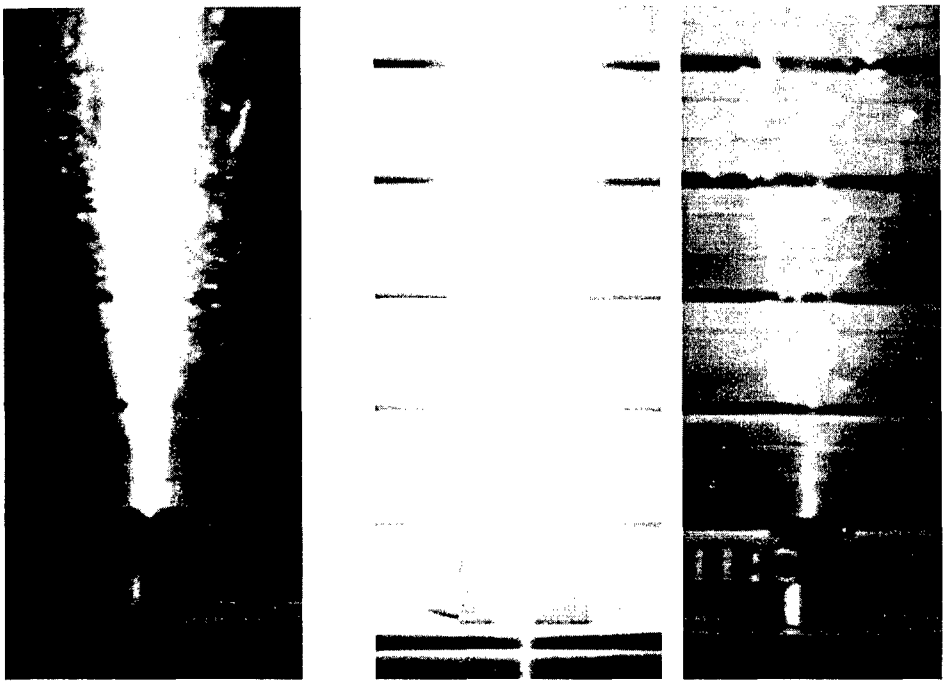

a) b) c)

Bild 5 Vergleich des Schwadenstrahls eines Schwarzpulvers (a) mit einem konventionel-len B/KNO3 Anzündmischung (b, c) zum Zeitpunkt maximaler Ausdehnung

In Bild 5 werden die Schwadenstrahlen zwischen einem Schwarzpulver (a) und einer konventionellen $BKNO_3$-AZM (b) zum Zeitpunkt maximaler Ausdehnung verglichen. Bild 5c zeigt den $BKNO_3$-Strahl 80 ms später. Die Klemmungsöffnung betrug 2 mm und die Ladedichte Δ=0.15. Schwarzpulver ergibt einen eng begrenzten, relativ schwach leuchtenden Strahl. Am Rand sind einige einzelne, leuchtende Partikel zu erkennen. Der Strahl erscheint nur in 3 aufeinanderfolgenden Videobildern; daraus ergibt sich eine Reaktionsdauer von etwa 100 ms. Der Strahl des $BKNO_3$ ist wesentlich heller und breiter. Augenscheinlich enthält er eine erheblich höhere Partikelmenge. Dies wird auch durch die Aufnahme 80 ms danach dokumentiert. Man erkennt viele, über die Fläche des ehemaligen Strahls verteilte Leuchtpunkte, die erst nach weiteren 200 ms vollständig erlöschen. Es handelt sich um Borpartikel, die in der Luft nachverbrennen.

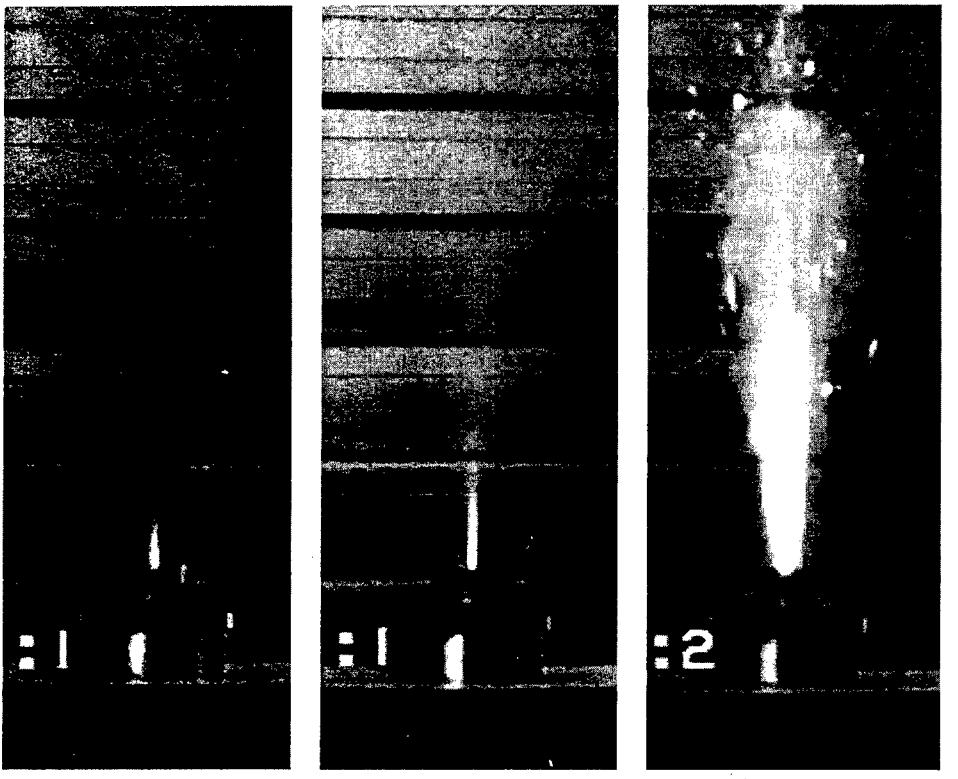

a) b) c)

Bild 6 Screenshot des Schwadenstrahls bei Schwarzpulver zum Zeitpunkt maximaler Ausdehnung bei unterschiedlichen Öffnungsdurchmessern; a) 1 mm, b) 2 mm, c) 4 mm.

Den Einfluß der Klemmung auf den Schwadenstrahl eines Schwarzpulvers (Δ=0.15) ist in Bild 6 dargestellt. Die Öffnungsdurchmesser betrugen 1, 2 und 4 mm. Die Länge des leuchtenden Schwadenstrahls verhält sich etwa proportional zur Klemmungsöffnung. Die hellgelbe Strahlung wird von heißen Kleinstpartikeln hervorgerufen, d. h. bei kleineren Öffnungen verbrennen die Schwarzpulverkörner schneller als bei großen. Dafür muß der höhere Innendruck im Modul verantwortlich gemacht werden, der ähnliche Effekte hervorruft, wie sie im Abschnitt 2 beschrieben sind. Bei kleinen Klemmungsöffnungen ändert sich die Strahlbreite nicht. Erst ab relativ großen Öffnungsradien fächert der leuchtende Anteil des Strahles auf. Wahrscheinlich werden mehr Partikel des AZM aus der Brennkammer geschleudert.

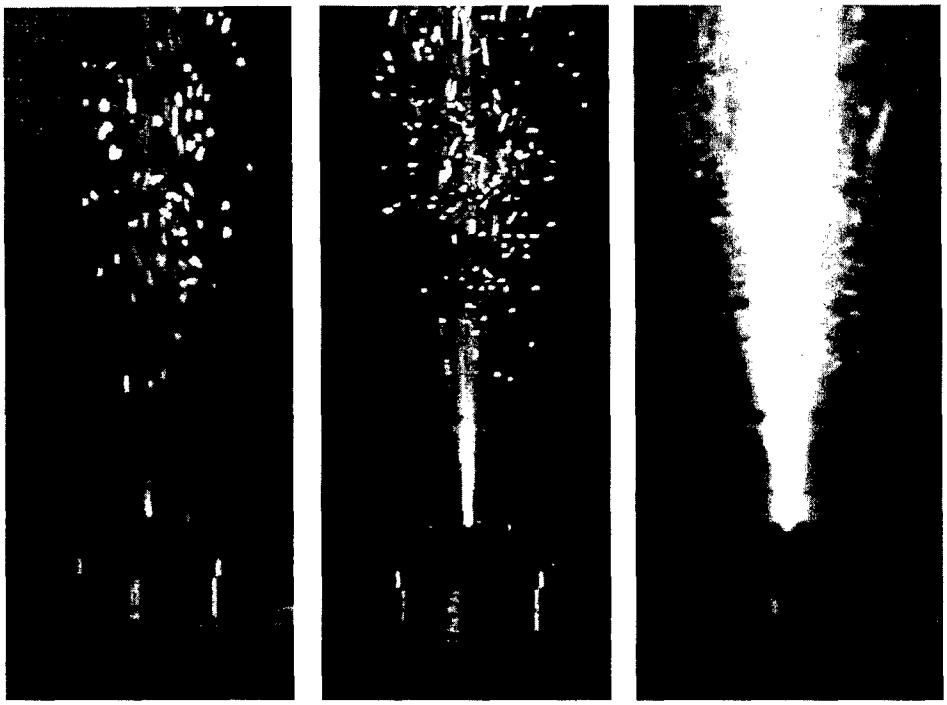

a) b) c)

Bild 7 Screenshot des Schwadenstrahls bei B/KNO3-Pulvern zum Zeitpunkt maximaler Ausdehnung und verschieden großen KNO_3-Partikeln a) x50(KNO_3) = 3 µm, b) x50(KNO_3) = 6 µm, c) x50(KNO_3) = 12 µm.

Auch die Partikelgröße des Kaliumnitratpulvers weist einen deutlichen Einfluß auf den Schwadenstrahl aus (Bild 7). Bei feinerer KNO_3-Aufmahlung endet die leuchtende Hauptreaktionszone kurz nach der Austrittsöffnung (Bild 7a). Erst einige Zentimeter darüber erscheinen einige leuchtende Partikel. Vermutlich handelt es sich hier wiederum um nicht verbrannte Borpartikel, die durch den heißen Gasstrahl erwärmt werden aber erst bei ausreichender Umgebungsluft anzünden und nachverbrennen. Der leuchtende Teil des Strahls ist um so länger, je größer die KNO_3-Partikel sind. Dabei steigt die Zahl der nachverbrannten Borpartikel an. Die Abbrandreaktion scheint langsamer abzulaufen, obwohl alle drei AZM die gleiche Zusammensetzung aufweisen. So führen die Beobachtungen zu der Annahme, daß nur die kleinen KNO_3-Partikel schnell genug ausreichend Oxidationssauerstoff abgeben können, um das Bor vollständig zu verbrennen. Nur bei hohen Kornaufmahlungen läuft die Reaktion vollständig in der inneren Kammer statt.

4 Literatur

[1] Berger, B.; Haas, B.; Reinhard, G.; Einfluss der Korngrösse des Reduktionsmittels auf die Reaktionsparameter pyrotechnischer Systeme; ICT-Jahrestagung 1996; 13-(1-16)

[2] V. Weiser, N. Eisenreich, W. Haberecht, W. Mex, K. Zilly; Neue Konzepte beim Aufbau einer modernen Crawford-Anlage; TM 6/96

[3] Müller, D.; Weiser, V.; Ebeling, H.; Eisenreich, N.; Neue Anzündmittel für TLANZ Kal. 76 mm, ICT-Bericht 9/95

[4] Müller, D.; Neue Anzündmittel für LOVA-TLP, ICT-Bericht, 24/93

EFFECT OF CRYSTAL DEFECTS ON REACTIVITY OF ENERGETIC MATERIALS: 1. THE EFFECT OF MECHANICAL DEFORMATION.

Rogers Longjohn† and Michael. Cartwright†

ABSTRACT

The impact sensitivity of mechanically deformed RDX have been performed on the Rotter Impact Tester. Mechanical deformation was brought about by dropping a 5 kg weight on the samples from a height below the Median Drop Height (M.D.H.) of pure RDX. Increasing the Initial Impact Height (I.I.H.) from 20 cm to about 80 cm produced a corresponding increase in sensitisation of the RDX as measured by a reduction in the M.D.H. for second and final impacts. Above an I.I.H. of 80 cm, reduced sensitisation occurred and a slightly higher impact height, although still less than that for the original RDX sample, was then required to bring about an ignition event.

These results can be explained assuming that the initial impact sensitises RDX by increasing the dislocation pile-up concentration (potential hot spots) and hence reducing the required height for a subsequent ignition event. The dislocation pile-up theory sufficiently describes the sequence of events from an I.I.H. of 20 cm up to an I.I.H. of 80 cm. Above an I.I.H. of 80 cm blunting of the initial pile-up sets in - effectively reducing the initial stress concentration which existed at the pile-up. Consequently, a slightly higher impact height was required to bring about an ignition event when compared to samples initially impacted just below 80 cm.

---

† Department of Environmental Ordinance Systems, Cranfield University, Royal Military College of Science, Shrivenham, Swindon, Wiltshire, UK SN6 8LA.

1. INTRODUCTION

During impact testing of solid explosives hot spots can be generated from the adiabatic compression of the trapped gases and friction between the crystal particles[1]. The hardness, particle size and habit of the explosive crystals can also act to enhance the explosive sensitivity. On the atomic scale crystal defects, such as substitutional and interstitial impurity atoms, dislocation lines, stacking faults and grain boundaries also affect sensitivity of crystalline explosives. This work was undertaken in an effort to understand the role of crystal defect in the sensitivity of energetic material.

There are a number of convenient techniques[2] that can be used to increase the concentration of defects above the thermal equilibrium concentration. These include plastic deformation, quenching from high temperature, alloying or doping and irradiation with energetic particles. This paper investigates the effect of mechanical deformation on the sensitivity response of RDX. Initiation of crystalline explosives by impact is via a mechanism in which extremely localised plastic deformation zones resulting from shear stresses cause a pile-up of dislocation and act as sources of hot spots[1&3]. Consequently, pre-existing dislocation pile-up, previously introduced by mechanical deformation, could be expected to enhance an explosive response to impact. Rotter impact testing is one of the standard method for the evaluation of impact sensitivity of energetic materials[4].

2. LITERATURE SURVEY

During the impact of most crystalline solids the resulting dislocation movement causes lattice perturbations which generate a phonon field. The radiated phonon can be locally concentrated to form hot spots which in turn can influence the mechanical strength, as well as other properties, of the solid. Early work on the heat generated by a moving dislocation[5&6] found small temperature increases in commercial grade aluminium - between 4.7 and 14.3 °C, and between 25.2 and 79.5 °C for a structural aluminium alloy.

Recent modification of these earlier results - through a correction factor - to allow for much higher temperature increases have been reported by Coffey and Armstrong[7]; their observations were based on experiments on rapidly deformed crystals of sodium chloride. More recently, C. S. Coffey[8] have derived a quantum mechanical expression for the phonon energy (É) generated by a moving dislocation and from the equation he estimated the local energy and temperature produced by a moving dislocation in RDX as 4.6 x 10^{-13} J and 185 °C respectively, stressing the fact that these are only approximate calculations since some of the imput values are not accurately known. However, from their rough estimate, a much higher temperature was predicted with this model. Figure 1 is a schematic representation of the microstructural changes within RDX explosive crystals during drop weight impact loading giving rise to the generation of localised hot spots[9]. On the microscale, localised heating in a material is believed to result from adiabatic collapse of dislocation pile-up avalanche[9 & 10]. This model predicts a greatly increased heating effect if the dislocations are first arranged in a static pile-up configuration within a slip band with subsequent sudden release as in a catastrophic avalanche. Other factors which can influence an explosive response to impact are discussed elsewhere[11, 12 & 13].

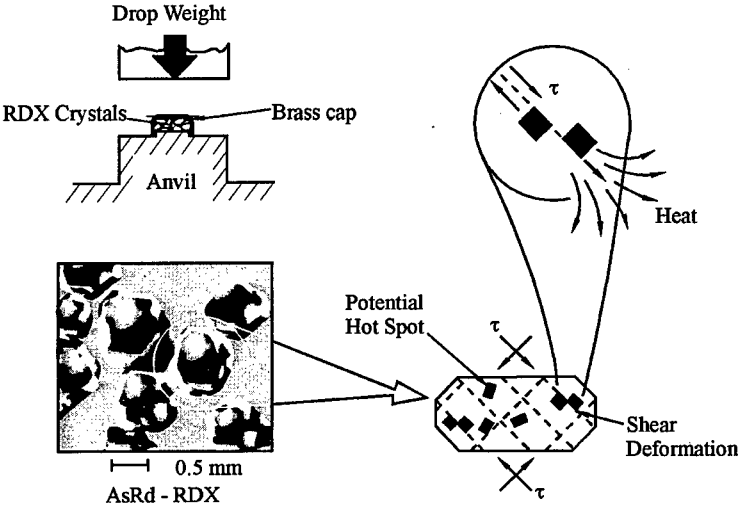

Figure 1. High Rate Localised Shearing of RDX Explosive Crystals.

3. EXPERIMENTAL PROCEDURES

MULTIPLE IMPACT TESTING

Standard RDX (AsRd-RDX) supplied by DERA, Fort Halstead was used for these experiments. It was oven dried at 80 °C under a vacuum of ≈ 900 mbar (675 Torr) and stored in a desiccator with no further treatment. The Rotter Impact Machine[4] was used to carry out the testing. Double impacts were carried out on each sample. The Initial Impact Height (I.I.H.) was chosen such that no ignition event was possible; i.e. a height well below or not higher than the Median Drop Height (M.D.H.) of RDX - which is 120 cm. A second and final impact on each batch of samples from each I.I.H. was then carried out to determine the 0 % ignition height and the 100 % ignition height, along with intermediate mixed response heights (Yes/No ignition events) at 10 cm intervals to obtain typical response curve of the type shown in Figure 2. A whole spectrum of I.I.H. was looked at; 0 cm to 120 cm, at 20 cm intervals. Evidence of a positive impact response was determined by using the usual standard gas evaluation criteria[4].

SCANNING ELECTRON MICROSCOPY (SEM)

Samples from two extremes, one from an I.I.H. of 20 cm and another from an I.I.H. of 80 cm, recovered from the multiple impact testing, were examined under the SEM (JOEL JSM - T300A) for structural damage resulting from the initial impact. An attempt was also made to obtain evidence of adiabatic shearing. In order to facilitate this, some of the sample was deliberately gently tapped into smaller half flakes to allow some sideways viewing and to allow the assessment internal damage; the rest of the samples were mounted with care to preserve the damaged surfaces as they were just after impact.

4. RESULTS AND DISCUSSION

MULTIPLE IMPACT TESTING

ROTTER IMPACT RESULTS

Figure 2 shows a typical response curve for the AsRd-RDX - Median Drop Height (M.D.H.) = 120 cm; obtained from single impact experiments i.e. Initial Impact Height (I.I.H.) = 0 cm. During multiple impact testing, the sample remained in the test cell after the first impact and the impacting weight was readjusted to a new height for the second and final impact. The second impact occurred within twenty seconds after the first impact. Some significant sensitisation of the AsRd-RDX occurred even at a very low I.I.H. of 20 cm. Figure 3 (a) and (b) show the combined effect impact loading on the AsRd-RDX as the I.I.H. is progressively increased from 0 to 120 cm, and Figure 4 is a trace of the M.D.H. for all the samples tested versus the corresponding I.I.H..

OPERATIVE MECHANISM DURING IMPACT LOADING

Ljungberg[14] first observed a sharp drop in pressure during the impact of PETN, but it was Heavens and Field[3] who correctly attributed this phenomenon to material flow resulting from the impact energy. The proposed mechanism to account for the changes observed in the sensitivity response of the AsRd-RDX at different I.I.H. is be based on the material flow of the sample resulting from the impact energy via the Dislocation Pile-up Theory. As the I.I.H. was progressively increased some energy localisation (dislocation pile-up) occurred up to a certain point depending on the magnitude of the impact energy. This energy localisation is possible due to the formation of adiabatic shear banding[15] resulting from the mechanical deformation; grain boundaries are also a good means of generating and pinning dislocations - leading to the formation of Unstressed Single Pile-up of dislocation on removal of the initial impacting load - Figure 5. Particle fragmentation resulting from the mechanical failure also brings about the creation of new surfaces or a mosaic structure which act as grain boundaries - effectively increasing

not only the number of dislocations but also the obstacles to pin these dislocations. The RDX sample, having undergone an initial impact, is in a highly strained state due to the

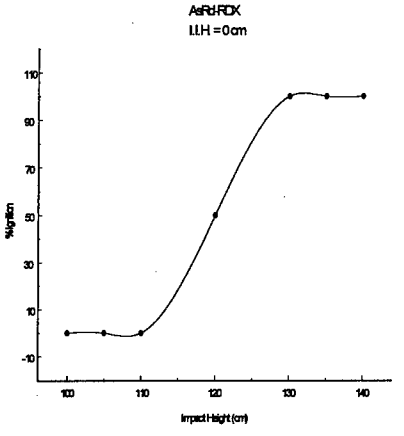

Figure 2. Impact Response Curve for AsRd-RDX.

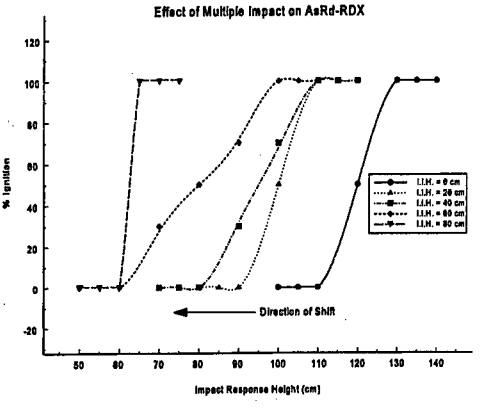

Figure 3 (a).Changes in Response of AsRd-RDX at Different I.I.H. - 0 to 80 cm.

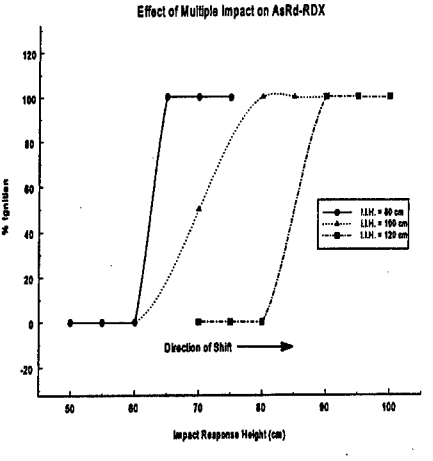

Figure 3 (b).Changes in Response of AsRd-RDX at Different I.I.H. - 80 to 120 cm.

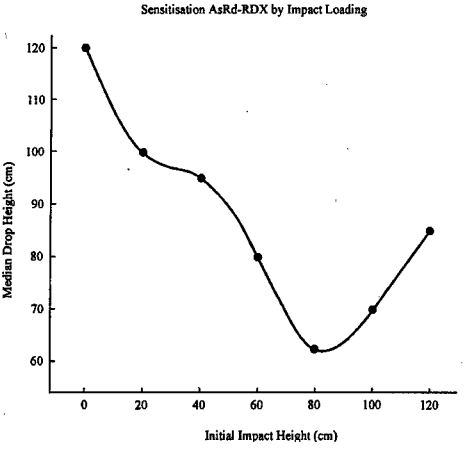

Figure 4. The Effect of Impact Loading on the M.D.H. of AsRd-RDX.

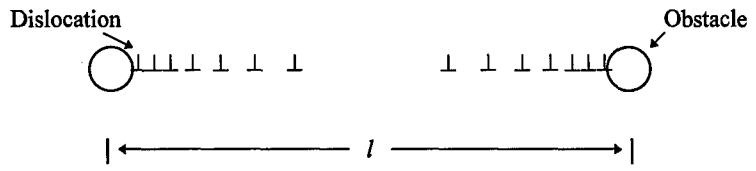

Figure 5. Single Pile-up in the Absence of Stress.

dislocation pile-up activity and as a result potential hot spots are thus created. Consequently, a moderately high subsequent impact height (between 15 and 50 % less than the M.D.H. of the AsRd-RDX - depending on the I.I.H. used) is required to bring about an explosion event.

With reference to the sensitisation curve of Figure 4, the above dislocation pile-up theory adequately describes the sequence of events from an I.I.H. of 20 cm up to an I.I.H. of 80 cm; i.e. increasing the I.I.H. from 20 cm to about 80 cm produces a corresponding increase in sensitisation of the AsRd-RDX by increasing the dislocation pile-up concentration (potential hot spots) and hence reducing the required drop height for a subsequent ignition event. Above an I.I.H. of 80 cm, reduced sensitisation (still greater than untreated RDX) occurs and a slightly higher impact height was then required to bring about an ignition event; hence, the pile-up theory breaks down at this point and a different mechanism is then required to account for the observed impact response above the I.I.H. of 80 cm.

OPERATIVE MECHANISM ABOVE I.I.H. OF 80 cm

Microhardness indentation studies on RDX crystals have been carried out by a number of worker including P. J. Halfpenny *et al.* [16], Elban and Armstrong[2] and J. K. A. Azumu *et al.* [17] and a well define primary slip system have been reported as (010) [16,18] with limiting possible dislocations with Burgers vectors[16], **b**, of [001], [100] and [101] (1.07, 1.359 and 1.690 nm, respectively). There is also evidence for a secondary slip system, but controversy surrounds the exact slip plane for this system. Elban and Armstrong[2]

proposed a {021} primary slip system following indentation and etching studies of only the {021} faces. P. J. Halfpenny *et al.* have put forward, from their extensive studies on different faces of RDX facets, a (021) or (011) secondary slip plane since both plane intersect the (001) faces in a line parallel to [100] direction. However, more evidence from their work have led them to nominate the (011) plane as the most likely slip plane rather than the (021) plane. A Molecule of RDX is shown in Figure 6 (a), and the unit cell of RDX is shown in Figure 6 (b). Figure 7 is a schematic diagram of the operative slip planes in RDX unit cell.

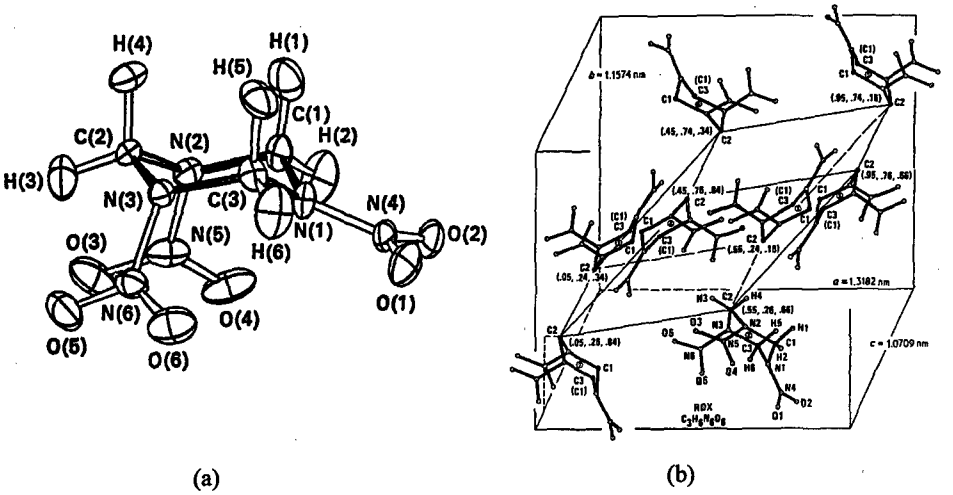

(a) (b)

Figure 6. Side View of the RDX Molecule[19] (a) and A Unit Cell of RDX (b) [20].

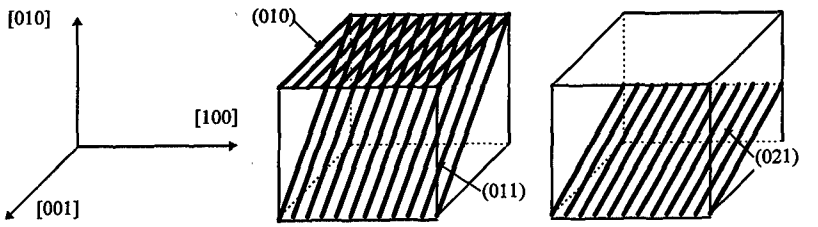

(a) (b) (c)

Figure 7. Directions and Planes in RDX. (a) Three Orthogonal Directions, (b) the (010) Primary Slip Plane, and the (011) Secondary Slip Plane, (c) the (021) Secondary Slip Plane.

For a crystalline material with a high stacking fault energy such as RDX, the possibility of glide dislocation pile-ups becoming BLUNTED are favourable at sufficiently high stresses during plastic flow. Cross slip (requiring a secondary slip system) or operation of new dislocation sources near the dislocation pile-up tip are responsible for such processes[21]. Figure 8 is a schematic representation of a glide pile-up blunting. Although the dislocation in tangle (i.e. blunted) do not resemble an ideal pile-up (Figure 5), the long-range stress field at distances greater than the length of the "tangled" pile-up is similar to the ideal pile-up results. Only at the spearhead of the tangle pile-up are the stresses reduced by blunting.

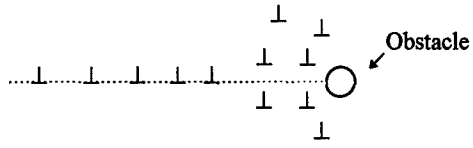

Figure 8. Blunting of a Glide Pile-up.

It is possible that as the I.I.H. is increased above 80 cm, blunting of the ideal dislocation pile-up occurs in these samples of RDX - thus reducing the stress concentration at the tip of the pile-up and hence a slightly higher subsequent impact height was required to initiate explosion events in these samples.

SCANNING ELECTRON MICROSCOPY (SEM) STUDIES

SAMPLES FROM AN I.I.H. OF 20 cm

Figure 9 (a) and (b) are electron micrographs of samples of AsRd-RDX recovered from the brass cap used in the Rotter testing. The remaining micrographs are selected areas of the above mentioned two samples. Figure 9 (c) is a magnified top central region (arrow pointing downwards) of Figure 9 (a). On this micrograph (Figure 9 (c)) a typical brittle fracture surface, multiple cleavage-type fracture, can be seen on the right; and on the top left - evidence of shear banding can clearly be seen; a magnified version is shown in

Figure 9 (d). At even higher magnifications, the flat surface of Figures 9 (a) appears to be completely covered with tiny line of cracks, and inclusions - highlighted with arrows - which were forced to the surface by the impacting load, can also be seen in Figure 9 (e). Figure 9 (f) is a magnified micrograph of an area of Figure 9 (b) (arrow pointing upwards) where a brittle fracture surface and particle inclusions (lighter in contrast) can be seen.

SAMPLES FROM AN I.I.H. OF 80 cm

Figure 10 (a) is an electron micrograph of recovered AsRd-RDX sample after an initial impact from 80 cm. A magnified region which is indicated by the arrow pointing upwards in Figure 10 (a) is shown in Figure 10 (b); a dense structure with what appears to be microcracks are obvious - a magnified version is shown in Figure 10 (c). At even higher magnifications, Figure 10 (d) reveals a whole series of tiny protrusions; they appears to be perfectly aligned in one direction. The reason for or the significance of these aligned protrusion are not clearly understood yet; work is in progress to find out more about this effect. What appeared initially as tiny microcracks are actually filled with previously molten material - they are mostly glassy in appearance. A large, previously liquefied region is also indicated by the arrow. Figure 10 (e) and (f) are images of a piece of sample on Figure 10 (a) indicated by the arrow pointing downwards. Here again there are a large collection of previously molten regions. It is highly likely that these were a result of melting at the tip of propagating cracks - causing the thermal decomposition of the surrounding material during mechanical deformation. P. G. Fox & J. Soria-Ruiz[22] have studied fracture-induced thermal decomposition in brittle crystalline solids. By relating the amount of decomposition to the fracture velocity and the kinetics of thermal decomposition of each material, a figure for the crack tip temperature was deduced in each case that was investigated. K. N. G. Fuller *et al.* [23] have also reported a temperature rise of about 500 K at the tip of fast-moving cracks in polymethyl-methacrylate. More recently, W. L. Elban *et al*[24-26] have reported on the observation of a decomposition product - R-Salt - from impacted samples of RDX.

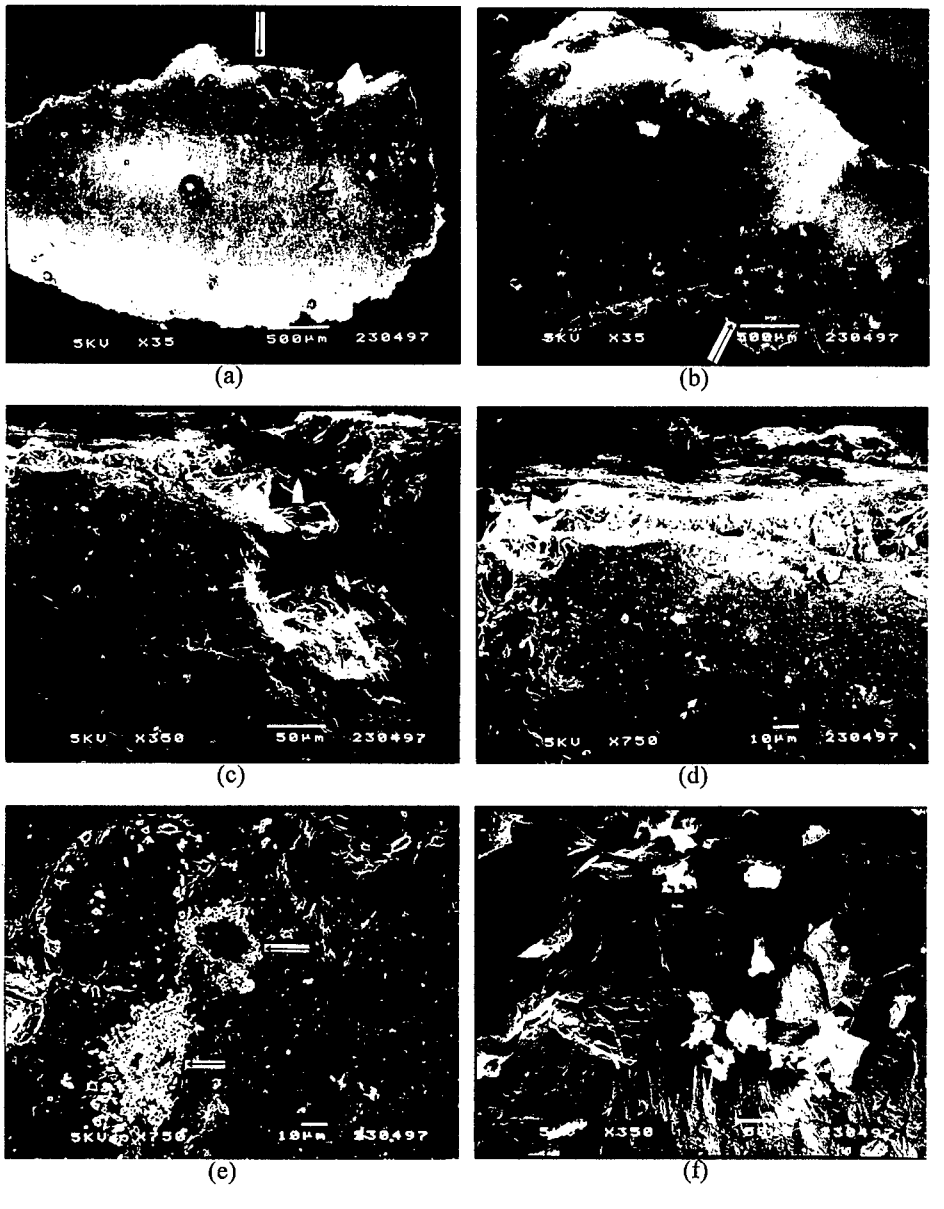

Figure 9. Recovered Samples of AsRd-RDX after an I.I.H. of 20 cm.

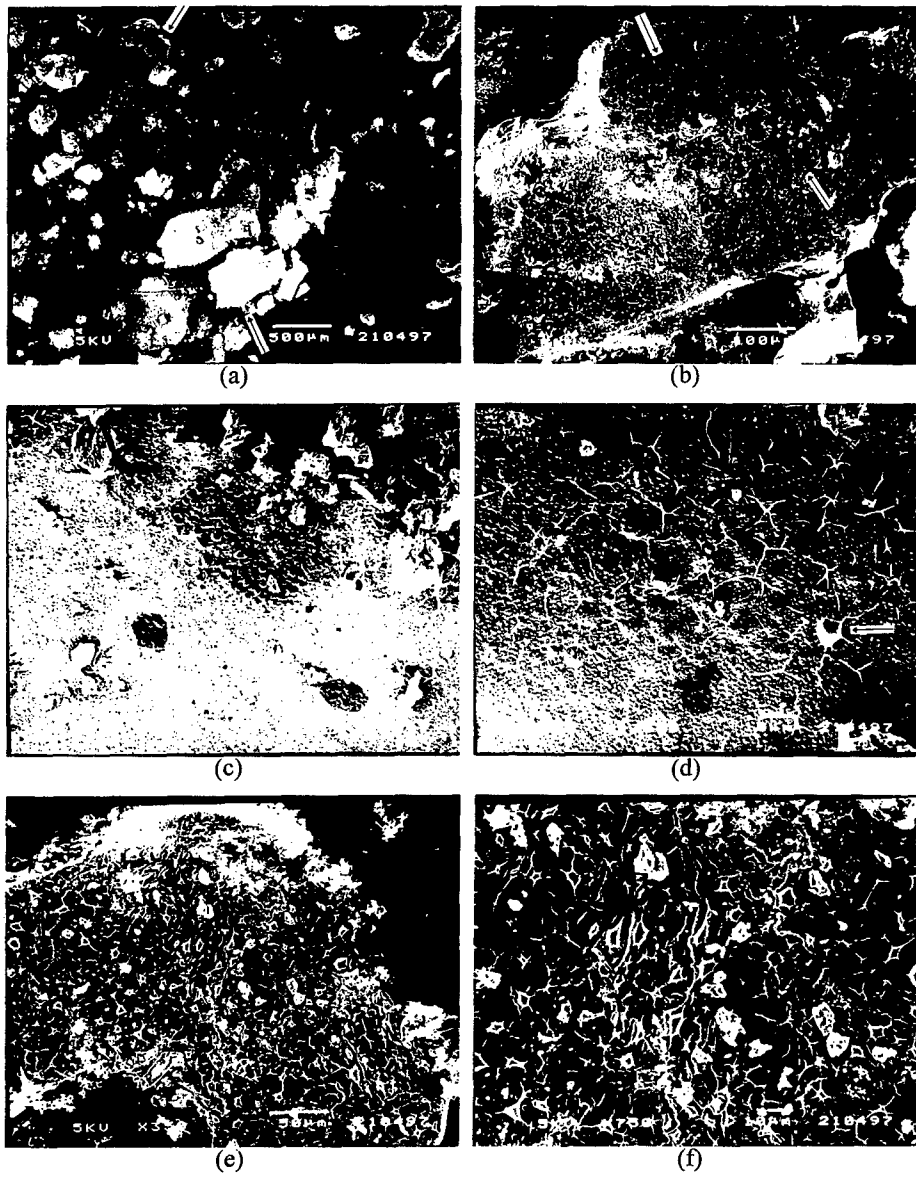

Figure 10. Recovered Samples of AsRd-RDX after an I.I.H. of 80 cm.

5. CONCLUSIONS

Mechanical deformation of RDX crystals via impact loading results in the RDX being sensitised. Increasing the I.I.H. from 20 cm to about 80 cm produces a corresponding increase in sensitisation of the AsRd-RDX by increasing the dislocation pile-up concentration (potential hot spots) and hence reducing the required drop height for a subsequent ignition event. Above an I.I.H. of 80 cm, reduced sensitisation occurs and a slightly higher impact height was then required to bring about an ignition event.

The dislocation pile-up theory sufficiently describes the sequence of events from an I.I.H. of 20 cm up to an I.I.H. of 80. Above an I.I.H. of 80 cm, reduced sensitisation may indicate the operation of a different mechanism where blunting of the initial dislocation pile-up occurs - effectively reducing the initial stress concentration which existed at the pile-up. Consequently a slightly higher impact height is required to bring about an ignition event.

SEM studies on samples impacted at an I.I.H. of 20 cm revealed typical brittle fracture surfaces; evidence of shear banding, cracks and foreign inclusion were also found. Studies on samples impacted at an I.I.H. of 80 cm showed, in addition to the observations mentioned for samples impacted at an I.I.H. of 20, that the cracks were filled with previously molten material believed to be a known decomposition product of thermally degraded RDX.

6. REFERENCES

1. W. L. Elban and R. W. Armstrong. 7th Symp. on Detonation, pp. 976-985, June 1981. "Microhardness Study of RDX to Assess Localised Deformation and its Role in Hot Spot Formation".

2. B. Henderson, "Defects in Crystalline Solids", Edward Arnold (Publishers) Ltd. ... (1972).

3. S. N. Heavens and J. E. Field. Proc. R. Soc. Lond. A. 338, pp. 77-93, 1974. "The Ignition of a Thin Layer of Explosive by Impact".

4. Sensitiveness Collaboration Committee: Manual of Tests; S.C.C. No 3, 1977. " Explosives Hazard Assessment".

5. A. M. Freudental and J. H. Weiner. J. Appl. Phys. Vol. 27, No. 1, pp. 44-50, 1956. "On The Thermal Aspect of Fatigue".

6. J. S. Eshelby and P. L. Pratt. Acta Metall. Vol. 4, pp. 560-562, 1956. "Note on the Heating Effect of Moving Dislocations".

7. C. S. Coffey and R. W. Armstrong in Shock Waves and High Strain Rate Phenomena in Metal. Editors: M. A. Meyers and L. E. Murr.
"Description of 'Hot Spots' Associated with Localised Shear Zone in Impact Tests ".

8. C. S. Coffey. Phys. Rev. B, Vol. 24, No. 12, pp. 6984-6990, 1981. "Phonon Generation and Energy Localisation by Moving Edge Dislocations".

9. R. W. Armstrong, C. S. Coffey and W. L. Elban. Acta Metall. Vol. 30, pp. 2111-2116, 1982. "Adiabatic Heating at Dislocation Pile-up Avalanche".

10. N. M. Madhava and R. W. Armstrong, Metall. Trans. Vol. 5, pp. 1517- , 1974.

11. F. P. Bowden and A. D. Yoffe. "Initiation and Growth of Explosion in Liquids and Solids" ...(1952).

12. J. Starkenberg, 7th Symp. on Detonation, pp. 3-16, June 1981. "Ignition of Solid High Explosives by the Rapid Compression of an Adjacent Gas Layer".

13. F. P. Bowden and O. A. Gurton, Proc. R. Soc. Lond. A. 198, pp. 337-349, ...(1974). "Initiation of Solid Explosives by Impact and Friction: The Influence of Grit".

14. S. Ljunberg, Nobel Hefte Vol. 24, pp. 40-, 1958.

15. G. Gibbons, Ballistic Res. Lab., private communication to J. Starkenberg[12].

16. P. J. Halfpenny, K. J. Roberts and J. N. Sherwood, J. Mat. Sci. Vol. 19, pp. 1629-1637, ...(1984). "Dislocations in Energetic Materials".

17. J. K. A. Azumu, B. J. Briscoe and M. M. Chaudhri, J. Phys. D. Appl. Phys. Vol. 9, pp. 133, ...(1976).

18. W. Connick and F. G. J. May, J. Cryst. Growth, Vol. 5, pp. 165 , ...(1969). "Dislocation Etching of Cyclotrimethylene-trinitramine Crystals".

19. C. S. Choi, Acta. Cryst., Vol. B28, pp. 2857-2862, ...(1972). "The Crystal Structure of Cyclotrimethylene-trinitramine".

20. W. L. Elban, J. C. Hoffsommer and R. W. Armstrong, J. Mats. Sci., Vol. 19, pp. 552-566, ...(1984). "X-ray Orientation & Hardness Experiments on RDX Explosive Crystals".

21. J. P. Hirth, "Theory of Dislocation", McGraw-Hill, ...(1968).

22. P. G. Fox and J. Soria-Ruiz, Proc. R. Soc. Lond. A. 317, pp. 79-90, ...(1974). "Fracture-Induced Thermal Decomposition in Brittle Crystalline Solids".

23. K. N. G. Fuller, P. G. Fox and J. E. Field, Proc. R. Soc. Lond. A. 341, pp. 537-557, ...(1974). "The Temperature Rise at the Tip of Fast-Moving Cracks in Glassy Polymers".

24. W. L. Elban, J. C. Hoffsommer, D. J. Glover, C. S. Coffey and R. W. Armstrong, "Microstructural Origins of Hot Spots in RDX Explosive and Several Reference Inert Materials", Report Number: NSWC MP 84-358, November 1984.

25. W. L. Elban, J. C. Hoffsommer, C. S. Coffey, K. C. Yoo and R. G. Rosemeier, "Microstructural Origins of Hot Spots in RDX Explosive and a Reference Inert Material", Report Number: NSWC MP 84-200, May 1984.

26. J. C. Hoffsommer, D. J. Glover and W. L. Elban, J. Ener. Mats. Vol. 3, pp. 149-167, ...(1985). "Quantitative Evidence for Nitroso Compound Formation in Drop-Weight Impacted RDX Crystals".

Characterization of electro-exploded aluminum (Alex)

Roland Sandén, Defence Research Establishment, FOA, Sweden

Abstract

A nanostructured aluminum material, "Alex", from the Argonide Corporation, USA, has been studied with the aim of using it both as fuel in high explosives and in rocket propellants.

The Alex material is much easier oxidized than ordinary aluminum is. Differential scanning calorimetry measurements show that, when heated in air, the Alex material is partly oxidized resulting in a large exotherm starting at around 450^0C. With an ordinary aluminum powder, A-100 from Carlfors Bruk, Sweden, a much smaller exotherm is obtained.

Microcalorimetry measurements, carried out at 65^0C and at 45^0C, show that Alex has good stability in dry air but that it reacts quickly, though not vigorously, at high relative humidity, releasing much heat.

The BET surface area for a sample of Alex was measured to about 12 m^2.

Drop weight tests indicate that the Alex material has a very low sensitivity to impact. Tests were carried out both on the pure material and on HTPB/AP propellants containing 10% Alex.

The experiments carried out so far shows that Alex reacts easily with oxygen and water. A substantial part of it is easily oxidized at temperatures far below the melting point. It can, however, be handled with safety. It seems to be well worth to continue with further studies on this material.

Introduction

The phenomenon of electro-explosion of a metal wire (EEW) has been much studied in recent years. Reports in international symposia and numerous articles in scientific magazines have been published. However, not much have been published on producing fine aerosols and on research on the properties of the materials produced. In 1996, properties of a type of ultra-fine aluminum powder, formed by the EEW process, was reported [1]. The material was called "Alex". According to this report, after 1970, studies started in the High Voltage Institute in Tomsk, Russia, on the production of ultra-fine aluminum particles by the EEW process. In these experiments the explosion of the wire was achieved by powerful impulses of electrical current in a vessel filled with a non oxidizing gas of either hydrogen, argon or helium, and the particles were collected by sedimentation. The material is now made also by the Argonide Corporation in Florida, USA. It is suggested to be used as a fuel in pyrotechnics, explosives and propellants. In 1996, studies of a superfine aluminum material, "SAl", was reported in China [2]. The SAl material may be similar to the Alex material.

By using ultra-high resolution scanning electron microscopy the Alex powder was shown to consist of irregular clumps of small particles, approximately 50-100 nm in size, with a substantial amount of crystal defects. In the act of exotherming, the recrystallization offers remarkable new surface for reactions with oxidizers as in propellant mixes, and even fast enough to contribute to reactions in high explosives" (letter from the Argonide Corp.). A coating of oxide of about 3 nm on the particles was also shown. Chemical analysis showed that the powder consisted of about 92-95% aluminum. Thermal analysis (DTA) indicated that the material contains some conserved energy which in these experiments was released when it was heated to about 450^0C.

Possible applications for the Alex material could be to increase the reaction rate in explosives. It is of special intererest for under-water weapons, where ordinary aluminum may react too slowly and in rocket propellants when high burning rates are of great importance. A problem that occures with aluminum containing composite propellants is that when the charges burn in rocket motors, the particles of aluminum melt and agglomerate to large droplets. These droplets generally do not burn completely within the engine resulting in a substantial loss in performance. In this case a type of aluminum with special burning properties like Alex, is of interest [1].

Experiments

The Alex material

The Alex material was used as received. It is a fine gray powder. It was delivered carefully sealed in polyethylene containers, with about 0.23 kg of the material in each. The bulk density is said to be about 1.0 g /cm^3 and the particle size about 70-100 nm. In preliminary experiments at FOA the volume weight was found to be 0.34 g/cm^3 when the powder was poured over into a graduated measuring glass and slightly shaken. By light compressing of the powder, manually in a cylinder, the volume weight was increased to 0.92 g /cm^3.

Results from elemental analysis performed at different laboratories differed a lot. At Carlfors Bruk, Sweden, a method based on treatment of the sample with sodium hydroxide was used.

The amount of hydrogen gas evolved is a measure of the aluminum content. The result for one batch was 95.6% aluminum.

A sample of Alex was studied by X-ray diffraction. The results were similar to those for ordinary pure metallic aluminum. The complicated internal structure was probably transformed to the ordinary aluminum structure by the strong X-ray radiation, similar to what may happen with this material in ordinary scanning electron microscopy (SEM) measurements (information from the Argonide Corp.). The only conclusions that can be drawn from these measurements are that the purity of the material is at least 90% metallic aluminum and that its internal structure is sensitive to the X-ray treatment.

For comparison a reference material of an ordinary fine particle size aluminum powder, type A-100, from Carlfors Bruk, Sweden, was used. The bulk density of this material is about 1.0 g/cm^3. More than 92% has a particle size of less than 60 μm and 70-90% has a particle size of less than 42 μm. Its aluminum content is at least 97.5%.

Drop weight tests

Tests were carried out on samples of Alex mixed with hydroxyl terminated polybutadiene (HTPB), cured with the diisocyanate IPDI. The samples contained 50% Alex. Tests were also carried out with the pure powder and a composite propellant of the HTPB/AP/Al type with 60% AP and 10 % Alex as the aluminum ingredient (AP= ammonium perchlorat, about 5 μm particle size). A 2.0 kg hammer was used, and it was dropped from heights of at most 140 cm.

Differential scanning calorimetry (DSC) and thermogravimetric analysis (TGA)

Experiments were carried out with Alex in air and in inert atmosphere (argon). If not otherwise said the heating rate was 10^{0}C/min. It was not easy to find an apparatus which gave reproducable results at high temperatures. Therefore experiments were carried out at different laboratories. The apparatuses used were Mettler DSC 820 and Seiko DSC 6200. For measuring up to 600^{0}C the Mettler 4000 apparatus was used. For thermogravimetric measurements the Mettler TGA 820 apparatus was used. Measurements were carried out at temperatures up to 700^{0}C in aluminum oxide crucibles.

Microcalorimetry

The measurements were performed with a computerized LKB 2277 instrument. Measurements were carried out at 45^{0}C and at 65^{0}C. The measurement vessels (2.5 ml glass ampoules) were charged with about 2.0 mg of Alex or about 20 mg of aluminum A-100. In some experiments after a stable power signal was reached, water was added to the vessels in very small open ampoules so that a 100% RH humidity was obtained without any direct contact of liquid water with the sample.

Surface BET measurements

The measurements were performed in a Micromeritics/Gemini apparatus. The active surface as well as the pore volume were measured.

Results

Drop weight tests

No reaction was seen for any of the samples, not even when the 2.0 kg hammer was dropped from a height of 1.40 m. See Table 1. The Alex material can be regarded as very insensitive to impact treatment.

Differential scanning calorimetry and thermogravimetric analysis

In all DSC experiments, when run in air, a large exotherm appeared at temperatures around 400^{0}C. This shows that no quick oxidation occurres in air up to about 400^{0}C. Figure 1 and 2 show typical thermograms in the temperature range of 400-700^{0}C of Alex and of A-100 in air. The amount of energy released differed at different experiments and was at the most 5.5 MJ/kg for Alex and 0.1 MJ/kg for A-100. In all cases the melting point endotherm appeared at around 630 to 660^{0}C. After cooling, the Alex residue was a gray powder looking rather similar to unreacted Alex. It could be initiated and burned in air.

It seems to be difficult to measure any structurally bound energy that may occur in the Alex material. With the equipment used for high temperature measurements, it was very difficult to avoid small amounts of air to penetrate into the sample. For measurements up to about 600^{0}C, it is possible to use sealed aluminum crucibles. When those were used no heat evolution was seen. Figure 3 shows thermograms of a sample of Alex which was first heated in a sealed aluminum crucible and then run a second time in air with the crucible punctured. With the crucible punctured a large exotherm, similar to what can be seen in Figure 1, appeared. The crucibles were weighed before and after every DSC was run. When the samples were heated in sealed crucibles there was no increase in weight. When the crucibles were punctured and heated in air the Alex samples increased their weight with about 15% and the A-100 samples with less than 1%. The A-100 material reacted, however, to some degree. Figure 4 shows a thermogram for a sample of A-100 in punctured crucible in air at high amplification.

The TGA experiments were carried out in argon atmosphere. It was difficult to avoid small amounts of air to reach the sample in the apparatus. The Alex material reacted with traces of oxygen, which could be seen as an increase in weight, beginning at a temperature of about 500 ^{0}C. To avoid oxidation from traces of air, the experiments had to be performed very carefully. Argon was added to the apparatus. The sample was added to the crucible in a flow of argon and the crucible was equipped with a lid. Figure 5 shows the increase in weight for a sample of Alex when heated in air and in argon. With no weight increase of the sample during the heating, no heat evolution was seen.

Microcalorimetry

Figure 6 shows the heat flow for samples of Alex when stored in the instrument at 45^{0}C and at 65^{0}C. It was stored for more than 9 days in dry oxygen. Only a small heat evolution can be seen. After the initial deviation the heat flow is very small. Even if the initial deviation is included the total heat evolved is small. In another experiment after one day in the microcalorimeter, the ampoule was opened and new dry oxygen was added. Here a similar curve was obtained with a new initial deviation similar to the first deviation. One of the samples was taken for DSC measurements. A thermogram similar to that for samples of fresh Alex was obtained. It seems that the endo- and exotherms which could be seen the first 1-2

hours from the start of the calorimeter do not emanate from the sample but from initial deviations of the instrument.

In other experiments, samples were kept for 20 hours at 45 ^{0}C in air atmosphere in sealed ampoules. Then the relative humidity was raised to 100 % by bringing small test tubes with water into the ampoules. No heat, or only small amounts of heat, were evolved before the humidity was raised. In humid atmosphere a large amount of heat was quickly evolved, though the reaction was not vigorous. See Figure 7. Because of the initial deviation the amount of heat evolved was difficult to estimate, but it seems to be near to the total reaction energy of the formation of aluminum oxide from aluminum. For comparison the sample of ordinary aluminum powder, A-100, was treated in the same way as the Alex samples. In this case only a very small heat flow was observed. Compared to what was obtained with the Alex samples the reaction rate for the A-100 material with water seemed to be much slower.

Surface BET measurements

The BET surface area for a sample of Alex was measured to 12 ±2 m^2/g and the adsorption total pore volume 0.011 cm^3/g. The same sample of the material was kept for about one month in open air in the laboratory and then measured again. This time the value obtained for the BET surface area was 4.7 m^2/g and the adsorption total pore volume 0.0024 cm^3/g. For a sample of ordinary aluminum powder, A-100, the BET surface area was measured to 0.10 m^2/g and the total adsorption pore volume was measured to 0.0002 cm^3/g.

Discussion

The drop weight tests indicate that the Alex material has a very low sensitivity to impact treatment.

The DSC results indicate that the Alex material, compared to ordinary aluminum, reacts very fast with oxygen when heated. In spite of this, the material is remarkably stable up to about 400^{0}C in air under dry conditions. In the DSC experiments the amount of energy evolved when heated up to 700^{0}C, could be as high as 5 MJ/kg. This is about the same as the heat of explosion for the well-known explosive TNT, which is 5.07 MJ/kg. The heat of combustion of ordinary aluminum is 31.0 MJ/kg. Aluminum melts at about 660^{0}C. The heat of melting is about 390 J/g. For the Alex material the melting is shown as an endotherm at around 630^{0}C-660^{0}C close to the foregoing exotherm. For measureing at high temperatures it is important to use proper types of crucibles. Copper crucibles are not useful because aluminum forms an alloy with the copper. Crucibles made of alumina are useful. When Alex was heated up to 600^{0}C in sealed aluminum crucibles, no weight change and no heat evolution was seen. If there is any structurally bound energy in Alex the amount of it seems to be very small.

The microcalorimeter experiments where Alex was treated with humid air shows clearly that Alex reacts very easily with water, so when handled it has to be protected from moist air. No clear reactions could be seen in dry air at 45^{0}C (RH was 30% at room temperature), but when the relative humidity was raised to 100%, strong exothermic reactions occurred quickly. The amounts of energy released in wet air was difficult to measure because of the initial deviations of the instrument, but it was estimated to about 15 MJ/kg. Theoretically 15.14 MJ/kg is evolved when aluminum reacts with water to give the oxide (Al_2O_3) and hydrogen. The reaction seemed to start as soon as the humid air appeared. With a sample of the ordinary

aluminum, Carlfors A-100, using the same conditions, only a very small reaction occurred. This shows that the Alex material reacts much easier with water than ordinary aluminum.

The results from the surface BET measurements show, as expected, that the surface area of the Alex material is much larger than the surface area of ordinary small particle size aluminum (Carlfors A-100). The pore volume of Alex is very small. When a sample of Alex was stored in an open vessel in the laboratory for one month the BET surface area decreased considerably. This indicates that Alex in open air and ambient temperature slowly deteriorates.

In summary, the main conclusions are as follows:

1. When the superfine aluminum material, Alex, is slowly heated in air it is partly oxidized and a substantial amount of heat is evolved. This reaction starts far below the melting point, leaving a metallic powder residue. With ordinary aluminum powder, only very little of this kind of heat evolution is seen.

2. The Alex material is very insensitive to impact treatment.

3. The Alex material is stable and easy to handle in dry conditions. In air at high humidity, and at slightly elevated temperature, it reacts quickly but not vigourosly under heat evolution.

4. The BET surface area for Alex was measured to about 12 m^2/g. For an ordinary fine particle size aluminum powder, Carlfors A-100, a value of 0.1 m^2/g was obtained.

5. The experiments carried out so far indicates that Alex is an interesting energetic material and that it is well worth to continue with further studies on this material.

References

1. Ivanov, G V and Tepper F 'Activated' Aluminum as a Stored Energy Source for Propellants, Conference in Challenges in Propellants and Combustion 100 Years After Nobel, Stockholm May 1996.

2. Deng, Kangqing and Wang, Guangtian The characteristics and mechanism for superfine aluminum powder combustion. Proc. int. Autumn Semin. Propellants, Explos. Pyrotech. 1996, 311-321.

Acknowledgement

Many thanks to Mr Frederick Tepper at the Argonide Corporation, USA, and to my colleague Mr Niklas Wingborg at the Defence Research Establishment, FOA, Sweden, for valuable discussions.

Table I. Drop weight tests on Alex containing compositions. Weight of hammer: 2.0 kg. Height of fall: 1.40 m.

Composition	Components (%)				Reaction
No	Alex	HTPB binder	AP (3-4 μm)	Iron oxide	
1	100	--	--	--	No reaction
2	10	30	60	--	No reaction
3	10	25	50	15	No reaction

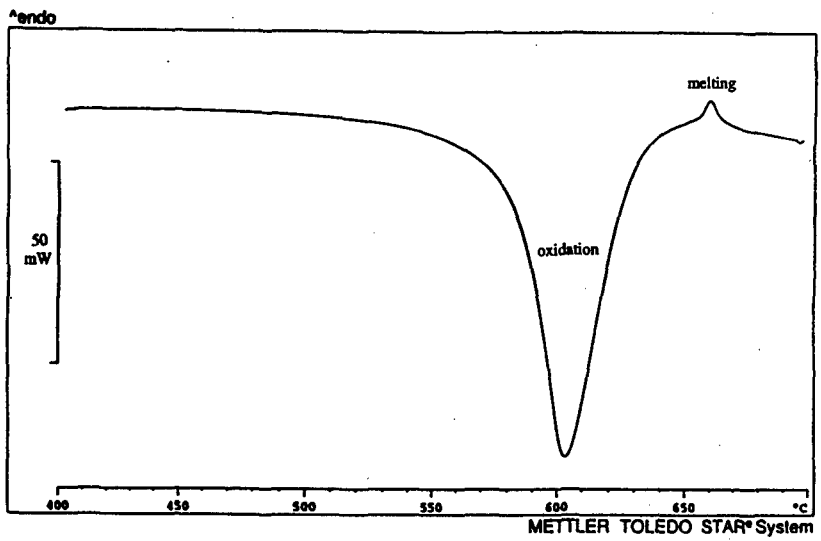

Figure 1. DSC thermogram for Alex in air.

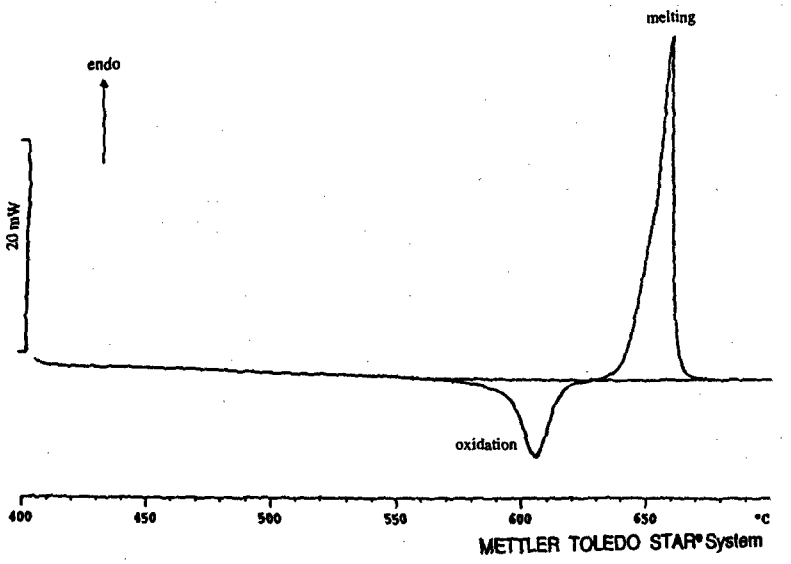

Figure 2. DSC thermogram for aluminum, A-100, in air.

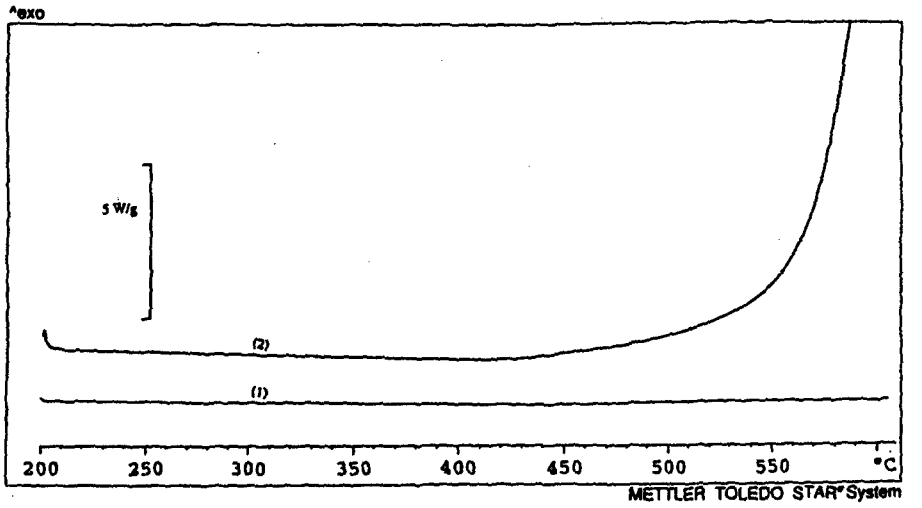

Figure 3. DSC thermograms for Alex in sealed crucible (1) and in air (2).

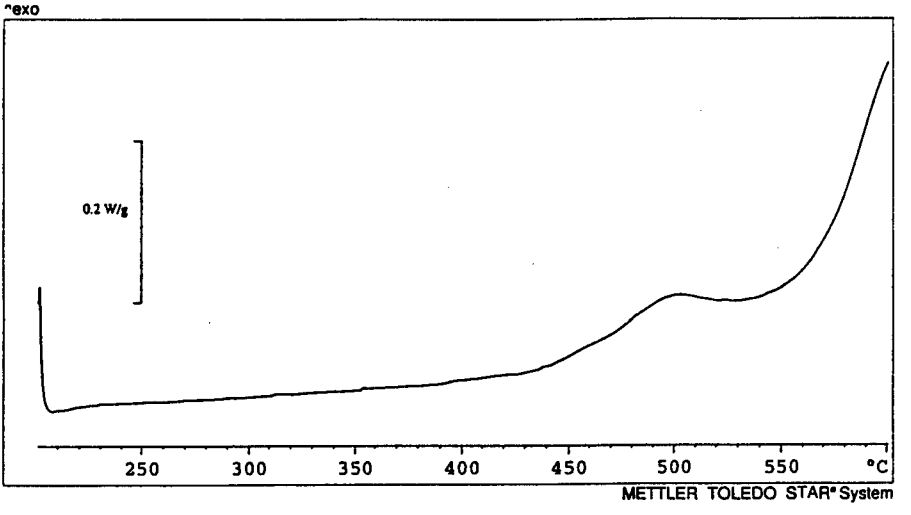

Figure 4. DSC thermogram for A-100 in air.

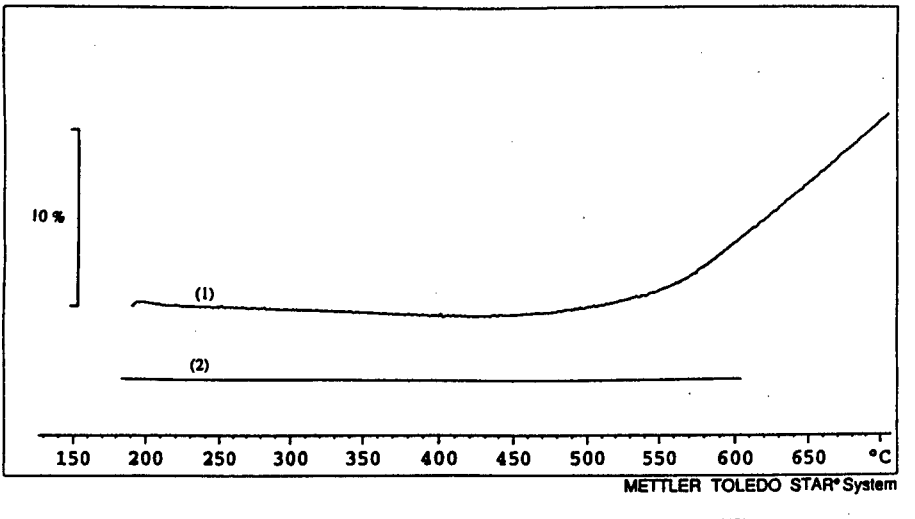

Figure 5. TGA experiments. Weight increase for Alex in air (1) and in argon (2).

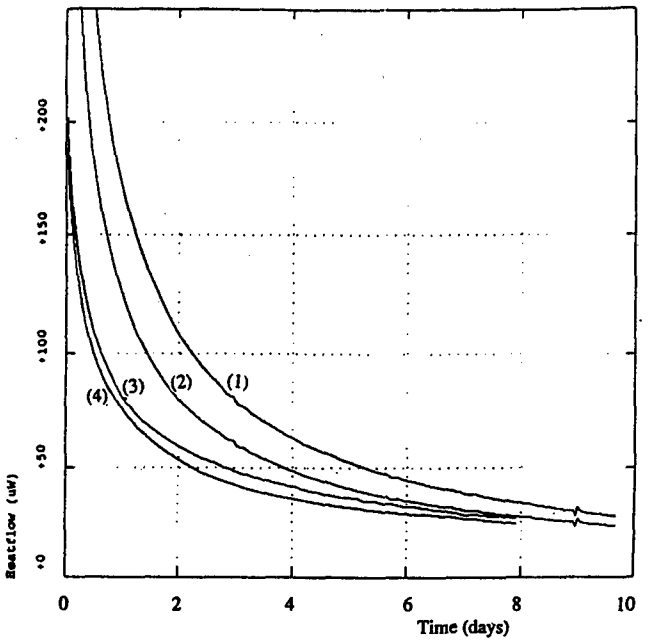

Figure 6. Microcalorimetry. Heat flow for samples of Alex in dry oxygen at 65°C (1, 2) and at 45°C (3, 4). The amounts of Alex were 36 mg, 42 mg, 74 mg and 18 mg in sample number 1, 2, 3 and 4, respectively.

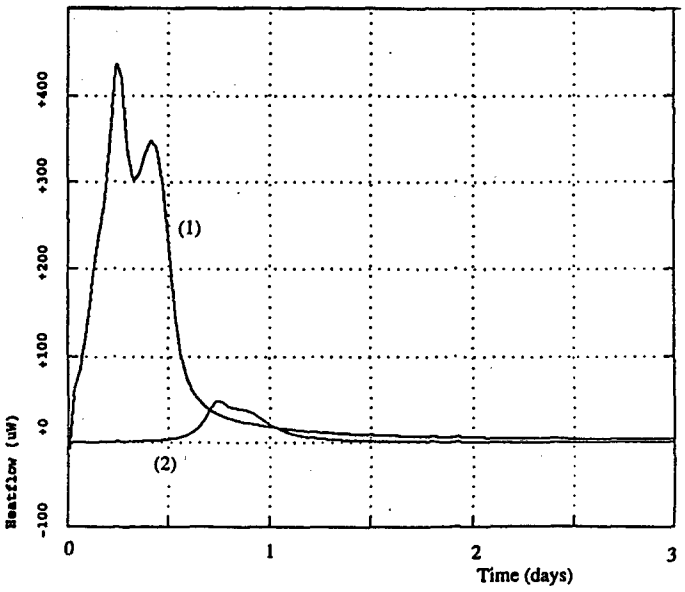

Figure 7. Heat flow for Alex (1), 1.90 mg, and for A-100 (2), 19.88 mg, in humid air at 45 °C.

Bestimmung der Oberflächenenergie von Polymerbindern und Explosivstoffpartikeln

U. Teipel, E. Marioth, T. Heintz, I. Mikonsaari
Fraunhofer Institut für Chemische Technologie (ICT), Pfinztal, D

Abstract

The surface free energy of the filler and the matrix considerably influences the quality of the coupling between these two components to a compound. This contributes to the processing properties and the ultimate properties of the composite. These characteristic values can only be measured indirectly. In case of polymers the determination of the surface free energy by measuring contact angles is a proven technique. The contact angles have been measured by a modified Wilhelmy-method. For HTPB and Viton A the surface free energy has been determined from the theory of Owens, Wendt, Rabel and Kaelble. Five different types of HTPB and Viton A as binder material for particles of explosives have been examined.

1 Einleitung

In vielen Bereichen finden partikuläre Polymersysteme ihre spezifische Anwendung. Der Füllstoff kann verschiedene Funktionen übernehmen, welche die Eigenschaften des Polymers anwendungsspezifisch unterstützen, bzw. erst den Einsatz ermöglicht. Füllstoffe können die optischen, mechanischen und chemischen Eigenschaften der Polymere entscheidend beeinflussen. Viele Anwendungen sehen das Polymer als Hilfsmittel, den eigentlichen Funktionsträger in Partikelform zu binden. Bei der Einarbeitung energetischer Materialien in eine Matrix steht der Füllstoff als reaktiver Teil eines Compositewerkstoffes im Vordergrund.

Die Herstellung solcher Systeme wird durch Beschichtung, Rühren oder Kneten der festen Phase in eine flüssige Phase erreicht. In jedem Fall wird die Grenzfläche Feststoff-Dampf durch eine Grenzfläche Feststoff-Flüssigkeit ersetzt. Dieser Vorgang wird als Benetzung bezeichnet. Geschieht der Vorgang der Benetzung spontan und vollständig, wird von vollständiger Benetzung oder Spreitung gesprochen. Muß zur Herstellung eines guten Verbundes zusätzliche Arbeit in das System gesteckt werden, ist die Benetzung unvollständig. Dabei besteht die Gefahr, daß Blasen an der Grenzfläche

eingeschlossen werden, die die Eigenschaften des Verbundes entscheidend negativ beeinflussen können. Durch Zugabe von oberflächenaktiven Stoffen in die flüssige Phase oder durch Aufbringen von Sorptionsschichten auf die Festkörperoberfläche läßt sich das Benetzungsverhalten in weiten Grenzen variieren.

Ein Maß für die Benetzbarkeit ist der Benetzungs- oder Randwinkel. Er ist jedoch keine stoffspezifische Eigenschaft, sondern abhängig von den grenzflächenenergetischen Größen der beteiligten Phasen. Um also Voraussagen über das Benetzungsverhalten von Stoffkombinationen treffen zu können, müssen die grenzflächenenergetischen Größen bekannt sein.

In diesem Beitrag wird die Methode zur Ermittlung der Freien Grenzflächenenergie polymerer Binder HTPB und Viton A vorgestellt und die Ergebnisse präsentiert.

2 Grundlagen

2.1 Definition der Freien Grenzflächenenergie

Die freie Oberflächenenergie ist die reversible Arbeit, die bei konstantem Volumen und konstanter Temperatur aufgewendet werden muß, um die Oberfläche zu vergrößern.

$$\gamma_{ij} = \left.\frac{\partial F}{\partial A_{ij}}\right|_{V,T} \tag{1}$$

mit A_{ij} = Grenzfläche zwischen den Phasen i und j

2.2 Grundlagen und Modelle

Während die Grenzflächenspannungen von Flüssigkeiten ohne großen Aufwand direkt meßbar sind, ist dies bei Festkörpern aufwendiger. Ein Weg erschließt sich aus der Young´schen Gleichung:

$$\cos\delta = \frac{\gamma_S - \gamma_{SI}}{\gamma_I} \tag{2}$$

mit: δ= Randwinkel [°], γ_I=Flüssigkeitsoberflächenspannung [mN/m], γ_{SI}=Grenzflächenspannung [mN/m], γ_S= Festkörperoberflächenspannung [mN/m]

Wenn der Kontaktwinkel einer Flüssigkeit mit bekannten Eigenschaften auf einem Festkörper gemessen werden kann, sind die Freien Grenzflächenenergien der

Phasengrenzen fest-gasförmig und fest-flüssig unbekannt. Um die Freie Grenzflächenenergie fest-gasförmig zu ermitteln, gibt es verschiedene Modelle. Für Polymeroberflächen wird das Modell von Owens, Wendt, Rabel und Kaelble empfohlen (WU, 1982) und dieser Arbeit angewendet. Dieses Modell formuliert die Freie Grenzflächenenergie als Summe aus dispersen und polaren Anteilen (Gleichung 3).

$$\gamma = \gamma^{\text{dispers}} + \gamma^{\text{polar}} \tag{3}$$

Ausgehend davon, daß nur die beiden polaren Anteile und die beiden unpolaren Anteile des Grenzflächenpaares miteinander in Wechselwirkung treten, wird folgende Beziehung für das geometrische Mittel der freien Grenzflächenenergie formuliert:

$$\gamma_{12} = \gamma_1 + \gamma_2 - 2 \cdot \left(\sqrt{\gamma_1^d \cdot \gamma_2^d} + \sqrt{\gamma_1^p \cdot \gamma_2^p} \right) \tag{4}$$

Indices: 1: Phase 1, 2: Phase 2; d; disperser Anteil, p: polarer Anteil

In der Praxis bedeutet dies, daß die polaren und dispersen Anteile der Meßflüssigkeiten bekannt sein müssen, um mit dieser Gleichung und der Kenntnis des Kontaktwinkels die Freie Grenzflächenenergie des Feststoffes ermitteln zu können. Als Ergebnis erhält man eine Geradengleichung, aus deren Achsenabschnitt der disperse Anteil und aus deren Steigung der polare Anteil der freien Grenzflächenenergie hervorgeht (Kombination von Gleichung 1 und 4):

$$y = m \cdot x + b \tag{5}$$

$$x = \sqrt{\frac{\gamma_l - \gamma_l^d}{\gamma_l^d}} = \sqrt{\frac{\gamma_l^p}{\gamma_l^d}} \Rightarrow m = \sqrt{\gamma_s^p} \tag{6}$$

$$y = \frac{1 + \cos\delta}{2} \cdot \frac{\gamma_l}{\sqrt{\gamma_l^d}} \Rightarrow b = \sqrt{\gamma_s^d} \tag{7}$$

Ein weiteres Modell der Bestimmung der Oberflächenenergie geht auf Zisman zurück. Hier werden Kontaktwinkel von Flüssigkeitsreihen an einer Feststoffoberfläche bestimmt und der cos δ gegen die Oberflächenspannung der Flüssigkeit aufgetragen (Abbildung 2.1).

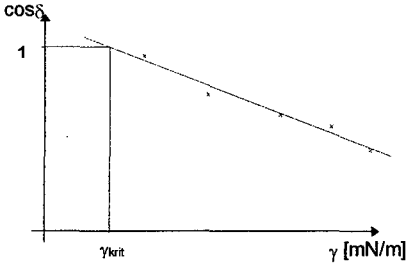

Abb. 2.1: Zisman-Auftragung zur Ermittlung der freien Grenzflächenenergie von Feststoffen

Für $\cos \delta = 1$ erhält man mit Hilfe der Ausgleichsgeraden den Wert γ_{krit}, der dem theoretischen Randwinkel von $\delta = 0°$ entspricht und als Freie Grenzflächenenergie des Feststoffs übernommen wird. Einschränkend für dieses Modell ist die Tatsache, daß es für die Verwendung ausschließlich unpolarer Flüssigkeiten entworfen wurde. Da das hier untersuchte Material HTPB die Neigung hat, in n-Alkanen zu quellen, konnte diese Auswertungsmethode nicht angewandt werden. Durch die Vielfalt der Modelle wird deutlich, daß das Verfahren der Kontaktwinkelmessung zur Bestimmung der freien Grenzflächenenergie nicht uneingeschränkt geeignet ist, quantitative Aussagen zu machen. Für die Bestimmung qualitativer Daten und zum Vergleich verschiedener Binder reicht diese Methode jedoch aus.

2.3 Ermittlung der Randwinkel

Um Randwinkel verschiedener Flüssigkeiten an Plättchen messen zu können, wurden Randwinkeluntersuchungen nach der Wilhelmy-Methode durchgeführt. Bei den Versuchen nach dem Prinzip der Wilhelmy-Platte wird ein Plättchen in eine Flüssigkeit eingetaucht und die Kraft gemessen, die durch die Oberflächenspannung der Flüssigkeit an dem Plättchen ausgeübt wird (Abbildung 2.2).

Der Randwinkel berechnet sich, wenn der Auftrieb der Platte und die Masse der angehobenen Flüssigkeit vernachlässigt werden kann, nach folgender Gleichung (8):

$$\cos\delta = \frac{F_W}{\gamma_l \cdot L} \tag{8}$$

mit L = benetzte Länge, F_W = Wilhelmy-Kraft

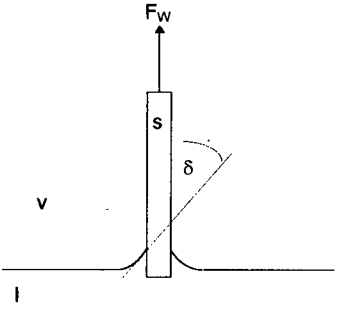

Abb. 2.2: Schema der eingetauchten Platte nach Wilhelmy

Wird die Platte in die Flüssigkeit getaucht und wieder zurück gezogen, lassen sich dynamische Randwinkel ermitteln. Als Resultat der Versuche erhält man einen dynamischen Vorrückrandwinkel und einen dynamischen Rückzugsrandwinkel. Die Vorteile dieser Randwinkelmessung im Vergleich zu der Vermessung eines liegenden Tropfens bestehen darin, daß sie reproduzierbar ist und der Randwinkel über einen vergleichsweise großen Bereich des Plättchens gemessen wird.

Aufgenommen wird die Kraft auf das Plättchen in Abhängigkeit von der Eintauchtiefe. Die Kraft, die auf das Plättchen wirkt, setzt sich aus zwei Komponenten zusammen. Die Wilhelmy-Kraft F_W wirkt nur an der Dreiphasengrenzlinie, also an der Flüssigkeitsoberfläche, und ist während des gesamten Eintauchvorganges bzw. während des Rückzugsvorganges konstant. Dies gilt nur unter der Voraussetzung, daß die Geometrie (Umfang entlang der Dreiphasengrenzlinie) des Plättchens konstant ist. Dann ist die Auftriebskraft F_A eine lineare Funktion der Eintauchtiefe (Gleichung 9):

$$F_A = \rho_l \cdot g \cdot l \cdot b \cdot d \tag{9}$$

mit l = Länge des Plättchens, b = Breite des Plättchens, d = Eintauchtiefe

Durch Trennung der Wilhelmy-Kraft (konstant) von der Auftriebskraft (abhängig von der Eintauchtiefe) kann jeweils für den Eintauchvorgang und das Herausziehen die Wilhelmy-Kraft berechnet werden. Der Randwinkel errechnet sich dann mit der Kenntnis der Flüssigkeitsdaten nach Gleichung (10).

$$\cos\delta(v) = \frac{1}{\gamma \cdot L} \cdot \left(F_W + F_A\right) \tag{10}$$

Die benetzte Länge der Probe, d.h. der Umfang der Dreiphasengrenzlinie, kann entweder unter Berücksichtigung von Rauhigkeiten durch Messung mit einer vollständig benetzenden Flüssigkeit ermittelt werden oder läßt sich bei glatter Oberfläche direkt messen.

2.4 Materialien

2.4.1 HTPB

Von HTPB (hydroxy-terminated-poly-butadien) wurden fünf verschiedene Rezepturen verwendet (Tabelle 2.1). Füllstoffe, wie Ruß oder Siliziumoxidpartikel wurden nicht eingesetzt.

Tabelle 2.1: Rezepturen der verwendeten HTPB-Proben

Bezeichnung	HTPB 1	HTPB 2	HTPB 3	HTPB 4	HTPB 5
HTPB R45 HT Eq: 1205	91,42	91,42	91,42	91,42	91,42
Irganox	1	1	1	1	1
IPDI difkt. Eq: 111	7,58	7,58	7,58	7,58	7,58
Summe	100	100	100	100	100
Katalysator	FeAA	FeAA	D22	TPB	FeAA
Menge	40 ppm	400 ppm	4 Tr./100g	200 ppm	200 ppm

2.4.2 Viton A

Viton A (Handelsname der Firma DuPont) ist ein Copolymerisat von Difluorovinyl und Hexafluorpropylen. Viton A zeichnet sich, wie alle Fluor-Kohlenstoff Elastomere, durch hohe Beständigkeit gegenüber Wärmeeinwirkung und Ölen aus und findet deshalb seine Hauptanwendung als Dichtungsmaterial.

Das Viton A lag als linsenförmiges Material (Durchmesser ca. 4 mm) vor.

2.4.3 Meßflüssigkeiten

Bei der Auswahl geeigneter Meßflüssigkeiten steht zum einen die chemische Verträglichkeit hinsichtlich der untersuchten Elastomere im Vordergrund, andererseits muß die Oberflächenspannungen der verwendeten Flüssigkeiten ein möglichst weites Spektrum abdecken. Zur Anwendung kam destilliertes Wasser und Dekanol p.A. (Tabelle 2.2).

Tabelle 2.2: Daten der Meßflüssigkeiten bei 20 °C

	Wasser, dest.	1-Dekanol (p.A.)
Dichte ρ [g/cm^3]	0,99	0,83
Oberflächenspannung γ [mN/m]	72,8	28,8
polarer Anteil γ_l^p [mN/m]	51,0	6,3
disperser Anteil γ_l^d [mN/m]	21,8	22,5

2.4.4 Probenpräparation

Um Randwinkel nach der Wilhelmy-Methode bestimmen zu können, ist eine konstante Probengeometrie unerläßlich. Um störende Einflüsse durch Kanten möglichst gering zu halten, muß die Probe ein hohes Breite/Dicke-Verhältnis haben. Andererseits werden elastische Plättchen mit zunehmendem Breite/Dicke-Verhältnis instabil gegen Verformung.

Diese Bedingungen führten zu der hier verwendeten Methode der Präparation auf ein starres Trägerplättchen.

Das nicht ausgehärtete HTPB wurde auf Deckgläschen aufgebracht, wie sie aus der Mikroskopie bekannt sind. Erst nachdem sich auf der Glasoberfläche ein gleichmäßiger HTPB-Film gebildet hatte, wurden die Proben im Ofen ausgehärtet. Die Viton A Plättchen wurden ebenfalls auf Glasplättchen präpariert, um den oben genannten Ansprüchen hinsichtlich konstanter Geometrie und Steifigkeit zu entsprechen.Dazu wurden die Viton A-Linsen zunächst in Butylacetat p.A. gelöst.

Nach Eintauchen der Glasplättchen und Verdampfen des Lösungsmittels verblieb ein dünner Film (Dicke < 0,1 mm) von Viton A auf der Glasoberfläche. Vorversuche, die mit massiven Viton A-Plättchen durchgeführt worden waren, lieferten identische Randwinkel. Auffallend ist jedoch die höhere Reproduzierbarkeit der mit den beschichteten Glasplättchen ermittelten Ergebnisse.

3 Ergebnisse und Diskussion

3.1 Dynamische Vorrückrandwinkel

Zur Auswertung kamen Benetzungsuntersuchungen an den oben beschriebenen Platten nach der Wilhelmy-Methode. Die errechneten dynamischen Vorrückrandwinkel sind in Tabelle 3.1 aufgeführt.

Tabelle 3.1: Dynamische Vorrückrandwinkel (Mittelwerte) von Wasser und 1-Dekanol an den HTPB und Viton A Proben

	Wasser, dest.	1-Dekanol p.A.
Viton A	111,5 °	52,6 °
HTPB 1	94,0 °	24,8 °
HTPB 2	91,2 °	10,0 °
HTPB 3	90,6 °	19,5 °
HTPB 4	93,2 °	19,4 °
HTPB 5	92,7 °	21,0 °

Bei den verschiedenen HTPB-Plättchen sind die Unterschiede im Benetzungsverhalten mit Wasser gering. Eine quantitative Aussage über den Einfluß der verschiedenen Katalysatoren oder deren Gehalte ist aufgrund dieser Werte nicht möglich. Auffällig ist jedoch die Tendenz, die sich bei den Plättchen mit HTPB 1, 5 und 2 zeigt: Mit in dieser Reihenfolge zunehmendem Gehalt an FeAA sinken die gemessenen Randwinkel von 94 ° bei 40 ppm über 92,7 ° bei 200 ppm bis auf 91,2 ° bei 400 ppm. Die gleiche Tendenz zeigt sich ebenfalls an den Randwinkeln, die mit Dekanol aufgenommen wurden. Hier sanken die Randwinkel von 24,8 ° über 21,0 ° auf sogar 10 °.

Das HTPB 3 zeigte mit 90,6 ° den geringsten mit Wasser gemessenen Randwinkel, weist jedoch mit Dekanol einen mittleren Wert von 19,5 ° auf.

HTPB 4 weist mit Wasser einen relativ hohen Wert mit 93,2 ° für den Randwinkel auf, während bei Dekanol ein mit HTPB 3 vergleichbarer Wert von 19,4 ° gemessen wurde.

Interessant ist der Vergleich der Größenordnung der Randwinkel, die mit HTPB und Viton A gemessen wurden.

Die Randwinkelwerte von Viton A liegen sowohl mit Wasser, als auch mit Dekanol deutlich über den gemessenen Werten der HTPBs. Während Wasser an HTPB den benetzenden Bereich mit Werten knapp über 90 ° gerade nicht mehr berührt, liegt das System Viton A mit Wasser schon deutlich im nicht-benetzenden Bereich. Ebenso liegt der Randwinkel bei Dekanol deutlich höher, als bei den HTPB-Proben.

3.2 Ermittlung der Freien Grenzflächenenergie nach Owens, Wendt, Rabel und Kaelble

Wie in Abschnitt 2.2 erläutert, wird auf Grundlage der Gleichung (4) eine Geradengleichung aufgestellt. Die Steigung führt auf den polaren Anteil der Freien Grenzflächenenergie des Festkörpers, während der Achsenabschnitt den dispersen Anteil angibt.
Jede Randwinkelmessung mit einer Flüssigkeit ergibt einen Punkt zur Bestimmung der Geraden.

$$y = m \cdot x + b \tag{11}$$

Die dimensionslosen x-Werte sind durch die Meßflüssigkeit vorgegeben (Gleichungen (6) und (7)) und betragen für

- Wasser: $x = 1{,}52953$
- 1-Dekanol: $x = 0{,}53271$.

Die y-Werte (Einheit $(mN/m)^{1/2}$), die sich aus den Messungen der Elastomere mit den Flüssigkeiten ergeben, sind in Tabelle 3.2 aufgeführt.

Tabelle 3.2: Aus den Randwinkelversuchen ermittelte y-Werte

	y-Werte [(mN/m)$^{1/2}$]	
	Wasser	1-Dekanol
Viton A	4,9414	4,8618
HTPB 1	7,2546	5,7700
HTPB 2	7,6351	6,0029
HTPB 3	7,7167	5,8754
HTPB 4	7,3632	5,8771
HTPB 5	7,4312	5,8480

Die aus den zwei x-Werten und den jeweiligen y-Werten errechneten Geradengleichungen lauten für die entsprechenden Elastomeren wie folgt (Tabelle 3.3):

Tabelle 3.3: Errechnete Geradengleichungen für die Systeme Viton A bzw. HTPB mit Wasser und 1-Dekanol

	Geradengleichung
Viton A	$y = 0{,}0799 \cdot x + 4{,}8192$
HTPB 1	$y = 1{,}4894 \cdot x + 4{,}9766$
HTPB 2	$y = 1{,}6375 \cdot x + 5{,}1306$
HTPB 3	$y = 1{,}8472 \cdot x + 4{,}8913$
HTPB 4	$y = 1{,}4908 \cdot x + 5{,}0829$
HTPB 5	$y = 1{,}5882 \cdot x + 5{,}0019$

Aus diesen Geradengleichungen gehen nach den Gleichungen (6) und (7) die polaren und dispersen Anteile hervor, deren Addition zur Freien Grenzflächenenergie der Elastomere führen.

In Tabelle 3.4 sind die polaren und dispersen Anteile, sowie die Freien Grenzflächenenergien der Elastomere dargestellt.

Tabelle 3.4: Polare, disperse Anteile und Gesamtsumme der Freien Grenzflächenenergie von Viton A und HTPB 1 bis 5

	Polarer Anteil der Freien Grenzflächenenergie γ_s^p [mN/m]	Disperser Anteil der Freien Grenzflächenenergie γ_s^d [mN/m]	**Gesamtsumme der Freien Grenzflächenenergie γ_s [mN/m]**
Viton A	0,01	23,22	**23,23**
HTPB 1	2,22	24,75	**26,97**
HTPB 2	2,68	26,32	**29,0**
HTPB 3	3,41	23,96	**27,37**
HTPB 4	2,22	25,84	**28,06**
HTPB 5	2,52	25,02	**27,54**

Das Viton A zeigt nach dieser Auswertung den geringsten Wert für die Freie Grenzflächenenergie und ist zudem fast völlig unpolar, was auch anhand der Struktur zu erwarten war. In der Literatur war ein Wert der Freien Grenzflächenenergie für Viton A von 23 mN/m angegeben und findet sich in den hier präsentierten Messungen bestätigt [Wu, Handbook of Polymer Science].

Für HTPB fand sich in der Literatur keine Angabe über die Freie Grenzflächenenergie. Im Vergleich liegen alle Werte über dem des Viton A. Der polare, wie der disperse Anteil steigt mit zunehmendem Gehalt an FeAA leicht an. Folglich ergibt sich in der Gesamtsumme ebenfalls eine ansteigende Tendenz. Der höchste polare Anteil wurde bei HTPB 3 ermittelt.

Der polaren Anteile bei HTPB 4 und 1 sind identisch, durch einen höheren dispersen Anteil bei HTPB 4 ist dessen Gesamtsumme höher.

Die höchste Gesamtsumme findet sich beim HTPB 2, die vor allem aus dem hohen Wert für den dispersen Anteil hervorgeht.

4 Zusammenfassung

Durch den Vergleich des Literaturwertes der Freien Grenzflächenenergie von Viton A und den in dieser Arbeit ermittelten Werten, kann die Anwendbarkeit des verwendeten Verfahrens bestätigt werden.

Für HTPB aus unterschiedlichen Rezepturen werden Werte für die Freie Grenzflächenenergie angegeben, mit denen der Verfahrensschritt Benetzung spezifischer gestaltet werden kann. Gehalte und Art der verwendeten Katalysatoren können die Höhe der Freien Grenzflächenenergie verändern. Dieser Punkt führt darauf, die Auswahl und Dosierung unter dem Aspekt der veränderten Wechselwirkungen mit dem Explosivstoffpartikel genauer zu betrachten. In weiteren Untersuchungen folgt die Erfassung der oberflächenenergetischen Größen von Explosivstoffpartikeln, um diese Grundlagen zu vervollständigen.

Liegen diese Daten vor, können mit Hilfe der Binder- und Partikeldaten Schwachstellen durch Blasen im Composite durch gezielten Eingriff in das Benetzungsverhalten verringert werden.

Microencapsulation of fine particles in a fluidized bed

M. Niehaus[1], W. Weisweiler[2]

[1]Fraunhofer Institute of Chemical Technology,
J. v. Fraunhofer-Str. 7, 76327 Pfinztal/Germany
Fax: +49(0)721/4640-111
E-mail: ni@ict.fhg.de

[2]Universität Karlsruhe, Institut für Chemische Technik (ICT),
Kaiserstr. 12, D-76128 Karlsruhe/Germany

Abstract

A microscale fluidized bed reactor for coating fine particles is being presented. In contrast to conventional organic solvents, supercritical carbon dioxide (sc CO_2) was used as a solvent. By injecting sc CO_2 loaded with wax through a nozzle into the fluidized bed, glass particles with diameters in the range of 40 to 60 µm diameter have been coated with stearylstearate. Analysis of the particles via scanning electron microscopy (SEM) as well as optical microscopy (OM) gives evidence that very smooth and regular coatings can be achieved. The experiments indicate that there exists a minimum Reynolds number for the nozzle (Re_P^n) of about 30 required to coat particles (diameter of 54 µm) without agglomeration. The measured thickness of the encapsulation can be satisfactorily correlated with the mass fraction of the coating material as well with process parameters like time or the collection efficiency of the fluidized bed.

Introduction

Usually, particles are encapsulated by spraying an organic solvent solution into a fluidized bed [1, 2]. However, significant problems are connected with this technique. Organic solvents are only applicable for particles with diameters above 100 µm due to strong capillary forces of the organic solvent resulting in defluidization of the bed [1]. Also high temperatures are necessary to perform this process thus limiting the technique to temperature-insensitive substances [2].
Using sc carbon dioxide as a solvent may be an attractive alternative because capillary forces are neglectible [3]. Additionally the fluidized bed material can be coated at mild thermal conditions due to the low critical point of carbon dioxide. In order to study the applicability of the proposed process a microscale fluidized bed reactor was built.

Experimental

Figure 1 shows schematically the apparatus being used for the experiments. Liquid carbon dioxide having a pressure of 11 MPa provides the pump in order to fill the autoclaves each with a volume of 100 ml at defined temperature and pressure. In these autoclaves the sc fluid is loaded with the coating material and then expanded through a nozzle into the reactor exhibiting a diameter of 1.4 cm.

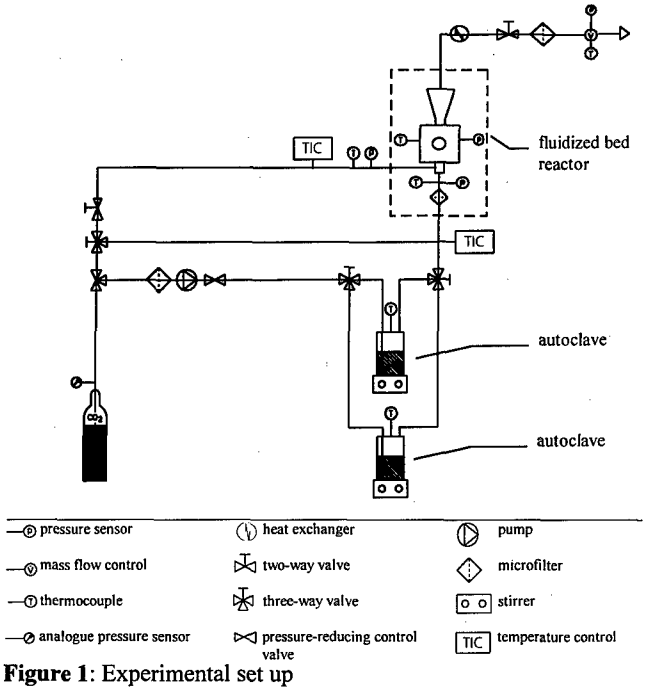

Figure 1: Experimental set up

By varying the nozzle diameter from 50 to 100 µm, different flow rates can be adjusted at a constant nozzle pressure and nozzle temperature. The support gas flow of the fluidized bed is also provided by the carbon dioxide tank. The pressure of the fluidized bed can be varied up to 10 MPa. Observation of the fluidized bed is enabled by using an optical cell which can be fixed in different heights of the reactor.

Results

Figure 2 shows the solubility of the coating material stearylstearate in sc carbon dioxide. It is evident that increasing the density at constant temperature enhances the solubility of the substance whereas the solubility decreases by varying the temperature from 333 K to 393 K at constant pressure.

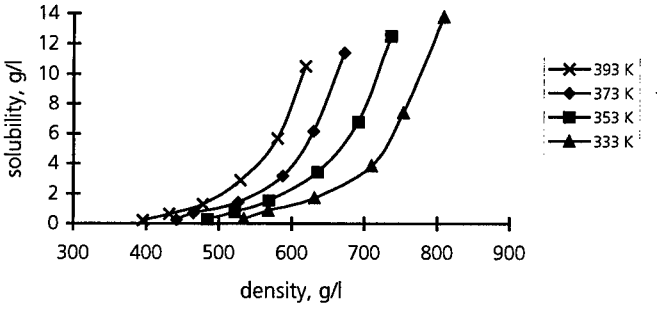

Figure 2: Solubility of stearylstearate in sc carbon dioxide as function of the pressure

The stearylstearate is an industrial product having a molecular weight distribution. Another problem in modeling the solubility is faced by the fact that at 333 K the substance begins to melt. Since most equations of state (EOS), for example the Peng-Robinson or Sanchez-Lacombe EOS [4], do need physical parameters like the accentricity or the molar volume, which for the material used are not available, the semi-empirical model proposed by Chrastil was used [5]. Hence the concentration of the wax can be calculated as follows with c being the concentration of the solute in weight percent and d being the density of the solvent:

$$c = d_{CO_2}^{k} \cdot \exp\left(\frac{a}{T} + b\right) \qquad (1)$$

c = solute concentration, w%
d_{CO2} = density of CO_2, kg/m³ k = coordination number
a, b = constants T = temperature, K

The mass flow of stearylstearate as a function of the density of the sc carbon dioxide at a temperature of 353 K is pointed out in figure 3. It is evident that the mass flow of stearylstearate increases with the extraction density. At a density of 15 MPa there is no difference of the amount of solved wax in the fluid in comparison to the amount of solved wax at equilibrium conditions, whereas at an extraction pressure of 20 MPa only 40 percent of the maximum wax loading is achieved.

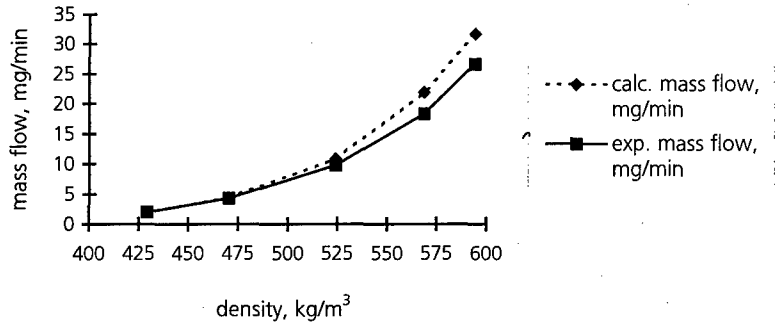

Figure 3: Mass flow of stearylstearate versus extraction density ($T_{extractor}$ = 353 K, d_{nozzle} = 50 µm)

Figures 4 and 5 present micrographs of encapsulated glass spheres with a diameter of 54 µm. In order to intensify the contrast of the wax layer with the background, polarized light was used. Both pictures display a very regular encapsulation of all particles. A comparison of the SEM picture of an untreated glass sphere presented in figure 6 with the SEM picture of a coated sphere depicted in figure 7 shows clearly that an intact coating can be achieved.

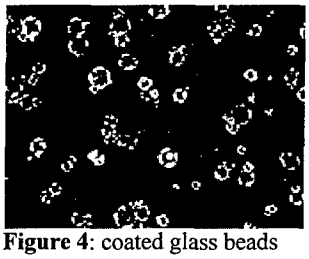

Figure 4: coated glass beads

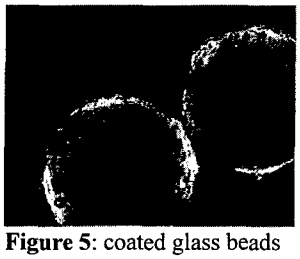

Figure 5: coated glass beads

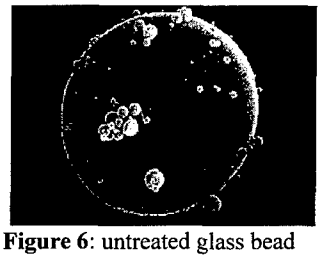

Figure 6: untreated glass bead

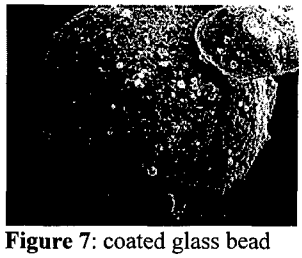

Figure 7: coated glass bead

Assuming that the collection efficiency of the fluidized bed remains constant with time, for spherical particles equation (2) can be derived. Hence, in equation (3) the coating thickness is a function of time as well as of coating parameters, namely the mass flow and density of the coating material, the density of the treated particles and the collection efficiency of the fluidized bed.

$$d_S = d_P \cdot \sqrt[3]{\frac{r_P}{r_W} \cdot \frac{m_W}{m_E}} \quad (2) \qquad d_S = d_P \cdot \sqrt[3]{\frac{r_P}{r_W} \cdot \frac{\dot{m}_W}{m_E} \cdot T_{(x)} \cdot t} \quad (3)$$

t = time, min
d_s = coating thickness, µm
d_p = particle diameter, µm
m_w = mass of wax, kg
$\dot{m}_W$ = mass flow of wax, kg/min
ρ_P = particle density, kg/m³
ρ_W = wax density, kg/m³
m_e = mass of particles
$T_{(x)}$ = collection efficiency

A comparison of the calculated encapsulation thickness as a function of the coating mass fraction with the experimental results is shown in figure 8. It is evident that there is good agreement of the calculated encapsulation thickness with the experimental encapsulation thickness if a nozzle with 100 µm diameter is used. Figure 8 also shows that by using a nozzle with 50 µm diameter considerable agglomeration occurs. Since the melting point of the extracted wax is below the temperature of the fluidized bed, agglomeration due to capillary forces can be excluded.

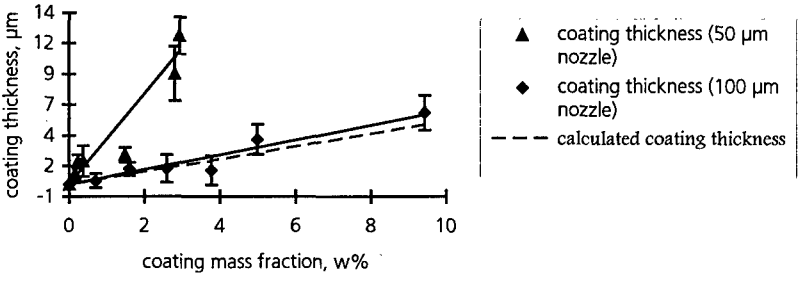

Figure 8: Coating thickness of encapsulated particles (diameter of 54 µm) versus the mass fraction of the coating substance
($T_{reactor}$ = 308 K, $p_{reactor}$ = 8,5 MPa, T_{nozzle} = 353 K, p_{nozzle} = 18 MPa)

It is well known in literature [6] that agglomeration in the fluidized bed occurs, if the kinetic energy of the particles is lower than the binding energy of a potential agglomerate. The Re_P^n number at the nozzle is connected with the circulation velocity of the fluidized particles and hence with the kinetic energy of the particles. A calculation shows that the Re_P^n number increases from 6 to 33 by changing the nozzle diameter from 50 to 100 µm. Therefore the validity of the proposed equations (2) and (3) is limited to Re_P numbers higher than 33. Also there is to be expected an upper limit of the Re_P^n number at the nozzle because attrition of the coating layer may occur.

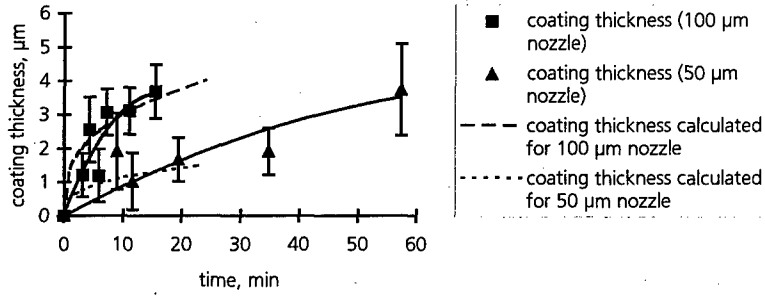

Figure 9: The coating thickness of encapsulated particles with a mean diameter of 54 µm versus time
($T_{reactor}$ = 308 K, $p_{reactor}$ = 8,5 MPa, T_{nozzle} = 353 K, p_{nozzle} = 18 MPa)

A comparison of the calculated coating thickness as a function of time with the experimental result shows qualitative agreement with respect to the 50 µm nozzle (figure 9), though the equation yields too high coating thicknesses for the first 4 minutes. According to the literature the collection efficiency increases with time. This is primarily due to an increase of the collection efficiency of the fluidized particles [7]. Also it is assumed that by adding a wax layer to the spheres, the electrostatic forces may be strongly increased and hence the electrostatic deposition as a very efficient collection mechanism may be getting dominant with time. Since for the calculation mean collection efficiencies were used this might result in an overestimation of the coating thickness of the treated glass spheres in the first minutes and an underestimation of the coating thickness at advanced time.

Conclusions

The encapsulation of fine particles with a diameter below 100 µm is connected with significant problems due to the adhesion forces of the particles. Consequently agglomeration of the particles and therefore the break down of the fluidized bed may occur. In this study it has been shown that an increase of the mass flow of the sc fluid through the nozzle reduces the agglomeration of the particles.

Also it has been proven that a theoretically derived equation predicts the coating thickness as a function of the processing time as well as the particle diameter and the mass of the fluidized bed material, the mass flow of the coating substance and the collection efficiency of the fluidized bed in fair agreement.

It is well known that agglomeration is avoided, if the kinetic energy of the fluidized bed particles is higher then the binding energy. The results indicate that the circulation velocity and hence the kinetic energy of the fluidized bed particles is beeing influenced by the mass flow of the sc carbon dioxide through the nozzle. Therefore the propability of coating the particles without agglomeration can be estimated by calculating the Re_P^n number of the expanded fluid at the nozzle. Hence agglomerationfree coating of particles with a diameter of 54 µm can be achieved, if the Re_P^n number exceeds a value of 33. It is the goal of further works, to investigate the Re_P^n number for different particle sizes in order to find an equation, which predicts the process parameters for agglomeration free coating in a fluidized bed.

Literature

[1] WURSTER D. J., Am. Phar. Assoc., Vol. 48, No. 8, **1959**, p. 451
[2] LIU L. et al., Powder Technology, No. 74, **1993**, p. 215
[3] TSUTSUMI A. et al., Powder Technology, No. 85, **1995**, p. 275
[4] MC HUGH M, KRUKONIS V., Supercritical Fluid Extraction, Butterworth-Heinemann, Boston, 2nd Ed. **1994**
[5] CHRASTIL J., J. Phys. Chem., No. 86, **1982**, p. 3016
[6] ENNIS B., TARDOS G., Powder Technology, No. 65, **1991**, p. 257
[7] LÖFFLER F., Staubabscheiden, Thieme Verlag, Stuttgart, New York, 1st Ed., **1988**

MONTE CARLO SIMULATION OF ALUMINUM AGGLOMERATION IN COMPOSITE SOLID PROPELLANTS COMBUSTION

SERGEY A. RASHKOVSKY
Moscow Institute of Heating Engr.
Russia 140056 Moscow region, Dzerzhinskij, Dzerzhinskaja st., 12-24

In metalized composite solid propellants combustion, agglomerates of metals are formed. Its possess a wide sizes spectrum significantly different from the original metal powder sizes. At present there doesn't exist a complete agglomeration theory, which is capable to predict all the array of experimental data. A pocket model allows to obtain only qualitative conformities as the very notion of pockets is to a certain extent conditional, and on the composite solid propellant burning surface it is impossible to exactly define the volume required for agglomerates spectrum formation. As a basis of a complete agglomeration theory must be a statistical model taking into account the agglomerates generation dynamics, it evolution on burning surface and separation from its. Such model for fusible metals (aluminum) has been presented in the paper. Experimental research results lie in the foundation of this model. Governing equations, describing the agglomerates sizes distribution function changes in the carcass layer and on the composite solid propellant burning surface, has been derived. It was shown that the given equations are, to a sufficient degree, fundamental and that it must be in the foundation of any complete statistical agglomeration theory. The distinction of possible agglomeration theory is connected with various models of agglomerates generation and separation from composite solid propellant burning surface. The exact solution of agglomeration equation for monodisperse initial metal powder are obtained. The properties of the developed agglomeration models were investigated. The Monte Carlo method for agglomeration investigation are considered. Several models of agglomerate-agglomerate and agglomerate-ammonium perchlorate particles interaction in solid propellants combustion were investigated. It was shown, that there are three mechanisms of agglomerate separation from burning surface. It is a aerodynamical, small-disperse and "collision" mechanisms. The "collision" mechanism of agglomerate separation take place at collision of agglomerate with ammonium perchlorate particles, which going to burning surface. For this case the Monte Carlo simulations are carried out. It was shown, that agglomerate sizes distribution function are bi-modal and polymodal for different spectrum of ammonium perchlorate powder. The correlations between average-mass diameter of agglomerates and average-mass diameter of ammonium pechlorate particles are obtained. The comparison of Monte Carlo solutions with exact solution of agglomeration equation and with well-known experimental data are carried out. The agglomerate evolution on burning surface vs time were investigated. Statistical nature of agglomerate generation was shown. The developed method are closed the new possibilities for theoretical investigations of agglomeration process and for control of agglomerates sizes in composite solid propellants combustion.

SIMULATION OF COMPOSITE SOLID PROPELLANTS STATISTICAL STRUCTURE

Serguei A. Rashkovsky

Moscow Institute of Heating Engr.
Russia 140056 Moscow region, Dzerzhinskij, Dzerzhinskaja st., 12-24

Abstract - Analog method of a random distribution of the hard spheres in the volume (hard disks on a plane), consisting in computation of spheres system evolution to an equilibrium condition, in which they are not crossed, is suggested. Using the suggested method a statistical structure of metalized composite solid propellants is investigated. Is shown, that all necessary statistical performances, required for modeling of various properties of propellant, can be received by computer simulation. The parametrical research of various properties of composite solid propellants at a wide range of aluminum particles sizes and concentration of components are carried out. Is shown, that average size of agglomerates, which form in composite solid propellants combustion, has linear dependence upon the size of an oxidizer particles. Is shown, that the statistical structure of solid propellants depends on mutual effect of components: the oxidizer particles correlation function much depends on aluminum concentration in propellant and upon sizes of its particles. Thus a correlation range of oxidizer particles is more large at presence in propellant of aluminum particles, than without them at identical volumetric concentration of an oxidizer. Is shown, that there is the critical aluminum concentration in propellant, is higher which after combustion of propellant there is the solid residue, formed by sintered aluminum particles, the shape of which repeats the grain shape. The suggested method opens new opportunities for statistical modeling of various properties of composite solid propellants and other composite materials, containing hard particles.

Introduction

Composite solid propellants are the complex composite materials, containing disperse components, distributed in continuous binder. Disperse components of composite solid propellants are an oxidizer (ammonium perchlorate, ammonium nitrate, etc.) and power additives, for example, nitramine HMX and RDX, and also powdery metals (aluminum, boron, etc.) or metals hydrides. The sizes of disperse components particles can change in ranges from a fraction of micrometer up to

hundreds of micrometers, and a total volumetric fraction of disperse components in composite solid propellants can reach of 80 %.

Thus, solid propellants are highly filled composites, the properties of which (physical and mechanical, thermal, ballistic, electromagnetic, etc.) are defined not only properties of components, their concentration and dispersion, but also distribution of disperse components in the volume of a material.

Modern computers allow to carry out direct numerical modeling of various properties of composite solid propellants, however thus it is necessary to be limited by assumptions about their regular internal structure. For development of more exact methods of direct computer modeling of composite solid propellants properties, it is necessary to reproduce their random internal structure.

From the mathematical point of view the problem is reduced to random distribution of given hard spheres in the space without crossing with each other.

The problem of hard spheres random distribution in the space (or hard disks on a surface), has not only applied, but also the basic importance and meets in many fields of a science. The problem concerns to the category of combinatorial problems, which investigate by methods of stochastic geometry [1-3]. The analytical solution of this problem, even in the elementary case, is absent, therefore the basic research method remains computer modeling. However and in this case there is no general method of particles distribution in the space, for any given particles diameter distribution. The basic difficulty consists that the distributed particles should not be crossed.

At present such methods of particles distribution in the space, as "the hard-core point processes", "Gibbs point processes", "the Strauss model", "the spatial birth-death processes", etc. [1-3], are known and are investigated in detail . However, the area of these methods application is very limited, as they have weak convergence for large volumetric density of space filling, close to maximum, and require of large computational time. The greatest difficulties arise at distribution in the space of particles, which have a wide spectrum of the sizes. The above-mentioned methods very frequently result in that the distribution of the placed particles sizes differs from the distribution of initial particles sizes.

The method of particles distribution in the space, suggested in the present work, does not depend upon an initial particles spectrum and upon a volumetric density of particles in the space. It has good convergence, allowing to investigate the systems with volumetric density of space filling,

close to maximum, and is, apparently, the most general method of the similar problems solution.

Physical model and computer realization

Abstract oneself from real investigated system, we shall consider the following model physical problem.

There is a system of N spherical particles with known radiuses r_i (i=1,...,N). We shall consider, that the particles can free move, to draw together on distances, smaller, than the sum of their radiuses and between them have repulsive force, equal zero for non-crossed particles. It allows to replace a system of spherical particles by a system of point particles, which interact by means of repulsive forces. The forces are central, pair and for two point particles i and j, which correspond to spheres with radiuses r_i and r_j, the force is defined by the following ratios

$$\bar{F}_{ij} = \frac{(\bar{x}_i - \bar{x}_j)}{|\bar{x}_i - \bar{x}_j|} F_{ij}$$

$$F_{ij}(r) = \begin{cases} F_0, \text{ for } r < r_i + r_j \\ 0, \text{ for } r \geq r_i + r_j \end{cases}$$

where $\bar{x}_i$ - radius-vector of the particle i; $r = |\bar{x}_i - \bar{x}_j|$ - spheres center to center distance, F_0 - some function, which in a general case depends on distance r.

The movement of particles in such system can be investigated numerically by a method of molecular dynamics [4]. The particles are in a continuous and chaotic movement. That this process could be used for random distribution of spheres in the space, it is necessary "freeze" system in some moment, i.e. to stop calculation and to fix of particles coordinates. Such method is possible to name as "molecular dynamics point process" and it can be considered as a molecular dynamics variant of "Gibbs point processes". These processes correlate among themselves same as a method of molecular dynamics and a method of Monte Carlo in statistical physics [4]. Obviously, in "frozen" condition of system some spherical particles will be crossed and additional complex thin out procedure are required, to receive system of non-crossed, random distributed particles.

This difficulty is displayed stronger, than closer is volumetric density of system filling to greatest possible. To remove it we shall consider, that viscous force, equal $(-\mu\bar{v})$, act to a particle,

where $\bar{v}$ - particle velocity, μ - factor of proportionality (viscosity). Under viscous force action the free (non-crossed) particles stop and at rather large value of factor μ the system should very quickly reach in an equilibrium condition, in which all particles are motionless and are not crossed.

Dynamics of such system is described by system of the equations

$$m_i \frac{d^2 \bar{x}_i}{dt^2} = \sum_{i \neq j} \bar{F}_{ij} - \mu \bar{v}_i$$

where m_i - mass of a particle i, t - time.

The resulted equation describes dynamics of viscous suspension, consisting from particles, between which repulsive forces act.

The equation of a system dynamics contains a number of uncertain parameters and functions (μ, m_i, F_0). These parameters are insignificant from the point of view of particles in the space random distribution problem, but rather are essential from the point of view of calculation method realization and convergence.

Taking into account, that in the given problem has interest final stationary particles distribution in the space, but not a system relaxation process to this condition, is possible essentially to simplify a model. System viscosity μ increase results in acceleration of system relaxation to an equilibrium condition, as the inertial member in the left part of the equation is of no importance. It allows to neglect the inertial member and to write the equation of system evolution as $\bar{v}_i = \frac{1}{\mu} \sum_{i \neq j} \bar{F}_{ij}$. At the appropriate definition of parameter F_0 it is possible to accept $\mu = 1$. We consider a case $F_0 = const$. The evolution equation can be written as

$$\bar{v}_i = F_0 \sum_{i \neq j} \frac{(\bar{x}_i - \bar{x}_j)}{|\bar{x}_i - \bar{x}_j|} \Delta_{ij}$$

where

$$\Delta_{ij} = \begin{cases} 1, \text{ if } |\bar{x}_i - \bar{x}_j| < r_i + r_j \\ 0, \text{ if } |\bar{x}_i - \bar{x}_j| \geq r_i + r_j \end{cases}$$

Assuming $F_0 = 1$, it is possible to redefine a time scale. Then the evolution equation of hard spheres system in a examined problem is following

$$\frac{d\,\vec{x}_i}{dt} = \sum_{i \neq j} \frac{(\vec{x}_i - \vec{x}_j)}{|\vec{x}_i - \vec{x}_j|} \Delta_{ij} \qquad (1)$$

This equation is basic in the suggested method and does not contain any insignificant parameters, describing particles or viscous medium.

The solution of the equations (1) converges to a condition, in which the right parts for all i is equal to zero. In this condition the system can be unlimited time. This condition is equilibrium.

The described process can be used for random distribution of particles in the space. We shall name the suggested method as a "viscous suspension" method, or, by analogy to other processes of distribution of hard spheres in the space [1-3], as " viscous suspension point process".

The equation system (1) describes regular dynamics of hard spheres system and does not contain the elements of fortuity. The random nature of hard particles equilibrium distribution is defined by the random initial conditions. The initial conditions are given by pseudo-random number generator, which defines initial coordinates of each particle. Thus, the centers of particles are randomly distributed in given area of space and further a system evolve to an equilibrium condition according to the equations (1).

In the viscous suspension method it is possible beforehand to generate system of particles with the given performances, which should be randomly distributed in the space. Thus, it is possible to hope, that even if one condition of system is available, in which the particles are not crossed, the system sooner or later it will reach. At present the strict mathematical proof of this statement is not obtained, however numerous calculations, executed for different systems down to volumetric density of space filling, equal 0.95 of maximum possible for given system, show that the process (1) always converges.

The computer realization of a viscous suspension method is similar to realization of a molecular dynamics method in statistical physics, however, it has the number of peculiarities.

In first, there is no necessity to apply the high order calculation methods to solution of the equations (1), it is enough to use the simple integration scheme $\vec{x}_i(t+\delta t) = \vec{x}_i(t) + \vec{v}_i \delta t$, where δt - temporal integration step, $\vec{v}_i$ - right parts of the equations (1). The integration step can be chosen rather large, for example $\delta t = 0.01$, being not feared of calculation instability.

The process calculation consists in a fingering on the given step of all particles of system and

calculation of new particles coordinates. At calculation of the right parts of the equations (1) for each particle is made fingering of the other particles of system. At simple fingering of all particles of system for determination of force, which acts on the given particle, the calculation time increase proportionally to a square of particles number in system.

For decrease of calculation time, it is necessary to finger only near neighbours of the given particle. For this purpose the whole calculation area was divided into cells with the size, equal to a diameter of the largest particle. It has allowed at calculation of force, which acts on the given particle, to consider only those particles, which were in 27 nearest cells for a 3D-problem or in 9 nearest cells for a 2D-problem.

As boundary conditions in a viscous suspension method, as well as in a molecular dynamics method either periodic conditions [6] are used, or it is considered, that volume, in which particles are distributed, is limited by hard, impenetrable walls.

Results and discussion

Below some results of numerical modeling of composite solid propellants structure by a viscous suspension method are adduced.

In the beginning of each calculation was carried out a random initial distribution of particles centers in calculation area. This distribution stopped as soon as given value of components volumetric fraction were reached.

In calculations the hard, impenetrable walls were chosen as boundary conditions.

The calculation stopped, when the right parts of all equations (1) turn into zero.

For simplicity the propellants, containing particles of two kinds: large particles of an oxidizer, e.g. ammonium perchlorate, and small particles of aluminum, were considered. The particles are considered spherical, and all particles of one kind have an identical diameter. Such simplification allows to avoid the difficult analysis, connected to dispersion of the particles sizes.

As the problem is geometrical, it is possible to abstract from real spatial scale of system and to introduce relative scale, in which the length unit is a diameter of large particles (oxidizer). Thus, it is considered, that the diameter of particles of an oxidizer is equal to unit, and the relative diameter of aluminum particles is equal $d < 1$.

The system is characterized by components volumetric fraction, equal to the ratio of given kind particles total volume to whole system volume. We shall introduce volumetric fraction of oxidizer particles ν_{AP} and aluminum particles ν_{Al}. In the present work the composite solid propellants, in which the aluminum mass fraction changed in ranges 10 ...25 % ($\nu_{Al} = 0.07...0.17$), and oxidizer mass fraction - in ranges 40 ...70 % ($\nu_{AP} = 0.38...0.66$), were considered . The rest of the propellant's weight is related to binder.

For understanding of composite solid propellants structure is of interest evidently to see as components in volume of system are distributed. Although the viscous suspension method allows to obtain coordinates of all particles of system, to show its 3D-picture in the present work it is difficult. To imagine distribution of particles in system, we shall consider a planar model of propellant, described by a set of hard disks on plane.

Fig.1 shows the structure of a planar model of composite solid propellants, containing particles of two kinds.

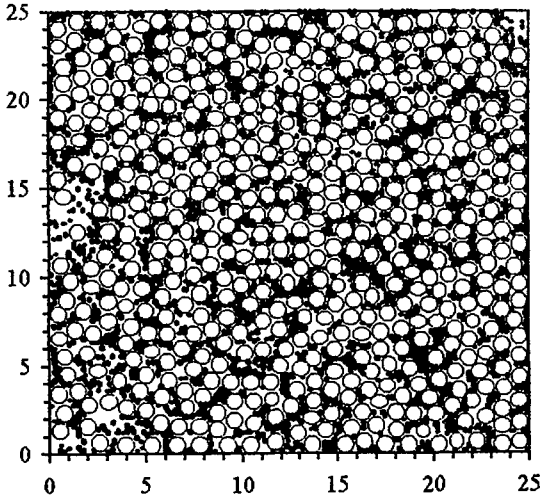

Figure1. Planar model of composite solid propellant. White circles-oxidizer; black circles-aluminum. (ν_{AP}=0.65; ν_{Al}=0.137; d=0.2).

The analysis shows, that at a microlevel the particles of components are distributed non-uniformly: the particles of large fraction are grouped in grains, containing a number of oxidizer particles, and the small fraction particles (aluminum) are distributed on borders of oxidizer particles grains, forming thin layers.

In composite solid propellants combustion on account of sintering and the melting of metal particles in a thermal wave the agglomerates form. They are connected with a burning surface and carried away from it under action of propellant gaseous burning products [5-9]. For agglomerates sizes prediction use a model of pockets [5-6].

The analysis of composite solid propellants structure, obtained by the viscous suspension method computer modeling, shows, that it is impossible to speak that in propellant the oxidizer particles form closed pockets, inside which the metal particles are capsulated. Nevertheless, modeling shows, that the aluminum particles in propellant are located compactly, forming isolated clusters of contacting particles. In combustion take place the sintering of contacting aluminum particles, their melting and fusion in a single, large particle, which can be a basis of agglomerate. We shall name such particle as sub-agglomerate. The agglomerate can consist several of sub-agglomerates, fused on burning surfaces.

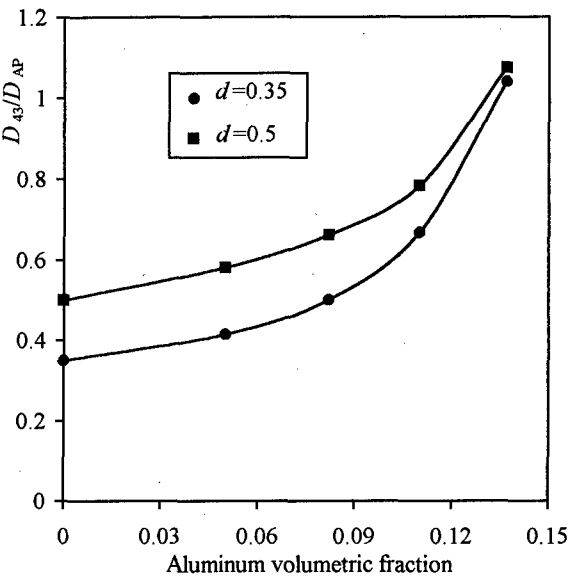

Figure 2. Dependence of non-dimensional average mass diameter of agglomerate upon aluminum volumetric fraction. (ν_{AP}=0.38).

If sub-agglomerates not crumble and do not merge with each other on a burning surface the agglomerates coincide with sub-agglomerates.

We determine the sizes of sub-agglomerates (agglomerates) in melted states, assuming, that the sub-agglomerates coincide with clusters of contacting aluminum particles.

The algorithm of clusters picking in the system is based on the following definition of cluster: the particle concerns to the given cluster, if it contacts though of one particle, belonging to this cluster. Inertness of the calculation scheme in a viscous suspension method, connected with final size of a step δt, results in that in a final equilibrium condition, strictly speaking, will be absent contacting particles, and, an average backlash between surfaces of particles will be about $\delta t/2$. Therefore it is hereinafter considered, that the particles have contact in propellant, if the backlash between them does not exceed δt, i.e., if a condition $|\bar{x}_i - \bar{x}_j| < r_i + r_j + \delta t$ is realized.

The statistical characteristic of clusters (agglomerates) system is function of clusters mass distribution. For considered propellant, containing aluminum particles of the identical sizes, it is meaningful to speak about a mass fraction of clusters (agglomerates), formed by equally k aluminum particles: $P(k) = \frac{k\,N(k)}{N_\Sigma}$, where $N(k)$ - number of clusters, containing equally k particles, N_Σ - total number of aluminum particles in propellant. The average mass diameter of agglomerate is determined by a ratio $D_{43}^1 = d \sum_{k=1}^{\infty} k^{1/3} P(k)$. The superscript "1" specifies on the fact, that the average mass diameter is related to unit oxidizer particle diameter. Taking into account a geometrical similarity of a problem, the agglomerate average mass diameter at any diameter of an oxidizer particle D_{AP} is determined by ratio $D_{43} = D_{43}^1 D_{AP}$, where factor of proportionality D_{43}^1 depends only on a relative diameter of aluminum particles d and volumetric fraction of components ν_{AP} and ν_{Al}. The obtained ratio correlate with well known experimental fact of proportionality between an agglomerate average mass diameter and an oxidizer particles average mass diameter [5-9].

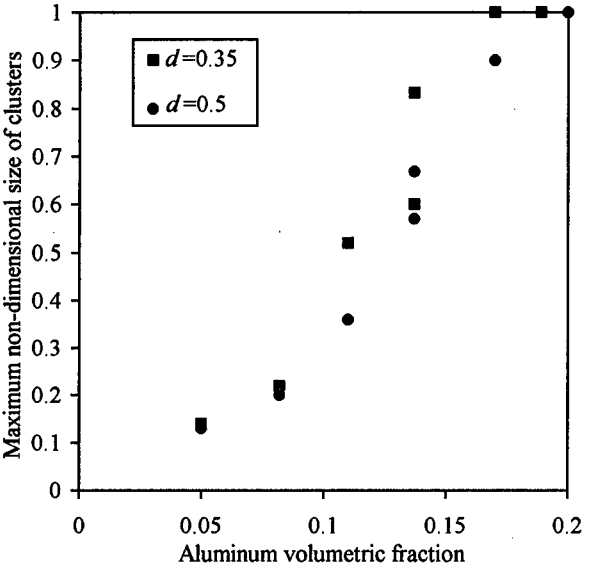

Figure 3. Dependence of maximum clusters size upon aluminum volumetric fraction. (ν_{AP}=0.38).

Fig.2 shows dependencies of agglomerates average mass diameter D_{43}^1 upon aluminum volumetric fraction ν_{Al} for different relative diameter of aluminum particles d.

The analysis of mass clusters distribution shows, that for small aluminum volumetric fraction

$\nu_{Al} \le 0.15$ great mass of aluminum is concentrated in clusters, containing no more than 10-30 particles. However already at $\nu_{Al} \ge 0.17$ more than 70 % of aluminum mass is concentrated in single large cluster.

For confirmation of this fact we consider as the size of the largest cluster in system change with increase of aluminum volumetric fraction and at which fractions there is the coherent structure, extending from one borders of system to other.

Fig.3 shows dependence of the maximum cluster size, referred to the size of system upon aluminum volumetric fraction.

For considered system, since concentration $\nu_{Al} \approx 0.17$, the sizes of the greatest cluster coincide with the sizes of whole system. Thus for $\nu_{Al} \ge 0.17$ in system there is cluster, extending per whole system and ensuring its connectedness. In combustion of such propellant remains solid, unburned residue, the shape of which repeats the propellant grain shape.

At volumetric fraction $\nu_{Al} < 0.14$ the probability of cluster formation, covering whole system, is close to zero. At volumetric fraction in the range $\nu_{Al} \approx 0.15...0.17$ the significant fluctuations of the sizes of the greatest clusters are observed: from test to test in system can be formed as small clusters, have the sizes much less than system sizes, and large clusters, covering whole system. The fluctuations decrease with increase of the system sizes. It is possible to contend that for system of infinite volume there is a threshold value of aluminum volumetric fraction, close to $\nu_{Al} \approx 0.17$, is higher which in system coherent cluster, covering whole system, will be formed. For volumetric fraction of aluminum in system, smaller 0.17, separate isolated clusters will be formed only, sizes of which there are less system sizes.

Many properties of composite solid propellants are defined by a mutual location of disperse component particles. To such properties concern first of all acoustic and electromagnetic: the mutual location of particles in propellant defines dispersion and attenuation of sonic and electromagnetic waves in a material.

One of the important statistical performances of propellant is pair correlation function $g(r)$, determined as $g(r) = \frac{dN(r,dr)}{4\pi r^2 n dr}$ for a spatial problem and $g(r) = \frac{dN(r,dr)}{2\pi r n dr}$ for a planar problem, where $dN(r, dr)$ - number of particles in spherical (circular) layer $[r, r + dr]$, average on all particles,

chosen as a centre of spherical (circular) layer; n - average number of particles per unit volume.

As real calculation volume has the limited sizes (in present work it is 10x10x10), for each particle the minimum distance up to volume borders was determined and contribution of the given particle in $dN(r,dr)$ was calculated for all r, smaller this distance. It allows to avoid distortions of function $g(r)$ for the account of boundary effects. At calculation of $dN(r, dr)$ and correlation function was assumed $dr = 0.1$.

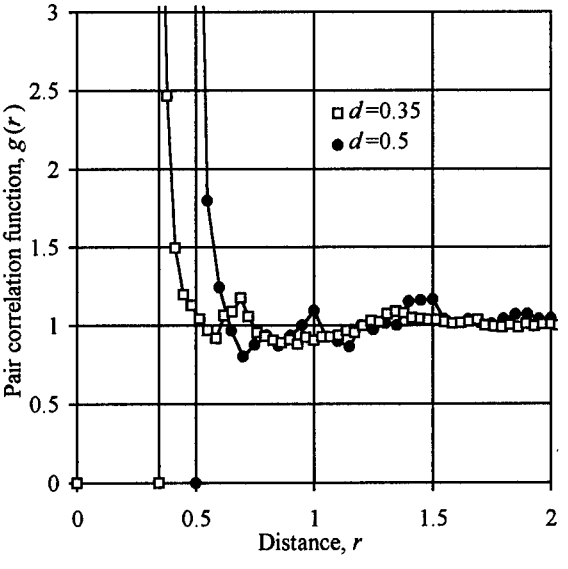

Figure 4. Pair correlation function of aluminum particles. ν_{AP}=0.38; ν_{Al}=0.137.

Fig.4 shows pair correlation function for aluminum particles.

The analysis shows, that at small volumetric fraction of aluminum particles the pair correlation function of an oxidizer particles quickly decreases and already on distances about 3-4 poorly differs from unit. Increase of aluminum particles fraction results in that the location of an oxidizer particles in propellant becomes more correlated and correlation range is increased in some times.

The conclusion

Thus, in work an analog model of random distribution of hard spheres in volume (hard disks on a plane), named by a viscous suspension method is suggested.

By the method of viscous suspension the statistical structure of metalized composite solid propellants are investigated. Is shown, that many properties, required for modeling of various performances of propellant can be obtained by computer simulation, using a suggested method.

Parametrical research of some properties of propellant in a wide range of the aluminum particles sizes and components concentration is carried out.

Is shown, that the agglomerates, formed in composite solid propellant combustion, have the

sizes, linearly dependent on the sizes of an oxidizer particles. This dependence is purely geometrical and, apparently, poorly depends on physical properties of components.

Is shown, that the statistical structure of propellants depends on mutual influence of components: the pair correlation function of an oxidizer particles much depends on aluminum concentration and size of its particles.

Is shown, that there is the critical value of aluminum volumetric fraction, is higher which after propellant combustion there is the solid residue, formed by sintered aluminum particles, shape of which repeats the shape of propellant grain.

The suggested method opens new possibilities for statistical modeling of various properties of composite solid propellants, composite explosives and other composite materials, containing hard particles.

References

1.Ambartsumyan R.V., Mecke, J., Stoyan, D. Introduction in Stochastic Geometry. - Moscow, Nauka, 1989, 400p. (in Russian).

2.Stoyan, D., Kendall, W.S., Mecke, J. Stochastic Geometry and Its Applications.- Akademie-Verlag Berlin, 1987, 345 p.

3.Ripley, B.D. Spatial Statistics. J.Wiley&Sons, New York/Chichester. 1981. 252 p.

4.Monte Carlo Methods In Statistical Physics. Edited by K.Binder. Springer-Verlag-Berlin-Heidelberg-New York. 1979. 400 p.

5.Grigor'ev, V.G., Kutsenogij, K.G., Zarko, V.E. *Fiz. Goreniya Vzryva*, 1981, 4, 9. (in Russian).

6.Cohen N.S. AIAA Journal. 1983. V.21, № 5. P.720 - 725.

7.Sambamurthi T.K., Price E.W., Sigman R.K. AIAA Journal. 1984. V.22. № 8. P1132 - 1138.

8.Grigor'ev, V.G., Zarko, V.E., Kutsenogij, K.G. *Fiz. Goreniya Vzryva*. 1981, 3, 3. (in Russian).

9.Kashporov, L.Ya., Frolov, Yu.V., Ostretsov, G.A. et al. *Fiz. Goreniya Vzryva*, 1975, 1, 33. (in Russian).

Finite Elemente Modellierung der Mikromechanik von Festtreibstoffen und Treibladungspulvern

E. Geißler, Ch. Hübner
Fraunhofer-Institut für Chemische Technologie ICT
Joseph-von-Fraunhofer-Str. 7
D-76327 Pfinztal (Berghausen)

Abstract

Modern rocket motor propellants and gun powders can be regarded as composite materials: hard filler particles are embedded in a soft matrix material. In these materials the adhesion between filler and matrix is very important. The influence of the dewetting, the detachment of the matrix from the filler surface, on the mechanical behavior of the composite material was simulated with the help of a Finite Elemente Model of an elementary cell of a filler particle in the matrix material. In this paper, the influence of the stage of dewetting on Poisson's Ratio is discussed.

Kurzfassung

Moderne Raketenfesttreibstoffe und Treibladungspulver können als Composite-Werkstoffe betrachtet werden: Harte Füllstoffpartikel sind in einem weichen Matrixmaterial eingebettet. Bei diesen Materialien spielt die Haftung zwischen Matrixmatrial und Füllstoff ein große Rolle. Die Auswirkung der Ablösung der Matrix von der Füllstoffoberfläche auf das Materialverhalten wurde an einem Elementarzellenmodell eines Füllstoffteilchens in dem Matrixmaterial mit der Methode der Finiten Elemente simuliert. Der Einfluß des Ablösegrades des Füllstoffes von der Matrix auf das Poissonverhältnis ist hier beschrieben.

1. Einleitung

Durch den Haftungszustand zwischen Füllstoff und Matrixmaterial werden die Gebrauchseigenschaften (Mechanik, Abbrandverhalten) von Raketenfesttreibstoffen und Treibladungspulvern sehr stark beeinflußt. Die Ablösung zwischen Matrixmaterial und dem eingearbeiteten Füllstoff äußert sich in einer Änderung der mechanischen

Eigenschaften, insbesondere auch durch die Änderung des Querdehnungsverhaltens. Zur experimentellen Analyse dieses Querdehnungsverhaltens wird im ICT ein berührungsloses Meßverfahren eingesetzt /1/.
Parallel dazu wird an einem Elementarzellenmodell der Einfluß des Ablösegrades des Füllstoffes von der Matrix auf das Poissonverhältnis untersucht.

2. Elementarzellenmodell

Das in /2/ entwickelte Elementarzellenmodell wurde als Grundlage für die Finite Elemente Berechnungen herangezogen. Der Treibstoff wird durch eine kubische Elementarzelle aus elastischem Matrixmaterial mit einem starren würfelförmigen Einschluß als Füllstoff beschrieben.

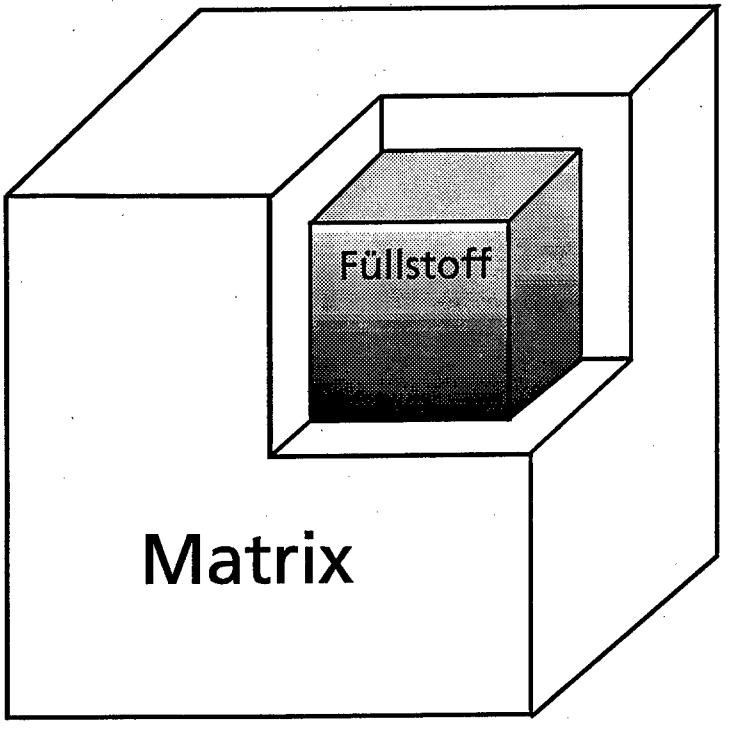

Bild 1: Modell der Elementarzelle

Zur Untersuchung des Einflusses von Matrix-Füllstoffablösungen auf das mechanische Verhalten der Elementarzelle werden die folgenden drei Zustände definiert und modelliert (Bild 2):

- pefektes Haften
- abgelöster Zustand
- totale Ablösung.

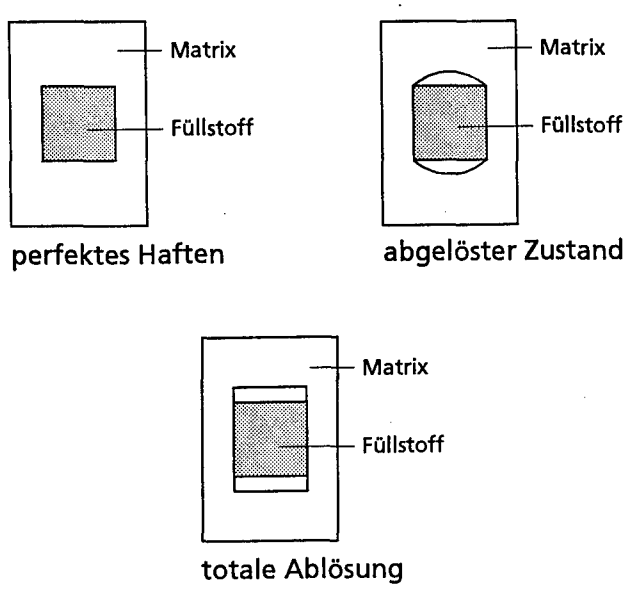

Bild 2: Modelle der drei Ablösezustände

Zu Beginn der Belastung haftet das Matrixmaterial am Füllstoff. Dieser Zustand wird als **perfektes Haften** bezeichnet. Hierdurch wird der Anfangszustand zu Beginn der Belastung beschrieben.

Wird die Elementarzelle weiter belastet, dann löst sich das Matrixmaterial an den horizontal liegenden Füllstoffoberflächen aufgrund von Normalspannungen ab. Es herrscht jedoch zwischen den vertikalen Grenzflächen des Füllstoffes und dem Matrixmaterial weiterhin Haftung. Der Eintritt dieses **abgelösten Zustandes** macht sich

in einer Abflachung der Spannungs-Dehnungskurve für die Elementarzelle bemerkbar. Das Material erscheint weicher.

Bei weiterer Belastungssteigerung löst sich die Grenzfläche zwischen Matrixmaterial und Füllstoff auch an den vertikalen Grenzflächen des Einschlusses ab. Hierdurch tritt eine weitere Erweichung des Materials ein. Es überträgt nur noch das weiche Matrixmaterial die Spannung. Dieser Zustand wird **totale Ablösung** genannt.

3. FE-Modell der Elementarzelle

Die in Abschnitt 2 beschriebenen Zustände „perfektes Haften", „abgelöster Zustand" und „totale Ablösung" wurden für Füllstoffanteile von 15 Vol% und 45 Vol% modelliert. Zur Reduzierung der Rechenzeit werden die Symmetrieeigenschaften des Bauteils bezüglich Geometrie und Belastung ausgenutzt. Es wurde ein Achtel-Ausschnitt der Zelle für die FE-Rechnung diskretisiert /3/. Hier wurde das Modell entlang seiner Symmetrieebenen bezüglich der Belastung und Geometrie aufgeteilt. Die Randbedingungen an den Symmetrieebenen wurden so gewählt, daß sich die in den Symmetrieebenen befindlichen Knoten nur innerhalb der Symmetrieebenen bewegen können. Die Zelle wird axial auf Zug belastet. Der Belastungszustand ist somit symmetrisch zu den Symmetrieebenen der Elementarzelle, deshalb bleiben die Symmetriebenen bei der Belastung eben.

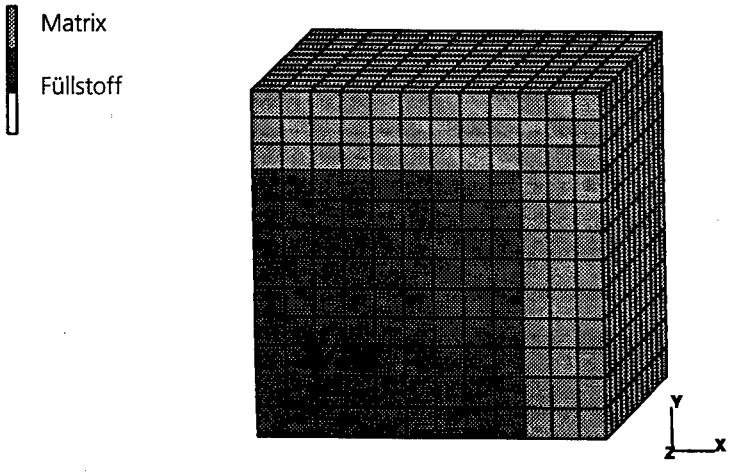

Bild 3: FE-Modell der Elementarzelle

Das FE-Modell für den Füllstoffanteil von 45 Vol% ist im Bild 3 dargestellt. Bei einem Füllstoffanteil von 15 Vol% ist die Elementeinteilung ähnlich, lediglich der Füllstoff nimmt entsprechend des kleineren Anteils weniger Raum ein. Für beide Füllstoffanteile wurde das weiche Matrixmaterial mit einem deutlich kleineren Elastizitätsmodul (4.2 N/mm^2) als der Füllstoff (40.000 N/mm^2) modelliert. Das Füllstoff verhält sich durch den deutlich größeren Elastizitätsmodul im Vergleich zur Matrix praktisch starr.

Die Elementarzelle wird zur Simulation des Zugversuches in der Finite Elemente Rechnung auf Zug belastet, und das mittlere Poissonverhältnis über die gesamte Elementarzelle wird numerisch berechnet. Die Belastung wird durch sogenannte Master-Slave-Knoten aufgebracht. Das heißt, an einem Knoten - dem Master-Knoten - wird die Belastung aufgebracht. Die anderen Knoten, die in der Belastungsebene liegenen, die sogenannten Slave-Knoten, werden durch die Master-Slave-Beziehung so gekoppelt, daß sie in Belastungsrichtung den gleichen Weg zurücklegen wie der Masterknoten. Die Belastungsebene bleibt somit eben. Diese Annahme entspricht den Einspannbedingungen beim Zugversuch.

Beim Zustand des perfekten Haftens besteht eine feste Verbindung zwischen Matrixmaterial und Füllstoff, d.h. daß die Knoten, die an der Grenzfläche zwischen Füllstoff und Matrixmaterial liegen, direkt miteinander gekoppelt sind.

Der abgelöste Zustand wurde so diskretisiert, daß zwischen der Deckfläche des Füllstoffwürfels und dem Matrixmaterial keine feste Verbindung vorlag.

Beim Zustand der totalen Ablösung waren alle seitlichen Grenzflächen zwischen Füllstoff und Matrixmaterial abgelöst. Bei der totalen Ablösung wurden die Matrix und der Füllstoff als Kontaktkörper modelliert /4/. Die Wechselwirkung zwischen Füllstoff und Matrixmaterial wird als Kontaktkörper berechnet.

4. Finite Elemente Berechnung des Poissonverhältnisses der Elementarzelle

Das Poissonverhältnis der Elementarzelle ergibt sich aus der mittleren Querdehnung der Elementarzelle, bezogen auf die Ausgangsbreite. Sie entspricht in der Modellvorstellung dem makroskopisch meßbaren Poissonverhältnis des Treibstoffes, das im Zugversuch ermittelt wird.

Das Querkontraktionsverhalten des Matrixmaterials wurde in den FEM-Berechnungen durch ein deformationsabhängiges Poissonverhältnis beschrieben, das mit der folgenden vereinfachten Geradengleichung definiert wird:

$$\nu(\varepsilon_l) = 0.5 - 0{,}34 \cdot \varepsilon_l \qquad (1)$$

Dies ist näherungsweise das Poissonverhältnis eines volumenkonstanten Materials, welches exakt der Formel

$$\nu(\varepsilon_l) = \frac{1}{\varepsilon_l} \cdot \left(1 - \frac{1}{\sqrt{1+\varepsilon_l}}\right) \qquad (2)$$

gehorcht, was im Zugversuch an reinem Matrixmaterial bestätigt werden konnte.

4.1 Definition des Poissonverhältnisses der Elementarzelle

Die experimentelle Ermittlung des Querkontraktionsverhaltens von Materialien erfolgt im ICT im Zugversuch mit einem berührungslosen Projektionsverfahren. Hierbei wird ein Probestab mit einer optischen Vorrichtung durch Weißlicht angestrahlt, und zur Bestimmung der Querkontraktion wird das Schattenbild vermessen /1/. Bei diesem Versuch wird die mittlere Querkontraktion über die Probenlänge gemessen. Die Bestimmung der Längsdehnung erfolgt ebenfalls berührungslos mit einem laseroptischen Verfahren /8/. Aus der Längsdehnung und der Querkontraktion wird das Poissonverhältnis berechnet.

Zur qualitativen Bewertung und Beurteilung der Finite Elemente Ergebnisse wird das Poissonverhältnis der Elementarzelle berechnet. Es hängt vom Ablösezustand und dem Füllstoffgehalt ab. Bei der Belastung der Elementarzelle in Längsrichtung verlängert sie sich. Durch den steifen Füllstoff, der die Querdehnung behindert, ist die Verschiebung quer zur Belastungsrichtung nicht über die gesamte Länge der Elementarzelle konstant. Im Bereich des Füllstoffes ist die Querkontraktion daher am kleinsten.

Das Poissonverhältnis $\bar{\nu}$ der Elementarzelle ergibt sich aus dem Verhältnis der mittleren Querdehnung $\bar{\varepsilon}_q$ und der Gesamtlängsdehnung ε_l der Elementarzelle:

$$\bar{\upsilon} = -\frac{\bar{\varepsilon}_q}{\varepsilon_l} \tag{3}$$

Aus der Diskretisierung der Elementarzelle (Bild 3) ergibt sich direkt eine Einteilung des Elementarzellenwürfels zur Berechnung des mittleren Poissonverhältnisses (Bild 4).

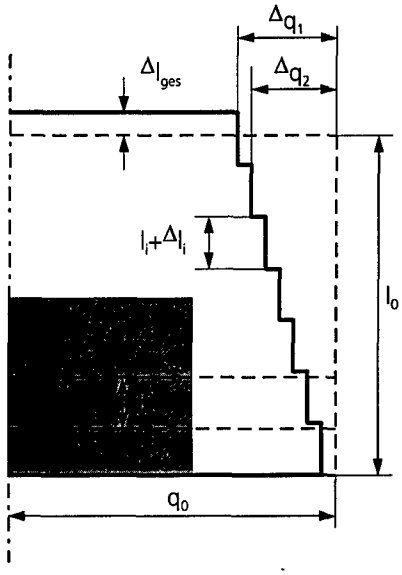

l_0	Höhe der unverformten Elementarzelle
l_i	Höhe eines unverformten Elementarzellenstreifens
Δl_i	Verlängerung der Elementarzellenstreifens in Längsrichtung
Δl_{ges}	Gesamtverlängerung der Elementarzelle in Längsrichtung
q_0	Breite der unverformten Elementarzelle
Δq_i	Querverschiebung des Elementarzellenstreifens (Verschiebung quer zur Belastungsrichtung)

Bild 4: Viertelausschnitt der Elementarzelle zur Berechnung des Poisonverhältnisses
unbelastete Struktur (– – – –), *belastete Struktur* (——)

Zur Einsparung von Rechenzeit genügt es, aus Symmetriegründen einen Viertelausschnitt aus der Mittelebene der Elementarzelle zu betrachten. Die Elementarzelle wird in Längsrichtung auf Zug belastet. Somit bleiben die Symmetrieebenen bezüglich der Geometrie und der Belastung nach Aufbringen der Last erhalten. Das heißt, die Symmetrielinien des Viertelausschnittes bleiben gerade.

Die mittlere Querdehnung $\bar{\varepsilon}_q$ der Elementarzelle ergibt sich aus dem Verhältnis des arithmetischen Mittelwerts der Querverschiebung $\Delta\bar{q}$ und der Breite der unverformten Elementarzelle q_0 :

$$\bar{\varepsilon}_q = \frac{\Delta\bar{q}}{q_0} \tag{4}$$

Der arithmetische Mittelwert der Querverschiebung der Elementarzellenstreifen berechnet sich aus den Querverschiebungen der einzelnen Streifen Δq_i, gewichtet mit dem relativen Längenanteil der Streifen:

$$\Delta\bar{q} = \sum_{1}^{\text{Anzahl der Streifen}} \Delta q_i \cdot \frac{l_i + \Delta l_i}{l_0 + \Delta l_{ges}} \tag{5}$$

4.2. Berechnung der mittleren Poisonzahl mit dem Elementarzellenmodell

Für die drei Zustände „perfektes Haften", „abgelöster Zustand" und „totale Ablösung" wurden mit dem deformationsabhängigen Poissonverhältnis für das Matrixmaterial nach Gleichung 1 Finite Elemente Berechnungen durchgeführt. Das Ziel dieser Berechnungen war es, den Einfluß des Ablösezustandes auf das mittlere Poissonverhältnis der Elementarzelle nach Gleichung 2 zu simulieren und mit experimentellen Ergebnissen zu vergleichen.

Die Ergebnisse der Finite Elemente Berechnungen sind in Bild 5 für die drei beschriebenen Zustände dargestellt. Es zeigt sich, daß mit zunehmendem Ablösegrad das berechnete Poissonverhältnis abnimmt.

Dieser Sachverhalt wird durch die experimentellen Ergebnisse unterstützt (Bild 6). Das Poissonverhältnis wurde experimentell in einem zyklischen Belastungsversuch ermittelt. Mikrospische Aufnahmen von gefüllten Probekörpern zeigten, daß mit zunehmender Belastung der Ablösegrad zwischen Matrixmaterial und Füllstoff zunimmt. Parallel dazu zeigt der zyklische Versuch, daß mit zunehmender Zahl der Lastwechsel das Poissonverhältnis abnimmt. Dies läßt sich dahingehend deuten, daß mit zunehmender Ablösung des Füllstoffes vom Matrixmaterial das Poissonverhältnis abnimmt. Dieser experimentell gefundene Sachverhalt wird durch die durchgeführte Finite Elemente Berechnung qualitativ bestätigt.

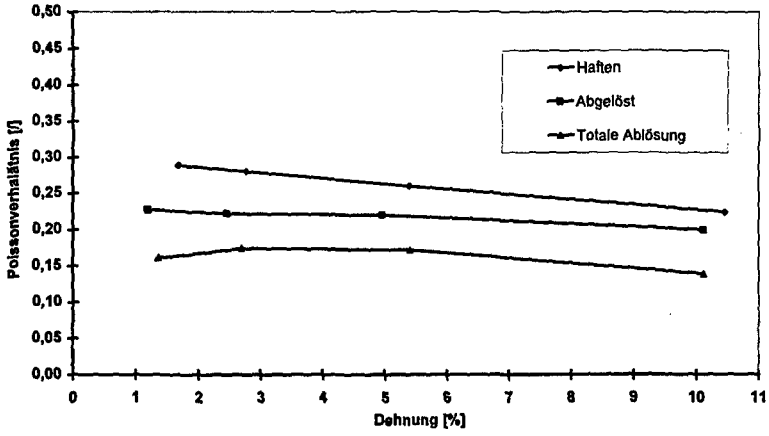

Bild 5: Mit der Finite Elemente Methode berechnete Poissonverhältnisse für verschiedene Ablösezustände

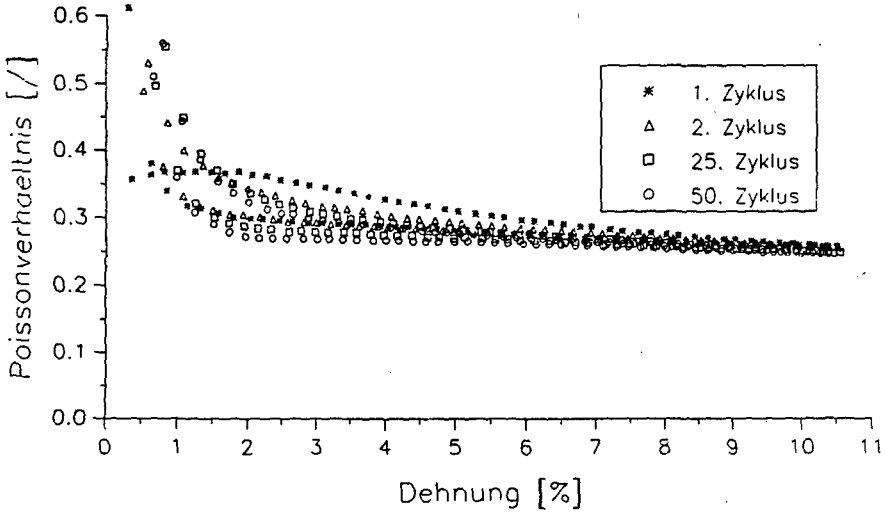

Bild 6: Im zyklischen Versuch experimentel ermittelte Poissonverhältnisse

5. Schlußfolgerung und Ausblick

Die Änderung des Poissonverhältnisses von Festtreibstoffen unter Belastung im Zugversuch wurde durch eine zunehmende Ablösung des Matrixmaterials von der Füllstoffoberfläche erklärt, wofür einige gewichtige experimentell ermittelte Indizien sprachen. Dieser Zusammenhang konnte durch eine FE-Rechnung einer Elementarzelle eines Füllstoffteilchens in elastischem Matrixmaterial qualitativ bestätigt werden.

Mit der Messung des Poissonverhältnisses von Festtreibstoffen ist es daher möglich, Schadensdetektion im Hinblick auf die Matrix-Füllstoff-Anbindung zu betreiben und damit deren Qualität zu beurteilen.

Die Arbeiten werden weitergeführt mit realistischeren Modellen (kugelförmiger Füllstoff) zur Verifikation des Zusammenhanges von Ablösezustand und Poissonverhältnis. Danach werden verschiedene Elementarzellen kombiniert, um die gegenseitige Beeinflussung der Elementarzellen untereinander zu studieren und zu einem realistischeren Materialmodell zu gelangen. Zur Berechnung höherer Füllgrade wird an eine Simulation bimodaler Verteilungen gedacht.

Literatur

/1/ A. Geißler, H. P. Kugler, W. Schmitt, Ch. Weingötz. *Qualitätskontrolle von Festtreibstoffen aufgrund des Querdehnungsverhaltens.* 17th International Annual Conference of ICT 1986, Karlsruhe.

/2/ Ch. Hübner. *Modellierung der deformationsbedingten Änderung der mechanischen Eigenschaften von Modelltreibstoffen unter besonderer Berücksichtigung von Phasengrenzflächenphänomenen.* ICT-Bericht B10/94, Pfinztal 1994.

/3/ K.-J. Bathe. *Finite Element Procedures in Engineering Analysis.* Prentice-Hall, New-Jersey, 1982.

/4/ A. L. Eterovic u. K. J. Bathe. *On the Treatment of Inequality Constraining Arising from Contact Conditions in Finite Element Analysis.* J. Compt. Struct. 40, 433-439, 1991

/5/ L. R. Herrmann. *Elasticity Equations for Incompressible and Nearly Incompressible Materials by a Variational Theorem.* AIAA 3, 1896-1900, 1965.

/6/ J. F. Debongnie. *Sur la formulation de Herrmann pour l'étude des solides incompressibles.* Journal de Mécanique 17, 531-558, 1978.

/7/ E. Geißler. *Implementierung eines speziellen Stoffgesetzes für nichtlinear viskoelastische Festtreibsätze in ein Finite Elemente Programm (Theoretische Vorüberlegungen),* ICT-Bericht B25/92, Pfinztal, 1992.

/8/ N. Eisenreich, C. Fabry, R. Fischer, A. Geißler, H. P. Kugler, F. Sinn. *Messmethode zur Bestimmung der Materialeigenschaften von Energieträgern bei hohen Dehngeschwindigkeiten.* 18th International annual Conference of ICT 1987, Karlsruhe.

CHARACTERIZATION FOR BONDING EFFICIENCY OF THE BONDING AGENTS IN COMPOSITE SOLID PROPELLANTS BY DYNAMIC MECHANICAL AYALYSIS

AIMIN PANG, JINHAN WU, HUIPING JIANG
(HUBEI RED-STAR CHEMISTRY INSTITUTE, XIANGFAN, 441003, CHINA)

ABSTRACT

Composite solid propellant is a highly filled elastomer, the fillers used extensively in today's composites solid propellants are AP, HMX or RDX, which are all non- reinforced fillers; Thus, the interaction between these filler and binder matrix will be very weak. This always results in dewetting under a certain load, which have a detrimental effect on the mechanical properties, combustion properties and aging properties of the propellants. Adding a dash of bonding agent is the most effective and economical method to ameliorate the interfacial binding.

Dynamic mechanical analysis is an effective approach in the investigation of visco-elastic response of polymers. The visco-elastic spectrum is a reflection of the molecular movement which can combine the microscopic structure with its microscopic mechanical properties.

The dynamic mechanical properties of composite solid propellants with and without a bonding agent were studied as a function of temperature in this paper. The propellants (HTPB/AP, Polyeter/HMX) was evaluated by establishing a mesophase or interphase model and introducing a characterization factor, A. The result shows that the lower the value of A, the higher the bonding efficiency is in this temperature range. This investigation provids a new method for the characterization of bonding efficiency of bonding agents in composite solid propellants.

Abstract for submission to 29th International Annual Conference of ICT

Contact details: Dr D A Tod
WX4 (Energetic Materials) Department
DERA, Fort Halstead
Sevenoaks, Kent
United Kingdom

Tel +44 (0) 1959 514492
Fax +44 (0) 1959 516041

Characterisation of Propellant Cure

L Cribb, A V Cunliffe and D A Tod

DERA, WX4
Fort Halstead
Sevenoaks, Kent, UK

Composite rocket propellants based upon hydroxy terminated polybutadiene cured with isophorone di-isocyanate are probable the most common systems used today. Little work has been conducted upon subtle changes in the mechanical properties of the material during the cure cycle. The way the material cures in-situ within the motor body will inevitable affect the mechanical integrity of the charge.

In this study we report the characterisation of the cure of rubbery composite propellants based upon HTPB cured with IPDI. The technique of dynamic stress rheometry has been used where small samples of the material have been cured in-situ whilst the dynamic viscosity has been monitored. The key element of the trials is the sensitivity of the transducer system used which allows very subtle changes in mechanical stiffness to be determined. The trials have included a range of different binder curative ratios with and without the incorporation of fillers. The cure temperature has also been investigated together with the influence of bonding agents.

PLASTICISERS FOR NEW ENERGETIC BINDERS

Paul Bunyan, Anthony Cunliffe & Peter Honey

DERA, FORT HALSTEAD, Sevenoaks, Kent TN14 7BP, UK

ABSTRACT

The physical and chemical behaviour of plasticisers for new elastomeric energetic binders are discussed. It is emphasised that a number of different properties need to be considered when choosing plasticisers, and the choice often depends upon a compromise between conflicting properties.

Experimental results for the lowering of the polyNIMMO binder glass transition temperature by a range of plasticisers, as measured by DSC, are presented. The experimental results can be described in terms of simple equations, relating the T_g of mixtures to those of the pure components. An expression is derived for the efficiency of a plasticiser in lowering the T_g and this is used to compare different plasticisers. However, high plasticising efficiency is not the only criterion for choice of plasticiser, since it is necessary to consider other properties, such as miscibility and migration properties.

One measure of migration is the diffusion rate. Experimental results for diffusion rates of plasticisers in polyNIMMO binders are presented. The results show that plasticisers which are good at lowering the T_g of the binder may also have high diffusion rates, leading to migration problems. Conversely, a plasticiser (BDNPA/F) which is relatively poor at lowering T_g has a particularly low diffusion rate. It is suggested that free volume theories provide the necessary link between the various physical properties.

The importance of stability considerations for the choice of plasticiser/binder systems is stressed. Examples of instability caused by plasticisers are given.

There is a need for better plasticisers, and one possibility is to use oligomeric plasticisers. DERA results for materials of this type are presented, and show encouraging properties. It is concluded that further work is required, to understand the behaviour of existing plasticisers, and to develop new ones.

1. Introduction

There has been considerable interest, over the past few years, in energetic binders based on elastomeric, energetic pre-polymers. Composite energetic materials, based on these binders, in conjunction with crystalline fillers such as HMX, have been proposed for most types of application, including rocket propellants, gun propellants and plastic bonded explosives (PBXs) [1]. The most developed systems are based on glycidyl azide polymer (GAP), poly(3-nitratomethyl-3-methloxetane) (polyNIMMO), and poly(glycidyl nitrate) (polyGLYN). In the UK, collaboration between DERA and ICI Explosives has resulted in extensive development of polyNIMMO and polyGLYN, and the materials show considerable promise. One aspect which has been the recognised from the outset with all currently available energetic pre-polymers is the need to use energetic plasticisers to obtain formulations with properties acceptable for service use. From UK experience, it has become clear that there are problems associated with currently-available plasticisers, which are all far from ideal. We have thus initiated a programme to address this problem. The programme is presently in progress; this paper describes some of the results to date, and also indicates future directions. It is concerned mostly with our attempts to understand the behaviour of existing plasticisers, and their implications for developing improved systems.

It is clear that plasticisers are required in energetic formulations for a number of reasons, and that the properties which need to be considered are even more numerous (Table 1).

1. Plasticisation - lower Tg
2. Improve processing - lower viscosity
3. Physical compatibility - polymer-plasticiser interaction parameter
4. Low migration - diffusion
5. Low migration - volatility
6. No adverse effects on cure reactions
7. Energy - plasticisers often added to increase energy.
8. Stability - long term stability can be crucial.
9. Chemical compatibility - adverse reactions between ingredients
10. Hazard properties - particularly in processing
11. Availability
12. Cost
13. Purity
14. Toxicity.

Table 1. Plasticiser Requirements

We may divide the properties required into three categories. Firstly, there are physical considerations, which would be similar to requirements for ordinary polymer systems, ranging from ability to lower the glass transition temperature (T_g) of the binder, to low migration properties, together with the requirement not to adversely effect the cure behaviour. Secondly, there are a whole set of considerations which arise because we are dealing with energetic materials, ranging from the plasticiser's ability to increase the overall energy, to considerations of stability, compatibility and hazard properties. Finally, there are the standard considerations of availability, cost, purity and toxicity. Many of these requirements are conflicting, and we therefore usually end up with the best compromise for a given situation. If a plasticiser is chosen on the basis of optimising a single property, then this will often lead to problems with other requirements.

2. Lowering of the T_g

The currently available energetic prepolymers all have T_g s above -35^0C, and the values are usually about 10^0 C higher for the cured binders. The UK temperature requirement for air carriage of munitions is approximately -55^0 C to $+70^0$ C, so that it was immediately apparent that a plasticiser was necessary to lower the T_g of polyNIMMO and polyGLYN binders. In order to preserve or improve the energy of the binder, this had to be energetic. This did not appear to be a great problem initially, since it was soon found that energetic plasticisers were effective in lowering the Tg. Data for K10/polyNIMMO is shown in Table 2 (all T_gs were measured by DSC). However, it was clear that different plasticiser had different abilities to lower Tg, and we therefore looked at the plasticiser efficiency of different plasticisers with polyNIMMO.

Plasticiser Concentration % w/w	Tg ^{0}C	Tg ^{0}K
0	-15.0	258.2
25	-36.4	236.8
33	-39.1	234.1
50	-49.3	223.9
100	-66.7	206.5

Table 2 Plasticisation of PolyNIMMO by K10

The first step is to develop a method to describe the behaviour of the plasticiser in the binder. Our approach is illustrated in figure 1. We measure the Tg of the cured polymer, the Tg of the pure plasticiser, and the Tg of cured plasticiser/polymer mixtures. (We found that all the plasticisers which we have studied so far readily form a glass on cooling, and therefore show a Tg). In order to understand the factors controlling the plasticiser behaviour, we wish to describe this behaviour. We therefore looked at theories of plasticiser behaviour. Firstly, we may take a purely empirical approach. The simplest assumption is that the Tg of the mixture lies between that of the pure components, and the simplest relationship is a linear one.

$$T_g = w_1 * T_{g1} + w_2 * T_{g2}$$

As with all problems of this type, the second approach is an inverse relationship;

$$1/Tg = w1/Tg1 + w2/Tg2$$

This is sometimes referred to as the Fox equation; I will call it the simple Fox equation. It is sometime successful in describing plasticiser behaviour and the similar problem of Tgs of copolymers, but does not in general fit our data..

We then looked at theories of Tg of plasticisers or co-polymers. There appear to be two equations commonly quoted. One is due to Gordon and Taylor [2].

$$c1(Tg-Tg1) + \lambda c2(Tg-Tg2) = 0$$

The quantity λ is given by

$$\lambda = \Delta\beta1/\Delta\beta2$$

where $\Delta\beta1$ is the difference between the expansion coefficients for the rubbery and glassy states for polymer 1.

The other equation is the generalised Fox equation [3];

$$1/Tg = 1/(c1+Bc2) *(c1/Tg1 + Bc2/Tg2)$$

It is easy to show that these two equations are the same, if we write;

$$\lambda = B*Tg1/Tg2$$

We find that we can fit our experimental data with equations of this type, by choosing a suitable value of B. A typical result is shown in figure 2. In general, the experimental data tend to have values of B greater than unity, so that the experimental points fall below the simple theories.

Clearly, we can describe the deviation from simple behaviour in terms of the quantity B. The nature of this quantity is indicated by the approach of Gordon and Taylor [2]. Their theory defined the Tg in terms of volume changes in the glassy and rubbery phases of the polymer. In general terms, it is possible to relate B to free-volume changes caused by plasticisation. The larger the value of B, the greater the free volume increase caused by the plasticiser. Thus, if the data deviates greatly from the simple Fox equation, then the plasticiser is causing a greater than expected increase in free volume.

We may define the plasticiser ε efficiency as

$$\varepsilon = -\left(\frac{\partial T_g}{\partial w_2}\right)_{w_2 = 0}$$

$$\varepsilon = \lambda (T_{g1} - T_{g2})$$

1 - Polymer 2 - Plasticiser

We see that there are two factors contributing to a high value of ε. Firstly , we require a large value of $(T_{g1} - T_{g2})$; that is, the plasticiser should have a much lower T_g than the polymer. Thus, for a given polymer system, we require a plasticiser with as low a T_g as possible. In addition, we require a large value of λ. Since λ (and B) represents the deviation from ideal behaviour in the Fox equation, large values of this quantity represent increased plasticiser efficiency over that expected for ideal behaviour. Thus, large deviations from ideal behaviour can give greater lowering of the T_g s of the binder. It will be seen, however, that this may lead to other, undesirable features when the total trade off between a range of properties is considered.

We have found that this simple approach describes very well our data on the effect of plasticisers on polyNIMMO binders. Typical results are shown in figures 2 and 3. The approach is a good way of characterising the plasticisation behaviour of the different plasticisers. We can thus characterise the behaviour in terms of the parameters described above. Values for a number of energetic and non-energetic plasticisers of interest are shown in Table 3. The approach so far is a good way of rationalising the experimental data, but we wish also to understand the relationships between chemical structure and behaviour. We hope to apply molecular modelling techniques to this end. Previous work [4] has shown the usefulness of the molecular modelling approach, and we are in the process of extending the techniques to our ore comprehensive and better understood experimental data.

PLASTICISER	Tg	Tg1-Tg2	λ	ε
K10	206.3	51.7	1.905	98.5
BuNENA	191.2	66.8	1.607	107.4
MEN42	193.9	64.1	2.334	149.6
BDNPA/F	210.8	47.2	0.891	42.0
LNP	223.2	34.8	1.415	49.2
DOS	167.6	90.4	2.338	211.4
DBP	180.0	78.0	1.342	104.7
DOP	190.2	67.8	1.927	130.7
NIMMO Monomer	178.0	80.0		

Table 3. Plasticiser Efficiencies

3. Miscibility and Migration Properties

From the results so far, it would appear that the best plasticisers are ones with low T_gs , and large values of λ (and B). It might appear that we require the largest value of λ, since this gives the lowest Tg for a given concentration. However, this is not necessarily the case. The reason is that other properties are also important.

I show two examples of this. If we consider plasticisation of polyNIMMO by DOS, then this shows a very large value of B (figure 4). However, the curve stops at 20 % of DOS. This is because at this stage the DOS becomes immiscible, and phase separation occurs. In general,

large plasticisation effects are associated with poor solvent systems, and there is thus a greater tendency for phase separation in materials which cause large reductions in Tg. Similarly, good capability for lowering the Tg is often associated with high migration rates. This is understandable in terns of free volume theories. Large free volume will produce large reductions in Tg, but it will also be associated with large diffusion rates. The free volume approach to plasticisation is particularly useful, as it links several of the important quantities. Thus, free volume theories can be used to describe the lowering of Tg, the diffusion rates and the viscosity of polymer/plasticiser compositions.

We hope to develop these ideas further to attempt to rationalise plasticiser data. It has always been recognised that migration problems are associated with plasticisers in energetic materials, the most important and longest-suffered case being "sweating" of NG. We wish to obtain reliable quantitative data to compare different plasticisers. One problem is that the actual practical behaviour depends upon a number of properties, such as diffusion coefficients, vapour pressure, polymer/solvent interaction parameters etc., as well as the actual configuration of the system, temperature and temperature gradients etc. However, as a starting point we have a programme to measure diffusion coefficients. In certain circumstances this will determine migration behaviour, and is a good first indication of the relative mobility of plasticisers.

The next table shows measured diffusion coefficients for a number of plasticisers in polyNIMMO binders at 75^0 C.

PLASTICISER	TEMPERATURE ^{0}C	D X10^8 cm^2 $secs^{-1}$	ACTIVATION ENERGY KJ $Mole^{-1}$
MEN 42	75	2.40	51.5
BuNENA	75	1.23	51.2
K10	75	1.15	56.6
BDNPA/F	75	0.45	59.6

Table 4. Coefficients & Activation Energies for Diffusion in PolyNIMMO Binders

We see that there is a considerable variation in the diffusion coefficients for the four materials.

It is of interest to compare these results with the better known example of nitro-cellulose migration. Results are shown in Table 5.

PLASTICISER/POLYMER	TEMPERATURE ^0C	D X $!0^8$ cm^2 $secs^{-1}$	ACTIVATION ENERGY KJ $Mole^{-1}$
K10/PolyNIMMO	75	1.15	56.6
BuNENA/polyNIMMO	75	12323	51.2
BuNENA/Nitro-cellulose	75	.013	72
NG/Nitro-cellulose	75	.014	95

Table 5. Diffusion Constants in PolyNIMMO and Cellulose Nitrate

We see that the diffusion constant for BuNENA in polyNIMMO is roughly two orders of magnitude greater in polyNIMMO than in cellulose nitrate. This is no surprise when we consider the nature of the two materials. Cured polyNIMMO is a soft, elastomeric material whereas un-plasticised nitro-cellulose is a thermoplastic, partially crystalline material at room temperature. The different behaviour can be understood in a general way in terms of the relative glass transition temperatures of the two materials. Thus, plasticiser migration problems can be rationalised in terms of the glass transition temperatures of the two materials.

These considerations illustrate that migration problems may be relatively more severe for any elastomeric binder system, whether energetic or non-energetic, and is one of the main reasons for the need for better (in this case, less mobile) plasticisers. On the basis of Table 4, it appears that BDNPA/F is the best material with regard to plasticiser migration, and this has been noticed already from practical weight loss tests on model formulations. However, it has other drawbacks. It is not very good at lowering the Tg, and another problem is indicated as follows.

We initially carried out diffusion measurements at higher temperatures, to obtain results rapidly. The experimental set up is such that we are effectively measuring the rate of diffusion of plasticiser out of the sample. The results are plotted as Arrhenius plots i.e. the log of the rate constant v 1/T. Most of the samples show reasonable Arrhenius plots, with activation energies similar to those obtained at lower temperatures. However, the BDNPA/F results are anomalous. The highest temperature measurements could not be analysed by the expected equations. For the two lower points, the activation energy of ~ 196 KJ $Mole^{-1}$ is

much too high for a diffusion process. In fact, it is typical of a value for chemical decomposition of an energetic material, and it is clear that this is dominating the sample weight loss at high temperatures. We are in the process of investigating this effect further, but at present we believe that it is decomposition of the acetal component which is the problem.

4. Stability Considerations

This question of the stability of the materials is one of the major areas of study within DERA. There are several aspects to this; for example, the stability of plasticiser alone, the compatibility of the plasticiser with other components of the energetic composition, and the effect of plasticiser on binder stability e.g. binder cross-link density & mechanical properties and gas production.

BDNPA/F is an example of the first type of behaviour. However, a lot of binders show the second type of behaviour, particularly when real formulations with a number of potentially reactive additives, added for various performance reasons, are considered.

For polyNIMMO binders, for example, the critical ageing mechanisms is oxidative chain scission of the binder, which causes a softening (figure 5). This is often accelerated by plasticisers, as shown in figure 5 for the changes in crosslink density of polyNIMMO binders plasticised with MEN42. It is seen that the softening, which also accelerates migration problems etc., is much more severe for the MEN42 binder, leading to a significant reduction in expected service lifetime. These types of behaviour is not confined to polyNIMMO. For example, it has been shown that propellants based on GAP, which is an azide-based energetic polymer, may suffer from high rates of gassing [5]. Some minimum smoke rocket propellants, based on GAP plasticised with nitrate ester stabilisers, have been shown to exhibit high rates of gas evolution at elevated temperatures [5].

5. Future Plasticisers

Our results so far indicate that there are problems with all the plasticisers which we have studied. Of particular concern are the migration and stability considerations, which cause doubts about the use of the lower molecular weight materials. One approach being pursued at DERA to address this problem is the use of oligomeric plasticisers e.g. NIMMO oligomers, and GLYN oligomers, to plasticise the energetic binders [6]. The development of oligomeric

plasticisers has a number of attractions. Oligomeric NIMMO is expected to show good physical and chemical compatibility with polyNIMMO, and can be prepared by a modification of the same process. Work has already been carried out on this material, and the preliminary indications are promising. In the case of NIMMO, either the cyclic tetramer, or linear oligomers may be prepared. The linear materials appear more promising at present. It is possible to prepare linear materials, based on a difunctional initiators, or branched materials with tri- or tetra-functional initiators. Initially, hydroxyl terminated oligomers are produced, and these are then nitrated. We are at present in the process of optimising the chain lengths and structures to obtain the best compromise between properties such as plasticisation efficiency, low migration and energy. Finally, it is clear that there are difficulties with all separate plasticisers, and a very attractive solution would be to achieve internal plasticisation. This would involve modification of the polymer structure to improve the properties without the use of a separate plasticiser.

6. Conclusions

We may draw a number of conclusion from our work so far.

1. It is necessary to consider a range of properties when assessing plasticisers
2. Plasticiser behaviour can be rationalised in terms of simple theories
3. We need to develop these further, and extend them to other plasticisers
4. No plasticiser is ideal
5. There is a need for new plasticisers

7. References

1. *New Energetic Formulations Containing Nitratopolyethers*, D Debenham, W B H Leeming and E J Marshall, "Proceedings of the Joint International Symposium on Energetic Materials Technology", ADPA, San Diego USA, 119 (1991).
2. Gordon M and Taylor J S, *J Applied Chem.* **2**, 493 (1952).
3. Fox T G and Loshaek S, *J Polym Sci* **15**, 371 (1955).
4. *Molecular Modelling of PolyNIMMO Plasticisation*, Robson E, Leiper GA & Cumming A S, "Life Cycles of Energetic Materials Conference", San Diego USA, November 1994.
5. *Life Time Assessment and Stability of AN/GAP Propellants*, M A Bohn, J Böhnlein-Mauss and K Menke, "Service Life of Solid Propellant Systems", AGARD PEP 87th Symposium, Athens, Greece, 10-14 May 1996, AGARD CP-586, 9.1 (1996).
6. *Synthesis and Characterisation of α,ω-hydroxy and nitrato telechelic oligomers of 3,3-(nitratomethyl) methyl oxetane (NIMMO) and Glycidyl Nitrate (GLYN)*, H J Desai, A V Cunliffe, J Hamid, P J Honey, M J Stewart and A J Amass, Polymer **37**, 3461 (1996).

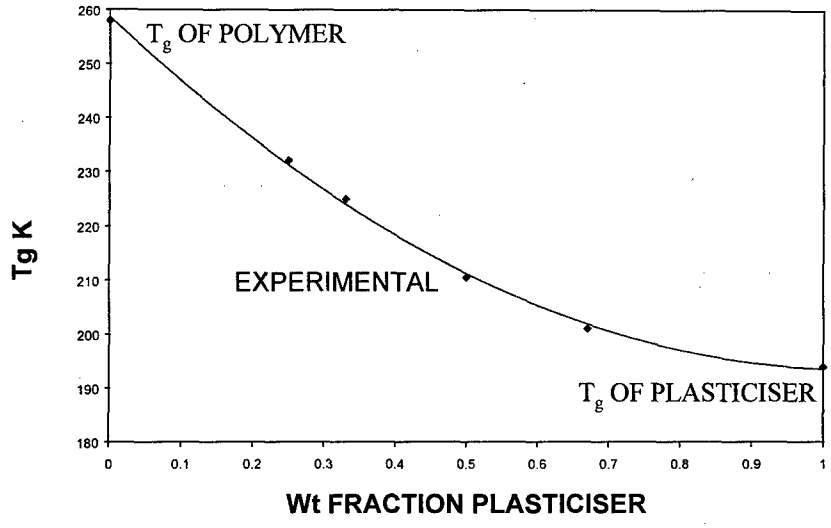

FIGURE 1 Tgs of POLYMER/PLASTICISER SYSTEMS

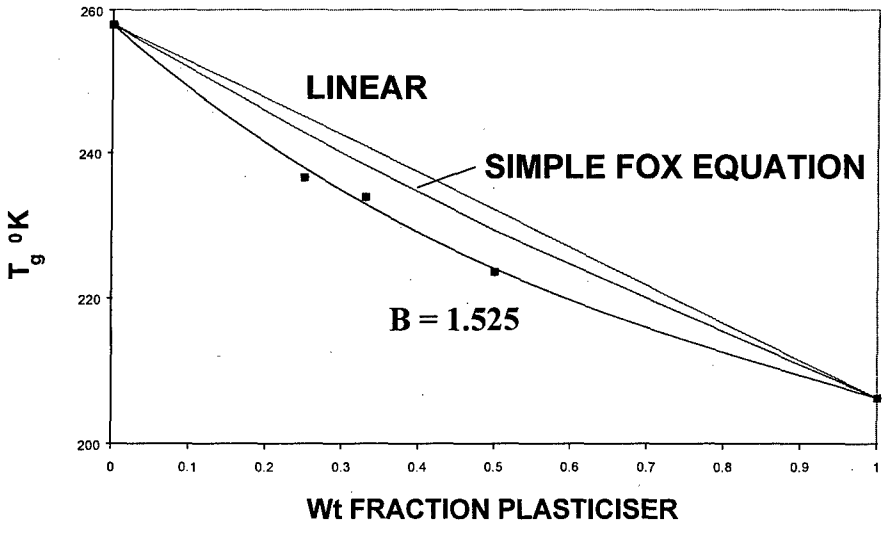

FIGURE 2 Tgs for PolyNIMMO/K10 SYSTEM

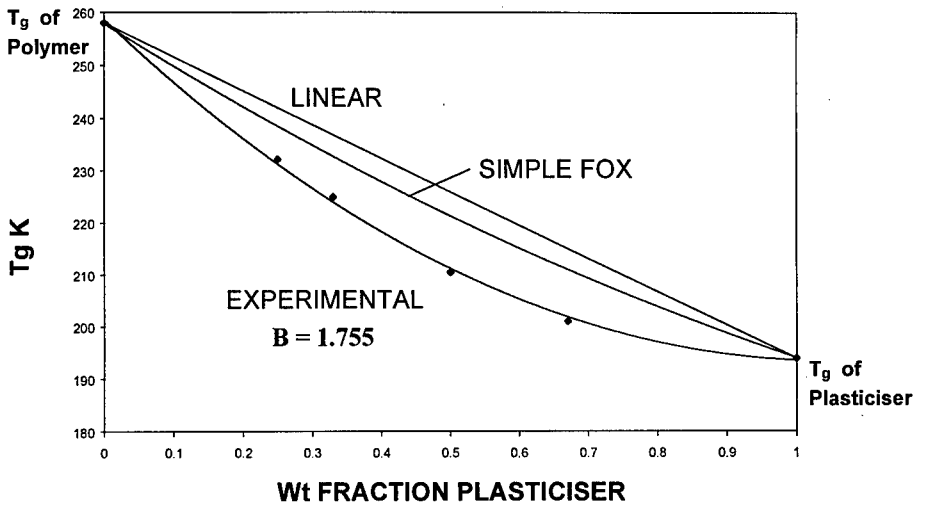

FIGURE 3 Tgs for PolyNIMMO/MEN42 SYSTEM

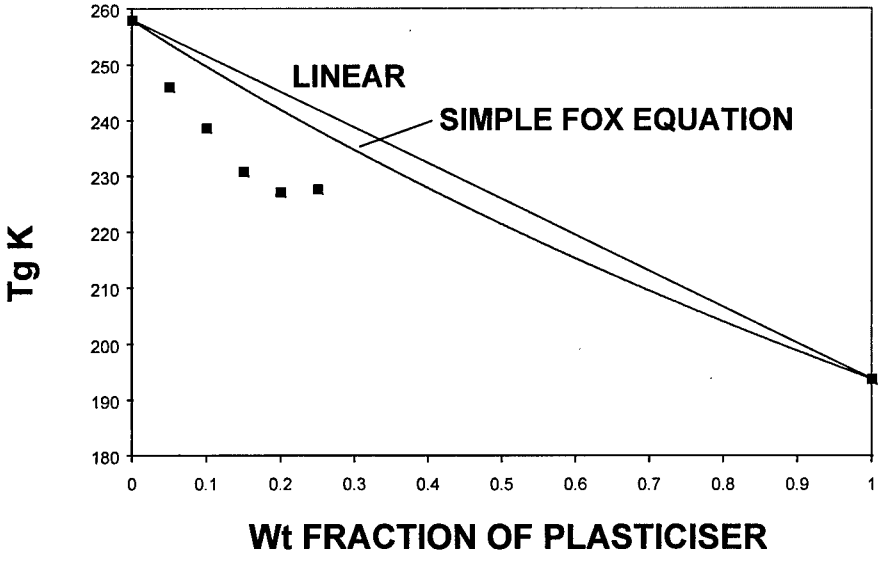

FIGURE 4 Tg of PolyNIMMO/DOS SYSTEMS

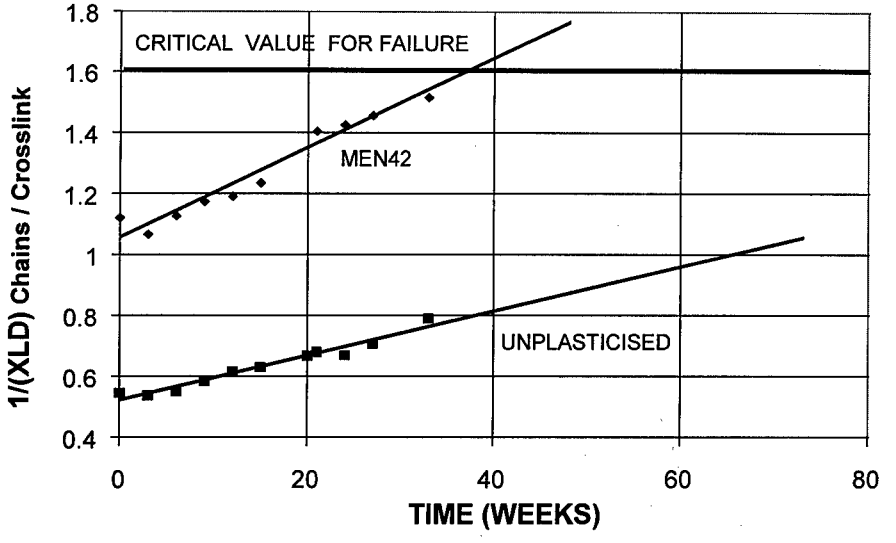

FIGURE 5 DRY AGEING AT 70C OF POLYNIMMO AND POLYNIMMO / MEN42 BINDERS

Evaluation of a Homologous Series of High Energy Oxetane Thermoplastic Elastomer Gun Propellants*

I.A. Wallace, P.C. Braithwaite, A.C. Haaland, M.R. Rose, R. B. Wardle
Thiokol Propulsion
Brigham City, Utah 84302

INTRODUCTION

Current state-of-the-art gun propellants produce energies slightly above 1100 J/g and loading densities of roughly 1.1 g/ml. In a standard grain configuration, this energy-density combination does not deliver the desired muzzle energy for future indirect fire support requirements. Similar shortfalls occur in using today's propellant in tomorrow's direct fire gun systems. Higher loading densities of hazardous ingredients (HMX, RDX) and unique grain geometries provide energy growth but only with great difficulty are the required muzzle energy levels achieved.

An alternate strategy for meeting the need for increased performance in impetus, ballistics, and density in advanced gun propellants is the use of high energy/density ingredients. As with the vast majority of emerging technologies, these materials have required considerable research and development prior to being mature enough for use in a developmental gun propellant system. This fundamental groundwork has been laid by extensive research under the auspices of the Office of Naval Research into the synthesis, characterization and exploratory formulation of novel high energy materials.

SUMMARY

Six TPE-based gun propellants were evaluated. The TPE's used included BAMO-AMMO (25% BAMO), BAMO-NMMO (25% BAMO), and BEMO-NMMO (25% BEMO). The monopropellants/oxidizers used included CL-20, RDX, TNAZ and NQ. The ingredients were vertically mixed and ram extruded into ½-in diameter cords. These were subsequently rolled into sheets from which 1-in by 1-in by 0.10-in "squares" were stamped. Closed bomb testing was done on the samples which had burn rates ranging from eight to nearly eleven inches per second (40ksi, 21°C) and impetus (calculated) between 1278 and 1349 J/g.

DISCUSSION

Theoretical Trade Study

A fairly large number of TPE's, mono-propellants and additives were available for use as gun propellant ingredients when this work began. Some prior knowledge of their effect on performance and ballistic properties in propellant formulations was available. For example, in propellants using BAMO-AMMO TPE, it was known that the use of CL-20 resulted in much higher burn rates and energy-densities than RDX did.

Theoretical calculations also indicated that energy-density increased with increasing BAMO/AMMO ratios. Six formulations were pursued. These formulations are shown in Tables I through VI along with calculated performance values and closed bomb data.

The NBLAKE thermodynamics code was used to perform the calculations. Impetus and closed bomb burn rate of most of these formulations are plotted in Figure 1. In general, the CL-20 formulations result in the highest impetus (and burn rates). A notable exception, however, is formulation ONR #5, a BAMO-NMMO/RDX/TNAZ formulation. Here the use of NMMO instead of AMMO and the use of 24 percent TNAZ instead of RDX add about 100 J/g to the impetus of a 76 percent solids BAMO-AMMO/RDX formulation (not plotted). BEMO is the least energetic of the three TPE's used for the ONR propellants and the performance of the BEMO-containing formulations reflect this.

Table I. Formulation ONR #1, Calculated and Measured Properties.

Ingredients	Wt. Percent	Hazards Characteristics			
BAMO	6.00	ABL Impact (cm, TIL)	33		
AMMO	18.00	ABL Friction (psi, TIL)	800@8ft/s		
NMMO		TC ESD (J)	>8		
BEMO		SBAT (Onset, °F)	304		
CL20 (3.8μ, bimodal)	76.00	**Mechanical Properties**			
RDX (7μ)		Not measured			
NQ (50μ, needles)					
TNAZ (11μ)					
Calculated Performance					
Impetus (J/g)	1291	**Ballistic Properties**			
Temperature (K)	3378	Pressure (ksi)	Rb (ips)		
TMD (g/cc)	1.78		-32°C	22°C	48°C
Gamma	1.267	30	6.13	6.54	6.81
Energy-Density (J/cc)	8588	40	8.24	8.74	9.07
Other		50	10.07	10.71	11.09
Density (g/cc)	1.733	n	0.98	0.97	0.96

Table II. Formulation ONR #2, Calculated and Measured Properties.

Ingredients	Wt. Percent	Hazards Characteristics			
BAMO	6.00	ABL Impact (cm, TIL)	26		
AMMO		ABL Friction (psi, TIL)	800@8ft/s		
NMMO	18.00	TC ESD (J)	>8		
BEMO		SBAT (Onset, °F)	290		
CL20 (3.8μ, bimodal)	64.00	**Mechanical Properties**			
RDX (7μ)		Not measured			
NQ (50μ, needles)	12.00				
TNAZ (11μ)					
Calculated Performance					
Impetus (J/g)	1280	**Ballistic Properties**			
Temperature (K)	3476	Pressure (ksi)	Rb (ips)		
TMD (g/cc)	1.75		-32°C	22°C	49°C
Gamma	1.254	30	6.99	7.14	7.34
Energy-Density (J/cc)	8793	40	9.74	9.66	9.89
Other		50	12.01	11.71	12.13
Density (g/cc)	1.732	n	1.07	0.97	0.99

Table III. Formulation ONR #3, Calculated and Measured Properties.

Ingredients	Wt. Percent	Hazards Characteristics			
BAMO	6.00	ABL Impact (cm, TIL)	33		
AMMO	18.00	ABL Friction (psi, TIL)	800@8ft/s		
NMMO		TC ESD (J)	>8		
BEMO		SBAT (Onset, °F)	304		
CL20 (3.8μ, bimodal)	52.00	**Mechanical Properties**			
RDX (7μ)		Not measured			
NQ (50μ, needles)					
TNAZ (11μ)	24.00				
Calculated Performance					
Impetus (J/g)	1278	**Ballistic Properties**			
Temperature (K)	3306	Pressure (ksi)	Rb (ips)		
TMD (g/cc)	1.74		-32°C	23°C	49°C
Gamma	1.267	30	6.88	7.57	7.70
Energy-Density (J/cc)	8322	40	9.18	10.01	10.20
Other		50	11.12	11.99	12.24
Density (g/cc)	1.698	n	0.94	0.90	0.91

Table IV. Formulation ONR #4, Calculated and Measured Properties.

Ingredients	Wt. Percent	Hazards Characteristics			
BAMO	6.00	ABL Impact (cm, TIL)	21		
AMMO		ABL Friction (psi, TIL)	800@8ft/s		
NMMO	18.00	TC ESD (J)	>8		
BEMO		SBAT (Onset, °F)	275		
CL20 (3.8μ, bimodal)	76.00	**Mechanical Properties**			
RDX (7μ)		Not measured			
NQ (50μ, needles)					
TNAZ (11μ)					
Calculated Performance					
Impetus (J/g)	1349	**Ballistic Properties**			
Temperature (K)	3794	Pressure (ksi)	Rb (ips)		
TMD (g/cc)	1.78		-33°C	22°C	48°C
Gamma	1.249	30	7.43	7.65	8.04
Energy-Density (J/cc)	9633	40	10.19	10.43	10.95
Other		50	12.54	12.70	13.21
Density (g/cc)	1.777	n	1.03	1.00	0.98

Table V. Formulation ONR #5, Calculated and Measured Properties.					
Ingredients	**Wt. Percent**	**Hazards Characteristics**			
BAMO	6.00	ABL Impact (cm, TIL)	26		
AMMO		ABL Friction (psi, TIL)	800@8ft/s		
NMMO	18.00	TC ESD (J)	>8		
BEMO		SBAT (Onset, °F)	264		
CL20 (3.8μ, bimodal)		**Mechanical Properties**			
RDX (7μ)	52.00	Not measured			
NQ (50μ, needles)					
TNAZ (11μ)	24.00				
Calculated Performance					
Impetus (J/g)	1283	**Ballistic Properties**			
Temperature (K)	3327	Pressure (ksi)	Rb (ips)		
TMD (g/cc)	1.626		-33°C	24°C	49°C
Gamma	1.254	30	6.41	6.66	7.00
Energy-Density (J/cc)	8205	40	8.69	9.08	9.40
Other		50	10.59	11.27	11.44
Density (g/cc)	1.646	n	0.99	1.03	0.96

Table VI. Formulation ONR #6, Calculated and Measured Properties.					
Ingredients	**Wt. Percent**	**Hazards Characteristics**			
BAMO		ABL Impact (cm, TIL)	21		
AMMO		ABL Friction (psi, TIL)	800@8ft/s		
NMMO	18.00	TC ESD (J)	>8		
BEMO	6.00	SBAT (Onset, °F)	269		
CL20 (3.8μ, bimodal)	76.00	**Mechanical Properties**			
RDX (7μ)		Not measured			
NQ (50μ, needles)					
TNAZ (11μ)					
Calculated Performance					
Impetus (J/g)	1290	**Ballistic Properties**			
Temperature (K)	3489	Pressure (ksi)	Rb (ips)		
TMD (g/cc)	1.76		-33°C	24°C	49°C
Gamma	1.254	30	5.75	5.99	6.75
Energy-Density (J/cc)	8926	40	8.27	8.26	9.36
Other		50	10.54	10.32	11.35
Density (g/cc)	1.732	n	1.19	1.07	1.02

Table VII. Ingredients and Thermochemical Data for ONR ETC Gun Propellants.			
Ingredient	**ΔH_f (kcal/mol)**	**Formula**	**Density**
BAMO	53.3	C 3.033, H 4.790, O 0.498, N 3.635	1.26
AMMO	4.32	C 3.967, H 7.180, O 0.723, N 2.400	1.26
NMMO	-79.67	C 5, H 9, N, 1, O, 4	1.26

BEMO	-164	C 9, H 18, O 3	1.10
CL-20	101	C 6, H 6, O 12, N 12	2.04
RDX	15.9	C 3, H 6, O 6, N 6	1.82
NQ	-22.1	C 1, H 4, O 2, N 4	1.73
TNAZ	2.8	C 3, H 4, O 6, N 4	1.84

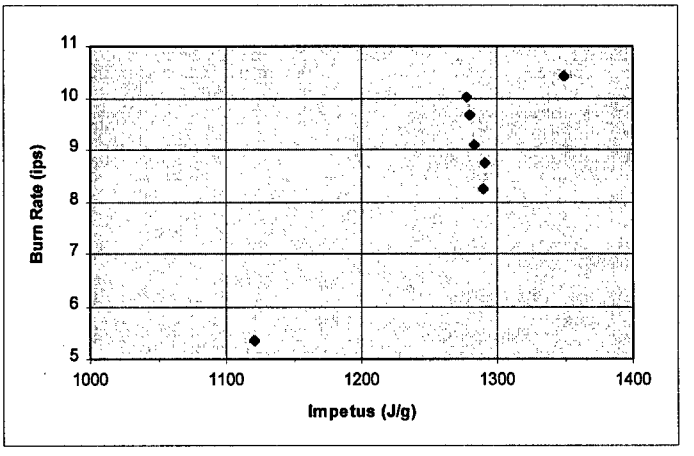

Figure 1. Impetus (calculated) and closed bomb burn rate (40 ksi, 21°C) of the propellants of this study and of a 72% solids RDX BAMO-AMMO propellant for comparison (impetus 1121 J/g, burn rate 5. 36 ips).

Propellant Processing

Each formulation manufactured for this program was processed using a three step process: 1) batch mixing, 2) ram extrusion, and 3) roller milling to final configuration. The overall goal of all propellant processing operations was to produce the most uniformly high density and homogeneous gun propellant possible. This processing method has been successfully used to produce the small quantities of propellant needed for analytical testing and closed bomb testing. A brief description of each processing step is found below.

All propellant mixes produced in this program were processed in a 1-pint vertical mixer.

The basic mix cycle used consisted of three steps:

1) Add polymer and solvent to the mix bowl and mix until the polymer is dissolved.
2) Add the solid ingredients and mix until uniform.
3) Slowly heat the mixer and mix until all of the solvent has been removed and the mix is of the proper consistency.

The goal of the batch mixing step was to thoroughly wet all of the solid particles with the TPE binder and to provide a consistent and homogeneous feedstock for ram extrusion. Fine adjustments (temperature, mix times, etc.) were made with each composition to compensate for differences in the processibility. As expected, formulations which had higher solids were more viscous than those with lower solids contents.

Once propellant was mixed it was immediately taken to a 2-inch ram extruder and extruded through a ½-inch diameter circular die. By controlling the extrusion rate, pressure and temperature it was possible to obtain extruded propellant with a smooth surface. It was found that the surface finish was an excellent indicator of final propellant quality. Therefore every effort was made to obtain the smoothest propellant surface possible. Formulation quality was verified by measurement of density and comparison to the theoretical value.

Following extrusion the final step in the process was roller milling. In this process the extruded cord was taken and cut into appropriate lengths and processed through a laboratory scale roller mill. Typically a piece of propellant would be processed several times through the mill in order to get it to the desired thickness and width (0.100-inch thick and a minimum of 1.1 inches in width). Once the propellant had been rolled to the desired dimensions it was cut into 1-inch squares which were 0.100-inches thick. All formulations were readily rolled and cut into squares.

Closed Bomb Testing

Gun propellant samples consisted 1-in by 1-in squares stamped from 0.100-in thick sheets. Several squares were loaded into a Harwood closed bomb. The bomb used is rated at 129 ksi and has an operating pressure of 100 ksi. The bomb was not equipped with a cooling jacket. Prior to ignition, the samples were conditioned for 4 hours. The ignitor used was a bag type ignitor with one gram of DuPont FFFG black powder secured to an electric match (Davey Corp.) with paper.

It was desired to obtain burn rate data in duplicate at three different temperatures for each of the six formulations chosen, and this was done. A sample of the data are presented in the propellant data sheets, Tables I through VI. The McVece thermochemical code along with the data of Table VII was used to provide the input required for the closed bomb data reduction.

Conclusions

A homologous series of oxetane-based gun propellants were prepared using a combination of mixing, extrusion and rolling to prepare reproducibly high quality samples. The series examined the effect of filler and characteristics of the binders on the ballistic properties. The high energy and flame temperature of the formulations led to generally high burn rates although a 26 percent range in burn rate was demonstrated

over a 5.6 percent range of impetus. This suggests these formulation changes can offer the ability to tailor ballistics at a constant performance and to manage the energy of a given charge to maximize ballistic performance.

THE MODELLING OF EXPERIMENTAL BUNENA/RDX/NC PROPELLANT PROPERTIES

Charles Frank Wiehahn, Martin Ayliff Jeremy Gantana and Jeffrey Charles Engel

Somchem, Division of DENEL, (Pty), Ltd, Gun Propulsion – R & D,
PO Box 187, Somerset West, 7129, South Africa

Abstract

In order to develop new generation propellants with improved properties various energetic components, and formulations thereof, were considered. One of the most promising components was BuNENA and it was decided to investigate a series of propellant formulations with BuNENA as energetic plasticiser, nitrocellulose as binder and RDX as oxidiser. Certain constraints were placed on the thermochemical, density and processing properties and this was used as a guideline in the experimental design.

This paper describes the experimental design matrix used to study various propellant properties (responses) as a function of propellant composition. These propellant properties were measured and evaluated and then used to generate response surfaces or contour maps that display the effect of the changing component levels of the formulation on the various propellant properties. The information so gained was of great importance in generating a comprehensive computer model to predict the various response trends as a function of the changing component levels of the BuNENA/RDX/NC propellant formulations.

1 INTRODUCTION

As part of the ongoing process to develop propellant formulations with improved properties, various energetic components and propellant formulations thereof, were investigated. BuNENA [N-n-butyl-N-(2-nitroxy-ethyl) nitramine] has been identified as one of the most promising components and it was decided to investigate a series of propellant formulations with BuNENA as energetic plasticiser, nitrocellulose as binder and RDX as oxidiser.

BuNENA has previously been synthesised and characterised with regards to its chemical, thermal and sensitivity properties. We needed to evaluate it as an energetic plasticiser in NC containing propellant formulations and an effective way of evaluation is the modelling of the

propellant properties as a function of BuNENA and its other components. Various families of propellant formulations containing BuNENA as energetic plasticiser and NC as binder were investigated for possible use in the modelling process. However, after applying the design criteria for new generation propellants only the propellant family containing NC, BuNENA, RDX and NQ remained as a viable option for the modelling of propellant properties.

In our experimentation a variation of the extreme vertices mixture design was used to study the propellant properties as a function of composition. A design matrix consisting of four components or variables was generated and consisted of 17 formulations. These formulations were processed and the initial model was constructed after analysing the propellant properties to determine the various responses. These responses were then used to generate response surfaces or contour maps that display the effect of the changing component level of the formulation on the propellant properties.

The response surface contours, which are generated for each property, are useful in predicting the effect of changing component levels on the various propellant properties. These optimisation plots offer the flexibility of making meaningful trade-offs between various propellant properties when confronted with the need to prioritise propellant properties according to user requirements. These models and all the response surfaces or contour maps generated, are discussed in detail.

1.1 CRITERIA FOR NEW GENERATION PROPELLANT PROPERTIES

The propellant properties that have been set as a guideline for the development of new generation propellant formulations are the following:

- Thermochemical properties:
  - ♦ Specific energy ≥ 1050 J/g
  - ♦ Flame temperature ≤ 2700 K
  - ♦ Molecular mass of combustion gasses ≤ 20 g/mole
- Theoretical density > 1.50 g/cm^3

1.2 PROCESSING PARAMETERS

In experimenting with mixtures it is often also necessary to constrain the components to avoid compositions which would be undesirable in terms of economic reasons, processability and/or mixture properties. Irrespective of the guidelines for all the other propellant properties, one of

the most critical parameters is that the propellant formulations must be processable. During this experiment we only concentrated on propellant formulations that are processable with the solvent process. The following processing parameters are used as a guideline for the solvent process with NC as the binder. They are basically as follows:

- Effect of binder : plasticiser ratio on propellant processing:
  - ♦ binder : plasticiser > 2 processing not possible
  - ♦ binder : plasticiser 1- 1.5 good processing
  - ♦ binder : plasticiser < 1 too soft, poor processing
- Crystalline concentration 10% - 60%

1.3 THERMOCHEMICAL DESIGN CONSTRAINTS

The above mentioned design constraints for new generation propellants were applied to various propellant formulations containing BuNENA as plasticiser and NC as binder. In order to be able to model the propellant properties as a function of the propellant composition, we strived to keep the composition or formulations as simple as possible. We attempted to model the effects of BuNENA and the BuNENA/NC ratio's on the propellant properties and only RDX as a third formulation variable was initially investigated. The thermochemical data that we initially had for BuNENA was considerably higher than the thermochemical data according to the latest ICT Database (third update, 1997). The formulations containing only BuNENA/NC/-RDX gave flame temperature values that were all above our guideline criteria. For this reason we introduced NQ as a fourth formulation variable to cool the formulations.

2 EXPERIMENTAL DESIGN

Propellant formulations that complied with the thermochemical and density criteria and that fell within the feasible processing range formed the framework for the construction of the experimental design matrix. A variation of the extreme vertices mixture design was used to construct models which were then used to generate response surfaces or contour maps that display the effect of the changing component levels of the formulation on the propellant properties. This type of design matrix minimises the number of formulations required for experimental processing and at the same time maximises the information obtained from the experiment.

The Design Expert Software Package was used to generate the design matrix and the various contour maps (models). The design matrix consisted of 17 formulations for the four component system under the constraints as given in Table 1.

Table 1: Constraint Levels For Each Of The Four Components

Component	Lower Level	Upper Level
NC (11.7% N)	25%	40%
BuNENA	20%	30%
NQ	15%	35%
RDX	10%	25%

The stabiliser concentration was kept constant for all the formulations.

3 TESTING AND EVALUATION

The 17 experimental NC/BuNENA/NQ/RDX propellant formulations were all successfully processed using the solvent process. The samples were evaluated for a wide range of chemical, stability, sensitivity, physical, mechanical and ballistic properties. The test and evaluation results are not presented in this paper and only the modelling of the results will be presented.

4 MATHEMATICAL MODELLING OF RESPONSE DATA

The objectives of the modelling of propellant properties are to:

- determine practical processing limits
- design formulations that comply with thermochemical constraints
- predict specific propellant properties
- manipulate propellant formulations to meet specific requirements

Computer-aided experimental design, multiple regression analysis and response surface methodology was used to study the influence of the independent variables (components) on the propellant properties (responses). From this analysis, empirical regression models for the properties of the propellant within the given experimental domain, were derived.

The design model consists of 4 variables namely the BuNENA, NC, RDX and NQ concentrations and each response is modelled as a function of these 4 variables. Only 3 of the 4 variables can be graphically depicted in a 2-dimensional presentation and therefore for each presentation one of the variables is kept at a constant value while the other 3 are varied between the upper and lower design concentration levels. A different value for the constant variable is then used and the modelling process repeated at that level.

The larger number of responses measured and the corresponding models generated, cannot all be reported in this paper and only the following responses or properties were included.

- stress
- strain
- impact strength
- Tg value (glass transition temperature)
- percentage die swell or shrinkage
- relative quickness
- burning rate at 350 MPa

Many of the other properties such as the specific energy, flame temperature and density can be calculated empirically from the formulation and modelling is therefore not necessary to predict these properties as a function of the component formulation. However, in order to predict the specific energy, flame temperature and density trends as a function of changing component level these properties can be modelled.

4.1 MODELLING OF MECHANICAL PROPERTIES

Stress Properties

The stress value of a propellant formulation is a direct indication of the mechanical strength of the propellant sample. The modelling of the stress values was done at a constant NQ concentration of 20% and repeated at a NQ concentration of 30%. The NC, RDX and BuNENA concentrations were varied between the upper and lower constraint levels. The graphical presentations of the models generated are presented in Figure 1.

The trends of the graphic models are as follows:

- both the NQ and RDX concentrations and the total crystalline concentration have negligible influence on the stress values

- the highest stress values occur at the highest NC values and when the BuNENA concentration is at its lowest level
- BuNENA has the largest influence on the stress values, but in a negative sense in so far as the lowest stress occurs at the highest BuNENA concentration and the corresponding lowest NC concentration
- there is basically no change in the range and the trend of the stress values for a NQ concentration of 20% or 30%
- the relations of stress versus component concentrations are all linear

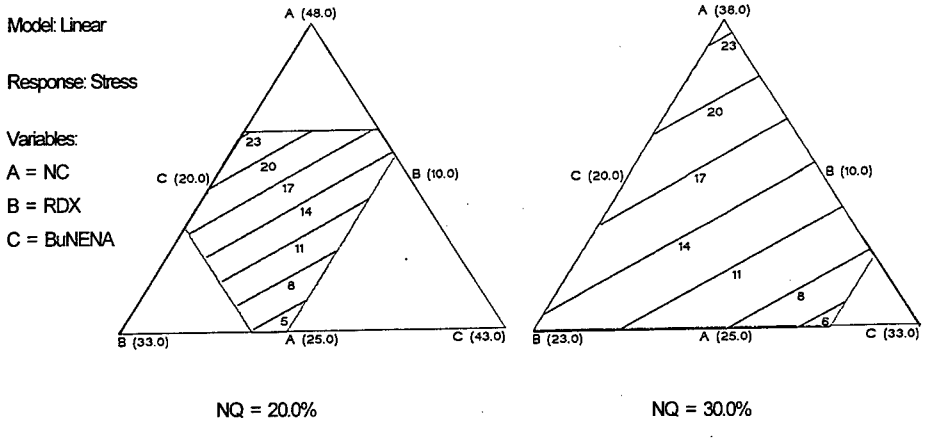

Figure 1: Modelling of Stress Values at Two NQ Concentration Levels

The stress value of any formulation that lies within the boundaries of the experimental design matrix can be predicted from the stress value model. The exact propellant formulation and its corresponding stress value can be "read" from the graphs at the two BuNENA concentration levels. For each of the graphical presentations the minimum and maximum stress values for that BuNENA concentration level can be determined from the graph.

Modelling of Strain Properties

The strain property of a propellant formulation is an indication of the elongation or elasticity of the propellant sample. The modelling of the strain properties was done at a constant NQ concentration of 20% and the NC, RDX and BuNENA concentrations were varied between the upper and lower constraint levels. This process was repeated at a constant NQ concentration of 30%. The graphical presentations of the models generated are presented in Figure 2.

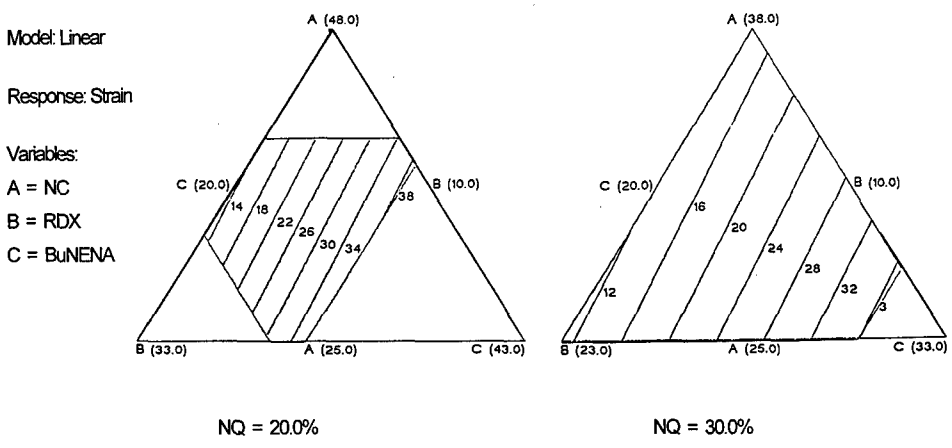

Figure 2: Modelling of Strain Values at Two NQ Concentration Levels

The trends of the modelling of the strain properties are as follows:

- the BuNENA concentration has by far the largest influence on the strain properties and the strain value increases linearly as the BuNENA increases
- both the NQ and RDX concentrations have a minor influence on the strain values and the strain values decrease gradually as the NQ or RDX increase respectively
- the strain values increase gradually as the NC value increases
- the strain value stays constant for a specific BuNENA contour line as the NQ increases and the NC proportionally decreases
- for a specific BuNENA contour line the influence of an increase in the crystalline concentration is exactly countered by the proportionally decrease of the NC
- the relations of strain versus component concentrations are all linear

Modelling of Impact Properties

The impact property of a propellant formulation is an indication of the hardness of the propellant sample. The modelling of the impact properties was done at a constant RDX concentration of 14% and the NC, NQ and BuNENA concentrations were varied between the upper and lower constraint levels. This process was repeated at a constant RDX concentration of 24%. The graphical presentations of the models generated are presented in Figure 3.

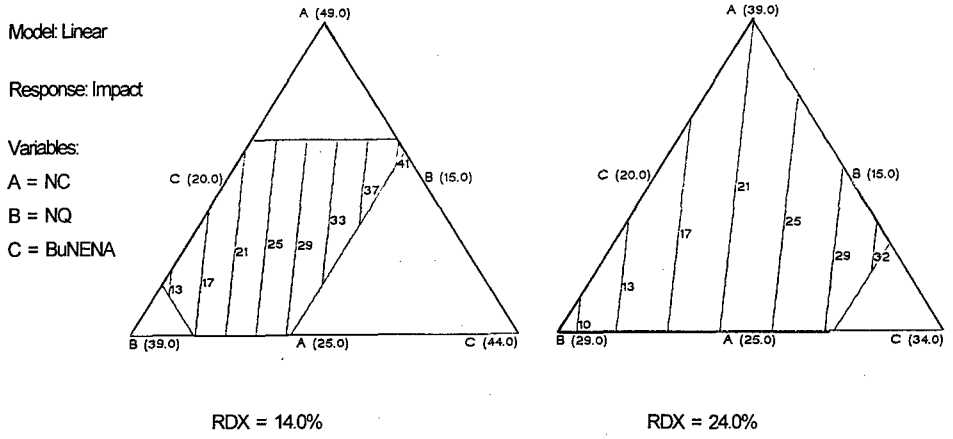

Figure 3: Modelling of Impact Values at Two RDX Concentration Levels

The basic trends are as follows:

- the NC concentration has no apparent influence on the impact values
- the highest impact values occur at the highest BuNENA values and when the NQ concentration is at its lowest level
- there is a basic shift in the impact values from the 14% RDX concentration level to the 24% RDX level with lower impact values at the increased RDX level
- the lowest impact levels are at the maximum crystalline level of 53%
- the relations of impact values versus component concentrations are all linear

In general the BuNENA concentration has the greatest influence on all three types of mechanical properties measured.

4.2 MODELLING OF GLASS TRANSITION TEMPERATURE

The primary glass transition temperature (Tg-1) of a propellant formulation is the temperature above which the propellant becomes soft with reduced tensile strength and the secondary glass transition temperature (Tg-2) is the temperature below which the propellant becomes hard and brittle – its glass point. The ideal propellant would have a Tg-1 above 63°C and a Tg-2 below – 40°C. The larger the Tg range the better.

The modelling of the glass transition temperatures was done at a constant RDX concentration of 14% and the NC, NQ and BuNENA concentrations were varied between the upper and lower levels. This process was repeated at a constant RDX concentration of 24%. The graphical presentations of the models generated are presented in Figure 4.

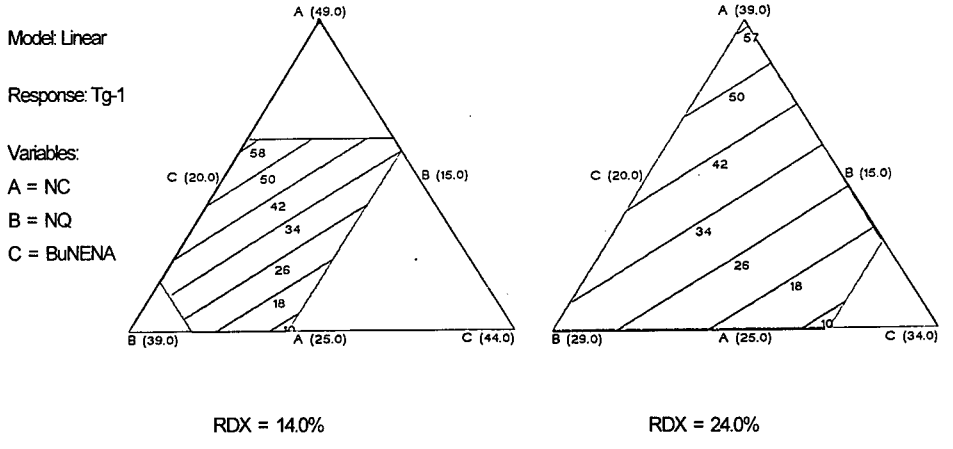

Figure 4: Modelling of the Glass Transition at Two RDX Concentration Levels

The trends of the graphic models are as follows:

- both the NQ and RDX concentrations have negligible influence on the Tg values
- the highest Tg-1 values occur at the highest NC values and when the BuNENA concentration is at its lowest level, namely when the NC : BuNENA ratio is 2 : 1
- the lowest Tg-1 values occur when the NC : BuNENA ratio is 1 : 1
- there is basically no change in the Tg-1 values for a RDX concentration of 14% or 24%
- the relations of Tg-1 values versus component concentrations are all linear

4.3 MODELLING OF DIE SWELL AND SHRINKAGE

The modelling of the percentage die swell or shrinkage was done at a constant NQ concentration of 20% and repeated at a constant NQ concentration of 34% while the NC, RDX and BuNENA concentrations were varied between the upper and lower constraint levels. The graphical presentations of the models generated are presented in Figure 5.

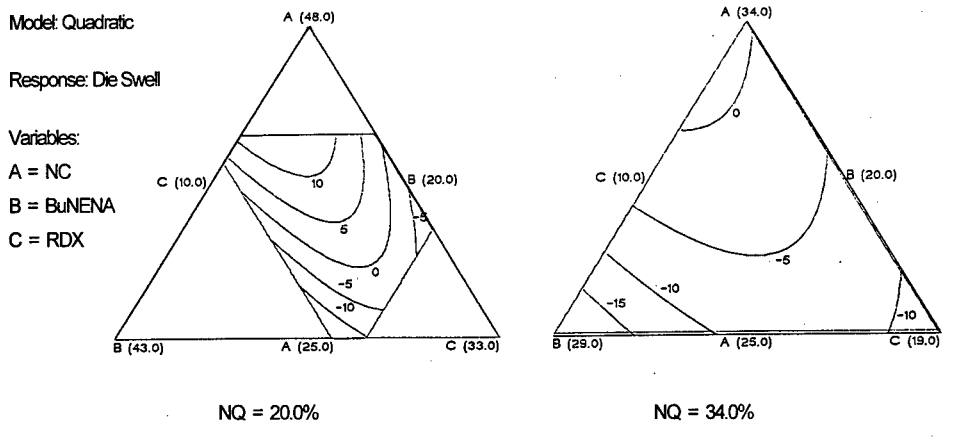

Figure 5: Modelling of Die Swell or Shrinkage at Two NQ Concentration Levels

The trends of the graphic models at the two NQ concentration levels are as follows:

- the relations of swell or shrinkage versus component concentrations are all quadratic
- at the NQ concentrations of 20% both die swell and shrinkage occur, but at the NQ concentration of 34%, where the minimum total crystalline concentration is 44%, only shrinkage occurs
- at the NQ concentration of 34% and the RDX at its minimum concentration of 10%, therefore total crystallinity at 44%, no die swell or shrinkage occurs when the BuNENA concentration is at its minimum level of 20%, and the NC at its highest level of 34%, but as the NC decreases and the BuNENA increases the shrinkage increases quite rapidly
- it seems that the percentage total crystallinity plays an important role, but that at a specific crystallinity level the NC : BuNENA ration has the biggest effect upon the die swell or shrinkage
- in general the total crystallinity and the NC : BuNENA ratio play the biggest role in determining the die swell or shrinkage
- die swell occurs below a total crystallinity of approximately 40% and shrinkage occurs above a total crystallinity of approximately 40%
- the maximum die swell occurs at the highest ratio of NC : BuNENA
- under certain conditions at a total crystallinity of approximately 40% and a NC : BuNENA ratio of approximately 1.5 : 1 basically no die swell or shrinkage occurs

4.4 MODELLING OF RELATIVE QUICKNESS

The modelling of the relative quickness was done at a constant NQ concentration of 20% and repeated at a constant NQ concentration of 30% with the NC, RDX and BuNENA concentrations varied between the upper and lower constraint levels. The graphical presentations of the models generated are presented in Figure 6.

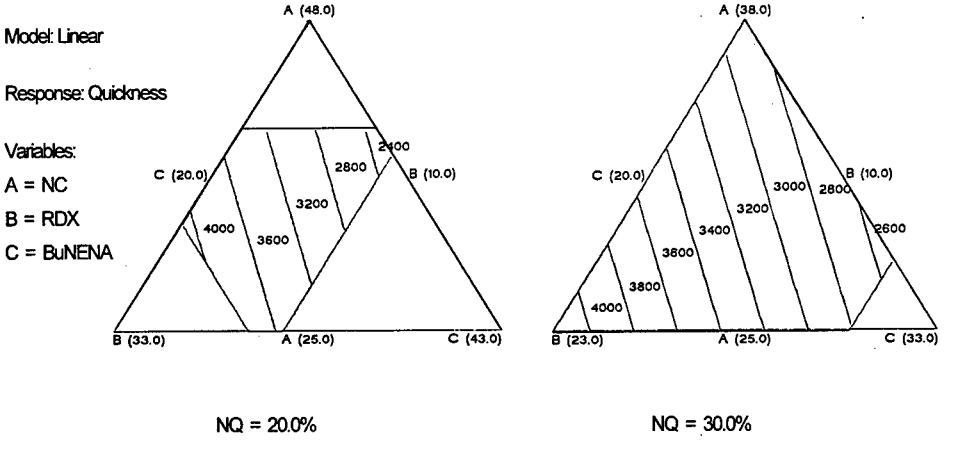

Figure 6: Modelling of Quickness Values at Two NQ Concentration Levels

The trends of the graphic models at the two NQ levels are as follows:

- the RDX concentration has the largest influence on the relative quickness
- the NC has a small negative effect
- the BuNENA has a larger, but also negative effect, than the NC
- the highest relative quickness values are at the highest RDX concentration and the lowest NC : BuNENA ratio
- there is basically no change in the range and the trend of the relative quickness for a NQ concentration of 20% or 30%
- the relations of stress versus component concentrations are all linear

4.5 MODELLING OF BURNING RATE

The modelling was done at a constant BuNENA concentration of 20% and repeated at a constant BuNENA concentration of 29% with the NC, NQ and RDX concentrations varied between the upper and lower constraint levels. The graphical presentations of the models generated are presented in Figure 7.

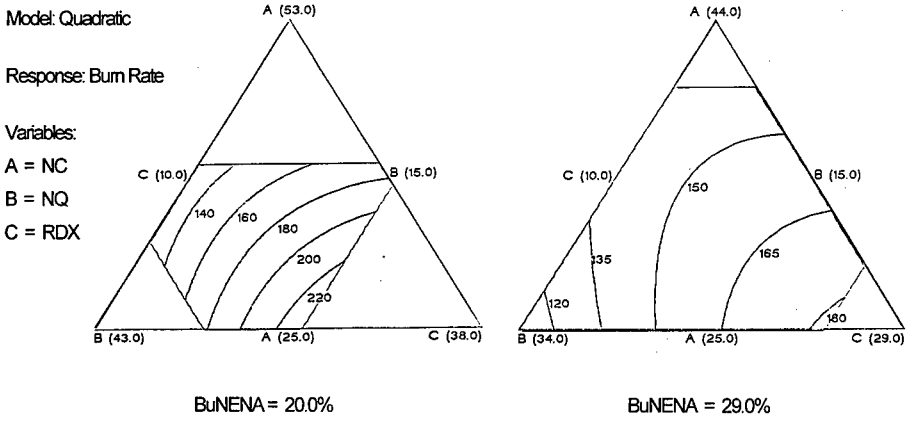

Figure 7: Modelling of Burning Rate Values at Two BuNENA Concentration Levels

The trends of the graphic models at the two BuNENA levels are as follows:

- the RDX has the greatest influence on the burning rate
- the effect of the NQ is minor
- there is a definite shift in the burning rate from a constant BuNENA concentration of 20% to a BuNENA concentration of 29% with the general burning rate being considerably higher at a 20% BuNENA concentration
- the relations of burning rate versus component concentrations are quadratic

4.6 PREDICTION OF OPTIMUM PROPELLANT FORMULATION ZONE

The model of a specific response can be used to determine the optimum propellant formulation for that specific response. The optimum formulation for a specific response can, however, be totally the opposite to the optimum formulation for a different type of response. In many cases a trade-off or compromise must be made between various responses or propellant properties in order to obtain the best overall formulation for a specific requirement. The models of the

various responses can be superimposed upon each other to find the formulation or formulation zone that will give the best compromise of the required propellant properties.

The following is an example of superimposing the models of various responses upon each other to find the optimum formulation range that complies with the requirements placed on the specific propellant formulation. The requirements are as follows:

- stress value > 12 MPa
- impact value > 20 kN/m^2
- relative quickness > 3300
- Tg-1 < 45°C
- a constant RDX concentration of 20%

The models of the 4 specific properties at a constant RDX concentration of 20% are superimposed over each other. The end result depicts the workable zone for propellant formulations that comply with all four these requirements at a RDX concentration of 20% and is graphically presented in Figure 8. In this specific case there is a central workable zone, enclosed by the R1, R2, R6 and R7 boundary lines, which complies with all four requirements. So often there will not be an overlap zone that complies with all the requirements and then a compromise will have to be found based on the priorities attached to each response or propellant property.

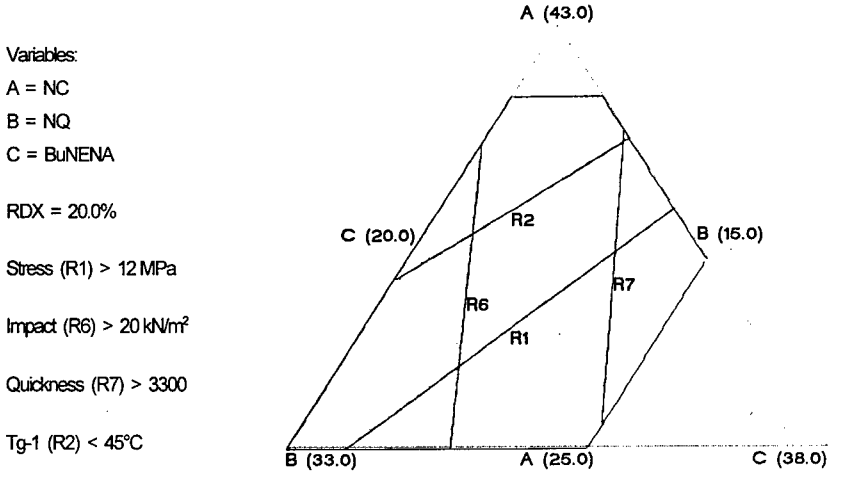

Figure 8: Modelling of Propellant Formulations with Restrictions on Stress, Impact, Quickness and Tg-1 Temperature Values Imposed

5 SUMMARY AND CONCLUSIONS

Various properties of propellant formulations containing NC as binder, BuNENA as energetic plasticiser and RDX and NQ as oxidisers were evaluated and modelled as a function of the formulation component variables. The experimental design matrix consisted of four component variables at two levels each plus a centre point formulation giving a total of 17 formulations. These experimental propellant formulations were processed, evaluated and the responses were used to generate response surface plots. The objectives of the modelling of the propellant properties (refer to **4**) were all met.

A summary of the experimental work, analysis, results and some of the trends are listed below:

- BuNENA has the greatest influence on the mechanical properties of the propellant formulations. As the BuNENA concentration increases, the stress values are reduced, but the strain values or elasticity of the formulations are increased.
- NC has the greatest effect on the glass transition temperature and the NC : BuNENA ratio also plays a major role.
- RDX has the largest influence on the relative quickness and on the burning rates.
- NQ has very little effect on most of the measured propellant properties.
- In general the tendency is that die swell occurs below approximately 40% total crystallinity and shrinkage occurs above 40% total crystallinity.
- Die swell/shrinkage and burning rate show an quadratic relationship versus changing component concentration levels whereas all the other properties show a linear relationship.
- The computer models of the various propellant properties can be used to predict and optimise the propellant formulations for each specific property. The models can also be used to predict the optimum propellant formulation zone when various propellant specifications require seemingly very different optimum propellant formulations.

AN INVESTIGATION INTO THE THERMAL STABILITY OF END - MODIFIED PolyGLYN

H Bull, P F Bunyan*,A V Cunliffe*, W B H Leeming , E J Marshall and M J Rodgers

ICI Explosives, Stevenston, Ayrshire, KA20 3LN, UK.
*DERA, Fort Halstead, Sevenoaks, Kent, TN14 7 BP, UK.

ABSTRACT

It has been reported[1,2,4] that end-modification of polyGLYN pre-polymer, by ring closure of the secondary hydroxyl group followed by hydrolysis to form a primary/secondary diol, gives rise to rubbers of very good cure stability when reacted with conventional isocyanates. However, even though the cured material showed no tendency to soften mechanically upon ageing, the modified polymers exhibited higher gas generation than desirable, in particular in the form of uncured prepolymer.

This paper reports the development of a more effective post-modification purification treatment for diol end-modified polyGLYN. The thermal stability of both the treated, modified polyGLYN prepolymer and the cured rubber is described using microcalorimetry, vacuum stability, thermomechanical analysis and nuclear magnetic resonance spectroscopy. The results show clearly that modified polyGLYN, manufactured by this process, exhibits far superior long-term chemical stability characteristics than shown by all earlier varieties of polyGLYN.

The stability of a longer chain variant of polyGLYN, formed by optimising the level and ratio of the catalyst/initiator in the polymerisation reaction and subjected to the same post-modification purification treatment, is also discussed.

These processes have been scaled up to pilot plant level and PolyGLYN, exhibiting excellent long term chemical stability characteristics, is now available in standard and higher molecular weight versions.

1. INTRODUCTION

Developments in the field of energetic binders have resulted in the appearance of polymers such as polyNIMMO, polyGLYN and GAP which can compensate to some extent for the reductions in performance associated with lower explosive filler levels and the replacement of more energetic oxidisers with Ammonium Nitrate. Although polyGLYN (Fig.1) is the most energetic and, in some applications, the most attractive of these new polymers, unmodified PG rubbers have been shown[3] to exhibit age-related softening resulting from breakdown of the polyurethane network. This behaviour has been attributed[3] to a low activation energy degradation mechanism associated with chain scission at the urethane linkage (Fig.2).

The H atom on the ß position to the urethane oxygen is slightly acidic due to the proximity of the O-nitro group. The geometry of the system is such that this proton can be abstracted by the weakly basic nitrogen in a favoured six-membered transition state reaction. It is also possible that an NO_2 radical becomes attached to the N, thus further increasing it's basicity. This, in turn, destabilises the C-O bond to the polymer chain and the group, fragments via a cyclic transition state.

This instability appears to be an inherent property of polyGLYN cured with any isocyanate and so in order to overcome this problem it was necessary to modify the chain ends (Fig.3). This is effected by ring closure of the secondary hydroxyl group into an epoxide followed by ring opening of the epoxide under sulphuric acid catalysis, water being the active nucleophilic species. This results in a very desirable secondary/primary diol prepolymer which is faster

curing and less sensitive to the presence of water, and which gives rise to rubbers of very good cure stability[3].

However, even though the cured material shows no tendency to soften mechanically upon ageing, the modified polymers exhibit higher gas generation than expected[1,4]. In an attempt to eradicate this behaviour, several post-modification purification treatments were investigated. The most effective, employing potassium carbonate, has now been incorporated into the standard method of manufacture for polyGLYN prepolymer.

2. MANUFACTURE OF POLYGLYN PREPOLYMER

The technologies involved in the laboratory preparation of polyGLYN and its scale up to pilot plant production rely on the now well proven application of dinitrogen pentoxide (N_2O_5).[5] An overview of the process is shown in Figure 4. Glycidol (vacuum distilled before use) is nitrated in a flow reactor to produce a dichloromethane (DCM) solution of GLYN in a very high yield (>95%) and of such a high purity (>99%) that no further purification is required prior to polymerisation.

2.1 Polymerisation

A classical ring-opening method is used to polymerise the energetic oxirane, GLYN, to give hydroxyl terminated polyGLYN. The initiator system employs tetrafluoroboric acid etherate combined with a di-functional alcohol to give a nominally di-functional polymer. The procedure involves the slow addition of monomer solution at 0°C to the initiator solution in a stirred reactor over a prescribed period of time. An activated monomer unit combines with the alcohol in a ring opening reaction which regenerates a proton which can then activate a further monomer unit which adds to the polymer chain. Complete monomer conversion is achieved by raising the temperature of the reaction to 20°C for several hours at the end of monomer addition. The polymerisation reaction is terminated by quenching in excess water and neutralisation is carried out by means of two separate sodium bicarbonate washes.

The molecular weight of the resulting polymer can be varied by altering the initiator/monomer ratio. Currently polyGLYN is made in two molecular weight ranges :-

	Mw	Mn
'Standard'	1000 - 2000	750 - 1100
'Longer Chain'	2000 - 3500	1100 - 2000

2.2 End Group Modification

The prepolymer dissolved in DCM obtained from the polymerisation reaction is reacted with a potassium hydroxide/ethanol solution in a stirred reaction vessel at room temperature. After stirring for the prescribed period, an excess of water is added and stirring continued for a further 30 minutes. The organic layer is then given a further wash with a 1% (w/w) aqueous sulphuric acid solution and the epoxidised polymer is isolated by separation and removal of the DCM.
The epoxidised polymer is then dissolved in tetrahydrofuran (THF) and refluxed with an aqueous sulphuric acid solution for several hours at 66°C. The THF is then removed to yield the crude end-modified polyGLYN.

2.3 Post - Modification Purification

Purification of the crude end-modified polyGLYN was originally carried out by re-dissolving the prepolymer in DCM and washing twice with an aqueous sodium bicarbonate solution. However an improved method is now employed whereby the crude DCM solution of polyGLYN is stirred for a period with solid potassium carbonate before drowning with an excess of water. After a further period of stirring, the solution is allowed to separate and the organic layer is given a further water wash. The purified polymer is then isolated by separation and removal of the DCM.

3. ASSESSMENT OF THERMAL STABILITY OF POLYGLYN

3.1 End modified PolyGLYN

A sample of polyGLYN (batch BX6), which had been end-modified using the sulphuric acid hydrolysis process described in section 2.2, but which had not received the post modification purification treatment outlined in section 2.3, was assessed for stability characteristics using the techniques of vacuum stability, microcalorimetry and NMR spectroscopy. Where indicated, the prepolymer was cured to form solid rubbers by reaction with Desmodur N100/IPDI (1 equivalent weight polyol mixed stoichiometricaliy with 0.5 equivalent weights of each isocyanate), or reacted stoichiometrically with BuNCO to form soluble urethane compounds.

VS tests were performed at 100°C on 5g samples of each polymer both in the form of liquid prepolymers and after being cured to form solid rubbers. Pressures were recorded manually every 4 hours. Both uncured and cured samples of this material exhibited excessive gas generation under these conditions and each test was curtailed before the scheduled 40 hour test period. This contrasts with the behaviour of earlier varieties of polyGLYN where high gas generation was found solely in cured rubbers. Figure 5 shows the gas generation profiles of modified polyGLYN BX6, along with those of unmodified (GLYN ended) polyGLYN and the earlier chlorohydrin-ended polyGLYN [1].

In order to allow tests of the normal 40 hours duration to be completed, VS tests were repeated using 2g samples of fully hydrolysed end-modified polyGLYN (BX6). Total gas generated during this test was 12.65 ml gas at STP for the uncured 2g sample and 6.62 ml gas at STP for the cured 2g rubber sample. These VS test results would suggest that the prepolymer is exhibiting marked instability whereas the curing process appears to improve the vacuum stability of the fully hydrolysed, modified material.

Heat generation from end-modified polyGLYN (BX6) samples held isothermally at 77°C was monitored for 90 hours using a Thermometric thermal activiy monitor. Results are summarised in Table 1 and illustrated in Figures 6-7.

These results on the sulphuric acid hydrolysed polyGLYN are in line with the VS behaviour of this material, which suggest that the prepolymer exhibits gas generation problems whereas curing the sample to a rubber appears to reduce the tendency to evolve gas. This is the opposite of what has been reported previously with all other types of polyGLYN, including the chlorohydrin-ended, modified material [1-4].

Clearly the VS and heat generation tests both reveal that the diol end group modification process results in increased chemical activity in polyGLYN prepolymer of a type which has not been seen in earlier types of polyGLYN.

^{13}C NMR spectra were recorded on modified polyGLYN (batch BX6), both unaged and after storage at 60°C for 6 weeks. The samples are described in Table 2 and the spectra illustrated in Figures 8-9.

The uncured, modified BX6 prepolymer shows two notable changes in its ^{13}C NMR spectrum when aged for 6 weeks at 60°C. First, a large, single peak appears at 109.5 ppm. Secondly, the peaks assigned to the primary hydroxyl end group carbons disappear almost entirely. These samples exhibit a very small peak at 191 ppm, which is a feature frequently observed in aged polyGLYN-urethane samples.

3.2 End Modified PolyGLYN with Post-Hydrolysis Purification

A later batch of end-modified polyGLYN (batch BX10), which had been subjected to the post-modification purification treatment described in section 2.3, was assessed for stability characteristics, again using the techniques of vacuum stability, microcalorimetry and NMR spectroscopy.

VS tests were performed at 100°C on 2g samples of each polymer, either as liquid prepolymers, or as cured rubbers. Pressures were recorded manually every 4 hours. Results are illustrated in Figures 10 and 11 and total gas generated during the test is summarised in Table 3. Results under similar conditions for a sample of unmodified polyGLYN are shown for comparison.

Heat generation measurements were made in the TAM at 77 °C, as described for earlier polyGLYN batches both in the form of liquid prepolymers and after being cured to form rubbers. The results are illustrated in Figures 12-13 and summarised in Table 4.

^{13}C NMR spectra were recorded on treated, modified polyGLYN (batch BX10), both unaged and after being stored at 60°C for 6 weeks. The samples are described in Table 5 and the spectra illustrated in Figures 14-15.

3.3 Longer Chain End Modified PolyGLYN with Post-Hydrolysis Purification

End-modified PolyGLYN has now been produced with a significantly higher molecular weight than was possible before - see section 2.1. Preliminary studies of the stability of 3 batches of this material (BX14, BX15 and BX16) have been performed, using vacuum stability (Fig.16) and microcalorimetry (Fig.17). It can be seen that the results are similar to the standard product which has been modified and treated and there is no evidence of any new instabilities introduced by the manufacturing process used to achieve the longer polymer chains.

4. DISCUSSION

Vacuum stability and TAM experiments on polyGLYN batch BX6 show that high gas and heat generation behaviour are introduced into the prepolymer when epoxidised polyGLYN is hydrolysed using sulphuric acid. The complicated, but reproducible appearance of the TAM traces indicate that the observed reactions differ in nature, as well as rate, from the "normal" exothermic decomposition which is exhibited by all nitrated polyethers. This is in agreement with the NMR evidence on aged, modified polyGLYN (BX6), which shows the aged material to be characterised by the appearance of a large peak at 109.5 ppm in the spectrum. This is thought to be caused by the production of an acidic species during ageing which catalyses a reaction between the modified end groups and the deuterated acetone solvent employed for the NMR analysis [1]. When diol ended polyGLYN has received the purification treatment described in 2.3, this type of instability is no longer observed.

The various experiments appear to be consistent with each other and to agree on the general features of the phenomena and, in particular, on the effectiveness of the K_2CO_3 treatment in eradicating this type of instability The overall picture appears to be very promising. The latest sulphuric acid hydrolysed / K_2CO_3 stabilised end-modified polyGLYN represents a significant advance, in terms of stability characteristics, on all earlier types of polyGLYN.

5. CONCLUSIONS

The immense promise of polyGLYN as the most energetic of the current range of energetic polymers for binder systems appears at last to have been realised. The problem of cure instability has been overcome with an elegant epoxidation / hydrolysis end modification reaction and an additional post-modification purification step has resulted in a very stable polymer which is compatible with all of the common fillers used in propellant and explosive formulations.

PolyGLYN is now routinely and consistently manufactured on a pilot plant scale in two molecular weight ranges - 'standard' and 'longer chain' - both of which exhibit excellent long term chemical stability characteristics.

6. REFERENCES

1 P F Bunyan, A V Cunliffe, B W Clements, S A Torry and H Bull, Stability Studies on End Modified PolyGLYN, Proc. of ADPA/NSIA Insensitive Munitions and Energetic Materials Symposium, Tampa, Florida, USA, October 6-9th, 1997.

2 N C Paul, H Desai, A V Cunliffe, M Rodgers and H Bull, An Improved PolyGLYN Binder Through End Group Modification, Proc. ADPA Joint Int. Symp. on Energetic Materials Technology, 24 - 27th Sept. 1995, Phoenix, Arizona, USA.

3 P F Bunyan, A V Cunliffe, W B H Leeming, E J Marshall and N C Paul, Stability of Cured PolyGLYN and End Modified PolyGLYN, Proc. ADPA Joint Int. Symp. on Energetic Materials Technology, Phoenix, Arizona, 24 - 27th Sept. 1995.

4 W B H Leeming, E J Marshall, H Bull, M J Rodgers and N C Paul, An Investigation Into PolyGLYN Cure Stability, Proc. 27th Int. Conf of ICT, Poster Presentation P99, Karlsruhe, FRG, June, 1996.

5 G Bagg, H Desai, W B H Leeming, N C Paul, D H Paterson and P F Swinton, Scale-up of PolyGLYN Manufacture; Process Development and Assessment. Proc. ADPA Int. Symp. on Energetic Materials Technology, New Orleans, 1992.

Table 1 Heat Flow Calorimetry - Diol ended polyGLYN; No stabilisation treatment

Sample[a]	Heat Evolution Rate After 90 Hours (μW/g)	Total Heat Generated in 90 Hours (Joules/g)
Uncured Prepolymer Samples		
BX6 IN AIR	127	19.3
BX6 IN NITROGEN	128	12.5
Cured Rubber Samples [b]		
BX6 IN AIR	31	19.9
BX6 IN NITROGEN	29	17.2

Table 2 NMR Spectroscopy - Diol ended polyGL YN; No stabilisation treatment

Sample Description	Spectrum no.
PolyGLYN BX6 prepolymer - end modified by hydrolysis with sulphuric acid - unaged	4909
PolyGLYN BX6 prepolymer - end modified by hydrolysis with sulphuric acid - aged 6 weeks at 60°C [a]	4942
PolyGLYN BX6 - end modified by hydrolysis with sulphuric acid and pseudocured with BuNCO - unaged	4997
PolyGLYN BX6 - end modified by hydrolysis with sulphuric acid and pseudocured with BUNCO - aged for 6 weeks at 60°C [b]	4940

a A large single peak appeared at 109.5 ppm in the spectrum of the uncured material when aged (Fig 4)

b A small peak appeared at 191 ppm in the pseudocured material, a feature seen in aged polyGLYN urethanes before. However, there was no sign of the 109.5 ppm peak which appeared in the aged, uncured sample (Fig 5).

Table 3 Vacuum Stability Tests on Straight and Modified/Treated PolyGLYN Blend BX10

Sample	Gas from 2g sample (ml STP)
UncuredPrepolymer Samples	
Straight GLYN-ended polyGLYN	1.8
Diol end modified polyGLYN (post-purified)	2.1
Cured Rubber Samples	
Straight GLYN-ended polyGLYN	13.3
Diol end modified polyGLYN (post-purified)	4.8

Table 4 **Heat Flow Calorimetry on Straight and Modified/Treated PolyGLYN Blend BX10**

Sample	Heat Evolution Rate After 90 Hours (uW/g)	Total Heat Generated in 90 Hours (Joules/g)
Uncured Prepolymer Samples		
Straight GLYNended polyGLYN	19.6	7.1
Diol end modified polyGLYN (post-purified	19.6	10.7
Cured Rubber Samples		
Straight GLYN-ended polyGLYN	42.4	29.8
Diol end modified polyGLYN (post-purified	27.0	13.2

Table 5 NMR Spectroscopy - diol ended/K2CO3 treated polyGLYN

Sample Description	Spectrum no.
PolyGLYN BX10 prepolymer - end modified by hydrolysis with sulphuric acid and then treated with K2CO3 - unaged[α]	5742
PolyGLYN BX10 prepolymer - end modified by hydrolysis with sulphuric acid and then treated with K2CO3 - aged 6 weeks at 60°C[α]	5860
Pseudocured PolyGLYN BX10/BuNCO - end modified by hydrolysis with sulphuric acid and pseudocured - unaged[β]	5733
Pseudocured PolyGLYN BX10/BuNCO - end modified by hydrolysis with sulphuric acid and pseudocured - aged for 6 weeks at 60°C[β]	5847

[α] No obvious change in spectrum observed in the prepolymer as a result of accelerated ageing - in particular, the 109.5 ppm peak associated with ageing untreated diol-ended polyGLYN, was absent - spectra illustrated in figure14.

[β] No obvious change in spectrum observed in pseudocured polymer as a result of accelerated ageing - in particular the urethane peaks at 155 ppm have not split into multiplets and the 191 ppm associated with aged, unmodified polyGLYN, has not appeared - spectra illustrated in figure 15.

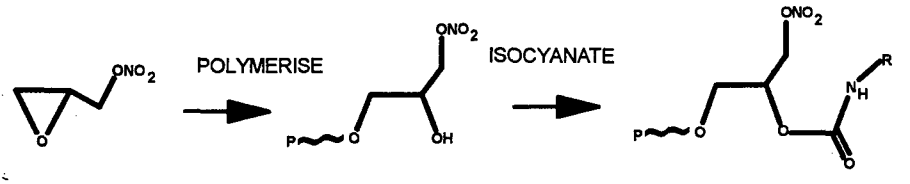

Figure 1 **PolyGLYN**

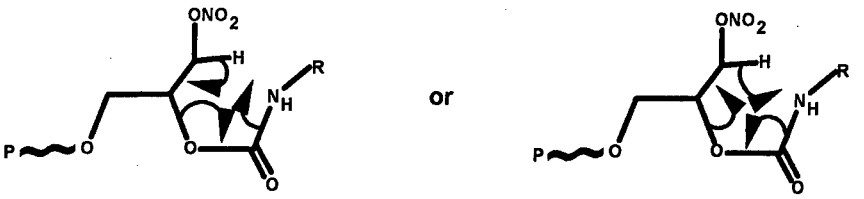

Or Perhaps Involving:

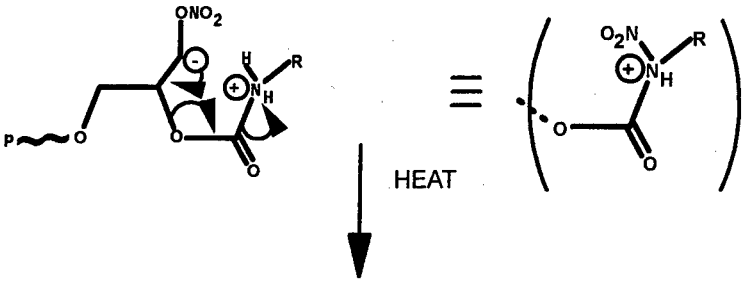

LOW VISCOSITY PRODUCTS

Figure 2 Postulated Decomposition Mechansim for polyGLYN

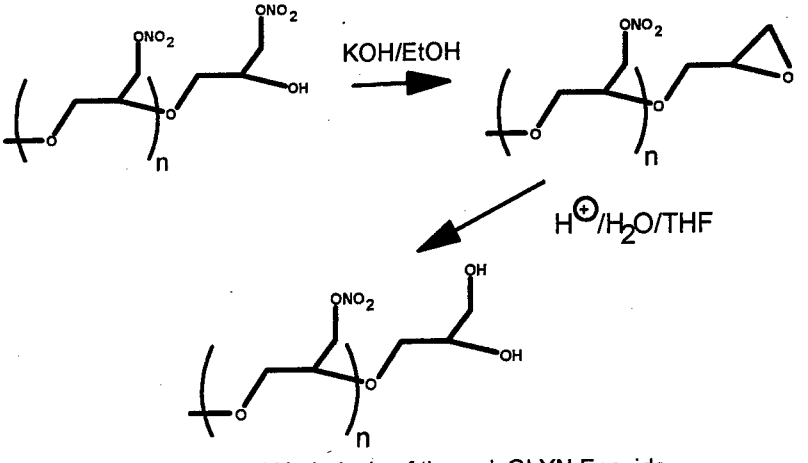

Figure 3 Formation and Hydrolysis of the polyGLYN Epoxide

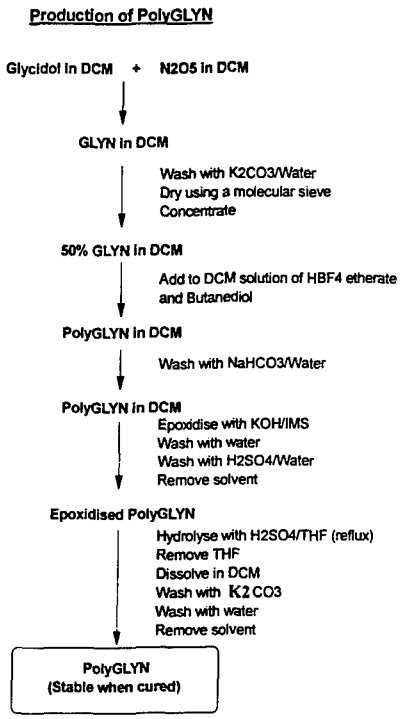

Figure 4 Manufacture of PolyGLYN

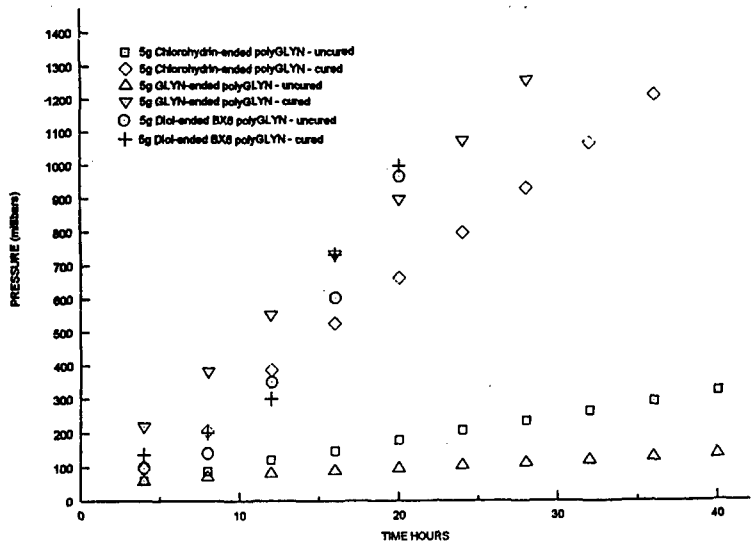

Figure 5 VS Tests of Various Types of PolyGLYN

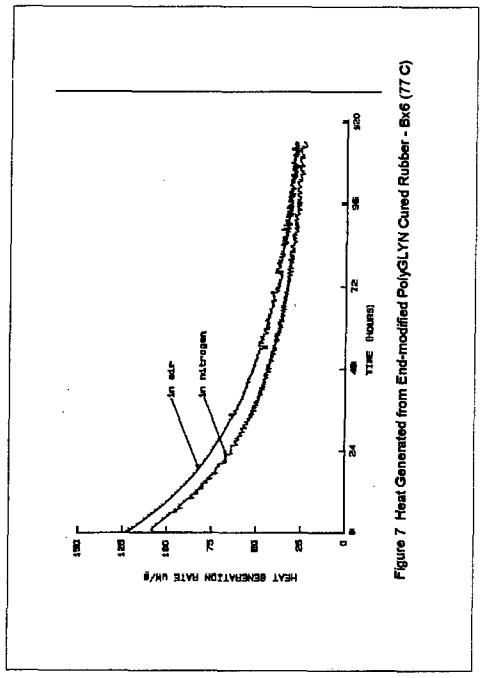

Figure 7 Heat Generated from End-modified PolyGLYN Cured Rubber - Bx6 (77 C)

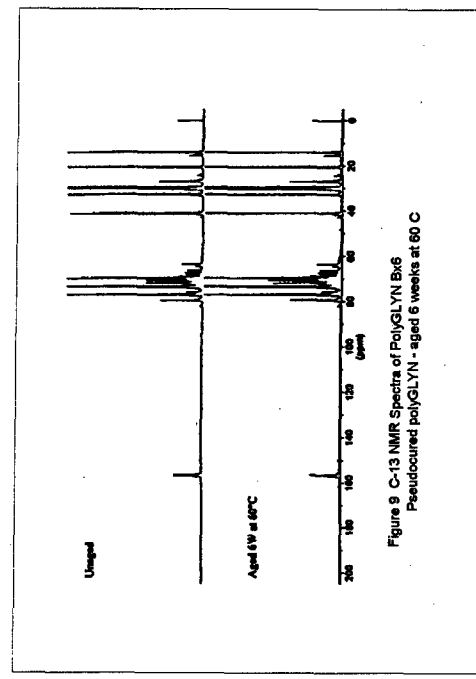

Figure 9 C-13 NMR Spectra of PolyGLYN Bx6
Pseudocured polyGLYN - aged 6 weeks at 60 C

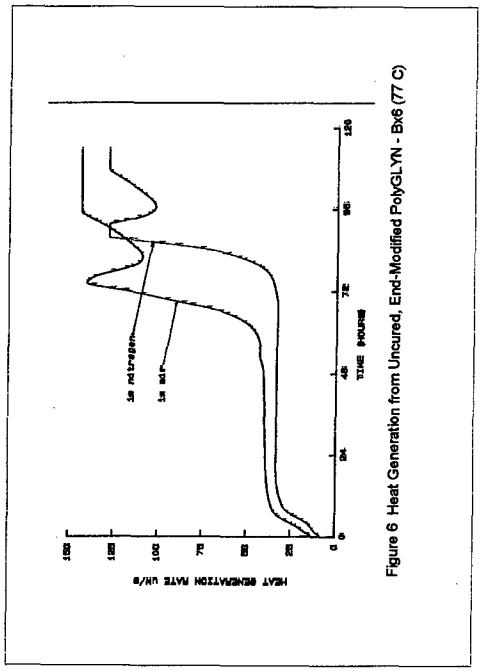

Figure 6 Heat Generation from Uncured, End-Modified PolyGLYN - Bx6 (77 C)

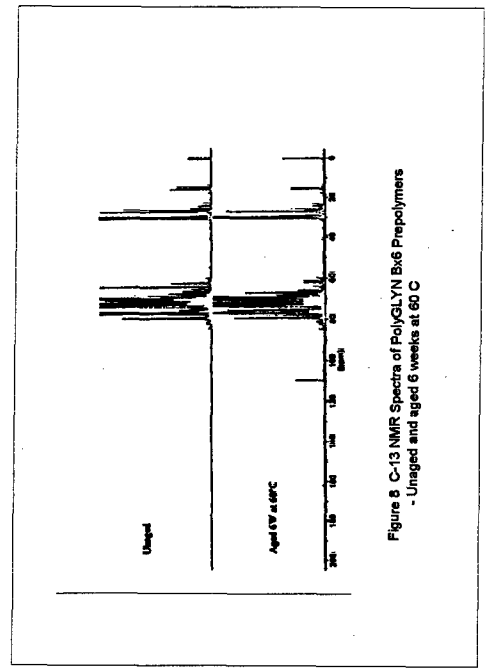

Figure 8 C-13 NMR Spectra of PolyGLYN Bx6 Prepolymers
- Unaged and aged 6 weeks at 60 C

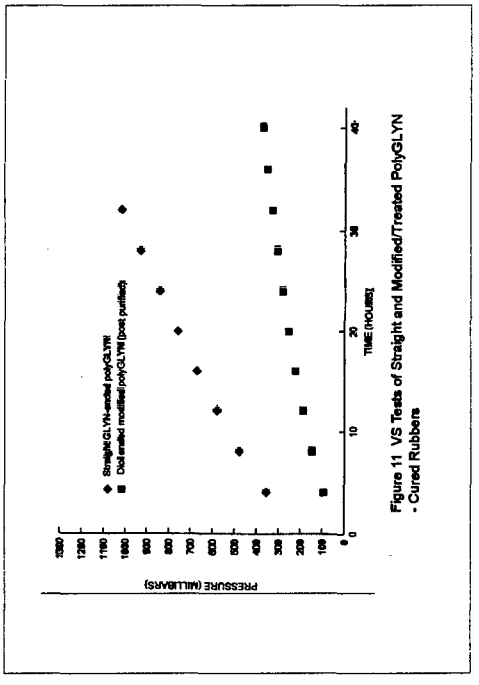

Figure 11 VS Tests of Straight and Modified/Treated PolyGLYN - Cured Rubbers

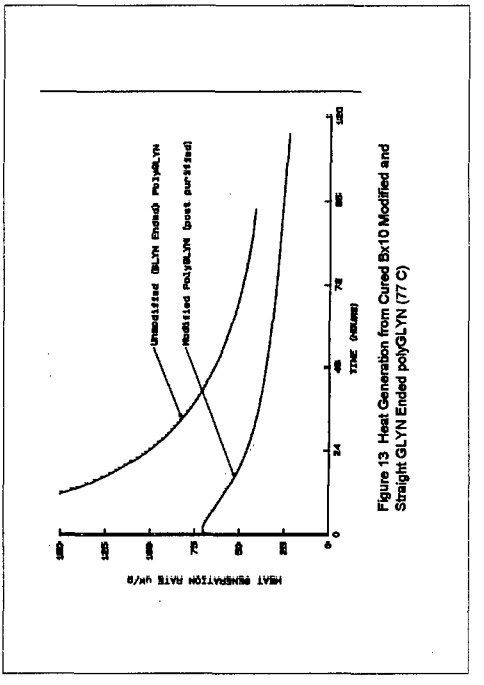

Figure 13 Heat Generation from Cured Bx10 Modified and Straight GLYN Ended polyGLYN (77 C)

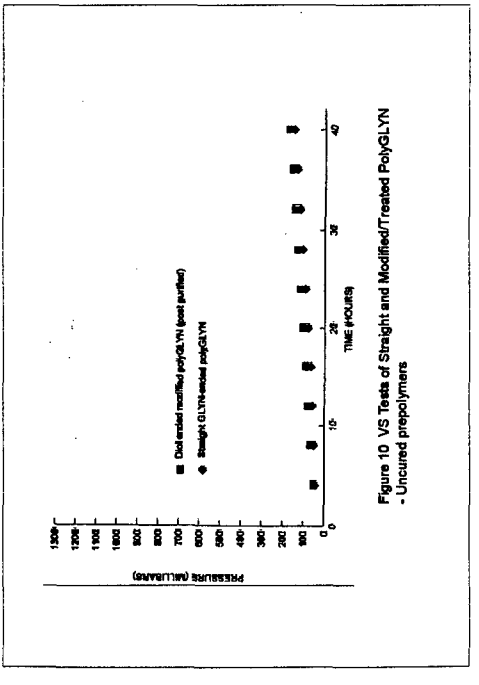

Figure 10 VS Tests of Straight and Modified/Treated PolyGLYN - Uncured prepolymers

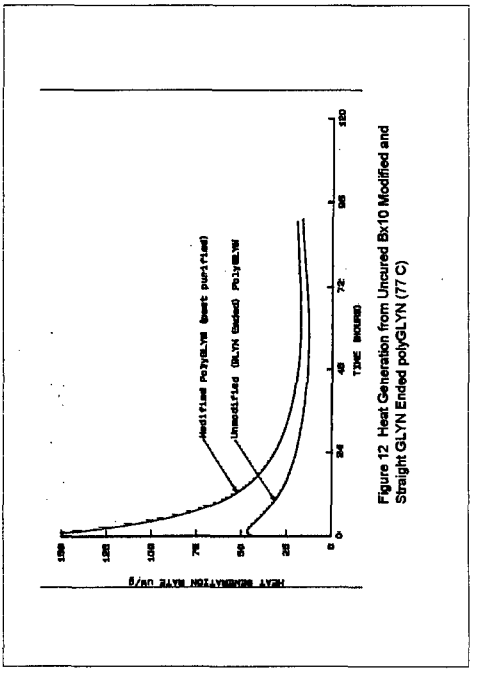

Figure 12 Heat Generation from Uncured Bx10 Modified and Straight GLYN Ended polyGLYN (77 C)

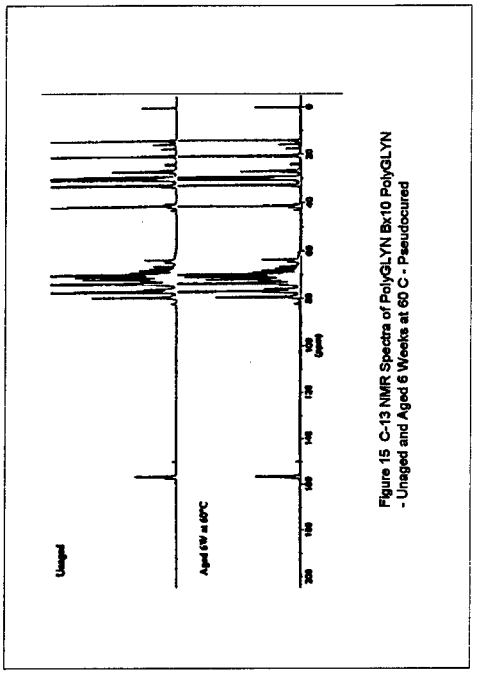

Figure 15 C-13 NMR Spectra of PolyGLYN Bx10 PolyGLYN
- Unaged and Aged 6 Weeks at 60 C - Pseudocured

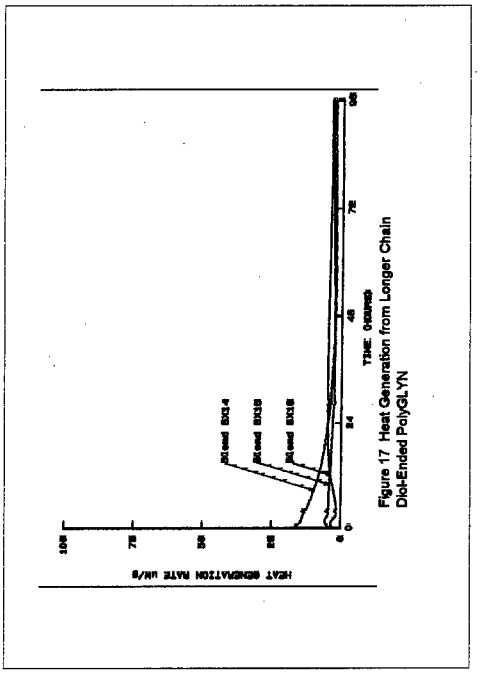

Figure 17 Heat Generation from Longer Chain
Diol-Ended PolyGLYN

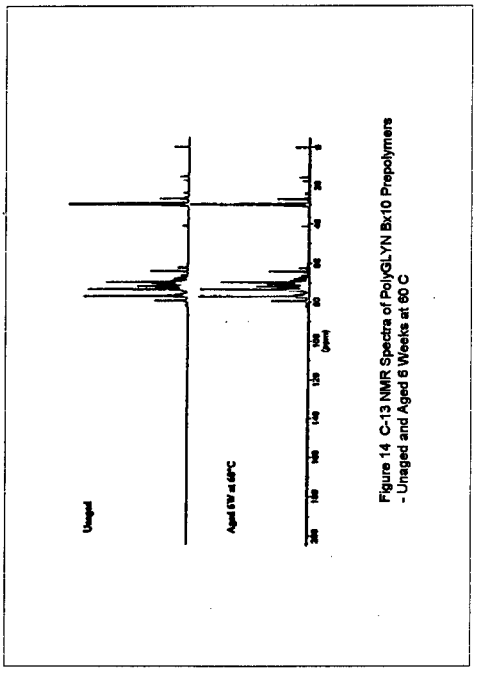

Figure 14 C-13 NMR Spectra of PolyGLYN Bx10 Prepolymers
- Unaged and Aged 6 Weeks at 60 C

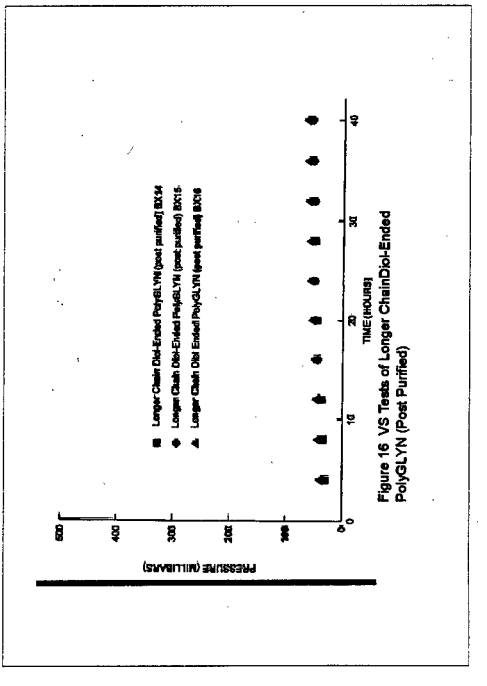

Figure 16 VS Tests of Longer ChainDiol-Ended
PolyGLYN (Post Purified)

STUDIES TO UNDERSTAND THE ROLE OF BALLISTIC MODIFIERS IN THE PLATONISATION OF DOUBLE BASE PROPELLANTS

MP Sloan
Royal Ordnance Rocket Motors
Summerfield, Kidderminster
Worcs., UK
DY11 7RZ

IA Duncan
ICI Explosives
2550 Eisenhower Avenue
Norristown PA 19403
USA

SF Dixon
ICI Explosives
Ardeer, Stevenston,
Ayrshire, UK
KA20 3LN

ABSTRACT:
The studies presented were carried out to enable a better understanding of the mechanism and hence control of plateau burning rate behaviour in double base propellants. The physical and chemical mechanisms underlying this behaviour were explored. It is hoped that the information gained on the operation of lead and copper based ballistic modifiers can be used to formulate less toxic and hence environmentally friendly alternatives.

Previous literature concerning mechanisms of platonisation is briefly discussed. These mechanisms are considered in terms of our current formulatory experience.

Experimental studies aimed understanding the operation of individual modifiers by defining some of their physical and chemical characteristics are detailed. The temperatures experienced by these organometallic compounds in burning propellant were modeled. Thermal ramp decomposition experiments of the modifiers and the roles of different ligands and carbon black were investigated. The conclusions of these in-virtro' experiments were tested by manufacture and ballistic characterization of extruded and case double base propellants.

It is considered likely that lead organometallic ballistic modifiers decompose to a metal oxide plus ligand with the precise form of oxide being determined by the physical, chemical and thermal properties of the individual modifier. The active superrate catalysis is hypothesized to be a PbO/C moiety with platonisation resulting from competitive oxidation of the carbon by NO. This behaviour will be compared with studies on copper modifiers where the specific surface area of the copper compound is a primary contributor to catalysis although the ligand is also important.

FAST BURNING ROCKET PROPELLANTS WITH REDUCED SMOKE

Klaus Menke, Siegfried Eisele,

Fraunhofer-Institut für Chemische Technologie (ICT)
D-76327 Pfinztal-Berghausen

1. Abstract

Rocket propellants with reduced smoke and high burning rates recommend themselves for use in a rocket motor for high accelerating tactical missiles. They serve for an improved camouflage on the battle field and may enable guidance control due to the higher transmission of their rocket plume compared to traditional aluminized composit propellants.

In this contribution the material based ranges of performance and properties of three non aluminized rocket propellants will be introduced and compared to each other. The selected formulations based on AP/HTPB; AP/PU/TMETN and AP/HMX/GAP/TMETN have roughly the same specific impulse of Isp = 2430 Ns/kg at 70:1 expansion ratio. The burning rates in the pressure range from 10- 18 MPa vary from to 26 - 33 mm/s for the AP/HTPB propellant, 52 - 68 mm/s for the formulation based on AP/PU/TMETN and 28 - 39 mm/s for the propellant based on AP/HMX/GAP. With 58 % and 20 % AP-content the propellants with nitrate ester plasticizers create a much smaller secondary signature than the AP/HTPB representative containing 86 % AP. Their disadvantage, however, is the connection of high performance to a high level of energetic plasticizer. For this reason, the very fast burning propellant based on AP/PU/TMETN is endowed with a low elastic modulus and is limited to a grain configuration which isn't exposed too much to the fast and turbulent airstream.
The mechanical properties of the AP/HMX/GAP-propellant are as good or better as those of the AP/HTPB propellant. The first one exhibits the same performance

and burn rates as the composit representative but produces only one fifth of HCl exhaust. For this reason it is recommended for missile applications, which must have high accelerating power together with a significantly reduced plume signature and smoke production.

Zusammenfassung

Rauchreduzierte Festtreibstoffe mit hohen Abbrandgeschwindigkeiten bieten sich für den Antrieb hochbeschleunigender taktischer Flugkörper an, da sie gegenüber aluminiumhaltigen Composits eine bessere Tarnung auf dem Gefechtsfeld und durch die höhere Transmission des Abgasstrahls u.U. Kommando-Lenkung ermöglichen.

In diesem Beitrag werden die stoffbezogenen Leistungsbereiche und Eigenschaften dreier metallfreier Raketentreibstoffe vorgestellt und miteinander verglichen. Die ausgewählten Formulierungen auf der Basis AP/HTPB, AP/PU/TMETN und AP/HMX/GAP/TMETN besitzen in etwa den gleichen spezifischen Impuls von 2430 Ns/kg bei einem Entspannungsverhältnis von 70:1. Die Abbrandgeschwindigkeiten im Druckbereich 10 - 18 MPa betragen für den AP/HTPB-Treibstoff 26 - 33 mm/s, für die Formulierung auf der Basis AP/PU/TMETN 52 - 68 mm/s und für den AP/HMX/GAP-Treibstoff 28 - 39 mm/s. Mit 58 % und 20 % AP-Anteil besitzen die Treibstoffe mit Nitratesterweichmachern eine geringere Sekundärsignatur als der AP/HTPB-Vertreter mit 86 % AP. Ihr Nachteil ist eine von einem hohen Anteil des energetischen Weichmachers abhängige Leistung. Der extrem schnellbrennende AP/PU/TMETN-Treibstoff erhält dadurch einen geringen E-Modul und bleibt in der Anwendung auf weniger strömungsbelastete Treibsatzgeome-trien beschränkt.
Der AP/HMX/GAP-Treibstoff besitzt ebenso gute und bessere mechanische Eigenschaften wie der AP/HTPB-Compositttreibstoff. Bei gleicher Leistung und Abbrandgeschwindigkeit stößt er nur ein Fünftel der HCl-Emission des Compositvertreters aus. Er empfiehlt sich damit für Flugkörperanwendungen, die eine hohe Beschleunigung zusammen mit einer beträchtlich reduzierten Rauchbildung und Abgasstrahlsignatur erfordern.

2. List of Symbols

Isp	Specific Impulse
Tc	Combustion temperature
κ	kappa =Cp/Cv ratio of specific heats
AP	Ammoniumperchlorate
BTTN	1,2,4 Butanetrioltrinitrate
DOA	Diisooctyladipate
FTS	Festtreibstoff - solid propellant
GAP	Glycidylazidopolymer
HDI	Hexamethylenediisocyanate
HMX	Octogen
HTPB	Polybutadiene, hydroxyterminated (R45 M)
IPDI	Isophorondiisocyanate
MPa	Megapascal
N100	trifunctional Isocyanate (Bayer)
NGl	Nitroglycerine
PU	Polyurethane (Desmophen Type)
TMETN	Metrioltrinitrate

3. Introduction

Composite propellants which have been specifically designed on the basis of ammonium perchlorate, aluminium and polybutadiene binders fulfil the demands for high specific impulse, high burning rate and high mechanical strength. However, their burning is accompanied by a great deal of smoke production.[1,2,3)]

Applications which include active guidance e.g. by means of radar or laser guidance or battle field applications which require the camouflage of the launch location, are made very difficult or even impossible by the vast amount of primary and secondary signatures and the consequent sight and absorption effects of the rocket plume.

For this reason rocket propellants with low smoke or reduced smoke rocket propellants with high specific impulse and high burning rates are of special interest for the development of high accelerating missiles.

This paper describes three types of fast burning, reduced smoke rocket propellants which under certain circumstances can be adapted to suit these applications and compares their properties.

4. Propellant systems

4.1 Basic components

In today's existing propellant technology, the rocket propellants used which have high specific impulse and high burning rates were and are connected with the presence of ammonium perchlorate in small particle size. Using smoke reduced double base and nitramine propellants, it has so far not been possible to achieve the high performance of composite propellants and high burning rates at the same time[1-5]. In order to compare their properties, three propellants were selected which represent systems with high, medium and low perchlorate proportions.

System 1 is based on traditional composite components:

AP / HMX / HTPB / DOA

System 2 replaces HTPB and DOA with a polyesterurethane and an energy rich nitrate ester as plasticizer:

AP / PU / TMETN

System 3 reduces the proportion of AP to 20% and introduces glycidyl-azidopolymer with nitrate ester as energetic binder and plasticizer apart from octogen as an energetic solid:

AP / HMX / GAP / TMETN / BTTN

4.2 Performance ranges

In order to present the performance ranges of the three propellant systems, up to 25 thermodynamic performance calculations were performed in each case using the thermodynamic program and the associated material database generated by Volk and Bathelt[6] within the following concentration limits:

System 1: AP : 84 - 92 %
HMX : 0 - 25 %
HTPB + DOA: 8 - 16 %
Composition of binder:
R45M + IPDI with R = NCO/OH = 1.0

System 2: AP : 50 - 80 %
PU : 4 - 20 %
TMETN : 12 - 40%
Composition of binder:
PU = Desmophen® prepolymer + HDI with R = NCO/OH = 1.0

System 3: AP : 20 %
HMX : 50 - 60 %
GAP / N100 : 6 - 18 %
TMETN : 8 - 21 %
Composition of binder:
GAP elastomer = 86.2 % GAP
13.8 % N100
GAP + TMETN = 20 - 30 %
with TMETN = 40 - 70 % of the binder

The calculated values for the specific impulse in Ns/kg with an expansion ratio of 70:1 were converted into two dimensional concentration diagrams to lines of the same impulse values with a distance of 10 - 20 Ns/kg. The results are represented in Figs. 1, 3 and 5.
Fig. 1 shows the isocurves of the specific impulse determined in this manner for the propellant system AP/HMX/HTPB. From this it can be seen that:

* The greater the solids loading, the greater the performance of the smoke reduced composite. The maximum is reached at approx. Isp = 2475 Ns/kg with 89% solids without HMX addition.
  Values up to and above 2500 Ns/kg are possible if more solids and HMX are applied.

* If up to 88% filler is added, the addition of HMX always results in a reduction of the thermodynamic performance. It is not until formulations include more than 88% solids that the addition of octogen increases performance

due to the performance improved oxygen balance. The maximum of 90% filler is approx. 2493 Ns/kg with a 12 % proportion of HMX.

* Regarding processibility, the maximium solids loading amounts to 86-88% up to which castability of the ready mixed propellant slurry can be achieved. In this case, the performance limit is marked at 2430 - 2460 Ns/kg by propellant formulations without HMX..

Fig. 3 shows the isocurves of the specific impulse for the propellant system AP/PU/TMETN. In this case the maximum for the specific impulse is dependent on the proportion of nitrate ester plasticizer and lies in the range between 55-70% ammonium perchlorate. Due to the improved oxygen balance of the binder/ plasticizer system, the Isp value quickly decreases with AP contents of greater than 70%.

In the case of a 60% AP proportion, the specific impulse is significantly increased by the increase of the TMETN content by only a few percent. However, if the nitrate ester proportion is increased, the propellants become soft, migration and sweating processes can take place. The maximum values for a stable propellant in this range lies with 30% TMETN, i.e. a 70 - 75% percentage of nitrate ester in the binder. The maximum possible specific impulse therefore is Isp = 2460 Ns/kg.

Fig. 5 shows the isocurves of the specific impulses for the system AP/HMX/GAP/TMETN. It can be seen that as is the case with system 2, the specific impulse increases with the proportion of the energetic plasticizer in the binder and with the solids loading. Due to the decreased oxygen balance of the binder and the nitramine solid, there is no maximum up to 80% solids loading, instead there is a constant increase of the specific impulse up to 2550 Ns/kg in regions which are usually only reserved for composite propellants containing metals. The cause of this is the very high energy of the system from nitramine, energetic binder and nitrate ester plasticizer. In order to make a castable, fast burning propellant it is virtually impossible to increase the 70% proportion of solid.

The limit of this propellant systems therefore lies at Isp = 2500 - 2510 Ns/kg without additives. However, further increases in performance are possible by

including the high energy BTTN into the plasticizer proportion of TMETN. In this manner a specific impulse of Isp = 2540 Ns/kg is possible for a propellant with a high amount of plasticizer[8].

5. Propellant formulations and properties

In order to discuss the properties of propellants of the systems presented, three formulations were chosen, the compositions of which are shown in table 1. Representative for propellant system 1, an AP/HTPB composite No. 27a with 86% AP in a bimodal particlesize distribution, 12% HTPB binder as well as 2% iron-III-oxide as burning catalyst were used.

Propellant system 2 is represented by formulation No. 130 with : 58% AP in very fine bimodal particlesize distribution, 30% TMETN, 10% PU binder content and 2% copper chromite as burning catalyst.

Propellant system 3 is represented by formulation No. 103 with 20% air jet ground AP, 45.5% ground octogen, 12% GAP binder, 18% TMETN and 4.5% iron-III-oxide as burning catalyst.
All three formulations make use of fine ground ammoniumperchlorate and burning catalysts in common. Because the latter are added as metal oxides and furthermore stabilising or wetting additives are necessary, the values for the specific impulses compared to the performance limits described in section 2, are reduced by 2 - 4%.

5.1 Thermodynamic properties

Tables 2 and 3 show that all three propellants have approximately the same specific impulse, but other densities, different oxygen balances and different compositions of the exhaust gases. Due to the lower oxygen balance and the lower AP proportion,

the average molecular weight of the gaseous combustion products is reduced from AP/HTPB propellant No. 27a to that of AP/HMX/GAP propellant No. 103. As the proportion of hydrochloric acid and steam in the exhaust gases decrease, the

hydrogen and CO proportions increase significantly.

The lower hydrochloric acid and steam proportion drastically reduces the resulting smoke formation for formulation No. 103. According to the new AGARD classification, this propellant is given the B-classification for secondary signature[7].

Due to a better O_2 balance, propellant no. 27a reaches a higher burning temperature compared to the propellants 130 and 103. In the case of propellant no. 103, mainly the high energy components HMX and GAP contribute towards higher values of Tc and Isp. Overall, the higher burning temperature and the smaller kappa = Cp/Cv of the HTPB propellant balance out the greater average molecular weight of the combustion gases. Therefore the three propellants all have approximately the same thermodynamic calculated specific impulse.

5.2 Sensitivity and stability

Tables 4 and 5 show the data of the propellants for the processing viscosity and mechanical properties, sensitivity and chemical stability. Due to the, in some cases, high proportion of very fine crystalline ground perchlorate, all three propellants are especially friction and impact sensitive compared to doublebase or nitramine propellants. This is noticeable most in the case of the traditional composite propellant which has the greatest AP proportion and therefore also the greatest friction and impact sensitivity. As octogen and nitrateesters are missing, AP/HTPB propellants belong to the safety classification group 1.3 not showing any detonation sensitivity in small dimensions. In the case of the formulations No. 130 and No. 103, the safety classification is 1.1.

The chemical stability of all three propellants, determined by the Holland test and vacuum stability, are good, they are especially high in the case of AP/HTPB propellant. The use of TMETN which is somewhat lower in energy but more stable compared to the energy richer but more unstable representatives NGI or BTTN, also results in good stability values for propellants No. 130 and No. 103.

5.3 Processibility and mechanical properties

All three propellants have a sufficiently low casting viscosity and can be processed well in the slurry casting procedure, i.e. can be processed in a manner in which they adhere to the walls of the chamber. In order to set a sufficiently long potlife, propellants No. 130 and No. 103 with the curing agents HDI and N100 are processed at 30°C, FTS 27A with IPDI at 60°C.

All three propellant types show viscoelastic mechanical properties in the temperature range between - 40°C to+ 50 °C, in each case the glass transition and freezing points lie below - 50°C, in each case the softening point lies above + 60°C.

All three propellant types were not optimised in their mechanical properties, all three can be adapted, within limits, to specific grain designs and requirements by changing the binder networking and curing cinetics. Differences which cannot be avoided are manifested in the details. They are caused by the different proportions of the solids, binder polymers and plasticizer contents.

At plus and minus temperatures, the HTPB Propellant No. 27A shows approximately the same tensile strength and E-module values as GAP bound formulations No. 103, but at + 20°C and + 50 °C it shows lower elongation at break. In the case of HTPB propellant, a lower proportion of plasticizer and improved curing cinetics result in improved elongation at break, tensile strength and E-module without changing the specific impulse and the burning behaviour of the formulation. In the case of the GAP propellant, this is only possible within certain limits , e.g. by changing the network density. As in the case of propellant No. 130, reducing the proportion of the plasticizer also results in a reduction in performance.

Due to its high plasticizer and low filler content, the mechanical strength, especially the E-module of propellant No. 130 lies significantly below the values of the other two propellant systems. Although the high stretchability indicates that the E-module can be increased by increasing the binder networking and therefore reducing the elongation at break, the high plasticizer content which is connected with performance limits very high tensile strengths and E module values being reached. Therefore in this case, the mechanical properties make a simple

grain configuration which is not exposed too much to the fast and turbulent airstream necessary for the use of this propellant.

5.4 Burning behaviour

One of the most important functional properties of the propellant is its burning behaviour, i.e. the interaction of burning rate, pressure exponents and temperature coefficients.

Figs. 2, 4 and 6 show the burn rate versus pressure diagrams in the range between 2 - 25 MPa, determined by using Crawford measurements at -40 °C, +20 °C and +50 °C together with their pressure exponents . The range between 10 - 18 MPa which is interesting for the applicational profile has been marked by two vertical green bars.

In the case of the HTPB propellant No. 27A, the burning rates between 10 and 18 MPa combustion chamber pressure lie just under and around r = 30 mm/s, the pressure components between n = 0.4 and 0.5.

Propellant No. 130 is set to be very fast burning due to the use of air jet ground perchlorate. Its burning rates lie between r = 52 mm/s and r = 68 mm/s with pressure exponents between n = 0.40 and n = 0.55.

Propellant No. 103 shows burning rates between r = 28 - 38 mm/s and somewhat greater unfavourable pressure exponents between n = 0.50 to n = 0.65 in the pressure range between 10 and 18 MPa. The high pressure exponents so far are a very significant disadvantage which limits the use of this propellant to simple grain configurations.

The temperature coefficients lie around $(\Pi r)_p$ = 0.03 - 0.42 for FTS 27 A and for FTS No. 130 around $(\Pi r)_p$ = 0.10 - 0.22.

6. Evaluation of property profiles

In this section we will try and compare the differences and limits of the system properties performance, burning behaviour, signature and mechanical properties of the propellants and to evaluate them for the application in high accelerating missiles.

The specific impulse of the AP/HTPB propellant No. 27A can be increased by increasing its filler content, however, if high burning rates are required, it very quickly reaches the limits of processability in the casting process. In the case of the HTPB representative, greater burning rates, such as for example are exhibited from propellant No. 130, are frequently achieved with a reduction in performance. The formulation described therefore represents a compromise between a high specific impulse and a sufficiently high burning rate. With regard to the latter property it cannot strike the other two propellants No. 130 and No. 103. Instead its advantages lie in its high chemical stability, lack of detonation sensitivity and good mechanical properties which can be improved compared to the values shown here for tensile strength, elongation at break and E-module. This makes the propellant accessible for high stress applications in the HFK sector.

Because of the lower solids loading necessary, propellant No. 130 has the greatest burning rates in combination with good specific impulse values when compared to the other systems. It seems possible that its performance can be increased with the use of high energy nitrateesters but this may be accompanied by a decrease in chemical stability and probably makes it necessary to add performance reducing, stabilising additives.

The disadvantage of this propellant type is the coupling of a high specific impulse with high proportions of energetic nitrateester plasticizers. This increases the sensitivity of the propellant, the tensile strength and E-module values are reduced. This type of propellant can release a great deal of energy in a very short period of time due to its high burning rate, but it is bound in its application to simple, less strained grain configurations. Compared to the HTPB propellant, propellant No. 130 has approximately one third less hydrochloric acid in its exhaust gases, but still has a secondary signature which is very dependent on air humidity.

Propellant No. 103 shows that it is possible to limit the perchlorate proportion in the propellant to 20%, to reduce the proportion of hydrochloric acid in the exhaust gases to the AGARD B classification and to combine good performance and high burning rates in one formulation. However, as the perchlorate propor-

tion cannot be increased without increasing the secondary signature, the burning rates achieved for propellant FTS No. 103 represent the maximum for this type of propellant. The disadvantage of the propellant representative described here consists of the high pressure exponents, which prevent its use in complex grain designs demanding a pretentious combustion behaviour. However, it should be possible to develop this propellant system further and to improve its combustion properties.

Further possibilities of improving the performance have so far only been possible by increasing the specific impulse with energy rich nitrateesters which bring with it new problems regarding chemical stability and sensitivity. Increasing the solids loading does not seem possible, because ingredients with coarser particles must be used to maintain castability of the propellant in the slurry casting process. Use of AP or HMX with greater particle size will however decrease the burning rates (with coarser AP) or increase the pressure exponents (with coarser HMX).

7. Conclusion

The observation and evaluation of the properties have shown that the smoke reduced composite propellants presented here can be used to drive high accelerating missiles if the grain configuration is compatible with the specific properties of the propellant. Compared to highly filled composite propellants containing aluminium, they have an approximately 5 % lower specific impulse, but the production of primary smoke is significantly reduced and the transmission of the exhaust plume is greater. For the system with the least smoke production the perchlorate proportion has been reduced to 20% and the HCl proportion in the plume has been reduced to one fifth of that of the AP/HTPB composite propellant. On the battle field this improves protection and camouflage of the launching location significantly and should enable active command guidance.

Literature, References

1) Hiltmar Schubert;
Propellants
Ullmann's Encycl. Vol.A22, p.185-209 VCH Weinheim 1993

2) A.E. Oberth;
Principles of Solid Propellant Development
US Government DAR clause 8-104.9, 1986
3) A.Davenas;
Solid Rocket Propulsion Technology
Pergamon Press, Oxford 1993
4) R.N. Kumar, L.D.Stand;
Combustion Problems of Nitramine Propellants
AIAA 13th Aerosp.Sc.Meeting, Pasadena, p. 75-239 (1975)
5) K.P. McCarty et al.:
Nitramine Propellant Combustion
AIAA Joint Prop. Conf.,Las Vegas 1979
6) F. Volk, H. Bathelt;
Application of the virial equation of state in Calculating Interior Ballistic Quantities
Prop. And Expl. 1, p 7-14 (1976)
7) P.A. Kessel
in AGARD-LS-188
Rocket Motor Plume Technology, p. 3-1 to 3-9
Neubiberg 1993
8) K. Menke, S. Eisele;
Rocket Propellants with Reduced Smoke and High Burning Rates
Prop. Expl. Pyrot. 22, 112-119 (1997)

Tables and Figures

Table 1:
Selected propellant formulations.

	Nr.27A	Nr.130	Nr.103
Ammoniumperchlorate 200µm/8µm HTPB-Binder (R 45 M / IPDI / DOA) Burning rate catalyst	86.00 % 12.00 % 2.00 %		
Ammoniumperchlorate 30µm/2µm Trimethylolethanetrinitrate (TMETN) PU-Binder Burning rate catalyst		58.00 % 30.00 % 10.50 % 1.5 %	
Ammoniumperchlorate 2µm Octogen 11µm GAP / N100 (NCO/OH =1.00) Trimethylolethanetrinitrate (TMETN) Burning rate catalyst			20.00% 45.50% 12.00% 18.00% 4.50%

Table 2:
Calculated thermodynamical properties

Thermodynamic Properties (Expansion Ratio 70:1)	Nr.27A	Nr.130	Nr.103
Spec. Impulse $I_{SP.EQ}$ in Ns/kg	2431	2435	2422
Spec. Impulse $I_{SP.FR}$ in Ns/kg	2368	2383	2391
Vol.Spec. Impulse $I_{SP.EQ} * \rho$ in Ns/dm^3	4174	3970	4239
Vol.Spec. Impulse $I_{SP.FR} * \rho$ in Ns/dm^3	4065	3884	4184
Char. Velocity c* in m/s	1489	1491	1516
Density ρ_{theor} in g/cm^3	1.72	1.63	1.75
Temperature T_C in K	3003	2865	2925
Adiabatic Coeff.	1.208	1.217	1.234
Mean Molecular Weight in g/mol	26.59	25.21	24.47
Oxygen Balance in %	-6.42	-16.93	-25.74

Table 3:
Calculated reaction products after expansion.

	Nr.27A		Nr.130		Nr.103	
Reaction Products Nozzle	Mol%	Ma%	Mol%	Ma%	Mol%	Ma%
CO_2	16.27	26.38	20.01	32.36	10.94	19.63
H_2O	43.23	28.69	38.20	25.27	20.71	15.21
N_2	10.12	10.48	11.83	12.18	23.85	27.24
CO	5.60	5.79	9.59	9.87	22.78	26.01
H_2	5.30	0.39	6.29	0.47	16.69	1.37
HCl	18.84	25.32	13.43	18.00	3.75	5.57
$FeCl_2$ G	0.51	2.38			0.21	1.10
$FeCl_2$ L						
FeO S					0.71	2.07
Cr_2O_3 S			0.18	0.99		
Cu L			0.17	0.41		
MgO S			0.30	0.45		
ZrO_2	0.13	0.60			0.36	1.79

Table 4:
Processing viscosity. mechanical properties.glass transition temperature and chemical stability of the selected propellant formulations

	Nr.27A	Nr.130	Nr.103
Processing Viscosity	112 Pas (+60°C)	84 Pas (+30°C)	184 Pas (+30°C)
Mechanical Properties (50mm/min)			
- 40° C Tensile strenght σ in N/mm²	2.01	2.56	2.92
Elongation ε in %	31.7	> 200	35.3
Modulus E in N/mm²	50.4	13.5	51.39
+20° C Tensile strenght σ in N/mm²	0.64	0.63	0.65
Elongation ε in %	19.5	> 300	39.5
Modulus E in N/mm²	5.59	0.57	6.43
+ 50° C Tensile strenght σ in N/mm²	0.59	>0.35	0.54
Elongation ε in %	16.9	> 300	29.3
Modulus E in N/mm²	5.20	0.57	5.67
Glass Transition Temperature	- 79 °C	- 61 °C	-57 °C
Chemical Stability:			
Weight Loss : (105 °C / 8-72h)	0.01 %	0.33 %	0.63 %
Gasevaluation: (40h / 100 °C)	0.02 ml/g	1.04 ml/g	1.44 ml/g
Deflagration Temperature (20°C/min)	256 °C	185 °C	188 °C

Table 5:
Mechanical sensitivity. safety- and signatureclassification

	Nr.27A	Nr.130	Nr.103
Safety Datas			
Impact Sensitivity	7.5 Nm	4 Nm	3 Nm
Friction Sensitivity	24 N	40 N	40 N
Safety Classification	Class 1.3	Class 1.1	Class 1.1
Signature Classification			
Primary AGARDP	B	A	B
Secondary AGARDS	C	C	B

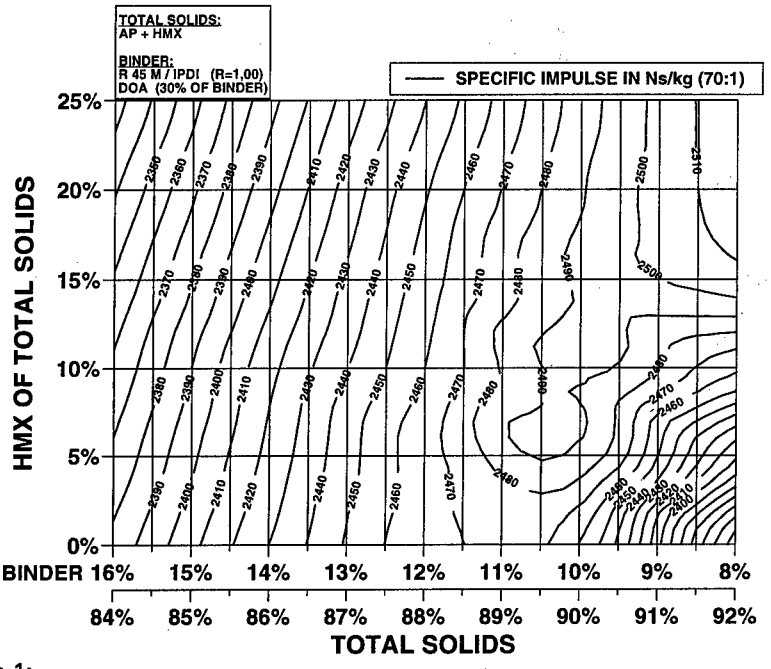

Figure 1:
Isocurves of the specific impulse in Ns/kg at an expansion ratio of 70:1 for the AP/HMX/HTPB propellant system.

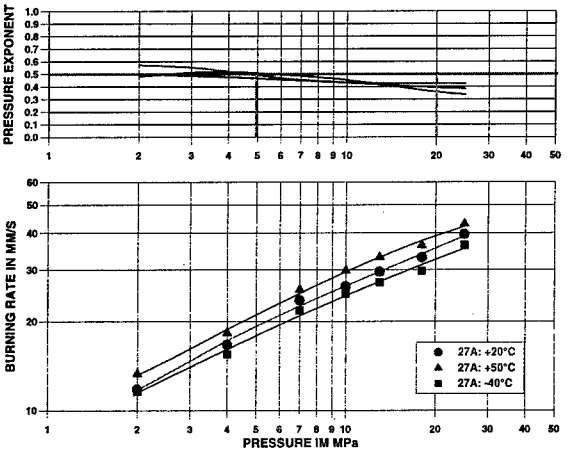

Figure 2:
Burning rates and pressure exponents for the AP/HTPB-propellant Nr. 27A

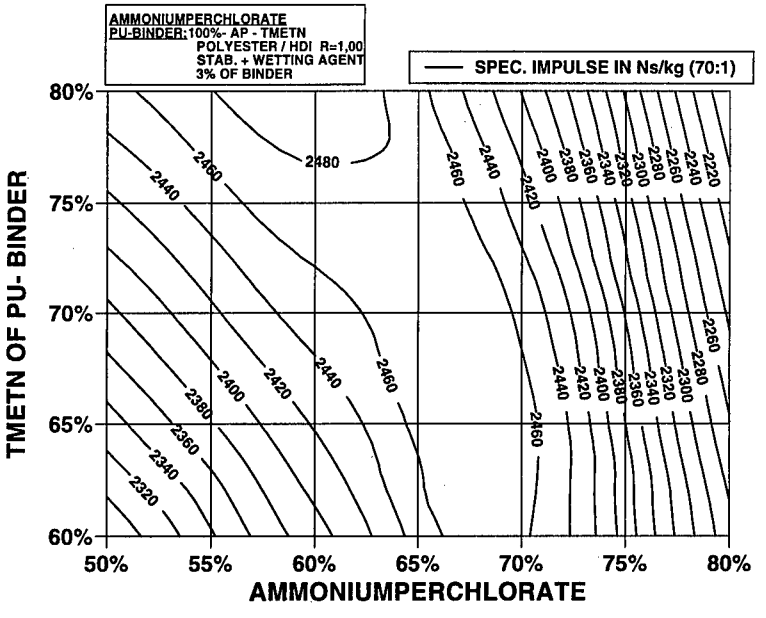

Figure 3:
Isocurves of the specific impulse in Ns/kg at an expansion ratio of 70:1 for the AP/PU/TMETN propellant system.

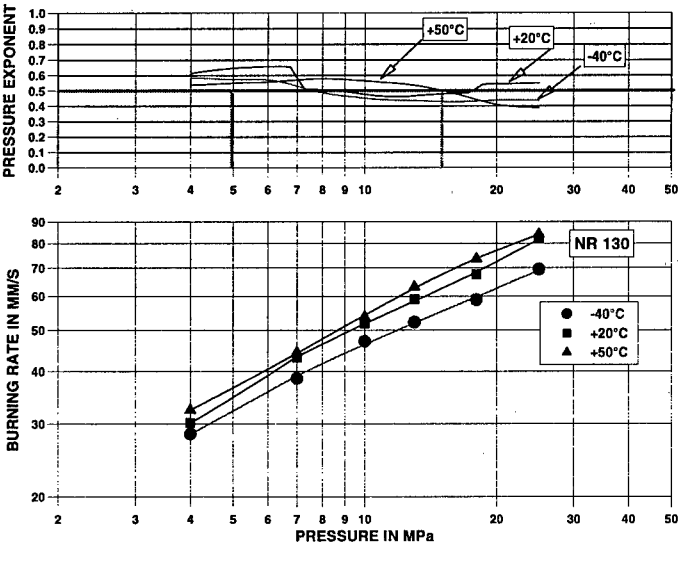

Figure 4:
Burning rates and pressure exponents for the AP/PU/TMETN-propellant Nr. 130.

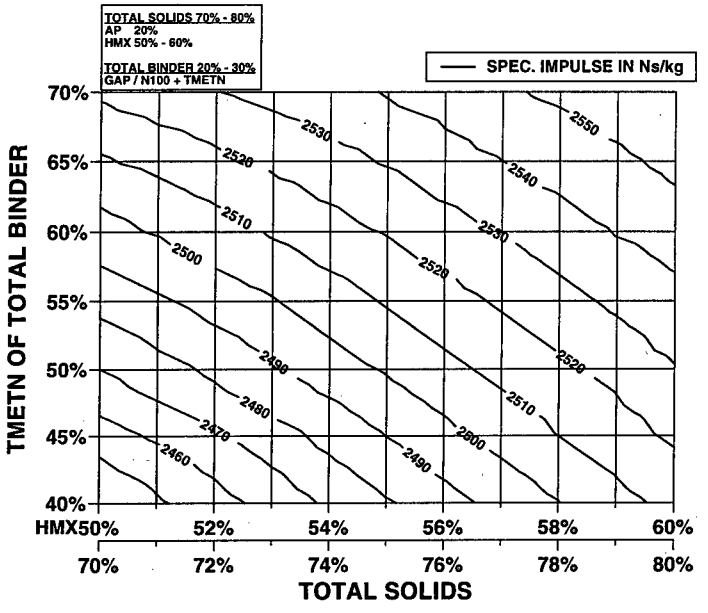

Figure 5:
Isocurves of the specific impulse in Ns/kg at an expansion ratio of 70:1 for the AP/HMX/GAP/TMETN propellant system from 70 % to 80 % solids loading.

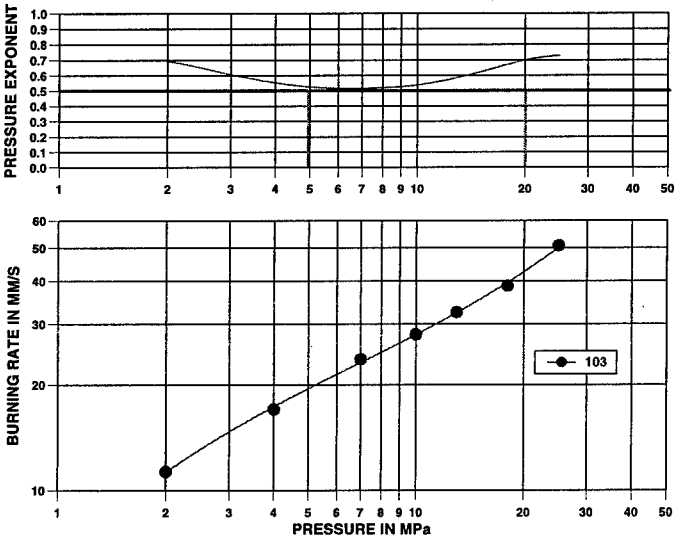

Figure 6:
Burning rates and pressure exponents for the AP/HMX/GAP/TMETN-propellant Nr. 103.

IMPROVING THE ELONGATION CAPABILITY OF HTPB-BASED COMPOSITE PROPELLANT

Gideon J. J. Steyn and Gideon J. van Zyl

Somchem, Division of Denel (Pty)Ltd
P.O. Box 187, Somerset West, 7129
South Africa

Abstract

The elongation capability of composite propellants plays an important role in the design of case-bonded end-burning solid propellant grains, as well as propellant grains with small inner bore diameters. This investigation focused on improving the elongation capability of a baseline HTPB-based composite propellant. A certain ratio of a tri-functional crosslinking agent (trimethylol propane) and a chain terminator (1-decanol), as well as a low polymer/curing agent ratio improved the elongation capability of the baseline propellant significantly. Results also indicate that propellant cured with the aliphatic curing agent dimeryl diisocyanate (DDI) have better elongation capabilities than corresponding propellants cured with the cyclic curing agent isophorone diisocyanate (IPDI). The tri-functional isocyanate curing agent Desmodur N100 was also part of the planned investigation, but due to the much shorter pot life of the N100 cured propellants, these propellants could not be processed and was subsequently not investigated.

1. Introduction

For more than twenty years, since the early seventies, composite propellants based on the hydroxy terminated polybutadiene resin, HTPB, have been the state of the art propellants for solid rocket motors. One of the several advantages of propellants based on HTPB is the superior mechanical properties of such propellants. The mechanical properties of HTPB-based composite propellants are a function of the properties of the HTPB prepolymer i.e. molecular weight, hydroxyl value, functionality, etc. Selection of a proper curing agent to form the three-dimensional binder network is also essential. Other ingredients such as bonding agents and plasticisers are normally included in the binder and are also beneficial in improving the propellant mechanical properties.

The range of available mechanical properties of composite propellants based on these basic ingredients is limited between certain boundaries, which, unless the binder system is modified, is fixed. Varying the molecular weight of the prepolymer and the crosslink density can induce drastic changes in the properties of the elastomer. Adjusting the ratio between various crosslinking agents can vary average molecular weight between crosslinks. Depending on the number of functional OH groups of the compound, these crosslinking agents can be divided into the following groups[1,2,3]:

- Crosslinkers, which are trifunctional alcohols like trimethylol propane (TMP), 1,2,6-hexanetriol and glycerol.
- Chain-extenders, which are difunctional alcohols like butanediol.
- Chain terminators, which are monofunctional alcohols like 1-decanol (DEC).

The essential requirement of composite propellants suitable for case-bonded end-burner configurations or configurations with small inner bore diameters are high strain capabilities with moderately high tensile strengths[4]. The objective of this investigation was to investigate to what limits the strain capability of a chosen baseline propellant can be improved without substantially decreasing the tensile strength.

There are three basic characteristics of the polymer network which determine along with two other factors the mechanical properties of the propellant[4]. These characteristics are (1) the degree of chain extension (2) the degree of chain branching and (3) the degree of chain

termination. Two other factors, (1) the degrees of freedom (or flexibility) of the basic polymer chain and (2) the concentration and type of non-network material (plasticisers and bonding agents), also have an effect on the mechanical properties of the propellant. Two different approaches were followed in this investigation to improve the elongation capability of the baseline propellant. The first approach was systematic variation of the trifunctional crosslinker (TMP) and the monofunctional chain terminator (DEC) concentrations to vary the extent of chain extension, chain branching and chain termination. The crosslinking density was also varied by variation of the equivalence ratio between the species with functional OH groups (HTPB, TMP and DEC) and the isocyanate curing agents (the NCO/OH ratio).

The second approach was evaluation of the two difunctional isocyanate curing agents, IPDI and DDI, as well as the trifunctional curing agent Desmodur N100.

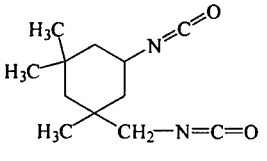

Isophorone diisocyanate

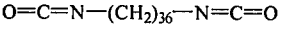

Dimeryl diisocyanate

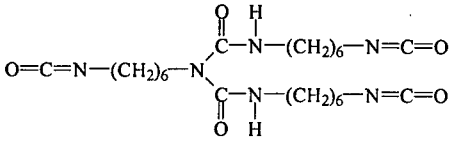

Desmodur N100

The main difference between the two difunctional curing agents is that DDI has a long chain molecular structure and that IPDI is a cyclic molecule. The chain length between the two isocyanate groups in the case of DDI is 37 while the chain length in IPDI is only 5. In the case of IPDI the chain between the two isocyanate groups forms part of a cyclohexane ring and therefor DDI has theoretically more degrees of freedom in terms of parameters such as bond rotation, bond angle deformation and molecular entanglement, compared to IPDI. The chain length between the isocyanate groups in the case of Desmodur N100 of

between 16 and 18 falls intermediate between that of IPDI and DDI. Desmodur N100 also does not have a rigid cyclic structure like IPDI, but have a chain molecular structure like DDI. Desmodur N100 can also function as a crosslinker in the binder network due to the trifunctional nature of this curing agent.

2. Experimental

A reduced smoke propellant composition with a total solids content of 83.0 % was chosen as baseline for this investigation. The propellant contained a binder system, a combustion stabiliser and a bimodal particle size distribution of ammonium perchlorate as oxidiser. The baseline binder system consisted of HTPB and a curing agent (IPDI/DDI/Desmodur N100). The tri-functional crosslinker (TMP) and/or a monofunctional chain terminator (DEC) were added to this baseline binder system in different ratios to manipulate the mechanical properties of the propellant. The binder system also contains a bonding agent and plasticiser. The general formulation of the baseline propellant is tabulated in Table 1.

Table 1. Baseline reduced smoke propellant composition

Component	Concentration (m/m %)
Binder system: HTPB TMP DEC IPDI/DDI/N100	14.7
Anti-oxidant	0.1
Bonding agent	0.3
Plasticiser	1.9
Combustion stabiliser	1.0
Ammonium perchlorate	82.0

Pilot plant mixes of 6 kg each were mixed on a 10-liter vertical mixer. Mechanical properties were determined with JANNAF samples at 21 °C on an Instron tensile test apparatus. End-of-mix viscosities at 60 °C were determined on a Brookfield viscometer.

3. Results and Discussion

3.1 Propellant cured with IPDI

The binder compositions of the propellant cured with IPDI with their respective properties are tabulated in Table 2. The relative concentrations of species that contains functional OH-groups (HTPB, TMP and DEC) are expressed in terms of percentage values.

Table 2. Binder compositions and mechanical properties of propellant cured with IPDI

No.	NCO/OH-ratio	HTPB-OH (%)	TMP-OH (%)	DEC-OH (%)	σ_m (MPa)	Σ_m (%)	Σ_b (%)	Y_m (MPa)
IPDI/1	0.80	100	-	-	1.02	43	48	5.1
IPDI/2	0.70	90	10	-	0.87	64	68	2.6
IPDI/3	0.75	90	10	-	1.07	44	50	4.5
IPDI/4	0.80	90	10	-	1.18	28	33	8.8
IPDI/5	0.70	80	20	-	1.05	59	64	3.5
IPDI/6	0.75	80	20	-	1.34	38	40	6.6
IPDI/7	0.80	80	20	-	1.43	28	31	9.7
IPDI/8	0.85	80	20	-	1.41	24	27	10.9
IPDI/9	0.70	80	15	5	0.60	71	83	1.4
IPDI/10	0.75	80	15	5	0.99	65	71	2.7
IPDI/11	0.80	80	15	5	1.22	56	61	4.8
IPDI/12	0.75	80	10	10	0.24	86	111	0.72
IPDI/13	0.70	75	20	5	0.57	72	83	1.3
IPDI/14	0.75	75	20	5	0.56	80	101	1.3
IPDI/15	0.75	75	15	10	0.26	107	163	1.1
IPDI/16	0.75	75	10	15	*	*	*	*
IPDI/17	0.75	70	25	5	0.91	71	75	2.1
IPDI/18	0.75	70	20	10	0.24	105	154	0.82
IPDI/19	0.75	70	15	15	*	*	*	*

** NCO/OH ratio was too low to cure the propellant properly*

The baseline propellant where the binder was not modified is represented by formulation IPDI/1. It was decided that all propellants developed as part of this investigation must have a tensile strength of between 0.8 and 1.0 MPa. The baseline propellant conforms to this requirement.

The second (IPDI/2 to IPDI/4) and third (IPDI/5 to IPDI/8) data sets in Table 1 represent formulations where the crosslinking density was increased by inclusion of the crosslinker TMP. The effect of increasing TMP concentration at various NCO/OH ratios on the tensile strength and elongation of the propellant are represented graphically in Figures 1 and 2 respectively. At the same NCO/OH ratio, the tensile strength increases while the elongation decreases with increasing TMP concentration. This trend is expected since inclusion of

TMP in the binder system increases the crosslinking density and leads to the formation of a more rigid polymer[4].

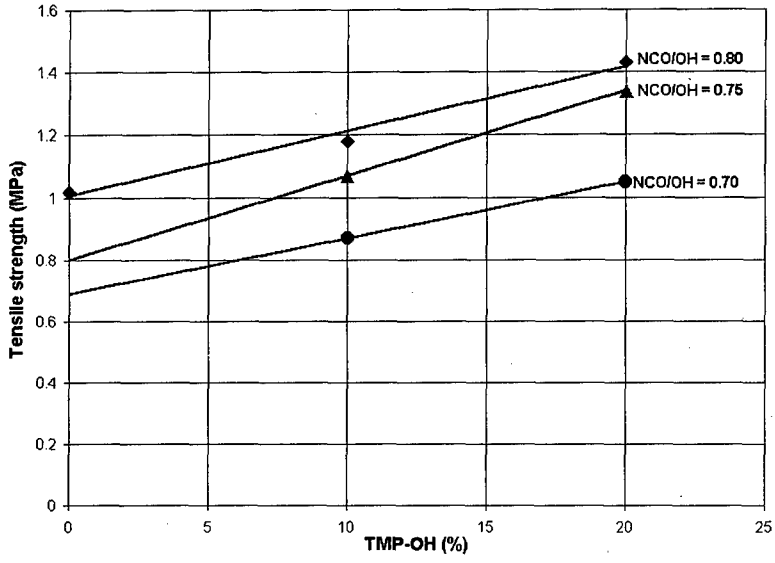

Figure 1. Relationship between Tensile Strength and TMP concentration at various NCO/OH ratios.

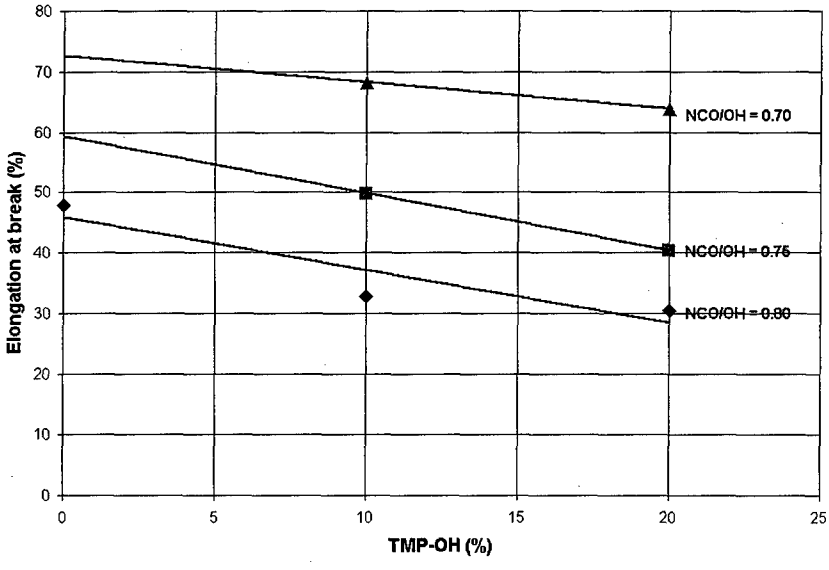

Figure 2. Relationship between Elongation and TMP concentration at various NCO/OH ratios.

In spite of this observed trend, it is also interesting to note that the elongation capability of the propellant can be improved by inclusion of TMP, while maintaining the required tensile strength. The tensile strengths of both formulations IPDI/2 and IPDI/5 conform to the requirement of 0.9 ± 0.1 MPa, but the strain capabilities of both these propellant compositions are substantially higher than that of the baseline propellant. The NCO/OH ratio has to be lowered substantially, from 0.80 to 0.70, to achieve this goal. These results are in line with those of Marsh and Udlock[4] where it was found that a combination of low crosslink density with flexible chains leads to a highly extensible rubber.

The last five data sets (IPDI/9 to IPDI/19) in Table 1 represent different combinations of the trifunctional crosslinker (TMP) and the monofunctional chain terminator (DEC). A large amount of chain termination interferes completely with formation of a network polymer. In the case where a small amount of chain termination exists, a network polymer is still produced, but there is a proportion of non-crosslinked branches. The main objective is to increase chain extension at the expense of crosslinking. The effect of chain termination on the tensile strength and elongation, at a fixed NCO/OH ratio of 0.75, is graphically represented in Figures 3 and 4 respectively.

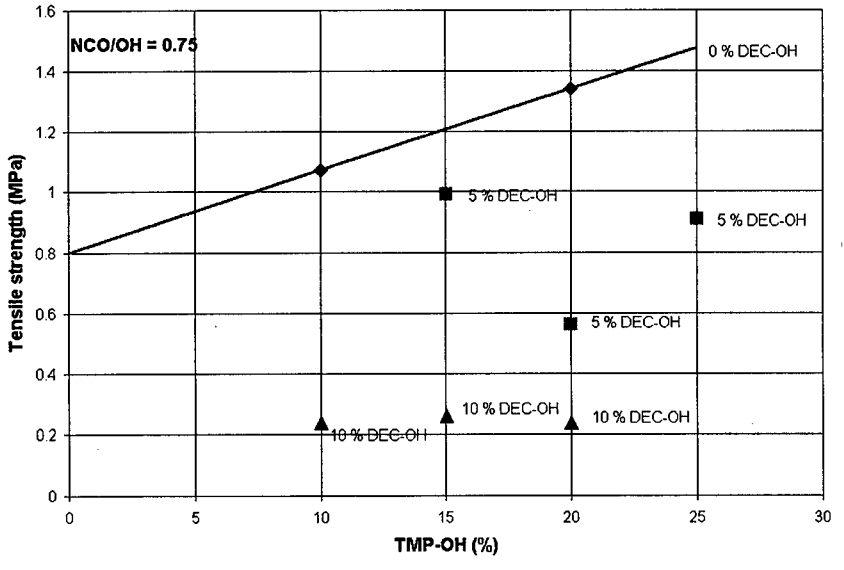

Figure 3. Relationship between Tensile Strength and TMP concentration at various DEC concentrations.

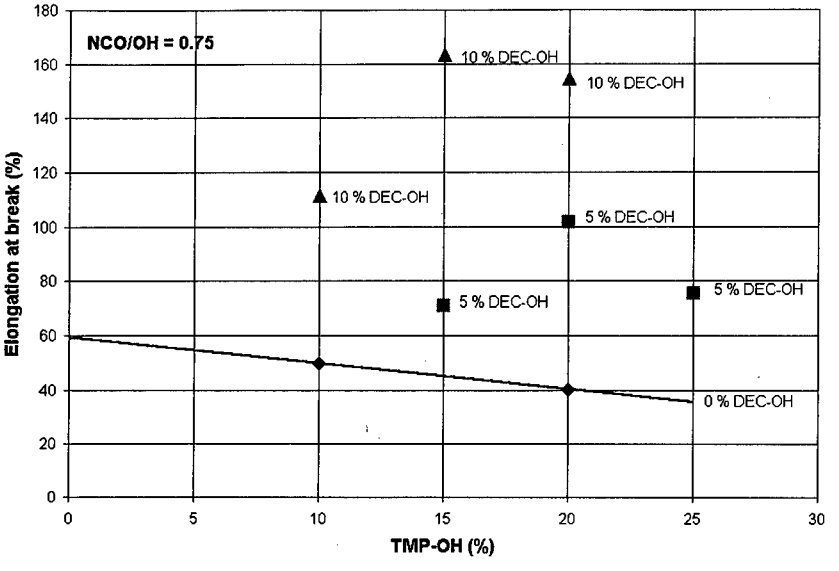

Figure 4. Relationship between Elongation and TMP concentration at various DEC concentrations.

The delicate balance between desired degree of crosslinking and chain termination is evident when comparing the results of formulations containing 5 and 10 % DEC-OH respectively. The inclusion of 5 % DEC-OH has a small decreasing effect on the tensile strength (IPDI/10 and IPDI/17), while the elongation capability increased substantially with more than 20 % when compared to that of formulations containing only TMP. When comparing the mechanical properties of these two propellant compositions with that of the baseline propellant (IPDI/1), it is evident that the required tensile strength (0.9 ± 0.1 MPa) is achieved by both formulations, but with substantially higher elongation capabilities.

It is also clear that when the DEC-OH is increased from 5 to 10 %, the extent of chain termination is so large that it almost prevents the formation of a three-dimensional polymer network. The result is a polymer with unacceptably low tensile strength and but high elongation capability (IPDI/12, IPDI/15 and IPDI/18). Increasing the NCO/OH ratio higher than 0.75 will help to increase the tensile strength, while maintaining good elongation capabilities.

3.2 Propellant cured with DDI

The binder compositions of the propellant cured with DDI with their respective properties are tabulated in Table 3.

Table 3. Binder compositions and mechanical properties of propellant cured with DDI

No.	NCO/OH-ratio	HTPB-OH (%)	TMP-OH (%)	DEC-OH (%)	σ_m (MPa)	Σ_m (%)	Σ_b (%)	Y_m (MPa)
DDI/1	0.8	100	0	0	1.02	60	65	3.2
DDI/2	0.8	87.5	12.5	0	1.11	39	40	4.8
DDI/3	0.7	80	20	0	0.696	83	94	1.6
DDI/4	0.75	80	20	0	1.26	55	58	4.2
DDI/5	0.8	80	20	0	1.28	30	34	7.6
DDI/6	0.85	80	20	0	1.39	30	35	8.8
DDI/7	0.7	80	15	5	0.16	116	185	0.60
DDI/8	0.75	80	15	5	0.41	87	107	0.76
DDI/9	0.8	80	15	5	1.02	69	77	2.7
DDI/10	0.85	80	15	5	1.19	33	41	5.7
DDI/11	0.8	70	25	5	1.14	47	51	4.3
DDI/12	0.8	75	20	5	1.05	66	70	2.9
DDI/13	0.8	77.5	17.5	5	0.98	72	81	2.4
DDI/14	0.8	80	15	5	1.02	69	77	2.7
DDI/15	0.8	85	10	5	0.931)	73	80	2.3
DDI/16	0.8	72.5	20	7.5	1.13	61	63	3.2
DDI/17	0.8	75	17.5	7.5	0.63	84	91	1.3
DDI/18	0.8	77.5	15	7.5	0.76	79	84	1.7
DDI/19	0.8	70	20	10	0.62	87	96	1.2
DDI/20	0.8	72.5	17.5	10	0.67	79	83	1.3
DDI/21	0.8	75	15	10	1.17	49	50	3.7
DDI/22	0.8	80	10	10	0.48	100	113	0.82
DDI/23	0.8	70	15	15	0.50	86	99	0.95

The relationship between the mechanical properties and increasing TMP-OH at different DEC-OH values is represented in Figures 5 and 6 respectively. The NCO/OH ratio of all formulations was held constant on 0.80. Similar to the IPDI formulations an almost linear trend is observed between the mechanical property (tensile strength and elongation) and increasing concentrations of the crosslinker TMP. This linear trend is also observed when the chain terminator DEC is added in 5 and 10 % quantities. It is also obvious that the effects of crosslinking and chain termination by the inclusion of varying quantities of TMP and DEC in the DDI cured formulations, are similar to those observed in the IPDI cured formulations. A small degree of chain termination (5 % DEC-OH) accompanied by chain branching and chain extension by the inclusion of 10 to 20 % TMP, forms a polymer

network with suitable tensile strength and excellent elongation capabilities (DDI/12 to DDI/15).

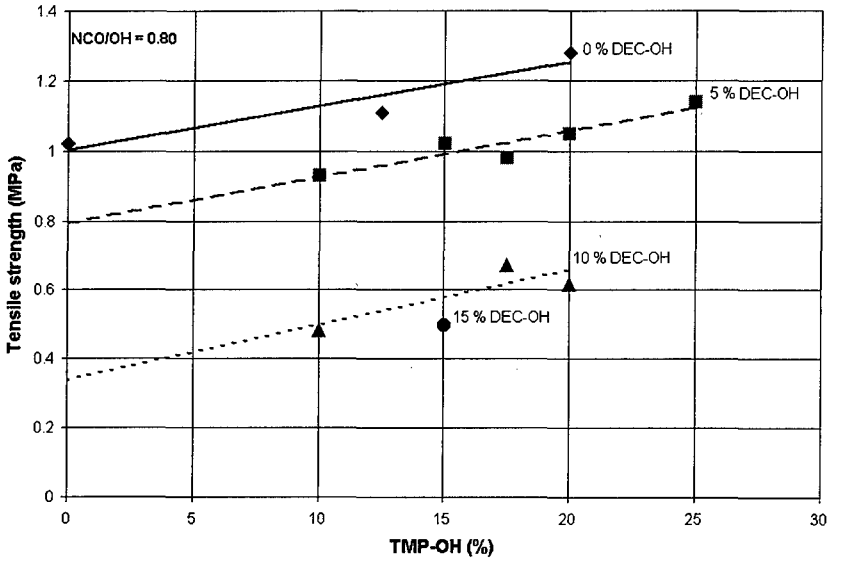

Figure 5. Relationship between Tensile Strength and TMP concentration at various DEC concentrations

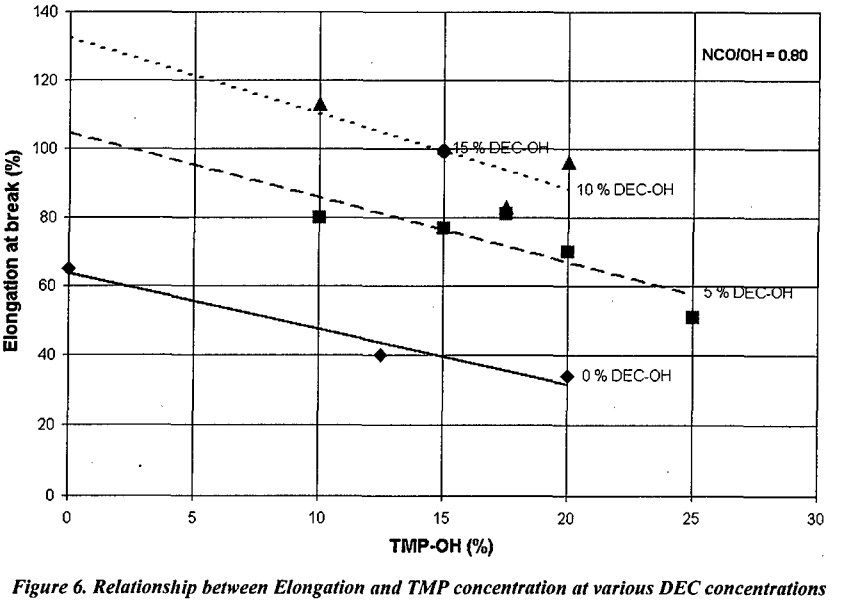

Figure 6. Relationship between Elongation and TMP concentration at various DEC concentrations

The mechanical properties of the latter formulations are also superior to that of the baseline propellant (DDI/1), which does not contain any TMP or DEC. The required tensile strength of 0.9 ± 0.1 MPa is achieved, but the elongation capabilities are improved by between 10 and 15 %. As is the case with the IPDI cured formulations, it is obvious that increasing the concentration of the chain terminator DEC to more than 5 %, prevents the formation of a suitable network polymer, due to the high degree of chain termination. The result is a polymer with high elongation capabilities, but unsuitably low tensile strengths (DDI/17 to DDI/23).

3.3 Comparison between propellants cured with IPDI and DDI respectively

The effect of the two different curing agents, IPDI and DDI, on the mechanical properties of formulations containing similar quantities of HTPB, TMP and DEC respectively, is represented graphically in Figures 7 and 8 respectively.

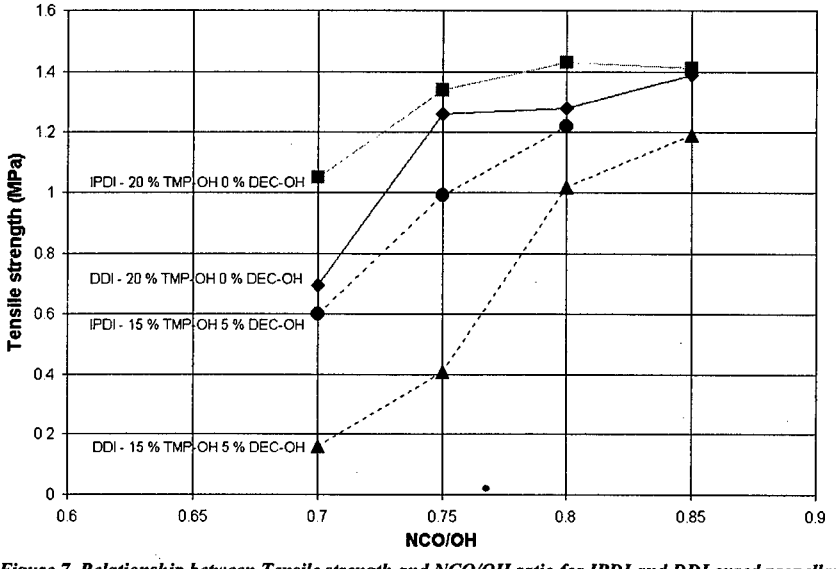

Figure 7. Relationship between Tensile strength and NCO/OH ratio for IPDI and DDI cured propellants

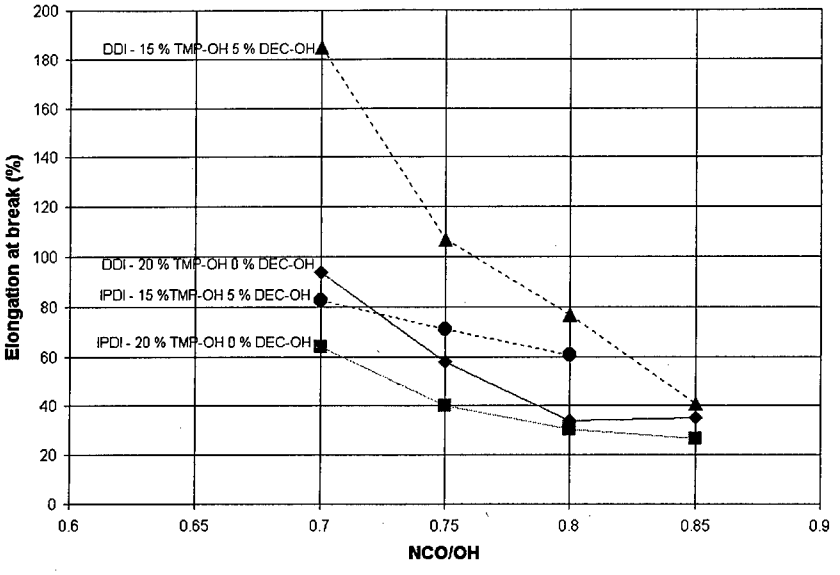

Figure 8. Relationship between Elongation and NCO/OH ratio for IPDI and DDI cured propellants

The same trend is observed at all NCO/OH ratios and for both formulations, the one containing 20 % TMP-OH, as well as the one containing 15 % TMP-OH and 5 % DEC-OH. The tensile strength of the formulation cured with IPDI is in every case higher than the corresponding DDI cured formulation. The elongation capabilities of the DDI cured formulations are however better than the corresponding IPDI cured formulations.

The benefit of using DDI as curing agent provides two essential characteristics to the polymer network that is beneficial for better elongation capabilities. The long chain molecular structure of the DDI molecule serves as chain extender in the polymer network, which as discussed earlier, improves the elongation capability of the polymer network. The other important characteristic of the DDI molecule is that is has substantially more degrees of freedom (more flexibility) when compared to the rigid cyclic structure of the much shorter IPDI molecule. Using DDI in the polymer network has the advantage of providing chain extension while simultaneously providing more degrees of freedom to the network.

3.4 Propellant cured with Desmodur N100

One of the initial objectives of this investigation was to evaluate the trifunctional curing agent Desmodur N100. The potential benefit of using Desmodur N100 is that the

trifunctional isocyanate will also function as crosslinker and in combination with TMP and/or DEC may provide interesting results. Unfortunately, it was not possible to process the Desmodur N100 propellant batches due to the short pot life of these formulations. An attempt to improve the pot life by excluding the combustion stabiliser was fruitless. Inclusion of a pot life extender was also unsuccessful in improving the pot life. One explanation for the short pot life of the Desmodur N100 formulations is that this isocyanate compound is more reactive towards the alcohol species in formation of urethane than either IPDI or DDI.

4. Conclusions

This investigation proved that it is possible to improve the elongation capability of HTPB-based propellants by manipulating the degree of chain extension and crosslinking in the polymer network. This is done by incorporating crosslinkers such as TMP as well as chain terminators such as DEC in the binder of the propellant. The best results are obtained with a small degree of chain termination (DEC-OH = 5 %) and a moderate degree of crosslinking (TMP-OH = 10 to 20 %). Less than stoichiometric quantities of the isocyanate curing agent (lower NCO/OH ratios) which produces a lower crosslinking density is also beneficial in obtaining propellant with better elongation capabilities. The target tensile strength of 0.8 to 1.0 MPa can be achieved, but the elongation capabilities of propellants with the modified binder systems are between 10 and 30 percent higher than those of the two baseline propellant compositions.

The curing agent also affects the elongation capability of the propellant. A curing agent with a long chain molecular structure and more degrees of freedom like DDI produces a polymer network with better elongation capabilities than one cured with IPDI. IPDI is a cyclic more rigid molecule with a very short chain length between the two isocyanate groups. The trifunctional curing agent Desmodur N100 could not be evaluated due to the short pot life of these formulations.

5. References

1. R. Manjari, V. C. Joseph, L. P. Pandureng and T. Sriram, *"Structure-Property Relationship of HTPB Propellants. 1. Effect of Hydroxyl Value of HTPB Resin"*, J. Appl. Pol. Sc., Vol. 48, 271 – 278 (1993).

2. R. Manjari, U. I. Somasundaran, V. C. Joseph and T. Sriram, *"Structure-Property Relationship of HTPB Propellants. II. Formulation Tailoring for Better Mechanical Properties"*, J. Appl. Pol. Sc., Vol. 48, 279 – 289 (1993).

3. R. Manjari, L. P. Pandureng, U. I. Somasundaran and T. Sriram, *"Structure-Property Relationship of HTPB Propellants. III. Optimization Trials with Varying Levels of Diol-Triol Contents"*, J. Appl. Pol. Sc., Vol. 51,435 – 42 (1994).

4. H. E. Marsh, Jr. and D. E. Udlock, *Formulating Propellants for Fully Case-Bonded End-Burning Motors"*, AIAA/SAE 7th Propulsion Joint Specialist Conference, Salt Lake City, Utah, AIAA Paper No. 71-654 (1971).

Acknowledgment

The Defense Research and Development Board (DRDB) as approved by the Armaments Technology Acquisition Secretariat (ATAS) have partially sponsored the work reported here.

Symbols and Abbreviations

HTPB	=	Hydroxy-terminated polybutadiene
TMP	=	Trimethylol propane
DEC	=	1-Decanol
IPDI	=	Isophorone diisocyanate
DDI	=	Dimeryl diisocyanate
NCO	=	NCO-value
OH	=	OH-value
HTPB-OH	=	Hydroxyl groups of HTPB
TMP-OH	=	Hydroxyl groups of TMP
DEC-OH	=	Hydroxyl groups of DEC
σ_m	=	Tensile strength
Σ_m	=	Elongation at maximum stress
Σ_{br}	=	Elongation at break
Y_m	=	Young's modulus

Use of Butacene In Composite Propellant

Ferrocene derivatives are well known as effective burning rate catalysts for solid composite propellants based on ammonium perchlorate and hydroxy-terminated polybutadiene (HTPB), both with and without aluminium. Low molecular mass ferrocenes such as 2,2-bis(ethyl ferrocenyl)propane (Catocene) are relatively volatile and introduce additional hazards during propellant manufacture. They also tend to migrate to the charge surface and to promote atmospheric oxidation during storage, thus reducing the life of the propellant due to the development of inconsistent burning rates, reduced strain capability, and increased sensitiveness.

Butacene is a ferrocenyl hydroxy functional polymer based on HTPB (R45M grade) manufactured by SNPE, which is non-volatile and migration free. This paper reviews work conducted at Royal Ordnance Rocket Motors on a range of formulations containing various levels of Butacene. Results are presented covering the following aspects.

1. Optimisation of processability through the use of polymer blends and processing aids.
2. Sensitiveness testing of Butacene propellants.
3. The effect of Butacene on burning rates compared to other iron compounds.
4. The effect of Butacene on the temperature sensitivity of burning rate.
5. The effect of Butacene on mechanical properties.
6. The relative efficiencies of antioxidants in Butacene propellants.

Authors
D. R. Fossey
D. G. Catton
W. G. Turner-Mutch

Properties of CL-20 based High Explosives

H.R. Bircher, P. Mäder, J. Mathieu

GR Gruppe Rüstung, Fachabteilung Waffensysteme und Munition,
Feuerwerkerstrasse 39, CH-3600 Thun 2

ABSTRACT

A new processing technology for PBX's, called „Isogen Pressing", is described. The equipment needed therfore, is a conventional press and an adapted pressing tool, so that its implementation can be realized without extensive investments. „Isogen Pressing" combines the advantages of high energetic filler content from pressed formulations with good mechanical properties as known in cast cured compositions. We have applied this technology on HMX and CL-20 based formulations using the binder systems GAP and HTPB.
Handling safety parameter are compared with other CL-20 and HMX based compositions, such and LX-19. Chemical compatibility of the compositions ingredients was checked with Micro Calorimetry. The thermal stability was investigated with Differential Scanning Calorimetry (DSC). Detonation velocities have been calculated and verified with experimental data.

EINLEITUNG

Die Zugänglichkeit von neuen Energieträgern, wie beispielsweise CL-20 [1,2,3], eröffnet im Bereich von Hochleistungssprengstoffen die Möglichkeit einer nicht unerheblichen Leistungssteigerung [4,5]. Auf der anderen Seite ist man aber auch bestrebt, die Empfindlichkeit von Explosivstoffen soweit zu reduzieren, dass diese in entsprechenden Munitionsanwendungen die geforderten Verwundbarkeitskriterien (IM, MURAT...) erfüllen [6,7,8]. Entscheidend für die Reduktion der Empfindlichkeit ist, neben der intrinsischen Empfindlichkeit des Energieträgers und der Optimierung von Kornform und Korngrössenverteilung, auch das auf den Energieträger abgestimmte Bindersystem, bzw. dessen mechanische Eigenschaften, sowie dessen Kornhaftungsvermögen.

Kunststoffgebundene Sprengstoffe auf der Basis von Harz/Härtersystemen, welche mit Hilfe der sogenannten „Cast-cure Technologie" verarbeitet werden, zeichnen sich neben den meist hervorragenden mechanischen Eigenschaften auch durch Dichten aus, welche nahe an den theoretisch erreichbaren liegen (>99% TMD). Diese Vorteile müssen jedoch durch eine Leistungsreduktion erkauft werden, da der Füllgrad eines Polymers aufgrund der zunehmenden Viskosität bei steigendem Energieträgeranteil, begrenzt ist. In sehr gut optimierten Systemen können Füllgrade von zirka 90% erreicht werden.

Auf der anderen Seite existieren zahlreiche pressbare kunststoffgebundene Sprengstoffformulierungen, welche mit Füllgraden von weit über 90% zwar sehr gute Leistungen aufweisen, deren Dichten jedoch, ohne die Anwendung besonderer Techniken, weit hinter den theoretisch maximal erreichbaren nachhinken (>95% TMD).

Ziel dieser Arbeit war die Vorteile von kunststoffgebundenen Ladungen auf der Basis von Harz/Härtersystemen mit denjenigen von verpressten Ladungen zu kombinieren, d.h. eine Technologie zu konzipieren, bei der ein konventionelles Harz/Härtersystem bis zu 98% (w/w) mit Oktogen oder CL-20 gefüllt werden kann. Neben einer ausgesprochen hohen Leistung (Füllgrad: >96%, Dichte: >97% TMD) sollten die entsprechenden Ladungen auch über gute mechanische Eigenschaften verfügen, welche eine spanabhebende Nachbearbeitung auf einer Drehbank ohne Probleme zulassen sollten.

Wie bereits erwähnt, wurden im Hinblick auf die anvisierte Leistungsoptimierung die Energieträger Oktogen (HMX) und Hexanitrohexaazaisowurtzitan (CL-20) verwendet. Als Harz/Härtersystem entschied man sich für die OH-endständigen Polymere HTPB (inert) bzw. GAP (energetisch) und den Härter Isophorondiisocyanat.

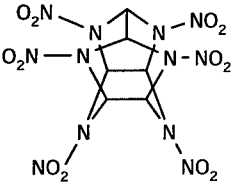

CL-20

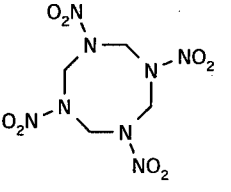

HMX

Dieser Beitrag umfasst sowohl die Beschreibung der Technologie (Isogenpressen), welche es ermöglicht, Sprengstoffe mit den beschriebenen Anforderungen herzustellen, wie auch die Diskussion der entsprechenden Sprengstoffeigenschaften.

ISOGENPRESSEN

Unter dem Begriff „Isogenpressen"[9] versteht man eine Verarbeitungstechnologie, bei der in einem ersten Schritt ein Energieträger (HMX, CL-20) durch Aufbringen eines Harz/Härtersystems zu einem rieselfähigen Granulat verarbeitet wird. In einem nächsten Schritt erfolgt die Herstellung eines Formkörpers. Dabei wird das Granulat bei erhöhter Temperatur unter Vakuum verpresst und zugleich ausgehärtet. Das Bindemittel bleibt bei Raumtemperatur während des Pressvorganges flüssig und kann durch vorgewählte Temperaturbereiche in seiner Aushärtung gesteuert werden. Das während der Verdichtung flüssige Bindemittel führt zu einer hohen Dichte und Homogenität der Sprengladung. Ein ähnliches Verfahren wurde in einem Patent von THIOKOL[10] beschreiben, wobei ein OH-endständiges Polymer zuerst durch einen Isocyanathärter zu einem „Extended Chain"-Polymer mit höherem mittlerem Molgewicht und höherer Viskosität umgesetzt wird. Dieses wird dann in Lösung durch Zugabe eines Antilösungsmittels auf das Sprengstoffkorn aufgetragen, das Granulat getrocknet und verpresst. Die beiden Verarbeitungsverfahren unterscheiden sich in zwei wesentlichen Punkten:

- Beim Isogenpressen wird das gesamte Bindersystem, als Gemisch von OH-endständigem Polymer, Härter und Reaktionsbeschleuniger durch Abdampfen des Lösungsmittels auf das Sprengstoffkorn aufgetragen. Beim THIOKOL-Verfahren wird ein bereits vernetztes Polymer durch einen Fällungsprozess auf das Korn des Energieträgers gebracht.
- Währenddem beim Isogenpressen das Polymer unter Druck zu einer Kunststoffmatrix aushärtet, welche sich über den gesamten Presskörper erstreckt, werden beim THIOKOL-Verfahren die plastischen Eigenschaften des „Extended Chain"-Polymers unter hohem Druck ausgenutzt. Dies entspricht der klassischen Funktion von Bindern in pressbaren Formulierungen. Zwei wesentliche Vorteile, wie die hohe Adhäsion der Bindermatrix an die Kristalle des Energieträgers und die hohen Dichten (% TMD) sind dadurch nicht mehr ohne weiteres gegeben.

a) Herstellung des Granulates

In einem ersten Schritt wird das OH-endständige Polymer (HTPB R-45-M, GAP) bei Raumtemperatur unter mässigem Rühren mit einem Reaktionsbeschleuniger homogen vermischt, in Aceton aufgenommen und mit einem Härter (IDPI) versetzt. Um

einen optimalen Vernetzungsprozess zu gewährleisten, ist darauf zu achten, dass unter möglichst wasserfreien Bedingungen (< 0.1% (w/w) Wasser) gearbeitet werden kann. Die Binderlösung wird mit Hilfe eines Trommelmischers auf die Sprengstoffkörner aufgebracht. Für Granulate auf der Basis von HMX wurde Oktogen, welches der Spezifikation des MIL-H-45444, Grade B, sowie STANAG 4284 genügt, verwendet. Das von uns verwendete CL-20 (ε-Polymorph) erfüllt die Anforderungen des entsprechenden STANAG-Entwurfs. Die von uns verwendeten Korngrössenverteilungen sind in Tabelle 1 dargestellt.

	HMX, Klasse C	CL-20
90 %	< 1340 µm	< 134 µm
50 %	< 460 µm	< 35 µm
10 %	< 90 µm	< 6 µm

Tabelle 1: Korngrössenverteilungen der verwendeten Energieträger

Nach der Beschichtung des Energieträgers lässt man das restliche Lösungsmittel bei Raumtemperatur unter Vakuum (1 mbar) während einer Stunde verflüchtigen. Das Granulat wird dabei rieselfähig (vgl. Abbildung 1) und lässt sich weiterverarbeiten, obwohl das Bindemittel auf der Kornoberfläche an sich bei Raumtemperatur noch flüssig ist.

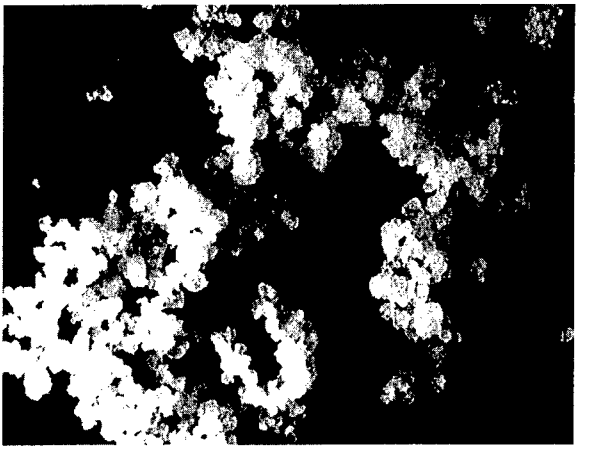

Abbildung 1: 20 fache Vergrösserung des Granulates (98% CL-20, 2% HTPB)

b) Verpressen des Granulates

Je nach Anwendung kann das Granulat axial oder isostatisch verpresst und ausgehärtet werden. Voraussetzung ist einzig, dass das entsprechende Presswerkzeug evakuier- und beheizbar ist. Die in dieser Arbeit beschriebenen Presskörper wurden schwimmend auf einer Axialpresse hergestellt, wobei das entsprechende Presswerkzeug über O-Ringdichtungen zur Evakuierung des Pressraumes und über einen Heizmantel zur Steuerung der Temperatur verfügte. Nach dem Einfüllen des Granulates und dem Anlegen eines Druckes von 2000 bar wird die Temperatur des Presswerkzeuges auf 80 °C bis 85 °C erhöht. Dadurch wird der Reaktionsbeschleuniger aktiviert und der Aushärtungsprozess eingeleitet. Die Temperatur wird je nach Gehalt an Reaktionsbeschleuniger während einer halben bis zu zwei Stunden aufrecht erhalten, dann während einer halben Stunde gekühlt und schliesslich der Druck entlastet. Der Sprengkörper liegt nun als hydrophobe, formstabile Ladung vor, welche zur vollständigen Aushärtung während weiteren 72 Stunden bei einer Temperatur von 65 °C unter Normaldruck gelagert wird. Die mit dieser Methode erreichten Dichten sind in Tabelle 2 dargestellt.

Energieträger		Binder	Körperdimensionen		Dichte	% TMD
Typ	Gehalt		ϕ	Länge		
HMX	96 %	HTPB	21.3 mm	35.04 mm	1.789 gcm^{-3}	98.1 %
HMX	98 %	HTPB	21.3 mm	15.03 mm	1.812 gcm^{-3}	97.3 %
HMX	96 %	GAP	21.3 mm	15.03 mm	1.822 gcm^{-3}	97.6 %
HMX	98 %	GAP	21.3 mm	15.03 mm	1.831 gcm^{-3}	97.2 %
CL-20	98 %	HTPB	21.3 mm	15.60 mm	1.943 gcm^{-3}	97.4 %
CL-20	98 %	GAP	21.3 mm	15.48 mm	1.964 gcm^{-3}	97.4 %

Tabelle 2: Dichten von isogengefertigten Presskörpern

Die Oberfläche der mit dem Isogenverfahren gefertigten Presskörper erscheint äusserst homogen und glatt. Die maschinelle Nachbearbeitung auf einer Drehbank ist aufgrund der sehr kompakten und homogenen Struktur problemlos möglich. Die Abbildung 2 zeigt einen mit Hilfe der Isogentechnik hergestellten Presskörper (links) im

Vergleich mit einem Pressling auf der Basis von Oktastit VIII. Die unterschiedlichen Oberflächen sind offensichtlich.

Abbildung 2: Oberfläche von isogen (links) und konventionell (rechts) gepressten Sprengstoffkörpern in 10-facher Vergrösserung

VERTRÄGLICHKEIT

Die chemische Verträglichkeit der Komponenten von Oktogensprengstoffen auf der Basis von HTPB und GAP wurde bereits in früheren Untersuchungen nachgewiesen. Obwohl aufgrund der Nitraminfunktionalität von CL-20 keine Inkompatibilitäten mit den verwendeten Binderbestandteilen zu erwarten sind, wurden zur Sicherstellung der Verträglichkeit mikrokalorimetrische Messungen durchgeführt.

Dazu wurde der Wärmefluss eines Gramms des jeweiligen Sprengstoffes bei einer Temperatur von 70 °C während eines Zeitintervalls von 60 Tagen gemessen. Dies entspricht einer Alterung um zirka 40 Jahre. Die während der Prüfung umgesetzte Wärme lässt sich durch numerische Integration des Wärmeflusses über die Zeit bestimmen. Ein Sprengstoff wird als chemisch stabil beurteilt, wenn über die gesamte Messdauer bei einer Prüftemperatur von 70 °C der Wärmefluss den Grenzwert von ±10µW nicht überschreitet und der integrierte Wärmeumsatz kleiner als 52 Joule ist.

Alle untersuchten Sprengstoffe zeigten während der ersten Tage ein endothermes

Verhalten, welches dann in ein exothermes übergeht. Innerhalb der Prüfzeit zeigte keine der Proben Anzeichen einer autokatalytischen Zersetzung. Der Grenzwert wurde von keinem der getesteten Isogensprengstoffe überschritten (vgl. Abbildung 3).

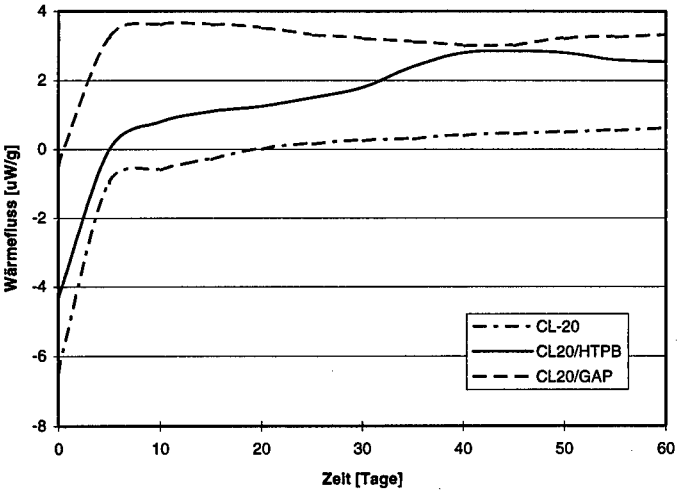

Abbildung 3: Wärmeflusskurve der Systeme CL-20 (96%)/HTPB (4%), CL-20 (96%)/ GAP (4%) und CL-20 (100%) bei einer Prüftemperatur von 70 °C.

Der integrierte Wärmefluss (d.h. die während der 60 Tage produzierte Wärme) beträgt 0.25 J/g bei CL-20, 8.8 J/g bei CL-20/4% HTPB und 16.75 J/g bei CL-20/4% GAP. Der Grenzwert von 52 J wurde in keinem der getesteten Formulierungen überschritten. Aufgrund dieser Tatsache kann angenommen werden, dass die untersuchten Isogenformulierungen über einen Zeitraum von zirka 40 Jahren chemisch stabil sein sollten.

Die chemische Verträglichkeit der Sprengstoffbestandteile mit eventuellen Kontaktmaterialien, wie Eisen, Kupfer und Aluminium ist für sämtliche Kombinationen mit HMX, CL-20 und HTPB gegeben. Hingegen zeigen die mikrokalorimetrischen Messungen beim Kontakt von GAP mit Eisen und insbesondere mit Kupfer einen erhöhten Wärmefluss und somit eine nicht akzeptable chemische Kompatibilität.

THERMISCHE STABILITÄT

Die thermische Stabilität wurde mit Hilfe von Differential Scanning Calorimetry (DSC) untersucht. Zur Messung stand ein METTLER TOLEDO Star System zur Verfügung. Die in Tabelle 3 aufgeführten Daten beziehen sich auf eine Heizrate von 5°C/Min und eine Probemenge von 5 mg bei HMX-Formulierungen, bzw. 1 mg bei CL-20-Kompositionen.

Komponenten	Zusammensetzung [%]	Phasenumwandlung (max)	Onset Temperatur	Max. Exotherm
HMX	100	$\beta \rightarrow \delta$: 180 °C	271 °C	276 °C
HMX/HTPB	98/2	$\beta \rightarrow \delta$: 180 °C	270 °C	271 °C
HMX/GAP	98/2	$\beta \rightarrow \delta$: 178 °C	265 °C	270 °C
HMX/ESTANE	LX-14	$\beta \rightarrow \delta$: 186 °C	265 °C	275 °C
CL-20	100	$\varepsilon \rightarrow \gamma$: 170 °C	232 °C	244 °C
CL-20/HTPB	96/4	$\varepsilon \rightarrow \gamma$: 168 °C	233 °C	236 °C
CL-20/GAP	96/4	$\varepsilon \rightarrow \gamma$: 169 °C	238 °C	241 °C
CL-20/ESTANE	LX-19	$\varepsilon \rightarrow \gamma$: 168 °C	220°C	227 °C

Tabelle 3: Differencial Scanning Calorimetry Daten von HMX, CL-20, sowie der entsprechenden HTPB, GAP und ESTANE-Formulierungen

Wie bereits die Daten der chemisch reinen Stoffe zeigen, erfolgt die exotherme chemische Zersetzung von CL-20 bei rund 30°C tieferer Temperatur als diejenige von Oktogen. Der Einfluss der Binder kann je nach Energieträger recht unterschiedlich sein. Während beispielsweise der Binder ESTANE in LX-14 die Onset-Temperatur um 6 °C und die Temperatur der maximalen exothermen Umsetzung um bloss 1°C erniedrigt, ist der Effekt bei der CL-20-Formulierung LX-19 bedeutend ausgeprägter. Die Onset-Temperatur wird um ganze 12 °C und die Temperatur des maximalen exothermen Wärmeflusses um nicht weniger als 17 °C erniedrigt. In den vorliegenden Sprengstoff-Formulierungen scheint der Einfluss des Binders unter den erwähnten Versuchsbedingungen keinen grossen Einfluss auf die Temperatur der endother-

men Kristallumwandlungen zu haben. Es wäre jedoch falsch, daraus in der jeweiligen Bindermatrix eine gute Stabilität der verwendeten Kristallmodifikationen ableiten zu wollen. Insbesondere im Fall von CL-20 wurde gezeigt, dass sowohl das Löslichkeitsvermögen des Binders[11,12], wie auch Verunreinigungen[13] massgeblich die Umwandlung in andere Kristallmodifikationen fördert.

Die Formulierungen auf der Basis der Binder GAP und HTPB zeigen bei Aufheizraten von 5°C/min eine exotherme Vorreaktion (vgl. Abbildung 4). Diese korrespondiert

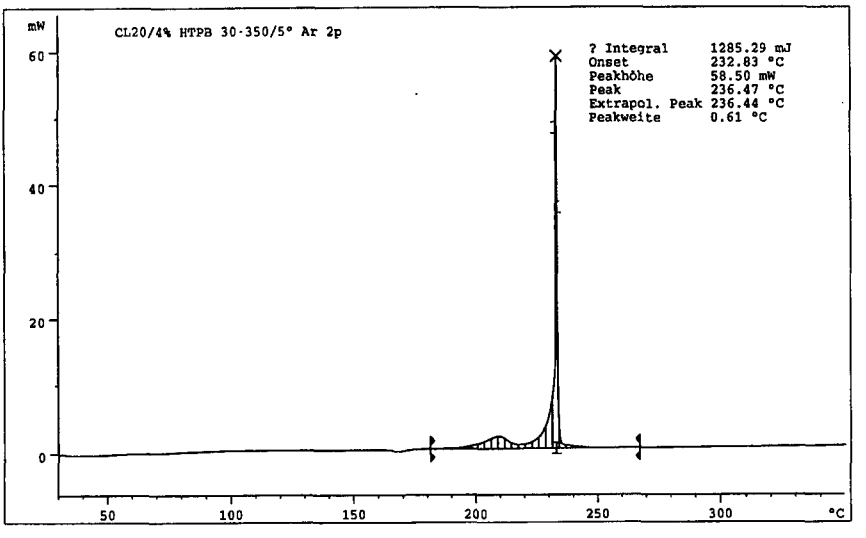

Abbildung 4: DSC von CL-20/HTPB (96/4), Aufheizrate: 5 °C/min

mit der exothermen Umsetzung des Binders. Die Reaktion der energetischen Komponente selbst findet dann sehr rasch in einem engen Temperaturbereich statt. Der Einfluss der Binder HTPB und GAP auf die Erniedrigung der Temperatur des maximalen Wärmeflusses ist für HMX und CL-20 in den untersuchten Konzentrationsbereichen kleiner als 8 °C.

HANDHABUNGSSICHERHEIT

Zur Ermittlung der Handhabungssicherheit wurde die Schlag- und die Reibempfindlichkeit bestimmt. Die Empfindlichkeit bezüglich Schlag wurde auf einem BAM-Fallhammer mit einem 2 kg Fallgewicht ermittelt. Zur Bestimmung der Reibempfindlichkeit stand ein Julius Peters Reibapparat zur Verfügung. Die Durchführung und Ermittlung der Resultate entspricht den Beschreibungen aus „UN Recommendations on Transport of Dangerous Goods", Tests 3(a)(ii) bzw. 3(b)(i).

Formulierung	Zusammensetzung	Reibempfindlichkeit	Schlagempfindlichkeit
HMX, Klasse C	100	8.0 kg	20 cm
HMX/HTPB*	98/2	9.6 kg	10 cm
HMX/GAP*	98/2	9.6 kg	10 cm
HMX/ESTANE	LX-14	28.8 kg	15 cm
CL-20	100	9.6 kg	15 cm
CL-20/HTPB*	96/4	14.4 kg	15 cm
CL-20/GAP*	96/4	9.6 kg	10 cm
CL-20/ESTANE	LX-19	14.4 kg	10 cm
* Binder ausgehärtet			

Tabelle 4: Reibungs- und Schlagempfindlichkeit von HMX und CL-20-Formulierungen auf der Basis von HTPB, GAP und ESTANE

Die Schlagempfindlichkeit aller Formulierungen bewegt sich zwischen 10 und 15 cm, in einem Bereich also, welcher typisch für die meisten hochbrisanten Oktogensprengstoffe ist. Bei der Reibungsempfindlichkeit gibt es gewisse Unterschiede. So scheinen die Binder HTPB und ESTANE eine eher phlegmatisierende Wirkung auszuüben, währenddem bei GAP kein eindeutiger Effekt festgestellt werden kann.

Die Empfindlichkeit bezüglich elektrostatischer Entladung[14] ist für alle in Tabelle 4 aufgeführten Formulierungen in einem für die Handhabung unproblematischen Bereich.

LEISTUNG

Zur Abschätzung der Leistung wurden einerseits Explosionswärmen bestimmt, andererseits aber auch Detonationsgeschwindigkeiten berechnet und teilweise experimentell verifiziert.

Formulierung	Zusammensetzung [%]	Explosionswärme
Oktogen (HMX)	100	5558 J/g
HMX/ESTANE	LX-14	5063 J/g
CL-20	100	6090 J/g
CL-20/HTPB	96/4	5443 J/g
CL-20/GAP	96/4	5799 J/g
CL-20/ESTANE	LX-19	5382 J/g

Tabelle 5: Explosionswärmen von CL-20- und HMX-Formulierungen

Wie bereits aus den Explosionswärmen der reinen Substanzen ersichtlich ist, kann aufgrund der Substitution von HMX durch CL-20 mit einer Erhöhung der Energieausbeute von zirka 10% gerechnet werden. Die Applizierung eines Binders vermindert diese zwar, doch der Energieverlust kann durch die Verwendung energetischer Binder, wie beispielsweise GAP, reduziert werden.

Die experimentelle Bestimmung der Detonationsgeschwindigkeiten liess sich mit Hilfe von Präzisionszeitmessern und Ionisationssonden durchführen, welche jeweils zwischen zwei Presskörpern plaziert wurden. Die Dicke (0.08 mm) der verwendeten

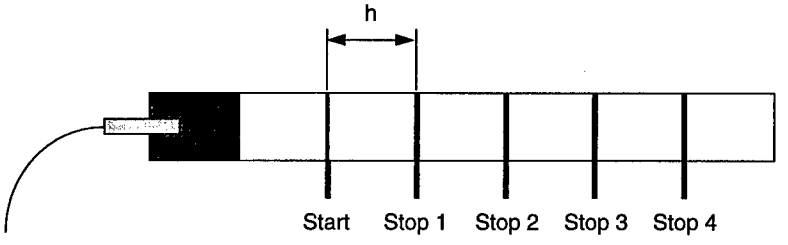

Abbildung 5: Experimenteller Aufbau für die Messung der Detonationsgeschwindigkeit

Kammfolie wurde bei der Bestimmung der Detonationsgeschwindigkeit berücksichtigt.

Formulierung	Zusammensetzung	Dichte	Geschwindigkeit
HMX/HTPB	96/4	1.789 gcm^{-3}	8710 ± 12 m/s
HMX/HTPB	98/2	1.812 gcm^{-3}	8763 ± 30 m/s
HMX/GAP	96/4	1.822 gcm^{-3}	8760 ± 35 m/s
HMX/GAP	98/2	1.831 gcm^{-3}	8833 ± 26 m/s
HMX/ESTANE	LX-14	1.800 gcm^{-3}	8760 ± 70 m/s
CL-20/HTPB	98/2	1.943 gcm^{-3}	9231 ± 7 m/s
CL-20/GAP	98/2	1.964 gcm^{-3}	9286 ± 6 m/s
CL-20/ESTANE	LX-19	1.929 gcm^{-3}	9124 ± 12 m/s

Tabelle 6: Experimentell ermittelte Detonationsgeschwindigkeiten von Sprengstoffen auf der Basis von CL-20 und HMX im Vergleich.

Die theoretische Berechnung der Detonationsgeschwindigkeiten erfolgte mit Hilfe der Sumin-Kondrikov-Zustandsgleichung[15] und entsprechenden Parametern aus der „Datenbank Thermochemischer Daten" (Version 3) des ICT, wobei die theoretisch maximale Dichte (TMD) von CL-20 auf den Wert von 2.04 gcm^{-3} korrigiert wurde.

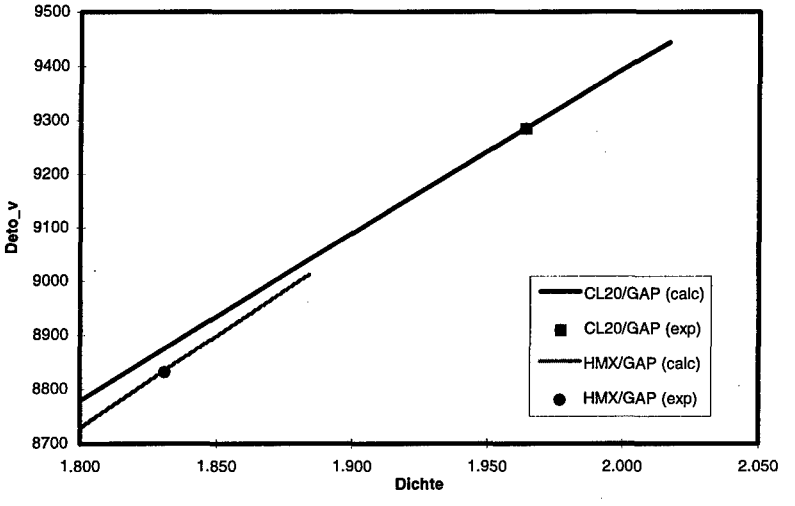

Abbildung 6: Berechnete und gemessene Detonationsgeschwindigkeiten der Formulierungen CL-20/GAP (98/2) und HMX/GAP (98/2).

Wie aus Abbildung 6 ersichtlich ist, könnten theoretisch bei isogenverpressten Formulierungen auf der Basis von CL-20 und GAP Detonationsgeschwindigkeiten von über 9400 m/s erreicht werden. Dies entspricht gegenüber den äquivalenten HMX-Formulierungen eine Steigerung von mindestens 400 m/s. Dieser Trend wurde auch durch experimentelle Daten bestätigt. Währenddem für das System HMX/GAP (98/2) eine Detonationsgeschwindigkeit von 8833 m/s gemessen wurde, erreichte die Formulierung CL-20/GAP (98/2) 9286 m/s, was einer Steigerung um 5% entspricht. Der selbe Trend konnte auch für die Systeme HMX/HTPB bzw. CL-20/HTPB nachgewiesen werden, wobei die erreichten Detonationsgeschwindigkeiten diejenigen der entsprechenden GAP-Formulierungen nicht ganz erreichten.

SCHLUSSFOLGERUNGEN

Die Technologie des Isogenverpressens lässt es zu Sprengstoffkörper herzustellen, welche trotz einem Energieträgergehalt (HMX/CL-20) von bis zu 98% hervorragende mechanische Eigenschaften aufweisen. Als Nachteil dieser Verarbeitungsmethode muss die beschränkte Haltbarkeit des Granulates, sowie die zeitliche Inanspruchnahme der Presswerkzeuge erwähnt werden. Dies sind jedoch Probleme, welche grundsätzlich technisch lösbar sein sollten.

Die untersuchten Systeme auf der Basis von HMX und CL-20 als Energieträger sowie HTPB und GAP als Bindersysteme zeichnen sich durch gute Langzeitstabilität aus. Wie bereits aus der Literatur bekannt war, ist einzig der Kontakt von GAP mit bestimmten Metallen (z.B. Kupfer) problematisch. Die Thermostabilität von CL-20-Formulierungen ist im Vergleich zu entsprechenden HMX-Systemen leicht vermindert, jedoch bei weitem in einem akzeptablen Bereich. Die Stabilität der bei CL-20 verwendeten ε-Kristallmodifikation in verschiedenen Bindermatrizes ist Gegenstand noch laufender Untersuchungen.

Die Handhabungssicherheit bewegt sich aufgrund der ermittelten Schlag- und Reibempfindlichkeit im Rahmen heute verwendeter hochbrisanter Oktogensprengstoffe. Die Empfindlichkeit bezüglich elektrostatischer Entladung ist sowohl für die untersuchten Oktogen-, wie auch für die CL-20-Sprengstoffe unproblematisch.

Wie die Messung der Explosionswärme zeigt, ist durch die Verwendung von CL-20 anstelle von Oktogen eine Steigerung der Energieausbeute um fast 10% zu erwar-

ten. Aufgrund der theoretischen Berechnungen, wie auch der experimentell ermittelten Leistungskenndaten ist absehbar, dass mit Hilfe der Isogentechnologie und aufgrund einer weiteren Optimierung der Ausgangsprodukte, CL-20-Sprengstoffe mit Detonationsgeschwindigkeiten im Bereich von 9400 m/s hergestellt und verarbeitet werden können. Die höchste bis anhin experimentell ermittelte Detonationsgeschwindigkeit von 9286 m/s wurde für das System CL-20/GAP (98/2) gemessen.
Da die Isogentechnologie auch ein Aushärten des Binders unter isostatischer Druckverteilung zulässt, sollte die erreichte Leistungssteigerung bei den Sprengstoffen auch im Bereich grosskalibriger geformter Ladungen umzusetzen sein.

---

[1] „Neue Zürcher Zeitung", 18. Mai 1994

[2] J.F. Bottaro, Chemistry & Industry, 249 (1996)

[3] A.T. Nielsen, US Patent 5,693,794 (1997)

[4] S.M. Nicolich et al.,"High Energy PATHX CL-20 Formulations", Insensitive Munitions & Energetic Materials Symposium, Tampa FL (1997)

[5] R.L. Simpson et al., Prop. Expl. Pyrotech. **22**, 249 (1997)

[6] STANAG 4439, Draft Edition 1 (1995)

[7] Military Standard 2105B, Hazard Assessment Tests for Non-Nuclear Munitions (1994)

[8] International Defense & Technologie, „Insensitive Munitions", October 1992, ISSN 1155-3480

[9] J. Mathieu, P. Mäder, CH Patent 685 118 A5 (1995)

[10] P.C. Braithwaite, G.K. Lund, R.B. Wardle, UK Patent Application GB 2 307 906 A (1995)

[11] M.F. Foltz et al., Prop. Expl. Pyrotech. **19**, 19 (1994)

[12] M.F. Foltz et al., Prop. Expl. Pyrotech. **19**, 133 (1994)

[13] M.F. Foltz, Prop. Expl. Pyrotech. **19**, 63 (1994)

[14] B. Berger et al., 18th International Conference of ICT, P55 (1987)

[15] B.N. Kondrikov et al., Fizika Goreniya i Vzryva 23, 114 (1987)

IMPROVEMENTS IN NTO BASED PBXs

Alain BECUWE - Alain DELCLOS - Georges DONZEL
Martine GOLFIER

S.N.P.E.

Centre de Recherches du Bouchet
91710 VERT-LE-PETIT
France

ABSTRACT

For more than ten years SNPE has been looking for insensitive high explosives for IM. The way chosen to achieve this target was to use NTO as an insensitive filler in a PBX. The first result of these studies was the preparation of B2214 (NTO/HMX/binder) which has been described during the ninth symposium on detonation (Portland, 1989).

Besides its very low sensitivity, B2214 shows two major difficulties which are its large failure diameter (around 75 mm) and its relatively limited performances (Detonation pressure 22.5 GPa).

To improve these properties the first way was to increase the HMX content while still being EIDS. This was described during an ADPA meeting (Phoenix, 1995).

The second one is to replace the inert binder by an energetic one. Using this method two PBXs called B3017 (NTO/Binder) and B3021 (NTO/HMX/Binder) were formulated and characterised.

This presentation will report and summarise those results.

1. INTRODUCTION

For many years, S.N.P.E. has been looking for insensitive ammunitions (IM). EIDS (Extremely Insensitive Detonating Substance) seemed to be the best way to obtain intrinsic insensitivity. Among different available technologies, it has been shown (1, 2) that NTO based cast cured PBXs was the more accurate in terms of processability, cost, performances and vulnerability.

On this basis a cast cured PBX named B2214 using HTPB as binder and filled with a mixture of NTO and HMX was manufactured and characterised (3). It showed a high insensitivity to FCO, SCO, bullet impact, shock (gap test, heavy fragment impact) and shaped change.

More, the resistance to sympathetic detonation has been demonstrated up to a stack test using ∅ 248 mm - l 450 mm confined (0,5" of steel) model.

Unfortunately such wonderful insensitivity has a price which has to be paid in terms of high critical diameter (≈ 75 mm unconfined) and poor initiability.

This B2214 is suitable for large ammunitions such as general purpose bombs but has to be improved for other applications.

2. *IMPROVEMENT OF B2214*

As we were looking for EIDS one way was to increase the HMX content and to optimise the ratio NTO/HMX while still having a extra large gap test lower than 70 mm of PMMA.

This way was explored and lead to define B2248 whose properties had been described earlier (4).

The performances have been increased by 20 % (as ρD^2), the failure diameter divided by 7 (11 mm) but if this PBX is still an EIDS, its sensitivity has been increased a lot and cannot insure sympathetic detonation of large ammunitions.

This B2248 can be used in missile warheads up to 140 or 150 mm diameter.

3. *THE ENERGETIC BINDER WAY*

The target of the study reported hereafter was to process a PBX having the same shack sensitivity than B2214 with a lowered failure diameter and increased amorcability and performances. It was choosen to use an energetic binder for the two last properties and NTO alone as filler for the first one.

3.1. *Composition :*

Looking for processability, mechanical properties and energy, the best compromise was found to be 74 % of fillers in a classical energetic binder (i.e. inert polymer with a large amount of energetic plasticizer). This PBX named B3017 has been formulated with a classical process to prepare cast cured PBX.

Processability was optimised by using available classes of NTO particle size manufactured by SNPE. Samples were obtained directly by casting and curing or by machining after curing. Compositions of B3017, as well as B2214 and ORA86A as references are shown in table 1.

% MASS	*NAME*		
	B3017	B2214	ORA86
% Binder	26	16	14
% NTO	74	72	-
% HMX	-	12	86
Specific mass (g/cm^3)	1.75	1.63	1.71

Table 1 : Composition of PBX

3.2. *Detonation velocity*

The detonation velocity of B3017 extrapolated to infinite diameter was found to

be 7.780 m/s. Comparison with references is given in table 2 :

	B3017	*B2214*	*ORA86*
D∞ (m/s)	7780	7440	8380
$\rho D^2/4$ (GPa)	26.5	22.5	30.0
Ratios	1.17	1	-
Ratios	0.88	-	1

Table 2 : Performances

The failure diameter was found to be between 10 and 15 mm.

3.3. Fast cook off

For the three compositions, the fuel fire tests were performed using the French MOD model (3.0 l - ∅ 123 mm - e = 10 mm steel). The result was type V reaction for the three composition which means only smooth combustion of the HE without any violent event.

3.4. Slow cook off

Using the same model and a heating of 3.3°C/h (6°F/h) the same result i.e. type V reaction was observed on all of the three compositions.

3.5. Bullet impact test

For the three compositions the same model was used and one bullet (12.7 AP) was shot at different velocities. Once again for all velocities from 600 m/s to 1140 m/s the same results was found i.e. type IV / type V reaction (type V for B2214) depending on the exact configuration.

3.6. Extended large scale gap test

The gap test is used to determine the threshold of the propagation of detonation in a solid substance. A inert barrier of PMMA is placed between an initiating booster (hexo-wax 95/5 - ∅ 75 mm) and a sample of explosive to be tested (∅ 75 mm - l 280 mm) confined in a 4 mm thick steel pipe.

Results are given in table 3. They are expressed in thickness of PMMA needed to stop the transmission of detonation from the booster to the sample to be tested.

	Thickness of barrier (mm)	*Pressure (kbar)*
ORA86	80	30
B2214	40	80
B3017	35	90

Table 3 : Extended large scale gap test

It can be seen that although it is more performant, B3017 is slightly less shock sensitive than B2214 and twice less than ORA86.

3.7. Heavy fragment impact

This test, usually performed in France, is another mean to measure the shock sensitivity. The sample is confined in the same model than hereabove and a steel ball (∅ 39.5 mm - m = 252 g) is shot at it. The velocity can be increased up to 2300 m/s.

The result is expressed as the higher velocity which didn't lead to the detonation of the sample (table 4).

	Velocity (m/s)	*Pressure (kbar)*
ORA86	1910	60
B2214	> 2273	> 90
B3017	> 2240	> 90

Table 4 : Heavy fragment impact

3.8. Sensitivity to sympathetic detonation

Different experiments were performed using the kinds of models and configurations as described hereafter. No sympathetic detonation have been observed.

All the results are summarised in table 5 :

Configu -ration	*L*	*l*	*e*	*x*	*Result*
D/A	400	90	12.5	25	NSD
Stack	400	90	12.5	25	NSD
D/2A	400	90	6	25	NSD
Stack	400	90	6	35	NSD
D/2A	400	90	3	25	NSD
D/2A	260	123	10	25	NSD

NSD : No sympathetic detonation

Table 5

4. IMPROVEMENT OF B3017

Although the goal of the study had been fully reached, some more improvements seemed to be possible, looking for the most performant EIDS.

For this purpose HMX was progressively substituted to NTO and the sensitivity to gap test evaluated. The limit of the sensitivity to be EIDS was reached with an amount of 25 % of HMX.

This PBX, named B3021, has the same binder than B3017 and a content of 50 % of NTO and 25 % of HMX. Some properties of B3021 in comparison with B3017 are listed in table 6.

	B3021	*B3017*
Detonation velocity (m/s)	8050	7780
$\rho D^2 / 4$ (GPa)	28.7	26.5
Critical diameter (mm)	< 10	10 to 15
ELS Gap test	60	35
FCO	Type V	Type V
SCO	Type V	Type V
Bullet impact	Type IV/V	Type IV/V

Table 6

5. *CONCLUSIONS*

The target of this study made by SNPE was to improved performances, failure diameter and amorcability. This target has been achieved by processing B3017 which is a mixture of NTO and an energetic binder. It can be seen in the reported results than the shock sensitivity is equivalent to B2214 while the performance in terms of detonation pressure is increased by 17 %.

The comparison with a classical PBX such as ORA86 (86 % HMX - 14 % polyurethane binder) is the following : shock sensitivity is divided by three while the decrease of performances (as detonation pressure) is only 12 %.

The behaviour of such a PBX versus other stimuli (FCO, SCO, bullet impact) is still good and B3017 is a very good candidate to fill insensitive ammunitions.

Nevertheless it can be thought that performances are still a bit low. That's why B3021 has been conceived and its characteristics show that it is possible, using NTO based cast cured PBXs, to manufacture EIDS having performances very close to composition B.

REFERENCES

[1] A. BECUWE, A. DELCLOS

"L'oxynitrotriazole et son utilisation en tant qu'explosif insensible". Proceedings of the 18th International Annual Conference of I.C.T., KARLSRUHE (F.R.G.) 1-3 July 1987.

[2] A. BECUWE, A. DELCLOS

"Use of oxynitrotriazole as a low sensitivity explosive". Proceedings of the 1st International Symposium on Pyrotechnics and Explosives, BEIJING (China) - 12-15 October, 1987

[3] A. BECUWE, A. DELCLOS

"Use of oxynitrotriazole to prepare an insensitive high explosive". Proceedings of the 9th International Symposium on Detonation, Portland (USA) - 28 August - 1st September, 1989

[4] A. BECUWE, A. DELCLOS, J. ISLER

"E.I.D.S. High explosives for 1.6. munitions". ADPA Meeting, Phoenix, September 1995.

EXTRUSION TRIALS WITH A TSK045 TWIN SCREW EXTRUDER

Sabel, H.W.R. and Schonewille, E.

TNO Prins Maurits Laboratory, Pyrotechnics and Energetic Materials, P.O.Box 45, 2280AA Rijswijk, The Netherlands

ABSTRACT

In 1994 a 45mm twin screw extruder was introduced at the Prins Maurits Laboratory of TNO for the processing of energetic materials. Initial safety experiments were carried out by using inert compositions with small amounts of different energetic components and micro encapsulated chemical sensors to simulate solventless extrusion processing.

By this approach the internal shear forces and the thermal behavior during such type of extrusion processing could be assessed. As a consequence, some limiting and verifiable processing parameters as product temperature, product pressure, drive torque were found and used to avoid hazardous situations when processing energetic materials at similar conditions. The range of encountered shear stresses within the product during processing could be measured with CAMES™-particles and these too could be related to possible hazardous conditions.

Initial processing of some PBX compositions, which cannot be processed by existing casting techniques, based on monomodal RDX and a solid loading upto 86-87 w% showed promising results. To process the same type of compositions by casting the solids level has to be reduced to the range of 70-78 wt% depending on the crystal sizes and tapdensity.

1. INTRODUCTION

At the Prins Maurits Laboratory (PML/TNO) a project was started to investigate the process behavior during solventless extrusion processing of various composite materials. The main objectives were to determine which type of explosive substances can be safely used in the extruder by measuring the forces and by assessing the thermal behavior during the extrusion process. This is performed by testing different types of liquid prepolymer binders with small amounts of some high explosives and an inert filler. Furthermore, microencapsulated chemical sensors were used to indicate the range of shear stresses during the high-shear mixing and extrusion cycles of the same type of compositions.

2. TECHNICAL DETAILS OF EXTRUDER

The technical data of the Theysohn Maschinenbau GmbH (BRD) TSK045 extruder used during the experiments are as follows:

- Type: co-rotating self-wiping twin screw extruder (SWE)
- Capacity: 2 - 45 kg/hr
- Number of screws: 2
- Screw diameter: 45 mm (D)
- Screw length: 1305 mm (29 L/D)
- Processing unit length: 1260 mm (28 L/D)
- Number of barrel sections: 7 (each 4 L/D)
- Screw shaft rotational speed: 0 - 150 rpm
- Drive: frequency controlled flange motor, max.capacity = 7.5kW (50Hz/1500rpm)

This extruder is feeded by:

- Two gravimetric feeding units for solid ingredients (Brabender, 0-2 and 1-15kg/hr)
- One volumetric feeding unit for solid ingredients (Ktron, 0-26ltr/hr)
- Four volumetric feeding units for liquid ingredients (2 LDT single-piston dosing pumps, 0–2 ltr/hr and 2 Verderflex displacement pumps 2010, 4–100 ltr/hr)

The screw elements are interchangeable, with dispersive mixing elements (complete destruction of agglomerates) and distributive mixing cog-wheel elements (mechanical turbulence and re-orientation for good thermal homogenisation).

3. SAFETY MEASURES

IN HARDWARE:

- safety clutch on drive, with a set shifting torque of 480 Nm
- burst disc in last part of processing unit, which tears at pressures > 300 bar
- breaking bolts mounted in extrusion head construction, which tear at pressures > 250 bar

IN SOFTWARE:

- Continuously monitoring of product temperature and product pressure in process unit and in head construction, which are compared to the specified set points.

4. DETERMINATION OF SAFETY LIMITS

The safety limits were measured by extrusion trials during a process flow of 2-3 kg/hr, different rotational speeds (70-150 rpm) and a continuous temperature of 60°C in the process unit and head construction based on:

- [K_2SO_4 / HTPB + plasticizer]

or:

- [K_2SO_4 / PPG + plasticizer]

with:

- Solid Load: 83 - 92 %

and:

- 2-3% High Explosive additive as thermochemical sensor, with different friction sensitivities and thermal behaviour (TNT, RDX, HMX, and PETN)

or:

- 0.2% 'microspheres' CAMES™ as coloring sensor (Mach I Inc), of which the %-fracture is a function of wall thickness and shear stress

Since it was assumed that an accidental ignition of an energetic material during extrusion processing can be related to its thermal behaviour and friction sensitivity, it was decided to use in the experimental compositions some high explosives with remarkable differences in these two characteristics as shown in the following table :

High Explosive additive	*Thermal characteristics*	*BAM-friction 50%-value*
TNT	melting at 80°C, TG onset at 190°C $-\Delta H_c$ = 14980 kJ/kg	> 360 Nm
RDX	melting/exothermic reaction at 200°C TG onset at 200°C $-\Delta H_c$ = 9450 kJ/kg	250 Nm
HMX	exothermic reaction at 250°C TG onset at 240°C $-\Delta H_c$ = 9330 kJ/kg	100 Nm
PETN	melting at 140°C exothermic reaction at 170°C TG onset at 100°C $-\Delta H_c$ = 8140 kJ/kg	70 Nm

These high explosives were used as thermo-chemical reactive sensors in an inert medium with as close as possible comparable flow behavior during extrusion as is the case with high energetic compositions. As a start some prepolymer binder/inert filler 15/85 blends were prepared and mixed with 2.0 wt-% of these energetic components, whereafter the final compositions were tested by TG/DTA/DSC. As a selection criterion for these trials it was required that the compositions should only react to a degree comparable to the concentration of the HE ingredients included. A more violent reaction, in terms of a higher reaction enthalpy and/or a higher weight loss then should be expected based on the amount of HE, was not acceptable.

From these TG/DTA/DSC tests it was decided to perform all extrusion trials with the inert filler **Potassium Sulfate.** This filler was used earlier at the PML/TNO as an inert ingredient in energetic formulations. The high crystal density of this filler compared to most types of HE's (2.66 and 1.6-1.9 g/cm3 respectively) is a disadvantage, because this results in a lower specific surface area and thus in lower dynamic viscosities during the extrusion process. However, this material is less sensitive to moisture and shows also less or no corrosive reactions to metallic surfaces.

Potassium Chloride is mentioned in literature as an inert ingredient to simulate high explosives (crystal density of KCl: 1.98 g/cm3). It is however sensitive to moisture, which results in agglomeration (feeding problems) and corrosive reactions with metallic surfaces of the hardware. Powderous Sugar is also mentioned in literature as an inert filler for preparation of "mimics". The main advantages are a comparable crystal density as HE's (about 1.6 g/cm3) and a smaller particle size and distribution. However, it is known that this ingredient could also act as an oxidizer, which may lead to a follow-on reaction with the binder after a burning-type ignition has already started. Müller of ICT [6,7] used Powderous Sugar as an inert to measure the relationship between shear stress and shear rate during an extrusion process within a Continua twin-screw C-37E extruder to simulate the Gun Propellant XM-39. From the TG/DTA/DSC-results it was found that all compositions based on Powderous Sugar and HE-sensor showed much too high reaction enthalpies and weight losses as could be expected if the inert filler was really inert.

The thermal differences between the K_2SO_4- and KCl-compositions are however negligible, so it was decided to start the extrusion trials with K_2SO_4 as an inert filler because of a better feeding capability and negligible corrosive behaviour.

During the International Annual Conference of ICT (Karlsruhe BRD) in 1991 and in 1994 papers were presented [1,2], in which the use of spheres of micro-encapsulated dyes during extrusion processes was shown. These spheres rupture when a specified set of shear conditions is exceeded. The colour resulting from the released dye can be monitored to indicate the value of the highest shear stress on the extruded composition and/or alert for an impending critical situation.

The supplier, Mach I Inc., was willing to deliver some samples of these microencapsulated chemical sensors to the PML/TNO for testing purposes. Some characteristics of these sensors as presented by the supplier are summarized in the next table:

CAMES sample	particle diameter range	wall thickness	Shear stress at 10% rupture	Shear stress at 90% rupture
lot 19-67A	63-74μ	0.40±0.03μ	~ 110 kPa	~ 240 kPa
lot 25-11	< 44μ	0.87±0.00μ	~ 500 kPa	~ 2600 kPa

As a start CAMES™ Lot 19-67A was used by setting up a calibration curve. This was done by accurately preparing samples of inert filler and prepolymer binder with well-known fractions of ruptured and unruptured CAMES-particles. These samples were extracted and tested with a Spectrophotometric analysis technique (extraction liquid: xylene; extinction peak at 525 nm; overall concentration CAMES: 0.20%). The resulting calibration curve could be fitted with the exponential equation:

$$E(525) = 0.309 * e^{(1.85 * FRC)} \qquad [1]$$

In which:

E(525) = Photospectrometric extinction at 525nm

FRC = fraction ruptured CAMES-particles

Based on earlier presented data of the supplier, it was assumed that an almost linear relationship exists for the tested lot 19-67A with a maximum shear stress at 100% rupture of about 260 kPa. Based on this assumption the following equation approximates the relationship between shear stress and fraction of ruptured CAMES™-particles lot 19-67A:

$$\text{Shear stress} \approx 163 * FRC + 94 \text{ [kPa]} \qquad [2]$$

And, by combining these two equations, the following relationship between the shear stress and the extinction at 525nm can be derived:

$$\text{Shear stress} \approx 88 * \ln E(525) + 197 \text{ [kPa]} \qquad [3]$$

This lot CAMES™ was tested in similar extrusion trials as was performed with the HE-sensor additives. By this method the shear stresses at which reaction occured in the HE-sensor compositions can be determined quite accurately.

The following data were monitored continuously during these trials:

- absorbed power on the drive in kW
- drive torque
- pressure of product in process unit and head construction
- temperature of product in process unit and head construction
- feeding rates of components

5. RESULTS

Of all compositions with the prepolymer HTPB only those with PETN as HE-thermochemical sensor showed a heat-generating reaction. In comparison to the other HE-sensor compositions (RDX, TNT and HMX) with comparable SL-ratios[1], these results points of an effect *only caused by the higher sensitivity to friction* of PETN, because the TG/DTA/DSC-onset temperature of this type of PETN-composition is almost the same as for the TNT-composition.

The same behavior could also be extracted from the results with the PPG-prepolymer. In comparison with the RDX- and HMX-sensor compositions the PETN-compositions showed a remarkable heat generating effect and change of colour of the product. As with the HTPB-compositions, this could only be suppressed by increasing the liquid binder content.

However, another transition could be recognized, in which the RDX-sensor based compositions showed a remarkable temperature increase and change of colour of a part of the product at the lowest binder concentrations (about 10.5 wt%, SL-ratio 3.3). Such a reaction did not occur with the HMX-sensor compositions with comparable SL-ratios. This heat generating effect cannot be related to the friction sensitivity, because HMX shows the highest sensitivity between these two HE-components.

[1] SL-ratio: Solid/Liquid volume ratio, these values can be used for comparison purposes between different combinations of fillers and liquids

Some other remarkable reactions were observed during the trials with the TNT/PPG-compositions. In one test (8.5 wt% binder, SL-ratio 4.1) a moderate burning reaction occurred, while a second test with a higher liquid content (11 wt% binder, SL-ratio 3.1) was prematurely interrupted to avoid another hazardous reaction. Also, by comparison of the different trials, this heat generating effect cannot be related to the friction sensitivity of the specific HE-sensor. Besides, it can be assumed that the TNT-crystals are melted during the highest value of shear flow in the head construction since the recorded product temperatures exceeded this phase transition temperature.

The most likely explanation for these phenomenona is the *thermal behavior* of the extruded product, due to the heat-up of the material above the onset temperature of the composition. This heat-up is mainly caused by the rotational friction of both screw-tips with the pressurized product within the head construction.

The maximum peak-pressures during these trials ranged from 10 upto 60 bars. These values are lower than the pressures which are needed by statically pressing HTPB-based Gun Propellant strands (60-90 bar). In related literature comparable extrusion process pressures are summarized from 40 upto 90 bar (solvent extrusion processing of 7- and 19-holes Double Base, CAB/RDX-based, triple-based M30 and Kraton modified-M30 GP-strands in twin-screw extruders) [3,4,6]. The maximum product temperatures during the trials with no reactions at all (65-69□C) are comparable to literature data as well [6].

During the extrusion trials with the CAMES™ sensor (lot 19-67A) samples of the product were taken after running at an adjusted rotational speed of the screws for about 20 minutes, after which the samples were analysed with an extraction/spectrophotometric technique. These analysis results were incorporated in equation [3] to calculate the value of the shear stresses. From these measurements, values were found in between 80 and 190 kPa for SL-ratios from 3.5 to 4.3 and rotational speeds of 70 to 150 rpm.

From these experimental trials the following provisional **safety limit values** for solventless extrusion processing of RDX- and HMX-based energetic compositions were extracted:

- temperature rise product above last barrel temperature : < 10°C
- peak pressure of product in barrel : < 70 bar
- torsion main drive : < 25 Nm
- shear stress : < 150 kPa
- SL-ratio : < 3.3

7. PROCESSED ENERGETIC COMPOSITIONS

Besides process parameters, also the accuracy of the feeding process is very critical in respect to safety. Due to the periodical fluctuations of the solid and liquid feeding units an unsafe condition could arise recurrently, by exceeding the required SL-ratio upto or crossing the limit value. Most such irregularities from the feeding units are dimmed in this TSK045-extruder, since the periodical fluctuations of the gravimetric units are lower as about 20% of the mean residential time in the processing unit.

Based on the provisional safety limits the following first PBX-batches were processed safely on the TSK045-extruder:

CODE	RDX-wt%	TYPE RDX
ECX1001/1	79.9 ± 1.2	20µ
ECX1001/2	82.8 ± 1.0	20µ
ECX1001/3	84.0 ± 1.0	20µ
ECX1003	84.0 ± 1.2	20µ
ECX1004/1	86.2 ± 1.4	18µ
ECX1004/2	86.5 ± 0.7	18µ
ECX1005	86.7 ± 0.5	180µ

Binder/Curing Agent: HTPB/IPDI
Plasticizers: DOA, IDP
Additive: Dantocol DHE

The distribution values of the RDX-concentration are based on the periodical fluctuations of the feeding units and thus are only representative for the initial composition which enters the processing unit or in the case the extruder is considered as a tube reactor with no backmixing effects at all. In fact, due to backflow at some of the mixing elements and in front of the head construction most of these fluctuations are dimmed to a much lower value for the finally processed compositions.

6. MAIN CONCLUSION

Provisional safety limit values for extrusion processing of composite materials could be extracted by using "mimics" with small amounts of energetic ingredients and/or microencapsulated chemical sensors (Cames^{TM}).

By using these safety limits PBX-compositions based on unimodal RDX could be processed solventless on the TSK045-extruder with a solid loading upto 87wt% (SL-ratio $\approx$ 3.1).

REFERENCES

[1] A.C.Condo, B.M.Kosowski (Mach I Inc., US)
Microencapsulated chemical sensors for shear stress determination: a method to monitor PBX extrusion processing
22th Int.Annual Conference of ICT 1991, 119

[2] B.M.Kosowski, A.C.Condo (Mach I Inc., US)
Microencapsulated chemical sensors for on line shear stress determination during twin screw extrusion mixing of PBX simulants
25th Int.Annual Conference of ICT 1991, 19

[3] C.W.Fong (WSRL)
Manufacture of propellants and polymer bonded explosives by screw extrusion
Weapons Systems Research Laboratory (Australia), Technical report
WSRL-0456-TR, june 1986 (D89-0786)

[4] Stewart
Considerations for using twin-srew extruders for manufacturing propellants & explosives
15th Int.Annual Conference of ICT 1984, 119-129

[5] Haff Jr.
Extruded composite propellant technology development
J.Spacecraft, Vol.21, no.6 (dec.1984), 587-592

[6] Müller
Verarbeitung von LOVA-TLP im doppelschnecken-extruder
21th Int.Annual Conference of ICT 1990, 22

[7] Müller
Kontinuierliche herstellung von Anzündmitteln
16th Int.Annual Conference of ICT 1985, 42

Twin screw extrusion compounding of energetic materials - a small scale laboratory facility

P Q Flower [1], M J Gough [1], S E Gaulter [1], R Clift[1], B Murray [2]

(1) Weapons Systems,
DERA Fort Halstead,
Sevenoaks,
Kent, TN14 7BP,
United Kingdom.

(2) Prism,
The Old Stables,
Friars Alley,
Lichfield,
Staffordshire, WS13 6PN,
United Kingdom.

SUMMARY

The poster describes the design of a small scale laboratory twin screw extrusion compounding facility based upon a 24mm twin screw extruder now installed at DERA Fort Halstead. The design methodology of the extruder, and ancillary equipment such as loss in weight feeders, to ensure safety for energetics materials processing is discussed. The role of computer based process control systems is described together with an assessment of the safety of the total process.

INTRODUCTION

The development of new energetic materials formulations for gun and rocket propellants and high explosives which meet the various criteria of higher performance but with reduced vulnerability will need to make use of the new energetic binders and energetic solids now being researched and developed in the laboratory. Exploitation of new materials will require evidence of their usability in compositions and will therefore require appropriate formulation technology. Some materials, such as energetic TPEs, may not be readily processable using

conventional batch mixing techniques, whilst other materials may only be available in small laboratory scale quantities at high cost. The DERA therefore required to develop a process which was configurable for a wide range of materials and which could be used, both for initial processing studies with new ingredients and the small scale processing of formulations for early trials purposes.

A review of techniques used for processing conventional polymers indicated twin screw extrusion compounding to be a versatile technique which was also finding application in the explosives field. An analysis by the Thiokol Corporation at their Longhorn Division [1] has demonstrated that the use of a remotely controlled compounding extruder for the manufacture of flare compositions greatly reduces the risk to personnel when compared to more conventional batch processing techniques. The more intensive mixing regime generated in twin screw extruders also offered the potential of improved mixing and performance of formulations compared to those manufactured by conventional batch processes.

There are a number of designs of twin screw extruder based on the direction of rotation of the shafts, the degree of intermeshing between the screws and the screw profiles. After careful consideration of all aspects of design, and the implications on both safety and processing capabilities, a laboratory scale 24mm co-rotating machine with fully intermeshing self wiping screws was selected.

DESCRIPTION OF PLANT

The plant comprises four basic units :-

- extruder
- feeders
- control system
- post die operations

Extruder : One major design consideration was whether to select a segmented barrel or clam shell design. If it was necessary to rapidly vent the barrel the clam shell design offers

significant advantages. Firstly the complete length of the screw is exposed rapidly whereas with a segmented design there is a considerable time delay before the screw tips are exposed. Secondly the very act of withdrawing the barrel segments over the screws may in itself constitute a frictional hazard and cause an ignition. A clam shell design of barrel, with an l/d of 20/1, was finally selected.

To allow the greatest versatility in configuration for processing the screws are segmented. However for large scale manufacture monolithic screws would be chosen to minimise the risk of material becoming trapped between the segments and the shafts.

Feeders : The choice of feeders was based upon the presumption that a likely composition, similar to a PBX would be based on a liquid binder, a plasticiser with curative, and a bimodal filler. For accuracy two liquid and two powder loss in weight feeders were selected from Brabender. The standard design of the powder feeders is also being changed to incorporate low pressure blow out discs at the base of the hoppers to prevent any build up of pressure.

Control system : Control of the system is via a Supervisory Control And Data Aquisition (SCADA) software package (ex Eurotherm) loaded onto client and server PCs. All process parameters are controlled via the two computers, and in the event of one failing the other is capable of running the system. Set point values for all process parameters are input together with hi, hi-hi, lo and lo-lo alarms and actual values are data logged as the machine is running providing a history of the process. Once correct parameters are achieved and the process is running satisfactorily the recipe values may be saved to disc for future use. This aspect is particularly useful where repeat trials are required, or in a manufacturing environment where different formulations are processed.

If any parameter goes out of limit a warning is given automatically. Should the alarm not be corrected, or the hi-hi or lo-lo value be reached the complete process undergoes an automatic shut down procedure which results in all feeders stopped, the main drive stopped and the barrel open. If the process goes out of control very rapidly, then hard wire alarms on torque, pressure and temperature cause an immediate and automatic safe shut down. The barrel is

positively clamped under hydraulic pressure and safe shut down initiates dumping of the hydraulic oil, releasing the barrel.

The control hierarchy is depicted in Figure 1.

Post die operations : The extrudate is removed by the use of a pneumatically controlled haul-off system comprising a number of belts, onto which lengths up to 2m can be extruded and left to cure. The system is ideally suited to the production of high performance LOVA gun propellant cord.

SAFETY

Safety in operation is of course of prime importance. The fact that the plant is operated remotely significantly reduces the risk to operators but the risk to the plant is high. To minimise this risk the design philosophy has been to reduce the risk of an ignition occurring and if it does then to encourage rapid release of any pressure rise and to reduce containment thereby minimising the risk of an ignition running to detonation. It is to be hoped therefore that any event would be limited to a burn. If any heat source is detected by UV detectors then high pressure water drenchers are automatically activated.

In designing the equipment a number of areas were identified which represented a high risk of an ignition or event, in particular the inter-action between the screws/barrel and explosive in both the powder feeders and the extruder and the design of the extrusion die. Should such an event occur then it is hoped that the design of the control system and the safe shut down sequences would minimise any possible damage to the plant by limiting the event to, at worst, a fire.

Hazard data (F of I & F of F) : The inter-action between the screws of both the powder feeders and the extruder constitute an effect similar to a combined impact and rotary friction test due to rotational and possible sideways motions of the screws. Possible solutions rely on desensitisation of the nitramine filler and the use of materials of construction which reduce any hazard.

For reasons of safety it is not possible to process dry nitramines and for processing a desensitising agent is required. However for the feeders to accurately dispense the powder the addition of a liquid, such as binder or plasticiser, must not adversely affect the flow properties of the powder. A series of formulations, using RDX Grade 1 Fine with a specific surface of 5000 to 7000cm^2/cm^3, were prepared with per cent increments of dioctyl sebacate (DOS), and subjected to rotary friction, impact and electric spark hazard tests. Results, Table 1, indicated that whilst the DOS did not have an appreciable affect on the Figure of Friction a significant reduction in impact hazard was achieved at DOS additions $\geq$3%. Moreover at this level of addition the flow behaviour of the powder was not adversely affected. Therefore to desensitise the nitramine against an impact stimulus 3% DOS would be sufficient to significantly reduce the risk of ignition but other considerations would have to be applied to reduce the risk due to friction.

Work some years previously by Cooke [2] and reproduced in Table 2 indicated that the hardness of the anvils in a rotary friction test had a significant effect on the outcome of the test and the use of anvils with lower hardness than steel could significantly reduce the potential risk of ignition when a friction stimulus was applied. However the use of conventional engineering polymers with poor electrical conductivity properties could introduce a further hazard associated with electrostatic charging. An extensive survey of available materials resulted in a highly modified grade of polyetheretherketone (PEEK) being selected for the manufacture of both extruder screw elements and the feeder screws. This had good thermal, mechanical (including wear) and electrical conductivity characteristics. In a rotary friction test, with a conventional rotating steel wheel with modified PEEK anvils, a Figure of Friction >6 was obtained with RDX, a result which is in accordance with previous data. At present only limited trials have been conducted to ascertain the actual wear characteristics of the material, but early indications are encouraging.

Though the reported wear characteristics of PEEK are extremely good it must be remembered that further hazards may be produced by possible embedding of particulate fillers in the screw leading to wear and other chemical instabilities. Also particles produced by wear of the polymer may also introduce a stability problem with some energetic compositions.

Critical height : In operation the largest concentration of explosive materials, and therefore potentially the area of greatest risk, will be in the hoppers of the two powder feeders. A sample of RDX Grade 1 Fine with a specific surface of 5000 to 7000cm^2/cm^3 was prepared with 3% addition of DOS as shown in other trials to offer the optimum desensitisation. Initial trials used a 95mm internal diameter tube filled to a maximum height of 18.5 cms which equated to 1 Kg of RDX/DOS. Using an E Type fuze head with either CK2 or SR886F as an ignition system both dry RDX and RDX/DOS 97/3 burnt gently with no damage to the tube. A second series of tests was performed using a 50mm diameter tube which allowed a maximum height of 75cms with 1Kg of RDX, representing a severe 50% overtest compared to the maximum height in the feeder hopper of 50cms. In this series a cardboard disc was taped across the top and base of the tube to minimise ejection of unburnt material and the contents were firmly tamped down. At heights up to 75cms the explosive burnt vigorously. Only in the case of the dry RDX at maximum height (75cms) was there any event other than burning but this was of low order and not a detonation.

FUTURE PROGRAMME

Much of the immediate programme is concerned with characterising the process envelope of the various items of equipment and in particular the limits for safe processing with explosives. In particular :-

- Performance characteristics of the loss in weight feeders, e.g. the variation of feed rate with time
- Improvements in die design to minimise shear heating
- Wear characteristics of the polymer screw elements
- Extruder process parameters (including maximum throughput, particle comminution, safe operating envelope for explosive ingredients).

REFERENCES

1. *Processing Flare compositions,* D Turner, Continuous Mixer and Extruder Users Group, December 1990

2. *The manufacture of high performance composite propellants and novel charges by batch and continuous extrusion processes*, E M G Cooke, Propellants, Explosives, Pyrotechnics 15 235-242, 1990

ACKNOWLEDGEMENTS

The authors thank Mr L Featherstone for the critical height firing trials.

%RDX %DOS	99 1	98 2	97 3	96 4	95 5	94 6
F of I F of F	95 2.7	100 3.7	108 3.8	111 3.2	114 3.5	121 3.2
			Electric spark test (J)			
Ignition at 4.5J	yes	yes	yes	n/a	n/a	n/a
Ignition at 0.45 J	no	no	no	yes	yes	yes
Ignition at 0.045J	n/a	n/a	n/a	no	no	no

Table 1 : Effect of DOS as a Desensitiser of RDX Grade 1 Fine

Explosive	Materials tested under 70kg load				Velocity of wheel for a 50% explosion point (m/s)	
	Wheel		Anvil			
	Material	Hardness	Material	Hardness		
RDX	s/s	500	mild steel	200	2.5	0.1
RD2423	s/s	500	mild steel	200	2.5	0.2
RD2423	s/s	300-330	mild steel	200	2.7	0.1
RD2423	s/s	500	grp (across ends)	50	4.7	0.2
RD2423	s/s	500	grp (aligned)	50	4.5	0.2
RD2423	s/s	500	Japanese oak	n/a	no ignition at 7	
RD2423	s/s	500	Cablec 874	n/a	no ignition at 7	
RD2423	s/s	500	Tufnol	n/a	no ignition at 7	
RD2423	s/s	500	nylon 66	30	no ignition at 7	
RD2423	s/s	450	s/s	450	1.41	0.06
RD2423	s/s	500	tool steel	675-695	1.23	0.12
RD2423	s/s	450	mild steel	293-296	2.75	0.1

[Diamond hardness measured using Cabul penetrascope]

Table 2 : Variation of rotary friction with substrate hardness

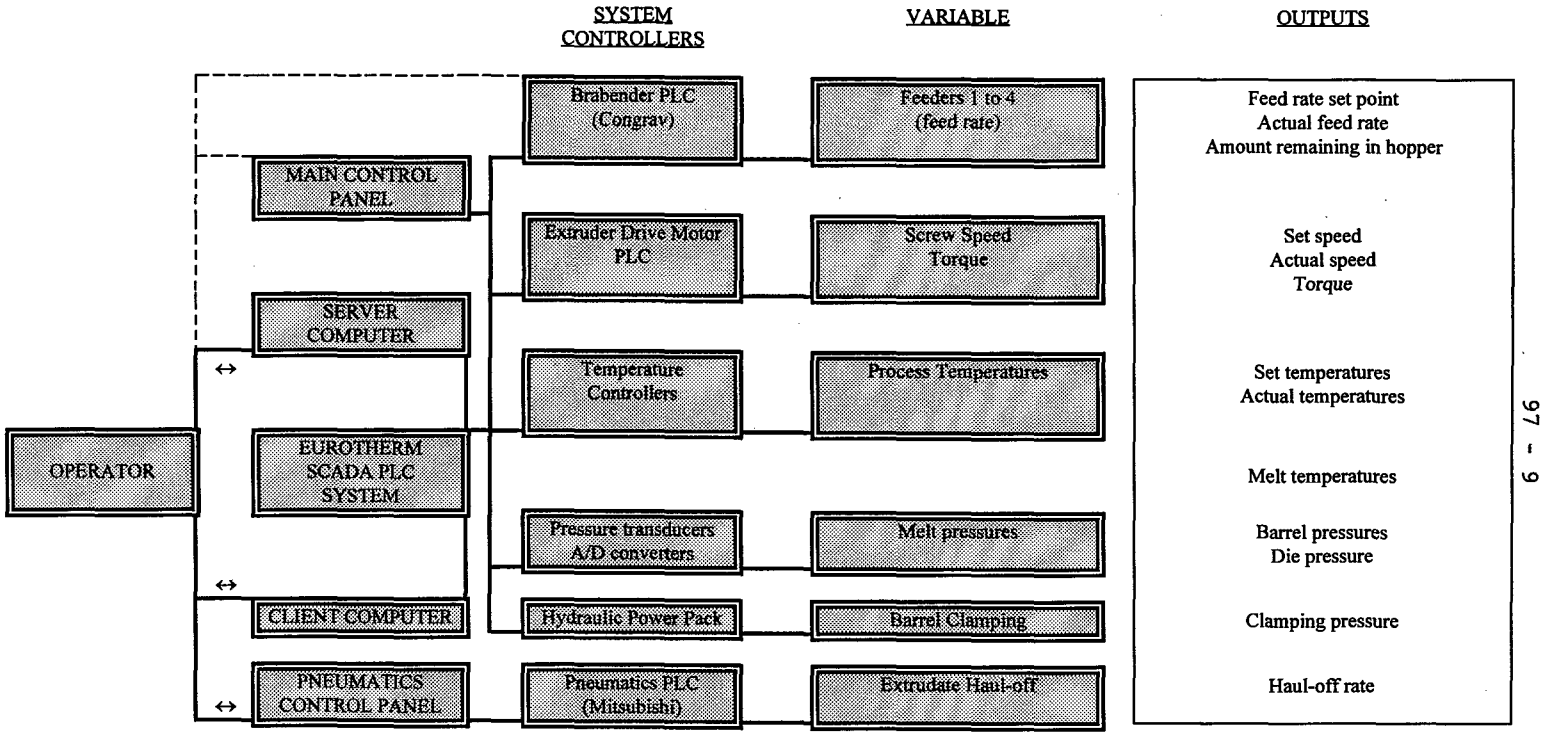

Figure 1 : Control hierarchy

ÜBERWACHUNG DES EXTRUSIONSPROZESSES MIT NAHINFRAROT (NIR)-SPEKTROSKOPIE

Thomas Rohe, Sabine Kölle, Helmut Nägele, Norbert Eisenreich

Fraunhofer-Institut für Chemische Technologie (ICT), Joseph-von-Fraunhofer-Straße 7, 76327 Pfinztal (Berghausen)

Abstract

In recent years near infrared (NIR) spectroscopy developed to a frequently used tool for analysis of chemical manufacturing processes, especially for determination of compositions or concentrations. These informations are of high interest for many processes in the chemical industry. A concrete example is polymer extrusion, where the extrusion of propellants and explosives, which themselves are highly filled polymers, play an important role. In this case the mentioned parameters decide on the quality of the final products (e.g. propellants) and therefore on the reliability of corresponding weapon systems. Hence a continuous quality control of the extrusion process by NIR spectroscopy will be a contribution to improved manufacturing processes.

In this paper the development of a suitable measurement technology for controlling extrusion processes is reported. The system itself is a transmission measuring system consisting of fiber optic probes and a flow cell, which can be adapted to different extruders for in-line measurements. First measurements at pure polymer extrusion processes demonstrate the applicability of the system. Use of multivariate data analysis allowed a first estimate on the accuracy of the developed method. Deviation between predicted and measured polymer composition of a PE/PP blend was below 2 %. An increase of the accuracy can be expected due to improved modelling.

1 Einführung

Moderne Treib- und Explosivstoffe sind zumeist kunststoffgebundene Explosivstoffe (plastic bonded explosives, PBX) [1]. Hierbei bildet ein Polymer, das sich bei der chemischen Reaktion zweier Komponenten bildet und als Brennstoff und Bindemittel dient,

das Matrixmaterial. In diese Matrix bettet man vor dem Aushärten kristalline Explosivstoffe, wie z.B. Hexogen oder Octogen, ein. Der Polymeranteil (10 bis 20 %) verleiht der fertigen Masse eine kautschukartige Elastizität, wodurch diese Massen z.T. auch extrudierbar sind. Bei der Herstellung und Verarbeitung dieser Stoffe ist besonderer Wert auf eine gleichbleibende Qualität zu legen, da diese die Eigenschaften des Endproduktes wesentlich beeinflußt. Um das sicherstellen zu können, bedarf es daher zusätzlicher Kontrollen im Herstellungsprozeß, die in- bzw. on-line (d.h. in bzw. an der Fertigungslinie) erfolgen müssen. Denn nur so können Stoffe minderer oder gar unzureichender Qualität noch vor der Weiterverarbeitung zum Produkt erkannt und verworfen werden. Solch eine Qualitätskontrolle kann mit Hilfe der Nahinfrarot (NIR)-Spektroskopie vorgenommen werden.

In den letzten Jahrzehnten ist die Nahinfrarot (NIR)-Spektroskopie zu einem intensiv genutzten analytischen Werkzeug in vielen verschiedenen Anwendungsfeldern geworden [2], u.a. auch bei Treib- und Explosivstoffen [3,4]. Die Prozeßanalyse und -überwachung mit NIR-Spektroskopie eröffnet dabei neue Möglichkeiten für verbesserte Prozesse, insbesondere bei der Polymerverarbeitung [5]. Diese neuen Kontrollkonzepte können zum Beispiel im Extrusionsprozeß genutzt werden, um das Wissen über das verarbeitete Material zu vergrößern. Derzeit werden hauptsächlich stichprobenartige off-line Messungen angewandt, um z.B. Zusammensetzung, mechanische Eigenschaften, Feuchte, etc. zu bestimmen. Dieses geringe Informationsniveau über das gerade verarbeitete Produkt kann zu großen Verlusten führen, was auf den Zeitverzug zwischen der Detektion unzureichender Produktqualität im Labor und der Reaktion im Prozeß selbst zurückzuführen ist. Dieser Zeitverzug kann bis zu einigen Stunden betragen und verursacht u.U. große Abfallmengen, da Produkte, die den vorgegebenen Qualitätsanforderungen nicht entsprechen, in vielen Fällen nur noch entsorgt werden können. Die NIR-Spektroskopie kann hier zusätzliche Informationen wie z.B. Feuchte oder Zusammensetzung in-situ liefern.

Die Möglichkeiten der in-line NIR-Spektroskopie zur Bestimmung von Extrudatzusammensetzungen werden im folgenden am Beispiel von Polymerschmelzen aufgezeigt. Hierbei stellt die Polymerschmelze lediglich ein Dummy-Material dar, an dem die Anwendbarkeit der Meßmethode als solche untersucht werden sollte. In einem späteren Schritt soll dann die Meßtechnik soweit weiterentwickelt werden, daß sie die Untersuchung von Treib- und Explosivstoffen im Verarbeitungsprozeß zuläßt.

Die Probleme bei der Realisierung der oben angeführten Meßtechnologie sind vielseitig:

- die Sensoren sind heißer und unter Druck stehender Polymerschmelze ausgesetzt, die auch korrosiv sein kann;
- das angewandte Spektrometer muß den rauhen Umgebungsbedingungen widerstehen;
- die Datenverarbeitung muß schnell und zuverlässig sein;
- das komplette System muß ökonomisch und sehr robust sein.

In dem vorliegenden Beitrag wird ein Meßsystem für in-line Transmissions-NIR-Spektroskopie bei Polymerextrusionsprozessen vorgestellt, das diesen Randbedingungen genügt. Die Anwendung zur Bestimmung der Extrudatzusammensetzung wird anhand eines PE/PP-Blends demonstriert. Die Ergebnisse werden besonders in Bezug auf die Anwendung bei der Extrusion von Treib- und Explosivstoffen bewertet und diskutiert.

2 Methode und Materialien

2.1 Ausrüstung

Für die Aufschmelzung von festem Kunststoffgranulat wird ein 20 mm Einschneckenextruder (Haake Rheomex 252) mit einem Länge/Durchmesser-Verhältnis von 25 benutzt. Das maximale Drehmoment beträgt 100 Nm, der maximale Schmelzedruck liegt bei 7 GPa. Das Temperaturprofil kann über vier unabhängige Heizzonen (inclusive Düse) eingestellt werden. Die maximale Wandtemperatur am Zylinder beträgt 400 °C. Eine Kontrolleinheit reguliert die Extrusionsbedingungen und registriert automatisch Drehmoment und Schneckendrehzahl.

Zwischen dem Ende der Schnecke und der Düse befindet sich ein Adapter, der zu einer Durchflußzelle umfunktioniert wurde, die ihrerseits Adapter und Sensoraufnahme in einem Bauteil vereinigt. In der Durchflußzelle sind zwei faseroptische Sensoren derart installiert, daß sie sich gegenüberliegen um Lichtstrahlung durch die Schmelze leiten zu können (Abb. 1). Daher passiert die Polymerschmelze die Meßzone noch im Extruder und wird somit einer echten in-line Messung unterzogen. Der Abstand zwischen den Sensoren kann durch das Einführen von Abstandshaltern variiert werden, woraus sich Weglängen zwischen 0 und 10 mm ergeben. Die Sensoren sind mittels Lichtwellenleiter mit einer Lichtquelle bzw. einem AOTF-NIR-Spektrometer (siehe Kap. 2.3) verbunden.

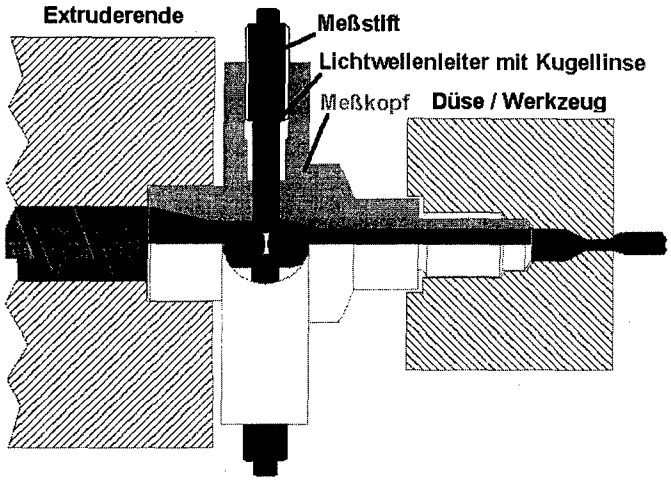

Abbildung 1: Schema des Meßkopfes mit integrierten faseroptischen Sensoren.

2.2 Sensoren

Faseroptische Sensoren für in-line Beobachtung von Polymerextrusionsprozessen müssen verschiedene Anforderungen erfüllen. Hierbei sind zunächst die normalen Extrusionsbedingungen wie hohe Temperatur, hoher Druck, hohe Viskosität und Korrosivität der Polymerschmelze zu nennen. Thermische Wechselbeanspruchung aufgrund von Prozeßan- und abfahrvorgängen stellt eine weitere Schwierigkeit bei der Entwicklung dar. Für die Messung müssen die Sensoren Strahlung effektiv transportieren, so daß die Dämpfung durch die optischen Komponenten gering ist. Chemische Anforderungen beziehen sich auf den Einfluß der Sensoren auf das Extrudat: es muß sichergestellt sein, daß die Sensoren die Extrudateigenschaften nicht beeinflussen. Auf der anderen Seite müssen die Sensoren robust und preisgünstig sein, um eine breite Akzeptanz in der industriellen Anwendung zu finden.

Das Konzept der Sensoren kann in zwei Teile unterteilt werden. Der erste Teil besteht aus einer Kugellinse, die auf einen Lichtwellenleiter aufgeschweißt ist. Beide Komponenten sind aus Quarz. Diese zentrale Optik ist in eine Hülse aus Edelstahl eingebettet. Der Raum zwischen Hülse und Optik ist mit einem Kleber ausgefüllt, der gegenüber hohen Temperaturen resistent ist. Ein schützendes Gehäuse in Form einer weiteren Hülse ist der zweite Teil des Sensors. Dieses Gehäuse beinhaltet den ersten Teil und hat eine Öffnung für die Kugellinse, so daß nur ein Teil der Linse in Kontakt mit der Polymerschmel-

ze steht. Auf der anderen Seite des Gehäuses ist eine Standard-SMA-Kupplung für einen Lichtwellenleiter angebracht. Die Verbindung zwischen den beiden Sensorteilen ist wiederum mit einem Kleber hergestellt worden. Die fertigen Sensoren sind in Abbildung 2 zu sehen.

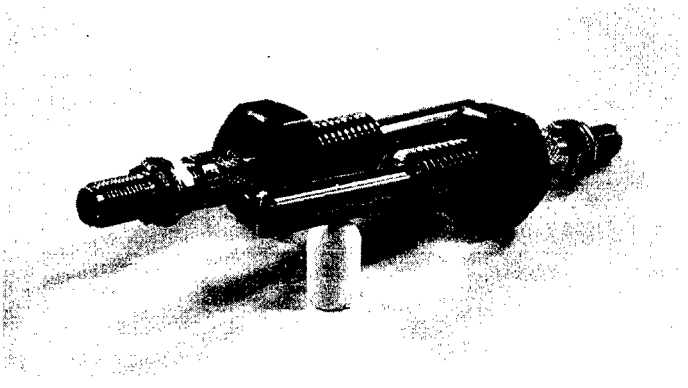

Abbildung 2: Faseroptische Sensoren. Anschlußseite mit SMA-Stecker (linker Sensor) und zur Polymerschmelze gerichtete Seite (rechter Sensor).

Die Auswahl dieser Anordnung hat mehrere Gründe. Der Gebrauch von Kugellinsen reduziert die Intensitätsverluste im Vergleich zur einfachen Gegenüberstellung von zwei Lichtwellenleitern. Dies resultiert in einer Gesamttransmission von 12 %. Durch die Wahl von Quarz als Linsenmaterial gibt es keine Probleme mit hohen Temperaturen, da Quarz bis zu 800 °C als optisches Material einsetzbar ist. Der Unterschied zwischen den thermischen Ausdehnungskoeffizienten von Quarz und Gehäusematerial wird durch den eingesetzten Kleber aufgefangen, so daß es keine internen Spannungen gibt. Auf der anderen Seite sind die Ausdehnungskoeffizienten des Gehäuses und der Durchflußzelle gleich, so daß eine Spielpassung zwischen diesen beiden Teilen ausreicht.

Die Nützlichkeit dieses Sensor-Designs ist offensichtlich. Es wird kein By-pass benutzt, so daß kein Ausschuß produziert wird, und das verarbeitete Material selbst untersucht wird. Die Kosten für einen Sensor sind gering, weil keine teuren Materialien (wie z.B. Diamant- oder Saphir-Fenster) verwendet werden. Die Handhabung dieser Sensoren ist einfach, da sie nur in die Durchflußzelle eingeschraubt werden brauchen. Die Adaption an andere Extruder ist ebenfalls unproblematisch, weil die Sensoren nur wenig Platz benötigen (leidglich ein M10 Bohrloch). Alles in allem lassen diese Vorteile dieses Sensor-Design günstig für den industriellen Einsatz erscheinen.

2.3 AOTF-NIR Spektrometer

Das benutzte AOTF-NIR Spektrometer wurde ebenfalls am ICT entwickelt [6]. Es besteht aus den Komponenten Halogen-Lichtquelle, Quarzfaseroptik, akustooptisch durchstimmbaren Filter (acousto-optic tunable filter, AOTF) aus Tellurdioxid (TeO_2), Germanium-Photodetektoren (1.000 bis 1.800 nm) und einer Kontroll- und Datenerfassungseinheit. Die Scan-Geschwindigkeit des Spektrometers beträgt 1.000 nm/ms mit einem Zeitverzug von 10 µs zwischen zwei Spaktralscans. Die Wellenlängenauflösung von 2 bis 3 nm kann für geringere Scan-Geschwindigkeiten erreicht werden.

AOTF-NIR-Spektrometer haben alle notwendigen Eigenschaften, um in einer industriellen Umgebung eingesetzt zu werden:

- Robustheit
- akzeptable Kosten
- hohe Scan-Geschwindigkeiten (bis zu 1.000 Spektren pro Sekunde)
- Unempfindlichkeit gegenüber Störungen durch Verwendung von Faseroptiken
- schnelle Datenerfassung und -verarbeitung mittels PC.

All diese Vorteile wurden bereits bei Kunststoffidentifikations-Prozessen in Recycling-Anwendungen geprüft [7]. Daher erscheint das entwickelte Spektrometer am besten für den industriellen Einsatz auf dem Gebiet der Polymerverarbeitung geeignet zu sein.

2.4 Materialien

Für die Untersuchungen wurden Kunststoffgranulate von Polyethylen (PE-LD) und Polypropylen (PP) eingesetzt (siehe nachstehende Tabelle). Diese Materialien wurden als reine Substanzen und als Mischungen eingesetzt. Die Mischungen wurden durch abwiegen hergestellt, wobei die Genauigkeit der Wiegung ± 0,01 g betrug. Daher sind alle Mischungsverhältnisse in Gewichtsprozent angegeben.

	Handelsname	**Hersteller**	**MFI**	
Polyethylen (PE-LD)	ESCORENE	EXXON Chemical	MFI (190 °C; 2,16 kg): 0,3 g / 10 min	hoch viskos
Polypropylen (PP)	Hostalen PP	Hoechst AG	MFI (230 °C / 2,16 kg): 47 g / 10 min	niedrig viskos

2.5 Experimentelles

Der Extruder wird auf ein vordefiniertes Temperaturprofil aufgeheizt, entsprechend dem zu verarbeitenden Material. Anschließend wird er mit polymerem Material beschickt. Nach der Verarbeitung im Schneckenbereich passiert die Schmelze die Durchflußzelle, wobei die Nahinfrarot-Spektren während dieses Vorganges aufgenommen werden. Die registrierten Spektren werden abgespeichert und auf einem separaten PC ausgewertet. Neben der spektroskopischen Messung werden zusätzlich die Parameter Schmelzetemperatur, Schmelzedruck, Drehmoment der Schnecke und Spektrometereinstellung dokumentiert. Die Meßzeit für ein Spektrum (wobei die Mittelung von 500 Einzelspektren eingeschlossen ist) beträgt etwa 0,5 Sekunden.

3 Datenanalyse

Die aufgenommenen Spektren wurden mit dem Software-Paket *The Unscrambler®* der Firma CAMO Inc. verarbeitet, ausgewertet und analysiert. Gebräuchliche statistische Analysen, wie z.B. Hauptkomponentenanalyse (principal component analysis, PCA), Hauptkomponentenregression (principal component regression, PCR), Partial-Methode der kleinsten Fehlerquadrate (partial least squares analysis, PLS), stehen innerhalb dieses Programms zur Verfügung. Für die Untersuchungen an Polymerblends wurde nur die PLS-Analyse [8] benutzt, die hier nur grob skizziert werden soll.

Bei der PLS-Analyse wird ein Satz von Spektren unterschiedlicher Polymermischungen für eine Art Lernprozedur verwendet. Die Spektren werden in ihre Hauptkomponenten zerlegt, d.h. die wesentlichen spektralen Informationen in Bezug auf die Zusammensetzung des Polymerblends werden herausgefiltert. Mit diesen Hauptkomponenten können nun andere, unbekannte Spektren derart angefittet werden, daß sich daraus über ein Regressionsverfahren die Zusammensetzung des untersuchten Gemisches vorhersagen läßt. Diese Vorhersage wird mit einem zweiten Satz von Spektren überprüft (validiert), um die Zuverlässigkeit des PLS-Modells zu bestimmen. Auf diese Weise kann die Qualität des Modells bereits im Vorfeld ermittelt werden.

Die für die oben genannte Vorgehensweise verwendeten Spektren bzw. Datensätze wurden schnell hintereinander aufgenommen, so daß die Spektren die gleiche Mischung repräsentieren. Für die Erstellung des PLS-Modells wurden je 20 Spektren von 10

Mischungen verwendet, wohingegen für die Validierung je 20 Spektren von 8 Mischungen genutzt wurden.

4 Ergebnisse und Diskussion

4.1 Technische Ergebnisse bezüglich der entwickelten Sensoren

Die entwickelten Sensoren widerstehen den normalen Extrusionsbedingungen. Schmelzetemperaturen von 300 °C und Drucke von bis zu 35 MPa waren unproblematisch. Der komplette Meßkopf war abgedichtet, so daß keine Schmelze austreten konnte. Die Änderung der Transmissionsstrecke zwischen den beiden Sensoren konnte problemlos durch unterschiedliche Einschraubtiefe der Sensoren herbeigeführt werden und beeinflußte dieses Ergebnisse nicht: der Meßkopf war immer noch dicht und die Sensoren waren unbeschädigt. Obwohl die Sensoren in den Schmelzekanal hineinragen, wird der Schmelzefluß in Bezug auf Durchsatz und offensichtliche Fließinhomogenitäten nicht gestört.

Die optischen Eigenschaften der Sensoren sind für die hier beschriebene Anwendung vollkommen ausreichend. Das Licht, das die Sensoren verläßt, bildet einen Kegel mit einem Fokuspunkt bei etwa 2,5 mm, ist also nicht parallel. Daher eignen sich diese Sensoren nicht für hochpräzise spektroskopische Untersuchungen, die exakte Extinktionswerte zum Ziel haben. Jedoch sind sie absolut tauglich für spektroskopische Messungen, die lediglich eine relative Aussage über einen Prozeß liefern sollen, z.B. ob ein Prozeß gut oder schlecht abläuft oder ob ein bestimmter Parameter aus dem zulässigen Schwankungsbereich herausläuft. Für diese Art der Anwendung ist die Gesamttransmission von 12 % wichtiger als eine hohe Spektrenqualität, da eine hohe Transmission längere Absorptionswege zuläßt, z.B. um zu höheren Extruderdurchmessern zu gehen oder um die Oberflächeneffekte bei den Sensoren zu verringern.

4.2 PE/PP-Blends

Als Untersuchungsobjekt wurde ein leicht zu verarbeitender Polymerblend (Kunststoffgemisch) gewählt, um die prinzipielle Bestimmung der Extrudatzusammensetzung auszutesten. Dazu wurden verschiedene PE/PP-Blends hergestellt und vermessen (s.o.), wobei der PE- (bzw. PP-) Gehalt von 0 bis 100 % in unterschiedlichen prozentualen Schritten variiert wurde. In Abbildung 3 sind exemplarisch die Spektren für 20 %

Schritte dargestellt. Besonders auffällig sind der zweite Oberton der C-H-Streckschwingung bei 1,2 µm und die Kombinationsbande bei 1,4 µm [9].

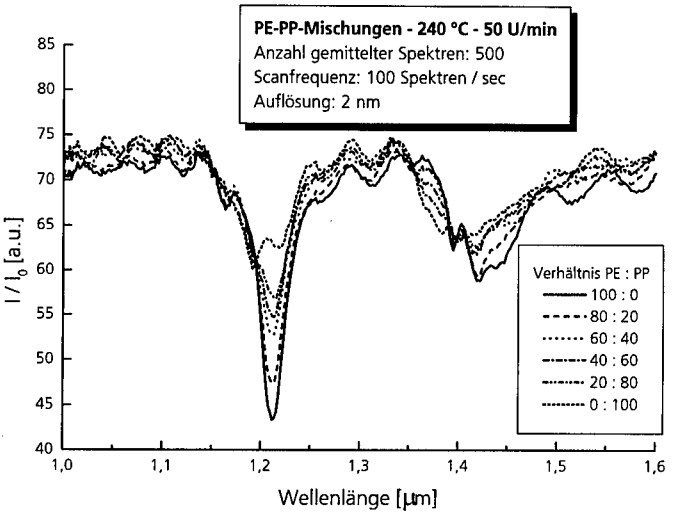

Abbildung 3: Spektren von PE/PP-Blends mit unterschiedlichen Mischungsverhältnissen, die von reinem PE bis zu reinem PP in Schritten von 20 % variieren.

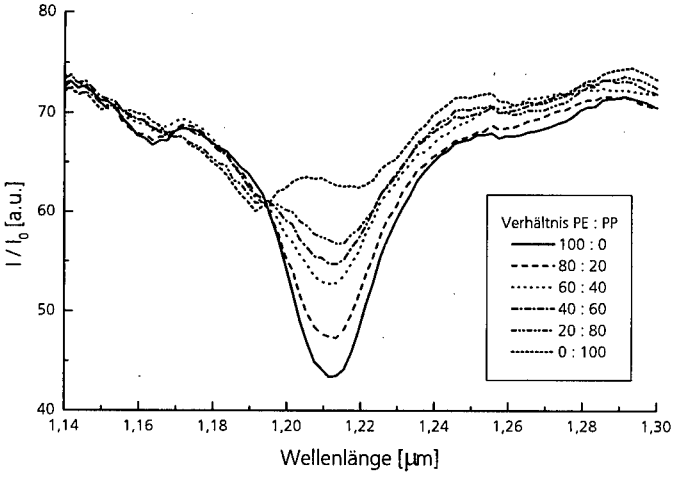

Abbildung 4: Spektren von PE/PP-Blends (Detail).

Es ist offensichtlich, daß die spektrale Hauptinformation in Bezug auf die Blend-Zusammensetzung im zweiten Oberton der (C-H)-Streckungsbande um 1,21 µm liegt (Abb. 4). Die Transmission fällt hier mit zunehmendem PE-Gehalt ab. Ein gegensätzlicher Effekt kann kann im im Bereich 1,19 µm beobachtet werden, wo sich mit zunehmendem PP-Gehalt eine Bandenschulter zu einem Nebenmaximum entwickelt. Dieses Nebenmaximum von PP kann dadurch erklärt werden, daß neben (C-H)-Schwingungen der CH_2-Gruppen auch Schwingungen von CH- und CH_3-Gruppen auftreten, die im Vergleich zu den CH_2-Gruppenschwingungen leicht versetzt sind. Dies führt zu einer Bandenaufspaltung und einer Verschiebung der Bandenschwerpunkte.

Anhand dieser Spektren wird bereits deutlich, daß eine Bestimmung der unterschiedlichen Konzentrationen prinzipiell möglich ist. Unklar ist dagegen, bis in welchen Bereich man eine solche Unterscheidung vornehmen kann. Im Falle der 20 %-Mischungen kann dies einfach durch Bildung eines linearen Regressionsmodells erfolgen. Für geringere Unterschiede in den Spektren ist diese einfache Analyse nicht mehr ausreichend und es muß auf andere Verfahren ausgewichen werden muß.

Daher wurde für die Vorhersage der Polymermischung, d.h. des Verhältnisses von PE zu PP, ein PLS-Modell angewandt. Die für dieses PLS-Modell benutzten Mischungen variierten zwischen 100 % PE und (90 % PE + 10 % PP) in Schritten von 1 % und wurden ausgesucht um a) verschiedene Additivanteile in einer Polymermatrix und b) das blenden zweier verschiedener Polymere zu simulieren. Daher umfaßt das PLS-Modell 11 verschiedene PE/PP-Blends, mit je 20 Spektren pro Mischung für die Kalibrierung und 20 Spektren von 8 Mischungen für die Validierung.

Die gemittelten Spektren des Kalibriersatzes sind in Abbildung 5 dargestellt. Für eine erste Näherung des Mischungsverhältnisses war es ausreichend, diese Rohspektren (ohne jede weitere Datenaufbereitung) und die limitierte Spektrenanzahl zu benutzen. Für das PLS-Modell waren vier Hauptkomponenten ausreichend.

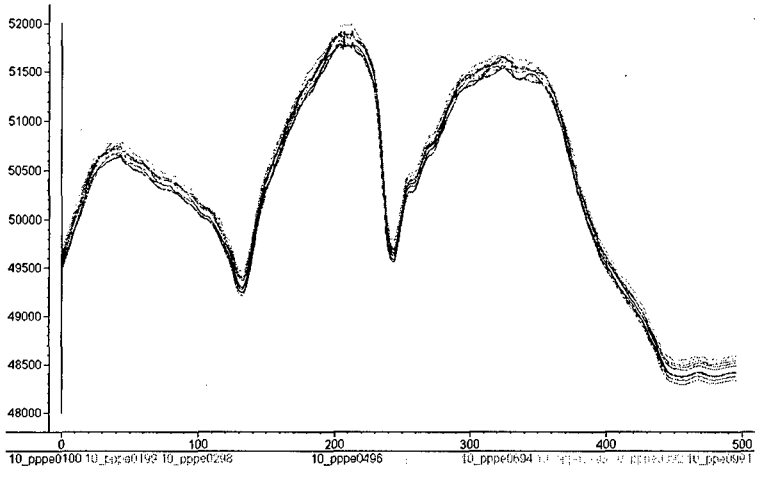

Abbildung 5: Gemittelte Transmissionspektren des Kalibrationssatzes (y-Achse: Transmission in willkürlichen Einheiten, x-Achse: Wellenlängenkanal).

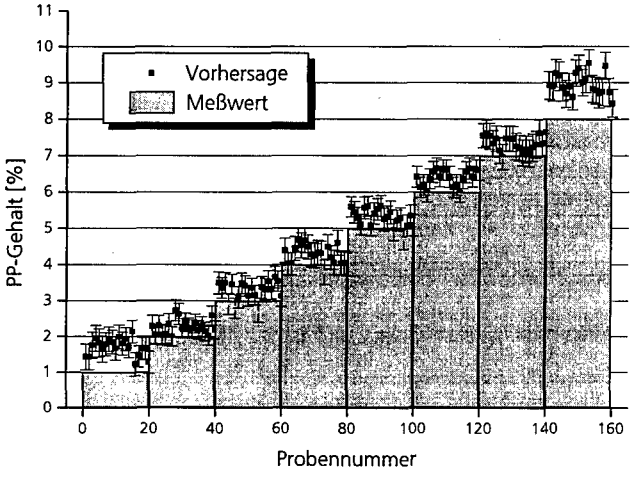

Abbildung 6: Validierungsplot mit der Gegenüberstellung von vorhergesagtem (Punkt mit Fehlerbalken) und gemessenem (Säule) Wert des PP-Anteils im PE/PP-Blend für die Spektren des Validierungssatzes.

Die Vorhersagemöglichkeit des Modells wurde mit dem Validierungssatz getestet. Die Resultate sind in Abbildung 6 zu sehen, in der die vorhergesagten und gemessenen

PE/PP-Verhältnisse verglichen werden. Der quadratische mittlere Fehler der Vorhersage (root mean square error of prediction, RMSEP) des PLS-Modells beträgt 0,402, was ein recht guter Wert für ein derart grobes Modell ist. Mit Ausnahme der Mischungen mit 1 % und 8 % PP liegen alle Vorhersagen nur leicht über den gemessenen Werten. Dies kann durch die grobe Datenbearbeitung erklärt werden, die nicht darauf abzielte ein präzises PLS-Modell zu generieren. Trotzdem variieren die Wolken der vorhergesagten Verhältnisse für jede Mischung nur innerhalb von 1 % und sind deutlich voneinander getrennt. Eine Verbesserung der Bearbeitung der spektralen Daten, die durch dieses neue Meßsystem erhalten werden, und ein differenzierteres PLS-Modell kann die Auflösung von Blendverhältnissen in der Zukunft stark erhöhen.

5 Zusammenfassung und Ausblick

Ein Meßsystem für die in-line NIR Spektroskopie bei Extrusionsprozessen wurde am ICT entwickelt. Es besteht aus einem Meßkopf, der an einen Einschneckenextruder adaptiert wurde, mit integrierten faseroptischen Sensoren und einem AOTF-NIR-Spektrometer. Transmissionsmessungen bei typischen Extrusionsbedingungen (Temperatur 300 °C, Druck 35 MPa) lieferten gute Ergebnisse in Bezug auf mechanische und optische Eigenschaften der Sensoren. Das entwickelte System ist in der Lage verschiedene Extrudatzusammensetzungen zu vermessen, wie am Beispiel von PE/PP-Blends gezeigt wurde. In diesem Fall lag die Vorhersagemöglichkeit eines PLS-Modells im Bereich von 1 bis 2 %.

Es wurde gezeigt, daß sich die In-Line-NIR-Spektroskopie sehr gut für die Beobachtung von Extrusionsprozessen eignet, was auf die hohe Meßgeschwindigkeit und die Berührungslosigkeit der Messung zurückgeführt werden kann. Somit können Fehlfunktionen innerhalb des Prozesses rechtzeitig detektiert und schnell korrigiert werden. Dies führt zu verbesserter Produktqualität und höherer Prozeßeffizienz.

In weiteren Untersuchungen sollen Materialien eingesetzt werden, die reale Treib- und Explosivstoffe besser simulieren als reine Polymerblends, nämlich gefüllte Polymere. Hierbei kommen vor allem einfache Polymermatrices (z.B. Polyethylen oder thermoplastische Elastomere) und kristalline Füllstoffe (z.B. Zucker) in Betracht. Auch hier soll geprüft werden, in wieweit sich die Extrudatzusammensetzung on-line bestimmen läßt. Erst danach kann daran können reale extrudierbare Treibstoffe untersucht werden.

6 Literatur

1. A.Homburg, N.Fiederling, P.Elsner, T.Keicher, P.Eyerer, H.Schubert, G.Bunte, G.Hambitzer, M.Krausa, F.Volk, *Spektrum der Wissenschaft* **8**, 92 (1996)
2. J.Workman, Jr., *Journal of Near Infrared Spectroscopy* **1**, 221 (1993)
3. L.G.Weyer, Making light work, ed. Ian Murray, Weinheim, 430 (1992)
4. T.Rohe, E.Grünblatt, N.Eisenreich, *27. Int. Jahreskonferenz des ICT*, 85-1 (1996)
5. M.G.Hansen, A.Khettry, *Polymer Engineering and Science* **34**, 1758 (1994)
6. A.Blanc, N.Eisenreich, H.Kull, W.Liehmann, *19. Int. Jahreskonferenz des ICT*, 74-1 (1988)
7. N.Eisenreich, J.Herz, H.Kull, W.Mayer, T.Rohe, *ANTEC '96*, 3131 (1996)
8. H.Martens, S.A.Jensen, Progress in Cereal Chemistry and Technology, Part A, eds. J.Holasand J.Kratochvil, Elsevier, 607 (1983)
9. H.W.Siesler, K.Holland-Moritz, Infrared and Raman Spectroscopy of Polymers. Practical Spectroscopy Series, Vol.4, Marcel Dekker, New York (1980)

DETERRENT COATING OF SINGLE BASE POWDERS

Václav Puš

S Y N T H E S I A a.s.
Research Institute of Industrial Chemistry - VÚPCH
53217 Pardubice - Semtín
CZECH REPUBLIC

S u m m a r y

The submitted paper gives the results of experiments that help to clear up the process of phlegmatization of powder grain for large calibre ammunition. This is a matter of method that can be called „internal phlegmatization". The experiments have been carried out with single base powders. Distribution of various substances with phlegmatizing effect in powder grain has been observed.

The manner is given here, how the concentration of individual phlegmatizing substances was found in various depths of powder grain.

Determination of different phlegmatizers in individual layers of powder grain has been carried out by means of gas and liquid chromatography.

Introduction

Phlegmatization of the surface layer of powder grain is a wide spread method aimed at modifying burning rate of powder grain. With classical method of phlegmatization, the phlegmatizer is applied on the grain from external environment no matter if the process is lead in dry or wet way. This method is called „external phlegmatization".

This work deals with finding out of phlegmatizer distribution in powder grain after phlegmatization that can be called „internal phlegmatization". When carrying out this phlegmatization, the phlegmatizer is introduced into powder mass in the kneader at mixing and the phlegmatizing layer is formed during the next technological process of powder production.

Theory

To carry out external phlegmatization in both wet and dry way requires expensive facilities and in both cases it is necessary to perform very dangerous operations especially at the dry way, which makes production of gun powder more expensive.

The aim of this work is to find distribution of phlegmatizing substances in powder grain prepared in the way that can be called „internal phlegmatization". In this way of carrying out phlegmatization, some very dangerous operations come off the technological process because phlegmatizing substances are introduced into powder grain already during the basic technological steps of production of single base powders. Accordingly to the course of these steps, the kind and quantity of the used phlegmatizer, various concentration profiles arise inside the grain.

Knowledge from the works observing movement of phlegmatizers in powder grain in nitrocellulose environment in dependence on length of hydrogen bond in the observed compounds [1] or on length of the bond between carbonyl group of the described compounds and non-esterified -OH group of NCL [2,4] were employed at the experiments.

The works where the authors give various ways of measuring of concentration profiles arising due to diffusion of phlegmatizers in the environment of NCL mass [3,5,6,7,8,9] then influenced selection of the method used in this work. Liquid and gas chromatography have been used here to identify and determine the phlegmatizer in the individual layers of powder grain.

Experimental

All specimens were prepared in the same way. The calculated quantity of NCL [2,4], ether, diphenylamine and the appropriate phlegmatizer (2,4 - DNT, CI, DBP or camphor) were fed into the kneader. The temperature was maintained at 20°C and the speed of the stirrers was during the whole time of kneading maintained at constant value 24 r.p.m.The whole process of kneading took 60 minutes. After that time interval the powder mass was taken out of the kneader and placed into the cylinder of the extruding facility and then the mass was extruded at constant speed of the piston 10mm/min. through the extruding die.The extruded thick-walled tubular thread was cut to 10cm and then subjected to pre-drying, dipping and drying.

The final product was tubular NCL powder with 2mm wall thickness. Layers of 0.4 mm thickness in radius were turned off from the dried powder. In this way always 5 layers were obtained.Determination of the used phlegmatizer was then carried out in each layer. Liquid or gas chromatography was used in dependence on the used phlegmatizer.

Results

Distribution of phlegmatizer (2,4 - DNT) that proved to be a characteristic one for NCL tubular single perforated powder is shown in Figure 1.

Fgure 1 Distribution of 2,4-DNT at initial concentration 5,0%

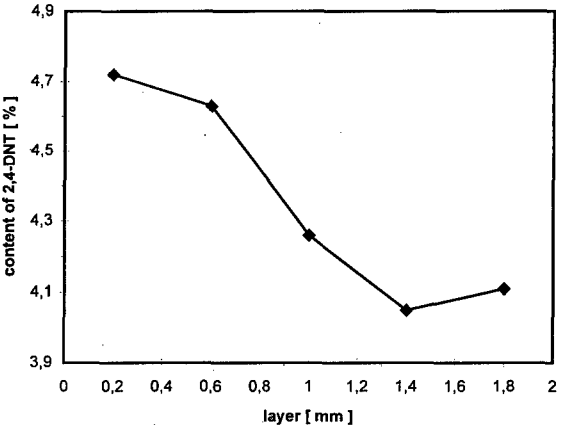

Figure 2 represents the case when initial concentration of phlegmatizer 2,4 - DNT influenced the course and size of the maximum concentration profile inside the powder grain. The maximum concentration profile in case of 5.0% content of phlegmatizer in a batch is 0.55% for 2.5% content of phlegmatizer it is 0.39%.

Figure 2 Distribution of 2,4-DNT in dependence on initial concentration

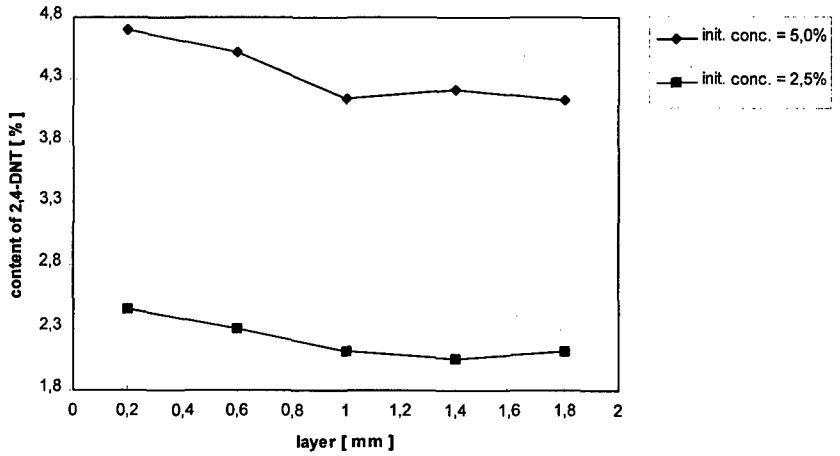

The influence of time interval of pre-drying on phlegmatizer distribution is given in Figure 3, which represents the case when a change in technology of powder production was performed.

Figure 3 Influence of time interval of pre-drying on 2,4-DNT distribution at initial concentration 5,0%

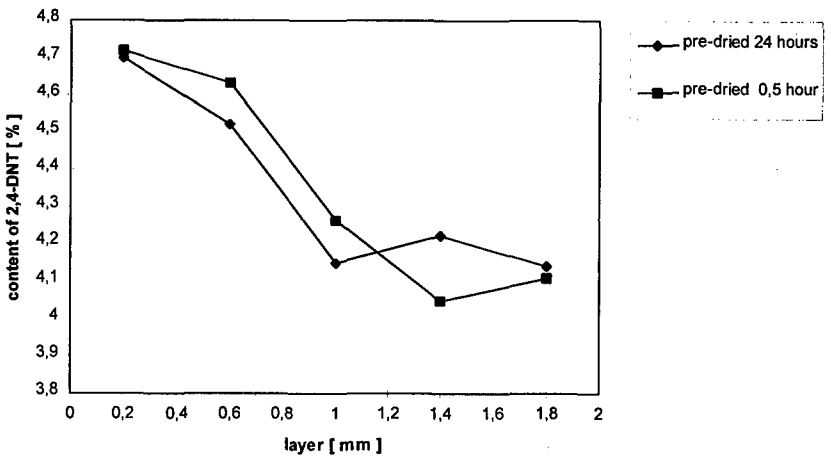

Apart from the experiments with 2,4 - DNT , the influence of time interval of pre-drying on phlegmatizer distribution in powder grain wall was also observed in the cases when Centralite I, DBP and camphor were used. The results of those experiments are given in Figure 4.

Figure 4 Comprehensive graph - distribution concentrations of the observed phlegmatizers

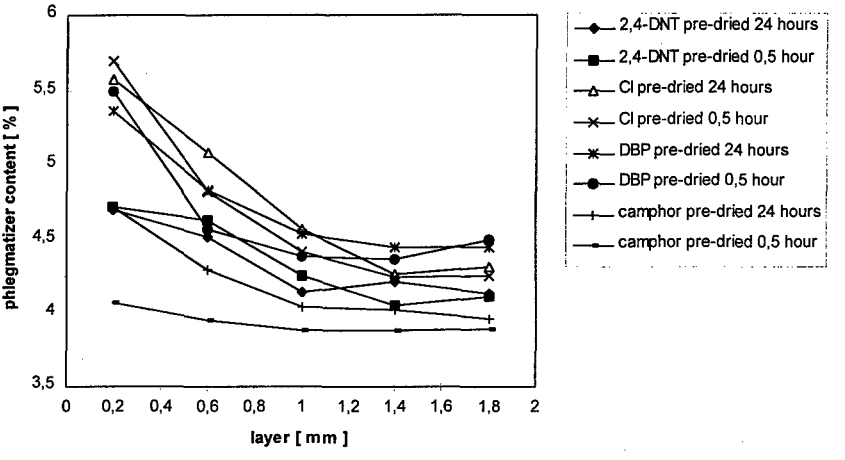

Conclusion

Existence of an uneven distribution of phlegmatizers in powder grain walls was proven and characteristic distribution of phlegmatizer in NCL tubular powder (Figure 1) was found.
The phlegmatizer distribution can be influenced by a quantity of the introduced phlegmatizer (Figure 2) but also by changes in technology at powder production (Figure 3).
By comparison of concentration profile curves of various phlegmatizers it is possible to find the suitability of the given phlegmatizer for this way of phlegmatization (Figure 4).

References

1. Nakamoto K., Marghoses M., Rundle R.E. : J. Amer. Chem. Soc., Vol. 77, 6480 - 6486
2. Brodman B.W., Devine M.P., Gurbarg M.T. : J. Appl. Polym. Sci., Vol. 18, 943 - 946 (1974)
3. Louden J.D., Kelly J. : Anal. Appl. Spectrosc. 2, 2nd 1990, (Pub. 1991), 90 - 95
4. Brodman B.W., Lampner N. : J. Appl. Polym. Sci., 1982, 27(9), 3621 - 3
5. Fong C.W., Cooke C. : J. Appl. Polym. Sci., 1982, 27(8), 2827 - 32
6. Varriano-Marston E. : J. Appl. Polym. Sci., 1987, 33(1), 107 - 16
7. Louden J.D., Kelly J. Phillipson J. : J. Raman Spectrosc., 1987, 18(2), 137 - 40
8. Meier H. et al. : Report 1983, BMVg-FBWT-83-7, 102s., Energy Res. Abstr., 1984, 9(17), a.c34159
9. Wilken J. : CA 121, 1994, 13186g

Temperature Sensitivity of Small Arm Propellant

Jan Petrzilek, Ladislav Valenta, Ladislav Velebradsky

Synthesia a.s.
Research Institute for Industrial Chemistry
53217 Pardubice-Semtin
CZECH REPUBLIC

The temperature sensitivity of interior and exterior ballistic parameters is discussed with respect to the effects of shape, deterrent coating and chemical composition of propellant. Spherical and tubular small arm propellants were prepared and the ballistic performance tested in various weapons at various temperatures.

A Road Map to Very High Impetus Gun Propellants ... Some Intriguing Possibilities ...

Ronald L. Simmons
Naval Surface Warfare Center
Indian Head, Maryland 20640
301-743-4521
E-mail: RonSimmons@wpnengr.ih.navy.mil

Abstract

As the urgency increases for hypervelocity guns, i.e., velocities > 1600 m/sec, the propellant chemist will eventually need to seek propellants of higher impetus than currently available with RDX or HMX, i.e., 1250-1300 Joules/g. Ingredients such as CL-20, TNAZ, and ADN offer promise to slightly higher values, but a ceiling begins to appear near 1350 Joules/g, beyond which new compounds are required. In this poster, possibilities will be discussed for attaining impetus values substantially greater than 1400 Joules/g, i.e., > 40% above current operational double-base propellants.

A class of compounds known as diazido nitramines offer significantly more impetus than RDX. Some well-known examples are: DADNH (1,6-diazido-2,5-dinitrazahexane), DADZP (1,5-diazido-2,4-dinitrazapentane), and DANP (1,3-diazido-2-nitrazapropane), which have impetus values as neat ingredients ranging from 1500 to 1750 Joules/g. Unfortunately, these nitramines have very high isochoric flame temperatures (Tv) > 4000°K, and hence, are of limited usefulness. New compounds are required which have the proper stoichiometry to generate lower molecular weight gases, and a suitable ΔHf to provide a reasonable flame temperature.

A number of energetic compounds are being examined to significantly increase the performance of explosives, but unfortunately, these are not suitable for gun propulsion. The figure of merit for explosives is C-J detonation pressure, which is a function of the square of the density and a high flame temperature. Compounds of very high density (> 2 g/cc) are being synthesized, but these have little or no hydrogen, and consequently have very poor gas output. Not only is high gas output or low gas MW relatively unimportant for explosives, but the need for high density precludes the presence of hydrogen.

For gun propellants, on the other hand, density is relatively unimportant, and high flame temperature is intolerable. High gas output and low gas MW is all important to high impetus. Compounds best suited for gun propulsion are quite different than those designed for high performance explosives, and compounds that make outstanding explosives do not necessarily make good propellants ... because of the lack of hydrogen.

Two families of C-H-O-N compounds have been identified to illustrate the potential increase in impetus possible via a radical change in stoichiometry and ΔHf. The first is a baseline $C_1 H_1 O_1 N_3$, which has a theoretical gas output of 42.23 moles/kg, equivalent to a gas MW of 23.7, approximating that of conventional double-base. At a flame temperature of 3400°K (near that of the 120mm propellant JA-2), the system has an impetus of 1180 Joules/g.

The second family is $C_1 H_4 O_1 N_4$, which has a theoretical gas output of 56.77 moles/kg, equivalent to a gas MW of 17.6, representing a "quantum" leap in improvement. At a flame temperature of 3400°K, the new system has an impetus of 1565 Joules/g. At a slightly higher flame temperature of 3600°K, the system has an impressive impetus of 1660 Joules/g.

It is important to consider both the stoichiometry and ΔHf in combination. Neither one alone provides a complete answer. Stoichiometry is a predictor of gas output (or gas MW), while flame temperature is a strong function of ΔHf. Gas output is not especially sensitive to ΔHf, and in general, as ΔHf increases, gas output increases only very gradually.

A number of similar C-H-O-N compounds have been examined to illustrate the behavior possible for various performance gains. The objective has been to provide guidelines, i.e., a road map, for the synthesis chemist to pursue new possibilities and to identify key functional groups as target molecules. Some of these may not be practical, but should provide a fundamental basis to search for new compounds.

* * * * *

Combustible Cases for RMK 30

F. Schedlbauer, A. Meßmer
Fraunhofer-Institut für Chemische Technologie - ICT
76327 Pfinztal

U. Steffens, I. Reuter
Mauser Werke Oberndorf
Waffensysteme GmbH
78727 Oberndorf a. N.

Abstract

New results of the cooperation between Fraunhofer ICT and Mauser Weapon Systems concerning combustible cases and weapon concept for the Recoilless Automatic Cannon RMK 30 will be presented.
The recoillessness of the new weapon designed by Mauser could be realized by a telescoped ammunition with combustible case developed by Fraunhofer ICT. Firing tests brought up good results in muzzle velocity at the required maximum pressure, and the hit pattern showed very low deviation. Applications of the recoilless cannon RMK system are light carriers and helicopters.

A Combustible cases for RMK 30

Introduction

Since many years combustible cases are wellknown for the 120 mm tank gun and for modular charges for the 155 mm howitzer. They mainly consist of pressed nitrocellulose fibers with a special after-treatment. These combustible cases serve the purpose of loading conventional gun powders but do not contribute to the energy of the ammunition.
The new generation of combustible cases are intended for machine guns of middle caliber. In contrast to the cases mentioned above the new type of combustible cases must have an additional high performance.

The cases for RMK 30 consist of plastic bonded explosives. The required performance is reached by combining the case with a conventional gun powder. Using different types of single or double base propellants the internal ballistic properties can be adjusted very accurately.

A new concept is the inductive ignition which allows a very high rate of firing. Another big advantage is the fully telescoped projectile. Because of the lower weight of this type of ammunition the platform can store more rounds.

Combustible Case

Fig. 1 and 2 show the conventional ammunition, caliber 30 mm, in comparison to the telescoped ammunition with combustible case.

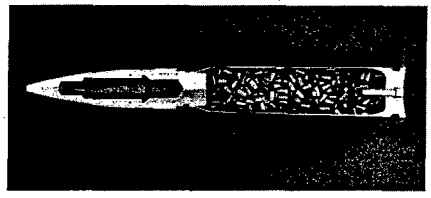

Fig. 1: Conventional ammunition

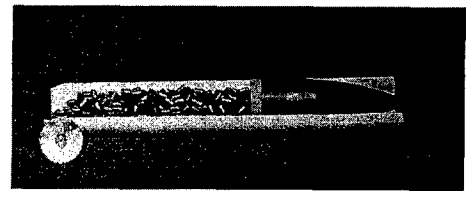

Fig. 2: Combustible case.

Fig. 3 compares the telescoped ammunition to conventional cartridges with calibers in the range of 20 to 35 mm. The telescoped ammunition has the same length than the conventional 30 mm cartridge, but possesses higher energy because of the combustible case. Fig. 4 shows different types of combustible cases (caliber 30 mm).

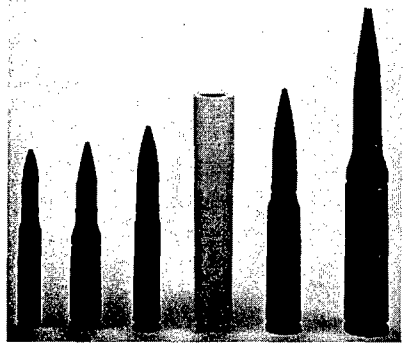

Fig. 3: Comparison of 20 - 35 mm cartridges and telescoped ammunition.

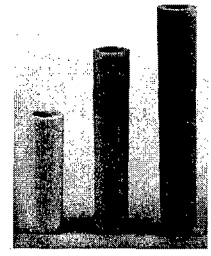

Fig. 4: Telescoped ammunition with combustible case and inductive ignition.

Telescoped ammuntion with inductive ignition and combustible cases has several advantages:

- low production costs because no metall cartridge is needed
- no ejection of cartridges
- recoillessness
- no firing pin because of inductive ignition
- high performance
- high rate of fire
- transferable to other calibers.

The combustible case developed by FhG ICT had to fulfill essential requirements like:

- muzzle velocity > 1000 m/s
- maximum pressure of 400 MPa
- perfect flight of the projectile
- residueless combustion
- reproducibility
- good mechanical properties
- no cook-off behaviour
- chemical and thermal stability
- low cost production.

The designed combustible case is based on plastic bonded explosives. Specific energy and burning characteristics of the case depend on parameters like

- type and quantity of explosives
- particle size of explosives
- additives
- density and porosity of the case.

In order to adjust force and internal ballistic behaviour of the telescoped ammunition, the case is combined with different single or double base propellants, further influencing parameters are

- type and amount of additional propellant
- type and amount of igniter material
- performance of the fuze.

Results of firing tests

Performance and functioning of the ammuntion could be demonstrated in several firing tests. Fig. 5 and 6 show some results of firings tests of cases combined with a double base propellant.

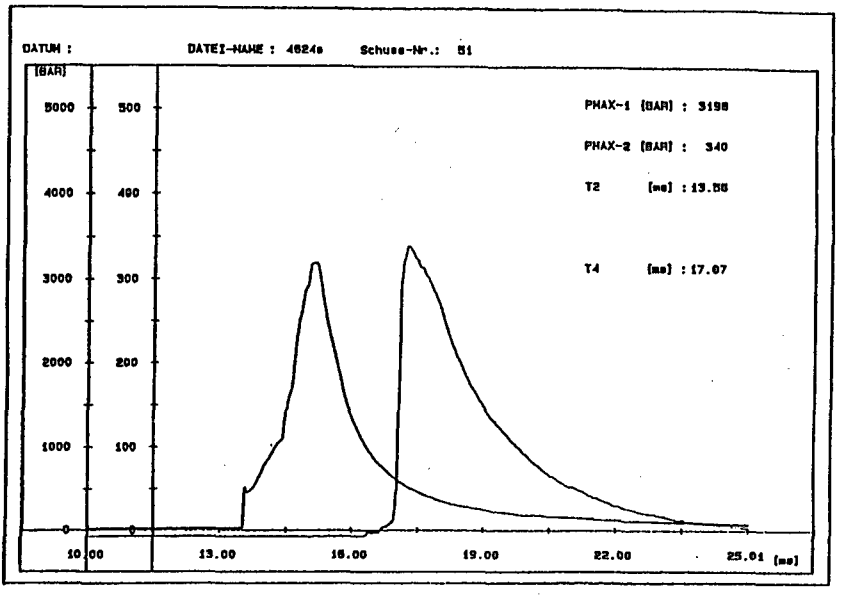

Fig. 5: Pressure-time curve of the telescoped ammuntion.

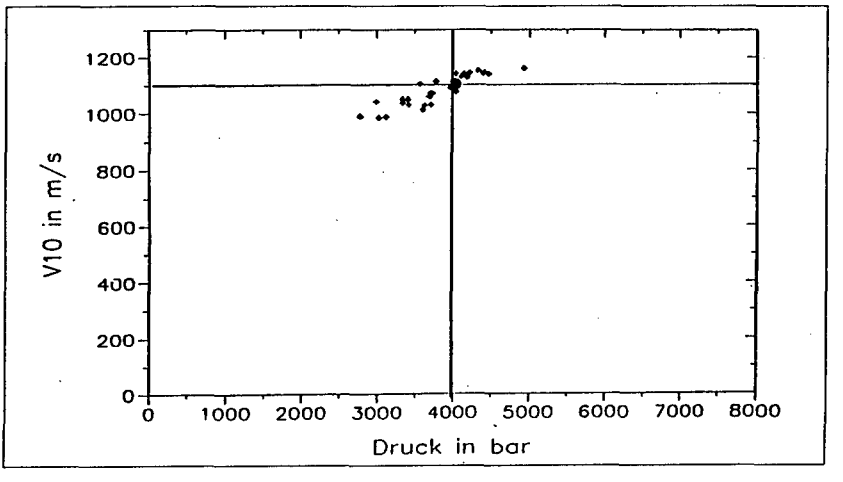

Fig. 6: Muzzle velocities at different pressures.

B RECOILLESS AUTOMATIC CANNON RMK 30

Introduction

The projekt RMK 30 has been started in 1993 with the goal of designing a recoilless weapon system for use on helicopters or other light weapon carriers.

In the past, such low recoil or recoilless weapons have only been designed for operation in single fire. In fact, an automatic cannon that is able to operate in burst fire has not yet been presented recoilless until now.

During the feasibility study a prototype of the RMK 30 has been built which in 10/96 was presented for the first time in full operation. For this firing demonstration the weapon was integrated in the light armoured vehicle WIESEL. Optimization procedures concerning weapon and ammunition are currently being carried out aiming to start production after the year 2002.

The weapon system RMK 30 with its new concepts of gun and ammunition opened a completely new field of applications [see Fig. 7]

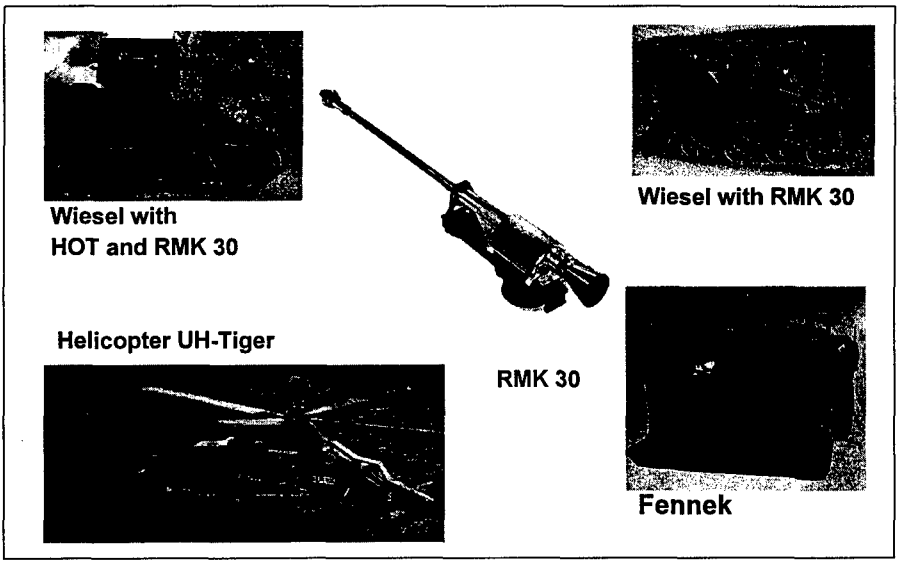

Fig. 7: Field of applications of the RMK 30.

Weapon Concept and Basic Principles

The new weapon concept had to satisfy the requirements of low weight, compactness, and simple design - features that are needed for a helicopter weapon or other light carriers. To realize this concept, Mauser had to use some totally new technologies:

- Recoillessness in combination with high performance
- Ammunition feeding from the front, to get the shortest possible gun length
- Telescoped cartridge to enable the front feeding system
- A new compact solid propellant and a combustible case
- Inductive electrical priming system.

The results of the new design [see Fig. 8] are

- accurate action of the weapon
- smallest possible dimensions and low weight.

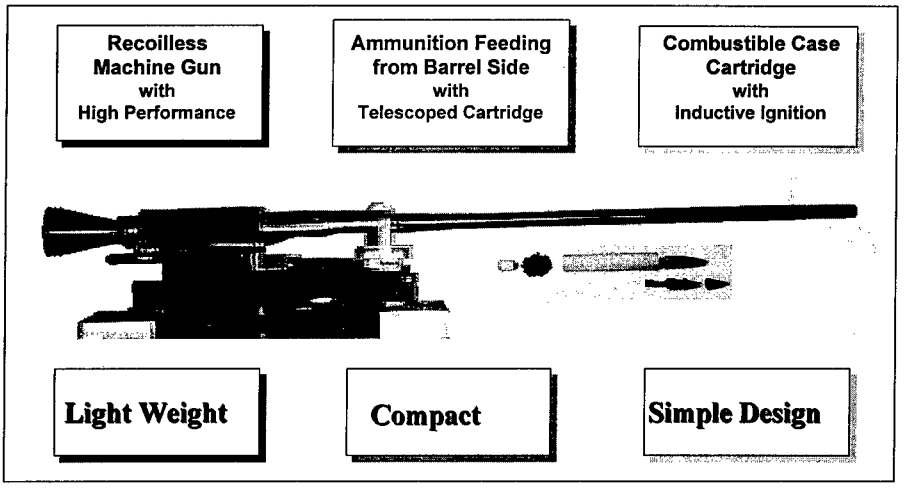

Fig. 8: Design Concept of the Recoilless Automatic Cannon RMK 30.

Fig. 9 gives details of the weapon concept with the 3-chamber breech cylinder, the ammunition feeding from the barrel side, and the gas jet nozzle. The Jet-cannon combines the rocket propulsion principle with the features of a conventional revolver type machine gun like the Mauser BK 27mm.

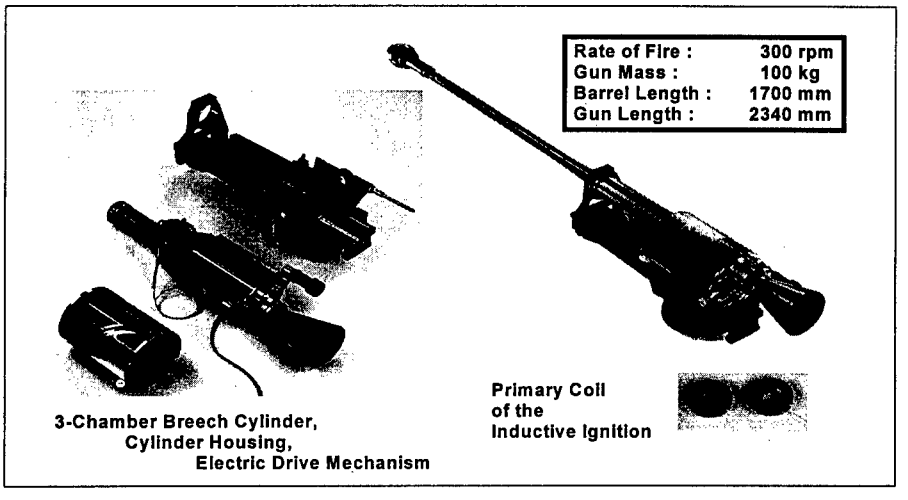

Fig. 9: Gun lay-out of the RMK 30.

The principle of recoillessness is based on the idea that the rear outstream of firing gases through a gas jet nozzle compensates the recoil impulse of the weapon. It has been demonstrated, that the remaining recoil is a simple function of the nozzle diameter, and that it is also possible to get a counter recoil [see Fig. 10].

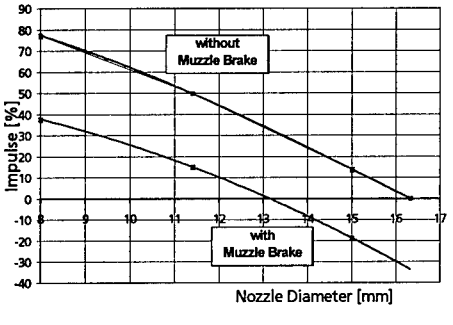

Fig. 10: Impulse Compensation according to the Nozzle Diameter.

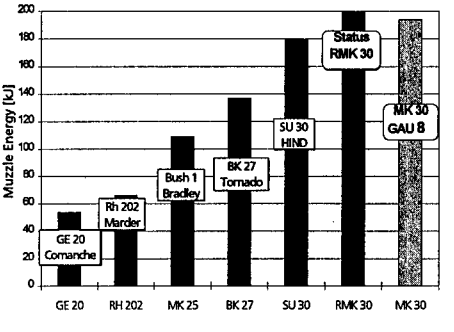

Fig. 11: Comparison of Muzzle Energies.

When the project was started at Mauser, the ammunition performance of the RMK 30 was expected to be considerably reduced compared to other conventional cannons with the same caliber. Nevertheless, by using ammunition with suitable propellants, even higher muzzle velocities or higher muzzle energies, respectively, could be achieved [see

Fig. 11]. The performance of the existing prototype is even higher than the conventional MK 30 mm with GAU 8A Ammunition. This new weapon can be used for the same missions as classic automatic cannons.

Advantages and System Applications

The recoillessness of the weapon has the following advantage:
Because of the low or nonexistent recoil forces on the carrier the cannon shows a significantly higher accuracy [see Fig. 12]. When being integrated into a weapon system the hit probability is improved especially during burst firing.
The consequences of this higher accuracy are:

1. The amount of ammunition used can be considerably reduced.
2. A very high rate of fire, that usually is requested of conventional automatic cannons to compensate for their lack of precision, is not needed.
3. Due to the low total firing disturbances, the Fire Control System can be integrated closer to the weapon, which suppresses the standard problems in harmonization.

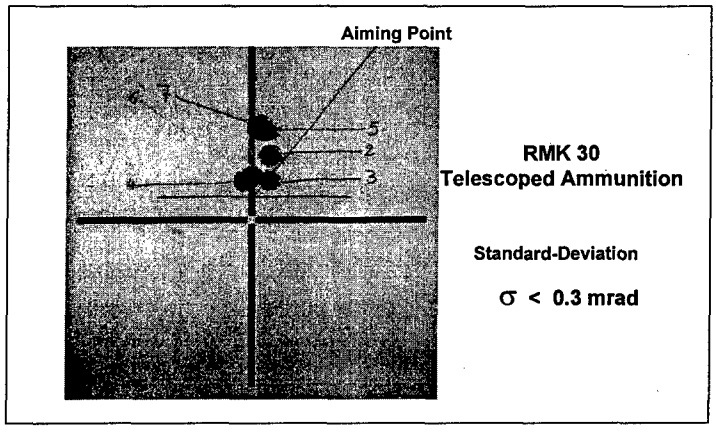

Fig. 12: Hit Pattern.

A sensor integrated weapon system allows a dispersion of the complete dynamical system of less than 1.5 mrad. Therefore, a high maneuvering air target in the range up to 1500 m (like a combat helicopter) can be effectively intercepted with only 3 rounds. The RMK 30 posseses the advantage of a short reaction gun system with "Fire and Forget" missile technology, in a range, where a missile itself cannot operate.

Summary

Recoillessness and good performance of the RMK 30 could be reached with a new designed telescoped ammunition with combustible case and inductive ignition.

By combining new technologies the RMK enlarges the application spectrum of classic automatic cannons with respect to the field of precisely operating weapon systems, which until today has only been applied to guided missiles.

Hence, this new type of weapon - allocated in between automatic cannon and missile - represents an interesting alternative to both effective systems.

LASER CUTTING OF PRESSED EXPLOSIVES

J. P. Armstrong, P. S. Banks, M. D. Feit, R. S. Lee,
M. D. Perry, F. Roeske, B. C. Stuart

Lawrence Livermore National Laboratory
Livermore, California 94550

ABSTRACT

We have used a femtosecond laser beam to make cuts through small pressed pellets of six common high explosives (HE's). The laser system produced 100 - 150 fs pulses of 820 nm light at a repetition rate of 1 kHz. Maximum energy per pulse was 5 mJ. The samples were 6.35-mm-diameter, 2-mm-thick, pressed pellets of various explosives mounted on stainless steel substrates whose thickness ranged from 0.1-1.2 mm. Various cutting rates were used, with average power varying from 0.1W to 3W. The HE was easily cut at low power levels. At 0.5W average power, one or two sweeps sufficed to cut most of the pellets. Experiments were also performed where we cut through both the HE pellet and the stainless steel substrate from either direction. Explosives that were cut included high-surface-area PETN, LX-16 (96%PETN/4% FPC 461 binder), LX-14 (95.5% HMX/4.5% Estane), LX-15 (95% HNS/5% Kel-F), LX-17 (92.5% TATB/7.5% Kel-F), PBX-9407 (94% RDX/6% Exon 461), and pressed TNT. Absorption of femtosecond pulses transfers virtually no heat to the material being cut and no evidence of HE burning or decomposition was observed on the cut surfaces. Numerous applications appear feasible for the processing of energetic materials, including HE machining and demilitarization operations.

INTRODUCTION

Cutting and machining operations on energetic materials present significant safety challenges. If conventional machine tools are used, improper fixturing of the work, improper tool configuration and improper cutting speeds have resulted in violent reactions

**Work performed under the auspices of the U.S. Department of Energy by the Lawrence Livermore National Laboratory under Contract W-7405-Eng-48.*

during machining operations. In addition, significant hazardous waste is generated from the machining chips and the necessity of using cutting fluids to cool the cutting tool.

Ablation of the energetic material by femtosecond laser pulses may offer an attractive alternative to conventional machining. Absorption of these ultra-short pulses occurs on such a short time scale that the material is ablated with virtually no heat transfer to the surrounding material, resulting in a "cold" laser cutting process. In contrast, cutting with laser pulses longer than ~10 ps is a thermal process which proceeds by first melting and then vaporizing the material with significant heat transfer to material outside of the cutting region. The waste products from short-pulse laser cutting are, for the most part, solid carbon or benign gases, which can be released into the atmosphere. If the quantity of chlorine and fluorine from the binder is a problem, these gases are easily removed.

ULTRA-SHORT-PULSE OPTICAL ABLATION

Laser heating of a solid occurs when incident radiation is absorbed in electronic states and is subsequently transferred to the lattice. When a dielectric absorbs a laser pulse of duration τ, a thermal conduction model predicts that the threshold fluence for damage (melting or vaporization) has a $\tau^{1/2}$ dependence on pulse length,[1,2] in good agreement with experiment for pulses in the range 20 ps to >100 ns.[3-10] For pulses shorter than 20 ns, the damage threshold for dielectrics deviates from the thermal scaling law.[5,9] Stuart et al.[11] report a continuously decreasing damage threshold and a gradual transition from the thermal regime to an ablative regime dominated by collisional and multiphoton ionization and plasma formation. After formation of the plasma, no further energy is transferred to the dielectric during the laser pulse because the plasma strongly absorbs the laser beam. Heat transfer to the lattice does not occur because the entire duration of the laser pulse is comparable to a single period of the highest frequency lattice vibrations. HE is a good dielectric and in the work reported here, the 100-150 fs pulses are well within the ablative regime.

In the case of metal targets, the laser pulse initially produces Joule heating, as the electromagnetic fields of the laser beam diffuse into the metal. When the temperature becomes high enough for plasma formation, the plasma shields the metal from the electromagnetic fields and absorbs the laser pulse. For pulses in the 100-150 fs range, virtually no energy is transferred to the metal after plasma formation and heat transfer does not occur because of the short duration of the pulse..

Subsequent to the laser pulse, the material that has been converted to a plasma moves away from the surface by hydrodynamic expansion and cools adiabatically. For the laser pulse energies we employed, the plasma temperatures are of the order of a few eV and expansion occurs very rapidly. Each pulse typically removes a few microns of material and if the plasma expands at a speed of a few km/s, it will cool in a few ns, leaving no time for significant heat transfer. This means that in the ablative regime (100-150 fs) where our laser operates, the cutting process is "cold" with no significant heat transfer to the material being cut. Care must be taken to ensure that the plasma can expand rapidly away from the region being cut, otherwise heat could be transferred by condensation of the plasma onto surfaces close to the cutting region.

LASER CHARACTERISTICS

The laser used in these experiments produced up to 5 W average power at 1 kHz in 120 fs pulses at 825 nm. The system, which was based on the technique of chirped-pulse amplification,[12,13] consisted of an oscillator to generate the initial short pulses, a pulse stretcher to temporally stretch the pulse and avoid nonlinear effects during amplification, a regenerative amplifier, and a pulse compressor to return the pulse width to near transform-limited duration. Seed pulses for this system were generated by a Kerr-lens mode-locked Ti:sapphire oscillator (Coherent Mira) which produced 0.8 W of transform-limited 100-fs pulses at 80 MHz. The seed pulses were stretched to 500 ps in a four-element all-reflective pulse stretcher. The seed pulses were switched into a Ti:sapphire linear regenerative amplifier where they were amplified by approximately 10^8 to 7 mJ. The

Ti:sapphire crystal was pumped on each end by 20 W from a frequency-doubled Nd:YLF laser running at 1 kHz. Switching in and out of the amplifier was done with two quarter-wave Pockels cells. After amplification, the stretched pulses were compressed in a four-pass, single-grating compressor, yielding up to 5 mJ, 120-fs pulses at 1 kHz.

EXPERIMENTAL ARRANGEMENTS

It was necessary to develop a safe procedure for performing experiments on small amounts of HE in the laser laboratory, which was not designed to allow the handling of explosives. Protection from accidental reaction of the HE was provided by performing the cutting experiments inside a portable steel firing chamber, shown in Fig.1, that has been designed and tested to safely contain the detonation of two grams of HE. To further reduce the risk from the HE, the samples for our initial experiments were limited to 100-125 mg, 6.35-mm-diameter, 2-mm-thick, pressed pellets of various explosives. These were mounted in the chamber on stainless steel substrates whose thickness ranged from 0.1-1.2 mm. To avoid nonlinear effects as the beam passed through the optical port into the chamber, it was necessary to use a thinner window than was usual. We determined that a 6-mm-thick quartz window outer window and a 3-mm-thick quartz blast shield inside the chamber gave adequate protection in the event of a sample detonation.

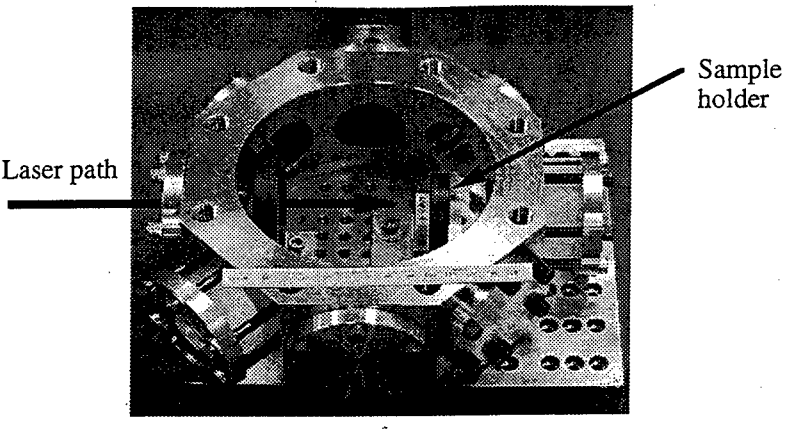

Figure 1. Portable firing chamber, shown without its steel lid in place.

For each experiment the HE sample was loaded into the chamber in a HE-handling area and the chamber was closed and evacuated to a pressure of ~ 5 Pa (40 mTorr). Evacuation of the chamber is important to avoid air breakdown from the high electric fields in the laser beam when it is focused on the target and it also greatly increases the safety margin of the chamber. The chamber was then transported to the laser laboratory, which was located in another building. The laser beam was introduced into the chamber through an optical port with a 6-mm-thick fused quartz window and passed through a 3-mm-thick blast shield inside the tank. Both the outer window and blast shield had anti-reflection coatings. Before the beam entered the chamber it was reflected from a tilted mirror that could be translated to scan the beam back and forth across the sample. The laser beam was focused to a line 300 μm long and 25 μm across. Various cutting rates were used with average power varying from 0.1W to 3W. The sample was also monitored, through another optical port, by a video camera and video recorder. The video camera recorded the plasma plume as the beam swept back and forth. Multiple cuts on a sample were made by repositioning the beam and repeating the scanning process. When the requisite number of cuts had been made, the chamber was transported back to the HE facility, unloaded, and the sample was inspected and photographed.

RESULTS OF HE CUTTING EXPERIMENTS

We used LX-16 explosive (96%PETN/4% FPC 461 binder) for our initial experiments because PETN is one of the most sensitive of the secondary explosives. In some of the experiments the beam first cut through the HE pellet and then into the stainless steel substrate and in other experiments the beam first cut through the stainless steel and then into the HE pellet. In either case, no reaction was observed in the LX-16 pellets. We also cut through pellets that were not backed by a substrate. In addition to LX-16 we cut pellets of LX-14 (95.5% HMX/4.5% Estane), LX-15 (95% HNS/5% Kel-F), LX-17 (92.5% TATB/7.5% Kel-F), PBX-9407 (94% RDX/6% Exon 461), and pressed TNT.

HMX and RDX are high-performance explosives used in many types of explosive ordnance, PETN and HNS are initiating explosives, TATB is an insensitive explosive and TNT is ubiquitous in conventional ordnance

The HE was easily cut at low power levels. At 0.5W average power, one or two sweeps sufficed to cut most of the pellets. The LX-14 required more sweep than the other HE materials. No reaction was observed in any of these materials. In experiments where the pellets were cut on a stainless steel backing, the metal plasma produced discoloration of the pellet surface, particularly when the cuts were made through the pellet into the metal substrate. When LX-16, LX-14 and PBX-9407 were cut without the stainless steel backing, the cut was clean with no discoloration or other visible evidence of reaction but the TNT, LX-15 and LX-17, which have solid carbon in their reaction products, showed some soot deposition on the cut surfaces. Figure 2 shows some typical cuts made in different explosives.

The only experiment in which reaction was observed was in cutting a LX-16 pellet when we did not compress the pulse after amplification (a factor of 5000 increase in pulse length). Using 500 ps pulses, 10 sweeps at 1W average power barely marked the surface of the pellet, but with a single sweep at 3W, the video record of the experiment clearly showed that some material was reacting, as is shown in Fig 3. Examination of the pellet afterward revealed that the edges of the cut were melted, although the pellet was still intact. Figure 4 shows a photo of the cut made with the uncompressed pulse. It is clear that ultra-short pulses are essential to laser cutting and machining of explosive materials.

We performed a second series of experiments where the purpose was to explore hole drilling and to try to measure cutting rates more precisely. For these experiments we used LX-16 because of its sensitivity and used compressed pulses for all of the experiments. Figure 5 shows a photo of several holes drilled in a 2-mm-thick sample. As before, we observed no evidence of reaction in the LX-16. Our cutting rate experiments consisted on performing parallel cuts on a sample and varying the number of sweeps or the power on

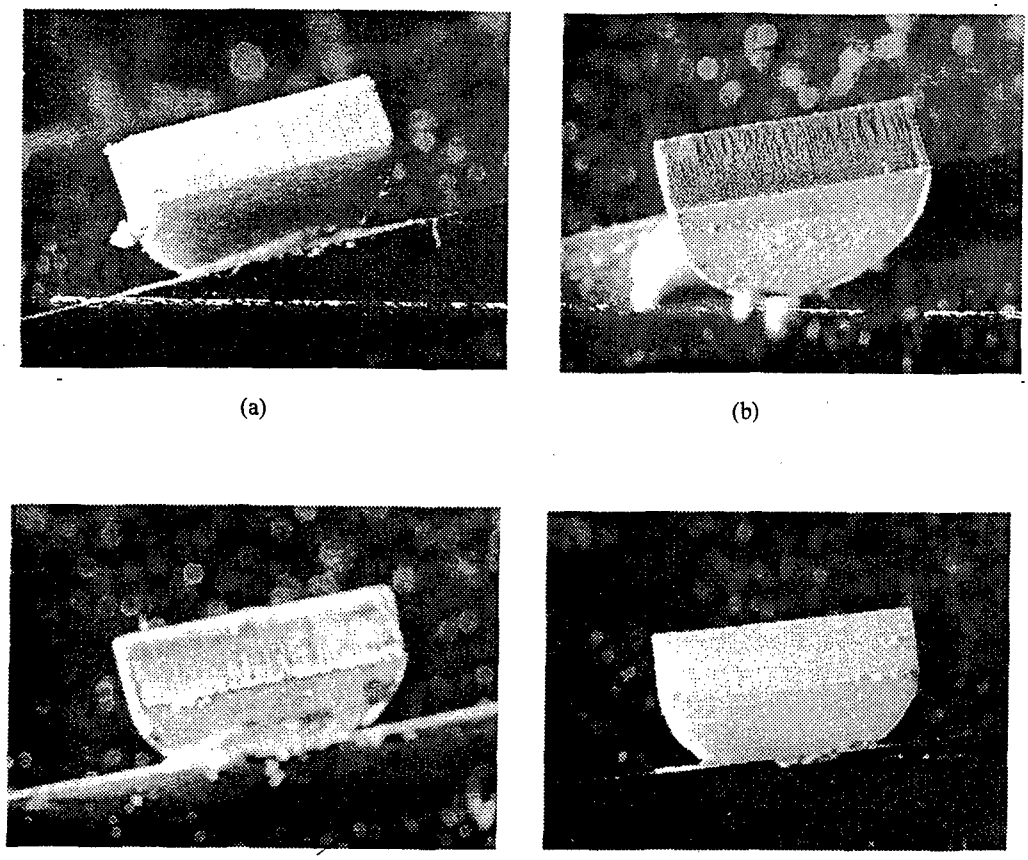

Figure 2. Cuts made at 0.5 W average power: (a) LX-14, 9 sweeps, (b) LX-15, 1 sweep, (c) LX-17, 2 sweeps, (d) LX-16, 1 sweep.

each cut. We then rotated the sample by 90° and cut all the way through to expose the depths of the cuts. Unfortunately, this was not entirely successful because it appeared that stress relaxation in the pressed pellets was closing up the cut at the bottom so we could not measure the true depth of the cut. For these experiments the laser beam was only 25 μm across. For a future series we will use a wider beam. Figure 6 shows a photo of a sectioned LX-16 sample with two parallel cuts.

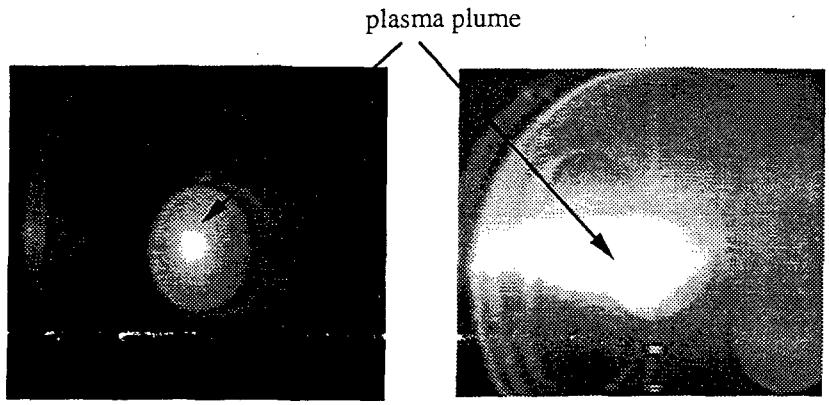

(a) (b)

Figure 3. LX-16 being cut with (a) 100 fs pulses (0.5 W) and (b) 500 ps pulses (3 W). HE reaction is clearly contributing to the plume in (b).

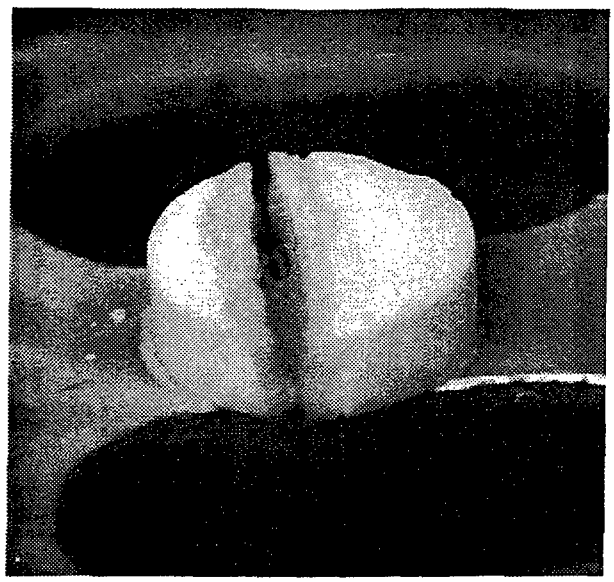

Figure 4. LX-16 cut with uncompressed laser pulses with average power of 3 W.

In the second series of experiments we also explored the range of materials that could be cut using femtosecond laser pulses. We chose diamond for a material that is extremely difficult to cut. Diamond does not absorb at 820 nm, but the beam intensity is sufficient to

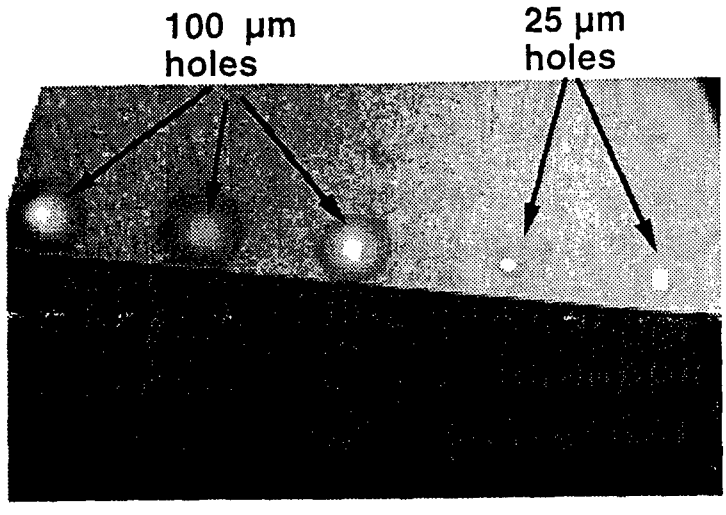

Figure 5. Holes were drilled in a LX-16 sample in less than a second. The 25 µm holes were drilled at 0.1 W average power and the 100 µm holes at 0.3 W average power.

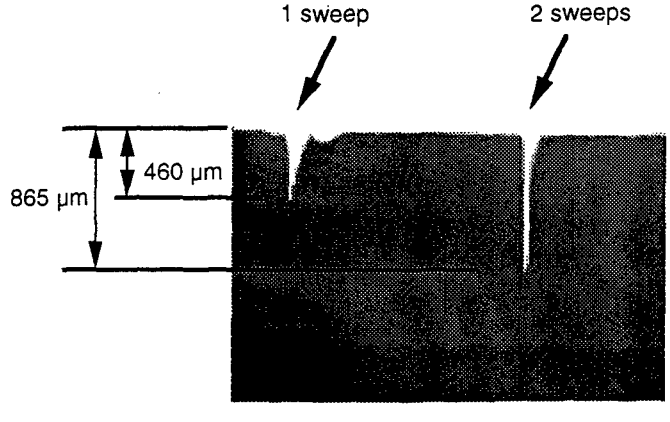

Figure 6. Two ~ 25-µm-wide cuts made in LX-16 at an average power of 0.4 W.

produce charge carriers by multiphoton processes. These carriers can produce other carriers by avalanche breakdown in the strong electric field and a plasma is thus formed, as discussed above. Our interest was to see if it might be possible to machine features on a diamond surface. Figure 7 shows some lines scribed on the surface of a diamond wafer.

For a fragile material we chose a low-density SiO_2 aerogel with a density of 0.02 g/cm^3. The femtosecond laser beam made clean cuts as shown in the photo of Figure 8. The two cuts on the left were made in vacuum, the cut on the right was made in air. The damage around the cut made in air is probably due shock waves from laser-induced air breakdown.

DISCUSSION

The initial experiments we have performed on cutting HE with a femtosecond laser beam show that ultra-short laser pulses have great promise for machining HE parts and for demilitarization operations on munitions and munition components containing energetic materials. One of the greatest potential advantages in machining operations is that laser machining would produce virtually no waste. Most of the products formed from the laser-produced plasma will be benign gases. Chlorine and fluorine from binders can be scrubbed and carbon particulates can be easily collected. Because the laser pulse can be adjusted so as to remove only a few microns of material with each pulse, precision machining should be possible. Obviously, more studies and a great deal of engineering will be needed to develop laser machining of HE into a practical tool for HE processing..

Another area that shows great promise is demilitarization. Two important features that the femtosecond laser brings to this arena are "cold" cutting of both metal and high explosives and the surgical precision with which the cuts can be made. When cutting open a metal munitions casing, the casing does not get hot, and our results so far indicate that one could safely continue cutting into the HE. If one wishes to salvage high-value components, the focused laser beam offers unprecedented precision of cutting with little loss of material.

Figure 7. Three ~ 40-μm lines scribed in a diamond wafer. Laser power was 0.13 - 1 W.

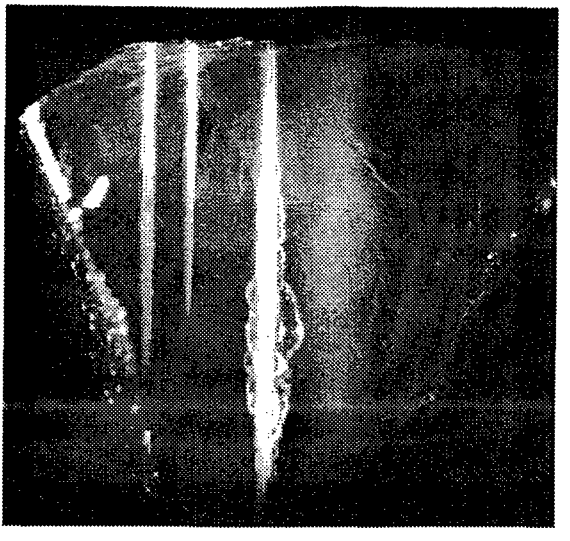

Figure 8. Cuts made in 0.02-g/cm^3-density SiO_2 aerogel. The two cuts on the left were made with 0.5 W in vacuum and the cut on the right was made at 1 W in air.

It is clear that much work remains to be done to explore the capabilities and limitations of femtosecond laser processing of explosives and explosive components. We have demonstrated that the laser beam cuts a wide range of explosives and that it cuts through steel/HE interfaces from either direction with no evidence of thermal effects. We need to obtain more information on the interaction of the laser-produced plasma with the HE. The plasma itself is at a very high temperature and carries thermal energy. As long as the plasma expands and cools on a time scale short enough to preclude heat transfer, the explosive will remain cool. For the experiments we have performed, this has been the case, but we need to understand, both by experiments and modeling, the conditions under which the plasma can transfer heat to nearby surfaces and the extent of HE reaction that can be produced by such transfer. This is important in setting limits on laser peak power, scan rate and depth of cut. We need to be sure that there are no unexpected pitfalls such as cutting into internal voids or gaps at interfaces. It is important that we understand how the plasma interacts with HE when we cut metals other than steel. We need to look at other explosives, including aluminized explosives.

Working in the laser laboratory we are severely limited in the quantity of HE that we can use in our experiments. We plan to obtain a portable femtosecond laser system that we can use in our High Explosives Application Facility at Livermore, where we can safely work with up to 10 kg of HE in enclosed firing tanks. The larger quantities of HE will allow us to perform realistic tests of the safety limits on the operating parameters.

SUMMARY

We have used a femtosecond laser beam to make cuts through small pressed pellets of six common high explosives (HE's). The laser system produced 100 - 150 fs pulses of 820 nm light at a repetition rate of 1 kHz. Maximum energy per pulse was 3.5 mJ. The samples were 6.35-mm-diameter, 2-mm-thick, pressed pellets of various explosives mounted on stainless steel substrates whose thickness ranged from 0.1-1.2 mm. Various cutting rates were used with average power varying from 0.1W to 3W. The HE was easily cut at low

power levels. At 0.5W average power, one or two sweeps sufficed to cut most of the pellets. Experiments were also performed where we cut through both the HE pellet and the stainless steel substrate from either direction. Explosives that were cut included high-surface-area PETN, LX-16 (96%PETN/4% FPC 461 binder), LX-14 (95.5% HMX/4.5% Estane), LX-15 (95% HNS/5% Kel-F), LX-17 (92.5% TATB/7.5% Kel-F), PBX-9407 (94% RDX/6% Exon 461), and pressed TNT. Absorption of such short pulses transfers virtually no heat to the material being cut and no evidence of HE burning or decomposition was observed on the cut surfaces. Numerous applications appear feasible for the processing of energetic materials, including HE machining and demilitarization operations. Further experiments are planned to study and model the cutting process. We will measure the cutting rate as we vary the peak power and scan rate of the beam. We will cut through metal/HE interfaces using metals other than steel, e.g. aluminum and copper. A particular concern will be to understand the interaction of the laser-produced plasma with the HE. Longer-range plans include installing a portable femtosecond laser system in our High Explosives Application Facility so that we can perform more realistic experiments and verify the scaling behavior of the cutting process.

REFERENCES

1. E. S. Bliss, Opto-Electronics **3,** 99 (1971).
2. J. R. Bettis, R. A. House II, and A. H. Guenther, in *Laser-Induced Damage in Optical Materials: 1976,* A. J. Glass and A. H. Guenther, eds., Natl. Bur. Stand. (U.S.) Spec. Publ. **462**, 338 (1976).
3. W. H. Lowdermilk and D. Milam, IEEE J. Quantum Electron. **QE-17**, 1888 (1981).
4. T. W. Walker, A. H. Guenther and P. E. Nielsen, IEEE J. Quantum Electron. **QE-17**, 2042 (1981).
5. M. J. Soileau, W. E. Williams, E. W. Van Stryland, T. F. Boggess and A. L. Smirlin, in *Laser-Induced Damage in Optical Materials: 1982,* H. E. Bennet, A. H. Guenther, D. Milan, and B. E. Newnam, eds., Natl. Bur. Stand. (U.S.) Spec. Publ. **669**, 387 (1984).

6. S. R. Foltyn and L. J. Jolin, in *Laser-Induced Damage in Optical Materials: 1986,* H. E. Bennet, A. H. Guenther, D. Milan, and B. E. Newnam, eds., Natl. Bur. Stand. (U.S.) Spec. Publ. **752**, 336 (1988).
7. J. Campbell, F. Rainer, M. Kozlowski, C. R. Wolfe, I Thomas and F. Milanovich, in *Laser-Induced Damage in Optical Materials: 1990,* H. E. Bennet, L. L. Chase, A. H. Guenther, B. E. Newnam, and M. J. Soileau, eds., Proc. Soc. Photo-Opt. Instrum. Eng. **1441**, 444 (1991).
8. K. Mann, H. Gerhardt, G. Pfeifer and R. Wolf, in *Laser-Induced Damage in Optical Materials: 1991,* H. E. Bennet, L. L. Chase, A. H. Guenther, B. E. Newnam, and M. J. Soileau, eds., Proc. Soc. Photo-Opt. Instrum. Eng. **1624**, 436 (1992).
9. D. Du, X. Liu, G. Korn, J. Squier, and G. Morou, Appl. Phys. Lett. **64**, 3071 (1994).
10. B. C. Stuart, M. D. Feit, A. M. Rubenchik, B. W. Shore and M. D. Perry, Phys. Rev. Lett. **74**, 2248 (1995).
11. B. C. Stuart, M. D. Feit, S. Herman, A. M. Rubenchik, B. W. Shore and M. D. Perry, Phys. Rev. B, **53**, 1749 (1996).
12. D. Strickland and G. Mourou, Opt. Comm **56**, 219 (1985).
13. P. Maine, D. Strickland, P. Bado, M. Pessot and G. Mourou, IEEE J. Quantum Electron.,**QE-24**, 398 (1988)

29th Int. Annual Conf. of ICT "Energetic Materials", Karlsruhe, Germany, June 30, 1998

METHOD FOR EXPERIMENTAL STUDY OF FLAME SPREAD ALONG COMBUSTIBLE NARROW CHANNELS

Igor G. ASSOVSKII and Oleg A. KUDRYAVTSEV***

*Semenov Institute of Chemical Physics, The Russian Academy of Sciences;
Kosygin St. 4, Moscow 117977, Russia.; Fax: (7-095) 938 2156;
E-mail: assov@chph.rc.ac.ru
**PVAIU, Penza 440005, Russia.

The purpose of this paper is an experimental investigation of gas flow patterns and ignition mechanism by flame penetration into narrow channels or pores of combustible porous materials. An original experimental method is proposed for such investigations. This method includes the independent and simultaneous measurement of gas-pressure, -temperature, and -velocity at several points of gas flow along the channel. A distinguishing feature of this method is the registration of ignition front position during the inflammation, using small inert insets in the channel. The transition of ignition front through that inset makes the typical mark on the pressure time curve.

The capabilities of the method are demonstrated on the inflammation of semi-closed cylindrical channels in solid-propellant grains. It is shown that the flame penetration process can be accompanied by pressure oscillations having two modes of frequency. The amplitude of the low-frequency fluctuations is much more than amplitude of high frequency pressure oscillations. It is founded how the diameter and length of channel, the initial gas-pressure in chamber, and initial temperature of propellant influence the process of channel inflammation.

29th Int. Annual Conf. of ICT "Energetic Materials", Karlsruhe, Germany, June 30, 1998

EROSIVE BURNING OF ENERGETIC MATERIALS. EXPERIMENTAL CHARACTERIZATION.

Igor G. ASSOVSKII
Semenov Institute of Chemical Physics RAS
Kosygin St. 4, Moscow 117 977, Russia
e-mail: iga@icp.msk.ru

Combustion products flowing over the burning surface can significantly increase the rate of solid propellant combustion. This phenomenon (so-called "razduvaniye" [1] or "erosive burning" [2]) is one of the main factors (together with gas pressure and initial temperature of propellant) governing the combustion rate in propulsion systems. That is why the propulsion systems design needs data on erosive burning obtained with high accuracy. Meanwhile it meets some principal problems, as determination of the rate needs constancy of all mentioned factors during a test time.

A traditional experimental method is a fire-test of propellant in a model rocket motor. Majority of such data is based on direct measurement of a part of propellant grain burnt during respectively long time interval (between ignition and extinction). Thus it is impossible to obtain the instant local rate with high accuracy, especially for thin propellant elements. In addition, the erosive burning takes place coincidentally with the effect of unsteady accelerated combustion after ignition [3]. These obstacles cause wide scattering of experimental data for erosive burning. Therefore it is necessary to devise a method to derive the instant local rate without any interruption of combustion process and gross error of averaging.

The main purpose of this paper is to propose such an experimental-calculating method to derive the erosive burning law using correlation between the burning rate and the pressure-time curve of combustion chamber. Such a correlation is established employing a theoretical model that takes into account dependence of the instant rate on local values of pressure and gas flow velocity, as well as on ignition conditions. This method gives a possibility to obtain new data on the combustion and ignition processes or to correct the data obtained from the tests in closed bombs. Capability of this method is demonstrated for example of double base propellant charges having tubular elements.

1. Lcypunskii O.I. On Physical Fundamentals of Interior Ballistics of Missiles. Doct dissertation, Moscow, Inst. Chem. Phys., 1945. Reprinted in: "Theory of the Combustion of Powders and Explosives", Moscow, Nauka, 1982, p.226 (in Russian).
2. Wimpress R. N. Internal Ballistics of Solid-Fuel Rockets, NY, 1950, McGrow-Hill.
3. Assovskii I.G., Theory of Non-steady-state Combustion of Fuel at High Pressure, Dokl. Phys. Chem., Proc. Acad. Scien. USSR, Vol. 294, Nos. 1-3, pp. 421-424, (1987).

TECHNISCHE HARMONISIERUNG IN DER EUROPÄISCHEN GEMEINSCHAFT – CE – KENNZEICHNUNG FÜR ZIVILE TREIBMITTEL

Dr. Heike Michael-Schulz
Bundesanstalt für Materialforschung und –prüfung
Unter den Eichen 87
D-12205 Berlin

Abstract:

The attempt to harmonization of regulations in Europe keep on. With coming into force of the Council Directive 93/15/EEC of 5 April 1993 on the harmonization of the provisions relating to the placing on the market and supervision of explosives for civil uses the regulations of the rules of the separate member states are changed, the proceeding will be standardized within Europe. It will have two parts; the proceeding of EU - conformity of type and the proceeding of quality system for the products. The propellants for civil uses will be characterized by a representative example, by performing the requirements the propellants get a CE-mark and could be transfer in the community.

Zusammenfassung:

Die Bestrebung zur Harmonisierung von Rechtsvorschriften innerhalb Europas schreitet immer weiter voran. Mit Inkrafttreten der Richtlinie 93/15/ EWG des Rates vom 5. April 1993 zur Harmonisierung der Bestimmungen über das Inverkehrbringen und die Kontrolle von Explosivstoffen für zivile Zwecke ändern sich die gesetzlichen Vorschriften der Regelwerke der einzelnen Mitgliedstaaten - das Verfahren wird innerhalb Europas vereinheitlicht. Es gliedert sich in zwei Bereiche; das Verfahren der EG- Baumusterprüfung und das Qualitätssicherungssystem für die Produkte. Die Treibmittel für zivile Zwecke werden durch ein vorgelegtes Baumuster charakterisiert, erhalten bei Erfüllung der Anforderungen ein CE - Zeichen und können innerhalb der EU inverkehrgebracht werden.

Einleitung:

Innerhalb der europäischen Gemeinschaft erfolgen technische Harmonisierungen nach einem einheitlichen Konzept.
Mit Einführung des Binnenmarktes am 1. Januar 1993 wird der freie Warenverkehr im Gemeinschaftsgebiet ermöglicht. Voraussetzung hierfür ist die Anwendung gemeinschaftlicher Richtlinien zur Harmonisierung im technischen Bereich, die Gruppen von Industrieerzeugnissen wie z.B. Maschinen, Bauprodukte, persönliche Schutzausrüstung, Telekommunikation oder auch Spielzeug betreffen.

Die Richtlinie 93/15/EWG des Rates vom 5. April 1993 zur Harmonisierung der Bestimmung über das Inverkehrbringen und die Kontrolle von Explosivstoffen für zivile Zwecke regelt den Warenverkehr mit Explosivstoffen.
Die Mitgliedstaaten sind verpflichtet den Inhalt der Richtlinie innerhalb einer festgelegten Frist in nationales Recht umzusetzen.
Das Umsetzen der Richtlinie 93/15/EWG, die Rechte und Pflichten der Beteiligten begründet, erfolgt in der Bundesrepublik Deutschland durch Gesetze oder Verordnungen.
In der Bundesrepublik Deutschland wird deshalb ein Änderungsgesetz zum Sprengstoffgesetz vorbereitet, das Änderungen im Sprengstoffgesetz und in der 1.SprengV beinhalten wird.

Von der Richtlinie werden nur die Explosivstoffe für die zivile Verwendung erfaßt.
Alle Treibmittel, Sprengstoffe, Zünder und Sprengschnüre, die als Explosivstoffe in der 8. revidierten Fassung der „Empfehlungen der Vereinten Nationen über die Beförderung gefährlicher Güter" als solche betrachtet werden und die in diesen Empfehlungen der Klasse 1 zugeordnet sind, unterliegen der Richtlinie. Künftig sind alle diese Explosivstoffe mit einem CE - Zeichen zu kennzeichnen.

Unter die Treibmittel fallen Treibladungspulver, Raketenmotoren und Festtreibstoffe. Auch Schwarzpulver unterliegt der Pflicht zur CE - Kennzeichnung bei Verwendung als Treibladungspulver, Sprengpulver und in gepreßter Form als Antrieb für Modellraketen
Ausgenommen von der Richtlinie sind pyrotechnische Erzeugnisse und Munition sowie Explosivstoffe die nach einzelstaatlichen Bestimmungen zur Verwendung durch die Streitkräfte und die Polizei bestimmt sind.

Inverkehrbringen und Verbringen

Unter Inverkehrbringen wird jede erstmalige entgeltliche oder unentgeltliche Bereitstellung eines unter die Richtlinie fallenden Explosivstoffes auf dem Gemeinschaftsmarkt für den Vertrieb und/oder die Benutzung im Gebiet der Gemeinschaft – aber nicht die Verwendung der Explosivstoffe selbst - verstanden.
Vom Inverkehrbringen ist das Verbringen zu unterscheiden.
Unter Verbringung ist jede tatsächliche Verbringung innerhalb des Gemeinschaftsgebiets unter Ausschluß der Verbringungen, die an ein und dem selben Ort stattfinden, zu verstehen.
Das Befördern von Explosivstoffen innerhalb einer Betriebsstätte ist somit kein Verbringen und setzt deshalb auch nicht die Pflicht zur CE – Kennzeichnung der beförderten Explosivstoffe voraus.
Export und Import beziehen sich künftig nur noch auf den Warenverkehr zwischen der Gemeinschaft und Drittländern.
Mit Inkrafttreten der Richtlinie dürfen in der Gemeinschaft nur noch Produkte in den Verkehr gebracht werden, die die Anforderungen der Richtlinie erfüllen. Derartige Produkte sind durch das CE – Zeichen erkennbar.

Die Verbringung von Explosivstoffen innerhalb der Europäischen Gemeinschaft unterliegt durch den Wegfall der Binnengrenzen, der Kontrolle der national zuständigen Behörden.
Der Verbringensvorgang bedarf somit der Genehmigung durch die zuständigen Behörden. Eine Voraussetzung für die Verbringensgenehmigung ist ein rechtmäßig mit

dem CE – Zeichen gekennzeichneter Explosivstoff. Außerdem müssen die beteiligten Personen zum Verbringen befugt sein.
Die Genehmigung zur Verbringung muß der Empfänger des Explosivstoffes beantragen.
Jeder am Verbringensvorgang beteiligte Mitgliedstaat muß der Verbringung zustimmen. Der Empfänger sorgt für die Übersendung der Genehmigungen an den Absender.
Die Verbringensgenehmigung begleitet den Explosivstoff bis zu seinem Bestimmungsort.

CE – Kennzeichnung und die unterschiedlichen Module

Ein unter die Richtlinie 93/15/EWG fallender Explosivstoff kann nur in Verkehr gebracht werden, wenn er die Anforderungen der Richtlinie erfüllt.
Eine hierfür benannte Stelle überprüft anhand eines Baumusters, ob die Anforderungen der Richtlinie erfüllt sind (EG – Baumusterprüfung oder Modul B).
Innerhalb Europas wird es mehrere benannte Stellen geben, diese werden von den Mitgliedstaaten gegenüber der Kommission für die jeweilige Aufgaben benannt.

Den Antrag auf eine EG-Baumusterprüfbescheinigung kann nur der Hersteller oder sein in der EU - ansässiger Bevollmächtigter nur bei einer der dafür benannten Stellen in Europa stellen.

Erfüllt das Baumuster die Anforderungen der Richtlinie, erstellt die benannte Stelle eine EG – Baumusterprüfbescheinigung. Diese ist die Voraussetzung dafür, daß der Hersteller die dem Baumuster nachgefertigten Produkte mit einem CE – Zeichen versehen kann.
Mit Hilfe eines geeigneten Verfahrens muß der Hersteller sicherstellen, daß die nachgefertigten Produkte dem Baumuster entsprechen.
Die Richtlinie legt für diesen Zweck mehrere Verfahren fest, der Hersteller kann zwischen diesen Verfahren, auch als Module bezeichnet, wählen.
Für die Explosivstoffe kommen im Prinzip nur die Module C, D, E und F in Betracht.

Die Module C und F gehen davon aus, daß der Hersteller über kein zertifiziertes Qualitätssicherungssystem verfügt. Der Hersteller beauftragt in diesem Fall durch Vertrag eine für diese Aufgabe benannte Stelle mit der Überprüfung der Konformität zwischen Baumuster und nachgefertigten Produkten.
Die benannte Stelle prüft stichprobenartig bestimmte sicherheitsrelevante Aspekte an den nachgefertigten Produkten und bescheinigt bei Übereinstimmung die Konformität der nachgefertigten Produkte mit dem Baumuster.

Die Module D und E setzen ein zertifiziertes Qualitätssicherungssystem des Herstellers voraus. Eine für diese Aufgabe benannte Stelle überprüft regelmäßig das Qualitätssicherungssystem. Der Hersteller bescheinigt die Konformität von Baumuster und nachgefertigtem Produkt.

Die EG – Baumusterprüfbescheinigung (Modul B) und die Sicherung der Konformität der nachgefertigten Produkte mit Hilfe eines der Module C, D, E oder F ergeben die Berechtigung zur CE – Kennzeichnung eines Explosivstoffes.

Betrachtungen hinsichtlich der behelfsmässigen Anwendung von selbsthergestellten explosiven Materialien.

Author: DDr.Ing.Othmar Tueller, Th.D., Budapest Ingenieur-Gerichtssachverständiger.

Hinter der eigenartigen Formulierung geht es eigentlich nicht um die Praktiken der terroristischen,kriminellen Selbstlaboraten. Vor einiger Zeit kamen Veröffentlichungen zum Tageslicht, die sich u.a. mit Herstellung von nicht üblichen industriellen-militärischen Sprengstoffen befassen. Im Zweiten Weltkrieg verwendete z.B. der amerikanische militärische Geheimdienst /siehe z.B. das Buch von J.W.Brunner: OSS Weapons/solche Proterten, die backbar,essbar sind, aber dennoch Explosivstoffe sind. In verschiedenen Armeen untersuchte man die Situation, die entsteht, wenn ein Truppenkommandeur ohne Sprengstoffe dasteht, aber sprengen muss. Es entstand - teilweise basiert auf den "terroristischen Erfahrungen" - eine lange Liste, die solche Materialien enthält, die im Notfalle als "Behelfssprengstoffe" dienen könnten, allgemein aber als Ingredienzmischungen. Die lange Liste wird natürlich angeführt von ANO /AN+ jeweiliges Öl/, Aluminiumgries und Pulver, Puderzucker und dann weiterhin über Holzkohle,Wachs,Zündholzköpfe,Glyzerin bis Kunststoffzerkleinerungen, Instant-Kaffeepulver, Watte,Nitromethan,usw. Die in Tabellenform vorzuführenden Materialien sind eigentlich keine "anergetische Materialien", sind aber ggf. "Behelfssprengstoffkomponente". Diese eigenartige Situation soll vorgestellt werden im Beitrag.

/DDr.Ing.Othmar Tueller/ Th.D.
H-1118 Budapest, Villányi ut 47.
Tel./Fax: /36-1/-1660-931.
Fax nach 5 Klingelzeichen, bin allgemein nachmittags ab 14 Uhr zu erreichen.

The Paper for 29th International Annual Conference of ICT

A NEW DETONATION MODEL

Hu, Shaoming
Xian Modern Chemistry Research Institute People,s Republic of China

ABSTRACT

As the basis of detonation model, C-J theory has been proposed for near one hundred years and has been successfully used in detonation study and practice. At the same time, some imperfections of this theory are also found: for C-J point is an instant and intermediate condition, the measured so-called C-J pressure and temperature deviate from theoretical result obviously; it is hard to explain the situation in expansion area (rarefaction) with C-J theory; etc… All of these weakness of C-J theory are thoroughly discussed in this paper.

Based on theoretically analysis, a new detonation model has been proposed by this paper. The C-J condition, i.e. u=D+C is not cited in this theory. Comparing with the C-J theory, the advantage of this model is that the aft-explosion condition is described clearly and definitely. Because the properties of original explosives and final products have been fully considered, the result obtained are more reasonable and significant in both theory and practice.

Key words: Detonation model, C-J theory

NUMERICAL EXPERIMENT ON DETERMINATION OF LIQUID EXPLOSIVES INITIATION BY IMPACT

A. V. Dubovik
Semenov Institut of Chemical Physics RAS
Kosygin Str. 4, 117977 Moscow, Russia

Numerical experiment on determination of minimal energy initiation E_m depending on thickness of liquid explosive (LE) charges h_0, locating in the clearance between plane surfaces of striker and anvil, is presented. Statement of the experiment simulates the conditions of real testings any explosives on sensitivity to impact. Obtained results are evidenced that there are exist LE layer with "soft" type of mechanical behavior, which more intensive takes up the energy from striker. Soft layer is heated up stronger than other layers at given energy of impact. This layer formes the critical thickness layer h_c, which characterized by absolute minimum of initiation energy E_c. The existing in charges under test more thicker layer with "stiff" type of mechanical behavior explaines a non-monotonic variation of $E_m(h_0)$ dependence. Necessary experimental data on non-monotonic $E_m(h_0)$ dependence for row of liquid and solid explosives are presented in [1,2].

Two-dimensional mathematical model of spreading and heating LE during the impact is developed in [3]. This model includes the hydrodynamical equations for average (along layer's thickness) and local (Lagrangian) values of velocities, pressures and temperatures in liquid flow. These equations is completed by the equations for striker's braking which determines the values on the contact boundary with striker (anvil) and velocity for striker's center of attraction. Dynamic viscosity is assumed to change according to exponential low

$$\mu = \mu_0 \exp[-(U/GT_0)(T/T_0-1)+\beta(P-P_0)]$$

where U- activation energy for viscous flow, β- piezocoefficient of viscosity, G - gas constant. Initial values are marked by interior indexes 0.

Numerical experiment on LE initiation was carried out like that. For given layer's thickness h_0 it is assumed the initial velocity of impact V_0 and Lagrangian (particle) coordinates (r_0, z_0). Under explosion condition the law of particle temperature variation T(t) must be

so as

$$f = \int_0^{t_b} dt/\tau[T(t)] = 1$$

where $\tau(T)$- induction period under temperature T, t_b- time of explosion. The explosion condition must be fulfilled under next limitations on particle state in the flow: 1) point of explosion r_b must be in the limits of striker ($r_b < R$- radius of striker); 2) time of explosion must be lower than time of impact ($t_b < t_k$); 3) for all particles $f<1$ except of "the hotest" one. Further after variation of independental values V_0, r_0, z_0 it is determined the minimal energy of initiation $E_m = MV_0^2/2$ for given h_0. By analogy with that case it is determined all dependence $E_m(h_0)$.

Connecting equation's system of hydrodynamics, dynamics of impact and explosion delay was integrated on personal computer in according to modified program STIFFR from MATHCAD 5.0+. Accuracy of determination r_0 was not more than 100 μm, z_0- 10 μm, V_0 - 1 mm/s.

As known from the experiment [1,2] LE charge of any thickness h_0 may be exploded by impact with minimal energy $E_m = MgH_0$ ($V_0 = \sqrt{2gH_0}$). Empirical dependence $E_m(h_0)$ has a form of strong dropping curve for $0 < h_0 < h_c$. For $h_0 > h_c$ initiation energy is roughly constant $E_m = E_c$ (type 3) or it is increased to value E_s. For $h_0 > h_s$ initiation energy may be roughly constant $E_m = E_s$ (type 2) or it is decreasing function to value $E_m = E_n \geqslant E_c$. For $h_0 > h_n$ initiation energy is roughly constant E_n (type 1). Thus curves type 2 or 3 may be obtained from one type 1 when $h_n \to h_s$ or $h_n \to h_c$ accordingly (fig.1).

Numerical simulation of impact initiation LE charges shows $E_m(h_0)$ dependeces as empirical ones. For example we consider the results of numerical experiment on hypothetical explosive with ρ=1500 kg/m^3, c_p=1,25 kJ/(kg.K), μ_0=50 Pa.s, U=80 kJ/mol, β=5 GPa^{-1}, thermochemical and kinetic parameters Q=4,3 MJ/kg, E=165 MJ/mol, $Z = 4*10^{15}$ s^{-1}, coefficient of heat removal from LE to striker (anvil) 3 kW/(m^2.K). Parameters of impact system : mechanical stiffness 0,35 GN/m, diameter of striker 2R=19 mm, drop weight 5 kg.

Calculated curve $E_m(h_0)$ and experimental points are presented on fig.2. Real experiment was made with pasteous mixture fine-grained HMX, Al and binder. Obtained dependence $E_m(h_0)$ belongs to 1-rd type ones. The curve has absolute minimum E_c=34,5 J in point h_c=0,225 mm

and characteristic maximum E_s=49,1 J in h_s=0,35 mm. For all $h_0 > h_n$=0,5 mm the value E_n=40 J is approximately constant and $E_n > E_c$.

In order to better understand the reason of non-monotonic curve change we turn to fig.3 where is shown time-dependent picture the changing of impact parameters under critical conditions: h_c=0,225 mm, V_c=3,715 m/s. Observed particle, which "the hotest" one, is placed in point with r_0 =3,0 mm and z_0=0,06 μm. At the beginning of impact the viscosity is increased because of the pressure rises and elastic energy of striker is increased also. LE temperature is increased very small. However because of strong temperature-viscosity dependence the viscosity drops and after it the pressure breaks down also from value p_c=0,495 GPa. Elastic energy of striker transits to energy of liquid stream and LE temperature is increased to maximum T_m=668 K. Note the main heating of particle take place not in time of maximum striker's surface velocity w_m=11,4 m/s but in time of coming the spreading wave in point r_0. At that time inertial forces is negative and viscous pressure rises above middle pressure p. Maximal velocity of dissipation energy q_m is 20,4 kW/μl. Immidiately after maximums q and T value $f \to 1$ what meanes the initiation of explosion in time of t_b=0,6 t_k. At that time the particle is stopped in 0,2 R from the border of striker and approximately in the middle of compressed layer which thickness is 95 nm. Maximal value of Reynolds number Re_m in spreading flow is 28,2.

Consider fig.4 where are presented the extremal parameters of impact with critical energy E_c for different h_0. All curves have characteristic extremums in points of h_c=0,225 mm and h_s=0,35 mm. The charge of thickness h_c names "soft" as it is compressed to minimal thickness h_k=92 nm and it absorbs maximal part of impact energy e_l=0,725 E_c (viscous part of energy e_v is 0,47 e_l). After impact the striker rebounds from h_k with velocity V_k=0,52 V_c. This charge is heated the strongest and the fastest than other charges.

In contrast to h_c the charge of thickness h_s names "stiff" as it is compressed to maximal thickness h_k=130 nm and it absorbs only 58% E_c. The velocity of rebound is 0,65 V_c, maximal velocity of heat dissipation is 13,7 kW/μl, temperature T_m =619 K. Therefore maximum f_m=0,14 and the explosion is absent. For all $h_0 > h_n$=0,5 mm the values of extremal parameters is roughly constant.

For all $h_0 \neq h_c$ the explosins are absent. In order to explode its it is necessary to lift the impact energy E_0 more than E_c and the most

level of this lifting must be made for $h_0=h_s$. For all $h_0>h_n$ the lift of E_0 must be roughly constant.

Considering fig.2 we may convince in justing of this conclusion. In fact the local maximum of initiation energy E_s take place for "stiff" layer h_s, absolute minimum of initiation energy E_c - in h_c and for all $h_0>h_n$ the initiation energy E_n is roughly constant. As one would expect from condition f=1 along curve $E_m(h_0)$ the values T_m=668±0 K, q_m=20,8±0,4 kW/μl, h_b=98±2 nm are conserved as constants. Although impact time t_k increases with h_0 but the time Δt from beginning of pressure drop t_p to moment of explosion t_b has a week minimum Δt_m=86 μs under $h_0=h_c$.

It was made other numerical experiments on initiation LE with different rheology but the same explosion characteristics. These calculations shown the 5-fold decreasing μ_0 brings to $E_m(h_0)$ dependence 2-nd type and additional 2-fold decreasing U brings to $E_m(h_0)$ dependence 3-rd type (fig.1). Some obtained results are presented in Table.

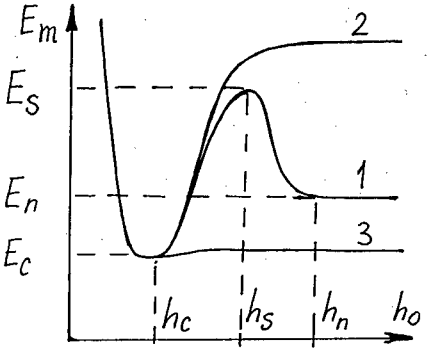

Fig.1. Schematic diagram of $E_m(h_0)$ dependences

Table

Type $E_m(h_0)$		1	2	3
μ_0	Pas	50	10	10
U	kJ/mol	80	80	40
E_c	J/cm^2	12,2	10,2	4,97
p_c	GPa	0,495	0,448	0,257
h_c	mm	0,225	0,11	0,20
Re_m		28,2	28,5	0,762
q_m	kJ/μl	20,4	34,3	6,09
T_m	K	668	674	629
Δt	μs	86,0	63,8	218
E_n	J/cm^2	14,0	22,2	6,11

As follows from the Table, the 5-fold decreasing μ_0 brings into slightly increasing of LE sensitivity which is characterized by the values of E_c and p_c. But additional 2-fold decreasing U increases LE sensitivity most visible. Small U equivalent to weak dependence $\mu(T)$. Therefore LE type 3 may be considered as isoviscous liquid. The impact compression of this LE runs in noninertial regime ($Re\ll1$). The viscosi-

ty plays a two-fold role in explosion initiation of LE. It increases dissipation velocity of impact energy but it increases the crushing strength of liquid layer. In result the maximal impact temperature may be small. Often great impact time t_k and concerned with its long time of dissipation heating Δt plays a dominant part in the explosion initiation.

In the case of a strong temperature-viscosity dependence (high U) the pressure dropping due to heat instability of LE layer under load [1] has a break down character. In the break down moment t_p the striker accumulates up to 80 % impact energy E_c and break down pressure p_c is about 0,5 GPa. This high pressure may be produced only at very thin layer of LE. The less μ_0 the less must be h_c to produce the same pressure under roughly the same E_c. Therefore it is observed a weak dependence of LE sensitivity on the μ_0, if the value μ_0 is not so big.

Thus the variation of rheological characteristics LE only gives a possibility to explain qualitative the origine of different types $E_m(h_0)$ dependences and LE sensitivities to impact. All extremums at these dependences may be explained due to new insight about substatially different mechanical behavior of LE charges under impact, in particular the existence of soft and stiff layers. To obtain quantitative characteristic of LE sensitivity it is necessary to have an accurate data about its rheological and explosive properties.

After all it is necessary to discuss one principal conclusion from this work about the justification of the choice E_c (or p_c) as an absolute index of explosive sensitivity to impact. As per fig.2 the interval of h_0 near h_c is narrow in comparison with wide range $h_0 \gg h_n$. In this range h_0 the initiation energy $E_n > E_c$ but the change E_n is not coinciding with E_c change (see Table). Therefore the using only E_c as a characteristics of impact sensitivity may bring into some overestimation (or underestimation) of real explosive hazard.

LITERATURE

1. Dubovik A.V., Lisanov M.V. Heat instability of deformation and initiation of HE charges under impact / In: "Detonation and Shock Waves. Proc.8-th Allunion Symp.on Combustion and Explosion". Tchernogolovka, 1986, p.6-9.

2. Dubovik A.V., Denisaev A.A. Analogy between a solid and vis-

co-flowing explosives initiation by impact / In: "21-th Intern. Pyrotechn. Seminar". Moscow, 1995, p. 182-186.

3. Dubovik A.V., Bobolev V.K. Schlagempfindlichkeit Flussiger Explosionsfahiger Systeme /Transl. from Russian. Ed. Dr. C.-O. Leiber/ FBWT, 1996.

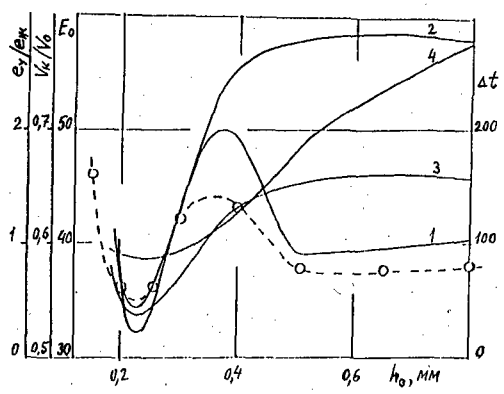

Fig. 2. Initiation parameters according to h_0: 1- E_m (in J), 2- rebound velocity V_k/V_0, 3- striker elastic energy-liquid energy ratio e_s/e_l, 4-explosion delay $\Delta t=t_p-t_b$ (in μs), t_p- moment of pressure break down beginning.

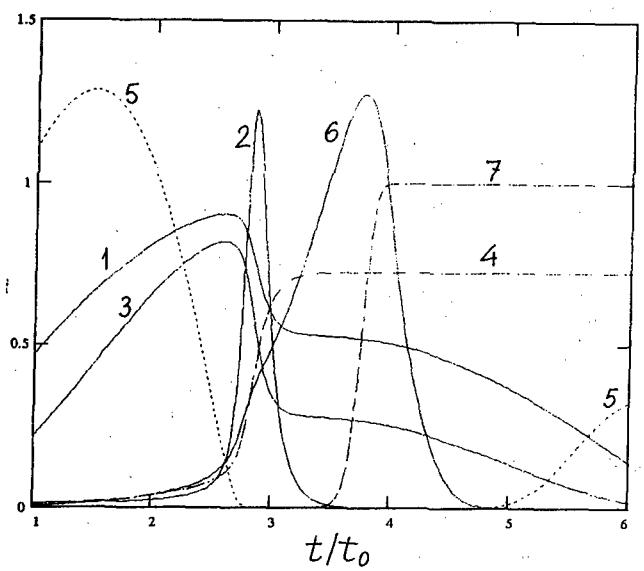

Fig. 3.

Time-dependent parameters of impact with E_c=34,5 J: 1- p/p_x; 2- w/V_c; 3- e_s/E_c; 4- e_l/E_c; 5- μ/μ_0·0,4 6- (T/T_0-1); 7- f. Scale values: p_x=0,548 GPa, μ_0=50 Pas, T_0=293 K, Vc=3,71 m/s, t_0=60,6 μs.

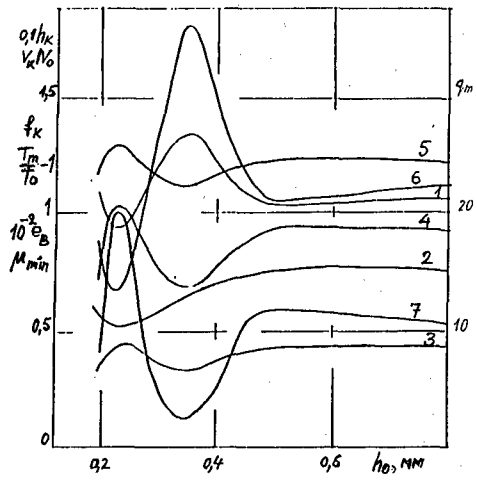

Fig. 4. Extremal impact parameters according to h_0 under E_c =12,2 J/cm^2: 1- h_k (in μm), 2- V_k/V_0, 3- e_v (in J/μl), 4- q_m (in kW/μl), 5- (T_m/T_0-1), 6- μ_{min} (in μPas), 7- f_k.

ANOMALOUS DETONATION OF CONDENSED EXPLOSIVES WITH THE CJ CONDITION VIOLATION AND CHANGE IN CARBON PHASE STATE

Sergey B. Victorov and Sergey A. Gubin

Moscow State Engineering Physics Institute (Technical University),

31, Kashirskoe shosse, Moscow, 115409, Russia

Previous theoretical investigations of TNT detonation associate a break in the D vs ρ_0 slope at initial density ρ_0 = 1.55 g/cm^3 with the graphite to diamond transition and assume that both phases of solid carbon (i.e. graphite and diamond) are present in the TNT detonation products at $\rho_0 \geq 1.55$ g/cm^3. We have computed the detonation properties of two explosives, carbon-rich TNT and carbon-poor RDX. The size and structure effects of solid carbon clusters were taken into account. The results of this study show that coexistence of both the graphite and diamond phases of solid carbon in the detonation products of considered explosives is impossible at any ρ_0. Depending on ρ_0, the condensed detonation products consist of either graphite or diamond. Both explosives have a range of ρ_0 where their detonation occurs in anomalous mode: the CJ condition of equality between sound and detonation products velocities is not satisfied but the detonation is stable. Our calculations yield sharp increase of temperature and pressure of the detonation products at the beginning of the «anomalous region» of ρ_0. The predicted values of ρ_0 corresponding to the anomalous mode of detonation are sensitive to size and structure of the graphite and diamond clusters. We suggest experiments on detonation pressure of porous explosives that should reveal whether the predicted anomalous mode of detonation occurs and that will help us specify the parameters of solid carbon clusters in detonation products.

1. INTRODUCTION

Condensed carbon presents in detonation products of many high explosives (HE). Its principal phase states are graphite, diamond and liquid. Carbon phase state in detonation products depends on their temperature and pressure and affects to detonation parameters of explosives because distinct carbon phases have different thermodynamic properties. Therefore, knowledge of carbon phase state in detonation products is important for accurate prediction of HE detonation characteristics.

We have researched the detonation properties of carbon-rich TNT and carbon-poor RDX to show how changes of carbon phase state in detonation products influence HE detonation parameters.

Besides different carbon content several other factors motivate the study of these two explosives. There are a lot of precise experimental data on detonation parameters of TNT and RDX. Hence, it is possible to compare calculated detonation parameters with experimental ones. Both explosives have breaks in their experimental dependencies of detonation pressure and velocity slope on initial charge density. These breaks seem to be result of phase transitions in the detonation products. Thus, the choice of TNT and RDX for studying effects of carbon phase transitions on HE detonation behavior is quite justified.

2. THEORY

The chemical formula of TNT is $C_7H_5N_3O_6$ and of RDX is $C_3H_6N_6O_6$. The standard heats (enthalpies) of formation of TNT and RDX are equal to −17.8 and 14.7 kcal/mole, respectively. We assume that both explosives produce the only gaseous phase and a solid carbon phases, i.e. graphite or diamond. The gaseous phase consists of 14 gaseous species (C, C_2, C_5, CH_4, CO, CO_2, H_2, H_2O, N_2, N_2O, NH_3, NO, NO_2, O_2).

The Gibbs free energy G of k reacting species is

$$G(T,p,n_1,...,n_k) = \sum_{j=1}^{k} n_j\mu_j(T,p,n_1,...,n_k),$$

where T - temperature, p - pressure, n_j - molar concentrations, μ_j - chemical potentials for gas and solid species.

We have used BKW equation of state (EOS) for the gaseous phase with our own set of EOS coefficients BKW-RR [1].

To describe thermodynamic properties of solid carbon phases more accurately we have obtained new EOS for graphite and diamond with the Grüneisen gamma depending on specific volume only. All available experimental data on thermal expansion, heat capacity, shock-wave and static compression have been used to determine the best EOS parameters. These EOS have been applied to calculate the

graphite-diamond equilibrium line in a wide range of pressures and temperatures. The computed phase equilibrium line fits available experimental data and theoretical calculations.

Condensed carbon in form of graphite or diamond clusters is a major detonation product of many HE. The regions of phase stability and synthesis conditions of carbon clusters are little investigated. While the phase diagram of non-disperse carbon is well established even at high pressures and high temperatures, researches devoted to properties of small carbon clusters almost are not present.

In this work it is supposed, that the sizes of clusters are not small so, that a qualitative state (internal structure) of substance has appreciably changed. Therefore, we consider that the structure, lattice parameters, bond energies and heat capacity of small clusters are equal to corresponding parameters of non-disperse crystals.

The distinction consists only of high surface energy of clusters, that causes respective changes of enthalpy ΔH and entropy ΔS of substance:

$$\Delta H = \int_A \left[\sigma - T\left(\frac{\partial \sigma}{\partial T}\right)_p \right] dA,$$

$$\Delta S = \int_A \left[\left(\frac{\partial \sigma}{\partial T}\right)_p \right] dA,$$

where σ - surface energy, A - molar surface area.

It is supposed, that the surface energy linearly depends on temperature and does not depend on pressure. Such assumption is convenient for carbon clusters with number of atoms more than thousand and size above 10 nm [2].

Within the framework of offered model changes of enthalpy and entropy of carbon clusters caused by its small size do not depend on temperature and pressure, and are defined only by shape and size of crystals. Thus, the effect of structure and size of clusters on the thermodynamics of solid carbon particles can be described by correction of the standard-state heat of formation and entropy of carbon phases. The corrections to the heat of formation and entropy depend on shape and size of crystals.

We have used compact shape (a regular hexagonal prism) of carbon clusters for calculations of TNT and RDX detonation parameters. Our results show increasing

of graphite-diamond cluster equilibrium pressure in comparison with one of non-disperse carbon phases.

A new computer code (TDS) has been developed to carry out multi-phase equilibrium calculations of HE detonation. The TDS code allows to determine all local minima of detonation velocity and to find the only point of the HE Hugoniot (absolute or global minimum) which corresponds to the real state of products behind the detonation wave.

3. RESULTS

The theoretical detonation parameters calculated by the TDS code are in satisfactory agreement with experimental data for a lot of HE. We have used this code to compute detonation of porous TNT and RDX in a wide range of initial charge density.

The Hugoniots of TNT and RDX were carefully researched by means of the TDS code. The size and structure effects of graphite and diamond clusters were taken into account. These parameters of solid carbon clusters have been determined to obtain the best agreement between calculated and experimental detonation properties.

The experimental data on porous TNT are in [3]. The summary of experimental data on porous RDX is in [4].

Previous theoretical investigations of TNT detonation associate a break in the detonation velocity D vs ρ_0 slope at initial charge density $\rho_0 = 1.55$ g/cm^3 with the graphite to diamond transition and assume that both phases of solid carbon (i.e. graphite and diamond) are present in the TNT detonation products at $\rho_0 \geq 1.55$ g/cm^3.

Our researches confirm that this break in the D vs ρ_0 slope is really caused by the graphite to diamond transition but the assumption about graphite-diamond coexistence in the detonation products was found to be quite incorrect.

In fact, coexistence of both the graphite and diamond phases of solid carbon in detonation products of the considered explosives is impossible at any ρ_0. Depending on ρ_0, the condensed detonation products consist of either graphite (at $\rho_0 < 1.55$ g/cm^3 for TNT and at $\rho_0 < 1.43$ g/cm^3 for RDX) or diamond (at $\rho_0 \geq 1.55$ g/cm^3 for TNT and at $\rho_0 \geq 1.43$ g/cm^3 for RDX). Both explosives have a range of ρ_0 where their detonation occurs in an anomalous mode [5]: the CJ condition of equality between

sound velocity and velocity of detonation products is not satisfied but the detonation is stable.

The stability of anomalous detonation is due to global minimum of detonation velocity on the detonation Hugoniot. The experimental data on porous TNT and RDX also indicate to stability of their detonation.

Our calculation predicts sharp increase of temperature and pressure of the detonation products and break in the D vs ρ_0 slope at the beginning of «anomalous region» of ρ_0 (i.e. at ρ_0 = 1.55 g/cm^3 for TNT and at ρ_0 = 1.43 g/cm^3 for RDX). The calculated detonation properties of TNT and RDX fit available experimental data (Fig.1-3). The predicted values of ρ_0 corresponding to the anomalous mode of detonation are sensitive to size and structure of the graphite and diamond clusters. We suggest experiments on detonation pressure of porous explosives that should reveal whether the predicted anomalous mode of detonation occurs (i.e. the beginning and the end of «anomalous region» of ρ_0).

The anomalous mode of detonation exists due to the following difference between graphite and diamond thermodynamic properties: at the same temperature and pressure entropy of diamond always appears less than entropy of graphite. At some HE initial densities this feature of carbon thermodynamics causes solid carbon to change its phase state in the detonation products (graphite to diamond transition occurs) and results in appearance of the anomalous detonation.

4. CONCLUSION

The results of this study show that solid carbon clusters are required to explain the experimental detonation data of porous TNT and RDX.

Both explosives have a range of ρ_0 where their detonation occurs in anomalous mode: the CJ condition of equality between sound and detonation products velocities is not satisfied but the detonation is stable. Our calculations yield sharp increase of temperature and pressure of the detonation products at the beginning of the «anomalous region» of ρ_0. The predicted values of ρ_0 corresponding to the anomalous mode of detonation are sensitive to size and structure (shape) of the graphite and diamond clusters. We suggest experiments on detonation pressure of porous explosives that should reveal whether the predicted anomalous mode of detonation

occurs and that will help us specify the parameters of solid carbon clusters in detonation products.

The anomalous detonation seems to be "the rule rather than the exception" even for explosives containing relatively small amounts of carbon. We expect that many high explosives have a range of initial charge densities where their detonation occurs in the anomalous mode.

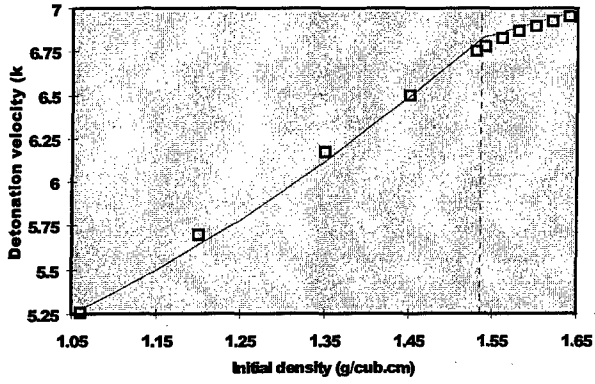

FIG. 1. Detonation velocity vs initial TNT density. Vertical dotted line indicates the beginning of initial density region where detonation occurs in the anomalous mode. Solid line - our calculation, square markers - experiment [3].

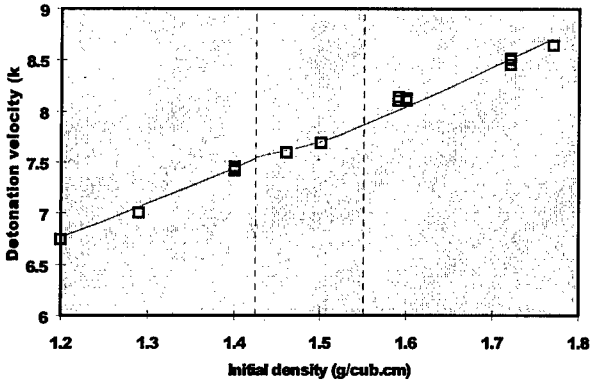

FIG. 2. Detonation velocity vs initial RDX density. Vertical dotted lines indicate the beginning and the end of initial density region where detonation occurs in the anomalous mode. Solid line - our calculation, square markers - experiments summarized in [4].

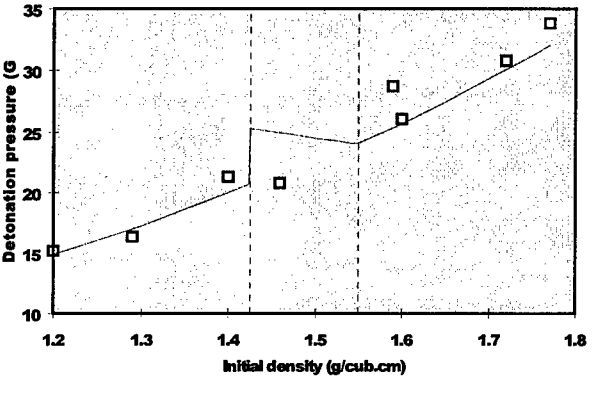

FIG. 3. Detonation pressure vs initial RDX density. Vertical dotted lines indicate the beginning and the end of initial density region where detonation occurs in the anomalous mode. Solid line - our calculation, square markers - experiments summarized in [4].

REFERENCES

1. S.A.Gubin, V.V.Odintsov, V.I.Pepekin Khimicheskaya Fizika, Vol.5, No.1, 1986, p.111 (in Russian).

2. V.V.Odintsov, S.A.Gubin, V.I.Pepekin Determination of Form and Size of Diamond Crystals behind Detonation Wave in Condensed HE. Khimicheskaya Fizika, Vol.10, No.3, 1991, p.687 (in Russian). (There is translation in English CHEMICAL PHYSICS REPORTS the former Russian Journal of Chemical Physics, cover-to-cover translation of "Khimicheskaya fizika").

3. M.J.Urisar, E.Jr.James, L.C.Smith Physics of Fluids, Vol.4, 1961, p.262.

4. F.H.Ree Supercritical fluid phase separations: Implications for detonation properties of condensed explosives. J.Chem.Phys., 84(10), 1986, p.5845.

5. S.B.Victorov, S.A.Gubin The anomalous regime of the TNT detonation caused by change in the carbon phase state in the products. International Conference «Shock Waves in Condensed Matter». St.Petersburg, Russia, September 2-6, 1996, p.13.

Development and optimisation of the Fiber Optic Probe; a new optic method for measuring the shock velocity in energetic materials

R.J. van Esveld, M.P. van Rooijen, W.C. Prinse, A.C. van der Steen

TNO Prins Maurits Laboratory, P.O. Box 45, 2280 AA Rijswijk, The Netherlands

The TNO Prins Maurits Laboratory uses an electric gun to characterize the behaviour of energetic materials on impact with a flyer plate. The electric gun generates a powerful electromagnetic field, which makes the use of electrical measuring methods like resistance wire or ionisation pins problematic. The need for accurate measurement of shock and detonation velocities in a strong electomagnetic environment has led to the development of the Fiber Optic Probe (FOP), which is an optical method.

The FOP is an optic fiber, in which several holes are drilled. This fiber is placed in the sample normal to the shockfront. When a shockwave travels through the sample, the air in the drilled holes is compressed and will emit light through the process of ionisation. This light is recorded with a digital signal analyzer (DSA), on which a peak in light intensity will be visible each time the shockfront passes a hole. The distance between two holes (measured during the construction of the FOP) divided by the time between the two corresponding peaks gives the average shockwave velocity in between two holes.

Initially the FOP has been used for solid energetic materials, for example RDX and HMX based plastic bonded explosives, pressed HNS II and pressed TATB. Recent optimisations have extended the use of the FOP to powder (guanidine nitrate) and liquid (nitromethane) energetic materials. The velocity range, in which the FOP has proven to work correctly, ranges from 3 km/s to 12 km/s. The error in the measured velocity is mainly influenced by the distance between the holes, and is usually less than 0.3 km/s.

The FOP has some distinct advantages relative to other methods of shock velocity measurement. One advantage is the small scale on wich experiments can be performed. Usually only 2.5 to 10 grams of energetic material is used, but at large scale the FOP also performs excellent. Furthermore, the FOP is capable of monitoring the shock to detonation transition in explosives. These advantages, combined with the insensitivity of the FOP to electromagnetic fields, make the FOP an excellent tool for the characterisation of energetic materials used in Exploding Foil Initiators (EFIs).

CHARACTERISATION OF BOOSTER EXPLOSIVES BY FLYER IMPACT

W.C. Prinse[1], T. Jordan[2], A. Cardell[2], R.H.B. Bouma[1], A.C. van der Steen[1]

[1] TNO Prins Maurits Laboratory, P.O. Box 45, 2280 AA Rijswijk, The Netherlands
[2] DERA, Fort Halstead, Sevenoaks, Kent TN14 7BP, United Kingdom

DERA and TNO are both interested in the response of new explosives candidates to flyer impact for application in Insensitive Munitions. The objective of a joint research programme is to analyse, and eventually optimise, the response of new explosives to flyer impact initiation. The type of explosive and the influence of crystal size distribution are investigated in this programme. As the explosives are typically applied in exploding foil initiators or in parts of an explosive train, the dimensions of the flyer are also changed in the flyer impact initiation experiments.
In the design of exploding foil initiator both the explosive's crystal size[1,2], and pulse length[1] of the input shock wave, are crucial to its reliable operation, the pulse length being proportional to flyer thickness.

DERA has prepared charges of explosives that show good thermal characteristics and low explosiveness. At TNO the flyer impact initiation of these charges has been investigated. In the experiments the run-to-detonation or initiation distance is determined optically, as a function of the velocity of the impacting flyer. From the experiments one can determine the initiation threshold of an explosive; the initiation threshold being characterised by a pressure or energy, specific for the applied flyer thickness. Experiments are then repeated at various flyer thicknesses, and plots of the initiation energy at the threshold versus the corresponding initiation pressure will be constructed. These plots show a curve that separates the two regions of detonation and no-detonation, which is important to the design of an electric foil initiator. Two asymptotes are found, a critical initiation energy for thin flyer impact initiation, and a critical initiation pressure for thick flyer impact initiation.

Results will be shown on the flyer impact initiation of HNS II and HNS IV, TATB C and TATB superfine. The thicknesses of the flyers are 125 μm and 250 μm.
Due to the relatively high shock sensitivity of HNS, difficulties are encountered in the determination of the shock initiation threshold. The capacitorbank used in the initiation experiments operates reliably between 10 kV and 40 kV, which in turn determines the range of attainable flyer velocities, specific for each combination of flyer thickness and flyer diameter. In order to lower the velocity of the impacting flyer, a primary flyer hits a PVC barrier with a relatively low velocity, on top of which a secondary flyer has been placed. Because of the damped shock wave in the PVC barrier, the secondary flyer is released at a lower velocity. In this way the lower limit of attainable flyer velocities has been altered successfully, allowing for the determination of the shock initiation threshold of HNS. The dimensioning of the PVC barrier is determined from an analysis of shock and release wave propagation in both the primary flyer and the PVC barrier. The velocities of the secondary flyers have been determined by calibration in separate experiments applying the Fabry-Perot velocity interferometer system[3].

At the moment experiments are being carried out on the shock initiation behaviour with 25 and 50 μm thick flyers, which requires also a new flyer velocity calibration procedure at respective flyer thicknesses. Furthermore the detonation pressure of HNS and TATB will be determined with the Fabry-Perot velocity

interferometer system by measuring the time-evolution of the particle velocity at the explosive/PMMA interface, as described in reference 3.

At small flyer thicknesses typically small size crystals should be employed for the reliable functioning of an electronic foil initiator, as the critical initiation energy is larger for the larger crystal sizes.

1 W.C. Prinse, M.P. van Rooijen, B. Coleau, J.M. Mul, H.J. Verbeek, A.C. van der Steen, Shock sensitivity testing of explosives with the gap test and the thin flyer impact test,EuroPyro 95, Tours, France, 5 - 9 June 1995.

2 H. Moulard, Particular aspect of the explosive particle size effect on shock sensitivity of cast PBX formulations, Proceedings of the Ninth Symposium (International) on Detonation, Portland, USA, 28 August - 1 September 1989, pp 18-24.

3 L.K. Cheng, A.J.A. Bruinsma, W.C. Prinse, C. Smorenburg, A Fabry-Perot Interferometer System for high-speed velocity measurement, High Speed Photonics Congress, 28 October - 1 November 1996, Santa Fé, USA.

Ict symposium 1998
abstract

29 th INTERNATIONAL ANNUAL CONFERENCE OF ICT

JUNE 30 – JULY 3, 1998

KARLSRUHE, FEDERAL REPUBLIC OF GERMANY

DETERMINATION OF THE DETONATION ENERGY AND SOME OF THE ENERGETIC CHARACTERISTICS OF VARIOUS NTO-BASED FORMULATIONS

Gideon J Ellis and Hendrik C Bezuidenhout

NASCHEM (A Division of DENEL, Private Bag X1254, Potchefstroom, 2520, Republic of South Africa)

ABSTRACT

The behavior of condensed media under detonation loading is classically investigated through free-surface and final velocity V reached by a liner coating one side of an explosive mass, detonating parallel to its surface. The liner mass constitutes an available parameter to be related with V. This method of observation of flow boundaries, provides important information on detonation and the flow behind it.

It is used to calculate parameters of some equations of state for the detonation gas, and also in the present work, whose aim was to characterize and classify NTO-formulated high explosives on the basis of the maximum kinetic energy transferred to the liner in the lateral projection geometry.

By varying the thickness of the inert plate and measuring the free surface velocity, data is obtained which is extrapolated to zero plate thickness. The acoustic approximation is used to calculate the Chapman-Jougeut explosive pressure. The polytropic exponent, the chemical energy released in the detonation, and the maximum fraction of this energy transferred to the liner, can also be calculated.

Ict symposium 1998
abstract

NTO (3-Nitro1,2,4-Triazol-5-one) was identified as a relatively insensitive explosive with a calculated performance near that of RDX. Several experiments were performed. NTO was incorporated into TNT and RDX-mixtures. The experiments used various combinations of charge mass and plate mass, and various types of explosive charges, such as NTO/TNT (40/60), RDX/NTO/TNT (25/25/50), RDX/TNT (60/40), TNT, and various PBX formulations. The determination of the energetic characteristics of the explosives was determined from the registration (performed by X-ray apparatus) of the projection of the metal plate driven by the detonation products. Detonation velocity was also measured.

Theoretical predictions (based on the conservation of momentum and energy) are compared with the experimental results. Although used in small-scale experiments, the present method has been successfully used to characterize various NTO compositions.

SHOCK INITIATION OF NITROMETHANE BASED EXPLOSIVES IN GAP TEST CONFIGURATION

Stanisław CUDZIŁO, Andrzej MARANDA, Waldemar Andrzej TRZCIŃSKI

Military University of Technology
Kaliskiego 2, 01-489 Warsaw, POLAND
Fax: +48 22 6669041

Abstract

A process of shock initiation of nitromethane and its mixtures with ammonium nitrate or hexogen or aluminium powder or copper powder was investigated. A modified gap test was employed to measure the mean velocity of explosion propagation at different depths in an acceptor charge and to determine the length of a plexiglass gap for which the probability of detonation initiation is equal 50%. The experimental results show that the critical velocity of propagation of explosion that leads to detonation is independent of a kind of addition and it coincides with the value for pure nitromethane but it is reached for different lengths of the plexiglass gap. An observed increase of shock sensitivity cannot be explained only on the basis of physical phenomena connected to shock wave propagation in a heterogeneous medium. A hypothesis is made that in the first stage of initiation the thermal explosion of nitromethane in hot-spots placed at solid inclusions occurs and after that the decomposition products of nitromethane react with adjacent material of inclusion.

1. Introduction

The process of shock initiation of nitromethane (NM) has been a subject of many experimental and theoretical investigations [1-10]. Their results show that the chemical reactions in NM under shock initiation conditions have an induction period and that the length of time induction decreases with increasing the shock pressure. In many works devoted to the shock initiation of liquid explosives, it was showed that experimental results could be interpreted using a homogeneous thermal explosion theory. On the basis of this theory, the qualitative relationships were found between time to detonation or an amplitude of initiation pressure and the chemical kinetics of the heat releasing reactions.

Addition of solid inclusions to the homogeneous liquid explosive turns it into a heterogeneous explosive and radically changes the mechanism of initiation of detonation. In consequence of inclusions attendance (with different wave impedance), the shock compression energy is localised in particular areas. Multiple reflections of shock wave and collision its curved front create inhomogeneous fields of temperature and pressure with many regions of elevated values of the parameters. After exceeding critical values by local temperatures, the regions act as ignition sites (hot-spots) in which the exothermic decomposition of NM begins. Decomposition of the hot-spots leads to energy release that is proportional to their volume. If the concentration of hot-spots is high enough, the chemical energy strengthens the shock wave and transforms it into a self-sustaining detonation wave. In their classic work on the shock initiation of solid particles suspension in nitromethane, Howe, Frey, Taylor and Boyle [7] showed that shock sensitivity of the explosive mixtures is proportional to total surface area of inclusions in wide range their individual size (0.5÷200 μm) and concentration (0.15÷20% vol.). Furthermore, at a constant surface area, the sensitivity increases with increasing the shock impedance of the inclusions.

According to the authors' knowledge there have been done very limited studies on the shock initiation of NM mixtures with chemical active solid additives which are nominally able to react with nitromethane decomposition products in hot-spots. Since the elevated temperature regions are placed in a neighbourhood of inclusions, a chemical interaction between initial decomposition products and the material of addition may occur. In case of appearing that reactions, the shock sensitivity should be not only a function of addition concentration and its dispersity or density but should depend also on its chemical nature. To check this hypothesis, 40% in mass of powdered aluminium (Al) or crystalline ammonium nitrate (AN) or hexogen (RDX) or powdered copper (Cu) were added to nitromethane. The addition of 2% in mass of polymethylmethacrylate (PMMA) to NM was also added to obtain stable suspension of additives in it. The shock sensitivity of explosives tested was investigated with modified gap test technique. In succeeding shots, the mean velocity of explosion process propagation at different depths in the tested charge was measured by short-circuit sensors. Moreover, the length of plexiglass gap was determined for which the probability of detonation initiation was equal 50%.

2. Experimental approach and results

Commercial grade nitromethane, aluminium powder (size of grains < 150 μm), crystalline ammonium nitrate (size < 500 μm), hexogen (size < 50 μm) and powdered copper (mean size of grain = 63 μm) were used to prepare explosive mixtures. The addition of 2% in mass of PMMA to NM increased its viscosity sufficiently to obtain stable suspension of 40% additives in it. To avoid air bubbles, the explosive mixtures were prepared by mixing the additive with homogeneous, viscous NM/PMMA mixture at least two hours before the shot. Before the main experiments, the density of the mixtures was characterised by a pycnometric method and the detonation velocity was determined under the same conditions as during the experiments. The detonation velocity was measured by short-circuit sensors located in the 36-mm-diameter charge. The composition of the explosive mixtures tested and the results of preliminary measurements are given in Table 1.

Table 1. Composition and properties of the explosive mixtures

Explosive mixture	Composition [% mass]	Density* ρ [kg/m^3]	Detonation velocity D_e [m/s]
NM/PMMA	98/2	1140	6350
NM/PMMA/Al	58.8/1.2/40	1470	5870
NM/PMMA/AN	58.8/1.2/40	1305	5800
NM/PMMA/RDX	58.8/1.2/40	1335	6850
NM/PMMA/Cu	58.8/1.2/40	1748	5300

* - initial density at the temperature T = 293 K

The charge configuration used in main experiments is shown in Fig. 1. It conformed to the usual large-scale gap test [11], except that the short-circuit sensors to measure the mean velocity of explosion process propagation were employed. A booster made of phlegmatised hexogen served as a shock wave generator. From shot to shot, the length of plexiglass attenuator was changed with 2-mm step. The highest and the least gap values were appointed for which the complete detonation and failure of explosion process were observed. The complete detonation of explosive charge was indicated when a clean hole was cut in the steel witness plate that was 5-mm thick. The mean shock wave velocity in plexiglass gap and mean value of explosion process

propagation in the acceptor charge was measured by short-circuit sensors. The manner of the sensor location is shown in Fig. 1.

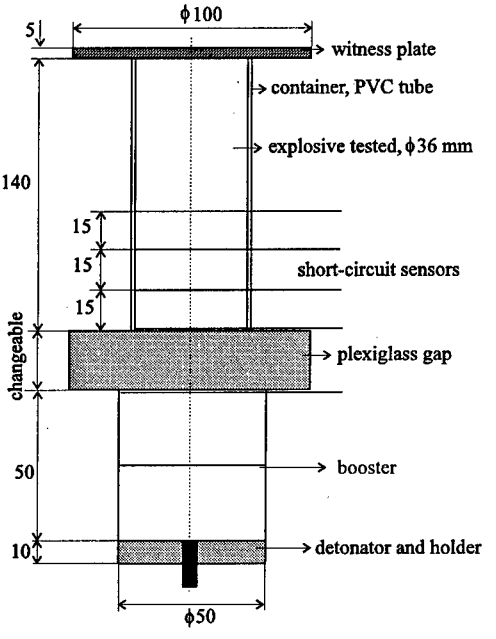

Fig. 1. Scheme of the charge configuration to determine the shock sensitivity and to measure the mean velocity of explosion process propagation.

The shock sensitivity of explosives tested as the usual gap test results in the form „detonation-no detonation" are presented in Table 2 and the results of measuring the mean velocity of explosion process propagation are shown in Figs. 2, 3, 4 and 5. The curves illustrate changes of the velocity values as a function of distance from the loaded surface for different length of the plexiglass gap. The value of mean velocity obtained on a given measured distance is shown as the point corresponding to the centre of the distance. On all the graphs, there are also points (⊙) which correspond to the value of mean shock wave velocity in the plexiglass attenuator (for different its length). The values of shock wave velocity that are marked as black points (•), were obtained at the first measured distance in the NM/PMMA charge for different length of the gap. Two of them which are described as NM+ and NM– correspond to the critical values of velocity for that complete detonation and failure of NM explosion process were observed. The values were obtained for the length of the plexiglass gap equal adequately 30 and 32 mm.

Table 2. The length of the plexiglass gap as a measure of the shock sensitivity.

Explosive	Length of the plexiglass gap [mm]		
	detonation	no detonation	50%
NM/PMMA	30	32	31
NM/PMMA/Al	40	42	41
NM/PMMA/AN	36	38	37
NM/PMMA/RDX	34	36	35
NM/PMMA/Cu	28	30	29

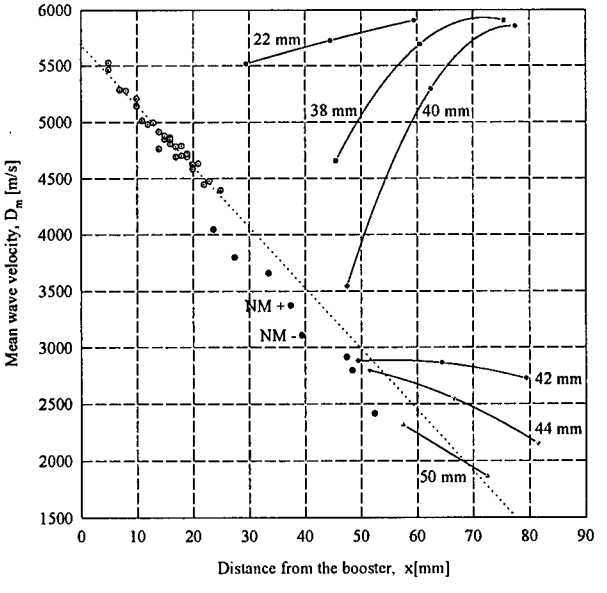

Fig. 2. Mean velocities of wave in the plexiglass gap (⊙), in NM/PMMA (•) at the first measuring distance and in NM/PMMA/Al (—) at the consecutive measuring distances as a function of distance from the end of the booster for different lengths of the gap.

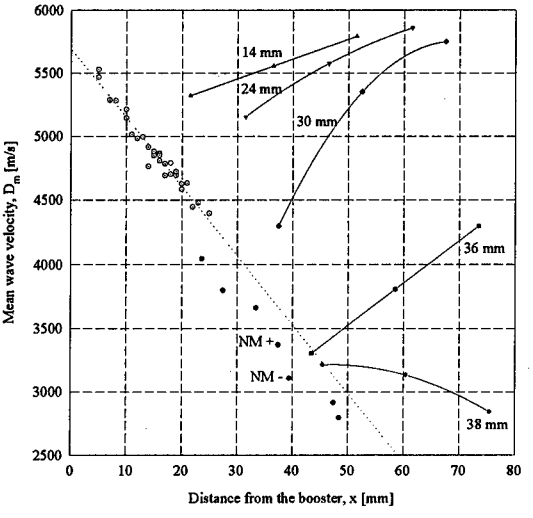

Fig. 3. Mean velocities of wave in the plexiglass gap (⊙), in NM/PMMA (•) at the first measuring distance and in NM/PMMA/AN (—) at the consecutive measuring distances as a function of distance from the end of the booster for different lengths of the gap.

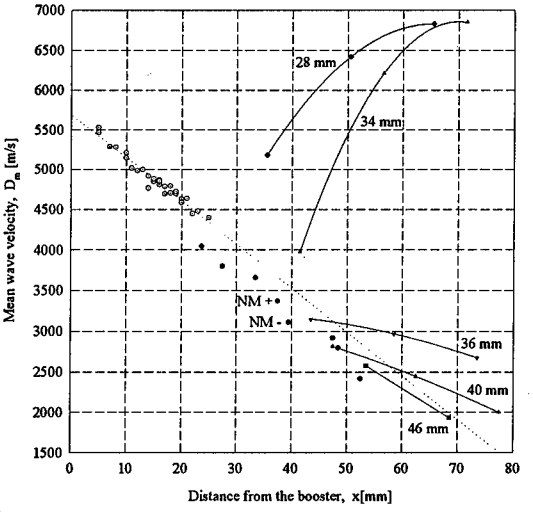

Fig. 4. Mean velocities of wave in the plexiglass gap (⊙), in NM/PMMA (•) at the first measuring distance and in NM/PMMA/RDX (—) at the consecutive measuring distances as a function of distance from the end of the booster for different lengths of the gap.

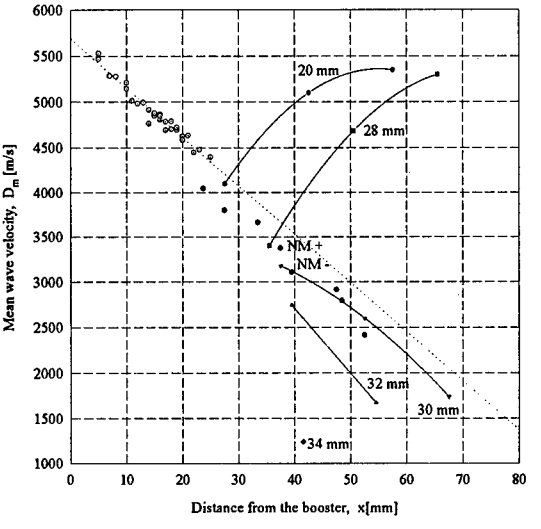

Fig. 5. Mean velocities of wave in the plexiglass gap (⊙), in NM/PMMA (•) at the first measuring distance and in NM/PMMA/Cu (—) at the consecutive measuring distances as a function of distance from the end of the booster for different lengths of the gap.

4. Calculations

Detonation velocities of explosive tested were calculated by assuming the neutrality of additives in the zone of chemical reactions or their activity in this zone. Calculations of the detonation velocity in the first case (D_i) were performed by the method described in Ref. 12 and calculations in the second one (D_a) were done by means of a program for thermochemical calculations TIGER - [13] with the set of parameters in the BKW equation of state recommended in [14]: $\alpha = 0.50$, $\beta = 0.176$, $\kappa = 11.80$, $\Theta = 1850$. The results of calculations are presented in Table 3. For comparison, the experimental results (D_e) are also given in this table.

On the basis of the measured values of time of propagation of shock waves across the plexiglass gap of different thickness, the time-dependence of a shock wave velocity (D_s) can be determined. Thus, the shock wave velocity against distance from the plexiglass surface can be obtained (Fig. 6).

Table 3. Experimental and calculated detonation velocities for the mixtures tested

Explosive mixture	D_e [m/s]	D_i [m/s]	D_a [m/s]
NM/PMMA	6530	6360	6670
NM/PMMA/Al	5870	5910	6060*
NM/PMMA/AN	5800	5635	7280
NM/PMMA/RDX	6850	5870	7320
NM/PMMA/Cu	5300	5280	-

* maximal value obtained for 13 % chemically active aluminium

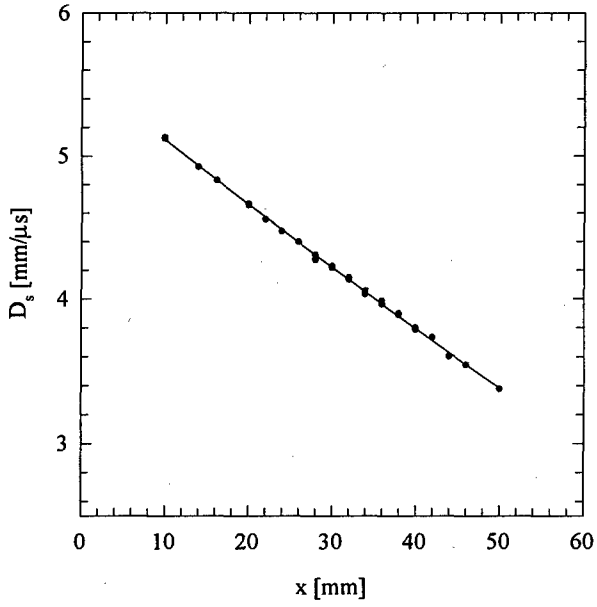

Fig. 6. Shock wave velocity, D_s, in plexiglass as a function of distance, x, from the loaded surface.

If shock adiabates of the explosive mixtures are known then initial parameters of shock wave generated in the explosive may be calculated on the basis of the value of shock wave velocity at the end of plexiglass block. Shock adiabates of NM/additive mixtures were determined by the method of constructing the shock adiabate of a multi-component medium proposed in [13]. The

values of parameters characterising the properties of plexiglass, NM, and additives are given in Table 4. The parameters ρ_0, a , λ and γ_0 are the density of a pure material, the coefficients of a shock adiabate $D_N = \alpha + \lambda u_N$ (D_N and u_N denote normal shock wave and mass velocities in a pure additive), and the Grüneisen coefficient, respectively.

Table 4. Parameters of shock adiabates and Grüneisen coefficients for materials used in tests

Material	ρ_0 [kg/m^3]	a [m/s]	λ	γ_0
Plexiglass	1186	2598	1.516	0.97
NM	1140	2650	1.64	1.25
Al	2710	5250	1.39	2.13
AN	1690	1800	1.8	1.55
RDX	1800	2870	1.61	1.29
Cu	8920	3940	1.489	1.99

The calculated values of the initial shock pressure (p*) leading to the detonation of given mixture are presented in Table 5.

Table 5. Calculated critical shock pressures leading to detonation

Explosive mixture	p* [GPa]
NM/PMMA	4.75
NM/PMMA/Al	3.55
NM/PMMA/AN	4.00
NM/PMMA/RDX	4.45
NM/PMMA/Cu	5.95

5. Discussion

The results of experiments and calculations presented in Table 3 give an answer to the question if the reactions between additives and the products of decomposition of NM take place in the reaction zone of the detonation wave. Comparison of the measured and computed values of the detonation velocity shows that the values of D_e for the mixtures with Al, AN or Cu additives are similar to those of D_i which are calculated by assuming the chemical inertia of the additives. Discrepancies between the values of D_e and D_i are much lower than those between the values of D_e

and D_a. This fact enables us to formulate a conclusion that possible reaction, in which Cu, Al and the products of AN decomposition participate, proceeds behind the reaction zone of the detonation wave. In case of NM/PMMA/RDX mixture the value of D_e is higher than that of D_i and only insignificantly lower than that of D_a. This means that the decomposition of RDX takes place in the reaction zone and reactions between the products of NM and RDX are possible.

From the gap test results presented in Table 2 and the calculated critical shock pressures shown in Table 5 it follows that there is no correlation between a shock sensitivity of the NM mixtures and the dispersity and shock impedance of additives' material. If only physical phenomena influenced the sensitivity of explosive tested then copper powder would be the best sensitizer because of its high dispersity and high density. But aluminium and ammonium nitrate are better sensitizer in spite of their greater particles and lower shock impedance. This fact enables us to drawn a conclusion that higher sensitivity of the NM mixtures with Al or AN is caused by chemical reactions of the additives with the products of NM decomposition. These reactions lead to an increase of a rate of heat release behind the initiating shock wave. Strong influence of aluminium and ammonium nitrate on the sensitivity of NM means that the NM decomposition products are able to react with reductants as well as oxidizers. Unexpected weak influence of RDX on the NM-mixture sensitivity is caused by the fact that RDX is not strong reductant nor strong oxidizer as well. That is why the heat effect of reactions between the products of decomposition of RDX and NM is lower than that in the NM mixtures with Al or AN.

Copper powder decreases the shock sensitivity of NM in a significant degree. Presence of Cu particles affects positively the shock sensitivity of the mixture by the formation of hot spots but simultaneously copper absorbs the heat energy and reduces a probability of occurring of chemical reactions in the shocked nitromethane.

Thus, on the basis of experimental results, a conclusion can be drawn that the sensitivity of explosives tested decreased in series NM/PMMA/Al > NM/PMMA/AN > NM/PMMA/RDX > NM/PMMA > NM/PMMA/Cu. This changes do not correlate with total surface area and shock impedance of the inclusions but they can be explained with assumption that the shock initiation process consists of two stages, the thermal explosion of NM in hot-spots and the heterogeneous combustion of the inclusion material.

References

[1] A. W. Campbell, W. C. Davis, J. R Travis., *Shock initiation of detonation in liquid explosives*, Proc. 3rd Symp. on Detonation, Princenton University, 1960.

[2] W. A. Gey, K. Kinga, *The shock initiation of detonation in liquid explosives*, Proc. 3rd Symp. on Detonation, Princenton University, 1960.

[3] J. E. Hay, J. Ribovich, Scott F. H., F. C. Gibson, *The effect of physical and chemical properties on the sensitivity of liquid explosives*, Proc. 4th Symp. (Int.) on Detonation, White Oak, 1965.

[4] I. G. Berke, R. Shaw, D. Tegg, L. B. Seely, *Shock initiation of nitromethane, methyl nitrate and some bis difluoroamino alkanes*, Proc. 5th Symp. (Int.) on Detonation, Pasadena, 1970.

[5] F. E. Walker, R. I. Wasley, *Initiation of nitromethane with relatively long-duration, low-amplitude shock waves*, Combustion and Flame, **15**, 233, 1970.

[6] D. R. Hardesty, *An investigation of the shock initiation of liquid nitromethane*, Combustion and Flame, **27**, 229, 1976.

[7] P. Howe, Frey R. , B. Taylor, V. Boyle, *Shock initiation and the critical energy concept*, Proc. 6th Symp. (Int.) on Detonation, White Oak, 1976.

[8] K. Mohan, J. E. Hay, *Effect of caviation on the shock sensitivity of liquid explosives*, Proc. 7th Symp. (Int.) on Detonation, Annapolis, 1981.

[9] G. I. Pangilinan, C. P. Constantinou, Y. A. Gruzdkov, Y. M. Gupta, *Investigation of shock-induced chemical decomposition of sensitized nitromethane through time-resolved raman spectroscopy*, Materials Research Society, Symp. Proc., v. 418, Pittsburgh, 1996.

[10] X. Hong, R. I. Hill, D. D. Dlott, *Vibrational energy transfer in high explosives: Nitromethane*, Materials Research Society, Symp. Proc., v. 418, Pittsburgh, 1996.

[11] M. Suceska, *Test methods for explosives*, Springer-Verlag, New York, 1995.

[12] R. Trębiński, W. Trzciński, E. Wlodarczyk, *A method for determining detonation adiabates of explosives with admixture of inert additions*, J. Tech. Phys., **31**, 1, 1990.

[13] Ch. L. Mader, *Numerical modelling of detonations*, University of California Press, Berkeley-Los Angeles-London, 1979.

[14] P. Crawford, *Getting Started with TIGER*, Lawrence Livermore National Laboratory, 1986.

DETECTION OF IMPACT TIME IN DROP-HAMMER TEST *

Lu Zijian, Hu Qingxian
Institute of Chemical Materials, CAEP
P.O.Box 513-108, Chengdu 610003, China

ABSTRACT

Drop-hammer test is a well known method for characterization of explosive safety and the test result obtained therefrom is one of the most important data concerned in the explosive application. But there are few methods which can be used to accurately reflect the impact process. The accurate time of the hammer striking the impact set with sample is essential for the further research and application of explosives, but this accurate time is very difficult to detect. We have designed a device and procedure to gain the impact time by using a Data Acquisition System to record the acceleration variation of the hammer striking upon the impact set. A series of data related to the acceleration variation of impact can be obtained under different conditions, including

- impact set without any sample:
- impact set with non-explosive sample;
- impact set with explosive sample;
- impact with different drop-hammer height, etc.

According to comparison and analysis of the acceleration vs time ($a \sim t$) curves scanned in the tests said-above, the impact time under different conditions were obtained for a series of explosives. The preliminary results of the experiments indicate that this device could be used as a new method to evaluate the impact sensitivity of granular explosives and describe their mechanism from the impact time and the shape of the corresponding $a \sim t$ curves.

KEYWORDS impact sensitivity of explosive impact time drop-hammer test

1. INTRODUCTION

The drop hammer test is still a widely used method to describe the impact sensitivity [1] and usually for granular explosives [2]. In general, the test results are evaluated by two ways, one is the sensitiveness of the

* This work is supported by the Science Foundation of China Academy of Engineering Physics.

explosive in terms of 50% drop height to cause ignition [3], the other is the explosion probability under a specified hammer weight and drop height. Both ways are on the basis of statistical principle which can show nothing of the impact process. It is impossible, therefore, to give the answer about how long a time has gone for the sample to ignite after it was impacted.

Based on the " hot spot " theory which is usually used to explain the mechanism of explosive ignition by impact, we thought it should be necessary to find a way to reflect the response of the explosive sample while being impacted by a hammer, at the same time the factors influencing on the response should be easily detected by means of some devices and not disagreed with the " hot spot " mechanism. The acceleration variation of the hammer striking the impact set is taken as a criteria describing the response process of the test sample. According to this idea, we have designed a device and procedure to scan the acceleration process of the striking hammer and a series of acceleration vs time ($a \sim t$) curves were obtained. After analyzing the curves, it can be found apparent differences in the impact process among the explosives of different types such as PETN; HMX and RDX [5]; Teryl and TNT etc..

2. TEST DEVICE AND PROCEDURE

The experiments are carried out on the drop-hammer device with a 5kg weight. The impact set consists of two steel rollers of 10mm diameter in a close-matched sleeve on a pedestal as shown in Fig. 1. The sample is placed in-between the adjacent ends of the two rollers. An accelerometer YJ-5 is fixed on the hammer and the signals produced are transmitted into the Data Acquisition System DAS-820 through a charge amplifier YE5852. The impact time under different conditions can be obtained by computer analyzing the $a \sim t$ cures recorded.

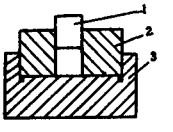

Fig. 1 Impact set

1. roller 2. Sleeve 3. Pedestal

3. TEST RESULT

3.1 Blank test

In order to verify the function stability of the device, the tests without any sample in-between the rollers were carried out at the drop height of 20, 50 and 70cm and repeated at each one. The curves picturing the relationship between the impact acceleration, a, and time, t, were scanned as in Fig. 2, 3 and 4. The range of

the impact time is marked by letters " a " and " b " in each of the curves. Since all the experiments below were made on the same device with the same procedure, the curves obtained from different group of tests will be shown in the same manner.

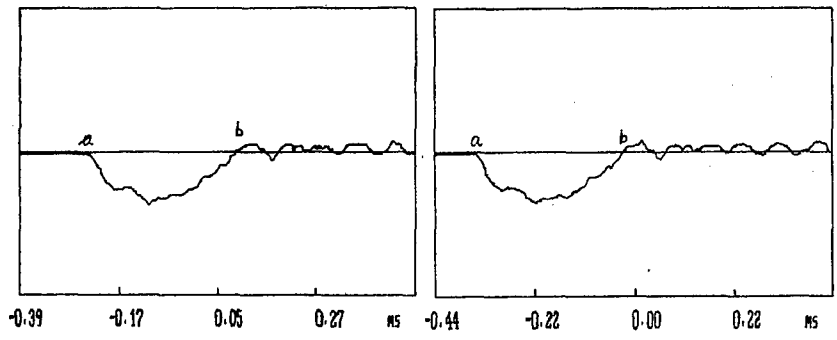

t_{ab} = 0.324ms t_{ab} = 0.326ms

Fig. 2 *a* vs *t* curves of blank test at drop height 20cm

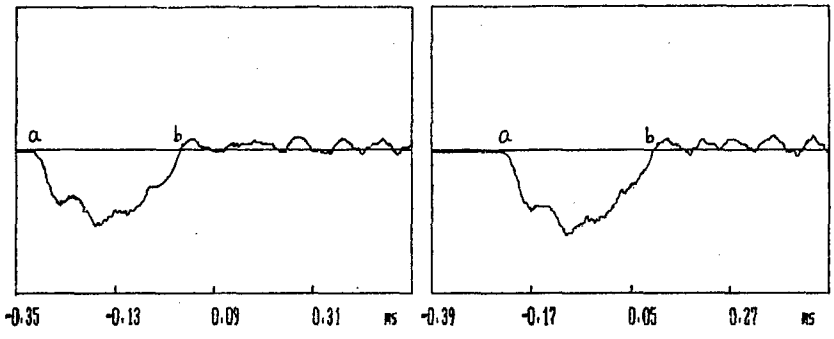

t_{ab} = 0.330ms t_{ab} = 0.330ms

Fig. 3 *a* vs *t* curves of blank test at drop height 50cm

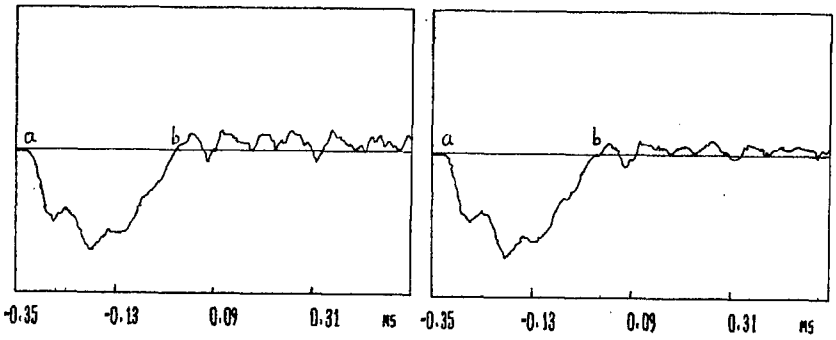

t_{ab} = 0.332ms t_{ab} = 0.330ms

Fig. 4 *a* vs *t* curves of blank test at drop height 70cm

The small deviation among the t_{ab} values in three groups of blank test shows an acceptable reproducibility of the device.

3.2 Non-explosive test

Graphite and wax were selected to examine their behaviors under impacting, because they are often used as additives to reduce the sensitivity of polymer bonded explosives (PBXs). The $a \sim t$ curves of graphite and wax with different quantity at drop height of 40cm are as below.

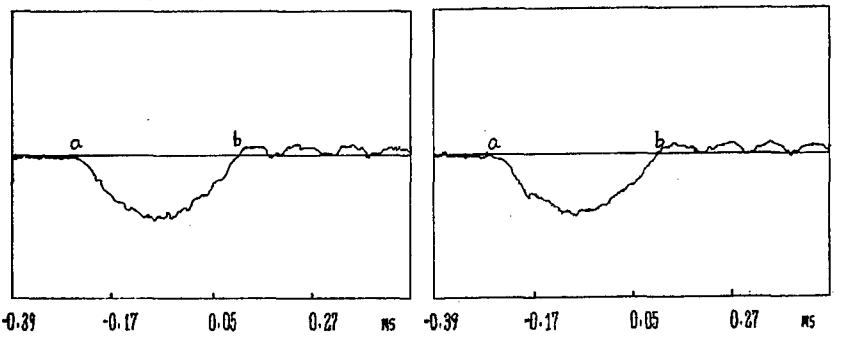

(a) t_{ab} = 0.364ms (b) t_{ab} = 0.368ms

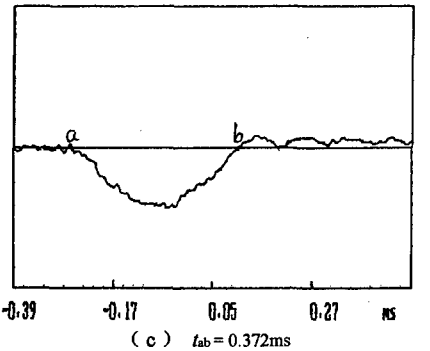

(c) t_{ab} = 0.372ms

Fig. 5 a vs t curves of graphite with (a) 10mg, (b) 30mg, (c) 50mg

It can be seen that the sample quantity of graphite shows little influence on the impact time.

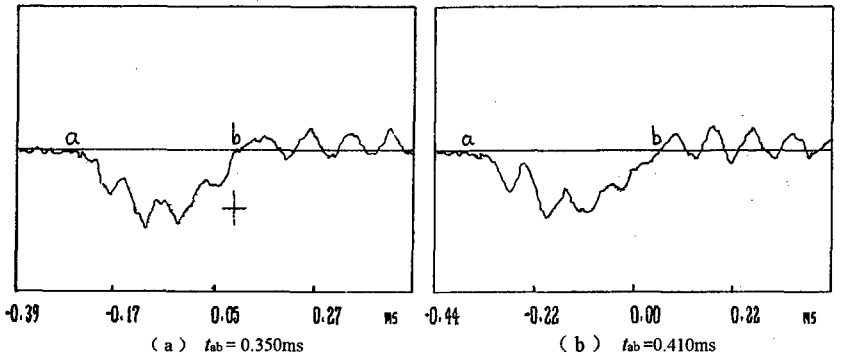

(a) t_{ab} = 0.350ms (b) t_{ab} =0.410ms

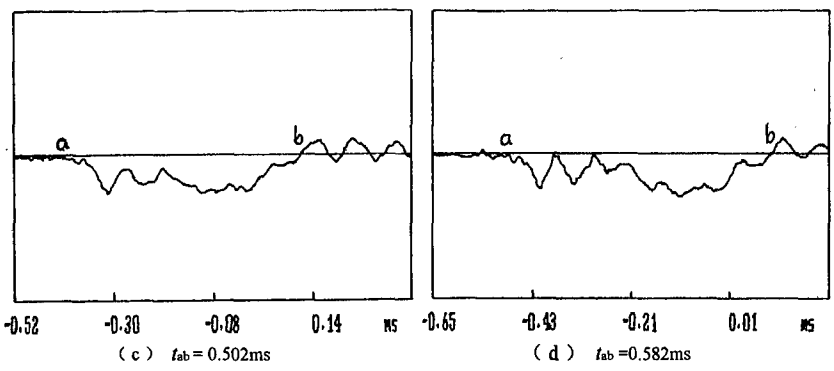

(c) t_{ab} = 0.502ms (d) t_{ab} =0.582ms

Fig. 6 *a* vs *t* curves of wax with (a)10mg , (b) 20mg , (c) 30mg , (d) 40mg

The results show that the quantity of wax apparently increases the range of impact time, which should be resulted from some melted sample squeezed out of the rollers after impact.

3.3 Explosive test

It is well known that different explosive shows different impact sensitivity in the drop-hammer test. In order to record the responses of both explosion and non-explosion of the sample tested on our device under a certain condition, the drop height of the hammer should not be the same.

When 50mg of PETN was tested under drop height of 10cm, explosion responded with both " yes " and " no " as shown in Fig. 7 and 8, respectively.

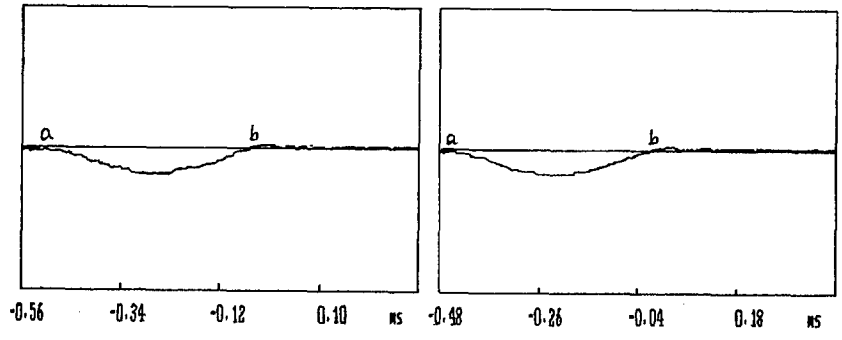

T_{ab} = 0.434ms t_{ab} = 0.438ms

Fig. 7 *a* vs *t* curves of PETN at drop height 10cm (no explosion)

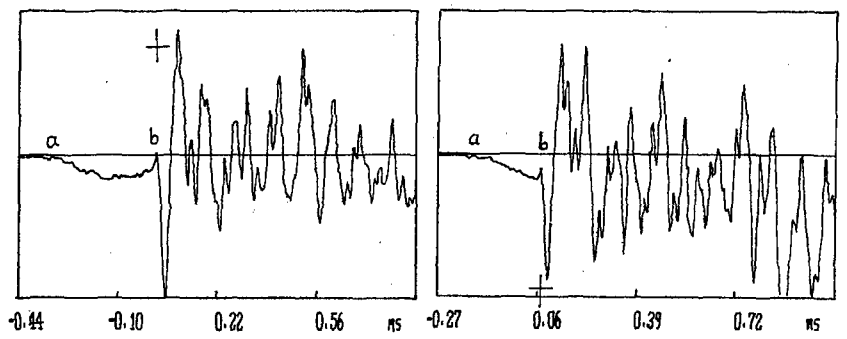

t_{ab} =0.384ms t_{ab} = 0.222ms

Fig. 8 *a* vs *t* curves of PETN at drop height 10cm （explosion）

It can be seen from the figures, in the case of "no", the t_{ab} of two tests are well agreed to each other, while the "yes" responses in Fig. 8 give much shorter impact time and show an apparent difference between the two tests. When 50mg PETN was impacted by a hammer from 40cm high, all samples gave much violent explosion within a very short time as shown in Fig. 9.

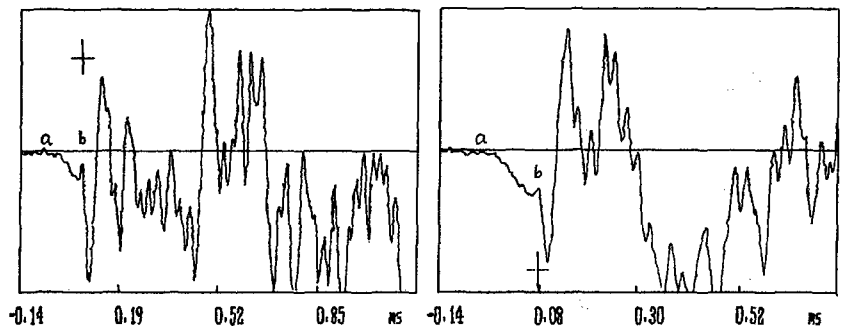

t_{ab} =0.075ms t_{ab} = 0.100ms

Fig. 9 *a* vs *t* curves of PETN at drop height 40cm

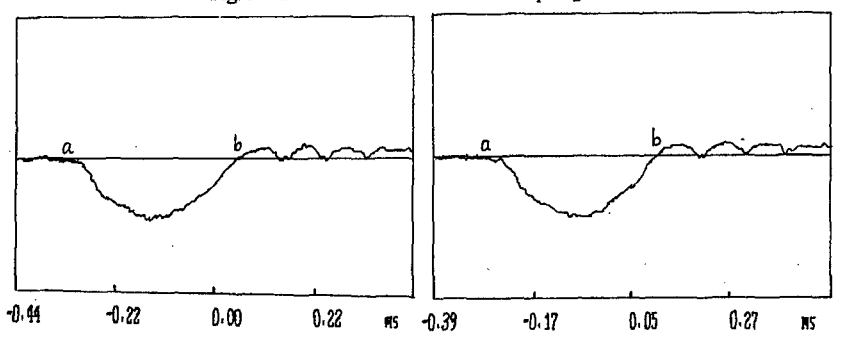

t_{ab} = 0.346ms t_{ab} =0.348ms

Fig. 10 *a* vs *t* curves of 50mg HMX at drop height 40cm （no explosion）

To compare their behaviors with that of PETN, the tests of HMX, RDX, Tetryl and TNT were carried out at the same conditions of 50mg sample and 40cm drop height. All the explosives except TNT responded with "yes" and "no" explosion as shown in Fig. 10 to 15, while the different shape of the curves scanned in the experiments should imply different reaction process in each group of samples.

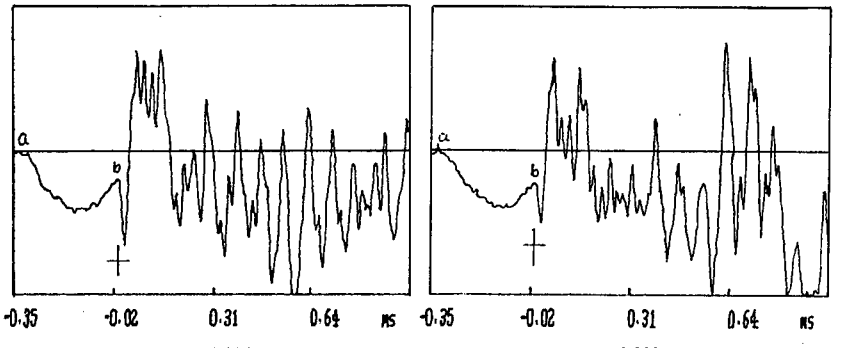

t_{ab} = 0.306ms t_{ab} =0.303ms

Fig. 11 *a* vs *t* curves of 50mg HMX at drop height 40cm (explosion)

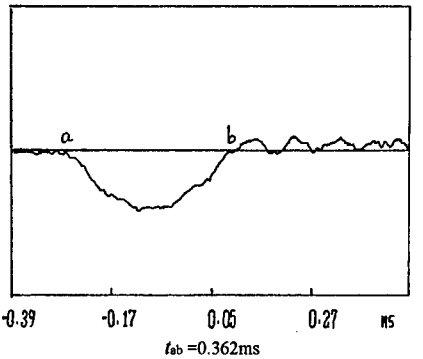

t_{ab} =0.362ms

Fig. 12 *a* vs *t* curves of 50mg RDX at drop height 40cm (no explosion)

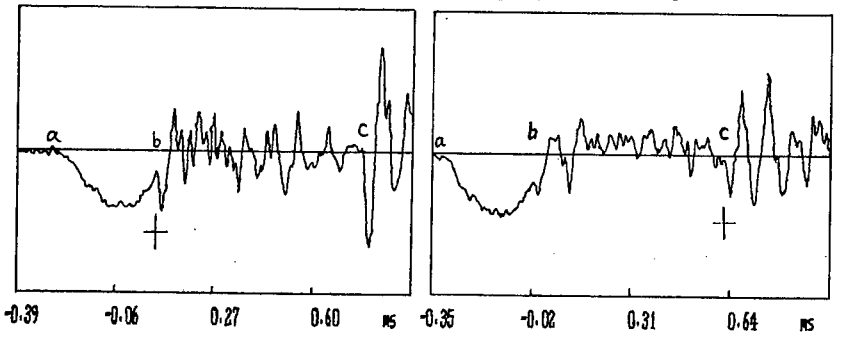

t_{ab} = 0.330ms; t_{ac} = 1.044ms t_{ab} = 0.330ms; t_{ac} = 0.933ms

Fig. 13 *a* vs *t* curves of 50mg RDX at drop height 40cm (explosion)

Because of the special behavior of RDX while being impacted , a further time interval is marked as " ac " in the figures.

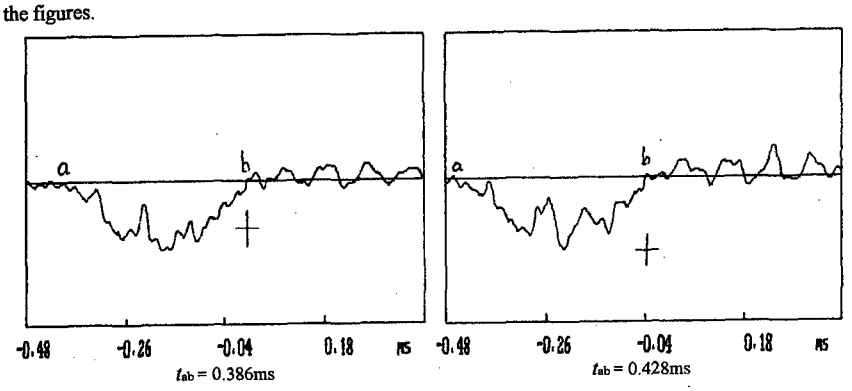

Fig. 14 *a* vs *t* curves of 50mg Tetryl at drop height 40cm （no explosion）

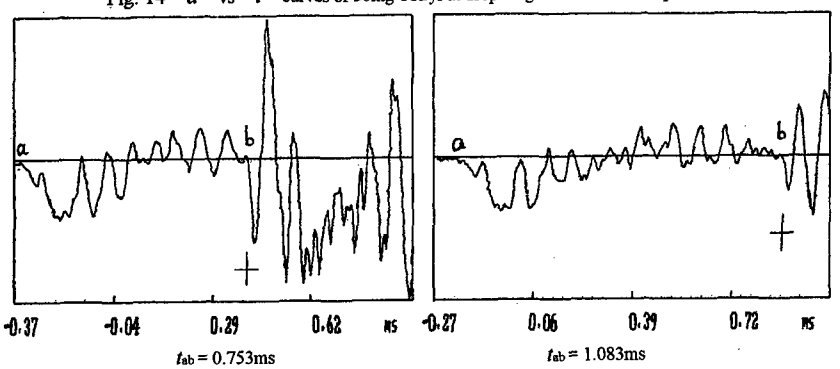

Fig. 15 *a* vs *t* curves of 50mg Tetryl at drop height 40cm （explosion）

TNT did not explode under the same conditions above, but its behavior were quite different in the time intervals of ab, bc and cd as shown in Fig. 16.

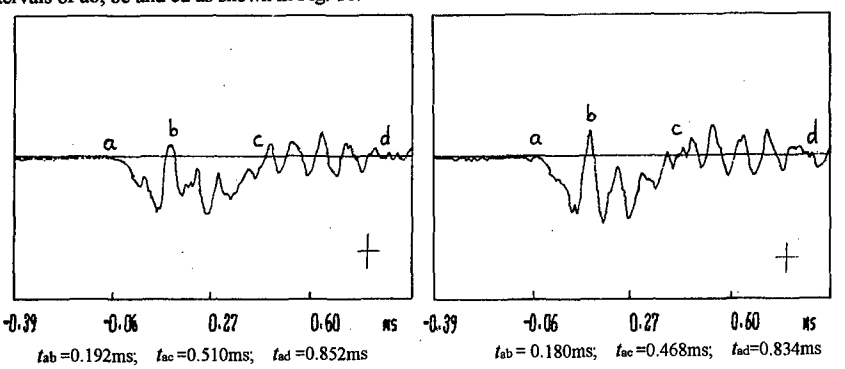

Fig. 16 *a* vs *t* curves of 50mg TNT at 40cm drop height

4. ANALYSIS AND DISCUSSION

4.1 Impact process

The impact is actually an instant process consisting of two stages, i.e. the hammer striking the roller and consequently rebounding away. In the first stage at the moment of the hammer contacting the roller, the acceleration of the hammer coming from its potential will continually increase due to the elastic strain of the roller. Until the elastic strain reaches its limit, the hammer can not move down any more and its acceleration will get up to the maximum. At this moment the compression stress of the roller will make the hammer rebounding away, decreasing its acceleration down to zero at the moment of their disengagement. We define, therefore, the impact time, t_{sb}, as the duration of the hammer acceleration from zero to maximum and then to zero. If there is sample in-between the two rollers of the test device, its response to the impact should affect the shape of $a \sim t$ curve scanned by the DAS, implying the reaction characteristics in some extent.

4.2 Reproducibility of test results

The blank tests as shown in Fig. 2, 3 and 4 indicate that the device can fairly reproduce the impact time. Fig. 5 show that the results of the test with graphite under different conditions are also well-reproducible, even in the case of no explosion of PETN, HMX and RDX after impact, the reproducibility of the test under corresponding conditions is acceptable as the shape of $a \sim t$ curves shown in Fig. 7, Fig. 10 and 12. The $a \sim t$ curves in Fig. 11 and 13 indicate that if HMX or RDX exploded in the test, the deviation of their impact time is quite agreed with each other, respectively.

The sample of PETN or Tetryl exploded after impact could give similar results but not fairly reproducible as shown in Fig 8, 9 and 15. These phenomena can be explained by " hot-spot " mechanism of explosive ignition as the heat energy coming from the mechanical shock could not evenly distribute over all the sample grains but on some local points and as a result to form " hot-spots ", while the position and time of hot-spot formation are random rather than the same.

4.3 Impact time and low melting point

Unlike the results said-above, the test reproducibility of the samples with low melting point such as wax （Fig.6）, Tetryl （Fig.14） and TNT （Fig.16） are not satisfied. The complex picture of their $a \sim t$ curves must be resulted from the squeeze and scatter of the melted sample. These processes will fluctuate the pressure in-between the rollers and, therefore, the acceleration of the hammer. This fluctuation will last until the hammer rebounding away, lengthening the impact time.

4.4 Hammer drop height

Fig. 8 and 9 indicate that the drop height increases the explosion probability as usual, but shortens the impact time.

4.5 Reaction propagation

Compared Fig. 11, 13 and 15, there seemed to be different ignition mechanisms for different explosives. It can be supposed that friction among the explosive grains is the main source of the heat energy for the hot spot forming, but the behavior of the said explosives are quite different at the end of impact time. The reaction of HMX immediately grows up to deflagration even explosion, while RDX gives a period of reaction propagation from point " b " to " c " before the violent explosion comes and whether the intervals of " ab " and the sum of " ac " are close to each other in the parallel experiments. The fluctuation in the range of " ab " in Fig. 15 implies that the ignition of Tetryl should be mainly due to its viscous heating caused by rapidly squeeze of the sample in-between the impact rollers or capillary flow among the non-melted grains.

5. CONCLUSION

From the results of the preliminary experiments it can be concluded

- The test by using Data Acquisition System (DAS) combined with the drop hammer device is promising to be used as a new method for evaluating the impact sensitivity of granular explosives, especially, the high melting point samples because of the fine reproducibility of the impact time recorded.

- The reaction process of low melting point material can also be explained based on their $a \sim t$ curves and the longer impact time seems to agree with the desensitizing effect of the well-known substances like this kind.

- As discussed in 4.2 ~ 4.5, the length of impact time and the smooth or fluctuating shape of $a \sim t$ curves scanned by DAS attached with the drop hammer device can be used to describe the impact sensitivity of explosives and their response mechanism to impact in some extent. The further experiments and examination are going on.

ACKNOWLEDGEMENT

The authors cordially thank Profs. Han Duxin and Li Changqing, Ms. Huang Yue and Zhang Yanli for their valuable help in the work.

REFERENCE

[1] Alf Prytz A More Efficient Method of Evaluating Results from Impact Sensitivity Test. Proceedings of the 17th international pyrotechnics seminar combined with the 2nd Beijing international symposium on pyrotechnics and explosives, 1991.

[2] MIL-STD-1751(USAF), 1982.

[3] Liu Baoguang A Method of Ascending and Descending, Fireworks, No.3, 1982.

[4] F.P.Bowden and A.D.Yoffe, Initiation and Growth of Explosions in Liquids and Solids, Cambridge University Press, 1952.

[5] Robert A. Rhein, Russell Reed, and Ngo Q.Vu, Propellants, Explosives, Pyrotechnics 18, 184-187, 1993

[6] Dong Haisan, Zhou Fenfen, Properties of High Explosives and Its Relative, Science Publishing House, 1989.

COMPUTER MODEL TO PREDICT THE ENVIRONMENTAL HAZARD AFTER EXPLOSIONS

Nickolai N.Belyaev, Natalia E. Kalinina ,Victor K..Khrutch
State University of Transport Engineering,
Acad. Lazaryan Str. 2, Dnipropetrovsk, Ukraine

ABSTRACT

Dispersion of pollutants in the case of the complex terrain or in the very near-field vicinity of buildings is difficult to predict due to the complex flow patterns. The authors have proposed the new 2-D computer model for predicting the wind flow field and pollution dispersion near urban and industrial sites. The model permits to take into account the arbitrary geometrical form of buildings, orography , different types of pollutant ejections and different disposition of sources of pollution. The results of the numerical simulation of the pollutant dispersion after explosions are shown.

INTRODUCTION

In Ukraine and other countries of the former USSR the ground-level concentrations are estimated by the Berlyand's method which is called now "Method OND-86". This method gives very rough results because it does not take into account the effect of complex terrain , buildings, their geometrical form, different regimes of sources of ejections on the pollutant dispersion. That is why this method is subjected to sharp criticism. It is well known that an application of Navier-Stokes equations , K-ε model and others "high level" models to describe the flow field among buildings , in the case of complex terrain and to create the robust computer model for solving real problems of air pollution which the designers face is now out of the question. That is why the development of the appropriate computer models capable of predicting pollution under varying factors is of great interest. In this work to describe the 2-D wind flow between buildings or in the case of complex terrain the model of the inviscid separated vortex flows is used. The computational procedure is based on the implicit difference schemes.

MATHEMATICAL MODEL

Wind flow between the buildings or in the case of complex terrain (See Fig.1) is described by the equation of vorticity transfer and Poisson equation

$$\frac{\partial \omega}{\partial t}+\frac{\partial u\omega}{\partial x}+\frac{\partial v\omega}{\partial y}=0$$

$$\frac{\partial^2 \psi}{\partial x^2}+\frac{\partial^2 \psi}{\partial y^2}=-\omega \qquad (1)$$

$$\omega=\frac{\partial v}{\partial x}-\frac{\partial u}{\partial y}$$

The solution of these equations is used to determine the components of the wind flow vector. The assumption is made that the separation of flow takes part in the corner points of buildings or terrain and this causes the formation of vortices the intensity of which is determined.

The computational procedure is carried out using the rectangular computational mesh. The vorticity is determined in the centres of the cells, the flow function is determined in the knots of the mesh and the velocity components **u**, **v** are determined on the sides of the cell. The geometrical form of the buildings , terrain is formed by "markers" in the discrete model. These "markers" help to differ the cells which correspond to buildings , terrain from the computational cells where the equations of the model are solved. The implicit "time-splitting" difference scheme to calculate the vorticity is as following:

$$\left(E+\frac{\Delta t}{2}\left(L_x^+ + L_y^+\right)\right)\omega^{n+\frac{1}{2}} = \left(E-\frac{\Delta t}{2}\left(L_x^- + L_y^-\right)\right)\omega^n$$
$$\left(E+\frac{\Delta t}{2}\left(L_x^- + L_y^-\right)\right)\omega^{n+1} = \left(E-\frac{\Delta t}{2}\left(L_x^+ + L_y^+\right)\right)\omega^{n+\frac{1}{2}} \qquad (2)$$

where, E: the identical operator,

$$L_x^+\,\omega \approx \frac{\partial u^+\omega}{\partial x} \approx \frac{u^+_{i+1,j}\,\omega_{i,j} - u^+_{i,j}\omega_{i-1,j}}{\Delta x}; \quad u^+ = \frac{u+|u|}{2};$$
$$L_x^-\,\omega \approx \frac{\partial u^-\omega}{\partial x} \approx \frac{u^-_{i+1,j}\,\omega_{i+1,j} - u^-_{i,j}\omega_{i,j}}{\Delta x}; \quad u^- = \frac{u-|u|}{2};$$

This scheme is used to determine the vorticity field on the new time step. To determine the intensity of free vortex in the corner points of buildings , terrain the following procedure is used. In the area ABCD near the corner point (See Fig. 2) the summary intensity of vortices is equal to

$$v_1(y_c - y_b) - u_2(x_c - x_d) = G_0 + \frac{1}{4}(\omega_b \Delta S_b + \omega_c \Delta S_c + \omega_d \Delta S_d),$$

where, G_0: intensity of the vortex in the corner point; ω_b, ω_c, ω_d: the intensity of the vorticity in the computational cells; ΔS_b, ΔS_c, ΔS_d: the square of the computational cells.

From this expression we can obtain the intensity of the vortex in the corner point

$$G_0 = v_c(y_c - y_b) - u_2(x_c - x_d) - \frac{1}{4}(\omega_b \Delta S_b + \omega_c \Delta S_c + \omega_d \Delta S_d)$$

We assume that at the separation of flow in the corner point the vortex formed is free. The direction of its movement can be obtained if we use the approximate value of the velocity in the corner point

$$u_0 = \frac{(u_2 + u_4)}{2} = \frac{u_2}{2}; \quad v_0 = \frac{(v_1 + v_3)}{2} = \frac{v_1}{2}$$

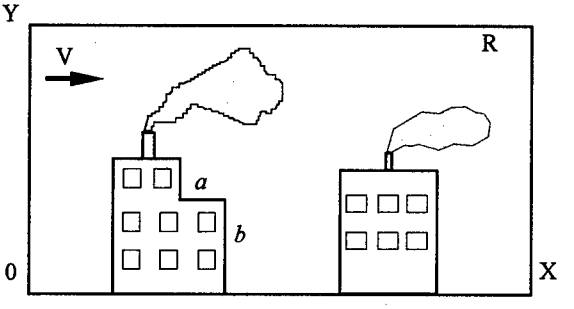

Figure 1. View of the computational region.

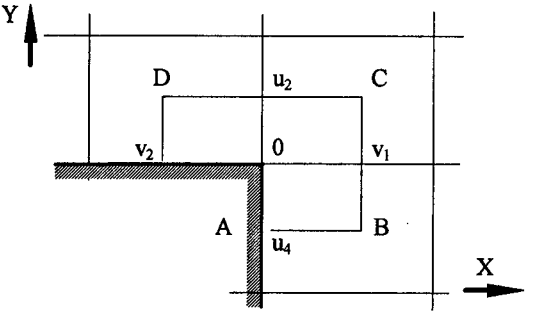

Figure 2. Calculation of the vorticity in the corner point.

The vortex displacement results in changing of the vorticity value in the cells which are situated nearby the corner point. This new value of the vorticity can be expressed as

$$\begin{aligned}
\overline{\omega}_b &= \omega_b + \frac{G_0}{\Delta x \, \Delta y}, \quad \text{if} \quad u_0 < 0, \quad v_0 > 0 \\
\overline{\omega}_c &= \omega_c + \frac{G_0}{\Delta x \, \Delta y}, \quad \text{if} \quad u_0 > 0, \quad v_0 > 0 \\
\overline{\omega}_d &= \omega_d + \frac{G_0}{\Delta x \, \Delta y}, \quad \text{if} \quad u_0 > 0, \quad v_0 < 0
\end{aligned} \tag{3}$$

To determine the velocity field the Poisson equation having the form

$$\frac{\partial \psi}{\partial \tau} = \frac{\partial^2 \psi}{\partial x^2} + \frac{\partial^2 \psi}{\partial y^2} + \omega$$

is calculated by following implicit scheme

$$\overline{\omega}_{i,j} = \frac{1}{4}(\omega_{i,j} + \omega_{i-1,j} + \omega_{i,j-1} + \omega_{i-1,j-1}),$$

$$\psi^{l+1/4} = \psi^{l} + \overline{\omega}\frac{\Delta t}{2},$$

$$\left(E - \frac{\Delta t}{2}\left(L^{+}_{xx} + L^{+}_{yy}\right)\right)\psi^{l+1/2} = \left(E + \frac{\Delta t}{2}\left(L^{-}_{xx} + L^{-}_{yy}\right)\right)\psi^{l+1/4},$$

$$\left(E - \frac{\Delta t}{2}\left(L^{-}_{xx} + L^{-}_{yy}\right)\right)\psi^{l+3/4} = \left(E + \frac{\Delta t}{2}\left(L^{+}_{xx} + L^{+}_{yy}\right)\right)\psi^{l+2/4},$$

$$\psi^{l+1} = \psi^{l+3/4} + \overline{\omega}\frac{\Delta t}{2},$$

where

$$L^{-}_{xx}\,\psi + L^{+}_{xx}\,\psi \approx \frac{\partial^2 \psi}{\partial x^2} \approx \frac{\psi_{i+1,j} - \psi_{i,j}}{\Delta x^2} - \frac{\psi_{i,j} - \psi_{i-1,j}}{\Delta x^2}.$$

The complete algorithm to solve equations (1) is as following. At the initial time step t^n the values of **u**, **v**, ω are known. At first the vorticity ω is determined by using scheme (2). At the next step the intensity of the vortices in the corner points and their displacement is determined. Then the new value of vorticity in the cells which are near by the corner point is determined using expressions (3). Then the Poisson equation is calculated and the new value of **u**, **v**, ω on the new time step $\mathbf{t^{(n+1)}}$ is obtained. The obtained velocity field is used at the next computational step to calculate the pollutant dispersion . The governing equation which is used at this step is the equation of the gradient transport model:

$$\frac{\partial \varphi}{\partial t} + \frac{\partial u\,\varphi}{\partial x} + \frac{\partial (v - w_s)\varphi}{\partial y} + \sigma\,\varphi = \mathrm{div}(\mu \nabla \varphi),$$

where φ: is concentration; σ: represents the chemical reactions; w_s: velocity of pollutant fall; μ: is the coefficient of the turbulent diffusion.

To solve this equation the implicit scheme like scheme (2) is used. To create the form of the cloud formed in the place of the accident after the explosion the "markers" are used.

CALCULATION RESULTS

The results of the pollutant dispersion after explosions in the case of the different typical situations , which occur in practice are shown below . In all examples the geometrical form of the pollutant cloud , the concentration of the pollutant in it were given at the place of the explosion.

Example 1. The explosion on the industrial site.

This type of explosion occurs while transporting , loading of explosives on the industrial site or in the case of accidents in the storage of explosives .This example illustrates the possibility to apply the model developed to predict the environment pollution with the account of buildings and reliefs .The explosions took place between the buildings and after the second building (Fig.3,4) .The initial form of all the clouds formed after explosion was like the "column". One can see that both buildings and the slope form the stagnant zones where the pollutant is accumulated.

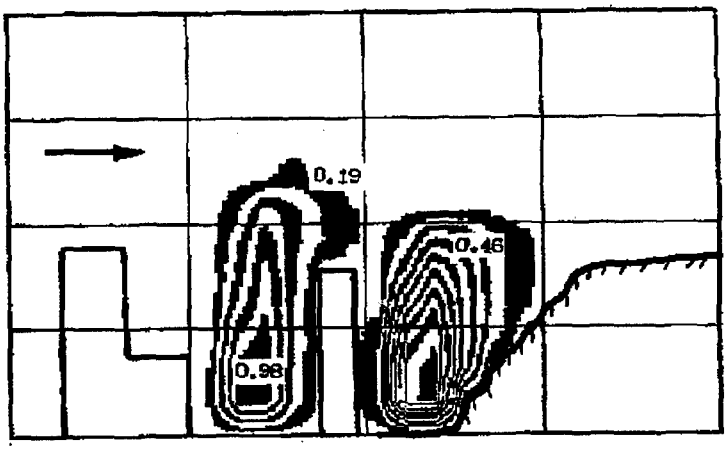

Fig.3. The isolines of pollutant concentration at t=0.5

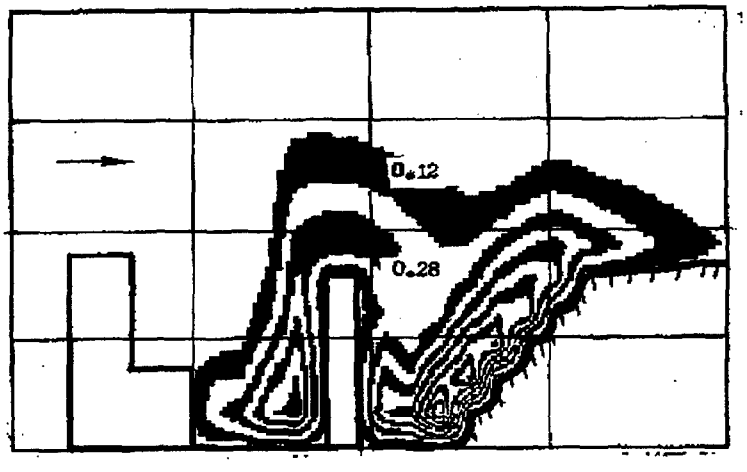

Fig.4. The isolines of pollutant concentration at t=0.8 .

Example 2. The explosion at the storage situated in the hollow.

Very often the storage's of the explosives are situated in the "negative" places of reliefs (in the hollows) The dynamic of the air pollution when the explosion occurred at the storage are shown in Fig.5.

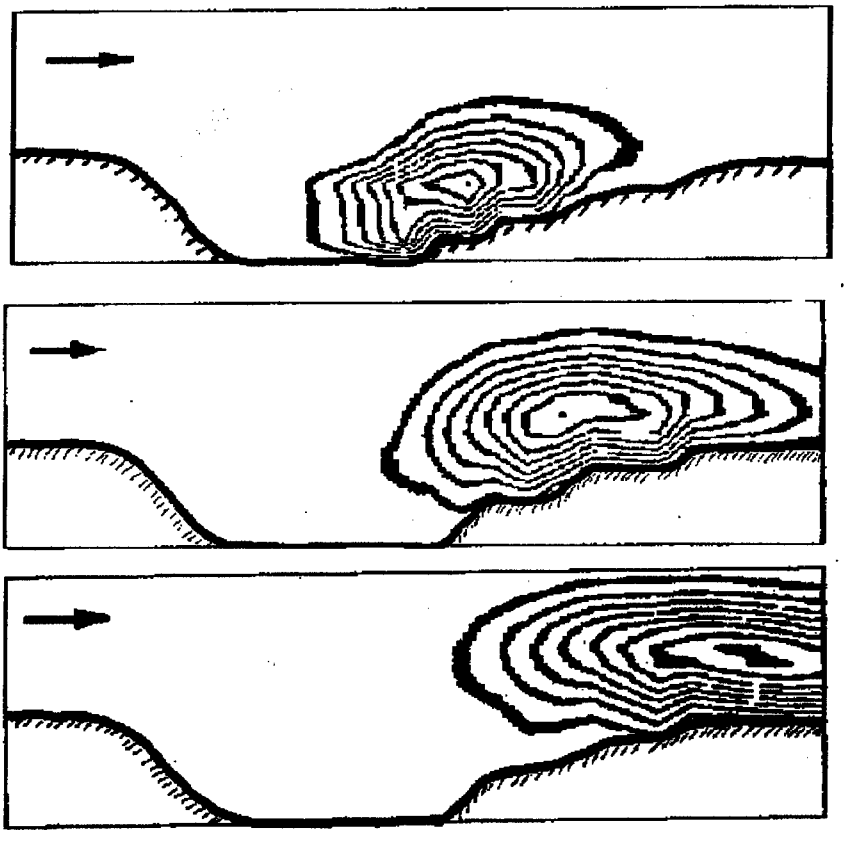

Fig.5. Isolines of the pollutant concentration for three time moments

Example 3. The explosion in the buildings.

The situation when the explosion took place in the buildings and this caused the ejection of pollutant outside of them is considered. The place of the pollutant ejection on the buildings is shown with the help of designation "*" (Fig. 6) . In this example two clouds of pollutant appeared on the first building and one on the second. The clouds are seen to become larger during the time and a part of pollutant is accumulated in the stagnant zone between the buildings .The polluted air tends to go to the ground after the second building.

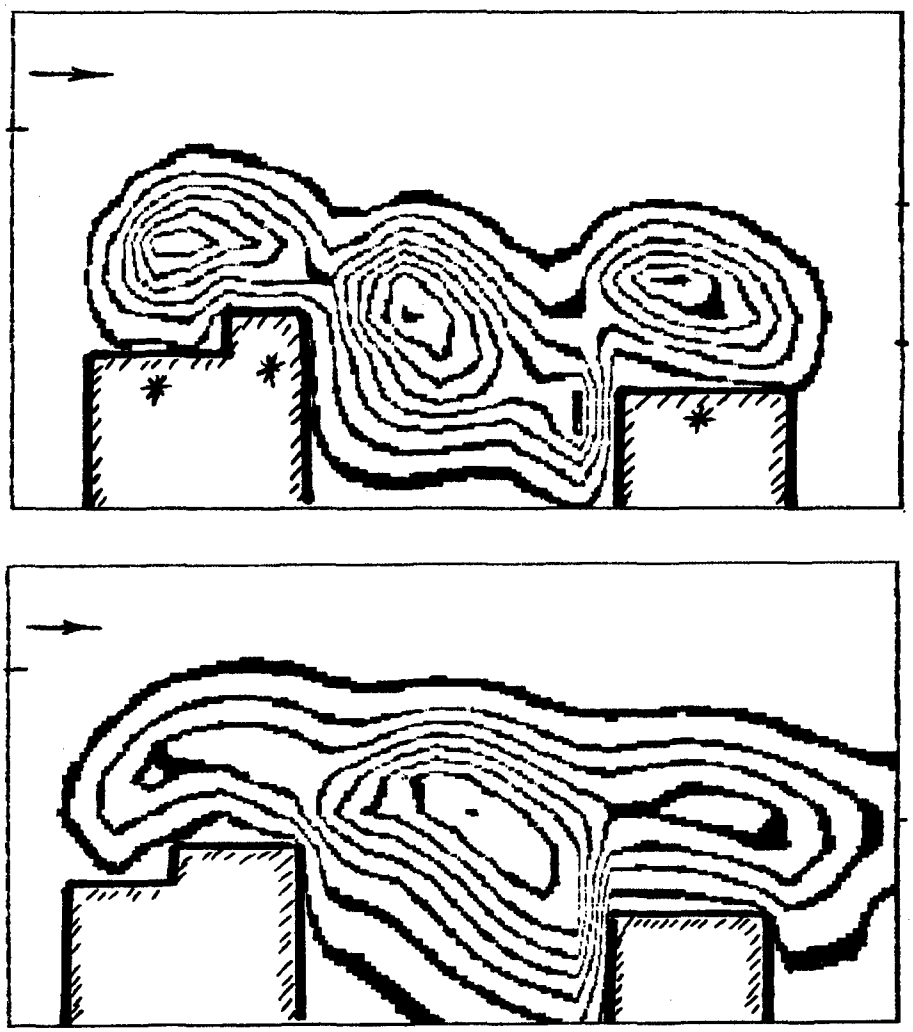

Fig.6. Isolines of the pollutant concentration for two time moments

CONCLUSION

The computer model developed was used at the State Research Institute of the Chemical Industry (Shostka, Ukraine) and Chemical plant "Desna" (Shostka, Ukraine) for solving the forecast problems of the air pollution in the case of different accidents with explosives.

EXPLOSIVE HAZARD OF GASOL MIXED WITH FLUORINE AGENT

Xuezhong Xu Degui Wang Baotian Hao
mingjing Pei Ruifu Yang Xuefeng Zheng
Northwest Institute of Nuclear Technology XIAN 710024 China

ABSTRACT

The explosive characteristics of a gasol mixed with fluorine agent were investigated in a vertical detonation tube. Filling the tube with a premixed gasol-air-oxygen, a fluorine agent was sprayed by a jet installed at the bottom of the tube and generated rapidly a lot of free –radical. This free- radical induced the rapid reaction of the gasol-air mixture, then transition to detonation was realized. Detonation wave parameters piezoelectric and infrared transducers were recorded. At a point, 2.2m away from the jet, the maximum overpressure was about 2.8Mpa and the temperature was more than 2500℃ in these laboratory tests. In unconfined field tests, the experimental apparatus was plastic bag in 1m diameter. To obtain a very rapid dispersing rate an effective push force can be got by a blast-generating piston apparatus. It took less than 1 millisecond to mix gasol-oxygen with the fluorine agent, detonation can be achieved immediately. 12cm away from the edge of the bag, the overpressure of shock was 1.2Mpa. When the agent was sprayed into gasol-air mixture in the same size bag, only deflagration phenomena was observed by high-speed photography. Influence factor might include:(1) the size of the bag.(2) the initial concentration and volume of gasol.

1. INTRODUCTION

The accidental release of combustible gases or evaporating liquid can lead to devastating explosions. Gaseous detonation research up until the early 1970s focused on theoretical and laboratory studies of detonation phenomena in fuel-oxygen mixtures. Very few experimental data were available on detonations in fuel-air mixtures. The energy and the cloud volume required to establish a self-sustained detonation in most fuel-air mixtures are too large for laboratory testing. Fuel-air detonations were studied in laboratory tubes and channels. Since 1980s large-scale field tests have been performed to determine the detonablity and the behaviors of detonations in fuel-air mixtures. In such research detonation can be achieved by two models, These include:(i) Direct ignition. The initiating explosion is provided by an external high-energy source. (e.g., a high explosive charge) The strong shock waves produced by such explosions directly initiate a self-sustained detonation without going through a deflagration phase. (ii) weak ignition. The flame is accelerated to high speeds and to cause transition to detonation within such clouds. In these case the ignition is delayed so that a potentially explosive fuel-air cloud has been formed.

According to a different concept, Browser KR· and co-workers[1] studied the chemical initiation in unconfined fuel-air mixtures. In this case, the detonation can be obtained by mass flow, which was generated by very rapid fuel and fluorine agent dispersion, and an ignition delay for mixing fuel with air didn't require, that is, it seems possible to obtain detonation in fuel-air mixtures by flow generated by very rapid dispersion and energy release. This paper presents results of an investigation on the explosive phenomena of gasol mixed with fluorine agent (e.g., BrF3).

2. TEST CONCEPT

A rapid chemical energy release proceeds after hydrocarbon fuel mixed with fluorine agents, for example,

$$BrF_3 + 2[CH_2] = 2C + 2HF + HBr$$

The reaction releases heat energy and accelerates the following combustion process.

$$2[CH_2] + 3O_2 \rightarrow 2CO_2 + 2H_2O + Q_v$$

G·Ven Elbe and E·T·McHale[2] studied the chemical kinetics of the proceeds. The chemical energy release proceeds via collisions of free radicals, that is, molecules carrying a free chemical bond, with neutral molecules of fuel, oxygen and intermediate reaction products. The probability of occurrence of chemical reaction in such collisions at ordinary temperatures exceeds the probability in collisions between neutral molecules by at least twenty orders of magnitude, due to the comparatively low activation energies E of the free-radical reactions and the correspondingly large Arrhenius factors exp. (-E/RT). In the reaction the free chemical bond is transferred to one of the product molecules and may thus continue the reaction chain. The chain is broken if the product free radical is substantially non-reactive, as for example the radical HO_2, or if two free radicals combine to form a neutral molecule. The latter process becomes significant only at the high free-radical concentration in the final stage of the combustion process. The chain branches of the reaction is sufficiently energetic to break a chemical bond and to separate the molecular fragments, this generating two new free radicals.

Taking butane, C_4H_{10}, for example, this is explained by chain branching in collisions of BrF3 with radical C_4H_9, i.e. ,

$$C_4H_9\cdot + BrF_3 = C_4H_7\cdot + 2HF + BrF + Q$$
$$F\cdot + C_4H_9H \rightarrow HF + C_4H_9\cdot$$
$$C_4H_9\cdot + O_2 \rightarrow C_4H_9OO\cdot$$
$$C_4H_9OO\cdot + BrF_3 \rightarrow C_4H_9 + neutralmolecules$$

It is certain that at the high O_2 - concentration in flammable gaseous hydrocarbon–air mixture C_4H_9OO predominates over C_4H_9.and the chemical consideration suggest that reaction of C_4H_9OO with BrF_3 produces a molecule HF and breaks the peroxidic band O-O, with BrF_3 the molecular fragments apparently combine with two of the available atoms, i.e., Br and F, to form neutral molecules.

3. EXPERIMENTAL APPARTUS

3.1 Detonation Tube

A vertical detonation tube is shown in Figure 1. The apparatus consisted of a 4. 5 meter long tube with internal diameter of 120mm. In the experiments whole tube was filled with gasol-air or gasol-air-oxygen mixtures, the fluorine agent was sprayed by a nozzle installed at the bottom of the tube.

The diagnostic system consisted of piezoelectric pressure transducer (1#, 2#,3#,4#,5#,6#) and Infrared temperature transducers (1′,2′) . The locations of the transducers are shown is Figure 2. The signals from the pressure and temperature transducers were recorded on TEK644.

3.2 Field Test Apparatus

The test apparatus shown in Fig.3, was plastic bag in 1meter diameter. The bag was filled with gasol-oxygen or gasol-air mixtures. To obtain a very rapid dispersing rate, a blast-generating piston apparatus, was used. When the powder was ignited, a very powerful push force drove a metal piston so that the fluorine agent was spurted to the gasol-air or gasol-oxygen mixtures.

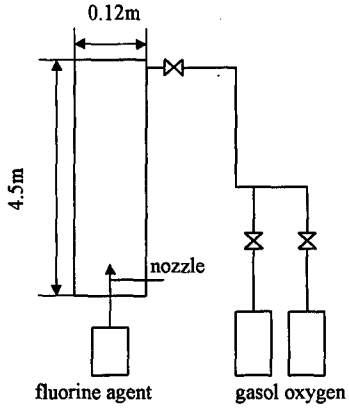

Figure1: A schematic of the detonation tube

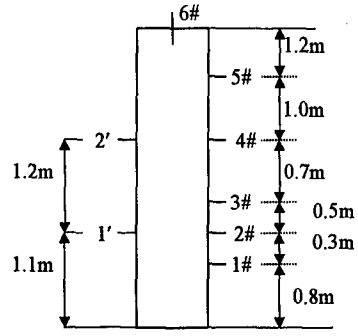

Figure2: Location of pressure and temperature transducers

The overpressure of shock wave was measured by six PCB piezoelectric pressure transducers, which were placed in an array as shown in Figure 4.

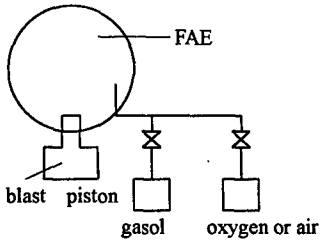

Figure 3: Schematic of the bag test

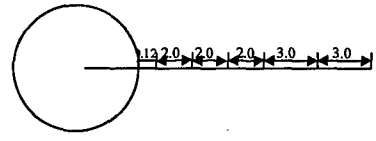

Figure 4: transducers array of bag test

4. EXPERIMENTAL RESULTS

4.1.Reaction products

Using Magna 750 and HP 5890II/5971A, Qian-Yong Xu[3] analyzed the composition of the gasol sample. The content of the gasol sample were listed in Table 1. The infrared spectrum for gasol sample is shown in Figure 5.

Table 1: Content of gasol sample

	Ethane	Propylene	Butane	Butene	Isopentane
Content	14%	62%	12%	10%	2%

Notice that there are absorption peaks of methyl (3000~2800, 1500~1350cm^{-1}) and alkene bond.

The gasol reacted with fluorine agent BrF3 in a cylindrical vessel. In which the initial pressure was 130Pa.That is, in the vessel oxygen was absence. In the tests, the gasous reaction

products were froge out by liquid nitrgen and the infrared spectrum are shown in Figure 6. Spectrum of the products at ordinary temperatures is shown in Figure 7. The absorption peaks of the methyl (see Fig6) are visible and the peaks of dangling bond don't exist. At ordinary temperatures the products consists of propane, butane, isopentane and dibromine-propane (see Fig 7).

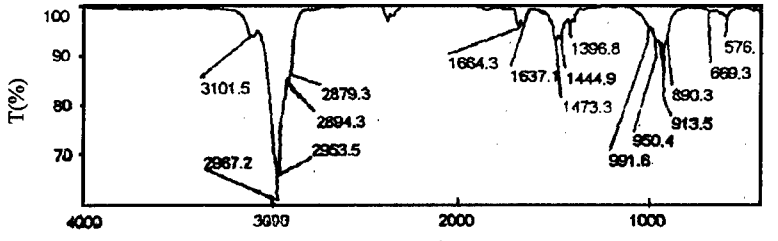

Figure 5: Infrared spectrum of gasol sample

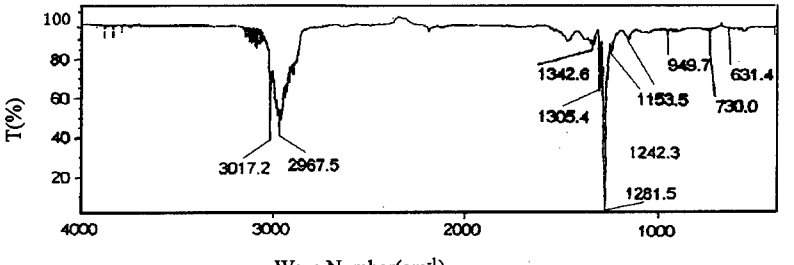

Figure 6: Spectrum of products(froge by liquid nitrgen)

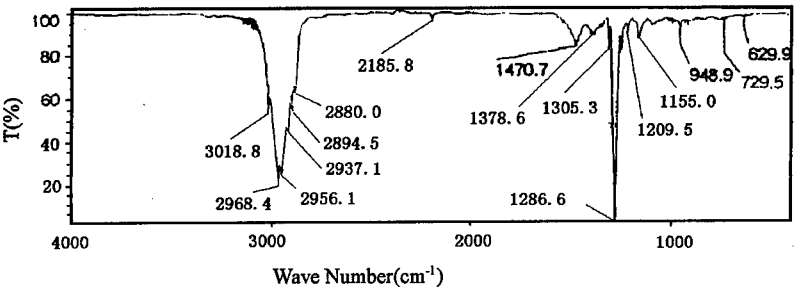

Figure 7: Spectrum of products(atmospheric temperature 298k)

4.2 Explosion behaviour in the tube

Table 2 contains the summary of tests, The results show the deflagration and detonation behaviour achieved in the detonation tube for the chemical initiation of gasol-air and gasol-air-oxygen mixtures.

In the vertical detonation tube BrF3 mixed with gasol-air mixtures generated a lot of free radical. These free radical induced rapid reaction of gasol, the deflagration regime was detected. If

the gasol was added (gasol and oxygen at stoichiometric composition). Transition to detonation was realized. Detonation wave overpressure and temperature(see Table 2) measured by piezoelectric and infrared transducers.

Table 2: Results of tests to mix gasol with BrF3

Trial	%content by volume			Flourine Agent(ml)	Overpressure (Mpa)	Temperature k	Result
	Gasol	air	Oxygen				
1	3.8	96.2	0	10			Deflagration
2	7	93		10			Deflagration
3	12	88		10			Deflagration
4	5	86	9	10	2.2	2570	Detonation
5	6	78	16	10	2.8	2773	Detonation

4.3. Detonation parameters of filed tests

As shown in Table 3 the detonation parameters are valid for the gasol-oxygen mixture at stoichiometric composition. But the detonation was unavailable for the gasol-air mixture. The overpressure was measured by PCB piezoelectric transducers placed in 12cm away from the edge of the bag, and the deflagaration or detonation phenomena was observed by high-speed photography.

Table 3: Results of bag tests

Trial	%content by volume			Flourine Agent(ml)	Overpressure (Mpa)	Result
	Gasol	Oxygen	Air			
1	16	84		25	0.82	Detonation
2	17	83		25	1.2	Detonation
3	18	82		25	0.62	Detonation
4	3.8		96.2	25		Deflagration

5. CONCLUSIONS AND RECOMMENDATIONS

A series of experimental study for explosive hazard of gasol mixed with flourine agent has been performed. In laboratory tests, that is, in confined experiment, detonation was easily achieved. In the filed tests, that is, in the unconfined tests, the agent mixed with gasol-air, deflogaration was merely obtained unless the volume of the mixtures was big enough for DDT. in the gasol-oxygen mixtures detonation was realized. Detonation wasn't achieved in the gasol-air mixture. The influence factor of transition to detonation might include: (1) the size of the bag. (2) the initial concentration and volume of gasol.

Further work should be done to measure the middle products of gasol reacted with fluorine agent to determine the limit concentration and voloum of the gasol by using fluorine agent as a chemical initiation charge.

6. ACKNOWLEDGEMENT

We wish to thank Ms Haiying Wei, Ms Yang-Fong, Mr Yihe Zhang and Mr Li Ming who undertook the actual experimental measurement.

7. REFERENCES

1. Brower K R. Explosive Reactions of liquid mixtures of chloring Trifluride with Hydrocarbons and Halocarhons , Journal of Flourine Chemistry, 1986, 31:333~349.
2. Von Elbe G, McHale E T. Chemcal Initiation of FAE clouds. AD-A082610 1979.11.
3. Qianyong Xu et al. Analysis of Reaction Product of Gasol With Bromine Trifluride. Journal of Test and Study. 1993.5: 58~64.

DETPAR - THE CATALOGUE OF DETONATION PARAMETERS OF EXPLOSIVES

Jiří Majzlík, Václav Dusík

SYNTHESIA a.s.
Research Institute of Industrial Chemistry (VÚPCH)
532 17 Pardubice - Semtín
CZECH REPUBLIC

ABSTRACT

A short description of the structure of detonation parameters data base and some further characteristic data of the concerned condensed explosives are presented in the paper.

The data registered in the form of charts have mostly been drawn from the professional publications. The smaller part of the data set has been obtained from a series of experiments realized at the VÚPCH workplace. The DETPAR Catalogue can be employed in both printed form and live (operable) form. Among others, the following data are stored: reference, the name of the substance in question, its composition, density and Chapman - Jouguet (C-J) parameters. If available in the original source, the dimensions of the specimen, the figure describing the method or the arrangement of specimen for measurement of C-J parameters, and the results of PDT and Gap Test evaluation are presented as well.

The DETPAR data base offers a possibility of filtering the collected data. Consequently, it is possible to separate reliable C-J parameters from the data loaded by some methodical error.

The enclosed examples of figures, charts, and references represent the contents and graphical arrangement of the DETPAR Catalogue.

1. INTRODUCTION

For any design process concerning explosives, detonation parameters expressing the performance of detonation products of the used charge, are of fundamental importance. For this reason, the data base DETPAR comprising C-J parameters and some other basic characteristics of broad spectrum of condensed explosives has been drawn up. Now it contains some 1,000 charts. Data archived were mainly drawn from tens original sources, above all from Dremin's work [1], from publications that were issued in printed form by LASL, see [2], [3], and from the reports produced in the VÚPCH workplace.

2. STRUCTURE OF THE DATA BASE

A chart is used in the information system, referred to hereinafter as DETPAR, as the most convenient way of presentation of the stored data. The chart represents a combination of graphic part and texts - see Table 1. The concerned data were primarily inserted into the table created in dBASE IV environment that is tabulated of fields (vertical columns of corresponding meaning) and lines. The content of a line represents the contents of one chart.

Table 1. Invariable texts and contents of individual fields of the chart.

CLASS	*COMP*					
Refer.:	*CONT*				ρ_o =	kg/m^3
C-J parameters	D =	m/s	$u_{pc\text{-}j}$ =	m/s	$P_{c\text{-}j}$ =	GPa
	Exp. k =		E_g =	$\times 10^3$ m^2/s^2	a =	mm
	Figure No.		d_{sp} =	mm	L =	mm
HEAT	Q =	cal/g	*TEXT*			
PDT	Y =	mm	d_{expl} =	mm	d_{pl} =	mm
GT	b =	mm	P_b =	GPa	*TEXT*	
TEXT *TEXT* *TEXT* *TEXT*						

It follows from Table 1. that the chart comprises both invariable texts as e.g. C-J parameters, PDT etc., and symbolism, values and dimensions of variables.

The contents of individual fields and meaning of the symbols in Table 1. are defined as follows:

CLASS

In principle, the explosives given here are, in accordance with Table 2, divided into seven classes. The first four classes represent the types of explosives containing TNT, RDX, PETN, or HMX as a predominant compound. Industrial explosives are stored under the class PRUM.

Table 2. Classification of explosives in the *CLASS* field

Filename	Class	File contents
DPTNT	TNT	Explosives containing predominantly TNT
DPRDX	RDX	- " - RDX
DPPETN	PETN	- " - PETN
DPHMX	HMX	- " - HMX
DPVBTZ	VBTZ	Other explosives of known composition
DPVBTN	VBTN	Explosives of unknown composition
DPPRUM	PRUM	Industrial explosives and other explosive substances

In case the explosive is composed of two components present in equal portions, the data are usually mentioned in both appropriate classes.

The field ***COMP*** is designated to store the data concerning composition, name or brand of explosive here.

The field containing invariable text **Refer.** is designated for inserting the obligatory reference to the source of information.

The field labelled as ***CONT*** serves for inserting the content of individual compounds expressed in % by weight.

Density of the specimen is given in ρ_o field.

The fields with invariable texts **D**, $\mathbf{u_{pcj}}$, $\mathbf{P_{cj}}$, and **Exp. k** are designated for storing the following values:

D - detonation velocity

$\mathbf{u_{pcj}}$ - particle velocity at the C-J plane

$\mathbf{P_{cj}}$ - detonation pressure of products, and

Exp. k - polytropic exponent of gas products of the given explosive.

At present, a series of methods is used, developed for measurement of C-J parameters:

- If the time contour of particle velocity, $u_p = f(t)$ is measured by the inductive method, then the curve in the form similar to that of the ideal curve presented in Figure 1 and also a fairly detailed view into the process observed may be obtained [1].

- C-J pressure of products can be determined using Manganin piezoresistive gauge, which is directly embedded into the measured specimen. Then the change in electric signal, which is proportional to the change in resistivity of the gauge due to the acting pressure of products is registered - see Figure 2.

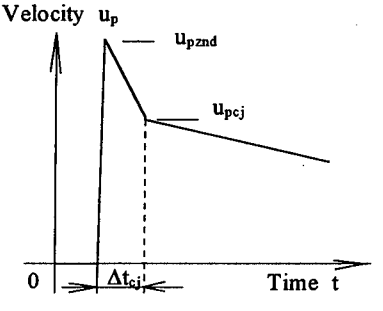

Figure 1

Idealized particle velocity contour behind the front of detonation wave (DW)

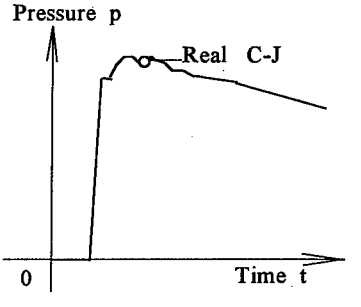

Figure 2

Typical pressure-response of Manganin gauge inserted into the HE specimen

- C-J parameters may be evaluated by means of various types of indirect methods. Their basis usually consists in measurement of planar shock wave front velocity $U_o = f(x)$ or particle velocity behind the shock front $u_p = f(x)$ along the calibrated inert material, which is tightly contacted to the scoped specimen. As the second step, the impedance mismatch is processed and the set of C-J parameters is evaluated in accordance with theoretical postulate [3].

Detonation velocity is usually measured using the charge of cylindric geometry with length, L, several times outnumbering the diameter, d_{sp}. More information about the technologies and advantages or problems of various methods is given in [2], [3].

The relation between pressure P_{cj}, density, detonation velocity and particle velocity, u_{pcj} is expressed by the equation of conservation of momentum (1):

$$P_{cj} = \rho_o D u_{pcj} \quad (1)$$

The polytropic exponent is defined by the equation (2):

$$k = \left(\frac{D}{u_{pcj}}\right) - 1 \quad (2)$$

The next field, $\mathbf{E_g}$, is designated for the Gurney energy value, which is calculated from C-J parameters set, as theoretically defined by equation (3):

$$E_g = \frac{D^2}{k^2 - 1}\left(\frac{k}{k+1}\right)^k \quad (3)$$

This relation is suitable mainly in the area of small ballistic ratios.

E_g data, experimentally determined by means of any type of ballistic method, are usually presented in the bottom text part of the chart.

The width of reaction zone, **a**, is defined by the equation (4):

$$a = \left(D - \overline{u_p}\right)\Delta t_{cj} \quad (4)$$

where $\overline{u_p}$, in accordance with Figure 1, represents the value of median particle velocity in the interval $(t_{cj} - t_o) = \Delta t_{cj}$.

The number of illustration showing the appropriate method of measurement C-J parameters is given in the field **Figure No.**

The dimensions of diameter and length of the specimen are put into the fields labelled as $\mathbf{d_{sp}}$, **L.**

The **HEAT** field serves to record there experimentally determined or calculated specific detonation heat, **Q,** of the explosive.

The line labelled with the **PDT** abbrevation is designated to insert there Plate Denting Test data (the depth of steel plate dent), **Y**, and specimen and plate diameters, $\mathbf{d_{ex}}$, $\mathbf{d_{pl}}$.

In the line labelled with **GT** symbol, the height of barrier, **b**, and the value of pressure behind the shock wave front in barrier at boundary, $\mathbf{P_b}$, are inserted. Both these parameters represent the sensitivity of the observed specimen to shock wave, determined by means of Gap Test.

Other data characterising the explosive concerned are possible to be given in the text fields using accessible alpha-numerical symbols. The data drawn from other sources are always accompanied with reference to the source of these information.

3. CONCLUSION

Comparation of the data stored enables, to a certain extent, to distinguish influences of measuring system and the way of interpretation of primary data from the influences of conditions of individual experimental procedure on the reliability of the resulting data obtained. In such a case it is necessary to avoid the application of simple statistic access into the process of fitting of data compared, because e.g., the dimensions of specimen, planarity/nonplanarity and stability/instability of detonation regime play a very important role here.

C-J data obtained at the self-sustaining planar detonation regime may serve as basic input data for a numerical simulation of product effects on the surroundings. The data obtained at the measurement of cylinder shaped specimen describe another, but natural and frequently generated regime of detonation. The apparent distinction between those two detonation systems is necessary to be taken into account whenever the DETPAR Catalogue or any similar database collecting C-J parameters is processed or analysed.

The printed form of DETPAR Catalogue in English language, designed for specialists in this branch, is prepared at present time.

4. REFERENCES

[1] Dremin, A.N., Savrov, S.D.: Detonacionnye volny v kondensirovannych sredach. Moskva, Nauka, 1970

[2] Gibbs, T.R., Popolato, A.: LASL Explosive Property Data. UC Press Berkley, 1980

[3] Mader, Ch,L., Johnson, J.N., Crane, S.L.: Los Alamos Explosives Performance Data, UC Press Berkley, 1982

[4] Majzlík, J.: The Measurement of Parameters of Plane High-Pressure Dynamic Phenomena. (in Czech), VÚPCH, 1994

[5] ASHTON -TATE: Program DBASE IVa, 1988 (Handbook)

EXAMPLE OF THE REFERENCES

[73] So-young Song, Jun Wung Lee: A Deton System Employing High Resistance Manganin Foil Gauge ernat.) on Detonat., Portland, 1989, pp. 471 - 477

[74] Dong Haishan: Properties of Bis (2,2,2 - Trinitroethyl-N-Nitro) ethyleneamidine and Formulations Thereof. "In: Proc. 9th Sympos. (Inter.) on Detonation. Portland, Oregon, 1989, pp. 995 - 1000

[75] Li Hailing, and add.: Displacement Gradient Method for Measuring Detonation Parameters Using Flash X-Ray Photography. "In: Proceed. 8th Sym. (Inter.) on Detonation, Albuquerque, N.M., 1985, pp. 1 - 5

[76] Stanjukovič, K.P., and add.: Fizika vzryva. Nauka, Moskva, 1975

[77] Jacobs, S.J.: ARSJ 30, 1966, 151

[78] Altšuler, L.V., Ašajev, V.K., and add.: Experimentalnoje issledovanie sostojanij v zoně chemičeskoj reakcii detonacionnoj volny. "In: Detonacia - Mat. VI. Vsesojuznovo simpoz. po gor. i vzryvu, Alma-Ata, 1980, pp. 8 - 11

[79] Cowperthwaite, M., and Rosenberg, T.J.: Lagrange Gage Studies of Detonation in Some Intermolecular EA Based Explosives. "In: Proc. 8th Sympos. (Inter.) on Detonat., 1985, pp. 987 - 998

[80] Altšuler, L.V., Ašajev,V.K., and add.: "In: Tretij Vsesojuz. simpozium po impuls. davlenijam. Moskva, 1979, pp. 9

[81] Gill, R., Asaoka, L., and Baroody, E.: On Underwater Detonations, I. A New Method for Predicting the CJ Detonation Pressure of Explosives. "In: Journal of Energet. Mater., 5, 1987, no. 3 - 4, pp. 287 - 307

[82] Zukas, J.A.: High Velocity Impact Dynamics, John Wil., N.Y., 1990, 935 pp.

[83] Dobratz, B.M.: LLNL Explosive Handbook. Properties of Chemical Explosives and Explosive Stimulants, LLNL Report UCRL - 52 997, 1981, 1992

[84] Seitz, W.L., Stacy, H.L., and add.: Detonation Reaction - Zone Structure of PBX 9502. "In: Proceed. 9th Symposium (Inter.) on Detonat., 1989, Portland, Oregon, pp. 657 - 669

[85] Green, L.G., Tarver, C.M., and Erskine, D.J.: Reaction Zone Structure in Supracompressed Detonating Explosives. "In: Proc. 9th Sympos. (Inter.) on Deton., 1989, Portland, pp. 670

[86] Švedov, K.K.: O registracii parametrov Čepmena - Žuge pri detonacii kondensirovannych VV. "In: Fizika gor. i vzryva, 23, 1987, no. 4, pp. 94 - 104

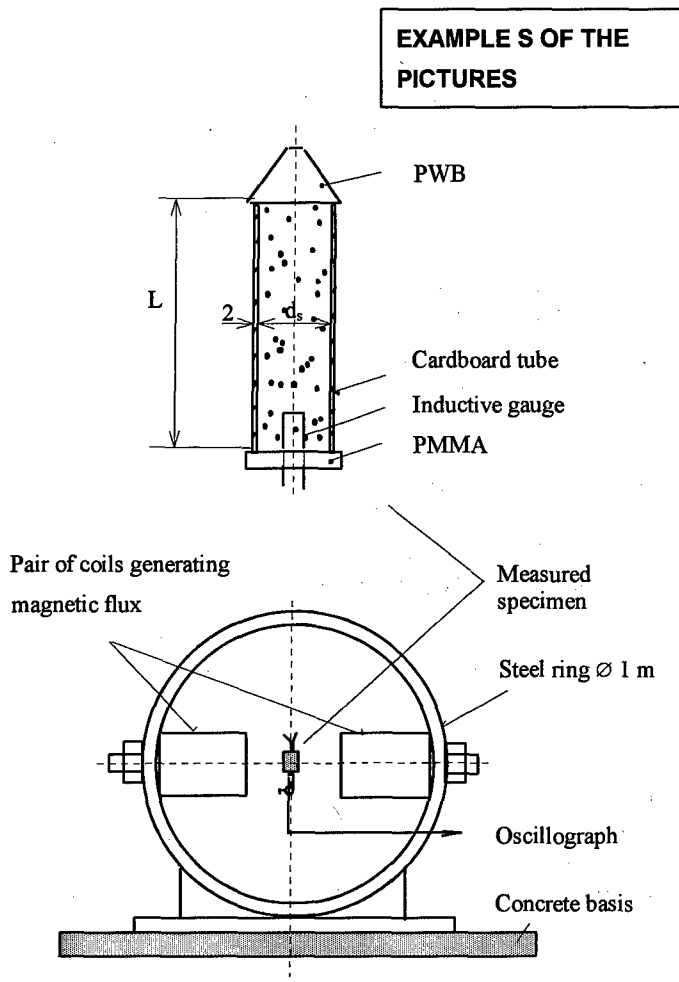

Figure 14. Measurement of particle velocity contour behind the DW of an industrial explosives. Construction of magnetic flux generator.

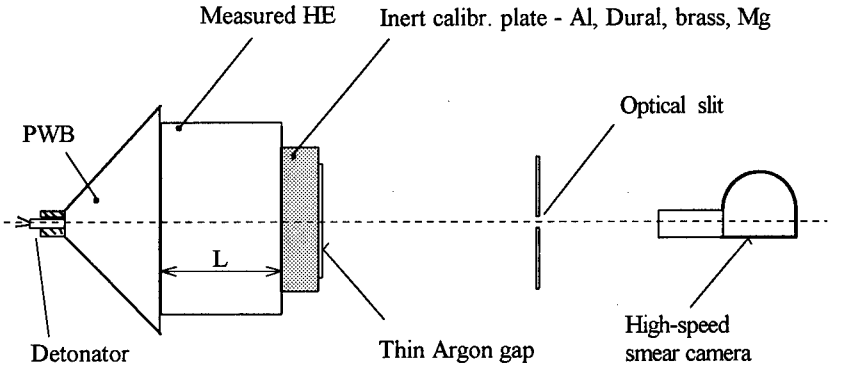

Figure 21. Measurement of shock wave front velocity along the inert calibrated plate according to [29]

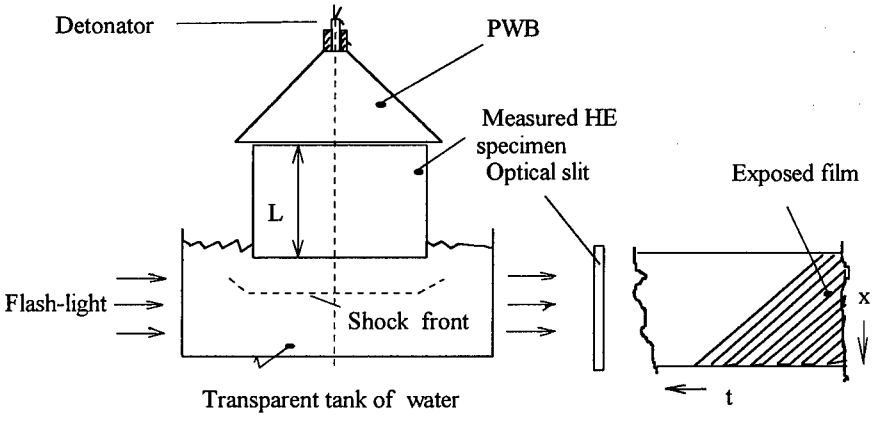

Figure 22. Measurement of shock wave velocity in water using high-speed camera according to [30]

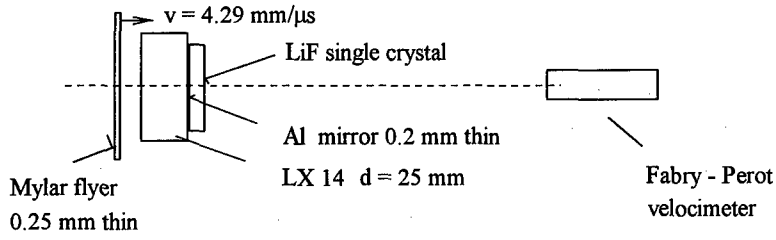

Figure 23. Measurement of velocity of the HE - LiF window boundary using Fabry - Perot interferential device [35]

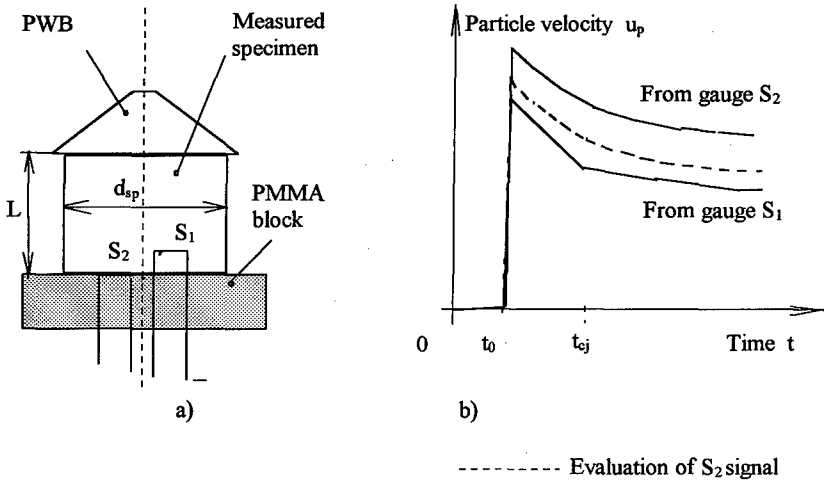

a) Arrangement of a specimen with couple of embedded inductive gauges, S_1, S_2
b) Comparation of a rather idealized response of the gauge S_1, which is embedded into HE, with a response of the boundary gauge S_2

Figure 24. Simultaneous measurement of particle velocity in the specimen and at the HE -PMMA boundary by means of inductive gauges.

EXAMPLE S OF THE DATA STORED

TNT	**TNT**		
Refer.: **93**			
C - J parameters	D = 3450 m/s	u_{pc-j} = 966 m/s	
	Exp. k = 2.57	$E_g = 904\times10^3$ m^2/s^2	
	Figure No. 33	d_{sp} = 40 mm	
HEAT	Q =		
PDT	Y =	d_{expl} =	d_{pl} =
GT	b =	P_b =	
Simultaneous measur. of DV and U_s velocity along PMMA			

TNT	**TNT**		
Refer.: **93**			$r_0 = 640$ kg/m^3
C - J parameters	D = 3850 m/s	u_{pc-j} = 974 m/s	P_{c-j} = 2.4 GPa
	Exp. k = 2.95	$E_g = 813\times10^3$ m^2/s^2	a =
	Figure No. 33	d_{sp} = 40 mm	L =
HEAT	Q =		
PDT	Y =	d_{expl} =	d_{pl} =
GT	b =	P_b =	
Simultaneous measur. of DV and U_s along PMMA			

TNT	**TNT**		
Refer.: **93**			$r_0 = 710$ kg/m^3
C - J parameters	D = 4100 m/s	u_{pc-j} = 1133 m/s	P_{c-j} = 3.3 GPa
	Exp. k = 2.62	$E_g = 1227\times10^3$ m^2/s^2	a =
	Figure No. 33	d_{sp} = 40 mm	L =
HEAT	Q =		
PDT	Y =	d_{expl} =	d_{pl} =
GT	b =	P_b =	
Simultaneous measur. of DV of specimen and U_s along PMMA For TNT in accordance with [93] is valid: $D = 4340 + 2830(r_0 - 800)$; [m/s, kg/m^3]			

RDX	**RDX/NH_4NO_3/U/Water DH 50**		
Refer.: **114**	50/28/7/15		r_0 = 1450 kg/m^3
C - J parameters	D = 7250 m/s	u_{pc-j} = 1690 m/s	P_{c-j} = 17.7 GPa
	Exp. k = 3.3	E_g = 2200×10^3 m^2/s^2	a =
	Figure No. 15	d_{sp} = 70 mm	L =
HEAT	Q =	E_g - experiment. determined value	
PDT	Y =	$d_{expl.}$ =	$d_{pl.}$ =
GT	b =	P_b =	
U - urea Filled into PVC tube			

RDX	**RDX/NH_4NO_3/U/Water DH 70**		
Refer.: **114**	70.0/16.8/4.2/9.0		r_0 = 1530 kg/m^3
C - J parameters	D = 7900 m/s	u_{pc-j} = 1620 m/s	P_{c-j} = 19 GPa
	Exp. k = 3.89	E_g = 3170×10^3 m^2/s^2	a =
	Figure No. 15	d_{sp} = 70 mm	L =
HEAT	Q =	E_g - experiment. determined value	
PDT	Y =	$d_{expl.}$ =	$d_{pl.}$ =
GT	b =	P_b =	
U - urea Filled into PVC tube			

RDX	**RDX/NH_4NO_3/Water**		
Refer.: **113**	70/18/12		r_0 = 1530 kg/m^3
C - J parameters	D = 7510 m/s	u_{pc-j} = 1680 m/s	P_{c-j} = 19.3 GPa
	Exp. k = 3.46	E_g =	a =
	Figure No. 15	d_{sp} = 70 mm	L =
HEAT	Q =		
PDT	Y =	$d_{expl.}$ =	$d_{pl.}$ =
GT	b =	P_b =	
Filled into PVC tube			

HMX	**HMX**		
Refer.: **71**			r_0 = 1900 kg/m^3
C - J parameters	D =	u_{pc-j} =	P_{c-j} =
	Exp. k =	E_g =	a =
	Figure No.	d_{sp} =	L =
HEAT	Q =		
PDT	Y =	d_{expl} =	d_{pl} =
GT	b =	P_b =	

HMX single crystal, nonreactive shock adiabat: $U_s = 5800 + 0.59\ u_p$; [m/s]

U_s [m/s]	7200	7350	7550
u_p [m/s]	2610	2490	2930
P [GPa]	35.705	34.773	42.031

HMX	**HMX Phlegmat.**		
Refer.: **78**			r_0 = 1770 kg/m^3
C - J parameters	D = 8690 m/s	u_{pc-j} = 2028 m/s	P_{c-j} = 31.2 GPa
	Exp. k = 3.28	$E_g = 3227\times10^3$ m^2/s^2	a =
	Figure No. 28	d_{sp} = 64 mm	L = 120 mm
HEAT	Q =		
PDT	Y =	d_{expl} =	d_{pl} =
GT	b =	P_b =	

PMMA slices cca 0.3 mm thin, contacted to HMX
Device LIVS described in source [80]
Δt_{cj} = 40 ns, P_{znd} = 46.8 GPa,
Shock velocity at the interface PMMA - HE: U_{so} = 8060 m/s

HMX	**HMX Phlegmat.**		
Refer.: **78**			r_0 = 1770 kg/m^3
C - J parameters	D = 8690 m/s	u_{pc-j} = 2028 m/s	P_{c-j} = 31.2 GPa
	Exp. k = 3.28	$E_g = 3226\times10^3$ m^2/s^2	a =
	Figure No. 18	d_{sp} = 64 mm	L = 120 mm
HEAT	Q =		
PDT	Y =	d_{expl} =	d_{pl} =
GT	b =	P_b =	

Velocity of interface between HE products - PMMA measured by laser and photomultiplier devices,
Time interval Δt_{cj} = 40 ns

THE

ICT - THERMOCHEMICAL DATABASE

Version 1998 (Fourth update)

H. Bathelt
F. Volk
M. Weindel

Fraunhofer Institut
Chemische Technologie (ICT)
Joseph-von-Fraunhofer-Str. 7
D-76327 Pfinztal

e-mail: hb@ict.fhg.de
Fax 0049-721-4640-111

The calculation of chemical equilibria is not only of interest for the evaluation of the performance of rocket and gun propellants. It is being used also for optimization purposes of different combustion processes with regard to temperature, pressure and product formations. Such calculations can be performed for example with the ICT-Thermodynamic Code, which is running on PC.

The reliability of the results of thermochemical calculations depends primarily on the accuracy of the data used. Therefore the Fraunhofer-Institut für Chemische Technologie (ICT) began very early to collect data on energetic materials. In 1971, tables with properties of substances related with the preparation of rocket and gun propellants were published[1]. This publication contains besides enthalpies of formation other data like heat of combustion, molecular weight, oxygen balance, density and structure formula of some 500 substances. Data of 147 additional substances was published in 1981[2].

Meanwhile, properties of a lot of new energetic substances have been published. Therefore, instead of compiling an additional supplement, the main properties of all these substances are stored in a Thermochemical Database. Compared with printed tables, this has the advantage that data can be retrieved very fast; updates can be made easily and regularly.

The first published database of 1994 contained data of 1850 substances; this fourth update is containing data of more than 3800 substances.

The database is available in a MS-DOS-Version and now also in a Windows-Version (to be used with Windows 95 / Windows NT 3.51 and higher). With the new Windows-Version the structure formulas can be seen at the screen, they can be printed together with the data and are easily transferred to the clipboard.

---

[1] *F. Volk, H. Bathelt, R. Kuthe: Thermodynamische Daten von Raketentreibstoffen, Treibladungspulvern sowie deren Komponenten*

[2] *H. Bathelt, F. Volk: Thermodynamische Daten von Raketentreibstoffen, Treibladungspulvern und Sprengstoffen sowie deren Komponenten 1. Ergänzungsband, ICT-Bericht 1/81*

The Thermochemical Database

→**contains data of more than 3800 substances**

→**contains especially data of energetic materials**

→**is available in English and German**

→**is updated regularly**

The following data is stored:

- **Sum formula**
- **State of aggregation**
- **Name(s)**
- **Molecular weight**
- **Oxygen balance**
- **Density**
- **Melting point**
- **Boiling point**
- **Enthalpy of formation (up to four values)**
- **Energy of formation**
- **Energy of combustion**
- **References**

Structure formulas of the stored organic substances are given in the manual (MS-DOS-Version) or are shown at the screen in the Windows-Version

w238.doc

The Thermochemical Data Base

allows to search for

- Names
- Sum formulas
- Parts of names
- Parts of sum formulas
- Names beginning with a certain letter
- Substances consisting of certain elements
- Substances containing certain elements
- Substances with certain properties

(for example with a positive oxygen balance or with a positive enthalpy of formation)

- Substances belonging to certain classes

for example: Primary explosives
Stabilizers
Liquid fuels
Pyrotechnics
...

w239.doc

Windows - Version: **Search for names:** w381.doc

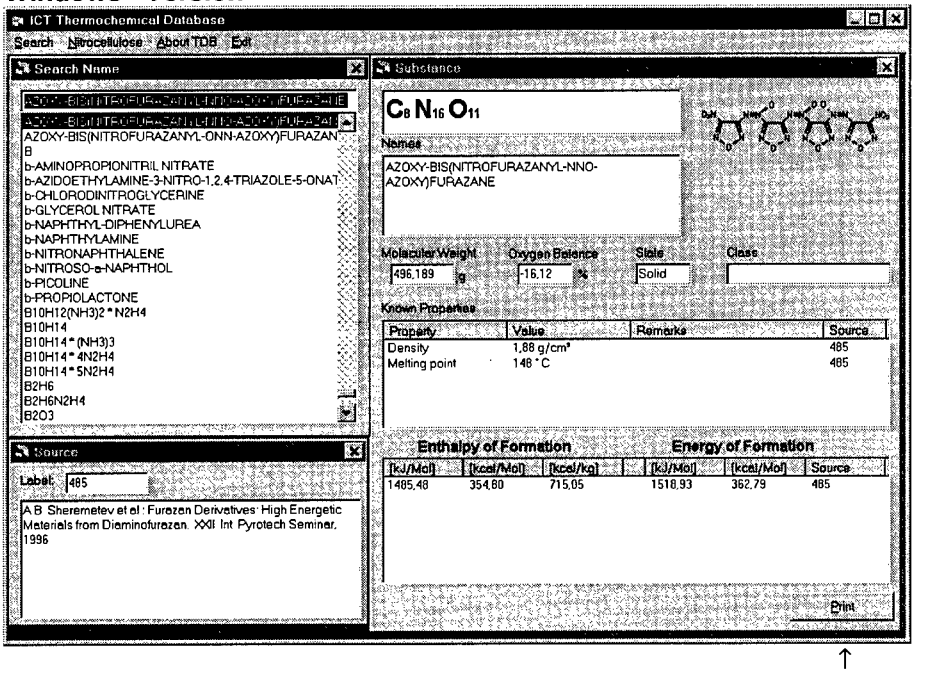

By clicking on the Print button in the lower right corner the stored data including the structure formula and sources can be printed.

Search for part of names: Example: Search for -hexanitro- (63 names found)

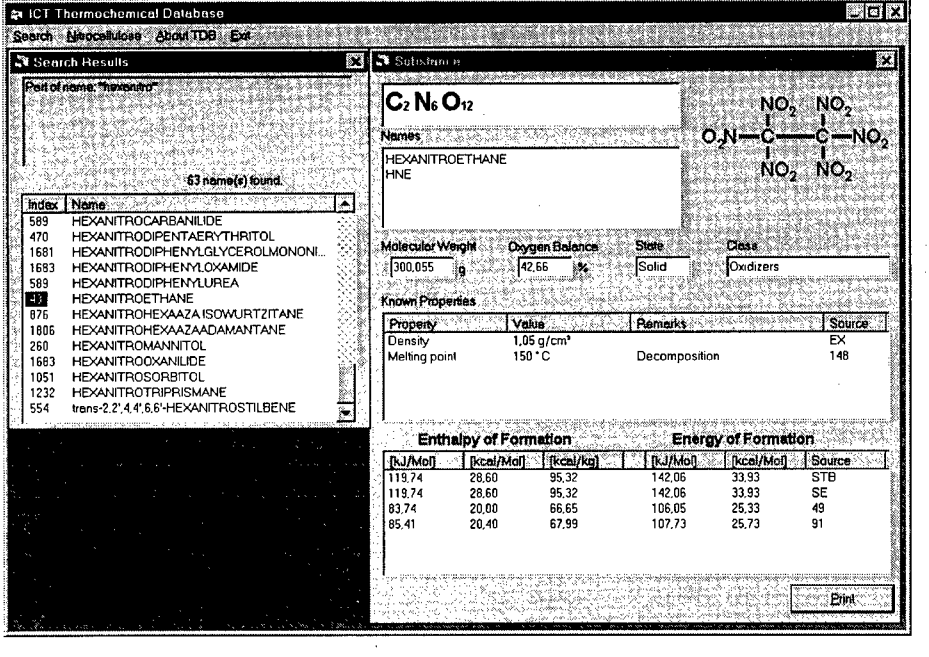

Windows - Version: Example for Partial Element Search

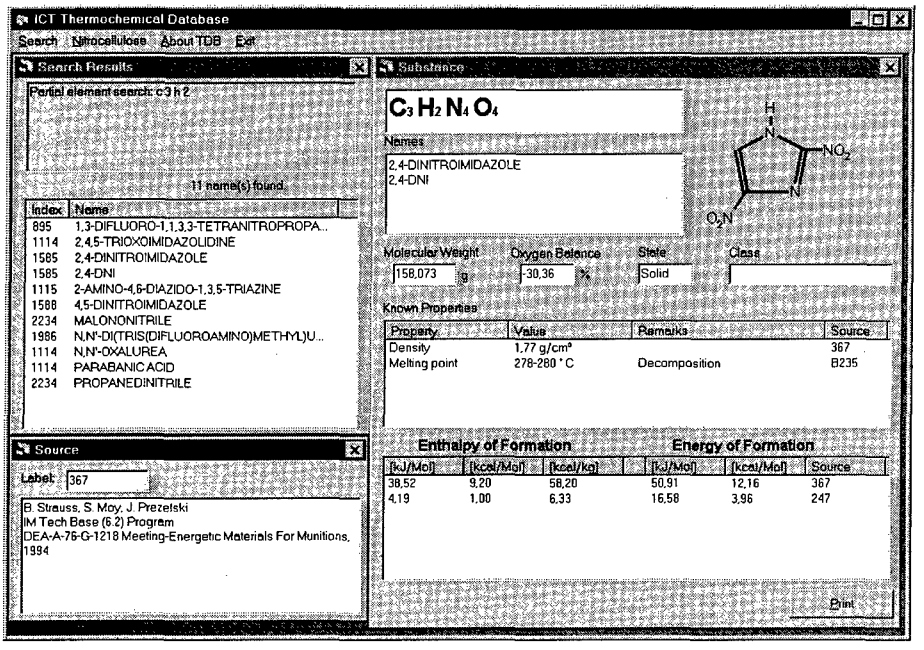

Nitrocellulose:

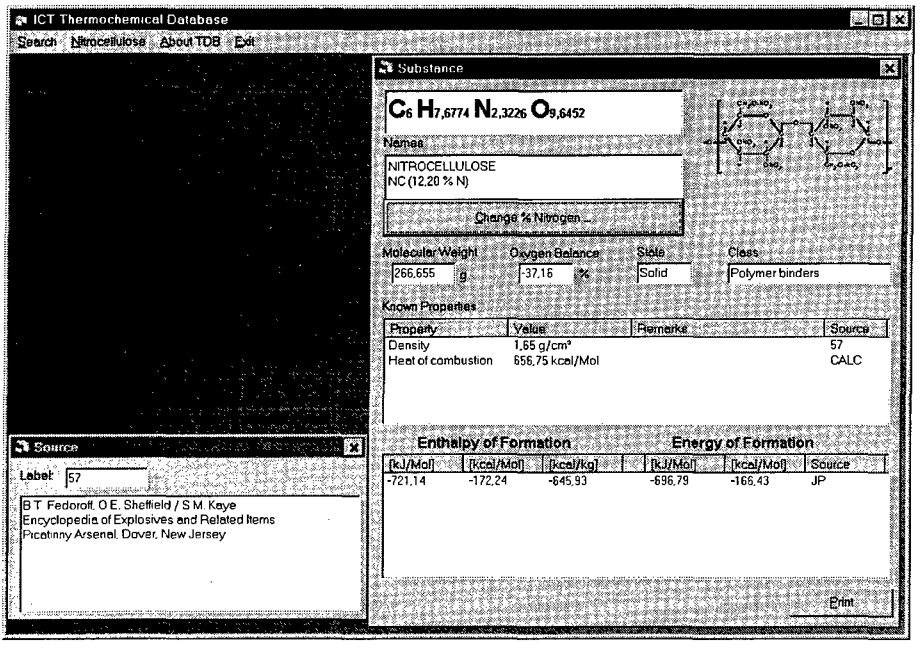

Windows - Version: Search for substances with certain properties

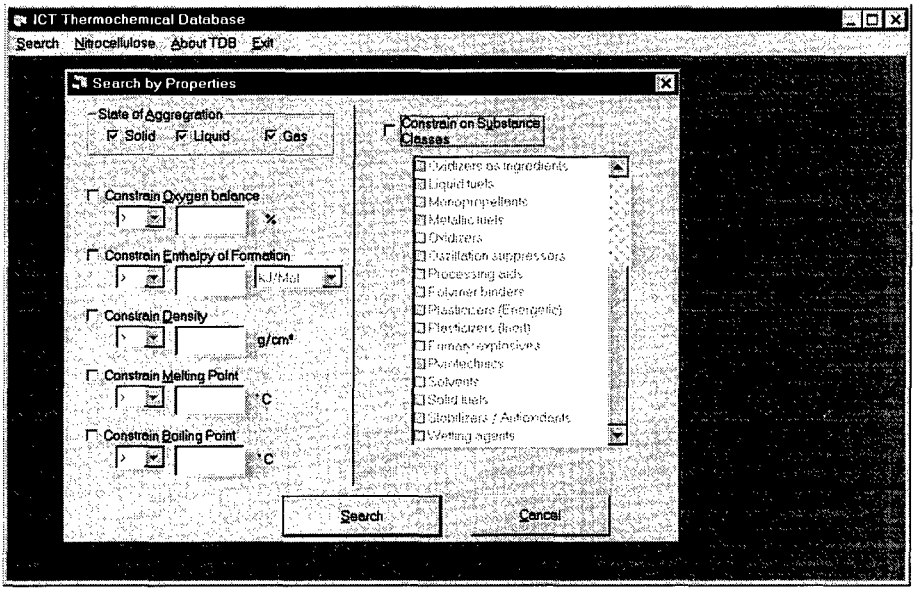

It is possible to choose:

- **State of aggregation: Solid and / or liquid and / or gaseous**
- **Classes of substances**

Choosing the other options

- **Oxygen balance**
- **Enthalpy of Formation**
- **Density**
- **Melting Point**
- **Boiling Point**

you can decide whether the values shall be greater, equal or less than the entered value. Besides this, the Enthalpy of Formation can be entered in Kcal/mol or in KJ/mol.

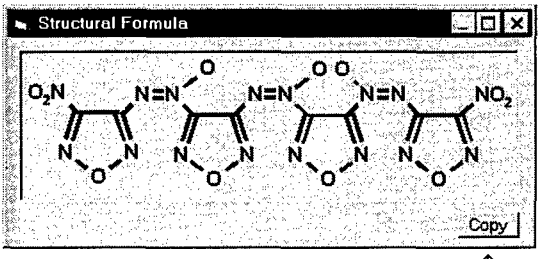

↑

By clicking on the Copy button the structure is copied to the clipboard.

Samples
of the stored values

C 4 H 4 N 8 O 14 — Solid

N-NITROBIS(2,2,2-TRINITROETHYL)AMINE
1,1,1,3,5,5,5-HEPTANITRO-3-AZAPENTANE HOX BTNENA
BIS(2,2,2-TRINITROETHYL)NITRAMINE

Molecular Weight: 388.121 [g] Oxygen Balance: 16.49 [%]
Density [g/cm3]: 1.96 at 20°C Source: 93
Melting Point [°C]: 94-95 Source: 93
Boiling Point [°C]: 175.7 D Source: 420

Enthalpy of Formation [KJ/Mol]	Enthalpy of Formation [Kcal/Mol]	Enthalpy of Formation [Kcal/kg]	Energy of Formation [KJ/Mol]	Energy of Formation [Kcal/Mol]	Source
-28.03	-6.70	-17.26	4.17	1.00	72
-27.20	-6.50	-16.75	5.01	1.20	34
20.29	4.85	12.50	52.50	12.55	358
-136.82	-32.70	-84.25	-104.61	-25.00	STB

Energy of Combustion: Source: 93
506.1 [Kcal/Mol] = 1304.0 [cal/g] — 1- 182

C 5 H 9 N 1 O 4 — Liquid

POLY-3-NITRATOMETHYL-3-METHYLOXETANE POLYNIMMO PN
pNMMO

Molecular Weight: 147.131 [g] Oxygen Balance: -114.18 [%]
Density [g/cm3]: 1.26 Source: 253
Boiling Point [°C]: 187 D Source: 484

Enthalpy of Formation [KJ/Mol]	Enthalpy of Formation [Kcal/Mol]	Enthalpy of Formation [Kcal/kg]	Energy of Formation [KJ/Mol]	Energy of Formation [Kcal/Mol]	Source
-309.20	-73.90	-502.27	-291.86	-69.76	349
-309.20	-73.90	-502.27	-291.86	-69.76	253
-393.30	-94.00	-638.89	-375.96	-89.86	465
-334.72	-80.00	-543.73	-317.38	-75.86	390

1-1594

H 4 N 4 O 4 — Solid

AMMONIUM DINITRAMIDE NH4N(NO2)2 ADN

Molecular Weight: 124.056 [g] Oxygen Balance: 25.79 [%]
Density [g/cm3]: 1.812 at 20°C Source: 396
Melting Point [°C]: 92.9 Source: 467
Boiling Point [°C]: 135 D Source: 226

Enthalpy of Formation [KJ/Mol]	Enthalpy of Formation [Kcal/Mol]	Enthalpy of Formation [Kcal/kg]	Energy of Formation [KJ/Mol]	Energy of Formation [Kcal/Mol]	Source
-149.79	-35.80	-288.58	-134.92	-32.25	364
-150.62	-36.00	-290.19	-135.76	-32.45	278
-146.44	-35.00	-282.13	-131.58	-31.45	243
-140.16	-33.50	-270.04	-125.30	-29.95	226

405 M.E. Grice, Dept. of Chemistry, University of New Orleans, USA
Personal communication, 1995

406 A. Gunasekaran, M.L. Trudell, J.H. Boyer
Dense Energetic Compounds of C,H,N,and O Atoms
IV Nitro and Azidofurazan Derivatives
Heteroatom Chemistry, Volume 5, No. 5/6, 1994

407 J. Meulenbrugge, A.vd Steen, A. vd Heyden
Crystallisation of energetic materials;
the effect on stability, sensitivity and processing properties
Proc. Int. Symp. on Energetic Materials Technology,
Sept. 24-27, 1995, Phoenix, Arizona

408 K.Y.-Lee, M. Chan
The Two Polymorphs of N-DNAT, A High Nitrogen Molecule
Proc. Int. Symp. on Energetic Materials Technology,
Sept. 24-27, 1995, Phoenix, Arizona

409 B. Wang, C. Zhu, Q. Longl
Synthesis and Properties of 1,3,3-Trinitroazetidine
Hanneng Cailiao, 3(1), 7-9 (Chinese), 1995

410 J.R. Cho, J.S. Kim, Y.G. Cheun
An Improved Synthetic Method of Poly(NMMO) and PGN Prepolymers
Proc. Int. Symp. on Energetic Materials Technology,
Sept. 24-27, 1995, Phoenix, Arizona

411 M.R. Buehler, S.A. Aubert
Characterization of the Sensitivity and Performance Properties
of Bis-(2,2-Dinitropropyl)Fumarate and 1,3,5-Trinitrobenzene
Proc. Int. Symp. on Energetic Materials Technology,
Sept. 24-27, 1995, Phoenix, Arizona

412 S.T. Peters, R.B. Wardle, I.A. Wallace, A.C. Haaland
The Selection, Processing and Characterization of a Set of
Gun Propellants Utilizing Novel Ingredients
Proc. Int. Symp. on Energetic Materials Technology,
Sept. 24-27, 1995, Phoenix, Arizona

413 P.C. Braithwaite, W.W. Edwards, R.M. Hajik, T.K. Highsmith,
G.K. Lund, R.B. Wardle
TEX: A Promising New Insensitive High Explosive
Proc. Int. Symp. on Energetic Materials Technology,
Sept. 24-27, 1995, Phoenix, Arizona

414 V.N. Gamezo, S. Odiot, M. Blain, S. Fliszar, A. Delpuech
Theoretical analysis of the effects of nitration of the
explosive properties of triazoles: 4-nitro-2H-1,2,3-triazole
and 4,5-dinitro-2H-1,2,3-triazole
Journal of Molecular Structure (Theochem) 337 (1995), 189-197

415 J.P. Ritchie, S.M. Bachrach: Molecular Models for Explosives
Journal de Physique, Colloque C4, Tome 48, Sept. 1987, 377-391

416 T. Glowiak, L. Sobczyk, E. Grech
Chemical Physics Letters 34, 292 (1975)

417 L.A. Camerman, L.H. Jensen, A.T. Balaban
Acta Cryst., Sect. B25, 2623 (1969)

418 S. Zeman
On the Physical Thermal Stability of Some Cyclic Nitramines
Proc. 21. Int. Pyrotechnics Seminar, Moscow, 1995

419 V.P. Sinditskii, A.E. Fogelzang et al.
Combustion of 5-Aminotetrazole Salts
Proc. 21. Int. Pyrotechnics Seminar, Moscow, 1995

420 Yan Hong, G. Xiao-Pei, Chen Bo-Ren: Comparison of Thermal
Stabilities of Azidomethyl-gem-Dinitromethyl Compounds...
Proc. 21. Int. Pyrotechnics Seminar, Moscow, 1995

421 M.E. Walsh, T.F. Jenkins, P.G. Thorne
Laboratory and Analytical Methods for Explosives Residues in Soil
Journal of Energetic Mat. Vol. 13, 357-383 (1995)

Sample page
of the list of substances
(Manual)

1-1688 TETRAMETHYLLEAD
1- 468 TETRAMETHYLOLCYCLOHEXANOL PENTANITRATE
1- 467 TETRAMETHYLOLCYCLOHEXANONE TETRANITRATE
1- 441 TETRAMETHYLOLCYCLOPENTANOL PENTANITRATE
1- 440 TETRAMETHYLOLCYCLOPENTANON TETRANITRATE
1- 747 TETRAMETHYLOLMETHANE
1- 187 TETRAMETHYLOZONIDE
1-2454 TETRAMETHYLTETRAZENE
1-2449 TETRAMETHYLTHIACYCLOPROPANE
1-2701 TETRAMMINE-cis-BIS(5-NITRO-2H-TETRAZOLATO-N2)COBALT/3/PERCHLORATE
1-2032 1,2,4,7-TETRANITRAMINOCUBANE
1-1886 2,6,8,10-TETRANITRAZA-4,8-DIAZA-TRICYCLO(7.3.0.0)DODECANE
1-1885 2,6,8,10-TETRANITRAZA-4,8-DIAZA-TRICYCLO(7.3.0.0)DODECANE-5,11-DIONE
1-2730 2,4,5,7-TETRANITRO-1-(2,4,6-TRINITROPHENYL)NAPHTHALENE
1- 159 1,3,5,7-TETRANITRO-1,3,5,7-TETRAAZACYCLOOCTANE
1-1946 trans-1,3,5,7-TETRANITRO-1,3,5,7-TETRAAZADECALIN
1-1945 cis-1,3,5,7-TETRANITRO-1,3,5,7-TETRAAZADECALIN
1-1944 1,3,7,9-TETRANITRO-1,3,7,9-TETRAAZASPIRO(4.5)DECANE
1- 868 1,3,5,5-TETRANITRO-1,3-DIAZACYCLOHEXANE
1- 868 1,3,5,5-TETRANITRO-1,3-DIAZINE
1- 323 trans-1,4,5,8-TETRANITRO-1,4,5,8-TETRAAZADECALIN
1-1241 1,4,5,8-TETRANITRO-1,4,5,8-TETRAAZADIFURAZANO-(3,4-c)(3,4-h)DECALIN
1-2686 1,4,5,8-TETRANITRO-1,4,5,8-TETRAAZAFURAZANO(3,4-b)DECALIN
1-1153 2,4,6,8-TETRANITRO-2,4,6,8-TETRAAZACYCLOOCTANON-1
1- 198 2,4,6,8-TETRANITRO-2,4,6,8-TETRAAZADICYCLO(3,3,0)-OCTANDIONE-(3,7)
1-1152 2,4,6,8-TETRANITRO-2,4,6,8-TETRAAZADICYCLO(3,3,0)OCTANE
1-1143 2,4,6,8-TETRANITRO-2,4,6,8-TETRAAZADICYCLO(3,3,0)OCTANON-3
1-1941 2,4,8,10-TETRANITRO-2,4,8,10-TETRAAZASPIRO(5.5)UNDECANE
1-2458 2,5,7,9-TETRANITRO-2,5,7,9-TETRAAZABICYCLO[4.3.0]NONANE-8-ONE
1-1167 1,3,5,7-TETRANITRO-2,6-DIOXO-1,3,5,7-TETRAAZACYCLOOCTANE
1-1263 1,3,6,8-TETRANITRO-3,6-DIAZA-n-OCTANE
1-2107 1,1,1,3-TETRANITRO-3-AZABUTANE
1- 872 2,2,6,6-TETRANITRO-4-AZAHEPTANE
1-1878 2,2,6,6-TETRANITROADAMANTANE
1- 238 2,3,4,6-TETRANITROANILINE
1-1240 1,2,3,4-TETRANITROBENZENE
1- 312 1,2,4,5-TETRANITROBENZENE
1-1239 1,2,3,5-TETRANITROBENZENE
1-2652 2,2',4,4'-TETRANITROBENZIL
1-1736 4,5,6,7-TETRANITROBENZOFUROXANE
1- 789 1,3,8,10-TETRANITROBENZOTRIAZOLO[1,2-a]BENZOTRIAZOLE
1- 507 1,3,7,9-TETRANITROBENZOTRIAZOLO[2,1-a]BENZOTRIAZOLE
1- 204 1,1,1,4-TETRANITROBUTANE
1- 967 1,1,3,3-TETRANITROBUTANE
1- 171 2,2,3,3-TETRANITROBUTANE
1- 491 1,3,6,8-TETRANITROCARBAZOLE
1-2041 1,3,5,7-TETRANITROCUBANE
1-2642 1,2,3,4-TETRANITROCUBANE
1-2648 2,4,4',6-TETRANITRODIBENZYL
1-2646 2,2',4,4'-TETRANITRODIBENZYL
1-1537 TETRANITRODIGLYCEROL
1-1413 2,2',4,4'-TETRANITRODIPHENYLAMINE
1- 154 TETRANITROERYTHROL
1- 198 1,3,4,4-TETRANITROGLYCOLURIL
1- 868 1,3,5,5-TETRANITROHEXAHYDROPYRIMIDINE
1-1881 2,2,6,6-TETRANITRO-HEXAMETHYLENE TETRAMINE
1-2685 1,3,4,7-TETRANITROIMIDAZOLINE(4,5-b)-FURAZANO(3,4-e)PIPERAZINE
1- 2 TETRANITROMETHANE
1- 487 1,4,5,6-TETRANITRONAPHTHALENE
1- 474 1,3,6,8-TETRANITRONAPHTHALENE
1- 483 1,4,5,8-TETRANITRONAPHTHALENE
1-1295 2,2,7,7-TETRANITRONORBORNANE

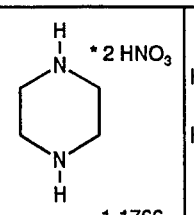

1-1766

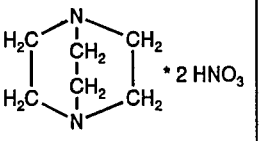

1-1767

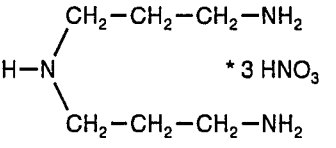

1-1768

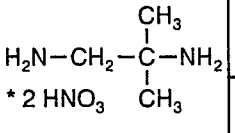

1-1769

Samples of structure formulas (Manual MS-DOS-Version)

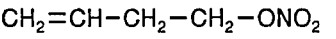

1-1771

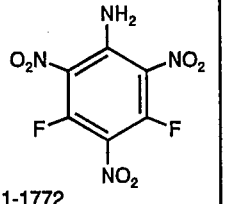

1-1772

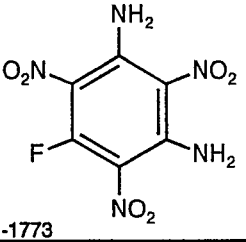

1-1773

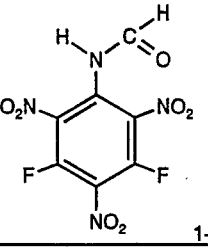

1-1774

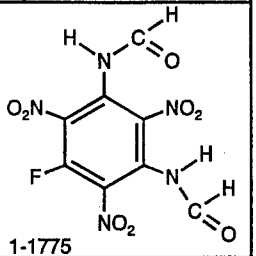

1-1775

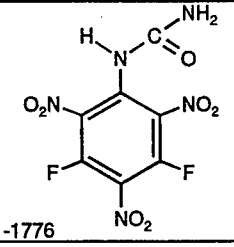

1-1776

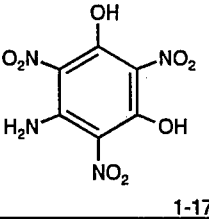

1-1777

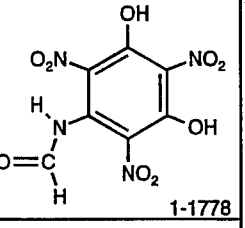

1-1778

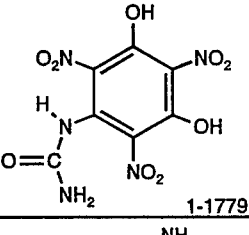

1-1779

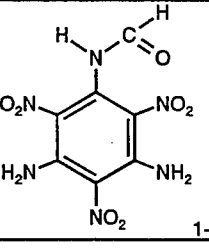

1-1780

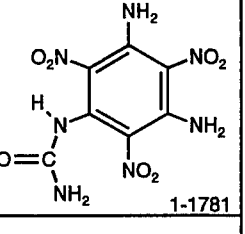

1-1781

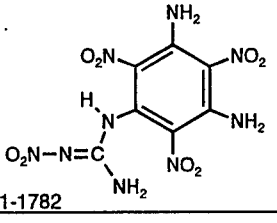

1-1782

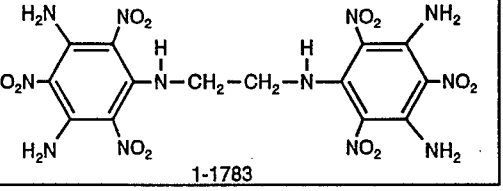

1-1783

ETC Plasma-Propellant Interactions

P.J. Kaste, R.A. Rodriguez-Pesce, M.A. Schroeder, G.L. Katulka, K.J. White, M.L. Leadore, A.E. Kinkennon

U.S. Army Research Laboratory (ARL), AMSRL-WM-BD, APG, MD, 21005-5066, USA

Abstract

Characterization of propellants after treatment with ETC plasmas was undertaken to understand the mechanisms of plasma-propellant interaction. Samples of various chemistries were studied, including JA2, composite propellants containing RDX and CL20, and propellants with energetic thermoplastic elastomeric (ETPE) polymers as the binders. The plasma source was characteristic of that used in ETC ignition, except that the power was reduced so that reaction, but not ignition, occurred for most samples, and material remained for analysis. Samples were exposed to the following plasma treatments: a) direct exposure to the plasma, b) shielding with polyethylene terephthalate (Mylar) films to screen a large fraction of the UV component and reduce convective heating, and c:) shielding with aluminum foil to reduce the radiative, but not conductive, component. Morphological and chemical characterization studies were performed on the treated samples, and compared with the virgin material. Scanning electron microscopy of some treated JA2 samples showed that melting and probably degassing occurred. Through reflectance Fourier transform infrared (FTIR) spectroscopy, the following changes in treated propellant samples were observed: denitration of nitrate esters, hydrolysis of cellulosic binders and a reduction of the nitramine level. Desorption-gas chromatography-mass spectrometry was used to determine that some treated samples suffered a loss of nitrate ester plasticizer. X-ray fluorescence spectroscopy showed that tungsten is deposited on the propellant after plasma treatment.

Background

Electrothermal chemical (ETC) gun concepts are being explored for improving gun performance in propelling charges with high energy densities. High energy plasmas are used as igniters in ETC firings. The goal is to enhance propellant burning rates through interaction of the plasma with the propellant. Experimentally, ignition times are shorter and more reproducible with ETC igniters compared to conventional igniters (1,2). Moreover, if propellant temperature sensitivity could be reduced so that firings over a range of temperatures would yield similar gun pressures, then a concomitant improvement in performance could be realized. However, to exploit the potential of plasma igniters, it is necessary to understand the mechanisms involved in plasma-propellant interactions. These mechanisms could include radiative, conductive, and convective transfer, as well as chemical interaction of the plasma species with the propellant. This paper is a summary of efforts to date at the ARL in the area of plasma propellant interaction. Samples were generated in three different series of experiments and under different conditions, therefore it is not possible to correlate the results of the different experiments. It is possible to make observations from each regarding the role of plasma mechanisms.

Moreover, the studies have been valuable in developing the methodology and strategies to be used in future systematic experiments for understanding plasma propellant interaction, which will be an integral part of a basic ETC research program.

Experimental

A 100 kJ capacitor-based pulsed power supply (PPS) was used for generating the high energy plasmas in these experiments. The power supply consists of two capacitors (11 kV, 830 *u*F), interconnected with a 10 *u*H inductor and an ignitron switch. The plasma generator has an inner diameter of 0.6 cm and an overall length of about 10 cm. Power levels for the different experiments ranged from 60 to 125 MW, depending on the initial capacitor voltage level. In response to a pulse from the plasma generator, a metal (commonly aluminum) fuse positioned between the anode and the cathode is rapidly vaporized and ionizes the polyethylene liner to form a dense plasma in which a high current discharge is sustained (3). The desired ignition effect is to increase the propellant gas generation rate so that the pressure profile is optimized (lowered in amplitude and broadened in time), compensating for the propellant burning rate temperature sensitivity.

Three types of experiments, involving different plasma-propellant exposure mechanisms, were performed. In all experiments, JA2 (consisting of nitroglycerin, NG; diethylene glycol dinitrate, DEGDN; and nitrocellulose, NC) was used as a sample. Additionally in the third experiment, a matrix of a variety of propellant materials was examined. These experiments are described below:

1. JA2 Exposed through a Polyethylene Tube: The first experiment involved exposure of sheet JA2 through a polyethylene tube; Figure 1 shows a schematic of the experimental setup (4). The plasma cartridge was fired into a polyethylene centercore tube (OD-44 mm; wall thickness-3mm; length-235 mm). Small rectangles of the JA2 sheet were located at the same axial position along the outside of the polyethylene centercore tube which provided a physical barrier between the plasma and propellant. The JA2 was therefore not subjected to the convective flow of the gases, but was exposed to some radiant energy. The polyethylene tubing is largely transparent in the visible and infrared regions, but has a cut-off at wavelengths lower than 200 nm, as shown in Figure 2. Although the propellant samples were located at the same axial position along the length of the tube, they were located at various stand-off distances from the tube outer surface. Thus, the conductive effect of the plasma was virtually eliminated. The power output of the PPS was 60 MW; peak energy is delivered by 250-300 *u*sec, with a total pulse duration of about 500 *u*sec.

2. JA2 in a Freely-Expanding Plasma: In the second experiment granular JA2 was used. A schematic for the experimental setup is shown in Figure 3. The propellant was exposed to the plasma in three different ways:

a) direct exposure to the freely propagating electrical plasma

b) shielding of the grains by covering with aluminum foil. This allowed the propellant to be subjected to the conductive heat, but diminished the effects of radiation and convective gas flow.

c) shielding of the grains by a sheet of Mylar film. The latter is transparent in the visible region, but is an effective filter of UV radiation below 300 nm- at least down to 190 nm- the lowest wavelength measurable with the spectrometer used (Figure 2). Thus, the Mylar would allow the propellant to be subjected to visible radiation, but would diminish the convective and conductive gas flow effects, and exposure to UV radiation.

3. Propellant Array: The third experiment was performed in August, 1997, and consisted of a matrix of propellants which were exposed simultaneously to a single plasma output. Samples were positioned with adhesive to a sheet of Plexiglas. An array of fourteen samples, consisting of two sets of seven different formulations, were tested as shown in Figure 4. The top set of samples was exposed to the plasma directly, whereas the bottom, "twin", set was covered by a sheet of Mylar film. The distance from the plasma output nozzle to the Plexiglas center was 30 cm, and the direction of propagation of the plasma was normal to the sample surfaces. The PPS power level was 125 MW; it is estimated from computer simulations (5) that the plasma temperature inside the generator core and prior to expansion in the open air, reached about 30,000 K. The spatial distribution of the plasma across the Plexiglas sheet (nom. 7 mm x 15 mm) is not known, thus it is not certain that all the samples were exposed to the same plasma intensity. Not only were the samples exposed to the plasma, but also to the heat and reaction products of the surrounding samples, several of which burned. Thus, this experiment is not meant to determine the relative reactivity of the samples, but rather to identify chemical changes in a variety of formulations caused by direct, or indirect, interaction with the plasma.

The propellants which were tested include the following types: a) M9, containing NC and NG; b) JA2, containing NC, NG and DEGDN; c) a HELP variation containing cellulose acetate-butyrate (CAB) binder, NC, RDX and an energetic plasticizer, EP; and d) energetic thermoplastic elastomeric (ETPE) binders containing either RDX or CL20 as the nitramine solids fill.

Chemical Characterization

Plasma-treated samples were analyzed by D-GC-MS, reflectance FTIR and XRF spectroscopies:

Thermal desorption gas chromatography-mass spectrometry (D-GC-MS): D-GC-MS was used to heat uniformly prepared propellant samples in a pyroprobe at 175 C for 20 sec to release nitroglycerin (NG) and diethyleneglycol dinitratrate (DEGDN). The desorbed plasticizers are injected simultaneously through an interface onto a GC column for separation, and passed through a mass-spectrometer for identification. Desorption was achieved via a CDS Model 122 Pyroprobe (coil type) connected to a heated interface chamber to the splitless injector of a Hewlett Packard GC-FTIR-MS system (Model 5890 GC and Model 5970 mass selective detector), as shown in Figure 5. The pyroprobe interface temperature was 175C and the sample was pulsed at 175 C for 20 seconds. The GC column was a J & W Scientific capillary column (0.25 mm x 15 m; 0.25 μm DB5 film). The GC injector temperature was 200 C. The oven temperature program used was as follows: 50 C isothermal for 1 min; 70 C/min to 250 C for 4 min (total run time 7.9 min). This D-GC-MS method has been used previously for quantitative analysis of energetic materials (6).

Micro-Reflectance Fourier Transfer Infrared (FTIR) Spectroscopy: FTIR was used to obtain spectra of the surface (i.e. about top 10 microns) of the propellant samples. The spectrometer used for all the IR measurements was a Mattson Polaris. The reflectance spectra were obtained using a Spectra-Tech microreflectance attachment and were run at 4 cm^{-1} resolution, with 200 scans signal averaged for background and sample spectra.

X-Ray Fluorescence (XRF): XRF was performed on the Mylar film used to shield the matrix of propellant samples, in order to determine what metals are present in the plasma, and whether they penetrate the film. Spectra were obtained on a Kevex Delta 1 x-ray fluorescence spectrometer attachment to a JEOL 820 SEM using Quantex V software.

Results

The results from the three different experiments will be presented in the same order in which they were described in the Experimental Section.

1. JA2 Exposed Through a Polyethylene Tube: In this experiment, an attempt was made to mitigate the conductive, convective and far-UV components of the plasma to which the JA2 sample was exposed, by channeling the bulk of the plasma output through a polyethylene tube and locating samples on the outside, up to a couple of centimeters away from the tube. Post-testing analysis of the recovered propellant indicated that a subsurface reaction was initiated which resulted in the propellant changing from a green translucent color to a creamy opaque green-yellow color. An SEM analysis of the reacted propellant showed that the reaction extended to a depth of approximately 1 mm into the sample, and that voids within the sample became larger at greater depths (7). The JA2 plasticizers, DEGDN and NG, are known to be volatile and are readily diminished at temperatures used in aging studies (up to 75 C). Thus, if heating and subsurface reactions occurred, the levels of NG and DEDGN might easily be diminished.

The NG and DEGDN levels were determined by D-GC-MS as a function of depth below the surface which had been exposed to the plasma. For comparison, a virgin JA2 sample was depth profiled in the same manner. The results are shown in Figure 6. Both the virgin and plasma-treated samples showed that the same level of NG was present. However, the level of DEGDN in the treated sample was reduced about 5-10% from its original level in the virgin samples.

2. JA2 in a Freely Expanding Plasma: In this experiment the samples were characterized by reflectance spectroscopy, in order to determine if decomposition of the JA2 occurred. D-GC-MS analysis was performed to determine plasticizer levels in the treated and virgin samples.

a) direct exposure to the freely propagating electrical plasma: The effect of full plasma exposure was definitive, and showed that significant denitration of the nitrate esters of JA2 occurred. This is evident from the IR spectra shown in Figure 7b, in which a band at 1740 cm^{-1} appears, due to the aldehyde carbonyl which is

formed when nitrogen dioxide is released. The spectrum of virgin JA2 is provided for comparison (Figure 7a), and shows that the only significant bands are at 1650 cm^{-1} and 1290 cm^{-1}, and are due to the asymmetric and symmetric stretching modes of N-O, respectively. Components which could be the source of the nitrogen dioxide include NC, DEGDN and NG.

b) shielding of the grains by Mylar film: As mentioned above, the Mylar film diminishes the conductive and the convective flows of the plasma, and filters UV radiation below 300 nm. The Mylar was very effective in mitigating the effect of the plasma on the propellant. This spectrum is virtually identical to JA2, and is not shown here.

c) shielding of the JA2 by aluminum foil: The aluminum foil allowed the propellant to be subjected to the conductive heat, but would diminish the effects of radiation and convective gas flow. This sample was non-uniform, with a gradient over the surface which could be detected visually. One end had the same color and flatness of the virgin sample, while the opposite end appeared darkened and pitted, as did the directly exposed sample. The spectra confirmed the visual assessment (Figure 8). The darkened end gave a spectrum very similar to that found in Figure 7b, showing the aldehyde carbonyl formed from denitration, while the opposite end appeared much like JA2, with no evidence of oxidation. This gradient in the level of reaction suggests that plasma effects were not uniform over the sample.

The three samples exposed to the freely expanding plasma were analyzed by D-GC-MS. The results are shown in Figure 9, and indicate that, within the error of the analysis, the NG and DEGDN levels were the same for the treated and virgin samples. The D-GC-MS and IR data indicate that the plasticizer level is not affected by plasma treatment, but in the directly exposed and aluminum covered samples, denitration occurs to some extent in NC, NG, and/or DEGDN.

3. Propellant Array: This experiment was done as a preliminary screening to explore how samples might react, and to develop the methodology to characterize the decomposition products and reaction mechanisms of propellants with a wide variety of chemistries. Conclusions regarding the relative reactivity of the propellants can not be made based on these results because: a) the spatial distribution of the plasma intensity over the dimensions of the Plexiglas plate is not known, and is currently being investigated and b) the samples were not run independently, and were in close proximity to one another. Thus, samples which ignited could generate heat and reactive products which could, in turn, react with other samples in an uncontrolled and unpredictable manner. Thus, further experiments will be performed to determine whether the reactions observed are direct or secondary effects of the plasma.

Of the array propellants shown in Figure 4, only the samples directly exposed to the plasma appeared to have reacted or ignited. As in the freely expanding plasma experiment described above, those shielded with Mylar film did not appear to react. The samples which burned included: JA2, and three of the four samples which had BAMO-AMMO (BA) as the binder (two containing CL20 and one containing RDX and NQ). The samples

which partially reacted and for which material was recovered included: RDX-BA (without NQ), HELP and M9. Reflectance IR was performed on: a) the partially reacted samples, b) the Mylar shielded samples, and c) the virgin samples for comparison. Chemical changes can only be discussed for the samples which partially reacted, i.e RDX-BA, HELP and M9:

RDX-BAMO/AMMO without NQ: The exposed sample appeared deep grey at one end, and light grey at the other. The spectra for dark grey area differed most from those for the virgin material (Figure 10), and bands unique to RDX and BAMO-AMMO are readily distinguished. The RDX bands diminish significantly for the exposed, dark grey sample, relative to the virgin sample; the light grey RDX bands were intermediate in intensity (not shown). Thus, the reflectance data shows that RDX is reduced significantly, at least at the surface, upon plasma treatment. The decomposition of AMMO polymer was previously reported (8) and showed that heating to 260C in an Argon atmosphere, virtually eliminated the azide group (i.e. disappearance of the IR band at 2100 cm^{-1}) through the loss of nitrogen and formation of the imine (R-C=NH) group (appearance of the 1660 cm^{-1} band). Both the azide and imine bands are sharp and are easily monitored; the azide is present in BAMO as well. The fact that the imine is not observed in the spectrum of the treated sample shows that under the conditions of this experiment, the RDX level begins to diminish, while the BAMO-AMMO polymer remains intact.

HELP Propellant: The virgin and Mylar-shielded samples appeared yellow, while the exposed sample was light green at the surface (underneath was yellow). The spectra of the unshielded sample was only slightly different from the virgin and shielded samples (Figure 10); band assignments agree with those reported previously using ATR microscopy (9). The differences are subtle, but the unshielded sample has reduced bands at 1750 cm^{-1} and 1660 cm^{-1}, which are assigned to the ester C=O of CAB and the nitrate N-O of NC respectively. (Nitrate ester plasticizers were not present in the HELP sample.) It is known that the acetic and butyric acids esters of CAB diminish under relatively mild thermal exposure. Moreover, the acids resulting from CAB decomposition can, in turn, promote the decomposition of the nitrate esters, accelerating the release of nitrogen oxides. The green color may arise from reaction of the nitrogen dioxide with the stabilizer. The latter is present at a level too low to be detected in the infrared, but can be a very powerful visible chromophore. Although the unshielded sample reacted only very slightly, spectroscopic changes were detectable. At greater plasma intensities and increased levels of reaction, IR spectroscopy should be a valuable monitor of chemical changes. Moreover, D-GC-MS will also be very useful to quantify hydrolysis of the CAB esters and the denitration of NC.

M9 sample: The virgin and shielded spectra of M9 look identical to that of JA2, the main features being the nitrate esters which dominate both formulations (JA2 containing NC, DEGDN and NG; M9 containing NC and NG). The unshielded sample yielded a small but distinct peak at 1740 cm^{-1}, indicative of carbonyl formation, analogous to that found in JA2 (Figure 12). Although neat DEGDN, found in JA2 but not M9, has a strong ether C-O-C band at 1135 cm^{-1}, this band is not evident in the propellant spectrum. Thus, for propellants rich

in nitrate esters, e.g. single and double base formulations, IR spectroscopy is not useful for quantitative analysis of the nitrate esters, but it is a quick tool for assessing if their oxidation has occurred.

For the samples which burned, it was only possible to compare the virgin with the Mylar-shielded samples, and in every case the spectra were identical. Future studies are planned, however, in which samples with varying propellant chemistries will individually be exposed to the ETC-plasmas at appropriate intensities so that the sample will partially decompose. For this purpose, the spectra of the virgin propellants are of interest to determine if bands are present which can serve as indicators that specific components are decreased or undergo chemical reaction initiated by the plasma. Thus, the virgin spectra for the samples that burned to completion are presented below:

a) RDX-BAMO-AMMO with NQ: The virgin spectrum appeared much like that of the RDX BAMO-AMMO sample shown in Figure 13, except that a few bands due to NQ are present. The intensity of the bands is detectable, although not great, since the NQ is present at less than 20 weight percent in the sample; the band at 1640 cm^{-1} could be enhanced if the water vapor were more completely purged. The sample with NQ had the coarsest surface of any virgin material, and that is reflected by a baseline which more irregular than the other propellants.

b) JA2 sample: Spectra of a virgin and denitrated sample of JA2 were shown in Figure 6; the formation of the aldehyde can be readily monitored in the IR.

c) CL20 BAMO-AMMO samples: The spectra of the two different virgin samples showed much different relative band intensities of CL20 vs the BAMO-AMMO, reflecting a difference in the solids fill level. Strong sharp bands for CL20 and BAMO-AMMO are evident (Figure 14), which will facilitate monitoring of these components in future plasma propellant interaction studies.

Conclusions

Three experiments were performed, under different conditions, to begin to understand the effect of ETC plasma on ignition. In the first experiment, JA2 was exposed to plasma radiation (60 MW) through a polyethylene tube which shielded the convective and conductive effects of the plasma. The treated sample showed evidence of subsurface reaction, and the level of DEGDN plasticizer was reduced to 15-20% from the 25% measured for the virgin material. In this case, plasma radiation (filtered below 200 nm by polyethylene) appears to have been effective altering the propellant composition.

The second experiment involved grains of JA2 which were exposed to a freely expanding plasma (60 MW). Grains were either unshielded, or shielded with aluminum foil or a Mylar film. None of the grains had a significant change in plasticizer level after treatment. However, IR spectroscopy of the surface showed that for the unshielded sample, some denitration of the nitrate esters (either NC, NG or DEGDN) occurred. The aluminum-shielded sample showed a gradient of denitration, with one end having significant reaction and the

other end having no reaction. The aluminum foil did not appear disturbed, and it is believed that it did block the plasma radiation. Thus, conduction also appears to be a factor in plasma propellant interaction. The Mylar shielded sample showed no evidence of denitration. In this case radiation which passed through the Mylar film was not sufficient to generate reaction of the propellant, and the thermal insulation provided by the Mylar film reduced conductive heating.

Although the power levels used in the above two experiments were the same, other important parameters are different. Mylar (polyethylene terephthalate, used in the freely-expanding plasma experiment) cuts off below 300 nm, whereas polyethylene (used in the tube experiment) begins to cut off below 200 nm; thus the two samples are not exposed to the same spectral distribution. Also, the form of the plasma is much different in each case. For the tube experiment the plasma is channeled through a confined region, whereas in the second experiment, the plasma expands freely into open air. A third variable is that the sheet JA2 sample was used in the polyethylene tube experiment, whereas JA2 grains were used in open air configuration. Thus, it is not possible to directly correlate the results of both experiments, but the conclusion which can be drawn is that there is experimental evidence for both radiation (as evidenced in the polyethylene tube experiment) and conduction (as evidenced from the samples shielded with aluminum foil) as being important mechanisms in plasma-propellant interaction.

The third experiment consisted of an array of samples exposed directly to a freely expanding plasma (125 MW). The intensity of the plasma impacting each sample is not known, so further work is needed to assess relative reactivity of the various samples. Samples shielded with Mylar film all appeared unreacted; IR analysis of the surfaces confirmed that no degradation occurred. Samples which burned included JA2, and three samples with a BAMO-AMMO binder (two containing different CL20 levels and one containing RDX and NQ). The three samples which remained all showed some evidence of decomposition: a) reduction of the nitramine level in the RDX-NQ-BAMO/AMMO sample; b) reduced carbonyl band of CAB and nitrate ester band of NC, respectively; and c) denitration of nitrate esters in M9 (analogous to that described above for JA2). For the samples which burned, IR spectra were obtained for the virgin samples, and bands are evident which can be monitored for identification and quantifying components in future plasma-propellant studies under conditions which result in partial decomposition.

Future Work

The results described in this paper were a summary of several plasma-propellant studies which were done as auxiliary parts of other programs. Future experiments will have as a goal, the understanding of the mechanisms involved in plasma propellant interaction. An important element of that understanding is characterization of the plasma, and work is in progress to measure the spatial distribution of the plasma in terms of pressure, temperature and spectral content. Metal particles may be generated from fuse and nozzle erosion, and contribute to the plasma composition; such effects will be investigated and minimized. Alternative

materials will be used to pass or block radiation, such as quartz or sapphire, rather than reactive materials such as polyethylene and Mylar which might complicate interpretation of the data.

The mechanisms involved in plasma-propellant interaction can be expected to be quite sensitive to sample chemistry. Future efforts will focus on treating a single sample with a well-characterized plasma. Samples will be well characterized in terms of their processing history and morphology, which can result in physical differences between samples of even the same composition. For example, samples with solids fill will be well characterized in terms of final particle size and coating, particularly at the surface. Also, as the plasma levels are better tuned to each propellant type, more complex decomposition products may result. For better characterization of the products, additional analytical methods will be performed. Gel permeation chromatography will be used to analyze changes in the length of polymeric components such as CAB, NC and the ETPE binders. Other FTIR methods will be investigated, such as attenuated total reflectance (ATR) and photoacoustic spectroscopies (PAS). ATR offers advantages in quantitative analysis, and PAS offers advantages for non-destructive depth profiling. Moreover, full use of the pyroprobe-GC-MS instrumentation for identification and quantification of decomposition products will be made. Thermal analyses and X-ray techniques sensitive to organic species will be applied as appropriate.

References

1. Juhasz, A.A., private communication, U.S. Army Research Laboratory, APG, MD, 1996.

2. Katulka G.L. and Dyvik, J., "Experimental Results of Electrical Plasma Ignition in 120-mm Solid Propellant Tank Gun Firings", 32nd JANNAF Combustion Subcommittee Meeting, Vol. 1, CPIA Pub. 631, pp. 113-122, October 1995.

3. Powell, J.D. and A.E. Zielinski, "Theory and Experiment for Ablating-Capillary Discharge and Applicaiton to Electrothermal-Chemical Guns", BRL-TR-3355, June 1992.

4. White, K.J., G.L. Katulka, and S. Driesen, "Electrothermal Chemical Plasma Interaction with Propellants", 32nd JANNAF Combustion Subcommittee Meeting, Vol. 1, CPIA Pub. 631, pp. 113-122, October 1995.

5. Katulka, G.L., "Parametric Study of High Energy Plasmas for Electrothermal-Chemical Propulsion Applications", IEEE Transactions on Plasma Science, Vol. 25, No. 1, February 1997.

6. Pesce-Rodriguez, R.A., P.J. Kaste, J.B. Morris and K.L. McNesby "Qualitative and Quantitative Analysis of A Foreign Explosive", ARL-TR-1624, March 1998.

7. Lieb, R.J., private communication, U.S. Army Research Laboratory, Aberdeen Proving Ground, MD, 1995.

8. Bazaki, H., and N. Kubota, "Energetics of Ammo", Proceedings of the 21st International Conference of the ICT, 45/1-12, Karlesruhe, FHG, July 1990.

9. Pesce-Rodriquez, R.A., C.S Miser, K.L. McNesby, R.A. Fifer, S. Kessel, B.D. Strauss, "Characterization of Solid Propellant and Its Connection to Aging Phenomena", Applied Spectroscopy, Volume 46, No. 7,1992.

10. White, K. private communication, U.S. Army Research Laboratory, Aberdeen Proving Ground, MD, 1998.

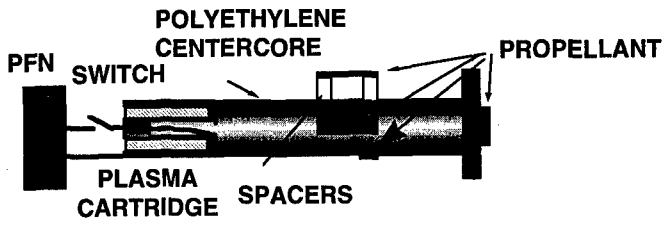

Figure 1. Schematic of experiment for plasma exposure of JA2 through a polyethylene tube.

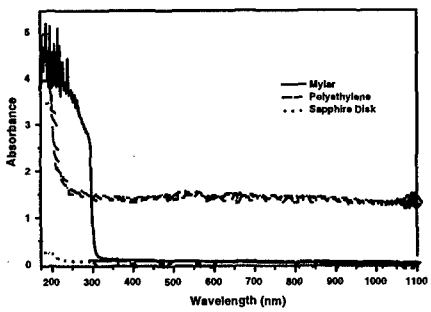

Figure 2. UV-visible absorbance spectrum of polyethylene tubing and Mylar film; sapphire was run as a reference material.

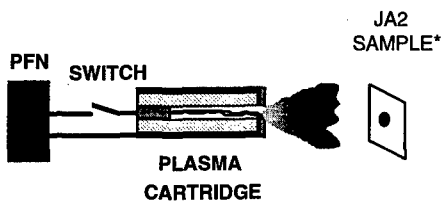

Figure 3. Schematic of the experimental setup used in the treatment of JA2 to a freely expanding plasma. *JA2 sample was either unshielded, or shielded with aluminum foil or a Mylar film.

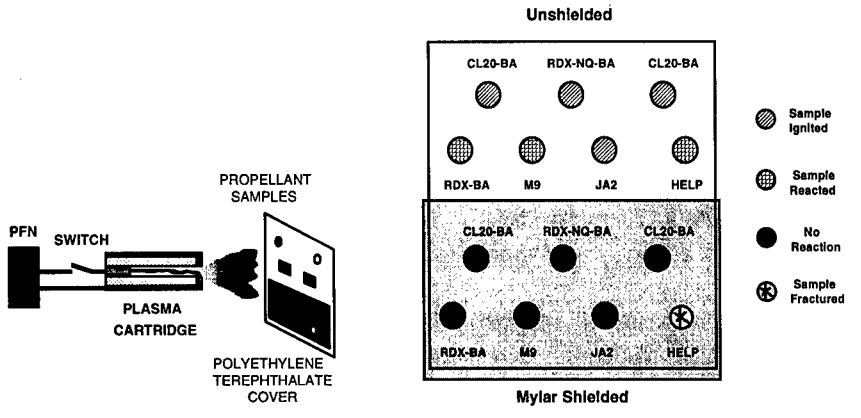

Figure 4. Arrangement of samples exposed to plasma in the propellant array experiment.

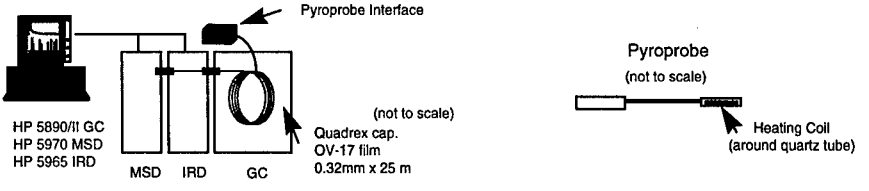

Figure 5. Schematic of the D-GC-MS instrumentation used in the analysis of NG and DEGDN.

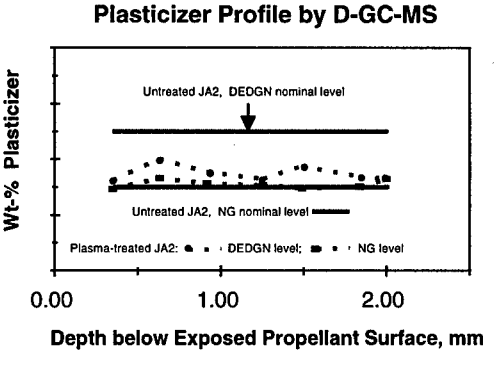

Figure 6. Analysis of plasticizers in virgin and plasma treated JA2.

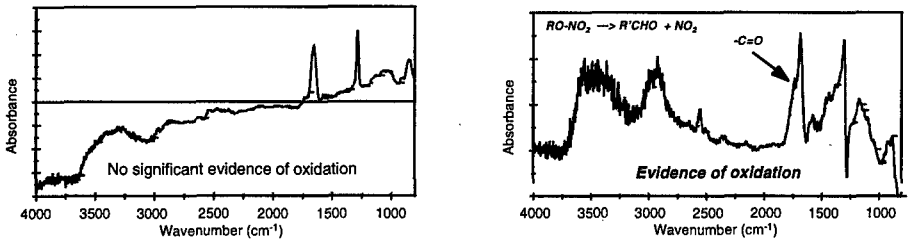

Figure 7. FTIR microreflectance spectrum of a) virgin JA2 and b) a sample exposed directly to the output of the freely expanding plasma.

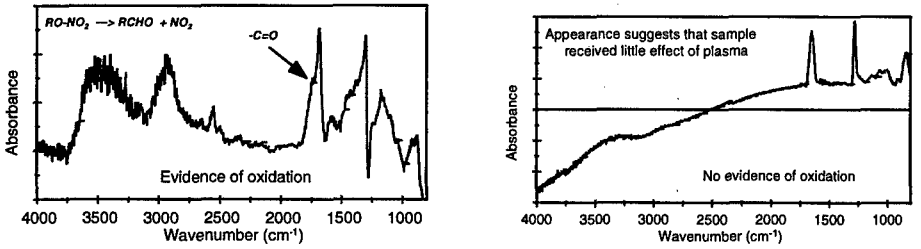

Figure 8. FTIR microreflectance spectra of opposite ends, a and b, of an aluminum-shielded sample of JA2 in the output stream of the freely expanding plasma.

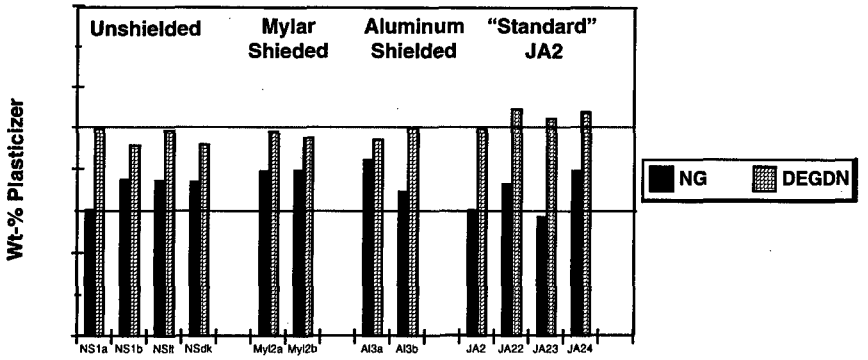

Figure 9. Analysis of plasticizers in virgin JA2 and the three samples exposed to the freely expanding plasma: 1) unshielded; 2) Mylar shielded and 3) Aluminum foil shielded.

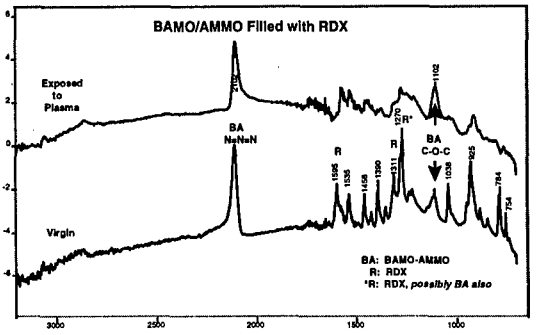

Figure 10. FTIR microreflectance spectra of virgin and the plasma treated RDX-BAMO/AMMO propellants.

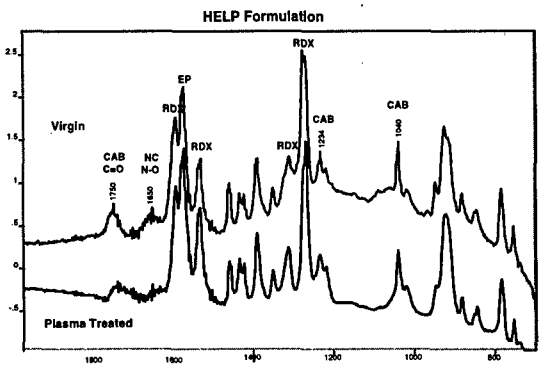

Figure 11. FTIR microreflectance spectra of virgin and the plasma-treated HELP propellants.

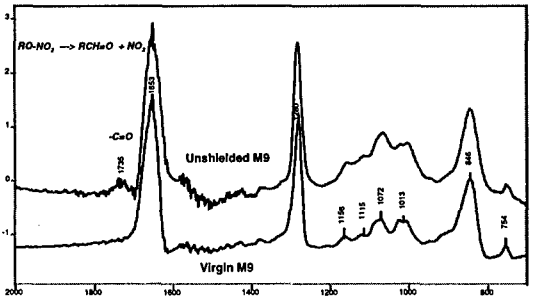

Figure 12. FTIR microreflectance spectra of virgin and unshielded M9 sample.

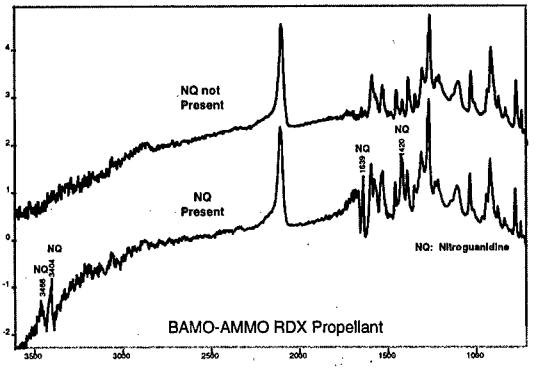

Figure 13. FTIR microreflectance spectra of the virgin RDX-NQ-BAMO/AMMO sample.

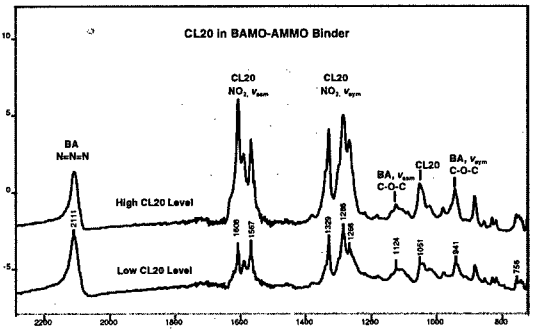

Figure 14. FTIR microreflectance spectra of the virgin BAMO/AMMO with high and low CL20 solids fill.

Text proposed to the
29th International Annual Conference of ICT
June 30 - July 3, 1998, Karlsruhe
Federal Republic of Germany

IGNITION AND PYROLISIS OF EXPLOSIVE COMPONENTS

S. Almada*, J. Campos and J.C. Gois****

Lab. of Energetics and Detonics
*Naval Expl. Laboratory, Alfeite - 2800 Almada,
***Mech. Eng. Depart. – Fac. of Sciences and Technology –*
Polo II - University of Coimbra – 3030 COIMBRA - PORTUGAL

ABSTRACT

Pyrolisis reactions, existing in explosives components and mixtures, are very hard to follow by experiments, because these processes are very fast and proceed with increasing pressure and temperature. The thermogravimetric analysis (TGA), differential scanning calorimetry (DSC) and conventional cook-off methods, do not give precise and correct answer to the problem of detecting the level of life time of any chemical explosive or powder, by the beginning of its decomposition reaction. The method, here presented, is based in thermogravimetric analysis, correlated with a simple ignition and transition to combustion model. The original experimental set-up, presented in a previous paper, is based in classical thermogravimetry equipment (TGA), recording the evolution of sample mass as a function of temperature, for samples larger enough to solve heterogeneity problems. The sample is enclosed in an open cylindrical container, inside a glass column, where the products of combustion of propane/air flow. Different heating levels can be selected as a function of the distance from the propane/air burner. The temperature and the mass of the sample are continuously measured and recorded during heating process. The warming transient regime and the ignition zones are clearly visible in obtained results, in range of 800 - 1000 K.

The selected energetic materials are Ammonium Nitrate (AN), pentaerythritol tetranitrate (PETN) and cyclo-1,3,5-trimethylene-2,4,6-trinitramine (RDX), very well known energetic components of industrial and military plastic bonded explosives.

A reaction path, final composition and thermodynamic properties of products, are predicted as a function of temperature and pressure, for isobar and isochor adiabatic combustion conditions, using a thermochemical computer code, named THOR. The results are discussed with theoretical prediction of ignition temperature and time

delay, based in Semenov criteria for one single particle. The ignition criteria is based on the changement of reaction intensity, during heating regime, showing the start of combustion or explosion regime. Experimental results prove the validity of this ignition criteria. Kinetics parameters are based on Coats and Redfern approach. From the selected materials, PETN and RDX present an interesting temperature jumping phenomena, after ignition, predicted in theoretical model and observed in experimental results.

EXTENDED ABSTRACT

1. Introduction

For people safety, environmental control and adequate strategy during storage and transportation of energetic compounds, is very important to know its thermal decomposition behaviour. The existing run-away phenomena, generating explosions, are complex. Past experiences have shown that there are neither simple nor universal predictive methods. Small-scale tests could be desirable because all explosion phenomena start in a single or multiple small flame kernels. Thermal decomposition of AN, PETN and RDX, in a silica sand bed, showing its ignition temperature and delay and its pyrolysis behaviour, were already presented [Cardao et al., 1997]. Thermal response of those energetic materials were discussed in such a way to relate thermal behaviour, from the small scale DSC and TGA samples (3 mg) with those obtained from an intermediate scale experiment with larger samples (100 mg). A cylindrical brass container, inside a glass column, where the combustion products of propane/air flow, was used to heat the sample up to its ignition. The silica sand bed was used to clarify ignition mechanism, reducing the violence of the decomposition stage and its blasting effects. The temperature and mass of the sample were continuously measured. Selected external temperature range was 800 - 1000 K and obtained results have been discussed according to a simple theoretical model based in Semenov ignition criteria [Cardao et al., 1997].

Based on previous work, the theoretical model and discussion of thermal flow of each energetic material, for several compositions, in order to determine when the regime of the decomposition reaction is going to change, showing its ignition and explosion

regime, is now presented and discussed. The kinetic parameters are based on Coats and Redfern, 1964, theoretical approach.

2. Selected energetic materials and thermal characterization

Selected energetic materials are Ammonium Nitrate (AN), pentaerythritol tetranitrate (PETN) and cyclo-1,3,5-trimethylene-2,4,6-trinitramine (RDX) used respectively in industrial and military plastic bonded explosives.

The particle range size of AN was obtained using laser diffraction spectrometry. PETN, RDX and inert silica particle sand sizes were measured by Coulter Counter (Cardao et al., 1997).

Simultaneous thermal analysis (heat flow DSC and TGA) was also employed to investigate the thermal decomposition of the selected energetic materials, in non-isothermal conditions (using a *Rheometric Scientific* STA 1500 equipment). The nominal heating rate of 10 ^{0}C/min (covering the temperature range from 298 K to 623 K) was employed using samples size of 3 mg . The samples were loaded into open crucibles and a dry nitrogen purge flow of 50 ml/min at 0.1 MPa absolute pressure was used in all measurements. A resume of the more relevant experimental results comparatively with the ones theoretically predicted is presented in the following figure.

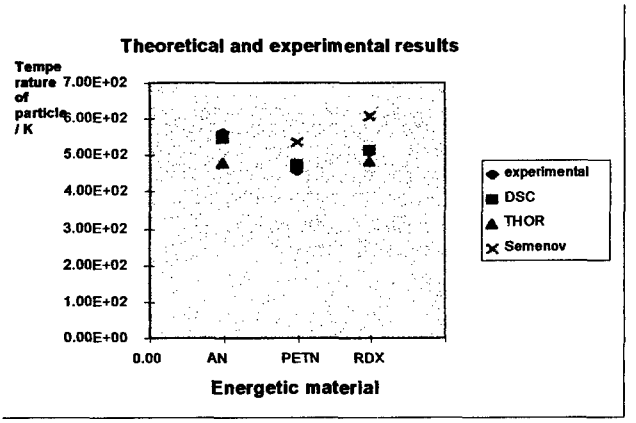

Figure 1 - Theoretical and experimental results of ignition temperature of AN, PETN and RDX samples.

3 Experimental equipment and results

The original thermal analysis equipment was already presented [Cardao et al., 1997]. A propane/air burner and a glass column make the experimental apparatus. Different temperature levels can be obtained depending on the distance from the burner and in the propane/air ratio. An open brass cylinder container, suspended by a spindle, fixed in a digital balance, is used to confine the sample. The temperature and the mass of the sample are continuously measured. Two thermocouples are placed at different levels inside the sample. A third thermocouple measure the flow temperature at the level of the container.

Two independent valves previously calibrated as a function of the upstream pressure controlled the mass flows of propane and air. The glass column has an internal diameter of 44 mm and a thickness of 3 mm, for a length of 68 mm, divided in five stages. The external temperature inside the glass column at fifth level was calibrated for two propane/air ratios, Tg=857 K and Tg=959 K, and recorded using K-type thermocouples, using a system composed by two digital signal acquisition and analyser system.

In order to protect the original thermal analyser equipment, the energetic particles were mixed with silica sand particles, in a bed, with total mass of 500 mg. A calibration of the bed warming evolution temperature, without energetic particles, was performed. Mass fractions of energetic materials ranging, from 5 to 20%, were tested for each selected energetic material.

The thermal flow analysis is presented in figures 2 to 4, showing the thermal flow regime as a function of time, for different concentrations of energetic materials in the bed (with silica sand particles). These results allow to calculate the mean value of observed thermal flow regime immediately before and after the ignition instant (vd. Table 1).

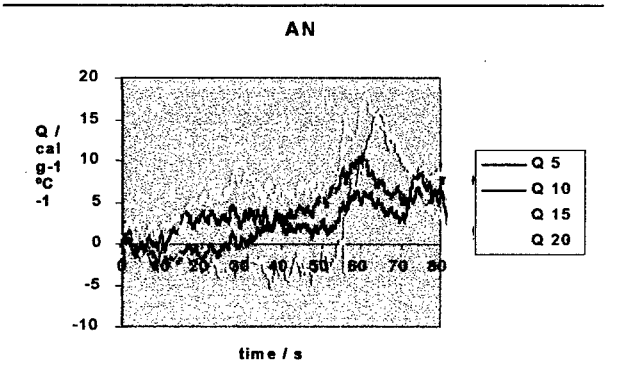

Figure 2- Thermal flow for AN 5, 10, 15 and 20 %.

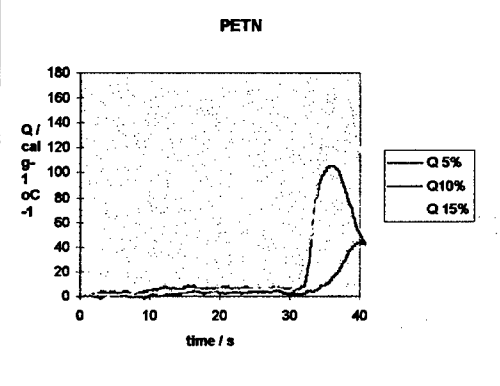

Figure 3- Thermal flow for PETN 5, 10, and 15 %.

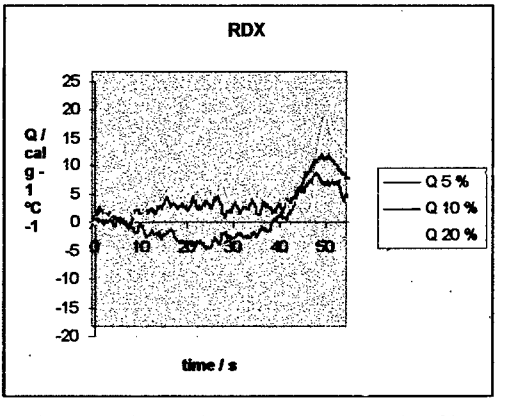

Figure 4- Thermal flow for RDX 5, 10 and 20 %.

Q	Before "Ignition"	After "Ignition"
AN		
5 %	8.7	8.78
10 %	8.78	8.78
15 %	8.78	17.56
20 %	5.85	17.56
PETN		
5 %	4.2	52.7
10 %	5.0	193.2
15 %	5.9	216.6
RDX		
5 %	8.78	17.56
10 %	4.18	8.78
20 %	5.85	35.13

Table 1- Average of the thermal flow before and after the "explosion", for AN, PETN and RDX.

4. Kinetics analysis

Several authors have discussed the kinetic parameters based on thermogravimetric data. In the present text Coats e Redfern, 1964, approach is applied to the experimental curves of temperature and weight evolution.

For a reaction like aA (s) $\rightarrow$ bB (s) + cC (g) the rate of consumption of reagent A is given by:

$$\frac{d\alpha}{dt} \equiv k(1-\alpha)^n \qquad (1)$$

with $\alpha=(m_0-m/m_0)$ the fraction of A that undergo decomposition during time t, n the reaction order and k the rate constante.

A linear heating rate allows $\beta \equiv \frac{dT}{dt}$ $\beta=dT/dt$ (2)

Combining the last expressions it can be obtained:

$$\int_0^{\alpha} \frac{d\alpha}{(1-\alpha)^n} \equiv \frac{A}{\beta}\int_0^{T} e^{-E\ RT} dT \qquad (3)$$

With several approaches and simplifications, the expression becomes:

$$\ln\left\{\frac{1-(1-\alpha)^{1-n}}{T^2(1-n)}\right\} \equiv \ln\frac{AR}{\beta E}\left[1-\frac{2RT}{E}\right]-\frac{E}{RT} \qquad (4)$$

To n=1 the graphical representation of $\ln\left[\frac{-\ln(1-\alpha)}{T^2}\right]$ function of $\frac{1}{T}$ gives, if the chosen order is correct, a straight line with inclination -E/R. This is true since in the temperature interval chosen the expression $\frac{AR}{\beta E}\left[1-\frac{2RT}{E}\right]$ is constant.

For each energetic material the bigger zone of linearity were chosen. The kinetic parameters can then be obtained through a linear regression. The presented results correspond to the average of the kinetic parameters obtained for the different tested compositions.

	AN	PETN	RDX
E /Jmol^{-1}	2.10×10^5	1.16×10^5	1.10×10^5
A / s^{-1}	2.38×10^{17}	1.17×10^{19}	4.95×10^{12}
Temperature zone /K	564 – 620	465 – 570	520 – 598
1 - α	0.85 – 0.47	0.95 – 0.76	0.91 – 0.56
E / Jmol^{-1} *[DOBRATZ, 1981]*	1.96×10^5	1.96×10^5	1.97×10^5
A / s^{-1} *[DOBRATZ, 1981]*	4.00×10^{19}	6.30×10^{19}	2.02×10^{18}

Table 2 – Correlation between experimental and referenced kinetic parameters [DOBRATZ, 1981] for AN, PETN e RDX .

5. Discussion and conclusions

A good agreement, in ignition temperature, was found between theoretical approaches and the experimental results. The experimental results were really more concordant with the obtained by DSC, the theoretical results from Semenov criteria were slightly above and the predicted values using THOR code were slightly under the experimental.

Relatively to the thermal flow, PETN shows a higher jumping of the thermal flow before and after the "explosion" reaction. For AN that difference only appears for composition near 20 %, which is in accordance with the previous results.

The strongest thermal reaction, among the selected energetic materials, was observed for PETN. This energetic material presents a higher trend for the "temperature

jumping phenomena ". This trend increases with the increase of PETN concentration in silica sand bed. This temperature jumping corresponds to a run-away followed by fast reaction rate. The ignition temperature of PETN and RDX is independent both of the sample mass concentration in silica send bed and external temperature. On the other hand, the ignition temperature of AN has a tendency for slightly decrease with increasing concentration and increasing external temperature.

The kinetic parameters, based on the experimental results, appear to be very coincident with the presented by other authors. These results prove the validity of the presented experiment method and theoretical approach.

References

Bandyopadhyay, S., Bhaduri, D. 1972, Prediction of ignition temperature of a single coal particle, *Combustion and flame* , n° 18 p. 133-136.

Brigite Dobratz, 1981 - *LLNL Explosives Handbook*, Lawrence Livermore Laboratory.

Campos, J., 1991, Thermodynamic calculations of solid and gas combustion pollutants using different equations of state, in Proc. of the *1st International Conference on Combustion Technologies for a Clean Environment*, Vilamoura, Algarve, p. 30.4-1.

Cardão, P.; Góis, J.C.; Almada, S.; Simões P. , Durães, L.; Campos, J., 1997, Thermal decomposition of energetic materials, in Proc. of the *28th International Annual Conference of ICT.*

Coats, A.W.; Redfern, J.P., 1964, *Nature*, January 4, 68.

Durães, L., Campos, J., Gois, J. C., 1995, Deflagration and detonation predictions using a new equation of state, in Proc. of the *26th International Annual Conference of ICT*, p.67-1.

Hongtu F., P. G. Laye, D. J. Rose, 1991, Ignition Temperatures by Thermal Analysis, in Proc. of the *17th International Pyrotechnics Seminar*, p.31.

Liza F. D., Ilzoo Lee, Frank E. Hudson III, 1996, Thermal Response and Parametric Analysis of Aluminized AP/HTPB Based Propellants With Varying Composition, in Proc. of the *27th International Annual Conference of ICT.*

PROTOCOL FOR THE CHARACTERIZATION OF EXPLOSIVES-CONTAMINATED SITES

Thiboutot, S., Ampleman, G., and Dubé, P., DREV

J. Hawari, BRI

T.F. Jenkins and M.E. Walsh, CRREL

Defence Research Establishment, Valcartier (DREV)
Department of National Defence, Canada
2459, Pie-XI Blvd North, Val-Bélair, Québec, G3J 1X5

Biotechnology Research Institute, NRC Canada (BRI)
6100 Royalmount Avenue
Montreal, Quebec, H4P 2R2

U.S. Army Cold Regions Research and Engineering Laboratory (CRREL)
72 Lyme Rd, Hanover, NH 03755-0127

Presented at the 29th International ICT Conference, June 1998

ABSTRACT

Many activities of the Canadian Forces such as firing, demolition procedures and destruction of obsolete ammunition by open burning and open detonation may lead to the dispersion of energetic compounds in the environment. These compounds are being closely examined due to their highly specific physical, chemical and toxicological properties. In Canada, limited effort has been spent to examine this particular environmental threat. In this context, R&D was dedicated towards the establishment of a protocol that allows reliable and safe characterization of sites contaminated with explosives. This protocol is based on DREV research efforts and expertise in the chemistry of energetic materials, on the current existing literature, on the experience gained in practical field sampling and on collaborative work with Biotechnology Research Institute and Cold Regions Research and Engineering Laboratory. The protocol covers all aspects related to surface and sub-surface sampling, extraction, analysis, field screening methods and environmental fate related with these specific contaminants. Furthermore, safety procedures are described that take into account the explosive and toxic nature of these compounds. This protocol will serve as a reference guide for sampling campaigns on sites that are potentially contaminated with explosives.

1.0 INTRODUCTION

Identifying and developing economical and effective methods to eliminate undesirable contaminants from soil and groundwater is of increasing environmental interest and importance, worldwide. The task is all-the-more critical and complicated when the contaminants are energetic materials, main components of gun powders, explosives warheads and solid rocket propellants. The new international context with the end of the Cold War has resulted in the closing of many military bases and a growing awareness in environmental issues. This awareness has led many countries to integrate R&D programs related to the environmental impacts of energetic materials. It is within this context that the Canadian Research and Development Branch has directed some of its resources to assess the environmental risks associated with explosive compounds.

Many sites such as impact areas, training ranges, demolition and open burning/open detonation (OB/OD) ranges used to destroy the out-of specification materials are highly suspected to be contaminated by energetic substances as described in the literature (Refs. 1-2). Explosive manufacturing sites are also contaminated with energetic compounds. In order to evaluate the extent of contamination of DND sites, the sampling and characterization of various types of ranges have been performed in the last four years. All standard sampling, analysis and data management techniques should be applied when characterizing explosives contaminated sites. However, the overall work within this task has led to the establishment of a specific sampling protocol addressing different aspects related to these unique crystalline organic contaminants.

Our efforts were first targeted towards the characterization of secondary explosive compounds in soil and groundwater, since they represent the major threat. TNT and/or RDX are major ingredients in nearly every munition formulation and are the secondary explosives used in the greatest quantities (Ref. 3). Several other organic chemical explosives have also been used in specific munition formulations, including 2,4-dinitrotoluene (2,4-DNT), HMX, tetryl and trinitrobenzene (TNB). In addition to chemicals added to explosive formulas, munition residues often contain other chemicals impurities from production or as environmental transformation by-products. As an example, military grade TNT often contains a number of impurities, including 2,4-DNT and other isomers of dinitrotoluene. In addition TNT is prone to photo and microbial degradation from which a variety of

transformation products have been identified. The extraction and characterization protocol should include all these co-contaminants and should also take into account the sensitive nature of these molecules toward biotic and abiotic transformations. More details related to the protocol described in the present paper can be found in reference 4.

2.0 SAMPLING

Accurate chemical characterization of a hazardous waste site requires the development and implementation of a well-designed sampling plan. After defining the area of interest, which might be an entire site or several defined areas within a site, samples are collected according to one or several possible schemes. Distribution of contaminants are very site specific, depending on the manner in which the contamination occurred, the physical and chemical properties of the contaminant involved, soil type, and the geology and hydrogeology of the site.

The particular nature of explosives as contaminants must be taken into consideration for all aspects related to the sampling, preservation and analysis of soil or water matrixes. Explosives are solids at ambient temperature, dissolve slowly and sparingly in aqueous solution and have low vapour pressure (table I). These properties limit their mobility compared to other organic contaminants such as fuel or solvents. These contaminants demonstrate a pattern of high degree of heterogeneity in their distribution because of their low solubility and their crystalline nature. A protocol which will minimize this heterogeneous waste distribution must be implemented. The use of field screening methods is of high value since it will help in establishing a sampling pattern and in reducing laboratory analytical costs. The sampling of soil and groundwater and preservation of these samples must also take into account the particular nature of these contaminants.

2.1 Soil Sampling

A minimum of 500 g of soil must be sampled for each discrete or composite sample. Explosives are not volatile compounds (see table I) and therefore, no specific precautions such as the use of sealed containers have to be taken. The containers that are recommended for use are 1 litre amber glass bottles with a polypropylene or black phenolic baked polypropylene cap.

2.2 Spatial Heterogeneity

Several papers have been published by CRREL scientists on short range spatial heterogeneity of explosive concentrations in surface soils (Refs. 5-7). A collaborative study between CRREL and DREV has also led to the study of spatial heterogeneity at an HMX contaminated site (Refs. 8-10). Overall we found that sampling error greatly exceeds analytical error, and that the homogenization and compositing approach minimizes the sampling error. Thus, a characterization campaign of an explosives contaminated sites should involve the collection of composite samples using the sampling pattern previously described (Ref. 4), or a composite sampling pattern which will lead to the collection of representative samples.

2.3 Groundwater Sampling

Sampling the groundwater plume of a potentially contaminated site is often the best way to monitor the environmental impact. Operational ranges are often very large areas for which systematic griding and soil characterization can result in large expenditures. Thus, a sampling plan involving groundwater can minimize the associated sampling and analytical costs. If contamination is not found in detectable levels neither in the groundwater on-site, down and up-gradient of the site, it means that the potential contamination does not leach from the site and does not represent a threat to the watertable. If contamination is found in the groundwater, a more detailed sampling plan for the soil must be undertaken. However, depending of the future use of the site, surface soil contamination can represent a threat and might have to be evaluated. A detailed protocol for sampling explosive contaminated groundwater was developed as part of a natural attenuation study conducted in the US by Waterways Experiment Station (Ref. 11). All details related to well water sampling can be found in references 4 or 11.

2.4 Field Screening Methods

Field analytical chemistry is a growing area of chemical analysis in which the analytical measurement is accomplished at the site. Traditionally, analysis has been accomplished by collecting a sample from a site, transporting the sample to an analytical laboratory and, finally storing the sample until laboratory testing. This delay in data

availability delays decisions about the sampling site. Some decisions, such as those concerning human safety and product liability, are desired in real time. This is particularly true when explosives are the targeted contaminants. In addition to time saving and increased safety, the use of on-site methods can significantly reduce analytical costs. The site can be mapped with respect to analyte concentrations, decreasing the total number of samples required to characterize a site. For explosives, the cost of on-site analysis is much lower than laboratory analysis and this approach eliminates the need for transportation and storage. Two field methods designed for explosive compounds are currently available. Both methods were tested by DREV and CRREL under many different conditions and strong and weak points of both methods have been methodically assessed. These methods can be used to pre-screen the extent of contamination, ensure human safety, provide accurate and reliable results and reduce the total analytical costs. These methods are based either on colorimetric or on enzyme immunoassays. All details related to the use of these two methods are covered in reference 4.

2.5 Sample Preservation

The maximum holding time (MHT) for soil and water samples are critical to determine shipping and storage requirements. These factors are important in order to obtain reliable analytical results from field sampling. Table II presents the MHTs for soils and groundwater samples which have been determined based on references 12-14.

2.6 Other Co-Contaminants

When sampling an explosive contaminated site, parameters other than explosive compounds might be of interest. Activities which might have led to the contamination of soil and groundwater by explosives might also have led to the dispersion of other contaminants in the environment. The most probable one is contamination by metals, since they are either part of the ammunition casing, the ignition system or the target. Screening for metals and heavy metals should be conducted simultaneously at ranges where metallic shrapnel is generated and spread on the ground. Mercury should also be investigated where munitions fired at the ranges include this chemical. Also, some activities such as the open burning of obsolete ammunitions may lead to the accumulation of polycyclic aromatic

hydrocarbons in the environment and they should be monitored when their presence is suspected.

3.0 EXTRACTION AND ANALYSIS

At present, the established extraction/analysis method is the EPA SW846 Method 8330 (Ref. 12). Briefly, it uses solvent extraction by sonication for soils, salting-out pre-concentration for groundwater followed by an isocratic HPLC separation and UV detection. Detection limits for 15 individual compounds (HMX, RDX, TNB, DNB, tetryl, NB, TNT, 2-ADNT, 4-ADNT, 2,6-DNT, 2,4-DNT, 3,5-dinitroaniline, and the three isomers of NT) are all less than 1 μg/g. Analytical explosive standards for method EPA 8330 are available from AccuStandard® and other commercial sources.

3.1 Soil Preparation

A soil preparation method was developed in order to improve the availability and to minimize the heterogeneity problem of nitroaromatic and nitramine residues in soil. Soil samples (~500g) are air-dried to a constant weight at room temperature. The air-drying process should be done away from sunlight. The sample is then saturated with lab-grade acetone to minimize its heterogeneity and to optimize the availability of the contaminants. The soil is ground with a mortar and the soil/acetone slurry is thoroughly mixed. The sample with acetone is air-dried again until no traces of acetone are detectable (24 hours). The soil is then grounded to pass a 25-30 mesh sieve and then extracted.

3.2. Acetone Extraction

Another possible extraction method is the direct extraction by shaking the soil sample in acetone. Dried soil (20g) is placed in an extraction bottle with 100 ml of acetone and shaken vigorously for 30 minutes by vortex. This extraction procedure was recently compared with EPA sonication (Ref, 8-9) and proved to be equally effective at extracting explosive compounds. Acetone extracts can also be injected directly for HPLC/UV analysis. The limitation is the fact that acetone absorbs in the UV, and the separation used needs to take this into account. LC-CN columns can be used for acetone extracts but it is not appropriate for all applications.

3.3 Groundwater Extraction

Aqueous samples require an initial pre-concentration step before analysis in order to enable measurements in the low parts-per-billions (μg/L) range. This preconcentration step can be performed by using a salting-out method or by a solid phase extraction (SPE) method. In the past, EPA salting out method has been the predominant method to preconcentrate contaminants. Today, many laboratories are also employing the SPE technique due to many advantages brought per this technique. Solid phase cartridge extraction has been recently studied as an alternative pre-concentration method for explosives in water (Ref. 15). Prepacked cartridges of Porapak RDX Sep-Pak, 6cc, 500mg (Waters Corporation) can be used and will maximize the efficiency of pre-concentration.

4.0 ENVIRONMENTAL FATE OF EXPLOSIVES

Explosives are organic, crystalline compounds and have low vapour pressure and low water solubility. Their crystalline properties result in heterogeneous dispersion in the soil matrix. Explosives behave differently from each other, depending on the water solubility and structure. TNT is more soluble in water than RDX which in turn is more soluble than HMX. Also, TNT dissolves more rapidly compared to RDX and HMX, which dissolves slowest. TNT has a tendency to degrade by photolysis while RDX and HMX do not. In addition, TNT can degrade into at least 21 metabolites, which possess their own solubilities and toxicities. Some of these metabolites can be stabilized by the formation of amides with organic content of the soil. Moreover, sorption mechanisms with soils containing clays are stronger with TNT and its metabolites than for RDX and HMX (Ref. 16). Therefore, a soil multi contaminated by these three explosives would lead to a complex situation and as a result, RDX would leach out faster than TNT which would leach out faster than HMX. Relative environmental fate of explosives must be taken into account when sampling explosives contaminated sites.

5.0 SAFETY PROCEDURES

High explosives have specific chemical, physical and toxicological properties. Their explosive characteristics must be carefully integrated in the risk analysis and safety protocol.

They can lead to either reactions of: detonation, deflagration or burning under various stimuli such as heat, shock, friction and electrostatic charge. Thus, specific safety procedures have been developed for sampling at explosive-contaminated site. Their toxicological characteristics also have to be considered to ensure proper safety of the sampling team. A final consideration is the potential presence of unexploded ordnance. This represents a unique and important risk which has to be understood and properly managed.

5.1 Explosive Nature of Contaminants

Safety precautions must be taken at sites contaminated with explosive wastes. The United States has been involved in sampling and treating explosive wastes for many years. They have developed safety protocols and handling procedures for sites potentially contaminated. They determined that soils containing more than 12 percent secondary explosive by weight are susceptible to initiation and propagation. As a conservative limit, it is suggested that a soil containing more than 10 percent secondary explosives by weight (100,000 mg/Kg) has to be considered as explosive and a number of safety precautions have to be implemented during sampling and treatment (Ref. 1).

When a site is suspected of being contaminated with high levels of explosives, a preliminary sampling of the worst contaminated area should be carried out. Only surface soil samples should be taken and no drilling should take place. Representative composite samples of the worst area should be built and analysed. This is a good example of where the field methods may be applied. In the case where levels higher than 10% by weight are encountered, safety precautions will have to be implemented. The most important safety precaution is to minimize exposure, by reducing the number of workers exposed to the hazardous situation. To reduce the hazard at explosives wastes sites, physical activities should be carried out on materials that have been diluted to a wet slurry. If needed, water should be added to the soil to achieve the desired moisture content. Another safety precaution is the use of non sparking tools, conductive and grounded plastics and no screw tops, which have been developed for manufacturing explosives. If an operation involving mechanical shovelling is needed, remotely controlled operations would offer the best protection. When this is not possible, armoured safety glasses must be installed in the operator compartment. Drilling operations should only be permitted after removing the soil layer that is contaminated above the safety level. Equipment used in treatment must have sealed bearings

and shielded electrical junction boxes. The equipment must also be decontaminated frequently to prevent the build-up of explosive dust.

5.2 Toxicity Associated with Explosives

In addition to the explosivity associated with energetic compounds, some toxicological aspects must be taken into consideration. Secondary explosives are considered carcinogenic and mutagenic. Human health toxicity of explosive chemicals has been studied extensively by the U.S. Army Biomedical Research and Development Laboratory and a summary of these investigations has been published (Refs. 17,18). No general recommendations have been issued for explosive contaminant levels in soils. In the United States, threshold levels in soils are evaluated on a site by site basis, depending on factors such as the proximity of the contaminated soils to other locations and the use of surrounding groundwater.

Generic criteria for soils and groundwater were calculated by Daniels and Knezowitch in 1994 (Ref. 19). The same human health based criteria were calculated using a Canadian model 1997 (Ref. 20).The latest threshold criteria are very severe and do take into account all possible intakes of these compounds by humans. Many exposure pathways considered in the calculation of the criteria are not encountered in real site situations and therefore, the levels recommended are probably too severe. The evaluation of site by site threshold criteria as it is done in the U.S. appears to be the best choice to obtain threshold criteria that are realistic and will still protect human health. This can be achieved by a detailed site risk assessment which considers all possible exposure pathways relative to the site.

Explosive compounds are not volatile with the exception of nitroglycerine (NG). Therefore, no specific precautions have to be taken to prevent the inhalation of explosive vapour. If NG is a possible contaminant, an organic vapour protective respiratory mask should be worn at all times during sampling and manipulation of these soils or water samples. For other explosives, this protective equipment is not needed. However, explosive crystals dispersed in the soil might be carried away with soil dust, and a dust mask must be worn by the sampling team when dry sandy or clay type soils are encountered. Protective

clothing, gloves and glasses should be worn in all situations to avoid dermal contacts with the contaminated media.

5.3 Unexploded Ordnance Clearance

In many contaminated sites such as firing ranges, there is a high probability of contamination by unexploded ordnance. These dispersed duds are often still fused and armed and represent a high risk level when carrying out site investigation. Specially trained military personnel such as an ammunition specialist, field engineer or specialist contractors have the required expertise to take care of this situation. They can perform clearance of the contaminated site at three different levels of safety: Level one clearance: consisting of identifying only surface duds by visual observation of the site. Level two clearance: Consisting of clearing a layer of soil of 30-45 cm depth from duds with the help of a magnetic detector. Level three clearance: Consisting of completely cleaning the area of the site to any depth until nothing is detected.

Ideally, a level three clearance of a contaminated area should be performed before a soil characterization program or remedial action plan is undertaken. However, this operation might be economically or physically unfeasible and level one or two clearance may still provide a safe working environment. In addition, level 3 clearance disturbs the soil profile and it is impossible afterward to characterize depth distribution of explosives. No drilling operations should be conducted until a level three clearance has been done, or remotely-controlled drilling could be conducted. Cautious surface sampling can still be accomplished after one or two level clearance operations but an ammunition specialist or a field engineer must be present at all times during the sampling operation in order to ensure that proper procedures are followed. When shovelling or implanting grids on the site, the verification by a specialist of the absence of metallic debris underneath the surface soil must be done with the help of a portable metal detector. In conclusion, the characterization of these unexploded ordnance contaminated sites can still be carried out, with the active participation of ammunition specialists that will ensure the safety of workers.

6.0 CONCLUSION

The ultimate goal of site characterization is to provide effective and sufficient information to assess the environmental risks and to allow a decision making process about development of an optimal remediation plan. Explosives are just now gaining recognition as possible sources of soil or groundwater contamination and specific actions for effective and safe characterization of explosive contaminated sites have to be taken.

The best approach to assess the environmental impacts of sites contaminated with explosives is to begin with a hydrogeological characterization of the site. The screening of groundwater up and down gradient of the site will provide the first indication of whether or not there is an environmental impact. The first step is to evaluate the potential of finding unexploded ordnance on the range and if yes, no well should be drilled on the range without proper clearance and specific precautions (level 3 clearance). This groundwater sampling will indicate if leaching of explosive and explosive metabolites have contaminated the watertable. At the same time, random composite soil samples may be taken to get preliminary results. If an environmental impact is detected and traces of explosives are also detected in the groundwater samples, a more detailed soil sampling plan must be implemented. The soil characterization should then follow the procedures recommended to minimize the large heterogenous pattern demonstrated by explosives. Subsurface sampling on the range should be conducted when possible.

Field screening methods should be used in many situations in order to decrease the risk and cost associated with sampling. The most useful application of field screening methods are: 1) Establishment of safety levels for the manipulation of highly potentially contaminated samples in relation with the 10% threshold safety limit. 2) Screening of soil or water samples for the absence/presence of explosive compounds to discriminate samples that will or will not be sent to the laboratory for HPLC analysis. 3) For the establishment of the most effective sampling plan to delineate the area and depth of contamination for both soil and groundwater. 4) For the safe disposal of pumped groundwater.

The collection, conservation and treatment of samples should follow the recommendations detailed in section 2. The extraction and analysis with the HPLC laboratory method should be carried out following recommendations provided in section 3.

Soils should be extracted by the standard sonication method while water extraction should be done using the salting-out or the SPE. All aspects related to the environmental fate and soil/explosive interactions as described in section 4 should be integrated in the sampling strategy. Finally, the specific chemical and physical properties of explosive must be taken into consideration and safety precautions outlined in section 5 should be carefully followed. Certain military activities may lead to the accumulation of explosives in the environment which represent a threat to human health and to the surrounding environment. Thus, screening of potentially contaminated ranges should be conducted.

The goal of this characterization work is not to stop any operational activities. It should be conducted to assess the environmental impacts of these activities so that proper remedial action and safety precautions could be taken when operating at ranges. Recommendations could be drafted in order to pursue these activities while minimizing their environmental impacts. In conclusion, the protocol described in the present paper will help the Canadian Forces to pursue its activities in an environmentally responsible manner.

7.0 REFERENCES

1. "Approaches for the Remediation of Federal Facility Sites Contaminated with Explosives "; EPA Handbook # EPA/625/R-93/013, September 1993.
2. Jenkins, T.F., Walsh, M.E., "Development of an Analytical Method for Explosive Residues in Soil"; CRREL Report 87-7, June 1987.
3. Walsh, M.E., Jenkins, T.F. and Thorne, P.G., "Laboratory and Field Analytical Methods for Explosives Residues in soil"; Proceedings of the Symposium on Alternatives to Incineration for Disposal of Chemical Munitions and Energetics, Vol. 2, p.17, June 1995.
4. Thiboutot, S., Ampleman, G., Dubé, P., Hawari, J., Spencer, B., Paquet, L., Jenkins, T.F., Walsh, M.E., "Protocol for the Characterization of Explosives-Contaminated Sites ", DREV-R-9721, April 1998.
5. Jenkins, T.F., Grant, C.L., Brar, G.S., Thorne, P.G., Schumacher, P.W. and Ranney, T.A., "Assessment of Sampling Error Associated with the Collection and Analysis of Soil Samples at Explosives Contaminated Sites"; Field Analytical Chemistry and Technology, 1, 151-163,1997.
6. Jenkins, T.F., Grant, C.L., Brar, G.S., Thorne, P.G., Schumacher, P.W. and Ranney, T.A., "Assessment of Sampling Error Associated with the Collection and Analysis of Soil Samples at Explosives Contaminated Sites"; CRREL Special Report 96-15.

7. Walsh, M.E., Jenkins, T.F.., Schnitker, P.S., Elwell, J.W. and Stutz, M.H., "Evaluation of Method 8330 for Characterization of Sites Potentially Contaminated with Residues of High Explosives"; CRREL Report 93-5.

8. Jenkins, T.F., Walsh, M.E., Thorne, P.G., Thiboutot, S., Ampleman, G., Ranney, T.A., Grant, C.L., "Assessment of Sampling Error Associated with Collection and Analysis of Soil Samples at a Firing Range Contaminated with HMX"; CRREL Special Report #97-22, September 1997.
9. Thiboutot, S., Ampleman, G., Jenkins, T.F., Walsh, M.E., Thorne, P.G., Ranney, T.A. and Grant, G.L., "Assessment of Sampling Strategy for Explosives-Contaminated Soils"; Proceeding of the 90th Annual Air & Waste Management meeting, Paper # 94-WP 101.08, Toronto, June 1997.
10. Jenkins, T.F., Thorne, P.G., Walsh, M.E., Grant, C.L., Thiboutot, S., Ampleman, G., Ranney, T.A. and Stutz, M.H., "Sampling Strategy for Site Characterization at Explosives-Contaminated Sites"; Proceedings of the Second Tri-service Environmental Technology Workshop, St-Louis, Missouri, June 1997.
11. Pennington, J.C., "Natural Attenuation of Explosives in Groundwater, Technology Demonstration Plan"; SOP#13, August 1996.
12. "Nitroaromatics and Nitramines by HPLC"; SW846 EPA Method 8330.
13. Grant, C.L., Jenkins, T.F. and Golden, S.M., "Evaluation of Pre-Extraction Analytical Holding Times for Nitroaromatics and Nitramines Explosives in Water"; CRREL Special Report #93-24, August 1993.
14. Maskarinec, M.P., Bayne, C.K., Johnson, L.H., Holladay, S.K., Jenkins, R.A. and Tomkins, B.A., "Stability of Explosives in Environmental Water and Soil Samples"; Oak ridge National laboratory, Report ORNL/TM-11770, 1991.
15. Jenkins, T.F., Thorne, P.G., Myers, K.F., McCormick, E.F., Parker, D.E. and Escalon, B.L., "Evaluation of Clean Solid Phases for Extraction of Nitroaromatics and Nitamines from water"; U.S. Army CRREL Special Report, 1995
16. Li, A. Z., Marx, K. A., Walker, J. and Kaplan, D. L., "Trinitrotoluene and Metabolites Binding to Humic Acid"; Environ. Sci. Technol., 31, 584, 1997.
17. Burrows, E.P., Rosenblatt, D.H., Mitchell, W.R. and Palmer, D.L., "US Army Biomedical Research and Development Laboratory"; Report Number 8901, Fort Detrick, Frederik, MD, 1989.
18. Rosenblatt, D.H., "US Army Medical Bioengineering Research and Development Laboratory"; Report Number 8603, Fort Detrick, Frederick, MD, 1986.
19. Daniels, J.I. and Knezowich, J.P., "Human Health Risk from TNT, RDX and HMX"; in Environmental Media and Considerations of the US Regulatory Environment, Proceedings of the Luxembourg Int. Symp. on the Rehabilitation of Former Military Sites and Demilitarization for Explosive Ordnance, November 1994.
20. Rouisse, L., "Élaboration de critères génériques pour le sol et l'eau souterrainne pour le TNT, le RDX et le HMX"; DREV contract report, January 1997.

Table I

Physical and Chemical Properties of Nitroaromatics and Nitramines.

Analyte	Molecular Weight	Melting Pt (°C)	Boiling Pt (°C)	Water Solubility (mg/L)	Vapour Pressure at 20°C/torr
TNT	227.13	80.1-81.6	240 (explodes)	130 @ 20°	1.1×10^{-6}
RDX	222.26	204.1	(decomposes)	42 @ 20°	4.2×10^{-9}
HMX	296.16	276-280	(decomposes)	5.0 @ 25°	3.3×10^{-14}
TNB	213.11	122.5	315	34 @ 20°	2.2×10^{-14}
DNB	168.11	89.6	300-303	460 @ 15°	3.9×10^{-3}
Tetryl	287.14	129.5	(decomposes)	80	5.7×10^{-9} @ 25
2,4-DNT	182.15	70	300 (decomposes)	270 @ 22°	2.2×10^{-4} @ 25°
2,6-DNT	182.15	64-66		206 @ 25°	5.67×10^{-4}
2-A-DNT	197.17	176		2800	4×10^{-5}
4-A-DNT	197.17	171		2800	2×10^{-5}

Table II

Maximum Holding Time (MHT) for Nitroaromatics and Nitramines.

Target analyte	MHT Water (4°C)	MHT Water (-20°C)	MHT Soil (4°C)	MHT Soil (-20°c)
Nitroaromatics	28 days*	6 months	7 days	8 weeks
Nitramines	50 days	6 months	8 weeks	6 months

* (Stabilized with $NaHSO_4$, 1.5g/L)

Influence of the Primary Nitramines' Structure on their Thermostability

Rudolf S. Stepanov, Alexander M. Astachov, Ludmila A. Kruglyakova

Krasnoyarsk State Technological Academy
660049, Krasnoyarsk, prosp. Mira, 82, Russia

Abstract

The manometric method combined with chromatography and chromato-mass spectrometry was used for detailed analysis of kinetics and products of thermal decomposition for the homological series of primary nitramines in the melted state with general formula $R–NHNO_2$, where R = *Me*, *Et*, *n-Pr*, *n-Bu*, *i-Bu*, *t-Bu*, $O_2NHN(CH_2)_3$, $NC(CH_2)_2$, O_2NHNCH_2, $O_2NHNCH_2N(NO_2)CH_2$, with the objective to find how nitramines' structure influences decomposition rate. Arrhenius' equation parameters vary in the following limits: E_a=106.3-129.9 kJ·mol^{-1}, lgA=9.55-12.72. A linear correlation, found between the decomposition rate constant logarithm and nitramines' *pKa*, indicates nitramines' primary ionization under thermal decomposition. The proposed mechanism of thermal decomposition is based on ionization and the following decomposition of a nitramine's molecule, protonated by aminonitrogen.

Introduction

The application of primary nitramines as energy-supplying compounds is restricted because of their relatively low thermal stability. The earlier research, conducted by various authors, shed no light on how primary nitramines' thermal stability depends on their structure [1]. The systematic studies of aliphatic primary nitramines, conducted by us during the last several years, made it possible to determine the decomposition mechanism for nitramines in condensed state and also allowed to understand how nitramines thermal stability depends on their structure. Present article summarizes the results of studies on thermal decomposition kinetics and decomposition products for the homological series of primary nitramines in the melted state with general formula $R–NHNO_2$, where $R = Me$ (I), Et (II), *n-Pr* (III), *n-Bu* (IV), *i-Bu* (V), *t-Bu* (VI), $O_2NHN(CH_2)_3$ (VII), $NC(CH_2)_2$ (VIII), O_2NHNCH_2 (IX), $O_2NHNCH_2N(NO_2)CH_2$ (X).

Experimental Results and Discussion

We used manometric method (Bourdon-type compensation manometer) combined with chromatography and chromato-mass spectrometry. Thermal decomposition of nitramines (I-X) is described by the first-order equation of reaction in the temperature range of 120-180°C. The thermal decomposition rate constant depends neither on the size of reactionary vessel's surface area nor on the ratio of substance's mass to the volume of reaction. This proves reaction is homogeneous. Table 1 lists Arrhenius parameters for compounds (I–X). These parameters are smaller than those observed during radical decomposition on $N\text{-}NO_2$ bond for primary nitramines in the gas phase [2].

Table 1. Arrhenius Parameters for Thermal Decomposition of Primary Nitramines in the Melted State with General Formula $R\text{–}NHNO_2$ (I-X)

	Substitute *R*	ΔT, °C	E_a, kJ·mol^{-1}	*lg A*	$k_{150}\cdot10^5$, s^{-1}	pK_a
I	*Me*	120-170	106.3	9.55	26.9	6.23
II	*Et*	130-170	111.8	10.19	24.8	6.30
III	*Pr*	120-170	111.4	10.15	25.2	6.35
IV	*Bu*	130-180	109.3	9.87	24.3	6.43
V	*i-Bu*	140-180	116.0	10.66	22.4	6.50
VI	*t-Bu*	130-170	117.2	10.78	20.4	6.59
VII	$O_2NNH(CH_2)_3$	120-160	116.4	11.18	66.3	5.59
VIII	$NCCH_2CH_2$	140-180	119.7	11.43	44.7	5.27
IX	O_2NNHCH_2	110-150	128.9	12.72	61.4	5.00
X	$O_2NNHCH_2N(NO_2)CH_2$	150-160	127.7	12.42	45.4	3.80

The kinetic compensation effect shows in the series (I-X) (Fig.1). This is characteristic for catalytic reactions.

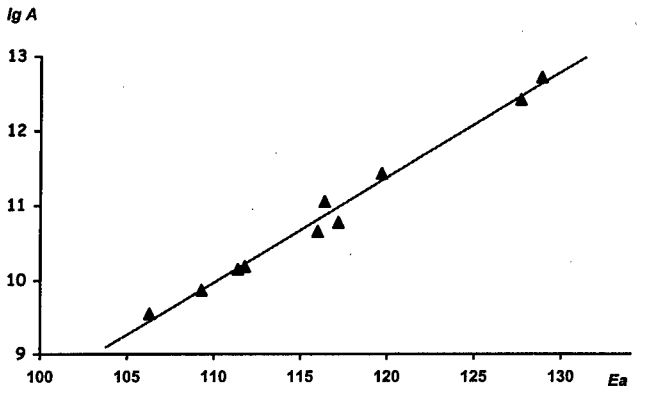

Figure 1. Plot of all Arrhenius parameters for primary nitramines' (I-X) thermal decomposition showing that a kinetic compensation effect exists.

$$Lg\,A = (0.14 \pm 0.01)E_a - (5.53 \pm 0.05) \qquad (1)$$

$$r=0.993;\ S_y=0.14;\ n=10$$

Almost all nitrogen, contained in (I-X), goes out as N_2O as a result of thermal decomposition. Some *NO* (12-14%) is contained in the thermal decomposition products in case of (X). The corresponding alcohols are found in the condensed residue after decomposition of nitramines (I-VII). Thus, for instance, butanol-1 (46%) and butanol-2 (37%) are the main products of decomposition for (IV) at 170°C and conversion of 97% [3]. The main products of decomposition for nitramines (IX) and (X), except for N_2O, are formaldehyde and water, while for (VIII) these products are acrylonitrile, acrylic acid, water and molecular nitrogen. Generally, the observed decomposition products differ only slightly from products found earlier for decomposition in aqueous acid medium [4].

Therefore, results obtained are treated within the scheme of the acid catalysis mechanism in which autoprotolysis of a nitramine is followed by the nitramine's fast decomposition on N_2O and alcohol.

$$RNHNO_2+RNHNO_2 \rightleftharpoons \overset{\oplus}{R}NH_2NO_2+[RNNO_2]^{\ominus} \quad (2)$$

$$\overset{\oplus}{R}NH_2NO_2 \longrightarrow R^{\oplus}+NH_2NO_2 \quad (3)$$

$$NH_2NO_2 \longrightarrow H_2O+N_2O \quad (4)$$

$$R^{\oplus}+H_2O \longrightarrow ROH+H^{\oplus} \quad (5)$$

Reaction (2) plays a decisive role in the mechanism (2)-(5). This is proved, in particular, by the relationship between the decomposition rate constant logarithm and nitramines *pKa* found in experiment (Fig.2). Opposite to the results obtained for primary nitramines decomposition in the aqueous acid medium [4], the rate of decomposition in the melted state goes up with the increase in electron-acceptor properties for the substituent R.

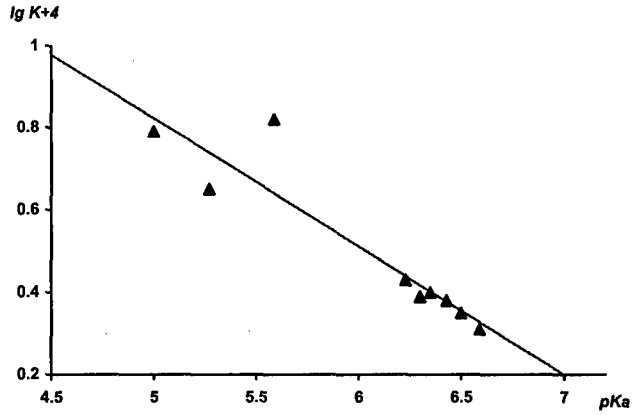

Figure 2. Dependence of the thermal decomposition rate constant logarithm on *pKa* value for primary nitramines (I-X) in the melted state.

$$Lg\ k_{150°C} = -(0.31\pm0.05)\,pKa - (1.62\pm0.03) \qquad (6)$$

$$r=0.928;\ S_y=0.08;\ n=9$$

The best correlation is found for alkylmononitramines (I-VI) [5]. Although nitramines (VII-IX) have a slightly worse correlation coefficient, the general trend still remains. Note, that data for compound (X) were not used in these calculations.

Reaction (2)-(5) is thought to proceed in a cell in a weakly salvationed ionic pair. The logic is that dissociation into ions does not occur after ionization (2) because of the medium's low dielectric coefficient which is lower than that of water. Not only structure of the forming carbcation influences the decomposition products composition for (I–X) but the reactionary ability of nitramine's anion does so too. Although anion is ambident and carbcation alkylation proceeds both on amino-type and on nitrogroup's oxygen, the latter appears to be the preferable direction for the reaction under those conditions. The forming *O*-alkyl ethers are unstable and break up into free radicals. Reaction between these radicals explains formation of some propionic aldehyde and tetrahydrofuran (8.4%), for example, in case of decomposition of (IV) [3].

The anion's reactionary ability in reaction of oxidation-reduction increases as the experiment's temperature goes up. At relatively low temperatures (below 100°C), the proportion of *N*-alkylation reactions increases and, accordingly, secondary nitramines show up in decomposition products.

$$R^{\oplus} + [RNNO_2]^{\ominus} \longrightarrow R_2N{-}NO_2 \qquad (7)$$

Therefore, the process of primary nitramines thermal decomposition in the melted state differs from the one in water solution because in the melted state autoprotolytic decomposition goes on in non-divided ionic pair. This fact explains phenomena described above.

References

[1] Dubovitskii, F. I., Korsunskii, B. L., *Usp. Khim.* **1981,** 50, 1828 (in Russian).

[2] Kekin Yu. V., Shan'ko, V. N., Stepanov R. S., *Kinet. Katal.* **1989,** 30, 963 (in Russian)

[3] Stepanov R. S., Astachov A. M., Kekin Yu. V., Kruglyakova L. A., *Zh. Org. Khim.* **1997,** 33, 1632 (in Russian).

[4] (a) Barrott, J., Denton I. N., Lamberton A. H., *J. Chem. Soc.* **1953,** 7, 1998.

(b) Denton, I. N., Lamberton A. H., *J. Chem. Soc.* **1955,** 6, 1655.

(c) Xiao, H.-M., Li, Y.-M., Li, Y.-F., *Acta Chim. Sin.* **1995,** 53, 438.

[5] Stepanov R. S., Astachov A. M., Kekin Yu. V., Kruglyakova L. A., *Izv. Vyssh. Uchebn. Zaved. Khim. Khim. Technol.* **1998,** 41, in press.

THERMAL DECOMPOSITION OF 1,9-DIAZO-2,4,6,8-TETRANITRO-2,4,6,8-TETRAAZANONANE IN LIQUID AND SOLID PHASE

Yuri M.Burov, Genadii M.Nazin

Institute of Chemical Physics Research
(Institute of Chemical Physics in Chernogolovka)
Russian Academy of Sciences,
142432 Chernogolovka, Moscow Region, Russian Federation.
Fax: +007 (096) 515 3588 E-mail: jubur@icp.ac.ru

ABSTRACT

This investigation is devoted to a comparative study of thermal decomposition of organic compound in liquid and solid states. The compound 1,9-diazido-2,4,6,8-tetranitro-2,4,6,8-tetra-azanonane (I) is linear analog of HMX. The kinetics was studied by the manometrical method. The reaction rate in liquid was described by the first-order equation. The activation parameters are: in solvent in m-DNB - lgA_l=14.59 ± 0,7 (s^{-1}), E_l = 36.3 ±1,3 kcal/mol, T = 120-180°C and lgA_m = 14.73 (s^{-1}), E_m = 36.3 kcal/mol in melt. The decomposition rate of solid **I** is independent of m/v, and the gas and liquid products do not affect the first stage rate. Activation parameters are: lgA_s = 12.86 (s^{-1}), E_s = 36.7 kcal/mol, T= 120-175°C. It is possible that both homogeneous and located reactions in solid I take place.

INTRODUCTION

Different models of monomolecular reactions in the solid state [I-3] predict a depends of the retarded effect of crystal state (RECS), that is the ratio of rate constants, k_l/k_s (k_l is the rate constant of the reaction in liquid state and k_s - in solid state, correspondingly, on as activated volume of reaction $\Delta V^{\#}$. There is a deficit of experimental data for checking this deduction. Therefore, the collecting of information on both k_s and $\Delta V^{\#}$ is important. For this problem the research of thermal decomposition of azidocompounds RN_3 that must have little $\Delta V^{\#}$ and should be weakly retarded by solid state is of interest.

Monofunctional azides have comparatively low melting points and do not decompose in a crystal state. Therefore, the polyfunctional compound $N_3(CH_2NNO_2)_4CH_2N_3$ (I) was chosen as the object of study. The most reactivity groups in **I** are azido-groups. It follows from comparison of stability of nitramine- and azido- groups in monofunctional compounds [2,4,5] and from the data on primary decomposition products of compound $N_3(CH_2NNO_2)_3CH_2N_3$ [6] which is the nearest analog of **I**. The high melting

point (177°C) and absence of phase transition in solid state (as has been shown by DSK method) allow studying of the decomposition of **I** below m.p. in the wide temperature range. Its advantage is that it can be easily purified from impurities and studied by manometrical method which is highly sensitive and accurate. This allows the rates to be determined at early stages of a convertion starting from 0,01%.

EXPERIMENTAL AND RESULTS

The purity of **I** was controlled on melting and decomposition curves. After two-stage recrystallization in water-aceton mixture and drying in vacuum at 40°C the rate constant of the gas evolution was abtained without showing any signs of impurity processes.

The kinetics of thermal decomposition of **I** was studied by manometrical method in a solid state at 120-175°C, in a liquid state at 180-185°C and in solution at 120-180°C.

Meta-dinitrobenzene which has low vapour pressure has been chosen as an inert solvent. The reaction proceeds by the first-order equation both in solution and liquid state almost up to 100% conversion. The final evolve (ΔV_∞, cm^3/g) is 550 in the melted **I** and 480 - in 1-2% solvents. The first value was used for calculation of the first-order rate constants according to the time of 1% decomposition at low temperatures. The rate constant of decomposition in solution does not depend on concentration (see Table) and is described by Arrhenius equation with parameters: $lgA = 14.59 \pm 0.7$ (s^{-1}) and $E = 36.3 \pm 1.3$ kcal/mol. In a melted state the rate is higher by 40% than in a solution and is described by equation

$$k_l = 10^{14.73} \exp(-36300/RT),\ s^{-1}. \qquad (1)$$

The rate constants of the decomposition in a solid state (k_s) were obtained at an early stage of convesion. It has been assumed that $\Delta V_{\infty,s} = \Delta V_{\infty,l} = 550$ cm^3/g. In a solid phase k_s does not depend on the degree of filling the substance in the vessel (m/v). This is explained by low volatility of **I**, gas decomposition and catalysis of gas products are absent. Condensed products are chemically inert, which is confirmed for the liquid phase data, but they increase the rate due to dissolving the initial substance. Therefore, the whole kinetic curves at temperature close to the melting point have an S-image pattern.

Table 1. The rate constants of decomposition of **I**

T,°C	Concent-ration, % mass	k_l s^{-1}	k_s s^{-1}
120,5	5	$2.84 \cdot 10^{-6}$	$4.86 \cdot 10^{-8}$
140	5	$2.46 \cdot 10^{-5}$	$3.75 \cdot 10^{-7}$
145	5	$4.09 \cdot 10^{-5}$	-
150	5	$6.71 \cdot 10^{-5}$	$1.06 \cdot 10^{-6}$
155	5	$1.09 \cdot 10^{-4}$	-
160	5	$1.75 \cdot 10^{-4}$	$2.65 \cdot 10^{-6}$
170	5	$4.35 \cdot 10^{-4}$	$6.78 \cdot 10^{-6}$
175	5	$8.95 \cdot 10^{-4}$	$1.02 \cdot 10^{-5}$
180.5	1	$1.04 \cdot 10^{-3}$	-
180.5	5	$1.06 \cdot 10^{-3}$	-
180.5	100	$1.35 \cdot 10^{-3}$	-
185	100	$2.52 \cdot 10^{-3}$	-

Due to melting influence k has been determined at the earlyest stages (<l%). The obtained k_s are described by the Arrhenius equation within 120-175°C:

$$k_s = 10^{12.86} \exp(-36700/RT),\ s^{-1}. \qquad (2)$$

Therefore, the activated energies E_l and E_s are approximately equal to one another and at all temperatures $k_l/k_s = 70$.

DISCUSSION

The combination of two facts: $E_l = E_s$ and $k_l/k_s = 70$ allows one to confirm that decomposition of solid **I** takes place at inequilibrium defects and on the surface but not in the bulk. Therefore, the true RECS does not equal 70, it much exceeds this magnitude. This conclusion follows from the analysis of different monomolecular reactions in solid state models [1-3]. The retardation of reaction in a crystal lattice is always due to energy factors and, if RECS exceeds unity, then $\Delta E = E_s - E_l > 0$. The supplementary energy ΔE is necessary for producing near the reacting molecule a free cavity with volume ΔV_c, within which decomposition with activated energy E_l is possible. The magnitude of ΔE can be estimated [l-3] by equation

$$\Delta E = RT \cdot \ln (k_l/k_s) = (\gamma \Delta V^{\#})/(2\beta V_0), \qquad (3)$$

where β is compressibility of a crystal, $V_0 = M/\rho$ - molar volume, M - molar massa, ρ- density, γ- structural factor that takes account of the mismatch of an activated complex and a free cavity in form and dimension $\gamma \Delta V^{\#} = \Delta V_c$.

If the true RECS > 100 for **I** and $\beta = 1.0 \cdot 10^{-10}$ Pa^{-1} (the average magnitude for organic compounds), $V_0 \approx 200$ cm^3/mole from (3) we can find that $\gamma \Delta V^{\#} > 13$ cm^3/mole.

The activated volume for decomposition of **I** can be estimated as follows. Assuming that the azide group ia a cylinder with a radius equal to intermolecular radius of a nitrogen atom R_N, and that in a transition state the extension of bond (Δl) is 0,18 Å (in RN-N_2 l= 1,24 Å, Δl is usually 10-15% [7], we have $\Delta V^{\#} = \pi R_N^2 \times \Delta l = 0{,}52$ cm^2/mole and $\gamma = 25$.

The decomposition of **I** indicates thus, that the effective value of activated volume in solid phase considerably exceeds the true activated volume. Moreover, the magnitude of $\Delta V^{\#}$, comprises about 5% of the substance mole volume, and can be compared with free volume in liquids (about 10% of V). In order to react the molecule should eliminate general intermolecular interaction and not the local one (near the reaction center) and acquire a considerable oscillatory freedom of motion.

LITERATURE

1. Burov Yu.M., Manelis G.B., Nazin G.M. - Doklady Akademii Nauk SSSR, 1984, V.279, N 5, p.1142 (in Russian).
2. Manelis G.B., Nazin G.M., Rubsov Yu.I., Strunin V.A. - Thermal decomposition and combustion of explosives and pouders, - M, Nauka, 1996, 223p, ill, (in Russian).
3. Burov Yu.M., Nazin G.M. - Some lows of thermal decomposition of solid organic compounds. - in "The Internation Autumn Seminar on Propellants, Explosives and Pyrotechnics, Shenzhen, China, October 8-11, 1997.
4. Geiseler G., Konig W. - Z. Phys. Chem. (DDR), 1964, Bd.227, N 1, P.81.
5. Burov Yu.M., Nazin G.M. - Kinetika i Katalis, 1982, V.23, N 1, p.12. (in Russian).
6. Oyumi Y., Rheingold A., L., Brill T.B. - J. Phys. Chem., 1987, V.91, N 4, p.920.
7. Gonikberg M. G. - Chemical equalibrium and rates of reaction at high pressures, M; Chimia, 1969, p.180. (In Russian).

Characterization of ADN and CL20 by NMR spectroscopy

Manfred Kaiser, Bert Ditz, Wehrwissenschaftliches Institut für Material-, Explosiv- und Betriebsstoffe (WIWEB), Großes Cent, D-53913 Swisttal, Germany

Summary

The new explosives ammonium dinitramide (ADN) and 2,4,6,8,10,12-hexanitro-hexaazaisowurzitane (CL20) were explored by NMR spectroscopy under high resolution conditions. The measurements were performed with a NMR spectrometer at 400.13 MHz proton resonance frequency. The ^{1}H, ^{13}C, ^{14}N, ^{15}N and ^{17}O NMR spectra were measured and the signals were assigned. With the help of the ^{13}C NMR spectroscopy the $^{1}J_{C-H}$ coupling constants could be determined for CL20.

Zusammenfassung

Die neuen Explosivstoffe Ammoniumdinitramid (ADN) und 2,4,6,8,10,12-Hexanitro-hexaazaisowurzitan (CL20) wurden NMR-spektroskopisch unter Hochauflösungs-bedingungen untersucht. Die Messungen erfolgten an einem NMR-Spektrometer mit 400.13 MHz Protonenresonanzfrequenz. Es wurden ^{1}H-, ^{13}C-, ^{14}N-, ^{15}N- und ^{17}O-NMR-Spektren aufgenommen und die Signale zugeordnet. Mit Hilfe der ^{13}C-NMR-Spektroskopie konnten die $^{1}J_{C-H}$-Kopplungskonstanten für CL20 bestimmt werden.

Introduction

The compounds ammonium dinitramide (ADN) and 2,4,6,8,10,12-hexanitro-hexaazaisowurzitane (CL20) are relatively new explosives that are up to now not used in German ammunition. ADN is a new compound, which has very promising properties for the formulation of new propellants. CL20 is interesting as a component for main charges because of its high density. For blast investigations an exact characterization of the materials is of particular importance. This can be accomplished for example with chromatographic and/or spectroscopic methods. One of the spectroscopic methods is NMR spectroscopy. It is very interesting, since it provides information on the structure of the compounds and on mixtures of substances. In the following both products are explored with the help of different NMR techniques and with the aid of different NMR active nuclei.

Instruments and methods

The investigations were accomplished with a Bruker DMX 400 NMR spectrometer with a proton resonance frequency of 400.13 MHz. The resonance frequency for the ^{13}C nucleus lies at 100.62 the one for ^{14}N at 28.91 and for ^{15}N at 40.56 MHz. The ^{17}O NMR spectra were measured at a resonance frequency of 54.24 MHz.

For the measurement, the substances were dissolved in D_2O (ADN) or acetone-d $_6$ (CL20). A 5 mm and a 10 mm multinuclear high resolution probe were used. The amount of the data points totaled characteristically 32 K and/or 64 K. All measurements were executed at ambient temperature. ^1H and ^{13}C spectra were calibrated relatively to tetramethyl silane (TMS). The chemical shifts in the ^{14}N and ^{15}N spectra refer relatively to external nitromethane, which was measured before the measurement of the substances. It was calibrated to the value of $\delta = 0$. Before the measurement of ^{17}O spectra deionizised water was measured and its chemical shift was fixed at $\delta = 0$. The CL20 samples were technical products of Thiocol (USA) and SNPE (France). ADN was synthesized by ICT (Pfinztal-Berghausen).

^1H NMR spectroscopy

CL20 shows two signals at $\delta = 8.34$ and $\delta = 8.20$ in the ^1H - NMR spectrum. The assignments can be accomplished through integration of the signals. The first signal corresponds to 4 protons and the second to 2 protons (figure 1). The measurement of the ^1H NMR spectrum of ADN was omitted, since an exchange between the NH_4^+ signal and the signal of the HDO appears in the spectrum. Thus a mean value of the signal appears in the spectrum, whose chemical shift depends on the ADN concentration.

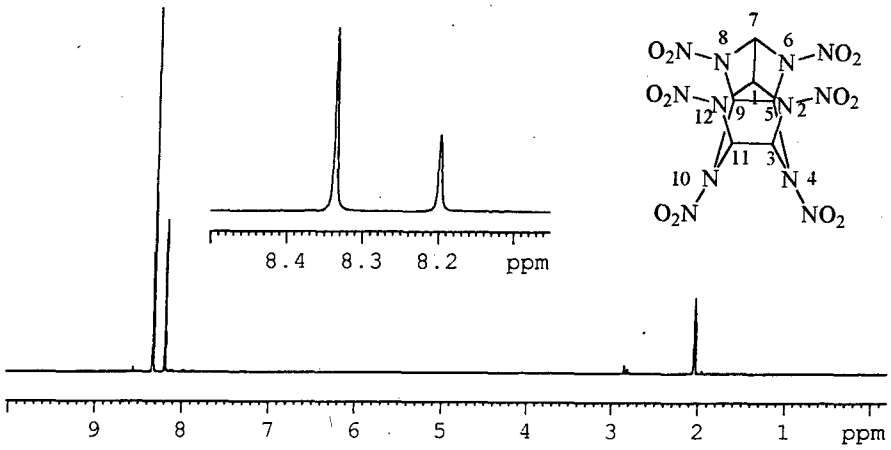

Figure 1: ^1H NMR spectrum of CL20 in acetone-d $_6$

^{13}C NMR spectroscopy

In contrast to proton NMR spectroscopy the ^{13}C NMR spectroscopy is less sensitive because of the natural abundance of 1.1 % of the ^{13}C nucleus.

The ^{13}C NMR spectrum of CL20 shows two signals at $\delta = 72.1$ and $\delta = 75.1$ (figure 2). An assignment can be carried out by quantitative Inverse Gated NMR spectroscopy /1,2/. In this case one signal corresponds to 2 and the other to 4 carbons. The $^{1}J_{C-H}$ coupling constants were determined by means of a Gated NMR spectrum /1,2/ (figure 3). The ^{13}C NMR signal at $\delta = 75.1$ shows a coupling constant of $^{1}J_{C-H} = 175.9$ Hz and at $\delta = 72.1$ a $^{1}J_{C-H} = 176.6$ Hz. Both coupling constants hardly deviate from each other, since the chemical environment of the carbon atoms is very similar.

In the case of ADN no ^{13}C spectrum was acquired, since no carbon is available in the substance.

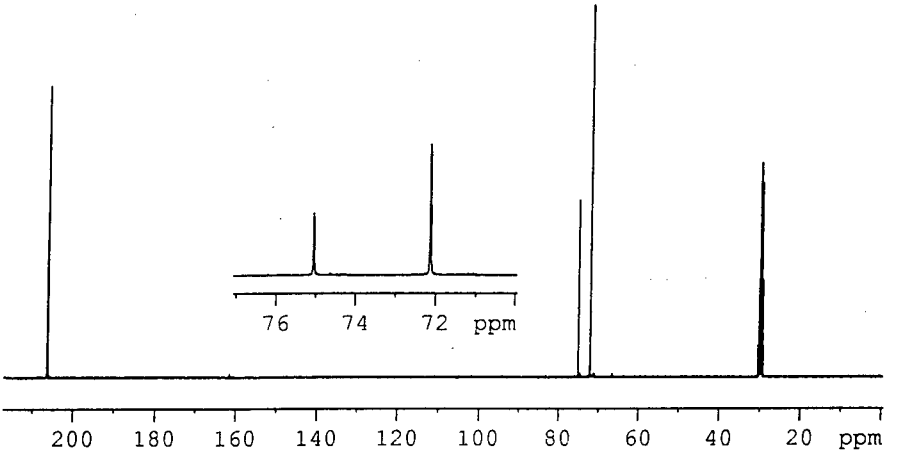

Figure 2: ^{13}C NMR spectrum of CL20 in acetone-d_6

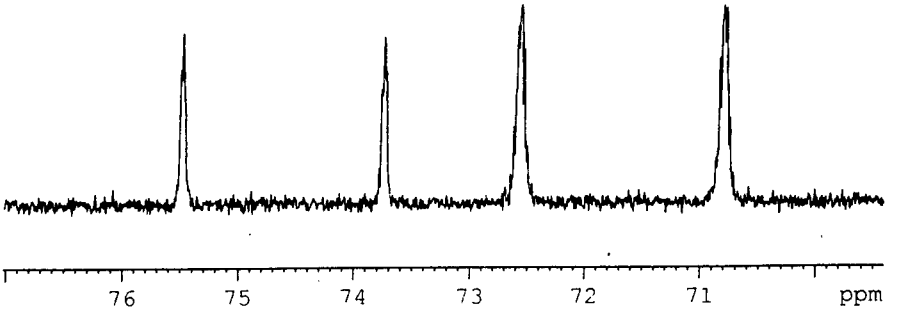

Figure 3: ^{13}C Gated NMR spectrum of CL20 in acetone-d_6

^{14}N NMR spectroscopy

Although the ^{14}N nucleus has a large natural abundance of 99.63 %, the measurement of ^{14}N nuclei is not simple, because the nuclear spin is I = 1 and thus the nucleus shows a quadrupole moment /3,4/. This leads to broadening of the signals and a loss of the signal to noise ratio.

The ^{14}N NMR spectrum of ADN shows three signals at δ = -12.0, δ = -60.2 and δ = -360.1. The signal at δ = -12.0 can be associated with the nitro group in the dinitramide. At δ = -60.2, the central nitrogen atom of the dinitramide appears and at δ = -360.1 the nitrogen atom of the ammonium ion is visible. A small signal at δ = -3.9 is a nitrate impurity of the ADN. The line widths of the signals of ADN are very different, whereby the signal of the ammonium ion shows the smallest line width, followed by the nitro groups and the central nitrogen atom of the dinitramide. The line widths correlate with the quadrupole moment of the ^{14} N nucleus. Sharp lines will only be obtained in a symmetrical environment of the ^{14}N nucleus and with very fast rotating groups around the nitrogen nucleus.

The ^{14}N NMR spectrum of CL20 shows two signals at δ = -41.6 and at δ = -180.6. The signal at δ = -41.6 is assigned to nitro groups. The signal at δ = -180.6 corresponds to the nitramine nitrogens. Both lines are quite broad, whereby the signal at δ = -180.6 is so broad, that it disappears almost in the baseline. So again the quadrupole moment of the ^{14}N is responsible for the broad lines and for the missing splitting of the signals.

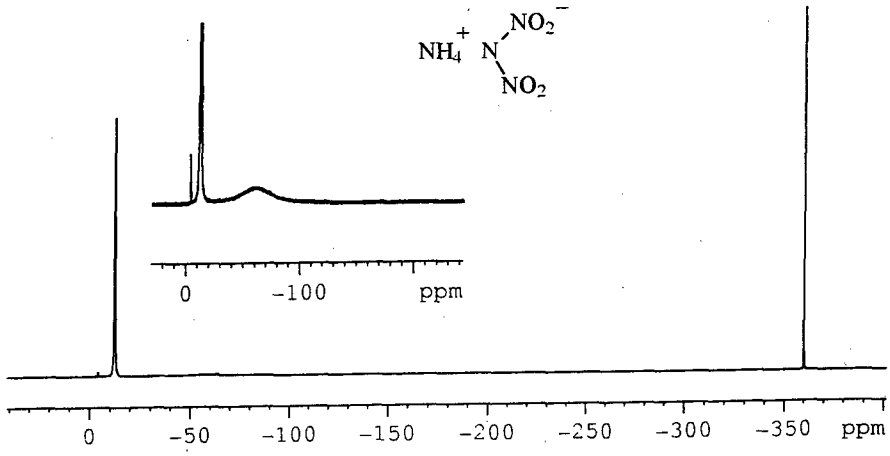

Figure 4: ^{14}N NMR spectrum of ADN in D_2O

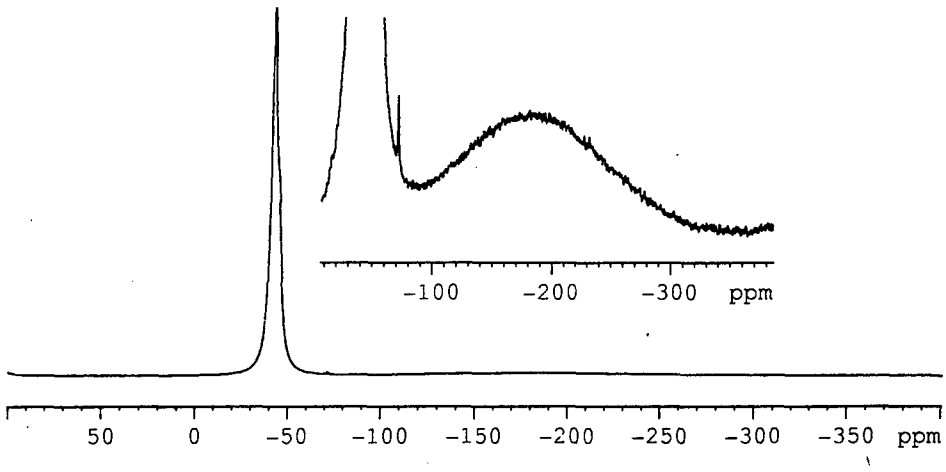

Figure 5: ^{14}N NMR spectrum of CL20 in acetone-d $_6$

^{15}N NMR spectroscopy

In contrast to ^{14}N NMR spectroscopy ^{15}N NMR spectroscopy has the advantage of very sharp lines in the spectrum /5,6,7/. The reason lies in the missing quadrupole moment, since the nuclear spin quantum number is I = ½. Yet the measurement of ^{15}N spectra is very time consuming, because the natural abundance of this isotope is only 0.36 %. So a measuring time of 1 day with a sample amount of 1 gramm is needed for the spectrum in fig. 6. Additional reasons are the long relaxation times and the negative nuclear Overhauser effect because of the negative gyromagnetic ratio.

The ammonium dinitramide shows three signals at δ = -12.2, δ = -60.8 and at δ = -360.1 in the ^{15}N spectrum. The signal at δ = -12.2 corresponds to the nitro group and the one at δ = -360.1 to the ammonium ion. The signal of the central nitrogen atom of the dinitramide at δ = -60.8 is broadened in the spectrum because of chemical exchange.

The ^{15}N spectrum of the CL20 is much more resolved than the ^{14}N spectrum. Four lines can be seen at δ = -40.3, δ = -43.4, δ = -179.5 and δ = -199.0. The two signals at δ = -40.3 and δ = -43.4 are assigned to nitro groups. The signals at δ = -179.5 and δ = -199.0 correspond to the nitramine nitrogen atoms. An assignment by intensity of the signals is indicated in figure 7.

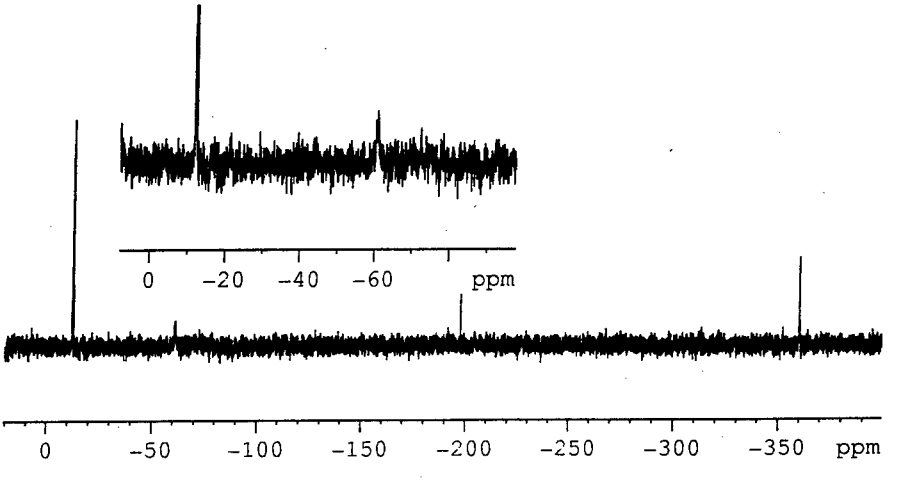

Figure 6: ^{15}N NMR spectrum of ADN in D_2O

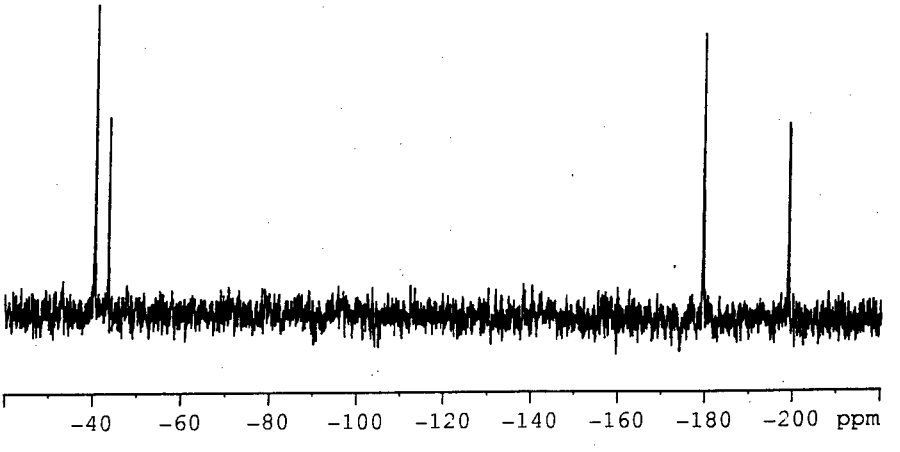

Figure 7: ^{15}N NMR spectrum of CL20 in acetone-d $_6$

^{17}O NMR spectroscopy

The NMR active ^{17}O nucleus has some unfavorable characteristics in NMR spectroscopy /8/. One reason is its small natural abundance of 0.037 %, the other is its nuclear spin quantum number of I = 5/2. This leads to a quadrupole moment, which has a negative effect on the line widths.

The oxygen signal of the nitro groups in ADN appears at δ = 469.6. In the spectrum the water is visible at δ = -3.0. The calibration was performed by measuring external H_2O. Since the sample is dissolved in water the chemical shift of the water differs from the external calibration. The small signal at δ = 414.2 is a nitrate impurity of ammonium dinitramide.

The ^{17}O signal of the nitro groups of CL20 is visible at δ = 468.7. The large signal in the spectrum is caused by the carbonyl group of the acetone, which was used as solvent.

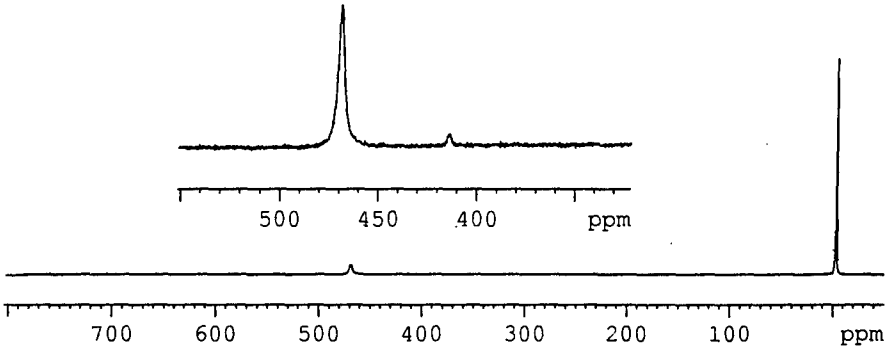

Figure 8: ^{17}O NMR spectrum of ADN in D_2O

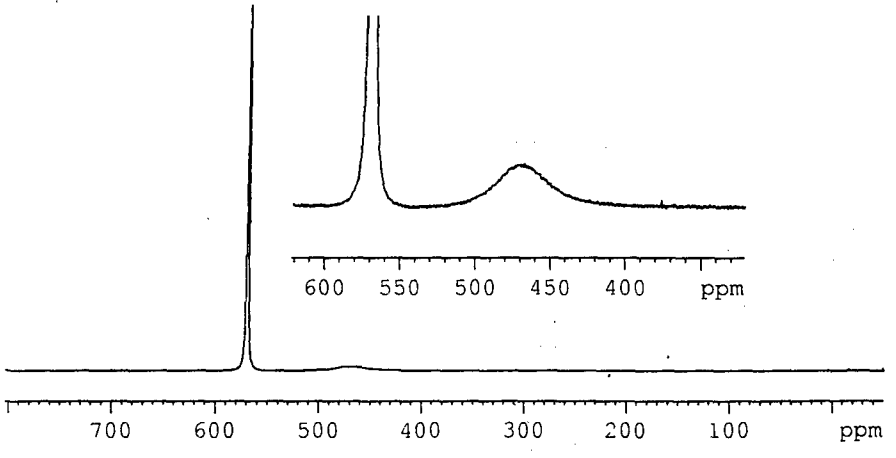

Figure 9: ^{17}O NMR spectrum of CL20 in acetone-d_6

Summary

The following table shows all NMR signals of ADN and of CL20.

nucleus	MHz	ADN	CL20
^{1}H	400.13	--	8.20 (2H) (H-1, H-7) 8.34 (4H) (H-3, H-5, H-9, H-11)
^{13}C	100.62	--	72.1 ($^{1}J_{CH}$ = 175.9) (C-1, C-7) 75.1 ($^{1}J_{CH}$ = 176.6) (C-3, C-5, C-9, C-11)
^{14}N	28.91	-12.0 ($N\underline{N}O_2^-$) $\Delta 1/2$ = 12.4 Hz -60.2 ($\underline{N}NO_2^-$) $\Delta 1/2$ = 940 Hz -360.1 ($\underline{N}H_4^+$) $\Delta 1/2$ = 4.5 Hz	-41.6 ($N\underline{N}O_2$) $\Delta 1/2$ = 140 Hz -180.6 ($\underline{N}NO_2$) $\Delta 1/2$ = 4.3 kHz
^{15}N	40.56	-12.2 ($N\underline{N}O_2^-$) -60.8 ($\underline{N}NO_2^-$) -360.1 ($\underline{N}H_4^+$)	-40.3 ($N\underline{N}O_2$) -43.4 ($N\underline{N}O_2$) -179.5 ($\underline{N}NO_2$) -199.0 ($\underline{N}NO_2$)
^{17}O	54.24	469.6 ($NN\underline{O}_2^-$) $\Delta 1/2$ = 204 Hz	468.7 ($NN\underline{O}_2$) $\Delta 1/2$ = 2.1 kHz

References

1.) H.-O. Kalinowski, S. Berger, S. Braun, ^{13}C-NMR-Spektroskopie, Georg Thieme Verlag Stuttgart, New York (1984).

2.) H. Günther, NMR-Spektroskopie, Georg Thieme Verlag Stuttgart, New York (1983).

3.) R. K. Harris, B. E. Mann, NMR and the Periodic Table, Academic Press, London, New York, San Francisco 96-98 (1978).

4.) C. H. Yoder, C. D. Schaeffer, Jr., Introduction to Multinuclear NMR, The Benjamin/Cummings Publishing Company, Inc., Menlo Park (California), Reading (Massachusetts), Don Mills (Ontario), Wokingham (U.K.), Amsterdam, Sydney, Singapore, Tokyo, Madrid, Bogota, Santiago, San Juan (1987).

5.) G. J. Martin, M. L. Martin, J.-P. Gouesnard, ^{15}N NMR Spectroscopy, Springer Verlag, Berlin, Heidelberg, New York (1981).

6.) M. Witanowski, G. A. Webb, Nitrogen NMR, Plenum Press, London and New York (1973).

7.) S. Berger, S. Braun, H.-O. Kalinowski, NMR-Spektroskopie von Nichtmetallen-^{15}N-NMR-Spektroskopie (Band 2), Georg Thieme Verlag Stuttgart, New York (1992).

8.) S. Berger, S. Braun, H.-O. Kalinowski, NMR-Spektroskopie von Nichtmetallen-Grundlagen, ^{17}O-, ^{33}S- und ^{129}Xe-NMR-Spektroskopie (Band 1), Georg Thieme Verlag Stuttgart, New York (1992).

Untersuchung der Zersetzung von Pulvervorkonzentrat

Stephan Wilker, Uldis Ticmanis, Manfred Kaiser, Gabriele Pantel, Gerhard Holl
(WIWEB, ASt Heimerzheim, Großes Cent, 53913 Swisttal),

Karl-Friedrich Elshoff (WASAG Chemie, Werkstr. 111, 45721 Haltern)

Kurzfassung

Pulvervorkonzentrate (PVK) bestehen aus Mischungen von Sprengölen (Nitroglycerin oder DEGN) und Nitrocellulose im Verhältnis 85/15 und werden zur Herstellung zweibasiger TLP und FTS verwendet. Frisch hergestellte PVK enthalten ca. 5-7 % Alkohol und sind in dieser Form lagerstabil. Gegebenenfalls enthalten sie zusätzlich noch Amine oder Harnstoffderivate als Stabilisatoren (ca. 0,5 %). Wenn sie getrocknet werden, gehen die stabilisatorfreien PVK bei 80°C innerhalb von ein bis zwei Tagen im Wärmeflußkalorimeter in eine heftige Autokatalyse über, deren Kinetik berechnet wurde.

Die Zersetzung des Nitroglycerins setzt an der mittleren Nitratestergruppe ein, wie 1D- und 2D-NMR-Untersuchungen belegen. Anschließend folgen die endständigen Nitratestergruppen, wobei sich unter den Reaktionsbedingungen zunächst Alkohole und danach Carbonsäuren bilden, die mit den Alkoholen Ester entstehen lassen, die dann polymerisieren. Diese Masse weist unter NO_x-Atmosphäre eine intensiv grünliche Färbung auf, an Luft ist sie weiß. Bei Unterbrechung der Messung im autokatalytischen Zustand und Abkühlen der Reaktionsmischung auf Raumtemperatur wird diese grüne oder weiße Masse innerhalb von einigen Wochen durch den dichten Verschluß des Meßgefäßes nach außen gedrückt. Treibende Kraft ist hierbei die Bildung von NO_x und damit verbunden ein erheblicher Druckaufbau. Diese Autokatalyse bei Raumtemperatur wird durch eine eindrucksvolle Bilderserie belegt.

Die Stabilisierung durch 2-NDPA kann die Autokatalyse des getrockneten PVK lediglich verzögern, aber nicht verhindern. Dagegen zeigen Untersuchungen von mit Akardit-stabilisiertem PVK keine Autokatalyse innerhalb von 25 Tagen bei 80°C. PVK mit DEGN als Sprengöl sind im Vergleich stabiler als PVK mit Nitroglycerin.

Abstract

Primitive masses (PVK) are a mixture of nitroglycerin or DEGN (85%) and nitrocellulose (15%). They are used for the production of double base propellants. Freshly synthetised PVK contain about 5-7 wgt% ethanol. In this form they are sufficiently stable at room temperature. Some PVK contain additionally amines or urea derivatives (0,5%) as stabilisers. When the unstabilised PVK are dried they decompose within 1-2 days at 80°C showing a severe autocatalysis in the microcalorimeter. The kinetics of the decomposition was calculated.

1D and 2D-NMR spectra show that the decomposition starts at the central nitrate ester group of nitroglycerin. After that the terminal nitrate ester groups follow. At first alcohols are formed which are oxidised under the reaction conditions to carboxylic acids. These acids react with the primary and secondary alcohols to esters, which form a polymeric mass showing a greenish colour under NO_x atmosphere. It loses its colour under air. If the autocatalysis at 80°C is stopped and the reaction mixture is cooled to room temperature this greenish mass comes out of the measuring ampoule within a few days or weeks forced by huge amounts of gases (NO_x) produced. An impressive series of photos documents this behaviour.

The stabilising of PVK with 2-NDPA can only delay the autocatalysis but not prevent it. Akardite II stabilised PVK don't show an autocatalysis within 25 days at 80°C. PVK containing DEGN are more stable than PVK containing nitroglycerin.

Einleitung

PVK's dienen als Rohstoffe für die Herstellung zweibasiger TLP und FTS. Sie bestehen in der Regel aus einer Mischung aus Sprengöl (Nitroglycerin oder DEGN; 85% in der Trockenmasse) und Nitrocellulose (15% in der Trockenmasse). Frisch hergestellte PVK enthalten ca. 5-7 % Alkohol und sind in dieser Form lagerstabil. In den vergangenen Jahren ist es trotzdem immer wieder zu folgenschweren Unfällen mit PVK in Lagern der explosivstoffverarbeitenden Industrie gekommen, deren Ursache oft nicht restlos geklärt werden konnte. Obwohl stabilisatorfreie PVK bei Raumtemperatur hinreichend lagerstabil sind (s. Abschnitt „Bewertung"), wird seit 1997 PVK nur noch stabilisiert hergestellt und ausgeliefert.

Uns interessierte die Frage, ob PVK ein ähnliches Verhalten wie Pulverrohmassen [1] zeigen und ob es möglich ist, den Verlauf der Autokatalyse durch chemische Analysen zu verfolgen. Dies gelang durch NMR-Analysen belasteter PVK in verschiedenen Abbaugraden. Durch die Untersuchung verschiedener PVK-Typen (Variation des Feuchtegehalts, des Sprengöls und der Stabilisatoren) wollten wir den Einfluß dieser Faktoren auf die Stabilität der PVK ermitteln. Durch die Untersuchung der PVK bei verschiedenen Temperaturen konnte die Kinetik der Zersetzungsreaktion ermittelt werden und das Ergebnis auf die relevante Lagertemperatur von PVK extrapoliert werden.

Versuchsdurchführung

Das PVK (stabilisiert und unstabilisiert) wurde sowohl im Originalzustand als auch getrocknet im Wärmeflußkalorimeter (Typ TAM) bei verschiedenen Temperaturen untersucht. Die Trocknung erfolgte im Trockenschrank bei 40°C über Nacht. Die Proben wurden bei jeder Temperatur frisch in das Kalorimeter eingesetzt. Darüberhinaus wurde die Explosionswärme nach TL 1376-0600, 3.41.1 bestimmt.

Die NMR-Spektren wurden bei 400 MHz (^{1}H-NMR) und 100 MHz (^{13}C-NMR) in geeigneten deuterierten Lösemitteln (meist Aceton-d_6) mit einem Bruker-NMR-Spektrometer (400 MHz) aufgenommen.

Proben

Tabelle 1 zeigt die untersuchten Proben und ihre chemische Zusammensetzung

Tab. 1: Untersuchte PVK-Proben

Bezeichnung	Inhaltsstoffe	Stabilisator	Herstellungsmonat
PVK A	85/15 NGL/Nc	Ak II	8/97
PVK B	85/15 NGL/Nc	keiner	10/96
PVK D	85/15 DEGN/Nc	Ak II	12/96
PVK N	85/15 NGL/Nc	2-N-DPA	2/97
PVK Q	85/15 NGL/Nc	keiner	4/88

Ergebnisse

Wärmeflußmessungen an feuchten PVK

Die durchgeführten Messungen (s. Abb. 1 und 2) zeigen, daß bei allen Temperaturen nach kurzer Zeit eine nahezu konstante Zersetzungsrate erreicht wird.

Eine Langzeitmessung bei 40°C ergab auch nach 14 Tagen keine meßbare Wärmeproduktion, so daß davon ausgegangen werden kann, daß bei diesen Temperaturen eine nur sehr geringe Zersetzung der Proben eintritt. Dies gilt natürlich analog für alle darunter liegenden Temperaturen.

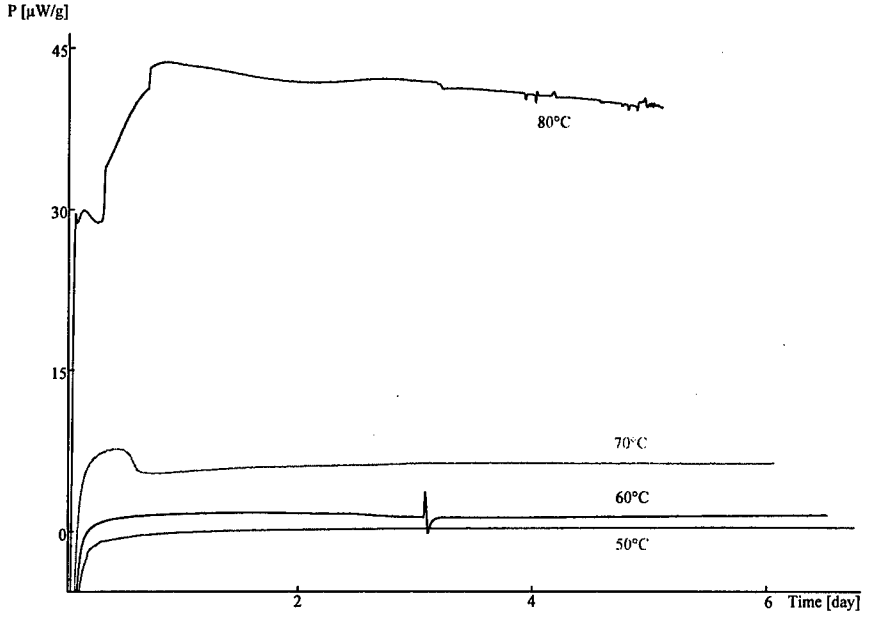

Abb. 1. Spezifische Wärmeproduktionsrate von nicht stabilisiertem feuchtem PVK B; bei jeder Prüftemperatur frisch eingesetzt.

Tab. 2: Konstante Meßwerte der spezifischen Wärmeproduktion feuchter PVK

Temperatur	unstab. PVK B	Meßzeit	stab. PVK N	Meßzeit
[°C]	[µW/g]	[Tage]	[µW/g]	[Tage]
80	41,8	5,1	nicht konst. (s. Text)	6,8
70	6,32	6,0	7,88	8,0
60	1,50	6,5	1,60	8,5
50	0,36	8,0	n.b.	
40	< Best.grenze	16,2	n.b.	

n.b. = nicht bestimmt

Im Gegensatz zum nicht stabilisierten feuchten PVK zeigt das stabilisierte feuchte PVK bei 80°C eine deutlich geringere spezifische Wärmeproduktionsrate (16 µW/g statt 40 µW/g). Diese steigt jedoch im Zeitraum zwischen zwei und sechs Tagen von 14 auf 16 µW/g an, ohne daß jedoch eine Beschleunigung dieses Anstiegs zu beobachten ist. Die Messung bei 60°C (s. Abb. 2) zeigt keine signifikanten Unterschiede zwischen dem stabilisierten und dem unstabilisierten feuchten PVK B und N.

Die aus dem Arrheniusplot (Abb. 3) berechneten kinetischen Parameter (Aktivierungsenergie und vorexp. Faktor) betragen für das nicht stabilisierte feuchte PVK B 132 kJ/mol bzw. $7 \cdot 10^{17}$ W/kg (Tieftemperaturbereich (70-50°C)) bzw. 191 kJ/mol bzw. $7 \cdot 10^{26}$ W/kg (Hochtemperaturbereich (80 und 70°C)).

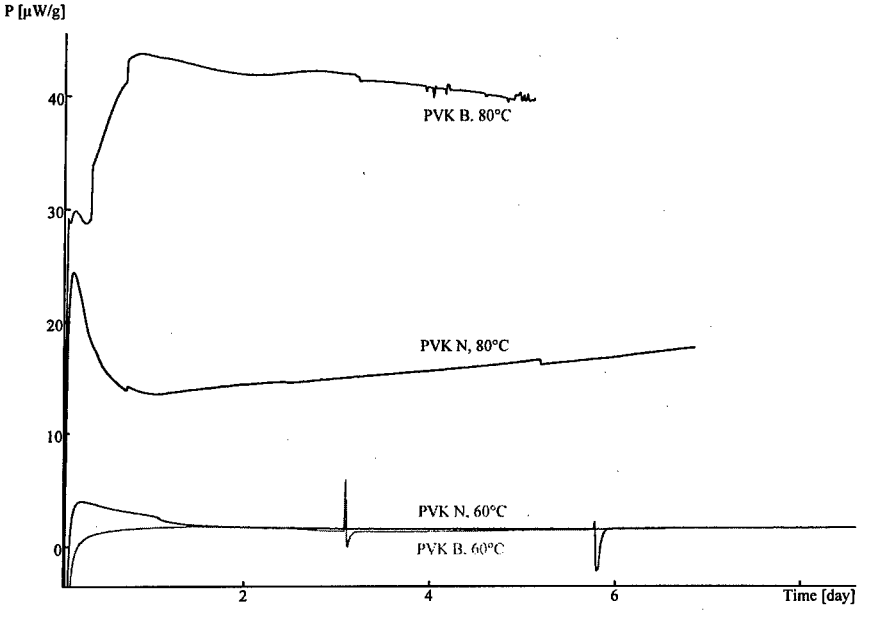

Abb. 2. Vergleich zwischen stabilisiertem und nicht stabilisiertem feuchten PVK

Wärmeflußmessungen an getrockneten PVK

Im Gegensatz zu den alkoholfeuchten Proben kommt es bei 80°C bei den **getrockneten, nicht stabilisierten Proben** innerhalb von ca. 15 h (abhängig vom Trocknungsgrad und der Einwaage) zu einer den Pulverrohmassen (PRM) vergleichbaren heftigen autokatalytischen Zersetzung. Sie weist – wie schon bei den PRM beobachtet – eine vorgelagerte exotherme Reaktion auf [1], die etwa einer Energieabgabe von 2 J/g entspricht. Die Abb. 4 und 5 zeigen den Verlauf der Zersetzungsreaktion; die Ergebnisse entstammen verschiedenen Versuchsreihen, die alle eine sehr hohe Reproduzierbarkeit aufwiesen.

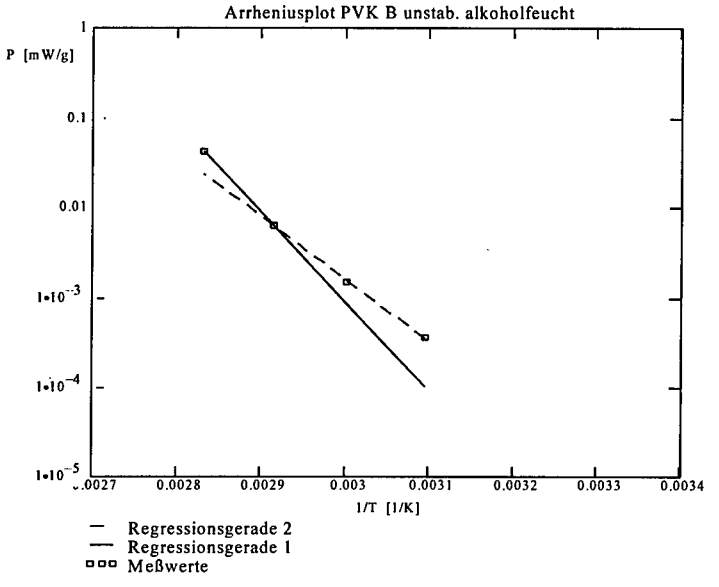

Abb. 3. Arrhenius-Plot des nicht stabilisierten, alkoholfeuchten PVK. Eingetragen sind die konstanten Endwerte der spezifischen Wärmeproduktionsrate.

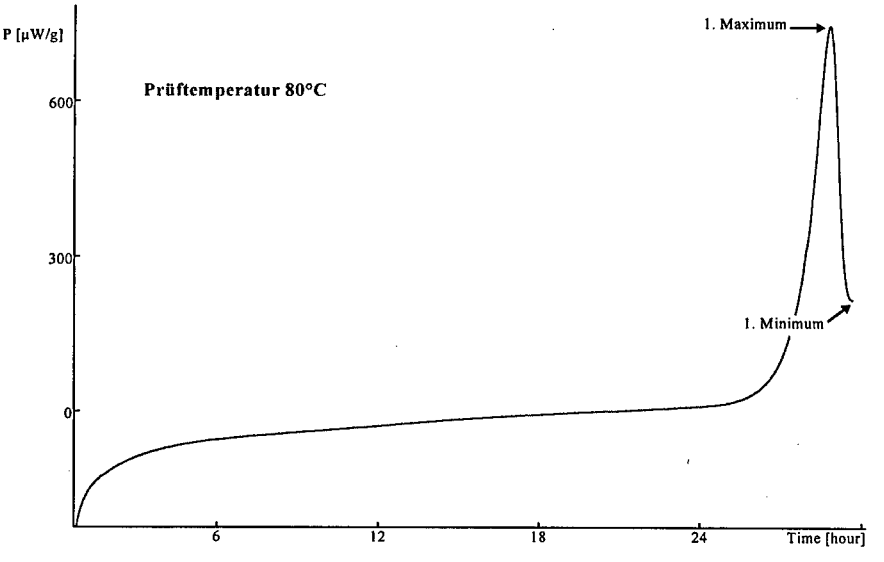

Abb. 4. Zersetzung getrocknetes PVK B bis zum ersten Minimum (Einwaage ca. 150 mg).

Da die autokatalytische Zersetzung einer gefüllten Ampulle (3,5 bis 4 g) durchaus eine Gefahr für das Meßsystem und den Operator darstellt, wurden die meisten Versuche mit geringen Probenmengen (s. Tab. 3) durchgeführt. Diese Meßanordnung erlaubt außerdem, den vollständigen Ablauf der Zersetzungsreaktion zu verfolgen (maximal erfaßbarer Gesamtwärmefluß 30 mW/ Probe). Dabei zeigte sich im Vergleich zu denen komplett gefüllter Ampullen ein etwas späterer Eintritt in die Autokatalyse. Bei Mehrfachbestimmungen mit ähnlicher Einwaage wurden vergleichbare Zeiten ermittelt. Der Gewichtsverlust bei diesen Versuchen liegt nach vollständigem Durchgang der Autokatalyse bei 90-95%. Die Probengläschendeckel sind nach der Messung aufgerissen, die Gummidichtung ist angeschmolzen und aufgebogen.

Tab. 3a: Eintritt in die Autokatalyse bei 80°C, 70° und bei 60°C (PVK B); sortiert nach Meßtemperatur und Einwaage.

Versuch	Einwaage [mg]	T [°C]	1. Maximum [µW/g]	1. Maximum [Tage]	1. Minimum [µW/g]	1. Minimum [Tage]
91	143	80	765	1,39	210	1,24
88	151	80	698	1,29	398	1,39
83	151	80	825	1,04	272	1,09
90	154	80	712	1,15	385	1,19
85	159	80	748	1,20	216	1,24
84	161	80	782	1,17	-	-
86	162	80	680	1,30	350	1,45
89	169	80	850	1,60	490	1,70
87	172	80	635	1,15	300	1,31
81	1635	80	427	1,23	329	1,27
82	3743	80	161	0,71	106	0,75
93	4075	80	120	0,79	86	0,83
71	3920	70	68	3,07	51	3,45
64	4046	60	31	16,3	29	16,4

-) Messung im 1. Maximum abgebrochen

Die Abhängigkeit des Zeitpunkts des Eintritts der Autokatalyse von der Einwaage führte zu der Frage, ob der sich über dem PVK aufbauende Gasdruck zu einer Beschleunigung der Zersetzungsreaktion führt. Daher wurde das PVK Q mit verschlossenem und nicht gasdicht verschlossenem Ampullendeckel bei 80°C gemessen. Das Resultat ist Abb. 6 zu entnehmen. Es zeigte sich, daß der Verschluß der Meßampullen im Rahmen der Streuung der Meßergebnisse keinen Einfluß auf die Zersetzungsgeschwindigkeit hat.

Das bedeutet, daß es nicht der sich aufbauende Gasdruck ist, der Ampullen mit höherer Einwaage früher in die Autokatalyse geraten läßt. Hier spielen offensichtlich andere Vorgänge eine Rolle (z.B: die NO_x-Konzentration im PVK selbst). Interessant ist auch die Korrelation zwischen Energieabgabe und Gewichtsverlust (s. Tab. 3b). Es zeigt sich, daß ein merklicher Gewichtsverlust erst bei einer Energieabgabe von etwa 500 J/g einsetzt. Vorher baut sich offensichtlich ein erheblicher Druck auf. Erst nach dem Aufspringen der Dichtung (Maximaldruck nach Herstellerangaben: 2 bis 3 bar) können die gasförmigen Reaktionsprodukte entweichen.

Tab. 3b: Gewichtsverluste und Energieabgaben bei 80°C, 70° und bei 60°C (PVK B); sortiert nach Temperatur und Energieabgabe

Versuch	T [°C]	Meßzeit [Tage]	Gewichts-verlust [mg]	Gewichts-verlust [%]	abgegebene Energie [J/g]
84	80	1,17	1	< 1	2,70
93	80	0,94	1	< 1	3,60
85	80	1,24	1	< 1	3,82
82	80	0,93	0	0	5,35
81	80	1,39	1	< 1	12,4
91	80	2,04	0	0	68
88	80	2,09	1	< 1	224
89	80	2,22	1	< 1	281
90	80	1,80	1	< 1	317
86	80	2,06	55	34	630
87	80	2,08	85	49	1400
83	80	5,83	146	95	> 1000 a)
71	70	4,00	1	< 1	11,4
64	60	21,4	n.b.	n.b.	31,7

a) Wegen Überschreitung des Meßbereichs ist eine genaue Aussage nicht möglich (s. Abb. 5).

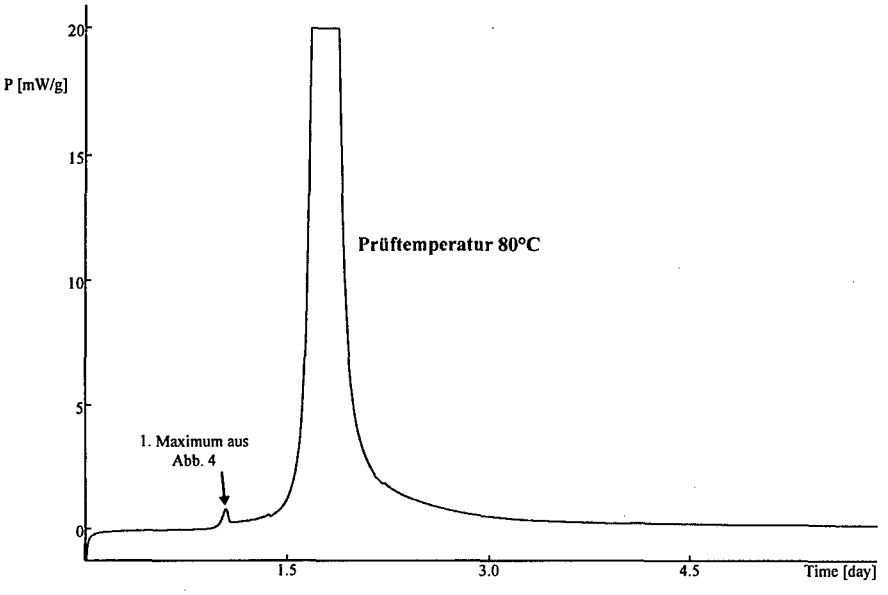

Abb. 5. Zersetzung getrocknetes PVK B (gesamter Zerfallsvorgang; Einwaage ca. 150 mg)

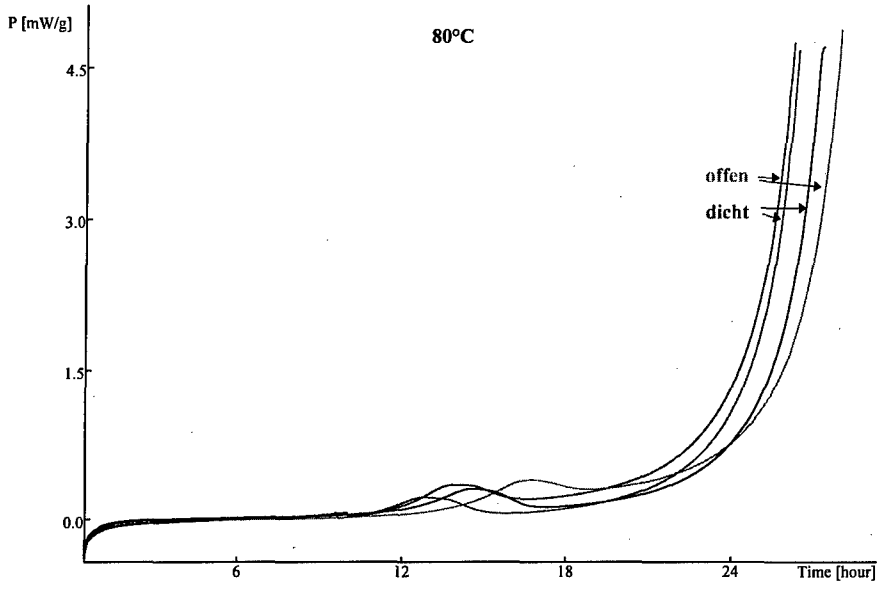

Abb. 6. Spezifische Wärmeproduktionsrate PVK Q (85% NGL, 15% NC, < 0,1% EtOH) mit geschlossener und nicht geschlossener Meßampulle. Einwaage je ca. 0,6 g.

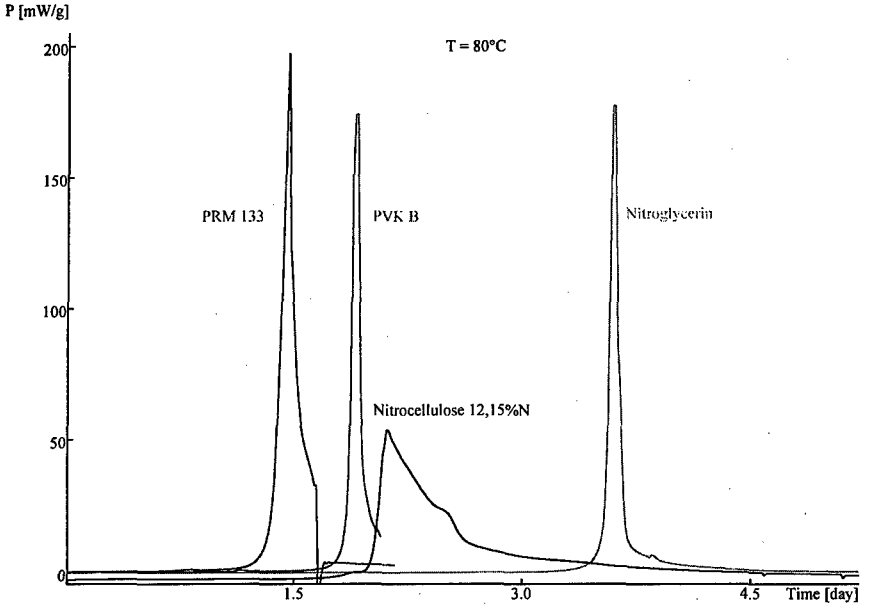

Abb. 7. Vergleich des PVK mit PRM 133E aus [1] sowie mit Nitrocellulose sowie Nitroglycerin bei 80°C (Einwaage je ca. 150 mg)

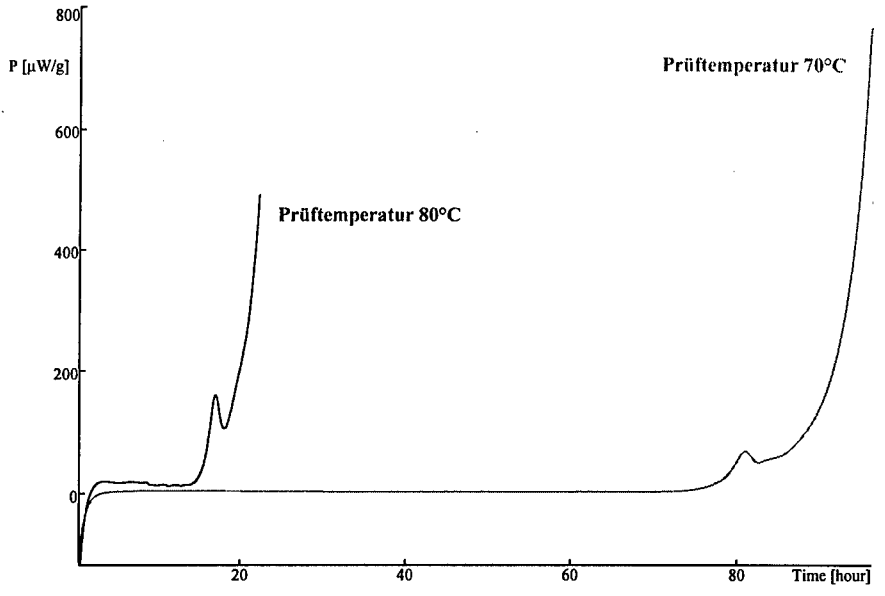

Abb. 8. Zersetzung getrockneter PVK B bei 80 und 70°C (Einwaage ca. 4 g)

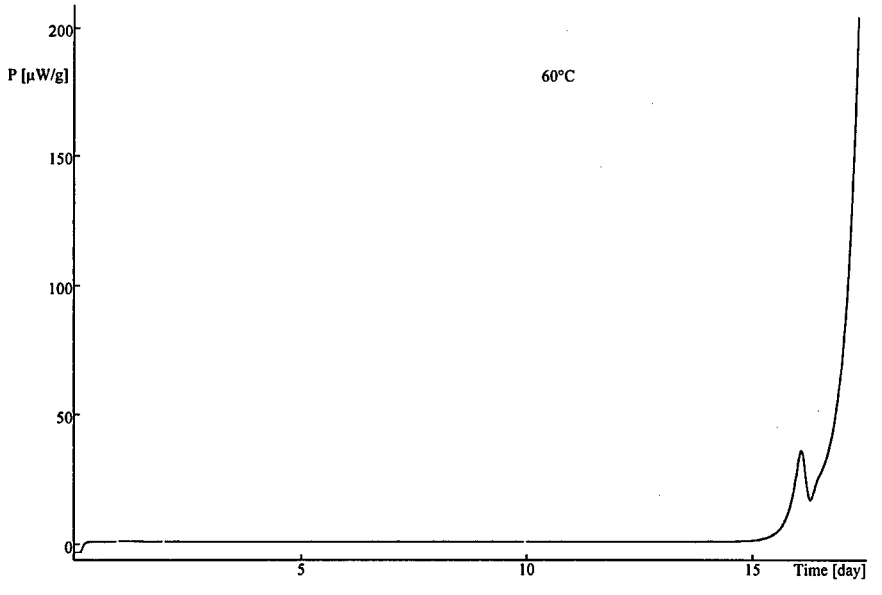

Abb. 9. Zersetzung getrockneter PVK B bei 60°C. Einwaage ca. 4 g.

Der Vergleich zwischen PVK, unstabilisierter PRM, reiner nicht stabilisierter Nitrocellulose und von reinem Nitroglycerin ist Abb. 7 zu entnehmen. Es zeigt sich, daß PRM (mit einem Nitrocellulosegehalt von ca. 60%) bei vergleichbarer Einwaage schneller die Autokatalyse erreicht. Reine Nitrocellulose (Stickstoffgehalt 12,15%) weist eine „schwächere" Autokatalyse auf, die zu einem späteren Zeitpunkt auftritt; reines Nitroglycerin schließlich bildet mit einer Zeit bis zur Autokatalyse von gut 3½ Tagen das „Schlußlicht". Interessanterweise zeigt Nitroglycerin ein sehr frühes erstes Maximum von 250 µW/g nach 6 Stunden. PVK, PRM und Nitroglycerin haben prinzipiell die gleiche Kurvenform.

Der Gewichtsverlust nach der Messung des Nitroglycerins beträgt 74%. Die Energieabgabe beläuft sich auf ca. 1500 J/g.

Die autokatalytische Zersetzungsrektion tritt auch bei 70°C und bei 60°C ein. Während das erste Maximum des PVK B bei 80°C nach 17,1 h (0,71 Tagen) eintritt, beträgt die Zeit bis dahin bei 70°C 3,1 Tage (s. Tab. 3 und Abb. 8) und bei 60°C knapp 16 Tage (Abb. 9). Das zehn Jahre alte PVK Q erreicht das erste Maximum schon nach 13 Stunden (0,54 Tagen; 80°C), 1,6 Tagen (70°C) bzw. 3,9 Tagen (60°C); Abb. 10.

Die Form des Wärmeflußsignals bleibt bei tieferen Temperaturen – wenn auch mit veränderten Zeit- und Wärmeflußachsen – im wesentlichen gleich. Dies bedeutet, daß die verschiedenen für diese Wärmetönung verantwortlichen chemischen bzw. physikalischen Reaktionen vergleichbare Aktivierungsenergien aufweisen. Dies ermöglicht somit auch, Extrapolationen zu tieferen Temperaturen hin durchzuführen (s. Abschnitt „Bewertung").

Die Reaktion des **getrockneten 2-NO_2-DPA-stabilisierten PVK** bei 80°C zeigt zunächst nur einen allmählichen Anstieg des Meßwertes (s. Abb. 11). Anschließend erfolgt hier eine autokatalytische Zersetzung, ohne daß eine Vorreaktion wie bei den unstabilisierten PVK eintritt.

Im Vergleich mit nicht stabilisiertem PVK findet der Eintritt in die Autokatalyse bei sonst identischen Meßbedingungen um den Faktor 20 (14 statt 0,7 Tage) später statt. Der Stabilisator hat in den ersten Stunden der Messung keinen Einfluß auf das Niveau der Wärmeproduktionsrate.

Dagegen zeigen **Akardit-stabilisierte PVK** (sowohl mit Ngl als auch mit DEGN) innerhalb von 25 Tagen keine Autokatalyse. Interessanterweise liegt die spezifische Wärmeproduktionsrate der DEGN-PVK deutlich unter der der Ngl-PVK. Dies deutet auf eine geringere Zersetzungsgeschwindigkeit des DEGN im Vergleich zum Nitroglycerin hin und somit auf eine größere Stabilität dieses Sprengöls (Abb. 12). Der gesamte Gewichtsverlust nach der Messung beläuft sich beim PVK D auf 2,8 %.

Der Stabilisator 2-NO_2-DPA ist im PVK N nach 14 Tagen nicht mehr nachweisbar, sondern hat sich in Tetranitro-DPA umgewandelt. Das PVK A (akardit-stabilisiert) weist nach 25 Tagen ebenfalls keinen originären Stabilisator mehr auf; hier sind die Reaktionsprodukte Di-, Tri- und Tetranitro-DPA, d.h. die stabilisierende Wirkung von Akardit II ist etwas besser als die des 2-NDPA, was sich auch in der fehlenden Autokatalyse zeigt. Im Gegensatz dazu ist im PVK D Akardit II auch nach 25 Tagen noch in fast der Ausgangsmenge enthalten. Im Vergleich zwischen PVK A und D (beide Akardit-stabilisiert) ist der Abbau des Akardits im PVK A schneller (Nitroglycerin zersetzt sich schneller als DEGN).

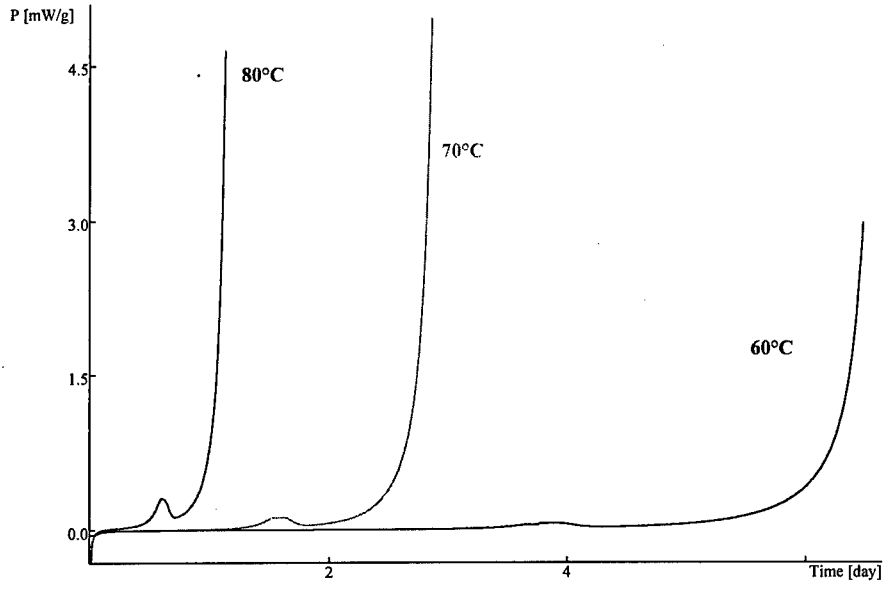

Abb. 10. Einfluß der Zersetzungstemperatur auf das WFK-Signal (PVK Q). Einwaage ca. 0,6 g.

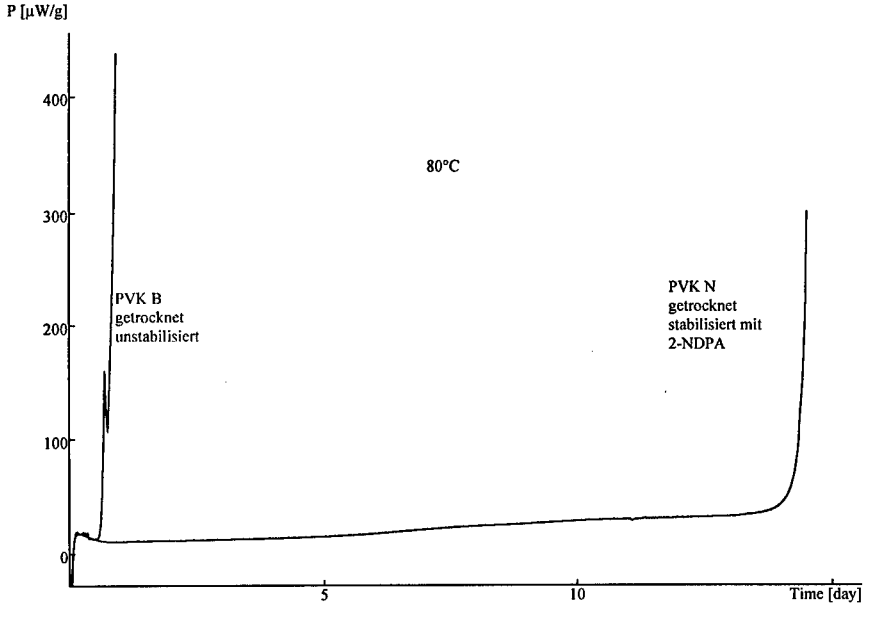

Abb. 11. Zersetzung getrockneter stabilisierter und nicht stabilisierter PVK bei 80°C (hohe Einwaage)

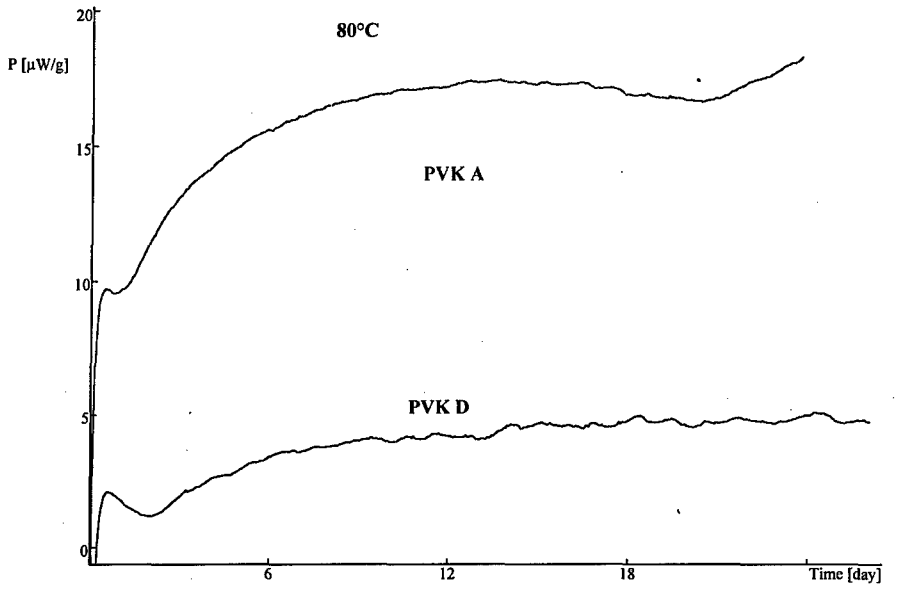

Abb. 12. Zersetzung getrockneter stabilisierter PVK bei 80°C (je ca. 600 mg Einwaage, Stabilisator Ak II)

NMR-Untersuchungen belasteter Proben

Thermisch belastete Proben aus der Wärmeflußkalorimetrie wurden NMR-spektroskopisch untersucht. Fernziel dieser Untersuchungen war es, die chemische Struktur der entstehenden Zerfallsprodukte zu ermitteln und den zeitlichen Verlauf ihrer Konzentration in Abhängigkeit von der Lagerzeit zu ermitteln. Zu diesem Zweck wurden verschiedene NMR-Techniken angewandt, so (eindimensionale) ^{1}H- und ^{13}C-NMR-Spektroskopie und 2D-NMR-Spektroskopie (^{1}H-^{1}H-Korrelation und verschiedene ^{1}H-^{13}C-Korrelationstechniken). Detaillierte Angaben werden in [2] veröffentlicht.

Die NMR-Spektren unbelasteter PVK's in Aceton-d_6 zeigen drei Multipletts für die Protonen des Nitroglycerins bei 5,9; 5,1 und 4,9 ppm. Im ^{13}C-NMR liegen die Signale bei chemischen Verschiebungen von 76,5 (**C**H-) und 69,8 ppm (**C**H_2-Gruppe).

Die Resonanzen der Nitrocellulose sind sowohl im ^{1}H- als auch im ^{13}C-NMR nur als breite kleine Hügel sichtbar. Qualitative oder gar quantitative Aussagen oder Zuordnungen dieser Signale zu bestimmten funktionellen Gruppen sind nicht möglich. Insofern kann der Einfluß der Zersetzung der Sprengöle auf die Nitrocellulose nicht ermittelt werden. Der Einfluß der Nitrocellulose auf die Zersetzung der Sprengöle ist nur indirekt über den Vergleich der PVK mit reinem Nitroglycerin möglich (vgl. Abb. 7).

Geringfügig belastete Proben zeigen ein charakteristisches ^{1}H-NMR-Spektrum (s. Abb. 13). Es konnten mit Hilfe der oben angegebenen Kopplungstechniken die sieben in Abb. 14 genannten Stoffe identifiziert werden. Im Beginn der Zersetzung (Energieabgabe 0,4 J/g noch vor dem ersten Maximum) sind Signale einer bislang nicht identifizierten Verbindung zu sehen, die im ersten Maximum wieder verschwunden sind.

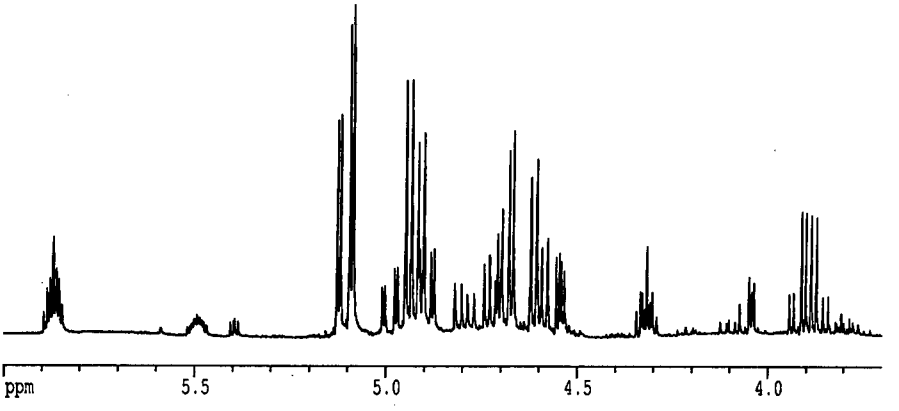

Abb. 13. ^{1}H-NMR-Spektrum (Ausschnitt) einer belasteten Probe (PVK B)

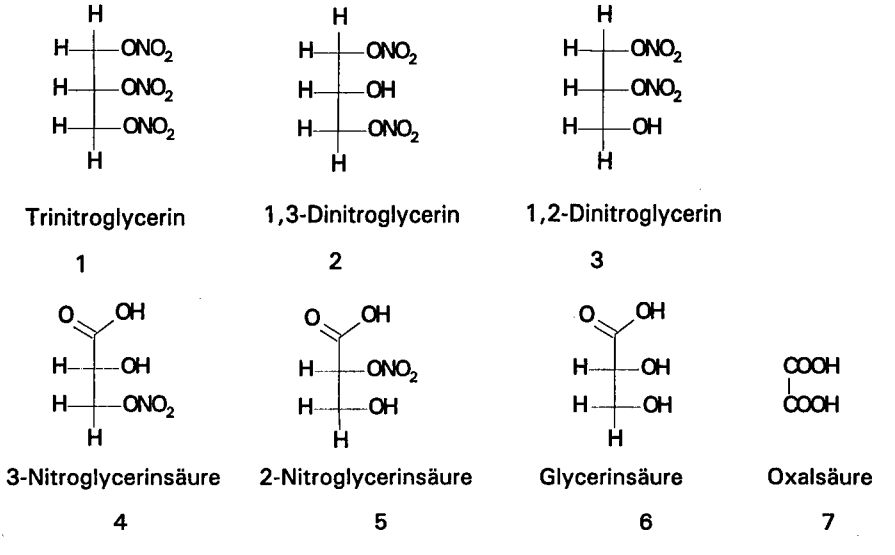

Abb. 14. Mittels NMR-Spektroskopie identifizierte Verbindungen (Reaktionsprodukte des Ngl)

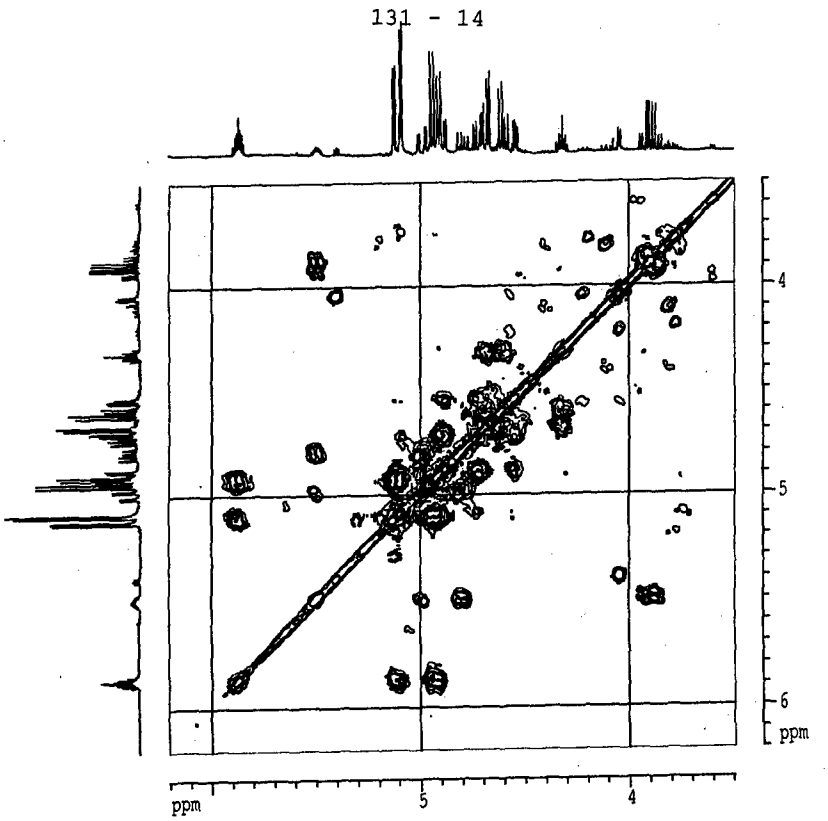

Abb. 15. 2D-NMR (^{1}H-/^{1}H-Korrelation) der belasteten PVK B (Energieabgabe ca. 280 J/g)

Diese Stoffe bilden sich nicht alle zur gleichen Zeit. Um die zeitliche Entstehung zu dokumentieren, haben wir die Autokatalyse nach verschiedenen Zeitpunkten (bzw. Energieabgaben) abgebrochen und die löslichen Reaktionsprodukte NMR-spektroskopisch quantitativ erfaßt. In Tabelle 4 sind die Ergebnisse dieser Untersuchungen zusammengestellt.

Tabelle 4: Relativer Gehalt der Dinitroglycerine bezogen auf den Nitroglyceringehalt nach Lagerung bei 80°C, bezogen auf 100% = Summe der drei Verbindungen (Der Absolutgehalt ist mittels NMR nur schwierig zu bestimmen, da ein vielfältiges Produktgemisch vorliegt und das entstehende polymere Material unlöslich ist).

Energieabgabe [J/g]	Anteile Trinitroglycerin **1**	Anteile 1,3-Dinitroglycerin **2**	Anteile 1,2-Dinitroglycerin **3**
0	100	0	0
5	94	6	0
68	50	30	20
281	59	26	15
630	26	48	26
1400	19	54	27

Alle Messungen wurden mit PVK B durchgeführt.

Nach kurzzeitiger Belastung bis zum ersten Minimum (Abb. 4; Energieabgabe ca. 5 J/g) haben sich etwa 6 % des Nitroglycerins in 1,3-Dinitroglycerin umgewandelt und eine Spur von 1,2-Dinitroglycerin ist erkennbar.

Im weiteren Verlauf nimmt der Nitroglyceringehalt rasch ab; in der Nähe des Maximums setzt ein erheblicher Gewichtsverlust ein (vgl. Tab. 3b). Gleichzeitig bildet sich eine polymere pastöse Masse, die gemäß NMR-Spektrum[1] zahlreiche Ester- oder Carbonsäuregruppierungen aufweist und vermutlich aus einer Reaktion von entstandenen Glycerinmono- oder -dicarbonsäuren mit Glycerin o. ä. gebildet wurde. Diese Masse weist unter NO_x-Atmosphäre eine intensiv grünliche Färbung auf, an Luft ist sie weiß. Bei Unterbrechung der Autokatalyse und Abkühlen der Reaktionsmischung auf Raumtemperatur wird diese grüne oder weiße Masse innerhalb von einigen Wochen durch den dichten Verschluß des Meßgefäßes nach außen gedrückt. Treibende Kraft ist hierbei die Bildung von NO_x und damit verbunden ein erheblicher Druckaufbau. Diese Autokatalyse bei Raumtemperatur wird durch eine eindrucksvolle Bilderserie (auf dem Poster) belegt.

Qex-Untersuchungen

Die Bestimmung der Explosionswärme ergab für das nicht stabilisierte feuchte PVK B 6587 J/g, für das stabilisierte feuchte PVK N 6151 J/g. Die bei der Umsetzung entstehende polymere Masse hat dagegen nur noch eine Explosionswärme von rund 4300 J/g. Die Differenz entspricht größenordnungsmäßig dem Energieverlust während der Wärmeflußkalorimetrie.

Bewertung

Die **feuchten** [2] PVK zeigen – sowohl stabilisiert als auch unstabilisiert – keine Neigung zu autokatalytischer Zersetzung innerhalb von 5 Tagen bei 80°C. Bei Temperaturen > 50°C können die spezifischen Wärmeproduktionsraten nach Arrhenius ausgewertet werden (s. Abb. 3 und Tab. 2). Die durchgeführten Messungen (s. Abb. 1 und 2) zeigen, daß bei allen Temperaturen nach kurzer Zeit eine konstante Zersetzungsrate erreicht wird. Eine Autokatalyse bei Lagertemperatur ($15 < T < 30$°C) kann für die feuchten Pulvervorkonzentrate innerhalb der üblichen Lagerzeit von maximal 3 Jahren mit an Sicherheit grenzender Wahrscheinlichkeit ausgeschlossen werden.

Die adiabatische Selbstaufheizung des **getrockneten** PVK ist im doppelten Sinne eine „worst case"-Betrachtung, da

1) im Realfall immer eine Ableitung der durch die Zersetzungsreaktion erzeugten Wärme des PVK an die Umgebung erfolgt und

2) das PVK alkoholfeucht vorliegt (was wie oben dargelegt, einen Eintritt in die autokatalytische Zersetzungsreaktion verhindert oder zumindest stark verzögert).

Bewertung PVK B

Bei 70°C wurde – vor Beginn der Autokatalyse – ein über 68 h konstanter Wärmefluß von 2,8 µW/g gemessen (s. vorletzter Eintrag in Tab. 3), der einer Wärmemenge von 0,69 J/g entspricht. Die spezifische Wärme des Systems beträgt bei 30°C 1,55 J/(g·K). Die maximal mögliche (adiabatische) Erwärmung des PVK ist daher lediglich 0,69/1,55 = 0,44 K. Nimmt man (wiederum als

[1] Problematisch ist die geringe Löslichkeit dieser Masse, so daß zur Zeit nur der in Aceton lösliche Anteil aufgrund seiner NMR-Signale beurteilt werden kann.

[2] Feucht bedeutet in diesem Zusammenhang alkoholfeucht. Ein Mindestgehalt muß eingehalten werden, da eine Verringerung des Alkoholgehalts z.B. von 7% auf 1% eine wesentliche Beschleunigung der Zersetzungsreaktion bewirkt.

„worst case") die niedrigsten berechneten Aktivierungsenergien von 130 kJ/mol, so entsprechen 68 h Lagerzeit 3,2 Jahren bei 30°C (bzw. von 2,9 Jahren bei adiabatischen Lagerbedingungen). Das bedeutet, daß die Zeit bis zur Autokatalyse der trockenen PVK selbst unter adiabatischen Lagerbedingungen bei einer Starttemperatur von 30°C länger als 2,9 Jahre ist.

Somit ist für eine Selbstentzündung von PVK selbst unter „worst case"-Bedingungen eine Vorlaufzeit von Jahren notwendig und damit die Wahrscheinlichkeit einer Selbstentzündung außerordentlich gering. Dies gilt nur für den Zustand vor der Autokatalyse. Sobald diese eingetreten ist, erreicht das PVK einen Reaktionszustand, in dem bei üblichen Geometrien der Packgebinde und Lagertemperaturen durchaus mit einer Selbstentzündung zu rechnen ist.

Die kritische Temperatur für ein Gebinde aus 4 · 5 Packeinheiten, das als unendliche Platte mit einer Dicke von 0,42 m angenommen wurde, liegt bei 21°C im Maximum der Reaktion (spezif. Wärmeproduktionsrate bei 80°C 200 mW/g, E_a 130 kJ/mol, vorexp. Faktor $3.5 \cdot 10^{21}$ W/kg, Wärmeleitfähigkeit 0,21 W/(m·K)).

Zusammenfassung

Es wurde die autokatalytische Zersetzung verschiedener PVK-Typen mittels Wärmeflußkalorimetrie untersucht. Dabei wurde festgestellt, daß – nach einer Periode mit vergleichsweise sehr geringen Wärmeproduktionsraten – eine kurze Vorreaktion und anschließend eine heftige autokatalytische Zersetzungsreaktion eintritt. Der Zeitpunkt dieser Autokatalyse hängt von folgenden Faktoren ab:

- Alkohol- (Feuchte-) Gehalt der Proben (alkoholhaltige PVK neigen nicht zur Autokatalyse)
- Lagertemperatur (es liegt in etwa der Faktor 2½ bis 3½ pro 10°C Temperaturunterschied)
- enthaltener Stabilisator (die stabilisierende Wirkung von Akardit II ist größer als die von 2-NO_2-DPA)
- enthaltenes Sprengöl (nitroglycerinhaltiges PVK zeigt deutlich höhere Wärmeproduktionsraten als DEGN-haltiges PVK)
- Versuchsaufbau (höhere Einwaagen führen zu einem rascheren Eintritt in die Autokatalyse; bei Einwaagen < 100 mg wird keine Autokatalyse mehr beobachtet)

Bei der Zersetzung entsteht zunächst eine unbekannte Verbindung geringster Konzentration, danach 1,3-Dinitroglycerin, später wird auch 1,2-Dinitroglycerin gebildet. Unter den Versuchsbedingungen entstehen dann Nitroglycerin-carbonsäuren sowie Oxalsäure und eine weiße polymere Masse, deren Struktur noch nicht endgültig aufgeklärt werden konnte.

Eine Autokatalyse bei Lagertemperatur kann für die feuchten Pulvervorkonzentrate mit an Sicherheit grenzender Wahrscheinlichkeit ausgeschlossen werden. Zu beachten ist jedoch, daß sich der Alkohol in nicht dicht geschlossenen Behältnissen relativ leicht verflüchtigt. Eine regelmäßige Kontrolle des Alkoholgehalts des PVK ist daher notwendig. Die vorgeschriebenen Lagertemperaturen sind einzuhalten.

Trockene PVK zeigen, wenn sie unter hinreichend lange und hohe Temperaturbelastung geraten, eine außerordentlich heftige Autokatalyse. Bis diese Autokatalyse eintritt, vergeht jedoch unter vorgegebenen Lagerbedingungen ein Zeitraum von mindestens einigen Jahren, selbst wenn man den „worst case" einer adiabatischen Selbstaufheizung zugrundelegt. Wird diese Autokatalyse jedoch erreicht, so ist mit einer Selbstentzündung der Packeinheiten zu rechnen.

Durch die Verwendung des Stabilisators 2-NDPA kann der Zeitraum bis zur Autokatalyse noch einmal um etwa den Faktor 20 verlängert werden. Die Verwendung von stabilisiertem PVK ist daher empfehlenswert. Die Stabilität Akardit II-haltiger PVK's ist noch einmal um mindestens das zweifache besser; hier konnte innerhalb von 25 Tagen kein Übergang in die Autokatalyse beobachtet werden.

Literatur

[1] S. Wilker, U. Ticmanis, G. Pantel, M. Kaiser, T. Fox, „Sicherheitslebensdauer von Pulverrohmassen", *ICT-Jahrestagung* **1996**, *27*, .

[2] M. Kaiser, B. Ditz, S. Wilker, „Identifizierung von Zersetzungsprodukten des Nitroglycerins mittels mehrdimensionaler NMR-Spektroskopie", *Propellants, Explosives, Pyrotechnics*, in Vorbereitung.

Weiterführende Literatur zum Thema Nitroglycerin, PVK, Nitrocellulose und deren Stabilität und Zersetzung ist folgender Literaturliste zu entnehmen.

1. VBG 55f „Sprengöle und Nitratsprengstoffe" sowie die dazugehörige Durchführungsanweisung (1.4.1996).
2. K. Mehlhose, „Die mikroskopische Untersuchung der Gelatinierung von Treibladungspulvern", *BICT-Bericht* 1.3-3/3872/75.
3. G. Mavel, L. Nicolas, S. Wevert, „Untersuchung der Stabilität der Nitrocellulose-Nitroglycerin-Gele", *Bericht Institut National de Recherche Chimique Appliquée* (1.) (1966).
4. J. Hansson, „Microcalorimetric measurements on substances having self-ignited", *Symp. Chem.Probl.Connected Stabil.Explos.* **1985**, *7*, 87-98.
5. L.E. Paulsson, L.-G. Svensson, T. Lindblom, „Degradation of Nitrocellulose. Some Microcalorimetric Studies", *Symp.Chem.Probl.Connected Stabil.Explos.* **1992**, *9*, 69-75.
6. L.-G. Svensson, L.E. Paulsson, T. Lindblom, „A Microcalorimetric Study of Temperature and Stabilizer Effects on the Heat Generation in Gun Propellants", *Vortrag 4. Gun Propellant Conf. Mulwala AUS* **1990**.
7. Leider, H.R., Pane, A.J., „Evidence for Differences in Stability between Nitrate Ester Positions on the Cellulose Nitrate Ring", *USArmy Report UCRL 94049* (1986), Vortrag American Defense Preparedness Association Symposium, Long Beach, CA (1986).
8. R. Böhn, „Kritische Einflußgrößen auf den Abel-Test bei der großtechnischen Herstellung der Salpetersäureester Ethylenglykoldinitrat und Glycerintrinitrat", Diplomarbeit Univ./GH Siegen, **1997**.
9. D.M. Baaske, N.N. Karnatz, J.E. Carter, „HPLC Assay for Partially Nitrated Glycerins in Nitroglycerin", *J. Pharm. Sci.*, **72**, 194-196 (1983).
10. Servent, M. Delaforge, C. Ducrocq, D. Mansuy, M. Lenfant, „Nitric Oxide Formation During Microsomal Hepatic Dentration of Nitroglycerin: Involvement of Cytochrome P-450", *Biochem. Biophys. Res. Comm.* **163**, 1210-1216 (1989).
11. T. Krasiejko, „Spektrofotometryczne oznaczanie 1,3-dwuazotanu gliceryny w technicznej nitroglycerynie", *Organika* **1976**, 69-77.
12. Baaske, J.E. Carter, A.H. Amann, „Rapid and Accurate Stability-Indicating Assay for Nitroglycerin", *J. Pharm. Sci.* **68**, 481-483 (1979).
13. Camera, P. Penco, „Abel Stability of Nitroglycerin versus Dinitroglycerin Content", *Proc. Int. Pyrotech. Sem.* **8**, 772-790 (1982).
14. Gumbleton, J.R. Cashman, L.Z. Benet, „1,2- and 1,3-dinitrate metabolites of nitroglycerin: spectroscopic characterization and initial administration to man", *Int. J. Pharm.* **71**, 175-186 (1991).

International Round Robin Test to Determine the Stability of DB Ball Propellants by Heat Flow Calorimetry

Stephan Wilker [#], Pierre Guillaume [*]

Abstract

In this paper a method for the determination of the slow decomposition of propellants by heat flow calorimetry (HFC) was tested amongst ten laboratories in eight countries. As it is known that small changes of sample preparation and measuring procedure affect the HFC signal very much it was very easy to detect whether the operational procedure was conducted in a comparable way. The results show that – besides the initial effects – the standard deviation of the HFC curves at 80°C were very low which means that the measuring principle proposed by PB Clermont and WIWEB was good enough to be reproduced. This method should thus be integrated into a STANAG „HFC of DB ball propellants".

Zusammenfassung

In dieser Publikation wird eine Methode zur Bestimmung der langsamen Zersetzung von TLP mittels Wärmeflußkalorimetrie beschrieben, die in zehn Laboratorien in acht Ländern durchgeführt wurde. Aus früheren Arbeiten ist bekannt, daß geringfügige Änderungen bei der Probenvorbehandlung und der Meßdurchführung einen großen Einfluß auf das Meßsignal haben. Somit ermöglichen die erhaltenen Ergebnisse eine einfache Überprüfung der Übereinstimmung der Meßdurchführung. Die Ergebnisse zeigen, daß – abgesehen von unterschiedlichen Anfangseffekten – die Standardabweichung der Wärmeflußkurven bei 80°C sehr gering ist, was nichts anderes bedeutet, als daß die von PB Clermont und WIWEB vorgeschlagene Meßmethode sehr gut in anderen Laboratorien reproduziert werden kann. Daher sollte diese Methode Eingang in eine STANAG-Vorschrift „Wärmeflußkalorimetrie von zweibasigen Kugelpulvern" finden.

Introduction

In April 1997 ten scientists agreed to participate in a Round Robin Test dealing with microcalorimetric measurements of double base ball propellants. The aim was to harmonize the measurement conditions and the evaluation procedure and to compare the obtained data. The DPA stabilised propellant K 6210 was chosen because the decomposition of this propellant was intensively investigated during the past three years [1]. Lot 225 was taken for this test.

The participants of this Round Robin Test are collected in table 1. Only the results that were available in March 1998 are collected in this paper.

[#] Wehrwissenschaftliches Institut für Werk-, Explosiv- und Betriebsstoffe (WIWEB), ASt Heimerzheim, Großes Cent, D 53913 Swisttal
[*] PB Clermont SA., Rue de Clermont, 176, B-4480 Engis

Table 1. Participants of the Round Robin Test „Heat Flow Calorimetry"

Affilation	Name	Address		
Celsius Materialteknik	Dr. L.-G. Svensson	Gammelbackavägen 6	S-69151	Karlskoga
DERA	J. Dodds	Fort Halstead	TN1 47BP	Sevenoaks
ETBS	Dr. C. Balès	Route de Guerry	F-18015	Bourges
ICT	Dr. M.A. Bohn	J-v-Fraunhofer-Str. 7	D-76327	Pfinztal
PB Clermont S.A.	Dr. P. Guillaume	Rue de Clermont, 176	B-4480	Engis
Puolustusvoimien Tutkimuskeskus	Mrs. M. Hihkiö	PL 5	SF-34111	Lakiala
Schweizerische Munitionsunternehmung	Mrs. R. Sopranetti		CH-3752	Wimmis
SNPE – CRB	Mme M. Rat	Boîte Postale N° 2	F-91710	Vert-le-Petit
TNO P.M. Laborat.	Dr. N. v.d.Meer	Postbus 45	NL-2280AA	Rijswijk
WIWEB	Dr. S. Wilker	Großes Cent	D-53913	Swisttal

Program

To conduct a Round Robin Test it is necessary to define as exactly as possible the measuring conditions. This includes sample preparation, preconditioning, measurement temperature and time and calibration.

The following method was evaluated at PB Clermont and WIWEB/BICT during the past years and has proved to be satisfactory for HFC measurements of DB ball propellants. Its advantage is that it's very convenient, reproducible and it gives results within a few weeks. The measuring conditions are well-defined and are – what is very important – analogous to the conditions in small caliber ammunition. We describe the measuring instruction in this paper.

Sample Preparation and Measurement

The ball propellant grains are taken as they are (no cutting necessary). From former experience we know that there is a dependence of the HFC signal from the moisture content. Thus a preconditioning of the propellant is recommended. The sample should be stored in 60-69% relative humidity (21°C) environment for some days and – for comparison reasons – used unconditioned under ambient conditions. However the moisture content of the samples has to be known (Karl-Fischer titration).

The HFC signal is also dependent from the degree of filling (this is due to oxidation reactions). The measuring ampoules are filled up to the top so that the amount of air inside is minimal. The loading density is thus approximately 0,9 to 1,0 g/ml (2,7 - 3,0 g for a 3 ml ampoule). If other ampoules (e.g. 4 ml) are used the amount of propellant is of course higher. The closing of the ampoules must be complete so that the top can not be turned around manually. The closing can be easily controled by looking at the HFC curve (see fig. 1).

The measurements are done by a TAM microcalorimeter. Always double or triple measurements are recommended. They start at 80°C, followed by 60°C, 50°C and 40°C. Measurements at temperatures below 50°C are quite tricky and depending on a good room temperature constance. An inverse temperature program (from 40 up to 80°C) is not useful because the initial effects last very long at lower temperatures. But it is possible to control the values at 50 or 60°C after the descending temperature program.

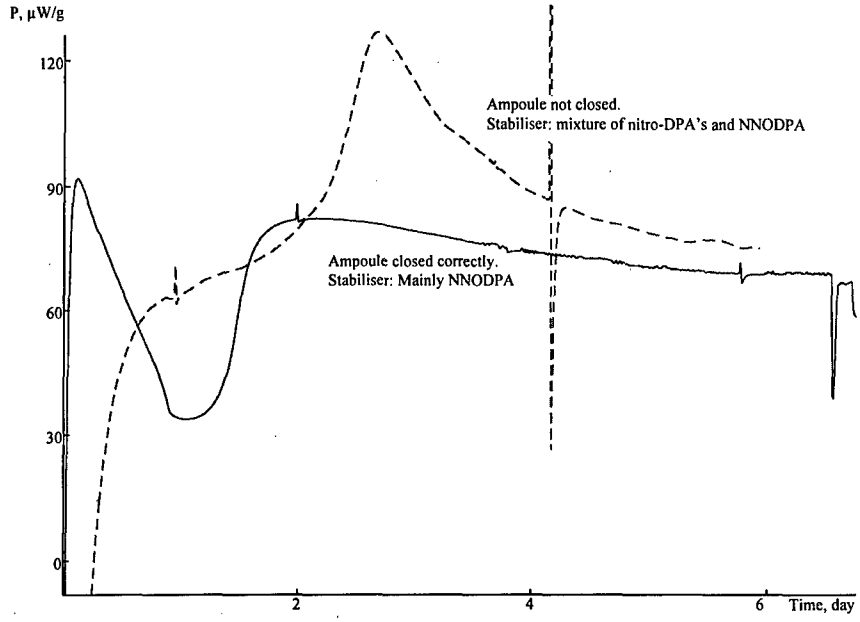

Fig. 1. One example of closed and non-closed ampoule measurements of K 6210, lot 219, (stabiliser content analysed at the end of the measurement).

Before measurement the system is calibrated. A stable baseline (minimum 12 h of stability) must be waited for, that means the base line drift and the noise should be below the specification of the TAM apparatus. On the reference side empty ampoules are used (inert material like sand on the reference side has no effect on the stability of the signal, but in this case the time for equilibration is much longer). The lowest possible measuring range for calibration and measurement should be used (e.g. 300 µW for 80°C, 100 µW for 60°C, 30 µW for 50°C and 10 µW for 40°C).

The „Switch technique" must be used to be sure of the niveau of the true baseline at 50/40°C measurements. Switch technique means exchanging sample and reference ampoule to obtain the negative signal. The „Switch technique" needs a time of at least 20 min in the park position before putting the switched samples down into the measuring position. Otherwise the thermal equilibrium might be disturbed too much. The same is true for the „re-switch". The switched measurement should last at least several hours (e.g. over night). Alternatively both sample and reference can be put up into the park position. Thus a „zero against zero" baseline measurement is possible. For data evaluation the measured values have to be corrected with the „real zero". Fig. 2 shows a Switch and a Switch/baseline experiment.

The measuring time of 8 days at 80°C is recommended to reach a constant niveau. The lower temperature HFC measurements should be run until a constant level is reached. Constant level in this case means a variation of <10 % of the signal within a period of 24 h. The use of the park position for about 20 minutes prior to a measurement is possible but not really necessary.

If endothermic peaks due to gas evolution occur at the end of the 80°C measurement the control – and if necessary the correction – of the closing of the ampoules is recommended before the samples are measured at lower temperatures.

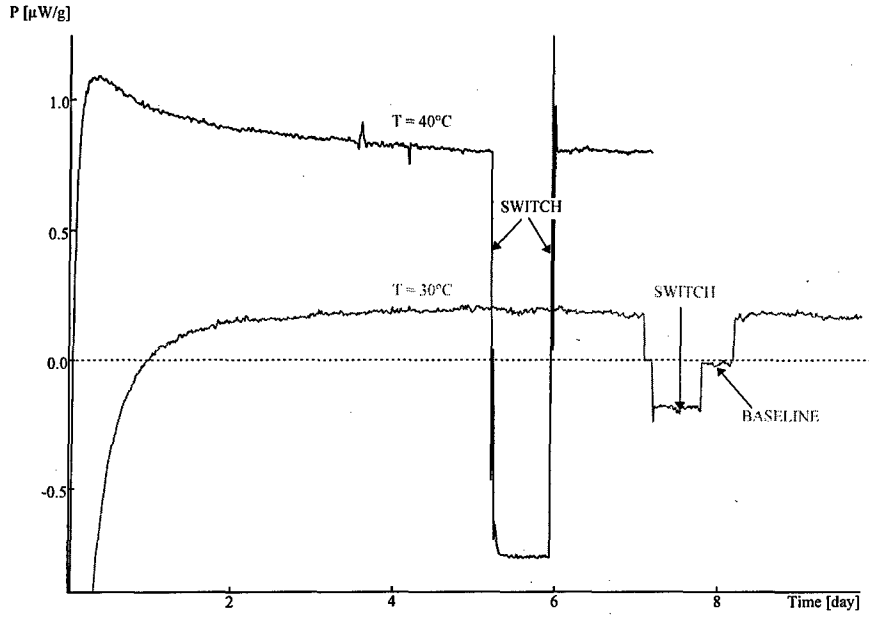

Fig. 2. Measurements showing a Switch and a combined Switch-baseline experiment

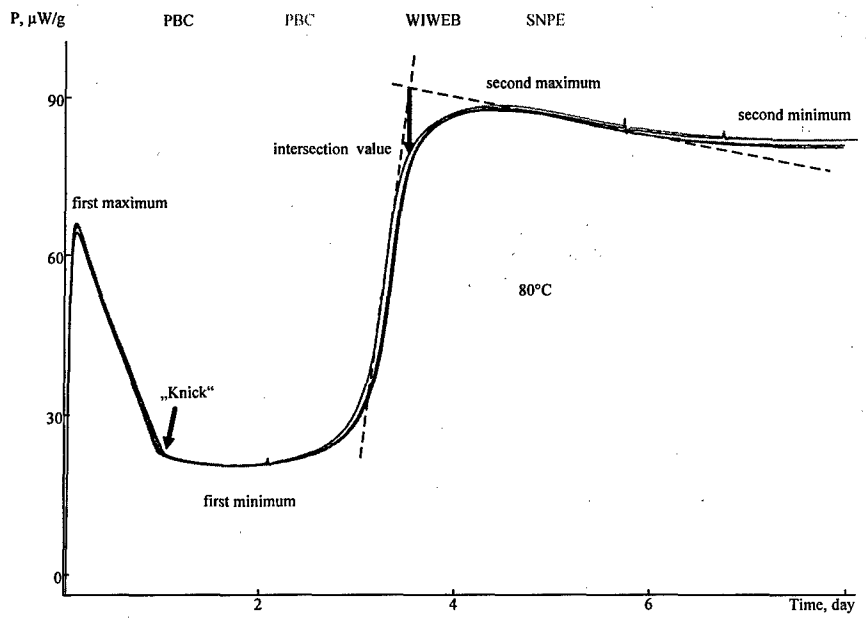

Fig. 3. Explanation of maxima, minima, „Knick", and 90% value (see text). K 6210, lot 223.

HFC Results

At first the values at different temperatures deriving from all laboratories are compared to look at the „qualitiy" of measurement. As mentioned before the shape of the 80°C curve is very dependent on the humidity of the propellant, on the degree of filling and on the closing of the ampoules. So we separated the evaluation into samples with and without preconditioning. We took out values and time of some very special points of the curve (1st maximum, „Knick", 1st minimum, intersection value, 2nd maximum and the 2nd minimum) and compared the results from different laboratories. The intersection point is consistent with the graphically estimated point of intersection where the tangent of the decreasing part of the curve meets the tangent going through the point of inflexion between the first minimum and the second maximum (see fig. 3). It is taken because it is much easier to determine in time and heat flow than the second maximum itself. Its value is about 90% of the heat flow of the 2nd maximum.

All average values are collected in table 2 (80°C). The results of the 60/50/40°C measurements are collected in tables 3-5.

See fig. 3 for explanation of minima, Knick and maxima.

Table 2. Averages of measurements at T = 80°C

labs A-F	precond.	P/1. max.	t/1. max.	P/Knick	t/Knick	P/1. min.	t/1. min.
		[µW/g]	[h]	[µW/g]	[d]	[µW/g]	[d]
Average	Y	68,2	2,62	22,2	1,09	20,4	1,74
Standard deviation	Y	8,32	1,24	1,20	0,10	1,33	0,15
Rel. standard dev.	Y	12,2%	47,4%	5,4%	8,8%	6,5%	8,5%
Average	N	65,9	2,26	22,7	1,12	20,7	1,70
Standard deviation	N	5,54	1,37	0,81	0,23	0,93	0,10
Rel. standard dev.	N	8,4%	60,5%	3,6%	20,2%	4,5%	5,7%

Explanation: labs A-F: laboratories participated in these measurements; precond. = preconditioning (Yes/No); P/1.max. = value at the 1st maximum; t/1. max = time of 1st maximum; P/Knick = value of Knick; t/Knick = time of Knick; P/1. min. = value at 1st minimum; t/1. min. = time of 1st minimum

Table 2 (contd). Averages of measurements at T = 80°C

labs A-F	precond.	P/inters	t/inters	P/2. max.	t/2. Max.	P/end	t/end	Qg
		[µW/g]	[d]	[µW/g]	[d]	[µW/d]	[d]	[J/g]
Average	Y	79,4	3,56	87,2	4,13	78,3	7,68	42,2
Standard deviation	Y	4,72	0,13	6,02	0,13	a)	a)	a)
Rel. standard dev.	Y	5,9%	3,6%	6,9%	3,1%	a)	a)	a)
Average	N	78,1	3,46	87,0	4,27	79,6	7,93	41,9
Standard deviation	N	1,47	0,23	1,73	0,26	a)	a)	a)
Rel. standard dev.	N	1,8%	6,7%	2,0%	6,2%	a)	a)	a)

a) not useful (different times of end of measurement)

Explanation: P/inters = value at the intersection point; t/inters = time of the intersection point; P/2.max. = value at the 2nd maximum; t/2. max = time of 2nd maximum; P/end = value of the end of measurement; Qg = total energy released during measurement.

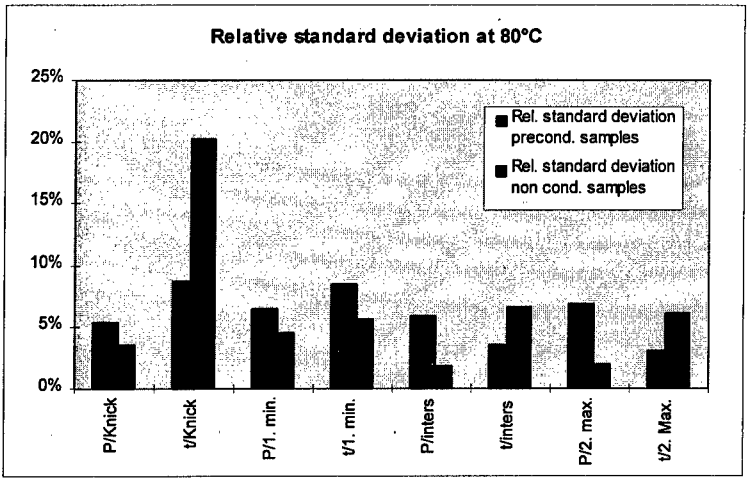

Fig. 4. Comparison of preconditioned and non-conditioned samples at 80°C

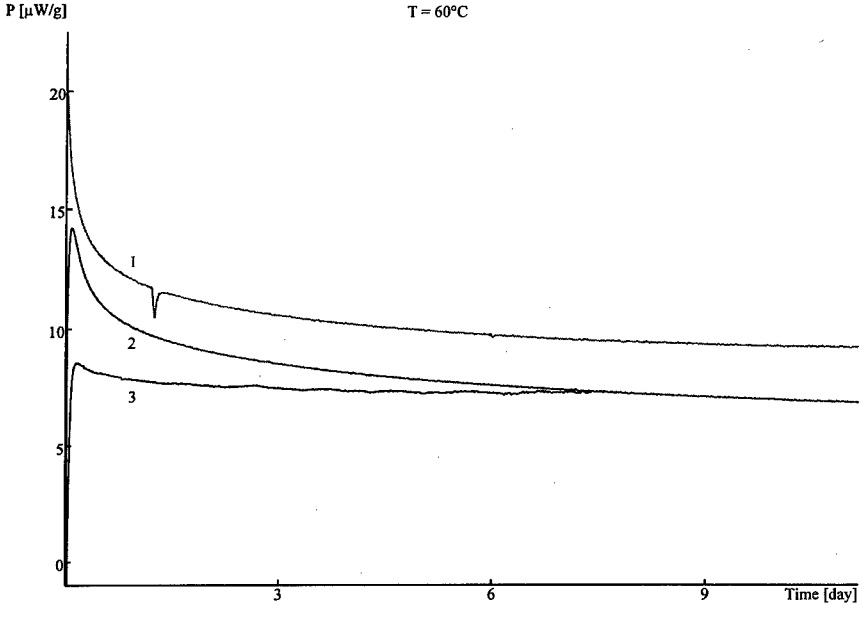

Fig. 5. Comparison of results at 60°C.

1 = lab. A; conditioned sample; measured at 80 → 60°C

2 = lab. B; unconditioned sample; measured at 80 → 60°C

3 = lab. C; unconditioned sample; measured at 80 → 70 → 60°C

Table 3. Averages of measurements at T = 60°C

labs A-D, F	precond.	P/2d	P/4d	P/6d	P/8d	meas. time	Qg
		[µW/g]	[µW/g]	[µW/g]	[µW/g]	[d]	[J/g]
average	Y	8,73	7,85	7,61	7,77	4 - 12	2 - 10
std. dev.	Y	1,48	1,44	1,50	1,79	-	-
average	N	7,77	7,18	6,92	6,72	4 - 11	1 - 8
std. dev.	N	1,03	0,98	1,17	0,53	-	

Table 4. Averages of measurements at T = 50°C

labs A-D, F	precond.	P/2d	P/4d	P/6d	P/8d	meas. time	Qg
		[µW/g]	[µW/g]	[µW/g]	[µW/g]	[d]	[J/g]
average	Y	2,58	2,42	2,30	-	6 - 9	1 - 2,3
std. dev.	Y	0,48	0,49	0,52	-	-	-
average	N	1,86	1,71	1,65	1,67	6 - 23	0,8 - 4,8
std. dev.	N	0,20	0,20	0,20	-		

Table 5. Averages of measurements at T = 40°C [a)]

labs A-D, F	precond.	P/2d	P/4d	P/6d	P/8d	meas. time	Qg
		[µW/g]	[µW/g]	[µW/g]	[µW/g]	[d]	[J/g]
average	Y	0,870	0,789	0,757	-	6 - 20	0,3 - 1,0
std. dev.	Y	0,085	0,108	0,110	-	-	-
average	N	0,689	0,586	0,560	-	6,5 - 20	0,2 - 1,0
std. dev.	N	0,049	0,074	0,078	-	-	-

a) all values are corrected by Switch and/or baseline experiments (see fig. 1)

Discussion

After all the data were collected and analysed by comparison (see tables 2-8) and by statistical analysis (see table 9). To find out the differences between samples with and without preconditioning they were evaluated separately. It was also necessary to give details of the measuring conditions (type of cell used). The details of all measurements are published in the final report of the Round Robin Test [5]. Some examples are picked out in the following tables.

The preconditioning has large effects at **80°C** only on the samples of laboratory D because the measurements were conducted in winter with a very low humidity in the laboratory. Especially the value of the second maximum of the 80°C measurement differs between conditioned and unconditioned samples. In all other cases the effects of preconditioning were negligible and differ in both directions (higher and lower values can be found) from the values of unconditioned samples.

Whereas the first maximum is quite dependent of the experimental procedure in the beginning the following points of the 80°C curves are quite indifferent towards it. So there are big standard deviations of heat flow and time of the first maximum. The best agreement was the time

and the value of the second maximum. This is the period where the DPA is nearly totally consumed.

The second maximum indicates the maximum of N-NO-DPA content and the reduction of DPA to a very low value. DPA reaches nearly zero after 8 days at 80°C. Comparing the measurements of conditioned and unconditioned samples there is no big difference between the two (neither in value nor in time; and the standard deviation is quite comparable) except for the measurements in laboratory D as mentioned earlier. It is probably not useful to discuss in detail small differences in HFC value. What can be seen is that the standard deviation of HFC values is somewhat smaller using nonconditioned samples whereas the standard deviation of the measuring times to reach the different points of the curve is smaller with preconditioned samples.

Interestingly there is nearly no difference between measurements in glass or in steel (Inox) ampoules if the other parameters like closing, degree of filling and preconditioning are comparable.

Table 6. Details of 80°C measurements. (Average = average of all measurements of precond. samples). Abbreviations see table 2.

Sample N°	ampoule	V	precondition.	K.F.	P/1. max.	t/1. max.	Knick	t/Knick
		[ml]		[%]	[µW/g]	[h]	[µW/g]	[d]
A1	INOX	5	65%r.H./3 d	0,60	73,4	3,18	23,6	1,23
B6	Glass	3	65%r.H./3 d	0,62	62,0	3,08	22,8	1,07
C23	Glass	3	no	n.d.	66,0	3,22	22,9	0,96
D24	Glass	3	no	n.d.	62,4	0	22,0	1,46
F16	Glass	20	0%r.H.	0,20	59,0	5,02	19,7	1,34
Average					**68,2**	**2,62**	**22,2**	**1,09**

Table 6 (contd.)

Sample N°	P/1. min.	t/1. min.	P/inters	t/inters	P/2. max.	t/2. Max.	P/end	t/end	Qg
	[µW/g]	[d]	[µW/g]	[d]	[µW/g]	[d]	[µW/d]	[d]	[J/g]
A1	22,5	1,67	86,1	3,45	-	-	87,2	8,00	44,3
B6	21,0	1,75	77,3	3,49	85,6	4,08	72,5	7,94	40,1
C23	20,4	1,79	78,4	3,56	87,9	4,36	80,8	7,89	40,8
D24	20,6	1,83	60,6	3,17	67,2	3,83	54,3	6,33	41,1
F16	18,4	1,91	60,2	3,70	66,9	4,18	46,6	8,00	30,0
Average	**20,4**	**1,74**	**79,4**	**3,56**	**87,2**	**4,13**	**78,3**	**8,83**	

The difference between preconditioning and no preconditioning is much bigger at **60°C**. After 6 days for example the average value differs between 7,6 µW/g (precond.) and 6,9 µW/g (no precond.). The increase in average value after 6 and 8 days is due to the reduced number of samples, there is no increase in value itself. To show the slow decrease we put the values at the end of the measurement and at one day before the end in two columns. The reduction of the value is about 60 nW in the last 24 hours so it can be regarded as being constant enough.

Table 7. Detailed values at 60°C.

lab.	V	ampoule	precond.	meas. program	P/2d	P/4d	P/6d	P(end-1d)	P/end	meas. time	Qg
	[ml]		[%r.H]		[µW/g]	[µW/g]	[µW/g]	[µW/g]	[µW/g]	[d]	[J/g]
A	5	INOX	65	80 → 60	11,30	10,41	9,88	9,48	9,44	11,01	10,1
B	3	GLASS	65	80 → 60	8,48	7,37	6,87	6,12	6,04	12,21	7,75
D1	3	GLASS	69	80 → 60	7,43	7,10	7,00	6,99	7,02	6,50	4,25
D2	3	GLASS	69	80,60,50, 40 → 60	5,71	5,47	-	5,79	5,47	4,00	1,81
C	3	GLASS	no	80 → 70 → 60	7,56	7,21	7,21	7,21	7,31	7,02	4,46
F	20	GLASS	0	80 → 60	4,75	4,23	3,93	3,93	3,81	7,13	2,72
average [a)]		-	-	-	**8,73**	**7,85**	**7,61**	-	-	-	-

a) average of all preconditioned samples. precond. = %rH of preconditioning; meas. program = temperature program; P/2d = heat flow after 2 days; P(end-1d) = heat flow one day before the end of the measurement; P/end = heat flow at the end. See also table 2.

Interestingly laboratory D had measured the sample again at 60°C after the whole temperature program (table 7, entry D2). The HFC value has dropped down to about 4 µW/g, reaching a constant level quite fast. Even the sample C (no preconditioning) that had been measured at 70°C prior to 60°C shows a lower heat flow value than the others. The time to reach a constant niveau is also much faster. The (possible) reason for this is explained later on. The dried sample (lab. F) shows severe differences in HFC value compared to the other samples.

The same is true for the **50°C measurement** (tables 4 and 8). Here we also find bigger differences between the samples' preconditioning: 2,30 µW/g (precond.) and 1,65 µW/g (no precond.) after 6 days. At the end the signal was constant enough for evaluation (decrease of 20-50 nW in the last 24 hours).
If the sample comes directly from 80°C to 50°C the HFC value is much higher (see entry C1) and the time to rach a constant level is much longer whereas if 70°C had also been measured this time is much shorter. This shows that an exact temperature program must be kept.

Table 8. Detailed values at 50°C. Abbreviations see table 7.

lab.	V	ampoule	precond.	meas. program	P/2d	P/4d	P/6d	P (end -1d)	P/end	meas. time	Qg
	[ml]		[% r.H.]		[µW/g]	[µW/g]	[µW/g]	[µW/g]	[µW/g]	[d]	[J/g]
B	3	GLASS	65	80,60,50	2,23	2,13	2,03	2,00	1,98	7,60	1,48
F	4	GLASS	65	80,60,50	1,89	1,71	1,77	1,66	1,67	8,04	1,17
A	5	INOX	no	80,60,50	1,94	1,77	1,65	1,63	1,61	8,00	1,31
C1	3	GLASS	no	80,50	3,50	2,90	2,58	1,76	1,72	**22,68**	4,69
C2	3	GLASS	no	80,70,60, 50	2,03	2,00	1,98	1,98	2,01	6,86	1,09
F	20	GLASS	no	80,60,50	2,23	2,06	1,97	1,94	1,91	8,05	1,32
average					**2,58**	**2,42**	**2,30**	-	-	-	-

The averages of the preconditioned samples (0,76 vs. 0,56 µW/g after 6 days) at **40°C** (see table 5) are still higher than those of the unconditioned ones. Nearly all measurements are

corrected with the Switch. The baseline is never at zero but differs about 50 to 80 nW in both directions. This is in the range of the value of the detection limit which we know from calibration experiments we conducted in the last months [2]. They show that the „correct" values can be slightly different from the observed ones. If the data evaluation is done by Arrhenius plot these small differences can cause a change in slope and though in activation energy and preexponential factor, especially at lower temperatures.
At the end the signal was constant enough for evaluation (decrease of 20-50 nW per day).

Statistical evaluation of data

By calculating the performance index using formula (1) the quality of the obtained data can be checked. As the 80°C measurement does not deliver a single value (like in HPLC tests) but a complex curve we took out the intersection point (see explanations to table 2) and looked at the value and at the time of it. The results are divided into conditioned and unconditioned samples.

$$PI = \sum_{i=1}^{N}\left[\frac{c_i}{c_i^*} - 1\right]^2 * \frac{10.000}{N} \qquad (1)$$

c_i = average of laboratory; c_i^* = average of all laboratories; N = number of samples; s_i = standard deviation of all samples

Because there is no „true value" for the HFC measurement we took the average of all measurements (but conditioned and unconditioned separately) as c_i^*. The $|z|$ score is calculated with formula (2); the average value of the unconditioned samples does not contain the µW values of lab D, because they are much lower due to low humidity of the propellant (see above). A performance index < 100 and a $|z|$ score < 2 can be regarded as satisfactory. In fact for both value and time of the intersection point all laboratories reach this goal.

$$|z| = \frac{\left(c_i - c_i^*\right)}{s_i} \qquad (2)$$

Table 9. Performance index and $|z|$ scores for the intersection value and time at 80°C

	cond. samples				uncond. samples			
Lab.	PI value	PI time	|z| score value	|z| score time	PI value	PI time	|z| score value	|z| score time
A	25,57	2,00	1,47	-0,69	1,90	30,94	-1,27	-1,43
B	0,54	0,05	-0,30	0,15	0,72	1,60	0,90	0,38
C	49,10	7,12	-1,67	1,06	0,00	5,54	0,05	0,70
D	2,49	10,82	-0,38	-1,31	*239,57* [a]	26,10	*-11,63* [a]	-1,07
E	7,81	1,64	0,67	0,51	-	-	-	-
F	0,86	4,97	0,16	0,63	0,02	4,09	0,08	-0,30

PI = performance index; a) = value not in average

The higher performance index and $|z|$ score of time of the intersection value of the unconditioned samples is due to some differences between early (labs A, D) and late (labs B, C) second maximum, which is also visible in the relatively high standard deviation.

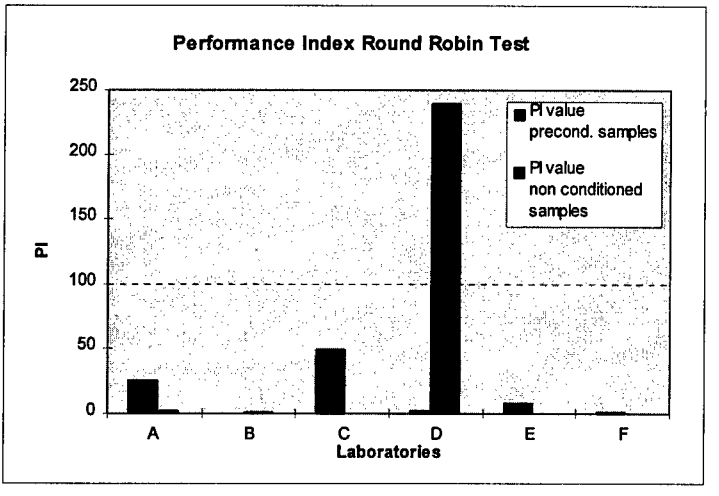

Fig. 6. Performance Index of heat flow at the intersection point

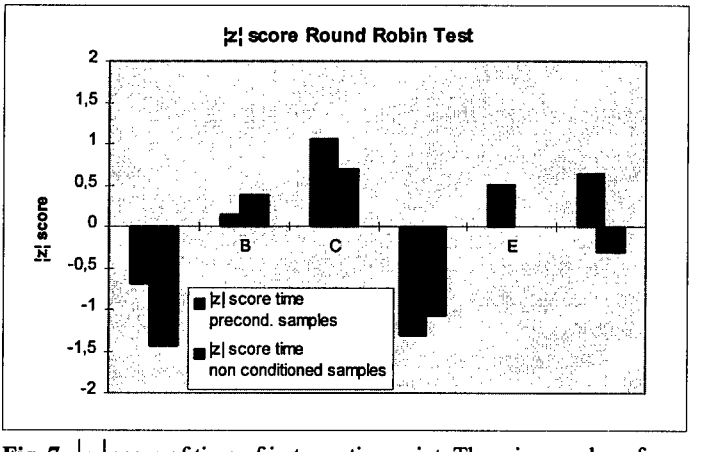

Fig. 7. $|z|$ score of time of in tersection point. There is no value of non conditioned sample from lab. E available. All laboratories fit the limit of $-2 < |z| < 2$, which is also true for the heat flow at the intersection point.

Evaluation of stability of propellants

There are two possibilities of evaluation for this purpose.

The first is the calculation of service life analogously to the formula presented in the TL and at the TTCP workshop [1]. The first step is to establish an Arrhenius plot (formula 3). The determination of the correlation coefficient from all measurements is useful to get a feeling

for the quality of the data [1]. As in nearly all cases a change in slope at about 60°C occurs two Arrhenius plots (the first with the 80/60°C values; the second with the 60/40°C values) have to be established.
The calculation of the time of 3% energy loss according to formula (4) as always done by WIWEB is not useful any more because there is no direct evidence between 3% energy loss and a significant and limiting loss of v_0 at this stage of decomposition. Moreover, long time experiments show that the decomposition rate does not remain constant over this range of energy loss (≈ 120 kJ/mole) [3].

$$P = C * e^{\frac{-E_a}{R*T}} \qquad (3)$$

$$t_{40} = \frac{Q_{ex} * 0{,}03}{P_{40} * 86400 * 365{,}25} \qquad (4)$$

using

P = heat flow [µW/g]
C = preexp. factor [W/kg]
E_a = activation energy [kJ/mol]
T = temperature [K]
R = universal gas constant [8,31 $J \cdot K^{-1} \cdot mol^{-1}$]
t = time [years]
P_{40} = from (1) calculated heat flow at 40°C
Q_{ex} = heat of explosion [4075 J/g]

The calculation of the kinetic parameters had been done by MathCad® program using every single value (for tab. 10a) resp. average values of the measurements (for table 10b) at the end (80°C) or after 6 days (60/50/40°C). In the following table it can be seen that there are differences in activation energy and pre-exponential factor between conditioned and unconditioned samples. It is also of importance that not always all values could be taken after 6 days (some measurements had been stopped earlier; in these cases the last value has been taken).

If the values 80, 60 and 50°C are taken together, the activation energy changes a little bit (see an example in table 10b). In the case of non conditioned samples the correlation coefficient is even a little bit better if the 50°C measurement is integrated into the higher temperature area.

The grey marked values are not taken for the average calculation.

Table 10a. Calculation of kinetic parameters from different laboratories

	Ea 80-60	pF 80-60	Ea 60-40	pF 60-40	KK 80-60	KK 60-40
sample precond.						
Lab.	[kJ/mole]	[W/kg]	[kJ/mole]	[W/kg]	-	-
A	106	4E14	106	4E14	0,9994	0,9990
B	125	2E17	96	6E12	0,9994	0,9990
D	128	6E17	120	4E16	0,9995	0,9937
F	125	2E17	110	1E15	1,0000	0,9999

[1] As a general rule it can be said that if KK > 0.999 all values can be described by the same straight line. If KK < 0.999 then a change in slope must be assumed which means there is no constant activation energy in the whole temperature range.

sample uncond.						
A	125	2E17	104	1E14	0,9999	0,9874
B	122	8E16	105	2E14	0,9999	0,9933
C	115	7E15	112	2E15	0,9972	0,9980
D	118	1E16	120	3E16	0,9998	0,9999
F	121	6E16	114	5E15	0,9999	0,9987
sample dried						
F	132	2E18	120	3E16	0,9996	0,9987

Ea = activation energy, pF = pre-exponential factor, KK = correlation coefficient

There is a small change in slope of the Arrhenius plot at about 50-60°C. This can be found with any gun propellant as far as we know. The „detection limit" of the activation energy is about 3 kJ/mole [2] which means that these effects are real.

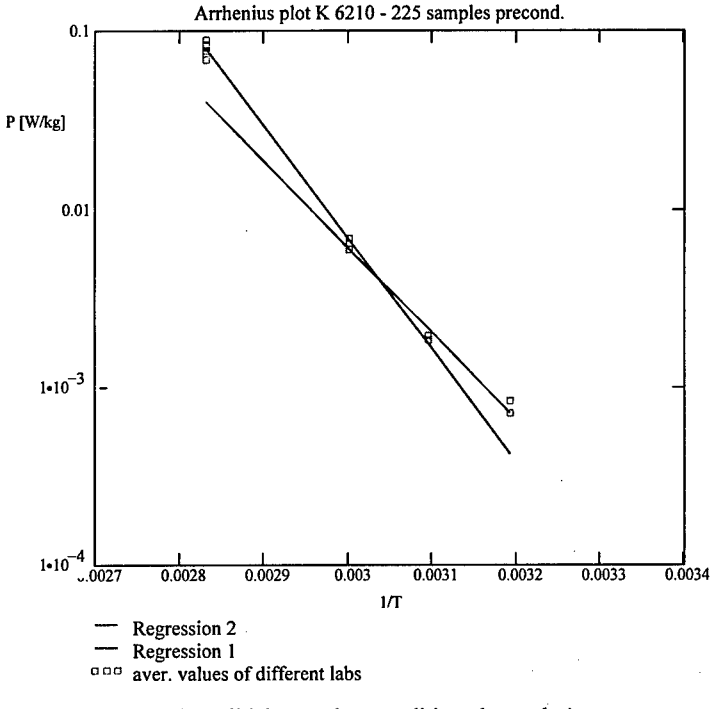

Fig. 5. Arrhenius plot (all laboratories; conditioned samples)

The second method for evaluation of stability is to measure the time of the 2nd minimum and extrapolate it with the activation energy on storage temperatures of e.g. 30°C. As we know that the shape of the curve of fresh samples is very comparable also at 70, 60, and 50°C [1] the time of the 2nd minimum is an „iso-α-point" and therefore the calculation method is reliable. The problem of this method is the long measuring time of fresh samples at 60°C or 50°C.

Table 10b. Activation energy and preexp. factor from all measurements

	sample precond.			sample non cond.		
temp. range	activation energy	preexp. factor	corr. coeff.	activation energy	preexp. factor	corr. coeff.
[°C]	[kJ/mole]	[W/kg]		[kJ/mole]	[W/kg]	
60-40	108	6E14	0,9917	112	2E15	0,9942
80-60	126	4E17	0,9995	120	5E16	0,9981
80-50	120	3E16	0,9987	120	6E16	0,9986

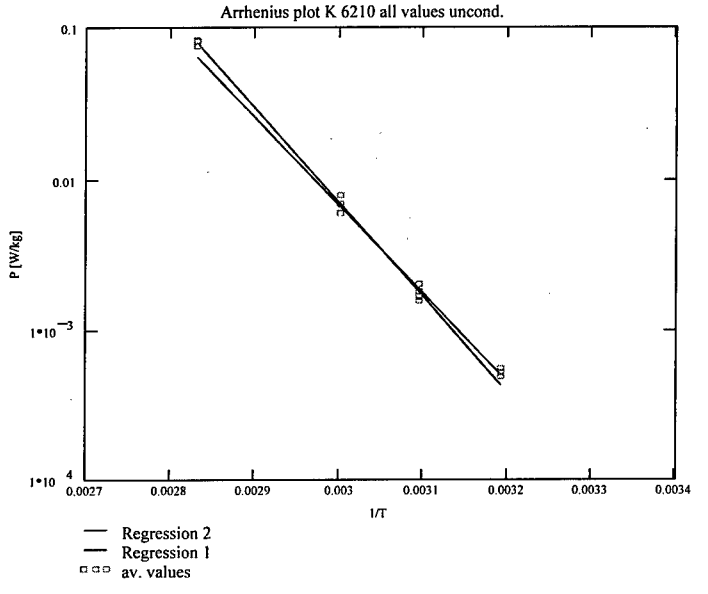

Fig. 6. Arrhenius plot (all laboratories; unconditioned samples)

Chemical analysis after measurement

To be sure of the correctness of closing of the ampoules the samples were analysed after the HFC measurements by HPLC and/or GPC to look at the changes of the stabiliser content and its reaction products and at the molecular mass decay under the measured conditions. The results will be presented on the poster and in [5], which also include the total energy lost during the measurement and the actual heat of explosion after measurement, which show a comparable reduction.

Conclusion

The results show a very good comparability and reproducibility leading to the conclusion that the Round Robin Test was a success. Thus a STANAG method „HFC of DB ball propellants" should be established using the HFC method described in this paper.

Very surprising was the fact that the standard deviation of all measurements at 80°C was – besides the initial effects – very low and that even the preconditioning of the propellant is not really necessary. This is not true if the measurement is prepared and conducted in a cold winter (then the humidity of the propellant is too low). At measuring temperatures below 80°C the preconditioning has a bigger effect, which is not fully understood. If the evaluation of data is done by Arrhenius equation the preconditioned samples show a lower activation energy and a lower preexponential factor making the propellant a little bit „less stable".

What is as well surprising is that a measurement at e.g. 60°C after the whole temperature program shows different results than the first 60°C measurement because between both measurements there are only some J/g energy difference in the propellant. That means that both measurements are done nearly at the same stage of decomposition (iso-α). One explanation for this might be that the thermal decomposition is superimposed by long lasting endothermic evaporation and exothermic condensation or diffusion processes probably of moisture and/or nitroglycerin. If the equilibrium is not completely established deviations of the total signal in both directions may occur depending on the conditions of the experiment (e.g. duration of the experiment, the measuring temperature before, the treatment and the time between two measurements). A hint in this direction has been obtained by HFC testing of single base propellants [4] where an equilibrium is reached within 1-2 days, which is faster than here.

The stabiliser consumption measured after HFC measurements shows that the closing of the ampoules was good enough (mainly N-NO-DPA), because if the ampoule is not closed correctly then dinitro- and trinitro-DPAs are dominating.

Acknowledgements. The authors want to thank all participants for their engagement and time they spent into this project.

References

[1] P. Guillaume, A. Fantin, M. Rat, S. Wilker, G. Pantel, „Stability Studies of Spherical Propellants", *ICT-Jahrestagung* **27**, 16-1 - 16-14 (1996); M. Rat, P. Guillaume, S. Wilker, G. Pantel, „Practical Application of the HFC for the determination of the Stability of Propellants", *Proc. TTCP Workshop Leeds* 4/**1997**; P. Guillaume, M. Rat, S. Wilker, G. Pantel, „Microcalorimetric and Chemical Studies of Propellants", *ICT Jahrestagung* **28** (1998).

[2] S. Wilker, U. Ticmanis, G. Pantel, P. Guillaume, „Detailed investigation of sensitivity and reproducibility of HFC measurements", *11. Symp.Chem.Probl.Conn. Stabil. Explos.*, Båstad **1998**.

[3] D.S. Ellison, A. Chin, „Common Factors that May Affect the Accuracy of Microcalorimetric Data" *Proc. TTCP Workshop Leeds* 4/**1997**; A. Chin, D.S. Ellison, „20 mm Gun Propellant Safety Service Life Study Using Microcalorimetry/HPLC Correlation Diagrams", *Proc. TTCP Workshop Leeds* 4/**1997**.

[4] U. Ticmanis, G. Pantel, L. Stottmeister, „Stabilitätsuntersuchungen einbasiger Treibladungspulver – Mikrokalorimetrie im Grenzbereich", *ICT Jahrestagung* **28** (1998).

[5] S. Wilker, P. Guillaume, „Ringversuch Mikrokalorimetrie – Abschlußbericht", *WIWEB-Bericht* **1998**.

MICROCALORIMETRY AND CHEMICAL STUDIES OF DOUBLE BASE PROPELLANTS

Pierre GUILLAUME[1], Mauricette RAT[2], Stephan WILKER[3], Gabriele PANTEL[3]

1. P.B.CLERMONT s.a., Rue de Clermont 176, B-4480 Engis, Belgium
2. SNPE, Centre de Recherche du Bouchet, Rue Lavoisier, Le Bouchet BP N°2, F-91710 Vert-Le-Petit, France
3. Wehrwissenschaftliches Institut für Werk-, Explosiv- und Betriebsstoffe (WIWEB), Groβes Cent, D-53913 Swisttal, Germany

Abstract

In order to standardise a test procedure and to minimise the errors, a detailed study of various factors affecting the heat flow calorimetry (HFC) results like the moisture content of the propellants or the loading density of the cell.
Besides those effects on HFC measurements, the correlation of HFC with stabiliser consumption has been worked out.
The results show that HFC measurements are an easy, reproducible and sensitive method for the determination of the slow decomposition of propellants.

Zusammenfassung

Um die Testmethode zu standardisieren und die möglichen Felher bei der Meβdurchführung zu minimieren, wurde eine Studie verschiedener Faktoren, die die Wärmefluβkalorimetrie beeinflussen, durchgeführt. Zu diesen Faktoren zählen z.B. der Feuchtegehalt des TLP und die Ladedichte der Meβampulle.
Parallel dazu wurde der Stabilisatorgehalt der Tribladungspulver untersucht und der Stabilisatorabbau mit den Wärmefluβmessungen korreliert.
Die Untersuchungen zeigen, daβ die Wärmefluβkalorimetrie eine einfache, reproduzierbare und sehr empfindliche Meβmethode für die Bestimmung der langsamen Zersetzung von Treibladungspulvern ist.

1. INTRODUCTION

The Heat Flow Calorimetry (HFC) is one of the most useful technique for assessing a service lifetime of nitrocellulose based propellant [1], [2], [3], [4].

The fundamental principle of HFC is that all chemical or physical reactions which produce or absorb heat are recorded during the whole measuring time.

The measurements are conducted at different temperatures between 80 and 30°C. The values of constant heat production rates are taken for the calculation of the activation energy and the preexponential factor according to Arrhenius kinetics.

It is important to know what chemically happens during HFC measurements of a propellant. A previous study has already showed that the HFC results can be correlated with stabiliser consumption results [5].

Moreover, assuming a maximum loss of energy of the propellant that still delivers an acceptable ballistic behaviour, it is possible to evaluate a service lifetime of the propellant [6].

However, the error in lifetime calculation depends on the correctness of the measurements of the heat production rates.

In order to minimise the errors, a detailed study of various factors affecting the HFC results has been undertaken.

Spherical propellants were used for this study.

We have considered the following factors.

I. the moisture of the propellant

II. the loading density of the cell.

Those 2 parameters are encountered in the real life of the propellant in the cartridges and can affect the rate of decomposition of the propellant.

Beside those two parameters we have to consider the reproducibility of the measurements.

Measurements in three different laboratories were carried out in order to check the reproducibility of the results, to standardise the test procedure and hence to minimise the errors in service life calculations [7].

2. EXPERIMENTAL PROCEDURE

For the purpose of this study, double base spherical propellants were used. Most of the work has been done with the double base spherical propellant K6210. The mean composition is 20% Nitroglycerine, 4.5% dibutylphtalate, 0.9% diphenylamine, 0.5% potassium nitrate and the remaining % is nitrocellulose.

The experiments were runned in a TAM calorimeter with glass ampoules. Three different working ampoules were used : 3 cm^3 (WIWEB and PB Clermont), 4 cm^3 (SNPE) and 20 cm^3 (SNPE) At least double measurements were recorded on each samples. The measurements were started as soon as the samples were introduced into the microcalorimeter.

The measurements were started with a fresh sample at 80°C for at least 8 days. Then the samples are measured at lower temperatures until they reach a constant HFC signal that is used for the evaluation of the kinetic parameters. The measuring temperatures lie in the range between 80 and 30°C (mostly excluding 70°C).

Some measurements have been made with fresh samples at temperature below 80°C in the range between 70 and 50°C.

A few measurements have also been recorded in a CALVET calorimeter with a sample vessel of 92 cm^3.

In parallel we have analysed the stabiliser products at different times of samples that had been aged under the same conditions. The analysis of stabilisers and derivatives were performed by HPLC.

3. RESULTS AND DISCUSSIONS

3.1. Analysis of the shape of the HFC curves

In the case of double base propellants (see FIG 1), we have a certain and reproducible structure of the curves of freshly introduced samples which can be described by

a first maximum

a first minimum

a second maximum

a second minimum

an increase of the heat flow

Combining HFC measurements with stabiliser analysis we can better understand what chemically happens during HFC measurements.

As it can be seen on FIG 2, the DPA concentration decreases while the measurement goes on. In the minimum only a few percent of the original of DPA remains while N-NO-DPA is increasing rapidly reaching a maximum value at the second maximum of HFC (all DPA has disappeared at that point). Other derivatives of DPA are also measured : 4-N-DPA, 2-N-DPA, N-NO-2-NDPA, N-NO-4-NDPA and 2,2'DN-DPA. The three last appear mainly when the N-NO-DPA has reached its maximum and start to decrease (TABLE 1).

The same shape is recorded at lower temperature (e.g. 70, 60 or 50°C) when a fresh sample is introduced (FIG 3). However as expected, the time to reach the different stages is much longer and the heat flux much lower, but the energy release is comparable (TABLE 2). That means that the decomposition mechanism is unchanged for all these temperatures.

TABLE 1

T (d)	DPA	N-NO-DPA	4-N-DPA	2-N-DPA	N-NO-2-NDPA	N-NO-4-NDPA	2-2'DNDPA	HFC (µW/g)
0	0.5	0.59	0.033	0.031	0.0027			133
1	0.29	0.76	0.038	0.038	0.0099			32
2	0.26	0.68	0.045	0.048	0.016			25.5
3	0.022	0.95	0.046	0.056	0.0324	0.0424		28.6
4	0.019	1.06	0.02	0.035	0.0476	0.0638		51
6	0.018	1.04	0.021	0.012	0.1078	0.0757		48.3
7	0.013	1.04	0.024	0.008	0.1259	0.1047		46
8	0.004	0.94	-	0.01	0.1568	0.3426	0.01	43.3
10	-	0.81	-	-	0.148	0.4101	0.045	N.A.

TABLE 2

T (°C)	1st minimum (J/g)	2nd maximum (J/g)	2nd minimum (J/g)
80	5.2	14.5	42.2
70	5.2	14.3	44.6
60	5.4	15.4	- (*)

(*) the second minimum is nearly reached and the value is approximately 41 J/g

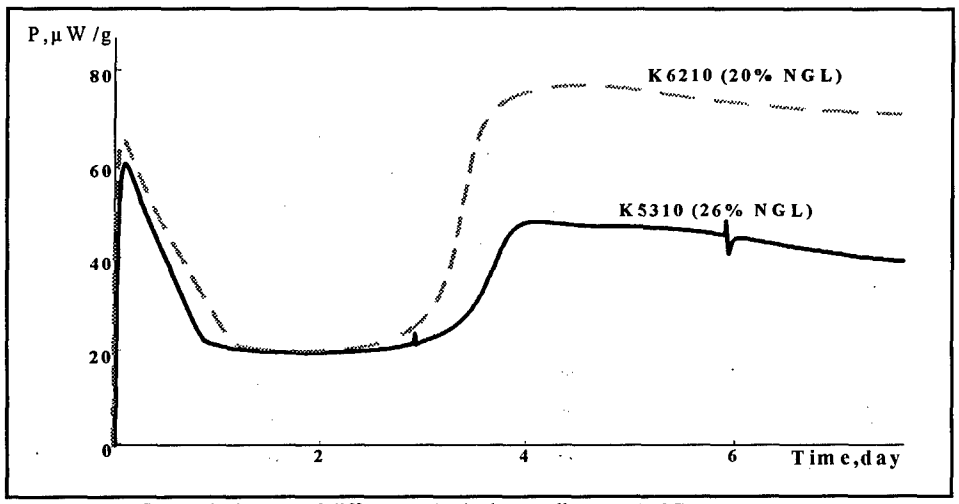

FIG 1: Heat flow calorimetry of different spherical propellants at 80°C

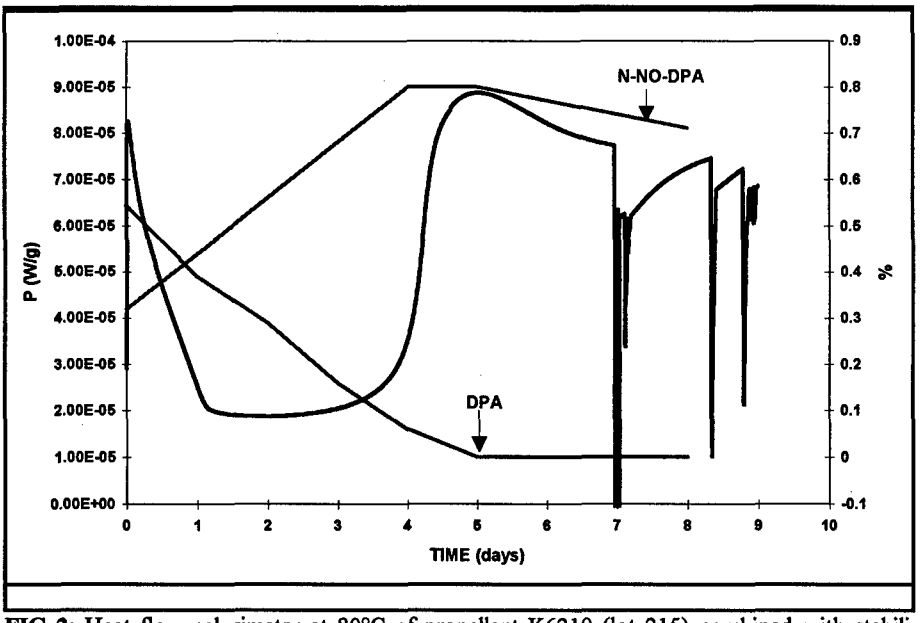

FIG 2: Heat flow calorimetry at 80°C of propellant K6210 (lot 215) combined with stabiliser loss.

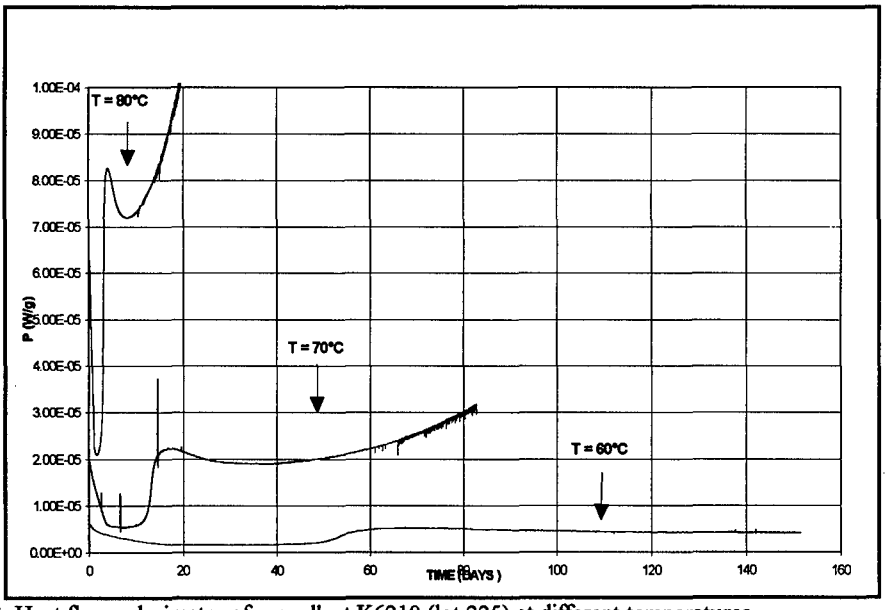

FIG 3: Heat flow calorimetry of propellant K6210 (lot 225) at different temperatures.

Using a zero order reaction the heat production rate can be described by the following equation

$$q = A \cdot e^{-E/RT} \qquad \text{eq. 1}$$

At the same stage of decomposition of the reaction (same energy release) at 2 different temperatures T1 and T2 we have

$$t1 \cdot e^{-E/RT1} = t2 \cdot e^{-E/RT2} \qquad \text{eq 2}$$

and hence combining (1) and (2)

$$q_1 t_1 = q_2 t_2 = \text{constant} \qquad \text{eq.3}$$

$$\text{or } \ln q = -\ln t + \text{constant} \qquad \text{eq.4}$$

On a graph we can draw the curves ln q as a function of ln t for the different temperatures (FIG 4). The intersection of the various curves with a straight line of slope -1 corresponds to a same stage of the reaction.

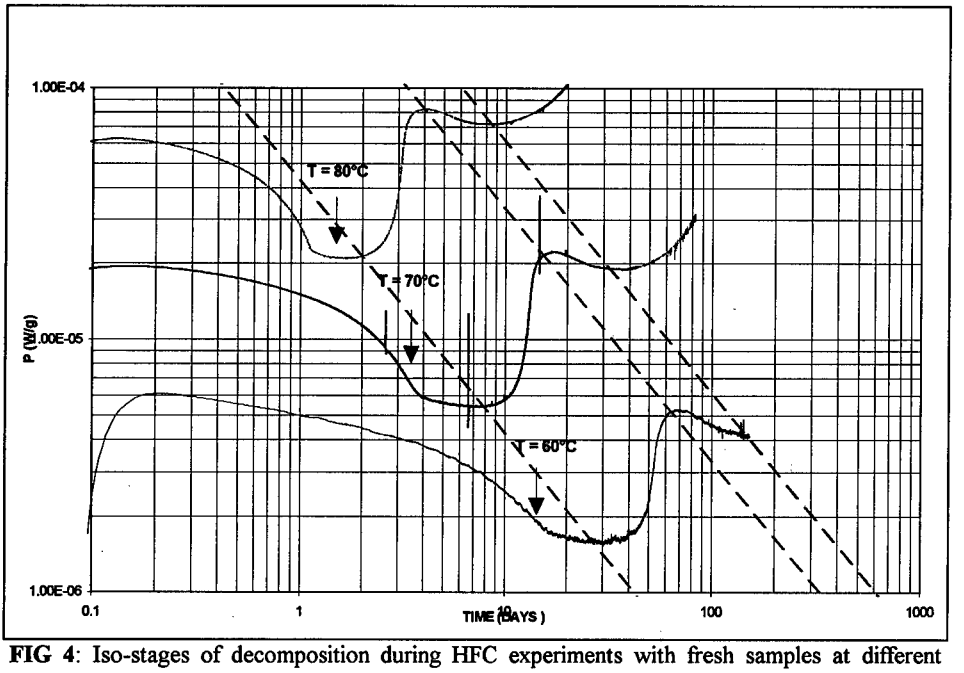

FIG 4: Iso-stages of decomposition during HFC experiments with fresh samples at different temperatures.

On FIG 4 you can see the results of the plot for the HFC measurement presented in FIG 3. This shows that when you reach the same part of the HFC curve at different temperatures you reach the same degradation point.

From those plot one can calculate the activation energy from the plot of ln q as a function of 1/T. Values between 126 and 138 kJ/mole are calculated.

Those values are in good agreement with the values calculated by Shin and al. [9]. They are also in the same range as those calculated when we start the measurements at 80°C and continue the measurements with the same sample at 70°C and 60°C (see table 4).

3.2. Influence of the moisture content

The propellant K6210 has been conditioned for several days at different relative humidity before measurements. The moisture content is determined by Karl-Fisher tiration (KF).

1. drying on P_2O_5 or $CaCl_2$: RH = 0 % (KF = 0.02%)
2. conditioning at 65 % RH (KF = 0.65%)
3. conditioning at 80 % RH (KF = 0.85%)

The HFC results are presented on FIG 5 and the values reached at different stages of the HFC reactions in TABLE 3.

The differences observed by HFC are confirmed by the measurement of stabiliser consumption where the same trend is recorded (see FIG 6 and 7). That is to say :

1. the rate of consumption of DPA decreases when the moisture content of the propellant increases.
2. the maximum of N-NO-DPA increases with moisture in time and value.
3. the steady state reached after the second maximum increases with the moisture. This is also true for the constant values measured at lower temperatures

When one calculates the activation energy and the preexponential factor (TABLE 4) according to equation 5, it appears that the activation energy remains nearly constant but the preexponential factor differs significantly leading to different service life (equation 6).

$$P = C * e^{-Ea/RT} \qquad \text{eq. 5}$$

$$t_{40} = \frac{Q_{ex} * 0.03}{P_{40} * 86400 * 365.25} \qquad \text{eq. 6}$$

P = heat flow (μW/g)

C = preexp. factor (W/g)

Ea = activation energy (kJ/mol)

T = temperature (K)

R = universal gas constant (8.31 J. K^{-1}.mol^{-1})

t time (years)

P_{40} = from eq 5 calculated heat flow at 40°C

Q_{ex} = heat of explosion (4075J/g)

The value of the activation energy calculated for the 60-40°C range beeing lower that for the 80-60°C range, the service life is calculated only for the range 60-40°C for safety reason. In addition the activation energy calculated for the temperature range 80 to 60°C is in agreement with the activation energy calculated from experiments with fresh samples (see above).

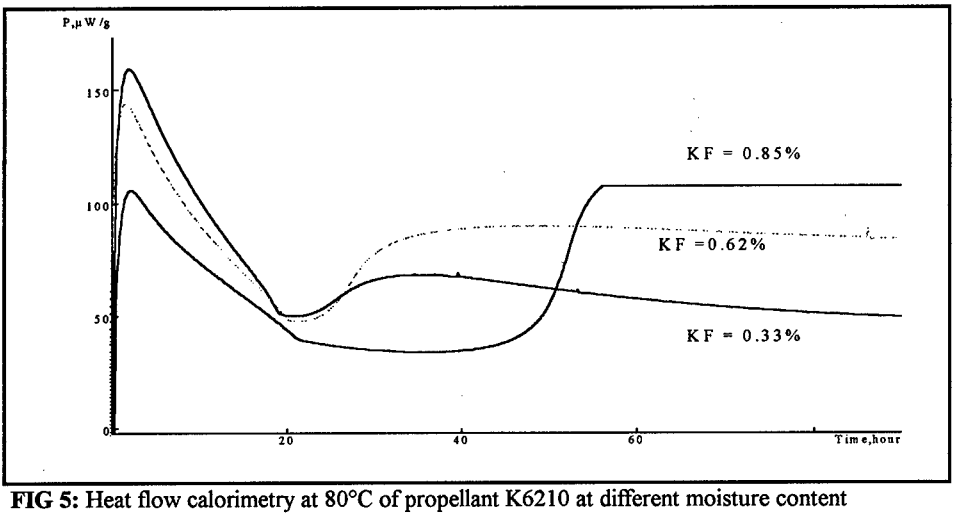

FIG 5: Heat flow calorimetry at 80°C of propellant K6210 at different moisture content

Table 3: Important values of HFC measurements of fig 5 for propellant K6210

MOISTURE (%)	1. Max [µW/g]	1. Min [µW/g]	2. Max [µW/g]
0.05	164 [2.0h]	52 [20.3h]	67.8 [1.4d]
0.33	158 [2.1h]	50 [19.5h]	68.3 [1.5d]
0.62	145 [2.3h]	49 [22.2h]	91 [2.04d]
0.85	106 [2.6h]	34 [37.7h]	[3.12d]

Table 4: Kinetic parameters for the fig 6

moisture content (KF)		activation energy (60-40)	pre-exp. factor (60-40)	correlation coefficient	SERVICE LIFE AT 40°C	SERVICE LIFE AT 30°C
(%)	(%)	(kJ/mol)	(W/kg)		(Years)	(Years)
start	end					
0.05	0.20	98	$1.1*10^{13}$	0.977	9.3	32
0.33	0.24	88	$2.5*10^{11}$	0.996	7.7	23
0.62	0.61	101	$4.4*10^{13}$	0.993	6.2	22
0.85	0.86	106	$4.5*10^{14}$	0.996	4.2	16
		activation energy (80-60)	pre-exp. factor (80-60)	correlation coefficient		
0.05	0.20	125	$1.2*10^{17}$	0.999		
0.33	0.24	118	$1.3*10^{16}$	0.999		
0.62	0.61	121	$5.8*10^{16}$	0.998		

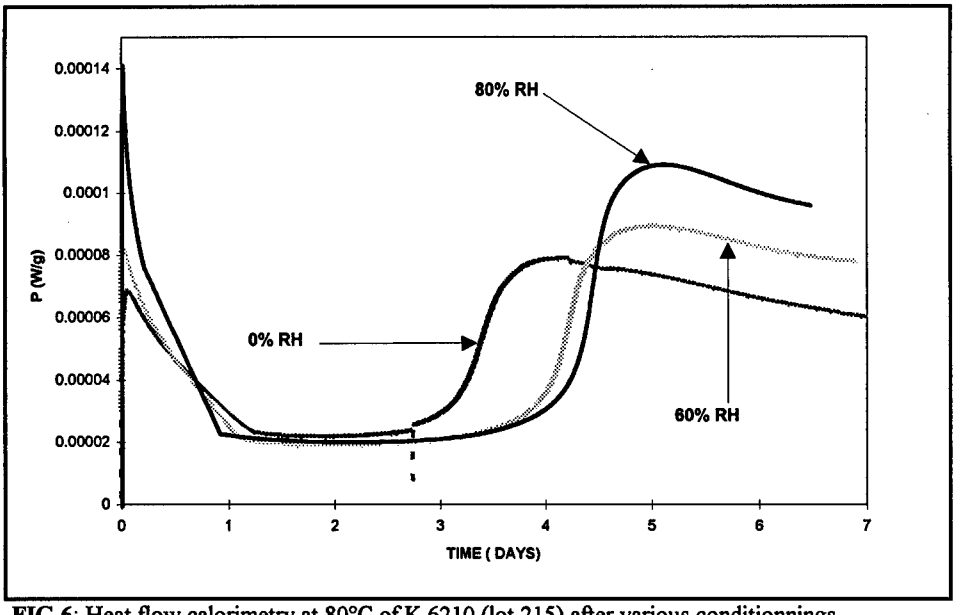

FIG 6: Heat flow calorimetry at 80°C of K 6210 (lot 215) after various conditionnings

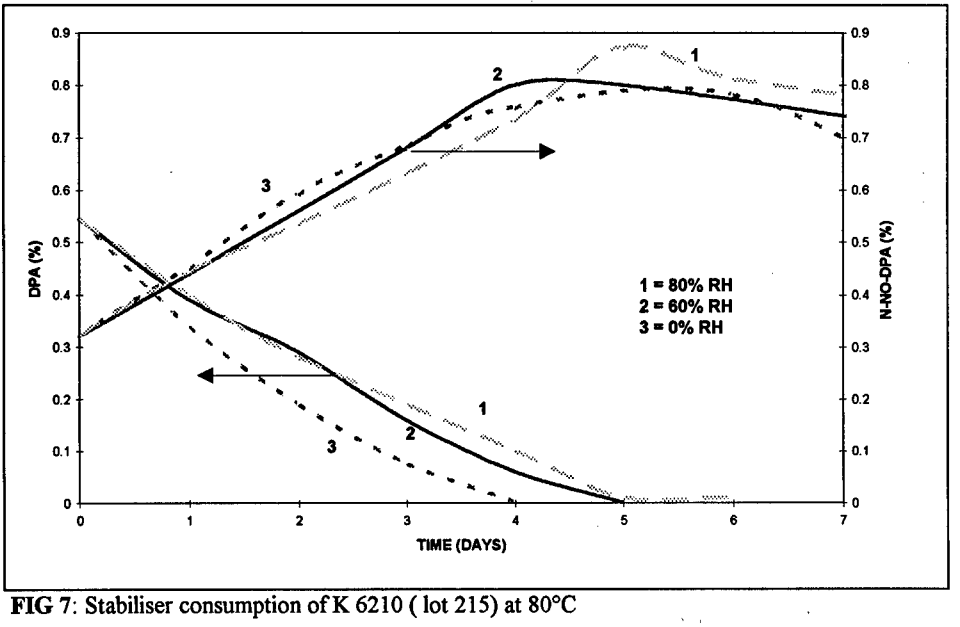

FIG 7: Stabiliser consumption of K 6210 (lot 215) at 80°C

3.3. Influence of the loading density

In order to see the ability of HFC measurements to show reproducible values within different laboratories having different cells, we have undertaken a study of the loading density of the cells. Indeed if one is using a larger cell, with an unknown propellant, it is interesting to know the evolution of HFC curves in order to avoid any damages to the apparatus that may arise from a large build up of pressure inside the cell. To reduce this risk one way is to reduce the amount of propellant in the cell, the other way is to start at lower temperature but then the time to reach a constant heat flow will be much longer.

An other point is to see if a different filling grade of the ampoule can lead to different results for the sample studied.

On FIG 8 one can see the evolution of the HFC curves for different filling grades of the ampoule. When the loading density of the ampoule is decreasing, the shapes of the HFC curves vary from the shape described earlier to the following shape :

1. first maximum
2. first minimum
3. second sharp maximum
4. second minimum
5. increase to a nearly constant value

This last increase leads to a higher heat flux value when the loading density decreases.

The time to reach a nearly constant value increases also when the loading density decreases.

The change of the shape of the HFC curves may be due to the fact that all DPA is transformed before oxygen has been consumed.

In order to verify this hypothesis, some experiments have been run with an full filled ampoule where the air has been replaced by pure oxygen.

As it can be seen from FIG 9, the same shape of curve arises with an oxygen atmosphere.

When the kinetics parameters are calculated, the main difference is due to the preexponential factor (see TABLE 5).

We can suppose that additional reactions with oxygen occur increasing the consumption rate of the stabiliser leading to a diminution of the service life of the propellant.

Table 5:Kinetic parameters for propellant K6210 lot222

CELL	Activation energy (60-40)	pre-exp. factor	TIME AT 40°C
	(kJ/mol)	W/Kg	(Years)
FULL	97	$1 *10^{13}$	6.1
HALF	94	$4. *10^{12}$	4.3

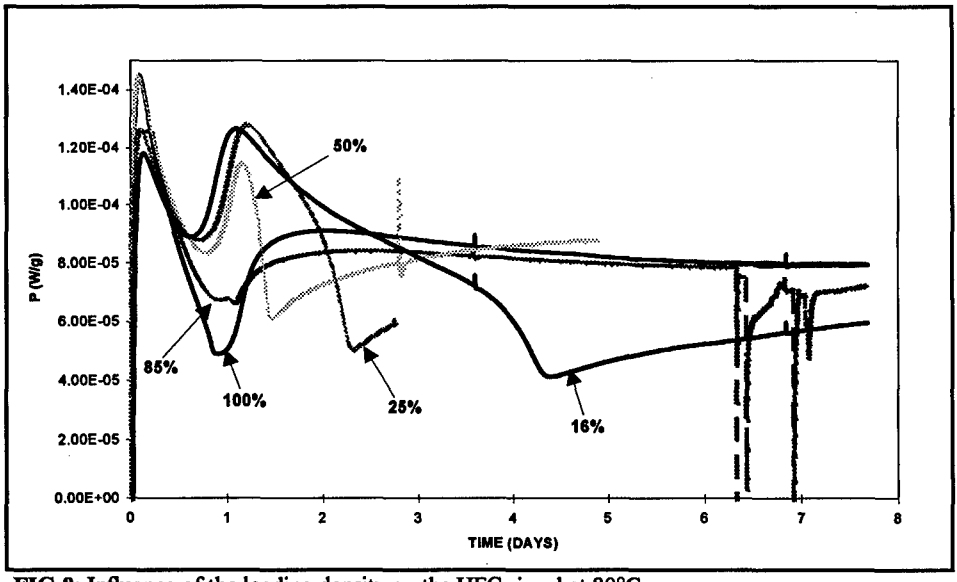

FIG 8: Influence of the loading density on the HFC signal at 80°C.

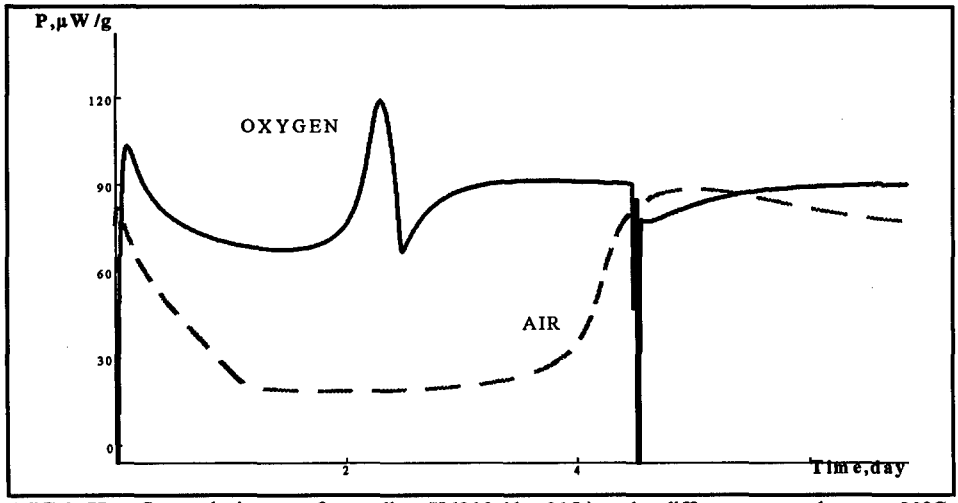

FIG 9: Heat flow calorimetry of propellant K6210 (lot 215) under different atmospheres at 80°C

3.4. Influence of the sealing of the ampoule

In some experiments an "abnormal" shape of the HFC curve is recorded [7][8] or some endothermic peaks are observed (e.g. fig 2 or 9).

The "abnormal" shapes are much like the shapes observed at low loading density or when air is replaced by oxygen. It can be concluded that those "abnormal" shape arises when the ampoule is not firmly sealed and then air can enter.

The endothermic peaks arise only after a few days at high temperatures. During the measurement a build up of the pressure occurs due to the degradation process of the propellant. According to the quality of the sealing of the glass ampoule, the ampoule will hold a pressure of a few bars before it leaks. The appearance of those endothermic peaks is thus the results of the leaks.

3.5. Comparison between two types of calorimeters

A few experiments have been run in 2 different calorimeters : TAM and CALVET (Setaram). The comparison of the results is given on FIG 10 for lot 215.

The results obtained in the CALVET are for 46 g. of propellant in a 92 cm^3 cell and for the TAM in a 4 cm^3 cell with 2 g. of propellant. The results obtained show a good agreement especially if one takes into account the differences in sample size. The loading density is comparable (see chapter 3.3).

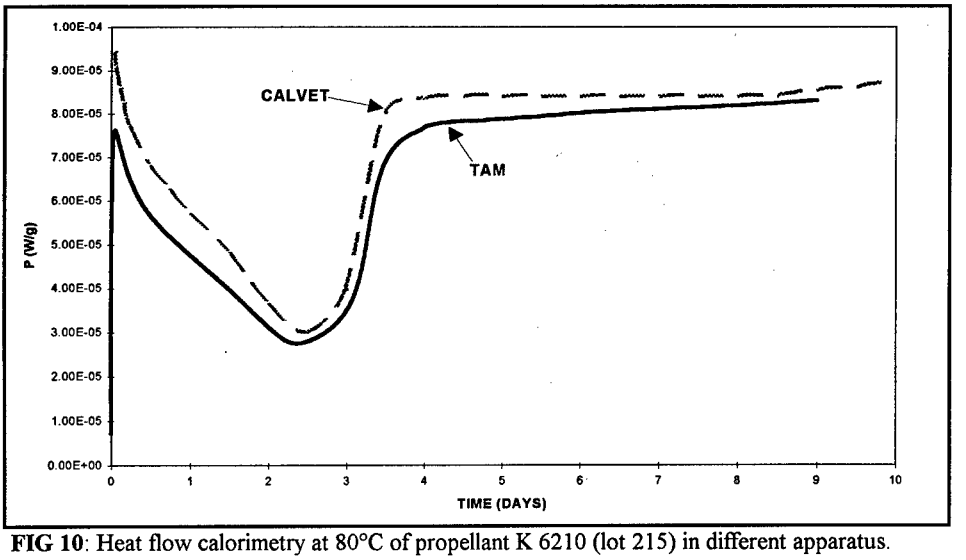

FIG 10: Heat flow calorimetry at 80°C of propellant K 6210 (lot 215) in different apparatus.

4. CONCLUSIONS

In this paper we have discussed different parameters that have an incidence for the reliability and reproducibility of the results.

At the start, HFC test which gives you the rate at which the reaction is going forward has to be combined with stabiliser consumption experiments or molar mass degradation that give the actual stage of the decomposition reaction. Then it is possible to calculate the service life of the propellant.

It is still unknown what the service life would be if a not preaged sample is used for HFC experiments for all the temperature lower than 80°C.

But it is impossible to do HFC measurements within an acceptable time frame with unaged samples.

The same problem arises with stabiliser comsumption experiments but the HFC allows to determine the Arrhenius factors in an acceptable time frame .

In order to standardise a test procedure one has to take into account all the different parameters.

This means that

1) the propellant has to be conditioned before measurement or the moisture content of the propellant has to be fixed.
2) the filling of the ampoule has to be kept constant in the ampoules for all measurements of the different samples. A completely filled ampoule is to be preferably used because it is more close to the situation encountered in the cartridges.
3) great care must be devoted to the sealing of the measuring ampoule.
   To be sure of the quality of the measurements at least duplicate experiment have to be made.
4) special care must be paid for HFC measurements at low temperature for the calibration of the apparatus (a more detailed investigation is presented in [10]).

As a conclusion it can be said that HFC measurements can be run with an excellent reproducibility in different laboratories and/or vessels if the parameters like loading density, moisture content and measuring method are fixed [7].

REFERENCES

[1] C.J. Elmqvist, P.E. Lagerkvist, L.G. Svensson, « Stability and compatibility Testing Using A microcalorimetric Method » J.Haz.Mat. 7, 281-285 (1983).

[2] M.Rat « Application de la microcalorimetrie isotherme à l'étude de la stabilité des poudres pour armes » Symp.Chem.Probl.Conn.Stabil.Explos 361-380 (1979)B. Vogelsanger, R. Sopranetti, « Sicherheits-, Stabilitäts- und Lebendaueruntersuchungen im Lebenszyklus von Treibladungspulvern », Vortrag Mikrokalorimetrie-/Thermoanalyse-Workshop BICT,p.27-43 (1995)

[3] Bohn M.A, Volk F., « Aging Behavior of Propellants Investigated by Heat Generation, Stabilizer Consumption and Molar Mass Degradation » Propellants, Explosives, Pyrotechnics **17**,171-178 (1992)

[4] S.Wilker, G.Pantel, U.Ticmanis, « Wärmeflußkalorimetrische Untersuchungen an Anzündhüchten » Proc.Int.Conf.ICT **26**, 84 (1995)

[5] P. Guillaume, A. Fantin, M. Rat, S. Wilker, G. Pantel, « Stability Studies of Sperical Propellants », Proc. Int. Conf. ICT **27**, 16-1 - 16-14 (1996)

[6] G.Holl, S.Wilker, M. Kaiser, P.Guillaume, «Former and modern methods of the determination of the service life of propellants »,Proc. 87th AGARD Conference on Service Life of Solid Propellant Systems, Athens 1996, p.18-1 - 18-13

[7] S. Wilker, P. Guillaume, « International Round Robin Test to Determine the Stability of DB Ball Propellants by Heat Flow Calorimetry, Proc. Int. Conf. ICT 29,1998

[8] M. Rat, P. Guillaume, S. Wilker, G. Pantel, « Practical Application of the Microcalorimetry to the Stability Studies of Propellants », Proc. TTCP Workshop Leeds 4/1997

[9] A. Chin, D.S. Ellison, « 20mm Gun Propellant Safety Service Life Study Using Microcalorimetry/HPLC Correlation Diagram, Proc. TTCP Workshop Leeds 4/1997

[10] S. Wilker, U. Ticmanis, G. Pantel, P. Guillaume, « Detailed Investigation of Sensitivity and Reproducibility of Heat Flow Calorimetric (HFC) Measurements », 11. Symp. Chem. Probl. Connected Stabil. Explos., Båstad 1998

Physical Chemical Characterization and Explosive Properties of Hydrazine azide

W.-H. Walther und T.M. Klapötke
Institut für Anorganische Chemie Ludwig-Maximilians-Universität, 80333 München

G. Holl
Wehrwissenschaftliches Institut für Werk-, Explosiv- und Betriebsstoffe
53913 Swisttal-Heimerzheim (ASt)

1 Abstract

The synthesis of hydrazine azide is reported. Physical and chemical characterization was done by IR-, Raman-, mass-, NMR- and X-ray spectroscopy comparing and completing well known datas of this compound. In addition we determined the purity and thermal stability with TG, DTA, DSC and calorimetry. With a drop hammer, friction device, steel tube and an electric discharge device we tested the explosive properties.
By the time we could produce new derivatives (alkyl-, aryl-) of this very potent molecule in an aspiration to fit the thermal and explosive properties of this class of compounds.

2 Introduction

Hydrazine azide $N_2H_5N_3$ is since 1891 a well known compound and was first prepared by professor THEODOR CURTIUS by adding hydrazine hydrate to an aqueous solution of hydrogen azide[a]. In the following years many scientists could improve the synthesis and purity[b,c,d,e], but only J.H. KOCH could prepare in 1959 a 1,1-dimethylhydrazine azide, the only known derivative of this inorganic azide till today[f]. But he could not purify and characterise this new compound. In the same time a few studies on the explosive properties of hydrazine azide were done[g,h,i,j]. Hydrazine azide was tested as an explosive, gun and rocket propellant showing good efficiencies. In later times many data about IR-, NMR-, mass- and X-ray spectrometry were collected. In this context the present study is a summery of all known

data on hydrazine azide and is the starting point of a systematic evolution of the potentials of this substance class.

3. Hydrazine Azide: Synthesis and physical chemical characterization

3.1 Synthesis

Hydrazine azide was synthesized by blowing gaseous hydrogen azide, made from stearic acid and sodium azide at 130 °C (1), in an ice-salt-cooled ethanolic solution of hydrazine hydrate (2). The crude ionic colourless salt can be recrystalized in absolute methanol getting crystals with a melting point of 72 °C.

$$CH_3(CH_2)_{16}COOH + NaN_3 \xrightarrow{130\text{-}160\ ^\circ C} CH_3(CH_2)_{16}COONa + HN_3 \quad (1)$$

$$HN_3 + N_2H_5OH \xrightarrow[-15\ ^\circ C]{EtOH} \left[\begin{array}{c} H \\ H \end{array}\!\!>\!\bar{N}\!-\!\overset{+}{N}\!<\!\begin{array}{c} H \\ H \\ H \end{array}\right] \; {}^{-}N{=}N^{+}{:}N^{-} + H_2O \quad (2)$$

3.2 Infrared spectrum

Figure 1 shows the infrared spectrum of hydrazine azide. The typical bands from deformation and stretching vibration of the functional groups are in good agreement with earlier publications[al,an].

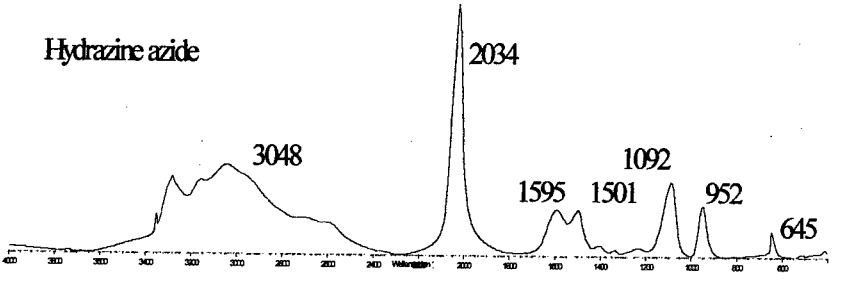

Figure 1: Infrared spectrum of hydrazine azide (wavenumbers/absorbance)

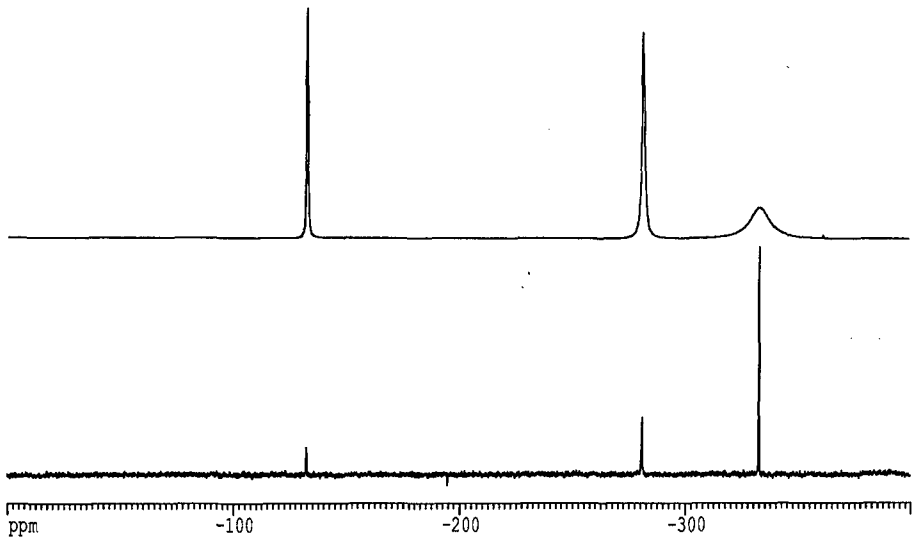

Figure 3: ^{14}N-NMR- and ^{15}N-NMR-spectrum of hydrazine azide.

3.6 X-Ray diffraction investigations

The structure of hydrazine azide (N_5H_5) was investigated by means of x-ray diffraction. Investigations at various temperatures were carried out using a x-ray diffractometer. Due to the hygroscopic nature of hydrazine azide, the specimens were preserved in an exsiccator.

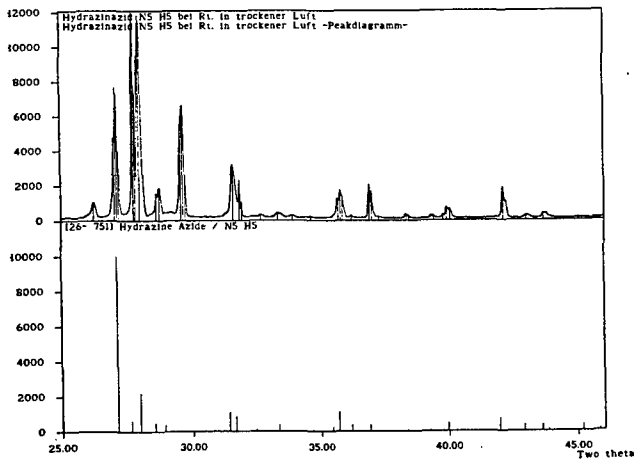

Figure 4 : X-Ray diffraction diagramme of hydrazine azide at room temperature with a peak-diagramme of the JCPDS-Database (literature values for comparison).

X-ray diffraction measurement of hydrazine azide taken at room temperature showed no agreement with the structural data of the literature (Figure 4). Phase transition of hydrazine azide were observed at higher temperatures. Further investigations are necessary to clasify this phenomena.

3.7 DTA-TGA, DSC and HFC

As indicated by the TGA-DTA curves in figure 5, hydrazine azides exhibits a very unsharp melting point at 72 °C. The peaks are interpreted as follows: The first peak at 4,7 °C corresponds to the melting point of residual water., the next two peaks are due to the crystal structure transformations, followed by the melting of the substance. In the first TGA-DTA measurement, carried out some weeks before, the solid state transformation was not observed, and the melting point was found at a considerably higher temperature. In the meantime the sample was stored in an open pan in an exsiccator. Taking into consideration the different values of the melting points in the literature (up to 80 °C), it can be assumed that the substance reacts during storage in air. It is often be observed that crystal transformations are hindered in the pure compound.

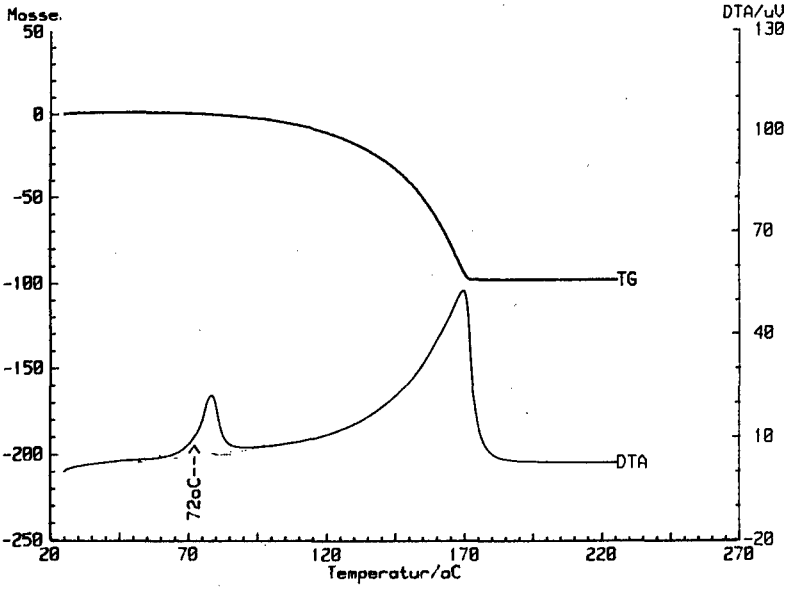

Figure 5: TGA-DTA diagramm of hydrazine azide (heating rate: 5 °C/min).

Figure 6 shows the heating of hydrazine azide in a pierced aluminium tube meassured by DSC. The peaks before the melting point (65.9 °C) could not be identified. The DSC-diagramm in figure 6 makes clearly, that hydrazine azide which was stored in an exsiccator, shows a different as one would expect from the TGA experiment. In the cooling curve the whole exothermic changes are shifted to lower temperatures.

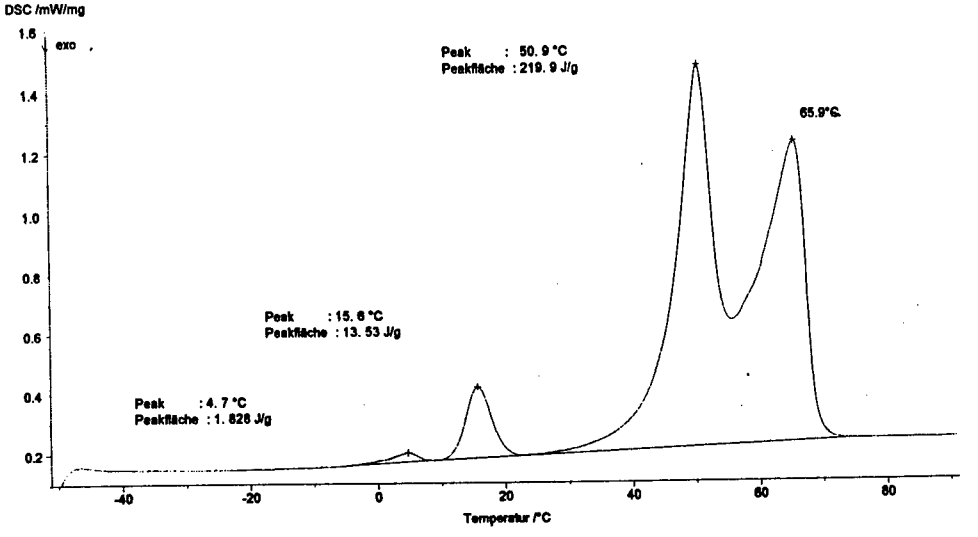

Figure 6: DSC of hydrazine (heating rate: 5 °C/min).

To check the ability of chemical decomposition, three samples were meassured by heat flow calorimetry (HFC)[p] at constant temperature of 60 °C. The first tube (4 mL) was filled with hydrazine azide under normal conditions. To exclude the interaction with oxygen and water, hydrazine azide was filled in the second tube (4 ml) under argon. The corresponding thermogramm shows a similar effect at the beginning as observed under normal condition. To give an evidence, that the reaction may be influenced by the free volume in the tube, a third sample of hydrazine azide was filled in a larger tube (20 ml). The reaction starts slower and is not competed before eight days. But the area under the curve (= lost energy of an exothermic process) after more than one week is nearly the same as for the specime 1,2 and 3. This may point to an impurity of hydrazine azide. Further investigations are necessary.

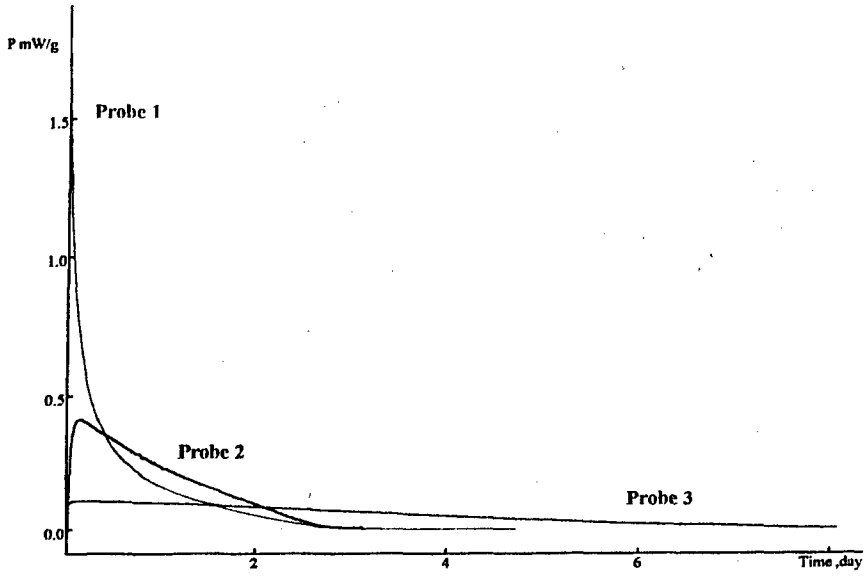

Figure 7: Heat flow calorimetry of hydrazine azide (storage temperatur: 60°C).

3.8 Impact-, friction-, electrostatic- and thermal sensitivity

Using BAM drop hammer and friction devices for the determination of the impact and friction sensitivity [o] , it was shown that hydrazine azide has an impact sensitivity at about 40 Nm which is not very sensitive. The friction sensitivity of the pure crystalyzed material was found to be at 80 N. For the determination of the electrostatic sensitivity[o] the material (approx. 25 mm^3) was subjected to an electric discharge of 32 Joule. No reaction accured in a series of ten tests. The electrostatic sensitivity is very low.

The sensitivity to a thermal stimulus[o] was determined by means of Koehnen test. The investigations were done with orifice plates of 2 and 6 mm. Tests with the 6 mm plates showed no reaction where as with the 2mm orifice plate the steel tube was fragmented into a lot of small pieces (Figure 8).

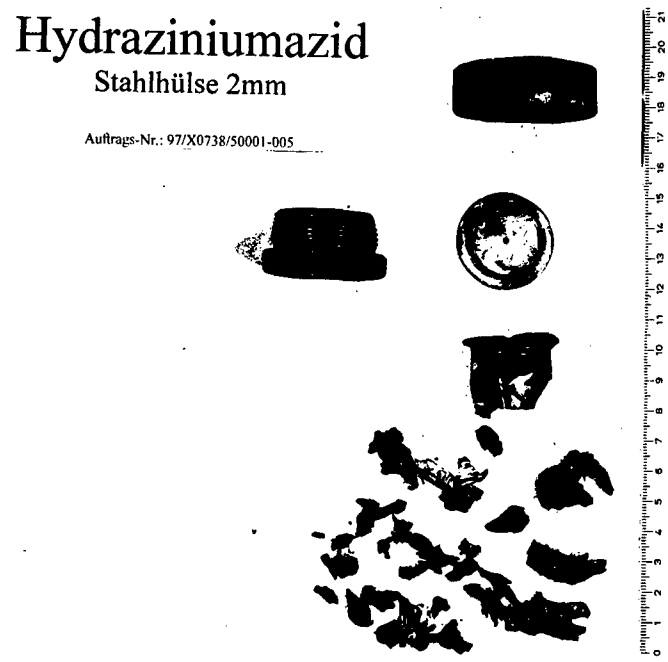

Figure 8: Steel tube after heating hydrazine azide with an orifice plate diameter of 2 mm

4. New derivatives of hydrazine azide: Synthesis and physical chemical characterization

The equations (3) and (4) show the general chemical reaction to produce new derivatives of hydrazine azides.

$$CH_3(CH_2)_{16}COOH + NaN_3 \xrightarrow{130\text{-}160\ ^\circ C} CH_3(CH_2)_{16}COONa + HN_3 \qquad (3)$$

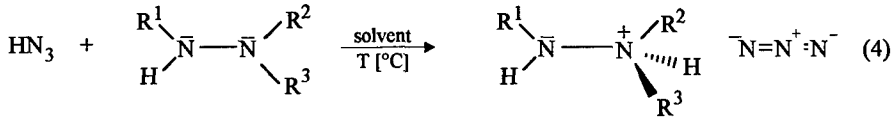

Table 1 gives a survey on the new derivatives of hydrazine azide with reaction conditions and the physical chemical analysis. We will report on the characterization of these new compounds shortly.

Substance name	Conditions	Physical chemical characterization
Monomethylhydrazine azide $R^2 = -CH_3$	T = 0 °C solvent = THF	m.p.; element analysis; IR; Raman; NMR: ^1H, ^{13}C, ^{14}N, ^{15}N.
1,1-Dimethylhydrazine azide $R^2 = -CH_3$; $R^3 = -CH_3$	T = -25 °C solvent = CH_2Cl_2	m.p.; element analysis; IR; Raman; NMR: ^1H, ^{13}C, ^{14}N, ^{15}N; X-ray.
Phenylhydrazine azide $R^1 = C_6H_5$-	T = RT solvent = Et_2O	m.p.; IR; Raman; NMR: ^1H, ^{13}C, ^{14}N, ^{15}N.
Acetylhydrazine azide $R^1 = CH_3CO$-	T = RT solvent = i-prop.	IR; NMR: ^1H, ^{13}C.

Table 1: New derivatives of hydrazine azide with reaction conditions and physical chemical characterization.

5. Conclusion

Energetic materials, designed by the elements of N and H are of general interest.
The observed properties of hydrazine azide pertaining to its chemical variability, the explosive character and the thermochemical behaviourr can not be chraracterized in all details. Of particular interest is the question, as through new derivatives of hydrazine azide, its properties may be influenced. 'Further investigations will follow.

Acknowledgegment

The authors wish to thank Dr. Kaiser, Dr. Ticmanis and Dr. Gupta from WIWEB for their great support of this investigations.

References

[a]: T. Curtius, *Ber.*, 1891, 24, 3341.

[b]: J. Rissom, T. Curtius, *J. Prakt. Chem.*, 1898, 58, 261.

[c]: H.E. Riegger, *Ph. D Theses: Hydronitric acid and hydrazine trinitride*, 1910, Cornell Univeristy, Ithaca, New York.

[d]: A.L. Dresser, A.W. Browne, *J. amer. chem. Soc.*, 1933, 55, 1963.

[e]: E. Muller, *Ger. Patent*, 1936, Nr. 634688.

[f]: J.H. Koch, *Chem.Abstr.*, 1962-1966, 56, P13153a.

[g]: D.A. Rausch, *U.S. Patent*, 1966, Nr. 3,288,659.

[h]: D.A. Rausch, *U.S. Patent*, 1967, Nr. 3,309,248.

[i]: J.E. Paustian, M.M. Fein, *U.S. Patent*, 1969, Nr. 3,459,607.

[j]: G.S. Yakovleva, R.Kh. Kurbangalina, L.N. Stesik, *Fizika Goreniya i Vzryva*, 1974, 10 (2), 270.

[k]: G. Pannetier u. F. Margineanu, *Bull. Soc. Chim. Fr.*, 1972, 7, 2621.

[l]: H. Holfter, T.M. Klapötke, A. Schulz, *Eur. J. Solid State Inorg. Chem.*, 1996, 33 (9), 855.

[m]: H. Holfter, T.M. Klapötke, A. Schulz, *Propellants, Explosives, Pyrotechnics*, 1997, 22, 51.

[n]: G. Pannetier, F. Margineanu, A. Dereigne, R. Bonnaire, *Bull. Soc. Chim. Fr.*, 1972, 7, 2623.

[o]: Beschreibung des Prüfverfahrens: Arbeitsschutz (Fachteil des Bundesarbeitsblattes), Heft 3/1961, S. 53..57

[p] M. Rat, P. Guillaume, S.Wilker, G. Pantel, Practical Application of Microcalometry to the Stability Studies of Propellants in „Proceeding of the workshop on the microcalometry of energetic materials", The Technical Cooperation Program (TTCP) 1997 Leed, United Kingdom

BEURTEILUNG DER VERSPRÖDUNGSNEIGUNG VON TLP MIT HILFE DES SCHLAGSCHERVERSUCHS

Burkhard Nicklas

WIWEB Außenstelle Swisttal
Großes Cent
53913 Swisttal

ABSTRACT

A new test method was develloped to measure the transition to brittle behaviour of gun propellants. The test method is called impact shear test. With this test it is possible to measure the work necessary to shear a gun propellant grain with high shearing velocity as a function of temperature. A pendulum for measuring the izod impact strength was reconstructed with a new specimen holder for propellant grains (instead of the original clamping system) and a new striking edge. The striking edge hits the grain 0.1 mm above the specimen holder. A first test series shows, the impact shear test is a good method to determine the temperature region where the gun propellant becomes brittle.

ZUSAMMENFASSUNG

Um Aussagen über das Versprödungsverhalten von TLP-Körnern machen zu können, wurde eine neue Prüfmethode entwickelt, die es ermöglicht einzelne TLP Körner mit hoher Verformungsgeschwindigkeit zu untersuchen: der Schlagschertest. Die Versuchseinrichtung gestattet es (in Abhängigkeit von der Temperatur), die Arbeit zu messen, die notwendig ist um ein TLP Korn abzuscheren. Dazu wurde ein vorhandenes Pendel mit einer neuen Probenaufnahme und einem neuen Pendelarm ausgestattet. Der Einbau erfolgte so, daß die Hammerscheide 0,1 mm oberhalb der Probenhalterung auf die Probe trifft. Erste Versuche zeigen, daß dieses Verfahren geeignet ist, den Temperaturbereich zu bestimmen, bei dem ein TLP versprödet.

1. EINLEITUNG

Beim Abbrand in einem für die sich bildenden Gase geschlossenen System, wie es in einem Waffenrohr vorliegt, werden die TLP-Körner durch den Gasdruck sehr stark mechanisch belastet. Neben einem großen hydrostatischen Druck belasten auch Druckwellen das TLP, z. B. eine Körnerdruckwelle, die das TLP am Geschoßboden komprimiert. Die TLP-Körner werden mechanisch verformt, wenn sie eine gewisse Duktilität aufweisen. Ist die Duktilität zu gering, tritt im Extrem-

fall der Sprödbruch ohne Verformung auf. Dabei wird Oberfläche für den Abbrand neu geschaffen; dies muß soweit wie möglich vermieden werden. Daraus folgt, TLP Körner müssen eine gewisse Duktilität aufweisen und zwar bei realen sehr großen Belastungsgeschwindigkeiten.

Werkstoffprüfgeräte, die mit relativ hohen Verformungsgeschwindigkeiten arbeiten (außer Zugprüfgeräte), sind spezielle Druckprüfmaschinen (1) Pendelschlagwerke und jede Art von Fallgerüsten (2). Wegen der vertretbaren Anschaffungskosten und der leichteren Handhabbarkeit wurde für diese Untersuchungen an TLP das Schlagpendel gewählt. Mit einem speziellen Umbau, der im Hause vorgenommen wurde, ist es nun möglich, TLP über einen großen Temperaturbereich im Schlagscherversuch zu testen.

Da Treibladungspulverlose immer aus mehreren Ansätzen bestehen, muß bei der Messung an Einzelkörnern immer mit einem rel. großen Streuband gerechnet werden. Für diese Untersuchung wurden pro Temperatur immer 5 Körner gemessen.

2. KONSTRUKTION DER VERSUCHSAPPARATUR

Für die Durchführung der Tests wurde ein vorhandenes 50 J Pendelschlagwerk umgebaut, d.h. mit einer neuen Probenhalterung und einem neuen Pendelhammer versehen. Das 50 J Pendelschlagwerk besitzt die notwendige Steifigkeit für Versuche dieser Art. Abbildung 1 zeigt die wesentlichen Teile des Pendelschlagwerks. Die Probenhalterung besteht aus einem Grundgestell und einer Probenaufnahme. Das Grundgestell (aus Stahl) wird auf dem Aufspanntisch des Pendelschlagwerks aufgeschraubt. Es enthält eine Bohrung zur Aufname der eigentlichen Probenhalterung, einem Messingzylinder mit zentraler Bohrung für das TLP Korn. Dieser Messingzylinder wird mittemperiert und trägt somit dazu bei, das das TLP Korn die Temperatur der Vortemperierung bis zur Abscherung hält. Durch eine Schraube im Boden der Bohrung im Grundgestell kann eingestellt werden, wie tief die Probenaufnahme in diese Bohrung abgesenkt werden. Damit wird die Höhendifferenz zwischen Oberkante Probenhalterung und Hammerschneide eingestellt (z. B. mit einer Fühlerlehre). Die Hammerschneide wurde ebenfalls neu gestaltet. Dort, wo der vorderen Teil des Pendelhammers auf die Probe trifft wurde ein Hartmetalleinsatz. mit definierter Auftrefffläche eingefügt.

Die Auftreffgeschwindigkeit des Hammers auf der Probe beträgt 3,9 m/s. Gemessen wird die Arbeit, die benötigt wird, um das TLP Korn abzuscheren.. Die Ermittlung der Schlagarbeit erfolgt mit der vorhandenen Meß- und Auswerteeinheit. Da das Pendelschlagwerk mit den Umbauten

noch nicht kalibriert wurde, ist in den Diagrammen als Einheit [xx] anstelle von mJ/mm² angegeben. Die Bestimmung der Versprödungstemperatur erfolgt als Schnittpunkt der Geraden durch die Meßwerte bei tiefen bzw. hohen Temperaturen analog zu dem Verfahren für Schlagbiegeversuche an FTS in der entsprechenden TL (1). Von einer Versprödungstemperatur kann allerdings nur gesprochen werden, wenn die Schlagzähigkeit bei tiefen Temperaturen kleine Werte annimmt. Zum Vergleich wurden auch Messungen mit der Dynamisch Mechanischen Analyse (DMA) gemacht.Die Durchführung und Auswert der DMA erfolgte nach STANAG 4540 (2). Die Glasübergangstemperatur wird als Maximum der Verlustmodul (E'') - Temperatur - Kurve ermittelt

3.VORVERSUCHE

Als erstes wurde untersucht, wie sich die Höhe des Auftreffpunktes der Hammerscheide auf die Probe oberhalb der Probenaufnahme auswirkt. Wird die Probe nicht direkt oberhalb der Probenaufnahme getroffen, so kann außer Scherung auch noch Biegung auftreten. Nachstehende Skizze zeigt schematisch das Aussehen der Körner nach dem Versuch, links ist noch Biegung vor dem Bruch beteiligt, während rechts das Korn glatt abgeschert wurde. Abb. 2 zeigt die ermittelten Meßwerte.

Skizze 1 : Schematische Darstellung eines TLP Korns nach dem Bruch

Korn bei 1,5 mm freier Höhe Korn bei 0,1 mm freier Höhe

Da bei größeren freien Höhen zusätzlich zur Scherung auch Biegung auftritt, wurden alle weiteren Versuche mit 0,1 mm freier Höhe durchgeführt.

Um einen Vergleich der Meßergebnisse mit denen anderer Meßmethoden zu erhalten, wurde anschließend eine Untersuchung mit Proben (∅ 8 mm) aus doppelbasigem FTS durchgeführt. Die Messungen können dann mit Ergebnissen aus Schlagbiegeversuchen und DMA am gleichen Material verglichen werden. Die Ergebnisse sind in den Abb. 3 und Abb. 4 dargestellt. Die ermittelten Kennwerte lauten: Glasübergangstemperatur (DMA) T_g = 238 K; Versprödungstemperatur (Schlagbiege) T_v = 242 K und Versprödungstemperatur (Schlagscher) T_v = 234 K Die ermittelten Werte mit drei unterschiedlichen Verfahren liegen innerhalb von 8 K, ein recht gutes Ergebnis.

4. TESTERGEBNISSE AN TLP UND VERGLEICH MIT DMA MESSUNGEN

Um einen Anhaltspunkt zu haben, ob die Messungen zum richtigen Temperaturbereich führen, wurde die Versprödungstemperatur mit der Glasübergangstemperatur aus DMA - Messungen verglichen.

Als erstes TLP wurde ein dreibasiges Pulver untersucht. Abb. 5 zeigt die entsprechenden Diagramme. Versprödungstemperatur (242 K) und Glasübergangstemperatur (243 K) liegen sehr nahe beisammen, jedoch zeigen auch die rel. großen Meßwertstreuungen, daß diese sehr gute Übereinstimmung nicht bei jeder Messung erwartet werden kann.

Als zweites wurde ein zweibasiges Pulver untersucht (Abb. 6). Die Übereinstimmung zwischen Glasübergangstemperatur (248 K) und Versprödungstemperatur (238 K) ist zwar nicht so gut wie bei den Messungen am dreibasisen TLP, jedoch ist auch hier die Tatsache zu berücksichtigen, daß es sich um Messungen am Einzelkorn handelt. Mit 238 K beim zweibasigen TLP liegt der Wert der Versprödungstemperatur gegenüber 242 K am dreibasigen TLP im erwarteten Bereich.

Das einbasige TLP zeigt erwartungsgemäß keine Versprödungsneigung. Selbst bei 210 K liegt der Mittelwert der Schlagzähigkeit noch über 50 mJ/mm².

Abschließend noch die Ergebnisse von Untersuchungen an zwei Versuchs-TLP, die mit TLP A (Abb. 7) und TLP B (Abb. 8) bezeichnet wurden. Die ermittelten Temperaturwerte für Glasübergang bzw. Versprödung liegen innerhalb von 10 K, wobei besonders bei der DMA zu erkennen ist, daß durch Überlagerung der Effekte der Einzelkomponenten eines TLP oft die Bestimmung eines Maximums in der E´´- T- Kurve sehr schwierig ist. Die Ergebnisse des Schlagscherversuchs sind in diesem Fall eindeutiger.

(1) Robert J. Lieb, Mechanical Response and Morphological Charakterization of Gun Propellant, ARL-TR-1205, 1996

(2). R.C.Warren, Dynamic Mechanical and Fracture Properties of Some Double And Triple Base Gun Propellants, MRL-TR-93-40 Report, 1994

(3) TL 1376- 0701 Arbeitsvorschrift 2.7, Bestimmung des Versprödungsverhaltens von Festtreibstoffen im Schlagbiegeversuch

(4) STANAG 4540, Explosives, Procedures for Dynamic Mechanical Analysis (DMA) and Determination of Glass Transition Temperature

Prüfvorrichtung für Schlagscherversuche

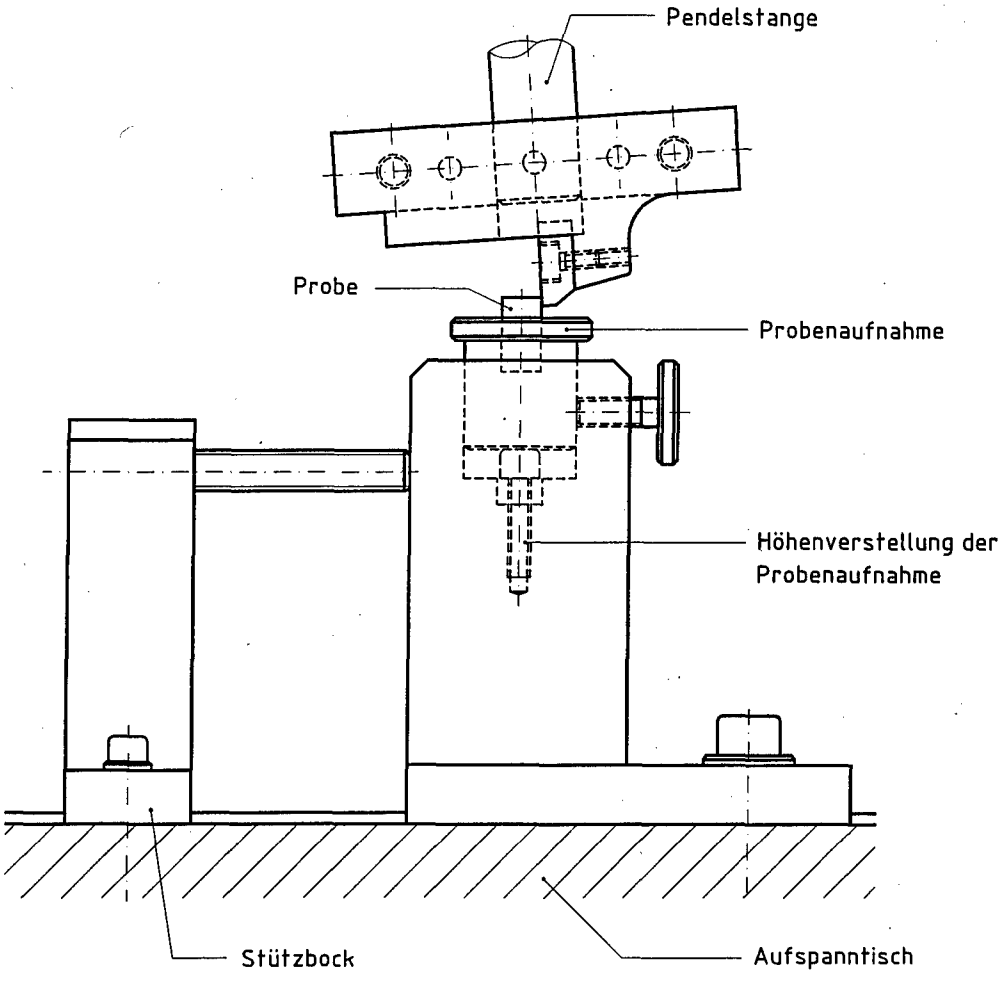

Abb. 1 Skizze des Versuchsaufbaus

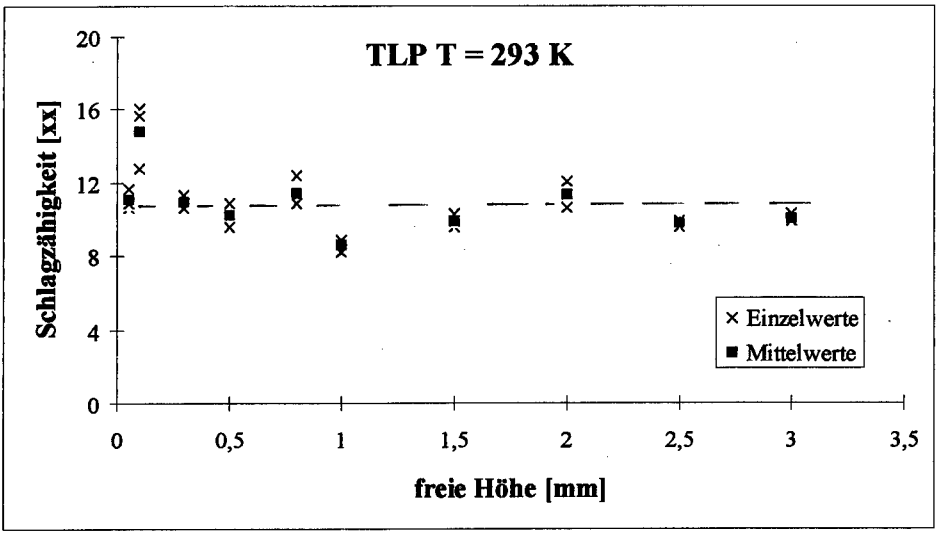

Abb. 2 Schlagzähigkeit als Funktion der Auftreffhöhe der Hammerschneide oberhalb der Probenaufnahme gemessen an jeweils drei Einzelkörnern

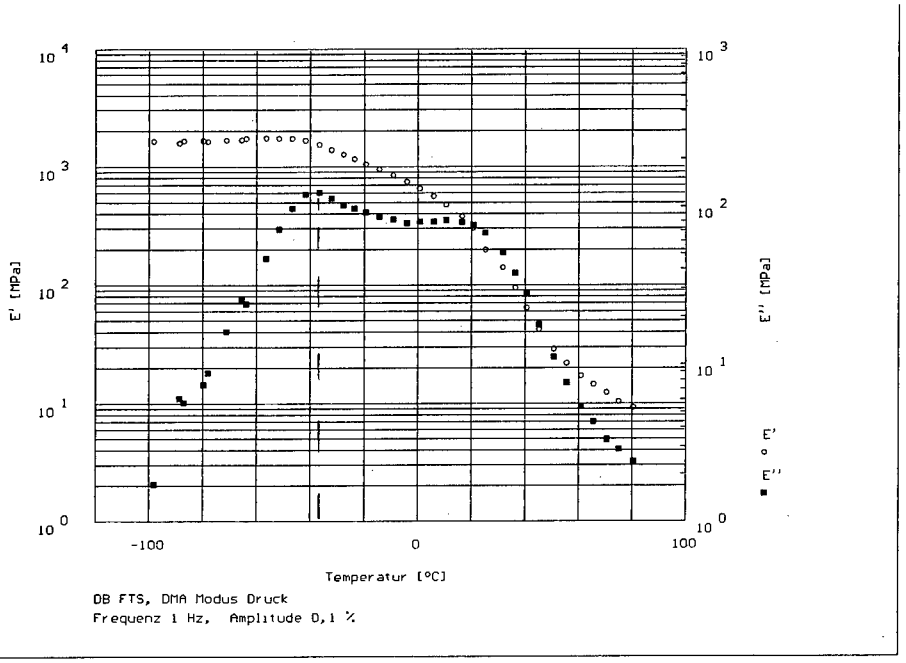

Abb. 3 Ergebnisse aus DMA, Glasübergangstemperatur -35 °C (238 K)

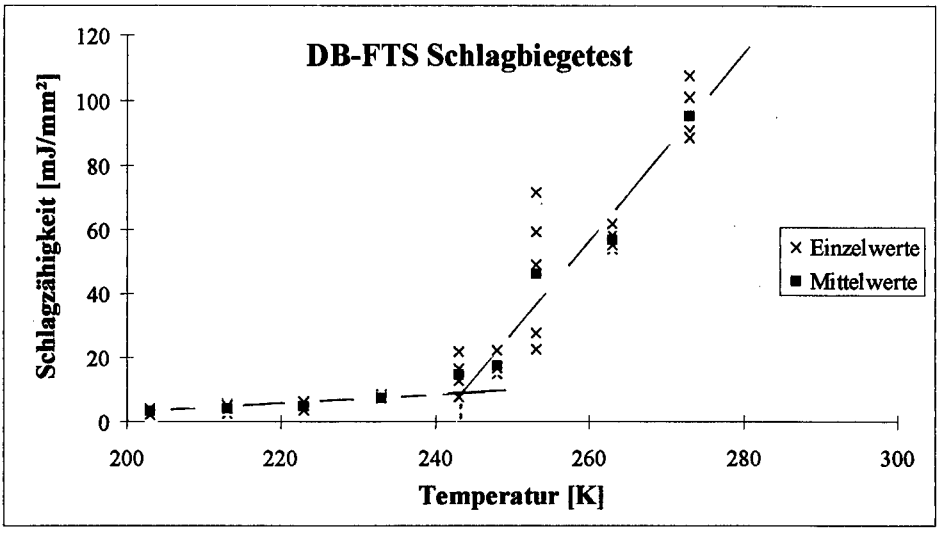

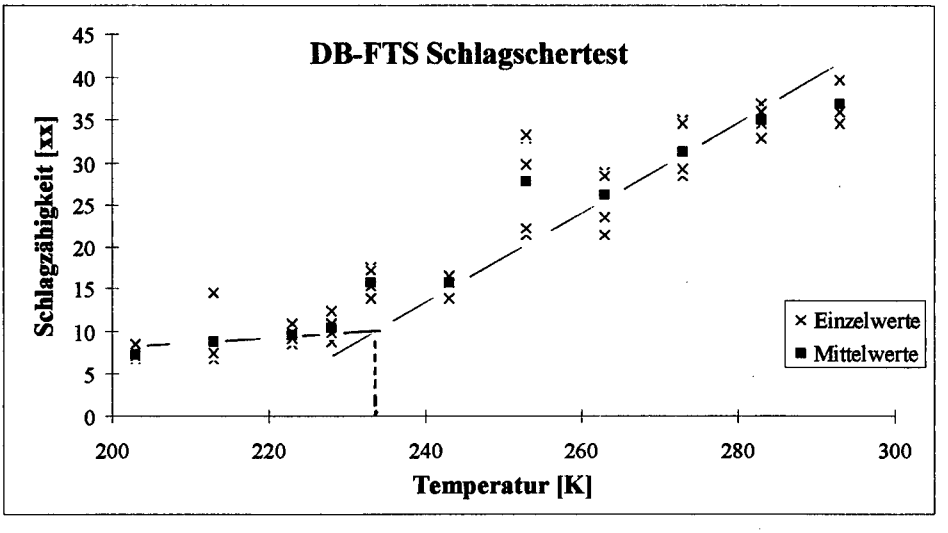

Abb. 4 Vergleich der Schlagzähigkeiten ermittelt im Schlagbiegeversuch (Probe 6 x 6 x 70 mm) und im Schlagscherversuch (Probe ∅ 8 mm).
Versprödungstemperaturen : Schlagbiege 242 K , Schlagscher: 234 K

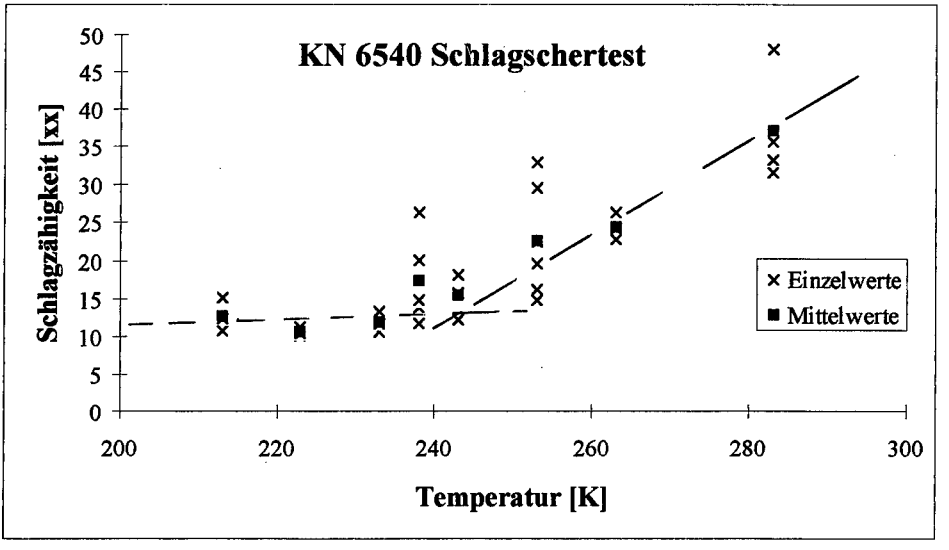

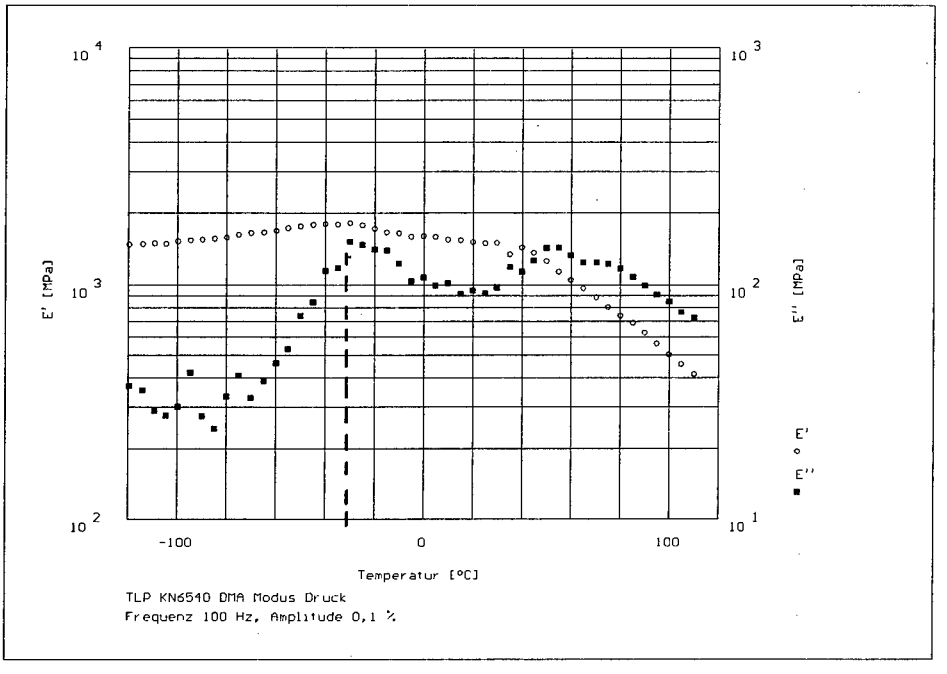

Abb. 5 Dreibasiges TLP, Vergleich der Messergebnisse aus Schlagscherversuchen und DMA Glasübergangstemperatur 243 K, Versprödungstemperatur 242 K

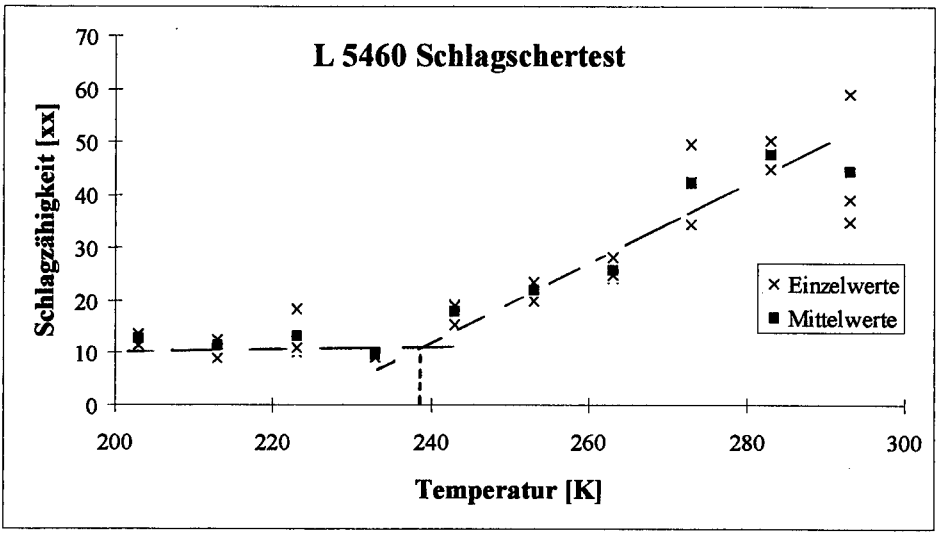

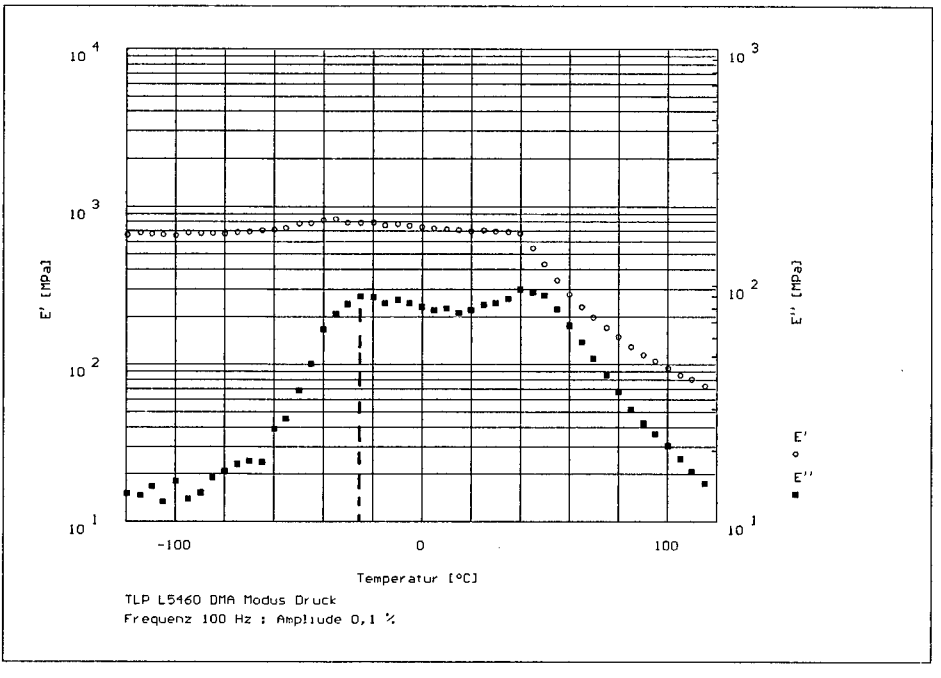

Abb. 6 Zweibasiges TLP, Vergleich der Messergebnisse aus Schlagscherversuchen und DMA Glasübergangstemperatur 248 K Versprödungstemperatur 238 K

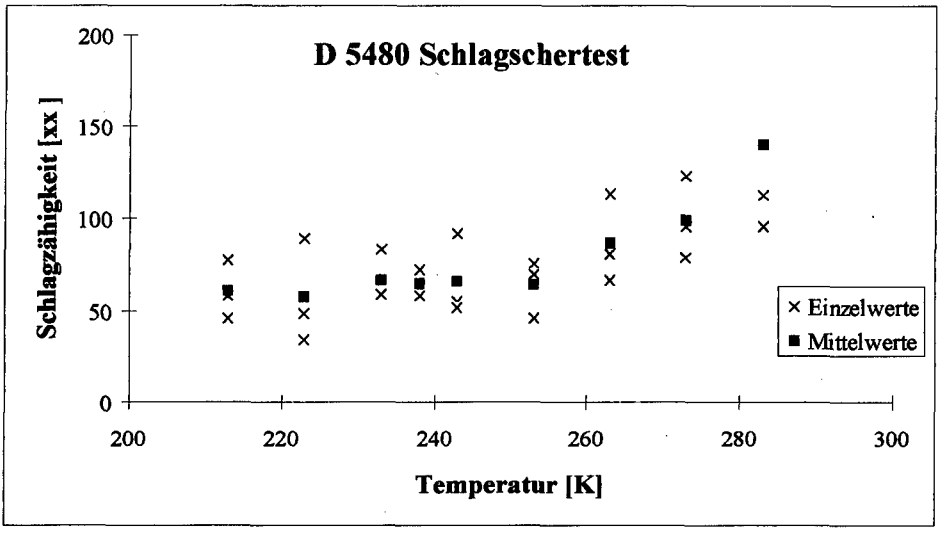

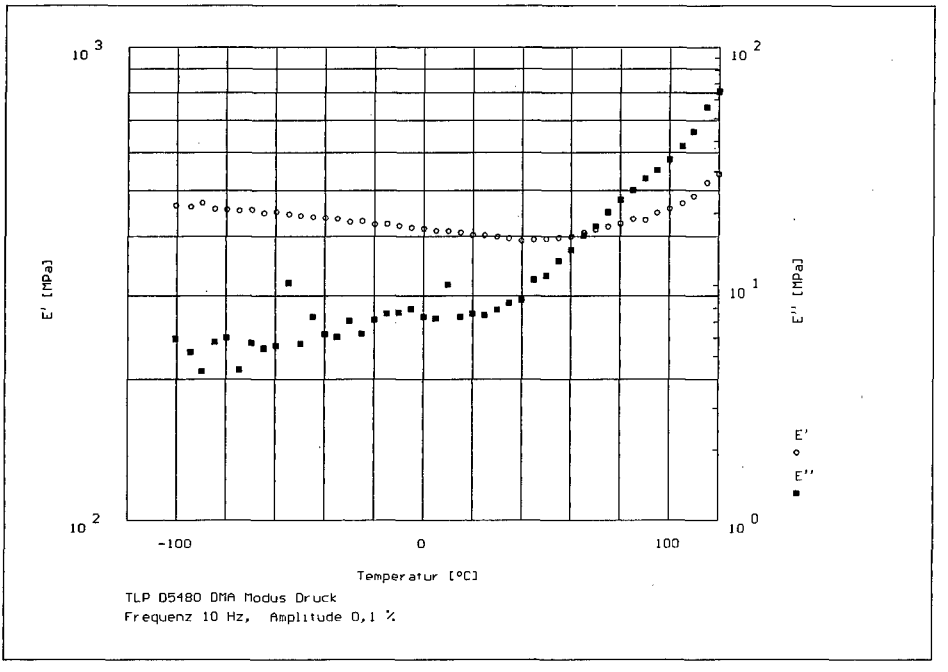

Abb. 7 Einbasiges TLP, Vergleich der Meßergebnisse aus Schlagscherversuchen und DMA
Weder Glasübergang noch Versprödung zu erkennen, bis zu tiefen Temperaturen sehr große Schlagzähigkeit .

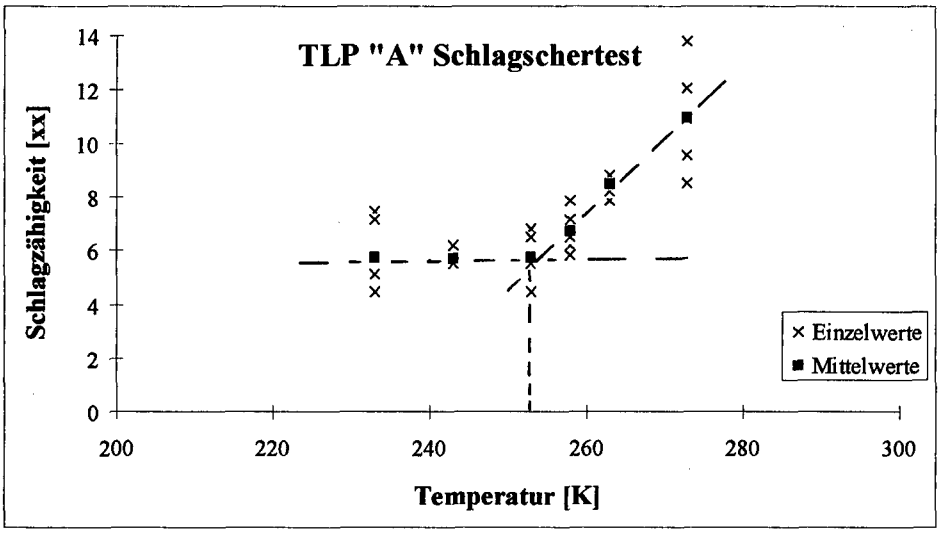

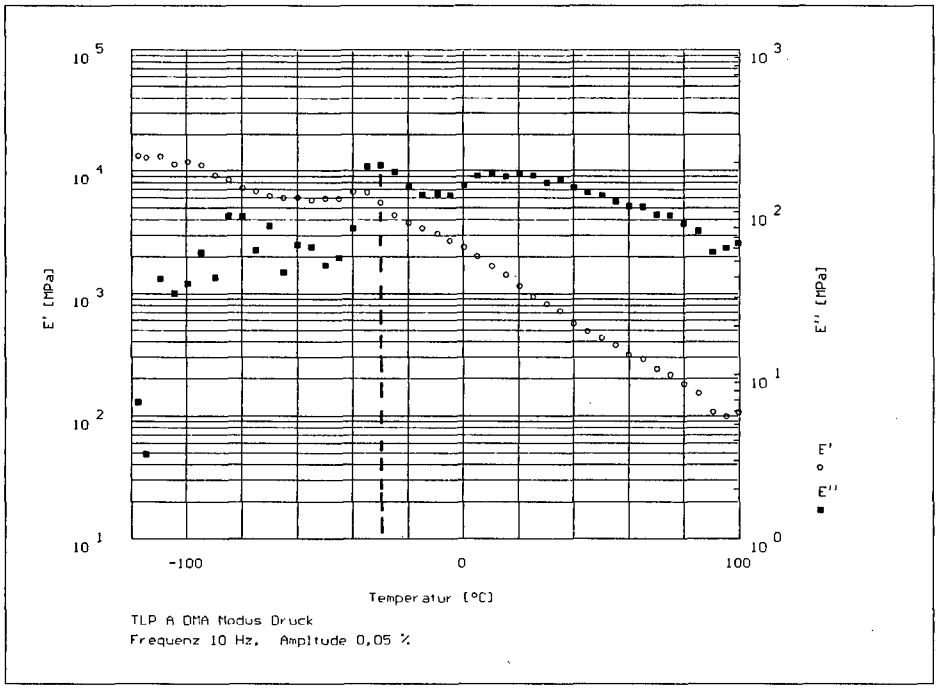

Abb. 8 Ergebnisse von Schlagscherversuchen an einem Versuchs - TLP Glasübergangstemperatur 243 K; Versprödungstemperatur 253 K Außerdem im Schlagscherversuch zu erkennen: sehr kleine Schlagzähigkeiten unterhalb 260 K

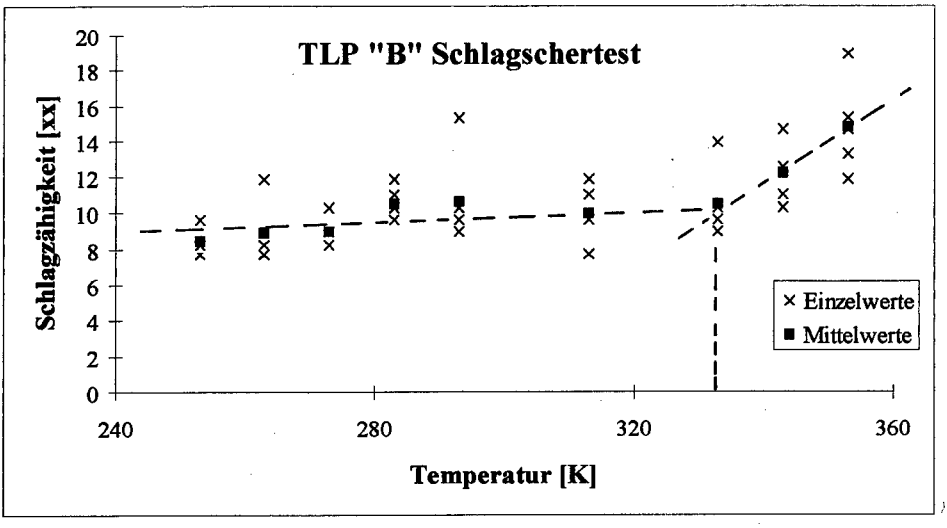

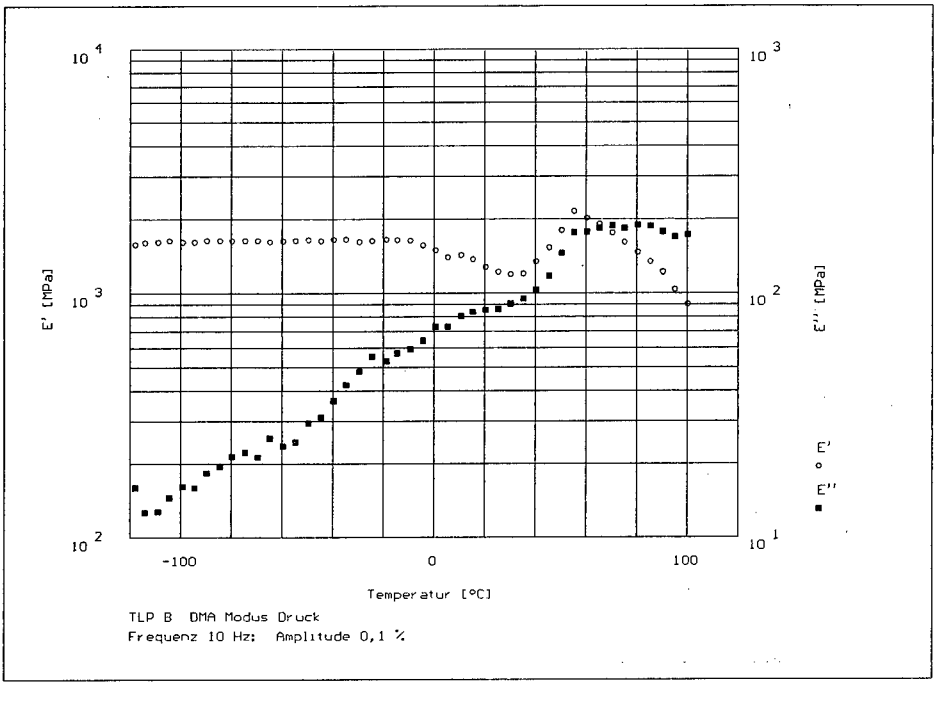

Abb. 9 Ergebnisse von Schlagscherversuchen an einem Versuchs - TLP Glasübergangstemperatur: etwa 343 K (schwer zu bestimmen) Versprödungstemperatur 333 K , Schlagzähigkeit nimmt unterhalb von T_v kaum noch ab

BDNPA/F AS ENERGETIC PLASTICIZER IN PROPELLANT FORMULATIONS

G.M.Gore , R.G. Bhatewara , K.R. Tipare , N.M. Walunj,V.K.Bhat

High Energy Materials Research Laboratory, Pashan, Sutarwadi,

Pune, India 411021

ABSTRACT

A study on energetic plasticisers have been carried out for their use as a desensitiser for nitroglycerine(NG) in the propellant formulations. Two reported nitroplasticisers bis (2,2 dinitropropyl) acetal (BDNPA) and bis (2,2 dinitropropyl) formal (BDNPF) were synthesised using oxidative nitration route for converting nitroethane to gem-dinitroethane. The compounds were characterised using IR and NMR techniques. Impact and friction sensitivity data generated with mixed plasticisers showed desensitisation of nitroglycerine on incorporation of these plasticisers. Propellant processed using these plasticizers in double-base (DB) and composite modified double-base (CMDB) formulations gave improved energetics and burn-rate as compared to propellant containing inert plasticiser such as diethyl phthalate (DEP). BDNPA and BDNPF gave better mechanical and thermal properties in combination, rather than when used singly. Plasticiser viscosity however was found to be higher than DEP, and thus lowered solid loading capability in CMDB propellant. BDNPA and BDNPF thus appear to be promising candidates for high energy, minimum smoke propellant formulations

INTRODUCTION

Plasticizers have an important role in rocket propellant development because of their potential to modify the propellant characteristics particularly mechanical properties and energetics. Plasticizers having energetic groups in their molecular structure enhance propellant performance. Research work is being conducted on compounds with nitro, nitroso, fluro, fluronitro, azido or fluroamino groups for application in propellant field as energetic polymers and plasticizers[1,2,3]. However, nitroglycerine (NG) is one of the earliest energetic plasticizer and is still being used on large scale in double base (DB), composite modified double base (CMDB) and elastomer modified double base (EMCDB)

propellants. But hazardous nature of NG dose not permit its use as such during propellant processing. For handling NG, its desensitization is necessary and is conventionally done by mixing NG with inert plasticizers such as diethyl phthalate (DEP), triacetine (TA) etc. However, incorporation of these inert plasticizers adversely affect the propellant energetics. Search for insensitive but energetic plasticizers led to synthesis and characterization of nitroplasticizers such as Bis (2,2 dinitropropyl) formal (BDNPF) and acetal (BDNPA)[4]. Most of the data on the propellant compositions using these nitroplasticizers and their performance are available in patent form[5] and very few results of studies on desensitizing effect with NG and propellant performance characteristics are available in open literature. In the present study these plasticizers have been synthesized, characterized and used in DB and CMDB propellant formulations in combination with NG. Data on propellant parameters using mixed plasticizer are also included in the paper.

EXPERIMENTAL

1.Synthesis of plasticizers:

Energetic plasticisers BDNPA and BDNPF were synthesized following the reported[6,7] methods involving oxidative nitration of nitroethane (EtNO2) with aqueous $NaOH\text{-}NaNO_2\text{-}AgNO_3$ and its condensation with aqueous HCHO to get 2,2 dinitropropanol. Condensation of this compound with paraformaldehyde in H_2SO_4 and para acetaldehyde in BF_3 etherate gave BDNPF and BDNPA respectively. The overall sequence of reaction involved is shown in fig-1. The plasticisers were prepared on laboratory scale and characterized by IR, ^{1}HNMR and elemental analysis. FTIR, Perkin-Elmer model 1605 and Bruker 90MHz were used for IR and NMR respectively. IR spectra of liquid compounds were recorded by smear method where as NMR were recorded using CDCl3 as a solvent with tetra methyl silane(TMS) as an internal standard.

Thermal decomposition and sensitivity properties were determined for these nitrocompounds seperately and for mixed plasticizer before using in the propellant formulations. Thermal decomposition pattern were determined in air and recorded using locally fabricated Micro DTA apparatus. Heating rate and sample size were maintained at 10^0 C /min and 10 mg respectively in all the DTA experiments. Friction and impact sensitivity were determined using Julies peter apparatus and fall hammer method.

2.Propellant Processing:

Ingredients used in propellant formulations are nitrocellulose (12.2% nitrogen content) in dense spheroidal form of 25-45 micron size, nitroglycerine desensitized(DNG) with

insensitive plasticizers such as diethyl phthalate(DEP) or nitroplasticizer(BDNPA/F), ammonium perchlorate (AP) of 8-11 micron size, and minor amounts of stabilisers, curing agents and curing catalysts. All the solid ingredients are dried to moisture level of less than 0.5% before processing. Desensitized nitroglycerine(DNG) is deaerated under vacuum for half an hour at 10mm of mercury before using. Non energetic plasticizer DEP, curing agent toluene diisocyanate(TDI), stabiliser 2-nitro diphenyl amine(2-NDPA) and curing catalyst ferric acetyl acetonate(FAA) are procured from trade and are used as such. Propellant processing was done by slurry cast process[8] in 1 kg batch size by mixing all ingredients in DNG and casting in aluminium moulds. The slurry was evacuated for ½ hour at less than 10 mm of mercury before curing in oven at 60^0 C for minimum 3 days. Propellant slabs were processed both in DB and CMDB formulations.

Cured propellant samples were cut to generate data on mechanical properties, thermal stability, burn rates, cal-val, etc. and propellant energetics were calculated by thermochemical calculations using NASA -273 programme[9]. Propellant mechanical properties were determined using universal test machine (INSTRON) on tensile samples as per ASTM standard. Heat test was conducted at 160^0F as per BS standard. Burning rate was determined by burning 6.0 mm strands in an indigenously built up equipment using acoustic signal for determining burn time. Cal-Val was determined using Julius Peter calorimetric bomb at 0.01 g/cc loading.

RESULTS AND DISCUSSION

1.Plasticizer characterisation:

IR traces of BDNPF and BDNPA are given in fig 3 where as NMR traces are given in Fig-4 & 5 respectively.

The IR spectrum of BDNPF and BDNPA showed the characteristic peaks of gem-dinitro group frequencies at 1576 cm^{-1} (asymmetric C-NO2 stretching) and 1328 cm^{-1} (symmetric C-NO2 stretching) as well as at 1142 cm^{-1} and 1018 cm^{-1} for >C-O-C< ether linkage.

^{1}-HNMR for BDNPF gives peaks for three different types of protons at 2.2 δ (6H singlet), 4.2 δ (4H singlet), 4.8 δ (2H singlet), whereas for BDNPA peaks are observed at 2.1 δ (6H singlet), 1.3δ (3H doublet), 4.2 δ (4H singlet), 4.8 δ (1H quarterlet).

Fig-2 shows the DTA decomposition pattern for BDNPA and BDNPF. Both the plasticizers show exothermic decomposition with a peak at around 248-250^0 C indicating the energetic nature of the plasticizers.

2. Plasticizer Parameters:

The plasticizer and propellant formulations taken up in the present study are given in Table - 1 and 2 . The comparative physical properties and plasticizer parameters affecting the propellant performance are given in Table -3 and 4 respectively for these plasticizers. As compared to energetic plasticizer NG, these nitro-plasticizer are stable as seen from the data in table-3. Boiling points have been reported at pressures of 0.01 mm for BDNPA/F at around 150°C whereas NG decomposes on heating. Both BDNPF and BDNPA have higher melting points as compared to DEP and NG while 1:1 mixture of BDNPA and BDNPF exhibit lower melting point and can be used as a liquid plasticizer in this combination.. Density values of BDNPA/F are higher than DEP which is an added advantage. However higher viscosity values as compared to DEP, affect the solid loading capability of these nitroplasticizers in propellant formulations. The pararmeters affecting propellant performance such as heat of formation(Hf), cal-val, Oxygen balance(O.B.) are given in Table -4. Cal-val and O.B.of nitroplasticizer and nitroplasticizer-NG combinations are either positive or less negative respectively as compared to NG-DEP combination indicating the energetic nature of mixed plasticizer. On the contrary sensitivity values are comparable with the mixture of NG- DEP making the NG-BDNPA/F highly attractive energetic plasticizer and an alternative to the inert NG-DEP combination.

3.Propellant performance :

Preliminary studies on processing and curing using nitroplasticizer was done using NG-BDNPF combination as a plasticizer in a DB formulation. Data generated on mechanical properties and stability as seen from the Table-4 and 5 indicate comparable values both in mechanical properties and thermal stability results as compared to composition containing DEP. Increase in energetics were found to be substantial as seen from cal-val and specific impulse(Isp) data in table-6. Cal-val increased by 20-30% where as Isp increased by 10%.

BDNPF when used singly as NG-BDNPF plasticizer in filled propellant formulations of CMDB showed decrease in mechanical properties and further studies were conducted using eutectic combination of BDNPA/F as NG-BDNPA/F plasticizer in CMDB formulations. In this case comparable mechanical properties were obtained to NG-DEP formulations. Increase in cal-val and Isp were seen to be as obtained in case of DB formulations(30% & 10%

respectively) indicating the advantage of these nitroplasticizer combinations in CMDB propellant. Thermal stability as indicated by the heat test results show comparable values with the NG-DEP composition indicating no adverse effect of nitroplasticizers in CMDB propellant. Burn rate results showed in table-5 indicate a remarkable increase upto 40% in burn-rate in the pressure range of 50 - 100 kg/cm^2 and further studies on combustion aspect may be necessary to understand this increase in burn-rate.

CONCLUSIONS

BDNPA/F combination appears to be promising energetic plasticizer in propellant formulations. The preliminary study conducted with thermal stability and processability of propellant compositions showed no adverse effect as compared to inert plasticizer such as DEP. BDNPA/F may thus find application in high burn-rate, energetic low solid loaded propellant formulations.

REFERENCES

1.Simmons, R.L., 'Thermochemistry of NENA plasticizers', Int. Annu. Conf., ICT., 1994

2.Flanagan, J.E., et.al., '1,5 diazido-3-nitraza pentane and its preparation', USP 5,013,856 (1991)

3.Sitzmann, M.E., '2-polynitro alkyl- 5- perfluoro alkyl 1,3,4 oxadiazolane as plasticizer for explosives,' USP 901621 (1993)

4.Hammel, E.E., 'Research in polynitro aliphatics for use in solid propellants,' ICT, Jahrestag, (1982)

5.Klager, K. and Winkler, J.,'Explosives and propellant compositions', Brit. Pat. 1522593 (1978)

6.Ungnade, H.E.,and Kissinger, L.W., Tetrahedron 19(1), 121 , (1963)

7.Stojkovie, B., Stojanovic, N.,'Synthesis of nitroacetal plasticizers', Naucno- Tech. Pregl. 40(10), 41-6 (1990)

8.Bhat, V.K., et.al.,' Processing of high energy crosslinked CMDB propellants', Int. Jehrestag. Fraunhoffer Institut. ICT, (1987)

9. Gordon, S., and McBride, B.C., 'Computer program for calculation of complex equillibrium compositions, rocket performance, incident and reflected shocks and jouquoet detonation', No. NASA-SP-273, NASA , Washington , DC, (1971)

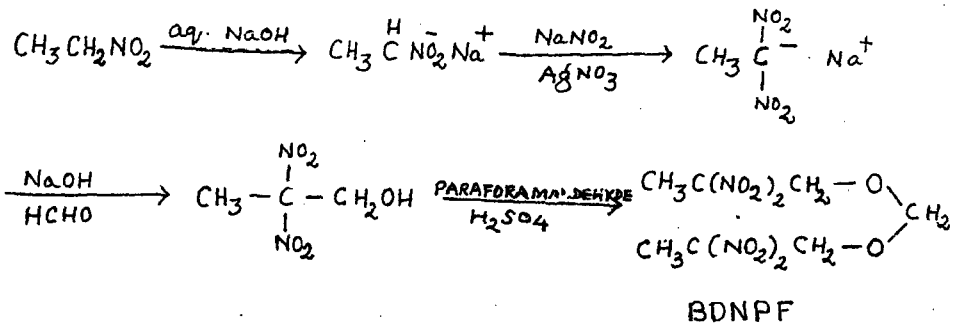

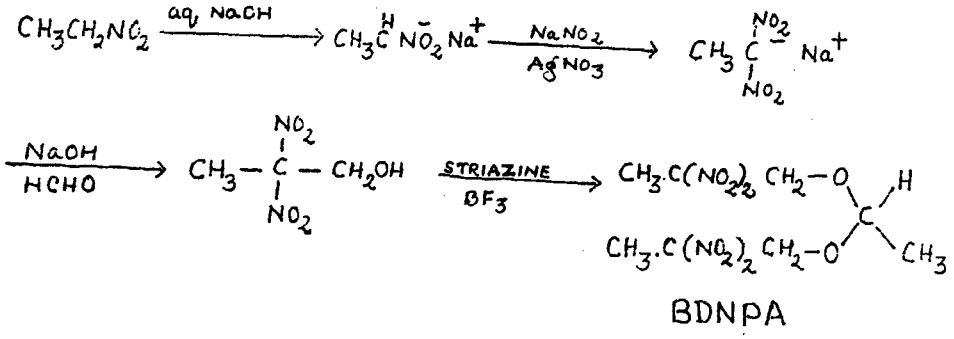

Fig 1 : Reaction sequence for synthesis of BDNPF and BDNPA.

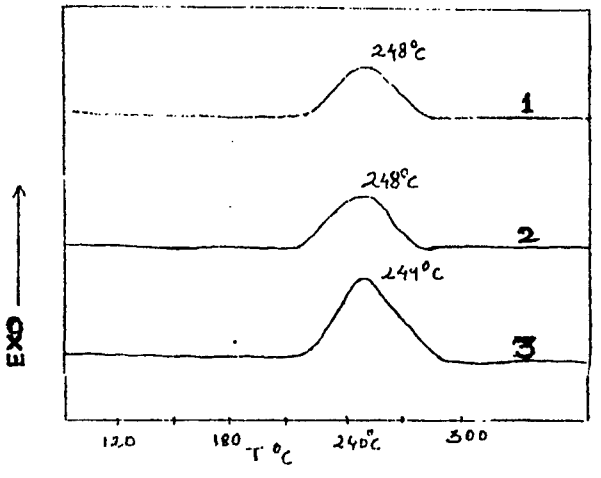

Fig 2 : DTA Thermographs, 1) BDNPA 2) BDNPF 3) BDNPA/

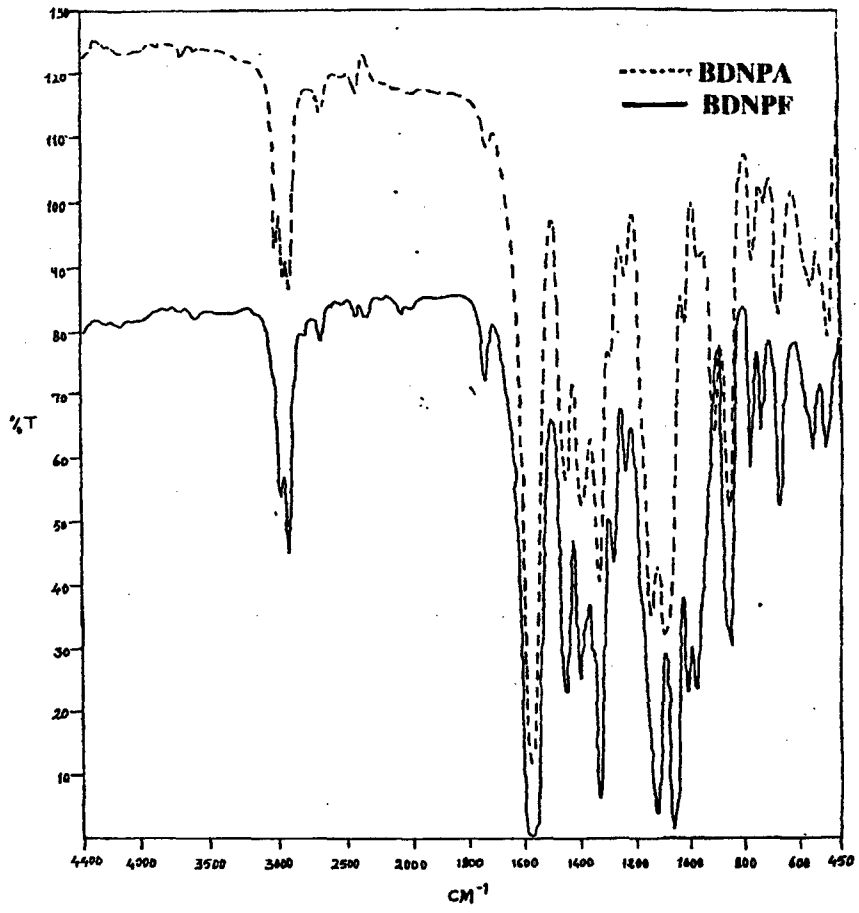

Fig 3 : I R Spectra of BDNPA and BDNPF

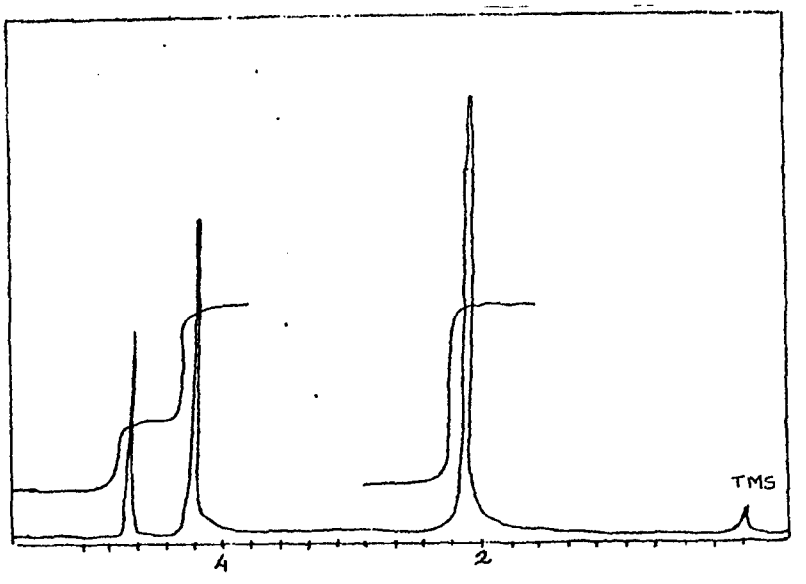

Fig 4 : ^{1}H NMR Spectra of BDNPF

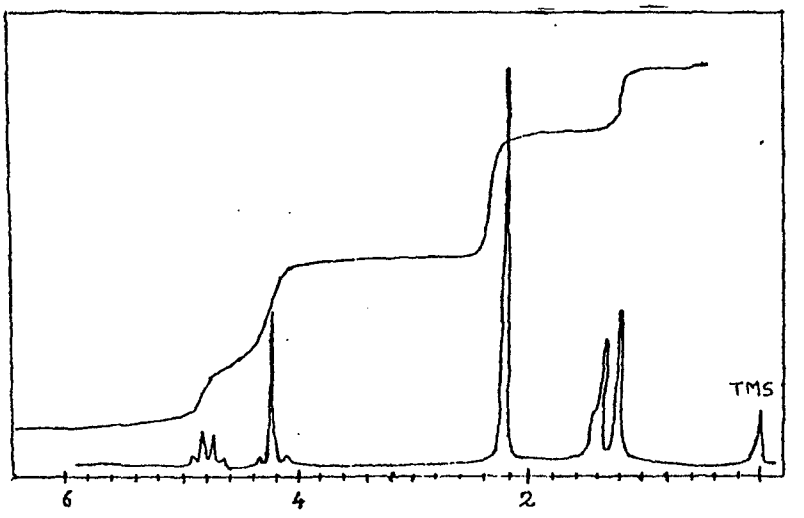

Fig 5 : ^{1}H NMR Spectra of BDNPA

NG
DEP
BDNPF
BDNPA
NG-DEP
NG/BDNPF
NG/BDNPA/F
Note: mixed plasticizers contain 78% NG and 2% 2-NDPA

Table 1- List of plasticizers and their combinations

Sr. No.	Propellant Class	Composition DNC	NG	DEP	BDNPF	BDNPF/A	2-NDPA	AP	TDI
1.	DB (control)	50	39	10			1		0.5
2.	DB (BDNPF)	50	39		10		1		0.5
3.	DB (BDNPA/F)	50	39			10	1		0.5
4.	CMDB (Control)	40	31.2	8			0.8	20	0.5
5.	CMDB (BDNPF)	40	31.2		8		0.8	20	0.5
6.	CMDB (BDNPA/F)	40	31.2			8	0.8	20	0.5

Table 2- Propellant compositions

Sr. No.	Plasticizer	B.P. ^{0} C	M.P. ^{0} C	Density at 27^0 C g/cc	Viscosity at 27^0 C cps
1.	NG	Decomposes	2.2 &13.2	1.59	-
2.	DEP	298	-40	1.12	28
3.	BDNPF	149/0.01 mm Hg	31	1.41	-
4.	BDNPA	150/0.01 mm Hg	33-35	1.36	-
5.	BDNPA/F	150/0.01 mm Hg	-18	1.39	250

Table 3 - Physical properties of plasticizers

Sr. No.	Plasticizer	- Hf cal/g	Cal-Val cal/g	Oxy-Bal %	Sensitivity Impact cm	Friction > kg
1	NG	392	1785	+ 3.5	1	36
2	DEP	806	-1765	- 194	170	36
3	BDNPF	457	700	- 51	170	36
4.	BDNPA	484	700	-63	170	36
5.	NG-DEP	464	1003	-39	90	36
6.	NG-BDNPA/F	395	1496	-11	85	36

Table 4 - Plasticizer parameters affecting propellant performance

Propellant Class	Density g/cc	Mechanical properties T.S.kg/cm^2	% E	Modulus(kg/cm^2)	Burn rate(mm/s) 50kg/cm^2	70kg/cm^2	110kg/cm2	Pressure index 50-70	70-110
DB (Control)	1.48	17	75	65					
DB(BDNPF)	1.50	24	65	140					
CMDB(Control)	1.54	12	36	195	9.2	11.0	14.5	0.53	0.61
CMDB(BDNPF)	1.58	6	14	250	12.4	15.3	20.1	0.62	0.60
CMDB(BDNPA/F)	1.58	14	22	325	12.3	15.2	20.0	0.63	0.61

Table 5- Propellant parameters - Mechanical properties & Burn-rates

Propellant class	Oxy-bal %	Cal-val cal/g	Isp s	Char.vel m/s	Flame temp ^{0}K	Stability test Heat test(min)	M.V.Test(min)
DB (Control)	-40	920	227	1417	2454	8	45 no explosion in 5 hrs
DB (BDNPF)	-28	1141	246	1520	2997	8	45 no explosion in 5 hrs
CMDB(Control)	-26	1056	239	1483	2833	8	45 explosion after 4 hrs
CMDB(BDNPF)	-16	1234	251	1540	3149	7.5	45 explosion after 4 hrs
CMDB(BDNPA/F)	-15	1260	251	1540	3149	7.5	45 explosion after 4 hrs

Table 6 - Propellant parameters - Stability properties & energetics

USE OF HEADSPACE GAS CHROMATOGRAPHY - MASS SPECTROMETRY TO IDENTIFY AND MONITOR GASES EVOLVED DURING AGING OF ENERGETIC MATERIALS

Anjum N Agha, John M Bellerby and Christopher S Blackman

Department of Environmental and Ordnance Systems
Cranfield University
RMCS Shrivenham
Swindon SN6 8LA, Great Britain

ABSTRACT

Automatic headspace sampling in conjunction with capillary gas chromatography employing a dual-column switching system coupled to a mass spectrometer has been investigated as a means of identifying gases evolved from energetic materials and of monitoring their evolution as a function of time. Four of the principal gases arising from nitrate ester propellant degradation during accelerated aging (CO, CO_2, N_2O and N_2) can be successfully separated using this approach and the sensitivity of the detection system allows gas monitoring to be carried out at temperatures close to ambient. Evolution rates of individual gases can therefore be determined over a wide range of aging temperatures. An example of the application of the system is presented.

INTRODUCTION

Gas chromatography has been extensively used[1-4] to separate and detect permanent gases evolved from propellants and other energetic materials during natural and accelerated aging. Such investigations can help in understanding the decomposition mechanisms of a range of established and novel energetic

materials and are of particular value in the study of double base rocket propellants which are susceptible to gas cracking.

Various types of gas sampling equipment have been used but in most cases the energetic material is held in an evacuated vessel with the gases being sampled periodically and injected onto the GC. Separation has been achieved with a single packed column using temperature programming[3] or with a system involving two packed columns in series[2] maintained at widely different temperatures. The gases have been detected using either a thermal conductivity detector (TCD) or by mass spectrometry.

Recently the use of headspace sampling gas chromatography for analysing gases evolved from solid propellants aged in air has been reported[5]. In this study a number of identical propellant samples were held in standard crimp top glass vials under normal atmospheric conditions and the vials were sampled in turn after increasing aging periods using a headspace autosampler. Separation of gases was achieved by column switching using two capillary columns and detection was by TCD. As part of a continuing investigation into the aging properties of energetic materials we have sought to extend this approach by using narrower bore columns to improve chromatographic separation and by interfacing the GC to a mass spectrometer to give greater sensitivity.

EXPERIMENTAL

Apparatus

Analyses were performed using a Dani 3950 HSS automatic headspace sampler interfaced to a Fisons MD800 gas chromatograph - mass spectrometer running under Masslab software. A Chrompack PoraPLOT Q fused silica porous layer open tubular (PLOT) column (30 m long x 0.32 mm internal diameter x 10 µm film thickness) and a Chrompack Molsieve 5 Å fused silica PLOT column (25 m long x 0.32 mm internal diameter x 30 µm film thickness) were installed in series on the GC. Column switching

was achieved by means of a Valco EH4N10WE 10-port valve and attempts were made to reduce pressure fluctuations during switching by incorporating a J&W DB1 restrictor (15 m long x 0.32 mm internal diameter x 1 μm film thickness) in line with the PoraPLOT Q column when the latter was used alone. A deactivated fused silica column (15 m long x 0.32 mm internal diameter) was used as a transfer line to connect the outlet of the 10-port valve to the mass spectrometer. Samples were injected onto the GC using a split-splitless injector held at 250°C and the carrier gas was helium.

Procedure

Column switching was set up to achieve baseline separation of CO, CO_2, N_2O and N_2. These gases could be successfully separated from O_2 although it was found that the latter co-elutes with argon (Ar) if that gas is also present.

Initially the system was configured to allow the injected gas sample to pass first through the PoraPLOT Q column (column 1) and then through the Molsieve 5Å column (column 2). This configuration (valve Position A) is shown schematically in Figure 1 (where P1 and P2 are the carrier gas pressures in the two parts of the system) and was maintained until the co-eluting N_2/CO/O_2 had passed onto the Molsieve 5Å column. The valve was then switched so that the remaining gas sample flowed through the PoraPLOT Q column (column 1) and the restrictor only (Position B, Figure 2). It was kept in Position B until the CO_2 and N_2O peaks had been detected whereupon the valve was switched back to Position A to allow the gases which had passed onto the Molsieve 5Å column to elute from the system. Under the the GC conditions normally employed it was found that the first switch was required at about 6.5 minutes and the second at just under 10 minutes.

Calibration gas mixtures were injected directly onto the GC using a gas tight syringe. Propellant samples were loaded into separate

20 cm^3 vials and aged for various periods before being placed in the headspace sampler for automatic programmed analysis.

RESULTS AND DISCUSSION

Injection of a $N_2O/N_2/CO/CO_2$ calibration gas mixture showed that the column switching system was capable of achieving complete baseline separation of these gases under isothermal conditions (50°C) to give an elution order of CO_2, N_2O, N_2, CO. The approximate retention times for a typical carrier gas pressure of 50 kPa were: CO_2 - 7.8 mins, N_2O - 8.3 mins, N_2 - 14.8 mins and CO - 36.0 mins. O_2 and Ar elute together after 11.2 mins under the same conditions. It was possible to shorten the analysis time by setting up a simple temperature programme about 14 minutes into a run. This involved raising the oven temperature to 140°C at a rate of 10°C min^{-1} and then holding it there for one minute. The retention time of CO was thereby reduced to less than 25 minutes.

The technique has been used for investigating gas evolution from a number of different propellants undergoing accelerated aging in air and two typical total ion chromatograms from different stages of one such study are presented in Figures 3 and 4. In this case the propellant yielded increasing quantities of N_2O with time and it was important that the column switching system could successfully separate this gas from CO_2. No CO was evolved and the chromatograms do not extend to the point where CO would have eluted.

The monitoring of each gas in the aged air-filled vials was carried out by comparing the peak area for the selected gas with the peak area for Ar from each headspace sample and then plotting this ratio as a function of the aging time of the vial. Although Ar was not able to be separated chromatographically from O_2 its GC peak is readily identified by using the mass filter function in the Masslab software and it can therefore be used as an internal calibrant.

The column switching system described herein has been used successfully for monitoring gases evolved at temperatures as low as 30°C. Further work is underway in an attempt to increase the range of examinable gases and to extend the applications of the technique.

ACKNOWLEDGEMENT

One of us (CSB) thanks the Defence Research and Evaluation Agency (Fort Halstead) for financial support.

REFERENCES

1. F I H Tunstall, "The Determination of Gases Evolved from Propellant Compositions by Gas Chromatography", *Chromatographia*, 3, 411 (1970).

2. R J Powell, B Downes and J Rowley, "Precise Mass Spectrometric Determination of Gas Evolution from Propellants", *Proceedings of the 6th Symposium on Chemical Problems Connected with the Stability of Explosives, Kungälv, Sweden,* 329 (1982).

3. M Marshall and N MacLeod, "Characterisation of Gases Evolved from Propellants at Elevated Temperatures", *Proceedings of the 18th International Annual Conference of ICT, Karlsruhe, Germany,* 69-1 (1988).

4. J M Bellerby, M H Sammour, P F Bunyan and I A Carmichael, "The Effect of Ballistic Modifiers on Gas Evolution from Cast Double Base Propellants", *Proceedings of the 9th Symposium on Chemical Problems Connected with the Stability of Explosives, Margretetorp, Sweden,* 309 (1992).

5. M D Judge, "Solid Propellant Degradation Kinetics via Headspace Sampling Gas Chromatography", *Propellants, Explos., Pyrotech.*, 22, 11 (1997).

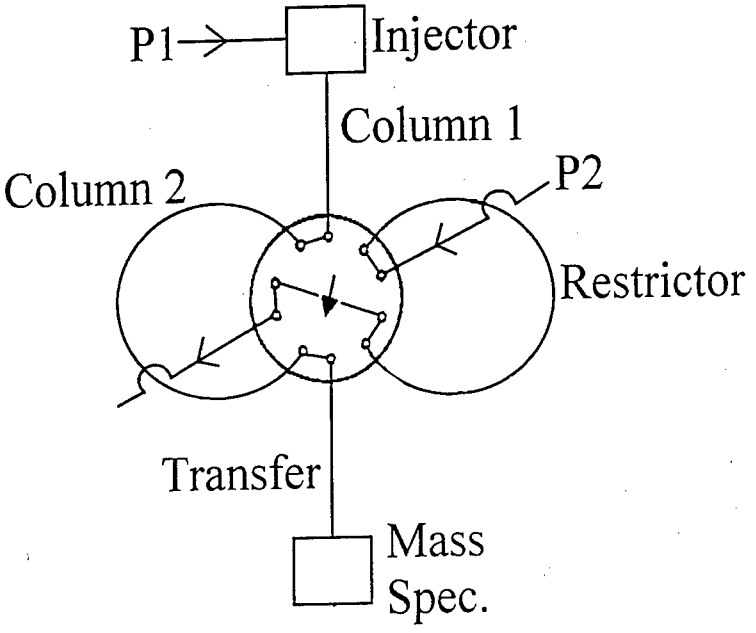

Figure 1. GC Column Configuration for Valve Position A

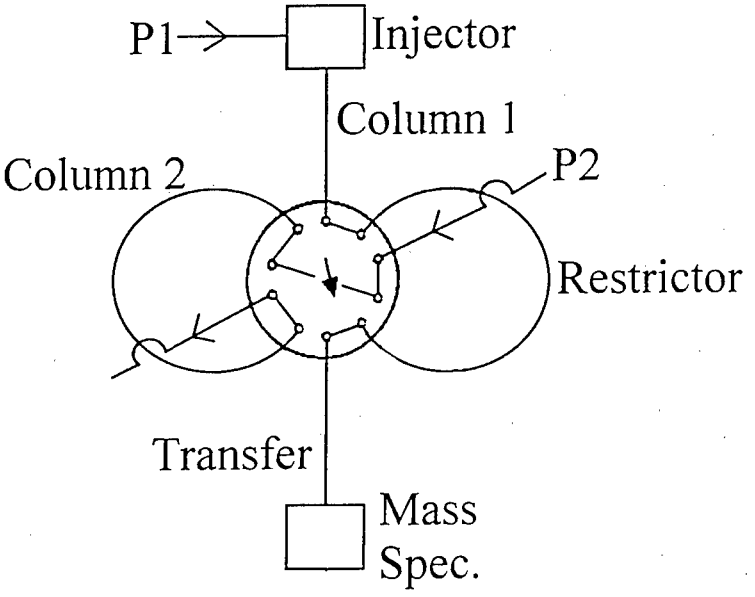

Figure 2. GC Column Configuration for Valve Position B

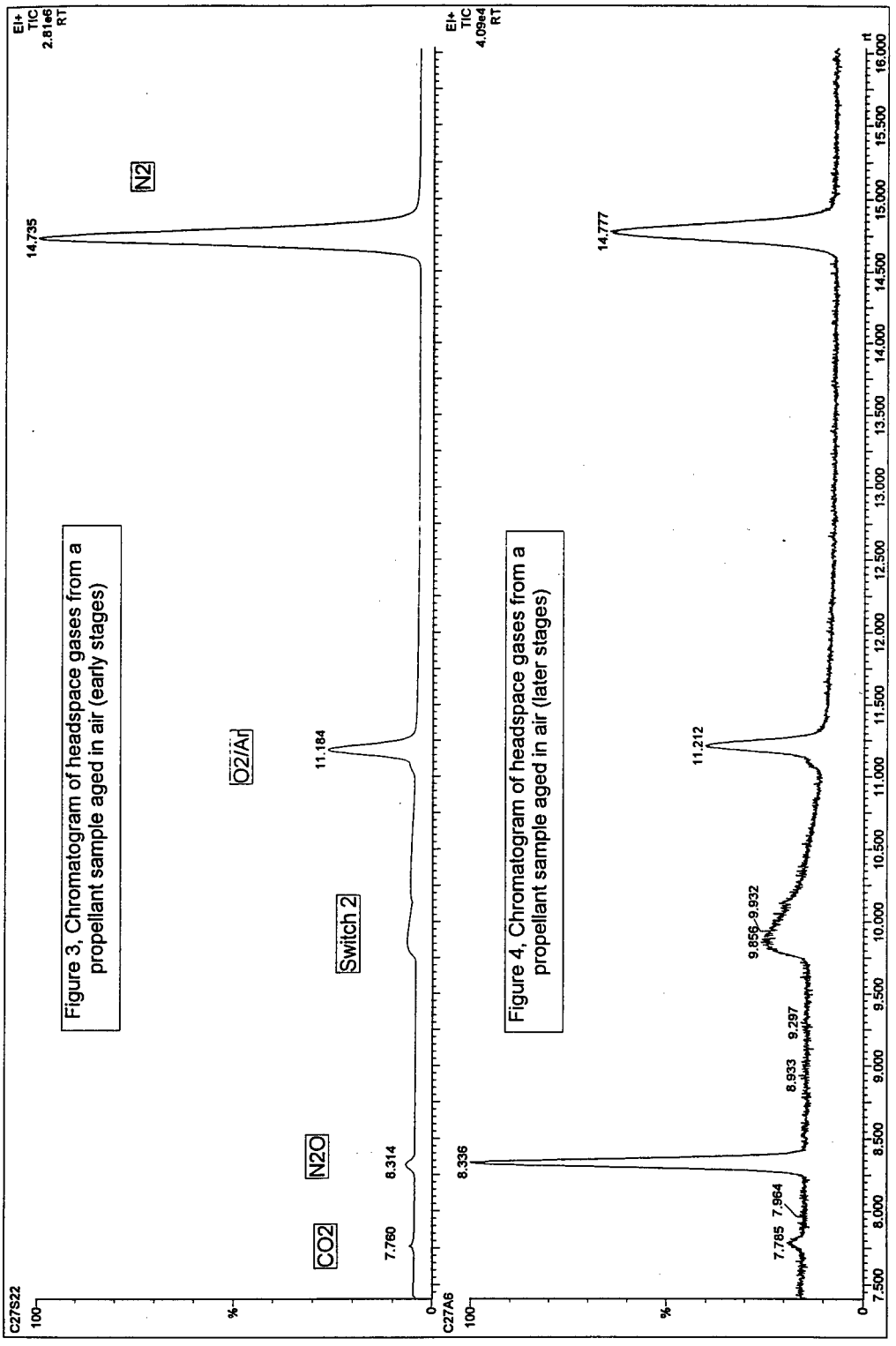
C27S22
EI+
TIC
2.81e6
RT
100
%
0
14.735
N2
O2/Ar
11.184
Switch 2
CO2
N2O
7.760
8.314
Figure 3, Chromatogram of headspace gases from a propellant sample aged in air (early stages)
C27A6
EI+
TIC
4.09e4
RT
8.336
7.765
7.964
8.933
9.297
9.856
9.932
11.212
14.777
Figure 4, Chromatogram of headspace gases from a propellant sample aged in air (later stages)
7.500
8.000
8.500
9.000
9.500
10.000
10.500
11.000
11.500
12.000
12.500
13.000
13.500
14.000
14.500
15.000
15.500
16.000
rt

INVESTIGATION OF LATTICE IMPERFECTIONS IN ENERGETIC MATERIALS USING X-RAY DIFFRACTION

Michael Herrmann and Walter Engel

Fraunhofer Institut für Chemische Technologie / Joseph-von-Fraunhofer-Straße 7
D-76327 Pfinztal / Berghausen

Abstract

Lattice imperfections play an important role in the production and quality assurance of energetic materials as they influence properties like the mechanical sensitivity, elasticity and stability. However, the quantitative detection of lattice imperfections is difficult. Direct methods measure small areas that are often not representative, and the preparation is troublesome and could induce imperfections by itself. Integral methods characterize larger sample volumes and deliver average values that are useful for quantitative detection. Especially suited is X-ray diffraction, as the imperfections effect the diffration to a reasonably observable extent.

The paper gives the theoretical background for the investigation of lattice imperfections with X-ray diffraction that should be introduced as a method for the characterization of energetic materials like HMX, CL20 and ADN.

Zusammenfassung

Gitterdefekte spielen eine wichtige Rolle bei der Herstellung und Qualitätssicherung von energetischen Materialien, da sie wichtige Eigenschaften wie die mechanische Empfindlichkeit, Elastizität und Stabilität beeinflussen. Ihre quantitative Erfassung ist schwierig. Direkte Methoden beleuchten kleine, oft nicht repräsentative Ausschnitte, und sie sind meist mit aufwendigen Präparationen verbunden, die selbst Defekte erzeugen können. Integrale Methoden charakterisieren größere Probenvolumen und liefern Mittelwerte, die eine quantitative Erfassung unterstützen. Besonders bietet sich die Röntgenbeugung zur Untersuchung an, da hier aussagekräftige Effekte von Gitterdefekten auf die Beugungsphänomene auftreten.

Die Arbeit gibt die theoretischen Grundlagen für Untersuchungen von Gitterfehlern mit Hilfe der Röntgenbeugung. Die Methode soll für die Untersuchung von kristallinen energetischen Materialien wie Oktogen, CL20 und ADN Anwendung finden.

Introduction

The requirements to energetic systems increase continuously. Especially systems with increased performance and LOVA characteristics are needed. Therefore new energetic materials as CL20 are proposed for applications in solid propellants. On the other hand high performance materials as HMX could be used, if the material properties are improved for example by recrystallization procedures avoiding lattice imperfections (Heijden et al. 1996).

Lattice imperfections influence properties like mechanical sensitivity, elasticity and stability. Their characterization should be envisaged for the characterization of energetic materials as HMX, CL20 and ADN as well as for the evaluation of recrystallization procedures.

Lattice Imperfections

There are three important types of lattice imperfections influencing material properties: Thermal and chemical imperfections and dislocations. Thermal lattice imperfections are vacancies or interstitial atoms. They belong to the thermodynamical equilibrium and can not be avoided by careful preparation. Chemical lattice imperfections are impurities on lattice sites or interstitials. For example a volume of $1cm^3$ with a purity of 99,9999% includes about 10^{17} foreign atoms.

Dislocations are lattice imperfections that extend through crystallites as edge or screw dislocations built by plastic deformations or misfits in crystallization processes (Bohm 1995). The dislocations glide easily perpendicular to the dislocation edge causing plastic properties of solids. However, dislocations often settle down at chemical imperfections, which explain the hardening of steal caused by impurities (Gerthsen et al. 1989).

The dislocation density ρ (cm^{-3}) is defined as the length of all dislocation lines per volume. Typical values of metals amount to 10^6 per cm^3, where dislocation lines add to a length of 10 km (Bohm 1995).

The lattice imperfections distort the lattice and change lattice distances. They are described by the strain which is defines by $\varepsilon=\Delta d/d$, where Δd is the difference between distorted and undistorted lattice distance d . The distorting force per area is called stress.

Detection of Lattice Imperfections

The detection and quantitative determination of lattice imperfections is difficult. Direct methods as high resolution electron microscopy or scanning tunnel microscopy include small areas that are often not representative, and at low imperfection densities the probability to find imperfections is rather small. Besides, the preparation of thin films for the high resolution electron microscopy is troublesome and may induce imperfections by itself. On the other side scanning tunnel microscopy measures only surfaces.

Direct or integrated methods base on measurements of the density, intrinsic energy, specific heat or electric conductivity. However, the most informative integral effects of dislocations rely on their influence on diffraction phenomena especially of X-ray diffraction (Bohm 1995).

X-ray Diffraction

The use of diffraction line profiles for the investigation of micro crystalline properties is nearly as old as the powder diffractometry itself. In 1918 Scherrer reported, that the breadth of diffraction lines are inverse to the size of crystallites. Van Arkel found 1925, that lines are broadened by micro strains. The evaluation of these effects is based on the kinematic theory of the X-ray diffraction by polycrystalline structures. X-rays are diffracted by electrons under special geometrical conditions, described by the Bragg law and the Laue equations. The theory proposes sharp reflection lines or peaks for perfect large crystallites. However, such sharp lines are not found in real experiments, as the lines are broadened by geometrical and physical effects.

Therefore the first task of a peak profile analysis is the determination of the pure diffraction profile due to the diffraction at the sample (Klug and Alexander 1974).

Determination of the pure Line Profile

The superposition of geometrical and pure line profile is described by the convolution as shown in equation 1.

$$h(\varepsilon) = g * f = \int_{-\infty}^{+\infty} g(\eta) f(\varepsilon - \eta) d\eta \qquad [1]$$

The pure line profile *f* can be determined by deconvolution of the measured profile *h* and the geometrical profile *g*. Useful methods are the Fourier-method (Stokes 1948) and the method of the iterative deconvolution (Ergung 1968).

The Fourier method yields the pure line profile as a Fourier series and their Fourier coefficients

$$f(\varepsilon) = \frac{1}{60} \sum_{\zeta} F_r(\zeta) \cos \frac{2\pi\varepsilon\zeta}{60} + \sum_{\zeta} F_i(\zeta) \sin \frac{2\pi\varepsilon\zeta}{60} \qquad [2]$$

The iterative deconvolution uses the difference between the measured profile and the convolution *g*h* as a first approximation of the effect of the convolution *g*f*. The method starts with

$$f_1 = f_0 + (h - g * f_0) = h + (h - g * h) \qquad [3]$$

and approximates the pure line profile with

$$f_{n+1} = f_n + (h - g * f_n) \qquad [4]$$

The method deliver a curve of the pure line profile.

Both methods need geometrical profiles, that are practically obtained from measurements of nearly perfect crystals.

Analysis of the pure Line Profile

The pure line profile includes the effects of the sample on the breadth and profile shape due to micro strain and particle size simultaneously. The most used method for the separation and evaluation of the strain and stress effects is based on the theory of Warren and Averbach (1950). Besides, the method of Williamson and Hall will be used for the separation.

Fourier-Method of Warren and Averbach

Warren and Averbach start with the assumption, that for a given crystallite the vector location of the origin of a particular unit cell $m_1m_2m_3$ is defined as

$$R_m = ma_1 + ma_2 + ma_3 + \partial(m_1m_2m_3) \qquad [5]$$

where the m_1, m_2 and m_3 are the number of unit cells along a_1, a_2 and a_3 and $\delta(m_1m_2m3)$ allows distortion displacements. Using the powder pattern power theorem the profile is expressed as the Fourier series

$$P'(2\theta) = \frac{KNF^2}{\sin^2\theta} \sum_{n=-\infty}^{+\infty} \left(A_n \cos 2\pi n h_3 + B_n \sin 2\pi n h_3\right) \qquad [6]$$

with the Fourier coefficients

$$A_n = \frac{N_n}{N_3}\left\langle \cos 2\pi l Z_n \right\rangle \quad \text{and} \quad B_n = -\frac{N_n}{N_3}\left\langle \sin 2\pi l Z_n \right\rangle \qquad [7]$$

The coefficients are obtained by the deconvolution with the Fourier method.

The cosine coefficient A_n is the product of N_n/N_3 which depends only on the size and $\langle cos2\pi\ lZ_n\rangle$ which depends only on the distortion. Denoting size and distortion by superscripts S and D, respectively, we have then

$$A_n^S = \frac{N_n}{N_3} \quad \text{and} \quad A_n^D = \left\langle \cos 2\pi l Z_n \right\rangle \quad \text{with} \quad A_n = A_n^S A_n^D \qquad [8]$$

The separation of A_n^S and A_n^D is based on the fact that the size coefficient is independent of order l, whereas the distortion coefficient is a function of l and approach unity as l goes to zero. On the assumption that l and n are small the logarithm of the measured Fourier coefficients may be written as

$$\ln A_n(l) = \ln A_n^S - 2\pi^2 l^2 \left\langle Z_n^2 \right\rangle \qquad [9]$$

Now for each fixed value of n the value of $ln\ A_n(l)$ is plotted against l^2 (see fig. ...), whereupon the l^2 zero intercepts give the size coefficient A_n^S and the slopes give values of $-2\pi^2\langle Z_n^2\rangle$, where $\langle Z_n^2\rangle$ can be replaced by $n^2\langle\varepsilon_L^2\rangle$, from which the mean-square values of the component of $\langle\varepsilon_L^2\rangle$ strain may be calculated.

Williamson-Hall-Plot

An other method for the separation of strain and size effect is the Williamson-Hall plot (1953). Starting with a strain contribution with an integral breadth ξ the corresponding integral line breadth β_s due to strain is

$$\beta_s = 2\xi \tan\theta \qquad [10]$$

where θ is the Bragg angle. In terms of the reciprocal lattice strain broadens the reciprocal lattice points to a breadth β^*_s

$$\beta^* = \frac{\beta}{\lambda}\cos\theta \quad \text{and} \quad d^* = \frac{2}{\lambda}\sin\theta$$

$$\beta_s^* = \xi d^* \qquad [11]$$

Particle size broadening has been shown to obey the relation

$$\beta_p = \frac{\lambda}{t\cos\theta} \quad \text{or} \quad \beta_p^* = 1/t \qquad [12]$$

where λ is the X-ray wavelength and t is a mean linear dimension of the particle. The reciprocal lattice breadth due to particle size is a constant independent of d^* and equal to $1/t$.

However, the method consists essentially in plotting the breadth of the reciprocal lattice points against their distances from the origin. Small particles alone then give a horizontal plot with an intercept at 1/t and strain alone gives a line through the origin with a slope ξ, if the strain distribution is isotropic. The composite broadening produced by simultaneous small particle size and strain depends to some extend on the broadening functions of the separated effects.

Measuring Systems

The measuring systems consist of Siemens diffractometers equipped with a primary or a channel-cut monochromator to minimize the line broadening due to the measuring geometry. With the channel-cut monochromator peak widths are reduced to about 0.02 degree two theta, which is near the values obtained by synchrotron radiation. The measuring systems will be optimized for the investigation of lattice imperfections. First results will be presented at the poster.

References

Bohm J., Realstruktur von Kristallen, Stuttgart : Schweizerbart, ISBN 3-510-65160-X, (1995)

Ergun S.; Direct Method for Unfolding Convolution Products - Ist Application to X-Ray Scattering Intensities; J. Appl. Cryst. 1, 19 (1967)

Gerthsen C., Kneser H.O., Vogel H.;Physik; ISBN 3-540-51196-2; (1989)

Klug H.P., Alexander L.E.; X-Ray Diffraction Procedures, ISBN 0-471-49369-4, J. Wiley & Sons Inc., (1954)

Heijden A.E., Duvalois W., Characterization of the Internal Quality of HMX Crystals, 27. Int. Annu. Conf. of ICT, 32,1-11, (1996)

Stokes A.R.; Proc. Phys. Soc. (London), A61, 382, (1948)

Van Arkel A.E.; Physica 5, 208-12, (1925)

Warren B.E., Averbach B.L.; The effect of Cold-Worked Distortion on X-Ray Patterns; J. Appl. Phys., Vol. 21, 595-599, (1950)

Williamson G. K., Hall W. H.; X-ray Line Broadening from filed Aluminium and Wolfram; Acta Metall., Vol 1, 22-31 (1953)

THERMOCHEMICAL AND RADIATIVE CODES LINKAGE USING AN EXPERIMENTAL DESIGN METHOD

Rémi BOULANGER, Luc BRUNET et André ESPAGNACQ

Giat Industries - Centre de Bourges
7, Route de Guerry
Service DSAM/DT/PYRO/EME/L
BP 265
18023 BOURGES Cedex

I. SUBJECT:

The aim of this work is to replace the linkage of two computation codes by simple analytical formulae elaborated using an experimental design method. These formulae are then applied to the combustion of propellants and their erosion characteristics are evaluated.

The two computation codes are:

- ALJAN in its isobaric version (previous version of ALJAN_EP)
- RADCAL which calculates the IR emission spectra of a combustion and its total directional radiation in the correct spectral band.

II. CODES USED:

II-A. ALJAN

The physical following terms are defined by:

Product	Chemical species formed at the end of the combustion
Reactant	Chemical species existing at ignition
Energy of formation	Energy used to form a reactant or a product, under isochoric conditions and at standard temperature, from the elements taken in their stablest state
Enthalpy of formation	Energy used to form a reactant or a product, under isobaric conditions and at standard temperature, from the elements taken in their stablest state

a_{ik}	number of atoms k in the chemical species i.
A_k	number of atoms k in the reactant medium.
X_k	atom name from species k
n_i	mole number of species i.
μ_i	chemical potential of species i
Φ	fugacity
$\hat{\Phi}$	standard fugacity
P	pressure

P°	standard pressure
Γ	magnitude of the gaussian perturbation
R	perfect gases constant (8,314 J/mol/K)
T	temperature (K)
V	Volume (m^3)
ξ	random integer number
ζ	random real number taken between 0 and 1

II-A-1. GENERAL PRESENTATION

The purpose of this software is to compute the thermodynamic variables of the combustion:

- Flame temperature or balance
- Combustion energy
- Composition of reactant products

It can be used for every pyrotechnic composition, powder or explosive.

II-A-2. EQUATIONS OF THE MODEL

In this report, only the case of the composition of products as a function of temperature or pressure will be considered. Isochoric (u=uo, v=vo) and isobaric (h=ho, p=po) cases are easily solvable once the distribution of combustion products is known.

Two equations have to be solved simultaneously:

1- Mass law action :

For the chemical reaction

$$X^1_{A_1}X^2_{A_2}X^3_{A_3}\cdots X^k_{A_k} \rightarrow n_1 X^1_{a_{11}}X^2_{a_{12}}X^3_{a_{13}}\cdots X^k_{a_{1k}} + n_2 X^1_{a_{21}}X^2_{a_{22}}X^3_{a_{23}}\cdots X^k_{a_{2k}} + \cdots + n_{nespèces} X^1_{a_{nespèces1}}X^2_{a_{nespèces2}}X^3_{a_{nespèces3}}\cdots X^k_{a_{nespèces k}}$$

the conservation balance of matter can be written:

$$\forall k \in [1..natomes] \Rightarrow \sum_{i=1}^{nespeces} a_{ik} n_i = A_k \qquad (I)$$

Every vector n has to answer to this equation.

2- Minimal free enthalpy:

Free enthalpy is related to the entropic balance of the reaction. A minimum value exists for the best thermodynamical reaction. This approach does not take into account the chemical kinetics of the reaction.

$$F = \sum_{i=1}^{nespeces} \mu_i . n_i \quad \text{minimale} \qquad (II)$$

The chemical potential μ is calculated following:

$$\mu_i = \mu_i^\circ + RT \ln\left(\frac{\Phi}{\bar{\Phi}}\right) \qquad (III)$$

In case of a perfect gas (PV=nRT), this equation becomes:

$$\mu_i = \mu_i^* + cd.\left(RT \ln\left(\frac{n_i}{\sum_i n_i} \right) + RT \ln(P/P^\circ) \right) \quad \text{(IV)}$$

where

cd = 1 for gaseous species

cd = 0 for condensed phases

These equations are easily solved using Lagrange's multiplicator method. This method consists in writing the sum of (I)*λ(II) and then deriving it with respect to all the unknown variables.

II-B. RADCAL

The physical terms employed for this part of the computation are:

Intensity I_λ (W/cm²/sr/μm)	Monochromatic energy radiated by the medium
Total directional Intensity I (W/cm²/sr)	Total directional intensity integrated in the spectral band considered
Blackbody Intensity $I°_\lambda$ (W/cm²/sr/μm)	Energy radiated by the reference emitter (blackbody)
Absorption coefficient κ (m^{-1})	Part of the emitted energy absorbed by the gaseous medium
Scattering coefficient σ (m^{-1})	Part of the energy scattered by the medium
Extinction coefficient β (m^{-1})	Sum of the absorption and scattering effects
Optical pathlength *s* (m)	Optical length along which the computation of radiative transfer is made
Temperature T (K)	Temperature of the homogeneous path considered in the medium
Transmittivity τ	Transmittivity of the gaseous column considered

II-B-1. GENERAL PRESENTATION AND HYPOTHESIS OF THE MODEL

The aim of this computation code is to determine the infrared emission spectra (1 to 200μm) of hydrocarbon combustion from the gaseous and particle concentration of the medium. At first sight, this type of computation can be made with isobaric combustion; this thermodynamic computations have been made with this configuration.

The gaseous species taken into account are: CO_2, H_2O, CH_4, CO, O_2, N_2. Carbon particles, most commonly called soot, found in a more or less substantial quantity in hydrocarbon combustion, radiate in a continuous and stronger manner than the gaseous species which radiate in specific spectral bands. The volume fraction of soot particles is needed to carry out the computation.

The scattering effects of soot are negligible; absorption is the only effect considered for this type of computation and it is evaluated using a theory similar to the Mie scattering theory: Rayleigh's theory.

The basic equation of the model is the Radiative Transfer Equation (RTE) applied to combustions. A gradient temperature and concentration of species can be taken into account.

II-B-2. PHYSIC EQUATIONS OF THE MODEL

The thermochemical computations have shown that no soot was encountered in our application cases and that only gases radiate in these powder combustions. Moreover, radiative computations have been made on homogeneous gaseous pathlength.

The RTE in its most general form can be written as :

$$\underbrace{\frac{\partial I_\lambda(s,\vec{u})}{\partial s}}_{\text{Variation of the intensity}} + \underbrace{\left[\kappa_\lambda(s)+\sigma_\lambda(s)\right]\cdot I_\lambda(s,\vec{u})}_{\text{Absorption of the radiation}} = \underbrace{\kappa_\lambda(s)\cdot I_\lambda^{\circ}\left[T(s)\right]}_{\text{Emission}} + \underbrace{\frac{\sigma_\lambda(s)}{4\pi}\int_0^{4\pi} P_\lambda(\vec{u}',\vec{u})\cdot I_\lambda(s,\vec{u})d\Omega'}_{\text{Scattering}} \qquad \text{(V)}$$

In equation (V), the different parameters of the radiative transfer are detailed for a combustion. For the combustion of powders, scattering effects are negligible because of the small size the particles in comparison with the computation wavelength. The equation (V) becomes :

$$\underbrace{\frac{\partial I_\lambda(s,\vec{u})}{\partial s}}_{\text{Variation of the intensity}} + \underbrace{\kappa_\lambda(s)\cdot I_\lambda(s,\vec{u})}_{\text{Absorption of the radiation}} = \underbrace{\kappa_\lambda(s)\cdot I_\lambda^{\circ}\left[T(s)\right]}_{\text{Emission}} \qquad \text{(VI)}$$

To solve this equation, two computation options are possible: determining the radiative energy using the tabulated data (function of temperature and wavelength) of the absorption coefficient[1], or calculating it using models directly issued from quantum mechanics theory. These models have been studied by several authors[2,3,4] and exploited by Grosshandler[5].

Thus, equation (2) has been solved and rendered discrete as follows:

$$\overline{I_\nu}(s) = \overline{I_\nu}(0)\cdot\overline{\tau_\nu}(0,s) + \sum_{i=1}^{N} I_\nu^{\circ}(T_i)\left[\overline{\tau_\nu}(i,N) - \overline{\tau_\nu}(i-1,N)\right] \qquad \text{(VII)}$$

the transmittivity of the gaseous column being obtained directly using the classical formulation :

$$\tau(0,s) = \exp\left[-\int_0^s \kappa(s')ds'\right] \qquad \text{(VIII)}$$

[1] "Handbook of Infrared Radiation from Combustion Gases" - C.B. Ludwig, W. Malkmus, J.E. Reardon & J.A.L. Thomson - NASA SP-3080 (1973)

[2] "The Spectral and Total Emissivity of Carbon Dioxide" - B. Leckner - Combustion & Flame, Vol. 17, pp. 27-44 (1971)

[3] "Thermal Radiation of Methane Gas" - Ind. Eng. Chem. Fundamentals 3, pp. 167-176 (1964)

[4] "Infrared Emissivity of Diatomic Gases for the Anharmonic Vibrating-Rotator Model" - W. Malkmus, A. Thomson - JQSRT 2, 17 (1961)

[5] "A Narrow Band Model for Radiation Computations in a Combustion Environment" - W. L. Grosshandler - Fire Sci. Div. Natl. Stand. Technol. (BFRL), NIST/TN-1402, 57 p. (1993)

which is integrated on the optical pathlength considered for the computation. The different values of the intensity are obtained at the different wavelengths of the computation path ($\approx 2.5 \times 10^{-3}$ µm) making it possible to constitute a complete emission spectrum which can be integrated on the required spectral band; the total directional intensity is computed in this manner.

III. EXPERIMENTAL DESIGN

III-A. SELECTED CASES

For this report, a hadamard's experimental design based on an alteration of the JA2 powder formula has been used. This type of matrix is relatively efficient because of its isovariance by rotation and its uniform accuracy on the domain. In this study, the interactions will not be considered.

C	H	O	*N*	Qf=-Hf
21	31	37	*8,93*	2000
20	31	37	*9,79*	2200
20	30	37	*9,86*	2200
21	30	36	*10,14*	2200
20	31	36	*10,93*	2000
21	30	37	*9,00*	2000
21	31	36	*10,07*	2200
20	30	36	*11,00*	2000

This experimental design leads to 8 formulae of powders and the reduced centered variables are:

X1 : Carbon number in ATG/kg (C)
X2 : Hydrogen number in ATG/kg (H)
X3 : Oxygen number in ATG/kg (O)
X4 : Enthalpy of formation (kJ/kg) (Qf)

The nitrogen quantity is calculated knowing that molecular mass of the powder is 1000 g/mol.

Those variables correspond to the following domain:

	C	H	O	*N*	Qf=-Hf
max	21	31	37	*11,00*	2200
min	20	30	36	*8,93*	2000

Knowing the maximum (VM) and minimum (Vm) values of the real variable, the reduced centered variables X are expressed by :

$$X = \frac{2V - (VM + Vm)}{(VM - Vm)}$$

So, for the following conditions:

V=VM => X=+1
V=Vm => X=-1

the previous matrix becomes:

$$\begin{bmatrix} 1 & 1 & 1 & 1 \\ 1 & 1 & 1 & 1 \\ -1 & -1 & 1 & 1 \\ 1 & -1 & -1 & 1 \\ 1 & 1 & 1 & 1 \\ 1 & -1 & 1 & -1 \\ 1 & 1 & -1 & 1 \\ -1 & -1 & 1 & -1 \end{bmatrix}$$

III-B. ANALYTICAL FORMS

ALJAN and RADCAL computations are made on every point of the domain in order to establish the analytical forms after an analysis of the experimental design:

C	H	O	*N*	Qf=-Hf	T(K)	N(mol/kg)	F (MJ/kg)	Intensity (W/cm²/sr)
21	31	37	*8,93*	2000	2732	41,807	0,95	0,923
20	31	37	*9,79*	2200	2715	41,204	0,93	0,97
20	30	37	*9,86*	2200	2725	40,776	0,92	0,98
21	30	36	*10,14*	2200	2608	41,528	0,90	0,856
20	31	36	*10,93*	2000	2700	41,7	0,94	0,908
21	30	37	*9,00*	2000	2743	41,378	0,94	0,941
21	31	36	*10,07*	2200	2593	41,97	0,90	0,836
20	30	36	*11,00*	2000	2712	41,27	0,93	0,92

The studied answers are:

T : Isobaric flame temperature at 1 atm.

N : Mole number produced by 1 kg of powder

F : Force = NRT

I : Gas intensity between 1 and 200 µm.

Yi=	Temperature (K)	N (mol/kg)	Force (MJ/kg)	Intensity (W/cm²/sr)
β0	2691	41,4541	0,92737	0,91675
β1	-22	0,21662	-0,00275	-0,02775
β2	-6	0,21612	0,00276	-0,0075
β3	37,75	-0,16287	0,00941	0,03675
β4	-30,75	-0,08463	-0,01259	-0,00625

The analytical formulae are:

$$Yi = \beta 0 + \beta 1\, X1 + \beta 2\, X2 + \beta 3\, X3 + \beta 1\, X4$$

The differences between calculated values with the analytical forms and those computed with the computation codes are very low (0,030 % on T; 0,006 % on N; 0,03 % on F et 0,02 % on I).

IV. APPLICATION TO PROPELLANTS

To validate these analytical forms both inside and outside the analysed domain with the hadamard matrix, several powders have been computed using ALJAN/RADCAL codes and the analytical forms previously determined.

Propellant	area in-out C-H-O-Hf
P1	I-I-I-I
P2	I-O-I-O
P3	I-O-I-O
P4	O-O-I-O
PX1	O-O-O-O
PX2	O-O-O-O
P5	O-O-O-O
P6(1)	I-O-O-O
P6(2)[6]	O-I-O-O

I indicates that the variable is within the domain (interpolation case); O indicates that the variable is out of the domain (extrapolation case). Two computation results can be seen in Figure 1 at the end of the article.

	Temperature(K)			Gases (mol/kg)			Force (MJ/kg)			Intensity (W/cm²/sr)		
Propellant	Aljan	diff%	Exp. design	Aljan	diff%	Exp. design	Aljan	diff%	Exp. design	RADCAL	diff%	Exp. design
P1	2692	0,17%	2688	41,18	-0,03%	41,20	0,92	0,15%	0,92	0,931	0,09%	0,93
P2	2684	0,26%	2677	40,04	-0,06%	40,06	0,89	0,24%	0,89	0,955	0,53%	0,95
P3	2678	0,24%	2672	40,31	-0,05%	40,33	0,90	0,23%	0,90	0,936	0,26%	0,93
P4	2386	-2,06%	2436	41,28	0,40%	41,12	0,82	-1,49%	0,83	0,773	-4,27%	0,81
PX1	2384	-4,37%	2490	47,60	0,89%	47,18	0,94	-4,55%	0,99	0,35	29,53%	0,26
PX2	2818	-2,01%	2875	48,00	0,56%	47,73	1,12	-0,78%	1,13	0,49	9,78%	0,44
P5	2862	-3,16%	2954	44,58	0,57%	44,32	1,06	-2,15%	1,08	0,69	-5,82%	0,73
P6(1)	2756	-0,45%	2768	42,77	0,10%	42,73	0,98	-0,31%	0,98	-	-	0,83
P6(2)	2783	-0,70%	2803	42,35	0,17%	42,28	0,98	-0,51%	0,98	-	-	0,87

The deviations between the analytical forms and the results of complete computation codes are once more very slight, except, however, for two composite powders.

V. CONCLUSION

This way of computation easily allows slow codes to be replaced by simple analytical formulae. It can be noted that even if the chemical formulae are not completely included in the experimental design domain, the variation of the results is not illogical.

It seems that the range of intensities follows that of erosion. However, the intensity of composite powders is low whereas they have a high power of erosion.

This can be explained by the remarkable heterogeneity of the materials (the intensity of RDX grains is very high) and because of their formulation, which is out of the experimental design and which influences the results more than the other powders.

The intensity of the new ISL powders (nitramine based powders P6(1) and P6(2)) radiates in the same range as P4 but with a higher force.

The P5 is also an interesting formula, with a force of 1,08 and a spectral intensity of 0,73.

[6]LICHT H.H, BRAUN S.; Poudre haute puissance à plusieurs bases à érosivité réduite; ISL RT 506/96F

FIGURE 1 : Comparison between the emission spectra calculated on two different powders

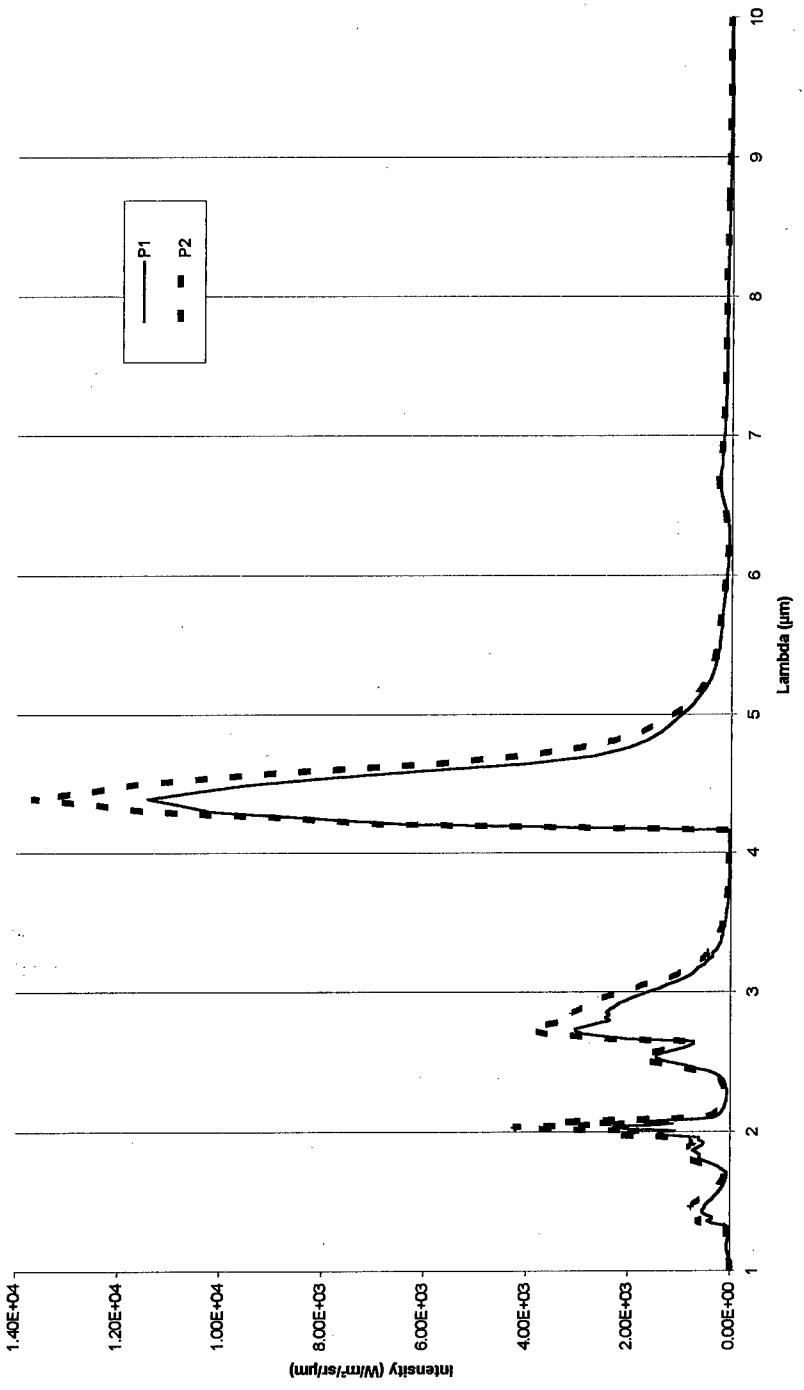

RADIATIVE CALCULATIONS ON COMBUSTION OF PYROTECHNIC COMPOSITIONS

Rémi BOULANGER*, Jean-Michel SOUIL**, Philippe GILLARD**, Michel ROUX**, André ESPAGNACQ*.

(*) Giat Industries - Centre de Bourges - 7, Route de Guerry - BP 265 - 18023 BOURGES Cedex (FRANCE)

(**) Laboratoire de Combustion et de Détonique - Université de Poitiers - ENSMA -Téléport 2 - B.P. 109 - Site du Futuroscope - 86960 FUTUROSCOPE Cedex (FRANCE)

ABSTRACT

Here is presented the elaboration of a model able to compute the radiative effects generated by the combustion of hydrocarbon fuels or pyrotechnic based compositions. A brief bibliography has been made on the different ways to realise such a modelisation. The justification of our choice in the way to model these phenomena is presented. The main equations of the solved problem are recalled. The first validations made thanks to data found in the literature are shown for the two types of combustions.

NOMENCLATURE

a : Albedo.
f_v : Soot volume fraction [m^3/m^3].
k : Absorption index of particle.
$L_\lambda(s,\vec{u})$: Monochromatic intensity towards $\vec{u}$ along the path s [W/m²/sr/µm].
$L^\circ_\lambda(s,\vec{u})$: Monochromatic blackbody intensity towards $\vec{u}$ along the path s [W/m²/sr/µm].
$L^+(s)$: Forward calculated intensity along the path s [W/m²/sr/µm].
$L^-(s)$: Backward calculated intensity along the path s [W/m²/sr/µm].
m : Complex index of particles.
n : Refraction index of soot particle.
$P_\lambda(\vec{u}',\vec{u})$: Phase function characterising scattering from $\vec{u}'$ towards $\vec{u}$
X : Optical depth parameter.
κ_λ : Monochromatic absorption coefficient [m^{-1}].
σ_λ : Monochromatic scattering coefficient [m^{-1}].
$d\Omega'$: Solid angle [sr].
λ : Radiation wavelength [µm].

INTRODUCTION

Pool fires have been studied for many years in lots of domains : industrial flames hazards of chemicals and various oil-derived fuels. In the defence industry also, in particular for pyrotechnic applications, the limitations of the development of a fire is at the heart of interest. In this domain, pool fires of gelified hydrocarbons, sodium or sodium/potassium eutectic fires, phosphorus or phosphorus based compositions fires, thermit fires, ignition compositions, combustion of powders, ... can be encountered. In all these cases, radiation emitted by flames is a dominant factor in fire development. The objective of this work is to discuss about the possibility to model the radiative effects generated by the combustion of such energetic materials. A radiation model has been performed, accounting for both contributions of gases and particles. Some validations of our computations are carried out using literature data.

THEORETICAL CONSIDERATIONS

The Radiative Transfer Equation

A few applications concerning radiation computations in pyrotechnic situations can be found in literature. In a related domain, some work has been done to evaluate infrared signatures of exhaust plumes [1, 2]. In these media, extinction (including absorption and scattering) phenomena have to be considered depending upon radiative species of interest (gas and particles). The general Radiative Transfer Equation (RTE), accounting for these phenomena has an integro-differential form. It can be written as :

$$\underbrace{\frac{\partial L_\lambda(s,\vec{u})}{\partial s}}_{\substack{\text{Variation}\\ \text{of the intensity}}} + \underbrace{\left[\kappa_\lambda(s)+\sigma_\lambda(s)\right]\cdot L_\lambda(s,\vec{u})}_{\substack{\text{Absorption}\\ \text{of the radiation}}} = \underbrace{\kappa_\lambda(s)\cdot L_\lambda^{\circ}\left[T(s)\right]}_{\text{Emission}} + \underbrace{\frac{\sigma_\lambda(s)}{4\pi}\int_0^{4\pi} P_\lambda(\vec{u}',\vec{u})\cdot L_\lambda(s,\vec{u})\,d\Omega'}_{\text{Scattering}} \qquad (1)$$

At the sight of this equation, it appears that the radiation intensity results from a combination of two different phenomena : on the one hand, the contribution of gases (emitting and absorbing in particular spectral bands) and, on the other hand, the contribution of large size particles which scatter (in a continuous way, but anisotropically).

When combustion situations involving hydrocarbons are considered, the scattering term can be neglected, the radiative medium being a melting between gases and small generally non-scattering particles : soot. So the RTE (1) becomes :

$$\underbrace{\frac{\partial L_\lambda(s,\vec{u})}{\partial s}}_{\substack{\text{Variation}\\ \text{of the intensity}}} + \underbrace{\kappa_\lambda(s)\cdot L_\lambda(s,\vec{u})}_{\substack{\text{Absorption}\\ \text{of the radiation}}} = \underbrace{\kappa_\lambda(s)\cdot L_\lambda^{\circ}\left[T(s)\right]}_{\text{Emission}} \qquad (2)$$

For pyrotechnic combustion situations, the products of combustion are more various and imply the generation of metal oxide particles of important size and the scattering effect can not be neglected in the radiative computation.

Radiative effects modelisation

The resolution of RTE for a non-scattering medium (Eq. 2) leads to consider the gaseous radiation first. In this perspective, different degrees of resolution can be used; one consists in a line by line treatment which is the most precise way, but very expensive in time computation. Moreover, it becomes quickly prohibitive when complex geometries are involved and this is why approximated solutions have been developed. Among these methods, Statistical Narrow-Band (SNB) models can solve (Eq. 2) with acceptable accuracy. Two algorithms are strongly recommended : the Single Line Group (SLG) algorithm which considers the line strengths constant in a spectral interval, and the Multi Line Group (MLG) model which details the spectral interval grouping the lines of equivalent strengths.

The spectroscopic parameters needed to perform SNB models can be found in the literature [3]. For non-isothermal gaseous media, the Curtis-Godson approximation [3] is commonly added to the band model.

Other ways to apprehend the radiation of gases can be mentioned. Some models expressing the radiative properties of gases in terms of absorption coefficients or more precise models depending on the distribution function of the absorption coefficient exist : the correlated-K (CK) model [4] and the Correlated-K Fictitious Gases (CKFG) model [5]. For the CK model, the notion of histogram of the absorption coefficient values into a spectral band is important but for a non-isothermal medium, the correlation of the spectra between two points where the properties are different is necessary. To avoid the "over-correlation", main default of the CK model, in a column of gases with a great temperature gradient, the CKFG model has been created [5]. The method consists in to consider the real gas as a melting of fictitious gases.

Concerning particles radiation, the contribution of small size (generally soot) particles which do not scatter can be considered together with gases; this contribution is accounted in terms of an absorption coefficient.

Considering the large size particle radiation implies the resolution of the complete RTE (Eq. 1). A few solutions can be recalled here; it is important to note that these methods are not necessarily used with the scattering term of the RTE but they do not exclude this opportunity.

We can mention:

- Exact solutions: the resolution is complex in most of the cases. Some results are obtained with very simple monodimensional configurations like gray media with uniform boundary conditions [6].
- Statistical methods: the best known is the Monte-Carlo method which is more useful to apply for complex geometries and non-gray media [8, 9]. The degree of precision increases with the number of statistic samples but it often costs a lot in time computation.

- Zone methods: this calculation way [10] is most of the time used to estimate the radiation in the industrial ovens or combustion in enclosures. The aim is to divide the space and bounds into surface and volume zones with isothermal and constant thermophysical properties.

At the present time, the flux methods are the most frequently used methods. This category of modelisation of the RTE includes three distinct principles: the basis of the process is that the integro-differential equation is replaced by a system of partial differential equations. The different methods are :

- Multi-flux methods: they consist in rendering discrete the angular space into elementary solid angles where the intensity is uniform within.
- Discrete ordinate method (or S_N-approximation): it is based on a discrete representation of the directional variation of the radiative intensity. The RTE is solved choosing a set of discrete directions, the integral terms being approximated by a quadratic sum of intensities.
- Method of spherical harmonics (or P_N-approximation): another technic considering the angular variation of the intensity. Low-order approximation are usually accurate in optically thick media, but accuracy improves slowly for higher-order approximation while mathematical complexity increases extremely rapidly.

Most of these methods are described in details in the book written by Modest [11].

In the present work, a simple two-flux method coupled with a SNB model has been chosen to solve the general RTE. Being aware that at the present time the discrete ordinate method is often used, most of the published works using this last method concern applications for which a linear anisotropic scattering phase function is considered. The aim of this work is to provide a convenient mean to calculate radiation of anisotropically scattering oxide particles encountered in pyrotechnic applications, for which the optical properties are not clearly established. Thus starting with a simple method will lead to a more sophisticated one depending on the adequation between the computations and first experimental results.

PARAMETERS OF THE MODEL

Gaseous Radiation Parameter

Concerning the gaseous band model, tabulated parameters can be used [3]. Narrow-band gas parameters can be also computed using formulations issued from quantic mechanical considerations. The bases of the work undertaken by Grosshandler [7] and the principles of his calculations have been followed, especially for CO_2, CH_4 and CO band modelling [12, 13 & 14]. The bandwidth parameter, the mean line intensity of the lines in the band and the line spacing are determined in order to calculate the absorption coefficient. For H_2O spectroscopic parameters, the tabulated data of [3] have been used. The SLG algorithm is used.

Emission spectra of hydrocarbon based compositions can be calculated by adding the contribution of absorption from soot particles to the gaseous absorption coefficient. The soot absorption coefficient can be obtained from the Rayleigh theory :

$$\kappa_\lambda = \frac{36\pi}{\lambda} \cdot \frac{n \cdot k}{\left(n^2 - k^2 + 2\right)^2 + \left(2 \cdot n \cdot k\right)^2} \cdot f_v \tag{3}$$

Considering that soot optical parameters (n, k) do not vary strongly with wavelength, the following simple correlation can be used:

$$\kappa_\lambda = \frac{C}{\lambda} \cdot f_v \tag{4}$$

with C taken equal to 7.

Particle Radiation Parameters

For most of pyrotechnic combustion applications, the radiating medium may include large size particles for which the extinction and scattering parameters must be known. These parameters (extinction and scattering coefficients, albedo, phase function) can be calculated from Mie theory assuming spherical particles. Mie computations require the knowledge of the complex index of particles. Data concerning this last parameter may be found in literature [15] for aluminium oxide, carbon and magnesium oxide. Unfortunately, the variations of the complex index with wavelength and temperature are not well established and the choice of the appropriate values is difficult.

TWO FLUX METHOD.

Dividing equation (1) by $X = \left[\left(\kappa_\lambda(s) + \sigma_\lambda(s)\right) \cdot s\right]$ leads to:

$$\frac{\partial L_\lambda(s)}{\partial X} = -L_\lambda(s) + (1-a) \cdot L'_\lambda(s) + \frac{a}{4\pi} \cdot \int_{4\pi} P_\lambda(s,s') \cdot L_\lambda(s') d\Omega(s') \tag{5}$$

where X is the optical depth parameter and a the albedo. A two-flux method permits to integrate radiation along a line of sight as it can be done in the absence of scattering. Anisotropic scattering can be considered by introducing two integrated average fractions for forward and backscattering:

$$f = \frac{1}{2} \cdot \int_0^{\pi/2} P(\theta) \sin(\theta) d\theta \tag{6}$$

$$b = \frac{1}{2} \cdot \int_{\pi/2}^{\pi} P(\theta) \sin(\theta) d\theta \tag{7}$$

The two-flux formulation leads to the following system for radiation intensity in the positive and negative direction respectively:

$$\begin{cases} \dfrac{dL^{+}(s)}{dX} = -L^{+}(s) + (1-a)\cdot L^{*}(s) + a\cdot\left[f\cdot L^{+}(s) + b\cdot L^{*}(s)\right] \\ -\dfrac{dL^{-}(s)}{dX} = -L^{-}(s) + (1-a)\cdot L^{*}(s) + a\cdot\left[f\cdot L^{-}(s) + b\cdot L^{*}(s)\right] \end{cases} \quad (8)$$

For an heterogeneous medium, n homogeneous "slabs" can be considered. Then a system of 2n equations should be solved, the radiative intensity being calculated between each "slab" in the positive and negative direction. In general, one of the two bounds intensity is looked for. The algorithm loops on the wavelength to compute a complete emission spectrum in the infrared.

COMPUTATION RESULTS

In order to appreciate the behaviour of the model calculating the emission spectra of hydrocarbon fuels, different sets of data found in the combustion literature have been considered, allowing spectra comparisons.

For the combustion of pyrotechnic compositions, published experimental or theoretical data are quite difficult to find. Consequently, the first computations presented in this paper concern simulations consisting in adding assumed particle oxide (Al_2O_3) concentrations of given size to gaseous concentration profiles.

Computations without scattering

A tentative of validation has been carried out using published experimental results concerning spectral radiant emission from pool fires of various fuels [16]. The given data for the combustion of a 113 mm diameter isooctane pool fire have been selected for computations. Measurements reported in reference [16] were given for two different heights in the flame. We present here a computation concerning data at 20 mm above surface, assuming equal concentration for H_2O and CO_2 because the concentration for H_2O was not directly measured. NO_x concentration was neglected.

Table 1 shows the set of gaseous concentrations. Temperature can be approximated with the curve of [16] which shows its evolution as a function of time. A mean temperature value was then taken to 1600 K. The radiation pathlength for computation has been taken equal to the pool diameter (113 mm). As the soot volume fraction was not easily accessible too, a value of 0.4×10^{-6} has been considered for this parameter, according to a previously reported value for the combustion of isooctane [17].

	Height	CH_4	CO	CO_2	O_2	H_2O
Isooctane	20 mm	14	5	7	0.5	7

TABLE 1 : Gaseous Species Concentration in Flames (% mol)

The results of computation are drawn in Figure 1.

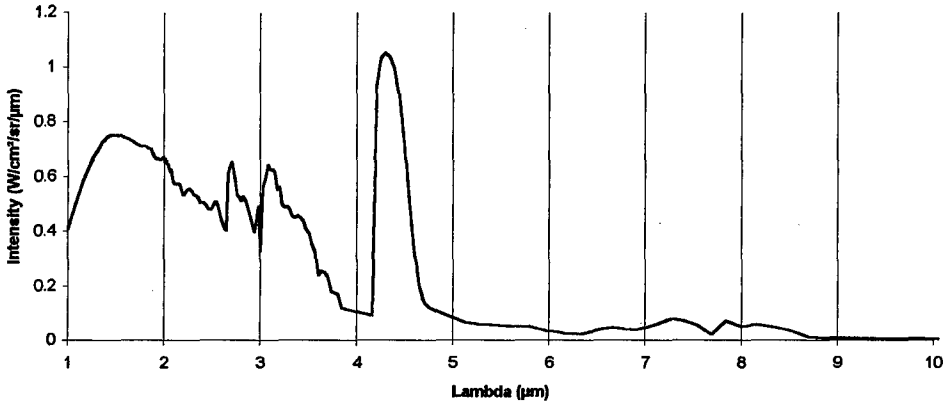

FIGURE 1 : Calculated Emission Spectrum of an Isooctane Flame at 20 mm Height

The main gaseous bands (2.7 µm for H_2O, 2.7 and 4.3 µm for CO_2 and 3.3 µm for CH_4) can be identified in Figure 1. The computed spectrum agrees quite well both on qualitative and quantitative level with the experimental time-mean spectrum from reference [16] and reported in Figure 2. The high emission level for shortest wavelengths in Figure 1 leads to think that soot concentration has been probably overestimated in our calculations.

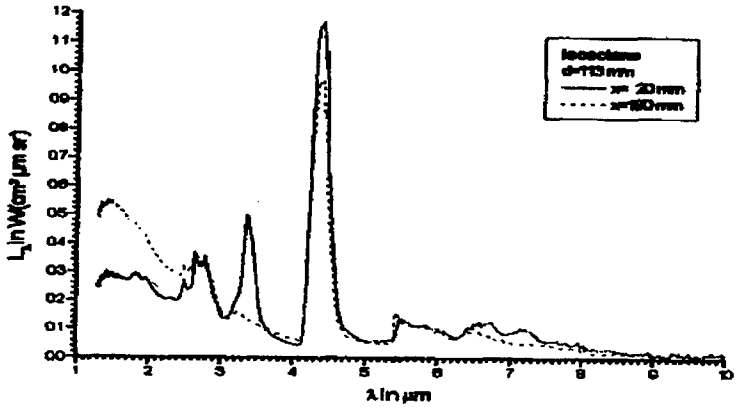

FIGURE 2 : Emission Spectrum Measured in Reference [16]

Computations including scattering

Computations have been made on a simulated 1 m diameter fire containing CO_2, H_2O and soot considered by Grosshandler [7]. The simple radial profile for concentrations and temperature can be seen in Table 2 (soot has been removed in our simulation).

Dist. (m)	T (K)	CO_2 (kPa)	H_2O (kPa)	N_2 (kPa)
0.05	899	7.07	7.07	86.8
0.1	1158	10	10	81
0.2	1438	13.1	13.1	74.7
0.3	1637	15.4	15.4	70.3
0.5	1770	16.1	16.1	67.3
0.7	1637	15.4	15.4	70.3
0.8	1438	13.1	13.1	74.7
0.9	1158	10	10	81
0.95	899	7.07	7.07	86.8

TABLE 2 : Temperature and Gaseous Concentration Profile.

In a first step, we have calculated the spectral radiant intensity distribution resulting from gaseous pathlength of TABLE 2. In a second step, an uniform concentration of Al_2O_3 have been introduced (1 µm diameter) in the preceding simulated profile in order to study the influence of scattering.

Two spectral calculations have been performed considering two different values for Al_2O_3 volume fraction : $0.5x10^{-6}$ and $2x10^{-6}$. The results can be observed on Figure 3 and 4; on both figures, the comparison with gaseous spectrum is made to display the influence of scattering.

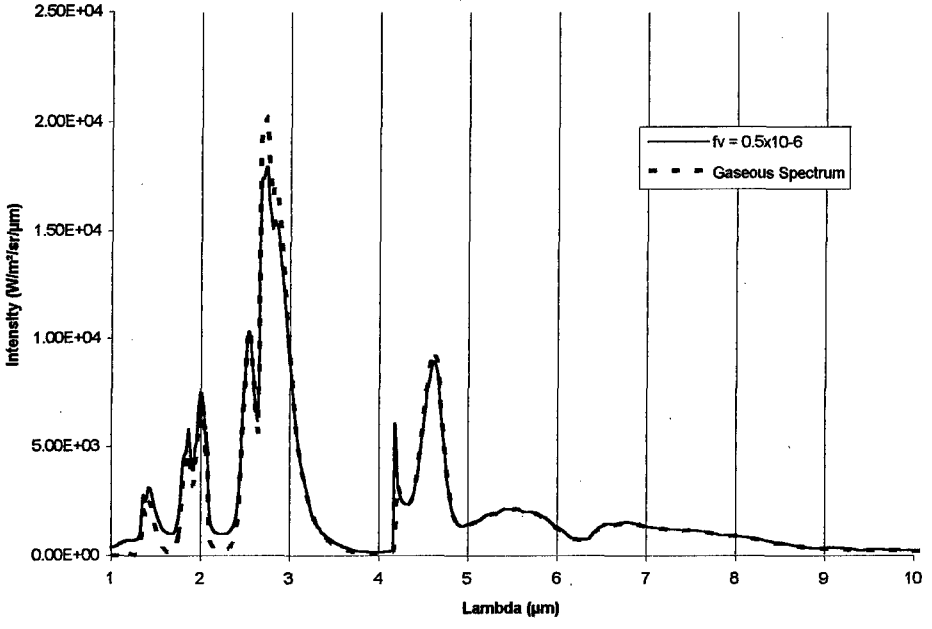

FIGURE 3 : Effect of Scattering with a Low Al_2O_3 Concentration

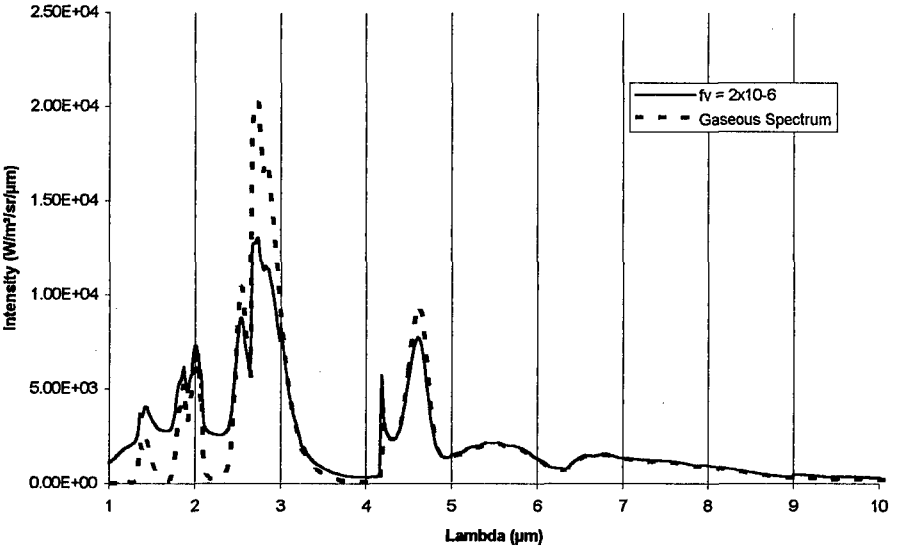

FIGURE 4 : Effect of Scattering with a Higher Concentration of Al_2O_3

The effects of scattering are much more marked when the concentration of Al_2O_3 is more important. It can be seen on Figure 4 that particles give a contribution to emission in regions where gases do not emit and absorb (especially in the short wavelengths region). On the contrary, the radiative intensity is lowered in band regions (especially around 2.7 µm) because a part of energy emitted by gases is scattered by particles.

CONCLUSIONS

We have presented in this report the first computation results concerning hydrocarbon fires and simulated pyrotechnic flames. A model has been completed to compute the radiative emission spectra for these two types of combustions. The computations for hydrocarbon fuels show a satisfying agreement with experimental published data. Concerning pyrotechnic combustion, we hope to undertake a deeper prospecting in literature and to carry out some tests in order to validate the first results presented here. We intend also to study the effects of the data choice for particles optical properties on the emission spectrum computation.

REFERENCES

1- "A Physico-Mathematical Model of Rocket Exhaust Plumes" - E.I. Vitkin, V.G. Kirillov, A.S. Suprun & Ju. V. Khadyra - Int. J. of Heat & Mass Transfer, Vol. 40, n°5, pp 1127-1241 (1996).

2- "Radiation Emitted from Rocket Plumes" - L. Deimling, W. Liehman, N. Eisenreich & W. Eckl - Propellant, Explosives & Pyrotechnics 22, 152-155 (1997).

3- "Handbook of Infrared Radiation from Combustion Gases" - C.B. Ludwig, W. Malkmus, J.E. Reardon & J.A.L. Thomson - NASA SP-3080 (1973)

4- Ph. Rivière, D. Scutaru, A. Soufiani, J. Taine - Proc. 10th Int. Heat Transfer Conf., Vol. 2, Brighton (1994).

5- "Correlated-k Fictitious Gas Model for H_2O IR Radiation in the Voigt Regime" - Ph. Rivière, A. Soufiani, J. Taine - J. Quant. Spectrosc. Radiat. Transfer, Vol. 53, n°3, pp 335-346 (1995)

6- "Radiative Transfer and Interaction with Conduction and Convection" - M.N. Ozisïk - New York : J. Wiley & Sons (1973)

7- "A Narrow Band Model for Radiation Calculations in a combustion environment" - W. L. Grösshandler - Fire Sci. Div. Natl. Stand. Technol. (BFRL), NIST/TN-1402 (1993)

8- "The Radiative Transfer of Gas in a Three-Dimensional System Calculated by Monte-Carlo Method" - H. Taniguichi - Bull. of the Japan Society of Mechanical Engineers, Vol. 12, pp. 67-68 (1969)

9- "The Calculation of Radiative Heat Flux in a Cylindrical Furnace Using the Monte-Carlo Method" - F.R. Steward, P. Cannon - Int. J. of Heat & Mass Transfer, Vol. 14, n°2, pp. 245-262 (1971)

10- "Radiative Transfer" - H.C. Hottel, A.F. Sarofim - New York : Mc Graw-Hill (1967)

11- "Radiative Heat Transfer" - Michael F. Modest - Mc Graw-Hill (1993)

12- "The Spectral and Total Emissivity of Carbon Dioxide" - B. Leckner - Combustion & Flame, Vol. 17, pp. 27-44 (1971)

13- "Thermal Radiation of Methane Gas" - Ind. Eng. Chem. Fundamentals 3, pp. 167-176 (1964)

14- "Infrared Emissivity of Diatomic Gases for the Anharmonic Vibrating-Rotator Model" - W. Malkmus, A. Thomson - JQSRT 2, 17 (1961)

15- "Handbook of The Infrared Optical Properties of Al_2O_3, Carbon, MgO & ZrO_2" - SAMSO, El Segundo, Calif. SAMSO-TR-75-131, Vols. I and II (June 1975)

16- "Spectral Emission from Pool Fires of Various Fuels Considering Transient Structures" – V. Weiser, M. Weindel, A. Hoffman, N. Eisenreich - 26th International Annual Conference of ICT, Karlsruhe (Germany), p 79-1,79-9 (1995).

17- "Carbon Particulate in Small Pool Fire Flames" - S. Bard, P.J. Pagni - J. of Heat Transfer, Transactions of the ASME, Vol. 103, pp. 357-362 (1981).

A NEW ASPECT OF RELATIONS BETWEEN DIFFERENTIAL THERMAL ANALYSIS DATA AND THE DETONATION CHARACTERISTICS OF POLYNITRO COMPOUNDS.

Svatopluk ZEMAN

Department of Theory and Technology of Explosives, University of Pardubice,
CZ-532 10 Pardubice, The Czech Republic
fax: 00420 40 603 8024 *E-mail: svatopluk.zeman@upce.cz*

ABSTRACT: An attempt is made to explain previously published relationships between the DTA data and detonation characteristics of polynitro compounds in terms of the entropy of their thermolysis onsets. It is concluded that primary fragmentation of these compounds in their detonation is most likely identical with the primary fragmentation in their low-temperature thermolysis.

Recently the non-isothermal differential thermal analysis (DTA) was realized in the case of polynitroarenes [1-7], nitramines [8], nitrosamines [8], and nitrate esters [8] with the evaluation of the corresponding records by the method of Piloyan [9] modified in the sense of refs. [2,3,10] - see. Figs. 1 and 2. The values of activation energies $\mathbf{E_p}$ following from these measurements for the low-temperature intervals immediately at the beginning of thermal decomposition $\mathbf{T_D}$ corresponded to the non-autocatalyzed start of thermolysis: this is documented by the existence of relationships between the values of $\mathbf{E_p}*\mathbf{T_D}^{-1}$ ratios and the characteristics of molecular structure, namely the moments of inertia of alkyl groups in N-alkyl-2,4,6-trinitroanilines [2,10] or the R_M factors in paper chromatography of N-alkyl- and N,N-dialkyl-polynitroanilines [2,11-13]. From what has been given it then appears logical that there also exist relationships between the values of $\mathbf{E_p}*\mathbf{T_D}^{-1}$ ratios and the values of Arrhenius parameters resulting from application of the Soviet manometric method (SMM) to studies of thermolysis of polynitroarenes [1,3-6]. With regards to the homolytic nature of primary fragmentations in the thermolysis of organic polynitro compounds (in general) the values of activation energies $\mathbf{E_p}$ and decomposition onsets $\mathbf{T_D}$ depend also on the construction materials which are in contact with the substance thermolyzed [10]. More definite dependencies result from the DTA method where the sample thermolyzed is in contact with glass [14] - the method

was called „method B" in refs. [1-7,10-14]. That is why this paper adopts the results of DTA measurements of this type.

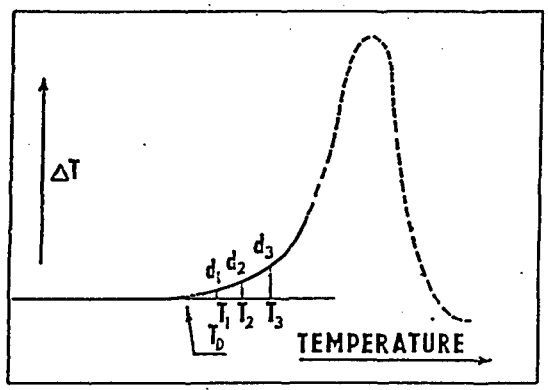

Figure 1: A modified Piloyan method of the DTA-curve treatment [2,3,10].

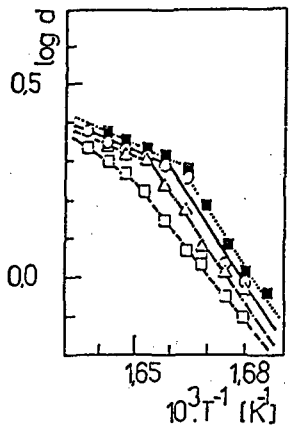

Figure 2: An linearization of the initial part of the exotherm of TPT according to the modified Piloyan method (*taken from ref.* [3]).

The physical meaning of $E_p*T_D^{-1}$ expression can be specified by using the definition equation of activation enthalpy of an endothermic reaction:

$$\Delta H^{\neq} = E_p - T_m*R \qquad (1)$$

where T_m is the mean temperature of the temperature interval for E_p. A modification then leads to:

$$(\Delta H^{\neq}/T_D) = \Delta S_{pt} = E_p*T_D^{-1} - (T_m*T_D^{-1})*R \qquad (2)$$

where ΔS_{pt} can be referred to as the entropy of thermolysis onset. With respect to magnitude of those values and experimental error in determination of E_p the value of expression $(T_m/T_D)*R$ (*from 8.4 to 8.5 J.mol^{-1}K^{-1}*) has an only slight mathematical meaning. Therefore,

in the first rough approximation, the expression $E_p*T_D^{-1}$ can be considered a representative of the above-mentioned entropy.

Mutual comparison of the $E_p*T_D^{-1}$ values with the corresponding characteristics of detonation of polynitroarenes and their derivatives valid for the maximum theoretical crystal densities (TMD, *i. e. for a monocrystal*) has led to the following general relationship [14]:

$$\ln(E_p/T_D) = a*X + b \qquad (3)$$

where X can be square of detonation velocity, D^2, or the heat of detonation, Q, or the ratio of detonation pressure P_{CJ} and density ρ of the given nitro compound, $P_{CJ}*\rho^{-1}$.

A graphical representation of relationship 3 for polynitroarenes and for $X = P_{CJ}.\rho^{-1}$ is given in Fig. 3, that for nitrosamines, nitramines and nitric esters in Figs. 4 ($X = D^2$) and 5 ($X = Q$). The last picture given adopts the theoretical heats of explosion (Q_{max}) calculated by method of Kamlet & Jacobs [15] as well as the values Q_p calculated by means of the semiempirical relationships by Pepekin et al. [16] to give the real experimental values.

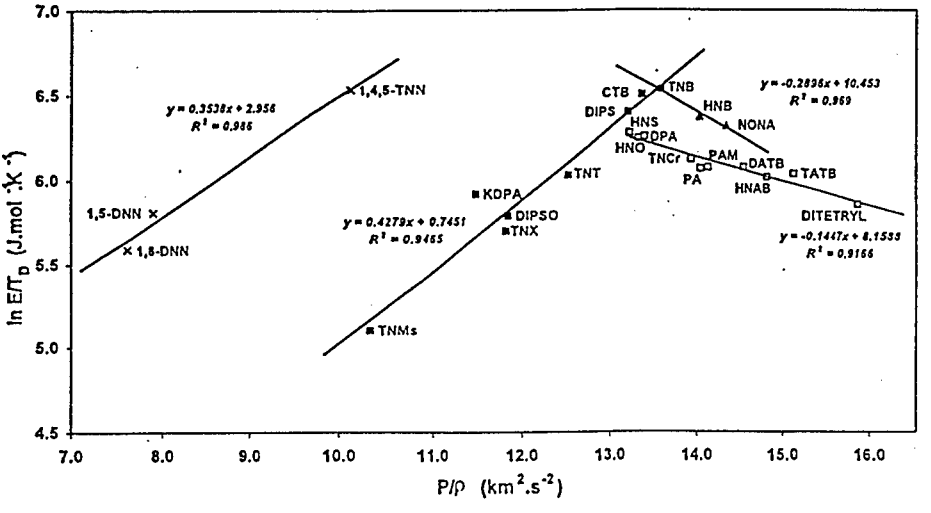

Figure 3: Graphic representation of the relationship 3 for $X = P_{CJ}*\rho^{-1}$ (*constructed on the basis of E_p and T_D values which were taken from ref. [14]*).

Substances studied in the sense of Fig. 3 and Table 2 (*substance - code design.*):
1,3,5-Trinitrobenzene- **TNB**, 1-Methyl-2,4,6-trinitrobenzene- **TNT**, 1,3-Dimethyl-2,4,6-trinitrobenzene- **TNX**, 1,3,5-Trimethyl-2,4,6-trinitrobenzene - **TNMs**, 1-Amino-2,4,6-trinitrobenzene- **PAM**, 1,3-Diamino-2,4,6-trinitrobenzene- **DATB**, 1,3,5-Triamino-2,4,6-trinitrobenzene - **TATB**, 1-Chloro-2,4,6-trinitrobenzene- **CTB**, 1-Hydroxy-2,4,6-trinitrobenzene-**PA**, 1-Hydroxy-3-methyl-2,4,6-trinitrobenzene-**TNCr**,1,5-Dinitronaphthalene - **1,5-DNN**, 1,8-Dinitronaphthalene - **1,8-DNN**, 1,4,5-Trinitronaphthalene - **1,4,5-TNN**, 1,4,5,8-Tetranitro-naphthalene-**TENN**, 1,3-bis(Methylnitramino)-2,4,6-trinitrobenzene- **Ditetryl**, 2,2',4,4',6,6'-Hexanitrobiphenyl-**HNB**, 2,2',4,4',6,6'-Hexanitrodiphenylsulfide - **DIPS**, 2,2',4,4',6,6'-Hexanitrodiphenylsulfone - **DIPSO**, 2,2',4,4',6,6'-Hexanitrodiphenylamine - **DPA**, Potassium 2,2',4,4',6,6'-hexanitrodiphenylaminate - **KDPA**, 2,2',4,4',6,6'-Hexanitrostilbene - **HNS**, 2,2',4,4',6,6'-Hexanitroazobenzene - **HNAB**, 2,2',4,4',6,6'-Hexanitro-oxanilide - **HNO**, 2,2',2'',4,4',4'',6,6',6''-Nonanitro-m-terphenyl - **NONA**, 2,4,6-tris(2,4,6-Trinitrophenyl-amino)-1,3,5-triazine - **TPM**, 2,4,6-tris(2,4,6-Trinitrophenyl)-1,3,5-triazine - **TPT**.

A more detailed analysis [14] of the relationship 3 shows that classification of polynitroarenes in the sense of Fig. 3 is given [14] by thermochemical factors, and beside that, by steric conditions and electron configuration in the ground state of the reaction centre of the molecule. In this context, by the reaction centre is meant the grouping of atoms and/or functional groups in the molecule whose mutual chemical interaction initiates the thermal decomposition of this molecule at the given experimental conditions.

Relationship 3 can also be applied to the specification of the centre of primary thermolysis in the molecule, e.g. participation of hydroxyl group in the primary splitting in the case of trinitro-m-cresol (TNCr).

Figures 4 and 5 document the validity of relationship 3 also for nitramines, nitrosamines and nitric esters [8], and it has been proved that the correlation is much closer for $X = D^2$ than for $X = Q$.

A significant generalization of relationship 3 was achieved by Bhide et al. who extended it to the thermolysis of a mixed explosives of hexolite type [17]: these authors applied here both the calculated and the experimental D values. Similarly, in works by Prabhakaran et al. [18] or Makashir &Kurian [19], relationship 3 is applied to the thermal decomposition of nitrosamines, nitramines, nitrates of quanidine derivatives and other energetic materials.

In connection with the findings quoted [i.e. refs. 8,14,17-20], Thesis [20] has checked the validity of relation 3 for $X = P_{CJ}*\rho^{-1}$ (see Fig. 3) and the ρ values lower than TMD (examples see in Table 1): on transition from a monocrystal to lower charge densities the fit of correlation in the sense of the relationship mentioned markedly decreases. A likely reason can lie in the comparison of thermolysis characteristics of crystals and/or melt (*i.e. undiluted substances*) with the explosive characteristics of the „as-if diluted" polynitroarenes (*the*

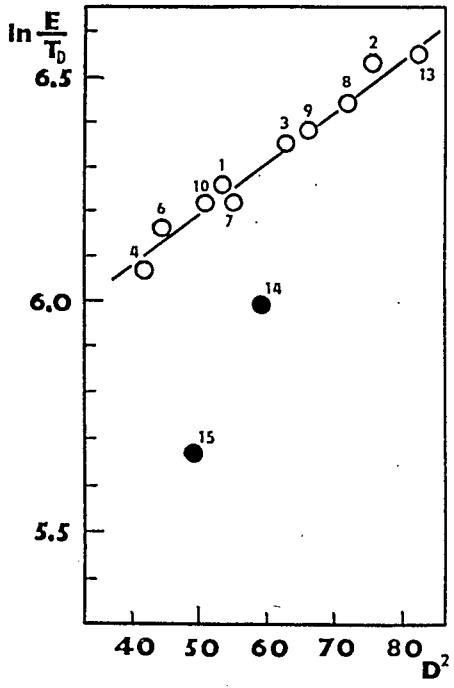

Figure 4: Graphic representation of the relationship 3 for $X = D^2$ and for nitramines, nitrosamines, and nitric esters (*taken from ref. [8]*).

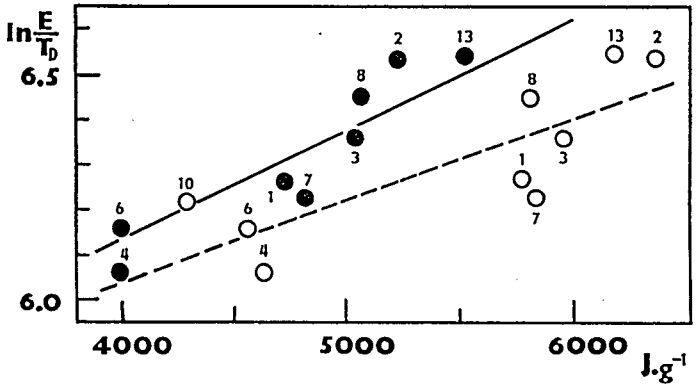

Figure 5: Graphic representation of the relationship 3 for X = Q and for nitramines, nitrosamines, and nitric esters (*taken from ref. [8]*):
points ● correspond to Q_p values
points ○ correspond to Q_{max} values

Substances studied in the sense of Figs. 4 and 5 (*substance - No.*):
1,1,1-Trimethylolpropan trinitrate - **1**, Pentaerythritol tetranitrate - **2**, Dipentacrythritol hexanitrate - **3**, ,4-Dinitroso-1,4-diazacyclohexane - **4** 1,5-Endomethylene-3,7-dinitroso-1,3,5,7-tatraazacyclooctane - **6**, 1,3,5-Trinitroso-1,3,5-triazacyclohexane - **7**, 1,4-Dinitro-1,4-diaza-cyclohexane - **8**, 1,4-Dinitrotetrahydroimidazo[4,5-d]imidazol-(1H,3H)dione - **9**, 1,5-Endomethylene-3,7-dinitro-1,3,5,7-tetraaza-cyclooctane - **10**, 1,5-Diacetyl-3,7-dinitro-1,3,5,7-tetraazacyclooctane - **11**, 1,3,5-Trinitro-1,3,5-triazacyclohexane - **12**, 1,3,5,7-Tetranitro-1,3,5,7-tetraazacyclooctane - **13**, 2,2,3,3-Tetranitrobutane - **14** Monomethylamonium nitrate - **15**.

theoretical increase in the number of all possible realization of molecules in space which should be different for different molecular structures). The facts given signalize **the significance of entropy** in evaluation the mutual relationships between properties of an explosive system (in general) and its explosive characteristics. On this basis, Prof. Urbanski [21] tried to interpretation the temperature dependence of impact sensitivity of TNT and the detonation velocity of two-component explosives, but this work [21] remained at the stage of a short communication.

On the basis of what has just been said and with regard to relationship 2 a relationship was derived [20] in the following general form:

$$\Delta S_{pt} = \alpha * \ln X + \beta \qquad (4)$$

where X can be either $P_{CJ}*\rho^{-1}$ or the heat of explosion, Q. In the sense of this relationship (for $X = P_{CJ}*\rho^{-1}$), polynitroarenes of Fig. 3 were reclassified [20] - resulting groups are presented in

Table 1: Coefficients of the relationship 3 for a transition from TMD to lower charge densities of some polynitroarenes - for $X = P_{CJ}*\rho^{-1}$ [20] (*corresponding E_p and T_D values taken from ref. [14]*).

Group of polynitroarenes	% TMD	Coefficient a	b	r^2
TATB, DATB, PAM, PA, HNO, HNS, HNAB, DPA, TNCr, Ditetryl	**100**	-0.1447	8.1588	**0.9166**
	95	-0.1246	7.7714	0.7777
	90	-0.1296	7.7514	0.7490
	85	-0.1397	7.7770	0.7722
TNB, HNB, NONA	**100**	-0.2896	10.4530	**0.9690**
	95	-0.5070	13.1980	0.7670
	90	-0.5309	13.1410	0.7579
	85	-0.5778	13.3310	0.7555

Table 2. Compositions of the groups are almost identical with those defined by modified relationship of Evans-Polanyi-Semenov [20] (*i.e. by the relationship between activation energies of low-temperature thermolysis from SMM and heats of detonation of polynitro compounds* [22]). The nitramines, nitrosamines and nitric esters from Fig. 4 correspond to a

single form of relationship 4 [20]. Also here a transition from a monocrystal to lower charge densities causes an abrupt decrease in the correlation fit (see in Table 2).

In the context of interpretation of the meaning of relationship 3 the following opinion was published in 1981 [23]: A stable detonation is characterized by constant parameters, i.e. constant detonation velocity, detonation pressure, and detonation energy throughout this explosion transformation. That means a constant production of fragments and/or radicals in the primary fragmentation processes at the shock compression of that particular explosive throughout the detonation time, which must be characterized by a constant chemical mechanism of the whole process. Similarly, constant chemical mechanisms and their relative

Table 2: Coefficients of the relationship 4 - for $X = P_{CJ}*\rho^{-1}$ [20] *(corresponding E_p, T_m, and T_D values taken from ref. [14])*.

Group of polynitroarenes	% TMD	Coefficient α	β	r^2
TNB, HNB, NONA, HNAB	**100**	-3063.70	8681.9	**0.9729**
	95	-3987.10	10950.0	0.9468
	90	-4051.20	10901.0	0.9364
	85	-4022.60	10599.0	0.9351
PAM, DATB, TATB	**100**	-259.18	1122.6	**0.8210**
	95	-221.19	1008.7	0.7552
	90	-167.84	860.7	0.4763
HNS, HNO, DPA, TNCr, PA, PAM	**100**	-1540.70	4508.7	**0.9873**
	95	-713.30	2299.1	0.3602
	90	-702.90	2235.6	0.3379
TNT, TNX, TNMs, CTB, DIPS, DIPSO, KDPA	**100**	1858.50	-4228.1	**0.8832**
1,5-DNN, 1,8-DNN, 1,4,5-TNN	**100**	1445.70	-2667.8	**0.9994**
	95	1447.10	-2596.8	0.9996
	90	1447.10	-2596.8	0.9946
	85	1454.40	-2451.1	0.9989
TPM, TENN, TPT	**100**	1443.20	-3234.4	**0.9939**
	95	3486.00	-8266.2	0.7522
	90	3672.00	-1295.8	0.1027

ratios in mutual interaction of fragments and/or radicals must be present in the zone of throughout the detonation time, which must be characterized by a constant chemical mechanism of the whole process. Similarly, constant chemical mechanisms and their relative ratios in mutual interaction of fragments and/or radicals must be present in the zone of chemical reaction of the detonation wave. From these conditions of stable detonation it follows that e.g. the heat of reaction of the primary splitting processes must be regularly related to the overall reaction (*explosion*) heat. If the thermochemical kinetic characteristics of primary fragmentation processes in low-temperature non-autocatalyzed thermolysis of explosives correlate with the reaction heat of detonation transformation, then it in an identity of, or a regular context between, the primary mechanism of a low-temperature and a detonation reactions. The opinion presented is, however, in a better correspondence with relationship 4 (*see ref. [20]*).

The identity of the primary mechanisms of low-temperature and detonation reactions of polynitro compounds is also confirmed by the most striking pieces of experimental evidence. First of all they include the evidence (*obtained with the help of XPS*) of primary splitting of N-NO_2 bond in 1,3,5-trinitro-1,3,5-triazacyclohexane (RDX) exposed to a shock wave [24] (*homolysis of this bond is the primary step of thermolysis of nitramines in general*). On the basis of deuterium kinetic isotope effect (DKIE) it was proved [25] that the rate-limiting step of thermolysis of TNT (*in condensed state*) and that of initiation of its detonation are identical. It is also possible to give the evidence provided by furoxanes and furazanes in the XPS spectrum of TATB exposed to shock [26,27] (*the pyrolysis of ortho-nitroaniline is a method of synthesis of benzofurazane [28], in the case of DATB this reaction leads to 4-amino-5,7-dinitrobenzofurazane [29]*).

The said identity is, however, in far the best correspondence with the modified Evans-Polanyi-Semenov equation [20] (*it might determine the bond which is the first split in detonation - preliminary study see ref. [22]*). Thesis [20] gives more detail analysis of the above-mentioned facts and also of other relations between thermal reactivity and the detonation characteristics of polynitro and polynitroso compounds, taking ito account some newest findings due especially to Prof. Dremin in the field of detonation theory [30, 31]. The following conclusion resulted from this analysis [20]:

The primary fragmentation of polynitro and polynitroso compounds in their detonation transformation proceeds at milder conditions than those present at the front of detonation wave or in its reaction zone. That means that the detonation transformation

itself of the given substance should be preceded by an induction period. The course of the fragmentation mentioned is not random but is characterized by a chemical mechanism which is most likely identical with that of the primary fragmentation of the compounds given in their low-temperature thermolysis.

It must be stated here that this primary fragmentation is not probably thermally initiated: the newest findings confirm that explosives sensitivity to shock and impact is related to electronic excitation of their molecules by both these mechanical stimuli (*e.g. see refs. [27,30, 32-34]*).

REFERENCES

[1] S. Zeman: *Thermal Stabilities of Polynitroaromatic Compounds and their Derivatives.* Thermochim. Acta **31**, 269-283 (1979).

[2] S. Zeman: *Thermostable Polynitro Arenes.* Ph.D. Thesis, Univ. Pardubice, June 1973.

[3] S. Zeman: *Possibilities of Applying the Piloyan Method of Determination of Decompn. Activation Energies in the Differential Thermal Analysis of Polyniroaromatic and of their Derivatives: Part I. Polymethyl and Polychloro Derivatives of 1,3,5-Trinitrobenzene.* J. Thermal Anal. **17**, 19-29 (1979).

[4] S. Zeman: *dtto [3], Part II. Polyamino and Polyhydroxi Derivatives of 1,3,5-Trinitrobenzene.* J. Thermal Anal. **19**, 99-105 (1980).

[5] S. Zeman: *dtto [3], Part III. Derivatives Containing Two Picryl Groups in the Molecule and Melamine Derivatives.* J. Thermal Anal. **19**, 107-115 (1980).

[6] S. Zeman: *dtto [3], Part IV. 1,3,5-Trinitrobenzene, 2,2',4,4',6,6'-Hexanitrobiphenyl, 2,2',2'',4,4',4'',6,6',6''-Nonanitro-m-terphenyl, 1,4,5,8-Tetranitronaphthalene and 2,4,6-Tripicryl-1,3,5-triazine.* J. Thermal Anal. **19**, 207-214 (1980).

[7] S. Zeman: *dtto [3], Part VIII. Polynitro Derivatives of Toluene and Naphthalene.* Thermal Anal. **21**, 9-14 (1981).

[8] S. Zeman, J. Fedak and M. Dimun: *The Relationship Between Differential Thermal Analysis Data and the Detonation Characteristics of Thermodynamically Unstable Aliphatic Series Compounds.* Zbornik Radova (Coll. Papers, Tech. Fac. Bor) **18**, 119-135 (1982).

[9] G. O. Piloyan, I. D. Ryabchikov and O. S. Novikova: *Determination of Activation Energies of Chemical Reactions by Differential Thermal Analysis.* Nature **212**, 1229 (1966).

[10] S. Zeman: *Non-Isothermal Differential Thermal Analysis in the Study of the Initial Stage of the Thermal Decomposition of Polynitroaromatic Compounds in the Condensed State.* Thermochim. Acta **39**, 117-124 (1980).

[11] S. Zeman and E. Zemanova: *dtto [3], Part V. The Relationship Found Between Chromatographic and Thermal Analysis Data of N-Substituted 2,4-Dinitroanilines.* J. Thermal Anal. **19**, 417-424 (1980).

[12] S. Zeman and E. Zemanova: *dtto [3], Part VI. The Relationship Found Between Chromatographic and Thermal Analysis Data of N-Substituted 2,6-Dinitroanilines.* Thermal Anal. **20**, 87-92 (1981).

[13] S. Zeman and E. Zemanova: *dtto [3], Part VII. The Relationship Found Between Chromatographic and Thermal Analysis Data of N-Substituted 2,4,6-Trinitroanilines.* Thermal Anal. **20**, 331-337 (1981).

[14] S. Zeman: *The Relationship Between Differential Thermal Analysis Data and the Detonation Characteristics of Polynitroaromatic Compounds.* Thermochim. Acta **41**, 199-212 (1980).

[15] M. J. Kamlet and S. J. Jacobs: *Chemistry of Detonation: Simple Method of Calculation Detonation Properties of CHNO Explosives.* J. Chem. Phys. **48**, 23-29 (1968).

[16] V. I. Pepekin. M. N. Makhov and Yu. A. Lebedev: *Teploty vzryvchatogo razlozheniya individualnykh VV.* Dokl. Akad. Nauk SSSR **232**, 852 (1977).

[17] N. M. Bhide, S. R. Naidu, E. M. Kurian and K. R. K. Rao: *Kinetics of Initial Thermal Decomposition and Detonation Parameters Studies on RDX:TNT System.* J. Thermal Anal. **35**, 1181-1189 (1989).

[18] K. V. Prabhakaran, N. M. Bhide and E. M. Kurian: *XRD, Spectroscopic and Thermal Analysis Studies on trans-1,4,5,8-tetranitrosotetraazadecalin (TNSTAD).* Thermochim. Acta **220**, 169-183 (1993).

[19] P. S. Makashir and E. M. Kurian: *Spectroscopic and Thermal Studies on the Decompn. of 1,3,5-Triamino-2,4,6-trinitrobenzene (TATB).* Thermal Anal. **46**, 225-236 (1996).

[20] S. Zeman: *The Study of Chemical Micromechanism Governing Detonation Initiation of Organic Polynitro and Polynitroso Compounds.* D.Sc. Thesis, Inst. of Chemical Technology, Prague, Sept. 1997.

[21] T. Urbanski: *On Entropy and Free Energy of Explosives (preliminary communication).* Bull. L'Acad. Polonaise Sci., Ser. Sci. Chim., **28**, 511-513 (1980).

[22] S. Zeman, M. Dimun and S. Truchlik: *The Relationship Between Kinetic Data of the Low-Temperature Thermolysis and the Heats of Explosion of Organic Polynitro Compounds.* Thermochim. Acta **78**, 181-209 (1984).

[23] S. Zeman: *Kinetic Data from Low-Temperature Thermolysis in the Study of the Microscopic Initiation Mechanism of the Detonation of Organic Polynitro Compds.* Thermochim. Acta **49**, 219-246 (1981).

[24] F. J. Owens and J. Sharma: *X-Ray Photoelectron Spectroscopy and Paramagnetic Resonance Evidence for Shock-Induced Intramolecular Bond Breaking in some Energetic Solids.* J. Appl. Phys. **51**, 1494 - 1497 (1980).

[25] S. Bulusu and J. R. Autera: *Initiation Mechanism of TNT: Deuterium Isotope Effect as an Experimental Probe.* J. Energ. Mater. **1**, 133 - 140 (1983).

[26] J. Sharma, J. W. Forbes, C. C. Coffey and T. P. Liddiard: *The Physical and Chemical Nature of Sensitization Centers Left from Hots Spots Caused in Trinitrotriaminobenzene by Shock or Impact.* J. Phys. Chem. **91**, 5139 -5144 (1987).

[27] J. Sharma: *Chemistry of Energetic Materials under Shock Caused via Electronic Excitation.* in S. C. Schmidt, R. D. Dick, J. W. Forbes and D. G. Tasker (Eds.): *Shock Compression of Condensed Matter*, Elsevier Sci. Publ. B. V., 1992, p. 639-645.

[28] J. M. Prokipcak, P. A. Forte and D. D. Lennox: *Thermal Decomposition of Alkyl-(o-nitrophenyl)carbamates: A Novel Synthesis of Benzofurazan.* Canad. J. Chem **47**, 2482-2484 (1969).

[29] T. P. Hobin: *Some Aminodinitro Derivatives of Benzofurazan and Benzofurazan Oxide.* Tetrahedron **24**, 6145-6148 (1968).

[30] A. N. Dremin: *Shock Discontinuity Zone Effect: the Main Factor in the Explosive Decomposition Detonation Process.* In J.E. Field and P.Gray (Eds.): *Energetic Materials* Phil. Trans. R. Soc. Lond. **A 339**, 355-364 (1992).

[31] V. Yu. Klimenko, M. A. Yakovencev and A. N. Dremin: *Mnogoprotsessnaya model' detonatsii* Khim. Fizika **12**, 671-680 (1994).

[32] F. Williams: *Electronic States of Solid Explosives and Their Probable Role in Detonations.* In : Hirschfelder (Ed.): *Chemical Dynamics*, J. Wiley and Sons, 1971, pp 289-302.

[33] J. J. Gilman: *Chemical Reactions at Detonation Fronts in Solids.* Phil. Magazine B **71**, 1057-1068 (1995).

[34] R. N. Mulford, J. J. Dick and D. R. Pettit: *Shock Initiation of Penterythritol Tetranitrate Crystals: Optical Absorption and Emission Studies.* In S. C. Schmidt, R. D. Dick, J. W. Forbes and D. G. Tasker (Eds.): *Shock Compression of Condensed Matter 1991,* Elsevier Sci. Publ. B. V., 1992, pp. 725-728.

EVALUATION OF THERMOCHEMICAL PARAMETERS OF SOME ENERGETIC MOLECULES.

Vladimir G. Prokudin

Institute of Chemical Physics Research
(Institute of Chemical Physics in Chernogolovka)
Russian Academy of Sciences,
142432 Chernogolovka, Moscow Region, Russian Federation.
Fax: +007 (096) 515 3588 E-mail: prokud@icp.ac.ru

Abstract

Kinetic data on thermal decomposition reactions, generating 1,3-dipoles [named due to R.Huisgen] or including intermediate ones, create unique possibilities of the numerical estimations of thermochemical parameters of that highly reactive molecules or thermochemical increments for their fragments. Up to now there is a deficiency of such data on heat formations and bond energies for azides, nitriloxides and etc.

Using known data and obtained kinetic information for recyclization of dimethylfurazan and dimethylfuroxan the bond energy for N-->O in alkylnitriloxides was evaluated. The scheme of evaluation and the values of bond energy are discussed.

Using thermochemical and kinetic data for monomolecular thermal decomposition of 1,5- and 2,5-disubstituted tetrazoles the increments of heat formations of groups $\Delta_fH°[C_d-(C)(N_3)]$, $\Delta_fH°[C_d-(C_b)(N_3)]$ and $\Delta_fH°[C_d-(C_d)(N_3)]$ [according to additivity rules by S.Benson] were evaluated. The scheme of evaluation, the values of increments and obtained heats of formation for some azides are discussed.

***

Activation energy E of thermal decomposition reaction, that rate is controlled by stage of weakest σ-bond breaking, as, for example, for many C-NO_2 compounds, practically equial strength bond $D(R_1\text{-}R_2)$, calculated from equation:

$$E \cong D(R_1\text{-}R_2) = \Delta H_f^\circ(R_1) + \Delta H_f^\circ(R_2) - \Delta H_f^\circ(R_1R_2),$$

where ΔH_f° - enthalpies of formation. Here and below data correspond to standard conditions in gas phase.
This simple equation is correct under small activation energy for reverse recombination of radicals into initial molecule, and often is used for calculating of enthalpies of radicals formation [1].

In 1963 year R. Huisgen [2] represent the definition of 1,3-dipolar molecule and 1,3-dipolar cycloaddition reactions, i.e. reaction of formation of heterocyclic compound due to interaction between 1,3-dipole and dipolarophile. Now huge number of papers is devoted to reactions of this kind. In the meantime, data, especially thermochemical parameters for 1,3-dipoles, remain difficult of access due to their high reactivity.

For multicentered heterocycle decomposition reaction **1** (cycloreversion, reaction retro-1,3-dipolar cycloaddition) and for reverse reaction **-1,** that is really 1,3-dipolar cycloaddition, can be written equation (in terms of workability of detailed equilibrium principle [3])

$$\Delta H_f^\circ(\text{heterocycle}) + E_1(\text{cyclodecomposition}) = E_{-1}(\text{cycloreversion}) + \Delta H_f^\circ(\text{1,3-dipole}) + \Delta H_f^\circ(\text{dipolarophile}) \qquad (*)$$

We use such equation (*) for estimation of enthalpy of formation nitriloxides - 1,3-dipolar compounds, so often these energetic compounds have high reactivity.

For irreversible cycle opening (reaction 1) in tetramethylenefurazan (TMF)

$$TMF \Rightarrow NC\text{-}(CH_2)_4\text{-}CNO$$

experimental activation energy E_1=44.1 Kcal/mol [4].
Enthalpy of tetramethylenefurazan formation must be near equal to value for tetramethylenefuroxan, known from [5], ΔH_f°=22.3 Kcal/mol because bond strength N->O in furoxans D(N->O)≈60 Kcal/mol [6]. From [7] the experimental activation energy E_{-1}=21.1 Kcal/mol is known for 1,3-cyclization NC-(CH=CH)$_2$-CNO into benzfurazan (BF). This value corresponds well-known data [8] on relation between reagents structure and rates of cycloaddition reactions. The assumption on almost same value of activation energy (E_{-1}) for 1,3-cyclization NC-$(CH_2)_4$-CNO into TMF corresponds data [8] also.

From equation type (*) for TMF we can calculate

$\Delta H_f^\circ(NC(CH_2)_4CNO)$=45.3 Kcal/mol

Using known data [3], we can calculate increment

$\Delta H_f^\circ[C\text{-}(H)_2(C)(CNO)]$=32.8 Kcal/mol

and from equation

$D(N\text{->}O)= \Delta H_f^\circ[C\text{-}(H)_2(C)(CN)]+\Delta H_f(O)-\Delta H_f^\circ[C\text{-}(H)_2(C)(CNO)]$

strength bond N->O in nitriloxide group, binded to methylene link D(N->O)=49.3 Kcal/mol.

In recent paper [9] by determining combustion heat of 1,4-dicyanobenzene and 1,4-dicyanobenzene-di-N-oxide the value D(N->O)=53.3 Kcal/mol was calculated according equation:

$$D(N->O)= \Delta H_f^\circ(1,4\text{-dicyanobenzene})+\Delta H_f^\circ(O)-\Delta H_f^\circ(1,4\text{-dicyanobenzene-di-N-oxide})$$

Inspite of made assumptions, our estimation scheme leads to result that corresponds value D(N->O) from [9] within the summary accuracy of estimation (near ±5 Kcal/mol).

Using value D(N->O)=49.3 and data [3] we can calculate the formation heat of intermediate compound

$$\Delta H_f^\circ(NC(CH=CH)_2CNO)=98.7 \text{ Kcal/mol}$$

Again the experimental activation energy E_{-1} for 1,3-cyclization NC-$(CH=CH)_2$-CNO into benzfurazan is equal 21.1 Kcal/mol [7].
The enthalpy of formation $\Delta H_f^\circ(BF)$=70.1 Kcal/mol [6].
As experimental value of activation energy E_1 of BF decomposition is is equal 58.7 Kcal/mol [4] and we have

$$\Delta H_f^\circ(БФ)+E_1>E_{-1}+\Delta H_f^\circ(NC(CH=CH)_2CNO) \quad \text{or}$$

$$E_1> E_{-1}+\Delta H$$

this is mean, that thermal decomposition of benzfurazan is running in stepwise manner. Most probable second stage of decomposition is monomolecular isomerization of nitiloxidic fragment into isocyanatic one. If we can consider, that another following steps runs sufficiently fast and don't contribute appreciable addition in observed rate constant of decomposition, then we have estimation for second stage E_2=30.1 Kcal/mol.

Using D(N->O)=49.3 Kcal/mol and known data on decomposition kinetics of dimethylfuroxan [4] for estimation of activation energy for

dimerization methylnitriloxides into dimethylfuroxan we find value near 7 Kcal/mol.

Mechanism of thermal decomposition 1,5-disubstituted tetrazoles, as for benzfurazan is stepwise. Azidoazomethine that is the result of tetrazolic ring opening Образующийся в результате раскрытия гетероциклического фрагмента azidoazomethine (reaction 1) способен can close heterocycle quickly into initial structure (reaction -1) and can eliminate nitrogen from azidic fragment (reaction 2). Detailed analysis of the decomposition mechanism is discussed in paper [11]. Using analogous scheme we estimate the heat formation for intermediate azidoazomethines:

$\Delta H_f^\circ[(CH_3)(N_3)C{=}N(CH_3)]$=84.5 Kcal/mol

$\Delta H_f^\circ[(C_2H_3)(N_3)C{=}N(CH_3)]$=110.1 Kcal/mol

$\Delta H_f^\circ[(C_6H_5)(N_3)C{=}N(C_6H_5)]$=143.7 Kcal/mol

and increments of azidic groups in heat formation:

$\Delta H_f^\circ[C_d\text{-}(C)(N_3)]$=83.4 Kcal/mol

$\Delta H_f^\circ[C_d\text{-}(C_d)(N_3)]$=85.8 Kcal/mol

$\Delta H_f^\circ[C_d\text{-}(C_b)(N_3)]$=88.4 Kcal/mol.

Before the next values were estimated [10]:

$\Delta H_f^\circ[C_d\text{-}(H)(N_3)]$=81.4 Kcal/mol

$\Delta H_f^\circ[(C_b)\text{-}(N_3)]$=75.8 Kcal/mol

REFERENCES

1. Gurvich, L. V.; Karachevtsev, G. V.; Kondrat'ev, V. N.; Lebedev, A.; Medvedev V. A.; Potapov, V. K.; Hodeev, Yu. S. *Bond dissociation energies. Ionisation potentials and electron affinities.*; Moscow: "Nauka", 1974. (in Russian).

2. Huisgen R., "1,3-Dipolar Cycloadditions. Past and Future." 563. "Kinetics and mechanism of 1,3-Dipolar Cycloadditions" 633. *Angew. chem. Intern. Ed. Engl.*, v.2, (1963).

3. Benson, S. W. *Thermochemical Kinetics*; J. Wiley & Sons: New York, 1968.

4. V. G. Prokudin, G. M. Nazin and G. B. Manelis, "On Mechanism of Thermal Decomposition of Furazans and Furoxans", *Dokl. Akad. Nauk USSR*, **1980**, *255*, 917-920. (in Russian).

5. Kchmelnitsky, L. I.; Novikov, S. S.; Godovikova, T. I. *The Chemistry of Furoxans v.1 Structure and Synthesis*; Nauka: Moskow, 1981. (in Russian).

6. Pepekin, V. I.; Matyushin, N.; Feschenko, A. G.; Smirnov, S. P. "Bond N->O dissociation energy in benzfuroxane"; *Dokl. Akad. Nauk USSR*, **1972**, *202*, 91. (in Russian).

7. Heinzelmann, W.; Gilgen, P. "Zum Mechanismus der Photochemie des Benzfurazans"; *Helv. Chim. Acta* **1976**, *59*, 2727-2737.

8. *1,3-Dipolar Cycloadditions Chemistry*, Ed. A. Padwa, J. Wiley & Sons, New York, 1984 v. 1, 817 p., v. 2, 704 p.

9. W. E. Acree, J.; Tucker, S. A.; Pilcher, G. "Enthalpies of combustion of 1,4-dicyanobenzene di-N-oxide and 1,4-dicyanobenzene: The mean dissociation enthalpy of the (N-O) bonds"; *J. Chem. Thermodynamics* **1992**, *34*, 213-216.

10. Shaw, R. "Thermochemistry of diazo compounds and organic azides" In *Chemistry of Diazonium and Diazo Groups*; Patai, S., Ed.; J. Wiley and Sons: New York, 1978; p. 137-147

11. Prokudin, V. G.; Poplavsky, V. S.; Ostrovsky, V. A. " Mechanism of the monomolecular thermal decomposition of 1,5- and 2,5-disubstituted tetrazoles "; *Russian Chemical Bulletin*, **1996**, *45*, 2209-2215.

DETERMINATION OF REACTION KINETICS DATA FROM THERMODYNAMIC MEASUREMENTS OF CATALYSED COMPOSITE PROPELLANTS

M.A.BENMAHAMED,
BP 17 EMP (ENITA), Bordj-El -Bahri, 35320 BOUMERDES, ALGERIA

ABSTRACT

The propellant formulation is an essential physicochemical parameter for the improvement of its energetic and kinetic performances. It exists also other properties and more particularly the incorporation of specific additives that have generally for role, in one hand to modify mechanical properties, in other hand to increase ballistic characteristics [1].

The present work consists in study the effect of the nature of some combustion catalyst as copper chromite, ferric oxide and ferrocen on thermoanalytical properties of PVC-plasticised propellants and also the determination of reaction kinetics data from thermodynamic measurements : temperature and enthalpy of decomposition, by using kinetic methods of OZAWA [2] and KISSINGER [3]. They allow the determination of the activation energy and the frequency factor.

The reaction model based on the work of L. Wilhelmy [4] is usually employed here :

$$\frac{d\alpha}{dt} = k(1-\alpha)^n \quad ,$$

where $\frac{d\alpha}{dt}$ is the reaction rate in s^{-1}, k is the rate constant in s^{-1} and n is the order of the reaction.

The reaction constant is generally assumed to have a temperature dependence of

$$k = k_0 . \exp(-E_a / RT),$$

where k_0 is the frequency factor in s^{-1}, E_a is the activation energy of the reaction in J/mol, R is the gas constant and T is the absolute temperature of the reaction mixture in K.

The appropriate apparatus for these analysis is the differential scanning calorimeter (DSC) [5]. The chemical reaction of interest is measured with several heating rates β. The sample temperature at the peak tip is determined for every curve. The activation energy can be obtained from the slope of the graph of log β versus $1 / T_{peak}$ (OZAWA) or $\ln \beta / (T_{peak})^2$ versus $1 / T_{peak}$ (KISSINGER).

The determination of kinetic parameters of thermally hazardous materials, by OZAWA and KISSINGER methods, allows finally to define the mechanism of the reaction.

REFERENCES :

[1]. DAVENAS.A & Coll, Technologie des propergols solides, MASSON, Paris 1989,
[2]. DOYLE.C.D, J. Appl. Polym.Sci, 1961,
[3]. WENDLANDT.W, Thermal analysis, Vol.19 third edition, John Wiley & Sons,USA 1986,
[4]. WIDMANN.G, RIESEN. R, Thermal analysis, Huthig, Heidelberg 1987,
[5]. McNAUGHTON.J.L, MORTIMER.C.T, Differential scanning calorimeter, PERKIN-ELMER, USA 1975.

CHARACTERISATION AND QUANTITATIVE DETERMINATION OF TRINITROTOLUENE IN MIXTURES WITH HEXOGEN BY DIFFERENTIAL SCANNING CALORIMETRY

Muhamed Sućeska, Maša Rajić and Ružica Čuljak*

Brodarski institut – Marine Research & Special Technologies, Av. V. Holjevca 20, 10020 Zagreb, Croatia (E-mail: suceska@brod.hrbi.hr)
* MoD - Ammunition and Weapons Testing Department, Stančićeva 4, 10000 Zagreb, Croatia

ABSTRACT

Mixtures of 2,4,6-trinitrotoluene (TNT) and cyclo-1,3,5-trimethylene-2,4,6-trinitramine (RDX, Cyclonite, Hexogen), standard high explosives, in different mass proportions, are widely used as an explosive fill for different types of projectiles.

The mass fraction of TNT in such mixtures may be easily determined by a standard analytical method based on the selective solution of one of the components in suitable solvent. This method is precise, but time consuming.

The procedure and the results of quantitative determination of TNT in mixtures with RDX by the use of Differential Scanning Calorimetry (DSC) are described in the paper. The obtained accuracy (error less than ±3 mass percents), as well as the fact that the method is fast and that it simultaneously gives several pieces of information about a sample to be tested (e.g. temperature and heat of melting, temperature and heat of decomposition, calorimetric purity, etc.) make it applicable for fast and rough quantitative determination of TNT in a mixture with RDX.

The described method can be also used for the determination of TNT in a mixtures with HMX and PETN.

1. INTRODUCTION

Mixtures of trinitrotoluene and hexogen are known under various names: Cyclotols (USA), Hexotol (Sweden), Hexolite (France), Füllpulver (Germany), Tritolite (Italy), etc. [1,2]. The content of TNT and RDX in such mixtures may vary in broad limits, depending on technological requirements, detonation performances required, etc.

A usual way to determine TNT content in such mixtures is by the selective solution of TNT by using a suitable solvent. This method is very precise, but time consuming [3].

Today, in the field of explosive materials the methods of thermal analysis have found widespread use. This refers in particular to Differential Scanning Calorimetry (DSC), Differential Thermal Analysis (DTA), and Thermogravimetry (TGA). Their application is, however, directed mostly to the characterisation of explosive materials and studying their thermal properties (e.g. melting process, polymorphic transformations, thermal stability, thermal decomposition kinetics, etc.) [1,4,5,6,7].

Since these methods give qualitative and quantitative information about the physical or chemical changes in a sample tested, associated with the heat liberation or absorption, they may be successfully applied for the quality control, as well as for some analytical purposes (e.g. identification thanks to a compound specific thermogram), for compositional analysis of mixture, etc. [8,9,10,11,12].

The determination of a component content in a mixture, as an important quality control test, may be for some types of mixtures done by DSC [13]. The determination is based on the fact that the heat of melting (crystallisation, phase transition, etc.) of a sample is in simple relation with the heat of melting of 100% pure compound.

To determine TNT content in a TNT/RDX mixture, a weighted sample is heated from well below TNT melting temperature to well over it. The area under the melting endotherm is then integrated and the heat of melting calculated. Rationing the so obtained heat of melting with the heat of melting obtained for a 100% TNT sample, the mass percent of TNT in the mixture is obtained.

2. EXPERIMENTAL

To perform the experiment, the TNT and RDX samples of a commercial grade of quality (the melting point of TNT was 80.66 °C, and the melting point of RDX 203.48 °C) were chosen.

The mixtures of TNT and RDX were prepared by hand mixing of previously finely ground explosives.

The DSC curves were obtained with TA Instruments model DSC 2910 by placing a sample, about 5 mg in mass, in an aluminium sample pan covered by an aluminium cover without crimping, with a heating rate of 5 °C/min, and under nitrogen pouring with a flow rate of 100 ml/min.

The TGA curves were obtained with TA Instruments model SDT 2960, using the same sample masses, aluminium sample pans, the same heating rate, and nitrogen pouring, as for the DSC curves.

3. RESULTS AND DISCUSSION

The temperature and the heat of melting of pure chemical compound may be easily determined by the DSC technique. However, the melting behaviour of the samples containing more than one chemical component may be more complex, and thus the determination of the sample temperature and the heat of melting. For example, if one pure solid component does not dissolve at all in other pure solid component in a mixture, they form an eutectic mixture; two solid components very similar in structure may form solid solution; one solid component may be partially soluble in other component of the mixture; two components may chemically react and form a compound, etc. [8].

A usual way to study the phase behaviour of a mixture by the methods of thermal analysis is to obtain the DSC or DTA curves of the components forming the mixture, and the mixtures having a different mass ratio of components. Thus, in order to estimate the possibility of quantitative determination of TNT in TNT/RDX mixtures by the DSC technique, the first step was to obtain DSC curves of TNT, RDX, and the mixtures with different TNT/RDX ratios (Fig. 1).

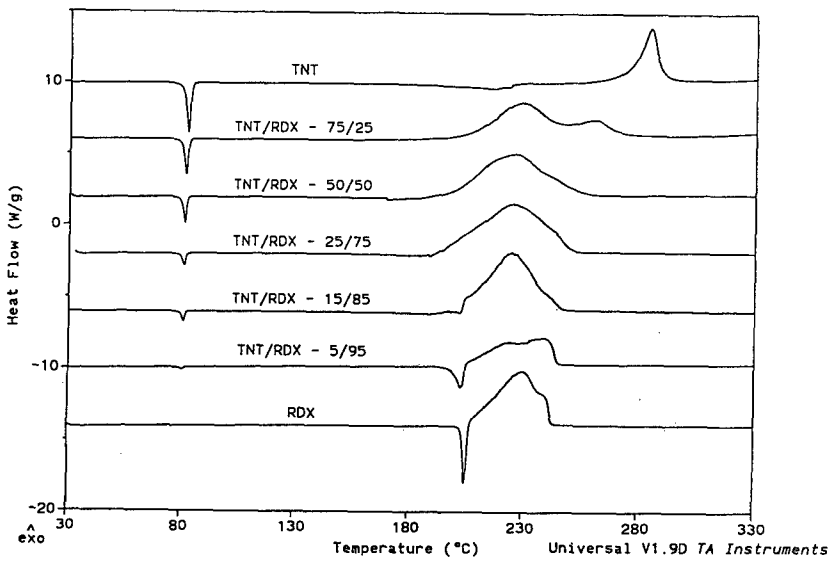

Figure 1. DSC curves of TNT, RDX and TNT/RDX mixtures

It can be seen from Fig. 1 that TNT shows a sharp melting endotherm in the temperature range of 75-85 °C, and an exothermic peak corresponding to decomposition in the range of 250-300 °C (the shape of TNT thermogram, particularly over 130 °C, depends strongly on testing conditions: heating rate, whether a sample cup is hermetically crimped or not, etc.).

The DSC curve of pure RDX shows a sharp melting endotherm in the range of 200-210 °C. Immediately after melting, decomposition takes place, and an exothermic peak is observed in the range of 210-250 °C.

The DSC curves of TNT/RDX mixtures show two separate melting peaks; one corresponding to TNT melting , and the other to RDX melting processes. Such behaviour is typical for eutectic mixtures [8]. The peak corresponding to RDX melting decreases rapidly with the decrease of RDX content in the mixture, and disappears completely below about 50% RDX. This is a consequence of two processes: dissolution of solid RDX in melted

TNT at higher temperatures [14], and overlapping with the exothermic decomposition of the mixture.

It is also evident from Fig. 1 that there are no other peaks overlapping the TNT melting peak, and from Fig. 2 that there are no mass losses in the range of TNT melting process (75-85 °C). These facts are important preconditions for the quantitative determination of TNT in a TNT/RDX mixture on the basis of TNT heat of melting.

Enthalpy of melting

From the DSC curves showing TNT melting endotherms (Fig. 3) it is clear that the decrease of TNT content in the mixture results with the decrease of the area under the melting endotherm, i.e. decrease of specific enthalpy of melting. The relation between sample mass (m_S), area under peak (A), and specific enthalpy of melting ($\Delta_m h$) is given by the equation:

$$\Delta_m h = \frac{A \cdot K}{m_S} \tag{1}$$

where: K - DSC calibration constant

Mass percent of TNT (w%TNT) in the mixture is calculated from specific enthalpy of melting of 100% TNT ($\Delta_m h_{TNT}$), and specific enthalpy of TNT melting in TNT/RDX mixture ($\Delta_m h_{TNT/RDX}$), according to the following equation [13]:

$$w\%\text{TNT} = \frac{\Delta_m h_{TNT/RDX}}{\Delta_m h_{TNT}} \cdot 100 \tag{2}$$

The specific enthalpies of melting are obtained from the DSC curves given in Fig. 1 (integration of melting endotherm and calculation of enthalpy by Eq. 1). The values obtained are given in Table 1.

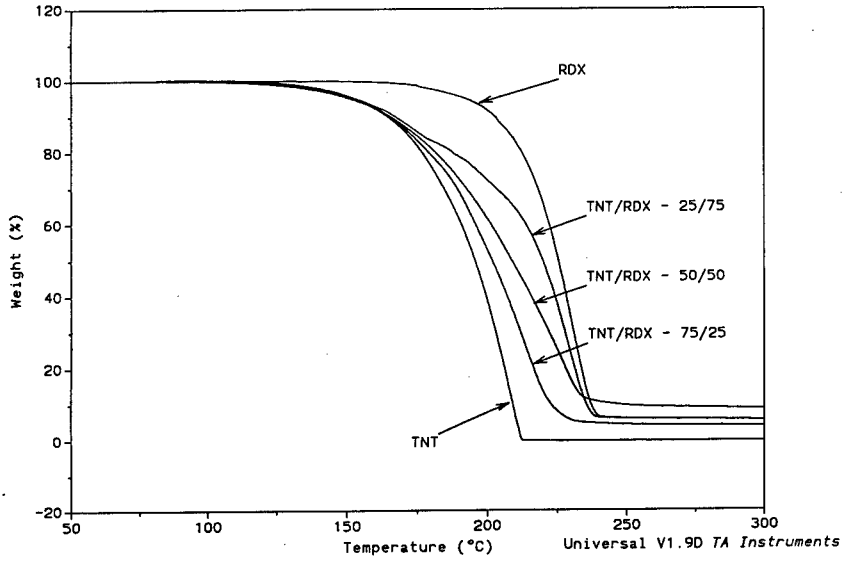

Figure 2. TGA curves of TNT, RDX and TNT/RDX mixtures

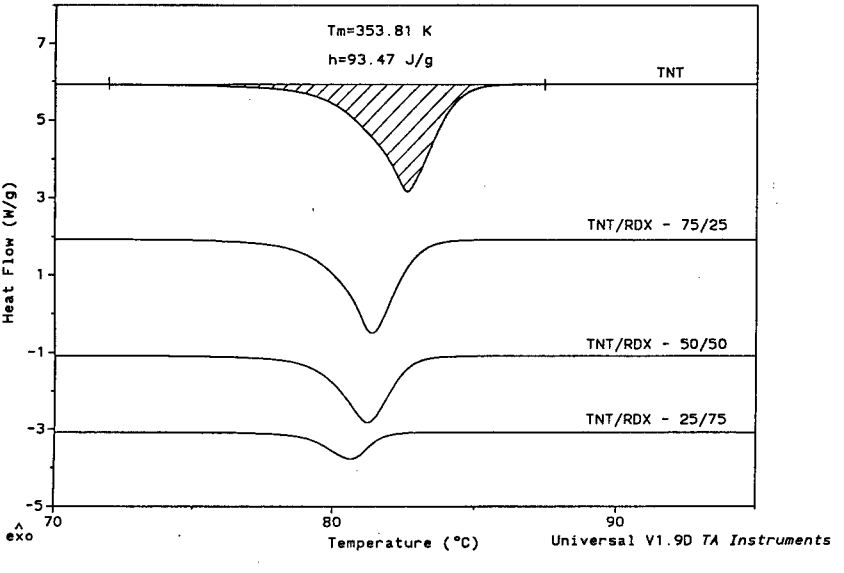

Figure 3. Endothermic peaks corresponding to TNT melting process as a function of TNT content in the mixture

Table 1. Experimentally obtained enthalpies of melting

TNT/RDX mass ratio	Specific enthalpy of melting	
	Mean value J/g	Standard deviation J/g
100/0	93.47	2.01
85/15	80.11	1.87
75/25	67.45	2.70
50/50	46.52	1.55
25/75	20.57	1.26
15/85	12.64	2.15
5/95	2.99	–

The specific enthalpy of melting of 100% TNT of 93.47 J/g is obtained as a mean value of seven measurements, with standard deviation of 2.01 J/g. This value is quite close to some literature values for pure (recrystallised) TNT of 99.5 and 103.2 J/g [15], and 98.51 J/g [1]. The values of specific enthalpies of melting, given in Table 1, are obtained as a mean values of 3-5 measurements.

From Fig. 4, showing the dependence of the experimentally obtained values of specific enthalpy of melting, and the values of the enthalpy of melting calculated by Eq. 2, upon actual (as prepared) TNT content, it follows that there is a good agreement between the experimentally obtained and the calculated values of melting enthalpies (difference less than 3 J/g). The experimentally obtained values are consistently slightly lower than the calculated ones, and result with a slightly non-linear dependence of melting enthalpy on TNT content. Such result should be attributed to the partial solution of RDX in melted TNT (about 4.5% at 81 °C, according to [14]). Because of that, the experimentally obtained values of enthalpy of melting should be lower than expected, i.e. calculated by Eq. 2 for actual TNT content (because of enthalpy of mixing and enthalpy of solution).

From the experimentally obtained values of the specific enthalpy of melting, TNT content (found) is calculated applying Eq. 2. The comparison of the so obtained TNT content, and the actual content (Fig. 5), shows that a satisfactory agreement exists between them (error less than ±3%)

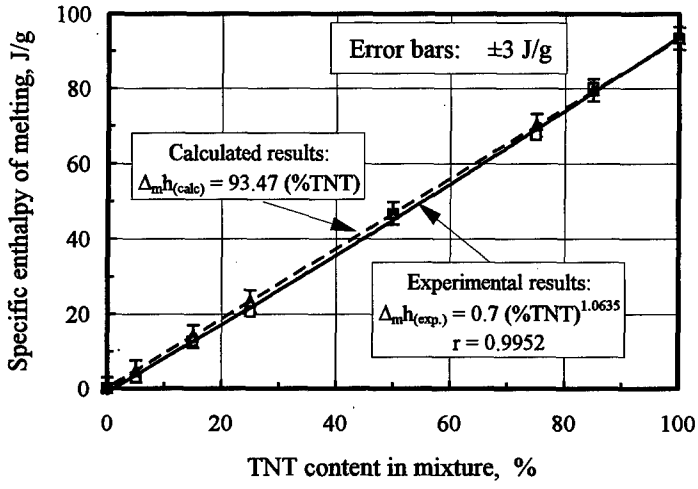

Figure 4. Specific enthalpy of melting *vs.* TNT content in TNT/RDX mixture

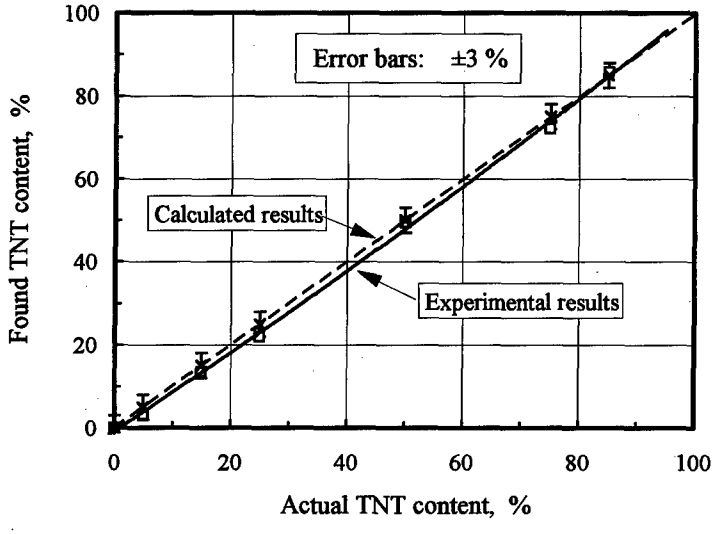

Figure 5. Comparison of found and actual TNT content in TNT/RDX mixture

However, instead of applying Eq. 2 for the calculation of TNT content, one may use experimentally obtained relationship between the enthalpy of melting and the actual TNT content in the mixture (Fig. 4), i.e. calibration curve:

$$\Delta_m h_{(exp.)} = 0.7 \cdot (\%TNT)^{1.0635} \qquad (r = 0.9952) \qquad (3)$$

Calculating TNT content in such a way, the error between the actual and the found TNT content may be decreased below 1.8 mass percents.

Melting temperature

The melting temperatures of TNT and RDX, given in Table 2, are obtained from DSC curves.

Table 2. Melting temperatures of TNT and RDX

TNT/RDX mass ratio	Melting temperature of TNT		Melting temperature of RDX °C
	Mean value °C	Standard deviation °C	
100/0	80.66	0.10	–
85/15	80.00	0.05	–
75/25	79.86	0.03	–
50/50	79.32	0.24	169.3
25/75	79.15	0.01	188.0
15/85	79.02	0.13	198.1
5/95	78.99	–	199.4
0/100	–	–	203.48

The melting temperature of 100% TNT of 80.66 °C (obtained as a mean value of seven measurements, with a standard deviation of 0.099) decreases with TNT content decrease, approaching asymptotically about 79 °C. This melting temperature is stated in literature as the melting temperature of Comp B (60 % RDX) and Cyclotols having 70 and 80% RDX [1].

The melting temperature of RDX decreases more rapidly with RDX content decrease. Below 50% of RDX melting endotherm corresponding to RDX disappeared completely: as mentioned earlier, this is connected with RDX dissolution in melted TNT, as well as with the overlapping of the melting endotherm with the exothermic decomposition processes.

It is known that the melting temperature shows the effect of soluble impurities on a pure compound: a small amount of soluble impurity lowers the melting temperature [8]. Thus the melting temperature depression may serve as a measure of a substance purity. In this paper, TNT melting temperature depression is applied for the calculation of the content of RDX dissolved in melted TNT (in the range of TNT melting endotherm: 75-85 °C), according to the van't Hoff equation in the following form [11,12]:

$$mol\%\text{RDX} = 100 \cdot \frac{\Delta_m H_{TNT}}{R T_m^2} \cdot \left[T_{m,TNT} - T_{m,TNT/RDX} \right] \qquad (4)$$

where: *mol*%RDX - mol percent of soluble RDX

$T_{m,TNT}$ - melting temperature of pure TNT

$T_{m,TNT/RDX}$ - melting temperature of TNT in TNT/RDX mixture

$\Delta_m H_{TNT}$ - molar enthalpy of melting of 100% TNT

It follows (Fig. 6) that the mol percent of RDX soluble in melted TNT is dependent on its content in the mixture. The amount of soluble RDX increases with increase of RDX content in the mixture, approaching asymptotically a value of about 3.5%. This value is close to the value of 4.5% at 81 °C, cited in literature [14].

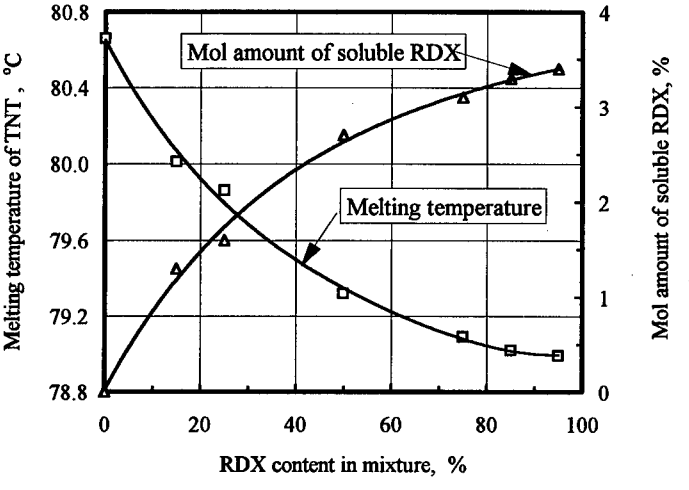

Figure 6. Dependence of TNT melting temperature and RDX solubility in melted TNT on RDX content in the mixture

4. CONCLUSIONS

The results of the presented show that Differential Scanning Calorimetry may be applied for a rough quantitative determination of TNT content in mixtures with RDX. The difference between the actual and the found TNT content less than 3 mass percents was obtained. If the calibration curve, expressing the dependence of the enthalpy of melting on TNT content, is used, the difference may be lowered below 1.8 mass percents.

The advantage of the described method is in its simplicity, quickness, and in the fact that it gives at the same time several pieces of information about the tested sample. This makes the method suitable for fast and rough quantitative determination of TNT in mixtures with RDX. Following the same principle, the method may be applied for the determination of TNT in mixtures with HMX and PETN.

5. LITERATURE

1. T. Gibbs, A. Popolato, LASL Explosive Property Data, Berkeley, 1980, pp. 11-33, 143-151, 172-187
2. J. Kohler, R. Mayer, Explosives, VCH, Weinheim, 1993, pp. 63-64, 70-73
3. Croatian Military Standard, Heksotol, HRVN-1131, 1970
4. J. Yunon, S. Zitrin, The Analysis of Explosives, Pergamon Press, New York, 1981, pp. 133-140
5. W. Beckmann, J. S. Wilkes, R. R. McGuire, Thermochim. Acta 19 (1977) 111-118
6. S. Zeman, Thermochim. Acta 290 (1997) 199-217
7. J. R. Quintana, J. A. Ciller, F. J. Serna, Propellants, Explosives, Pyrotechnics 17 (1992) 106-109
8. J. Haines, Thermal Methods of Analysis. Principles, Applications and Problems, Blackie Academic & Professional, Glasgow, 1995, pp. 84-97
9. B. Brill, K. J. James, J. Phys. Chem. 97 (1993) 8759-8763
10. G. Krien, Propellants, Explos. Pyrotech. 4 (1979) 53-55
11. E. Marti, Thermochim. Acta 5 (1972) 173-220
12. C. Plato, A. R. Glasgow, Anal. Chem. 41 (1969) 330-336
13. L. Blaine, Wax Content of Lubricants, Thermal Analysis Technical Literature, TA Application Brief, TA-44
14. M. Prpich, Explosive devices filling by casting and pressing process (in Croatian), Masters thesis, CVTŠ Zagreb, 1985, pp. 8-10
15. G. Edwards, Trans. Faraday Soc. 46 (1950) 425-429

Thermal Behavior and Stability of HNIW (CL 20)

S. Löbbecke, M.A. Bohn, A. Pfeil, H. Krause

Fraunhofer-Institut für Chemische Technologie ICT
P.O. Box 12 40, 76318 Pfinztal, Germany

Introduction

2,4,6,8,10,12-hexanitrohexaazaisowurtzitane (HNIW; also known as „CL 20") is a relatively new polycyclic strained-cage nitramine which was first synthesized in 1987 by A.T. Nielsen at the former Naval Surface Weapons Center at China Lake, California.
The molecular structure of HNIW (exact chemical name: 2,4,6,8,10,12-hexanitro-2,4,6,8,10,12-hexaazatetracyclo[5.5.0.$0^{5,9}$.$0^{3,11}$]dodecane) consists of a basic isowurtzitane cage with one nitro group attached to each of the bridging nitrogen atoms as shown in Figure 1.

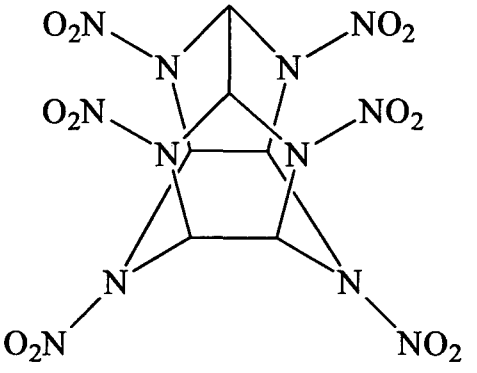

Fig. 1: molecular structure of HNIW („CL 20")

Although HNIW is chemically similar to the well-known monocyclic nitramines, RDX and HMX, it has remarkable advantages due to its cage structure. Table 1 shows that the cage structure of HNIW effects a high molecular density as well as a significant increase in the heat of formation caused by additional ring strain.

Tab. 1: physicochemical properties of HNIW compared with RDX and HMX

	RDX	HMX	ε-HNIW („CL 20")
sum formula	$C_3H_6N_6O_6$	$C_4H_8N_8O_8$	$C_6H_6N_{12}O_{12}$
molecular weight	222.12 g/mol	296.16 g/mol	438.19 g/mol
density	1.81 g/cm³	1.90 g/cm³	2.04 g/cm³
heat of formation	70 kJ/mol	88 kJ/mol	415 kJ/mol
oxygen balance	-21.61%	-21.61%	-10.95%

Four stable polymorphs of HNIW (α, β, γ and ε) are known to exist at ambient conditions from which the ε polymorph is the one with the highest density (2,04 g/cm³). The application of ε-HNIW in energetic formulations, for example as a substituent for RDX or HMX, requires reliable information on its thermal and energetic properties. This work presents first results investigating thermal decomposition, thermal stability and thermal phase behavior of ε-HNIW.

Experimental

ε-HNIW was purchased from Thiokol Corporation, Brigham City, Utah (USA), with a particle size of $d_{(0.5)}$ = 163 µm. A portion of the sample was ground at ICT to particle sizes of $d_{(0.5)}$ = 5 µm [1]. An additional sample of ε-HNIW was received from SNPE, Vert-le-Petit (France), having a particle size of $d_{(0.5)}$ = 16 µm.

The chemical and polymorph purity of the samples was characterized by FTIR, X-Ray diffraction, HPLC, NMR and other analytical techniques that are described in detail elsewhere [2, 3]. Main chemical impurities were lower nitrated derivates of HNIW as well as different solvent residues.

The thermal behavior of ε-HNIW was investigated by Thermogravimetric Analysis (TGA; TA Instruments, New Castle, DE, USA), Differential Scanning Calorimetry (DSC; TA Instruments, New Castle, DE, USA) and infrared spectroscopic Evolved Gas Analysis (EGA; for detailed description see ref. [4]) under isothermal conditions or by using slow linear heating rates (0.5 to 10.0 K/min). The experiments were performed under argon atmosphere. DSC experiments were carried out in sample pans with pierced lids made

of aluminum. Visual monitoring of the thermal behavior of HNIW was realized by a video CCD camera which was adapted to a self-constructed thermo-microscope, again working with slow linear heating rates or under isothermal conditions.

Results

The thermal behavior of ε-HNIW is dominated by two main thermal effects, illustrated by a typical DSC measurement of ε-HNIW in Figure 2:

1. solid-solid phase transition from the ε- to the γ-polymorph, followed by:
2. thermal decomposition of the γ-polymorph at higher temperatures

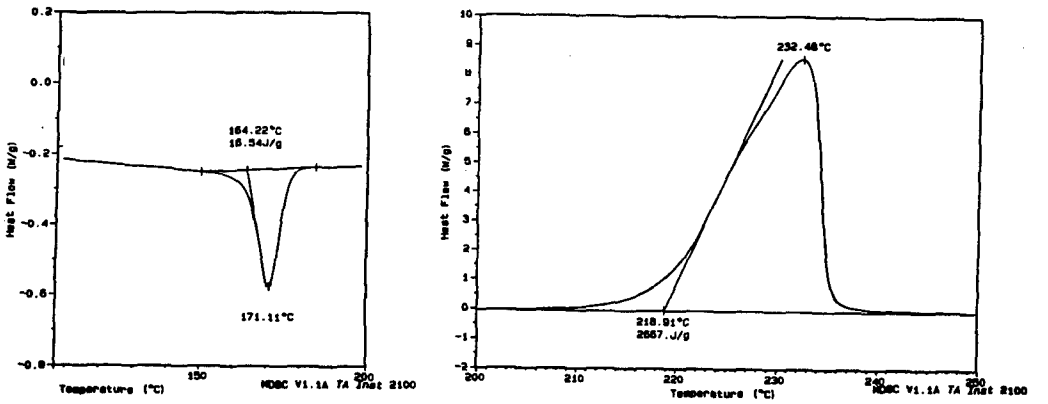

Fig. 2: endothermic phase transition and exothermic decomposition of ε-HNIW measured by DSC

phase behavior of ε-HNIW:

Heating of ε-HNIW to temperatures above 164°C (onset temperature) effects a solid-solid phase transition to the γ-polymorph detected as an endothermic signal in DSC experiments (Fig. 3). The ε → γ transition is irreversible; cooling and heating again of γ-HNIW effects no polymorphic conversion. The different polymorphs of HNIW can be easily identified and distinguished using FTIR spectroscopy, especially in the spectral range between 1200 cm^{-1} and 600 cm^{-1} (see Fig. 4).

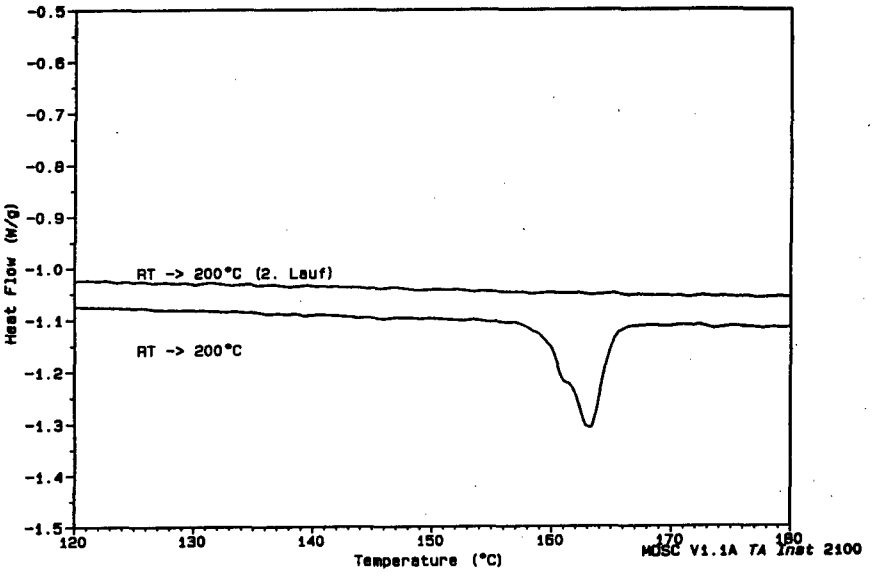

Fig. 3: twofold heating and cooling of HNIW between 25°C and 200°C demonstrating irreversible $\varepsilon \rightarrow \gamma$ solid-solid phase transition (measured by DSC)

In addition to the fast and quantitative $\varepsilon \rightarrow \gamma$ transition of HNIW under conditions of linear heating also a slow $\varepsilon \rightarrow \gamma$ transition was observed at temperatures < 164°C. For example, more than 15% γ-polymorph was observed after 20 hours storage of ε-HNIW at 140°C (Fig. 4). Indication of a slow polymorphic conversion of ε-HNIW at temperatures below 164°C is also described by Foltz et al. who measured $\varepsilon \rightarrow \gamma$ transition of dissolved HNIW already at $T = 64 \pm 1$°C [5].

Since the $\varepsilon \rightarrow \gamma$ solid-solid phase transition is combined with a decrease in molecular density as well as an increase in volume the knowledge of HNIW phase stability even at lower temperatures has a significant importance for the application of HNIW in energetic formulations and will be investigated much more in detail in future work.

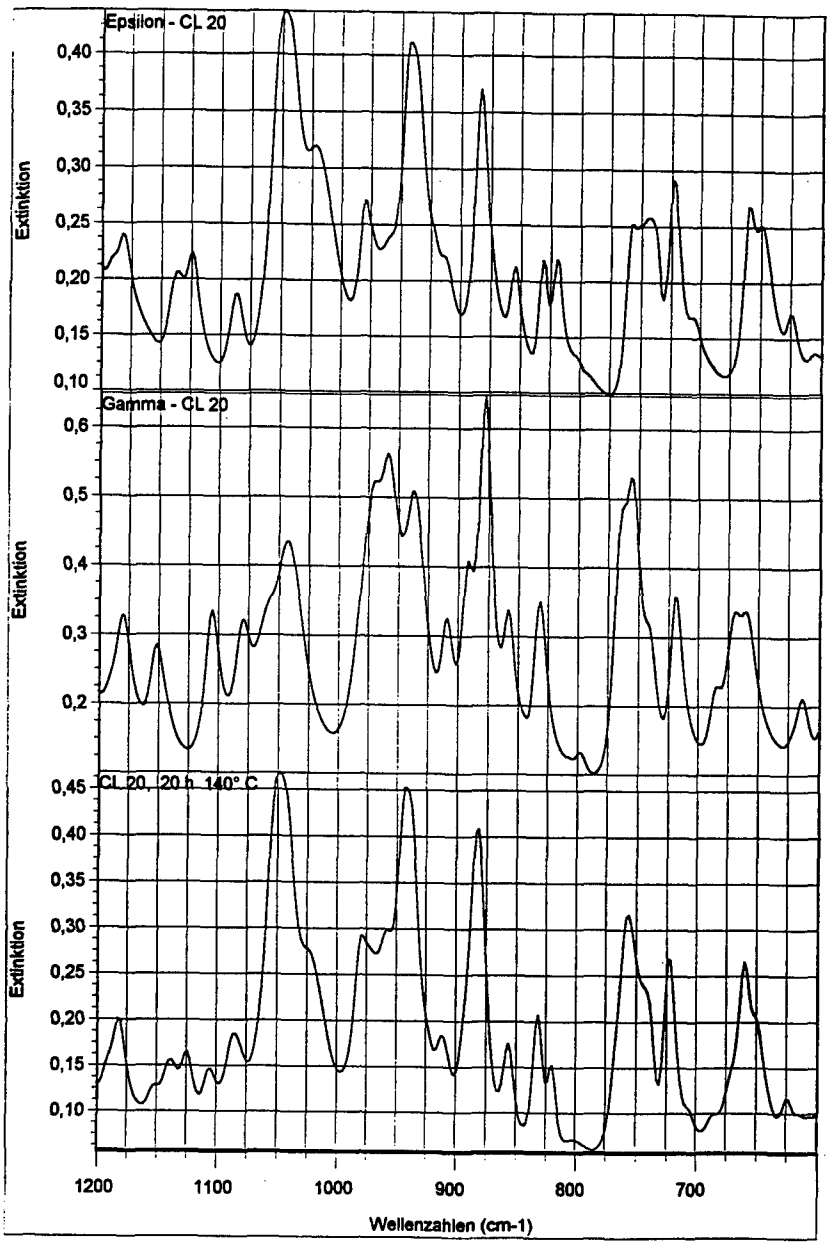

Fig. 4: Infrared spectra of pure ε-HNIW, pure γ-HNIW and original ε-HNIW 20 hours after storage at 140°C, containing significant amounts of γ-HNIW due to polymorphic conversion

thermal decomposition of γ-HNIW:

As shown in Figure 2 further heating of polymorphic converted γ-HNIW to temperatures above 210°C causes the exothermic decomposition of the polycyclic nitramine. On closer inspection of the exothermic DSC peak a low-temperature shoulder can be observed indicating two superimposed decomposition steps.
Since the few DSC data of ε- resp. γ-HNIW found in literature show no reliable accordance [6, 7], and even in some cases uncontrolled decomposition [7] Table 2 summarizes mean values of ten DSC experiments carried out at a linear heating rate of 2 K/min with sample sizes between 0.669 and 0.945 mg.

Tab. 2: DSC data of ε- resp. γ-HNIW decomposition (2 K/min, argon atmosphere, Al sample pans with pierced lids; mean values of ten DSC runs)

calculated onset temperature of decomposition	temperature at maximum heat flow	maximum heat flow	heat of decomposition
218.87 ± 0.43 °C	232.36 ± 0.18 °C	3.75 ± 0.17 kW/mol (8.55 ± 0.39 W/g)	1133.9 ± 29.4 kJ/mol (2588 ± 67.1 J/g)

TGA experiments confirm the two-step decomposition of HNIW. Figure 5 show TGA measurements of the large particle fraction ($d_{(0.5)}$ = 163 µm) indicating a significant influence of the heating rate on the two-step mass loss. Since the 5 and 16 µm fractions of HNIW show no two-step decomposition at lower heating rates (Fig. 6) (but still at higher heating rates ≥ 10 K/min) it can be supposed that the initial decomposition of HNIW is - at least partly - kinetically controlled by particle size. (Furthermore, the slower the heating rate, the more complete polymorphic conversion to the γ-phase takes place, combined with volume expansion as well as micro-cracking and fracturing of the crystals, as it was observed by thermo microscopy; see also [7]).

In contrast to the monocyclic nitramines RDX and HMX which produce only gaseous decomposition products, polycyclic HNIW produces a solid residue of 9 - 14 mass% at T = 300°C (Fig. 5 and 6). The infrared spectrum of the residue is shown in Figure 7.

A broad absorption band centered at 3237 cm^{-1} can be identified as a secondary amine fragment. Further absorption bands are located between 1750 and 1200 cm^{-1} that could be used as evidence for carbonyl (resp. amide fragments), C=N, C-C, C=C, NO or polymeric fragments like azines and melon-like fragments, as it was also suggested by Brill and Patil [8 - 9].

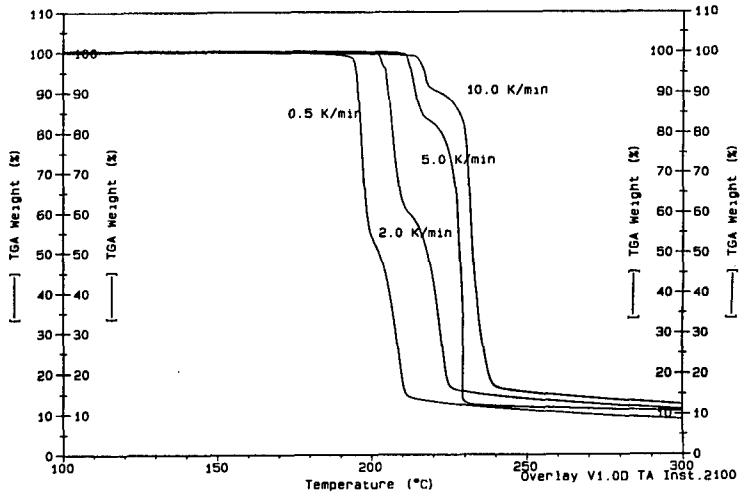

Fig. 5: TGA measurements of ε-HNIW ($d_{(0.5)}$ = 163 µm) at different heating rates

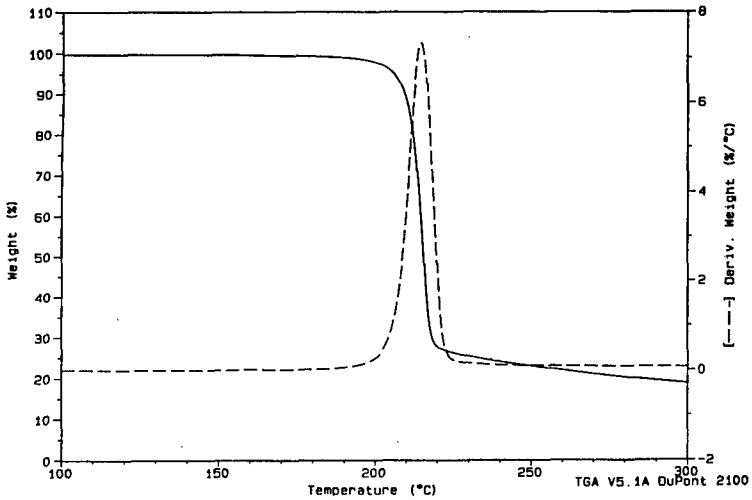

Fig. 6: TGA measurement of ε-HNIW ($d_{(0.5)}$ = 5 µm) at 2 K/min

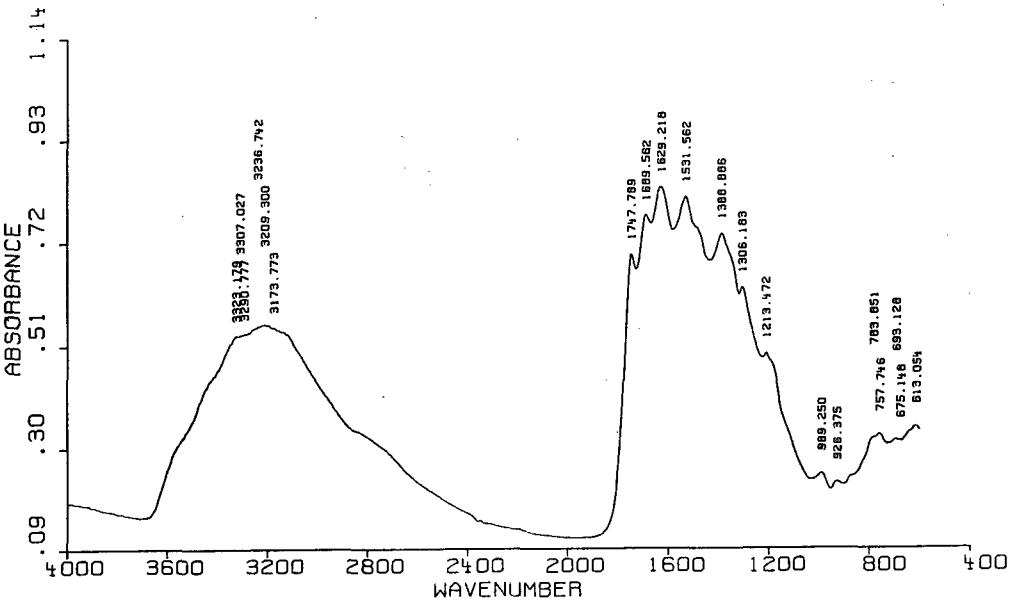

Fig. 7: Infrared spectrum of solid HNIW decomposition residue

Gaseous decomposition products of HNIW which were detected by rapid scan FTIR spectroscopy are shown in Figure 8. Main decomposition products are CO_2, N_2O, NO_2 and HCN, in addition traces of NO and CO were detected. The evaporation profiles show a nearly parallel evolution of the four main decomposition products until the maximum of NO_2 and N_2O concentration was reached. NO_2 is liberated from HNIW by N-NO_2 homolysis which is a typical mechanism of nitramine thermolysis [10]. The NO_2 release effects a weakening of HC-NNO_2 bonds adjoining to the position of N-NO_2 homolysis. The weak C-N bond can be stabilized by the evaporation of N_2O and by forming a carbonyl containing residue [8] (Fig. 9).

The concerted evaporation of NO_2 and N_2O can be clearly seen in the EGA profiles. While the concentration of the stable decomposition product N_2O keeps constant after reaching the maximum, the NO_2 concentration decreases due to reactions with the cage structure backbone. Further amounts of CO_2 and HCN are evaporated (Fig. 8) and the solid residue containing amine, amide and/or other azine fragments is formed.

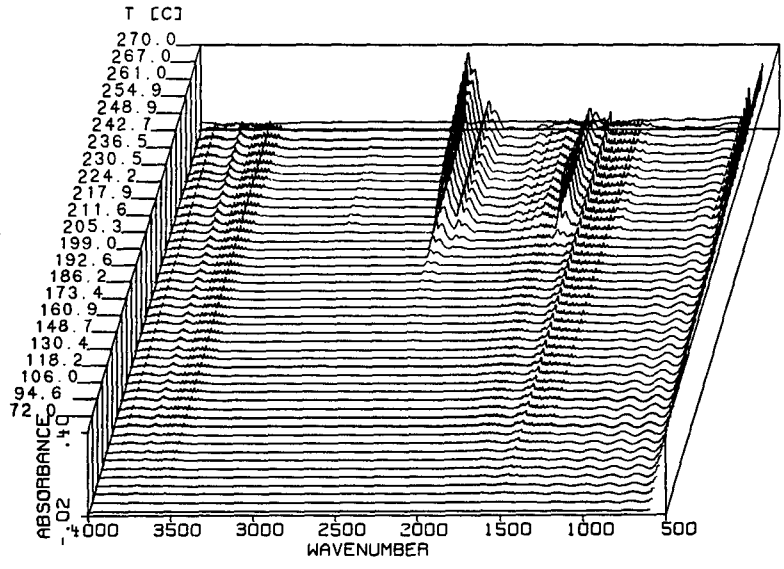

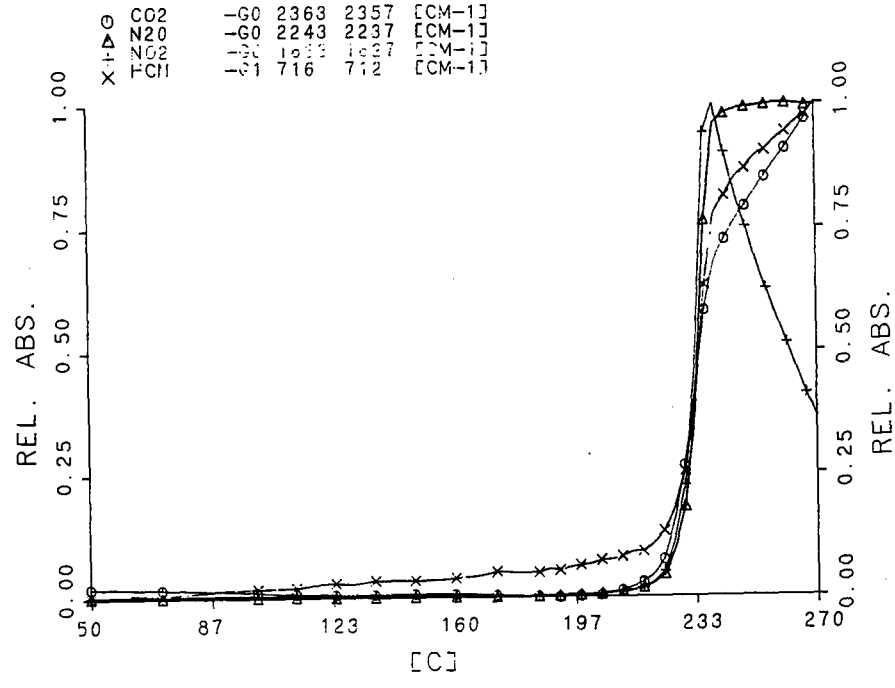

Fig. 8: IR spectroscopic Evolved Gas Analysis of HNIW decomposition (HR: 5 K/min)

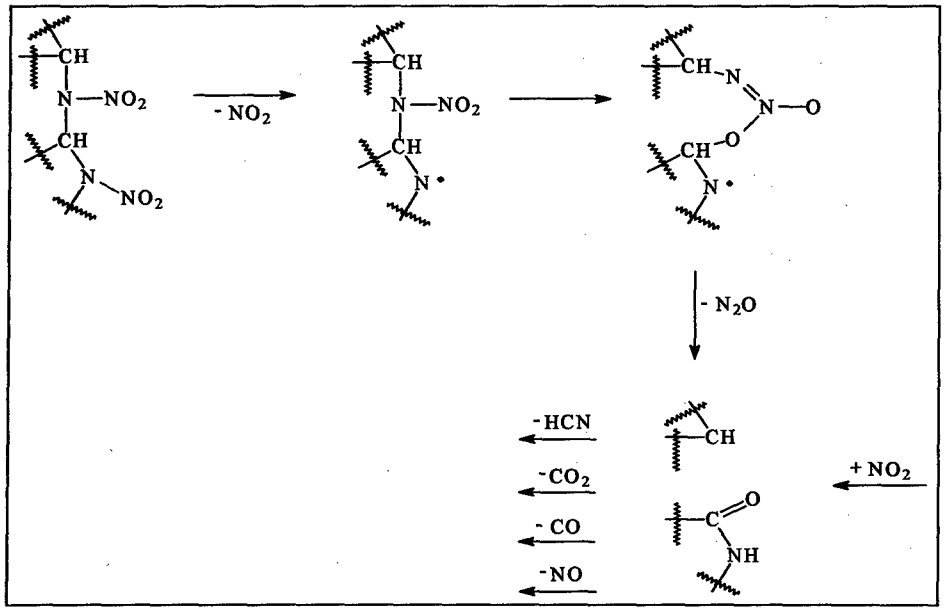

Fig. 9: schematic illustration of possible HNIW decomposition pathways

thermal stability of ε-HNIW:

Beside quantitative thermal decomposition of ε-HNIW at temperatures above 210°C also a slow thermal decomposition at lower temperatures was observed by isothermal TGA experiments. Conversion times measured for 5% mass loss are summarized in Table 3.

Tab. 3: Conversion times measured for 5% mass loss during isothermal storage of ε-HNIW ($d_{(0.5)}$ = 163 µm) at different temperatures

temperature / °C	5% mass loss conversion time / min
160	1141.9
165	697.8
170	360.7
175	215.4
180	99.6

With some of these isothermal TGA mass loss measurements kinetic calculations were performed. HNIW shows an autocatalytic decay which can be generally described by the reaction scheme (RS 1):

(RS 1)

$$A \xrightarrow{k_1} B + C + S \qquad \text{unimolecular decomposition}$$
$$A + B \xrightarrow{k_2} 2\,B + C + S \qquad \text{autocatalytic decomposition}$$

B is the autocatalyticly effective decomposition product, C represents all volatile decomposition products and S summarizes all non-volatile decomposition products.
With A = HNIW eq.(1) is obtained from reaction scheme 1.

(1) $$\left(\frac{dA(t,T)}{dt}\right)\Bigg|_T = -k_1(T)\cdot A(t,T) - k_2(T)\cdot A(t,T)\cdot B(t,T)$$

The unimolecular decomposition of HNIW is a reaction of first-order whereas the autocatalytic reaction represents a second-order kinetics. (RS 1) and eq.(1) are formulated by using the molar amounts of the reactants. Because the HNIW decomposition was investigated by isothermal TGA mass loss measurements, eq (1) has to be re-formulated by using the masses of the reactants. With the conditions of the formation of B and C by the decomposition of A,

$B(t,T) = A(0) - A(t,T)$ and $B(0) = 0$
$C(t,T) = A(0) - A(t,T)$ and $C(0) = 0$

and with the molar masses m_A, m_B, m_C, m_S as well as by dividing A(t,T) with the starting amount A(0) in eq.(1), the eq.(2) is obtained with A expressed as the relative mass $M_{Ar}(t,T) = M_A(t,T)/M_A(0)$ [11].

(2) $$\left(\frac{dM_{Ar}(t,T)}{dt}\right)\Bigg|_T = -k^1_{ML}(T)\cdot M_{Ar}(t,T) - k^2_{ML}(T)\cdot M_{Ar}(t,T)\cdot\left(1 - M_{Ar}(t,T)\right)$$

The reaction rate constants of eq.(2) are connected to those of (RS 1) and eq.(1) according to eq.(3), their dimensions are now 1/time.

(3) $$k^1_{ML}(T) = k_1(T) \quad and \quad k^2_{ML}(T) = k_2(T)\cdot A(0)$$

Integration of eq.(2) leads to eq.(4), also known as „1st order + autocatalytic"-model.

$$(4) \qquad M_{Ar}(t,T) = \frac{k^1_{ML}(T) + k^2_{ML}(T)}{k^2_{ML}(T) + k^1_{ML}(T) \cdot \exp\left(\left(k^1_{ML}(T) + k^2_{ML}(T)\right) \cdot t\right)}$$

The actual mass loss during a TGA experiment can be generally expressed by eq.(5) [11].

$$(5) \qquad M(t,T) = M(0) - \frac{m_A - m_B - m_S}{m_A} \cdot \left(M_A(0) - M_A(t,T)\right)$$

Due to the formation of the residue S and the possiblity of non-reacting components be present in the sample, the actually measured mass M(t,T) and the mass M_A(t,T) of the reacting substance A may not be equal. In the case of HNIW decomposition, pure HNIW is assumed to be the starting material. Hence, with M(0) = M_A(0) the eq.(6) can be derived from the eq.(5).

$$(6) \qquad M_r(t,T) = 1 - \frac{m_A - m_B - m_S}{m_A} \cdot \left(1 - M_{Ar}(t,T)\right) = 1 - \frac{m_C}{m_A} \cdot \left(1 - M_{Ar}(t,T)\right)$$

The mass loss ML is calculated by using eq.(7):

$$ML(t,T) = O + \left(1 - M_r(t,T)\right) \cdot 100\%$$

(7)

$$ML(t,T) = O + \frac{m_C}{m_A} \cdot \left(1 - M_{Ar}(t,T)\right) \cdot 100\%$$

In eq.(7) the parameter O stands for an offset caused by the evaporation of volatile compounds and may not be generated by the decomposition of A. As mentioned above HNIW forms a solid residue after thermal decomposition. Until now the values for the molar masses m_B, m_S und m_C of the corresponding reactants B, S and C are not known and eq.(7-1) in combination with eq.(4) was used to evaluate the measurements in the temperature range 160°C to 180°C. The data that had been recorded during the equilibration of the TGA system have been removed, which sets O to zero. For the use in propellants only the first few percentages in the decomposition of an energetic ingredient is of importance. This determines already the performance limits and eq.(7-1) is a suitable approximation to describe this very first part of the HNIW decomposition,

here between 0 and 3% in mass loss. The results of the modelling are presented in Figure 10 and Table 4. The solid lines in Figure 10 represent the calculated values according to the model, dots represent a reduced number of the experimental data used in the calculations, there numbers have been about 700 up to 1000 for each temperature.

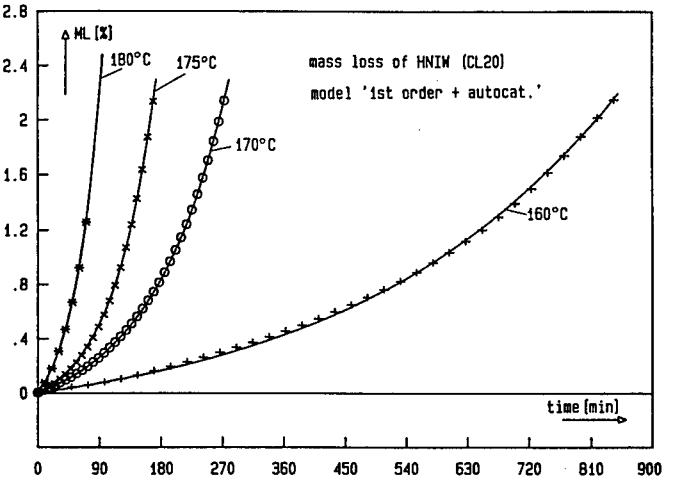

Fig. 10: correlation of isothermal TGA measurements of ε-HNIW ($d_{(0.5)}$ = 163 µm) with the „1st order + autocatalytic" model (solid line: calculated data, dots: selected measured data).

Tab. 4: reaction rate constants and Arrhenius parameters of isothermal decomposition of ε-HNIW at temperatures between 160°C and 180°C, calculated with the „1st order + autocatalytic" model

T / °C	k^1_{ML} / (1/min)	k^2_{ML} / (1/min)	correl.coeff.
160	7.3108 E-6	2.5639 E-3	0.99983
170	1.9450 E-5	8.7134 E-3	0.99991
175	2.6188 E-5	1.5603 E-2	0.99992
180	6.8665 E-5	2.4130 E-2	0.99997
Ea^i_{ML} / (kJ/mol)	172 ± 26	185 ± 7	
Z^i_{ML} / (1/s)	6.527 E+13	9.740 E+17	
$lg(Z^i_{ML}$ [1/s])	13.8 ± 3	18.0 ± 0.8	
correl.coeff.	0.9781	0.9985	

Correlation coefficients close to 1 indicate the good description of the experimental data by the model. Therefore, one can conclude that the thermal decomposition of HNIW is autocatalyticly accelerated. The activation energies of the two reaction rate constants are 172 kJ/mol and 185 kJ/mol. These values are lower compared with activation energies for the decomposition of RDX and HMX found in the literature [12]. The reported values are 198 kJ/mol and 220 kJ/mol for RDX, respectively HMX for their decomposition in the liquid state, evaluated by first order kinetics only. It is assumed that the values for their solid state decomposition are somewhat higher. In [10] Arrhenius parameters of the decomposition of HNIW in solution of acetone (1 mass %) are given: Z = 4 E+17 1/s and Ea = 177 kJ/mol. The temperature range was 146°C to 226°C. Again only a first order kinetics was applied. Even lower values of the activation energy have been reported by Brill [8], about 150 to 160 kJ/mol.

Due to the significant higher preexponential factor the autocatalytic reaction is dominating the unimolecular decomposition in solid HNIW. The correlation coefficient for the calculation of the Arrhenius parameters is somewhat smaller in the case of the unimolecular decomposition than in the case of the autocatalytic reaction (Tab. 4). Reasons herefore could be:

- influence of the solid-solid phase transition
- chemical impurities of HNIW
- influence of particle size

First results obtained from isothermal TGA measurements on small particle size ε-HNIW fractions and purified material seem to confirm this interpretation.

References

[1] P. Gerber, B. Zilly, U. Teipel,
Fine grinding of explosives, this proceeding, P 71

[2] M. Kaiser, B. Ditz,
Characterisation of ADN and CL 20 by NMR spectroscopy, this proceeding, P 130

[3] G. Bunte, H. Pontius, M. Kaiser,
Characterisation of impurities in new energetic materials, this proceeding, P 148

[4] H. Krause, A. Pfeil, N. Eisenreich,
Thermochim. Acta 149 (1989) 349

[5] M.F. Foltz, C.L. Coon, F. Garcia, A.L. Nichols III,
The thermal stability of the polymorphs of hexanitrohexaaza-isowurtzitane. Part I,
Propellants, Explos., Pyrotechn. 19 (1994) 19

[6] R.B. Wardle, J.C. Hinshaw, P. Braithwaite, M. Rose, G. Johnston, R. Jones, K. Poush,
Synthesis of the caged nitramine HNIW (CL-20),
Int. Annu. Conf. ICT (1996), 27th (Energetic Materials), 27.1-27.10, Karlsruhe, Germany

[7] M.F. Foltz, C.L. Coon, F. Garcia, A.L. Nichols III,
The thermal stability of the polymorphs of hexanitrohexaaza-isowurtzitane. Part II,
Propellants, Explos., Pyrotech. 19 (1994) 133

[8] D.G. Patil, T.B. Brill,
Thermal decomposition of energetic materials. 53. Kinetics and mechanism of thermolysis of hexanitro-hexazaisowurtzitane,
Combust. Flame 87 (1991) 145

[9] D.G. Patil, T.B. Brill,
Thermal decomposition of energetic materials. 59. Characterization of the residue of hexanitro-hexaazaisowurtzitane,
Combust. Flame 92 (1993) 456

[10] J.C. Oxley, A.B. Kooh, R. Szekeres, W. Zheng,
Mechanisms of nitramine thermolysis,
J. Phys. Chem. 98 (1994) 7004

[11] M.A. Bohn,
Systematische Darstellung der Alterung von Rohrwaffentreibmitteln und Raketenfesttreibstoffen,
Int. Annu. Conf. ICT (1997), 28th (Combustion and Detonation), 109.1-109.46, Karlsruhe, Germany

[12] R.A. Fifer,
Chemistry of Nitrate Ester and Nitramine Propellants,
in: Fundamentals of Solid-Propellant Combustion, Ed. K.K. Kuo; Vol. 90 of the series: Progress in Astronautics and Aeronautics, Editor: M. Summerfield, American Institute of Aeronautics and Astronautics, New York, 1984

Correlations between Theoretical and Experimental Determination of Heat of Formation of Certain Aromatic Nitro Compounds

P.C Chen*, S.C. Tzeng, J.C. Wu

Department of Applied Chemistry

Chung Cheng Institute of Technology

Tashi, Taoyuan, Taiwan (R.O.C.)

Abstract

Heats of formation of energetic materials can be obtained either experimentally or theoretically. In order to compare the results of the two method, a correlation method is proposed in this study. The molecular structures and heats of formation of nitrobenzenes and nitrotoluenes were calculated by Dewar's AM1 and Stewart's PM3 methods. Correlation for heat of formation between the theoretical calculations and experimental results was evaluated by the weighted least square multivariable method. Results indicate that there are very precise correlations. Based on these correlations, the heat of formation of some aromatic nitro compounds can be predicted without experimental analysis. The PM3 method provides a better results than the AM1 method because of its better calculation of the molecular structure. The weighted least square multivariable fitting to theoretical gas-phase and experimental crystal heats of formation for nitrobenzenes and nitrotoluenes is also presented. From these results, heat of sublimation can be predicted theoretically.

Introduction

Aromatic nitro compounds are widely used in various fields, especially explosives and these compounds are generally classified as secondary explosives [1,2]. For example, 2,4,6-trinitrotoluene (TNT), 2,4,6-trinitroaniline (TNA), and 2,4,6-

trinitrophenol (TNP) are well known for use in ammunitions. In order to investigate the characteristic of an explosive, the heat of formation is indispensable. There are two ways to determine the heat of formation : experimentally or theoretically. Heat of formation can be experimentally determined by using an adiabatic calorimeter, and this process is described in any physical chemistry textbook. Recently, a reduced pressure differential scanning calorimeter has been applied for use with nitro derivatives of benzene and toluene for estimating heat of formation [3]. However, certain aromatic nitro compounds are difficult to synthesis and some of them are highly unstable. Hence, it would be useful to develop a reliable theoretical means to calculate the heat of formation of energetic materials. If the theoretical calculations and experimental data have a reliable degree of correlation, some highly unstable and difficult to synthesize explosives can be analyzed and that data would be useful to study the properties of those explosives.

Various theoretical methods have been selected to calculate the heat of formation of a molecule. Among them, the semi-empirical and ab initio methods are the most commonly used. Although the ab initio approaches can calculate the heat of formation of a molecule, they only apply to "small to medium size" systems [4-11]. Furthermore, in order to develop a precise ab initio calculation, more complicated electron correlation methods must be considered. Hence, this method can require huge amounts of calculation time. Recently, the ab initio approach by using selection of the isodesmic reaction to calculate the heat of formation for the studied molecule has been reported extensively [11-13]. However, it is difficult to find the heat of formation for some reactants or the products of the isodesmic reaction for an aromatic nitro compound.

Semi-empirical methods are especially designed to obtain heat of formation of chemical systems [14-20]. In spite of their usefulness and their low computational cost,

semi-empirical methods have some drawbacks. However, most of these problems can be corrected by an "ad hoc" correction to the semi-empirical heat of formation, adding -9 kcal/mol to the AM1 and 3.5 cal/mol to the PM3 heat of formation for each adjacent lone pair-lone pair repulsion of nitro substituted compounds [21]. Successive NO_2 substitution in a given skeleton presumably will require additional corrections, thus favoring the continued use of the additive models are still in use [22,23].

The scope of this study develops semi-empirical calculations of the heat of formation of aromatic nitro compounds in various phases by selecting the AM1[24] and PM3 [25,26] levels. Firstly, we choose the families of nitrobenzenes and nitrotoluenes to calculate their geometries and heat of formation. Secondly, a weighted least square multivariable fitting of the experimental heat of formation to theoretical heat of formation in each system is applied. Finally, the corrected heat of formation of the most stable conformer of the discussed molecules are presented, including those whose experimental results are not available.

Computational Aspects

The Spartan version 4.1 software package [27] was selected as the tool for calculation of the molecular structures and heat of formation of 33 benzene and toluene, as well as their nitro isomers. The molecular geometries of all isomers are fully optimized at the semi-empirical AM1 and PM3 theoretical levels of theory without any sort of geometrical restrictions. Second derivatives were calculated by verifying the vibrational frequencies so that a local minimum was be located for each molecule.

Correlation of heats of formation between the theoretical and experimental results was performed by a statistical SPSS version 7.0 software [28], considering the number and the position of the nitro groups. From the scatter diagram of the experimental heats

of formation against the number of C-NO_2, a piecewise linear regression model is proposed. For inference in regression analysis, the weighted least square (WLS) method was selected and the fitted model was obtained. After analyzing the process of the fitted model, a 95% predictive interval was found, thus giving a prediction for the heat of formation for aromatic nitro compounds whose experimental value is unknown.

Results and Discussion

1.Molecular geometries

Fig. 1 presents the geometry of thirteen nitrobenzene isomers, and significant bond lengths, bond angles, and dihedral angles are listed in Table 1. For nitrobenzene, AM1 and PM3 give the excellent agreement with the experimental results [29-31]. It is generally accepted that, because of the inductive and resonance effects, the nitro group is coplanar with the phenyl ring. However, when two or more groups are held close together, steric effect must be considered. In order to avoid steric crowding, distortion of the nitro group is necessary. Hence, we observe that nitrobenzene, 1,3-dinitrobenzene, 1,4-dinitrobenzene, 1,3,5-trinitrobenzene are planar molecules, but the other isomers are nonplanar molecules and the distortion angles of these nitro groups are listed in Table 1. The nitro groups of 1,2-dinitrobenzene are distorted at 37.2^0 and 38.7^0 (AM1) and 47.7^0 and 47.2^0 (PM3), respectively to the same direction from the plane of the phenyl ring, while the experimental values were both in 31.1^0 [32]. In the hexanitrobenzene molecule, the six nitro groups are distorted at 53^0 to the same direction as determined experimentally [16]. However, the six distortional angles of the nitro groups are 52.8^0, 52.9^0, 52.5^0, 52.8^0, 52.8^0, and 52.5^0, respectively for AM1 method and 54.8^0, 55.1^0, 54.4^0, 55.1^0, 54.9^0, and 54.6^0, respectively for PM3 method. Those distortions are also the same directions from the plane of phenyl ring.

The O-O distance between the neighboring nitro groups is essential to determine whether the calculated geometry represents a true molecule. For example, as shown in Fig. 2, if the O_9 and O_{11} atoms are held closely, a bonding is expected to exist between them and a cyclic molecule can be obtained, although this cyclic molecule also has a local minimum. Hence, it is necessary to carefully examine all O-O bonds. To prevent formation of a cyclic molecule, the O-O bond must more than twice the length of the oxygen's Van der Waals radius. All the O-O distances between the neighboring nitro groups are listed in Table 1, indicating that these distance are significant. Therefore, the molecules studies are not cyclic.

No further discussion of nitrotoluenes is given here because the ab initio study of their geometries have been extensively reported by us [33-39].

2.Heats of formation

Theoretical AM1 and PM3 calculations of heats of formation of nitrobenzenes and nitrotoluenes in gaseous phase are listed in Table 2. Plotting AM1 and PM3 calculated heats of formation versus the experimental values, no correlation was found because the coefficient of correlation is 0.422 in both methods. De Paz et al. [21] have corrected the relationships for nitrobenzenes and nitrotoluenes by estimating the lone pair-lone pair repulsion proximity effects. They observed that the best regression coefficients were obtained at the AM1 and PM3 levels corresponding to the correction for each C-NO_2 group of -9 kcal/mol and 3.5 kcal/mol, respectively. However, since their model lacks regression diagnosis and prediction intervals, its reliability is questionable. Hence, further study is necessary. In this study, we use the weighted least square multivariable fitting for the experimental and theoretical values and consider the number of the nitro group in order to find a proper regression model. Furthermore, the prediction interval for the experimental values is proposed.

The scatter diagram of the experimental heats of formation in gaseous phase for nitrobenzene against the number of nitro group is presented in Fig. 3. From this figure, a "piecepwise" regression must be selected instead of "simple" linear regression. Hence, we consider the regression models (1) and (2) and obtain the fitted model (3) and (4) by least square method.

$$AM1\Delta H_f(exp)=\beta_0+\beta_1\,(AM1\Delta H_f)+\beta_2 n+\beta_3(n-1)m+\varepsilon \quad (1)$$

$$PM3\Delta H_f(exp)=\beta_0+\beta_1\,(PM3\Delta H_f)+\beta_2 n+\beta_3(n-1)m+\varepsilon \quad (2)$$

where β_0, β_1, β_2, and β_3 are undetermined parameters

n = number of $C-NO_2$

$$m=\begin{cases}1, & n>1\\ 0, & \text{otherwise}\end{cases}$$

ε is a random error term obeying normal distribution $N(0, \sigma^2)$

$$AM1\Delta H_f(exp)=-5.677+1.185\,(AM1\Delta H_f)-8.593n-3.076(n-1)m \quad (3)$$

$$PM3\Delta H_f(exp)=-3.222+1.019\,(PM3\Delta H_f)+3.821n-0.368(n-1)m \quad (4)$$

Assessing the fitted models, the coefficient of multiple determination R^2 and the adjusted coefficient of multiple determination Ra^2 are 0.980, 0.960 (AM1) and 0.974, 0.948 (PM3), respectively. Fig. 4 gives a SPSS residual plot against the fitted values and tends to be of the "megaphone" type. This suggests that error terms have nonconstant variance and the error variance decreases with the fitted values. To make the variances of the error terms more nearly equal, the WLS is selected to fit the regression models and the fitted equations are presented in (5) and (6).

$$AM1\Delta H_f(exp)=-6.572+1.204\,(AM1\Delta H_f)-7.921n-4.398(n-1)m \quad (5)$$

and

$$PM3\Delta H_f(exp)=-2.825+1.039\,(PM3\Delta H_f)+3.810n-0.468(n-1)m \quad (6)$$

After examing the aptness of the models (5) and (6) , we note that R^2 and Ra^2 are 0.999 (AM1,PM3) and 0.998(AM1), 0.997(PM3) in both and methods, respectively. The p-

value of the F-test is 0.000, which is less than significant level 0.05. The above results show that there exists a good regression relationship between the response and explanatory variables. Moreover, the Durbin-Watson statistics are 2.124 (AM1) and 1.990 (PM3); the residuals are randomly around the base line 0, and the normal probability plot is nearly linear. Those values suggest that there is an agreement with normality and independence of error terms. Finally, we proposed the predictions and 95% predictive intervals for AM1 and PM3 methods for all nitrobenzenes and nitrotoluenes, as given in Tables 2 by using models (5) and (6).

Similar statistical regressions are selected to study the AM1 and PM3 heats of formation of nitrobenzenes and nitrotoluenes in condensed phase and the fitted equations and data are given in Equations (7) and (8) and Table 3.

$$AM1\Delta H_f(exp)=-16.083+1.197\ (\Delta H_f\ AM1)-12.987n-1.335(n-1)m \quad (7)$$

and

$$PM3\Delta H_f(exp.)=-13.722+1.036\ (\Delta H_f\ PM3)-0.408n+1.356(n-1)m \quad (8)$$

When the previous fitting model was selected, there are unreasonable heats of formation of 3,4-dinitrotoluene, 2,3,4-trinitrotoluene and 2,4,6-trinitrotoluene were found. And the Ra^2 only have 0.649 (AM1) and 0.640 (PM3). Similar results were also reported by De Paz et al. [21]. Since the nitro groups of these molecules are held close together, the steric effect may play an important role to affect the prediction of their heats of formation. Hence, the steric effect must be considered and we included an variable which is the number of nitro groups are held together, and used WLS to fit regression model. A multivariant fitting model can be obtained :

$$AM1\Delta H_f(exp)=-11.820+0.963\ (\Delta H_f\ AM1)-12.347n-1.429(n-1)m+4.840I \quad (9)$$

and

$$PM3\Delta H_f(exp.)=-10.278+0.853\ (\Delta H_f\ PM3)-2.189n+0.858(n-1)m+4.747I \quad (10)$$

where N = number of $C-NO_2$

I = the number of nitro groups are held close together

Because there exists serious collinearity in models (9) and (10), we consider their reduced model and conclude the reduced models, which are given by (11) and (12), by F-test.

$$AM1\Delta H_f(exp)=-10.412+0.965\ (\Delta H_f\ AM1)-13.786n+4.882I \quad (11)$$

and

$$PM3\Delta H_f(exp.)=-10.858+0.865\ (\Delta H_f\ PM3)-1.524n+4.837I \quad (12)$$

Statistical analysis, such as $R^2 = 0.993$ (AM1), 0.997 (PM3), residual, and normal plots, suggest that the above models are reasonable and suitable. In Table 4, the corresponding fitted values and 95% predictive intervals are illustrated. Especially notable is that the estimated heats of formation in crystal phase of 3,4-dinitrotoluene, 2,3,4-trinitrotoluene and 2,4,6-trinitrotoluene were -3.808, 2.463 and -11.773 (AM1), and -4.492, 3.602 and -12.527 (PM3), respectively. These results are superior to the values predicted by De Paz et al.[21].

Conclusion

The molecular structures of 33 nitrobenzene and nitrotoluene isomers were calculated by AM1 and PM3 semi-empirical methods. Calculated geometries were found to be similar to experimental data. The deformation of the benzene ring is affected by the substituted groups and the distortional angle of the substitute groups is affected by the steric effect. The weighted least square multivariable fittings on the calculated heats of formation by either the AM1 or the PM3 approach against the experimental approaches were presented. For the correlation, the number and position of the nitro groups were considered. After finishing these fittings, there is a 95%

predictive interval in each fitting. Based on these precise correlations, the heats of formation of some aromatic nitro compounds for which experimental data are not available, can be predicted and these values are useful to study the properties of explosives.

Acknowledgments

This work was support by the National Science Foundation (NSC 87-2113-M-014-005). The calculation facility was supported by the Computer Center of Chung Cheng Institute of Technology.

References:

1.T. Urbanski, Chemistry and Technology of Explosives, Pergamon Press, New York, 1984.

2.J. Kohler and R. Meyer, Explosives, VCH, New York, 1993.

3.D. R. Hwang, M. Tamura, T. Yoshida, N. Tanaka and F. Hosofa, J. Energetic Materials, 8 (1990) 85.

4.J. M. Schulman and R. L. Disch, J. Am. Chem. Soc., 106 (1984) 1202.

5.L. R. Schmitz, I. Motoc, C. Bender, J. K. Labanowski, and N. L. Allinger, J. Phys. Org. Chem., 5 (1992) 225.

6.N. L. Allinger, L. R. Schmitz, I. Motoc, C. Bender, and J. K. Labanowski, J. Comput. Chem., 13 (1992) 838.

7.B. J. Smith, J. A. Pople, L. A. Curtiss and L. Radom, Aust. J. Chem., 45 (1992) 285.

8.N. L. Allinger, L. R. Schmitz, I. Motoc, C. Bender, and J. K. Labanowski, J. Am. Chem. Soc., 14 (1992) 2880.

9.E. A. Castro, J. Mol. Struct. (Theochem), 304 (1994) 93.

10.D. A. Good and J. S. Francisco, Chem. Phys. Letters, 266 (1997) 512.

11.J. Espinosa-Garcia, Chem. Phys. Letters, 278 (1997) 209.

12.W. J. Hehre, L. Radom, P. v. R. Schleyer and J. A. Pople, Ab Initio Molecular Orbital Theory, John Wiley & Sons, New York, 1986.

13.J. B. Foresman and A. Frisch, Exploring Chemistry with Electronic Strcuture Methods, 2nd Ed., Gaussian, Inc., Pittsburgh, U. S. A., 1996.

14.L. P. Davis, D. Storch and R. M. Guidry, J. Energetic Materials, 5 (1987) 89.

15.Y. Akutsu, J. Takayama and M. Tamura, J. Energetic Materials, 10 (1992) 173.

16.T. Matsunaga, Y. Nakayama, M. Iida, S. Oinuma, N. Ishikawa and K. Tanaka, Propellants, Explosives, Pyrotechnics, 17 (1992) 63.

17.Y. Akutsu and M. Tamura J. Energetic Materials, 11 (1993) 205.

18.Y. Akutsu, R. Che and M. Tamura, J. Energetic Materials, 11 (1993) 195.

19.H. Xiao, X. Gong and B. Yu, Acta Chemica Sinica, 52 (1994) 750.

20.X. Gong, J. Wang and H. Xiao, Chem. J. Chinese University, 12 (1994) 1817.

21.J. G. De Paz and J. Ciller, Propellants, Explosives, Pyrotechnics, 8 (1993) 33.

22.S. Bourasseau, J. Energetic Materials, 8 (1990) 266.

23.S. Bourasseau, J. Energetic Materials, 8 (1990) 416.

24.M. J. S. Dewar, E. G. Zoebisch, E. F. Healy and J. P. Stewart, J. Am. Chem. Soc., 107 (1985) 3902.

25.J.J.P. Stewar, J. Comput. Chem., 10 (1989) 201.

26.J.J.P. Stewart, J. Comput. Chem. 11 (1990) 543.

27.Spartan Version 4.1, Wavefunction, Inc., 18401 Von Karman Ave., #370, Irvine, CA 92715 USA, 1995.

28.SPSS Release 7.0, SPSS Inc., 444 N. Michigan Avenue, Chicago, IL, 60611, 1995.
29.P. Nosberger, A. Bauder and Hs. H. Gunthard, Chem. Phys., 8 (1975) 245.
30.I. F. Shishkov, N. I. Sadova, V. P. Novikov and L. V. Vilkov, Zh. Strukt. Knim., 25 (1984) 98.
31.L. E. Sutton (Ed.), "Table of Interatomic Distance and Configuration in Molecules and Ions", Special Publication No. 18, The Chemical Society, London, 1965.
32.N. P. Penionzhkevich, N. I. Popik, L. V. Vilkov and Yu. A. Pankrushev, Zh. Strukt. Khim., 20 (1979) 603.
33.P. C. Chen and C. C. Huang, J. Mol. Struct. (Theochem.), 282 (1993) 287.
34.P. C. Chen, Chemistry (The Chinese Chem. Soc. Taiwan), 52 (1994) 147.
35.P. C. Chen and C. W. Wu, J. Mol. Struct. (Theochem.), 357 (1995) 87.
36.P. C. Chen, J. Chin. Chem.. Soc., 42 (1995) 755.
37.P. C. Chen, W. Lo and K. H. Hu, J. Mol. Struct. (Theochem.), 389 (1997) 91.
38.P. C. Chen, W. Lo and K. H. Hu, Theor. Chim. Acta., 95 (1997) 99.
39.P. C. Chen and W. Lo, J. Mol. Struct. (Theochem), 397 (1997) 21.

Table 1 Some geometry parameters of nitronenzenes

parameter	nitrobenzene		1,2-dinitrobenzene		1,3-dinitrobenzene	
	AM1	PM3	AM1	PM3	AM1	PM3
C1-X1	1.487	1.497	1.495	1.516	1.490	1.505
C2-X2	1.103	1.099	1.495	1.516	1.109	1.105
C3-X3	1.101	1.096	1.105	1.100	1.490	1.505
Y2-Y3	-	-	2.689	3.042	-	-
C2-C1-C6	121.0	119.8	119.7	119.6	121.3	120.1
C1-C2-C3	119.0	119.8	119.8	119.6	118.1	119.6
C2-C3-C4	120.4	120.3	119.9	120.4	121.3	120.1
X1-C1-C6-C2	180.0	180.0	-178.7	178.4	180.0	180.0
Y1-X1-C1-C6	-0.4	0.6	-37.2	47.7	0.3	0.8
X2-C2-C1-C3	180.0	180.0	178.6	-178.3	180.0	180.0
Y3-X2-C2-C1	-	-	-38.7	47.2	-	-
Y5-X3-C3-C2	-	-	-	-	0.5	-1.3

(continue)

parameter	1,4-dinitrobenzene		1,2,3,-trinitrobenzene		1,2,4-trinitrobenzene	
	AM1	PM3	AM1	PM3	AM1	PM3
C1-X1	1.492	1.508	1.499	1.523	1.500	1.526
C2-X2	1.105	1.100	1.505	1.540	1.499	1.523

C3-X3	1.105	1.110	1.499	1.523	1.110	1.105
C4-X4	1.492	1.508	1.199	1.208	1.495	1.514
Y2-Y3	-	-	2.793	3.026	2.695	3.049
Y4-Y5	-	-	2.792	3.036	-	-
C2-C1-C6	121.2	119.9	120.5	120.3	120.0	119.7
C1-C2-C3	119.4	120.1	118.7	119.0	120.0	119.8
C2-C3-C4	119.4	120.1	120.5	120.3	119.0	120.1
C3-C4-C5	121.2	119.9	119.9	120.2	121.3	120.1
X1-C1-C6-C2	180.0	180.0	179.4	-178.9	-178.8	178.4
Y1-X1-C1-C6	0.0	-1.0	36.8	-42.0	-39.8	50.9
X2-C2-C1-C3	180.0	180.0	180.0	180.0	178.9	-178.6
Y3-X2-C2-C1	-	-	53.0	-59.3	-37.5	45.4
X3-C3-C2-C4	180.0	180.0	179.4	178.8	-179.8	179.8
Y5-X3-C3-C2	-	-	38.5	-44.6	-	-
X4-C4-C3-C5	180.0	180.0	179.9	-179.8	179.8	-179.8
Y7-X4-C4-C3	0.1	-2.2	-	-	-1.4	1.4

(continue)

parameter	1,3,5-trinitrobenzene		1,2,3,4-tetranitrobenzene		1,2,3,5-tetranitrobenzene	
	AM1	PM3	AM1	PM3	AM1	PM3
C1-X1	1.493	1.513	1.503	1.532	1.503	1.530
C2-X2	1.111	1.106	1.509	1.545	1.510	1.550
C3-X3	1.493	1.513	1.509	1.545	1.503	1.530
C4-X4	1.111	1.106	1.503	1.532	1.112	1.106
C5-X5	1.493	1.513	1.108	1.101	1.498	1.520
Y2-Y3	-	-	2.860	3.015	2.796	3.029
Y4-Y5	-	-	2.589	3.031	2.795	3.029
Y6-Y7	-	-	2.881	3.016	-	-
C2-C1-C6	121.6	120.4	120.4	120.2	120.8	120.5
C1-C2-C3	118.4	119.6	119.5	119.7	118.9	119.1
C2-C3-C4	121.6	120.4	119.5	119.7	120.8	120.5
C3-C4-C5	118.4	119.6	120.4	120.2	119.0	120.0
C4-C5-C6	121.6	120.4	120.1	120.2	121.4	120.0
C1-C6-C5			120.1	120.2	119.0	120.0
X1-C1-C6-C2	180.0	180.0	-179.9	-178.6	-179.6	-179.1
Y1-X1-C1-C6	0.0	0.3	33.9	-45.5	-36.5	-42.5
X2-C2-C1-C3	180.0	180.0	-177.7	179.6	180.0	180.0
Y3-X2-C2-C1	-	-	-57.3	-55.7	-54.1	-60.1

X3-C3-C2-C4	180.0	180.0	-177.8	-179.0	179.6	179.0
Y5-X3-C3-C2	0.0	-0.2	-60.8	-55.8	-38.3	-43.7
X4-C4-C3-C5	180.0	180.0	-179.9	178.5	-179.9	180.0
Y7-X4-C4-C3	-	-	-37.0	-47.1	-	-
X5-C5-C4-C6	180.0	180.0	-179.3	-179.5	180.0	180.0
Y9-X5-C5-C4	-0.5	-0.6	-	-	-2.5	-15.2

(continue)

parameter	1,2,4,5-tetranitrobenzene		1,2,3,4,5-pentanitrobenzene		1,2,3,4,5,6-hexanitrobenzene	
	AM1	PM3	AM1	PM3	AM1	PM3
C1-X1	1.503	1.532	1.507	1.538	1.517	1.560
C2-X2	1.503	1.532	1.513	1.555	1.517	1.560
C3-X3	1.110	1.105	1.514	1.551	1.517	1.560
C4-X4	1.503	1.532	1.513	1.555	1.517	1.560
C5-X5	1.503	1.531	1.507	1.538	1.517	1.560
C6-X6	1.111	1.105	1.113	1.106	1.517	1.560
Y2-Y3	2.692	3.036	2.791	3.007	2.902	2.996
Y4-Y5	-	-	2.893	3.014	2.899	2.995
Y6-Y7	-	-	2.893	3.015	2.898	2.997
Y8-Y9	2.683	3.027	2.792	3.007	2.901	2.998
Y10-Y11	-	-	-	-	2.898	2.995
Y12-Y1	-	-	-	-	2.897	2.993
C2-C1-C6	120.0	119.7	120.6	120.1	120.0	120.0
C1-C2-C3	120.0	119.6	119.4	119.5	120.0	120.0
C2-C3-C4	119.8	120.7	120.2	120.3	120.0	120.0
C3-C4-C5	120.0	119.7	119.4	119.5	120.0	120.0
C4-C5-C6	120.0	119.6	120.6	120.1	120.0	120.0
C1-C6-C5	119.9	120.6	119.8	120.4	120.0	120.0
X1-C1-C6-C2	-179.1	-178.8	179.7	179.1	180.0	180.0
Y1-X1-C1-C6	-37.4	-47.3	36.1	42.6	-52.8	-54.8
X2-C2-C1-C3	179.1	178.8	-179.5	-179.8	180.0	180.0
Y3-X2-C2-C1	-38.8	-47.0	52.6	52.2	-52.8	-55.1
X3-C3-C2-C4	180.0	180.0	180.0	180.0	180.0	180.0
Y5-X3-C3-C2	-	-	53.3	53.9	-52.5	-54.4
X4-C4-C3-C5	-179.2	178.8	179.6	179.8	180.0	180.0
Y7-X4-C4-C3	-37.6	-47.3	53.2	57.2	-52.8	-55.1
X5-C5-C4-C6	179.1	178.8	-179.6	-179.0	180.0	180.0
Y9-X5-C5-C4	-38.1	-46.4	38.0	44.1	-52.8	-54.9

X6-C6-C5-C1	180.0	180.0	180.0	180.0	180.0	180.0
Y11-X6-C6-C5	-	-	-	-	-52.5	-54.6

Table 2 Heats of formation of various nitro derivatives of benzene and toluene in gaseous phase from model (5),(6)

	Exp.	AM1(cal.)	Predict(AM1)	PM3(cal.)	Predict(PM3)
Benzene	19.81	22.022	19.942	23.453	21.543
Nitrobenzene	16.1	25.292	15.959	14.535	16.087
1,2-dinitrobenzene	20.2	38.609	19.673	15.228	20.149
1,3-dinitrobenzene	11.3	33.132	13.079	9.128	13.811
1,4-dinitrobenzene	13.3	33.289	13.268	10.134	14.856
1,2,3-trinitrobenzene		53.912	25.779	18.222	26.602
1,2,4-trinitrobenzene		50.026	21.1	13.176	21.359
1,3,5-trinitrobenzene	14.9	44.875	14.898	6.941	14.881
1,2,3,4-tetranitrobenzene		73.88	37.502	23.962	35.908
1,2,3,5-tetranitrobenzene		68.337	30.828	18.301	30.026
1,2,4,5-tetranitrobenzene		69.391	32.097	18.886	30.634
1,2,3,4,5-pentanitrobenzene		92.441	47.53	31.271	46.844
1,2,3,4,5,6-hexanitrobenzene		117.233	65.061	45.788	65.269
Toluene	11.99	14.41	10.778	14.09	11.815
o-nitrotoluene	9.3	18.919	8.285	8.001	9.298
m-nitrotoluene	4.1	17.593	6.689	5.071	6.254
p-nitrotoluene	7.4	17.249	6.275	4.682	5.85
2,3-dinitrotoluene		31.776	11.446	8.024	12.664
2,4-dinitrotoluene	4.7	26.196	4.728	2.025	6.431
2,5-dinitrotoluene		26.729	5.37	3.027	7.472
2,6-dinitrotoluene	9.6	30.105	9.434	6.382	10.958
3,4-dinitrotoluene		30.455	9.856	5.29	9.823
3,5-dinitrotoluene		25.297	3.646	-0.387	3.925
2,3,4-trinitrotoluene		46.593	16.967	10.815	18.906
2,3,5-trinitrotoluene		42.914	12.537	5.652	13.541
2,3,6-trinitrotoluene		45.963	16.208	9.812	17.864
2,4,5-trinitrotoluene		42.83	12.436	5.642	13.531
2,4,6-trinitrotoluene	12.3	41.222	10.5	3.356	11.156
3,4,5-trinitrotoluene		45.623	15.799	8.147	16.134
2,3,4,5-tetranitrotoluene		64.451	26.149	16.248	27.893
2,3,4,6-tetranitrotoluene		63.778	25.339	14.739	26.325
2,3,5,6-tetranitrotoluene		65.04	26.858	15.47	27.084
2,3,4,5,6-pentanitrotoluene		87.265	41.298	27.95	43.393

Table 3 Heats of formation of various nitro derivatives of benzene and toluene in condense phase from model (7),(8)

	Exp.	Cal.(AM1)	Predict(AM1)	Cal.(PM3)	Predict(PM3)
Benzene	10.130	22.022	10.288	23.453	10.581
Nitrobenzene	0.200	25.292	1.216	14.535	0.932
1,2-dinitrobenzene	-0.430	38.609	2.840	15.228	2.599
1,3-dinitrobenzene	-6.023	33.132	-3.719	9.128	-3.723
1,4-dinitrobenzene	-9.230	33.289	-3.531	10.134	-2.680
1,2,3-trinitrobenzene		53.912	6.842	18.222	6.649
1,2,4-trinitrobenzene	6.800	50.026	2.189	13.176	1.420
1,3,5-trinitrobenzene	-8.481	44.875	-3.979	6.941	-5.041
1,2,3,4-tetranitrobenzene		73.880	16.430	23.962	13.545
1,2,3,5-tetranitrobenzene		68.337	9.793	18.301	7.679
1,2,4,5-tetranitrobenzene		69.391	11.055	18.886	8.285
1,2,3,4,5-pentanitrobenzene		92.441	24.334	31.271	22.067
1,2,3,4,5,6-hexanitrobenzene		117.233	39.699	45.788	38.059
Toluene	1.330	14.410	1.173	14.090	0.879
o-nitrotoluene	-0.400	18.919	-6.416	8.001	-5.839
m-nitrotoluene	-6.000	17.593	-8.003	5.071	-8.875
p-nitrotoluene	-11.500	17.249	-8.415	4.682	-9.278
2,3-dinitrotoluene	-3.806	31.776	-5.342	8.024	-4.867
2,4-dinitrotoluene	-16.298	26.196	-12.024	2.025	-11.083
2,5-dinitrotoluene	-8.195	26.729	-11.386	3.027	-10.045
2,6-dinitrotoluene	-10.489	30.105	-7.343	6.382	-6.568
3,4-dinitrotoluene	-3.496	30.455	-6.924	5.290	-7.700
3,5-dinitrotoluene	-10.398	25.297	-13.100	-0.387	-13.582
2,3,4-trinitrotoluene	3.611	46.593	-1.922	10.815	-1.026
2,3,5-trinitrotoluene	-5.496	42.914	-6.327	5.652	-6.376
2,3,6-trinitrotoluene	-3.997	45.963	-2.676	9.812	-2.066
2,4,5-trinitrotoluene	-3.702	42.830	-6.428	5.642	-6.387
2,4,6-trinitrotoluene	-14.194	41.222	-8.354	3.356	-8.756
3,4,5-trinitrotoluene	-1.204	45.623	-3.084	8.147	-3.791
2,3,4,5-tetranitrotoluene		64.451	5.140	16.248	5.552
2,3,4,6-tetranitrotoluene		63.778	4.334	14.739	3.988
2,3,5,6-tetranitrotoluene		65.040	5.845	15.470	4.746
2,3,4,5,6-pentanitrotoluene		87.265	18.136	27.950	18.626

Table 4 Heats of formation of various nitro derivatives of benzene and toluene in condense phase from model (11),(12)

Predict(AM1)	Low limit of 95% predict interval	Up limit of 95% predict interval	Predict(PM3)	Low limit of 95% predict interval	Up limit of 95% predict interval

Benzezne	9.789	7.639	11.946	9.429	7.364	11.506
Nitrobenzene	-0.212	-1.834	1.420	0.191	0.038	0.351
1,2-dinitrobenzene	3.522	-4.389	11.449	4.103	-4.612	12.827
1,3-dinitrobenzene	-6.105	-6.680	-5.517	-6.010	-6.210	-5.806
1,4-dinitrobenzene	-5.964	-12.649	0.734	-5.140	-13.805	3.529
1,2,3-trinitrobenzene	9.043			10.006		
1,2,4-trinitrobenzene	0.845	-12.090	13.801	0.804	-12.712	14.327
1,3,5-trinitrobenzene	-8.489	-8.595	-8.364	-9.426	-11.325	-7.524
1,2,3,4-tetranitrobenzene	18.757			18.284		
1,2,3,5-tetranitrobenzene	9.070			8.550		
1,2,4,5-tetranitrobenzene	10.018			9.056		
1,2,3,4,5-pentanitrobenzene	27.206			27.919		
1,2,3,4,5,6-hexanitrobenzene	41.257			43.790		
Toluene	2.946	0.372	5.524	1.330	1.181	1.486
o-nitrotoluene	-5.942	-18.532	6.656	-5.461	-15.758	4.840
m-nitrotoluene	-7.134	-10.465	-3.796	-7.996	-11.642	-4.347
p-nitrotoluene	-7.443	-15.436	0.556	-8.332	-15.620	1.042
2,3-dinitrotoluene	-2.620	-4.532	-0.696	-2.128	-5.356	1.104
2,4-dinitrotoluene	-12.341	-20.483	-4.188	-12.154	-21.516	-2.793
2,5-dinitrotoluene	-11.862	-20.141	-3.570	-11.288	-17.266	-5.309
2,6-dinitrotoluene	-8.827	-12.103	-5.538	-8.386	-13.135	-3.633
3,4-dinitrotoluene	-3.308	-5.254	-2.349	-4.493	-6.796	-2.187
3,5-dinitrotoluene	-13.149	19.549	-6.738	-14.241	-21.566	-6.916
2,3,4-trinitrotoluene	2.463	-0.732	5.677	3.599	2.028	5.176
2,3,5-trinitrotoluene	-5.548	-6.068	-5.011	-5.704	-6.615	-4.791
2,3,6-trinitrotoluene	-2.807	-5.159	-0.437	-2.106	-5.485	1.279
2,4,5-trinitrotoluene	-5.624	-10.018	-1.212	-5.713	-10.314	-1.108
2,4,6-trinitrotoluene	-11.773	-17.009	-6.520	-12.527	-16.408	-8.645
3,4,5-trinitrotoluene	1.591	-3.849	7.050	1.291	-3.008	5.595
2,3,4,5-tetranitrotoluene	10.280			11.612		
2,3,4,6-tetranitrotoluene	4.971			5.469		
2,3,5,6-tetranitrotoluene	6.106			6.102		
2,3,4,5,6-pentanitrotoluene	22.553			25.047		

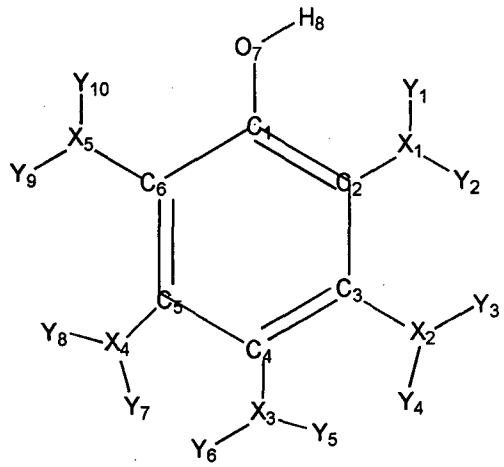

X= N or H atom, Y= O atom

Fig. 1. The molecular structures of the dinitrophenols and trinitrophenols

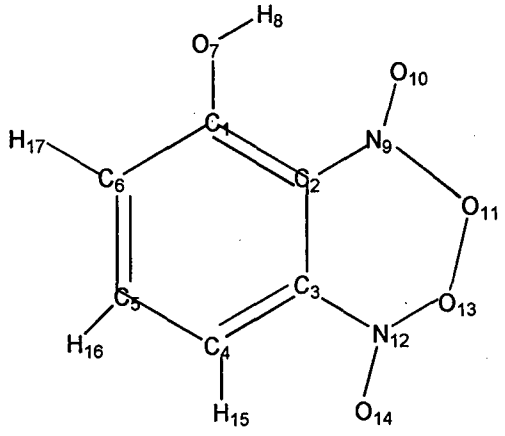

Fig. 2. A cyclic molecule of 2,3- dinitrophenol which the O11 and O13 atoms are bonding

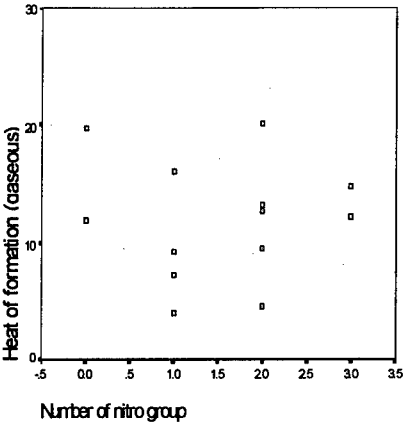

Fig.3 The scatter diagram of exp. heats of formation (gaseous) for nitrobenzene and nitrotoluenes against the number of nitro group

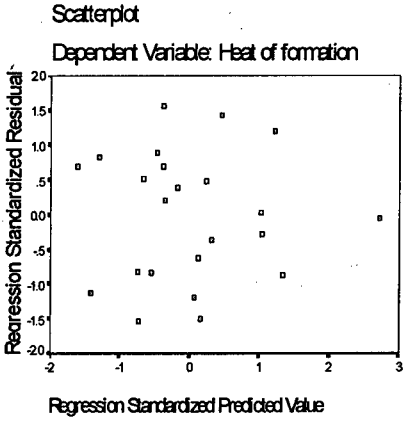

Fig.4 The SPSS plot for residual vs. Predictive value from model (3)

Untersuchung zur Stabilität und Reaktivität von reinem NTO, NTO/RDX- und NTO/TNT-Gemengen zur Beurteilung ihrer sicheren Verwendung

Investigation on Stability and Reactivity of NTO and the mixtures NTO/RDX and NTO/TNT to Assess Their Safe Use

Manfred A. Bohn, Heike Pontius, Stefan Löbbecke

Fraunhofer-Institut für Chemische Technologie (ICT)
Postfach 1240, D-76318 Pfinztal-Berghausen, Germany

Stephan Wilker, Gabriele Pantel

Wehrwissenschaftliches Institut für Werk-, Explosiv- und Betriebsstoffe (WIWEB)
Außenstelle Swisttal Heimerzheim
Großes Cent, D-53913 Swisttal-Heimerzheim, Germany

Kurzfassung

NTO (3-Nitro-1,2,4-triazol-5-on) hat mindestens ein als Proton abspaltbares Wassersoffatom von zwei Wasserstoffatomen gebunden an zwei Ringstickstoffatomen. Eine Unverträglichkeit mit anderen Explosivstoffen oder Kontaktmaterialen ist daher möglich. Von den beiden Instituten WIWEB und ICT wurden in einer gemeinsamen Untersuchung Methoden angewendet, um chemische Reaktionen zwischen NTO und RDX und zwischen NTO und TNT aufzudecken, welche einen Einsatz des NTO in Sprengladungen fraglich werden lassen oder gar ausschließen könnten. Um Reaktionen zu beschleunigen und eine Alterungsabhängigkeit der Unverträglichkeit zu erkennen, wurden die Einzelsprengstoffe und die massenbezogenen 1:1-Mischungen NTO/RDX und NTO/TNT bei 65,5°C über zwei und vier Monate gealtert. Die Untersuchungsmethoden waren: Thermoanalyse mit TGA/DTA und DSC, isotherme Wärmestrom-Mikrokalorimetrie gemessen mit einem TAM™, adiabatische Selbstaufheizung gemessen mit einem ARC™, Infrarotabsorption, sowie Massenverlust nach der Lagerung und eine Wasserbestimmung nach der Karl-Fischer-Methode.

Mit den thermoanalytischen Methoden TGA/DTA und DSC konnten erst im Temperaturbereich 160°C bis 220°C chemische Zersetzungsreaktionen festgestellt werden, die Zersetzungsbereiche lagen in der DSC noch höher. Die Probenmengen waren 10mg bis 20mg mit der TGA/DTA und um 0,4mg mit der DSC. RDX reagiert deutlich mit NTO. Die isotherm bei 65,5°C mit Einwaagen von 3g bis 3,5g durchgeführten mikrokalorimetrischen Wärmestrommessungen ließen keine signifikante reaktive Aktivität zwischen NTO und RDX und zwischen NTO und TNT erkennen. Kleine

Paper presented at the 29th Internat. Annual Conference of ICT, Karlsruhe, Germany, June 30 - July 3, 1998.

Wärmeströme im Bereich 100nW/g bis 200nW/g wurden gefunden, welche aber schon im Grenzbereich der Methode liegen. Die adiabatischen Selbstaufheizraten wurden mit Probenmengen von 250mg bis 400mg gemessen. Alle Anfangstemperaturen der Selbstaufheizraten lagen zwischen 170°C und 195°C und die Übergangstemperaturen zur Deflagration lagen zwischen 15°C (RDX-Proben) und 40°C (NTO, TNT) darüber. Die Ergebnisse zeigen, daß sich die NTO/RDX-Mischung RDX-kontrolliert zersetzt und die Selbstaufheizrate der Mischung bei niedrigeren Temperaturen liegt als die der Einzelkomponenten, was eine erhöhte Reaktivität zwischen NTO und RDX bedeutet. Die Zersetzung der NTO/TNT-Mischung ist NTO-kontrolliert, eine relative Reaktivitätszunahme zwischen beiden Komponenten macht sich über 200°C bemerkbar. IR-Absorption, Massenverlust und die Wasserbestimmung konnten keine Unverträglichkeit aufzeigen. Deutliche Reaktivitäten zwischen NTO und RDX und zwischen NTO und TNT konnten somit erst bei Temperaturen über 150°C nachgewiesen werden. Allerdings verfärbten sich die TNT-haltigen Proben alle, wobei die NTO/TNT-Mischungen beider Institute nach 16 Wochen bei 65,5°C bräunlich verfärbt und sinterartig fest waren.

1. Einleitung

Das ICT und das WIWEB sind übereingekommen, gemeinsam Fragen aus der Explosivstoffchemie zu bearbeiten. Das erste ausgewählte Projekt dazu ist die Untersuchung der Stabilität des NTO und seine Verträglichkeit in Mischungen mit Nitraminen, am Beispiel des RDX, und mit Nitroaromaten, am Beispiel des TNT. Dieses Thema wurde gewählt, weil das NTO durch zwei N-H-Bindungen an den Ringpositionen 1 und 4, Abb. 1, saure Reaktionen zeigt, d.h. Protonen H^+ abspalten kann, insbesondere an der Ringposition 4. Abspaltung des H^+ an dieser Stelle läßt NTO als Anion in Salzen mit NH_3 und Metallen fungieren. Quantenmechanische Rechnungen zeigten, daß für beide Wasserstoffatome energetisch eine Abgabe als Proton in Frage kommen könnte /1/. Die Reaktionen von herkömmlichen Sprengstoffen mit sauren Komponenten oder sauren Kontaktmaterialien ist noch nicht genügend untersucht, um eine Unverträglichkeit definitiv ausschließen zu können. Sollte sich NTO mit diesen Referenzsprengstoffen als unverträglich erweisen, wäre seine Anwendung in Munition und Sprengladungen sehr fraglich.

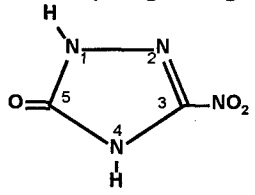

Abb.1: Chemische Struktur des NTO (3-Nitro-1,2,4-Triazol-5-on, alternativ findet man auch die Nummerierung 5-Nitro-1,2,4-Triazol-3-on).

Protonenübertragungen vom NTO auf die Nitrogruppen des TNT oder des RDX wären eine Möglichkeit, daß deren Nitrogruppen als salpetrige Säure HNO_2 bei Zeit-Temperatur-Belastungen abgespalten werden können und somit eine Zersetzung eingeleitet werden würde. Solche Reaktionen wurden für TNT und andere

Nitroaryle nachgewiesen, untersucht bei Temperaturen über 180°C /2/. Untersuchungen der thermischen Zersetzung mit reinem NTO und NTO in Mischung mit TNT wurden schon durchgeführt /3,4,5/. Die Untersuchungstemperaturbereiche waren 225°C bis 245°C in /4/ und 220°C bis 280°C in /4,5/. In diesen Untersuchungen wird durch einen intermolekularen Deuterium-Kinetischen-Isotopeneffekt mit 2D-NTO die These des H-Transfers von NTO zu einer Nitrogruppe gestützt. Sowohl erhöht NTO die Zersetzungsrate des TNT als auch das TNT die Zersetzungsrate des NTO.

2. Untersuchungsmethoden

Zur Klärung der Frage einer möglichen Unverträglichkeit zwischen Sprengladungskomponenten müssen Untersuchungsmethoden eingesetzt werden, welche eine chemische Zersetzungsaktivität zwischen den Komponenten nachweisen können. Zudem muß die wahrscheinliche Einsatzzeit in der Beurteilung enthalten sein, so daß eine Zeit-Temperatur-Belastung der Proben durchzuführen ist. Um im realistischen Belastungsbereich zu bleiben, wurde als Alterungstemperatur 65,5°C gewählt. Diese Temperatur ist noch so niedrig, daß ein Schmelzen des TNT ausgeschlossen werden kann. 65,5°C (= 150°F) ist eine Standard-Surveillance-Temperatur. Die gewählten Lagerzeiten sind mit 2 und 4 Monaten bzw. 8 und 16 Wochen ausreichend lang und bieten das Erkennen der Alterungsabhängigkeit einer möglichen Unverträglichkeit. Bei einer mittleren Einsatztemperatur von 25,5°C errechnet sich mit einem Beschleunigungsfaktor 3 pro 10°C Temperaturänderung ein Skalierungsfaktor von 81 für die Extrapolation von 65,5°C zu 25,5°C. Die zwei und vier Monate Alterung bei 65,5°C entsprechen somit 13,5 und 27 Jahren bei 25,5°C. In der Tabelle 1 sind die von beiden Instituten durchgeführten Arbeiten und Untersuchungsmethoden zusammengestellt.

Tabelle 1: Arbeiten und verwendete Untersuchungsmethoden.

Arbeit und Untersuchungsmethode	ICT	WIWEB
Herstellen (Mischen) der Proben	X	X
Alterung bei 65,5°C mit lose aufgesetztem Stopfen über 2 und 4 Monate	X	X
DSC und TGA/DTA	X	X
Wärmestrom-Mikrokalorimetrie bei 65,5°C		X
adiabatische Selbstaufheizung mit ARC	X	
Infrarotabsorption	X	
Massenverlust nach Lagerung	X	
Wassergehalt nach Karl-Fischer-Methode		X

3. Untersuchte Einzelstoffe, Mischungen und Probenvorbereitung

Folgende Einzelsprengstoffe und Sprengstoffmischungen wurden untersucht, wobei die Substanzen so wie geliefert (außer der Trocknung) verwendet wurden:

- NTO
- RDX
- TNT
- 1:1-Mischung NTO / RDX
- 1:1-Mischung NTO / TNT

Die massenbezogenen 1:1-Mischungen stellte jedes Institut mit den bei ihm vorhandenen Substanzen her, dadurch können leichte Unterschiede wegen verschiedener Reinheit in die Ergebnisse eingehen, jedoch ist damit die Beurteilungsbreite vergrößert. Die Proben wurden in Gefäßen mit lose aufgesetztem Stopfen (Lagergläser aus Duranglas mit Normschliffstopfen) für zwei und vier Monate bzw. acht und sechzehn Wochen bei 65,5°C gelagert. Die Korngrößenverteilungen waren für NTO (200µm bis 400µm) und RDX (mps 100µm) vergleichbar. Damit befriedigende Homogenität erreicht wird, wurden die TNT-Schuppen per Hand im Achatmörser verrieben. Die ausgelagerten Proben wurden ebenfalls durch Verreiben im Achatmörser zerkleinert und homogenisiert, da speziell bei TNT und NTO/TNT die Proben zusammenbackten. Die TNT-Proben beider Institute zeigten einen Schmelzbeginn nach DTA bzw. DSC von etwa 79°C bzw. 80°C. Dies läßt auf leicht verunreinigtes TNT schließen, was als Verschärfung der Bedingungen der Verträglichkeitsbeurteilung zu sehen ist.

4. Ergebnisse und Diskussion

4.1 Thermoanalyse mit TGA/DTA und DSC

Die unbelasteten und belasteten Sprengstoffe und Gemische wurden mit einer kombinierten TGA/DTA-Apparatur bei einer Aufheizrate von 1 K/min in offenen Al-Tiegeln mit Einwaagen zwischen 10mg und 20mg geprüft. Bei den WIWEB-Untersuchungen sind die Geräte von Netzsch, bei denen des ICT von Mettler. Geräte- und Versuchsparameter können den entsprechenden Abbildungen entnommen werden. Die charakteristischen Daten der Zersetzungen und Phasenumwandlungen sind in den Thermogrammen Abb. 2 bis Abb. 12 angegeben. Hingewiesen wird nocheinmal auf den relativ niedrigen Schmelzpunkt des verwendeten TNT, 79°C bei WIWEB, Abb. 4, und 80°C (Peakmaximum) bei ICT.

Die Thermogramme wurden auf folgenden Informationsgehalt analysiert:
- werden die Einzelstoffe durch die Lagerung bei 65,5°C instabiler?
- wird die Verträglichkeit der Gemische durch die Lagerung bei 65,5°C beeinflußt?

Die thermoanalytischen Methoden erlauben wegen ihrer begrenzten Empfindlichkeit Aussagen zur chemischen Zersetzung der Sprengstoffe erst bei Temperaturen über 150°C. Zudem zeigte sich, daß nur mit den TGA-Daten eine sinnvolle Bewer-

tung durchzuführen war. Die DTA-Temperaturen des Beginns der exothermen Zersetzung sind als Bewertungskriterium in diesem Fall ungeeignet, da unter den Versuchsbedingungen die Zersetzung des TNT wegen Verdampfen nicht und die des RDX erst in der flüssigen Phase erkennbar ist. Folgende Interpretationstechnik wurde angewendet: Es wird aus den TGA-Thermogrammen die Temperatur bestimmt, welche als Ausgangstemperatur zur Bestimmung des Massenverlusts geeignet ist, diese wird MV-$T_{ref,A}$ genannt. Sie wird bei den unbelasteten Einzelsprengstoffen bestimmt wird. Von da ausgehend wird eine Endtemperatur MV-$T_{ref,E}$ bestimmt, bei der die unbelasteten Sprengstoffe einen Massenverlust von 3% erreichen, siehe Abb. 2, 3 und 4. Die Ergebnisse der Auswertung der TGA-Messungen an unbelasteten und belasteten Sprengstoffen sind in der Tabelle 2 zusammengefaßt.

Tabelle 2: Massenverlustbewertung der Zersetzungsneigung der unbelasteten und belasteten Einzelsprengstoffe mit TGA-Messungen.

Sprengstoff	Lagerzeit bei 65,5 °C [Monate]	Abb. -Nr.	MV-$T_{ref,A}$ [°C]	MV-$T_{ref,E}$ [°C]	Massen-verlust [%]	D_z
NTO	0	2	179	219	3,0	-
RDX	0	3	145	196	3,0	-
TNT	0	4	125	161	3,0	-
NTO	4		179	219	1,7	0,57
RDX	2		145	196	2,6	0,87
TNT	4		125	161	3,5	1,2

In der letzten Spalte der Tabelle 2 ist die Kenngröße D_z angegeben. Sie ist das Verhältnis der Massenverluste der belasteten zur unbelasteten Probe, Gl.(1).

$$(1) \qquad D_Z = \frac{MV_B}{MV_U}$$

D_Z wird größer als 1 für eine 'Destabilisierung' oder eine Zunahme der Zersetzungsneigung durch die Alterung und kleiner als 1 für formal gesehen eine Reduzierung der Zersetzungsneigung aufgrund der Lagerung bei 65,5°C. Innerhalb des Methodenfehlers hat danach die Alterung bei RDX und TNT keinen Einfluß, während NTO scheinbar etwas stabiler wird, möglicherweise durch die Zersetzung einer Verunreinigung oder durch Verdampfen von Wasser, welches NTO über Wasserstoffbrücken binden kann. Dadurch zeigt bei 65,5°C gelagertes NTO einen geringeren Massenverlust als ungelagertes.

In Anlehnung an die STANAG 4147, Test 2 /6/, wird in dieser Arbeit die Verträglichkeit zwischen den Gemischkomponenten mit der Verträglichkeitskenngröße D_{MV} als dem Quotienten des Massenverlustes MV_G der 1:1-Mischung zur Summe der Massenverluste MV_1 und MV_2 der Einzelkomponenten bestimmt.

$$(2) \qquad D_{MV} = \frac{\frac{M_G}{M_G} \cdot MV_G}{\frac{M_{G,1}}{M_G} \cdot MV_1 + \frac{M_{G,2}}{M_G} \cdot MV_2} = \frac{M_G \cdot MV_G}{M_{G,1} \cdot MV_1 + M_{G,2} \cdot MV_2}$$

Gl.(2) gilt allgemein für beliebige Massenverhältnisse in der Mischung. $M_G = M_{G,1} + M_{G,2}$ ist die Gesamtmasse der Mischung. Die Massenverluste MV_1 und MV_2 können mit davon unterschiedlichen Massen bestimmt worden sein. In Gl.(2) werden die Beiträge der Einzelstoffe mischungsmassenbruchgewichtet berücksichtigt. Ist der Massenanteil einer Komponente in der Mischung null wird $D_{MV} = 1$. Mit der Bedingung $M_{G,1} = M_{G,2} = M$ folgt $M_G = 2\,M$ und die Gl.(3) resultiert für die Verträglichkeitskenngröße D_{MV}.

$$(3) \qquad D_{MV} = \frac{2 \cdot MV_G}{MV_1 + MV_2} = 2 \cdot \frac{\frac{\left[M_{G,1}(0) - M_{G,1}(t) + M_{G,2}(0) - M_{G,2}(t)\right]}{M_{G,1}(0) + M_{G,2}(0)}}{\frac{M_1(0) - M_1(t)}{M_1(0)} + \frac{M_2(0) - M_2(t)}{M_2(0)}} = 2 \cdot \frac{\frac{\Delta M_G}{2 \cdot M}}{\frac{\Delta M_1 + \Delta M_2}{M}}$$

mit $M_1(0) = M_2(0) = M_{G,1}(0) = M_{G,2}(0) = M$

Der Ausdruck in eckigen Klammern in oberen Zähler des mittleren Teils der Gl.(3) ist nur formal aufgespalten. Diese Aufspaltung gilt, wenn die Komponenten indifferent zueinander sind, dann ist $D_{MV} = 1$. Ein $D_{MV} > 1$ bedeutet eine Zunahme der Reaktivität zwischen den Gemischkomponenten und ein $D_{MV} < 1$ formal eine Abnahme der Reaktivität zwischen den Gemischkomponenten. Die untere Grenze für D_{MV} ist null. Aber wenn Werte deutlich kleiner 1 erhalten werden, muß mit anderen Methoden geprüft werden, weil eine reaktive Wechselwirkung zwischen den Komponenten dann nicht auszuschließen ist. Ist bei einer Komponente der Massenverlustwert MV_i null, resultiert bei 1:1-Mischungen ebenfalls $D_{MV} = 1$ für indifferentes Verhalten. Als Beurteilungskriterien gelten für die D_{MV}-Werte nach Gl.(3) mit MV_1 und/oder MV_2 ungleich null:

$D_{MV} > 2$	unverträglich
$D_{MV} < 0{,}5$	unverträglich bzw. prüfen mit anderen Methoden
$0{,}5 \leq D_{MV} \leq 2$	keine definierte Aussage möglich, andere Methoden mit heranziehen
$D_{MV} = 1$	indifferent bzw. verträglich

Die Kriterien sind noch in der Entwicklung. Die Datenbasis für D_{MV} ist bei weitem kleiner als die der Verträglichkeitsprüfung mit dem Vakuumstabilitätstest.

Bei den Sprengstoffmischungen wird zu deren Bewertung als Referenztemperatur $MV\text{-}T_{ref,G}$ jeweils die Einzelstoff-Referenztemperatur $MV\text{-}T_{ref,E}$ gewählt, bei der die instabilere unbelastete Einzelkomponente 3% Massenverlust aufweist. Die Ergebnisse sind in der Tabelle 3 zusammengestellt. Die Messungen an den unbelasteten Gemischen zeigen die Abbildungen 5 und 6.

Tabelle 3: Verträglichkeitsbewertung mit den Massenverlusten aus den TGA-Messungen der unbelasteten und belasteten Sprengstoffmischungen.

Sprengstoff-gemisch	Lagerzeit bei 65,5°C [Monate]	Abb. Nr.	MV-$T_{ref,G}$ [°C]	MV_G [%]	MV_1 [%]	MV_2 [%]	D_{MV}
NTO/RDX	0	5	196	10,5	0,97	3	5,3
NTO/TNT	0	6	161	1,6	0	3	1,07
NTO/RDX	4		196	10,3	0,90	2,6	5,9
NTO/TNT	4		161	1,8	0	3,5	1,03

Innerhalb des Methodenfehlers und bei der relativ niedrigen Referenztemperatur MV-$T_{ref,G}$ = 161°C reagiert NTO nicht mit TNT und die Vorlagerung hat auf die Reaktivität zwischen NTO und TNT keinen Einfluß. Bei der Referenztemperatur MV-$T_{ref,G}$ = 196°C hingegen reagieren RDX und NTO merklich miteinander, die Zersetzungsneigung oder Reaktivität wird jedoch durch die 65,5°C-Lagerung auch nicht erhöht. Diese so festgestellten Zersetzungsreaktionen zwischen NTO und RDX dürften bei normalen Lager- und Einsatzbedingungen keine Rolle spielen. Die thermogravimetrische Analyse kann somit keine relevante Reaktivität zwischen NTO und RDX sowie zwischen NTO und TNT für die vorgesehene Einsatzbelastungen feststellen.

DSC-Wärmestrom-Thermogramme von unbelastetem NTO, von 16 Wochen bei 65,5°C gealtertem NTO, von RDX und von der Mischung NTO/RDX, beide bei 65,5°C über 16 Wochen gealtert und von unbelastetem TNT und von der unbelasteten Mischung NTO/TNT zeigen die Abbildungen 7 bis 12. Die Einwaagen lagen zwischen 0,3mg und 0,5mg. Die Aufheizrate war immer 10°C/min. Die TNT-haltigen Proben wurden im geschlossenen Al-Tiegel gemessen. Die DSC-Diagramme Abb. 7 und Abb. 8 zeigen keinen signifikanten Unterschied zwischen unbelastetem und gealtertem NTO. Die kleine Verschiebung der Exotherme des gealterten NTO zu höheren Temperaturen ist auf die um 20% verringerte Einwaage zurückzuführen. Die Abb. 9 und 10 zeigen im Vergleich die RDX-kontrollierte Zersetzung der Mischung NTO/RDX, bei der Mischung NTO/TNT erkennt man mit den Abb. 11 und 12 die NTO-kontrollierte Zersetzung.

4.2. Wärmestrom-Mikrokalorimetrie

Zur Messung der Wärmeströme dQ/dt der Sprengstoffproben wurde ein Wärmestrom-Mikrokalorimeter mit Zwillingsmeßprinzip Typ TAM™ der Fa. Thermometric, Schweden verwendet. Die Proben wurden wie in /7/ beschrieben in nicht vorkonditionierte Meßampullen mit 3ml Volumen gefüllt. Die Meßampullen wurden fest mit einem Crimp-Verschlußdeckel mit teflonüberzogener Elastomerdichtung verschlossen und nach dem Verschließen in das Mikrokalorimeter eingebracht. Als Referenz in der Zwillingsmeßanordnung diente eine leere Meßampulle, um das Rauschen durch Temperaturschwankungen im isothermen Bad zu reduzieren. Der Meßbereich wurde zu 10µW gewählt, die Kalibrierung erfolgte mit zwei Punkten,

0µW und mit der im Meßzylinder eingebauten Widerstandskalibrierheizung mit festeingestellten 9,9µW. Gemessen wurden die Wärmeströme bei 65,5°C Badtemperatur des Mikrokalorimeters. Folgende Ausdrücke werden synonym zum Wärmestrom verwendet: Wärmefluß, Wärmeflußrate, Wärmeproduktionsrate, Wärmeproduktion, Wärmeentwicklung, Wärmeentwicklungsrate, Leistung, Wärmeleistung. Der im Deutschen zutreffendste Ausdruck ist Wärmestrom, welcher von oder zur Probe gerichtet sein kann. Der Begriff Wärmeentwicklungsrate impliziert eine exotherme Reaktion in der Probe, was bei Explosivstoffen häufig ist und er stellt einen Bezug zur Reaktionswärme oder Wärmetönung der chemischen Reaktion her. Im Englischen ist 'heat flow' der zutreffende Begriff für den 'Wärmestrom', daneben wird auch 'heat generation rate' verwendet.

Alle Messungen wurden mit der 'Switch'-Technik aufgenommen, da bei allen Proben nur sehr kleine spezifische (meint bezogen auf die Einwaage) Wärmeströme zu beobachten waren, meistens zwischen ±0,5µW/g und nahe der Nullinie. 'Switch'-Technik bedeutet den Wechsel der Meßposition der Probe von der Probenmeßstelle A zur Referenzmeßstelle B in der Zwillingsmeßanordnung und umgekehrt. Damit kann das Nullsignal bestimmt werden als halber Wert des Abstands zwischen den Meßkurven vor und nach dem Switch. Diese Methode arbeitet dann optimal, wenn die Probe einen konstanten Wärmestrom zeigt. Die vom Hersteller des Mikrokalorimeters angegebene Nachweisgrenze beträgt 50nW (nano-Watt), was nach /7/ für die meisten Meßkanäle dieses verwendeten Mikrokalorimetertyps in einem Ringversuch bestätigt wurde. Als Kriterium der Bestimmungsgrenze gilt die 3-fache Nachweisgrenze, somit hier 150nW absolut. Die Ladedichte bei den Messungen war nahezu 1, d.h. es wurden 3g bis 3,5g an Substanz eingewogen. Demnach kann die probenbezogene oder spezifische Bestimmungsgrenze mit ca. 50nW/g angegeben werden.

Die Abbildungen 13 bis 17 zeigen die erhaltenen Wärmeströme. Die spike-artigen Elemente der Meßkurven sind bei der Anwendung der Switch-Technik entstanden, dabei kommt das Mikrokalorimeter für 2 bis 4 Stunden aus dem thermischen Gleichgewicht. Das unbelastete NTO, Abb. 13, zeigt eine deutliche endotherme Wärmetönung in der Größenordnung von –400nW/g. Nach 4-monatiger Lagerung bei 65,5°C ist dieser Effekt allerdings verschwunden. Die negative Wärmetönung kann durch das Abspalten von über Wasserstoffbrücken gebundenem Wasser im NTO herrühren. Das reine RDX zeigt unbelastet keine endotherme Wärmetönung, Abb. 14, die Werte der Wärmeströme liegen nahe bei null. Das unbelastete NTO/RDX-Gemisch hat einen endothermen Effekt von etwa –200nW/g, die Hälfte des Wertes des NTO. Nach 4-monatiger Lagerung bei 65,5°C, Abb. 15, ist dieser endotherme Effekt nicht mehr erkennbar. Die belasteten NTO/RDX-Mischungen zeigen mit 100nW/g Wärmeströme im Grenzbereich des Geräts /8,9/. Störeffekte sind nicht auszuschließen. Ungelagertes TNT zeigt innerhalb der ersten 40 Stunden ein deutlich exothermes Signal mit einer maximalen Höhe von 4,2µW/g, Abb. 16. Dieser Anfangseffekt tritt auch bei der NTO/TNT-Mischung in entsprechend „verdünnter" Form auf. Wahrscheinlich handelt es sich bei der im unbelasteten TNT ablaufenden Reaktion nicht um eine Zersetzungsreaktion des TNT, sondern um die einer Verunreinigung, da dieser Wärmestrom bei den 2 und 4 Monate gelagerten Proben des reinen TNT sowie der 1:1-Mischung NTO/TNT nicht mehr auftritt, Abb. 17. Die ARC-Messungen weisen bei unbelastetem TNT gegenüber bela-

stetem ebenfalls auf erhöhte Reaktivität hin, Abb. 21. Die Wärmeströme der belasteten NTO/TNT-Mischungen haben mit etwa 200nW/g leicht positive Werte, aber wiederum im Grenzbereich des Geräts.

Alle Messungen zeigen, daß weder NTO noch TNT noch RDX sowohl unbelastet als auch belastet Wärmetönungen aufweisen, die eindeutig auf eine chemische Zersetzung dieser Stoffe bei der Mikrokalorimeter-Meßtemperatur von 65,5°C schließen lassen. Das Gleiche gilt für die 1:1-Mischungen NTO/RDX und NTO/TNT. Im Temperaturbereich bis 65,5°C gibt die Wärmestrom-Mikrokalorimetrie keinen Hinweis auf chemische Reaktionen in diesen Sprengstoffmischungen, die mit einem entscheidenden Wärmestrom erkennbar wären.

4.3 Adiabatische Selbstaufheizung

Die Methode der adiabatischen Selbstaufheizung wurde in einem der Institute bei Treib- und Explosivstoffen wurde schon angewendet /10/. Ein weiterer Beitrag dazu ist in /11/ zu finden, in welchem die Methode nochmals beschrieben ist. Die adiabatische Selbstaufheizung der Sprengstoffe und der Mischungen wurde mit einem Accelerating Rate Calorimeter (ARC^{TM}) bestimmt. In den folgenden Abbildungen 18 bis 23 werden die adiabatischen Selbstaufheizraten h in °C/min als Funktion der adiabatisch erreichten Temperatur gezeigt, welche als 1/T in 1/K eingetragen ist, jedoch wurden °C-Werte zugeordnet. Die Einwaagen waren um 300mg, bei RDX-haltigen Proben um 250mg, gemessen wurde in kugeligen Titanmeßzellen mit einem Zoll Durchmesser. Die thermische Inertheit des Systems Meßzelle-Probe ausgedrückt als ϕ-Faktor lag zwischen 6 und 8,2. Alle Selbstaufheizungen zeigten einen Übergang von der kontrolliert verfolgbaren Selbstaufheizung zur Deflagration, dem jeweiligen Endpunkt der gezeigten Meßkurven.

In der Abb. 18 sind die unbelasteten Proben zu sehen. Die Kurven des NTO und des TNT liegen nahe zusammen und haben für die Hauptexotherme der Selbstaufheizung eine um etwa 20°C höhere Anfangstemperatur als das RDX. Die Mischung NTO/TNT wird etwas zu niedrigeren Temperaturen verschoben, ihre Selbstaufheizrate scheint NTO-kontrolliert, wie auch DSC-Messungen zeigen, Abb. 11 und 12. Die Verschiebung zu niedrigeren Temperaturen ist nur mit einer Zersetzungsreaktion zwischen NTO und TNT erklärbar. Die Mischung NTO/RDX ist klar erkennbar RDX-kontrolliert in ihrem Verhalten. Ihre Selbstaufheizkurve liegt bei niedrigeren Temperaturen als die des RDX, was auf eine Reaktivität zwischen NTO und RDX hindeutet, jedoch erst bei höheren Temperaturen. Der exothermen Zersetzung des RDX kann eine endotherme vorgelagert sein. In der Abb. 19 sind die Messungen an den unbelasteten und belasteten NTO-Proben dargestellt. Die bei tieferer Temperatur liegende Messung an unbelastetem NTO mit der Markierung 0,1 wurde mit einer Einwaage von 400mg durchgeführt, alle anderen Messungen mit 300mg Einwaage. Die Messung 0,1 zeigt den Einfluß des ϕ-Faktors, der bei dieser Messung wegen der höheren Einwaage kleiner ist als bei den anderen, 4,9 zu 7. Dies führt zu einem schnelleren Ansteigen der Temperatur in der NTO-Probe mit 400mg Einwaage. Die Messungen lassen keinen Einfluß der Alterung erkennen. Die adiabatischen Selbstaufheizungen von unbelastetem RDX, zwei Mesungen 0,1 und 0,2, und 16 Wochen bei 65,5°C gelagertem RDX zeigt die Abb. 20. Es kann ein leichter

Alterungseffekt erkannt werden. Eine These ist, daß durch die Alterung Produkte gebildet werden, welche die Zersetzungsreaktionen des RDX leicht inhibieren oder Inhaltsstoffe des technisch reinen RDX wurden zersetzt, welche bei unbelastetem RDX dessen Zersetzung fördern. Die Ergebnisse für unbelastetes TNT und belastetes TNT zeigt die Abb. 21. Auch hier verschieben sich die Selbstaufheizratenkurven mit der Belastung zu höheren Temperaturen, allerdings scheint der Alterungseinfluß schon nach den ersten Lagerungswochen einzutreten. Zwischen den Kurven für 8 und 16 Wochen ist kein Unterschied mehr feststellbar.

Die Selbstaufheizkurven der Mischung NTO/RDX zusammen mit denen der Komponenten sind in der Abb. 22 zu sehen. Die Alterung der Mischung ändert nur marginal die Selbstaufheizratenkurven der Proben. Sie gehen jedoch schon bei deutlich niedrigeren Selbstaufheizraten in die Deflagration über. Die Abb. 23 zeigt die Messungen an den NTO/TNT-Mischungen. Auch hier sind die Änderungen der gealterten Mischungen gegenüber der ungealterten nur marginal. Zu erwähnen ist allerdings, daß die über 16 Wochen gealterte Mischung NTO/TNT streuende Meßkurven lieferte, sie waren sowohl zu tieferen wie zu höheren Temperaturen verschoben, die gezeigte Kurve ist etwa die Mittellage. An dieser Stelle sei auch auf die deutliche bräunlicher Verfärbung dieser Probe hingewiesen. Mit der adiabatischen Selbstaufheizung der Sprengstoffmischungen ist zu erkennen, daß die Mischungen gegenüber den reinen Komponenten eine erhöhte Reaktivität aufweisen. Diese wird aber durch die Alterung nicht signifikant verändert. Die erhöhte Reaktivität wird erst bei höheren Temperaturen meßbar.

4.4 Infrarotabsorption

Für die Aufnahme der Infrarotabsorptionsspektren wurden KBr-Peßlinge mit den Proben hergestellt. Gemessen wurde mit einem Fouriertransform-IR-Spektrometer Typ 60SX der Fa. Nicolet, im Mittleren IR mit einer Auflösung von 4 cm^{-1}. Dargestellt sind immer spezifische Absorptionsspektren (Extinktion oder Absorbanz). Durch die Subtraktionstechnik wurde versucht, im Rahmen der Genauigkeit der Methode Unterschiede zwischen unbelasteten und belasteten Proben zu erkennen. Die Abb. 24 und die Abb. 25 zeigen das IR-Absorptionsspektrum des unbelasteten NTO und in der Abb. 25 auch das von NTO über 16 Wochen gealtert. Es kann kein Unterschied in den Spektren der Abb. 25, hervorgerufen durch Absorptionsbanden von Zersetzungsprodukten, festgestellt werden. Dasselbe gilt für die Mischung NTO/RDX, unbelastet und 16 Wochen belastet, Abb. 26 und Abb. 27, letztere zeigt das Fingerprint-Gebiet der Spektren der unbelasteten und der 16 Wochen belasteten Mischung. An Hand der Spektren der NTO/TNT-Mischung ist letzlich die gleiche Schlußfolgerung zu ziehen, obwohl hier bei der über 16 Wochen belasteten Mischung erhebliche Unterschiede in dem Subtraktionsspektrum zu sehen sind, Abb 29. Auch die Abb. 28 für den Vergleich der unbelasteten mit der 8 Wochen belasteten Mischung zeigt einige Unterschiede, die aber auf Ungenauigkeiten der Aufnahmetechnik mit den KBr-Preßlingen zurückgeführt werden kann. Den Haupteffekt im Differenzspektrum der Abb. 29 dürften Konzentrationsunterschiede bei den beiden Proben im KBr-Preßling sein, da qualitativ die Spektren nahezu gleich sind. In Bereich der N-H oder O-H-Schwingungen bei 3200 cm^{-1} und bei der Bande um 1720 cm^{-1} zeigt sich ein größerer Unterschied, doch der

Vergleich mit der Bandenlage und der bandenform des reinen NTO, Abb. 24, läßt keinen Rückschluß auf eine N-H···O_2N-Gruppenwechselwirkung zwischen NTO und TNT zu. Beide genannten Banden im Subtraktionsspektrum sind als NTO-Banden zu erkennen.

4.5 Wassergehaltsbestimmung nach der Karl-Fischer-Methode

Die Sprengstoffe wurden vor und nach der Lagerung auf ihren Wassergehalt hin untersucht. Damit sollte eine eventuelle Hygroskopizität und/oder eine Bildung von Wasser als Reaktionsprodukt aus einer möglichen chemischen Zersetzung ermittelt werden. Tabelle 4 zeigt die Ergebnisse.

Tabelle 4: Wassergehalt in Mass.-% nach Karl-Fischer (K.F.) und Massenverlust nach Lagerung.

Probe	Lagerzeit bei 65,5°C	K.F.-Wert [Mass.-%]	Massenverlust nach Lagerung
NTO	unbelastet	0,15	-
NTO	2 Monate	0,13	0,04 %
NTO	4 Monate	0,07	0,09 %
RDX	unbelastet	0,09	-
RDX	4 Monate	0,04	0,07 %
TNT	unbelastet	0,01	-
TNT	4 Monate	0,09	0,09 %
NTO/RDX	4 Monate	< 0,01	0,09 %
NTO/TNT	4 Monate	< 0,01	0,08 %

Die Entstehung von Wasser durch Zersetzungsreaktionen konnte nicht nachgewiesen werden, auch keine Hygroskopizität der Stoffe oder Gemische. Die Massenverluste nach Lagerung haben so kleine Werte, daß sie zu vernachlässigen sind, d.h. auch damit sind keine den Einsatz der Mischungen begrenzenden Zersetzungsreaktionen nachweisbar.

5. Zusammenfassung

In einer gemeinsamen Untersuchung zwischen den Instituten WIWEB und ICT zur Klärung der Frage einer Reaktivität zwischen NTO und RDX als Beispiel eines typischen Nitramins und zwischen NTO und TNT als Beispiel eines typischen Nitroaromaten wurden folgende Methoden eingesetzt: die Thermoanalyse mit TGA/DTA und DSC, die Wärmestrom-Mikrokalorimetrie gemessen mit einem TAM^{TM}, die adiabatische Selbstaufheizung gemessen mit einem Accelerating Rate Calorimeter (ARC^{TM}), die IR-Absorption im Mittleren Infraroten sowie der Massenverlust nach Lagerung und die Wasserbestimmung nach Karl-Fischer. Um eventuelle Reaktionen

zwischen den Komponenten zu beschleunigen wurden, die Proben bei 65,5°C über 2 und 4 Monate gealtert.

Die Bewertung mit den thermoanalytischen Methoden wurde mit den TGA-Messungen quantifiziert durchgeführt. Über die Definition einer Verträglichkeits- oder Reaktivitätskenngröße D_{MV} wurden die Daten der TGA-Thermogramme ausgewertet. Es konnte keine relevante Reaktivität zwischen NTO und RDX und zwischen NTO und TNT für die üblichen Lager- und Einsatztemperaturen festgestellt werden. RDX reagiert aber bei erhöhten Temperaturen deutlich mit NTO. Innerhalb des Methodenfehlers reagiert NTO nicht mit TNT bei etwa 160°C, auch die Belastung bei 65,5°C über 4 Monate änderte die Reaktivität der Mischungen nicht. Die Wärmestrommessungen bei 65,5°C mit dem Mikrokalorimeter mit einer spezifischen Bestimmungsgrenze von 0,05µW/g konnten keine offensichtlichen Unverträglichkeitsreaktionen zwischen NTO und RDX und zwischen NTO und TNT aufzeigen. Die Wärmeströme waren so klein, meistens zwischen ±0,5µW/g und nahe der Nullinie, daß mit der Switch-Technik gemessen werden mußte.

Mit der adiabatischen Selbstaufheizung wurde festgestellt, daß sich die Mischung NTO/RDX RDX-kontrolliert zersetzt und die Selbstaufheizrate der Mischung bei niedrigeren Temperturen liegt als die des RDX. Bei NTO und TNT allein liegen die Anfangstemperaturen der Selbstaufheizraten etwa 20°C über der des RDX. Die Zersetzung der Mischung NTO/TNT ist NTO-kontrolliert, eine Reaktivität zwischen beiden Komponenten kommt bei höheren Temperaturen zum Tragen, so daß die Selbstaufheizratenkurve der Mischungen bei niedrigeren Temperaturen als die der Komponenten liegt. Die Alterung bei 65,5°C über 8 und 16 Wochen änderte die Grundreaktivität der beiden Mischungen nicht mehr signifikant. Mit der IR-Absorption konnte keine Reaktivität in den Sprengstoffmischungen erkannt werden. Verglichen wurden die spezifischen Absorptionsspektren der unbelasteten und der belasteten Mischungen. Mit der Subtraktion der Spektren als empfindliche Unterscheidungstechnik zwischen zwei sehr ähnlichen Spektren konnten keine neuen Absorptionsbanden von eventuell entstandenen Zersetzungsprodukten gefunden werden. Auch bei NTO konnte in den Spektren keine Veränderung mit der Alterung festgestellt werden.

Die Massenverluste durch die Lagerungen bei 65,5°C sind so klein, daß Zersetzungsreaktionen damit nicht zu belegen sind. Auch die Änderungen im Wassergehalt der Proben war sehr gering.

Mit den verwendeten Untersuchungsmethoden der beiden Institute WIWEB und ICT konnten, außer bei Temperaturen über 150°C, keine offensichtlichen chemischen Reaktivitäten zwischen den Mischungskomponenten in den 1:1-Mischungen NTO/RDX und NTO/TNT festgestellt werden. Bei NTO/TNT kam es allerdings bei den Proben beider Institute nach 4 Monaten Lagerung zu einer deutlichen Braunfärbung und zum Zusammenbacken. Bei der WIWEB-Probe war dies mit einer teilweisen Entmischung verbunden. Wahrscheinlich ist das TNT etwas angeschmolzen und gesintert. Eine entscheidende Wärmetönung oder höhere Massenverluste wurden jedoch auch für diese NTO/TNT-Mischung nicht beobachtet.

6. Abbildungen

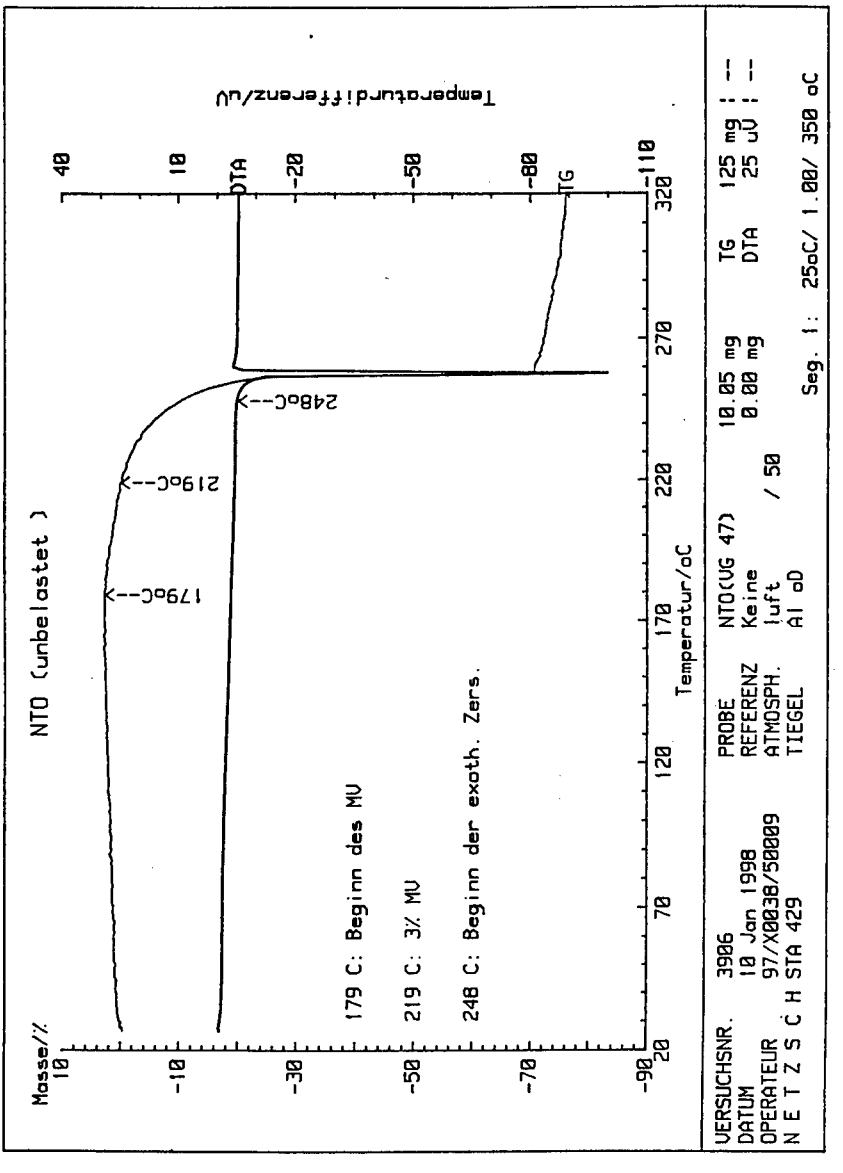

Abb. 2: TGA/DTA-Thermogramme von unbelastetem NTO.

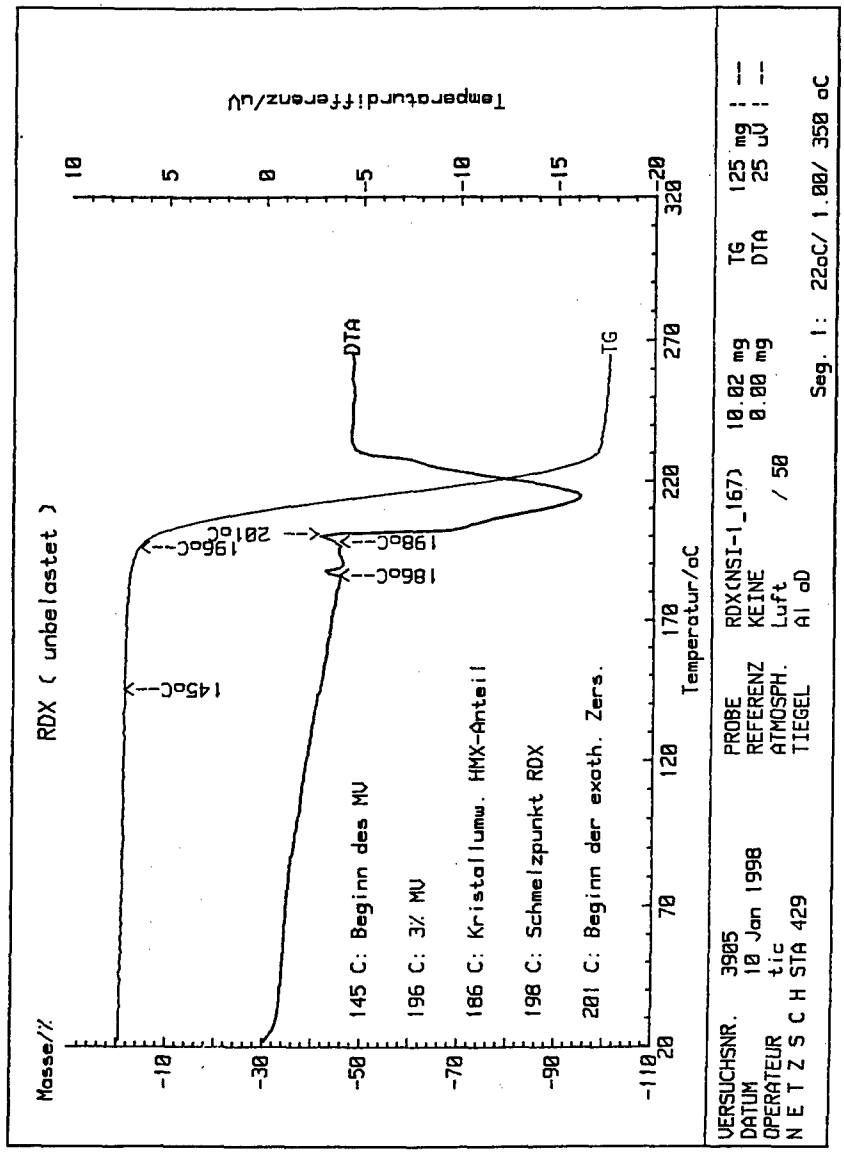

Abb. 3: TGA/DTA-Thermogramme von unbelastetem RDX.

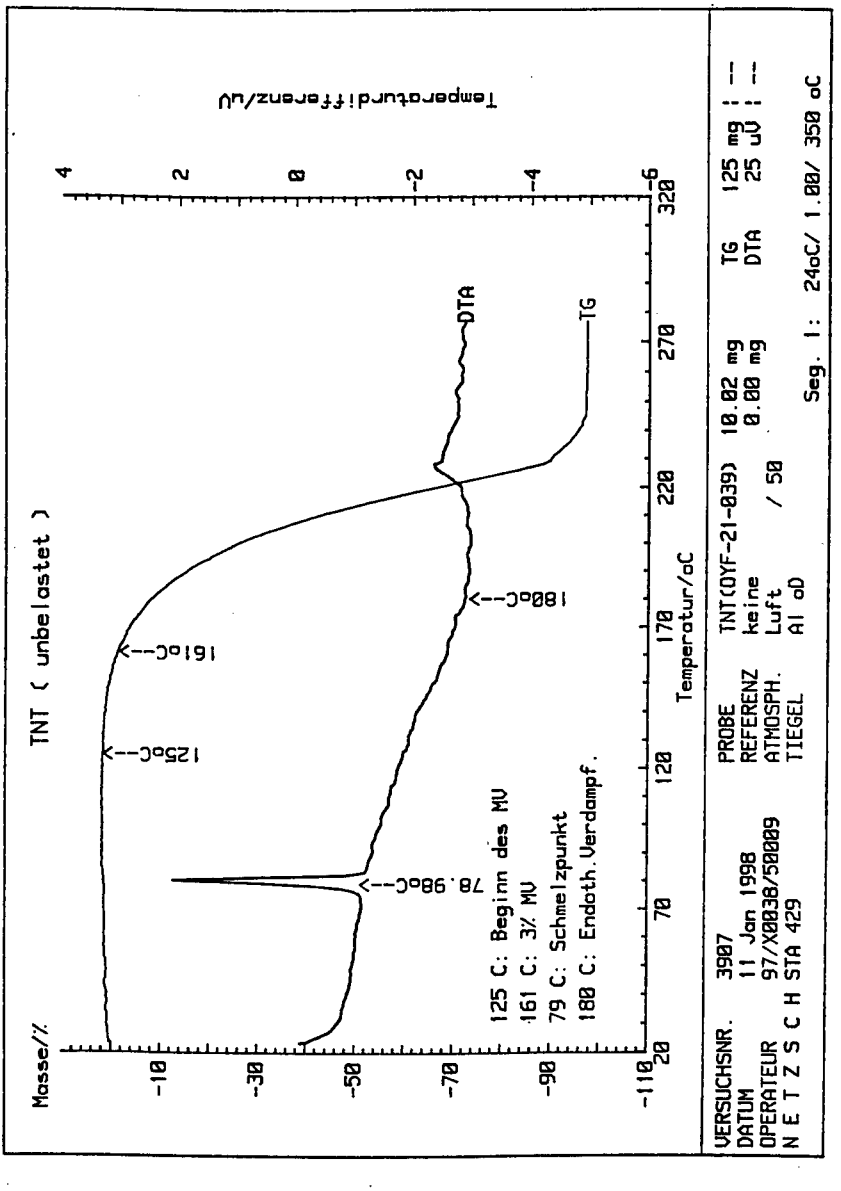

Abb.4: TGA/DTA-Thermogramme von unbelastetem TNT.

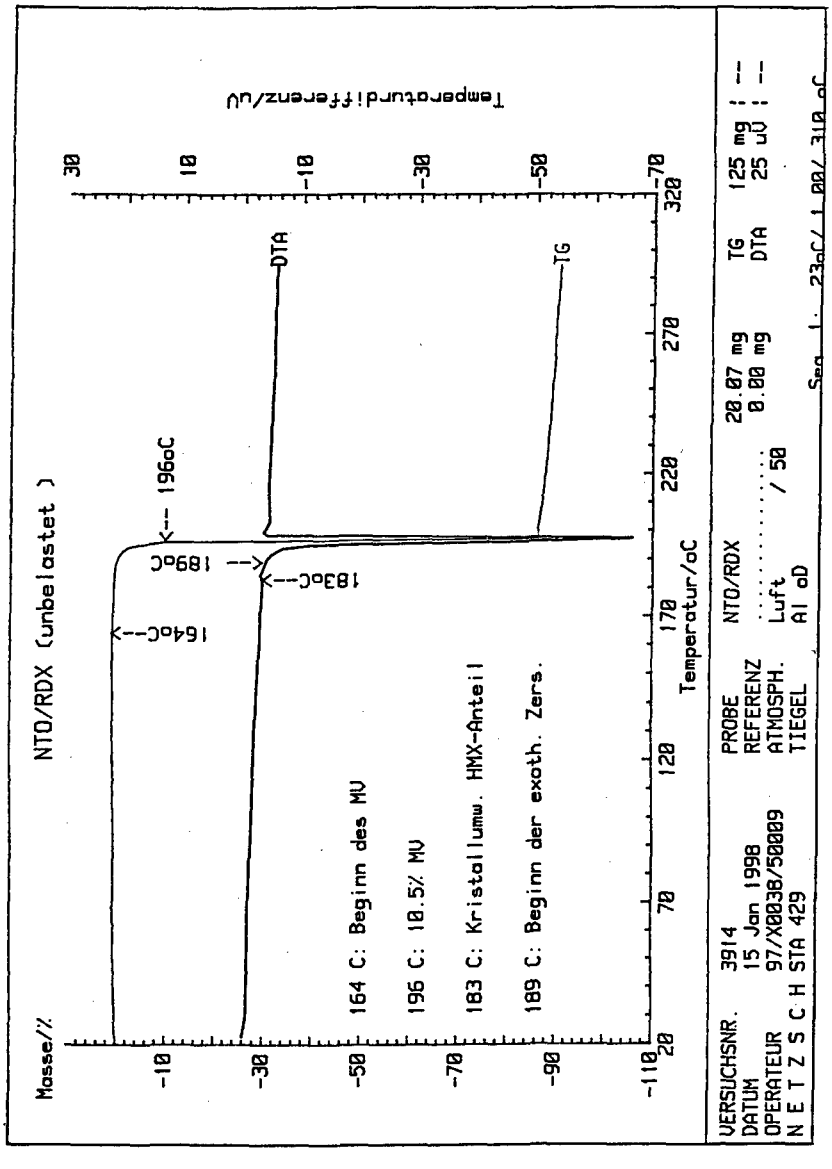

Abb. 5: TGA/DTA-Thermogramme der unbelasteten 1:1-Mischung NTO/RDX.

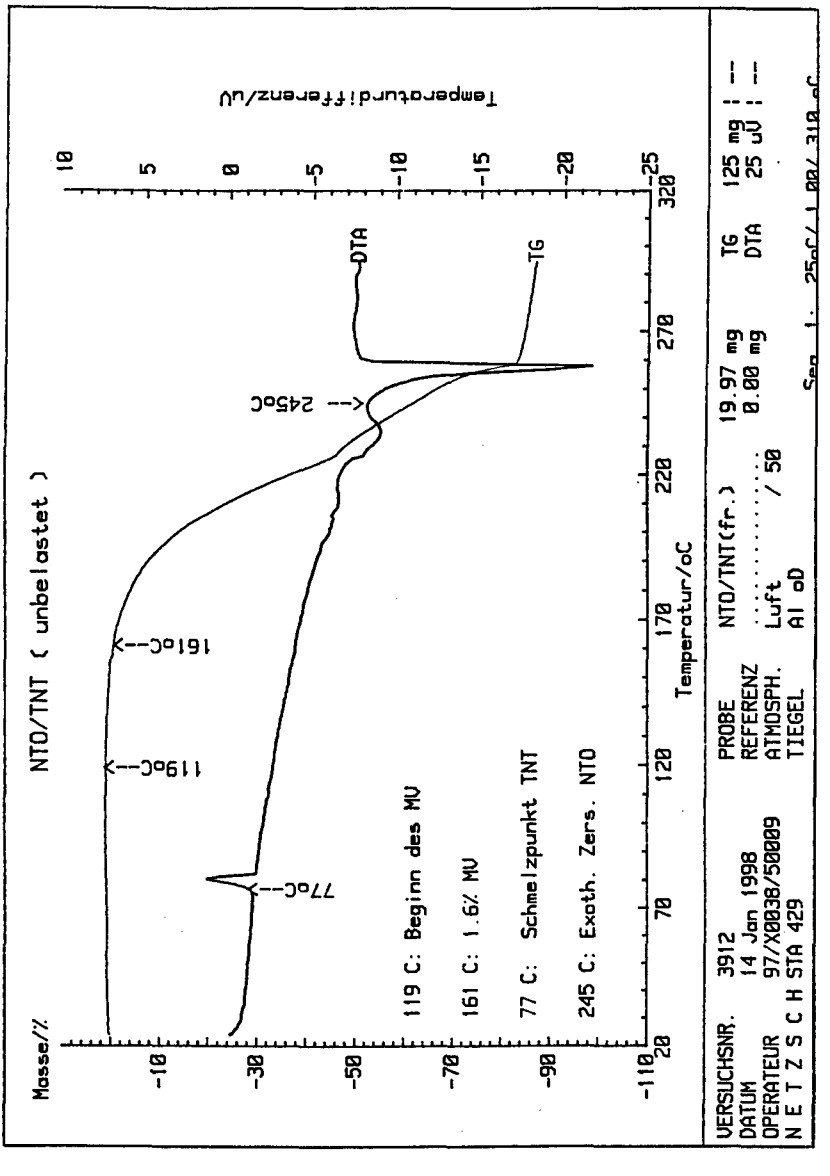

Abb. 6: TGA/DTA-Thermogramme der unbelasteten 1:1-Mischung NTO/TNT.

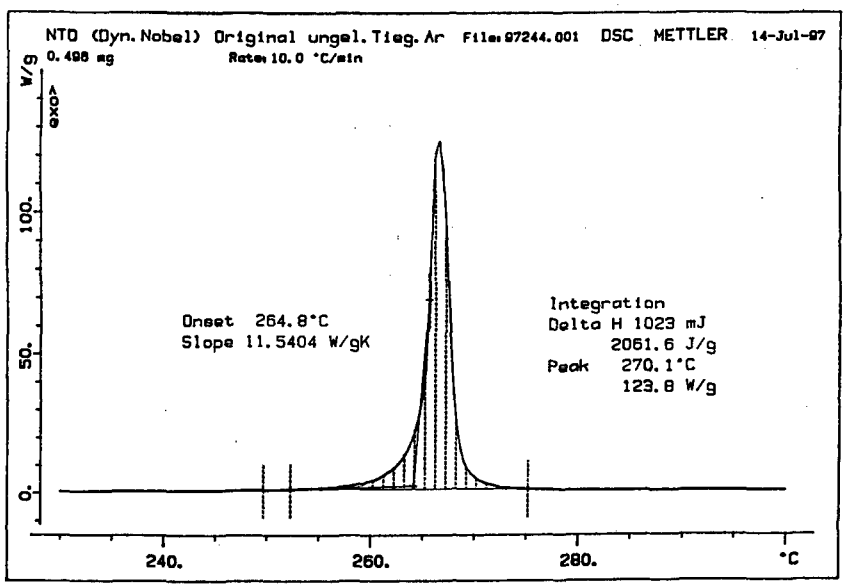

Abb. 7: DSC-Thermogramm von unbelastetem NTO.

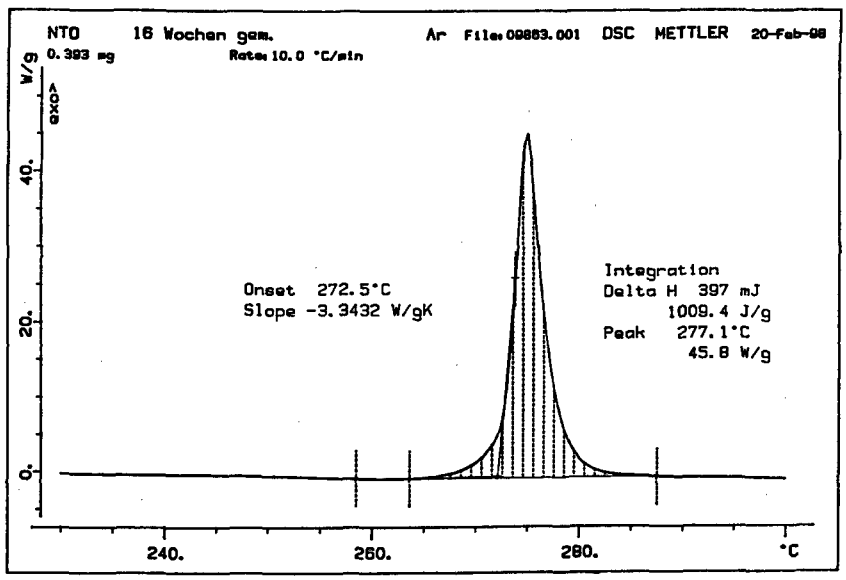

Abb. 8: DSC-Thermogramm von bei 65,5°C über 16 Wochen belastetem NTO.

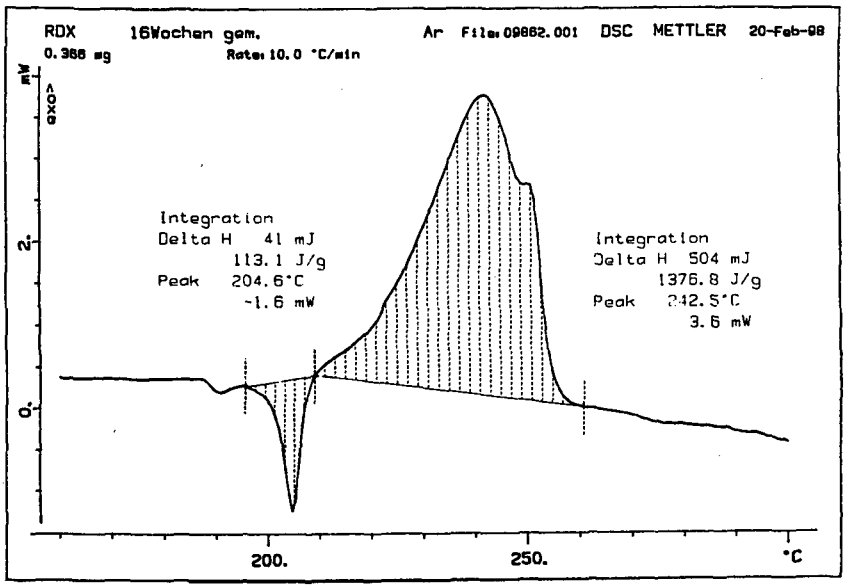

Abb. 9: DSC-Thermogramm von bei 65,5°C und 16 Wochen belastetem RDX.

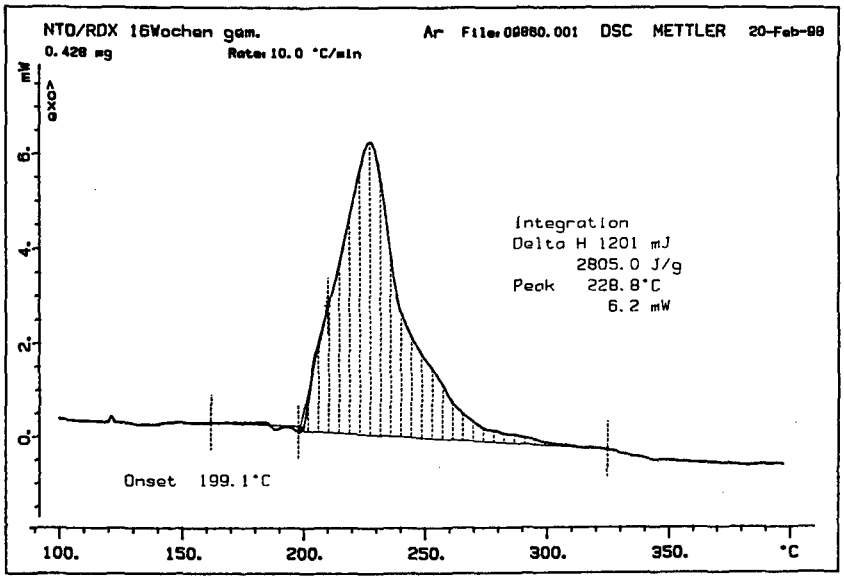

Abb. 10: DSC-Thermogramm der bei 65,5°C und 16 Wochen belasteten 1:1-Mischung NTO/RDX.

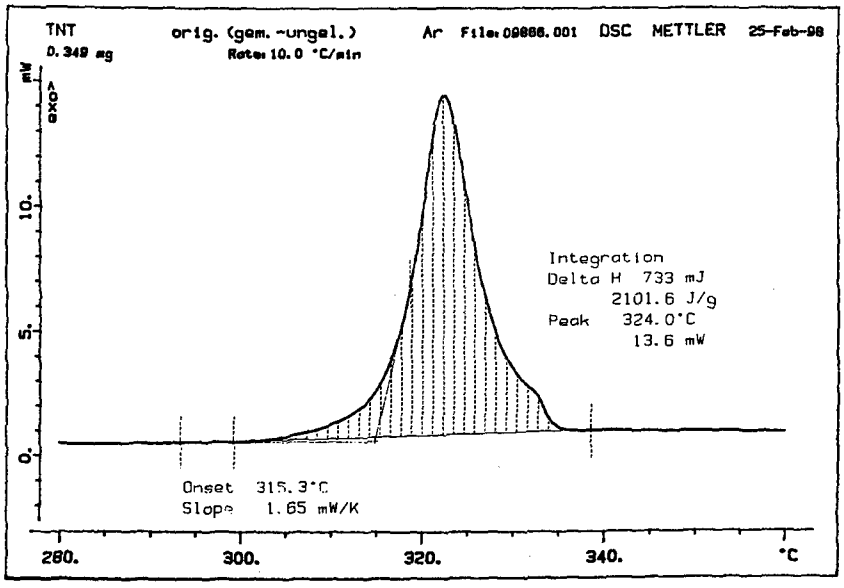

Abb. 11: DSC-Thermogramm von unbelastetem TNT, gemessen im geschlossenen Al-Tiegel.

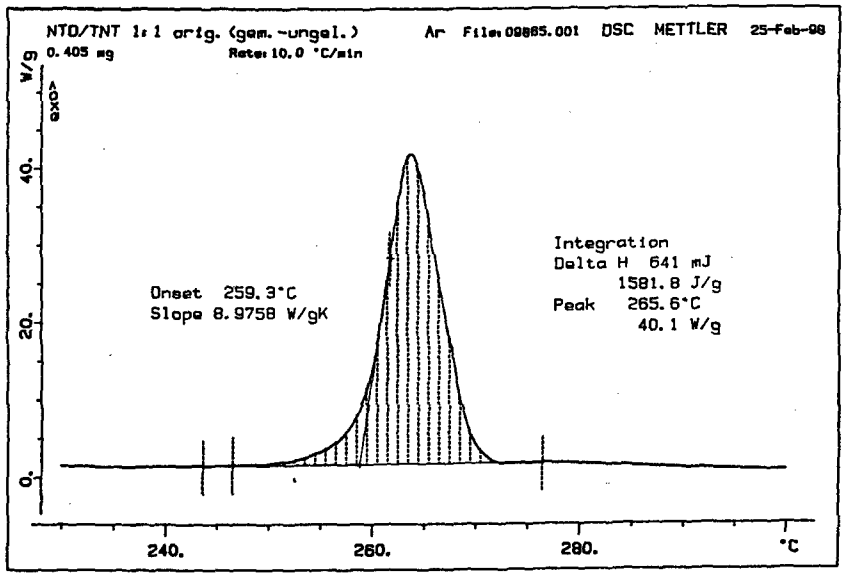

Abb. 12: DSC-Thermogramm der unbelasteten 1:1-Mischung NTO/TNT, gemessen im geschlossenen Al-Tiegel.

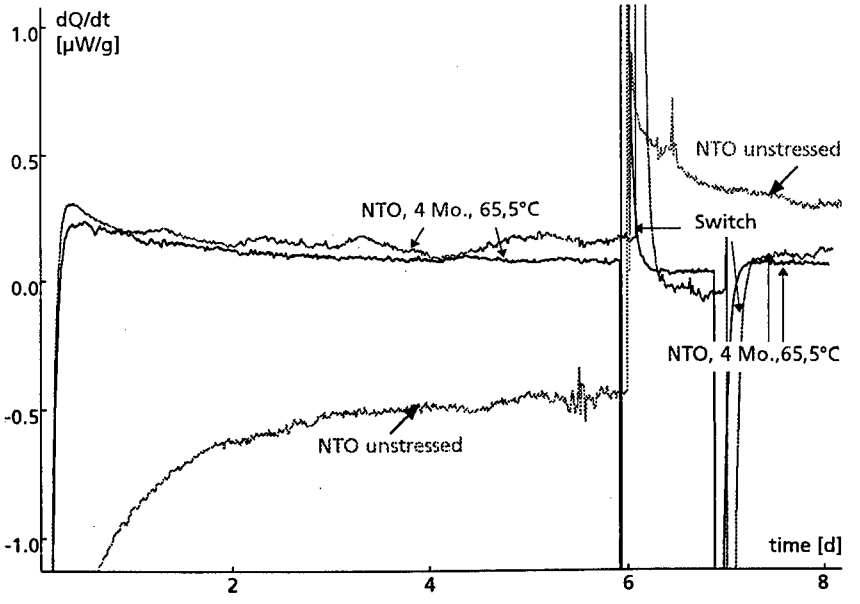

Abb. 13: Spezifische Wärmeströme von unbelastetem NTO und von 4 Monate gelagertem NTO.

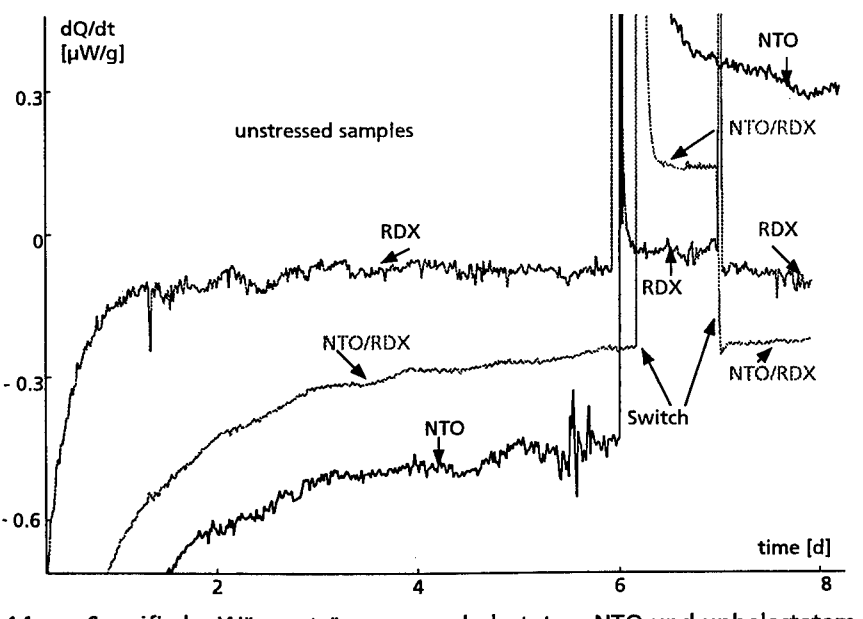

Abb. 14: Spezifische Wärmeströme von unbelastetem NTO und unbelastetem RDX und der unbelasteten 1:1-Mischung NTO/RDX.

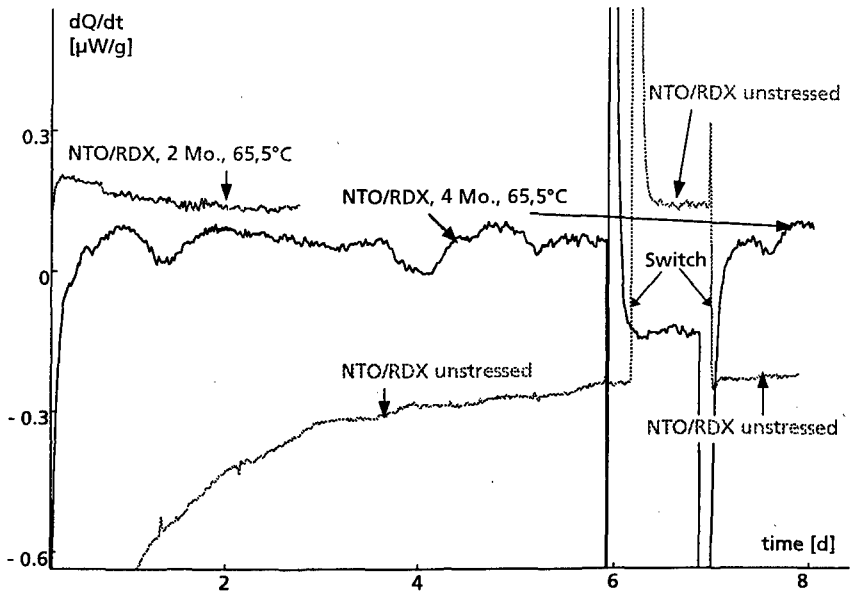

Abb. 15: Spezifische Wärmeströme der 1:1-Mischung NTO/RDX, unbelastet und nach Lagerung bei 65,5°C über 2 und 4 Monaten.

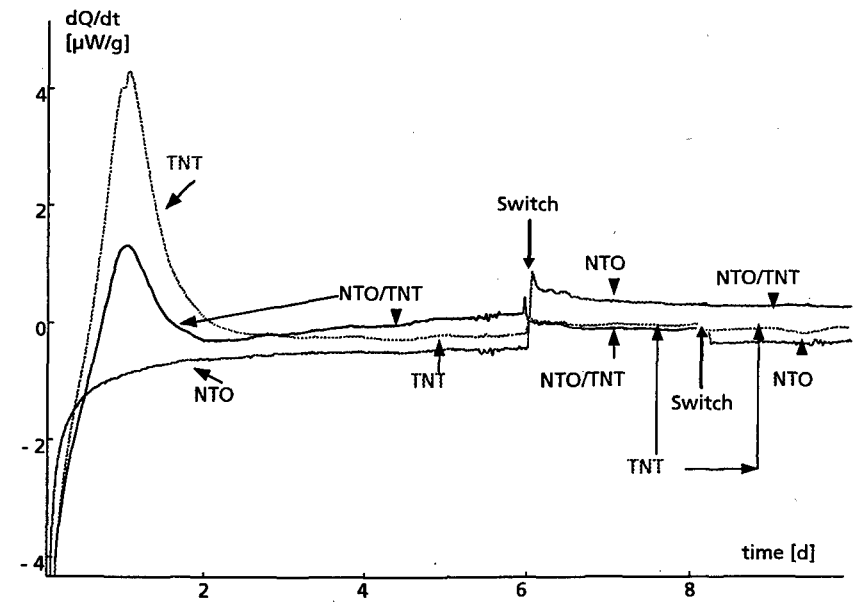

Abb. 16: Spezifische Wärmeströme von unbelastetem TNT und von unbelastetem NTO sowie von der unbelasteten 1:1-Mischung NTO/TNT.

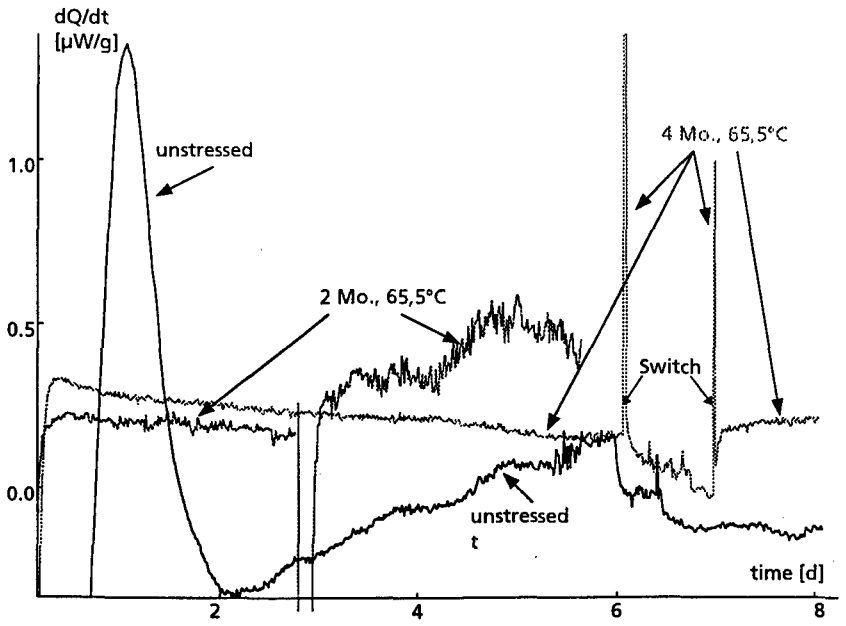

Abb. 17: Spezifische Wärmeströme der 1:1-Mischung NTO/TNT, unbelastet und nach Lagerung bei 65,5°C über 2 und 4 Monaten.

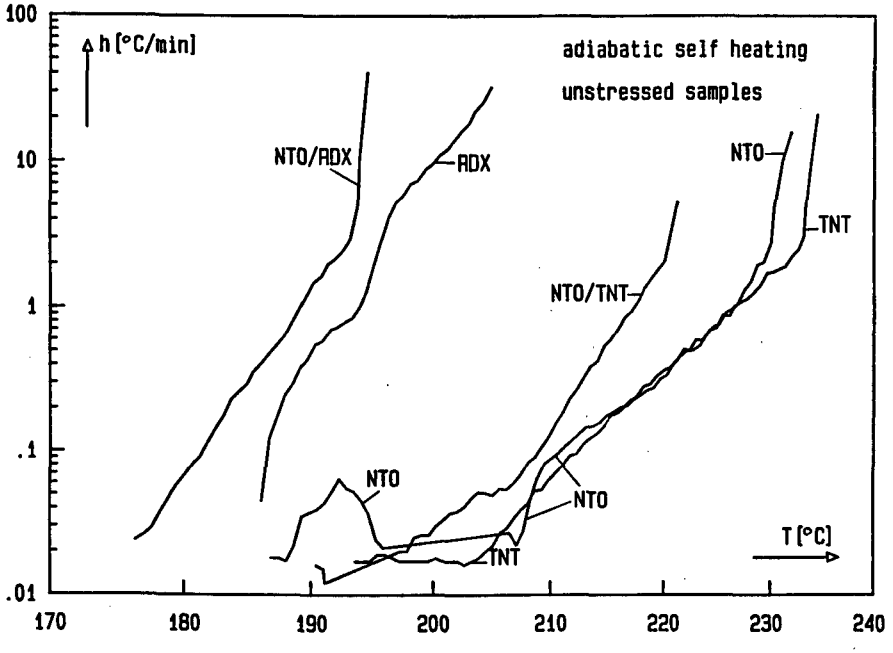

Abb. 18: Adiabatische Selbstaufheizrate von NTO, RDX und TNT und der beiden 1:1-Sprengstoffmischungen NTO/RDX und NTO/TNT.

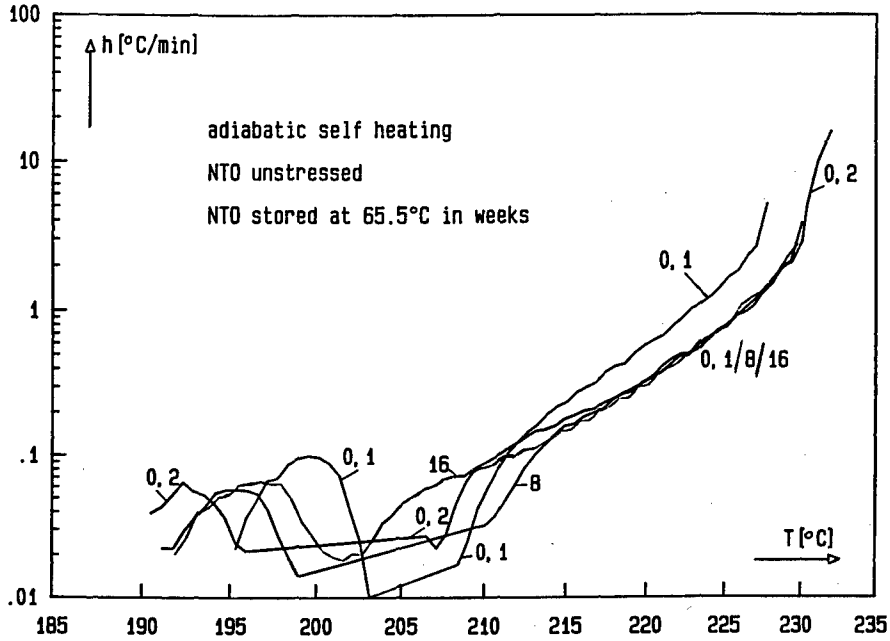

Abb. 19: Adiabatische Selbstaufheizrate von NTO und von bei 65,5°C über 8 und 16 Wochen gealtertem NTO. Zwei Messungen am unbelasteten NTO, 0,1 mit 400mg Einwaage, alle anderen Proben mit 300mg.

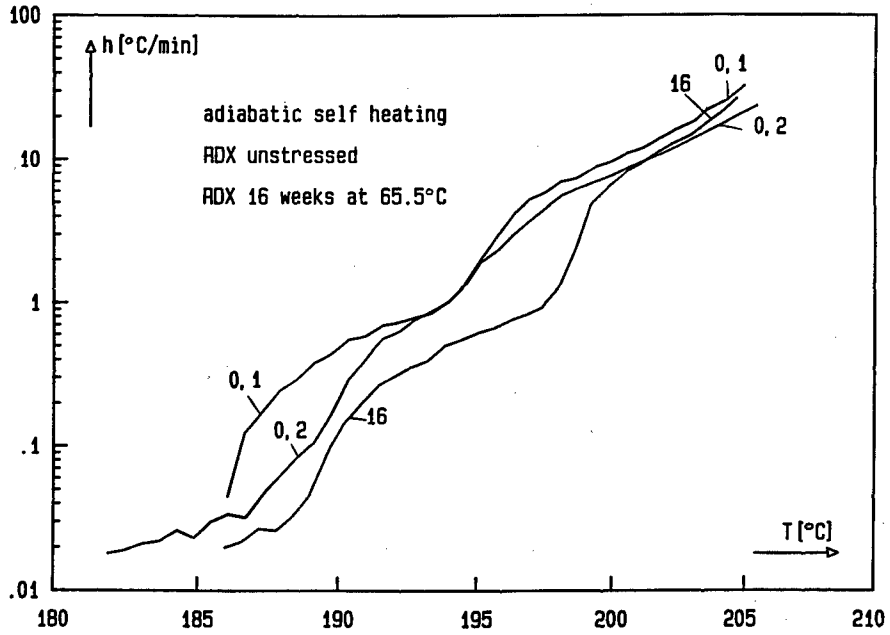

Abb. 20: Adiabatische Selbstaufheizrate von RDX und von bei 65,5°C über 16 Wochen gealtertem RDX. Zwei Messungen mit unbelastetem RDX.

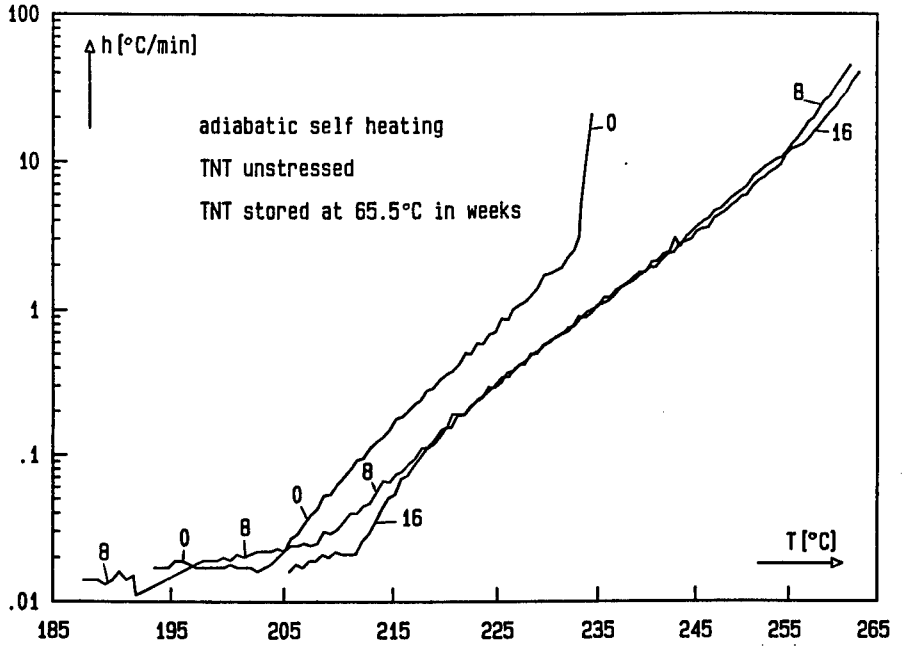

Abb. 21: Adiabatische Selbstaufheizrate von TNT und von bei 65,5°C über 8 und 16 Wochen gealtertem TNT.

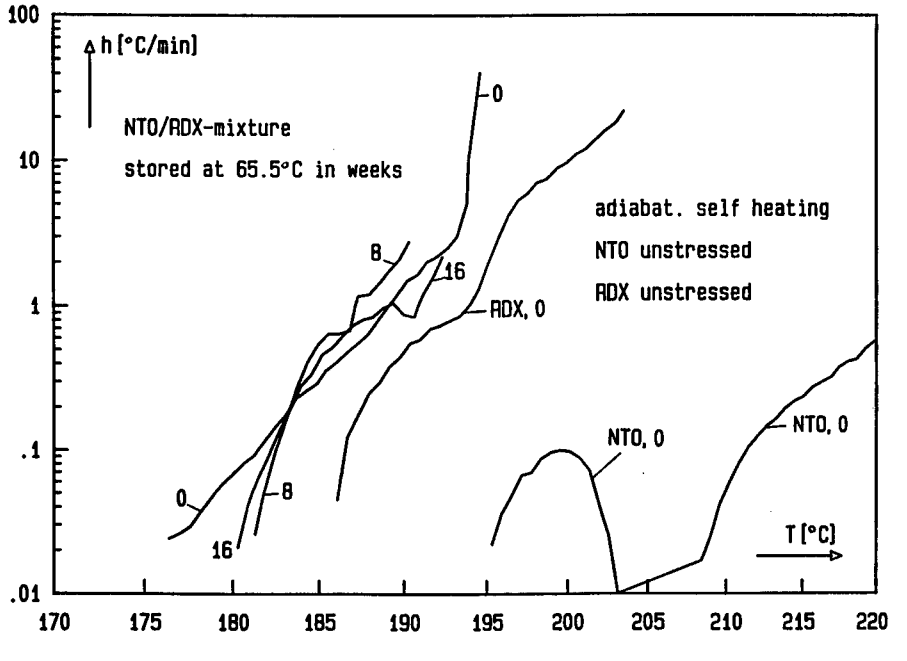

Abb. 22: Adiabatische Selbstaufheizrate von unbelastetem NTO und RDX und von der 1:1-Mischung NTO/RDX, unbelastet und belastet.

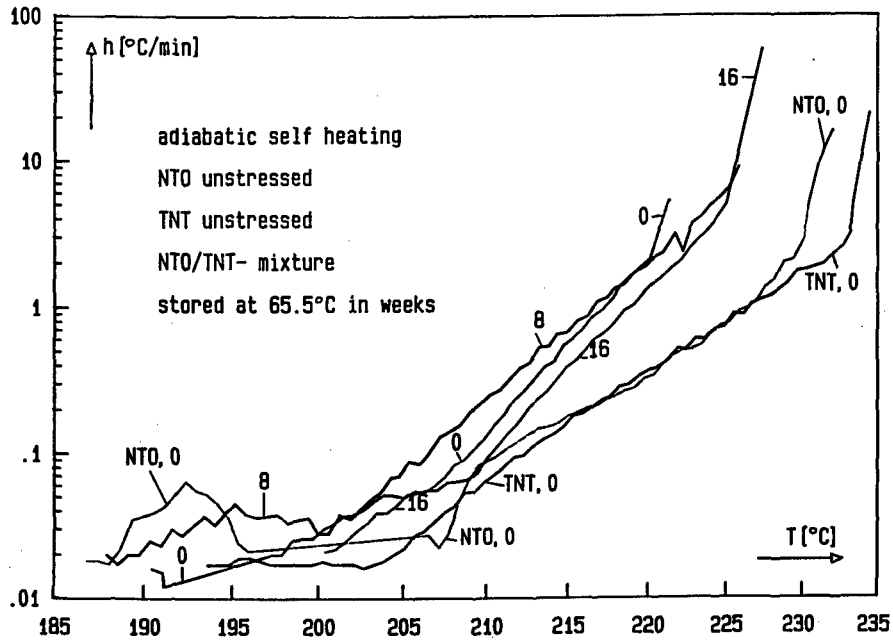

Abb. 23: Adiabatische Selbstaufheizrate von unbelastetem NTO und TNT und von der 1:1-Mischung NTO/TNT, unbelastet und belastet.

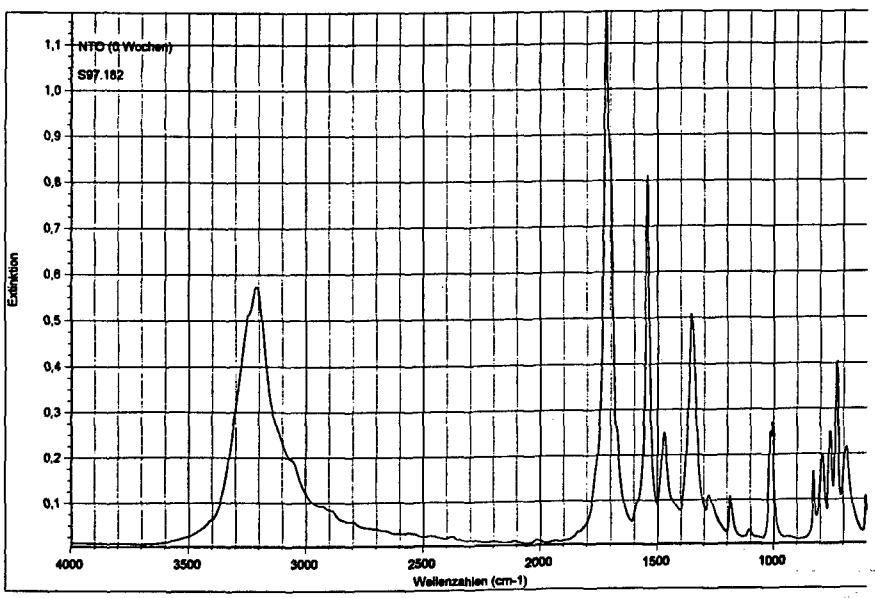

Abb. 24: IR-Absorptionsspektrum von unbelastetem NTO.

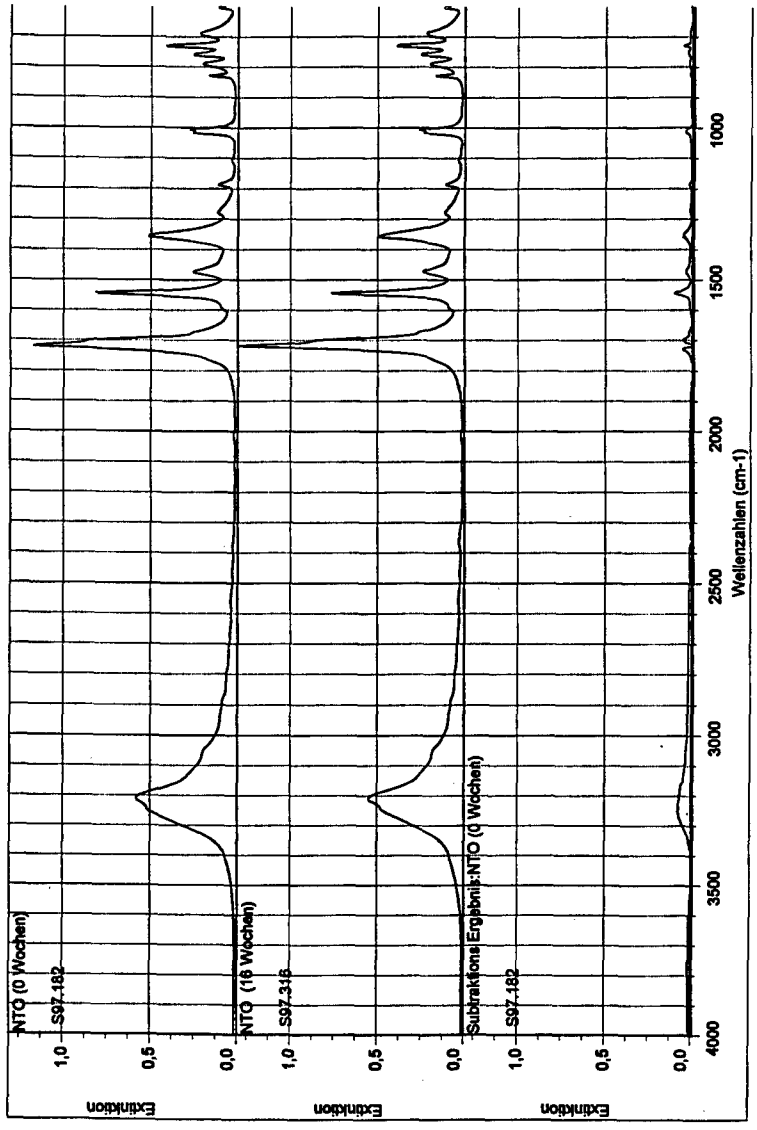

Abb. 25: IR-Absorptionsspektren von unbelastetem NTO und von bei 65,5°C über 16 Wochen gealtertem NTO. Das Subtraktionsspektrum zeigt keine Änderung der belasteten Probe an.

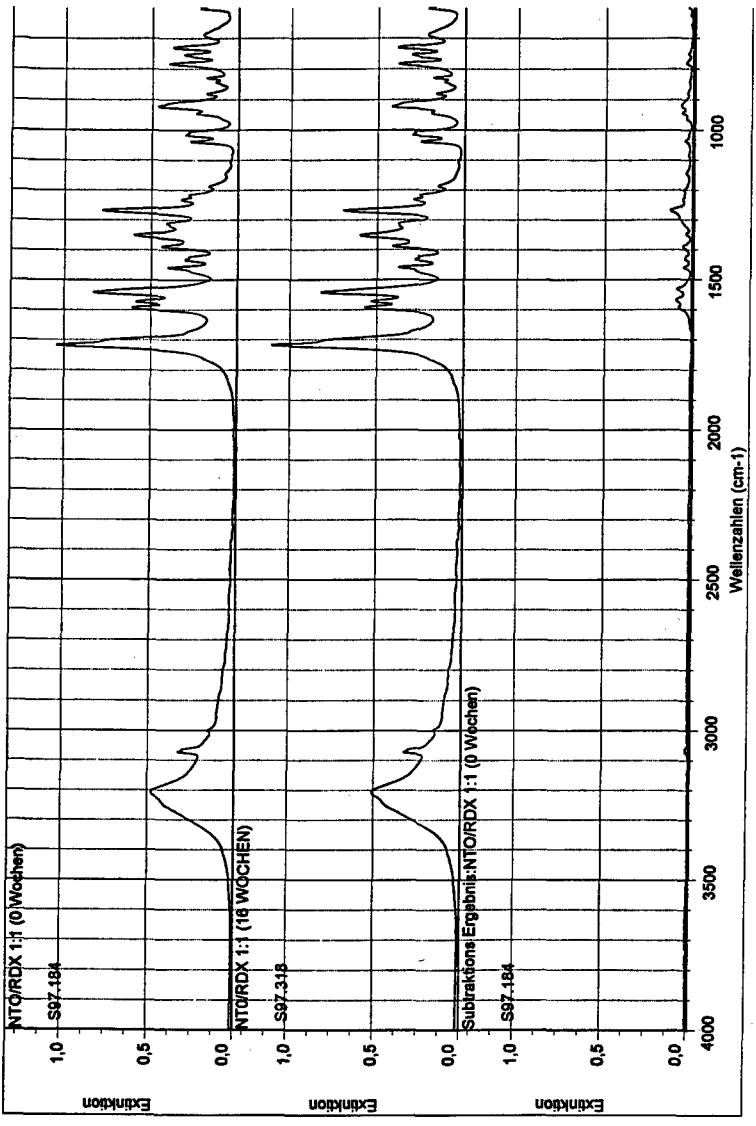

Abb. 26: IR-Absorptionsspektren der unbelasteten Mischung NTO/RDX und der bei 65,5°C über 16 Wochen gealterten Mischung NTO/RDX. Das Subtraktionsspektrum zeigt keine Änderung der belasteten Probe an.

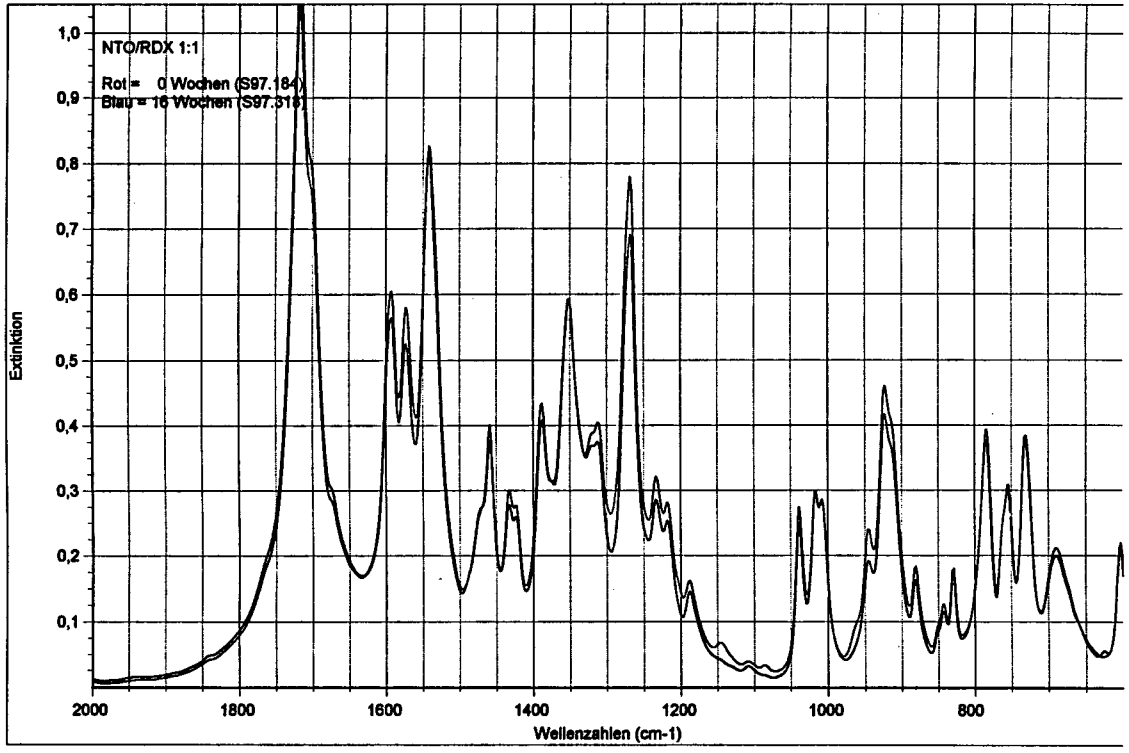

Abb. 27: IR-Absorptionsspektren der unbelasteten Mischung NTO/RDX und der bei 65,5°C über 16 Wochen gealterten Mischung NTO/RDX im Fingerprintgebiet. Das Spektrum mit den etwas kleineren Extinktions- (Absorbanz-) werten ist von der belasteten Probe. Die Spektren sind bezüglich der Banden identisch.

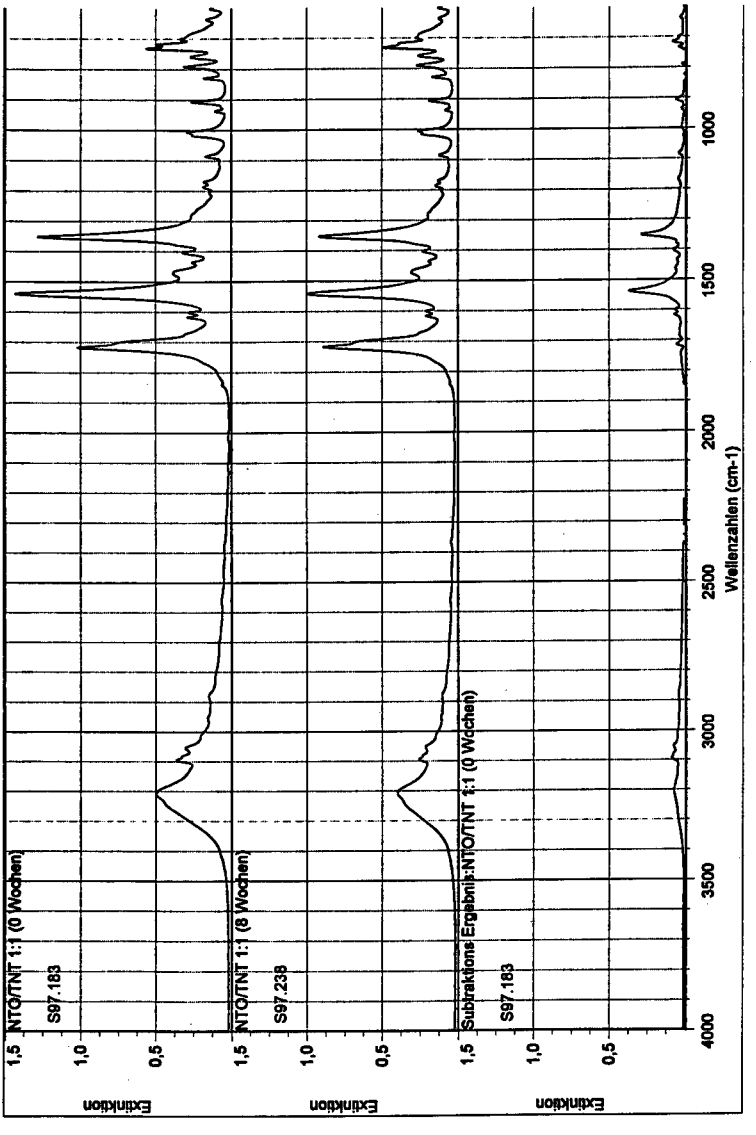

Abb. 28: IR-Absorptionsspektren der unbelasteten Mischung NTO/TNT und der bei 65,5°C über 8 Wochen gealterten Mischung NTO/TNT. Das Subtraktionsspektrum zeigt keine signifikanten Änderung. Die Unterschiede im Fingerprintgebiet sind auf Streuungen in der Probenpräparationstechnik rückführbar.

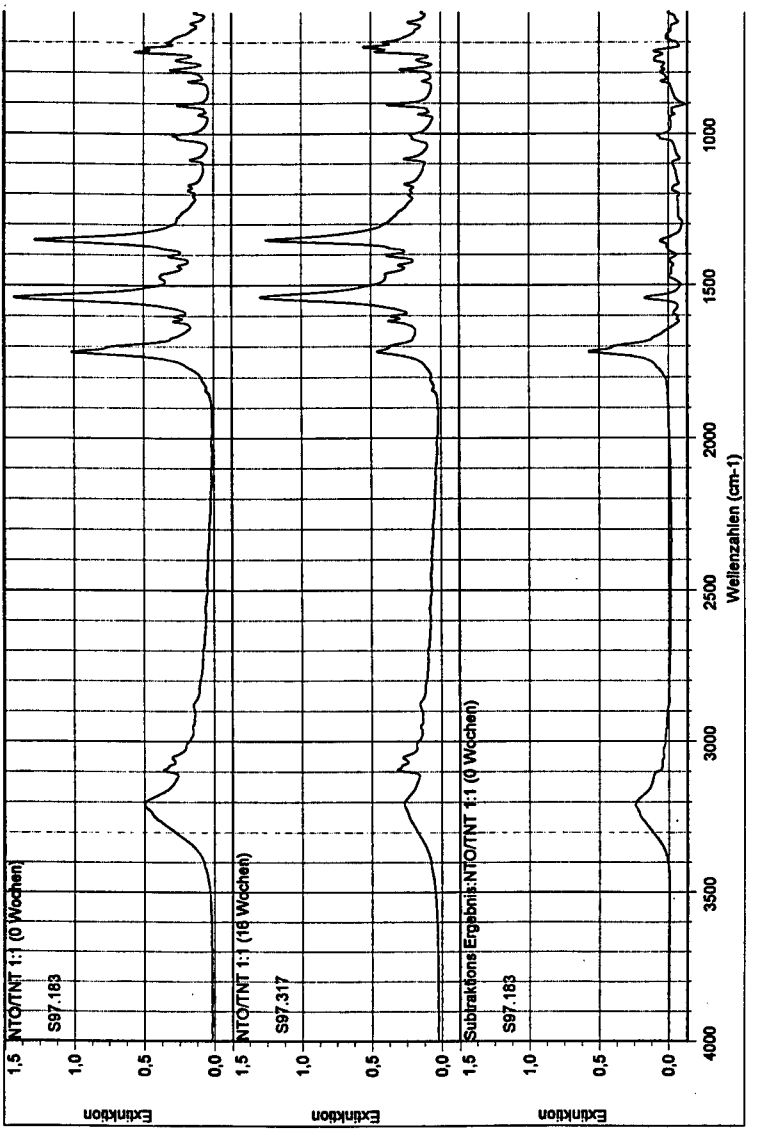

Abb. 29: IR-Absorptionsspektren der unbelasteten Mischung NTO/TNT und der bei 65,5°C über 16 Wochen gealterten Mischung NTO/TNT. Das Subtraktionsspektrum zeigt erhebliche Unterschiede, aber es ist nicht eindeutig, ob diese alterungsbedingt sind. Es können auch Abweichungen vom 1:1-Mischungsverhältnis sein.

7. Literatur

/1/ J.P. Ritchie
„Structures and Energies of the Tautomers and Conjugate Bases of some 1,2,4-triazolones"
J. Org. Chem. 54, 3553 (1989).

/2/ L.M. Minier, K.R. Brower, J.C. Oxley
„Role of Intermolecular Reactions in Thermolysis of Aromatic Nitro Compounds in Supercritical Aromatic Solvents"
J. Phys. Chem. 56, 3306 (1991).

J.C. Oxley, J.L. Smith, W.Wang
„Compatibility of Ammonium Nitrate with Monomolecular Explosives"
Part I: J. Phys. Chem. 98, 3893 (1994)
Part II: Nitroarenes ,J. Phys. Chem. 98, 3901 (1994).

/3/ J. A. Menapace, J.E. Marlin, D.R. Bruss, R.V. Dascher
„Photochemical and Thermochemical Decomposition of 3-nitro-1,2,4-triazol-5-one and perdeuterio-3-nitro-1,2,4-triazol-5-one in neat and mixed mixtures"
J. Phys. Chem. 95, 5509 (1991).

/4/ J.C. Oxley, J.L.Smith, Z. Zou, R.L. Kennedy
„Thermal Decomposition Studies on NTO"
Proceed. 26th Internat. Annual Conference of ICT, Paper 28, July 4-7, 1995, Karlsruhe, Germany, Fraunhofer-Institut für Chemische Technologie, ICT.

/5/ J.C. Oxley, J.L. Smith, Z. Zou, R.L. Kennedy
„Thermal Decomposition Studies on NTO and NTO/TNT"
J. Phys. Chem. 99, 10383 (1995).

/6/ NATO-STANAG 4147
„Chemical Compatibility of Ammunition Components with Explosives"
Final Draft 1997.

/7/ S. Wilker, P. Guillaume
„International Round Robin Test to Determine the Stability of DB Ball Propellants by Heat Flow Calorimetry"
Proceed. 29th Internat. Annual Conference of ICT, Paper 132, June 30-July 3, 1998, Karlsruhe, Germany, Fraunhofer-Institut für Chemische Technologie, ICT.

/8/ U. Ticmanis, G. Pantel, L. Stottmeister
„Stabilitätsuntersuchungen einbasiger Treibladungspulver - Mikrokalorimetrie im Grenzbereich"
Proceed. 29th Internat. Annual Conference of ICT, Paper 37, June 30-July 3, 1998, Karlsruhe, Germany, Fraunhofer-Institut für Chemische Technologie, ICT.

/9/ S. Wilker, U. Ticmanis, G. Pantel
„Detailed investigation of sensitivity and reproducibility of HFC measurements"
11th Symposium on 'Chemical Problems Connected with the Stability of Explosives', May 24-28, 1998, Båstad, Sweden.

/10/ M.A. Bohn, F. Volk
„Adiabatische Selbstaufheizung bei Treib- und Explosivstoffen"
Proceed. 24th. Internat. Annual Conference of ICT, Paper 8, June 29 - July 2, 1993, Karlsruhe, Germany, Fraunhofer-Institut für Chemische Technologie, ICT.

/11/ M.A. Bohn
„Thermisches Zersetzungsverhalten von neueren Weichmachern und Bindern untersucht mit der adiabatischen Selbstaufheizung"
Proceed. 29th Internat. Annual Conference of ICT, Paper 29, June 30-July 3, 1998, Karlsruhe, Germany, Fraunhofer-Institut für Chemische Technologie, ICT.

Characterisation of impurities in new energetic materials

G. Bunte[1], H. Pontius[1], M. Kaiser[2]

[1] Fraunhofer-Institut für Chemische Technologie (ICT), D-76327 Pfinztal 1

[2] WIWEB, Swisttal-Heimerzheim

ABSTRACT

In the last years several new explosives have recently attracted attention as possible alternatives e.g. for the nitramines RDX and HMX. Hexanitrohexaazaisowurtzitane (HNIW), also known as CL 20 is one of them. Objective of the study was to analyse three different CL 20 samples from different suppliers (ε - CL 20 from Thiokol , USA and ε- and β- CL 20 from SNPE, France) with chromatographic and spectroscopic techniques to characterise the chemical and polymorph purity of the materials in order to compare the different samples to eachother.

From IR-spectroscopic measurements it was determined that all three materials have polymorph purities > 95 %. To get informations about the chemical purity and possible byproducts or residual solvents the samples were analysed by HPLC, NMR and GC-MSD. For the last a new technique, the so called Solid Phase Micro Extraction, SPME was applied fro sample preparation. The chemical purity estimated by HPLC analysis was for all CL 20 samples > 96 % while the ε-charge of SNPE had the highest purity (98.3 %). From NMR-measurements a formyl-substituted byproduct was identified. From NMR as well as from GC-MSD analyses residual amounts of organic solvents have been detected (ethanole or tetrahydrofurane). Furthermore different spare amounts of other organic components were identified after SPME-treatment and characterization with GC-MSD.

1. INTRODUCTION

In the last years several new explosives have recently attracted attention as possible alternatives e.g. for the nitramines RDX and HMX. Hexanitrohexaazaisowurtzitane (HNIW), also known as CL 20 is one of them. Advantages of CL 20 for example are the higher energy value related to HMX and RDX. CL 20 is predicted to significantly enhance performance in the areas of specific impulse and / or density in propellants and in detonation velocity and pressure in explosives /2/.

Like HMX the nitramine CL 20 exists in different polymorph structures with slightly different densities whereby the epsilon-phase has the highest density. The phase stability depends on or could be influenced respectively by several conditions like /3/:

- temperature
- tace amounts of other polymorphs
- chemical impurities
- organic solvents.

The characterisation of chemical impurities and / or spare amounts of organic solvents could give informations about the synthesis steps or the crystallisation conditions. Objective of study is to analyse three different CL 20 samples with chromatographic and spectroscopic techniques to characterise the chemical and polymorph purity of the materials in order to compare the different samples to eachother.

2. EXPERIMENTAL

Three different CL 20 samples (ε - CL 20 MNPCL 157 from Thiokol , USA and ε- and β-CL 20 from SNPE, France, ε-charge-no.: A981) were analysed in this study. Like HMX and RDX the nitramine CL 20 is thermally lable meaning that this compound itself could not be analysed with gaschromatographic methods for estimating the purity. Nevertheless residues of organic solvents from the crystallization process or thermally stabil, volatile organic compounds from the synthesis should be detectable after using a suitable enrichment / extraction techniques. The chemical purity of CL 20 was analysed by liquid chromatography while the polymorph purity was analysed by IR-spectroscopy.

- HPLC-analysis was carried out with a Novopak C18 column (3,9 mm x 150 mm) using a Waters HPLC with PDA-detection (225 nm). Injection volume was 15 µl. Seperation of the peaks were obtained by using a specific methanol : water - gradient.
- To analyse probable spare compounds by GC-MSD a new micro extraction technique, SPME (solid phase micro extraction), was applied and optimized. SPME is a solventless extraction procedure in which a phase-coated silica fiber (picture 1) is immersed in a liquid sample or exposed to the headspace above a liquid or solid sample. Analytes adsorb to the phase , and then are thermally desorbed in the injection port of a GC and transferred to the column. Different SPME-phases (SUPELCO) were tested for CL 20 „solutions" in water or dichloromethane. The gaschromatographic characterisation was made with a SPB-5-column using different temperature programs. The measurements were made with a HP 5890 and a MSD 5971.
- NMR-spectroscopic measurements were made at the WIWEB with a BRUKER-spectrometer at 400,13 MHz (^{1}H-NMR) and at 100,62 MHz (^{13}C-NMR). As solvent acetone-d6 was used.
- KBr-pellets were measured with a NICOLET 60 SX IR-spectrometer.

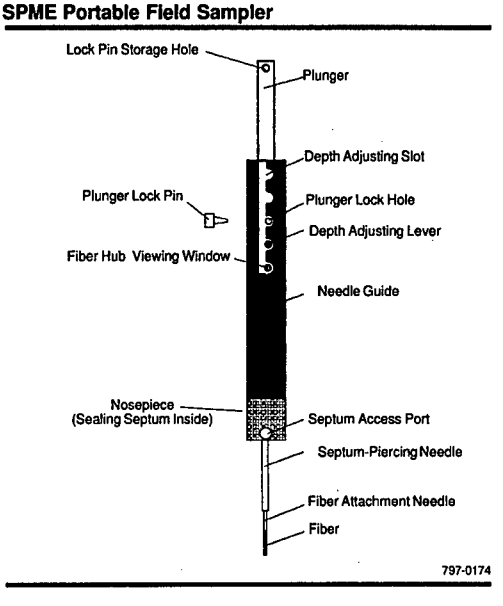

Figure 1: schematic view of the SPME-technique /1/

3. RESULTS AND DISCUSSION

The IR-absorption spectra of the three different CL 20 samples are shown in figure 2. Both epsilon-modifications show the same typical „ε-IR bands" in the finger-print region while the β-sample differs from both showing the specific bands for the β-modification /3/. From these IR-measurements the samples could be denotes as pure modifications which means that no more than 2 to 5 % of another polymorph modification should in the samples.

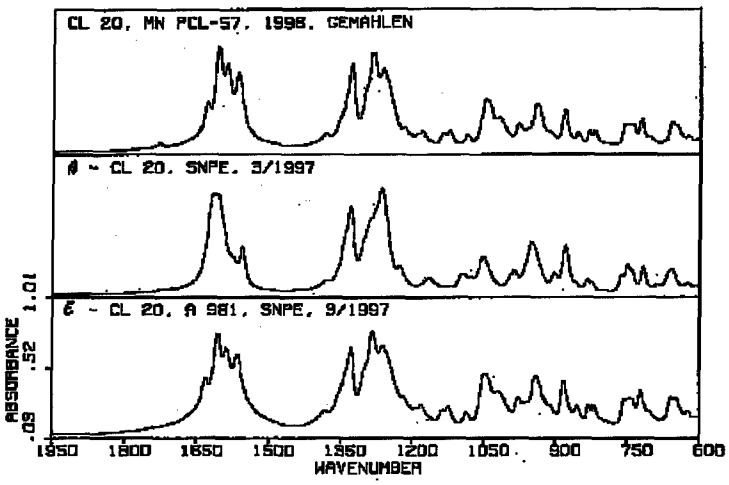

Figure 2: IR-spectra of the different CL 20 samples

In order to get information about the chemical purity several measurements were carried out. The HPLC chromatogram of CL 20 - MNPCL57 is shown in figure 3. It is clearly seen that the main product elutes as the last of four peaks (12.01 min), having major intensity of all. There are three byproducts at retention times of 8.86, 9.99 and 11.19 minutes. Assuming that all components have the same sensitivity for the PDA detector (225 nm) we get a chemical purity of 96.3 % for this CL 20 charge. The main byproduct elutes at 9.99 minutes with a portion of about 3.1 %.

Figure 4 shows a comparison of the HPLC chromatograms of the three different CL 20 samples emphasising the peak intensities of the byproducts. As for the Thiokol material both SNPE samples show four peaks in the HPLC chromatogram with the main peak at

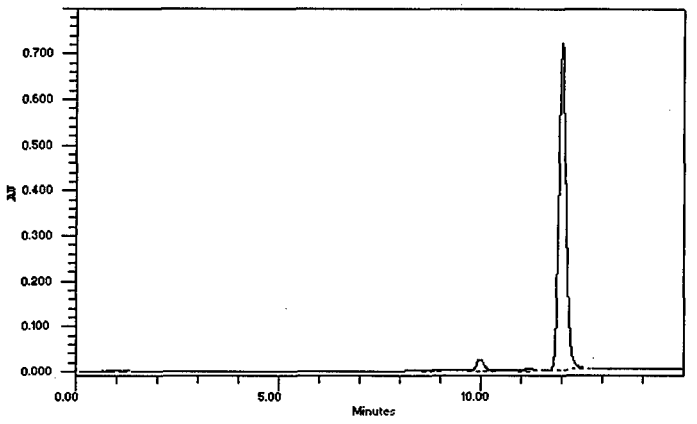

Figure 3: HPLC-chromatogram of CL 20 MNPCL57, Thiokol

about 11.9 minutes. There were also three byproducts detected but the peak with the major intensity appears for both modifications at a retention time of about 8.6 min. Using also the peak areas to determine the relative percentages of the four components the epsilon-charge of SNPE seems to have the highest chemical purity (98.3 %) of all three analysed materials. For the beta-modification a chemical purity of about 96.2 % was detected with a main byproduct of about 3.4 %. The results are summarized in the following table whereby the peaks are designated as 1 to 5 in the ordere of increasing retention time:

Peak-No.	retention time [min]	peak area [%]		
		ε-CL 20 (Thiokol)	ε-CL 20 (SNPE)	β-CL 20 (Thiokol)
1	**7.7**	-	0.05	0.13
2	**8.7**	0.26	1.58	3.39
3	**10.0**	3.11	-	-
4	**11.2**	0.35	0.08	0.25
5	**12.0**	96.28	98.29	96.22

Table 1: relative peak area percentages determined by HPLC measurements for the three analysed CL 20 charges

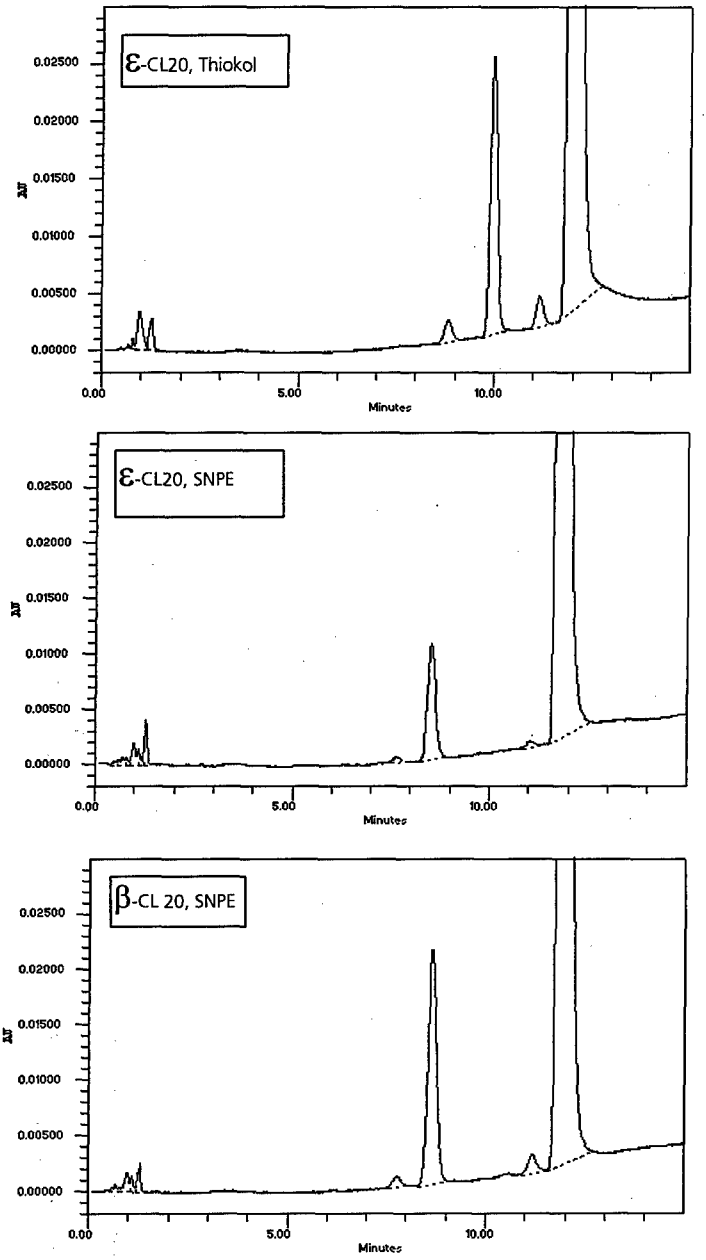

Figure 4: Comparison of the HPLC chromatograms of the three different CL 20 samples with emphasis of the peak intensities of the byproducts

The ^{13}C- and ^{1}H-NMR-spectra measured for both epsilon samples show similar main signals for both charges. CL 20 has two signals in the ^{1}H-NMR-spectrum at $\delta = 8,34$ and $\delta = 7,83$ and also two signals in the ^{13}C-NMR-spectrum at $\delta = 72,1$ and $\delta = 75,1$. Detailed spectra are given in /4/. The material from Thiokol shows a small ^{13}C-NMR-signal at $\delta = 161,6$ whereas for the SNPE sample a small signal appears at $\delta = 167,8$. In both cases this signal could be interpreted as a carbonyl-C-atom in the neighbourhood of a proton. This means that in both CL 20 samples a byproduct exists which has one formyl-group instead of a nitro-group. The different δ-values probably resulted because of different ring-positions.

Furthermore the ^{1}H-NMR-spectra of both materials show small amounts of signals coming from ethanole which perhaps was used for the recrystallization of the samples. Looking especially at the ^{1}H-NMR-region between $\delta = 7.0$ to 9.0 the byproducts in both epsilon-samples differ from each other. This corresponds to the HPLC results noticed above. For the Thiokol-sample the small proton-signals could be better interpreted yielding to a chemical purity for CL 20 of about 97 mol-% which is the same value compared to the HPLC-purity. In the case of the SNPE-material the NMR-spectrum is to complex to give exact concentration values of all components. Nevertheless the chemical purity of ε-CL 20 from SNPE is higher regarding the results of the seperated HPLC-peaks.

The ^{1}H-NMR-spectrum of the beta-SNPE-CL 20 was also measured. Here small amounts of tetrahydrofurane were detected. The GC-MSD measurements (figures 5a and 5b) after enrichment with a SPME fibre (SUPELCO CW/DVB) also showed that β-CL 20 from SNPE contains residual THF amounts. Furthermore a branched heptanol and a di-tert-butyl-benzochinone were identified as thermally stabil, volatile components.

The GC-MSD chromatograms of different SPME-treated „water solutions" of both ε-modifications were also measured. Only with a CW/DVB fibre GC-detectable peaks appeared. For the Thikol-sample relatively more small peaks were detected in comparison to the SNPE-material. Some of the peaks of the last noted sample were also recognized in the chromatogram of the first (figure 6) . Nevertheless until now only for the peak at a retention time of about 39.5 minutes the library search comparison gave

possible structure informations (figure 7). With a match quality of 78 % a derivative of a long chain paraffinic diethyester was identified.

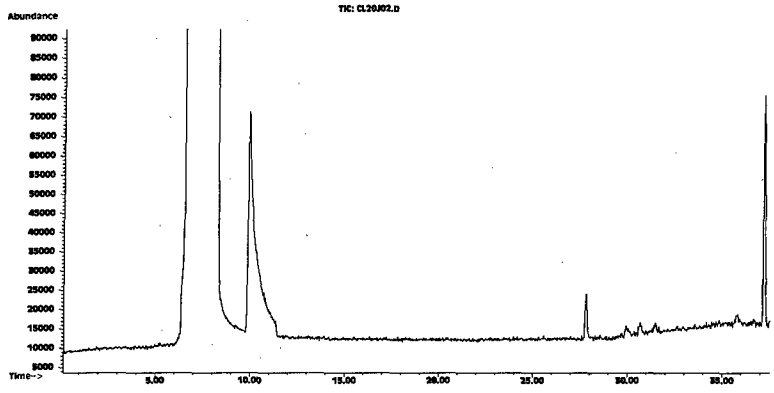

Figure 5a: GC-MSD total ion chromatogram after SPME-treatment of the „water solution" of β-CL 20 (SNPE)

For „dichloromethane solutions" of CL 20 no GC-detectable peaks have been measured after SPME enrichment. Other organic solvents were not tested since in this case thermal degradation products of CL 20 would be produced in the GC-injector. Despite of this further GC-MSD analysis of SPME-treated solutions with solvents in which CL 20 is soluble could probably give further informations about the byproducts provided they are more soluble than in water or CH_2Cl_2.

4. LITERATURE

/1/ SUPELCO product specification, T497105 (1997)
/2/ R. B. Wardle, J. C. Hinshaw, P. Braithwaite, M. Rose
Synthesis of the caged Nitramine HNIW (CL 20)
27. ICT-Jahrestagung 1996, Karlsruhe
/3/ E. v. Holtz, D. Ornellas, M. F. Foltz, J. E. Clarkson
The solubility of ε-CL 20 in selected materials
Propellants, Explosives, Pyrotechnics 19, 206-212 (1994)
/4/M. Kaiser, B. Ditz
NMR-spektroskopische Charakterisierung von ADN and CL 20
29. ICT-Jahrestagung 1998, Karlsruhe

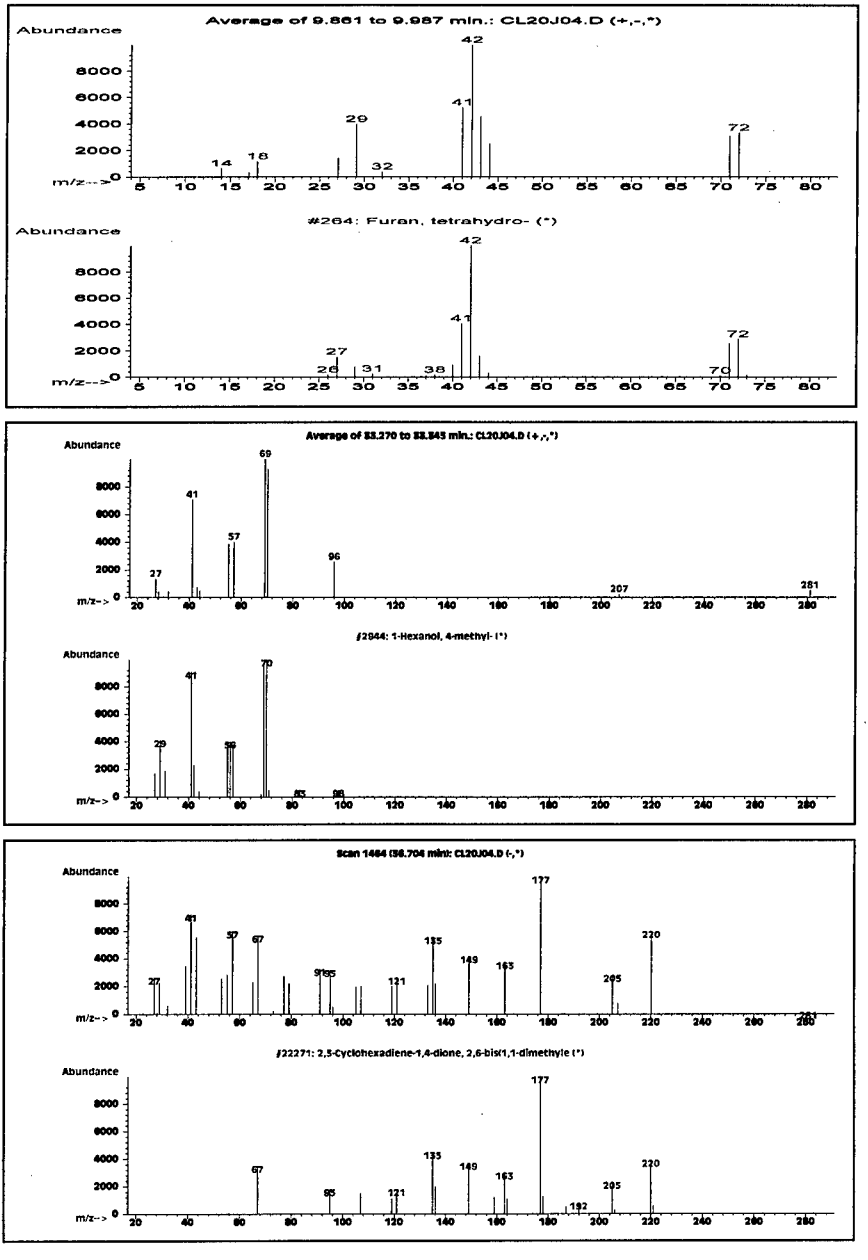

Figure 5b: Library search results for three peaks in the GC-MSD chromatogram after the SPME-treatment of the „water solution" of β-CL 20 (SNPE)

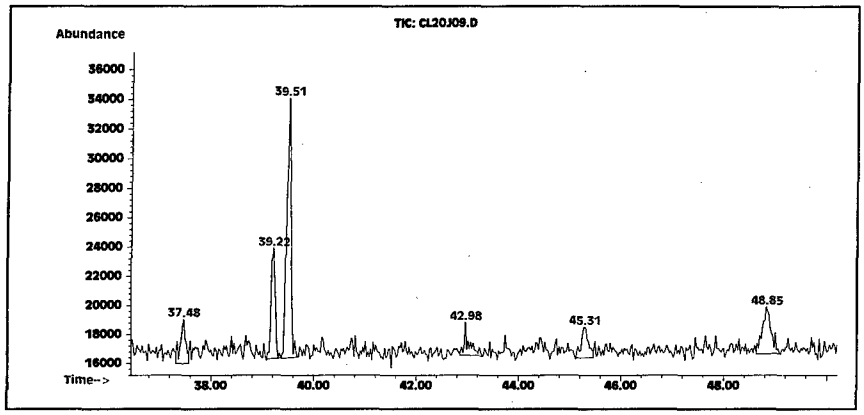

Figure 6: GC-MSD total ion chromatogram after the SPME-treatment of the „water solution" of ε-CL 20 (Thiokol)

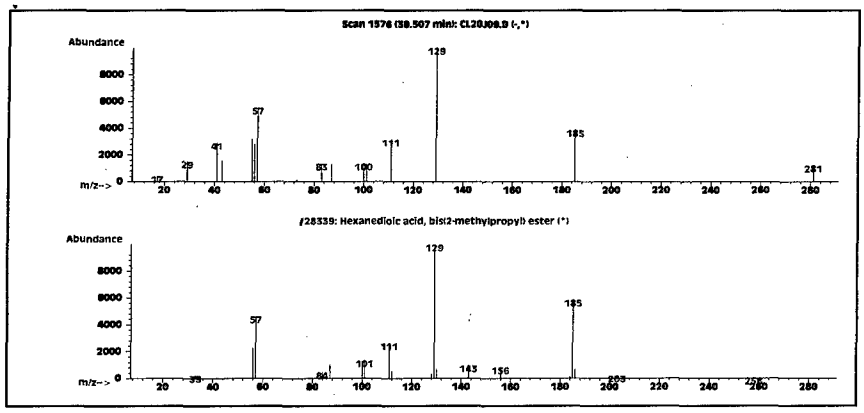

Figure 7: GC-MSD-library search result for the peak at 39.7 min after the SPME-treatment of the „water solution" of ε-CL 20 (Thiokol and SNPE)

AFTERBURNING OF TNT DETONATION PRODUCTS IN AN EXPLOSIVE CHAMBER

Józef PASZULA, Radosław TRĘBIŃSKI, Waldemar A. TRZCIŃSKI
Military University of Technology
Kaliskiego 2, 01-489 Warsaw, POLAND

Piotr WOLAŃSKI
Warsaw University of Technology
Nowowiejska 25, 00-665 Warsaw, POLAND

Abstract

The process of afterburning of TNT detonation products in an explosion chamber of a volume of 0.15 m^3 was investigated. The chamber was filled with argon or air under normal pressure (0.1 MPa). Charges of 50 or 100 g of TNT were fired. Signals of overpressure in the chamber were recorded by two pressure gauges. Scattering and consecutive compression of detonation products in the chamber was also modelled. The results of gasdynamical modelling as well as those of thermochemical calculations were compared with the overpressure records. As a result, the additional energy released during afterburning of the TNT detonation products in air atmosphere was estimated.

1. Introduction

Trinitrotoluene (TNT) is one of the most commonly used explosive of strong negative oxygen balance (B_O = -75 %). Detonation heat of TNT is about 1100 cal/g, but the oxidation of the unreacted carbon, carbon oxide and hydrogen contained in the detonation-produced gases can release additional 2500 cal/g [1]. This effect can increase the late-time pressure in confined explosions by a factor 3.5. However, conditions of the afterburning process of TNT are not known.

In this work a series of experiments for charges of different mass of TNT in an explosion chamber of a volume of 0.15 m^3 has been conducted. The chamber was filled with argon or air under pressure of 0.1 MPa. Signals of overpressure at the chamber wall after detonation of TNT charge were recorded by two pressure gauges. The results of gasdynamical modelling and thermochemical calculations were compared with the overpressure records. In consequence, the

energies released during the detonation of TNT charges in argon and air closed in the explosion chamber were determined. A rate of heat losses to the wall of the chamber was also estimated.

2. Experimental approach and results

Explosion tests with TNT charges were performed in a chamber which schematic diagram is shown in Fig. 1. The chamber consists of a cylindrical part of height 180 mm and internal diameter 580 mm and two spherical parts of internal diameter of 580 mm. The chamber volume is about 0.15 m^3.

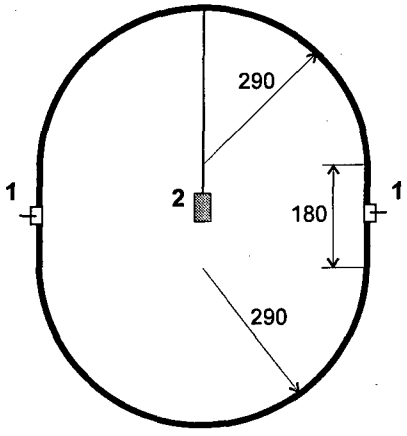

Fig. 1. Schematic diagram of an explosion chamber; 1- pressure gauges, 2 - TNT charge.

Charges of flaked TNT of 50 or 100 g weight were used. Samples of TNT were pressed in cylindrical matrices of inner diameter of 30 mm (50 g samples) or 40 mm (100 g samples). Each charge had a fuse cavity 8 mm in diameter and 15 mm long. Density of the charges varied in the range 1.57-1.58 g/cm^3.

The chamber was filled with argon or air under a pressure 0.1 MPa. The charge with a fuse was hung in the centre of the chamber. Signals of overpressure from two pressure gauges located at opposite walls of the chamber (see Fig. 1) were recorded by a digital storage scope DS-8621 (Iwatsu Electric Co., Ltd.). Chosen overpressure records from the chamber are presented in Figs. 2-3 for argon atmosphere and in Figs. 4-5 for air atmosphere in the chamber. The records from Figs. 2 and 4 were made at 1 V/div. sensitivity and 20 μs/div. sweep rate and those from Figs. 3 and 5 at 0.1 V/div. and 500 μs/div.

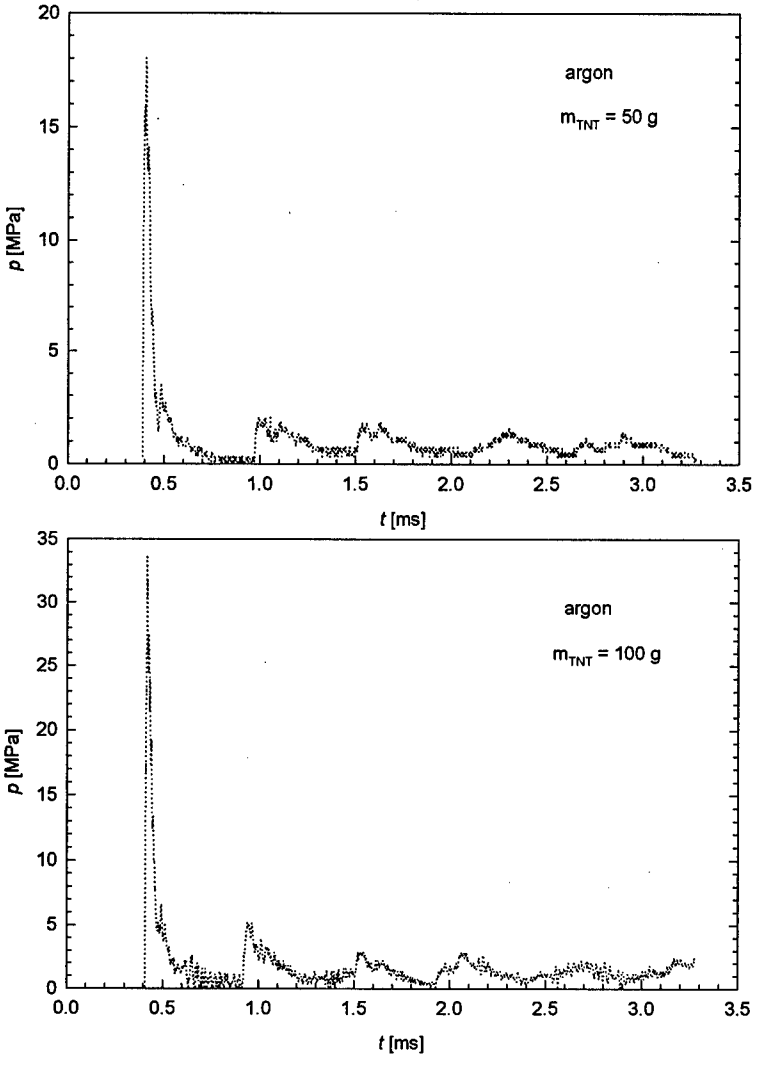

Fig. 2. Overpressure records in the chamber filled with argon; 1 V/div. sensitivity, 20 μs/div. sweep rate.

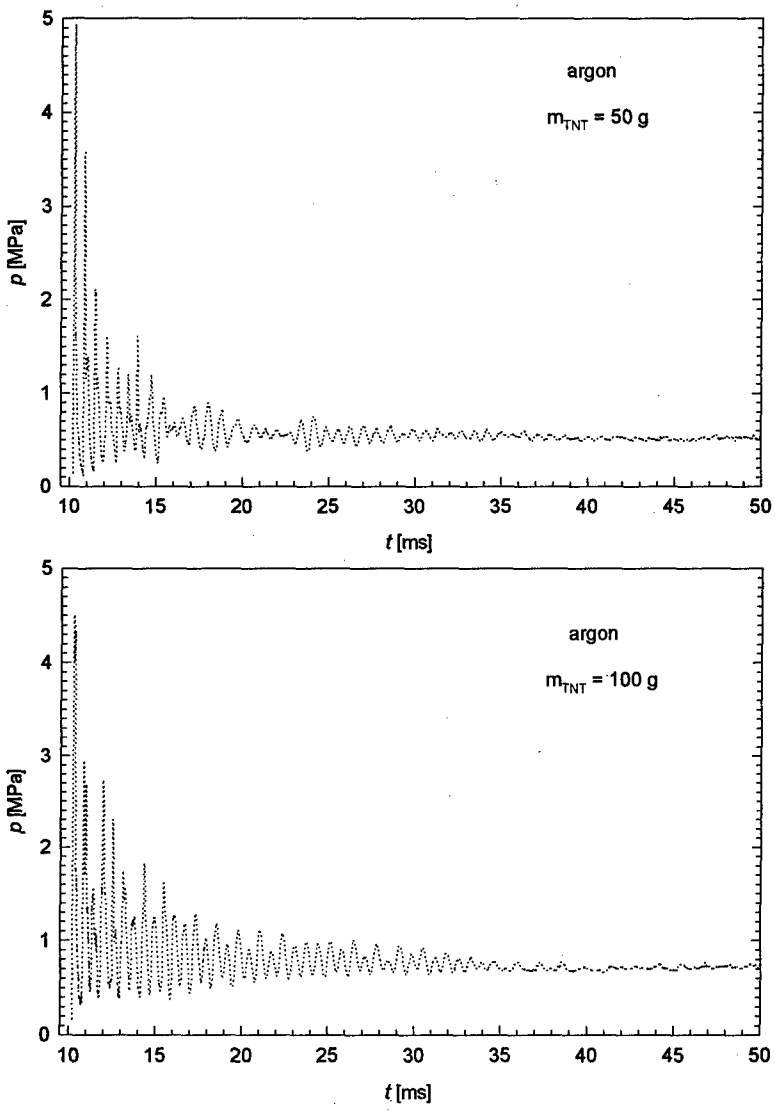

Fig. 3. Overpressure records in the chamber filled with argon; 0.1 V/div. sensitivity, 500 μs/div. sweep rate.

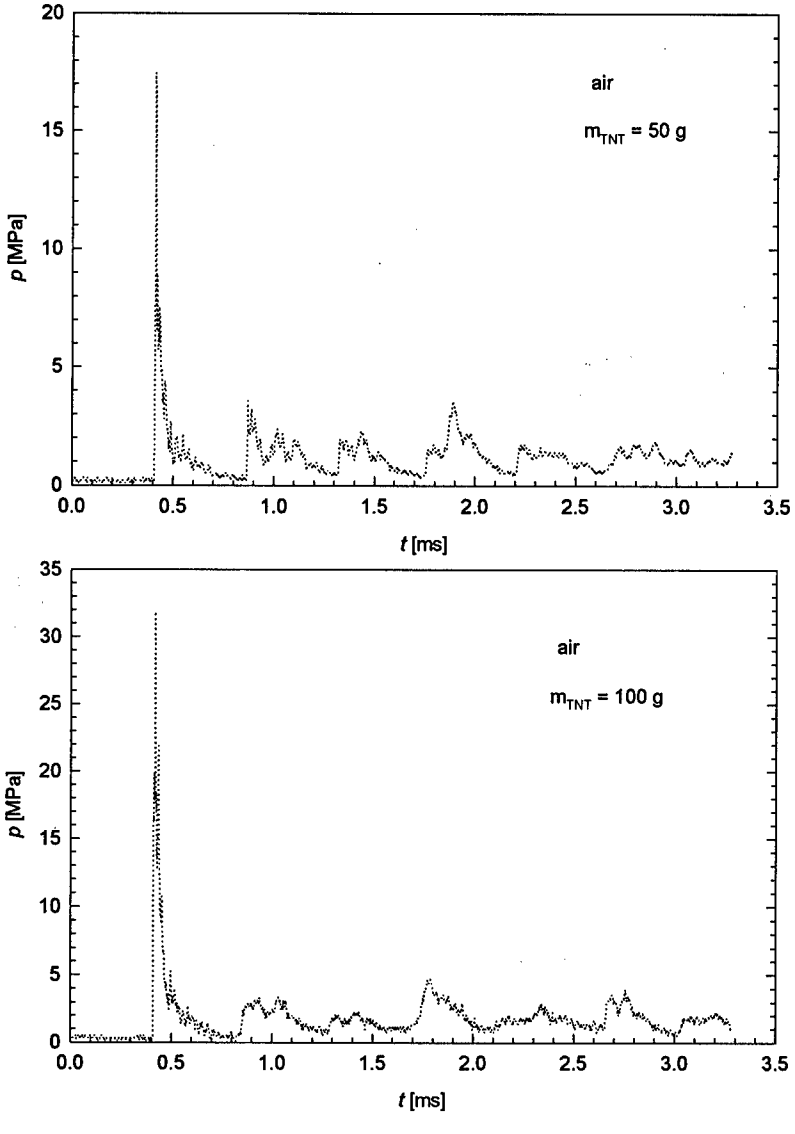

Fig. 4. Overpressure records in the chamber filled with air; 1 V/div. sensitivity, 20 μs/div. sweep rate.

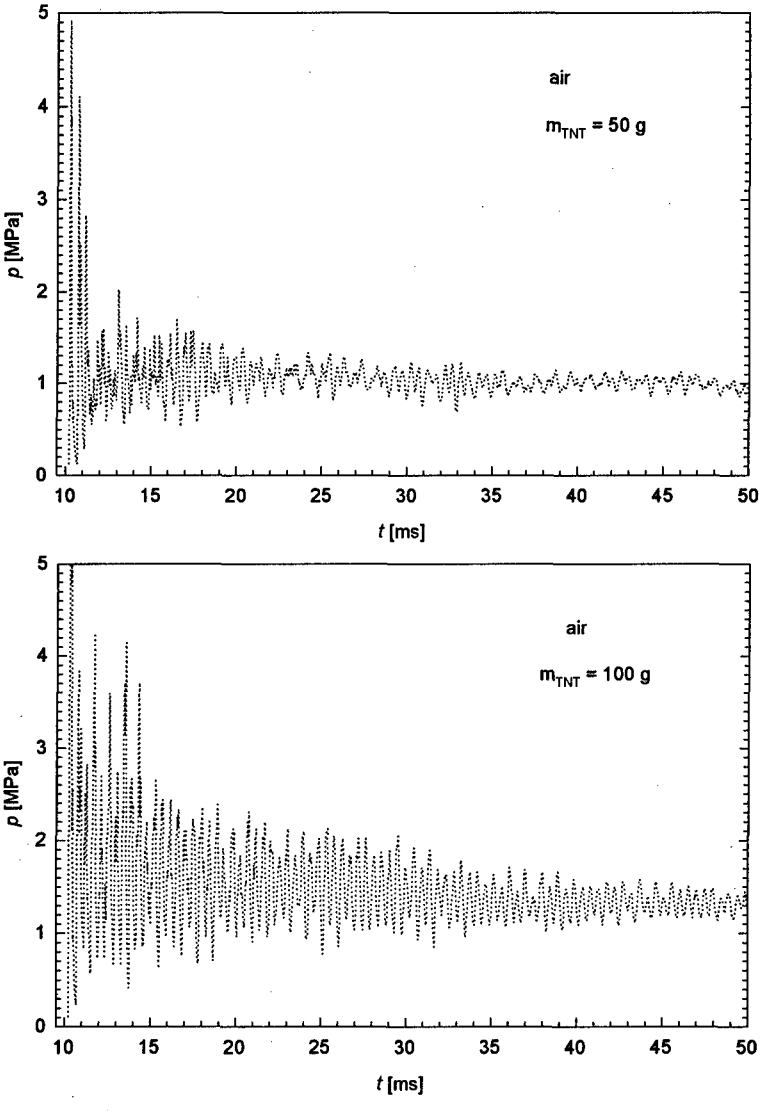

Fig. 5. Overpressure records in the chamber filled with air; 0.1 V/div. sensitivity, 500 μs/div. sweep rate.

The overpressure records have the oscillating nature. The amplitudes of oscillations decrease with increasing the time of recording. After the first reverberations of shock waves at the chamber wall also averaged value of overpressure decreases. This phenomenon is caused by the heat losses to the wall.

From 5 to 7 tests were made for each mass of TNT charge for given filler of the chamber. The overpressure records were averaged by the method described in Ref. [2]. The mean overpressure was obtained by the following equation

$$p_{aver}(t) = \frac{1}{\tau} \int_{t-\frac{\tau}{2}}^{t+\frac{\tau}{2}} p(t')\, dt' \qquad (1)$$

A value τ = 1 ms was chosen. This value is about two times longer than the time-duration of a single peak of overpressure recorded in the chamber filled with argon or air. Simultaneously, the records were modified by adding of 0.1 MPa to the overpressure values. In this way the pressure records were obtained.

To determine a rate of decreasing of the average pressure, the initial dynamical part of the pressure records was rejected. It was assumed that the first dynamical stage of shock wave reverberations at the wall lasted about 5 ms. The average pressure are shown in Fig. 6 in the form of dotted-plots. A drop of the mean pressure is caused mainly by the heat flow to the chamber wall. Thus, a time-dependence of the mean pressure can be approximated by the following function

$$p_{aver}(t) = p_0\, e^{-a(t-t_0)} \qquad (2)$$

where t_0 is the time of the first reflection of the shock wave from the chamber wall, p_0 and a are constants. To determine these constants, the records of all shots for given TNT mass and type of gas filling the chamber were used. It was assumed that t_0 = 10.25 ms, although the time of the first shock reflection varied from 10.22 to 10.28 ms. The calculated values of p_0 and a are presented in Table 1. The functions (2) with these constants are represented in Fig. 6 by solid lines.

The parameter a represents the rate of the pressure decrease at the chamber wall. There is no correlation between the value of average pressure at the wall and the rate of drop it.

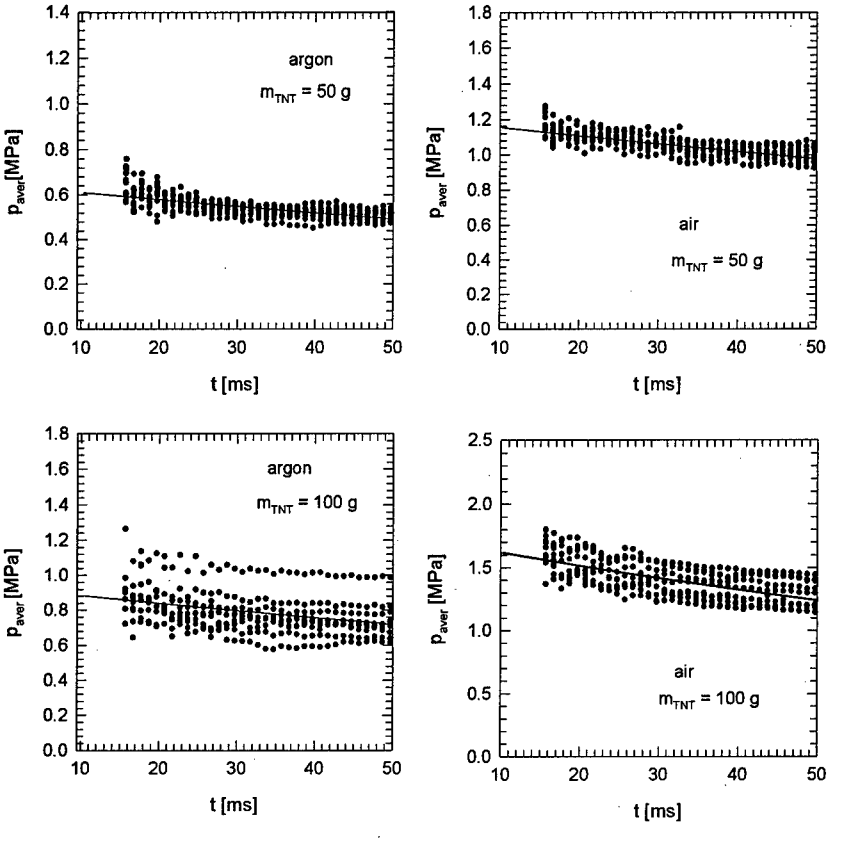

Fig. 6. Time-dependencies of an average pressure at the chamber wall

Table 1. Calculated parameters for the function (2)

Type of gas in the chamber	Mass of TNT [g]	p_0 [MPa]	$a \cdot 10^3$ [1/s]
argon	50	0.610	5.36
argon	100	0.880	5.15
air	50	1.154	4.18
air	100	1.618	6.72

The parameter p_0 can be treated as a mean value of pressure at the chamber wall at the moment of the first shock wave reverberation. In reality, the mean pressure at the wall during the initial phase of expansion and mixing of the detonation products and gaseous medium is higher due to the gasdynamical processes (acceleration, reflection and reverberation of shock waves) occurring in the chamber. However, it can be assumed that p_0 denotes the final pressure in the chamber after mixing and afterburning without heat losses to the chamber wall. A comparison of the values of p_0 presented in Table 1 with calculated pressures for different fractions of unreacted carbon in the chamber will give us an answer to the question if the afterburning process takes place in the chamber

3. Calculations

3.1 Modelling of scattering and compression of the detonation products

To describe the process of scattering and consecutive compression of the detonation products in the explosion chamber a theoretical model described in Ref. [3] was applied. In this model it is assumed that the spherical charge (of radius r_1) is located at the centre of a spherical explosion chamber of radius r_k (Fig. 7). The chamber is filled with inert gas, i.e., no reactions take place between this gas and the detonation products.

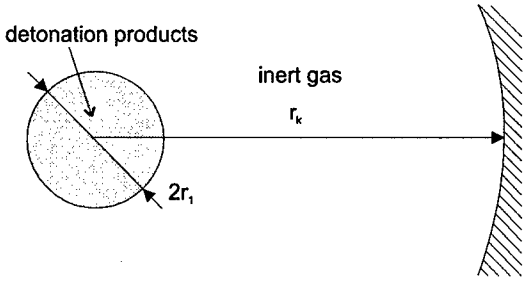

Fig. 7. Schematic diagram of a spherical chamber.

The motion of the gaseous medium in the chamber was described by the equations of continuity of mass, momentum flux and energy. The JWL (Jones-Wilkins-Lee) equation of state was assumed for describing the thermodynamical properties of the detonation products and a polytropic gas model was used for inert gas. The equations of motion with approximate initial and boundary conditions were solved numerically by the Godunov's method [4]. The spherical chamber had the same volume as the chamber used in experiments. Densities of 1.78 and 1.29 kg/m^3

and politropic exponents 1.67 and 1.4 were assumed for argon and air, respectively. The results of modelling are presented in Figs. 8 and 9.

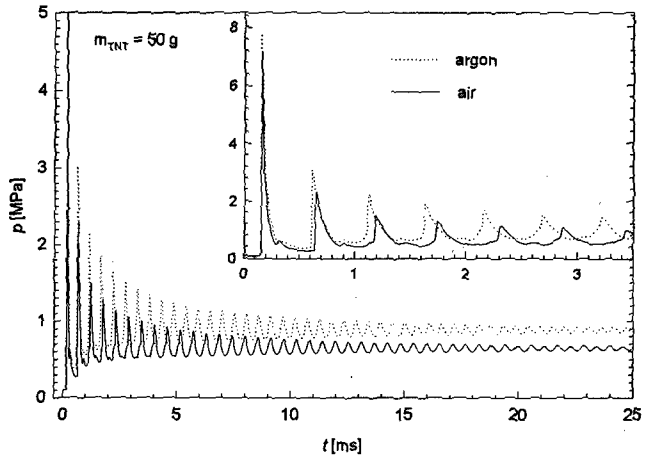

Fig. 8. Calculated pressure variations at a spherical chamber wall for 50 g TNT

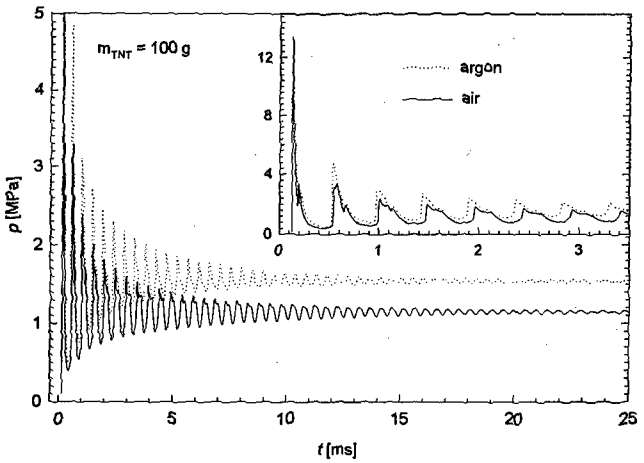

Fig. 9. Calculated pressure variations at a spherical chamber wall for 100 g TNT

Comparison of the average pressures in argon and air atmospheres for the same mass of TNT (Fig. 6) shows that the average pressure in the chamber filled with air is higher than that in argon filler. An inverse relation was obtained from calculations by assuming an inert nature of gases (Figs. 8, 9). Thus, an inference can be drawn that reactions between the detonation products of TNT and air take place and the additional energy, increasing the pressure in the chamber, is released.

3.2. Thermochemical calculations

Thermochemical calculations were made by using TIGER - [5]. The set of values of the parameters $\alpha = 0.50$, $\beta = 0.298$, $\kappa = 10.50$, $\Theta = 6620$ for the BKW equation of state and covolumes factors for species were taken from Refs. [6-7]. The detonation velocity of 6780 m/s was calculated for TNT of density 1.58 g/cm^3. The compositions of the detonation products at the C-J point and at 1800 K on the C-J isentrope are presented in Table 2.

Table 2. Products of detonation of TNT

	T_{CJ} = 3250 K	T_{IS} = 1800 K
Detonation products[mol/kg]:		
CO_2	9,1645	6,6608
CO	0,8433	9,7009
H_2O	6,0961	3,3633
N_2	5,7383	6,3398
H_2	0,8971	2,2770
CH_4	0,4227	2,2848
NH_3	1,7298	0,5193
HCOOH	0,5734	0,0149
HCN	0,0006	0,0089
NO	0,0005	0,0
C(s)	19,8141	12,1474

The calculations of explosion parameters of the TNT/argon or TNT/air mixtures were performed by using TIGER code. It was assumed in the first approximation that carbon from the detonation products is the main fuel. The influence of mass of unreacted (frozen) carbon, m_C, in 1 kg of the mixture on the final pressure in the explosion chamber was checked. The results are presented in Figs. 10 and 11. Symbols EQ, IS, and CJ denote the values of carbon mass in the mix-

ture at an equilibrium state, at the temperature 1800 K on the C-J isentrope, and at the C-J point, respectively.

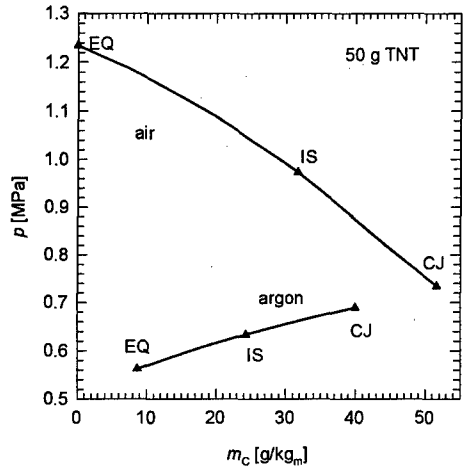

Fig. 10. Pressure as a function of mass of unreacted carbon for 50 g TNT

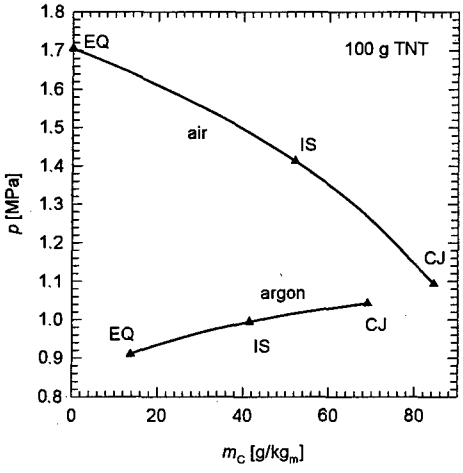

Fig. 11. Pressure as a function of mass of unreacted carbon for 100 g TNT

By comparison of values of p_0 given in Table 1 with plots in Figs. 10 and 11, the final values of carbon mass in the mixtures were established. Then, these masses were frozen and the compositions of products and heats of reactions were calculated. The results are presented in Table 3.

Table 3. Compositions of reaction products corresponding to the pressure (p_0) in the chamber

Gas in the chamber	argon		air	
Mass of charge [g]	50	100	50	100
Carbon mass in mixture [g/kg_m]	15	20	10	0
Products [mol/kg_m]:				
N_2	1.1227	1.9151	22.117	19.497
H_2O	0.3211	0.2868	2.3597	3.4598
CO_2	0.1805	0.1018	5.0562	3.6903
CO	3.8102	7.1704	0.7967	7.2974
C(s)	1.2490	1.6653	0.8326	0.0
H_2	1.5506	2.9051	0.0279	0.4643
NO	0.0	0.0	0.7825	0.3533
NO_2	0.0	0.0	0.0007	0.0001
O_2	0.0	0.0	1.5199	0.1324
Ar	20.777	17.773	0.2714	0.2230
Reaction heat [cal/g_{TNT}]	730	612	2880	2080

From Table 3 it follows that the reaction heats of TNT charges detonated in the chamber with argon atmosphere are lower than the explosion heat of TNT (about 1100 cal/g). Similar effect was observed in calorimetric experiments performed in Ref. [1]. Detonation of unconfined charges of TNT in an evacuated calorimetric bomb produced energy from 582 to 669 cal/g. According to author of Ref. [1], the detonation products of TNT were reshocked strongly and the composition of products re-equilibrated under conditions of high temperature and relatively low pressure. This re-equilibration led to an increase of CO and H_2 and a decrease of CO_2, H_2O and solid C in the products. The compositions presented in Table 3 show that the same phenomenon occurs in the chamber with argon filler.

In the case of air in the chamber, the reaction effects are higher, as compared with the TNT explosion heat, of about 1800 and 1000 cal/g for 50 and 100 g charges of TNT, respectively. Despite of a present of some amounts of oxygen in the final compositions of the reaction products, the afterburning process of the products has been stopped. This means that mixing of the detona-

tion products with air is not full or heat losses to the chamber wall cause a decrease of the temperature of gaseous medium below the critical temperature of oxidation reactions.

4. Summary

1. The overpressures recorded at the chamber wall after detonation of TNT charges have the oscillating nature. The amplitudes of oscillations decrease with time. The average overpressure also drops off.
2. For the same mass of TNT the average pressure in the chamber filled with argon is lower than that in the chamber with air. An inverse relation is obtained from calculations when a model of inert gas is assumed for argon and air.
3. Estimated heats released in the chamber filled with argon are lower than the explosion heat of TNT.
4. The reaction effects in the chamber filled with air are higher than the heat of explosion of TNT (about 1800 and 1000 cal/g_{TNT} for 50 and 100 g TNT, respectively).

Acknowledgments

This work was supported by the DSWA Contract No. DSWA01-97-C-0051

References

[1] D. L. Ornellas, *Calorimetric determinations of the heat and products of detonation for explosives*, Lawrence Livermore Laboratory, Livermore, 1982.

[2] P. Neuwald et al., *Self-Similar Combustion of Turbulent Fuel Jets in Air*, Fraunhofer Institut für Kurzzetdynamik, 1997.

[3] R. Trębiński, W. Trzciński, E. Włodarczyk, *Solution of the problem of scattering of the detonation products of a spherical explosive charge with solid particles,* J. Techn. Phys., **32**, 2, 1991.

[4] S. K. Godunov, *Numerical solution of multi-dimensional problems of gasdynamics* (in Russian), Nauka, Moscow, 1976.

[5] Ch. L. Mader, *Numerical modelling of detonations*, University of California Press, Berkeley-Los Angeles-London, 1979.

[6] M. L. Hobbs, M. R. Baer, *Nonideal thermoequilibrium calculations using a large product species data base*, Shock Waves (1992), 2: 177-187.

[7] M. L. Hobbs, M. R. Baer, *Calibration of the BKW-EOS and aplication to aluminized composite explosives*, Proceedings of EUROPYRO 93, Strasbourg 1993.

COMPARISON OF HEAT EFFECTS OF COMBUSTION AND DETONATION OF EXPLOSIVES IN A CALORIMETRIC BOMB

Stanisław CUDZIŁO, Radosław TRĘBIŃSKI, Waldemar A. TRZCIŃSKI

Military University of Technology
Kaliskiego 2, 01-489 Warsaw, POLAND

Piotr WOLAŃSKI

Warsaw University of Technology
Nowowiejska 25, 00-665 Warsaw, POLAND

Abstract

The process of heat releasing during combustion and detonation of condensed explosives in a calorimetric bomb of 3.6 l in volume was investigated. TNT, RDX and HMX-based explosives were used in tests. The bomb was filled with argon or air under pressure 1 MPa. The combustion and detonation heats were measured for both the bomb fillers. Thermochemical calculations were also performed for the explosive systems tested. The calculated heat effects of combustion and detonation were compared with measured ones. The degree of afterburning of the detonation products of explosive used in the bomb calorimeter tests was estimated.

1. Introduction

Most conventional explosives used in military and commercial operations are not oxygen balanced. For example, the oxygen balance of TNT is about -75 % and that of RDX or HMX is about -21.6 %. Consequently, the detonation products of such explosives mixed with air will afterburn and additional energy will be released.

An influence of detonation conditions on a heat effect of explosive was investigated by D. L. Ornellas [1]. Among others, the calorimetric heats of TNT were measured in [1] and the values of 1093, 1116 and 3575 cal/g were obtained for TNT charges located in the bomb with vacuum or filled with carbon dioxide and oxygen, respectively. Moreover, different heats were measured after detonation of heavily confined and unconfined charges, for instance, 1093 and 632 cal/g for TNT and 1479 and 1334 cal/g for HMX charges.

In this work the effect of a type of gaseous filler of the calorimetric bomb on the heat released during combustion or detonation was examined. TNT, phlegmatized hexogen (RDX_{phl}) and phlegmatized octogen (HMX_{phl}) were used in tests. The values of calorimetric heats were compared with those obtained from thermochemical calculations.

2. Experimental approach and results

A spherical steel bomb of a volume of 3.6 l was used to measure heat effects of combustion and detonation. The bomb was placed in a calorimetric vessel. The heat capacity of a calorimeter system was 12 944 ± 6 cal/°C.

TNT of 1.58 g/cm^3, RDX_{phl} ($RDX/(CH_2)_n$ 94/6) of 1.68 g/cm^3 and HMX_{phl} ($HMX/(CH_2)_n$ 96/4) of 1.78 g/cm^3 density were tested. Weighed samples of explosives were pressed in matrices of inner diameter of 16 or 20 mm. Each charge destined for detonation had a fuse cavity 8 mm in diameter and 15 mm long. The charge was suspended in the centre of the bomb. The bomb was evacuated and filled with argon or air to the pressure of 1 MPa.

The sample of explosive destined for combustion had a resistance wire to ignite the combustion process. The results of measuring of the combustion heats of explosives tested are presented in Table 1.

Table 1. Combustion heat effects of explosives for different fillers of the bomb

Explosive	Mass of sample [g]	Gas	Total heat effect [cal]	Specific heat effect [cal/g]
TNT	10.206	argon	no burning	-
	9.244	air	33 430	3616
RDX_{phl}	8.128	argon	9 060	1115
	9.495	air	26 680	2810
HMX_{phl}	8.317	argon	10 130	1218
	9.286	air	24 960	2688

Electrical fuses were used to initiate detonation of charges. The fuse was made of primary and secondary explosives closed in an aluminium cup. To estimate the energy released by the fuse the TNT charges of different mass was detonated in the bomb filled with argon or air. If the degree of reaction of aluminium and the explosion products of the fuse with the gaseous products of TNT

and gas filling the bomb is independent of the mass of TNT then the dependence of the total explosion heat of TNT charge with the fuse on the TNT mass should have a linear form. The heat released from the fuse explosion can be obtained from this dependence. The values of the total heat effect per unit mass of TNT are presented in Fig. 1 for argon and in Fig. 2 for air filling the bomb. For the latter, the results measured for 12 and 13 g TNT were rejected in a procedure of estimation of the linear dependence $Q = Q(m_{TNT})$, because there was too small amount of oxygen in the bomb to burn the explosion products of TNT and fuse.

From a linear approximation of the calorimetric results presented in Figs. 1 and 2 the energy effects of the fuse can be calculated. The values of 2802 ± 109 cal and 14253 ± 80 cal were obtained for argon and air in the bomb, respectively. This values were assumed for further calculations of explosion heats on the basis of the results of calorimetric experiments.

The detonation heat effects of the explosives tested are shown in Table 2. As compared with argon atmosphere the heat effect of detonation in air increased about 272 % for TNT, 118 % for RDX_{phl} and 99 % for HMX_{phl}.

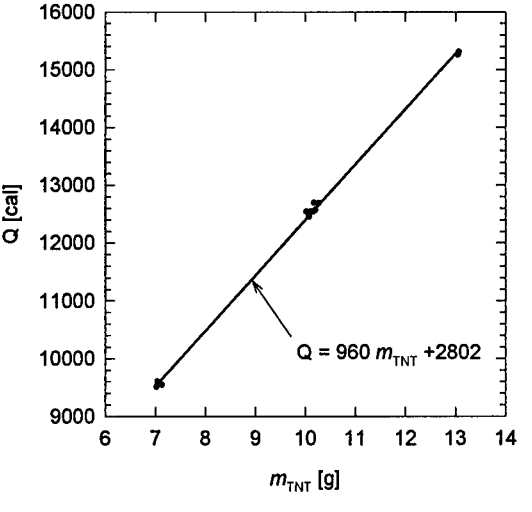

Fig. 1. Total heat, Q, of TNT charges detonated in argon as a function of TNT mass, m_{TNT}.

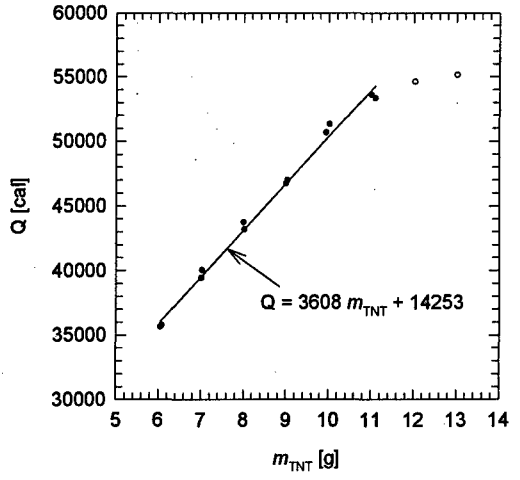

Fig. 2. Total heat, Q, of TNT charges detonated in air as a function of TNT mass, m_{TNT}.

Table 2. Detonation heat effects of explosives for different fillers of the bomb

Explosive	Mass of sample [g]	Gas	Total heat effect [cal]	Specific heat effect [cal/g]
TNT	10.318	argon	12 790	968
	9.007	air	46 710	3604
RDX_{phl}	8.068	argon	12 950	1258
	8.106	air	36 470	2741
HMX_{phl}	8.267	argon	13 850	1336
	8.105	air	35 790	2657

3. Calculations and discussion

Thermochemical calculations were performed by using TIGER -[2]. The set of values of the parameters $\alpha = 0.50$, $\beta = 0.298$, $\kappa = 10.50$ and $\Theta = 6620$ for the BKW equation of state and co-volumes factors for gaseous species were taken from Refs.[3-4].

Calculated detonation parameters, compositions of products and heats of detonation for the explosive used in experiments are presented in Table 3. The compositions of the detonation products at the C-J state and at the temperature 1800 K on the isentrope beginning at the C-J state are

shown. The detonation products set at 1800 K is suggested to be close to the final composition of the products [1, 5]. The heat effect corresponding to the products set was calculated on the basis of values of a standard enthalpy of formation for given explosive and its products.

Table 3. Calculated detonation parameters, products sets and heat effects of the explosive tested

Explosive	TNT		RDX_{phl}		HMX_{phl}	
Detonation velocity [m/s]	6780		8445		8880	
Detonation temperature [K]	3250		3690		3780	
Detonation pressure [GPa]	17,1		27,6		31,8	
State of products	C-J	1800 K*	C-J	1800 K*	C-J	1800 K*
Products [mol/kg_{expl}]:						
N_2	5,7383	6,3365	10,5509	12,1167	10,8822	12,3946
H_2O	6,0961	3,3960	7,6925	5,3460	7,0139	5,8203
CO_2	9,1645	6,6774	7,7341	6,3459	8,1908	6,9230
CO	0,8433	9,6348	0,2155	7,3170	0,1260	6,2251
C(s)	19,8141	12,2228	7,5009	0,0	5,8975	0,0
H_2	0,8971	2,2827	0,8138	3,3115	0,5573	2,9816
NH_3	1,7298	0,5260	4,2855	1,1498	4,1623	1,1366
CH_4	0,4227	2,2596	0,5167	3,2845	0,4003	2,6440
HCN	0,0006	0,0089	0,0001	0,0077	0,0	0,0055
HCOOH	0,5734	0,0153	1,0057	0,0181	1,2025	0,0199
NO	0,0005	0,0	0,0031	0,0	0,0043	0,0
O_2	0,0	0,0	0,0001	0,0	0,0001	0,0
Heat effect [cal/g_{expl}]	1306	1090	1436	1262	1449	1314

* temperature of the detonation products rarefied from the C-J state by isentropic means

Comparison of calculated heats with those obtained in calorimetric experiment with argon filler shows that good agreement is obtained when the composition frozen at 1800 K was assumed for calculations. This fact confirms the hypothesis presented in Refs. [1, 5]. Only explosion heat measured for TNT in argon atmosphere is slightly smaller than that calculated. A possible cause of this discrepancy is the construction of the experimental set-up used for determining the detonation heat. In the experiments, unconfined charges were suspended at the centre of the bomb and shock wave reverberations can influences the equilibration process of the detonation products. Ornellas ([1]) tested the influence of confinement and no confinement on the explosion heat of TNT charges in the bomb evacuated to a pressure of about 50 μm Hg. Values of 1093 and 632

cal/g were obtained for gold confinement and no confinement, respectively. According to Ornellas, the detonation products of TNT were reshocked strongly when unconfined charge was used. In our opinion, the argon atmosphere with the pressure of 1 MPa plays the similar role during the expansion of the detonation products as confinement of the charge. But, the argon layer surrounding the charge absorbs smaller amount of the explosion energy than a solid confinement. Thus, the shock wave reflected from the wall of the bomb causes only partial equilibration of solid carbon content and the calorimetric explosion heat of carbon riched TNT is slight smaller than the theoretical one and that obtained in [1] for confined charge.

Table 4. Calcutated parameters of self-sustaining combustion of the explosive tested

Explosive	TNT	RDX_{phl}	HMX_{phl}
Combustion temperature [K]	1830	2725	2950
External pressure [MPa]	1	1	1
Freeze-out temperature [K]	1800 K*	1800 K*	1800 K*
Products [mol/kg_{expl}]:			
N_2	6,1284	12,6952	12,9656
H_2O	0,0004	7,0286	8,2309
CO_2	0,0001	1,3946	1,9084
CO	26,4154	15,5821	13,9259
C(s)	3,4312	0,0	0,0
H_2	10,5202	9,9488	7,6086
NH_3	0,0004	0,0005	0,0004
CH_4	0,0058	0,0	0,0
HCN	0,9644	0,0	0,0
Heat effect [cal/g_{expl}]	597	1057	1149

* temperature of frozen composition of the reaction products

Temperatures of a self-sustaining combustion process were calculated by assuming an external pressure of 1 MPa. The results are presented in Table 4. The compositions of combustion products frozen at 1800 K and the heat effects corresponding to these compositions are also given in Table 4. The compositions differ insignificantly from the products sets at the combustion temperature and discrepancies in the heat effects do not exceed 5 cal/g. Heat effect calculated for given explosive is lower than that measured during combustion of the explosive in argon. This

difference is caused by the assumption of constant pressure of combustion products. In reality, this pressure increases with a development of combustion

Table 5. Calculated parameters of reaction with air closed in the bomb.

Explosive	TNT	RDX_{phl}	HMX_{phl}
Explosion temperature [K]	2706	2222	2125
Explosion pressure [MPa]	10,9	9,3	8,9
Frozee-out temperature [K]	1800 K*	1800 K*	1800 K*
Products[mol/kg_m]:			
N_2	23,3679	24,3927	24,4355
H_2O	1,8933	2.9197	2,7209
CO_2	5,3011	2.9195	2,7207
CO	0,0005	0,0002	0,0002
NO	0,1117	0,1569	0,1640
NO_2	0,0010	0,0019	0,0021
O_2	1,9713	3,7286	4,0691
Ar	0,2861	0,2861	0,2861
Heat effect [cal/g_{expl}]	3572	2791	2597

* temperature of frozen composition of the reaction products

Close values of measured heat effects of detonation and combustion of given explosive in air atmosphere indicate that in both the cases the explosive products and air equilibrate under similar conditions of high temperature and relatively low pressure. Accordingly, the products of reaction of the explosive and air closed in the bomb can be calculated by assuming that an explosion of the mixture of explosive and air takes place in a constant volume. The 3.6 l bomb contained 32.67 g nitrogen, 10.05 g oxygen and 0.60 g argon at the temperature 21.5 °C and under the pressure 1 MPa. The TNT charge of 9 g mass was chosen for calculations. It was assumed that, after explosion, the products were cooled in a constant volume and the composition was frozen at 1800 K. The results of calculations are presented in Table 5. In this case the fractions of the products are given in moles per one kilogram of the mixture of explosive and air.

From comparison of the heat effects shown in Table 5 with calculated detonation heats (Table 3) it follows that the additional energies released due to afterburning of the detonation are about 228, 121 and 98 % of the detonation heats of TNT, RDX_{phl} and HMX_{phl}, respectively.

4. Summary

1. Afterburning of the products of explosives detonated in the calorimetric bomb filled with air leads to releasing additional energy as compared with the bomb filled with argon. These additional energies are 272, 118 and 99 % of those measured in argon atmosphere for TNT, RDX_{phl} and HMX_{phl}, respectively. Calculated effects of afterburning of the detonation products are 228, 121 and 98 % of calculated detonation heats for these explosives.
2. In the case of argon filler, the value of combustion heat is lower than the value of detonation heat for all explosive tested. Results of calculations indicate that the initial temperature and pressure of the detonation products are higher than those of the combustion products. Conditions of high temperature and pressure facilitate oxidation of carbon and hydrogen from the explosive.
3. In the case of air filler, the value of heat effect of combustion is higher than the value of heat effect of detonation for all explosive. In this case the time-duration of the process is a main factor influencing the effectiveness of the afterburning phenomena in the bomb.
4. Good agreement between measured and calculated heat effects was obtained when the composition of reaction products frozen at 1800 K was assumed for the heat estimation.
5. The heat of detonation of RDX_{phl} or HMX_{phl} can be measured by use of unconfined charge in a calorimetric bomb filled with argon, but a solid confinement for charge must be apply to measure the detonation heat of TNT.

This work was partially supported by the DSWA Contract No. DSWA01-97-C-0051 and internal Project PBZ 019-12 financed by the PolishScientific Research Committee.

References

[1] D. L. Ornellas, *Calorimetric determinations of the heat and products of detonation for explosives*, Lawrence Livermore Laboratory, Livermore, 1982.

[2] Ch. L. Mader, *Numerical modelling of detonations*, University of California Press, Berkeley-Los Angeles-London, 1979.

[3] M. L. Hobbs, M. R. Baer, *Nonideal thermoequilibrium calculations using a large product species data base*, Shock Waves (1992), 2: 177-187.

[4] M. L. Hobbs, M. R. Baer, *Calibration of the BKW-EOS and aplication to aluminized composite explosives*, Proceedings of EUROPYRO 93, Strasbourg 1993.

[5] P. C. Souers, J. W. Kury, *Comparison of cylinder data and code calculations for homogeneous explosives*, Propellants, Explosives, Pyrotechnics 18 (1993), 175-183.

STUDIES OF HIGH ENERGY COMPOSITES CONTAINING POLYTETRAFLUOROETHYLENE

Stanisław CUDZIŁO, Waldemar Andrzej TRZCIŃSKI

Military University of Technology
Kaliskiego 2, 01-489 Warsaw, POLAND
Fax: +48 22 6669041

Abstract

Two-component mixtures containing magnesium (Mg) or aluminium (Al) or their alloy (Al_3Mg_4) and polytetrafluoroethylene (TF) have been investigated. The heat of combustion and linear burning rate were determined as well as differential thermal analysis (DTA) was performed for mixtures containing different mass concentration of metal and TF. On the basis of experimental results concentration limits of combustibility and initiation temperatures of exothermic reactions in combustion wave were appointed. The analysis of combustion of metal-TF mixtures was performed on the basis of theoretical model given in literature for the combustion process of mixtures with classical oxidiser.

1. Introduction

Pyrotechnic effects (e.g. white or coloured light, black or white or coloured smoke, continuous or pulsating sound, compressed gases, heat and so on) are produced in combustion processes of pyrotechnic mixtures, which are mainly composed from a fuel and an oxidiser. Additives or modifiers have also been included to produce more saturated coloured flames, to adjust burning rates, to produce coloured smoke clouds, and to increase storage life and processing safety [1,2]. Qualitative and quantitative optimisation of composition of pyrotechnic mixtures is aimed to maximise a needed effect by using minimal quantity of mixture. In high energy compositions the creating of the highest possible chemical combustion energy is based either partly or wholly on metal powders, as for example aluminium (Al) or magnesium (Mg), oxidising into an oxide (Al_2O_3, MgO). As an oxidiser there are often used different nitrates, chlorates, and perchlorates as well as different oxides or peroxides. Sometimes presence of the oxygen in combustion products of some mixtures may be unprofitable. Such a situation takes place

in compositions that are destined for generating of screen clouds to stop infrared radiation [3-6]. An improvement of effectiveness in camouflage in IR-region may be reached by increasing of quantity of carbon particles in combustion products, thus a presence of oxygen carrier in the composition is undesirable because a part of carbon is oxidised to carbon oxides (CO, CO_2). In order to avoid oxidising of carbon, a mixture of organic polychloride compounds and/or fluorocarbon polymers and metal powders may be used as a system supporting combustion of pyrotechnic compositions. The metal powders should be able to highly exothermic reactions with chlorine (fluorine) bound previously with carbon atom. As an oxidiser, in such a mixture, can be employed hexachloroethane, hexachlorobenzene, polytetrafluoroethylene, polyvinylidyne fluoride.

The burning rate and sensitivity characteristics of pyrolants containing some metals and polytetrafluoroethylene (TF) have been studied by a number of researchers [7-10]. However, there have not been published any results of measurements of combustion heat and burning rate for pyrolants containing an alloy of aluminium and magnesium (Al_3Mg_4). In this study the characteristics were determined and the thermal decomposition process was measured for the Al_3Mg_4/TF mixtures made up of different mass concentration. The same investigations were performed for Mg/TF pyrolants. On the basis of experimental results concentration limits of combustibility at 0.1 and 0.5 MPa and initiation temperatures of exothermic reactions in combustion wave were appointed. Furthermore a theoretical analysis of combustion of the metal/TF mixtures was performed by making use of the model given in literature for the combustion process of pyrolants with classical oxidisers.

2. Experimental

Powders of Al_3Mg_4 or Mg and powder of TF were used to prepare the mixtures. The mean size of metal grains was equal to 75÷105 μm and the contents of active metal exceeded 95%. The contents of TF was changed with a step of 5% within the range from 20.5 to 80.5% for Al_3Mg_4/TF pyrolants and from 27.3 to 77.3% for mixtures containing Mg.

2.1. Heat of combustion

Heat of combustion was measured with a water calorimetric set in a bomb filled with argon at 0.5 MPa. The samples were prepared in the form of about 5-gram tablets having density of 1500

kg/m^3. The combustion process was initiated by an electrically heated igniter. Its heat of combustion had been exactly known. Fig. 1 shows the relationship between the heat of combustion (Q) and the concentration of TF (η) in Al_3Mg_4/ TF and Mg/TF mixtures.

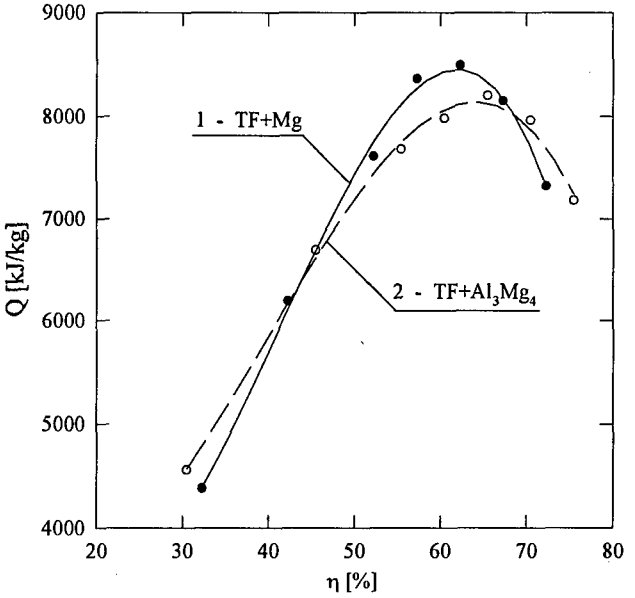

Fig. 1. Heat of combustion as a function of the concentration of TF.

The heat of combustion (Q) increases with increasing contents (η) of TF within the range from 30 to 65%. Further increase of η causes decrease of Q. The maximum Q values were obtained for the following mixtures

62.3% TF + 37.7% Mg

65.5% TF + 34.5% Al_3Mg_4

Both of the compositions correspond to contents of TF which are poorer (on 5%) than the following stechiometric reactions

$2Mg + C_2F_4 = 2MgF_2 + 2C$; (Mg/TF = 67,3/32,7)

$4Al_3Mg_4 + 17C_2F_4 = 16MgF_2 + 12AlF_3 + 34C$; ($Al_3Mg_4$/TF = 70,5/29,5)

The reason for maximisation of Q in compositions which contained less metal than the stechiometric ones is an use of partly oxidised metals to prepare mixtures.

In the tests no reactions took place in the mixtures containing less than 30% and more than 75% of TF, so the range of η from 30 to 75% is the concentration area of combustibility under the pressure of 0.5 MPa.

2.2. Decomposition characteristics

The thermal decomposition processes of TF/metal pyrolants were measured with differential thermal analysis technique (DTA). Nitrogen at 0.1 MPa was used as an atmosphere and the heating rate was 10 K/min. The temperature in the DTA increased up to 1300 K. Concentrations of TF were 67.3 or 52.3% in the Mg/TF mixtures and 70.5 or 55.5% in the Al_3Mg_4/TF mixtures. The 0.2-gram samples were not pressed to tablets. Fig. 2 shows the DTA curves for TF and for investigated pyrolants.

The endothermic peak between 600 and 630 K which is observed on all curves coincides with the melting temperature of TF (curve 1). Then the TF decomposes within the range from 780 to 900 K. On the curves 2 and 2' there is the second endothermic peak within the range from 900 to 930 K. This range of temperatures corresponds to the melting temperature of Mg, so Mg has not reacted completely with TF. Melting of Al_3Mg_4 takes place between 710÷740 K and this temperature is lower then the initial temperature of TF decomposition (780 K). The very intensive exothermic peaks (especially for Al_3Mg_4/TF pyrolants) which begin at about 780 K are results of exothermic reactions between metals and TF, so T_r = 780 K can be found as an initiation temperature of exothermic reactions in burning wave.

The DTA curves show that the reactions start after decomposition of TF and they are much faster when the metal is already in liquid state. In other words, the rate of heat production just on and behind the burning surface increases rapidly due to suitable form of fuel to react (droplets of Al_3Mg_4 instead of solid particles). That is why the exothermic heat capacity for Al_3Mg_4/TF is much higher then that for Mg/TF and why the initiation temperature decreases and exothermic effect increases meaningfully with increasing concentration of Al_3Mg_4 in the mixture. In case of solid Mg particles, the influence of their concentration on decomposition characteristics is rather small. The oxidation reaction of the Mg particles is considered to occur from the surface and reaction completes at far-downstream of the pyrolant burning surface, so the heat is mostly released in gas phase and cannot be registered in DTA technique.

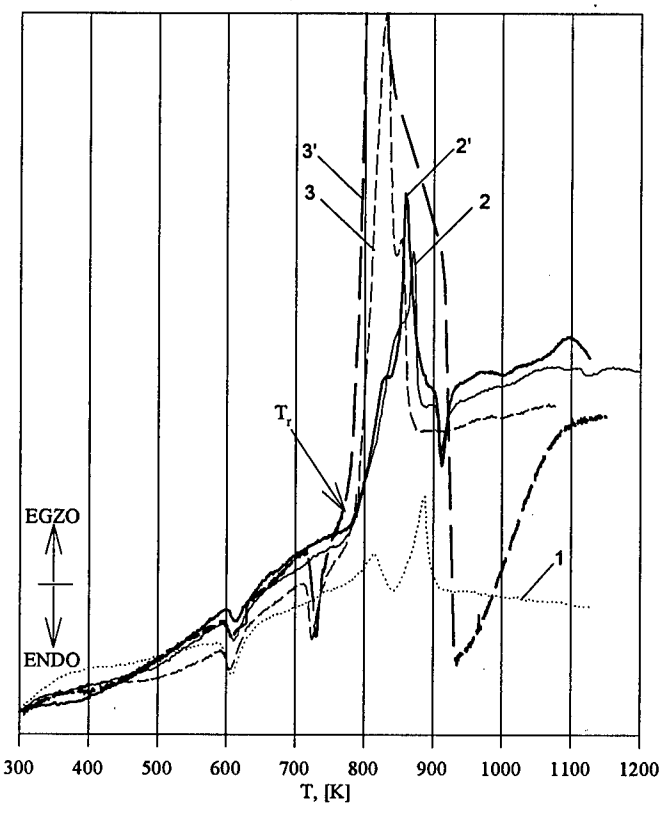

Fig. 2. DTA-curves for TF (1) and for its mixtures with: 32.7% of Mg (2), and 47.7% of Mg (2') and 29.5% of Al_3Mg_4 (3) and 44.5% of Al_3Mg_4 (3').

2.3. Burning rate

To measure the linear burning rate the samples of metal/TF pyrolants were made as pressed pellets. The size of each pellet was 30 mm in diameter and 60 mm in length and the density was 1500 kg/m^3 or 2000 kg/m^3. The burning rate (u) of the pellets was measured under atmospheric pressure with a set shown in Fig. 3. Each pellet (1) was ignited by an electrically heated igniter which was attached to the top of the pellet (2 and 3). Time of covering the distant between crevices (5) in screen (4) by burning wave was measured by a time recorder (7) that was started and stopped by photodiodes (6).

The results of burning rate measurements for each composition and density are shown in Fig. 4.

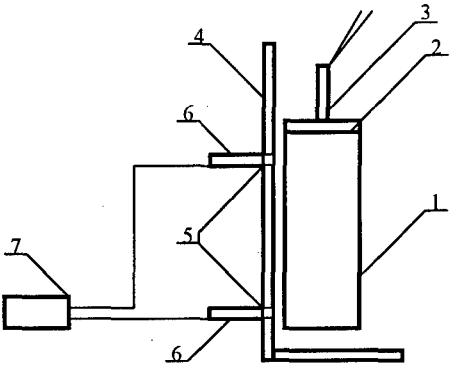

Fig. 3. Scheme of the set to measure burning rate. 1 - pellet of pyrolant, 2 and 3 - igniter, 4 - screen, 5 - crevices, 6 - photodiodes, 7 - time recorder.

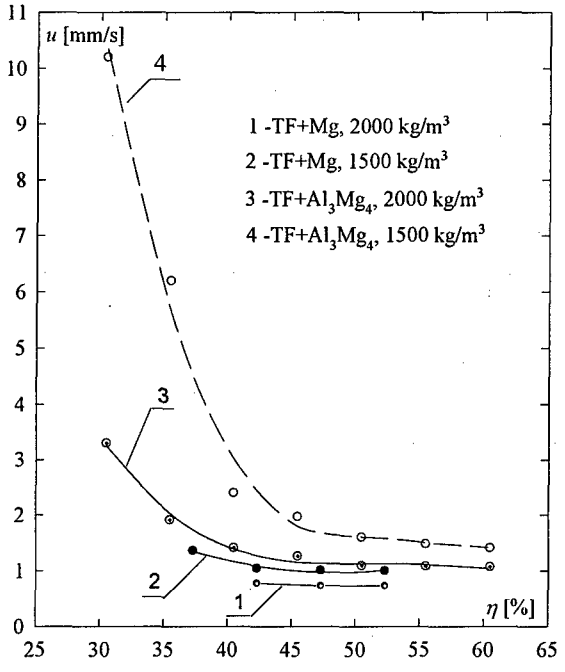

Fig. 4. Burning rate versus the contents of TF for different density of the pellets.

The burning rate decreases with increasing density and contents of TF. The Mg/TF pyrolants burn slower than composition containing Al_3Mg_4 and the burning rate of Mg/TF mixtures depends weakly on TF contents. The same relationship for Al_3Mg_4/TF pyrolants is much stronger, especially for low density of pellet. When the content of Al_3Mg_4 is high the burning rate is about ten times faster than that for composition being close to stechiometric one. At 0.1 MPa the Mg/TF pyrolants can combust in stable manner when the contents of TF is within the range from 37.3 to 52.3%. For Al_3Mg_4/TF mixtures the range of admissible composition changes is twice as wide as for the previous ones. But in order to assure a stability of combustion process at 0.1 MPa it is necessary to use compositions which contain more Mg or Al_3Mg_4 (on 10÷15%) than in stechiometric ones.

Like as the decomposition characteristics, the relationship $u = f(\eta)$ shows that liquid state of fuel makes easier combustion initiation and exothermic reactions just on and behind the burning surface of the Al_3Mg_4/TF pyrolants. The amount of heat released next to the burning surface in consequence of this reaction is significantly higher than for Mg/TF mixtures. Solid particles of magnesium are considered to be borne by TF decomposition products from burning surface and they are oxidised less or more completely far from it. The highest temperature is at some distance behind the burning surface and for that reason the heat flux feedback from the gas phase to the burning surface is relatively small and the burning rate is relatively small too (Fig. 4).

3. Calculation of a burning wave velocity

A schematic representation of the combustion wave of metal/TF pyrolats is shown in Fig. 5. In zone I, no chemical reactions occur and a fuel (metal) and an oxidiser (TF) are in solid phase. Temperature increases from the initial temperature T_0 due to the conductive heat flux (Q_k). A burning wave front separates the solid phase and liquid phase of metal. In zone II, a part of metal can react with oxidiser in solid phase and the heat (Q_f) from condensed phase is released. At the burning surface a phase change of oxidiser from solid to gas occurs and behind this surface metal particles are overflowed by gaseous products of oxidiser decomposition. In zone III, temperature increases rapidly from T_f at the burning surface to the flame temperature T_g due to exothermic reactions in gas phase.

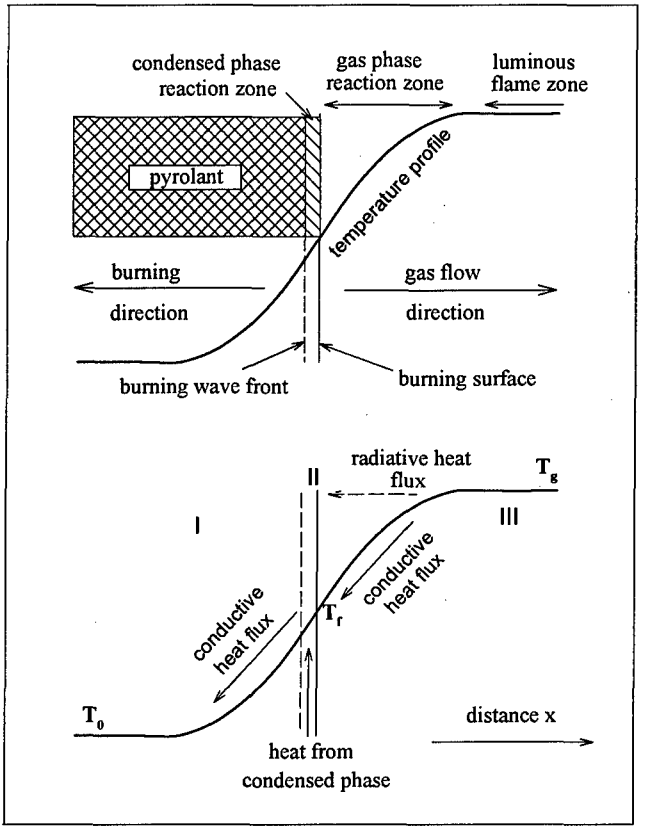

Fig. 5. Combustion wave structure and heat transfer model of a solid propellant

It is assumed that the burning process is stationary in the frame of reference fixed at the burning surface. Then the overall heat balance at the burning surface can be written as follows [11]

$$u\rho_0\left[\eta l_u + (1-\eta) l_m^t + c_T\left(T_f - T_0\right)\right] = Q_k + Q_r + Q_f \qquad (3.1)$$

where u denotes a linear burning rate, ρ_0 - density of the metal/TF mixture, η - mass fraction of TF, l_u - heat of melting and decomposition of TF, l_m^t - melting heat of metal, c_T - specific heat of

the mixture, Q_k, Q_r - conductive and radiative heat flux, respectively, Q_f - heat from condensed phase.

The expression for Q_k, Q_r and Q_f are given in paper [11]. Equation (3.1) was solved numerically for the TF/metal mixtures with parameters given in Table 1. The results are presented in Figs. 6 and 7.

Table 1. Parameters used in calculations

Parameter	Mg/TF	Al_3Mg_4/TF
particle diameter d_0 [mm]	90	90
initial temperature T_0 [K]	293	293
temperature at the burning surface T_f [K]	780	780
flame temperature T_g [K]	2540	2540
melting and decomposition heat of TF l_u [kJ/kg]	1137.3	1137.3
combustion heat of metal in gaseous C_2F_4 H_u [kJ/kg]	32482	33493
metal density ρ_m [kg/m^3]	1740	2150
melting heat of metal l_m^t [kJ/kg]	368.2	152.9
dynamic viscosity of C_2F_4 at T_g temperature μ_f [kg/(s m)]	$23.8\ 10^{-6}$	$23.8\ 10^{-6}$
specific heat of a TF/metal mixture c_T [kJ/kg]	1.224	1.225
heat conductivity of C_2F_4 λ [kJ/(k s m)]	0.1	0.1
fraction of fluoride in the mixture ξ	0.76	0.76
emission of condensed products of combustion ε	0.8	0.8
fraction of metal burned in condensed phase ζ	0	0

Satisfactory agreement between measured and calculated velocities of burning wave in the Mg/TF mixtures was obtained for whole tested range of TF concentration. But significant discrepancies between experimental and theoretical results appear for the Al_3Mg_4/TF mixtures of density of 1500 kg/m^3. However, quite good agreement was obtained also in this case, when the reaction of 12 % Al_3Mg_4 ($\zeta = 0.12$) with TF in condensed phase was assumed. This assumption is justifiable because the DTA curves of Al_3Mg_4/TF mixtures of high contents of metal show that the initial temperature (T_r) of exothermic reaction is lower than the temperature of TF decomposition (curve 3' in Fig. 2).

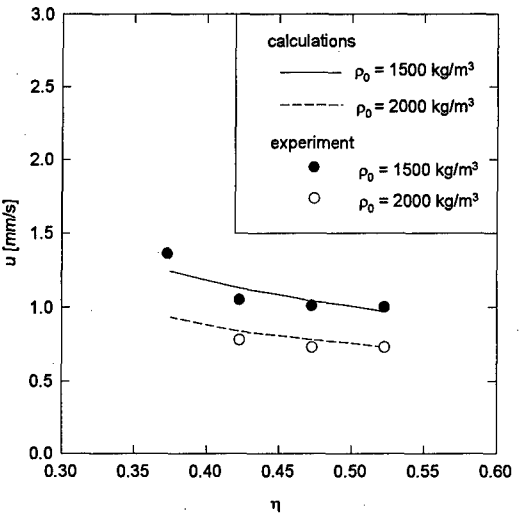

Fig. 6. Experimental and calculated velocities of burning wave in the Mg/TF mixture

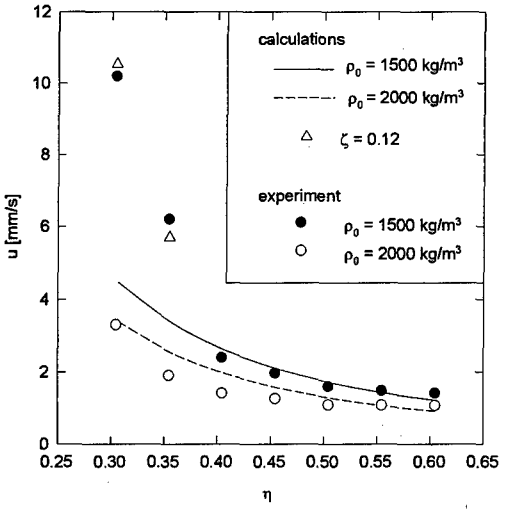

Fig. 7. Experimental and calculated velocities of burning wave in the Al_3Mg_4/TF mixture

Experimental and calculated values of the linear velocity of burning wave of the metal/TF mixtures are very low. From analysis of the calculation results it follows that the radiative heat flux is a main way of heat transport to the burning surface. The radiative heat flux divided by the total heat flux and the reaction zone widths in gaseous phase are presented in Table 2 for the metal/TF mixtures of 1500 kg/m^3 density. Heat from condensed phase was neglected in calculations.

Table 2. Calculated burning velocities, widths of reaction zone and fractions of radiative flux in total heat flux for the mixtures of density 1500 kg/m^3

Mixture	η	u [mm/s]	Δx [mm]	$\frac{Q_r}{Q_r + Q_k}$ [%]
Mg/TF	0.523	0.97	1.52	98
	0.473	1.04	0.93	96
	0.423	1.13	0.58	94
	0.273	1.25	0.37	91
Al_3Mg_4/TF	0.605	1.22	0.30	76
	0.505	1.72	0.13	58
	0.405	2.64	0.08	41
	0.305	4.52	0.05	26

The results presented in Table 2 show that an increase of the metal concentration causes increasing of the velocity of burning wave and a decrease of the reaction zone width and the conductive heat flux. Moreover, the widths of reaction zone are much lower for the Al_3Mg_4/TF mixture than those for the Mg/TF mixture. This means that exothermic reactions proceed in near vicinity of the burning surface in Al_3Mg_4/TF pyrolants. In this case the metallic component is in liquid phase and this fact facilitates the exothermic reactions with the gaseous oxidiser.

4. Summary

1. Stable combustion of the Mg/TF and Al_3Mg_4/TF mixtures is possible for a wide range of TF concentration from 30 to 70 %.
2. DTA curves for the mixtures tested show that the exothermic reaction begin when gaseous products of TF decomposition occur at the temperature of about 780 K. Alloy Al_3Mg_4 is in

liquid phase at this temperature and this fact facilitates its reaction with TF decomposition products.

3. Stable combustion under atmospheric pressure is possible when concentration of TF is from 37.3 to 52.3 % or from 30.5 to 60.5 % for the mixtures with Mg and Al_3Mg_4, respectively. Pyrolants containing Mg burn slowly than those with Al_3Mg_4.
4. Similar to the decomposition characteristics of the pyrolants tested, also a relationship between the linear velocity of burning and the concentration of TF shows that metal in liquid phase makes combustion process easier.
5. The theoretical model applied in calculations of the burning velocity describes in saticfactory manner the process of combustion of metal/TF mixtures. There is a good qualitative agreement between the experimental and calculated linear velocities of combustion of the Mg/TF and Al_3Mg_4/TF mixtures.

This paper was accomplished within the framework of the Project PBZ 019-12 financed by the Scientific Research Committee.

References

[1] A. A. Shydlowsky, *Basis of pirotechnics* (in Russian), Nauka, Moscow, 1970.

[2] J. H. Mc Lain, *Pyrotechnics*, The Franklin Institute Press, Philadelphia 1980.

[3] J. F. Vega, et al., US Patent 4698108, October 1987.

[4] A. Espagnacq, Suwestre G., D., US Patent 4697521, October, 1987.

[5] A. Espagnacq et al., US Patent 4724018, February 1988.

[6] M. Weber, *Pyrotechnische Nebelsatze*, B. D. Patentschrift, DE 3238444, 30.10.1986.

[7] T. Kuwahara, S. Matsuo, N. Shinozaki, *Combustion and sensitivity characteristics of Mg/TF pyrolants*, EUROPYRO 1995, Tours, France, 5-9.06.1995.

[8] N. Kubota, C. Serizava, *Combustion process of Mg/TF pyrotechnics*, Prop. Expl. Pyrotech., 12, 1987.

[9] P. Gongpei, et al., *A study on the infrared radiation of pyrotechnic compositions*, 2nd Beijing International Symposium of Pyrotechnics and Explosives, Beijing, China, 28-31.10.1991.

[10] N. Kubota, C. Serizava, *Combustion of magnesium/polytetrafluorethylene*, J. Propulsion and Power, **3**, 4, 1987.

[11] L. Ya. Kashporov et al., Combustion of mixtures of magnesium and sodium nitrate (in Russian), Fiz. Gor. Vzr., **30**, 5, 1994.

LDV-Vermessung reaktiver Strömungsfelder in einer Brennkammer

J. Backhaus, A. Brock, L. Deimling

Abstract

An existing combustion chamber with fuelinjection against the main airstream was modified for performing flowmeasurements by the application of the Laser-Doppler-Velocimetry (LDV). Test measurements in a turbulent free jet were performed to prove the correct function of the measuring system. They showed a good aggreement with literature values. Flowfieldmeasurements in the combustion chamber indicated high turbulenceratios in the entrance area and near to the injection nozzle as it was expected. The Variation of the air to fuel ratio showed, that in any case the fuelinjection velocity was too low for getting a complete mixing with the air over the full range of the chamber radius. By using the calculated waste gas volumestream the air ratio of the combustion was obtained and showed that the reaction was incomplete.

1 Einführung

Die Entwicklung und Erprobung neuer Antriebskonzepte für feste Brennstoffe ist ein wichtiger Forschungsschwerpunkt am Fraunhofer Institut für Chemische Technologie.
In diesem Zusammenhang wird die Einsatzfähigkeit von Festbrennstoffen wie Bor in luftatmenden Kombinationsantrieben, die eine Weiterentwicklung des Staustrahlkonzeptes darstellen, untersucht.
Neben dem Nachweis der prinzipiellen Eignung von Bor bei Staustrahlverbrennung zeigt sich, daß bei diesem Brennstoff die Strömungs- bzw. Mischungsverhältnisse in der Brennkammer von besonders großem Einfluß sind. Chemische Vorbehandlungen, wie z. B. ein Überziehen der Feststoffpartikel mit speziellen verbrennungsfördernden Substanzen (Coating) zeigen bei Bor entgegen den Erfahrungen mit anderen Festtreibstoffen kaum eine Wirkung [1]. Daher stehen die Strömungsverhältnisse in der Brennkammer bei der weiteren Optimierung im Mittelpunkt des Interesses.
Die Realisierung der Borverbrennung in einer eigens dafür konstruierten Versuchsbrennkammer war Teil vorangegangener Arbeiten am ICT, wobei die Strömungsverhältnisse aber zunächst unberücksichtigt blieben. Ziel der vorliegenden Untersuchung ist

es daher, die bestehende Brennkammer für die Strömungsvermessung zugänglich zu machen, um mit den Meßergebnissen die der Konstruktion zu Grunde legenden Annahmen zu verifizieren und Optimierungsmöglichkeiten aufzuzeigen.

Auf Grund der hohen Verbrennungstemperaturen und der weitgehend stationären Verbrennungsverhältnisse wurde die Laser-Doppler-Velocimetrie für die Vermessung der Brennkammerströmung ausgewählt. Bei dieser Methode wird am Meßpunkt bzw.-Volumen durch die Interferenz zweier Laserstrahlen ein Streifenmuster bekannter Geometrie erzeugt. Eigens zu diesem Zwecke der Strömung zugesetzte Tracerpartikel blinken beim Durchflug durch dieses Muster mit einer ihrer Geschwindigkeit direkt proportionalen Frequenz. Mit einer geeigneten Auswerteelektronik kann somit die Strömungsgeschwindigkeit im Meßvolumen kalibrierfrei ermittelt werden.

Die direkte Anwendung dieses Verfahrens auf die Borverbrennung ist aber sehr problematisch, da mit dem Bor bereits Partikel in der Strömung sind, die die Streulichtmessung der Tracerpartikel sehr erschweren. Der Einsatz der Borpartikel selbst als Tracer ist zwar denkbar, aber wenig sinnvoll, da im Falle der beabsichtigten vollständigen Verbrennung hinter der Flammenfront die Partikelkonzentration stark abnehmen und somit eine Messung in dieser besonders interessanten Zone unmöglich würde.

Daher wurden die befeuerten Strömungsmessungen mit einem gasförmigen Modellbrennstoff (Acetylen) durchgeführt, wobei mit MgO eine Tracersubstanz zur Anwendung kam, deren Dichte und mittlerer Partikeldurchmesser in der selben Größenordung, wie die von Bor liegen. Durch die Eindüsung dieses Tracers an Stelle von Bor kann somit auch das Eindringverhalten der Partikel in die Luftströmung untersucht werden.

2 Experimenteller Aufbau

Die Abbildung 1 zeigt den grundsätzlichen Aufbau der Versuchsanlage:

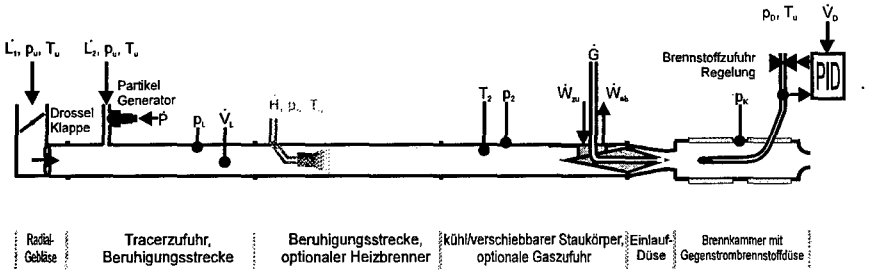

Abb. 1: Schematischer Aufbau der Versuchsanlage

Die über ein Radialgebläse angesaugte Luft wird über einen Preßluftstrom mit zwischengeschalteten Bürstenpartikelgenerator mit MgO-Tracern angereichert. Nach einer ersten Beruhigungsstrecke erfolgt die Eingangsdruck- und Volumenstrommessung. Die anschließende zweite Beruhigungsstrecke kann bei späteren Untersuchungen den für die Borverbrennung nötigen Vorheizbrenner aufnehmen. Von hier gelangt die Luftströmung in den Einlaufbereich der Brennkammer, in dem der Strömungsquerschnitt mit Hilfe eines Staukörpers zu einem Ringspalt verjüngt wird, dessen Fläche gleich dem halben Querschnitt der Brennkammeraustrittsdüse ist.

Um bei späteren Messungen mit Vorheizbrenner ein Überhitzen des Staukörpers zu vermeiden, ist dieser wasserkühlbar ausgeführt. Außerdem wurde eine weitere Gaszufuhr vorgesehen, mit der auch Versuche mit konzentrischem Doppelstrahl gefahren werden können. Die für die Messungen verwandte Gegenstromgaszufuhr kann mittels Regelelektronik auf den gewünschten Volumenstrom eingestellt werden.

Einen Schnitt durch die Brennkammer zeigt Abbildung 2

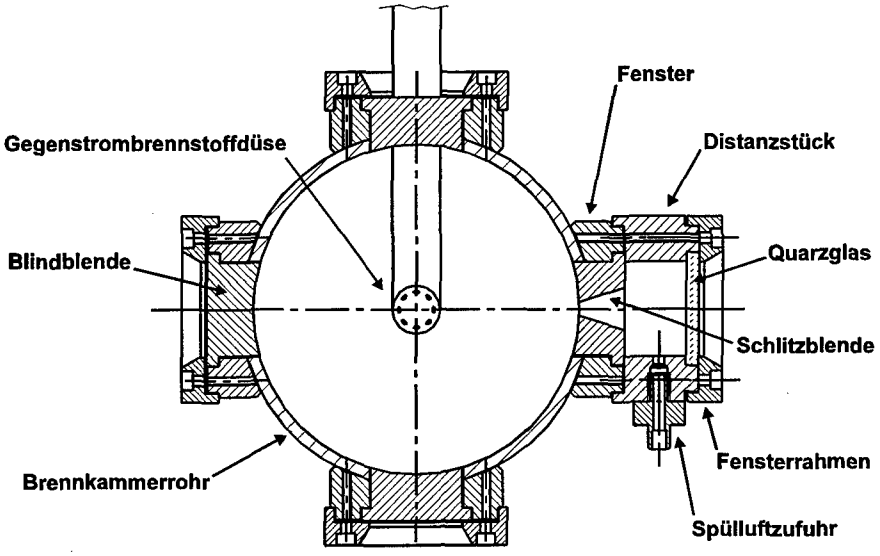

Abb. 2: Schnitt durch die Brennkammer (in Strömungsrichtung)

Die Gegenstrombrennstoffdüse ist mittig im Kammerrohr montiert, welches mit bis zu acht optischen Zugängen ausgestattet werden kann. Um die Strömungsverhältnisse im interessierenden vorderen Kammerbereich so wenig wie möglich zu stören, wurden die

drei nicht benötigten Öffnungen mit der Kammerkontur angepaßten Blindblenden verschlossen.

Bei der Ausführung des optischen Zugangs für das LDV mußten folgende Probleme berücksichtigt werden, die bei Vorversuchen mit einfachen Fenstereinsätzen auftraten:

- Tracerpartikelniederschlag auf den Fensterscheiben, der die LDV-Messungen schon nach wenigen Minuten stark beeinträchtigte.
- Verrußen der Fensterscheiben in der Zündphase (manchmal schon nach 30 Sek.)
- Verformung und Springen der Quarzglasscheiben nach Versuchszeiten > 20 Min.

Außerdem beeinflussen diese Zugänge die zu vermessende Brennkammerströmung erheblich, da sie unstetige Querschnittserweiterungen darstellen.

Eine einfache Lösung dieser Probleme konnte gefunden werden, weil zur eindimensionalen Vermessung der Axialgeschwindigkeiten in der waagerechten Durchmesserebene der Brennkammer prinzipiell nur ein länglicher Schlitz erforderlich ist, dessen Höhe etwas größer als der Durchmesser der beiden hindurchtretenden Strahlen sein sollte.

Daher wurde eine Schlitzblende gefertigt, wie sie in Abb. 2 zu sehen ist. Um ein Ausblocken der Laserstrahlen an Schlitzkanten für den Fall von leichten Dejustierungen zu verhindern, wurde der Schlitz sich nach außen öffnend vorgesehen.Auf der Kammerseite hat die Blindblende wieder die Wölbung des Kammerrohres, womit die Störung der Kammergeometrie auf ein Minimum reduziert ist. Um Tracer- bzw. Rußablagerungen auf der Quarzglasscheibe zu verhindern, wurde zwischen Fenster und Fensterrahmen ein Distanzstück eingesetzt, durch welches hinter dem Schlitz ein Totvolumen entsteht. Über eine Spülluftzufuhr kann ein schleichender Spülstrom in die Hauptströmung erzeugt werden, der das Eindringen von Partikeln und die Wärmeübertragung an die Quarzglasscheibe erschwert.

3 Messungen

Um die einwandfreie Funktionsweise des Meßaufbaus nachzuweisen, wurden zunächst isotherme und befeuerte Freistrahlmessungen an der Brennkammeraustrittsdüse durchgeführt, deren Ergebnisse Abbildung 3 zeigt:

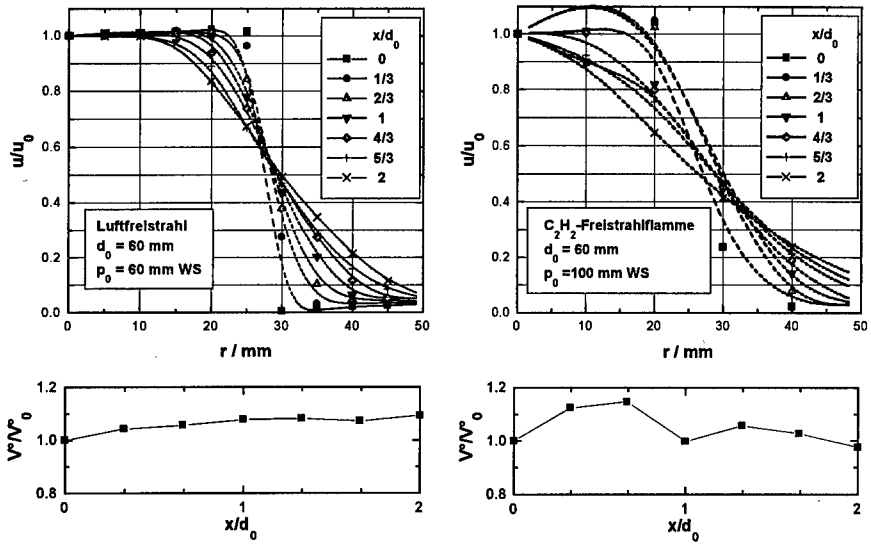

Abb. 3: Normierte Axialgeschwindigkeitsverläufe (oben) und Volumenströme (unten) im isothermen (links) und befeuerten Freistrahl (rechts)

Für den isothermen Fall (Abb 3, links unten) ergab sich ein leichter Anstieg des Volumenstromes V°, der das Entrainement von Umgebungsluft wiedergibt. Der erwartete starke Volumenstromanstieg bei Verbrennung (Abb. 3, rechts unten) wurde aber nicht gemessen, was auf unvollständige Verbrennung hindeutet.

Um Meßmethode und -werte zu verifizieren, wurden letztere mit Literaturwerten von Lenze [2] verglichen:

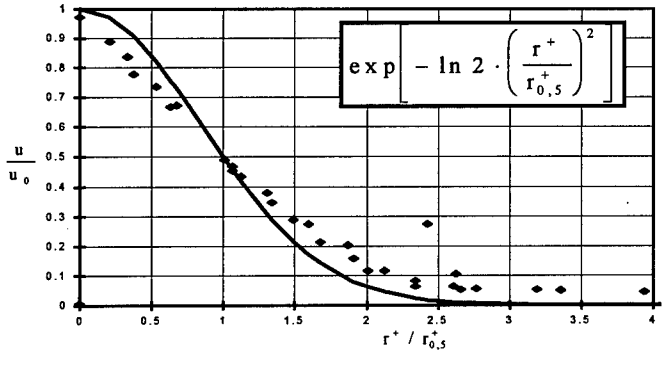

Abb. 4: Vergleich der gemessenen (Punkte) und den nach Lenze berechneten normierten Geschwindigkeitsmittelwerte im isothermen Freistrahl

Wie Abbildung 4 zeigt, wurde eine weitgehende Übereinstimmung festgestellt.

Bei den Messungen im Innern der Brennkammer sollten die Profile der Axialgeschwindigkeiten in der Mischungszone zwischen Luft im Hauptstrom und dem eingedüsten Brennstoff im Gegenstrom aufgenommen werden. An Hand dieser sollte geklärt werden:

1. ob sich eine äußere Rückströmzone am Brennkammereintritt ausbildet
2. welche Turbulenzgrade durch die Gegenstromeindüsung erzeugt werden
3. wie tief der Brennstoffstrom in den Luftstrom eindringt

Das für diese Messungen verwandte Meßfeld und die geometrischen Verhältnisse zeigt Abbildung 5:

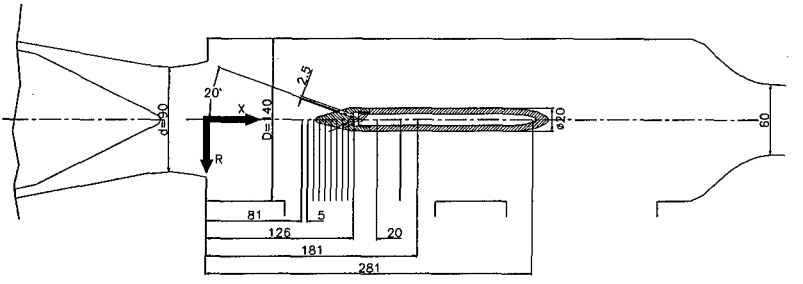

Abb. 5: Geometrische Verhältnisse und Position der Meßradien in der Brennkammer

4 Ergebnisse

Entgegen den Erwartungen nehmen die einlaufnahen Axialgeschwindigkeitsverläufe (Abb. 6, schwarz) in Wandnähe keine negativen Werte an. Die hohen Turbulenzgrade in dieser Zone deuten aber darauf hin, daß sich eine äußere Rückströmzone zwar direkt nach der Einlaufkante bildet, jedoch nicht bis in den Meßbereich hineinreicht.

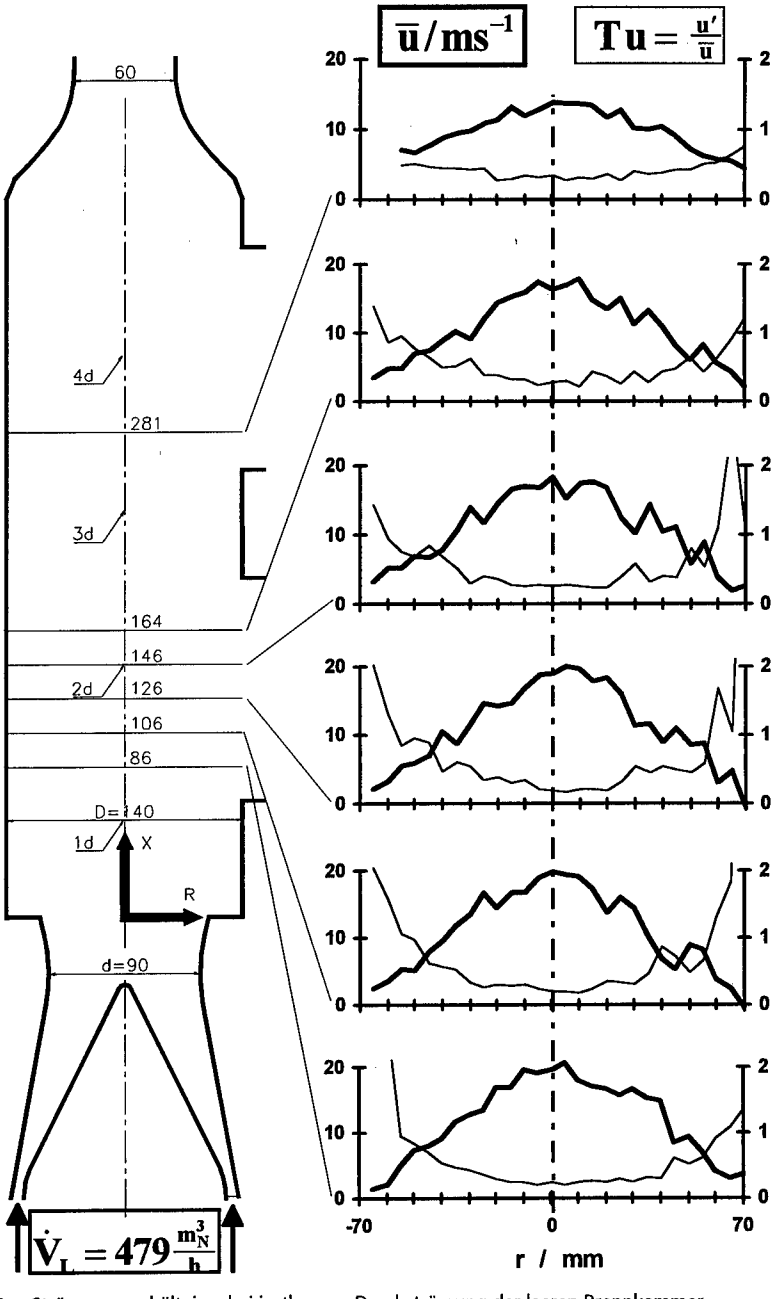

Abb. 6: Strömungsverhältnisse bei isothermer Durchströmung der leeren Brennkammer

Das isotherme Eindringverhalten des Brennstoffgegenstroms bei drei unterschiedlichen Hauptluftvolumenströmen ist in Abbildung 7 aufgetragen:

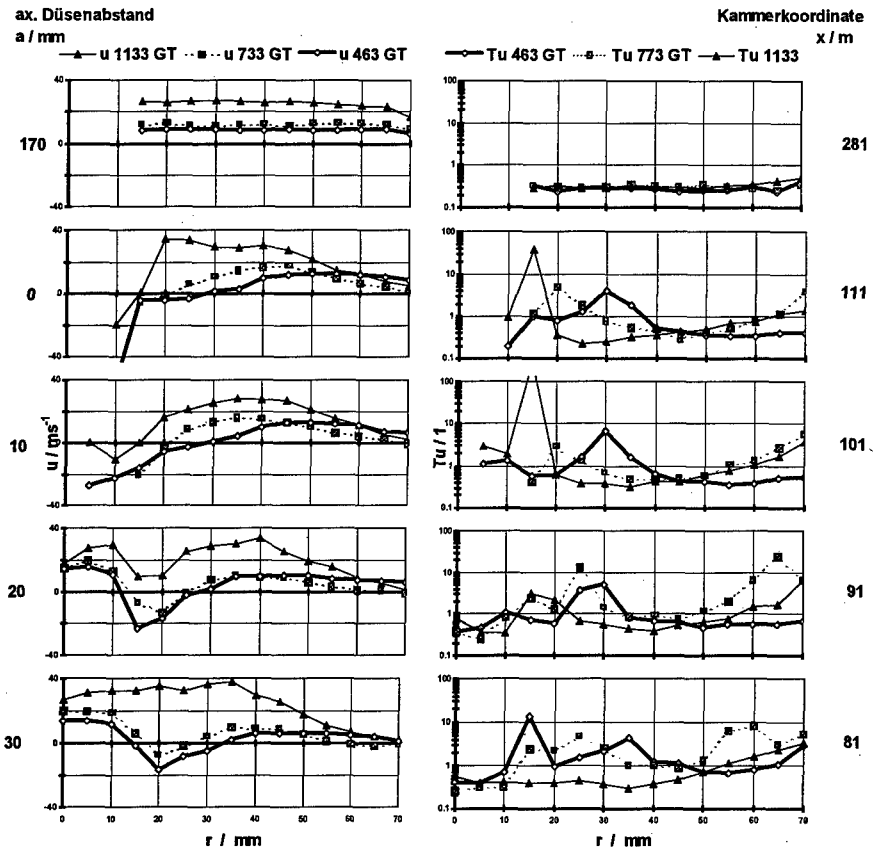

Abb. 7: Verläufe der mittleren Geschwindigkeit (links) und des Turbulenzgrades (rechts) bei verschiedenen Hauptluftvolumenströmen

Je kleiner der eingestellte Hauptluftvolumenstrom, umso stärker werden die Geschwindigkeitsprofile u in der Nähe der Gegenstromdüse vermindert bzw. zu negativen Werten verschoben. Besonders aufschlußreich ist die Auftragung der zugehörigen Turbulenzgrade Tu: Hierbei zeigen sich zwei Zonen erhöhter Turbulenz: am Rand und in Düsennähe. Bei einem Radius zwischen 35 und 45 mm haben alle Turbulenzverläufe ein Minimum, was darauf schließen läßt, daß auch die turbulente Durchmischung von Luft- und Brennstoffstrom nur bis zu diesem Radius reicht. Diese Vermutung bestätigt sich in Abbildung 8, in der Geschwindigkeits- und Turbulenzgradverläufe jeweils für den isothermen und den befeuerten Fall aufgetragen sind:

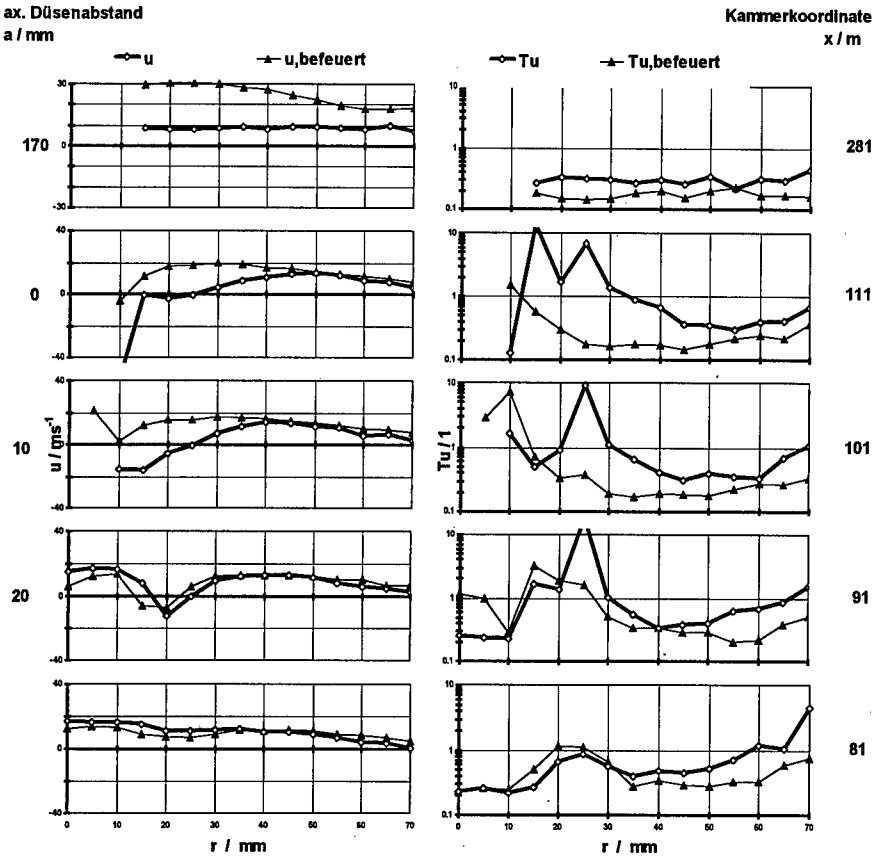

Abb. 8: Verläufe der mittleren Geschwindigkeit (links) und des Turbulenzgrades (rechts) bei isothermer und befeuerter Messung

Die expansionsbedingte Erhöhung der Axialgeschwindigkeit gegenüber dem isothermen Verlauf erstreckt sich in Düsennähe nur bis zu einem Mischungsradius von etwa 40 mm von dort bis zur Wand zeigen sich jedoch keine größeren Geschwindigkeitsdifferenzen. Erst sehr viel weiter stromabwärts (a = 170 mm) dehnt sich die beschleunigte Strömungszone über den gesamten Radius aus. Bei dieser Kammerkoordinate hat sich der befeuerte Turbulenzgrad Tu,befeuert bereits über dem Radius ausgeglichen, während er in Düsennähe schon bei kleineren Radien abnimmt als der isotherme.

Aus diesen Werten konnte der Verlauf des integralen Volumenstromes bei Gegenstromacetylenverbrennung errechnet werden (Abb. 9):

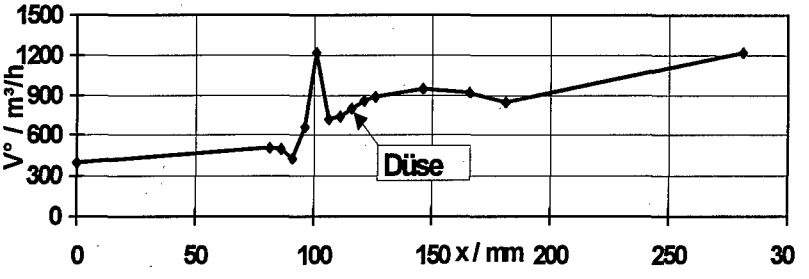

Abb. 9: Volumenstromverlauf entlang der Kammerachse bei Gegenstromacetylenverbrennung

Die maximale Volumenstromerhöhung beträgt danach etwa Faktor drei, was einem Wert von ca. 1200 m_N/h^3 entspricht. Aus der Verbrennungsbilanzrechnung ergibt sich jedoch ein Abgasvolumenstrom von 1430 m_N/h^3, was einer theoretischen Luftzahl von 2,8 gleichkommt. Dieses Mißverhältnis konnte nachvollzogen werden, nachdem der in den Messungen festgestellte Mischungsradius, bei dem die Turbulenzgrade ihr Minimum durchlaufen in die Berechnung miteinbezogen wurde:

$$\dot{V}_{Ab,ges} = \left(\dot{V}_L - \dot{V}_L(r_M)\right) + \dot{V}_{Ab,M}\left(\lambda(r_M)\right)$$

Damit konnte iterativ die zu dem gemessenen Abgasvolumenstrom gehörige Luftzahl ermittelt werden. Sie beträgt danach etwa 0,75 bei einem Mischungsradius von 37 mm. Entsprechend ergab sich für stöchiometrische Verbrennung ein Mischungsradius von 42,5 mm.

5 Zusammenfassung und Ausblick

Mit der Vermessung der Strömungsverhältnisse bei Acetylenverbrennung wurde zunächst nachgewiesen, daß die aufgebaute Anlage den Anforderungen der Strömungsmessung in der befeuerten Brennkammer gewachsen ist. Mit Hilfe der LDV Meßtechnik konnte gezeigt werden, daß die im Einlaufbereich der Brennkammer vermutete Rückstromzone nur geringe Ausmaße besitzt und auf die beabsichtigte Durchmischung von Luft- und Brennstoffstrom kaum Einfluß hat. Eine stöchiometrische Verbrennung kann bei sonst gleichen Parametern durch größere Mischungsradien erreicht werden. Dazu stehen ein größerer Anstellwinkel der Gegenstromdüsen oder eine eine erhöhte Eindüsgeschwindigkeit, die durch ein Verkleinern der Düsenbohrungen realisiert werden könnte, zur Auswahl.

Durch die besondere Konstruktion des Staukörpers im Brennkammereinlauf ist es außerdem möglich, statt der Gegenstrombrennstoffeindüsung eine Brennstoffzufuhr

durch den Staukörper nach dem Prinzip des konzentrischen Doppelrohres mit Staukörperstabilisierung zu realisieren und so den Ausbrand zu verbessern.
Neben diesen Optimierungsmöglichkeiten bestehen die nächsten Schritte in für die geplante Strömungsmessung bei der Borverbrennung in der Konstruktion eines für LDV-Messungen ausreichend kontinuierlich arbeitenden Borpartikelgenerators und im Einbau eines Vorwärmbrenners, mit dem die Verbrennungsluft auf die zur Borverbrennung notwendigen Zündtemperaturen gebracht werden kann.

6 Literatur:

[1] Liehmann, W.: Combustion of Boron-based Slurries in a Ramburner, 22. International Annual Conference of ICT, 1991

[2] Lenze, B.: Bestimmung der Geschwindigkeits- und Konzentrationsprofile im Kern- und Übergangsbereich von Freistrahlen, Chemie-Ingenieur-Technik 49, H 12, S. 983 ff, 1977

TITLE : Generic Qualification of Pyrotechnic Compositions

AUTHOR : P Fincham,
DGTS/POB, Ordnance Board, MOD(PE), Abbey Wood, Bristol, UK

DATE : 5th January 1998

ABSTRACT

Pyrotechnic Compositions are UK Qualified in accordance with UK MOD Ordnance Board Proceedings which call up well defined tests aimed at characterising a composition in terms of its physical, theological, thermal and chemical properties, together with its sensitiveness to various stimuli, and its explosiveness.

Pyrotechnic Compositions are used in a wide variety of roles, and more often than not, the combustion and burning characteristics are tailor-made, by compositional modifications, to deliver specific performance parameters. In addition, such compositional modifications may also affect the sensitiveness and explosiveness characteristics.

As a consequence of the compositional modifications, there tends to be a large array of formulations with only minor variations of ingredients and percentages .

The purpose of this paper is to examine factors which could affect the characterisation of the Pyrotechnic Composition, with a particular view to applying the concept of " Generic Qualification " with the aim of reducing the level of testing, whilst still maintaining a high degree of confidence.

Einfache Modelle der Anzündung von Festtreibstoffen

W. Eckl, S. Kelzenberg, V. Weiser, N. Eisenreich

Fraunhofer-Institut für Chemische Technolgie
Postfach 1240, D-76318 Pfinztal

Abstract

The combustion of energetic materials is governed in the solid or condensed phase mainly by the heat flow equation including phase transitions and exothermic reactions. In addition, in the gaseous phase the heat flow and the diffusion equation have to be considered for each species accounted for in the reaction scheme. Simplified models deliver some results on ignition delay and the dependence of the burning rate on initial temperature useful for practical application. The treatment of more complex aspects can describe transient behaviour during ignition or the influence of externally supplied energy transfer.

Kurzfassung

Die Verbrennung von energetischen Materialien wird in der kondensierten Phase im wesentlichen durch die Wärmeleitungsgleichung bestimmt wobei Phasenumwandlungen und exotherme Reaktionen eine Rolle spielen. In der Gasphase ist zusätzlich der Stofftransport durch Diffusion zu berücksichtigen. Mit vereinfachten Modellen für die kondensierte Phase kann man bereits wichtige Ergebnisse, wie Anzündverzugszeiten und die Abhängigkeit der Abbrandgeschwindigkeit vom Druck abschätzen. Aufwendiger Modelle erlauben die Beschreibung von komplexeren Phänomenen, wie den Verlauf der Anzündung oder die Reaktion der Abbrandgeschwindigkeit auf externen Energieübertrag.

1 Einleitung

Bei Festtreibstoffen für Rohrwaffentreibmittel oder Raketenantriebe bestehen für die Praxis wichtige Zusammenhänge in den Abhängigkeiten der Abbrandgeschwindigkeit von Druck und Ausgangstemperatur oder der Anzündverzugszeit vom eingebrachten Energiefluß. Diese lassen sich zwar experimentell bestimmen, aber eine Bestätigung durch theoretische Herleitungen ist wünschenswert, da sie erst den Einfluß von physikalischen und chemischen Stoffdaten wie Dichte, spezifische Wärme, Wärmeleitungskoeffizient aufzeigen, bzw. aufzeigen, wie Phasenumwandlungen und chemische Reaktionen bei der Pyrolyse der kondensierten Phase und in der Gasphase wirken. Nachdem lange Zeit nur vereinfachte Modelle [1-3] betrachtet wurden, sind inzwischen von Zarko und Mitarbeitern [4-6] komplexere Modelle betrachtet worden, mit denen transiente Phänomene wie Anzündung oder Auswirkung externer Energieübertragung untersucht werden können.

In diesem Beitrag wird dargestellt, wie aus der Wärmeleitungsgleichung einige für die Anwendung nützliche Formeln herzuleiten sind, in denen sich der Einfluß physikalischer und chemischer Daten ausdrückt. Auch werden Berechnungen der Wirkung von externer Strahlung mit einem komplexerem Model (nach Zarko et al.) wiedergegeben.

2 Feststoffaufheizung

2.1 Definitionen

Um die Darstellung zu vereinfachen und die Übersichtlichkeit der Formeln zu verbessern, werden folgende Definitionen angewandt:

$$\mathbf{t} = \frac{\lambda}{c\rho}\mathbf{t^*}, \qquad \mathbf{a} = \frac{\lambda}{c\rho}, \qquad \mathbf{Q} = \mathbf{Q^*}/\lambda, \qquad \mathbf{q} = \mathbf{q^*}/\lambda$$

2.2 Größen und ihre Einheiten

Bei der Benutzung der im vorigen Abschnitt definierten Größen ergeben sich in zwei Fällen ungewöhnliche Einheiten: die Zeit erhält die Einheit einer Fläche und die Wärmquellen und -senken die Einheit einer Temperatur pro Flächeneinheit (damit wird Zeit in die Dimension m^2 überführt, da sich bei Diffusionsvorgängen, wie der Wärmeleitung die Zeit proportional dem Quadrat des Ortes verhält).

[λ]	= W / (m * K)	Wärmeleitfähigkeit
[c]	= J / (kg * K)	Wärmekapazität
[ρ]	= kg / m³	Dichte
[a]	= m² / s	Temperaturleitfähigkeit
[t*]	= s (Sekunden)	Zeit
[t]	= m²	Zeit
[Q*]	= W / m³	
[Q]	= K / m²	

3 Inerter Feststoff

Ausgangspunkt für die Untersuchung des Verhaltens eines Feststoffes bei Zuführung von Wärme ist die Wärmeleitungsgleichung:

$$\frac{\partial T}{\partial t} - \frac{\partial^2 T}{\partial x^2} = Q[x,t] \qquad (1)$$

In dreidimensionaler Form:

$$\frac{\partial T}{\partial t} - \Delta T = Q[\vec{x},t] \qquad (2)$$

Die inerte Feststoffaufheizung durch äußeren Energieübertrag läßt sich am einfachsten über die Green'sche Funktion darstellen [7]. Die Green'sche Funktion von (1) ist für die unbegrenzte Abszisse (d.h. Ränder im unendlichen, Q[x,t]=0):

$$G_U[x,x',t,t'] = \frac{e^{-\frac{(x-x')^2}{4(t-t')}}}{\sqrt{4\pi(t-t')}} \qquad (3)$$

und für die dreidimensionale (3D) Form:

$$G_U[\vec{x},\vec{x}',t,t'] = \frac{e^{-\frac{(\vec{x}-\vec{x}')^2}{4(t-t')}}}{(4\pi(t-t'))^{3/2}} \qquad (4)$$

Die Lösung von (1) entsteht durch Faltung der Quellfunktion Q[x,t] mit der Green'schen Funktion:

$$T[x,t] = \int_0^t \int_{-\infty}^{\infty} \frac{e^{-\frac{(x-x')^2}{4(t-t')}}}{\sqrt{4\pi(t-t')}} Q[x',t']dx'dt' \qquad (5)$$

Im 3D-Fall ist das Ortsintegral entsprechend über alle drei Raumrichtungen auszuführen. Die Integration über x in (5) kann für eine Reihe von Funktionen analytisch durchgeführt werden. Solche Funktionen sind z. B. die Dirac'sche Deltafunktion, eine Konstante, eine Exponentialfunktion, eine Gaußfunktion. Einige dieser ausführbaren Beispiele sind im folgenden wiedergegeben.

Für Anzünd-und Abbrandphänomene wird der Feststoff auf der positiven Halbachse liegend angenommen. Für diesen Bereich ergibt sich die Green'sche Funktion zu:

$$G_{hu}[x\text{-}x',t\text{-}t'] = G_{u\text{-}}[x\text{-}x',t\text{-}t'] + G_{u+}[x+x',t\text{-}t']$$

3.1 Kontinuierliche Aufheizung

Anzündung erfolgt durch eine zeitlich begrenzte kontinuierliche Energieübertragung von einem Anzünder auf ein energetisches Material. Der Energieübertrag kommt durch Wärmeleitung, -strahlung, konvektive heiße Gase oder durch heiße Partikel zu Stande.

3.1.1 Konstanter Wärmefluß auf eine Feststoffoberfläche

In einfachster Betrachtung der Anzündung trifft ein konstanter Wärmestrom auf die Feststoffoberfläche bei x_0, wo er absorbiert wird. Damit ist:

$$Q[x,t] = Q_R \cdot \delta[x - x_0] \qquad (6)$$

mit:

$$T[x,t] = \int_0^t \int_0^{\infty} 2 \frac{e^{-\frac{(x-x')^2}{4(t-t')}}}{\sqrt{4\pi(t-t')}} Q_R \cdot \delta[x' - x_0]dx'dt' \qquad (7)$$

Im Falle der Dirac'schen Deltafunktion reduziert sich die Summe aus G_{u-} und G_{u+} auf einen Faktor 2 mit der Lösung:

$$T[x,t] = Q_R\left(2\sqrt{\frac{t}{\pi}}e^{-\frac{x^2}{4t}} + x \cdot Erf\left[\frac{x}{\sqrt{4t}}\right] - x\right) \qquad (8)$$

Von der Oberfläche fällt die Temperatur steil in x-Richtung ab.

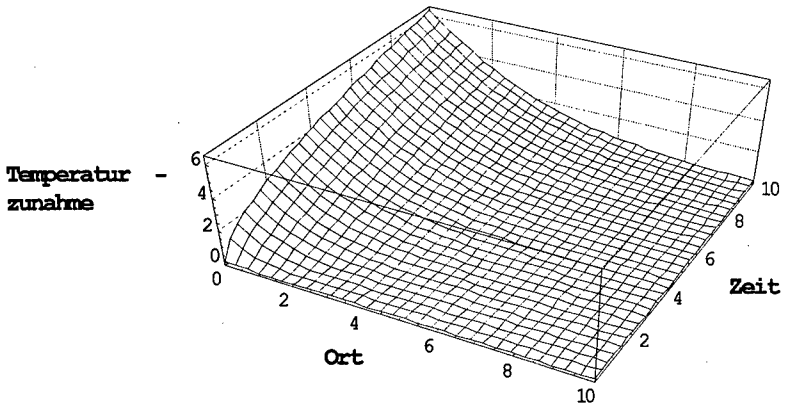

Abbildung 1: Temperaturprofil. Die Einheiten hier und in den folgenden Abbildungen sind willkürlich gewählt.

An der Oberfläche (x=0) steigt die Temperatur parabolisch mit der Zeit an.

$$T[0,t] = 2Q_R\sqrt{\frac{t}{\pi}} \qquad (9)$$

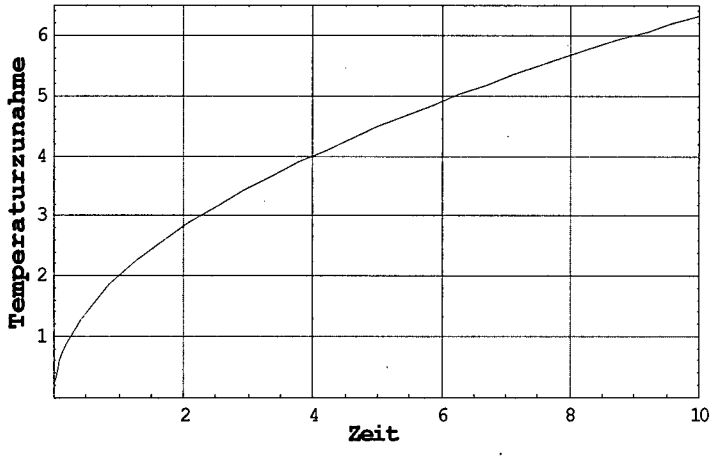

Abbildung 2: Temperaturverlauf an der Oberfläche

Häufig beansprucht die Zeit zum Aufheizen der Oberfläche auf eine bestimmte Temperatur durch externe Quellen, bei der Feststoff- oder/und Gasphasenreaktionen einsetzen den wesentlichsten Teil der Anzündverzugszeit. Deshalb ist in einfachster Näherung diese Verzugszeit durch folgende Formel gegeben:

$$t_{ign} \approx \frac{\pi T_p^2}{4 Q_R^{\ 2}} \tag{10}$$

3.2 Strahlungsaufheizung

Strahlung wird in einem homogenen Medium nach dem Lambert-Beer'schen Gesetz absorbiert. Die Wämeübertragung Q_R erzeugt ein exponentielles Profil mit dem Absorptionskoeffizienten b. Bei einer nur kurzzeitigen Energieübertragung zum Zeitpunkt t_0, wie z.B. mit einem Laser entsteht folgende Temperaturverteilung.

$$Q[x,t] = bQ_R e^{-bx} \cdot \delta(t - t_0)$$

$$T[x,t] = \int_0^t \int_0^\infty \frac{e^{-\frac{(x-x')^2}{4(t-t')}} + e^{-\frac{(x+x')^2}{4(t-t')}}}{\sqrt{4\pi(t-t')}} bQ_R e^{-bx'} \cdot \delta[t' - t_0] dx' dt' \tag{11}$$

mit der Lösung:

$$T[x,t] = \frac{bQ_R}{2}\left(e^{b(bt-x)}\left(1 - Erf\left[\sqrt{t}b - \frac{x}{2\sqrt{t}}\right]\right) + e^{b(bt+x)}\left(1 - Erf\left[\sqrt{t}b + \frac{x}{2\sqrt{t}}\right]\right)\right) \tag{12}$$

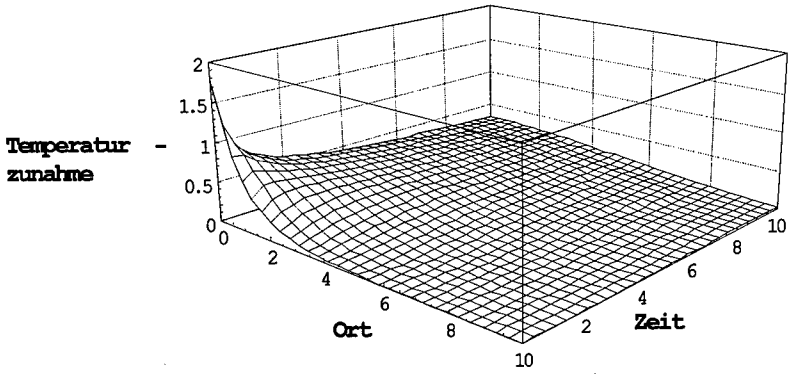

Abbildung 3: Temperaturprofil

und für x=0:

$$T[0,t] = Q_R b e^{b^2 t}\left(1 - \mathrm{Erf}\left[b\sqrt{t}\right]\right)$$

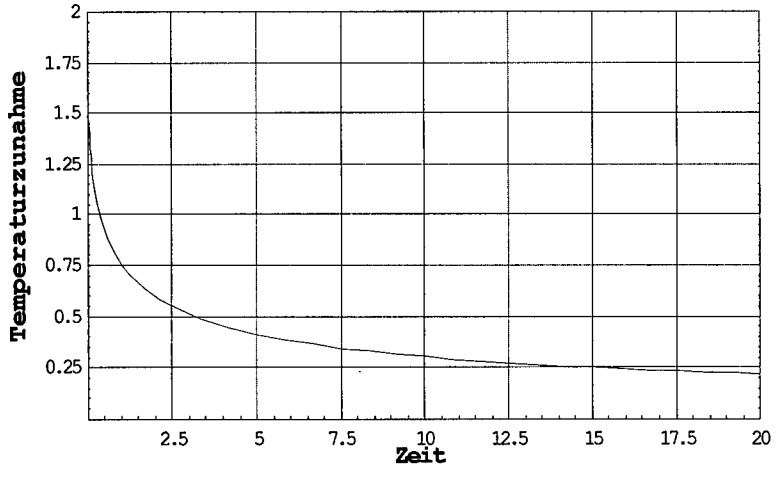

Abbildung 4: Temperaturverlauf an der Oberfläche

Für zeitlich ausgedehnte, konstante Bestrahlung ergibt sich mit

$$Q[x,t] = Q_R b e^{-bx}$$

folgendes Temperaturprofil:

$$T[x,t] = \int_0^t \int_0^\infty \frac{e^{-\frac{(x-x')^2}{4(t-t')}} + e^{-\frac{(x+x')^2}{4(t-t')}}}{\sqrt{4\pi(t-t')}} bQ_R e^{-bx'} dx'\, dt' \qquad (13)$$

Auch dieses Integral ist noch ausführbar:

$$T[x,t] = \frac{Q_R}{2b}\left(e^{b(bt-x)}\left(1 - \mathrm{Erf}\left[\sqrt{t}b - \frac{x}{2\sqrt{t}}\right]\right) + 2bx \cdot \mathrm{Erf}\left[\frac{x}{2\sqrt{t}}\right] + e^{b(bt+x)}\left(1 - \mathrm{Erf}\left[\sqrt{t}b + \frac{x}{2\sqrt{t}}\right]\right) + 4b\sqrt{\frac{t}{\pi}} e^{-\frac{x^2}{4t}} - 2bx - e^{-bx}\right) \qquad (14)$$

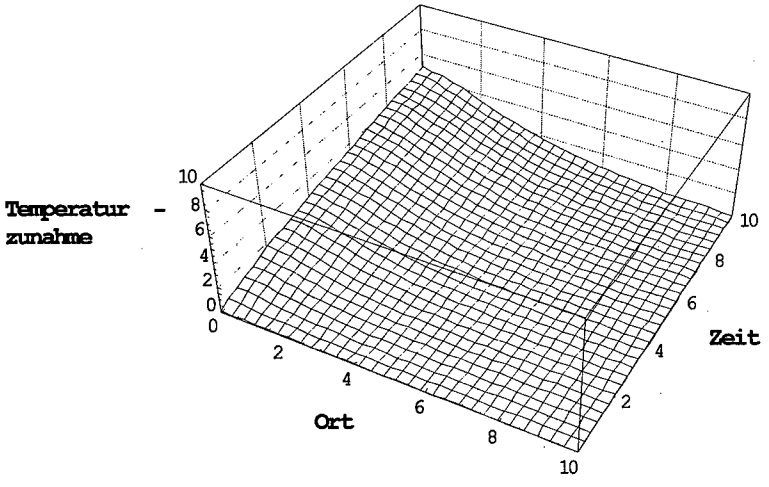

Abbildung 5: Temperaturprofil

Im Grenzfall eines sehr großen Absorptionskoeffizienten geht dieses Temperaturprofil in das Profil bei konstanter Energieübertragung auf die Oberfläche über. In Oberflächennähe ist die Temperatur immer geringer als bei reiner Oberflächenabsorption. Ansonsten ist der Temperaturverlauf S-förmig. An der Oberfläche steigt die Temperatur nach folgender Formel mit der Zeit an, die für b->∞ in (9) übergeht:

$$T[0,t] = \frac{Q_R}{b}\left(e^{b^2 t}\left(1 - \mathrm{Erf}\left[b\sqrt{t}\right]\right) + 2b\sqrt{\frac{t}{\pi}} - 1\right) \qquad (15)$$

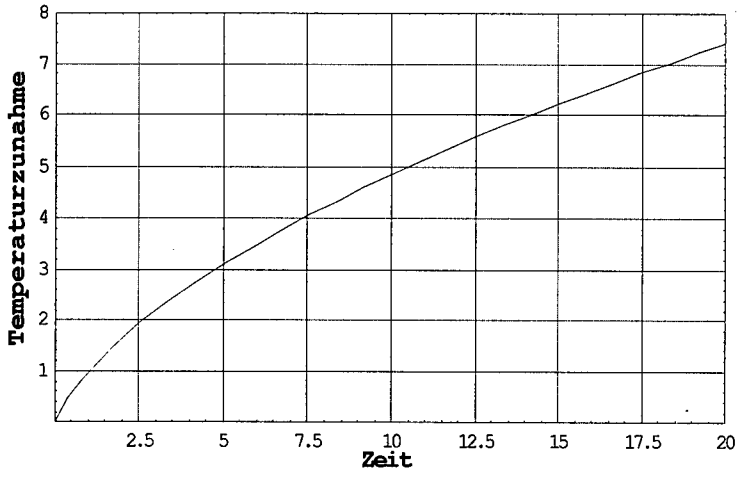

Abbildung 6: Temperaturverlauf an der Oberfläche

4 Reaktiver Feststoff

In einem Feststoff sind bei Temperaturänderung Phasenumwandlungen, endotherme und exotherme Reaktionen möglich. Nach Aufheizen auf gewisse Temperaturwerte setzen diese ein und verändern das Temperaturprofil. Bei einem Anzündvorgang ist es das Ziel exotherme Reaktionen in Gang zu setzen.

Die Reaktionen wirken als Quellterme in der Wärmeleitungsgleichung, Veränderungen der physikalischen Stoffeigenschaften werden hier nicht berücksichtigt. Die c_i sind hier Stoffkonzentrationen.

$$\frac{\partial T}{\partial t} - \frac{\partial^2 T}{\partial x^2} = Q[x,t] + \sum_i q_i \frac{\partial c_i}{\partial t} \tag{16}$$

$$\frac{\partial c_i}{\partial t} = -\sum Z_{i,j} e^{-\frac{E_{i,j}}{RT}} f[c_i, c_j] \tag{17}$$

Zur Vereinfachung wird im weiteren meist eine einzelne Reaktion 0.ter Ordnung angenommen:

$$\frac{\partial c}{\partial t} = -Z e^{-\frac{E}{RT}} \tag{18}$$

Das Gleichungssystem (16) und (17) ist wegen des Arrheniusterms stark nichtlinear und damit nicht analytisch lösbar. Das Integral über die Arrheniusfunktion wird mit folgender semikonvergenter Reihe angenähert, da E/RT meist wesentlich größer als 1 ist (RT/E sollte kleiner sein als 0.2):

$$S[E,T] = T e^{-\frac{E}{RT}} \sum_{n=1}^{N} n!(-1)^{n-1} \left(\frac{RT}{E}\right)^n$$

die Summe für endliches nicht zu großes N (d.h. n zwischen 1 und 5).

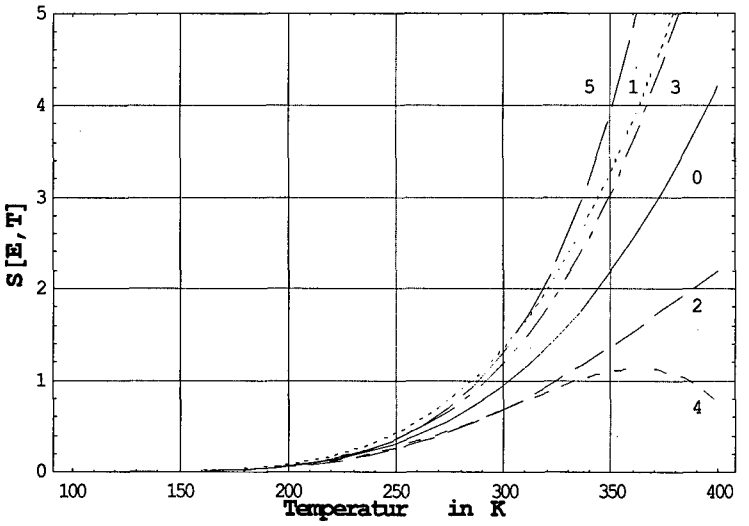

Abbildung 7: Näherung E / R = (10 000 J/ mol) / (8,31 J / mol / K) ≈ 1200 K. Kurve 0 exakte Lösung, Kurven 1-5 Näherung mit Polynomen S[E,T] der Ordnung 1-5.

4.1 Adiabatische Selbsterhitzung

$$\frac{dT}{dt^*} = \frac{Zq^*}{c\rho} e^{-\frac{E}{RT}} - a(T - T_0) \qquad (19)$$

Der erste Term rechts mit der Exponentialfunktion beschreibt die chemische Reaktion, der zweite Term den Wärmeübergang an der Oberfläche mit dem Übergangskoeffizienten a. Die Lösung lautet:

$$t^* - t_0^* = \int_{T_0}^{T} \frac{c\rho dT}{Zq^* e^{-\frac{E}{RT}} - a(T - T_0)} \qquad (20)$$

Für adiabatische Selbsterhitzung ist a=0 und das Integral kann gelöst werden:

$$t^* - t_0^* = \frac{c\rho}{Zq^*} \cdot \left(Te^{\frac{E}{RT}} - \frac{E}{R} Ei\left[\frac{E}{RT}\right] - T_0 e^{\frac{E}{RT_0}} + \frac{E}{R} Ei\left[\frac{E}{RT_0}\right] \right) \qquad (21)$$

Ei ist die Exponentialintegralfunktion

$$Ei[x] = \int_{-\infty}^{x} \frac{e^t}{t} dt$$

4.2 Kritischer Durchmesser

In einer weiteren Näherung vernachlässigt man die Zeitableitung, d.h. man betrachtet die Fälle, bei denen sich für ein lineares Problem noch ein stationäres Temperaturprofil einstellt. (Beispiele: ein Reaktor, ein reaktiver Festkörper bei gegebener Außentemperatur).

$$\frac{\partial^2 T}{\partial x^2} = Zqe^{-\frac{E}{RT}} \tag{22}$$

$$x - x_0 = \int_{T_0}^{T} \frac{dT}{\sqrt{2Zq\left(Te^{-\frac{E}{RT}} + \frac{E}{R}Ei\left[-\frac{E}{RT}\right]\right)}}$$

eine einfache Näherung ergibt:

$$x - x_0 = \int_{T_0}^{T} \frac{dT}{\sqrt{2ZqS[E,T]}} \tag{23}$$

$$x - x_0 = \sqrt{\frac{E}{2RZq}} \int_{T_0}^{T} \frac{e^{\frac{E}{2RT}} dT}{T}$$

$$x - x_0 = -\sqrt{\frac{E}{2RZq}} \cdot \left(Ei\left[\frac{E}{2RT}\right] - Ei\left[\frac{E}{2RT_0}\right]\right) \tag{24}$$

Der Verlauf von (23) und (24) ergibt den kritischen Durchmesser, wenn die Temperatur gegen unendlich geht. Für zylindrische und sphärische Geometrie sind (23) und (24) noch mit Faktoren zu multiplizieren [9].

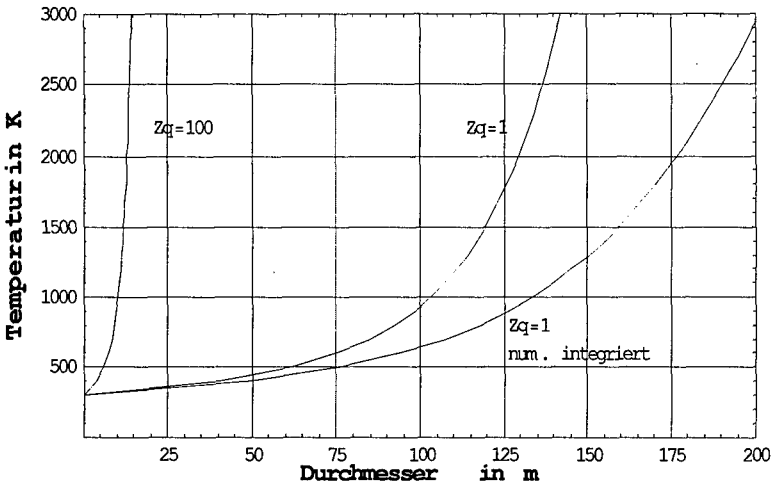

Abbildung 8: Kritischer Durchmesser E / R = (10 000 J / mol) / (8,31 J / mol / K) ≈ 1200 K wie oben, T_0 = 300 K.

5 Stationäre Feststoffreaktion/-verbrennung

Nach einer Anfangsphase der Feststoffaufheizung durch extern zugeführte oder intern durch Reaktion entstandene Energie stellt sich ein stationärer Reaktionsfortschritt ein, wenn gewisse Bedingungen erfüllt sind. D.h., die Reaktionsfront bewegt sich als stationäres Temperaturprofil mit einer konstanten Geschwindigkeit r in den Feststoff hinein. Wegen der konstanten Geschwindigkeit kann das Koordinatensystem so transformiert werden, daß das Temperaturprofil ruht. Mit der Transformation $\bar{x} = x - rt$ wird aus:

$$\frac{\partial T[\bar{x},t]}{\partial t} = \frac{\partial T[x,t]}{\partial t} - r\frac{\partial T[x,t]}{\partial x} \tag{26}$$

und damit:

$$\frac{\partial T}{\partial t} - r\frac{\partial T}{\partial x} - \frac{\partial^2 T}{\partial x^2} = Q[x,t] + \sum_i \left(q_i \frac{\partial c_i}{\partial t} - r q_i \frac{\partial c_i}{\partial x} \right) \tag{27}$$

Für die Umsatzrate $\frac{\partial c_i}{\partial t}$ benutzt man für gewöhnlich den Arrhenius-Ansatz:

$$\frac{\partial c_i}{\partial t} = -\sum_j Z_{i,j} e^{-\frac{E_{i,j}}{RT}} f[c_i, c_j] \tag{28}$$

Wenn jede weitere Zeitabhängigkeit ausgeschlossen ist, entsteht folgendes System gewöhnlicher Differentialgleichungen:

$$r\frac{dT}{dx} + \frac{d^2T}{dx^2} = -Q[x] + r\sum_i q_i \frac{dc_i}{dx} \tag{29}$$

$$r\frac{dc_i}{dx} = \sum Z_{i,j} e^{-\frac{E_{i,j}}{RT}} f[c_i, c_j] \tag{30}$$

Die Green'sche Funktion von (27) im unendlichen Raum ist ebenfalls durch Koordinatentransformation zu erhalten:

$$G_u[x, x', t, t'] = \frac{e^{-\frac{(x-rt-x'+rt')^2}{4(t-t')}}}{\sqrt{4\pi(t-t')}} \tag{31}$$

Dreidimensional sieht die Green'sche Funktion analog zu (4) aus.

Im folgenden wird zur Darstellung mit Wärmeleitung und spezifischer Wärme (temperaturabhängig) zurückgegriffen:

$$r\rho c[T]\frac{dT}{dx} + \lambda\frac{d^2T}{dx^2} = -Q^*[x] + r\sum_i q_i^*\frac{dc_i}{dx} \qquad (32)$$

folgende Randbedingungen sind zu berücksichtigen:

$T[\infty] = T_\infty$; $T[0] = T_s$;

$\lambda dT/dx = -Q_0$ an der Stelle $x = 0$

$c_i[\infty] = 0$(oder 1) $c_i[0] = c_i^*$ (je nach Reaktionsmodell)

Die Energiebilanzgleichung entsteht aus (32) durch Integration von T_∞ bis T_s:

$$r\rho\int_{T_\infty}^{T_s} c[T]dT + \lambda\left.\frac{dT}{dx}\right|_{x=\infty}^{x=0} = -\int_\infty^0 Q^*[x]dx + r\sum_i q_i^*\int_0^1 dc_i \qquad (33)$$

5.1 Beispiel 1: Abbrandgeschwindigkeit r für einen quasi-stationären Abbrand

$c(T) = c + L\delta[T-T_L]$; (Phasenumwandlung als Polstelle)

$\lambda dT/dx = -Q_0$, bei $x = 0$ und $\lambda dT/dx = 0$ für $x \to \infty$ (vgl. Randbedingungen)

$Q^*[x] = ble^{-bx}$; Strahlungsaufheizung

$c_i[0] = 1$ und $c_i[\infty] = 0$; (vollständiger Stoffumsatz)

Dabei bedeuten:

L = Phasenumwandlungswärme

T_L = Phasenumwandlungstemperatur

Q_0 = Wärmefluß an der Oberfläche

$$r\rho\left(c\left(T_s - T_\infty\right) + L\right) - Q_0 - 0 = I - 0 + r\sum_i q_i^*\left(1 - 0\right)$$

$$r = \frac{Q_o + I}{\rho\left(c\cdot\left(T_s - T_\infty\right) + L - \sum_i q_i^*\right)} \qquad (34)$$

Der Temperaturgradient $\lambda dT/dx$ hat an der Stelle x = 0 einen Sprung. Die zweite Ableitung von T[x,t] kann deshalb auch mit einer Dirac'schen Deltafunktion dargestellt werden: $\lambda d^2T/dx^2 = - Q_0 \delta[0 - x]$.

5.2 Beispiel 2: Temperaturprofil für einen quasi-stationären Abbrand

Wieder ausgehend von Gleichung (42) mit Berücksichtigung von Strahlung $Q^* = I\, b\, e^{-bx}$ aber ohne chemische Reaktion:

$$\lambda\frac{\partial^2 T}{\partial x^2} + r\rho\left(c_p + L\delta[T - T_L]\right)\frac{\partial T}{\partial x} = -Ibe^{-bx}$$

Integration über den Ort x ergibt die Energiebilanzgleichung

$$\lambda\frac{\partial T}{\partial x} + r\rho\left(c_p\left(T[x] - T_{t=0}\right) + L\right) - Ie^{-bx} = 0 \qquad \text{für } x = 0 \qquad (35)$$

und

$$\lambda\frac{\partial T}{\partial x} + r\rho c_p\left(T[x] - T_{t=0}\right) - Ie^{-bx} = 0 \qquad \text{für } x > 0 \qquad (36)$$

Das Temperaturprofil wird unter dem Einfluß von Strahlung sigmaoid. Die Oberfläche habe die Phasenumwandlungstemperatur T_L und der Temperaturgradient an der Oberfläche sei durch den Wärmefluß Q_0 gegeben:

$$T[x = 0] = T_L \qquad \text{und} \qquad \lambda\left.\frac{\partial T}{\partial x}\right|_{x=0} = -Q_0$$

Die erneute Integration über den Ort x ergibt:

$$T[x] - T_{t=0} = \frac{e^{-bx}}{r\rho c_p - b\lambda}I - \frac{h}{c_p} + e^{-\frac{r\rho c}{\lambda}x}\cdot const \qquad (37)$$

$$T[x] - T_{t=0} = \frac{e^{-bx}}{r\rho c_p - b\lambda}I + e^{-\frac{r\rho c}{\lambda}x}\cdot const \qquad (38)$$

Die Integrationskonstante const wird durch Einsetzen der Randbedingungen in Gleichung (35) und (37) bestimmt:

$$\mathbf{const} = \frac{1}{r\rho c_p} Q_0 - \frac{b\lambda}{r\rho c_p\left(r\rho c_p - b\lambda\right)} I \qquad (39)$$

einsetzen in (38) gibt:

$$T[x] - T_{t=0} = \frac{e^{-\frac{r\rho c_p}{\lambda}x}}{r\rho c_p} Q_0 + \left(\frac{e^{-bx}}{r\rho c_p - b\lambda} - \frac{b\lambda e^{-\frac{r\rho c_p}{\lambda}x}}{r\rho c_p\left(r\rho c_p - b\lambda\right)}\right) I$$

6 Instationäre Feststoffreaktion

Ein Modell mit Berücksichtigung einer Phasenumwandlung in der kondensierten Phase und chemischer Reaktionen darin wie auch des Wärme- und Stofftransports mit Reaktionen in der Gasphase wurden von Zarko et al [4-6] ausgearbeitet. Damit können dynamische Effekte bei der Anzündung und beim Energieeintrag durch externe Quellen berücksichtigt werden. Beispiele sind in den Abb. 9 und 10 wiedergegeben, wobei externer Energieübertrag zunächst die Anzündung bewirkt und eine Steigerung des Energieflusses dynamisch die Abbrandgeschwindigkeit beeinflußt. Temperaturanstieg, Anzündverzugszeiten und asymptotische Abbrandgeschwindigkeiten entsprechen den Ergebnissen aus den oben hergeleiteten Formeln. Interessant ist jeweils die dynamische Reaktion an den Flanken des Energieflußpulses. Bei Absorption der Energie an der Oberfläche ergeben sich Überschwinger, bei Absorption in der Tiefe eine verzögerte Annäherung.

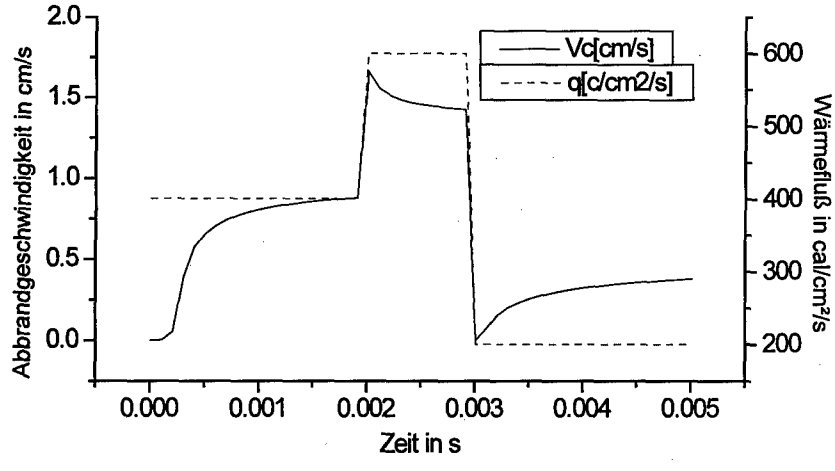

Abbildung 9: Verlauf der Abbrandgeschwindigkeit beeinflußt durch externe Energieübertragung bei Absorption an der Oberfläche.

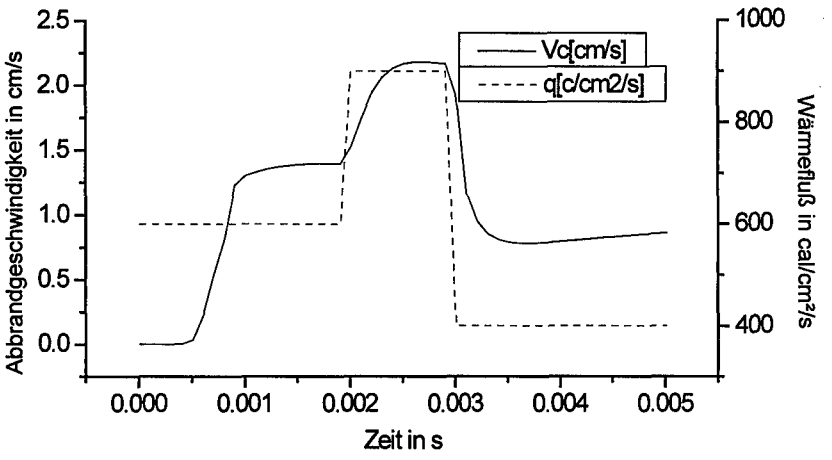

Abbildung 10: Verlauf der Abbrandgeschwindigkeit beeinflußt durch externe Energieübertragung bei Absorption der Energie in der Tiefe der kondensierten Phase.

Literatur

[1]Eisenreich N.; Theoretische Untersuchungen über den Abbrand von Festtreibstoffen ICT-Bericht 5/76, Pfinztal 1976.

[2]Eisenreich N.; Vergleich Theoretischer und Experimenteller Untersuchungen über die Anfangstemperaturabhängigkeit der Abbrandgeschwindigkeit von Festtreibstoffen ICT-Bericht 8/77, Pfinztal 1977.

[3]DeLuca L. Pagani C.D., Verri M.; A Review of Solid Rocket Propellant Combustion, ISTS paper No 94-a-30v, Int. Symp. Space Techn. Sci. Yokohama, Japan 15-24 may 1994

[4]Zarko, V.E.; Gusachenko, L.K. and Rychkov, A.D.;Simulation of Combustion of Melting Energetic Materials; Defence Science Journal; 46 No.5, pp425-433, 1996.

[5]Gusachenko, L.K.; Zarko, V.E. and Rychkov, A.D.;Modeling of Gasification of Evaporated Energetic Materials under Irradiation; INTAS Workshop, Milan, July 1996.

[6]Gusachenko, L.K.; Zarko, V.E. and Rychkov, A.D.;Instability of a Combustion Model with Evaporation on a Surface and Overheat in the Condensed Phase; Combustion, Explosion and Shock Waves, 33 No.1, 1997.

[7]Carslaw, H.S. and Jaeger,J.C.; Conduction of Heat in Solids, 2. Edition, Oxford University Press, London 1973.

[8]Wolfram S; The Mathematica Book, 3rd Edition, Wolfram Media Inc. Champaign, IL, USA 1996.

[9]Frank-Kamenetskii D.A.; Diffusion and Heat Exchange in Chemical Kinetics; Princeton University Press, Princeton 1955.

[10]Eisenreich, N. Weiser V.; Phenomena of Energy Transport in Pool Fires; 1st Internet Conference on Process Safety, 27.-29. January 1998, Hamm, Germany

CHARACTERIZATION OF COMBUSTION AND STABILITY BEHAVIOR OF SOLID PROPELLANTS

Matt M. Mench and Kenneth K. Kuo

Department of Mechanical Engineering
The Pennsylvania State University
University Park, PA 16802 USA

Abstract

Before implementation of new solid propellants, a great deal of parameters must be experimentally determined. Among the most basic of ballistic parameters that need to be described are the burn rate characteristics, temperature sensitivities, Arrhenius form of burning rate law, and stability behavior of propellants in terms of the Novozhilov parameters. Obtaining these data for a single propellant ordinarily requires a large number of experiments. By determining the burning surface temperature as a function of chamber pressure and initial temperature, stability maps of two propellants were generated, without using a very large set of surface temperature and temperature sensitivity data. An experimental study has been performed to determine the burning rate and stability characteristics of two similar composite propellants (propellant M, with a significant percentage of metal additive, and propellant N with no metal additive). Samples were tested in an optical strand burner at pressures up to 30.0 MPa and initial propellant temperatures from -60 to around 100 °C. An Arrhenius form of burning rate correlation was deduced for both the metalized propellant M and the non-metalized propellant N. An analytical expression for temperature sensitivity and Novozhilov stability parameters as functions of pressure and initial propellant temperature was developed for each propellant.

Introduction

In the design and utilization of modern solid propellants, a great deal of experimentally determined parameters must be defined in order to characterize the burning behavior of the propellant. Among the most basic of ballistic parameters that need to be determined are the burn rate characteristics, temperature sensitivities, and an Arrhenius form of burning rate law. Increasingly, the stability behavior of propellants in terms of the Novozhilov parameters κ and r, defined in the Method of Approach section of this paper, are being examined. The conventional method for deducing these parameters is to use either a constant-volume (Crawford) bomb or a

constant-pressure strand burner. The methodology for producing this data is straightforward: burning rate measurements are taken as a function of both pressure and propellant initial temperature. In addition, ultra-fine wire thermocouples need to be embedded in the propellant for measuring propellant burning surface temperature as a function of operating conditions. In theory, this is a simple task, and requires a set matrix of tests varying in pressure and propellant initial temperature. In practice, however, enormous labor is required to obtain reliable surface temperature measurements and other data over a complete operating domain, especially for propellants which do not follow a Saint Robert's burning rate law ($r_b=aP^n$).

In this research, the steady-state strand burner tests were conducted for two propellants with different metal content. Propellant M has a significant percentage of metal, and propellant N is of similar ingredients except it contains no metal additive. Neither propellant exhibits a Saint Robert's burning rate law over the entire pressure domain. The purpose of this paper is to describe and illustrate the method used to efficiently characterize these propellants in terms of burning rate, temperature sensitivity, Arrhenius burning rate law and Novozhilov stability parameters. This methodology provides a reasonable description of the propellant characteristics over a large domain with significantly less time and resources than would normally be required.

Method of Approach

A schematic diagram of the test setup used in this study is shown in Fig. 1. A high-pressure, optical strand burner equipped with access for micro-thermocouples, breakwires and pressure transducers was used to obtain data including:

a) the surface regression rate by both video imaging and breakwire techniques;
b) the chamber pressure-time history with a fast-response (on the order of 10 μs) Kistler pressure transducer; and
c) the sub-surface temperature profile of the propellant with the use of micro-thermocouples.

The high-pressure, optical strand burner is capable of pressures up to 69 MPa (~10,000 psig) and temperatures ranging from -100 °C to around 100 °C. Details of the operating procedure for this setup can be found in Refs. 1 and 2. For the strand burner tests, cylindrical propellant samples (diameter ~ 1 cm, length ~ 8 cm) were cut from blocks of cast propellants. Figure 2 is a sketch of a prepared propellant sample. A tapered cup was cut into the bottom of

the sample having an initial length of around 4-5 cm. A matching truncated cone was cut on the top portion of a shorter 1-2 cm

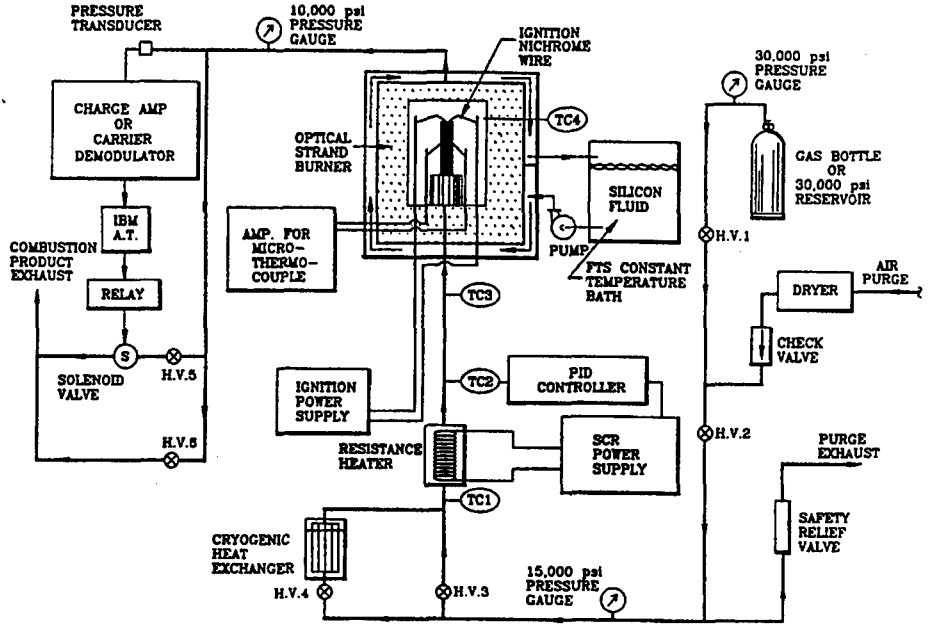

Fig. 1 Schematic diagram of the optical strand burner

base piece. A Zenin-type [3,4] rolled micro-thermocouple with a typical flat bead thickness of < 5μm was manufactured by the authors and placed directly on the top surface of the truncated cone by laying the flat bead portion on the flat top of the truncated cone. The upper portion of the propellant was lowered onto the truncated cone portion to secure the thermocouple at the interface of the matched cup and cone assembly. In order to ensure that the thermocouple stayed in direct contact with the propellant surface, a small needle was pressed through the propellant which penetrated through the cup and cone assembly at the height slightly above the interface of the two segments. Due to the fact that the truncated cone section was approximately 2.5 mm in

height and the deduced thermal wave thickness was on the order of 100 μm, the needle will have no effect on the thermal wave profile in the propellant near the thermocouple location.

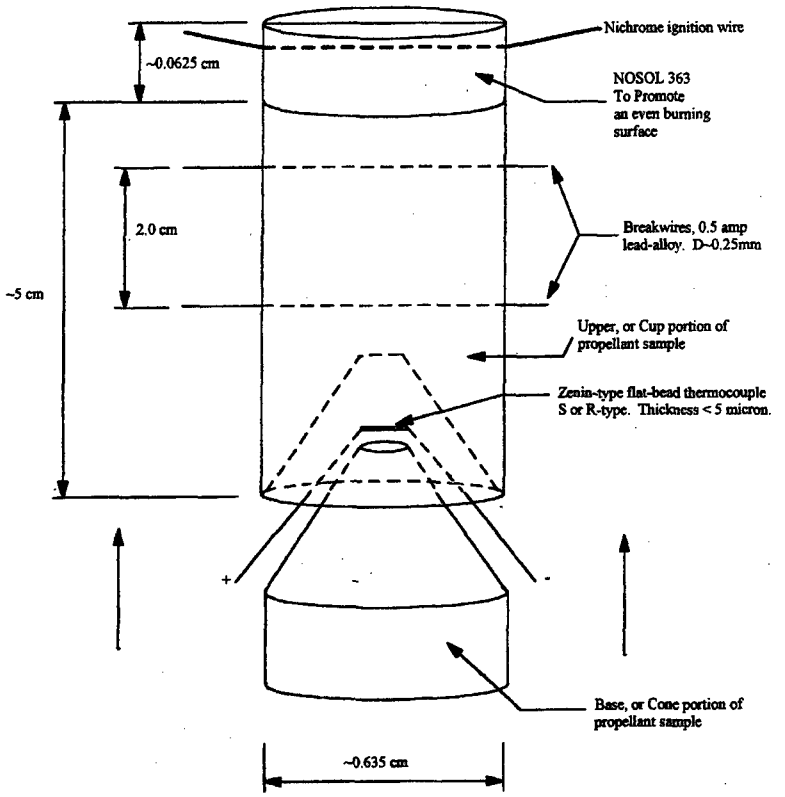

Fig. 2 A schematic of a typical propellant sample with cup and cone configuration and Zenin-type ribbon micro-thermocouple.

Two breakwires were also installed radially at 2 cm apart from one another in the upper portion of the propellant sample. The diameter of the breakwire is approximately 0.25 mm. The purpose for these two breakwires is to obtain a second set of burning rate data for comparison with optical measurements. In order to achieve uniform surface ignition, a small piece of

homogeneous propellant with nearly the same diameter as the propellant samples was glued to the top portion of the propellant sample. A nichrome wire for ignition was inserted radially through the homogeneous propellant piece. This provided a uniform heating of the propellant sample surface prior to ignition.

Burning Rate Data Reduction

The primary method for deducing the burning rate of the propellant sample was by direct video imaging of the instantaneous burning surface location. A Pulnix color video camera was used to record the propellant regression event at a framing rate of 60 frames per second. A regression distance versus time history was deduced from the video image data in order to determine the regression rate of the propellant. The propellant burning surface location was measured at several times during a test and a linear curve-fit of the distance versus time plot for each test was used to determine the burning rate. In the case of non-flat burning surface, the breakwire method was utilized to compare with the video image data.

Due to the fact that the breakwires are installed in the propellant at room temperature, while some tests were conducted at much higher or lower than ambient temperatures, using the pre-test distance between the two breakwires is a source of error. In order to correct for this error, a measurement of the linear thermal expansion coefficient (α) of the propellant was made. Video images of a propellant sample, with marks 2 cm apart at room temperature, were taken at various temperatures ranging from -60 to 80 ^{o}C. The results were plotted and fitted to a straight line. The α value for the propellant was used to correct the initial distance between the breakwires for tests at initial propellant temperatures differing from the ambient.

Surface Temperature Data Reduction

A natural log plot of temperature versus distance measured from propellant surface was used to determine the surface temperature. Since the subsurface temperature profile was assumed to be exponential until reaching the surface [5], the point of departure from linearity was taken to be the location of the burning surface. A representative plot of this type is shown in the Discussion of Results section of this paper.

Test Matrix

In order to obtain a wide range of surface temperature data covering a broad range of test conditions, it is desirable to conduct tests at many different propellant initial temperatures and chamber pressures. This is different from conventional testing procedures, in which typically five to ten pressures and only three to five propellant initial temperatures are selected for testing. In other words, the particular propellant initial temperature and pressures selected are not important, so long as they are accurately measured and conducted over a wide range. It is therefore desired to obtain data at many propellant initial temperatures and pressures tested as input information for the correlation development. Several tests at the same pressure and propellant initial temperature were conducted only to verify the accuracy of the burning rate and surface temperature measurement.

Stability Parameter Data Reduction

The intrinsic stability characteristics of propellants M and N were examined based upon the determination of the Novozhilov parameters κ and r [6]. Where:

$$\kappa \equiv \left(T_s - T_i\right) \times \sigma_p \tag{1}$$

and

$$r \equiv \left(\frac{\partial T_s}{\partial T_i}\right)_p \tag{2}$$

These two stability parameters are very useful in determining the stable operating regimes of a given propellant. According to Novozhilov [6], a given propellant is stable if one of the following conditions is met:

a) $\kappa < 1$ or

b) $\kappa > 1$ *and* $r > r^*$ where $r^* = (\kappa\text{-}1)^2/(\kappa+1)$

According to Novozhilov [6], the condition of stability implies that the propellant burning will be stable despite any small perturbations in operating parameters such as gas-phase pressure and temperature. Using the surface temperature data recorded with the embedded micro-thermocouples and the Arrhenius burning rate law parameters derived from many tests at

different initial propellant temperatures and pressures, these stability parameters were deduced for both the metalized propellant M and non-metalized propellant N.

Discussion of Results

Burning Rate Behavior under Various Pressures

The burning rate behavior of both the metalized and non-metalized propellants was examined as a function of chamber pressure at various initial propellant temperatures. A comparison of the burning rate behavior of propellants M and N is shown in Figs. 3a and 3b. It can be seen that the burning rate behavior of the non-metalized propellant N was nearly identical to that of the metalized propellant M. The burning rate versus pressure relationship shown in Fig. 3 clearly indicates that the burning rate do not follow the conventional Saint Robert's burning rate law. The estimated error of $\pm$ 1% for the deduced burning rate is based upon the measurement of the instantaneous propellant sample length from the video image (which has a framing rate of 60 frames per second) and the accuracy of the pressure and initial temperature measurements.

The addition of metal to the propellant formulation for replacing a portion of oxidizer content has two major effects on burning rate. One is to increase the burning rate by the enhanced thermal conductivity to the unburnt propellant. The other effect is the reduction of heat feedback to the unburnt propellant zone. This reduction is believed to be associated with the decrease of oxidizer-to-binder ratio with metal addition, the higher energy required for metal liquefaction near the burning surface and metal particle combustion at locations relatively far above the propellant surface. It is believed that these two effects counteract each other resulting in the relatively small difference between the burning rates of the non-metalized and metalized propellants.

Figure 4 is a photograph of propellant M showing metal particle combustion at locations far from the burning surface. It can be seen clearly that the metal particle is burning far from the propellant surface, reducing heat feedback from the metal-oxidizer combustion. The multiple bright streaks represent the trajectories of burning metal particles during the recording interval of 1/60 second. It is interesting to note that the length of each streak is on the order of 2 mm. This translates to an average particle velocity of around 12 cm/s, which is many times smaller than the expected gas velocity. This implies that the metal particles have velocities much lower than the

gaseous products. The reasons for many distributed streaks covering a vertical distance of approximately 3 cm is believed to be caused by the difference in ignition delay times for various particles. The number of bright streaks shown in Fig. 4 is around 25; this is less than the actual number of burning particles, due to the blockage of views of other metal particles burning in direction perpendicular to the plane of view.

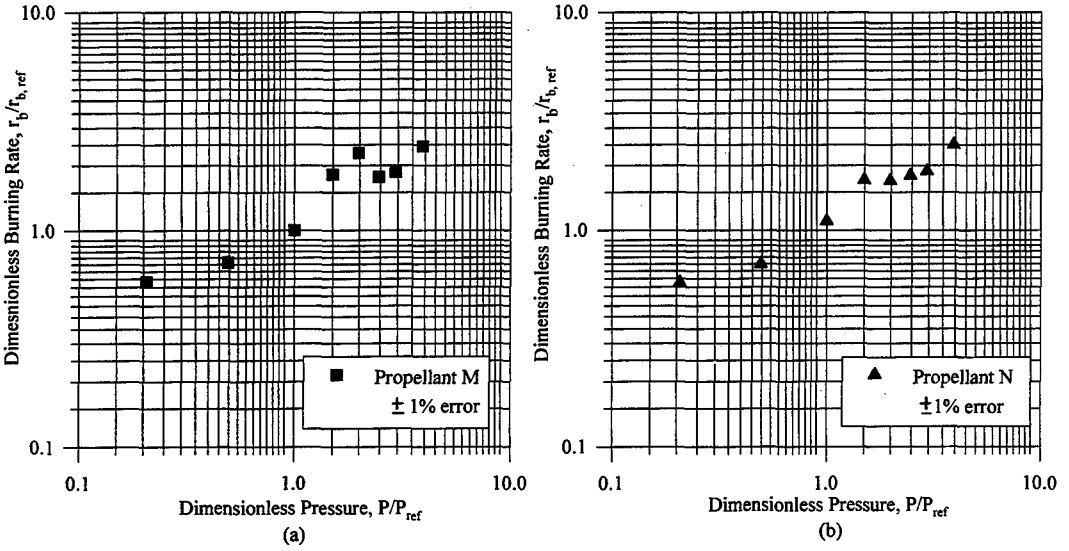

Fig. 3 Comparison of dimensionless burning rate data for propellants M and N at various pressures

Temperature Sensitivity to Burning Rate

The temperature sensitivity to burning rate (σ_p) is defined as:

$$\sigma_p \equiv \left.\frac{\partial \ln r_b}{\partial T_i}\right|_p \tag{3}$$

By constructing a plot of deduced burning rate versus initial propellant temperature (measured with micro-thermocouples inserted directly in the propellant), the experimental σ_p value for propellants M and N was determined for the pressures tested.

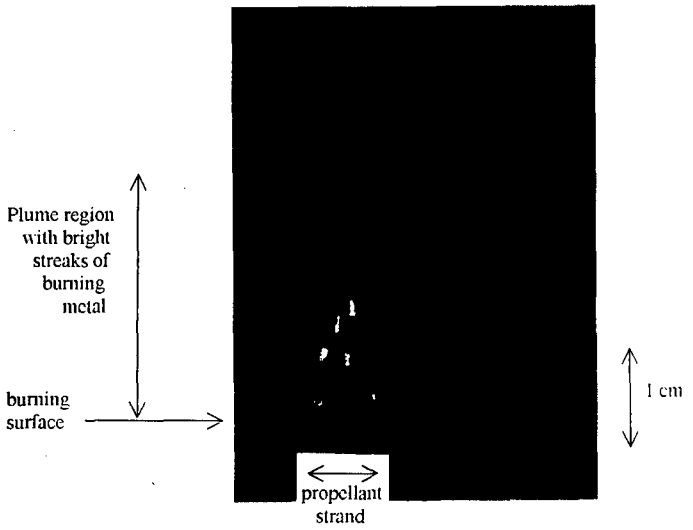

Fig. 4 Photograph of propellant M showing metal particle combustion at locations far from the propellant burning surface

Figure 5 is a plot of dimensionless temperature sensitivity versus dimensionless pressure for propellants M and N. Deduced results indicate that σ_p of M drops significantly from a relatively high value at low pressures to a much lower value for higher pressures. The temperature sensitivities of the propellant N were also deduced according to Eq. (3). From Fig. 5 it can be seen that the propellant N follows a general trend of decreasing temperature sensitivity with increasing pressure in the lower pressure range. At higher pressures, the σ_p increases slightly over the remaining range of pressure tested. In comparing propellants M and N, it can be seen that the σ_p of the metalized propellant M is slightly higher than that of the non-metalized propellant N for most pressures. The σ_p of the metalized propellant M is also a stronger function of pressure in the middle pressure range tested. The estimated errors for deduced temperature sensitivities are ± 5%. This estimation is based upon the errors involved in initial temperature and chamber pressure measurements. In general, the σ_p is a function of initial temperature and pressure, namely:

$$\sigma_p = \sigma_p(T_i, P) \tag{4}$$

The error of σ_p was obtained from the chain-rule described by:

$$\Delta\sigma_P = \left.\frac{\partial\sigma_P}{\partial T_i}\right|_P \Delta T_i + \left.\frac{\partial\sigma_P}{\partial P}\right|_{Ti} \Delta P \qquad (5)$$

where the two partial derivatives of σ_p with respect to T_i and P were calculated based upon the analytical function of burning rate, r_b, in terms of burning propellant initial temperature and pressure described in a later section of this paper. The error of the initial temperature measurements is around ± 3 K. The error in chamber pressure measurement is around 0.07 MPa.

Overall, the effect of metal addition to the propellant formulation on the temperature sensitivity to burning rate is slight, and it can be stated that the controlling mechanisms of the temperature sensitivity are more strongly coupled to the binder-oxidizer interaction than the metal particle-propellant interaction, since both propellants N and M have similar σ_p characteristics. It should be noted that the unexpectedly high values of σ_p at low pressures could be associated with the uneven burning surface phenomenon resulting from relatively low heat feedback from the gaseous flame zone. Uneven burning surface phenomena were observed at the lowest pressure tested and it was difficult to obtain a flat burning surface at this low pressure, therefore, although the semi-log plot of burning rate data at the lowest pressure showed a linear correlation with respect to the initial temperature, the result could be somewhat influenced by this uneven burning surface phenomenon observed at the lowest pressure tested. At all other pressures, this phenomenon was not observed and the corresponding σ_p results are more reliable.

Surface Temperature Data

A natural log of temperature versus distance from propellant surface plot can be used to determine the surface temperature, since the subsurface temperature profile is assumed to be exponential until reaching the surface [6]. A representative plot of this type for Propellant M is shown in Fig. 6. Similar plots were obtained for the Propellant N. It can be seen that a clearly defined departure point from a linear profile can be determined as the surface temperature. The

location of this break is defined as the surface location, and the distance coordinate is found by multiplying the recorded time of event by the measured burning rate. At low temperatures, the plot may not always be totally linear due to endothermicities involved in oxidizer decomposition.

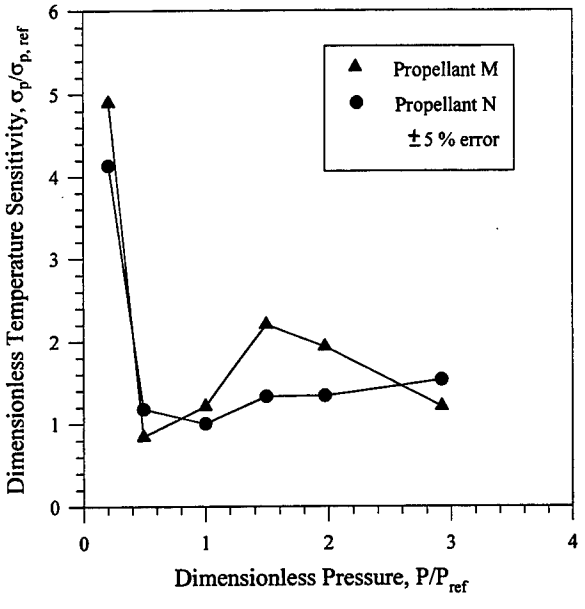

Fig. 5 Deduced dimensionless temperature sensitivities versus pressure for propellants M and N

Arrhenius Burning Rate Law

By plotting burning rate versus surface temperature, the Arrhenius form of burning rate law:

$$r_b = A \exp\left(\frac{-E_a}{R_u T_s}\right) \tag{6}$$

can be deduced, where E_a is the activation energy and A is the pre-exponential factor. Using the burning surface temperature determined from the traces of micro-thermocouples embedded in the propellant strand and the measured burning rate data, the Arrhenius forms of the burning rate correlation were deduced for both the metalized propellant M and the non-metalized propellant

N. A plot of the data used to deduce the Arrhenius burning rate law for both propellants M and N is shown in Fig. 7. It is useful to note that surface temperature data were obtained under conditions with various initial temperatures and pressures. In general, the data correlates reasonably well with the exponential curve-fit. The E_a of the metalized propellant M is lower than that that of the non-metalized propellant N. This is related to the phenomenon of lower burning surface temperature of the metalized propellant M at the same test conditions as propellant N. Due to the fact that the burning rates are similar for these two propellants, it can be seen from Eq. (6) that the E_a for propellant M must be lower than that of propellant N.

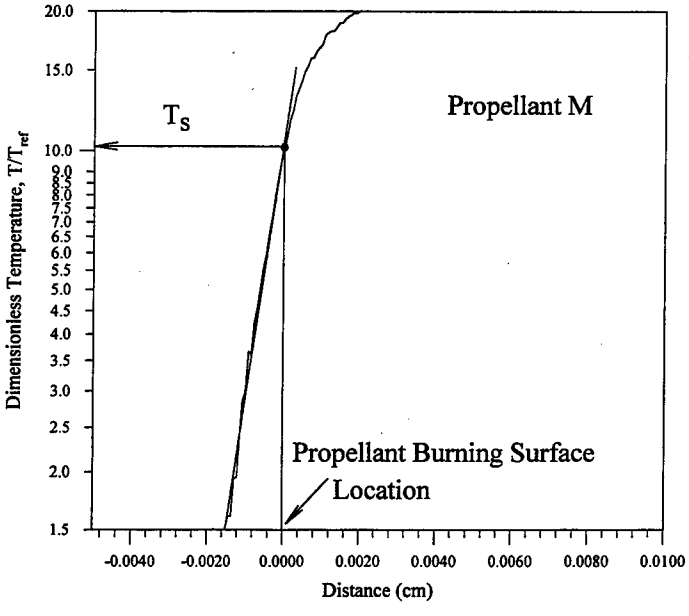

Fig. 6 A typical log temperature versus distance plot to determine surface temperature

Stability Analysis

The intrinsic stability of propellants M and N was examined based upon the determination of the Novozhilov stability parameters κ and r [6], shown in the Method of Approach section of this paper. Using the surface temperature data recorded with the embedded micro-thermocouples and the σ_p data derived from many tests at different initial propellant temperatures, stability parameters were deduced for propellants M and N. Due to the fact that tests were conducted for

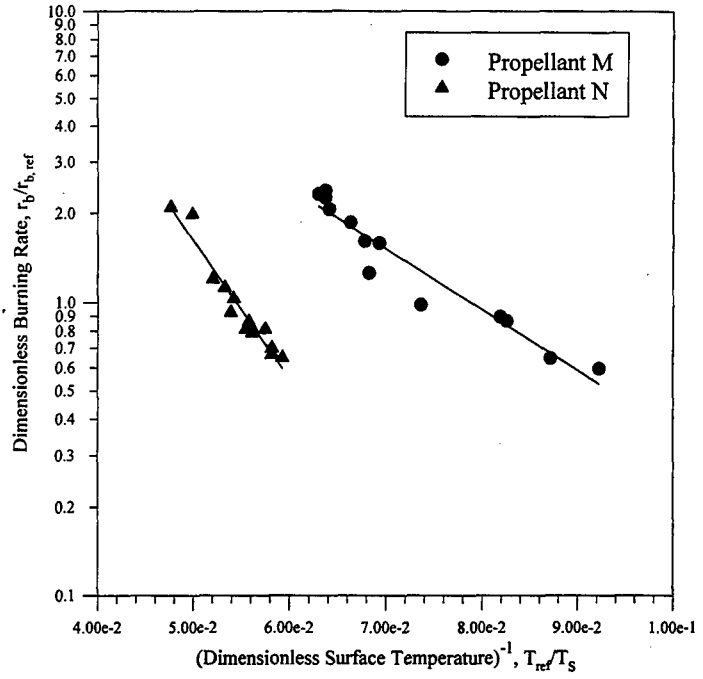

Fig. 7 Deduced Arrhenius burning rate law for Propellants M and N

two different propellants at eight different pressures, and only about one third of the tests resulted in a usable sub-surface thermocouple trace, a limited number of surface temperature data points were available to determine the stability parameters directly from Eqs. (1) and (2). Nevertheless, the surface temperature data were sufficient for the development of a correlation with pressure and initial temperature because all data points at various pressures and initial temperatures were utilized together. This surface temperature correlation was then used in the determination of stability parameters, discussed in the following section.

Development of a Functional Expression for Surface Temperature

Using all the deduced surface temperatures for both propellants at various initial propellant temperatures and pressures, the following functional form of the surface temperature was obtained. This equation relates surface temperature to pressure in a linear functional form

with coefficients independent of initial propellant temperature and pressure and is shown below as:

$$T_s = a_0 + a_1(T_i - T_{i,ref}) + [b_0 + b_1(T_i - T_{i,ref})]P \quad (7)$$

where $T_{i,\,ref}$ can be chosen arbitrarily. The a_0 term can be thought of as a base surface temperature and the a_1 term can be considered as a propellant initial temperature amplification factor. The b_0 term represents the change of surface temperature with respect to pressure independent of initial propellant temperature, and the b_1 term can be regarded as the amplification factor of the combined effects of initial propellant temperature and pressure. Figure 8 is a plot of the deduced surface temperature versus predicted surface temperature using Eq. (7) for propellants M and N. It can be seen that the data fit the predicted behavior for a variety of initial propellant temperatures and pressures to within ± 5% error. This expression can be used with other parameters deduced in this study to evaluate the temperature sensitivity to burning rate and the intrinsic stability of both propellants as functions of initial temperature and pressure. It should be noted that only 10-15 data points per propellant are needed for this correlation. Also, it is evident that the functional form of this correlation is applicable to both metalized and non-metalized propellants which exhibit non-Saint Robert's burning rate law characteristics.

Functional Expression for Temperature Sensitivity, σ_p

Substituting the deduced Arrhenius burning rate law into Eq. (3), an expression for σ_p of both propellants can be written as:

$$\sigma_p = \frac{E_a}{R_u T_s^2} \frac{\partial T_s}{\partial T_i}\bigg|_P \quad (8)$$

Since T_s as a function of T_i is known from Eq. (7), one can directly substitute the algebraic form of T_s into Eq. (8) and perform the differentiation to obtain the following equation:

$$\sigma_P = \frac{E_a}{R_u T_s^2}\left[a_1 + b_1 P\right] \quad (9)$$

Using the T_s expression given in Eq. (7), σ_p can be calculated from Eq. (9) when the pressure and initial temperature are known. The σ_p values calculated from this equation are in general agreement with those data shown in Fig 5., except at very low pressures, where non-

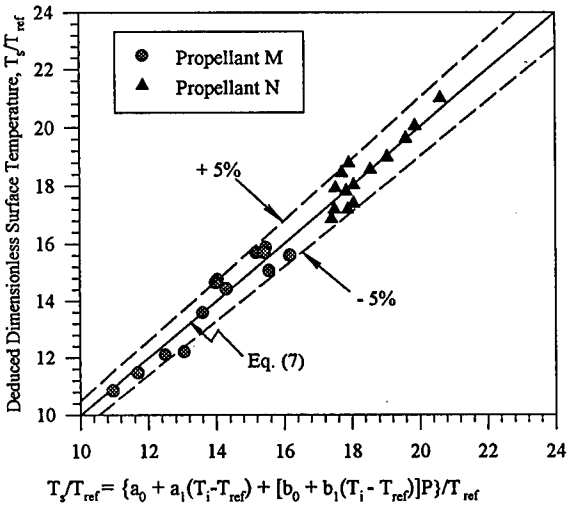

Fig. 8 Experimentally determined surface temperature versus predicted surface temperature for propellants M and N

planar burning surfaces were observed. This unsteadiness could be associated with the relatively high σ_p values determined experimentally at the lowest pressure tested. It is worthwhile to mention that Eq. (9) was also utilized for obtaining the partial derivatives of σ_p in Eq. (5) in the error analysis.

Novozhilov Stability Parameters

Using Eq. (7) as an expression for surface temperature, and Eq. (9) as an expression for σ_p, the functional forms of both Novozhilov stability parameters κ and r can be derived as:

$$\kappa = \frac{E_a(T_s - T_i)}{R_u T_s^2}\left[a_1 + b_1 P\right] \tag{10}$$

and

$$r = \left[a_1 + b_1 P\right] \tag{11}$$

where Eq. (7) is substituted in for T_s with the appropriate parameters for each of the two propellants in Eq. (10). Figures 9a and 9b show four relevant surfaces for propellant M in three-dimensional plots with different scales to enhance clarity. It can be seen that the κ stability

criterion (a) of $\kappa < 1$ is not satisfied for all pressures and initial temperatures. However, for most operating conditions (P, T_i), the r surface is above the r^* surface, indicating the second stability criterion (b) is satisfied. Only at very low initial temperatures and pressures both criteria (a) and (b) are not satisfied. This region is indicated by an ellipse and designated as unstable combustion zone.

The values for the stability parameters of propellant N were determined with the same method as for the propellant M. Figures 10a and 10b are a similar set of stability plots for the propellant N, except that Fig. 10b is also rotated for clarity. It can be seen that except for a small region of low pressure and high initial temperature, the κ surface is above the $\kappa = 1$ plane. However, the r surface is above the r^* surface for all values of P and T_i in the calculation domain; therefore, propellant N is stable for all operating regimes depicted in these two figures.

In order to derive a similar stability map for any given propellant without the use of Eq. (7), hundreds of tests would be required at all regions of the operational domain. The stability maps shown in Figs. 9 and 10 were derived with the use of around twenty surface temperature data points at various operating conditions. It should be noted, however, that the uncertainty in the stability maps shown in Figs. 9 and 10 is a cumulative function of the uncertainty in deriving the parameters in Eq. (7) and the Arrhenius burning rate law. It should be noted that care must be taken into consideration when extrapolating stability data beyond the range of actual test conditions due to the highly coupled nature of the gas and solid-phase phenomena. Therefore, as stated in the Method of Approach section of this paper, it is desired to have surface temperature data points that survey a large domain of operating pressure and propellant initial temperature as input for determination of the parameters in Eq. (7). However, the tremendous decrease in total number of tests required to deduce a stability map for a given propellant justify the usage of this method.

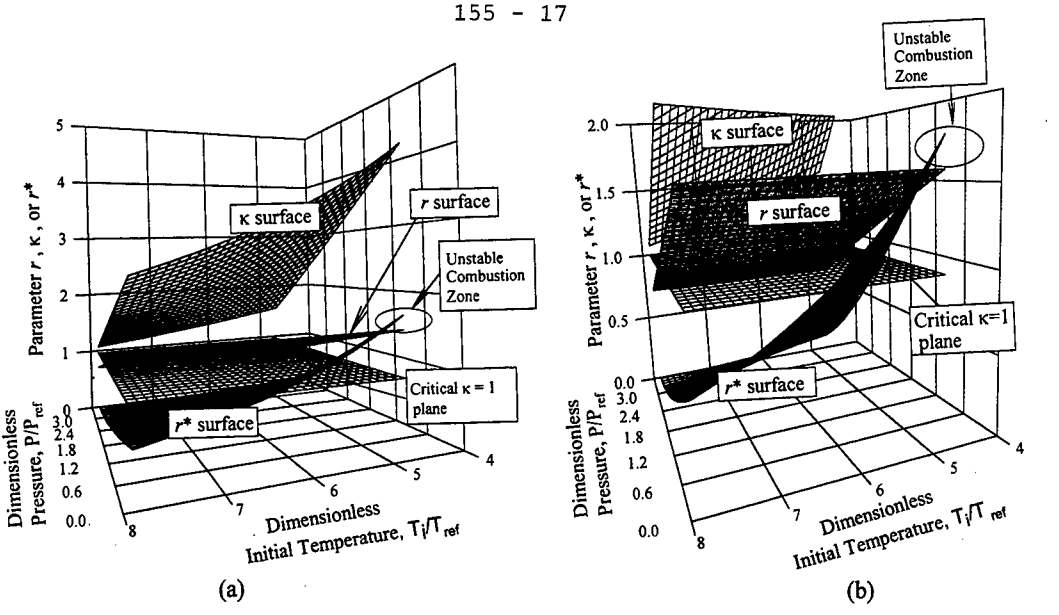

Fig. 9 Stability plots for propellant M showing broad stability region except at very low initial temperature and pressure conditions

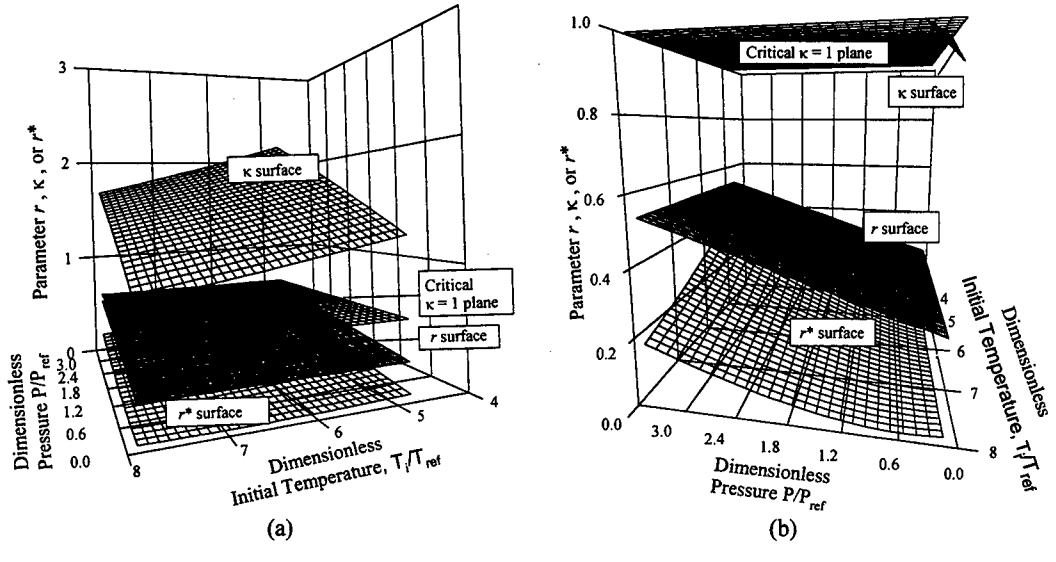

Fig. 10 Stability plots for propellant N showing complete stability in all regions of the operational domain

Conclusions

Many interesting and useful observations were made in terms of the burning rate behavior, temperature sensitivity, and stability characteristics of the two similar propellants (a metalized propellant M and a non-metalized propellant N) studied under broad ranges of initial temperature and pressure. Major results are summarized below.

- A general method was introduced for deriving an analytical expression for Novozhilov stability parameters using an experimentally deduced surface temperature correlation, which is applicable to the entire operating domain. This method greatly reduces the number of tests required to achieve reliable results as compared to conventional methods. This method has been shown to be applicable to both metalized and non-metalized propellants which do not exhibit typical Saint Robert's burning rate law behavior.
- The key steps of this method involve 1) determination of Arrhenius burning rate law parameters, 2) correlating burning surface temperature as a function of propellant initial temperature and pressure, and 3) using this surface temperature correlation with the Arrhenius parameters to describe the Novozhilov stability parameters of the propellants as a function of initial conditions.
- The addition of metal to the propellant formulation for replacing a portion of oxidizer content has two major effects on burning rate. One is to increase the burning rate by the enhanced thermal conductivity to the unburnt propellant. The other effect is the reduction of heat feedback to the unburnt propellant associated with 1) reduction of oxidizer-to-binder ratio, 2) higher energy required for metal liquefaction near the surface, and 3) combustion of metal particles in locations relatively far above the propellant burning surface. It is believed that these opposing heat-transfer effects counteract each other resulting in the relatively small difference between the burning rates of propellant M and N.
- The T_s correlation was used with the deduced Arrhenius burning rate expressions for both propellants to derive an analytical expression for temperature sensitivity as a function of pressure and initial temperature. Results obtained from the correlation were in agreement with those deduced directly from the burning rate data, except at very low pressures, where non-planar burning surface behavior limited the number of surface temperature data points available as input to the correlation.

Acknowledgments

This work was funded through Dr. Richard S. Miller of the Mechanics & Energy Conversion S&T Division of the Office of Naval Research under Grant No. N00014-96-1-0785. The authors wish to express their gratitude to Dr. Miller for his support and encouragement of this work. The propellants used in this study were supplied by Dr. Carol Campbell of Thiokol Corporation. The authors would also like to thank Dr. Y. C. Lu of PSU for his assistance in the initial phases of this work.

References

1. Salizzoni, R. M., Hsieh, W. H., and Kuo, K. K., "Temperature Sensitivity Measurements and Regression Behavior of a Family of Boron-Based Very High Burning Rate Propellants," Combustion of Boron-Based Solid Propellants and Solid Fuels, Begell House and CRC Press, pp. 438-452, 1993.
2. Kopicz, C., Watson, T. J., Kuo, K. K., and Thynell, S. T., "Combustion Behavior and Thermochemical Properties of JA2 Propellant," Challenges in Propellants and Combustion 100 Years after Nobel, Begell House, pp. 559-573, 1997.
3. Zenin, A., "Thermal Wave Profiling Measurements Using Fine-Wire Thermocouples," *An Invited Presentation at Penn State University,* August 10, 1994.
4. Kopicz, C. F., "Combustion Behavior and Thermochemical Properties of JA2 Propellant," *Masters Thesis in Mechanical Engineering,* May, 1995.
5. Kubota N. , "Survey of Rocket Propellants and Their Combustion Characteristics", Chapter 1 of *Fundamentals of Solid Propellant Combustion,* Edited K. K. Kuo, and M. Summerfield, *Progress in Astronautics and Aeronautics,* AIAA, Vol. 90, 1994, pp. 1-52.
6. Novozhilov B. V., "Theory of Nonsteady Burning and Combustion Stability of Solid Propellants by the Zeldovich-Novozhilov Method," Chapter 15 of *Nonsteady Burning and Combustion Stability of Solid Propellants,* Edited by L. De Luca, E. W. Price, and M. Summerfield, *Progress in Astronautics and Aeronautics,* AIAA Vol. 143, 1990, pp. 601-641.

STUDY OF THE FLAME STRUCTURE OF ADN/HTPB COMPOSITE PROPELLANTS USING MOLECULAR-BEAM MASS-SPECTROMETRY

Alexander A.Paletsky, Oleg P.Korobeinichev

Institute of Chemical Kinetics and Combustion Siberian Branch Russian Academy of Sciences 630090 Novosibirsk, Russia.

ABSTRACT

Flame structure of propellants based on HTPB (3%) and ADN (97%) at pressures of 0.5, 0.75, 1 and 6 atm was studied using such methods as probing molecular-beam mass-spectrometry (MBMS), of thin thermocouples and videorecording. Burning zone width at 1 atm is about 1.5 mm. Thermocouple research has shown temperature fluctuations of about ±400°C at 1 atm in flame zone within 1.5-4 mm from the burning surface. Along with temperature fluctuations, fluctuations in the intensities of mass peaks 17 (NH_3), 28 (CO, N_2), 30 (NO),46 (HNO_3, NO_2), 44 (CO_2, N_2O) take place as well. These observation is a consequence of the combustion process of the propellant under investigation spatial-time heterogenity and non-stationarity. Video-recording demonstrates the existence of several brightly illuminating torches of about 1 mm at the burning surface disappearing at one site and appearing at another. One torch life time is 0.2 sec. The nature of these torches is discussed. The combustion products composition was found away from the burning surface and in its immediate vicinity using MBMS. The composition of oxygen-nitrogen-hydrogen containing products of propellant combustion at 1 atm is close to this of ADN combustion at 6 atm. The main carbon- containing propellant combustion product at 1 atm is CO_2, CO was not found in the combustion products.

INTRODUCTION

ADN is a powerful ecologically safe oxidizer with extraordinary properties. It has found its application when developing composite solid rocket propellants [1]. A large number of papers is concerned with the combustion mechanism of pure ADN [2-5]. However there are very few works studying composite and sandwich systems based on ADN. In [6] the combustion of ADN mixtures with paraffin (90:10) was studied using spectroscopic technique. In [7] ADN combustion in paraffin mixtures was studied as well. In [8,9] the combustion of sandwiches based on ADN and a binder was studied in an effort to

understand the combustion mechanism of ADN based composite systems. Sandwiches are known to model composite systems combustion.

The study of diffusion flames structure of sandwiches ADN/energetic binder using the PLIF method [8] and measurement of ADN based sandwiches burning rate [9] testifies the absence or insignificant effect of diffusion flames on the processes controlling propellant burning rate within the pressure range up to ~15 atm. However the burning rates of sandwiches such as ADN/ADN:HTPB/ADN and ADN/PBAN/ADN rise nearly 1.5 fold with pressure rise from 15 to 70 atm [9], which is indicative of diffusion flames ADN-binder influence in this pressure range on sandwiches burning rate. This paper is aimed at studying combustion characteristics, chemical and thermal flame structure of composite propellants based on ADN and HTPB using molecular beam mass-spectrometry, thin thermocouples technique and video-recording.

EXPERIMENTAL TECHNIQUE

The methods applied to the study of ADN solid composite propellant (SCP) flame structure include probing mass-spectrometry (PMS) [10-14] and thermocouple measurements. The PMS method consists in the following: a burning strand of SCP moves with a speed exceeding the burning rate toward a probe so, that a probe is continuously sampling gaseous species from all the zones including those adjacent to the burning surface. In the case of thermocouple measurements a burning strand moves to touch a immovable thermocouple to the contact with the surface. The gaseous sample is transported to an ion source of a time-of-flight mass-spectrometer (TOFMS) as a molecular beam. When studying SCP flame structure an aluminum probe with a surface covered with Al_2O_3 was used. The probe represents a cone with a hole at its top (ø70, 100 microns at 1 atm, ø110 microns at p<1 atm), the cone inner angle is 40 °, the external one is 50-60°, walls thickness nearby the top is 100 microns. The MBMS system shows in Fig.1, which has been used to examine SCP flame structures. It includes: an apparatus for probing a flame containing a molecular beam sampling system, a TOFMS type MSCh-4 as a detector, a combustion chamber, a scanning system, a data acquisition system and an experiment controller based on CAMAC equipment and a computer. At the experiment start the ignition spiral (see Fig.1) is automatically or manualy removed from the combustion zone after ignition. A control system and a stepper motor are required to scan SCP flame. Video camera Panasonic NV-M3000EN has been used to visualize the combustion process. Temperature profiles have

been measured with WRe(5%)-WRe(20%) thermocouple 50 microns in diameter. The thermocouple was protected with an anticatalytic coating Ceramobond 569. The coating was 35 microns wide.

ADN (ammonium dinitramide) used in this work have been synthesized at Zelinsky Institute of Organic Chemistry Russian Academy of Sciences. The main impurity was AN (less than 3%). Melting started at 90-94^{0}C. HTPB (hudroxyl-terminated polubutadiene) was produced by the firm *elf atochem*/ATO, Philadelpia.

In all experiments non-cured propellant strands 8 mm in diameter and ~15 mm in length were used. Crystalline ADN powder with particles average dimension of ~ 40 microns was taken to prepare propellant. Samples prepared from HTPB (liquid) and ADN (powder) immediate mechanical mixing were also used in the work. At low fuel content (3%) HTPB dissolved in hexane (ADN is not dissolved in hexane) was used to prepare homogeneous propellant. Composite propellant was prepared by drying the mixture in a dry cell at room temperature under multiple mixing providing HTPB uniform distribution around ADN crystals.

Stoichiometric propellant formulation corresponds to ADN/HTPB components composition 7.67%:93.2% (by mass). Fuel amount in a mixture of formulation under consideration ranged from 20% to 3% (by mass).

RESULTS AND DISCUSSION

Table 1 represents some visual flame characteristics, burning rates and final flame temperature for the propellants under consideration. For the propellants of high fuel content (20 and 10%) at 1 atm black resinous formations at the burning surface shaped as craters and carboneous skeleton cropping out from the burning surface into gas phase were observed. The burning rate was increasing therewith from ~0.9 mm/sec to ~1.5 mm/sec with the fall in fuel content (from 20 to 10%). The temperature of HTPB decomposition start (~450 °C) is much more the temperature of ADN decomposition start (~130 °C). One can suggest that having a high fuel content in a formulation (20%) with a readily melting oxidizer (ADN melting point is ~90 °C) rubber can play a role of inert filler incapable to react completely at condition of experiment. With insignificant pressure rise from 1 to 3 atm for propellant 10/90 (HTPB/ADN) the burning rate increased more than two fold. Stoichiometric propellant composition at 6 atm provides the burning rate of ~7,3 mm/s and the temperature of final combustion products of ~3000°C. The length of

luminous zone above the strand was ~ 5 cm. For propellant 3/97 (HTPB/ADN) at 6 atm video-recording nearby the burning surface allowed the reveal of dark zone of ~0,3 mm, which was in agreement with the data found when studying ADN-based sandwiches [8]. The dark zone width increases up to 1.5 mm with pressure fall to 1 atm. Propellant 3/97 (HTPB/ADN) combustion was jetting in nature. Video-recording demonstrated the existence of several brightly luminous torches (jets) of about 0.5÷1 mm in diameter at the burning surface disappearing at one site and appearing at another. One torch (jet) life time is 0.2 s. The spatial heterogeneity and non-stationary nature of the propellant combustion process is in agreement with mass-spectrometric and temperature measurements. Thermocouple investigations have shown temperature fluctuations (Fig.2) of about ±400°C at 1 atm in flame zone within 1.5-4 mm from the burning surface. Along with the temperature fluctuations in the intensities of mass peaks 17 (NH_3^+), 28 (CO^+, N_2^+), 30 (NO^+), 46 (HNO_3^+, NO_2^+), 44 (CO_2^+, N_2O^+) take place as well (Fig.3). The data on mass peaks relative intensities of combustion products nearby the burning surface of ADN/HTPB 97/3 propellant and pure ADN at 1 atm are close by their values and represented in Table 2. One can suggest that mainly pure ADN combustion products are found in dark zone on propellant combustion, and when mixing them with HTPB decomposition products luminous jets are formed in gas phase. Mass peaks relative intensities in mass-spectra of samples withdrawn from an luminous zone for 3/97 propellant at pressures of 0.5; 0.75; 1 atm were represented in Table 3. Combustion nature did not change with pressure variation, it remained jetting. The rise of jets number formed at the burning surface, the increase of peak amu 28 (CO^+, N_2^+) intensity and the decrease of peak 44 amu (CO_2^+, N_2O^+) intensity are observed with the pressure fall. This bears a witness to the fall in combustion completeness and inefficient binder interaction with an oxidizer in condensed phase. One of the explanations to the existence of luminous jets with mean size of ~0,5- 1 mm at the burning surface exceeding the size of fuel powder particles (~0.04 mm) can be agglomeration of small ADN particles into large ones at the burning surface. Similar phenomenon has been found when observing ADN particles behavior in non-cured HTPB [9]. On heating melted ADN moved together, and on cooling it is crystallized in large particles of ~1 mm. Similar processes can take place on propellant combustion as well.

Element composition of the propellant HTPB/ADN (3/97) is as follows: $N_{3.129}H_{3.567}O_{3.131}C_{0.22}$. Additional calibration experiments by CO_2 were carried out

I_{22}/I_{44}=0.93 %. In the conducted experiments :$I_{22}(CO_2^{++})/I_{44}(CO_2^{+},N_2O^{+})$=0.3%. This value was close to the limits of TOFMS sensitivity. However the background spectrum is free from peak with m/e=22, which allows us to measure this peak in our experiments at the highest accuracy, that is 0.30±0.06%. Identification of CO_2 was conducted by mass m/e 22 (CO_2^{++}) and refined using peak m/e 12. The measured peaks 12 and 22 intensities were found to exclude CO^+ input into m/e 28. The calculations performed allowed the following gas phase composition of HTPB/ADN (3/97) composite propellant combustion products in mole fraction:

NH_3	H_2O	N_2	NO	N_2O	CO_2
0.01	0.35	0.13	0.26	0.18	0.06

The following (N/O) products ratio normalized per (N/O) ratio in the propellant was taken to test the fulfillment of material balance. The data obtained for all elements are cited below:

$(N/O)_{products}/(N/O)_{propellant}$ =0.98; $(H/O)_{products}/(H/O)_{propellant}$=0.72;

$(C/O)_{products}/(C/O)_{propellant}$ =0.94. This ratio is to approach to 1.

The combustion products composition of a composite propellant ADN/HTPB 97/3 at 1 atm approaches the products composition of pure ADN combustion at p=6 atm [4] by the content of nitrogen-contain components (Table 4.).

CONCLUSION

Composite propellants ADN/HTPB (with HTPB content by mass from 3% to 20%) at 0.5÷6 atm show non-homogeneous jet combustion . As distinct from AP-based propellants , ADN propellant flame is far from the burning surface (which is apparent from temperature, mass-spectrometric measurements and video-recording) and most possibly does not effect the propellant burning rate due to low temperature gradients. Individual luminous jets with the average time life of ~0,2 sec can emerge above the propellant surface within ~0.5÷2 mm. The generation of such torches (jets) the size of 0.5÷1 mm is attributable to 1) small melted ADN particles agglomeration into the large ones at the burning surface; 2) generation of a diffusion flame torch. At the same time small ADN particles decomposition at the burning surface is likely to be inhibited by the binder. This can bring an explanation to the fact that adding even small fuel amount (3% of HTPB) provides the fall (and not the rise as in the case of AP) of the fuel burning rate several times (2÷3) as compared with pure ADN burning rate within 1÷6 atm pressure range. At the same time the

final temperature of composite propellant combustion products (~2100 °C) far exceeds the temperature of pure ADN combustion (~350 °C) at 1 atm. The composition of nitrogen-containing final products of the same propellant is close to pure ADN combustion products composition at 6 atm.

ACKNOWLEDGMENT

This work was supported by the US Army Aviation and MICOM under Contract № DAAHO195CR141.

REFERENCES

1. Pak, Z., "Some ways to higher environmental safety of solid rockets propellant application", *AIAA Paper*, 1993, pp. 93-1755.
2. Fetherolf, B.L., Litzinger, T.A., "Physical and Chemical Processes Governing the CO_2 Laser-Induced Deflagration of Ammonium Dinitramide (ADN)". Proceeding of the 29th JANNAF Combustion Meeting, 1992, pp. 329- 338.
3. Fogelzang, A.E., Sinditskii, V.P., Egorshev, V.Y., Levshenkov, A.I., Serushkin, V.V., Kolesov, "Combustion behavoir and flame structure of ammonium dinitramide", Combustion and Detonation, 28-th Annual Conference of ICT, Karlsruhe, FRG, 1997, pp. 99-1-99-14.
4. Korobeinichev, O.P., Kuibida, L.V., Paletsky, A.A., Shmakov, A.G., "Study of Flame Structure, Kinetics and Mechanism of the Thermal Decomposition of Solid Propellants by Probing Mass-Spectrometry" in "Challenges in Propellant and Combustion. /100 years after Nobel/" (editor Kenneth K. Kuo), Begell House Inc., New York, Wallingford (U.K.), 1997, pp. 38-47.
5. Korobeinichev, O.P., Kuibida, L.V., Paletsky A.A., Shmakov, A.G., "Combustion Chemistry of Energetic Materials Studied by Probing Mass-Spectrometry", Decomposition, Combustion and Detonation of Energetic Materials, Materials Research Society.(Editors T.B.Brill et al); Vol. 418, 1996, pp. 245-255.
6. Weiser, V., Eisenreich, N., Bayer, A., Weindel, M., Menke, K., "Burning Behavior of ADN-Mixtures", Combustion and Detonation, 28-th Annual Conference of ICT, Karlsruhe, FRG, 1997, pp. 99-1-99-14.
7. Fogelzang, A.E., Sinditskii, V.P., Egorshev, V.Y., Levshenkov, A.I., Serushkin, V.V., Kolesov, "Combustion behavoir of ADN and Related Compaunds", MURI Workshop on ADN, Reno, Nevada, January 15, 1998.

8. Parr, T., Hanson-Parr, D.M., "Solid Propellant Diffusion Flame Structure", *Twenty-Sixth Symposium (International) on Combustion*, The Combustion Institute, Pittsburgh, PA, 1996.

9. Price, E.W., (private communication).

10. Korobeinichev, O.P., "Dynamic probe mass spectrometry of flames and the decomposition of condensed systems", *Combustion, Explosion and Shock Waves,* Vol. 23, 1988, pp. 565-576.

11. Korobeinichev, O.P., "A study of condensed system flame structure", *Pure & Appl. Chem.*, Vol. 65, 1993, pp. 269-276.

12. Korobeinichev, O.P., Kuibida, L.V., Paletsky, A.A., Chernov, A.A., "Study of Solid Propellant Flame Structure By Mass-Spectrometric Sampling", *Combustion Science and Technology.*, Vol. 113-114, 1996, pp. 557-571.

13. Litzinger, T.A., Lee, Y.J., Tang, C.J., "A Study of Solid Propellant Combustion Using a Triple Quadruple Mass Spectrometer with Microprobe Sampling", Proceedings Workshop on Application of Free-Jet, Molecular Beam, Mass Spectrometric Sampling, Estes Park, Colorado, October 11-14, 1994. pp. 128-135.

14. Fetherolf, B.L., Litzinger, T.A., "Physical and Chemical Processes Governing the CO_2 Laser-Induced Deflagration of Ammonium Dinitramide (ADN)". Proceeding of the 29th JANNAF Combustion Meeting, 1992, pp. 329- 338.

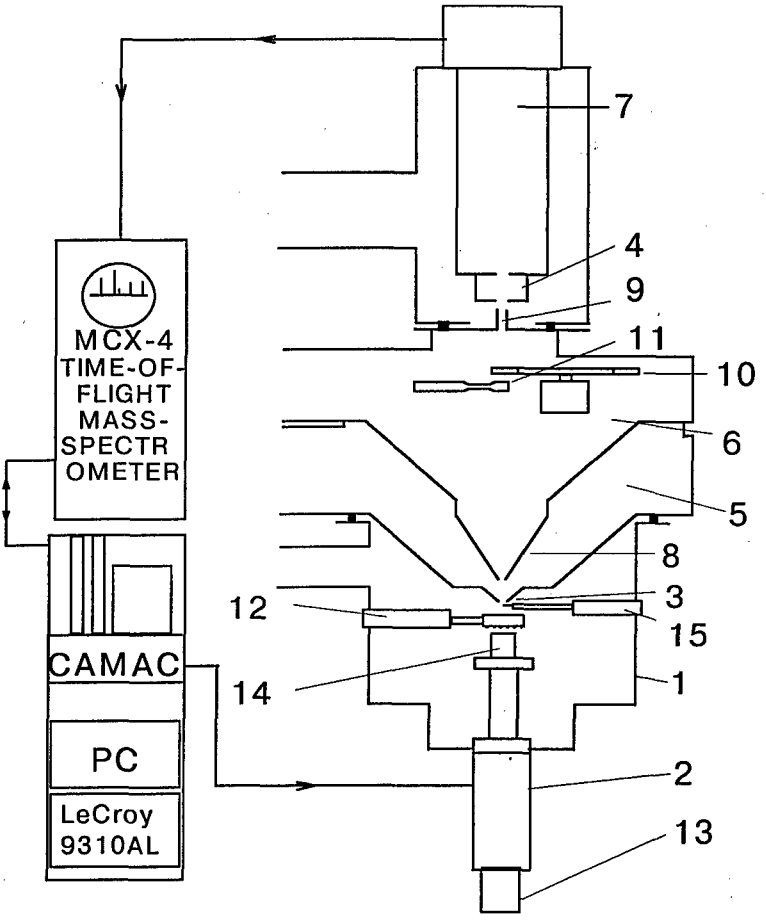

Fig.1 MBMS system for studying the flame structure of solid propellants with TOFMS.

1) combustion chamber; 2) scanning system; 3) probe; 4) ion source; 5) skimmer chamber; 6) collimator chamber; 7) drift tube; 8) stainless steel skimmer; 9) collimator; 10) slotted disk; 11) electromagnetic chopper; 12) ignition spiral; 13) stepper motor; 14) burning strand; 15) thermocouple.

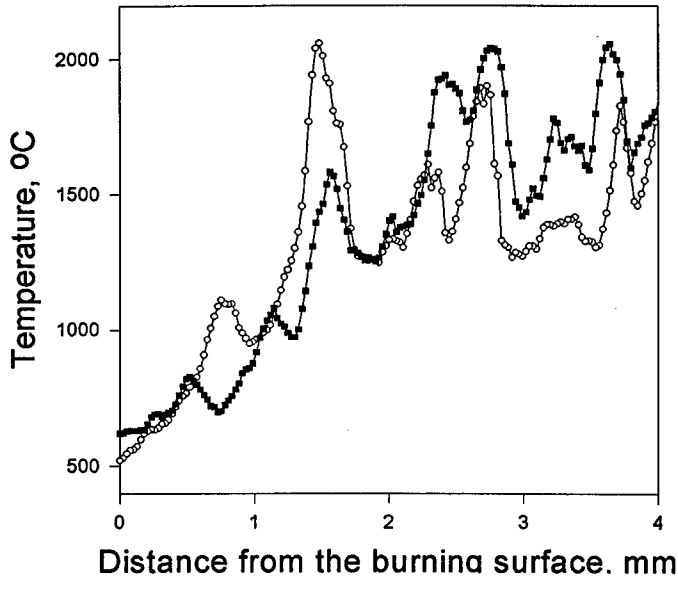

Fig.2. Temperature profiles in HTPB/ADN (3/97) flame at 1 atm.

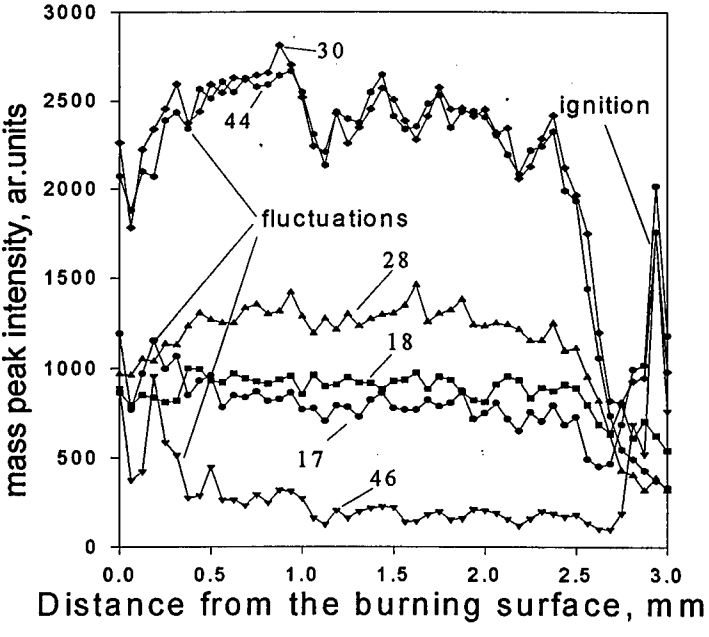

Fig.3. Mass peak intensity profiles in HTPB/ADN (3/97) flame at 1 atm.

Table 1.

Composition of propellants HTPB/ADN	Pressure, atm	Burning rate, mm/s	Final temperature, °C	Visual characteristics
20/80	1	~ 0.9	*	carbonaceous bubbles on the surface
10/90	1	~ 1.5	*	carbonaceous skeleton in some places of the strand
10/90	3	~ 3.4	*	
7/93	6	~ 7.3	above 3000	the height of luminous zone is about 5 cm
3/97	6	~ 7.5	*	dark zone is about 0.3 mm (by video)
3/97	1	~ 1.2	≈2100	luminous sprays with the characteristic dimensions less than 1 mm in diameter and characteristic lifetime ~0.2 s.

* Were not measured

Table 2.Relative mass peaks intensities in HTPB/ADN (3/97) composite propellant flame at the pressure 1 atm (dark zone near the burning surface).

amu / p,atm	17	18	30	44	46	28
ADN/HTPB 1	0.15	0.10	0.27	0.25	0.12	0.11
ADN 1	0.15	0.07	0.26	0.16	0.23	0.06

Table 3.Relative mass peaks intensities in HTPB/ADN (3%:97%) flame at the pressure 1, 0.75, 0.5 atm (luminous zone, ~8mm from the burning surface).

p, atm	amu	17 NH_3^+, H_2O^+	18 H_2O^+	30 NO^+,N_2O^+, HNO_3^+,NO_2^+	44 N_2O^+, CO_2^+	46 NO_2^+, HNO_3^+	28 N_2^+, CO^+, CO_2^+
1	$I_i/\Sigma I_i$	0.05	0.14	0.30	0.29	<0.01	0.21
0.75	$I_i/\Sigma I_i$	0.05	0.18	0.25	0.15	<0.01	0.35
0.5	$I_i/\Sigma I_i$	0.05	0.15	0.20	0.18	<0.01	0.41

ΣI_i - a sum of I_i

Table 4. Comparative table of the flame temperature and the combustion products final composition of pure ADN and ADN/HTPB composite propellant.

composition	p, atm	T,K	NH_3	H_2O	N_2	NO	N_2O	CO_2
ADN/HTPB (97/3)	1	2370	0.01	0.35	0.13	0.26	0.18	0.06
ADN	6	1420	0	0.45	0.11	0.25	0.20	-

Entwicklung von Hotspots in energetischen Materialien
Development of Hot Spots in Energetic Materials

G. Langer, N. Eisenreich
Fraunhofer-Institut für Chemische Technologie, ICT
D-76327 Pfinztal 1

Abstract

The transition between deflagration and detonation is not only of interest in understanding the initiation of a detonation but also of practical importance. Many problems in the field of vulnerability depend on DDT and there are also some applications in the field of new charge technologies . In the case of porous materials hot spots seem to be responsible for the transition of deflagration to detonation. Here hot spots are defined theoretically as a short, focused energy input which is caused by a shock wave or penetrating hot gas. Solving the heat flow equation some interesting cases can be discussed. An inert material can only spread out the heat pulses to a uniform distribution. A reactive material pyrolyses by formation of craters or ignites. Depending on the density of the hot spots and the intensity of the energy input the reacting front follows the generating wave immediately or delayed.

Kurzfassung

Der Übergangsbereich zwischen Deflagration und Detonation ist einerseits von grundlegendem Interesse, um die Initiierung der Detonation zu verstehen, andererseits aber auch von praktischer Bedeutung, da viele Fragen der Empfindlichkeit damit verknüpft sind und Anwendungen für neue Antriebe möglich scheinen. Bei porösen Materialien werden meist Hotspots für den Übergang Deflagration/Detonation verantwortlich gemacht.
Hotspots werden hier theoretisch durch sehr kurzen, punktförmigen Energieeintrag definiert, der als Ursache z.B. eine Stoßwelle oder in Poren eindringendes Heißgas hat. Durch numerische Lösung der Wärmeleitungsgleichung können einige interessante Fälle diskutiert werden. In einem inerten Feststoff kann sich der Energiepuls, der sukzessive das Material erfaßt, nur verteilen, bei einem reaktiven Feststoff kann er auch zur Pyrolyse, Kraterbildung oder Anzündung führen. Abhängig von der Hotspotdichte folgt die Reaktionsfront der erzeugenden Welle unmittelbar oder verzögert.

Einleitung

Die Umsetzungsgeschwindigkeit energetischer Stoffe variiert je nach Initiierung, Dichte und Formulierung erheblich. Bei der Verbrennung liegt sie im Bereich zwischen 0.01 cm/s und 100 cm/s, bei der sog. langsamen Detonation erhält man 1000 bis 2500 m/s und erreicht bei idealer Detonation Werte bis zu 10000 m/s. Der Übergangsbereich zwischen Deflagration und Detonation ist einerseits von grundlegendem Interesse, um die Initiierung der Detonation zu verstehen, andererseits aber auch von praktischer Bedeutung, da viele Fragen der Empfindlichkeit damit verknüpft sind /1,2/.
Für neue Antriebstechnologien wären ebenfalls Bereiche schneller Verbrennung und lansamer Detonation wünschenswert - wenn der massive Druckanstieg im System kontrollierbar ist. Solche stabilen Zustände können unter gewissen Randbedingungen reproduzierbar realisiert werden, wie Samirant für Ladungen mittleren Dichte zeigte /3,4/. Mögliche Anwendungsgebiete ergeben sich bei der Umsetzung von kompakten Ladungen oder bei Impulsgebern.
Es eröffnen sich damit eine Reihe von Problemstellungen, die geklärt müssen. Von der experimentellen Seite her stellen z.B. die Abhängigkeit von der Ladungsgeometrie und der Anzündung wichtige Punkte dar. Von theoretischer Seite interessieren die Mechanismen, die zu den hohen Verbrennungs- oder langsamen Detonationsgeschwindigkeiten führen und für einen stabilen Zustand sorgen /1,2,5-11/. Letzteres ist auch von sicherheitstechnischer Bedeutung.
In dieser Arbeit wird anhand eines einfachen thermischen Modells qualitativ untersucht, wie Hotspots, die sukzessive durch einen nicht weiter spezifizierten Mechanismus, z.B. durch eine Stoßwelle, entstehen, die chemische Umsetzung eines energetischen Materials initiieren.

Modellvorstellung

Als Reaktionsmedium dient ein hoch idealisiertes energetisches Material, von dem Konstanz aller physikalischen und chemischen Stoffgrößen angenommen wird. In diesem Medium soll eine Welle voranschreiten, die sukzessive Hotspots erzeugt, die in einer chemischen Reaktion für die Umsetzung des Materials sorgen /14/. Solch ein Mechanismus könnte z.B. eine Stoßwelle, die Poren adiabatisch aufheizt oder in poröse Strukturen eindringende heiße Gase sein. Der Wärmeeintrag ins Material wird als δ-Funktion oder Gaußfunktion angenommen, wobei im Prinzip jede beliebige Form Verwendung finden könnte. Die weitere Entwicklung dieser und der durch die Reaktion erzeugten Temperaturverteilung erfolgt durch die Wämeleitungsgleichung.

$Q(x,t)$:	Wärme von einer externen Quelle
q_i^* :	Wärme erzeugt durch den Umsatz des Spezies c_i
λ:	Wärmeleitfähigkeit
ρ:	Dichte
c:	spezifische Wärme
c_i:	Konzentration der Spezies

$$t = \frac{\lambda}{c\rho} t^*, \quad Q = Q^*/\lambda, \qquad q_i = q_i^*/\lambda$$

$$\frac{\partial T}{\partial t} - \Delta T = Q(\vec{x},t) + \sum_i q_i \frac{\partial c_i}{\partial t}$$

In einem inerten Medium ohne chemische Reaktion ergibt sich die Lösung von eingebrachten Wärmequellen sofort über die Greensfunktion (siehe z.B. /12/):

$$T(\vec{x},t) = \int_{0-\infty}^{t} \int^{\infty} \frac{Q(\vec{x},t) e^{-\frac{(\vec{x}-\vec{x}')^2}{4(t-t')}}}{(4\pi(t-t'))^{3/2}} \delta(\vec{x}')\delta(t')d\vec{x}'\,dt'$$

Wenn Wärmequellen $Q_{i,j,k}\delta(x-x_{i,j,k})\delta(t-t_{i,j,k})$ eingebracht werden, läßt sich die Lösung sofort hinschreiben (für einen einen einzelen Puls siehe /13,14/):

$$T_{hs}(\vec{x},t) = \sum_{i,j,k=1}^{I,J,K} \frac{Q_{i,j,k} e^{-\frac{(\vec{x}-\vec{x}_{i,j,k})^2}{4(t-t_{i,j,k})}}}{\left(4\pi(t-t_{i,j,k})\right)^{3/2}} \qquad t_{i,j,k} > t$$

Auch für Gaußfunktionen als Wärmequellen ergibt sich noch eine analytische Lösung, da wiederum Gaußfunktionen entstehen.
Bei Ausbreitung einer ebenen Stoßwelle mit der Geschwindigkeit v_S in x-Richtung ergeben sich die Zeiten sukzessiv mit einer eventuellen Reaktionszeit t_R:

$$t_{n,j,k} = t_{n-1,j,k} \frac{x_{n,j,k} - x_{n-1,j,k}}{v_S} + t_R$$

Im inerten Medium stellt sich nach längerer Zeit ein konstanter Temperaturwert ein, der bei äquidistanten Hotspots vergleichbar dem Abklingen einer gedämpften Welle erreicht wird.
Der Umsatzmechanismus ist im Prinzip beliebig zu wählen, wobei hier Reaktionen nach Arrhenius angesetzt werden:

$$\frac{\partial c_i}{\partial t} = -\sum Z_{i,j} e^{-\frac{E_{i,j}}{RT}} f(c_i, c_j)$$

Bei chemischer Reaktion mit Arrheniuskonstanten kann die Lösung nicht mehr analytisch gefunden werden, sodaß numerisch integriert werden muß. Im Gegensatz zu häufig verwendeten FEM-Verfahren wird hier eine Integration über die Greensfunktion versucht:
Es sei eine Anfangstemperaturverteilung $T_0(x,0)$ gegeben. Diese entwickelt sich in einem Zeitschritt Δt einerseits über das Faltungsintegral (siehe oben) weiter. Andererseits entsteht an jedem Ort eine Temperaturveränderung, entsprechend der chemischen Reaktion, die zum Faltungsintegral addiert wird, womit $T_1(x,t_1)$ entsteht. Dieses wird als momentan eingebracht angesehen und entwickelt sich ebenfalls zeitlich über das Faltungsintegral weiter. $T_n(x,t_n)$ erhält man durch n-fache Anwendung eines solchen Schrittes.

$$T_0(\vec{x},0) \Rightarrow Q_0(\vec{x})\delta(t)$$

$$T_1(\vec{x},t_1) = \int_{-\infty}^{\infty} \frac{e^{-\frac{(\vec{x}-\vec{x}')^2}{4\Delta t_1}}}{\sqrt{4\pi\Delta t_1}} \left(Q_0(\vec{x}') + \Delta t_1 \sum_i q_i \frac{\partial c_i\left(T_0\left(\vec{x}',0\right)\right)}{\partial t} \right) d\vec{x}'$$

$$T_{n-1}(\vec{x},0) + \sum Q_{i,j,k} \Rightarrow Q_{n-1}(\vec{x})\delta(t)$$

$$T_n(\vec{x},t_n) = \int_{-\infty}^{\infty} \frac{e^{-\frac{(\vec{x}-\vec{x}')^2}{4\Delta t_n}}}{\sqrt{4\pi\Delta t_n}} \left(Q_{n-1}(\vec{x}') + \Delta t_n \sum_i q_i \frac{\partial c_i\left(T_{n-1}\left(\vec{x}',t_{n-1}\right)\right)}{\partial t} \right) d\vec{x}'$$

Einige Beispiele, die mit den kinetischen Daten stabilisierter Nitrocellulose gerechnet wurden, sind in den Abbildungen 1 bis 4 dargestellt. Die berechneten Temperaturprofile sind zu verschiedenen Zeiten zweidimensional aufgetragen.

Im wesentlichen sind folgende Fälle zu unterscheiden:

- Die Hotspots überlagern sich, wobei eine gleichmäßige Temperaturerhöhung erfolgt und eine übergreifende Anzündung (bei geringem Energieeintrag keine Reaktion) stattfindet.
    - Die chemische Reaktionswelle folgt unmittelbar der erzeugenden Welle
    - Die chemische Reaktionswelle folgt verzögert der erzeugenden Welle

- Die Hotspots überlagern nur zum Teil, so daß ein stark verzögertes heterogenes Reaktionsmuster entsteht.

- Die zeitlich auseinanderlaufenden Hotspots überlappen nicht oder nur wenig, so bleibt die Temperaturerhöhung entweder ohne Konsequenzen oder führt nur zur lokalen Anzündung.

Entscheidend für den zu beobachtbaren Effekt ist die Dichte der Hotspots und die Intensität der eingebrachten Wärme.

Literatur

1. C. O. Leiber: A Microscopic Model of Detonation, Heimerzheim (1994)
2. C. O. Leiber: Critical Dimension Phenomena- Asymptotic Considerations, in Proceedings.Physics of Explosives, DEA - AF- 71 - F/G - 7304, April 27-29, 1994
3. M. Samirant, Proceedings 9th Int. Symposium on Detonation, Portland 1989, p. 259
4. M. Samirant, Proceedings 15th Int. Symposium on Ballistics, Jerusalem, May 21-24, 1995

5. Kondrikov B.N. Theory of Hydrodynamic Burning Instability of Granular Porous Energetic Materials, 28th Annual Int. Conf. of ICT, June 24 -27 1997
6. M. R. Baer, J. W. Nunziato: Int. J. Multiphase Flow 12, 6 (1986) 861
7. M. R. Baer, J. W. Nunziato: Proc. 9th (Int.) Det. Sysmp. (1989) 293
8. R. Saurel: Determination of Decomposition Rates in Non Ideal Explosives, in Proceedings Physics of Explosives, DEA - AF- 71 - F/G - 7304, Gramat, June 19-21 1996
9. R. H. Guirguis: Modeling Non-ideal Explosives, in Proceedings Physics of Explosives, DEA - AF- 71 - F/G - 7304, Gramat, June 19-21 1996
10. P. M. Howe, D. Benson, P. Conley: Microstructural Effects in Shock Initiation, in Proceedings Physics of Explosives, DEA - AF- 71 - F/G - 7304, Gramat, June 19-21 1996
11. B. Veyssiere, B.A. Khasainov: Non-Ideal Detonations: Different Structures and Multiple Regimes, Proc. Physics of Explosives, DEA - AF- 71 - F/G - 7304, Gramat, June 19-21 1996
12. H. S. Carslaw, J. C. Jaeger: Conduction of Heat in Solids, 2nd ed., Clarendon Press, Oxford 1973
13. N. Eisenreich, A. Pfeil: Pyrolysis Craters Produced by Laser Pulse Irradiation on Propellant Solids, Appl. Phys. 15 (1978) 47
14. N. Eisenreich, A. Pfeil, H. H. Weidlich: Laser Pyrolysis of High Energetic Materials, in Fast Reactions in Energetic Systems, Proceedings NATO Advanced Study Institute, Preveza, Greece, (1980) 523
15. N. Eisenreich, Successively Initiated Arrays of Hot Spots in a Reactive Medium, Proceedings Physics of Explosives, DEA - AF- 71 - F/G - 7304, Berchtesgaden, September 29 - October 1,1997

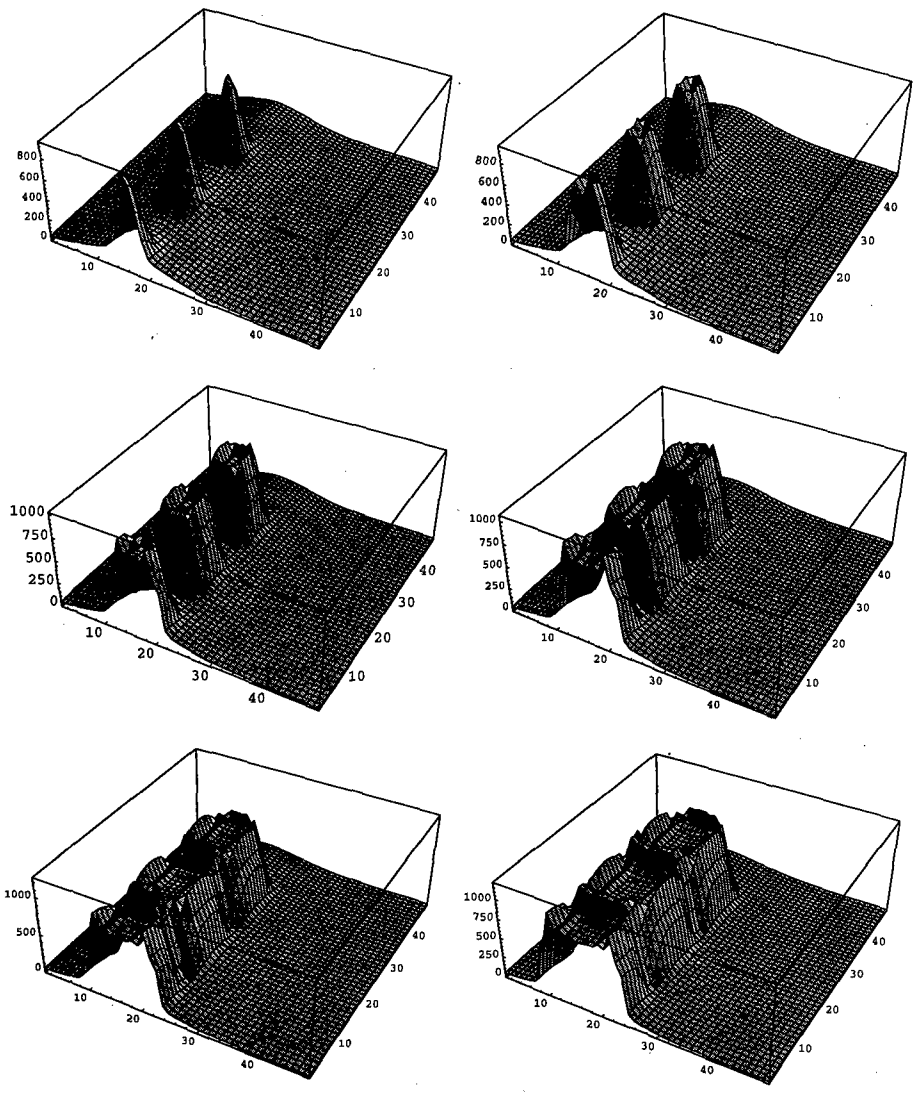

Abb. 1: Lineare Arrays die bei nahezu gleichen Abständen in einem reaktiven Medium (3-dimensional) von einer ebenen Welle erzeugt werden. Aufgetragen ist 2-dimensional die Temperaturverteilung zu verschiedenen Zeiten.

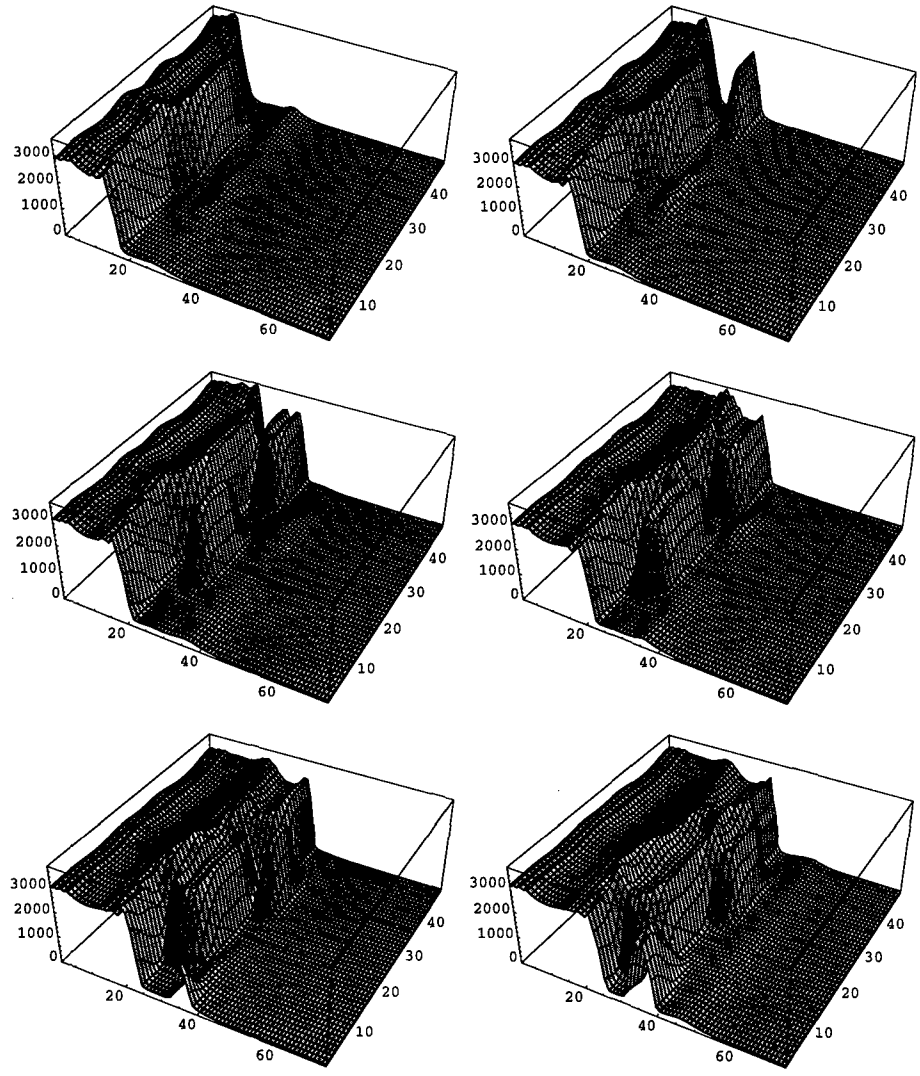

Abb. 2: Die Reaktionsfront folgt unmittelbar der erzeugenden Welle. Aufgetragen ist 2-dimensional die Temperaturverteilung zu verschiedenen Zeiten.

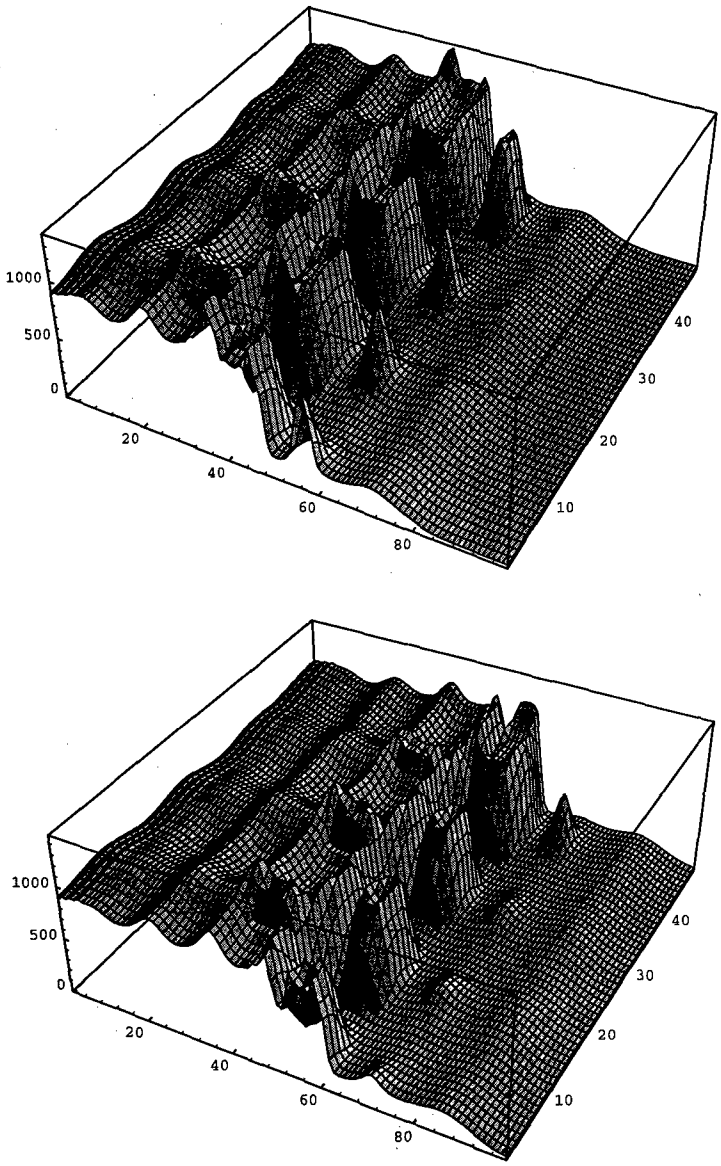

Abb. 3: Verzögerte Reaktion der Hotspots auf die generierende Welle.

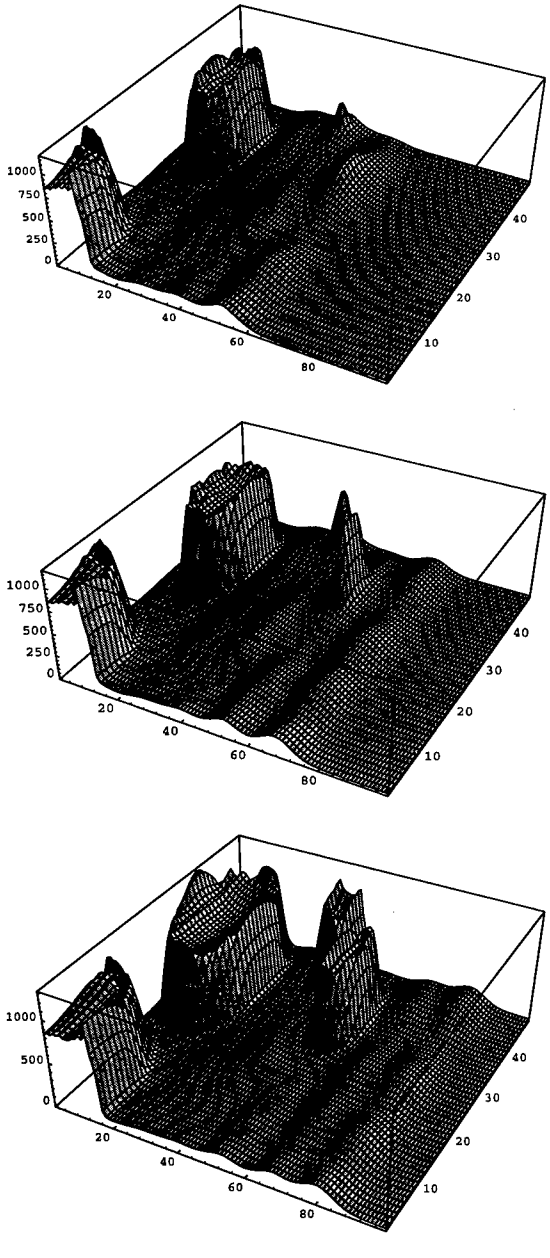

Abb. 4: Reaktion in isolierten Zentren.nach Durchlauf der Welle

TIME HISTORY OF RADIATIVE HEATFLUX FROM POOL FIRE

V. Weiser, M. Weindel, N. Eisenreich, W. Eckl

Fraunhofer-Institut Chemische Technologie (ICT)
P. O. Box 1240; D-76318 Pfinztal
E-Mail: vw@ict.fhg.de

Abstract

Damages by hazardous fires are caused by oxidation and pyrolysis, contamination from combustion products and convective and radiative heat flux. An effective risk assessment needs quantitative data of these effects on different flammable materials to make an effective and safe design of buildings and industrial structures. To reach such data many experiments with pool fires have been done in a moderate scale. To transfer the results on real fires the time history and non-homogenous structure of the flame has taken into account. This investigations need robust, non-intrusive and fast scanning measuring techniques like pyrometry, spectroscopy and cinematography. They have to be applied together to get an comprehensive image of the heat transfer dependent on time and location. Various methods, experimental set-ups and characteristic results are described like a fast scanning 2-colour-pyrometer to measure simultaneously the heat flux and flame temperature with a time resolution up to 10 kHz. Concentrations of intermediate flame radicals and combustion products in short time flame structures are sampled (with less than 10 ms) using UV/Vis- and IR-spectrometers. The distribution of heat radiation was determined using a simple video system and a thermo camera equipped with a special data analysing software. On the results non-stationary radiation model was derived to estimate heat flux on an endangered target.

Introduction

The damaging effect of hazardous fires comprises the chemical conversion of materials, the emission and deposition of pyrolysis and combustion residues and the radiant heat. The latter is the main hazardous source of energy transfer to the near objects resulting. The calculation of the heat q_T radiated from a fire to a target at distance y_T demands a realistic model of the contours of the flame and the local and temporal distribution of the zones emitting the radiation.

Although recently the radiation source pool fire was simulated by sophisticated numerical calculations [1,2,4,6], practical application use two simplified models [3,7].

The model using point sources assumes the radiation to be emitted by central point and as the radiation at a distance y_T to be inversely proportional to y_T^2.

$$q_T(y_T) = \frac{Q_R}{4\pi y_T^2}$$ Eq. 1

$Q_R = \chi_R \, m'' \, H_C$ consists of the burn rate m'', the heat of combustion H_C and an empirical factor χ_R, which accounts for the fraction of energy radiated.

The surface emission model assumes constant emission E from the surface A_{SEP} of a regular body e.g. a cylinder or a sphere [8]. The radiant heat incident on a target q_T is obtained by the viewing factor φ_{12} which depends on the distance and the atmospheric transmission τ.

$$q_T(y_T) = \varphi_{12}(y_T)\tau(y_T)E$$ Eq. 2

φ_{12} is given by the solid angles of source and target [14, 15]. The atmospheric absorption is normally neglected ($\tau \approx 1$).

Both models assume a constant shape of the flame body which emits averaged radiation with respect to time and position. However, time-resolved optical investigations show that this approach oversimplifies the situation [13, 16, 17]. Rasbash [17] emphasises that the flame of pool fires can periodically change its visual height by a factor of 2 within short time intervals of less than a second.

The emitted radiation fluctuates even by an order of magnitude. It depends strongly on the temperature distribution and the chemical composition of the flame [18]. In principle, two types appear:

- continuous radiation from soot particles
- molecular bands from hot gases

The continuous emission the radiance L_λ is described by blackbody radiation

$$L_{\lambda B}(\lambda,T) = \frac{c_1}{\lambda^5\left(\exp\left(\frac{c_2}{\lambda T}\right)-1\right)}\frac{1}{\Omega_0}$$ Eq. 3

or more correctly modified by an emissivity ε depending on wavelength λ and temperature T:

$$L_\lambda(\lambda,T) = \varepsilon(\lambda,T)\cdot L_{\lambda B}(\lambda,T)$$ Eq. 4

In the case that a grey body radiation is assumed the emissivity does not depend on wavelength and temperature.

$$L_\lambda(\lambda,T) = \varepsilon \cdot L_{\lambda B}(\lambda,T)$$ Eq. 5

It was shown that sooty flame can be described by a grey body radiator in [11]. The integration of $L_{\lambda B}$ results in the Stefan-Boltzmann law of radiation which relates the total radiance to the 4th power of temperature.

$$E = \varepsilon\sigma T^4$$ Eq. 6

ε depends on the soot concentration and on the volumes of the emitting body. It is very low for lean and small flames ($\cong 0.001$) and close to 1 for large and sooty fires.

In the following pool fires are investigated at a small scale where strong fluctuations of the flame body and the radiation are observed. The variation of the radiating flame contours and volumes were measured and the intensity and dependence on the wavelength of the radiation analysed to obtain flame temperature distributions. The results lead to a dynamic model of the flame body, its emission of radiation and the related effect on irradiated objects.

Experimental

The experiments were performed in a cylindrical steel pool (113 mm diameter, 40 mm height) studying various fuels (iso-octane, 2-propanol, methanol, nitromethane) using an automatic fuel supply to substitute consumed fuel.

A video and a thermal imaging camera observed the contours of the flames. The video camera had a time resolution of 25 frames/s the thermal imaging camera 30 /s. A band filter allowed to select the spectral region of the CO_2-band from 4.1 to 4.4 µm. The video data were transferred to a PC by a frame grabber and evaluated by a computer code AVICOR which was developed to process the images of the fluctuating flames. AVICOR allows a statistical evaluation of the video images with respect to intensity distributions of single frames or frame sequences. The statistical evaluation comprises sums of lines and columns, variances and histograms.

The radiation of the pool fires was recorded by fast scanning spectrometers in the ultraviolet, visible and infrared spectral range:

- IDARRS: UV/Vis (280 to 900 nm), grating spectrometer with1024 intensified diodes, recording up to 100 spectra/s
- FiRa: IR (2400 nm to 15000 nm) InSn/HgCdTe-detector, fast scanning filter wheel with continuous wavelength variation up to 130 spectra/s

The spectra were quantitatively calibrated with respect to intensity by the use of a black body radiator.

Results

Flame Geometry

The flames of pool fires of diameters higher than 5 cm show complicated contours strongly varying with time and non-homogeneous distributions of radiance. This flickering is not irregular but repeats periodically similar structures. Fig. 1 shows a sequence of video frames of a iso-octane pool flame. The flame height varies quasi-periodically in time intervals of 0.2 s. A flame ball produced at the flame base moves upwards. It disappears at a height of about 5 to 10 diameters of the flame base after the subsequent flame ball was produced at the base. The frequency of the period depends strongly on the pool diameter and to some extend on the temperature of the pool. This behaviour is similar for all fuels investigated and agrees with that of other self-stabilising diffusion flames [7, 12].

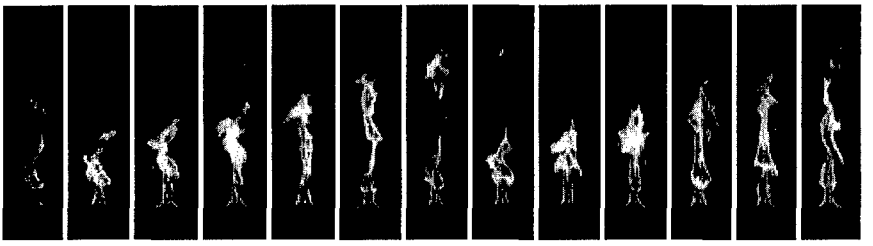

Fig 1: Transient structures of an iso-octane pool fire with a diameter of 113 mm (time intervals of frames 0.04 s, 60 s after ignition)

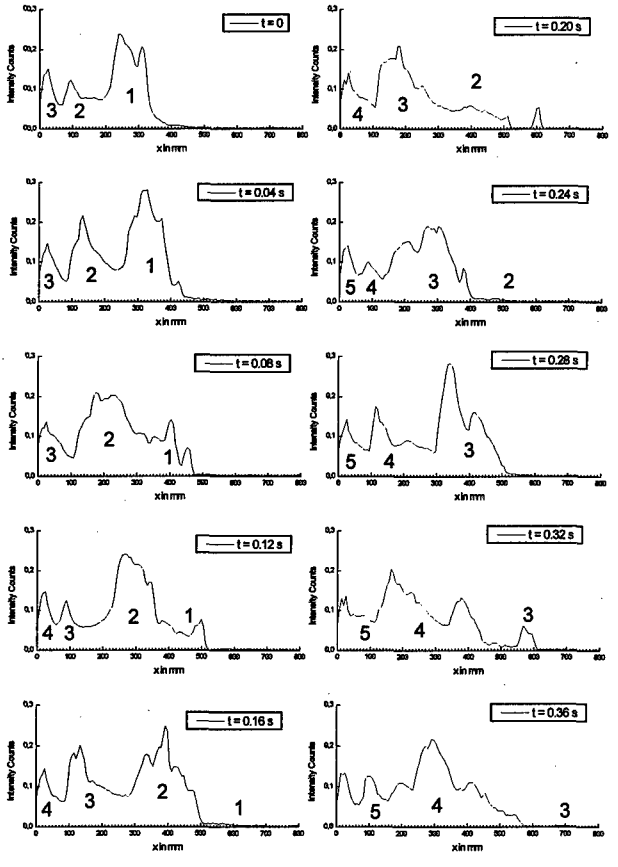

Fig. 2 Distribution of the accumulated brightness of the flame in axial direction, the numbers tag flame balls to be recognised at different frames (evaluation of a sequence of video frames)

The rising flame ball is not only enlarged with respect to the flame base but shows higher brightness which is indicated by the time evolution of it over the flame height depicted in fig. 2. The data were obtained by an evaluation of the video frames accumulating intensities transversal to the flame axis. Centres are observed which emit maxima of radiation. A stable centre is located at the flame base at a height of half of the pool diameter d. It seems to emit luminous maxima which ascend with increasing velocity and disappear later. The luminous centres are identical to the luminous flame balls as indicated by a comparison of the video evaluation with the video frames itself. Fig. 3 shows the position-time curves of several flame maxima whereas the time of formation of each is set to 0. The brightness of the flame in the visual spectral range is similar to the brightness in the IR which is illustrated in fig.4 by comparing the video frames with thermo camera frames. The agreement is good for the sooty flames. However, the thermo camera observes also similar structures for non-sooty flames compared to the structures of sooty flames (e.g. with methanol as fuel). The reason is that water and carbon dioxide mainly emit the radiation of non-sooty flames with strong bands only in the IR.

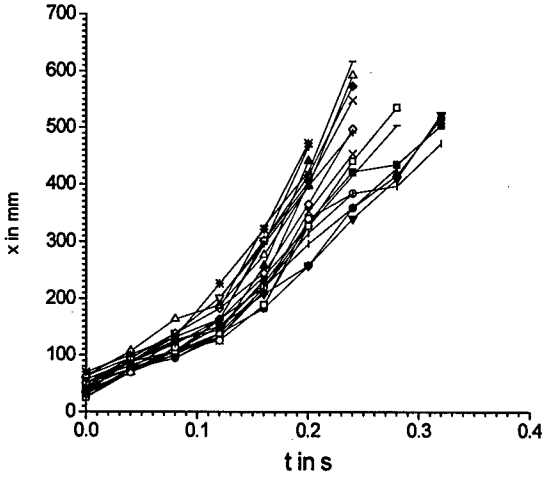

Fig. 3: Typical position-time curves of flame balls after their formation

Time Resolved Spectroscopy of the Pool Flame

Focusing a fixed spot above the pool onto the entrance slit of a spectrometer it records successively the transient emission from passing flame balls. As expected by the analysis of the video frames the flame balls also show strong emission when spectrally resolved. Fig 5 shows a series of spectra in the visible spectral range measured at a height of 220 m above the pool surface. The spectra vary periodically with time and are dominated by a continuum obviously emitted by the soot. Continuous spectra are especially emitted by the flames of iso-octane and 2-propanol.

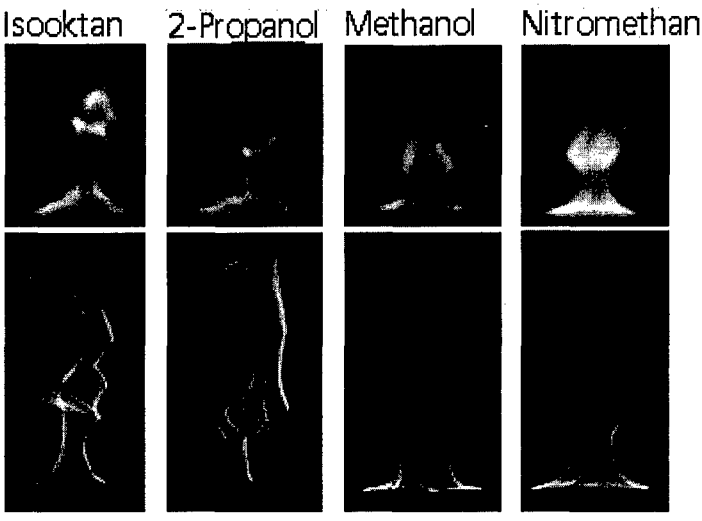

Fig. 4: Comparison of frames from video (bottom) and thermo camera (top)

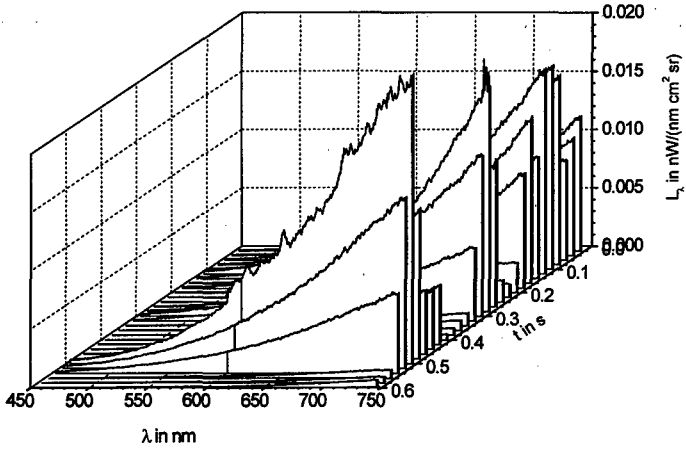

Fig. 5: Sequence of spectra in the visible range measured 220 mm above a iso-octane pool surface

These continuous spectra were analysed by a least squares fit on the formula Eq. 5 of the grey body radiation. Temperature T of the flame and emissivity ε were used as fit parameters. Fig 6 shows the analysis of an iso-octane spectrum measured 220 mm above the pool surface. The solid line represents the calculated spectrum obtained from the fit. The close agreement of experimental and calculated curve demonstrate that the emission

of the iso-octane pool fires above the flame base can be assigned to the emission of a grey body. The time characteristics of the temperature, the emissivity and the radiance obtained for the same flame is plotted in fig. 7. The emissivity varies between 0.05 and 0.15 and is highest at the flame balls which are given by the maxima of brightness. In the zone of the flame base (below 50 mm) it lies significantly lower between 0.02 and 0.1. High values of ε up to 0.8 are found at the top of the flame where smoke formation is observed. The temperature oscillates between 1500 K and 1700 K. High temperatures coincide with low values of ε. The temperature of the flame balls in fig. 7 is characteristic also for the other flame zones above the flame base.

The fuel 2-propanol gives higher temperatures which lie between 1600 and 1800 K and the emissivity between 0.03 and 0.1. The intensity of the flame emission of methanol and nitromethane is one order of magnitude lower than that of iso-octane. Therefore a time resolution as used in the case of iso-octane is more difficult. The emission in the visible range is composed of bands of the radicals OH, NH, CN and CH. These radical bands can be in general used to obtain temperatures but the low intensities and the insufficient time resolution do not allow a reliable evaluation. In addition, a broad band is observed in the blue wavelength range which can be assigned to chemoluminescence of the reaction of CO to CO_2. This band cannot be used for a temperature evaluation. A grey body radiation was very low or not found.

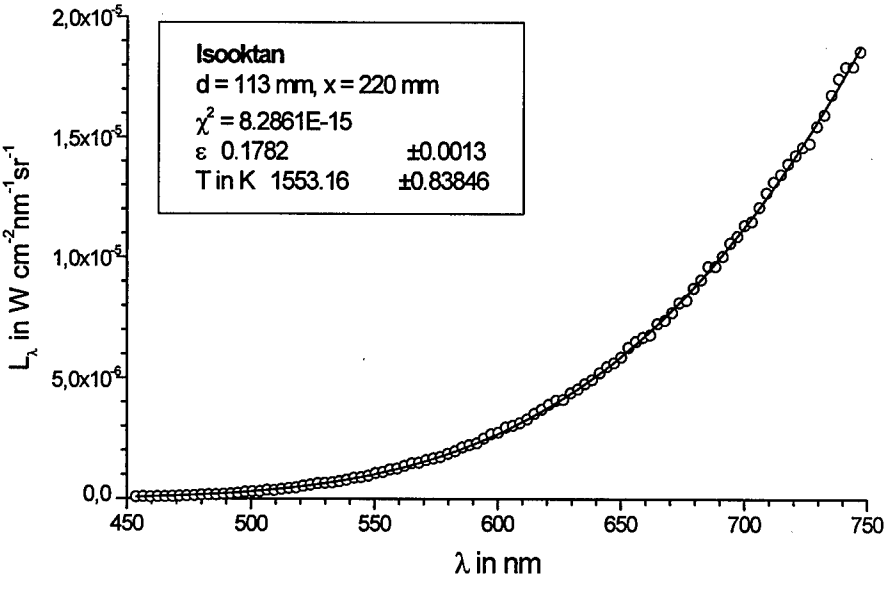

Fig. 6: Continuous spectrum of an isooctane pool flame and its least squares fit by grey body radiation

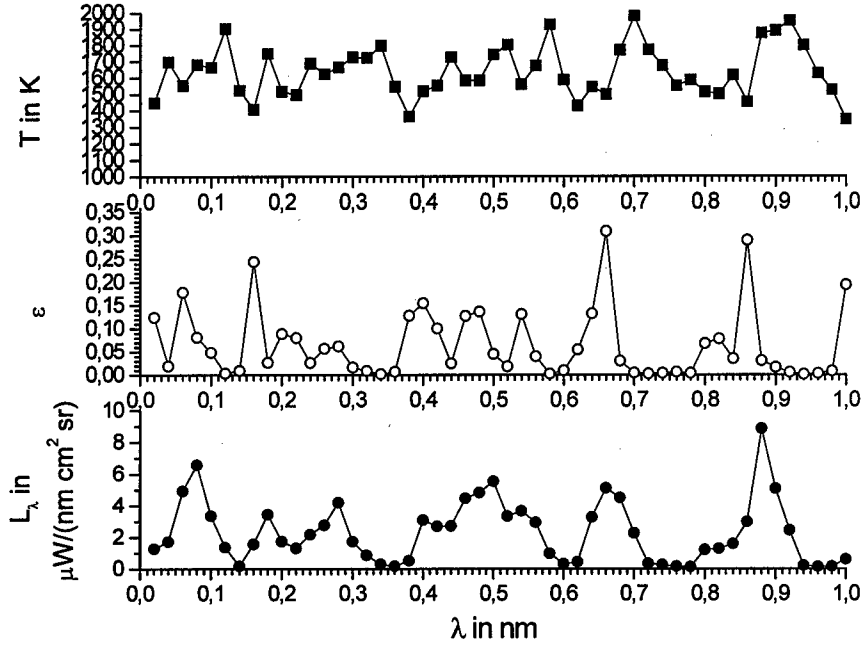

Fig. 7: Plot of the time characteristics of an iso-octane pool flame (220 mm above pool surface) temperature, emissivity and radiance.

Similar fluctuations can be found regarding series of IR-spectra like shown in Fig. 8. A semi-quantitative data analysis was applied by using band modelling. A computer code calculates IR-spectra (1 - 10 µm) of non-homogeneous gas mixtures of H_2O (bands near 1.3, 1.8, 2.7 and 6.2 µm), CO_2 (near 2.7 and 4.3 µm), CO, NO and HCl and can take into account emission of soot particles. It is based on a single line group model using also tabulated data of H_2O and CO_2 [18]. Because there are many unknown parameters affecting the emission spectrum of a non-homogeneous gas mixture, only a simplified model can be employed. Therefore we have assumed that there is just one emitting layer of undefined thickness, constant temperature, constant concentration of the various gases and soot particles in thermal equilibrium. These assumptions lead to a reduced number of parameters, which can be determined by fitting calculated spectra to experimental data. Fig. 9 gives a characteristic example and fig. 10 shows also exemplary the time characteristics of parameters of an iso-octane pool flame measured 100 mm above the pool surface. It is obvious that the variations of luminous intensity correlate to the radiation of soot and combustion products like water and CO_2. Temperature values of IR-radiation are in the same magnitude of size like the fits to the visible spectral range.

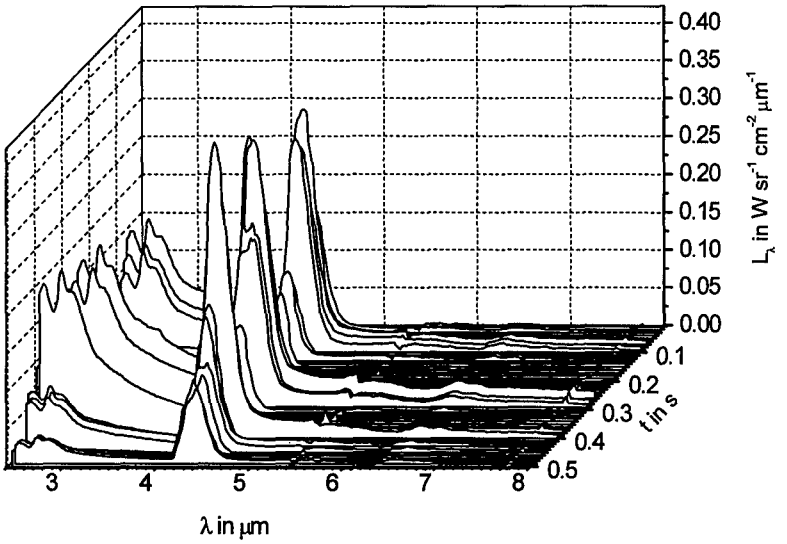

Fig. 8: Sequence of spectra in the IR range measured 180 mm above a iso-octane pool surface

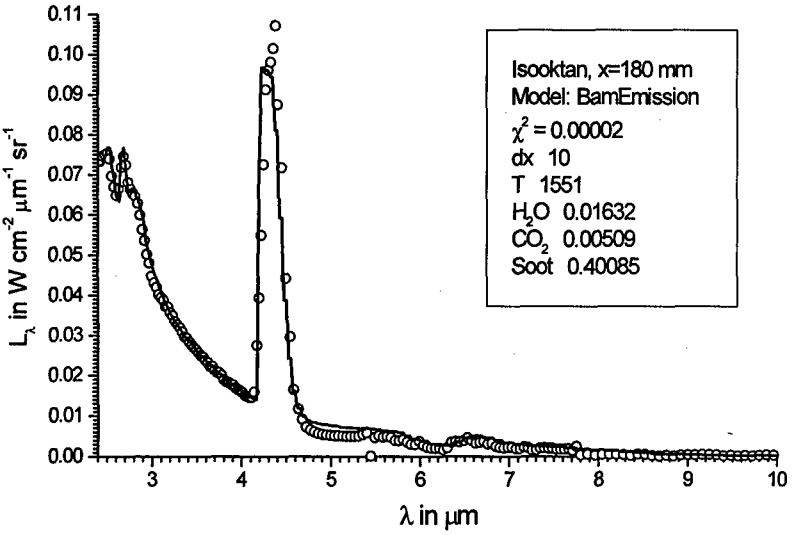

Fig. 9: Least squares fit of a IR spectrum of an iso-octane pool flame modelling the bands of H_2O, CO_2 and of a grey body emitter

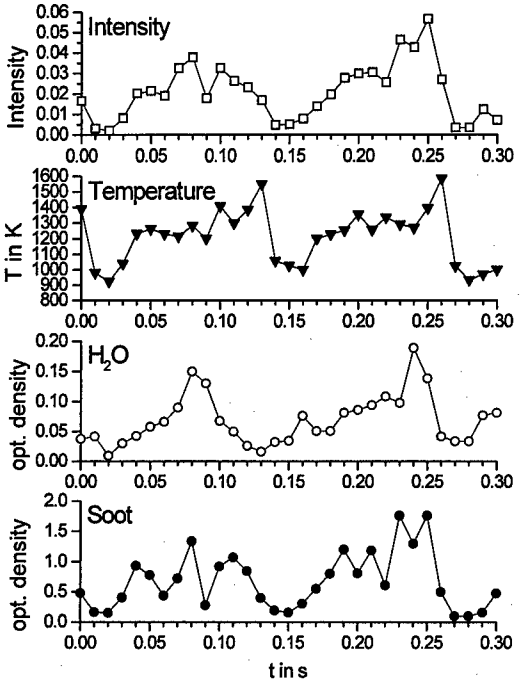

Fig. 10: Time characteristics of parameters of an iso-octane pool flame measured 100 mm above the pool surface

Discussion

The radiation from the investigated pool fires is dominated by the emission of flame balls which are formed quasi-periodically above the flame base and ascend with acceleration. They are also the dominant part of the transient flame structure which emits the main part of energy. Therefore a simplified model of radiation of pool fires which could act on flammable surrounding objects can be reduced to the consideration of the radiation from ascending flame balls. The flame balls are approximated by spheres of diameters d_{FB}. The flame ball is formed a pool diameter above the pool surface, moves upwards accelerated by buoyancy forces (see curves fig. 3) and burns out more than 5 pool diameters above the pool surface. The radiation incident on a neighboured object is described by eq. 5. The viewing factor is calculated according to Seeger [8] It reduces to an emitting disc with a diameter d_{FB} perpendicular to the straight line connecting flame ball and the centre of the object.

The radiation flux incident on a target area at a distance y_T depend on the geometry of the flame shape according to the flame model assumed. The total energy Q_R emitted by the surface A_{SEP} must be the same for all flame models compared. In the case of a grey body radiator:

$Q_R = E\ A_{SEP} = \varepsilon\ \sigma\ T^4\ A_{SEP}$ Eq. 7

If constant homogeneous flame temperatures T are assumed it is sufficient to adjust emissivity ε and surface to fulfil $\varepsilon\ A_{SEP}$ = const.

Fig. 11 compares the radiation incident on a target area emitted from the static point source model, cylinder model of Seeger and the model of an ascending spherical flame ball. The data used were taken from the results of a iso-octane pool fire of a pool diameter of 113 mm.

The flame ball diameter d_{FB} is set equal to the pool diameter as plausible from the video frames of fig. 1. From fig. 7 results an emissivity ε = 0.1. The temperature was assumed to be T = 1600 K (see fig. 7 and 10). The total emitted power was obtained then by $Q_R = 0.1 \times \sigma \times 1600^4\ K^4 \times \pi \times 0.113^2\ m^2$ = 1500 W for all models. The viewing factors are derived according to Seeger [8].

Fig. 11 shows the irradiance at a distance y_T on a area parallel to the flame axis at a height x=0 (height equal to the pool surface). The flame ball model predicts that more than twice of the power can fall onto objects when compared with the cylinder model, especially in the case the flame ball is close to flame base. If the flame ball is at higher positions the difference is lower and the cylinder model estimates quite well the irradiation on the average. Depending on the position of the flame ball the cylinder model predicts to low irradiation onto an endangered object.

The point source model overestimates the irradiation to objects close the pool fire. For distance higher than 4 d it agrees well with the maximum irradiation by the flame ball model. It is useful for to estimate the worst case.

If safety distances have to be estimated it should be carefully proved what model to use. In case where special materials cannot be exposed to radiation exceeding well defined limits the static models of surface radiators should be avoided.

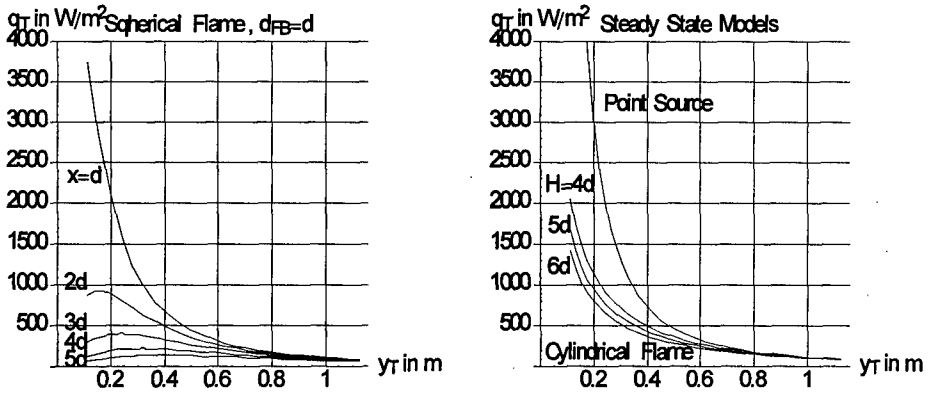

Fig. 11: Irradiation onto objects at distances y_T by the dynamical flame ball model (left side) and the static point source and cylincer flame model (parameters are derived from a isooctane pool flame of a diameter 113 mm)

References

[1] Adiga, K.C.; Ramaker, D.E.; Tatem, P.A.; Williams, F.W.; Modeling pool-like gas flames of propane; Fire Safty Journal, 14(1989)241-250

[2] Annarumma, M. O.; Most, J. M.; Joulain, P.; On the numerical modeling of buoyancy-dominated turbulent vertical diffusion flames; Combust. Flame (1991), 85(3-4), 403-15

[3] Bagster, D. F.; Pitblado, R. M.; Thermal hazards in the process industry; Chem. Eng. Prog., 85(7), 69-75 (1989)

[4] Baum, H.R.; McGrattan, K.B.; Rehm, R.G.; Simulation of smoke plumes from large pool fires; 25th Symp. (Int.) Comb. 1994/pp. 1463-1469

[5] Burgess, D.; Hertzberg, M.; Radiation from pool flames; Heat Transfer in Flames, John Wilkey, New York, pp. 413-430, 1973

[6] Di Blasi, C.; Crescitelli, S.; Russo, G.; Model of pulsating flame spread across liquid fuels; 23rd Symp. (Int.) on Comb., The Combustion Inst., 1990/pp. 1669-1675

[7] Schönbucher, Axel; Brötz, Walter; Balluff, Christoph; Goeck, Dietmar; Schieß, Norbert; Erforschung von Schadenfeuern flüssiger Kohlenwasserstoffe als Beitrag zur Sicherheit von Chemieanlagen; Chem.-Ing.-Tech., 57(10), 823-34 (1985)

[8] Seeger, P.G.;Wärmeübertragung durch Strahlung und Konvektion bei Bränden in Flüssiggaslagern; VFDB 1/87 S.7-13

[9] Weiser, V.; Franchin, I.; Eisenreich, N.; Temperature Profiles and Burning Rates of Pool Fires; 27th International Annual Conference of ICT, 1996, Karlsruhe, pp. 82-(1-10);

[10] Weiser, V.; Eckl, W.; Eisenreich, N.; Hoffmann, A.; Weindel, M.; Spectral Characterisation of the Radiative Heat Flux from Dynamic Flame Structures in Pool Fires; The Ninth International Symposium on Transport Phenomena in Thermal-Fluids Engineering (ISTP-9), Singapore, June 25-28, 1996, pp. 274-279

[11] Weiser, V.; Eisenreich, N.; Heat Feedback in Model-Scaled Pool Fires; 8th International Symposium on Transport Phenomena in Combustion, 1995, San Francisco; p. 8-C-2

[12] Brötz, W.; Schönbucher, A.; Wärme- und Stofftransport in Tankflammen; Chem.-Ing.-Tech. 50 (1978) Nr. 8, S. 573-585

[13] Markstein, G. H.; Radiative properties of plastics fires; Symp. (Int.) Combust., [Proc.] (1979), Volume Date 1978, 17, 1053-62

[14] Siegel, R.; Howell, J. R.; Lohrengel, J.; Wärmeübertragung durch Strahlung (Teil 2); Springer Verlag, Berlin, 1991

[15] Verein Deutscher Ingenieure - Berechnungsblätter für den Wärmeübergang (VDI-Wärmeatlas); 6. edition 1991

[16] Rasbash, D. J.; Rogowski, Z. W.; Stark, G. W. V.; Properties of fires of liquids; Fuel, 35, 94-106 (1955)

[17] Weiser, V.; Eisenreich, N.; Krause, H.; Experimentelle Untersuchungen von Flammengeometrie, Temperaturverteilung und Konzentrationsfeldern in Modell-Tankflammen verdampfender, flüssiger Brennstoffe; 22nd International Annual Conference of ICT 1991, S. 101-(1-14)

[18] Ludwig, C.B.; Malkmus, W.; Reardon, J.E.; Thomson, J.A.L.; Handbook of Infrared Radiation from Combustion Gases, NASA SP-30980 (1973)

NORMAL BURNING RATE OF POLYMERS

Prof. Nikolai N. Bakhman

Instiute of Chemical Physics, Russian Academy of Sciences
Kosygin str 4, 117977 Moscow GSP-1, Russia
e-mail: posv @ center.chph/ras.ru
FAX: (007 095) 9382156; (007 095) 9397417

ABSTRACT

The experimental data are presented relevant to normal burning rate (NBR) of PMMA in the course of flame spreading over the surface of specimens for three following cases: 1) horizontal slabs burning in still air; 2) vertical rods burning downward in still air; 3) PMMA slabs contacting with $KClO_4$ slabs and burning in N_2 at $p \leqslant 3$ MPa. The data just mentioned are compared with those in the available literature concerning NBR of PMMA spherical particles burning in still air, NBR during internal burning of PMMA blocks with coaxial canal in a stream of gaseous O_2, and NBR of PMMA rods burning on the top end in air flow.

Normal burning rate, u , i.e. normal regression rate of polymer specimens surface is an important characteristic of polymer flammability. Indeed, the higher is u, the greater is heat evolution rate, $J/cm^2 s$. NBR was investigated under two different conditions: 1) in the course of flame spreading over specimen surface (an unsteady-state process in laboratory system of coordinates) 2) on the entirely burning surface (a quasi-stationary process).

1. NBR in the Course of Flame Spreading.

We have measured profiles of cavities formed in PMMA slabs (case 1) or rods (case 2) burning in still air at atmospheric conditions or PMMA slabs contacting with $KClO_4$ or NH_4ClO_4 slabs and burning in N_2 atmosphere at pressure $p \leqslant 3$ MPa (case 3). In the cases 1 and 2 the specimens were extinguished with a jet of N_2 and in the case 3 a depressurization extinguishment was used. The profiles of cavities were

measured with a microscope. The micrometric screws shifted the extinguished specimens along three rectangular axes. NBR was calculated as $u = w \sin \varphi$ where w is flame spread velocity over polymer surface and φ is the angle between the tangent to cavity profile and flame spread direction. In the cases 1 and 2 only mean value of NBR was measured: in the case 1 - over interval x = 0-3 mm where x is the distance from the flame tip (x axis is turned along $\vec{w}$ vector, but in the opposed direction) and in the case 2 - over all the burning surface (nearly conical). In the case 3 a step of measurement of NBR was equal $\delta y = 0.1$ mm (where y axis is normal to x axis and directed inside the specimen).

1.1. PMMA slabs burning in air.

Experiments were conducted with flat horizotal specimens on various underlays (Al alloy, copper, textolite) at near-critical specimens thickness, Δ_{cr}, (such as at $\Delta = \Delta_{cr}$ the burning was stable, but at $\Delta < \Delta_{cr}$ it failed). In these conditions NBR ranged from $1.5\ 10^{-3}$ to $4.7\ 10^{-3}$ mm/s. NBR decreased with underlay thickness, Δ_u, increasing (for copper underlay - from $3.8\ 10^{-3}$ mm/s at $\Delta_u = 0.3$ mm to $2.0\ 10^{-3}$ mm/s at $\Delta_u = 1.0$ mm). NBR was nearly 20 times smaller than w (the ratio u/w ranged from 1/16.8 to 1/20.7).

1.2. PMMA rods burning in air.

The downward burning of vertical cylindrical rods was investigated at various rod diameter, d. The following data were obtained:

d, mm	6.8	11.7	15.0	20.4	25.0	35.2	40.7
w, mm/s	0.082	0.058	0.046	0.037	0.040	0.044	0.042
u, mm/s	0.020	0.015	0.011	0.0091	0.0091	0.0090	0.0086
w/u	1/4.1	1/3.9	1/4.2	1/4.1	1/4.4	1/4.9	1/4.9

Thus, NBR diminishes approximately twice with d increasing from 6.8 to 20.4 mm but then becomes nearly independent of d. As for the ratio u/w, it decreases slightly with d increasing (from 1/4.1 at d = 6.8 to 1/4.9 at d = 35.2-40.7 mm).

1.3. PMMA slabs contacting with $KClO_4$ slabs.

In this case the dependence of u on cavity depth, y , and pressure, p, were examined. NBR decreased strongly with y (and thus on x) increasing. For example, at p = 1 MPa it was obtained:

y, mm	0.2	0.3	0.4	0.5	0.9	1.0
u, mm/s	0.60	0.50	0.41	0.35	0.16	0.15
u/w	1/2.9	1/3.4	1/4.2	1/4.9	1/10.8	1/11.5

This is a principal feature of diffusion flames: indeed, the path of diffusion of oxygen (formed in the course of $KClO_4 = KCl + 2\ O_2$ reaction) and MMA (monomer) to the flame through a layer of combustion products augments with x and y. This results in decreasing NBR. Hence, the ratio u/w also decreases with y increasing (from 1/2.9 at y = = 0.2 mm to 1/11.5 at y = 1 mm).

The dependence u(p) is much more weak than w(p) dependence. For example, an increase of pressure from 1.0 MPa to 3.0 MPa augments w 2.1 times whereas NBR augments only 1.35 times at y = 0.2 mm and 1.1 times at y = 0.5 mm. Moreover, at great enough y NBR is pressure-independent. As a consequence, the ratio u/w is the smaller, the greater is y (see above) and pressure:

p, MPa	1.0	2.5	3.0
u/w (at y=0.2)	1/2.9	1/4.1	1/4.4

2. NBR on the Entirely Burning Surface.

2.1. Burning of spherical particles of PMMA.

The well-known equation for the diffusion burning of spherical drops of liquid fuels: $d^2 = d_0^2 - Kt$ (where d_0 is initial diameter of a drop, K is a constant and t is the time) may be used also for spherical particles of solid polymers. It follows from this equation that $u = 0.5|\delta d/\delta t| = K/4d$. So, NBR for spherical particles is proportional to K and inversely proportional to d. Unfortunately, the experimental

data for PMMA obtained in Ref.1 ($K = 6.9\ 10^{-3}$ cm^2/s at $d_0 = 2$ mm) differ drastically from those of Ref.2 ($K = 28\ 10^{-3}$ at $d_0 = 1$-2 mm).

2.2. Burning of a canal in PMMA blocks in O_2 flow.

The internal burning of PMMA specimens with a cylindrical opening was investigated in Refs.3,4. Specimens studied in Ref.3 consisted of 12 blocks (each 50.8 mm long) pressed together. A flow of gaseous O_2 was delivered in the concentric opening ($d_0 = 25.4$ mm). The mean value u was measured on the basis of mass-loss of each block during the time, t, of a run. The value of NBR decreased significantly with t increasing (1), but augmented lengthwise (2). So, at O_2 flux equal 22g/s the following values u were obtained for the first (u_1) and the eleventh (u_{11}) blocks:

t, s	10	30	60	120	150
u_1, mm/s	0.13	0.084	0.066	0.053	0.050
u_{11}, mm/s	0.22	0.11	0.078	0.055	0.050

The effect (1) may be connected with an increase of opening diameter and hence a decrease O_2 flux density, g/cm^2s. The effect (2) may be due to an increase of gas temperature. However, the effect (2) was very considerable at small t and practically disappeared at great t.

Cylindrical specimens of PMMA (8 mm i.d., 30 mm o.d., and 70 mm long) were investigated in Ref.4 at oxygen flux density ρv = 11-40 g/cm^2s (at $t \approx 0$). The following expression was used for NBR: $u = A(\rho v)^m p^\nu d^n$. In the range p = 0.5-5 MPa and ρv = 11-30 g/cm^2s the exponents m and ν were equal 0.40-0.42 and 0.10, respectively. The following values NBR were obtained at ρv equal 11 and 30 g/cm^2s (denote its here as u_{11} and u_{30} :

p, MPa	1.0	2.0	3.0	4.0	5.0
u_{11}, mm/s	0.36	0.38	0.40	0.41	0.42
u_{30}, mm/s	0.54	0.58	0.60	0.62	0.63

2.3. Polymeric rods burning on the top end.

The burning of flat top of vertical rods (12.7 mm dia) of several polymers was studied in Ref.5. Air (at normal conditions) flowed out a nozzle normal to specimen surface at volume flux density 100 $cm^3/cm^2 s$. The following values of NBR were obtained:

Polymer	PMMA[1]	PMMA[2]	PP	PE[3]	PE[4]
u, mm/s	0.036	0.028	0.022	0.018	0.016

Notes: 1;2 - nozzle type A and B, respectively
3;4 - PE of low and high density, respectively

3. CONCLUSIONS.

The data, considered above show that the difference between the values u measured at various conditions may be as much as two order of magnitude and even more:

Specimens configuration and burning conditions	Measured values $u\ 10^2$, mm/s
1.1. Burning of horizontal sheets of PMMA on various underlays in still air	0.15-0.47
1.2. Downward burning of vertical rods of PMMA in still air	0.86-2.0
1.3. PMMA slabs contacting with $KClO_4$ slabs and burning in N_2 at p = 1-3 MPa	15-81
2.2. Internal burning of PMMA specimens in gaseous oxygen flux	4.4-63
2.3. Polymeric rods burning on the top end in air flux	2.8-3.6

NBR depends strongly on the specimen dimensions (thickness or diameter), oxygen content in the ambient atmosphere, velocity of gas stream over burning surface. Such dependences are typical for diffusion

burning of solid fuels.

The maximum NBR values were obtained for internal burning in oxygen flux of specimens with opening as well as for PMMA slabs burning in contact with $KClO_4$ slabs. The minimum NBR was observed for thin enough flat specimens on thick metal underlays.

REFERENCES

1. A.S.Steinberg, V.B.Ulybin, E.I.Dolgov, and G.B.Manelis, in: Gorenie i Vzryv, Nauka, Moscow, p.124 (1972)
2. R.H.Essenhigh and W.L.Dreier, Fuel, Vol.48, p.330 (1969)
3. T.J.Houser and M.V.Peck, in: Heterogeneous Combustion, Academic Press, New York-London, p.559 (1964)
4. Yu.S.Kichin, S.A.Osvetimskii, and N.N.Bakhman, Fizika Goreniya i Vzryva, Vol.9, p.384 (1973)
5. D.J.Hove and R.F.Sawyer, 15th Symposium (Int.) on Combustion, The Combustion Institute, p.351 (1974)

UNTERSUCHUNGEN ZUM VERBRENNUNGSVERHALTEN VON FESTBRENNSTOFFEN MITTELS EINER FARBSCHLIERENAPPARATUR

Helmut K. Ciezki und Emmanuel Kehringer

DLR - Deutsches Zentrum für Luft- und Raumfahrt
Hauptabteilung Raumfahrtantriebe
Langer Grund
D-74239 Hardthausen, F.R.G.

Abstract

The combustion behaviour of solid fuel slabs in a planar step combustor has been investigated with a Colour-Schlieren technique under ramjet relevant conditions concerning the air inlet temperature. Large windows on both sides give access to the combustion processes above the surface of the slabs. Large scale vortical structures are conspicuous in the outer zone above the diffusion flame in the developing boundary layer behind the recirculation zone. The superimposed thermal emission from the flame region on the Colour-Schlieren pictures gives additional information of the location of the flame front.

1. Zusammenfassung

Für die Untersuchung des Verbrennungsverhaltens von Festbrennstoffplatten unter stauantriebsrelevanten Randbedingungen bezüglich der Lufteinlaßtemperatur wurde eine Farbschlierenapparatur aufgebaut. Diese wurde an einer ebenen Stufenbrennkammer eingesetzt, die es erlaubt durch große seitliche Fenster den Verbrennungsvorgang unmittelbar über der abbrennenden Festbrennstoffplatte zu beobachten. Die bei den Versuchen erhaltenen Aufnahmen zeigen großskalige Wirbelstrukturen im äußeren Bereich oberhalb der Diffusionsflamme in der sich hinter der Rezirkulationszone bildenden Grenzschicht. Die auf den Farbschlierenaufnahmen sichtbare Überlagerung des thermischen Leuchtens der Diffusionsflamme zeigt deren Position als zusätzliche Information.

2. Einleitung

Luftatmende Antriebe, die mit Festbrennstoffen arbeiten, wie zum Beispiel Feststauantriebe (SFRJ) und Ducted Rockets, sind für volumenlimitierte Systeme von großem Interesse. Hierbei versprechen vor allen Dingen Metallpartikelzusätze wie Bor oder Aluminium wegen ihres hohen volumetrischen Heizwertes im Vergleich zu den kohlenwasserstoffhaltigen Bindern (wie beispielsweise HTPB) Vorteile. Leider stehen diesen theoretischen Vorzügen praktische Probleme bei der Umsetzung dieser Partikel in einem Triebwerk entgegen, was sich z.B. in einem schlechten Verbrennungswirkungsgrad, Schlackenablagerungen und somit letztendlich in schlechten Flugleistungen äußern kann. Hierbei wären als Ursache z.B. Oxidkappenbildung bei Aluminiumpartikeln oder die Bildung eines flüssigen Boroxidfilmes auf den Borpartikeln unmittelbar nach der Entzündung zu nennen [1 - 5]. Die diesen Vorgängen zugrunde liegenden Prozesse, sowie die in der Brennkammer ablaufenden mehrphasigen Verbrennungsvorgänge sind bis heute noch nicht vollständig verstanden. Desweiteren sind diese Vorgänge in einer Staubrennkammer meßtechnisch schwierig zu erfassen.
Für die hier vorgestellte Untersuchung wurde eine Stufenbrennkammer ausgewählt, die es ermöglicht über große seitliche Fenster den Verbrennungsprozeß unmittelbar über der Festbrennstoffplatte zu beobachten. Hierfür wurde eine Farbschlierenapparatur aufgebaut, die es ermöglichen soll, Strukturen des Verbrennungsvorganges sichtbar zu machen.

3. Versuchsanlage

Abbildung 1 zeigt die Skizze der Versuchsanlage mit der ebenen Stufenbrennkammer, die einen rechteckigen Querschnitt von 150 mm Breite und 45 mm Höhe besitzt. Unmittelbar hinter der Stufe von 20 mm Höhe werden die Festbrennstoffplatten von 200 mm Länge und 100 mm Breite bündig zur Oberfläche in den Brennkammerboden eingelassen. Der mittels eines H_2/O_2-Brenners erhitzte Luftstrom wird über zwei Strömungsgleichrichter und Siebe der Brennkammer zugeführt. Hierbei wird über den Brenner soviel Sauerstoff zusätzlich zugeführt, daß der Sauerstoffgehalt der heißen Gasströmung dem von normaler Luft entspricht. Eine genauere Beschreibung der Versuchsanlage ist in [6,7] gegeben.
Für die hier präsentierte Untersuchung wurden Quarzscheiben als Fenster eingesetzt, die es erlauben, einen Bereich mit der Brennkammerhöhe von 45 mm über fast der gesamten Brennstoffplattenlänge von 200 mm und zusätzlich ca. 20 mm vor dem Rücksprung der Stufe einzusehen, wie dies in Abb. 1 skizziert ist. Als Festbrennstoff wurden Platten aus 91,6 Gew.-% HTPB und 8,4 Gew.-% IPDI eingesetzt. Der für die Versuche eingestellte Luftmassenstrom betrug 0,15 kg/sec und die zugehörige Temperatur 800 K. Dies entspricht

einer Reynolds-Zahl von $2{,}3 \cdot 10^4$, die mit der Stufenhöhe gebildet wurde. Der Druck innerhalb der Brennkammer betrug 1 bar.
Zu Versuchsbeginn wurde der Lufterhitzer gezündet und die Anlage zwei Minuten lang mit der heißen Luft durchströmt um die Anlage selbst und die Festbrennstoffplatte aufzuheizen. Hiernach wurde die Brennstoffplatte durch einen weiteren H_2/O_2-Brenner, der unterhalb der Stufe montiert ist, gezündet.

4. Farbschlierenapparatur

4.1 Grundlagen

Schlierenverfahren finden in der Strömungstechnik seit langem vielfache Anwendung um Zustandsänderungen in transparenten Medien darzustellen. Sie beruhen darauf, daß Lichtstrahlen, die ein Gebiet mit einem senkrecht zu ihrer Ausbreitungsrichtung verlaufenden Brechungsindexgradienten passieren, abgelenkt werden [8,9]. Bei homogenen Gasgemischen ist der Brechungsindex n mit der Dichte ρ gemäß Gleichung (1) gekoppelt, wobei K die stoffspezifische wellenlängenabhängige Gladstone-Dale-Konstante ist.

$$n - 1 = K(\lambda)\rho \qquad (1)$$

Somit kann im Idealfall bei einem ebenen Strömungsproblem für jeden Ort x_0,y_0 ein Zusammenhang zwischen dem Dichtegradienten z.B. in x-Richtung und dem Ablenkwinkel ε in gleicher x-Richtung des Lichtstrahles geschaffen werden, wie dies bei Born und Wolf [9] dargestellt ist.

$$\left(\frac{\partial \rho}{\partial x}\right)_{x_0,y_0} \approx \frac{1 + K(\lambda)\rho}{L \cdot K(\lambda)} \varepsilon_x \qquad (2)$$

Dies führt bei Schwarz/Weiß-Schlierenverfahren (S/W), bei denen weißes Licht benutzt wird, auf dem Schlierenbild zu lokalen Aufhellungen oder Abdunkelungen, durch die die Zustandsänderungen sichtbar gemacht werden können. Liegt nun ein mehrphasiges Problem vor, bei dem z.B. Partikel einer Gasströmung zugegeben sind, so tritt hier zusätzlich zum Schlierenеffekt der Gasphase eine Transmissionsminderung des durchstrahlenden Lichtes durch die Partikelphase infolge Streuung und z.T. auch Absorption auf. Dies erschwert die Interpretation der ablaufenden Vorgänge wesentlich.
Ein Farbschlierenverfahren hingegen, welches z.B. auf der von Cords [10] entwickelten Dissection-Technik beruht, weist verschiedenen Ablenkungswinkeln verschiedene Farben zu, wobei die Partikelphase lediglich die Intensitäten der einzelnen Farben abschwächt.

Somit können in erster Näherung die darzustellenden Brechungsindexgradienten in der Gasphase getrennt betrachtet werden. Abbildung 2 zeigt links ein S/W-Schlierenbild und rechts ein Farbschlierenbild eines partikelbeladenen Gasstrahles. Auf beiden Bildern sind ähnliche Strukturen zu erkennen. Das Farbschlierenbild zeigt vollständig grüne Farbe, die hier für keine oder äußerst geringe Ablenkungen steht, wobei die Strukturen als „Schatten" sichtbar werden. Dies weist daraufhin, daß die Strukturen auf dem S/W-Schlierenbild hauptsächlich durch die Absoption der Partikelphase hervorgerufen werden.
In einer Brennkammer treten nun zu den Strömungsprozessen zusätzlich Verbrennungsvorgänge hinzu, sodaß Gleichung (2) nicht mehr benutzt werden kann, da sich sowohl Dichte als auch Temperaturen und Konzentrationen lokal ändern. Infolgedessen gibt ein Schlierenbild hier lediglich einen qualitativen Eindruck der ablaufenden Vorgänge.
Farbschlierenverfahren sind in der Vergangenheit in verschiedenen Varianten entwickelt worden. Der Artikel von Settles [11] gibt einen Überblick über die Arbeiten bis etwa zum Jahre 1980. Auch wurden verschiedentlich Schlierenverfahren zur Darstellung der Verbrennungsvorgänge im Bereich Festbrennstoffe eingesetzt. So benutzten Netzer und Mitarbeiter [12] erfolgreich eine Farbschlierenapparatur zur Untersuchung des Abbrandes von Ammoniumperchlorat. Bei Prozessen, die ein starkes Eigenleuchten erzeugen, ergaben sich allerdings Probleme.

4.2 Aufbau

Das hier vorgestellte Verfahren beruht auf der von Cords entwickelten Dissection-Technik, bei der die üblicherweise benutzte Lichtquelle durch ein Areal von Farbfeldern (Farbmaske) ersetzt wird und einer Spaltblende im Brennpunkt des zweiten Hohlspiegels, wie dies in Abb. 3 dargestellt ist. Die Farbflächen der Farbmaske wurden nun so gewählt, daß auf den Schlierenaufnahmen die Farbe grün den Bereich um den Nullwert des Ablenkwinkels bzw. Brechungsindexgradienten wiedergibt. Die Abfolge der Farben wurde der Abfolge des Regenbogens entlehnt, um eindeutige Farbzuweisungen zu erhalten. Dies zeigt Abb. 4, bei dem eine langbrennweitige Linse als Kalibrierobjekt benutzt wurde. Desweiteren wurden Blitzlampe, Farbflächen und Farbfilm so aufeinander abgestimmt, daß sich gute Farbwiedergaben auf den Bildern ergaben. Diese hier vorgestellte Anordnung wurde in einer Variante bereits 1985 für den Einsatz an einem Stoßwellenrohr entwickelt und eingesetzt [13].
Für die Untersuchungen an der Stufenbrennkammer wurde ein modifiziertes Blitzgerät von Drello mit einer Halbwertszeit von etwa 13µsec benutzt. Im Strahlengang zur Kamera wurde zusätzlich ein schneller ansteuerbarer Verschluß positioniert um den Anteil der Lichtemission des Verbrennungsvorganges auf den Farbschlierenaufnahmen zu reduzieren. Der Aufbau der Schlierenapparatur wurde als Töpler´sche Z-Anordnung ausgeführt, wobei aus Platzgründen zwei zusätzliche Planspiegel benutzt wurden.

5. Ergebnisse und Diskussion

Abbildung 5 zeigt im oberen Bild eine Schlierenaufnahme mit dem Dichtegradienten in y-Richtung des Verbrennungsprozesses einer HTPB-Platte in der Stufenbrennkammer. In der zugehörigen unteren Skizze sind die charakteristischen Merkmale dieses Strömungs- und Verbrennungsvorganges dargestellt. Diese Darstellung ist an die Einteilung von Natan und Gany [14] für den Grenzschichtverbrennungsprozeß in einer Feststaubrennkammer angelehnt. Großskalige wirbelförmige Strukturen sind in der äußeren Zone oberhalb der Diffusionsflamme in der sich hinter der Rezirkulationszone entwickelnden Grenzschicht sichtbar. In diesem Bereich wird kälteres Gas aus der Außenströmungszone durch die Wirbel in tiefere Bereiche geführt und mit den heißen Verbrennungsgasen gemischt. Die Existenz dieser kälteren Gasbereiche in der Mischungszone konnte auch in einer früheren Untersuchung, bei der Temperaturmessungen mittels CARS durchgeführt wurden, durch eine bimodale Temperaturverteilung mit zwei ausgeprägten Maxima gezeigt werden [15].
Im unteren Bereich des Bildes erkennt man ein gelblich leuchtendes Band, das der Farbschlierenaufnahme überlagert ist. Der Ursprung kann dem thermischen Leuchten des Rußes zugeschrieben werden und ist nach Gany dem Ort der Kohlenwasserstoff-Diffusionsflamme zuzuordnen. Am Ende der Rezirkulationszone ist der Abstand der HC-Diffusionsflamme zum Brennkammerboden geringer als in den anderen Bereichen. Frühere Geschwindigkeitsmessungen mittels LDA [16] zeigen hier eine nach unten gerichtete Strömung mit einer Verzögerung auf den freien Sattelpunkt hin. In dieser verzögerten Strömung kann die Flamme fixiert werden.
Desweiteren erscheinen auf der Farbschlierenaufnahme große Bereiche der Rezirkulationszone schwarz. Hier wurde nach Versuchsende eine starke Schwärzung der Fenster durch Ruß festgestellt, der hier für eine starke Lichtabsorption verantwortlich erscheint. Somit kann in diesem Bereich keine Aussage über die dort ablaufenden Vorgänge gemacht werden.

6. Nomenklatur

K	Gladstone-Dale-Konstante
L	optische Weglänge
x	Koordinate parallel zur Brennkammerbodenfläche
x'	freie Koordinate
y	Koordinate senkrecht zur Brennkammerbodenfläche
ε	Ablenkwinkel
λ	Wellenlänge
ρ	Dichte

7. Literaturverzeichnis

1. Timnat, Y.M.
   Recent Developments in Ramjets, Ducted Rockets and Scramjets, Prog. Aerospace Sci., 1990, Vol. 27
2. Gany, A.
   Combustion of Boron-Containing Fuels in Solid Fuel Ramjets, in: Combustion of Boron-Based Solid Propellants and Solid Fuels (K. K. Kuo, R. Pein, Eds.) CRC Press, Boca Raton, 1993
3. King, M.K.
   A Review of Studies of Boron Ignition and Combustion Phenomena at Atlantic Research Corporation over the past Decade, in: Combustion of Boron-Based Solid Propellants and Solid Fuels (K. K. Kuo, R. Pein, Eds.) CRC Press, Boca Raton, 1993
4. Faeth, G.M.
   Status of Boron Combustion Research, Proceedings of the Specialist Meeting on Boron Combustion AFOSR, Oct. 1984
5. Yeh, C.L., Kuo, K.K.
   Ignition and Combustion of Boron Particles, Prog. Energy and Combust. Sci, Vol. 22, pp. 511-541 (1996)
6. Ciezki, H.K., Hensel, C., Liehmann, W.
   Spectroscopic Investigation of the Combustion Behaviour of Boron Containing Solid Fuels in a Planar Step Combustor, 13th ISOABE, September 7-12, 1997, Chattanooga, Tennessee, USA, pp. 582-590
7. Ciezki, H. K., Schwein, B.
   Investigation of Gaseous and Solid Reaction Products in a Step Combustor Using a Water-Cooled Sampling-Probe, AIAA 96-2768, 32nd Joint Propulsion Conference, July 1-3, 1996, Lake Buena Vista, FL, USA
8. Merzkirch, W.
   Density sensitive Flow Visualisation, Methods of Experimental Physics, Vol. 18A, Academic Press, 1981
9. Born, M., Wolf, E.
   Principles of Optics, Pergamon Press, London, 1959, 3. Auflage, 1965
10. Cords, P.H.
    A High Resolution, high Sensitivity Colour Schlieren Method, S.P.J.E. Journal, Vol. 6, 1968
11. Settles, G.S.
    Colour Schlieren Optics - A Review of Techniques and Applications, in: Flow Visualisation (Merzkirch, W., Ed.), Hemisphere Publishing Corporation, New York, 1980
12. Netzer, D.W., Andrews J.R.
    Schlieren Studies of Solid-Propellant Combustion, in: Experimental Diagnostics, in: Combustion of Solids (Th. Boggs, B.T. Zinn, Eds.), Progress in Astronautics and Aeronautics, Vol. 63, AIAA, 1978
13. Ciezki, H.
    Entwicklung eines Farbschlierenverfahrens unter besonderer Berücksichtigung des Einsatzes an einem Stoßwellenrohr, Diploma Thesis, Technical University Aachen, F.R.G., 1985
14. Natan, B., Gany, A.
    Ignition and Combustion of Boron Particles in the Flowfield of a Solid Fuel Ramjet, J. Propulsion, Vol. 7, No. 1, 1991, pp.37-43
15. Clauß, W., Vereschagin, K., Ciezki, H.K.
    Determination of Temperature Distributions by CARS-Thermometry in a Planar Solid Fuel Ramjet Combustion chamber, 36th Aerospace Sciences Meeting, Jan. 12-15, 1998, Reno, NV, USA
16. Sender, J., Ciezki, H.K.
    Velocities of reacting Boron Particles within a solid Fuel Ramjet Combustion Chamber, Int. Seminar on High Energy Materials (HEM), 19-21 Sept. 1996, Pune, India

Anmerkung

Für die Hilfe von Herrn A. Feinauer bei der Versuchsdurchführung, die Produktion der Festbrennstoffplatten durch Herrn J. Liebl, die Entwicklung der Ansteuerungselektronik durch Herrn K: Möhler, sowie für die Fotolaborarbeiten von Herrn W. Eith sei an dieser Stelle herzlich gedankt.

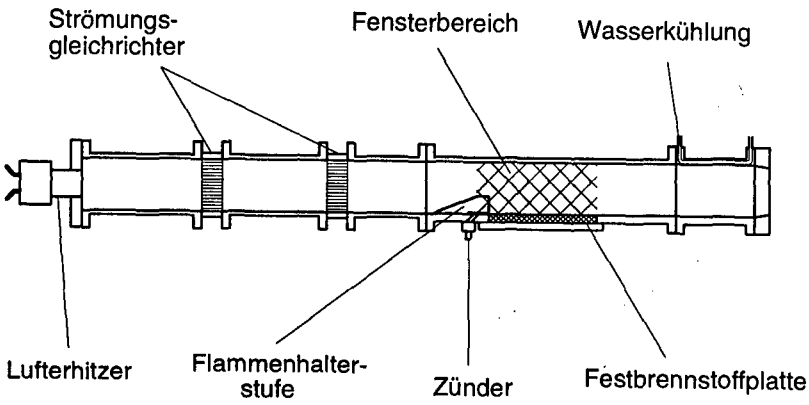

Abb. 1: Skizze Versuchsanlage mit ebener Stufenbrennkammer

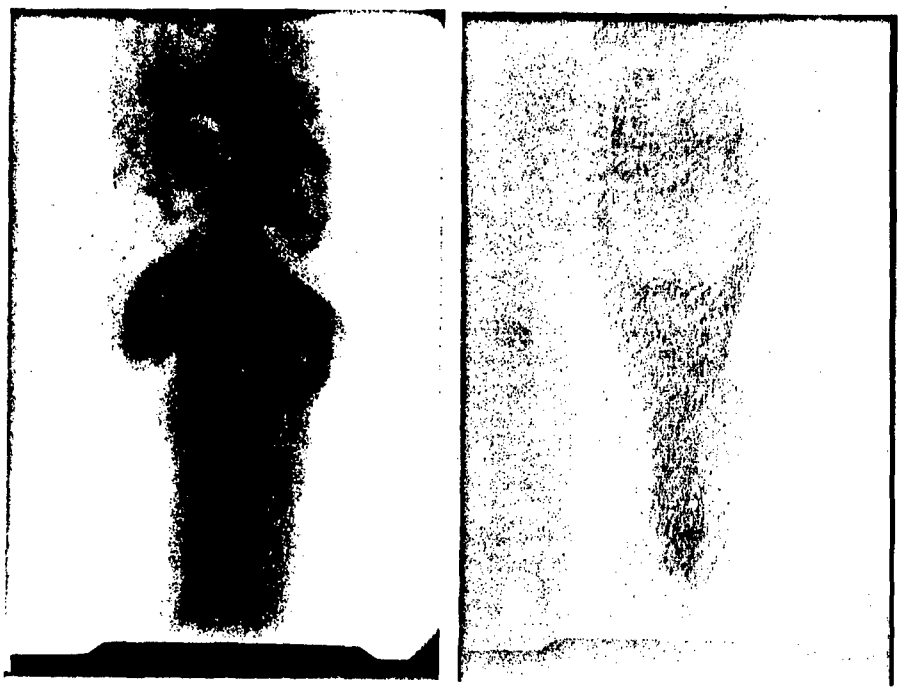

Abb. 2: Gegenüberstellung Schwarz/Weiß-Schlierenaufnahme (links) und Farbschlieren aufnahme (rechts) am Beispiel eines partikelbeladenen Luftstrahles

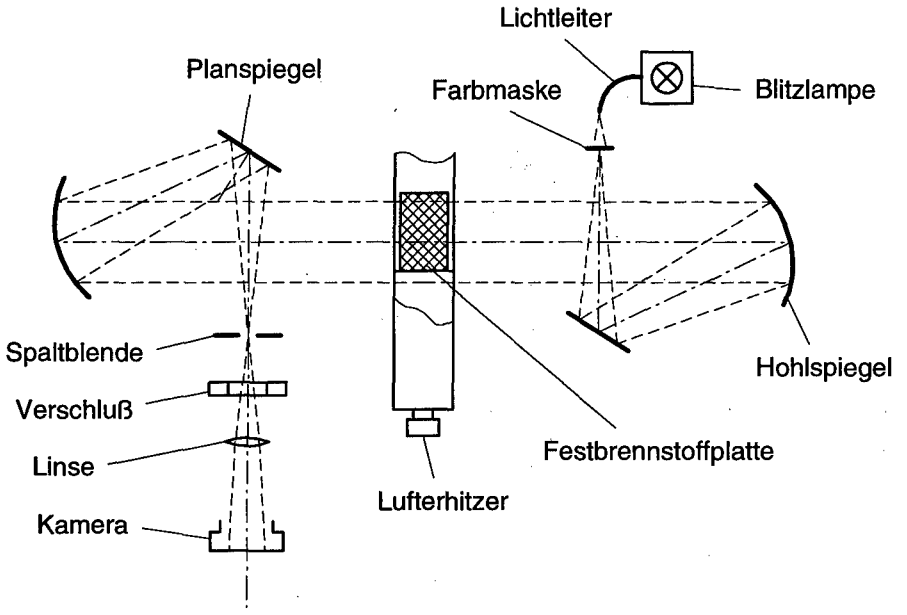

Abb. 3: Farbschlierenaufbau auf dem Prüfstand

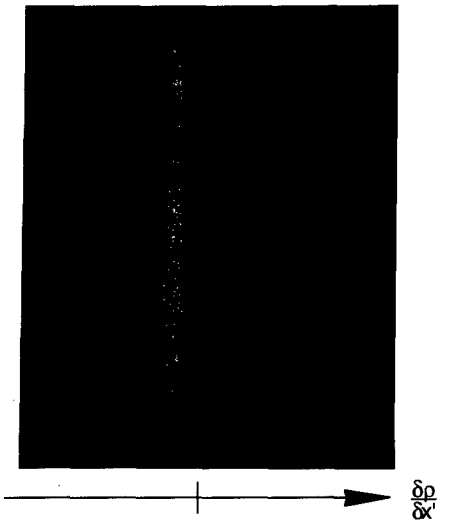

Abb. 4: Farbschlierenbild einer langbrennweitigen Linse

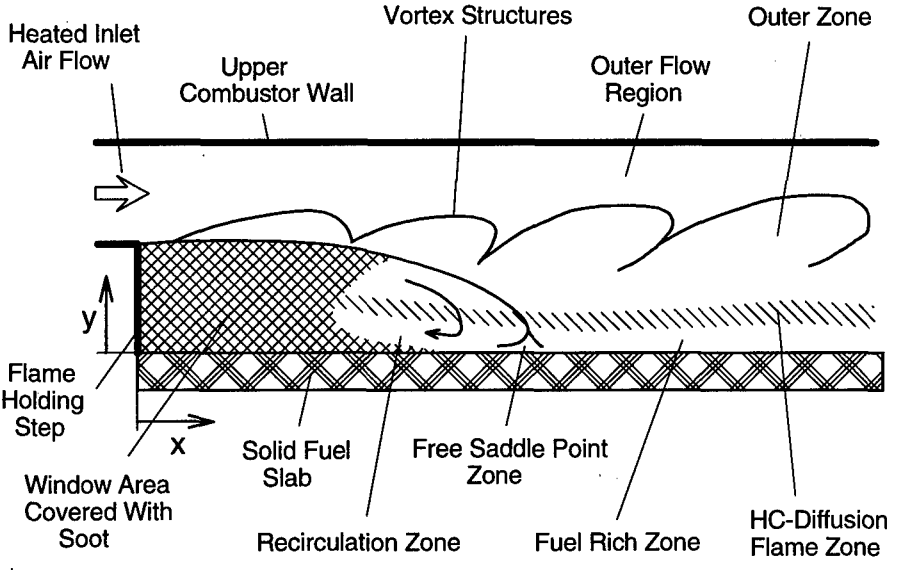

Abb. 5: oben: Farbschlierenaufnahme vom Abbrand von HTPB ohne Partikelzusatz

unten: Prinzipskizze der ablaufenden Strömungs- und Verbrennungsvorgänge

OBTAINING SUBMICRON ABRASIVE POWDERS BY PNEUMATIC PROCESSING OF ELECTRIC CORUNDUM AND PRODUCTS OF SOLID ROCKET PROPELLANTS COMBUSTION.

Yuri Biryukov, Alexander Vorozhtsov, Leonid Bogdanov
Tomsk State University, 36, Lenin 630050 Tomsk, Russia

Abstract: This report gives brief review of our research into production of superfine powders of organic and non organic materials, presents parameters of experimental series of powders based on aluminium oxide and products of combustion of solid propellants.

In many processes, such as pharmacological preparation production, the precise processing of surfaces, obtaining of superconductors or components of functional ceramics, production of superfine particles of metals and pharmacological preparations etc., the specific requirements to powder technology are placed: the maintenance of size uniformity of submicron particles and their mixes, shape and strict granulometric composition, moisture content.

In connection with topicality of the problem, in many countries intensive researches are performed and the various ways of the problem solution was created. The essential results in this area are achieved by firms of Japan, Germany and USA. Parameters of their abrasive powders, offered for approving on largest in Russia enterprise on production of ball - bearings (Vologda) are presented at table 1. In the last few years in the Tomsk State University emphasis is made also on the production of fine and submicron powders from inorganic and organic materials. The parameters of some trial series of powders based on electric corundum, produced by TSU are also shown in table 1, figure 1.

Considering that reduction of strategic armament as well as completion of their guarantee periods and removal from service of some arm types put a pressing problem of elaboration of economically acceptable technologies of their liquidation not only without any damage to environment, but with economic advantage, product of solid rocket propellant combustion (Al_2O_3) of abrasive submicron powders. In TSU a method of charges recovery by their combustion in chemically active environment, namely in a saturated water solution of ammonium perchlorate is elaborated. Using water solution of aluminium perchlorate as liquid in the pool for combustion allows to increase the completeness of combustion and Al_2O_3 powder output in comparison with known procedures.

The result of researches and industrial realisation of technology built upon controlled circulating movement of the flow "gas-solid particles" in closed volumes with help of gas jets displayed possibility of execution of the following operations:

- grinding is brought about by interaction of dense circulating layer of material with underexpanded gas jets;
- the classification of particles to fractions is provided by built-in separative elements of centrifugal type of various design with circulation of two-phase environment in their contours, that permits to receive narrow fractions;
- high-efficient mixing of components of varying granulometric composition and phase condition of components is performed on macrolevel (beds, aggregates of particles) by optimization of function of distribution of the particles throughout their residence time in circulating contour (the separative elements pass only gas), and on microlevel by dispersion of components in gas jets;
- convection drying is achieved in jets and flow of heat-transfer agent;
- granulation with at injection of dispersed liquid binder in circulating bed of material;
- the enrichment and separation of impurities is carried out by selective grinding and separation of materials on density;
- the fine clearing of gas in bag filters and in cyclones of special design.

We shall touch briefly on the description of technological processes, results of experiments and industrial realisation.

1. Intensity of grinding in complex pneumatic units (hereinafter "Combi", figure 6), in the first place is determined by working pressure, parameters of speedup chamber and nozzles, intensity of circulating motion, physical and mechanical properties of initial powders and size of particles of product. Our study shown that the process of particles self-abrasion is determining whereas the nozzles profiling and installation of obstacles did not influence noticeably on the process, The high purity of end product at grinding of hard and superhard materials (carbides, nitrides, oxides of some metals) is also explained by domination of particles interaction (self-abrasion), instead of interaction of particles with working surfaces. On dispersion of beryllium oxide the pollution with impurities was measured. The initial powder had specific surface 7200 cm^2/g and the end product 12300 cm^2/g, (table 2).

The experiments at pressure of more than 10 kg/cm^2 (up to 100 kg/cm^2) have not given any qualitative change of characteristics and increases of processes efficiency, but further investigations along this line are conducted. Specific expenditure of energy at production of submicron powder of electric corundum with initial $\delta_{50} \approx 30$ mkm and with use of complex

technology is 3-5 kWt hour/kg. The capacity of the unit then is 15 kg/hour, working pressure is 7-8 kg/sm^2. The potential opportunities of improvement of the powder technology processes of submicron and ultradispersive powders such as aluminium oxide and other ceramic powders exist. It requires more in-depth study of gasdynamics of flows "gas - solid particles" in unit "Combi".

The production of such of such strictly normalized submicron powders from Al_2O_3 with a required crystal structure resolve the ecological problem in technology of precise processing of details in ball-bearing industry, electronics, optics and fine mechanics, as at present pastes on basis rather toxic chrome oxide are mostly used.

The production of strictly normalized submicron of powders from Al_2O_3 with a required crystal structure, including that from products, receiving at liquidation of solid propellant, solves the ecological problem in technology of precise processing of details in ball-bearing industry, electronics, optics and fine mechanics, as at present pastes on basis rather toxic chrome oxide are mostly used.

The combining of pneumatic grinding Al_2O_3 with fractionation in multicontour separative units provided the production of abrasive powders with comparatively high characteristics (table 1), that has enabled to raise as the class of accuracy at manufacturing of ball-bearings as productivity, also to remove the problems, connected with liquidation of toxic wastes and harmful effects of production.

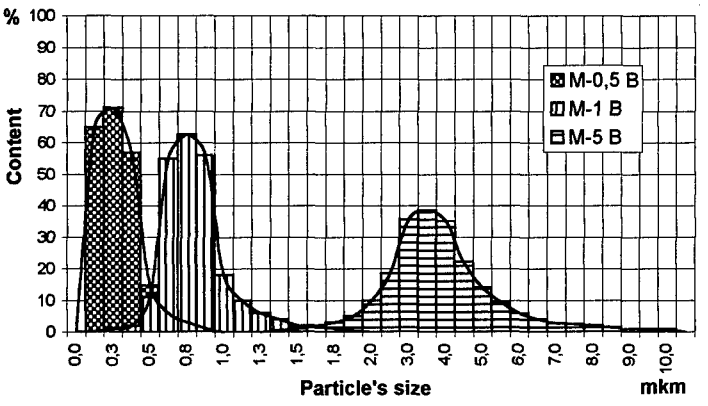

Figure 1 The mass distribution of polishing powders of electric corundum Al_2O_3 (granulometric composition is determined by optic microscope).

The pneumatic technology of separation of large inclusions in ultradispersive powders of copper, obtained by method of electrical discharge, has allowed to produce high-efficient oil and grease additives.

The similar characteristics are obtained also at combining of processes grinding and fractionation of wide class of materials (organic: polyethylene, polyvinylchloride, nozepami, cinnarizin, sorbite, vitamin concentrates, vitamin meal; inorganic: the aluminium, niobium, boron, tantalum, **Ni-Cr** alloy, talc, chalk, ammonium perchlorate).

2. Intensity of blend process in unit "Combi" is determined by character of convective transfer, namely by function of distribution of particles residence time in the bulk bed over a cycle - $f(t_{max}/t_{min})$, and quality of mixing on microlevel by effect underexpanded gas jet on incoming in it aggregates of particles. On figure 2 the variation of the key component concentration (**C**) with number of displasements to blend (**N**), needed to achieve the given heterogeneity coefficient (V_c=5%) are shown.

On figure 3 the results of mathematical modeling and experimental relationship between **N** and t_{max}/t_{min} - ratio of maximal particles' residence time to minimal, where $V_c = \frac{100}{\bar{c}}\sqrt{\frac{1}{n-1}\sum_{i=1}^{n}(c_i-\bar{c})^2}$ % are presented. Referring to figure 3, the maximal efficiency of process is reached at t_{max}/t_{min} =2,2-2,4. During experiments the particles velocity and trajectories distribution were registered with help of variable-induction and capacitive pickups (through injection of bench mark particles).

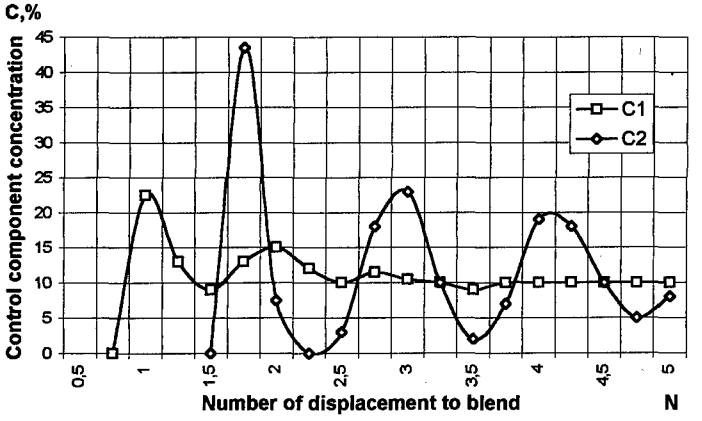

Figure 2 Variation of the control component concentration with number of displacement to blend (C1: $\frac{t_{max}}{t_{min}}$=2.4; C2: $\frac{t_{max}}{t_{min}}$=1.7).

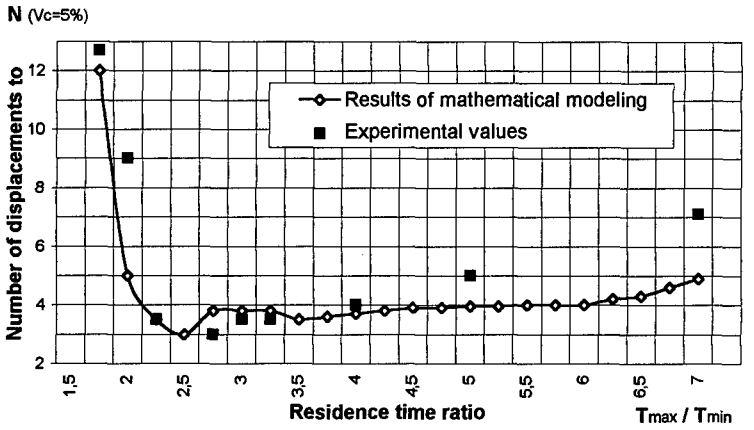

Figure 3 Results of experiments and mathematical modeling of residence time distribution at blending

On base of combined processes of blending and dispersion the technology for obtaining high-homogeneous compositions with small additives was developed. An example is production of medicinal composition on base **Na** benzoat and salbutamol at ratio 98:2 with dispersive composition 85% to 5 mkm and heterogeneity coefficient V_c<3%. figure 4 gives the results of tests. The work with pectin lend support to validity of proposed technology.

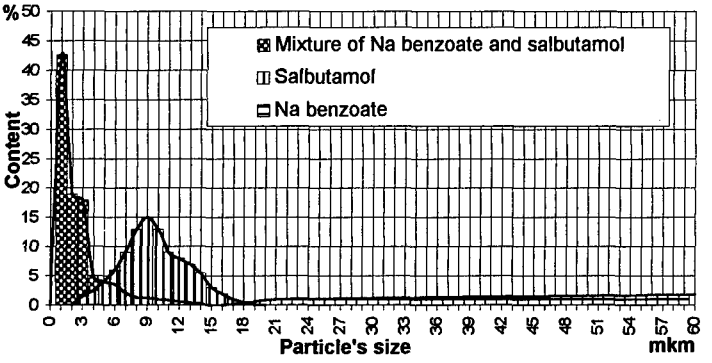

Figure 4 Results of combined blending and dispersion of salbutamol and Na benzoate components. The resulting coefficient of heterogeneity is V_c =2,7%

One of essential moment in production of finely dispersed powder materials on pneumatic circulation apparatuses is neutralization of influence of adhesive and cohesive properties of loose material, which hinder the motion of bulk bed over the internal surfaces of apparatus, cause bridging and give no way to control the circulating motion. Therefore the given problem

is worked for each specific material. The obtained results have allowed to develop the commercial plants for processing of moist materials (moisture content up to 25%).

3. The soft drying equipment and process for moist thermodestruction-prone materials are developed. The cooling of gas at its expansion and intensive flow around particles prevents thermodestruction. This permits to grind some high-molecular compounds and organic medicinal: polyethylene, polyvinylchloride, vitan, nozepami, pentocsifilin, pectin Acorus calamus, Thermopsis lanceolata, etc.

4. Efforts are underway to solve the problem of granulation in unified production line. The complexity of the problem consists in necessity of unition in one working volume almost all processes of powder technology: dispersion, fractionating, mixing of particles with liquids and simultaneous drying.

5. Analysis of the current tendencies of development of ores dress technology shows, that on its final stage the use of pneumatic methods is perspective. They permit to combine the process of selective grinding of raw material up to fine fractions level and their separation. It simplifies the operation and completely excludes losses of fine and submicron product as slurry with pulp, which accompany to hydroseparation.

For example, at dressing and separation of iron ore concentrate on various regimes of dispersion and separation were allocated following fine fractions of pigment: №1 - $0 \leq \delta_{95} \leq 2$ mkm, №2 - $2 \leq \delta_{95} \leq 4$ mkm, №3 - $4 \leq \delta_{95} \leq 7$ mkm, and 80% concentrate of **Fe** (powder). The researches on dressing of loparite ore, containing niobium, tantalum etc. are carried out at present.

Now we have also other realizations of pneumatic powder technology:

- the production of high-melting compounds powders on levels 1 mkm for functional ceramics; from compound of zirconium oxide (figure 5) and aluminium oxide fractions with size up to 0,3 mkm were received;
- production of powders for production of accumulators;
- the production of polyethylene powders with strictly preset granulometric composition for production of filters and membranes;
- the production of narrow fractions from talk and chalk for splendid cosmetic powders and rouge.

The experimental researches were conducted on specially designed laboratory stands and model units. The analysis of particles sizes was conducted as in laboratory, as on equipment of customers enterprises.

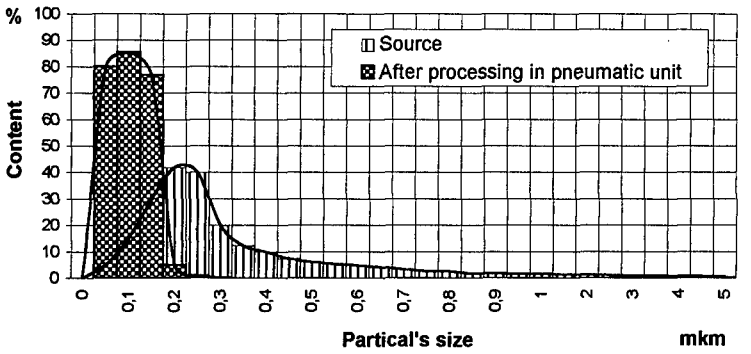

Figure 5 The mass distribution of ZrO_2 particles (granulometric composition is determined by electron and optic microscope)

In authors opinion the existing in the world instruments for analysis of dispersive composition: sedimentometers, laser counters and instruments for determinations of specific surface do not give objective characteristic of particles on submicron level. Therefore the control for updating of results with helps optical and electronic microscopes, as well as their computer processing is practical always necessary. As the example, in table 3 presented the granulometric analysis of the same consignment of monocorundum powder on photosedimentometer "SKC-200" and on laser counter "SEISIN". The chemical analysis of products, as a rule, was conducted on equipment of special enterprises.

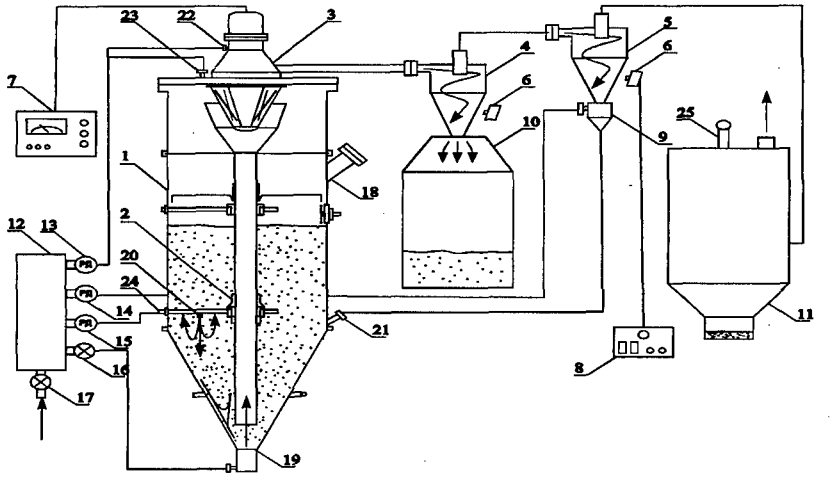

Fig. 6 Scheme of the "Combi" unit.

1 - blending hopper
2 - circulation tube
3 - classifier
4,5 - cyclone
6 - projectiles
7 - classifier control console
8 - projectiles control console
9 - ejector of earge fraction return
10 - receiving hopper for end product
11 - fine filter
12-17- gas distribution centre
18 - loading hatch
19 - nozzle block
20-24 - blow system
25 - mechanical shaker

Table 1. Comparative characteristics of granulometric composition of abrasive powders on the base of electric corundum by USA and TSU (Tomsk) firms.

PRODUCTING FIRM	GRANULOMETRIC COMPOSITION OF MICROPOWDERS,%														
	<0,5 mkm	<0,7 mkm	<1 mkm	1-2 mkm	2-3 mkm	3-4 mkm	4-5 mkm	5-6 mkm	6-7 mkm	7-8 mkm	8-10 mkm	10-12 mkm	12-14 mkm	14-16 mkm	16-20 mkm
MICRO ABRASIVE COMPANY			1,1	33	12,5	15,4	1,6	17,8	1,5	7,9	5,5	2,0	1,8	0,2	0,2
K.C. ABRASIVE COMPANY			37		12	19	15		6		9	1	-	-	-
--- """ ---			37		19	11	10		5		10	2	2	2	5
TREIBACHER SCHLIFMITTEL CORPORATION			2,3	29	12,5	13,3	3,1	15,6	2,3	7,8	10,9	3,1	-	-	-
MICRO ABRASIVE CORPORATION				96			3				1		-	-	-
TSU -TOMSK M 0,5 - B	78	97	100	-	-	-	-	-	-	-	-	-	-	-	-
--- """ --- M 0,75 -B	56	65	86	14	-	-	-	-	-	-	-	-	-	-	-
--- """ --- M 1 - B			69	31	-	-	-	-	-	-	-	-	-	-	-
--- """ --- M 2,5 - B			3	12	52	28	5	-	-	-	-	-	-	-	-
--- """ --- M 5 - B				1,5	18,5	42	18	15, 5		0,5		-	-	-	-
--- """ --- M 7 - B					2,5	12	25		47		10	3	0,5	-	-
--- """ --- M 10 - B					1	3,5	29		43		13	7	2,5	1	-

Table 2. Grinding and fractionation of beryllium oxide .
Percentage of foreign chemical element's impurities pre- and post- processing on the"Combi" unit (TSU).

ELEMENT	Initial percentage, %	Percentage in end product, %
Br - boron	$3{,}6\cdot10^{-5}$	$9{,}4\cdot10^{-5}$
Si - silicon	$4{,}7\cdot10^{-3}$	$7{,}2\cdot10^{-3}$
Mn - manganese	$3{,}6\cdot10^{-4}$	$5{,}0\cdot10^{-4}$
Fe - ferrum	$4{,}3\cdot10^{-2}$	$5{,}4\cdot10^{-2}$
Mg - magnesium	$5{,}0\cdot10^{-3}$	$3{,}9\cdot10^{-3}$
Cr	$5{,}4\cdot10^{-3}$	$6{,}8\cdot10^{-3}$
Ni - nickel	$1{,}5\cdot10^{-2}$	$7{,}2\cdot10^{-3}$
Al - aluminium	$1{,}2\cdot10^{-2}$	$1{,}7\cdot10^{-2}$
Cu - cuprum	$4{,}7\cdot10^{-4}$	$4{,}3\cdot10^{-4}$
Zn - zinc	$4{,}7\cdot10^{-3}$	$4{,}7\cdot10^{-3}$
Ca - calcium	$5{,}7\cdot10^{-3}$	$5{,}7\cdot10^{-3}$
Ag - silver	$1{,}1\cdot10^{-5}$	$1{,}1\cdot10^{-5}$
Li - lithium	$1{,}1\cdot10^{-3}$	$1{,}1\cdot10^{-3}$
Na - sodium	$3{,}6\cdot10^{-3}$	$4{,}3\cdot10^{-3}$

Table 3. Grinding and fractionation of monocorundum powder.
Granulometric composition on foreign firm's evalution.

"SKC - 200"		**"SEISIN"**	
δ, **mkm**	**%**	δ, **mkm**	**%**
0 - 0,5	78,27	0 - 1	52,8
0,5 - 1	18,05	1 - 1,5	19,8
1 - 1,5	1,84	1,5 - 2	11,9
1,5 - 2	1,84	2 - 3	15,0
δ_{50} **= 0,32 mkm**		δ_{50} **= 0,9 mkm**	

References:

- 2nd World Congress "Particle Technology", Kyoto, Sept. 19-22, 1990. Pt 1. Plenary lect.: 1. Mechanical powder properties, 2. Particle characterization.-[Tokyo]: Soc. Powder Technol., 1990. - IX, 571p.-Eng.
- Rosljak A, Biryukov Y, Pachin V 1990 Pneumatic methods and units of powder technology Tomsk State University 1990
- The method of pneumatic separation of powder-like materials and device for it realisation, Russia patent №1273193

COMBUSTION OF AMMONIUM NITRATE-BASED COMPOSITIONS
I. MIXTURES OF AMMONIUM NITRATE WITH CATALYSTS AND HIGH EXPLOSIVES

B. N. Kondrikov, V. E. Annikov
Mendeleev University of Chemical Technology
9 Miusskaya Square, 125047 Moscow, Russia

L. De Luca
Dipartimento di Energetica, Politecnico di Milano
32 Piazza Leonardo da Vinci, 20133 Milan, MI, Italy

Abstract

The subject of this paper is to describe the experimental facts in the field of steady state burning and to estimate the critical burning conditions of three categories of AN-based compositions:. Neat AN with minor additives to lower the pressure deflagration limit (PDL), compositions based on AN/TNT 80/20 mixture, materials containing RDX or liquid nitric esters.

It is shown that combustion of almost all of the substances studied is characterized by the usual for many propellants and high explosives burning rate and dependence of the rate on ambient pressure but at the same time it is connected with the very low level of burning stability: PDL and critical diameter of burning in the majority of cases are much higher than the corresponding values observed for the standard double base and composite propellants as well as for the variety of nitrocompounds investigated earlier.

The preliminary explanation proposed for this peculiarity takes into consideration the experimental observation that in the moderate pressure region, reactions of thermal decomposition of AN proceed in a liquid layer which comprises a mixture of melted AN, water, nitric acid, ammonia, nitrogen oxides, and some other less pronounced constituents. Reactions in this layer go on slowly and release the correspondingly low quantities of heat at relatively low characteristic temperature. Reactions in the secondary flame are separated from the liquid/solid interface by a layer of the rather inert fluid and do not participate significantly in formation of the burn rate of the composition. They strongly influence however PDL and d_c values. A theoretical description of the influence of melting, intermediate layer of liquid formation and heat of reactions evolved in the liquid layer, on the one side, and in the secondary flame, on the other side, is assumed to be presented in one of the next papers.

1.Introduction

Ammonium nitrate, AN, is a widely used oxidizer yielding in the mixtures with usual organic fuels the burning products which do not contain, under conditions of thermodynamic equilibrium, any environmentally harmful constituents. The relatively low enthalpy of formation of this oxidizer is expiated by the very low cost of the commercial grade product which may provide correspondingly the very cheap unit of specific impulse. Another essential advantage of AN-based compositions consists in

comparatively low sensitivity to mechanical stimuli. Accidental explosions of the compositions of this type still had taken place in the course of the long history of their production, transportation and application that allowed to construct however the well developed approach to the safety provision of the materials of this sort as a whole. Obviously this long, hard and hazardous way must be passed through with every new, or may be relatively old but less assimilated, oxidizer. One might say that for the specialists in the field of safety AN-based EM constitute rather boring subject of study. Nevertheless, at this stage of development of a new kind of compositions on the base of AN for rocket propulsion it would be necessary to consider all the information concerning the fundamental performances of AN-based EM, bearing in mind both clarification of their advantages as suggested rocket propellants and estimation of possibly dangerous behavior as the subjects of the technology. Very important in this respect obviously is the possibility of explosive substances of this sort to burn, in general, and the ballistic properties of their burning, in particular. It is the main goal of this paper.

Several categories of AN-based model propellants were studied in this paper:

1. Neat AN, burning as a solid monopropellant, with minor additives to lower the pressure deflagration limit (PDL).
2. Compositions based on AN/TNT 80/20 mixture under influence of the catalysts, carbonaceous materials including carbon black, and some suppressants of burning.
3. Materials containing, besides AN and TNT, RDX or liquid nitric esters.

Preliminary results indicate that, up to pressures of the order of hundreds atm, the essential part of reactions responsible for heat evolution during the combustion proceed mostly in the liquid layer near the solid/liquid interface for pure AN and AN with organic fuels (including TNT and RDX), as well as for AN water impregnated compositions; studied earlier [Egorshev-91KY], whereas, at higher pressures, the gas phase flame certainly plays an important role in controlling the burn rate.

2. Burning of AN mixtures with mineral additives

K. Andreev and A. Glaskova [Andreev-52G, Glaskova-67, Andreev-67Ga, Andreev-67Gb] in Russia were among the first who extensively investigated burning of AN and AN-based compositions. The main goal of their study was to clarify mechanisms of burning and elucidate the influence of possible catalysts (considered at that time by Andreev as one of the main factors determining safety of AN-based explosives as applied in coal mines).

2.1. Experimental results

At room temperature neat AN did not burn in experiments carried out by Glaskova [Glaskova-67], by means of a constant pressure bomb, in glass tubes of relatively large diameter - up to 30 mm - even at 1000 atm. In PMMA tubes of 7 mm inner diameter (AN density 1.1 g/cm^3) burning waves propagated following ignition by a tablet of dynammon, supposedly due to partial reaction of AN with PMMA walls. The measured mass burning rate at 1000 atm was 0.8 g/cm^{2}s. In accordance with previous investigations [Taylor-48, Taylor-49S, Shidlovsky-58], it was found that a variety of small mineral additives makes burning of AN possible without PMMA.

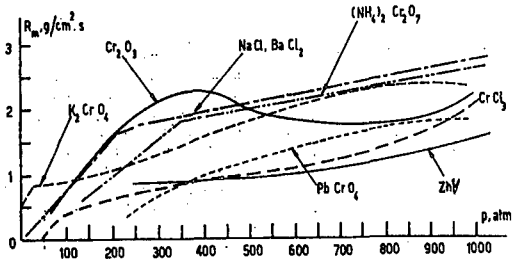

Fig.1. Burning of AN containing 5-7% additives [Glaskova-67] in a pressure interval from 1 to 1000 atm.

Typical burning rates in a pressure interval from 1 to 1000 atm are presented in Fig. 1 (taken from [Glaskova-67]). Content of the additives is 5% by mass. All experiments were carried out in PMMA tubes, inner diameter 7 mm and outer diameter 9 mm, with charge porosity close to zero. A similar behavior was observed in the course of experiments with AN/TNT 80/20 mixture (denoted as Am in Fig. 2). This composition burns rather slowly and has also very high pressure deflagration limit (although much less than for pure AN), about 130 atm. The presence of AN deflagration catalysts enhances burn rates of AN/TNT 80/20 and reduces PDL.

Similar experiments were performed by the authors of this paper, by means of a constant pressure bomb in PMMA tubes of 7 mm inner diameter. It was found that: burning rates of mixtures containing KCl are slightly lower than those of NaCl compositions, Am catalyzed by 7% NaCl burns faster than similar AN/NaCl mixtures, and faster also than Am + 20% NaCl; but overall the results of our measurements are very close to the data by Glaskova [Glaskova-67].

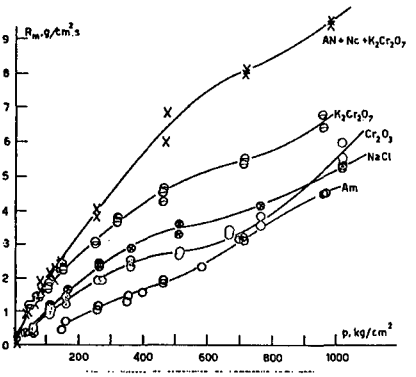

Fig.2 Burning of Am (AN/TNT 80/20) with and without catalysts (5%) in a pressure interval from 1 to 1000 atm. AN+NaCl+ $K_2Cr_2O_7$ is a mixture of AN and nitrocellulose (70/20) catalyzed by $K_2Cr_2O_7$ (10%). [Glaskova-67].

2.2.Instability and catalysis

Only a new fact should be noted. It was detected that deflagration of AN containing KCl or NaCl is characterized by a strong distortion of the condensed phase surface. At 100-200 atm pressures, the surface bents during combustion - sometimes forming a platform of 1-2 cm height - as a result of accumulation of the liquid, including dissolved catalyst, at the sites of the solid/liquid interface that occasionally turns out lower than the other regions of the interface. During combustion, phase interface is not smooth, but rough and irregular. The lower part of the interface forms a cavern collecting all the new portions of the liquid flowing down from the upper parts, and reaction proceeds preeminently in the thick layer of the liquid in the cavern. At high pressures, 200 atm and even more, when burn rates become higher and the liquid layers on top of the solid surface become thinner, burning wave stability increases. A similar behavior was disclosed during burning of mixtures AN/$K_2Cr_2O_7$ 90/10 at atmospheric pressure .

The previous observations are centered around a peculiar form of unstable burning, which might be called gravitational burning instability of the condensed materials containing catalyst with a liquid layer on the surface. As a consequence of this liquid/solid interface instability, attempts to measure temperature profiles during burning of AN-based compositions were not successful. The liquid layer reaches the thermocouple joint sometimes backward or from the sides, and no definite T(x) curve can be obtained.

The most effective catalysts of AN burning are probably dichromates [Taylor-48]. However, it was stated by Glaskova [Glaskova-67] that some of the usual participants in the redox reactions may sensibly promote the dichromate effects. One of the most effective promoters of potassium dichromate was proven to be potassium oxalate $K_2C_2O_4$: the addition of 0.5% potassium oxalate increases burn rate of AN/$K_2Cr_2O_7$ 90/10 by more than twice. For 2% $K_2C_2O_4$ the maximum effectiveness is reached, being the mass burn rate 0.26 - 0.33 g/(cm^{2}s) at 2 atm (while with no oxalate the mass burn rate is 0.13 g/(cm^{2}s)). For further addition of $K_2C_2O_4$, burn rate is reduced and a strong addition of 10% $K_2C_2O_4$ does not allow AN to burn. Presumably the potassium oxalate promotes evolution of active oxygen for the dichromate to chromate conversion, but does not influence itself the HNO_3/NH_3 reactions as $K_2Cr_2O_7$ does.

3. Burning of AN mixtures with explosives and organic fuels

3.1. Experimental procedure

The most effective fuels of AN and AN-based compositions in the sense of burning promotion are charcoal and activated carbon. Burning of this kind of mixtures will be the object of another compilation by the authors. Here we consider the mixtures of AN with nitrocompounds, mostly (TNT) - as a model composition of the oxidizer with an active binder capable to melt - and partly with RDX, Nitroglycerin, wood flour and carbon black. In addition to pure AN, a commercial grade product containing several tenths of a percent of ferrous salts of stearic acids was used, imparting to AN some kind of water resistance and at the same time working as a weak catalyst of burning reaction. This waterproof material is called AN ZhV or ANZ. Some of the mixtures contained NaCl and Na_2SO_4 as the catalysts, and LiF as the burning retardant. The full compositions and basic characteristics of material tested are given in Table 1.

The compositions were prepared by mixing of AN (at most 100 mcm) with TNT (50 mcm) and additives by shaking them in a glass bulb containing a dozen of the rubber plugs during about 20 min. The mean particles dimensions of NaCl and Na_2SO_4 were at most 200 mcm, LiF 20 mcm, wood flour 10 mcm, and carbon black at most 1 mcm. Aquanit № 2, SK № 1 and Detonit 10A are the commercial products.

Mixtures in the dry powder form were pressed into PMMA tubes of 7 mm inner diameter and 9 mm outer diameter at a pressure of about 0.2 GPa giving practically zero porosity of the specimen. 12/14 mm glass tubes were also used for AmZ burn rate estimation. Relative density of the mixture was about 0.8 in this particular case. The length of the cylinder of the mixture in the tube was about 20 mm. Aquanit № 2 and Detonit 10A were pressed into the tubes by means of a plastic punch manually. Relative density was about 1.0 in the case of Aquanit and 0.8÷0.9 in the case of Detonit.

Burn rate measurements were implemented in the constant pressure bomb at a pressure from several atm to 360 atm. Drum photoregister FR-10 was used to obtain the streak photographs of the process in the course of the burn rate measurements.

Critical diameter was measured in conical glass tubes of 0.5 to 1 mm wall thickness placed, wide ends up, into the glass beaker filled with water. The beaker was installed in the constant pressure bomb. The tube was filled in by the substance under investigation by means of a set of punches, manually, to receive the highest possible density. After burning had extinguished, the tube was taken from the bomb, the residual layer (usually covering the inner surface of the tube walls) was carefully removed, and critical diameter was measured as the diameter of the upper part of the unburned column.

3.2. Burn rate measurements

Table 1

The compositions and basic characteristics of the materials tested

Designation	Components content, % by mass				u_m, g/cm^{2}s at 30 MPa	T_f,K at 30 MPa
	AN	TNT	NaCl and other mineral additives	Hydrocarbons and other combustibles		
Am	80	20			1.2	2609
AmZ	79.7	20.0		~0.3	1.8	2623
Am+7NaCl	74.4	18.6	7.0		3.0	2439
Am+20NaCl	64	16	20		2.3	2232
AmZ+20NaCl	63.8	16.0	20.0	~0.2	2.3	2234
Am+10Na_2SO_4	72	18	10		1.9[a]	2325
Am+10LiF	72	18	10		1.0	2250
Am+5WF	76	19		5 WF	1.2	2466
Am+5CB	76	19		5 CB	1.3	2322
ANFO	96			4	-	2072
ANFO+NaCl	76.8		20.0	3.2	2.7	1802
Aquanit №2	44.2+ 7.4CaN	5.0	6.5 H_2O	0.8+35.0RDX+1.1SC	5.5[a]	2449
SK 1	66	5		24RDX+5 Al	4.0	3017
Detonit 10A	76.0	8.0		0.8+5.2Al+10.0NE	2.8	2868

Notes: CaN is calcium nitrate, WF is wood flour, SC is sodium carboxymethylcellulose, NE is liquid nitric esters (NG/DEGDN 60/40), [a] Extrapolated

Burn rates of Am, AmZ and their mixtures with NaCl (20%), having oxygen balance close to zero, are shown vs pressure in Fig. 3. Measurements were made, in a constant pressure bomb, in PMMA tubes with porosity of the specimens close to zero. For the neat AN/TNT mixture the data collected by Glaskova [Glaskova-67] are reported. experimental measurements reveal a fair scatter presumably connected with the kind of AN-based propellants burning instability mentioned in Section 2. Burn rates of AmZ is about 1.5 times higher than that of AN/TNT. The addition of 20% NaCl leads to further augmentation, about 30 to 40%. NaCl as a catalyst is so effective that suppresses influence of the ferrous salts introduced into AN, thus burn rates of AN/TNT and AmZ with NaCl are almost equal. The mass burn rate dependence on pressure is almost direct proportionality with the exception of Am (AN/TNT 80/20) at P<300 atm and Am+20NaCl at P>300atm. In the last case, at P>300 atm the effect of NaCl on AN/TNT burning becomes weaker, and thus the $u_m(p)$ line gets closer to that of the neat AN/TNT mixture almost overlapping with it at $p \approx 1000$ atm.. Neat Am demonstrates rather peculiar $u_m(P)$ dependence. At high pressure, it is the usual straight line, n=1. In the pressure interval from PDL to about 300 atm it is the curve characterized by the n-value

variation stipulated probably by the complex behavior of the reactions in the condensed phase. The strange effect of the tube diameter on the burn rate of AmZ is connected probably, with its burning instability and a reaction of AN with PMMA

The high value of PDL needs a special attention. For AN/TNT it is about 130 atm (while most of the common rocket or gun propellants can burn at atmospheric pressure or even lower) and the corresponding mass burn rate is about 0.6 g/(cm^{2}s) (10 to 20 times larger than the common propellants have at PDL conditions). Ferrous salts and NaCl seem to diminish considerably the PDL value, but the corresponding critical burn rate at PDL is still too high compared with the common propellants. This peculiarity of AN-based propellants, i.e. quite usual burn rate values and pressure dependence but unusually high PDL and corresponding critical burn rate value, will be discussed elsewhere.

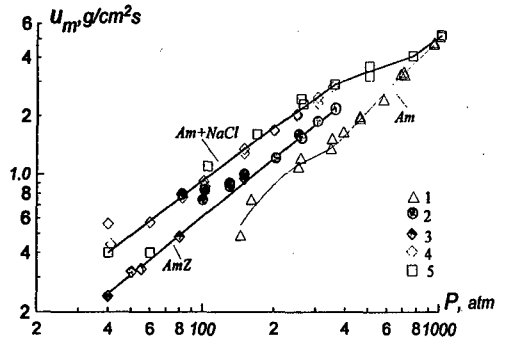

Fig.3. Burn rates of Am (1), AmZ (2,3) and mixture of Am with 20%NaCl (4,5), (2) in the PMMA tubes of 7 mm i.d., (3) in glass tubes of 12 mm i.d., (1,5) are A. P. Glaskova data [Glaskova-67]

An important burning characteristic of the mixtures is the shining bright yellowish-white flame indicating condensed carbon evolution during burning. In spite of the close to zero oxygen balance of the mixtures in Fig. 3, thin stripes of carbon black cover the walls of the tube after burning and the upper sample surface, after occasional extinguishment, form the peculiar cellular patterns.

Introducing NaCl into the composition sensibly increases burn rates. The special set of experiments demonstrates that maximum value is reached for 5% NaCl indicating the

outstanding influence of sodium and chlorine ions on the process. Interaction between NaCl and NH_4NO_3 is considered the leading reaction.

At 10-20 atm the pellets pressed from AN/TNT+7%NaCl mixture extinguish usually after a small space of burning, several mm, disclosing the curved surface of the upper part of the pellet. This surface as well as the edges of the meniscus and, at least partly, the lateral surface of the cylinder are covered by the layer of crystalline residue. Its color changes from yellow to brown or black. This layer was removed by a blade, dissolved in dry toluene, and after filtration a yellowish solution containing almost neat TNT was obtained. The residue on the filter (about 6% of the layer mass) consisted of carbon black and several grains of NaCl. Almost pure TNT can be found after AN in the surface layer is fully consumed. AN and NaCl react decidedly much faster than TNT does. At low pressures, TNT absorbs the heat released by AN decomposition, reduces the concentration of the main reactants (NH_4NO_3 and NaCl), and acts preferably as an obstacle against further reactions. However, at higher pressures, when steady state burning develops, TNT participates considerably in the overall process of deflagration: mixture of AN/TNT + 7%NaCl burns markedly faster than the mixture AN + 7%NaCl does.

The influence of other additives on burning of AN/TNT and ANZ/TNT 80/20 mixtures is shown in Figs. 4-6. The addition of 10% Na_2SO_4 (Fig.4) increases the burn rate of AN/TNT 80/20 but NaCl effect is substantially stronger. The addition of 10% LiF, on the contrary, decreases the burn rate of Am. Admixture of 5% wood flour (WF) almost does not change the burn rate of AN/TNT 80/20, if one compares the points at the same pressure, but as a whole the curve $u_m(P)$ for AN/TNT 80/20+5%WF acquires its peculiar shape and form. The main effect of WF addition consists however in the strong decrease of PDL and critical mass burn rate, respectively from 130 atm and 0.6g/(cm^2s) for neat Am to 50 atm and 0.2 g/(cm^2s).

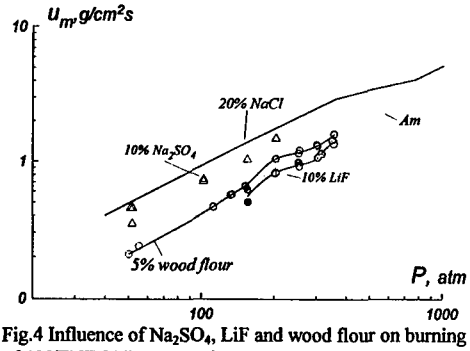

Fig.4 Influence of Na_2SO_4, LiF and wood flour on burning of AN/TNT 80/20, Am, mixture.

Still more pronounced in this respect seems to be carbon black influence (Fig. 5). Even added in quantity as small as 5%, it diminishes the mass burn rate of AN/TNT 80/20 at high pressures; but for small pressure the mass burn rate increases, to 0.02 g/(cm^2s). A difference between AN and

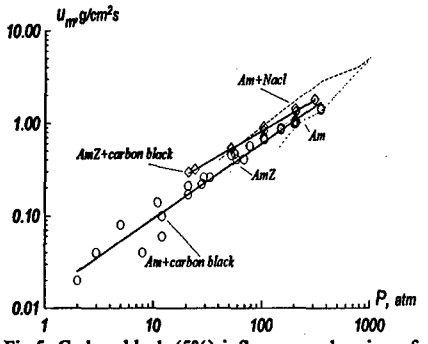

Fig.5. Carbon black (5%) influence on burning of compositions of AN/TNT (80/20), Am, and ANZ/TNT (80/20), AmZ

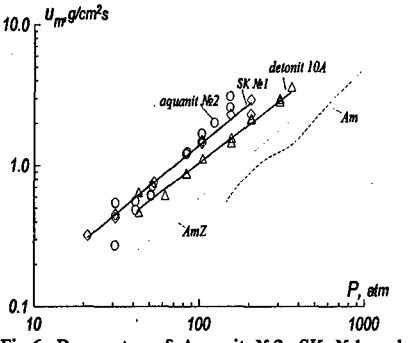

Fig.6. Burn rates of Aquanit №2, SK №1 and Detonit 10A. Lines with no points are the compositions of AN/TNT (80/20), Am, and ANZ/TNT (80/20), AmZ

ANZ-based materials consists in the fact that carbon black increases the AmZ burning rate at least up to 300 atm whereas PDL is reduced from 130 to 10-15 atm, and the critical mass burn rate from 0.6 to 0.02 (g/cm^{2}s).

Fig. 6 represents the data for two AN-based formulations, containing 10% of commercial grade NG/DEGDN 60/40 mixture (called Detonit 10A) or 24% RDX (called SK1). Both compositions contain also 4-5% aluminum powder. Aquanit №2 contains RDX (35%) and about 10% water gelatinized by sodium carboxymethylcellulose. All of them burn faster than AN/TNT 80/20, and even than the AN/TNT/NaCl 64/16/20 mixtures.

ANFO explosive does not burn steadily, at least up to 40 MPa. 20% NaCl addition makes it possible to burn, and the burn rate at P = 30 MPa becomes even higher than that of Am+NaCl (see Table 1).

3.3. Critical diameter of burning

Estimation of critical diameters, d_c, of high explosives was implemented earlier [Annikov-67K] to obtain further information about the burning mechanisms.

Dependencies of $d_c(p)$ are shown in Figs. 7-8. They are mostly hyperbola like lines, and usually can be plotted as straight lines in the coordinates p vs $1/d_c$ (see Fig.9). Processing of AN in presence of iron ferrous sulfate and organic acids giving ANZ demonstrates strong decrease of d_c (p) curve position in the p *vs* d_c plane, especially at moderate pressures (Fig. 7). NaCl addition works about as AN to ANZ transformation at moderate pressures

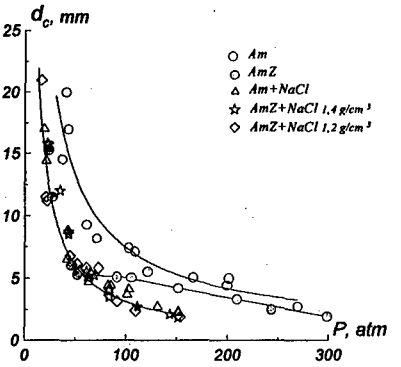

Fig.7. Critical diameter vs. pressure of Am, AmZ and Am+20NaCl.

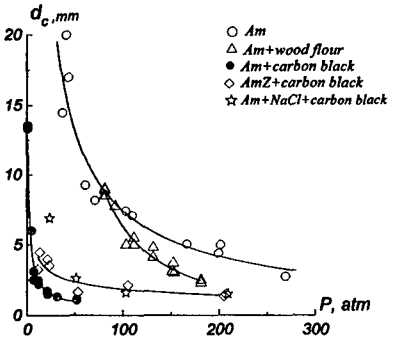

Fig.8. Comparison of wood flour (5%) and carbon black (5%) influence on d_c of compositions of AN/TNT (80/20), Am, ANZ/TNT (80/20), AmZ, and AN/TNT/NaCl (64/16/20), Am+20NaCl.

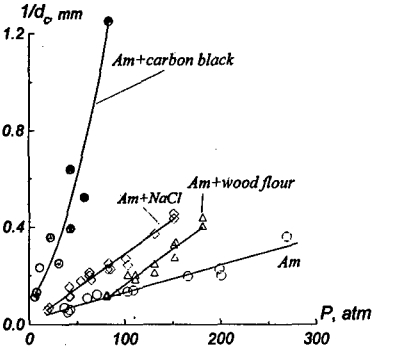

Fig 9. Inverse critical diameter vs. pressure for AN-based compositions.

(up to 60 atm) and more strongly at higher pressures. NaCl addition to AN/TNT and to ANZ/TNT 80/20 mixtures gives about the same curve (Fig. 7). Variation of density within the limits of 1.2 to 1.4 g/cm^3 discloses the absence of any appreciable effect. The most pronounced decrease of d_c is realized by means of carbon black to Am admixture; see Fig. 8. This effect is not so strong in the case of AmZ and AmZ + 20NaCl mixtures, but nevertheless it is evident in both cases. Wood flour addition increases burning stability of Am but much weaker than carbon black does (Fig. 8).

3.4. Temperature measurements

The main reaction in the course of burning of AN-based materials under consideration, at least in the region of several tens to several hundreds atm, is supposed to proceed preeminently in condensed phase, at the surface liquid layer, containing NH_4NO_3, dissolved catalyst, liquid fuel and the products of decomposition thereof. In the absence of a catalyst the reaction develops presumably as a result of interaction between the primary products of NH_4NO_3 decomposition, NH_3 and HNO_3, promoted by the carbon itself and the carbon containing substances produced at a fuel pyrolysis.

The leading role played by the processes in the liquid layer may be demonstrated by the results of temperature profile determination. Measurements were carried out in cooperation with A.E. Fogel'zang using flat Pi-shaped thermocouples Tungsten/

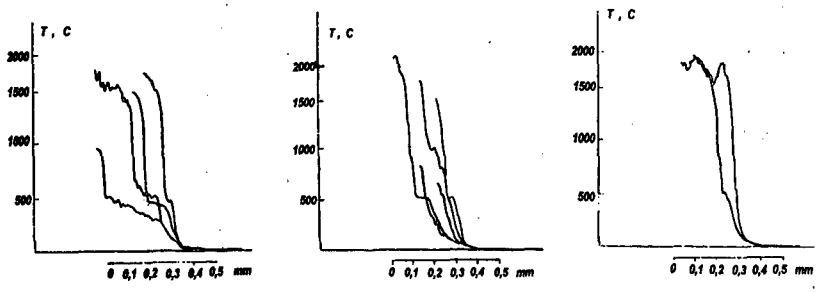

(a) (b) ©

Fig.10. Temperature profiles at burning of: (a) AN/TNT (80/20), (b) AN/TNT (80/20) containing 5% NaCl, and © AN/TNT (80/20) containing 5% wood flour. P=200 atm.

Table 2

Burning of AN/TNT compositions at p=200 atm

Composition	N	Burn rate, mm/s	δ_{calc}, mm	N	δ_{exp} mm	$\frac{\delta_{exp}}{\delta_{calc}}$	N	T_f, K
AN/TNT 80/20	17	6.1±0.5	0.016	5	0.26±0.07	16	2	2383±37
AN/TNT/WF 76/19/5	13	6.5±0.4	0.015	2	0.17±0.02	11	4	2183
AN/TNT/NaCl76/19/5	12	11.8±0.8	0.0085	5	0.17±0.05	20	2	2633

Notes: N is number of runs, δ is thickness of the preheated zone.

5%Rhenium - Tungsten/20%Rhenium. The thermocouple was placed in the central part of the charge inside a PMMA tube 8 mm diameter, 2 mm wallets of the mixtures of AN/fuel/additive were used. Thermocouples of 7 mcm wire thickness were used to determine T(x) dependence, 50 mcm wire thickness to detect the maximum burning temperature. Experimental results are presented in Fig. 10 and Table 2. Experimental curves obtained under the same operating conditions vary considerably. This is a consequence of the burning instability phenomena. However, one may note that almost all of the curves contain, for temperatures near 500^0C, a small flat plateau especially well developed when burning the AN/TNT 80/20 material without additives. A similar observation was first made in [Whittaker-64B] and explained as a surface tension effect causing the liquid to ''hang onto the thermocouple''; on the other hand, thermal profiles without plateau are reported as well [Alspach-91H] (AN/TMETN/GAP 67/12/21). The thickness of the liquid layer, separating the original solid substance from the gaseous products of the reaction, varies from 0.03 to 0.3 mm for AN/TNT 80/20. The mean value of 0.15 mm is about ten times higher than the calculated thickness of the preheated Michelson layer as a whole. This obstacle cannot be overcome by any heat flux from the gas phase. Thus, the source of heat release responsible driving the mixture burning is located in the liquid layer quite near the solid phase surface. NaCl diminishes the thickness of the liquid, wood flour decreases it still more. At any rate, the presence of the almost horizontal platform on T(x) curves does mean that the place of the leading heat release is positioned, with reference to Fig.10, on the right side of the platform, and the gaseous flame has little but perceivable influence on burn rate as well as other relevant burning parameters, especially d_c.

3.5. Comparison of the results with data for nitrocompounds

Chemistry of processes in condensed phase, at elevated pressures is very complicated matter, and will be considered in detail in the next paper of the series. In the high pressure region the results are easily generalized [Kondrikov-73RS]. Relation between the reduced burn rate and adiabatic combustion temperature at P = 30 MPa is shown in Fig. 11 in the same coordinates, as used in [Kondrikov-73RS]. The straight line in Fig.

11 is taken from [Kondrikov-73RS] and corresponds to the burning velocity dependence on the flame temperature for nitrocompounds at p = 30 MPa. It can be assumed that in

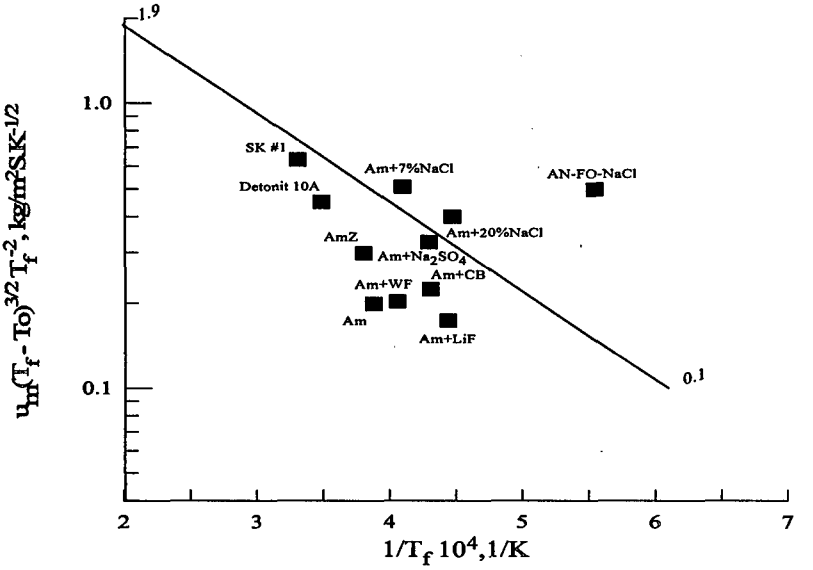

Fig.11. Dependence of the reduced burning rate of AN-based compositions at P=30 MPa on calculated inverse temperature of flame. Straight line corresponds to the same dependence for nitrocompounds [Kondrikov-73RS]

the case of nitrocompounds, the $u_m(T_f)$ variation is determined by the effective activation energy of the interaction between the nitrogen oxides and the combustible gases (CO, H_2 and similar). All of the other substances, with no catalysts or with minor content of it, (Am, AmZ, Am+WF, Am+CB and even Detonit 10A) are positioned in Fig. 11 plane much lower than the line is, demonstrating in fact that the leading reaction both in condensed7 and in gas phase at burning of these compounds proceeds much slower than that at the regular nitrocompounds burning. Quite probably it is the result of the big ammonia concentration in the mixture. NH_3 retardation influence on burning of explosives was postulated by A.P.Glaskova [Glaskova-76]. She was being considered this as a result of the reverse reaction of the type of equilibrium (1). The real influence of ammonia is probably much more complicated problem, and may be stipulated preeminently by the reactions

$$NH_3 + H \rightarrow NH_2 + H_2$$

$$NH_3 + OH \rightarrow NH_2 + H_2O$$

$NH_2 + H \rightarrow NH + H_2$

which eliminate active hydrogen and hydroxyl radicals in flame to exchange them by the relatively passive species NH_2 and NH. Correspondingly, the gas flame does not take part in the burning wave propagation, while the reaction in the condensed phase where influence of H and OH is relatively small becomes the leading process determining the overall burn rate.

The catalysts influence leads to acceleration of the reactions in the condensed phase and correspondingly burn rate of Am, AmZ and even AN-FO compositions is enhanced to reach the reference point at corresponding temperature or even to exceed it. Especially strong this effect is in the AN-FO case where no burning without NaCl might be observed up to 40MPa, meanwhile the very high u_m value is reached in the presence of NaCl.

5.Conclusions

The subject of this paper is to describe the experimental facts in the field of steady state burning and to estimate the critical burning conditions of three categories of AN-based compositions.

1. Neat AN, burning as a solid monopropellant, with minor additives to lower the pressure deflagration limit (PDL).
2. Compositions based on AN/TNT 80/20 mixture under influence of the catalysts, carbonaceous materials including carbon black, and some suppressants of burning.
3. Materials containing, besides AN and TNT, RDX or liquid nitric esters.
4.

It is shown that combustion of almost all of the substances studied is characterized by the usual for many propellants and high explosives burning rate and dependence of the rate on ambient pressure but at the same time by the very low level of burning stability: PDL value and critical diameter of burning in the majority of cases are much higher than the corresponding values observed for the usual double base and composite propellants as well as for the variety of nitrocompounds investigated earlier.

The preliminary explanation proposed for this peculiarity takes into consideration the experimental observation that in the moderate pressure region, related to the PDL, and d_c values, reactions of thermal decomposition of AN proceed in a liquid layer which comprises a mixture of melted AN, water, nitric acid, ammonia, nitrogen oxides, and some other less pronounced constituents. Reactions in this layer go on slowly and release the correspondingly low quantities of heat at relatively low characteristic temperature. Reactions in the secondary flame are separated from the liquid/solid interface by a layer of the rather inert fluid and do not participate significantly in formation of the burning process as a whole. They strongly influence however PDL and d_c values. A theoretical description of the influence of melting, intermediate layer of liquid formation and heat of reactions evolved in the liquid layer, on the one side, and in the secondary flame, on the other side, is assumed to be presented in one of the next papers.

Generally speaking, the ammonium nitrate compositions are created by Nature for practical utilization in the form of high explosives, not propellants. They react slowly

and have no tendency to burn at low pressures and correspondingly display the outstanding safety characteristics. At the same time they react very eagerly at high pressures, and accordingly behave under these conditions as very effective explosives. This does not mean absolutely that the problem of accidental explosion hazard in the case of AN-based explosives and propellants has no practical sense. Versus versa, it is extremely actual problem. On the one hand, psychologically, the safe explosives have the strong tendency to give accidental explosions more often than relatively more hazardous materials. On the other hand, our main objective is to force AN-based compositions to burn properly at the relatively low pressures, and when this goal will be reached, the main, in the sense of safety, advantage of these compositions, low burning stability, will be automatically avoided, and the problem of safety will arise undoubtedly again.

In the presence of some additives, first of all carbon black, the burning stability of AN-based formulations may be essentially augmented. PDL is decreased to atmospheric pressure, d_c numbers get to the usual for the rocket and gun propellants figures, secondary flame is assumed to begin to play an essential role during burning of AN-based compositions.

Problems to be discussed in the next papers include influence of the thin dispersed metals (aluminum and magnesium), structure of the gas phase flame, details of the burning surface, burning stability problems, and more.

Acknowledgments

Professor Boris N. Novozhilov is highly acknowledged for many helpful comments to the text of the paper. Contribution of Dr. A.E.Fogel'zang into temperature profile measurements is remembered with pleasure and gratitude. Russian part of the team of the authors is indebted to Russian Basic Research Foundation (RBRF) for the financial support of this study within the framework of the Grant N 98-03-32167a.

References

Alspach, D.A., and Hall, G.M., Temperature profile measurements in solid propellant flames, Technical Report AIAA Preprint 91-2192, 1991.

Andreev, K.K., Glaskova, A.P., A comment to the theory of permissible explosives Proc. Acad. Sci. USSR (Doklady) 1952, v.86, 801.

Andreev, K.K., Glaskova, A.P., Influence of some additives on burning of AN, in Theory of Explosives, K.K.Andreev, editor, Moscow, Higher School Publishing House, 1967, 314-321 (in Russian). [Andreev-67Ga]

Andreev, K.K., Glaskova, A.P., Burning of dinammones and ammatol, ibid., 321-328. [Andreev-67Gb]

Annikov, V.E., Kondrikov, B.N., Influence of pressure on burning ability of high explosives, in: Theory of Explosives, Higher School Publishing. House, Moscow, 1967, 300-306 (in Russian).

Glaskova, A.P., Effet des catalyseurs sur la deflagration du nitrate d'ammonium et de ses melanges, Explosifs, 1967, N 1, 5-13.

Egorshev, V.Yu., Kondrikov, B.N., and Yakovleva, O.I., Combustion of water-impregnated explosive compounds, Comb., Expl. & Shock Waves, 1991, v.27, N5, 565-572.

Kondrikov, B.N., Raikova, V.M., and Samsonov, B.S., Reaction kinetics in the burning of nitrocompounds at a high pressure, Comb., Expl. & Shock Waves, 1973, N 1, 84.

Shidlovsky, A.A., Izvestia visshich Utchebnich Zavedenii, Khimia I Khimitcheskaya Technologia, 1958, N 3, 105 (in Russian).

Taylor, J., Low temperature reactions of burning in the solid state, Indust. Chemist. and Chem. Manufacturers, 1948, v.24, 289-296.

Taylor, J., and Sillito, G., The use of ammonium nitrate as a solid fuel to provide gas for propulsive purposes, 3rd Symposium (International) on Combustion, 1949, 572-579.

Whittaker, A.G., and Barham, D.C., Surface temperature measurements on burning solids. The Journal of Physical Chemistry, 1964, v.68, N 1, 196-199.

Burning of Liquid Aliphatic Azides

B.N. Kondrikov, M.S. Kozhukh, I.N. Ohotskaya,

Mendeleev University of Chemical Technology
9 Miusskaya Sq., Moscow 125047, Russia

Burning of 16 aliphatic azides is investigated in glass tubes of different diameter at a constant pressure. Constants of burn rate vs pressure law $u = u_o p^n$ in the region of steady-state combustion are estimated. For several of the substances temperature profiles in the burning wave are measured by the method of thin thermocouples.

Thermodynamic analyses of the alyphatic azides is carried out. Heats of formation and evaporation of the substances and their boiling points are determined. Adiabatic flame temperatures T_p are calculated using the modern computer code REAL-1, and correlation of u data with T_p is performed.

Comparison of calculated temperature of a leading chemical reaction T_f with experimentally observed effective temperature T_{ef} is made in suggestion of the first order kinetics for several azides of different chemical structure. Values of T_f for monoazido-propionic ester of acetic acid eventually coincide with the T_{ef} data. Thus the first order of the leading chemical reaction is quantitatively supported in this particular case. In some of the other cases this suggestion might be also at least substantiated.

Azidoethanol demonstrates very interesting peculiarity at comparison of experimental and calculated effective burning temperatures vs pressure curves. In the interval of 4 to 20kPa the curves essentially coincide if the first order reaction mechanism is used for the calculations, whereas the progressive increasing difference between them ($T_f > T_{ef}$) can be noted at 20 to 50kPa. Presumably this incostistency between T_{ef} and T_f may be connected with Landau instability effect that usually results in T_{ef} to decrease.

Calculation of the burn rate of droplets of azidoethanol is carried out in the interval of pressures of 0.005 to 0.1MPa in the framework of F.Williams approach. The calculation results agree very well with the experimental data previously reported. Corresponding comparison of calculated and experimentally observed data for a series of diazides thoroughly studied earlier by C.K.Law and coworkers demonstrates significant difference between mono- and diazides probably due to influence of the reaction in condensed phase at a high temperature of the liquid in the last case.

Results of these investigations are used, in particular, for interpretation of the experimental data received in our Laboratory and related to sensitivity of liquid (and melted) EM assessment. It was stated recently that constants of the burning law are the essential factors stipulated the sensitivity of a liquid EM. Very good results in elucidation of the sensitivity level of the compounds studied were achieved. The data now determined allow to calculate, in accordance with the values eventually measured, the figures of sensitivity for polyazides,1,3-diazidopropyl-azidoacetate, and 2-azidoethoxy-4,6-diazido-s-triazine.

Catalysis of Modern Solid Propellant Combustion

A.A.Zenin, S.V.Finjakov, N.G.Ibragimov, E.K.Afiatullov
Semenov Institute of Chemical Physics,
Russian Academy of Sciences. Moscow, RUSSIA.

Abstract

Actions of different catalysts on the combustion mechanism of nitramine containing double base propellants have been investigated by microthermocouple techniques. A theory of thermocouple measurements in combustion waves of solids is briefly outlined. The catalysts containing oxides of Fe, Pb, Ni and soot and complex compounds of Co, K, Cu, S and Pb were used. Burning wave parameters of the propellants with and without these catalysts were found at pressures 20, 50 and 100atm. Differences between these parameters constitute blocks of new parameters which present multiparametric actions of the catalysts. These blocks of the new parameters have been presented as matrixes for each catalyst. The matrixes are useful for description of the multiparametric actions of the catalysts in combustion waves of the modified propellants.A possible uses of the matrixes is discussed. The places of the catalytic actions in combustion waves and the character of their actions were established. Four modes (types) of catalytic actions in combustion waves were identified: mode of normal catalytic action, catalytic mode of blowing off, catalytic mode of heat compensation and gas phase catalytic mode. It was revealed that a significant increasing of burning rate is associated usually with an increase of heat release in solid or on the burning surface.

Introduction

Modern propellants contain various nitramines which improve the ballistic characteristics [1-4]. As a rule the propellants contain also different catalysts for regulation of burning rate laws. The actions of these catalysts usually can be determined only by the trial-and-error method. An understanding the mechanism of catalytic effect in combustion waves is necessary to creating a more productive method of catalyst searching. The paper aims to obtain changes of burning wave parameters due to catalysts including into a typical double base modern propellant, to classify these changes and to suggest a method of the catalytic action presentation which probably can be useful for catalyst searching. A possible method of prediction of actions of used catalysts by computer simulation is discussed.

Burning wave parameters of the propellants have been obtained by microthermocouple techniques [5-9]. The parameters of combustion waves are as follows: mass burning rate, burning surface temperature, heat feedback from gas to solid, heat release in solid, heat release rate in gas near to the burning surface, sizes and temperatures of zones in gas and solid. The catalytic action is investigated by comparing the burning wave parameters obtained for catalyzed and noncatalyzed (base) propellants: the differences between the parameters comprise blocks of catalytic actions.

The paper continues the investigations which were made in [5-7, 10]. The content of the paper is as follows: methods of investigations, combustion mechanism of base propellant, mechanism of catalytic actions in propellant combustion waves,

classification of catalytic actions in combustion waves and discussion about predictions of catalytic actions.

Methods of Investigations

Temperature profiles of the combustion waves were obtained by microthermocouples imbedded into solid. Thermocouples went through combustion waves when the waves propagated through the solid samples and registered temperature profiles. Microthermocouples made of alloys W+5%Re/W+20%Re were used. The ribbon U-shaped thermocouples 3.5-7 mkm thick were imbedded into samples which were cut along the axis and then were glued by acetone. Every sample had inside 2-3 thermocouples placed one above the other. Distances between junctions were 2-4 mm. The samples had been burned in a bomb of constant pressure in atmosphere of nitrogen at pressures 20, 50 and 100atm. The ignition was performed by a heated nickel-chromium wire. Burning rate was registrated by time delay between the thermocouple signals, by pressure increase in the bomb during sample combustion and by photo-registrations. Thermocouple signals were registered by the amplifier and oscillograph. Burning surface temperatures were measured by thermocouples pressed to the burning surface by special device (at low pressures) or by establishing the locations of slope breaks on temperature profiles registered by thermocouples (see below).

In combustion waves there exist high temperature gradients and thermocouple measurements can give temperature profiles with significant errors due to thermocouple heat inertia. Because of that it is necessary to find conditions under which thermocouple measurements in combustion waves will introduce small errors. These conditions have been found by numerical simulations of the process of heat exchange between thermal layer of solid and the thermocouple inside the layer when the combustion wave propagates. The thermocouple partially absorbs the heat of the thermal layer and decreases the temperature at the point of the measurement. The condition of small temperature decrease (less than 10%) is indicated by the following formula : $h \le 0.2\ \chi/r_b$; (1)

Here: h - thermocouple thickness (in cm), χ - heat diffusivity of the solid (in cm^2/s), r_b - linear burning rate (in cm/s). $\chi/r_b = l_t$, where l_t is the thickness of the thermal layer of the condensed phase. Expression (1) implies that thermocouple measurement can be successful only if thermocouple thickness is at least 5 times less than l_t. It is an obligatory requirement upon reliable thermocouple measurements in combustion waves. There is another requirement: the thermocouples must have U-shape form. It is necessary because of great difference between heat conductivity coefficients of metallic thermocouple wire and that of solid or gas (the difference comprises 3 order). In U-shaped thermocouples the junctions do not experience large temperature decrease. The decrease is caused by heat losses into wires when the thermocouple is in the field of large temperature gradient. Angle-shape thermocouples can not be used just because of the indicated heat losses. There are experimental confirmations of significant temperature errors introduced by angle-shape thermocouples. Modelling experiments and numerical simulations show that decrease of junction temperature for condensed and gas phases will be small (≤3%) if the horizontal part l_2 of U-shaped thermocouple is as follows: $l_2 \ge 100\ h$; (2)

Consideration of displacement of junction when U-shaped thermocouple passes the boundary of solid-gas and the thermocouple is subjected to the gas stream from the burning surface shows that the displacement is much less than h if condition (2) is fulfilled.

Thermal inertia of the thermocouple in gas phase must be eliminated by a special procedure. The procedure implies the use of the following equation:

$$dT_{ex}/dx = (r_b \cdot \tau_o)^{-1} \cdot (T - T_{ex}); \qquad (3)$$

Here: T - the real temperature of gas in combustion wave; T_{ex} - the temperature registrated by thermocouple; τ_o - time response of thermocouple in gas. Time response τ_o depends on mass burning rate m ($m=\rho \cdot r_b$) and on T. Values τ_o for used thermocouples can be found by expression $\tau_o = c_2 \cdot \rho_2 / 2\alpha$, where $c_2 \cdot \rho_2$ - volume specific heat capacity coefficient of thermocouple ($c_2 \cdot \rho_2 = 0.614 cal/cm^3 s$ for W,Re/W,Re), α - heat exchange coefficient between gas and thermocouple. Values α can be found by the following equation: $Nu = 0.72\sqrt{Re}$; (4)

Here: $Nu = 20\alpha \cdot h/\lambda_1$; (Nu - Nusselt criterion); $Re = 20mh/\mu_1$ (Re - Reynolds criterion), where - λ_1 and μ_1 - heat conductivity and viscosity coefficients of gas phase.

The above outlined short theory of thermocouple measurements in combustion waves of solids was tested and confirmed by measurements of combustion wave temperature profiles by thermocouples with gradually decreased thickness (method of "zero diameter"). All the above mentioned requirements have been met. Calculations show that for used propellants and microthermocouples all distortions of burning waves due to thermocouple imbedding are small under the investigated conditions.

Different types of metal wires for thermocouples were used (We,Re and Pt/Pt+13%Rh) to test the catalytic effect on thermocouples. The effect of this type of catalysis has not been observed.

The above mentioned method of burning surface temperature T_s measurement by determining the locations of slope breaks on temperature profiles registered by thermocouples (method of "slope break") is based on the existence of the delay ($r_b \cdot \tau_o$). The delay is due to the change of heat exchange laws between medium and thermocouple: contact heat exchange in solid is transformed into heat exchange by Newton law in gas.

The received profiles allow the following parameters of propellant combustion waves to be evaluated: heat feedback from gas to solid (q) by heat conductivity, heat release in solid (Q), heat release rate in gas near to burning surface (Φ). Heat flux by heat conductivity from gas to the burning surface can be obtained by the slope of the temperature profile near to the burn surface and by the use of the following formula:

$$q_m = -\lambda_1(T) \cdot (dT/dx)_o; \qquad (5)$$

Heat feedback from gas into solid by heat conductivity can be obtained by the following expression: $q = -\lambda_1(T) \cdot \varphi / m$;

Heat feedback by flame radiation is small.

Heat release in the reaction layer of the solid phase (and on the solid surface) is as follows:

$$Q = c \cdot (T_s - T_o) - q + q_m; \qquad (6)$$

Here q_m is the heat of nitramine melting.

This parameter Q includes heat release inside the reaction layer of solid and heat release on the burning surface as well. Existing methods Q obtaining do not allow these two types of heat release separately to be measured. It is highly probable that the heat release on the burning surface from the gas side plays a very significant role in combustion waves of catalyzed propellants.

Heat conductivity equation for gas phase of stable combustion waves is as follows:

$$(\lambda_1 \cdot T_x')_x' - m \cdot c_p \cdot T_x' + \Phi(T) = 0 ; \qquad (7)$$

Here: c_p , λ_1 - specific heat capacity and heat conductivity coefficients of gas phase correspondingly. Generally distribution of volumetric heat-release-rate $\Phi(T)$ in gas can be received by using experimentally obtained temperature profile T(x), eq.(7) and by a special calculation procedure. However an approximate expression can be obtained for Φ close to the surface when there exists a significant heat release in the solid phase. It is just the case observed here. The first term of eq.(7) for propellant profiles is small and thus the following expression is valid: $\Phi = c_p \cdot m \cdot \varphi$; (8)

Combustion Mechanism of the Base Propellant

The typical modern double base propellant was chosen as the basic one. It contains 34% nitrocellulose, 33% nitroglycerine, 15% HMX, 15% nitrosoamine and 3% technological additions. Caloric power 1085cal/g, flame temperature T_f=2450°C. Diameter of cylindrical samples 8mm, length 30mm. Back side was protected by thin layer of polymer. Figs.1, 2 and 3 show the obtained averaged temperature profiles (averaging 8-12 experimental registrations). It can be see that at 20atm gas phase has a typical for double base propellants two-zone structure: dark zone and flame zone []. At 50atm both zones are very close and at 100atm they merge. Table I presents obtained averaged burning wave parameters. The following coefficients were used: for solid c=0.36cal/g·K, ρ=1.6g/cm^3, q_m=4cal/g; for gas c_p=0.465-83.3/T (T in K), λ_1=[0.167$\sqrt{T}$ -2.67]·10^{-4}cal/cm·s·K (T in K). The used nomenclature is as follows: T_1 - mean dark zone temperature; T_f - flame temperature; l_f - thickness of heat layer in solid (i.e. distance between surface and section T*, where $T^* = (T_s - T_o)/2.72 + T_o$;); l_{mf} - heat conductive size in solid ($l_{mf} = \chi / r_b$, $\chi = 10^{-3}$cm^2/s); δ - relative thickness of heat layer in solid ($\delta = l_f / l_{mf}$); l_g - thickness of gas phase zone of variable temperature (i.e. distance between section $0.9T_1$ and T_s or, when gas zones merge, - between $0.9T_f$ and T_s); l_{mg} - heat conductive size in gas ($l_{mg} = \lambda_1 / c_p \cdot m$); Ω - relative thickness of gas phase zone of variable temperature ($\Omega = l_g / l_{mg}$); L_1 - thickness of dark zone; L - distance for surface till flame (till section $0.95T_f$).

It can be seen that parameters m, T_s, φ, q and Q monotonically grow when pressure increases. Value T_f also increases and achieves maximum between 50 and 100atm. Distances L_1 and L are over heat conductive sizes of gas phase zone 20 - 200 times (see values Ω). It is important to stress since it implies that a large heat resistance exists between burning surface and high temperature regions of the gas phase. It implies also that burning rate control stage can be only heat release in solid and a very thin low-temperature gas layer (l_{mg} thick) close to the burning surface. In other words investigated propellant has a very thick reaction region in gas with heat release rate distributed along the gas phase.

Obtained values δ can be assumed as close to 1 because value of heat diffusivity of solid $\chi=10^{-3}cm^2/s$ used for the appraisal δ was taken from the determinations of that parameter at normal temperature. It is obvious that at elevated heat layer temperatures χ have to be higher. In fact values δ obtained from temperature profiles in solid allow χ determination at elevated temperatures. Thus obtained values δ imply that $\chi=(2-3)\cdot10^{-3}cm^2/s$ in heat layer. It implies also that this layer can be assumed as heat conductive size and that subsurface heat release is concentrated inside thin reaction layer close to surface.

It is necessary to note that all the obtained peculiarities of combustion of the studied nitramine propellants are inherent ones for all double base propellants [8, 9].

Table I

Base Propellant Burning Wave Parameters

pressure, atm	20	50	100
m, g/cm^2s	0,71	1,65	2,31
T_s,°C	365	442	478
$\varphi.10^4$, K/cm	4,6	11	16,6
q, cal/g	10	12	13,7
Q, cal/g	115	140	151
T_1,°C	1200	-	-
T_f, °C	190	2400	2450
l_t, mkm	44	28	20
l_{mt}, mkm	23	10	7
δ	1,9	2,8	2,8
l_g,mkm	200	1000	480
l_{mg},mkm	10	5	3
Ω	20	200	166
L_1,mm	1,2	-	-
L,mm	-	1,5	0,5
Φ, $Kcal/cm^3s$	12	68	150

The investigation shows that catalyzed propellants have the same qualitative peculiarities of combustion waves as noncatalyzed propellants (in particular, large values Ω and values δ close to 1). Because of that the investigations of the pointed above catalysts in combustion waves of catalysed propellants will be conducted by the analyses of the behaviour of the main wave parameters: m, T_s, q, Q, Φ and L.

It is convenient to present the main parameters in the form of the following matrix:

$$\begin{pmatrix} p_1 & m_1 & T_{s1} & q_1 & Q_1 & \Phi_1 & L_{,1} \\ p_2 & m_2 & T_{s2} & q_2 & Q_2 & \Phi_2 & L_{,2} \\ p_3 & m_3 & T_{s3} & q_3 & Q_3 & \Phi_3 & L_{,3} \end{pmatrix}$$

The matrix of main burning wave parameters of the base propellant has the following form:

$$\begin{pmatrix} 20 & 0{,}71 & 365 & 10 & 115 & 12 & - \\ 50 & 1{,}65 & 442 & 11 & 140 & 68 & 1{,}5 \\ 100 & 2{,}31 & 478 & 13{,}7 & 151 & 150 & 0{,}5 \end{pmatrix}$$

Standard deviations of the obtained parameters are as follows: $\vartheta m=\pm 5\%$, $\vartheta T_s=\pm 5\%$, $\vartheta\varphi=\pm 10\%$, $\vartheta q=\pm 15\%$, $\vartheta Q=\pm 5\%$, $\vartheta\Phi=\pm 15\%$, $\vartheta L=\pm 15\%$.

Mechanisms of Catalytic Actions in Propellant Combustion Waves

The following catalysts have been studied:

1. Fe_2O_3 (particles of 5mkm, addition **3%** by weight above 100%);
2. CSCP (partic. 2-5mkm, addit. **2%**); **3. 1%CSCP+1%soot (C);**
4. CSNP (2-5mkm, **2%**); **5.** 1%**CSNP+1%C; 6. 1%PbO_2** (5mkm)**+1%C;**
7. 0.7%PbO_2+1%C+0.15%SR; 8. 9.1%PbO_2+1%C; 9. 1%**PbO** (5mkm)**+1%C;**
10. 1%**PbO+1%NiO** (5mkm)**+1%C;**
11. 0.37%PbO+1.5%HCP (10-20mkm)**+0.45%C;**
12. 1.5%**PbO+5.5%HCP+2%C;**

Here: CSCP is combined salts of Cu and Pb of 1,4-benzoldicarbon asides,
CSNP is combined salts of Ni and Pb of 1,4-benzoldicarbon asides,
SR is sulphurresorzinate,
HCP is hexanitrocobaltate of potassium - $K_3[Co(NO_2)_6]$;

Actions of the catalysts have been described by differences between the main burning wave parameters of catalyzed and noncatalyzed propellants. These differences constitute block of multiparametric action of each catalyst and that block ("portrait" of catalyst) can be presented as a special matrix having the following form:

$$\begin{bmatrix} p_1 & \Delta m_1 & \Delta T_{s1} & \Delta q_1 & \Delta Q_1 & \Delta\Phi_1 & \Delta L_{,1} \\ p_2 & \Delta m_2 & \Delta T_{s2} & \Delta q_2 & \Delta Q_2 & \Delta\Phi_2 & \Delta L_{,2} \\ p_3 & \Delta m_3 & \Delta T_{s3} & \Delta q_3 & \Delta Q_3 & \Delta\Phi_3 & \Delta L_{,3} \end{bmatrix}$$

Here, for example, Δm_1 is equal to difference between mass burning rates of catalyzed and noncatalyzed propellants at pressure p_1.

Values which lie within the standard deviations will be designated by italic figures. It is obvious that in these cases only tendencies of the value changing can be discussed. The portraits of the studied catalysts is presented below in the corresponding sections. In addition all the portraits are presented in Fig.II.

1. Action of Fe_2O_3 (3%)

Figs. 1-3 show the obtained averaged temperature profiles. The portrait of Fe_2O_3 can be presented as follows:

$$\begin{bmatrix} 20 & \textit{0,03} & \textit{3} & 15{,}7 & -14{,}6 & 20 & - \\ 50 & -0{,}33 & \textit{-20} & 5{,}2 & -12{,}3 & \textit{-4} & \textit{-0,5} \\ 100 & 0{,}33 & \textit{15} & -4{,}1 & 9{,}4 & -22 & 0{,}15 \end{bmatrix} \qquad \{1\}$$

It can be seen that action of Fe_2O_3 depends on pressure. At pressures 20atm m practically doesn't change, at 50atm m decreases and at 100atm m grows when Fe_2O_3 is added. However at 20atm significant increase of q takes place and simultaneously Q is reduced practically to the same value. Because of that m does not change. Fig.1 shows that the temperature profile of propellant with Fe_2O_3 is much steeper inside the dark zone and T_1 and Φ are much higher. The reason of the indicated effect of Fe_2O_3 on process of burning is the presence of carbon (soot) lattice on the surface which captures catalyst particles moving from the surface. The capturing increases residence time of the particle close to surface (this effect was noted by different investigators). Thus at 20atm Fe_2O_3 particles catalyse gas phase reaction and inhibit the reactions in solid. On the contrary at 100atm (see **{1}**) Fe_2O_3 increases Q and decreases q. Carbon lattice is lacking here and particles of Fe_2O_3 can go off without delay. But the action of the particles on the burning surface leads to a significant additional heat release Q. Because of that the increasing of m takes place. Pressure 50atm presents intermediate case: the decreased Q is not compensated by the increased q. Because of that m diminishes.

Thus at low pressures Fe_2O_3 acts in gas phase and this action has a weak influence on m and at elevated pressures Fe_2O_3 acts in solid (or on the surface) and its action increases m.

In [11] no influence of Fe_2O_3 on m was established. Possibly it is a consequence of a small amount of addition (1-1.5% Fe_2O_3) and of absence of nitramines in that double base propellant.

Actions of CSCP and CSNP With and Without Soot

2. CSCP (2%);.

Figs. 1-3 show the obtained averaged temperature profiles. The portrait of CSCP can be presented as follows:

$$\begin{bmatrix} 20 & 0{,}45 & 42 & 2{,}5 & 12{,}2 & 24 & - \\ 50 & 1{,}07 & 55 & -5{,}5 & 24{,}8 & 22 & 0{,}1 \\ 100 & 0{,}66 & 29 & -7{,}3 & 17{,}4 & -43 & 0{,}25 \end{bmatrix} \quad \{2\}$$

It can be seen that 2% CSCP increases m, T_s and Q at all pressures and it leads to m increasing. Heat feedback q decreases at 50 and 100atm but the decreasing can not compensate Q grow. The high temperature gas reactions are blown off through larger distances from the burning surface at 50 and 100atm. Heat release rate Φ increases at 20 and 50atm and decreases at 100atm. The obtained results show that CSCP acts at 20atm in the solid and in a significant part of the gas phase, at 50atm it acts in the solid and in a thin gas layer close to the surface and at 100atm this action occurs in solid.

3. 1%CSCP+1%C.

The portrait of 1%CSCP+1%C can be presented as follows:

$$\begin{bmatrix} 20 & 0{,}03 & 3 & -0{,}1 & 1{,}2 & 0{,}5 & - \\ 50 & 0{,}16 & 9 & 0{,}8 & 2{,}3 & 18 & 0{,}1 \\ 100 & 0{,}16 & 7 & 1{,}4 & 1{,}0 & 35 & 0{,}1 \end{bmatrix} \quad \{3\}$$

It can be seen that substitution of 1%CSCP for 1%C practically destroys the catalytic effect of the remaining part of CSCP. It is the first observation of the effect of inhibit action of soot in Cu-Pb catalyst. In [12] for propellants without nitramines it was stated that large amount of soot can act as an inhibitor but small amount of soot increases catalytic activity. Possibly the presence of nitramines accounts for the effect observed in our work.

4. CSNP (2%);

Figs. 1-3 show the obtained averaged temperature profiles. The portrait of CSNP can be presented as follows:

$$\begin{bmatrix} 20 & 0{,}64 & 57 & 9 & 11 & 60 & - \\ 50 & 0{,}66 & 36 & 9{,}1 & \textit{3,5} & 150 & -0{,}35 \\ 100 & 0{,}49 & \textit{22} & -3{,}1 & 10{,}8 & \textit{10} & 0{,}15 \end{bmatrix} \quad \{4\}$$

It can be seen that CSNP increases m at all pressures and particularly notably at 20atm (about two times). It is due to growth Q and q at 20 and 50atm and due to significant growth Q at 100atm which compensates here decreasing q. CSNP decreases L more strong than CSCP.

5. 1%CSNP+1%C;

Figs. 1-3 show temperature profiles. The portrait of 1%CSNP+1%C can be presented as follows:

$$\begin{bmatrix} 20 & 0{,}69 & 60 & 7{,}9 & 13{,}1 & 61 & - \\ 50 & 0{,}66 & 36 & 8{,}7 & \textit{3,9} & 148 & -0{,}45 \\ 100 & 0{,}99 & 42 & -4{,}6 & 19{,}3 & 36 & 0{,}15 \end{bmatrix} \quad \{5\}$$

The substitution of 1%CSNP for 1%C does not depress CSNP action at 20 and 50atm and significantly enhances the action at 100atm. It is due to Q increasing.

Conclusions About Actions CSCP, CSNP and Soot:

1) CSCP and CSNP increase m of the base propellant, CSNP being more effective at low pressures and CSCP more effective at elevated pressures;
2) As a rule CSCP catalyses more effectively low-temperature reactions (on the surface) and CSNP catalyses more effectively high-temperature reactions (in the gas);
3) The substitution of 1% catalysts (CSCP or CSNP) for 1%C as a rule inhibits action of CSCP and enhances action of CSNP.

Actions of PbO_2 With Soot and With and Without SR

6. 1%PbO_2+1%C;

Figs. 4-6 show the obtained averaged temperature profiles. The portrait of 1%PbO_2+1%C can be presented as follows:

$$\begin{bmatrix} 20 & 0{,}115 & \textit{12} & \textit{-0,76} & \textit{5} & 2 & - \\ 50 & 0{,}41 & 23 & -3 & 11{,}2 & \textit{7} & 0{,}25 \\ 100 & 0 & 0 & 18 & -18 & 187 & 0{,}2 \end{bmatrix} \quad \{6\}$$

This catalyst increases m significantly only at 50atm due to increase Q (q diminishes). At 100atm m does not change however the temperature profile is notably transformed. The transformation causes significant growth q and decrease Q; in this case the parameters have the same values and opposite signs. The

phenomenon is named as "heat compensation effect" (the effect can exist in the combustion waves not only because of catalytic action).

7. 0.7%PbO_2+1%C+0.15%SR;

Figs. 4-6 show the obtained averaged temperature profiles. The portrait of 0.7%PbO_2+1%C+0.15%SR can be presented as follows:

20	0,115	*12*	2,3	*1,9*	179	-
50	0,16	*10*	7,2	*-4,1*	60	0,15
100	0,99	50	5,3	9,4	234	0,2

{7}

The addition of surface-active substance SR causes more uniform distribution of catalytic particles in the propellant volume and leads to improvement of the catalyst action in the gas phase. Indeed a significant increase Φ takes place in **{7}** in comparison with **{6}**. This increasing causes rise of q at 20 and 50atm and rise of the gas phase temperature. However Q has a week growth at 20atm and a tendency of decreasing at 50atm. Because of that the change of m is small at 20-50atm and only at 100atm m increases significantly due to growth Q (possibly due to a more uniform distribution of catalyst particles on the surface).

8. 9.1%PbO_2+1%C;

Figs. 4-6 show the averaged temperature profiles. The portrait of 9.1% PbO_2+1%C can be presented as follows:

20	0,775	66	12,2	10,9	88	-
50	0,99	51	4,1	13,8	138	0,4
100	0,99	42	5,3	9,4	220	0,1

{8}

The increased addition of PbO_2 up to 9% increases m at the whole pressure region (the increase is particularly notable at 20atm) - due to combined growth Q and q (and Φ). Significantly rises T_1 at 20atm (till 1500-1600°C). It is interesting to note that increasing m, q and Q at 100atm in **{8}** are the same as in **{7}**. It shows how it is important to have the uniform distribution of catalyst particles inside the propellant volume.

Conclusions About Actions PbO_2, Soot and SR:

1) Small addition of PbO_2+C acts mainly in the solid at 20-50atm and inside the gas layer close to the surface at the elevated pressures;

2) Surface-active addition SR improves action of PbO_2+C in solid and gas phase especially at elevated pressures;

3) Large amount of PbO_2+C provides strong catalytic action in solid and gas phase.

Actions of PbO With Soot, NiO and HCP

9. 1%PbO+1%C.

Figs. 7-9 show the obtained averaged temperature profiles. The portrait of 1%PbO+1%C can be presented as follows:

20	*0,03*	*3*	5,1	*-4*	7	-
50	-0,17	*-11*	2,2	*-6,5*	*-2*	*0,05*
100	1,815	72	*0,5*	24,7	276	0,3

{9}

It can be seen that at 20 and 50atm catalyst does not act. Catalytic action is observed only at 100atm mainly due to Q increasing. In spite of Φ growth L increases. The increase L shows that strong blowing off of the reacting gas from the burning surface takes place.

10. 1%**PbO+1%NiO+1%C;**

Figs. 7-9 show the obtained averaged temperature profiles. The portrait of 1%PbO+1%NiO+1%C can be presented as follows:

20	0,66	58	13,2	7,1	80	-
50	1,65	78	5	22,2	271	*-0,02*
100	2,65	97	6,1	27,8	690	1,0

{10}

The portrait shows that the catalyst doubled m at 20-100atm due to significant increasing Q. Parameter Φ significantly increases. However q grows slightly because of the above pointed effect of blowing off of the reacting gas from the burning surface. This effect leads even to temperature decrease in gas at 50-100atm in comparison with the temperature of the base propellant profiles and only at 20atm temperature profile above the base profile.

11. 0.37%PbO+1.5%HCP+0.45%C;

Figs. 7-9 show the averaged temperature profiles.

The portrait of 0.37%PbO+1.5%HCP+0.45%C can be presented as follows:

20	0,45	42	*0,3*	14,4	17	-
50	0	*1*	6,7	*-6,8*	35	-0,35
100	0,99	42	2,7	12	176	0,38

{11}

It can be seen that at 20atm catalytic effect takes place due to the increase of Q and it leads to m growing. At 50atm the profile changes but m does not change. At 100atm the joint increase of q and Q lead to a significant increase of m. At this pressure in spite of the growth of Φ the mentioned above effect of blowing off of the gas phase takes place: see L increase in **{11}** and gas temperature decrease on the corresponding profile in Fig.9 (in comparison with the base temperature profile).

12. 1.5% **PbO+5.5%HCP+2%C;**

Figs. 7-9 show the obtained averaged temperature profiles.

The portrait of 1.5%PbO+5.5%HCP+2%C can be presented as follows:

20	1,1	87	20,3	10,2	187	-
50	3,79	147	*1,0*	50,2	575	-0,75
100	4,29	140	-4,0	53	533	0,3

{12}

The addition of this catalyst creates a fast-rate propellant. Indeed burning rates increase here approximate 3 times. A very significant growth of T_s (90-150K) takes place. The heat release rate in gas near surface Φ increases one order. Burning rate m increases at 50-100atm due to Q increasing only. At 20atm growth of q is observed as well.. A very significant effect of blowing off of the gas phase at elevated temperatures at 100atm is observed - see increased L in **{12}** and on the corresponding profile on Fig.9.

Conclusions About Actions PbO With Soot, NiO and HCP:
1) Additions of 1%PbO+1%C and 0.37%PbO+1.5%HCP+0.45%C increase burning rate and can significantly catalyse reactions in solid and in gas only at elevated pressures (100atm);
2) Addition of 1%Ni to the catalytic system 1%PbO+1%C makes it most effective: it can redouble burning rate due to the reaction increasing in solid and gas phases;
3) Addition of 5.5%HCP to the catalytic system 1.5%PbO+2%C greatly enchances its action and creates a fast-rate propellant due to a significant increase of reactions in solid and gas phases.

Modes of Catalytic Actions in Propellant Combustion Waves

Four modes (types) of catalytic actions in propellant combustion waves can be identified on the base of the obtained results: mode of normal catalytic action, catalytic mode of blowing off, catalytic mode of heat compensation and gas phase catalytic mode.

Normal Mode of Catalytic Action

It is a more wide-spread mode of catalytic activity (12 regimes from the studied 36 ones). Significant increase of burning rate observed here is mainly due to the increase of heat release in solid or on the burning surface. Heat feedback also increase here but 2-4 times less than Q. This type of catalytic activity is nominated as "normal" because of the normal reasoning that the most effective place of the catalytic heat release is the burning surface (due to subsurface or on-surface heat release). The following regimes of the studied propellant combustion have the normal mode of catalytic action (nominations: after the portrait number is pointed the number of pressure -1 for 20atm, 2 - for 50atm, 3 - for 100atm; for example [**{12}**3] means that it is the regime of combustion of propellant catalysed by 1.5%PbO+5.5%HCP+2%C - see portrait **{12}** - at pressure 100atm):
[{2}1], [{4}1], [{5}1], [{7}3], [{8}2], [{8}3], [{9}3], [{10}2], [{10}3],[{11}1], {11}3], [{12}2].

Catalytic Mode of Blowing Off

It is the case of a very high burning rate growth which is caused exclusively by the heat release Q in solid or on the burning surface. Heat feedback q even decreases in this case since the acceleration of chemical processes in solid is much higher than in gas phase. Because of that accelerating of the solid gasification the gas phase reactions blow off on a larger distances from the burning surface. The additional feature of the mode is an elongating of the temperature profiles. 8 regimes from the studied 36 ones have the mode of blowing off. They are as follows:
[{1}3], [{2}2], [{2}3], [{4}3], [{5}3], [{6}1], [{6}2], [{12}3].

Catalytic Mode of Heat Compensation

The decrease heat release in solid is observed in this mode. However heat feedback from gas to solid increases and compensates this decreasing. Burning rate does not change significantly here. 7 regimes from the studied 36 ones have the catalytic mode of heat compensation. They are as follows:

[{1}1], [{1}2], [{6}3], [{7}2], [{9}1], [{9}2], [{11}2].

Gas Phase Catalytic Mode

Increasing burning rate which is observed here owes its existence to the fact that mainly heat feedback from gas phase to solid increases. Heat release in solid can be increased also but it much less than q. This catalytic mode exists as a rule at low pressures when carbon (soot) lattice forms on the burning surface. 5 regimes from the studied 36 ones have the gas phase catalytic mode. They are as follows:
[{4}2], [{5}2], [{8}1], [{10}1], [{12}1].

About Predictions of Catalytic Actions in Propellant Combustion Waves

A reasonable assumption as to the predictions of catalytic actions in solid combustion wave on the base of obtained portraits of catalysts can be made. This assumption started from the procedure which was used for numerical simulation of the propellant combustion when hot gas flows along the burning surface. Propellant burning rates and temperature profiles in erosive burning were calculated by using burning wave parameters obtained without blowing: functions Φ, T_s and Q were used [13, 14]. Possibly a similar approach can be used for calculations of catalytic actions. It is necessary in this case to have functions T_s, Q and q of the base propellant. The numerical simulation for each catalyst must use the portrait of that catalyst: the members of the portrait of that catalyst have to be added to the main parameters of the base propellant (the main parameters of the base propellant must be obtained before). The advantage of the suggested simulation is that one does not have to make experimental work.

Presented work was performed by financial support of the Russian Found of Fundamental Investigations, grant № 97-03-32076a.

Table II

Portraits of the Catalysts

№	catalysts	p, atm	Δm, g/cm²·s	ΔT_s, °C	Δq, cal/g	ΔQ, cal/g	ΔΦ, Kcal/cm³s	ΔL, mm
1	Fe_2O_3 (3%)	20	*0,03*	*3*	15,7	-14,6	20	-
		50	-0,33	*-20*	5,2	-12,3	*-4*	-0,5
		100	0,33	*15*	-4,1	9,4	-22	0,15
2	CSCP(2%)	20	0,45	42	2,5	12,2	24	-
		50	1,07	55	-5,5	24,8	22	*0,1*
		100	0,66	29	-7,3	17,4	-43	0,25
3	1%CSCP+1%C	20	*0,03*	*3*	*-0,1*	*1,2*	*0,5*	-
		50	0,16	*9*	*0,8*	*2,3*	18	*0,1*
		100	0,16	*7*	*1,4*	*1,0*	35	0,1
4	CSNP(2%)	20	0,64	57	9	11	60	-
		50	0,66	36	9,1	*3,5*	150	-0,35
		100	0,49	*22*	-3,1	10,8	*10*	0,15
5	1%CSNP+1%C	20	0,69	60	7,9	13,1	61	-
		50	0,66	36	8,7	*3,9*	148	-0,45
		100	0,99	42	-4,6	19,3	36	0,15
6	1%PbO_2+1%C	20	0,12	*12*	*-0,76*	*5*	2	-
		50	0,41	23	-3	11,2	*7*	0,25
		100	0	0	18	-18	187	0,2
7	0,7%PbO_2+1%C+ +0,15%SR	20	0,12	*12*	2,3	*1,9*	179	-
		50	0,16	*10*	7,2	*-4,1*	60	0,15
		100	0,99	50	5,3	9,4	234	0,2
8	9,1%PbO_2+1%C	20	0,78	66	12,2	10,9	88	-
		50	0,99	51	4,1	13,8	138	0,4
		100	0,99	42	5,3	9,4	220	0,1
9	1%PbO+1%C	20	*0,03*	*3*	5,1	*-4*	7	-
		50	-0,17	*-11*	2,2	*-6,5*	*-2*	*0,05*
		100	1,82	72	*0,5*	24,7	276	0,3
10	1%PbO+1%C+ +1%NiO_2	20	0,66	58	13,2	7,1	80	-
		50	1,65	78	5	22,2	271	*-0,02*
		100	2,65	97	6,1	27,8	690	1,0
11	0,37%PbO+0,45%C+ +1,5%HCP	20	0,45	42	*0,3*	14,4	17	-
		50	0	*1*	6,7	*-6,8*	35	-0,35
		100	0,99	42	2,7	12	176	0,38
12	1,5%PbO+2%C+ +5,5%HCP	20	1,1	87	20,3	10,2	187	-
		50	3,8	147	*1,0*	50,2	575	-0,75
		100	4,3	140	-4,0	53,0	533	0,3

References

1. **Boggs T. L.** "The Thermal Behaviour of RDX and HMX". *Fundamentals of Solid-PropellantCombustion.* Eds. K.K. Kuo, M. Summerfield (eds). New York: Acad. Press, 1984. p.121-175. (Progress in Astronautics and Aeronautics; 90).
2. **Fifer R. A.** "Chemistry of Nitrate Esters and Nitramine Propellants". Ibid. p.177-237.
3. **Raman K. V., Singh H.** "Ballistic Modification of RDX-Based CMDB Propellants". *Propellants, Explosives and Pyrotechnics.* 1988. v.13. p.149-151.
4. **Fong C. W., Smith R. F.** "The Effect of Binder, Particle Size and Catalysts on the Burning Rates of PETN and RDX Composite Propellants". *Combust. Sci. Techn.* 1988. v.57, №1, p.1-15.
5. **Zenin A.A., Finjakov S.V., Puchkov V.M., Ibragimov N.G., Okhrimenko E.F.** "Influence of Octogen on the Combustion Mechanism of Double Based Propellants". *Fizika Gorenia I Vzriva*, 1996. v.32, №3, p.42-52. (in Russian)
6. **Zenin A.A., Puchkov V.M., Finjakov S.V.** "Combustion Mechanism of Nitramines as Monopropellants and as Additives to Double-Base Propellants". *Aerotecnica Missili e Spazio. Rivista Dell'Associazione Italiana Di Aeronautica e Astronautica.* Luglio-Decembre 1995, v.74, № 3-4, p.80-92.
7. **Zenin A. A.** "HMX and RDX: Combustion Mechanism and Influence on Modern Double-Base Propellant Combustion". *Journal of Propulsion and Power.* 1995. v.11, №4, p.752-758.
8. **Zenin A. A.** "Processes in Combustion Zones of Double Base Propellants". *Physical Processes in Combustion and Explosion. Collection of Papers.* Moscow. Atomizdat. 1980. p.68-104. (in Russian)
9. **Zenin A. A.** "Thermophysics of Stable Combustion Waves of Solid Propellants". *Nonsteady Burning and Combustion Stability of Solid Propellants.* Eds. L. De Luca, E. W. Price, M. Summerfield. New York: Acad.Press, Chapter 6, p.197-231. (Progress in Astronautics and Aeronautics; V. 143).
10. **Leipunsky O.I., Zenin A. A., Puchkov V.M.** "Influence of Catalyst on Burning Zone Characteristics of Solid". *Combustion and Explosion. Proceeding of the III USSR Symposium on Combustion and Explosion.* Moscow. 1972. p.1357-1359. (in Russian)
11. **Denisjuk A.P., Zhevlakov A.F.** " Influence of Iron Oxide and Cobalt Oxide on Propellant Combustion Dependencies". *Fizika Gorenia I Vzriva.* 1974 v.10, №2, p.197-201. (in Russian)
12. **Denisjuk A.P., Margolin A.D. et al.** "Soot Role in Combustion of Double Base Propellants with Lead Containing Catalysts". *Fizika Gorenia I Vzriva.* 1977 v.13, №4, p.576-584. (in Russian)
13. **Zenin A.A., Finjakov S.V.** "Influence of Blowing Off on Physics of Double Propellant Combustion". *Problems of Combustion and Explosion. Proceeding of the IX USSR Symposium on Combustion and Explosion.* Chernogolovka. 1989. p.21-26. (in Russian)
14. **Beljaev A.A., Zenin A.A., Kuleshov V.V., Leipunsky O.I., Novozhilov B.V., Posvjansky V.S.** "Propellant Combustion in Gas Stream". *Chimicheskaja Fizika.* 1982. №10, p.1421-1427. (in Russian)

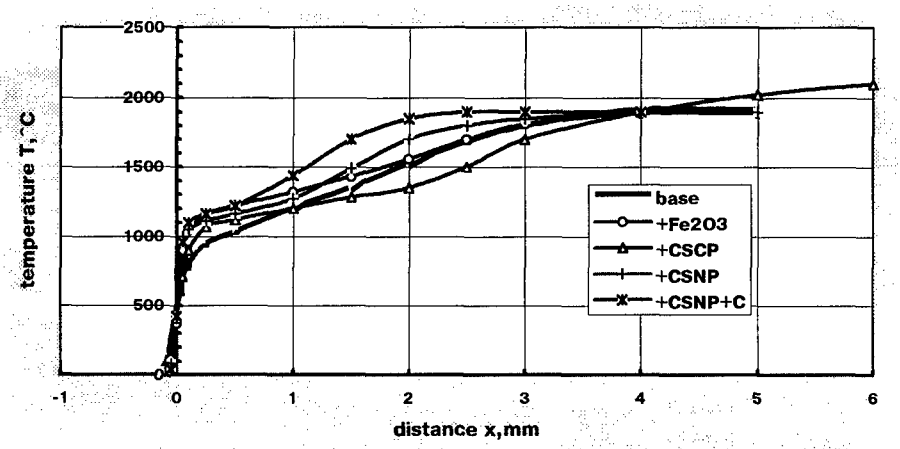

Fig.1. Averaged temperature profiles T(x). 20atm.

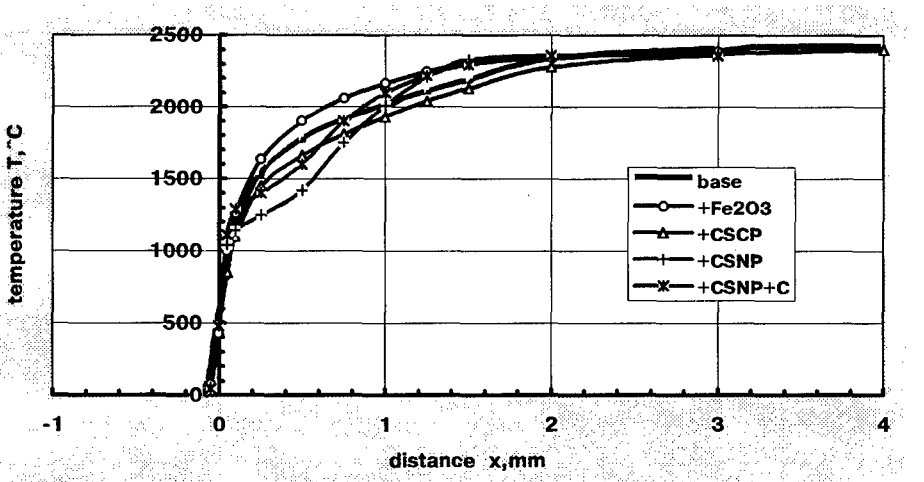

Fig.2. Averaged temperature profiles T(x). 50atm.

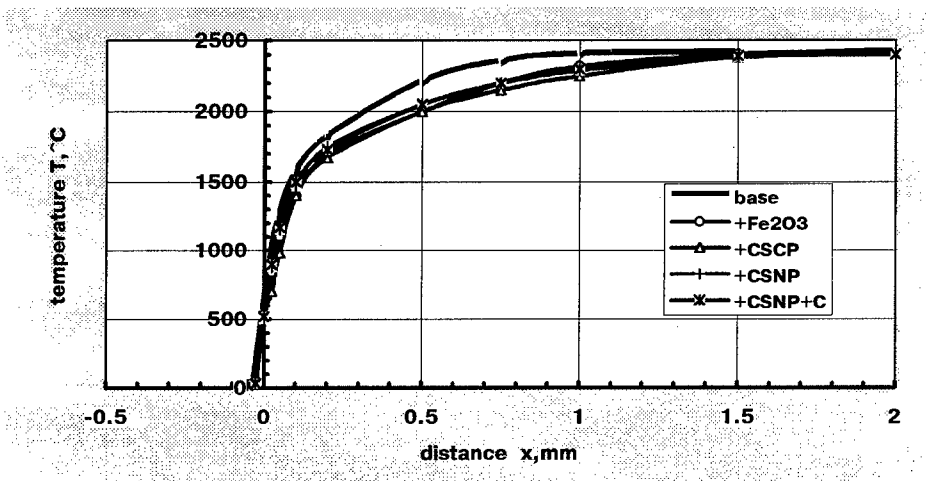

Fig.3.Averaged temperature profiles T(x). 100 atm.

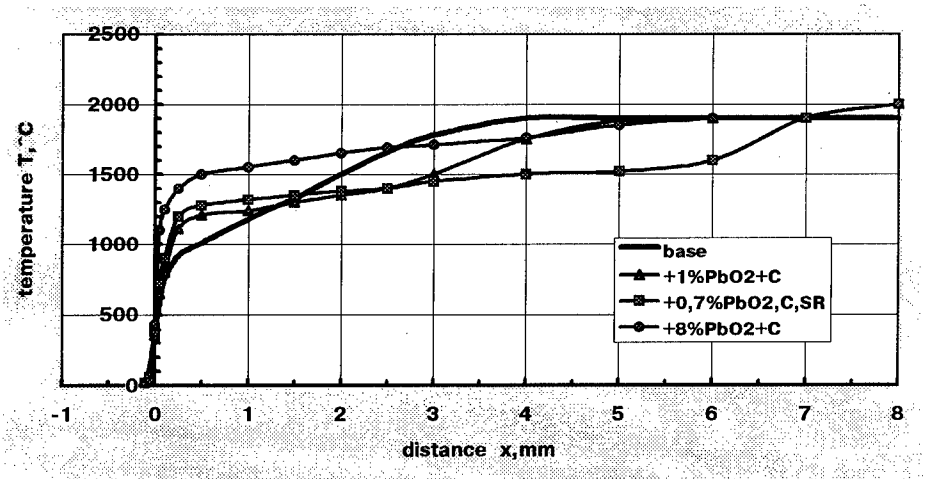

Fig.4. Averaged temperature profiles T(x). 20atm

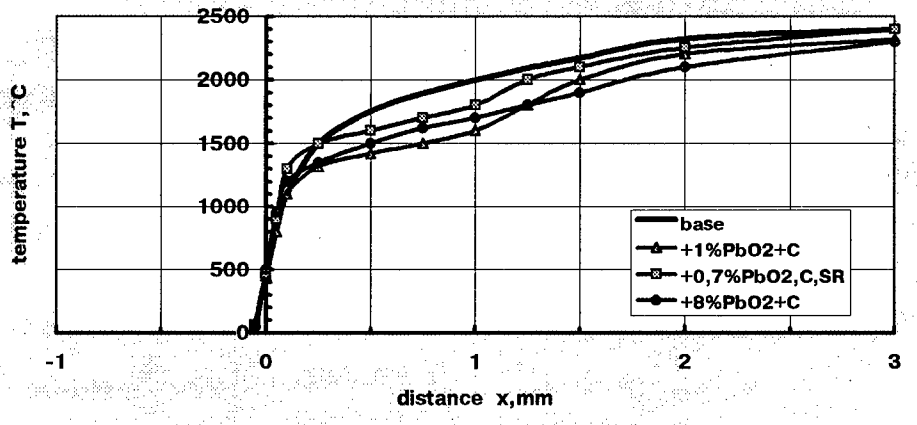

Fig.5. Averaged temperature profiles T(x). 50atm

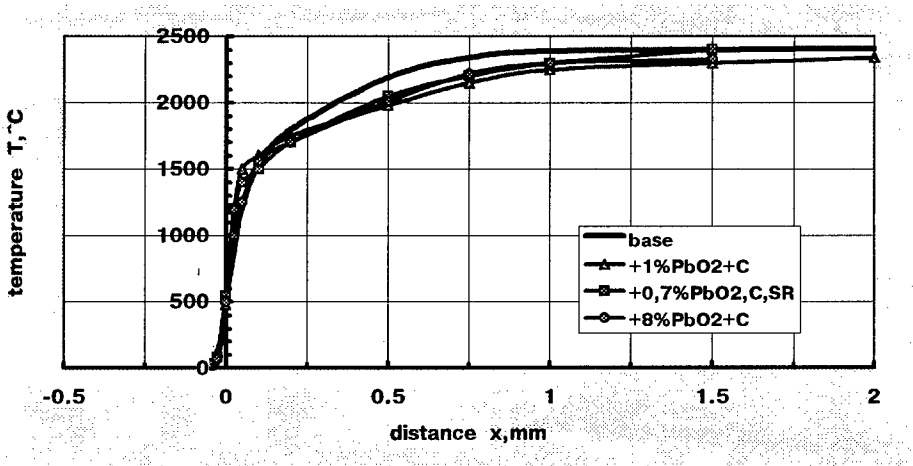

Fig.6. Averaged temperature profiles T(x). 100atm

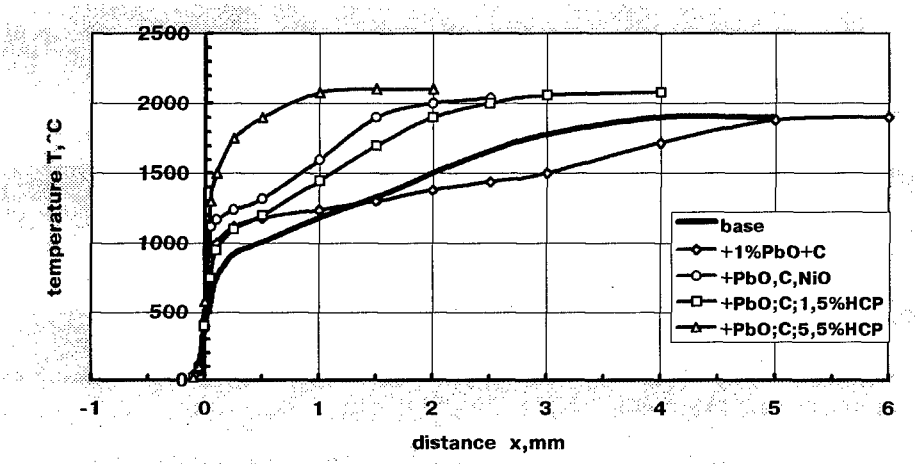

Fig.7.Averaged temperature profiles T(x). 20atm

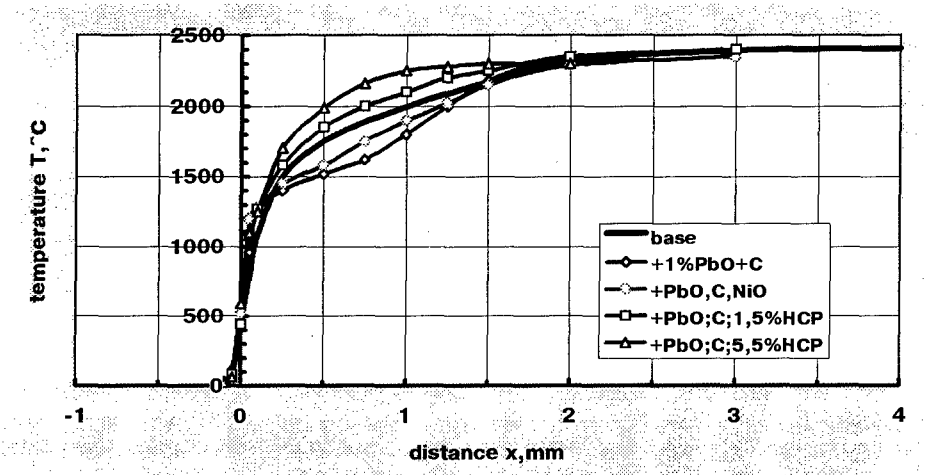

Fig.8. Averaged temperature profiles T(x). 50atm

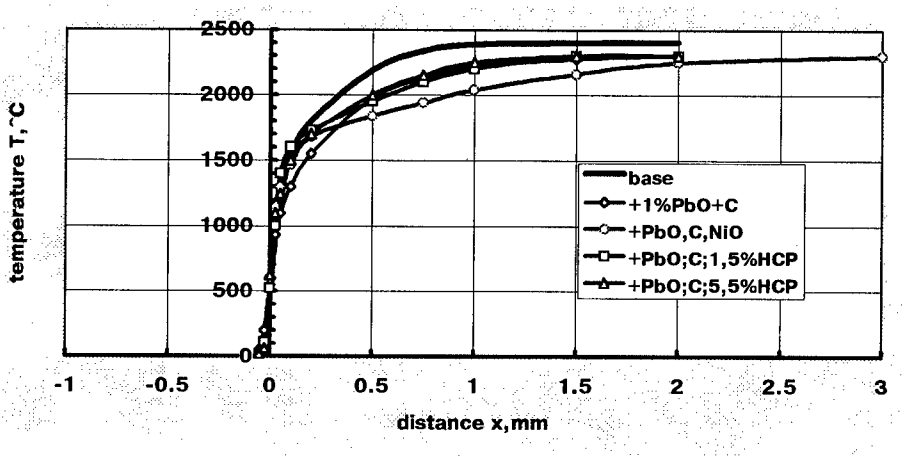

Fig.9. Averaged temperature profiles T(x). 100atm

NUMERICAL MODELLING OF CONVECTIVE COMBUSTION TRANSITION TO DETONATION

Alexander N. Ischenko, Jury P. Khomenko

Institute of Applied Mathematics and Mechanics at Tomsk State University
36 Lenin pr., GSP-14, Tomsk, 634050, RUSSIA

A new model is proposed for the convective combustion of a porous fuel, which incorporates the deformation and dispersal of the porous matrix as well as the dissipative heating. Parametric studies have been made on the combustion of low-porosity and granulated charges. An experimental test agrees well with the model

Convective combustion (CC) in a porous fuel is a mode of combustion, in which forced gas combustion ignites the cold fuel. The phenomenon occurs widely. Practically all combustible porous materials burn on that mechanism at elevated pressures. Convective combustion and low-velocity explosive conversion (LVEC) are successive stages in the passage from combustion to detonation. It is necessary to research these processes to overcome anomalous effects when porous fuels are used and to provide explosion safety in production.

A large volume of experimental data on these processes has been surveyed in /1/. Early attempts were made in /2, 3/ to give a theoretical interpretation of convective combustion from the mechanics of multiphase media, which were extended in /4, 5/. In existing models, it is usual to describe the thermal and strain states in the matrix rather arbitrarily. One uses effective intergranular stresses /4, 5/, which is not the case for low-porosity monoblock specimens, since it does not enable one to determine the amount of energy dissipated on deformation in transient burning states. In /6/, an approach was used in which the fuel is deformed elastically. Here we propose a model for describing various modes of convective combustion, particularly the transition to low-speed explosive transformation, when the fuel can be considered as a viscoplastic medium.

The following assumptions are made. All the pores are connected. As the porosity increases to a certain given value Φ_1^*, the skeleton is dispersed into a set of identical particles, and the pressure in the particles is taken as equal to the pressure in the gas. The pressures in the phases do not coincide in the undispersed porous matrix. It is not possible to consider the geometrical features of real pores, so they are replaced by effective cylindrical channels with equivalent volumes and surfaces. The viscosity and thermal conductivity of the gas are incorporated only in the phase interaction, and then the porous skeleton is assumed to consist of effective spherical particles. The combustion rate is considered stationary and determined by combustion in a closed volume.

When the fuel moves through a channel with a variable cross section, the model includes the following equations of motion, thermal conduction in the pore wall, and closure formulas:

$$\frac{\partial}{\partial t}(\rho_1 \Phi_1 S) + \frac{\partial}{\partial x}(\rho_1 \Phi_1 u_1 S) = I_1 S; \qquad (1)$$

$$\frac{\partial}{\partial t}(\rho_2 \Phi_2 S)+\frac{\partial}{\partial x}(\rho_2 \Phi_2 u_2 S)=-I_1 S; \tag{2}$$

$$\frac{\partial}{\partial t}(\rho_1 u_1 \Phi_1 S)+\frac{\partial}{\partial x}(\rho_1 u_1^2 \Phi_1 S)=-\Phi_1 S\frac{\partial P_1}{\partial x}-FS+I_1 u_2 S; \tag{3}$$

$$\frac{\partial}{\partial t}(\rho_2 u_2 \Phi_2 S)+\frac{\partial}{\partial x}(\rho_2 u_2^2 \Phi_2 S)=S\frac{\partial \sigma_{xx}\Phi_2}{\partial x}+P_1\frac{\partial \Phi_2}{\partial x}+$$
$$+F I_1 u_2 S+\frac{\partial S}{\partial x}\Phi_2(\sigma_{xx}-\sigma_{nn})-2\sigma_{n\tau}\Phi_2\sqrt{\pi S}; \tag{4}$$

$$\frac{\partial}{\partial t}(\rho_1 \Phi_1 E_1 S)+\frac{\partial}{\partial x}(\rho_1 u_1 \Phi_1 E_1)=-\frac{\partial}{\partial x}(\Phi_1 u_1 P_1 S)-F u_2 S+I_1 S(E_2+Q)-$$
$$-q_1 S-P_1 S\left(\frac{\partial \Phi_1}{\partial t}-\frac{I_1}{\rho_2}\right),\qquad E_i=e_i+\frac{u_i^2}{2};\quad i=1,2; \tag{5}$$

$$\frac{d_2 e_2}{dt}=-P_2\frac{d_2\left(1/\rho_2\right)}{dt}+\frac{Q_d(r_c)}{\rho_2}+Qze^{-E_a/(RT_2^*)}; \tag{6}$$

$$\frac{d_2 N_1 S}{dt}=0,\quad \frac{d_2}{dt}=\frac{\partial}{\partial t}+u_2\frac{\partial}{\partial x}; \tag{7}$$

$$P_1=\frac{\rho_1(\gamma-1)e_1}{1-a\rho_1},\qquad T_1=P_1\frac{1-a\rho_1}{\rho_1 R}; \tag{8}$$

$$e_2=\frac{P_2-c_{20}^2(\rho_2-\rho_{20})}{(\gamma_2-1)\rho_2},\quad e_2=c_{p2}(T_2^*-T_0), \tag{9}$$

$$\Phi_1+\Phi_2=1,\ \Phi_1=\pi r_1^2 N_1,\ S_{sp}=2\pi r_1 N_1; \tag{10}$$

$$c_{p2}\rho_2\left(\frac{\partial T_2}{\partial t}+v\frac{\partial T_2}{\partial r}\right)=\lambda_2\left(\frac{\partial^2 T_2}{\partial r^2}+\frac{1}{r}\frac{\partial T_2}{\partial r}\right)-$$
$$-c_{p2}u_2\rho_2\frac{\partial T_2}{\partial x}+Q_d(r)+Qz\,\rho_2 e^{-E_a/(RT_2)}; \tag{11}$$

$$\sigma_{xx}=\begin{cases}-P_2+\tau_{xx}, & \Phi_1<\Phi_1^*,\\ -P_1+k(\Phi_1)\tau_{xx}, & \Phi_1\ge\Phi_1^*;\end{cases} \tag{12}$$

$$\tau_{xx}=\frac{2}{3}\left(\mu_2\frac{\tau_s\sqrt{3}}{\sqrt{\left(\frac{B}{r_1\Phi_2}\right)^2+\left(\frac{A r_1}{\Phi_2 r_c^2}\right)^2}}\right)\left(2\frac{\partial u_2}{\partial x}-\frac{S_{y\partial}}{\Phi_2}\left(u_r-\frac{d_2 r_1}{dt}\right)-\frac{u_2}{S}\frac{\partial S}{\partial x}\right);$$

$$A=\sqrt{3}\left(\frac{d_2 r_1}{dt}-u_r-\frac{r_1\Phi_2 u_2}{2S}\frac{\partial S}{\partial x}\right);\ B=\left(\frac{\partial u_2}{\partial x}-\frac{1}{2\Phi_2 S}\left(\frac{I_1 S}{\rho_2}+\frac{d_2\Phi_2 S}{dt}\right)\right)r_1\Phi_2; \tag{13}$$

$$\sigma_{xx}-\sigma_{nn}=\left(\mu_2+\frac{\tau_S}{\sqrt{2I_2}}\right)\left[2\frac{\partial u_2}{\partial x}-\frac{1}{\Phi_2 S}\left(\frac{d_2\Phi_2 S}{dt}+\frac{I_1 S}{\rho_2}\right)+\right.$$

$$\left.+\frac{2r_1}{r_c^2\Phi_2}\left(\frac{d_2 r_1}{dt}-u_r\right)-\frac{r_1^2 u_2}{r_c^2 S}\frac{\partial S}{\partial x}\right]\Big/\left(1+\left(\frac{\partial R_c}{\partial x}\right)^2\right); \tag{14}$$

$$I_2=\frac{2}{3}\left(\left(\frac{B}{r_1\Phi_2}\right)^2+\left(\frac{Ar_1}{r_c^2\Phi_2}\right)^2\right), \tag{15}$$

$$I_1=\begin{cases}0, & t<t_{ign},\\ 2\pi r_1 N_1 u_r\rho_2, & t>t_{ign},\\ S_{sp}^d u_r\rho_2, & t\ge t_{ign},\ \Phi_1\ge\Phi_1^*,\end{cases} \tag{16}$$

$$u_r=bP_1;\quad S_{sp}^d=4\pi r_{ed}^2 N_e;$$

$$F=\pi r_e^2 N_e C_d\rho_1\frac{(u_1-u_2)|u_1-u_2|}{2}; \tag{17}$$

$$C_d=\begin{cases}C_1=\dfrac{24}{\mathrm{Re}_F}+\dfrac{4.4}{\mathrm{Re}_F^{0.5}}+0.42,\ \Phi_2<0.08\\ C_2=\dfrac{(\Phi_2-0.08)C_3+(0.25-\Phi_2)C_1}{0.17},\ 0.08\le\Phi_2<0.25\\ C_3=2.33+\dfrac{200\Phi_2}{\Phi_1\,\mathrm{Re}_F},\ 0.25\le\Phi_2\le 0.6\\ C_4=\dfrac{0.7}{\Phi_1-0.1}+\dfrac{66.4\Phi_2}{(\Phi_1-0.068)\Phi_1\,\mathrm{Re}_F},\ 0.6<\Phi_2<0.88\\ C_5=\dfrac{1}{\Phi_1-0.054}\left(2.24+85.12\left(\dfrac{\Phi_2}{\Phi_1\,\mathrm{Re}_F}\right)^n\right),\ 0.88\le\Phi_2\le 0.945\\ n=1+7.07(\Phi_1-0.12)\end{cases} \tag{18}$$

$$\frac{4}{3}\pi r_e^3 N_e=\Phi_2;\quad S_{sp}=4\pi r_e^2 N_e;$$

$$\mathrm{Re}_F=\frac{\rho_1|u_1-u_2|2r_e}{\mu_1}$$

$$q_1=\begin{cases}4\pi r_e^2 N_e\alpha_1(T_1-T_{2S}), & t<t_{ign},\\ 0, & t\ge t_{ign};\end{cases} \tag{19}$$

$$Nu = \begin{cases} 2 + 0.106\,\mathrm{Re}_q\,\mathrm{Pr}^{0.33}, \mathrm{Re}_q \le 200, \\ 2.274 + 0.6\,\mathrm{Re}_q{}^{0.67}\,\mathrm{Pr}^{0.33}, \mathrm{Re}_q > 200; \end{cases}$$

$$\mathrm{Re}_q = \Phi_1\,\mathrm{Re}_F;$$

$$\mathrm{Pr} = \frac{c_{p1}\mu_1}{\lambda_1}; \quad \alpha_1 = \frac{\lambda_1 Nu}{2r_e};$$

$$r_c = r_1\left(1 + \frac{1}{\sqrt{\Phi_1}}\right)\Big/2.$$

Here p, u, P, e, and T are correspondingly the density, velocity, pressure, internal energy, and temperature; e_2 is the thermal component of the fuel's internal energy; Φ - volume fraction; σ_{xx} the stress on an area normal to the 0X axis; τ_{xx} component of the stress tensor deviator; σ_{nn} and $\sigma_{n\tau}$ correspondingly the normal and tangential stresses on an elementary area having normal n at the channel wall; R_c channel radius in the relevant cross section; S channel area, Q_d the heat influx due to energy dissipation on deformation; ν the speed of the radial fuel motion in unit cylindrical pore in the skeleton; μ dynamic viscosity, τ_S yield point in pure shear; r_1 and r_e the radii of the effective cylindrical pores and spherical particles; N_1 number of pores in unit cross section; N_e number of particles in unit volume; T_2^* the mean fuel temperature; Q calorific value of fuel; z preexponential factor; E_A activation energy; R the gas constant; a covolume; γ isentrope parameter; c_{20} speed of sound in the skeleton in the initial state; λ thermal conductivity; Re, Nu, and Pr Reynolds, Nusselt and Prandtl numbers for the flow; u_r layerwise combustion rate; Φ_1^* specified porosity; S_{sp} and S_{sp}^d specific surfaces of pores in the undispersed and dispersed skeleton; r_c mean value of radius in an individual cylindrical pore; and b an empirical coefficient. Subscripts: 1 - gas, 2 - solid phase, 0 - initial state, s - pore surface.

Equations (1) and (2) are those of continuity; (3) and (4) are for momentum conservation; (5) and (6) are for energy conservation in the gas and condensed phases; (7) is for conservation of the number of pores in a mobile Lagrange particle of fuel; and (8) and (9) are the phase state equations. The expressions for the resistance force in a low-porosity system have been taken from /7/ (coefficients C_1-C_3), and /8/ (coefficients C_4, C_5 – own authors data) and for the convective heat flux q_1 from /9/.

System (l)-(19) is closed by the equation for the deformation of an effective cylindrical pore and by expressions for the radial component of the fuel particle velocity and the dissipated energy:

$$\frac{d_2 r_1}{dt} = \frac{(P_1 - P_2)r_1}{2\mu_2} + u_r + \frac{r_1\Phi_2 u_2}{2S}\frac{\partial S}{\partial x} \pm \frac{r_1\tau_S}{2\mu_2}\ln\left(\frac{A + \sqrt{A^2 + B^2}}{\Phi_1\left(A + \sqrt{A^2(B/\Phi_1)^2}\right)}\right); \qquad (20)$$

$$v = \frac{1}{\Phi_2}\left(\frac{d_2 r_1}{dt} - u_r\right)\left(\frac{r_1}{r} - r\pi r_1 N_1\right) - \frac{\partial S}{\partial x}\frac{u_2}{2S}\left(\frac{r_1^2}{r} - r\right), \tag{21}$$

$$Q_d = \frac{1}{\Phi_2}\left(\frac{4}{3}\frac{\mu_2}{\Phi_2}\left(\frac{B}{r_1^2} + \frac{Ar_1^2}{r^4}\right) + \sqrt{2}\tau_s\sqrt{\frac{B^2}{r_1^2} + \frac{A^2 r_1^2}{r^4}}\right). \tag{22}$$

These formulas have been derived on the assumption that the skeleton deformation in any cross section is adequately described by the deformation of an individual pore in that cross section and that one can neglect the nondiagonal components in the stress and strain rate tensors. The equations for the condensed phase are written in a local cylindrical coordinate system, while the kinematically permissible motions are defined in accordance with (4). The mode of deformation is considered as highly viscous, with "+" taken for compression and "-" - for expansion in (20).

A similar technique has been used in deriving (14) and (15) with the complex motion in a channel of variable cross section replaced by one-dimensional motion with averaged parameters.

Two regions are distinguished in describing the temperature pattern in the condensed phase: boundary and main ones. The first consists of a thin layer of fuel adjoining the pore walls, in which the temperature distribution is dependent on the convective heat flux q_1 and is defined by (11). The main one includes the rest of the fuel, where the effects of q_1 can be neglected. The energy-conservation equation for it is taken as the heat influx equation (6). The ignition condition for the pore surface is $T_{2S} \to \infty$.

This system allows one to pass to the limit $\Phi_1 \to 0$ and $\Phi_2 \to 0$. In the first case, one obtains the equations for a continuous fuel, and in the second, for the combustion products. This feature distinguishes this model from existing ones /4, 5, 9/ and enables one to use it when the pores collapse during deformation, as well as to describe a monoblock with law initial porosity.

Changes are made in the model after the fuel dispersal, which simplify it substantially and enable one to avoid describing effects that are minor under the new conditions. Instead of (6), one uses the integral obtained on neglecting the dissipation:

$$\rho_2 = R_2\left(P_2 / \Pi + 1\right)^{1/\gamma_2}, \quad \Pi = R_2 c_0^2 / \gamma_2$$

in which R_2 and Π are defined from the condition that the isentrope passes through the point P_2, R_2 at the instant when the given skeleton particle is dispersed. We do not use the equations and formulas related to the effective cylindrical: pores, while N_e is subject to the condition $d_2 N_e S/dt = 0$.

In a granulated medium, there are repacking effects in the porous matrix around the gravimetric density, where the true rheology of the skeleton is of minor importance. To do this model suitable for describing the states of strain in granular and powder systems it is necessary to introduce the effective yield point,

$$\tau_S^e = \tau_S(\Phi_2 - \Phi_2^0)/(1 - \Phi_2^0) \tag{23}$$

which tends to the true value τ_S as the pores collapse.

This approach has been used in researching the combustion of a monoblock containing undispersed porous skeleton in the initial state and placed in a rigid closed shell with length L_C. The calculations define the main points in the combustion, its transition to detonation and the effects of the initial parameters on the general pattern.

The cross-sectional area of the channel is taken as fixed, and the following initial and boundary conditions are defined for (1)-(22):

$$t = 0,\ 0 \le x \le L_c,\ u_1 = u_2 = 0,\quad P_1 = P_2 = P^0$$

$$\Phi_1 = \Phi_1^0,\quad S_{SP} = S_{SP}^0,\quad T_2 = T^0$$

$$x = 0,\quad x = L_C\ :\ u_1 = u_2 = 0$$

$$r = r_1 :- \lambda_2 \frac{\partial T_2}{\partial r} = \alpha_1 \left(T_1 - T_{2S}^*\right)$$

$$r = \infty : T_2 = T_2^*$$

The initial porosity is $0.05 \le \Phi_1^0 \le 0.3$, initial specific surface $5 \cdot 10^3$-$15 \cdot 10^3$ 1/m, and the yield point $0 \le \tau_S \le 50$ MPa. Thermodynamic parameters of the combustion products and fuel: ρ_2=1600 kg/m^3; $c_{P1} = I$ kJ/kg K; T^0 = 300 K; $\lambda_1 = 8.33 \cdot 10^{-2}$ kg m/sec^3 K; $\lambda_2 = 0.25$ kg m/ sec^3 K; $\mu_1 = 2 \cdot 10^{-5}$ kg/m sec; $\mu_2 = 10^4$ kg/m sec; $Q = 4.54$ MJ/kg; $\Phi_1^* = 0.37$.

We used an explicit difference scheme with a mobile net, whose nodes moved with speed u_2.

Figure 1 shows the parameter distribution along the charge. The most typical characteristics are the extensive deformation in the entire nonburning matrix, the rapid stress transmission through the skeleton from the combustion zone to the nonburning end of the shell and the characteristic combination of initial matrix compression and subsequent stretching, which ends with dispersal into individual particles, with a wide zone of final combustion in the dispersed mixture.

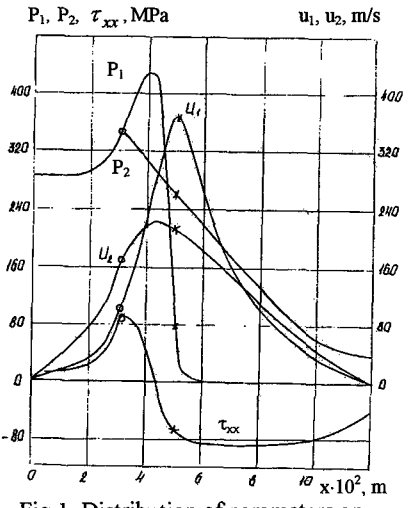

Fig.1. Distribution of parameters on length of a charge
×- ignition front, o - dispersion front

The parametric studies showed that the combustion was most sensitive to the initial specific pore surface. Any increase in this produced a sharp rise in the rate of gas input and increased the rate of the convective ignition, while reducing the predetonation length.

Figure 2 shows how the rheological characteristics affect the combustion. An increase in yield point raises the stress level in the skeleton and the pressure in the gas, and also accentuates the matrix deformation. As the viscosity falls, the skeleton compression front becomes narrower, while the stresses are reduced and become localized near the ignition front.

The offered model of CC allows to describe transition of CC in a mode LVEC and normal detonation /1/. The analysis of ignition prosess of a surface shows, that on the initial stage of burning the conducting mechanism of ignition is the outstriping filtration of hot products, then it replaces by convective heat exchange with gas which is taking place in pores originally, and warming up at the expense of high-speed friction and shock compression /10/. After this on the foreground there is a warming up for the account of dissipative processes in a plastic compression wave previous zone of CC. The change of the mechanism means a beginning of transient of CC to LVEC. The accounts have shown, that depending on a way of the description of force interaction it can occur on any other business. If to use (17) with C_4 and C_5, then received spasmodic change of speed of ignition with transition of CC to LVEC (fig.3) more than twice. At a LVEC stage U_{IGN} varies poorly, in a range 1100-1250 m/s. Thus, the wave, illustrated by fig.1 is distributed on the fuel. The structure of pressure at the front has the brightly expressed triangular kind. Length wave from a point of deformation beginning before complete burning out of fuel makes about 20 cm. This size, certainly, varies depending on the initial characteristics of a charge. If to use the traditional formulas with only C_1 – C_3 from (17) /2,5/ then transition occurs smoothly, without jumps, and the U_{IGN} meanings appreciably distinguish from the first case (up to 25%). This fact gives basic importance to use of authentic dependences for F in the description of transients.

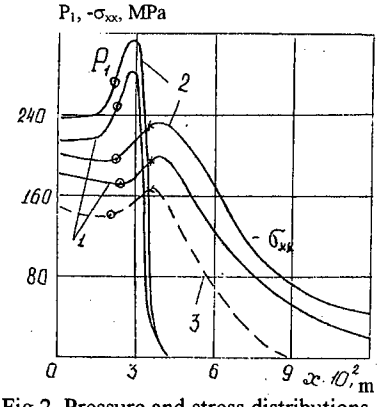

Fig.2. Pressure and stress distributions along charge: $\tau_S = 0$ (curves *1* and *3*) or 30 MPa (curve *2*); $\mu_2 = 10^4$ Pa sec (curves *1* and *2*) or 2.5 10^3 (curve *3*)

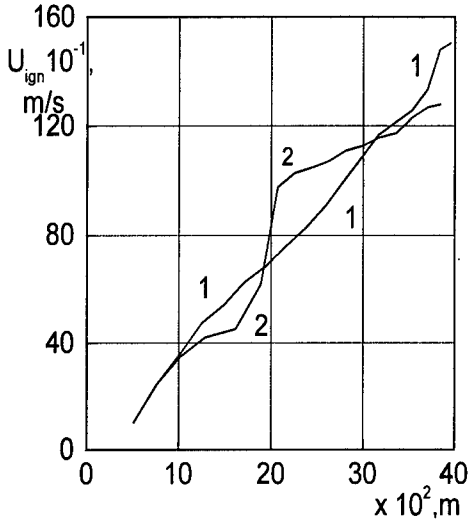

Fig.3. Distribution of pressure and voltage on length of a charge:
1 – calculanion with C_1-C_5 in (17);
2 – calculanion with C_D from /2,5 /, without C_4, C_5.

On fig.4 are given *x-t* diagram of a front ignition situation and point of the maximal plastic deformations, where greatest dissipative warming up is observed. *Up* to section x = 20 cm the front of ignition lags behind a plastic wave, and after it outstrips it a little. This point corresponds to jump on fig.3, that confirms change of the mechanism of ignition. The similar type of transition CC to LVEC is described in /1,5/.

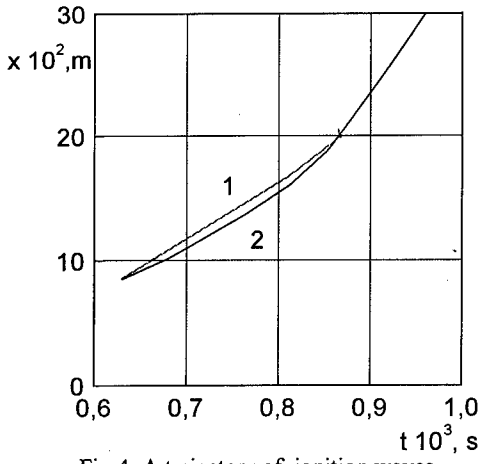

Fig.4. A trajectory of ignition waves and point of the maximal plastic deformations:
1 - plastic wave; *2* - wave of ignition

We calculated the combustion in a granular charge with poured density in a closed shell under the conditions described in /11/ to illustrate the performance in describing transient processes, where we used the (23) effective yield point.

Figure 5 shows the ignition rate distribution for the pore surfaces along the charge. The $U_{IGN}(x)$ curve has several characteristic parts, which are commonly observed by experiment: AB, developed convective combustion; BC, stabilized convective combustion, where U_{IGN} varies only slightly (within 5%); and DE, low-speed explosive conversion. The stabilized state is maintained by the pressure rise in the combustion zone and the compensating increase in resistance in the porous skeleton. Then U_{IGN} in that period is 460 m/sec. The corresponding value in the experiment was 430 m/sec /11/. The stabilized combustion length also correlated with the experimental value.

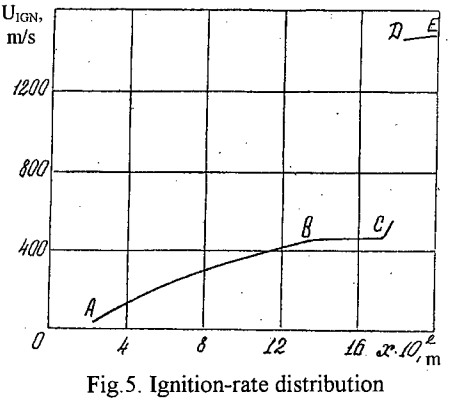

Fig.5. Ignition-rate distribution

The transition to low-speed explosive transformation is characterized by a step in U_{IGN} to 1480 m/sec (1400 m/sec in the experiment). The ignition rate subsequently varies only slightly. The point for the start of the transition is a head of the ignition front. The porosity near it is ~3%. At the time of transition, there is a change in the ignition mechanism from convective heat transfer to ignition by viscoplastic heating of the skeleton-ahead of the combustion zone.

On fig.6 the comparison curve $U_{IGN}(x)$ of different limits of fluidity of fuel is given. The tendency is revealed, according to which, with increase, length of a

predetonation site of burning is reduced, and, than it is less, especially delay the stabilized site of CC and stronger jump of speed of ignition is expressed with

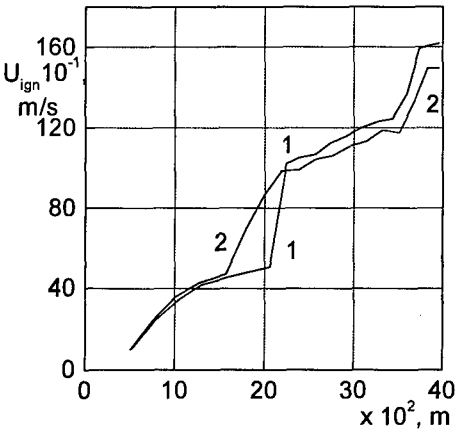

Fig.6. Distribution of ignition speed on length of a charge:
τ_s = 50 (*1*), MPa (*2*)

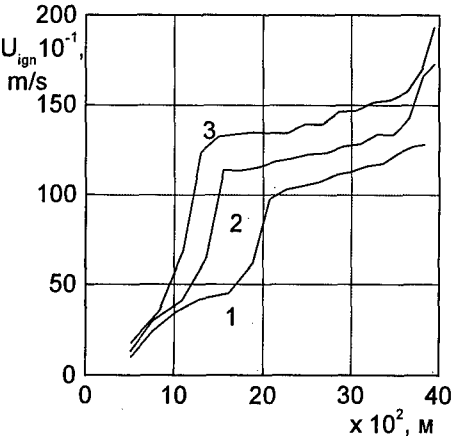

Fig.7. Influence of initial porosity on distribution of ignition speed on length of a charge: Φ_1^0 =0,2 (*1*), 0,3 (*2*), 0,4(*3*)

transition of CC to LVEC. After transition at fuel with small τ_S the LVEC speed is little bit higher. Apparently, it is because the process is distributed on more compressed and dense environment.

Fig.7 illustrates change of ignition character depending on initial porosity of a sample. With downturn Φ_1 from 0.4 up to 0.2 lengths of a predetonation site is reduced, the mode of stabilized CC disappears, and the speed of ignition on a LVEC site is essentially increased (up to 40 %).

Change of an initial specific surface (fig.8) has an similary effect. In a range

$$\Phi_1^0 \le 0.3 \quad S_{sp}^0 > 40\ cm^{-1}$$

CC practically at once after ignition is broken in LVEC. The structure similar shown on fig.1, is distributed on whole length of a charge with poorly growthing speed. Near to the bottom the wave speed is increased because of general pressing and increase of average density of environment.

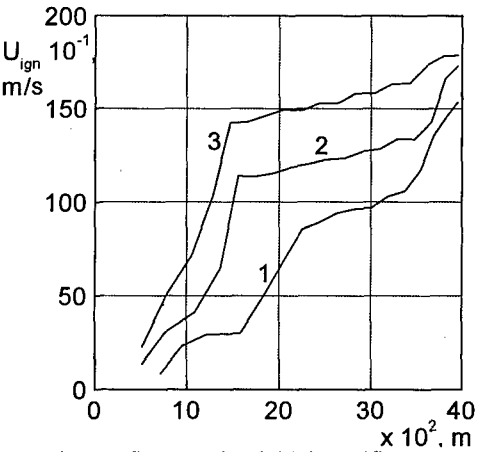

Fig.8. Influence of an initial specific pore surface on distribution of ignition speed on length of a charge:
S_{sp}^0 = 80 (*1*), 42 (*2*), 20 cm^{-1} (*3*)

The main results are that we have a new model for the combustion of a porous fuel, in which one can describe the transition from combustion to detonation. The

theoretical studies have been made on the convective combustion of low-porosity monoblocks and poured charges in closed volumes. The results agree well with the available experimental evidence.

LITERATURE CITED

1. A.F. Belyaev, V. K. Bobolev, A.B. Korotkov, A.A. Sulimov The Transition from Combustion to Explosion in Condensed Systems [in Russian], Nauka, Moscow (1973).
2. K. K. Kuo, M. Sommerfield The theory of stationary burning gase-permeable fuels. Raketnaya Tekhnika Kosmonavtika, II, N 4, 8-16 (1973).
3. H. Crier, M. Ryan, Van Tassell Flame spreading and combustion in packed beds of propellant grains. AIAA J. N 4, 58-69 (1976).
4. P. S. Gough, F. T. Zwarts Modelling heterogeneous two-pfase reacting flow. AIAA J. N 1, 19-28 (1979).
5. Sh. Akhatov, P. B. Vainshtein Non-stationary modes of burning of porous gunpowders. Fiz. Gor. Vzryva, 19, N 3, 53-62 (1983).
6. N. N. Smirnov, I. D. Dimitrienko A mode of convective combustion in deformable firm fuel with longitudinal channels. Fiz. Gor. Vzryva, 12, N 3, 59-67 (1986).
7. S. Ergun, A.Orning Fluid flow through randomly packed columns and fluidized beds. Ind. Eng. Chem., 49, 1179-1184 (1949).
8. I.M. Barishev, V.N. Voronin, A.N. Ischenko, J.P. Khomenko An experimental research of the resistance laws with current of gas in lowporous environments in a wide range of Reynolds numbers. News of High Schools. Physics, N 4, 101-110, (1993).
9. V. N. Timofeev Heat exchange in a layer. Izv. VTI, N 2, 12-18, (1949).
10. B. S. Ermolaev, B. V. Novozhilov, S. V. Posvyanskii, A. A. Sulimov Results of numerical modeling convective combustion of powder explosive systems with growing pressure. Fiz. Gor.Vzryva, 21, N 5, 3-12 (1985).
11. A.A. Sulimov, B. S. Ermolaev, A.B. Korotkov Laws of distribution of convective combustion waves in closed volume. Fiz. Gor. Vzryva, N 6, 9-19, (1987).

ASH INFLUENCE ON CONVERSION OF SPHERICAL COAL PARTICLE REACTING WITH AMBIENT OXIDIZING GAS.

T.A.Yarovoy*, A.N. Zolotko, N.I. Poletaev, Y.I. Vovchuk

Institute of Combustion of the Odessa State University,
270026, st. Dvoryanskaya 2, Odessa, Ukraine.

*Author to whom correspondence should be addressed:

Taras A. Yarovoy
ul. Malinovskogo 35/2, kv. 51
Odessa 270074,
Ukraine.

home tel +38 048 2651419
work tel +38 048 2633633
e-mail: vov@ictg.intes.odessa.ua

ABSTRACT

The problem of ash coal combustion has a special significance, as in present time there is a change for the worse in extracted coals quality observed. It is especially difficult to reach high levels of char conversion in case of low ash fusion temperature. In a burning process ash is able to cover a surface of the coal particle and act as a diffusion barrier for oxygen (particularly liquid ash).

A model is presented to describe spherical ash coal particle combustion in quiescent oxidizing gas and reveal the main factors of an ash influence on this process. System behavior was determined by equations of heat and mass balances. Heat was released by two parallel heterogeneous carbon-oxygen first order chemical reactions

1. $C+O_2=CO_2$
2. $2C+O_2=2CO$

Mass balance equation described the rate alteration of the coal particle weight loss. Assumption of quasi-steady oxygen diffusion towards the char particle surface from ambient oxidizing gas was used. Also the oxidant diffusion through the ash layer and its dependence from an ash aggregative state was taken into account.

The equations system was solved numerically. Calculated temperature dynamics of burning particle is in agreement with the measurement of Robert H. Hurt, where combustion of $\approx 200\mu m$ Illinois #6 coal particle in 6 mole-% oxygen at a steady gas temperature of 1250 K were studied.

Obtained results analysis demonstrates that a fusibility of the inorganic matter is one of the most significant ash coal characteristics. High-fusing ash has a weak influence on the conversion dynamics and burning time of an ash coal in the comparison with an ash free coal. In such case an ash can be considered as a thermal dead matter. The qualitative change of an ash coal combustion mechanism is able to appear if the temperatures reached in the combustion process exceed the ash fusing temperature even under the relatively low inorganic matter fraction (A=11%). That, in its turn, leads not only to considerable increasing of the particles burning times but to appearance of the qualitatively new, with extreme, dependences of the burning time as a function the coal particle initial size and oxidizer mass fraction.

It seems to be very significant for a practice of ash coal combustion.

INTRODUCTION

Study of ash coal combustion problem is important both for expansion of the fundamental

knowledge about possible regimes of char burning and for elucidation of the profitable conditions of low quality coal use in furnaces. In present time carbon conversion of 90% and more are typically required for the economic operation of pulverized coal-fired boilers. Last years there was a change for the worse of extracted chars quality observed. It is connected with coal inorganic inclusions quantity increase.

On early stages of char burning its mineral components form ash. Further coal conversion depends on ash physical and chemical properties such as fusibility, porosity and so on. It is naturally to expect that the influence of an ash is connected to the next factors.

Part of the heat produced in chemical reactions warms the ash. This heat loss grows with the increase of an ash quantity.

Mineral components presence leads to exception of certain coal particle surface from the reaction process. That reduces the macroscopic rate of char oxidation.

Especially it is important in case of the low ash-fusion temperature. Liquid ash layer on the coal particle surface acts as a diffusion barrier for the oxygen. It is a very difficult condition for oxidizer diffusion. As a result total carbon oxidation rate and coal conversion level decrease and the time required for the full carbon conversion increases. Therefore ash-fusion temperature value is one of the important char ash characteristic.

Properties and conversion process of chars were studied during many years but mineral inclusions influence has been examined insufficiently wide.

Previous works

Theoretical research of ash influence on coal particle combustion was conducted by Vulis and Frank-Kameneckii [1-3]. They took into account diffusion resistance of the solid ash cover to the oxygen flux flowing towards the reaction surface and showed that it is possible to neglect solid ash layer influence in such case.

Ash coal bed burning was studied by Kantorovich [4]. In his model an ash of the consumed coal occupies places between char particles. It leads to decrease of the oxidant diffusion rate and specific reaction surface.

The theoretical and experimental researches of the ash-rich coal burning were done by Kiro and coauthors [5]. In that paper it was shown that an ash can has a fatal influence on char conversion and confirmed the possibility of the different regimes of an ash coal ignition in dependence of an ash content and aggregative state.

Enumerated studies did not take into account ash layer formation stage and change of its aggregative state. Also inorganic inclusions size influence on the coal conversion process was not

examined.

Suggested model takes into account influence of the inorganic inclusions size and ash aggregative state alteration in the time of char conversion.

BACKGROUND

Qualitative and quantitative composition of the coal inorganic inclusions is highly wide and different for various chars. However there is a certain correlation. In the main char ash consists of the metal oxides [8-12]. It has following typical composition: SiO_2 40-60%, Al_2O_3 20-60%, Fe_2O_3 5-25%, CaO 1-15%, MgO 0.5-4%, Na_2O+K_2O 1-4%. Ash fusion temperature depends on ash composition. It can be evaluated by the next expression [10]:

$$\frac{SiO_2 + Al_2O_3}{CaO + MgO + Fe_2O_3};$$

here chemical formula of each substance implies mass fraction of its material in ash. Ash fusion temperature grows with increase of the above expression. According to [10-12] the range of the inorganic inclusions particles size is from 0.01μm to 1mm except partings, which have much more sizes. It is very difficult to find a connection between definite ash chemical substance and its particles size. Probably it can be explained by characteristic conditions of coals formation different for each coalfield.

Analytical model

Spherical ash coal particle of radius r burning in a quiescent oxidant-inert mixture is considered. Oxygen is assumed to diffuse quasi-steady towards the surface of the coal particle and react heterogeneously with the carbon to form gaseous products, which diffuse outwards without any further reaction. Also it is assumed that:

Oxygen reacts with the carbon only by the parallel reactions of the first order

$$C+O_2=CO_2$$
$$2C+O_2=2CO$$

Homogeneous reactions, volatile and moisture release, possible catalytic effects of an ash are not considered in present paper.

Ambient gas has a constant temperature T_g, density ρ_g and oxidant mole fraction C_∞.

The particle is isothermal at its surface temperature T. This is reasonable for small particles or for particle having a high thermal conductivity.

Transfer coefficients: thermal conductivity λ and diffusivity D, as well as ambient gas density ρ_g have the next temperature dependences: $\lambda=\lambda_0(T^*/T_0)^{0.75}$, $D=D_0(T^*/T_0)^{1.75}$, $\rho_g=\rho_{g0}(T_0/T^*)$, here λ_0, D_0 and ρ_{g0} were determined under temperature T_0; T^* - arithmetic average between coal particle temperature T and gas temperature T_g.

Heat capacities of the coal particle and gas are constant. Carbon and ash heat capacities are equal.

Ash particles are spherical with radius r_z. They distributed uniformly inside coal particle. These assumptions are based on the experimental data [9,12,15].

Ash and coal densities are equal. In that case inorganic inclusions mass fraction $A=m_z/(m_z+m_c)$ is equal to an ash volume fraction which can be find by the same way. m_z, m_c - ash and carbon masses of a coal particle.

Ash particles accumulate and cover reaction surface as coal particle burning. A ratio of the surface area covered by inorganic substance to the total coal particle surface area is z. When z value is 1 all reaction surface covered by ash layer.

Considering all assumptions the energy balance at the coal particle surface is

$$\frac{d(C_p m T)}{dt} = 4\pi r^2 (1-A)(k_1 q_1 + k_2 q_2)[C^1_{O_2} \cdot (1-z) + C^2_{O_2} \cdot z]\rho_g -$$
$$- 2\pi Nu(r+h)(T-T_g) - 4\pi(r+h)^2 \sigma[\varepsilon_c(1-z) + \varepsilon_a z](T^4 - T_\infty^4)$$

where C_p is the coal heat capacity, h is the thickness of ash layer, Nu=2.

The carbon weight loss equation is

$$\frac{dm}{dt} = -4\pi r^2 (1-A)(k_1 \nu_1 + k_2 \nu_2)[C^1_{O_2} \cdot (1-z) + C^2_{O_2} \cdot z]\rho_g$$

where m is the coal particle mass. According to the geometrical considerations:

$$z = A(r_0^3 - r^3) / 4r^2 r_z$$

Considering quasi-steady diffusion of the oxidizer its mass fraction on the clean char surface is

$$C_{O_2}^1 = \frac{C_\infty}{(k_1 + k_2)\left[(1-A)\frac{1}{\beta} + \frac{1}{(k_1+k_2)}\right]}$$

And oxidant mass fraction on the coal particle surface under ash layer is

$$C_{O_2}^2 = \frac{C_\infty}{(k_1 + k_2)\left[(1-A)(\frac{1}{\beta} + \frac{1}{\chi}) + \frac{1}{(k_1+k_2)}\right]}$$

here $\chi=D_z/h$ - oxygen diffusion rate through ash layer [1,2]. Diffusion coefficient D_Z magnitude does not depend on ash chemical composition. It determined by ash cover aggregative state

$D_z=\Omega D$	for solid ash layer;
$D_z=D^*\exp(-E_z/(RT))$	for liquid ash layer;

here Ω is the porosity of the ash cover, D^* - preexponential factor, E_z - activation energy of the oxidant diffusion through the liquid ash layer.

An ash is considered as a high-fusing (HFA) when the char burning temperature during combustion does not overhead the ash fusion temperature. There are two possible variants in that case: a) ash particles, which appear on the coal surface, do not accumulate on it; definite part of the reaction surface is covered by ash and b) solid ash accumulates on the coal surface. Thus oxygen must to diffuse to the char through a porous ash layer which covers the definite part of the reaction surface.

Ash is considered as low fusing (LFA) when the char particle burning temperature overheads the ash fusion temperature. In that case ash accumulates and can form a liquid layer on the coal surface.

Moreover, the equations system gives a possibility to obtain solution for the limit case of an ash free coal.

DESCUSSION

Above equations system was solved numerically. All values of parameters were taken from [5], [13].On the first stage of the research calculations were aimed on the comparison of the obtained solutions for the temperature dynamics with the experimental data [14].

Figure 1 shows the calculated temperature dynamics for three above-mentioned variants. Here the experimental dependence [14] is also presented and as it is emphasized by author it was observed in experiment that "...a period of bright incandescence from 0.8 to 1.2 seconds, followed by a relatively abrupt drop in temperature of 125 K and a long, slow, nearly-isothermal, final burnout to a carbon-free ash particle." It could be seen from the figure that calculations give the similar result only in case of the fusible ash. In works [14-18] authors did not give the ash fusion temperature value of the Illinois #6 coal. But captive particle images for a typical Illinois #6 coal char particle surface [15] testify that an ash is able to stay on the char particle surface and to form fused framework.

It is necessary to note that given experimental temperatures [14] are radiance but not true temperatures. However, it is not essential for the behavior comparison of the calculated coal particle temperature dynamics with the measured one. Experimental temperature increase rate is less than calculated one. It can be explained by the volatile and moisture release influence, which detains ignition process.

That comparison testifies the LFA release can lead to the thermal extinction and increase of the complete burning time. Presented model is able to consider it.

On the next stage of the present work the burning times of an ash coal as a function of the particle and environment parameters were investigated (the conversion level was set as 99%).

Figure 2 presents the characteristic burning time (t_b/r_0^2) dependence on the initial radius of the ash coal particle for different assumptions about aggregative state of the ash (curves 1-3). As it can be seen, the ash fusing possibility leads to abrupt increasing of the burning times in comparison with the HFA cases. The results for HFA coal particles (curves 1,2) with sizes more than 100 μm indicate the diffusion control of the burning rate: characteristic burning time value is practically constant. Influence of the kinetics for the smaller particles size is displayed by some increase of the t_b/r_0^2 values. The behavior of the curve 3 for a LFA does not allow to determine the leading mechanism of such coal combustion and demonstrates that the diffusion barrier of the liquid ash

layer strongly reduces the macroscopic reaction rate in all investigated particles sizes range.

It is interesting to compare the burning time of an ash coal with the one's of an ash-free coal. Figure 3 shows these times ratio as a function of the initial particle size. For a LFA the ratio exceed 3 and has an extreme (curve 3) where as for a HFA (curves 1,2) they are close to 1 and slightly decrease with a particle size increasing. Curve 3' obtained for a LFA without the radiation heat losses accounting is presented to explain above-mentioned extreme. Radiation heat losses hinder the surface coal particle temperature growing above the ash fusion temperature. It leads to decrease of the particle surface fraction covered by a liquid ash layer for the coal particles which radius is more than 75 μm and as a result to the burning times decrease.

Figure 4 shows the burning time as a function of the oxygen mass fraction. Curves 1 and 2 for the HFA represent a typical for the heterogeneous combustion decreasing dependence of a burning time under oxidizer mass fraction growth. Otherwise, the dependence for a LFA (curve 3) has a minimum. Fact of the burning time increase for the oxygen mass fraction greater than 10 % can be explained by the above mentioned influence mechanism of the correlation between the maximum particle surface temperature reached in the combustion process and the ash fusion temperature value.

CONCLUSION

Presented above results make it possible to conclude that fusibility of the inorganic matter is one of the most significant ash coal characteristics. HFA has a weak influence on the conversion dynamics and burning time of an ash coal in the comparison with the ash free coal. In such case an ash can be considered as a thermal dead matter. The qualitative change of an ash coal combustion mechanism is able to appear if the temperatures reached in the combustion process exceed the ash fusing temperature even under the relatively low inorganic matter fraction (A=11%). That, in its turn, leads not only to considerable increasing of the particles burning times but to appearance of the qualitatively new, with extreme, dependences of the burning time as a function the coal particle initial size and oxidizer mass fraction.

It seems to be very significant for the practice of ash coal combustion.

This work was supported by the Ministry of Education of Ukraine, project №673-96.

REFERENCES

1. Vulis,L.A., Journal of the Technical Physics, vol 10 iss 24-26 (1940).
2. Vulis,L.A., Journal of the Technical Physics, vol 16,1 (1946).
3. Frank-Kamenetskii,D.A., Diffusion and Heat Transfer in Chemical Kinetics (3rd ed) Nauka, Moskow, 1987.
4. Kantorovich,E.V., Fundamentals of Theory of Combustion and Gasification of Solid Fuels AN USSR, Moskow 1958, pp 380-385.
5. Kiro,S.A., Vovchuk,Y.I., Zolotko,A.N., Klyachko,L.A., The Physics of Combustion and Explosion, 5: 36-39 (1983).
6. Lavrov,P.V., Shurigin,A.P., Introduction in Theory of Combustion and Gasification of Fuels AN USSR, Moskow, 1962, pp 204-204.
7. Pomerantsev,V.V., Fundamentals of Practical Theory of Combustion Energiya, Leningrad, 1973, pp 164-169.
8. Hoffman,E.J., Coal Conversion Energoatomizdat, Moskow, 1983, pp 64-76.
9. Yurovskii,A.Z., Mineral Components of Solid Combustible Minerals Nedra, Moskow, 1968.
10. Agroskin,A.A., Chemistry and Techology of Coal Nedra, Moskow, 1969.
11. Parks,B.C., Mineral Matter in Coal, Sec. Conf. on the Origin and Const. of Coal, Crystal Cliffs, Nova Scotia, 1952, pp 272-299.
12. Dutcher,R.R., White,E.W., Spackman,W., Elemental Ash Distribution in Coal Components - Use of Electron Probe, Ironmaking Conference, Iron and Steel Div. Metal. Sos., American Institute Min. Metal. Perd. Engs. Proc., New York - London, 1963,1964, 22 pp 463-483.
13. Vilenskii,T.V., Hzmalyan,D.M., Dinamics of Dust Fuel Combustion Energiya, Moskow, 1978.
14. Hurt,R.H., Davis,K.A., *Twenty-Fifth (International) Symposium on Combustion*,"Near-Extinction and Final Burnout in Coal Combustion", The Combustion Institute, Pittsburg, 1994.
15. Hurt, R.H., Davis,K.A., Yang,N.Y.C., Headley,T.H., Mitchell,R.E.,"Residual Carbon from Pulverised Coal Fired Boilers 2: Morphology and Physicochemical Properties", Fuel, v 74, #9, 1297-1306 (1995)
16. Hurt,R.H., Energy & Fuel 7 :721-733 (1993)
17. Davis,K.A., Hurt,R.H., Yang,N.Y.C., Headley,T.J., "Evolution of Char Chemistry, Crystallinity, and Ultrafine Structure during Pulverised-Coal Combustion", *Twenty-Fifth (International) Symposium on Combustion*, The Combustion Institute, Pittsburg, 1994.
18. Hurt,R.H., Mitchell,R.E., *Twenty-Fourth (International) Symposium on Combustion*, The Combustion Institute, Pittsburg, 1992, pp 1243-1250.

NOMENCLATURE

T -coal particle temperature, K

$\mathbf{T_g}$ -gas temperature, K

M -coal particle mass, g

r -coal particle radius, cm

$\mathbf{r_0}$ -coal particle initial radius, cm

$\mathbf{r_z}$ -ash particle radius, cm

t -time, s

$\mathbf{t_b}$ -complete burning time, s

$\mathbf{t_{baf}}$ -complete burning time of an ash free coal, s

A -ash content

H -ash layer thickness, cm

Z -fraction of the reaction surface area covered by ash

$\mathbf{C_\infty}$ -ambient gas oxidant mole fraction

$\mathbf{C^1_{O_2}}$ -oxidant mole fraction on clean coal surface

$\mathbf{C^2_{O_2}}$ -mole fraction on coal surface covered by ash

$\mathbf{\nu_i}$ -stoichiometric coefficients

$\mathbf{k_i}$ -reaction rate coefficients, cm/s

$\mathbf{E_i}$ -activation energy, cal/mole

$\mathbf{Q_i}$ -heat release by i reaction, cal/g of carbon

λ -thermal conductivity of gas, cal/(cmsK)

$\mathbf{C_p}$ -coal heat capacity, cal/(gK)

D -gas diffusion coefficient, cm^2/s

$\mathbf{D_z}$ -coefficient of gas diffusion through ash layer, cm^2/s

ε_c -carbon emissivity

ε_a -ash emissivity

$\mathbf{T_\infty}$ =300 K

Ω -ash layer porosity

$\mathbf{D^*}$,$\mathbf{E_z}$ -preexponential factor and activation energy of the oxygen diffusion through the liquid ash layer

FIGURE CAPTIONS

Figure 1.

Calculated temperature dynamics of the coal particle combustion. T_g=1250K, C_∞=6 mole-%, r_0=100μm, r_z=0.5μm, A=11%, ε_c=0.78, ε_a=0.4. (•)- experiment [14], 1 - LFA, 2 - HFA leaves coal particle, 3 - HFA covers coal particle.

Figure 2.

Characteristic time (t_b/r_0^2) vs initial coal particle radius. T_g=1250K, C_∞=6 mole-%, r_z=0.5μm, A=11%, ε_c=0.78, ε_a=0.4. 1 - HFA leaves coal particle, 2 - HFA covers coal particle, 3 - LFA.

Figure 3.

Relative burning time (t_b/t_{baf}) vs initial coal particle radius. T_g=1250K, C_∞=6 mole-%, r_z=0.5μm, A=11%, ε_c=0.78, ε_a=0.4. 1 - HFA leaves coal particle, 2 - HFA covers coal particle, 3 - LFA, 3' - LFA, radiation heat losses absence.

Figure 4.

Burning time vs oxygen mass fraction. T_g=1250K, r_0=100μm, r_z=0.5μm, A=11%, ε_c=0.78, ε_a=0.4. 1 - HFA leaves coal particle, 2 - HFA covers coal particle, 3 - LFA.

Figure 1

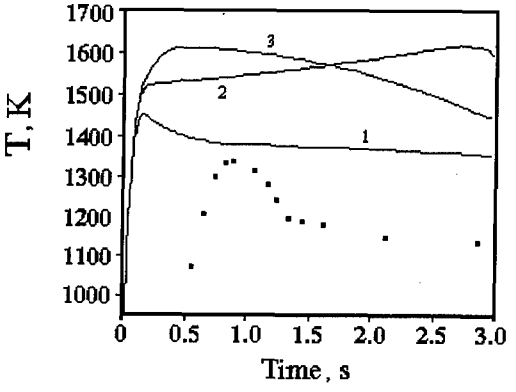

Figure 2

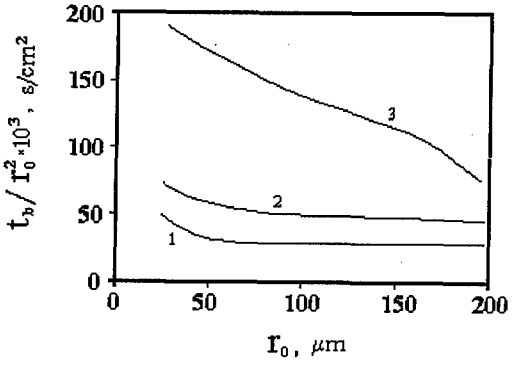

Figure 3

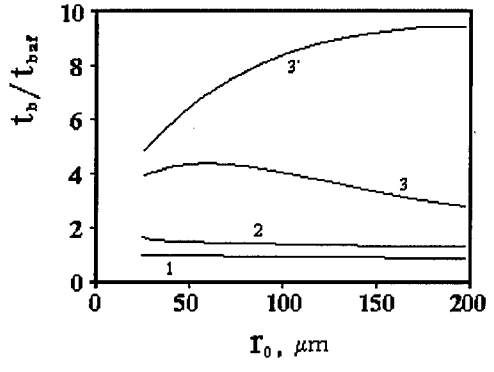

Figure 4

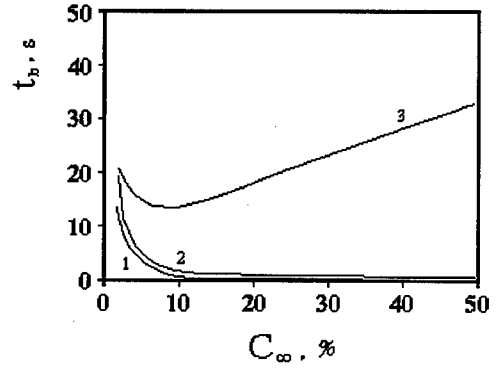

CHARACTERIZATION OF SELF-SUSTAINING COMBUSTION OF CYCLIC NITRAMINES

Vladimir N. Simonenko, Vladimir E. Zarko and **Alexander B. Kiskin**

Institute of Chemical Kinetics and Combustion,
Institutskaya 3, Novosibirsk, 630090, Russia

Abstract

A transducer of the reactive force of the combustion products was used to study experimentally the peculiarities of combustion of RDX and HMX in the range of 1-4 atm. It has been established that at atmospheric pressure in addition to the usually recorded flame combustion regime, RDX has the regime of flameless gasification under irradiation. Both of the regimes are followed by high-frequency oscillations in the reactive force exceeding 600 Hz. The source of these oscillations is assumed to be the process of boiling and rupture of bubbles at the surface.

It has been established that in the pressure range of 1-3 atm the HMX combustion has pronounced auto oscillating character. Under harmonically modulated radiant flux the response of reactive force for HMX displays the resonance character. Even at small modulation depths the character of this response is nonlinear.

For both HMX and RDX the dependencies of the steady-state burning rate on initial temperature and on external radiant flux have been determined.

Introduction

The detailed models available in the literature [1-3] for describing steady-state combustion of the simplest monopropellant - cyclic nitramines, contain a great number of matching parameters. The verification and justification of combustion models are commonly performed by comparing with the experimental data on the dependence of steady-state burning rate on the initial temperature and pressure. As mentioned earlier [4], this approach fails to provide the reliability of verification due to large "flexibility" of theoretical descriptions due to existence of numerous of matching parameters. In this connection, of importance are the experimental results for nonsteady-state combustion which make it possible to compare adequately the theory with experiment because they correspond to a variety of combustion conditions.

One of the types of nonsteady-state combustion is the regime of self-sustaining combustion near the stability limit of steady-state combustion. It is known that small perturbations near the stability limit give rise to the undamped oscillations of the burning rate which become nonlinear with distance from the limit [5]. The experimentally

observed pulsations of either temperature or component concentration in the gas phase performed by local measuring at a point using microthermocouples or microprobes, in most cases cannot be identified with predicted by theory periodical oscillations of the burning rate and are determined by predominantly either micro inhomogeneities in the composition of condensed substances or the formation of gas bubbles in the surface layer. We may mention only one reliable fact [6] of revealing oscillations of the burning rate of the catalyzed double base propellant in the self-sustaining combustion regime.

This report gives the results of a study of RDX and HMX combustion in self-sustaining regime and under the action of periodical changes in the external radiation flux.

Preparation of samples

In experiments we used cylindrical samples with length 0.6-0.8 cm and diameter 0.8,1 and 1.6 cm pressed at a pressure of 5000-6000 kg/cm^2. The density of pressed specimens reached 95% of crystal density.

To decrease transparency of material and reflection of radiant energy from the sample surface we added 0.5% of fine-dispersed carbon black (CB). According to special tests, the addition of CB up to 3% fails to change the combustion behavior and burning rate of RDX and HMX. We used three sources of radiant energy: CO_2-laser with a wavelength of 10.6 μm, Nd:YAG - laser with a wavelength of 1.06 μm and Xenon lamp with emissivity spectrum in the range of wavelengths 0.2-1.4 μm. A set-up with Nd:YAG - laser has been used to perform the programmed control over the radiation power. We used the sinusoidal and step-wise changes in the flux recording simultaneously the reactive force of flowing combustion products and the signal of photodiode that measures the integral flame radiation. To provide one-dimensional flow of gaseous combustion products the specimens were tightly inserted into protecting tube of quartz that also served as inhibition of lateral surface. In some experiments we recorded the temperature profile by means of a WRe 20/ WRe 5 thermocouple made of wires of 50 and 150 μm diameter. The reactive force F is related to the burning rate r_b via the expression below (if the frequency of the burning rate oscillations does not exceed 100-150 Hz):

$$F = (\rho_c \ r_b)^2 / \rho_g$$

where ρ_c is the propellant density; ρ_g is the density of gaseous combustion products. The method of investigation is described in [6-8].

Preliminary experiments

In a special series of experiments the samples were pressed by a pressure of 1500 and 3000 kg/cm^2. In this case, the sample density reached 0.88-0.9 of the crystal one. The difference from the maximum value (pressing at 5000-6000 kg/cm^2) amounts to 5-6%. When the relative density varies within the range of 0.88-0.95, the burning rate remains constant.

In a series of experiments we tested the influence of inhibition layer material on the character of combustion behavior. It was revealed that the character of RDX combustion is actually independent of the inhibitor type. HMX is more sensitive to the type of inhibitor. When the inhibition layer is combustible (glue, iditol, shellac), the pilot flame originates at the edge of the sample and the character of HMX combustion changes. For the main series of experiments, as inhibition material, we used both linoleum and quartz tubes or we performed the blowing with nitrogen along the lateral surface of the sample.

Self-sustaining combustion regime

The character of HMX and RDX combustion is quite different. When samples of RDX doped with CB are irradiated by with Nd:YAG laser by constant flux in the range 10-18 cal/cm^{2}s the flameless gasification regime is established with relatively small regression rate. Flame does not appear neither in air nor in nitrogen environment. All these experiments were conducted with unprotected and non-inhibited RDX samples. Even slow deradiation up to zero level during 0.6-1.0 sec could not provide conditions for flame appearance. It merely led to total extinguishing and gradual cooling of the sample.

The data on flameless gasification rate for CB doped RDX samples versus incident (Nd:YAG laser) radiant flux can be described by relationship

$$r_{\text{gasification}}\ [\text{cm/s}] = 0.001\ q$$

where q should be taken in cal/cm^{2}s.

In the case of laser radiative heating of RDX samples supplied with protection tube the ignition in gas phase (flame appearance) occurred in arbitrary moments of time. This fact indicates that the reason for gas flame ignition is overheating of the glass tube or the edge of inhibiting layer.

In the ignition of RDX in air by Xenon lamp the flame combustion regimes (samples with quartz protection tube) were initiated with $q > 8$ cal.cm^{2}s. The burning rate in regime with a developed flame is 0.039±0.003 cm/s. A characteristic feature of the recorded signal of reactive force is the existence of a high-frequency component with an oscillation frequency of about 600 Hz that corresponds to the eigen frequency of a mechanical unit of the transducer. This behavior is supposedly determined by the fact that the measured reactive force contains oscillations whose frequency exceeds the eigen frequency of the mechanical unit of the transducer. The photodiode signal trace has a smooth character (Fig. 1).

It is assumed that the source of the reactive force oscillations is the process of rupture of bubbles forming in the surface RDX layer upon combustion. According to our temperature measurements and to the literature data [9], upon combustion in air the melted layer of RDX equals to 0.04 cm which is 2-3 times larger than that of HMX.

The HMX combustion in self-sustaining regime has a pronounced auto oscillatory character (Fig. 2). This behavior is recorded by both the transducer of the reactive force and the photodiode. The unsteadiness of HMX combustion at atmospheric pressure was reported in [10]. The oscillatory regime of HMX combustion is established either in the case of radiant flux switch-off or in the case of initiation by the burning RDX sample (combustion of two samples in contact). Note that in the composite charge the combustion wave passes steadily (without delay) in the direction RDX→HMX and back. After ignition, in HMX the oscillatory combustion regime develops with a frequency of 6-8 Hz.

Upon radiative ignition after removal of external energy source the reactive force decreases substantially for 0.5-1 s (depending on the igniting flux value) with subsequent transition to the auto oscillatory regime. Further, upon combustion the oscillation amplitude may increase with decreasing frequency. The frequency of reactive force oscillations may decrease to 3-4 Hz and the amplitude may increase to the values close to 100%. In most cases, this process leads to extinction.

The HMX combustion behavior is very sensitive to impurities. The oscillatory character of combustion vanishes completely if RDX is added to HMX in amounts of more than 5%. The presence of the combustible inhibition layer (glue) decreases the oscillation amplitude. The addition of the inert component (Al_2O_3 or soot) up to 5% has no effect on the HMX combustion behavior.

Figures 3 and 4 show the dependencies of RDX and HMX burning rates on the radiant flux. The data are given for three sources of the radiation. When the samples contain 0.5 to 1% of carbon black, the $r_b(q)$ dependencies are not distinguished under the action of various energy sources. Figure 5 shows the dependencies of the steady-state burning rate of RDX and the averaged burning rate of HMX on initial temperature at atmospheric pressure. In this case, the value of the coefficient of burning rate temperature sensitivity $\sigma_p = \partial ln(u)/\partial T_0$ almost const for both compounds and equals approximately to $\sigma_p = 0.0026$ 1/K.

Combustion under external radiation

The burning rate response to the radiant flux has been studied by flux step-wise and sinusoidal changes. Upon cut off (during $\approx 10^{-3}$ s) of the radiant flux, RDX transforms to self-sustained combustion regime without noticeable time delays. In this case, the high frequency oscillations of the reactive force are preserved. HMX is more sensitive to the changes in radiant flux. When a radiant flux of (10 – 14) cal/cm^{2}s is cut off abruptly, the burning rate decreases almost to zero and the duration of transition period amounts to 0.5 s. Thereafter, the auto oscillatory combustion regime develops if there is no complete extinction.

Under the action of harmonically modulated radiant flux the reactive force response for HMX exhibits a pronounced resonance character. Experiments were performed at T_0=20^{o}C, the mean radiant flux q = 14 cal/cm^{2}s. The resonance frequency observed was 10 - 12 Hz (Fig. 6) and the resonance response amplitude was 60-70% for a 30% depth of radiation modulation. The character of the response of reactive force signal is nonlinear which is manifested in both the shape of response signal and the dependence of the response amplitude on modulation depth. As the modulation depth decreases to 10% and even 5%, the response amplitude in the vicinity of resonance frequency remains

constant. In these two cases the response uniformity is lost with distance from the resonance frequency and then (at large frequencies) HMX combustion passes to the oscillatory regime at resonance frequency. Note that at constant radiant flux equal 14 cal/cm^{2}s the HMX combustion was steady in most experiments. However, in some cases we observed the oscillatory combustion regimes under constant irradiation with an oscillation frequency of reactive force of 10 - 13 Hz.

The resonance frequency of reactive force response for RDX is 5 - 7 Hz at q = 14 cal/cm^{2}s and modulation depth 20% and the response amplitude is lower than that of HMX. These low resonance frequencies were not detected in [13] where experiments with the HMX and RDX were conducted in the range (15 – 100) Hz.

Combustion under elevated pressures

In the experiments under elevated pressures the self-sustained combustion regimes were analyzed on the basis of reactive force signal records. As the pressure increases, the amplitude of high-frequency oscillations in the reactive force signal of RDX decreases and with the pressure exceeding 4 atm the recorded signal becomes smooth. In HMX, as the pressure increases, the oscillation frequency increases and the relative amplitude of the reactive force decreases. At 3 atm the frequency reaches 40 Hz and with further increase in pressure the reactive force oscillations are actually not recorded.

Figure 7 shows the dependencies of burning rate on pressure and Figure 8 shows a change in the dimensionless oscillation frequency of HMX burning rate with varying pressure.

Discussion

The experimental study revealed variety of important features of the RDX and HMX combustion behavior at atmospheric pressure. It gives a basis for improvement and validation of existing theoretical models for combustion of melted energetic materials.

An existence of flameless low rate radiation–driven gasification regime for RDX upon radiative ignition at atmospheric pressure reflects the fact that the rate of chemical reactions in the gas phase for this compound is rather low. It means that the characteristic time for chemical reactions in the flame may become comparable with the residence time

of gaseous species in the flow of vapor and decomposition products. Consequently, the flame can be formed at a finite distance from reacting surface but in conditions of radiative heating the gases cool down going away from the surface that prevents appearance of flame. In the case of forced ignition of gases above the surface, e.g. with external flame torch or via propagating combustion wave (samples in contact) the RDX samples burn in flame regime with enhanced burning rate.

The flameless gasification regime of RDX should be studied experimentally in more details. The dependence of gasification rate on initial temperature, radiant flux and pressure may give valuable information about global parameters of chemical transformations in the condensed phase. Measurement of surface temperature in flameless gasification regime may also provide information on boiling temperature that is known to be very difficult measurable in direct way for reacting substances.

Another important feature of self-sustaining RDX combustion is high frequency oscillatory behavior of the burning rate/reactive force at pressures 1-3 atm. It has been mentioned above that the very possible cause of oscillations is the rupture of bubbles in the melted surface layer of RDX. The formation of separate bubbles at the reacting surface of RDX was observed in our experiments and mentioned in literature [10]. However, to prove statement about cause of reactive force oscillations one needs to perform experiments with visualization of combustion along with determining the dependence of frequency of oscillations on the magnitude of reacting surface and combustion conditions. It will be useful to conduct experiments with other melted energetic materials in order to establish correlation on oscillations existence with the width of the melted layer.

In the case of HMX the most interesting finding is an existence at pressures 1-3 atm of low-frequency regular burning rate oscillations that is very similar to the predicted by theory [11] for the system burning close to the limit of steady-state combustion. The observed occasional extinction of HMX self-sustaining oscillating combustion at atmospheric pressure gives the evidence of intrinsic instability of this combustion regime. Note that comparison with prediction by original version of phenomenological theory of nonstationary combustion (the Zeldovich - Novozhilov approach) [11] reveals contradiction with experimental observations. Indeed, according to the linear analysis [11]

the combustion regimes with auto oscillations of burning rate exist at the limit of stability of steady-state combustion when parameter $k = \sigma_p (T_S - T_0) > 1$. With $k < 1$ the auto oscillations of the burning rate must not exist. However, if we take experimental value σ_p=0.0026 1/K and T_S = 633 K [9], the calculated value $k = 0.88 < 1$ at T_0= 293 K. The first explanation of this discrepancy is that measured experimentally value of σ_p corresponds, in fact, to oscillating but not steady-state combustion regime which should only be used for determining σ_p.

It can be mentioned that according to the model developed by Ward et al. [12] the self-sustaining combustion of HMX at atmospheric pressure should be unstable and it becomes stable at elevated pressures. However, it is known that the model [12] is based on oversimplified assumptions and efforts on theoretical simulation of nitramines combustion should be continued. The experimental dependencies for the frequency and amplitude of auto oscillations of the burning rate on initial temperature and pressure may serve good job for validation of theoretical models and for determining needed global kinetic parameters. It is interesting to note that an improved version of the Zeldovich - Novozhilov approach that takes into consideration the latent heat of melting gives for unstable combustion regimes the limiting value k<1 depending on the magnitude of melting heat [14]. In fact, to check theoretical predictions one needs to obtain precise experimental data that can be used in theoretical calculations.

Conclusions

The findings of the present work are as follows:

1. The flameless radiation-driven gasification regime of RDX at atmospheric pressure is revealed.

2. High frequency oscillations (> 600 Hz) of recoil force are recorded in combustion/gasification of RDX at atmospheric pressure.

3. The regime of low-frequency auto oscillating HMX combustion is recorded at pressures 1-3 atm with frequencies increasing from 6 – 8 Hz to 37 – 40 Hz in the pressure range studied.

4. The resonance response of burning rate to sinusoidal oscillations of the radiant flux (q = 14 cal/cm^{2}s, modulation depth 20%) is recorded at atmospheric pressure. The frequency of resonance equals to 10 – 12 Hz for HMX and 5 – 7 Hz for RDX.

The results obtained give background for improving and validation of theoretical combustion models and better understanding of the mechanism of nitramines combustion. It should be underlined the significance of using the methods of recording transient combustion parameters (recoil force, flame radiation) in getting new information about combustion mechanism. It is believed that new experimental data will be helpful in deriving the values of global kinetic parameters characterizing combustion of nitramines at conditions under study.

Acknowledgment

Partial support of this work from the ONR and ERO, USARDSG-UK (N68171-95-C-9009) is gratefully acknowledged.

Literature

1. Melius C.F. "Thermochemical modeling: I & II", Chemistry and Physics of Energetic Materials, Ed. by S.N. Bulusu, Kluwer Academic Publishers, Netherlands, 1990.

2. Liau Y.-C., Yang V., "Analysis of RDX monopropellant combustion with two-phase subsurface reactions" JPP, 1995, Vol. 11, No. 4, pp. 729-739.

3. Erikson B., Beckstead M.W., "A numerical model of monopropellant deflagration under unsteady conditions", AIAA Paper, 96-0652.

4. Gusachenko L.K., and Zarko, V.E., "Analysis of Contemporary Models of Steady State Combustion of Composite Solid Fuels", Combustion, Explosion, and Shock Waves, 1986, Vol.22, No. 6, pp. 643-653.

5. Zarko V.E., Simonenko V.N., and Kiskin A.B., "Nonstationary combustion of Condensed Substances under the Influence of Radiation", Fizika Goreniya i Vzryva [*Combustion, Explosion and Shock Waves*], Vol. 23, No. 5, 1987, pp. 16 - 26.

6. Zarko V.E., Simonenko V.N., and Kiskin A.B., "Radiation - Driven Transient Burning: Experimental Results", Progress in Astronautics and Aeronautics, Ed. L. De Luca, E.W. Price, and M. Summerfield, New-York, AIAA Inc., Vol. 143. 1992, pp. 363 - 398.

7. Simonenko V.N., Zarko V.E., "The Reactive Force of Combustion Products as a Measure of Propellant Transient Burning Rate", Fizika Goreniya i Vzryva [*Combustion, Explosion and Shock Waves*], Vol. 17, No. 3, 1981, pp. 129-132.

8. Zarko V.E., Simonenko V.N., and Kiskin A.B., "Unsteady Burning of Double Base Propellants", in Progress in Astronautics and Aeronautics, Ed. by J.R. Bowen, N. Manson, A.K. Oppenheim, and R.I. Soloukhin, New-York, AIAA, Inc., Vol. 88. 1983.

9. Zenin A. A., "HMX and RDX: Combustion Mechanism and Influence on Modern Double – Base Propellant Combustion", JPP, Vol. 11, No. 4, 1995, pp. 752 – 758.

10. Parr T.P., Hanson-Parr D.M., "Solid Propellant Flame Structure", In: Decomposition, Combustion, and Detonation Chemistry of Energetic Materials, Materials Research Society Symposium Proceedings, Ed. by T.B. Brill, T.P. Russel, W.C Tao. and R.B. Wardle, Pittsburgh, MRS, Vol. 418, 1996, pp. 207 - 219

11. Novozilov B.V., "Theory of Nonsteady Burning and Combustion Stability of Solid Propellants by the Zeldovich – Novozilov Method", Progress in Astronautics and Aeronautics, Ed. L. De Luca, E.W. Price, and M. Summerfield, New-York, AIAA, Inc., Vol. 143. 1992, pp. 601 – 642.

12. Ward M.J., Son S. F., and Brewster M. Q., "Deflagration of HMX with Simple Kinetics: A New Modeling Steady Paradigm", submitted to Combustion and Flame.

13. Finlinson J.C., "Laser Recoil Response Function of HMX, RDX, N5, GAP/BTTN and Others from 1 to 6 atm", AIAA Paper 97 – 0698.

14. Gusachenko, L.K., "Effect of Melting on the Combustion Stability of Quasi Homogeneous Propellants", Fizika Goreniya i Vzryva [*Combustion, Explosion and Shock Waves*], Vol. 34, No. 2, 1998.

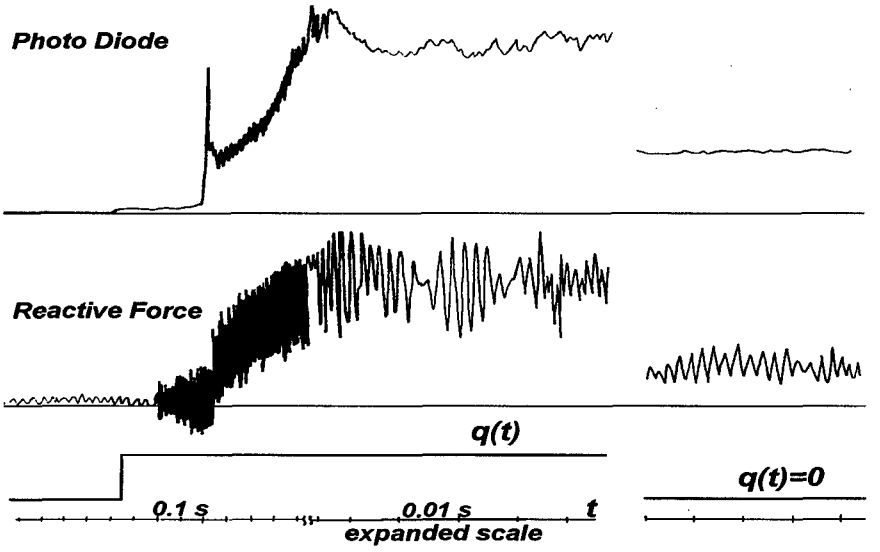

Fig. 1. The records of RDX radiation driven combustion; To = 20°C, P=1 atm.

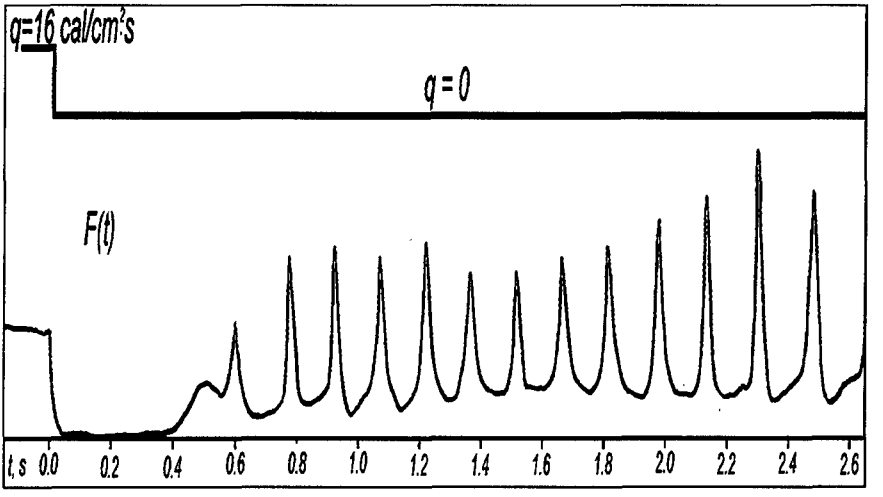

Fig. 2. The records of HMX radiation driven combustion; To = 20°C, P=1 atm.

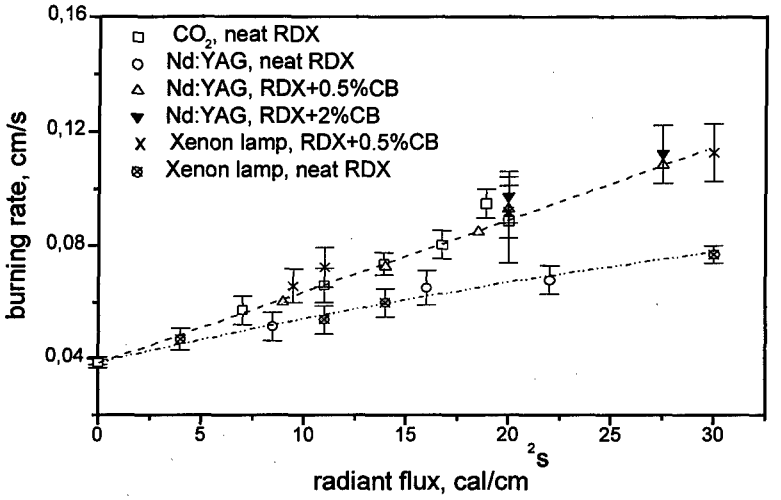

Fig. 3. RDX burning rate vs radiant flux; To = 20°C, P=1 atm.

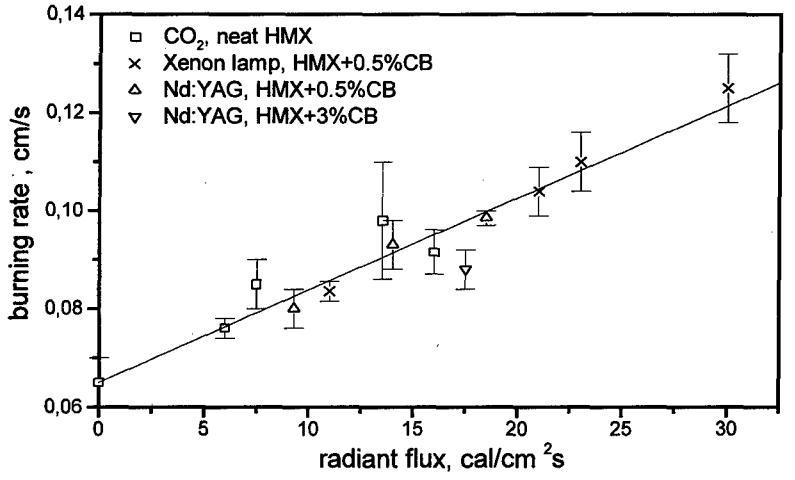

Fig. 4. HMX burning rate vs radiant flux; To = 20°C, P=1 atm.

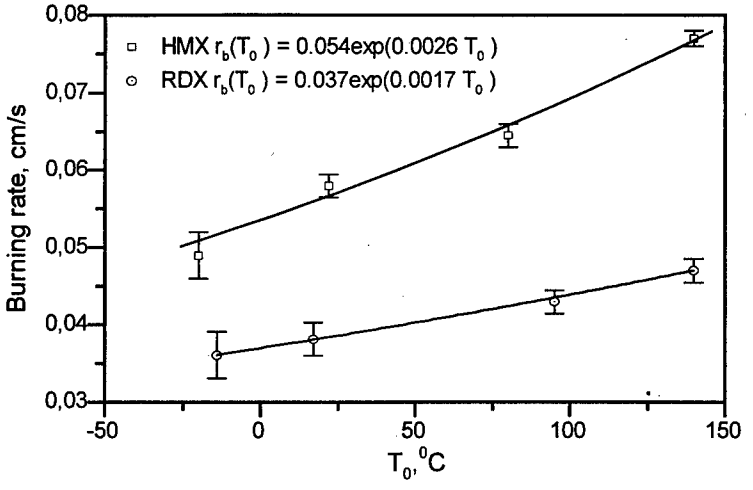

Fig. 5. RDX and HMX burning rates vs ambient temperature; P=1 atm.

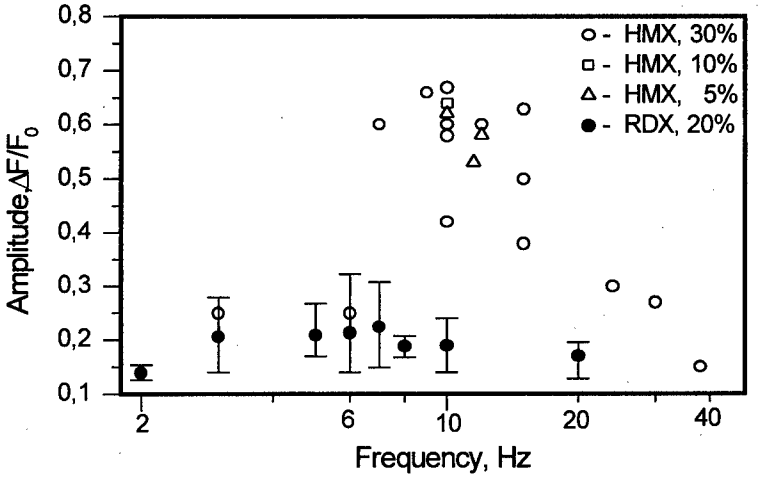

Fig. 6. RDX and HMX recoil force response vs Frequency; To = 20°C, P=1 atm.

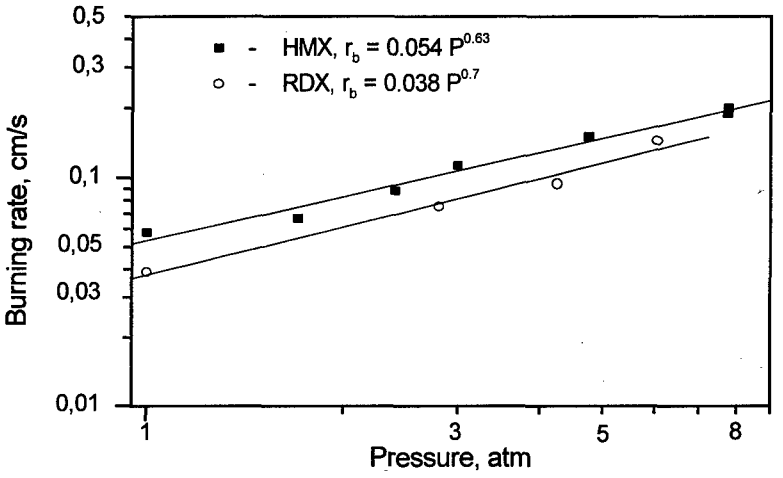

Fig. 7. RDX and HMX burning rate vs pressure; To = 20°C.

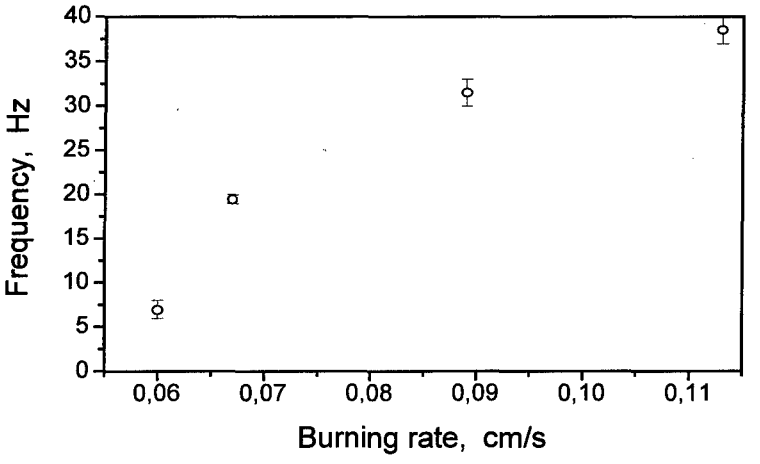

Fig. 8. RDX and HMX auto oscillation frequency vs burning rate, To = 20°C.

STUDY ON COMBUSTION OF NEW ENERGETIC FURAZANS

Valery P.Sinditskii, He Wei Dong, Valery V.Serushkin,
Alexander E.Fogelzang
Department of Chemical Engineering, Mendeleev University of Chemical Technology,
9 Miusskaya Sq., 125047, Moscow, Russia
and

Alexey B.Sheremetev
N.D.Zilinskiy Institute of Organic Chemistry, Russian Academy of Science, Leninsky Prosp., 47,
Moscow 117913, Russia

ABSTRACT

Burn rate characteristics of monopropellant combustion of furazan derivatives, an aromatic endothermic five-membered ring, were studied. Three furazan series: furazans, azofurazans, and azoxyfurazans, substituted with NH_2, OH, OCH_3, CH_3, CN, and NO_2 groups, were under investigation. Within each of the three furazan series, the burning rate of a furazan derivative containing nitro group has been found to be much higher than that of the rest, even exceeding the burning rate of traditional high-energy materials (HMX, RDX). For the compounds without active oxygen in the substituent, thermocouple-aided measurements showed results well below calculated adiabatic combustion temperatures. Nitrile-containing compounds formed during decomposition of the heterocycle in the absence of an oxidizer is assumed to remain unreacted among combustion products and to be responsible for incomplete energy release. For combustion of compounds of this type, the main source of heat release is suggested to be isomerisation of the nitriloxide formed during furazan decomposition to isocyanate rather than an oxidation reaction.

INTRODUCTION

Performance, stability and sensitivity are three of the most obvious criteria that can be used in evaluating energetic ingredients, but many other factors come into play in determining whether a compound ever finds its way into usage. Combustion characteristics are among them. Derivatives of furazan, an aromatic five-membered ring with one oxygen atom between two nitrogen atoms, are being investigated intensively as they can be thought of to contribute to propellant performance due to high enthalpy of formation of furazan ring. The present work was aimed at studying burn rate characteristics of monopropellant combustion of furazan derivatives to evaluate a combustion mechanism and to allocate this new class of compounds among other energetic materials.

EXPERIMENTAL

Furazan derivatives, 3,4-diaminofurazan [1,2], 3-aminofurazan-4-carboxamidoxime [3], 3-amino-4-nitrofurazan [4], 3-amino-4-cyanofurazan [5], 4,4'-dimethylazofurazan [6], 4,4'-dimethoxy-azofurazan [7], 4,4'-dicyanoazofurazan [8], 4,4'-dinitroazofurazan [4], 3,3'-diaminoazoxyfurazan [9], 4,4'-dinitroazoxy-furazan [4] were synthesized by methods published elsewhere. Analytic data confirmed the assigned structures.

Table 1. Physical Properties of Furazan Derivatives.

Abbreviation	Structural Formula	ΔH°_{f}, kcal/mol	Density g/cm^3	Melting Point, °C	Adiabatic Flame Temperature, K (100 atm)
DAF	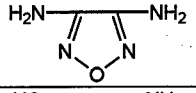	24.8	1. 61	180	1590
CNAF	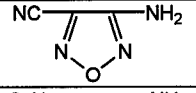	67*	1.57**	187	2425
NAF	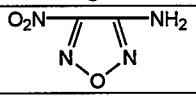	27.1	1.86	126	3280
AOAF	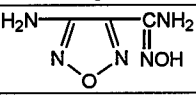	10*	1.58**	190	1520
DCNAZF	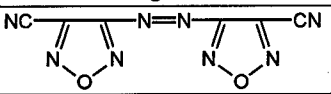	225	1.58**	152	3710
DMOAZF	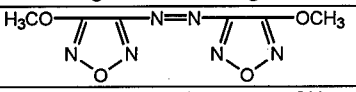	62.7	1.67**	175	1725
DOHAZF	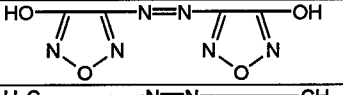	59*	1.75**		2750
DMAZF	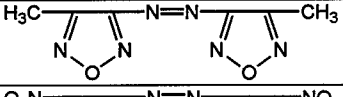	137*	1.57**	105	2365
DNAZF	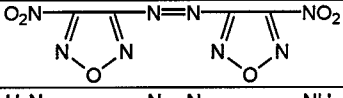	168.4	1.73	56	4130
DAAZOF	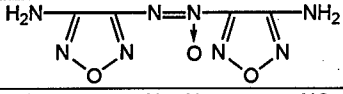	127.2	1.6**	246	2655
DNAZOF	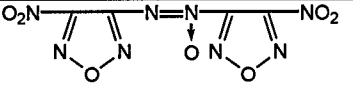	154.7	1.82	112	4030

* Calculated enthalpies (the other enthalpies were determined by Dr. V.P.Lebedev from Institute of Chemical Physics of Russia); ** Density of pressed strands.

Burn rate measurements were carried out in a window constant pressure bomb of 1.5 liter volume in the pressure range of 0.1-36 MPa. A slit camera was used to determine a character of the combustion process as well as burning rate values.

The combustion strands were prepared by pressing thoroughly comminuted substances in transparent acrylic tubes of 4 or 7 mm i.d. at 150-200 MPa.

Temperature profiles in the combustion wave of furazans were measured using Π-shaped thermocouples. The thermocouples were welded from 25μm diameter tungsten/5%-rhenium and tungsten/20%-rhenium wires, rolled in bands to obtain 7 μm bead size, and embedded into pressed strands of 7 mm diameter.

RESULTS AND DISCUSSION

Combustion behavior

Three furazan series: furazans, azofurazans, and azoxyfurazans, substituted with NH_2, OH, OCH_3, CH_3, CN, and NO_2 groups, were under investigation. The effect of pressure on the burning rate of the furazans is presented in Figs.1-3. Mononuclear furazan derivatives except for aminonitrofurazan burn with a very weak luminescence, forming a plenty of smoke, especially at low pressures. In the case of azo- and azoxyfurazans much smoke is observed also, but the flame in combustion is brighter, of reddish color. All of furazan nitroderivetives give a smokeless bright white flame.

Furazan derivatives appeared to demonstrate burning rates typical for of usual nitrocompounds, but not nearly so rapid as derivatives of tetrazole, another high-energy heterocycle. Thus, diaminofurazan DAF burns at approximately the same rates as dinitrophenol isomers of close combustion temperature [10] but below than slow-burning tetrazole derivatives, 5-amino- and 5-hydroxytetrazole [11]. This is not surprising since except the heat of oxidation by the active oxygen atom the energy in combustion of furazans can be only released during decomposition of nitrile fragments "built-in" the heterocycle, which are extremely slow to decompose in the absence of an oxidizer.

Within each of the three furazan series, the burning rate of the furazan derivative containing nitro-group appears to be much higher than that of the rest, approaching or even exceeding the burning rate of traditional N-NO_2 energetic materials such as HMX and RDX. This is connected with higher combustion temperatures of furazan nitroderivetives (see Table 1).

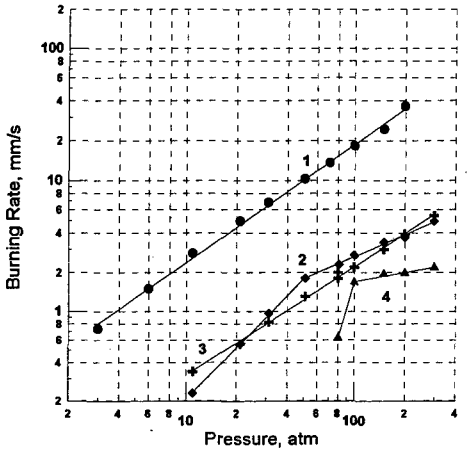

Fig. 1. Pressure dependence of the burning rate of furazan derivatives:

3-amino-4-nitrofurazan - (1)
3-amino-4-cyanofurazan - (2)
3,4-diaminofurazan - (3)
3-aminofurazan-4-carboxamidoxime - (4)

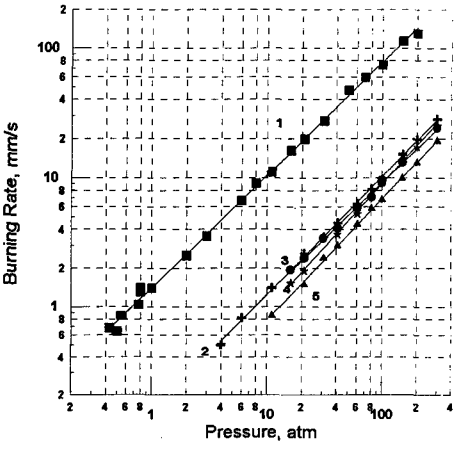

Fig. 2. Pressure dependence of the burning rate of azofurazan derivatives:

4,4'-dinitroazofurazan - (1)
4,4'-dihydroxyazofurazan - (2)
4,4'-dimethylazofurazan - (3)
4,4'-dicyanoazofurazan - (4)
4,4'-dioxymethylazofurazan - (5)

However, no correlation between the burning rate of others furazan derivatives and adiabatic flame temperatures is observed. For example, the calculated combustion temperature of aminocyanofurazan is more than 800 K higher than that of temperature of diaminofurazan (see Table 1), whereas the burning rates of these compounds are close to each other (see Fig. 1). While the burning rates of a large group of furazan azo derivatives are closely related (see Fig. 2), the corresponding calculated combustion temperatures are different. This situation is believed to reflect the difficulty with energy release from nitrile-containing decomposition products in a deficit of an oxidizer, with the result that the greatest possible combustion temperature is not achieved.

In contrast to nitrile group the inner energy reserved in azo and azoxy groups has an opportunity to be released in the combustion wave as evidence by higher burning rates of azo- and azoxyfurazans in comparison with mononuclear compounds (compare Figs.1-3).

A comparison of burning rates of azo and azoxy derivatives (see Fig. 4) shows the less burning rate of the latter in the whole pressure range despite of additional active oxygen atom (capable of participating in oxidation reactions) in the molecule. At first glance it seems to be connected with somewhat lower combustion temperature of azoxy compound as compared with combustion

temperature of azo analog, however, the difference is insignificant. The lesser burning rate of azoxy compound is conceivable to be associated with the formation of N_2O molecule in decomposition of azoxy compound. N_2O retains some internal energy evolved during the decomposition (ΔH°_f = 19.5 kcal/mole) and is usually reduced in the most high-temperature and farthest from the combustion surface flame zones [12], producing a weak effect on the burning rate.

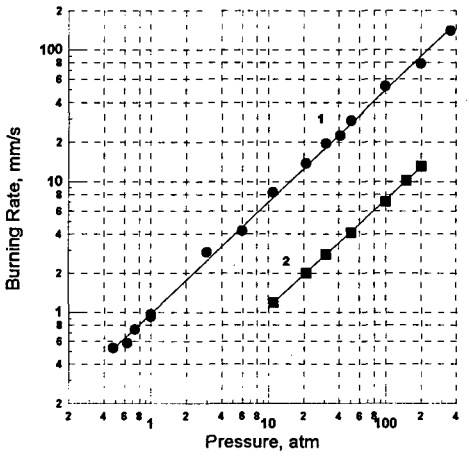

Fig. 3. Pressure dependence of the burning rate of azoxyfurazan derivatives:
4,4'-dinitroazoxyfurazan - (1)
3,3'-diaminoazoxyfurazan - (2)

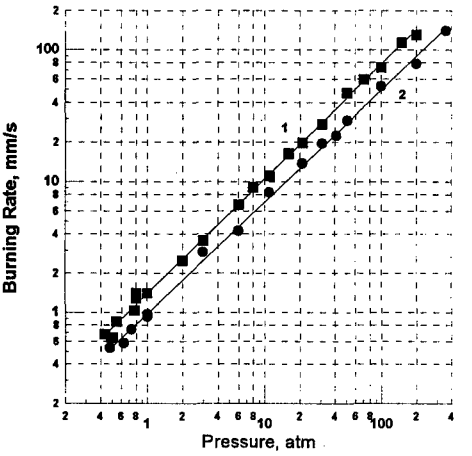

Fig. 4. Comparison of burning rates of azo- and azoxy- furazan derivatives:
4,4'-dinitroazofurazan - (1)
4,4'-dinitroazoxyfurazan - (2)

Combustion temperatures

To elucidate combustion features of furazans derivatives more closely tungsten-rhenium fine microthermocouple technique was employed to measure combustion temperatures and investigate the temperature distribution in the combustion wave at various pressures. The results of thermocouple studies are presented in Tables 2- 4.

As noted above there is no correlation between the burning rate of furazan derivatives and their adiabatic flame temperature. The data of Tables 2- 4 show that in all cases measured temperatures is below calculated adiabatic ones. For furazan nitroderivatives, which combustion temperatures were measured only at low pressure because of high burning rates, the incompleteness of energy release is known to be connected with incomplete reduction of nitrogen oxides just at low pressures. For compounds containing active oxygen in the furazan ring only, the reason for incompleteness of the heat release in combustion should be searched for formation of high-energy

products. Such compounds are most likely nitrile derivatives **I**, which are known [13] to be formed during slow thermal decomposition of furazans:

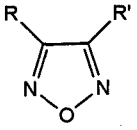

$$\longrightarrow \quad \underset{\mathbf{I}}{RCN} + \underset{\mathbf{II}}{R'CNO} \qquad (1)$$

Nitriloxides **II** can undergo isomerisation to isocyanates **III** or decompose to form nitrile and oxygen atom:

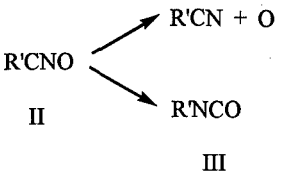

Calculation of the combustion temperature of furazan derivatives on the assumption that both of nitrile groups formed in heterocycle decomposition remain in the combustion products, gives very low values (see Table 2 and Table 4). This allows considering the route of nitriloxide decomposition as well as transfer of the oxygen atom to any particle other than CN as insignificant pathway in the combustion process.

Table 2. Comparison of measured and calculated temperatures of furazan combustion.

Compound	Pressure, atm	Measured Temperature, K		Calculated Flame Temperature, K		Nonequilibrum Products, Mole per Mole of Furazan
		T_s	T_f	Equilibrum	Nonequilibrum	
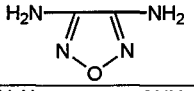	80	750	1030	1580	620 1175 1080	$(CN)_2$ 0.5 $(CN)_2$ H_2NCN, CO
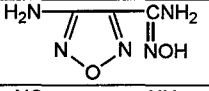	120	750	1090	1530	625 1120 1255	1.5 $(CN)_2$ NH_2CN, 0.5$(CN)_2$ NH_2CN, 2CO, NH_3
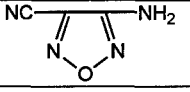	80	–	970	2425	700 835 980	1.5 $(CN)_2$ $(CN)_2$, CO $(CN)_2$, CO, 0.5NH_3

At the same time, calculated temperatures for one nitrile group "frozen" per one heterocycle (plus nitrile groups of the substituents) prove to be closed to the measured ones. For the given temperatures and the set of reducing fragments (CN- and NH_2-groups) the isomerisation reaction to isocyanate seems to dominate over the reaction of oxidation of these fragments by nitriloxide

or oxygen. It is interesting that calculated combustion temperature for compound AOAF with the oxime group as the substituent is in a good agreement with measured one only when oxime is proposed to produce nitrile during decomposition.

Table 3. Comparison of measured and calculated temperatures of nitrofurazans combustion

Compound	Pressure, atm	Measured Temperature, K		Calculated Flame Temperature, K		Nonequilibrum Products, Mole per Mole of Furazan
		T_s	T_f	Equilibrum	Nonequilibrum	
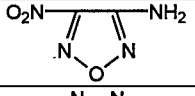	5	580	2610	3090	2520 2620	0.5 NO 0.5 N_2O
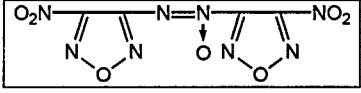	1	570	2650	3365	3210 2680 2590	2 NO 2NO, N_2O 3 N_2O

The incompleteness of the heat release in combustion of nitrocompounds at low pressure is usually due to formatting of NO which is reduced in the second flame located far from the surface and unachievable by the thermocouple. The combustion temperature of NAF calculated on the assumption that the nitro group is reduced only partially (2520 K) might be in a good agreement with measured one (2610 K). Experimental (2650 K) and calculated (2680 K) combustion temperatures of DNAOF at atmospheric pressure are also in a good agreement if one assumes two molecules of NO from two nitro groups and one molecule of N_2O from the azoxy group remain unreacted in the combustion products. However, a unique set of primary decomposition products of the furazan cycle (RCN and RNCO) cast doubt on the presence of unreacted NO in the combustion products. The point is that NCO known to be a major product of oxidation of nitrile derivatives by NO_2 and serves as a perfect scavenger of NO, transforming it to N_2O [14]. Table 3 demonstrates a good agreement between measured temperatures and calculated ones on the assumption of unreacted N_2O among the combustion products.

A comparison of the measured and calculated combustion temperatures for bicyclic furazans (see Table 4) suggest formation of one mole of dicyan (two moles of cyanamide for DAAZOF) per mole of initial substance as responsible for heat release incompleteness. In contrast to dinitroazoxyfurazan DNAZOF, diaminoanalog DAAZOF does not suggest the definite composition of combustion products if comparing calculated and measured temperatures. However in any case the share of unreacted N_2O is less than expectable. This is probably connected with the large contents of reducing fragments in the molecule of DAAZOF.

Table 4. Comparison of measured and calculated temperature of azo- and azoxyfurazans

Compound	Pressure, atm	Measured Temperature, K		Calculated Flame Temperature, K		Nonequilibrum Products, Mole per Mole of Furazan
		T_s	T_f	Equilibrum	Nonequilibrum	
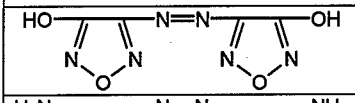	20	–	2115	2730	280 2630 1930	2 $(CN)_2$ $(CN)_2$ 2 HOCN, 2 CO
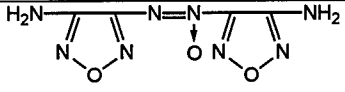	20	–	2110	2640	1490 2320 1955 2100 2200	2 $(CN)_2$ $(CN)_2$ 2 NH_2CN, 2CO $2NH_2CN$, 1.8CO $2NH_2CN$, $0.5N_2O$

Combustion mechanism

Temperature distribution in the combustion wave at various pressures was investigated by the example of DAF, one of the simplest representatives of furazans. The results of the measurements are presented in Table 5. A typical recording of temperature distribution in the combustion wave of DAF is shown in Fig. 5. Based on of the temperature profiles measured the combustion wave can be divided into the following typical zones:

- melting layer zone extending from the melting point (T_m) to the surface temperature (T_s);
- gas phase zone where the temperature increases abruptly from T_s to T_f within the very thin region;
- final gas phase interval where the temperature remains practically constant over some distance.

Table 5. Temperature distribution in the combustion wave of diaminofurazan.

Pressure, atm	Surface Temperature, K	Maximal Flame Temperature, K
20	650	970
50	700	1010
80	750	1030
200	795	1050

Temperature profiles in the gas phase is rather uneven, temperature fluctuations observed are probably due to the presence of condensed combustion products in the flame. The thermolysis of DAF is known [15] to produce ammonium dicyanamide and thermally stable cyclic azines, melamine and melon. Combustion of DAF at 80 atm leads to formation about 40% of the condensed residue which, according to IR-spectroscopy data (wide strong bands 3435, 3330 and 3130 cm^{-1} (νN-H), small band 2120 cm^{-1} (νC≡N) and absorbance in the range of 1500 -1650 cm^{-1}

(δNH_2 and $\nu C{=}N$)), consists of the condensation products of cyanamide: melamine with an admixture of dicyandiamide. It almost quantitatively corresponds to the amount of cyanamide which can be formed in the decomposition of DAF by the reaction (1).

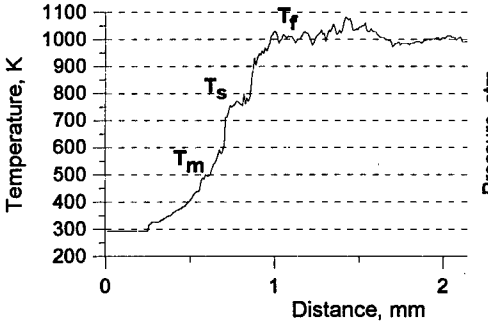

Fig. 5. Temperature distribution in the combustion wave of diaminofurazan at 80 atm.

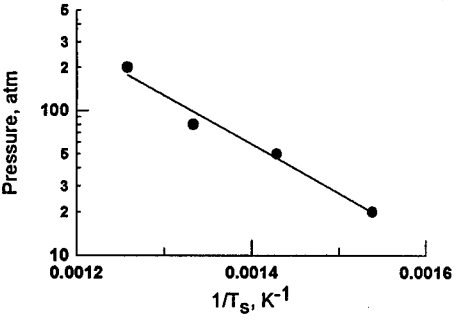

Fig. 6. Relationship between vapor pressure and surface temperature of diaminofurazan.

The value of thermal diffusivity (χ) in the condensed phase of DAF ($4.52 \cdot 10^{-3}$ cm^2/sec) calculated from thermocouple data using Michelson relation and calculated value of specific heat c_p (0.57 cal/g·K) allow calculating thermal conductivity in the condensed phase λ_c ($9 \cdot 10^{-4}$ cal/sec·sm·K). Using the thermophysical data obtained and kinetic parameters of diaminofurazan decomposition determined in [16] (preexponential factor is $10^{14.15}$ sec^{-1}, activation energy of the decomposition is 47.8 kcal/mole), it is possible to estimated a degree of DAF decomposition in a superficial layer at the surface temperature. At all investigated pressures and corresponding burning rates, as little as 1% of DAF has had time to decompose in the condensed phase. Therefore, the surface temperature may be conceived to be the boiling temperature of DAF. The data on T_s plotted in the coordinates pressure *vs.* reciprocal temperature fall on a straight line. The slope of the line yields the enthalpy of evaporation of 15.1 kcal/mole, quite reasonable value for similar compounds [17].

Since the profile of temperature distribution in the gas phase is not smooth, it is difficult to obtain exact values of the temperature gradient above the combustion surface. A comparison of profiles recorded at various pressures clearly demonstrates, however, that the temperature gradient in the gas phase also grows with pressure.

All these data suggest the following combustion mechanism of diaminofurazan. The leading combustion reaction proceeds in the gas phase, with the surface temperature being the boiling

temperature of DAF. Decomposition of DAF in the flame results in formation of cyanamide NH_2CN and aminonitriloxide NH_2CNO, the former undergoes condensation in the flame and basically on cooling to give melamine $(NH_2CN)_3$ and dicyandiamide $NCNHC(NH_2)=NH$. The isomerisation of aminonitriloxide to isocyanate presumably defines the combustion temperature and the burning rate of DAF.

CONCLUDING REMARKS

Some distinctive characteristics of combustion of furazan derivatives can be revealed from the analysis of burning rate data and thermocouple-aided measurements. Furazan cycle itself possesses a high thermal stability, and therefore, its simple derivatives in the absent of thermally unstable substituents decompose at high temperatures achieved in the gas phase. Nitrile-containing compounds formed during the decomposition of the heterocycle have no time to decompose fully in the oxygen-deficient flame zone, resulting in incomplete release of energy stored in the furazan cycle. For this type of compounds, the basic source of heat release in combustion is nitriloxide formed during furazan decomposition. In contrast to other energetic materials containing active oxygen, such as nitrocompounds, the main heat release reaction is not an oxidation reaction but the reaction of isomerisation of nitriloxide to isocyanate rather than oxidation reaction.

The introduction of azo- and azoxy groups as the substituents results in increase of furazan combustion temperatures, because of the lower thermal stability of these endothermic groups leads to a release of their energies in combustion, however nitrile derivatives still do not decompose fully. The complete energy release from the furazan cycle during combustion is achievable only in the presence of oxidizer: the introduction of nitro groups allows compounds with very high combustion temperatures exceeding 4000 K.

REFERENCES

1. Coburn, M.D. Picrylamino-substituted Heterocycles. II Furazans. *J.Heterocycl. Chem.*, 1968, v.5, pp.83-87
2. Sheremetev, A. B., Kniagina, V. O., Batog, L. V., Lebedev, O. V., Yudin, I. L., Pivina, T. S., Andrianov, V. G. and Starchenkov, A.B. High Energetic Materials from Diaminofurazan, *Proc. 22nd Inter. Pyrotechnics Seminar*, July 15-19, 1996, Colorado, USA, pp. 377-388.
3. Ichikawa, T., Kato, T., Takenishi, T. *J.Heterocycl.Chem.*, 1965, v.2, p. 253.
4. Novikova, T.S., Melnikova, T.M., Kharitonova, O.V., Kulagina, V.O., Aleksandrova, N.S., Sheremetev, A.B., Pivina, T.S., Khmelnitskii, L.I., Novikov, S.S. Effective Method for Oxidation of Aminofurazans to Nitrofurazans, *Mendeleev Commun.*, 1994, pp.138-140.
5. Andrianov, V.G., Eremeev, A.V. *Khim.Geterotsikl.Soedin.*, 1994, pp.693-696 (in Russ.).

6. Ponzio, G., Ruggeri, G. *Gazz.Chim.Ital.*, 1923, v.53, pp.297-305.

7. Sheremetev A.B., Novikova T.S., Mel'nikova T.M., Khmel'nitskii L.I. The synthesis of 3-nitroso-4-R-furazans. *Izv. Akad. Nauk SSSR, Ser.Khim.*, 1990, (5), p.1193. [*Bull. Acad. Sci. USSR, Div. Chem. Sci.*, 1990, v.39 (5), p.1073].

8. Sheremetev, A.B., Kulagina, V.O., Aleksandrova, N.S., Novikova, T.S. and Khmelnitskii, L.I. Aminofurazans as Key Synthons for Construction of High Energetic Materials". *Proc. 3th (Beijing) International Symposium on Pyrotechnics and Explosives.* November 6-9, 1995, Beijing, China, pp.249-254.

9. Solodyuk, G.D., Boldyrev, M.D., Gidaspov, B.V., Nikolaev, V.D. *Zh.Org.Khim.*, 1981, v.17, p.861 (in Russ.).

10. Fogelzang, A.E., Sinditskii, V.P., Serushkin, V.V., Egorshev, V.Yu., Shchipin, Yu.K., Tropynin, V.A., Combustion of Propellants and Energetic Materials, *Database FLAME*, 1990-1996.

11. Fogelzang, A.E., Egorshev, V.Yu., Sinditskii, V.P. Influence of Chemical Nature of Substituent on the Burning Rate of 5-Substituent Tetrazoles. *Proc. 17th Inter. Pyrotech. Sem.*, Oct., 28-31, 1991, Beijing, China, Vol.2, pp.618-623.

12. Melius C.F., The Gas-Phase Flame Chemistry of Nitramine Combustion, *Proc. 25th JANNAF Comb. Meeting*, Oct., 1988, Hantsville, USA.

13. Manelis, G.B., Nazin, G.M., Rubtzov, Yu.I., Strunin, V.A. Thermal decomposition and combustion of explosives and propellants, Moscow, Nauka, 1996, pp. 82-87 (in Russ.).

14. Miller, J.A., Bowman, C.T., Mechanism and Modeling of Nitrogen Chemistry in Combustion. *Prog. Energy Combust. Sci.*, 1989, vol.15, pp.287-333.

15. Stoner Jr, C.E., Brill, T.B. Thermal Decomposition of Energetic Materials 46. The Formation of Melamine-like Cyclic Azines as a Mechanism for Ballistic Modification of Composite Propellants by DCD, DAG, and DAF. *Comb. and Flame*, 1991, vol. 83, pp.302-308.

16. Prokudin, V.G., Nazin, G.M., Manelis, G.B. *Dok. Akad. Nauk SSSR*, 1980. vol. 255. pp. 917—920 (in Russ.).

17. Khmel'nitskii, L.I., Novikov, S.S., Godovikova, T.I. Chemistry of furoxans: Structure and synthesis. Revised and enlarged edition, Moscow, Nauka, 1996, 383p., (in Russ.).

COMBUSTION BEHAVIOR AND FLAME STRUCTURE OF TETRAZOLE DERIVATIVES

Valery P.Sinditskii, Viacheslav Y.Egorshev, Alexander E.Fogelzang, Valery V.Serushkin, Vasilii I.Kolesov

Mendeleev University of Chemical Technology, 9 Miusskaya Square, 125047, Moscow, Russia

ABSTRACT

Combustion behavior of tetrazole and 5-chlorotetrazole was studied in the form of pressed strands in a window constant pressure bomb in the pressure range of 0.1-36 MPa. Temperature profiles in the combustion wave were measured using thin tungsten-rhenium thermocouples embedded in the strands. Analyses of condensed combustion products were carried out by means of IR spectrophotometry.

The principal feature of tetrazole combustion has been shown to consist in formation of stable energetic nitrile derivatives in the combustion products rather than equilibrium adiabatic composition, resulting in incomplete heat release. In spite of decomposition nature of the rate-controlling reactions, they prove to be different than those in slow thermal decomposition at 150-250 °C.

By the example of tetrazole, a new combustion regime has been suggested, characterized by variations in the surface temperature. The periodic process involves a gradual accumulation of a product of high decomposition/boiling temperature at the burning surface, followed by ejecting thereof in the gas and clearing the surface.

INTRODUCTION

Tetrazoles, high-nitrogen heterocyclic compounds, are of special interest as energetic components of propellants and gas-generating systems. Having high internal energy content, many of tetrazole derivatives are capable of sustain burning at the expense of heat produced at thermal decomposition of the heterocyclic ring [1-2]. The stationary combustion of the parent compound, tetrazole, and temperature distribution in its combustion wave at atmospheric pressure were investigated in [1-3], some thermophysical characteristics were determined in work [3]. Recent data on thermal decomposition of tetrazole and its derivatives were published in [4 - 8]. Since just the decomposition reactions are at the basis of combustion of compounds of this class, the new data stimulate further study of tetrazole combustion, providing deeper understanding of the processes, what is important in predicting its performance in practical use. Besides, a knowledge of the combustion mechanism of tetrazoles is important for understanding combustion behavior and mechanism of other endothermic

compounds which burning is also governed by decomposition reactions. The main goal of the present work was to study flame structure and burn rate characteristics of tetrazole derivatives in an attempt to discover combustion mechanism.

Tetrazole, which thermodynamic and physical properties had been extensively investigated (see Table 1), was chosen as the basic object of the study. 5-Chlorotetrazole, having the electronegative substituent at the carbon and higher burning rate, was investigated simultaneously.

EXPERIMENTAL

Tetrazole was prepared from ethylortoformiate, sodium azide and ammonium chloride by the method [9]. It had melting point of 156 ° C after the crystallization from alcohol.

Chlorotetrazole were prepared by the diazotization of 5-aminotetrazole at the presence of copper chloride [10]. It had a melting point of 73°C after the crystallization from benzene.

Table 1. Thermodynamic and physical properties of tetrazole and 5-chlorotetrazole

Properties	Tetrazole	5-Cloro-tetrazole
Melting point, ° C	156.4[3]	73 [11]
Density, g/cm^3	1.632	
Strand density, g/cm^3	1.54	1.79
Enthalpy of formation, kJ/mol	237.07[12], 236.0[13]	201(calc.)
Enthalpy of fusing, kJ/mol	17.7[3]	
Enthalpy of boiling, kJ/mol	79.6[3]	
Enthalpy of sublimation, kJ/mol	97.3[12]; 90.1; 88.0[14]	
Heat of decomposition, kJ/mol	162[3], 216[15]	
Activation energy of the decomposition in the condensed phase(E_c), kJ/mol	157[3], 156[8]	
Preexponential factor (lgA_c), sec^{-1}	14.7[3], 14.1[8]	
Activation energy of the decomposition in the gas phase (E_g), kJ/mol	135[8]	
Preexponential factor (lgA_g), sec^{-1}	11.5[8]	
Thermal conductivity (λ_c), J/sec · cm · K	0.0125[3]	
Specific heat (c_p), J/g · K	2.43[3]	

Burn rate measurements were carried out in a window constant pressure bomb of 1.5 liter volume. The pressure range studied was 0.1-36 MPa. A slit camera was used to determine a character of the combustion process as well as burning rate values. The combustion strands were prepared by compacting thoroughly comminuted substances in transparent acrylic tubes of 4 or 7 mm i.d. at 150-200 MPa.

Temperature profiles in the combustion wave of tetrazoles were measured using Π-shaped thermocouples. The thermocouples were welded from 25 or 50 μm diameter tungsten—5% rhenium and tungsten—20% rhenium wires and rolled in bands to obtain 7 or 20 μm bead size.

RESULTS AND DISCUSSION

At atmospheric and close pressures, tetrazole burns under nitrogen atmosphere with crackling, forming copious white vapours, which condense as fine yellowish drops inside tube and at cold surfaces of the bomb. As pressure increases above 2 MPa, flowing off gases become almost transparent, the condensed products of combustion are not observed. The IR-spectroscopy data of condensed combustion products of tetrazole combustion, wide band in the range of 3080 - 3330 cm^{-1} (νN-H), strong band in the range of 2130 - 2245 cm^{-1} (νC≡N), as well as the absorbances in the range of 1400 -1620 cm^{-1} (δNH_2 and νC=N), show that condensed products consist of a mixture of the cyanamide and its condensation products: dicyandiamide and, probably, melamine.

Burning rates of tetrazole, chlorotetrazole and some other derivatives in form of 4 mm diameter strands were measured in [1]. In the present work, burning rates of tetrazole in the form of strands with diameter of 7 mm have been further measured (see Fig. 1a). The data obtained are in a good agreement with data obtained in [3] for strands of 10-20 mm diameter covered with varnish by use of strain gauge technique. The discrepancy between burning rates for strands of different diameters at low pressure indicates that heat losses play a significant role in combustion of tetrazole in the form of strands of 4 mm diameter.

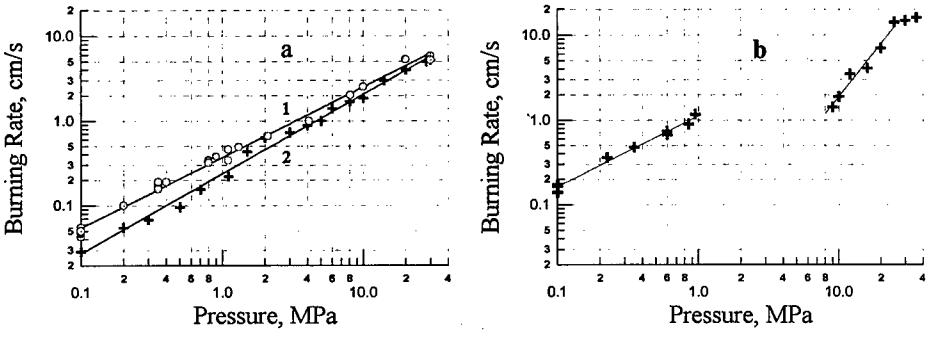

Fig. 1. *Pressure dependence the burning rate of tetrazole derivatives: a - tetrazole, strands of 7 mm i.d.(1) and 4 mm i.d.(2); b - chlorotetrazole.*

Chlorotetrazole, which has higher burning rate at atmospheric pressure burns at invariant speed both in tubes of 4 and 7 mm i.d. Its burning is not accompanied by formation of condensed combustion products. At the same time, a very interesting feature is inherent for the combustion of chlorotetrazole in the range of 1-9 MPa: pressed strands are not capable of sustained burning (see Fig. 1b).

Thermocouple-aided measurements allow the following typical zones on the tetrazole temperature profile (see Fig. 2):

- molten layer extended from the melting point (T_m) to the surface temperature (T_s); both length of layer and value of T_s are subject to significant variations;
- gas phase zone where the temperature increases abruptly from T_s to T_1 within the very thin region;
- final gas phase zone where the temperature is relatively slow to increase from T_1 to maximal value T_{max}. As pressure increase from 1 atm to 8 atm somewhat regular drops in temperature are observed in this zone as well as in the subsequent region of gas cooling, which are strongly smoothed out at 13 atm.

Similar structure of the flame (see Fig. 3) is typical of chlorotetrazole combustion too. However, in contrast to tetrazole, the scatter in the measured lengths of zones and T_s is significantly less; the areas of temperature fall in the gas phase region are absent.

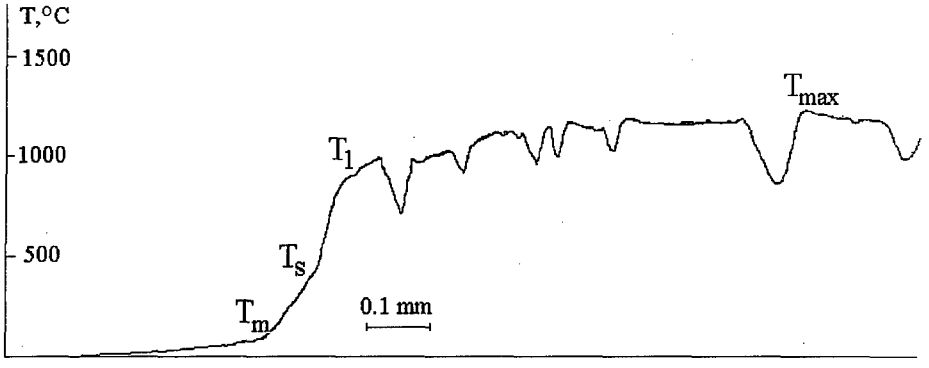

Fig. 2. *Temperature distribution in the combustion wave of tetrazole at 8 atm.*

The value of thermal diffusivity (χ) in the condensed phase of tetrazole ($3.38 \cdot 10^{-3}$ cm^2/sec) calculated from thermocouple data using Michelson relation is in a good agreement with value ($3.34 \cdot 10^{-3}$ cm^2/sec) calculated from thermal conductivity and specific heat directly measured in [3].

At 300 atm, only maximal temperature of burning T_{max} is measurable using thermocouples with 20 μm bead size. All data of temperature measurements are collected on Fig. 4 and Table 2.

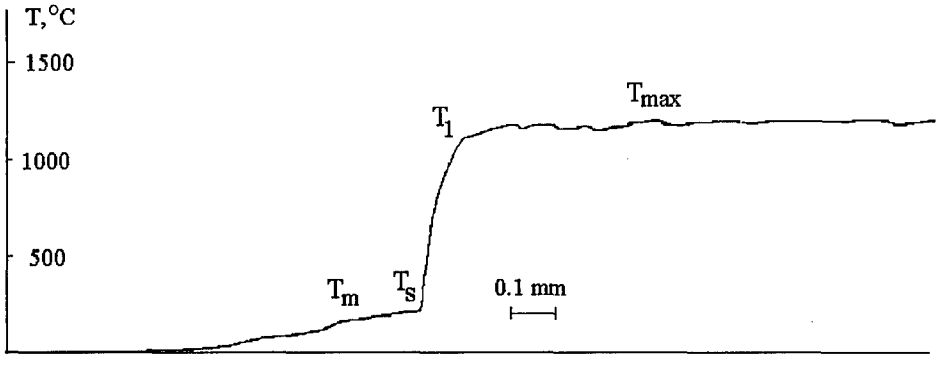

Fig. 3. *Temperature distribution in the combustion wave of chlorotetrazole at atmospheric pressure.*

Table 2. Surface temperature T_s, temperature of a gas zone near the surface T_1, and maximal temperature T_{max}, thickness of the molten layer (L_{cond}), length of gas zone from T_s to T_1 (L_{gas}) and temperature gradient in the gas phase for combustion of tetrazole and chlorotetrazole.

Compound	P, atm	T_s, °C[a]	T_1, °C	T_{max}, °C	dT/dx, K/cm ($\cdot 10^{-4}$)[a]	L_{cond}, μm[a]	L_{gas}, μm[a]
Tetrazole	1	250-302	968±15	1138±33	2.9 - 9.2	200-400	50-135
	3.5	300-422	978±12	1200±8	4.9 - 9.2	70-170	80-130
	8	368-515	971±13	1224±33	3.3 - 8.7	65-160	100-170
	13	328-600	985±33	1097±11	2.7 - 10.0		
	300			1065±8			
5-Chlorotetrazole	1	251±10	1125±17	1260±23	15.1±2.0	95±5	60±10
	2.5	260±18	1150±18	1310±14	10.8±1.0	50±10	85±15

[a] For tetrazole, minimal and maximal measured values are given.

It is interesting to note that T_1 practically does not vary with pressure, while maximal combustion temperature of tetrazole shows a peculiar behavior: with increasing pressure from 1 to 8 atm it grows and then T_{max} falls on 120-160°C at 13 and 300 atm. The dependence of tetrazole boiling temperature on pressure calculated from Nernst's equation [16] is also presented in Fig. 4:

$$\lg\frac{P}{P_0}=\frac{LM}{19.155}\left(\frac{1}{T_0}-\frac{1}{T}\right)$$

where L is latent heat of evaporation, kJ/kg; M is molecular weight, kg/mole, T and T_0 are boiling temperatures at pressure P and P_0 = 1 atm, respectively. The heat of evaporation of 79.6 kJ/mole was obtained as the difference between heat of sublimation of 97.3 kJ/mole [12] and heat of melting of 17.7 kJ/mole [3]. The calculation was carried out on the assumption that the measured surface temperature of tetrazole at atmospheric pressure corresponds to its boiling temperature. In our opinion, this assumption is supported by the presence of an endotherm at 237°C at the ascending branch of the decomposition curve found out during tetrazole thermolysis in [3].

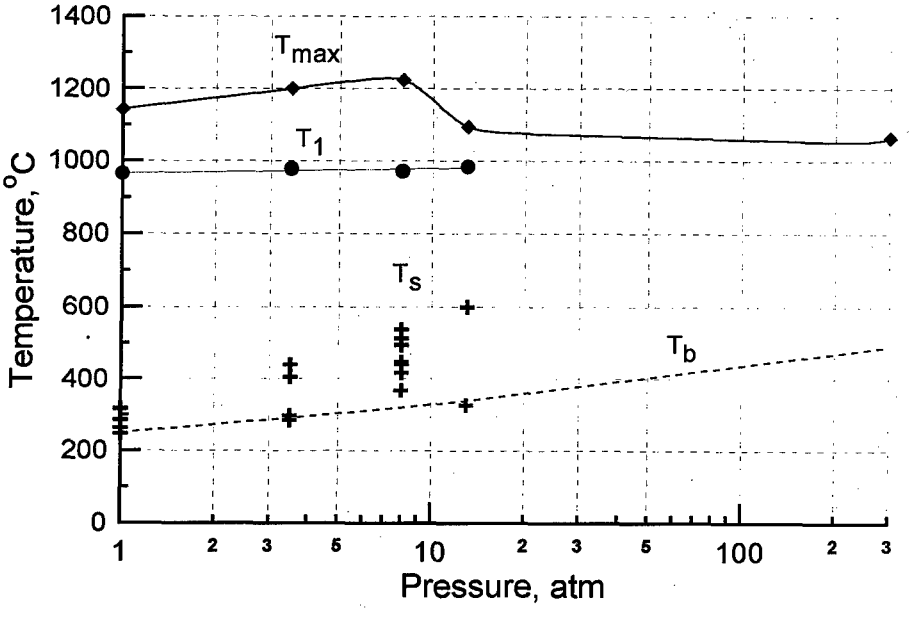

Fig. 4. *Pressure dependence of characteristic temperatures in the combustion wave of tetrazole. Dashed line is calculated boiling temperature of tetrazole.*

Furthermore, using kinetic parameters of tetrazole thermal decomposition [8] it is possible to estimate that no more than 3 % of tetrazole decomposes in the surface reactive zone during combustion at 1 atm. All experimental data on the surface temperature are summarized on the Fig. 4. The minimal measured values are evident to lay practically on the calculated boiling temperature of tetrazole, whereas the maximal values are more and more exceed the boiling temperature with increasing pressure.

It is interesting that the maximal measured temperatures of combustion of both tetrazole (~1140 °C) and chlorotetrazole (~1260 °C)at atmospheric pressure are much below calculated adiabatic combustion temperatures of these compounds, 1925 and 2180 °C, respectively. The difference between calculated and measured temperatures could be attributed to either nonequilibrum composition of combustion products or the incompleteness of the combustion due to dispersing of initial substance from the surface. However, the last assumption was not proved by analysis of the condensed combustion product, in which there was no initial tetrazole detected.

To anticipate a nonequilibrum composition of combustion products, there is a need to examine possible ways of thermal decomposition of tetrazole derivatives. Recent studies devoted to kinetics and mechanism of thermal decomposition of tetrazole and its derivatives in the interval 150-230 °C [7,8] show the first reaction order of the process. For both the gas phase, where tetrazole *2H*-tautomer **II** is dominate, and melt or solutions, where tautomer equilibrium is shifted to more polar *1H*-tautomer **I**[17], the *2H*-form of tetrazole cycle is supposed to liberate N_2 molecule, whereas the *1H*-form is almost stable under these conditions. The decomposition mechanism includes fast reversible transformation of the *1H*- и *2H*-forms, reversible opening of the *2H*-form **II** following by the formation and decomposition of intermediate diazo compound **III** to form N_2 and nitrilimine **IV**, further transformations of which are not discussed in [8] as having little effect on the decomposition kinetics under the experimental conditions:

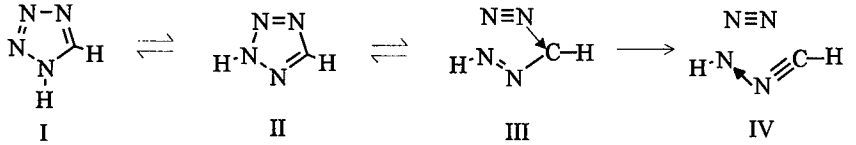

I II III IV

The parallel routes of the decomposition are not supposed to contribute considerable to the observed rate constants.

The formation of intermediate nitrilimine has been proposed by many authors. For thermolysis products of 5-phenyltetrazole [18], analysis of reaction products suggests that about 80% of tetrazole decomposes to form nitrilimine $PhC^{+}=N\text{-}N^{-}H$ and only 20% of it destroys to give PhCN and HN_3.

The authors of work [19] also point out insignificant (~ 5 %) contribution of tetrazole decomposition in melt to form HN_3 and HCN. The decomposition scheme, however, includes isomerization of the *1H*-form **I** to azidoazomethyne **V** followed by the formation of nitrene **VI**. This scheme is based on the fact that tetrazole thermolysis leads to formation a high-thermostable compound **VIII** representing a polymerization product of the cyanamide **VII** :

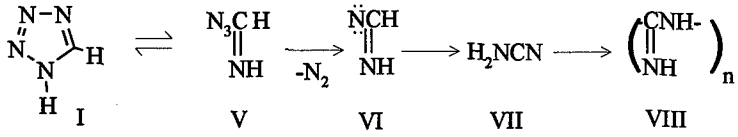

Rapid thermal decomposition of 5-aminotetrazole in an interval 25-300°C was studied in [4] with rapid-scan FTIR-spectroscopy to result in formation of HN_3 and H_2NCN in the gas phase above a sample surface at the beginning of decomposition followed by appearance of a condensation product which was identified as melamine (trimer of cyanamide).

When thermolysis of tetrazole takes place in the gas phase, only minor amounts of polymer **VIII** are formed. The main gas products are hydrogen, nitrogen and hydrogen cyanide produced in the opinion of authors of work [19] in the decomposition of nitrilimine **IV**:

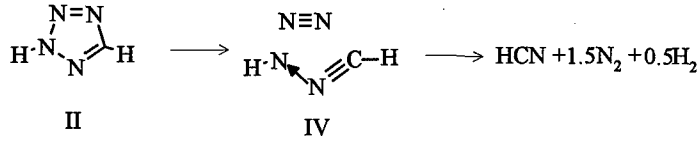

A correlation between combustion temperatures calculated for various tetrazole decomposition channels and measured combustion temperatures allows choosing between possible decomposition routes. Table 2 and Table 3 show that temperature in the gas phase directly

above the surface (T_1) is in a good agreement with the calculated temperature of the decomposition to give HCN, H_2 and N_2.

Table 3. Combustion temperatures calculated for various decomposition routes of tetrazole

Combustion products	**Combustion temperature, °C**
Equilibrium composition	
0.97 H_2, 1.99 N_2, 0.95 C(cond.), 0.05 HCN	1925
Non-equilibrium composition	
0.5 H_2, 1.5 N_2, HCN	990
0.5 H_2, 1.5 N_2, 0.33 $(HCN)_3$ (1,3,5-triazine)	1707
N_2, H_2NCN	1770
N_2, 0.5 $NCNHC(=NH)NH_2$	2100
N_2, 0.33 $(H_2NCN)_3$ (melamine)	2420

This is surprising at first glance result because the tetrazole thermolysis in the melt at temperatures close to the surface temperature is bound to proceed through the main decomposition route to form condensation products of nitrilimine rather than HCN. This decomposition route is supported by formation of condensed products during combustion as well as significant difference between maximal experimental values of the surface temperature and calculated tetrazole boiling temperature. This difference is likely to be connected with accumulation of high-boiling decomposition products in the tetrazole molten layer. Since these are compounds less endothermic than HCN, calculated combustion temperatures prove to be significantly (>500°C) above experimental ones. The contribution of these decomposition routes can be estimated by comparing the maximal tetrazole combustion temperatures T_{max} (see Table 2) with ones provided by decomposition to HCN to be 10-20%.

The difference between thermolysis at 150-250°C and burning is in particular conditions of the latter: short residence time of substance in the reaction zone and the fact that the reaction products and unreacted substance are thrown in the high-temperature gas zone immediately after a reaction in the molten layer. At high temperatures reactions with higher activation energy go faster. Therefore it may be suggested that the tetrazole decomposition pathway to HCN, giving a small contribution to the general decomposition at surface temperatures, due to the high energy of activation [7], becomes determining one in high-temperature flame zone.

For the same reason decomposition of the formed polymeric products has a low rate in the molten zone, whereas in the flame zone it proceeds very quickly to form NH_2CN and then HCN. The formation of nitrilimine condensation products under these conditions, on the contrary, proceeds with low rate because the concentration decreases more than 1000 times when passing from the condensed to the gas phase.

The distinction in rate-determining reactions between combustion process and decomposition in the interval of 150 - 300 °C is additionally supported by different electronic effects of the substituents in the tetrazole molecule on the rate of burning and thermal decomposition. Kinetics parameters of thermal decomposition of 5-tetrazolyltetrazole (Hammett's constant of the tetrazolyl-substituent $\sigma \sim 0.4$) and 5-phenyltetrazole ($\sigma = -0.01$), as well as 5-(m-nitrophenyl)-, methyl- and ethyltetrazole given in [8] do not practically differ, while the mass burning rate of 5-substituted tetrazoles varies 4-5 times with change of Hammett's constant by approximately 0.4 [1, 2].

Combustion of 5-chlorotetrazole has much in common with burning of tetrazole. The measured combustion temperature is closest to the temperature of chlorotetrazole conversion to nitrile-containing products of dicyan type (see Table 2 and Table 4.). In contrast to tetrazole the decomposition of chlorotetrazole does not result in formation of more high-boiling or thermostable products: cyanuric chloride $(ClCN)_3$, a possible condensation product boiling temperature of 190°C that is below the measured surface temperature. Smooth appearance of chlorotetrazole temperature profiles confirm this suggestion.

Table 4. Combustion temperatures calculated for various decomposition routes of 5-chlorotetrazole

Combustion products	**Combustion temperature, °C**
Equilibrium composition	
0.9 HCl, 0.1 Cl, 0.04 H_2, 1.99 N_2, 0.02 HCN, 0.97 C(cond.)	2180
Non-equilibrium composition	
0.5 H_2, 1.5 N_2, ClCN	625
0.5 H_2, 1.5 N_2, HCl, 0.5 $(CN)_2$	1220
0.5 H_2, 1.5 N_2, 0.33 $(ClCN)_3$	1300

According to [20] the temperature gradient of in the gas phase ($\frac{dT}{dx}$) depends on rate of reaction responsible for heat release (W_g), which, in turn, depends on the concentration of reacting substances [C]:

$$\frac{dT}{dx} = \frac{W_g Q_g}{U_m c_g} = \frac{k[C]^n (T_f - T_s)}{U_m}, \qquad (1)$$

here k is constant of reaction rate at flame temperature T_f, n is reaction order, U_m is mass burning rate, c_g is specific heat of gas, Q_g is heat evolved in gas phase.

Since tetrazole combustion is characterized by surface temperature cycling, the share of the substance to be decomposed in the condensed phase will also be variable will effect on the temperature gradient in the gas phase. As evident from Table 2, a wide scatter in the measured values of the temperature gradient is observed, with larger gradients corresponded to the least values of the surface temperature, and vice versa. Using equation (1), it is possible to estimate a ratio between temperature gradients at various pressures and, by comparing the calculated values with experimental ones, to assess a reaction order in the gas phase. Substituting boiling temperature as T_s, and T_1 as T_f in (1), and neglecting decomposition in the condensed phase (i.e., $[C] = \frac{P}{RT_1}$) one can easily find that changing pressure 1 to 8 atm will result in increase in temperature gradient by factor 1.1 for the first reaction order and 8.8 for the second reaction order. As seen from Table 2, the maximal values of the temperature gradient in the gas phase of tetrazole (i.e., at the surface temperature close to the boiling temperature) differ slightly. A weak dependence of the temperature gradient on pressure is likely to suggest the first order of heat release reaction in the gas phase, which can be attributed to the reaction of tetrazole decomposition to HCN.

Similar estimation of gradient variation for chlorotetrazole when pressure changes from 1 to 2.5 atm gives a value 1.16 for the first order. An unusual decrease in the temperature gradient with pressure is indicative of a decrease in the rate of heat release in the gas phase caused by reducing vapor concentration because of increasing decomposition in the condensed phase.

It is significant that a role of the gas phase in combustion of both tetrazole and chlorotetrazole reduces considerably as pressure increases from 1 to 10-20 atm, that can be judged from magnitudes of the temperature gradient as well as its peculiar dependence on pressure.

A pattern of tetrazole combustion can be conceived of as follows: the surface temperature of tetrazole is initially the boiling temperature, with the main heat for combustion coming from the gas phase. As combustion proceeds, the decomposition product, despite of an insignificant share of decomposition in the condensed phase, accumulates in the boiling layer owing to its high boiling (or decomposition) temperature thus increasing its temperature and resulting in an increased share of decomposition in the melt. At some time the surface temperature achieves such a value that gas evolution [1] in the condensed phase increases to point where an ejection of the accumulated layer of high-boiling condensed products (melamine) happens. The surface temperature returns back to the tetrazole boiling temperature and the process is repeated again. A portion of the condensed products having been thrown into a high-temperature zone undergoes to endothermic decomposition to NH_2CN and further to HCN. However at low pressures, the drops do not all have time to be decomposed. Small regular temperature falls, seen on profiles in the pressure region of 1 - 8 atm are likely to result from hitting colder drops to the thermocouple. Since the formation of both cyanamide and its condensation products (dicyandiamide and melamine) is more favorable from the energetic standpoint than the formation of HCN, the maximal combustion temperature T_{max} exceeds one that can be obtained in decomposition to HCN when a part of the condensed product do not decompose in the flame zone. Besides, if a part of the condensed products passes through the flame zone accessible for the thermocouple without evaporating, it will also promote overestimating the gas-phase temperature. As the maximal surface temperature at which the ejection of tetrazole decomposition products to the gas can happen, grows with pressure (solubility of gas in the melt increases with pressure), there comes a point at the pressure more that 13 atm, where the tetrazole decomposition reaction in the condensed phase to form HCN becomes dominant. Besides, increasing pressures favorable for more effective evaporating the drops which have taken off from the surface, resulting in homogeneous gas-phase zone observed in profiles at high pressures. At the same time, the maximal temperature is reduced and approaches to tetrazole combustion temperature to produce HCN.

As with tetrazole, the basic reaction proceeding in combustion of 5-chlorotetrazole is also decomposition reaction to form nitrile derivatives. The absence of thermostable substances

[1] In this case the surface temperature cannot be equal to boiling temperature of the formed decomposition product because the calculated enthalpy of evaporation from the maximal measured surface temperatures gives 36 kJ/mole. approximately 2 times less than enthalpy of low-boiling tetrazole.

among the combustion products simplifies physico-chemical processes during burning. A large temperature gradient at atmospheric pressure is indicative of the leading role of the gas phase. As the pressure grows, however, a significant drop in the gradient in parallel with increasing surface temperature is likely to testify a transition of the main heat release reaction from gas to the condensed phase. The absence of steady-state combustion of 5-chlorotetrazole within the region of 10-90 atm can probably be connected with total transition of the heat release reaction to the condensed phase at pressures more than 10 atm. Unfortunately, the lack of information on kinetic data of 5-chlorotetrazole decomposition does not allow clear explanation of the reason for its combustion instability.

CONCLUSION

Combustion mechanism of energetic materials which burning proceeds at the expense of heat evolved during decomposition reactions has been shown to differs significantly from the combustion mechanism of redox systems. The main feature of burning of tetrazoles, as well as related organic azides [21], lies in the fact that in the absence of oxidizing agents the combustion process is accomplished by formation of thermostable high-energy nitrile derivatives rather than adiabatic equilibrium combustion products, resulting in incomplete heat release. In spite of decomposition nature of the rate-controlling reactions, they prove to be different than those in slow thermal decomposition at 150-250 °C.

By the example of tetrazole, a new combustion regime has been suggested, characterized by variations in the surface temperature. The periodic process involves gradual accumulation of a product with high temperature of decomposition/boiling at the burning surface, followed by ejecting thereof in the gas and clearing the surface.

ACKNOWLEDGMENTS

The authors are grateful to A.I.Levshenkov for assistance with tetrazole preparation. The work was supported by Russian Fund of Fundamental Researches (grant 97-03-32402).

REFERENCES

1. Fogelzang, A.E., Egorshev, V.Yu., Sinditskii, V.P., Dutov, M.D., Solov'ev, M.Yu. Research of Combustion of Tetrazole and its Derivatives, *Proc.IX All-union. Symp. on Combustion and Explosion. Combustion of condensed system.* Chernogolovka, 1986, pp. 3-5, 129-131(in Russ).
2. Fogelzang, A.E., Egorshev, V.Yu., Sinditskii, V.P. Influence of Chemical Nature of Substituent on the Burning Rate of 5-Substituent Tetrazoles. *Proc. 17 Inter. Pyrotech. Sem.*, Oct., 28-31, 1991, Beijing, China, vol.2, pp.618-623.

3. Lesnikovich, A.I., Printsev, G.V., Ivachkevich, O.A., Lutsko, V.A., Kovalenko, K.K. Combustion of Tetrazole. *Fizika gorenia i vzryva*, 1988, vol.24, N 5, pp.48-51 (in Russ.).

4. Gao, A., Oyumi, Y., Brill, T.B. Thermal Decomposition of Energetic Materials 49. Thermolysis Routes of Mono- and Diaminotetrazoles. *Combustion and Flame*, 1991, vol. 83, pp.345-352.

5. Lesnikovich, A.I., Levchik, S.V., Balabanovich, A.I., Ivachkevich, O.A., Gaponik, P.N. *Thermochim. Acta*, 1992, vol. 200, pp. 427-441.

6. Nikichev, Yu.Yu., Siafullin, I.Sh., Klushnikov, O.P. Quantum-chemical Index of Reactivity of Heteroaromatic Compounds in Homolytic Cyclodecomposition Reactions. *Kinetics and Catalysis*, 1993, vol. 34, N 6, pp.969-971 (in Russ.).

7. Prokudin, V.G., Poplavsky, V.S., Ostrovsky, V.A. The Mechanism of Monomolecular Thermal Decomposition of 1,5- and 2,5- Disubstituted Tetrazoles. *Izvestia Akademii Nauk. Seria khim.*, 1996, N 9, pp.2209-2215 (in Russ.).

8. Prokudin, V.G., Poplavsky, V.S., Ostrovsky, V.A. The Mechanism of Monomolecular Thermal Decomposition of Tetrazole and its 5-Substituted Derivatives. *Izvestia Akademii Nauk. Seria khim.*, 1996, N 9, pp.2216-2219 (in Russ.).

9. Gaponik, P.N., Karavai, V.P. *Vestnik BGU, seria khim.*, 1980, vol.3, p.51(in Russ.).

10. Stolle, R., *Ber.*, 1929, vol.62, p.1123.

11. Benson, F.R. The Chemistry of the Tetrazoles. *Chem.Rev*, 1947, vol.41, p. 1.

12. McEvan, M.S., Riss, M.W. *J. Amer.Chem.Soc.*, 1951, vol. 73, pp.4725-4727.

13. Matushin, Yu.N., Lebedev, V.P. Thermochemical Properties of Mononitroderivatives of Azoles and Oxadiazoles, Proc. 28th Int. Annual Conference of ICT, Karlsruhe, 1997, June 24-27, pp.98-1÷98-10.

14. Kozyrev, A.A., Simirskii, V.V., Krasylin, A.P. et al. *Russ. J. Phys. Chem*, 1990, vol.64, N 3, pp. 656-661(in Russ.).

15. Matsuzawa, T., Itoh, M., Arai, M., Tamura, M. *Proc 22 Inter. Pyrothech. Sem.*, 15-19 July 1996, Colorado, pp.317-323.

16. Brodskii, A.I. Physical Chemistry, Moscow, Nauka, 1948, vol.1.

17. Wong, M.W., Leung-Toung, R., Wentrup, C. Tautomeric Equilibrium and Hydrogen Shifts of Tetrazole in Gas Phase and in Solution. *J.Am.Chem.Soc.*, 1993, vol.115, pp.2465-2472.

18. Huisgen, D.R. *Angew.Chem.*, 1960, Bd. 72, No.11, pp.359-390.

19. Ivachkevich, O.A., Krasitsky, V.A., Lesnikovich, A.I., Astashinsky, V.M., Kostyukevich, E.A., Khusid, B.M., Mansurov, V.A. Liquid-Flame Combustion II. *Combustion and Flame*, 1997, vol.110, pp.113-126.

20. Kubota, N., Ishihara, A. Analysis of the Temperature Sensitivity of Double-based Propellants, *Proc. 20th Symp. on Comb.*, 1984, pp.2035-2041.

21. Fogelzang, A.E., Egorshev, V.Yu, Sinditskii, V.P., Dutov, M.D. Combustion of Nitroderivatives of Azidobenzenes and Benzofuroxans. *Combustion and Flame*, 1991, vol.87, pp.123-135.

POLYURETHANES AS A BASIS FOR NEW MATERIALS AND NEW PROCESS ENGINEERINGS

Vladimir A. Vilensky,* Ludmila A. Goncharenko,*
Sergey I. Azarov,+ Ludmila N. Vilenska+
* Institute of Macromolecular Chemistry of National Academy of Sciences of Ukraine, Kharkov Chausse, 48, Kyiv, 253160, Ukraine
+ Institute for Nuclear Reaserches of National Academy of Scieces of Ukraine, pr. Nauki, 47, Kyiv, 252026, Ukraine

It is shown in this paper how modern methods of synthesis and modification of polyurethanes permit to give them the properties of thermosensitive ion-conducting materials or polymer composites.

Among polyblock systems the special place belongs to block-copolyurethanes or segmented polyurethanes, in which alternating soft and hard segments are bonded by urethane or urethane urea groups. The possibility of inclusion into makromolecular chain of blocks (segments) with polar groups, energy of which can differ by a factor of 10^2 - 10^3 distinguishes the urethane containing block copolymer into the special class of polymers, having no analogs. The progress in the field of the research of the structure and properties of segmented polyurethanes develops both on a path of synthesis of polymeric materials, including on a base of new intermonomers, and on a path of their physicochemical and physical modification. The examples of similar modification are stated below.

In papers [1-4] it was shown, that crown-containing polymers are capable to sorb the salts of univalent metals from their aqueous and alcoholic solutions, incidentally crown ethers coordinate cations and thus limit their mobility (μ). The charge transport is carried out by anion [4], being in intermolecular space and possessing a greater degree of freedom; the solutions of cation-active polyurethane ionomers, "charged" by potassium perchlorate, gain high ionic conductivity. However till now very few systematic researches on influence of changes in the structure of macrochain of crown-containing polyurethanes and their hydrophilic and hydrophobic component ratio on ionic conductivity in condensed state are known [3-5].

In this connection the objective of the given paper was synthesis of polyurethanes (PU) and polyurethane semicarbazides (SPU), fragments

of hard blocks of which are macrocycles, the research of their structure, thermal properties and ionic conductivity.

Phosphor containing PU and SPU were synthesized by prepolymer method [6], at the first stage of which macrodiisocyanate was obtained at the temperature 333-353K on the base of 4,4'-diphenylmethane diisocyanate (4,4'-DPhMDI) or mixture of isomers 2,4- and 2,6-tolylene diisocyanate (TDI) and one of oligoethers - oligotetramethylene glycol with molecular mass 1000 (OTMG-1000) or 2000 (OTMG-2000) at oligoether-diisocyanate proportion 1:2. On the second stage of synthesis we have carried out extending of macrodiisocyanate by tetrahydrazides or macrodiols DB18K6 and DB24K8. Synthesis have been carried out at the temperature 350-360K until exhaustion of free NCO-groups, what have been determined by disappearance of the absorption band 2270 cm^{-1} in IR-spectra. Transparent sparkling films with high physicochemical characteristics were preparated from 20% solutions of SPU. The metal salts $CuCl_2 \star 2H_2O$ and $FeCl_3 \star 6H_2O$ were introduced in crown-containing polymers in dimethyl phormamide solution in the ratio crown-ether - metal 1:1. Conductivity of the samples of PU and SPU was investigated in solution and in condensed state with the help of of the instrument E6-13A in specially made containers and cells. Supermolucular structure was investigated by X-ray small angle scattering with the help of installation KRM-1 with beam collimation by Kratky. Calorimetric researches have been carried out by scanning microcalorimeter in temperatures range 170-420K, mass of the sample was 0,07 g at the speed of heating $2^{\circ}C$/min. An evaluation of ionic conductivity crown-containing polymers should begin from study of sorption ability of film-forming materials. With this objective complex formation was estimated by imbedding of polymeric films in hot (333K) 20% a aqueous metal chloride solution. After the endurance during 30 min films were dried and investigated, the data of these researches are offered in table 1.

Table 1. Complexing ability of phosphorus-containing polyurethane semicarbazides based on DB18K6 and DB24K8.

Cation	Ionic diameter, Å	Cation bonding, % (mol)	
		SPU - 1 DB18K6	SPU - 1 DB24K8
Li^+	1,20	20	17
Na^+	1,90	28	23
Ca^{+2}	1,98	40	28
K^+	2,66	80	35
Ba^{+2}	2,70	81	47
Cs^+	3,34	29	50
Ni^{+2}	3,38	16	55
Pb^{+2}	3,40	15	67

From table 1, where data on ionic diameters of alkaline and alkaline-earth metals are also given, the manifestation of selective absorption by crown ethers is visible. Proceeding from a character of dependence of absorption on a diameter of a cation, it is possible to consider, that complex formation crown ether - metal occurs by absorption of metal, instead of sandwich compound forming. An accuracy of this supposition we see in that the mobility of crown ether is limited by its covalent bonds in macrochain of polymer. In development of the research of extractive ability of our polymers we used the method of equilibrium distribution of picric acid salts in two incompatible solvents water - chloroform. The constant of extraction equilibrium was calculated by expression:

$$K_{exp} = \alpha / [a^+ * (1 - \alpha)(L_0/(A_0 - \alpha))], \qquad (1)$$

where α - metal picrate share, which was extracted into the organic phase, and a^+ - activity of the cation in aqueous phase; L_0 and A_0 - initial concentrations of crown-containing polymer and picrates of investigated metals accordingly. In table 2 data on extraction ability of investigated polymers are offered.

Table 2. Extraction and extraction equilibrium constants of phosphorus-containing PU with DB18K6 and DB24K8 fragments.

Polymer	K^+		Na^+		Li^+	
	Extraction %	K_e*10^{-3} m^{-2}	Extraction %	K_e*10^{-3} m^{-2}	Extraction %	K_e*10^{-3} m^{-2}
PU-1 DB18K6	70	840	54,2	408	41,4	234
PU-1 DB24K8	76,8	987	64,2	584	46,7	293

From the table it is possible to observe the dependence, showing that the selectivity of metal ions is reduced in a sequence:

$$K^+ > Na^+ > Li^+ > Ni^{+2} > Ca^{+2} > Ba^{+2} > Ce^+ > Pb^{+2} .$$

At the same time this sequence will badly agree with the selective ability of the ether DB18K6 and polymers with its involvement, as it follows from data [3].

The researches have shown, that phosphorus - containing PU, distinguishing by the ratio between hydrophilic and hydrophobic components and "charged" by sorbed electrolytes, possess ionic conductivity. Specific conductivity of PU was estimated on the technique, used for the study of ionites conductivity. The obtained data were put into a base of calculations of electrochemical mobility of ions in polymers, being in an equilibrium with 0,01M KCl, NaCl and LiCl solutions in ethanol (table 3).

Table 3. The influence of polyurethane structure on charge carriers mobility in polyelectrolytes based on metal chlorides.

Polymer	Electrolyte	$\mu_{Me} * 10^{-7}$	$\mu_{Cl} * 10^{-7}$
		$cm^2 V^{-1} sec^{-1}$	
PU-1	LiCl	4,8 ±0,6	3,8 ±0,6
OTMG-1000	NaCl	5,8 ±0,8	4,0 ±0,8
	KCl	6,2 ±1,6	4,5 ±1,6
PU-2	LiCl	3,9 ±0,5	3,0 ±0,5
OTMG-2000	NaCl	5,2 ±0,7	3,9 ±0,7
	KCl	5,9 ±1,2	4,0 ±1,2

It is possible to make a conclusion from the data of the table, that for small concentration of an electrolyte the cations exhibit smaller mobility, than anions, and this outcome will be agreeed with the data for crown containing polymers of other structure. Basically such outcome can be considered as natural, as the mobility of cations is limited by complex Me - crown-ether, whereas the mobility of an anion is determined by such factors, as its building, concentration and the structure of condensed medium.

The unsufficiency of experimental data about the role of the structure of condensed state of crown-containing PU and SPU in ionic conductivity [3] has determined the necessity of such research. In [4] crown-containing SPU, distinguished by the structure of hydrophilic and hydrophobic components of polymer, crown-ether and complex crown ether - metal were inwestigated. The date permit to conclude, that the specific resistance does not exhibit the strong dependence on a chemical building of units of SPU structure. This regularity is broken when transition to polymer, containing the complex crown-ether - metal. Thus the value of a specific resistance is reduced by a factor of 10^3 - 10^4 in dependence on nature of metal, i.e. a ferromagnetic metal in the structure of complex renders the greater influence upon decrease of the value of specific resistance of SPU in

comparison with metal diamagnetic. In paper [4] it was shown by us, that in polyurethane ureas based on DB18K6 and DB24K8 specific resistance of polymers decreases in the event of increasing the difference $T_i - T_g$ (T_i - temperature of resistance measuring).

In this connection it was of great interest to investigate the temperature dependence of specific resistance of SPU (U=10V) in the range of temperatures 290 - 370K, where segmental relaxation of hard (hydrophobic) component of polymer occurs. In fig.1 temperature dependences of logarithm of specific resistance of number of crown containing PU, distinguishing by the structure of soft segment and its molecular mass (curves 1,2 and 3) and structure of hard segment (curves 3 and 4) are offered. The curves of specific resistance (ρ) are good approximated by the logarithmic function. From figure it is visible, that an interval of change of log ρ is more in polymers, oligoetrher segment of which is not declined to microphase separating with hard blocks of PU (compare curves 1 and 2). The amplification of microphase separating owing to crystallization processes in oligoether segment OTMG-2000 promotes the extension of interval of temperature dependence of log ρ, however a more effective method of the amplification of thermosensibility of PU is the substitution of symmetrical DPhMDI for asymmetrical 2,4-TDI (comp. curves 1, 3 and 4). Above we mentioned the role of the magnetic characteristics of metal in the structure of complex crown-ether - metal at isothermal measurements of ρ. The data of fig. 2 spread these results on area of segmental relaxation of hard blocks of crown-containing polymers, macrochelates of which contain various metals. From figure it is possible to conclude, that for carry of charge with involvement of the iron cation (ferromagnetic) the greater current is necessery, however the temperature range of change of log ρ is much less, than in case of diamagnetic - copper, and practically does not depend on the structure of the repeated unit of polymer (comp. curves 2,4 with curves 1,3).

It is natural, that such unique dependence of specific resistance on temperature in ion- containing polymers has predetermined the necessity of study of mobility of current carriers. For the evaluation of mobility (μ) the expression [7] was used:

$$\mu = d^2/\tau\ U, \qquad (2)$$

where d - width of film, U - potential, affixed on a sample, τ - peak of maximum on time dependence of motion of space charge at constant potential U=0,8V. Fig. 3 shows, that the detected feature of

temperature dependence of ionic conductivity of SPU has more deep essence, than it is characteristic to the conductors or semiconductors. It is known, that basically the growth of ion mobility results in dissipation of energy owing to processes of impact of cariers and decrease of free range. In given case the increasing of current in researched range of temperatures is accompanied by increase of mobility of copper ions in the range 303-363K and consequent decrease of it in the range 333-363K. This naturality is kept irrespective of structure of repeated PU unit.

The substitution of copper cations by iron in complex is accompanied by antibatic change of mobility of current carriers in considered ranges of temperatures. It is possible to suppose, that this process is stipulated by features of the gain by iron cations of magnetization in a continuum of moving dipoles of polar groups of hard PU segments. It is possible to assume, that the frequency of dipole oscillations in a temperature range 303-333K promotes the increase of magnetization of iron particles and it conditioned the limitation of cation mobility. Rise of oscillation frequency of dipoles of chains under the influence of temperature results in, in our opinion, demagnetization of iron particles, as promotes growth of their mobility.

In summary it should be noticed, that detected features of metal sorption, temperature dependence of conductivity and mobility of ions in considered consequence of polymers we connect with their segmental building, processes of thermodynamic incompatibility of soft and hard segments, and at the same time magnetic characteristics of metal ions.

The next part of proceeding demonstrates the new possibility of process engineerings in PU synthesis with the attraction of constant magnetic filds. Over the last several years the quantity of work, in which the electrical and magnetic fields are used for modification of polymer properties or,what is more important, for study of the influence of the intensity of its fields upon of polymerization processes, control of molecular weight, chemical or physical structure formation, constantly grows.

Analysis of this work,in which electrical or magnetic fields,were used shows the pragmatic character of these research projects. This is displayed in a statement of the objective to obtain the polymer with certain physicochemical or mechanical properties, without the preliminary construction of interaction model of the initial monomer

units with physical fields and the influences of such interactions on final product. The necessity of creation of similar models becomes obvious. When considering of the initial charging symmetry, for example, molecule of methanol, charges can be calculated by non-empirical methods:

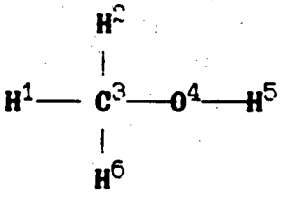

atom	q^*	atom	q
1,6	-0.006	4	-0.350
2	0.014	5	0.211

q^* - atom charge

or of phenyl isocyanate, calculated by the HMO method:

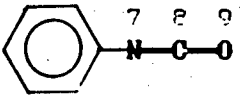

atom	$q^*\pi$	atom	q
1	-0.049	7	-0.495
2,6	0.003	8	1.329
3,5	0.006	9	-1.096
4	0.013		

These molecules differ in their charging symmetry and will interact in different way with magnetic field when imposing it on reaction mixture. Let us represent the reaction of polyaddition as a bonded set of <N> dipoles as follows:

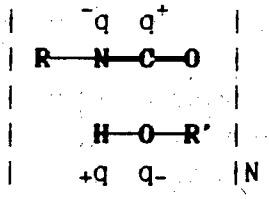

As far as each monomers X_i and Y_i consist of the group of segments and by being in thermal motion, the set <N> will be characterized by statistical distribution of orientations of the dipoles. If constant magnetic field with intensity H_j is imposed upon such system it became obvious that the interaction between field and the quadrupoles <K> is imposed on the processes of polyaddition. One of these quadrupoles in form of linked dipoles C=O and O-H can be presented as:

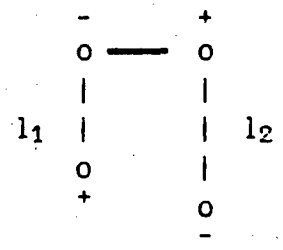

with dipole moment P_e, equal:

$$\vec{P}_e = q\vec{l}_i \qquad (3)$$

where l_i - is the distance between corresponding charges and $l_1 \neq l_2$ because of the different Van der Vaals radii of atoms N, C, H and O. Such quadrupol can be considered as some closed circuit with current i_k, existing during the time of migration of hydrogen atom from oxygen to nitrogen and opening of double bond between nitrogen and carbon. If such circuit with current is placed in a homogenous magnetic field with magnitude of magnetic induction B_1 then in accordance with the moment of forces M_1 will act upon it:

$$\vec{M}_1 = [\vec{P}_m \vec{B}_1] \qquad (4)$$

and

$$\vec{B}_i = \vec{H}_i \mu \qquad (5)$$

where P_m - is the vector of the magnetic moment of the circuit. Vector M_1 is directed perpendiculary to the vectors P_m and B_1, so that from its end the shortest rotation from P_1 to B_1 takes place counterclockwise. Under the action of M_1 the circuit will take the new position of stable equilibrium. It is clear that magnitude of displacement of urethane groupings relatively to axis of macrochain is proportional to magnitude B_i. Concerning B, in accordance to eq.(5) it is alwais proportional to H - magnetic field intensity and μ-the magnetic permeability of environment, which remain constant in the

given investigation. If our preconditions are true the change of H of EMF should be reflected on structure and properties of segmented PU. Such picture of the mechanism of influence of constant magnetic field on monomers which participate in reactions of polyaddition, is confirmed by our first studies [8-10].

The dependence of changing of the specific heat capacity from magnitude of EMF intensity at the middle of the glass transition interval of SPU-1 is shown in Fig.4. It is seen synthesis of SPU in magnetic fields in range of intensity $1,5\text{-}6,0\star10^{-5}$ A/m is accompanied both increasing of specific heat capacity of oligoether polyurethane matrix and stable tendency to limitation of its segmental relaxation (T_g middle of interval increases). These changes permit to conclude that the magnetic field leads to rearrangement of structure in regions of segregated oligoether matrix of SPU.

Increasing of the intensity of EMF to $H=7,5\star10^5$ A/m leads to jump change of influence of EMF upon polyurethane structure as it is seen from changing of position of the specific heat capacity curve in Fig.4. The results of SAXS studying indicate the value $H = 6\star10^5$ A/m is threshold magnitude of influence upon SPU structure (Fig.5). Comparison of Fig.4 and Fig.5 permits to do the same conclusions about the influence of H_j(A/m) upon soft and hard components of SPU-1. The analysis of these figures shows that the increasing of H (A/m) to its threshold value H_{th} leads to that the forming of PU structure in polyaddition processes takes place with the increasing of packing density in segregated hard blocks i.e. in rigid domains. Oligoether matrix micro regions on the contrary undergo rearrangement processes. The crossing through H_{th} leads to antibatic change of state of soft and hard SPU components. Decreasing of C_p magnitude, corresponding to increasing of oligoether matrix packing density and X-rays scattering intensity ($I\star10^3$ imp) by rigid domains of SPU-1 indicates that the EMF deformation og chains of forming hard blocks is transmitted upon oligoetheric chains and in such a way influences upon oligoether macromolecule packing density.

The trustworthiness of the offered model of interaction of EMF with the system of virtual quadrupols of polyaddition reactions is confirmed by the date of study of elasticity modulus at stretching (E_{el}) of polyurethanes, synthesized at various intensities of EMF. The results of this study are presented in Fig.6. It is possible to conclude from the analysis of the curve of E_{el} that supermolecular

structure of polyurethanes prepared at the intensities 1,5 - $3*10^5$ A/m forms the set of fragments of chains, having various degree of orientation by action EMF and that is equal to action of dispersial fillers, the results of which usually improve strength properties of polymers [11].The subsequent increasing of intensity of EMF results in that the ratio between fragments of chains, formed in natural way and in conditions of EMF is decreased. The transition throjh extremum of curve of dependence of elasticity module indicates that the structure formed at the interval of the intensity of EMF 4,5-7,$5*10^5$ A/m is more plastic in comparison with the initial polymer. The influence of external magnetic field of such intensities may be compared with the action of plastisizer an polyurethane.

REFERENCES

1. Hiraoka Michio /Crown compounds/ Elsevier Scientific Publishing Company. Amsterdam-Oxford-New-York. P.362.
2. Host Guest Complex Chemistry Macrocycles, Synthesis, Structure, Application /Editors:F.Vögtle, E.Weber, Springer-Verlag. Berlin, Heidelberg, New York, Tokyo, 1985
3. Vilensky V.A., Shtompel V.I., Goncharova L.B., Kercha Yu.Yu. /Ukrainian Chem J.,V.62,N12,1996
4. Veselov V., Jurilo A., Grekov A., Korviakov S./Composites,-1988, N36, P.12
5. Vilensky V., Goncharenko L., Kercha Yu., Shtompel V., Savel'ev Yu., Veselov V., Ogorodova T. / Vysokomolecularnye soedineniya /Russia -1996, Ser.A,- V.38, N11. P.1865
6. Saunders J.H.,Frish K.C./Polyurethanes/ John Wiley and Sons, New Yirk - London, 1962.
7. Lampert M.A., Mark P./Current injection in solids/Academic Press, New York - London, 1970.
8. Vylensky V.A. / Dokld.Akad.Nauk Ukraine,1996,N12,142-147
9. Vilensky V.A. / in Proceeding,8-th Ukrainian Conference on Macromolecules,Kyiv,24-26 September,1996,p.150
10. Vilensky V.A. / Patent application. Priority in Ukraine 21.05.1996 N96051993
11. Polymer Blends/Edited by D.R.Paul, S.Newman,Academic Press Inc., 1978, V.2.

Fig.1.Temperature dependence of log on PU with complexes of crown-Cu

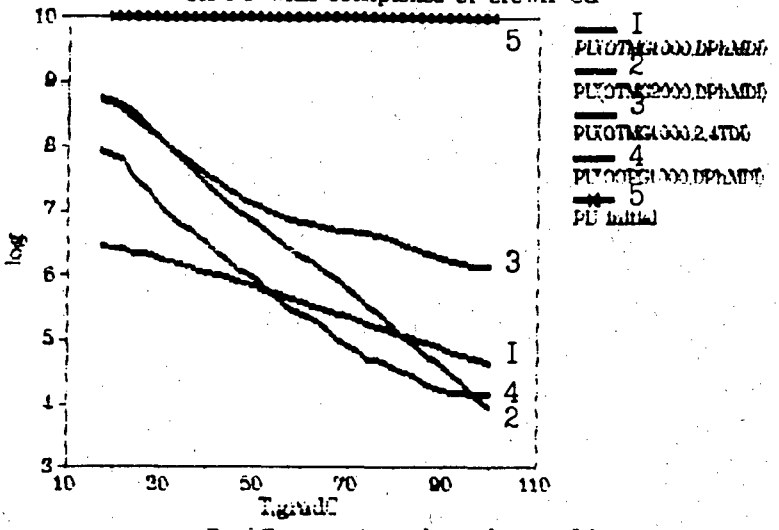

Fig.2.Temperature dependence of log of PU with complexes crown-ble

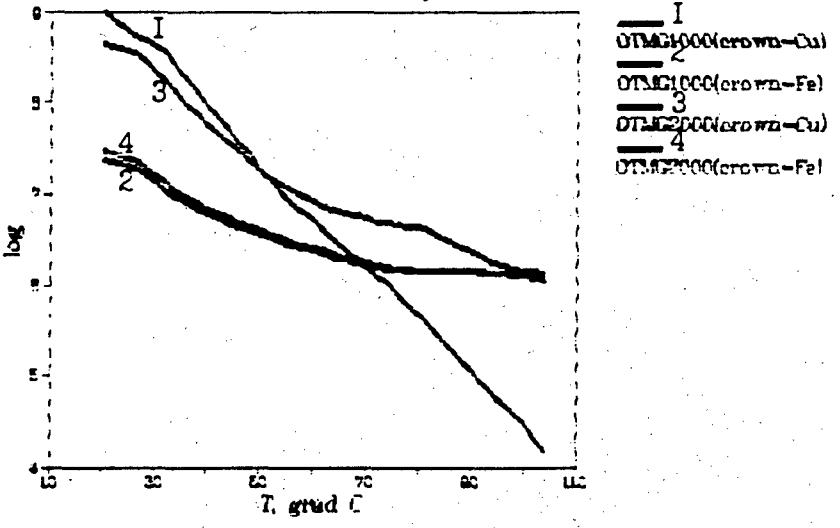

Fig.3.Temperature dependence of carriers mobility of various complexes

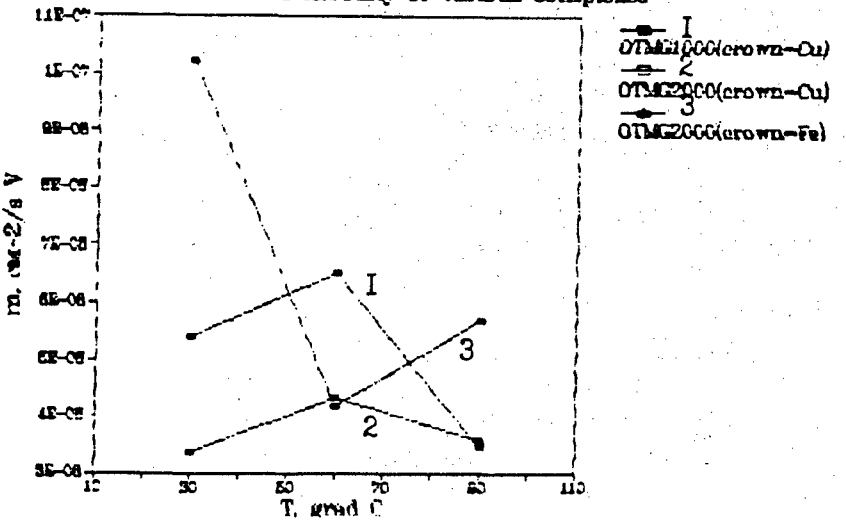

Fig.4 Dependence of Cp (1) and Tg (2) of PC from intensity of EMF

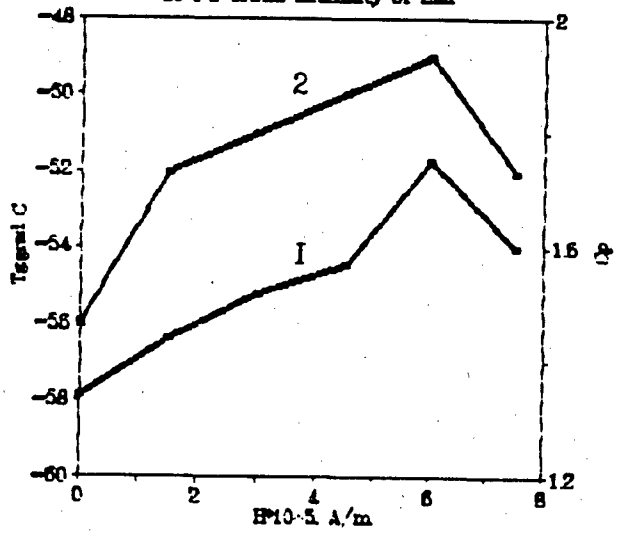

Fig.5 SAXS curves of SPU-1 synthesized at different EMF intensities

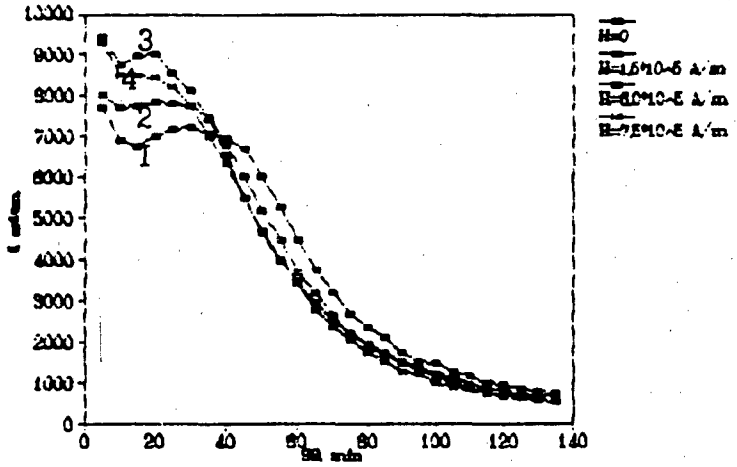

Fig.6 Dependence of elasticity modulus of PC from intensity of EMF

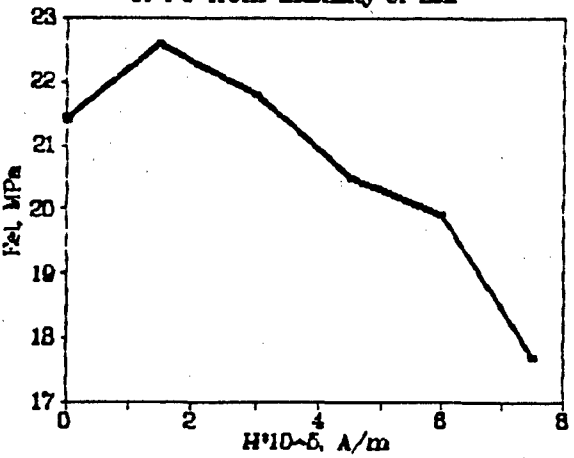

POLYURETHANE COMPOSITES FOR PERSONAL SAFETY FEATURES AND RECREATION OF SOILS,CONTAMINATED BY RADIONUCLIDES

Vladimir A. Vilensky*, Sergey I. Azarov+, Ludmila N. Vilenska+
*Institute of Macromolecular Chemistry National Academy of Sciences, Kharkov Chausse, 48, Kyiv, 253160, Ukraine
+Institute for Nuclear Researches National Academy of Sciences of Ukraine, pr. Nauki, 47, Kyiv, 252028, Ukraine

The results of the study of polyurethane compositions, the modification of component content of which permits to use them as individual means of protection or artificial protective grounds, are offered.

As is well known, as a result of the accident in ChNPP rediative contamination of the ground more than 2000 sq.kms areal with population more 250.000 persons appears.Therefore for our country one of the most actual task is the providing with individual and collective means on protection of the people, which not only took part in liquidation on the accident consequence, but in daily work in conditions of ionizing radiation effects. The second so very actual task is the re-entry into the normal reproductive activity of gradually rehabilitated plots of the territory.Our vision of the solution methods of these problems is the objective of the present work.

The elaborating and study of the materials for manufacturing of individual means of protection (IMP) from combined effect of different nature (penetrating radiation, light radiation etc.) dangerous and harmful factors (DHF) is a complex task. Present-day means and ways of personal protection for everyday purpose, applied when working with radioactive substances or in conditions of high temperature and light radiation action, are of little use for personnel protection when combined acting of radiation and radioactive contamination, open fire and elevated temperature, toxic radioactive burnig products etc.

In the majority of cases these protective means and ways are manufactured of lead and don't secure necessary protective effectiveness and are difficult in opperating. Besides lead is the toxic substance and it is necessary to exclude the possibility of its contact with a person. In consequence of it emergency and fire

division personnel and at the same time special-purpose units when liquidating of radiative accidents find themselves without IMP of short-term use The fitness of materials for manufacturing of IMP of short-term use when combined effecting of different nature DHF is determined by following characteristics:

- possession by complex of physico-mechamical properties, assuring IMP effectiveness when operating (thermo- and radiative stability, strength and elasticity, refractoriness, arc rezistance etc.);
- minimal sorption ot radioactive substances, air- and gas-impermeability, moisture- resistance etc.;
- stability to corrosive media action and technological effectiveness when manufacturing;
- cofirmity to sanitary requirements.

Several DHF can simultaneously act on IMP materials at following permissible levels:

- thermal flux surface density - (0,3 - 5,0) kW/m^2;
- temperature - (70 -100)^oC;
- toxic burning products:part by volume CO_2 - 6,0%, CO - 0,1%; mass concentration NO, NO_2- 0,015 mg/m^3, SO_2 - 0,5 mg/m^3;
- permissible radionuclide concentration in air, Ci/l: ^3H - $6,0\star10^{-5}$, ^{14}C - $3,5\star10^{-9}$, ^{90}Sr - $1,2\star10^{-12}$, ^{137}Cs - $1,4\star10^{-11}$, ^{235}U - $6,0\star10^{-14}$, ^{239}Pu - $9,0\star10^{16}$.

Radiation power density of α-particles is 10^6MeV/$cm^3\star$sec in energy range (1,0-7,0) MeV. Power density of γ-radiation is $0,5\star10^8$ MeV/ $cm^3\star$sec in energy range (0,01 10,0) MeV, for β-radiation - $0,2\star10^8$ MeV/$cm^3\star$sec in energy range (0,02 - 3,5) MeV.

For those cases,when low energy γ-radiation (with energy to 150 keV) acts on the personnel, the approach to working out of protective materials, excluding application of lead, is realized by us [inventor's certificate of USSR #1620460, 1991].

As is well known, in the range of low energy γ-quantum the main process of interaction of ionizing radiation with a matter is photoeffect. Photoeffect cross-section has maxima at γ-quantum energy equal bond energy of electrons in atom. In maximum photoeffect increases 2-4 times. There- fore for effective attenuation of low-energy γ-radiation it is expediently to use the material, including mix of elements with various sites of maxima in cross-section. The composition of element mix depends on radiation spectrum and thickness of materials.

Adduced calculative - experimental researches have shown that the use of the material with optimum content of elements allows to elevate attenuation multiplicity of low-energy γ-radiation (whith energy to 150 keV) to two times in comparison with lead (at similar mass).

The investigations on the modification of polyurethanes have shown certain oxide compositions (TiO_2, Fe_2O_3, CuO, ZnO, BaO, Cr_2O_3, SiO_2, Al_2O_3) permit to create high filled (to 80% by weight) elastic film materials, tensile strength of which increases by adding of filler, and specific elongation is lovered (see Table 1).

Table 1. Physicomechnical properties of filled PU

Filling, %	Tear strength, kg/cm	Tensile strength, kg/cm^2	Specific elongation, %	Strength at 100% elongation
10	150	430	450	130
30	265	600	430	190
50	270	620	400	200

These oxydes (or their mixtures) in the form of powder were introduced into polyurethane binders. Then after corresponding treatment polymer plates with various physicochemical properties were prepared.

Soft segment and hard segment glass temperatures (T_g) of polyurethane composites are presented in Table 2.

Table 2. Temperatural characteristicks of soft and hard blocks of filled polyurethanes

Filling, %	Soft segments		Hard segments	
	T_g, K	ΔC_p, kJ/kg K	T_g, K	ΔC_p, kJ/kg K
0	216	0,47	333	0,30
1	221	0,37	340	0,91
5	217	0,28	364	0,60
10	219	0,43	357	0,80
20	216	0,73	353	1,11
50	222	0,32	361	0,32

It follows from the Table that filling degree doesn't practically influence on mid-interval changes of glass temperature, i.e.specific interactions between filler and soft segment of polymer are absent. On the other hand, polar hard segments display strong interaction with oxydes, as a result glass transition of which increases. These interactions find their reflection in viscoelastic characteristics of initial and filled polyurethane specimens (Table 3).

Table 3. Viscoelastic properties of initial and filled polyurethane

Filling, %	E_1* MPa	τ_1** s	E_2 MPa	τ_2 s	E_3 MPa	τ_3 s	E_4 MPa	τ_4 s	rms error, %
0	54,6	551,4	7,5	11,5	14	1,0	-	-	0,8
1	25,9	729,2	5,6	8,7	5,9	0,4	-	-	0,7
5	27,6	506,8	5,4	8,4	4,4	1,2	-	-	0,9
10	26,1	571,0	6,5	6,1	3,4	2,6	5,5	0,3	0,85
20	28,5	879,0	5,3	13,9	4,8	2,4	6,3	0,25	1,0
50	26,9	706,5	6,0	12,8	2,7	4,0	7,8	0,35	0,85

where * E_i - modulus of elasticity of i-th relaxation oscillator
** τ_i - time relaxation of i-th relaxation oscillator

Analysis of the data given in Table 3 on the basis of segmented polyurethane structure model allows to include, that the filler is localized mainly in hard segments and their associates regions. Saturation of interaction between hard segments and the filler results in release of filler into transition regions between flexible matrix and hard domains.

The investigations of supermolecular structure of these composites allow to determine their such specific property as substantial attenuation of roentgen rays. Following more detailed study of this effect allows to determine that attenuating property of composites shows concentration dependence.

Carried out radiative investigations of EFM with density 1,6 g/cm^3 (Table 4), that γ-radiation attenuation ratio multiplicity is 1,5 - 2,5 times.

Table 4. Dependence of low energy γ-radiation attenuation coefficient $k\alpha$ of EFM on oxyde content by weight

Filling, %	$K\alpha$, cm^2/g
10	2,3
20	15,9
50	34,6

Worked out materials may be used when manufactirung of different systems of local, collective and at the same time personal protection. The details of desired configuration for use as shields or assembling on cabin walls of special equipment etc., when working out and projecting of protection from γ-, δ- and α-radiation, open fire and elevated temperatures may be prepared from denoted materials by molding. As is well known, for post-chernobyl situation in Ukraine the main sources of radionuclide admission in human organism exept for direct penetration from air are flora and drinking water. Therefore the research of the ways and methods of minimization of radioative contamination consequences of soils, vegetation and wells in regions with elevated radionuclide content is the permanent problem of our country.

Rather wide series of measures, directed on decreasing of soil contamination by radionuclides exists at the present time.

The use of different type sorbents as one of the effective methods of decreasing of radionuclide content in the soil-plant system is one of the main directions in which the selection of plants is the predominant. In so far as one of the channels via radionuclides admit into the plant is their assimilation from the soil when root feeding, the choise of plants as the sorbent is determining. For example, gramineous crops in a less degree collect radionuclides than beans. At the same time various degree of their accumulation may be revealed in different species of a family. Thus, in paper [8] on research of the gramineous crop family, namelly of wheat, oats, rue, barley, represented by two varieties, it was shown that minimum accumulation of radionuclides is typical for barley. Lupine accumulates maximum amount of radionuclides among beans. It is assumed, that effectiveness of such decreasing of contamination degree of soils by radionuclides will depend on such factors as soil properties, agricultural technology measures, and at the same time on used varieties of plants.

It should admit that this direction may be considered as main one in soil recreation processes of contaminated soils, whereas it may be subdivided into two ingredients. One of them is the optimal choice of agricultural crops, accumulating comparatively small amounts of radionuclides, but fixing them in soil and on the contrary, plants, carrying out from the soil great amount of radionuclides. However there is a situation in this important direction when carried out onto the surface radionuclides can be transferred in case of wind soil erosion and contaminate new territories.

The comprehension of the importance of this program has predetermined the idea of the project on creation of artificial grounds with the purpose of protecting of soil plots, contaminated by radionuclides. The initial materials for preparation of artificial soils is elaborated by us polyurethane composition which include with the exception of above-mentioned ingredients various types of fertilizers, rippers and binders.

In the last few years such models were tested by us for intergrowth of some species of gramineous and bean crops in the capasity of the experiment. Preliminary results give us the grounds to suggest the given direction as one of possible ingredients of collective means of flora and fauna protection from radionuclides transfer by air flows.

PHENOMENOLOGICAL ASPECTS OF DETONATION IN NON-IDEAL HETEROGENEOUS EXPLOSIVES

Allen J. Tulis, James L. Austing, Remon J. Dihu, and Richard P. Joyce
IIT Research Institute
Chicago, Illinois, 60616, U.S.A.

and

Divyakant L. Patel, James Dillon, and David C. Heberlein
U.S. Army CECOM-NVESD
Fort Belvoir, Virginia 22060, U.S.A.

ABSTRACT

The detonation of highly-insensitive hybrid extruded heterogeneous compositions has been characterized in terms of the detonation characteristics. The compositions investigated were glycerine (CHO), aluminum (Al), and ammonium perchlorate (AP), in most cases sensitized with small amounts of RDX. The extruded compositions were confined in steel tubes of up to nominally 100-mm in diameter at densities as high as 1.7 kg/m^3. These compositions were also detonated in fiber canisters of nominally 150-mm diameter upon a blast-pad to assess blast output in terms of overpressures and impulses, and as previously reported, provided blast performances comparable or greater than TNT. Here attention was directed to the detonation characteristics of pressure, velocity, and temperature. These characteristics were monitored using carbon-resister gauges for pressures, fiber-optic light detector diodes for reaction-front phenomenology, and three-color radiometry for temperatures. The reaction-front durations demonstrated the non-ideal behavior of these compositions, and the temperature measurements confirmed the phenomenological aspects of these highly complex hybrid heterogeneous compositions. Analytical CHEETAH Code CJ computations were conducted to guide the experimental effort. Particle size of the components was also a factor, and influenced the chemical reaction mechanisms to some extent, but not detonation performance in general. Major factors of processing these compositions was their rheological properties in regard to homogeneity and quality. Particle size and shape of the solid components in the formulation/extrusion of these high performance insensitive explosive compositions was critical and required special extrusion techniques.

UNDERWATER EXPLOSIVES (I) - INFLUENCE OF ALUMINIUM AND AMMONIUMPERCHLORATE ON THE PERFORMANCE

A.Happ, A. Kretschmer, U. Meyer, T. Keicher; Fraunhofer ICT, Pfinztal, D
U. Sirringhaus, R. Wild; WIWEB, Swisttal, D

ABSTRACT

This paper shows the influence of aluminium (Al) and ammonium perchlorate (AP) in GAP- and RDX-based explosives on the underwater explosion performance and reaction behavior. The studied explosives varied in formulation, aluminium particle size and aluminium arrangement in the matrix. The different explosives were characterized by the plate-dent-test, measurement of detonation velocity, testing of stability and sensitivity, and analyses of the detonation products after blasting in a closed vessel. The performance was measured by underwater explosions of charges with weights of 70, 250, 500 and 1000 g.

Al and AP increased the bubble energy while the pressure remained constant. The maximal bubble energy was reached with aluminium contents ranging from 40 to 50 %. Surprisingly the pressure and the impuls were constant for Al-contents from 15 to 40 %. Decreasing pressure and impulse was observed only for the exotic formulations containing 50 % Al. As a consequence maximal bubble energy with no loss in pressure and impuls is obtained with charges containing about 40 % aluminium.

Charges with a specific geometrical arrangement of aluminium in a layer between the explosive charge and the water caused lower bubble energy than those with homogeneously incorporated aluminium. The energy released by reactions between water and aluminium was less than expected and did not dominate.

There was no remarkable difference in performance of formulations with aluminium particle sizes varying from 5 µm to 150 µm.

EINLEITUNG

Metallpulver in Unterwassersprengstoffen setzen bei ihrer Umsetzung beträchliche Mengen an thermischer Energie frei und erhöhen die Temperatur und somit den Druck der Reaktionsgase. Der für die Umsetzung der Metalle notwendige Sauerstoff kann prinzipiell direkt vom Sprengstoff und zugesetzten Oxidatoren wie Ammonium-

perchlorat (AP) oder aber in einer sog. Nachreaktion vom umgebenden Wasser stammen.

Der Energiebeitrag aus der Metallumsetzung führt grundsätzlich zu einer Steigerung der Gasblasenschwingungsenergie aber der genaue Einfluß auf die Energieverteilung zwischen Gasblasenschwingungsenergie und der Schockwellenenergie in Abhängigkeit von Aluminium und AP bei RDX/GAP-haltigen Sprengstoffkompositionen ist bisher nicht untersucht.

Die folgenden Zusammenhänge und Fragestellungen werden in der vorliegenden Arbeit untersucht:

- Einfluß der Komponenten RDX, AP, Al auf das Leistungsverhalten von Unterwassersprengstoffen
- Einfluß der unterschiedlichen Kompositionen auf Verteilung der Wirkleistung in Schockwelle und Gasblasenenergie
- Untersuchungen zum Umsetzungsverhalten von Aluminium in Unterwassersprengstoffen
- Einfluß von verschiedenen Aluminiumsorten auf das Umsetzungsverhalten
- Einfluß eines Aluminiummantels auf die Unterwasserleistung

DURCHGEFÜHRTE ARBEITEN UND ERGEBNISSE

Zusammensetzung der Ladungen:

Aus Gründen einer guten Verarbeitbarkeit bei möglichst hohen Füllstoffgehalten wurde bei den meisten der hergestellten kunstoffgebundenen Unterwasserladungen einheitlich ein GAP - Bindersystemanteil von 18 % eingestellt. Das Bindersystem bestand aus Glycidyazidpolymer-Diol, dem Weichmacher BDNPA/BDNPF und dem Härter Desmodur N100. Als Vergleichssprengstoff wurde TNT verwendet.

Ladung	GHX 86	GHX 78	GHX 83	GHX 84	GHX 85	GHX 87	GHX 89
RDX [%]	82	67	62	57	52	42	27
Al [%]	-	15	20	25	30	40	50
AP [%]	-	-	-	-	-	-	-
GAP-Binder [%]	18	18	18	18	18	18	23

Tabelle 1

Bei den Ladungen der Tabelle 1 steigt der Aluminiumanteil von 0 % bis 50 % jeweils auf Kosten des RDX an. Diese Reihe soll den Einfluß des steigenden Al-Gehaltes bei gleichzeitiger Abnahme des brisanten Sprengstoffanteiles RDX auf das erzielbare Leistungsvermögen aufzeigen. Mit den "extremen", in der Praxis der Unterwassersprengstoffe nicht üblichen Formulierungen GHX 87 und GHX 89, die 40 bzw. 50 % Al enthalten, soll gleichzeitig die Grenze des maximal zur Umsetzung anregbaren Al-Gehaltes in solchen Systemen aufgezeigt werden.

Ladung	**GHX 76**	**GHX 80**	**GHX 81**	**GHX 82**	**GHX 99**	**GHX 100**	**GHX 101**
RDX [%]	42	37	32	27	47	47	47
Al [%]	15	20	25	30	30 [1)]	30 [2)]	30 [3)]
AP [%]	25	25	25	25	-	-	-
GAP-Binder [%]	18	18	18	18	23	23	23

1): Spez. Oberfläche: 0,134 m²/g; Mittl. Korngröße: 150 µm
2): Spez. Oberfläche: 0,229 m²/g; Mittl. Korngröße: 50 µm
3): Spez. Oberfläche: 1,144 m²/g; Mittl. Korngröße: 5 µm
Tabelle 2

Die Formulierungen in der Tabelle 2 (Reihe GHX 76/-80/-81 /-82) enthalten alle konstant 25 % AP und Al-Gehalte von 15 % bis 30 %. Wie in der Reihe der Tabelle 1 erfolgt die Zunahme des Al-Anteils auf Kosten des RDX-Gehaltes.

Diese Reihe soll ebenfalls den Einfluß des steigenden Al-Gehaltes bei gleichzeitiger Abnahme des brisanten Sprengstoffanteiles RDX auf das erzielbare Leistungsvermögen aufzeigen. Durch Vergleich der Leistungsdaten dieser AP-haltigen Sprengstoffe mit den AP-freien Formulierungen der Tabelle 1 wird zusätzlich der Einfluß des "Nicht-idealen" Sprengstoffs AP auf das Leistungsvermögen solcher Systeme im Zusammenhang mit der Aluminiumumsetzung studierbar.

Die Ladungen GHX 99/-100/-101 enthalten drei verschiedene Al-Sorten mit Partikelgrößen zwischen 5 - 150 µm bei sonst gleicher Zusammensetzung. Aus Gründen der besseren Vearbeitbarkeit wurden für diese drei Formulierungen jeweils 23 % GAP-Binderanteil eingesetzt. In dieser Reihe soll der Einfluß von unterschiedlich großen Al-Partikeln auf die Wirkleistung untersucht werden.

Ladung	GHX 86 mit Al-Mantel	
	Kernladung	Mantelladung
RDX [%]	82	-
Al [%]	-	70,3
AP [%]	-	-
GAP-Binder [%]	18	29,7

Tabelle 3

Die in homogener Mischung verarbeiteten Bestandteile der Formulierung GHX 101 wurden bei Ladungen unter der Bezeichnung GHX 86 mit Al-Mantel in zwei unterschiedliche Ladungsteile getrennt (Tabelle 3). Die zylindrische Kernladung bestand aus der Al-freien Mischung GHX 86 (= GAP, RDX) und die umschließende Mantelladung bestand aus einer Mischung von 70,3 % Al und 29,7 % Binder. Durch Vergleich der jeweils in der Gesamtsumme aus den gleichen Komponenten aufgebauten Ladungen GHX 101 und GHX 86 mit Al-Mantel sollte der Einfluß des vollständig im Mantel angeordneten Aluminium auf das Unterwassersprengverhalten untersucht werden.

Untersuchungen im Sprengkessel:

In einem dickwandigen zylindrischen Stahlkessel mit einem Volumen von 1,5 m³ wurden verschiedene Sprengstoffkompositionen mit jeweils 300 g Ladungsmasse unter Argonatmosphäre gesprengt und die Rückstände sowie die Gasschwaden analysiert. Die experimentelle Durchführung erfolgte analog wie in Lit. (1) beschrieben. Von jeder untersuchten Formulierung wurden zwei Sprengungen durchgeführt.

Tabelle 4 zeigt die Untersuchungsergebnisse der festen Detonationsrückstände und der gasförmigen Detonationsprodukte. Die gemessenen RDX-Gehalte (Zeile 1) belegen eindeutig, daß die untersuchten Ladungen im Sprengkessel vollständig detonierten.

Die Aluminiumgehalte der Rückstände von den Ladungen GHX 76/78/82/85 lagen alle deutlich unter 1 % und belegen somit, daß bei den untersuchten Formulierungen Al-Gehalte von bis zu 30 % ohne zusätzlichen Fremdsauerstoff aus umgebendem Wasser oder Luft komplett umgesetzt werden. Bei der Umsetzung des Sprengstoffs hat offensichtlich das Al als starkes Reduktionsmittel die höchste Priorität im Hinblick auf seine Oxidation. Die weiteren Reduktionsmittel wie Wasserstoff und Kohlenstoff konkurrieren um den vom Aluminium nicht verbrauchten Sauerstoff.

	GHX 76	GHX 78	GHX 82	GHX 85	GHX 87
RDX-Gehalt [%]	0,003 < 0,0004	0,002 0,001	< 0,0004 < 0,0004	< 0,0004 < 0,0004	-- --
Al-Gehalt [%]	< 0,3 / < 0,3	< 0,3 / < 0,3	< 0,3 / 0,8	< 0,3 / < 0,3	6,8 / 6,9
H_2 [Vol.-%]	28,86 /28,49	29,88 /29,64	38,86 /39,17	33,65 /34,78	36,21 /33,05
(Berechn.)*	(28,29)	(24,09)	(40,08)	(38,76)	(51,00)
N_2 [Vol.-%]	34,52 /33,71	32,78 /34,06	31,52 /31,17	35,37 /33,29	35,17 /40,09
(Berechn.)*	(31,74)	(34,47)	(35,51)	(45,49)	(38,00)
CO [Vol.-%]	30,42 /31,74	34,71 /34,13	29,30 /29,40	30,70 /31,46	28,26 /26,45
(Berechn.)*	(30,99)	(32,32)	(14,84)	(6,49)	(0,03)
CO_2 [Vol.%]	5,95 / 5,61	2,29 / 1,94	0,09 / 0,10	0,11 / 0,11	0,11 / 0,21
(Berechn.)*	(6,35)	(3,11)	(0,36)	(0,07)	(0,00)
KW + Restgase [Vol.-%]**	0,25 / 0,45	0,34 / 0,25	0,29 / 0,16	0,17 / 0,36	0,25 / 0,20
(Berechn.)*	(2,63)	(6,01)	(9,21)	(9,19)	(10,97)

* Berechnet nach ICT-Thermodynamik-Code
** Kohlenwasserstoffe
Tabelle 4

In den Rückständen der Formulierung GHX 87 wurde Restaluminium gefunden. Dies ist nicht überraschend, da bei einem Al-Gehalt von 40 % der primär in der Formulierung vorhandene Sauerstoff für die komplette Oxidation des Al's nicht ausreicht.

Für die Sprengschwadenzusammensetzungen ergaben sich die folgenden Abhängigkeiten:

Mit steigendem Al-Gehalt (GHX 76 - GHX 87) steigen die Anteile an H_2 und N_2 an. Die Berechnungen ergeben allerdings für den Wasserstoff beim Übergang von GHX 85 (Al 30%) zu GHX 87 (Al 40%) eine deutlichere Steigerung, die durch die Messungen in der berechneten Größenordnung nicht bestätigt werden konnte.

Der CO_2-Gehalt der Sprengschwaden sinkt mit zunehmendem Al-Gehalt der Formulierung.

Deutliche Abweichungen zwischen den Berechnungen und den Messungen ergeben sich für die Gase CO und die Kohlenwasserstoffe. Nach den Berechnungen müßte der CO-Anteil mit steigendem Al-Gehalt bis auf 0% absinken und der KW-Wert gleichzeitig ansteigen. Diese Tendenz wird von den Messungen nicht bestätigt.

Unter Zusammenfassung der vorstehenden Ergebnisse ergibt sich das folgende Gesamtbild:

Das Al hat für seine Oxidation den ersten Anspruch auf den im Sprengstoff vorhandenen Sauerstoff und wird komplett umgesetzt solange genügend Sauerstoff vorhanden ist. Die anderen im Sprengstoff vorhandenen Elemente konkurrieren um den verbleibenden Restsauerstoff. Deshalb verschieben sich einige Reaktionsgleichgewichte bei zunehmendem Al-Gehalt jeweils in Richtung sauerstoffreier Reaktionsprodukte (Zunahme von H_2 unter vermutlicher Abnahme von H_2O und Zunahme von N_2 unter vermutlicher Abnahme von NO_x sowie Abnahme von CO_2). Das CO bildet hierbei eine Ausnahme. Die Sauerstoffaffinität des Aluminiums ist offentsichtlich nicht groß genug, um den Gehalt an CO entsprechend den Berechnungen zu reduzieren. So beträgt der CO-Gehalt fast unabhängig vom Al-Gehalt konstant ca. 30% und sinkt erst bei extremen Al-Gehalten langsam ab. Auch die Reduzierung des CO_2-Gehaltes durch das Al führt eher zur Rußbildung als zur Veränderung der CO-Konzentration.

Sprengungen unter Wasser

Die Unterwassersprengleistungen wurden vom WIWEB nach der von Cole vorgeschlagenen Methode gemessen (2) und ausgewertet (3) (4). Hierzu wurden zylindrische Ladungen mit Länge/Durchmesser = 1:1 und den Gewichten 70 g, 250 g, 500 g und 1 kg in einer Wassertiefe von 3 m gesprengt und die auftretenden Stoßdrücke in einem Abstand von jeweils 5 m mit 2 Turmalindruckaufnehmer gemessen. Für alle Formulierungen wurden pro Ladungsmasse jeweils vier Ladungen gesprengt und die Streubreite der Ergebnisse in den Diagrammen in Form von Fehlerbalken angegeben.

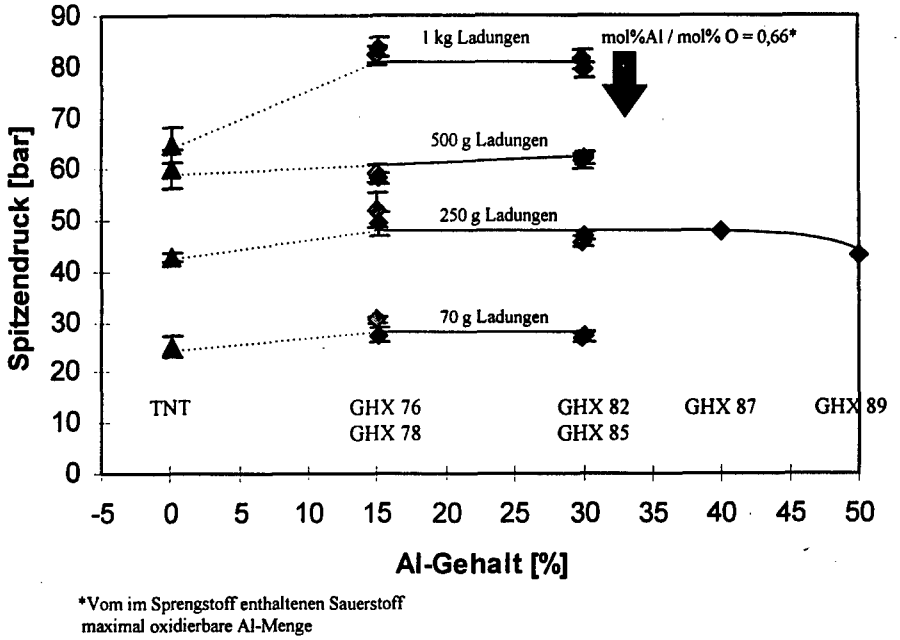

Diagramm 1: Spitzendruck in Abhängigkeit vom Al-Gehalt

Die untersuchten Ladungen mit gleichen Massen zeigen überraschenderweise über weite Bereiche des Aluminiumgehaltes kaum Änderungen für den Spitzendruck. So weisen die Ladungen mit 15 und 30 % Al jeweils ähnliche Spitzendrucke auf und erst bei weiterer Steigerung des Aluminiumgehaltes auf über 40 % kommt es zu einer geringfügigen Abnahme des Spitzendrucks (s. eingezeichneter Kurvenverlauf). Im Diagramm markiert ein Pfeil den Grenzbereich für die maximal oxidierbare Al-Menge, wenn man von der theoretischen Annahme ausgeht, daß der im Sprengstoff enthaltene Sauerstoff ausschließlich für die Al-Oxidation verwendet wird. Diese Annahme entspricht natürlich nicht der Praxis, da sich die sonstigen im Sprengstoff enthaltenen Elemente dann zu sauerstofffreien Verbindungen wie elementarem Kohlenstoff, Kohlenwasserstoffe, N_2, NH_3, HCN, H_2 usw. umsetzen müßten, was die Analysen der Sprengschwaden widerlegen. Die Markierung der maximal oxidierbaren Al-Menge verdeutlicht lediglich, daß eine angenommene Reaktion zwischen Al und dem umgebenden Wasser keinen Einfluß auf den Spitzendruck hat. Sowohl unterstöchiometrische Al-Gehalte von 15% Al als auch weit überstöchiometrische Al-

Gehalte von 40% Al ergeben gleiche Werte für die Spitzendrucke. Bei 0 % Aluminiumgehalt ist als Referenzsprengstoff TNT aufgetragen. Die Spitzendruckwerte für TNT liegen in der Größenordnung der kunststoffgebundenen GHX-Ladungen. Warum die TNT-Spitzendrucke der 1 kg-Ladungen tiefer als erwartet lagen kann bisher nicht erklärt werden.

Die engen Streubereiche für die jeweils vier gleichen Ladungen je Ladungsmasse (siehe Fehlerbalken im Diagramm) belegen den repräsentativen Charakter der dargestellten Mittelwerte.

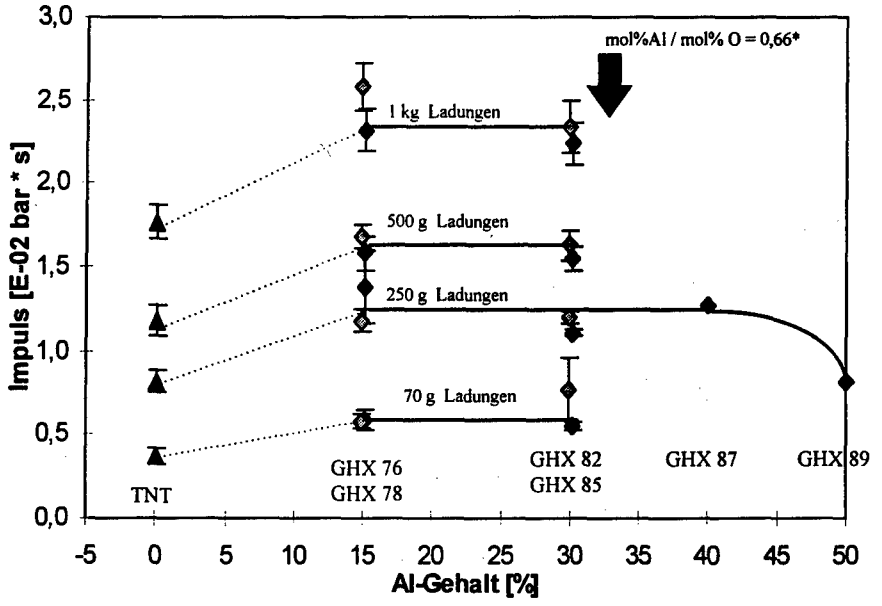

*Vom im Sprengstoff enthaltenen Sauerstoff maximal oxidierbare Al-Menge

Diagramm 2: Impuls in Abhängigkeit vom Al-Gehalt

Diagramm 2 zeigt die Abhängigkeit der Impulswerte vom Aluminiumgehalt auf. Wie der Spitzendruck ist auch der Impuls abhängig vom Ladungsgewicht; höhere Ladungsmasse bedingt größeren Impuls. Auch der Einfluß des Aluminiumgehalts auf den Impuls ist ähnlich wie beim Spitzendruck. Für Aluminiumgehalte im Bereich von 15 - 40 % ändert sich interessanterweise der Impuls kaum und sinkt erst bei weiterer Steigerung des Al-Anteils zwischen 40 % und 50 % deutlich ab (s. eingezeichneter Kurvenverlauf).

Für Ladungsgewichte von 70 g, 250 g und 500 g ist zwischen den AP-haltigen und AP-freien Ladungen kein signifikanter Unterschied erkennbar. Erst für Ladungsgewichte von 1 kg scheinen die Ammoniumperchloratladungen höhere Impulswerte aufzuweisen. Diese Tendenz müßte allerdings durch Messung von Ladungen mit Massen von 5 kg und mehr untermauert bzw. verdeutlicht werden.

Beim Aluminiumgehalt von 0 % ist TNT als Referenzsprengstoff aufgeführt

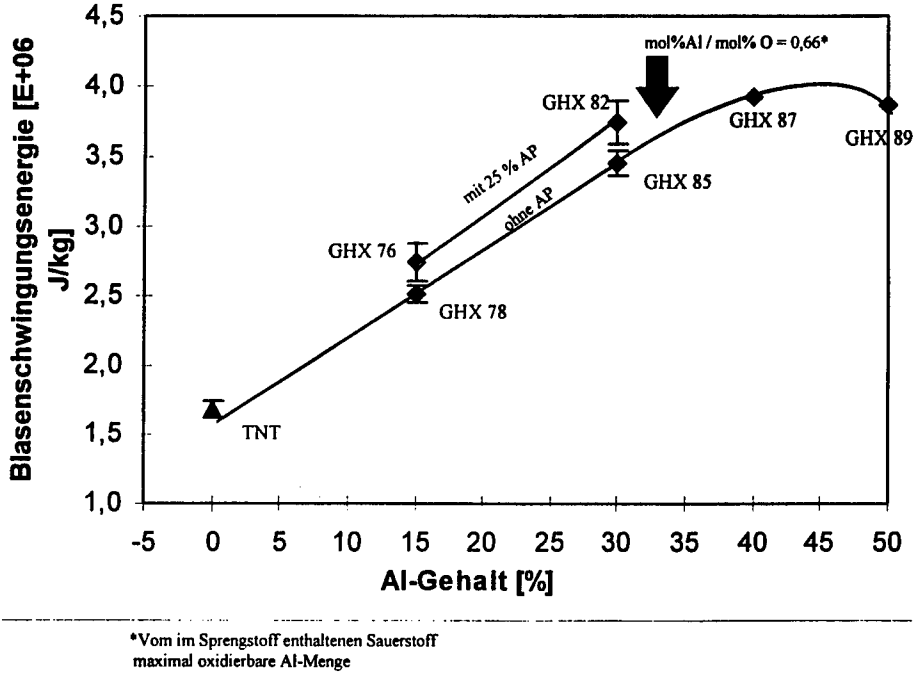

Diagramm 3: Blasenschwingungsenergie in Abhängigkeit vom Al-Gehalt

Diagramm 3 zeigt die Abhängigkeit der Blasenschwingungsenergie unterschiedlicher Formulierungen vom jeweiligen Al-Gehalt. Da die Blasenschwingungsenergie entsprechend ihrer Definition nach der von Cole (2) angegebenen Formel in Joule/kg ermittelt wird, besteht hier keine Abhängigkeit der Blasenschwingungsenergie von der Ladungsmasse.

Die Abhängigkeit der Blasenschwingungsenergie vom Al-Gehalt ist deutlich ausgeprägt. Erwartungsgemäß steigt mit zunehmendem Aluminiumgehalt die jeweils gemessene

Blasenschwingungsenergie an und erreicht bei 40 % ihr Maximum. Erst die weitere Erhöhung des Al-Gehalts auf 50 % führt zu einer geringfügigen Abnahme der Blasenschwingungsenergie.

Weiterhin führt die Verwendung von AP zu einer Steigerung der Blasenschwingungsenergie. Die Ladungen mit jeweils 25 % AP (GHX 76 / 82) liegen mit ihren Werten um 8 bis 9 % höher als ihre analogen Vertreter ohne AP. Interessant wäre in diesem Zusammenhang die Möglichkeit einer weiteren Steigerung der Blasenschwingungsenergie bei Aluminiumgehalten von 40 - 50 % durch Zusatz von Ammoniumperchlorat.

Die Streuung der Meßwerte bewegt sich in allen Fällen in engen Grenzen und bestätigt den repräsentativen Charakter der Mittelwerte.

Einfluß unterschiedlicher Al-Partikelgrößen und mantelförmiger Al-Anordnung auf die Unterwasserleistung

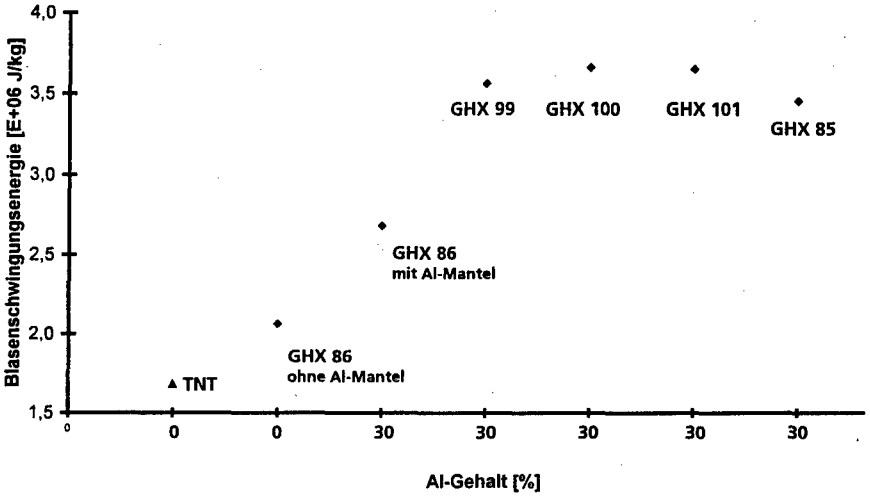

Diagramm 4: Blasenschwingungsenergie in Abhängigkeit vom Al-Gehalt

Diagramm 4 zeigt die Blasenschwingungsenergie in Abhängigkeit vom Al-Gehalt. Die Blasenschwingungsenergie der Al-freien Formulierung GHX 86 liegt im erwarteten Bereich, d.h. über den TNT-Ladungen. Durch Ummantelung dieser Ladung mit Al steigt die Blasenschwingungsenergie signifikant an. Der erreichte Wert bleibt allerdings

deutlich unterhalb von GHX 101, bei dem gleiche Al-Mengen homogen in den Sprengstoff eingearbeitet sind. Offensichtlich führt die mantelförmige Anordnung des Aluminiums nicht zu der erhofften Steigerung der Blasenschwingungsenergie gegenüber Ladungen mit homogen eingearbeitetem Al.
Die Ladungen GHX 99/100/101 mit drei unterschiedlich Al-Partikelgrößen zwischen 5 µm und 150 µm weisen vergleichbare Werte für ihre Blasenschwingungsenergie auf.

ZUSAMMENFASSUNG UND AUSBLICK

Die eingesetzten Komponenten zeigten bei den Sprengungen der untersuchten Formulierungen das folgende Umsetzungsverhalten und hatten auf die Unterwassersprengleistungen die folgenden Einflüsse:

- **Aluminium**

Bei der detonativen Umsetzung hat das Aluminium auf den im Sprengstoff vorhandenen Sauerstoff den ersten Anspruch und wird komplett umgesetzt solange genügend Sauerstoff vorhanden ist. Die anderen im Sprengstoff vorhandenen Elemente konkurrieren um den verbleibenden Restsauerstoff.

Die Messwerte für Spitzendruck und Impuls sind für weite Bereiche des Al-Gehalts konstant und sinken erst bei Extremformulierungen mit 50 % Al ab.

Die Blasenschwingungsenergie erreicht ihr Maximum bei Al-Gehalten von 40 - 50 %. Das bedeutet für die Praxis, daß bei den untersuchten Formulierungen der Al-Gehalt bis in den Bereich der maximalen Blasenschwingungsenergie gesteigert werden kann, ohne daß gleichzeitig Einbußen beim Spitzendruck und beim Impuls in Kauf genommen werden müssen.

Die mantelförmige Anordnung des Aluminiums führte nicht zu der gewünschten Steigerung der Blasenschwingungsenergie. Es wurden die Leistungswerte von Ladungen mit homogen eingebrachtem Al bei weitem nicht erreicht. Offensichtlich findet die erwartete zusätzlich energieliefernde Al-Wasser-Reaktion bei der untersuchten Ladungskonfiguration nicht statt.

Die drei untersuchten unterschiedlichen Al-Sorten zeigten keinen erkennbaren Zusammenhang zwischen Al-Partikelgröße und Leistungsausbeute. Das bedeutet für die Praxis, daß in den untersuchten Systemen Al-Partikel im Größenbereich zwischen 5 µm

und 150 µm eingesetzt werden können, ohne nachteilige Auswirkungen auf die Leistungsausbeute in Kauf nehmen zu müssen.

- **Ammoniumperchlorat**

Bei den untersuchten Ladungsmassen führte ein AP-Gehalt von 25% zu einer Steigerung der Blasenschwingungsenergie.

Beim Spitzendruck ergab sich durch das AP keine Veränderung im Vergleich zu den AP-freien Ladungen; beim Impuls dagegen, war ein Trend zu höheren Werten zu beobachten, was allerdings noch durch Sprengungen mit größeren Ladungsmassen bestätigt werden muß.

LITERATUR

(1) "Analysis of the Detonation Products of Insensitive High Explosives";
F. Volk; 25th International Annual Conference of ICT, Karlsruhe 1994

(2) Cole R.H. "Underwater Explosions"
Princeton University Press, Princeton, NJ, 1948

(3) Sirringhaus, Wild: "1. Teilbericht Unterwasserleistung der Sprengstoff-mischungen GHX 76, GHX 78, GHX 82 und GHX 85 des ICT-Berghausen"
BerichtsNr. 220/15309/95 (v. 01/12/95); BICT

(4) Sirringhaus, Wild: "Unterwassersprengleistung der Sprengstoff-mischungen GHX 86, GHX 87, GHX 89, GHX 91, GHX 99, GHX 100 und GHX 101 des ICT-Berghausen"
BerichtsNr. 220/16012/96 (v. 14/11/96); BICT

MODIFIED SYNTHESIS OF DIETHYLALUMINUM AZIDE AND THE CHARACTERIZATION THEREOF *

Zhou Keyan[1], Gao Zhenxian[1], Sun Yu[1]
Li changqing[2], Huang Yue[2], Xia Zhongjun[2]

ABSTRACT

The synthesis method of diethylaluminum azide (DEAA) is modified by optimizing the reactant ratio, reaction time, temperature and other conditions. The yield of DEAA is increased from 54% to 75% compared with that reported in the references abroad. The final product and its molecular structure are verified by means of elemental analysis, IR spectra, ^1H NMR and other methods. The results indicate that DEAA is a trimer with stable 6-membered ring structure under ordinary conditions. This structure is consistent with the behavior of DEAA in distillation at high temperature up to 420 ℃ under 400Pa without any decomposition. It can be concluded, therefore, DEAA is a compound with acceptable thermal stability promising to be used as a self-ignition agent in some special application. While heating up to 460 ~ 570 ℃ in vacuum, DEAA rapidly decomposes without explosion, releasing low-molecular hydrocarbons and forming microcrystallite identified to be aluminum nitride (AlN) with particle size in the range of nanometer. This property shows another prosperity of DEAA as a nice precursor for preparation of ceramic materials with high purity.

KEYWORDS diethylaluminum azide (DEAA) pyrophoric agent aluminum nitride

1 INTRODUCTION

As a new family of energetic materials, organic azide compounds are widely researched and developed in recent two decades, but organometallic azides are rather less noticed in this technology field. After the synthesis of diethylaluminum azide (DEAA) reported by Karl[1] in 1961 and Prince[2] in1966, only a few references related to this compound.

The molecular formula of $(CH_3CH_2)_2AlN_3$ and the corresponding structure would give DEAA the properties like both triethylaluminum (TEA) and azides, i.e. self-ignition as a pyrophoric agent in the presence of any kind of oxidizers and self-explosion because of the oxidation reaction. Due to its

* This work is supported by the Science Foundation of China Academy of Engineering Physics (CAEP).

1 College of Chemical Engineering, Dalian University of Technology, Dalian 116012, China

2 Institute of Chemical Materials, CAEP, P.O.Box 513-100 Chengdu, China

low melting point (-130 ℃), DEAA would be a promising pyrophoric agent with acceptable safety used for propellants and some oil-taking device in deep well.

It is reported that DEAA exists as a trimer in the liquid state with a 6-membered Al-N plane cyclic structure with D_{3h} symmetry, while the structure in gas state is not known so far[3-5]. The properties of DEAA had not reported in detail and the known data are not all agreed with each other. Mole T. et al [6] took it as a non-explosive but high-sensitive substance to air and moisture.

In order to clear these confusions, we have made a comprehensive study of the synthesis modification and characterization of DEAA, including its structure and properties.

2 SYNTHESIS OF DEAA

There are three synthesis methods reported so far as below:

The first method is a two-phase reaction of diethylaluminum chloride (Et_2AlCl, abbr. as DEAC) with sodium azide (NaN_3) in benzene. Karl[1] reported if the reaction was carried out at the temperature of benzene reflux and then distilled under reduced pressure, DEAA would be obtained as a solid with yield of 32%. Prince[2] made the synthesis at ambient temperature. After filtering the reaction mixture, a transparent liquid remained. Distilled out the solvent and filtered again, a viscous liquid DEAA was obtained with yield of 54%.

The second way[4] is based on the reaction of TEA with chlorine azide (ClN_3) in benzene as solvent at 0 ℃. After distillation of the reacted mixture under conditions of 63 ℃ and 10^{-1} Pa, a colorless and hygroscopic liquid is obtained with yield of 50%. The melting point (-130 ℃) of the purified product agrees with the reported data of DEAA.

The third method[7] is based on TEA and HN_3 as starting materials and the reaction undergo in chloroform under -78 ℃, after distillation out of the solvent, the reaction mixture is directly put into the further reaction with α,β-unsaturated carboxylic compound to form DEAA.

Concerned about the toxicity, operation unsafety and other factors in the former two methods, we took the first as the principle route to synthesize DEAA and improve the reaction conditions so that to increase the yield and quality. All syntheses were operated in the cleaned and dried Schlenk reaction system under the protection of purified nitrogen. The influence of different factors on the reaction in benzene were examined as below, including reaction time, temperature, reactant ratio and solvent.

2.1 Reaction time

When the starting material ratio is NaN_3 : DEAC = 1.5 : 1 （mole） and the reaction undergoes at ambient temperature, the yield of DEAA is close to its maximum in 24hrs and no further apparent benefit after then as the data in Table 1. The IR spectrum of the purified product is shown as Fig. 1..

Table 1. Influence of reaction time on DEAA yield

reaction time / h	yield / %	DEAC residue / %（mole）
2	40.6	6.90
12	47.5	4.16
18	50.6	2.46
24	52.6	0.05
48	53.6	0.11

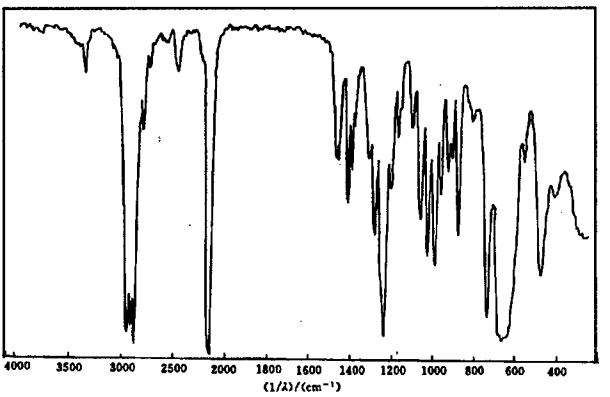

Fig. 1 IR spectrum of DEAA

2.2 Reactant ratio

It can be seen from Table 2, when the mole ratio of NaN_3 to DEAC is 1.05:1, the yield of DEAA can

Table 2. Influence of reactant ratio on DEAA yield

NaN_3 : DEAC	yield / %	DEAC residue / %（mole）
1.05 : 1	74.6	0.93
1.20 : 1	70.2	0.24
1.30 : 1	71.0	0.34
1.40 : 1	70.8	0.05
1.50 : 1	52.6	0.05

be enhanced up to 75% at ambient reaction temperature in 24 hours, 21% higher than that of ref. [2].

2.3 Reaction temperature

It is reported that one of the reactant DEAC exists usually as a dimer which hinders itself to smoothly react with other compounds under ordinary conditions. It can be suggested that some suitable solvent or

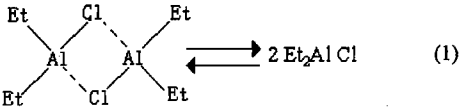

(1)

higher temperature would promote the dissociation of the dimer into monomers and, consequently, speed up the electrophilic substitution of −Cl by $-N_3$. Our experiments indicate that in the same reactant ratio the reaction is faster in some extent under the condition of reacting mixture reflux, but the yield of DEAA is hardly to increase after 12 hrs and can not reach the maximum as that at ambient temperature. The reaction time, h, temperature, t, and yield, y, are listed in Table 3.

Table 3. Influence of reaction temperature on DEAA yield

t \ h / y	2	4	6	8	12	24	36
20 ℃					65.0	74.6	75.0
30 ℃		63.3		65.4			
80 ℃	66.7		69.1		71.3	73.7	

2.4 Effect of solvent

Different solvents such as n-hexane, cyclohexane, benzene, toluene, dimethyl benzene, trimethyl benzene and tetrahydrofuran （ THF ） are, respectively, used as the reaction medium at 30 ℃ to examine their effect on the yield of DEAA. The experimental results verify the existence of the dissociation equilibrium （ 1 ） and it seems to be the key factor to control the azidation of DEAC.

In n- or cyclohexane, the DEAC dimer does not dissociate and the Cl atoms in the bridge state are difficult to react with solid NaN_3. But if the electron-rich THF of the same mole as DEAC is added into the hexane, an apparent exothermic effect appears and the substitution reaction will go on. The reacted mixture is filtered and distilled after 4 hrs, a colorless liquid is obtained with 71% yield and identified as an adduct of DEAA • THF as reported by Prince[2].

If THF is used as the reaction medium, the yield of DEAA • THF is increased up to 87.39% in 4 hrs,. It

can be suggested from these results that the electron-rich THF promote the dissociation of DEAC dimer into the corresponding monomer adduct which is favorable for the electrophilic displacement of -Cl by $-N_3$ as follows:

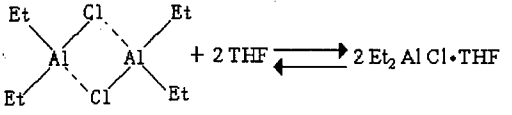

(2)

The characteristic strong absorption at $1230cm^{-1}$ and $2145cm^{-1}$ for symmetric and asymmetric N_3 stretching, at $860cm^{-1}$ and $1060cm^{-1}$ for symmetric and asymmetric C-O-C stretching, respectively, in the IR spectrum of Fig. 2 conform to the structure of DEAA•THF.

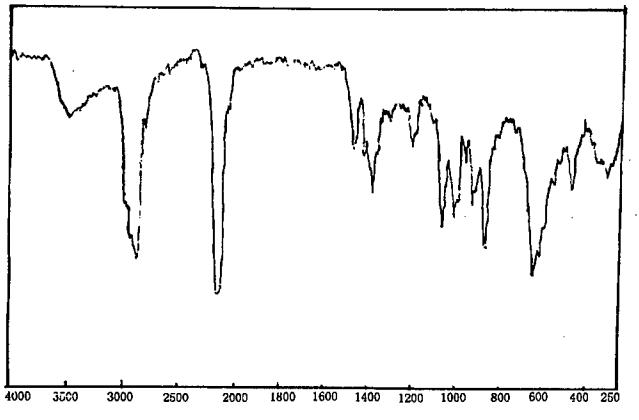

Fig. 2 IR spectrum of DEAA•THF

Since it has not found a proper method so far to separate DEAA from its complex with THF, benzene and some of its derivatives are still the best solvents for DEAA synthesis. Benzene presents some ability of electronation because of its conjugated π-bond, it, therefore, can couple in some extent with the electron-lack Al in the DEAC dimer, promoting the dissociation of the Al-Cl bond and, consequently, the formation of DEAA. With the increase of electron-rich methyl group in the ring of toluene, methyl-, dimethyl- and trimethyl benzene, their electron donor function are sequentially increased. When all the reactions are carried out with the same reactant ratio at 30 ℃ for 4 hrs, the yield of DEAA also increase correspondingly in these mediums as the experimental data presented in Table 4.

Table 4. Effect of reaction solvent on DEAA yield

solvent	n-C_6H_1	n-$C_6H_{14}C_6H_6$/THF	C_6H_6	CH_3-C_6H_6	$(CH_3)_2$-C_6H	$(CH_3)_3$-C_6H_6	THF
yield / %	0	45.3*	63.3	68.0	69.2	71.2	55.8*

* Conversed from the yield of DEAA•THF

3. DISTILLATION OF DEAA

Mueller[4] and Boyd[5] determined that the boiling point of DEAA was 63 ℃ at 0.125Pa and 65 ~ 69 ℃ at 0.375Pa, respectively. This operation is difficult to do in ordinary laboratories. We have succeeded in distillation of DEAA at higher temperature and pressure without using the expensive oil-diffusion pump as the data listed in Table 5.

Table 5 Boiling range (℃) of DEAA vs its vapor pressure (Pa)

Pa	0.5	2	3	3.5	213.5	266.6	333.3	799.9
℃	74 ~ 76	76 ~ 78	76 ~ 79	76 ~ 80	100 ~ 102	104 ~ 108	108 ~ 112	122 ~ 124

Plotting the data in Fig. 3, two linear lines with a large difference of slope are obtained, which implies that there is a state conversion in the vapor system. The point of intersection is close to 90 ℃. When lower than this temperature and pressure in stage (I), the distillate should be DEAA trimer; when the temperature raises above 100 ℃ in stage (II), the trimer would dissociate into dimer and monomers. In fact, this phenomenon is found to be general in the alkyl-aluminum compounds[8,9,10].

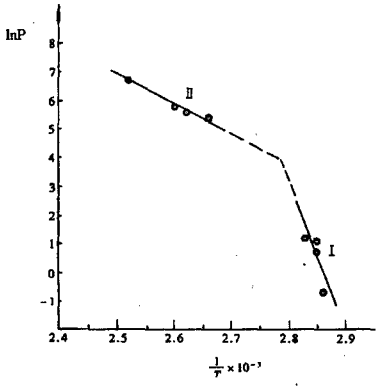

Fig.3 Boiling range of DEAA vs vapor pressure

4. DEAA STRUCTURE

By using the cryoscopic method Mueller[11] determined the molecular weight of DEAA as 379 with a very small deviation from the its trimer weight 381. He suggested, therefore, the structure of the trimer was a plane with D_3h symmetry. The structure of $Me_2AlN(CH_2)_2$ [12], $Me_2AlNHMe$[13] and Me_2AlN_3[6] reported later show that the 6-membered $(Al-N)_3$ ring skeleton seem to be a general configuration for the nitrogen-containing organometallic derivatives.

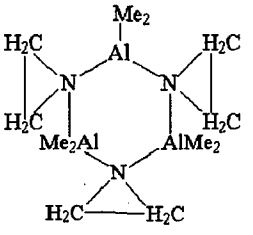

$Me_2AlN(CH_2)_2$

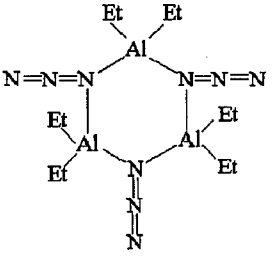

DEAA

Referring to the IR spectra data of 6-membered cyclic Et_2GaN_3[10] and $MeAlN_3$, the data from analysis of Fig. 1 also indicate the structure of DEAA under ordinary conditions is $(Al-N)_3$ ring.

Table 6. Analysis of data from Fig. 1

wavenumber/cm^{-1}	3350	2930	2980	2850	2450	2145	
intensity*	W	UI	UI	UI	W	UI	
belong to	2145+1230	$\nu_{as}(CH_2)$ $\nu_s(CH_3)$	$\nu_{as}(CH_2)$	$\nu_s(CH_3)$	1230 × 2	$\nu_{as}(N_3)$	
wavenumber/cm^{-1}	1460	1405	1230	1020	980	920	875
intensity*	MI	MI	UI	MI	MI	W	MI
belong to	$\delta_{as}(CH_3)$	$\delta_s(CH_2)$	$\nu_s(N_3)$	P(C-C)	ν(C-C)	$\delta_s(CH_3)$	$\delta_s(N_3)$
wavenumber/cm^{-1}	650	542	462	400	300	290	
intensity*	UI	W	W	W	W	W	
belong to	$\delta_{as}(Al-C_2)$	$\nu_s(Al-C_2)$	$\delta_r(N_3)$	$\delta(Al-C_2)$	Al-N	$\nu_{as}(N_3)$	δ(ring)

* W, MI and UI are the abbreviations of intensity, middle and ultra intensity, respectivly.

From the ^1H NMR spectrum of DEAA (Fig. 4.) it can be seen that there are only two proton chemical shifts, i.e. the 4-fold peak of δ = 0.078ppm for 2H and 3-fold peak of δ = 0.986ppm for 3H. This means only one kind of alkyl group, $-C_2CH_3$,existing in DEAA molecule.

Summing up the experimental results of distillation, IR and ^1H NMR together, it can be further confirmed that DEAA is undoubted in a trimer structure at ordinary conditions.

5. THERMAL STABILITY

$Al-N_3$ in DEAA is combined with covalent bond, the electronation effect of two methyl groups on Al atom would make the molecule rather unstable, but the distillation experiments show DEAA can bear heating at 190 ℃ under 266 ~ 400Pa for a long time without explosion; when the temperature raises

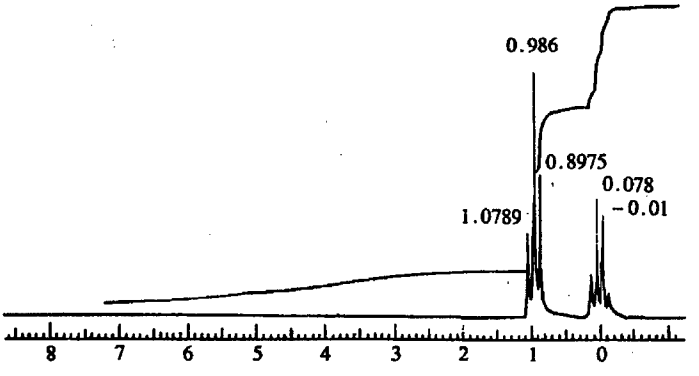

Fig. 5 ^{1}H NMR Spectrum of DEAA

to 420 ℃, an intensive reflux occurs but no decomposition until the temperature up to 460 ~ 570 ℃. This thermal stability of DEAA must related to its trimer structure, because in its 6-membered ring structure the isolated electron pair on each N_a in the structure unit Al-N_a=N_b=N_C of one DEAA would form a coordinate bond with the Al atom in another molecule. This coordination meets both the electron octet requirement on the outer orbit of Al atom and decrease of the electron density on the N atoms in -N_3, the later is the principle factor to the high stability of DEAA.

When heated to 460 ~ 570 ℃, DEAA will rapidly decompose, releasing nitrogen and low molecule hydrocarbons like ethylene and ethane etc.; by means of IR and scanning electronmicroscope the remained solid is identified to be aluminum nitride （AlN） with particle size in the range of nanometer. Besides nitrogen and low molecule hydrocarbons in the released gas are easy to pump out, the low decomposition temperature is not possible to result in carbonized residue. It can be predicted, therefore, DEAA could be used as a precursor to prepare high quality AlN ceramic materials.

Compared with DEAA, the DEAA•THF is much unstable, because the electron-lack orbit on Al atom in DEAA is coupled with the isolate electron pair on the oxygen atom in THF molecule to form an adduct monomer, which is not favorable for the dispersion of the electron density on -N_3. When stimulated by sunlight, heat, impact or other impulse, DEAA•THF would respond with violent decomposition even explosion.

6. CONCLUSION

By using the improved synthesis method and convenient distillation procedure herein, diethylaluminum azide （DEAA） is prepared with a higher yield and purity. Addition to IR and ^{1}H NMR analysis

results, the behavior of DEAA in distillation at high temperature and pressure convincibly verify that DEAA exist as a 6-membered cyclic trimer under ordinary conditions. The experimental results indicate DEAA is a promising pyrophoric agent for some special purposes and its thermal stability is acceptable for storage and transportation with low pressure nitrogen protection. Since it can be heated up to 570 ℃ in vacuum without explosion, DEAA is also a nice candidate for making high purity AlN ceramic material by means of chemical vapor deposition （CVD）.

ACKNOWLEDGEMENT

The authors thank Ms. Ye Yaping, the doctoral student, and Ms. Sun Zhumei for their valuable work in the synthesis and characterization of DEAA.

REFERENCES

1 Karl W, et al. U.S. Dept. Con., Office Tech. Serv., AD 274 499 （1961）.

2 Prince M. I, et al. J. Organometallic Chem., 584, vol. 5, No. 6 （1966）.

3 Dehnicke K, et al. J. Organometallic Chem. 298, vol. 5, No. 3 （1966）.

4 Mueller J, et al.. Z. Anorg. Allg. Chem. 261, Vol.384, No.5-6 （1996）.

5 Boyd D.C, et al. Chem. Mater., 119, vol. 1, No. 1 （1989）.

6 Mole T, et al. Organoaluminum Compounds, 41 （1972） Elsevier, New York

7 Bong Young Chung, et al. Bull. Karean. Chem. Soc., 269, vol. 9, No.4 （1998）.

8 Gosling K, et al. Chem. Sco. Am. 1738 （1969）.

9 Gallais F, et al. Compt. Rent. 785, vol. 259 （1964）.

10 Mole T, et al. Organoaluminum Compounds, 25 （1972） Elsevier, New York

11 Mueller J, et al. J. Organometallic Chem. 37, vol. 2 （1968）.

12 Atwood J.L, et al. J. Am. Chem. Soc. 285, vol. 92 （1972）.

13 Gosling k, ET AL. Chem. Commun. 1617 （1970）.

SYNTHESIS AND INITIATION SPOT-SIZE TESTING OF SONOCHEMICALLY-AMINATED TATB

K.-Y. LEE, J.E. KENNEDY AND J. R. STINE*

MS C920, HE Science & Technology
Los Alamos National Laboratory
Los Alamos, New Mexico, 87545, USA

ABSTRACT

The synthesis of 1,3,5-triamino-2,4,6-trinitrobenzene (TATB) from 1,3,5-trichloro-2,4,6-trinitrobenzene (TCTNB) by amination with ammonium hydroxide under the influence of ultrasonic irradiation was studied for the ease of preparation and for a finer-grain materials. Results from powder characterization indicated that this sonochemically-aminated TATB (SA-TATB) have particle size comparable to that of ultrafine TATB (UF-TATB), an IHE booster material. SEM micrographs of SA-TATB powders showed that the surface is extremely porous.

To evaluate the shock initiation, samples of SA-TATB were pressed to high density and subjected to initiation spot-size testings, and the results were compared with those for UF-TATB. The test involved initiation of a pressed TATB pellet by the impact of an explosively driven steel flyer plate. The flyer plate diameter was varied to determine the initiation spot-size sensitivity of the TATB acceptor. Depth of the dent on a copper witness plate was measured as an indication of the output of the test material. The SA-TATBs produced slightly deeper dents than the UF-TATB, suggesting a higher initiation sensitivity.

1. *INTRODUCTION*

The compound 1,3,5-triamino-2,4,6-trinitrobenzene (TATB) is an explosive with a high melting point and thermal stability that has been applied in situations where insensitivity to impact hazards is important. In the past, production grade TATB was prepared by amination of 1,3,5-trichloride-2,4,6-trinitrobenzene (TCTNB) in toluene with anhydrous ammonia gas in a pressurized reactor.[1] TATB thus produced is suitable for most applications having particle size ranging from 30 to 60 micrometers. However, for applications requiring higher sensitivity to shock initiation, fine-grain TATB is desirable. TATB with an arithmetic median of 6 micrometers, produced by 9Lawrence Livermore National Laboratory (LLNL) and Pantex, has been qualified as an insensitive high explosive (IHE) according to U.S. Department of Energy (DOE) standards.[2] Unfortunately, the processes involved in the production of such TATB (UF-TATB) are complicated and time consuming.[3]

Ultrasound is a sound with frequencies beyond human hearing, i.e. above 20 kHz. When ultrasound is applied to liquids of either a homogeneous or heterogeneous reaction system, acoustic cavitation results. Rate enhancement of chemical reactions accompanied by higher production yield has been demonstrated under the influence of ultrasonic irradiation.[4] Ultrasound is also known to generate extremely fine emulsions from mixtures of immiscible liquids. Such fine emulsions provide enormous interfacial contact areas between immiscible liquids and thus the potential for greater

reaction between the two phases. Recently, the synthesis of nanostructured catalysts with selective hydrogenation reactivity by ultrasonication was reported by Suslick and his coworkers.[5]

In an attempt to develop a simple method to produce TATB that will have particle size and shock initiation sensitivity comparable to UF-TATB, we have studied the synthesis of TATB by amination of TCTNB in toluene with ammonium hydroxide solution under the influence of ultrasonic waves. In this article, the synthesis of sonochemically-aminated TATB (SA-TATB) will be described. Results from the powder characterization of both UF-TATB and SA TATB powders will be reported. Results from initiation spot-size testings of TATB samples will also be presented.

2. *EXPERIMENTAL AND RESULTS*

2.1 Synthesis

2.1.1 Preparation of FP-TATB (KYL-I-58s)

An ultrasonic liquid processor (Misonix XL2020) equipped with a 0.5-inch probe, operating at 20 kHz with a variable amplitude power-supply output was used for the preparation of SP-TATB. The power output was set at 60% of maximum 550 watts.

In a 300 ml beaker (Pyrex No. 1040) containing ammonium hydroxide solution was added a solution of TCTNB in toluene. The amination reaction began by immersing the sonicator horn into the two-phase mixture followed by turning on the processor power. To avoid potential ammonia gas escaping to the air, the beaker was covered with a piece of aluminum foil. After a 40-minute sonication time, the resulting emulsion was left at ambient temperature overnight. The resultant FP-TATB was collected by filtration, followed by washing the solids sequentially with hot water, toluene and acetone. The lemon-colored solids thus obtained were then dried at 98°C in a vacuum oven overnight. The amination reaction which produces TATB is shown in Reaction 1.

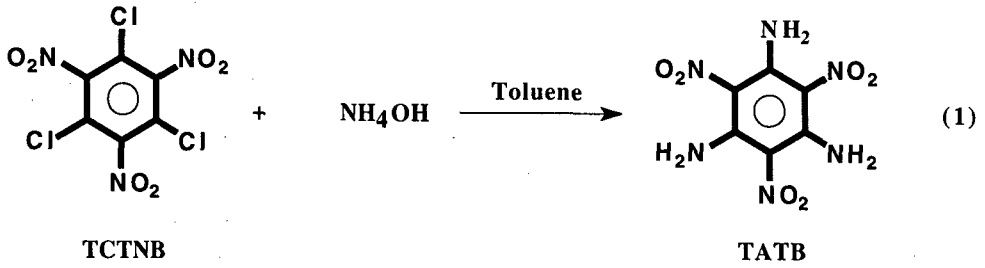

TCTNB TATB (1)

2.1.2 Preparation of FP6-TATB (KYL-I-89H)

The amination reaction which produced FP6-TATB took place in an air sealed sonicator reactor, instead of in an open beaker. The reaction time and temperature were 30 minutes and 1°C respectively.

2.2 Powder Characterization

2.2.1 Particle size analysis of TATB samples

Particle sizing was done on a Coulter LS 230 particle size analyzer with a Small Volume Module which measures size distributions of particles from 0.04 to 2000 micrometers. The Module is an integrated system which consists mainly a sample vessel and a centrifugal pump. To analyze the particle sizes, suspension of TATB sample in water is placed into the suspension fluid (water) in the sample vessel. The suspension fluid and dispersed particles flow through the sample cells and hoses in a closed-loop system. The sample cells stand contain a diffraction sample cell and a PIDS sample cell. Light passes through the sample cell during measurement. TATB refractive index of 2.1 was used for size calculation throughout the analysis studies. The data is displayed in volume percent. The particle size distribution of FP-, FP6-, and UF-TATBs are shown in Fig. 1. For comparison, the particle size distribution of the production grade TATB (PG-TATB) is also included. The arithmetic median diameters of the four powders are compared in Table 1. It can been seen that the median particle diameters of both FP- and FP6-TATBs are comparable to that of UF-TATB, inspite of the significant difference in the preparation process. As expected, the particle size of TATB produced by the traditional method is much larger than any of the other three.

2.2.2 SEM study of TATB samples

The surface sturcture of TATB powders was studied by scanning electron microscopy (SEM), using a Joel 6300 FXV. Samples were coated for examination and was carried out at room temperature. Figure 2 and 3 are SEM micrographs of FP-and UF-TATB respectively, taken at 2.0KV. SEM micrograph of FP6-TATB is shown in Figure 4. It can be seen that the particles of UF-TATB powders are smaller as compared to that of the FP-TATB. The edges of the UF-TATB crystals are noticeably round, indicating that the particles have undergone a severe mechanical treatment

Samples	Median Particle Diameter (μm)
FP-TATB (KYL-I-58s)	14
UF-TATB (91190-135M-003)	6
FP6-TATB (KYL-I-89H)	6
PG-TATB (hercules)	51

Table. 1. Particle Diameters of TATB Powders

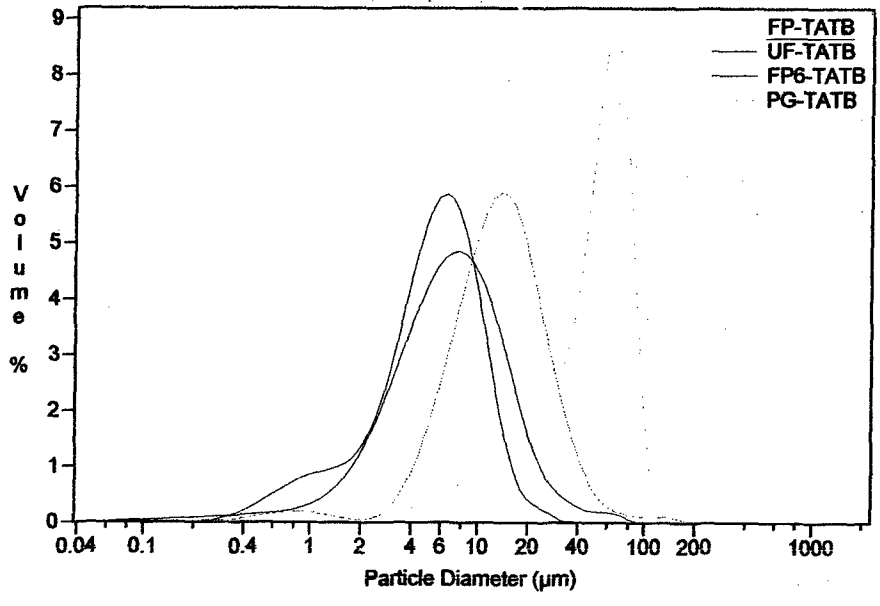

Fig. 1. Particle Size Distribution of TATB Samples

Fig. 2. SEM micrograph of FP-TATB, obtained on a Joel 6300 FXV

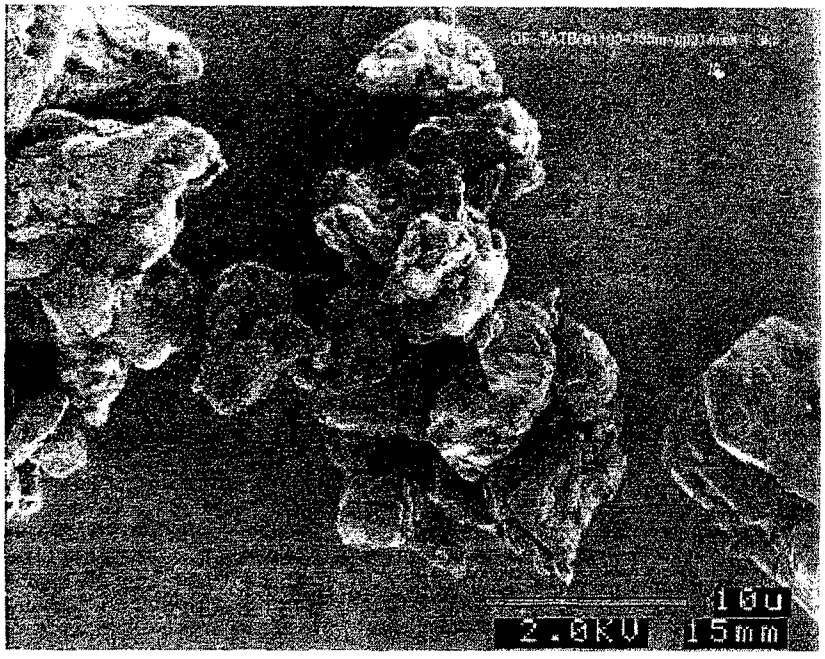

Fig. 3. SEM micrograph of UF-TATB, obtained on a Joel 6300 FXV

Flyer Diam. (mm)	Dent Depth (mm)			
	UF-TATB (91190-135m-003)	FP-TATB (KYL-I-58s)	PG-TATB (Hercules)	FP6-TATB (KYL-I-69H)
3.0	0.56	0.63	—	0.65
4.0	0.66	0.83	0.41	0.91

Table 2. Initiation Spot-Size Test Data on TATB Samples

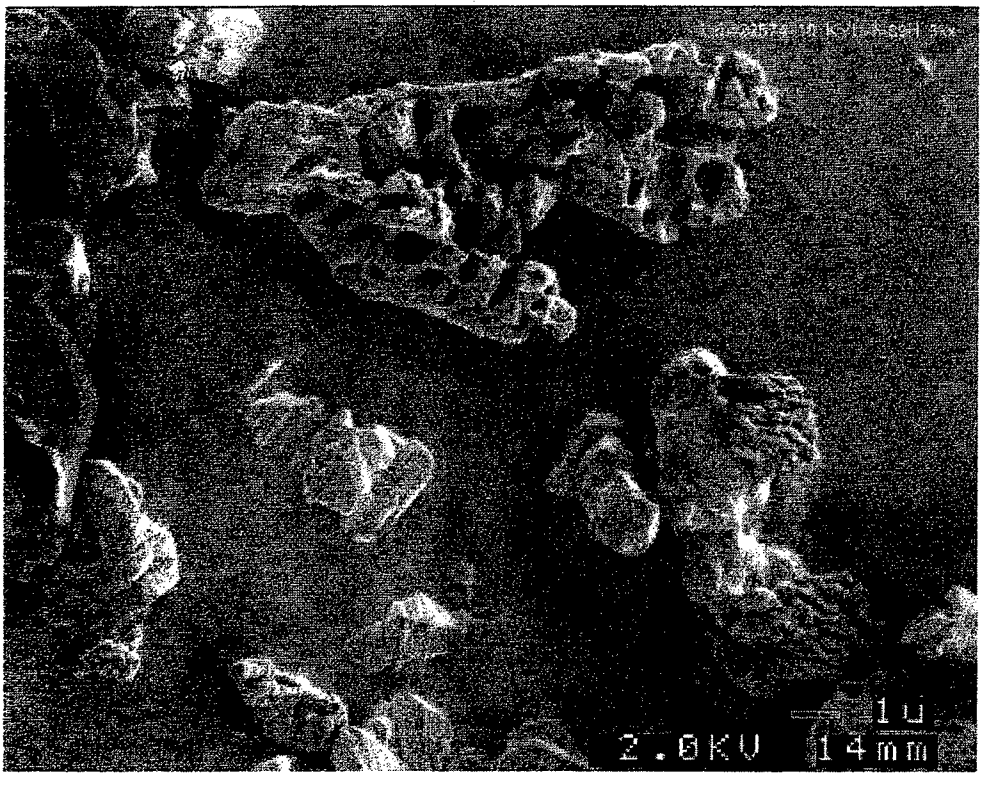

Fig. 4. SEM micrograph of FP6-TATB, obtained on a Joel 6300 FXV

(milling). Note the unusual "Indian ruins" formation on the surface of both the FP-and FP6-TATB crystals. In addition to the extensive porosity on the surface, the particles appear to be mechanically fragil.

2.3 Impact initiation testing of fine-grain TATBs with variable flyer plate diameters

Testing of the spot-size sensitivity of TATB was done, based on information from W. Hemsing that this style of testing reveals differences in shock sensitivity of different explosive materials.[6] The intent is to rank the detonation spreading behaviors of various fine TATBs. The test fixture is sketched in Figure 5. The parameters for the test are outlined as following:

1. Donor Explosive
   - 1.63 g/cc PETN
   - 6.35mm x 3mm
   - initiated by electrical slapper
2. Flyer Plate
   - 0.127-mm-1.0mm stainless steel
   - Diameter -- 3.0 -4.0 mm, controlled by cutter's plate
   - Velocity -- 2.5 km/s
   - Flight distance -- 1.5mm
3. TATB Acceptor Samples
   - Size -- 12.7mm-dia x 4 mm
   - density (g/cc) -- 1.808 $\pm$ 0.002

The TATB acceptor sample configuration was short and large in diameter so that impact from smaller flyer plate would not be able to spread to consume the entire TATB pellets. There was a large-diameter relief hole in the cutter plate so that shock from the detonating PETN could not pass through that plate into the TATB acceptor pellet, arrive before the flyer plate impact occurred, and cause desensitization of the acceptor by dynamic precompression. This relief step was 0.75mm in the axial direction. The sample pellet was in contact with a copper witness plate, and the depth and the diameter of the dent in the plate were used as a measure of the detonation spreading responses of test samples. Testing was done at room temperature,

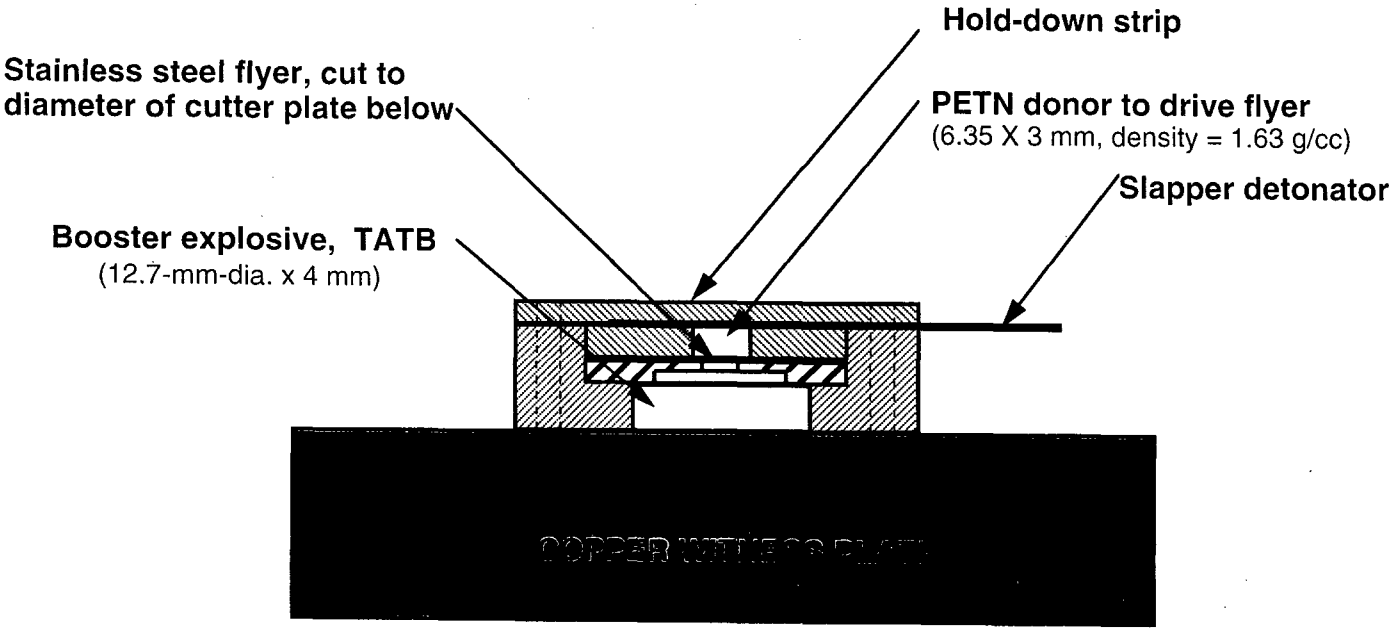

Fig. 5. Setup of Spot Size Test for Detonation Spreading

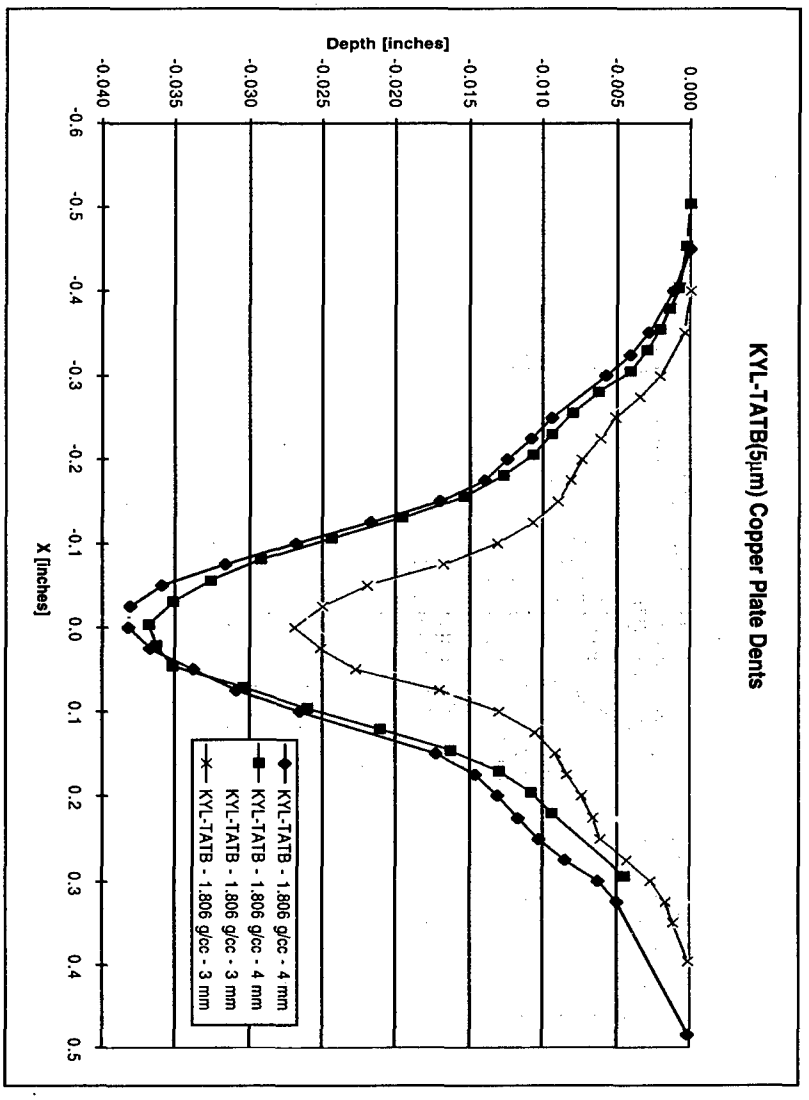

Fig. 6. Detonation spreading of FP6-TATB samples, compacted by both 3 and 4 mm flyer diameters

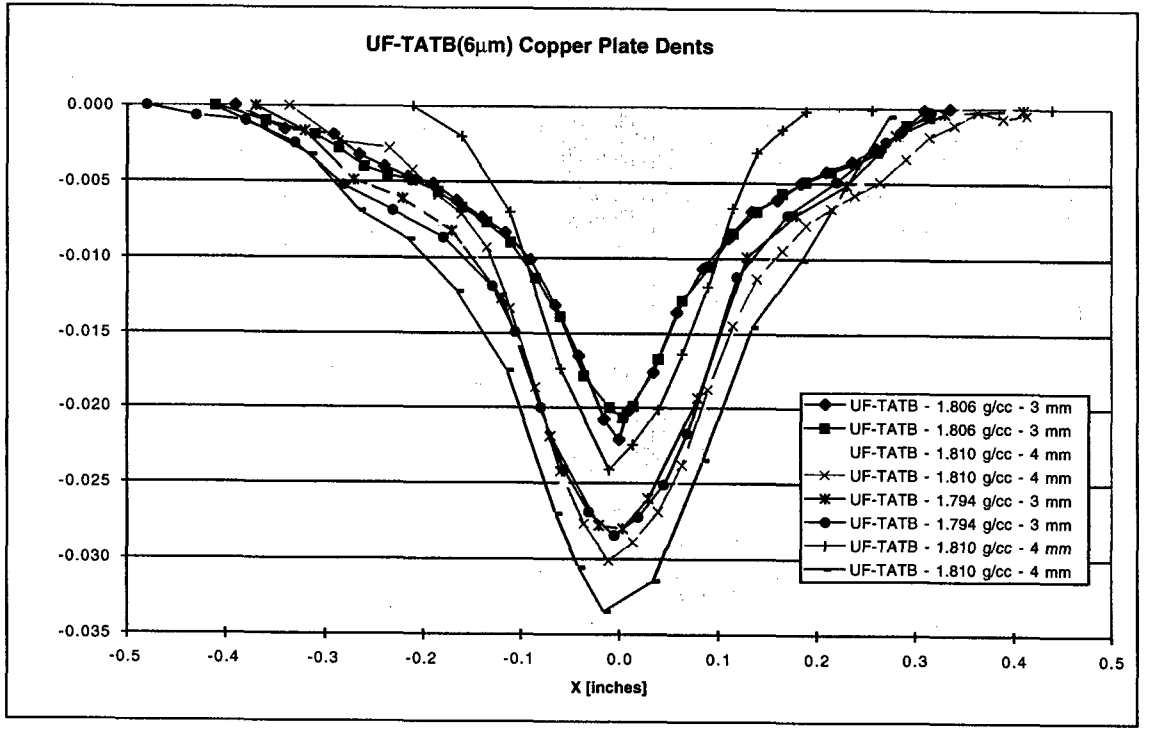

Fig. 7. Detonation spreading of UF-TATB samples, compacted by both 3 and 4 mm flyer diameters

approximately 22°C. Results of tests conducted on two batches of ultrasonically-aminiated TATBs, one lot of UF-TATB (91190-135M-003) and one lot of PG-TATB are shown in Table 2. It is interesting to observe that the dents of both SA-TATB samples are deeper than that of UF-TATB, either compacted by 3mm or 4mm flyer diameter, even though the particle sizes of the three samples are similar. As expected, the dents of TATB powders compacted by 4mm are deeper than that by 3mm flyer diameter. However, the dent of PG-TATB is significantly smaller than any of the other three, even compacted by 4mm flyer diameter. The detonation spreading of FP6-TATB samples, compacted by both 3 and 4mm flyer diameters is illustrated in Figure 6, showing the dent depth as well as the diameters of the dent. The sample also shows a good symmetry in blast effects on the copper witness plate. The detonation spreading of UF-TATB samples is shown in Figure 7. It appears that there is considerable variation in detonation spreading shown by the LLNL booster material, impacted by either 3 or 4mm flyer plate diameter. The variation may due to the material or density variation within the pellets.

CONCLUSIONS

We have demonstrated that fine-particle TATB can be made by a simple, one-step amination from TCTNB and ammonium hydroxide solution under the influence of ultrasonic irradiation (ultrasonication). This sonochemically-aminated TATB (SA-TATB) has particle size comparable to UF-TATB, an IHE booster material. Results from powder characterization on TATB samples illustrated that the arithmetic median particle diameters of FP-and FP6-TATB are 13 and 6 micrometers respectively, while that of UF-TATB is 5 micrometers. Results from initiation spot-size testing indicated that both SA-TATBs are slightly more sensitive to shock initiation than UF-TATB, as measured by the dent depth of the witness plate. Hence, this simpler process

can be considered to produce shock sensitive TATB for booster applications, in lieu of the more extended process used to produce UF-TATB.

ACKNOWLEDGMENTS

Work was performed under the auspices of the Department of Energy by the Los Alamos National Laboratory under Contract Number W-7405-ENG-36. Special thanks to Joe Romero for his excellent SEM micrographs of TATB samples.

REFERENCES

1. B. M. Dobratz, The Insensitive High Explosive Triaminotrinitrobenzene (TATB): Development and Characterization—1888 to 1994, Los Alamos National Laboratory, LA-13014-H, August 1995.
2. R. Lee, et al.,The Relationship Between the Shock Sensitivity and the Solid Pore Sizes of TATB Powders Pressed to Various Densities, Proc., Eighth Symposium (Intl.) on Detonation, pp. 3-14, NSWC MP 86-194, Albuquerque, NM, July 1985.
3. A. G. Osborn and T. L. Stallings, Ultrafine TATB - Lot No. 91190-135M-003, PXET-92-03, Mason & Hanger - Silas Mason Co., Inc., Pantex Plant, Amarillo, TX, August, 1992.
4. K.-Y. Lee, Study of Chemical Reactions Under the Influence of Ultrasound, Ultrasonics International 93 Conference Proceedings, pp. 743-746, Vienna, 1993.
5. K. S. Suslick, et al., Sonochemical Synthesis of Nanostructured Catalysts, Mater. Sci. Eng., A204 (1-2), pp. 186-92, 1995.
6. J. E. Kennedy et al., Initiation spot-size testing of EA-TATB, ADPA, Energetic Materials Symposium, #680, p. 227-231, Phoenix, AZ., Sept. 1995.

Fragment Mine Characterized by a Directional Effect

Karel Hel

Synthesia Joint-Stock Co., Res. Inst. Ind. Chem.,
532 17 Pardubice-Semtín, Czech Republic

Entwurf einer durch den Richtungseffekt charakterisierten Splittermine

Die vorliegende Arbeit befaßt sich der mit dem vorläufigen Entwurf einer Splittermine, die durch die Richtungswirkung charakterisiert wird, unter Anwendung der Prinzipien der Explosionsbeschleunigung von Masse. Es wird ein Beispiel des Entwurfs angeführt, und die Resultate der Berechnung werden im Vergleich mit den Ergebnissen der praktischen Versuche ausgewertet.

D' une Mine fragmenté avec effect directionel

L' article s'occupe d'project preliminaire d une mine fragmenté avec effect directionel á l'aide de l'accelération de la masse, par explosion. Un example d'une mine é cité dans l'article et les résultats du calcul sont comparés avec l' expériment.

Summary

The paper deals with a preliminary design of Fragment Splinter Mine characterized by a directional effect using the regularities of explosion-induced mass acceleration. There is given an example of the design concerned, and the results of calculation are evaluated by comparison with experiments.

1. Introduction

The splinter mines with a directional effect are used against the living force and also against light armoured technique[1-5]. As a rule they complete the system of barricades. In such a case they are used for the protection of important military objects. The landing air-borne forces can use the splinter mines with directional effects as "withdrawal mines" (i.e. mines for defensive applications), fitted with a simple, e.g., mechanical time-delay element, the intruding forces being thus destroyed. The effect manifests itself in a horizontal direction above the

ground, and the mines of this type are, therefore, designated as horizontal splinter mines (HSM).
The best known representatives of the HSM involve the American M18Al (Claymore) with ball-like splinters, loaded with the plastic explosive Composition C-4[2]. The Swedish HSM of the FFV Wehrtechnik Company belongs with respect to its dimensions and mass data to the biggest ones. These multipurpose war means, FFV - 013 and FFV - 013R, create from the prefragmented steel shell about 1200 hexagonal splinters, which cover, as reported, a surface of 7500 m^2 at a fragment density of 2 splinters per a m^2. The effect on a living force extends to a distance of 150 m. In that distance the splinters cover a surface of 100 m in width and 4 m in height. The fragments protrude (pierce) a steel armour of 6 mm in thickness at a distance of 50 m. The HSM of the FFV-13 is positioned on a tripod, and the whole set has a weight of 35 kg, the proper mine weighting 20 kg. The splinter body has a weight of 7,5 kg. The dimensions of a prefragmented steel shell are 420 by 250 mm[1].
The examples given for the HSM-type weapons represent simple and effective tools, which can be activated by means of tripwires, electric contact wires, seismic sensing elements, optical gates, wireless initiation means induced by a coded signal, and the like.

2. Horizontal Splinter Mine (HSM) Design

The HSM considered from the point of view of accelerating the mass by an explosive effect can be represented by an open assymetrical sandwich structure, which can be described by the Gurney acceleration scheme, especially then when we want to evaluate the effect of shell on accelerating the splinters. The Gurney's formulas cannot be used for describing the directional effect of splinters[6].
The velocity of splinter body under conditons of acceleartion having the form of prefragmented steel plate can be described by the relation (1) and the deflection angle defined by the relation (2), as given in the following:

$$v_{os} = 2\ D \sin \varphi/2 \ , \qquad (1)$$

$$1/\ = 1/\varphi_o + b/r \ , \qquad (2)$$

wherein $1/\varphi_o$ and b are empirical constants, D is the velocity of detonation, and r is the the ballistic ratio as defined by the following relation:

$$r = m_e/m_z \ , \qquad (3)$$

wherein m_e is the mass of explosive and m_z is the mass of the splinter body under the acceleration.
Figure 1. shows the direction of flight of the splinters created from the prefragmented steel plate being accelerated by an explosion.

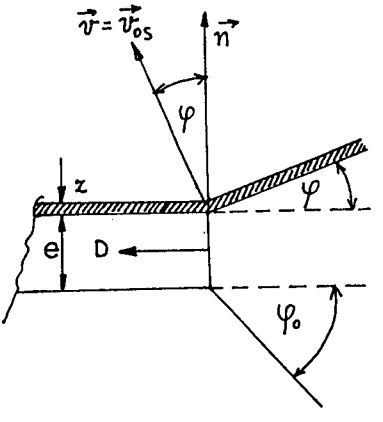

Figure 1. Direction of flight of the splinters created from the prefragmented plate being accelerated by the explosive acceleration

For the RDX/TNT 50/50 explosive the empirical relation assumes the form as follows:

$$1/\varphi = 1.728 + 3.55/r \quad (\mathrm{rad}^{-1}) \tag{4}$$

With the splinter-forming body of z in thickness there exists for a given explosive column e an optimum thickness value, $z_{opt.}$, corresponding to the optimum ballistic ratio value, which can be related to an optimum utilization of explosive energy, as characterized by a deflection angle $\varphi = \varphi_o/2$, wherein φ_o is the angle of expansion of the detonation products into the atmosphere[8], as given by the following relation:

$$\varphi_o = \pi \left[\left[(\gamma + 1)/(\gamma - 1)\right]\right]^{1/2} - 1\}/2 \ , \tag{5}$$

wherein γ is the polytropic exponent. For $\gamma = 3$ is $\varphi_o = 37^o15'$.

Fig. 2 shows the dependence of the velocity and kinetic energy of the plate being accelerated reduced to the unit mass of the explosive on the ballistic ratio according to the relations (3) and (4).

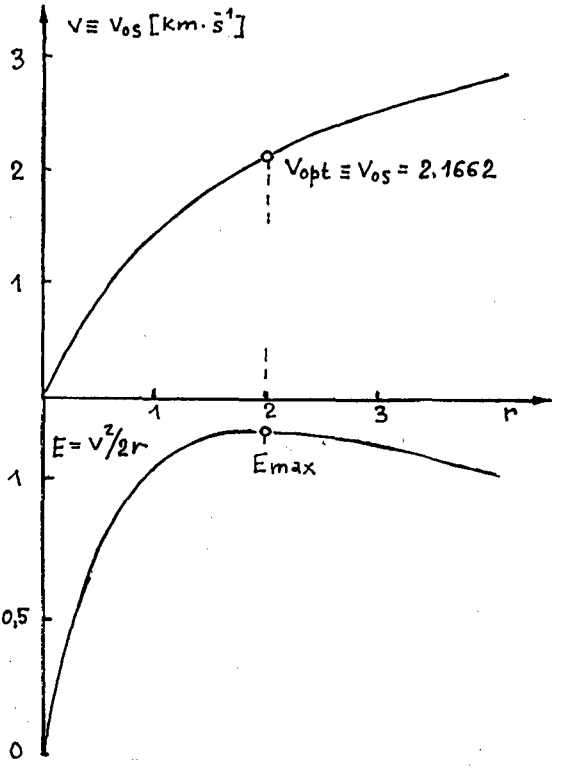

Figure 2. The ballistic ratio dependence of velocity and kinetic energy of the accelerated plate reduced to the unit mass of explosive

The fragments separated from the prefragmentd plate are given the velocities given by the relation (1).
If we denote the initial velocity of fragment as v_{os} then the drop of velocity follows an approximate relation given by the following equation (6)

$$v_s = v_{os} \exp\left(- c_D A_s \rho_{vz} x / m_s\right) , \qquad (6)$$

wherein c_D is the coefficient of resitance, A_s is the surface area of the fragment cross section, ρ_{vz} is the density of air,

x is the distance, and m_s is the mass of the fragment. The effective distance necessary for putting the target out of action is given by the relation

$$x_N = - (\mathrm{Ln}\ v_{xN}/v_{os})/k_v \ , \qquad (7)$$

wherein $k_v = c_D A_s \rho_{vz}/m_s$, v_{xN} is the velocity necessary for destroying the targets at a given mass of fragment m_s

$$v_{xN} = (2\ A_s E_{xN}/m_s)^{1/2} \ , \qquad (8)$$

wherein E_{xN} is the specific energy for destroying the targets.

In Table 1. there are given some approximate values of E_{xN} for individual targets

Table 1. Specific energies for destroying the targets

Target	E_{xN} ($J.m^{-2}$)
living force	1×10^6
living force with a protective jacket	7.7×10^6
nonarmnoured military equipment	1.3×10^6
carrier	1.5×10^6

In Table 2. there are given the geometrical characteristics of the freagments considered and the coefficient of resistance c_D values[9].

Table 2. Geometrical characteristics of the fragments considered

Parameter	Sphere a(radius)	Rhombic prisms of the dimensions (2a , a) 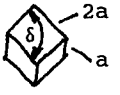
Volume $V_s(cm^3)$	$0.5236a^3$	$3.464a^3$
Surface area $S_s(cm^2)$	$3.1416a^2$	$11.464a^2$
Cross section $A_s(cm^2)$	$0.7854a^2$	$2.866a^2$
m_s/A_s	$2a\ \rho_s/3$	$1.209a\ \rho_s$
c_D	0.47	1,15

The drag coeffient is shown by the balls. In the fact the drag coefficient depends on the velocity, and at a Mach number value M < 1 the coeffient drops below the values as given in Table 2.
It is useful to express the destruction coeffient v_{xN} from the relations (7) and (8) by means of the starting velocity v_{os}, the destruction distance x_N, and the energy of destruction E_{xN} as follows:

$$v_{xN} = v_{os} \exp(- \tau v_{xN}^2) , \qquad (9)$$

wherein $\tau = c_D \rho_{vz} x_N / 2 E_{xN}^2$

The probability of hitting the target is given by the following expression:

$$P = 1 - \exp(- \Delta S_{red}) , \qquad (10)$$

wherein Δ is the density of fragments expressed as the number of fragments impinging a surface area of 1 m^2. The reduced target surface S_{red} can be determined from the target outline.

3. Example of the desing of HSM

We will try to design an HSM, which is able to pierce with its fragments a steel plate of 6 mm in thickness. For this purpose we consider as appropriate to use a hexogene and tritol based explosive with an RDX/TNT weight ratio of 50/50.
According to (1) and (2) we can write for a ballistic ratio r of 2

$$\varphi = 2/(1.728x2 + 3.33) = 0.2855 \text{ rad} = 16°21$$

$$v_{os} = 2x7.6 \sin 0.2855 = 2.1622 \text{ km.s}^{-1}$$

On using the relation (9) we can write the following relations for the fragments shaped as follows:

a) as a ball: $\tau = 0.47x1.3x50/2x1,5x10^{-6} = 1.018x10^{-6}$
b) as a rhombic prism: $\tau = 1.15x1.3x50/2x1,5x10^{-6} = 2.491x10^{-6}$

and further, using the relation (8), we get the following relations for the fragments shaped as follows:

a) as a ball: $v_{xN} = 2162 \exp(- 1.018x10^{-6}) v_{xN}^2$

b) as a rhombic prism: $v_{xN} = 2162 \exp(- 2.491x10^{-6}) v_{xN}^2$

These equations solved give us the values of destruction velocity for

a) a ball fragment: $v_{xN} = 917 \text{ m.s}^{-1}$

b) a rhomboid fragment: $v_{xN} = 680 \text{ m.s}^{-1}$

From the equation (8) we get:

a) for a ball fragnent $A_s/m_s = 917^2/2x1.5x10^{-7} = 0.028\ m^2.kg^{-1}$

and $m_s/A_s = 35.68\ kg.m^{-2} = 3.568\ g.cm^{-2}$

b) for a rhomboid fragment $A_s/m_s = 680^2/2x1.5x10^{-7} =$

$= 0{,}0154\ m^2.kg^{-1}$

and $m_s/A_s = 6.488\ g.cm^{-2}$

The killing velocities are then as follows:

a) a ball fragment $v_{sM} = (2x0{,}028x10^6)^{1/2} = 236.6\ m.s^{-1}$

b) a rhomboid fragment $v_{sM} = (2x0.0154x10^6)^{1/2} = 175.5\ m.s^{-5}$

The killing distances are given as:

a) for a ball fragment $x_{sM} = Ln(236.6/2162)/(-0.0171) = 129$ m

and $k_v = 0.47x1.3x0.028 = 0.0171\ m^{-1}$

b) for a rhomboid fragment $x_{sM} = Ln(175.5/2162)/(-0.0230) = 109$ m

and $k_v = 1.15x1.3x0.0154 = 0.02302\ m^{-1}$

For a ball-like fragment the values of interest are as follows: a = 1.19 cm and for a rhomboid fragment showing a geometry (2a, a, $\delta = 60^o$) a = 0,659 cm and m_s = 7,77 g. The balls are used as a rule in a fragment body manufactured of a plastic.
Considering a design of HSM with a rhomboid fragment and assuming a mass of HSM of 30 kg the mass of prefragmented plate will be 10 kg and and the explosive charge mass 20 kg, provided a ballistic ratio r = 2.

The thickness of explosive charge will be

$$e = 2 \times 0{,}659 \times 7.85/1.67 = 6.195\ cm$$

on using steel with a density of 7.85 $g.cm^{-3}$ and an explosive with a density of 1.67 $g.cm^{-3}$.
The fragment has then a surface area of

$$A_s = 2.866x0.659^2 = 1.245\ cm^2$$

The prefragmented plate surface will then be given by the following equation

$$S = 10^4/0.659x7.85 = 1935\ cm^2$$

When we select a prefragmented plate size of 35 by 55 cm (S = 1925 cm^2), then the number of fragments $N_s = 1925/1.245 = 1546$.

With respect to the dimensions of prefragmentation scratches the number of fragments is appropriately lower (area of scratches S_v = 1.5 cm^2)

$$N_s = 1925/1.5 = 1280$$

Scattering geometry of the fragments

For example, at the demand provided that at a distance of 100 m from the place of activation of the HSM a surface of 150 m by 4 m = 600 m^2 is covered the values of sector angles will be as represented in Fig. 3 as follows

$$\vartheta_1 = \text{arctg } 75/100 = 0.6435 \text{ rad} = 36°52$$
$$\vartheta_2 = \text{arctg } 2/100 = 0.0199 \text{ rad} = 1° 8$$

In case when the focus distance f≡IF = $0.225/\sin \vartheta_{1,2}$ is much lower than the distance from the target surface it is possible to use the above mentioned procedure for determining $\vartheta_{1,2}$.
0.225 m is a half of the length of the prefragmented plate.
At an angle of deflection φ = 0.2855 rad = 16°21 the angles ε_1 and ε_2 of the structure profile of the prefragmented plate represented in Fig. 4 for the convergent and divergent geometries are given by the following relations

$$\varepsilon_1 = \vartheta_1 + \varphi = 0.6434 + 0.2855 = 0.929 \text{ rad} = 53°13$$
$$\varepsilon_2 = \vartheta_1 - \varphi = 0,6434 - 0,2855 = 0.358 \text{ rad} = 20°30$$
$$\varepsilon_3 = \varphi - \vartheta_2 = 0,2855 - 0.0199 = 0.2655 \text{ rad} = 15°12$$

In Fig. 3 there are represented the scheme of the target surface coverage by the fragments and the determination of sector angles, and Fig. 4 represents the geometrical and structural parameters of HSM according to the requirements of the task definition.

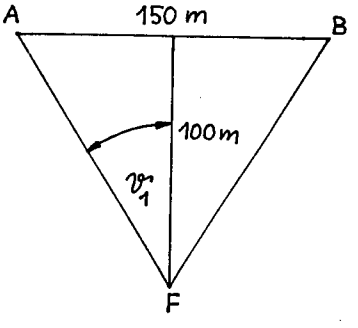

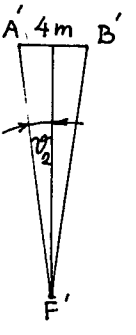

Ground plan

Side elevation

Figure 3. Coverage ot the target surface by the fragments and the determination of sector angles

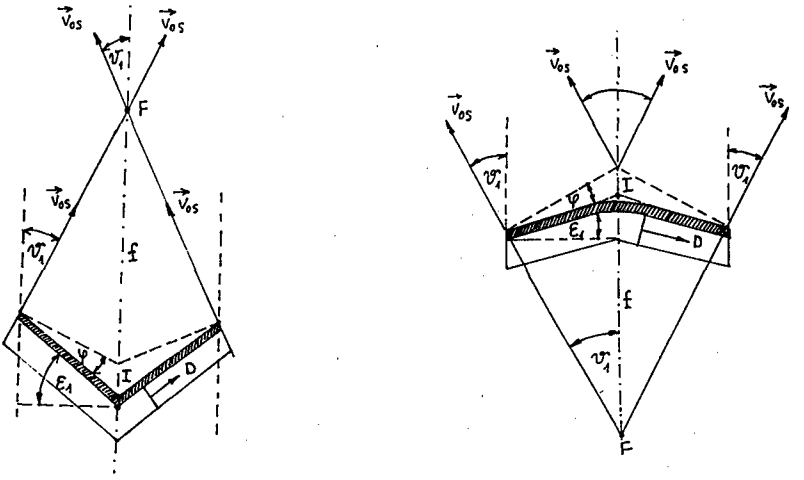

Ground plan

Convergent geometry
(f = 0.225/sin 0.6445 =
= 0.375 m)

Divergent geometry
(f = 0.225/sin 0.6435 =
= 0.375 m)

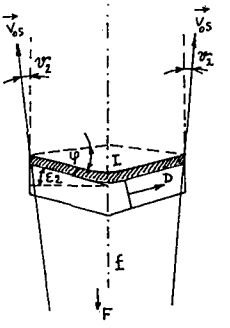

Side elevation
(f = 0.225/sin 0.0199 = 11.36 m)

Figure 4. Geometrical structure parameters of HSM according to the task definition

The density of fragment coverage at a distance of x from the place of initiation and the probability of deactivation of a living target are given in Table 3.

Table 3. Probability of deactivation of living force for the HSM designed

Distance x(m)	Surface of coverage for the target area $S_c(m^2)$	Density of fragments $\Delta = N_s/S_c$	Probability of hitting the target (P)	
			standing	lying
100	600	2.13	0.63	0.34
50	150	8.55	0.986	0.86

The design arrangement of the HSM can vary in accordance with the requirements for the coverage of target area with the fragments, the methodological procedure of design preparation will be, however, analogical. We want to turn your attention to the fact that the relation (2) giving the angle of deflection is correct only for the accelerated steel class 11 plates. For the splinter bodies prefragmented mechanically or by application of laser rays the angle of deflection is lower than that for the case of undisturbed plates.
Having this in mind we cannot use this relation in calculations for the HSM designs in case of splinter bodies prepared from, e.g., polystyrene containing balls. Here it is possible to determine the conditions of detonations and accelerations of splinter bodies experimentally by means of argon flashes and a rapid scanning camera[11]. The regularities (1) and (2) keep their validities also in case of accelerating a splinter body having a radius of curvature R_o, the preliminary design of HSM will be, however, more complicated.

4. Experimental Verifications of the HSM performance

For manufacturing the prefragmented steel splinter bodies a material according to ČSN 42 5310, grade 11 373, having a size of 200 by 150 by 5 mm was selected, the optimum cutting depth and cuttting width being 3 resp. 0.5 mm, with a rhombic pattern of side by side size of 7 by 7 mm, the sharp angle amounting to 45^o. The prefragmentation can be performed by means of milling operations or by a laser cutting procedure.
Table 4. gives the results of mneasuring the splinter velocities observed on parting the prefragmented steel plates using the military-purpose explosives RDX/TNT 50/50, a plastic explosive P1 Np 10 of a density 1.48 $g.cm^{-3}$ and a detonation velocity D = 7.5 $km.s^{-1}$, an aluminized plastic explosive VÝKON (POWER) with a density of 1.62 $g.cm^{-3}$ and D = 7.1 $km.s^{-1}$, and a commercial plastic explosive SEMTEX 1A showing a density of 1.48 $g.cm^{-3}$ and D = 7.4 $km.s^{-1}$. The velocities of first splinters parted from

a prefragmented steel plate on detonating the experimental HSM were measured using a single-channel procedure on the base of 9 m the piezoelectric sensors KA MAG as designed by the Res. Inst. Ind. Chem.

Table 4. Results obtained on measuring the velocities of fragments generated by the experimental HSM using various explosives[11, 12].

Explosive	Ballistic ratio r	Experimental average velocity of fragments $v(m.s^{-1})$	Initial fragment velocities $V_{os}(m.s^{-1})$	Acceleration equivalent %
RDX/TNT 50/50	2.86-2.9	2262	2332	100
SEMTEX 1A	2.7-2.81	2010	2072	88.9
VÝKON	2.808	2110	2130	91.3
Pl Np 10	2.8	2136	2144	91.9

On testing the partability of a prefragmented steel plate there was experimentally determined the optimum scratch depth as equal 3 mm at a plate thickness of 5 mm; a good partability of the plate was found in case when the explosive was in contact with the prefragmented plate side.
Also a qualitative finding was taken showing that the partability of a prefragmented plate to the splinters is improved when the direction of propagating front coincides with the axis of sharp angle of prefragmentation pattern, which allows to conclude on the optimum way of initiating by a planar detonation wave generator (PDWG) and an attached explosive charge, as shown in Fig. 5. The initiation of HSM according to Figure 5b) is a simpler one of the two possibilities.

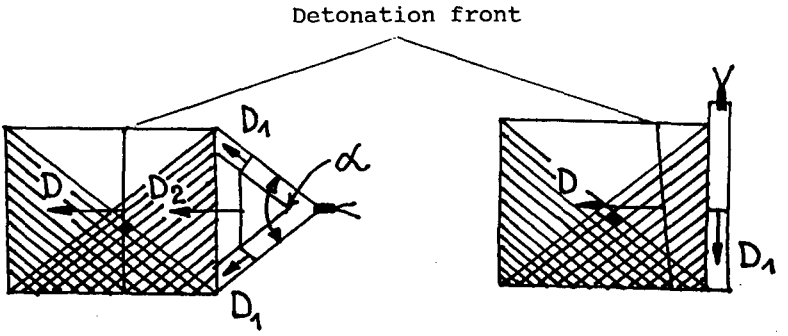

$D_1 > D_2$ $D_1 > D$

a) by means of the PDWG b) by means of an attached charge

Figure 5. The preferred ways of initiating the explosive HSM charge[12]

The angle α in the plane detonation wave generator is defined by the following formula[15]:

$$\alpha = 2 \arcsin (D_1^2/D_2^2 - 1)^{1/2} , \qquad (11)$$

wherein $D_{1,2}$ denotes the detonation velocities of explosives. The position of impingement of splinters followed on the target corresponded to the angle of deflection as calculated according to the relation (4).
The splinter bodies of poly(methyl methacrylate) containing steel balls gave on the acceleration at the same ballistic conditions the substantially identical starting velocities and do not follow the earlier defined regularity (4). The geometry of scattering of the fragments is determined sooner by the geometry of fragment body, which seems simpler for the purposes of designing the splinter mines with a directional effect. The fragment bodies containing balls allow to reach higher fragment densities.

5. Conclusions

Known types of HSM and also the preliminary design shown consist in that a fragment mine body with an explosive charge is profiled by various ways according to the requirements put on the space coverage with the splinters. Such solutions represent an disadvantage for a stuggle situation as it is not possible to change the scope of coverage of a target area with the splinters and their density at a required distance and direction by using a single HSM.
The given disadvantages of comparatively large HSM types can be

removed by the design adaptions consisting in using a structure having two independent combat parts, which revolve round a stand ending in a tripod[12].
The priming system of combat parts of the explosive charges consists of plane detonation wave generator and/or a booster charge attached.

Fig. 6 shows a structural HSM embodiment thus comprised, wherein the key symbols used have the following meanings:

1 - a fragment body
2 - an explosive charge
3 - plane detonation-wave generator and/or an attached primary charge
4 - initiation chain fuse
5 - rotary joints of combat HSM parts
6 - initiation system comprising a fuse, a primary charge, and a detonation cord, wchich transfers the detonation into the initiation system consisting of positions 3 and 4
7 - rotary joints of combat HSM parts, giving possibility of varying the angle of opening of combat parts
8 - carrying middle rod
9 - HSM stand
10 - ring for gripping the tilting legs
11 - tripod
12 - protracting scale for adjusting the angle of opening of both combat HSM parts

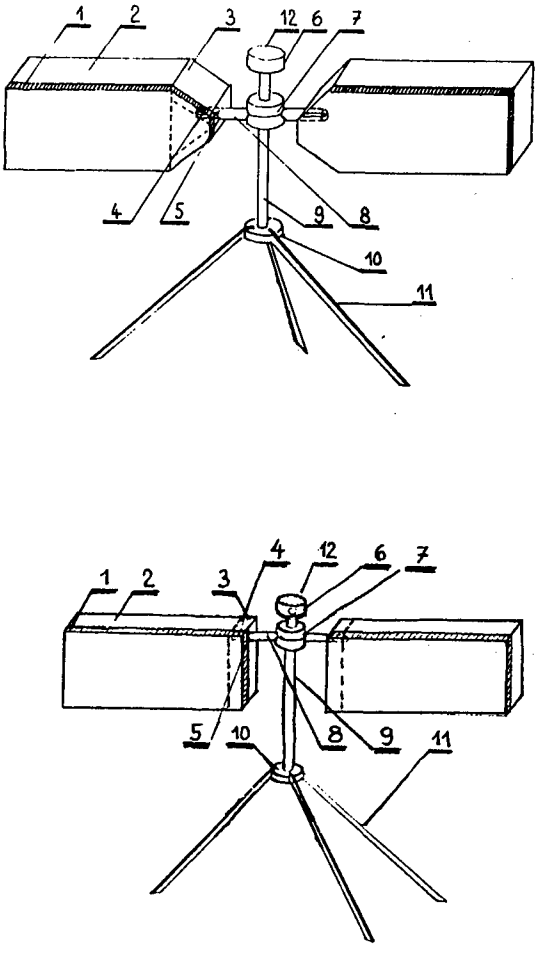

Figure 6. The HSM consisting of 2 parts

An advantage of the design represented in Fig. 6. consists in the fact that on using two independent combat parts it is possible to create the divergent and convergent streams of fragments and to adapt the shooting to local terrain conditions and to cover the target area as appropriate.
The parachute troops can find as practical mining means for individuals the splinter mines characterized by a directional effect; as a sample of this kind of mining means the afore-mentioned American M18 A1 (Claymore) mine can serve.
Recently the systems of heavy fragments have been used in the active dynamic protection charges for armoured vehicles[16,17].

6. References

(1) "Ein horizontal wirkendes Mehrzweck-Kampfmittel" (A horizontally acting multi-purpose Combat Means), *Soldat und Technik* 4, 221 (1982)

(2) Richter H., "Schützenabwehrrichtminen kapitalistischer Armeen" (Directional Infantry Defence Mines Used in the Armed Forces of Capitalist Countries), *Militärtechnik 3, 162 (1989)*

(3) Garstka J. and Janiak A.,"Miny Kierunkove" (Splinter Mines). *WPT* 17, 509 (1984)

(4) "Miny s usměrněným a horizontálním účinkem" (Mines Characterized by Oriented and Horizontal Effects), *Atom 4 (1984)*

(5) Opilát V., "Oskolochnaya mina napravlennogo deistviya" (Fragment Mine of the Oriented Effect), *Zarubeznoe voennoe obozrenie No. 10, 46-8 (1976)*

(6) Jones G. E., Kennedy J. S. and Bertholf L. D., *Am. J. Phys. 48, 4, 364-9 (1980)*

(7) Richter H., *"Sur la théorie des charges creuses. Mouvement de revétement minces en matériau plastique á la surface d un explosif plan"* , Rapport LRBA (I.S.L.) no. 42/46, 1946

(8) Defourneaux M. and Jacques L.," Étude théorique et expérimentale de la propulsion par explosif, et application á une classification balistique des explosifs", *Mém.* de *l artillerie franc. 41, 3, 69 (1969)*

(9) Baker W. S., et al., *" Explosion Hazards and Evaluation"*. Elsevier Sci. Publ. Comp., Amsterdam-Oxford-New York 1983

(10) Malkovský K.,*"Urychlování hmoty s využitím energie výbušin"* (Acceleration of Mass by using the explosives energy). XIth Partial Report, Annual Report, Res. Inst. Ind. Chem. No. 754/C 1986

(11) Hel K., " *Urychlování hmoty výbuchem*" (Explosive Mass Acceleration). Ph.D. Degree Thesis, VŠCHT at Pardubice (1989)

(12) Hel K., "*Urychlování hmoty výbuchem*" (Explosive Mass Acceleration), XIIIth Partial Report, Annual Report, Res. Inst. Ind. Chem. No. 807/C/1989

(13) Komenda J., "*Optimalizace tříštivosti protipěchotní munice s řízeným rozkladem na střepiny*" (Optimization of Scattering Power of Antiinfantry Ammunition Characterized by Directed Decomposition to Fragments), Military Academy at Brno (1991)

(14) *Jane's Military Logistics 1990/1991*, Butler Tanner, Londýn (1990)

(15) Baum F. A. et al., "*Fizika vzryva*" (Physics of Explosion), Nauka Publishing House, Moskva, 1975

(16) Ogorkiewicz R.M., "Future tank armors revealed Developments in electric and explosive reactive armor", *Jane s International Defense Review 5, 50-51 (1997)*

(17) Held M., "Plate Velocities for Asymmetric Sandwiches", *Propellants, Explos., Pyrotechn. 22, 218-220 (1997)*

TO THE QUESTION ON THE ENTHALPY OF FORMATION FOR THE NITROCELLULOSE

Yuriy N. Matyushin, Tatjana S. Konkova, Lidiya I. Korchatova

N.N.Semenov Institute of Chemical Physics,
Russian Academy of Science
4 Kosygin Street, Moscow, 117977, RUSSIA

ABSTRACT

The difference in enthalpies of formation of a nitrocellulose (NC) with the identical contents of nitrogen at the various authors reaches 60 kcal/kg. It is connected with first of all to a nature of source cellulose, as well as with the factious composition, degree crystallinity, molecular - mass distribution and other factors. On the measured energy of combustion NC renders also significant influence presence of the remaining moisture in samples in consequence of its hygroscopicity and contents of impurities.

By the method of a calorimetry of combustion the energies of combustion are measured of 6 samples NC with the contents of nitrogen from 10.24 before 13.65 %, received from highclean cotton cellulose. From the received experimental data the enthalpies of formation of the investigated samples NC are calculated. For preventing an influence absorb moisture on the value of the energy of combustion the samples NC are dried in high vacuum under 110° C. Dried up samples carried without the contact with atmosphere in the dry box, placed in the previously weighed polyethylene packages, which then hermetically sealed.

Combustion of the samples NC carried out on the calorimeter of the design ICP RAS, developed specially for burning energetic materials on small quantities of samples.

The profound analysis of works on the determination of the enthalpies of formation NC is carried out. The regressive equation for dependence the enthalpies of formation NC from percentage of nitrogen is received on the basis of the received enthalpies of formation and the most reliable literary values by the method of the least squares.

INTRODUCTION

The nitrocellulose (NC) is major in the practical plan of substances. The NC is the basis for development of the extremely wide nomenclature of the ammunition, and she far has not exhausted the yet not opportunities. She serves the basic component of the artillery and ballistic gunpowders and largely determines quality of the ammunition. In spite of the important significance for a theoretical estimation of efficiency solid propellants and gunpowders on the basis NC the value its enthalpy of formation is known with smaller accuracy, than for other components. It is connected both to specific features the NC, and with difficulties of definition of its thermochemical characteristics. The value of the enthalpies of formation NC depends first of all on percentage in it of nitrogen (% N), describing the degree replacement of hydrogen atoms in cellulose with nitrogroups. In turn, the quality NC basically depends on properties of initial cellulose, methods of its processing and conditions of realization of process nitration.

Despite of significant quantity of works, in which by the calorimetric methods investigated various properties cellulose and NC (enthalpy of combustion, heat of wetting to water and solvents, heat capacity, interaction with plasticizer and so on), it is impossible to consider these researches exhaustive, in a row of cases reliable, and conclusions unequivocal. Very much frequently measurements were carried out on the not characterized samples, the methods of preparation of samples to experiences are not indicateded in the majority works. At the same time, the properties of these substances very

strongly depend on initial raw material, methods of its processing and conditions of the drying out.

The discrepancy in values of the enthalpy of formation NC at the various authors reaches more than 60 kcal/kg. On measured the energy of combustion is rendered by influence presence of a residual moisture NC, contents of metals and organic impurity, index crystallinities, factious composition, degree polymerization, molecular - mass distribution and other factors.

For the first time the enthalpy of formation NC with N = 13,46 % is received in 1881 year equal -573,8 kcal/kg [1]. In 1921 year Kast has received for a sample NC with N = 12,99 % the enthalpy of formation equal -594,6 kcal/kg [2]. Prettre [3] has received for the first time linear dependence the enthalpies of formation NC from percentage of nitrogen in the substance. In the further similar dependence were received by the row of the authors [4 – 10]. It is necessary to note, that the works are executed basically in 30-th-years, and last publication concerns to 1950. The results of these measurements are given on pic.1. From the diagram it is visible, that the character of dependences appreciablly differs: direct 2 and 7 practically coincide; 3 and 6 are almost parallel them, direct 1,4 and 5 have various inclinations.

Most energetically advantageous values of the enthalpies of formation are received in works Miles [8] and Taylor [9,10] from calorimetric measurements of heats of explosive decomposition NC. In work [8] the total volume of the gaseous products of explosion is measured and their analysis on CO_2, CO, CH_4, H_2 is made, the quantity formed water is determined. In result the author calculated enthalpies of formation of four samples NC in the interval 12,62 —

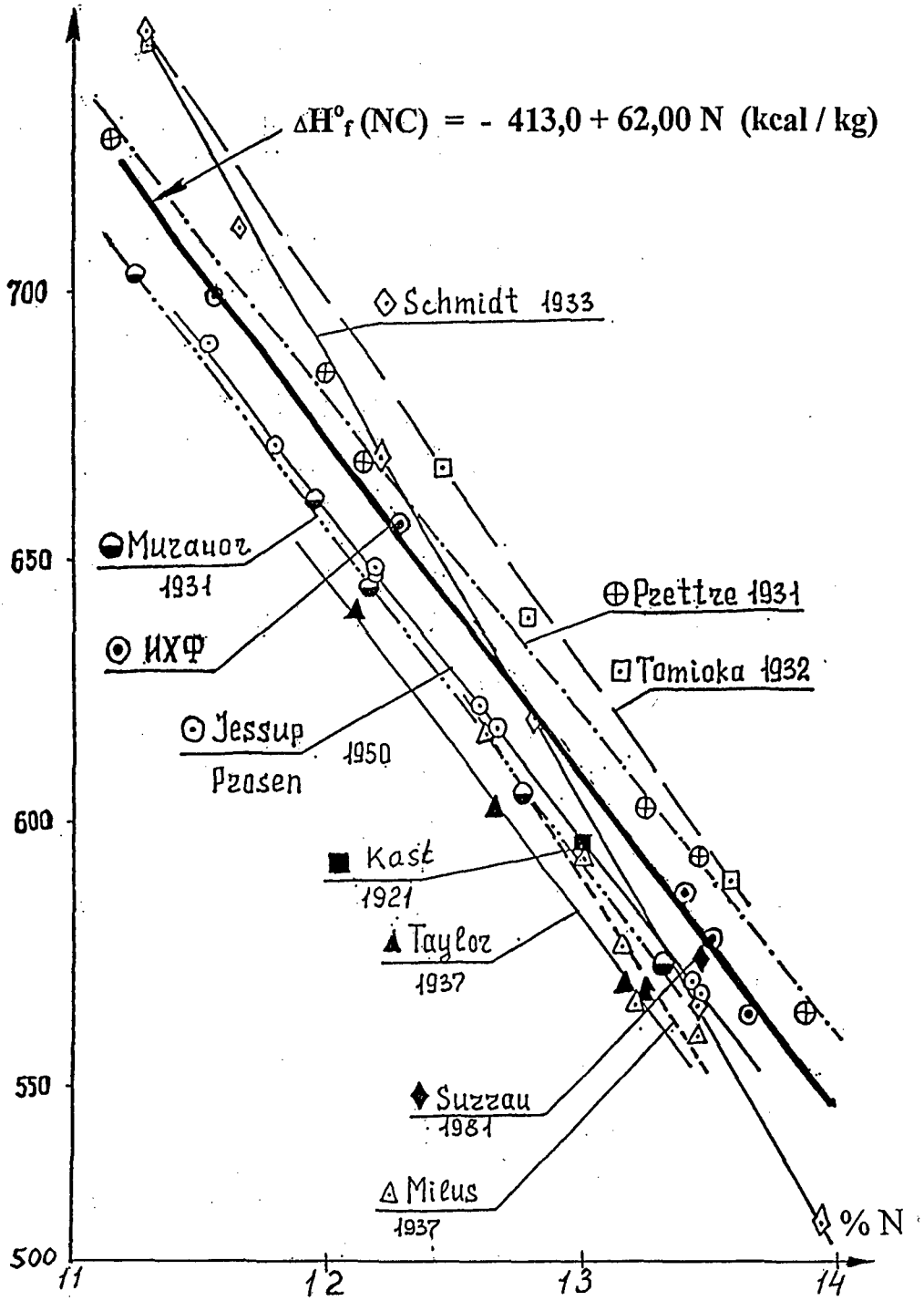

Pic.1 The dependence of the enthalpy of formation NC from percentage nitrogen.

13,45 % N. The author indicates that the error of definition of heat of explosive decomposition NC and gas analysis make up about 1%.

In work [10] volume of gases and quantity of water formed with combustion of samples NC in vacuum is determined, the humidity of initial samples was controlled. As the gas analysis of products of reaction was not carried out, calculated on the basis of these measurements the enthalpies of formation NC cannot be considered reliable. In work [6] the influence of the residual moisture in samples is not taken into account. It is doubtless that data [7] in area above than 13 % N and below 12% N are erroneous.

In work [11], executed in NBS USA, the energies of combustion of samples of wood and cotton cellulose are measured. The authors took into account the amendments on heats of wetting NC, the quantity of the burned down substance undertook on the basis of results of the gas analysis on formed CO_2. All impurity in samples (0,4 — 0,9 %) the authors considered as inert materials, which did not give the contribution to the energy of combustion, that is rather disputable.

EXPERIMENTAL

The analysis of work has shown, that for reliable definition the enthalpies of formation NC the important significance has not only purity of substance, but also method of definition, and condition of preparation. We produced conditions of combustion NC by two ways. In the first case the samples NC dried with 110° C in high vacuum within one hour, then transferred to dry box

Table 1.

Determination of the thermochemical properties NC

% N	Condition of preparation of samples	$\Delta U'_B$ (NC) kcal / kg	$-\Delta H^\circ_f$ (NC) kcal / kg
10.24	Dried at110° C in vacuum, 3 hours, sealed in polyethylene packages	2732.4	778.1
11.56	Dried at110° C in vacuum, 3 hours, sealed in polyethylene packages	2545.2	696.3
12.28	Not dried	2397.9	
	Dried on air	2408.4	
	Dried at110° C in vacuum, 1 hour, pressed as tablets	2437.5	656.0
13.41	Dried on air	2261.2	
	Dried at110° C in vacuum, 3 hours, sealed in polyethylene packages	2282.2	586.4
13.49	Dried at110° C in vacuum, 1 hour, maintained day on air	2265.9	
	Dried at110° C in vacuum, 1 hour, sealed in polyethylene packages	2271.4	576.9
13.65	Dried at110° C in vacuum, 3 hours, sealed in polyethylene packages	2255.2	562.6

without contact to the atmosphere, placed in previously weighed packages from polyethylene. Packages hermetically sealed and again weighed for definition of weight substance. In the other case a NC pressed as the tablet, which dried in the vacuum cupboard, then placed in previously weighed weighing bottle with a cover and again weighed. The tablet NC placed in platinum tigel , which determined in the calorimetric bomb. The sorption heat of water took into account on the data of work [11].

As the speeds of burning NC and films did not coincide, in the first case it was very difficult to achieve completeness of combustion. The second method technically is much easier.

The results of measurements of energies of combustion NC and received the enthalpies of formation are given in tabl. For comparison samples sustained on air with room temperature before and after drying out in vacuum. were burned. It is visible, that the energies of combustion of samples NC which are not having the contact to the atmosphere after drying, have higher values the energies of combustion.

On the basis of received the enthalpies of formation NC with the account of the most reliable literary data by [3,5,11] method of the least squares is received the following regressive equation

$$\Delta H^{\circ}_{f}(NC) = - 413{,}0 + 62{,}00\ N \ \ (kcal / kg) \qquad (1)$$

The equation allows to calculate the enthalpies of formation NC with the contents of nitrogen from 10 up to 14%.

REFERENCES

1. Sarrau and Vielille, Compt. Rend., V. 93., P. 269, 1881 [Quote by 11].

2. H. Kast, Spreng und Zundstoffe, P.71, 1921 [Quote by 11].

3. M. Prettre, *Determination des chaleurs de combustion des nitrocelluloses et de la cellulose*, Memorial des poudres, V. 24, P. 223-233, 1931.

4. V.G.Cvetkov, M.Ya.Ielovich, I.F.Kaimin et al., *Enthalpy of interaction of cellulose of a various degree crystallinities with water*, Kristallizaciya polisakharidov i ih vzaimodeistvie s vodoi, Tezisi dokladov, Riga, Zinantne, P. 6-8, 1979.

5. D. Muraour [Quote by 11].

6. K. Tomioka, J. Cellulose Inst., Tokio, V. 8, P. 88-93, 1932 [Quote by 11].

7. A. Schmidt, F. Becker, Z. Des Sciess und Sprengstoff, V. 28, P. 280-283, 1933.

8. F.D. Miles, *Thermochemical examination of nitrocellulose*, Ind. Eng. Chem., 29, N 1, P. 492-494, 1937.

9. J. Taylor, C.R.L. Hall, *Determination of heat of combustion of nitroglycerin and the thermocemical constant of nitrocellulose*, J. Phys. Chem., V. 51, N 2, P. 593-611, 1947.

10. J. Teylor, C.R.L. Hall, H. Thomas, *Thermochemistry of propellent explosives, J. Phys. Colloid. Chemie*, V. 51, N 2, P. 580-592, 1947.

11. R.S. Jessup, E.J. Prosen, *Heats of combustion and formation of cellulose and nitrocellulose*, J. Res. NBS, V.44, N 4, P. 387-393, 1950.

Thermochemical and explosive properties of nitropyrazoles

V.P.Lebedev, Yu. N.Matyushin, Ya. O.Inozemtcev

N.N.Semenov Institute of Chemical Physics - RAS, Moscow, RUSSIA

I.L.Dalinger, S.A.Shevelev, I.V.Fomenkov

N.D.Zelinsky Institute of Organic Chemistry - RAS, Moscow, RUSSIA

ABSTRACT

The enthalpy of formation - main power characteristic of energetic materials, which is necessary with thermodynamic calculations of their power efficiency, and also in technological and heatphysical calculations. In the present work the calorimetric method energies of combustion are measured and the standard enthalpies of formation for a row derivatives of nitropyrazole are calculated. The influence of number and place of connection amine and nitrogroups to the pyrazole cycle on the thermochemical and physicist-chemical properties of the investigated compounds is analysed. On the basis of experimental values of enthalpies of formation and calculated densities are calculated the heat of explosion and the detonation velocity of the investigated derivative nitropyrazoles by the method ICP RAS.

Is shown, that on the basis of the pyrazole cycle the explosives with a wide spectrum of element structure, enthalpy, density and physicist-chemical properties can be synthesized.

INTRODUCTION

The pyrazole cycle contains high-enthalpy double bonds carbon - carbon and unary bond nitrogen-nitrogen, that provides the increased enthalpy of formation of this cycle,

and its flat without bends the structure allows to expect the increased density of the compounds with this fragment.

The specific enthalpy of formation of a pyrazole (406.9 kcal/kg) [1] is little bit higher, than at 1,2,4-triazole (380.7 kcal/kg) [2], and in the row of azoles the pyrazole occupies an intermediate position between the high-enthalpy tetrazole (806.0 kcal/kg) [1] and low-enthalpy imidazole (205.2 kcal/kg) [1]. It is possible to expect, that the combination in the molecule endothermic and, at the same time, the stable pyrazole cycle with various energetic fragments suffices will result in creation of energetic materials with a wide spectrum of change of the element structure, enthalpy, density and physicist-chemical properties, including, and compounds with the given properties..

In the literature there are no items of information on the enthalpies of combustion and formation for the nitropyrazoles.

Among pyrazoles of separate attention deserve amino- and nitroderivatives, as these functional groups, interactioning with the heterocycle and among themselves, stabilize the molecule, and at the expense of formation inside and intermolecular hydrogen bonds promote increase of density of substance.

EXPERIMENTAL

Investigated derivative of the pyrazole are synthesized in Institute of organic chemistry RAS specially for thermochemical researches. The substances are cleared repeated recrystallization, their identity and cleanliness are confirmed by results of the element analysis, spectral and chromatographic measurements.

The enthalpies of formation of substances is received from energies of their combustion in the calorimetric bomb at the abundance of oxygen. The energies of com-

bustion are measured on the hermetic calorimeter with the magnetic stirrer developed in ICP RAS specially for researches of energetic materials [3]. The calibration of the calorimeter is executed on burning the reference standard - benzoic acid of the mark K-1, certificated in D.I.Mendeleev Institute of Metrology. The absence of the systematic error of the measurements on the given calorimeter is confirmed by burning of the secondary reference standard – succinic and hippuric acids. The calorimeter allows to measure the thermal effects of the combustion reactions of the substances with the error 0.02 - 0.03%. The bases of a technique of burning of energetic materials are stated in work [4].

The investigated energetic derivative of the pyrazole are complicated objects for the thermochemical researches., The molecules of the investigated compounds contain the high-enthalpy pyrazole cycle with joined to it of the nitrogroups. With burning such compounds in the calorimetric bomb with abundance of oxygen the spontaneous transition of burning in explosion is possible. It results in destruction of the internal fixture of the calorimetric bomb and change of parameters of the thermometer of resistance.

With the purposes of stabilization of the burning process the weighed portion of researched pyrazoles reduced at the expense of addition of auxiliary substances – the dimethylphtalate or the benzoic acid. The ratio between weights of researched and auxiliary substances determined experimentally, and it was individually for each derivative pyrazole.

With calculation of the combustion enthalpies the amendments on heat exchange of the calorimetric vessel with the cover, on the incendiary energy and the combustion

energy of auxiliary substance, on the thermal effect of formation of the nitric acid, Washburn and work of expansion of gases are entered.

With calculation of the standard enthalpies of formation derivatives of the pyrazole the following the enthalpies of formation of the combustion products are used:

$\Delta H^\circ_f [CO_2]_g = -94.051$ kcal/mol [5]

$\Delta H^\circ_f [H_2O]_l = -68.315$ kcal/mol [5].

RESULTS AND DISCUSSION

The results of measurements of enthalpies of formation of nitroderivative pyrazoles are submitted in table 1. The calculated data of the density, the heat of explosion and the detonation velocity for the row of the investigated compounds are submitted at this table. The calculations are carried out on methods developed in ICP RAS [6].

In the table the following designations are accepted:

$\Delta U'_B$ - energy of combustion in conditions of the calorimetric bomb, cal/g;
ΔH°_c - standard enthalpy of combustion, kcal/mol;
ΔH°_f - standard enthalpy of formation, kcal/mol;
ρ - density of compounds, g/c^3;
Q - heat of explosion, kcal/kg;
D - detonation velocity, km/c.

As shown in [2], the energetic effect of introduction of the nitrogroup in azole cycles (ΔE) grows in the row pyrrole - imidazole - pyrazole - triazole - tetrazole. The energetic effect of the introduction of the nitrogroup in azoles is determined as the difference between the enthalpies of formation of the nitroderivative azoles and the initial

Table 1.

The thermochemical properties of the nitropyrazoles

Compounds	$\Delta U'_B$	ΔH°_c	ΔH°_f	ρ	Q	D
1	2	3	4	5	6	7
I. 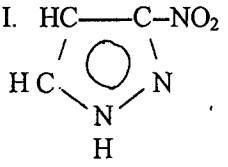	3565.5± 2.6	401.7± 0.3	17.1			
II. 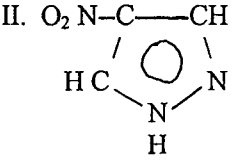	3558.2± 1.8	400.9± 0.2	16.2			
III. 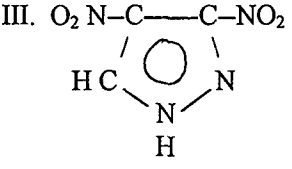	2415.6± 1.5	379.1± 0.2	28.7	1.81	1249	8.24
IV. 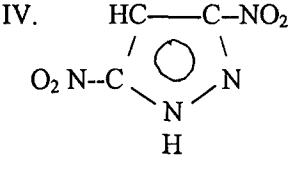	2376.0± 3.7	372.9± 0.6	22.4	1.80	1212	8.15
V. 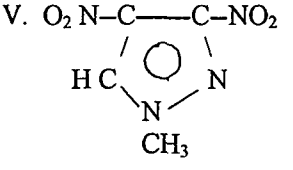	3140.6± 4.6	538.1± 0.8	25.2			

Continuation table 1.

1	2	3	4	5	6	7
VI. 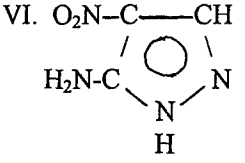	3310.3± 2.2	422.3± 0.3	3.6	1.67	769	7.21
VII. 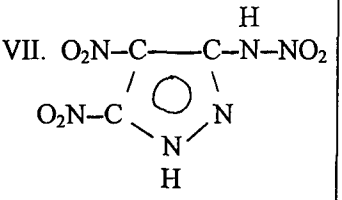	1762.5± 2.8	380.3± 0.6	29.8	1.97	1375	9.25
VIII. 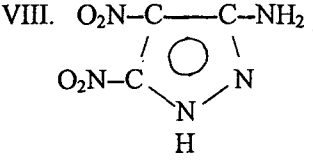	2321.9± 3.3	399.0± 0.6	14.4	1.90	1116	8.53
IX. 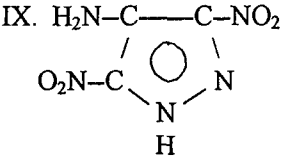	2237.7± 3.2	384.4± 0.6	- 0.2	1.93	1045	8.49
X. 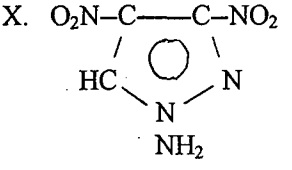	2478.2± 1.4	426.1± 0.3	41.5	1.76	1232	8.25

Continuation table 1.

1	2	3	4	5	6	7
XI. 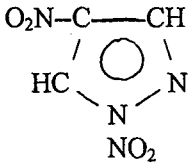	2501.0± 3.8	392.6± 0.6	42.2			
XII. 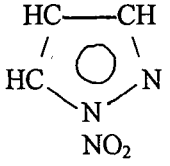	3798.0± 1.8	428.0± 0.2	43.4			
XIII. 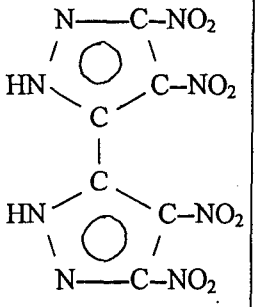	2193.5± 2.8	683.3± 0.9	50.7	1.87	1393	8.38
XIV. 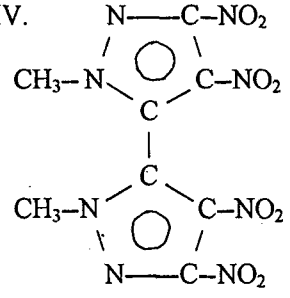	2967.5± 4.2	1010.2± 1.4	52.9			

Continuation table 1.

1	2	3	4	5	6	7
XV. 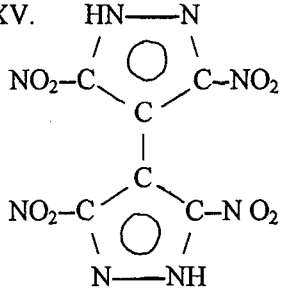	2207.0± 3.4	687.5± 1.1	54.9	1.85	1407	8.33

Table 2.

Energetic effect of introduction of the nitrogroup in the azole cycles

Compounds	ΔH^{o}_{f}	ΔE
I. 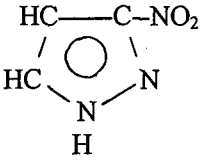	17.1	-11.2
II. 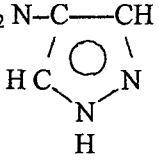	16.2	-12.1
III. 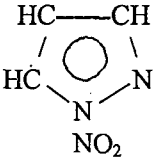	43.4	15.1

azoles.

The enthalpies of formation of C-mononitroderivatives of the pyrazole weakly depend on the place of connection of the nitrogroups (table 2). The enthalpies of formation the 3-nitropyrazole and the 4-nitropyrazole differ less, than on 1 kcal/mol. Accordingly energetic effect of introduction of the nitrogroup in a pyrazole for these compounds lays in the same limits. The enthalpy of formation of the pyrazole is accepted equal 28.3 kcal/mol [1].

Other picture of change of the value the formation enthalpy is observed with connection of the nitrogroup in the position of 1 pyrazole cycle to the atom of nitrogen. Thus the high-enthalpy bond nitrogen - nitrogen will be formed, and the increase the enthalpy of formation of the 1-nitropyrazole on 15.1 kcal/mol is observed in comparison with the pyrazole and on ~ 27 kcal/mol in comparison with the C-mononitropyrazoles.

In dinitropyrazoles the tendency of change of the formation enthalpies is other, than in the mononitropyrazoles. With connection of the second nitrogroup to the nitropyrazole the increase of enthalpies of formation mononitropyrazoles is observed. So the introduction of the nitrogroup in the position 4 is resulted in growth with the enthalpies of formation on 11.6 kcal/mol, and in the position 5 - on 5.3 kcal/mol (table 3). Thus, the introduction of the nitrogroup in the 3-nitropyrazole in the position 4 energetically is more advantageous, than in the position 5 on 6.3 kcal/mol. The similar picture is observed in the dinitrobenzene, where o-isomer energetically is more advantageous, than m-isomer on 8.9 kcal/mol and on 11.8 kcal/mol, then p-isomer [1].

In dinitropyrazoles most energetically advantageous structure, when the second nitrogroup is joined to the atom of nitrogen of the heterocycle, as in this case enthalpy

Table 3.

Energetic effect of introduction of the nitrogroup in the 3-nitropyrazol

Compounds	ΔH^{o}_{f}	ΔE
I. 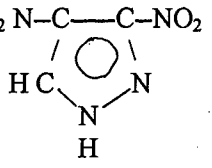	28.7	11.6
II. 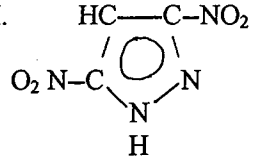	22.4	5.3
III. 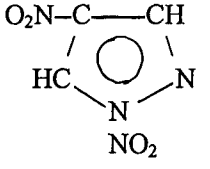	42.2	26.0

of formation is increased on 26 kcal/mol (table 3).

In the literature there are no items of information on the enthalpies of formation of the aminopyrazoles, but it is known, that with connection of aminogroup to atom of carbon of the aromatic cycle there is some decrease of the enthalpy of formation of this cycle. So, in aniline the enthalpy of formation is reduced on 4.3 kcal/mol, and in aminotetrazole on 7.0 kcal/mol in comparison with the not replaced compounds [1].

With introduction in the 4-nitropyrazole aminogroup to atom of the carbon in the position 5 enthalpies of formation formed 4-nitro-5-aminopyrazole are reduced on 12.6 kcal/mol concerning the mononitroderivative pyrazole (table 4).

Table 4.
Energetic effect of introduction of the aminogroup in the nitropyrazoles

Compounds	ΔH°_f	ΔE
I. 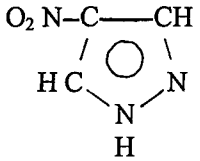	16.2	12.6
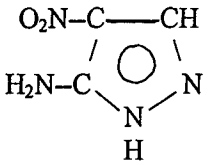	3.6	
II. 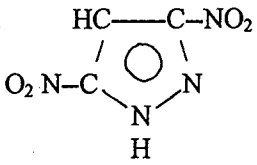	22.4	- 22.6
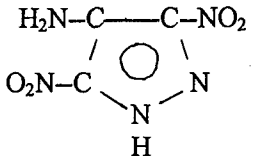	- 0.2	
III. 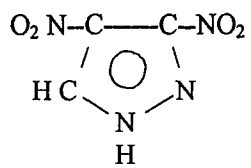	28.7	12.8
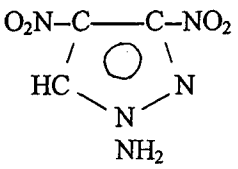	42.5	

Such reduction the enthalpy of formation is caused not only stabilizing influence of aminogroup, but also by the intramolecular hydrogen bond.

The enthalpy of formation the 3,5-nitro-4-aminopyrazole is lower the enthalpies of formation 3,5-nitropyrazole on 22.6 kcal/mol as a result of introduction aminogroup in the position 4. Connection of the amine group in pyrazole cycle to the atom nitrogen energetically is more favourable. Thus in the molecule there is the high-energy bond nitrogen - nitrogen and the increase the enthalpy of formation of formed compound is observed in comparison with 3,5-dinitropyrazole.

The carried out thermochemical analysis of the received enthalpies of formation of the nitroderivative pyrazole allows to understand the reasons influencing to change of values of the formation enthalpies.

Work was made under support of Russian Fund of Fundamental Investigations. Grant number 97-03-32254a.

REFERENCES

1. Stull D.R., Westrum E.D., SinkeG.C. The chemical therodynamics of organic compounds, J.Wiley & sons, INC., New-York – London – Sydney – Toronto, 1969, 807 p.

2. Matyushin Yu.N., Lebedev V.P. Thermochemical propities of mononitroderivatives of azoles and oxadiazoles, Combustion and Detonation, 28-th International Annual Conference of ICT, Karlsruhe, FRG, 1997, P. 98-1 – 98-10.

3. Matyushin Yu.N., Vorob'ev A.B., Kon'kova T.S. et al. Combustion calorimeter, Inventor's Certificate of the USSR, SU, No 1221568 A, G 01 N 25/50, Bull. Izobret. No 12, 1986 (in Russian).

4. Lebedev Yu.A., Miroshnichenco E.A., Knobel Yu.K. Thermochemistry of the nitrocompounds, Ed. "Nauka", Moscow, 1970, 168 p. (in Russian).

5. Cox J.D., Vagman D.D., and Medvedev V.A. (Eds.) Codata Key Values for Thermodynamics, New-York – Washington, 1989.

6. Pepekin V.I., Lebedev Yu.A. The criterion of estimation of the detonation parameters. DAN SSSR, 1984, T. 277, N 2, P. 429-433 (in Russian)..

Malvern Instruments Ltd
Enigma Business Park
Grovewood Road
Malvern
Worcs WR 14 1XZ
UK
Tel.: +44 (0) 1684 892456
Fax: +44 (0) 1684 892789

Malvern Instruments GmbH
Rigipsstraße 19
D-71083 Herrenberg

Tel.: +49 (0) 7032 9777-0
Fax: +49 (0) 7032 77854

http:\\www.malvern.co.uk

Particle Sizing and Zetapotential Measurement Technology

Malvern Instruments is one of the biggest manufacturers worldwide of particle size distribution and zetapotential measurement instruments.
For more than 28 years we support our systems in more than 50 countries.

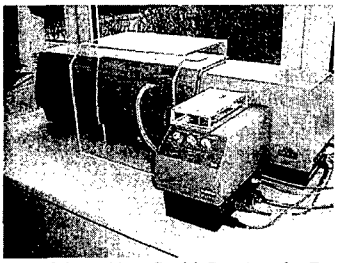

Figure 1: MasterSizer S with Dry Powder Feeder

Three different families of instruments solve every problem:

1. The **MasterSizer**-Family is a group of Laser Diffraction Instruments to measure emulsions, dispersions and powders in the range of 0.05 µm up to 3500 µm.
2. The **ZetaSizer**-Family enables to measure particle sizes from 2 nm to 3000 nm using Photon-Correlation-Spectroscopy. These instruments measure the Zetapotential of emulsions and dispersions.
3. The **Spraytec** systems measure sprays and aerosols between 0.5 µm and 850 µm using Laser Diffraction with a maximum resolution of 2500 measurements per second.

Partikelgrößen- und Zetapotentialmeßtechnik

Malvern Instruments ist einer der größten Hersteller von Partikelgrößen- und Zetapotentialmeßgeräten.
Seit über 28 Jahren werden die Geräten nun direkt in über 50 Länder der Welt vertrieben und betreut.

Drei unterschiedliche Gerätegruppen decken alle Fragen und Probleme ab:

1. Die **MasterSizer**-Familie beinhaltet Laserbeugungsspektrometer, die in dem Größenbereich zwischen 0,05 µm und 3500 µm Emulsionen, Dispersionen und Pulver vermessen.
2. Die Geräte der **ZetaSizer**-Serie sind in der Lage die Partikelgröße von Emulsionen und Dispersionen zwischen 2 und 3000 nm zu vermessen.
3. Die **Spraytec**-Laserbeugungsspektrometer analysieren Sprays und Aerosolen in dem Größenbereich 0,5 µm bis 850 µm mit einer Zeitauflösung von 2500 Messungen pro Sekunde.

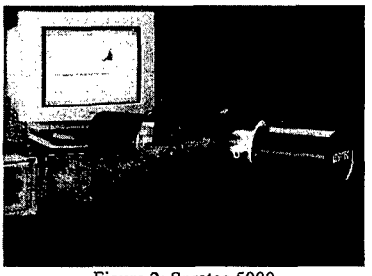

Figure 2: Spratec 5000

Topics of previous conferences:

1982	Use of Plastic Materials for Propellants and Explosives
1983	Production Control and Surveillance of Propellants and High Explosives
1984	Technology of Propellants and High Explosives
1985	Pyrotechnics: Basic Principles, Technology, Application
1986	Analysis of Propellants and Explosives - Chemical and Physical Methods
1987	Technology of Energetic Materials - Manufacturing and Processing, Valuation of Product Properties
1988	Combustion and Detonation Phenomena
1989	Environmental Testing in the 90's
1990	Technology of Polymer Compounds and Energetic Materials
1991	Combustion and Reaction Kinetics
1992	Waste Management of Energetic Materials and Polymers
1993	Energetic Materials - Insensitivity and Environmental Awareness
1994	Energetic Materials - Analysis, Characterization and Test Techniques
1995	Pyrotechnics - Basic Principles, Technology, Application
1996	Energetic Materials - Technology, Manufacturing and Processing
1997	Combustion and Detonation